

About this CD-ROM

Recommended platform

Operating System

Windows computers operating on Windows®2000 (SP 2 or higher) or XP (SP1/SP2).

Macintosh computers operating on Mac OS X (10.2.8/10.3/10.4).

CPU

Windows Intel Pentium Processor

Macintosh Power PC G3, G4 or G5 Processor

System operation tested and confirmed with the English version of these operating systems.

Memory

128MB or more (256MB or more recommended)

This CD-ROM contains PDF files (portable document format files) which require the use of the Adobe Reader® 7.0.8 or higher.

If not installed, Adobe Reader may be downloaded from <http://www.adobe.com/>.

Usage

For Windows, the CD-ROM will run automatically when the disk is inserted.

If it does not run automatically, open the CD-ROM Drive from My Computer and double click the file "MicroTAS2006.pdf."

For Macintosh, CD-ROM folder automatically opens when the disk is inserted. If CD-ROM folder do not open automatically, double click the CD-ROM icon on the desktop and open the folder. Then double click the "MicroTAS2006.pdf" file.

©2006 CHEMINAS. Personal use of this material is permitted. However, permission to reprint/republish this material for advertising or promotional purposes or for creating new collective works for resale or redistribution to servers or lists, or to reuse any copyrighted component of this work in other works must be obtained from the CHEMINAS.

Duplication of this CD-ROM and its content in print or digital form for the purpose of sharing with others is prohibited without permission from CHEMINAS.

Windows is a registered trademark of Microsoft Corp.

Macintosh is a registered trademark of Apple Computer, Inc.

Pentium is a registered trademark of Intel Corporation.

Power PC is a registered trademark of the International Business Machines Corp.

Adobe Reader is a registered trademark of Adobe Systems Inc.

Micro Total Analysis Systems 2006

Proceedings of μ TAS 2006 Conference

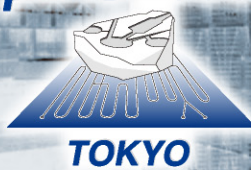
Volume 1

Tenth International Conference on Miniaturized Systems for Chemistry and Life Sciences
November 5-9, 2006
Tokyo, Japan

Editors:

Takehiko Kitamori
Hiroyuki Fujita
Shinji Hasebe

μ TAS 2006



Micro Total Analysis Systems 2006
Proceedings of μ TAS 2006 Conference
Volume 1 & Volume 2

Tenth Anniversary International Conference on
Miniaturized Systems for Chemistry and Life Sciences

November 5 - 9, 2006
Tokyo, Japan

Copyright and Reprint Permission:

Abstracting of items in this volume is permitted with credit to the source. No part of this book may be reproduced in any form or by electronic or mechanical means without prior permission. For copying, reprint or replication permission, write to JAACC.

Japan Academic Association Inc. for Copyright Clearance (JAACC)
9-6-41 Akasaka, Minato-ku, Tokyo 107-0052, JAPAN
Phone: 81-3-3475-5618 Fax: 81-3-3475-5619 E-mail: info@jaacc.jp

For users in USA write to:
Copyright Clearance Center Inc.
222 Rosewood Drive, Danvers, MA 01923, USA
Phone: 1-978-750-8400 Fax: 1-978-646-8600

© Society for Chemistry and Micro-Nano Systems (CHEMINAS), 2006
All rights reserved.
Printed in Japan. 2006.

ISBN: 4-9903269-0-3-C3043

PREFACE

μ TAS 2006 is celebrating its 10th anniversary, and the official name is The 10th Anniversary International Conference on Miniaturized Systems for Chemistry and Life Sciences. The first μ TAS was held in 1994 with 160 participants and the conference has rapidly and delightfully grown up through the ten conferences. The participants are reaching almost 1000, and μ TAS has become the largest and the highest quality international conference in this field. Professor Thomas Laurell, Chairman of the 8th μ TAS , described the brief history of the conference in the PREFACE of μ TAS 2004 proceedings.

The number of the participating nations is around 30. The conference sites have been rotating among the three regions of North America, Asia and Europe since the 8th conference. This year, the number of submitted abstracts increased to 881, the largest ever. 66 orals and 473 posters, therefore 539 abstracts in total were selected. The noteworthy tendency of this year is that the number of both submitted and accepted abstracts from Asian countries has exceeded those from the other two areas for the first time. Another characteristic is that the conference has formed a tie with "Micro Machine Exhibition 2006", the largest and oldest MEMS related exhibition, which attracts more than ten thousand people. This tie will produce reciprocal benefits between the two related fields of technology.

As the tenth anniversary event, "History of Microchips" is exhibited. The epoch-making microchips, devices and other components are exhibited in showcases, with the brief explanation panels. People visiting this anniversary exhibition, especially the young generation, will be impressed by the rapid progress in the field and may see its promising future with scientific ambition in their mind.

The management and support system of μ TAS has changed this time. The Steering Committee used to organize and operate the conference and select the abstracts. Now, the technical program committee (TPC) which selects the abstracts and organizes the program is separated from the newly established managing organization Chemical and Biological Microsystems Society (CBMS). The present President of CBMS is Professor Jed Harrison, and the board meeting steers the general direction of the conference. Another role of CBMS board meeting is organizing the TPC. The members of TPC are selected five persons each from North America, Asia and Europe regions respectively, with holding the balance between the scientific areas. This new management and operation system copes with the rapid expansion and accompanying financial difficulties of the conference. This year, the Japanese domestic society "Society for Chemistry and Micro-Nano Systems (CHEMINAS)" co-sponsors the conference with CBMS, and operates the local organizing committee. All the members of CBMS board, TPC committee and the local organizing committee are listed later.

These two volumes of proceedings cover all of the sciences and technologies ranging from the matured to the newly growing areas. Micro fluidics and devices, detection, and cell handling and analysis are the major areas occupying over 45% of these large volumes indeed. The cell handling and analysis area has shown outstanding progress in these couple of μ TAS conferences, while the micro fluidics and device area is the matured traditional one. The detection area suddenly becomes conspicuous, although everyone has recognized the importance from the beginning. Nano fluidics and nano

chemistry are allegro following the nano-bio area. Genomics and proteomic application is going into maturation, but still forms large application group exceeding 10% of the abstracts in case the area puts together with the medical and clinical applications. In my personal opinion, chemical synthesis and combinatorial applications accounting for only 2% of whole volume should be encouraged. Anyway, these two volumes exhibit the results of progress through the ten μ TAS conferences, and show the solid evidence of further development of practical applications and the opening of new horizon of the science and technologies.

I would like to thank all of those who have supported and contributed to organizing the 10th Anniversary μ TAS. The sincere and serious but laborious work of TPC for abstract selection and premeditative direction of CBMS boards are the most grateful efforts. Also, I should express my hearty gratitude to the local organizing committee for the continuous contribution to the planning and organizing the conference. Dr. Shigetoshi Seta's great contribution as Chairman of the Financial Committee was indispensable to make it possible to hold this large-scale international conference in the center of Tokyo, and especially we are grateful to the contribution of President Katsuji Fujimoto of Nippon Sheet Glass Co., Ltd. Ms. June Echizen and her company Echizen and Associates expertly handled the organization. I am also deeply thankful to Co-Chairman Professor Hiroyuki Fujita for his truly cooperative leading of the organization and handling of the committees. And it must be noted Secretary General Dr. Tadashi Fujinuki and Ms. Yoshiko Ogawa of CHEMINAS devoted themselves to this conference and I would express my deepest thank to them. Finally, I would like to thank the community of μ TAS for scientific, financial, cultural and every kind of contribution making the conference success, and I do hope continuous progress, prospect and evolution of all of these contributors.

Takehiko Kitamori
 μ TAS 2006 Chairman
October 6, 2006

Previous μ TAS Conferences:

1994	Enschede, The Netherlands
1996	Basel, Switzerland
1998	Banff, Canada
2000	Enschede, The Netherlands
2001	Monterey, California, USA
2002	Nara, Japan
2003	Squaw Valley, California, USA
2004	Malmö, Sweden
2005	Boston, Massachusetts, USA

CONFERENCE OUTLINE

The 10th Anniversary International Conference on Miniaturized Systems for Chemistry and Life Sciences (μ TAS2006)

November 5 - 9, 2006

Tokyo International Forum, Tokyo, Japan

Co-Sponsored by:

Society for Chemistry and Micro-Nano Systems
Chemical and Biological Microsystems Society

Supported by:

Japan National Tourist Organization

In cooperation with:

The Biophysical Society of Japan
The Chemical Society of Japan
The Electrochemical Society of Japan
The Food Hygienics Society of Japan
The Institute of Electrical Engineers of Japan
The Institute of Electronics, Information and Communication Engineers
Japan Analytical Instruments Manufacturers Association
The Japan Society for Analytical Chemistry
Japan Society for Bioscience, Biotechnology, and Agrochemistry
The Japan Society for Precision Engineering
Japanese Society of Animal Science
The Japan Society of Applied Physics
The Japanese Biochemical Society
The Japanese Society of Microscopy
The Mass Spectrometry Society of Japan
The Pharmaceutical Society of Japan
Spectroscopical Society of Japan
The Society for Chromatographic Sciences
The Society of Chemical Engineers, Japan
The Society of Instrument and Control Engineers

The Royal Society of Chemistry, Lab on a Chip
American Chemical Society, Analytical Chemistry
Institute of Physics, Journal of Micromechanics and Microengineering

ORGANIZERS

Board of Directors, Chemical and Biological Microsystems Society

D. Jed Harrison (President)	University of Alberta
Takehiko Kitamori (Vice President)	The University of Tokyo
J. Michael Ramsey (Treasurer)	University of North Carolina at Chapel Hill
Albert van den Berg (Secretary)	University of Twente
Yoshinobu Baba	Nagoya University
Klavs F. Jensen	Massachusetts Institute of Technology
Thomas Laurell	Lund University
Andreas Manz	Institute of Analytical Sciences
Allen Northrup	MicroFluidic Systems, Inc.
Shuichi Shoji	Waseda University

μ TAS 2006 Conference Officials

Conference Chair

Takehiko Kitamori The University of Tokyo

Conference Co-Chair

Hiroyuki Fujita The University of Tokyo

Program Committee

Takehiko Kitamori (Chair)	The University of Tokyo
Yoshinobu Baba	Nagoya University
Zhao-Lun Fang	Northeastern University
Hiroyuki Fujita	The University of Tokyo
Stephen Jacobson	Indiana University
Klavs F. Jensen	Massachusetts Institute of Technology
Tae Song Kim	Korea Institute of Science and Technology
Jorg P. Kutter	Technical University of Denmark
James P. Landers	University of Virginia
Thomas Laurell	Lund University
Laurie Locascio	National Institute of Standards & Technology
Andrew de Mello	Imperial College
Minoru Seki	Osaka Prefecture University
Sabeth Verpoorte	University of Groningen
Jean-Louis Viovy	Curie Institute

Local Organizing Committee

Takehiko Kitamori (Chair)	The University of Tokyo
Hiroyuki Fujita (Co-Chair)	The University of Tokyo
Yoshinobu Baba	Nagoya University
Long-Sheng Fan	National Tsing Hua University
Zhao-Lun Fang	Northeastern University
Teruo Fujii	The University of Tokyo

Shinji Hasebe	Kyoto University
Akihide Hibara	The University of Tokyo
I-Ming Hsing	Hong Kong University of Science and Technology
Koji Ikuta	Nagoya University
Noritada Kaji	Nagoya University
Yoshiki Katayama	Kyushu University
Tae Song Kim	Korea Institute of Science and Technology
Haeng-Boo Kim	The University of Tokyo
Katsuki Kusakabe	Fukuoka Women's University
Liu Ai Qun	Nanyang Technological University
Ryo Miyake	Hitachi, Ltd.
Hiroaki Nakanishi	Shimadzu Corp.
Koji Otsuka	Kyoto University
John Ralston	University of South Australia
Minoru Seki	Osaka Prefecture University
Shigetoshi Seta	Tokyo University of Agriculture & Technology
Shuichi Shoji	Waseda University
Eiichi Tamiya	Japan Advanced Institute of Science & Technology
Hiroshi Terada	Tokyo University of Science
Manabu Tokeshi	Nagoya University
Masao Washizu	The University of Tokyo

CONTRIBUTORS

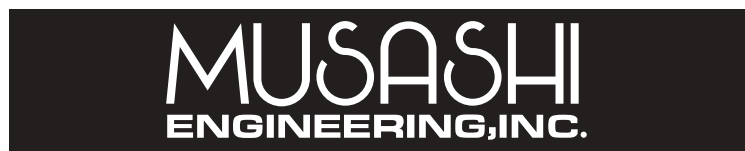
We gratefully acknowledge the support from the following companies and organizations.

Commemorative Organization for the Japan World Exposition '70
Japan Society for the Promotion of Science
Nanotechnology Researchers Network Center of Japan, Ministry of Education, Culture, Sports, Science and Technology
The Federation of Pharmaceutical Manufacturers' Associations of Japan
Tokyo Ohka Foundation for the Promotion of Science and Technology

Asahi Kasei Corporation
Dainippon Ink and Chemicals, Inc.
DKK-Toa Corporation
Fujirebio Inc.
Hitachi Chemical Co., Ltd.
Hitachi High-Technologies Corporation
Hitachi Ltd.
Horiba, Ltd.
Inabata & Co., Ltd.
Institute of Microchemical Technology Co., Ltd.
Itoham Foods Inc.
JEOL Ltd.
KRI, Inc.
Kyoto Electronics Manufacturing Co., Ltd.
Matsushita Electric Industrial Co., Ltd.
Mitsubishi Chemical Corporation
Musashi Engineering Inc.
Nagase & Co., Ltd.
Nichia Corporation
Nippon Kayaku Co., Ltd.
Nippon Sheet Glass Co., Ltd.
Nippon Sheet Glass Foundation for Materials Science and Engineering
Nissan Chemical Industries, Ltd.
NOF Corporation
NTT Data Corporation
Olympus Corporation
Osaka Gas Co., Ltd.
Sharp Corporation
Shimadzu Corporation
Shiseido Co., Ltd.
Starlite Co., Ltd.
Sumita Optical Glass, Inc.
Sumitomo Bakelite Co., Ltd.
Sumitomo Chemical Co., Ltd.
Sumitomo Corporation
Sumitomo Electric Industries, Ltd.
Tanaka Kikinzoku Kogyo K. K.
Tokuyama Corporation
Tokyo Chemical Industry Co., Ltd.
Tosoh Corporation



世 界 の デ イ ス ペ ン サ ー



武藏エンジニアリング株式会社



AsahiKASEI
旭化成株式会社

 FUJIReBIO INC.

Hitachi High-Technologies

HORIBA

IK
INABATA & CO., LTD.

JEOL

KEM
KYOTO ELECTRONICS
MANUFACTURING CO.,LTD.

NAGASE

 NIPPON KAYAKU

OLYMPUS®

Your Vision, Our Future

SHARP

 Starlite Co., Ltd.

SUMITOMO CHEMICAL

 SUMITOMO ELECTRIC



 DKK-TOA CORPORATION

Chemistry with a heart
TOKUYAMA 

TOSOH CORPORATION

TABLE OF CONTENTS

Volume 1

Pages 1- 1031

Volume 2

Pages 1032 - 1592

MICRO TOTAL ANALYSIS SYSTEMS 2006

DAY 1 - MONDAY, NOVEMBER 6, 2006

PLENARY LECTURE 1

- Sub-Diffraction Limit Imaging of Single Molecules and Single Cells1**
Edward S. Yeung, Yang He, Hungwing Li, Seong Ho Kang, Dragan Isailovic,
Jinjian Zheng
Iowa State University and DOE Ames Lab, U.S.A

Session 1A1 Micro & Nano Biology

- Single Protein Molecule Analysis in Single Cells in a Microfluidic Chip4**
Jonas Jarvius, Jonas Melin, Henrik Johansson, Malin Jarvius, Yuki Tanaka, Mats
Nilsson, Ulf Landegren
Uppsala University, Sweden

- Single Cell Transcriptome Analysis Using a PDMS Microchip7**
Nathalie Bontoux¹, Luce Dauphinot², Tania Vitalis², Vincent Studer², Yong Chen¹,
Jean Rossier², Marie-Claude Potier²
¹Laboratoire de Photonique et de Nanostructures-CNRS, France, ² Laboratoire de
Neurobiologie et Diversité Cellulaire-ESPCI-CNRS, France

- Genotyping of Single DNA Molecules in Single Cells in Microfluidic
Chips.....10**
Yuki Tanaka¹, Henrik Johansson², Chatarina Larsson², Jonas Jarvius², Jonas
Melin², Takehiko Kitamori³, Ulf Landegren², Mats Nilsson²
¹Japan Society for the Promotion of Science, Japan, ²Uppsala University, Sweden,
³The University of Tokyo, Japan

Session 1B1 Micro & Nano Fabrication

- Nano-Acoustic Interactions Governing High Aspect Ratio Nanochannel
Femtosecond Laser Machining13**
Sanghyun Lee, Ernest F. Hasselbrink, Alan J. Hunt
University of Michigan, USA.

- DNA Nano-Stamping for Molecular Surgery16**
Masafumi Fuke, Osamu Kurosawa, Hidehiro Oana, Masao Washizu
University of Tokyo, Japan

- Exponential Size Reduction of Chemical Patterns Using Repetitive
Microcontact Printing19**
Kenji Suzuki, Kazuo Hosokawa, Mizuo Maeda
RIKEN, Japan

Session 1A2 Cell Handling & Analysis 1 (Electroporation)

- Gene Transfer and Characterization of Protein Dynamics in Stem Cells
Using Single Cell Electroporation in a Microfluidic Device22**
Ana Valero, Janine N. Post, Jan W. van Nieuwkaastele, Wiebe Kruijer, Helene
Andersson, Albert van den Berg
University of Twente, The Netherlands

Selective High Efficiency In-Flow Electroporation with Focused Electric Fields in a Microsystem.....	25
Aniruddh Sarkar ¹ , Ashutosh Shastry ¹ , Bhaskar Mitra ¹ , Rita Mulherkar ² , Rakesh Lal ¹	

¹Indian Institute of Technology Bombay, India, ²Cancer Research Institute, ACTREC, Navi Mumbai, India

Molecular Size Effect on Micro Electroporation by Using Microchip with a Three-Dimensional Electrode Array	28
Huiqi He, Yi-Kuen Lee, Donald C. Chang	
Hong Kong University of Science and Technology, Hong Kong	

Session 1B2 Particle 1

Micro Particle Sampling on a Perforated Filter Membrane by EWOD-Actuated Droplet Sweeping.....	31
Sang K. Chung, Yuezun Zhao, Sung K. Cho	
University of Pittsburgh, USA	

Optical Manipulation of Microparticles Using a Liquid Crystal Display	34
Wonjae Choi ¹ , Sehwan Kim ² , Jin Jang ² , Je-Kyun Park ¹	
¹ Korea Advanced Institute of Science and Technology (KAIST), Korea, ² Kyung Hee University, Korea	

A Microfluidic Chip with a Nanoscale Array for Analysis of Viral Particles.....	37
Kidong Park, Demir Akin, Rashid Bashir	
Purdue University, USA	

PLENARY LECTURE 2

Suspended Microchannel Resonator (SMR) for Biomolecular and Cellular Detection	40
Thomas Burg, Michel Godin, Scott Knudsen, Scott Manalis	
Massachusetts Institute of Technology, USA	

POSTER SESSION 1

Micro & Nano Fluidics

An Electrokinetic Sandwich Injection Technique for Microchip Capillary Electrophoresis	41
Gui-Sheng Zhuang	
Shanghai Institute of Microsystem and Information Technology, Chinese Academy of Science, China	

A PDMS Diffusion Pump for On-Chip Fluid Handling in Microfluidic Devices	44
Mark A. Eddings, Bruce K. Gale	
University of Utah, USA	

Full-Image Micro-PIV Analysis of Transient and Stationary Flow Patterns in Microfluidic Structures Under Piezo Actuation	47
Melker Sundin, Thomas Glasdam Jensen, Henrik Bruus, Jörg P. Kutter	
Technical University of Denmark, Denmark	

Efficiency Controllable Sample Preconcentration Chips Based on Nano Ion Depletion Bridge	50
Jing Liu, GuiSheng Zhuang, MengSu Yang, QingHui Jin, JianLong Zhao	
Shanghai Institute of Microsystem and Information Technology, Chinese Academy of Sciences, China	
3D-Simulations of Aggregating Beads in Microfluidic Chambers on High Performance Computers Compared to Experiments	53
Thomas Glatzel ¹ , Claudio Cupelli ¹ , Uwe Küster ² , Roland Zengerle ¹ , Mark Santer ¹	
¹ University of Freiburg, Germany ² University of Stuttgart, Germany	
High-Performance Droplet Generation Via Integrated 3-D Circular Constrictions	56
Wee-Liat Ong ¹ , Stefan Martens ² , Nagarajan Ranganathan ¹ , Levent Yobas ¹	
¹ Institute of Microelectronics, Singapore, ² University of Applied Sciences, Wiesbaden, Germany	
Simulation Examination for Multilayer Flow System	59
Ryo Anraku ¹ , Takahiro Asai ¹ , Kenji Uchiyama ¹ , Akihiko Hattori ¹ , Manabu Tokeshi ² , Takehiko Kitamori ³	
¹ Nippon Sheet Glass Co., Ltd., Japan, ² Nagoya University, Japan, ³ The University of Tokyo, Japan	
Computational Modelling of Pneumatic Particle Capture Device	62
Ok Chan Jeong, Satoshi Konishi	
Ritsumeikan University, Japan	
Three-Dimensional Measurement of Circulation Flow in a Droplet Moving in a Microchannel	65
Haruyuki Kinoshita, Marie Oshima, Shohei Kaneda, Teruo Fujii	
University of Tokyo, Japan	
An Optically Driven Pump for Microfluidics	68
Hasan M. Mushfique ¹ , Jonathan Leach ¹ , Miles Padgett ¹ , Roberto Di Leonardo ^{1,2} , Jon Cooper ¹	
¹ University of Glasgow, UK, ² INFM-CRS SOFT, Dipartimento di Fisica, Roma, Italy	
Stereo-Scopic Observation and Its Application to Three Dimensional Flow Measurements in a Microchannel	71
Naoki Ichikawa, Peter M.-Y. Chung, Ryutaro Maeda	
National Institute of Advanced Industrial Science and Technology (AIST), Japan	
Spatio-Temporal Tuning of Stimuli-Responding Surfaces for Dynamic Control of Electroosmotic Flows	74
Jan Sudor ¹ , Guillaume Paumier ¹ , Anne-Marie Gue ¹ , Francoise Vinet ² , Alain Esteve ¹ , Mehdi Djafari-Rouhani ¹	
¹ LAAS-CNRS, France, ² CEA-Leti, France	
Producing Droplets in Parallel Microfluidic Systems	77
Hervé Willaime ¹ , Valessa Baribier ¹ , Patrick Tabeling ¹ , Fabien Jousse ²	
¹ CNRS-ESPCI Paris, France, ² Unilever Center of Research, UK	

Controlling PDMS Surfaces Properties: To Generate Double Emulsions	80
Valessa Barbier ¹ , Michaël Tatoulian ² , Patrick Tabeling ¹ , Hong Li ¹ , Hervé Willaime ¹ , Farzaneh Arefi-Khonsari ²	
¹ CNRS-ESPCI Paris, France, ² ENSCP Paris, France	
Transient Charging of the Electric Double Layer in Field Effect-Flow Control of Electro-Osmotic Flow.....	83
Egbert J. van der Wouden, J.G.E. Gardeniers, Albert van den Berg University of Twente, The Netherlands	
Meshless Simulation for Micro Droplet Generation	86
Takahiro Harada ¹ , Yukihito Suzuki ² , Takahiro Arakawa ³ , Shuichi Shoji ³ , Seiichi Koshizuka ¹	
¹ The University of Tokyo, Japan, ² Japan Science and Technology Agency, Japan, ³ Waseda University, Japan	
Use Micro-PIV to Measure Transient Electroosmotic Flow and Zeta Potential of Channel Wall	89
D.G. Yan, N.T. Nguyen, X.Y. Huang Nanyang Technological University, Singapore	
Simulations of a Microfluidic Variable Resistor.....	92
Bozhi Yang ¹ , Qiao Lin ²	
¹ Carnegie Mellon University, USA, ² Columbia University, USA	
Electrokinetic Control of Droplet Break-Up and Switching of Droplet Movement Direction in an Aqueous Two-Phase System	95
Young Hoon Choi, Do Hyun Kim KAIST, Korea	
Droplets Break-Up in Junctions: the Concept of a Critical Length.....	98
Laure Ménétrier, Patrick Tabeling ESPCI, France	
Nanoscale Laser Induced Fluorescence Imaging of Zeta-Potential Affected by Ion Motion in Microchannel	101
Yutaka Kazoe, Yohei Sato Keio University, Japan	
Micropump and Micromixer Driven by Laser and AC Electric Field	104
Michihiko Nakano ¹ , Kazunori Takashima ¹ , Shinji Katsura ² , Akira Mizuno ¹	
¹ Toyohashi University of Technology, Japan, ² Gunma University, Japan	
Pressure Balance at Liquid-Liquid Interface for Elucidation of Anomalous Phenomena in Micro Counter-Current Flow.....	107
Arata Aota ^{1,2} Akihide Hibara ^{1,3} Yasuhiko Sugii ³ , Takehiko Kitamori ^{1,3}	
¹ The University of Tokyo, Japan, ² Japan Society for the Promotion of Science, Japan, ³ Japan Science and Technology Agency, Japan	
Magnetic Levitation of Microdroplets in Air	110
Vincent Haguet ¹ , Christian Jeandey ¹ , Hichem Chetouani ² , Gilbert Reyne ² , François Chatelain ¹	
¹ CEA, France, ² ENSIEG, France	

Automatic Design of Optimal Fluidic Components	113
David R. Mott, Keith S. Obenschain, Peter B. Howell, Joel P. Golden	
Naval Research Laboratory, USA	
Laminar Flow Mixing Using Acoustic Microcavitation Streaming	116
John Collin, Jeff Fan, Reza Moghbel, Albert Tsung-Hsi Hsieh, Abraham P. Lee	
University of California, Irvine, USA	
Precise Characterization of Liposome Populations Formed in a 5-Channel Flow-Focused System	119
Andreas Jahn ¹ , Wyatt Vreeland ¹ , Laurie Locascio ¹ , Don DeVoe ² , Michael Gaitan ¹	
¹ National Institute of Standards and Technology, USA, ² University of Maryland, USA	
Bounds on Contact Angle Hysteresis of Textured Super-Hydrophobic Surfaces	122
Ashutosh Shastry, Aziel Epilepsia, Marianne J. Case, Shaghayegh Abbasi, Karl F. Bohringer	
University of Washington, Seattle, USA	
Electromechanical Forces Effecting Droplet Movement in a Twoplate Microfluidic Device	125
Debalina Chatterjee, Heather Shepherd, Robin L. Garrell	
University of California Los Angeles, USA	
Electrically-Induced Splitting and Generation of Sub-Nanoliterdroplets in Air on a Digital Microfluidic Device	128
Sang Uk Son ¹ , Debalina Chatterjee ² , Robin L. Garrell ²	
¹ Korea Advanced Institute of Science and Technology, Korea, ² University of California Los Angeles, USA, ² University of California Los Angeles, USA	
Fast Pulsatile Flow Included in Net Continuous Flow Generated by a Traveling Wave Micropump	131
Takaaki Suzuki ¹ , Hidetoshi Hata ¹ , Hirofumi Shintaku ¹ , Isaku Kanno ¹ , Satoyuki Kawano ² , Hidetoshi Kotera ¹	
¹ Kyoto University, Japan, ² Osaka University, Japan	
Nanoliter Droplet Creation by EWOD and LDEP	134
Yen-Chen Lin, Yu-Chi Chang, Kai-Cheng Chuang, Shih-Kang Fan	
National Chiao Tung University, Taiwan	
Micro & Nano Fabrication	
Optimized Reactive Ion Etching Process for the Fabrication of High-Aspect-Ratio Silicon Nanopillar Arrays	137
Yu-Fen Chang ¹ , Qiong-Ru Chou ² , Jiunn-Yuan Lin ² , Chau-Hwang Lee ¹	
¹ Academia Sinica, Taiwan, ² National Chung-Cheng University, Taiwan	
Study of Masking Materials Using in Powder Blasting for Low Cost Microfluidic Chip Fabrication	140
Adisorn Tuantranont, Sakon Rahong, Nisaporn Porntheerapat, Tanom Lomas, Anurat Wisitsoraat	
National Electronics and Computer Technology Center, Thailand	

Electrostatic Force Driven Micro and Nano Imprint Lithography	143
Isabel Rodriguez, Saman Dharmatilleke	
Institute of Materials Research and Engineering (IMRE), Singapore	
Hybrid Tooling by Combination of UV-LIGA and CNC-Milling for Microfluidic Disposables	146
Reinhold Jurischka, Christoph Blattert, Isam Tahhan, Andreas Schoth, Claas Mueller, Holger Reinecke	
University of Freiburg, Germany	
A Nanoimprint Lithographic Method for Fabrication of Three-Dimensional Sealed Nanofluidic Channel Arrays	149
Jarrett J. Dumond, Hong Yee Low, Isabel Rodriguez	
Institute of Materials Research and Engineering, Singapore	
Glass Microfabricated Nebulizer Chip for Mass Spectrometry	152
Ville Saarela ¹ , Markus Haapala ² , Risto Kostiainen ² , Tapio Kotiaho ² , Sami Franssila ¹	
¹ Helsinki University of Technology, Finland, ² University of Helsinki, Finland	
Low Distortion, High Strength Bonding of Polymer Microfluidic Chips Exploiting Case II Permeation.....	155
Alfredo M. Morales ¹ , Blake A. Simmons ¹ , Thomas I. Wallow ² , Karen L. Krafcik ¹ , Linda A. Domeier ¹	
¹ Sandia National Laboratories, USA, ² Advanced Micro Devices, USA	
Fabrication of Highly Dimension Controlled Pmma Microchip by Hot Embossing and Low Temperature Direct Bonding	158
Hidetoshi Shinohara ¹ , Jun Mizuno ¹ , Fumihiko Kitagawa ² , Koji Otsuka ² , Shuichi Shoji ¹	
¹ Waseda University, Japan, ² Kyoto University, Japan	
Fabrication of Superhydrophobic Surface by Nanomolding	161
Ming-Hung Chen, Yun-Ju Chuang, Fan-Gang Tseng	
National Tsing Hua University, Taiwan	
Pressure-Assisted Micropatterning of Non-Photodefinable Polymers.....	164
Yi Zhao, David L. Mabius, Jonnathan Regis, Xin Zhang	
Boston University, USA	
Creating Silicon Nanostructures with Controllable Sidewall Profiles by Using Fluorine-Enhanced Oxide Passivation	167
Yi Zhao, Xiaoyu Zheng, Jonnathan Regis, David L. Mabius, Xin Zhang	
Boston University, USA	
Characterization of the Fluidic Properties of In-Situ Polymerized Monolith in Microfluidic Device.....	170
Mei He, D. Jed Harrison	
University of Alberta, Canada	
Microplasma Technogogy Developed for Micromachining and Surface Patterning in Microbiosystem Applications	173
Helen M. L. Tan, Takanori Akagi, Takanori Ichiki	
University of Tokyo, Japan	

Plasma-Based Microfabrication of Sub-Micron-Aperture Parylene Nozzles	176
Po-Jui Chen, Yu-Chong Tai	
California Institute of Technology, USA	
Solvent-Resistant and Transparent Polysilazane Glass Microfluidics for Photochemical Reactions	179
Hong-Joo Lee, Amit Asthana, Jayakumar Perumal, Jun-Hong Park, Dong-Pyo Kim	
Chungnam National University, Korea	
Batch Fabricated Micro and Nanopores in Silicon for Particle Translocation Detection	182
Christophe Yamahata ¹ , Agnès Tixier-Mita ² , Bruno Le Pioufle ² , Hiroaki Suzuki ¹ , Edin Sarajlic ¹ , Momoko Kumemura ¹ , Shoji Takeuchi ¹ , Dominique Collard ² , Hiroyuki Fujita ¹	
¹ Institute of Industrial Science, The University of Tokyo, Japan,	
² LIMMS-CNRS/IIS, The University of Tokyo, Japan	
Packaging & Interface	
Fabrication of a Microfluidic Bioarray Using 2-D Array of Microbeads Fixed Within Laser-Machined Surface Microstructures	185
Tadatake Sato, Thomas Gumpenberger, Ryozo Kurosaki, Aiko Narazaki, Yoshizo Kawaguchi, Hiroyuki Niino	
National Institute of Advanced Industrial Science and Technology (AIST), Japan	
Development of a 3D Hybrid Si/Polymer Technology for Integrating Active Si Chips in Microfluidic Systems	188
Samuel Charlot, Anne-Marie Gue, Josiane Tasselli, Antoine Marty, Patrick Abgrall, Daniel Esteve	
LAAS-CNRS, France	
Dead Volume Free and User-Friendly One Touch Lock and Detachable Microfluidic Connector (2).....	191
Kenji Katayama ¹ , Keisuke Morisima ² , Yoshikuni Kikutani ³ , Mitsuo Kitaoka ⁴ , Takehiko Kitamori ⁵	
¹ Chuo University, Japan, ² Tokyo University of Agriculture and Technology, Japan,	
³ Kanagawa Academy of Science and Technology, Japan, ⁴ The Research Association of Micro Chemical Process Technology, Japan, ⁵ University of Tokyo, Japan	
Material & Surface	
Patterning Hydrophobic and Hydrophilic SAM's in Microfluidic Devices Using a UV Photolithography-Technique	194
Eric Besson ¹ , Anne-Marie Gue ¹ , Hafsa Korri-Youssoufi ² , Jan Sudor ¹ , Nicole Jaffrezic ³	
¹ LAAS-CNRS, France, ² Université Paris Sud, France, ³ Ecole Centrale de Lyon, France	
Addressable Protein and Cell Patterning Via Switchable Superhydrophobic Microarrays.....	197
Jau-Yeh Shiu, Peilin Chen	
Academia Sinica, Taiwan	

Superhydrophobic Surfaces for Microfluidic Applications	200
Yasemin Koc ¹ , Paul Roach ² , Carol C. Perry ² , Michael I. Newton ² , Glen McHale ² , Andrew J. deMello ¹ , Neil J. Shirtcliffe ²	
¹ Imperial College London, UK, ² School of Biomedical and Natural Sciences, Nottingham Trent University, UK	
Surface Modification and Photografting of COC with Trypsin for Proteolytic Digestion of Protein Samples	203
Mohamed Bedair, Roxanne Lewis, Ballios Brian, Richard Oleschuk Queen's University, Canada	
Surface Plasmon Resonance Imaging Clarifies Non-Cross-Linking Interaction Between DNA Duplex on a Substrate and Duplex on Gold Nanoparticles.....	206
Yasunobu Sato, Kazuo Hosokawa, Mizuo Maeda RIKEN, Japan	
RNA-To-Protein Chip: An Integrated Microarray Platform to Bridge Genomics and Proteomics	209
Manish Biyani ¹ , Naoto Nemoto ¹ , Yosuke Hosoi ² , Takanori Ichiki ²	
¹ Saitama Small Enterprise Promotion Corporation, Kawaguchi, Saitama, Japan, ² The University of Tokyo, Tokyo, Japan	
Non-Biofouling Surface for Microchannel Device by Grafting with Biocompatible 2-Methacryloyloxyethyl Phosphorylcholine for Obtaining High S/N Ratio	212
James Sibarani, Tomohiro Konno, Madoka Takai, Kazuhiko Ishihara The University of Tokyo, Japan	
Protein Antiadsorption Modification by Negatively Charged Phospholipid Polymer for Microsystem Needing Electroosmotic Flow	215
Yan Xu, Madoka Takai, Tomohiro Konno, Kazuhiko Ishihara University of Tokyo, Japan	
Polymeric Actuating Materials for Micro-Fluidic Manipulation Using External Stimuli	218
Hans T.A. Wilderbeek, Anthony J. Van der Linden, Titie Mol, Judith De Goede, Wim Talen, Murray Gillies, Dirk J. Broer, Jaap M.J. Den Toonder Philips Research, Netherlands	
Photo-Patternable Liquid Crystal Actuators with High Work Output Through Optimization of Molecular Configuration	221
Casper L. van Oosten ¹ , Kenneth D. Harris ¹ , Cees W.M. Bastiaansen ¹ , Dirk J. Broer ^{1,2}	
¹ Eindhoven University of Technology, The Netherlands ² Philips Research Laboratories, The Netherlands	
Generation of Permanently Hydrophilic Poly(Dimethylsiloxane) Microfluidic Devices	224
Charles S Henry, Jonathon J Vickers, Brian M Murphy, Xinya He, David W Grainger, David S Dandy Colorado State University, USA	

Hydrophilic, Protein-Resistant Surface Modification of Polymer Monoliths Via Photografting for Multifunctional Microfluidic Devices	227
Timothy B. Stachowiak ¹ , Frantisek Svec ² , Jean M. J. Fréchet ¹	
¹ University of California, Berkeley, USA, ² Lawrence Berkeley National Lab, USA	
Microfluidic Generation of Tunable Monodisperse Double Emulsions for Templated Silica Particles	230
Frank J. Zendejas ¹ , Uthara Srinivasan ² , William J. Holtz ¹ , Jay D. Keasling ¹ , Roger T. Howe ³	
¹ University of California at Berkeley, Berkeley Sensor & Actuator Center, USA, ² University of California at Berkeley, Energy and Resources Group, USA, ³ Stanford University, Department of Electrical Engineering, USA	
3D Manipulation of Lipid Nanotubes with Photo-Crosslinkable Gel Micro-Beads for Nano-Assenby	233
Fumihito Arai ¹ , Toshiaki Endo ² , Ryuji Yamauchi ² , Toshio Fukuda ² , Toshimi Shimizu ³ , Shoko Kamiya ⁴	
¹ Tohoku University, Japan, ² Nagoya University, Japan, ³ AIST, Japan, ⁴ JST-CREST, Japan	
Dynamic Coating of Poly(Methyl Methacrylate) Chips with N-Dodecyl-B-D-Maltoside and Cellulose for Separation of Glycans from Glycoproteins	236
Fuquan Dang	
Health Technology Research Center, AIST, Japan	
Effects of Surface Modification on Electroosmotic Flow and Zeta Potential in Microchannel.....	239
Seiichi Sasaki, Yohei Sato	
Keio University, Japan	
Stable Poly(Ethylene Glycol) Microwell Arrays for Long-Term Cell Patterning	242
Hideaki Tsutsui, Chih-Ming Ho	
University of California, Los Angeles, USA	
Sub-Nano Litter Micro Batch Operation Systems with Multi-Step Laplace Pressure Valves Prepared by Photocatalytic Analog Lithography	245
Go Takei ¹ , Mari Nonogi ¹ , Akihide Hibara ^{1,2,3} Takehiko Kitamori ^{1,2,3} Haeng-Boo Kim ^{1,2,3}	
¹ University of Tokyo, Japan, ² Kanagawa Academy of Science and Technology, Japan, ³ Japan Science and Technology, Japan	
'On the Fly' Production of Microtubes for the Artificial Micro Vessel	248
SungRak Kim ¹ SangHoon Lee ²	
¹ Korea Artificial Organ Center, Korea University, Korea, ² Korea University, Korea	
Microfluidic-Directed Molecular Self-Assembly and Templating of Bio-Inspired Nanoparticles	251
Wyatt N. Vreeland ¹ Jennifer S. Hong ¹ Andreas Jahn ¹ Srinivasa R. Raghavan ² , Laurie E. Locascio ¹ Michael Gaitan ¹	
¹ National Institute of Standards and Technology, USA, ² University of Maryland, USA	

Microfabrication of Graphitic Carbon Materials Via Electrochemical Etching.....	254
Mark T. McDermott, Solomon Ssenyange, Justine Taylor, Jed Harrison, Rongbing Du University of Alberta, Canada	
Integrated Microreactor for Continuous Colloid Synthesis and Surface-Coating	257
Saif A. Khan, Klavs F. Jensen Massachusetts Institute of Technology, U.S.A	
Photopatterned Polyelectrolyte Multilayers for Cell Culture	260
Darwin R. Reyes, J. Brian Hutchison, Laurie E. Locascio, Michael Gaitan National Institute of Standards and Technology, USA	
Hydrophobic Non-Fouling Surfaces for Droplet Based Microfluidicbioanalytical Systems	263
Ashutosh Shastry, Sidhartha Goyal, Buddy Ratner, Karl F. Bohringer University of Washington, Seattle, USA	
Comparison of Micro/Nano Pore Platinum Electrodes for CMOS Integrated Non-Disposbale Biosensor Applications.....	266
Hye K. Seo, Dae J. Park, Jae Y. Park Kwangwoon University, Korea	
Plasma Surface Modification with the Aid of Colloidal Surface Modification for Polymer Microchip	269
Masahiro Matsumoto, Matsuhiro Nishizawa, Takashi Abe Tohoku University, Japan	
Microchip-Based DNA Purification in a Two-Stage, Dual-Phase Microchip Containing a Derivatized Photo-Polymerized Monolithic	272
Jian Wen, Christelle Guillo, Jerome P. Ferrance, James P. Landers University of Virginia, USA	
Experimental Study of the Shrinkage Ratio of PDMS and Its Alignment for the Wafer Level Process	275
Seok Woo Lee, Seung S. Lee KAIST, Korea	
Basic Technologies & Science - Others	
Micro and Nano Fluidic Devices Using Electroactive Polymer Artificial Muscle.....	278
Ron Pelrine, Roy Kornbluh, Harsha Prahlad, Richard Heydt, Seiki A. Chiba SRI International, USA	
Optimal Microchannel Design by Genetic Algorithms	281
Hyunwoo Bang ¹ Won Gu Lee ¹ Junha Park ² , Hoyoung Yun ¹ Joonmo Lee ¹ Seok Chung ³ , Keunchang Cho ² , Chanil Chung ² , Dong-Chul Han ¹ Jun Keun Chang ² ¹ Seoul National University, Korea, ² Digital Bio Technology, Korea, ³ Massachusetts Institute of Technology, USA	

Localized Optical Activation of Therapeutic Gene Release in Breast Cancer Cells Using Photothermal Nanocrescents as Oligonucleotide-Carriers	284
Eunice S. Lee, Gang L. Liu, Luke P. Lee University of California, Berkeley, USA	
High Power Biofluid-Activated Laminated Batteries for Bio-Applications	287
Ki B. Lee KB Lab, Singapore	
Numerous Water-in-Oil Droplets as Microreactors in Microchamber Array.....	290
Hiroaki Kitagawa, Wei-Heong Tan, Shoji Takeuchi The University of Tokyo, Japan	
Geometric Optimization of a Thin Film ITO Heater to Generate a Uniform Temperature Distribution.....	293
Jungkyu Kim, Bruce Gale University of Utah, United State	
Reliability and Consistency of Microchip Based Analysis -Validation at Nano Litter Analysis-	296
Tomohiko Kawakami ^{1,2} , Katsumasa Sakamoto ^{2,3} , Yoshinori Matsuoka ^{2,4} , Yoshikuni Kikutani ^{2,5} , Kazuma Mawatari ^{2,5} , Kiyoko Kurosawa ¹ Mitsuo Kitaoka ² , Takehiko Kitamori ^{5,6}	
¹ Kaken Inc., Japan, ² The Research Association of Micro Chemical Process Technology, Japan, ³ Shimadzu Corporation, Japan, ⁴ Nippon Sheet Glass Co., Ltd., Japan, ⁵ Kanagawa Academy of Science and Technology, Japan, ⁶ The University of Tokyo, Japan,	
Medical & Clinical	
Multiple Immunoassay on a Capillary-Assembled Microchip (CAs-Chip) Integrating Valving and Immuno-Reaction Functions	299
Terence G. Henares, Shun-ichi Funano, Hideaki Hisamoto, Shigeru Terabe University of Hyogo, Japan	
Improvement of the Detection Limit in a Surface Plasmon Resonance Immunosensor for the Rapid On-Site Measurement of a Cardiac Marker in Blood Samples.....	302
Ryoji Kurita, Yoshimi Yokota, Yukari Sato, Fumio Mizutani, Osamu Niwa National Institute of Advanced Industrial Science and Technology, Japan	
An Electro-Microchip for Immunoassay Using Gold Nanoparticle and Silver Enhancement	305
Keng-Shiang Huang, Hao-Hsuan Huang, Tsung Chain Chang, Hong-Ping Lin, Yu-Cheng Lin National Cheng Kung University, Taiwan	
Development of a Piezoelectric Microjet Injector for Transdermal Drug Delivery	308
Jeanne C. Stachowiak, Julia Rasooly, Wilbur Lam, Daniel A. Fletcher University of California, Berkeley, USA	

A Microfluidic Device Based on the Heat-Sensitive Structural Transition of Poly (N-Isopropylacrylamide) for Controlled Surface Patterning of Proteins	311
Dae-Sik Lee ¹ Kwang Hyo Chung ¹ Hyeon-Bong Pyo ¹ Sung Il Jeon ² , Seung Yeon Song ² , Jung Woo Hong ² , Hyun C. Yoon ²	
¹ Electronics and Telecommunication Research Institute (ETRI), Korea, ² Ajou University, Korea	
Whole Blood Plasmapheresis Using Acoustic Separation Chips	314
Andreas Nilsson, Filip Petersson, Thomas Laurell	
Lund University, Sweden	
Micro-Extraction of Viral Ribonucleic Acid (RNA)	317
Levent Yobas ¹ , Hongmiao Ji ¹ , Yu Chen ¹ , Saxon Liw ¹ , Wing-Cheong Hui ¹ , Siti Rafeah ¹ , Ser Choong Chong ¹ , Ling Xie ¹ , Lim-Jing Jing ² , Sek-Man Wong ²	
¹ Institute of Microelectronics, Singapore, ² National University of Singapore, Singapore	
Magnetophoretic Immunoassay for Allergen-Specific Immunoglobulin E (IgE) in Patient Samples	320
Young Ki Hahn ¹ , Zongwen Jin ¹ , Joo H. Kang ¹ , Eunkeu Oh ¹ , Hak-Sung Kim ¹ , Jung-Tak Jang ² , Jinwoo Cheon ² , Hae-Sim Park ³ , Je-Kyun Park ¹	
¹ KAIST, Korea, ² Yonsei University, Korea, ³ Ajou University School of Medicine, Korea	
Silicon-Based Microfilters for Whole Blood Cell Separation	323
Hong Miao Ji ¹ Victor Samper ¹ Levent Yobas ¹ Yu Chen ¹ Chew Kiat Heng ² , Tit Meng Lim ²	
¹ Institute of Microelectronics, Singapore, ² National University of Singapore, Singapore	
Evaluation of a PDMS-Based Sensor for Human Cd4+-Cell Count	326
Sara Thorslund ¹ , Rolf Larsson ² , Fredrik Nikolajeff ¹ Jonas Bergquist ¹ , Javier Sanchez ²	
¹ Uppsala University, Sweden, ² Uppsala University Hospital, Sweden	
Centrifugal Processor for Standard Microarray Slides	329
Sascha Lutz ¹ , Markus Grumann ¹ , Oliver Gutmann ¹ , Markus Dube ¹ , Lutz Riegger ¹ , Jürgen Steigert ¹ , Claas Müller ² , Martina Daub ¹ , Roland Zengerle ^{1,2} , Jens Ducrée ^{1,2}	
¹ IMTEK-University of Freiburg, Germany, ² HSG-IMIT, Germany	
A Palm-Sized Real-Time (RT) PCR	332
Lukas Novak, Pavel Neuzil, Juergen Pipper, Chunyan Zhang	
Institute of Bioengineering and Nanotechnology, Singapore	
Electrosprayed Phospholipid Polymer Surface for Enhanced Sensitive ELISA Chip	335
Kazuki Nishizawa, Madoka Takai, Kazuhiko Ishihara	
University of Tokyo, Japan	
Bio-Detection System with Bacterial Spore Collection & Detection Chip.....	338
Hisao Inami ¹ , Mitsuhiro Matsuzawa ¹ , Yasuhiko Sasaki ¹ , Shigenori Togashi ¹ , Ryo Miyake ¹ , Masahiro Kurihara ¹ , Kouichiro Tsuge ² , Yasuo Seto ²	
¹ Hitachi, Ltd., Japan, ² National Research Institute of Police Science, Japan	

Precipitation Biosensor Based on Lab-Chip Accomplishing Self-Fluid Replacements Via Capillary Force	341
Kwang-Hyo Chung ² , Jung-Woo Hong ¹ , Jun-Hwang Lee ¹ , Hyeon-Bong Pyo ² , Byung-Woo Kim ³ , Hyun C. Yoon ¹	
¹ Ajou University, Korea, ² Electronics and Telecommunication Research Institute, Korea, ³ Sungkyunkwan University, Korea	
Simultaneous Bioassays on Several Plugs of Magnetic Particles	344
Ben J.K. Brown, Nicole Pamme	
The University of Hull, UK	
Single Chamber Based Cell Concentration, DNA Extraction and Real-Time PCR for Rapid Pathogen Identification	347
Yoon-Kyoung Cho, Jeong-Gun Lee, Young-Sun Lee, Jong-Myeon Park, Beom-Seok Lee, Christopher Ko	
Samsung Advanced Institute of Technology, Korea	
Microfluidic Device Based on Self-Organized Magnetic Beads: Application to the On-Chip Analysis of the Prion Protein.....	350
Anne Le Nel ² , Lucie Korecka ³ , Marcela Slovakova ³ , Nicolas Minc ¹ , Claire Smadja ² , Jean-Michel Peyrin ² , Jean-Louis Viovy ¹ , Myriam Taverna ²	
¹ Curie Institute, France, ³ University of Paris XI, France, ² University of Pardubice, Czech Republic	
Separation Science	
Electokinetic Preconcentration and Highly Stacking Gel Electrophoresis for Analysis of High Molecular Weight Protein Complexes on a Plastic Microchip	353
Mohamad Reza Mohamadi ¹ , Laili Mahmoudian ¹ , Noritada Kaji ¹ , Manabu Tokeshi ¹ , Hiroshi Chuman ² , Yoshinobu Baba ¹	
¹ Nagoya University, Japan, ² The University of Tokushima, Japan	
Fabrication of the Chemically-Functionalized Capillary-Electrophoresis Microchip Based on Capillary-Assembled Microchip (CAs-Chip) Technique	356
Seigi Takeda, Hideaki Hisamoto, Shigeru Terabe	
University of Hyogo, Japan	
Improved Plasma Yield by a New Design of Microchannel Bend Structures	359
Christoph Blattert, Reinhold Jurischka, Isam Tahhan, Andreas Schoth, Holger Reinecke	
University of Freiburg, Germany	
High Performance Electrophoretic Analysis on Cycloolefin Polymer Microchips	362
Fumihiko Kitagawa ¹ , Takafumi Suzuki ² , Jun Mizuno ² , Shuichi Shoji ² , Koji Otsuka ¹	
¹ Kyoto University, Japan, ² Waseda University, Japan	
One-Step Immobilization of Cationic Polymer Onto a Poly(Methyl Methacrylate) Microchip for High Performance Electrophoretic Analysis of Proteins	365
Kei Kubota, Kenji Sueyoshi, Fumihiko Kitagawa, Koji Otsuka	
Kyoto University, Japan	

A Microliter Electrokinetic Deionizer for Rapid Processing	368
Charlotte C. Kwong, Adam A. Huang, Chih-Ming Ho	
University of California, Los Angeles, USA	
Flow Rate Independent Particle Focusing and Separation by Chaotic	
Advection	371
Sungyoung Choi, Je-Kyun Park	
Korea Advanced Institute of Science and Technology (KAIST), Korea	
Application of Partial Filling Technique and Sweeping to Electrophoretic	
Analysis on T-Cross and 5 Way-Cross Microchips	374
Kenji Sueyoshi ¹ , Hidenori Nagai ² , Shin-ichi Wakida ² , Junji Nishii ² , Fumihiro	
Kitagawa ¹ , Koji Otsuka ¹	
¹ Kyoto University, Japan, ² National Institute of Advanced Industrial Science and	
Technology, Japan	
tRNA Purification by Electrophoretic Filtration for Genomic	
Identification of Bacteria On-A-Chip	377
Paul Vulto, Christoph Klaunick, Günter Igel, Gerald A. Urban	
Albert-Ludwigs-Universität Freiburg, Germany	
SU-8 Microchips for Biomolecule Analysis Using Free Zone	
Electrophoresis	380
Tiina M. Sikanen ^{1,2} , Liisa Heikkilä ¹ , Santeri Tuomikoski ² , Raimo Ketola ¹ Risto A.	
Kostiainen ¹ , Sami Franssila ² , Tapio Kotiaho ¹	
¹ University of Helsinki, Finland, ² Helsinki University of Technology, Finland	
Fast Separation of Lambda- and T2-DNA with Electrodeless	
Dielectrophoresis	383
Jan Regtmeier, Thanh Tu Duong, Alexandra Ros, Dario Anselmetti	
Experimental Biophysics, Bielefeld University, Germany	
Ni Pattern for Guiding Magnetic Beads Self-Organization: Application To	
Long DNA Electrophoresis in Dilute Arrays	386
Antoine-Emmanuel Saliba ¹ , Charlie Gosse ² , Nicolas Minc ³ , Christophe Roblin ² ,	
Kevin Dorfman ⁴ , Jean-Louis Viovy ¹	
¹ Institut Curie, France, ² Laboratoire de Photonique et Nanostructures, LPN-CNRS,	
France, ³ Columbia University, USA, ⁴ University of Minnesota, USA	
Multiplex Affinity Capillary Electrophoresis in a Single Microfluidic	
Channel for Gene Mutation Analysis.....	389
Akira Inoue ¹ , Kazuo Hosokawa ¹ , Toshiyuki Ito ¹ , Kae Sato ¹ , Kimiko Makino ² ,	
Mizuo Maeda ¹	
¹ RIKEN, Japan, ² Tokyo University of Science, Japan	
Miniaturized Two-Dimensional Gel Electrophoresis of Proteins Using	
Low-Concentration Multifilament-Supporting Gel for Isoelectric	
Focusing.....	392
Tamao Odake ¹ , Kazutoshi Kamezawa ¹ , Kozue Miyata ¹ , Hiroki Hotta ¹ , Yasuaki	
Kojima ² , Kin-ichi Tsunoda ¹	
¹ Gunma University, Japan, ² Mitachi Co. Ltd, Japan	

A New Exploration in Enhancing the Resolution for High-Performance Analysis of Mono-Sulfate Glycosaminoglycan Disaccharide Isomers on a Poly(Methyl Methacrylate) Chip	395
Yong Zhang ^{1,2} , Guichen Ping ³ , Bingmei Zhu ² , Noritada Kaji ² , Manabu Tokeshi ² , Yoshinobu Baba ^{2,4}	
¹ University of Tokushima, Japan, ² University of Nagoya, Japan, ³ Waseda University, Japan, ⁴ AIST, Japan	
Selective Particle Separation and Deposition by 3-D Insulator-Based Dielectrophoresis	398
Kai-Cheng Chuang ¹ , Li-Yu Chu ¹ , Maw-Shiuan Jiang ² , Tzu-Han Chuang ² , Chien-Chung Fu ² , Shih-Kang Fan ¹	
¹ National Chiao Tung University, Taiwan, ² National Tsing-Hua University, Taiwan	
Novel Physically Adsorbed Polymer Coating on PMMA Microchip with Multi Channel Array for High-Throughput Protein Analysis	401
Hiroki Okada ¹ , Noritada Kaji ¹ , Manabu Tokeshi ¹ , Yoshinobu Baba ^{1,2}	
¹ Nagoya University, Japan, ² HTRC, AIST, Japan	
DNA Separation Based on the Gyration Radius Employing Nano-Pillar with Square Allocation	404
Ryo Ogawa ¹ , Noritada Kaji ² , Sou Wakao ² , Shingi Hashioka ¹ , Yoshinobu Baba ^{2,3} , Yasuhiro Horike ¹	
¹ National Institute for Materials Science, Japan, ² Nagoya University, Japan, AIST, Japan	
Cell Handling & Analysis	
μ-Hotplate Array for Manipulation of Adhesive Cells by Means of IR Diode Laser Light	407
Helke Reinhardt, Petra S. Dittrich, Joachim Franzke, Andreas Manz ISAS - Institute for Analytical Sciences, Dortmund, Germany	
High Throughput Single Cell Clone Analysis	410
Sara Lindstrom ¹ , Rolf Larsson ² , Helene Andersson ¹	
¹ Royal Institute of Technology, KTH, Sweden, ² Uppsala University, Sweden	
On-Chip High Accuracy Evaluation of Cellular EPM Variation with the Cell Cycle Progress Through S-Phase	413
Takanori Akagi, Masae Suzuki, Takanori Ichiki University of Tokyo, Japan	
Magneto-Microfluidic Device for Apoptotic Cell Separation	416
Hyun-Seok Kim ¹ , Oh-Taek Son ¹ , Kunhong Kim ¹ , Sang Hyeob Kim ² , Sung-Lyul Maeng ² , Hyo-II Jung ¹	
¹ Yonsei University, Korea, ² Cambridge-ETRI Joint R&D Center, ETRI, Korea	
Microbial Cells Trapping and Detection Through Filter-Based Microfluidic Devices	419
Liang Zhu, Xue Li Peh, Homg Miao Ji, Han Hua Feng, Wen-tso Liu Institute of Microelectronics, Singapore	

Disposable Thermoplastic Microchips for Cell andbiomolecular Analysis.....	422
Jonas Melin, Henrik Johansson, Malin Jarvius, Ola Soderberg, Jenny Goransson, Ulf Landegren, Mats Nilsson, Jonas Jarvius University of Uppsala	
The Micro Petri Dish: a Highly Subdivided Microbiological Growth Format Fabricated by Micro-Engineering A Highly Porous Ceramic for Diagnostics, Counting and Screening Applications	425
Colin J. Ingham ¹ , Ad Sprenkels ² , Johan Bomer ² , Albert van den Berg ² , Willem M. de Vos ¹ , Johan E.T. van Hylckama Vlieg ¹ ¹ Wageningen Centre for Food Sciences, Netherlands, ² MESA+ University of Twente, Netherlands	
Magnetic On-Chip DNA Extraction in a Droplet-Based Microsystem.....	428
Ulrike Lehmann, Caroline Vandevyver, Virendra K. Parashar, Martin A.M. Gijs Ecole Polytechnique Federale de Lausanne (EPFL), Switzerland	
Development of a Microchip-Based Fertilization and Cultivation System for in Vitro Production of Blastocysts	431
Kiichi Sato ¹ , Manabu Ozawa ² , Kazuhiro Kikuchi ² , Takashi Nagai ³ , Takehiko Kitamori ¹ ¹ The University of Tokyo, Japan, ² National Institute of Agrobiological Sciences, Japan, ³ National Institute of Livestock and Grassland Science, Japan	
Fully-Round Buried Microchannels in Glass for Lateral Patch Clamping	434
Wee-Liat Ong, Jack-Sheng Kee, Ajay Agarwal, Nagarajan Ranganathan, Kum-Cheong Tang, Levent Yobas Institute of Microelectronics, Singapore	
The Rolling Motion of Cardiomyocytes on a Dielectrophoresis Chip.....	437
Yiling Qiu ¹ , Ronglih Liao ² , Xin Zhang ¹ ¹ Boston University, USA, ² Harvard University, USA	
Cell Growth Control Using Chemical Stimulation Regulated by Microvalve Switching	440
Yuta Nakashima, Takashi Yasuda Kyushu Institute of Technology, Japan	
Single Microbe Dispensing System with Micro Machined Particle Sensor	443
Tadashi Sano ¹ , Yasuhiko Sasaki ¹ , Hajime Ikuta ² , Tatsuo Sumino ² ¹ Mechanical Engineering Research Laboratory, Hitachi, Ltd., Japan, ² Hitachi Plant Technologies, Ltd., Japan	
Ultrasonic Manipulation in a Microfluidic Chip for Individual Handling of Particles and Cells.....	446
Martin Wiklund, Jessica Hultström, Otto Manneberg, Hans M. Hertz Royal Institute of Technology, Sweden	
Proliferation of COS-7 Cells Trapped by Standing-Wave Ultrasound in a Microfluidic Chip	449
Jessica Hultström, Otto Manneberg, Hans M. Hertz, Hjalmar Brismar, Martin Wiklund Royal Institute of Technology, Sweden	

Multiparametric Optimization of Silicon Chip Properties for Consistent Success in Ion Channel Recordings	452
Thomas Sordel ¹ , Yann Sinquin ¹ , Frederique Marcel-Kermarec ¹ , Fabien Sauter-Starace ² , Catherine Pudda ² , Francois Chatelain ¹ , Nathalie Picollet-D'hahan ¹	

¹CEA Life Science Division, France, ²LETI, CEA Grenoble, France

Rapid Concentration of Bacteria Using 3-D Electrodeless Dielectrophoresis in a Plastic Chip	455
Yoon-Kyoung Cho, Suhyeon Kim, Chinsung Park, Kyusang Lee, Jeong-Gun Lee, Christopher Ko	
Samsung Advanced Institute of Technology, Korea	

High-Yield Electroporation Using RF-Modulated Field Constriction.....	458
Osamu Kurosawa ¹ , Hidehiro Oana ² , Hidetoshi Kotera ³ , Masao Washizu ²	
¹ Advance Co., Japan, ² University of Tokyo, Japan, ³ Kyoto University, Japan	

Red Blood Cell Deformation Under Extensional Flow Using Hyperbolic Converging Shape Microchannel	461
Sung S. Lee ¹ , Yoon J. Yim ¹ , Kyung H. Ahn ¹ , Seong J. Lee ¹	
¹ Seoul National University, Korea	

Miniaturized Cell Culture Devices for Spiral Ganglion Neurons.....	464
Peter Norlin ¹ , Tommy Schönberg ¹ , Beata Kostyszyn ² , Christian Vieider ¹ , Mats Ulfendahl ²	
¹ Acro AB, Sweden, ² Karolinska Institutet, Sweden	

Environmental

A Polymer Biochip for Detecting Inorganic and Organic Phosphate Using Planar Cobalt Microelectrodes	467
Zhiwei Zou, Jungyoup Han, Am Jang, Paul L. Bishop, Chong H. Ahn	
University of Cincinnati, USA	

Autonomos Label Free Optical Detection of Spores Trapping in An Insulator-Based Dielectrophoretic Concentrator	470
Poorya Sabounchi, Alfredo M. Morales, Blake A. Simmons, Rafael V. Davalos	
Sandia National Laboratories, USA	

Alternative Method for Current Collector of Micro Direct Methanol Fuel Cell Using Carbon Papers	473
Soo Ho Kim ¹ , Jermim Noh ¹ , Min Ku Jeon ¹ , Luke P. Lee ² , Seong Ihl Woo ¹	
¹ Korea Advanced Institute of Science and Technology, Korea, ² University of California, USA	

Semi-Automatic Microsystem Based Sample Preparation for the Detection of Biological Agents	476
Marion Ritzi, Dalibor Dadic, Frank Doffing, Frithjof von Germar, Rainer Gransee, Klaus S. Drese	
Institut fuer Mikrotechnik Mainz GmbH, Germany	

Microfluidic Glucose Biofuel Cells for Power Generation From Biofluids	479
Makoto Togo, Akimasa Takamura, Tatsuya Asai, Takashi Abe, Matsuhiko Nishizawa Tohoku University, Japan	
Genetic Conversion of Bacteria and its Application to Micro Direct Photosynthetic/Metabolic Bio-Fuel Cell (DPMFC)	482
Keisuke Morishima ¹ , Akihiro Furuya ¹ , Takeyuki Moriuchi ¹ , Makoto Yoshida ² , Masahiro Ota ² , Yuji Furukawa ¹ ¹ Tokyo University of Agriculture and Technology, Japan, ² Tokyo Metropolitan University, Japan	
Development of Handy Environmental Atmospheric Particle Measurement Device Based on On-Chip Two-Channel Micro Coulter Counter	485
Kazuhiro Miyamura ^{1,2} Yoshikuni Kikutani ^{2,3} , Kazuma Mawatari ^{2,3} , Mitsuo Kitaoka ² , Takehiko Kitamori ^{3,4} ¹ Horiba, Ltd, Japan, ² The Research Association of Micro Chemical Process Technology, Japan, ³ Kanagawa Academy of Science and Technology, Japan, ⁴ The University of Tokyo, Japan	
Effects of Fluidic Conditions on the Diffusion-Based Bioluminescent Detection of ATP in Microfluidic Device	488
Thuan-Hieu Tran ¹ , Young-Bum Kim ¹ , Yoon-Mo Koo ¹ , Jin-Hwan Kim ² , Eun-Ki Kim ¹ , Woo-Jin Chang ¹ ¹ Inha University, Korea, ² M&B GreenUs, Korea	
Micro FIA Using Segmented Laminar Flow in Microchanneland Its Applications to Multi-Component Environmental Analyses.....	491
Katsumasa Sakamoto ^{1,2} , Tomohiko Kawakami ² , Yoshikuni Kikutani ^{2,4} , Kazuma Mawatari ^{2,4} , Hiroaki Nakanishi ¹ , Mitsuo Kitaoka ² , Takehiko Kitamori ^{4,5} ¹ Shimadzu Corporation, Japan, ² The Research Association of Micro Chemical Process Technology, Japan, ³ Kaken Inc., Japan, ⁴ Kanagawa Academy of Science and Technology, Japan, ⁵ The University of Tokyo, Japan	
Dissolved Oxygen Microelectrode Sensor for in Situ Biological Applications	494
Jin-Hwan Lee, Xingtao Wei, Tae-Sun Lim, Ian Papautsky University of Cincinnati, USA	
Numerical Analysis and Mineral Water Measurement in Confined Liquid Electrode Plasma-Optical Emission Spectrometry	497
Isao Kumagai ¹ , Hirokazu Matsumoto ¹ , Tamotsu Yamamoto ² , Eiichi Tamiya ¹ , Yuzuru Takamura ^{1,3} , ¹ Japan Advanced Institute of Science and Technology (JAIST), Japan, ¹ Tenor Inc., Japan, ³ PRESTO, Japan Science and Technology Agency (JST), Japan	

Session 1A3 Microfluidic Device 1

Passive Distributing Method for Cellular Diagnostic Microwell Array Using Self-Regulating Pinched Flow.....	500
Kentaro Kawai ¹ , Masaki Kanai ¹ , Tatsuya Munaka ² , Hirohisa Abe ² , Shuichi Shoji ¹	
¹ Waseda University, Japan, ² Shimadzu Corporation, Japan	

Polymer Microvalves with Pre-Stressed Membranes for Tunable Flow-Pressure Characteristics.....	503
Detlef Snakenborg, Henning Klank, Jorg P. Kutter	
Technical University of Denmark, Denmark	

Programmable Pneumatic Logical Circuits for Microfluidic Device Control	506
William H. Grover, Erik C. Jensen, Robin H. C. Ivester, Richard A. Mathies	
University of California, Berkeley, USA	

Session 1B3 Particle 2

An Optical Retrieval Microfluidic System for Microarray Applications.....	509
Wei-Heong Tan, Shoji Takeuchi	
Institute of Industrial Science, The University of Tokyo, Japan	

Accurate and High Speed Particles and Biomolecules Sorting Microsystem Using 3-Dimensional Sheath Flow	512
Takahiro Arakawa ¹ , Tokihiko Aoki ¹ , Yoshitaka Shirasaki ² , Takashi Funatsu ² , Shuichi Shoji ¹	
¹ Waseda University, Japan, ² The University of Tokyo, Japan	

Microfluidic Particle Alignment for Flow Cytometric Applications Utilizing Hydrodynamic Filtration.....	515
Ryota Aoki ¹ , Masumi Yamada ² , Masahiro Yasuda ¹ , Minoru Seki ¹	
¹ Osaka Prefecture University, Japan, ² The University of Tokyo, Japan	

DAY 2 - TUESDAY, NOVEMBER 7, 2006

PLENARY LECTURE 3

Harnessing Biological Motors and Nanoswitches for Technical Applications	518
Viola Vogel	
ETH Zurich, Switzerland	

Session 2A1 Nanofluidics 1

Continuous-Flow Biomolecule Separation Through Patterned Anisotropic Nanofluidic Sieving Structure	519
Jianping Fu, Jongyoon Han	
Massachusetts Institute of Technology, USA	

Nonlinear Electrokinetic Flow Pattern Near Nanofluidic Channel	522
Sung Jae Kim, Ying-Chih Wang, Jongyoon Han	
Massachusetts Institute of Technology, USA	

Observing and Taming Brownian Motion of Silicon Nanoneedle in Micromachined PDMS Chamber	525
Ersin Altintas ¹ , Karl F. Bohringer ² , Hiroyuki Fujita ¹	
¹ The University of Tokyo, Japan, ² The University of Washington, USA	
Sesssion 2B1 Materials & Surface (Cell Characterization & Membrane Chips)	
Optical Detection of Living Cells' Refractive Index Via Buffer Modulation of Microfluidic Chip	528
Wuzhou Song ¹ , X.M. Zhang ¹ , L. K. Chin, Ai Qun Liu ¹ , Eric Peng Huat Yap ² , H.M. Hosseini ¹	
¹ Nanyang Technological University, Singapore, ² DSO National Laboratories, Singapore	
Integrated Microfluidic Bilayer Lipid Membrane (BLM) Arrays	531
Lou Hromada ¹ , John Kasianowicz ² , Michael Gaitan ² , Donald L. DeVoe ¹	
¹ University of Maryland, College Park, USA, ² National Institutes of Standards and Technology, USA	
'Blowing Vesicles': a Simple Method for Direct Microencapsulation in Lipid Vesicles	534
Kei Funakoshi, Hiroaki Suzuki, Shoji Takeuchi	
Institute of Industrial Science, The University of Tokyo, Japan	
2A2 Microfluidics	
Multiphase Microfluidics Near the Speed of Sound	537
Axel Guenther, Klavs F. Jensen	
Massachusetts Institute of Technology, USA	
Acoustic Separation of Particles with Similar Acoustic Properties by Means of Medium Density Manipulation	540
Filip Petersson, Lena Åberg, Thomas Laurell	
Lund University, Sweden	
Microfluidic Centrifugations in a Spiral Microchannel	543
Wei Wang, Dongsheng Xu, Zhihong Li	
Peking University, China	
Session 2B2 Nanofluidics 2 (Phenomenology)	
Water Confined in Extended-Nano Spaces Studied by NMR Spectroscopy: A Three-Phase Model -	546
Takehiko Tsukahara ^{1,2} , Wataru Mizutani ¹ , Akihide Hibara ¹ , Takehiko Kitamori ^{1,2}	
¹ The Univeristy of Tokyo, Japan, ² JST-CREST, Japan	
Voltage-Gated Protein Transport Through Nanoporous Membranes.....	549
Anson V. Hatch, Anup K. Singh	
Sandia National Laboratories, USA	

Nanomechanical Protein Presence and Concentration Detectors Based on the Mechanical Stiffness of Proteins in Squeezed Nano-Gaps.....	552
Won Chul Lee ¹ , Young-Ho Cho ¹ , Albert P. Pisano ²	

¹Korea Advanced Institute of Science and Technology, Korea, ²University of California at Berkeley, USA

PLENARY LECTURE 4

Industrial Production by Micro Chemical Plants	555
Shinji Hasebe	
Kyoto University, Japan	

POSTER SESSION 2

Micro & Nano Fluidic Devices

Customized Trapping & Assembly of Magnetic Carriers in Single & Multiple Potential Wells	558
--	-----

Qasem Ramadan¹, Daniel P Poenaru², Victor Samper¹, Chen Yu¹

¹Institute of Microelectronics, Singapore, ²Nanyang Technological University, Singapore

Nature-Inspired Micro-Fluidic Manipulation Using Artificial Cilia	561
---	-----

Jaap M. den Toonder, Dirk J. Broer, Murray Gillies, Judith de Goede, Titie Mol, Wim Talen, Hans Wilderbeek

Philips Research, The Netherlands

An Optical Injection System Used for Optimization Studies of High Aspect Ratio LC COMOSS Columns	564
--	-----

Wim De Malsche², Hamed Eghbali¹, Jan De Smet¹, J.G.E. Gardeniers², Gert Desmet¹

¹Vrije Universiteit Brussel, Belgium, ²Twente University, The Netherlands

Lateral Cell Separation in Microfluidic Channel by 3D Electrode Dielectrophoresis	567
---	-----

Lisen Wang, Steven Marchenko, Noo Li Jeon, Edwin Monuki, Lisa Flanagan, Abraham Lee

University of California, Irvine, USA

A Digital Centrifugal Droplet-Switch for Routing of Liquids.....	570
--	-----

Stefan Haeberle¹, Lars Naegele¹, Roland Zengerle¹, Jens Ducrée²

¹University of Freiburg, Germany, ²HSG-IMIT, Germany

Pneumatic Micropumps Utilizing Time-Delay Peristaltic Actuation.....	573
--	-----

Chun-Wei Huang, Song-Bin Huang

National Cheng Kung University, Taiwan

Microfluidic Integration of Gel-Based Reference Electrodes for Electrophysiological Measurements on Chip.....	576
---	-----

Elodie Dahan¹, Mariam Benabderrazik¹, Thomas Lehnert¹, Vincent Bize², Jean-Daniel Horisberger², Martin A. M. Gijs¹

¹Ecole Polytechnique Fédérale de Lausanne, EPFL, Switzerland, ²University of Lausanne, UNIL, Switzerland

Inkjet Micropump for Parallel Microfluidic Testing	579
Fumio Takagi, Hiroshi Koeda, Rie Miyazaki, Shinichi Kamisuki	
Seiko Epson Corporation, Japan	
Ultrarapid Droplet Mixer for Digital Microfluidics	582
Kevin P. Nichols, J.G.E. Gardeniers	
University of Twente, The Netherlands	
Control of Droplets in Microchannels through Laser-Induced Thermocapillarity	585
Charles N. Baroud ¹ , Jean-Pierre Delville ²	
¹ LadHyX, Ecole Polytechnique, France, ² CPMOH, Universite de Bordeaux, France	
A Disposable On-Chip Pressure Actuator Using IR-Induced Thermolysis for Sample Transport	588
Jungyup Han, Soo Hyun Lee, Chong H. Ahn	
University of Cincinnati, USA	
A Monolithic 3D Flow-Focusing Device for the Formation of Single/Double Emulsions in a Closed/Open Microfluidic System	591
Shih-hao Huang ¹ , Fan-Gang Tseng ¹ , Wei-Heong Tan ² , Shoji Takeuchi ²	
¹ Institute of MicroElectroMechanical System, National Tsing Hua University, Taiwan, ² Institute of Industrial Science, University of Tokyo, Japan	
Checkered Electrostatic Actuator for Two-Dimensional Manipulation of Liquid Droplets	594
Kei Takenaka, Yasushi Goto	
Hitachi, Ltd., Japan	
Spontaneous Microflow of Micropillar Array Electrospray Ionization Microchip	597
Teemu J. Nissila ¹ , Lauri Sainiemi ² , Tiina Sikanen ¹ , Tapio Kotiaho ¹ , Risto Kostiainen ¹ , Sami Franssila ² , Raimo A. Ketola ¹	
¹ University of Helsinki, Finland, ² Helsinki University of Technology, Finland	
Micromixing Biologically Crowded Agents by Folding Plugs Through Pillars	600
Kum Cheong Tang ¹ , Rachmat Multi Wibowo ² , Levent Yobas ¹	
¹ Institute of Microelectronics, Singapore, ² Nanyang Technological University, Singapore	
Multi-Reagents High Speed Exchange Flow System for Single Biomolecular Dynamics Real Time Monitoring	603
Yukiko Sato ¹ , Takahiro Arakawa ¹ , Taro Ueno ² , Tomoya Sameshima ² , Takashi Funatsu ² , Shuichi Shoji ¹	
¹ Waseda University, Japan, ² The University of Tokyo, Japan	
Bead Immobilisation in a Planar Polymer Microfluidic Electrocapture Device	606
Mats Jönsson, Ulf Lindberg	
Uppsala University, Sweden	
Moving, Mixing, and Filtration of Droplets by Magnetic Fields	609
Juergen Pipper, Pavel Neuzil, Tseng-Ming Hsieh	
Institute of Bioengineering and Nanotechnology, Singapore	

Advanced Flow Control of Liquids in Microfabricated Capillary Pumps	612
Martin Zimmermann ¹ , Patrick Hunziker ² , Emmanuel Delamarche ¹	
¹ IBM Research GmbH, Zurich Research Laboratory, Switzerland, ² University Hospital Basel, Switzerland	
Nanochannels with Integrated Fabry-Perot Interferometry: a New Tool for Nanofluidics.....	615
Jan C.T. Eijkel, Koen M. van Delft, Dragana Mijatovic, Niels R. Tas, Frieder Mugele, Albert van den Berg	
MESA+ Institute, Twente University, Netherlands	
A Delayed Micro Mixer Module for Continuous Flow Immunoassay with Preloaded Reagent.....	618
Jaephil Do, Junhai Kai, Chong H. Ahn	
University of Cincinnati, USA	
Nature-Inspired Active Mixing in a Microchannel	621
Vinayak V. Khatakkar, Patrick D. Anderson, Han E.H. Meijer, Jaap M.J den Toonder	
Eindhoven University of Technology, The Netherlands	
Centimeter-Scale, Diagnostics Incubator with Integrated Perfusion.....	624
Jelena Vukasinovic, Ari Glezer	
Georgia Institute of Technology, USA	
Improved Carrier Medium Exchange Efficiency in Acoustic Standing Wave Particle Washing	627
Per Augustsson, Filip Petersson, Thomas Laurell	
Lund University, Sweden	
The Spatially Focused Reagent Injection System Using 3-D Sheath Flow Scanner Integrated with SiO₂ Mesh Strainer.....	630
Yasuo Suzuki ¹ , Masaki Kanai ² , Takahiro Nishimoto ² , Shuichi Shoji ¹	
¹ Waseda University, Japan, ² Technology Research Laboratory, Shimadzu Corporation, Japan	
Electrolysis-Driven Drug Delivery for Treatment of Ocular Disease.....	633
Ellis Meng ¹ , Jason Shih ² , Po-Ying Li ¹ , Ronalee Lo ¹ , Mark S. Humayun ¹ , Yu-Chong Tai ²	
¹ University of Southern California, USA, ² California Institute of Technology, USA	
A Rapid Field-Free Electroosmotic Micropump Incorporating Charged Microchannel Surfaces	636
Segyeong Joo ¹ , Hee Chan Kim ¹ , Taek Dong Chung ²	
¹ Seoul National University, South Korea, ² Sungshin Women's University, South Korea	
Microfluidic Control for Gravity-Driven ELISA Apparatus	639
Jhy-wen Wu, Nan-kuang Yao	
Industrial Technology Research Institute, Taiwan	
A Novel Integrated Microfluidic SERS-CD with High-Throughput Centrifugal Cell Trapping Array for Quantitative Biomedicine	642
Hansang Cho, Jeonggi Seo, Luke P. Lee	
University of California, Berkeley, USA	

Electrophoretic Manipulation and Electrochemical Analysis of Single Cell with the Microfluidic Device	645
Kuniaki Nagamine ¹ , Tomoyuki Yasukawa ¹ , Hitoshi Shiku ¹ , Masahiro Koide ² , Tomosato Itayama ² , Tomokazu Matsue ¹	
¹ Tohoku University, Japan, ² National Institute for Environmental Studies, Japan	
Acceleration of Absolute Negative Mobility for Particle Sorting in Microfluidic Devices	648
Alexandra Ros, Jan Regtmeier, Ralf Eichhorn, Peter Reimann, Dario Anselmetti	
Bielefeld University, Germany	
Enhanced Protein Capture by Ultrafast Saw Droplet Micromixing	651
Alan Renaudin, Elisabeth Galopin, Vincent Thomy, Jean-Christophe Camart, Pierre Tabourier, Christian Druon	
Institut d'Electronique, de Microelectronique et de Nanotechnologie, France	
Giant Amplification of Redox Current in a Nanofluidic Channel	654
Marcel A.G. Zevenbergen ¹ , Diego Krapf ¹ , Marc Zuiddam ² , Serge G. Lemay ¹	
¹ Kavli Institute of Nanoscience, Delft University of Technology, the Netherlands,	
² Delft Institute of Microelectronics and Submicron Technology, Delft University of Technology, the Netherlands	
Microfluidic Bubble Actuators Based on Hydrogels.....	657
Joerg Nestler ¹ , Karla Hiller ¹ , Thomas Otto ² , Thomas Gessner ¹	
¹ Chemnitz University of Technology, Germany, ² Fraunhofer Institute for Reliability and Microintegration (IZM), Germany	
Micro & Nano Fabrication	
Fabrication of Novel Hydrophilic Polymer Nanofluidic System for Biomolecules Separation in Aqueous Flow	660
Tae-Ho Yoon, Lan-Young Hong, Chang-Soo Lee, Dong-Pyo Kim	
Chungnam National University, South Korea	
Photodefinable PDMS for Rapid Prototyping of Disposable Lab-on-A-Chip Systems.....	663
Ali Asgar S. Bhagat, Preetha Jothimuthu, Ian Papautsky	
University of Cincinnati, USA	
Fabrication and Optical Characterization of Nano-Hole Arrays for Molecular Detections.....	666
Oana M. Piciu, Andre Bossche	
TU Delft, Netherlands	
Three-Dimensional Microstructuring of PDMS Inside a Microchannel for Functional Microfluidic Devices	669
Shoji Maruo, Takuya Hasegawa, Kosuke Oishi	
Yokohama National University, Japan	
Soft Lithography Without Using Photolithography	672
Shih-hui Chao ¹ , Robert Carlson ² , Deirdre Meldrum ¹	
¹ Microscale Life Sciences Center, University of Washington, USA, ² University of Washington, USA	

Single Cell Capture with Ferromagnetic Elements Grown on PDMS	675
John H. Koschwanez, Robert H. Carlson, Deirdre R. Meldrum	
University of Washington, USA	
Fabrication and Characterization of Nanometer Sized Graphitic Carbon Electrodes	678
Rongbing Du, Mark T. McDermott	
University of Alberta and National Institute for Nanotechnology, Canada	
A Low Temperature Bonding Technique for Microfluidic Chip Fabrication Using Soft-Cure SU-8 Sheet	681
Hirofumi Shintaku, Yasutoshi Hirabayashi, Takaaki Suzuki, Isaku Kanno, Hidetoshi Kotera	
Kyoto University, Japan	
Three-Dimensional Microfabrication for Biodegradable Polymers Toward Implantable Micro Devices	684
Akira Yamada, Fuminori Niikura, Koji Ikuta	
Nagoya University, Japan	
Fabrication of Robust Biocompatible In-Plane Microneedle with Sharp 3-D Tip	687
Chun Yan Jin, Seung S. Lee	
Korea Advanced Institute of Scence and Technology, Korea	
Fast Pattern Formation of Polymer Microstructures Induced by Ultrahigh Electric Field	690
Brian Pow, Mo Yang	
Hong Kong Polytechnic University, Hong Kong	
The Membrane Micro Emboss (MeME) Process for Fabricating 3-D Microfluidic Device formed From Thin Polymer Membrane	693
Masashi Ikeuchi, Koji Ikuta	
Nagoya University, Japan	
Single-Step NIL of Micro and Nanochannels Combined with Opticalwaveguides for Characterization of DNA Molecules.....	696
Soeren Jacobsen ¹ , Jason Beech ¹ , Mikkel Schoeler ¹ , Anders Kristensen ² , Jonas O. Tegenfeldt ¹	
¹ University of Lund, Sweden, ² Technical University of Denmark (DTU), Denmark	
Solvent-Resistant Microfluidic Device Fabrication Using Rapid Molding Technique	699
Lung-Hsin Hung, Rita Kuo, Kenneth J. Shea, Abraham P. Lee	
University of California at Irvine, USA	
Vivo Study of Mechanical Properties of the Monolithic Silicon Probes with Flexible Parylene Cables for Neural Prostheses.....	702
Changlin Pang, Sam Musallam, Daniel Rizzuto, Cevat Ustun, Yu-Chong Tai, Joel W. Burdick, Richard A. Andersen	
California Institute of Technology, USA	

Fabrication of Silicon Nanowire Bridge	705
Kook-Nyung Lee, Suk-Won Jung, Won-Hyo Kim, Min-Ho Lee, Woo-Kyeong Seong	
Korea Electronics Technology Institute(KETI), Korea	

Detection Technology

Electronic Drop Sensing in Microfluidic Devices Using Air-Liquid Interface Detection: Automated Operation of a Nanoliter Viscometer.....	708
Nimisha Srivastava, Mark A. Burns	
University of Michigan Ann Arbor, USA	

Electrochemical Real-Time PCR.....	711
Thomas MH Lee, Siu-Wai Yeung, I-Ming Hsing	
Hong Kong University of Science and Technology, Hong Kong, China	

Ultrasensitive and High Resolution UV Absorbance Detection of Proteins Via Integrated Polymer Microfluidics	714
Likun Zhu, Cheng S Lee, Don L DeVoe	
University of Maryland, USA	

Integrating a Molecularly Imprinted TiO₂ Modified Microelectrode in a Microfluidic System for Detection of Nicotine.....	717
Chen-Hsun Weng ¹ , Cheng-Tar Wu ² , Kuo-Chuan Ho ²	
¹ National Cheng Kung University, Taiwan, ² National Taiwan University, Taiwan	

Monolithically Integrated Dye-Doped PDMS Optical Filters for Disposable On-Chip Fluorescence Detection.....	720
Oliver Hofmann ¹ , Xuhua Wang ² , Alastair Cornwell ² , Stephen Beecher ² , Amal Raja ² , Donal D.C. Bradley ² , John C. deMello ² , Andrew J. deMello ²	
¹ Molecular Vision Ltd, UK, ² Imperial College London, UK	

Microfluidic Data Acquisition for Digital Quantification Using Amplified Single Molecule Detection	723
Jonas Jarvius, Jonas Melin, Jenny Göransson, Mats Nilsson	
University of Uppsala, SWEDEN	

Fabrication of Liquid Core Waveguide Analytical Chips Using Teflon AF and Their Analytical Features.....	726
Hiroki Hotta ¹ , Hiromi Takiguchi ¹ , Tamao Odake ¹ , Tomonari Umemura ² , Kin-ichi Tsunoda ¹	
¹ Gunma University, Japan, ² Nagoya University, Japan	

Integrated Electrochemical Sensor Array for On-Line Monitoring of Yeast Fermentations	729
Erik E. Krommenhoek ¹ , Han G.E. Gardeniers ¹ , Albert van den Berg ¹ , Xiaonan Li ² , Marcel Ottens ² , Luuk A.M. van der Wielen ² , Gijs W.K. van Dedem ² , Michiel van Leeuwen ² , Walter M. van Gulik ² , Sef J. Heijnen ²	
¹ University of Twente, Netherlands, ² Delft University of Technology, Netherlands	

Integrated Polydimethylsiloxane Waveguide for Optical Detection.....	732
Jack S. Kee ¹ , Daniel P. Poenaru ² , Levent Yobas ¹	
¹ Institute of Microelectronics, Singapore, ² Nanyang Technological University, Singapore	

Padlock Probe-Mediated Rolling-Circle Amplification in Microchambers, Monitored at the Single Molecule Level and in Real-Time.....	735
Jonas Jarvius, Olle Ericsson, Mats Nilsson, Ulf Landegren Uppsala University, Sweden	
Ultra Wide Band Dielectric Spectroscopy of Single Cell in Microfluidic Devices	738
Vincent Senez ¹ , Anthony Treizebré ¹ , Erwan Lennon ^{2,3} , Hala Ghandour ¹ , Tahsin Akalin ¹ , Dominique Legrand ⁴ , Yasuyuki Sakai ^{5,2,3} , Joel Mazurier ⁵ , Teruo Fujii ^{2,3,1} Bertrand Bocquet ¹	
¹ IEMN/CNRS-USTL-ISEN University of Lille, France, ² UTRC/IIS The University of Tokyo, Japan, ³ LIMMS/CNRS-IIS University of Tokyo, Japan, ⁴ UGSF/CNRS-USTL University of Lille, France, ⁵ CSE-OBE/IIS University of Tokyo, Japan	
Corrosion Resistant Integrated Optical Microsensor for NIR Spectroscopy and Its Application in Microreactors.....	741
Sylwester Bargiel, Jan Dziuban, Rafal Walczak, Paweł Knapkiewicz, Anna Gorecka-Drzazga Wrocław University of Technology, Poland	
A Room Temperature CMOS Single Photon Sensor for Chemiluminescence Detection	744
Marek Gersbach ¹ , Yuki Maruyama ² , Cristiano Niclass ¹ , Kazuaki Sawada ² , Edoardo Charbon ¹	
¹ Ecole Polytechnique Federale de Lausanne (EPFL), Switzerland, ² Toyohashi University of Technology (TUT), Japan	
Neurotransmitter Sensing Device with Molecule-Permeable Platinum Filled in Nano-Holes	747
Takashi Yasuda, Kazuyuki Shinohara, Tetsunori Hirata Kyushu Institute of Technology, Japan	
Nanoparticle-Based SERS Imaging of Biological Arrays	750
Francis Nsiah, Jed D. Harrison, Mark T. McDermott University of Alberta, Canada, National Institute of Nanotechnology, Canada	
High-Sensitivity Low-Cost On-Chip Chemiluminescence Detection Based on Intergrated Organic Photodiodes	753
Rupa Das, Xuhua Wang, Oliver Hofmann, John C. deMello, Andrew J. deMello, Donal D.C. Bradley Imperial College London, UK	
Detection of Antibodies in 10µm Wells on Micro-Arrayed Cell Chips by 2D-SPR Affinity Imaging	756
Masayasu Suzuki ¹ , Shintaro Hane ¹ , Toyohiro Ohshima ¹ , Yasunori Iribe ¹ , Tatsuya Tobita ²	
¹ University of Toyama, Japan, ² NTT Advanced Technologies Corp., Japan	
Pyrolyzed Carbon for Detection of Biomolecular Interactions Using Electrochemical Impedance Spectroscopy	759
Jung a Lee ¹ , Seong P. Hwang ¹ , Kwang -C. Lee ² , Ju H. Kwak ¹ , Se I. Park ² , Seung S. Lee ¹	
¹ Korea Advanced Institute of Science and Technology, Korea, ² Korea Research Institute of Standards and Science, Korea	

Non-Surface-Binding Label-Free Quantification of PCR Product with Fast and Sequential Detection Capability.....	762
Maesoon Im ¹ , Seong-Jin Kim ¹ , Kyutae Yoo ² , Jeoyoung Shim ² , Kyusang Lee ² , Younja Cho ² , Wonseok Chung ² , Christopher Ko ² , Euisik Yoon ³	
¹ Korea Advanced Institute of Science and Technology, Korea, ² Samsung Advanced Institute of Technology, Korea, ³ University of Minnesota, USA	
A New Approach To the Evaluation of Dielectrophoresis	765
Yukihisa Wada, Yoshio Tsunazawa, Kenji Takubo, Naoji Moriya Shimadzu Corporation, Japan	
Peptide Based Protein Kinase Detection Using a Nanomechanical Dynamic Microcantilever	768
Kyo Seon Hwang ¹ , Jeong Hoon Lee ¹ , Dong Won Chun ¹ , Byung Hak Cha ¹ , Ga Young Han ¹ , Jung Ho Park ² , Dae Sung Yoon ¹ , Tae Song Kim ¹	
¹ Korea Institute of Science and Technology, Korea, ² Korea University, Korea	
Nanostructured Surface as EWOD Counter Electrode for Matrix-Free Mass Spectrometry Analysis.....	771
Nicolas Verlpanck ¹ , Yannick Coffinier ^{1,2} , Maxence Wisztorski ³ , Gaelle Piret ^{1,2} , Caroline Delhaye ³ , Vincent Thomy ¹ , Isabelle Fournier ³ , Jean-Christophe Camart ¹ , Pierre Tabourier ¹ , Rabah Boukherroub ¹	
¹ Institut d'Electronique de Microelectronique et de Nanotechnologie, France, ² Institut de Recherche Interdisciplinaire, France, ³ Laboratoire de Neuroimmunologie des Annelides, France	
MEMS-Based Picoliter Electrochemical Cell Array for the Fabrication of Oligonucleotide Chips	774
Thierry Leichle ¹ , Emeline Descamps ² , Bruno Corso ² , Sébastien Laurent ² , Pascal Mailley ² , Thierry Livache ² , Jean-Bernard Pourcel ¹ , Christian Bergaud ¹ , Liviu Nicu ²	
¹ Laboratory of Analysis and Architecture of Systems CNRS, FRANCE, ² SPRAM CNRS-CEA, FRANCE	
Novel Fluorescence Detection Technique for Non-Contact Temperature Sensing in Microchip PCR	777
Sudip Mondal, V. Venkataraman Department of Physics, Indian Institute of Science, India	
Development of a Gold-Capped Nanoparticle Layer-Based Optical Biosensor for Label-Free Detection of Biomolecular Interaction Studies.....	780
Do-Kyun Kim, Mihn Heip Ha, Tatsuro Endo, Yuzuru Takamura, Eiichi Tamiya Japan Advanced Institute of Science and Technology, Japan	
Micro & Nano Chemistry	
Pressure and Supercritical CO₂ Conditions Improve the Esterification Reaction of Phthalic Anhydride with Methanol in Glass Microreactors	783
Fernando Benito-Lopez, Roald M. Tiggelaar, Richard J.M. Egberink, Han J.G.E. Gardeniers, Willem Verboom, Albert van den Berg, David N. Reinhoudt MESA+ Institute for Nanotechnology, University of Twente, The Netherlands	

A Digital Microfluidic System to Facilitate Presteady State Kinetics Studies Using MALDI-TOF MS.....	786
Kevin P. Nichols, J.G.E. Gardeniers University of Twente, The Netherlands	
Electrokinetic Transport with Stokes Flow in Microfluidic-Chip Under Asymmetric Conditions of Channel Surface	789
Myung-Suk Chun, Tae Seok Lee, Il Tae Kim Korea Institute of Science and Technology (KIST), Korea	
Confocal Microscopic Measurement of Proton Diffusion in Chemical Reacting Flow	792
Mitsuhisa Ichiyanagi, Yohei Sato, Koichi Hishida Keio University, Japan	
Rapid Phase Surface Generation Using an Integrated Microfabricated Device Reaction Detection System and Automated Control.....	795
Christopher J. Cullen ¹ , Siva Krishnadasan ¹ , John C. de Mello ¹ , Robert C.R. Wootton ² , Andrew J. de Mello ¹	
¹ Imperial College London, UK, ² Liverpool John Moores University, UK	
Simulation Examination for Extraction on Oil/Water Surface.....	798
Ryo Anraku ¹ , Takahiro Asai ¹ , Kenji Uchiyama ¹ , Akihiko Hattori ¹ , Manabu Tokeshi ² , Takehiko Kitamori ³	
¹ Nippon Sheet Glass Co.,Ltd., Japan, ² The University of Nagoya, Japan, ³ The University of Tokyo, Japan	
Measurement of Ion Diffusivity at the Electrolyte-Glass Interface by Evanescent Wave Molecular Tagging.....	801
Hiroki Fukumura, Mitsuhisa Ichiyanagi, Yohei Sato Keio University, Japan	
Photoreactions in Microreactors.....	804
Teijiro Ichimura ¹ , Kosaku Sakeda ¹ , Yoshihisa Matsushita ¹ , Tadashi Suzuki ¹ , Kazuki Tanibata ² , Toshiaki Murata ³	
¹ Tokyo Institute of Technology, Japan, ² Mitsui Engineering & Shipbuilding Co., Ltd., Japan, ³ Mitsui Zosen Plant Engineering, Inc., Japan	
Streaming Currents as a Means to Study the Surface Charge in Nanofluidic Channels.....	807
Frank H.J. Van der Heyden, Derek Stein, Douwe J. Bonthuis, Koen Besteman, Serge G. Lemay, Christine Meyer, Cees Dekker Kavli Institute of Nanoscience, Delft University of Technology, The Netherlands	
Medical & Clinical	
In-Situ Monitoring of C-Reactive Protein (CRP) Antigen-Antibody Binding in a Liquid Environment Using a Micromechanical PZT Thick Film Cantilever	810
Tae Yun Kwon ¹ , Jae Hong Park ¹ , Dae Sung Yoon ² , Hong Lim Lee ¹ , Tae Song Kim ¹	
¹ Microsystem Research Center, Korea Institute of Science and Technology, Korea, ² Yonsei University, Korea	

Determination of Blood Sugar Using Microchip Electrophoresis	813
Eiki Maeda ^{1,2} , Masatoshi Kataoka ³ , Yasuo Shinohara ^{1,2} Noritada Kaji ⁴ , Manabu Tokeshi ⁴ , Yoshinobu Baba ^{3,4}	
¹ The University of Tokushima, Japan, ² IGR,The University of Tokushima, Japan,	
³ HTRC AIST, Japan, ⁴ Nagoya University, Japan	
A Microchip-Based Fluorescence Polarization Immunoassay	816
Tomoya Tachi ¹ , Noritada Kaji ¹ , Manabu Tokeshi ¹ , Yoshinobu Baba ^{1,2}	
¹ Nagoya University, Japan, ² HTRC, AIST, Japan	
Disk-Based Parallel Chemiluminescent Detection of Diagnostic Markers for Acute Myocardial Infarction.....	819
Lutz Rieger ¹ , Juergen Steigert ¹ , Markus Grumann ¹ , Sascha Lutz ¹ , Goeran Olofsson ² , Masoud Kayyami ² , Wolfgang Bessler ³ , Klaus Mittenbuehler ³ , Roland Zengerle ^{1,4} Jens Ducree ^{1,4}	
¹ University of Freiburg - IMTEK, Germany, ² Prolight Diagnostic AB, Sweden,	
³ University of Freiburg - IMMZ, Germany, ⁴ HSG-IMIT, Germany,	
Controlled Microfluidic Generation of Lipid Shell-Based Perfluorocarbon Microbubbles for Use as Ultrasound Contrast Agents	822
Kanaka Hettiarachchi ¹ , Esra Talu ² , Marjorie L. Longo ² , Paul A. Dayton ² , Abraham P. Lee ¹	
¹ University of California, Irvine, USA, ² University of California, Davis, USA	
Rapid, Multiplexed Competitive Immunoassays Using Disposable Microfluidic Devices and SPR Imaging	825
Kjell E. Nelson, Neil Geisler, Karman L. Tandon, Paul Yager	
University of Washington, USA	
A Cross-Flow Electrophoresis Microfluidic Device DNA Sample Concentration	828
Pedro Ortiz, Calum McNeil, Alun Harris	
University of Newcastle upon Tyne, UK	
A Rapid High-Sensitivity Immunoassay Utilizing a Novel On-Chip Electrokinetic Analyte Transport Method	831
Tomohisa Kawabata ¹ , Chen Li ² , Xiahui Bi ² , Celeste Kirby ² , Yihshing Shih ² , Luc Bousse ² , H. Garrett Wada ² , Mitsuo Watanabe ¹ , Shinji Satomura ¹	
¹ Wako Pure Chemical Industries, Osaka Research Laboratory, Japan, ² Wako Pure Chemical Industries, Mountain View R&D Center, USA	
In Vivo Characterizations of Implantable Unpowered Parylene MEMS Intraocular Pressure Sensors.....	834
Po-Jui Chen ¹ , Damien C. Rodger ¹ , Rajat Agrawal ² , Ellis Meng ² , Mark S. Humayun ² , Yu-Chong Tai ¹	
¹ California Institute of Technology, USA, ² University of Southern California, USA	
An Empirical Model for a Piezoelectric Tissue Contrast Sensor Embedded in a Biopsy Tool.....	837
Tao Li, Yogesh B. Gianchandani	
University of Michigan - Ann Arbor, USA	

Single Chamber DNA Extraction and Amplification for Prosthetic Joint Infection Detection	840
Lindsay A. Legendre ¹ , Weidong Cao ¹ , Kerryl Piper ² , Jerome P. Ferrance ¹ , Robin Patel ² , James P. Landers ¹	
¹ University of Virginia, USA, ² Mayo Clinic, USA	
Simplified Microfluidic Procedure for Biotinyl-Oligonucleotide Based Micro-Immunoassay System	843
Yuichi Oku ¹ , Shuichi Akaba ¹ , Ryotaro Hara ¹ , Mamoru Umeda ¹ , Manabu Tokeshi ² , Takehiko Kitamori ³	
¹ Nissui Pharmaceutical Co., Ltd., Japan, ² Nagoya University, Japan, ³ The University of Tokyo, Japan	
Integration of Antibody Arrays Into a Preassembled Microfluidic Device for On-Demand Immunoassay	846
Masahiko Hashimoto, Hirokazu Kaji, Emilia M. Kemppinen, Matsuhiko Nishizawa	
Tohoku University, Japan	
Temperature Gradient Focusing for On-Chip Monitoring of Enzyme Reaction Product in Complex Sample Mixtures	849
Matthew S. Munson, Jonathan G. Shackman, Laurie E. Locascio, David Ross	
National Institute of Standards and Technology, USA	
Single Bead Analysis on Compact Disk Shaped Microfluidic Device	852
Hidegori Nagai ¹ , Yuka Narita ² , Masayuki Matsubara ¹ , Takashi Irie ¹ , Keiitsu Saito ² , Shin-ichi Wakida ¹	
¹ National Institute of Advanced Industrial Science and Technology (AIST), Japan, ² Kobe University, Japan	
A Bead Based DNA Diagnostic Assay Using Nanoparticle Mediated SERRS Detection Within a Lab-On-A-Chip Format	855
Paul B Monaghan ¹ , Karen M McCarney ² , Alistair Ricketts ² , Rachel E Littleford ² , Frances Docherty ² , W Ewen Smith ² , Duncan Graham ² , Jonathan M Cooper ¹	
¹ University of Glasgow, UK, ² University of Strathclyde, UK	
Automated Micro-ELISA System for Allergy Checker: a Prototype and Clinical Test.....	858
Toshinori Ohashi ¹ , Yoshinori Matsuoka ¹ , Kazuma Mawatari ¹ , Mitsuo Kitaoka ¹ , Tadao Enomoto ² , Takehiko Kitamori ^{1,3}	
¹ The Research Association of Micro Chemical Process Technology, Japan, ² Japan Red Cross Society, Wakayama Medical Center, Japan ³ University of Tokyo, Japan	
Chemical Synthesis	
Parallel Synthesis in An EOF-Based Micro Reactor	861
Charlotte Wiles	
The University of Hull, UK	
Organic Solvent Microdroplets in Surface-Modified PDMS Microchannels	864
Daniel J Holt, Florian Hollfelder, Wilhelm T S Huck, Chris Abell	
University of Cambridge, UK	

Screening Multi-Phase Enzymatic Reactions in a Microreactor Setup	867
Kaspar Koch ¹ , Rutger J.F. van den Berg ¹ , Pieter J. Nieuwland ¹ , Hans E. Schoemaker ² , Marcel G. Wubbolts ² , Floris P.J.T. Rutjes ¹ , Jan C.M. van Hest ¹	
¹ Radboud University Nijmegen, The Netherlands, ² DSM Research, Geleen, The Netherlands	
Ionic Liquids in a Microreactor: Palladium Catalysis	870
Pieter J. Nieuwland, Kaspar Koch, Jan C.M. van Hest, Floris P.J.T. Rutjes	
Radboud University Nijmegen, The Netherlands	
High Surface Area Anatase Microreactors for Photocatalysis and Chemical Synthesis	873
Alexander Iles ¹ , Henrik Lindstrom ¹ , Robert C.R. Wootton ²	
¹ National Institute for Materials Science, Japan, ² John Moores University, UK	
Rapid Gas-Liquid Palladium Catalysed Carbonylative Cross-Coupling Reactions Using a Glass Fabricated Microfluidic Chip for Applications in ¹¹C-Radiolabelling	876
Philip W. Miller ¹ , Nicholas J. Long ¹ , Andrew J. de Mello ¹ , Ramon Vilar ¹ , Jan Passchier ² , Antony Gee ²	
¹ Imperial College London, UK, ² GlaxoSmithKline, UK	
Development of a NMR Measurement Chip for In-Site Monitoring of Chemical Synthesis	879
Yutaka Takahashi ¹ , Ryo Sakai ² , Masamichi Nakakoshi ³ , Satoshi Sakurai ¹ , Ryoji Tanaka ¹ , Hiroto Suematsu ¹ , Hiroaki Utsumi ¹ , Takehiko Kitamori ⁴	
¹ JEOL Ltd., Japan, ² Nippon Kayaku Co. Ltd., Japan, ³ Yokohama National University, Japan, ⁴ University of Tokyo, Japan	
Experiences with Meso and Microfluidics-Based Flow Reactors Filled with Heterogenous Catalysts, Using High Temperature and High Pressure.....	882
Ferenc Darvas, Csaba Csajagi, Richard Jones	
Thales Nanotechnology Inc., Hungary	
Separation Science	
DNA Separation on Nanochannel with Phospholipid Polymers	885
Madoka Takai ¹ , Kyousuke Shimizu ² , Yu Nagase ² , Kazuhiko Ishihara ¹	
¹ The University of Tokyo, Japan, ² Tokai University, Japan	
Desalting of Urea From Salt-Rich Protein Sample Facilitated by Copper(II) Ion in Microfluidic Device.....	888
Yun Suk Huh ¹ , Kwangsuk Yang ¹ , Yeon Ki Hong ² , Do Hyun Kim ¹ , Won Hi Hong ¹	
¹ KAIST, Korea, ² Chungju National University, Korea	
Microchip Solid-Phase-Enhanced Liquid-Liquid Extractions Utilising Highly Selective Molecularly Imprinted Polymers as Chemorecognition Solvent Extraction Agents	891
Oliver Castell, Chris Allender, David Barrow	
Cardiff University, UK	
Toward Denaturing Gradient Gel Electrophoresis on a Chip	894
Tomoyuki Morita ¹ , Takashi Matsumura ¹ , Akiko Miya ¹ , Juan G. Santiago ²	
¹ Ebara Research Co., Ltd., Japan, ² Stanford University, USA	

On-Chip Isotachophoresis Using Electrophoretic Spacers	897
Tarun Khurana, Juan G. Santiago	
Stanford University, USA	
Biomolecule and Organelle Trap Using Electric and Hydrodrag Force	
Fields in Taper Shaped Microchannel	900
Yuichi Tomizawa ¹ , Hiroaki Oose ¹ , Kunimitu Ueno ¹ , Md Shameen Ahsans ¹ , Naoki Nagatani ¹ , Wako Nagasaka ¹ , Eiichi Tamiya ¹ , Yuzuru Takamura ²	
¹ Japan Advanced Institute of Science and Technology, Japan, ² PRESTO and JAIST, Japan	
Microchip Electrophoretic Mobility Shift Assay for Detecting	
Interactions of DNA-Transcription Factor NFκB.....	903
Sonoko Inoue ¹ , Masatoshi Kataoka ^{2,3} , Yasuo Shinohara ² , Noritada Kaji ³ , Manabu Tokeshi ⁴ , Yoshinobu Baba ^{3,4}	
¹ The University of Tokushima, Japan, ² IGResearch, The University of Tokushima, Japan, ³ Health Technology Research Center, AIST, Japan, ⁴ Nagoya University, Japan	
Continuous Particle Manipulation in Microchannel Using Laser Radiation Pressure.....	906
Takatsugu Moriya, Koichiro Saiki, Yohei Sato	
Keio University, Japan	
High Throughput Continuous Separation by Electrodeless	
Dielectrophoresis	909
Lujun Zhang, Florin Tatar, Peter Turmezei, Jeroen Bastemeijer, Jeff Mollinger, Andre Bossche	
Delft University of Technology, the Netherlands	
Electrophoretic Separations in Small Spaces: Gradient Elution	
Moving-Boundary Electrophoresis (GEMBE)	912
Jonathan G. Shackman, David Ross	
National Institute of Standards and Technology, USA	
On-Chip Temperature Gradient Focusing Via Joule Heating: Low-Power	
Sample Concentration and Separation	915
Greg J. Sommer, Sun Min Kim, Mark A. Burns, Ernest F. Hasselbrink	
University of Michigan - Ann Arbor, USA	
Continuous-Flow Phase-Separation of Polymer Solutions in Microfluidic	
Aqueous Two-Phase Extraction System	918
Woo-Jin Chang, Hye-Mee Park, Thuan-Hieu Tran, Yoon-Mo Koo	
Inha University, Korea	
Multi-Stage Free-Flow Isoelectric Focusing for Enhanced Separation	
Speed and Resolution.....	921
Jacob W. Albrecht, Klavs F. Jensen	
Massachusetts Institute of Technology, USA	
Sensitivity Improvement for Peptide/Protein Analysis in Microchip	
Electrophoresis-Mass Spectrometry	924
Takahide Kameda ¹ , Fumihiko Kitagawa ¹ , Akihiro Arai ² , Koichi Suzuki ² , Shin Nakamura ² , Koji Otsuka ¹	
¹ Kyoto University, Japan, ² Shimadzu Corporation, Japan	

Automated All-Fractions Collection for Microfluidic Separation	927
Dawid R. Zalewski, Stefan Schlautmann, Richard B.M. Schasfoort MESA+ Institute, University of Twente, The Netherlands	
Pushing the Limits of Deterministic Lateral Displacement Devices	930
Asger V. Larsen ¹ , Jason Beech ² , Veysel Özkapici ¹ , Brian Bilenberg ¹ , Anders Kristensen ¹ , Jonas O. Tegenfeldt ²	
¹ Technical University of Denmark (DTU), Denmark, ² University of Lund, Sweden	
Flow Control in Microfluidic Devices with a Planar Separation Format	933
Stephen C. Jacobson, Margaret A. Lerch Indiana University, USA	
Microchip-Based Rapid Sample-Preparation for Gas-Chromatography Assay of Amphetamine-Type Stimulants in Urine Specimens	936
Hajime Miyaguchi ¹ , Manabu Tokeshi ² , Yoshikuni Kikutani ² , Akihide Hibara ^{2,3} , Hiroyuki Inoue ¹ , Takehiko Kitamori ^{2,3}	
¹ National Research Institute of Police Science, Japan, ² Kanagawa Academy of Science and Technology, Japan, ³ The University of Tokyo, Japan	
A Protein-Analysis Chip Integrating Affinity Chromatographic Column and Isoelectric Focusing Channel	939
Yutaka Koyama, Takehiko Kitamori, Kiyohito Shimura The University of Tokyo, Japan	
Cell Handling & Analysis	
Development of Negative Dielectrophoretic Cellular Patterning System for Co-Culturing of Two Different Cell Types	942
Masato Suzuki ¹ , Tomoyuki Yasukawa ¹ , Mariko Komabayashi ² , Akiko Inagaki ² , Yoshio Hori ² , Hitoshi Shiku ¹ , Tomokazu Matsue ¹	
¹ Tohoku University, Japan, ² Tohoku University Biomedical Engineering Research Organization, Japan	
Microsystems for Electrophysiological Study of Invitro Neurodermatological Cultures	945
Laurent Griscom ¹ , Ulysse Pereira ² , Jean-Pierre Pennec ² , Mathieu Ben ¹ , Laurent Misery ²	
¹ CNRS, France, ² Université de Brest Occidental, France	
A Multiple Electrode Microcompartment Platform (MUMP) for Spatiotemporal Localization of Neuronal Injury Potentials	948
Surendra K. Ravula ¹ , Maxine A. McClain ¹ , Min S. Wang ² , Jonathan D. Glass ² , A. Bruno. Frazier ¹	
¹ Georgia Institute of Technology, USA, ² Emory University, USA	
Perfused Multiwell Tissue Culture Plates with Integrated Microfluidic System	951
Karel Domansky, Walker Inman, Jim Serdy, Bryan Owens, Megan Whittemore, Laura Vineyard, Linda G. Griffith Massachusetts Institute of Technology, USA	

Stack and Measurement of Zeptomole Neurotransmitters Released from Living Single Cells on a FASS-Nano-Fluidic Chip with Electrochemical Detection	954
Ren-Guei Wu ¹ , Fan-Gang Tseng ¹ , Chung-Shi Yang ²	
¹ National Tsing Hua University, Taiwan, ² National Health Research Institutes, Taiwan	
Novel Picoliter Compartmental Microfluidic Chip Devices for High-Throughput Single-Cell Sorting and Analysis	957
Ramachandra Rao Sathuluri ¹ , Masahito Kitamura ² , Yamamura Shohei ² , Tamiya Eiichi ²	
¹ Toyama New Industry Organization, Japan, ² Japan Advanced Institute of Science and Technology, Japan	
Single-Cell Array Chip with Chambers Which Can Encase and Release B-cells Using Thermoresponsive Polymer.....	960
Yoshiyuki Yokoyama ¹ , Shohei Yamamura ² , Satoshi Fujiki ¹ , Katsumi Tanino ¹ , Eiichi Tamiya ²	
¹ Toyama Industrial Technology Center, Japan, ² Japan Advanced Institute of Science and Technology, Japan	
Mechanical Stimulation of Adult Ventricular Myocytes in Microfluidic Channels	963
Norbert Klauke	
University of Glasgow, UK	
Fabrication of a Flow-Type Micro Cell Chip Based on Photo-Induced Cell Capturing	966
Yuichi Tada ¹ , Jun-ichi Edahiro ¹ , Kimio Sumaru ¹ , Yoshiyuki Kanamori ¹ , Shinji Sugiura ¹ , Yoshiyuki Takagi ¹ , Toshio Shinbo ¹ , Yasuo Yoshimi ²	
¹ National Institute of Advanced Industrial Science and Technology (AIST), Japan, ² Shibaura Institute of Technology, Japan	
Single Cell Transfection Dynamics in a Microfluidic System	969
Na Li, Pak Kin Wong, James Lin, Chih-Ming Ho	
University of California, Los Angeles, USA	
Development of a Cell Culture System for Dynamically Controlling Cell Motility.....	972
Hirokazu Kaji, Takeaki Kawashima, Matsuhiro Nishizawa	
Tohoku University, Japan	
Screening of Molecular Libraries Using the Continuous-Flow Micro-Magnetic Cell Sorter	975
Sang-Hyun Oh, Amerendra K. Singh, Paul H. Bessette, Sophia A. Kenrick, Jeffrey J. Rice, Jiangrong Qian, Patrick S. Daugherty, H. T. Soh	
University of California-Santa Barbara, USA	
Micro Cell Incubator Which Can Control the pH of Culture Media Through On-Chip Integrated Carbon Dioxide Generator	978
Yo H. Choi, Sang U. Son, Seung S. Lee	
Korea Advanced Institute of Science and Technology, Korea	

A Reversibly Assembled Microfluidic Chip for Culture and Analysis of Single Cell Array.....	981
Cecile Crozatier, Issa Tapsoba, Mael Le Berre, Stephane Arbault, Christian Amatore, Yong Chen	
Ecole Normale Supérieure, Paris, France	
Rapid Fluorescence-Activated Cell Sorting with Optical-Force Deflection in a Microfluidic Device	984
Kamlesh D. Patel, Thomas D. Perroud	
Sandia National Laboratories, USA	
A Bioparticle Detector and Enrichment Platform Using Integrated Insulator-Based Dielectrophoresis and Bioimpedance Measurements	987
Pierre Ponce, Michelle Khine, Blake A. Simmons, Rafael V. Davalos	
Sandia National Laboratories, USA	
Soft-State Biomicrofluidic Pulse Generator for Fast Endocytic Recycling Analysis of Single Cells	990
Poorya Sabourchi, Navid Ghorashian, Cristian Ionecu-Zanetti, Luke P. Lee	
University of California Berkeley, USA	
Micro/Nano-Patterned Surfaces for Control of Cell Adhesion and Cell Functions: Differentiation Into Adipocytes	993
Makiko Goto, Kae Sato, Takehiko Tsukahara, Tomohiro Konno, Kazuhiko Ishihara, Takehiko Kitamori	
The University of Tokyo, Japan	
Evaporation- and Pressure- Driven Closed-Loop pH Control in a Microliter Bioreactor for High-Throughput Bioprocessing	996
Zhiyu Zhang, Patrick Boyle, Ruben Kolfschoten, Paolo Boccazzì, Anthony Sinskey, Klavs Jensen	
Massachusetts Institute of Technology, USA	
Drug Discovery	
Drop in Drop Nanoliter Kinase Assay Made with Hot Embossed Disposable Multi Channel Dispenser	999
Reinhard Steger ¹ , Christian Mehne ² , Nicolai Wangler ¹ , Mathias Heckele ³ , Roland Zengerle ¹ , Peter Koltay ¹	
¹ University of Freiburg - IMTEK, Germany, ² University of Karlsruhe - IMT, Germany, ³ Forschungszentrum Karlsruhe - IMT, Germany	
Synthesis of Spherical Microcapsules with Nano-Pores and Use as a Potential Encapsulant	1002
Eun H. Jeong ¹ , Sinoj Abraham ² , Takahiro Arakawa ³ , Il Kim ² , Shuichi Shoji ³ , Kyung C. Kim ¹ , Jeung S. Go ¹	
¹ Pusan National University, Korea, ² Pusan National University, Korea, ³ Waseda University, Japan	

On-Chip Construction of a Multifunctional Envelope-Type Nano Device for a Non-Viral Gene Delivery System.....	1005
Hiroshi Kuramoto ¹ , Noritada Kaji ² , Kentarou Kogure ³ , Yasuo Shinohara ¹ , Hideyoshi Harasima ³ , Yosinobu Baba ²	
¹ The University of Tokushima, Japan, ² Nagoya University, Japan, ³ Hokkaido University, Japan	
Microchip-Based Osteosis System for Rapid Drug Screening for Osteogenesis.....	1008
Kae Sato, Kazuyo Igawa, Yuki Tanaka, Kiichi Sato, Ung-il Chung, Takehiko Kitamori	
University of Tokyo, Japan	
Microfluidic Self-Assembly of Tumor Spheroids for Studies of Anticancer Drug Actions and Interactions	1011
Liz Y. Wu, Dino Di Carlo, Luke P. Lee	
University of California, Berkeley, USA	
Session 2A3 Nanofluidics 3 (Separation)	
Nanoimprinted Fluidic Device for Continuous Separation of Nanoparticles.....	1014
Keith J. Morton, James C. Sturm, Robert H. Austin, Stephen Y. Chou	
Princeton University, USA	
Effects of Applied Voltage and Channel Configurations on DNA Size Separation Using Nano Fence Matrix.....	1017
Yoichi Tagaya ¹ , Masakazu Baba ² , Kenji Fukuzawa ¹ , Yasunaga Mitsuya ¹	
¹ Nagoya University, Japan, ² NEC Corporation, Japan	
Self-Assembled Three-Dimensional Nanofluidic Sieves for Biomolecule Separation	1020
Yong Zeng, D. Jed Harrison	
University of Alberta, Canada	
Session 2B3 Chemical Synthesis	
Integrated Microreactors for Sequential and Parallel Reactions.....	1023
Guodong Sui, Hsian-Rong Tseng	
University of California, Los Angeles, USA	
Protein Synthesis in a Plastic Device for Toxin Detection.....	1026
Hugh Fan, Qian Mei, Andrew Simon, Carl Fredrickson, Wei Lian, Shouguang Jin	
University of Florida, USA	
Multi-Step Continuous Microchemical Synthesis and Separation.....	1029
Hemantkumar R. Sahoo, Jason G. Kralj, Klavs F. Jensen	
Massachusetts Institute of Technology, USA	

DAY 3 - WEDNESDAY, NOVEMBER 8, 2006

PLENARY LECTURE 5

Capillary Electrophoresis and Microchip	1032
Shigeru Terabe	
University of Hyogo, Emeritus Professor, Japan	

3A1 Separation 1

Stretching the Limits of Separation	1034
Jason Beech, Jonas O. Tegenfeldt	
University of Lund, Sweden	

Integrated High-Pressure 4-Stage Micro Pump for High Speed Micro Chromatography	1037
Hanseup Kim, William H. Steinecker, Gordon R. Lambertus, Aaron A. Astle, Khalil Najafi, Edward T. Zellers, Luis P. Bernal, Peter D. Washabaugh, Kensall D. Wise	
Center for Wireless Integrated MicroSystems (WIMS), University of Michigan, USA	

Integration of Surface Microfluidics to Closed-Channel Fluidics to Realize a Valveless Multi-Layer Genetic Analysis Chip	1040
Thirukumaran T. Kanagasabapathi, A. Ranjit Prakash, Karan VIS Kaler	
University of Calgary, Canada	

Session 3B1 Droplet

Droplet-Based High-Throughput Live/Dead Cell Assay	1043
Eric Brouzes ¹ , Jeffrey Branciforte ² , Mariusz Twardowski ² , Dave Marran ² , Yue Suo ² , Yves Charles ² , Laurent Boitard ² , Michael P. Weiner ² , Jonathan M. Rothberg, Norbert Perrimon ¹ , Darren Link ²	
¹ Harvard Medical School, USA, ² RainDance Technologies, USA, ³ Howard Hughes Medical Institute, Harvard Medical School, USA	

Real-Time Feedback Control of Droplet Generation for EWOD Digital Microfluidics	1046
Jian Gong, Chang Jin (CJ) Kim	
University of California Los Angeles, USA	

Production of Biphasic Organic Droplets and Particles of Geometrical Anisotropy Using a Tri-Phase Liquid Flow in Microchannels	1049
Takasi Nisisako ¹ , Toru Torii ²	

¹Tokyo Institute of Technology, Japan, ²The University of Tokyo, Japan

Session 3A2 Separation 2

Microfluidic Device for Continuous and Hydrodynamic Separation of Blood Cells	1052
Masumi Yamada ^{1,2} , Miyuki Matsuda ³ , Minoru Seki ³	
¹ University of Tokyo, Japan, ² Tokyo Women's Medical University, ³ Osaka Prefecture University, Japan	

Using Acoustic Differential Extraction to Enhance Analysis of Sexual Assault Evidence on a Valveless Glass Microdevice	1055
Mikael Evander ¹ , Katie M. Horsman ² , Christopher J. Easley ² , James P. Landers ² , Johan Nilsson ¹ , Thomas Laurell ¹	
¹ Lund University, Sweden, ² University of Virginia, USA	

Iso-Dielectric Separation: a New Method for Continuous-Flow Screening of Cells	1058
Michael D. Vahey, Joel Voldman	
Massachusetts Institute of Technology, USA	

Session 3B2 Microfluidic Device 2 (Electro/Magnetic Fluid Control)

Low-Voltage Microfabricated Pump Based on Electroosmosis of the Second Kind	1061
Trond Heldal ¹ , Tormod Volden ¹ , Janko Auerswald ² , Helmut Knapp ²	
¹ IQ Micro Inc., USA, ² Swiss Center for Electronics and Microtechnology (CSEM SA), Switzerland	

Directional and Frequency-Dependent Flow Control in Microfluidic Circuits Using Passive Elastomeric Components.....	1064
Christopher J. Easley, James M. Karlinsey, Daniel C. Leslie, Matthew R. Begley, James P. Landers	
University of Virginia, USA	

Gold Microwire Brushes from Nanoparticle Suspensions for Magnetohydrodynamic Pumping in Microfluidic Chips.....	1067
Jian-Bin Bao, D. Jed Harrison	
University of Alberta, Canada	

PLENARY LECTURE 6

On-Chip Cellomics Assay: Artificial Re-Construction of Tissue Model for Cell Based Drug Discovery	1070
Kenji Yasuda	
Medical and Dental University of Tokyo, Japan	

POSTER SESSION 3

Micro & Nano Fluidic Devices

Generation and Delivery of Monodisperse Pico-Liter Droplets Out of PDMC Microchip Into Accelerator Mass Spectrometry (AMS)	1076
Sung Jae Kim, Yong-Ak Song, Paul L. Skipper, Steven R. Tannenbaum, Jongyoon Han	
Massachusetts Institute of Technology, USA	

Diffusion-Based Free Solution DNA Hybridization and Transport in a Nanofluidic Device	1079
Sumita Pennathur, Kamlesh Patel	
Sandia National Laboratories, USA	

Miniturization of a High-Throughput Multi-Antigen Microfluidic Fluorescence Immunoassays	1082
George Maltezos ¹ , Emil P. Kartalov ² , Vinh Nguyen ¹ , Jiang F. Zhong ² , W. French Anderson ² , Axel Scherer ¹	
¹ California Institute of Technology, USA, ² University of Southern California, USA	
Optofluidic Particle Transport in Liquid Core Photonic Crystal Fibers.....	1085
Sudeep Mandal, David Erickson	
Cornell University, USA	
PCR by Moving a Free Droplet Over Different Temperature Zones.....	1088
Tseng-Ming Hsieh, Zhang Yi, Juergen Pipper, Pavel Neuzil	
Institute of Bioengineering and Nanotechnology, Singapore	
Numerical and Experimental Investigations into a Novel Cell Sorter Utilizing Continuous Cascade Squeeze-Jumping Effect.....	1091
Che Hsin Lin ¹ , Cheng Yan Lee ¹ , Lung Ming Fu ²	
¹ University of Kaohsiung, Taiwan, ² University of Pingtung, Taiwan	
A Novel Artificial Renal Microchip Employing Polymeric Nanofibers Membrane	1094
Kwang Ho Lee ¹ , Duck Joong Kim ³ , Jae Gwan Kim ² , Sang Hoon Lee ³ , Byoung Goo Min ⁴	
¹ Seoul National University, Korea, ³ Korea University, Korea, ² Seoul National University, Korea, ³ Korea University, Korea, ⁴ Seoul National University, Korea	
Continous Microfluidic Cell/Particle Separation Via Combination of Electroosmotic and Hydrodynamic Spreading	1097
Zhigang Wu ¹ , Ai Qun Liu ¹ , Eric Yap ²	
¹ Nanyang Technological University, Singapore, ² DSO National Laboratories, Singapore	
Towards Microchip Biosensors: Passive Microchamber Washing Using Inlet-Pressure Difference.....	1100
Byung-Kwon Kim ¹ , Sang-Youn Yang ¹ , Sung-Jin Kim ² , Haesik Yang ¹	
¹ Pusan National University, Korea, ² Electronics and Telecommunications Research Institute, Korea	
AC Electroosmotic Micromixer: Viscosity and Ionic Strength Dependence of Mixing Time	1103
Naoki Sasaki ¹ , Takehiko Kitamori ^{1,2,3} Haeng-Boo Kim ^{1,2,3}	
¹ The University of Tokyo, Japan, ² Kanagawa Academy of Science and Technology, Japan, ³ CREST, Japan Science and Technology Corporation, Japan	
Reciprocating Diaphragm Micropump for High Pressure Micro-Chemical Processes.....	1106
Takanori Aono ¹ , Akira Koide ¹ , Ryo Miyake ¹ , Mitsuo Kitaoka ² , Takehiko Kitamori ³	
¹ Mechanical Engineering Research Laboratory, Hitachi, Ltd., Japan, ² The Research Association of Micro Chemical Process Technology, Japan, ³ The University of Tokyo, Japan	
The Digital Generation of Analog Chemical Signals	1109
Li Chen, Farouk Azizi, Carlos Mastrangelo	
Case Western Reserve University, USA	

Pneumatic Micro Dispenser System with No Dead Volume for Portable Micro Chemical Device	1112
Tadahiro Hasegawa ¹ , Fumiayuki Omatsu ¹ , Toshiyuki Tsuji ¹ , Koji Ikuta ²	
¹ Osaka Institute of Technology, Japan, ² Nagoya University, Japan	
Manufacturing Size-Controlled Gelatin Microparticles Using a Microfluidic Chip	1115
Yu-Cheng Lin ¹ , Keng-Shiang Huang ¹ , Po-Wen Lin ^{1,2} , Shian-Chin Lai ² , Yu-Jen Lai ² , Po-Wen Lin ^{1,2} , Chih-Hui Yang ²	
¹ National Cheng Kung University, Taiwan, ² I-Shou University, Taiwan	
Hydrophobic Plating Technique for Fabrication of MEMS Slide Valve.....	1118
Michio Takayama, Yoshikuni Kikutani ³ , Kazuma Mawatari ³ , Mitsuo Kitaoka ² , Takehiko Kitamori ⁴	
¹ Olympus Corporation, Japan, ² The Research Association of Micro Chemical Process Technology, Japan, ³ Kanagawa Academy of Science and Technology, Japan, ⁴ The University of Tokyo, Japan	
Laser Controlled Pico-Fraction Unit for Nano-Biodevices	1121
Toshihiko Ooie ¹ , Masato Tanaka ¹ , Tomonori Nakahara ¹ , Shinji Hyodo ² , Yasuo Shinohara ³ , Yoshinobu Baba ^{1,4}	
¹ AIST, Japan, ² Toyo Manufacturing Co., Ltd., Japan, ³ University of Tokushima, Japan, ⁴ Nagoya University, Japan	
Micro Fluidic Devices in 1 mm Cube Shape for Flow Control in a Micro Chemical Chip	1124
Yukimitsu Sekimori ¹ , Takehiko Kitamori ²	
¹ Naganokeiki Ltd., Co., Japan, ² University of Tokyo, Japan	
Polymer Based Membrane Devices for Solid-Liquid Extraction	1127
Yuji Murakami ^{1,2} , Katsumasa Sakamoto ^{1,3} , Kazuma Mawatari ^{1,4} , Yoshikuni Kikutani ^{1,4} , Masashi Higasa ² , Hiroaki Nakanishi ³ , Mitsuo Kitaoka ^{1,3} , Takehiko Kitamori ^{4,5}	
¹ The Research Association of Micro Chemical Process Technology, Japan, ² New Frontiers Research Laboratories, Toray Industries, Inc., Japan, ³ Technology Research Laboratory, Shimadzu Corp., Japan, ⁴ Kanagawa Academy of Science and Technology, Japan, ⁵ The University of Tokyo, Japan	
Sliding Micro Valve Device for Nano Liter Handling in Microchip	1130
Masahiro Kuwata ^{1,2} , Takehiko Kitamori ³	
¹ Toshiba Corporation, Japan, ² Research Association of Micro Chemical Process Technology, ³ The University of Tokyo, Japan	
Fabrication of Primitive Spherical Micropump Powered by Cardiomyocytes: Micro Spherical Heart.....	1133
Yo Tanaka ¹ , Kae Sato ¹ , Tatsuya Shimizu ² , Masayuki Yamato ² , Teruo Okano ² , Takehiko Kitamori ¹	
¹ University of Tokyo, Japan, ² Tokyo Women's Medical University, Japan	
High Throughput Enzyme Inhibition Assays on a Capillary Based Sequential Injection System	1136
Wen-Bin Du, Qun Fang, Zhao-Lun Fang	
Zhejiang University, China	

Novel 3-D Impellor-Shaped Ferromagnetic Micro-Stirrer Bar and Its Use for Active Micromixing	1139
Arun K. Nallani ¹ , Jeong-Bong Lee ² , Danid B. Wallace ³ , Donald J. Hayes ³	
¹ Intel Corporation, USA, ² University of Texas at Dallas, USA, ³ MicroFab Technologies, USA	
High-Efficiency In-Vitro Selection of DNA Aptamers Using a Dielectrophoresis-Activated Cell Sorter (DACS)	1142
Eric T. Lagally ¹ , Xiaoyuan Hu ¹ , Yanting Zhang ¹ , Lisan Viel ¹ , Jeffrey B.-H. Tok ² , Theodore M. Tarasow ² , H.T. Soh ¹	
¹ California Nanosystems Institute, UC - Santa Barbara, USA, ² Chemistry and Materials Science Directorate, Lawrence Livermore National Laboratory, USA	
Fabrication of an On-Chip NMR Microfluidics Device	1145
Lydia L. Sohn ¹ , Julie L. Herberg ² , Bruce D. Harteneck ³ , David R. Myers ¹ , J. Alexander Liddle ³	
¹ University of California, Berkeley, USA, ² Lawrence Livermore National Laboratory, USA, ³ Lawrence Berkeley National Laboratory, USA	
A Low Power, Micromachined, Proportional Valve for Drug Delivery.....	1148
Allan Evans ¹ , Jong Park ¹ , Ryan Taylor ² , Tyler Brosten ² , Gregory Nellis ² , Sanford Klein ² , Jeffrey Feller ³ , Louis Salerno ³ , Yogesh Gianchandani ¹	
¹ University of Michigan, Ann Arbor, USA, ² University of Wisconsin, Madison, USA, ² NASA Ames Research Center, USA	
A Microfluidic Device for Droplet-Based DNA-PNA Hybridization and Separation	1151
Shohei Kaneda ¹ , Kotaro Somei ² , Koichi Ono ³ , Takatoki Yamamoto ¹ , Teruo Fujii ¹	
¹ The University of Tokyo, Japan, ² Tokyo Institute of Technology, Japan, ³ Enplas Laboratories, Japan	
Continuous Separation of Blood Plasma Using Sedimentation in Microchannel.....	1154
Joon-Ho Moon ¹ , Sang Youl Yoon ¹ , Sung Yang ² , Kyung Chun Kim ¹	
¹ Pusan National University, Korea, ² Pennsylvania State University, USA	
Flow Characteristics of Nanochannel Electroosmotic Pumps.....	1157
Duckjong Kim, Sang-Jin Park, Eui Soo Yoon	
Korea Institute of Machinery and Materials, Korea	
The Serial Dilution Chip for Cytotoxicity and Cell Differentiation Test.....	1160
C. Kim ^{1,2} , Sung S. Ryu ¹ , Su K. Chae ¹ , In H. Lee ¹ , Kyeong S. Shin ¹ , Kyu J. Lee ² , Ji Y. Kang ¹	
¹ Korea Institute of Science and Technology, Korea, ² Korea University, Korea	
Fluid Flow Study in a Rotary Gate Microvalve.....	1163
Rajesh Luharuka, Peter J. Hesketh	
Georgia Institute of Technology, Atlanta, USA	
Electroactive Nanowell Sensors for Parallel Particle Trapping and Detection	1166
Bernardo Cordovez, David Erickson	
Cornell University, U.S.A	

On-Site Size-Selective Particle Sampling Using Mesoporous Polymer Membrane Microfluidic Device.....	1169
Masashi Ikeuchi, Koji Ikuta	
Nagoya University, Japan	
Picoliter-Sized Gel Compartment Array for High-Throughput Cellular Analysis	1172
Tetsuya Shibanuma ¹ , Masumi Yamada ² , Masahiro Yasuda ¹ , Minoru Seki ¹	
¹ Osaka Prefecture University, Japan, ² University of Tokyo, Japan	
Venous Valve Like Mono-Leaflet Micro Valve and Its Integration with Pumping System	1175
Jeongyun Kim ¹ , Juyeoul Baek ² , Yongdoo Park ¹ , Kyung Sun ² , Sanghoon Lee ¹	
¹ Korea University, Korea, ² Korea Artificial Organ Center, Korea University, Korea	
Microfluidic Flow Distributors Generating Concentration Gradients for Biochemical Assay.....	1178
Takaya Hirano ¹ , Masumi Yamada ² , Masahiro Yasuda ¹ , Minoru Seki ¹	
¹ Osaka Prefecture University, Japan, ² University of Tokyo, Japan	
'Wet' AC Actuated Microfluidic Micropore Array for Patterning Diffusible Gradients During Cell Culture.....	1181
Tushar Bansal, Meng-Ping Chang, Michel M. Maharbiz	
University of Michigan, USA	
A Microelectrolytic Device for Electronically Controlled Nitric Oxide Microgradient Generation	1184
Prashant Padmanabhan, Zhengrong Zhou, Biyun Wu, Jaehyun Park, Michel M. Maharbiz	
University of Michigan, USA	
Continuous-Flow Particle Sorting at Low Applied Electric Fields Using Electrodeless Dielectrophoresis in Ridged Polymeric Microstructures.....	1187
A. Ezekial Smith, Benjamin G. Hawkins, Yusef A. Syed, Brian J. Kirby	
Cornell University, USA	
A Passive Microfluidic Droplet Fusion Device with 100% Fusion Efficiency	1190
Wei-Yu Tseng, Yung-Chieh Chen, Lung-Hsin Hung, Abraham P Lee	
University of California, Irvine, USA	
A Simple Composite Cap Sealing of Integrated Nano/Microfluidic Channel Devices Below 20 nm at Room Temperature	1193
Chia-Fu Chou ¹ , Jian Gu ² , Ravi Gupta ² , Qihuo Wei ²	
¹ Academia Sinica, Taiwan, ² Arizona State University, USA	
System Technology	
Palm Top Sized Detection System with Micro Chemical Chip	1196
Akihiko Hattori ¹ , Yoshinori Mastuoka ² , Mitsuo Kitaoka ² , Takehiko Kitamori ³	
¹ Nippon Sheet Glass Co., Ltd., Japan, ² MCPT, Japan, ³ University of Tokyo, Japan	

Integration of Multiple Analytical Principles on a Capillary-Assembled Microchip (CAS-Chip): Multiple Protease Activity and Electrolyte Sensing	1199
Terence G. Henares, Masayuki Takaishi, Naoya Yoshida, Hideaki Hisamoto, Shigeru Terabe	
University of Hyogo, Japan	
Chemiluminescent Detection in a Customised Microfluidic Chip with Integrated Protein Micro-Array.....	1202
Christophe A. Marquette ¹ , Alexandra Homsy ² , Kevin Heyries ¹ , Daniel Hoffmann ² , Loic J. Blum ¹ , Michael G. Loughran ²	
¹ Laboratoire de Genie Enzymatique et Biomoleculaire, Universite Lyon, France,	
² Tyndall National Institute, Ireland	
Three-Dimensional Biologically-Active Nanostructured Architectures in Polymer-Based Microfluidic Devices for Biomarker Detection	1205
Guofang Chen, Catherine Situma, Steven A. Soper, Robin L. McCarleyd	
Louisiana State University, USA.	
Integrated CMOS-Compatible Silicon Nanowire Sensor with Efficient Sample Delivery	1208
Ieng Kin Lao, Ajay Agarwal, Han Hua Feng, Narayanan Balasubramanian, Dim Lee Kwong	
Instituite of Microelectronics, Singapore	
Development of Automated Liquid Handler for Microfluidic Reactor Array for High-Throughput Screenings of Protein Crystallization Conditions.....	1211
Tetsu Isomura ¹ , Toshiharu Shiraishi ² , Seiichiro Kishishita ³ , Mikako Shirouzu ³ , Michiteru Nishino ¹ , Atsushi Someya ² , Shigeyuki Yokoyama ³ , Minoru Seki ⁴ , Shigetoshi Sugio ¹	
¹ ZOEGENE Corporation, Japan, ² ARBIOTEC, Ltd., Japan, ³ RIKEN Genomic Sciences Center, Japan, ⁴ Osaka Prefecture University, Japan	
Microfabrication of Barcoded Microparticle Arrays for Miniaturized and Multiplexed Single Nucleotide Polymorphism Detection.....	1214
Zheng-liang Zhi ² , Shouhei Yamamura ¹ , Takamura Yusuru ¹ , Tamiya Eiichi ¹	
¹ Japan Advanced Institute of Science & Technology, Japan, ² University of Liverpool, UK	
Spot-In-Spot Hybridization of Oligonucleotides Deposited on a Glass Slide by a Microcantilever Based Depositing Device.....	1217
Nathalie Berthet ¹ , Thierry Leichle ² , Emmanuelle Trevisiol ¹ , Jean-Bernard Pourcel ² , Daisuke Saya ² , Christian Bergaud ² , Liviu Nicu ² , Jean Marie Francois ¹	
¹ INSA Toulouse, France, ² CNRS, Toulouse, France	
Automated Continuous Flow Polymerase Chain Reaction (PCR) in Independent Microdroplets	1220
Max Chabert, Kevin D. Dorfman, Jean-Louis Viovy	
Institut Curie, France	

A Discontinuous, Embedded Waveguide and Microlens System for Multiplex Single Molecule Detection in Polymer Microfluidic Systems	1223
Jason M. Emory, Ren Yang, Wanjun Wang, Steven A. Soper	
Louisiana State University, USA	
Disposable Single-Use Pumps Based on a Wafer-Level Process	1226
Björn Samel, Julien Chretien, Rui Feng Yue, Patrick Griss, Göran Stemme	
Microsystem Technology Lab, School of Electrical Engineering, Royal Institute of Technology, Sweden	
A Handheld Immunosensing Device Based on Low-Cost Self-Contained Microchips and Ferromagnetic Actuation	1229
Cedric Robillot ¹ , Jane Fitzpatrick ¹ , Stephen Grimmer ¹ , Brett Kettle ¹ , Dalibor Dadic ² , Klaus Dreser ²	
¹ Cleveland Biosensors Pty Ltd, Australia, ² Institut fur Mikrotechnik Mainz GmbH, Germany	
Microfluidic Flow Injection Analysis System with an On-Chip Integrated Pump Drive Based on Capillary and Evaporation Effects	1232
Zhang-Run Xu, Chong-Hui Zhong, Yan-Xia Guan, Jian-Hua Wang, Zhao-Lun Fang	
Northeastern University, China	
Development of a Micro Elisa System for Rapid Colon Cancer Diagnosis from Tissue Cells.....	1235
Hisao Nakanishi ¹ , Mitsuo Kitaoka ² , Takehiko Kitamori ³	
¹ Sumitomo Bakelite Co., Ltd., Japan, ² The Research Association of Micro Chemical Process Technology, Japan, ³ University of Tokyo, Japan	
Efficient Miniaturized Systems for Microwave Heating on Microdevices	1238
Angelique Sklavounos, Daniel J. Marchiarullo, Susan L. R. Barker, James P. Landers, N. Scott Barker	
University of Virginia, USA	
Microbead Based Total Analysis System for Hepatitis C Detection	1241
Tae Seok Sim, Bo-Rahn Lee, Sang-Myoung Lee, Min-Soo Kim, Yoon-Sik Lee, Byung Gee Kim, Yong-Kweon Kim	
Seoul National University, Korea	
Detection Technology	
Fabrication of PMMA Microchip Integrated with Gold Nanoparticle Working and Decouple Electrode for High Performance CEEC Application	1244
Ching-Mou Chen ¹ , Guan-Liang Chang ¹ , Kuo-Tang Liao ² , Hsuan-Jung Huang ² , Che-Hsin Lin ²	
¹ National Cheng Kung University, Taiwan, ² National Sun Yet-Sen University, Taiwan	
On-Chip pH Sensing with Gel Microbead Positioned by Optical Tweezers.....	1247
Hisataka Maruyama ¹ , Fumihito Arai ² , Toshio Fukuda ¹	
¹ Nagoya University, Japan, ² Tohoku University, Japan	

A Biomimetic MEMS Neurotransmitter Detector	1250
Stephan T. Koev ¹ , Li-Qun Wu ² , Gregory F. Payne ² , Reza Ghodssi ¹	
¹ University of Maryland, USA, ² University of Maryland Biotechnology Institute, USA	
Fabrication of Polydimethylsiloxane(PDMS) Microlens for Cell Detection by Light Scattering.....	1253
Sewan Park, Yongwon Jeong, Jinseok Kim, Kihwan Choi, Hyeon Cheol Kim, Doo Soo Chung, Kukjin Chun	
Seoul National University, Korea	
A Novel Low-Cost Compact, Laser Pointer Driven Surface Plasmon Resonance System	1256
Rahber Thariani, Paul Yager	
University of Washington, USA	
Capacitive Surface Stress-Based Chemo-Mechanical Sensor	1259
Si-Hyung Lim ¹ , Srinath Satyanarayana ² , Arun Majumdar ¹	
¹ UC Berkeley, USA, ² Intel, USA	
Potentiometric Drug Transport Analysis Using Oocyte-Based Field Effect Transistor	1262
Toshiya Sakata, Yuji Miyahara	
National Institute for Materials Science, Japan	
Biomolecular Motor-Driven Selective Binding and Concentrating of Protein Analytes.....	1265
T. S. Kim, L. J. Cheng, M.-T. Kao, E. F. Hasselbrink, L. J. Guo, E. Meyhofer	
The University of Michigan, USA	
Development of Low-Cost Surface Enhanced Raman Scattering Substrates with Silver Nano-Particles Using the Modified Silver Mirror Reacion for Ultra-Sensitive and On-Site Detections	1268
Katsuhiro Kurooka, Norihisa Miki	
Keio University, Japan	
Flowing Thermal Lens Micro Flow Velocimeter with On-Chip Microlens and Detachable Optical Fibers.....	1271
Yoshikuni Kikutani ^{1,2} Kazuma Mawatari ^{1,2} Kenji Katayama ^{1,2} Yoshinori Matsuoka ^{2,3} Takashi Fukuzawa ³ , Akihiko Hattori ³ , Mitsuo Kitaoka ² , Manabu Tokeshi ^{1,4} , Takehiko Kitamori ^{1,4,5}	
¹ Kanagawa Academy of Science and Technology, Japan, ² The Research Association of Micro Chemical Process Technology, Japan, ³ Nippon Sheet Glass Co., Ltd., Japan, ⁴ Institute of Microchemical Technology, Japan, ⁵ The University of Tokyo, Japan	
Photothermal Spectroscopy Using Diffraction Grating Nano Channels for Detection in Nano Space	1274
Kotaro Oda ¹ , Kazuma Mawatari ² , Kenji Katayama ³ , Takehiko Kitamori ¹	
¹ The University of Tokyo, Japan, ² Kanagawa Academy of Science and Technology, Japan, ³ Chuo University, Japan	

Photothermally Enhanced Phase-Contrast Microscope for Sensitive Visualization of Non-Fluorescent Samples	1277
Ken Oikawa, Akihide Hibara, Takehiko Kitamori	
University of Tokyo, Japan	
Microfluidic Spotting Chip for Label-Free Protein Microarrays.....	1280
Eric Flaim, Mark T. McDermott, D. Jed Harrison	
University of Alberta	
Nanocavity Network-Based Impedance Sensor for Molecular Diagnostics	1283
J. Tanner Nevill, Dino Di Carlo, Luke P. Lee	
University of California at Berkeley, US	
Spreading Small Signals Over Large Areas: Electrochemical Amplification in an SPR Imaging Sensor Array.....	1286
Melissa S. Hasenbank, Elain Fu, Paul Yager	
University of Washington, USA	
Nanoparticle Enhanced SPR Imaging for Protein Microarrays	1289
Chris F Grant, Francis Nsiah, D. Jed Harrison, Mark T. McDermott	
University of Alberta, Canada	
Single Cell Differential Impedance Spectroscopy Analysis Using High Density Hydrodynamic Cell Trapping Arrays	1292
Daniele Malleo ¹ , Dino Di Carlo ² , J. Tanner Nevill ² , Luke P. Lee ² , David Holmes ¹ , Hywel Morgan ¹	
¹ University of Southampton, UK, ² University of California at Berkeley, US	
Surface Modification of Silicon Nanowires for the Development of Biosensor Chip	1295
Mira Kim ¹ , Kook-nyung Lee ¹ , Suk-won Jung ¹ , Dong-sik Shin ² , Yoon-Sik Lee ²	
¹ Korea Electronics Technology Institute, Korea, ² Seoul National University, Korea	
In-Situ Flow Velocimeter in Microchip Using Near-Field Heterodyne Grating Method	1298
Kenji Katayama ¹ , Yoshikuni Kikutani ² , Takehiko Kitamori ³	
¹ Chuo University, Japan, ² Kanagawa Academy of Science and Technology, Japan,	
³ University of Tokyo, Japan	
Microfluidic Impedance Assay for Monitoring Endothelin Induced Cardiomyocyte Hypertrophy.....	1301
Mo Yang ¹ , Xin Zhang ²	
¹ The Hong Kong Polytechnic University, Hong Kong, ² Boston University, USA	
Quantitative Temperature Measurement of Micro-Electrophoretic Flow Using Two-Color Laser-Induced Fluorescence.....	1304
Hiroyuki Akimoto, Souichi Saeki, Takashi Saito, Teruo Nishida, Kazuyuki Nakamura	
Yamaguchi University, Japan	

Optical and Impedance Detection for Analysis of DNA Hybridisation on Encoded Micro-Particles	1306
David Holmes, Gerasim Galitonov, Shahanara Banu, Hywel Morgan	
University of Southampton, UK	
Transit Time of Colloids in Chemically Functionalized Artificial Pores	1309
Andrea Carbonaro ¹ , Lucy Godley ² , Lydia L. Sohn ¹	
¹ University of California Berkeley, USA, ² University of Chicago, USA	
A Micro SPR (Surface Plasmon Resonance) Sensor with an Integrated Photodetector	1312
Hyung-Seok Pang, Patrick L. LiKamWa, Hyoung J. Cho	
University of Central Florida, USA	
Micro & Nano Chemistry	
Extraction Behavior of Lanthanoid (III) Species Using Dihexyl-<i>N,N</i>-Diethylcarbamoylmethylphosphonate in the Microchemical Chip	1315
Yuya Takahashi, Hiroyasu Hotokezaka, Yasuhisa Ikeda	
Tokyo Institute of Technology, Japan	
Development of Liquid/Liquid Optical Waveguide with Miscible Solvents and its Application to the Observation of 1-Anilino-8-Naphthalene Sulfonate at the Tetrahydrofuran/Water Interface	1318
Hiromi Takiguchi, Sohto Asanuma, Hiroki Hotta, Tamao Odake, Kin-ichi Tsunoda	
Gunma University, Japan	
Evaluation of Hybridization Kinetics of Molecular Beacons with Nucleic Acids Using Picoliter Microfluidic Droplet with Millisecond Resolution	1321
Albert T.H. Hsieh, Jen-Hao Pan, Yuh A. Lin, Abraham P. Lee	
University of California, Irvine, USA	
NMR Study on the Tautomeric Equilibrium of Acetylacetone Confined in Extended-Nano Space	1324
Kyousuke Nagaoka ¹ , Takehiko Tsukahara ^{1,2} , Akihide Hibara ^{1,3} , Haeng-Boo Kim ^{1,2,3} , Takehiko Kitamori ^{1,2,3}	
¹ The University of Tokyo, Japan, ² Japan Science and Technology Agency, Japan	
³ The University of Tokyo, Japan	
Fundamental Properties of Micro Supercooling Flow	1327
Akihide Hibara ^{1,2,3} , Shinya Matsuoka ¹ , Masaharu Ueno ¹ , Takehiko Kitamori ^{1,2}	
¹ University of Tokyo, Japan, ² Kanagawa Academy of Science and Technology, Japan, ³ PRESTO, Japan Science and Technology Agency, Japan	
In-Situ Measurement of the Photooxidation Process of Alkanethiol Self-Assembled Monolayers Using Dual-Channel Quartz Crystal Microbalance	1330
Takashi Abe, Hiroshi Kato, Xinghua Li, Matsuhiro Nishizawa	
Tohoku University, Japan	
A New Microstructured Reaction-Calorimeter as Screening Tool for Thermokinetic and Safety Parameters	1333
Juergen Antes, Daniel Schifferdecker, Stefan Löbbecke, Horst Krause	
Fraunhofer ICT, Germany	

Mechanism of Reaction Efficiency Enhancement in Microchannels Studied by Spectroscopic Visualization and Numerical Simulation	1336
Hirofumi Kawazumi ¹ , Kenichi Kanno ¹ , Masayuki Fujii ¹ , Yoshiko Yamaguchi ² , Hideaki Maeda ²	

¹Kinki University Kyushu, Japan, ²Micro-space Chemistry Lab., AIST, Japan

The Effect of Superhydrophobic SU-8 Patterned Surfaces on the Response of the Quartz Crystal Microbalance	1339
Paul Roach, Carl R. Evans, Glen McHale, Neil J. Shirtcliffe, Michael I. Newton	
Nottingham Trent University, UK	

Micro & Nano Biology

Controlled Delivery of Calcium-Gated MthK Channels Into an On-Chip Bilayer Lipid Membrane for Electrophysiology Measurements.....	1342
Michele Zagnoni ¹ , Robert J. Wood ² , Mairi E. Sandison ¹ , Peter L. Roach ² , Hywel Morgan ¹	

¹ECS, University of Southampton, UK, ²School of Chemistry, University of Southampton, UK

Viability after On-Chip Single-Cell Microelectroporation for the Study of Macrophage Signaling Pathways.....	1345
Eunice S. Lee ^{1,2,3} Sheri-Michele S. Bachelor ¹ , Zohora Q. Iqbal ¹ , Luke P. Lee ^{2,3} , Rafael V. Davalos ^{1,4}	

¹Sandia National Laboratories, USA, ²Berkeley Sensor and Actuator Center, University of California, Berkeley, USA, ³University of California, Berkeley, USA,

⁴Virginia Tech-Wake Forest University, USA

Microfluidic Systems Integrated with Pumping/Mixing and Separation Devices for Virus Detection	1348
Kang-Y. Lien, Cheng-Y. Liu, Jr-L. Lin, Hao-Y. Tseng, Wan-C. Lee, Huan-Y. Lei, Gwo-B. Lee	
National Cheng Kung University, Taiwan	

Electrotransfection in Microchannel: A Shortcut to Its Uptake Mechanism	1351
Won Gu Lee ¹ , Hyunwoo Bang ¹ , Jeong Ah Kim ² , J. Lee ¹ , H. Yun ¹ , J. Park ² , Keunchang Cho ² , Asif Riaz ³ , Young Shik Shin ⁴ , Neon C. Jung ² , Chanil Chung ² , Dong-Chul Han ¹ , Jun Keun Chang ²	

¹Seoul National University, South Korea, ²Digital Bio Technology, Inc., South Korea, ³University of California, Berkeley, USA, ⁴California Institute of Technology, USA

Giant Proteoliposome Array in Microchambers.....	1354
Nozomu Yamanaka, Shoji Takeuchi	
Institute of Industrial Science, The University of Tokyo, Japan	

Nanoneedle Fields for Biological Interaction with Cells.....	1357
Matthieu J. Denoual ¹ , Magali Chiral ¹ , Olivier De Sagazan ² , Bruno Le Pioufle ¹	
¹ Biomis/SATIE ENS-Cachan, France, ² ST Microelectronics, France	

Simulating Kinesin/Microtubule-Based Molecular Shuttle Movements	1360
Takahiro Nitta ¹ , Akihito Tanahashi ¹ , Motohisa Hirano ¹ , Henry Hess ²	
¹ Gifu University, Japan, ² University of Florida, USA	

Development of an Assay System for ABC Transporters Reconstituted in an Artificial Lipid Bilayer	1363
Hiroaki Suzuki ¹ , Kazuhito V. Tabata ² , Hiroyuki Noji ² , Shoji Takeuchi ¹	
¹ The University of Tokyo, Japan, ² Osaka University, Japan	
Lipid Bilayer Membrane Formation by Solvent Extraction in a Microfluidic Channel	1366
Noah Malmstadt, Michael Nash, Robert Purnell, Jacob J. Schmidt	
University of California, Los Angeles, USA	
Monodisperse Liposomal Gene Carrier Formulation in Picoliter Micro-Reactor for Consistent and Efficient Gene Delivery	1369
Albert T. H. Hsieh, Yuh A. Lin, Jen-Hao Pan, Abraham P. Lee	
Biomedical Engineering, University of California, Irvine, USA	
Hand-Operable Micro Fluidic Arrays for Single Cell Trapping, Precise Drug Dosage by 3D's Passive Micro Valves and Snares	1372
Tsung-Ju Chen, Fan-Gang Tseng, Chung-Shi Yang	
National Tsing Hua University, Taiwan	
Formation of Three-Dimensional Lipid Membrane Structures on a Microchip	1375
Petra S. Dittrich ¹ , Thomas Braschler ² , Philippe Renaud ² , Andreas Manz ¹	
¹ ISAS - Institute for Analytical Sciences, Germany, ² Swiss Federal Institute of Technology of Lausanne (EPFL), Switzerland	
Dynamic Single Cell Culture Array.....	1378
Dino Di Carlo, Liz Y. Wu, Luke P. Lee	
University of California, Berkeley, USA	
Influence of Apoptotic Cells on Macrophages and Induction of Phagocytosis Studied in PDMS Chips Using Photostable Staining.....	1381
Severine Le Gac ¹ , Istvan Vermes ² , Albert van den Berg ¹	
¹ University of Twente, The Netherlands, ² Medisch Spectrum Twente, The Netherlands	
Modeling the Behavior of Microtubule in the Presence of Electric Fields for Biomolecular Motor-Driven μTAS	1384
T. S. Kim, M.-T. Kao, E. F. Hasselbrink, E. Meyhofer	
The University of Michigan, USA	
Microfluidic Cell Culture Chip Employing Polymeric Nanofiber Membrane.....	1387
SungRak Kim, YongDoo Park, KiHwa Lee, SangHoon Lee	
Korea University, South Korea	
SAXS in a Microtas, a New Approach To Structure: Function Studies of Biological Macromolecules	1390
Bente Vestergaard ¹ , Lise Arleth ² , Detlef Snakenborg ³ , Katrine N. Toft ¹ , Jes K. Jacobsen ⁴ , James M. Flink ⁴ , Michael Gajhede ¹ , Jorg P. Kutter ³	
¹ Danish University of Pharmaceutical Sciences, Denmark, ² The Royal Veterinary and Agricultural University, Denmark, ³ Technical University of Denmark, Denmark, ⁴ Novo Nordisk A/S, Denmark	

Low Cost Microfabricated Silicon Chip for Membrane Protein Monitoring	1393
Bruno Le Pioufle ¹ , Christophe Yamahata ² , Kei Funakoshi ² , Hiroaki Suzuki ² , Agnès Tixier-Mita ¹ , Hiroyuki Fujita ¹ , Shoji Takeuchi ¹	
¹ LIMMS CNRS/IIS University of Tokyo, JAPAN, ² Institute of Industrial Science, University of Tokyo, JAPAN	
Direct Monitoring of B- to A-DNA Conformational Transition at a Single Molecule Level Induced by Ethanol in Microfluidic Devices	1396
Kentaro Fujiyoshi ¹ , Noritada Kaji ¹ , Manabu Tokeshi ¹ , Yoshinobu Baba ^{1,2}	
¹ Nagoya University, Japan, ² Health Technology Research Center, AIST, Japan	
Preparation of Cell-Sized Liposomes of Controlled Size Containing Long Genomic DNA	1399
Mael Le Berre ¹ , Marie-Alice Guedea-Boudeville ² , Yong Chen ¹ , Damien Baigl ¹	
¹ Ecole Normale Supérieure, France, ² Université Paris 7, France	
Intracellular Recording and Calcium Measurement in a Single Neuron of <i>Aplysia</i> Using a Nano-Probe	1402
Masaki Shuzo, Tomoki Kazawa, Koutaroh Okada, Ryohei Kanzaki, Isao Shimoyama	
The University of Tokyo, Japan	
Bio-Actuated Power Generator Using Cultured Cardiomyocytes on a Polymer Wire	1405
Tomoji Ishisaka ¹ , Hiroshi Sato ² , Yoshitake Akiyama ¹ , Yuji Furukawa ¹ , Keisuke Morishima ¹	
¹ Tokyo University of Agriculture and Technology, Japan, ² National Institute of Advanced Industrial Science and Technology, Japan	
Artificial Life Forms in Microfluidic Computers	1408
Goran Goranovic ¹ , Steen Rasmussen ² , Peter E. Nielsen ³	
¹ University of Southern Denmark, Denmark, ² Los Alamos National Laboratory, USA, ³ University of Copenhagen, Denmark	
Microfluidic In-Vivo Thermal Perturbation of Self-Assembled Drosophila Embryos to Study the Robustness of Cellular Genetics.....	1411
Weon Gyu Shin, Gabriel T. Dagani, Jean R. Fakhoury, John C. Sisson, Xiaojing Zhang	
The University of Texas at Austin, USA	
Bio-Actuated Bulb-Shaped Fluidic Dispenser Powered by Heart Muscle Cells	1414
Keisuke Morishima, Yoko Hori, Yoshitake Akiyama, Yuji Furukawa	
Tokyo University of Agriculture and Technology, JAPAN	
Dynamic Studies of Pore Forming Toxins Using a Microfluidic Cell Array	1417
Dino Di Carlo, Josephine Shaw, Luke P. Lee	
University of California, Berkeley, USA	

Genomics & Proteomics

Electric Field Induced Protein Crystallization	1420
Muhammad Imran Al-Haq ¹ , Hidenori Tsuchiya ¹ , Toru Torii ¹ , Hiroki Yamazaki ² , Etsuo Shinohara ²	
¹ The University of Tokyo, Japan, ² TechnoMedica Co., Ltd., Japan	
Micro SU-8 Chamber for PCR and Fluorescent Real-Time Detection of Salmonella Spp. DNA.....	1423
Janette L. M. Schulze ¹ , Dolores Verdoz ² , J Berganza ² , Garbié Olabarria ² , Javier Berganza ¹ , Jorge Elizalde ¹ , J M. Ruano-López ¹	
¹ IKERLAN-IK4 S.Coop., Spain, ² Gaiker-IK4, Centro Technológico, Spain	
Continuous-Flow Polymerase Chain Reaction (PCR) Device Using a Disposable Polymer Disk	1426
K. H. Chung, S. H. Park, D. S. Lee, H. B. Pyo Electronics and Telecommunications Research Institute (ETRI), Korea	
Restriction Enzyme Assay in Femtoliter Microchamber	1429
Liza Lam, Koji Ishizuka, Shouichi Sakakihara, Hiroyuki Noji Osaka University, Japan	
A Plastic Lab-On-A-Chip for HIV Diagnostics Using RT-PCR and Dynamic Detection	1432
Soohyun Lee ¹ , Chong H. Ahn ¹ , Sung-Woo Kim ² ¹ University of Cincinnati, USA, ² McLean Hospital, Harvard Medical School, U.S.A	
Characterization of mRNA Detection Device in Liquid Phase	1435
Ryuji Yokokawa ¹ , Soichiro Tamaoki ¹ , Takashi Sakamoto ² , Akira Murakami ² , Susumu Sugiyama ¹	
¹ Ritsumeikan University, Japan, ² Kyoto Institute of Technology, Japan	
Different Distribution of Lysozyme, GdnCl, and CTAB During Protein Refolding in Microfluidic Channel	1438
Toshiro Kobori, Toshio Ohtani, Yukio Magariyama National Agricultural and Food Research Organization, Japan	
Homogenous DNA Melting Analysis for Mutation Scanning Using Nanoliter Volumes	1441
Scott O. Sundberg, Jenny Greer, Carl T. Wittwer, Robert J. Pryor, Oluwole Elenitoba-Johnson, Bruce K. Gale University of Utah, USA	
Integrated PCR and Thermal Melt Analysis on a Microfluidic Chip	1444
Deborah J. Boles ¹ , Michele R. Stone ¹ , Esther Huang ² , Roger Dettloff ² , Aaron Rulison ² , Javier Farinas ² , Ivor T. Knight ¹	
¹ Canon U.S. Life Sciences, Inc., USA, ² Caliper Life Sciences, Inc., USA	
A Mini Automatic Protein Fractionator and Collector	1447
Zhen Wang, D Jed Harrison University of Alberta, Canada	

Microchip-Based Electrophoretic Analysis of Low Abundant Unknown Mutations Using Site-Specific Nicking and Ligation Enzymes 1450
Rondedrick Sinville¹, Shawn Llopis¹, Hanna Pincas², Francis Barany², Steven A. Soper¹

¹Louisiana State University, USA, ²Weill Medical College of Cornell University, USA

Multichannel Reverse Transcription-PCR Microdevice for Rapid Multiplex Gene Expression Analysis 1453
Nicholas M. Toriello, Chung N. Liu, Richard A. Mathies
UC Berkeley, USA

Integrated Microfluidic System for the Processing of Membrane Proteins Isolated from Stem Cells 1456

Malgorzata A. Witek¹, Guofang Chen¹, Hamed Shadpour¹, Indu Kheterpal², Darwin Prockop³, Carl A. Gregory³, Robin L. McCarley¹, Steven A. Soper¹

¹Louisiana State University, USA, ²Pennington Biomedical Research Center, USA,

³Center for Gene Therapy, Tulane University, USA

Rapid Protein Crystallization by Micro Osmotic Screening System 1459

Po-Hsiung Chan, Yu-Chuan Su

National Tsing Hua University, Taiwan

A Single Human Chromosome Manipulation and Gene Detection Via Trace Volume PCR Amplification Using Microtweezer Probe and Microchamber Array 1462

Masato Saito¹, Kazuhisa Nakagawa², Tetsuya Takekawa³, Keiichiro Yamanaka¹, Yuzuru Takamura¹, Gen Hashiguchi³, Eiichi Tamiya¹

¹Japan Advanced Institute of Science and Technology, Japan, ²Institute of Industrial Science, University of Tokyo, Japan, ³Kagawa University, Japan

Microfluidic Method for Thermal Cycling by Microwave Dielectric Heating 1465

Pierre-Alain Auroux¹, Jayna J. Shah¹, James Booth³, Mulpuri V. Rao², Michael Gaitan¹

¹National Institute for Standards and Technology, USA, ²Mason University, USA,

³National Institute for Standards and Technology, USA

Microfluidic Polymeric Integrated Selective Enrichment Target for MALDI MS Peptide Profiling 1468

Simon Ekström¹, Lars Wallman¹, Göran Helldin², Görgy Marko-Varga³, Thomas Laurell¹

¹Lund Institute of Technology, Lund University, Sweden, ²MicroPlast AB, Sweden,

³Lund University, Sweden

Cell Handling & Analysis

Encapsulation of Mouse Stem Cells in Alginate Bead by Microfluidic Chip 1471

Su Kyong Chae^{1,2}, In Hye Lee¹, Choong Kim¹, Chang Ha Lee², Ji Yoon Kang¹, Tae Song Kim¹

¹Korea Institute of Science Technology (KIST), Korea, ²Yonsei University, Korea,

³Korea University, Korea

A Cell Switching Microsystem for Single Cell Sorting Application Via Enhanced Dielectrophoresis Design	1474
Wen-Yu Chang, Cheng-Hsien Liu	
National Tsing Hua University	
High-Density Spheroid Arrays for 3-D Liver Cell Culture and Secretion Analysis	1477
Mimi Y. Zhang, Dino Di Carlo, Liz Y. Wu, Shira M. Lee, Luke P. Lee	
University of California, Berkeley, USA	
A Single-Cell Electroporation Lab Chip Via the Integration of Dielectrophoresis Manipulation and AC Electrokinetic Pump.....	1480
Pang-Chih Liu, Cheng-Hsien Liu	
National Tsing-Hua University, Taiwan	
Facile Image-Based Cell Sorting Using OPTO-FluCS (Opto-Fluidic Cell Sorting)	1483
Joseph R. Kovac, Joel Voldman	
Massachusetts Institute of Technology, USA	
Microcarrier Enabled Microfluidic Assays of Anchorage Dependant Cells	1486
Jamil El-Ali, Klavs F. Jensen	
Massachusetts Institute of Technology, USA	
Cell Synchronization Using Dielectrophoresis	1489
Unyoung Kim ¹ , Chih-Wen Shu ² , Karen Y. Dane ¹ , Jean Y. J. Wang ² , H. T. Soh ¹	
¹ University of California, Santa Barbara, USA, ² University of California, San Diego, USA	
Microfluidics for Controlled Single Cell Microinjection.....	1492
Andrea Adamo, Klavs F. Jensen	
Massachusetts Institute of Technology, USA	
96-Well Single-Cell Electroporation Arrays: Real-Time Monitoring and Feedback Control of Membrane Resealing Kinetics	1495
Michelle Khine ¹ , Lee-Ping Wang ¹ , Cristian Ionescu-Zanetti ¹ , Luke Lee ²	
¹ Fluxion Biosciences Inc., USA, ² University of California, Berkeley, USA	
High Throughput Electroporation Microchip Fabricated by Single-Mask Inclined UV Lithography.....	1498
Takaaki Suzuki ¹ , Hideo Yamamoto ¹ , Masataka Ohoka ² , Atsuhito Okonogi ³ , Hiroyuki Kabata ³ , Isaku Kanno ¹ , Masao Washizu ⁴ , Hidetoshi Kotera ¹	
¹ Kyoto University, Japan, ² Advanced Software Technology & Mechatronics Research Institute of Kyoto, Japan, ³ HMRO, Kyoto University, Japan, ⁴ The University of Tokyo	
Flow-Less Centrifugation-Free Washing and Incubation with Single-Cell Resolution.....	1501
Gianni Medoro ¹ , Antonio Fittpaldi ¹ , Alessandro Simoncelli ¹ , Luigi Altomare ² , Roberto Guerrieri ² , Nicoló Manaresi ¹	
¹ Silicon Biosystems, Italy, ² ARCES - University of Bologna, Italy	

Method for Selective Cell Lysis Based on Dielectrophoresis	1504
Gianni Medoro ¹ , Melanie Abonnenc ¹ , Antonio Fittipaldi ¹ , Alessandro Simoncelli ¹ , Aldo Romani ² , Roberto Guerrieri ² , Nicoló Manaresi ¹	
¹ Silicon Biosystems, Italy, ² ARCES - University of Bologna, Italy	
A Cell-Relevant Microgradient Environment	1507
Thomas W Frisk, Susanna Rydholm, Helene Andersson, Hjalmar Brismar, Göran Stemme	
Royal Institute of Technology, Sweden	
Microfabricated Device for Controlled Stimuli of Primary Cilia	1510
Susanna Rydholm, Thomas Frisk, Helene Andersson, Göran Stemme, Hjalmar Brismar	
Royal Institute of Technology, Sweden	
Insights into Neutrophil Polarization Mechanisms Through the Use of Microfluidic Devices	1513
Daniel Irimia, Mehmet Toner	
Harvard Medical School, Massachusetts General Hospital, USA	
Trapping & Chemical Dosing of Suspended Cells in Hydrodynamic Tweezer Arrays	1516
Barry R. Lutz, Jian Chen, Daniel T. Schwartz, Deirdre R. Meldrum	
University of Washington, USA	
Microfluidic Devices for the Assembly and Culture of Three-Dimensional Multi-Cellular Constructs with Diffusion-Limited Microenvironments	1519
Mike Pinelis ¹ , Rachel W. Kasinskas ² , Ruba T. Borno ¹ , Jaehyun Park ¹ , Eric Chu ³ , Neil S. Forbes ² , Michel M. Maharbiz ¹	
¹ University of Michigan, Ann Arbor, USA, ² University of Massachusetts, Amherst, USA, ³ Johns Hopkins University, USA	
Applications - others	
Sample Preparation for the Analysis of Gluten from Foodstuff in a Modular Chip-Platform	1522
Frithjof von Germar, Frank Doffing, Ines Frese, Rainer Gransee, Klaus S. Drese Institut für Mikrotechnik Mainz, Germany	
DNA Stretching Method Using a Flow Induced by Laser Irradiation under AC Electric Field	1525
Michihiko Nakano ¹ , Kazunori Takashima ¹ , Shinji Katsura ² , Akira Mizuno ¹	
¹ Toyohashi University of Technology, Japan, ² University of Gunma, Japan	
Metaphase Chromosome Manipulation Using Newly Developed AFM Probes.....	1528
Keiichiro Yamanaka ¹ , Tetsuya Takekawa ² , Kazuhisa Nakagawa ³ , Masato Saito ¹ , Yuzuru Takamura ¹ , Gen Hashiguchi ² , Eiichi Tamiya ¹	
¹ Japan Advanced Institute of Science and Technology, Japan, ² Kagawa University, Japan, ³ University of Tokyo, Japan	

A Novel Framework of Making PLA/PLGA Polymer Micro Needles Patch for Better Skin Piercing and Drug Release	1531
Shao-Yin Chiu, Heng-Chi Huang, Cheryl CY Chuang, Chien-Chung Fu	
National Tsing-Hua University, Taiwan	
Hydrodynamic Manipulation and Selective Immobilization of Giant Liposomes.....	1534
Kaori Kurabayashi ¹ , Bruno Le Pioufle ² , Shoji Takeuchi ¹	
¹ CIRMM-IIS, The University of Tokyo, Japan, ² LIMMS/CNRS-IIS, The University of Tokyo, Japan	
3A3 Cell Handling & Analysis 2 (Cell Culture)	
Rapid On-Chip Heterogeneous Bone-Cell Patterning Via the Enhanced Dielectrophoresis Trap for Tissue Engineering Application.....	1537
Chen-Ta Ho, Ruei-Zeng Lin, Hwan-You Chang, Cheng-Hsien Liu	
National Tsing-Hua University, Taiwan	
Microfluidic Cell-Based Assays by 3D Cell Culture in a Peptide Scaffold	1540
Minseok S. Kim, Sunki Chae, Wonhye Lee, Je-Kyun Park	
Korea Advanced Institute of Science and Technology (KAIST), Korea	
A Pneumatic Micro Cell Stimulator for the Differentiation of Human Mesenchymal Stem Cells (hMSCs)	1543
Woo-Young Sim, Sin-Wook Park, Sang-Sik Yang, Sang-Hyug Park, Byoung-Hyun Min	
Ajou University, Korea	
Session 3B3 Packaging and Interface	
Temperature, Flow and Glucose Sensors Integrated with a Spirally-Rolled Polymer Tube for Cardiovascular Monitoring.....	1546
Chunyan Li, Jungyoup Han, Pei-Ming Wu, Chong.H Ahn	
University of Cincinnati, USA	
A Fluidic Motherboard Including Fluidic and Optical Interconnections, Having Modular Functionality for Optical Anlaysis in Microfluidic Systems	1549
Gerardo Perozziello ¹ , Detlef Snakenborg ¹ , Zhiyu Zhang ² , Jörg P Kutter ¹ , Oliver Geschke ¹	
¹ Technical University of Denmark, Denmark, ² Massachusetts Institute of Technology, USA	
Directed Fluidic Self-Assembly of Microscale Tiles	1552
Michael T. Tolley, Victor Zykov, Hod Lipson, David Erickson	
Cornell University, USA	

DAY 4 - THURSDAY NOVEMBER 9, 2006

Session 4A1 Medical & Clinical

Microfluidics on a Conventional, 10-\$ CDROM Drive: All-In-One Determination of the Hematocrit	1555
Lutz Rieger ¹ , Markus Grumann ¹ , Juergen Steigert ¹ , Roland Zengerle ¹ , Jens Ducree ²	
¹ University of Freiburg-IMTEK, Germany, ² HSG-IMIT, Institute for Micromachining and Information Technology, Germany	
Calorimetric Measurement Clinical Chip for Home Medical Diagnosis.....	1558
Yasuhiro Horiike ¹ , Hiroko Koda ¹ , Chia-Hsien Chang ¹ , Ryo Ogawa ¹ , Shingi Hashioka ¹ , Masao Nagai ² , Hiroki Ogawa ²	
¹ National Institute for Materials Science, Japan, ² Adbic Incorporation, Japan	

A Microfluidic Device for Practical Label-Free CD4+ T Cell Counting of HIV-Infected Subjects.....	1561
Xuanhong Cheng ¹ , Daniel Irimia ¹ , Meredith Dixon ² , Kazuhiko Sekine ¹ , Utkan Demirci ¹ , Lee Zamir ² , Ronald Tompkins ¹ , William Rodriguez ² , Mehmet Tomer ¹	
¹ Mass. General Hospital, Harvard Medical School, and Shriners Hospital for Children, USA, ² Mass. General Hospital, Harvard Medical School, and Brigham and Women's Hospital, USA	

Session 4B1 System Technology

High Throughput Microfluidics	1564
Ivar Meyvantsson, Jay Warrick, David J. Beebe	
University of Wisconsin - Madison, USA	
Microfabricated Bioprocessor for Nanoliter-Scale Sanger DNA Sequencing	1567
Robert G. Blazej, Palani Kumaresan, Richard A. Mathies	
University of California, Berkeley, USA	

Integrated Microfluidic System for Proteomics Using Mixed-Scale Structures and MALDI-TOF-MS.....	1570
Harrison K. Musyimi, Hamed Shadpour, Goufang Chen, Kermit K. Murray, Steven A. Soper	
Louisiana State University, USA	

Session 4A2 Proteomics

Microfluidic Platform for Liquid Chromatography - Tandem Mass Spectrometry (LC-MS/MS)	1573
Jason Shih ¹ , Yunan Miao ² , Terry D. Lee ² , Yu-Chong Tai ¹	
¹ California Institute of Technology, USA, ² Beckman Research Institute, USA	
Microfluidic Device for High-Throughput Immunofluorescent Staining of Signaling Proteins in Attachment-Dependent Cells	1576
Chiaochun Joanne Wang, Raymond Cheong, Andre Levchenko	
The Johns Hopkins School of Medicine, USA	

Automated Two Dimensional Microfluidic Protein Profiling Combining IEF and SDS Gel Electrophoresis	1579
Jesse Buch ¹ , Shuang Yang ² , Chia-Wen Tsao ² , Ponniah Sivanesan ¹ , Koustubh Phalnikar ¹ , Tao Song ¹ , Cheng S. Lee ² , Don L. DeVoe ²	
¹ Calibrant Biosystems Inc., USA, ² University of Maryland, USA	

Session 4B2 Detection Technology

Sensitive Chiral Analysis Method for Microchip by Circular Dichroism Thermal Lens Microscope (UV-CD-TLM)	1582
Kazuma Mawatari ¹ , Shun Kubota ² , Takehiko Kitamori ^{1,2}	

¹Kanagawa Academy of Science and Technology, Japan, ² The University of Tokyo, Japan

Single-Nucleotide Polymorphism Detection with Thin Membrane Transducer	1585
Misun Cha, Ilchaek Kim, Junbo Choi, Junghoon Lee	
Seoul National University	

Measurement and Modeling of DNA Motion in Microchannel Including Frequency Dependent Electrophoresis and Electro-Osmotic Flow	1588
Momoko Kumemura ¹ , Christophe Yamahata ¹ , Naoyoshi Sakaki ¹ , Gen Hashiguchi ² , Dominique Collard ³ , Hiroyuki Fujita ¹	

¹Institute of Industrial Science, The University of Tokyo, Japan, ²Kagawa University, Japan, ³LIMMS-CNRS/IIS, The University of Tokyo, Japan

PLENARY LECTURE 7

A Human Protein Atlas Based on Normal and Cancer Tissue Profiles	1591
Mathias Uhlen	
KTH, Stockholm, Sweden	

Sub-Diffraction Limit Imaging of Single Molecules and Single Cells

Edward S. Yeung*, Yan He, Hungwing Li, Seong Ho Kang,
Dragan Isailovic, Jinjian Zheng

Ames Laboratory-USDOE and Department of Chemistry,
Iowa State University, Ames, IA 50011, USA, yeung@ameslab.gov

As micro-TAS transitions to the nanoscale, new measurement approaches will need to be developed. We will discuss applications of two different types of microscopies to imaging single molecules and single cells at or below 100 nm. The depth of penetration of the evanescent field at a liquid/solid interface depends on the incidence angle. The vertical resolution can be around 1/10 the wavelength of light while maintaining the horizontal (planar) resolution to the wavelength of light. In differential interference contrast microscopy (DIC), objects as small as microtubules (25 nm diameter) have been recorded. The vertical resolution remains at the wavelength of light.

Evanescence Field Fluorescence Microscopy. A variable-angle total internal-reflection fluorescence microscope (VATIRFM) capable of providing a large range of incident angles was constructed for imaging single DNA molecule dynamics at a solid/liquid interface. An algorithm using a public-domain image processing program, ImageJ, was developed for single-molecule counting. The experimental counts at various incident angles with different evanescent field layer (EFL) thickness are affected by molecular diffusion. The dynamics of molecules near the surface and the observed counts in VATIRFM are elucidated using a limited one-dimensional random walk diffusion model. The simulation fits well with the experimental counting results. Further analysis using the simulation reveals the details of single-molecule motion. One implication is that the measured intensities cannot be used directly to determine the distances of molecules from the surface, though the majority of fluorescence does come from the EFL. Another implication is that rather than providing molecular concentrations within EFL, the experimental counting results depict the distance-dependent dynamics of molecules near the surface. Thus VATIRFM could be a powerful technique to study the surface repulsion/attraction of molecules within a few hundred nanometers of the surface. Further studies show that molecules at low ionic strengths experience electrostatic repulsion at distances much further away from the surface than the calculated thickness of the electrical double layer (Figure 1).

To generate a large range of $\Delta\theta$, initially we adapted a beam steering design that consisted of a rotatable mirror, two parallel achromatic convex lenses, and a SF11 half-cylindrical prism, where the available $\Delta\theta$ range is determined by the F/# of the lens adjacent to the prism. For our purpose, a 12.7 mm diameter lens with F/# = 1.5 was used to achieve $\Delta\theta = 24^\circ$. However, the strong focusing effect of the lens caused unwanted angular dispersion of the laser beam and thus uncertainty in d within the

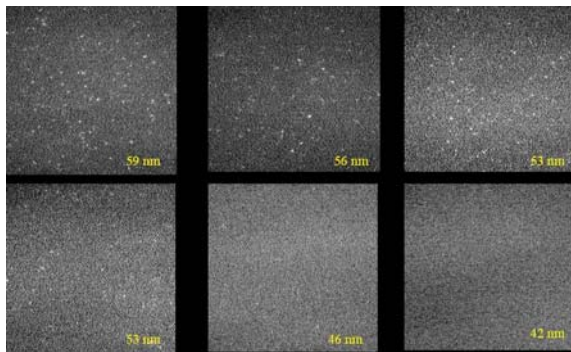


Figure 1. Variable-angle evanescent field microscopy. Single DNA molecules can be observed beyond 50 nm but not nearer the fused-silica surface because of charge repulsion from dissociated silanol groups.

probe area. Furthermore, it was very difficult to direct the laser beam to the same spot on the prism surface due to imperfection of curved optical surfaces. In comparison, all optical surfaces in the present setup are flat except for a long focal length convex lens to reduce the size of the laser spot to become smaller than the viewing area of the CCD. Thus, the angular dispersion is minimized and the optical alignment also becomes much easier. The $\Delta\theta$ range is determined by the maximum separation distance between the objective and the microscope stage and the minimum distance between the TIR prism and the vertical light path above the galvanometer. Currently, we achieve a range of 27°, the largest among all the VA-TIRFM instruments reported.

Sub-diffraction Limit 3-D Imaging by DIC. Real-time monitoring of the motion of individual λ -DNA in a PDMS/glass microchip is shown in Figure 2. The image of individual λ -DNA molecules appear sharp and distinct in DIC microscopy. Since the molecules are moving relative to the camera during exposure, the trajectories show up as streaks in the image. The trajectory of native λ -DNA molecules resemble an earthworm at an exposure time of 300 ms. Intercalator dyes affected the physical properties and dynamic behavior of DNA molecules. From the migration velocities in the microchannel it is evident that native DNA molecules migrated faster than DNA molecules labeled with YOYO-1. This is because YOYO-1 increases the molecular weight and size of λ -DNA and decreases the charge. This study underscores the superior x-y resolution of DIC and its ability to image even non-fluorescent species.

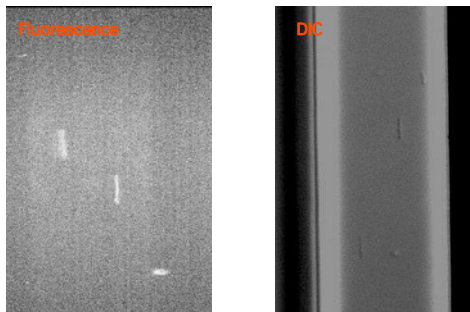
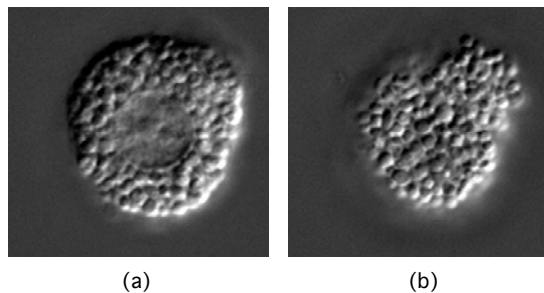


Figure 2. Images of YOYO- λ DNA molecules by fluorescence (left) and by DIC (right) at a PDMS/glass microchannel. Electric field, 10.2 V/cm; CCD exposure time, 300 ms; run buffer, 10 mM Gly-Gly (pH 8.2 with 0.1 M NaOH), DNA concentration, 20 pM.

Another major advantage of DIC microscopy is that it makes full use of the numerical aperture of the system and permits focusing in a thin plane section of a thick specimen, with reduced contributions from the specimen regions above or below the plane of focus. Therefore, DIC microscopy provides superior vertical resolution to phase-contrast microscopy and when coupled with other equipment, allows optical sectioning. Additionally, DIC has an advantage over standard phase-contrast microscopy in that the “halo” edge effect is absent. We coupled DIC with a motorized vertical stage so that we could track the dynamics of individual submicron granules inside a mast cell temporally and spatially. We were able to show that exocytosis is enhanced from the part of the cell membrane in contact with concanavalin A. Figure 3 shows that the top and the bottom layers of sub-micron granules in a 10- μm cell can be imaged without interference from the intermediate layers. The estimated vertical resolution is 0.5 μm .



(a)

(b)

Figure 3. An upright Nikon Eclipse 80i microscope equipped with a 100 \times objective and DIC slider was used. A motorized rotary stage (Sigma Koki) was coupled to the fine adjustment knob on the microscope. Travel for each frame is 0.5 μm . Light was from a 12V 100W halogen lamp. The CCD (Cool SNAP ES, Photometrics, pixel size = 6.4 μm) exposure time was 50 ms at 20 MHz digitization.

SINGLE PROTEIN MOLECULE ANALYSIS IN SINGLE CELLS IN A MICROFLUIDIC CHIP

Jonas Jarvius^{1,§}, Jonas Melin^{1,3}, Henrik Johansson¹, Malin Jarvius¹, Yuki Tanaka^{1,2}, Jenny Göransson¹, Mats Gullberg¹, Ola Söderberg¹, Mats Nilsson¹, Ulf Landegren¹

¹ Dept. of Genetics & Pathology, Uppsala University, Sweden

² Japan Society for the Promotion of Science, Tokyo, Japan

³ Dept. Engineering Sciences, Uppsala University, Sweden

[§]To whom correspondence should be addressed.

E-mail: mats.nilsson@genpat.uu.se

Abstract

Our group has developed a family of DNA ligation-based detection tools that allow for interrogation of complex biological samples, extending down to even individual molecules. In this contribution we report the recent progress of the in single-cell and single-molecule analysis projects carried out in microfluidic platforms.

Keywords: Single-molecule detection, padlock probes, proximity ligation, rolling-circle amplification

1. Introduction

We have developed highly selective molecular probing mechanisms for nucleic acid and protein targets based on ligation of oligonucleotides. Both these probing techniques allow for rolling-circle amplification, converting the nanometer-scale molecular recognition events to brightly fluorescent micrometer-sized DNA molecules suitable for optical detection.

Padlock probes

Linear synthetic oligonucleotide probes are designed so that their 5' and 3' ends hybridize in juxtaposition on target DNA [1] [2] or RNA [3] strands, positioning them for enzymatic joining by a DNA ligase, which creates unique amplifiable circular reporter molecules. Padlock probes are particularly useful tools for genetic analysis, since in contrast to PCR they can be combined in large numbers in single reactions without cross-reactivity problems [4] [5].

Proximity ligation

The probe ligation mechanism is not limited to the detection of nucleic acid sequences. In the proximity probe ligation technique, amplifiable DNA reporter molecules are created by an analogous mechanism resulting from dual recognition of protein molecules by specific

affinity probes equipped with oligonucleotide tails [6][7]. Thereby, amplifiable information-carrying DNA strands can be generated that serve as surrogate markers for any molecular targets bound by two such affinity reagents. Since it is possible to control which pairs of detection reagents that can be joined by ligation, the assay is suitable for multiplex protein detection, avoiding risks of cross reactivity.

Rolling-circle amplification

Both padlock and proximity probing mechanisms can be designed to result in the formation of circular DNA reporter molecules that include sequence motifs suitable for identification of the recognized target molecules. During rolling-circle amplification (RCA) each circular DNA molecule is copied by a DNA polymerase, generating a large DNA macromolecule of reverse polarity, concatenated about 1,000 times. A fundamental characteristic of RCA is that amplification products are confined in individual continuous random-coil DNA molecules that constitutes a spontaneously created compartment. The discrete nature of the molecular population is therefore preserved, enabling digital analysis. This is in contrast to PCR where numerous short and physically unlinked copies of the amplified region are created.

2. Experimental and discussion

Proximity ligation in situ

Proximity ligation followed by RCA can be used for localized *in situ* detection of individual target proteins or interacting sets of proteins (Fig 1) (Söderberg et al. *Nat.Methods*, in press). The microfluidic format offers the possibility to create laminar flow and thereby subject different fractions of cells on the chip surface to distinct treatments.

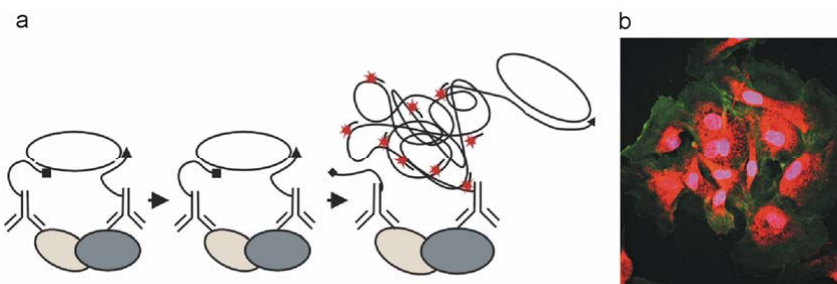


Figure 1. **a)** Schematic picture of the proximity ligation *in situ* assay. **b)** c-Myc/Max staining of the human endothelial cell line using proximity ligation *in situ* performed in microchip. The c-Myc/Max interactions (red dots, Alexa 555), nuclei (blue, DAPI) and actin filaments (green, FITC).

Amplified single-molecule detection in solution.

Rolling-circle amplification products (RCPs) derived from padlock or proximity probing can be detected in a homogenous format with no requirement for washes. The fluorophore density within a RCP corresponds to a concentration approximately 100 times higher than the surrounding solution. The signal to noise ratio is sufficient for direct observation of individual RCPs without removal of free fluorophores [8] (figure 2a). When observed by fluorescence microscopy the RCPs are visible as bright objects with a diameter of approximately 1 μm . This enables counting of individual RCPs by recording the fluorescence intensity when the solution is pumped through a microchannel [9]. The raw data files are thresholded to generate a binary output file in which each identified object corresponds to a detected target molecule (figure 2b).

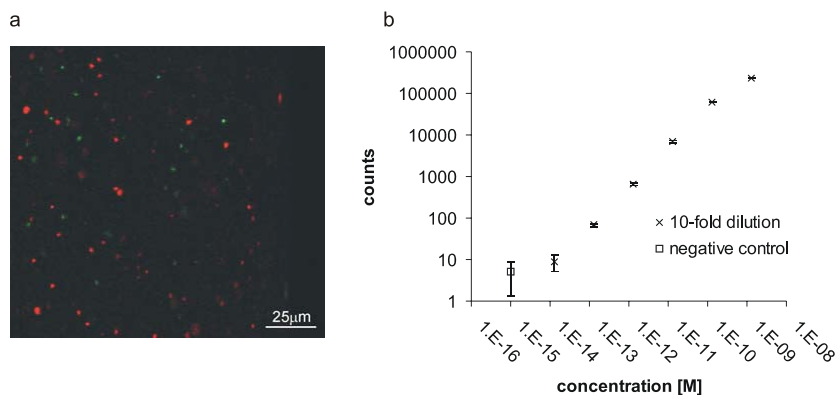


Figure 2. **a)** Direct observation of individual RCPs by fluorescence microscopy. **b)** Detection of *Vibrio cholerae* DNA. A serial dilution series of bacterial DNA was analyzed. The lowest concentration in the dilution series corresponds to DNA from 8 bacterial genomes.

References

1. Nilsson, M., et al., *Science*, 1994. 265(5181): p. 2085-8.
2. Nilsson, M., et al., *Nat. Genet.*, 1997. 16(3): p. 252-5.
3. Nilsson, M., et al., *Nat. Biotechnol.*, 2000. 18(7): p. 791-3.
4. Baner, J., et al., *Nucleic Acids Res.*, 2003. 31(17): p. e103.
5. Hardenbol, P., et al., *Nat. Biotechnol.*, 2003. 21(6): p. 673-8.
6. Fredriksson, S., et al., *Nat. Biotechnol.*, 2002. 20(5): p. 473-7.
7. Gullberg, M., et al., *Proc. Natl. Acad. Sci. U.S.A.*, 2004. 101(22): p. 8420-4.
8. Blab, G.A., T. Schmidt, and M. Nilsson, *Anal. Chem.*, 2004. 76: p. 495-498.
9. Jarvius, J., et al., *Nat. Methods*, 2006. 3(9).

SINGLE CELL TRANSCRIPTOME ANALYSIS USING A PDMS MICROCHIP

N.Bontoux¹, L. Dauphinot², T. Vitalis², V. Studer², Y. Chen¹, J. Rossier², M-C. Potier²

¹LPN-CNRS, Route de Nozay, Marcoussis, 91460 France

²Laboratoire de Neurobiologie et Diversité Cellulaire, ESPCI, 10 rue Vauquelin, Paris, 75005 France

Abstract

Whole transcriptome analysis can now be performed using DNA chips and recently developed amplification methods [1, 2]. In this paper, we demonstrate that all the steps of these protocols, i.e. cell lysis, DNase digestion of genomic DNA, reverse transcription and PCR amplification, can be performed either at the single-cell-scale or on a single cell using PDMS devices. Integrating all these microfluidic units into a lab-on-a-chip would certainly help improve the sensitivity of current analyses and provide a very efficient diagnosis tool.

Keywords : single cell, gene expression, lab-on-a-chip, PDMS, RT-PCR

1. Introduction

The recent development of global amplification protocols and DNA microarrays, as well as the human genome sequencing, have enabled whole transcriptome analysis of single cells, i.e. analysis of all the genes that are expressed by a cell at a given time and under given physiological or pathological conditions. Such studies will tremendously help understand differentiation mechanisms and characterize cellular heterogeneity [2]. They are also of significant interest for diagnosis and could prove a very efficient tool to identify new therapeutic targets [3]. Yet current methodologies do not seem adapted to single cells. The 10pg of total RNA contained initially in the picoliter-volume of a single cell are currently analyzed in several μL . Chances are that this does greatly limit efficiency of reactions as well as sensitivity of detection.

In our previous work [4], we demonstrated that reverse-transcription (RT) at the single-cell-scale (i.e. starting with 10pg of total RNA) was most efficient when performed in a 7nL PDMS rotary mixer rather than in tube. More specifically, we showed that all size mRNA, from 100bp to 6kb, were reverse-transcribed in the microfluidic device whereas only transcripts less than 700bp in size were reverse-transcribed and amplified in tube. In this paper, we show that all the other steps of global amplification protocols can be performed in PDMS microfluidic units. Cell capture, DNase treatment of genomic DNA and PCR amplification have been demonstrated.

2. Material and methods

All our microfluidic units embodied a rotary mixer [5] made out of PDMS using multi-layer soft-lithography [6]. Fluidic channels were 100 μm wide, 15 μm high and had a

parabolic cross-section. Control channels were $15\mu\text{m}$ high. The microchip for PCR was made of 3 layers of PDMS (figure 1(A)). The 2 top layers (A and B) form a rotary mixer. The bottom layer (C) is a hydration channel, used to prevent evaporation in the mixer during PCR.

All valves were pressure actuated and temperature was controlled using a flat-bed thermocycler. Experiments were performed using Lambda-phage DNA. No-enzyme control experiments were performed on-chip to evaluate the efficiency of PCR or DNase treatment: without the enzyme, DNA cannot be amplified or respectively digested.

3. Results and discussion

The amplification of a 6kb-long DNA fragment was investigated in our microfluidic unit for PCR (figure 1 (A)). The starting amount of DNA was 0.16pg. This quantity is comparable to the amount of cDNA that can be reverse-transcribed from a single cell mRNA content. Figure 1(B) shows that the off-chip quantitative PCR signal obtained after on-chip amplification is more intense than in the control experiment, where DNA is not amplified. This demonstrates that PCR is efficient in our microfluidic unit. Since on-chip amplification of a short (200-bp) DNA fragment has also been achieved (data not shown), we may conclude that all-size cDNAs, ranging from 100bp to 6kb, can be amplified in our PDMS device for PCR.

A microfluidic unit for digestion of genomic DNA prior to RT-PCR has also been developed. 10pg of DNA, which is about 10 times the genomic DNA content of a single cell, was treated on-chip. DNase treatment efficiency was measured after amplification of a 6kb-long DNA fragment. Figure 2 shows that DNA was selectively digested on-chip: after DNase treatment, no DNA could be amplified since no DNA was left (lane 3); DNA was not digested in the control experiment (lane 4). This unit could prove very useful for on-chip gene expression analysis; it will help eliminate amplification bias due to genomic DNA.

We also successfully injected cells in suspension and were able to trap one single cell in a cross-shaped microfluidic device (figure 3). Lysis is currently under investigation.

4. Conclusion

Several microfluidic units were presented, each corresponding to a specific step of global amplification protocols [1, 2]. We had previously reported that all size mRNA could be reverse-transcribed in a microfluidic PDMS device [4]. We now report PCR amplification of short and long DNA fragments in a PDMS microchip. These are indeed key steps for whole transcriptome analysis at the single cell level since all-size mRNA (from 100bp to 6kb) cannot be reverse-transcribed and amplified in tube for such small quantities.

We are currently working on the integration of all these units into a single microfluidic device. These new highly integrated microchips dedicated to the transcriptome analysis of single cells should prove very useful in many fields of biology where cell heterogeneity is a key paradigm, and also in diagnosis.

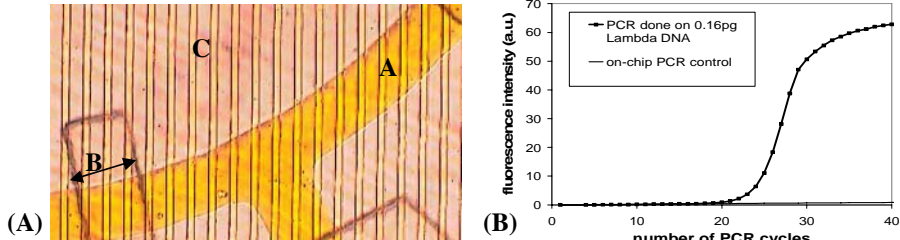


Figure 1 (A) Picture of our 3-layers PDMS device for PCR amplification.
 (B) Measure of PCR efficiency in our PDMS device using qPCR.

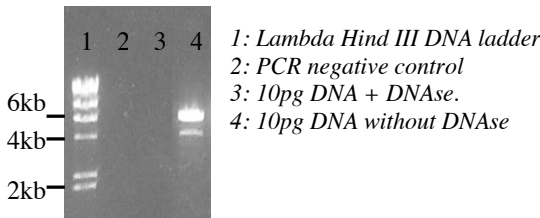


Figure 2: Measure of DNase efficiency in our PDMS device. Agarose gel (0.8%) electrophoresis of PCR products after 25 cycles of amplification. Starting quantity was 10pg of lambda DNA.

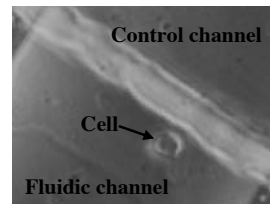


Figure 3: Neuronal cell in a 100 μ m wide and 15 μ m high PDMS fluidic channel

References

- [1] L. Petalidis *et al.*, *Nucleic Acids Research* **31** (2003)
- [2] C. Dulac *et al.*, *Cell* **83** (1995)
- [3] C.A. Klein *et al.*, *Nature Biotechnology* **20** (2002)
- [4] N. Bontoux *et al.*: In *Proceedings of Micro Total Analysis System* (2005)
- [5] H.P. Chou *et al.*, *Biomedical Microdevices* **3** (2001)
- [6] M.A. Unger *et al.*, *Science* **288** (2000)

GENOTYPING OF SINGLE DNA MOLECULES IN SINGLE CELLS IN MICROFLUIDIC CHIPS

Yuki Tanaka^{1,2}, Henrik Johansson², Chatarina Larsson², Jonas Jarvius², Jonas Melin², Takehiko Kitamori³, Ulf Landegren² and Mats Nilsson²

¹Japan Society for the Promotion of Science, Japan

²Dept. of Genetics & Pathology, Uppsala University, Sweden

³Graduate School of Engineering, The University of Tokyo, Japan

Abstract

This paper reports single DNA molecule analysis in single cells using a microfluidic platform. Single-nucleotide polymorphisms (SNPs) in individual mitochondrial DNA molecules were analyzed using padlock probes, made visible by rolling-circle amplification of the circularized padlock probes [1]. By combining microfluidics with padlock probes, individual cells can be manipulated and investigated with single-molecule sensitivity. The microfluidic format also gives us the possibility to subject a fraction of the cells on the device to specific treatment and to observe the response.

Keywords: Single cell study, SNPs, mitochondria, padlock probes

1. Introduction

Mitochondria are important organelles involved in many fundamental cellular maintenance processes and have been implicated in processes like aging, diabetes and neurodegeneration. The effects of mitochondrial mutations remain unclear, and an important question is how mutations influence mitochondrial phenotypes such as mobility and maintenance. Padlock probes, the oligonucleotide probes with one target-complementary sequence at each end allow analysis of single-nucleotide variation directly in genomic DNA molecules. In this research, we applied microfluidics to investigate genotype-phenotype correlations in mitochondrial biology.

2. Materials and Methods

The microfluidic device was made of thermoplastics by injection molding and bonded with a PDMS lid [2]. This microfluidic platform is suitable for mass production and has valuable features such as biocompatibility, optical transparency over a wide range, as well as low-cost and disposability. The microchip used for cell experiments is shown in Figure 1. By applying precise control of the laminar flow we can achieve multilayer flow for selective exposure of cells to reagents.

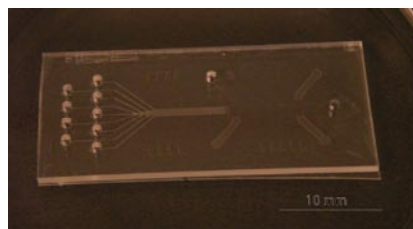


Figure 1. Microchip for cell culture and single molecule analysis.

To make visible the selective treatment of cells, we cultured homoplasmic cell line M50 in this microchip for 2 days. Then laminar flow was formed with Cell culture medium and genotoxic anticancer agent mitomycin C supplemented medium from the inlets at the left. After 2 hours of exposure, mitochondrial DNA molecules were detected with padlock probes and RCA (Figure 2). Damaged mitochondria DNA were not detected (Figure 3). Cell culture and the formation of laminar flow have been shown successfully.

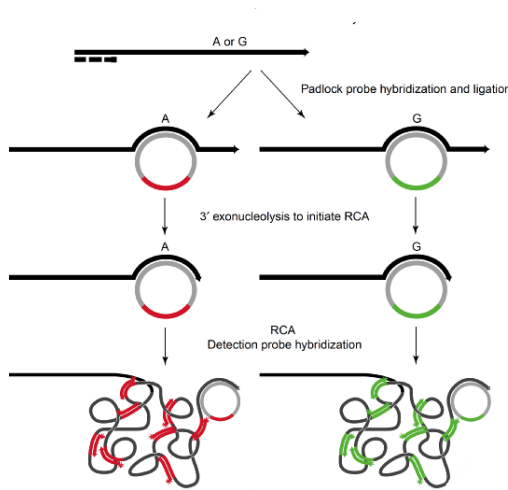


Figure 2. *In situ* genotyping of individual DNA molecules using padlock probes and RCA.
The single nucleotide mutation at the base pair 3243 (A to G) of the mitochondrial DNA is detected with these probes.

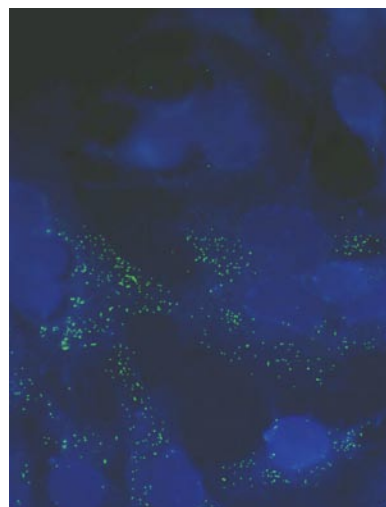


Figure 3. Image of cells after 2 hours partial (upper half) exposure to mytomycin C using laminar flow in microfluidic chip. Cell nuclei are shown in bright spots and normal mitochondrial DNA shown in small dots by padlock probes and RCA.

3. Results and Discussions

We have demonstrated the use of padlock probes for single nucleotide genotyping of individual mitochondrial DNA molecules [3] in the microfluidic format, by applying target-primed RCA of *in situ*-circularized padlock probes (Figure 2). This method can be applied to study sequence variation in the mitochondrial genome, enabling analysis of the distribution of mitochondrial genomes within cells. Figure 4 shows the results of mitochondrial genotyping of the heteroplasmic cell line G55.1.1, having two genotypes of mitochondria that differed in one base pair (A3243G point mutation) in microfluidic chip. Individual mitochondrial DNA molecules are visualized as discrete fluorescence-

labeled rolling-circle amplification products (seen as bright dots) and their genotype could be determined from the color; with mutant and wild-type probes reporting in green and red fluorescence, respectively. We succeeded *in situ* genotyping of mitochondrial DNA mutation in microfluidic device by optimizing surface modification and shear flow conditions.

4. Conclusions

In conclusion, we succeeded *in situ* genotyping of mitochondrial DNA mutation in microfluidic device by optimizing surface modification and shear flow conditions. This would be a first milestone for further development of a system for single-cell manipulation and analysis that can be combined with other molecular probing strategies and be applied for fundamental cell biology investigation in, e.g. cancer research.

Acknowledgments

This research was supported by a grant of Strategic Japanese-Swedish Cooperative Program on “Multidisciplinary BIO”.

References

- [1] Nilsson et al. (1994) *Science*, 265, 2085; Nilsson et al. (1997) *Nat. Genet.*, 16, 252; Nilsson et al. (2000) *Nat. Biotech.*, 18, 791; Hardenbol et al. (2003) *Nat. Biotech.*, 21, 673; Banér et al. (1998) *Nucleic Acids Res.*, 26, 5073; Dahl et al. (2004) *PNAS*, 101, 4548
- [2] Melin, J., Johansson, H., Söderberg, O., Nikolajeff, F., Landegren, U., Nilsson, M. & Jarvius, J., Thermoplastic Microfluidic Platform for Single-Molecule Detection, Cell Culture, and Actuation., *Anal. Chem.* 77, 7122-7130 (2005).
- [3] Larsson, C., Koch, J., Nygren, A., Janssen, G., Raap, A.K., Landegren, U. & Nilsson, M., In situ genotyping individual DNA molecules by target-primed rolling-circle amplification of padlock probes., *Nat. Meth.* 1, 227-232 (2004).

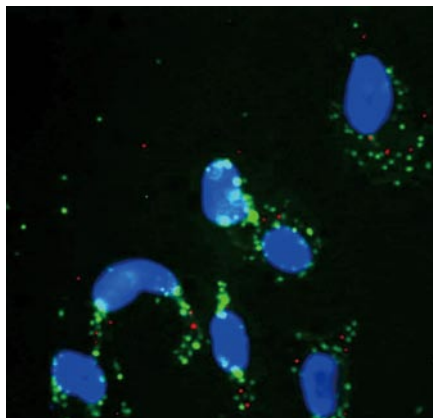


Figure 4. Image of *in situ* genotyping of the mitochondrial A3243G point mutation in microfluidic chip. Signals from the mutant mitochondrial DNA and the wild type DNA shown in dots with different colors (green and red, respectively) and the DAPI-stained cell nuclei are shown in bright spots.

NANO-ACOUSTIC INTERACTIONS GOVERNING HIGH ASPECT RATIO NANOCHEMEL FEMTOSECOND LASER MACHINING

Sanghyun Lee*, E. F. Hasselbrink*, Alan J. Hunt**

* Mechanical engineering, University of Michigan, Ann Arbor, U.S.A.

** Biomedical engineering, University of Michigan, Ann Arbor, U.S.A.

Abstract

Acoustic phenomena during nanochannel machining by *fs* laser pulses are found to have an unexpected strong influence on the machining efficiency. Analysis of acoustic nodes that strongly limit machining efficiency allows strategies to be identified for fabrication of high aspect ratio channels. Based on an analytic solution for node formation, it is found that increasing the speed of acoustic transmission can produce a two-fold increase in the length of the channels; this can be accomplished by maximizing the mole fraction of hydrogen in the gas phase. The model is further reinforced by the effects of varying pressure.

Keywords: femtosecond laser machining, high AR nanochannel, acoustic node formation

1. Introduction

Laser-induced optical ablation by *fs* (femtosecond) laser pulses constitutes a promising method for submicron scale fabrication in dielectric materials [1, 2], and has been applied to rapidly prototype surface and subsurface 3D nano features in glass using far-field nanoablation [3, 4]. For achieving a wider variety of micro/nanofluidics, high aspect ratio (**AR**=length/diameter) channel machining is required, but it is difficult to achieve because the debris extrusion becomes increasingly difficult as the machining progresses far into the material.

We find a major barrier to high **AR** channel machining arises from acoustic interactions that form pressure nodes at specific positions along the channel; this inhibits bubble and water circulation during the machining, resulting in the severe attenuation of machining.

2. Analytic model for the acoustic node formation

Fig. 1 (a) shows the first acoustic node formation, where machining is severely attenuated, resulting in termination of the primary channel. However, as the laser is scanned back and forth repetitively, a secondary channel forms visually discontinuous from the primary channel. With further scanning, the primary and secondary channels eventually unite, forming one longer channel as shown in fig. 1 (b).

The acoustic nodes form due to pressure cancellation, analogous to the nodes in standing wave, though physically distinct. When the channel is short, the two phase flow in nanochannel is unstable, but it becomes stabilized as the machining approaches

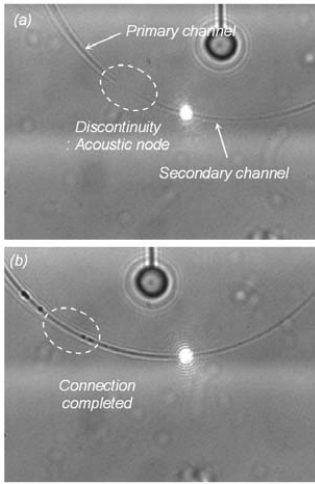


Fig.1. Acoustic node formation

decided by the speed of sound and length of the gas plug (k is specific heat ratio (c_p/c_v), R is the gas constant and T is temperature of gas plug).

When the f_n and f_{osc} are equal, the first acoustic node is formed, and the location of the first acoustic node is the total length of WGW structure ($=L_{wl}+L_g+L_{w2}$);

$$L_{node} = L_{wl} \left(1 + \frac{kRT}{16\pi^2 P_i} \right) + L_{w2} \quad (1)$$

3. Results

To solve equation (1), internal pressure and gas composition of bubble must be determined. Heat transfer analysis determines that the temperature of gas plug can be assumed as room temperature. And internal pressure was determined to be $P_i \approx P_o + 160$ [kPa] experimentally. This leaves to be determined k and R , which depend on the gas composition.

TABLE I. Gas composition of bubble by machining type

Machining type	Gas composition by mole fractions ($\alpha \leq 1$)
DWA, SWA	$\alpha(\frac{2}{3}\text{H}_2 + \frac{1}{3}\text{O}_2) + (0.99-\alpha)(0.65\text{N}_2 + 0.35\text{O}_2) + (0.01)\text{H}_2\text{O(g)}$
Cpt. DWA	$0.99(\frac{2}{3}\text{H}_2 + \frac{1}{3}\text{O}_2) + (0.01)\text{H}_2\text{O(g)}$

DWA – degassed-water-assisted; SWA – saturated-water-assisted; Cpt. DWA – completely degassed-water-assisted. Water was partially degassed by applying a vacuum and ultrasonic bath.

the first acoustic node; a large gas plug is formed in the middle of the channel while the inlet and terminal end of the channel are filled with water plugs.

When the resonant frequency of the stabilized WGW (Water-Gas-Water) structure matches the acoustic resonant frequency of the gas plug, energy delivered to the ablation site is readily transferred through the WGW structure, effectively canceling out bubble expansion at the ablation site, and attenuating fluid circulation.

As shown in fig. 2, the gas plug acts as a spring, and the water plug at the inlet port as a mass; the mass (m) and equivalent spring constant (k_s) decide resonance frequency f_n (m is equivalent mass of 1st water plug, P_i is internal pressure of gas plug, L_g and L_{wl} are the length of gas and 1st water plug). The pressure oscillation f_{osc} in the gas plug is

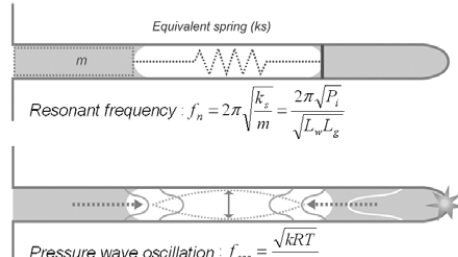


Fig.2. Model for the first acoustic node

As shown in Table I, three possible sources were considered for the gas composition of the bubble: 1) the dissociation of water molecules into hydrogen and oxygen, 2) dissolved gases in water such as nitrogen and oxygen, and 3) water vapor which is calculated at less than 1%. Fig. 3 shows trend of the first acoustic node formation follows the predictions of the analytic model well, when the pressure and gas composition are changed (custom built pressure controller is used for pressure control and degassing of water changes gas composition). Error bars on analytic solutions reflect observed variation of the WGW structure.

Two times the distance to the first node is suggested as a practical maximum of machining, after which the machining speed becomes very slow. Based on the analytic model and experimental verification, specific parameters such as mole fraction of hydrogen and pressure of the bubble are shown to be useful parameters for inhibiting first acoustic node formation.

4. Conclusion

We have characterized a strong, previously unrecognized, role of acoustic nodes during *fs* laser nanomachining. Experimental and theoretical description of these effects has allowed us to identify methods for machining high *AR* channels, which are critical for developing complex lab-on-a-chip and micro-total analysis devices. Understanding the role of acoustic nodes during *fs* laser nanomachining provides the basis to realize complex micro/nanofluidics with complete freedom to arbitrarily configure components in 3 dimensions.

Acknowledgements

This work was supported by a grant from IMRA corp.

References

- [1] Ajit P. Joglekar, Hsiao-hua Liu, Edgar Meyhöfer, Gerard Mourou, and Alan J. Hunt, *Proc. Nat. Acad. Sci. USA* 2004, **101**, 5856-5861.
- [2] Ajit P. Joglekar, Hsiao-hua Liu, Edgar Meyhöfer, Gerard Mourou, and Alan J. Hunt, *Appl. Phys. B-Lasers and Optics* 2003, **77**, 25-30.
- [3] K. Ke, E. F. Hasselbrink, and Alan. J. Hunt, *Anal Chem.* 2005, **77**, 5083-5088.
- [4] S. H. Lee, Kevin Ke, Alan J. Hunt and E.F.Hasselbrink, Proceedings of microTAS 2005 Conference, Vol.1, 524-526

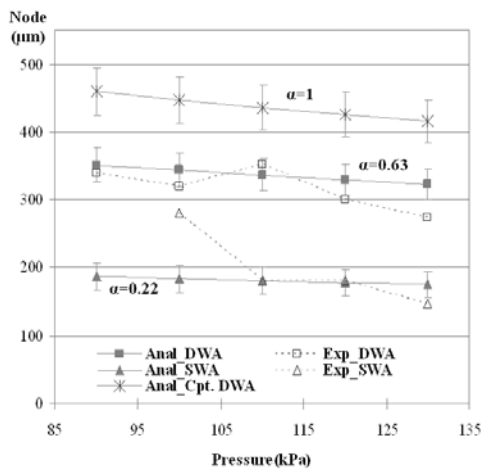


Fig.3. Acoustic node formation under different pressures and its analytic solution.

DNA NANO-STAMPING FOR MOLECULAR SURGERY

Masafumi Fuke¹, Osamu Kurosawa³, Hidehiro Oana¹ and Masao Washizu^{1, 2, *}

¹Department of Mechanical Engineering, ²Department of Bioengineering,

The University of Tokyo, 7-3-1 Hongo, Bunkyo-ku, Tokyo 113-8656 Japan

³Advance Co., 5-7 Nihonbachi-kobunecho, Chuo-ku, Tokyo 103-8354 Japan

*corresponding author: washizu@washizu.t.u-tokyo.ac.jp

Abstract

This paper reports a method to stretch and immobilize DNA onto a convex/concave micro-patterned periodical structure, where DNA strands are anchored onto the convex by adsorption, leaving the part above the concave freely suspended. The geometry allows DNA enzymes to work at the freely suspended parts, while the interaction is prevented at the adsorbed parts due to steric hindrance; hence the enzymatic activity is spatially modulated by the micropattern. An experimental demonstration is made by applying DNA-cutting enzymes to thus immobilized DNA, by which ordered DNA fragments are obtained, whose size is defined by the dimension of the structure.

keywords: DNA, DNA stretching, stamping, molecular surgery, restriction enzyme

1. Introduction

Molecular surgery here refers to the modification of a molecule with a spatial resolution provided by physical means. In [1] is demonstrated an example that, with a use of a microparticle coated with a DNA-cutting enzyme, which is laser-manipulated and made into contact with DNA, the strand can be dissected at any targeted position, with the molecular structure defined by the nature of the enzyme. It is reported that, if DNA is adsorbed onto a solid surface, the enzyme will lose its activity due to steric hindrance caused by the surface. In order to avoid such a hindrance, a special device is developed in [1] to suspend DNA strands with the termini anchored on a microstructure. However, with such geometry, the strands once dissected coil back towards anchoring points due to entropy elasticity, and no further operation can be performed.

The method presented in this paper aims at multi-point immobilization, as depicted in Fig.1. The substrate has a convex/concave structure, on which DNA strands are stretched and placed. The structure's surface is chemically modified to adsorb DNA, and cause steric hindrance to the enzymatic

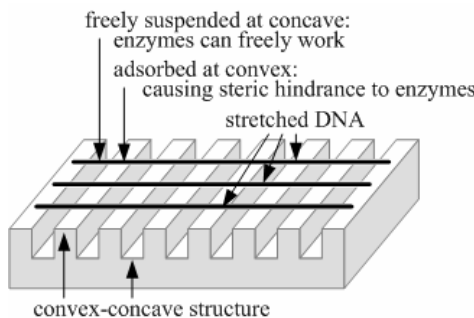


Fig.1 Immobilization of DNA onto a convex/concave micro-pattern for the modulation of enzymatic activities.

activity, so that enzymes can work only at the suspended part above the concave. With the use of the structure, the enzymatic activity is modulated by the periodicity of the micro-pattern, and if we apply a DNA-cutting enzyme to thus suspended DNA, we will have DNA fragments which are placed in order, whose size is defined by the dimension of the structure, with the clearly defined termini (e.g. cohesive ends etc.).

2. Experimental

A molding master is fabricated by a standard lithography of SU-8, and then transferred to PDMS, to fabricate the periodical convex/concave structure, with the convex width 3.0 μm , the concave width 1.5 μm and the depth 1.5 μm . Then its surface is treated with a positively charged amino-silane coupler to enhance adsorption.

For the immobilization of DNA onto the structure, we adopted the molecular stamping method originally developed by Ohtani's group [2], in combination with our electrostatic DNA stretching method [1]. Fig.2 depicts the process. DNA is first stretched and anchored between microelectrodes on a glass substrate (Fig.2 a) using the electrostatic method. The surface is etched down, in order to prevent the transfer of DNA not stretched but just adsorbed on the bottom. Then the substrate is flipped over (Fig.2 b), and "stamped" onto the PDMS structure (Fig.2 c). Then the substrate is carefully removed to leave DNA on the convex/concave structure.

3. Results and discussion

Two types of DNA-cutting enzymes are applied to thus immobilized DNA. One is DNaseI, which cuts DNA regardless of the sequence, and the other is HhaI, a 4-base cutter whose average cutting interval = $4^4 \times 0.34\text{nm/base} = 87\text{nm}$, adequately shorter than the concave width (1.5 μm) of the structure.

Fig.3 a) is a fluorescence image of immobilized DNA, where DNA strands are seen

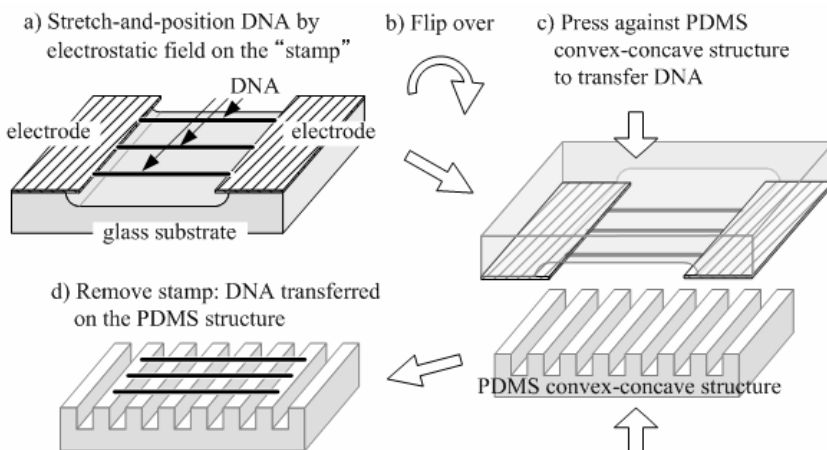


Fig. 2 DNA nano-stamping onto the convex/concave micro-pattern.

as curved horizontal lines. Fig.3 b) is just after DNaseI is fed. Instantaneous cutting of DNA occurred selectively above the concaves (indicated by arrows in the figure), which is observed as discontinuities in fluorescence at these locations. However, after a few minutes, cutting occurred even where DNA is adsorbed, so that all DNA disappeared.

Fig.4 a) and b) are before and after feeding the restriction enzyme HhaI. In this case also, the cutting occurred selectively above the concaves in a few minutes (fig.4 b). However, even after the elapse of 20 minutes, no cutting was observed on the convexes where DNA is adsorbed. The resultant length of the fragments is determined by the periodicity of the structure, and the fragments after cutting are maintained in its original order due to adsorption.

The difference between these two cases can be interpreted in terms of the strictness of fitting requirements. The restriction enzyme must go into DNA groove to recognize its restriction site, so that DNA adsorption onto a solid surface is likely to have more prominent effect on the enzyme's activity.

4. Conclusion

A method is developed to modulate enzymatic activities through steric hindrances created by a microfabricated convex/concave structure, and is experimentally demonstrated by cutting DNA into uniform-sized fragments. The multi-point DNA anchoring method should also serve for high-yield single-fiber Fluorescence *in-situ* Hybridization (FISH) by alleviating adsorption issues while firmly anchoring DNA.

Acknowledgements

This work is supported by Center for Nano Bio Integration, the University of Tokyo, and Kakenhi No.18048008 from the Ministry of Education Japan.

References

1. T. Yamamoto, O. Kurosawa, H. Kabata, N. Shimamoto and M. Washizu: "Molecular surgery of DNA based on electrostatic micromanipulation", IEEE Tran IA, Vol.36, No.4, p.1010-1017 (2000)
2. H. Nakao, M. Gad, S. Sugiyama, K. Otobe and T. Ohtani: "Transfer-Printing of Highly Aligned DNA Nanowires", J. Am. Chem. Soc., 125, 7162-7163 (2003)

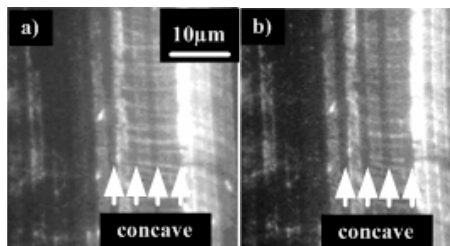


Fig.3 Cutting of DNA on the convex/concave micro-pattern using DNaseI: a) before and b) after.

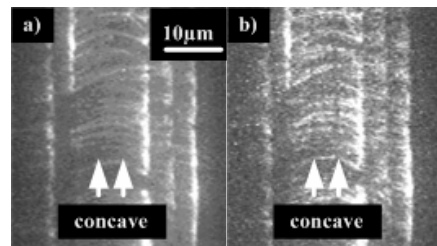


Fig.4 Cutting of DNA on the convex/concave micro-pattern using a restriction enzyme HhaI: a) before

EXPONENTIAL SIZE REDUCTION OF CHEMICAL PATTERNS USING REPETITIVE MICROCONTACT PRINTING

Kenji Suzuki, Kazuo Hosokawa and Mizuo Maeda

Bioengineering Laboratory, RIKEN, 2-1 Hirosawa, Wako, Saitama 351-0198, Japan

ABSTRACT

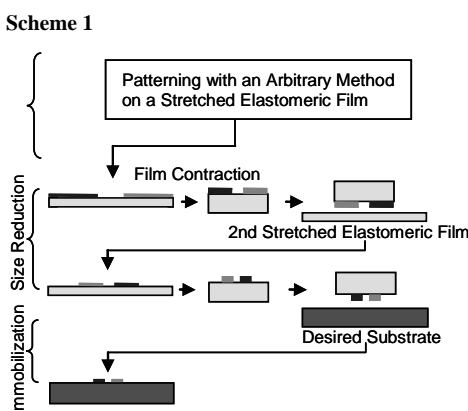
We have developed a modified version of microcontact printing for reduction in feature size of chemical patterns by exploiting contraction of stretched elastomeric films. Using the method, one can repeat size reduction of an original chemical pattern to achieve a desired reduction ratio. We carried out proof-of-concept experiments using DNA micropatterns with size reduction ratios down to ~1/20.

Key Words: PDMS, size reduction, DNA, microarray, microcontact printing

1. INTRODUCTION

Microcontact printing (μ CP) is a promising method for patterning various materials, such as self-assembled monolayers, colloidal particles, and biomolecules on an arbitrary substrate using a relief pattern on an elastomeric stamp [1]. About ten years ago, two types of modified μ CP techniques for high-throughput and cost-effective miniaturization of chemical patterns were developed by exploiting physical deformation of the stamp or the substrate [2, 3]. Xia et al. showed that μ CP with an elastomeric stamp under mechanical compression generates patterns with feature size smaller than that of original relief patterns on the stamp [2]. Hidber and co-workers reported size reduction of patterns of Pd colloid on a heat-shrinkable polymer substrate [3]. However, in these methods, the chemical patterns were shrunken only once; the size reduction was limited by the maximum contraction of the material (the elastomer or the heat-shrinkable polymer).

In this paper, we will describe a method for repetitive size reduction of chemical patterns. The basic idea is illustrated in Scheme 1. First, original chemical patterns are made on a stretched elastomeric film with an arbitrary method. Next, the patterns are shrunken by the film contraction, and are transferred to another stretched film by μ CP between the films. This cycle can be repeated any number of times without decrease in



surface density of inks, if each of the pattern shrinkage sufficiently condensed the inks. Finally, the shrunken patterns are transferred to a desired substrate. As a first demonstration, we examined size reduction of DNA micropatterns made originally by μ CP onto a stretched elastomeric film.

3. EXPERIMENTAL

Two types of 5'-amine-terminated 21-mer single stranded DNAs (ssDNAs) were used as the molecular inks. The elastomeric films were made by spin-coating of prepolymer of a silicone elastomer (SH 9555 clear base) from Dow Corning Toray Silicone (Tokyo, Japan) on silicon substrates. Fresh surfaces of the films were treated with glycerol at 110°C for 1 h and rinsed thoroughly with pure water just before use. The stamps for μ CP were made by replica molding of poly(dimethylsiloxane) (PDMS) on microfabricated silicon substrates. The stamps were inked with a solution of the ssDNA containing cetyltrimethylammonium chloride. DNA micropatterns were made on a stretched elastomeric film by μ CP with the inked stamp. After some cycles of pattern shrinkage and transfer between elastomeric films, the shrunken patterns on the final elastomeric film were transferred onto a glass slide or silicon wafer, the surface of which had been chemically activated with 3-aminopropyltriethoxysilane and glutaraldehyde in advance. The DNA patterns immobilized on the solid substrates were hybridized with fluorescently-labeled or gold nanoparticle-labeled complementary ssDNAs and then observed by fluorescence microscopy or atomic force microscopy.

4. RESULT AND DISCUSSION

As shown in Figure 1, repetition of pattern transfer without any film contraction resulted in a rapid decrease in surface density of hybridization signal in each square dot. In contrast, with the film contraction by a factor of 1.8, no significant decrease in surface density of hybridization signal was observed as shown in Figure 2(a)-(e), and (g). The stability of the hybridization signal can be explained by the increase in surface density of ssDNAs with film contraction. Through the five cycles of shrinkage-transfer, average size of the square dots were reduced from 0.21 mm to 11 μ m, and average interval of the square dots from 0.97 mm to 47 μ m. This means that the exponential size reduction was successful. Naturally, this method is compatible with multicolor patterns (see Figure 2(f)), indicating

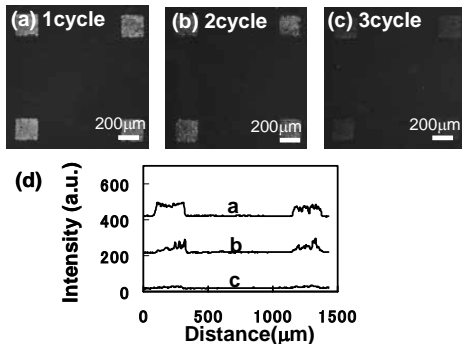


Figure 1. Fluorescence images of hybridized DNA micropatterns on glass slides after the following number of pattern transfer cycles without film contraction: (a) 1 cycle, (b) 2 cycles, and (c) 3 cycles. All observations were performed after hybridization with FITC-labeled complementary ssDNAs. (d) Intensity profiles of DNA patterns in (a) to (c).

sequence-specific hybridization of transferred ssDNAs even after the three cycles of size reduction. Figure 3 shows an example of size reduction of a striped pattern with smaller feature size. These results indicate the applicability of the method for size reduction from micrometer to submicrometer scale.

5. CONCLUSIONS

The repetitive microcontact printing for exponential size reduction of chemical patterns offers an attractive shortcut to make multicomponent submicron patterns because of the three advantages: (1) the high reduction ratio which is not limited by the maximum contraction of the deformable material, (2) wide choice of the final substrate materials, and (3) the applicability to multicolor patterns. Our results confirmed that the ink condensation with film contraction enabled the successful repetition of the microcontact printing. Further studies for other transferred molecules as well as for other formation methods of original patterns are needed to demonstrate the versatility of this method.

REFERENCES

- [1] Kumar, A.; Whitesides, G. M. *Appl. Phys. Lett.* **1993**, 63, 2002. Hidber, P. C.; Helbig, W.; Kim, E.; Whitesides, G. M. *Langmuir* **1996**, 12, 1375. Bernard, A.; Renault, J. P.; Michel, B.; Bosshard, H. R.; Delamarche, E. *Adv. Mater.* **2000**, 12, 1067.
- [2] Xia, Y.; Whiteside G. M. *Adv. Mater.* **1995**, 7, 471. Xia, Y.; Whiteside G. M. *Langmuir* **1997**, 13, 2059.
- [3] Hidber, P. C.; Nealey, P. F.; Helbig, W.; Whitesides, G. M. *Langmuir* **1996**, 12, 5209.

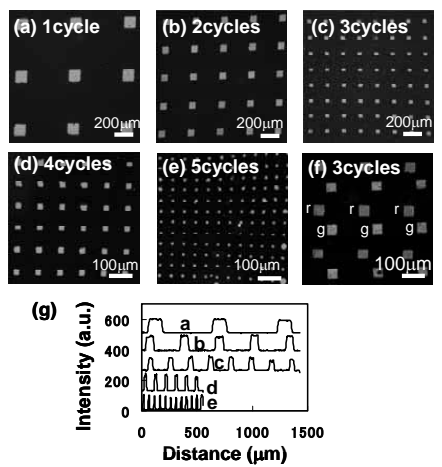


Figure 2. Fluorescence images of hybridized DNA micropatterns on glass slides after the following number of shrinkage-transfer cycles: (a) 1 cycle, (b) 2 cycles, (c) 3 cycles, (d) 4 cycles, and (e) 5 cycles. (f) multicolor DNA pattern shrunken 3 times. The inserted letters *g* and *r* indicate square dots with green (FITC) and red (Alexa fluor 594) fluorescence, respectively. (g) Intensity profiles of DNA patterns in (a) to (e).

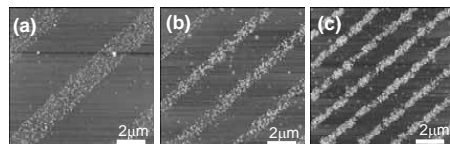


Figure 3. Atomic force microscopic images of DNA micropatterns after hybridization with gold nanoparticles modified with thiol-terminated complementary ssDNAs. DNA micropattern (a) directly printed from a stamp, (b) after a single cycle of, (c) after two cycles of size reduction.

GENE TRANSFER AND CHARACTERIZATION OF PROTEIN DYNAMICS IN STEM CELLS USING SINGLE CELL ELECTROPORATION IN A MICROFLUIDIC DEVICE

A. Valero¹, J.N. Post², J.W. van Nieuwkastele¹, W. Kruijer², H. Andersson¹ and A. van den Berg¹.

¹MESA⁺ Institute for Nanotechnology, BIOS group, University of Twente,
The Netherlands

²Molecular Cell Biology, Faculty of Science and Technology, University of
Twente, Enschede, The Netherlands
(a.valero@ewi.utwente.nl)

Abstract

We have developed a flow-through cell trapping device for the study of gene transfection by electroporation and characterization of protein dynamics in individual stem cells.

Keywords: Gene transfection, single cell manipulation, protein translocation, electroporation, stems cells.

1. Introduction

Transfer of DNA molecules into mammalian cells using electric field pulses, electroporation, is a powerful and widely used method that can be directly applied to gene therapy. Different layouts for on-chip electroporation have been reported [1-2]. These devices either address flow-through operation or single cell capture, but all lack the ability to address an individual cell from a pre-defined cell batch by microfluidic or electronic means. We have developed a flow-through chip that can immobilize, electroporate and transfect individual cells while being imaged using an inverted fluorescent microscope. With these chips we demonstrate transfection by electroporation of a green fluorescent-erk1 fusion protein and subsequent erk1 protein tracking in mouse myoblastic cells (C2C12) and in human mesenchymal stem cells (hMSCs). Our silicon-glass chip enables, to our best knowledge for the first time, the immobilization, electroporation and real-time monitoring of protein dynamics in single cells.

2. Experimental

The microfluidic cell trap device consists of two channels of asymmetric width (50µm/20µm) and details of the trapping feature are shown in figure 1b. All channels are 15µm deep, dry etched in silicon and covered by glass. To initiate the experiments, 100µl of cell sample is placed in inlet (1). Cells are transported through the channel by means of pressure driven flow. To trap single cells a negative pressure is applied to the suction reservoir (4) using a pump. Once the cells have been trapped, the pump is

switched off and cells are localized at the traps (Figure 1c). Using strategically positioned electrodes, a DNA construct encoding green fluorescent protein fused to erk1, pEGFP-erk1 was electroporated into C2C12 cells. Extracellular signal-regulated kinase, ERK1, is a protein that is important for transducing signals from the cells' environment to the cell nucleus [3]. Binding of growth factors to receptors on the cell membrane results in ERK1 activation and subsequent nuclear translocation.

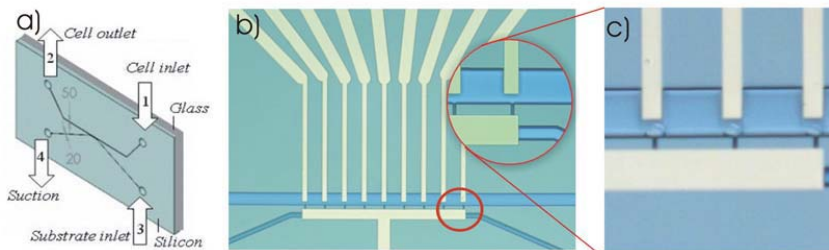


Figure 1: a) Schematic drawing of the microfluidic chip; b) image of the microfluidic chip with electrodes integrated and a zoom of the trapping sites ($4\mu\text{m}$ width) c) a close-up of a trapping feature showing three cells being trapped and awaited to be electroporated.

3. Results and discussion

Twenty-four hours after electroporation, eGFP-ERK1 expression is visible mainly in the cytoplasm of the cells. The cells were then starved by removing all growth factors from the medium, resulting in localization of eGFP-ERK1 protein to the cytoplasm.

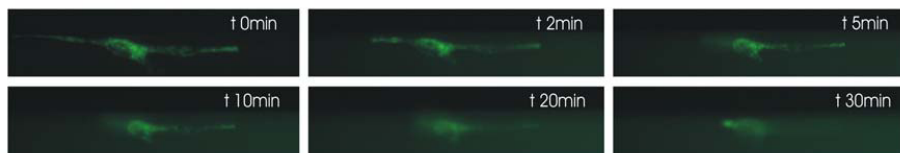


Figure 2: Nuclear translocation of eGFP-ERK after bFGF stimulation in C2C12 cells. eGFP-ERK1 is visible in cytoplasm while the nucleus remains dark (ERK1 is excluded from the nucleus, $t = 0$ min). After adding growth factors to the microfluidic chip, nuclear translocation of GFP-ERK1 is observed ($t = 2$ min to 30 min).

Forty-eight hours after electroporation, the medium was replaced for medium with serum (10%) and 10 ng ml⁻¹ bFGF to stimulate ERK phosphorylation and nuclear translocation. Addition of these growth-factors significantly increased the nuclear localization of ERK1 (Figure 2 and 3). Immediately after the addition of the growth factors, track images were taken every 5 minutes using a wide field fluorescence microscope with 488nm excitation and a 527/30 emission filter. Fluorescence intensity changes in either the cytoplasm or nucleus of the cells was determined using ImageJ software [4]. The maximum intensity of eGFP-ERK1 in the nucleus was reached 30 minutes after addition of growth factors, which corresponds with nuclear translocation in response to activation of extracellular signaling in a wide variety of cell types [3].

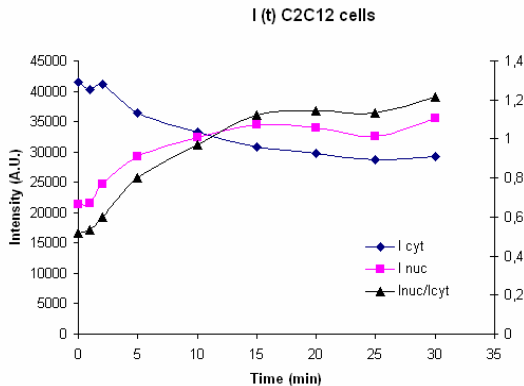


Figure 3: In the graph time courses for GFP-ERK1 translocation following growth factor stimulation of C2C12 cells are plotted: fluorescence intensity of the cytoplasm (\blacklozenge), the nucleus (\blacksquare) and the ratio between eGFP intensity in nucleus and cytoplasmic (\blacktriangle) was measured in time after adding growth factors. It can be observed that the maximum nuclear translocation was reached 30 min after addition of growth factors.

4. Conclusions

To our best knowledge, in this work for the first time the use of microfluidics devices is shown to efficiently transfer genes by single cell electroporation and protein expression in single cells. In addition, the dynamics of the introduced protein can be followed in real-time for each individual cell. The long-term survival and responsiveness of the cells to external stimuli demonstrates the bio-compatibility of the device. We are currently applying this technique for transfection of genes into adult stem cells. Because of the limited availability of adult stem cells, this method is a powerful tool for personalized gene therapy, tissue engineering and regenerative medicine.

Acknowledgements

Agrotechnology and Food Innovations, Wageningen University and Research Center as well as Technology Foundation STW are thanked for financial support of this project. Assistance in cell culturing is gratefully acknowledged to P.M. ter Braak.

References

1. M. Khine, A. Lau, C. Ionescu-Zanetti, J. Seo and L.P. Lee, A single cell electroporation chip, *Lab on a chip*, 5, pp. 38-43, (2005).
2. H. Lu, M.A. Schmidt and K.F. Jensen, A microfluidic electroporation device for cell lysis, *Lab on a chip*, 5, pp. 23-29, (2005).
3. M. J. Robinson and M. H. Cobb - Mitogen-activated protein kinase pathways; *Current Opinion in Cell Biology*, 9 (2), (1997), pp 180-186
4. <http://rsb.info.nih.gov/ij/>

SELECTIVE HIGH EFFICIENCY IN-FLOW ELECTROPORATION WITH FOCUSED ELECTRIC FIELDS IN A MICROSYSTEM

Aniruddh Sarkar¹, Ashutosh Shastry¹, Bhaskar Mitra¹, Rita Mulherkar² and Rakesh K. Lal¹

¹Department of Electrical Engineering, IIT Bombay, India

²Genetic Engineering Lab, Cancer Research Institute, TMC, Navi Mumbai, India

Abstract

We present a new technique for delivery of macromolecules into biological cells in suspension by in-flow electroporation which achieves reproducible high delivery efficiency with excellent post-electroporation viability and enables delivery to selected cell types in mixtures. We detect cells via impedance change as they flow through a microfabricated *sense-porate aperture* and then electroporate them by creating a transient zone of focused high electric field by applying a low voltage pulse. We describe here the device principle and demonstrate the delivery of FITC-labelled 150kD Dextran molecules to large numbers of cells of a human squamous cell carcinoma line with very delivery efficiency (~98%) and very low cell mortality (~1%).

Keywords: Electroporation, Targeted delivery, High Efficiency, High Viability

1. Introduction

Electroporation is a method for delivering cell membrane impermeant charged or polar molecules such as DNA, RNA, proteins and drugs to cells by transiently breaching their membranes using high electric fields. In conventional ‘plates-in-vial’ electroporators, this usually needs high voltages (~kVs) and yields poor and irreproducible delivery efficiencies (~50-60%) and poor cell viabilities (~30-40%) due to excessive heating and lack of control on the field experienced by individual cells [1]. Furthermore, cell-specific targeted delivery is inconceivable in this method. Recent chip-based electroporators [2,3] have used visually assisted cell trapping at orifices or junctons which limits their usefulness as tools for practical biological research requiring large number of cells.

2. Principle

We perform in-flow electroporation of cells in suspension as they pass at a controlled rate through a tapered hole in silicon that we refer to as the *sense-porate aperture*. This is depicted in Figure 1. The small-signal ac impedance of the aperture is continuously monitored using electrodes placed across it. Cells are detected by a rise in this impedance as they approach the narrow end of the aperture. A pre-programmed impedance-based parameter is evaluated for each incoming cell and if it lies within a specified window, a voltage pulse is applied to the electrodes to create a high electric field zone at the narrow end of the aperture. As the cell passes through this zone, it undergoes electroporation and the suspended macromolecules are delivered to its cyto-

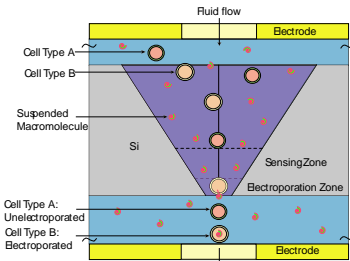


Figure 1. Principle of in-flow selective electroporation in a microfabricated *sense-pore* aperture. Cells moving through the tapered aperture are sensed and identified by their impedance and then electroporated in a selectively triggered controlled electric field zone.

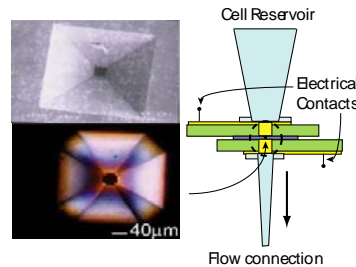


Figure 2. SEM and optical micrographs of the fabricated *sense-pore* aperture – a thermally oxidized anisotropically etched through hole in silicon. This is mounted between PCBs with gold-plated electrodes and plastic flow connectors.

-plasm. This impedance-signature-triggered transient generation of a small zone with adequately high electric field enables automated, continuous and controlled, in-flow electroporation of individual cells from a suspension containing a large number of cells without the need for any optical tagging and manual cell trapping.

3. Experimental Methods

The *sense-pore* aperture is an anisotropically etched, thermally oxidised through hole in silicon which was fabricated using standard microfabrication techniques as described in [4]. Figure 2 shows optical and SEM micrographs of the fabricated aperture which is designed to be 40 μm \times 40 μm at the narrow end. This is packaged in a flow-cell for electrical and flow connections. An electroporation setup with custom hardware and software [4] is then used to implement the scheme. The cell line used in the study is a human squamous carcinoma cell line (NT8e) which was grown using standard cell culture methods and harvested and finally suspended in the run buffer i.e. 1XPBS with 1% Bovine Serum Albumin (BSA) and kept on ice.

4. Results and Discussion

Impedance sizing of two particle sizing standards and the target cells was performed to calibrate the impedance sensing electronics. Voltage peak height distributions obtained for a mixture of 10 μm and 20 μm diameter particles and for the target NT8e cell population are shown in Figures 3 & 4.

The electroporation voltage was set to 8V and the cell suspension flow rate was set to 20nL/sec to achieve sufficient transmembrane potential (~0.2-1V) and electroporation time (~1ms) for this cell size. NT8e cells were electroporated in a suspension with a cell-membrane impermeant green fluorescent FITC-tagged dextran (MW=150kD). Cells kept in an identical suspension without electroporation were used as a control sample. Propidium iodide, a live-cell impermeant red fluorescent dye, was then added to both samples for viability estimation. Dual-color flow cytometry was performed to quantify the dextran delivery efficiency and cell viability. A delivery efficiency of ~98% along with a post-electroporation cell viability of 89% has been measured reproducible across

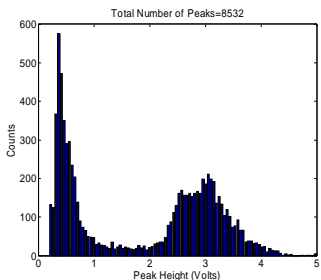


Figure 3. Distribution of voltage peaks obtained with a mixture of polystyrene particles with nominal diameters of $10\mu\text{m}$ and $20\mu\text{m}$. The mean peak heights roughly scale according to particle volume ($\propto r^3$) as expected theoretically.

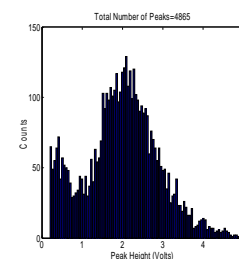


Figure 4. Distribution of voltage peaks obtained with a suspension of NT8e cells (1×10^5 cells/ml). Compared with the standard particles, using particle volume scaling, the mean cell diameter can be estimated from to be $\sim 17\mu\text{m}$.

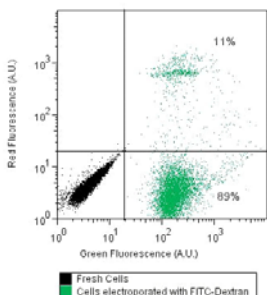


Figure 5. Dual-color flow cytometry results for NT8e cells electroporated with 0.5 mg/ml FITC-Dextran (MW=150kD). The percentage of green fluorescent cells i.e. the delivery efficiency is $\sim 98\%$ and the percentage of cells negative in red fluorescence i.e. the post-electroporation cell viability is $\sim 89\%$.

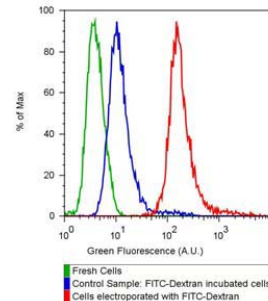


Figure 6. Green-fluorescence intensity distribution for FITC-dextran electroporated cells, control sample cells kept with FITC-dextran and fresh cells. An order of magnitude change in mean fluorescence is seen in the electroporated cells above the non-specific binding in the control cells.

batches of cells. Representative results are shown in Figures 5 & 6.

5. Conclusion

We have developed a novel non-viral delivery method which achieves very high efficiency and post-electroporation cell viability even for a large number of cells. This would be especially useful for applications in which the cells are difficult to culture such as in cancer gene therapy. Experiments are on to demonstrate impedance-selective electroporation which would then enable *ex-vivo* targeted delivery of genes and drugs in mixed suspensions obviating the need for laborious separations and post-transfection selection.

References

1. E. Neumann, *Electroporation & Electrofusion in Cell Biology*, Plenum Press, NY, 1989.
2. Washizu et al., MicroTAS 2005, pp. 1401-1403, 2005
3. Khine et al., Lab on a Chip, 5, pp. 38-43, 2005
4. A. Sarkar et al., IEEE MEMS 2004, pp. 375-378

MOLECULAR SIZE EFFECT ON MICRO ELECTROPORATION BY USING MICROCHIP WITH A THREE-DIMENSIONAL ELECTRODE ARRAY

Huiqi He¹, Donald C. Chang² and Yi-Kuen Lee^{3*}

¹Bioengineering Graduate Program, ²Dept. of Biology,

³Dept. of Mechanical Engineering

Hong Kong University of Science and Technology

Clear Water Bay, Kowloon, Hong Kong SAR, China

*E-mail: meyklee@ust.hk

Abstract

In this study, a new micro electroporation (EP) cell chip with three-dimensional (3D) electrodes was fabricated by means of MEMS technology, and tested on HeLa cervical cancer cells. Large statistical data of loading efficiency for five different size molecules and cell viability were determined under various voltage and duration time. Based on more than 2000 single cell measurements, the critical size of molecule was found to be approximately 40 kD.

Keywords : Micro electroporation, three-dimensional electrode, HeLa cell, size effect, dextran

1. Introduction

Electroporation (EP) is a widely-used technique for intra-cell delivery of many impermeable molecules, such as drugs, oligonucleotides and plasmids [1]. In recent years, novel micro EP chips, including flow-through types [2,3], single-cell type [4], etc., have been reported to increase EP efficiency. However, a systematic investigation of the molecular size effect on micro EP has never been performed. We developed a new micro EP chip with a 3D electrode array to enable such studies. Our micro EP chip with planar electrodes [5] can realize large-scale micro EP at the single-cell level. However, the sputtered planar electrodes ($< 0.5 \mu\text{m}$) can cause nonuniform electric field across a cell chamber. Thus, higher voltage is required to induce EP. This often resulted in electrolysis which can either generate undesirable bubbles, or change pH value. To solve these problems, we developed a new micro EP chip with a 3D gold electrode array with a height comparable to a cell's diameter.

2. Experimental

A modified electroplating process was adopted to avoid damage to the gold structure during wet etching process in an iodide bath. The microfabrication process is shown in Fig. 1. Twelve pairs of 3D electrodes were made of 100 nm-thick sputtered Ti, 200 nm-thick sputtered gold and 12 μm -thick electroplated gold. A packaged micro EP chip and the SEM image of the 3D microelectrodes were shown in Fig. 2. To understand the

electric field difference between the planar and 3D electrode designs, the numerical simulations were conducted using CFD-ACE+ (ESI CFD Inc., AL, USA).

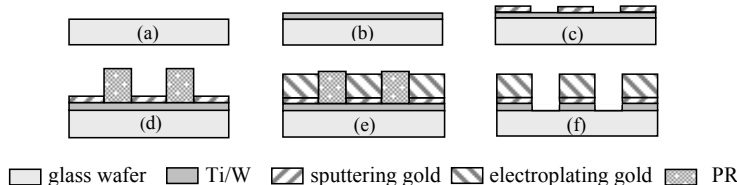


Fig. 1. Fabrication process flow of a micro EP chip with 3D electrodes: (a) Glass wafer Pyrex 7740, (b) Sputter Ti/W, (c) Pattern Au layer by lift-off, (d) Pattern thick photoresist for electroplating, (e) Electroplating gold electrode, (f) Remove PR and Ti/W.

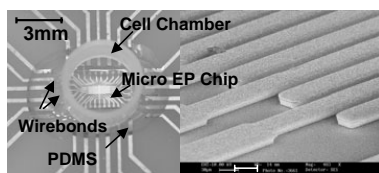


Fig. 2. A photo of a packaged micro EP chip (left) and the SEM close-up view of the 3D microelectrodes (right)

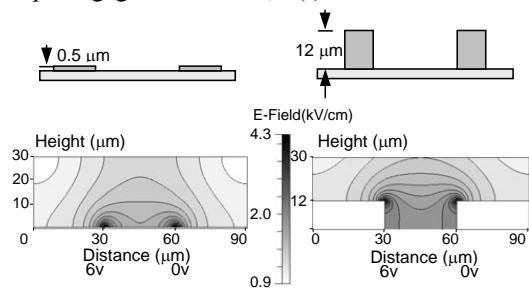


Fig. 3. Simulation results of the electric field distribution on a cross-section of 2D electrodes (left) and 3D electrodes (right).

3. Results and discussion

Five different molecules, including propidium iodide (668.4 Dalton), 10 kD, 20 kD, 40 kD and 70 kD Fluorescent dye labeled Dextran (corresponds to the diameters of *ca* 4.6nm, 6.6nm, 9nm and 12nm, respectively), were introduced into HeLa cells on a microchip (Fig. 4). The loading efficiency of these molecules as a function of the average electric field is illustrated in Fig. 5. Obviously the permeability of dextran highly depends on its molecular weight (MW). The higher the dextran's MW, the lower its permeability. Furthermore, the increasing uptake of these molecules is accompanied by lower cell viability. Large dextran (40 kD & 70kD) cannot reach a 50% efficiency, while the cell viability dropped to lower than 20%. In addition, the uptake of large molecules is pulse-duration dependent (Fig. 6). For a short electric pulse, the loading efficiency of the molecules with the MW larger than 40 kD decreases sharply, while for a longer pulse the efficiency of these molecules are similar. As shown in Fig. 6, the critical size of the molecules for micro EP lies between 9 nm (20kD) and 12 nm (40 kD).

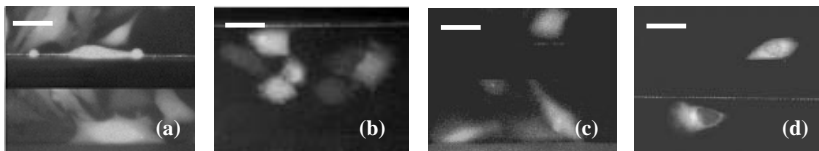


Fig. 4. Fluorescence micrographs of HeLa cells after electroporation on micro EP chips, using 4 different macromolecules. (a) 10 kD Rhodamine B-Dextran, (b) 20 kD RITC-Dextran, (c) 40 kD FITC-Dextran, (d) 70 kD FITC-Dextran (All scale bars = 30 μ m).

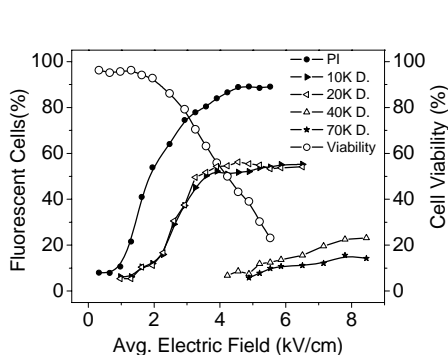


Fig. 5. Loading efficiency of macromolecules with different molecular weights (D. for Dextran) (Pulse duration = 400 μ s, single pulse).

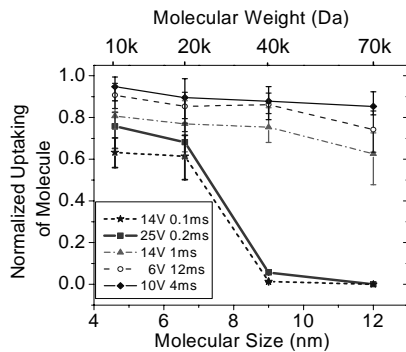


Fig. 6. The normalized uptake of molecules as a function of molecular size (each data point from the average of 10 HeLa cell experiments).

4. Conclusion

In summary, we demonstrated, for the first time, the molecular size effect on single-cell EP under different electric field and pulse duration conditions, using a new micro EP chip. This study will be very useful for parameter optimization of electroporation with large DNA molecules in the future. Comparing to the conventional instrument, MEMS based micro electroporation chip can greatly shorten the experimental time.

Acknowledgements

This work is supported by Hong Kong Research Grants Council (Project Ref No. 616205 and HKUST6466/05M).

References

- [1] D. C. Chang, Guide to Electroporation and Electrofusion, Academic Press, 1992.
- [2] Y.-C. Lin and M.-Y. Huang, J. Micromech. Microeng, Vol. 11, pp.542-547, 2001.
- [3] A. Valero, *et al.*, MicroTAS'05, pp.1395-1397.
- [4] M. Khine, *et al.*, Lab on a Chip, Vol. 5, pp.38-43, 2005.
- [5] H. He, D. C. Chang and Y.-K. Lee, MicroTAS'05, pp.382-384.

MICRO PARTICLE SAMPLING ON A PERFORATED FILTER MEMBRANE BY EWOD-ACTUATED DROPLET SWEEPING

Sang Kug Chung, Yuezun Zhao and Sung Kwon Cho*

Department of Mechanical Engineering, University of Pittsburgh

Abstract

This paper describes two major achievements in the course of developing a micro particle sampler: (1) reliable driving of liquid droplets *on a perforated membrane* by electrowetting-on-dielectric (EWOD); (2) particle sweeping and sampling on the membrane by EWOD-actuated moving droplets. These two achievements will allow us to realize a handheld environmental monitoring system integrated with the lab-on-a-chip technology.

Keywords: Micro particle sampler, EWOD, perforated membrane, lab-on-a-chip

1. Introduction

Recently, we experimentally showed that EWOD-actuated moving droplets can efficiently sweep and sample various micro particles *on a flat surface*[1-4]. However, it has been wondered whether or not this sampling method is also effective *on a perforated surface* since some EWOD actuations on micro structured surfaces were shown *irreversible*[5]. The irreversible operations do not promise reliable droplet transports. For the first time, to our knowledge, we show in this paper that water droplets can be *reversibly* actuated and transported by EWOD *on a perforated membrane*, and furthermore micro particles on the membrane can be swept and sampled by the EWOD-actuated moving droplets.

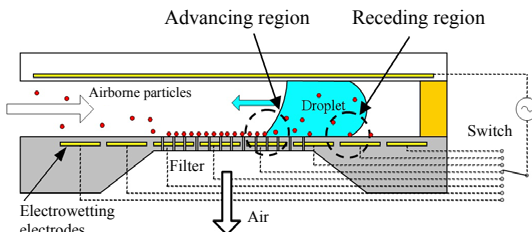


Fig. 1 Envisioned airborne particle sampler. Note that particles can be swept and sampled into the droplet driven by electrowetting-on-dielectric (EWOD) principle. The electrodes for EWOD are placed in the perforated filter membrane. The filter membrane surface in the advancing region turns hydrophilic with EWOD on, while the surface in the receding region remains hydrophobic. The particle sampling occurs in both advancing and receding regions of the droplet.

2. Reversible EWOD operations on a perforated membrane

Figure 2(a) shows a configuration for fundamental EWOD operation testing with a sessile droplet on a perforated structure. A commercially available filter membrane that has a rectangular array of perforated holes ($60 \mu\text{m} \times 128 \mu\text{m}$ hole area, see Fig. 3) is first passivated by a parylene layer and then coated with a Cr/Au layer for the EWOD electrode. For the EWOD dielectric layer, another parylene layer is deposited, followed by a Teflon layer. For grounding, a sharp tip is penetrated into the droplet. Under electrical potential (165 VAC, 1 kHz) applied, the contact angle is changed from 120° to 60° (Fig. 2(b)). Also, the top views (Fig. 2(b)) confirm corresponding droplet spreading. This 60° angle change was shown highly reversible and repeatable, and is large enough to guarantee reliable droplet transports with patterned electrodes[6-8].

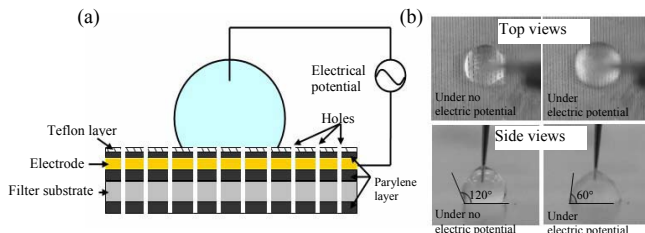


Fig. 2 Reversible EWOD operations with a sessile droplet on a *perforated* filter membrane: (a) Configuration of EWOD actuators. The volume of the droplet is about 5 μl . The filter membrane (hole size 60 $\mu\text{m} \times$ 128 μm , see Fig. 3 for hole geometry) is coated with a Parylene layer (10 μm) for passivation, Cr (100Å)/Au (1000Å) metal layers for EWOD electrodes, another Parylene layer (2 μm) for EWOD dielectric, and a Teflon layer (2000Å) for hydrophobic layer; (b) Contact angle is reversibly and repeatedly changed from 120° to 60°.

3. Droplet transportation on a perforated membrane

To test droplet transportation and particle sampling, testing devices are fabricated (Fig. 3) that mainly consist of a perforated filter membrane and a transparent top plate.

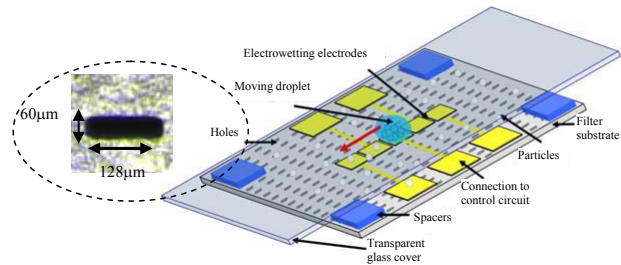


Fig. 3 Testing devices for particle sampling (not to scale). A linear array of square electrodes is patterned on the filter membrane. The transparent top plate is covered with an Indium Tin Oxide (ITO, 1000Å) layer for EWOD grounding and a Teflon layer (2000Å).

The membrane structure is the same as that in Fig. 2(a), except a linear array of square electrodes ($1.5 \times 1.5 \text{ mm}^2$) are patterned for EWOD droplet transports. The ground electrode (Indium Tin Oxide layer) for EWOD entirely covering the top plate is coated with a Teflon layer. Sequential activations of the patterned electrodes generate continuous movements of the droplet perpendicular (Fig. 4(a)) as well as parallel (Fig. 4(b)) to the hole pattern line, implying that droplets may move in any directions on the current membrane regardless of hole arranging pattern.

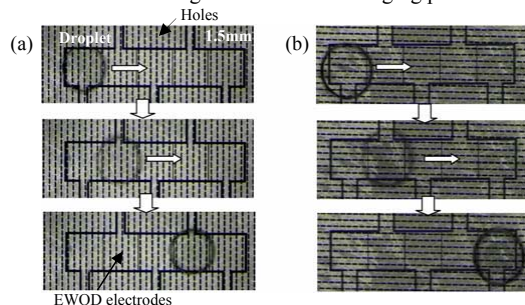


Fig. 4 Sequential pictures of successful EWOD droplet transports on a perforated filter membrane. Sequential activations of the electrodes make droplets move right, perpendicularly (a) as well as in parallel (b) to the hole pattern line.

4. Particle sampling

Finally, particle sampling is tested with hundreds of glass beads (80 μm in diameter) deposited on the membrane (Fig. 5(b)). A droplet moves from the right to the left along the electrodes, simultaneously sweeping and sampling the particles into the droplet (Figs. 5(c-d)). It is seen that no particle remains on the path where the droplet has previously passed (Figs. 5(c-d)). Finally, the sampled particles are suspended inside the droplet (Figs. 5(d-e)). The sampled particles can pile up by completely evaporating the water droplet (Fig. 5(f)).

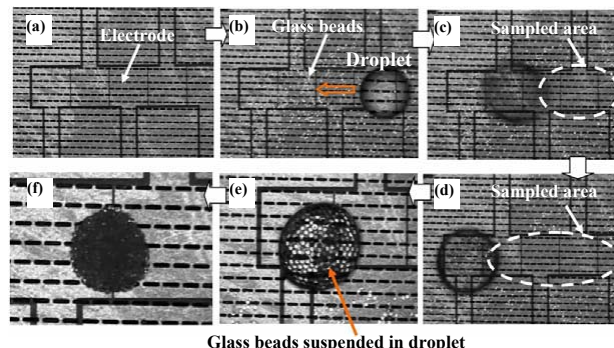


Fig. 5 Sequential pictures of glass beads sampling viewed through the transparent top glass plate: (a) The filter membrane without particles; (b) glass beads (white dots, 80 μm diameter) and a droplet are deposited on the perforated membrane. Note that the droplet looks smaller than those in Figs. 5(c-d) since it is not sandwiched yet by the top plate; (c-d) the droplet moves left when the EWOD electrodes are activated sequentially to the left. Glass beads are picked up by the moving droplet. After the droplet passes, the membrane surface becomes clean with no bead left behind; (e) Collected beads are suspended in the droplet (close-up view). Note that the top plate is removed to enhance evaporation; (f) Beads pile up after the water droplet is completely evaporated (close-up view).

5. Conclusion

Reversible operation of liquid droplets on a perforated membrane by EWOD and particle sweeping and sampling on the membrane by EWOD-actuated moving droplets have been demonstrated. The achievements will make the handheld environmental monitoring system integrated with the lab-on-a-chip technology possible.

References

- [1] Y. Zhao, and S. K. Cho, *J. of Lab on a Chip*, Vol. 6, pp. 137-144, 2006.
- [2] A. Desai, S.-W. Lee and Y.-C. Tai, 13th MEMS Conference, 2000, pp. 733-738.
- [3] X. Yang, J. M. Yang, X. Q. Wang, E. Meng, Y.-C. Tai, and C. M. Ho, 11th MEMS Conference, 1998, pp. 137-142.
- [4] Y. Zhao, and S. K. Cho, 13th International Conference on Solid-State Sensors, Actuators and Microsystems(Transducers 2005), Seoul, Korea, pp. 129-134.
- [5] T. N. Krupenkin, J. A. Taylor, T. M. Schneider, and S. Yang, *Langmuir*, Vol. 20, pp. 3824-3827, 2004.
- [6] S. K. Cho, H. Moon, and C.-J. Kim, *J. of MEMS*, Vol. 12, pp. 70-80, 2003.
- [7] M. G. Pollack, R. B. Fair and A. D. Shenderov, *Appl. Phys. Lett.*, 2000, 77, 11, 1725-1726.
- [8] F. Muggele and J.-C. Baret, *J. Phys. : Condens. Matter*, 2005, 17, R705-R774.

OPTICAL MANIPULATION OF MICROPARTICLES USING A LIQUID CRYSTAL DISPLAY

Wonjae Choi¹, Sehwan Kim², Jin Jang², and Je-Kyun Park¹

¹ Dept. of BioSystems, Korea Advanced Institute of Science and Technology (KAIST), ² Dept. of Information Display, Kyung Hee University, Korea

Abstract

We report a new microfluidic system, ‘lab-on-a-display,’ that microparticles can be manipulated by dielectrophoretic forces generated from the optoelectronic tweezers (OET) on a liquid crystal display (LCD). In this study, the lab-on-a-display is first realized by a conventional LCD module and an OET device including a ground layer, a liquid chamber, and a photoconductive layer. The lab-on-a-display is successfully applied to the programmable manipulation of polystyrene microparticles.

Keywords: lab-on-a-display, dielectrophoresis, optoelectronic tweezers, liquid crystal display (LCD), virtual electrode

1. Introduction

Dielectrophoresis (DEP) technique has become a promising approach for parallel manipulation of microparticles in biological and medical applications. Recently, two DEP-based approaches have been reported using a complementary metal-oxide-semiconductor (CMOS) circuit-driven technique [1] and a digital micromirror display (DMD) image-driven OET [2]. However, these techniques have potential drawbacks for disposable biomedical applications, due to the high manufacturing cost and complex optical system. Here we present a new portable microfluidic DEP platform, providing a low fabrication cost of the driving circuit, portability, and compatibility for disposable applications.

2. Principle

The lab-on-a-display has an OET device on the top of a LCD (Figure 1). In the OET device, the liquid layer containing microparticles was sandwiched between the photoconductive and the ground layers. When an AC bias voltage is applied between two layers, the transmitted LCD image forms virtual electrodes on the surface of photoconductive layer. As the illuminated light increases the conductivity of photoconductive layer in comparison

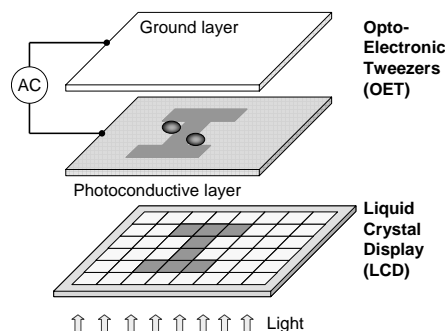


Figure 1. Schematic of a lab-on-a-display.

with the non-illuminated regions, a virtual electrode effectively forms at the illuminated region. This virtual electrode can be used to make a DEP force. The simulated electric field distributions in the liquid layer prove that microparticles are movable by the LCD-driven DEP (Figure 2A). In order to transport particles across a long distance, the LCD image pattern should be continuously changed (Figure 2B).

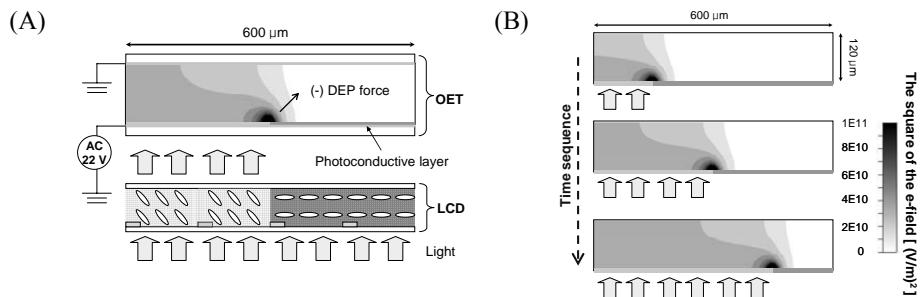


Figure 2. The electric field strength calculated using CFD-ACE; (A) a cross-sectional view and (B) the liquid layers at three sequential moments.

3. Experimental

The photoconductive layer was fabricated on a ITO glass substrate and was comprised of three layers: a 20 nm thick silicon nitride, a 1 μ m thick intrinsic hydrogenated amorphous silicon (a-Si:H), and a 50 nm thick n⁺ a-Si:H (Figure 3). After these layers were consecutively deposited by plasma enhanced chemical vapor deposition (PECVD), some regions were etched by reactive ion etch (RIE) to expose the ITO for bias connections. A 1.3-in monochromatic LCD module (26 \times 20 mm image area) from the conventional projector (EMP-5300; Epson, Japan) was used in this study. It was consisted of 800 \times 600 pixel array with 33- μ m pixel pitch. We used two illumination of the microscope: one for actuation and the other for observation (Figure 4). The movements of beads were observed and recorded using an upright microscope (Zeiss Axioskop 40; Carl Zeiss, Germany) with a camera.

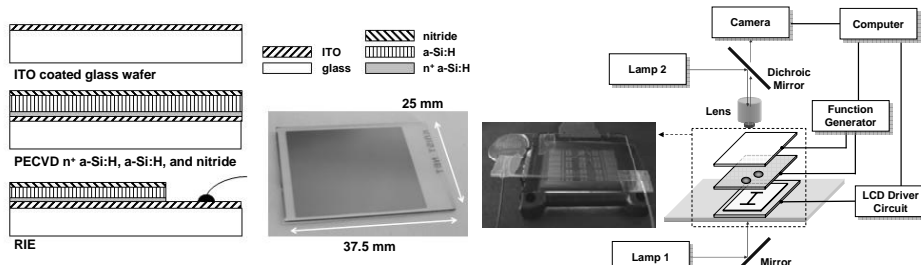


Figure 3. Microfabrication of a photoconductive layer

Figure 4. Experimental setup.

4. Results and discussion

Figure 5 shows videoclips representing the transport of $45\text{ }\mu\text{m}$ beads, finally forming a $1.8 \times 2.4\text{ mm}$ -size letter "I". It was observed that the beads follow the moving edge of the image at every moment. To measure the particle speed, we recorded the manipulation action and analyzed the video images frame by frame. Figure 6 shows the measured speeds of $75\text{-}\mu\text{m}$ polystyrene particles versus the ac bias voltage at the frequency of 100 kHz . The speed increases while the voltage increases, eventually reaching a speed of $36\text{ }\mu\text{m s}^{-1}$ at 10 V_{pp} bias.

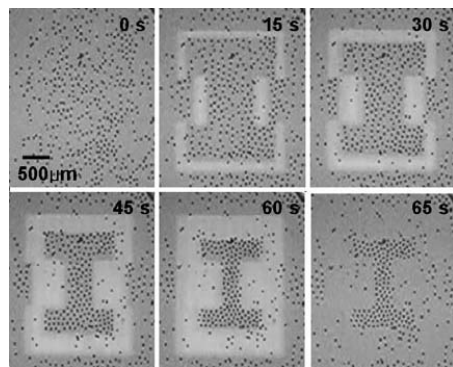


Figure 5. An example of LCD-driven optical manipulation of microbeads with a diameter of $45\text{ }\mu\text{m}$.

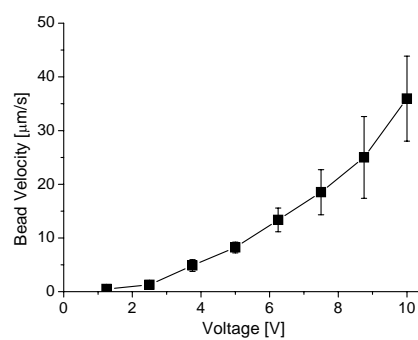


Figure 6. The relationship between the particle speed and the bias voltage.

5. Conclusions

Numerical simulation and experimental results on the basic capabilities of particle manipulation have been described. A number of polystyrene microparticles were transported by the prototype lab-on-a-display technology which used the LCD and light-patterned virtual electrodes. Transport speed of $36\text{ }\mu\text{m s}^{-1}$ was measured with 10 V_{pp} bias voltage. Since the virtual electrodes used in the lab-on-a-display are movable and reconfigurable, this platform may be potential for programmable particle manipulation or chip-based bioprocessing including cell separation and bead-based analysis.

Acknowledgements

This research was supported by the Nano/Bio Science & Technology Program (M10536-90002-05N3609-00210) of the Ministry of Science and Technology (MOST), Korea.

References

1. N. Manaresi, et al, IEEE J. Solid-St. Circ. Vol. 38, No. 12, pp.2297-2305, 2003.
2. P. Y. Chiou, A. T. Ohta, M. C. Wu, Nature Vol. 436, pp. 370-372, 2005.

A MICROFLUIDIC CHIP WITH A NANOSCALE ARRAY FOR ANALYSIS OF VIRUS PARTICLES

Kidong Park, Demir Akin, Rashid Bashir

Birck Nanotechnology Center, School of Electrical and Computer Engineering,
Weldon School of Biomedical Engineering, Purdue University, West Lafayette,
IN. USA

Abstract

In this work, an individually addressable nano-probe array within a micro-fluidic channel is developed. The probe array captured the viral particles from fluid flow with dielectrophoresis (DEP) force and the same probes are then used to investigate the effect of strong electric field on the virus particles. A number of biologically important particles, such as vaccinia virus, lambda virus and polystyrene beads can be captured, and can be conveniently observed via optical microscope.

Keywords: Nano-scale probe array, virus, micro-fluidics, dielectrophoresis, lysis

1. Introduction

Valuable information on the biological entities, such as cell, bacteria and virus, can be obtained by individually observing them under given stimulus in real time. However, those entities are usually suspended in the fluid and it's difficult to keep track of a single entity or a small number of them. A combination of micro-fluidics and the DEP technology has been used for this purpose [1, 2]. This paper presents a nano-scale probe array, which captures virus and enables real time observation. Also, the probe array can be used for the study on the effects of the strong electric fields on these particles, produced by its ultra sharp lateral probe tips.

2. Theory

Dielectrophoresis (DEP) is the electrokinetic motion of dielectrically polarized particles in non-uniform electric fields due to the difference in the strength of the polarization between the media and the particles. The DEP force is determined by the particle size, Clausius-Mossotti factor, and the electric filed, as in Eq. 1. Vaccinia virus is modeled with multi-shell model [3] to calculate the Clausius-Mossotti factor, as in Fig. 1. ξ_p , ξ_s , ξ_{mem} , and ξ_{in} is the complex permittivity of viral particle, media, viral particle's membrane and viral particle's bulk, respectively [4].

$$F_{DEP} = 2\pi\epsilon_s R^3 \operatorname{Re}\left(\frac{\xi_p - \xi_m}{\xi_p + 2\xi_m}\right) \nabla E^2, \quad \xi_p = \xi_{mem} \frac{\left(\frac{R}{r}\right)^3 + 2\left(\frac{\xi_{in} - \xi_{mem}}{\xi_{in} + 2\xi_{mem}}\right)}{\left(\frac{R}{r}\right)^3 - \left(\frac{\xi_{in} - \xi_{mem}}{\xi_{in} + 2\xi_{mem}}\right)} \quad (1)$$

3. Experimental

The starting substrate is a highly-doped Silicon on Insulator (SOI) wafer. The fabrication flow starts with reactive ion etching to define the probe array shape as shown in Fig. 2. Then the probe array is released and the probe tips are further

sharpened by repeated oxidation steps. After that, a metal contact layer is deposited and patterned. The scanning electron microscope image of the finished probe array is shown in Fig. 3. The device is then attached and wire bonded to a printed circuit board, and the PDMS cover is bonded. The ends of each probe is about 1-2 μm and electric fields of up to 10^5 V/cm can easily be generated using this probe arrays. The device is connected to a syringe pump for precise flow control and two function generators with opposite phase supply the DEP signal for each side of the probe, to maximize the electric field.

4. Results and Discussion

The DEP-mediated capture of 3 μm polystyrene microspheres was performed. The microspheres exhibit negative DEP in DI water. Without the applied DEP voltage, the microspheres freely pass over the electrodes and the tips. After applying the DEP voltage, the microspheres were captured in front of the probe and accumulated, as shown in Fig. 4.

Next Lambda viruses are captured by positive DEP. The lambda virus were dual-labeled differentially with green (DiOC63, Molecular Probes) and red (DiL, Molecular Probes) and suspended in DI-water, with concentration of $1 \times 10^9 \text{ pfu/ml}$. The average velocity of the DI water flow was 0.1mm/sec, and the applied voltage was 20 Vpp at 100 kHz. The images of the captured virus are shown in Fig. 5. After capturing, the PDMS cover was carefully removed and the surface was observed via SEM as shown in Fig. 6.

The vaccinia viruses were captured with positive DEP, and the effect of electric field on the viruses was investigated. The vaccinia virus particles were dual-labeled with its capsid green (DiOC63) and its DNA blue (Hoescht33342, Molecular Probes). The concentration of the vaccinia virus used was $1 \times 10^{10} \text{ pfu/ml}$. The capturing condition is same as above. The progress of the capture is shown in Fig. 7. In Fig. 8, we can see the co-localization of the blue and the green signal, with the blue signal comes out in the direction of line1, which shows the partial release of the DNA from the capsid.

5. Conclusion

In this paper, the nano-scale probe array, integrated with micro-fluidic channel is presented and the capture of the virus particles is shown with colocalization of the two different fluorescence signals. Also by applying high electric filed, produced by its ultra sharp probe tips, the effect of the electric field on virus particle can be studied.

Acknowledgement

This material is based upon work supported by the National Science Foundation under Grant # 0404107 and Grant # EEC-0425626 (NSEC at OSU).

References

1. B.M. Taff & J. Voldman, A Scalable Addressable Positive-Dielectrophoretic Cell-Sorting Array, Analytical Chemistry 77, 7976-7983 (2005).
2. D. Akin, H. Li, R. Bashir, Real-Time Virus Trapping and Fluorescent Imaging in Micro-fluidic Devices, Nano Letters, 4 (2), 257 -259, 2004.

3. Ying Huang, et al, Differences in the AC electrodynamics of viable and non-viable yeast cells determined through combined dielectrophoresis and electrorotation studies, *Phys. Med. Biol.*, 1992, Vol. 37, No 7, 1499~1517.
4. M. P. Hughes, Hywel Morgan, Frazer J. Rixon, Measuring the dielectric properties of herpes simplex virus type 1 virions with dielectrophoresis, *Biochimica et Biophysica Acta* 1571 (2002) 1-8

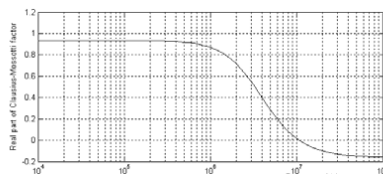


Figure. 1 Clausius-Mossotti factor.

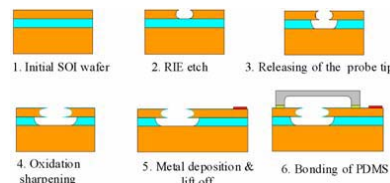


Figure 2. Process Flow

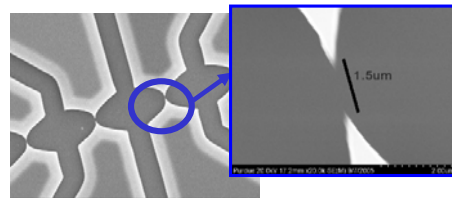


Figure 3. SEM images of the probe. The gap between each probe pair is about 1-2 μm .

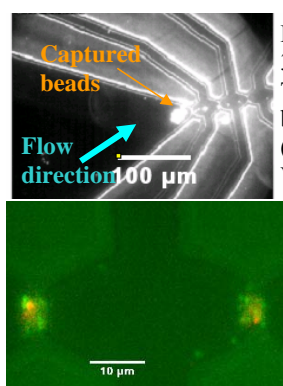


Figure 4. The collected 3um polystyrene beads. The beads are collected between the electrodes. ($v_{\text{fluid}}=1 \text{ mm/s}$, $V_{\text{DEP}}=20 \text{ V}_{\text{pp}}$ @ 100 kHz)

Figure 5. Lambda virus captured between the probe tips.

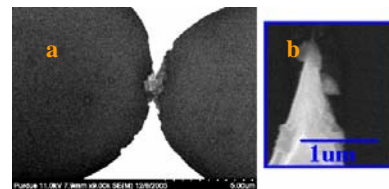


Figure 6. SEM images of the captured lambda virus. (a) The probe pair with captured virus. (b) The magnified image of the lower probe.

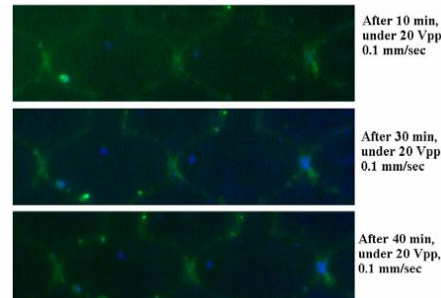


Figure 7. Series images of the progression of the viral capture, in 10, 30 and 40 min. The flow direction is from right to left.

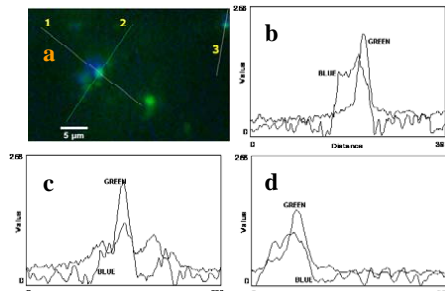


Figure 8. (a) Fluorescence image of the captured vaccinia virus. (b), (c), (d) Plot of the fluorescence signal on line 1, 2 and 3 respectively. The y-axis is the intensity of the each fluorescence signal and the x-axis is the distance (pixels).

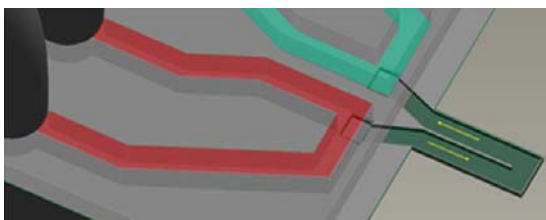
SUSPENDED MICROCHANNEL RESONATOR (SMR) FOR BIOMOLECULAR AND CELLULAR DETECTION

Thomas Burg, Michel Godin, Scott Knudsen, and Scott Manalis
Biological Engineering, Massachusetts Institute of Technology,
Cambridge, MA 02139 USA
(scottm@media.mit.edu)

Abstract

The most sensitive assays today generally rely on fluorescent or radioactive labeling, requiring multistep sample preparation and in some cases large sample volumes. Hence, assay development and throughput can represent critical bottlenecks for large-scale or point-of-use applications.

To reduce the impediment of these bottlenecks, we are exploiting silicon-based microfabrication for developing robust and real-time sensors for biomolecular and cellular detection. In many cases, our goal is to provide an alternative to fluorescent optical readout while achieving sensitivity and selectivity that is commensurate with benchtop assays. Non-optical alternatives have potential for point-of-use applications where robustness, small package size, and low cost are desirable.



Here we present a new detection concept for measuring mass known as the Suspended Microchannel Resonator (SMR). In SMR detection, target molecules flow through a vibrating suspended microchannel and are captured by

receptor molecules attached to the interior channel walls. What separates the SMR from other resonant mass sensors is that the receptors, targets, and their aqueous environment are confined inside the resonator, while the resonator itself can oscillate at high Q in an external vacuum environment, thus yielding extraordinarily high sensitivity.

We have demonstrated that the SMR can achieve a detection limit in fluid of 0.2 fg of total mass and 0.02 ng/cm² of surface mass density. When compared to the commercial quartz crystal microbalance, these limits are over 1000x more sensitive in terms of total mass and nearly 100x more sensitive in terms of surface mass density. We will present results on biomolecular detection and show how such a high mass resolution can enable single cells and single nanoparticles to be weighed with high precision.

Keywords: resonator, gravimetric, suspended microchannel

AN ELECTROKINETIC SANDWICH INJECTION TECHNIQUE FOR MICROCHIP CAPILLARY ELECTROPHORESIS

Gui-Sheng Zhuang^{1,2}, Gang Li^{1,2}, Jing Liu^{1,2}, Qing-Hui Jin¹, Jian-Long Zhao¹

¹Shanghai Institute of Microsystem and Information Technology, Chinese
Academy of Sciences, Shanghai 200050, China

²Graduate School of the Chinese Academy of Sciences, Beijing 100049, China

Abstract

In this paper, a novel electrokinetic sandwich injection technique for delivering high-quality sample plugs into the separation channel of a microchip capillary electrophoresis (μ -CE) system is developed. The microchip designed involves four focusing channels in which symmetrical potentials are loaded to form a unique parallel electric field distribution to confine the spreading of sample plugs and prevent sample leakage. Numerical simulation results show that well-defined and non-distorted sample plugs can be delivered for high-performance separation purposes. The similar results are experimentally observed.

Keywords: microfluidics, numerical simulation, electrokinetic injection, sample plug

1. Introduction

In μ -CE, injection techniques play an important role in the sample-handling process, and separation performance achieved, which depends strongly on the shape of sample plugs delivered into the separation channel. Many injection techniques have been developed to deliver discrete sample plugs, such as the T-form, cross-form and double-T-form injection techniques. Tsai et al. [1] utilizes a numerical simulation approach to investigate these injection methods and study the control parameters. Ideal shape of the sample plug can be achieved by reasonable channel geometry design and electrokinetic control. Recently, a double-cross injection system [2] is developed to deliver improved sample plugs. Generally, these injection systems deliver distorted or slanted sample plugs, which have a negative impact on the separation performance. Here, we develop a sandwich injection system to deliver high-quality sample plugs for high-performance separation, which employs a unique parallel electric field distribution in the intersection of injection channel and separation channel to confine the diffusion of analyte in loading step and prevent the sample leakage in dispensing step.

2. Experimental

Details of geometry and reservoir labeling scheme of the sandwich injection system are shown in Figure 1. Figure 1a shows the schematic diagram and the dimension of a microchip. F1, F2, F3, and F4 channels are the focusing channels. Figure 1b shows the schematic diagram and the photograph of the intersection. The photograph of the microchip is shown in Figure 1c. The basic operating principle of the injection system can be described as follows: In the loading step, the sample is driven from sample reservoir (S) to sample waste reservoir (SW) by a loading electric field. Simultaneously, appropriate voltages are applied to the focusing channels to form a unique parallel electric field distribution. The parallel electric field forms virtual walls to confine the

spreading of sample plugs and prevent sample leakage. When the sample fills the intersection, the electric field switches immediately to the dispensing step. Then the sample in the intersection is delivered into the separation channel while the focusing channels are applied appropriate bias voltages for preventing leakage. Figure 2 presents the corresponding potential distributions and streamlines for the two steps.

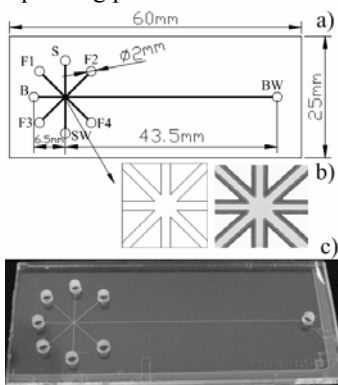


Figure 1. Design and photograph of the electrophoresis microchip with sandwich injection system.

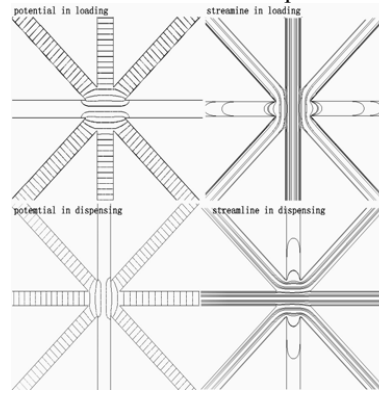


Figure 2. Numerical simulation of electrical potential contours and streamlines for the two steps.

3. Results and Discussion

Figure 3 shows the numerical and experimental flow contours. It can be seen that a well-defined sample plug is delivered into the separation channel. Figure 4 illustrates the three different simulated volumes of sample plugs introduced for three focusing voltages.

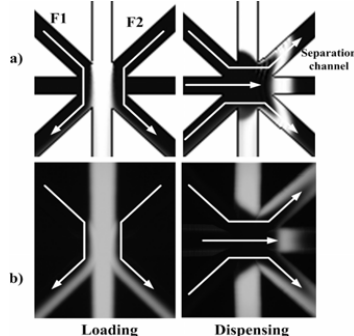


Figure 3. Comparison of the numerical and experimental flow distributions for the loading and dispensing procedures for three focusing voltages.

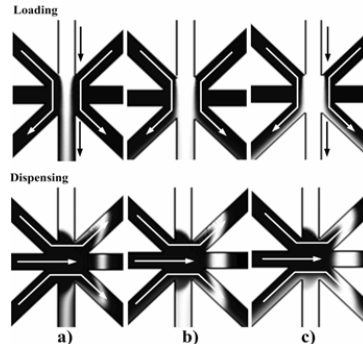


Figure 4. Simulated sample plug distributions for the loading and dispensing procedures for three focusing voltages.

Observation of the well-defined and rectangle-like sample plug delivered into the separation channel. The shape of the sample plug is prominently improved than that reported previously.

Figure 5 compares the sample shape and detected peak shape of the delivered sample plugs at the proposed sandwich injection system and the pinched cross-form systems. A narrower and higher sensitive peak than the pinched cross-from injection systems can be detected to improve resolution performance without leakage. Simulated electropherograms for two samples have affirmed the higher resolution with the proposed sandwich injection system (Figure 6c compared with figure 6a and b). The peak resolution of the peak quality is further improved, as expected.

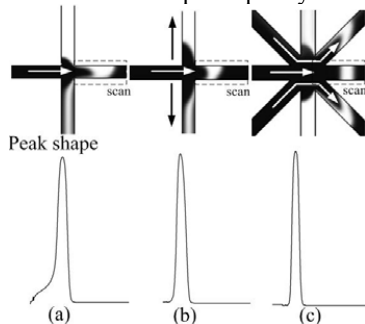


Figure 5. Comparison of the sample shape and detected peak shape of the delivered sample plugs. Pinched cross-form injection without pullback voltages a), pinched cross injection system with pullback voltages b) sandwich injection system c).

4. Conclusions

The sandwich injection technique proposed here prove to be a more efficient injection method, which can produce a high-quality sample plug with variable volumes and well-defined shape for high-performance detection purposes.

Acknowledgements

This work was supported by the STCSM Grant No. 051111019, and Shanghai-AM Research and Development Fund, Grant No. 0510.

References

- [1] Tsai, C. H., Yang, R. J., Tai, C. H., Fu, L. M., *Electrophoresis* 2005, 26, 674-686.
 - [2] Fu, L. M., Yang, R. J., Lee, G. B., *Anal. Chem.* 2003, 75, 1905-1910.
- Corresponding Author: Jian-Long Zhao, Nanotechnology Laboratory, Shanghai Institute of Microsystem and Information Technology, Chinese Academy of Sciences, Tel: +8621-62511070-5709, Fax: +8621-62511070-8714, E-Mail: jlzhao@mail.sim.ac.cn.

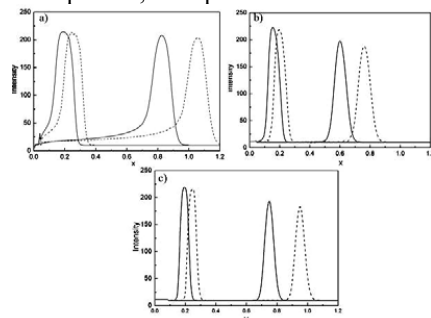


Figure 6. Electropherograms generated by simulation for two samples at 1s and 4s. Pinched cross-form injection without pullback voltages a), pinched cross injection system with pullback voltages b) sandwich injection system c).

A PDMS DIFFUSION PUMP FOR ON-CHIP FLUID HANDLING IN MICROFLUIDIC DEVICES

Mark A. Eddings¹ and Bruce K. Gale²

¹Department of Bioengineering, University of Utah, Salt Lake City, UT

²Department of Mechanical Engineering, University of Utah, Salt Lake City, UT

Abstract

A PDMS diffusion-based membrane pump has been developed for on-chip fluid handling within microfluidic devices. Vacuum and air pressure applied across a thin PDMS membrane were used to bi-directionally manipulate fluid at flow rates of 10-200 nl·min⁻¹. Flow rates can be altered by changing diffusion area, membrane thickness, and applied pressure or vacuum. The pump has been used to rapidly fill and evacuate dead-end channels and chambers. Desired volume plugs are easily isolated and manipulated. The pump can be integrated within densely arrayed microfluidic channels and chambers for mixing, separation, and analysis.

Keywords: PDMS, pump, dead-end filling, membrane, microfluidics

1. Introduction

A significant number of micropumps have been developed for PDMS microfluidic devices based on deflecting thin PDMS membranes through pneumatic actuation. [1-2] However, rapid off-chip valving is required to generate flow. In addition, mechanical actuation within the microfluidic channels may not be suitable for all biological applications. Other micropumps have focused on the gas permeability of PDMS to generate flow. The bulk of these methods have focused on applying pressure or vacuum to the bulk microfluidic device, rather than localized diffusion areas. The bulk degassing requires additional preparation time and limits the device to one-time fluidic control. [3] The diffusion-based membrane pump solves many of these problems by applying direct pressure or vacuum on the flow without mechanical actuation, enabling continuous fluidic control, and removing bulk-degassing preparation.

2. Experimental

In order to fabricate the diffusion membrane pump, previously reported multi-layer soft lithography methods were utilized [1-2]. Devices consisted of a microfluidic channel layer, a thin membrane layer, and the pressure/vacuum control layer. PDMS at 10:1 base to curing agent was poured into molds and was partially cured at 65 C° for 45 minutes. Reservoirs and tubing inlets were then cored in the channel and control layers using a 2mm diameter coring tool. A thin membrane layer was spun on a PMMA wafer and cured at 65 C° for 45 minutes. The three layers were combined and baked

overnight at 65 C° (See Figure 1a). Tests were run varying parameters such as diffusion area, membrane thickness, and applied pressure/vacuum to determine the change in flow rate. Separate devices were fabricated using soft lithography methods to demonstrate fluid handling and dead-end channel filling (See Figure 1b).

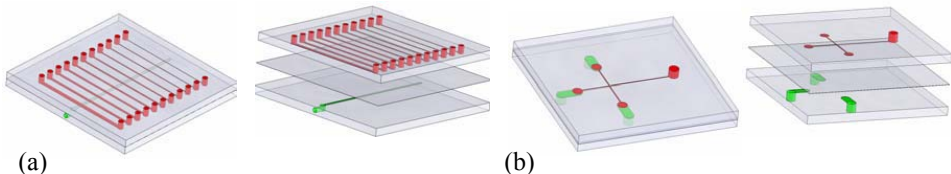


Figure 1- a) Drawing of a microfluidic device used for measuring flow rates. The three-layer PDMS device consists of a fluid channel layer, diffusion membrane, and vacuum source layer. Fluid was placed in each of the wells (red) and vacuum was applied at the control inlet (green). Flow rates were measured by determining fluid displacement after a fixed time for channels of varying widths, 200 μm to 1mm (red). b) Drawing of a microfluidic device used for demonstrating dead-end chamber filling. The chambers (red) are separated from the vacuum/pressure source by a 25 μm diffusion membrane. One well (red) is open to atmospheric pressure. Three pressure/vacuum inlets (green) are located below each of the three chambers.

3. Results and Discussion

As expected, the flow rate varied linearly with diffusion area and pressure/vacuum (Figure 2). Flow rates from 10-200 nl·min⁻¹ were achieved with the fabricated device. Higher flow rates should be possible with larger diffusion areas.

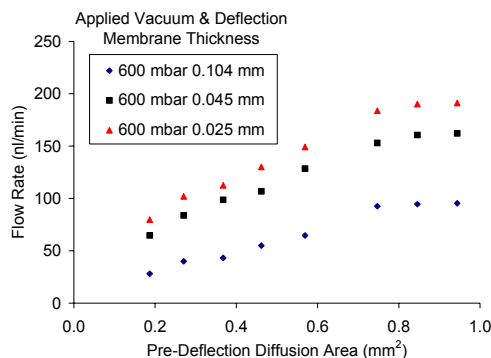


Figure 2- Measured flow rates at different diffusion areas for 600 mbar applied vacuum. Data was acquired for three different diffusion membrane thicknesses 0.104, 0.045, and 0.025 mm.

Also, fluid was easily manipulated through turns in cross intersections and filling dead-end channels and chambers (Figure 3). Individual chambers were filled with different colored fluids without mixing. Rapid fluid plug dispensing and fluid mixing was possible by toggling chambers between pressure and vacuum.

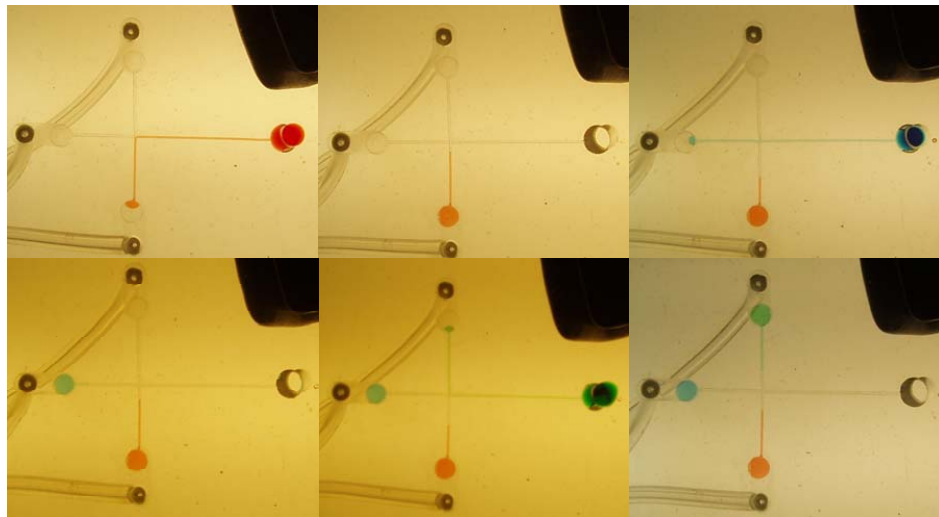


Figure 3- Pictures of three different fluids, red, green, and blue, filling dead-end chambers. Pressure differentials across the membrane below the chambers enabled the flow to make turns at the intersection. Each fluid was placed in the open well and pumped to each individual chamber. Each chamber can be individually returned to the well or can mix with the other wells at the intersection by toggling between pressure and vacuum below the membrane at each chamber. This technique also enables the isolation of fluid plugs for dispensing and metering similar to an electroosmotic flow setup.

4. Conclusion

The PDMS diffusion pump is a feasible option for complex lab-on-a-chip applications. The micropump is easily fabricated using existing methods and can be highly arrayed for multi-channel configurations. Rapid dead-end channel filling and flow rates in the $200 \text{ nl}\cdot\text{min}^{-1}$ range have been demonstrated.

Acknowledgements

The authors would like to acknowledge the support of the Utah State Center of Excellence for Biomedical Microfluidics and the NSF IGERT Program.

References

- [1] D. Duffy, J. McDonald, O. Schueller, G. Whitesides, Rapid Prototyping of Microfluidic Systems in Polydimethylsiloxane, *Anal. Chem.* 70, pp. 4974-4984
- [2] M. Unger, H. Chou, T. Thorsen, A. Scherer, S. Quake, Monolithic Microfabricated Valves and Pumps by Multilayer Soft Lithography, *Science*, Vol. 288, pp. 113-116
- [3] K. Hosokawa, K. Sato, N. Ichikawa, M. Maeda, Power-free PDMS microfluidic devices for gold nanoparticle-based DNA analysis, *Lab chip*, Vol. 4, pp.181–185

FULL-IMAGE MICRO-PIV ANALYSIS OF TRANSIENT AND STATIONARY FLOW PATTERNS IN MICROFLUIDIC STRUCTURES UNDER PIEZO ACTUATION

Melker Sundin, Thomas Glasdam Jensen, Henrik Bruus and Jörg P. Kutter

Technical University of Denmark

MIC - Department of Micro and Nanotechnology

DTU, Building 345 east

2800 Kgs. Lyngby, Denmark

Abstract

In this work a method for investigating acoustic forces in microfluidic structures is presented. By comparing, and combining, full-image micro-PIV measurements with CFD calculations, a higher understanding of acoustic coupling in microfluidic can be obtained.

Keywords: Micro-PIV, acoustic radiation force, acoustic streaming, microfluidic structures

1 Introduction

A plethora of suggestions exist on how to utilize acoustic forces for lab-on-a-chip applications. For the typical dimensions of microfluidic structures there are two acoustic effects that are mainly important: the acoustic radiation force, which moves particles either towards or away from pressure nodes depending on the established standing acoustic field, and acoustic streaming, which imparts movement onto the entire medium. In this study, two microfluidic chambers (one of quadratic and one of circular footprint, 2 mm on the side or in diameter) were investigated. Both chambers were connected to 400 μm wide inlet and outlet channels, and the depth was 200 μm throughout. While recent studies of acoustic behaviour have been reported for one-directional standing waves as well as for low-frequency acoustic streaming [1, 2], here the entire system is actuated, such that both vertical and horizontal standing waves can be formed. The coupling from the actuator to the structures and their acoustic resonances is a yet poorly understood mechanism. Coupling strengths vary for different resonances, and amplitude fluctuations across the structures are common. Therefore, full-image analysis is important in investigating acoustic effects. Streamlines can be employed to illustrate flow behaviour, but they are not sufficient in determining local variations in velocity. Thus, we have chosen to employ the micro-PIV technique. However, as particles under the influence of acoustic fields do no longer function as true independent tracers in all situations, extra caution and considerations have to be taken when applying micro-PIV for these types of studies.

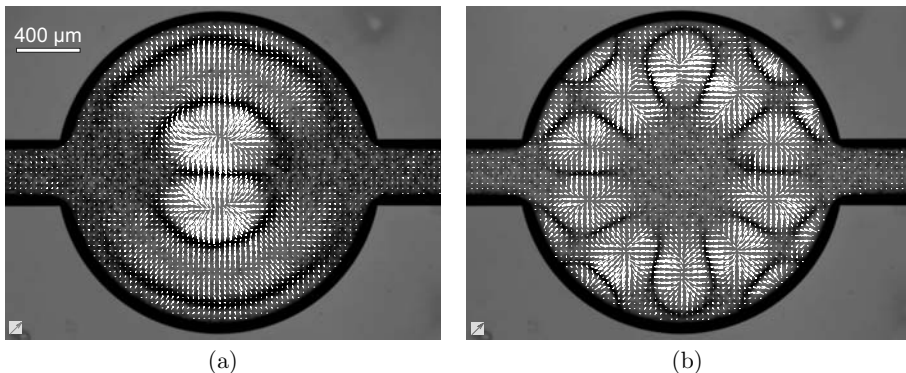


Figure 1: $10 \mu\text{m}$ beads at 1.936 MHz (a) and 2.417 MHz (b). Vector plots, showing the initial particle flow immediately after the piezo actuation is turned on, are positioned on top of the pattern obtained 3 seconds later. Acoustic radiation forces dominate. The length of the reference vectors in all figures equals $100 \mu\text{m}/\text{s}$.

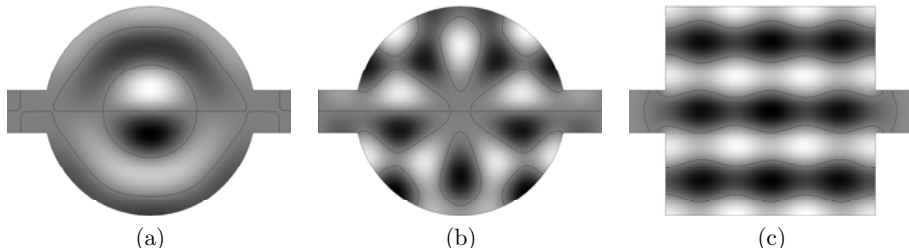


Figure 2: Calculated acoustic resonances for round chamber at 1.936 MHz (a) and 2.417 MHz (b), and quadratic chamber at 2.17 MHz (c).

2 Materials and Methods

The microfluidic chips were fabricated in silicon via deep reactive ion etching (DRIE). Anodic bonding was used to seal the structures by a glass lid on the channel side. The piezo actuator was pressed to the backside of the chip using a contact grease and biased by a 20 V ac voltage source. Images were captured with a CCD camera, with appropriate microscope magnification for capture of full-image vector fields. A LED was used as illumination source in a previously not described reflection backlit configuration.

3 Results and Discussion

The investigation was performed by scanning the spectrum from a tone generator, thus identifying those frequencies where strong coupling from the piezo actuator to the structures occurred. In Figure 1 vector plots at 1.936 MHz and 2.417 MHz in the circular

structure compared favourably with acoustic resonances calculated by use of COMSOL finite element method software (Figure 2). In Figure 3, the behaviour of 10 μm beads and 1 μm beads in the quadratic structure at 2.17 MHz are shown. The 6x6 pattern of vortices can only be seen for the smaller beads, since here the acoustic radiation force has less effect while the acoustic streaming dominates. A pronounced inhomogeneity in the strength of the vortices across the microfluidic chamber, for which chamber geometry cannot solely be accountable, is also apparent, illustrating the importance of full image analysis when acoustic effects are investigated. These little investigated irregularities are believed to stem from uneven coupling to the actuator.

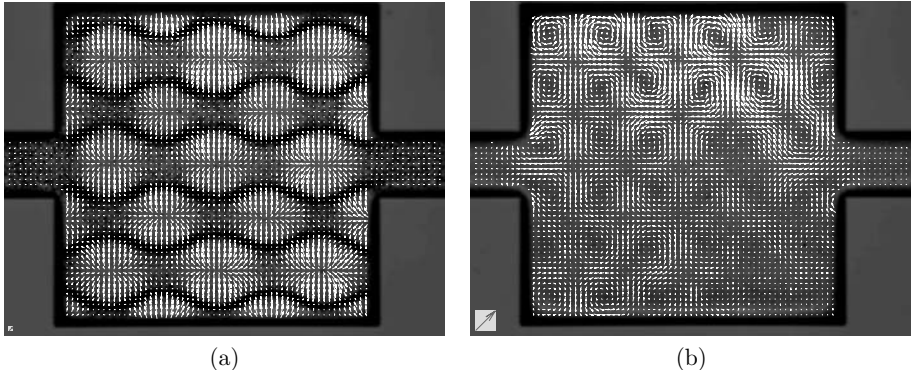


Figure 3: 10 μm beads (a) and 1 μm beads (b) at 2.17 MHz. For the large particles acoustic radiation forces dominate. For the smaller particles the effect of the acoustic radiation forces is weaker than the movement caused by streaming. Therefore, they function as tracers for the motion of the bulk fluid. Note the velocity difference between top left and bottom right corner (figure b).

4 Conclusions

In this study we have shown that full-image micro-PIV in combination with CFD calculations can be used for analysis of lab-on-a-chip applications where acoustics are applied.

References

- [1] L.A. Kuznetsova, S.P. Martin, and W.T. Coakley. Sub-micron particle behaviour and capture at an immuno-sensor surface in an ultrasonic standing wave. *Bioelectromagnetics*, 21(6):940–948, 2005.
- [2] L.S. Jang, S.H. Chao, M.R. Holl, and D.R. Meldrum. Microfluidic circulatory flows induced by resonant vibration of diaphragms. *Science*, 308(5725):141–148, 2005.

EFFICIENCY CONTROLLABLE SAMPLE PRECONCENTRATION CHIPS BASED ON NANO ION DEPLETION BRIDGE

Jing Liu^{1, 2}, Gui-Sheng Zhuang^{1, 2}, Qing-Hui Jin¹, and Jian-Long Zhao¹

¹Shanghai Institute of Microsystem and Information Technology, Chinese Academy of Sciences, Shanghai 200050, China

²Graduate School of the Chinese Academy of Sciences, Beijing 100039, China

Abstract

In this paper, quartz nanofluidic chips employing ion depletion bridges were developed for studying sample preconcentration efficiency. The nanostructures with a series of accurate nano depths were fabricated with two-step photolithography and nano wet etching techniques. Based on the electrokinetic trapping mechanisms, the chips could efficiently concentrate biological samples and the concentration efficiency could be optionally controlled through the adjustment of the nanostructure and buffer component.

Keywords: Ion depletion bridge, nanofluidic chip, preconcentration, nano wet etching, electrokinetic trapping

1. Introduction

Most microfluidic separation and sample processing devices suffers from the critical scaling problems, which can influence the detection ability and sensitivity. Recently, the electrokinetic trapping mechanism associated with nanostructure has been reported [1] and could be applied to the sample concentration system. Here we developed a series of nanofluidic chips and preconcentrated samples depending on the ion depletion bridges. The concentration efficiency could be controlled through the adjustment of the nanostructures and buffer component, which showed the application feasibility of nanofluidic preconcentration method.

2. Experimental

The process flow chart of nanofluidic chips was shown as Fig. 1. Sample transport channels (10μm depth) were fabricated by standard photolithography and wet etching. Then the nano bridges (12.0nm~45.6nm depth) (Fig. 2), which connected the transport channel, were fabricated with aligning photolithography and nano quartz wet etching (HF:HAC: H₂O₂=2:5:5, 40°C). The wet etching could be well used for the quartz nano structures' fabrication and could be exactly controlled: the etching velocity was described as the Fig. 3 and the surface roughness in the etched channel was tested, shown as the Fig. 4. Then hole-drilling and low-temperature bonding technique [2] were used to make quartz nanofluidic chips. For the preconcentration of biological samples, a two-step procedure was performed. Firstly, the channel was filled with the sample (Fig.5 (a)).

Then the DC voltage was applied between the nano bridge to form the ion-depletion trip and the sample was continuously massed nearby the ion-depletion trip (Fig.5 (b)).

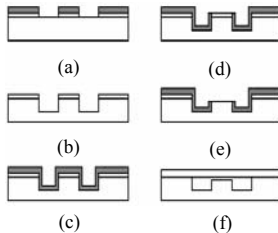


Figure 1. Process flow chart of nanofluidic chips. (a) First photolithography and chrome etching (b) Transport channel etching and photoresist striping (c) Photoresist coating (d) Twice photolithography for nano bridge (e) Twice chrome etching and nano wet etching (f) Bonding.

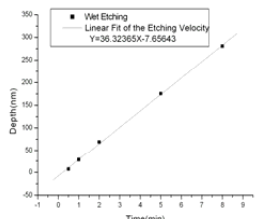


Figure 3. Nano wet etching velocity



(a)

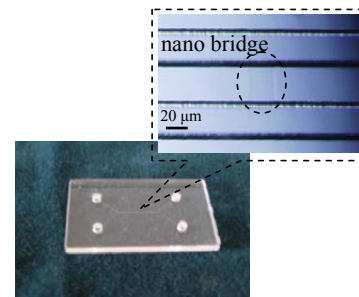


Figure 2. Picture of the nanofluidic chip and micrographs of 45.6nm-depth nano bridge

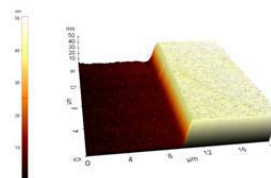
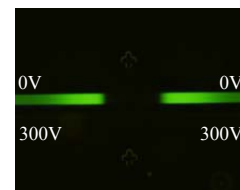


Figure 4. The AFM image of the nano bridge. The nano bridge was 45.6nm depth. The etching part's $R_a < 5.225$, while the initial R_a value of the quartz was 1.590.



(b)

Figure 5. Preconcentration process of the nanofluidic chip. (a) The initial form of the ion-depletion trip (b) The massing for the sample plug. 0.9 μ M FITC was used. The depth of the nano bridge was 12.0nm. And the running buffer was 0.1mM borax at pH 10.0.

3. Results and discussion

The electrokinetic trapping mechanisms associated with nanostructures are originated from the electric double layer overlapping [1]. The depths of the nano bridges affected

the overlapping degree of the electric double layer and then influenced the concentration efficiency. The comparison of FITC concentration results with different nano bridge depths was shown in Fig.6. The double layer thickness is inversely proportional to the square root of the electrolyte concentration, and then the concentration of the running buffer was regulated to control the concentration efficiency. The comparison of FITC and IgG concentration results with different buffer concentrations was described as Fig.7.

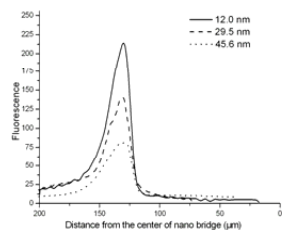


Figure 6. Comparison of FITC concentration results with different nano bridge depths. $0.9\mu\text{M}$ FITC was used and the running buffer was 0.1mM borax at pH 10.0.

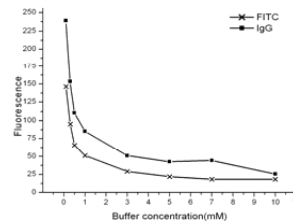


Figure 7. Comparison of FITC and IgG concentration results with different buffer concentration. $0.9 \mu\text{M}$ FITC and $1 \mu\text{M}$ IgG were used. The depth of the nano bridge was 12.0nm . The running buffer was borax with different concentration.

4. Conclusions

Without any physical barriers or reagents the controllable preconcentration experiments of FITC and protein were achieved in the nanofluidic chips. The fabrication and the experimental process were convenient. And the quartz chips could be used repeatedly.

Acknowledgements

This work was supported by the STCSM (Grant No: 051111019) and Shanghai AM. R&D. fund (Grant No: 0510).

References

- Qiaosheng Pu, Jongsin Yun, Henryk Temkin, and Shaorong Liu, *Ion-enrichment and ion-depletion effect of nanochannel structures*, Nano Letters, 4, pp.1099-1103, (2004).
- Jing Liu, Guisheng Zhuang, Qinghui Jin, and Jianlong Zhao, *A microchip electrophoresis system with UV detection for protein analysis*, Prog. Biochem. Biophys., 31, pp.1045-1049, (2004).

Corresponding Author: Jian-Long Zhao, Nanotechnology Laboratory, Shanghai Institute of Microsystem and Information Technology, Chinese Academy of Sciences, Tel: +8621-62511070-5709, Fax: +8621-62511070-8714, E-Mail: jlzhao@mail.sim.ac.cn.

3D-SIMULATIONS OF AGGREGATING BEADS IN MICROFLUIDIC CHAMBERS ON HIGH PERFORMANCE COMPUTERS COMPARED TO EXPERIMENTS

T. Glatzel^{*}, C. Cupelli^{*}, U. Kuester^{}, R. Zengerle^{*}, and M. Santer^{*}**

*** Laboratory for MEMS Applications, Department of Microsystems Engineering (IMTEK), University of Freiburg, Georges-Koehler-Allee 106, 79110 Freiburg, Germany (glatzel@imtek.de)**

****High Performance Computing Centre – HLRS, University of Stuttgart, Nobelstrasse 19, 70569 Stuttgart, Germany**

Abstract

We have developed a highly flexible computer code for studying rheological fluids in arbitrarily shaped micro channels based on a Fluid Particle approach [1-2]. As an application example, we show the aggregation of hundreds of polystyrene micro beads in a flat assay structure for fluorescent readout [3] and compare to corresponding experiments.

Keywords: simulation of complex fluids, microbead assays, high performance computing

Introduction

Understanding blood flow in micro capillaries, sorting bio-particles and aggregation of arbitrarily shaped objects is of great relevance for many μ TAS applications. These phenomena, however, cannot be studied with commercially available CFD tools which is a big problem in the design process of μ TAS devices. The Fluid Particle approach is a solution to this problem allowing for the implementation of arbitrary shaped objects regardless if they are stiff or flexible.

Theory of the fluid particle method

The simulation approach is based on discrete elements, so-called fluid particles (FP) [1]. In this method, hydrodynamics is represented in the continuum by FP interacting pairwise over conservative, dissipative and stochastic forces $\mathbf{F}_i = \sum (\mathbf{F}_{ij}^C + \mathbf{F}_{ij}^D + \mathbf{F}_{ij}^R)$ with a common cutoff distance r_c by solving Newtonian equations of motion. Channel walls, suspended objects etc. are made of FP and interact over similar force laws, allowing for a very efficient implementation of the simulation code on parallel computers. Arbitrarily shaped extended objects, e.g., spherical micro beads, bodies of cells and flexible tissue can be represented by compounds of FP. They may either form simple rigid bodies or elastic objects when connected by (non-)linear spring forces, such as FENE-models for polymers. The dynamics of the extended objects as a whole is determined by center of mass motion and that of the body axes that is efficiently described by quaternion dynamics [4].

Experiments and simulations

The experiments show the aggregation of polystyrene micro bead suspended in 5 % RBS flowing with flow rates between $I_F = 3 - 7 \text{ ml/min}$ in comparison with simulations (see Fig. 1). In the experiments as well as in the simulations beads are initially put in a collecting chamber (not shown) and are flowing through the inlet channel into the aggregation chamber. Capture of beads at walls and corners induces imperfections in the layering that are also present in the simulations (circle in Fig. 1) in particular the disturbance of the hexagonal order at round corners. Each simulation for a predefined number of aggregating beads takes about 10 hours for $\sim 2.5 \cdot 10^5 \text{ FP}$ on an Opteron Cluster calculated with eight CPUs. The rhomboidal aggregation part of the chamber can hold a maximum of 360 perfect hexagonal accumulated beads and has a height of $h_a = 190 \mu\text{m}$ in the aggregation area and $h_o = 80 \mu\text{m}$ in the outlet area (see Fig. 2). Due to the imperfect layering not all of the 360 beads are aggregated in the chamber and the pressure drop rapidly increases as beads entering the inlet channel (see Fig. 2).

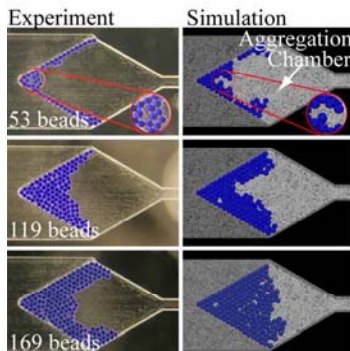


Figure 1. Comparison of the experimental (left) and simulated (right) aggregation of polystyrene micro beads. As in the experiments we reproduce the imperfect layering of beads (circle in the upper pictures).

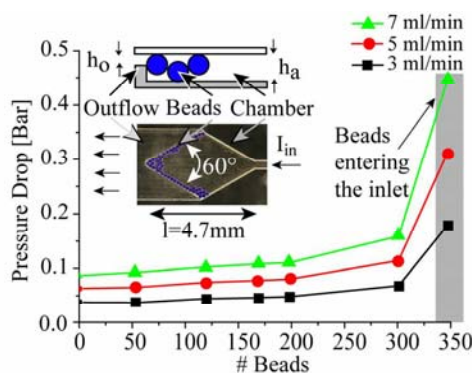


Figure 2. Measured pressure drop over the microfluidic geometry with increasing number of aggregated beads at flow rates I_{in} ranging from 3 - 7 ml/min. The polystyrene beads have a diameter of $d = 150 \mu\text{m}$ and a density of 1.05 g/cm^3 .

Performance, parallelisation and code structure

Our simulation code has been parallelized with a technique called Message-Passing Interface (MPI) employing a domain decomposition. The performance is significantly enhanced by a dynamic load balancing by weighting the actual workload on each processor. This ensures that particles are distributed evenly among all processors according to the predicted workload. The code has been tested on single processor workstations, PC-based clusters and high performance computers (HPC), showing an almost perfect super linear speed-up with increasing number of processors (see Fig. 3 as an example for PC-based clusters). Arbitrary shaped geometries such as the microfluidic chamber can be generated via external CAD tool (e.g. SolidWorksTM) subsequently

meshed, exported into the Patran-file format and then imported into the simulation code (see Fig. 4). The CAD file can further be used to fabricate the microfluidic structures or to accomplish simple CFD simulations without beads or biological cells.

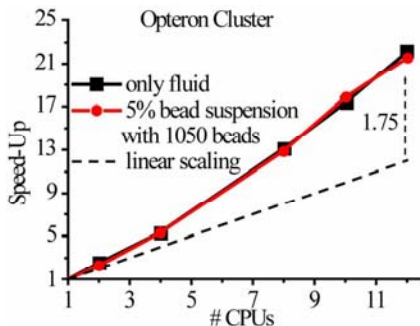


Figure 3. Relative speed-up of the simulation code with only fluid (squares) and with a 5 % bead suspension (circles) with $\sim 4.5 \cdot 10^6$ FP on a Dual-Core Opteron cluster (12 CPUs @ 2.2 GHz). The system shows a scaling which is a factor 1.75 better than linear scaling, indicating difficulties with handling large arrays on single processes.

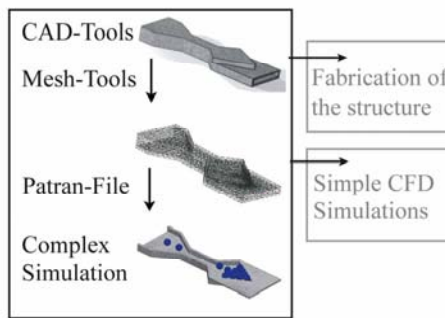


Figure 4. The interfacing to commercial tools is done via the Patran-file format. At first the geometry is constructed in SolidWorks™ (CAD), meshed with CFDRC-ACE+ and then imported into the simulation code. Complex simulations are done with our code whereas simple CFD simulations can be done with external tools (e.g. CFDRC-ACE+).

Conclusion:

We successfully implemented a highly flexible simulation code for the simulation of particle-laden flows in microfluidic geometries. The flexibility of the code allows for an easy extension of this simple example to more complicated problems such as flow of vesicles or blood cells in micro capillaries and other phenomena of great biological relevance. Our analysis of the code has shown that it can be run efficiently already on moderately sized, low-cost PC-clusters for efficient design of novel μTAS.

Acknowledgements

The support of the Landesstiftung Baden-Württemberg (HPC-Project) is gratefully acknowledged.

References

- [1] P. J. Hoogerbrugge and J. M. V. A. Koelman, *Europhysics Letters*, vol. 19, no. 3, pp. 155-160, (1992).
- [2] P. Espanol, *Physical Review e*, vol. 52, no. 2, pp. 1734-1742, (1995).
- [3] M. Grumann, et al., *Lab on A Chip*, vol. 4, no. 3, pp. 209-213, (2004).
- [4] D. J. Evans, *Molecular Physics*, vol. 34, no. 2, pp. 317-325 (1977). D. J. Evans and S. Murad, *Molecular Physics*, vol. 34, no. 2, pp. 327-331, (1977).

HIGH-PERFORMANCE DROPLET GENERATION VIA INTEGRATED 3-D CIRCULAR CONSTRICtIONS

Wee-Liat Ong, Stefan Martens[#], Nagarajan Ranganathan, Levent Yobas*

Institute of Microelectronics, 11 Science Park Road, S117685, Singapore

[#]University of Applied Sciences Wiesbaden, Germany

(*Contact: leventy@ime.a-star.edu.sg)

Abstract

This paper reports on high-performance droplet generation through a 3-D circular constriction integrated inside a planar flow-focusing geometry. Water-in-oil droplets show increased sensitivity against the total oil flow rate with a power of ~3.

Keywords: droplets, flow-focusing, orifice, integrated, shear stress

1. Introduction

Droplet generation via flow-focusing planar geometry has been introduced by Anna et al. [1] and improved by Tian et al. by a nozzle channel enforcing the droplet breakup at a fixed location [2]. These designs however are quasi-2-D (2-D) rectangular constrictions although a 3-D circular constriction would be ideal. The 2-D designs constrict the flow from two sides laterally since the channel height is uniform. Chan et al. created a step increase in the channel height at the flow-focusing region but preserved the rectangular constriction [3]. A circular constriction has been demonstrated earlier using replica-molding technique yet it is difficult to integrate such with planar microfluidics [4]. Here we introduce a novel flow-focusing design by integrating a lateral 3-D circular constriction directly inside a microchannel using planar fabrication.

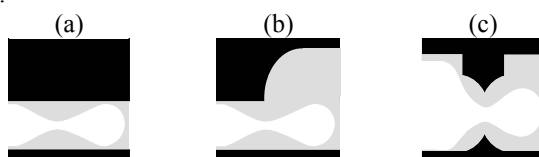


Figure 1. Side profile schematics of the flow-focusing constrictions: (a) rectangular 2-D [1]-[2] (b) rectangular 2-D with a step in channel height [3] (c) circular 3-D.

2. Chip Design

Figure 1 schematically compares the earlier 2-D and our 3-D constrictions. The 3-D constriction with a cusp-like edge imposes maximized shear at a single point. The constriction geometry being created by a simple lithographic silicon etching is controlled by the etching profile and layout parameters in figure 2 [5]. For the shown values, the constriction approaches a full circle with radius 22.5 μ m. Microchannels were deposited with a silicon-dioxide layer and capped with a glass anodic bonding.

The channels were then treated with octadecyltrichlorosilane to render them hydrophobic and hence suitable for generation of water-in-oil droplets.

3. Experimental

We used dyed distilled water and silicone oil (19.06mPa-s) as the dispersed and continuous phase, respectively. We also fabricated 2-D version of the same design in PDMS with constrictions' widths equivalent of the circular constriction's hydraulic diameter 32 μm and physical diameter 45 μm (figure 3). The designs all share the same channel height of 90 μm .

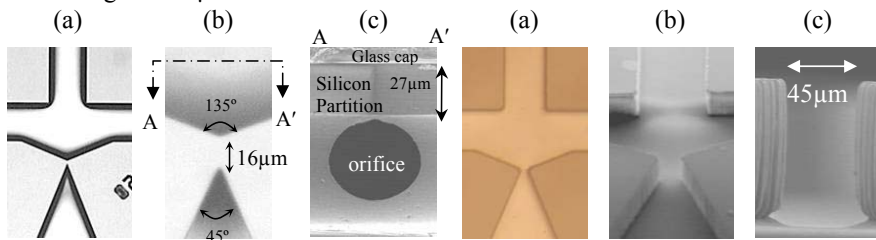


Figure 2. 3-D flow-focusing geometry in silicon: (a) planar view; (b) close-up view; (c) SEM image of the circular orifice. Water contact angle of treated surface: 112.5°

Figure 3. 2-D flow-focusing geometry in PDMS: (a) planar view; (b) and (c) SEM close-up of rectangular constriction without PDMS cap. Water contact angle of the surface: 114°.

4. Results and Discussion

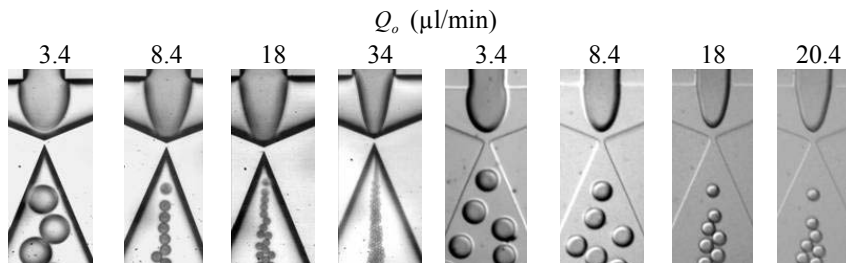


Figure 4. Phase diagrams showing water-in-oil droplets as generated in constrictions 3-D and 2-D having a width of 32 μm ($Q_w = 1.67\mu\text{l}/\text{min}$ for all).

Figure 4 shows phase diagrams of the 3-D and 2-D designs at the increasing total oil flow rates Q_o and fixed water flow rate Q_w of 1.67 $\mu\text{l}/\text{min}$. Droplet diameter D and frequency f derived from these images are compared as a function of Q_o in figure 5. Table 1 lists the equations pertaining to the trend lines ($R^2 \geq 0.9$ for all). Based on the results, one could deduce the characteristic relations $\{D \sim Q_o^{-1/3}, f \sim Q_o\}$ for the 2-D constrictions confirming the earlier reports [1-3], and $\{D \sim Q_o^{-1}, f \sim Q_o^3\}$ for the 3-D constriction.

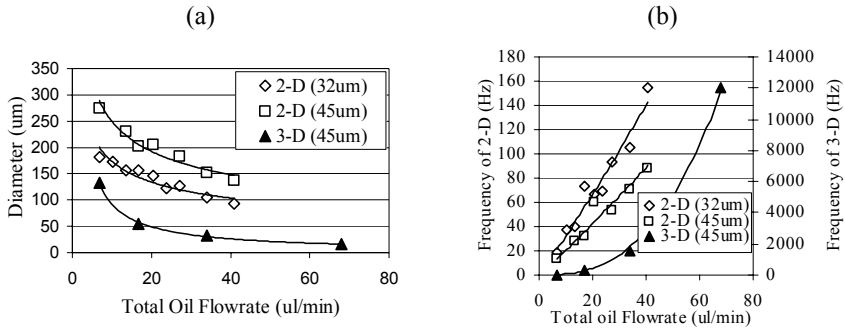


Figure 5. (a) Diameter D and (b) generation frequency f of water-in-oil droplets as a function of total oil flow rate Q_o and at Q_w 1.67 $\mu\text{l}/\text{min}$.

Table 1. Equations describing the trend lines in figure 5.

Constriction	type size	2-D		3-D
		32 μm	45 μm	45 μm
Droplets	diameter	$D = 409.01Q_o^{-0.372}$	$D = 593.94Q_o^{-0.376}$	$D = 737.61Q_o^{-0.905}$
	frequency	$f = 2.75Q_o^{1.06}$	$f = 1.81Q_o^{1.05}$	$f = 0.13Q_o^{2.7}$

5. Conclusion

Despite the similarity in the constriction size, water-in-oil droplets emerged from the 3-D constriction as compared to those from the 2-D constrictions show increased sensitivity in diameter and frequency against the total oil flow rate with power of ~ 3 .

References:

1. S.L. Anna, N. Bontoux, H.A. Stone, *Formation of dispersions using "flow focusing" in microchannels*, Appl. Phys. Lett., 82(3), pp. 364-366, (2003).
2. Y.C. Tan, V. Christini, A.P. Lee, *Monodispersed microfluidic droplet generation by shear focusing microfluidic device*, Sens & Act B, 114(1), pp. 350-356 (2006).
3. E.M. Chan, A.P. Alivisatos, R.A. Mathies, *High-temperature microfluidic synthesis of CdSe nanocrystals in nanoliter droplets*, J. Am. Chem. Soc., 127(40), pp. 13854-13861, (2005).
4. S. Takeuchi, P. Garstecki, D.B. Weibel, G.M. Whitesides, *An axisymmetric flow-focusing microfluidic device*, Adv. Mater., 17(8), pp. 1067-1072, (2005).
5. L. Yobas, R.K. Sharma, R. Nagrajan, V.D. Samper, P.S.R. Naidu, *Precise profile control of 3D lateral junction traps by 2D mask layout and isotropic etching*, J. Micromech. & Microeng., 15 (2), pp. 386- 393, (2005).

SIMULATION EXAMINATION FOR MULTILAYER FLOW SYSTEM

Ryo Anraku¹, Takahiro Asai¹, Kenji Uchiyama¹, Akihiko Hattori¹, Manabu Tokeshi², and Takehiko Kitamori³

¹NIPPON SHEET GLASS CO.,LTD., Japan

² The University of Nagoya, Japan

³The University of Tokyo, Japan

Abstract

In this study, we compared the observation experiment of a liquid-liquid interface with a simulation result about the three-phase micro channel used for an extraction reaction. As a result, each flow rate ratio greatly influences the formation of the three-phase flow. And the result of computing this multiphase flow model is corresponding to the experiment well, so the development of the unit chemistry operation model will become possible with the simulation in the future.

Keywords: Simulation, Multilayer flow, Microchannel, Microfluidics

1. Introduction

The formation of steady oil/water flow in a micro channel is indispensable to achieve the solvent extraction that is one of the chemical operations in the micro chemical system. In order to build a solvent extraction simulation model, it is required to establish the model of the oil/water flow in a micro channel. We previously reported on the fluid simulation model of the interfacial formation evaluation by used the oil/water flow in Y-shaped channel [1]. As there are also reports using the multi-phases as solvent extraction [2], we simulated water/oil/water flow model in this paper.

2. Experimental

Multi-Phase Flow Tests

Figure 1 shows the experiment system. We used the three confluence channel which were 70μm wide and 30μm deep in the glass chip. Water was poured on both sides of the channel with the syringe pump, and the ethyl acetate was made to flow in from the center channel. The interface in the confluence part at that time was observed with the microscope. The observation began from the state that the three-phase flow was not formed. The flow rate of water was decreased, and the flow rate was measured when the interface formed again.

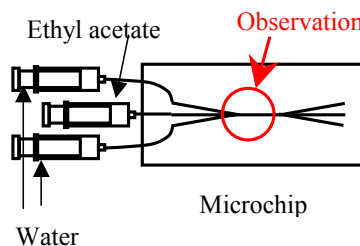


Figure 1. Experiment system

Moreover, the contact angles between oil/water interface and the channel wall for the calculation was estimated from the experiment result. The contact angles of the channel wall became about 10° from the meniscus when the interface vibrated. And this value was used as a calculation parameter.

Simulations

Behavior in the micro channel on water/oil interface was requested by the numerical analysis using the 3D model of Figure 2. The same inflow condition as the experiment was used about this model. To confirm the interface was formed, the confluence part neighborhood was modeled. A commercial CFD code (FLUENT6.2) solved the full Navier-Stokes equations using a Finite volume method approach. To reproduce the three-phase flow as consist of the three-phase of water and oil, we used the Volume of Fluid (VOF) method that was able to treat a complex transformation.

The free surface was analyzed in consideration of surface tension and the contact angle. The width of channel is $70\mu\text{m}$ and depth is $30\mu\text{m}$, and we changed each flow rate of the water and ethyl acetate.

3. Results and discussion

Comparison between experiment and calculation

When the three-phase flow forms the interface didn't return and advanced while making droplet because there were a lot of flow of the ethyl acetate at the center channel. The appearance that finally separated to the three-phase flow was confirmed from the experiment and the calculation result. An organic phase had been divided by narrowing of the width of this phase, and the contact of the interface when the three-phase flow was not formed. Therefore, the interface vibrated by droplet being made at almost the same position. Figure 3 shows the calculation result of interfacial behavior in the interfacial formation and non-formation.

When the flow rate of each phase is changed, it is shown in Figure 4 that right or wrong of the three-phase flow formation was plotted. The flow rate ratio of each phase

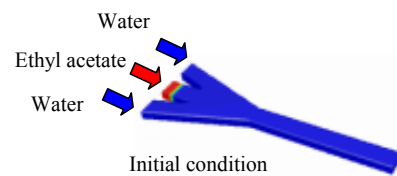


Figure 2. Simulation model

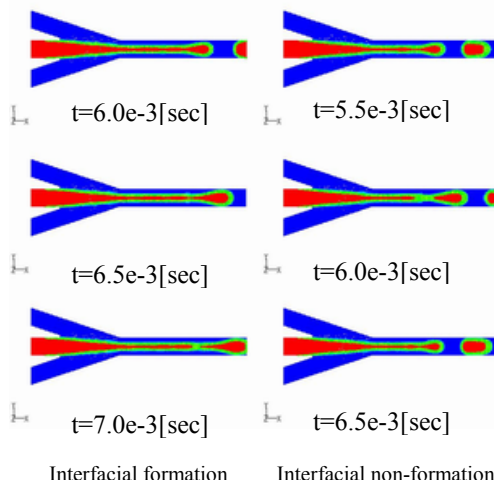


Figure 3. Interfacial position at each time

(water phase/oil phase) influence was large in the formation on the three-phase flow. And it had changed from the state of the three-phase flow non-formation into the formation when the ratio was 0.35-0.45 or less. Moreover, when having compared it with the calculation result, the borderline of an interfacial formation and non-formation is almost corresponding to the experiment result.

The sheath flow that was not contact with the channel wall was formed when the flow rate of oil phase was 11 μ L/min or more in the calculation, and the interface did not vibrate. However, this result was not confirmed by the experiment. As the reason, flow rate slightly changes actually while it is constant in the calculation. It was thought that the state that the interface has not come in contact with the channel wall was unstable, and the interface vibrated by the flow rate change.

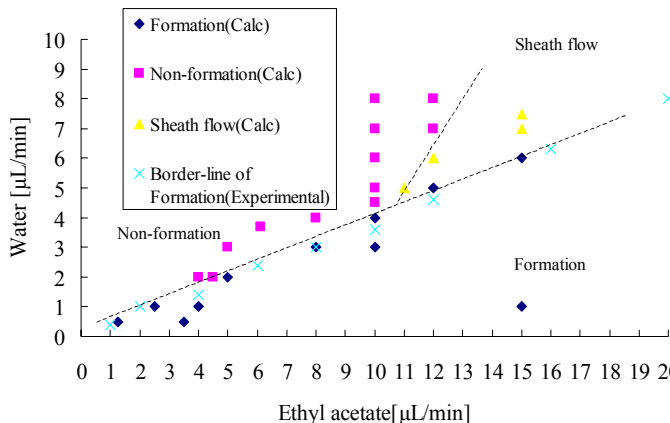


Figure 4. Relation between interfacial formation and flow rate

4. Conclusions

The flow rate ratio of water/oil has influenced interface formation greatly. The stable interface was formed in below a certain ratio. The result of computing this multiphase flow model is corresponding to the experiment well, so the development of the unit chemistry operation model will become possible with the simulation in the future.

References

- [1] R. Anraku, A. Hattori, T. Asai, T. Fukuzawa, M. Tokeshi, and T. Kitamori, MicroTAS2003, p151-153
- [2] A. Hibara, M. Tokeshi, K. Uchiyama, H. Hisamoto, and T. Kitamori, Anal.Sci., 2001, 17, 89

COMPUTATIONAL MODELLING OF PNEUMATIC PARTICLE CAPTURE DEVICE

Ok Chan Jeong¹ and Satoshi Konishi²

¹Center of Promotion of the COE program, Ritsumeikan University, JAPAN

²Dept. of Micro System Technology, Ritsumeikan University, JAPAN

Abstract

Improvements in manipulation of particles or cells are expected increasingly in microTAS field. This paper presents a computational modelling of particle motion induced by a pneumatic particle capture device through the fluid-structure analysis with the commercially available software.

Keywords: Computational modelling, Particle Capture, Pneumatic Vibrator

1. Introduction

Various working principles for the particle manipulation at a single cell level have been developing such as optical [1], dielectrophoretic [2], ultrasonic [3], and hydrodynamic [4]. Another interesting method is about all polymeric particle manipulator [5]. Forces generated by fluid flow have the potential to create relatively gentle trap actions and harmless manipulation. The capturing motion of single particle induced by pneumatic vibrators was successfully demonstrated [5]. This paper presents the computational modelling for particle capture devices since it is very important to understand particle motion influenced by the deformation of vibrator diaphragm.

2. Theory

Figure 1 illustrates a rigid sphere particle motion by single pneumatic vibrator. The particle and its surrounding fluid are in complete rest before actuation (a). If constant external pneumatic force is applied to vibrator diaphragm (b), the rigid particle motion is affected by the drag force (F_D) of the viscous fluid with velocity, $U(x, y)$ and the buoyancy force (F_B) [2]. Other force (F_E) on the particle defined in this paper is the force exerted by deformed diaphragm on the fluid. The equation of motion for the sphere particle becomes

$$ma = \sum F = F_D + F_B + F_E = 6\pi\eta R(U(x, y) - V(x, y)) + \frac{4}{3}\pi R^3 g\Delta\rho + F_E \quad (1)$$

where m , a , and R are mass, acceleration, and radius of the particle, respectively. η and $\Delta\rho$ are viscosity of fluid and density difference between the fluid and the particle, respectively. g is the acceleration of the gravity. Neglecting the minor inertial effect of mass, Eq. (1) is simplified by $V(x, y) = U(x, y) + 2R^2 g\Delta\rho/9\eta + F_E/6\pi\eta R$. The particle velocity is affected by all forces during the deformation of vibrator diaphragm. At the steady state of vibrator, it is only influenced by F_B and F_E , because $U(x, y) = 0$. To calculate particle velocity, two unknown values, $U(x, y)$ and F_E are computed through the fluid-structure analysis with FEMLAB software package.

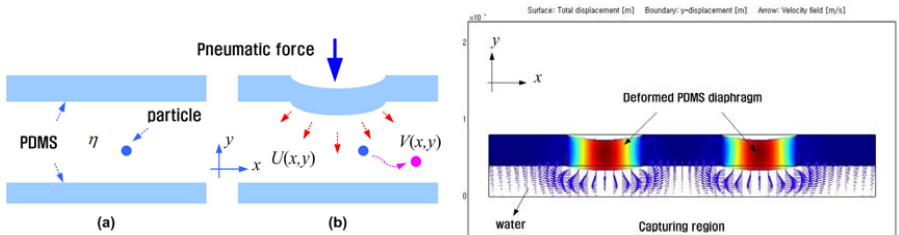


Fig. 1. Rigid sphere particle motion by pneumatic vibrator. η is the viscosity of the fluid. $U(x, y)$ and $V(x, y)$ are velocity of the fluid and the particle, respectively. (a) initial state of particle and viscous fluid at a complete rest, (b) particle motion affected by the velocity of its surrounding viscous fluid.

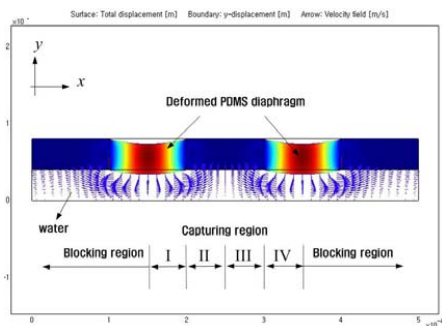


Fig. 2. Velocity field of water generated by the deformed of PDMS diaphragm. The capturing region between the center of two vibrator diaphragms is divided into four regions in order to investigate 2-dimensional particle velocity.

3. Simulation

Figure 2 shows computed velocity field of water caused by the deformed PDMS diaphragm of the pneumatic particle capture device. The multi-physics problem of that device is solved with Mooney-Rivlin material model for structural analysis of 20:1 PDMS diaphragm, moving mesh model, and incompressible Navier-Stoke model for fluid analysis. Two coefficients of Mooney-Rivlin model of PDMS elastomer are computed from the measured strain-stress relationship of PDMS film. The diameter and thickness of the circular diaphragm are 100 μm and 40 μm , respectively. The height of the liquid chamber is 40 μm . The calculated vertical deflection of PDMS diaphragm is about 6.24 μm when 125 kPa of the input pressure is applied. The capturing region between the center of two vibrator diaphragms ($150\mu\text{m} < x < 350\mu\text{m}$) is divided into four regions in order to investigate 2-dimensional particle velocity.

4. Results and Discussion

Figure 3 shows simulation results on the fluidic velocity and the force distribution along x -axis of the particle capture device. A polystyrene bead is used as a particle. Its diameter and density are 10 μm and 1.06 g/cm³, respectively. As shown in Fig. 3(a), at $x = 250\mu\text{m}$, U_x is zero and U_y becomes to be minimized because of the axial symmetry of vibrator structure. F_E is calculated from the computed pressure distribution of the fluid. It is found out that F_E is almost independent of the initial particle position (b). The magnitude of F_E is much smaller than other manipulation method [1].

Figure 4 shows the estimated axial-velocity of particle at $y = 20 \mu\text{m}$ and particle velocity diagram under the various initial positions of the particle. By inserting the simulation results into Eq. (1), the axial-velocity of particle, V_x and V_y can be calculated (a). Due to F_B and F_E , the axial-velocity components of the particle negatively increase. Fig. 4(b) shows the summary of the particle velocity diagram under various initial

position of the particle. V_x is the line symmetry at $V_x = 0$. It's easy to estimate the 2-dimensional particle motion by the vector summation of V_x and V_y . If the particle exists at the capturing regions, the particle moves to the central capturing region during periodic actuation of vibrator diaphragm and then is temporary trapped [5].

5. Conclusions

This paper describes the empirical formula based computational modelling on solid particle motion influenced by the deformation of vibrator diaphragms.

References

1. I. I. Smalyukh et al., *Applied physics letters*, **86**, 021913, 2005.
2. B. M. Taff and J. Voldman, *Anal. Chem.* 77(24), pp. 7976, 2005.
3. N. R. Harris et al., *Sens. & Actu. B* 111–112, p. 481-485, 2005.
4. B. R. Lutz and D. R. Meldrum, *Proc. u-TAS*, pp. 512-514, 2005.
5. O. C. Jeong and S. Konishi, 19th *IEEE MEMS Conf.*, pp. 782-785, 2006.

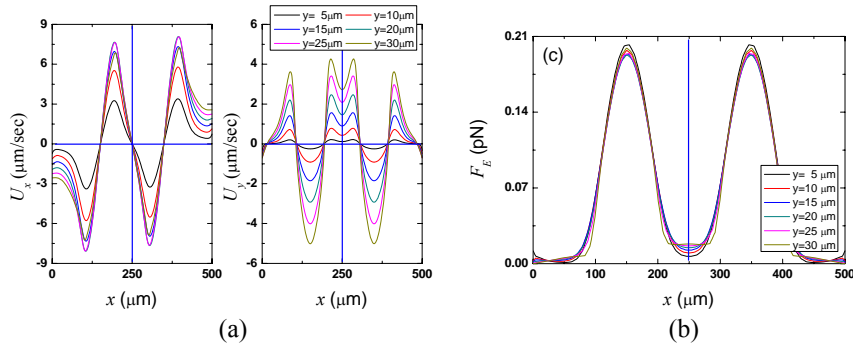


Fig. 3. Simulation results on the fluidic field and the generated force distribution along x -axis of the particle capture device. (a) U_x and U_y , (b) F_B

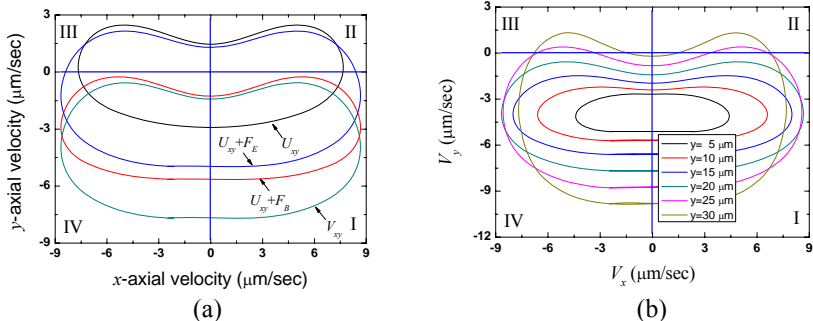


Fig. 4. Particle velocity diagram calculated from Fig. 3. (a) Axial-velocity at $y = 20 \mu\text{m}$, (b) Particle velocity diagram under various initial position of the particle.

THREE-DIMENSIONAL MEASUREMENT OF CIRCULATION FLOW IN A DROPLET MOVING IN A MICROCHANNEL

Haruyuki Kinoshita, Marie Oshima, Shohei Kaneda and Teruo Fujii

Institute of Industrial Science, The University of Tokyo, 4-6-1, Komaba, Meguro-ku, Tokyo, 153-8505 Japan
(hkino@iis.u-tokyo.ac.jp)

Abstract

The paper presents the measurements of three-components of three-dimensional flow velocities (3D3C) in a small liquid droplet using the confocal micro-PIV technique. The complex 3D flow structure is investigated which is generated inside the droplet when the droplet is transported through a square microchannel. The confocal micro-PIV technique enables us to measure 3D2C velocity distributions of micro flows with high accuracy and high resolution. Using those 3D2C velocity information and the equation of continuity, we can estimate the other vertical velocity component. As the result, we have successfully visualized the 3D flow pattern inside a moving droplet and have found out that 3D and complex circulating flow is formed inside the droplet.

Keywords: Confocal micro-PIV, droplet, 3D3C, equation of continuity

1. Introduction

The flow phenomenon in the droplet is of great significance for fluid handling in droplet-based microfluidic devices or systems [1]. In the microscale, the flow remains laminar due to a very low Reynolds number and never becomes turbulent flow. Therefore, fluid movement such as circulation or vortices reinforces acceleration of mixing and/or chemical reactions in droplet-based microfluidic devices [2]. In order to design a hydrodynamically-efficient droplet-based device or system, the key issue is to obtain a better understanding and controlling of the fluid flow phenomena inside a small droplet. In this study, we apply the confocal micro-PIV technique [3, 4] in order to investigate the three-dimensional complex flow field in the droplet.

2. Experimental setup

Figure 1 shows the schematic illustration of the confocal micro-PIV system [4]. The confocal imaging system enables us to obtain a sequence of sharp and high-contrast particle images within a thin layer of horizontal cross-sectional plane at 2,000 fps. Applying PIV method to this confocal system, we can measure the 2D2C velocity field in the region of $240 \mu\text{m} \times 180 \mu\text{m}$ with the depth-of-field of $1.88 \mu\text{m}$. Cross-sectional 2D2C measurements are conducted sequentially changing the focus position with the interval of $2.0 \mu\text{m}$ in vertical direction. A volumetric distribution of in-plane 2C velocities, u and v , is constructed by stacking those 2D2C cross-sectional velocity fields.

The other out-of-plane (vertical) component, w , is estimated analytically from the 3D distributions of u and v based on the equation of continuity. As a result, we can obtain the 3D3C velocity field information of micro flows with the grid resolution of 2.3 μm (x) \times 2.3 μm (y) \times 2.0 μm (z).

We use a T-shaped PDMS microchannel with 100 μm width \times 58 μm height in order to generate liquid droplets. Figure 2 shows sequential photographs of evolution of droplet formation process. Silicone oil is streaming in the main channel and glycerol solution is flowing into the main channel at the intersection, where small droplets of glycerol solution are generated repeatedly and transported to the measurement section. Glycerol solution contains fluorescent tracer particles of 500 nm in diameter for PIV.

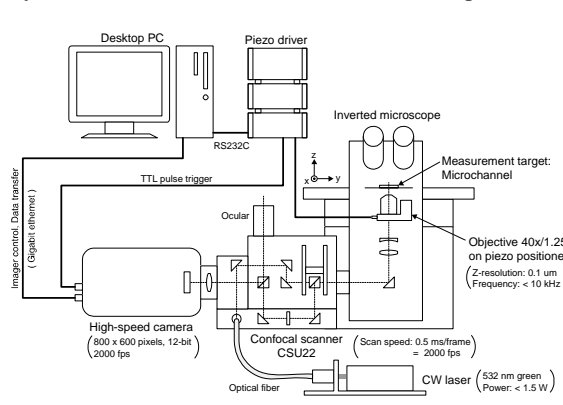


Figure 1. Confocal micro-PIV system

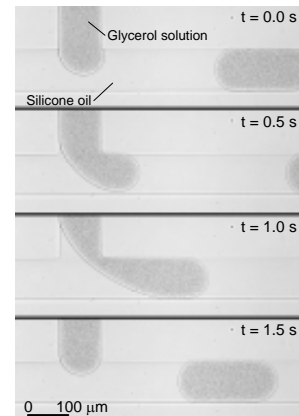


Figure 2. Droplet formation

3. Results and discussion

Figure 3 shows 3D3C velocity distributions inside the moving droplet. In order to elucidate the flow phenomenon inside the droplet, the velocities relative to the moving speed of the droplet are estimated and mapped in Fig. 3. Figure 4 also illustrates the flow pattern inside the droplet. Four contact surfaces with the surrounding channel walls are dragged by the walls and are moving backward when a round droplet is passing through the square channel. In contrast, surfaces near the four corners of the channel are flowing upstream. The round shape of the droplet forms gaps at the four corners, and these gaps are filled with another fluid, the oil phase. The fluid slips freely at the liquid-liquid interfaces between the water phase and the oil phase. Otherwise, the water phase fluid is dragged forward at the liquid-liquid interface by the oil phase flow, which overtakes the droplet. Anyway, the fluid which is dragged backward by the walls must return forward within the droplet since the fluid is forced to circulate when encaged in a closed volume such as the droplet. Therefore, the fluid inside the droplet circulates intricately and three-dimensionally in a closed volume due to the drag force on the contact surfaces with the surrounding walls of the channel.

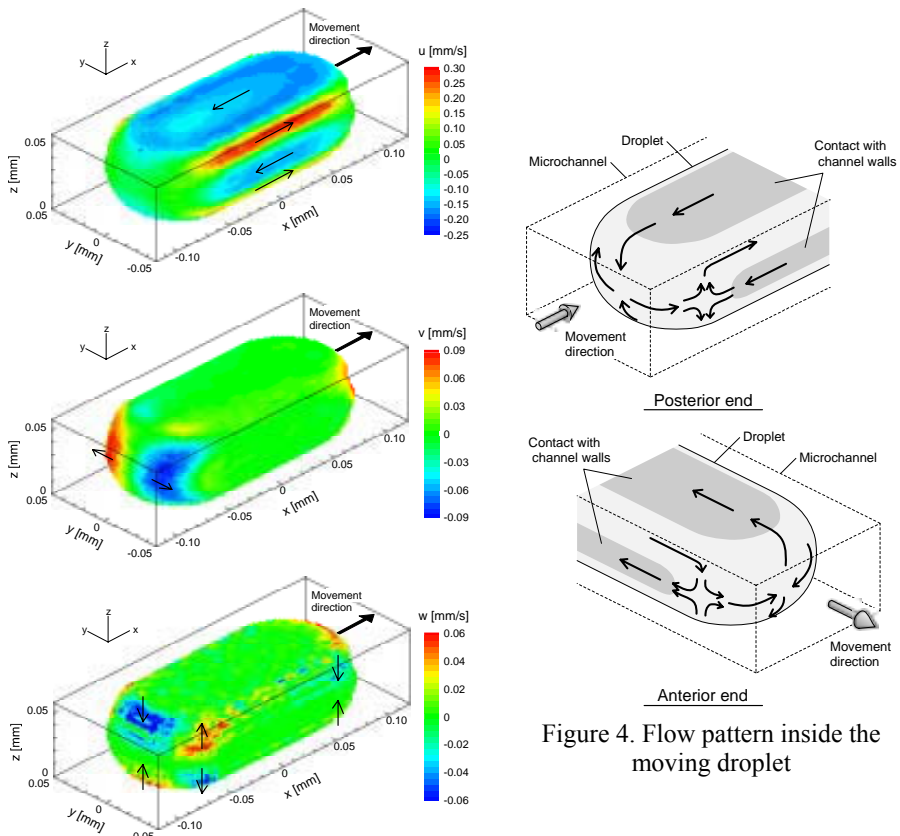


Figure 3. 3D3C velocity distributions (u , v , w)

4. Conclusions

We materialized the 3D3C measurement of micro flows using the confocal micro-PIV system and the equation of continuity. Using this technique, we have measured and investigated the internal flow of a droplet, transported in a square PDMS microchannel. We successfully obtained 3D3C velocity distribution and demonstrated the schematic diagram of the flow pattern inside the droplet. The fluid inside a droplet circulates intricately and three-dimensionally due to the drag force on the contact surfaces with the surrounding walls of the channel when the droplet moves in a square microchannel.

References

1. K. Hosokawa, et al., Analytical Chemistry, Vol. 71, pp. 4781-4785, (1999).
2. H. Song, et al., Angew. Chem. Int Ed, Vol. 42, No. 7, pp. 767-772, (2003).
3. J. S. Park, et al., Experiments in Fluids, Vol. 37, pp. 105-119, (2004).
4. H. Kinoshita, et al., Proc. μ TAS2005, Vol. 1, pp. 629-631, (2005).

AN OPTICALLY DRIVEN PUMP FOR MICROFLUIDICS

**Hasan Mushfique^{1,2}, Jonathan Leach^{1,2}, Miles Padgett²,
Roberto di Leonardo^{1,3} and Jon Cooper¹**

¹Electronics and Electrical Engineering, ²Physics and Astronomy,
University of Glasgow, Glasgow G12 8LT, UK.
³INFM-CRS SOFT, Dipartimento di Fisica, Roma, Italy.

Abstract

Central to the success of microfluidic and lab-on-a-chip systems has been the development of innovative methods for the manipulation of fluids within microchannels. We demonstrate a method for generating flow within a microchannel using an optically driven pump. The pump consists of two counter rotating birefringent vaterite particles trapped within a microfluidic channel and driven using optical tweezers. The transfer of spin angular momentum from a circularly polarised laser beam rotates the particles at up to 10 Hz. We show that the pump is able to displace fluid with flow rates of up to $200 \mu\text{m}^3 \text{s}^{-1}$ (200 fL s^{-1}). We also incorporate a novel optical sensing method, based upon an additional probe particle, trapped within a separate optical tweezers, enabling us to map the magnitude and direction of fluid flow within the channel. The techniques described in the paper have potential to be extended to drive an integrated lab-on-chip device, where pumping, flow measurement and optical sensing could all be achieved by structuring a single laser beam.

Keywords: lab-on-chip, microfluidics, pump, angular momentum, optical tweezers

1. Introduction

The miniaturisation of analytical processing as part of the development of lab-on-a-chip devices promises to revolutionise biological and chemical measurement. Fluid manipulation on such devices not only gives the possibility of automated analysis but has the advantages of providing faster and higher throughput, by reducing the volume of the materials used and by providing the ability to perform multiple processes simultaneously.

We report on a new system for driving fluid in microchannels using an optically driven pump [1] which does not require any specific channel design or scanning mirrors. Our approach uses the transfer of spin angular momentum from a circularly polarised beam to spin trapped birefringent particles resulting in a flow of the surrounding fluid. A novel optical sensing method [2] for mapping the magnitude and direction of flow in a microfluidic channel is also incorporated.

2. Experimental

The optical setup shown in Figure 1 is based on an inverted microscope in which the optical traps used for the pump were created with a tightly focused, circularly polarised $\lambda=1064 \text{ nm}$ laser beam. The circularly polarised beams were split with a Wollaston prism and brought to a focus, forming two optical traps with opposite angular

momentum in the image plane of the lens. The 1064 nm beam was used to trap and rotate two birefringent vaterite [3] particles in opposite directions.

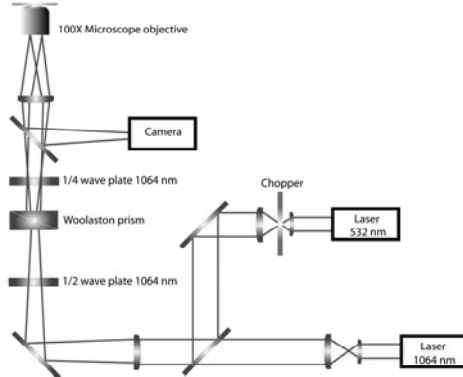


Figure 1. The optical tweezers set up required for the optical pump.

The microfluidic channels were made by photolithographic transfer of channel pattern onto a silicon wafer coated with a positive photoresist. The patterned wafer was then dry etched using an anisotropic deep silicon etch. Smooth, high aspect ratio masters, 15 μm deep were produced and subsequently used to cast the channels in a mixture of degassed poly(dimethylsiloxane) PDMS. Finally, the PDMS channels were sealed against a 150 μm thick coverglass producing the microchannels.

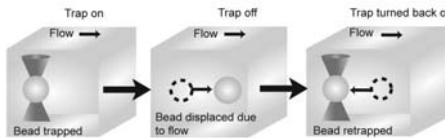


Figure 2. Flow measuring technique

As illustrated in Figure 2, a silica particle (1 μm) was trapped using a 532 nm beam and used to measure flow. The probe was repeatedly trapped and then released from a specific position within the channel. Images of the particle were taken on consecutive trigger signals with a relative delay using a chopper, rotating at 40 Hz, so that the magnitude and direction of the flow could be calculated at that point.

3. Results and Discussion

In order to measure fluid flow induced by the optically driven pump, we trapped and positioned a third silica bead at the entrance of the channel. When the trapping beam for the probe particle was blocked the particle was released into the fluid flow. Figure 3 is a sequence of images taken at 2 s intervals showing the probe particle being pumped through the channel. The average rate of flow generated by the pump through the channel was calculated to be 3.4 μms^{-1} and a maximum flow rate of 8.3 μms^{-1} was observed as the bead passed through the middle of the pump. Figure 4a shows a map of the flow field in the microchannel when the pump was active and Figure 4b shows the

measured flow produced at the centre of the pump as a function of both forward and reverse flow.

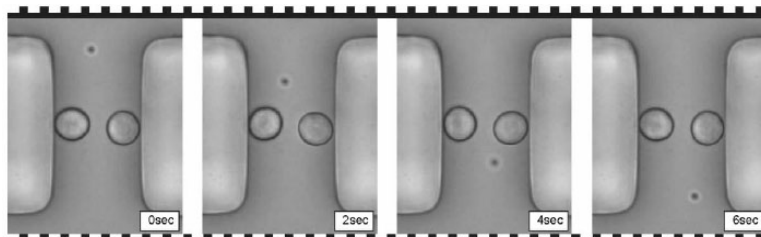


Figure 3. A silica bead is pumped along a microchannel (width: 15 μm , height: 27 μm)

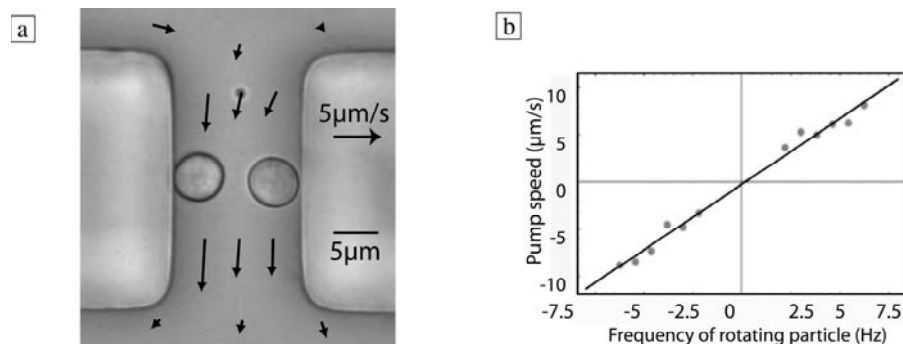


Figure 4 a) Measured flow field mapped while fluid is being pumped. (b) Fluid speed measured at the centre of the pump as a function of the rotation rate of the vaterite particles.

4. Conclusions

In conclusion we have demonstrated an optically driven pump in a microfluidic structure and a new method of sensing flow in the same channel. These methods of pumping and sensing flow can be used to accurately transport and measure the flow of small quantities of liquid. The technique could be extended to include a chain of pumps so that pumping in a more complex microfluidic system could be achieved. Whilst the present system requires large lasers coupled into a microscope, there is a possibility to integrate the optical tweezers system into a lab-on-a-chip device.

References

1. H. Mushfiq, J. Leach, R. Leonardo, M. Padgett and J. Cooper. *An optically driven pump for microfluidics*, Lab Chip, 6, 735 - 739, (2006).
2. R. di Leonardo, J. Leach, H. Mushfiq, J. Cooper, G. Ruocco and M. J. Padgett, *Multipoint holographic optical velocimetry in microfluidic systems*, Phys. Rev. Lett, 96(13), 134502, (2006).
3. A. Bishop, T. Nieminen, N. Heckenberg and H. Dunlop, *Optical Microrheology Using Rotating Laser-Trapped Particles*, Phys. Rev. Lett., 92(19), 198104 (2004).

STEREOSCOPIC OBSERVATION AND ITS APPLICATION TO THREE-DIMENSIONAL FLOW MEASUREMENT IN A MICROCHANNEL

Naoki Ichikawa¹, Peter Mang-Yu Chung¹ and Ryutaro Maeda¹

¹ National Institute of Advanced Industrial Science and Technology (AIST),
AIST Tsukuba East, 1-2-1 Namiki, Tsukuba, Ibaraki, 305-8564 Japan
e-mail: n.ichikawa@aist.go.jp

Abstract

This paper describes development of a stereoscopic observation system for three-dimensional (3-D) flow in a microchannel. The ultimate objective is construction of a particle tracking velocimetry (PTV) system to measure 3-D flows. There are several crucial points to developing the system: the requirement for a lens, darkness of images, and a calibration method. Using two lenses of long working distance and focal length along with high-speed cameras, we obtained two different angular images at 200 frames/s. A 3-D microchannel was fabricated from polydimethylsiloxane (PDMS). Distilled water with 2-μm-diameter fluorescent particles was used as the test liquid. Stereoscopic observation was performed. Then, 3-D particle motions in the microchannel were calculated.

Keywords: Microfluidics, Stereoscopic observation, Three-dimensional flow, PDMS

1. Introduction

Concomitant with the wide development of microfluidic applications, the importance of flow-field analysis in microchannels has continued to grow. Two-dimensional flow observations and measurements have been developing using microscopes after the early work of Santiago et al. [1]. In recent years, numbers of complicated three-dimensional (3-D) structures for microfluidic systems have been developed [2]. Although the necessity of measurements for 3-D flow fields is increasing, few papers have reported 3-D flow [3]. Therefore, we are developing a stereoscopic observation system with two cameras to realize a 3-D particle tracking velocimetry (PTV) system [4]. Technical problems and present results are discussed in this paper.

2. Stereoscopic Observation System and Test Channel

Several crucial points exist to develop the system, such as the requirement for a lens, darkness of images, and a calibration method. Using two lenses of long working distance and long focal length, two image intensifier units and two high-speed cameras that can capture images at 200 frames/s for 640 × 480 pixels, we constructed the system shown in Fig. 1. Image darkness is a serious problem because of the necessity for a small iris for long focal length and high shutter speed. We have adopted two kinds of lighting to obtain bright illumination, back-lighting, and fluorescence using laser irradiation. The former is

back-lighting with a 120 W mercury lamp or a 100 W halogen lamp used as the light source. An optical fiber and a plane light illuminator are used for back-lighting the test section. This lighting is used for obtaining reference positions. The latter is used for fluorescent observation with laser excitation. We used a 50 mW laser diode (LD) to irradiate an area of about 1 mm diameter. A pulse generator was used to synchronize the high-speed camera and laser. An optical and electrical diagram of this system is shown schematically in Fig. 2. Figure 3 shows a polydimethylsiloxane (PDMS) test chip with a groove of $100 \mu\text{m}$ (W) \times $75 \mu\text{m}$ (D) as the microchannel. The two chips are bonded such that the channels are perpendicular to each other, thereby creating the 3-D structure of the microchannel. Distilled water with 2- μm -diameter fluorescent particles was used as the test liquid.



Figure 1. Photographic view of stereoscopic observation system

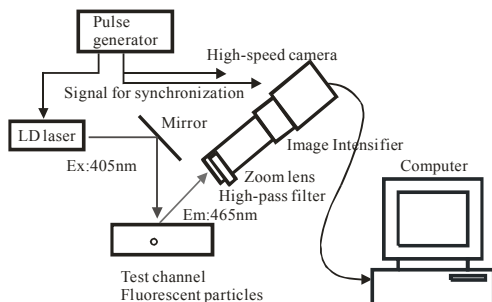


Figure 2. Optical and electrical diagram

3. Experimental results and Discussion

Examples of stereoscopic observation images for both left-hand and right-hand side cameras with back-lighting are shown in Fig. 4: they show a water bridge that is formed at the corner. Stereoscopic observation is realized clearly. By observing a position at a connection point of the 3-D test channel shown in Fig. 3, we can obtain eight reference points, as shown in Fig. 5, which are necessary to calculate the 3-D particle position. Points #1–#4 are on the top wall and #5–#8 are on the bottom wall of the microchannel under the assumption of the same channel height, which gives the same distance on the images for #5–#1 and #6–#2.

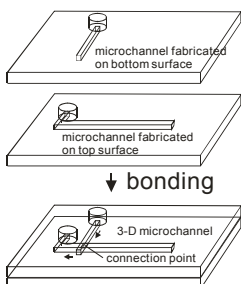
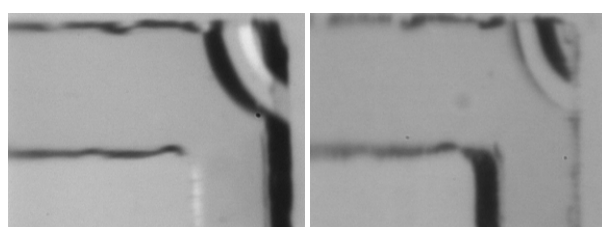


Figure 3. PDMS test chip



(a) Left-hand-side camera (b) Right-hand-side camera
Figure 4. Stereoscopic observation of a water bridge formed at a corner in a microchannel [4]

Images of tracer particles in the 3-D structure with the right hand camera and the left one are shown in Figs. 6(a) and 6(b). A calculated result of variation of the 3-D position for four tracer particles is shown in Fig. 7. Top and bottom channel walls are also indicated in the figure. The accuracy of the particle position is not confirmed, but the motion seems to be reasonable.

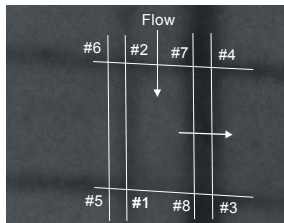
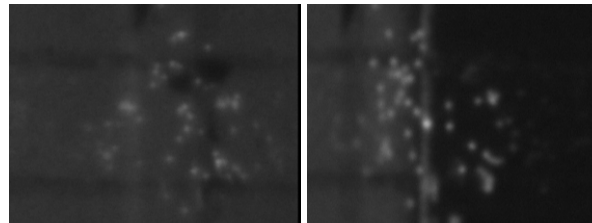


Figure 5. Reference points for 3-D position calculation



(a) Left-hand-side camera (b) Right-hand-side camera
Figure 6. Tracer particle images in a microchannel

4. Conclusions

In this study, we developed a stereoscopic observation system for observing 3-D flow behavior in a microchannel. Based on some aspects of this system, we will make improvements to a 3-D PTV system to measure complicated flow structure.

Acknowledgments

This work was partly supported by the New Energy and Industrial Technology Development Organization (NEDO).

References

- [1] J.G. Santiago, S.T. Wereley, C.D. Meinhart, D.J. Beebe and R.J. Adrian, A particle image velocimetry system for microfluidics, *Experiments in Fluids*, Vol. 25, pp. 316-319, (1998).
- [2] A.D. Stroock, S.K.W. Dertinger, A. Ajdari, I. Mezic, H.A. Stone and G.M. Whitesides, Chaotic Mixer for Microchannels, *Science*, Vol. 295, pp. 647-651, (2002).
- [3] S. Yoon and K.-C. Kim, A Detection Method of 3D Particle-Positions and 3D Microflow Diagnostic Method in a Microfluidics, *Micro Total Analysis System 2005*, Vol. 1, pp. 13-15, (2005).
- [4] N. Ichikawa, P. M.-Y. Chun and R. Maeda, Development of 3-dimensional PTV system in Microchannel, *Proc. of 4th World Congress on Industrial Process Tomography*, Vol. 2, pp. 1012-1017, (2005).

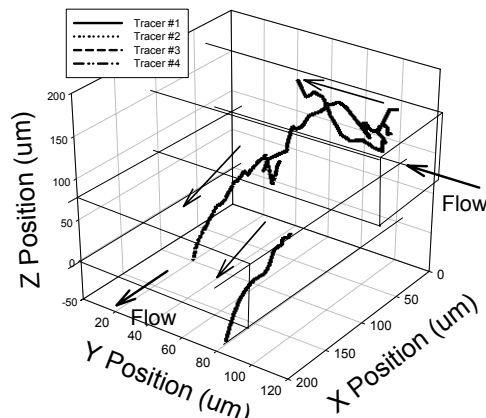


Figure 7. Calculated results of tracer position in 3-D coordinates

SPATIO-TEMPORAL TUNING OF STIMULI-RESPONDING SURFACES FOR DYNAMIC CONTROL OF ELECTROOSMOTIC FLOWS

Jan Sudor^{1,2}, Guillaume Paumier¹, Anne-Marie Gue¹, Françoise Vinet², Alain Estève¹ and Mehdi Djafari-Rouhani¹

¹ LAAS-CNRS, 7 avenue du Colonel Roche, 31077 Toulouse, France

² CEA-Leti, 17 rue des Martyrs, 38054 Grenoble, France

(jsudor@laas.fr)

Abstract

We report here on a novel approach for controlling, in space and time, nano-hydrodynamic properties at the liquid/solid interfaces through the use of end-grafted, stimuli-responding polymer brushes. Such brushes undergo a vertical phase separation upon external activation. A non-activated, swelled brush is thicker than the electrical double layer (EDL) and prohibits the ability of electrical effects to build into electro-osmotic flows (EOF), even on charged surfaces. On the contrary, an activated brush becomes thinner than the EDL and the electro-osmosis can build up unimpeded. It is shown here that, for given experimental conditions, the EOF velocity on the activated surface is 35-times greater than on the non-activated one. We propose to couple the stimuli-responding surfaces with dense arrays of thermal actuators in order to develop a novel family of micro- and nanofluidic components.

Keywords: Electroosmotic flow, stimuli-responsive polymers, micro- and nanofluidics

1. Introduction

Micro- and nanofluidics have been rapidly developing over the last several years. One of the major goals of this domain has been to develop highly integrated and automated fluidic systems for biology, chemistry and medicine. Such micro- or nanosystems operate from sub-micron to tens of microns length scales and manipulate nanoliter-volume samples. It is well known that the reduction of the scale of any fluidic system leads always to an increase of the influence of surface properties with respect to the bulk ones. Indeed, solid/liquid interfaces play a predominant role in many fluidic microsystems. It has been shown in the literature that neutral polymer brushes can effectively eliminate electroosmosis by hydrodynamic coupling of the electrical double layer with the bulk solution [1]. Since then, various polymers have been utilized for minimization of the EOF in channels with charged surfaces [2-4].

Here we go a step further and report on the use of surfaces decorated with active polymer brushes. The active polymers (e.g., poly (N-isopropyl acrylamide) (PNIPAM) employed in this study) exhibit lower-critical solution temperature (LCST) ($\sim 32^\circ\text{C}$ for PNIPAM) and undergo reversible coil-to-globule transition upon heating. When such polymers are end-grafted from/onto a surface, the thickness of the brush can repeatedly oscillate between a swollen ($\sim 10 \text{ nm}$; $T > \text{LCST}$) and a collapsed state ($\sim 1 \text{ nm}$; $T > \text{LCST}$). We demonstrate here that by using such active surfaces one can manipulate, in space and time, the flow-boundary conditions at the nano-meter scale within the electrical double layer and gain a control over the liquid flow on the macroscopic scale. We also propose to integrate the stimuli-responding surfaces into devices containing active elements such as heaters and to design and manufacture a novel family of fluidic building blocks (e.g., mixers, valves, sorters...) for complex microsystems.

2. Experimental

Fused silica capillaries (www.polymicro.com) were used for the electrokinetic measurements. The capillaries were 10-cm long with 75/385 μm inner/outer diameter. The inner surface of the capillaries was modified with linear polyacrylamide (PAM) and/or poly

(N-isopropyl acrylamide) (PNIPAM). The molecular weight of the grafted polymers was about 1 000 000 g/mol.

The EOF velocities were measured according to the method of Huang et al. [5]. All the chemicals employed in this study were obtained from Sigma-Aldrich (www.sigmadlrich.com). The experiments were performed on a home-built apparatus consisting of a high-voltage power supply (HVS448 3000V, www.labsmith.com), platinum electrodes and a thermostat (Memert; www.bioblock.com). The measurements of the EOF were carried out in the temperature range between 20 and 50°C.

3. Results and discussion

First, we modified solid surfaces (glass and Si) with PNIPAM polymer brushes and characterized them with dynamic contact angle measurements and multi-internal reflection (MIR) FTIR spectroscopy. The advancing contact angle increased from 65° to about 90° on the PNIPAM grafted surface by changing the temperature of the substrate from 25 to 50°C (results not shown).

Figure 1 shows the MIR FTIR spectrum of the PNIPAM layer. The absorption bands between 1500 and 1700 cm⁻¹ and 3300 and 3450 cm⁻¹ can be attributed to the Amide I groups and the C-H absorption bands between 2800 and 3000 cm⁻¹ to the backbone and isopropyl side-chains of the PNIPAM polymers.

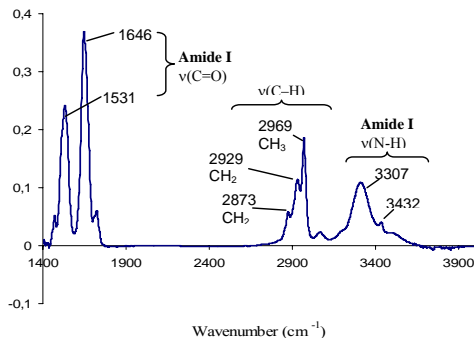


Figure 1. The MIR FTIR spectrum of the PNIPAM grafted on Si surface.

Next, we employed the same chemical protocols for the modifications of inner surfaces of the fused-silica capillaries. Three different capillaries were prepared: (i) capillaries silanized with 3-(Trimethoxysilyl) propyl methacrylate (TPM), (ii) capillaries modified with PAM and (iii) capillaries grafted with PNIPAM brushes. The TPM and PAM coated capillaries do not respond to any external activation in contrary to the PNIPAM capillaries. We measured the EOF velocities as a function of the buffer temperature in the three different capillaries and the results are summarized in the Figure 2. It can be seen in this figure that the EOF mobility increases almost linearly with the increasing buffer temperature in the capillary grafted with TPM (Fig. 2a). On the other hand, the EOF was completely blocked over the entire temperature range by the PAM coating (Fig. 2b). Finally; when the capillary surface was grafted with the PNIPAM chains, the EOF was close to zero up to about 30°C, and then it increased rapidly with the raising temperature (Fig. 2c). Beyond about 40°C, the increase in the EOF mobility was probably due to a change of the viscosity of the employed buffer.

What is of essential interest to us is that the amount of stretching of the brush seriously affects the ability of electrical effects in the nanometer scale EDL to build into electroosmotic flows. Schematically, if the brush is much thicker than the EDL (λ_D) (Fig. 2, top left), all the force electrically applied to the fluid is transmitted by hydrodynamic friction to

the polymer coating and thus back to the surface: we expect little electro-osmosis in this case, even if the surface is charged (Fig. 2c, $T < 30^\circ\text{C}$). On the contrary, if the brush is shrunken so that the EDL extends far beyond it (Fig. 2, top right), electro-osmosis can build up without hindrance (Fig. 2c, $T > 40^\circ\text{C}$). The low-temperature EOF mobility (@ 25°C) differs from the high-temperature one (@ 50°C) by a factor 35.

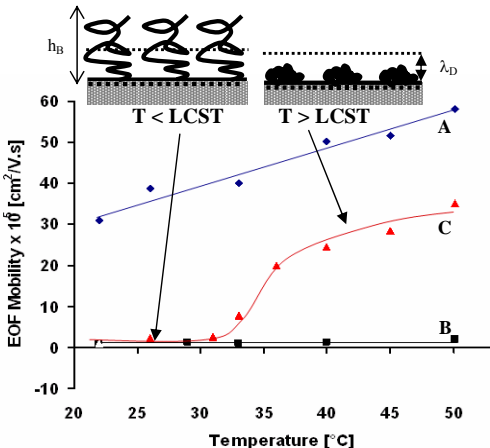


Figure 2: The evolution of the EOF mobility as a function of the buffer temperature for a fused silica capillary (A) modified with 3-(Trimethoxysilyl) Propyl Methacrylate (TPM), (B) end-grafted with PAM (~1MDa) and (C) end-grafted with PNIPAM (~1MDa)

We propose to go a step further and to couple the stimuli-responding surfaces with dense arrays of thermal actuators developed in our group [6] (Fig. 3) in order to design and manufacture a novel family of fluidic components, such as pumps, valves and mixers.

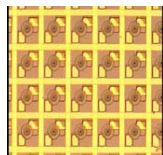


Figure 3: 2-D micro array of annular independent heating resistances ($4000/\text{cm}^2$).

Conclusions

We have demonstrated that by using stimuli-responding polymer brushes on charged surfaces, one can dynamically change the hydrodynamic screening of EOF and gain an active control of the dynamics of the liquid close to the solid substrate, which leads invariably to a control of the overall flow geometry.

Acknowledgements

This work was founded through a grant from the Agence Nationale de la Recherche (ANR) (NANODRIVE Project).

References

1. Hjertén, S., *J. Chromatogr.*, **347** (1985) 191.
2. Cobb, K.A., Dolnik, V., Novotny, M.V., *Anal. Chem.*, **62** (1990) 2478.
3. Nashabed, W., El Rassi, Z., *J. Chromatogr. A*, **559** (1991) 367.
4. Towns, J.K., Bao, J., Regnier, F.E. 1992. *J. Chromatogr. A*, **599**, 227.
5. Huang, X., Gordon, M.J., Zare, R.N. 1988. *Anal. Chem.*, **60**, 1837.
6. Gue, A.-M. D. Estève, V. Conédéra, N. Fabre, WO0205946.

PRODUCING DROPLETS IN PARALLEL MICROFLUIDIC SYSTEMS

H. Willaime¹, V. Barbier¹, P. Tabeling¹, F. Jousse²

¹Theorie et Microfluidique UMR CNRS-ESPCI 7083, ESPCI, Paris France

²Unilever –Center of Research, England

(herve.Willaime@espci.fr)

Abstract

We study the dynamics of two microfluidic droplets emitters placed in parallel. We observe complex dynamical behavior including synchronization, quasiperiodicity and chaos..

Keywords : digital microfluidics, droplets, emulsions, two phase flow, parallelization.

1. Introduction

Microfluidic technology has been shown to offer new capabilities for handling and transforming emulsions [1]. Compared to what is currently done in emulsion sciences, the volumes produced by a single droplet emitter are far too small for having a practical interest. This obviously calls for parallelization efforts in this direction were previously reported. In this paper we focus on the simplest case: two T-like droplets emitters placed in parallel on the same chip. We reveal for this case the surprising dynamical events that occur when parallelization of droplets emitters is carried out.

2. experimental system

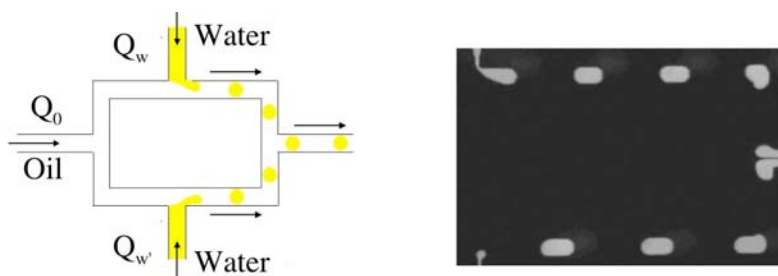


figure 1: Sketch of the parallelized system, and a typical flow pattern

Experimental systems are made in PDMS, and are represented in figure 1. They consist in 2 T-junctions placed in parallel on the same chip. Microchannels have

rectangular cross-sections ($30\mu\text{m} \times 100\mu\text{m}$) and water is injected on each side independently. Oil is the continuous phase and is injected in the main channel using a single entry. Flow-rates (for oil Q_o , Q_w and Q'_w , the water flow-rates in the upper and lower branch) lie between 0 and $20\ \mu\text{L}/\text{min}$. Droplets are formed at each T-junction. Visualizations are made by fluorescence microscopy (fluorescein is added to water). By real time image analyzes, we measure the frequency of generation of droplets and study the statistics of their sizes.

3. the symmetric case

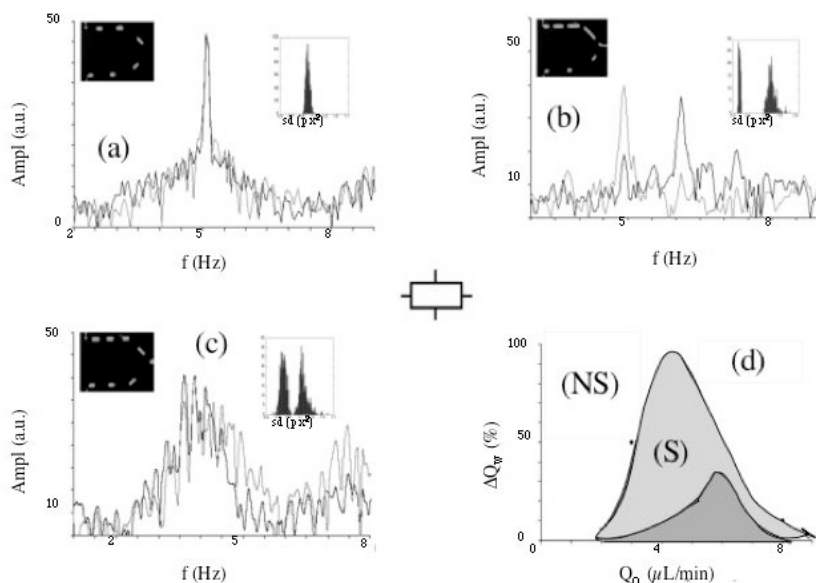


figure 2(a)-(c) Light intensity Fourier spectra, measured, respectively, in the upper (—) and lower branches (—); inserts : overall distributions of the droplet sizes (sd) in the same conditions, (a) $Q_o = 4\ \mu\text{L}/\text{min}$, $Q_w = 0.6\ \mu\text{L}/\text{min}$, $Q'_w = 0.5\ \mu\text{L}/\text{min}$; (b) $Q_o = 4\ \mu\text{L}/\text{min}$, $Q_w = 1.2\ \mu\text{L}/\text{min}$, $Q'_w = 0.5\ \mu\text{L}/\text{min}$; (c) $Q_o = 2.5\ \mu\text{L}/\text{min}$, $Q_w = 1.1\ \mu\text{L}/\text{min}$, $Q'_w = 0.5\ \mu\text{L}/\text{min}$. (d) Ranges of existence of synchronized (S) and non synchronized (NS) regimes as a function dQ_w/Q_w and the oil-flow rate; (light and dark gray region) $Q_w+Q'_w= 1\ \mu\text{L}/\text{min}$; (dark grey region) $Q_w+Q'_w= 2\ \mu\text{L}/\text{min}$.

In a first set of experiments, the branches of the system are symmetric with respect to the water entry. Depending on the difference $\delta Q_w = (Q'_w - Q_w)$, we observe either synchronized or non-synchronized (NS) regimes. The synchronized regime

is observed with small δQ_w (an example is given in fig 2a). In that case, emulsions are monodispersed with small dispersion. For larger δQ_w , one observes either quasiperiodical regimes (see fig 2b) or chaotic regimes (fig 2c). For both regimes, the mean sizes of droplets differ from one branch to the other and dispersion of their size is more than 30%. In fig 2d, these regimes are represented for two different Q_w . The domain of synchronization looks like a triangle. These observations provide evidence that the two emitters are dynamically coupled. The physical origin of the coupling is described in [2].

4. the asymmetric case

We also consider varying the branch lengths of the system (see figure 3). With unsymmetric bridges, the system may undergo chaotic regimes in all cases, giving rise to polydispersed emulsions with large distributions.

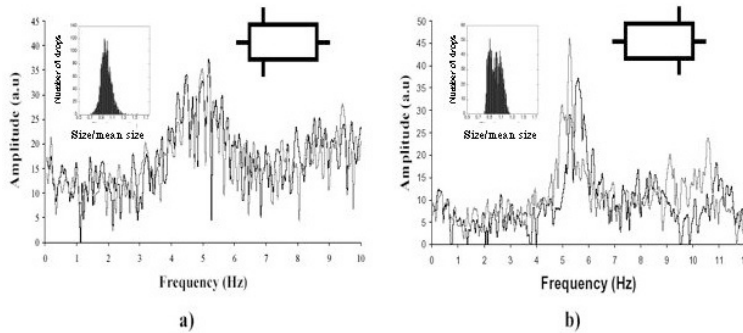


figure 3 : Frequency spectra of the light intensity signal measured in each branch (— upper branch, — lower branch) and overall droplet size distributions in various conditions, for bridges with unequal branch lengths; (a) $L_w/L_o = 5$; $Q_o = 4 \mu\text{L}/\text{min}$; $Q_w = Q'_w = 0.5 \mu\text{L}/\text{min}$; (b) $R_w/R_o = 1/5$; $Q_o = 4 \mu\text{L}/\text{min}$; $Q_w = 0.5 \mu\text{L}/\text{min}$, $Q'_w = 0.55 \mu\text{L}/\text{min}$.

Conclusion

In conclusion, we have shown with a simple parallel system that it is possible to produce synchronized emitters of droplets. The geometry of the system is exceedingly important. These results may lay down rules for building massively parallel droplet emitters, prone to produce emulsions in quantities of practical interest.

References

- [1] H. Song, J. Tice, R. Ismagilov .*Angew.Chem.Int.Ed.*, **42**, 767 (2003).
- [2] H Willaime, V Barbier, L Kloul, S Maine, P Tabeling *Phys. Rev. Lett.* **96**, 054501 (2006)

CONTROLLING PDMS SURFACES PROPERTIES : TO GENERATE DOUBLE EMULSIONS

Valessa Barbier¹, Michaël Tatoulian², Patrick Tabeling¹, Hong Li¹, Hervé Willaime¹, Farzaneh Arefi-Khonsari²

¹Théorie et Microfluidique UMR CNRS-ESPCI 7083, ESPCI, Paris France

²Génie des Procédés Plasma et des Traitements de Surface, ENSCP, Paris, France

Abstract : A new method for coating PDMS is presented, it is used to create long term stable hydrophilic surfaces. Applications are presented

Keywords : PDMS, surface treatment, double emulsions

Introduction

PDMS is a popular material, well adapted for the rapid fabrication of microfluidic systems. Its disadvantages are known: one of them is an inability to offer reliable and convenient-to-control surface properties [1]. For multiphase flows, this induces limitations on the type of emulsions we may produce, since the external phase must in all cases fully wet the channel walls [2].

1. PDMS surface treatment

In the present work, we propose a novel method for coating PDMS surfaces, in view of creating hydrophilic surfaces with long term stability *under dry conditions*, thus reverting the natural hydrophobicity of PDMS. In our approach, Plasma Polymerized Acrylic Acid coatings (PPAA) is deposited, cross-linked and post-backed on the PDMS surfaces. The protocol is the following: 1. *Pretreatment*: PDMS surface is activated by argon plasma. 2. *Polymer deposition*: a plasma of argon/acrylic acid is used to deposit an acrylic acid coating on PDMS. 3. *Post-treatment*: Cross-linking of the deposited polymer film and reinforcement of its cohesive strength by using helium flows. The result of the treatment is shown in fig 1, where wetting properties between coated and non-coated surfaces are shown. With coated surfaces, the contact angle for pure water in air is roughly 30°. Water can fully wet the coated PDMS by adding SDS, a feature that cannot be obtained with uncoated PDMS. This behavior is stable over several weeks *under dry conditions*. In similar conditions, popular treatments (such as oxygen plasma, or UV ozone) typically return to hydrophobicity after a few hours or so.

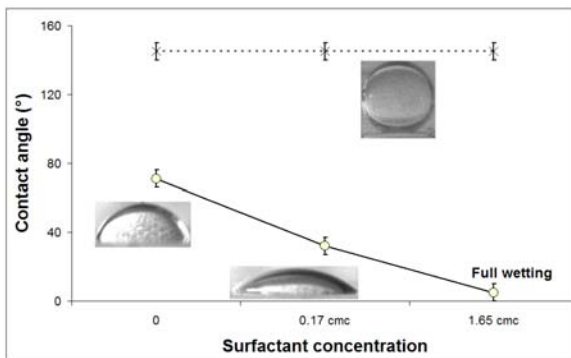


Figure 1 : Static contact angle measurements of a water drop immersed in oil (tetradecan). Contact angles are given for both uncoated PDMS (X) and PDMS coated with PPAA by plasma polymerization (O) and with increasing concentration of surfactant (Sodium dodecylsulfate, SDS)

2. Example of applicationof the treatment.

A more critical test for the stability of the PPAA coating can be undertaken by considering the still unsolved problem of forming double emulsions in PDMS: here we generate W/O/W emulsions in a double T-like junction system, such as the one shown in Fig 2. In the upper region of the chip, the channel walls are uncoated (hydrophobic) so as to generate W/O emulsions whereas in the second part (after the 2nd T junction), the channel has been locally coated with PAA – it is thus hydrophilic-. Results are shown in fig 3: In fig 3.a, oil in water droplets are formed in a coated PDMS channel. fig 3.d and e show detailed of 2 w/o/w double emulsion. To the best of our knowledge, this is the first time double emulsion is stably produced in PDMS

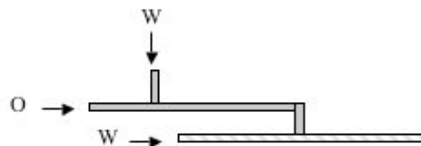


Figure 2 : scheme of the experimental in plain gray : the hydrophobic part, and in white the hydrophilic part of the channel.

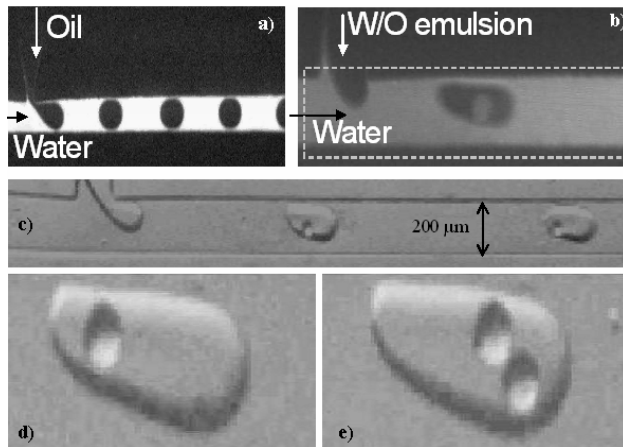


Figure 3: single O/W (a) and double W/O/W (b-e) emulsions made in a PDMS microsystem; Droplets are produced at T-junctions where both continuous and dispersed phases meet. The cross section of microchannels is $200 \times 50 \mu\text{m}_2$. Fluids are driven by syringe pumps with flow rates varying from 0.1 to $20 \mu\text{L}/\text{min}$. Observations are made using fluorescence video microscopy (water phases are labeled with fluorescein). For single O/W emulsions (a) tetradecan was used as dispersed phase and water with sodium dodecylsulfate (SDS, 0.4%) as continuous phase. The whole microsystem is coated with PAA. For O/W/O double emulsions (b-e), primary droplets of water in tetradecan (+SPAN 80, 0.75%) are produced at a first T-junction (uncoated, hydrophobic) and are then encapsulated with water and Tween (2%) at a second T-junction (coated with PAA, hydrophilic). The hydrophobic/hydrophilic patterning was achieved by masking the area of the first T-junction with a glass slide according to the dotted line on picture b/

Conclusion

In conclusion, we show here that by coating locally PDMS with PAA, it is possible to control its wetting properties and to produce under stable conditions W/O/W double emulsions.

References

- [1] Makamba H., Kim J.H., Lim K., Park N., Hahn J.H., *Electrophoresis*, **2003**, 24, 3607-3619
- [2] Dreyfus R., Tabeling P., Willaime H., *Physical Review Letters*, **2003**, 90(14).

TRANSIENT CHARGING OF THE ELECTRIC DOUBLE LAYER IN FIELD EFFECT-FLOW CONTROL OF ELECTRO-OSMOTIC FLOW

E.J van der Wouden, J.G.E. Gardeniers and A. van den Berg

*BIOS - Lab-on-a-Chip group, MESA+ Institute for Nanotechnology, University of Twente, NL-7500 AE, Enschede, The Netherlands
(e.j.vanderwouden@utwente.nl)*

Abstract

This paper describes the transient charging of the electrical double layer in Field Effect Flow Control (FEFC). It is shown that the buffer capacitance of the surface groups of the gate insulation and proton diffusion play a significant role in operation of a FEFC device in transient operation.

Keywords: FEFC, transient charging, EOF, buffer capacitance

1. Introduction

With the application of a dc gate potential the zeta potential at the insulator-liquid interface and therewith the electroosmotic flow (EOF) can be controlled [1]. However the use of EOF in integrated systems is limited by potential bubble formation at the open channel electrodes. Control of EOF by the ac-switching of a gate electrode, and the synchronized switching of the gate potential with the channel axial potential, has the advantage that potential gas formation at the electrodes that provide the axial electric field is suppressed, while the magnitude and direction of the flow can still be controlled [2]. The maximum frequency with which the EOF can be switched depends on the time for the EOF to develop [4] and the charging of the Electrical Double Layer (EDL).

2. Theory

The application of a FEFC structure will lead to an adjustment of the surface potential (Ψ) and a consequent change in the EDL capacitance (C_{edl}) as shown in Eq. 1 where σ is the surface charge.

$$\sigma = C_{edl} * \Psi \quad (\text{Equation.1})$$

In case of a positive potential step the EDL capacitance will decrease, which leads to a more negative surface potential and a corresponding flux of positive ions toward the EDL and thus a reversal of the current. The modification of the surface potential will lead to a change in proton concentration according to the Boltzmann equation (Eq.2)

$$[H^+]_s = [H^+]_0 \exp\left(\frac{-q\Psi_0}{kT}\right) \quad (\text{Equation. 2})$$

This change will induce a diffusion driven current with a time constant depending on the buffer concentration of the channel electrolyte.

3. Experimental

We have previously shown [1] that with a sequence of thin film deposition, etching, photolithography and chemical mechanical polishing steps, microfluidic structures with integrated insulator-covered gate electrodes can be fabricated. An example of a fabricated structure is shown in figure 1. The charging dynamics of a flowFET under transient operation has been investigated by monitoring the potential decay over a $1\text{M}\Omega$ resistance in series with the channel resistance. Figure 2 shows the electrical equivalent circuit of a FEFC structure. The circuit consists of the traditional applied three capacitor circuit [1] expanded with the buffer capacitance of the surface in series with a diffusion resistance to model the surface response to an applied gate potential.

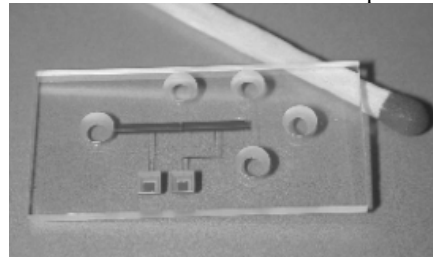


Fig. 1: FEFC microstructure with two gate electrodes channel width $150\mu\text{m}$, height $20\mu\text{m}$, length 1.5cm

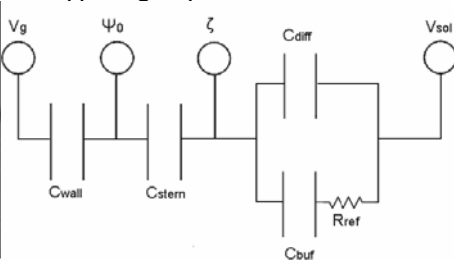


Fig. 2 equivalent electrical circuit
FEFC device.

4. Results and discussion

Figure 3 shows the potential response when a positive potential step is applied from -150 to 0 Volt at the gate electrode Figure 4 in case of a negative potential step from 150 -0 V. Both figures show a similar trend and can be subdivided in three regions. The first part shows a fast decay, linear in a semi-logarithmic plot, which can be explained by the charging of the double layer and gate insulation capacitances via the channel resistance. After the fast initial capacitive charging the EDL capacitance will adjust. The surface charge will initially remain constant after a gate potential step [5], so the modification of the EDL capacitance will lead to a proportional change in the surface potential as is illustrated by formula 1. Figure 5 shows the potential decay over the series resistance for different electrolyte pH and concentration. It shows that the slower diffusion limited relaxation increases with increasing pH and for a decrease in concentration. This effect is caused due to the increase of the buffer capacitance of the surface with an increase in pH and the resulting larger diffusion current. When the buffer concentration increases the flux of protons from the surface will have to travel a smaller distance to be buffered by the solution, which leads to a smaller diffusion limited time constant.

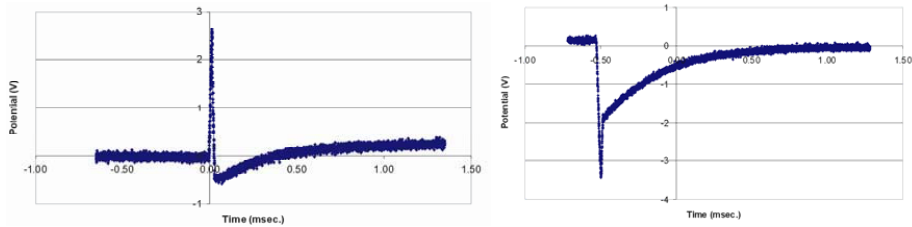


Fig. 3: -150-0 Volt 100 mM NaAc pH 2.7 Fig. 4: 150-0 Volt 100 mM NaAc pH

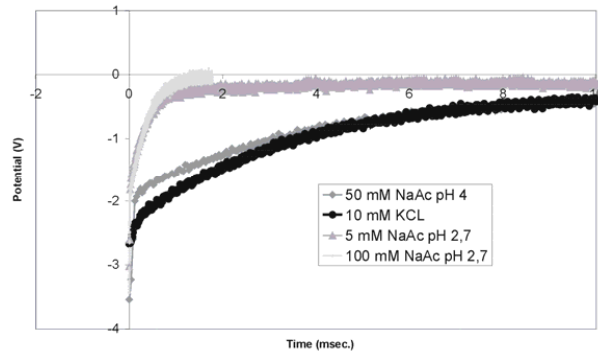


Fig.5 Charge relaxation as a function of pH for a gate potential step of 150-0 V.

5. Conclusions

It is shown that charge relaxation occurs over a time period of several tenths of milliseconds, depending on the buffer pH and concentration. However the slower diffusion limited relaxation leads to a counter potential of the silica surface. So for optimum performance in a Field-Effect Flow control structure the switching frequency should be matched with the RC charging of the EDL.

Acknowledgements

This research is supported by the Dutch Technology Foundation STW, applied science division of NWO and the technology programme of the Ministry of Economic Affairs.

References

1. 2] R.B.M. Schasfoort, S. Schlautmann, J. Hendrikse and A. van den Berg, Science 286 (1999) 942.
2. S. Mutlu, F. Svec, C. H. Mastrangelo, J. M.J. Frechet, and Y. B. Gianchandani, Proc. MEMS 2004, pp. 850-853.
3. D.C. Hermes, T. Heuser, E.J. van der Wouden, J.G.E. Gardeniers, A. van den Berg, Microsystem Technol. 12 (2005) 436-440.
4. E.V. Dose, G. Guiocchon, J. Chrom. A, 652, pp. 263-275, 1993.
5. J.C. van Kerkhof, J.C.T. Eijkel and P. Bergveld, Sens. Actuators B 18-19 (1994) 56-59.

MESHLESS SIMULATION FOR MICRO DROPLET GENERATION

**Takahiro Harada^{1*}, Yukihito Suzuki², Seiichi Koshizuka¹,
Takahiro Arakawa³ and Shuichi Shoji³**

¹Dept. of Quantum Engineering and Systems Science, The University of Tokyo,
7-3-1, Hongo, Bunkyo-ku, Tokyo, 113-8656, Japan

²Japan Science and Technology Agency,
7-3-1, Hongo, Bunkyo-ku, Tokyo, 113-8656 Japan

³Faculty of Science and Engineering, Waseda University,
3-4-1, Ookubo, Shinjuku-ku, Tokyo, 169-8555, Japan

*harada@mps.q.t.u-tokyo.ac.jp

Abstract

In this study, we developed a code which calculate three-dimensional micro multi-phase flow using Moving Particle Semi-implicit (MPS) method. To deal with large surface tension, a sub-time step algorithm is introduced. Three-dimensional micro droplet generation in a micro channel is calculated. The calculated results quantitatively agree with experimental ones.

Keywords: Simulation, droplet generation, particle method

1. Introduction

Micro total analysis systems(μ TAS) are micro scale devices which can be used for many kinds of fluid processes. They have advantages because of their sizes. Micro droplet generation is one of the key techniques of μ TAS. Micro droplets can be generated by injecting two immiscible fluids into a micro channel. There are many applications which uses micro droplets. For example, a drug delivery system is expected with micro droplets[1].

To promote efficiency of fluid processes, we have to optimize channel geometries. However, it is impossible to do in experimental try-and-error because of cost. If we can use simulation for optimization, it will be useful. However, there are two challenging points to simulate micro multi-phase flow. One is that the time steps have to be small because of extremely strong surface tension. This makes simulation time long. The other is that we have to deal with large interface deformation. It is difficult to calculate it with a method which uses a mesh.

Harada *et al.* calculated micro droplet generation in two dimensions with Moving Particle Semi-implicit (MPS) method, a particle method[2,3,4]. As the method needs no mesh, it can be applied easily to large interface deformation. They also developed a sub-time step algorithm to calculate strong surface tension efficiently. They could obtained qualitative agreement with experiment: effect of inlet flow ratio of two fluids etc.

In this study, we developed a three-dimensional micro multi-phase flow simulation code using the MPS method. To calculate large surface tension efficiently, we used the sub-time step algorithm. With this code, three-dimensional micro droplet generation is calculated. The calculated results quantitatively agree with experimental ones.

2. Method

In the MPS method, differential operators are discretized by particle interaction models. Without a mesh, it can deal with large interface deformation easily. Since particles themselves convect and express fluid, no surface tracking method is needed. Thus the interfaces are kept clear. We can find the details of the MPS method in [2].

To calculate strong surface tension efficiently in keeping numerical stability, we introduced a sub-time step algorithm developed by Harada *et al.*[3,4]. This algorithm divides a time step into sub-time steps and solve explicit terms with this sub-time steps.

3. Simulation Conditions

We made a simulation model which corresponds to a part of a channel geometry used in the experiment by Go *et al.*[5]. The cross-section of the channel is $100 \times 100 \mu\text{m}$. The channel has two inflows. One is inflow of organic phase and the other is that of water phase (fig.1).

Ratio of inlet flow rates R is defined as $Q_{\text{org}}/Q_{\text{water}}$ where Q_{org} is inflow volume of the organic phase and Q_{water} is that of the water phase. We used two values of Q_{water} and changed the ratio of inlet flow rates R .

4. Results

The simulated results are shown in fig.2. The organic phase delivered to the junction breaks up and droplets are generated. This behavior agreed with the experiment. The size of generated droplets are almost uniform. Then we measured the droplet size and compared it with that of the experiment. The simulation results quantitatively agree with experimental ones as shown in fig.3. The droplet size did not change if Q_{water} varies under the same condition of R . This behavior could be seen in experiment.

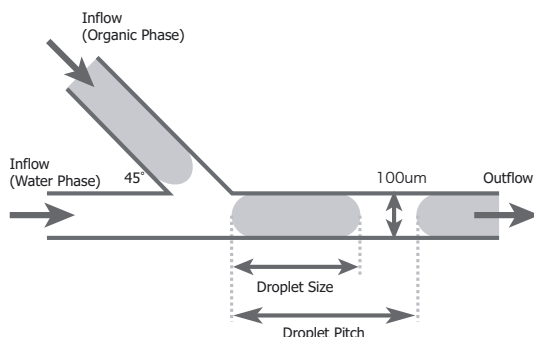


Figure 1. Calculation geometry

Both width and depth of micro channels are $100 \times 10^{-6}[\text{m}]$. Water and organic phases are delivered into the micro channels and droplets are generated at the Y-junction.

5. Conclusions

In this study, we developed a three-dimensional micro multi-phase flow simulation code using the MPS method. We introduced a sub-time step algorithm to calculate strong surface tension efficiently in keeping the numerical stability. Micro droplet generation was simulated and we compared the simulation results with the experimental results. We could obtain good agreement with the experiment quantitatively.

Acknowledgements

Financial support of Core Research for Evolutional Science and Technology (CREST) by Japan Science and Technology Agency (JST) is appreciated.

References

1. E.H.Jeong, S.Abraham, T.Arakawa, I.Kim, S.Saji, K.C.Kim and J.S.Go, "Functional Microcapsule for Drug Delivery," Proc. of Micro Total Analysis Systems, 2, 1440-1443 (2005)
2. S. Koshizuka and Y. Oka, "Moving-Particle Semi-implicit Method for Fragmentation of Incompressible Fluid," Nucl. Sci. Eng., 123, 421-434 (1996)
3. T.Harada, Y.Suzuki, S.Koshizuka, T.Arakawa and S.Shoji, "Simulation of Droplet Generation in Micro Flow using MPS Method," JSME International Journal Series B, to appear
4. T.Harada, Y.Suzuki, S.Koshizuka, T.Arakawa and S.Shoji, "Numerical Analysis of Micro Droplet Generation using a Particle Method", Proc. of Micro Total Analysis Systems, 1,638-640(2005)
5. J. S. Go,E. H. Jeong,T. Arakawa, M. Mori, K. C. Kim and S. Shoji, "Monolithic Microchemical Process Plant of Immiscible Microfluids," Proc. of 8th Int. Conf. Miniaturized Systems for Chemistry and Life Sciences, 1275-1278(2003)

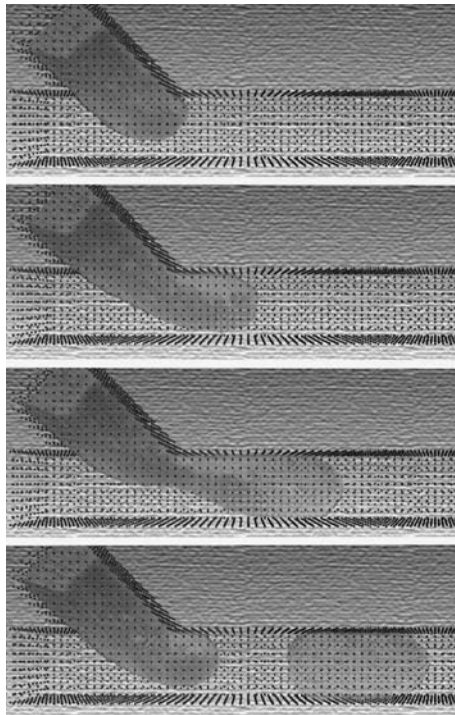


Figure 2. Formation of droplets.
Organic phase fluid surface is reconstructed from fluid particles. Black spheres are wall particles used in simulation. Time interval of each figure is 4.0×10^{-3} sec, $Q_{water} = 8.0 \times 10^{-3} \mu\text{L/sec}$ and $Q_{org} = 8.0 \times 10^{-3} \mu\text{L/sec}$.

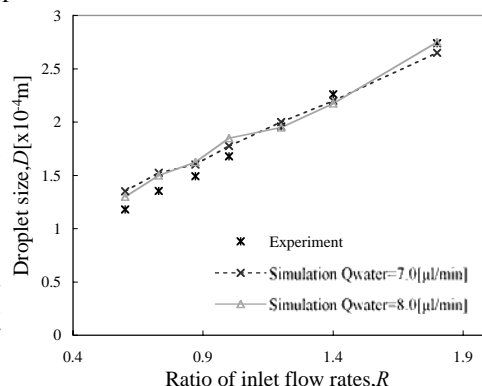


Figure 3. Ratio of inlet flow rates v.s. droplet size

USE MICRO-PIV TO MEASURE TRANSIENT ELECTROOSMOTIC FLOW AND ZETA POTENTIAL OF CHANNEL WALL

D.G Yan, H.Y. Gan, C. Yang*, N.T. Nguyen, X.Y. Huang, and Y.C. Lam

School of Mechanical and Aerospace Engineering
Nanyang Technological University, Singapore 639798
(*mcyang@ntu.edu.sg)

Abstract

In this paper, we demonstrated a micro-PIV based phase locking technique with an ordinary PIV CCD camera to measure the transient electroosmotic flow (EOF) in a microchannel by synchronizing different trigger signals for the laser, CCD camera, and in-house designed high-voltage switch. To obtain the EOF field, we further proposed a method to decouple the particle electrophoretic velocity from the micro-PIV measured velocity based on the rigorous analysis of the time scales. Then the zeta potential of the channel wall is determined using the measured EOF velocity at steady state. In addition, the theory of transient electroosmotic flow is first verified by our experimental data.

Keywords: Transient EOF, micro-PIV, zeta potential, particle electrophoresis

1. Introduction

Owing to numerous advantages, electroosmosis is utilized in many microfluidic devices as a pumping mechanism to manipulate liquid buffers and to transport solute samples for chemical and biomedical analyses. For optimal design and process control of microfluidic devices, it is imperative to characterize EOF in microchannels. Micro particle image velocimetry (micro-PIV) is a powerful tool for probing microchannel flows. The use of micro-PIV to characterize EOF has been reported, but only steady-state EOF fields have been obtained. In this study, we developed a transient micro-PIV technique to measure the time evolution of EOF in microchannels, which to our best knowledge has not been reported in the literature. Furthermore, based on the significant difference in time scales, we also proposed a novel method to decouple the particle electrophoretic velocity and the zeta potential of the channel walls. We believe such transient technique is important for characterizing the dynamic aspects of EOF which not only is of fundamental interest, but also has a wide spectrum of applications.

2. Experimental method and system

Theoretical analysis [1] suggests that the characteristic response time of a charged particle to an applied electric field is of order $\tau_{ep} = O(a^2 \rho_p / \mu)$, where a and ρ_p are the radius and density of the particle, respectively, and μ is the viscosity of the solution. In our experiment, latex particles of 465 nm in radius and 1050 kg/m³ in density were used, giving rise to a response time of $\tau_{ep} = O(10^{-6})$ s. In the same fashion, the characteristic response time of an EOF after switching on electric field can

be estimated from $\tau_{eo} = O(D_h^2 \rho / \mu)$, where D_h is the hydraulic diameter of the microchannel, and ρ is the density of the solution. For NaCl electrolyte in a typical microchannel of 100 μm hydraulic diameter, we can estimate the EOF relaxation time of order $\tau_{eo} = O(10^{-2})$ s. Such small response time poses a big challenge for the relatively low frame rates of the state-of-the-art PIV cameras. We therefore developed a novel micro-PIV technique which allows for measuring the transient developing process of EOF without the need of a high-speed camera. Figure 1(a) depicts the schematic of our experimental setup. The high-voltage switch, the laser, and the CCD camera can be synchronized by a PC-based timer unit to capture the particle velocity field at any time after switching on the high voltage, allowing for measuring particle velocity during the transient period, $\tau_{ep} < t \leq \tau_{eo}$. The synchronization scheme is depicted in Figure 1(b).

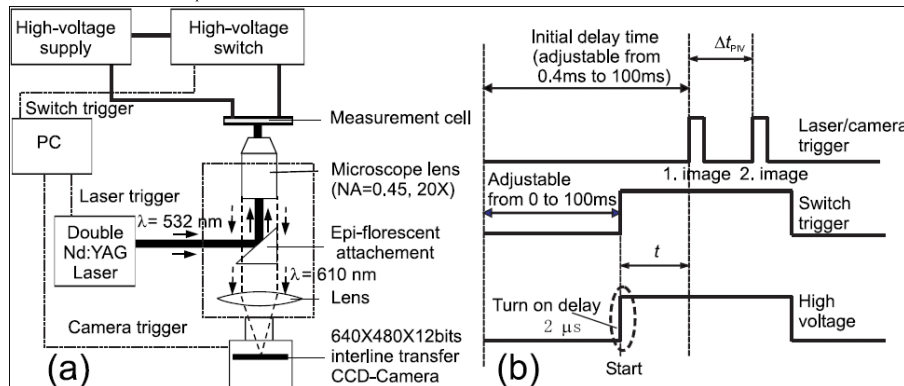


Figure 1 Schematic illustration of the transient micro-PIV technique developed in this study: (a) experimental setup, (b) timing and synchronization (not to scale)

3. Experimental results

Assuming that the flow development process is repeatable, the entire time evolution of the transient EOF can be found through recoding back-to-back images. Figure 2(a) show the micro-PIV measured transient particle vleocity field measured at the mid-plane of a microchannel filled with 1 mM NaCl electrolyte at $t = 0.5$ ms. However, the particle velocity, u_p evaluated from the micro-PIV measurement is a combination of the particle electrophoretic velocity, u_{ep} and the electroosmotic velocity, u_{eo} , namely $u_p = u_{ep} + u_{eo}$. In order to obtain the EOF velocity, a method was proposed to eliminate the contribution of particle electrophoresis in transient micro-PIV measurements. The method is based on the large difference between the response time scales of the particle electrophoresis and the bulk EOF. As analyzed earlier, the electrophoretic component can reach its steady-state velocity shortly after applying the electric field, e.g.,

$t = 0.5 \text{ ms} > \tau_{\text{ep}}$, while the electroosmotic component in the center part of the channel still remains stationary, i.e., $u_{\text{eo}} = 0 \text{ m/s}$ because $t = 0.5 \text{ ms} \ll \tau_{\text{eo}}$. Thus, at this moment, the particle electrophoretic velocity is equal to the measured particle velocity in the center region of the channel, $u_p = u_{\text{ep}}$, as shown by a dotted box in Figure 2(a). The corresponding EOF field can be obtained as shown in Figure 2(b).

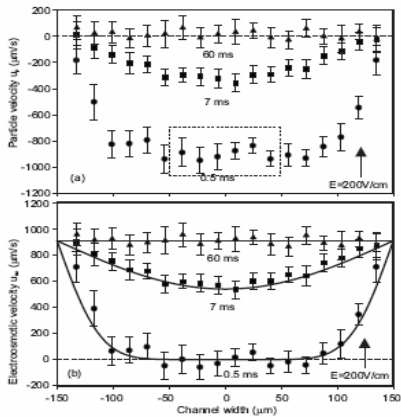


Figure 2 Temporal developing velocity profiles in 1 mM NaCl electrolyte: (a) Particle velocities evaluated from the micro-PIV measurement, (b) Electroosmotic velocity, the lines are theoretical velocity profiles calculated with the zeta potential evaluated from the experiment.

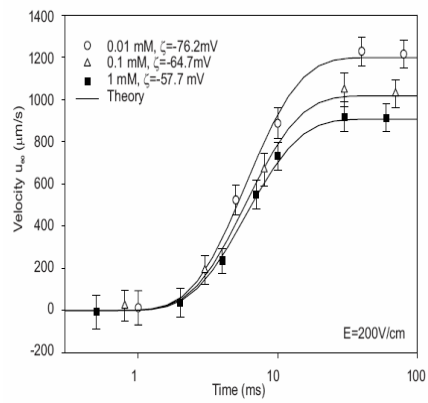


Figure 3 Transient response of electroosmotic velocity at the channel center for different NaCl concentrations. The symbols denote the experimental data. The lines represent the theoretical prediction of the electroosmotic velocity with the measured zeta potentials of the channel wall.

Furthermore, noting the fact that in a micron-sized channel, the EO velocity in the steady state can be described by the Smoluchowski equation, $u_s = u_{\text{eo}}(t \geq \tau_{\text{eo}}) = -\varepsilon \zeta_w E / \mu$, where ζ_w and ε are the channel wall's zeta potential and the dielectric constant of solution, respectively. Having obtained the steady-state EO velocity, the zeta potential of the channel wall can also be determined accordingly.

Figure 3 depicts the transient response of the electroosmotic velocity in NaCl electrolyte of three different concentrations used in our experiments. It shows a good agreement between the theory and the experimental data of the transient EOF velocity.

Acknowledgements: The graduate scholarships by Nanyang Technological University and A*Star of Singapore are greatly acknowledged.

References

- 1 C. Yang, in: F. Tay (Ed.), *Microfluidics and BioMEMS*. (Kluwer Academic, Boston, 2002).

SIMULATIONS OF A MICROFLUIDIC VARIABLE RESISTOR

Bozhi Yang¹ and Qiao Lin²

¹Dept. of Mechanical Engineering, Carnegie Mellon University,
Pittsburgh, PA 15213 USA

²Dept. of Mechanical Engineering, Columbia University, New York, NY 10027
E-mail: ql2134@columbia.edu

Abstract

This paper presents three-dimensional fluid-structure interaction (FSI) simulations of a microfluidic variable resistor featuring a thin flexible flap and a rigid stopper embedded inside a microchannel. Simulation of the structural deflection and CFD were carried out iteratively for each incremental pressure load step. The simulation results agree with the measurement results and provide insight to the device operations.

Keywords: Compliance, FEM, Fluidic Resistor, Fluid-Structure Interaction

1. Introduction

We have recently reported PDMS-based passive variable resistors, *i.e.*, microvalves and constant flow-rate regulators [1, 2], whose flow resistance changes drastically under different applied pressures. This paper presents the 3D finite-element analysis (FEA) simulations of the variable resistor considering the fluid-structure interaction (FSI) with ANSYS® [3]. The flap deflection, flow rate, pressure distribution and flow field under varying applied pressures were computed and compared with experimental results.

2. Design and Principle

The variable resistor consists of a thin flexible flap and a stiff stopper located closely in a microchannel (Fig. 1) [1, 2], both of which are anchored to the floor, ceiling, and one side wall of the microchannel. The flow resistance of the device depends on the applied pressure. Under forward pressure, the flow resistance will decrease as the gap between the flap and stopper widens. Under reverse pressure, the flow resistance will increase as the flap approaches and contacts the stopper forming two orifices. If the devices are carefully designed, the tendency of the increased reverse flow resistance to weaken the flow can cancel out the tendency of the increasing pressure to enhance the flow. Therefore, the flow rate can remain constant over certain range of reverse pressure [2].

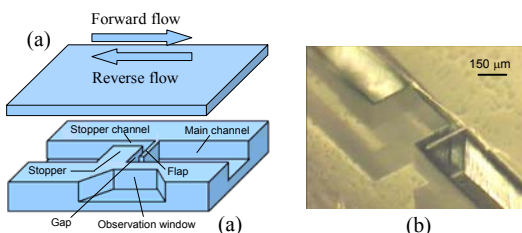


Fig. 1. (a) Schematic of a microfluidic resistor with an observation window for flap deflection measurement; (b) A fabricated PDMS sheet with the flap and stopper features.

3. Numerical Simulation Results

The simulations were conducted with the ANSYS® Multi-field™ solver [3], over pressure ranges in which there is no flap-stopper contact so that the physical problem is tractable for a first FSI study. In the simulations, the pressure load across device inlet and outlet was applied incrementally. And for each pressure step, simulations of the flow field and flap deflection were iteratively carried out. The fluid (water) was assumed to have constant density (1000 kg/m^3) and viscosity ($10^{-3} \text{ Pa}\cdot\text{s}$). PDMS was modeled as a nonlinear hyperelastic material with a nominal Young's modulus of 700 kPa.

Flap Deflection: We have measured and simulated the maximum flap deflection of a specially designed device (resistor A) with an observation window (Fig. 1a). The inlet and outlet channels were 300 μm wide, 275 μm high and 2 mm long. The compliant flap was 266 μm wide, 55 μm thick, and 30 μm from the stopper. The stopper channel was 40 μm wide and 500 μm long. Simulations show that the pressure drop over the inlet and outlet channels is less than 1% of the total pressure drop and hence negligible. The simulation and experiments agree within 15% and 20% for forward and reverse flow, and show nonlinear deflection-pressure relationship, consistent with the fact that the flap deformations are in the large-deflection regime [4].

Flow and Pressure Characteristics: Flow and pressure characteristics have been studied using resistor B, which had inlet and outlet channels 300 μm wide, 275 μm high and 2 mm long, a flap 275 μm high, 266 μm wide, 75 μm thick and 25 μm from the stopper, and a stopper channel 275 μm high, 40 μm wide and 500 μm long. At a given pressure, the calculated velocity field throughout the channel can be integrated to obtain the flow rate. Simulations were performed over 0–180 kPa for forward flow (Fig. 3a), and over 0 to 35 kPa, at which flap-

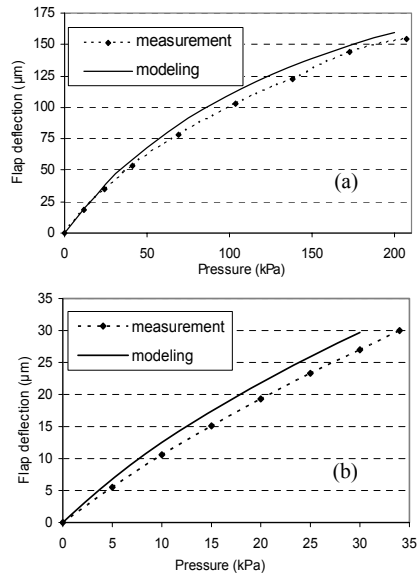


Fig. 2. Measured and simulated flap deflection of resistor A under (a) forward and (b) reverse flow.

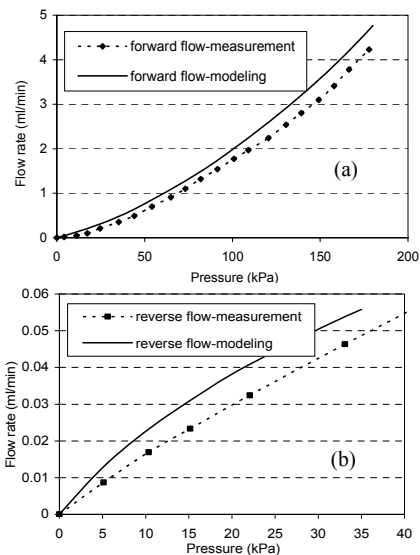


Fig. 3. Simulated and measured flow rates for the resistor B: (a) forward and (b) reverse flow.

stopper contact is imminent, for reverse flow (Fig. 3b). It can be seen from Fig. 3 that the forward flow resistance decreases with pressure, which can be attributed to the widening of the gap between the flap and the stopper. The reverse flow resistance increases with pressure because of the narrowing and orifice formation in the flap-stopper gap. The simulations correctly predict the trend of both the forward and reverse flow experiments, and agree with the experimental data within 15% for forward flow, and 17% for reverse flow. The deviations are likely caused by errors in device dimensions and PDMS's elastic properties, as well as deformations of the PDMS stopper and channel sidewalls that were not considered in the simulations.

We further calculated the pressure distributions of resistor B under forward and reverse pressure along a flow path (A-B-C-D-E-F-G-H in Fig. 4), where A, B, G and H are located on the main channel's centerline, C-D-E-F is the centerline of the flow path formed by the flap and stopper and the main channel walls, and B-C and F-G are normal to the main channel's centerline. The pressures were normalized with the total pressure applied over the device (50 kPa gauge pressure for forward flow and 35 kPa for reverse flow). It can be seen from Fig. 4 that the pressure drops along the main channel (A-B and G-H) are very small, less than 1% of the total pressure drop for both forward and reverse flow. On the other hand, the pressure drops in the flap-stopper gap and the stopper channel are significant. For forward flow, the pressure drop along flap gap (D-E) is 17% of the total pressure drop, compared with 78% for that along stopper channel (C-D). For reverse flow, the pressure drop along flap gap (D-E) is 70% of the total pressure drop, compared with 29% for that along stopper channel (C-D). This indicates an increased flow resistance associated with the flap-stopper channel for reverse flow than that for forward flow due to the gap narrowing under reverse flow.

6. Conclusions

A coupled three-dimensional FSI modeling has been conducted that accurately predicts the trend of the flap deflection, flow rate and pressure distribution of variable resistors. The simulations can help guide design of the future microfluidic resistors.

References

- [1] B. Yang and Q. Lin, "Planar Micro Check Valves Utilizing Large Compliance of PDMS," *IMECE2005-81958, 2005 ASME IMECE '05*, Nov., 2005, Orlando, FL.
- [2] B. Yang, J.W. Levis, and Q. Lin, "A PDMS-Based Constant-Flowrate Microfluidic Control Device," *IEEE MEMS '04*, Jan. 2004, the Netherlands, pp.379-382.
- [3] <http://www.ansys.com>
- [4] S. Timoshenko, et al., *Theory of Plates and Shells*, 2nd edition, New York: McGraw-Hill, 1959.

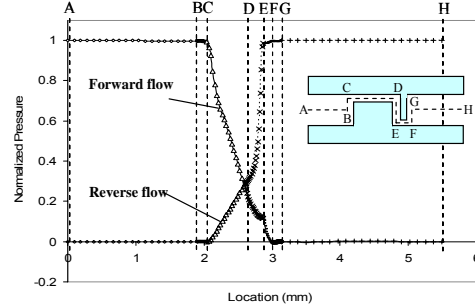


Fig. 4. Simulated normalized pressure distribution ($p_{\text{local}}/ p_{\text{total}}$) along resistor B. (p_{total} is the total pressure across device.)

ELECTROKINETIC CONTROL OF DROPLET BREAK-UP AND SWITCHING OF DROPLET MOVEMENT DIRECTION IN AN AQUEOUS TWO-PHASE SYSTEM

Young Hoon Choi, Young Soo Song and Do Hyun Kim

Korea Advanced Institute of Science and Technology and Center for Ultramicrochemical Process Systems, Daejeon 305-701 Korea

Abstract

Novel electrokinetic manipulation of dispersed micro droplets in an aqueous two-phase system (ATPS) is reported. Volume of broken droplets and the direction of droplet movement were effectively controlled by the applied DC electric field.

Key words: electrokinetic control, aqueous two-phase system, droplets

1. Introduction

Droplets in nanoliter volumes can be considered as microfluidic fluid carriers and reactors with enhanced surface-to-volume ratio. Droplets can accelerate and confine chemical reaction effectively inside them. Microfluidic technology has allowed the effective generation control of nanoliter droplets and many researchers have reported its applications such as protein crystallization and monodispersed emulsification. Recently, ATPS, which is usually formed by dissolving different kinds of polymers or salts in water, has drawn growing attention as a versatile liquid-liquid two-phase system for microfluidic applications, since its aqueous nature renders biocompatible conditions for the stable analysis of biomolecules [1]. Here, we report the ATPS droplet generation by shear force and the electrokinetic control of droplet break-up and movement direction.

2. Theory

It has been tried to explain the droplet electrophoretic mobility in ATPS [2]. There are two distinctive features of the electrokinetic phenomenon in ATPS; First, the mobility is directly proportional to drop radius. Second, the sign of the droplet mobility is opposite to that predicted from net charge distribution and Donnan potential. These differences are due to the internal circulation, the electroosmotic flow inside the droplet.

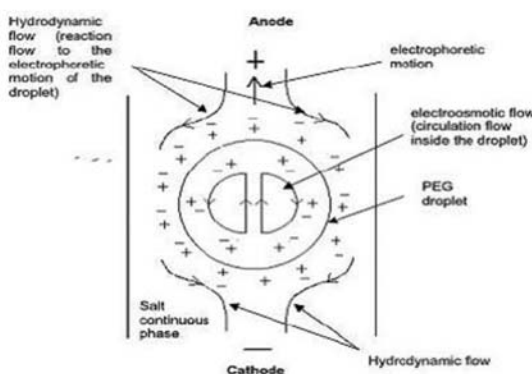


Figure 1. Conceptual diagram of electrophoretic flow PEG/salt ATPS droplet in the presence of an electric field (reprinted from [2]).

3. Experimental

PDMS/glass hybrid structure was fabricated by soft lithography. The width of the main channel was 200 μm and that of branched channels connected with two inlets and two outlets were 100 μm . For the control of break-up at the T-junction of the channel, stainless steel tube was drilled into the outlet, which is served as both electrode and outlet channel. ATPS used in this experiment was prepared by dissolving tetrabutylammonium bromide (TBAB) and ammonium sulfate (AS) in deionized water. When these two salts are dissolved in high concentrations, phase separation occurs. The binodal curve of TBAB/AS ATPS was determined experimentally in bulk system by turbidometric titration. In Figure 2, two-phase region is above the curve and the region at and below the curve is where only one aqueous phase is formed. In this experiment, the concentrations of TBAB and AS were fixed to 4.5M and 1M, respectively. The TBAB-rich phase and AS-rich phase were separated individually and introduced into each inlet at the microfluidic device shown in Figure 4(a). The TBAB-rich phase was continuous phase and the AS-rich phase was dispersed where plug-formed droplets were generated by shear force between the two phases. Two syringe pumps were used in controlling the flow rates of each phase independently. DC electric voltage in the range of 0~30V was applied between the electrodes located at the outlet reservoirs.

4. Results and Discussion

The size of droplets and pitch between droplets were controlled by varying flow rates and they are plotted with the appropriate parameter of flow rate combinations in Figure 3. With the flow rate of both phases fixed as

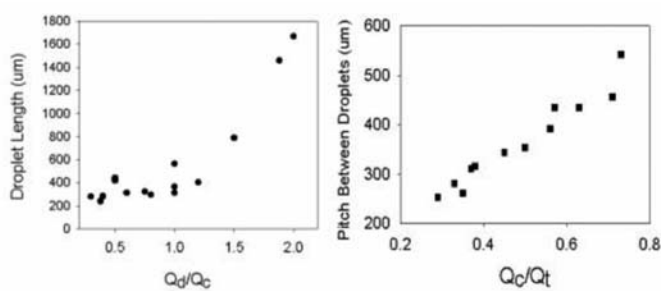


Figure 3. Bionodal curve of TBAB/AS ATPS.

0.3 $\mu\text{l}/\text{min}$, one single droplet was broken into two small droplets of equal volume at the T-junction, due to the effect of geometry. The droplets were broken with different volume ratios depending on the magnitude of the applied electric field as shown in Figure 4(b) and (c). The larger splinter was attracted toward the positive electrode. When sufficiently high voltage (higher than about 5V depending on the flow rate of each phase) was applied, the transportation of whole droplets was fully switched as

shown in the last two photographs of Figure 4(c).

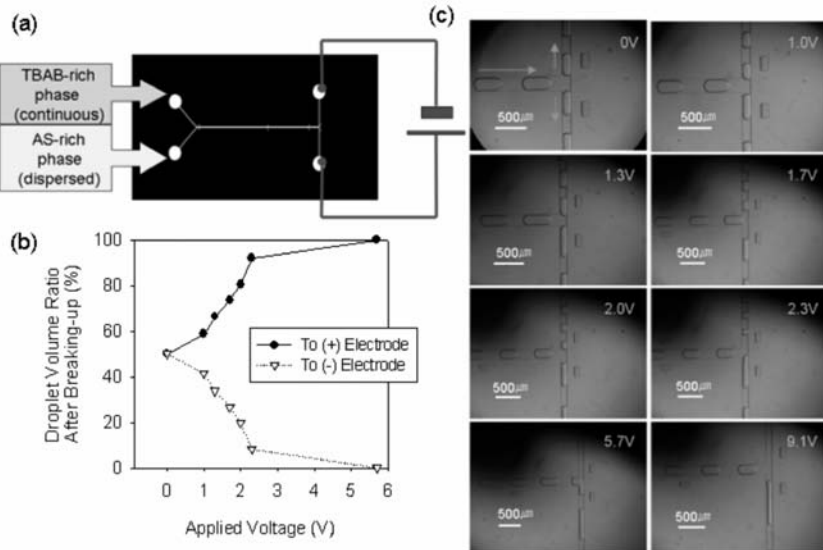


Figure 4. (a) Schematic diagram of microfluidic device and electric connection. (b) Droplet volume ratio after breaking-up as a function of applied voltage. (c) Microscopic photographs of controlled volume break-up and complete switching of direction of droplets.

5. Conclusions

We have demonstrated a novel method to manipulate ATPS droplets generated inside microfluidic channel. The breaking-up of droplets and the direction of droplet movement were controlled effectively by the applied DC electric field without any use of additional surfactant or moving part in the microfluidic device. This break-up and switching method is expected to be used in microfluidic reaction network where multiple chemical and biological species are involved since ATPS allows more room for handling hydrophilic molecules.

References

1. H. Walter, D.E. Brooks and D. Fisher, Ed., Partitioning in Aqueous Two Phase Systems: Theory, Methods, Uses and Applications to Biotechnology, Academic Press, Orlando, FL (1985).
2. N. Nagaraj, S. Chethana, and K.S.M.S. Raghavarao, Electrokinetic demixing of aqueous two-phase polymer/salt systems, Electrophoresis, **26**, 10–17 (2005).

Acknowledgements

This work was partially supported by the Center for Ultramicrochemical Process Systems at KAIST and BK21 project.

DROPLETS BREAK-UP IN JUNCTIONS : THE CONCEPT OF A CRITICAL LENGTH

¹L.Ménétrier, ¹P. Tabeling

¹Théorie et microfluidique, ESPCI 10, rue Vauquelin, 75231 Paris (France)

Abstract:

Experiments performed on droplets driven in microfluidic junctions of various angles show two types of break-up : direct and retarded. Direct break-up is controlled by a critical length that depends on the junction geometry and is independant of the flow conditions. A theory assuming small capillary numbers describes well the conditions that govern both types of break-up.

Keywords : microfluidics, digital microfluidics, droplets, emulsions, two phase flow.

A number of groups are currently revealing the potential offered by digital microfluidics, i.e microfluidics dealing with droplets moving through microchannels. Compared to “ordinary microfluidics”, digital microfluidics offers substantial advantages for screening chemical reactions [1], screening protein crystallization conditions [2], devising novel lab on a chips[3] ... In this context, it is desirable to lay down on firm grounds the physical bases of some of the elementary processes involved in this technology. This is what the present paper is dedicated to. Here, we concentrate on the phenomenon of droplet break-up through junctions with arbitrary angles. By studying a range of experimental conditions were interfacial tensions, viscosity, flow-rates, dimensions and junction angles are varied by one order of magnitude or so, we reveal the existence of a quantity that appears to control the breakup process. In substance, the quantity is a maximal finger length penetrating one side of the junction (see Fig 2). Using this quantity (we call “critical finger length”) allows to determine flow-rate conditions for which droplet breakup occurs in junctions of arbitrary angles. The concept is new; it extends previous work that applied to 90° junctions and large capillary numbers only [4]. We also propose a theoretical model that provides an explanation for our finding.

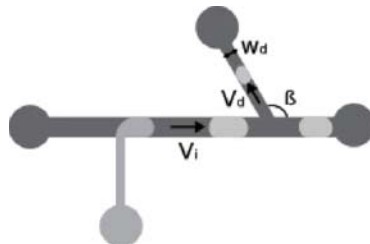


Figure 1: Sketch of the experimental setup. Water is in light gray and oil in dark.
The system is pressure controlled.

In our experiments, water droplets are formed in a continuous phase of hexadecane in PDMS microchannels (Fig 1). Pressure is measured and droplet deformations are characterized in real time by image processing techniques using fast cameras. In the experiments, velocities were varied from 50 to $10^4 \mu\text{m.s}^{-1}$, dispersed phase viscosities from 1 to 5 mP.s, interfacial tensions from 3 to 40 mN/m, widths of the channels from 50 to 150 μm and depths from 30 to 130 μm .

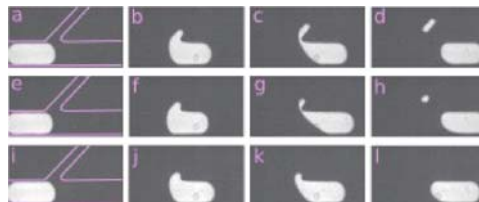


Figure 2: As it reaches the intersection (a,e,i), the droplet develops a finger in the derivation channel (b,f,j). If the finger is long enough (c), it will break. If it is shorter (g,k), it will partially retract and undergo a retarded break up (h) or fully retract (l).

As the droplets reach the junction, a transient finger develops into the side channel (see Fig 2). The experiments indicate the existence of a critical finger length above which fingers keep flowing downstream unavoidably provoking droplet break-up. This feature is revealed by the vertical lines on Fig 3, obtained for three different junction angles. The critical length is controlled by the width w_d of the side channel and the junction angle : a law in the form $l_{cr} = 1.5 w_d / (\cos\beta \cdot \sin\beta)$ is consistent with the data. Shorter fingers retract and, in most cases, eventually merge with the mother droplets. In some conditions, fingers may breakup as they retract, according to a process we called “retarded breakup” and that we documented.

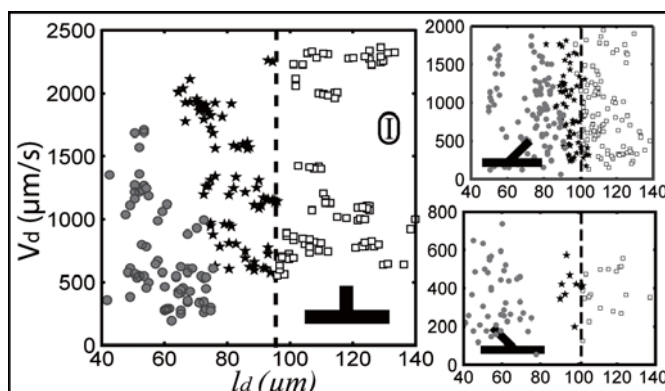


Figure 3 : Length of the finger in the derivation channel vs velocity in this channel. The experiments are carried out with channel angles β of 45° , 90° and 135° , and width $w_d = \sin(\beta) * 65 \mu\text{m}$. ● represents non-breaking droplets, ★ the droplets that undergo retarded break up and □ the droplet that break up. The vertical lines, separating the two breaking regimes, show the existance of a critical length $l_{cr} = 1.5 w_d / (\cos\beta \cdot \sin\beta)$.

This findings can be used to determine flow-rate conditions under which droplets breakup as they arrive in microfluidic junctions. This is shown in Fig 4 for a 90° junction angle. The full line is the theoretical line that one infers by assuming a critical finger length. Above the line, droplets breakup, below it, they mostly don't - except within a thin band that corresponds to what we called "retarded breakup" process.

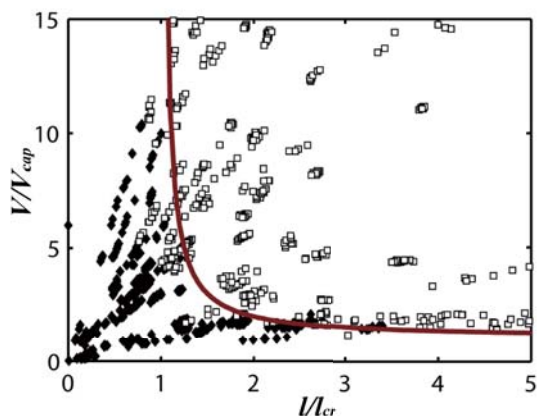


Figure 4: Control parameters: V_d as a function of $l=l_i$. V_d/V_i (l_i being the length of the incoming droplet). The values are normalized with l_{cr} and the characteristic capillary velocity V_{cap} . Blue is for droplets that do not break and red represents breaking droplets. Dashed line represents the theory based on the existence of a critical length.

We would like to thank Dan Angelescu and Philippe Salamitou for fruitfull discussions related to this work. Schlumberger, CNRS and ESPCI are gratefully acknowledged for their support.

REFERENCES:

- [1] H. Song and R.F. Ismagilov, *J. Am. Chem. Soc* 125(47):14613-14619
- [2] B. Zheng, L. Spencer Roach and R.F. Ismagilov, *J. Am. Chem. Soc* 125(37):11170
- [3] V.Srinivasan, V.K. Pamula, and R.B. Fair, *Lab on a chip* (2004) 4:310-315
- [4] D.R. Link, S.L. Ann, D.A. Weitz and H.A. Stone, *Phys. Rev. Lett.*, 92:054503

NANOSCALE LASER INDUCED FLUORESCENCE IMAGING OF ZETA-POTENTIAL AFFECTED BY ION MOTION IN MICROCHANNEL

Yutaka KAZOE¹ and Yohei SATO¹

¹Keio University, 3-14-1 Hiyoshi, Kohoku-ku, Yokohama, 223-8522 JAPAN

Abstract

A nanoscale laser induced fluorescence (nano-LIF) imaging was proposed by using the fluorescent dye and the evanescent wave. The present study focused on the measurement of zeta-potential distribution at the microchannel wall, which governs an electroosmotic flow field. A mixing flow field was formed by two-kinds of solution at different Na^+ concentration in a T-shaped microchannel. The zeta-potential distribution obtained from nano-LIF is quantitatively related to the transport of Na^+ in the flow field.

Keywords: Zeta-potential, Electric double layer, Fluorescence, Evanescent wave

1. Introduction

In microfluidic devices, electroosmotic flow (EOF) is generally used as a liquid driving force through a microchannel. Ion behavior in the microchannel and electrochemical characteristics of the wall yield a zeta-potential distribution and resulted in a complex flow structure. Therefore, the spatial and temporal sensing of zeta-potential is strongly required to realize the accurate flow control. The objective of the present study is to investigate the zeta-potential distribution by nano-LIF.

2. Nano-LIF Imaging for Zeta-Potential

In the nano-LIF imaging, Alexa Fluor 546 (Molecular Probes, Inc.), which is negative ion in the buffer solution, was selected as the fluorescent dye. The evanescent wave generated by total internal reflection of a laser beam and decays exponentially from the wall, was used as the excitation light of the fluorescent dye (Figure 1) [1]. Since the zeta-potential electrically affects the dye distribution in the vicinity of the wall, the detected fluorescent intensity is dependent on the zeta-potential. Figure 2 shows a

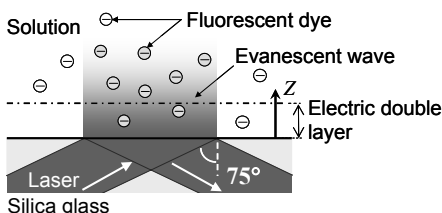


Fig. 1. Schematic of nano-LIF imaging. The laser beam ($\lambda = 532 \text{ nm}$) was totally reflected at the interface with an incident angle of 75° .

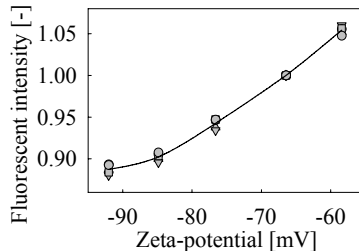


Fig. 2. Calibration curve between fluorescent intensity and zeta-potential.

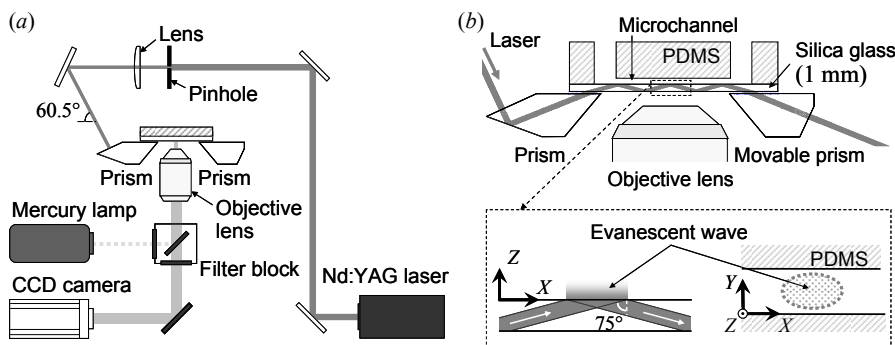


Fig. 3. Schematic of (a) the measurement system and (b) evanescent wave illumination in the microchannel.

calibration curve between the fluorescent intensity and the zeta-potential.

Figure 3 illustrates a schematic of the measurement system. The evanescent wave was generated at the silica glass-solution interface with a penetration depth of 93 nm [2] and excited the fluorescent dye in the vicinity of the glass wall (Fig. 3(b)). To obtain the high excitation intensity, a laser beam with a uniform intensity profile was utilized, which was generated by the diffraction from a pinhole. Fluorescence was collected through a 10 \times objective lens and captured by the CCD camera. The spatial resolution was 7.9 \times 7.9 μm and the measurement uncertainty was ± 5.3 mV in 95% confidence.

3. Results and Discussion

Figure 4 illustrates a schematic of T-shaped microchannel. Solution A and B (Table 1) were injected into the T-shaped microchannel at the equal flow rate from inlet I and II, respectively. The experiments were performed in two conditions in which the averaged velocity of pressure-driven flow, U_{ave} , was 575 $\mu\text{m}/\text{s}$ and 176 $\mu\text{m}/\text{s}$, respectively. In addition, a DC voltage of 150 V was applied from inlets to the outlet. The two-dimensional distribution of zeta-potential at the silica glass wall in the junction area is exhibited in Figure 5. The zeta-potential distributions were changed by the convection due to pressure- and electrokinetically driven flow. The Na^+ transport in the flow field was investigated by the velocity measurement using micron-resolution particle image velocimetry [3] and the numerical simulation by the scalar transport equation. Figure 6 shows the comparison of zeta-potential profiles at the silica glass wall ($z = 0$) to Na^+

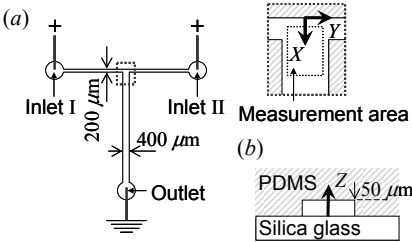


Fig. 4. (a) Top and (b) cross-sectional views of T-shaped microchannel.

Table 1. Properties of working fluids

	A	B
HEPES buffer [mM]	5	5
Alexa Fluor 546 [μM]	15	15
Na^+ [mM]	0.1	10
pH [-]	7.01	6.98

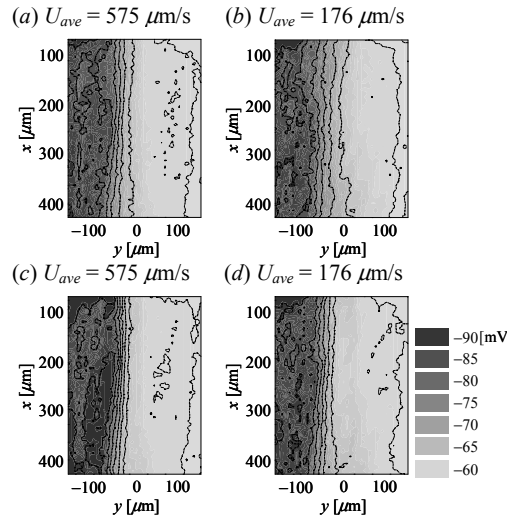


Fig. 5. Two-dimensional distribution of zeta-potential in pressure-driven flow ((a) $U_{ave} = 575 \mu\text{m/s}$, (b) $U_{ave} = 176 \mu\text{m/s}$), and on an application of 150V ((c) $U_{ave} = 575 \mu\text{m/s}$, (d) $U_{ave} = 176 \mu\text{m/s}$).

concentration profiles at $z = 25 \mu\text{m}$ in the Y -direction. The profiles of the zeta-potential at the silica glass wall show good agreement and a quantitative relationship with that of Na^+ concentration in the mixing flow field.

4. Conclusion

The nano-LIF imaging for zeta-potential was proposed by using the negative ion fluorescent dye and the evanescent wave. It is concluded that the zeta-potential distribution in the mixing flow was governed by the convection and diffusion of Na^+ . The present technique will contribute to understand the effect of zeta-potential distribution to EOF field and formation of the electric double layer.

Acknowledgements

The authors would like to thank Professor Hishida at Keio University for his technical assistance. This work was subsidized by the Grant-in-Aid for Young Scientists of Ministry of Education, Culture, Sports, Science and Technology (No. 14702030 and No. 17686017).

Reference

1. Kazoe, Y. and Sato, Y., *MicroTAS 2004*, Vol. 1, pp. 306-308, (2004).
2. Prieve, D. C. and Frej, N., *Langmuir*, 6, pp. 396-403, (1990).
3. Santiago, J. G., et al., *Exp. Fluid*, 25, pp. 316-319, (1998).

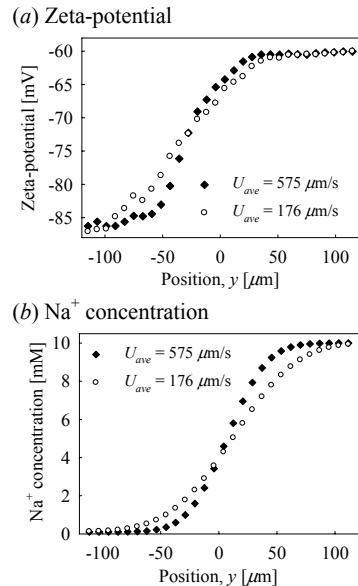


Fig. 6. Comparison of (a) zeta-potential profiles at the glass wall to (b) Na^+ concentration profiles at $z = 25 \mu\text{m}$.

MICROPUMP AND MICROMIXER DRIVEN BY LASER AND AC ELECTRIC FIELD

Michihiko Nakano¹, Kazunori Takashima¹, Shinji Katsura²
and Akira Mizuno¹

¹Toyohashi University of Technology, Toyohashi, Aichi, 441-8580 Japan

²Gunma University, Kiryu, Gunma, 376-8515 Japan

mizuno@eco.tut.ac.jp

Abstract

Fluid flow generated by laser irradiation in an AC electric field was investigated with a view to using it as the driving force for a micropump and a micromixer. We discovered an opto-electrostatic phenomenon known as opto-electrostatic micro vortex (OEMV) ten years ago. The OEMV is generated around the focal point of an infrared laser beam located in the center of an intense high-frequency electric field. The OEMV is an opposed flow. The direction of the flow is parallel to the AC electric field, and perpendicular to the sides of the electrodes. When the laser focus was positioned near one of the electrodes, a one-directional flow was generated toward the other electrode. These two flow patterns could be used as a micro-mixer and a micro-pump, respectively. The OEMV was generated in a microchannel by simultaneous application of an Nd:YAG laser (1064 nm) and an AC voltage. In this paper, it was investigated that the correlation between flow rate and laser power, AC voltage and AC frequency.

Keywords: Micropump, micromixer, opto-electrostatic micro-vortex, IR laser, electric field

1. Introduction

About a decade ago, we discovered that when an infrared (IR) laser is focused under an intense applied AC electric field, a circulating flow is generated around the laser focus as illustrated in Figure 1 [1]. We investigated this phenomenon, which is now known as opto-electrostatic micro-vortex (OEMV), to use as micropump and micromixer in a microchannel. The OEMV has two flow patterns that depend on a position of the IR laser spot. The opposed flow (Fig. 1 (A)) and the one-directional flow (Fig. 1 (B)) were generated by positioning the laser spot at center between the electrodes and beside the electrode, respectively. These flows can be used as micropump and micromixer without mechanical movement. In microchannel configuration, multi parallel fluid flow is generated due to low Reynolds number. Mixing of parallel flow is very important technique for rapid reaction. The OEMV (the opposed flow) is an easy way to generating vortex-like flow. Flow rate was investigated which varied with AC voltage, laser power and AC frequency.

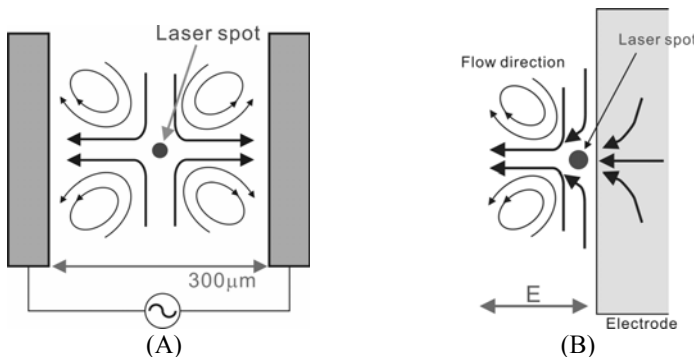


Figure 1. Schematic illustration of the flow, the OEMV, induced by laser irradiation and AC electric field. The flow direction changes with a position of the laser spot, center (A) and beside (B) the electrodes.

2. Experiment

The microchannel (300 μm wide and 100 μm deep) was made of polydimethylsiloxane (PDMS). The PDMS microchannel was mounted on the glass slide on which the chromium microelectrodes (gap between the electrodes was 300 μm wide) were patterned. The microchannel was mounted on an inverted microscope equipped with laser manipulation system. Nd:YAG laser (1064nm, cw) was focused through an objective lens (x100, N. A.: 1.30).

3. Results and discussion

In Table 1, the flow profiles around the laser focus were showed in the case of Milli-Q water and 10 mM NaCl solution. These results were in the case of the one-directional flow. In the case of the opposed flow, the flow profiles were similar to that of the one-directional flow. The flow velocity increased with about 2nd power of laser power and 1st power of AC voltage. A conductivity of the solution affected the correlation between flow velocity and laser power. The flow velocity was also varied with the AC frequency as illustrated in Figure 2. We think the OEMV was caused by an electro-thermal effect. Change of permittivity and conductivity of liquid around the laser focus caused by temperature rising due to the IR laser irradiation may generate the fluid flow under applied AC electric field.

4. Conclusions

Flow profiles were investigated in terms of the AC voltage, laser power and AC frequency. We consider that this fluid manipulation method is suitable for a micro-reaction system since it is easy to control flow velocity on a micro-scale. In addition, there are some advantages that a simple geometry for the electrodes and non-contact operation between the solution and the metal electrodes.

References

1. A. Mizuno, M. Nishioka, Y. Ohno, and L. D. Dascalescu, IEEE Trans. Ind. Appl. **31** 464 (1995).

Table 1. The correlation between the flow velocity and AC voltage and laser power.

Working liquid	Varied parameter	Experimental condition			Results	
		AC voltage [V _{0-p}]	Laser power [mW]	AC frequency [MHz]	Flow range [μm/sec]	Relation
Milli-Q (1.47 μS/cm)	AC voltage (V)	20 - 80	80	1	30 - 800	$u \propto V^{2.24}$
	Laser power (P _L)	70	20 - 200	1	5 - 200	$u \propto P_L^{1.53}$
10mM NaCl (1.28 mS/cm)	AC voltage (V)	30 - 90	135	1	20 - 500	$u \propto V^{2.63}$
	Laser power (P _L)	30	20 - 200	1	30 - 250	$u \propto P_L^{0.96}$

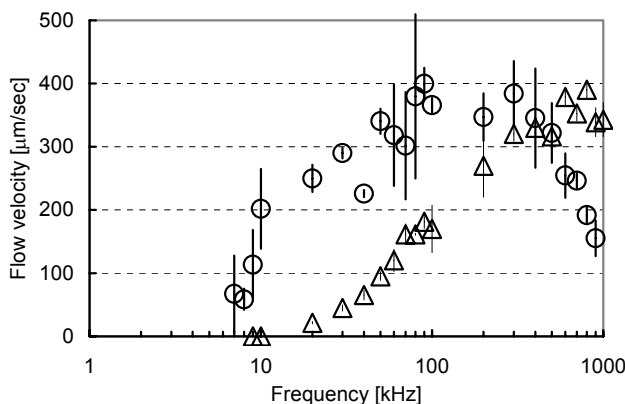


Figure 2. The correlation between the flow velocity and the AC frequency. The AC voltage was adjusted to 70 V_{0-p} and 30 V_{0-p} at 1 MHz in the Milli-Q water (open circle) and the 10 mM NaCl solution (open triangle), respectively. Laser power was adjusted to 35 mW in the both cases. The error bars indicate standard deviation.

PRESSURE BALANCE AT LIQUID-LIQUID INTERFACE OF MICRO COUNTER-CURRENT FLOW FOR PHASE SEPARATION

Arata Aota^{1,2}, Akihide Hibara^{1,3}, Yasuhiko Sugii³ and Takehiko Kitamori^{1,3}

¹The University of Tokyo, Bunkyo, Tokyo, 113-8656, Japan

²Japan Society for the Promotion of Science, Chiyoda, Tokyo, 102-8471, Japan

³Japan Science and Technology Agency, Kawaguchi, Saitama, 332-0012, Japan

Abstract

We report pressure balance model at the liquid-liquid interface of a micro counter-current flow for phase separation was proposed and verified. We focused on balance between dynamic pressure difference of two phases and Laplace pressure due to interfacial tension. Dynamic pressure difference and Laplace pressure were evaluated by measuring dynamic contact angles and interfacial tension, and examining pressure loss.

Keywords: Microfluidics, Surface Modification, Interfacial Tension, Multiphase flow, Contact Angle

1. Introduction

We have established a general method for integrating chemical and biological systems into a microchip by utilizing multiphase microflows, which is based on concepts of micro unit operations (MUOs) and continuous flow chemical processing (CFCP) [1]. Furthermore, we have achieved micro counter-current flow and micro counter-current extraction with high recovery efficiency [2, 3]. However, mechanisms of phase separation of the micro counter-current flow are not elucidated. Therefore, fundamental physical properties of the micro counter-current flow should be understood. In this paper, we proposed and verified an interfacial model of the micro counter-current flow focused on pressure balance at the liquid-liquid interface.

2. Theory

At the liquid-liquid interface, dynamic pressure difference (ΔP_{Flow}) of two phases and Laplace pressure ($\Delta P_{Laplace}$) due to interfacial tension are induced. When ΔP_{Flow} is lower than critical $\Delta P_{Laplace}$, the liquid-liquid interface is pinned at the boundary between the hydrophilic and hydrophobic surfaces. Figure 1 illustrates an interfacial pressure model. Critical $\Delta P_{Laplace}$ is characterized by dynamic contact angles. Laplace pressure can be estimated by Young-Laplace equation as follows.

$$\Delta P_{Laplace} = \frac{\gamma}{R} = \frac{2\gamma \sin(\theta - 90^\circ)}{d} \quad (1)$$

where R , γ , θ and d are radius of curvature, interfacial tension, contact angle and width of microchannel. ΔP_{Flow} can be estimated by utilizing Hagen-Poiseuille relationship.

$$\Delta P_{Flow} = P_{aq} - P_{org} = \frac{32 \mu_{aq} v_{aq} L_{aq}}{D^2} - \frac{32 \mu_{org} v_{org} L_{org}}{D^2} \quad (2)$$

where P , μ , v , L and D are pressure, viscosity, length and hydraulic diameter. Subscript corresponds to each phases.

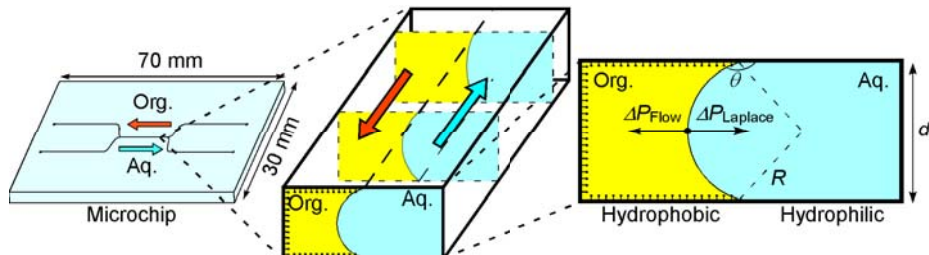


Figure 1. Interfacial pressure model of the micro counter-current flow.

3. Experimental

In order to estimate $\Delta P_{Laplace}$, we measured interfacial tension and dynamic contact angles of water droplet dipped in butylacetate and toluene on a hydrophilic bare glass and hydrophobic glass modified with octadecylsilane (ODS) group. The interfacial tensions are 15.5 mN/m (water-butylacetate) and 32.5 mN/m (water-toluene). Table 1 summarizes measured advancing and receding contact angles. $\Delta P_{Laplace}$ are estimated by utilizing advancing and receding contact angles of water on ODS surface and glass surface. In order to estimate ΔP_{Flow} , we examined the flow rate conditions of phase separation of the micro counter-current flow in microchannels with patterned surface modification where a width, a depth and liquid-liquid contact length were 120 μm , 25 μm and 500 μm , respectively. Figure 2 illustrates the microchip with patterned surface modification.

Table 1. Summary of measured dynamic contact angle of water

Organic solvent (substrate)	Advancing	Receding
Butylacetate (glass)	$72.2 \pm 2.2^\circ$	$7.5 \pm 2.9^\circ$
Butylacetate (ODS)	$172.6 \pm 2.4^\circ$	$153.3 \pm 8.2^\circ$
Toluene (glass)	$64.5 \pm 6.7^\circ$	$6.7 \pm 2.6^\circ$
Toluene (ODS)	$171.0 \pm 2.6^\circ$	$152.0 \pm 5.6^\circ$

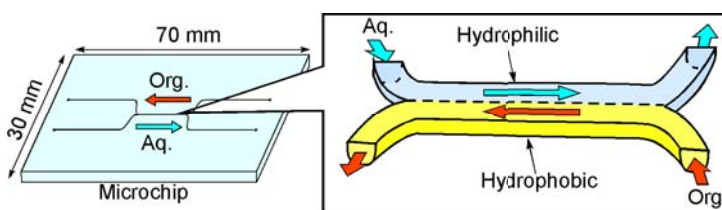


Figure 2. Microchip with patterned surface.

4. Results and discussion

Figure 4 shows the results of phase separation conditions of water-butylacetate and water-toluene micro counter-current flow. The obtained flow rates were converted to ΔP_{Flow} . The phase separation could be realized in the region between upper and lower limit. Upper and lower limit correspond to ΔP_{Flow} that water intruded onto the hydrophobic surface and the organic phase intruded onto the hydrophilic surface. Considering the proposed model, the micro counter-current flow can be formed under conditions between theoretical critical $\Delta P_{Laplace}$. Upper limit is agreed with the model although lower limit is not agreed with the model. This disagreement may be caused from theoretical critical $\Delta P_{Laplace}$ estimated from receding contact angle of water on glass surface instead of advancing contact angle of the organic solution. However, measuring dynamic contact angle of the organic solution in water is difficult because of buoyancy. Therefore, accurate $\Delta P_{Laplace}$ will be able to be evaluated by measuring the shape of the liquid-liquid interface in the microchannel. When this model is verified accurately, main physical parameters of formation of the micro counter-current flow and mechanism of the phase separation are expected to be understood.

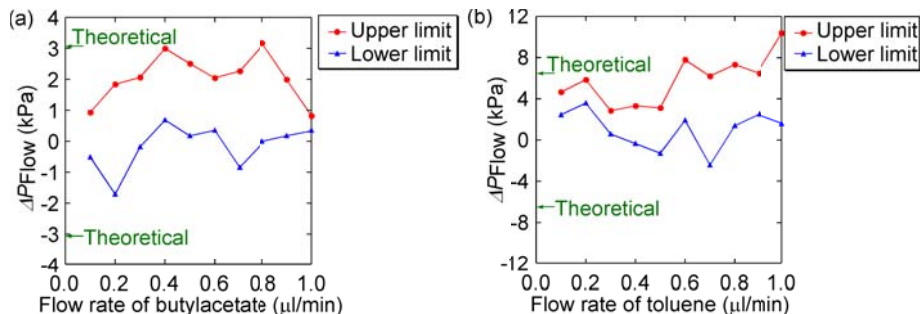


Figure 3. Relation between ΔP_{Flow} and theoretical critical $\Delta P_{Laplace}$ ((a) Water-butylacetate. (b) Water-toluene.).

5. Conclusion

We proposed and verified the interfacial pressure model of the micro counter-current flow for phase separation. The results indicate that the model is agreed when water intrude onto hydrophobic surface although that is not agreed when the organic phase intrude onto the hydrophilic surface. The model will be able to be verified accurately by measuring the shape of the liquid-liquid interface.

References

1. M. Tokeshi, et al., *Anal. Chem.*, **74**, 1565-1571 (2002).
2. A. Aota, et al., *Proceedings of Micro Total Analysis Systems 2003*, pp. 441-444 (2003).
3. A. Aota, et al., *Proceedings of Micro Total Analysis Systems 2005*, pp. 118-120 (2005).

MAGNETIC LEVITATION OF MICRODROPLETS IN AIR

Vincent Haguet*, Christian Jeandey*, Hichem Chetouani**,
Gilbert Reyne** and François Chatelain*

* Commissariat à l'Energie Atomique (CEA), Grenoble, France

** Laboratoire d'Electrotechnique de Grenoble, ENSIEG, France

Abstract

We show here the possibility to use permanent magnets to levitate microdroplets in air. This new microfluidic technique allows handling droplets within punctual or linear magnetic wells while avoiding contact of the droplets with any wall.

Keywords: diamagnetism, permanent magnets, levitation, microdroplet

1. Introduction

We propose levitation-based microfluidics as a new method for handling low-volume droplets. The diamagnetic levitation of liquids was first presented in the 1990s with very intense magnetic fields made by superconductor magnets (26.5 T) [1] or electromagnets (16 T) [2]. Indeed, as the magnetic susceptibilities of liquids are very low (e.g. $\chi = -9 \cdot 10^{-9} \text{ m}^3 \text{ kg}^{-1}$ for water), they were thus compensated by high magnetic fields. However, these two techniques involve large and complex equipments which are impossible to miniaturize, parallelize and integrate in lab-on-chip devices.

Here, we demonstrate the possibility to use small (centimeter-size) NdFeB magnets producing a magnetic field of only 1.2 T to levitate droplets of various liquids: water, ethanol, oil, glycerol 15%. The diamagnetic levitation of droplets in air can be obtained with standard permanent magnets without any supplementary equipment. In a first magnet configuration, the levitating droplets are spontaneously gathered (by a convergent radial magnetic force) and merge in a punctual magnetic well. In a second configuration, the droplets can move linearly along magnetic grooves, and also change their axis of levitation.

2. Punctual magnetic wells

The droplets are trapped in a punctual levitation well carried out by a permanent magnet made by 8 NdFeB sectors having radial magnetization and surmounted by a pole piece (Fig. 1). The levitation site is located between the pole piece and the permanent magnet at the center of the hole. Dispensing or spray techniques were used to eject droplets of 5 μm to 150 μm in diameter (65 fL to 1.8 nL) towards the permanent magnet. The magnetic force stops the droplet fall and pushes the droplets towards the magnetic well, where they finally merge.

Diamagnetic levitation was successfully obtained for droplets of water, ethanol, oil and glycerol 15%. Non-evaporating liquids such as oil can remain unchanged within the magnetic well for hours. Evaporation of other liquids can be compensated, for example by regularly dispensing small droplets which actually merge with the central droplet.

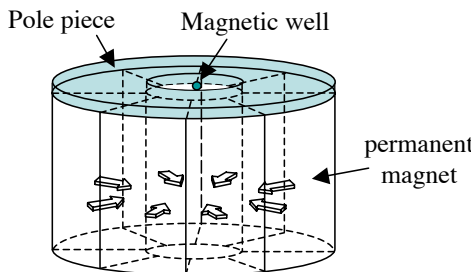


Fig. 1. Punctual magnetic well made by a permanent magnet with radial magnetization.

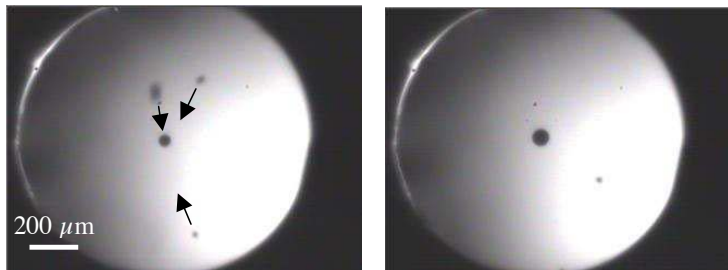


Fig. 2. Coalescence of droplets in levitation (top view of the device). The resulting droplet is bigger than the initial droplet due to the merging of microdroplets.

3. Linear magnetic wells

Droplets of $30\mu\text{m}$ in diameter can levitate in a stable manner within $150\mu\text{m}$ -large grooves made in a permanent magnet (Fig. 3). The microdroplets are guided along the groove axis under aerodynamic flow. Stability of the diamagnetic levitation is very high, even at the crossing of two perpendicular grooves where the magnetic force applied to droplets is reduced. As a result, the droplets can commute from one axis to another (Fig. 4), which makes likely achievable the individual control of any droplet trajectory.

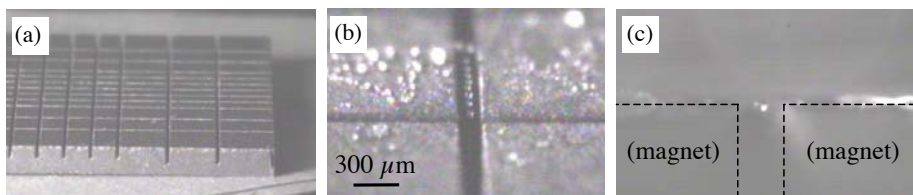


Fig. 3. (a) $150\mu\text{m}$ -large linear grooves in a planar permanent magnet having vertical magnetization. Levitation of microdroplets above the grooves, (b) view from above, (c) side view.



Fig. 4. Droplets turning from one levitation axis to another axis.

4. Discussion

Levitation-based microfluidics presents numerous advantages for handling samples. As the liquid is never in contact with any wall, there is no risk of cross-contamination between the sample and the walls of the device, as well as no unspecific adsorption of sample components onto the wall surface. The samples can be easily deposited, observed and quantified due to the absence of cover above the device. The droplets can be levitated at very precise positions with a micrometer-range accuracy. The microsystem needs no fluidic connection, has no dead volumes and the consumption of sample can be less than 1 nL. Moreover, diamagnetic levitation with permanent magnets is totally passive, which means that the droplets are moved, positioned and possibly merged without providing any energy (e.g. electricity) to the device.

The diamagnetic levitation in air was studied for moving and merging low-volume liquids. Nevertheless, it should be noticed that diamagnetism is an ubiquitous feature in nature. In particular, the diamagnetic levitation can also be applied to solid particles, such as solid diamagnetic (unlabelled) microparticles or any other particles having a strongly diamagnetic label.

5. Conclusions

We have presented the diamagnetic levitation of microdroplets in air which relies on permanent magnets producing a magnetic field of 1.2 T only. Two magnet configurations were presented: one magnet geometry forces the droplets to gather and merge within a punctual magnetic well; the second configuration allows linear motions of the droplets along magnetic grooves in the air gap. Moreover, the diamagnetic levitation of droplets is stable even at the crossing of two perpendicular linear magnetic wells, which thus allows switching of the droplets between linear wells.

References

1. E. Beaugnon and R. Tournier. Levitation of water and organic substances in high static magnetic fields. *J. Phys. III France*, 1423-1428 (1991).
2. M.V. Berry and A.K. Geim. Of flying frogs and levitrons. *Eur. J. Phys.*, 18, 307-313 (1997).

AUTOMATIC DESIGN OF OPTIMAL FLUIDIC COMPONENTS*

David R. Mott,¹ Keith S. Obenschain,¹ Peter B. Howell, Jr.,² and Joel P. Golden²

¹Laboratory for Computational Physics and Fluid Dynamics

²Center for Biomolecular Science and Engineering

US Naval Research Laboratory, Washington, DC 20375

(Corresponding author: david.mott@nrl.navy.mil)

Abstract

An approach to the automatic design of microfluidic components is described in which a novel method for the rapid characterization of individual components is combined with a genetic algorithm search of candidate designs. This approach delivers unprecedented capability for automatic optimization of microfluidic components based on performance criteria and does not require the user to provide a promising prototype to initialize the search.

Keywords: fluidics, automatic design, optimization, mixing

1. Introduction

Mott et al. [1] describe the automatic design of optimal microfluidic components based on performance criteria. Their approach constructs a complex component by adding geometric features, such as grooves of various shapes, to a microchannel. The net transport produced by each of these features in isolation was pre-computed and stored as an “advection map” for that feature, and the complex flow through a composite geometry that combines these basic features was calculated by applying the corresponding maps in sequence. A speed-up of approximately 10^5 was achieved relative to the time that would be required to solve the governing flow equations for the composite geometry using traditional computational fluid dynamics (CFD). Mott et al. developed optimal mixers of moderate sizes using an exhaustive search of all designs that met imposed geometric constraints. The software automatically determined which tested designs provided the best mixing based on several user-specified metrics.

In the current work, a genetic algorithm replaces the exhaustive search, enabling the optimization of components with far greater degrees of freedom. This approach is used to design a better mixer in less time than those previously published [1].

2. Genetic Algorithm

A genetic algorithm is a search algorithm that employs biological concepts such as breeding, mutation, and fitness to find a near-optimal solution to a problem in a fraction of the time required for an exhaustive search. [2]. The genetic algorithm

* This material is declared a work of the U.S. Government and is not subject to copyright protection in the United States.

evaluates the fitness for each solution in the current population and then generates a new population of solutions (crossover). Each solution is comprised of a list of chromosomes that is randomly generated in the initial population. In the current context, each solution is therefore a particular component design, i.e., an ordered list of grooves in the channel, and each chromosome is one particular groove. The fitness score for a solution is a user-specified metric for measuring the process of interest, such as the metrics for mixing used in Ref. 1. During crossover, the fittest members from the current population are used to generate a new population by combining chromosomes (grooves) from two parent solutions, with a slight chance for random mutation to prevent convergence on a local (rather than global) maximum for the fitness function.

3. Results and Discussion

Here we consider one optimization calculation performed in Ref. 1 for microchannel mixers that include 16 grooves in the mixer floor and 16 grooves in the mixer ceiling. The channel width is 3.11 times the height, and the groove depth is 0.42 times the channel height. Two streams to be mixed enter the component side-by-side. Choosing each of these 32 grooves independently from the options shown in Fig. 1 gives 8^{32} candidate designs. This number is too large for an exhaustive search, even using the advection maps to evaluate the performance of each design, so in Ref. 1 the designs were limited to particular pairings of grooves in the floor and ceiling and to a repeating pattern of grooves. These restrictions limited the number of candidate mixers to 331,776. The exhaustive search of these designs required approximately 8 CPU hours to complete, but improvements to the software implementation have reduced that time to approximately 2 CPU hours. Figure 2 shows the winning mixer designs and species distributions at outflow for two metrics that are described in Mott et al.

In contrast, using a genetic algorithm to search the full space of 8^{32} candidates finds a design that approximates the optimal design for this space in this same 2 CPU hours. We estimate an exhaustive search of all 8^{32} candidates would take approximately 10^{18} years. Figure 3 shows the outflow species distribution for the design chosen by the genetic algorithm search. Running in parallel on 16 processors of an SGI Altix, this optimal result is achieved in about 10 minutes. Note that this approach is not simply wrapping a genetic algorithm around a traditional CFD solver: if traditional CFD were used instead of the advection maps to characterize the fluid transport, we estimate that this 10-minute search would have required approximately 3 years.

4. Conclusions

The approach described here provides practical automatic design of fluidic components based on performance criteria. This software tests hundreds of thousands of candidate designs and finds the best feature combination for a specified task in the same time that traditional CFD approaches model a single user-specified geometry. The approach does not require the user to supply a promising prototype, and it can be applied to any process (mixing, surface delivery, dispersion mitigation) that can be quantified using the species transport through the candidate components.

Acknowledgements

This work was sponsored by NRL 6.2 Work Unit 6027. The views expressed in this paper are those of the authors and do not represent opinion or policy of the U.S. Navy, Department of Defense, or Federal Government.

References

1. Mott, D.R., Howell, P.B, Golden, J.P., Kaplan, C.R., Ligler, F.S., and Oran, E.S., "Toolbox for the Design of Optimized Microfluidic Components," *Lab on a Chip*, Vol. 6, No. 4, 2006, pp. 540-549.
2. Goldberg, David E. GENETIC ALGORITHMS in Search, Optimization and Machine Learning, Addison Wesley Longman, Incorporated, 1989.

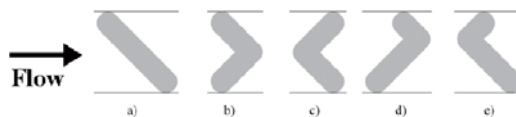


Figure 1: Allowed groove shapes that are added to the floor or ceiling of the channel to create a mixer. Note that vertical reflections of d) and e) provide additional options, so this collection represents eight choices.

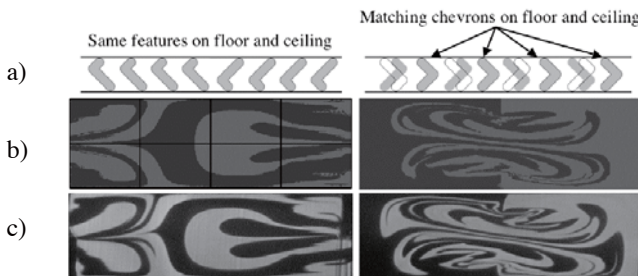


Figure 2: Optimal designs presented in Ref. 1 for the exhaustive search of 331,776 candidates using 2 mixing metrics. a: top view of the first 8 feature pairs; pattern repeats. b: simulation predictions of the outflow plane. c: experiments (from [1])



Figure 3: Outflow distribution for the new optimal mixer that chooses all 32 grooves in the mixer independently. Calculation performed in 10 minutes on 16 processors of an SGI Altix.

Laminar Flow Mixing using Acoustic Microcavitation Streaming

John Collin¹, Jeff Fan¹, Reza Moghbel¹,
Albert Tsung-Hsi Hsieh¹, Abraham P. Lee^{1,2}

¹Department of Biomedical Engineering, ²Department of Mechanical and Aerospace Engineering, University of California, Irvine, U.S.A.

Abstract

An active laminar flow mixer for chemical and biological reagents is developed using acoustic microcavitation streaming. The mixing is induced by the resonance frequency of the cavitative air bubble and the acoustic wave. The effects of different acoustic frequencies and flow rates for the mixing efficiency were tested using the same microfluidic channel and the results demonstrate conditions for good active mixing in laminar flows.

Keywords: Acoustic streaming, mixing, cavitation streaming, Low Reynolds Number

1. Introduction

In microfluidic systems for chemical and biochemical applications, the low Reynolds number flow leads to pure diffusion based mixing which will take many hours. Therefore, there have been much interest in passive and active mixers which uses complex geometry [1,2] and external energy [3,4] for improved mixing respectively. One of such active mixers is based on acoustic cavitation microstreaming [5,6] technique that utilizes acoustic frequency transducers to resonate cavitative bubbles.

2. Experimental

At resonance the frequency of the acoustic signal coincides with the natural frequency of the cavitative air bubble and is given by $2 \pi a f = \sqrt{3 \gamma P_o / \rho}$ where a is the bubble radius, γ is the ratio of specific heats for the gas, P_o is the hydrostatic pressure and ρ is the density of the liquid. Figure 1 shows schematic diagram of the micro cavitation streaming mixing device of inlet channels with 1.6 mm and mixing channel width 3mm. Here we present the enhanced mixing of two laminar streams and characterize an acoustic cavitation microstreaming mixing device. In our experiments, aqueous food dyes with two distinct colors are flown into a T-channel junction with flow rates at 10, 50 and 100 $\mu\text{L}/\text{min}$. The corresponding Reynolds

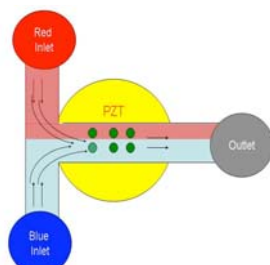


Figure 1. Schematic of the micro cavitation streaming mixing device of inlet channels with 1.6mm and mixing channel width 3mm.

numbers calculated using $R_e = \frac{\rho U H}{\eta}$ where... $H = \frac{2wd}{w+d}$ are 0.686 for 20 L/min, 3.43 for the flow rates 100 L/min and 6.86 for 200 μ L/min. The depth and width of the T channel are 500 μ m and 3mm, respectively.

3. Results and discussion

Due to low Reynolds number flow, at steady state a laminar flow pattern is established. The Peclet Number $P_e = \frac{Uw}{D}$ (D-diffusion coefficient) is directly proportion to the flow rate and hence diffusion between the two laminar streams is found to be more significant at lower flow rates. Mixing of the laminar streams is enhanced by turning on the external piezoelectric crystal at a constant voltage of 45Vpp. The cavitative bubble with a diameter of 400 μ m resonates at a frequency of 3.5 kHz. Figure 2 shows the rate of mixing of laminar streams at different flow rates with a constant resonant frequency of 3.5 kHz. The mixing parameter on the y-axis is the correlation coefficient of the image at the beginning of the mixing with subsequent images and the saturation point gives complete mixing. Figure 3 shows the rate of mixing of laminar streams at a frequency (3.3 kHz) slightly away from the resonant frequency. It is observed that the higher the flow rate, the longer time it takes for complete mixing. Figure 4 shows the time lapse shots of laminar streams under mixing at times 0 sec, 0.5 sec and 2 sec and flow rates. These snap shots are for a constant acoustic frequency of 3.5 kHz. Before switching on the acoustic frequency, diffusion between the fluids is observed at the interface between the two streams. The

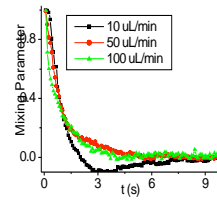


Fig. 2. Rate of mixing of laminar streams at different flow rates at the resonant frequency 3.5

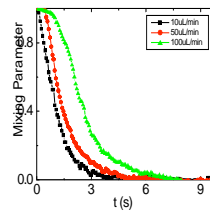


Figure 3. Rate of mixing of laminar streams at different flow rates at a frequency 3.3 kHz.

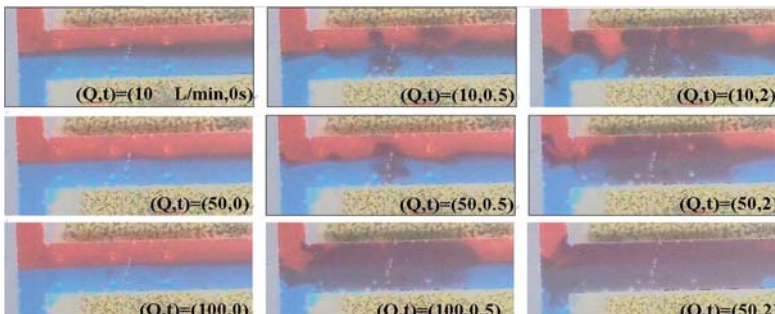


Fig. 4. Laminar streams under mixing. The labels on the figures corresponds to flow rates ((a) 10 (b) 50 (c) 100 μ L/min) and times ((a) 0 sec (b) 0.5 sec (c) 2 sec) after switching on the acoustics at f=3.5kHz.

higher the flow rate the less effective the diffusion is and a complete mixing is faster for higher flow rates. The dependence of geometry and location of the bubbles on the resonant frequency is investigated in an open well. The resonant frequency is identified by sweeping the acoustic signal for a narrow window between 100Hz and 10 kHz and recording the images corresponding to the swept frequency. In Figure 5 the detection of resonant frequency (F_r) using correlation coefficient of images is illustrated. Figure 6 shows the relationship between resonant frequency and diameter of the air bubbles. Figure 7 shows the resonant frequency dependence on the size of the air bubble array and on the inter-bubble distances. The well characterized acoustic streaming mixing device can be used to combine microfluidics with various biosensing applications including immunoassays and detection of DNA hybridization.

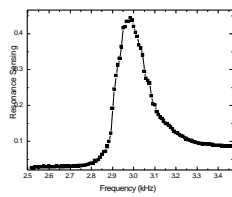


Fig. 5. Detection of resonance frequency (F_r) using correlation coefficient of images.

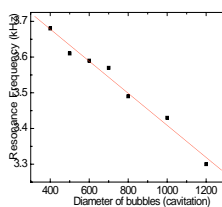


Fig. 6. Relationship between resonance frequency and diameter of the bubble.

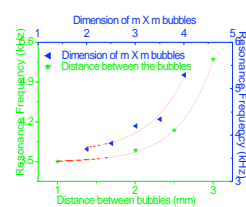


Fig. 7. Dependence of resonance frequency on the inter-bubble distances and the number dimension size of the air bubble array.

References:

1. S. Hardt, K. S. Drese, V. Hessel, and F. Schonfeld, Passive micromixers for applications in the microreactor and mu TAS fields. *Microfluid Nanofluid*, 2005. **1**(2): p. 108-118.
2. N. Y. Lee, M. Yamada, and M. Seki, Development of a passive micromixer based on repeated fluid twisting and flattening, and its application to DNA purification. *Anal Bioanal Chem*, 2005. **383**(5): p. 776-782.
3. K. Sritharan, C. J. Strobl, M. F. Schneider, A. Wixforth, and Z. Guttenberg, Acoustic mixing at low Reynold's numbers. *Appl Phys Lett*, 2006. **88**(5): p. -.
4. L. S. Jang, S. H. Chao, M. R. Holl, and D. R. Meldrum, Microfluidic circulatory flows induced by resonant vibration of diaphragms. *Sensor Actuat a-Phys*, 2005. **122**(1): p. 141-148.
5. R. H. Liu, R. Lenigk, R. L. Druyor-Sanchez, J. N. Yang, and P. Grodzinski, Hybridization enhancement using cavitation microstreaming. *Anal Chem*, 2003. **75**(8): p. 1911-1917.
6. R. H. Liu, J. N. Yang, M. Z. Pindera, M. Athavale, and P. Grodzinski, Bubble-induced acoustic micromixing. *Lab Chip*, 2002. **2**(3): p. 151-157.

PRECISE CHARACTERIZATION OF LIPOSOME POPULATIONS FORMED IN A 5-CHANNEL FLOW-FOCUSED SYSTEM

Andreas Jahn¹, Wyatt N. Vreeland¹, Don DeVoe², Laurie E. Locascio¹, Michael Gaitan¹

¹NIST, Gaithersburg Maryland 20899 USA

² Mech. Engineering Dept., University of Maryland, College Park 20742 USA

Abstract

Previously we demonstrated liposome formation using hydrodynamic focusing in a microfluidic network which enables us to produce liposomes of a controlled size and size distribution in a reproducible fashion [1]. Former measurements on liposomes were conducted with batch dynamic light scattering (DLS) and multi angle laser light scattering (MALLS) of unfractionated samples. However, this measurement only provides ensemble averages. In this paper a more detailed and accurate measurement technique that allows for precise characterization of liposome populations using asymmetric flow field flow fractionation (AFFFF) before MALLS and DLS is shown. Details about liposome size and size distribution allow further elucidation about the liposome self-assembly process.

Keywords: liposomes, nanoparticle, self-assembly, flow field fractionation

1. Introduction

The injection method for the formation of liposomes described previously [2] is used to produce liposome populations of particular size and size distribution. In short, a lipid mixture dissolved in isopropyl alcohol (IPA) is hydrodynamically focused between two streams of aqueous hydration buffer. Mixing between the sheathed streams occurs by molecular diffusion due to laminar flow conditions. As water and IPA interdiffuse lipids are no longer soluble and spontaneously self-assemble into liposomes. Combining DLS and MALLS with AFFFF allows for detailed characterization of the liposome population's size and size distribution. This provides more accurate characterization, which enables the determination of effects of the microfluidic flow conditions on the liposome preparation's physical characteristics.

2. Experimental

The microfluidic device depicted in Figure 1 consists of a central channel (channel 3), which contains the lipid tincture (2.5mM dimyristoylphosphatidylcholine, 2mM cholesterol, 0.5mM dicetylphosphate) in dry IPA and four oblique channels (channels 1, 2, 4, 5) containing hydration buffer (10mM phosphate, 2.7mM potassium chloride, 138mM sodium chloride, pH~7.4, 3mM sodium azide). The direction of the flow is indicated by arrows. The channels are fabricated in silicon (76.2mm silicon wafer, 305-350 μm thick) and sealed with an anodically bonded borofloat glass cover. The

dimensions of the channels are either 64 μm (channel 1, 5, 6) or 43 μm (channel 2, 3, 4) wide and 100 μm deep etched by standard deep reactive ion etching protocols. Rectangular fluid access through holes of the same width as the microchannels were etched from the backside of the wafer at each channel terminus and bonded to nanoports at the backside of the silicon wafer according to manufacturer directions. Fluid flow in the channel network was produced with syringe pumps. A 0.02 μm filter was placed inline to ensure that all fluids were dust free to prevent clogging of the microchannels.

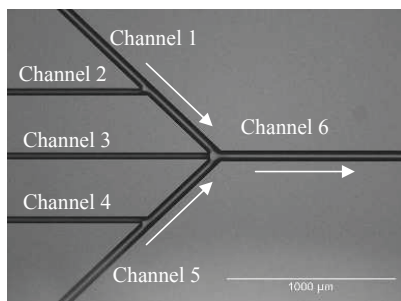


Figure 1. Optical micrograph of the multichannel microfluidic network.

The flow ratio, defined as the ratio of hydration buffer volumetric flow rate to lipid sample volumetric flow rate, was varied from 10 to 60 to produce liposomes of different sizes and size distributions. Following liposome generation within the focused flow stream, AFFFF was used to separate the population according to their hydrodynamic radius before characterizing them by MALLS and DLS with data processing using ASTRA software (all from Wyatt Technology, Santa Barbara, CA, USA) [3] to yield precise measurements of their unaveraged size and size distribution.

3. Results and discussion

As the sample stream is hydrodynamically focused by the two aqueous buffer streams the two streams begin to interdiffuse and amphiphilic lipid molecules begin to self-assemble into spherical liposomes. By modulating the flow rates in the microfluidic device, liposome size and size distribution change reproducibly [1]. The mean liposome radius varies between approximately 25 to 70 nm (Figure 2), a factor of ~2 smaller than earlier observations performed without AFFFF. The measurements also confirm a markedly low polydispersity of liposomes prepared by this new method.

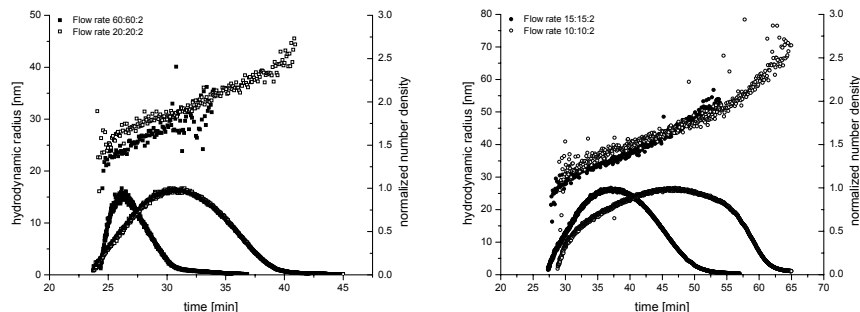


Figure 2. Hydrodynamic radius and normalized number density of fractionated liposome samples eluted over time generated at different flow rates.

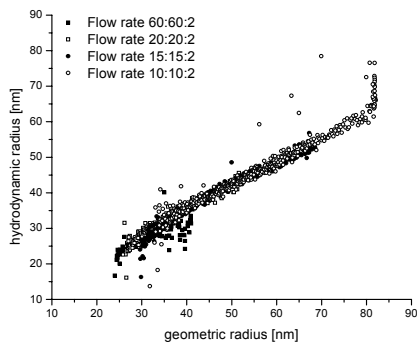


Figure 3. Hydrodynamic radius *vs.* geometric radius at different flow ratios

distribution. Larger particles, which bias the measurement and “hide” the smaller particles, are now measured separately.

Figure 3 shows a plot of hydrodynamic radius *vs.* geometric radius. The hydrodynamic radius is determined *via* DLS and is based on the particle’s diffusion coefficient. The geometric radius is measured *via* MALLS and fits the data to a model for the scattering expected for a hollow sphere. The two radii are roughly equivalent, indicative of liposomes being hollow spheres, as is expected with this method of formation.

4. Conclusion

We have presented an advanced characterization method to precisely measure populations of liposomes. Combining AFFFF with DLS and MALS provides details on the generated liposome population with respect to accurate measurement of particle size, size distribution, and the number of particles of each size. Further, comparison of DLS and MALLS results allows for determination of liposome shape and architecture.

Acknowledgments

Work was supported by NIST’s Single Molecule Measure and Manipulation Program.

References

1. A. Jahn, W.N. Vreeland, M. Gaitan, L.E. Locascio, MicroTAS 2004, Malmö, Sweden, Sept. 26-30, p 345, 2004.
2. A. Jahn, W.N. Vreeland, M. Gaitan, L.E. Locascio, *JACS*, 126(9), 2674-2675, 2004.
3. Certain commercial materials and equipment are identified in order to specify adequately experimental procedures. In no case does such identification imply recommendation or endorsement by the National Institute of Standards and Technology, nor does it imply that the items identified are necessarily the best available for the purpose.

Light scattering is a commonly used method to determine the size of particles such as liposomes in solution. However, a source of measurement inaccuracy is related to the fact that light scattering intensity strongly increases with particle size. Small numbers of larger particles in a distribution can result in a significantly overestimated average particle diameter over the full particle population. Applying AFFFF in combination with DLS and MALLS to a liposome population allows for the separation of liposomes according to their hydrodynamic radius and precise determination of their size and size

BOUNDS ON CONTACT ANGLE HYSTERESIS OF TEXTURED SUPER-HYDROPHOBIC SURFACES

Ashutosh Shastry, Aziel Epilepsia, Marianne J. Case, Shaghayegh Abbasi and Karl F. Böhringer

Department of Electrical Engineering, University of Washington, Seattle, USA

Abstract

This paper presents the fabrication of rough super-hydrophobic surfaces, dynamic measurements of sliding angles of water droplets, and a modeling approach to estimate bounds on contact angle hysteresis—the major dissipative mechanism in droplet based microfluidic systems. We investigate the dependence of hysteresis on texture parameters, evaluate the current model, propose a modification, and show that the two models—current and proposed—are useful bounds on the hysteresis of the surface.

Keywords: droplet microfluidics, contact angle hysteresis, surface characterization

1. Introduction

Droplet based systems make temporally and spatially resolved chemistries possible—creating exciting possibilities for lab-on-chip assay. A low hysteresis surface translates to low energy requirements for droplet actuation. For electrowetting based devices [1], low-hysteresis and low-drag surfaces [2, 3] could make sub-CMOS actuation voltages possible—enabling totally integrated microfluidic platforms. Understanding the quantitative relationship between the impeding force of contact angle hysteresis and surface parameters is therefore an important milestone in this pursuit.

2. Experimental

We built rough surfaces realized by pillars of controlled geometry in silicon. The texture is characterized by ϕ , the solid-liquid contact area fraction. The two states in which a sessile droplet can rest on a rough hydrophobic surface are explained in Fig. 1.

Pillars are fabricated in silicon using standard Bosch process for DRIE and Teflon AF 1600 is spin coated on them to create the test surfaces. We mounted the test surfaces on the goniometer stage and deposited measured droplets, ensuring Fakir state [4]. These droplets were expanded and contracted using a syringe pump. A video was recorded and contact angles measured in each frame.

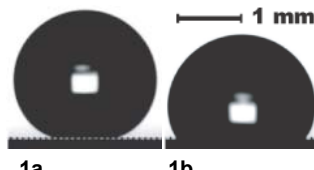


Figure 1: Droplets of volume $5 \mu\text{l}$, on a Teflon-coated silicon surface with $\phi = 0.05$ and $r = 1.4$ in a) Fakir state with a footprint diameter of 1 mm, $\theta_F = 156.6^\circ$ (expected: 164.5°) and b) Wenzel state with a footprint diameter of 1.96 mm, $\theta_W = 118^\circ$ (expected: 112.8°). Air pockets are visible between pillars under the Fakir state droplet. Pinning of the droplet edge causes significant deviations from the predicted equilibrium value.

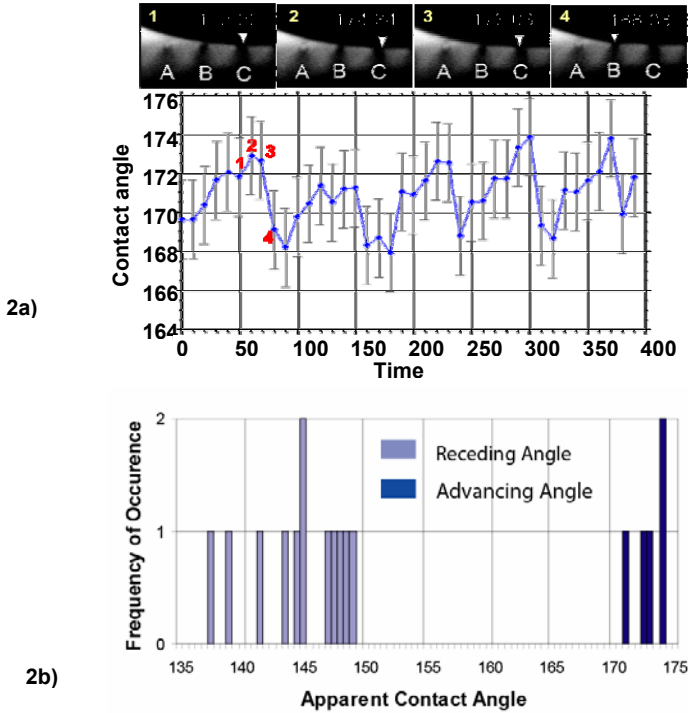


Figure 2: a) The advancing contact angle is plotted as a function of time for a sessile droplet (on a surface with $\phi = 0.04$). b) Contact angle values in the entire video for the advancing angle measurements were used to create the histogram shown.

In Fig. 2a, the contact angle of the expanding droplet increases till the advancing edge lands on the next pillar, at which point it drops. For the contracting droplet, the receding angle decreases till the edge snaps off a pillar. The mode value of contact angle is reported (Fig. 2b) for each case. Movies were made for surfaces of varying texture ϕ ranging from 0.025 to 1, data plotted, and trends analyzed.

3. Results and Discussion

The cosines of advancing and receding angles were observed to decrease linearly with ϕ (Fig. 3). The advancing angle model is $\cos\theta_A = -1 + \phi(1 + \cos\theta_{i,A})$, a heuristic relation proposed by He et al. [5] —obtained by replacing the intrinsic equilibrium contact angle θ_i with the intrinsic advancing angle $\theta_{i,A}$. These results provide the first experimental validation of this relation. The current model for receding angle in the Fakir state, $\cos\theta_R = 2\phi - 1$, is obtained assuming a trailing film remains on the pillar tops [5]. As seen in Fig. 4a, this assumption, originally proposed for hydrophilic surfaces [6], expectedly overestimates hysteresis—providing an upper bound (for $\phi > 0.1$).

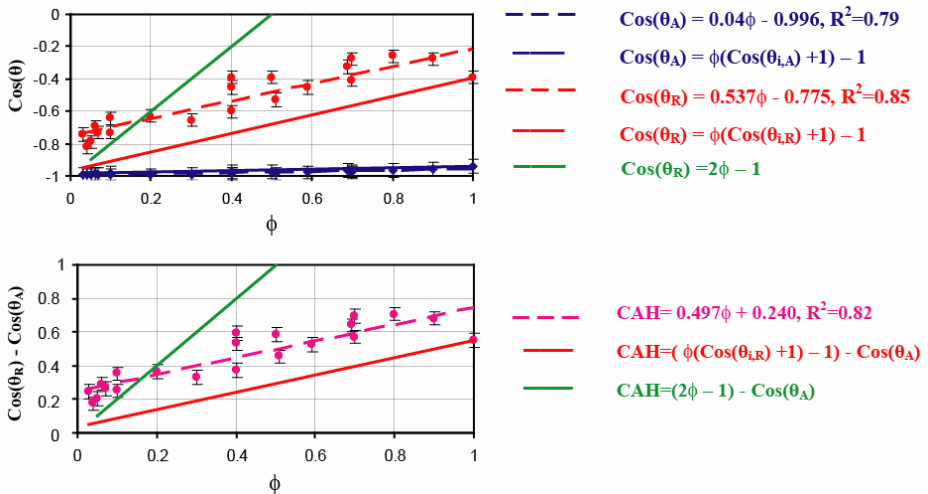


Figure 3: a) Mode values of advancing and receding contact angles obtained on Teflon coated surfaces are plotted as a function of ϕ along with the linear fit lines and model predictions. b) The contact angle hysteresis (CAH) is plotted as a function of ϕ for Teflon, as well as model lines and a fit line.

We re-derived the relation from first principles, heuristically replacing “1” ($=\cos 0$) by $\cos\theta_i$ in the coefficient of ϕ to obtain $\cos\theta_R = (1+\cos\theta_{i,A})\phi - 1$. The model accounts for partial coverage of pillars by the trailing film—which is expected for a hydrophobic coating. Our model provides the lower bound to hysteresis (Fig. 3b). For very low ϕ ($\phi < 0.1$), experiments are underway to validate our hypothesis that the perimeter per unit area and not ϕ controls the behavior.

This work marks an important step towards engineering droplet behavior on textured super-hydrophobic surfaces.

References

- [1] F. Mugele and J.-C. Baret, “Electrowetting: from basics to applications,” *Journal of Physics: Condensed Matter*, vol. 17, pp. R705–R774, 2005.
- [2] C. Cottin-Bizonne, J.-L. Barrat, L. Bocquet, and E. Charlaix, “Low-friction flows of liquid at nanopatterned interfaces,” *Nature Materials*, vol. 2, p. 237240, April 2003.
- [3] C.-H. Choi and C.-J. C. Kim, “Measurement of slip on nanoturf surfaces,” in *Proceedings of ASME NANO 2005: Integrated Nanosystems Design, Synthesis & Applications*, (Berkeley, CA, USA), p. 12, September 2005.
- [4] A. Lafuma and D. Quéré, “Superhydrophobic states,” *Nature Materials*, vol. 2, pp. 457–460, 2003.
- [5] B. He, J. Lee, and N. A. Patankar, “Contact angle hysteresis on rough hydrophobic surfaces,” *Colloid and Surfaces A: Physicochem. Eng. Aspects*, vol. 248, pp. 101–104, 2004.
- [6] P. Roura and J. Fort, “Equilibrium of drops on inclined hydrophilic surfaces,” *Physical Review E*, vol. 64, no. 011601, pp. 1–5, 2001.

ELECTROMECHANICAL FORCES EFFECTING DROPLET MOVEMENT IN A TWO PLATE MICROFLUIDIC DEVICE

Debalina Chatterjee¹, Heather Shepherd² and Robin L. Garrell^{1,2}

¹Biomedical Engineering Interdepartmental Program, University of California Los Angeles, 7523 Boelter Hall, Los Angeles, CA 90095-1600

²Department of Chemistry and Biochemistry, University of California Los Angeles, Box 951569, CA 90095-1569

ABSTRACT

A wide range of liquids can be actuated in droplet-based (digital) microfluidic devices [1]. This report presents a general electromechanical model that: (a) enables calculation of the forces acting on insulating and conductive fluids in two-plate devices, (b) illustrates that both electrowetting and dielectrophoresis simultaneously contribute to droplet actuation, and (c) shows how the device design parameters and operating conditions can be optimized to actuate particular liquids.

Keywords: Electromechanical, droplet, digital microfluidics, electrowetting, dielectrophoresis

INTRODUCTION

In digital microfluidics, liquid droplets in contact with dielectric surfaces are created, moved, merged and mixed by applying AC or DC potentials across electrodes patterned beneath the dielectric. We have recently shown that a wide range of liquids can be actuated in droplet-based microfluidic devices [1].

Droplet actuation has been attributed to electrocapillary or electrowetting (EW) forces for conductive liquids and dielectrophoretic (DEP) forces for dielectric liquids. For conductive liquids, droplet movement is associated with a corresponding voltage-induced contact angle change; for dielectric liquids, this is not the case. Many of the liquids we have actuated are neither perfect conductors nor perfect dielectrics. Some of these liquids have very small or no voltage-induced contact angle change, but are still movable. We have also observed that for some liquids, the movability depends on the applied frequency and gap. To explain our observations, we have developed a model for calculating the forces acting on droplets of liquids having a wide range of physical properties. The experimental variables are the complex permittivity of the liquid, the thickness and dielectric constant of each layer in the device, the gap D , and the applied voltage and frequency.

EXPERIMENTAL

We calculated the total electromechanical force acting on a droplet in a two plate digital microfluidic device as a way to explain and predict the feasibility of droplet

actuation. Our approach was inspired by Jones et al and Zeng and Korsmeyer [2-5]. We modeled the device in Figure 1 with the equivalent circuit model shown in Figure 2.

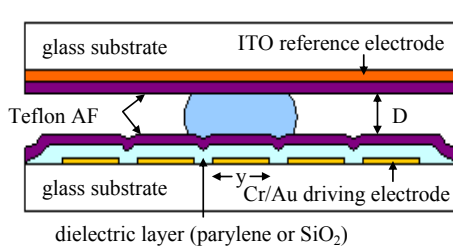


Figure 1: Device configuration

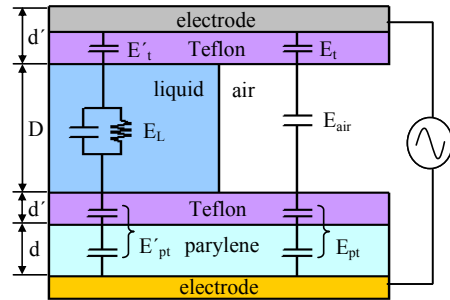


Figure 2: Circuit elements on either side of liquid-air interface, used to calculate the total electromechanical force on the liquid.

The total electromechanical force F acting on the liquid in the device (Figure 1) is calculated from simple circuit analysis:

$$F = \frac{1}{2} y \left[\epsilon_0 k_t d' (E'^2 - E_t^2) + D (\epsilon_L^* |E_L^2 - \epsilon_0 E_{air}^2|) + \frac{\epsilon_0 k_p k_t (d+d')^2}{k_p d' + k_t d} (E'^2 - E_{pt}^2) \right]$$

where y is the width of the electrode, ϵ_0 is the permittivity of vacuum, k_p and k_t are dielectric constants of parylene and Teflon AF, and E is the field across each layer. Note the ambient medium could be air (as here) or a second liquid. The total force has three distinct parts:

$\frac{1}{2} y \epsilon_0 k_t d' (E'^2 - E_t^2) = F_{EW}^{top}$ is the EW force acting on the three-phase contact line at the top plate; $\frac{1}{2} y \frac{\epsilon_0 k_p k_t (d+d')^2}{k_p d' + k_t d} (E'^2 - E_{pt}^2) = F_{EW}^{bottom}$ is the EW force on the three-phase contact line at the bottom plate, also referred to as the *line force* by Zeng & Korsmeyer [5], and $\frac{1}{2} y D (\epsilon_L^* |E_L^2 - \epsilon_0 E_{air}^2|) = F_{DEP}$ is the DEP force acting on the advancing edge of the liquid-air interface, referred to by Zeng and Korsmeyer as the *interfacial force* [5]. The relative contributions of these forces in effecting droplet movement depend on the frequency of the applied voltage and the gap D . This frequency dependence is taken into account in our model by using the complex permittivity of the liquid, $|\epsilon_L^*|$.

RESULTS AND DISCUSSION

Force calculations were performed for a variety of liquids, using 50 and 300 μm gaps and four different frequencies (10 Hz to 8 kHz)[1]. Figure 3 shows the total

calculated force vs. the modulus of complex permittivity. For liquids with $|\epsilon_L^*| < \sim 10^{-7}$, reducing the gap from 300 to 50 μm results in an increase in the total force acting on the liquid. This prediction is consistent with the experimental observation that liquids not movable at larger gaps could be moved with smaller gaps [1].

Figure 4 shows the DEP force, and also the EW force at each plate, for the two different gaps. As the liquid permittivity $|\epsilon_L^*|$ is increased, the interfacial force first rises then falls. For conductive liquids ($|\epsilon_L^*| > \sim 10^{-7}$), the line force dominates droplet actuation and is essentially constant. Summing the EW and DEP forces results in the crossover shown in Figure 3 at $|\epsilon_L^*| \sim 10^{-6}$.

Some liquids could not be actuated under the conditions/devices tested. The model shows the applied force was lower than that used to successfully actuate other liquids. The model can thus be used to predict the device design (gap height, dielectric material and thickness) and operating conditions (voltage and frequency) that will provide at least the minimum force needed to ensure facile movement of particular liquids.

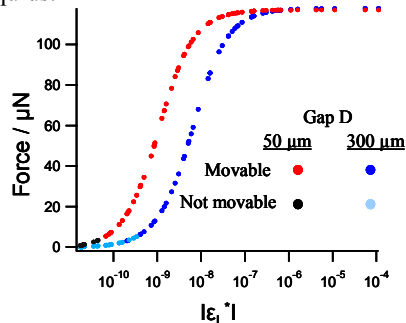


Figure 3: Total force as a function of modulus of complex permittivity. $V_{\text{rms}} = 100$ V.

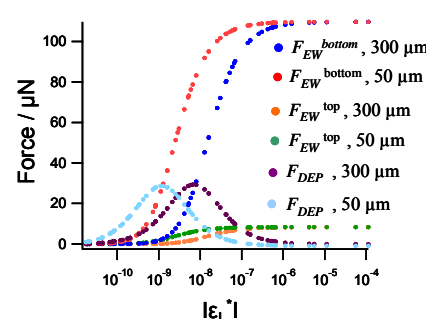


Figure 4: EW and DEP forces calculated for 50 and 300 μm gaps.

REFERENCES

- [1] D. Chatterjee, B. Hetayothin, A.R. Wheeler, D.J. King and R.L. Garrell, Droplet Based Microfluidics with Nonaqueous Solvents and Solutions, *Lab on a Chip*, Vol. 6, pp. 199-206 (2006).
- [2] T.B. Jones, On the Relationship of Dielectrophoresis and Electrowetting, *Langmuir*, Vol. 18, pp. 4437-4443 (2002).
- [3] T.B. Jones, J.D. Fowler, Y.S. Chang and C.-J. Kim, Frequency-Based Relationship of Electrowetting and Dielectrophoretic Liquid Microactuation, *Langmuir*, Vol. 19, pp. 7646-7651 (2003).
- [4] T.B. Jones, K.-L. Wang and D.-J. Yao, Frequency-Dependent Electromechanics of Aqueous Liquids: Electrowetting and Dielectrophoresis, *Langmuir*, Vol. 20, pp. 2813-2818 (2004).
- [5] J. Zeng and T. Korsmeyer, Principles of Droplet Electrohydrodynamics for Lab-on-a-Chip, *Lab Chip*, Vol. 4, pp. 265-277 (2004).

ELECTRICALLY-INDUCED SPLITTING AND GENERATION OF SUB-NANOLITER DROPLETS IN AIR ON A DIGITAL MICROFLUIDIC DEVICE

Sang Uk Son, Debalina Chatterjee, Robin L. Garrell*

Dept of Chemistry and Biochemistry, University of California, Los Angeles,
CA 90095-1569, USA

Email: garrell@chem.ucla.edu

KEYWORDS: *Microfluidics, droplet, electrowetting, splitting, EWOD*

ABSTRACT

Droplet-based (“digital”) microfluidics is attracting great interest as a platform for array-based chemical manipulations and assays, including MALDI-MS for proteomics and clinical diagnostics. We describe here the design and operation of a two-plate microfluidic device in which sub-nanoliter-size droplets are generated by successive splitting of larger droplets. The device operates on the principle of electrowetting-on-dielectric (EWOD), where voltages are applied successively to electrodes patterned underneath a dielectric surface, using air as the ambient medium. Groups of three electrodes are arranged perpendicular to one another. A 100 nL droplet of deionized water is placed on the middle electrode and split either symmetrically or asymmetrically to the two flanking electrodes by applying a 95 V_{rms} potential (2 to 8 kHz). One of the smaller droplets is then moved to the middle electrode of an adjacent group and split again. Four successive splittings yields, on the final electrode (240 × 240 µm, 13 µm gap between plates), a 750 pL droplet.

INTRODUCTION

Advantages of droplet-based microfluidic include the ease with which liquids can be moved and the ability to perform a sequence of manipulations on a single device, and to handle multiple samples either sequentially or in parallel. Droplets have been generated by electrowetting-on-dielectric (EWOD) [1-3], dielectrophoresis [4], or by breaking up a stream of liquid into droplets in air or in a second fluid [5]. Droplets as small as 500 nL have been actuated in air [2] and as small as 700-900 nL in silicone oil [6] by EWOD. Reducing the droplet size would reduce the required sample size and detection limits. We demonstrate here the generation of sub-nanoliter droplets by successive splitting and movement of droplets using EWOD, achieved by reducing the areas of adjacent electrodes and by arranging the electrodes to maintain droplet separation. Also, different-sized droplets can be generated by asymmetrical splitting.

SCHEMATIC

Fig. 1 shows the layout in which groups of three electrodes are arranged perpendicular to one another. The side electrodes have 70% and 80% of the middle electrode length, and the gap between the top and bottom plates is constant ordinarily

50 μm across the device. The initial droplet of deionized (DI) water is pipetted onto the device and the top cover put in place manually. Applying a potential simultaneously to both sides of the first middle electrode, A_0 , causes the droplet on A_0 to be split in two. One of these smaller droplets is moved to the next middle electrode, A_1 , and split in the same way. The volume of the split droplet decreases exponentially following the area of adjacent electrodes, i.e., $V(0.7)^{2n}$, $V(0.8)^{2n}$, or a combination of these, where n is the number of divisions and V the volume of the initial droplet on A_0 .

FABRICATION

The fabrication process for the two-plate ($15 \times 28 \text{ mm}$) device is shown in Fig. 2. For the bottom plate, 100 Å Cr and 1000 Å Au were deposited on a 500 μm -thick glass substrate using an e-beam evaporator. The bottom electrodes were defined by lithography with a 4 μm space between each electrode. 1 μm parylene was deposited as the dielectric layer by chemical vapor deposition, followed by a 500 Å Teflon AF hydrophobic coating. For the top electrode, Teflon AF was spin-coated on a transparent indium tin oxide-coated glass slide.

RESULTS

In each of the two experiments shown, a 100 nL droplet of DI water was pipetted onto the largest middle electrode ($1 \times 1 \text{ mm}$). The droplet was split by applying a 95 V_{rms} potential (2 to 8 kHz) simultaneously to the two adjacent electrodes; then one of the two smaller droplets was moved to the next electrode group to be split again. Fig. 3 shows an image of a 10 nL droplet made by three successive asymmetric splittings, where the flanking electrodes were $0.8 \times 0.8 \text{ mm}$ on the left and $0.7 \times 0.7 \text{ mm}$ on the right, with a 50 μm gap between plates. The co-generated 13 nL droplet could not be further divided because the force acting on the droplet was insufficient. To increase the applied force, the gap was narrowed from 50 to $\sim 13 \mu\text{m}$. Fig. 4 shows images of a sequence of one asymmetrical and three symmetrical splitting processes. The volumes of the two final droplets were approximately 2.2 nL on the $410 \times 410 \mu\text{m}$ electrode (left, Fig. 4d) and 750 pL on the $240 \times 240 \mu\text{m}$ electrode (right, Fig. 4d).

CONCLUSIONS

Droplets of DI water as small as 750 pL can be generated by successive splitting of a 100 nL droplet on an EWOD device, with air as the ambient medium. Droplet splitting can be symmetric or asymmetric depending on the electrode layout. Reducing the electrode and/or gap dimensions further should enable creation of even smaller droplets by this method.

REFERENCES

1. R. Mukhopadhyay, Diving into droplets, *Anal. Chem.*, 78, pp. 1401-1404, (2006).
2. A. R. Wheeler, H. Moon, C.-J. "CJ" Kim, J. A. Loo, and R. L. Garrell, Electrowetting-based microfluidics for analysis of peptides and proteins by matrix-assisted laser desorption/ionization mass spectrometry, *Anal. Chem.*, 76, pp. 4833-4838, (2004).
3. V. Srinivasan, V. K. Pamula, and R. B. Fair, An integrated digital microfluidic lab-on-a-chip

- for clinical diagnostics on human physiological fluids, *Lab Chip*, 4, pp. 310-315, (2004).
4. M. He, J. S. Edgar, G. D. M. Jeffries, R. M. Lorenz, J. P. Shelby, and D. T. Chiu, *Anal. Chem.*, Selective encapsulation of single cells and subcellular organelles into picoliter- and femtoliter-volume droplets, *Anal. Chem.*, 77, pp. 1539-1544, (2005).
 5. M. G. Pollack, A. D. Shenderov, and R. B. Fair, Electrowetting-based actuation of droplets for integrated microfluidics, *Lab Chip*, 2, pp. 96-101, (2002).
 6. R. Ahmed, D. Hsu, C. Bailey, and T. B. Jones, Dispensing picoliter droplets using dielectrophoretic (DEP) microactuation, *Microscale Therm. Eng.*, 8, pp. 271-283, (2004).

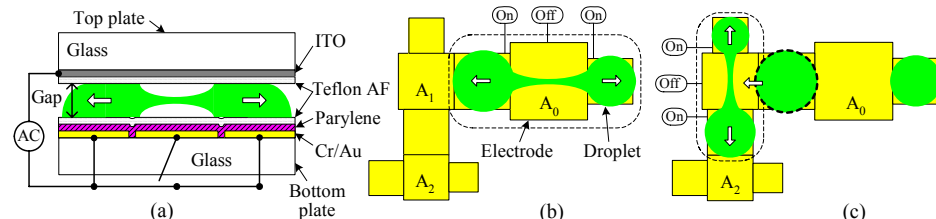


Fig. 1. (a) Device cross-section showing the addressing electrodes. (b) Schematic showing the splitting of a droplet initially placed on A₀, and (c) subsequent movement to A₁, followed by a second splitting.

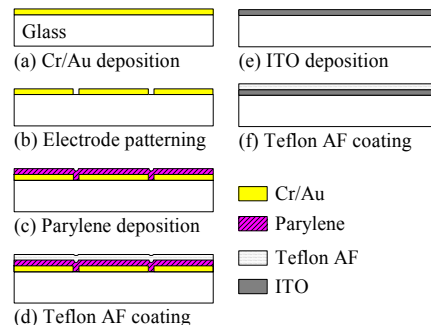


Fig. 2. Fabrication process. (a)-(d) are for the bottom plate and (e),(f) are for the top plate.

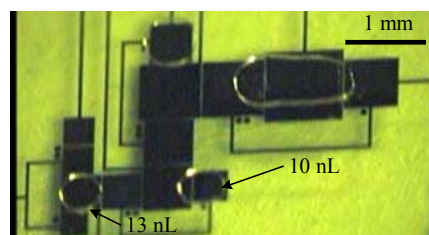


Fig. 3. A 10 nL droplet after three successive asymmetrical splittings with a 50 μ m gap between plates.

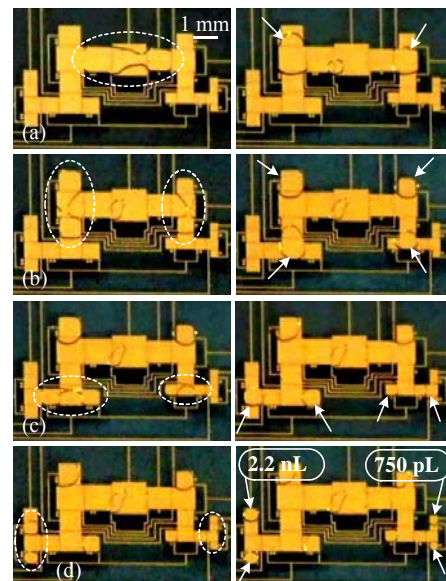


Fig. 4. Four successive splitting and movement steps, consisted of one asymmetrical and three symmetrical splittings (13 μ m gap between plates); final volume \sim 750 pL. Circles and arrows note the splitting and split droplets, respectively.

FAST PULSATILE FLOW INCLUDED IN NET CONTINUOUS FLOW GENERATED BY A TRAVELING WAVE MICROPUMP

Takaaki Suzuki¹, Hidetoshi Hata¹, Hirofumi Shintaku¹, Isaku Kanno¹,
Satoyuki Kawano² and Hidetoshi Kotera¹

¹ Kyoto University, Yoshida-honmachi, Sakyo-ku, Kyoto 606-8501, Japan,

² Osaka University, 1-3 Machikaneyama, Toyonaka, Osaka, 560-8531, Japan
(takaaki@me.kyoto-u.ac.jp)

Abstract

We observed the instantaneous fluid flow included in the net continuous flow simultaneously generated by traveling wave micropumps using a micro particle image velocimetry (microPIV) system with a high speed digital video camera and a confocal unit. It was measured that the instantaneous flow velocity was about 2.66 times higher than the time-averaged continuous flow in the traveling wave micropump.

Keywords: Traveling wave micropump, microPIV, pulsatile flow

1. Introduction

The specific flow induced by traveling wave micropumps is different from Hagen-Poiseuille's and plug flows induced by pressure pumps and electroosmotic flow (EOF). In previous research literatures, the authors have proposed a novel valveless traveling wave micropump composed of flexible microchannel and piezoelectric actuator array as shown in Fig.1, demonstrated its high efficiency flow [1], and measured the three-dimensional net fluid flow in the micropump using the microPIV system [2]. In this paper, instantaneous pulsatile flow induced by the traveling wave micropump was experimentally characterized using the microPIV with a high speed digital video camera in order to confirm the validity of the micropump for μ TAS applications.

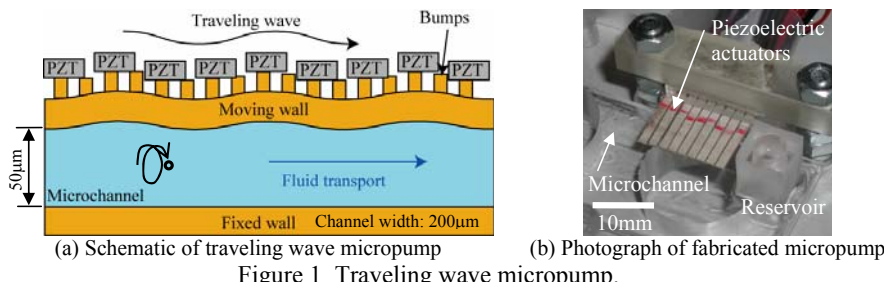


Figure 1 Traveling wave micropump.

2. Experimental

The valveless microchannels are made from PDMS using rapid and easy fabrication techniques, thus allowing it to be used as a low-cost disposable device (the piezoelectric actuators can be reused). The fabricated microchannel is the height of 50 μm and the width of 200 μm . A traveling wave is induced in the microchannel wall by applying different phased sinusoidal voltages to each of the piezoelectric actuators. When a wall surface of the microchannel oscillates in the form of the traveling sine waves, the fluid transports in the direction according to the traveling wave propagation. The instantaneous pulsatile flow induced by the micropump applying sine wave voltage of 20V_{p-p} at 100Hz to the actuators was observed using the microPIV system. The shift of the fluorescent tracer microparticles distributed in the fluid was observed by high-speed digital video camera with a confocal scanning unit to change the focal depth. The images under actuator array were obtained every 0.5msec (the frame rate of 2000fps), which corresponds to the 1/20 period of the traveling wave as well as actuator vibration.

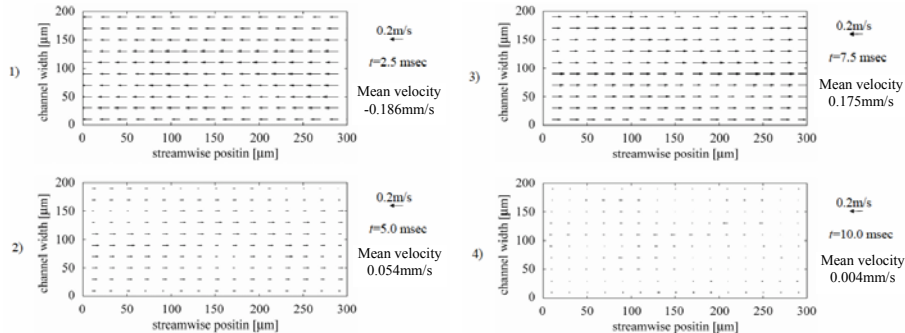


Figure 2 Periodical change of flow field.

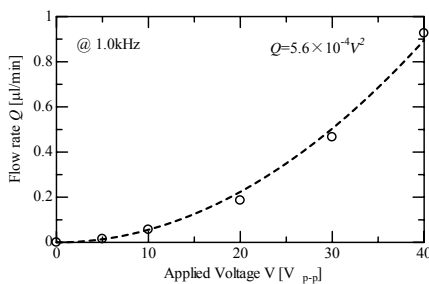


Figure 3 Flow rate as a function of applied voltage.

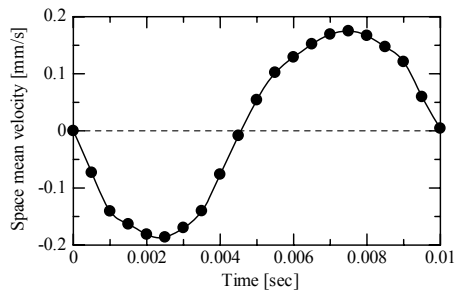


Figure 4 Space mean velocity at each period.

3. Results and discussion

Figure 2 shows the two-dimensional fluid flow time-mean velocity profiles every 1/4 period under 12 μm from the top moving wall. From these profiles, the velocity distribution is parabolic flow in the width direction, and the flow direction is periodically changed by the motion of the microchannel. It indicated that the trajectory of a fluid particle follows an elliptic path in the peristaltic transport [3]. After a period of the wave, the fluid particle slightly moves from the initial position due to the fluid viscosity. The net fluid transport is achieved by repeating such periodic motion as shown in Fig.3. To clarify the periodicity, the space mean velocity in the observed area is shown in Fig.4. The space mean velocity periodically changes with about 10msec corresponding to the period of the traveling wave. In this observed area, the maximum and minimum space mean velocities, and time mean velocity at a period are 0.175mm/s, -0.186mm/s and 7.0×10^{-2} mm/s, respectively. Therefore, the instantaneous flow velocity was 2.66 times larger than the net continuous flow. In flow velocity dominant phenomena such as a surface reaction between biosamples and solid surface [4], the fast pulsatile flow induced by the traveling wave micropump can improve the reaction rate under small sample volume resulting from the low net continuous flow.

4. Conclusions

The instantaneous pulsatile flow induced by the traveling wave micropump was observed using the microPIV system with the high speed digital video camera and the confocal scanning unit. Since the instantaneous flow velocity was 2.66 times larger than the net continuous flow, the proposed micropump can improve the reaction rate of velocity dominant phenomena under small sample volume.

Acknowledgements

This study is a part of Kyoto City Collaboration of Regional Entities for the Advancement of Technological Excellence of JST on the basis of research results supported in part by Scientific Research (A) (No. 15201033), and Center of Excellence for Research and Education on Complex Functional Mechanical Systems (COE) of MEXT, Japan.

References

1. I. Kanno, S. Kawano, S. Yakushiji and H. Kotera, *Characterization of Piezoelectric Micropump Driven by Traveling Waves*, Proc. MicroTAS2003, pp.997-100, (2003).
2. T. Suzuki, H. Hata, H. Shintaku, I. Kanno, S. Kawano and H. Kotera, *Visualization and optimization for fluid flow of traveling wave micropump using micropiv and numerical simulation*, Proc. MicroTAS2005, pp.1108-1110, (2005).
3. F.C.P.Yin and Y.C.Fung, *Comparison of theory and experiment in peristaltic transport*, J. Fluid Mech., Vol.47, pp.93-112, (1971).
4. J. Davies, *Surface Analytical Techniques for Probing Biomaterial Processes*, CRC-Press, (1996).

NANOLITER DROPLET CREATION BY EWOD AND LDEP

Yen-Chen Lin, Yu-Chi Chang, Kai-Cheng Chuang, and Shih-Kang Fan
Institute of Nanotechnology, National Chiao Tung University, Hsinchu, Taiwan

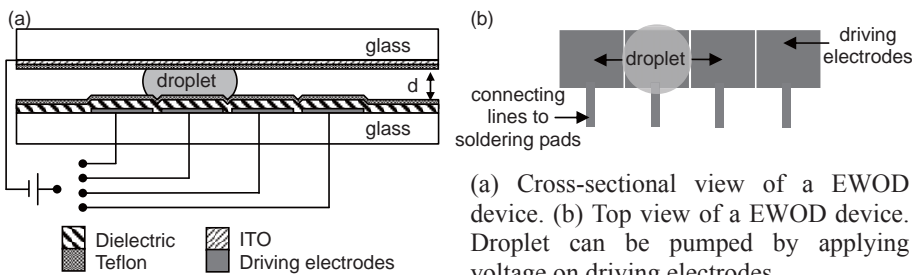
Abstract

Creation of droplets with consistent volume of 6.25 nL was achieved by using both EWOD and LDEP forces in the process. Creating droplets with precise volume is critical for the success of digital microfluidics. In this paper, we exploited LDEP to gradually pump liquid in a virtual microchannel to a droplet creation site. Combining LDEP and EWOD forces, precise volume of droplets can be consistently generated and subsequently transported by EWOD or LDEP.

keywords: EWOD, LDEP, Nanoliter Droplet, Droplet Generation

1. Introduction

EWOD (electrowetting-on-dielectric) has been widely used in manipulation of liquid droplets in the digital microfluidic applications [1]. Fig. 1 shows the configuration of a EWOD device. LDEP (liquid dielectrophoresis) is an electrokinetic force to drive liquid fingers toward high electric field region on coplanar electrodes [2]. Recently, we have demonstrated the integration of EWOD and LDEP on a single chip with the identical configuration of Fig. 1 [3]. Therefore, integrated digital and analog microfluidics would be realized. Digitized liquid droplets could be transported by EWOD, while continuous liquid columns were formed by LDEP.



(a) Cross-sectional view of a EWOD device. (b) Top view of a EWOD device. Droplet can be pumped by applying voltage on driving electrodes.

Figure 1. Digital microfluidics manipulated by EWOD.

2. Experimental

We found that on an oil-filled EWOD device, when altering the frequency of the applied voltage, a liquid column was projected on the thin connecting lines and proceeded until the excess liquid was consumed by LDEP. As shown in Fig. 2(a) and (b), by changing the frequency from 1 kHz (typical EWOD driving frequency) to 100 kHz, a water droplet, originally transported on square-shaped EWOD electrodes, was pumped on the thin connecting lines as in a virtual microchannel by LDEP. Based on

this phenomenon, a droplet creator was developed. Our scheme is to pump liquid from reservoir on the LDEP electrodes by LDEP, and create a droplet at the creation site by EWOD as shown in Fig. 3.

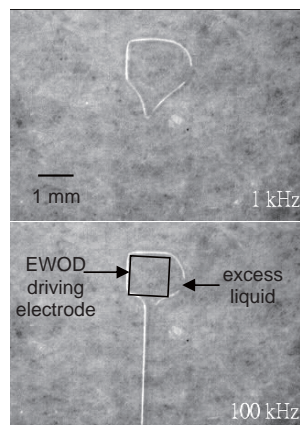


Figure 2. Frequency effect tested in an oil environment.

(a) 1 kHz and
140 V_{rms} were
applied
(EWOD).

(b) 100 kHz
and 140 V_{rms}
were applied
(LDEP).

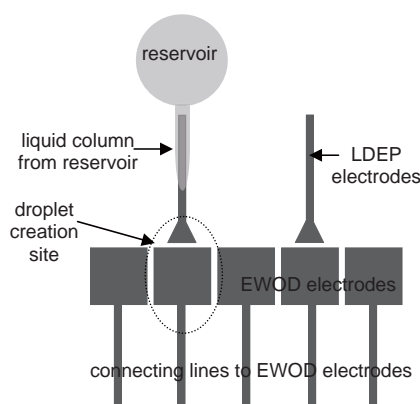
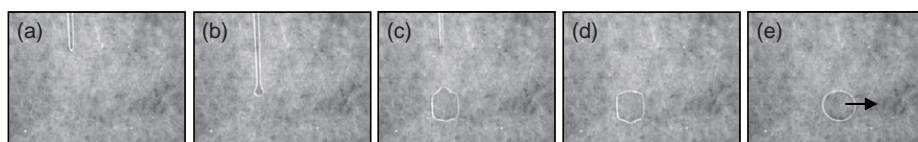


Figure 3. The top view of the electrode design to create droplets using EWOD and LDEP.

3. Result and discussion

Fig. 4(a) shows the liquid column proceeded when applying a 100 kHz signal on the 100- μm -wide LDEP electrode. When the frontier of the liquid column approached to the edge of the EWOD electrode (Fig. 4(b)), 1 kHz was applied on the EWOD electrode ($1 \text{ mm} \times 1 \text{ mm}$). Then, the LDEP electrode was switched off. The pulling force from reservoir by surface tension broke the thin liquid column, resulting in droplet creation (Fig. 4(c)). The created droplet was transported by EWOD as shown in Fig. 4 (d)-(g). With the same procedure, another droplet was created (Fig. 4(h)-(k)) and merged with the previous one (Fig. 4(l)-(m)). The merged droplet can be further pumped on the thin connecting line by LDEP when applying 100 kHz (Fig. 4(n)-(o)). Since the distance between glass plates (shown "d" in Fig. 1) was 100 μm , the droplet volume was 100 nL. From Fig. 4, two droplets of similar volume were achieved because the thin LDEP electrode reduced the volume uncertainty of the created droplet caused by the uncontrollable breaking point. More systematic study needs to be performed to obtain the individual volume deviation between droplets.



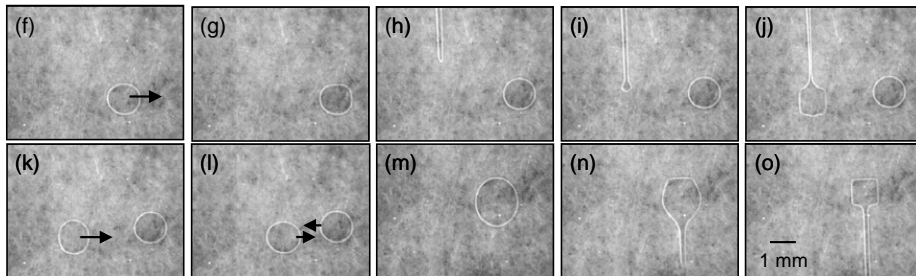


Figure 4. (a)-(b) Liquid column pumped by LDEP. (c) Creation of a 100 nL droplet by turning on EWOD electrode and turning off LDEP electrode. (d)-(g) Droplet transportation by EWOD. (h)-(j) Creation of the 2nd droplet. (k)-(m) Merging droplets. (n)-(o) Pumping liquid by LDEP.

Smaller droplets can be created on device with shrunk dimensions. Fig. 5 shows a 6.25 nL droplet created on a 500 $\mu\text{m} \times 500 \mu\text{m}$ EWOD electrode which a 25- μm -high spacer between plates. The width of the LDEP electrode in this device is 50 μm .

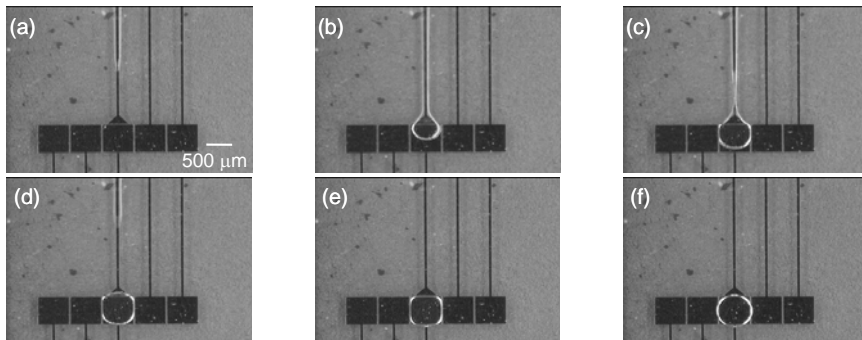


Figure 5. Creation of a 6.25 nL droplet by device with shrunk dimensions.

4. Conclusion

We successfully demonstrated the creation of nanoliter droplets by a novel procedure using both EWOD and LDEP. EWOD and LDEP can be selectively generated on the same electrode by simply changing the applied frequency. This creating mechanism can be investigated to create smaller droplet by further miniaturizing the device.

References

1. M. G. Pollack, R. B. Fair,; A. D. Shenderov, *Electrowetting-based actuation of liquid droplets for microfluidic actuation*, Appl. Phys. Lett., vol. 77, pp. 1725-1726, 2000.
2. T. B. Jones, *Liquid dielectrophoresis on the microscale*, J. of Electrostatics, vol. 51-52, pp. 290-299, 2001.
3. Y.-C. Lin, K.-C. Chuang, T.-T. Wang, C.-P. Chiu, and S.-K. Fan, *Integrated Digital and Analog Microfluidics by EWOD and LDEP*, IEEE Int. Conf. on NEMS, Zhuhai, China, Jan. 2006.

OPTIMIZED REACTIVE ION ETCHING PROCESS FOR THE FABRICATION OF HIGH-ASPECT-RATIO SILICON NANOPILLAR ARRAYS

Yu-Fen Chang¹, Qiong-Ru Chou², Jiunn-Yuan Lin², and Chau-Hwang Lee^{1*}

¹Research Center for Applied Sciences, Academia Sinica, Taipei 11529, Taiwan

²Department of Physics, National Chung Cheng University, Chia-Yi 62102, Taiwan

*E-mail address: clee@gate.sinica.edu.tw

Abstract

Silicon nanopillar arrays with pillar diameters smaller than 200 nm are made by using the conventional reactive ion etching process. Etching parameters including the chamber pressure, the rf power, and the gas mixture are optimized for the largest etching anisotropy. Silicon nanopillars with aspect ratios higher than 20 are demonstrated. After the treatment of aqua regia, the aspect ratio can be increased to 30.

Keywords: silicon nanopillar, reactive ion etching, etching anisotropy

1. Introduction

The applications of silicon nanopillar arrays have been proposed from micro-fluidic stretching devices of DNA or polymers [1] to molds of nanoimprint lithography [2]. These applications require pillars with smooth surface, accurate positioning, and high aspect ratios. Etching techniques such as deep reactive ion etching (DRIE) and inductively coupled plasma (ICP) etching have been employed to match these requirements. However, DRIE processes provide good results only for micrometer-scale structures. ICP etching processes are suitable for pillars of diameters smaller than 100 nm but the cost of an ICP facility is much higher than those of common RIE systems.

The conventional RIE technique is seldom employed for the fabrication of nanopillar arrays because its etching anisotropy is regarded worse than that of ICP etching. However, by properly choosing the mask material and adjusting the components of the etching agents, high resolution pillars of high aspect ratios can be fabricated with RIE. For example, we demonstrated lateral dimensions around 200 nm on silicon with aspect ratios ~ 9 by using the negative photoresist SU-8 masks defined by two-photon exposure [3]. In this work we use the conventional RIE technique with suitable gas mixture as well as careful control of the chamber pressure and the rf power to minimize the lateral dimension and to maximize the aspect ratios of silicon nanopillars.

2. RIE parameter optimization

The positions of the nanopillars are defined by using an e-beam writer to drill hole arrays on a PMMA layer coated on a silicon substrate. Next, a nickel layer is deposited by e-beam evaporation, and then the PMMA layer is lifted off with acetone. The remaining nickel disks on the silicon substrate serve as the masks.

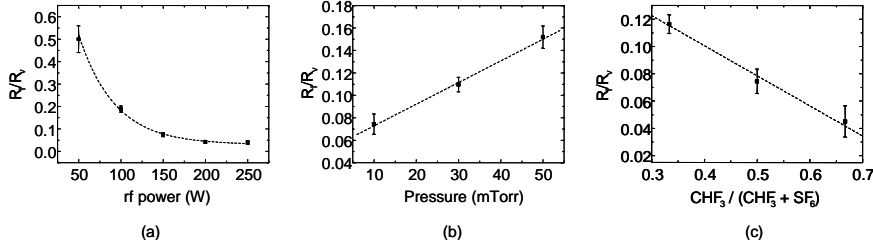


Figure 1. Controlling the values of R_v/R_v with the RIE parameters. (a) The values of R_v/R_v vs. the rf power. Flow rates of SF_6 and CHF_3 : 25 sccm. Chamber pressure: 10 mTorr. (b) The values of R_v/R_v vs. the chamber pressure. Flow rates of SF_6 and CHF_3 : 25 sccm. rf power: 150 W. (c) The values of R_v/R_v vs. the gas composition. Chamber pressure: 10 mTorr. rf power: 150 W.

To achieve aspect ratios higher than 10, we need to *minimize* the ratio between the lateral and the vertical etching rates (R_v/R_v). Figures 1 shows the relation between R_v/R_v and the rf power, the chamber pressure, and the composition of the etching gases. In Fig. 1(a), the value of R_v/R_v decreases exponentially with the rf power of the RIE chamber. This is because higher rf power generates ions of higher speed, and thus enhancing the vertical etching rates. Nevertheless, a very high vertical etching rate makes the control of pillar height difficult. Therefore we set the rf power at 150 W for later experiments. In contrast, the increase of chamber pressure raises the collision rate of the ions, such that the etching directionality becomes worse, as shown in Fig. 1(b). Hence for making nanopillar arrays the RIE chamber pressure should be set as low as possible.

For the etching of silicon, O_2 , SF_6 , and CHF_3 are the most common etching agents [4,5]. However, we do not use O_2 in this work because it produces micro-masks of nickel on the silicon substrate and results in rough surface. This effect of the mask residues has been known as the “black silicon method” [6]. Figure 1(c) shows the values of R_v/R_v as a function of the portion of CHF_3 in the mixture of $(CHF_3 + SF_6)$. We find the amount of CHF_3 is in favor of the etching anisotropy. But because a small portion of SF_6 would slow the etching rates [7], we use 1:1 SF_6/CHF_3 flow in our process of the nanopillars.

3. High-aspect-ratio silicon pillar arrays

By setting the rf power at 150 W, the chamber pressure at 10 mTorr, and the SF_6 and CHF_3 flow rates at 25 sccm, we make the nanopillar arrays as shown in Fig. 2. After 60 minutes of etching, the height of these pillars is ~ 3500 nm. We note that the surfaces of the pillars and the substrate are very smooth. Two packing densities of the pillars are shown in Figs. 2(a) and 2(b). In Fig. 2(b) the inter-pillar distance is only 150 nm. To achieve higher aspect ratios, we use aqua regia to treat the pillars in Fig. 2(a) for one day and find the diameter can be reduced to ~ 100 nm [Fig. 2(c)]. After the treatment of aqua regia the pillars are still upright, with an aspect ratio close to 30.

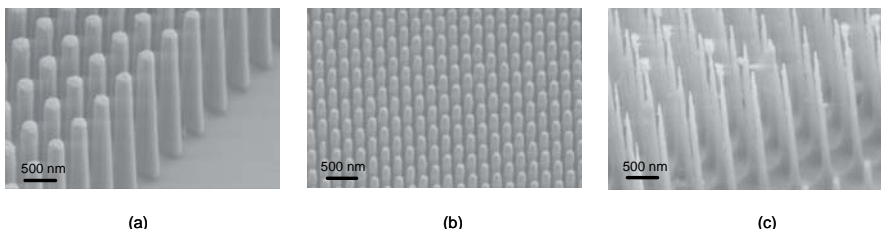


Figure 2. Silicon pillar arrays made with the optimized RIE parameters. (a) Pillar array of a 600 nm period. The diameter of the pillars is 250 nm, while the height is 3500 nm. (b) Pillar array of a 300 nm period. The diameter of the pillars is 150 nm, while the height is 3400 nm. (c) Silicon pillars in (a) after the treatment of aqua regia. The diameter of the pillars is reduced to 100 nm, while the height remains 3000 nm.

4. Conclusion

We develop a process for the mass production of high-aspect-ratio silicon nanopillar arrays based on the conventional RIE technique. With careful adjustments of the rf power and chamber pressure, we maximize the etching anisotropy while keeping a reasonable vertical etching rate. We demonstrate that $(CHF_3 + SF_6)$ can produce high-aspect-ratio pillars with vertical sidewalls and smooth surfaces. The aspect ratio can be increased up to 30 after the treatment of aqua regia. The processes in this work are more economical compared with the ICP etching.

References

1. W. Hattori, H. Someya, M. Baba, and H. Kawaura, "Size-based continuous-flow directional control of DNA with a nano-pillar anisotropic array," *J. Chromatogr. A* **1051**, 141-146 (2004).
2. X.-M. Yana, S. Kwonb, A. M. Contrerasa, M. M. Koebelc, J. Bokorb, and G. A. Somorja, "Fabrication of dense arrays of platinum nanowires on silica, alumina, zirconia and ceria surfaces as 2-D model catalysts," *Catal. Lett.* **105**, 127-132 (2005).
3. C.-H. Lee, T.-W. Chang, K.-L. Lee, J.-Y. Lin, and J. Wang, "Fabricating high-aspect-ratio sub-diffraction-limit structures on silicon with two-photon photopolymerization and reactive ion etching," *Appl. Phys. A* **79**, 2027-2031 (2004).
4. T. Syau, B. J. Baliga, and R. W. Hamaker, "Reactive ion etching of silicon trenches using SF_6/O_2 gas mixtures," *J. Electrochem. Soc.* **138**, 3076-3081 (1991).
5. R. Legtenberg, H. Jansen, M. de Boer, and M. Elwenspoek, "Anisotropic reactive ion etching of silicon using $SF_6/O_2/CHF_3$ gas mixtures," *J. Electrochem. Soc.* **142**, 2020-2028 (1995).
6. H. Jansen, M. de Boer, J. Burger, R. Legtenberg, and M. Elwenspoek, "The black silicon method II: the effect of mask material and loading on the reactive ion etching of deep silicon trenches," *Microelec. Eng.* **27**, 475-480 (1995).
7. S. Grigoropoulos, E. Gogolides, A. D. Tserepi, and A. G. Nassiopoulos, "Highly anisotropic silicon reactive ion etching for nanofabrication using mixtures of SF_6/CHF_3 gases," *J. Vac. Sci. Technol. B* **15**, 640-645 (1997).

STUDY OF MASKING MATERIALS USING IN POWDER BLASTING FOR LOW COST MICROFLUIDIC CHIP FABRICATION

A. Tuantranont, S. Rahong, N. Porntheerapat, T. Lomas, and A. Wisitsoraat
Nanoelectronics and MEMS Lab, National Electronics and Computer Technology
Center 112 Thailand Science Park, Pathumthani 12120 Thailand
Tel: +662-564-6900, Email: adisorn.tuantranont@nectec.or.th

Abstract

In this paper, we applied powder blasting for glass micromachining of microfluidic chips. The characteristics and performances of powder blasting were studied as a function of process parameters such as blasting pressure, time, and masking materials. Different masking materials including various kinds of polymers and elastomers, conventional PCB-grade dry film and BF-410 dry film containing urethane acrylate, were employed as masking materials.

Keywords: Powder blasting, Glass chip, Microfluidic, Masking

1. Introduction

In microfluidic applications, micro powder blasting has been considered a simple, fast, and low cost method suitable for glass and brittle material micromachining [1-2] because of high productivity and low heat transfer. The cost is considerably lower than other dry etching techniques including RIE etching, laser machining, however the aspect ratio is only limited to less than 3.

In powder blasting, a particle jet is directed towards a target for mechanical material removal. The material is selectively removed by an application of patterned masking material over the substrate. A major issue of powder blasting method is to find patternable masking materials that have high erosion resistance to powder blasting.

2. Experiment

2.1 Masking process

The masking process is used to prepare the specimens having required patterns for powder blasting. Various kinds of polymer and elastomers, including conventional PCB-grade dry film and BF-410 dry film containing urethane acrylate, were used as masking materials in this experiment. The photoresists were applied on glass substrate by laminating for both dry films. The photoresists were then exposed and developed to form the desired masking patterns. The minimum feature size attained by this masking method is generally larger than 50 μm .

2.2 Powder blasting process

The powder blasting process is shown in Fig. 1. The powder blasting was performed by Venturi-type powder blaster using glass bead powder. In this system, the glass bead powder was transported to the nozzle by under pressure generated by a venturi in the nozzle. The powder used is glass bead with the mean diameter of ~140 μm . After powder blasting, the remaining mask is removed by chemical etching. The polymer/elastomer mask can be removed by NaOH and/or H₂SO₄:H₂O₂ solutions. The powder blasting parameters are summarized in Table 1.

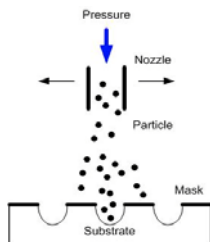


Figure 1. Powder blasting process

Table 1 Powder blasting parameters.

Air Pressure	4-7 bars
Time	2-8 mins
Particle size	Glass bead 140 μm
Distance	50 mm
Nozzle diameter	6 mm

3. Results and discussion

The optical micrograph of a typical glass chip with line-patterned urethane acrylate photoresist film before and after powder blasting are shown in Fig. 2. The corresponding 2D surface profile and SEM micrograph of the powder blasted microchannels are shown in Fig. 3. The pattern line width is increased after powder blasting, which corresponds to 12.5% line-width error. From the surface profile, the average surface roughness on blasted surface is approximately 7.5 μm with an etch depth of 50 μm . The surface roughness is relatively high due to large particle size (140 μm) being used. The line-width error is attributed to two main mechanisms, lateral etching and mask wear. The mask-wearing rate is directly a function of Young modulus and hardness of the mask. The etching depth, line width error, and surface roughness were then characterized as a function of blasting pressure as shown in Fig. 4.



Figure 2. The optical micrograph of a typical glass chip with line-patterned (a) before and (b) after powder blasting at a pressure of 6 bars.

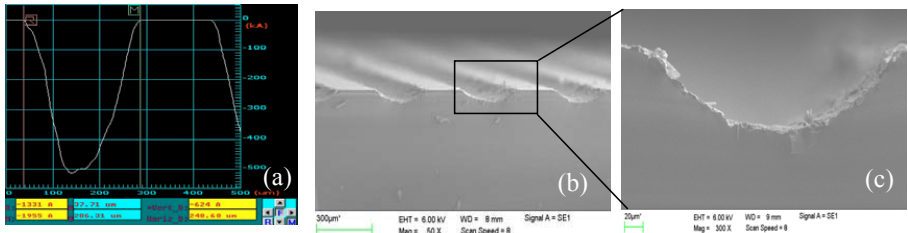


Figure 3. Surface profile across a powder blasted channel (a) and typical SEM micrographs of powder blasted microchannels (b) and enlarged cross-section (c).

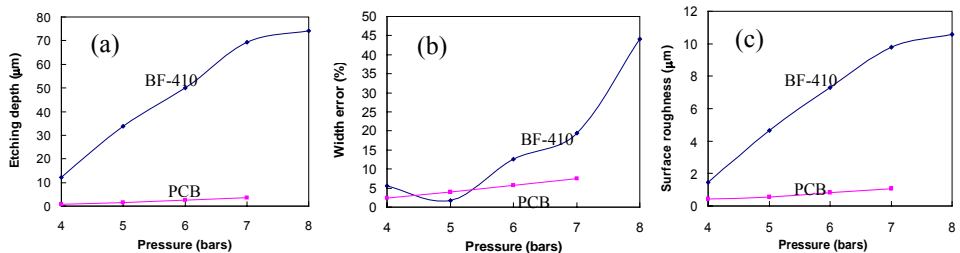


Figure 4. Plot of Etching depth vs. blasting pressure (a), Line width error vs. blasting pressure (b), Surface roughness vs. blasting pressure for a powder-blasted channel (c).

From experimental results, BF-410 dry film containing urethane acrylate that has very high abrasion resistance was found to have higher blasting resistance than a PCB-grade dry film. In addition, surface roughness, etching depth, and line-width errors are approximately linear functions of blasting pressure in the region investigated. Thus, we were able to satisfactorily control etching process of powder system for glass machining and successfully demonstrate glass chip for low cost microfluidic applications.

4. Conclusions

BF-410 dry film containing urethane acrylate was found to have higher blasting resistance than a PCB-grade dry film. In addition, it was found that surface roughness, etching depth, and line-width errors are approximately linear functions of blasting pressure in the tested operating parameter.

References

- [1] H. Wensink, J. W. Berenschot, H. V. Jansen, and M. C. Elwenspoek, *High resolution powder blasting micromaching*, Proc. of MEMS 2000, pp. 769-774, (2000).
- [2] E.Belloy, A.Sayah, and M.A.M.Gijs, *Sens. Actuators A, Phys.* 86, pp.231–237, 2000.

ELECTROSTATIC FORCE DRIVEN MICRO AND NANO IMPRINT LITHOGRAPHY

Isabel Rodríguez and Saman Dharmatilleke

Institute of Materials Research and Engineering (IMRE), 3 Research Link,
Singapore 117602
(e-mail: i-rodriguez@imre.a-star.edu.sg)

Abstract

With this work, we present a novel imprinting method to structure polymer films based on electrostatic induced pressure. The imprinting mechanism is based on the electrostatic force induced by charge migration and subsequent charge separation when a mold and substrate carrying the polymer to be imprinted are subjected to high voltages at high temperature. For this process, either the mold or substrate should contain a high concentration of mobile ions such as sodium. Doped substrates or naturally ion rich materials like soda lime glass are suitable for this process.

keywords: nano imprint lithography, hot embossing, nanofabrication

1. Introduction

Hot embossing, imprinting or nano-imprinting is a mechanical replication technology whereby micro or nano patterns are transferred into a polymer [1]. The process typically consists of pressing a rigid master mold or stamp with the desirable size features against a thin thermoplastic polymer that is softened by raising the temperature above its glass transition (T_g). Currently, this process is carried out using a mechanical hot press. Recently, an electrostatic force assisted nano imprint approach has been described by S. Chou and co-workers [2].

2. Experimental

A conventional anodic bonding system was employed to carry out this process. Typically a silicon mold carrying the nanostructures was used. The mold was treated with the releasing agent perfluorodecyltrichlorosilane to facilitate the de-molding process. The substrates used for imprinting were free standing films of polycarbonate (Lexan, $T_g = 150$) and polyethersulfone (Radel $T_g = 220^\circ\text{C}$). A substrate rich in sodium like soda lime glass was used to support the polymer films. In a typical imprinting process, soda lime glass wafers are placed at the anode side of an electric

field with the polymer film to be imprinted placed over it. The master mold is placed at the cathode side. Alternatively, a master mold highly doped with sodium ions can be positioned on the anodic side. Figure 1(a-c) shows a schematic representation of the arrangement. During the imprinting process (Fig. 1b), substrates are placed into contact and when the temperature is raised above the T_g of the polymer, voltage is applied across. The useful voltage range depends on the process temperature and is usually in the order of 1-2 kV.

Typical imprinting conditions for polycarbonate were temperature: 150° C; DC voltage 1500 V; Current read max: $1.3 \cdot 10^{-2}$ mA. The conditions for polyethersulfone were temperature: 220° C; DC voltage: 1500 V; Current read max : $2.8 \cdot 10^{-2}$ mA. Voltage was applied for a maximum time of 20 min with the current limited to a maximum of 0.1 mA to avoid overheating.

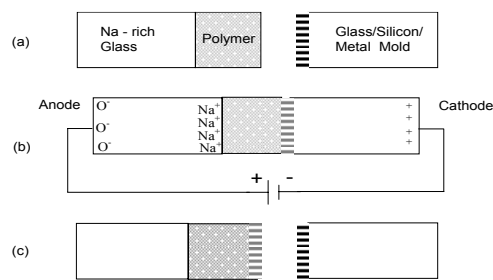


Figure 1. Fabrication steps for electric field driven nanoimprinting. (a) Substrates are assembled such that sodium rich wafers are placed at the anodic side of an electric field followed by the polymer to be imprinted and the mold at the cathode side. (b) The assembly is brought into contact, heated up above the T_g of the polymer and voltage is applied. Positive bias is applied to the doped glass substrate and negative bias to the substrate to be imprinted. (c) After the assembly has cooled down, the structures are released.

polymer and voltage is applied. Positive bias is applied to the doped glass substrate and negative bias to the substrate to be imprinted. (c) After the assembly has cooled down, the structures are released.

3. Results and discussion

The imprinting mechanism described in this work is based on the large electrostatic force developed across the polymer layer to be imprinted. At a temperature of 120° C and above, mobile ions like sodium experience high mobility in an electric field and migrate through the substrate matrix towards the negatively charged cathode to the interface with the polymer that acts as a diffusion barrier. As a result of the charge separation, a high electric field across the polymer layer is created. The resulting electric field generates a very strong electrostatic force between the substrates pulling the interfaces to a close contact and compressing the plastic film. The viscous polymer is then forced to flow into the cavities of the mold conforming to its relief. Upon cooling the assembly is separated and the imprinted polymer structures released. Figure 2 shows the SEM images of 500 nm pitch gratings imprinted in polycarbonate and Figure 3 shows the imprinted grating like structures on polyethersulfone films.

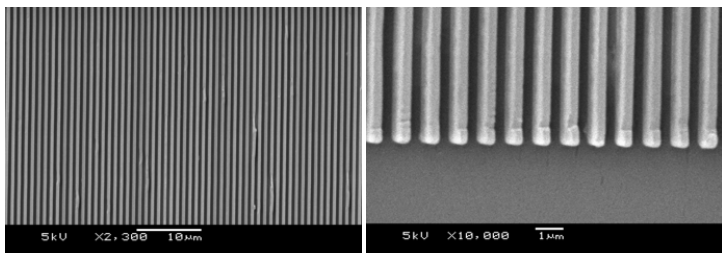


Figure 2. SEM images of grating like structures consisting of 500 nm elevated lines fabricated by electric field driven nanoimprint lithography on a 500 μm polycarbonate film. (Temperature, 160° C; DC voltage, 1500 V; Current max, $1.3 \cdot 10^{-2}$ mA)

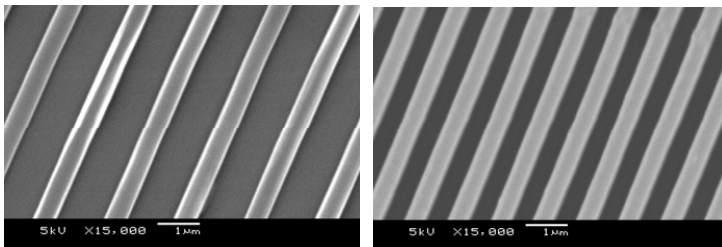


Figure 3. SEM micrographs of 500 nm grating like structures fabricated by electrostatic force driven nanoimprint lithography on polyethersulfone films. (Temperature, 220° C; DC voltage, 1500 V; Current max, $2.8 \cdot 10^{-2}$ mA)

4. Conclusions

We have presented a process to imprint thermoplastic substrates based on electrostatic pressure. Electrostatic induced pressure has the advantage over the commonly used hydraulic pressure that arises at every point of the polymer - mold interface. As a result, it is expected to be more homogenous across the entire substrate. Accordingly, this process can potentially solve major issues on imprinting lithography such as uniformity and reproducibility of the imprinted results. This process has also the advantage that can be carried out using anodic bonding systems existing in typical clean room foundries.

Acknowledgements

This work was performed at the Institute of Materials Research and Engineering which is supported by the Agency for Science, Technology and Research (A*STAR).

References

- [1] Chou, S. Y.; Krauss, P. R.; Renstrom, P. J. *Science* 272, 85 (1996).
- [2] Liang, X.; Zhang, W.; Li, M.; Xia, Q.; Wu, W.; Ge, H.; Huang, X.; Chou, S.Y. *Nano Lett.* 5, 527 (2005).

HYBRID TOOLING BY COMBINATION OF UV-LIGA AND CNC-MILLING FOR MICROFLUIDIC DISPOSABLES

R. Jurischka¹, C. Blatttert¹, I. Tahhan¹, A. Schoth¹, C. Mueller¹, H. Reinecke¹

¹ Laboratory for Process Technology, Department of Microsystems Engineering (IMTEK), University of Freiburg, Germany

Abstract

For the market of microfluidic devices is a strong need for low cost disposables, which can be produced in high volume by industrial technologies like injection molding. The tooling is a key technology for these devices. For interface purposes a microfluidic system need not only simple microchannels but also macro structures, like connectors or reservoirs for the analytical detection and for waste. This paper describes a novel and rapid hybrid tooling method for the fabrication of polymer-based microfluidic disposables containing micro and macro structures.

Keywords: UV-LIGA, milling, SU-8, hybrid tooling, injection molding, COC.

1. Introduction

There are different manufacturing techniques for micro molds like LIGA, UV-LIGA or CNC-milling. State of the art, LIGA or UV-LIGA [1] is one way to manufacture micro structures with high aspect ratio and high geometry accuracy but too restricted for macro structure with a height more than 2 mm and the necessary electroplating as well as the backside finishing are very time consuming. In contrast, CNC-milling is a fast and direct structuring method but generates higher roughness and burrs, and is limited on bigger micro structures. In this study we combine the advantages of UV-LIGA and CNC-milling in a hybrid tooling to overcome the limitations of the single methods and to decrease the tool fabrication time.

2. Experimental

Our hybrid tool consists of two parts, one with the micro structures and the second part with the macro structures which are finally combined by insertion. The micro structures are created by an UV-LIGA process [2] which is performed on metal substrates. Macro structures of the device like reservoirs are machined on an insert by CNC-milling. The overall fabrication sequence of our hybrid tooling method is illustrated schematically in figure 1. The substrate is a 2 mm thick polished brass wafer that is a low cost product in comparison to a silicon wafer. From the backside of the brass substrate, a opening is machined by CNC-milling for the insert with the macro structures (see figure 2). This opening is closed temporarily by PDMS (polydimethylsiloxane) to get a plane substrate before SU-8 lithography step with high resolution transparency or glass mask is carried out. After the lithography step, the PDMS is removed, and the insert is accurately placed in the opening of the substrate from their backside.

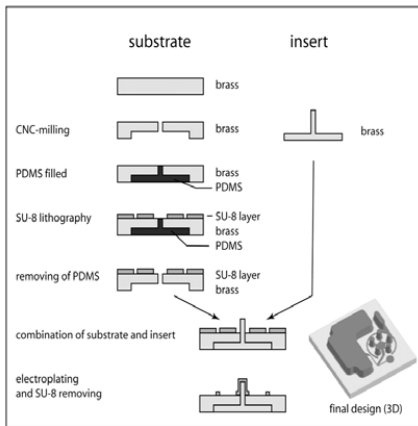


Fig.1: Fabrication sequence of hybrid tooling

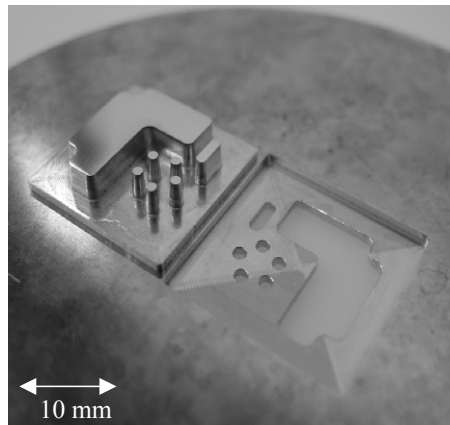


Fig. 2: CNC-milled insert on the backside of the machined brass wafer.

This results in a covering of the rough CNC machined surfaces. In the following electroplating step openings in the resist layer and the gaps between CNC-milled insert and substrate are filled by nickel. The micro structures are generated and gaps are closed. Finally, the resist is removed. The total tool fabrication time starting from lithography, CNC-milling and electroplating is about 20h.

4. Results and discussion

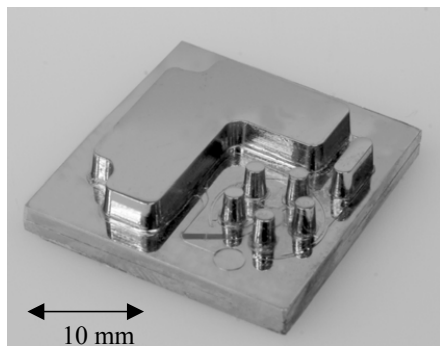


Fig. 3: Hybrid tool with 100 μm high micro and 2 mm high macro structures.

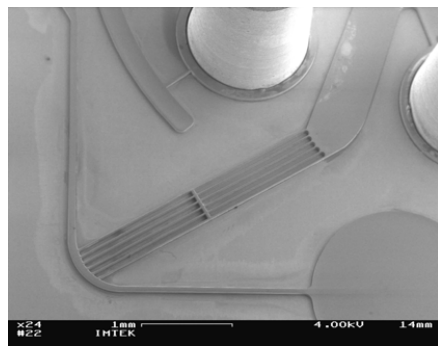


Fig. 4: SEM micrograph of the master micro structures, 6 parallel 20 μm wide ribs.

The hybrid tool and a detail view of the micro structures are shown in figure 3 and 4. With this novel tooling method, we are able to fabricate mold inserts that are used for the replication of microfluidic devices for blood analytics [3] in COC polymer by

injection molding (see figure 5). The dimensions of the structures, top surface roughness values, and the process times of the fabricated hybrid tool are summarized in Table 1.

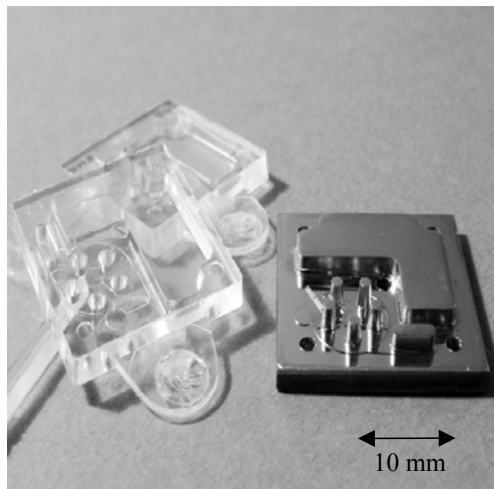


Fig. 5: Replicas in COC fabricated by the mold insert and injection molding.

micro structures	min. width	20 μm
	height	80 μm
	taper angle	2 – 4 degree
	roughness Ra	15 nm
macro structures	height	2 mm
	taper angle	5 degrees
	roughness Ra	40 nm
process	milling time	2 h
	electroplating time	3 h
	tool manufacturing time	approx. 20 h
	life time of fabricated tool	> 2000 cycles

Table 1: Summarisation of geometry, roughness and process values.

The crossover of micro and macro structures is free of burrs. The alignment of the different scale structures can be adjusted precisely by a maskaligner.

5. Conclusion

This novel tooling technology enables a cost effective, fast, and flexible manufacturing of microfluidic disposables. The combination of micro and macro structures leads to a new generation of lap-on-the-Chip devices. The injection molded chips have excellent surface quality and micro structures with high aspect ratio. This hybrid tooling process allows a seamless transition from prototyping to high-volume production, while using the same polymer material.

References

1. M. B. Chan-Park, J. Zhang, Y. Yan, C.Y. Yue, Sensors and Actuators B, 101 (2004), pp. 175-182.
2. R. Jurischka, C. Blattert, I. Tahhan, C. Müller, A. Schoth, W. Menz, Proc. of SPIE 2005, vol. 5718, pp. 65-72.
3. C. Blattert, R. Jurischka, I. Tahhan, A. Schoth, P. Kerth, H. Reinecke, Proc. of μ TAS 2005, pp. 1352-1354.

A NANOIMPRINT LITHOGRAPHIC METHOD FOR FABRICATION OF THREE-DIMENSIONAL SEALED NANOFUIDIC CHANNEL ARRAYS

Jarrett J Dumond¹, Hong Yee Low² and Isabel Rodriguez

Institute of Materials Research and Engineering (IMRE)

3 Research Link, Singapore 117602

¹j-dumond@imre.a-star.edu.sg, ²low-hy@imre.a-star.edu.sg

Abstract

We present a new approach toward fabricating isolated, sealed, high-density nanofuidic channel arrays using combinatorial-mold nanoimprint lithography (NIL). This method provides a means of stamping micro- to nanoscale channel arrays on a substrate from a thin polymer film patterned on both sides using a simple combination of two grating molds with proper feature geometries. Fabrication and characterization results are described herein.

Keywords: nanoimprint lithography, nanochannel, nanofuidic channel

1. Introduction

Nanoscale channels are crucial components of nanofuidic devices in the field of nanobiotechnology where the detection of single enzymes, proteins, and molecules is garnering considerable interest [1]. Commercialization of nanofuidic devices will require nanoscale channels to be fabricated using techniques that can be easily scaled-up to mass-production. Among the available techniques, conventional nanoimprint lithography (NIL) [2], a two-dimensional (2D) lithographic technique wherein a polymer film is spin coated onto a substrate and embossed with a hard mold, is particularly suited to these requirements. However, fabrication of three-dimensional (3D) structures such as nanofuidic channels is not straightforward with this approach.

We report herein the development of a three-dimensional (3D) imprint lithographic technique called combinatorial-mold NIL for fabricating sealed nanochannel enclosures. This technique employs simple yet precise combinations of 2D patterned molds to build up more complex 3D structures for specific applications. In this case, nanochannel enclosures are patterned directly into a thin polymer film, thus preserving the original templates (or molds) for further pattern replication, thereby retaining the most critical advantages of conventional 2D NIL such as scalability and low cost.

2. Experimental

As shown in figure 1, a polymer film is cast on a silicon grating mold and subsequently embossed with a second grating mold in an Obducat 4" imprinting machine so as to pattern the film on both sides. Transfer of the patterned film to an external support is achieved by manipulating surface energies via plasma treatment or

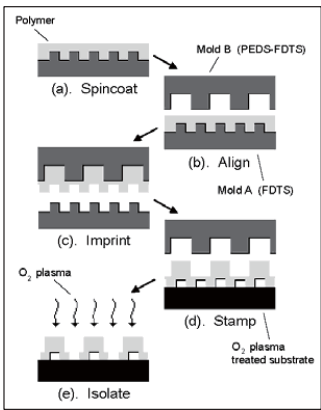


Figure 1. Five step schematic of the combinatorial-mold nanoimprint lithography process. Steps (a) and (b) are self-explanatory. In step (c) the polymer film is embossed above T_g and at high pressure (~ 5 MPa). The stamping step (d) against the substrate is carried out below the T_g of the polymer at lower pressure ($\sim 1\text{-}2$ MPa). In step (e), the sealed nanochannels are isolated by removing the suspended residual layer with oxygen RIE.

grating molds; one with 250 nm linewidth and 1:1 duty cycle (mold A), and the other with 500 nm linewidth and 1:1 duty cycle (mold B). We also investigated the integrity of the seal formed by the nanochannel enclosures. To that end, 250 nm square PMMA nanofluidic channel arrays were fabricated, sealed and isolated against a transparent plasma-activated surface such as indium tin oxide (ITO) glass using the same processing conditions listed above. Since in our imprinting process the mold-to-mold alignment was carried out manually, the residual layer etch created regions where the rotational misalignment of the PMMA gratings forced the channel enclosure to split open at approx. 20 μm intervals. These openings served as entry points for an aqueous fluorescent dye solution containing 70 μM fluorescein and 70 μM sodium dodecylbenzenesulfonate (SDS) surfactant. Figure 3 illustrates chronologically the application, spreading, and evaporation of a solution droplet applied on top of a set of nanochannel arrays under optical microscopy. Samples were left standing until the applied solution had completely evaporated after filling the nanochannels by capillary action (see figure 3, at 60

differing silane anti-stick coatings to achieve surface energy contrast. In figure 1(b), mold A was treated with liquid-phase 1H,1H,2H,2H-perfluorodecyltrichlorosilane (FDTs) and mold B was sequentially treated with phenethylmethyldichlorosilane (PEDS) followed by FDTs to obtain a ~ 6.5 mJ/m² surface energy contrast. This is sufficient to transfer the film cleanly from mold A to mold B (figure 1(b-c)). The stamping step (figure 1(d)) was carried out against a plasma-treated silicon wafer, the native oxide of which is ~ 115 mJ/m²; more than six-fold greater than the surface energy of mold B. The individual nanochannels were isolated in figure 1(e) by an oxygen reactive ion etch (RIE) to remove the suspended residual layer generated from imprinting. Further experimental details, including surface energy characterization results can be found elsewhere [3, 4].

3. Results & Discussion

A Representative SEM cross-section of isolated, sealed 250 nm square poly(methyl-methacrylate) (PMMA) nanochannels on a silicon substrate is shown in figure 2. These channels were fabricated from two

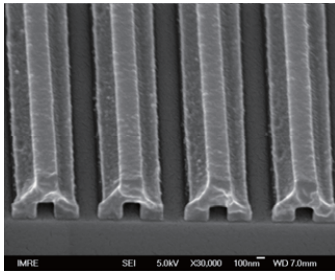


Figure 2. Cross-section SEM of a nanochannel array sealed against a silicon substrate. Each channel is 250 nm square, enclosed by a partially etched ~ 350 (width) \times 400 nm (height) PMMA line spanning two 250 \times 200 nm PMMA lines. The period spacing is approx. 1 μm .

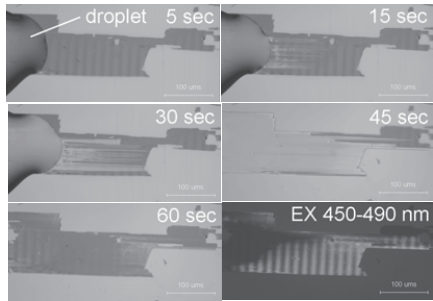


Figure 3. Chronologically arranged optical microscopy images showing the application of a fluorescein solution droplet to a set of nanochannel arrays on an ITO substrate. The scale bars are 100 μm . The sample is left standing until the exterior surface is dry before exposure to excitation radiation at 450-490 nm (lower right image).

and is not directly exposed to oxygen. Therefore the fluorescein molecules are considerably less likely to bleach or form aggregates and self-quench. Strong photoluminescence from the nanochannels is observed even several days after solution application, confirming that the nanochannel enclosures can form an effective barrier against transport to the external environment.

4. Conclusions

We have shown that isolated, sealed nanofluidic channels can be fabricated using inexpensive materials, an open architecture, and a scalable process. Combinatorial-mold NIL can also be used to construct fluidic channels with a wide range of different dimensions and spacings simply through the incorporation of the desired parameters into the hard molds used for the combinatorial imprint. This could prove instrumental toward interfacing micro- and nanoscale features on the same fluidic device.

References

1. H.G. Craighead, *Science*, **290**, 1532, (2000).
2. S.Y. Chou, P.R. Krauss and P.J. Renstrom, *Science*, **272**, 85, (1996).
3. Y.P. Kong, H.Y. Low, S.W. Pang and A.F. Yee, *J. Vac. Sci. Technol. B*, **22**, 3251, (2004).
4. J. Dumond, H.Y. Low, and I. Rodriguez, *Nanotechnology*, **17**, 1975, (2006).
5. L.L. Song, C. Varma, J.W. Verhoeven and H.J. Tanke, *Biophys. J.*, **70**, 2959, (1996).
6. C. Deka, B.E. Lehnert, N.M. Lehnert, G.M. Jones, L.A. Sklar and J.A. Steinkamp, *Cytometry*, **25**, 271, (1996).

seconds). Then, they were mounted on an Olympus BX51 epi-fluorescent microscope with a 150x objective lens (N.A. 0.9) and a Photometrics Cascade 512B cooled-CCD camera.

Figure 4 is a fluorescence microscope image showing photoluminescence from two discrete nanochannel arrays. Contrast is developed because the exterior of the nanochannels is coated with a dried fluorescein precipitate that photobleaches and self-quenches due to direct exposure to oxygen from the ambient and aggregation effects, respectively [5,6]. Fluorescein solution that is confined to the interior of the nanochannels, however, does not evaporate



Figure 4. 150x fluorescence microscope image showing two nanochannel arrays. The scale bar is 10 μm . Bright lines are sealed nanochannels with liquid fluorescein solution confined inside. Dark regions contain photobleached and self-quenched solid fluorescein. The misaligned region in the center of the image served as an entry point for the fluorescein solution (see figure 3).

GLASS MICROFABRICATED NEBULIZER CHIP FOR MASS SPECTROMETRY

Ville Saarela¹, Markus Haapala², Risto Kostiainen², Tapio Kotiaho³, Sami Franssila¹

¹ Microelectronics Centre, Helsinki University of Technology, Finland

² Department of Pharmaceutical Chemistry, University of Helsinki, Finland

³ Laboratory of Analytical Chemistry, University of Helsinki, Finland

(E-mail: ville.saarela@tkk.fi)

Abstract

A novel nebulizer chip for mass spectrometry is presented. It is fabricated fully in glass, enabling high temperature operation (up to 500 °C) for efficient vaporization. In the nebulizer chip, gas and vaporized liquid streams are mixed, and the spray is directed towards the inlet orifice of a mass spectrometer. The sample molecules in the spray are ionized using either corona discharge or a photoionization lamp. Fabrication process and interconnections scheme are presented with jet shape and mass spectrometric measurements.

Keywords: glass microfabrication, etching, fluidic interconnections, nebulizer, mass spectrometry

1. Introduction

Mass spectrometers are used to measure the mass-to-charge ratio of ions produced from a chemical compound. The components of the compound can be identified from the mass spectrum. Two different ionization methods have been coupled with a miniaturized nebulizer chip. Atmospheric pressure chemical ionization (APCI) uses a corona discharge [1], and in atmospheric pressure photoionization (APPI) mode the ionization is obtained with 10 eV photons [2]. Previously, the microfabricated nebulizers were made in silicon with an anodically bonded glass cover. In the new design, the component comprises of two fusion bonded glass wafers.

2. Experimental

The nebulizer chip fabrication process is illustrated in *Figure 1*. Through-wafer etching is done in 10:1 HF:HCl [3] using LPCVD silicon hard mask. To promote etch uniformity, the etching is done in a tank with magnetic stirring. After etching, the silicon hard mask is removed in 25 % tetra methyl ammonium hydroxide (TMAH) at 80 °C. The wafers are RCA-1 cleaned prior to fusion bonding at 650 °C. A 200 nm platinum film with chromium adhesion layer is sputtered on the wafer stack and patterned by wet etching platinum in 70 °C 3:1:2 HCl:HNO₃:H₂O and chromium in ceric ammonium nitrate based etchant. Typically, platinum patterning is done by lift-off, but etch patterning has its advantages. Etch patterning is insensitive to resist sidewall profile, enables thicker metal layers, and, unlike lift-off, produces no debris that may

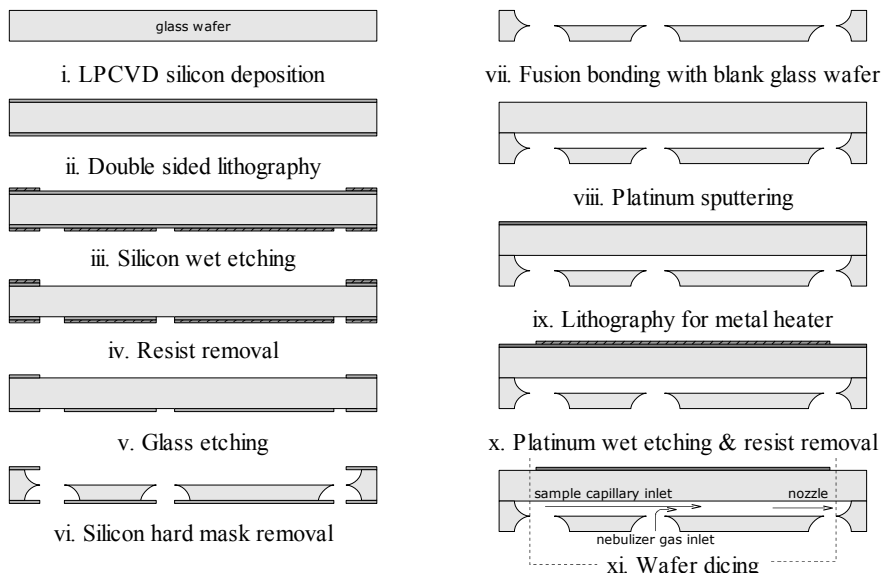


Figure 1. Fabrication process of the glass nebulizer chip.

clog the microchannels and nozzles. Deposition of platinum prior to bonding was also tested. Although a platinum layer on top of a glass wafer tolerates the glass fusion bonding temperature, the coefficient of thermal expansion mismatch causes deformation of the glass which prevents uniform bonding at least when the wafers are not compressed together.

The nebulizer chip has fluidic interconnections for liquid (1-10 $\mu\text{L}/\text{min}$) or gaseous (~1 sccm) sample and nebulizer gas (~100 sccm). Previously, NanoPortTM Assemblies (Upchurch Scientific) or a PDMS fluidic connector [4] have been used to make the interconnections. In the current inlet scheme, the sample capillary is inserted to the nebulizer channel from the side and sealed with high temperature epoxy glue (Duralco 4703, Cotronics). The nebulizer gas is introduced via a hole at the chip surface using a NanoPort connector or a custom made chip holder. Sample capillary connection induces no dead volume and for the nebulizer gas small dead volume is unimportant. Two different chip and inlet designs are shown in *Figure 2*.

The temperature distribution of the nebulizer plume was measured using a

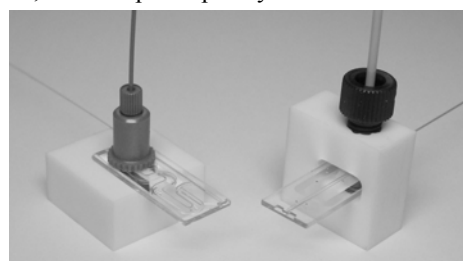


Figure 2. Two different gas inlet schemes: a NanoPortTM connector (left) and a custom made jig. Sample capillary is inserted directly to the nebulizer channel from the side and sealed with glue.

miniature thermocouple (KFT-25-100-200, ANBE SMT Co.) attached to a computer controlled micropositioning stage (F-206, PI (Physik Instrumente) GmbH & Co.). The measurement parameters (movement speed, measurement delays and averaging) were optimized for reasonable measurement time and accuracy.

3. Results and discussion

In mass spectrometric measurements, the new glass nebulizer chips have shown similar performance as the silicon-glass ones [1]. An example mass spectrum measured in APPI mode is shown in *Figure 3*. Sensitivity is higher compared to a commercial APCI source. This can be explained with smaller dimensions and better nozzle design that lead to narrow plume shape and higher ionization efficiency because in APCI the initial ionization occurs in a very small region near the corona needle tip. With the microchip nebulizer the jet stays well confined for at least 14 mm from the nozzle as shown by the measured temperature distribution in *Figure 4*.

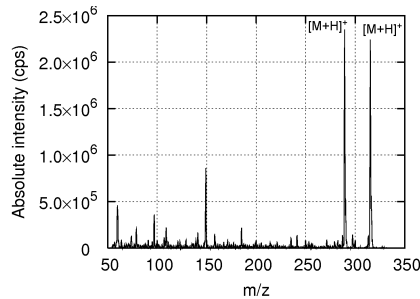


Figure 3. Mass spectrum of testosterone ($M=288$) and progesterone ($M=314$) in APPI mode. Concentration of both analytes was $1 \mu\text{mol/L}$ and sample flow rate was $5 \mu\text{L/min}$.

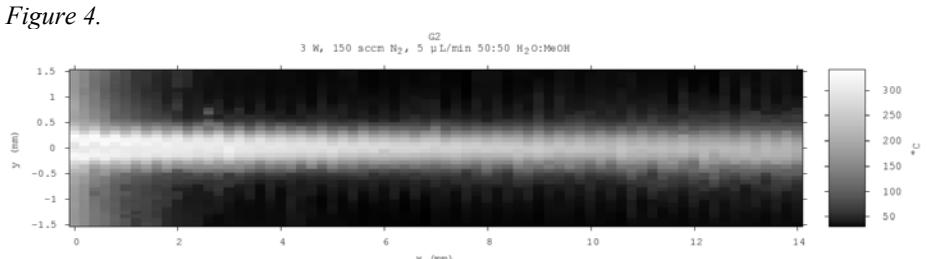


Figure 4. Measured temperature distribution of a nebulizer jet. The centre of the nozzle is at origin and the direction of the jet is to the positive x-axis.

Acknowledgments

This work is part of the Biofunctional Microchips project funded by the National Technology Agency of Finland. The thermocouple measurements were done at VTT Microelectronics (Espoo, Finland) with Ari Hokkanen and Markku Kapulainen.

References

1. P. Östman *et al.*, *Microchip Atmospheric Pressure Chemical Ionization Source for Mass Spectrometry*, Analytical Chemistry, 76 (22), pp. 6659-6664, (2004).
2. T. J. Kauppila *et al.*, *Atmospheric Pressure Photoionization-Mass Spectrometry with a Microchip Heated Nebulizer*, Analytical Chemistry, 76 (22), pp. 6797-6801, (2004).
3. C. Iliescu *et al.*, *Characterization of masking layers for deep wet etching of glass in an improved HF/HCl solution*, Surface & Coatings Technology, 198, pp. 314-318, (2005).
4. V. Saarela *et al.*, *Re-usable multi-inlet PDMS fluidic connector*, Sensors and Actuators B, 111, pp. 552-557, (2006).

LOW DISTORTION, HIGH STRENGTH BONDING OF POLYMER MICROFLUIDIC CHIPS EXPLOITING CASE II PERMEATION

Alfredo M. Morales^{*}, Blake A. Simmons, Thomas I. Wallow^a, Karen L. Krafcik, Linda A. Domeier

Sandia National Laboratories, P.O. Box 969, Livermore, CA 94551-0969.

^aCurrent address: Advanced Micro Devices, One AMD Place, Sunnyvale, CA 94088.

Email: amorale@sandia.gov

Keywords: Microfluidics, polymer, bonding, Zeonor™, case II diffusion.

1. Introduction

The cost to operate microfluidics based biological detection systems can be substantially reduced by using injection molded polymer microfluidic devices [1]. After injection molding a substrate wafer with microfluidic features and fabricating a lid wafer with matching vias, the two wafers must be bonded to each other without distorting the microfluidic features. Two simple, conventional polymer bonding techniques were initially investigated as potential techniques to yield low distortion, high bond strength Zeonor 1060R™ microfluidic devices. Conventional thermal diffusion bonding yielded devices with dimensional distortion (Fig. 1) and only moderate bond strengths (Table 1).

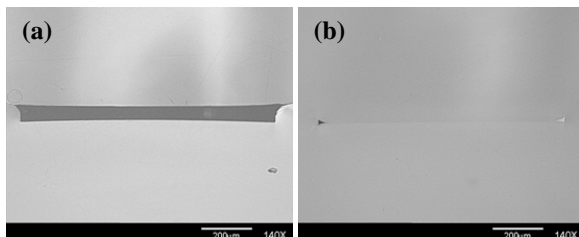


Figure 1: Optical micrographs showing cross-sections of nominally 1 mm x 70 micron microfluidic channels prepared by thermally bonding Zeonor 1060R™ at (a) 88 °C, and (b) 99 °C. Compressed mid-channel depth is 53 +/- 2 micron in (a); almost complete channel occlusion occurs in (b). The glass-transition temperature for Zeonor 1060R™ is 100 °C.

As the thermal diffusion bonding temperature approached the thermoplastic glass-transition temperature and bulk polymer viscous flow increased, more severe distortions were observed but the bonded surfaces still failed adhesively. In contrast, conventional solvent bonding can provide high bond strengths at temperatures that are low enough to avoid bulk viscous flow. Unfortunately, the depth of the solvent affected zone in

conventional solvent bonding can be comparable to the size of microfluidic features and attempts to solvent bond Zeonor devices resulted in microfluidic feature collapse.

Table 1. Failure levels of Zeonor 1060R™ bonded channels under hydrostatic pressure.

Bonding Method	Bonding Temperature (°C)	Failure Pressure (psi)	Failure Mechanism
Thermal Diffusion Bonding	88	930-1000	Adhesive
Case II Diffusion	99	600-1000	Adhesive
Case II Diffusion	60	1900-2340	Cohesive

2. Experiments and Results

Based on rheological studies of Zeonor, metrology of bonded devices, and studies of diffusion rates for aliphatic solvents into Zeonor, a modified solvent bonding method was developed and shown to be superior to conventional thermal diffusion bonding and solvent bonding. The new bonding method takes advantage of case II permeant diffusion to generate dimensionally controlled, activated bonding layers at the surfaces being joined. In case II diffusion, a permeant swollen zone forms at the polymer-permeant interface and advances into the polymer linearly with time: a sharply defined boundary separates the swollen layer from the dry polymer (Fig. 2a).

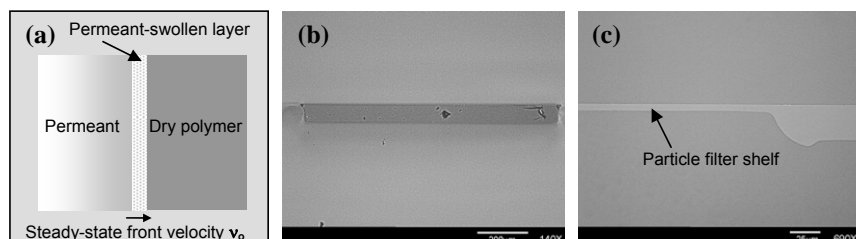


Figure 2: (a) Schematic of Case II diffusion. A well defined permeant diffusion front exist and thus the permeant swollen layer depth is given by $v_o \times t$, where v_o is the steady-state permeant front velocity and t is time. In order to simplify the schematic, permeant is shown interacting with the polymer only from one side. (b) Optical micrograph cross-section of case II diffusion bonded Zeonor 1060R™ microfluidic channel with the same nominal dimensions as the channels shown in figure 1. Actual bonded depth is 70 +/- 2 micron. (c) Optical micrograph cross-section of case II diffusion bonded Zeonor 1060R™ particle filter shelf. The shelf is nominally 6 micron deep, 1 mm wide, and 1 mm long. Actual bonded depth is 5.6 +/- 0.5 micron.

The depth of the permeant swollen zone is controlled by the immersion time. The technique was capable of producing bonds that exhibited cohesive failure while

preserving the fidelity of fine features in the bonding interface (Fig. 2b and 2c; Table 1). This approach is uniquely suited to production of layered microfluidic structures, as it allows the bond-forming interface between plastic parts to be precisely manipulated at micrometer length scales. Distortions in microfluidic device channels were limited to the size scale of the permeant-swollen layer; 6 micron deep channels were routinely produced with no detectable cross-sectional distortions. The bonding procedure is easily integrated in standard process flows, uses inexpensive reagents, and requires no specialized equipment. While this paper covers case II bonding of Zeonor 1060R™ devices only, this is likely to be a useful general bonding approach for thermoplastic materials used in microfluidics.

3. Acknowledgements

This work was performed by Sandia National Laboratories for the US Dept. of Energy, contract DE-AC04-94AL85000. Funding by the US Department of Homeland Security is acknowledged.

4. Reference

1. de Mello, A., "Plastic Fantastic?", *Lab on a Chip*, **2**, 31N-36N, 2002.

FABRICATION OF HIGHLY DIMENSION CONTROLLED PMMA MICROCHIP BY HOT EMBOSsing AND LOW TEMPERATURE DIRECT BONDING

Hidetoshi Shinohara¹, Jun Mizuno¹,

Fumihiko Kitagawa², Koji Otsuka² and Shuichi Shoji¹

¹Major in Nano-Science and Nano-Engineering, Waseda University, Japan

²Department of Material Chemistry, Kyoto University, Japan

(e-mail: h_shinohara@shoji.comm.waseda.ac.jp)

Abstract

In this paper, a PMMA (poly-methyl methacrylate) microchip, which has shallow dams of about 5 μm gaps, was fabricated and evaluated. Accurate dimension control of the micro-channels was realized by not only optimizing hot embossing conditions but also employing low temperature plasma activated bonding.

Keywords: Polymer microchip, hot embossing, surface activation bonding

1. Introduction

In our previous study, we developed a fabrication method for polymer microchip by combining hot embossing and direct bonding techniques using PMMA [1]. In this method, deformation of the channel was observed and shallow micro channels of less than 10 μm was not obtained. It is caused by the applied pressure under the heat around the glass transition temperature (T_g) of PMMA at the direct bonding process. Dimension control of about a few μm for the micro-channels is realized by the low temperature plasma activated bonding as well as the optimization of hot embossing conditions. In order to bond at lower than T_g , pretreatment was applied by oxygen plasma before bonding [2]. A PMMA microchip, which has shallow dams of about 5 μm gaps for efficient capillary electrophoresis, was fabricated.

2. Fabrication

Figure 1 shows the design of the microchip. Dimensions of the micro-channel are 50 μm wide and 19 μm deep. It has six ports (diameter: 1 mm) and two dams (50 μm wide and 4.3 μm gap). The fabrication process of the microchip is shown in Figure 2. The Si mold is fabricated by conventional photolithography and

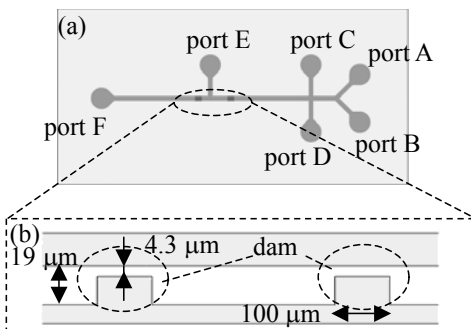


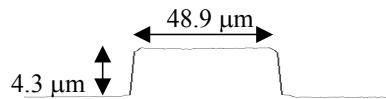
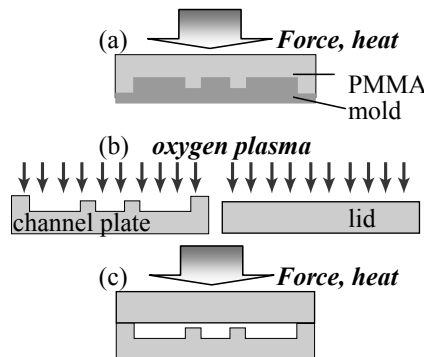
Figure 1. The design of the microchip; (a) whole view and (b) cross section of two dams.

Deep-RIE methods. Mold lubricant (EGC-1720 from Sumitomo 3M, Ltd.) is coated on the surface of the mold for easy demolding. The micro-channel region is fabricated by a PMMA (COMOGLASS from Kuraray Co., Ltd.) hot embossing using EVG520HE of EV Group Co. (Figure 2(a)). Next, six ports are drilled in appropriate positions on the micro-channel plate. Then the surface of the micro-channel plate and the PMMA lid are activated by a oxygen plasma activation bonding system (EVG810LT from EV Group Co.) (Figure 2(b)). Finally, the two PMMA structures are directly bonded. The typical bonding conditions are the temperature of 85 °C, the pressure of 3 MPa and the annealing time of 3 min (Figure 2(c)).

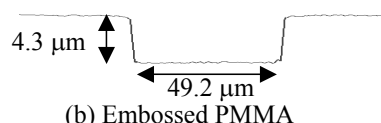
Figure 2. Fabrication process of the microchip.

3. Results and discussion

Figure 3 shows the cross-sectional profile of the mold and the embossed plate of the dam structure measured by a laser microscope (VK-8510 from KEYENCE Co.). SEM micrographs of the micro-channel regions are shown in Figure 4. Relative dimension differences between the Si mold and the embossed PMMA are smaller than 1 %. This result indicates the successful transfer from the mold to the PMMA plate. Figure 5 shows a whole view and a magnified photo micrograph of the micro-channel with dam



(a) Si mold



(b) Embossed PMMA

Figure 3. Cross sectional profile of the dam at the mold (a) and the embossed plate (b).

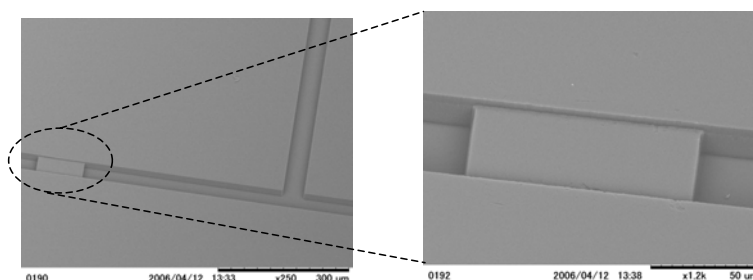


Figure 4. SEM micrograph of the micro-channel with dam structure.

structures. Void free structure of 2 cm x 4 cm is realized by this method. Since bond temperature is lower than T_g, deformation of the channel is negligible and shallow micro-channel of even less than 5 μm is obtained.

The flow behaviors of the dams were evaluated with fluorescent beads introduced from port E (see at Figure 1). Microbeads of $\phi 5.7 \mu\text{m}$ were completely trapped and filled between two dams, while microbeads of $\phi 1.0 \mu\text{m}$ were passed through the dams, as shown in Figure 6.

We are currently applying these microchips for capillary electrophoresis to separate various biomolecules.

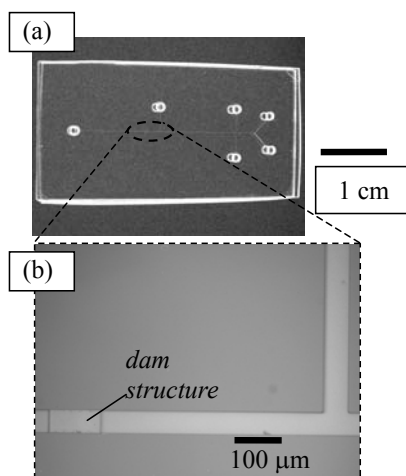


Figure 5. Whole view (a) and photo micrograph (b) of the fabricated microchip.

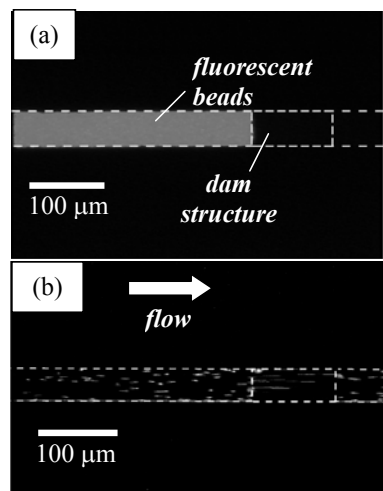


Figure 6. Flow behaviors of the dams using (a) $\phi 5.7 \mu\text{m}$ and (b) $\phi 1.0 \mu\text{m}$ fluorescent beads.

Acknowledgements

This work is partly supported by a Japan Ministry of Education, Culture, Sports Science & Technology Grant-in-Aid for COE Research "Molecular Nano-Engineering and Its Development into Microsystems," SCOE "ASMew," "The Foundation of Technology Promotion of Electronic Circuit Board", Scientific Basic Research (A) No.12450167 and SENTAN. JST. The authors thank for Nanotechnology Support Project of Waseda University.

References

1. J. Mizuno et al., *Fabrication of Micro-Channel Device by Hot emboss and Direct bonding of PMMA*, Proc. 2004 ICMENS, pp.26-29, (2004).
2. J. Mizuno et al., *Cyclo-Olefin Polymer Direct Bonding Using Low Temperature Plasma activation Bonding*, Proc. Transducers'05, pp.1346-1349, (2005).

FABRICATION OF SUPERHYDROPHOBIC SURFACE BY NANOMOLDING

Ming-Hung Chen¹, Yun-Ju Chuang², and Fan-Gang Tseng^{1,2}

¹ Institute of Microelectromechanical System,

² Department of Engineering and System Science,
National Tsing Hua University, Hsinchu 30013, Taiwan

Abstract

In this paper, a simple method of preparing superhydrophobic surface was proposed by nanomolding with lotus leaf as template. After two-step molding, micro and nano composite structures were transferred to poly(dimethylsiloxane) (PDMS) negative-mold and follow up positive replica of Parafilm® M, and there is no need of additional anti-stiction coating during demolding. After replication, PDMS negative-mold remained clean so as to reuse without repreparation. The results show that Parafilm® M replica, a wax material with transferred micro and nano structures could produce lotus-like superhydrophobic surface with contact angle larger than 150 degree and low hysteresis.

Keywords: molding, superhydrophobic, lotus leaf, PDMS, Parafilm® M

1. Introduction

In nature, some leaves with superhydrophobic surface, such as lotus, presented self-cleaning phenomenon to avoid surface contamination that raise the interest in surface modification to prevent biomolecules stiction on surface during reaction [1]. Several methods have been proposed to form a lotus-like surface composed of micro and nano structures to achieve superhydrophobicity [2, 3]. Recently, M. Sun et al. proposed a molding method with real lotus leaf as template and the surface structures were transfer to PDMS negative-mold and follow up PDMS replica [4]. However, the demolding process between PDMS/PDMS surface was difficult and anti-stiction coating was required that took time and might induce surface contamination or morphology change. Parafilm® M (Alcan Inc., USA), a wax material with thermoplastic and hydrophobic properties, commonly used as sealing or substrate of reagent mixing, was employed in this study. The micro and nano composite structures on PDMS negative-mold was transferred to Parafilm® M without anti-stiction coating and rapidly formed a lotus-like superhydrophobic surface.

2. Experimental

For lotus micro and nano composite structures transfer, two-step nanomolding was performed, as shown in Figure 1. In the first step, Sylgard 184 (Dow Corning Inc., USA), mixing with curing agent in proportion of 10:1 w/w and degassing in vacuum

chamber until no bubble formation, was poured on leaf surface and cured in oven at 50 °C for 10 hours. After curing, PDMS negative-mold was demolded from lotus leaf. The second step, Parafilm® M was covered on glass slide and pre-baking on hotplate with 80 °C for 1min. Then PDMS negative-mold fixed on another glass slide was brought to contact with the Parafilm® M substrate with contact pressure of 9.8×10^4 Pa and baked at 80°C for 3 mins. to ensure the completely pattern transfer. Finally, the sample was cooled down to ambient temperature naturally and Parafilm® M positive replica was formed by demolding gently. The contact angle was measured in contact angle analyzer (FTA-200, FTA Co., USA) and surface morphology was observed under scanning electron microscope (JEOL-6330F, JEOL Co., JP).

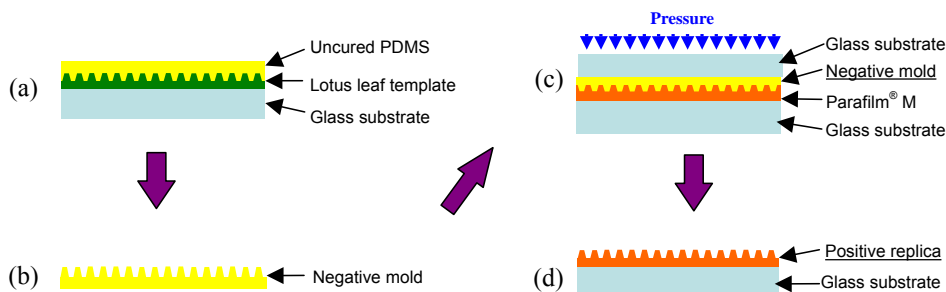


Figure 1. Two-step nanomolding processes: (a) PDMS molding with lotus leaf template; (b) cured PDMS negative-mold; (c) Parafilm® M molding with PDMS negative-mold; (d) positive replica of Parafilm® M.

3. Results and discussion

The SEM images of lotus leaf, PDMS negative mold and Parafilm® M replica surface morphologies are shown in Figure 2. The surface of Parafilm® M replica shows similar micro and nano structures as lotus leaf.

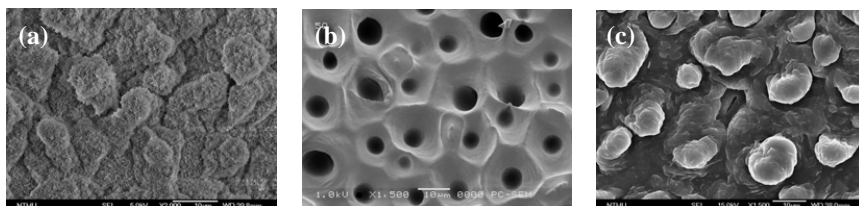


Figure 2. Surface morphologies of : (a) lotus leaf surface; (b) PDMS negative-mold; (c) positive replica of Parafilm® M.

The contact angle measurement results are shown in Figure 3, and the contact angle of Parafilm® M replica, 152.3 degree is comparable with lotus leaf, 154.5 degree. In the

replication process of Parafilm® M, the PDMS negative-mold without additional anti-stiction coating can remain original structure completeness and can be reusable, the SEM images of PDMS negative-mold surface before and after Parafilm® M replication are shown in Figure 4. And also, the Parafilm® M replica after demolding from PDMS negative mold can be still well adhered on glass substrate and offers a solid platform for further applications.

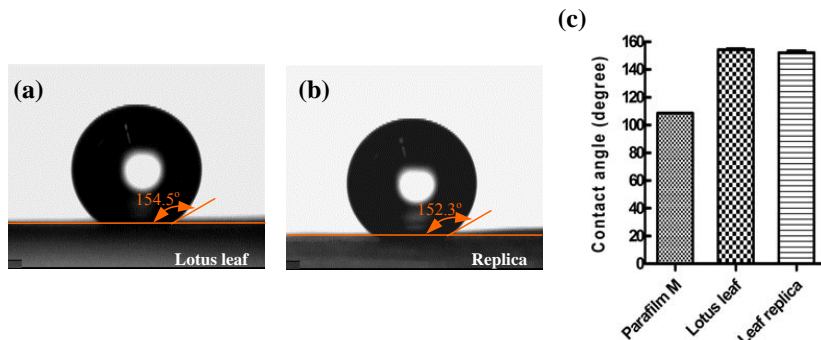


Figure 3. Contact angle measurement with 2 μ l DI water: (a) water droplet on lotus leaf; (b) water droplet on Parafilm® M replica; (c) the comparison of original Parafilm® M, lotus leaf, and replica.

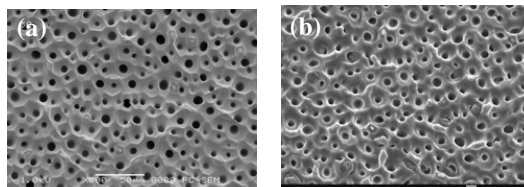


Figure 4. PDMS negative-mold surface: (a) before, and (b) after Parafilm® M molding. The surface remains the same even molding process without any anti-stiction coating.

4. Conclusions

In this study, we successfully demonstrate a simple, rapid, and low cost superhydrophobic surface preparation by nanomolding method. The artificial biomimic superhydrophobic surface has great potential on biomedical and microfluidics applications.

References

1. R. Blossey, *Nat. Mater.*, **2**, pp. 301-306, (2003).
2. H. Y. Erbil, A. L. Demirel, Y. Avci, and O. Mert, Vol. 299, *Science*, **299**, pp. 1377-1380, (2003).
3. W. Ming, D. Wu, R. van Benthem, and G. de With, *Nano Lett.*, **5**, pp. 2298-2301, (2005).
4. M. Sun, C. Luo, L. Xu, H. Ji, Q. Ouyang, D. Yu, and Y. Chen, *Langmuir*, **21**, pp. 8978-8981, (2005).

PRESSURE-ASSISTED MICROPATTERNING OF NON-PHOTODEFINABLE POLYMERS

Yi Zhao¹, David L. Mabius², Jonathan Regis², and Xin Zhang²

¹Department of Biomedical Engineering, The Ohio State University, USA

²Department of Manufacturing Engineering, Boston University, USA

Abstract

Patterning thin film polymer materials with controllable lateral dimensions is one of the main challenges in developing polymer-based micro total analysis systems because many polymers are not photodefinable. We introduce herein a microfluidic approach for patterning such materials using a pressure-induced process. Relying on the differential pressure induced by vacuum rather than the capillary force, this approach demonstrates wide material compatibility and fast channel filling. It thus offers an access for various polymer species to be readily adapted in miniaturized analytical systems.

Keywords: micropatterning, polymer, pressure-assisted

1. Introduction

Recent development of micro total analytical systems calls for functional polymer microdevices. Such devices usually require polymer microstructures on rigid substrates. Since many polymers are not photodefinable and thus not compatible with UV lithography process, alternative methods are needed. Micromolding in capillaries (MIMIC) [1] is the most widely used method. In this method, the polymer is patterned in predefined channels with the help of capillary effect and forms microstructures upon removal of the defining layer. This method works well with low-viscosity wetting polymers. It is, however, not as useful with polymers having weak wetting or even dewetting properties. Moreover, MIMIC also becomes problematic with high-viscous or quick-cured polymers, because relatively long filling time allows the polymers to set prematurely. Here, we report an alternative technology for robust construction of polymer microstructures on rigid substrates utilizing pressure-assisted microfluidics. This approach offers wider material compatibility, allowing polymers with various wetting properties and cure conditions to be molded into microdevices.

2. Fabrication

Figure 1 illustrates the process of pressure-assisted micropatterning. A photoresist layer was patterned on a glass substrate and covered with a polymer slab to form the

rectangular microchannels. We poured PDMS prepolymer around the channel openings to trap air inside the channels. After that, the stack was pumped to vacuum. The trapped air expanded and escaped to its surroundings with vacuum pressure applied. Then the chamber was vented to atmosphere when escaping bubbles were no longer observed. After conducting a secondary curing, we removed the polymer slab and the photoresist layer. PDMS microstructures were thus formed on the glass substrate.

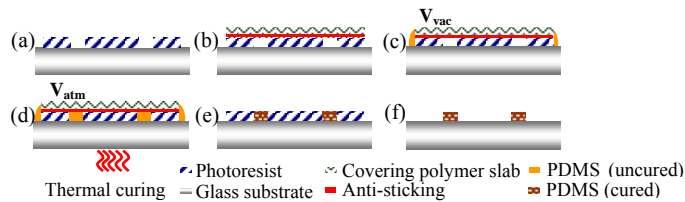


Figure 1. Illustration of pressure-assisted micropatterning process.

3. Theoretical Analysis

The filling is due to the vacuum-induced pressure and the capillary force, as illustrated in **Figure 2**. The prepolymer fills the channel from the left and pushes the air to the right (the center of the channel). The relationship between the pressure and the flowing velocity of the prepolymer along the length of the channel is given by coupling the Navier-Stokes equations with Poisson's equation. Assuming that the viscosity of the prepolymer is a constant during the filling, the velocity profile can be solved using Fourier series and the differential pressure between two ends of the prepolymer can be obtained, which is the driving force of the filling. Given numbers in this case, the differential pressure induced by vacuum is orders higher than that induced by capillary effect. This indicates that the filling can proceed even if the contact angle is greater than 90°. Therefore, the wetting process needed in prior techniques is no longer required.

Figure 3 shows comparison of pressure-assisted micropatterning and MIMIC. It is seen that with the help of vacuum, pressure-assisted micropatterning demonstrates an enhanced filling rate. This is especially important for patterning of highly viscous (or quick cure) polymers because these polymers are allowed to fill the channels before they become too viscous to flow.

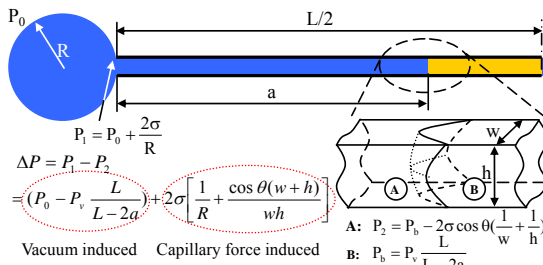


Figure 2. Principle of pressure-assisted micropatterning process (half channel).

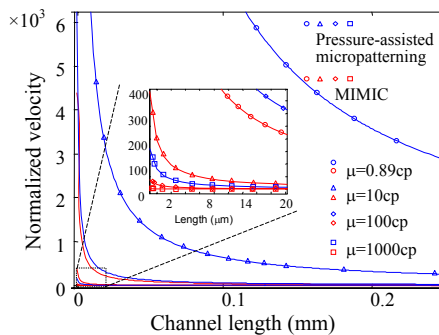


Figure 3. Comparison of pressure-assisted micropatterning and MIMIC.

4. Experimental Results

Several representative structures were demonstrated. **Figure 4a** shows a micro-stripe with the minimum feature size of less than $10\mu\text{m}$. Such features have a typical application as microfluidic components. **Figure 4b** shows a wheel-like structure with relative large features (over $200\mu\text{m}$). Such feature is hard to realize using MIMIC due to weak capillary force. Here, the feature was filled less than a minute utilizing a vacuum pressure of 0.2 mbar . Multi-layered microstructures were also demonstrated. The additional layers were formed by patterning photoresist layers and conducting pressure-assisted filling alternatively. **Figure 4c** shows the microchannels with a glass substrate. **Figure 4d** shows a bi-layered structure. The two layers with different lateral features and interlayer boundary are clearly viewed.

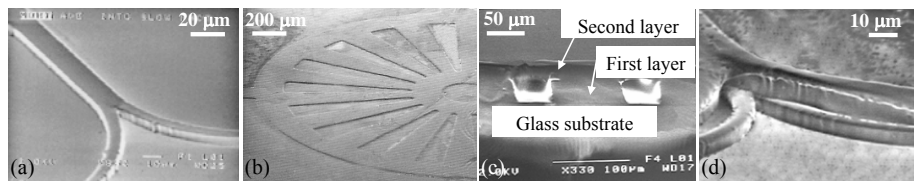


Figure 4. SEM micrographs of pressure-assisted micropatterned structures.

5. Conclusions

A pressure-assisted microfluidic approach is demonstrated for patterning non-photodefinable polymer. The filling of the polymer is dominated by differential pressure due to the applied vacuum rather than capillary force. This method demonstrates wide material compatibility and fast channel filling, as compared to prior techniques.

References

- [1] E. Kim; Y. Xia, G.M. Whitesides, Polymer Microstructures Formed by Molding in Capillaries, *Nature* 376, pp. 581-584 (1995).

CREATING SILICON NANOSTRUCTURES WITH CONTROLLABLE SIDEWALL PROFILES BY USING FLUORINE-ENHANCED OXIDE PASSIVATION

Yi Zhao¹, Xiaoyu Zheng², Jonathan Regis², David L. Mabius² and Xin Zhang²

¹Department of Biomedical Engineering, The Ohio State University, USA

²Department of Manufacturing Engineering, Boston University, USA

Abstract

This paper demonstrates development of silicon nanostructures with controllable sidewall profiles by fluorine-enhanced oxide passivation. The scheme of alternating reactive ion etching and air exposure protects the formed sidewall and ensures high aspect ratio nanostructures. This method adds flexibility of current nanofabrication and facilitates development of mechanical nanosensors.

Keywords: nanostructure, reactive ion etching, fluorine-enhanced oxidation

1. Introduction

Nanostructures are used for mechanical sensing due to the superior probing sensitivity and the enhanced spatial resolution. Cantilevers with high aspect-ratios are often desired. Unfortunately, currently-used deep reactive ion etching is problematic [1]. Since the etching rate of deep etching is relatively high, the etching depths for nanostructures, usually less than a few μm , are hard to be precisely controlled. Also, the lateral penetrations are comparable with the width of the nanostructures. Furthermore, the expensive facilities and expertise hinder wide application.

This paper reports fluorine-enhanced passivation for creating silicon nanostructures with controllable profiles. Reactive ion etching is utilized to form the sidewalls with different anisotropies, and fluorine-enhanced oxidation is utilized to protect the formed sidewalls and to enable high aspect-ratio structures. By avoiding the above limitations, this work provides an affordable nanofabrication and easy control of sidewall profiles.

2. Fabrication

Figure 1 illustrates the fabrication process. After patterning a masking layer, a brief reactive ion etching (CF_4+O_2) was performed. The sidewall anisotropy was controlled by operational pressure. The sample was then exposed to the atmosphere with moisture and heated, followed by another brief etching cycle. The procedure proceeds by alternating the etching cycles and air exposure cycles, forming the nanostructures with flexible sidewall profiles.

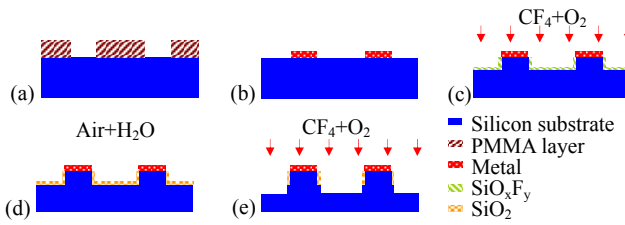


Figure 1. Fabrication process base on fluorine-enhanced oxide passivation.

3. Working Principle

The working principle is illustrated in **Figure 2**. During plasma etching, F being adsorbed on the surface breaks preexisting Si-O bonds and form Si-F group, thus forming a SiO_xF_y layer. When exposed to the coexistence of oxygen and moisture, the Si-F groups are quickly replaced by Si-OH groups from the water vapor ambient due to the similar ionicity. The Si-OH groups bridge and form layers of oxide. The oxide continues to grow due to field assisted Mott-Cabrera mechanism. The fluorine-enhanced oxide layer postpones the attack of the sidewalls during the following brief plasma etching. The sidewall passivation is thus enabled.

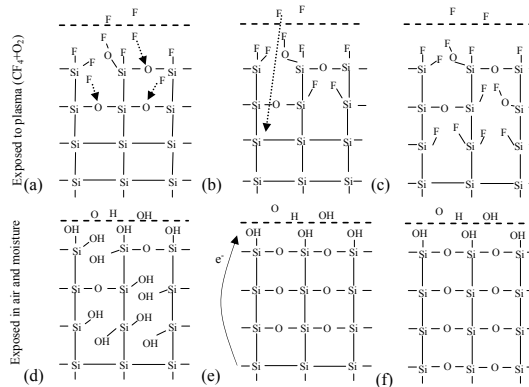


Figure 2. Reactions occurring at the interface during etching & passivation processes.

4. Experimental Results

Figure 3a shows the nanopillars with vertical sidewalls. The profile was achieved by performing etching cycles with high anisotropy. Smaller diameter associates with higher probing sensitivity. However, the diameter of the pillars can not be too small since too sharp pillars may pierce the specimen to be measured. Therefore, we selectively narrowed the bottom portion of the pillar less than 50 nm (**Figure 3b**). The profile was achieved by first performing etching cycles with high anisotropy, followed by etching cycles with somewhat isotropy.

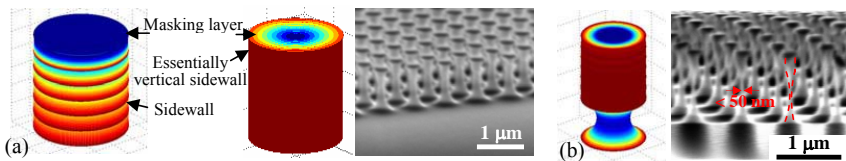


Figure 3. Nanopillars. (a) with vertical sidewalls, and (b) with narrowed sidewalls.

Figure 4 shows suspending nanocantilevers. The profile is formed by first performing etching cycles with high anisotropy, followed by etching cycles with severe undercut to suspend the structures. The probing sensitivity of the cantilevers can be adjusted by changing the thickness of the bottom silicon layer. Since the etchant availability differs spatially, the separation starts from the tip and expands towards the root (**Figure 5**). These nanostructures with flexible sidewall profiles have a potential application as force sensors for determination of mechanical response in small-scale objects, especially for biomedical applications.

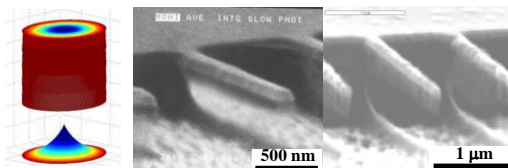


Figure 4. Suspending nanocantilevers.

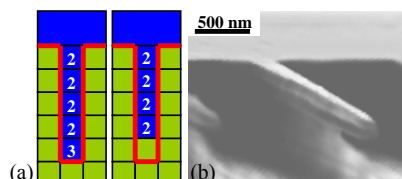


Figure 5. The cantilever is released from the tip to the root. (a) Schematics showing spatial difference of etchant; (b) A SEM micrograph.

5. Conclusions

We demonstrate herein an approach to fabricate silicon nanostructures with controllable sidewall profiles. By performing the alternative etching/passivation and controlling the sidewall anisotropy, nanopillars with vertical sidewalls, nanopillars with narrowed sidewalls and suspending nanocantilevers are realized. These structures can be potentially used for nanomechnosensors to probe at nanoscale with superior sensitivities.

References

- [1] A.A. Ayón, R.L. Bayt and K.S. Breuer, Deep Reactive Ion Etching: A Promising Technology for Micro and Nanosatellites, *Journal of Smart Materials and Structures* 10, pp. 1135-1144 (2001).

CHARACTERIZATION OF THE FLUIDIC PROPERTIES OF IN-SITU POLYMERIZED MONOLITHS IN MICROFLUIDIC DEVICES

Mei He and D. Jed Harrison*

Department of Chemistry, University of Alberta, Edmonton, Alberta T6G 2G2,
CANADA

Abstract

This paper reports the fluidic properties of monolithic beds as a function of preparation conditions. A photobleaching, time of flight linear flow rate measurement method was used to evaluate the stability of the monolithic bed, and bed to bed variation, which will be critical to the use of these materials in parallel microfluidic chip arrays.

Keywords: flow velocity measurement, polymer monolith, microfluidics

1. Introduction

Automated, high-throughput genomic and proteomic analysis calls for multiplexed, parallel and multichannel microfluidic systems. Reaction and separation beds for protein digestion, solid phase extraction (SPE) and liquid chromatography (LC) will be important components of such systems. Such beds can be prepared by packing conventional beads, coating channel walls, or creating monolithic columns. We fabricated 40 packed beds for protein digestion and SPE in 20 parallel channels, meant to feed into a mass spectrometer [1]. Unfortunately, it proved impossible to pack all 40 beds with conventional beads to obtain the same flow resistance. Monolithic columns provide a useful alternative for bed preparation in a highly multiplexed device. Monoliths have demonstrated reliable performance in a single-channel microchip [2]. However, the reproducibility of their fluidic properties has not been evaluated with the level of precision required for good performance in a parallel array of beds. Here we study in detail the effects of the preparation conditions and extent of column use on the flow properties, and report bed to bed reproducibility, which is critical to the use of these materials in parallel arrays.

2. Experimental

Monoliths were prepared by photo-polymerization of monomers of hydroxyethyl methacrylate (HEMA) and ethylene dimethacrylate (EDMA) in porogenic solvent, 1-octanol. A photo-mask was used for simultaneous photopatterning of several monolithic beds in individual channels on one wafer. A photobleaching, time of flight linear flow rate measurement method we developed previously [3] was used to study the fluidic properties of porous polymer monoliths in microfluidic channels.

3. Results and discussion

We found the recipe given in reference [4] did not, in our hands, yield a monolith in the microchannel with stable flow resistance over time. Bed to bed variation was in the range of \pm 20-30 % within the same wafer. Therefore, we sought an alternative recipe, investigating components that might give a more stable monolith. 1-octanol was chosen as the porogenic solvent. Figure 1 shows the porous structure formed within a microfluidic channel, and the bed-edge. The sharp interface indicates good photopatterning. The effects of monomer content on the flow resistance of the beds are shown in the Figure 2. Monomer content was varied from 20 to 70 wt% (monomer/solvent). Only beds with monomer content between 30 - 45 wt% gave desirable fluidic properties. Lower monomer content gave beds that crushed under pressure, while higher content gave gel-like, impermeable monoliths. Within the functional wt% range, a higher content of porogenic solvent resulted in material with higher permeability, allowing control of the flow resistance, as illustrated in Figure 2.

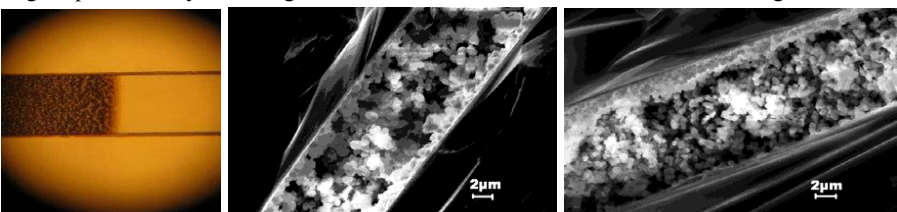


Figure 1. The morphologic images of porous polymerized monolith in microchannels. (A) Microscopic top view of the edge of the monolith. (B)-(C) SEM images of the cross-section of monolith photopolymerized for 6 mins and 11 mins. The monoliths were prepared in a 10 μm deep, 600 μm wide channel from 40 wt% monomer solution.

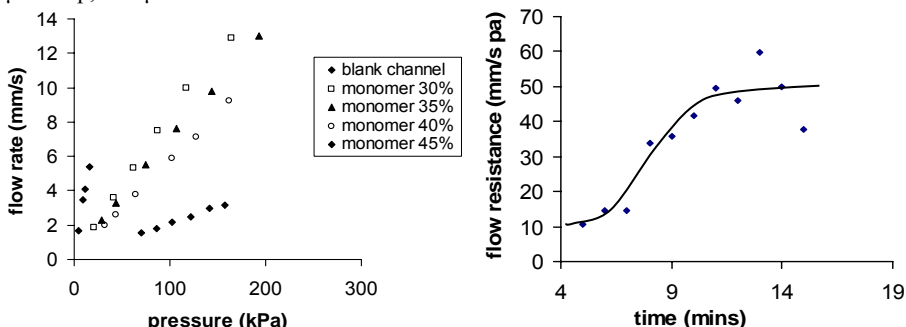


Figure 2. The effect of monomer content on the fluidic resistance, expressed as flow rate vs pressure.

Figure 3. The effect of exposure time on the flow resistance.

Figure 3 shows the effect of exposure time on the flow resistance of the beds, indicating higher flow resistance is achieved by longer reaction times, up to a point at which the

trend tends to plateau, presumably due to complete polymerization. The morphology of the monolith shown in Figure 1 (B) and (C) is consistent with the results in Figure 3. However, longer exposure times deteriorate the interface of the monolith in the channel. The beds shown in Figure 2 were tested for flow stability over time. Figure 4 shows that reproducible flow resistance was achieved for the 40 wt% composition. Five-day reproducibility for one bed was $\pm 1.9\%$ and bed to bed variation in one wafer was $\pm 5.3\%$, which is within the desired fabrication parameters. The wafer to wafer variation was 17.9%, which was less satisfactory. However, wafer to wafer variability is less important than bed to bed variation for multiplexed devices. The other compositions showed variation of 5-20% over 5 days.

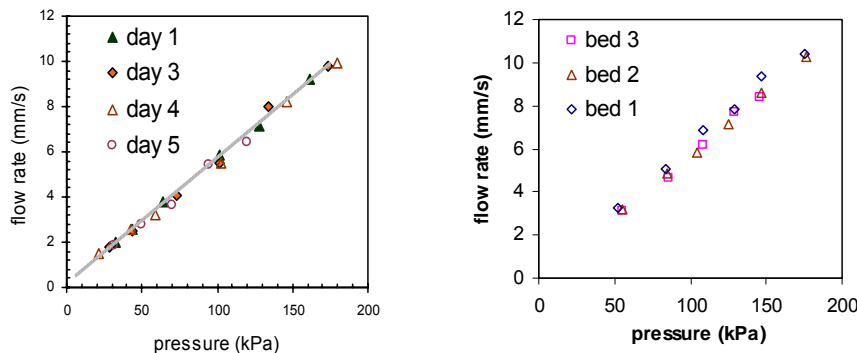


Figure 4. Flow properties measured on different days for one bed (left) and different beds in one microfluidic device (right). The HEMA-EDMA monoliths were prepared with 40 wt% monomers (HEMA-EDMA 40:60 wt/wt) and 9 mins exposure.

5. Conclusions

These results show that monolithic materials are good candidates for the formation of highly parallel beds within microfluidic devices, since the bed to bed variation of flow resistance within a single wafer could be adjusted to be highly reproducible. Flow resistance evaluation is an effective tool for designing suitable monolithic materials.

References

1. J. Taylor, C. Wang, D.J. Harrison, Micro-Total Analysis Systems 2002, Proceedings Volume, Kluwer Publishing, Netherlands, 2002, 344-346
2. C. Yu, M. H. Davey, F. Svec, J. M. J. Fréchet, Analytical Chemistry, 2001 (73), 5088-5096
3. J. B. Bao, D. J. Harrison, AIChE Journal, 2006 (52), 75-85
4. C. Yu, M. C. Xu, F. Svec, J. M. J. Fréchet, Journal of Polymer Science: Part A: Polymer Chemistry, 2002 (40), 755-769

MICROPLASMA TECHNOLOGY DEVELOPED FOR MICROMACHINING AND SURFACE PATTERNING IN MICROBIOSYSTEM APPLICATIONS

Helen M. L. Tan¹⁾, Takanori Akagi^{2,3)} and Takanori Ichiki^{1,2,3)}

¹⁾ Department of Materials Engineering, School of Engineering,
The University of Tokyo, Japan

²⁾ Department of Bioengineering, School of Engineering,
The University of Tokyo, Japan

³⁾ Center for NanoBio Integration, The University of Tokyo, Japan
Email: ichiki@bioeng.t.u-tokyo.ac.jp

Abstract

We report in this paper the development of a new type of plasma equipment for the rapid prototyping of microbiosystems, which consists of an on-chip microplasma jet source and a numerically controlled scanner. With this technology, localized and ultra high-speed micromachining and maskless surface patterning were achieved.

Keywords: microplasma, micromachining, scanning radical microjet, PDMS surface modification, cell patterning

1. Introduction

With the progress of micro total analysis systems (μ TASs) towards higher functionality and higher-order integration, advanced microfabrication technologies developed in the LSI industry will be increasingly applied in this field. In fact, much progress has been recently brought about by the introduction of advanced plasma microfabrication technologies to the fabrication of microelectromechanical systems (MEMS) and μ TAS. However, the current microfabrication process developed according to the requirements of the LSI industry is not sufficiently versatile for MEMS and/or μ TAS fabrication [1]. On the basis of this background, the authors' research group has recently developed a scanning microplasma system for establishing innovative micromachining. In this research study, a new type of plasma equipment has been developed, which consists of an on-chip microplasma jet source and a numerically controlled scanner. We report here the application of microplasma technology in the rapid prototyping of microbiosystems that involves the maskless pattern etching of silicon wafers and the patterned surface modification of biocompatible polymer surfaces.

2. Experimental

2.1. Apparatus

Figure 1 shows a schematic of a three-dimensional scanning microplasma jet etcher (SMPJE) whose plasma source can move independently of the x-, y- and z-axes. It consists of a miniaturized atmospheric-pressure inductively coupled plasma (ICP) jet source produced with a 144-MHz VHF power supplied to the plasma source that is kept constant at 50 W. The details of the plasma source can be found in ref. 2. Furthermore, we also developed a scanning radical microjet (SRMJ) [3, 4] treatment using oxygen radicals (Fig. 2) and applied it to the control of biological cells' attachment on biocompatible polymer material, poly(dimethylsiloxane) (PDMS) [5]. A fine argon plasma jet was emitted through the pinched end of a discharge tube, which had an inner diameter of 0.1 mm. Another small cylindrical tube was connected to the end of the

discharge tube for the introduction and subsequent dissociation of oxygen. The oxygen radicals were emitted through a 100- μm hole at the end of the cylindrical tube. The flow rate of argon was kept constant at 180 ccm. Subsequently, the effects of scanning speed on hydrophilic patterning were investigated for controlling HeLa cells' (human epitheloid carcinoma cell line) attachment.

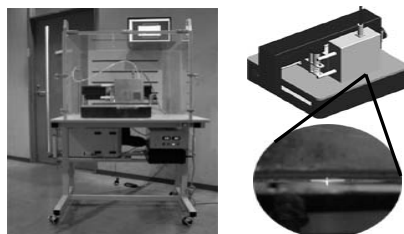


Fig. 1. Prototype of scanning microplasma jet etcher.

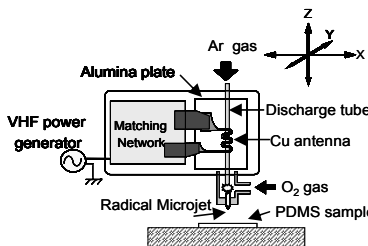


Fig. 2. Schematic of scanning radical microjet (SRMJ) employed in this study.

2.2. Sample Preparation and Cell Cultivation

SYLGARD 184 (Dow Corning), base and curing agent, was used to prepare thin PDMS films on glass substrates using a spin coater and cured at 100°C for 2 min. Line scanning in the x- or y-direction was then performed for hydrophilization using SRMJ equipment, and the water contact angle distributions of microscopic-size water droplets obtained from condensed steam of boiling water were measured across the scanned line using a home-made contact angle measurement system.

As a feasibility study, HeLa cells were cultured on treated PDMS films in Dulbecco's modified Eagle's medium supplemented with 10% fetal bovine serum, L-glutamine and penicillin-streptomycin, and incubated for 72 h at 37°C in 5% CO₂ in air atmosphere. The initial area density of seeded cells was constant at 30 cells/mm² in all experiments.

3. Results and discussion

Figure 3 shows a microreactor array fabricated on a silicon wafer using SMPJE. The diameter of the reactor hole is ca. 300 μm and is the minimum size that can be achieved using the present apparatus.

Figure 4 shows the water contact angle distribution measured across the scanned line. It is observed that as scanning speed increases from 0.5 to 6 mm/s, the minimal contact angle increases from 72 to 79 degrees while the treated line width decreases from 2.2 to 1.5 mm. This phenomenon could be ascribed to the shorter treatment time brought about by the oxygen radicals on the PDMS surface as scanning speed increases, hence resulting in decreasing hydrophilicity and thus a narrower line width and higher water contact angles. Figure 5 illustrates the cell proliferation profiles for four different scan speeds used in treating PDMS surfaces for day in vitro (DIV) 2 of the cell culture process. From the profiles, the scan speed of 0.5 mm/s shows the highest cell density of approximately 420 cells/mm².

Finally, maskless hydrophilic patterning using SRMJ has been demonstrated to be applicable to patterned cell cultivation by controlling the experimental condition parameters, as shown in Fig. 6. The cell line pattern was achieved using a scan speed of

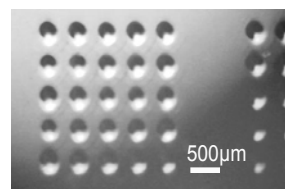


Fig. 3 Micrograph of the microreactor array etched on silicon wafer using scanning microplasma jet etcher.

0.5 mm/s and an oxygen flow rate of 90 ccm.

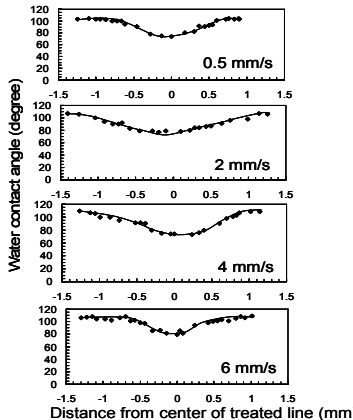


Fig. 4. Scanned line width profiles plotted from water contact angles measurements for different scanning speeds.

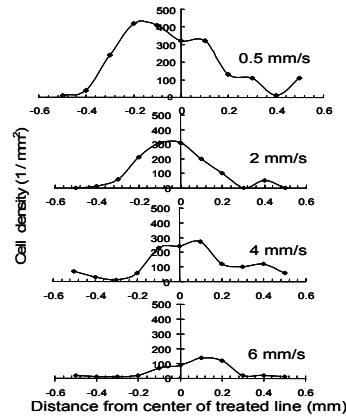


Fig. 5. Cell proliferation profile of different scanning speeds for DIV 2 of cell culture process.

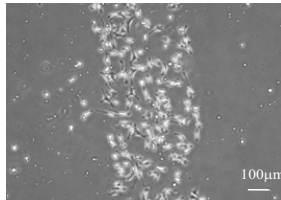


Fig. 6. Micrograph of cells cultivated in line on treated PDMS surfaces.

4. Conclusion

In this study, we demonstrated the practical usefulness of microplasma technology for the rapid prototyping of microbiosystems such as microreactors, microfluidics and biosensors. We developed a new plasma process using an atmospheric-pressure 3D-SMPJE and performed 3D micropatterning on silicon substrate. Moreover, surface treatments of PDMS for use in microbiosystems were also demonstrated.

Acknowledgements

This work was partially supported by Grants-in-Aid for Scientific Research on Priority Area: Generation of micro-scale reactive plasmas and development of their new applications from the Japanese Ministry of Education, Culture, Sports, Science and Technology.

References

- [1] T. Ichiki, Y. Sugiyama, R. Taura, T. Koidesawa and Y. Horiike, *Thin Solid Films*, **435**, 62(2003).
- [2] T. Ideno and T. Ichiki, *Thin Solid Films*, **506/507**, 235(2006).
- [3] H. M. L. Tan, H. Fukuda, T. Akagi and T. Ichiki, *Thin Solid Films* (accepted).
- [4] H. M. L. Tan, T. Akagi and T. Ichiki, *J. Photopolymer Sci. Technol.* **19**(2), 245(2006).
- [5] S. K. Sia and G. M. Whitesides, *Electrophoresis*, **24**, 3563(2003).

PLASMA-BASED MICROFABRICATION OF SUBMICRON-APERTURE PARYLENE NOZZLES

Po-Jui Chen and Yu-Chong Tai

California Institute of Technology, Pasadena, California, USA

E-mail: pjchen@mems.caltech.edu

Abstract

This paper presents the first submicron-aperture parylene nozzles fabricated with a convenient and economical plasma-based micromachining process. Batch fabrication of the devices can be realized by means of photolithography and plasma patterning, which totally obviates the need of complicated and expensive processing techniques such as ion-milling and nanofabrication. By using parylene (poly-para-xyllylene) as an exclusive structural material, the biocompatible microfabricated polymer nozzles with nanometer characteristic openings can be integrated into on-chip microsystems for electro-spray-ionization (ESI) and nanofluidic transport/analysis in life science research.

Keywords: Parylene, Nozzle, Sub-Micron-Aperture

1. Introduction

On-chip ESI nozzles generally require small apertures/orifices in order to form a efficient Taylor cone with a low applied electrical voltage for effective electrospray [1]. Many works have been done toward miniaturization of characteristic size of the on-chip nozzles. Giving a few examples, Fig. 1 shows conventionally microfabricated ESI nozzles from surface-micromachining [2] and focused-beam ion-milling [3] processes. Surface-micromachined nozzles can be batch-fabricated in an integration with other microdevices, while their orifices are in micron size due to photolithography limitation. Although a capillary slot in nanometer features can be achieved by using ion-milling, these nozzles are problematic with ability of batch-processing and their cost. Therefore, a convenient and economical wafer-level microfabrication technology has been developed to create on-chip nozzles with apertures smaller than one micron for high-performance ESI and nanofluidics.

2. Design

The foundation of our proposed nozzles is monolithic embedded channels [4]. As shown in Fig. 2, when the embedded channel are formed after a conformal layer deposition on determined trench openings with etch mask overhang, a nanometer-wide notch is naturally formed at the sealing point of the embedded channel. This notch can be etched through and exposed to outside as a nozzle aperture after patterning the top of the embedded channel. This fabrication method does not require any additional processes to define the nanometer features of the nozzles. Parylene C (poly-para-xylene C) is selected as a structural material because of its biocompatibility (USP Class VI grade) and conformal deposition that enables the novel nozzle fabrication technology.

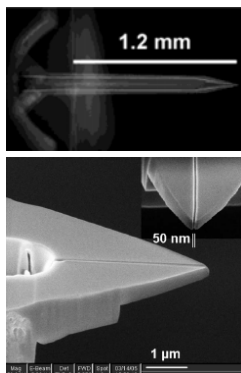


Figure 1. Micro/Nanofabricated nozzles by using surface-micromachining [2] (top) and ion-milling [3] (bottom) technologies.

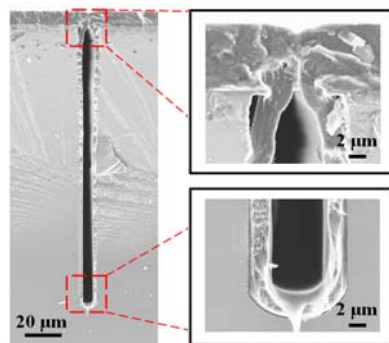


Figure 2. SEM images of a monolithic high-aspect-ratio embedded parylene channel [4]. Note the notch formed at the sealing point in the top cut-view of the channel.

3. Experimental

Fig. 3 illustrates the fabrication process of the parylene nozzles. Backside trenches were first created on the silicon wafer to define the fluidic ports. After the notches were created by using the process of the monolithic parylene channels, the parylene layer was patterned by using oxygen plasma etching with photoresist as a mask. At this step additional etching may be applied to undercut/sharpen the parylene tips. Finally the photoresist was stripped away with acetone and the parylene was etched back to create the nano-orifices. Fig. 4 shows SEM image of fabricated crater-shaped parylene nozzle.

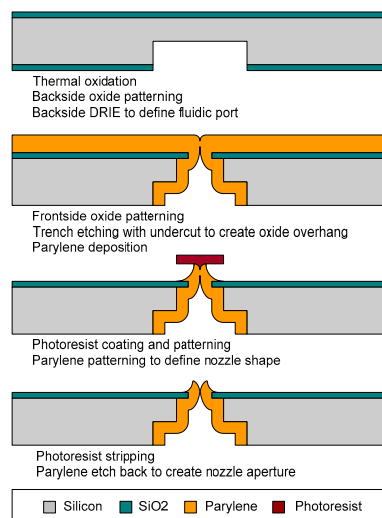


Figure 3. Process flow of nozzle fabrication.

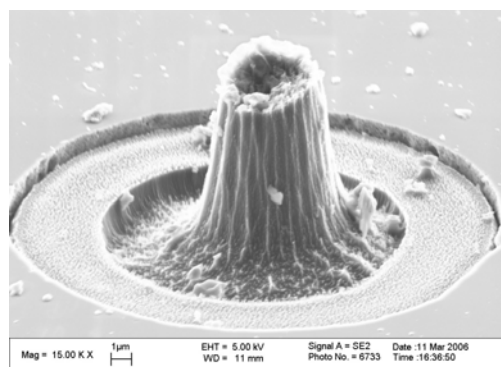


Figure 4. SEM image of the microfabricated crater-shaped parylene nozzle. Its submicron aperture is featured by the nano-orifice located at center of the nozzle tip.

4. Results and discussion

By controlling oxygen plasma etch and the notch size in correlation to trench opening in the monolithic embedded channel process, nozzles with different orifice sizes down to 200 nm and different shapes can be obtained as shown in Fig. 5.

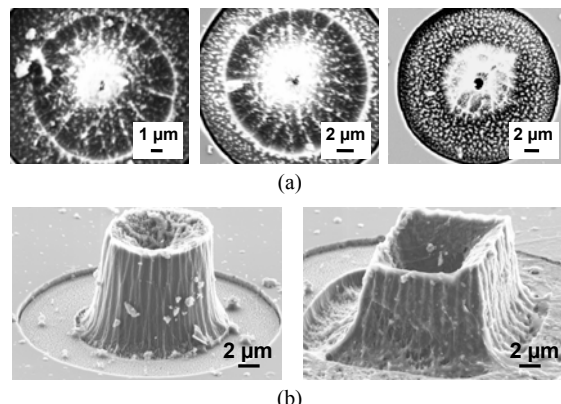


Figure 5. Control of nozzle profile: (a) Different resultant aperture sizes (top view; left: 200 nm, middle: 500 nm, right: 1 μm) after different time of oxygen plasma etching to the nano-notched parylene channels; (b) Different shapes of nozzle tips (left: circular, right: square) after parylene patterning using photoresist etch mask in different contours.

5. Conclusion

A novel micromachining process has been successfully developed to fabricate on-chip submicron-aperture parylene nozzles. Only lithography and plasma-etching techniques are employed so that the nozzles can be economically batch-fabricated. Fluidic characterization of the developed nozzles is currently underway to verify their performance in nanofluidic and lab-on-a-chip applications.

Acknowledgments

This work was supported in part by the Engineering Research Centers Program of the National Science Foundation under NSF Award Number EEC-0310723.

References

- [1] M. Wilm and M. Mann, "Electrospray and Taylor-Cone Theory, Dole's Beam of Macromolecules at Last?" *Intl. J. Mass Spec. Ion Processes*, 136, pp. 167-180, 1994.
- [2] J. Xie, Y. Miao, J. Shih, Q. He, J. Liu, Y.-C. Tai, and T.D. Lee, "An Electrochemical Pumping System for On-Chip Gradient Generation," *Anal. Chem.*, 76, pp. 3756-3763, 2004.
- [3] S. Arscott and D. Troadec, "Electrospraying from nanofluidic capillary slot", *Appl. Phys. Lett.*, 87, 134101, 2005.
- [4] P.-J. Chen, C.-Y. Shih, and Y.-C. Tai, Design, Fabrication, and Characterization of Monolithic Embedded Parylene Microchannels in Silicon Substrate, *Lab on a Chip*, 6, pp. 803-810, 2006.

SOLVENT-RESISTANT AND TRANSPARENT POLYSILAZANE GLASS MICROFLUIDICS FOR PHOTOCHEMICAL REACTIONS

**Hong-Joo Lee, Amit Asthana, Jayakumar Perumal, Jun-Hong Park,
Dong-Pyo Kim***

School of Applied Chemistry and Biological Engineering, Chungnam National
University, Daejeon 305-764, Korea, E-Mail: dpkim@cnu.ac.kr

Abstract

The microfabrication of ceramic material having thermal, chemical, and tribological stability is an inevitable demand for the devices in the fields of microfluidics. The study describes the preparation of micro/nano-sized patterns and microfluidic channels using soft lithographic technique from the UV and thermally cured preceramic polymer for the applicable potentials of the photochemical reaction.

Keywords: Soft lithography, Microfluidics, Polysilazane glass

1. Introduction

Soft lithography with elastomeric polydimethylsiloxane (PDMS) mold has been significantly facilitated for the micropattern transfer and fabrication of microfluidics in simple and efficient manners [1]. Among soft lithographic techniques, it is known that the imprint lithography makes it possible fabricate micro- or nanopatterns at high resolution, high throughput and low cost and can be applied to the fabrication of various shapes such as curved surfaces [2]. The preceramic polymer is heat-treated or pyrolyzed at ~1000 °C to convert it to a monolithic ceramic part for the useful potential of non-oxide ceramic MEMS (Microelectromechanical Systems). However, the polymer undergoes linear shrinkage of about 30 % during the heat treatment. Also, adhesion to a substrate during this stage can cause cracking or fracture as well as reduction of density [3]. It is suggested that the conversion of preceramic polymers into the cured polymers can be used for microfabrication because of low shrinkage compared with ceramic materials. As far as we know, the microfabrication of the cured polymer is rarely reported.

In our present study, we have successfully fabricated the polysilazane glass microfluidics with high optical transparency, thermal stability and chemical inertness via simple fabrication process using a commercially available preceramic polymer. Also, it was clearly shown that the fabrication of microchannels using the cured inorganic polymers holds tremendous potentials in the field of photochemical reaction.

2. Experimental

The solvent resistant polysilazane glass microfluidic channel was fabricated from a commercially available preceramic polymer of SiCN, polyvinylsilazane (VL-20, Kion Corp., USA) via the imprint lithography as shown in Fig. 1. A pre-cleaned glass substrate was first coated with liquid precursor polymer under nitrogen atmosphere. After a PDMS mold was coated with an appropriate mold release agent, it was placed on the preceramic polymer layer of the glass surface. The UV and thermal curation was executed after both channel and lid sides were attached together for making leak-free channels. Also, the influence of the curation on the thermal and chemical stability, optical properties and chemical structures were investigated for the cured polymer.

3. Results and discussion

In the thermal degradation with increasing temperature, the preceramic polymer was thermally degraded at higher temperature than 400 °C, the ceramic yield being 80 % at 600 °C or above. The thermal gravimetric result indicates that the polymer becomes ceramic properties at higher temperature than 600 °C. In the cross-linking phenomena for the UV-cured polyvinylsilazane, the absorption peak of vinyl group disappeared after curing at 150 °C for 3 h under nitrogen atmosphere, implying that complete cross-linking takes place above or around the maximum activity of a thermal initiator at 150 °C. The thermally cured polyvinylsilazanes were annealed at 300 °C and 400 °C for 1 hour in the N₂ atmosphere and their transmittances were observed for the UV transparency of the cured polyvinylsilazane, showing 93 % of transmittance in the longer wavelength than 280 nm (Fig. 2). For the solvent compatibility, all solvents did not show any notable change for the thermally cured polyvinylsilazane at 150 °C except for hexane, methanol and acetone. As shown in Table 1, the annealed polyvinylsilazane at 300 °C shows good solvent compatibility for all examined solvents. The characterized results imply that the polyvinylsilazane glass microchannels can be used for photochemical reactions.

At this work, the imprint lithography was considered to fabricate microfluidic channels. Microfluidics were examined by pumping isopropyl alcohol and two different kinds of dyes at the flow rate of 10 µl/min in the microfabricated channel having the width of 100 µm and the depth of 20 µm, as shown in Fig. 3. Based on this study, it is believed that transparent polyvinylsilazane glass derived microchannels hold tremendous potential in the

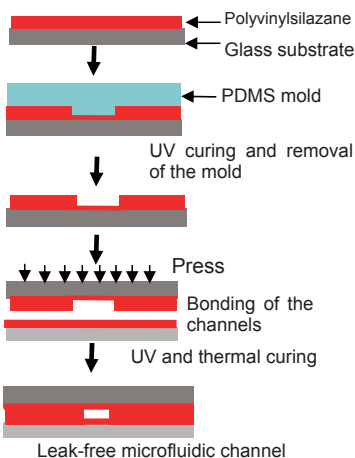


Fig. 1. Microfabrication of cured polysilazane channels by the imprint lithography

fields of micro total analysis system and photochemical reactions, where materials with high optical transparency, thermal stability and chemical inertness are in demand [4,5].

4. Concluding remarks

The study describes the preparation of nano-sized patterns and microfluidic channels having low shrinkage from the cured preceramic polymer using the imprint lithography. It is believed that the fabrication of microchannels using the cured inorganic polymers holds tremendous potential in the field of microfluidics, where materials with high optical transparency, thermal stability and chemical inertness are in demand as the obvious niche between conventional microfluidics using glass and polymer materials.

References

- Y. Xia and G.M. Whitesides, *Annu. Rev. Mater. Sci.*, 28, pp.153-184 (1998).
- H. Ooe, M. Morimatsu, T. Yoshikawa, H. Kawata and Y. Hira, *J. Vac. Sci. Technol. B*, 23, pp. 375-379 (2005).
- L.A. Liew, Y. Liu, R. Luo, T. Cross, L. An, V.M. Bright, M.L. Dunn, J.W. Daily and R. Rai, *Sens. Actuat. A*, 95, pp. 120-134 (2002).
- A. Asthana, Y. Asthana, I.K. Sung, D.P. Kim, *Lab Chip*, In Press (2006).
- P.S. Dittrich, K. Tachikawa, A. Manz, *Anal. Chem.* 78, pp. 3887-3908 (2006).

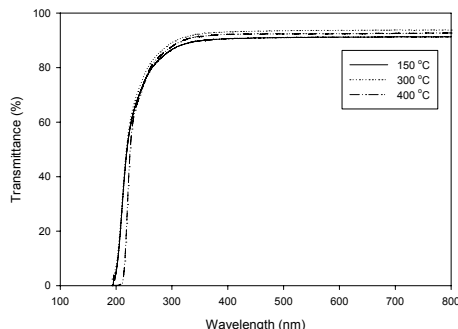


Fig. 2. Optical properties of the cured polysilazane.

Table 1 Solvent compatibility of the cured polysilazane

Solvent	Swelling ratio		Solvent	Swelling ratio	
	150 °C	300 °C		150 °C	300 °C
Water	0.95	1.0	THF	1.0	1.0
Hexane	1.2	1.0	Toluene	1.0	1.0
Methanol	Crack	1.0	Acetone	Crack	1.0
Ethanol	1.0	1.0	Acetonitrile	1.0	1.0
Isopropyl alcohol	1.0	1.0	Dimethyl sulfoxide	1.0	1.0

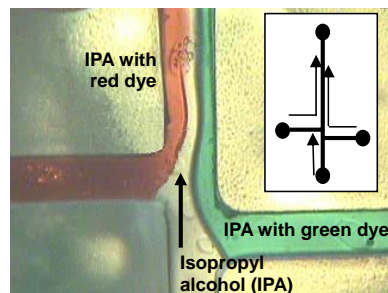


Fig. 3. Polysilazane glass microfluidic channel.

BATCH FABRICATED MICRO AND NANOPORES IN SILICON FOR PARTICLE TRANSLOCATION DETECTION

Christophe Yamahata¹, Agnès Tixier-Mita², Bruno Le Pioufle²,
Hiroaki Suzuki¹, Edin Sarajlic¹, Momoko Kumemura¹,
Shoji Takeuchi¹, Dominique Collard² and Hiroyuki Fujita¹

¹Institute of Industrial Science, The University of Tokyo, Japan

²LIMMS-CNRS/IIS, The University of Tokyo, Japan

Abstract

We describe a simple method for the batch fabrication of solid-state pores with controllable size ranging from few micrometers down to few hundred nanometers. Based on our method, a ‘Coulter counter’ device was developed and we could demonstrate the straightforward detection of particles translocation through the pore, opening possibility for the detection of biomolecules such as DNA.

Keywords: Micropore, Nanopore, V-groove, Coulter counter, Patch-clamp

1. Introduction

In the frame of the conception of a MEMS-based tool for the biomechanical characterization of DNA, we investigate strategies to detect and isolate a single DNA strand. The nanopore device¹ finds to be particularly attractive for DNA detection and could further be combined with currently under development microfluidic structures (for isolation of DNA) and micromachined tweezers (for manipulation of DNA) [1].

Most of the solid-state nanopores presented so far were fabricated by opening/closing a hole in a thin membrane with a Focused Ion Beam or a TEM [2,3]. However, such fabrication method is time consuming and inappropriate for mass production. A promising alternative to create a nanometer aperture is to take advantage of low temperature oxidation and selective etching of silicon [4].

2. Fabrication method

We use a fabrication method based on wet anisotropic etching of silicon in both KOH and TMAH solutions [5]. This approach is compatible with conventional UV photolithography and suitable for batch production. The process starts by making crossed V-grooves by wet anisotropic etching in KOH, one on each side of a standard (100)-oriented silicon wafer (Figure 1). Then, by etching one of the V-grooves in TMAH, a hole is created at the intersection. Its dimensions can be adjusted within tens of nanometers thanks to the slow etching rate of the {111} planes in TMAH (Table 1). Figure 2 shows two examples of micro- and nanopores fabricated with this method.

¹ The ‘Coulter counter’ (also known as ‘resistive-pulse’ sensor) is a commercially available system used to count particles, biological cells or molecules [2]. The principle was invented in the 1950’s and has regained interest in recent years thanks to its proven suitability for DNA detection through the use of a nanopore [3], thus finding applications at scales down to nanometer.

Table 1. Comparison of wet anisotropic etching rates for KOH and TMAH.

Material (etching rate or ratio)	Etching rate	
	KOH (33% w/w, 85°C)	TMAH (15% w/w, 85°C)
Si {100}	1.5 $\mu\text{m}/\text{min}$	0.8 $\mu\text{m}/\text{min}$
Si {111}/{100}	~1/300	1/30
SiO ₂ / Si {100}	1/200	1/1000
Si ₃ N ₄	almost no etching	

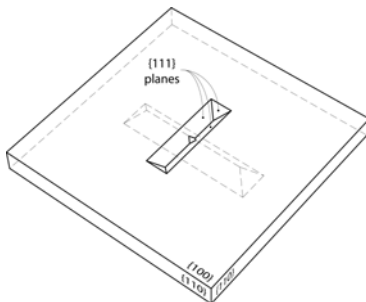


Figure 1. Three-dimensional schematic diagram showing crossed V-grooves in silicon forming a solid-state pore.

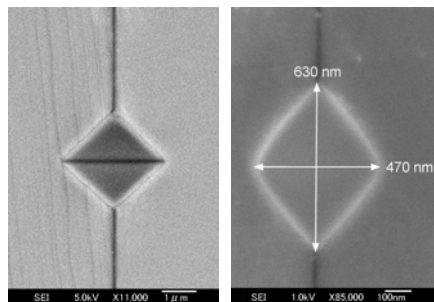


Figure 2. SEM photographs of a silicon micropore (left) and nanopore (right). The pictures were taken before removal of the oxide layer.

3. Experimental

The experimental setup, illustrated in Figure 3, consists of the silicon pore that divides two chambers containing a KCl electrolyte solution (100 mM); the electric potential is applied through Ag/AgCl electrodes. The resistive-pulse measurements were performed with a patch-clamp amplifier (Nihon Kohden, CEZ-2400, Japan) [6].

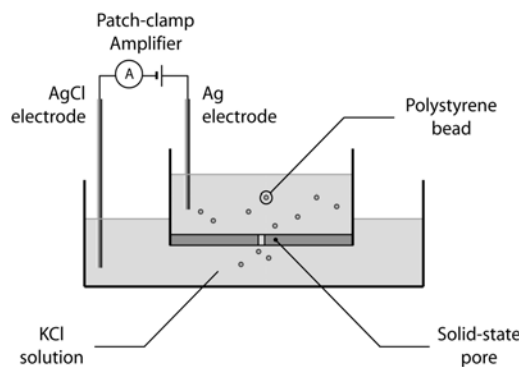


Figure 3. Setup of the ‘Resistive-Pulse’ electrical detection system.

Using different size combinations of beads and pores, we could verify the electrical detection of translocated beads. In Figure 4, for example, we show a current-step caused by a 15 μm polystyrene bead partially clogging a smaller pore. In Figure 5, we recorded a sequence of 2 μm beads flowing through a 20 μm (diagonal dimension) pore.

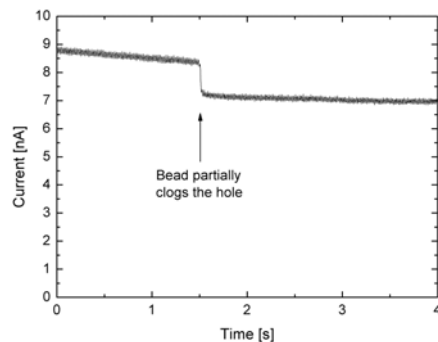


Figure 4. Patch-clamp measurement showing the effect of a 15 μm bead partially clogging a pore (diagonal length: 20 μm).

The experiment was achieved with a 100 mM KCl solution for an applied voltage of 1 mV.

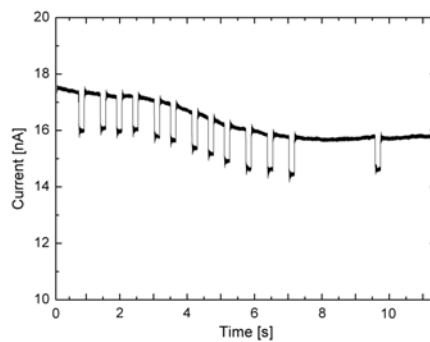


Figure 5. Detection of beads passing through a micropore (20 μm hole / 2 μm beads). The experiment was achieved with a 100 mM KCl solution for an applied voltage of 2 mV.

The data were filtered with a Tchebychev rejector around 50 Hz and a 4th order Butterworth low pass filter set at 1 kHz.

4. Conclusion and outlook

We have described a simple method that enables the fabrication of micro- and nanopores with dimensions ranging from few micrometers down to few hundred nanometers. Future work will focus on the preparation of nanopores with apertures around few tens of nanometers targeted to the detection of biomolecules such as DNA strands.

Acknowledgements

We are thankful to the VLSI Design and Education Center where the masks were fabricated (VDEC, University of Tokyo). This work was partially supported by the Swiss National Science Foundation.

References

1. G. Hashiguchi *et al.*, Anal. Chem. **75**, pp. 4347-4350, 2003.
2. H. Bayley and C.R. Martin, Chem. Rev. **100**, pp. 2575-2594, 2000.
3. J. Li, D. Stein, C. McMullan, D. Branton, M.J. Aziz and J.A. Golovchenko, Nature **412**, pp. 166-169, 2001.
4. P.N. Minh, T. Ono and M. Esashi, Applied Physics Letters **75**, pp. 4076-4078, 1999.
5. A. Tixier-Mita, Y. Mita and H. Fujita, Proc. Transducers '03, pp. 250-253, 2003.
6. H. Suzuki, K.V. Tabata, H. Noji and S. Takeuchi, Langmuir **22**, pp. 1937-1942, 2006.

FABRICATION OF A MICROFLUIDIC BIOARRAY USING 2-D ARRAY OF MICROBEADS FIXED WITHIN LASER-MACHINED SURFACE MICROSTRUCTURES

Tadatake Sato, Thomas Gumpenberger, Ryozo Kurosaki,
Aiko Narazaki, Yoshizo Kawaguchi and Hiroyuki Niino

Photonics Research Institute, National Institute of Advanced Industrial Science
and Technology(AIST), Tsukuba, Ibaraki 305-8565, Japan
sato-tadatake@aist.go.jp

Abstract

A microfluidic device incorporating a two-dimensional array of microbeads with 10 μm diameter was fabricated. Surface-modified microbeads used as detectors were arranged into laser-machined surface microstructures. The performance of the microfluidic bead array was confirmed by a capturing experiment of DNA.

Keywords: Laser-micromachining, microfluidic device, microbeads, bioarray

1. Introduction

The high precision surface micro-structuring of the transparent materials is a key technology for fabricating μTAS systems. As a solution, we have recently developed a technique for laser-micromachining of transparent materials using organic solution, named laser-induced backside wet etching (LIBWE) [1]. (Figure 1) This method employing mask projection system can fabricate microstructures with 1 μm resolution within an area of 1 x 1 mm^2 at single step.

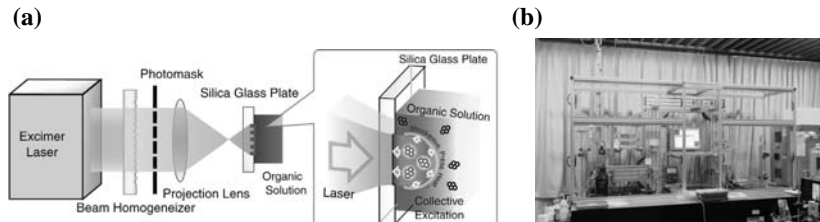


Figure 1 (a) Schematic illustration and (b) apparatus for the LIBWE method

Patterns of microstructures can be freely designed on photomasks, and the depth of the microstructures can be controlled by numbers of the laser pulses. In this work, we have prepared microstructures that can combine microfluidic system with array of microbeads [2]. Fabricated microstructures were sealed by a polydimethylsiloxane (PDMS) plate to form a novel microfluidic bioarray employing two-dimensional array of microbeads with 10 μm diameter [3]. In this device, the beads are arranged within microchannels regularly in two-dimensional manner without contacting each other, which makes extraction of beads' signals by image analyses easy.

2. Experimental

Microstructures were fabricated on synthetic silica glass plates by the LIBWE method employing toluene and a KrF excimer laser (Lambda Physik, EMG-201MSC, $\lambda = 248$ nm, FWHM ≈ 30 ns). Channels with 500 μm width and 40 μm depth connecting microstructures and through holes were also prepared by LIBWE. Through holes were drilled by means of a ultrasonic drill.

Surface modified beads were prepared from polystyrene beads with surface carboxyl group (10 μm diameter, Bangs Laboratories). To label bead itself, Eu(III)theonyl trifluoroacetate was introduced into the beads from tetrahydrofuran solutions. Then, probe DNA (20-mer) was immobilized onto the surface. The sequences of target and probe DNA (20-mer) was 3'-CGAAACTCCACGCACAAACA-5' and 5'-GCTTTGAGGTGCGTGTGTTG-3', respectively [4]. Target DNA was labeled with Cy3.

These microbeads were arranged into the microstructures by self- and force-loading. Then, the microstructures containing beads were sealed by a PDMS plate with pressing with a pressure of ca. 10 kPa to avoid leakage. On the rear side of the silica glass plate, PEEK tubing was connected and used for pressure-induced solution flow employing a syringe pump system. A pressure gauge and a connecting port were placed between the device and pump. The assembled device was set on the stage of inverted microscope (Nikon TE-2000U).

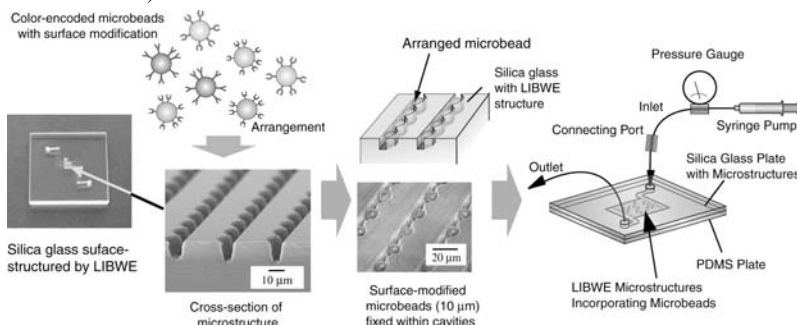


Figure 2 Beads array fabrication and device assembly.

3. Results and discussion

To fix the microbeads with 10 μm diameter, microstructures with depths of ca. 13 μm were fabricated by irradiation with 2640 pulses. Surface modified microbeads were successfully arranged with in the microstructures as shown in Figure 2. Up to 80% of cavities were filled with the beads. Beads fixed within the microstructures gave separated spots in fluorescent micrographs as shown in Figure 3.

For assembled device, sample solution was supplied by pressure-driven flow. Initially, solution was pumped at the flow rate of 40 $\mu\text{L min}^{-1}$. After the solution passed through the microstructures, flow rate was reduced to 2 $\mu\text{L min}^{-1}$ to achieve quasi-stationary flow. If flow rate did not reduced, pressure continued to increase and finally leakage occurred at around 40 kPa.

For examining the performance of the device, capturing of target DNA by surface-immobilized probe DNA(20 bps) was examined. In this experiment, two types of the beads was employed: one is a bead with target DNA, showing intense fluorescence of bead-labeling dye, the other is a surface-blocked beads showing weak

fluorescence of bead-labeling dye. Target oligoDNA labeled with Cy3 (1 μ M in TE buffer) was supplied through microchannels. 10 μ L of sample solution was sucked into the PEEK tube, then supplied to microbeads. Figure 3 shows fluorescent micrographs of signals from bead-labeling dye and target DNA (Cy3). Results on each bead (5,551 beads fixed on a chip) were obtained by image analyses. While 98 % of the beads with probe DNA showed fluorescent signals of target DNA, only 3 % of surface-blocked beads showed the signal. Thus, selective capturing of target DNA in this microfluidic bioarray was confirmed (Table 1).

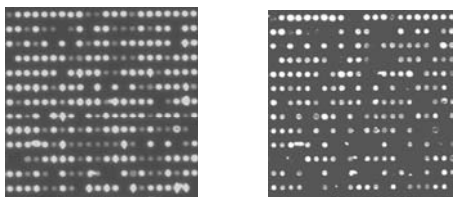


Figure 3 Fluorescent micrographs of signals from
(a) bead-labeling dye and (b) target DNA (Cy3).

Table 1 Numbers of the beads with each fluorescent signals.

Beads with Fl. from bead-labeling dye		Beads with Fl. from target DNA with Cy3	
Weak	1602	48	(3.0 %)
Intense	3949	3873	(98.1%)

5. Conclusions

Microstructures for fixing microbeads with 10 μ m diameter were designed and fabricated by LIBWE method. Microbeads can be successfully arranged into the microstructures. A microfluidic device could be fabricated by sealing the microstructures with a PDMS plate and coupled with PEEK tubing for supplying sample solution. Performance of thus fabricated microfluidic device was examined by fluorescent microscopic observations. Selective DNA capturing at the surface of microbeads were confirmed.

Acknowledgements

This work was supported in part by the Industrial Technology Research Grant Program in '05 from the New Energy and Industrial Technology Development Organization (NEDO) of Japan.

References

1. J. Wang, H. Niino and A. Yabe, *Appl. Phys. A*, **68**, pp.111-113, (1999).
2. D. R. Walt, *Science*, **287**, pp. 451-452 (2000).
3. T. Gumpenberger, T. Sato, R. Kurosaki, A. Narazaki, Y. Kawaguchi and H. Niino, *Chem. Lett*, **35**, pp.218-219 (2006).
4. T. Maruyama, L.-C. Park, T. Shinohara and M. Goto, *Biomacromolecules*, **5**, pp.49-53 (2004).

DEVELOPMENT OF A 3D HYBRID Si/POLYMER TECHNOLOGY FOR INTEGRATING ACTIVE Si CHIPS IN MICROFLUIDIC SYSTEMS

Samuel Charlot, Anne-Marie Gué, Josiane Tasselli, Antoine Marty, Patrick Abgrall, Daniel Estève
LAAS-CNRS, 7 Avenue du Colonel Roche, Toulouse, France
gue@laas.fr

Abstract

This paper describes a new technology permitting a hybrid integration of silicon chips in polymer (PDMS and SU8) microfluidic structures. This two steps technology starts with reporting and planarizing the silicon device on a rigid substrate (typically PCB) and then it proceeds with stacking of the polymer-made fluidic network onto the device. The technology is low cost, based on screen-print and lamination, can be applied to treat large surface areas and is compatible with standard photolithography and vacuum based approaches. We show, as an example, the integration of a thermal sensor inside channels made of PDMS or SU8. The developed structures had no fluid leaks at the Si/polymer interfaces and the electrical circuit was perfectly water-proof.

Keywords : Hybrid Si/polymer integration, 3D microfluidic integration

1. Introduction

Integrating small size devices, such as silicon sensors or actuators, into polymeric microfluidic systems is still a challenge even if several approaches have already been reported [1-3]: existing hybrid assembly technologies provide precision that is poorly compatible with characteristic channel dimensions and do not allow complex microfluidic integration. It is becoming obvious that different solutions for complete low cost silicon/polymer hybrid integration must be explored to obtain the full benefits of the advantages of integration. This paper proposes a new method to integrate silicon devices in complex networks of microfluidic channels on large areas. In order to meet high precision and low cost requirements this technology is based on classical photolithography and low cost screen-printing and roll to roll approaches.

2. Development of the integration technology

The general idea is to report the silicon devices onto a rigid substrate that will provide electrical connections to external instruments and then to planarize the silicon chips in order to get a perfectly flat surface on which we can perform standard microtechnology operations. A schematic description of the complete process is given in figure 1. The first step of the process is to glue the silicon device onto the rigid substrate on which conductive tracks and pads have already been patterned. In order to prepare inter level electrical vias, 3D pads of conductive ink are screen printed (Figure 1b; left). The ink is a highly thixotropic epoxy based paste and the pads typical diameter is 1mm corresponding to a 700 μ m height.

Figure 2 gives detailed and general view of those inter level connecting pads. In the next step, both silicon chip and 3D pads are planarized (fig.1-c, left) with an elastomer (PDMS) in order to bring the chip surface and the polymer surface at the same level. A screen-printing technology is also used to perform this task as it can process large areas (commonly required in microfluidics applications) with rather good precision (from 10 μ m to several 10 μ m). If necessary, an adhesion promoter can be sprayed over the PCB before screen-printing to allow a uniform coating. The PDMS viscosity and thixotropy have been carefully chosen in order that no polymer flows over the Si device. A PDMS roll, that never exceeded 10 μ m, has been frequently observed at the rim of the Si chip.

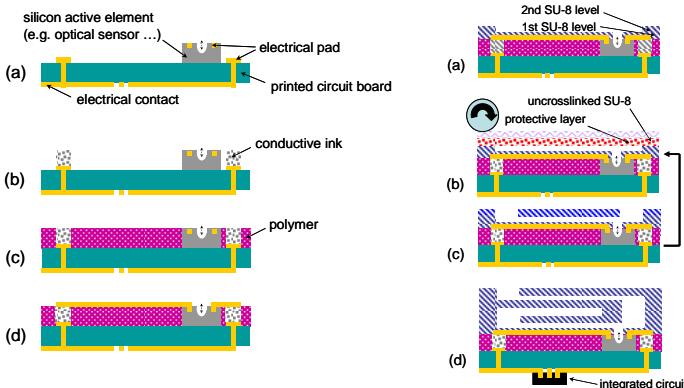


Figure 1: Schematic description of the integration process.
 Left: (a) assembly of the silicon chip onto the PCB, (b) realization of conductive pads,
 (c) planarization of the Si Chip, (d) patterning of electrical contacts.
 Right: (a) to (d) realization of the 3D channel network

Then, electrical contacts between the chip connecting pads and the PCB pads were made. Several methods, for making the electrical contacts, have been tested as illustrated in figure 3: screen printing of a conductive paste, spray of an Ag lacquer. Due to the planarity of the upper surface, photolithography or shadow mask techniques and vacuum deposition technologies as evaporation or sputtering can be used. The shadow mask technique has finally been selected as it is compatible with low dimensions ($<100\mu\text{m}$), high precision (several μm) and avoids the photolithographic step which is not very well suited for non silicon supports.

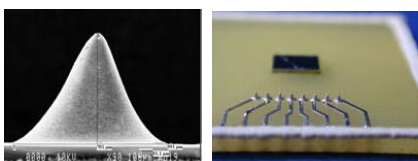


Figure 2: a) MEB photography of an epoxy based conductive pad after screen-printing, b) general view of screen-printed pads connected to the PCB tracks.

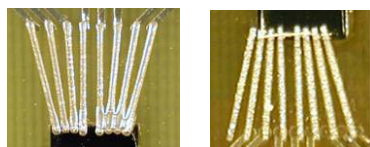


Figure 3: Electrical connection between the Si device and the PCB obtained by a) screen printing (note short-cut between tracks) and b) spray (note misalignment and poor quality of the deposited layer)

Then the channels network was realized (figure 1, right) either by reporting an already structured PDMS network or by stacking a 3D SU8 structure, layer by layer, as described previously in [4].

3. Validation of the technology

As an example, the integration of a thermal sensor in a simple microfluidic structure has been performed using this low cost technology. As shown in figure 4, the sensor has an overall dimension of $5000\mu\text{m} \times 3500\mu\text{m}$ and provides two sensing areas supported by a thin dielectric membrane (bright areas on the picture). Two types of microfluidic structures have been then reported onto the planarized sensor without breaking the membranes: a single channel previously molded in PDMS (Sylgard 184) and a SU8 structure which has been laminated level by level onto the sensor.

As the planarizing material is also an elastomer, sticking the PDMS microfluidic structure is straightforward and efficient. The electrical continuity between the sensor and the connecting pads of the PCB was verified and the channel was filled up with a fluorescent buffer. Figure 5 demonstrates clearly that the fluid flew strictly in the channel and that no leak occurs at the silicon/PDMS interface. The stability of the sensor electrical behavior indicated also that the electrical “network” is perfectly insulated from the fluidic network.

Stacking the SU8 microfluidic structure onto the planarized sensor was a little bit difficult as the SU8 layer has to be reported prior it is isolated and cross-linked. As a matter of fact, the solvent evaporating from SU8 degraded the PDMS/SU8 interface and it was necessary to process an intermediate SU8 layer prior the realization of the microfluidic channels.

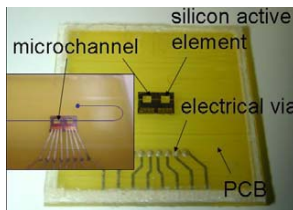


Figure 4. Si thermal sensor (sensitive areas in bright) in a microfluidic channel showing connecting tracks and pads

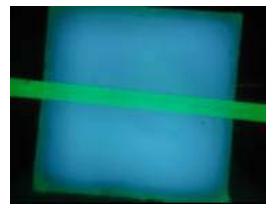


Figure 5. Fluid channel (in green) over the sensitive area (in blue). The perfect definition of the channel demonstrates that no leak occurs at the silicon/polymer interface

4. Conclusion

This study has shown that integrating Si devices in polymer fluidic system is achievable combining low cost approaches with conventional microtechnologies. A first and simple example has been performed that will open the ways to various improvements and opportunities. In particular, this technology can be easily extended to the integration of active devices into 3D systems at various levels or to the integration of hybrid flexible systems without rigid support.

Acknowledgments:

The authors would like to thanks the Novatec Society (Montauban, France) for its technical support for developing the screen-printing steps.

References

1. C.G.J. Schabmueller, M. Koch, A.G.R. Evans, A. Brunnenschweiler, Design and fabrication of a microfluidic circuitboard, *J. Micromech. Microeng.*, 9, 176 (1999)
2. J.M. Yang, J. Bell, Y. Huang, M. Tirado, D. Thomas, A.H. Forster, R.W. Haigis, P.D. Swanson, R.B. Wallace, B. Martinsons, M. Krihak, An integrated, stacked microlaboratory for biological agent detection with DNA and immunoassays, *Biosens. Bioelectron.*, 17, 605 (2002)
3. R.H. Liu, J. Yang, R. Lenigk, J. Bonanno, P. Grodzinski, Self-Contained, Fully Integrated Biochip for Sample Preparation, Polymerase Chain Reaction Amplification, and DNA Microarray Detection, *Anal. Chem.*, 76, 1824 (2004)
4. P. Abgrall, C. Lattes, V. Conédéra, S. Colin and A.-M. Gué, Journal of Micromechanics and Microengineering 16 (2006) 113-121

DEAD VOLUME FREE AND USER-FRIENDLY ONE TOUCH LOCK AND DETACHABLE MICROFLUIDIC CONNECTOR (2)

**Kenji Katayama¹, Keisuke Morisima², Yoshikuni Kikutani³,
Mitsuo Kitaoka⁴, and Takehiko Kitamori⁵**

¹Chuo University, 1-13-27 Kasuga Bunkyo Tokyo 112-8551, Japan

²Tokyo University of Agriculture and Technology, 2-24-16 Naka, Koganei, Tokyo 184-
8588, Japan

³Kanagawa Academy of Science and Technology,

3-2-1 Sakado, Takatsu-ku, Kawasaki City, Kanagawa, 213-0012, Japan

⁴The Research Association of Micro Chemical Process Technology,

Tamei Bldg., 3-22 Kanda Ogawamachi Chiyoda Tokyo 101-0052, Japan

⁵The University of Tokyo, 7-3-1 Hongo Bunkyo Tokyo 113-8551, Japan

E-mail: kkatayama@chem.chuo-u.ac.jp

Abstract

Solution for problems of connection between a microchip and tube was given. The holder with BNC-type connection adapters was developed for easy connection and positioning. Two types of detachable connectors was developed; One of them features high withstand pressure for liquid leakage and small dead volume, and the other features easy handling for connection and simple fabrication.

keywords: *micro connector, detachable connector*

1. Background

In the field of microchemistry much attention has been paid for methods for controlling a very small amount of liquid inside microchannels. Various types of devices such as valves, pumps and connectors have been developed for microchemical applications. Conventionally, micro connectors were attached to a microchip with adhesives or polymers, and it is difficult to reuse not only the connector but also a microchip. Most of micro connectors use a rubber o-ring at the contact between a connector and a microchip, and for this type of connector dead volume around a few micro liter cannot be negligible and it does not have enough leak withstand pressure.

To solve these problems, one-touch detachable microconnector has been developed, and it features no adhesives, one touch connection, and good corrosion resistance for chemicals. [1,2]. In this paper, we have developed two different kinds of micro connectors. One of them features high withstand pressure for liquid leakage and a small amount of dead volume (High performance connector). Although this gives a best performance for leak withstand pressure, precise positioning between a microchip and a connector is necessary, and complicated processing has been applied for the tip of a connector. Then, the other features easier positioning and machine-processing, while remaining the detachable mechanism (Simple connector).

2. Experiments and discussions

The pictures and drawings of a high-performance connector and simple connector are shown in fig.1, respectively. Both types of connectors have a connection mechanism similar to that of a BNC electric cable and they can be connected 90 degree turn after pushing down to a microchip. A holder for the BNC-type connector was developed, which has 8 connection holes with a female BNC connection adapters. The connection procedure is shown in fig.2, and it was simplified compared with the procedures for conventional screw-type or adhesive-type connectors. Furthermore, problems such as break of a microchip or liquid leakage were resolved because pushing force of a connector to a microchip remains constant and does not depend on user.

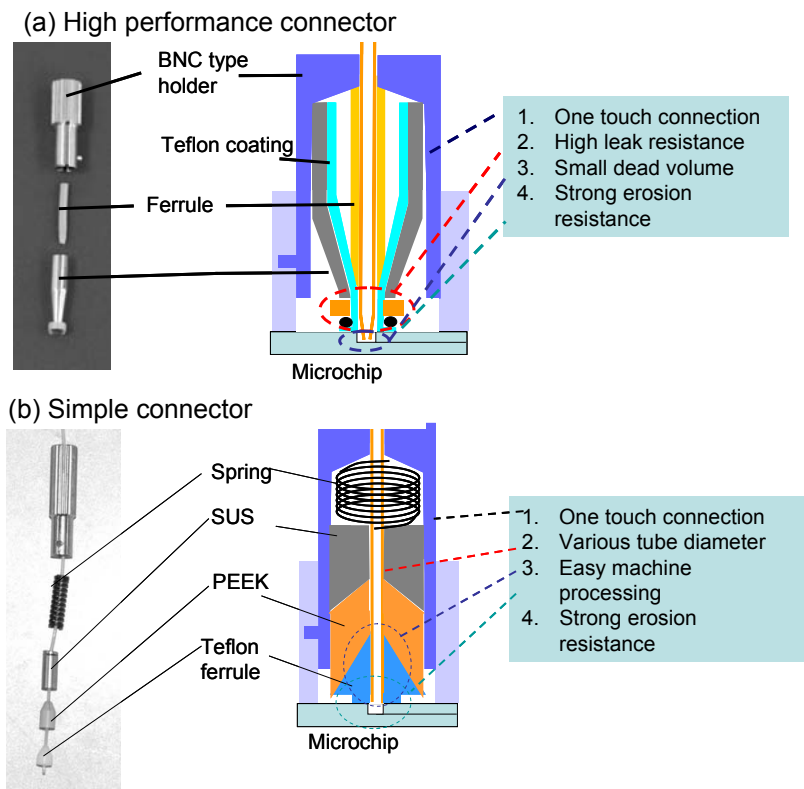


Fig.1 Pictures and drawings of a high performance connector (a) and simple connector (b).

In both types, a surface contacting a microchip was made of Teflon, and then it is strong resistance for chemicals corrosion. The high performance connector has a two-step flange

structure, which gives a high withstand pressure for liquid leakage. It was confirmed that the withstand pressure was 25 MPa on average, checked by repeated attachment test. Furthermore, the tip of the PEEK tube itself was tapered off and it can be directly put into a reservoir of a microchip, which gives a smaller amount of dead volume (30 nl). For the simple connector, the contact part to a microchip was a ferrule structure and this type of parts is easy to fabricate and then various tube types with different diameters can be used. The second ferrule made of PEEK was used for slip resistance between a tube and connector, and the tube is not slipped off by this structure. Force for pushing down to a microchip was added by a spring, and then longitudinal positioning deviation between a connector and a reservoir is allowed because the spring adjusts the strength of downward force. This connector has a withstand pressure for liquid leakage about 5 MPa.

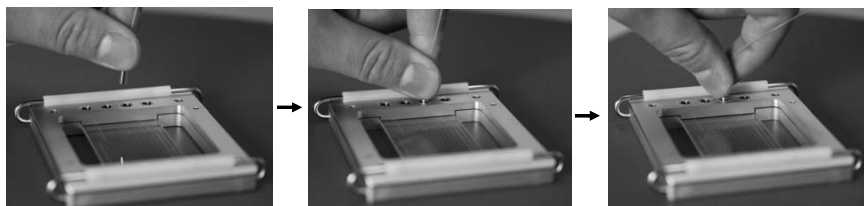


Fig.2 Connection procedures of one touch detachable connector.

Weak points for the high-performance connector is degradation after repeated detachment, and the simple connector does not have high withstand pressure and have a dead volume of 150 μ l. Thus, it is recommended that the high-performance connectors are used at the place where high pressure is loaded, and that the simple connectors are used at other normal places.

3. Summary

The whole solution for connection between a microchip and tube was given. The holder with a BNC-type connection adapter was developed for easy connection and positioning. Two type of connectors was developed and they can be used depending on purpose. Choosing one of these two types of connectors, connections under various conditions in microchemistry can be accomplished for high withstand pressure, small dead volume and simple connection.

Acknowledgement

This work has been supported by a grant-in-aid from the New Energy and Industrial Technology Development, Japan.

References

- [1] K. Morisima, Y. Kikutani, M. Kitaoka, T. Kitamori, MicroTAS'04 pp. 171-173, MicroTAS'05 pp. 647-649.

PATTERNING HYDROPHOBIC AND HYDROPHILIC SAMS IN MICROFLUIDIC DEVICES USING A UV PHOTOLITHOGRAPHY-TECHNIQUE

Eric Besson¹, Anne-Marie Gue¹, Jan Sudor¹, Hafsa Korri-Youssoufi², Nicole Jaffrezic³

¹ LAAS-CNRS, 7 Avenue du Colonel Roche, Toulouse, France

² ICMMO-LCBB UMR-CNRS 8124, Université Paris-Sud, 5 Rue Georges Clémenceau, Orsay, France

³ CEGETY, Ecole Centrale de Lyon, 36 Avenue Guy de Collonges, Ecully, France

Abstract

This work describes how selective patterning of hydrophobic and hydrophilic areas inside microchannels of microfluidic devices can be achieved combining thiol-ene reactions and standard photolithography process (365 nm). The modified surfaces have been characterized by contact angle measurements, AFM and MIR-FTIR. The difference in the contact angles on the hydrophilic and hydrophobic surfaces reached remarkable 77°. We have also demonstrated that this method is compatible with selective surface grafting inside microfluidic channels.

Keywords: Micropatterning, hydrophilic/hydrophobic contrast, wall-free microfluidics

1. Introduction

Patterned hydrophobic and hydrophilic regions inside microchannels typically requires modifying the surface in selected areas first, and then aligning and bonding substrates to form microchannel networks. Recently, Beebe et al. has reported on a patterning of surface free energies inside microchannels by the use of self-assembled monolayers (SAMs) in combination with either multistream laminar flow or photolithography [1, 2]. It was shown that the patterned surfaces in such microfluidic channels play the role of a flow guide. In this article, we describe a novel and simple method for producing hydrophilic / hydrophobic patterns on Si(100) or glass surfaces by UV irradiation. We show that our surface chemistry allows for a fast grafting, surface modification inside a microchannel and it is also compatible with standard photolithography apparatus.

2. Formation of hydrophobic and hydrophilic sams by thiols reaction

The strategy is based on the reaction known in the polymer field [3]: thiol-ene reaction using the benzophenone (BP) as photoinitiator [4] for the formation of hydrophobic surface. After formation of mercaptotripropyl SAMs on silicon wafers or glass, the substrates were UV grafted with aliphatic chains. Under UV treatment, benzophenone abstracted hydrogen from the thiol to generate surface radicals and semipinacol radicals. Subsequently, in presence of a -ene function, the grafting takes place. Figure 1 shows a schematic of the reaction procedure.

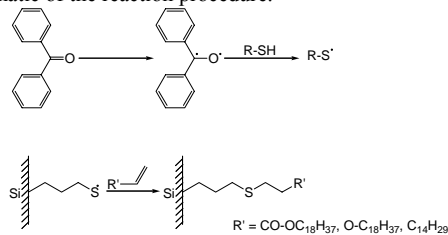


Figure 1: Simplified Schematic Overview of the Photo-Initiated Thiol-ene Free-Radical polymerization mechanism

With this approach, the thiol surfaces can easily be patterned with an aliphatic chain and become hydrophobic. On the other hand, the surfaces not grafted with aliphatic chains can subsequently be oxidized and become hydrophilic (sulfonic acid groups). Three different ene functions were tested for the formation of hydrophobic surfaces by thiol-ene reaction: octadecylvinyl ether, hexadecene and octadecylacrylate (ODA) derivative as it is known that the reactivity of alkenes towards thiol (RS^-) depends on the structure of alkenes groups. To graft the aliphatic chains on the MPTS coated SiO_2 substrates, the surfaces were irradiated using UV light (365 nm) for desired time periods in the presence of the benzophenone and the alkenes. The grafted surfaces were then cleaned in an ultrasonic bath in trichloroethylene and ethanol. Contact angle was used to study the quality of hydrophobic SAMs on glass or silicon.

The first group tested for the grafting reaction with alcene was the octadecylvinylether (0.2M in 1,4-Dioxane, benzophenone 2%w, irradiation time 15 min) but without positive results (may be due to the homopolymerization of the alcene). Then the second product tested was the hexadecene. The exposure time was fixed to 15 minutes. In diluted conditions, with three different solvents and 5% mol of photo-initiator, there is a weak modification of the contact angle but it is not very significant.

Then we studied the grafting of the octadecylacrylate. Different solvents and conditions were tested, such as the photoinitiator concentration, the relative amount of the methacrylate monomer and the reaction time. Both silicon wafer and glass substrates give the contact angles of about 112° and 105° respectively. This suggests that the film is relatively dense. Tapping mode AFM images (figure 2) showed the characteristic features of: silicon surfaces rms roughness of 0.3 nm, MPTS layer rms roughness of 0.45 nm and ODA UV grafted on MPTS rms value 0.55 nm.

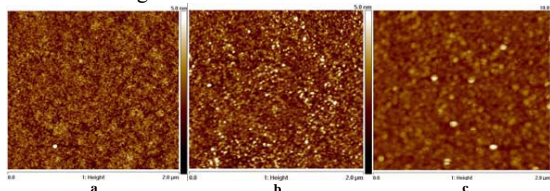


Figure 2: Tapping mode AFM images of a) silicon substrate, b) MPTS monolayer on silicon oxide and c) ODA UV grafted on MPTS.

The Figure 3 shows FTIR spectra of MPTS layer and ODA layer.

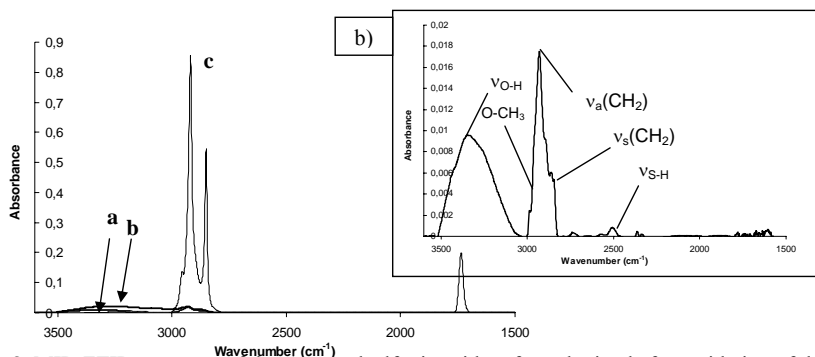


Figure 3. MIR-FTIR spectrum of the a) propylsulfonic acid surface obtained after oxidation of the b) MPTS monolayer and c) after UV grafting of ODA.

Two groups of absorptions can be distinguished in region c. Bandwidths and peak positions of the H-C-H stretch bands, at 2917 ($\nu_{as}(CH_2)$) and 2850 ($\nu_{as}(CH_2)$) cm^{-1} and methyl group of octadecyle at 2944 ($\nu_a(CH_3)$) cm^{-1} and the CH_2 peak intensity increase (compared to MPTS layer) indicate an organization of densely packed hydrocarbon chains. The band at 1733 cm^{-1} can be unambiguously assigned to the C=O stretch of the ester groups.

3. Selective patterning of surfaces with hydrophilic and hydrophobic areas

In order to demonstrate that direct patterning inside channels is feasible, simple microstructures have been manufactured. Channels 500 μm to 1mm wide, 250 μm deep and 8cm long were fabricated in 4" silicon wafers using Deep Reactive Ion Etching (DRIE) and then sealed with a pyrex plate by an anodic bonding technique. Inlet and outlet holes were machined in the pyrex lid prior to the bonding step. In these chips, the large channels acted as reservoirs that confined the reactive solution during the UV grafting step. First, the channels were piranha-cleaned, and a solution of MPTS in trichloroethylene solution (10^{-3} M) was flowed through the microchannels under a N₂ atmosphere. Then, the pyrex/silicon wafers were filled with a grafting solution (octadecylacrylate : 0.5M ; benzophenone : 0.5 %) in 1,4-dioxane. Then, they were positioned on a Karl Süss MA6 mask aligner and irradiated with UV light (20 mW/cm², 365 nm) through a mask. The irradiation time was adjusted to 120 seconds. Various patterns were realised on the same substrate that are shown in the Figure 4. Acetone was introduced inside the channels by capillarity.

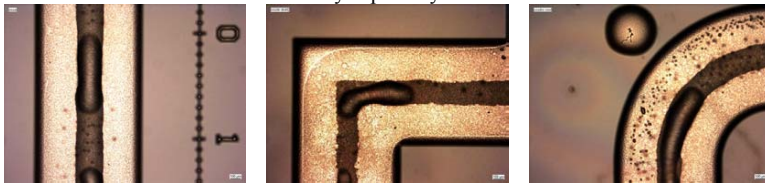


Figure 4. Images of microchannels of different geometries after UV grafting.

Figure 4 shows that acetone flow was clearly delimited to non exposed areas indicating that selective modification inside channels has been performed. The hydrophilic channel width is 300 μm while the micromachined channels are 1 mm wide. We observed that these monolayers allow guiding of the flow along 90° angles or curved virtual channels. We also noticed that edges of the flow pathways were not well defined. This may be a consequence of the diffraction effects during the UV grafting, as the distance between the photomask and the bottom of the silicon channel was about 300 μm . Noting that due to the short lifetime of the benzophenone radicals in their triplet state (80 – 120 μs), the distance diffused by the photoinitiator radicals ($D \sim 10^{-5} cm^2/s$) is negligible ($\sim 0.35 \mu m$) compared to the size of the surface defects (\sim few μm). We conclude that mainly the irradiation process has to be improved in order to overcome this effect.

Acknowledgments:

This work has been supported by the Programme "Nanoscience, nanotechnologies" of the French Ministère de la la Recherche. The authors would like to thank N. Rochat, F. Vinet and F. Martin from CEA-LETI for performing IR measurements.

References

1. Zhao, B.; Moore, J.S.; Beebe, D.J. *Anal. Chem.* **2002**, 74, 4259
2. Zhao, B.; Viernes, N.O.L.; Moore, J.S.; Beebe, D.J. *J. Am. Chem. Soc.* **2002**, 124, 5284
3. Hoyle, C.E.; Lee, T. Y.; Roper, T. *J. Polym. Sci. Part A : Polym. Chem.* **2004**, 42, 5301
4. Allen, N. S.; Hardy, S. *J. Appl. Polym. Sci.* **1991**, 42, 1169

ADDRESSABLE PROTEIN AND CELL PATTERNING VIA SWITCHABLE SUPERHYDROPHOBIC MICROARRAYS

Jau-Yeh Shiu and Peilin Chen*

Center for Applied Sciences, Academia Sinica, 128, Section 2, Academia Road, Nankang, Taipei 115, Taiwan

Abstract

We have fabricated a switchable superhydrophobic surface by a combination of a roughened surface and the electrowetting effect. Using such a switchable superhydrophobic device, we are able to pattern biomolecules such as IgG and cells in a microarray format. Our result indicated that the biomolecules patterned by this approach still retained their activity.

Keyword: superhydrophobic surface, protein array, cell array, nanostructure, cell adhesion

1. Introduction

There have been increasing research interests in the development of novel nano or micro-patterning techniques to create arrays of functional biomolecules for miniaturized assays, which could be used in various biomedical applications such as biosensors, proteomic, immunoassays or drug screening [1-2]. Several techniques have been demonstrated capable of “writing” or “printing” biomolecules with very high degree of spatial control including dip-pen lithography, nanopipet, inkjet printing, photolithography, micro contact printing etc. The serial writing techniques provide the individual addressability whereas the parallel printing processes offer easy and fast protein patterning. However, it remains difficult to create complex patterns, such as functional multicomponent protein arrays, in parallel with individual addressability. In this paper we describe a novel approach to fabricate functional multicomponent protein and cell arrays where the electrowetting effect was employed to convert a water-repellent superhydrophobic surface into a wettable one allowing fast but addressable protein and cell deposition on the otherwise protein- and cell-resistant superhydrophobic surface.

2. Experimental

To create a switchable superhydrophobic surface using electrowetting, a layer of 5 μm thick fluoropolymer poly [tetrafluoroethylene-co-2,2- bis(trifluoromethyl)-4,5-difluoro -1,3-dioxole] (Teflon AF, DuPont) was spin-coated on the ITO glass and followed by an oxygen plasma treatment. It was observed that depending on the period of oxygen plasma treatment, the water contact angle measured on the roughen fluoropolymer surface can be as high as 170^0 . To induce a transition from the superhydrophobic state to the completely

wetted state, an AC voltage (300V, 150 Hz) was applied to the ITO glass. As seen in figure 1, the water contact angle on the roughened fluoropolymer surface can be switched from ~167° to < 10°. In contrast, when the same voltage was applied to an ITO glass coated with a layer of flat fluoropolymer, the water contact angle was changed from 120° and 60°.

3. Results and Discussions

To pattern biomolecules and cells by the switchable superhydrophobic surfaces, a 4 x 4 microarray of electrodes ($200 \times 200 \mu\text{m}^2$) was created on the ITO glasses using a standard photolithographic process and wet etching. The electrode surfaces were converted to hydrophobic by coating a thin film of fluoropolymer (Teflon AF, DuPont). A microarray of superhydrophobic surfaces matching the patterns of the electrode array can be manufactured using an oxygen plasma treatment and a layer of patterned photoresist. The superhydrophobic microarray can be switched to the wetted state by applying proper voltage. To pattern proteins using a switchable superhydrophobic microarray, a drop (15 μl) of phosphate buffered saline (PBS) solution containing green-fluorescent FITC conjugated anti-chicken IgG (5 $\mu\text{g/ml}$, Sigma-Aldrich) was placed on the superhydrophobic microarray for 1 second with 150 V applied voltage, and then washed by PBS solution (Fig. 2a). To conduct complex assays on the microarray, it is advantageous to access each individual element in the microarray. Shown in figure 2b is a chip patterned with two different proteins: FITC conjugated anti-chicken IgG (5 $\mu\text{g/ml}$, green) and cy3 conjugated anti-rabbit IgG (10 $\mu\text{g/ml}$, red, Sigma-Aldrich). To show that the protein microarray produced by this approach did not lose its activity, goat IgG (50 $\mu\text{g/ml}$, Sigma-Aldrich) was first patterned on the microarray using the same process, and then a drop (15 μl) of red-fluorescent TRITC conjugated anti-goat IgG (20 $\mu\text{g/ml}$, Sigma-Aldrich) was placed on the microarray for 10 minutes without any applied voltage. Our result indicated that 55% of the patterned proteins retained their activity. The same patterning scheme can be extended for cell patterning. To pattern cells, fibronectin molecules were first patterned on the selective microarray elements and then the fibroblast cells were seeded on the chip and incubated in a CO₂ incubator at 37° C for 3 hours. The result is depicted in figure 3.

4. Conclusions

In conclusion, we have demonstrated a novel multicomponent protein patterning technique using the switchable superhydrophobic surfaces. It has been shown that each element on the switchable superhydrophobic microarray could be addressed individually and different types of functional biomolecules could be selectively deposited on the microarray. In addition, cells can also be patterned on the same chip using the same approach.

Acknowledgements

This research was supported in part by National Science Council, Taiwan under contract 95-2120-M-001-005

References

1. G. MacBeath, S.L. Schreiber, *Science* **2000**, 289, 1760-1763.
2. D.S. Wilson, S. Nock, *Angew. Chem. Int. Ed.* **2003**, 42, 494-500.

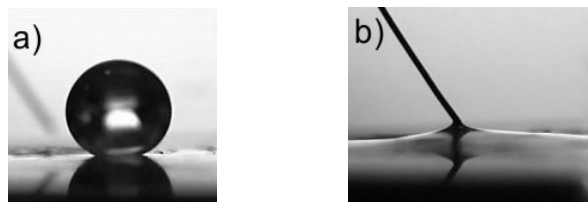


Figure 1. The contact angles measured on the roughened Teflon surface are a) 167° before and b) $<10^{\circ}$ after applying voltage to the substrate.

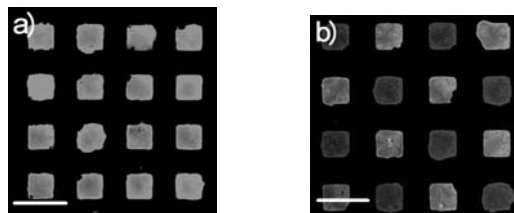


Figure 2. (a) Fluorescence image of the patterned FITC conjugated anti-chicken IgG on the switchable superhydrophobic microarray. The applied voltage was 150 V. (b) Fluorescence image of the patterned FITC conjugated anti-chicken IgG (green) and cy3 conjugated anti-rabbit IgG (red). Bar: 400 μm .

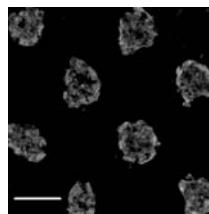


Figure 3. Fluorescence image of the patterned fibroblast cells. Bar: 400 μm .

SUPERHYDROPHOBIC SURFACES FOR MICROFLUIDIC APPLICATIONS

**Yasemin Koç¹, Paul Roach², Carole C. Perry², Michael I. Newton²,
Glen McHale², Andrew deMello¹, Neil J. Shirtcliffe²**

¹Imperial College London, South Kensington, London, SW7 2AZ, U.K.

²Interdisciplinary Biomedical Research Centre, School of Biomedical and Natural Sciences, Nottingham Trent University, Nottingham, U.K

Abstract

Protein adsorption is of major importance in many contemporary research fields including biotechnology and materials science. Chemical modification of surfaces provides a simple and direct way of controlling the nature of protein surface interactions. In the current studies, we demonstrate the use of superhydrophobic surfaces within microfluidic systems to allow almost complete removal of adsorbed protein under flow conditions. Our aim is to use such ‘surface technology’ in PCR microfluidic devices for continuous flow PCR to hinder enzyme loss due to adsorption and therefore increase the efficiency of the reaction.

Keywords: PCR, surface adsorption, superhydrophobic surfaces, ZnO

1. Introduction

The most investigated biological reaction within microfluidic systems is DNA amplification via the polymerase chain reaction (PCR). A variety of microfabricated devices for PCR have been reported and in most improvements in reaction times, sample throughput and reaction efficiency have been observed. An essential feature of all such developments is improved thermal and mass transfer on the small scale. Heat can be rapidly transferred to and removed from reaction environments allowing temperatures to be controlled uniformly throughout the sample volume. Unfortunately, when compared with conventional macroscale thermocyclers for PCR, microfluidic environments are typically characterized by extremely high surface-to-volume ratios. This means that surfaces play a dominant role in defining the efficiency of PCR through increased molecule-surface interactions. In a multi-component reaction system where the concentration of several components needs to be maintained the problem is particularly complicated. For example, inhibition of PCR is commonly observed due to polymerase adsorption at chip walls [1].

A number of surface passivation methods have been employed to reduce surface-molecule interactions within microchannels and thus create inactive surfaces that generate minimal interference with PCR. For example, silanization followed by dynamic coating [2][3][4] or polymerization steps [5] have been demonstrated with varying degrees of

success. Interestingly, surface treatments which involve a silanization step followed by coating with polyvinylpyrrolidone (PVP) and polyethylene glycol (PEG) have been performed to yield surfaces with contact angles of 95° and 70°. Since such coating methods often demonstrate inconsistent results we have investigated a new approach for generating superhydrophobic microchannel surfaces.

2. Experimental

In the current studies we have generated superhydrophobic surfaces with contact angles in excess of 150°, to hinder protein adsorption, particularly under flow conditions. Aqueous solutions in contact with some superhydrophobic surfaces are suspended by bridging-type wetting, and therefore the fraction of the surface in contact with the aqueous layer is significantly lower than for a flat surface, Figure 1. In addition, the non-wetted areas allow slippage between water and the surface, allowing zero flow boundary conditions to be broken and therefore greatly increasing flow rates near the wall for a given bulk flow rate or pressure drop. This would increase the shear stress on material, such as protein, adhered to the superhydrophobic surface.

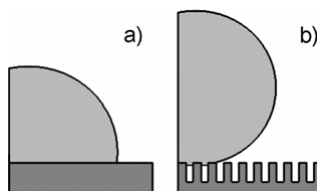


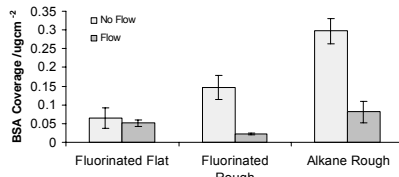
Figure 1. Wetting on a) hydrophobic and b) superhydrophobic surfaces

Glass microscope slides were used as flat substrates and slides coated with a porous silica sol-gel film were used as rough substrates. Surfaces were then chemically coated with either a fluorocarbon (Grangers Wash-In Solution) or trimethylchlorosilane (Aldrich). Adsorption of two serum proteins (fibrinogen and albumin) onto flat and rough surface was assessed using a Nano Orange fluorescent assay (Molecular Probes). This method allows accurate determination of protein concentration down to the ng/ml range. Further studies using albumin were conducted to examine the effects of flow on protein desorption and variation between alkane and fluorinated surfaces.

3. Results and Discussion

Albumin was found adsorb in higher amounts to rough surfaces than to flat. After surface washing the amount of protein remaining on flat surfaces is only slightly reduced, whereas for rough surfaces significant protein desorption is observed (Figure 2).

Additionally, albumin is observed to interact more strongly with fluorinated surfaces than alkane terminated surfaces. Under flow (washing) conditions adsorbed protein is removed



from the superhydrophobic surfaces more efficiently than from the hydrophobic surfaces.

Figure 2. Protein adsorption on hydrophobic and superhydrophobic surfaces with varying chemistry

4. Conclusion

It is observed that under flow conditions protein can be removed from superhydrophobic surfaces, with more pronounced desorption occurring from fluorinated surfaces. Presented studies also include protein adsorption measurements on superhydrophobic surfaces containing copper hydroxide or zinc oxide needles (Figure 3). It is expected that nanostructured surfaces of this kind can be used to precisely control surface molecule interactions within microfluidic systems. Moreover, it is hoped that control of the morphology of such nanostructured surfaces can be used to significantly reduce the strength of protein-surface binding under both static and flow conditions.

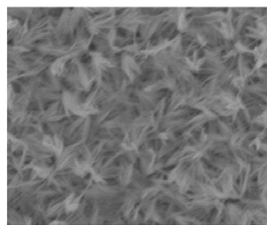


Figure 3. TEM image of copper hydroxide needles

Acknowledgements

The author's would like to thank Smiths Detection Plc for the provision of a research studentship

References

1. Krishnan, M., D.T. Burke, and M.A. Burns, .Analytical Chemistry, 2004. **76**(22): pp. 6588-6593.
2. Obeid, P.J., et al., Analytical Chemistry, 2003. **75**(2): pp. 288-295.
3. Kopp, M.U., A.J. de Mello, and A. Manz, Science, 1998. **280**(5366): pp. 1046-1048.
4. Chiem, N. and D.J. Harrison, Analytical Chemistry, 1997. **69**(3): pp. 373-378.
5. Munro, N.J., A.F.R. Huhmer, and J.P. Landers, Analytical Chemistry, 2001. **73**(8): pp. 1784-1794.

SURFACE MODIFICATION AND PHOTOGRAFTING OF COC WITH TRYPSIN FOR PROTEOLYTIC DIGESTION OF PROTEIN SAMPLES

Mohamed Bedair, Roxanne Lewis, Brian Ballios and Richard Oleschuk

Department of Chemistry, Queen's University, Kingston, Canada

Abstract

Microfluidic devices provide an inexpensive, rapid, low sample consumption means of protein digestion. Here, cyclic olefin copolymer chips have been photografted with either glycidyl methacrylate or acrylic acid and following trypsin was immobilized on the grafted structure. Cytochrome C and bovine serum albumin were digested through the microfluidic channels and studies were performed to determine the concentration and residence time limitations of the enzyme reactor.

Keywords: photo-patterning, surface modification, proteomics, cyclic olefin co-polymer

1. Introduction

Polymeric microfluidic devices have been increasingly utilized in sensors and lab-on-a chip fabrication. The ability to modify or pattern molecules in the channels of bonded chips is advantageous for the construction of separation columns, electrophoretic mixing elements and microreactors. We report the development of a patterned enzyme micro reactor fabricated by covalently immobilizing trypsin on photografted regions of the cyclic olefin copolymer COC channels. Following hot embossing and thermal bonding of the COC microfluidic chip, trypsin was photo patterned for 50 mm of the COC channel surface using two different immobilization chemistries. The first method utilizes COC photografted with glycidal methacrylate(GMA) followed by acid hydrolysis of the epoxy group to glycol, and the subsequent oxidation to an aldehyde using periodic acid. Following the trypsin was then covalently bonded using reductive amination. The second method used COC photografted with acrylic acid (AA), followed by activation of the carboxylic group with *N*-(3-Dimethylaminopropyl)-*N'*-ethylcarbodiimide in presence of *N*-hydroxysuccinimide, which formed an amide bond with trypsin.

The performance of the enzyme microreactors were studied in terms of amount of protein digested, residence time of the protein and flow rate through the micro-reactor. All digested protein fragments were analyzed using matrix-assisted laser desorption ionization time-of-flight mass spectrometry. Cytochrome C was identified with residence times as short as 4.5 sec and as little as 15 femtomoles of protein. Both methods of immobilization

created enzyme micro-reactors that performed protein digests, although the GMA reactor yielded higher sequence coverage for cytochrome C digests (80% with 3 missed cleavages) as shown by the MALDI-MS analysis. A maximum sequence coverage was obtained using a cytochrome C solution concentration of 2 μ M digested through a GMA enzyme microreactor with a flow rate of 0.5 μ L/min for 2 hours. It was also possible to digest bovine serum albumin with a residence time of 48 seconds however it required denaturation with dithiothreitol to facilitate reasonable sequence coverage 23%.

Figure 1: Immobilization of trypsin on GMA derivatized surface

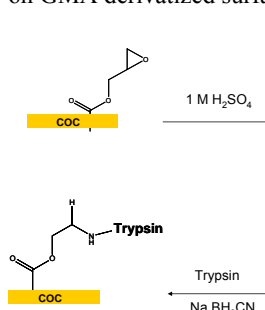


Figure 2: Immobilization of trypsin on AA derivatized surface

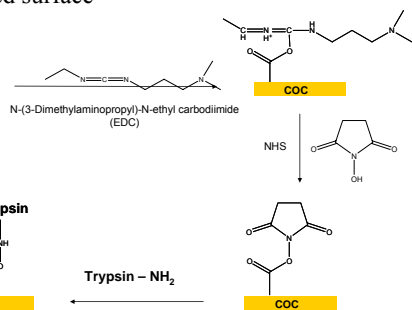


Table 1: Effect of photo-grafting conditions on the contact angle of the COC

Monomer	Solution 1 ^a 20 min	Solution 1 40 min	Solution 2 ^b 40min/PEGDA	Bulk 1 ^c 40 min	Bulk 2 ^d 40 min/PEGDA
AMPS	72.1 (\pm 5.7)	65.2 (\pm 5.7)	39.8 (\pm 5.7)		
GMA	75.3 (\pm 2.7)	64.5 (\pm 6.7)	59.2 (\pm 5.9)	75.7 (\pm 4.9)	70.8 (\pm 5.1)
AA	70.8 (\pm 5.7)	64.9 (\pm 5.0)	54.4 (\pm 5.7)	60.6 (\pm 5.4)	61.3 (\pm 5.0)

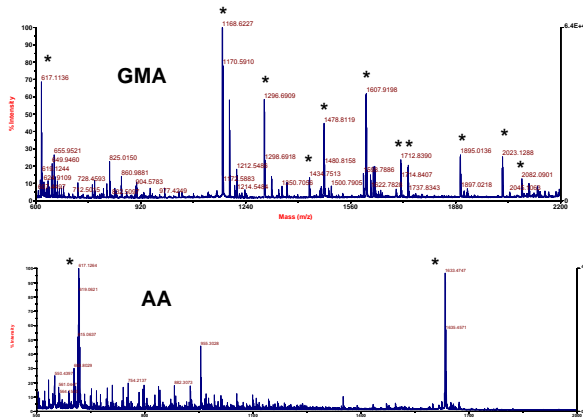
^a Solution 1: 15 wt% monomer in 3:1 t-BuOH : H₂O

^b Solution 2: 15 wt% monomer + 15 wt% PEGDA in 3:1 t-BuOH : H₂O

^c Bulk: pure monomer

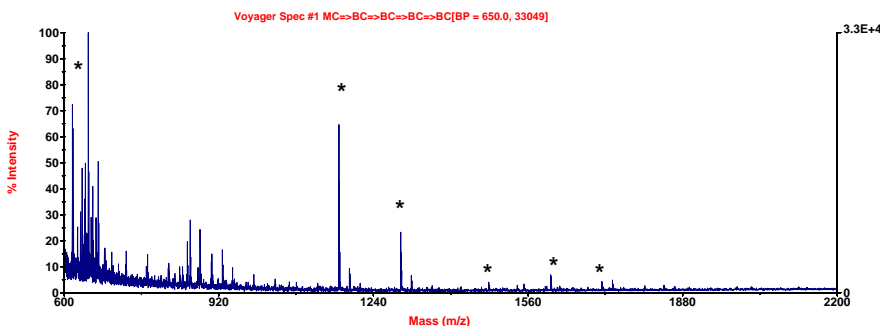
^d Bulk 2: pure monomer + 15 wt% PEGDA.

Figure 3: MALDI-MS Analysis of peptide fragments resulting from proteolytic digestion of cytochrome c in enzyme micro-reactor prepared with two different grafting methods.



Cytochrome C was identified with resident times as short as 4.5 sec and as little as 15 femtomoles of protein. The duration of enzyme microreactor activity was also investigated. After 28 days of inactivity while stored at 4°C, the activity of the enzyme reactor was reduced. The percent sequence coverage with cytochrome C was 33%. These results show the ability to fabricate an integrated enzyme microreactor on-chip, which would be an aid to the development of polymeric lab-on-a-chip devices for proteomic analysis.

Figure 4: COC-GMA-EMR 100 μm channel. Cytchrome c, 500 femtomole, 200 nL/min, resident time 132 sec.



SURFACE PLASMON RESONANCE IMAGING CLARIFIES NON-CROSS-LINKING INTERACTION BETWEEN DNA DUPLEX ON A SUBSTRATE AND DUPLEX ON GOLD NANOPARTICLES

Yasunobu Sato, Kazuo Hosokawa, and Mizuo Maeda

Bioengineering Laboratory, RIKEN, Wako, Saitama, 351-0198 JAPAN

yasunobu_sato@riken.jp

Abstract

Non-cross-linking (NCL) interaction between DNA duplex on a gold substrate and duplex on gold nanoparticles was studied using surface plasmon resonance (SPR) imaging. NCL interaction between different sequences was investigated for the first time. Attractive interactions were observed only with combinations of two matched termini. The order of the attraction strengths was as follows: GC/GC > GC/AT > AT/AT.

Keywords: DNA detection, SPR imaging, Gold nanoparticles, Non-cross-linking interaction

1. Introduction

We previously reported that NCL interaction between gold nanoparticles show selective aggregation of the nanoparticles with fully-matched DNA duplexes (FM-Au) [1]. The application of the NCL method using a microchip was also conducted. It showed selective deposition of FM-Au on a bare gold substrate at high salt concentration [2]. However, both previous studies confirmed interactions only between identical DNA duplexes. In this paper, DNA duplexes were immobilized to the gold substrate as shown in Figure 1. With this setup, NCL interactions between different DNA sequences have been clarified for the first time.

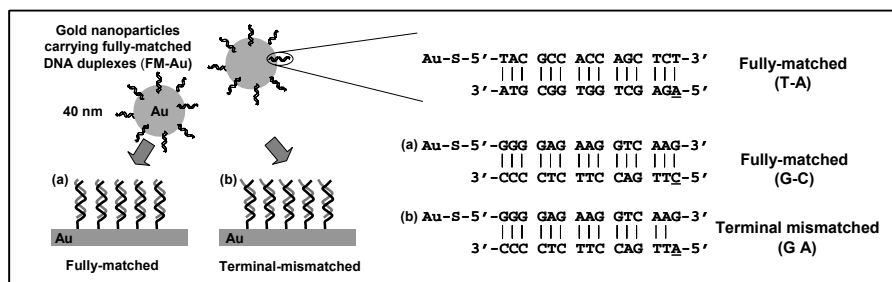


Figure 1. Schematic representation of non-cross-linking interaction applied to a planar surface to investigate hetero-interactions between DNA duplexes.

2. Experimental

A colloidal solution of gold nanoparticles with a diameter of 40 nm was used for preparing DNA conjugated gold nanoparticles. Single-stranded 5'-hexylthiol modified 15 mer oligonucleotide probe was immobilized onto the surfaces of the nanoparticles as described elsewhere [1]. DNA targets were hybridized to the DNA conjugated nanoparticles so that the terminus of the DNA duplex showed fully-matched base-pairing (T-A). We prepared two types of DNA target sensing surfaces: a single DNA probe surface (Figure 2) and a surface showing two different DNA probes in a line array (Figure 4). The single DNA probe surface was prepared by immersing a clean gold substrate to a thiol-modified DNA probe solution. The whole sensing surface was modified with a single DNA probe. The surface was washed and a PDMS microchip with a double Y-shaped microchannel was attached ontop. The line array was prepared using a set of microchannels to create two separate areas with two different DNA probes. After immobilization of the DNA probes the microchannel was detached and a second set of microchannels was attached to the surface perpendicular to the DNA line array. The prepared line array can detect two types of DNA targets on a single microchip.

All SPR experiments were carried out by dispensing the DNA target solution into inlet A and dispensing FM-Au into the other inlet B. Results were analyzed by SPR differential images which show a rise in intensity where refractive index increases. SPR images were taken at the beginning of the mixing of the two solutions (0 min) and at 3 min. A differential image was created by subtracting the 0 min image from the 3 min image using image analysis software.

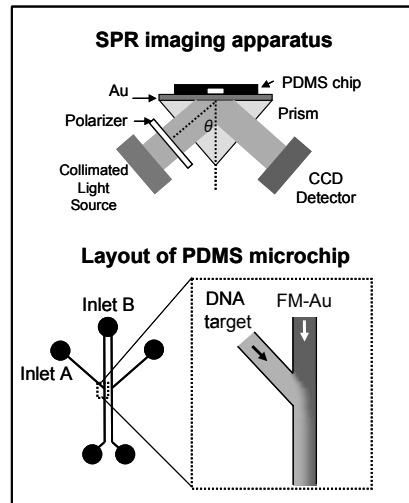


Figure 2. Representation of SPR imaging apparatus and the layout of the PDMS microchip. Channel description: 100 μm (width) \times 25 μm (height).

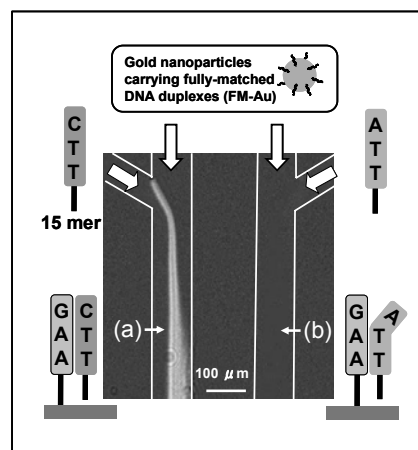


Figure 3. SPR differential image of the double Y-shaped microchannel showing the interaction of FM-Au with (a) fully-matched and (b) terminal-mismatched DNA duplexes.

3. Results and discussion

Figure 3 shows the result of interaction between FM-Au and the DNA duplex surface. The two injected solutions formed a stable laminar flow at the intercept. A significant increase in intensity was observed where DNA probe hybridized with its fully-matched target showing a blunt end (Figure 3(a)). This is a result of FM-Au adsorption onto the surface showing G-C terminus. In contrast, no change in intensity was observed with the single-base mismatched DNA duplex showing GA mismatch (Figure 3(b)). The FM-Au specifically recognized whether the terminal base-pairing was fully-matched or mismatched at the sensor surface. The interaction between different blunt ends (hetero interaction) was confirmed for the first time. A possible explanation of the phenomenon is that DNA duplexes attract each other as a result of helix-stacking which has been observed in DNA molecular self-assembly [3].

Figure 4 shows the result of FM-Au interacting with two different DNA probes in a line array. FM-Au adsorbed onto the two specified areas (c) and (f) showing fully-matched DNA-duplexes. No adsorption of FM-Au to the areas (d) and (e) showing single-base mismatched DNA at the terminus was observed. This result shows possibility of applying the NCL method to detect fully-matched DNA-duplexes on DNA arrays.

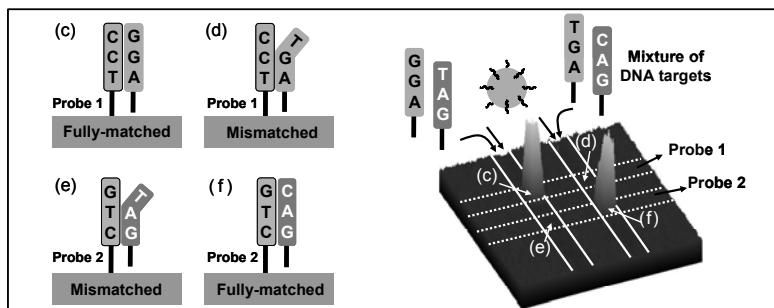


Figure 4. SPR differential image showing a line array detecting two types of DNA targets on a single microchip. (c) and (f) show fully-matched DNA duplexes and (d) and (e) show terminal-mismatched DNA duplexes.

4. Conclusions

We have examined the interaction between DNA duplexes using a planar gold substrate and gold nanoparticles. This format clarified the interaction between different DNA duplexes. Attractive interactions were observed only with combinations of two matched termini. The NCL interaction recognizes whether the terminal base pairing is fully-matched or mismatched.

References

- [1] K. Sato, K. Hosokawa and M. Maeda, *J. Am. Chem. Soc.*, **125**, 8102-8103 (2003).
- [2] Y. Sato, K. Sato, K. Hosokawa and M. Maeda, *Anal. Biochem.*, **355**, 125-131 (2006).
- [3] H. Yan et al, *Proc. Natl. Acad. Sci. U. S. A.*, **100**, 8103-8108 (2003).

RNA-TO-PROTEIN CHIP: AN INTEGRATED MICROARRAY PLATFORM TO BRIDGE GENOMICS AND PROTEOMICS

Manish Biyani¹, Naoto Nemoto¹, Yosuke Hosoi² and Takanori Ichiki²

¹Rational Evolutionary Design of Advanced Biomolecules, Saitama Small Enterprise Promotion Corporation (CREATE), Saitama, Japan

²Center for NanoBio Integration, The University of Tokyo, Tokyo, Japan
(email:sts101@saitama-j.or.jp)

Abstract

A novel protein microarray technique is described in which individual strands of mRNA are anchored and covalently linked to their translated protein product in order to simultaneously synthesize and directly immobilize proteins onto solid-surface. In the resulting mRNA-protein complex, mRNA provides genetic information about the functionally active protein which is insured to adhere onto the surface while properly retained their correctly folded functional content. Therefore, the convergence of microarray technology to RNA-protein fusion techniques enables to embrace the concept of the transformation of DNA/RNA chip-to-Protein chip and thus to the development of high-throughput microarray platform to the field of functional proteomics.

Keywords: Solid-phase mRNA-Protein fusion, Protein immobilization, Protein chip

1. Introduction

Following the completion of genomic DNA sequencing (genetic information) projects, protein microarrays are emerging as an innovative approach with the potential to rapidly profile the entire proteome (functional information) and thus is capable of providing a deeper understanding of protein abundance and revealing novel protein functions.

However, compared with DNA microarray, protein bio-chips provide more challenges and have yet to be perfected due to the complexity and inherent difficulties with protein immobilization. First, in contrast to DNA chips, it is impossible to amplify proteins and thus hard to get enough purified proteins on chip. Second, proteins tend to adsorb non-specifically to solid surfaces, leading not only to the inaccessibility of active sites but also to the possibility of denaturation and loss-of-function. Third, protein-ligand interactions are highly dependent upon the orientation and integrity of the protein conformation. Thus, advancing the cell-free protein synthesis systems to yield functional active protein and subsequent protein immobilization are a significant bottleneck in the advancement of protein microarray technology. In this context, we are focusing on engineering and converging microarray surfaces and protein display techniques to create high-throughput functional protein arrays directly from encoding mRNA, such that the encoded proteins are immobilized on a surface as they are synthesized (see Fig.1).

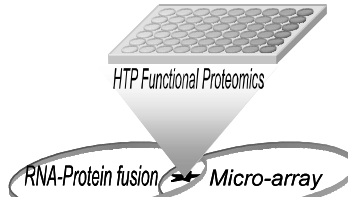


Figure 1. Convergence of display-technology and microarray-technology.

2. General Concept for RNA-to-Protein chip

We present a novel concept and miniaturized platform for simultaneously synthesize and directly immobilize a cell-free translated protein onto solid-surface in more native-state using a joint and solid-phase approach of cell-free translation and puromycin-assisted mRNA-protein fusion technique [1] (Fig.2). A newly constructed biotinylated linker-DNA, that enables puromycin-assisted RNA-protein fusion, is immobilized onto avidin-coated surface. The 3'ends of the mRNA molecules is then ligated to the 5'ends of linker-DNA and thus anchored onto support to enable the subsequent reactions of solid-phase cell-free translation and RNA-protein fusion on surface. The protein products are therefore directly immobilized onto solid-surfaces and synthesized in more native state with proper protein folding and stabilized form.

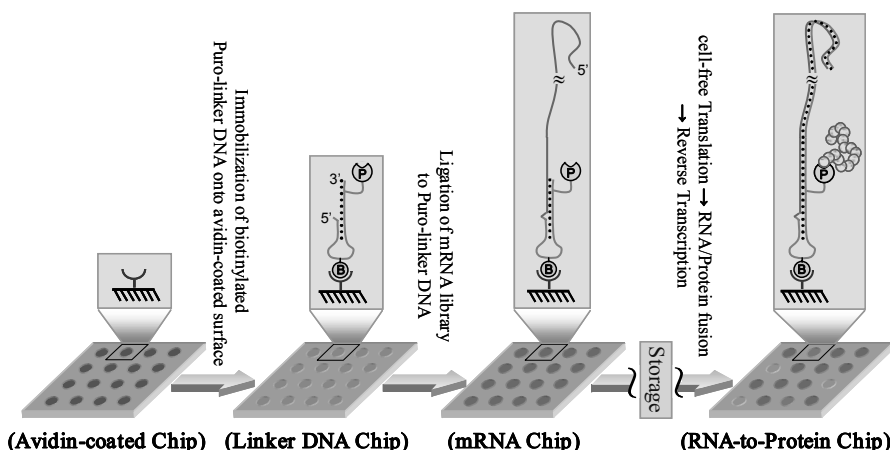


Figure 2. Schematic flow diagram of conceptual scheme of RNA-to-Protein chip. Following the immobilization of biotinylated linker-DNA, which is bearing puromycin at 3'-terminal end, onto avidin-coated surface, the 3'-UTR ends of mRNA is hybridized and ligated to the 5'-terminal end of linker-DNA and thus anchored on surface to use as template for succeeding steps of novel solid-phase cell-free translation and puromycin-assisted mRNA-Protein fusion approach.

3. Results

To build the platform, we have fabricated microreactor array chips comprising of uniformly distributed sub-picoliter scale reactors of $6\mu\text{m}$ in diameter (Fig.3a). Streptavidin (StAV)-coated paramagnetic beads of $3\mu\text{m}$ in diameter were used as solid-surface and arranged into the wells of chip with the best filling ratio of more than 99% by swaying method [2]. Prior to coupling the mRNA to a solid-surface via ligation to a biotinylated linker-DNA which is immobilized to surface of StAV-coated beads, the efficiency of ligation between the mRNA and linker-DNA molecules was optimized with more than 90% efficiency for various length of mRNA ranging from 0.3-1.2 kb. Furthermore, the efficiency of linker-DNA to generate RNA-protein complex was confirmed for shorter (POU-domain of Oct-1, 70 amino acids) and larger (ALR enzyme, 325 amino acids) proteins. For concept validation, we used GFP as the model protein and

constructed a template genome consisting of GFP-mRNA without a stop codon, a requirement for puromycin-assisted RNA-protein fusion. Following ligation and immobilization, bead-bound mRNA was incubated in a wheat germ-based translation system to synthesize an amino-acid chain, and then in high-salt buffer to convert the translation product into the fusion product. The beads were separated from the reaction solution, washed and directly observed by fluorescence microscopy (Fig.3b). Few discernible beads were found to emit green fluorescence. Protein thus immobilized onto solid surface while remain physically linked to their corresponding coded nucleic acids sequences. For confirmation, the solid-phase products were removed from the beads and then analyzed by SDS-PAGE. To further characterize the background or auto-fluorescence effects of beads or artifacts if any, non-fluorescent protein was tested in this system and confirmed. Very intriguingly, we discovered that the proteins synthesized in such-a-manner adopt a more native state and thus the more biological activity in comparison with the conventional liquid-phase approaches.

4. Conclusions

The acquisition of an integrated platform of genome chip and proteome chip, termed as RNA-to-Protein chip, and an effective solution for displaying fully functional proteins in a microarray format with the advantage of robustness, storage, ease of production are developed which are likely to revolutionize the future of proteomics.

Acknowledgements

This research was performed as part of the Rational Evolutionary Design of advanced biomolecules, Saitama (REDS, CREATE) and the PRESTO projects supported by JST.

References

1. N. Nemoto, E. Miyamoto-Sato, Y. Husimi and H. Yanagawa, FEBS Lett. 1997, pp. 405-408.
2. Y. Hosoi, K. Takahashi, M. Biyani, N. Nemoto, T. Akagi and T. Ichiki, Proc. MicroTotal Analysis Systems 2005, Boston, USA, pp. 232-234.

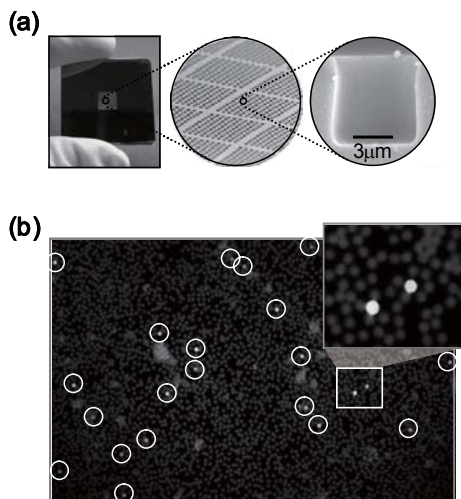


Figure 3. (a) Design and magnified photographs of microchip comprising 10^6 wells with a well volume of 0.15 pl (1chip = 10×10 units; 1 unit = 10×10 subunits; 1 subunit = 10×10 wells). (b) Proof-of-concept validation. Fluorescence microscopy image of bead-bound GFP molecules expressed using solid-phase RNA-protein fusion and visualized in scattered form on glass microscope slide by inverted fluorescent microscope using standard emission filters. White spheres indicate the green fluorescence beads (image with higher magnification are shown in inset). The avidin-coated polystyrene beads are 3 μm in dimension.

NON-BIOFOULING SURFACE FOR MICROCHANNEL DEVICE BY GRAFTING WITH BIOCOMPATIBLE 2-METHACRYLOYLOXYETHYL PHOSPHORYLCHOLINE FOR OBTAINING HIGH S/N RATIO

James Sibarani, Tomohiro Konno, Madoka Takai, Kazuhiko Ishihara

Department of Material Engineering and Center for NanoBio Integration
The University of Tokyo 7-3-1 Hongo, Bunkyo-ku, Tokyo, 113-8656, Japan
Email: ishihara@mpc.t.u-tokyo.ac.jp

Abstract

Preparation of non-biofouling surface for polymer-based microchannel was conducted by constructing biocompatible poly(MPC) brushes on polymer substrates based on living radical polymerization using photoiniferter. Protein adsorption on these modified surfaces significantly reduces compared to on PET substrate and control surfaces.

Keywords: non-biofouling surface, microfluidic device, poly(MPC) brushes, photoiniferter, grafting

1. Introduction

The chemistry and topography of a surface affect biological response and are of fundamental importance, especially when living system encounter synthetic surfaces. To create useful material for many biotechnology applications, interfaces are required that have both enhance specific binding and reduced non specific bonding. Thus, in application such as biosensors, the tailoring of surface chemistry and the use of micro or nanofabrication techniques becomes an important avenue for the production of surface with specific binding properties and minimal background interference [1]. It has already well known that cell-membrane-like surfaces based on 2-methacryloyloxyethyl phosphorylcholine (MPC) is very effective to inhibit blood coagulation on the medical devices or to prevent non-specific biological interactions at the interface of biosensors [2,3]. The aims of this study are to prepare non-biofouling surfaces bearing highly biocompatible poly(MPC) brushes (Fig.1) and to construct micropatterned recognition layers on microfluidic system for enhancing high signal/noise (S/N) ratio in biosensors using living radical polymerization based on dithiocarbamate as photoiniferter (initiator, transfer, and terminator)[4].

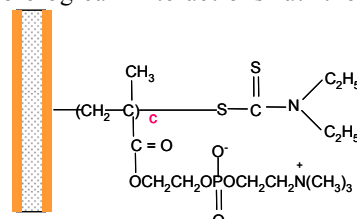


Figure 1 Schematic illustration of the non-biofouling poly(MPC) brush surface

2. Experimental

The Macrophotoiniferters comprised of 2-ethylhexyl methacrylate(EHMA) and 4-vinylbenzyl *N,N*-diethyldithiocarbamate(VBDC) (PEV as shown in Fig. 2) were synthesized with variation of VBDC content of 10% - 40% (PEV10, 20, 30, 40). Ultrasonically cleaned PET substrates were coated by dipping in 0.25% (by weight) of the macrophotoiniferter solutions in toluene. The photoiniferter-coated plates with aqueous solution of 0.3M MPC were irradiated with UV lamp (360 nm) at room temperature with variation of time. The surface characterization of the poly(MPC)-modified surfaces (represented as PEV-g-MPC) was conducted by water contact angle, X-ray photoelectron spectroscopy (XPS), ellipsometry and atomic force microscope (AFM) observation. Protein adsorption resistance of these modified surfaces was investigated by using FITC-labeled bovine serum albumin (BSA) and human plasma fibrinogen (HPF) in PBS solution (pH 7.1).

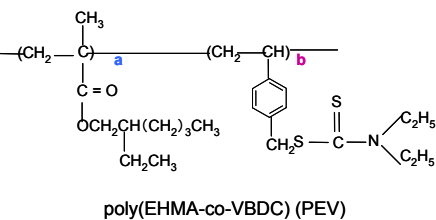


Figure 2 Chemical Structure of macrophotoiniferter

3. Results and Discussion

The non-biofouling surfaces based on biomimetic poly(MPC) brushes were prepared. The density and length of the poly(MPC) brushes which are the very important factors in suppressing the non specific protein adsorption were controlled by composition of VBDC on the macrophotoiniferter and irradiation time respectively. Figure 3 shows the static contact angle of poly(MPC) brush surfaces as a function of iniferter composition. The hydrophilicity of the modified surfaces is greatly improved as can be seen from the decreasing of contact angle from more than 88° to around 20° after 1 hour irradiation indicating that the poly(MPC) chains are well-oriented on the surface and completely covers the surface. Better covering also can be achieved by increasing the density of the poly(MPC) chains. Increasing the length of the

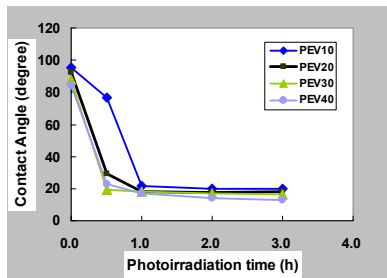


Figure 3 Water contact angle of MPC-grafted PET as a function of photoirradiation time and iniferter density.

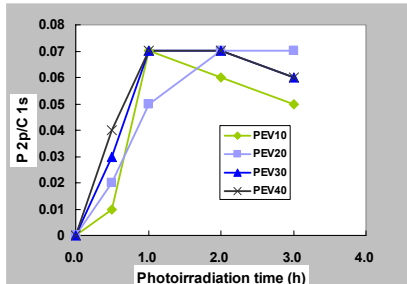


Figure 4 The value of P_{2p}/C_{1s} as a function of photoirradiation time and iniferter density.

poly(MPC) chains only slightly decreases the contact angle (became plateau) due to the complete covering of the surface. Every modified surface had XPS signals at 285 eV, 288 eV, 133 eV, and 403 eV attributed to C_{1s} methylene, C_{1s} carbonyl, P_{2p}, and N_{1s} from grafted poly(MPC) chains. The value of phosphorus/carbon (P/C) ratio increases by grafting time and composition of VBDC unit on the surface, especially in the lower grafting time (Fig. 4). The highest P/C value (0.07) is close to the theoretical one (0.09) indicates the well oriented states of the poly(MPC) layer. The thickness and molecular weight of the grafted layer also increase by grafting time as characteristic for living radical polymerization and reach at 100±14.4 nm and 320 kDa after 3 hours photoirradiation time respectively. Figure 5 shows the morphology of modified surfaces. It is confirmed that the poly(PMC) grafted surface has brush shape on the smooth PET substrate.

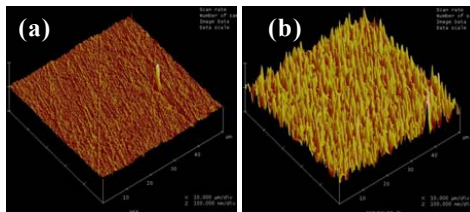


Figure 5 Surface morphology of 50 μm x 50 μm of PET substrate (a) and PEV40-g-MPC_{3h} (b) in dry condition

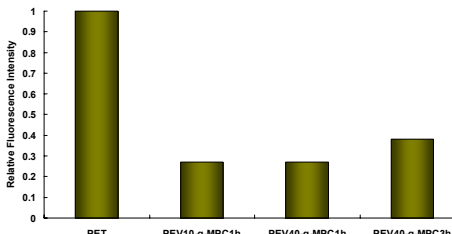


Figure 6 Fluorescence intensity of FITC-albumin adsorbed on PET substrate and some modified surfaces

Protein adsorption repellence of these poly(MPC)-modified surfaces was evaluated as can be seen in Figure 6. Protein adsorption significantly reduces on all poly(MPC)-modified surfaces compared to control one (PET substrate).

4. Conclusions

Preparation of non-biofouling surface by living radical polymerization for modification in polymer-based microchannel has successfully conducted. The modified surfaces significantly prevent protein adsorption. Furthermore, surface modification and micropatterning in microchannel by photochemical process will be achieved for evaluation the S/N ratio.

References

1. W. Senaratne, L. Andrucci, C.K. Ober, *Biomacromolecules*, 6, pp 2427 (2005)
2. M. Sakakida, K. Nishida, M. Shichiri, K. Ishihara and N. Nakabayashi, *Sensor and Actuators B*, 13, pp 319-322 (1993)
3. S. Zhang, Y. Benmakroha, P. Rolfe, S. Tanaka, K. Ishihara, *Biosensors and Bioelectron*, 11, pp 1019-1029 (1996)
4. T. Otsu, M. Yoshida, *Macromol. Chem., Rapid Commun.*, 3, pp 127 (1983).

PROTEIN ANTIADSORPTION MODIFICATION BY NEGATIVELY CHARGED PHOSPHOLIPID POLYMER FOR MICROSYSTEM NEEDING ELECTROOSMOTIC FLOW

Yan Xu, Madoka Takai, Tomohiro Konno, and Kazuhiko Ishihara

Department of Materials Engineering, School of Engineering,
and Center for NanoBio Integration,

The University of Tokyo, 7-3-1, Hongo, Bunkyo-ku, Tokyo 113-8656, Japan

Abstract

Biointerface with cell-membrane-like structure was constructed on the quartz microfluidic chip to suppress the non-specific protein adsorption as well as to retain the electroosmotic flow (EOF) effect through one-step modification. The PMBSSi, a negatively charged phospholipid copolymer containing 2-methacryloyloxyethyl phosphorylcholine (MPC) units, was synthesized to introduce such cell-membrane-like segments as well as surface charges onto the silica based microchannels via chemical bonding of the silane coupling units in the copolymer with the substrates. At neutral pH, the interface constructed by PMBSSi modification retained a significant cathodal EOF. Although the PMBSSi possesses negative charges, the nonspecific adsorptions of several kinds of proteins were effectively suppressed.

Key words: Surface modification, protein antiadsorption, electroosmotic flow, phospholipid polymer

1. Introduction

Protein and cell adsorption are seriously problem which would make it particularly difficult to realize micro-TAS on quartz and glass substrates for biological applications. Although surface coating is effective to suppress the adsorptions, many coatings result total suppression of EOF. For the applications needing EOF, it is unfavorable. Thus, it is necessary to construct a surface not only of protein anti adsorption but also retaining a certain extent of EOF effect. The phospholipid polymers containing 2-methacryloyloxyethyl phosphorylcholine (MPC) were bioinspired from the cell membrane structure and can construct bioinert interfaces or a non-adsorption biointerfaces by modification [1]. Here, a negatively charged MPC polymer PMBSSi (shown in Fig.1, left) was prepared and its protein antiadsorption effect and EOF effect were evaluated.

2. Experimental

The PMBSSi (Fig.1, left) was synthesized by a conventional radical polymerization of the corresponding monomers. In order to control the ξ -potential, another non-charged phospholipid polymer PMSi (Fig.1, right) was also prepared. The single-

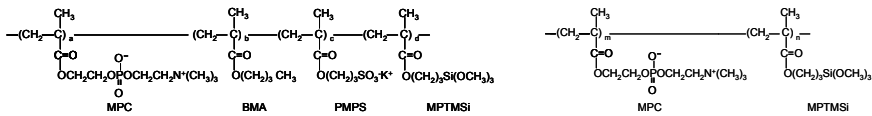


Fig. 1 The chemical structures of PMBSSi (left, a/b/c/d=50/35/5/10) and PMSi (right, m/n=90/10).

channel chip described as Fig.2 was fabricated on quartz plates. A dip-coating procedure and a filling method were applied to one-step modify the quartz plate and the microchannel, respectively. Two methods, qualitative and quantitative, were used to evaluate the protein adsorption. Qualitative evaluation was done by visually observing the fluorescence intensity of a fluorescein isothiocyanate labeled bovine serum albumin (FITC-BSA) absorbed onto the microchannel. Qualitative evaluation was processed on the quartz plates with several proteins by employing a micro BCA protocol [2]. The surface ξ -potential was measured by an electrophoretic light-scattering spectrophotometer with a plate cell. The measurements of EOF behavior were performed with the single-channel chip by observing the migration time of neutral beads at neutral pH [3].

3. Results and discussion

Like the other members of the MPC polymer family, both the PMBSSi and the PMSi have high ability to decrease the non-specific protein adsorption. The result (Fig.3) showed that in the case of the microchannel without PMBSSi coating, the FITC-BSA was strongly adsorbed to the inner surface of the microchannel, yielding bright and homogeneous fluorescence emission even after 4 time rinses totally using 1.2 ml PBS(pH 7.1). In contrast, the microchannel with a really low concentration of 0.03wt% PMBSSi coating, showed very low fluorescence emission after venting the protein solution and nearly no fluorescence emission was observed

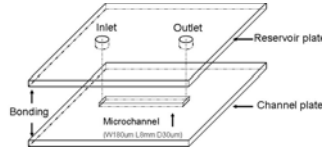


Fig.2 Schematic of the single-channel chip fabricated on quartz plates

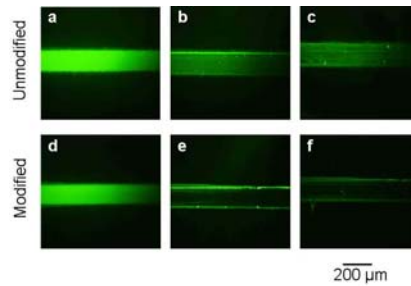


Fig. 3 Fluorescence images of protein adsorption in microchannels modified (d, e, f) or not modified (a, b, c) with 0.03wt%PMBSSi. Firstly, the microchannels were full filled with 0.045g/dL FITC-BSA solution (a, d), then incubated for 1h at 4°C. After venting the FITC-BSA solution out (b, e), the microchannels were rinsed 4 times totally using 1.2ml PBS (pH7.1) (c, f).

after 4 time rinsing. To make further quantitative evaluation, several proteins with 1% human plasma concentration level were used. The result (Fig.4) demonstrated that the protein adsorptions on quartz/glass plates were drastically reduced after PMBSSi coating ($<0.5 \mu\text{g}/\text{cm}^2$). Moreover, the surfaces coated by PMBSSi and by PMSi had no distinct difference in anti protein adsorption, although the conditions of surface charge were markedly different from each other (Fig.5).

To generate EOF, the surface of the capillary should have a certain extent of charge density. The unmodified quartz surface is negatively charged with a ξ -potential of $-47.4 \pm 0.9 \text{ mV}$ as determined by an electrophoretic light-scattering approach at neutral pH. Accordingly, the quartz microchannel showed a quite large cathodal EOF with a mobility of $(1.9 \pm 0.1) \times 10^{-4} \text{ cm}^2/\text{V}\cdot\text{s}$ at pH 7.0. The EOF determination also indicated that the quartz surface modified by PMBSSi retained a significant cathodal EOF. For example, in the condition of PBS, pH 7.0, the EOF mobility of the 0.3 wt% PMBSSi modified microchannel was $(1.0 \pm 0.1) \times 10^{-4} \text{ cm}^2/\text{V}\cdot\text{s}$, which was roughly more than the half (53%) of the EOF of the unmodified microchannel at the same buffer condition. Besides, this was consistent with the result of ξ -potential very well (Fig. 5). After modified by 0.3 wt% PMBSSi, the ξ -potential changed to $-24.2 \pm 2.5 \text{ mV}$ (at neutral pH), which was approximately 51% of that of unmodified quartz plate.

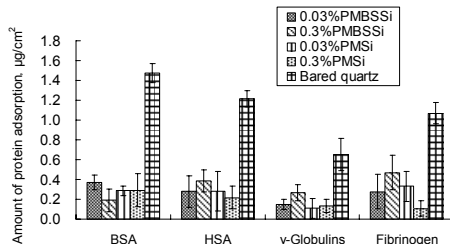


Fig.4 Amounts of different protein adsorption on the quartz plates with and without modifacaton of PMBSSi and PMSi.

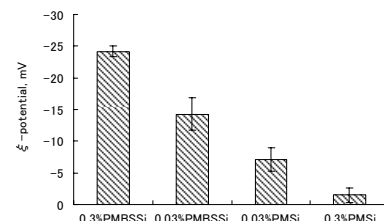


Fig. 5 The ξ -potential of quartz surfaces modified by PMBSSi and PMSi with different concentration.

4. Conclusions

The PMBSSi modified microfluidic surface retained a significant cathodal EOF at neutral pH. Although the PMBSSi possesses negative charges, the nonspecific protein adsorptions were effectively suppressed to a very small amount of less than $0.5 \mu\text{g}/\text{cm}^2$. As a conclusion, PMBSSi coating is a simple but highly effective modification for providing protein antiadsorption, and promising for applications needing some EOF.

References

1. K. Ishihara, T. Ueda, N. Nakabayashi, Polym. J., 22, pp. 355-360, (1990).
2. PIERCE Applications Handbook and Catalog, Pierce Biotechbology Inc. USA, pp. 241-243, (2003-2004).
3. A. S. Rathore, Electrophoresis, 23, pp. 3827-3846, (2002).

POLYMERIC ACTUATING MATERIALS FOR MICRO-FLUIDIC MANIPULATION USING EXTERNAL STIMULI

Hans T.A. Wilderbeek, Anthony J. van der Linden,

Titie Mol, Judith de Goede, Wim Talen,

Murray Gillies, Dirk J. Broer, Jaap M.J. den Toonder

Philips Research Laboratories, 5656 AE Eindhoven, The Netherlands

(hans.wilderbeek@philips.com)

Abstract

Responsive polymeric, micron-sized materials are described that can locally manipulate fluids by reversible micro-actuation. Selected examples of external stimuli, such as the use of a magnetic field are shown.

keywords: polymer micro-actuators, micro-fluidics, polymer chemistry & physics

1. Introduction

The anticipated increasing load on the healthcare system will stimulate a shift of the diagnosis from a more laborious, time-consuming and expensive hospital-based central lab to near-patient monitoring. This will bring about a need to downscale the analysis platforms with respect to physical size, cost and time to diagnosis. In this context, lab-on-a-chip devices such as cartridge-based biosensors attract substantial interest, both from academic and industrial point of view.

These cartridge-based devices require the combination of multiple micro-fluidic functions on a small area, such as mixing and displacement of liquids, controlled chemical and physical reactions, and the separation and detection of components. Although significant progress has already led to a variety of individual micro-fluidic components and principles, by and large it is still difficult to integrate the individual components in a device, and with respect to mixing and displacement of liquids, the area of manipulation is still pre-determined. In particular, the selective on-demand mixing, displacement and routing of liquids, at designated yet non-fixed locations has not yet been demonstrated. One way to fulfill the abovementioned functions on demand is to integrate versatile responsive materials in micro-fluidic devices.

In this contribution, a number of selected novel responsive polymeric, micron-sized materials are described that can manipulate fluids by reversible micro-actuation. These nature-inspired actuators, inspired by the motion and propulsion of asymmetric beating cilia of for instance microorganisms such as Paramecium [1], can be incorporated into micro channels. The actuation can be effected by various external stimuli, such as the use of heat, electrical stimulation [1], magnetism, and the interaction with light [2], as well as other stimuli. In this contribution, we address by means of example actuation using magnetism. Other stimuli are discussed on the accompanying poster as well.

2. Magnetically addressed micro-actuators

The use of magnetic addressing rather than for instance electrostatic addressing does eliminate possible intrinsic problems with electrolysis when using typical biological fluids. However, in order to minimize the required magnetic field strengths, and simultaneously realize substantial actuation of the employed elements, highly elastic polymeric materials are required exhibiting low Young's moduli in fluidic environment. Ideal candidates meeting these boundary conditions are rubber-like materials such as hydrogels. Figure 1a depicts the Young's moduli of readily photo-patternable crosslinked polyacrylic acid-based hydrogels in completely swollen state, tailored to exhibit values in the low megapascal range.

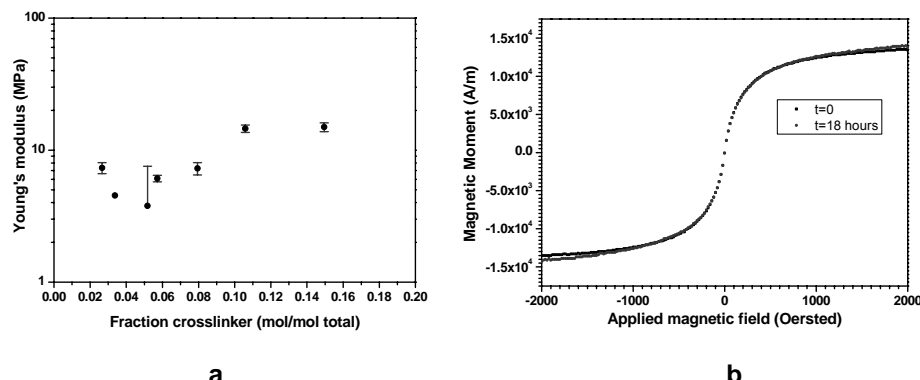


Figure 1. (a) Young's modulus as measured in extension using thermal gravimetric analysis of completely swollen polyacrylic acid-based hydrogels containing various amounts of polyethyleneglycol crosslinker. (b) Magnetic moment of completely swollen hydrogels containing 18% w/w superparamagnetic particles versus applied magnetic field, at $t = 0$ hours and after immersion in water for 18 hours.

Figure 1b depicts the magnetic moment of these swollen hydrogels containing super-paramagnetic nanoparticles resulting from an applied external magnetic field. The graph clearly shows that the nanoparticles are effortlessly retained in the completely swollen network even after continuous immersion in water for 18 hours. Moreover, the measured magnetic susceptibility (~ 3.50) is well within the desired range required for practical actuation. Despite the incorporation of superparamagnetic nanoparticles, the measured Young's moduli are still within the low megapascal range (~ 10 MPa).

Patterning of the hydrogels can be readily realized using standard photo-lithographic processing, and micron-sized features can be realized reproducibly (Figure 2), thus enabling the actual fabrication of micron-sized elements in micro-channels.

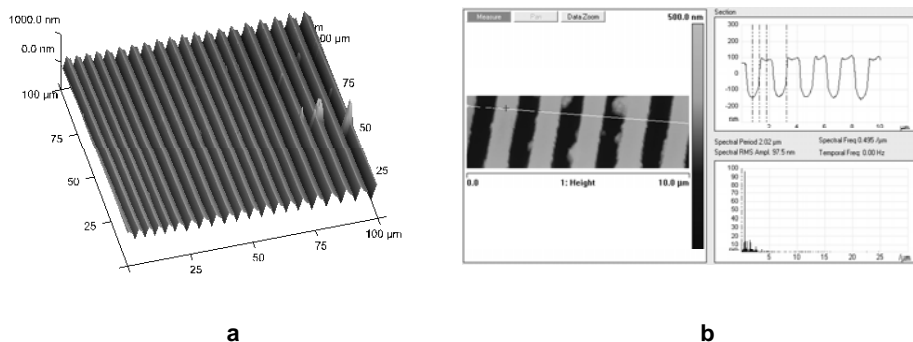


Figure 2. Atomic force micrographs showing micron-sized features in hydrogel-based systems using standard photolithographic processing techniques. (a) Lateral surface scan. (b) The analysis of the surface topography illustrates dimensional resolutions of approximately 2 μm laterally and 200 nm in depth, which is more than sufficient for the fabrication of elements within micro-channels.

4. Conclusions

The desired ability to manipulate fluids on a micro-scale, aimed at micro-fluidic devices, is addressed by using novel responsive polymeric, micron-sized materials. The actuation can be effected by various external stimuli, and in this contribution actuation using magnetic fields is illustrated by means of example. The concept introduced here enables the local manipulation of fluids and the generation of complex fluid patterns, thus opening new ways for the transportation, and mixing of liquids as well as for the selecting, sorting, deforming and rupturing of cells in lab-on-a-chip type of devices.

References

1. J.M.J. den Toonder, D.J. Broer, M. Gillies, J. de Goede, T. Mol, W. Talen, and H. Wilderbeek, *Nature-inspired micro-fluidic manipulation using artificial cilia*, Proc. Micro Total Analysis Systems 2006.
2. K.D. Harris, R. Cuypers, P. Scheibe, C.L. van Oosten, C.W.M. Bastiaansen, J. Lub, and D.J. Broer, *Large amplitude light-induced motion in high elastic modulus polymer actuators*, J. Mater. Chem., 15, pp. 5043-5048, (2005).

Photo-patternable liquid crystal actuators with high work output through optimization of molecular configuration

Casper L. van Oosten¹, Kenneth D. Harris¹, Cees W.M. Bastiaansen¹, Dirk J. Broer^{1,2}

¹Department of Chemistry and Chemical Engineering, Technische Universiteit Eindhoven, P.O. Box 513, 5600 MB, Eindhoven, The Netherlands

²Philips Research Laboratories, Prof. Holstlaan 4, 5656 AA, Eindhoven, The Netherlands
c.l.v.oosten@tue.nl

Abstract

In light driven liquid crystal network (LCN) actuators, large performance improvements can be obtained by varying the molecular director through the thickness of the film actuator. Experiments show that these systems are efficient and have an internal work density of 50 kJ/m^3 , orders of magnitude larger than that of the uniaxial planar film with the same chemical composition. The material is easy to process using standard photopatterning techniques and can be easily integrated in microsystems.

Keywords: Polymer actuator, UV-light actuation

1. Introduction

Liquid crystal based polymer actuators have several advantages as active elements in microfluidic devices: the materials are easy to process, the chemical composition provides a wide control over the properties and they are capable of deformations orders of magnitude larger than inorganic actuators. It will be shown that by using liquid crystal network (LCN) actuators, these properties can be combined with photopatterning processing techniques and that these systems offer the potential for performing useful work. Furthermore, a number of stimuli can be chosen as input for these systems, e.g. temperature [1], chemical agents such as humidity [2], pH and solvents [3] and electrical fields. Here, light induced actuation will be demonstrated, allowing for operation in both dry and aqueous environments.

2. Theory

In LCN actuators, shape deformation can be induced by a reduction of the molecular order of the aligned system, leading to a contraction along the director of molecular orientation and expansion perpendicular to it. In our case, the photoisomerization of azobenzene is used to reversibly decrease the order of the system using UV radiation [4]. In the uniaxial planar configuration, a gradient in absorbed intensity creates expansion differences, causing bending of the film. By using a splayed alignment of the molecules, a gradient in the preferred deformations through the thickness of a single

film is created. With decreasing order, one side of the film will contract and the opposite side will expand. For this splayed molecular alignment, small in-plane expansions are sufficient to produce large out-of plane deformations, resulting in a strong amplification of the rate and magnitude of bending. Schematic representations of the alignment configurations are shown in Figure 1.

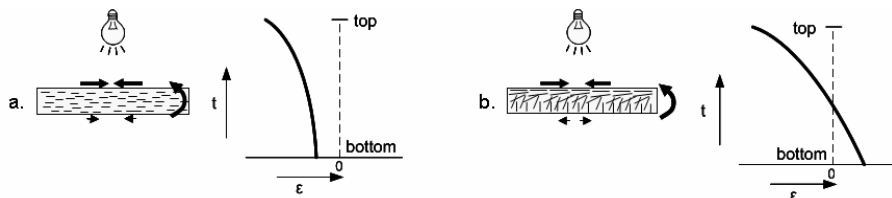


Figure 1. Schematic representations of the molecular alignment configurations. The strain ϵ caused by order decrease as a function of the thickness t is sketched on the right. Figure a. shows a planar configuration with only contraction through the cross-section, Figure b. a splayed configuration.

3. Results

A mix of reactive mesogenic host material containing 2% of the azobenzene compound and a photoinitiator was cured under splayed and planar alignment conditions. The material can be patterned by curing through a photomask and washing away the excess monomer, as was done for the structures shown in Figure 2. The typical elastic modulus of LCN actuators is 1 GPa.

The actuator motion for the two systems was measured on 7mm long, 4mm wide and 10 μm thick actuators, using a UV-light source with intensity of 60mW/cm² at the position of the actuator. Figure 3 shows images taken at 0, 0.20 and 0.50 seconds of exposure with UV light, at maximum deformation and after 40 seconds of recovery in ambient conditions. From these measurements, the maximum achieved strain difference between top and bottom is calculated to be 1.4% for the splayed actuator and less than 0.1% for the planar uniaxial actuator. When the splayed actuator film is turned over with the planar aligned side facing down, the film will bend downwards. In contrast, the uniaxial planar aligned film will always bend towards the light source.

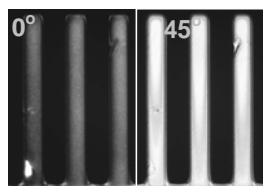


Figure 2. Crossed-polar view of 400 μm long, 50 μm wide flaps at 0° and at 45° made using photolithographic techniques. Due to the birefringent nature of the material, the flaps light up at 45° with the polarization angle, indicating the high level of molecular ordering in the structures.

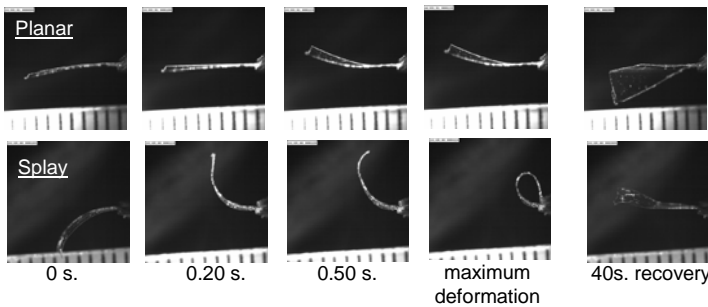


Figure 3. Movement of 7mm long, 10 μ m thick actuators containing 2% of the azobenzene compound. Images taken at 0, 0.20, 0.50, seconds of illumination, at the maximum deformation and after 40 seconds of recovery in ambient conditions. The bar at the bottom indicates millimeters.

4. Conclusions

The large and fast deformations in this experiment demonstrate the ability of the actuator to perform high internal work at a high rate. The material can be photopatterned, making it suitable for use in microsystems. For the case of the splayed, UV-driven actuator containing 2% azobenzene the internal work/volume ratio is calculated to be 50kJ/m³, which is in the same order of magnitude as the human muscle [5]. By controlling the molecular alignment, the direction of motion can be controlled independent of the light source. With an increasing number of mechanisms capable of molecular order manipulation of similar magnitude, the class of LCN actuators offers great potential to perform work in practical applications such as MEMS and lab-on-a-chip systems.

References

1. G. N. Mol, K. D. Harris, C. W. M. Bastiaansen and D. J. Broer, Thermo-mechanical responses of liquid crystal networks with a splayed molecular organization, *Adv. Funct. Mater.*, 2005, 15, 1155–1159.
2. K. D. Harris, C. W. M. Bastiaansen, J. Lub and D. J. Broer, Self-assembled polymer films for controlled agent-driven motion, *Nano Lett.*, 2005 Vol. 5, No. 9, 1857-1860.
3. K.D. Harris, C.W.M. Bastiaansen, and D.J. Broer, A glassy bending-mode polymeric actuator which deforms in response to solvent polarity, *Macromol. Rapid Commun.*, In Press, (2006).
4. H. Finkelmann, E. Nishikawa, G. G. Pereira and M. Warner, A new opto-mechanical effect in solids, *Phys. Rev. Lett.*, 2001, Vol. 87, No. 1, 015501.
5. J.D.W. Madden, N.A. Vandesteeg, P.A. Anquetil, P.G.A. Madden, A. Takshi, R.Z. Pytel, S.R. Lafontaine, P.A. Wieringa and I.W. Hunter, Artificial Muscle Technology: Physical Principles and Naval Prospects, *IEEE J. of Oceanic Eng.* 2004, 29 (3), 706-728

GENERATION OF PERMANENTLY HYDROPHILIC POLY(DIMETHYLSILOXANE) MICROFLUIDIC DEVICES

**Jonathon J. Vickers,* Xinya He,* Brian M. Murphy,* David W. Grainger,*
David S. Dandy,** Charles S. Henry***

*Department of Chemistry, Colorado State University, Fort Collins, CO, 80523.

**Department of Chemical Engineering, Colorado State University, Fort Collins,
CO, 80523.

Abstract:

Miniaturized total analysis systems (μ TAS) have potential for an exciting new class of Point-of-Care analysis technologies. To achieve this goal, however, inexpensive multifunctional microchips must be produced. Glass has always provided the best performance for microchip separations, but requires expensive cleanroom facilities for fabrication and is limited to non-mechanical pumping forces. Poly(dimethylsiloxane) (PDMS) is a soft elastomeric material that allows rapid prototyping of complex μ TAS devices outside of the cleanroom setting. PDMS is limited by its inherent hydrophobicity which causes significant adsorption and absorption of hydrophobic molecules. Here we report a surface modification protocol that generates a permanently hydrophilic PDMS that can self-wet and is stable in air for days. The improved PDMS material provides diffusion limited separation efficiencies as well as providing an excellent material for microfluidic patterning.

Keywords: Microfluidics, Microchip Electrophoresis, Polymer Materials,
Immunoassays, Electrochemical Detection

1. Introduction

Point-of-Care (POC) technologies have the potential to revolutionize modern medicine by making it more accessible through primary care physicians and emergency response personnel while at the same time, making it more affordable through low cost engineering methods. Our laboratory is developing modular multi-functional tools for analysis of disease biomarkers from serum, plasma, and urine. To accomplish this task, we are developing POC systems that integrate optical and/or electrochemical detection with chemical separations (electrophoresis and/or heterogeneous immunoassays) to provide selective detection of biomarkers.

One major challenge in the development of POC devices is selection of substrate material. Glass is considered to be the best material for generating high separation efficiencies and providing stable surfaces for immunoassays. Glass is not ideal in many other ways, requiring extensive and costly cleanroom space for fabrication. Furthermore, the size and shape of structures are limited by the etching technique. As a result, many groups have explored the use of polymeric substrates, with poly(methylmethacrylate) (PMMA)

and poly(dimethylsiloxane) (PDMS) being the most common [1]. PDMS is particularly attractive because the fabrication is very simple and the material is inexpensive and flexible [2]. PDMS is not a good material for separations however because the surface is hydrophobic and unstable. Here, we report a modified PDMS that is hydrophilic and stable with storage in air for days. We have used this material for both microchip electrophoresis and microfluidic patterning.

2. Experimental

Microchip Electrophoresis: The fabrication of poly(dimethylsiloxane) (PDMS) microchips using SU-8 molding has been described in detail previously [3, 4]. The PDMS was modified by placing it in a series of 3 organic solvents for extraction of unreacted short chain oligomers in the bulk polymer matrix and designated eoPDMS[5]. After extraction electrodes were aligned in pre-designated electrode channels and the chips were irreversibly sealed together via air plasma oxidation for use in microchip capillary electrophoresis with electrochemical detection (MCE-EC) [6]. Commercially available potentiostats (CHI812 and CHI660b, CH Instruments) in a two electrode configuration were used for the amperometric detection of catecholamines. The Au microwire (25 μ m diameter) working electrode was held at a constant 0.8 V detection potential. Noise was determined by measuring peak-to-peak current at $n \geq 30$ random points along the baseline.

Patterning. A PDMS stamp containing a micro-channel with a 250 μ m width, 60 μ m depth and 1.3 cm length was treated by plasma for 45 s. Then it was placed onto substrate surface. 2 μ l FITC-labeled HSA solution (1mg/ml) was dropped into the inlet reservoir. The protein solution spread along the channel instantly. After a 45-min incubation, the stamp was peeled off quickly under PBS flow. The substrate was rinsed by PBS, 0.5% Tween-20 (in PBS) and deionized water three times, respectively. The substrate surface was dried by air blast. The fluorescent images of the patterned protein were acquired using a Nikon Eclipse TE2000-U inverse microscope equipped with a CoolSNAP^{cf} CCDcamera.

3. Results and Discussion

Surface Analysis: The effect of air plasma oxidation on the surface composition of native and extracted PDMS was studied by SEM and XPS. Figure 1 shows a SEM image of the PDMS surface for native PDMS (A) and eoPDMS (B). Fits of the Si 2p peaks of native and eoPDMS are shown under their corresponding SEM image. Each Si 2p peak is fit with a siloxane ($(Si((CH_3)_2O)_n$) peak (green) with a known binding energy of 101.8 – 102.4 eV and a silicon dioxide (SiO_2) peak

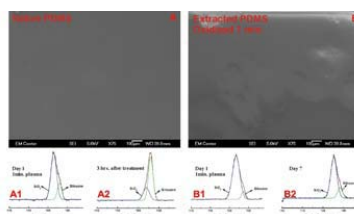


Figure 1: SEM and XPS of oxidized PDMS.

(blue) with a known binding energy of 103.2 – 104.1 eV. Si-CH₃ bonds on the surface of PDMS can be easily oxidized to form a hydrophilic surface. Native PDMS displays a hydrophobic recovery of the polymer surface in as little as three hours after a plasma oxidation (Figure 1-A1 and A2) while the eoPDMS does not display this characteristic by maintaining its silicate composition for up to 7 days (Figure 1-B1 and B2).

Microchip Electrophoresis: In addition to characterizing the surface chemistry of the PDMS, we also performed electrophoresis experiments using dopamine, catechol, and ascorbic acid as model analytes. An 8-fold improvement in separation efficiency from 50,000 N/m on native PDMS to 400,000 N/m on eoPDMS for ascorbic acid was seen using a 1.2 nL injection volume.

Microfluidic Patterning. Protein patterning was carried out on two different substrates: polystyrene and silicon nitride-coated Si wafer (SN-Wafer). On both substrates, the extracted PDMS channels provide better signal intensity than native PDMS channels. Being wettable, the hydrophilic PDMS adsorbs less protein than original PDMS, which leads to a higher protein concentration in the bulky solution. A higher protein concentration contributes a faster protein attachment on substrate. Therefore, a stronger fluorescent intensity was observed (Figure 2) for these experiments.

4. Conclusions

We have developed a simple robust method for generating permanently hydrophilic PDMS that can be used for both microchip electrophoresis and microfluidic patterning.

5. References

- [1] Soper, S. A., Ford, S. M., Qi, S., McCarley, R. L., Kelly, K., Murphy, M. C., *Anal Chem* 2000, 72, 545A.
- [2] McDonald, J. C., Whitesides, G. M., *Acc Chem Res* 2002, 35, 491-499.
- [3] Liu, Y., Fanguy, J. C., Bledsoe, J. M., Henry, C. S., *Anal Chem* 2000, 72, 5939-5944.
- [4] McDonald, J. C., Duffy, D. C., Anderson, J. R., Chiu, D. T., Wu, H., Schueller, O. J., Whitesides, G. M., *Electrophoresis* 2000, 21, 27-40.
- [5] Lee, J. N., Park, C., Whitesides, G. M., *Anal Chem* 2003, 75, 6544-6554.
- [6] Vickers, J. A., Henry, C. S., *Electrophoresis* 2005, 26, 4641-4647.

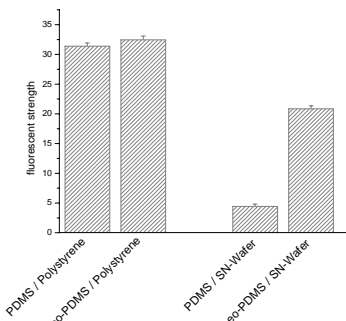


Figure 2: Comparison of fluorescent intensity for native and extracted PDMS stamps.

HYDROPHILIC, PROTEIN-RESISTANT SURFACE MODIFICATION OF POLYMER MONOLITHS VIA PHOTOGRAFTING FOR MULTIFUNCTIONAL MICROFLUIDIC DEVICES

Timothy B. Stachowiak,¹ Frantisek Svec,^{2,3} and Jean M. J. Fréchet^{1,2,3}

¹Department of Chemical Engineering, University of California, Berkeley, USA;

²The Molecular Foundry, Lawrence Berkeley National Laboratory, Berkeley, CA, USA; and ³Department of Chemistry, University of California, Berkeley, USA

Abstract

Polymer monoliths that resist the adsorption of proteins were prepared using both single- and two-step photografting of hydrophilic monomers. The adsorption of protein was measured using a fluorescent assay based on bovine serum albumin labeled with fluorescein. By photografting hydrophilic monomers such as poly(ethylene glycol) methacrylate onto polymer monoliths, protein adsorption was reduced by 98% relative to unmodified surfaces.

Keywords: Surface modification, photografting, polymer monolith, adsorption

1. Introduction

Porous polymer monoliths have been shown effective for creating many of the components needed in an integrated micro-analytical system such as preconcentrators, chromatographic stationary phases, and immobilized enzymatic microreactors [1]. However, no effective technique for the prevention of non-specific adsorption of species onto monolith surfaces has yet been demonstrated. As a result, localization of chemical/biological functionality is difficult and integration of monolith-based functional modules has been limited.

Photografting is an attractive approach for the *in situ* surface modification of polymer monoliths. Since grafting is a photoinitiated process, the location of grafts can be precisely controlled using masks, allowing different sections of a single monolith to be functionalized with different surface chemistries [2]. In this work, we utilize both sequential [3] and single-step photografting processes in order to create hydrophilic surface-modified polymer monoliths that resist protein adsorption (Fig. 1).

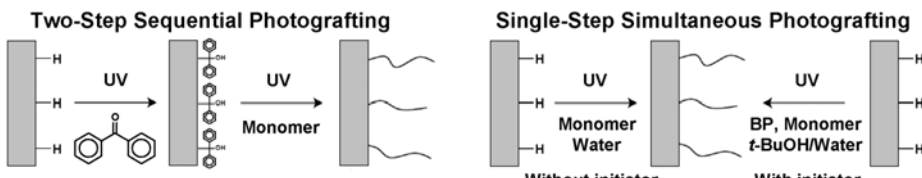


Figure 1. Schema of the photografting techniques.

2. Experimental

Poly(butyl methacrylate-co-ethylene dimethacrylate) monoliths were prepared via photopolymerization in fused silica capillary columns [4]. For sequential photografting, pores of the monoliths were first filled with a solution of 5 wt% benzophenone in methanol and then irradiated with UV light to create surface-bound photoinitiators. In the second step, the pores were filled with a 0.1 mol/L solution of hydrophilic monomer in water and then irradiated with UV light to initiate graft polymerization. For conventional single-step photografting, the grafting mixture contained monomer and initiator in a water/*tert*-butyl alcohol solvent. Initiator-free grafting was performed using a solution consisting of only hydrophilic monomer in water.

A fluorescence assay was utilized to determine the effectiveness of the different grafted layers to limit protein adsorption on the polymer monolith. A 0.5 mg/mL solution of fluorescein-labeled bovine serum albumin (BSA) was passed through the monolith for 1 h at a flow rate of 0.25 μ L/min. Then the monolith was rinsed with water for 1 h to remove excess BSA. After rinsing the monoliths, photomicrographs were taken and the fluorescent intensity analyzed across the width of the monolith.

3. Results and Discussion

A variety of monomers was screened for effective prevention of protein adsorption; poly(ethylene glycol) methacrylate (PEGMA) outperformed other neutral, hydrophilic monomers such as acrylamide, 2-hydroxyethyl methacrylate, and vinyl pyrrolidinone (Fig. 2a). Protein adsorption was reduced by 98% in PEGMA-photographed regions compared to unmodified polymer monolith surfaces. A study of the parameters in the two-step grafting process revealed that the most critical variables are the monomer concentration and the second-step exposure time (Fig. 2b).

In addition to the sequential method, single-step photografting techniques were also evaluated (Fig. 3a). The conventional single-step method provided very little prevention of protein adsorption. However, initiator-free photografting prevented protein adsorption in extent equal to the sequential two-step technique given sufficient grafting time. Finally, we demonstrated the utility of the hydrophilic grafted monolith for

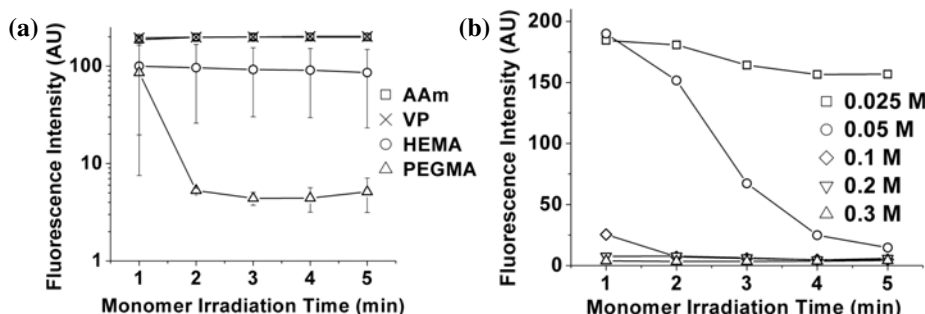


Figure 2. (a) Fluorescent intensity of adsorbed fluorescein-BSA on monoliths grafted with different hydrophilic monomers; (b) Intensity of adsorbed fluorescein-BSA on PEGMA-modified monolith at different monomer concentrations and graft times.

creating enzymatic microreactors. First, we used a fully PEGMA-modified monolith and in selected areas defined by a mask we photografted reactive chains of poly(vinyl azlactone) [2]. These regions were then used to immobilize green fluorescent protein (GFP) (Fig. 3b). This protein was well-patterned with very little fluorescence outside the patterned region, indicating good prevention of nonspecific adsorption by the layer of grafted PEGMA.

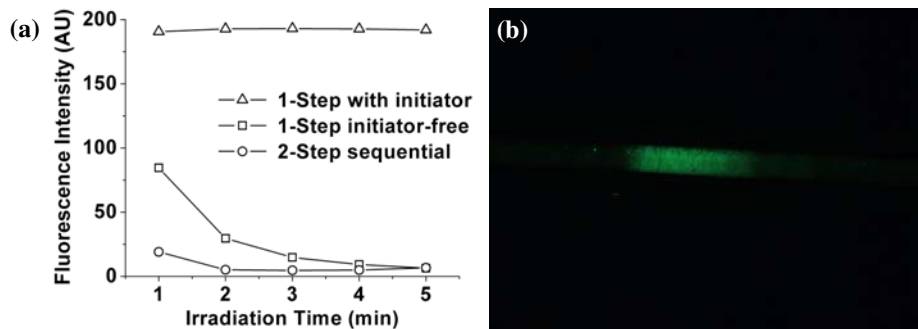


Figure 3. (a) Fluorescent intensity of adsorbed fluorescein-BSA on monoliths grafted using different photografting techniques; (b) Fluorescent micrograph of GFP immobilized onto a PEGMA-modified polymer monolith.

4. Conclusions

Photografting hydrophobic polymer monoliths with hydrophilic monomers is an effective means of reducing protein adsorption. Monomer concentration and irradiation time during photografting were found to be the most important parameters for optimization of the two-step process. For simultaneous single-step photografting, the solvent and the presence of photoinitiator were the key variables. Initiator-free single-step photografting was less efficient than the two-step technique, yet resulted in similar prevention of protein adsorption after grafting for an extended period of time.

Acknowledgement

Financial support of this work by the National Institute of Biomedical Imaging & Engineering, National Institutes of Health (EB006133) is gratefully acknowledged.

References

1. D.S. Peterson, *Lab-on-a-Chip*, 5, pp. 132-139, (2005).
2. T. Rohr, E.F. Hilder, J.J. Donovan, F. Svec, and J.M.J. Fréchet, *Macromolecules*, 36, pp. 1677-1684 (2003).
3. H. Ma, R.H. Davis, and C.N. Bowman, *Macromolecules*, 33, pp. 331-335 (2000).
4. E.F. Hilder, F. Svec, and J.M.J. Fréchet, *Anal. Chem.*, 76, pp. 3887-3892 (2004).

MICROFLUIDIC GENERATION OF TUNABLE MONODISPERSE DOUBLE EMULSIONS FOR TEMPLATED SILICA PARTICLES

Frank J. Zendejas¹, Uthara Srinivasan², William J. Holtz¹,
Jay D. Keasling¹ and Roger T. Howe³

¹ University of California at Berkeley, Berkeley Sensor & Actuator Center, Berkeley CA.

² University of California at Berkeley, Energy and Resources Group, Berkeley CA.

³ Stanford University, Department of Electrical Engineering, Stanford CA.

frank.zendejas@cal.berkeley.edu

Abstract

This paper describes a new approach to the formation of macroporous silica particles generated through a two-step emulsification process using a single microfluidic device. Between the first and second emulsification steps the microfluidic device has integrated channels that provide added flexibility of introducing reactive chemistries within the intermediate fluid. With control over the size of both the inner and outer emulsion droplets, we are able to precisely tailor the porosity of the resulting monodisperse silica particles. The overall size of the fabricated silica particles range from 40-120 μm in diameter with measured polydispersity less than 4.8 %. The innermost droplets each have pores with diameters on the order of 5 μm . Currently, there is great demand for such porous silica materials/particles in applications such as bioseparations, biocatalytic processes and photonic crystals within lab-on-a-chip systems.

Keywords: emulsion-templating, double emulsions, porous silica, biosilification

1. Introduction

Early work on double emulsions consisted of a two step process where the first emulsion is produced by vigorously stirring two immiscible fluids. The second step consists of taking the first emulsion and dispersing it in a third immiscible fluid by using low shearing forces to create the outer most droplets without disrupting the first emulsion. However, this technique leads to poor control of droplet size distributions since both the first and second emulsification steps have a large polydispersity. Several promising microfluidic devices for double emulsion generation have been described in recent literature [1,2]. These systems generate droplets with highly monodisperse inner and outer droplets with polydispersity near 3%. The authors in ref. [1] generated encapsulation structures by crosslinking a photopolymerizing polymer that made up the intermediate fluid of the double emulsion. However, their system at times suffers since the orifices of two capillary tubes must be aligned correctly to insure proper double emulsion droplet generation. Using silicon-based microfabriaction we avoid any alignment issues between the two emulsification steps. In this paper we combine biomimetic chemistry to modify the intermediate fluid of the double emulsion and microfluidics to produce high-quality template-directed macroporous silica particles. In the future these three dimensional porous particles may be produced *in-situ* within lab-on-chip systems for reaction and separation modules, or collected and dispensed from an ink-jet system to produce complex arrangements such as scaffolds.

2. Experimental

It has been hypothesized that diatoms use similar micro/nanoemulsions to template the synthesis of their nanostructured silica frustules [3]. Here we used triethylenetetramine as a biomimetic catalyst inspired by diatoms [4] to induce a gelation reaction within the intermediate phase of the double emulsion. This reaction occurs within minutes under benign conditions (neutral pH and ambient temperature) in contrast to conventional sol-gel routes [5]. To generate the monodisperse double emulsions, we employ a microfluidic flow-focusing configuration along with a T-junction configuration as described in refs. [6,7]. Deep reactive ion etching of a silicon (100) substrate is used to create the

microfluidic channels with a depth of 30 μm in the flow-focusing area and 120 μm at the T-junction area as well as the fluidic ports, through-etched from the backside of the wafer. The wafer is sealed by anodic bonding with a Pyrex wafer. A micrograph of our fabricated device is shown in Fig. 1a. Operation of the microfluidic double emulsion chip is based on a two-step emulsification process, where a water phase finally serves as the intermediate fluid. The first emulsification step (oil-in-water) is generated using flow-focusing, and the subsequent emulsification step (water-in-oil) occurs at a T-junction downstream. In order to create the water-in-oil emulsions at the T-junction, the hydrophilic silicon/Pyrex channels are selectively functionalized with a hydrophobic coating (Aqua-Sil), while the flow-focusing channels are left hydrophilic similar to [2].

3. Results and Discussion

Generation of hexadecane droplets in water, stabilized using 2% (w/v) polyvinyl alcohol in the water phase, is shown in Fig. 1b [7], and generation of water droplets in hexadecane, stabilized using 0.5% (w/v) lecithin in the hexadecane phase, is shown in Fig. 1c.

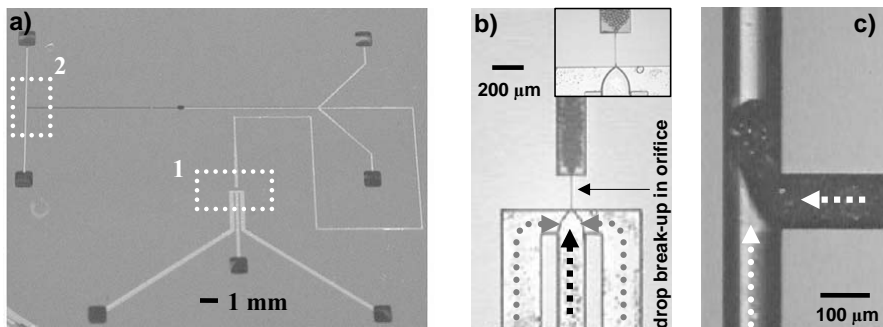


Fig. 1. a) Fabricated chip highlighting the flow focusing (1) and T-junction (2) regions. b) A continuous phase (●) flowing through the two outer channels focuses a stream of the dispersed phase (■) from the inner channel into an orifice, resulting in droplet break-up. Close-up of the emulsion generation is shown in the inset image. c) The initial emulsion (□) is subsequently re-emulsified by a continuous phase (○) at the T-junction, creating the double emulsion.

By setting a constant volumetric flow rate of both the inner oil flow ($Q_{\text{hexadecane}} = 0.4 \mu\text{L}/\text{min}$) and the outer water flows ($Q_{\text{water}} = 0.55 \mu\text{L}/\text{min}$), we produce the initial monodisperse oil-in-water emulsions that have a droplet polydispersity less than 2.4% as previously characterized [7] while maintaining a high droplet volume fraction. Once the flow-focusing region is stable we image the double emulsion droplet generation using a high speed Cohu 2700 video camera with exposure times as short as 100 μs . Fig. 2 shows a plot of the average double emulsion droplet diameter as a function of the lecithin/hexadecane flow rate.

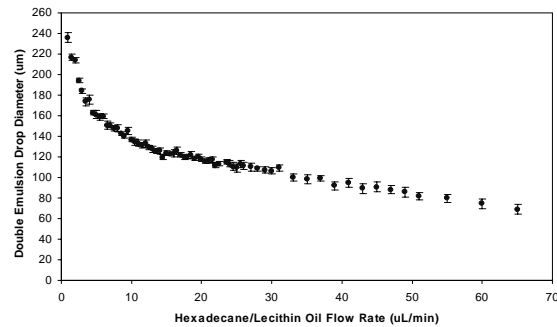


Fig. 2. The average outer diameter of the double emulsion droplets as a function of the hexadecane/lecithin flow rate. The hexadecane/lecithin oil represents the final continuous phase that is responsible for re-emulsifying the initial emulsion into a double emulsion at the T-junction. Polydispersity is less than 4.8% were measured.

Between the formation of the first and second emulsification steps, orthosilicic acid (1 M) and the biomimetic catalyst triethylenetetramine (6.7 mM) are introduced into the intermediate phase, causing it to form a templated silica gel around the inner monodisperse oil droplets (Fig. 3). Subsequent calcining of the gelled droplets at 400°C for 8 h removes the organic content and converts the material into glassy porous silica particles [5]. After calcining, we observe a densification of ~50-70%. A SEM of a double-emulsion-templated porous silica particle is shown in (Fig. 4).

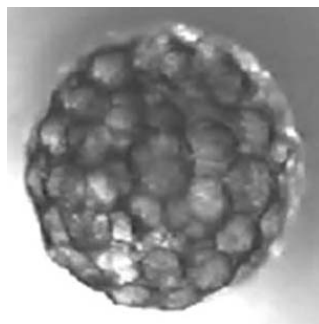


Fig. 3. Micrograph of a gelled double emulsion droplet. The intermediate phase inside the larger droplet forms a silica gel templated around the inner emulsion droplets of diameter ~30 μm .

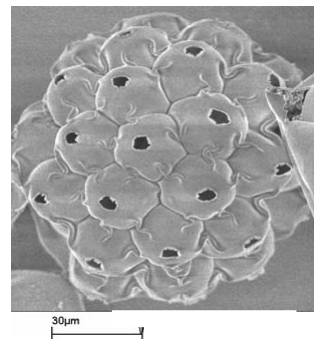


Fig. 4. SEM micrograph of emulsion-templated double emulsion porous silica particle. Inner droplets have a diameter of ~30 μm , with smaller pore diameters of ~5 μm .

4. Conclusions

We have demonstrated a new technique to create ordered macroporous particles efficiently, by combining template-directed synthesis and biomimetic chemistry with microfluidics. With the addition of the channels between emulsification steps we have added the flexibility of not only introducing the reactive chemistries but also the functionality of introducing other materials such as nanoparticles to the silica particles. If synthesized within lab-on-a-chip systems, functionalized porous silica will also be extremely valuable for microsystems, in particular for reaction, separation, and sample preparation modules. In future work, we will investigate the incorporation of nanoparticles into the intermediate phase of the double emulsion so as to stud the silica and form nanocomposite materials/particles. This technique may open possibilities of controlling the overall physical properties of the material and lead to particles that could effectively scatter light and as a result be used as pigments.

Acknowledgements

This work has been funded by a DARPA contract award N66001-04-1-8919. The authors would like to thank Noel Arellano for his SEM expertise, and the staff of the Berkeley Microfabrication Facility for their support.

References

- [1]. A.S. Utada, E. Lorenceau, D.R. Link, P.D. Kaplan, H.A. Stone, and D.A. Weitz, *Science* 308, 537 (2005).
- [2]. T. Nisisako, S. Okushima, and T. Torii, *Soft Matter* 1, (2005).
- [3]. M. Sumper, *Science* 295, 5564 (2002).
- [4]. F. Noll, M. Sumper, and N. Hampp, *Nano Letters* 2, 91 (2002).
- [5]. A. Imhof and D. J. Pine, *Nature* 389, 948 (1997).
- [6]. S. L. Anna, N. Bontoux, and H.A. Stone, *Applied Physics Letters* 82, 364 (2003).
- [7]. F.J. Zendejas, U. Srinivasan, W.J. Holtz, J.D. Keasling, and R.T. Howe, *Transducers* 05 conf., (2005)

3D MANIPULATION of LIPID NANOTUBES with PHOTO-CROSSLINKABLE GEL MICRO-BEADS for NANO-ASSEMBLY

Fumihito Arai¹, Toshiaki Endo², Ryuji Yamuchi², Toshio Fukuda²
Toshimi Shimizu³, Shoko Kamiya³

¹ Department of Bioengineering and Robotics, Tohoku University, JAPAN

² Department of Micro-Nano Systems Engineering, Nagoya University, JAPAN

³ Nanoarchitectonics Research Center, AIST, JAPAN

Abstract

It is suitable to use a micro to nano scaled object as a tool for measurement of cell and local environmental control around it. However, it is difficult to manipulate a nano scaled object stably using optical tweezers. Therefore, we aim to develop 3D manipulation technique that can manipulate several nanometer scale objects with different shapes. We developed a novel technique to **handle lipid nanotubes by optical tweezers** in water solutions. We succeeded in controlling the position and orientation of a lipid nanotube by using 3D Synchronized Laser Micromanipulation and novel functional gel-microtools.

Keywords: *Micromanipulation, Lipid nanotube, Optical tweezers, Gel, Microtool*

1. Introduction

With recent developments in biotechnology, several methods for observing and manipulating bio-molecules and cells under the microscope have been developed. Single cell manipulation is important for biological research works, and advanced techniques such as 3D manipulation are much useful for measurement and environmental control [1,2]. Recently, in particular, measurement of cell of μm order and local environmental control around it are requested. For this purpose, it is suitable to use micro to nano scaled objects as a functional tool. However, it is difficult to manipulate a nanometer scaled object, such as a lipid nanotube [3]. Therefore, here we developed functional gel-microtools for indirect manipulation of the lipid nanotube.

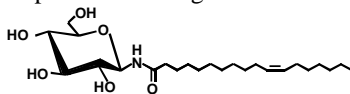
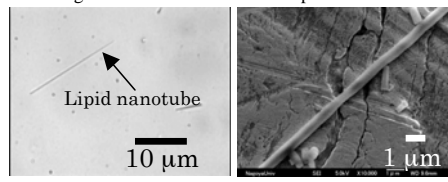


Fig. 1 Structural formula of a lipid molecule



(a) Optical microscope view (b) SEM view
Fig. 2 Microscope views of lipid nanotube

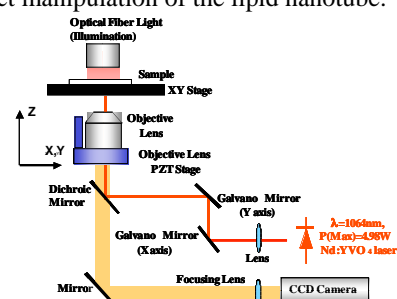


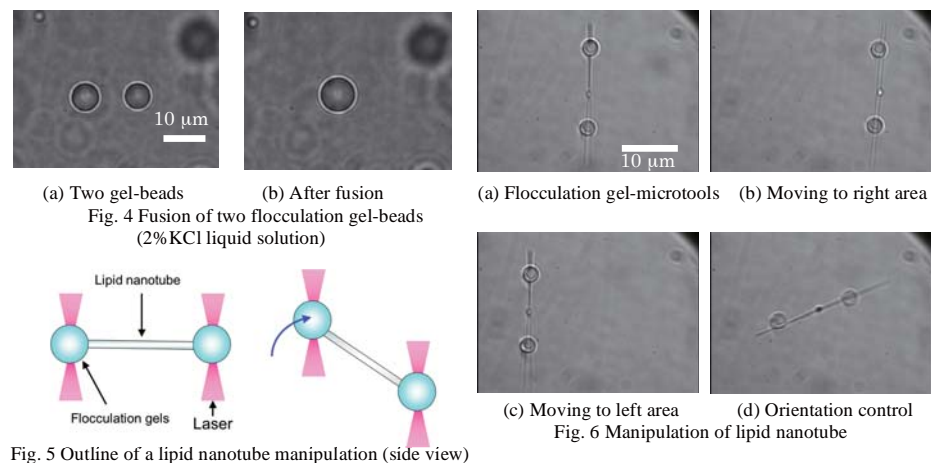
Fig. 3 Schematic diagram of optics for 3D laser trapping

2. Experimental

Figure 3 shows a schematic diagram of the optical system used in this study. An image of the target is obtained using a microscope equipped with a $\times 100$ (numerical number 1.35) oil-immersion objective lens and CCD camera. Nd:YVO₄ laser emission (1064 nm, continuous wave, max: 4.98 W) for laser trapping is introduced into the microscope. The X-Y stage and objective lens (Z axis) are actuated by a stepping motor. The laser is scanned in 2D observation plane by controlling the angle of a pair of galvanometer mirrors with DC motors. In addition, a piezo stage (PIFOC P-721, PI-Polytec) was used to drive an objective lens for scanning the laser in the Z axis. As a result, high-speed movement of the focal point in 3D space was achieved. Moreover, we newly developed an observation system to improve blurring of image by synchronization of shutter timing of the CCD camera and laser scanning. With this system, we can obtain clear image of the targets for 3D manipulation.

3. Result and discussion

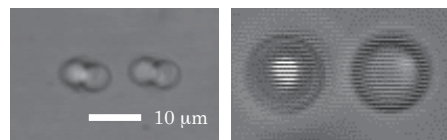
Manipulation of a nanometer scale object is possible by using laser trapped micro-beads. We developed a novel **flocculation gel micro-bead**, which is made by flocculation of gel, for indirect manipulation of the target. It is produced easily by mixing a small amount of **electrolyte** with a droplet made of **photocrosslinkable resin** (ENTP). The droplet is generated by mixing ENTP-4000 with the aqua pura. We also mixed electrolytes such as NaCl or KCl by 1% or more. Its size is adjusted to an arbitrary size (Fig. 4). The flocculation gel micro-bead takes in the nanotube (Fig. 5, 6). It doesn't adhere to the glass surface. We can manipulate nano scaled objects easily by the optical tweezers with the flocculation gel micro-beads. We succeeded in controlling **position and orientation of a lipid nanotube** by using 3D Synchronized Laser Micromanipulation [1] with the flocculation gel micro-beads (Fig. 6).



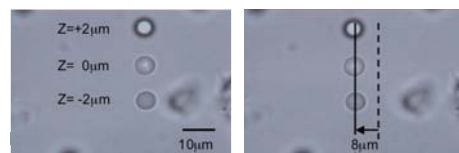
With this method, we achieved manipulating **ten times faster** than direct laser manipulation of lipid nanotube. Moreover the gel is cured by UV ray irradiation, and we can connect several nanotubes.

Second, we developed a new observation system to **improve blurring of image** (Fig. 7) by synchronization of shutter timing of the CCD camera and 3D laser scanning (Fig. 8). In this study, the shutter speed timing is raised to 1/250 sec. When the shutter is open, a clear image is obtained because the laser scanning is stopped. Transportation of three micro-beads that exist in a different plane was achieved easily with this system (Fig. 9). We can move them at speed of **26.7 $\mu\text{m}/\text{s}$** with **clear image** in 3D manipulation.

With these achievements, we succeeded in 3D position and orientation control of a rod-like nano material. We also established basic techniques for assembly of complex 3D nano structures.



(a)Scanning at different height (b) Interlace stripe
Fig. 7 Blurring in z axis rapid scan



(a) $T=0 \text{ sec}$ (b) $T=0.3 \text{ sec}$
Fig. 9 Photos of 3 microbeads
by synchronization of shutter and scanner

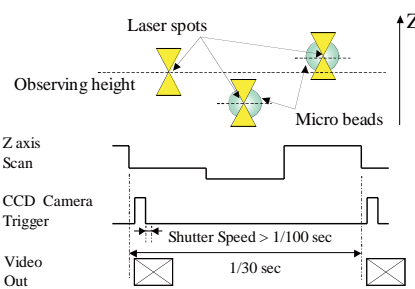


Fig. 8 Schematic of Z axis scanning and shutter

ACKNOWLEDGMENTS

This work was supported by JSPS.KAKENHI(17360113)

REFERENCES

- [1] F. Arai, K. Yoshikawa, T. Sakami, and T. Fukuda, Applied Physics Letters, 85-19, pp. 4301 – 4303, 2004
- [2] F. Arai, T. Endo, R. Yamuchi, T. Fukuda, Journal of Robotics and Mechatronics Vol.18 No.2, pp. 153-159, 2006
- [3] Toshimi Shimizu, Mitsutoshi Masuda, Hiroyuki Minamikawa, Chemical Reviews, 105, 4, pp. 1401-1443, 2005

DYNAMIC COATING OF POLY(METHYL METHACRYLATE) CHIPS WITH N-DODECYL- β -D-MALTOSIDE AND CELLULOSE FOR SEPARATION OF GLYCANS FROM GLYCOPROTEINS

Fuquan Dang¹, Mitsuru Ishikawa¹ and Yoshinobu Baba¹

¹ Nano-bioanalysis Team, Health Technology Research Center, National Institute of Advanced Industrial Science and Technology (AIST), Hayashi-cho 2217-14, Takamatsu 761-0395, Japan

Abstract

We developed a hybrid dynamic coating method using *n*-dodecyl- β -D-maltoside (DDM) and methyl cellulose (MC) for poly(methyl methacrylate) (PMMA) microfluidic chips. Hybrid dynamic coating with 0.25% DDM and 0.03% MC was found to minimize both analyte adsorption and electroosmotic flow (EOF) in a PMMA channel to a negligible, while still keeping a low viscosity of the solution. High-speed and high-throughput profiling of the N-linked glycans derived from glycoproteins was achieved in both single-channel and 10-channel PMMA chips.

Key words: Dynamic coating, adsorption, PMMA, DDM, cellulose, glycans

1. Introduction

Polymer materials have recently attracted much attention in mass fabrication of microfluidic chips because the low cost, ease of fabrication, and diversity of mechanical and chemical properties. However, the surfaces of many polymer materials are quite hydrophobic and not compatible with aqueous separation media, causing poor separation performance due to serious analyte adsorption on the channel surface. Therefore, surface modification is a critical issue for polymer-based microfluidic chips in electrophoresis applications.

Dynamic coating represents a simple and convenient surface modification technique, in which surface modifiers, such as polymers or surfactants dissolved in running buffers, physically adsorb on channel walls to form a coating layer for suppression of analyte adsorption and regulation of EOF. Although numerous approaches utilizing different surface modifiers have been reported for polymer microfluidic devices [1,2], we still do not fully understand the surface chemistry of polymer materials and the mechanism of dynamic coating on the polymer surface.

In this work, the coating performance of *n*-dodecyltrimethylammonium chloride (DTAC), DDM, and MC on a PMMA channel was systematically investigated using 8-aminopyrene-1,3,6-trisulfonate (APTS)-labeled maltriose (G_3) as a model analyte. We found that hydrophobic and hydrogen-bonding interactions rather than electrostatic interactions between surface modifiers and the PMMA surface are crucial to forming an efficient and stable dynamic coating on a PMMA channel. Thus, a hybrid dynamic coating using 0.25% DDM and 0.03% MC was developed for suppression of both analyte adsorption and EOF in a PMMA channel while still keeping a low-viscosity solution.

High-speed and high throughput profiling of the N-linked glycans released from glycoproteins was achieved in both single channel and multichannel PMMA chips.

2. Experimental

The experiments on single channel PMMA chips were performed on an SV1100 Microchip CE system (Hitachi Electronics Engineering Co., Ltd., Japan) [1]. The experiments on 10-channel array PMMA chips were carried on the stage of an inverted fluorescence microscope (Olympus IX70, Olympus, Japan) with LIF detection [2].

3. Results and discussion

Although widely used in fabrication of microfluidic chips, PMMA has a very hydrophobic surface, causing strong adsorption of analytes, especially for fluorescence dyes. As shown in Figure 1A, the separation of APTS labeled G₃ was impossible in an uncoated PMMA chip due to strong interactions between APTS and the PMMA surface. Through systematic study, we found that DDM obviously suppressed the adsorption of APTS-labeled G₃ in a PMMA channel, but EOF was reduced only by a factor of ~25%, resulting in irreproducible separations (Figure 1A). In contrast, DTAC did not show observable effects on reducing analyte adsorption under alkaline or acidic conditions (Figure 1B), although it has the same hydrophobic alkyl chain as DDM. Interestingly, both analyte adsorption and EOF in a PMMA channel was efficiently minimized with hydrophilic cellulose polymers like MC; however, concentrated MC above 0.3% was required to achieve good separations (Figure 1B). Because multiple hydroxyl groups of DDM and MC obviously facilitates hydrogen-bonding interactions with surface negative charges, whereas the positive charged ammonium groups of DTAC with favors electrostatic interactions in a 20 mM phosphate at pH 6.93, we concluded that hydrophobic interactions combined with hydrogen-bonding interactions play a critical role in forming an efficient and stable dynamic coating on the PMMA surface.

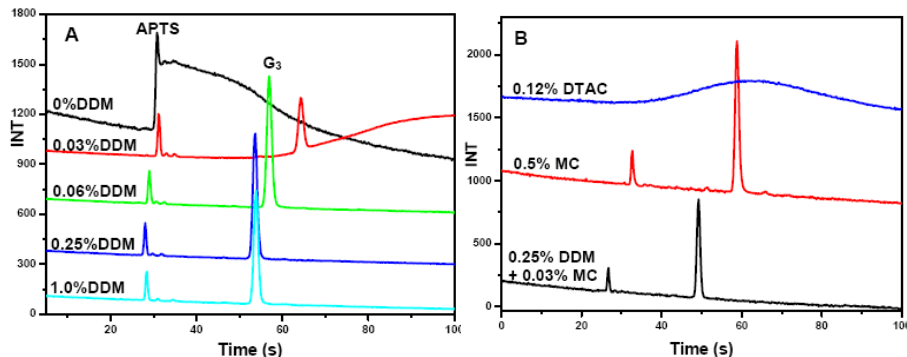


Figure 1. Electropherograms of APTS- G₃ in PMMA channels dynamically coated with various concentrations of DDM (A), and with 0.12% DTAC, 0.5% MC and 0.25% DDM- 0.03% MC (B). Conditions: E_{sep} = 200 V/cm; 20 mM phosphate buffer, pH 6.93.

A hybrid dynamic coating method using DDM and MC was explored to achieve an efficient dynamic coating on the PMMA surface with a low viscosity of the solution for ease of operation. As expected, separations with 0.25% DDM and 0.03% MC hybrid

coating were comparable to those obtained with 0.5% MC coating, and EOF was also found to be negligible with 0.25% DDM and 0.03% MC hybrid coating (Figure 1B). Note that no separation can be obtained with 0.03% MC coating without DDM. Because very small amounts of DDM and MC can efficiently minimize both analyte adsorption and EOF in a PMMA channel, indeed, a running buffer containing 0.25% DDM and 0.03% MC is still a dilute and low-viscosity solution (smaller than 30 cP at 25°C), which is easy to handle in PMMA MCE devices. High-speed and high-throughput profiling of the N-linked glycans derived from glycoproteins was thus achieved in both single-channel and 10-channel PMMA chips using DDM-MC hybrid coating (Figure 2).

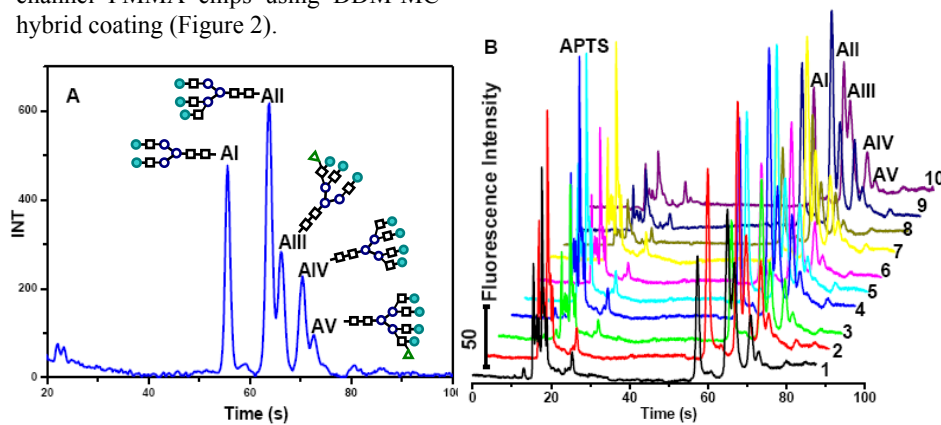


Figure 2. Electropherogram of N-linked glycans derived from α_1 -acid glycoprotein on a single PMMA chip (A), and on a 10-channel PMMA chip. Conditions: $E_{sep} = 300$ V/cm; 0.25% DDM and 0.03% MC in 20 mM phosphate buffer, pH 6.93.

4. Conclusions

Comparing the dynamic coating performance of DDM, DTAC and MC with their molecular structures, we found that hydrophobic and hydrogen bonding interactions are crucial to achieving efficient and stable dynamic coating on the PMMA surface. A hybrid dynamic coating using 0.25% DDM and 0.03% MC was developed for suppression of both analyte adsorption and EOF in a PMMA channel while still keeping a low-viscosity solution.

Acknowledgements

This research is supported in part by the CREST program of JST; a grant from NEDO of the Ministry of Economy, Trade and Industry, Japan; a Grant-in-Aid for Scientific Research from the Ministry of Education, Science and Technology, Japan.

References

1. F. Dang, L. Zhang, H. Hagiwara, Y. Mishina and Y. Baba, *Electrophoresis*, **24**, 714-721, (2003).
2. F. Dang, K. Kakehi, J. Cheng, O. Tabata, M. Kurokawa, K. Nakajima, M. Ishikawa, Y. Baba, *Anal. Chem.*, **78**, 1452-1458, (2006).

EFFECTS OF SURFACE MODIFICATION ON ELECTROOSMOTIC FLOW AND ZETA POTENTIAL IN MICROCHANNEL

Seiichi SASAKI¹ and Yohei SATO¹

¹Keio University, 3-14-1 Hiyoshi, Kohoku-ku, Yokohama, 223-8522 JAPAN
E-mail: yohei@sd.keio.ac.jp

Abstract

Surface modifications on a poly(dimethylsiloxane) (PDMS) microchannel were conducted by O₂ plasma treatment, silanization with silane coupling agent and PEGylation with poly(ethyleneglycol) (PEG) sequentially. The effects were quantitatively examined by measuring the electroosmotic flow velocity using micron-resolution particle image velocimetry (micro-PIV) and the zeta-potential. The electroosmotic flow velocity and the zeta-potential were changed significantly due to the surface compositions.

Keywords: Electroosmotic flow, Micro-PIV, Surface Modification, Zeta-potential

1. Introduction

Specific DNA, protein, and cells are separated on a miniaturized microfluidic device for chemical analysis by applying external forces, e.g., acoustic, electric, and optical force. Accurate control of electroosmotic flow is important for separation in microfluidic devices. Since an electroosmotic flow is generated by a complex interaction between surface compositions and buffer characteristics under an external electric field, specific kinds of surface modification are one of convenient and effective methods to control electroosmotic flow. The objective of this study is to demonstrate the alternation of electroosmotic flow velocity on various surface compositions.

2. Experimental section

Equipment Experimental setup illustrated in Figure 1 was composed of an inverted epi-fluorescent microscopy (Nikon) and a cooled CCD camera (Hamamatsu Photonics). Captured image data by the CCD camera at 37 ms frame interval were analyzed by micro-PIV [1]. An I-shaped microchannel shown in Figure 2 (a), whose inlets and outlets were connected to a power supply, was set on a microscope stage for measuring electroosmotic flow velocities. It was fabricated by using a soft lithography technique, sealing PDMS (ShinEtsu Chemical Co. Ltd) on a borosilicate cover slip glass. Figure 2 (b) illustrates a borosilicate microchannel for a closed cell experiment [2] to measure an electrophoretic velocity of tracer particles.

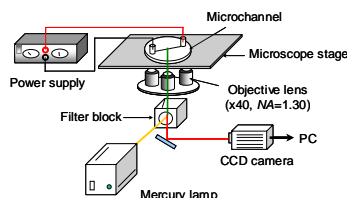


Figure 1. Experimental setup.

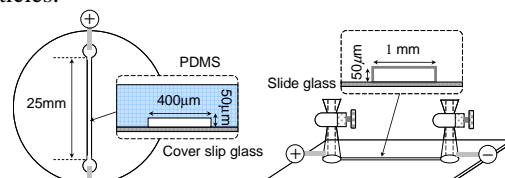


Figure 2. (a) Schematic of (a) an I-shaped microchannel and (b) a closed cell microchannel.

Table 1. Properties of fluorescent particles and chemical agents

Particle	
Material	Polystyrene
Diameter	1 μm
Solution	HEPES
pH	7.0
Silane coupling agent	
Substance	3-aminopropyl triethoxysilane
Solution	Ethanol
Terminal group	Amino group (-NH ₂)
Poly (ethylene glycol) (PEG) solution	
Substance	<i>p</i> -nitrophenyl PEGs
Solution	Ethanol
Terminal group	Methyl group (-CH ₃)

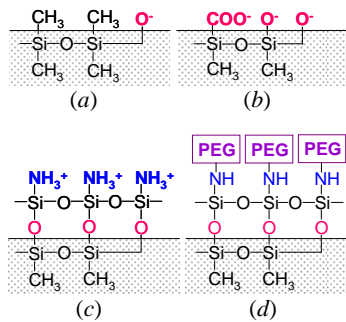


Figure 3. Chemical structures of each surface modification procedure. (a) Native PDMS, (b) O₂ plasma treated PDMS, (c) Silanized PDMS and (d) PEGylated PDMS.

Reagents Properties of fluorescent particles and chemical agents for surface modification experiment are listed in Table 1. Tracer particles were selected 1 μm carboxylate modified particles and added to HEPES buffer at 0.1% volumetric ratio. Silane coupling agent was composed of 3-aminopropyl triethoxysilane (ShinEtsu, KBE-903), ethanol and ion exchanged water at 1:9:1 volumetric ratio, and PEG solution was composed of *p*-nitrophenyl PEGs (NOF CORPORATION, SUNBRIGHT MENP-50H), whose molecular weight is 5000 Da, and heated ion exchanged water (approximately at 35°C).

Surface modification procedure Figure 3 shows each step of surface modification process on a PDMS microchannel. To activate the PDMS surface, O₂ plasma treatment was performed by irradiating O₂ plasma for 10 seconds using a plasma etcher. After the activated condition, silane coupling agent with added amino group was poured into the microchannel to bind onto O₂ plasma treated PDMS under nitrogen condition. Next, PEG solution was added to graft onto the amino group. After the treatment, the modified microchannel was dried for 6 hours naturally. Surface modification effect was evaluated by measuring electroosmotic flow velocity at the end of each step.

3. Results and discussions

Electroosmotic flow velocity An observed particle velocity in a microchannel is the sum of an electrophoretic (EP) and an electroosmotic flow (EOF) velocity. In a closed cell experiment for measuring an EP velocity of tracer particles, the EP velocity was calculated to be -64.8 $\mu\text{m}/\text{s}$ by applying Mori and Okamoto's equation [3] to the fitted parabolic curve on an application of 40 V/cm. The obtained EP velocity was applied to measure the EOF velocity in an I-shaped microchannel. The EOF velocity was measured under the same electric field intensity just after each surface modification was conducted. Each EOF velocity profile was shown in Figure 4. As shown in Figure 4 (a), the EOF field flow was influenced by surface compositions significantly. For an EOF velocity of O₂ plasma treated PDMS, the velocity became about three times faster than that of native PDMS. This indicates that PDMS surface was charged highly negative.

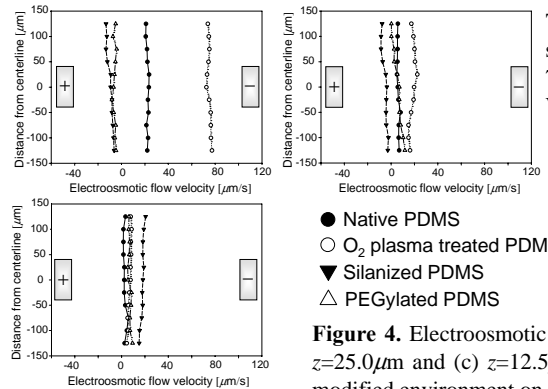


Table 2. Zeta-potentials of modified surfaces in HEPES buffer solution (pH 7.0) with applied electric field of 40 V/cm

Native PDMS	-69 mV
O ₂ plasma treated PDMS	-233 mV
Silanized PDMS	30 mV
PEGylated PDMS	18 mV

Figure 4. Electroosmotic flow velocities at (a) $z=37.5\mu\text{m}$, (b) $z=25.0\mu\text{m}$ and (c) $z=12.5\mu\text{m}$ in a microchannel under surface modified environment on an applied field of 40V/cm.

Silanized PDMS suppressed the EOF velocity, though the amino groups are attached to the terminal. Vezenov *et al.* [4] reported that adjoining amino groups are bonding each other with hydrogen bond. PEGylated PDMS also suppressed the EOF velocity because of choosing non ionic PEG in this study.

Zeta-potential Table 2 shows zeta-potentials on modified surfaces calculated from the Helmholtz-Smoluchowski equation by applying averaged EOF velocity. Since surface modification was conducted on PDMS walls totally in this study, each zeta-potential in a pH 7.0 solution was influenced by the surface compositions directly.

4. Conclusions

Under the modified surface environment, the fluid flow was altered dramatically by changing EOF velocity. By measuring EOF velocity at each depth of a microchannel, the EOF field flow in vertical and horizontal direction was investigated. As the result, alteration of EOF field in modified microchannels was examined spatially.

Acknowledgements

This work was subsidized by the Grants-in-Aid for Scientific Research of Ministry of Education, Culture, Sports, Science and Technology (No.17686017) and Keio Leading Edge Laboratory of Science and Technology.

References

1. C.D. Meinhart, S.T. Wereley, J.G. Santiago, *Experiments in Fluid*, **27**, (1999), 414-419.
2. Ichiyanagi *et al.*, Proc. 12th Int. Symp. Appl. Laser Tech. Fluid Mech. (CD-ROM).
3. S. Mori, H. Okamoto, *Fusen*, **27**, (1980), 117-126.
4. Vezenov, D.V., *J. Am. Chem. Soc.*, **119**, (1997), 2006-2015

STABLE POLY(ETHYLENE GLYCOL) MICROWELL ARRAYS FOR LONG-TERM CELL PATTERNING

Hideaki Tsutsui¹, Hong Wu², and Chih-Ming Ho¹

¹Department of Mechanical & Aerospace Engineering, University of California, Los Angeles, 420 Westwood Plaza, Los Angeles, CA 90095, USA

²Department of Molecular and Medical Pharmacology,
UCLA School of Medicine, Los Angeles, CA 90095, USA

Abstract

This paper reports development of stable poly(ethylene glycol) (PEG) micowell arrays for maintaining cell patterning for an extended period of time. By formulating copolymer of PEG-diacrylate (PEG-DA, Mn~575) and pentaerythritol tetraacrylate (PETA), we have achieved non-biofouling microstructures that stay intact for up to one month in 0.1M phosphate buffered saline (PBS). Micromolding in capillaries (MIMIC) [1] was employed to fabricate an array of 50,000 micowell in 1cm² area. The PEG micowell demonstrated accurate patterning of proteins and cells (>98% patterning fidelity). Combination of extensive stability and patterning fidelity allows long-time experiments with regulated cell patterning.

Keywords: PEG hydrogel, micowell array, copolymer, cell patterning

1. Introduction

PEG is used as a non-biofouling material for many biomedical applications. Various cells have been patterned on solid substrates by self-assembled monolayer of PEG (PEG-SAM) [2] or PEG microstructures [3]. However, the PEG-SAM degrades through both cell-dependent / independent oxidation, thus cell pattern fails in about 10 days [2]. PEG microstructures have advantages of topological features allowing physical confinement and three-dimensional assembly of cells. However, excessive swelling of PEG hydrogel causes stress at the PEG-substrate interface, delaminating the microstructures in a short time. To avoid excessive swelling of PEG hydrogel, while maintaining its non-biofouling property, we formulated copolymer hydrogel of PEG-DA and PETA.

2. Experimental

Four types of PEG precursors were prepared: (a) PEG-DA only, (b) PEG-DA + water, (c) PEG-DA + PETA, and (d) PEG-DA + water + PETA. Amounts of water and PETA

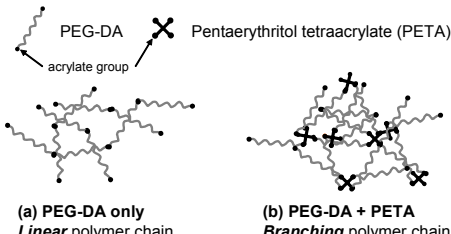


Figure 1 Cross-linked PEG-DA hydrogels (a) without PETA and (b) with PETA. PETA introduces branching of PEG chains to yield a denser mesh structure.

were 20% v/v and 20% w/w of PEG-DA, respectively. PETA, a crisscross molecule with four acrylate terminals, cross-links with PEG-DA, resulting in branched and tighter

PEG mesh (figure 1). Addition of water to the precursor also reduces relative swelling at equilibrium in aqueous solutions after UV photopolymerization. 1% w/w of 2,2-dimethoxy-2-phenylacetophenone was used as the photo initiator. MIMIC was employed to fabricate PEG microwell arrays (figure 2) [1]. In short, a glass substrate was acrylated with 3-(trymethoxysilyl) propyl methacrylate (TSM). A polydimethylsiloxane (PDMS) mold was placed on the substrate, forming a channel network. A droplet of PEG precursor was introduced from one side of the mold, and the precursor fills in the network by capillary motion. The precursor was cross-linked by UV photopolymerization, followed by removal of the mold.

3. Results and Discussion

The fabricated microwell arrays were tested for stability in PBS at room temperature (figure 3). Addition of either of PETA or water significantly improved the adhesion, and combination of the two yielded the best result. This copolymer hydrogel successfully stayed bound to the substrate up to 1 month; 85 times longer than conventionally used PEG-DA monomer hydrogel in this experiment.

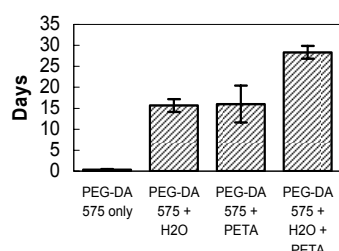


Figure 3 Stability of PEG microwell array in PBS at room temperature. A widely used composition, PEG-DA 575 mono macromer, resulted in delamination of the hydrogel within 12 hours. Addition of PETA and/or water significantly improved adhesion. The average and standard deviation were obtained from three samples for each condition.

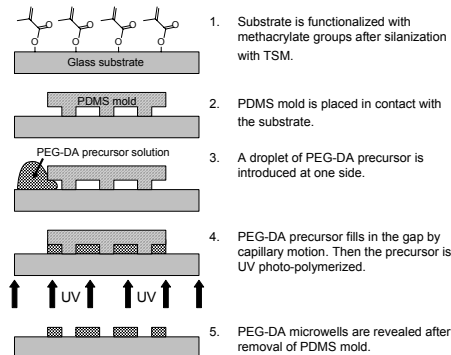


Figure 2 Fabrication of PEG-DA microwells. A glass substrate is functionalized with methacrylate groups after silanization with TSM. A polydimethylsiloxane (PDMS) mold is placed in contact with the substrate, forming a channel network. A droplet of PEG precursor is introduced at one side. The precursor fills in the gap by capillary motion. Then the precursor is UV photo-polymerized. Finally, the PDMS mold is removed to reveal the microwells.

Non-biofouling of the PEG microstructures was tested by patterning bovine serum albumin conjugated with Texas-Red fluorescein (BSA-TR) and HeLa cells. Figure 4 shows successful staining of the microwells where the glass substrate was exposed. Figure 5a demonstrates successful patterning of HeLa, with >98% of cells patterned inside the microwells. The patterning was maintained after 6 days in the

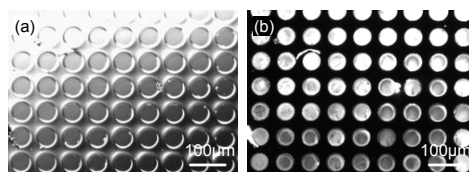


Figure 4 (a) Phase contrast image of 50 μ m-diameter microwell array and (b) BSA-TR staining of the same array.

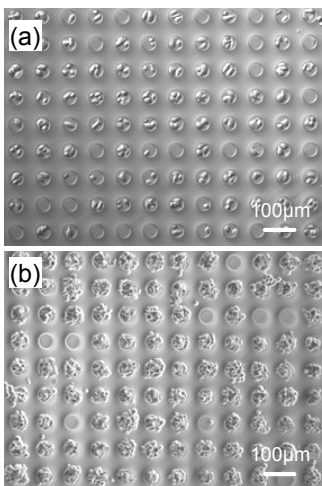


Figure 5 HeLa cells patterning in 50 μm -diameter microwell array. (a) 12 hours after initial plating. Array of 50,000 microwells are fabricated in 1 cm^2 area with high pattern fidelity. (b) After 6 days patterning fidelity was still maintained.

distributions (calculated from experimental average values), clearly indicating stochastic nature of cell patterning process under current experimental conditions.

4. Conclusions

We developed stable PEG microwells by formulating copolymer of PEG-DA and PETA. The fabricated microwells demonstrated significant improvement of physical stability without compromising its non-biofouling property. We believe combination of extensive stability and patterning fidelity allows long-time experiments with regulated cell patterning.

Acknowledgement

This work is partially supported by NASA Institute of Cell Mimetic Space Exploration (CMISE, NCC2-1364) and NIH NIDCR (UO1DE15018)

References

- [1] E. Kim, Y. Xia, and G.M. Whitesides, *Nature*, Vol. 376, pp. 581, 1995.
- [2] C.M. Nelson, S. Raghavan, J.L. Tan., and C.S. Chen, *Langmuir*, Vol. 19, pp. 1493, 2003.
- [3] A. Khademhosseini, S. Jon, K.Y. Suh, et al., *Advanced Materials*, Vol. 15, pp. 1995, 2003.

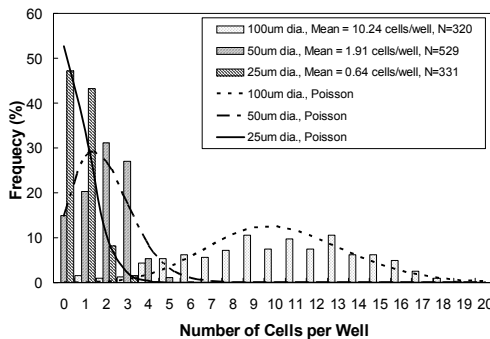


Figure 6 Frequency of a certain number of HeLa cells in microwells at 12 hours after seeding at 1.45×10^6 cells/ml. The histogram matches corresponding Poisson distributions because of the stochastic sedimentation of cells.

culture medium, with cells forming hemispherical aggregates (figure 5b). Figure 6 shows results of HeLa patterning in various microwells (25-100 μm diameter, seeded at 1.45×10^6 cells/ml). As anticipated the average number of cell per well increased almost proportionally to the area of individual microwells. The histogram matches Poisson

distributions (calculated from experimental average values), clearly indicating stochastic nature of cell patterning process under current experimental conditions.

SUB-NANO LITTER MICRO BATCH OPERATION SYSTEMS WITH MULTI-STEP LAPLACE PRESSURE VALVES PREPARED BY PHOTOCATALYTIC ANALOG LITHOGRAPHY

Go Takei¹, Mari Nonogi¹, Akihide Hibara^{1,2,3}, Takehiko Kitamori^{1,2,3} and
Haeng-Boo Kim^{1,2,3}

¹ School of Engineering, The University of Tokyo, Bunkyo, Tokyo, 113-8656, Japan

² Kanagawa Academy of Science and Technology, Kawasaki, Kanagawa, 213-0012, Japan

³ CREST, Japan Science and Technology Agency, Kawaguchi, Saitama, 332-0012, Japan

Abstract

This paper reports micro batch operation systems, which consists of two liquid dispensers and a chamber. To make them, Laplace pressure valves, which were prepared by photo patterning method to make wettability pattern, were utilized. Pattern of 5 pressure barriers was prepared in a microchannel. 900 pL and 450pL liquid fragments were measured, transported and mixed in the chamber.

Keywords: Photocatalyst, Patterning, Wettability, Laplace pressure, Titration

1. Introduction

We have developed various micro chemical processes on microchip according to the conception of continuous flow chemical processing (CFCP) [1]. In addition to CFCP, batch operations such as a quantitative sampling and a titration, is important for the further development of micro chemical systems. To prepare the batch operation systems, valves are important. However, it is difficult to fabricate mechanical valves in a microchip to handle sub-nano litter liquid. We have developed Laplace pressure valves utilizing surface wettability as stated in the following section. In this study, by utilizing the Laplace pressure valves, we prepared micro batch operation systems as shown in Figure 1. In the pL liquid dispensers, a fixed quantity of liquid was measured and dispensed into the chamber. The chamber kept the dispensed liquid fragment during mixing, reaction and detection processes. As a typical example of micro batch operations, titration was carried out.

2. Principle

As shown in Figure 2, by hydrophobic - hydrophilic patterned channel or narrower hydrophobic channel, a pressure barrier (P_B) was induced. P_B follows the Young-Laplace equation. [2-5]

$$P_B = \frac{2\gamma \cdot \cos\theta}{R} \quad \gamma: \text{interfacial tension} \quad R: \text{hydraulic radius}$$

To control the θ value, we have developed the photo patterning method (photocatalytic analog lithography) [2]. Microchannel is coated with TiO_2 nano particles and then modified with octadecylsilyl (ODS) group. Then UV irradiation makes the surface hydrophilic due to photocatalytic degradation of ODS. As shown in Figure 3, wettability is spatially patterned and controlled by the photo-irradiation area and the irradiation time, respectively. As a result, multi-step Laplace valves, which have different P_B s, are prepared. When an applied pressure (P_A) is less than P_B , the Laplace valves acts as a stop valve.

3. Experimental

$ODS-TiO_2$ modified microchannel (width: 60 μm , depth: 15 μm) was fabricated as shown in Figure 1. UV irradiation through the photomasks was carried out changing irradiation time stepwisely in the range from 0 to 16 min. Pattern of 5 pressure barriers as shown in Figure 4 was prepared. Aqueous liquid and air was introduced by using the pressure control system.

4. Results and discussion

Aqueous liquid was filled into the dispenser by the pressure less than V_2 (12.5 kPa) and V_6 (14.0 kPa). In the Dispenser I, 900 μl liquid was measured controlling the air pressure less than V_2 (Figure 5a). By applying the pressure (16.0 kPa) more than V_2 , the

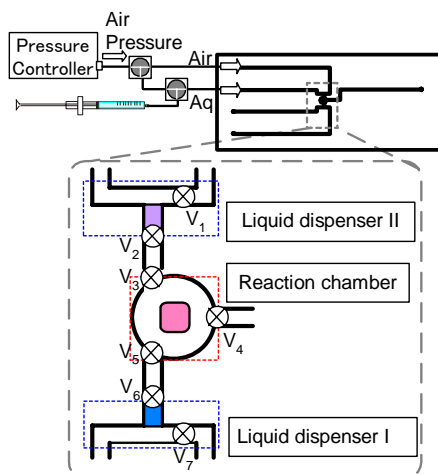


Figure 1. Conception of micro batch operation systems. The batch systems with two liquid dispensers and chamber was designed for titration. The system was equipped with 7 Laplace pressure valves prepared by novel photocatalytic analog lithography.

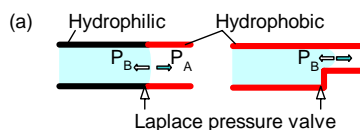


Figure 2. Laplace pressure valve
(a) Hydrophilic and hydrophobic patterned surface
(b) Narrower hydrophobic channel

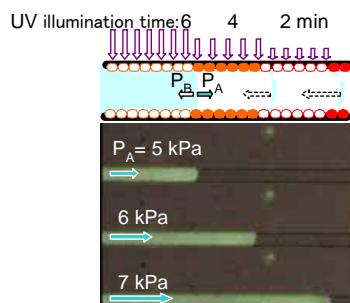


Figure 3. Multi-step Laplace pressure valves
By utilizing PAL, wettability can be patterned spatially and be controlled by UV illumination time. Pressure barriers of valves were controlled stepwisely.

liquid fragment was transported into the reaction chamber. In the same way, 450 pL liquid was dispensed into the chamber from Dispenser II (Figure 5b). During the liquid dispensing procedure, the 900 pL liquid fragment, which was dispensed from the Dispenser I previously, did not leak out from the chamber due to the valves (V_4). As a result, two dispensed liquid fragments were mixed in the chamber. We successfully performed the procedure for the titration.

5. Conclusions

We prepared micro batch operation systems utilizing multi-step Laplace pressure valves. Sub nano litter aqueous liquid fragments were measured and mixed in the chamber as a fundamental liquid manipulation for the titration.

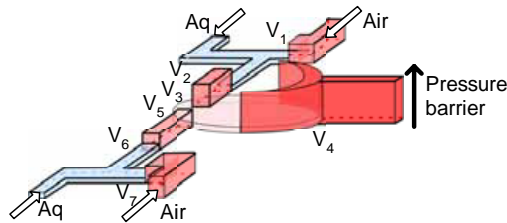


Figure 4 Schematic illustration of pressure barrier pattern prepared by PAL.

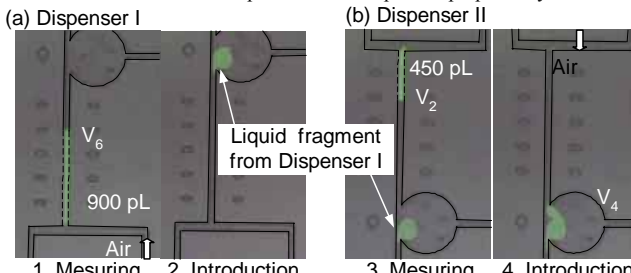


Figure 5 (a) 900 pL liquid was dispensed. (b) 450pL liquid fragment was dispensed and mixed.

Acknowledgements

The authors acknowledge a Grant-in-Aid from the Ministry of Education, Culture, Sports, Science and Technology (MEXT), Japan (no. 14050024 on Priority Areas (417)) for support in part of the research.

References

- [1] M. Tokeshi et al., *Anal. Chem.*, 2002, **74**, 1565 [2] G. Takei et al., *Micro Total Analysis Systems* 2005, 1273 [3] B. Zhao et al., *Science*, 2001, **291**, 1023 [4] A. Hibara et al, *Anal. Chem.*, 2005, **77**, 943 [5] T. Koide et al, *Micro Total Analysis Systems* 2003, 769

‘ON THE FLY’ PRODUCTION OF MICROTUBES FOR THE ARTIFICIAL MICRO VESSEL

SungRak Kim^{1,2,4}, DuckJoong Kim^{1,2}, HyunJung Jung³, JaeHoon Kim³,
DongKeun Han³, Kyung Sun^{1,2} and SangHoon Lee^{1,2}

¹Korea Artificial Organ Center, Korea Univ., South Korea

²Dept. of Biomedical Engineering, Korea Univ., South Korea

³Biomaterials Research Center, KIST, South Korea

⁴Korea Materials and Analysis Corp.(K-MAC), South Korea

Abstract

In this paper, we report a novel technique for the manufacture of artificial capillary having anticoagulant property. To use the blood compatible fabricated microtubes as the capillary, they were immobilized by heparin that has anticoagulant property. In addition, the blood compatibility of heparin-immobilized microtubes was evaluated by blood coagulation times and compared with the untreated control one.

Keywords: ‘on the fly’ photopolymerization, artificial vessel, microtube, heparin, blood compatibility

1. Introduction

The artificial blood vessels feasible for clinical use are fabricated by tissue engineering technology and most of their diameters are larger than 4mm [1]. However, smaller blood vessels with diameter less than millimeter size are as well as required, particularly in the peripheral circulation system. In this paper, we present a new method to create artificial capillary having diameter around 100 μm and the fabrication process was carried out using microfluidic chip and ‘on the fly’ polymerization method.

2. Principle of artificial micro vessel fabrication

To create micro vessel, microfluidic chip(MFC) was constructed using our pre-reported method [2] and hydrodynamic phenomena (e.g. laminar flow) were employed. The apparatus to fabricate the micro vessel is shown in Figure 1 and is fabricated by integrating the pre-punctured PDMS-based MFC and pulled glass pipette. Into 3 inlets, the photopolymerizable sample fluid (4-hydroxybutyl acrylate (4-HBA) mixed with photoinitiator and crosslinker) and non-polymerizable core and sheath fluid are introduced, and the coaxial flow is formed at the outlet pipette. By radiating UV light onto this coaxial outlet flow, we have polymerized the sample fluid, and the polymerized microtube is continuously produced. To add anticoagulant property at this microtube, we have developed the process to immobilize heparin on the surface 4-HBA. The heparinization was carried out by coupling heparin to -OH group of 4-HBA as illustrated in Figure 2.

3. Preparation of materials and experiments

The 4-HBA (81.605 wt%, Sigma-Aldrich) solution was mixed with crosslinker (ethylene glycol dimethacrylate(1.138 wt%, Sigma-Aldrich)) and photo-initiator (2,2'-dimethoxy-2-phenyl-acetonphenone(3.415 wt%, Sigma-Aldrich)) and this mixed solution was used as a sample fluid. The non-polymerizable core and sheath fluid were prepared by mixing 50 vol % polyvinyl alcohol (PVA) and 50 vol% DI water. To immobilize the heparin on the surface of microtubes, first, the tresylation reaction mixture was prepared by adding 200 ul of pyridine and 100 ul of dry tresyl chloride to 25 ml of dry acetone. The microtubes were soaked in the mixture and the reaction was allowed to proceed for 10 min at room temperature, after which the specimen was rinsed in 1 mM HCl and then 0.2 M sodium bicarbonate buffer (pH 10). The specimen was immersed in the buffer containing 1 wt% of heparin and incubated for 20 hr at room temperature. Subsequently, the buffer was removed, replaced with other buffer containing 0.8 M β -mercaptoethanol, and incubated for 2 hr.

4. Results and Discussion

Figure 3(a) and 3(b) demonstrates the continuously created microfiber and the lumen of the fiber. The inner and outer diameter of tube can be regulated via the change of flow rates (inner: sample flow rate, outer: sheath flow rate) as illustrated in Figure 4(a) and 4(b). We have introduced the water having air bubble into the microtube using syringe pump (Figure 5), and the flow moved well inside the microtube. In addition, Figure 6 demonstrates microtube FTIR spectra containing the specimen which has anti-coagulant property by heparin grafting. From the results of blood coagulation times measured by Blood Coagulation Analyzer, Sysmex CA-50, the coagulation time of heparin-immobilized specimen was more extended (78 sec) than that of untreated control one (40 sec), indicating that heparin-immobilized specimen is more blood compatible.

5. Conclusions

To use this microfiber as the capillary, we have embedded the heparin which is widely applied as an anticoagulant. We will investigate the blood compatibility by injecting the whole blood and biocompatibility by implanting the samples inside the skin in future. As conclusion, we have demonstrated a novel and simple method to fabricate the blood compatible micro polymeric vessels for the replacement of damaged vascular system, and we will prove its feasibility through the in-vivo test.

Acknowledgement

This study was supported by a grant of the Korea Health 21 R&D Project, Ministry of Health & Welfare, Republic of Korea (0405-ER01-0304-0001)

References

- [1] G. J. Wang, Y. F. Hsu, Vol. 10, Biomed. Microdevices (2005), pp. 51-58
- [2] Jeong W. J., Kim J. Y., Kim S. J., Lee S. H., Mensing G and Beebe D.J., Vol. 4, Lab Chip (2004), pp. 576-580

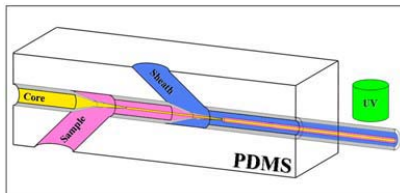


Figure 1. The apparatus to fabricate the micro vessel

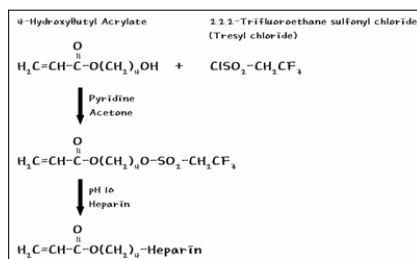


Figure 2. Heparin immobilization process

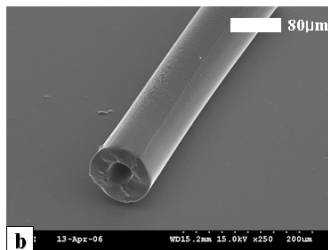
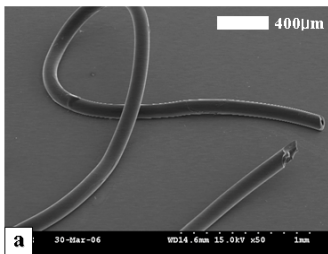


Figure 3. (a) The continuously created microfiber (microtube) and (b) The lumen of the fiber

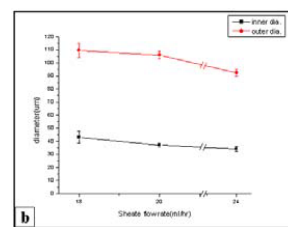
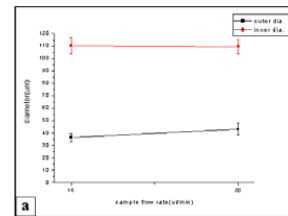


Figure 4. (a) Inner & outer diameter to the sample flow rate($\mu\text{l}/\text{min}$) change, (b) Inner & outer diameter to the sheath flow rate(ml/hr) change

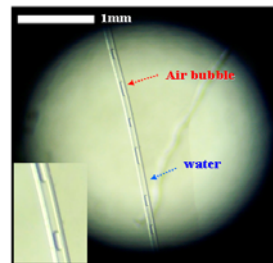


Figure 5. Introduced the water having air bubble into the microtube using syringe pump

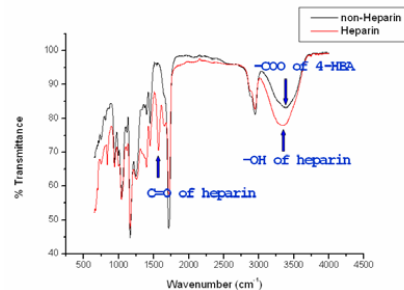


Figure 6. FTIR spectra of microtubes

MICROFLUIDIC-DIRECTED MOLECULAR SELF-ASSEMBLY AND TEMPLATING OF BIO-INSPIRED NANOPARTICLES

Wyatt N. Vreeland¹, Jennifer S. Hong¹, Andreas Jahn¹,

Srinivasa R. Raghavan², Laurie E. Locascio¹, and Michael Gaitan¹

¹National Institute of Standards and Technology, Gaithersburg, MD, 20899 USA

²University of Maryland, College Park, MD, 20742 USA

Abstract

Biology is replete with the motif of molecules self assembling into larger functional elements. In fact, a human being can be thought of as the product of the directed self-assembly of cells into a functional person. Here, we take a simple biologically inspired system, the liposome, and use it to template the self-assembly of biomolecules into nanoparticles of controlled size and architecture. We show that liposomes can be used to template the gelling of alginate into nanoparticles that have size equivalent to that of the parent liposome. This allows for the control of the nanoparticle size through modulation of the templating liposome's size. In contrast to liposomes and other vesicles, these nanoparticles appear to be extremely stable to temperature variations, detergent treatment, and changes in buffer osmolarity and pH.

Keywords: Self-assembly, nanoparticles, templating, liposomes

1. Introduction

Liposomes are spherical vesicles made of amphipathic lipids that self assemble in aqueous environments. They sequester an interior aqueous volume, are bathed in an aqueous extravesicular environment and are often used as "containers" for drug delivery, encapsulation of therapeutics, and flavorings. Liposomes exist in one of two thermodynamic phases, either liquid crystalline or gel. The phase is largely determined by the lipid formulation and the temperature of the system. When heating or cooling the system through the liquid crystalline-gel phase transition, grain boundaries between the coexisting phases in the liposome allow for the diffusion of small molecules through the lipid membrane and allowing for controlled modulation of the chemical environment of the liposome interior [1]. In this work we use the ability of liposomes to separate two distinct aqueous environments with controlled diffusion of small ions between these environments to template the self-assembly of alginate into spherical nanoparticles of controlled size.

In particular, we prepare liposomes that encapsulate a solution of sodium alginate suspended in an aqueous buffer containing Ca^{2+} ions. The encapsulated sodium alginate is "cross-linked" inside the liposome to form a gel through thermal permeabilization of the liposome membrane. This allows the Ca^{2+} ions to diffuse into the liposome causing gelation of the alginate. Subsequently the liposome "shell" is removed through aggressive treatment with the detergent octyl β -glucopyranoside (OBG); the resulting

alginate nanoparticles are then further characterized. This process is shown schematically in Figure 1.

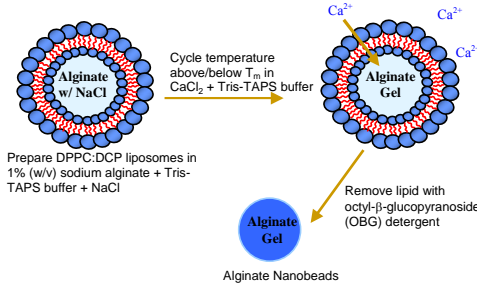


Figure 1. Schematic of the liposome template alginate gellation.

2. Experimental

Alginate particles were prepared by injecting 5μmoles of 1,2-dipalmitoyl-*sn*-glycero-3-phosphocholine (DPPC): dicetyl phosphate (DCP) lipid dissolved in isopropyl alcohol into an aqueous solution containing 1% w/v sodium alginate and Tris-TAPS-NaCl buffer. While injecting the lipids the solution was vortexed. After free alginate removal by centrifugation, the liposomes were resuspended in Tris-TAPS-CaCl₂ buffer and heated to the melting temperature to facilitate Ca²⁺ diffusion from surrounding buffer into the liposome for gelation of the encapsulated alginate. Removal of lipid shell with OBG detergent and buffer rinse resulted in templated calcium alginate nanogels.

3. Results and discussion

Nanoparticles were characterized with Asymmetric Flow Field Flow Fractionation (AFFFF) with tandem MultiAngle Laser Light Scattering (MALLS) and Dynamic Light Scattering (DLS) (Wyatt Technology, Inc, Santa Barbara, CA [2]) and Differential Interference Contrast (DIC) microscopy. AFFFF is a size based separation technique that is especially useful for colloidal systems. It separates particles by spatially partitioning them in different regions of a laminar parabolic flow profile according to the ratio of their diffusion rate to their Stokes drag. The MALLS detector then allows for both the detection of the presence of the particles as well as determination of their size through measurement of the angular dependence of the intensity of light scattered by the particles.

Figure 2 shows a fractogram showing the excess Rayleigh ratio measured at 90° as a function of time and the size as determined by MALLS for template liposomes containing ungelled alginate (panel A) and alginate nanoparticles prepared from liposomes as described in the experimental section (panel B). Comparing Figure 2a and 2b shows that the calcium alginate particles have radii and polydispersity similar to the original liposome template population with 90% of the alginate nanobeads having radii between 75 nm and 140 nm; the smaller radii are likely due to varying encapsulation efficiency of the alginate in liposomes. The ratios of hydrodynamic radius (as determined by DLS) to root mean square radii (as determined by MALLS) of empty liposomes are consistent with those expected for a hollow sphere and a solid isotropic sphere for the alginate nanoparticles.

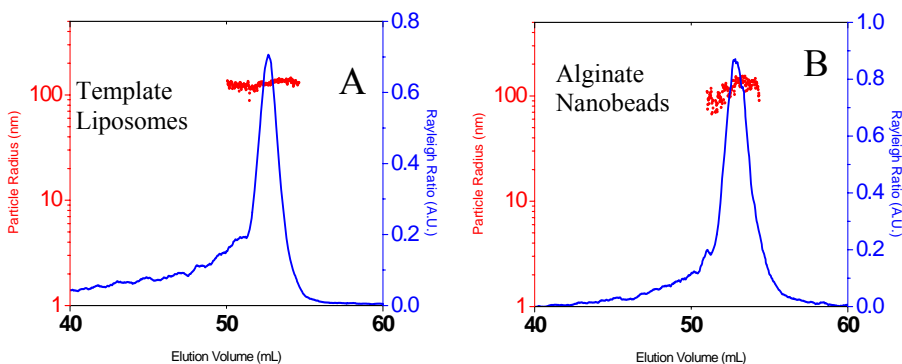


Figure 2. Tandem AFFF-MALLS fractograms of ungelled alginate liposomes (panel A) and alginate nanobeads (panel B). Conditions: buffer: 50 mM Tris-TAPS +15 mM NaCl. Elution flow 1 mL/min, Cross flow ramp of 2 mL/min to 0 mL/min over 45 minutes. 10 kDa regenerated cellulose membrane, channel height 250 μ m.

Figure 3 shows differential interference contrast micrograph of both liposomes (panel A) and self-assembled alginate nanoparticles (panel B). Visual inspection of the micrographs shows particles sizes that are consistent with MALLS and DLS measurements.

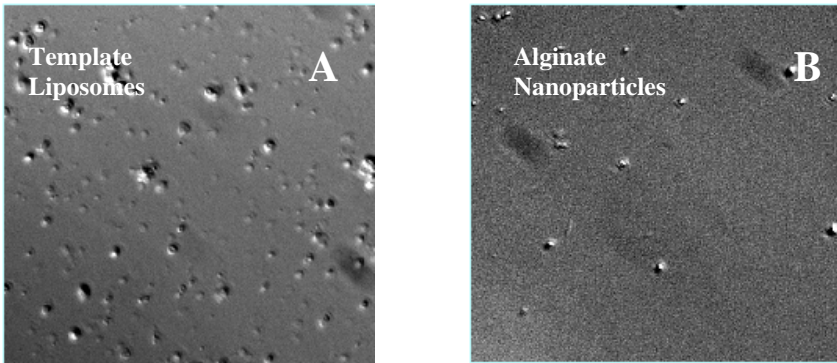


Figure 3. Differential interference contrast micrographs of template liposomes (panel A) and alginate nanoparticles (panel B). Features in the micrographs are below the diffraction limit of the imaging technique (500 nm) which is consistent with MALLS and DLS measurements

References

1. Vreeland W.N. and Locascio L.E. *Anal. Chem.* 75 (24): 6906-6911.
2. Certain commercial materials and equipment are identified in order to specify adequately experimental procedures. In no case does such identification imply recommendation or endorsement by the National Institute of Standards and Technology, nor does it imply that the items identified are necessarily the best available for the purpose.

MICROFABRICATION OF GRAPHITIC CARBON MATERIALS VIA ELECTROCHEMICAL ETCHING

**Mark T. McDermott, Solomon Ssenyange, Justine Taylor, D. Jed Harrison,
Rongbing Du**

Department of Chemistry and National Institute for Nanotechnology,
University of Alberta
Edmonton, Alberta T6G 2G2

Keywords: Etching, electrochemistry, graphitic carbon, electrospray mass spectrometry.

Abstract

We report here for the microfabrication of structures in carbon materials, particularly glassy carbon (GC) and thin carbon films. The procedure we employ combines lithographic pattern transfer and electrochemical etching to microfabricate features in carbon. We will discuss the etching mechanism, parameters that control the etching rate and the topography of the resultant etched surface.

1. Introduction

Microfabrication has had a considerable impact in many areas of chemistry and biology. The application of processes such as metal deposition, lithographic pattern transfer and etching techniques to a variety of materials has enabled, for example, the development of lab-on-a-chip devices, microelectromechanical systems (MEMS), miniaturized sensor systems, and methods to easily and reliably pattern surfaces. It is reasonable to believe that further developments of microfabrication processes and materials will lead to additional useful applications. We report here for the microfabrication of structures in carbon materials, particularly glassy carbon (GC) and thin carbon films.¹ The physical properties of GC such as good electrical conductivity, thermal stability, low gas permeability, low coefficient of thermal expansion, and low density provide a framework for GC as an appealing complementary material to glass and silicon for designing miniature systems. In addition, a number of convenient methods exist to chemically tailor the surface of GC opening pathways for the development of microsensors and microsystems for controlled fluid flow. Micromachined GC structures may also find applications as microbatteries, and microcapacitors.

2. Experimental

The procedure we employ combines lithographic pattern transfer and electrochemical etching to microfabricate features in carbon. A mask pattern is transferred into a layer of photoresist that had been deposited on a carbon surface. The substrate is then anodized in 0.1 M NaOH and the photoresist dissolved in an appropriate solvent. Due to the nanometer scale size of graphitic crystallites in GC, the electrochemical etching is isotropic

3. Results and discussion

Figure 1 demonstrates the result of our procedure. Figure 1A is a tapping mode (TM) SFM image of a GC electrode anodized at 3.0 V for 15 min. through a pattern transferred from a TEM grid consisting of 25 μm square openings. As highlighted in the cross sectional profile, the regions that were exposed to the anodization appear 400 nm lower in topography than those that were masked with the photoresist. Figure 1B is a SEM image of a similar GC substrate providing a different view of the well-like structures that can be fabricated with this procedure. The combination of lithographic patterning and electrochemical oxidation in basic solution results in spatially selected etching of GC and provides a pathway for microfabrication.

We are exploring a number of applications of microfabricated carbon materials. One application is that of microfluidic devices. As shown in Figure 2, channels of appropriate dimensions for microfluidic devices can be easily etched into GC. The channels in this device are 300 μm wide and 30 μm deep, similar to dimensions that are fabricated in glass substrates. A more complex channel system is shown in Figure 2B. We have been able to fabricate a number of complex channel systems into GC. For example, we have fabricated and tested a GC microfluidic device for electrospray mass spectrometry.² The advantage here is the ability to apply the electrospray voltage directly to the chip.

Another area we are pursuing is the fabrication of microelectrode arrays. The starting point for fabricating arrays of graphitic carbon structures that range in size from tens of microns to submicron is a thin (1–3 μm) graphitic carbon film on a conductive silicon substrate. Following lithographic transfer of a mask pattern, the carbon film is etched through to the silicon substrate. Arrays of carbon structures like that shown in Figure 3 can be prepared. The shape and size of the structures can be controlled by

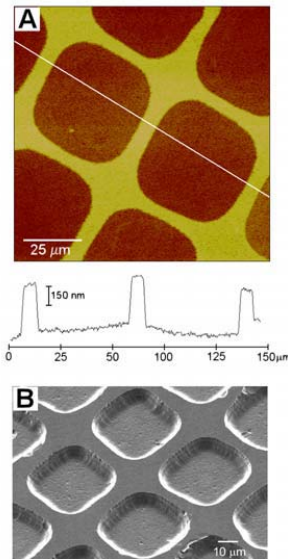


Figure 1: (A) 110 μm^2 TM-SFM image of the surface of a GC substrate after etching (B) SEM image of microwells etched in GC.

mask design and etching conditions. These structures provide electrochemical responses that are expected from microelectrode arrays of the appropriate geometry.

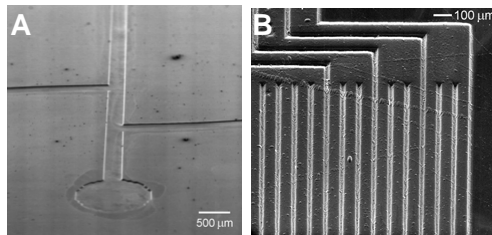


Figure 2: SEM images of microchannel structures etched in GC. The channels in both (A) and (B) were etched at 2.0 V for 30 min.

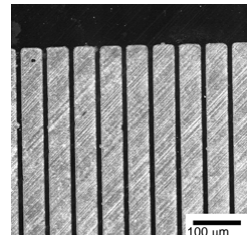


Figure 3: SEM image of a carbon microband electrode array fabricated via electrochemical etching.

4. Conclusions

We have demonstrated that lithographic pattern transfer and anodic etching in 0.1 M NaOH can be combined to microfabricate features in GC. In general, we employ an anodization potential between 2.0 and 2.5 V for between 30 and 120 min. to etch structures with depths on the order of tens of microns. We have demonstrated that a number of interesting structures can be etched into GC and are pursuing microfluidic devices and microelectrode arrays.

Acknowledgments

This work was supported by the Natural Sciences and Engineering Research Council of Canada (NSERC) and the Department of Chemistry, University of Alberta. We would like to thank the staff of the U of A NanoFab facility for training and useful discussions.

References

1. G. K. Kiema, S. Ssenyange, M. T. McDermott, *Microfabrication of Glassy Carbon by Electrochemical Etching*, *Journal of the Electrochemical Society* **2004**, *151*, C142-C148.
2. S. Ssenyange, J. Taylor, D. J. Harrison, M. T. McDermott, *A Glassy Carbon Microfluidic Device for Electrospray Mass Spectrometry* *Analytical Chemistry*. **2004**, *76*, 2393-2397.

INTEGRATED MICROREACTOR FOR CONTINUOUS COLLOID SYNTHESIS AND SURFACE-COATING

S. A. Khan, V. Gondoin and K.F. Jensen

Department of Chemical Engineering, Massachusetts Institute of Technology,
Cambridge, MA 01239, USA

Abstract

We report an integrated microreactor for continuous flow silica synthesis and subsequent titania overcoating. The microreactor consists of two stacked reactor layers fabricated in PDMS, the first layer consisting of microchannels for silica synthesis and the second layer consisting of microchannels for titania overcoating.

Keywords: Microreactor, colloids, silica, titania, segmented-flow

1. Introduction

Titania (TiO_2)-coated silica (SiO_2) particles are of considerable interest in a broad range of applications ranging from photocatalysis and pigments to photonic crystals. Sol-gel coating of titania on silica is a popular route to such core-shell particles. However, the rapid hydrolysis rates of titania precursors make the obtained coatings extremely sensitive to process parameters. Typically, multi-step batch processes have been employed with limited success. We have previously demonstrated microreactors for synthesis of monodisperse colloidal silica [1], as well as for coating thin layers of titania on pre-synthesized silica particles [2]. Here we report an integrated microreactor for the continuous silica-titania core-shell nanoparticle synthesis. It is possible to tune the relative sizes of the silica core and titania shell by simply varying the flow rates and residence times of the respective reactants. This microreactor therefore enables continuous synthesis of core-shell particles with engineered optical properties.

2. Experimental

Figure 1(a) is a schematic of the integrated microreactor. It consists of two stacked reactor layers, one for synthesis and the other for surface-coating. Both layers are fabricated in PDMS by standard soft lithographic techniques. The first layer is plasma-bonded to a glass substrate and the second layer is then aligned and plasma-bonded on top of the first. Figure 1(b) shows a photograph of a fabricated microreactor, and Figure 1(c) shows a cross-sectional schematic of the bonding and packaging scheme. Nucleation and growth of primary silica particles is accomplished in layer 1. A small amount of titanium tetraethoxide (TEOT) is then introduced at regular intervals through a manifold (Figure 1(a)) into the microreactor of layer 2 such that low concentration of alkoxide is maintained throughout. This ensures that uncontrolled precipitation of large titania particles does not occur, and only heterogeneous layer growth takes place on the silica surface. We use gas-liquid segmented flow that enables mixing of the added

reactant with the suspended particles in layer 2, and narrows particle size distributions throughout the integrated device.

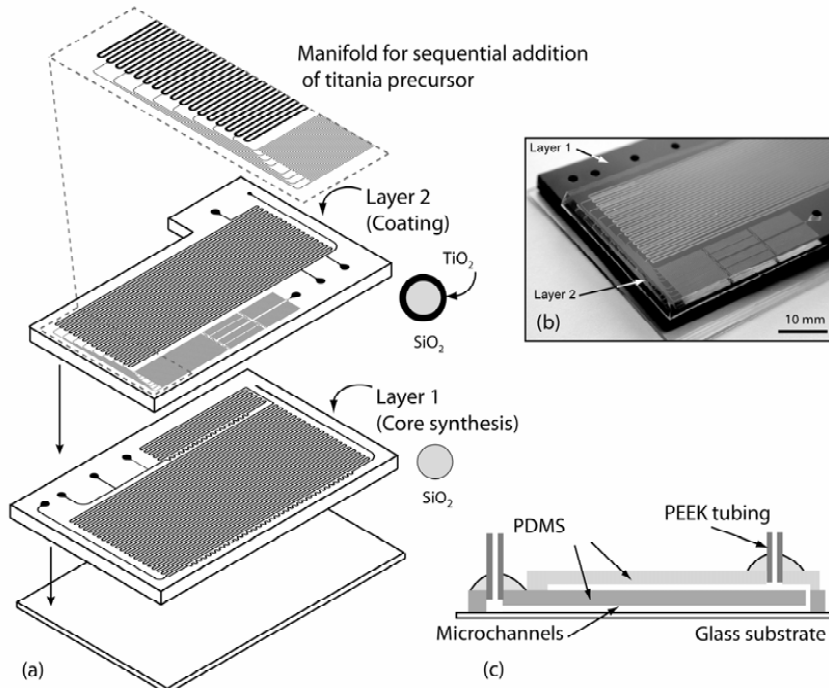


Figure 1: (a) Schematic of integrated microreactor. (b) Photograph of fabricated microreactor (c) Cross-sectional schematic illustrating packaging and bonding scheme.

3. Results and Discussion

There are several challenges associated with continuous alternating silica and titania sol-gel chemistry without intermediate particle separation. The silica synthesis reaction is typically slow, and requires both dissolved ammonia and excess water (~5 M to 15 M). Titanium alkoxide precursors, on the other hand, rapidly react with water leading to uncontrolled titania precipitation for water concentrations above 1 M. Hence, an integrated reactor that accomplishes series synthesis has to accommodate an intermediate quench/dilution step that adjusts the particle and water concentrations to values that are required for uniform titania (or silica) coatings without secondary precipitation and primary particle agglomeration. This ability to control layer growth without secondary homogeneous nucleation enables continuous multi-layer synthesis without the need for repeated separation steps that burden conventional synthesis techniques.

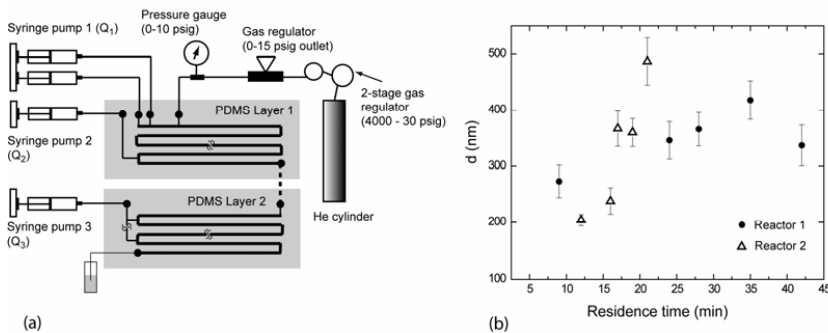


Figure 2: (a) Schematic of experimental setup (b) Tunable silica synthesis in integrated microreactor. The ‘Reactor 1’ conditions labeled in the figure correspond to $Q_1 = 2 \mu\text{L}/\text{min}$ and $Q_2=Q_3 = 18 \mu\text{L}/\text{min}$, with gas pressure as a parameter to adjust mean residence time. Similarly, ‘Reactor 2’ conditions labeled in the figure correspond to $Q_1 = 3 \mu\text{L}/\text{min}$ and $Q_2=Q_3 = 27 \mu\text{L}/\text{min}$.

The first set of experiments performed with the above microreactor consisted of ‘blank’ silica synthesis with no overcoating. Figure 2(a) is a schematic of the experimental setup. The important operating parameters were total inlet flow rate of silica reactants into layer 1 (Q_1), the inlet gas pressure and the flow rate of ethanol into the quench inlet of layer 1 (Q_2) and the feed manifold of layer 2 (Q_3). Figure 2(b) shows the results of these experiments. As expected, mean particle size increased with residence time in all cases. Tunable silica particle synthesis was thus demonstrated in the new microreactor. Subsequent experiments were carried out by feeding a TEOT solution through the manifold inlet of layer 2, in addition to the silica reactants and ethanol quench of layer 1. The main observation from these experiments is that extensive secondary titania precipitation occurs, with (qualitatively) different particle population distributions for the different synthesis conditions. There is a trade-off involved in these experiments. Increasing the quench flow rate dilutes the water concentration from the silica synthesis ($\sim 1 \text{ M}$) to levels that are acceptable for titania overcoating ($\sim 0.1 \text{ M}$). However, this also dilutes the particle concentration which increases the possibility of secondary nucleation. These counteracting considerations lead us to believe that there exists an optimum dilution of the synthesis mixture of layer 1 that will yield uniform titania coatings without secondary nucleation in layer 2. In addition, a smaller flow rate of titanium precursor feed is preferable for uniform titania coatings.

Acknowledgements

S. Khan acknowledges funding from CMSE at MIT and V. Gondoin acknowledges the support of Prof. Philipp Rudolf von Rohr.

References

1. Khan, S. A., Günther, A., Schmidt, M.A., and Jensen, K.F. *Langmuir* **2004**, *20*, 8604-8611.
2. Khan, S. A. and Jensen, K.F. *MicroTAS* **2005**, Vol.1, 265-267.

PHOTOPATTERNED POLYELECTROLYTE MULTILAYERS FOR CELL CULTURE

Darwin R. Reyes*, J. Brian Hutchison**,
Laurie E. Locascio** and Michael Gaitan*

*Semiconductor Electronics Division, and **Analytical Chemistry Division,
National Institute of Standards and Technology, Gaithersburg, MD USA

Abstract

A unique method for layer-by-layer patterning and crosslinking of polymers with dissimilar cell attachment characteristics is presented. Polyelectrolyte multilayers (PEMs) were deposited and exposed with UV light through a binary photomask to form a patterned upper stratum where cells are not viable and a lower cytophilic stratum. This work describes the facile synthetic procedures used to make crosslinkable polyelectrolytes, demonstrates photopolymerization of the functionalized polyelectrolytes, and reveals the cytophobic character of the new synthesized polyelectrolytes for future cell culture applications.

Keywords: cell culture, photopolymerization, polyelectrolyte, surface modification

1. Introduction

Deposition and spatial patterning of polyelectrolyte multilayers (PEMs) provides an avenue for constructing well-defined surface patterning with precise chemical properties that can serve as bioanalytical tools to address questions about cell-cell interactions, signaling, and migration, among others. Specifically, the depth of features is controlled by the number of layers in the PEM, and, in the case of this contribution, the lateral dimensions are controlled by 365-nm photolithography. Furthermore, the functionality and combination of various polyelectrolytes can be chosen to define the chemistry of the PEMs. Previous reports have demonstrated the stabilization of cytophobic PEMs, formed from commercially-available polyelectrolytes without modification, by exposure to UV light in the presence of a photoinitiator, but the mechanism for crosslinking is not obvious [1]. In contrast, the results described in this contribution demonstrate a facile means for functionalizing polyelectrolytes to introduce polymerizable groups for stabilizing cytophilic and cytophobic PEMs via radical chain photopolymerization.

2. Experimental

A. Functionalizing poly(allylamine hydrochloride) (PAH). Succinimidyl methacrylate (NHS-MA) (121 mg) in dimethylformamide was added to the PAH solution (5.3 mmol in 30 ml of water) and it was stirred for 30 minutes. The pH was adjusted to 9 and the solution stirred for 2 hours. The solution was dialyzed against water with 10,000 MWCO tubing for 3 days and lyophilized. The resulting foam-like white powder was characterized by NMR, and found to have approximately 10 % of the pendant amine functionality converted to methacrylamide groups.

B. Functionalizing poly(acrylic acid) (PAA). N-hydroxysuccinimide (NHS, 119 mg), dissolved in ethanol, and 2-aminoethyl methacrylate hydrochloride, (AEMA, 228 mg)

dissolved in water, were added to 50 % aqueous PAA solution diluted in water and stirred for 5 minutes. *N*-ethyl-*N'*-(3-dimethylaminopropyl)carbodiimide (EDC, 452 μ l) was added dropwise. After stirring for 2 hours, the solution was dialyzed against water with 10,000 MWCO tubing for 3 days and lyophilized. The resulting white powder was characterized by NMR. Approximately 10 % of the carboxylic acid functionality was converted to amide-tethered ethyl methacrylate groups.

C. Functionalizing polyacrylamide (PAAm). NHS (200 mg) in tetrahydrofuran, AEMA (250 mg), and 15 ml of water were added to an aqueous solution of PAAm-co-PAA (PAA is 10 % of total repeat units) and stirred for 5 minutes. EDC (280 μ l), dissolved in water, was added dropwise. After stirring for 2 hours at 50 °C, the solution was dialyzed against water with 10,000 MWCO tubing for 3 days and lyophilized. The resulting white powder was characterized by NMR. Approximately 1/3 of the carboxylic acid functionality (or 3 % of the total number of repeat units) was converted to amide-tethered ethyl methacrylate groups.

D. PEMs deposition and photopolymerization procedure. Multilayers were deposited by alternating immersion of a glass substrate in solutions of the polycation and polyanion. Figure 1 depicts the combination of polyelectrolytes used to make spatially-defined cytophilic and cytophobic surfaces. PAH, poly(sodium 4-styrenesulfonate) (PSS), and rinsing solutions were maintained at pH 5.1. After depositing 5 layers, the substrate was rinsed with water at pH 3. Then, up to 9 alternating layers of PAA and PAAm, which are held together by hydrogen bonding, were deposited at pH 3 [2]. Finally, an aqueous solution of photoinitiator (Irgacure 2959) was injected into a space between a photomask and the PEM-coated substrate defined by the thickness of a rubber gasket (typically, 200 μ m to 500 μ m) used to contain the photoinitiator solution.

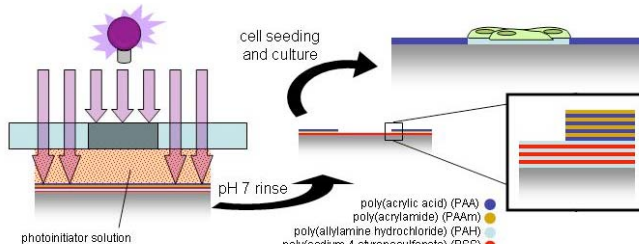


Figure 1. Schematic of method for patterning PEMs.

The substrate was exposed through the photo-mask with 365-nm light with a typical light intensity of ca. 20 mW/cm². After exposure, the substrate was rinsed with water to remove photoinitiator and uncrosslinked polyelectrolytes.

3. Results and Discussion

Figure 2 contains the results from analyzing the photopolymerization kinetics in a ca. 1 μ m film of methacrylate-functionalized PAA. The conversion of double bonds was measured by monitoring the disappearance of the absorbance at 950 cm⁻¹ using a grazing angle accessory with a FTIR spectrometer. The sample reached a maximum conversion of ca. 40 % after 20 minutes of exposure. This experiment yields two important conclusions. First, the functionalized polyelectrolytes are photopolymerizable. The kinetics and maximum conversion are within reason for meth-

acrylate polymerization within a solid thin film. Second, by employing the grazing angle accessory, FTIR spectroscopy can be used to measure polymerization in PEMs.

Figure 3 reveals the behavior of cells seeded on a conventional polystyrene culture flask (3A), on $(\text{PAH}/\text{PSS})_2\text{PAH}$ (3B), and on $(\text{PAA}/\text{PAAm})_4\text{PAA}$ (3C) to assess the cytophobic nature of the functionalized polyelectrolytes versus known cell adhesive surfaces. Figure 3A shows flattened, (i.e., well-attached, which is a key requirement for tissue culture cell survival) HeLa cells on a polystyrene surface. Cells seeded on $(\text{PAH}/\text{PSS})_2\text{PAH}$ show similar cell attachment behavior as on the polystyrene surface. On the other hand, cells on the photopatterned PEMs are mostly rounded and not well attached, indicating that this material does not promote cell adhesion. However, in areas where the material seemed to have small ruptures, cells appear flattened and strongly attached (white arrowheads in 3C). Nevertheless, the unreacted methacrylate groups that substituted about 10 % of the acrylic acid functional groups do not seem to affect the characteristic cell repellent behavior of PAA previously observed [3].

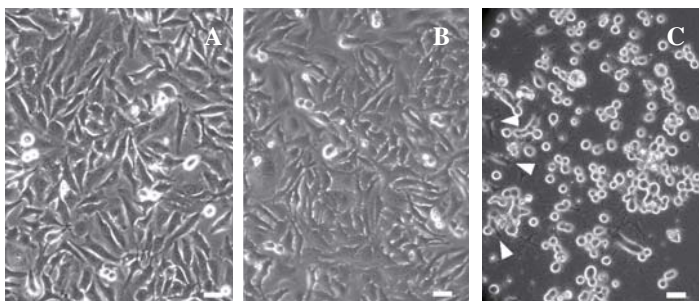


Figure 3. Images of HeLa cells on a polystyrene culture flask (A), on $(\text{PAH}/\text{PSS})_2\text{PAH}$ (B), and on covalently bound photopatterned PEMs (C). The three images show cells between 15 to 18 hours after being seeded. Scale bar: 20 μm .

4. Conclusions

This work demonstrates a photopolymerization method to generate crosslinked cytophobic PEMs having an underlying layer of cytophilic PEMs. Spatially-patterned PEMs with distinct chemical properties will ultimately be used for complex cell culture substrates and novel thin film hydrogels for separations or nanofluidics.

Acknowledgements

The authors thank the NIST/NRC Post-Doctoral Fellowship Program and NIST EEEL Director's Bioelectronics Initiative for financial support.

References:

- [1] Yang, S. Y.; Rubner, M.J. *J. Am. Chem. Soc.* **2002**, *124*, 2100.
- [2] Granick, S.; Sukhishvili, S. A. *J. Am. Chem. Soc.* **2000**, *122*, 9550.
- [3] Mendelsohn, J. D. et al. *Biomacromolecules* **2003**, *4*, 96.

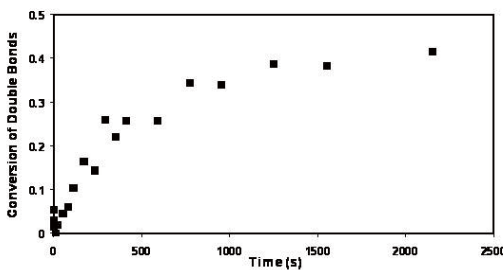


Figure 2. Photopolymerization of a PAA thin film.

HYDROPHOBIC NON-FOULING SURFACES FOR DROPLET BASED MICROFLUIDIC BIOANALYTICAL SYSTEMS

Ashutosh Shastry¹, Sidhartha Goyal¹, B.D. Ratner² and Karl F. Böhringer¹

¹Department of Electrical Engineering, ²Department of Bioengineering,
University of Washington, Seattle WA 98195

Abstract

This paper presents the principle, fabricated structure, characterization and results obtained for a new class of surfaces—"hydrophobic non-fouling surfaces"—for droplet-based microfluidics. Building on the theory of wetting of rough surfaces, we have developed novel surfaces which are chemically hydrophilic, i.e., the droplet is in contact with a non-fouling hydrophilic material but exhibits hydrophobic properties (high contact angle) as a result of thermodynamically stabilized air traps beneath the droplet.

Keywords: *non-fouling surfaces, bio-fouling, droplet microfluidics*

1. Introduction

Superhydrophobic surfaces [1, 2] —with low resistance to flow— seem promising candidates for any low energy scheme for manipulating fluids. Past studies have confirmed that hydrophobic interactions are involved in protein adsorption [4, 5]. Proteins being ubiquitous components of bioassays, the use of super-hydrophobic surfaces in microfluidic bioanalysis systems presents a challenge. Also, most non-fouling materials are hydrophilic [4].

2. Principle and Design

We designed a rough surface realized by pillars of controlled geometry in a silicon wafer.

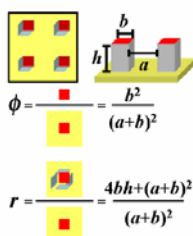


Figure 1: The texture parameters ϕ and r are expressed in terms of the design parameters a (gap length), b (pillar size) and h (pillar height).

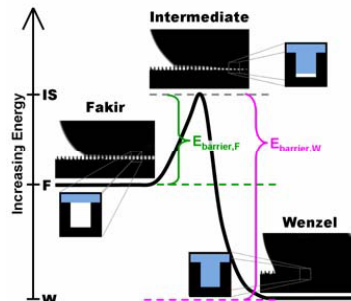


Figure 2: Photographs of droplets in Fakir and Wenzel states along with their energy levels. Substrate is designed to make Fakir state metastable.

The roughness is characterized by r , the ratio of rough to planar surface area (Fig. 1). As seen in Fig. 2, a droplet can sit on the pillar tops with air pockets trapped beneath, in the “Fakir” state [5] or in the Wenzel state where it is conformal with the topography. In the Fakir state, the base of the droplet contacts a composite surface of pillar tops and air—creating a contact angle θ_F given as: $\cos \theta_F = \phi(\cos \theta_i + 1) - 1$. Here θ_i is the intrinsic contact angle of the pillar tops. A Fakir droplet on a surface does not spontaneously transit to Wenzel state because of the presence of an energy barrier—analogous to the activation energy of a chemical reaction. We observed that the contact angle depends only on ϕ and θ_i : it is independent of the coating on the sidewall. But the energy barrier depends only on the coating of the sidewalls—it is independent of the θ_i of the pillar tops.

3. Experimental

Therefore, we proposed novel composite micro-textured surfaces with a hydrophobic material, alkanethiol coated gold, on the troughs and side walls of the pillars and a hydrophilic non-fouling material polyethylene glycol (PEG), on the pillar tops (Fig. 3).

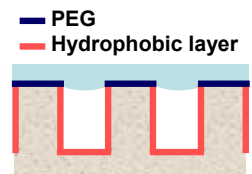


Figure 3: Schematic diagram of liquid deposited on the surface. The top surface is hydrophilic non-fouling polyethylene glycol (PEG). The trough and side-walls are hydrophobic. Although the liquid-vapor surface may be curved, the large size of the droplet relative to the spacing between pillars allows the profile to be approximated as spanning straight across surfaces in the derivation.

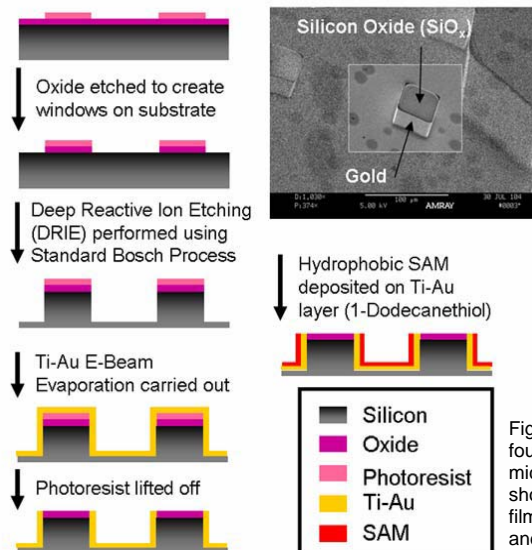


Figure 4: Fabrication steps for the non-fouling hydrophobic surface. In the SEM micrograph, the non-conducting oxide shows up dark while conducting metal film (Ti-Au) on the sidewalls of the pillars and on the trough shows up bright.

The fabrication process is detailed in Fig. 4. A self assembled monolayer of dodecanethiol on gold was used for the hydrophobic coating. A droplet was then placed on this surface and the contact angle measured using a goniometer. The light filtering through the air traps established that the droplet rested in the Fakir state, as expected, contacting only the hydrophilic oxide layer on the pillar tops, with the high contact angle as seen in Fig. 5. The measurements were repeated over several test surfaces—with a range of pillar widths and gaps—as summed up in Fig. 6.

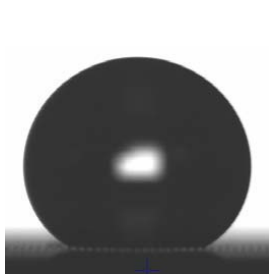


Figure 5: Even though the pillar tops are hydrophilic with $\theta_f = 32^\circ$, the droplet (of volume $7.68 \mu\text{l}$) is in the Fakir state with $\theta_F = 137^\circ$ as evident from the light seen below the droplet.

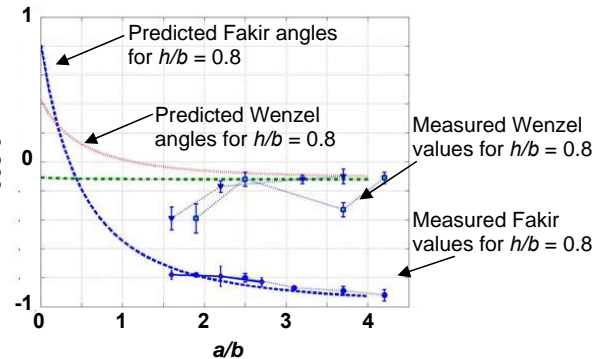


Figure 6: Measured contact angle values for Wenzel and Fakir are plotted along with the predicted angles based on the measured pillar dimension b and spacing a . Predicted values for (blue) Fakir, (pink) Wenzel with $h/b = 0.8$ and (green) Wenzel with $h/b = 1.9$ are plotted. The measured values for Fakir state closely match the predicted values while the measured Wenzel values expectedly deviate more.

4. Conclusion

The first phase of the project was thus successfully completed: the “proof-of-concept” results demonstrated “hydrophobic” surfaces where droplets contact only the “hydrophilic” region. Quantification of fouling, the ongoing second phase, entails using radio-labeled protein adsorption on well characterized PEG layer deposited on the oxide.

References

- [1] D. Quéré, A. Lafuma, and J. Bico, “Slippy and sticky microtextured solids,” *Nanotechnology*, vol. 1, pp. 14–15, 2003.
- [2] C.-H. Choi and C.-J. C. Kim, “Measurement of slip on nanoturf surfaces,” in *Proceedings of ASME NANO 2005: Integrated Nanosystems Design, Synthesis & Applications*, (Berkeley, CA, USA), p. 12, September 2005
- [3] V. Tangpasuthodal, N. Pongchaisirikul, and V. P. Hogen, “Surface modification of chitosan films. Effects of hydrophobicity on protein adsorption,” *Reviews of Modern Physics*, vol. 338, pp. 937–942, 2003.
- [4] D. G. Caster and B. D. Ratner, “Biomedical surface science: Foundation to frontiers,” *Surf. Sci.*, vol. 500, pp. 28–60, 2002.
- [5] D. Quéré, “Fakir droplets,” *Nature Materials*, vol. 14, pp. 1109–1112, 2002.

COMPARISON OF MICRO/NANO PORE PLATINUM ELECTRODES FOR CMOS INTEGRATED NON-DISPOSABLE BIOSENSOR APPLICATIONS

Hye-Kyoung Seo, Dae-Jun Park, and Jae-Yeong Park

Kwangwoon University, 447-1 Wolgye-Dong, Nowon-Gu, Seoul, 139-701 Korea

Abstract

In this paper, micro pore Pt, mesoporous Pt, and mesoporous Pt on micro pore Pt electrodes are fabricated and analyzed on a silicon substrate to check their usability as enzymeless sensing electrodes for non-disposable biosensors integrated with CMOS read out circuitry. The measured current responses at 10mM glucose solution of the fabricated plane Pt, micro pore Pt, mesoporous Pt, and mesoporous Pt on micro pore Pt electrodes are approximately 3.23nA/mm^2 , 14.2nA/mm^2 , $0.98\mu\text{A/mm}^2$ and $1.67\mu\text{A/mm}^2$, respectively.

Keywords: Mesoporous platinum, Nanostructure, Micro/nano pore, Glucose sensor

1. Introduction

Most of electrochemical biosensors are disposable due to the use of the enzymes that are living creatures. Thus, these are limited to use in the in-vivo and continuous monitoring biosensor system applications. The mesoporous (pores with a size of 2nm ~ 50nm) platinum electrodes formed on a Pt rod was reported for developments glucose sensors without any enzymes [1]. The structure and fabrication method of the mesoporous Pt electrode were first reported in 1997 and it was fabricated electrode on a Pt disk electrode (rod type) [2]. It was comprised of cylindrical hexagonally arrayed pores with a diameter of 2.5 nm and 5 nm of spacing distance between the pores.

2. Fabrication Method

The micro pore Pt electrode with approximately 10um in pore diameter and 20 um in height was fabricated by using deep RIE silicon etcher and DC sputtering system. The mesoporous Pt electrode with approximately 2.5nm in pore diameter and 150nm in height was fabricated by using a nonionic surfactant C_{16}EO_8 and an electroplating technique. And the mesoporus Pt on micro pore Pt electrode was fabricated by combining the above fabrication processes. The fabrication steps of the micro pore Pt electrode are represented in Fig. 1(a). The fabrication steps of the mesoporous Pt electrode are represented in Fig. 1(b). Ti and Pt layers are firstly deposited on top of SiO_2 of the silicon substrate. Liquid crystal templates of the C_{16}EO_8 are formed on the substrate at 85°C and Pt ions are electrodeposited on the silicon at 25°C . Finally, the templates are clearly removed in the deionized water. In Fig. 1(c), micro pore with mesoporous Pt electrode was fabricated by combining above two methods.

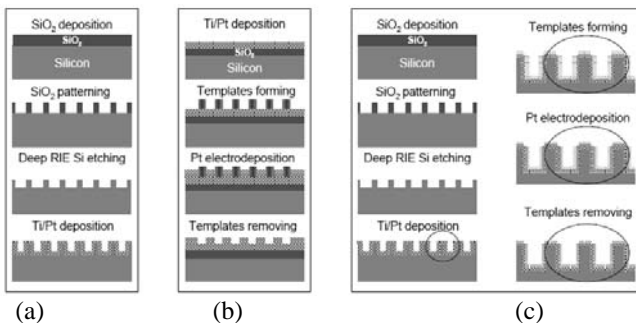


Figure 1. Fabrication steps of (a) micro pore Pt electrode, (b) mesoporous Pt electrode, and (c) micro pore with mesoporous Pt electrode.

3. Experimental Results and Discussions

All electrochemical measurements were performed in three electrodes system by using an electrochemical analyzer (CH Instruments Inc., USA) and an Ag/AgCl electrode was used as a reference electrode. For evaluation of the fabricated micro and mesoporous Pt electrodes, the current responses are measured and compared. Fig. 2 shows comparison of the cyclic voltammetry in 2M sulfuric acid solution of the fabricated micro/nano pore Pt electrodes. The current response of the micro pore with mesoporous Pt electrode is much larger than the other Pt electrodes. Fig. 3 shows comparison of current responses to the chronoamperometry in 1mM hydrogen peroxide solution of micro/nano pore Pt electrodes. These data also indicate that the micro pore with mesoporous Pt electrode is much more sensitive than the other Pt electrodes.

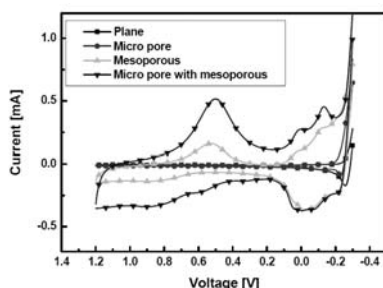


Figure 2. Comparison of the cyclic voltammetry of the fabricated micro/nano pore Pt electrodes in 2M sulfuric acid solution.

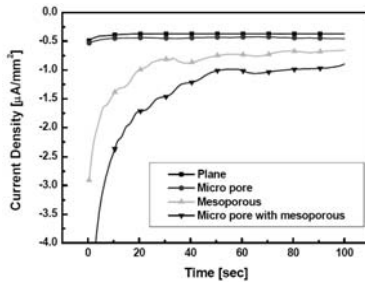


Figure 3. Comparison of current responses to the chronoamperometry of the fabricated micro/nano pore Pt electrodes in 1mM hydrogen peroxide solution.

The fabricated Pt electrodes were also evaluated to check their applicability for fabricating a enzymeless glucose sensor by varying the glucose concentrations in the

0.1M phosphate buffered saline solution. Fig. 4 shows the measured current response of the fabricated micro/nano pore Pt electrodes at various glucose concentrations. The measured current responses at 10mM glucose solution of the plane Pt, micro pore Pt, mesoporous Pt, and micro pore with mesoporous Pt electrodes are approximately 3.23nA/mm^2 , 14.2nA/mm^2 , $0.98\mu\text{A/mm}^2$ and $1.67\mu\text{A/mm}^2$, respectively. The current density of the fabricated micro/nano Pt electrodes relatively linearly increases as concentration of the glucose is increased. These data indicate that the micro pore with mesoporous Pt electrode is very sensitive to the glucose and strongly applicable for the non-disposable biosensor and electrochemical sensor applications.

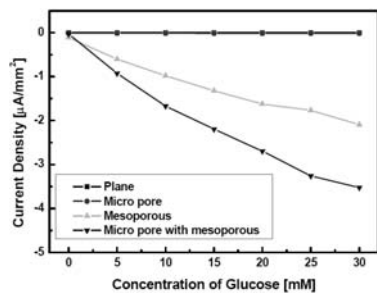


Figure 4. Comparison of the current response to various glucose concentrations of the fabricated micro/nano pore platinum electrodes.

4. Conclusions

The micro/nano pore platinum electrodes have been fabricated and characterized on a silicon substrate. In comparison of various micro/nano pore platinum electrodes, the micro pore with mesoporous Pt electrode has the best performance characteristics due to the largely expanded surface area. The measured current response of the micro pore with mesoporous Pt electrode was large enough to analyze the chemical substances without any enzymes. Thus, the micro pore with mesoporous Pt electrode is promising for non-disposable glucose sensors integrated with CMOS circuitry. These results also suggest that the mesoporous Pt electrode also have strong potential in use of chemical, environmental, and biological analysis systems.

Acknowledgments

This research was partially supported by the Korea Ministry of Information and Communication as a supporting project to form a Foundation of Advanced Leading Technology.

References

1. S. J. Park, T. D. Chung and H.C. Kim, Nonenzymatic glucose detection using mesoporous platinum, *Anal. Chem.*, vol. 75, pp. 3046-3049, 2003.
2. G. S. Attard, P. N. Bartlett, N. R. B. Coleman, J. M. Elliott, J. R. Owen and J. H. Wang, Mesoporous platinum films from lyotropic liquid crystalline phases, *Science*, vol. 278, p. 838-840, 1997.

PLASMA SURFACE MODIFICATION WITH THE AID OF COLLOIDAL SURFACE MODIFICATION FOR POLYMER MICROCHIP

Masahiro Matsumoto, Matsuhiko Nishizawa, and Takashi Abe

Tohoku University, 6-6-01, Aoba, Sendai 980-8579, Japan

Abstract

We report a novel plasma surface modification method with surfactant for hydrophobic polymers. Tetrafluoroethylene-perfluoroalkoxyvinyl ether copolymer (PFA) and cyclic olefin copolymers (COC) were employed as hydrophobic polymers. The modified surfaces were characterized by contact angle measurements, adhesion strength measurements and attenuated total reflection infrared (ATR-IR) spectroscopy. The water contact angle of the treated PFA surface decreased significantly from 110 to 66 degrees. Furthermore, no evolution of this surface property occurred over a period of at least 20 days after the treatment. This method allows us to bond directly the modified hydrophobic polymer plates under low temperature. Finally, we demonstrated the micropatterning and cell adhesion on the hydrophobic polymers.

Keywords: plasma surface modification, surfactant, wettability, micropatterning, cell adhesion

1. Introduction

Fluoropolymers possess excellent bulk properties including physical and chemical inertness, high temperature stability, low dielectric constant and biocompatibility. It has found many applications where these properties are desirable. For example, their utilization for microfluidics such as biomedical devices is attractive and adhesion to other materials at a low temperature is important for assembling polymer microchips. However, due to its poor wettability and adhesion property with other materials, some form of surface treatment and functionalization of the polymers is necessary. Various surface treatments such as electron beam [1], UV irradiation [2], corona discharge [3] and gas plasma [4] have been applied to modify the surface of fluoropolymers by incorporating polar groups on the surface. Plasma treatment is simple, easy to implement, reliable and cost effective, and H₂O plasma treatment seems to be effective [5,6]. But this method takes 30 min to modify and the water contact angle changes gradually with storage time. In addition, the introduction of water vapor into a vacuum system places high loads on the pumping system. Thus, novel and simple surface modification technique suitable for microchip fabrication is necessary.

In this paper, we describe a colloidal surface modification to improve oxygen ion beam treatment for introducing polar groups on hydrophobic polymer surfaces. It is well known that removal of water molecules from solid surface is not easy in vacuum. So we applied this phenomenon to our surface modification method, and we could effectively modify PFA and COC surfaces by introducing the water molecules close to the surface before ion beam irradiation.

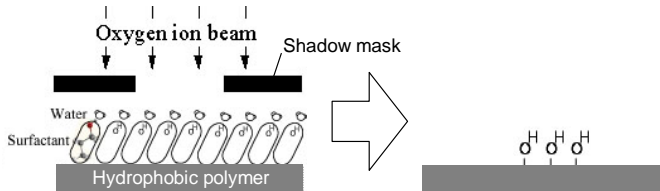


Figure 1. Schematic diagram of plasma surface modification with surfactant

2. Experimental

The process was shown in Figure 1. The native PFA and COC surfaces were exposed to oxygen plasma for 10 sec; then, the plates were dipping into surfactant solutions for several minutes. This pretreatment is necessary for improving the wettability of surfactant solutions. After the pretreatment, the plates were exposed to oxygen plasma for 10 sec again.

3. Results and discussion

Figure 2 shows the water contact angle on the plasma treated PFA surface with methanol, ethanol, propanol, butanol and cetyltrimethylammonium-bromide (CTAB) solution as surfactants. The contact angle decreased as the molecular weight increase. This result indicates that volatility in vacuum concerns the effectiveness of the treatment. The aging behavior of the plasma treated PFA surface with CTAB solution during storage in air at room temperature was shown in Figure 3. No contact angle changes were found for 20 days. Figure 4 shows the ATR-IR (Perkin Elmer, Universal ATR) spectrum measured for native PFA surface and the treated PFA surface with CTAB solution. We ascribe the broad peak measured at $3100\text{-}3600\text{ cm}^{-1}$ to the presence of hydroxyl groups. The appearance of this peak indicates that modification has penetrated into some depth inside the hydrophobic polymers, due to ATR-IR spectroscopy is not sufficiently sensitive to detect a hydroxyl group monolayer. This result supports the stability of the wettability property after the plasma treatment with surfactants. The shear tensile strengths of the plasma treated PFA with various surfactants were measured as shown in Figure 5. The treated PFA plates were adhered by hot emboss machine within 30 min after the treatment. The bonding pressure was 3 MPa and the temperature was 393 K. Under this condition, no deformation of the PFA plates was found. Though PFA plates could not bond each other below 583 K, the surface modified PFA plates could bond tightly at lower temperature. Furthermore, we carried out the micropatterning on a PFA plate with a shadow mask, as shown in Figure 6, and cell adhesion on a COC plate, as shown in Figure 7.

4. Conclusions

The method presented here is simple, reproducible and cost effective; nevertheless, its wettability property and adhesion strength were improved dramatically. In addition, the methodology combining a plasma ion irradiation with surfactant is unique. This technology can be applied to surface modification inside microfluidic devices, such as the manufacture of microvalve and separation parts.

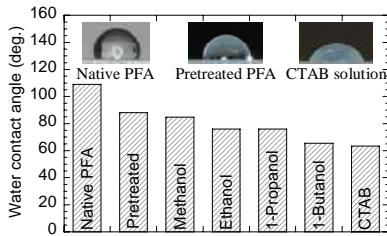


Figure 2. Water contact angle of native, pretreated PFA and treated with various surfactants.

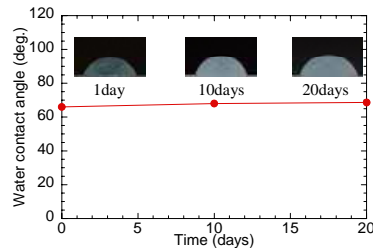


Figure 3. Wettability property of the plasma treated PFA with CTAB solution during storage in air.

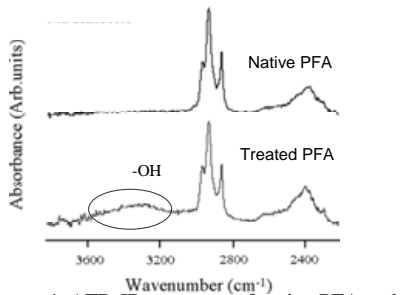


Figure 4. ATR-IR spectrum of native PFA and plasma treated PFA with CTAB solution.

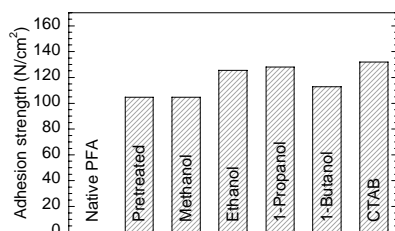


Figure 5. Adhesion strength of native, pretreated PFA and treated PFA with various surfactants under the temperature is 393 K and the pressure is 3 MPa.

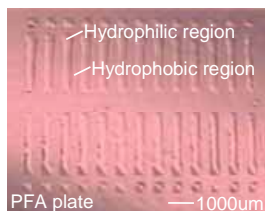


Figure 6. Micropatterning by surface modification with surfactant using a shadow mask.

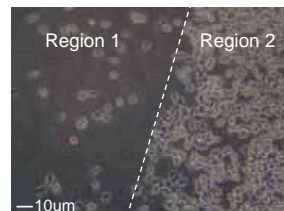


Figure 7. Adhesion of HeLa cell on Cyclic olefin copolymers plate. Region 1 is native surface and region 2 is the modified surface.

Acknowledgements

This work was supported by the Ministry of Education, Culture, Sports, Science and Technology, Grant-in-Aid for Young Scientists (A).

References

- [1]U. Lappan, et al., *Nucl. Instrum. Methods B*, **151**, pp.222-226, (1999)
- [2]L. J. Matienzo, et al., *J. Vac. Sci. Technol. A*, **12**, pp.2662-2671, (1994)
- [3]M. Kusabiraki, et al., *Jpn. J. Appl. Phys.*, **29**, pp.2809-2814, (1990)
- [4]Y. X. Da, et al., *Polymer*, **32**, pp.1126-1130, (1991)
- [5]U. Konig, et al., *Colloids and Surfaces B*, **25**, pp.313-324, (2002)
- [6]H. Xu, et al., *Mater. Chem. Phys.*, **80**, pp.278-282, (2003)

MICROCHIP-BASED DNA PURIFICATION IN A TWO-STAGE, DUAL-PHASE MICROCHIP CONTAINING A DERIVATIZED PHOTO-POLYMERIZED MONOLITHIC

Jian Wen^{1,2}, Christelle Guillo³, Jerome P. Ferrance² and James P. Landers^{2,4}

¹Departments of Molecular Physiology and Biological Physics and Department

of ²Chemistry and ⁴Pathology, University of Virginia Health Science Center,
Charlottesville, VA 22904

³Department of Chemistry, Florida State University, Tallahassee, FL 32306

Abstract

A novel two-stage, dual phase microdevice was developed to increase the capacity of a monolithic phase for extraction of DNA from blood. A reverse phase region was created in the microdevice for protein capture upstream of the monolith. Loading 10 μ L of whole blood on the two-stage microdevice resulted in capture of 70% of the protein by the C18 phase ($1,020 \pm 45 \mu\text{g}$) while allowing >97% of the DNA to reach the monolith for further purification. Of the roughly 350 ng of DNA in the original sample, $240 \pm 2 \text{ ng}$ DNA were recovered from the monolith, giving an overall extraction efficiency of $69 \pm 1\%$.

Keywords: Microfluidic, DNA Purification, Monolithic, Blood, Protein Capture

1. Introduction

One challenge in the development of integrated microfluidic devices that incorporate solid phases for the extraction (SPE) of DNA is the select localization of the solid phase in a specific region of the microchannel architecture of the device. Our previous work^[1] detailed a photopolymerized monolith for DNA extraction in a capillary that can now be fabricated in a microdevice. One problem with this monolith, however, is its affinity for proteins, which block DNA binding sites and decrease the capacity and efficiency with real biological samples such as blood. The work described here details the direct on-chip coupling of this monolith with a C18 reverse phase pre-column for capture the majority of the proteins present in a whole blood lysate. This was investigated with the goal of not only improving the efficiency of DNA extraction from whole blood, but increasing the volume (tens of microliters) of whole blood that could be loaded onto the microdevice without compromising DNA extraction efficiency.

2. Experimental

DNA extraction from a blood sample ($0.08 \mu\text{L}$ blood/ μL lysate) was performed on the two-stage platform shown in Figure 1. The lysate ($130 \mu\text{L}$ containing $10 \mu\text{L}$ of blood) was loaded onto the C18 pre-column, then the C18 phase was rinsed with equilibration buffer to ensure all of the DNA recovered from the C18 phase reached the monolithic phase. For protein capture studies, fractions were collected before the monolith to determine the amounts of protein and DNA passing through the C18 phase. For DNA extraction studies, elution of the DNA from the monolith was achieved by flowing elution buffer ($10 \text{ mM Tris}, 1 \text{ mM EDTA}, \text{pH } 8$) through the monolith after DNA loading.

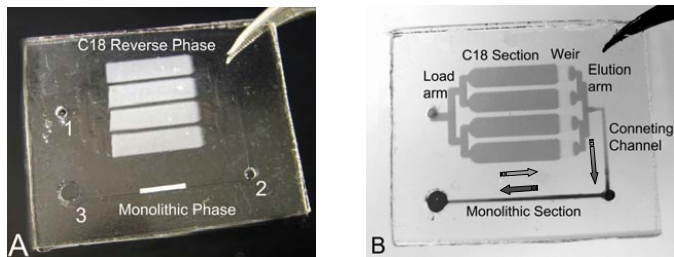


Figure 1. An integrated two-stage, dual-phase microdevice for protein capture/DNA extraction from whole blood. A) shows the filled C18 beads phase and monolithic phase in channels and B) shows a dye-filled view of the protein capture and DNA extraction sections. Arrows show the flow from stage 1 to stage 2.

3. Results and Discussion

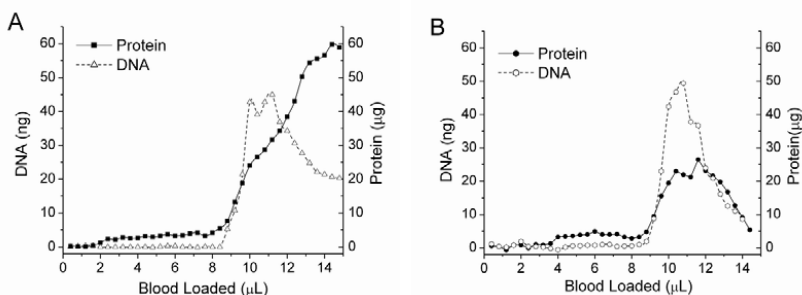


Figure 2. Elution of DNA and proteins from a C18 phase. A) continuous loading of a whole blood lysis solution; B) loading of a lysis solution containing $10 \mu\text{L}$ of blood.

Continuous loading of blood through the C18 phase generated the breakthrough curves shown in **Figure 2A**. While DNA is momentarily retained by the C18 phase, it is rapidly displaced by proteins that binds more avidly as loading continues, allowing the

vast majority of the loaded DNA to be recovered from the loaded sample. The breakthrough point for proteins is delayed, with only a minor fraction (the more hydrophilic proteins) passing unretained through the column, resulting in the shallower breakthrough curve. Optimal selectivity could be achieved with an unprecedented load of 10 μ L of whole blood - representing 350 ± 70 ng of DNA - resulting in capture of 70% of the proteins but allowing >97% of the DNA to exit to the stage 2 monolithic phase (**Figure 2B**).

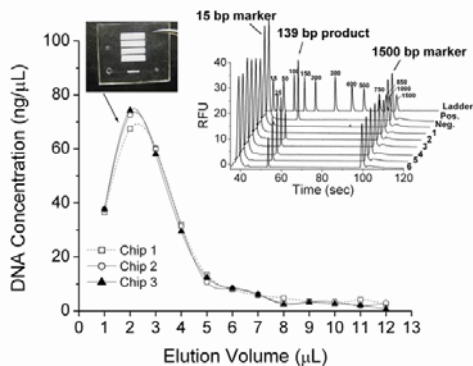


Figure 3. Device-to-device reproducibility for DNA extraction from whole blood using a two-stage, dual-phase microdevice. Inset picture shows the PCR profile produced from the amplification of a 139-bp gelsolin fragment without wash step applied.

shows successful amplification of a 139-bp gelsolin fragments from the extracted DNA.

4. Conclusions

A high capacity/high efficiency device for DNA extraction was developed utilizing two phases on an integrated device. The combination of these two phases allows for the purification of DNA from 10 μ L of whole blood with PCR amplification of the extracted DNA without a protein wash step, simplifying the process and reducing the overall time. This yields a microdevice for DNA extractions from whole blood for clinical and biomedical applications.

References

1. J. Wen, C. Guillo, J. P. Ferrance and J. P. Landers, *DNA Extraction Using a Tetramethyl Orthosilicate-Grafted Photopolymerized Monolithic Solid Phase*, Anal. Chem., **78**, pp. 1673-1681, (2006).

Figure 3 illustrates the reproducible results from three extractions of DNA from 10 μ L of blood on the two-stage device) - all three extractions provided essentially the same profile with similar fraction-to-fraction quantitative recovery of DNA. The extraction efficiency (EE) of $69 \pm 1\%$ compares favorably with other chip-based solid phases (EE 50-65%), but significantly more DNA is recovered than with other microchip SPE devices. The isopropanol wash step, usually required to remove PCR inhibiting components from the solid phase, is not required, and the use of PCR inhibiting isopropanol is also avoided in the two-stage device. The inset in **Figure 3**

EXPERIMENTAL STUDY OF THE SHRINKAGE RATIO OF PDMS ITS ALIGNMENT FOR THE WAFER LEVEL PROCESS

Seok Woo Lee and Seung S. Lee

*Dept. of Mechanical Engineering, KAIST, Daejeon, Korea

ABSTRACT

Shrinkage of PDMS is occurred when it is cured is the problem of alignment between PDMS layer and rigid substrate in the wafer level process. Measured shrinkage ratio of PDMS is 1.06%, 1.54%, 2.10% for curing temperature 65°C, 80°C, 100°C, respectively. Considering shrinkage ratio of PDMS, design offset applied in photomask is 1.07%, 1.57%, 2.14% for curing temperature 65°C, 80°C, 100°C, respectively.

Keywords: PDMS shrinkage, alignment, wafer level, batch process

1. INTRODUCTION

Poly-dimethylsiloxane(PDMS) is a popular material in the field of Micro Total Analysis Systems(μ -TAS) [1]. A shrinkage of PDMS induces a misalignment between shrank PDMS layer and a rigid substrate when PDMS is replicated patterns of a mold by curing. The shrinkage problem in the alignment is not severe in micro single devices because translation and rotation are dominant problem of misalignment compared with the shrinkage. But the misalignment induced by the shrinkage gets more significant in the wafer level process.

2. BASIC CONCEPT

In this paper, the shrinkage ratio of PDMS is measured and applied to the photo mask as a design offset to wafer level process between PDMS layer and a rigid substrate for a precision alignment. Figure 1 (a) shows the designed patterns of scale marks and align

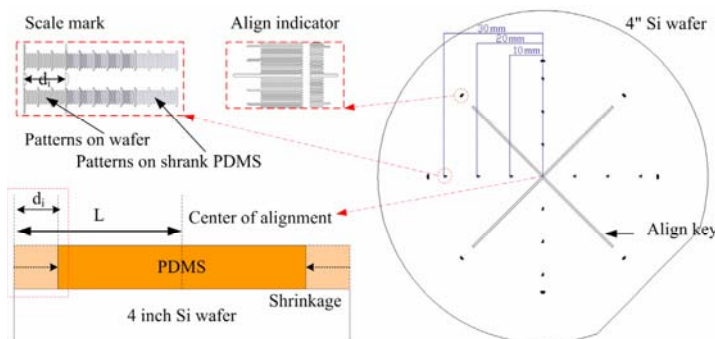


Figure 1: Schematic view of the measuring method of shrinkage ratio of PDMS.

indicators arranged on 4" silicon wafer for shrinkage ratio measurement. Distances between scale marks and the center of alignment, L, are 10, 20, and 30mm, respectively.

When the PDMS layer whose patterns of scale marks are replicated from patterns of the silicon wafer is bonded on the silicon wafer, the distance between shrank scale marks of PDMS layer and scale marks of silicon wafer, d_i , can be measured as shown in Figure 1 (b). Then, the shrinkage ratio of PDMS is calculated following the equation.

$$\text{Shrinkage_ratio}(\%) = \frac{1}{L} \times d \times 100 = \frac{1}{L} \times \frac{1}{4} \sum_{i=1}^4 d_i \times 100$$

d: average value of d_i

3. EXPERIMENT

Figure 2 shows the alignment method between grooved Si wafer and PDMS layer fabricated by the conventional PDMS fabrication process[2]. Scale marks are defined by photo lithography and molding on 4" silicon wafer and PDMS layer, respectively. The female key of the silicon wafer fabricated by anisotropic bulk micromachining and the male key of PDMS layer replicated from the female key of the silicon wafer is fitted spontaneously by structures of themselves. A PDMS curing condition is defined by temperature, thickness of PDMS layer, mixing ratio of curing agent and diluting solution. The conditions are labeled at Table 1 respectively. Figure 3 is the result of alignment between the PDMS layer whose curing condition is C and a 4" silicon wafer. The misalignment is less than $20 \mu\text{m}$ when substrates are aligned spontaneously by fitting of align keys. When a manual alignment is enhanced slightly, the misalignment is less than $10 \mu\text{m}$. Figure 3 shows the scale mark for measuring d_i of the PDMS layer compared with the Si wafer at $L=30\text{mm}$. Figure 4 shows displacement d, average value of d_i ,

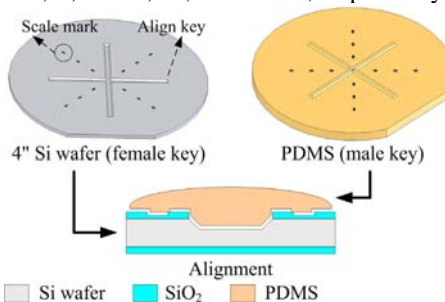


Figure 2: Alignment method between the PDMS layer and 4" Si wafer.

Table 1: PDMS curing conditions.

Condition	Temp.(°C)/time (h)	Thickness (mm)	agent (%wt)	dilutant (%wt)
a	65 / 4	1.2	10	0
b	80 / 3	1.2	10	0
c	100 / 1	1.2	10	0
a'	80 / 3	1.8	10	0
b'	80 / 3	2.4	10	0
a''	80 / 3	1.8	15	0
b''	80 / 3	1.8	20	0
a'''	80 / 3	1.8	10	10
b'''	80 / 3	1.8	10	20

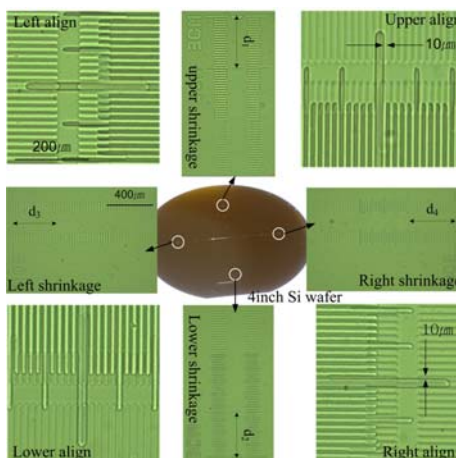


Figure 3: Results of alignment between 4inch silicon wafer and PDMS layer.

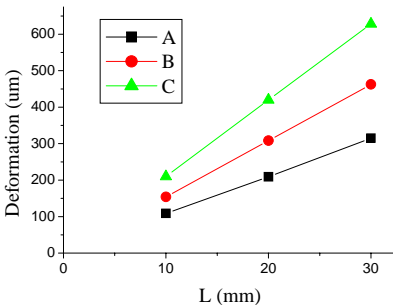


Figure 4: Displacement induced by PDMS shrinkage following positions and curing conditions.

Table 2: Shrinkage ratio following curing conditions.

Conditions	Shrinkage ratio (%) (100*d/L)	Photomask design offset (%)
a	1.06	1.07
b	1.52	1.54
c	1.94	1.98
a'	1.57	1.60
b'	1.61	1.64
a''	1.46	1.48
b''	1.64	1.67
a'''	2.05	2.09
b'''	2.46	2.52

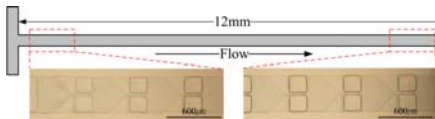


Figure 5: Microchannel based on PDMS 3D structure whose mask design is considered PDMS shrinkage ratio.

for L and curing condition. d is proportional to L and increases as curing temperature increases. Table 2 shows the shrinkage ratio of PDMS for curing conditions and the design offset of the photo mask considering the shrinkage.

Misalignment is decreased from 200 μm to 20 μm , for the curing temperature 80°C when the design offset is applied to fabrication of the micromixer[4].

4. CONCLUSIONS

In This paper, we demonstrate alignment method between PDMS layer and Si wafer using mechanical contact of their cross shaped female and male key. After alignment, 2-dimensional shrinkage ratios of PDMS for various curing temperature are obtained by measuring displacement between indicator of PDMS layer and Si wafer. The shrinkage ratios are 1.06%, 1.54%, and 2.10% for curing temperature 65°C, 80°C, and 100°C, respectively. The design offset applying photo mask for photolithography process are 1.07%, 1.57%, and 2.14% for curing temperature 65°C, 80°C, and 100°C, respectively. Applying this design offset, we expect that misalignment induced by shrinkage can be diminished.

REFERENCES

1. C. Wang, G. Jia, L. H. Taherabadi, and M. Madou, J. Microelectromech. Syst., 14 (2), 348 (2005).
2. M. Liger and Y-C. Tai, 19th IEEE Int. Conf. on MEMS, 106 (2006).
3. K. Naka, T. Hashishin, J. Tamake, and S. Konishi, 19th IEEE Int. Conf. on MEMS, 518 (2006).
4. S. W. Lee and S. S. Lee, Journal of micromech. microeng., 16 (5), 1067 (2006).

Seok Woo Lee, KAIST, Daejeon, Korea, e-mail: swlee81@kaist.ac.kr

MICRO AND NANO FLUIDIC DEVICES USING ELECTROACTIVE POLYMER ARTIFICIAL MUSCLE

Ron Peltine, Roy Kornbluh, Harsha Prahlad,
Richard Heydt, John Bashkin, Seiki Chiba

SRI International, 333 Ravenswood Avenue, Menlo Park, CA 94025, USA
(contact: schiba@sri.co.jp)

Abstract

Electroactive Polymer Artificial Muscle (EPAMTM [registered trademark of Artificial Muscle, Inc.]) poses unique challenges and opportunities in micro fluidics. EPAM has high strain, high actuation pressure, fast response, easy patternability, and low cost. This paper describes fundamental EPAM capabilities and devices demonstrated, and discusses EPAM microfluidic systems. The unique capabilities of EPAM for microfluidic systems include its ability to directly actuate surface features. An initially flat polymer surface can be actuated to form channels, pumps, and valves, all by computer control. To realize these advantages, however, various challenges in device design, electronics, and manufacturing must be addressed.

Keywords: electroactive polymers, microfluidics, artificial muscle, dielectric elastomers

1. Introduction

A wide variety of electroactive polymers have been investigated in recent years for microfluidics and other applications. One of the most promising is dielectric elastomers, or EPAM, originally developed by Peltine et al. [1]. The basic element is a polymer sandwiched between two compliant electrodes shown in Figure 1. When a voltage is applied between the electrodes, the electrostatic pressure squeezes the polymer in thickness and stretches in area [1].

Strains can be quite large (up to 380%), as can actuation pressures (up to 8 MPa). These numbers, however, represent peak performance, and as with any actuation technology, values in practical systems are typically much lower. Materials used in EPAM devices can often be tailored to the application. For example, silicone-based EPAM can be used for very high and low temperatures, an advantage for sterilization, freezing, and other temperature-sensitive functions.

Because of its performance potential and simplicity of structure, EPAM technology is being investigated worldwide by many organizations. Commercial development is being spearheaded by Artificial Muscle, Inc (AMI) [2], a company focused on large volume manufacturing of EPAM actuators, and development and commercialization of associated drive electronics. Excellent progress is being made toward practical

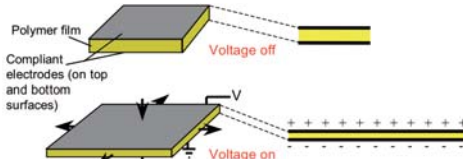


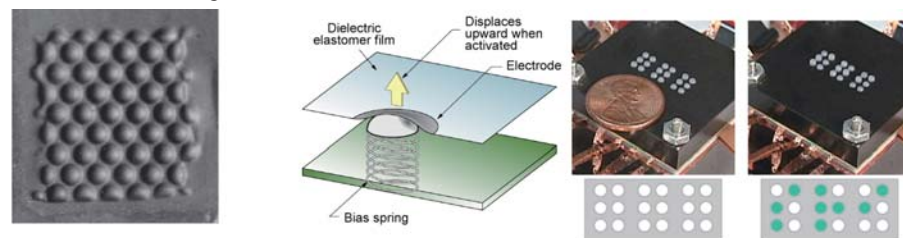
Figure 1. Principle of operation of EPAM.

applications of EPAM by AMI and others. However, most of the focus to date has been on macro actuators. Micro and nano applications are less visible but equally exciting with regards to their potential.

2. Microfluidic Actuator Types

Diaphragm actuators, such as those shown in Figure 2, are a common configuration for EPAM and larger sizes are in fact sold commercially [2]. EPAM diaphragm actuators make excellent pump and valve actuators because of their large stroke and good pressures. Diaphragm pumps on the order of 1 cm have been built, yet EPAM is applicable on much smaller scales. Fifty micrometer diaphragms have been demonstrated, and the fundamental lower limits are probably below 1 μm . EPAM diaphragms can achieve both slow and fast pumping, and even drop ejection.

Variable thickness mode actuators are shown in Figure 3 [3]. EPAM itself contracts in thickness as shown in Figure 1, but this effect can be enhanced using passive layers. Typical thickness changes are on the order of 10 to 25% of the total passive layer thickness. Complex patterns of thickness variation can be achieved and the system may achieve unique capabilities. An entire complex system of actuation can in principle be patterned on a disposable substrate. As shown in Figure 3, both channels and pockets can be actuated, and these are the key features needed to move drops. Alternately, a second surface can be placed above and in contact with the variable surface for sealing. In this design, the variable surface creates pumps, valves, and channels under computer control. Variable thickness mode can also be applied to greatly different scales on the same device, enabling a macro–micro interface, an issue with microfluidic devices.



a) Early array of 3 mm diaphragms

b) Braille device

Figure 2. EPAM diaphragm actuators (Braille device photo adapted from [4]).

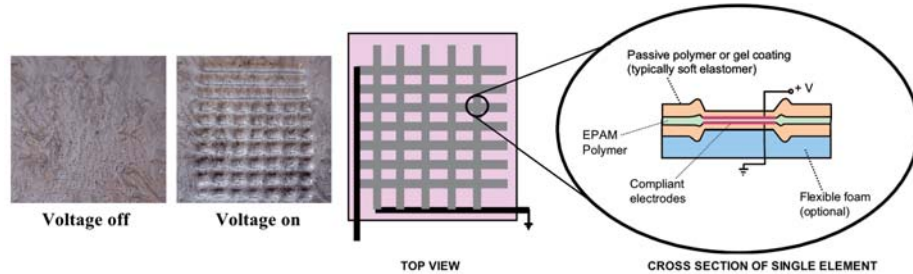


Figure 3. Variable thickness actuation.

3. Issues

Little is known about how EPAM behaves in the nano domain, yet the basic principle of operation is electrostatic in nature and scales to nano sizes. Films of 10 to 100 nm thickness can be fabricated. Such films should have low 1 to 10 V operating voltages but suitable electrode materials is an issue at these small scales.

EPAM currently requires relatively high voltage and low current, comparable to piezoelectric or electrostatic devices but less than voltages typically used for electrophoresis. At small scales, voltages of more than 100 V are currently easiest to implement although actuation has been demonstrated at less than 50 V. Microfluidic devices are typically too low power to present a safety issue, but in some cases the electronics needed for voltage conversion may be a cost issue.

Lifetime may also be an issue depending on drive levels. EPAM devices have been demonstrated for tens of millions of cycles, but testing is needed for specific applications. In general, smaller devices are expected to have longer lifetimes due to the statistics of electrical breakdown, the most common limit to EPAM lifetime.

4. Conclusions

EPAM offers exciting new opportunities in micro and nano fluidic devices. Pressures, displacements, patternability, and environmental tolerance are all attractive for fluidic applications. Perhaps the most interesting aspect of EPAM, however, is its ability to enable new types of microfluidic systems such as those using variable thickness mode actuation.

Acknowledgments

The authors would like to thank the Micromachine Center of Japan, METI, the New Energy and Industrial Technology Development Organization, the Defense Advanced Research Projects Agency, and the Office of Naval Research for their support of this general technology.

References

1. R. Pelrine, R. Kornbluh, Q. Pei, and J. Joseph, High-speed electrically actuated elastomers with over 100% strain, *Science*, Vol. 287, No. 5454, pp. 836–839 (2000).
2. See www.artificialmuscle.com
3. H. Prahlad, R. Pelrine, R. Kornbluh, P. vonGuggenberg, S. Chhokar, J. Eckerle, Programmable surface deformation: Thickness-mode electroactive polymer actuators and their applications, *Smart Structures and Materials 2005: Electroactive Polymer Actuators and Devices (EAPAD)*, San Diego, CA. Edited by Yoseph Bar-Cohen, Proceedings of SPIE Vol. 5759, pp 102–113, March (2005).
4. R. Heydt and S. Chhokar, Refreshable Braille display based on electroactive polymers, Proc. 23rd Intl. Display Research Conf., Phoenix, Arizona, 15–18 September (2003).

OPTIMAL MICROCHANNEL DESIGN BY GENETIC ALGORITHMS

Hyunwoo Bang¹, Won Gu Lee¹, Junha Park², Hoyoung Yun¹, Joonmo Lee¹, Seok Chung³, Keunchang Cho², Chanil Chung², Dong-Chul Han¹ and Jun Keun Chang²

¹School of Mechanical and Aerospace Eng., Seoul National University, Seoul, Korea

²Digital Bio Technology, Inc., Seoul, Korea

³Massachusetts Institute of Technology, Boston, MA, U.S.

Abstract

The design of a microsystem can evolve through the genetic algorithm (GA), a digital Darwinism. We applied the GA while optimizing a particle-suspended microchannel. A heuristic particle dynamics simulation was used for the fitness evaluation of the GA. The GA has been implemented to run in parallel on multiple computers connected via TCP/IP protocols using JAVA and SQL database technology. A commercial microchannel for imaging flow cytometry application has been selected for this optimization.

Keywords : genetic algorithm, microchannel, design optimization

Introduction

Partly due to its short history of the lab-on-a-chip industry, design problems have been solved by trial-and-error dictated by design specifications and guided by the experience and intuition of the engineer. The GA was selected to stochastically guide the algorithm through the solution space of available designs and arrive at an evolved one. It is a Darwinian “survival of the fittest” approach employed to search for optima in large multidimensional spaces [1, 2]. In the GA a genotype is a coded representation of a possible individual or problem solution. In our case, a genotype is a series of design variables for the microchannel geometry. GAs typically use populations of genotypes consisting of strings of binary digits or parameters. These are read to produce phenotypes which are then evaluated according to some fitness criteria and selectively reproduced. New genotypes are generated by copying, mutating, and/or combining the genotypes of the most fit individuals, and as the cycle repeats, the population ascends to higher and higher levels of fitness. We introduced a heuristic particle dynamics simulation developed for the fitness evaluation of the GA [3, 4]. In this study, we present a robust design methodology for optimizing the geometry of a particle-suspended microfluidic channel using GA.

Optimization Procedures

The microchannel system selected for this optimization is the imaging flow cytometry kit of Digital Bio Technology, Inc. As the device uses visual inspection, cells inside a microchannel should be sparsely distributed to avoid erroneous data acquisition [5]. The genetic algorithm was aimed at maximizing the distances between these blood cells by

optimizing its microchannel geometry. Fluid dynamics including solid walls, a liquid flow and buoyant solid particles inside it is so complex that plausible predictions cannot be easily acquired. So we developed a heuristic dynamics simulation based on object-oriented programming (OOP) paradigm. The heuristic simulation was used to simulate the emergent behaviors of particles resulting from their interactions with a virtual microchannel environment. The simulation is built on several simple rules but it simulates emergent group behaviors resulting from complex interactions of these entangled particles entangled with those rules [3]. Fitness evaluation based on this simulation was used to direct simulated evolutions towards an optimized design of the microchannel. The genetic algorithm has been implemented to run in parallel on multiple computers connected via TCP/IP protocols using JAVA and SQL database technology.

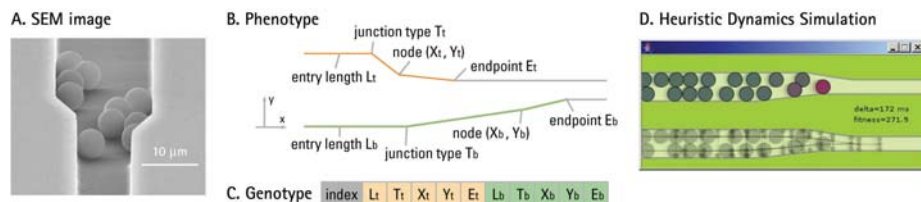


Fig.1. (A) SEM image (B, C) phenotype and genotype embodiment of the microchannel. The genetic representation of the microchannel morphology is a series of coordinates denoting all the geometry points. (D) Screenshot of the JAVA application for heuristic dynamics simulation

The final evolution was performed using 20 species of 5,000 genomes. The average fitness of the individuals of each species is inspected over 75 generations. The rate of evolutionary progress was similar for all species. All species took about 30 generations before they reached their plateau and the populations of each species converged toward homogeneity (see Fig.2.). Through the evolution process, the fitness values increased with about 40% of their initial values on average. Some examples of optimized microchannel morphologies (evolution tree) are shown in Fig. 2.

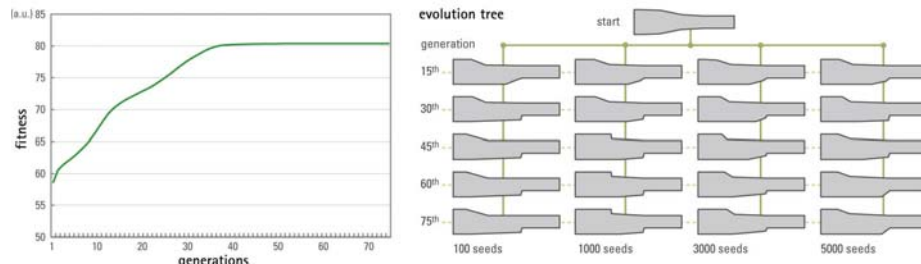


Fig.2. As the evolution converges, microchannel morphology becomes asymmetric having some skewness. Eventually all the wedges become the type of “flat line followed by a slope” and the second wedge of the channel becomes steeper than the first one.

Results and Discussion

The newly optimized microchannel was fabricated and compared with the existing one. The comparison between these two microchannels clearly proves the enhancement of the newly fabricated one. As in Fig. 3, RBCs in the newly fabricated microchannel are more sparsely distributed in observation channel without generating doublets of RBCs. The device was significantly enhanced showing that our approach can greatly surpass the traditional design methods.

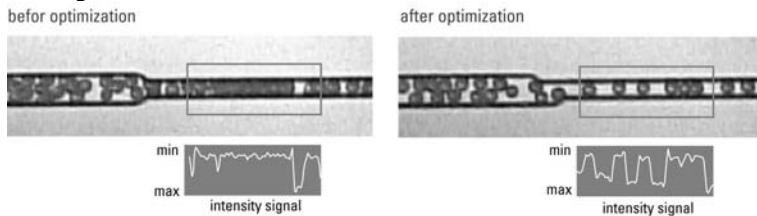


Fig.2. RBCs in the newly fabricated microchannel are more sparsely distributed without generating doublets.

This study is merely the beginning of GAs being applied to microchip designs. Although the design problem in this study was a simple one, the proposed methodology can be extended to resolve more complex design problems. By implementing simulations such as microchannel mixing, electro-osmosis and multiphase flows, this methodology will be applicable to even handling various microchannel design problems. This kind of design optimization will make new breakthroughs, consequently enhancing microchip devices. At the same time, it will give creative hints as to how we can overpass existing obstacles in designing microsystems in the industry.

Acknowledgement

This research has been supported by the Intelligent Microsystem Center (IMC; <http://www.microsystem.re.kr>), which carries out one of the 21st century's Frontier R&D Projects sponsored by the Korea Ministry Of Commerce, Industry and Energy.

References

1. C. Darwin, "The Origin of Species," New American Library, Mentor paperback, 1859.
2. D. E. Goldberg, "Genetic Algorithms in Search, Optimization, and Machine Learning", Addison-Wesley, 1989.
3. Craig W. Reynolds, "Flocks, Herds, and Schools: A Distributed Behavioral Model", Computer Graphics, 21(4), July 1987, pp. 25-34
4. Sims K., "Evolving Virtual Creatures", Computer Graphics (SIGGRAPH'94) Annual Conference Proceedings, July 1994, pp. 43-50.
5. J. Park, S. Chung, H. Yun, K. Cho, C. Chung, D.-C. Han and J. K. Chang, "Asymmetric nozzle structure for particles converging into a highly confined region", Current Applied Physics, 6(6), October 2006, pp. 992-995

LOCALIZED OPTICAL ACTIVATION OF THERAPEUTIC GENE RELEASE IN BREAST CANCER CELLS USING PHOTOTHERMAL NANOCRESCENTS AS OLIGONUCLEOTIDE-CARRIERS

Eunice S. Lee, Gang L. Liu, Franklin J. Kim, Angelee Kumar, Luke P. Lee

Biomolecular Nanotechnology Center, Berkeley Sensor and Actuator Center
Department of Bioengineering, University of California, Berkeley, CA 94720 USA

Abstract

Optical activation of photothermal nanoparticles permits remotely-triggered surface biomolecular reactions with high spatiotemporal resolution. We present a new method to selectively and locally control protein expression by internalizing photothermal nanocrescent particles carrying therapeutic genes within living cells.

Keywords: gene delivery, molecular nanomedicine, photothermal nanoparticles

1. Introduction

Remotely controllable nanoscale gene delivery vehicles can greatly benefit the study of molecular medicine. In particular, therapeutic gene delivery at specific locations is highly desired for precise gene therapy. We describe a new photoactive, nanoscale gene delivery vehicle based on the oligonucleotide-conjugated Au nanocrescents as photothermal nanoparticles. DNA hybridization and dehybridization has previously been triggered through the use of ultraviolet, photo-active chemical modifications [1] and inductive coupling of a radio frequency (RF) magnetic field to metal nanocrystals [2]. Our approach differs from other approaches in that our gene delivery method offers the combined advantages of high spatial resolution, remote gene release, longer penetration depth, and enhanced photothermal effect. Firstly, in order to provide quantitative control of gene delivery, improvements are needed in the area of spatial resolution (1 microns or less). This method could potentially be used to deliver genes from a single nanoparticle. In this way, we can selectively release genes with optical actuation at desired locations of cultured cells without disturbing the surrounding areas. Such selective gene therapy would be useful to treat cancerous cells in the presence of normal cells in tissue. Secondly, Au-nanocrescent (NC) particles are ideal for near infrared (NIR) activation. Because of the ideal geometry of the nanoparticles, large local field enhancement is seen at the crescent tips of the particle [3]. Finally, NIR activation is also ideal for remote gene delivery because NIR light has a longer penetration depth in human tissue.

Our method uses specialized nanocrescent (NC) particles, which specifically absorb NIR light, in order to optically activate oligonucleotides (OND), such as antisense OND and small interfering RNA (siRNA). Once the temperature on the NC particle reaches the critical melting temperature of ONDs due to photothermal heating, the double-stranded ONDs denature, thereby releasing the ONDs to interfere with mRNA translation within a cell (Fig. 1). We demonstrate the first demonstration of NIR activation of cancer therapeutic gene release using NC particles.

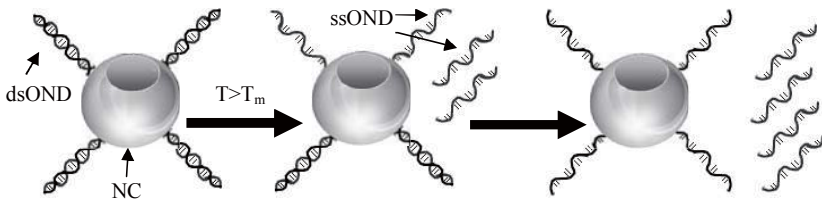


Fig.1 Concept of gene release using photothermal NC particles – Double-stranded ONDs (dsOND) are covalently attached to gold nanoparticles. Illumination is used photothermally heat the nanoparticles, causing the double-stranded OND to denature as the temperature reaches a threshold T_m on the nanoparticles. Because of the unique geometry of the NC particle, local field enhancement occurs at the tips of the crescents and ssONDs are first released from this area. Further photothermal heating will eventually cause all single-stranded ONDs (ssOND) to be released.

2. Experimental

OND-NC particle conjugation – Au NC particles are prepared as described elsewhere [3]. The oligonucleotides sequences for EGFR-2 (HER-2) were purchased from Integrated DNA Technologies (Coralville, IA). The sequences are 3'-GTGAGCACCATGGAG-5'-SH and 3'-CTCCATGGTGCTCAC-5'. In order to reduce disulfide bonds, thiolated oligonucleotides are incubated at room temperature with dithiothreitol (DTT) in a 1:100 (OND: DTT) ratio for two hours. To separate the DTT from the ONDs, the mixture is then run through NAP-5 gel column (GE Healthcare) and the eluted ONDs are collected. 70 μ l of 100 μ M reduced, thiolated ONDs is then incubated with 500 μ l of nanoparticles (3×10^8 particles/ml) on a rocker for 40 hours. 100 μ l of 0.5M PBS is added every 12 hours to decrease negative charge on the ONDs and increase the OND packing.

OND hybridization – Excess ONDs in solution are removed by centrifugation and the pellet is resuspended in PBS. 70 μ l of 100 μ M complementary ONDs are then added. For hybridization, this mixture is first heated in an 80°C water bath for 2 minutes and then heated in a 65°C water bath for 15 minutes. To allow enough time for hybridization of all ONDs on the particles, the mixture is incubated at room temperature for 24 hours.

3. Results and discussion

In vitro photothermal release – To demonstrate the *in vitro* release of therapeutic genes from NC particles, double-stranded ONDs are covalently attached to the NC particles through a thiol (-SH) group on the end of one strand. The conjugates are then immobilized on a glass microscope slide. When immersed in solution, the particles remain attached to the glass surface. Fluorescence dye, SYBR Green I, is used to stain double-stranded OND. Laser illumination (10 mW, 785 nm) is then used to locally excite and release the ONDs from the NC particles.

Figure 2 (b) and (c) show NC particles before and after excitation using laser NIR light. The arrow indicates the point of laser excitation. Decrease in the fluorescence is clearly limited to area of laser exposure, which is due to release of single-stranded antisense OND from the NC due to photothermal heating. This shows that ONDs can be successfully delivered with high spatial resolution.

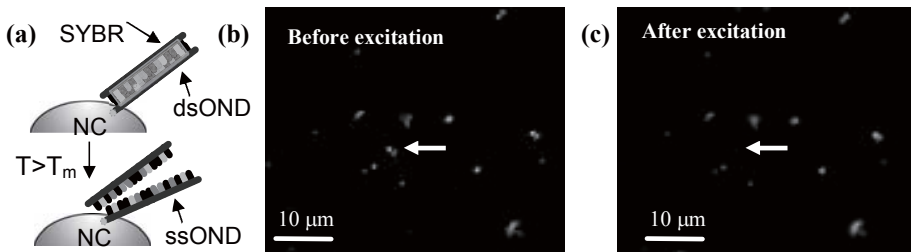


Fig 2. *In vitro* release of OND from NC particles. (a) Concept of double-stranded OND visualization using SYBR dye, and fluorescent images of OND attached to NC particles (b) before NIR excitation and (c) after NIR excitation.

Intracellular photothermal release – The OND-NC particles are internalized inside cultured MCF-7 breast cancer cells which overexpress membrane receptor protein EGFR-2 (HER-2). SYBR Green I staining is used to visualize double-stranded ONDs attached to the particles. A 10 mW laser beam (785 nm) is then used to induce photothermal heating at specific locations. When the temperature on the particle reaches the melting temperature of the OND, the double-stranded OND denatures.

We show that after 1 minute of illumination, the fluorescence intensity decreases dramatically, indicating that the double-stranded OND has denatured and the antisense ONDs have been released to subsequently interfere with HER-2 mRNA translation. Control experiments show that the decrease in fluorescence is not due to the photobleaching or thermal quenching. The cells were also viable after illumination since most of the thermal energy dissipates during the OND denaturing.

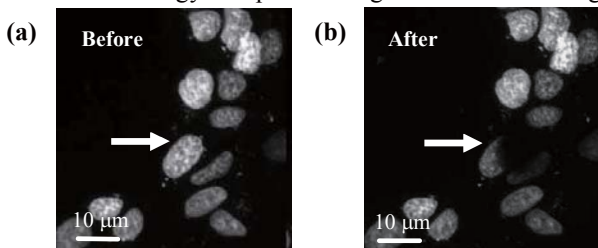


Fig. 3. Intracellular release of OND from NC particles. Fluorescence in cells is from double-stranded ONDs attached to NCs. Fluorescent images (a) before NIR excitation and (b) after NIR excitation.

4. Conclusions

The novel hybrid integration of NC particles and biomolecules has been developed for the optical activation of cancer therapeutic gene release. This work may also permit the remote triggering of surface-enhanced biomolecular reactions with high spatiotemporal resolution and minimal perturbation to surrounding cells, which can be applied in future quantitative systems biology and medicine.

References

- [1] Asanuma, et al. *Tetrahedron Letters*, 40 (1999) 7995-7998.
- [2] K. Hamad-Schifferli, et al., *Nature*, 415 (2002) 152-155.
- [3] G. L. Liu et al. *Nature Materials*, 5 (2006) 27-32.

HIGH POWER BIOFLUID-ACTIVATED LAMINATED BATTERIES FOR BIO-APPLICATIONS

Ki Bang Lee

KB Lab, 46B Toh Tuck Road #04-12, Singapore 596748

Email: kblee@kblab.biz, kibanglee@hotmail.com

ABSTRACT

High power battery with fast activation, fabricated by cheap paper/plastic lamination, has been successfully demonstrated to power disposable credit card-sized biosystems on a plastic chip. Two-step activation is presented for the prototype batteries to reduce the activation time and to supply high power. The batteries (paper area of 6cmx3cm) were activated by saliva, urine and even tap water, and the maximum voltage has been measured as 1.56V and the maximum power reached 15.6mW with load of 100Ω . As such, these high power biofluid-activated laminated batteries could be integrated with on-demand credit card sized biosystems such as healthcare test kit, biochip and lab-on-a-chip that require high power and fast response.

Keywords: biofluid-activated battery, paper battery, energy conversion, plastic lamination, and power source

1. INTRODUCTION

Micro power sources meeting the operation lifetime of disposable devices are attractive in contrast to the long-operation, miniature power source of micro internal combustion engine [1] or rechargeable, thin-film lithium battery [2]. Disposable on-demand, acid- and water-activated microbatteries, using chemical reactions in a cavity [3,4] were demonstrated for bioMEMS and microdevices, but the fabrication processes using silicon substrate hinders compatibility with plastic processes for microdevices. Urine-activated paper batteries [5] have been recently demonstrated to supply maximum power of 1.5mW with paper area of 4cmx2cm. However, the battery [5] requires more power and fast activation for fully-integrated biosystems that include several biosensors, electronic circuits, and even a display. The current work presents a high power laminated battery that uses two-step activation for high power and fast activation and that is activated by saliva-, urine- and even tap-water.

2. DESIGNS AND FABRICATION

Figure1 shows the schematic diagram of a high power battery. A stack of a magnesium (Mg) layer, facial tissue paper (fluid guide), heavily-doped filter paper with copper chloride (CuCl) and copper layer are laminated between two transparent laminating films into the battery. The facial tissue paper serves

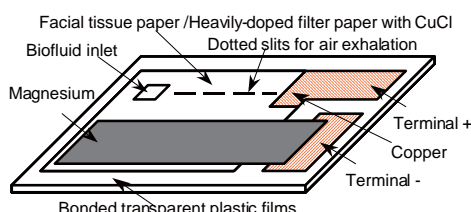


Fig.1. Schematic diagram of a high power biofluid-activated laminated battery.

as biofluid guide for high power battery while the heavily-doped paper with copper chloride acts as a cathode and the magnesium on the facial tissue paper acts as an anode. Figure 2 depicts the two-step activation of the high power battery. When biofluid such as saliva is introduced on the facial tissue paper in Fig.2(a), the biofluid first soaks through the paper, then the biofluid in the paper penetrates into the heavily-doped paper with CuCl to activate battery as shown in Fig.2(b).

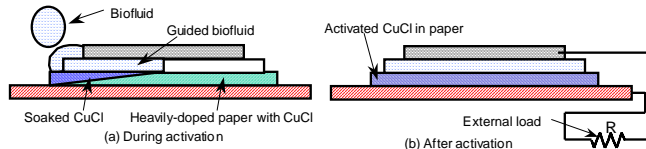


Fig.2. Two-step activation of the bio fluid-activated paper battery.

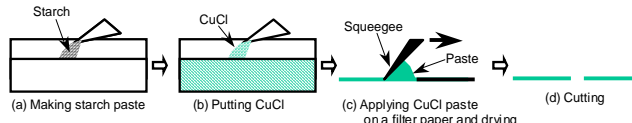


Fig.3. Preparation of the heavily doped filter paper with copper chloride (CuCl).

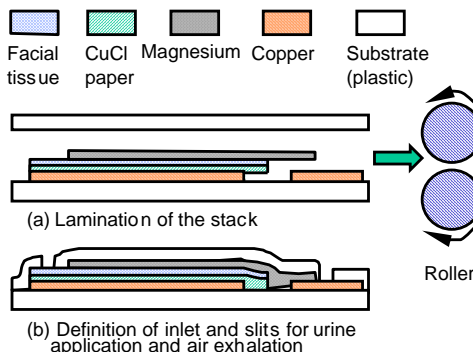


Fig.4. Fabrication process for the high power battery.

3. RESULTS AND DISCUSSION

Figures 6(a) and 6(b) are the measured voltage after saliva, urine and tap water of 0.3ml activates the batteries shown in Fig.5. Figure 6(a) compares voltages of batteries activated by saliva and urine when a load of $1\text{k}\Omega$ is used. The maximum voltages with urine and saliva are 1.54V and 1.48V, respectively. With urine, voltage reaches the maximum voltage of 1.54 within 10seconds and remains more than 1V for more than 2hour. Figure 6(b) shows voltages from the batteries with loads of 100Ω , $1\text{k}\Omega$ and $10\text{k}\Omega$ when tap water is used. Maximum power of 15.6mW is

Figure 3 shows preparation of the heavily-doped filter paper with CuCl. Using wheat starch in Fig.3(a), copper chloride (CuCl) paste is first prepared in Fig.3(b). After the CuCl paste is applied to a filter paper (Whatman, Cat No 1002 185), the paper is dried and cut into small pieces.

Using a laminator and lamination films, we can fabricate the battery as shown in Fig.4. After stacking patterned copper layer, heavily doped paper with CuCl, facial tissue paper, and magnesium between lamination films in Fig.4(a), all the layers (Fig.4b) are laminated into the battery while passing through the laminator at 115°C . Fig.5 shows the stacked copper layer, CuCl paper and facial tissue paper. Overall size of the fabricated battery (Fig.5) is $8\text{cm} \times 3\text{cm} \times 0.8\text{mm}$ (about half credit card size) and paper is $6\text{cm} \times 3\text{cm}$ in area.

achieved when 100Ω is used as a load.

Therefore, this environment-friendly high power battery, activated by biofluids(e.g. saliva and urine) and water, could be integrated with credit card-sized biosystems such as on-demand healthcare test kits.

4. CONCLUSIONS

An environment-friendly high power biofluid-activated battery, fabricated by cheap paper/plastic lamination, has been successfully demonstrated to power disposable credit card-sized biosystems on a plastic chip. The prototype batteries were activated by saliva, urine and even tap water, and the maximum voltage has been measured as 1.56V and the maximum power reached 15.6mW with load of 100Ω . As such, these high power biofluid-activated laminated batteries could be integrated with on-demand credit card sized biosystems such as healthcare test kit, biochip and lab-on-a-chip that require high power and fast activation.

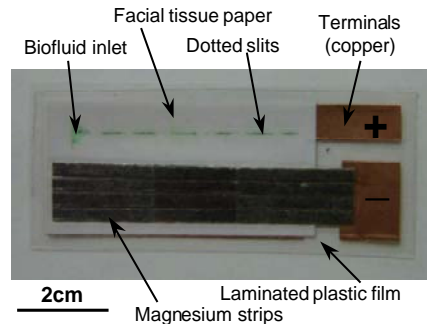


Fig.5. Photograph of the fabricated battery (6cm x 3cm)

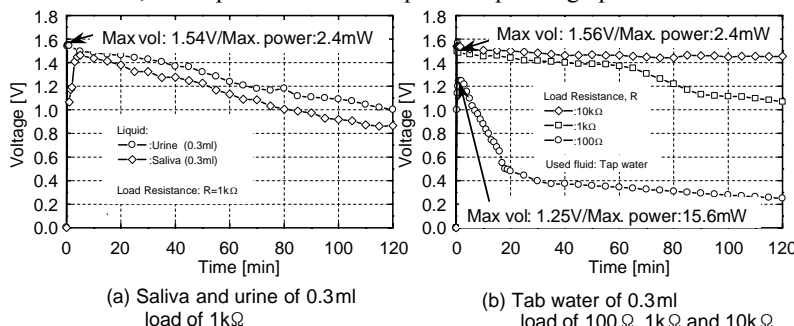


Fig.6. Measured voltages of the battery with different activation fluids and loads: (a) saliva and urine, load of $1k\Omega$ is used; (b) tap water, load of 100Ω , $1k\Omega$ and $10k\Omega$ are used. Fluid of 0.3ml is used for the battery activation.

REFERENCES

- [1] A. Mehra, X. Zhang, Arturo. A. Ayon, I. A. Waitz, M. A. Schmidt, and C. M. Spadaccini, "A Six-Wafer Combustion Systems for a Silicon Micro Gas Turbine Engine," *J. Microelectromechanical Systems*, V. 9, No. 4, pp.517-527, 2000.
- [2] S. D. Jones and J. R. Akridge, "A Microfabricated Solid-State Secondary Li Battery," *Solid State Ionics* 86-88, pp.1291-1294, 1996
- [3] Ki Bang Lee and Liwei Lin, "Electrolyte Based On-Demand and Disposable Microbattery," *IEEE/ASME Journal of Microelectromechanical Systems*, Vol. 12, No. 6, December 2003, pp.840-847.
- [4] Firas Sammoura, Ki Bang Lee and Liwei Lin, "Water Activated Disposable and Long Shelf Life Microbatteries," *Sensors and Actuators*, A111, March 1 2004, pp.79-86.
- [5] Ki Bang Lee, "Urine-Activated Paper Batteries for Biosystems," *Journal of Micromechanics and Microengineering*, 15, 2005, pp.S210-S214.

NUMEROUS WATER-IN-OIL DROPLETS AS MICROREACTORS IN MICROCHAMBER ARRAY

Hiroaki Kitagawa, Wei-Heong Tan and Shoji Takeuchi
CIRMM, Institute of Industrial Science, The University of Tokyo,
Meguro-ku, Tokyo 153-8505, Japan
kitagawa@iis.u-tokyo.ac.jp

Abstract

This paper describes an array of water-in-oil (W/O) droplets that can be used as microreactors. The droplets are created by sweeping water across a microchamber array with a non-water phase (Fluorocarbon); water left in the microchambers form droplets after the sweeping and remains trapped in the microchambers. With this method, more than 10,000 droplets are generated at once and placed in each microchamber. Also, we have succeeded in encapsulating beads in the droplets by mixing beads with water at the first step of this process. We believe this system will facilitate various chemical/biological experiments where ultra-large amount of observations with different conditions are required (e.g. protein expressions, crystallization, PCR).

Keywords: microreactor array, Water in oil (W/O), microchambers

1. Introduction

Small vessels such as liposomes, microchambers, and W/O droplets have been used as microreactors for detection and observation of chemical/biological reactions. Among the methods proposed, the method employing W/O droplets remains very promising, and represents an active area of research. Arraying of W/O droplets will make HTS possible by allowing massively parallel observation, detection, and analysis of these microreactors [1]. Here, we present a simple method for the formation and arraying of W/O droplets.

2. Theory

Figure 1. shows the conceptual sketch of our system. W/O droplet-based microreactors are arrayed in the microchambers. Closely-packed droplets allow detection and observation of large number of reactions simultaneously. In the future, we hope to extract specific droplets exhibiting interesting reactions from the array for post analyses such as PCR. Device operation is summarized in Figure 2. After filling with water, we introduced fluorocarbon (C_6F_{14}) phase into the PDMS device using syringe pumps. The formed W/O (strictly speaking C_6F_{14} is not an oil but an organic solvent) droplets were neatly arrayed in the microchamber. Fluorocarbon is very hydrophobic and its index of refraction (1.29) is lower than that of water (1.33). Therefore, water droplets in fluorocarbon phase can be trapped and manipulated with optical tweezers [2]. This technique may be useful for releasing these W/O droplets in the future.

3. Experimental

We prepared PDMS devices showed in Figure 3. The microchamber measures 5 μm in diameter and 5 μm in height. We filled the device with water containing suspended

fluorescent beads (ϕ 0.2 μm), and introduced the fluorocarbon phase into the device using syringe pumps. Flow rate of the fluorocarbon phase was varied and the relation between flow rate and the success rate (number of generated droplets / number of microchambers) was measured.

Water permeates into PDMS [3] and poses a problem in microscale. We observed that formed micro-droplets gradually disappeared after formation. The survival rate (number of remaining droplets / number of generated droplets during the first operation) over time was measured. To solve the water permeation problem and to extend the lifespan of the micro-droplets, we immersed the device in water for 12 hours before experiments to saturate the PDMS with water. We have also managed to produce W/O droplet array by introducing oil such as hexadecane (data not shown) instead of C_6F_{14} . But hexadecane is only suitable for short experiments because it penetrates PDMS and readily swells the microchambers.

4. Result and discussion

Sequential images of the droplet formation process are shown in Figure 4. Diameter of the generated droplets is the same as that of the chambers, and fluorescent beads were successfully encapsulated in water droplets. Figure 5 shows the relationship between the success rate and the flow rate. Both the saturated and non-saturated device shows the same general trend; high success rate at low flow rates that decreases at higher flow rates, albeit at different decreasing rates. The differences between the two cases are in the very low flow rate regime whereby the water-saturated device exhibited low success rate while the non-saturated device has extremely high success rate. This phenomenon is not yet fully understood and is still under investigation. Figure 6 shows the percentage of droplets that remain as a function of time for the two different cases. Saturating the PDMS device with water dramatically increases the lifespan of the droplets by around 27 folds (from around 10 mins to over 4.5 hrs).

5. Conclusions

Our proposed method for creating W/O droplets is simple, requiring only minute amounts of sample to cover the microchambers. Unlike conventional techniques using T-junctions [4] and flow focusing [5] for droplet formation, there is no need to wait for the system to stabilize. Moreover, formed droplets are arrayed, facilitating parallel observation and measurement. This simple device for the formation and arraying of W/O droplets could be the key for future development of a W/O droplet-based HTS system [6]. In addition, we are also currently developing an optical-based retrieval system to allow remote access to the droplets.

References

- [1] W. Tan and S. Takeuchi, *microTAS2005*, vol 1, pp. 506-508, 2005.
- [2] J. E. Reiner et. al., *Appl. Phys. Lett.* 89, 013904, 2006.
- [3] C. R. Greg and S. D. Patrick, *PNAS*, vol. 102, no. 31, pp.10813-10818, 2005
- [4] B. Zheng et. al., *Anal. Chem.*, 76, pp. 4977-4982, 2004.
- [5] S. Takeuchi et. al., *Advanced Materials*, vol. 17, no. 8, pp. 1067-1072, 2005.
- [6] M. Margulies et. al., *Nature*, 437, pp. 376-380, 2005.

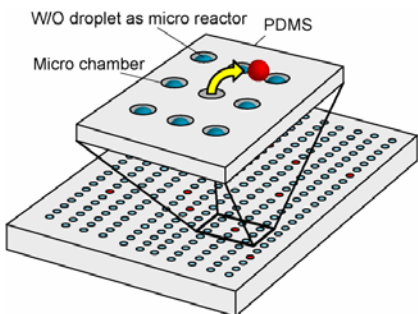


Figure 1. Conceptual sketch of Microchamber device

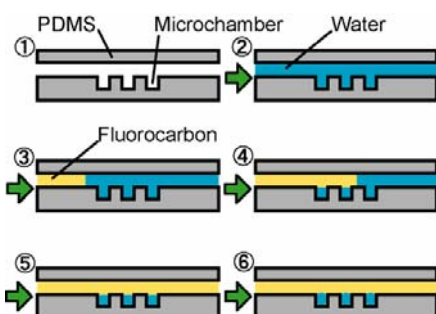
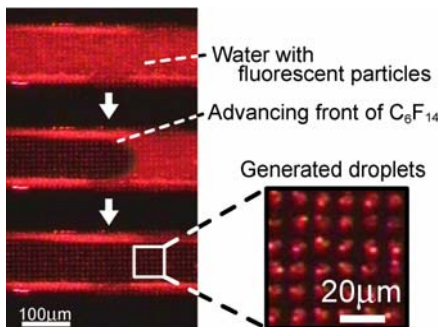


Figure 2. Device operation

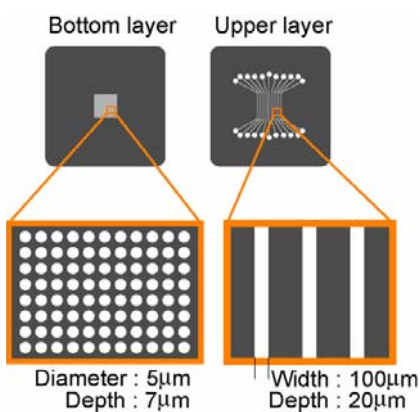


Figure 3. Device design

Figure 4. Sequential images of the droplet formation process. There are over 10000 droplets ($\phi = 5 \mu\text{m}$) formed in microchannels in each channel (channel length = 10 mm). Inset shows close-up view of the generated droplets.

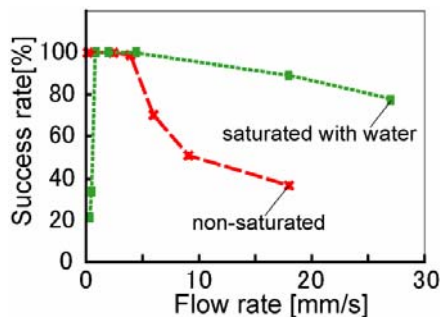


Figure 5. Success rate vs. Flow rate

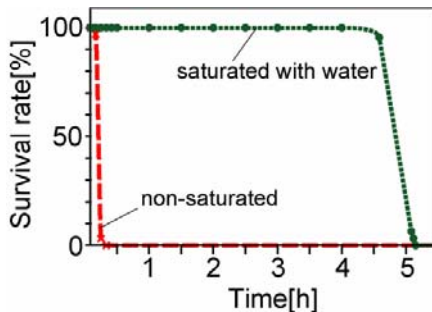


Figure 6. Duration of droplets

GEOMETRIC OPTIMIZATION OF A THIN FILM ITO HEATER TO GENERATE A UNIFORM TEMPERATURE DISTRIBUTION

Jungkyu Kim¹, Bruce K. Gale^{1,2}

¹Department of Bioengineering, University of Utah, Salt Lake City, UT 84112

²Department of Mechanical Engineering, University of Utah, Salt Lake City, UT 84112

Abstract

The shape of thin film ITO heater was designed and optimized to create a uniform temperature distribution across a specified area. COMSOL™ script language was used to solve the electrothermal problem and find the minimum temperature deviation for each variable (Gap size (g), center width (W_1) and reduction ratio of width ($R=W_{i+1}/W_i$)). Gap size and width did not strongly affect the temperature distribution, but reduction ratio was highly related with temperature distribution. At $R=0.8$, the standard deviation of temperature was found to be minimized at $\pm 0.21^\circ\text{C}$. Through this research, highly uniform temperature distributions for microsystems are made available.

Keywords: Optimization, thin film ITO, uniform temperature, Reduction ratio

1. Introduction

Biomedical microdevices that require precise temperature control, such as cell culture chips, PCR (Polymer Chain Reaction) chips and gas sensors need a microheater that has a uniform temperature distribution over a relatively large area. [1-3] Another typical requirement for these heating systems is transparency to allow optical detection of the reactions above the microheater system.[3-4] For this work, the microheater was designed to heat an array of PCR wells simultaneously in a consistent and reproducible manner. To implement the heaters, ITO was deposited on to a glass microscope slide. A uniform coating of ITO was found to not generate a uniform temperature distribution. To overcome this difficulty, a spiral type heater was designed and optimized with FEMLAB and MATLAB programming tools.

2. Simulation and Experiment

The geometric optimization for the microheater was performed by simulating a wide-range of possible geometries using COMSOL™, a commercial FEA (finite element analysis) package, and MATLAB™ programming. The desired function of the microheater was to minimize the standard deviation of temperature across an area 1 cm^2 where a PCR array would be located. The design variables are gap size (g), center width (W_1) and reduction ratio of width ($R=W_{i+1}/W_i$) as indicated in Figure 1. Using a numerical method, the global minimum point of standard deviation was found among the results of a series FEA experiments. Using the optimal design from these analyses,

the thin film ITO heater was fabricated by sputter depositing ITO through a shadow mask. To crystallize the ITO, it was annealed at 380 °C. Transparency of the ITO heater was measured with an Ocean Optics spectrometer after completion of the fabrication process. To compare the simulation result with experimental result, an IR (infrared) camera was used to measure the temperature across the heating surface.

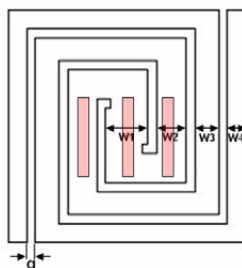


Figure 1. Geometry of thin film ITO Heater (3 variables (g , W_i and $R=W_{i+1}/W_i$) was used to acquire the uniform temperature distribution at specific areas (shaded)

3. Result and Discussion

The optimum geometry of a thin film ITO (Indium Tin Oxide) heater to be used for an array of PCR and DNA melting wells was determined using numerical analyses and compared to experimental data. The IR camera image and step response of ITO heater were compared with simulation data. The comparison showed very good agreement, and the step response of the system indicated that PCR should be able to be performed rapidly. (Data not shown) The transparency of the ITO heater was 82% between 450nm and 550nm, the wavelengths that are usually used for fluorescent dyes. At the minimum point, the standard deviation of temperature was $\pm 0.21^\circ\text{C}$ and gap size, width and reduction ratio were $g=2\text{mm}$, $W_1=2.8\text{mm}$ and $R=0.8$ respectively. The reduction ratio, which controls the resistance, was more sensitive than the other variables. The W_1 and g variables were highly correlated with the heat generation capacity of the ITO heater.

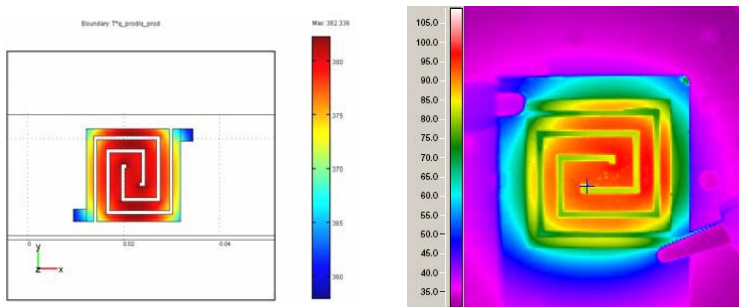


Figure 2. Validation of heater (Left: Simulation, Right: IR camera)

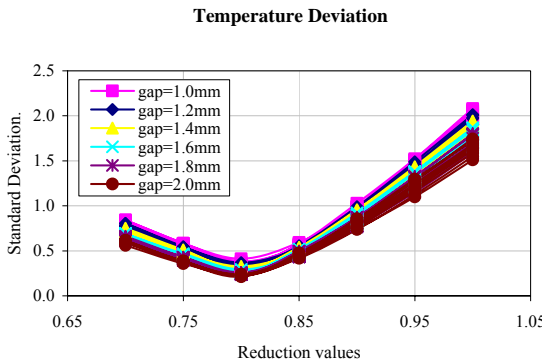


Figure 3. Temperature deviation of ITO heater with each case.

4. Conclusion

Shape optimization of a thin film ITO heater was completed to achieve a uniform temperature distribution. Three design variables were used to find the optimal geometry and among these variables, the reduction value was found to highly affect the temperature distribution. At Reduction value=0.8, the standard deviation of temperature profile was minimized at $\pm 0.21^{\circ}\text{C}$. Based on these results and concepts, we are able to make a uniform, small scale heater. If we change the scale of thin film ITO heater, the design values might change, but the trends should follow these results. This method has the potential to be applied to various electrothermal systems that involve the need for a uniform temperature.

Acknowledgements

The authors would like to acknowledge the financial support of the Utah State Centers of Excellence Program and the University of Utah.

Reference

1. Y. Mo, Y. Okawa, K. Inoue and K. Natukawa, *Low-voltage and low-power optimization of micro-heater and its on-chip drive circuitry for gas sensor array*, Sensor and Actuators A, 100(2002) 94-101
2. D. S. Yoon, Y-S. Lee, Y. Lee, H. J. Cho, S W Sung, K W Oh, J Cha and G Lim, *Precise temperature control and rapid thermal cycling in a micromachined DNA polymerase chain reaction chip*, J. Micromech. Microeng. 12(2002) 813-823
3. P. J. Hung, P. J. Lee, P. Sabourchi, N. Aghdam, R. Lin and L. P. Lee, *A novel high aspect ratio microfluidic design to provide a stable and uniform microenvironment for cell growth in a high throughput mammalian cell culture array*, Labchip, 5(2005). 44-48
4. B. G. Lewis and D. C. Paine, *Application and processing of transparent conducting oxides*, MRS bulletin, (2000) 22-27

RELIABILITY AND CONSISTENCY OF MICROCHIP BASED ANALYSIS - VALIDATION AT NANO LITTER ANALYSIS -

Tomohiko Kawakami^{1,2}, Katsumasa Sakamoto^{2,3}, Yoshinori Matsuoka^{2,4},
Yoshikuni Kikutani^{2,5}, Kazuma Mawatari^{2,5}, Kiyoko Kurosawa¹,
Mitsuo Kitaoka² and Takehiko Kitamori^{5,6}

¹Kaken Inc., 1044 Horimachi, Mito, Ibaraki 310-0903 Japan, ²The Research Association of Micro Chemical Process Technology, Japan, ³Technology Research Laboratory, Shimadzu Corporation, Japan, ⁴Nippon Sheet Glass Co., Ltd., Japan, ⁵Micro Chemistry Group, Special Research Laboratory for Optical Science, Kanagawa Academy of Science and Technology, Japan, ⁶Department of Applied Chemistry, Graduate School of Engineering, The University of Tokyo, Japan
(E-Mail: kawakami.tomohiko@jaea.go.jp)

Abstract

Validation studies of a microchip-based analysis system and its components for conformance to Japanese industrial standard (JIS) were carried out. Good correlation between micro-TAS and conventional scale analyses were observed and day-to-day variance was also small. These results are quite meaningful because validation would be a key for micro-TAS to become widespread in practical usage.

Keywords: validation, reliability, consistency, accuracy, trueness, industrial standard,

1. Introduction

Reduction in sample amounts has been one of the major targets in analytical chemistry for a long time, and recent progress in micro-TAS has made great contribution to this field of research.

Amounts of samples and reagents used in microchemical processes are sometimes as small as in nano litter levels, which are orders of magnitude smaller than those in corresponding conventional methods. And detection volumes in micro-TAS also tend to be much smaller than in normal analyses. Furthermore, in some micro assays, reaction times are much shorter than corresponding large scale ones. Whether it is really possible to obtain the same results as with the conventional methods is a question that many people might have for micro-TAS with such a small amounts of samples and reagents. Therefore it is critically important to verify that results obtained with micro-TAS are reliable enough and consistent with that with conventional methods. However, no complete validation study has been done on micro-TAS yet. In this paper we validate reliability of a microchip-based analysis system and its components in conformity with Japanese industrial standard (JIS).

2. Experimental

As one of the simplest examples of micro-TAS, we selected a system comprised of pumps, injectors, a microchemical chip, and a detector (Figure 1). Analyses of nitrous ion in water using 4-aminobenzenesulfamide and *N*-1-Naphthylethylenediamine dihydrochloride or

phosphate ion in water using sodium molybdate (JIS standard methods for industrial sewerage analysis K0102) were carried out with the microchemical system and with conventional glassware and a spectrometer for comparison. As a detector in the micro system, we used thermal lens microscope.

3. Results and Discussion

First, components of the micro system were validated. Flow rates of syringe pumps (KDScientific, Model 210) and gas pressure pumps (IMT, Japan IGP-11) were calibrated with balance weights. And then flow sensors (Sensirion, Inc., CMOSens) were calibrated with the calibrated syringe pumps. Coefficient of variation (CV) of the syringe pump flow rate was 1.7 ~ 3.5 % and strongly depended on the size of the syringe. CV of gas pressure pump flow rate was only 0.1 ~ 0.4 % and no pulsation in flow rate was observed (Figure 2). Next, reproducibility of the injector (Upchurch Scientific) was tested. CV was 2.9 % and no carryover was observed (Figure 3). In order to evaluate effects that variation in channel

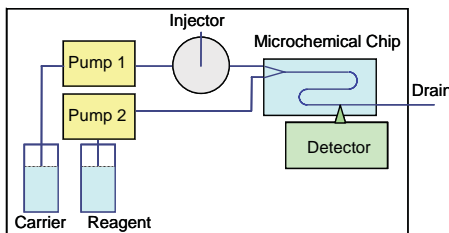


Figure 1. Structure of a micro total analysis system for nitrous or phosphate ion

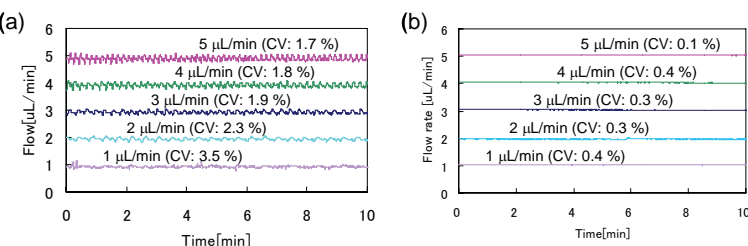


Figure 2. Fluctuations in flow rates of (a) a syringe pump with a 50 μL syringe and (b) a gas pressure driven pump

dimension would give upon reaction and detection, chip-to-chip variance was with seven glass microchips. About the detector, sensitivity, accuracy and stability of the thermal lens detection device were examined.

Finally, validation of the system as a whole was evaluated. Good correlation between micro-TAS and conventional scale analyses were observed for both in nitrous ion analysis (Figure 4, Table 1) and phosphate ion analysis (Figure 5, Table 2). Day-to-day variance was also small (CV: 3.2 % for nitrous ion analysis).

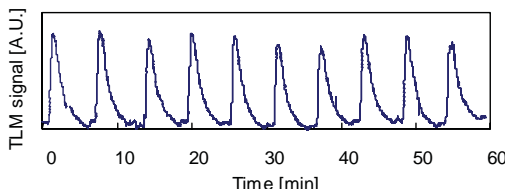


Figure 3. Reproducibility of a micro injector. 1 $\mu\text{g/mL}$ PO_4^{3-} standard solution was repetitively injected to the microchip-based analysis system.

4. Conclusion

In this study, it was proved that micro-TAS could be equally reliable as and consistent with the conventional industrial standard analyses. It is meaningful because validation would be a key for micro-TAS to become widespread in practical usage.

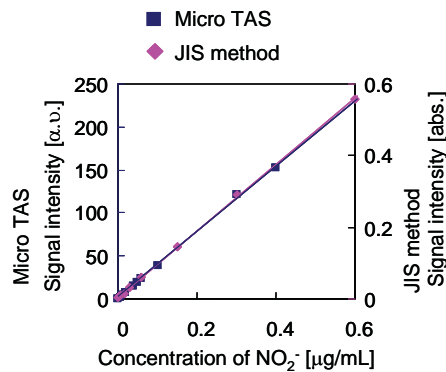


Figure 4. Correlation between micro TAS and conventional JIS method in analysis of nitrous ion

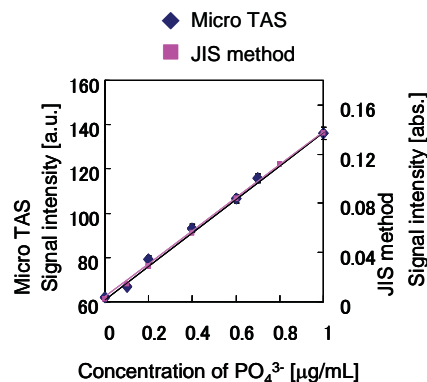


Figure 5. Correlation between micro TAS and conventional JIS method in analysis of phosphate ion

Table 1. Results of validation test of micro TAS in analysis of nitrous ion

	Micro TAS	JIS method
Linearity	$R^2=0.999$	$R^2=0.999$
Lowest detection limit S/N=3 ($\mu\text{g / mL}$)	0.002	0.02
Lowest determination limit S/N=10 ($\mu\text{g / mL}$)	0.006	0.06
Dynamic range ($\mu\text{g / mL}$)	0.006~6	0.06~2

Table 2. Results of validation test of micro TAS in analysis of phosphate ion

	Micro TAS	JIS method
Linearity	$R^2=0.998$	$R^2=0.999$
Lowest detection limit S/N=3 ($\mu\text{g / mL}$)	0.01	0.03
Lowest determination limit S/N=10 ($\mu\text{g / mL}$)	0.03	0.08
Dynamic range ($\mu\text{g / mL}$)	0.03~4.00	0.08~4.00
Reproducibility (CV)	1.5~3.2 %	2~10 %

MULTIPLE IMMUNOASSAY ON A CAPILLARY-ASSEMBLED MICROCHIP (CAs-CHIP) INTEGRATING VALVING AND IMMUNO-REACTION FUNCTIONS

**Terence G. Henares, Shun-ichi Funano,
Hideaki Hisamoto, and Shigeru Terabe**

Graduate School of Material Science, University of Hyogo, Japan
(e-mail: hisamoto@sci.u-hyogo.ac.jp)

Abstract

Multiple enzyme linked immunosorbent assay (ELISA) chip is developed by using capillary-assembled microchip (CAs-CHIP) technique [1-4], which involves the simple embedding of the multiple square capillaries possessing valving and immuno-reaction functions into the microchannels fabricated on a PDMS substrate. CAs-CHIP technique enables the integration of both fluid control parts and immuno-reaction parts in a single ELISA chip, thus, it leads to the flexible design of the multi-ELISA chip for many different medical and clinical purposes by using different immuno-reaction capillaries.

Keywords: capillary-assembled microchip, ELISA, immunoassay, PDMS, square capillary

1. Introduction

It is well-known that the integration of the immunoassay system on a microfabricated device is a very promising approach. Because the short molecular diffusion distance provided by the microchannel offers an advantageous feature in significant reduction of the analysis time from hours to minutes [5]. However, systematic and flexible integration of the valving operation and the different immuno-reaction systems in a single microchip is a crucial issue for realizing the multi-ELISA system required for different diagnostic purposes.

Here we demonstrated the multi-ELISA using the capillary-assembled microchip (CAs-CHIP) integrating valving and immuno-reaction functions in a single microchip.

2. Experimental

Here, a thermo-responsive polymer-immobilized capillary was used together with a small Peltier device, as valving part, and many different antibody-immobilized capillaries were used as immuno-reaction parts. These capillaries were cut into appropriate length (2-3 mm), and embedded as shown in Figure 1. Spin-coated PDMS prepolymer was used as final bonding. Sample solution and detecting reagent solutions were sequentially introduced through the valving capillary, and after introducing each solution, valve was closed by lowered the temperature of the Peltier device to start each reaction inside the immuno-reaction capillary. Detection was carried out by using the thermal lens microscope.

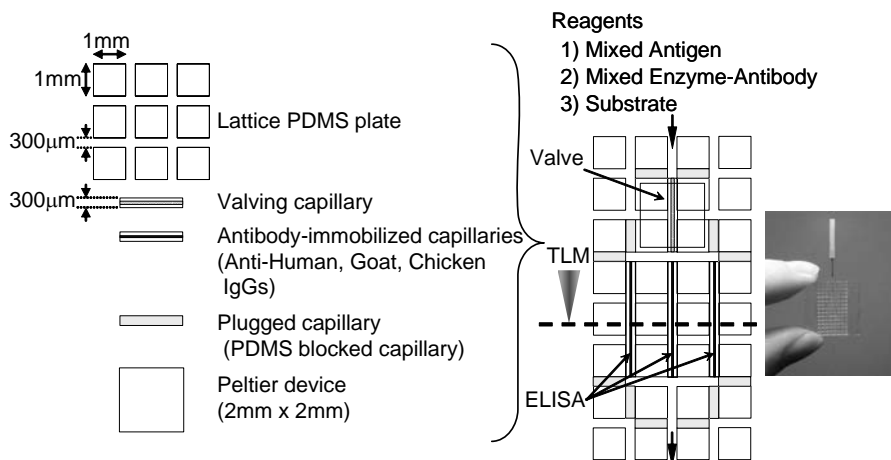


Figure 1. Design of the multiple ELISA CAs-CHIP integrating valving and immuno-reaction functions

3. Results and discussion

Figure 2 shows the typical response curve obtained by using anti-human IgG-immobilized capillary. Although, error bar is quite large, the results indicated that the determination of subnanogram per milli-liter human IgGs were successfully achieved. Anti-goat, or chicken IgG-immobilized capillaries also responded in the same concentration ranges to Figure 2.

When the mixed IgG solution (Human IgG: 100pg/ml, Goat IgG: 1 ng/ml, Chicken IgG: 10 ng/ml), mixed enzyme (HRP)-antibody solution and substrate solution were introduced through valving capillary, selective immuno-reactions and enzyme reactions took place in each antibody-immobilized capillary. Since the inner size of immuno-sensing capillaries was ca. 50 micron square, immuno reactions required for sandwich-type ELISA were significantly reduced to 30 minutes including two immuno-reactions and subsequent enzyme reaction steps.

Figure 3 shows the results of multi-IgG sensing using the chip together with those of single capillary responses. Three different IgG concentrations were successfully determined by scanning the focal point of thermal lens microscope.

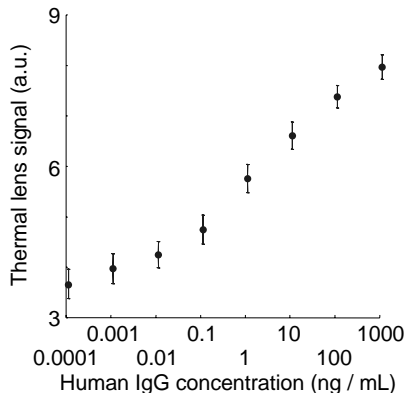


Figure 2. Typical response curve for Human IgG

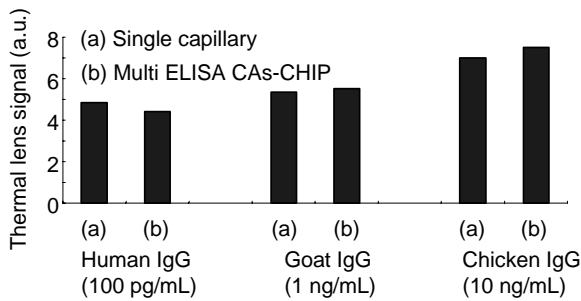


Figure 3. Comparison of the responses of multiple ELISA CAs-CHIP and corresponding single capillaries

4. Conclusions

Systematic and flexible integration of the valving operation and the different immuno-reaction systems in a single microchip was successfully achieved. Multi-ELISA chip developed here can be applied for many different medical and clinical purposes by using different immuno-reaction capillaries required for each purpose.

Acknowledgements

T. H. acknowledges for the Monbukagakusho Scholarship from the Japanese government and H.H. is grateful for the research funding sponsored by the New Energy and Industrial Technology Development Organization (NEDO, Grant for Industrial Technology Research, 05A37702a), the Grant-in-Aid for Scientific Research from the Ministry of Education, Culture, Sports, Science and Technology, Japan, and Hyogo Science and Technology Association, Japan.

References

- [1] H. Hisamoto, Y. Nakashima, C. Kitamura, S.-I. Funano, M. Yasuoka, K. Morishima, Y. Kikutani, T. Kitamori and S. Terabe, *Capillary-Assembled Microchip for Universal Integration of Various Chemical Functions onto a Single Microfluidic Device*, *Anal. Chem.*, 76, 3222-3228 (2004).
- [2] H. Hisamoto, S.-I. Funano and S. Terabe, *Integration of Valving and Sensing on a Capillary-Assembled Microchip*, *Anal. Chem.*, 77, 2266-2271 (2005).
- [3] H. Hisamoto, M. Yasuoka and S. Terabe, *Integration of Multiple-Ion Sensing on a Capillary-Assembled Microchip*, *Anal. Chim. Acta*, 556, 164-170 (2006).
- [4] H. Hisamoto, S. Takeda and S. Terabe, *Capillary-Assembled Microchip as a Deproteinization Device for Capillary Electrophoresis*, *Anal. Bioanal. Chem.* in press (2006).
- [5] K. Sato, M. Tokeshi, T. Odake, H. Kimura, T. Ooi, M. Nakao, T. Kitamori, *Integration of an Immunosorbent Assay System: Analysis of Secretory Human Immunoglobulin A on Polystyrene Beads in a Microchip*, *Anal. Chem.*, 72, 1144-1147 (2000).

IMPROVEMENT OF THE DETECTION LIMIT IN SURFACE PLASMON RESONANCE IMMUNOSENSOR FOR RAPID ON-SITE MEASUREMENT OF A CARIAC MARKER IN BLOOD SAMPLES

Ryoji Kurita¹, Yoshimi Yokota¹, Yukari Sato¹, Fumio Mizutani², Osamu Niwa¹

¹National Institute of Advanced Industrial Science and Technology (AIST)

1-1-1 Higashi, Tsukuba, Ibaraki, 305-8566 Japan

² University of Hyogo

3-2-1 Kouto, Kamigori-cho, Ako-gun, Hyogo 678-1297 Japan

Contact E-mail: r.kurita@aist.go.jp

Abstract

We developed a small volume immunoassay chip with very low detection limit (ppt level in 3 µL sample volume) based on surface plasmon resonance (SPR) detection by suppressing non-specific adsorption of interfering molecules in case of determining a blood B-type natriuretic peptide (BNP). This was achieved by a T-shaped microfluidic channel with BNP immobilized region for B/F separation of binded and unbinded antibody-enzyme conjugate located upstream of the junction and a gold thin film for SPR detection located downstream of the junction. This chip design is advantageous to avoid the blood samples pass over the gold film for SPR detection. Therefore, a low detection limit can be obtained since the detection region is free from non-specific adsorption.

Keywords; **Immunosensor, B-type natriuretic peptide (BNP), Surface plasmon resonance (SPR), Point-of-care testing**

1. Introduction

Various SPR immunosensors have been reported based on the SPR angle shifts caused by the formation of an immuno-complex on an antibody modified sensing surface. The SPR immunosensor has advantages as regards bedside monitoring and point-of-care testing because the method is a rapid, simple, safe and low power technique [1]. However, it is difficult to measure trace level biomolecules in real samples because of the non-specific adsorption when the sample solution is directly introduced onto the sensing surface. Since an SPR sensor simply responds to refractive index changes on the sensing surface, it is impossible to distinguish whether the SPR angle shift is caused by specific or non-specific adsorption. Various modifications of the film on the sensing surface have been used to suppress non-specific adsorption. Nevertheless, the complete prevention of non-specific adsorption is difficult at present. Thus, when monitoring trace level biomolecules, it is inappropriate to introduce the

blood sample directly onto the sensing surface during SPR measurement.

In this paper we propose a one-chip immunosensor with a small sample volume using a T-shaped microfluidic system that has a B/F separation chamber and a gold film for the SPR detection which is free from non-specific adsorption.

2. Experimental

Figure 1 is a schematic representation of our immunosensor. The immunosensor consists of poly-dimethylsiloxane cover with a T-shaped microchannel and a glass plate with two gold films. One is for BNP immobilized region and the other is for SPR detection. The T-shaped channel consists of a micro channel A (1 mm wide, 20 μm deep) and a micro channel B (2 mm wide, 20 μm deep). Assay protocol is described in figure caption 1.

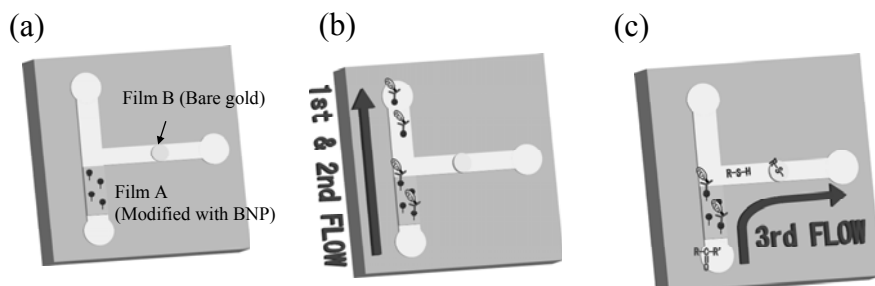


Figure 1 (a) Preparation of the immunosensor. Film A is modified with BNP for the collection of unreacted anti-BNP-AChE. Film B is a bare gold film for the SPR detection. (b); Introduction of a mixture solution containing sample BNP and 190 ng/mL of acetylcholine esterase labeled anti BNP antibody (anti-BNP-AChE) for 10 min. The unreacted anti-BNP-AChE was collected on BNP modified film A during the 1st flow. Then the channel was rinsed with phosphate buffer during the 2nd flow. (c); 1 mM acetylthiocholine was introduced toward the film B. Thiocholine was produced from acetylthiocholine by the collected anti-BNP-AChE on film A, then the thiocholine is accumulated on the film B surface located downstream in the microchannel, and monitored by the SPR angle shift during the 3rd flow.

3. Results and Discussions

Figure 2 shows the calibration curve of the immunosensor. When the BNP concentration was lower than 1 pg/mL, the SPR angle was almost unchanged. In contrast, the SPR angle started to decrease as increasing the BNP concentration when the BNP concentration was higher than 5 pg/mL. The proposed method could be used for determining BNP in wide dynamic range from 5 pg/mL to 100 ng/mL which covers

blood concentration of BNP required for clinical application. The proposed BNP sensing method has one of the most low detection limit yet reported based on an SPR detection system because both of sample solution and detection antibodies did not pass over the sensing surface by the T-shaped microfluidics. Table 1 compares SPR angle shift values obtained from BNP spiked in human serum with those obtained from BNP in a buffer solution. The SPR angle shift values in a buffer solution were estimated from the calibration curve in Fig. 2. Though good agreement could not be obtained when using unheated human serum because of a large amount of endogenous pseudocholinesterase in serum, we could obtain the satisfactory recovery using the spiked serum sample when we inactivate the esterase in the blood by pre-heat treatment. Our immunosensor is superior to commercially available immunoassay systems based on fluorescence or isotope detection since our immunosensor is portable and safe and employs a low power technique with a high sensitivity equivalent to that of conventional methods.

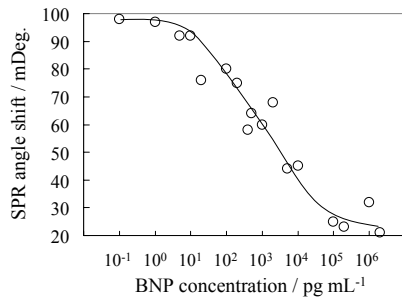


Figure 2 Calibration curve for BNP obtained with the immunosensor.

unheated human serum because of a large amount of endogenous pseudocholinesterase in serum, we could obtain the satisfactory recovery using the spiked serum sample when we inactivate the esterase in the blood by pre-heat treatment. Our immunosensor is superior to commercially available immunoassay systems based on fluorescence or isotope detection since our immunosensor is portable and safe and employs a low power technique with a high sensitivity equivalent to that of conventional methods.

Run no.	BNP added value	Calibration curve from fig. 2	Serum measurement	Ratio / %
1	0 pg/mL	99 mDeg.	96 mDeg.	97%
2	10 pg/mL	91 mDeg.	91 mDeg.	100%
3	100 pg/mL	75 mDeg.	76 mDeg.	101%
4	1 ng/mL	58 mDeg.	59 mDeg.	102%
5	10 ng/mL	38 mDeg.	32 mDeg.	84%
6	100 ng/mL	26 mDeg.	23 mDeg.	88%

Table 1 Comparison of SPR angle shift value in human serum with that in phosphate buffer for various concentrations of BNP spiked samples. The SPR angle shift values in buffer solution were estimated from the calibration curve in Fig. 2.

References

- [1] R. Kurita et al, Proc. Micro Total Analysis Systems 2005 vol. 1, pp.310-312 (2005)

AN ELECTRO-MICROCHIP FOR IMMUNOASSAY USING GOLD NANOPARTICLE AND SILVER ENHANCEMENT

Keng-Shiang Huang¹, Hao-Hsuan Huang¹, Tsung Chain Chang²,
Hong-Ping Lin³, Yung-Chiang Chung⁴, Yu-Cheng Lin^{1*}

¹Department of Engineering Science, ²Department of Medical Laboratory
Science and Biotechnology, ³Department of Chemistry,

National Cheng Kung University, 1 Ta-Hsueh Rd., 701 Tainan, Taiwan

⁴Department of Mechanical Engineering, Mingchi University of Technology, 243
Taishan, Taiwan

*Email: yuclin@mail.ncku.edu.tw

Abstract

This paper reports a novel immunoassay using an electro-microchip to detect the immuno-reaction signal and the silver enhancement reaction to magnify the detection signal. Moreover, gold nanoparticles (ANPs) play the roles of a label for antigen or antibody and a catalyst for silver precipitation. The change of the impedance to corroborate immuno-reaction is detected, amplified and analyzed. The results show that using the gap size of 20 μm electro-chip has the best sensitivity. The relationship between concentration and signal is established and the antigen detection limit is 100 ng/mL.

Keywords: immunoassay, gold nanoparticle, silver enhancement

1. Introduction

Immunogold silver staining (IGSS) technique is widely used in optical microscope observation [1, 2]. Herein, we combine IGSS, gold nanoparticles (ANPs) and an electro-microchip to construct a new immunoassay. The whole framework of the study is based on two major aspects: (i) direct immunoassay (two-layer format) is used for qualitative analysis (Fig. 1a), and (ii) sandwich immunoassay (three-layer format), which composed of a primary antibody, a secondary antibody and antigens, is used for qualitative and quantitative analysis (Fig. 1b).

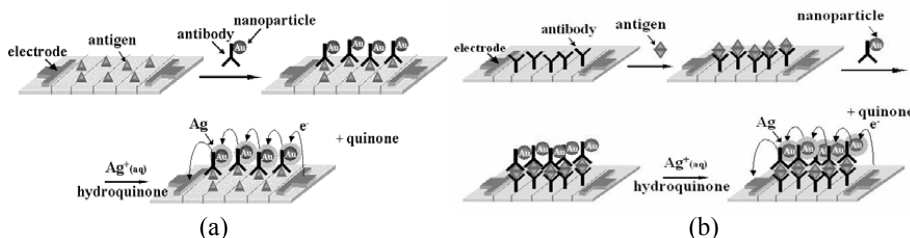


Fig. 1 Scheme of the signal amplification method: (a) two-layer format (direct immunoassay) and (b) three-layer format (sandwich immunoassay).

2. Experimental

The developed system, as shown in Fig. 2, includes: (i) a LCR meter, which is the main measurement instrument to measure the variation of the impedance, (ii) a Lab-VIEW® program for acquiring the data automatically and (iii) an electro-microchip. In SEM images, we find specific spaces between different sizes (5 nm and 20 nm) of ANPs, which indirectly prove the conjugation of the ANPs and IgG (Fig. 3a). Moreover, the IgG-ANPs conjugates have two specific absorption peaks at 270 nm and 530 nm in UV-Vis spectrum (Fig. 3b). These prove the conjugation of the ANPs and the IgG.

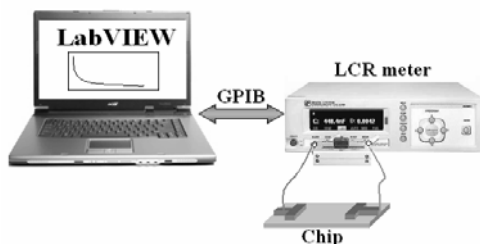


Fig. 2 Impedance measurement system including (i) a LCR meter: the main measuring instrument (ii) a Lab-VIEW® program for acquiring the data automatically, and (iii) an impedance microchip.

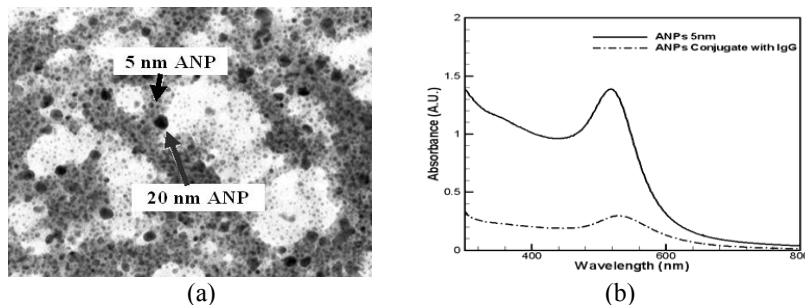


Fig. 3 (a) TEM images of IgG-ANPs (5 nm) conjugates bind with protein A-ANPs (20 nm) conjugates, and (b) The UV-Vis spectrum of 5 nm ANPs and IgG- ANPs conjugates.

3. Results and Discussions

The gap size of the parallel electrodes from 20 μm to 200 μm is designed to evaluate the relationship between the gap size of the electrode and the sensitivity. Experimental data show that the sensitivity is influenced by different gap sizes of the electrodes. An electro-microchip with a 20 μm gap electrodes has the best sensitivity among the others (Fig. 4). In immuno-experiment, the concentration of first antibody is fixed at 10 $\mu\text{g}/\text{mL}$ and the different concentration of antigen is set from 0.01 $\mu\text{g}/\text{mL}$ to 10 $\mu\text{g}/\text{mL}$. Experimental results show an apparently decreasing of the impedance, as shown in Fig. 5. The diversity of the impedance means that the developed immunoassay approach is work.

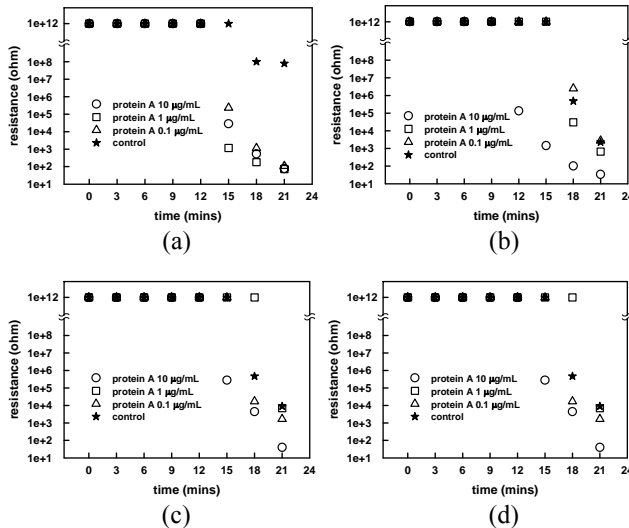


Fig. 5 The impedance spectrum of the direct immunoassay (two-layer format) in the gap size of (a) 20 μm (b) 50 μm (c) 100 μm , and (d) 200 μm . The chip with a 20 μm gap has the highest sensitivity.

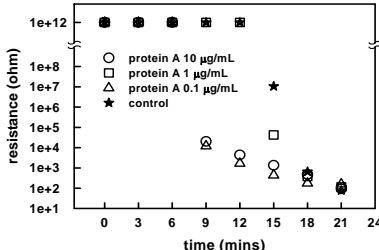


Fig. 5 The impedance spectrum of a chip with parallel electrodes with a 20 μm gap size in the sandwich immunoassay. The concentration of antigen is set from 0.1 $\mu\text{g/mL}$ to 10 $\mu\text{g/mL}$ and the detection limit is 0.1 $\mu\text{g/mL}$.

4. Conclusions

Changing the silver enhancement solution every 3 minutes restrains silver precipitation. The detection limit of the sandwich immunoassay is 100 ng/mL. The developed method has advantages of rapid, sensitive and convenient than conventional immunoassay ELISA.

REFERENCES

- [1] C.S. Holgate, P. Jackson, P.N. Cowen, C.C. Bird, Vol. **31**, Journal of Histochemistry & Cytochemistry, pp. 938-944.
- [2] M.L. Peter, Vol. **106**, Histochemistry and Cell Biology, pp. 9-17.

DEVELOPMENT OF A PIEZOELECTRIC MICROJET INJECTOR FOR TRANSDERMAL DRUG DELIVERY

Jeanne C. Stachowiak ¹, Thomas H. Li ¹, Julia Rasooly ²,
Wilbur A. Lam ², and Daniel A. Fletcher ²

¹ University of California, Berkeley, USA, Dept. of Mechanical Engineering,

² University of California, Berkeley, USA, Dept. of Bioengineering

Abstract

We present the development and characterization of a piezoelectric microjet. This needle-free drug delivery device is designed to deliver small, frequent drug doses that can be controlled by feedback from physiological sensors to create a closed-loop drug therapy system. Device performance is characterized using strobe imaging of injection speed, micro-scale force sensing, and measurement of penetration depth in skin surrogate materials. Penetration depth is found to correlate with the volume delivered above the critical pressure for material failure.

Keywords: drug delivery, needle-free, jet injector, piezoelectric

1. Introduction

Recently, autonomous micro-analytical systems have been developed that are capable of continuously monitoring patient physiology and drug response *in vivo* [1]. The availability of such devices suggests a new paradigm for transdermal drug therapy in which small, frequent drug doses given in response to sensor feedback create a closed-loop dose profile, replacing traditional transdermal drug therapy in which large, infrequent doses are delivered by hypodermic needles. This paradigm shift requires a new drug delivery technology capable of delivering small, precise drug doses through the skin. We present the development of a piezoelectric microjet injector for transdermal drug delivery. Here, a piezoelectric actuator is suddenly expanded, providing an impulse of momentum to the plunger of a syringe. As the plunger travels, a high-speed liquid jet capable of tissue penetration issues from a micro-nozzle and is imaged using strobe microscopy (Figure 1, Left). In this paper we experimentally and theoretically characterize the influence of nozzle diameter, an important device design parameter, on jet formation and penetration in polyacrylamide gel, a skin surrogate.

2. Experimental

The piezoelectric microjet consists of a conventional syringe (Hamilton, Reno, NV, USA) with the needle cut short and a glass micro-nozzle attached using epoxy. Nozzles are fabricated by heated mechanical pulling of glass pipettes followed by fire polishing and mechanical sanding to the desired orifice diameter. The piezoelectric actuator (Thorlabs, Newton, NJ, USA) is directly abutted to the syringe plunger prior to actuation. Jet speeds are measured using a 2-pulse strobe imaging technique [2], in which the pulses are of 5 ns duration and separated by 5 μ s (Fig. 1, left). A micro-scale

load cell (50g, Honeywell, 10kHz) is used to track the force generated by the impinging microjet (Fig. 1, bottom right). To measure penetration depth, FITC-conjugated latex beads are mixed with the ejected solution, creating contrast after injection into surrogate materials (4wt% polyacrylamide gel) (Fig. 1, top right).

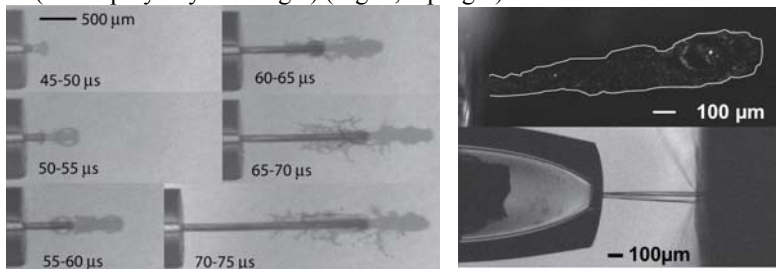


Figure 1. (Left) Strobe images of the developing microjet, from which the velocity is calculated. (Top Right) Image of jet penetration in polyacrylamide gel using 500nm FITC-latex beads. Outline added manually for contrast. (Bottom Right) Microjet impinging on micro-scale load cell.

3. Theory

A simple physical model of the microjet system is based on differential equation statements of mass and momentum conservation (Equations 1,2) [3]. This model focuses primarily on the exchange of energy between plunger momentum and liquid compression. Frictional losses are neglected.

$$(1) \quad \underbrace{\frac{du_o(t)}{dt}}_{\text{change in orifice velocity}} = \underbrace{\frac{(B + p(t)) \frac{dx_p(t)}{dt}}{L - x_p(t)}}_{\text{compressibility of liquid}} - \underbrace{\frac{BA_o}{A_p} \sqrt{\frac{2p(t)}{\rho}}}_{\text{loss through orifice}}$$

$$(2) \quad \underbrace{\frac{d^2x_p(t)}{dt^2}}_{\text{acceleration}} = - \underbrace{\frac{A_p p(t)}{m_p}}_{\text{pressure force}} \quad m_p - \text{plunger mass; } A_p - \text{plunger area; } B - \text{bulk modulus} \\ \rho - \text{initial density; } A_o - \text{orifice area; } L - \text{column length;} \\ x_p(t) - \text{plunger displacement; } p(t) - \text{pressure}$$

4. Results and Conclusions

The microjet device uses the rapid, brief expansion of a piezoelectric actuator (15 μm at 1m/s) to compress a small volume of liquid (4-10 μL). Actuator expansion results in the expulsion of a high-speed (50-200 m/s) stream of liquid of small total volume (50-700 nL). As the plunger moves forward the dynamic combination of system compression and losses causes jet velocity to oscillate, as observed when the jet impinges on a micro-scale load cell (Fig. 2, Left). Jet velocity increases as nozzle diameter decreases (Fig. 2, Middle). Comparison with the simple theory, where bulk modulus is adjusted to account for system compressibility, shows qualitative agreement in the observed trend (Fig. 2, Right).

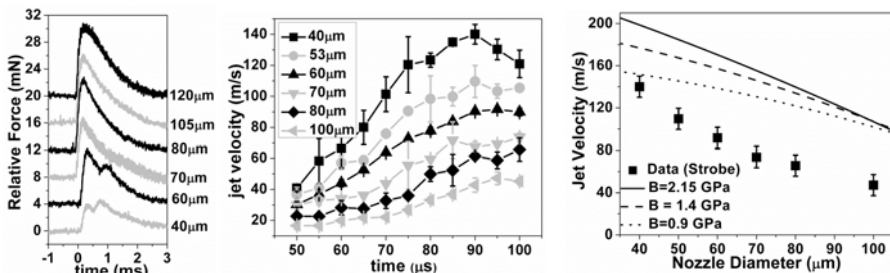


Figure 2. (Left) Load cell readings for various nozzle diameters. As nozzle diameter increases, an under-damped to over-damped transition occurs. (Middle) Jet velocity as a function of time and nozzle diameter. (Right) Maximum measured jet velocity as a function of nozzle diameter with comparison to model.

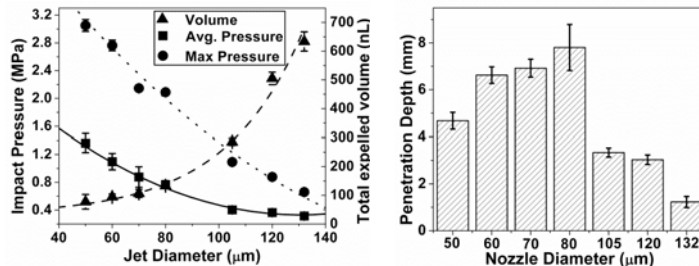


Figure 3. (Left) Impact pressure and volume measured as a function of nozzle diameter. (Right) Penetration depth in 4 wt% polyacrylamide gel as a function of nozzle diameter.

Two criteria must be met for material penetration to a given depth: (i) fluid impact pressure must exceed a critical value related to material fracture stress, and (ii) the total volume delivered at that pressure must be sufficient to create the fracture surface. As nozzle diameter increases, resistance to plunger motion decreases, increasing the total shot volume and simultaneously decreasing the maximum and average impact pressure (force per jet area) (Fig. 3, left). These effects act together, resulting in a maximum penetration depth for a nozzle diameter of 80 μm. Nozzles of smaller diameter suffer from insufficient volume delivered, while those of larger diameter suffer from insufficient pressure. Thus we conclude that penetration depth correlates with the shot volume delivered above the critical pressure for material failure.

Acknowledgements

We gratefully acknowledge Philips Semiconductor, Inc. for support of this work and Dr. Giovanni Nisato (Philips) for helpful discussions.

References

1. P. S. Petrou, I. Moser, G. Jobst, *Bios. and Bioelect.*, vol. 18, pp. 613-19, 2003.
2. D. A. Fletcher, D. V. Palanker, *Appl. Phys. Lett.*, 78, pp. 1993-1995, 2001.
3. A. B. Baker, J. E. Sanders, *IEEE Trans. on Biomed. Eng.*, 46, pp. 235-242, 1999.

A MICROFLUIDIC DEVICE BASED ON THE HEAT-SENSITIVE STRUCTURAL TRANSITION OF POLY (N-ISOPROPYLACRYLAMIDE) FOR CONTROLLED SURFACE PATTERNING OF PROTEINS

Dae-Sik Lee¹, Kwang Hyo Chung¹, Hyeon-Bong Pyo¹, Sung Il Jeon², Seung-Yeon Song², Jung Woo Hong², Hyun C. Yoon²

¹Biosensor Team, Electronics and Telecommunication Research Institute (ETRI), Korea

²Department of Molecular Science & Technology, Ajou University, Korea
[\(dslee@etri.re.kr\)](mailto:dslee@etri.re.kr)

key words: *Heat-controlled Microelectrode, Heat-sensitive polymer, Protein separation, Dendrimer, Microfluidic device*

1. Introduction

Since there is no PCR-like amplification in proteomics, sample preparation coupled with advanced sample separation and purification steps is necessary for detecting low-abundance protein species. In this study, we present a sample preparation microfluidic device for the controlled micropatterning of proteins with an intelligent polymer-modified temperature-controllable microelectrode. The device is composed of a micromachined Si chip and a hot-cast poly(dimethylsiloxane) (PDMS) chip. This paper will cover detailed results of the affinity microfabricated-device, including microfabrication, thermal analysis, enzyme-controlled patterning and bioelectrocatalytic sensing in a microfluidic chip.

2. Experimental

The development of microfluidic platforms that provide getting specific analytes purified or contaminants removed in complex fluid streams is critical for rapid and point-of-care testing systems [1]. Many techniques have been developed, including chemical modification of channel surfaces and packing with biochemical-coated beads [1-2]. These methods share several disadvantages in packaging like fouling. However, the novel integrated microfluidic device employing the heat-sensitive polymer, poly(*N*-isopropylacrylamide)(PNIPAAm) on the temperature-addressable electrodes, as shown in Figure 1, can overcome the problems and is very suitable for a mobile diagnostic system. Here, the controlled protein micropatterning in the microfluidic device by an external stimulus with an intelligent polymer-modified electrode is described. For the microfabrication, photolithography techniques were adapted. The 5-in wafer-level Si microfabrication processes were utilized for the implementation of the Si components, including the micropatterning of electrodes both for the temperature control (microheater

and temperature sensor) [3] and electroanalysis and the casting of a thin polymer microfluidic components with chamber, channel, and valve for a leak-free device, as shown in Figure 2.

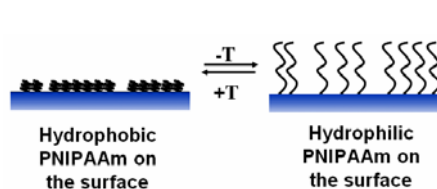


Figure 1. Schematic view of the heat-sensitive transition of PNIPAAm.

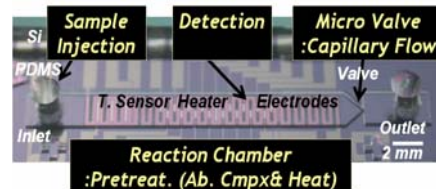


Figure 2. Photograph of the protein separation microfluidic device.

3. Results and discussion

Thermal distribution in the chamber was simulated by using CFD-ACE+ and thermal response of Si components was fast and reliable. For the controlled patterning and analysis of proteins including an enzyme (GOX), a NHS-esterified PNIPAAm was synthesized and functionalized on the gold electrode with dendrimer-conjugated SAM. Then, the electrode surface was manipulated using the structural transition of PNIPAAm by changing the surface temperature of electrodes across its lower critical solution temperature, as shown in Figure 3. The controlled patterning of GOX was evaluated from the bioelectrocatalytic signals by voltamograms as shown in Figure 4. And then the controlled patterning by employing fluorescence-labeled IgG was also demonstrated by fluorescence microscopy as shown in Figure 5. With in situ temperature control, fluorescence picture results indicated that the extended form of PNIPAAm below LCST on the surface inhibited the molecular approach and immobilization of GOX.

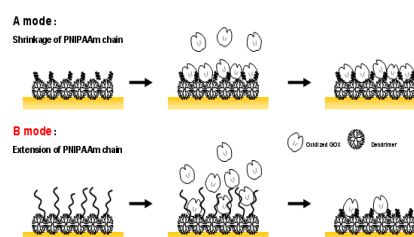


Figure 3. Diagram showing the processes for selective enzyme patterning evaluation: mode A(shrunken) and B(stretched).

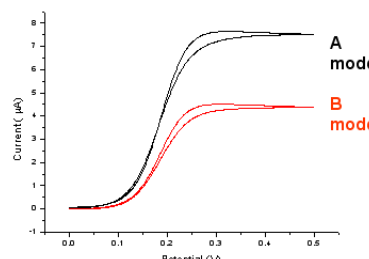


Figure 4. Electrochemical evaluation of the selective GOX adsorption between mode A and B.

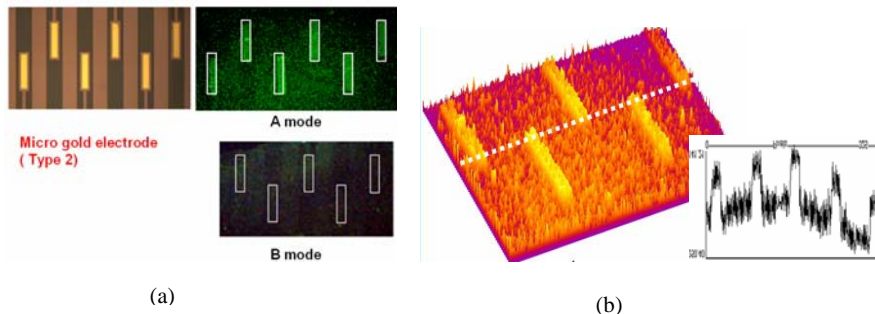


Figure 5. Photograph of fluorescence analysis of GOx adsorption with on-chip temperature control and its 3-D image with a line profile.

4. Conclusions

The smart affinity microfluidic device, including intelligent PNIPAAm polymer-modified temperature-controllable microelectrode in array, was designed and fabricated using Si bulk-micromachining MEMS protocols, hot casting of PDMS, and heat-sensitive polymer matrix. The device showed excellent thermal properties, including fast response and very low power consumption even though its wide area, good enzyme-controlled patterning. So, the device is directly applicable to a battery-powered portable immunoassay system.

Acknowledgements

This research was supported by grants from the Ministry of Information and Communication (MIC), the Basic Research Program of KOSEF (R01-2006-000-10240-0), the Regional Technology Innovation Program of MOCIE (RTI04-03-05), and the ERC(BSEP) of KOSEF, Korea.

References

1. D.L. Huber, R.P. Manginell, M.A. Samara, B. Kim, B.C. Bunker, *Programmed Adsorption and release of proteins in a microfluidic device*, Science, 2003, 301, pp. 352-354.
2. N. Malmstadt, A.S. Hoffman, and P.S. Stayton, *Smart mobile affinity matrix for microfluidic immunoassays*, Lab on a Chip, 2004, 4, pp. 412-415.
3. D.S. Lee, S.H. Park, K.H Chung, H. Yang, et al. *Bulk-micromachined submicroliter-volume PCR chip with very rapid thermal response and low power consumption*, Lab on a Chip, 2004, 4, pp.401-407.

WHOLE BLOOD PLASMAPHERESIS USING ACOUSTIC SEPARATION CHIPS

Andreas Nilsson, Filip Petersson and Thomas Laurell

Dept. of Electrical Measurements, Lund University, P.O. Box 118, S-221 00 Lund,
SWEDEN

Phone: +46 46 222 75 29, Fax: +46 46 222 45 27

Abstract

An acoustic separation system for producing pure blood plasma is presented. The separated plasma contains less than 1 % red blood cells from the original hematocrit of 40 %. A sequential separation system consisting of four separators is demonstrated.

Keywords: Acoustic separation, blood, plasma, radiation force, apheresis

1. Introduction

The need for pure blood plasma is of interest in diagnostic applications and in blood banking e.g. plasmapheresis. Blood plasma is usually generated by centrifugation or filtration. Plasmapheresis as realized by centrifugation in blood bank processes has hitherto not been addressed by μ TAS solutions as throughput is a major issue. Complementary techniques, such as mechanical filters, tend to saturate and though MEMS-solutions often offer attractive separation performance they commonly demonstrates a limited throughput, usually in the order of a few micro liters per minute [1]. This paper describes a method of extracting pure blood plasma from whole blood based on previously reported ultrasonic standing wave separation technique [2], offering a potential of up-scaling throughput to clinically relevant levels.

2. Theory

When whole blood is exposed to an acoustic standing wave, red blood cells (RBC) and white blood cells (WBC) are affected by an acoustic radiation force [3]. The radiation force will move the cells into the pressure node of the standing wave (Fig 1).

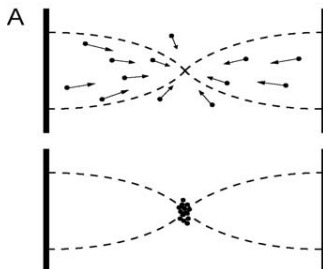


Figure 1. Particles exposed to an acoustic standing wave experience an acoustic radiation force and gather into the pressure backside node.

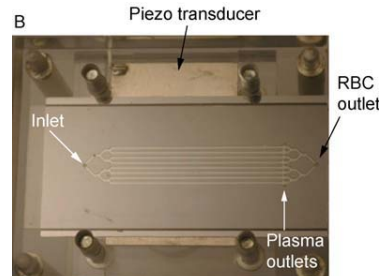


Figure 2. A single plasmapheresis chip actuated by a piezoceramic from the backside.

If a half wave length standing wave is exerted on blood in a microfluidic channel, red blood cells will be concentrated into a streaming band in the middle of the flow channel. If the channel is split into three outlets, the concentrated red blood cells exit through the centre outlet and the clear plasma trough the side outlets. To increase the throughput of the separation process, a separator of eight parallel channels in a bifurcation structure was made [4] (Fig. 2).

3. Experimental

Bovine blood was used and the flow rate of the eight channel chip was 0.6 ml/min (Fig. 3). The benefit of transversal mode ultrasonic excitation is that the same piezoceramic transducer is used to provide the ultrasonic separation in all eight channels. Consequently a further upscaling in a parallel channel bifurcation network is easily accomplished.

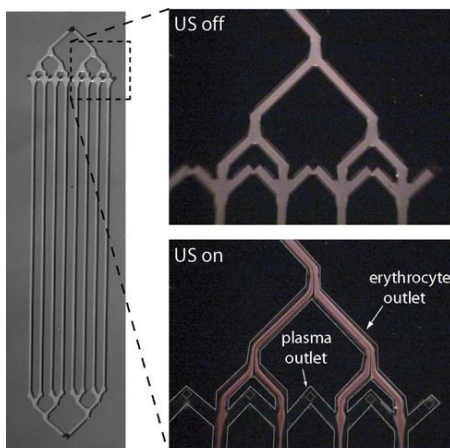


Figure 3. The eight channel separator. The top view to the right shows a channel segment with ultrasound turned off. The lower right view shows the acoustically controlled plasma extraction. White lines have been added to outline the separator channels.

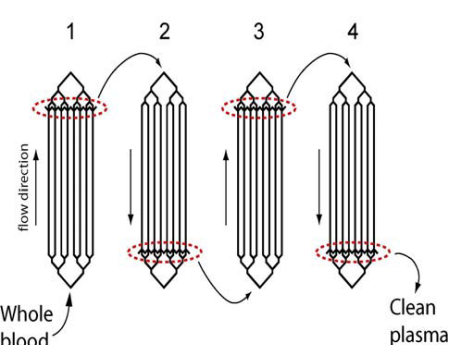


Figure 4. Sequential plasma extraction from whole blood. The plasma fraction from the first step is the input to the second step and so on.

4. Results and discussion

The RBC concentration in whole blood however, is too high to make a perfect acoustic separation in a single step. With a blood concentration of 40 %, forcing the full RBC volume into a channel taking only 50% of the flow is barely possible. A serial separation procedure containing four separation chips was therefore realized (Fig. 4). In the first step the RBC concentration was decreased from 40% to 30%. The 1st plasma fraction was then fed into the second separator where the RBC concentration was again decreased from 30% to 18%. In a similar way the third and fourth step decreased the RBC concentration from 18% to 6% and finally from 6% to less than 1% (Fig 5).

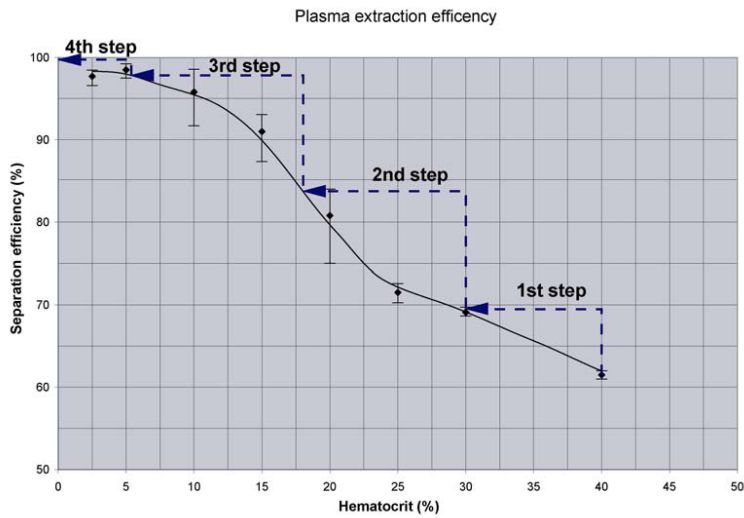


Figure 5. The diagram shows the removal efficiency of erythrocytes vs hematocrit (HCT) level. The HCT after each extraction step is followed by the step function. The process starts with whole blood of 40 % and end up with a plasma fraction containing less than 1 % erythrocytes.

References

1. Sethu, P., A. Sin, and M. Toner, *Microfluidic diffusive filter for apheresis (leukapheresis)*. Lab on a Chip, 2006. **6**(1): p. 83-89.
2. Nilsson, A., et al., *Acoustic control of suspended particles in micro fluidic chips*. Lab on a Chip, 2004. **4**(2): p. 131-135.
3. Petersson, F., et al., *Separation of lipids from blood utilizing ultrasonic standing waves in microfluidic channels*. Analyst, 2004. **129**(10): p. 938-943.
4. Jonsson, H., et al., *Particle Separation Using Ultrasound Can Radically Reduce Embolic Load to Brain After Cardiac Surgery*. The Annals of Thoracic Surgery, 2004. **78**(5): p. 1572-1577.

MICRO-EXTRACTION OF VIRAL RIBONUCLEIC ACID (RNA)

Levent Yobas*, Hong-Miao Ji*, Yu Chen*, Saxon Liw*, Wing-Cheong Hui*,
Siti Rafeah, Ser Choong Chong*, Ling Xie*, Lim-Jing Jing, Sek-Man Wong,
Tit-Meng Lim and Chew-Kiat Heng

*Institute of Microelectronics, 11 Science Park Rd, S117685, Singapore

National University of Singapore, Singapore

(Contact: leventy@ime.a-star.edu.sg)

Abstract

This paper reports on a microfluidic device and a portable automated system for micro-extraction of viral RNA from blood spiked with virus particles.

Keywords: Viral, RNA, nucleic acid, sample preparation

1. Introduction

Previously, we demonstrated a flow-through shear-type filter chip for isolation of plasma and virus particles from blood [1]. Here, we further expand the chip by integrating the subsequent sample preparation steps including lysis of virus particles and extraction of viral RNA (figure 1). The chip fabrication follows the simple process reported in [1]. The extraction is based on the fact that nucleic acid readily binds to silica surface in the presence of chaotropic salts [2]. Our device differs from the earlier biochips since others mostly demonstrated purification of DNA and used samples lysed outside the biochip [3], [4]. Some of the important infectious diseases arise from RNA viruses and require handling of complex samples such as blood.

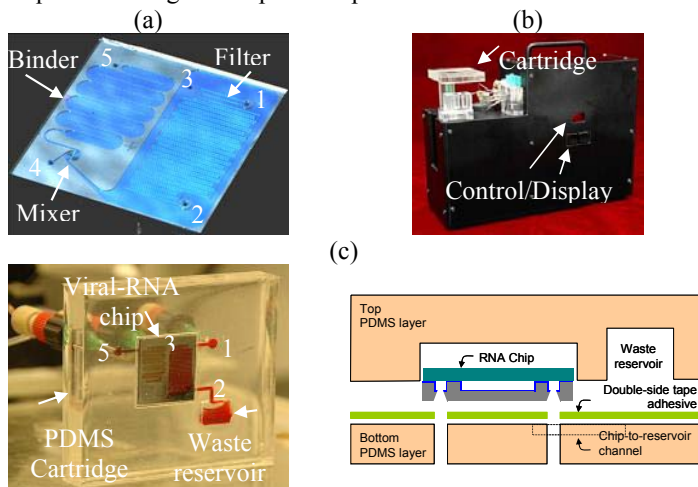


Figure 1. (a) viral RNA biochip (b) automated system and (c) the assembled cartridge.

2. Viral RNA Micro-extraction

Silicon-glass biochip in figure 1(a) integrates three parts: filter, mixer, and binder. Blood flows in and out of the filter through ports 1 and 2, respectively. Flow-through design of the filter allows the biochip to handle large volume of blood sample (e.g. 400 μ L). Screening adequate sample is crucial at the onset of disease as the host carries few viral copies. While blood flows through the filter, plasma and virus particles escape through 1.6- μ m gaps between the pillars. Meanwhile, lysis buffer which contains chaotropic salt (6M GuHCl) is introduced through inlet 3. The viral particles in plasma get lysed and nucleic acid binds to the silica surface of the chip as the plasma-lysis mixture flows through the mixer and binder. Further lysis buffer could be injected into the mixer through inlet 4. After washing away cellular debris with high-salt buffer, desalting of the chip can be realized with injection of absolute ethanol. After drying ethanol by passing air through the chip, a low-salt buffer is used to release purified nucleic acid from the chip surface through outlet 5. Fluidic control is provided by an automated portable system, shown in figure 1(b). Extraction protocol is encoded in software loaded into the system. The system is stand-alone and does not require computer unless a protocol revision is required. The system accepts blood in a dedicated syringe and physically isolates other reagents to prevent contamination. It injects the sample and reagents into a disposable cartridge containing the biochip. Figure 1(c) shows the assembly of the biochip in a cartridge replica-moulded in PDMS [poly(dimethylsiloxane)]. The cartridge is also shown while undergoing a test run using anticoagulated human blood. Waste blood from the filter is considered potentially infectious and poses health risk. Hence, it is stored in an enclosed reservoir.

3. Experimental Results and Discussion

Spiral mixer has been characterized by co-injecting fluorescent base (10 μ M fluorescein NaOH) and acid (1mM HCl) at the increasing flow rates. Due to adequate mixing of the acidic and basic solutions, pH gets less than 3 and the fluorescence starts to decay. As shown in figure 2, the mixer functions well in the flow range up to 50 μ l/min.

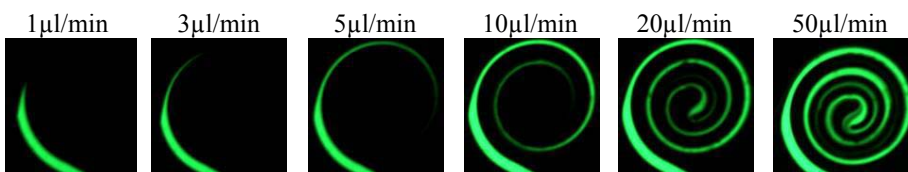


Figure 2. Spiral mixer efficiency at the increased flow rates.

As a test vehicle, virus particles were used to spike anticoagulated human blood to simulate an infected patient's sample. For safety, a plant virus Cymbidium Mosaic virus (*CymMV*) was used. Figure 3 shows parts of the biochip as it was injected by lysis buffer and 400 μ l of human blood spiked with 1000 *CymMV* particles. In figure 3(a), most blood cells are shown retained by the filter as they flow to the waste reservoir. For verification, elutions collected were subjected to nucleic acid sequence based

amplification (NASBA). NASBA is a homogenous isothermal (41°C) process already incorporates reverse transcriptase. NASBA products were detected by spectrometry via enzyme-linked probe that reacts with chromogenic substrate to form colored product. Lower limit of the micro-extraction was determined by differentially detecting internal controls spiked into NASBA. Based on the calibration curve by the internal controls in figure 4, we estimated that a total of 720 viral copies could be detected in the $40\mu\text{l}$ biochip elution. This shows that our biochip can extract viral RNA from a blood sample with a clinically relevant viral load.

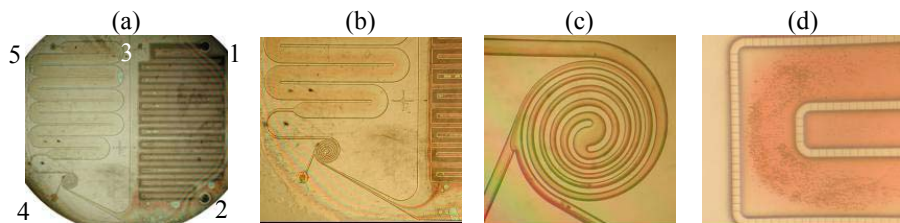


Figure 3. Photomicrographs of the biochip as blood and the lysis buffer pass through.

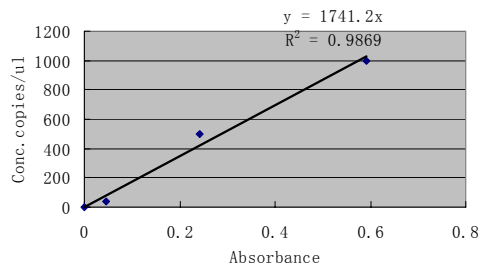


Figure 4. Calibration curve by internal controls RNA templates spiked into NASBA.

References:

1. L. Yobas, E.-L. Gui, H.-M. Ji, J. Li, Y. Chen, W.-C. Hui, S.R.B.M. Rafe, S. Swarup, S.-M. Wong, T.-M. Lim, and C.-K. Heng, *A flow-through shear-type microfilter chip for separating plasma and virus particles from whole blood*, Proc. Micro Total Analysis Systems, pp. 7-9, Vol. 2, 2004.
2. B. Vogelstein and D. Gillespie, *Preparative and analytical purification of DNA from agarose*, Proc. Natl. Acad. Sci., USA 76, 2, 615-619, 1979.
3. L.A. Christel, K. Petersen, W. McMillan, and M.A. Northrup, *Rapid and automated nucleic acid probe assays using silicon microstructures for nucleic acid concentration*, J. Biomech. Eng., 121 (1), 22-27 1999.
4. M.C. Breadmore, K.A. Wolfe, I.G. Arcibal, W.K. Leung, D. Dickson, B.C. Giordano, M.E. Power, J.P. Ferrance, S.H. Feldman, P.M. Norris, J.P. Landers, *Microchip-based purification of DNA from biological samples*, Analytical Chemistry 75 (8): 1880-1886, 2003.

MAGNETOPHORETIC IMMUNOASSAY FOR ALLERGEN-SPECIFIC IMMUNOGLOBULIN E (IgE) IN PATIENT SAMPLES

Young Ki Hahn¹, Zongwen Jin², Joo H. Kang¹, Eunkeu Oh²,
Hak-Sung Kim², Jung-Tak Jang³, Jinwoo Cheon³, Hae-Sim Park⁴,
and Je-Kyun Park¹

¹ Dept. of BioSystems, ² Dept. of Biological Sciences, Korea Advanced Institute of Science and Technology (KAIST), ³ Dept. of Chemistry, Yonsei Univ., ⁴ Dept. of Allergy and Clinical Immunology, Ajou University School of Medicine, Korea

Abstract

This paper reports a novel magnetophoretic immunoassay using a microbead conjugated with superparamagnetic nanoparticles under the enhanced magnetic field gradient. A ferromagnetic microstructure connected with a permanent magnet is used to increase the magnetic field gradient ($\sim 10^4 \text{ T m}^{-1}$) and successfully applied to detect allergen-specific IgEs samples obtained from 44 patients' serum in a hospital. The detectable ranges of human IgEs are 10.68 ng mL^{-1} to 151 pg mL^{-1} (*Dermatophagoides pteronyssinus*) and 19.47 ng mL^{-1} to 104 pg mL^{-1} (*Dermatophagoides farinae*).

Keywords: magnetophoretic immunoassay, superparamagnetic nanoparticles, human IgE, allergy

1. Introduction

Immunoglobulin E (IgE)-mediated type I allergic diseases are one of the most common causes of chronic illness in the populations of industrialized countries [1]. As IgE has been discovered as a key mediator of the allergic response in immune system, risk-free *in vitro* determination of IgE levels has significantly improved the diagnosis of allergy. However, the conventional *in vivo* allergy testing method, like skin prick test, has potential risk of causing adverse reactions, such as systemic reactions and anaphylactic shocks. In addition, due to the extremely low IgE level (less than 1/40,000 IgG) in serum, a highly sensitive IgE detection method is a prerequisite for accurate diagnosis of allergy.

2. Principle

In this detection scheme, microbeads are deflected from their own pathway in a microchannel as much as analytes are conjugated with microbeads and superparamagnetic nanoparticles by sandwich immunoreactions (Figure 1). Since the magnetophoretic deflection velocity of microbeads is proportional to the analyte concentration and magnetic field gradient [2], detection limit can be controlled by applying the higher magnetic field gradient [3]. To achieve lower detection limit, a

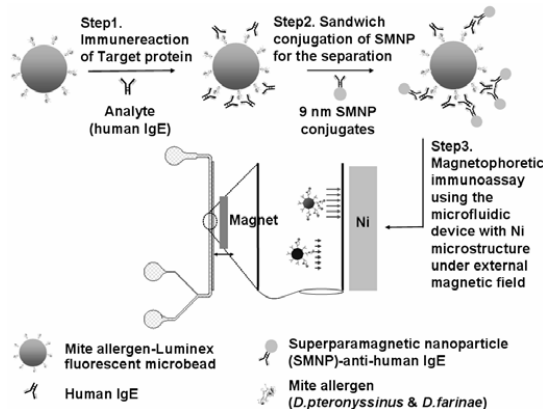


Figure 1. Sandwich immunoassay procedures based on the magnetophoretic migration in a microchannel.

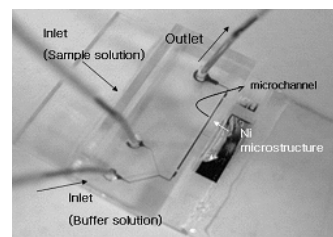


Figure 2. A photograph of the microfluidic device with a Ni microstructure.

ferromagnetic microstructure was used to increase the magnetic field gradient ($\sim 10^4 \text{ T m}^{-1}$).

3. Experimental

Figure 2 shows the microfluidic device fabricated by conventional poly(dimethylsiloxane) (PDMS) molding processes, where Ni microstructure was electroplated on a Pyrex glass wafer. For the sandwich immunoassay of allergen-specific human IgE, Luminex xMAP® Carboxylated Microspheres were conjugated with mite lysates by EDC (1-ethyl-3-(3-dimethylaminopropyl) carbodiimide hydrochloride)-NHS (N-hydroxysulfosuccinimide) activation. House dust mites, *D. pteronyssinus* and *D. farinae*, were used as the sources for allergen and human IgEs were obtained from 44 patients' serum in a hospital. Serum samples were grouped into five categories according to their mite allergen-specific IgE levels. To minimize the

Table 1. List of pooled sera used in the experiment and classification

	IgE (U mL^{-1})	IgE (ng mL^{-1})	No. of included serum	Class ^a (CAP system)
<i>D. pteronyssinus</i> 1	0.63	1.51	5	1
<i>D. pteronyssinus</i> 2	1.79	4.30	5	2
<i>D. pteronyssinus</i> 3	4.50	10.8	4	3
<i>D. pteronyssinus</i> 4	22.3	53.4	4	4
<i>D. pteronyssinus</i> 5	75.7	181.7	5	5
<i>D. farinae</i> 1	0.48	1.16	5	1
<i>D. farinae</i> 2	2.17	5.20	5	2
<i>D. farinae</i> 3	8.36	20.1	4	3
<i>D. farinae</i> 4	43.7	104.8	4	4
<i>D. farinae</i> 5	81.1	194.7	5	5

^a 1 U equals 2.4 ng of IgE.

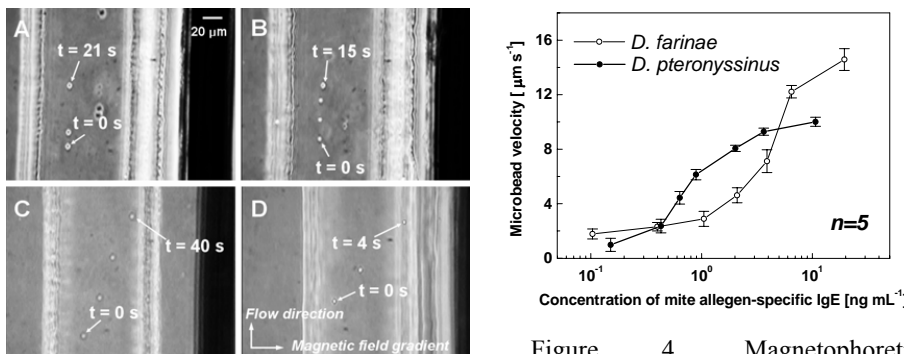


Figure 3. Superimposed CCD images of microbead movements; (A) a background control, (B) a negative control, (C) 104 pg mL^{-1} of *D. farinae*-specific human IgE ($1.78 \pm 0.36 \mu\text{m s}^{-1}$), (D) 19.47 ng mL^{-1} of *D. farinae*-specific human IgE ($14.6 \pm 0.8 \mu\text{m s}^{-1}$).

4. Results and discussion

Figure 3 shows the magnetophoretic movements of conjugated microbeads. The detectable range for *D. pteronyssinus*-specific IgE was from 10.68 ng mL⁻¹ to 151 pg mL⁻¹ and that for *D. farinae*-specific IgE was from 19.47 ng mL⁻¹ to 104 pg mL⁻¹. (Figure 4). The sensitivity of this system was comparable to that of a conventional allergy testing kit (CAP system) and incubation time of our method was reduced to 20 min with a serum sample of 10 µL.

5. Conclusions

We performed the magneto-phoretic immunoassays for the detection of mite allergen-specific human IgE in sera using an enhanced magnetic field gradient. This assay system has potential for multiple IgEs detection with fluorescently encoded microbeads.

Acknowledgement

This research was supported by the Nano/Bio Science & Technology Program (M10503000218-05M0300-21810) of the Ministry of Science and Technology (MOST), Korea.

References

1. M. Willis-Karp, J. Santeliz, C. L. Karp, Nat. Rev. Immunol. Vol. 1, pp. 69-75 (2001).
 2. K. S. Kim, J. -K. Park, Lab Chip, Vol. 5, pp. 657-664 (2005).
 3. J. H. Kang, Y. K. Hahn, K. S. Kim, J. -K. Park, MicroTAS'05, Vol. 1, pp. 25-27.

Figure 4. Magnetophoretic immunoassay for detection of *D. farinae* and *D. pteronyssinus*-specific human IgEs.

sample-to-sample variation of different categories in their protein contents, five samples in each group were mixed in the same volume (Table 1).

SILICON-BASED MICROFILTERS FOR WHOLE BLOOD CELL SEPARATION

Hong Miao JI, Victor SAMPER, Levent YOBAS, Yu CHEN,
Chew Kiat HENG*, Tit Meng LIM**

Institute of Microelectronics, Singapore

*Department of Pediatrics, National University of Singapore

**Department of Biological Sciences, National University of Singapore

Abstract

This paper presents comparison analysis on various silicon-glass microfilters which are used to trap white blood cells (WBC) from a given sample of blood. Four microfilter designs studied here includes weir filter, pillar filter, cross-flow filter and membrane filter. Fabrication process for the cross-flow and the pillar designs is simpler and more suitable for integration with other components. The cross-flow filter design offers the largest blood passing capacity and high WBC trapping efficiency.

Keyword: microfilter, separation, MEMS, cross-flow, pillar

1. Introduction

The microfilters for trapping WBC could play a crucial role for on-chip genomic analysis because the genetic code, deoxyribonucleic acid (DNA) is contained in nuclei of WBC. Various designs of the microfilter have been published [1]-[3]. But until now, no direct comparison on the trapping efficiency of these microfilters has been published, despite their different designs. In this paper, four different microfilters, the weir filter, the pillar filter, the cross-flow filter and the membrane filter, are being compared in term of their capacity of filtering human blood.

2. Design of Microfilter chip

Genomic analysis from whole blood requires extraction and purification of DNA from WBC. Red blood cells (RBC) have to be discarded as they contain no nucleus. Besides, RBC further contain hemoglobin which inhibits the subsequent step of nucleic acid amplification. Separation of the cells based on their size through filtration is a passive but simple approach and suitable for miniaturization. WBC (diameter $>5\mu\text{m}$) are typically larger than RBC (thickness $\sim 2\mu\text{m}$) and silicon-based technology can manufacture precise and uniform sieve structures with critical pore size ($<1\mu\text{m}$).

Four microfilter designs compared here are schematically described in figure 1. The four designs are the weir, the pillar, the cross-flow, and the porous membrane. The microfilters were fabricated using silicon micromachining mainly via deep reactive ion etching and silicon-glass anodic bonding. The inlet and outlet ports were created in silicon from backside by wet etching. A plain glass wafer was bonded to silicon to enclose the microfilters except the membrane design where the glass capping layer contains a microchamber. The critical pore size for all the designs is $3\mu\text{m}$ whereas the total pore area for each microfilter is listed in table 1.

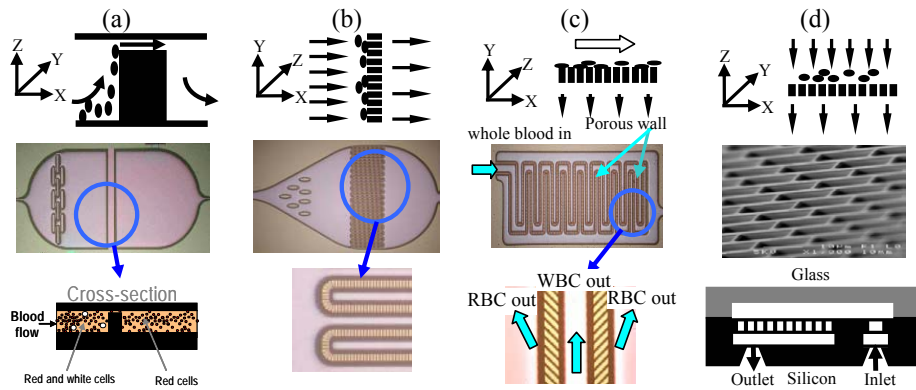


Figure 1. Four types of silicon-glass microfilter, (a). weir filter (b). pillar filter (c). cross-flow filter (d). membrane filter

Table 1. Total pore area and measured filter capacity

FILTER	Σ PORE AREA / CHIP	BLOOD PASSING CAPACITY
Weir	0.0105 mm ²	<50µl
Pillar	59.6 mm ²	300µl
Cross-flow	0.474 mm ²	>300µl
Membrane	12.67 mm ²	200µl

3. Experimental Results & Discussion

The microfilters were tested using human whole blood with WBC stained by methylene blue. The flow rate was varied between 10-50µl/min using a syringe pump and the blood was diluted 200× using phosphate buffered saline (PBS). The passing capacity for the different designs was compared by monitoring the input pressure. When the pressure increased more than 1.5atm, the filter was said to be clogged and the total volume of undiluted blood passed was recorded as the microfilter capacity (table 1).

The microfilters were evaluated for separation of WBC from RBC. The input and output fluids were sampled at 5min intervals using a hemocytometer. The results are summarized in table 2. All the microfilters show more than 50% trapping rate for WBC. In figure 2, it is found that the blood cells are being trapped on the membrane and weir microfilters. In terms of microfabrication process and ease of integration with other microfluidic components, the cross-flow and pillar designs are much simpler, and hence more advantageous. In figure 3, further experimental results support that the cross-flow design can pass through more RBC (60-95%) than the pillar design (20-55%) while trapping similar amount of WBC.

These empirical comparisons indicate that the cross-flow design has the largest blood passing capacity and high WBC trapping efficiency despite its small total pore and simple microfabrication process.

Table 2. Measured filter efficiency

FILTER	INPUT	FLOW RATE	VOLUME	TRAP WBC
Weir	Whole blood	10 μ l/min	1 μ l	~70%
Weir	Whole blood	50 μ l/min	1 μ l	~70%
Membrane	Whole blood	10 μ l/min	2 μ l	72-85%
Membrane	Whole blood	10 μ l/min	1 μ l	72-85%
Pillar	Whole blood	20 μ l/min	1 μ l	70-95%
Cross flow	Whole blood	20 μ l/min	1 μ l	70-95%

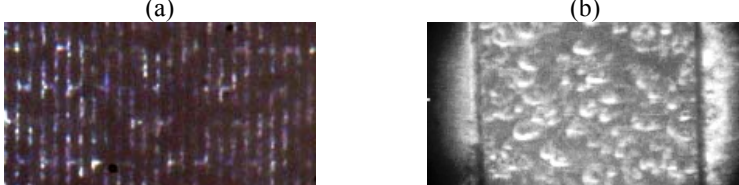


Figure 2. Trapping of cells on (a) the membrane and (b) weir filters

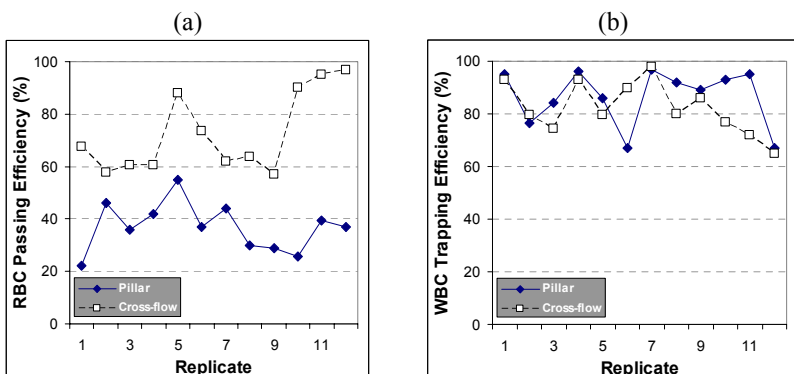


Figure 3. Comparison of pillar and cross-flow designs in terms of (a) RBC passing and (b) WBC trapping efficiency

References

1. L. Yobas, E.L Gui, H.M. Ji, J. Li, Y. Chen, W.C. Hui, S. Rafean, S. Swarup, S.M. Wong, T.M. Lim, C.K. Heng, *A flow-through shear-type microfilter chip for separating plasma and virus particles from whole blood*, Proc. Micro Total Analysis System 2004, Malmo, Sweden, pp. 7-9, Vol. 2, (2004).
2. P. Wilding, L.J. Kricka, J. Cheng, G. Hvichia, M.A. Shoffner, P. Fortina, *Integrated cell isolation and polymerase chain reaction analysis using silicon microfilter chambers*, Analytical Biochemistry, 1998, vol.257, pp95-100, (1998).
3. Y. Chen, Y.B. Miao, V. Samper, F.B. Mustafa, Q.X. Zhang, C.K. Heng, H.J. Lye, T.M. Lim, *Microfabrication of a Si mesh structure depth filter*, Proc. Micro Total Analysis System 2002, Nara, Japan, pp. 739-741, Vol. 2, (2002).

EVALUATION OF A PDMS-BASED SENSOR FOR HUMAN CD4⁺-CELL COUNT

Sara Thorslund¹, Rolf Larsson², Fredrik Nikolajeff¹, Jonas Bergquist³ and Javier Sanchez²

¹Dep. of Engineering Sciences, Uppsala University, Uppsala, Sweden

²Dep. of Clinical Immunology, University Hospital, Uppsala, Sweden

³Dep. of Physical and Analytical Chemistry, Uppsala University, Uppsala, Sweden

sara.thorslund@angstrom.uu.se

Abstract

Up to today, the number of CD4⁺ lymphocytes remains the most important biological marker to determine the clinical stage of an HIV-infection. Analysis by flow cytometry, the standard method used today, is unsuitable in many developing countries, because of high costs involved and practical inconveniences. We here describe a method where surface modified PDMS captures exclusively CD4⁺ cells from non-diluted human whole blood. A simple fluorescence microscope for stained leucocytes counting is the only detection equipment needed.

Keywords: CD4 cells, HIV, PDMS, heparin, point-of-care

1. Introduction

The number of CD4⁺ T-lymphocytes is today one of the most important biological markers for determining the clinical stage of an HIV-infection. The so-called CD4-count is used to decide when to initiate antiretroviral therapy and is the most relevant marker for disease progression. Up till today, flow cytometry is considered as the standard reference method for CD4-count. This method is because of practical inconveniences inappropriate for routine analysis in many developing countries and the need for low-cost CD4-counting facilities is urgent in order to fight AIDS [1].

2. Composition and evaluation of the sensor surface

The PDMS surface was initially coated with a heparin film, resulting in a surface that has been shown to have good thromboresistance as well as hydrophilic wetting properties [2]. Figure 1 shows how the biosensor channel is readily filled when a droplet of antibody incubated whole blood is held against the capillary inlet of the microchannel.

The heparin film was shown to bind avidin irreversibly, making it possible to exploit the strong avidin-biotin coupling chemistry. Biotinated CD4-antibodies capture CD4⁺ T-cells

from the blood and couple them to the avidin coated channel surface. Detection was performed by fluorescence microscopy, where HOECHST (stains cell nuclei) and CD3-FITC antibodies (stain all T-lymphocytes) were used to identify captured CD4^+ cells.

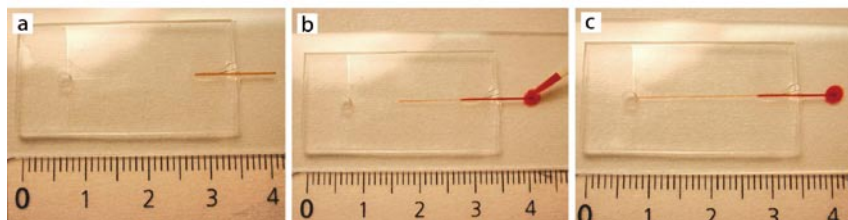


Figure 1. (a) A PDMS sensor chip, ready for cell capturing. (b-c) By holding a droplet of blood against the capillary ending, the empty microchannel was immediately filled with blood, due to its hydrophilic surface. The PDMS-part of the channel holds 0.1 μl blood.

A biosensor channel is shown in Figure 2, where six CD4^+ cells are visible, identified through complete agreement between HOECHST (Fig. 2a) and CD3-FITC (Fig. 2b) signal. The biosensor channel was rinsed with buffer, also accomplished by capillarity, leaving very few red blood cells behind.

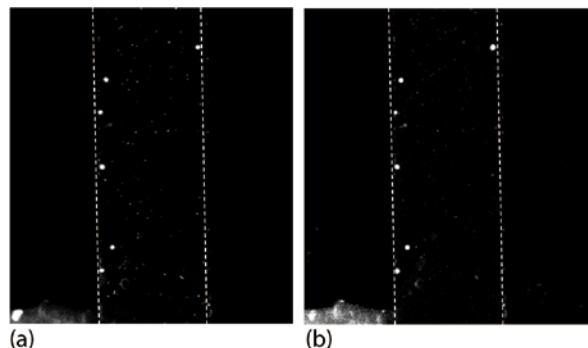


Figure 2. (a) HOECHST fluorescence, and (b) CD3-FITC fluorescence images from a part of a biosensor channel. Since the signals agree, all six cells are CD4^+ . The PDMS microchannel is 200 μm wide and 25 μm deep.

It was furthermore shown that the more easily detected HOECHST signal alone could be used for detection, since the number of non-specifically adsorbed CD4⁺ leucocytes was negligible (Figure 3).

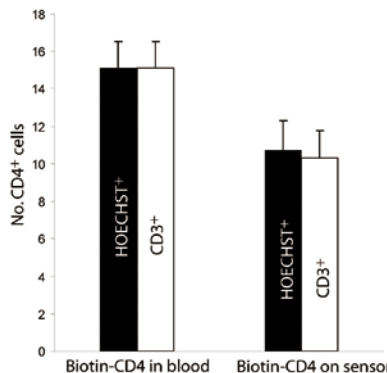


Figure 3. Diagram showing the agreement between HOECHST⁺ and CD3⁺ cells in biosensors having biotin-CD4 antibody, either added to the blood, or immobilized in the channel. From this it can be concluded that the non-specific adsorption of CD4⁺ leucocytes is negligible, and the detection can be based on HOECHST staining only. (N=8 and error bars represent standard error of the mean).

3. Conclusions

By combining the avidin-biotin coupling-chemistry with the bioactive heparin surface, we have constructed a PDMS-based biosensor for CD4-count. The active biosensor surface was designed and shown to capture only CD4⁺ cells from a non-diluted blood sample. Because the sensor surface has the ability to draw blood into the microchannel by pure capillarity, no external pumping sources are necessary. This makes the system highly suitable for a POC application. The main issue addressed in the present work, was to evaluate and optimize the CD4-capturing sensor surface in itself. As a next step, the microfluidic construction will be refined to create a more prototype-like system.

References

1. Z. Bentwich; *CD4 measurements in patients with HIV: are they feasible for poor settings?*, Plos Medicine, 2, pp. 595-596, (2005).
2. S. Thorslund, J. Sanchez, R. Larsson, F. Nikolajeff and J. Bergquist, *Bioactive heparin immobilized onto microfluidic channels in poly(dimethylsiloxane) results in hydrophilic surface properties*, Colloids and Surfaces B-Biointerfaces, 46, pp. 240-247, (2005).

CENTRIFUGAL PROCESSOR FOR STANDARD MICROARRAY SLIDES

S. Lutz¹, M. Grumann¹, O. Gutmann¹, M. Dube¹, L. Riegger¹, J. Steigert¹,
M. Daub¹, R. Zengerle^{1,2}, and J. Ducr  e^{1,2}

University of Freiburg - IMTEK, Department of Microsystems Engineering

¹Laboratory for MEMS-Applications, Germany

²HSG-IMIT, Villingen-Schwenningen, Germany

Abstract

We present a novel concept for the fully integrated centrifugal processing of microarray experiments using standard glass slides. Sample and reagent volumes are reduced to 50 µL in each step, and the overall processing time is reduced to 45 minutes [1,2]. All fluidic structures, e.g. for shake-mode incubation and siphon-based liquid handling, are incorporated in a disposable PDMS-chip which is reversibly clamped to the microarray slide. The slides can easily be transferred to a standard microarray reader or they can directly be investigated on the rotor by ATR principle.

Keywords: microarrays, microfluidics, centrifugal processing, ATR-readout

Introduction

Microarrays have become a powerful tool in the field of molecular biology. Arrays displaying a multitude of different capture proteins on a single substrate allow to simultaneously analyze a given sample with respect to a large set of different targets. Recent developments aim to adopt the microarray format for the field of medical diagnostics applications. Here it is crucial to achieve a short time-to-result as well as reduced volumes of samples and reagents. In our setup, we can realize a fully integrated and fast processing of a 3-step fluorescene immunoassay using a microarray format on a standard microscope slide within 45 minutes with a consumption of sample and reagents of 50 µL, only. Our microfluidic platform allows to exploit centrifugal forces for liquid transport and mixing processes.

The Centrifugal Processor

The processor features four rotor segments, each of them accomodating one standard microarray glass slide and a PDMS sheet on top featuring the microfluidic structures (Fig. 1-A). A bayonet clamps the glass slide against a PDMS to avoid leakage of the fluidic chip during spinning of the rotor for microarray processing. The reversible sealing proves to be leak-proof up to high spinning frequencies of 40 Hz. The frequency protocol $v(t)$ of the rotor is controlled by a PC.

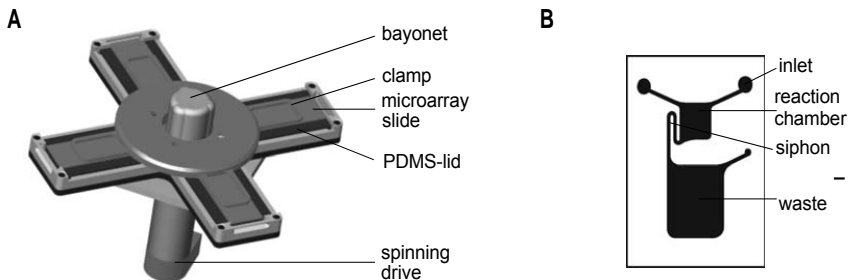


Fig. 1: Schematic view of the centrifugal microarray processor (CMP). (A) Four standard slides containing a microarray can be placed inside the CMP and processed in parallel. A bayonet locks the clamp on top of the glass slide to avoid leakage during the spinning process. (B) The micro-structured PDMS-chip features two inlets for sample and reagents which are connected to the 50- μL reaction chamber. The siphon ensures a permanent filling of the reaction chamber during the spinning process.

Experiments in the Centrifugal Microarray Processor

At first, capture probes containing BSA are printed onto the carrier slide and the resulting microarray is blocked using a casein solution. The self-adhesive and flexible PDMS lid (Fig. 1-B) incorporating a flat, 50- μL cavity displaying a siphon-based outlet are then introduced into one of four rotor arms and clamped against a slide (Fig. 2-A). Next, the sample of anti-BSA antibodies of a known concentration c is injected into the inlet reservoir of the PDMS chip (Fig. 2-A) and a designated frequency protocol $v(t)$ is started. This protocol implements our previously developed inertial “shake-mode” stirring [1] to appreciably increase the speed and homogeneity of the biochemical reactions. The siphon ensures a permanent liquid contact with the microarray during all washing and labelling steps.

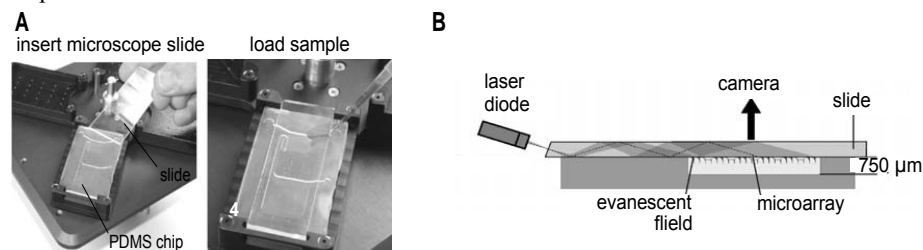


Fig. 2: (A) The rotor is first equipped with the PDMS chip and subsequently with the microarray slide. After fixing with the clamp unit, the inlet reservoir of the PDMS chip is filled with the sample. (B) Integration of processing and real-time readout: the microarray substrate acts as a waveguide for a laser beam. This concept bears the potential to conduct real-time measurements for kinetic studies or immunoassays without the need of intermediate washing steps.

In order to transfer the processed slide to a standard microarray reader, the mechanical clamp is released. For the integrated ATR readout, the slide is used as a wave guide for a beam coupled by a stationary laser diode through the edge of the slide (Fig. 2-B). Target

molecules bound to the surface-immobilized probes are specifically excited by the short-range evanescent field and their fluorescence signal is recorded by a camera mounted above the plane of rotation.

Results

A fluorescence detector reads out of the 3-step fluorescence immunoassay (Fig. 4-A). The results display an obvious correlation between the anti-BSA antibody concentration and the intensity of the fluorescence signal. For a dynamic range of dilutions between 10 µg/mL and 0.05 µg/mL, we obtain a *CV* of 5.2%, only (Fig. 2-C).

To examine the functionality of the ATR-readout device, we printed fluorescence-labelled oligonucleotides, streptavidin and BSA on a slide substrate. Fluorescent signals excited by ATR were recorded by a CCD-camera for a concentration *c* of 1 mg/mL of streptavidin and 50 µM of Cy5-labelled oligonucleotides.

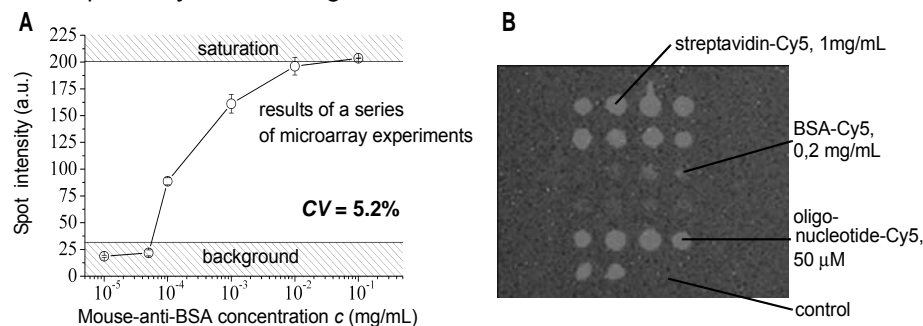


Fig. 3: (A) Results of the centrifuge-based fluorescence immunoassay. The error bars represent the internal standard deviation of six representative spots of each microarray. (B) Picture of ATR-exited fluorescence derived from Cy5 labelled oligonucleotides and proteins on the slide surface.

Conclusion and Outlook

We introduced a novel concept for running microarray experiments in parallel. Compared to our previous approach, all fluidic components are integrated in a reversibly attached disposable PDMS-chip. This way the user can adhere to the familiar standard slide format and standard readout devices while still taking full advantage of the rapid, reproducible and robust centrifugal liquid handling. We also demonstrated the feasibility of an on-board ATR readout which may, for instance, enable surface-specific on-line measurements for studies on reaction kinetics.

References

- [1] M. Grumann, M. Dube, O. Gutmann, S. Lutz, J. Ducr  e, Proc. of μ TAS 2005 conference, pp. 328–330
- [2] M. Grumann, A. Geipel, L. Rieger, R. Zengerle, and J. Ducr  e, Lab. Chip., vol. 5, 560–565, 2005
- [3] M. Madou, G. Kellogg, Proc. of SPIE 1998, vol. 3259, pp. 8093, 1998

A Palm-Sized Real-Time (RT) PCR

Lukas Novak, Pavel Neuzil*, Juergen Pipper, Chunyan Zhang

Institute of Bioengineering and Nanotechnology,
31 Biopolis Way, The Nanos, #04-01, 138669 Singapore
pneuzil@ibn.a-star.edu.sg

Abstract

We report the development of a miniaturized economical real-time PCR. The PCR device is made of micromachined silicon. The reaction is conducted on a disposable microscope cover slip. The miniaturized fluorescence system is integrated underneath the chip. The 12Ah battery can power the PCR system for 12 hours as its consumption is only 3W. The pocket size of the PCR system and its power consumption assure its portability. Its performance was demonstrated by performing a 50-cycle PCR process in 15 min.

Keywords: PCR, μ-optics, μ-PCR, droplet, Virtual Reaction Chamber

1. Introduction

A portable polymerase chain reaction (PCR) system was first reported about 13 years ago and further developed by the original inventors [1] as well as other groups.[2] Due to recent infection disease outbreaks, such as SARS and the current threat of Avian Influenza virus (H5N1), a truly portable real-time PCR (or RT-PCR)-based system is in high demand. [3]

2. Results and discussion

Here, we report on a compact real-time PCR (RT-PCR) system 7x7x3 cm in size (see fig. 1), with a weight of 75g. Its power consumption is only 3W, making this system suitable for long lasting field operations.

The real-time PCR system consists of four printed circuit boards (PCB) linked by connectors.

The top board hosts a micro machined PCR chip (see fig. 1) as described elsewhere. [4] The PCR chip contains a thin film gold heater and temperature sensor. The optical fluorescence unit (optical head) is attached beneath the PCR chip on this board. A light emitting diode (LED) with a peak emission wavelength of 490nm is used as a light source along with a photodiode as a light detector. Light was filtered by a fluorescein isothiocyanate (FITC) filter set. Signal processing for the fluorescent unit is conducted at the second board. The cross-section of the optical unit is shown in fig. 2.

The second board contains mostly analog circuits for thermal management and fluorescence data processing. The temperature of a PCR system is measured by an integrated resistance temperature detector (RTD) type of sensor connected to an AC powered Wheatstone bridge. The signal from this bridge is amplified and demodulated to provide a DC value for temperature feedback. The PCR temperature is controlled by modulating the amplitude of dissipated power within the heater using a proportional integrated derivative (PID) method.

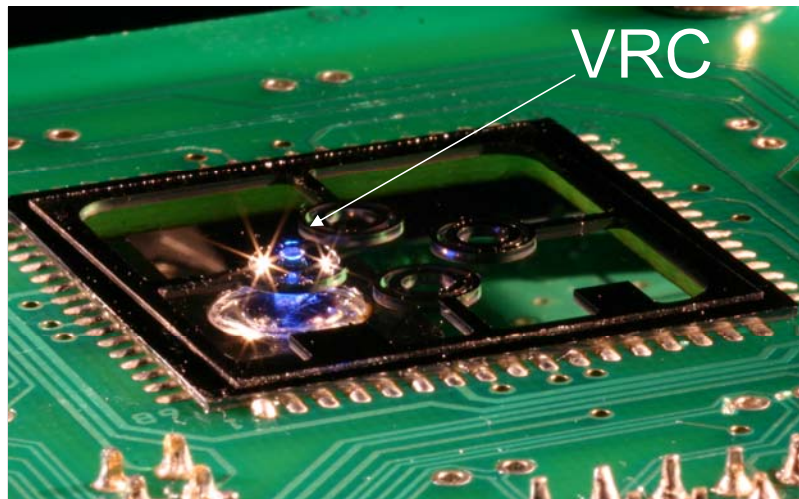


Figure 1: Photograph of a complete PCR system with an arrow pointing to a virtual reaction chamber (VRC). The system consists of three printed circuit boards (PCB) where the top board contains the PCR chip and integrated optical fluorescent system. The other two PCBs contain supporting electronics and power supplies.

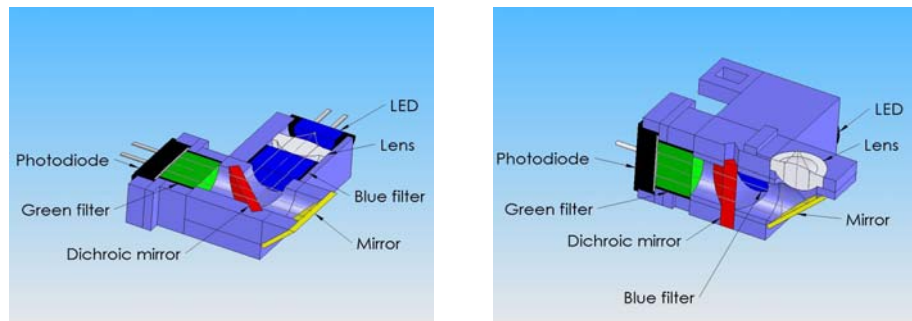


Figure 2: Cross section of the optical fluorescent system. The light comes from a 490nm wavelength LED, passes through blue filter, bounces of a dichroic mirror and is focused at the PCR sample. The fluorescent light is collected by the lens, passes through the dichroic mirror and green filter and is detected by a photodiode.

The LED inside the optical head is powered by current pulses with an amplitude of 100mA, a frequency of 1kHz and a duty cycle of 10%. The fluorescence signal from the photodiode is filtered by a high pass filter, amplified 10^8 times and fed into a lock-in amplifier. Therefore the fluorescent system can operate under ambient light. The PCR system is controlled by a PC computer with a LabView system. Instead of connecting the second PCB to a PC, a third board containing a single chip controller could be added, making the whole system totally autonomous. The fourth board is connected to a single battery or a charger and generates all the necessary power for the analog and digital blocks on the other boards.

3. Experimental verification

The real-time PCR data is shown in fig. 3. (6-FAM probe-based PCR system) demonstrating fast real-time PCR operation. The 50-cycle reaction is conducted in less than 15min.

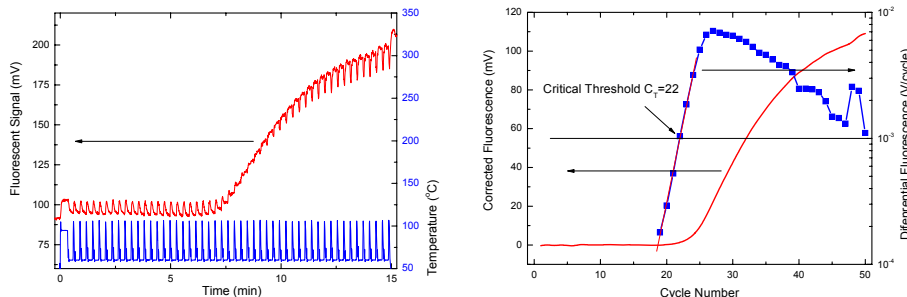


Figure 3: PCR fluorescent (red) and thermal (blue) profile (left). It demonstrates the high performance of the PCR detecting green fluorescence protein as the 50-cycle process was conducted in less than 15min. The extracted data (right) shows a critical threshold of 22, which is in agreement with the result obtained from a commercial thermocycler.

4. Conclusion

We have designed, fabricated and demonstrated a miniaturized real-time PCR system based on a previously described economical platform. [4] The optical head with a size of 30 x 30 x 11mm was attached to the PCR silicon micromachined chip. The performance was demonstrated by detecting a green fluorescent protein using a 6-FAM probe based PCR system.

-
- [1] Northrup, M.A., Bennet, B., Hadley, D., Landre, P., Lehew, S., Richards, J. and Stratton, P. A Miniature Analytical Instrument for Nucleic Acids Based on Micromachined Silicon Reaction Chambers. *Anal. Chem.*, 1998, **70**, 918 – 922.
 - [2] Higgins, J.A., Nasarabadi S., Karns, J.S., Shelton, D R., Cooper, M., Gbakima A., and Koopman, R.P. A handheld real time thermal cycler for bacterial pathogen detection, *Biosensors and Bioelectronics*, 2003, **18**, 1115-1123.
 - [3] http://www.who.int/csr/disease/avian_influenza/guidelines/labtests/en/index.html
 - [4] Neuzil, P., Ming, H.T. and Pipper, J., Disposable Real-time microPCR Device: Lab-on-a-Chip at low cost. *Mol. BioSyst.*, 2006, **2**, 292.

ELECTROSPRAYED PHOSPHOLIPID POLYMER SURFACE FOR ENHANCED SENSITIVE ELISA CHIP

Kazuki Nishizawa, Madoka Takai and Kazuhiko Ishihara

Department of Materials Engineering and Center for Nanobio Integration, The University of Tokyo, 7-3-1, Hongo, Bunkyo-ku, Tokyo, 113-8656, Japan

E-mail: takai@mpc.t.u-tokyo.ac.jp

Abstract

We developed a new solid biointerface by integrating a phospholipid polymer (PMBN) with a nanoscale surface modification process known as the electrospray deposition (ESD) method. In the enzyme immunoassay using this surface, the sensitivity was significantly enhanced. The surface prepared by ESD has a nanosphere-shaped structure and therefore the highly uneven surface causes a drastic increase in specific signals due to an increase in the surface area. The PMBN surface which can conjugate antibodies prevented the nonspecific protein adsorption. The stability of the antibodies immobilized on the PMBN surface was improved drastically. The PMBN surface sprayed by ESD can be used to yield a highly sensitive, stable, and reliable assay.

Keywords: immunoassay, electrospray deposition, MPC polymer, biointerface.

1. Introduction

One of the heterogeneous immunoassays, enzyme-linked immunosorbent assay (ELISA) has been widely used in the fields of biochemistry and clinical diagnosis. To shorten the assay time, to decrease the sample consumption, and to realize automated assay, microchip based immunoassay is useful. However, the significant decrease in sample volume results in low specific signals under the detection limit. Furthermore, in the microscale environment, the high surface area/volume ratio magnifies the influence of nonspecific binding of an analyte or a labeled antibody to the solid surface, arising high background or noise level. To develop a highly sensitive microchip-based ELISA system, both enhancement of specific signals and reduction of nonspecific signals should be achieved. In this study, we developed a new solid biointerface with a high sensitivity by integrating a novel phospholipid polymer with a nanoscale surface modification process known as the electrospray deposition (ESD) method [1].

2. Experimental

Poly [2-methacryloyloxyethyl phosphorylcholine (MPC)-*co*-*n*-butyl methacrylate (BMA)-*co*-*p*-nitrophenyloxycarbonyl diethylene glycol methacrylate (MEONP)] (PMBN) was synthesized (Figure 1) [2]. The MPC unit shows a high resistivity to

protein adsorption and effectively suppresses the denaturation of biomolecules [3]. The MEONP possesses active ester group, which can conjugate the antibody via dioxoethylene chain to enhance the antigen-antibody reaction efficiency.

The PMBN solution was sprayed by the ESD devise (ES-1000, Fuence, Tokyo, Japan). Au surface was used as a conductive substrate to impress the electric field between surface and polymer solution.

ELISA was carried out using the PMBN surface. First, anti-[human thyroid stimulating hormone (TSH)] mouse IgG was immobilized on the PMBN surface. Using human TSH as the antigen performed the antigen-antibody reaction. Biotinylated anti-TSH mouse IgG and streptavidin-conjugated horseradish peroxidase (HRP) was used to enhance the signal. Then, tetramethylbenzidine was applied as a substrate for HRP. Finally, the increase in absorbance at 450 nm based on the enzyme-substrate reaction was measured using a multilabel counter (Wallac ARVOsx1420, Perkin Elmer).

3. Results and discussion

The PMBN surface sprayed by ESD had large surface area comparing with the surface by dip coating (Figure 2). Therefore, it is expected that the number of immobilized antibodies is increased drastically.

ELISA was carried out using PMBN. The results are shown in Figure 3. The PMBN surface sprayed by ESD showed high specific signal because of a large number of conjugated antibodies by increasing surface area. Nevertheless, its back ground level

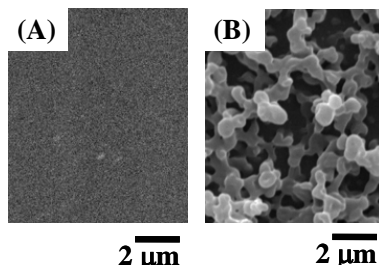


Figure 2. SEM images of the PMBN surfaces by dip-coating(A) and ESD(B) at 20 kV on sputtered Au/polyimide substrate.

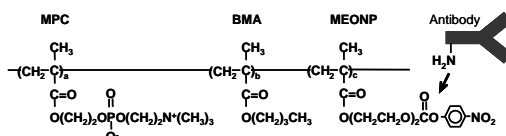


Figure 1. Chemical structure of PMBN.

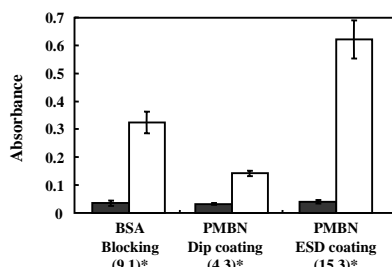


Figure 3. Absorbance values in the ELISA test using various solid surfaces. Open and close columns indicate TSH = 10 μ IU/mL(Signal), 0 μ IU/mL(background), respectively. * Signal/Background ratio.

kept low compared with bovine serum albumin (BSA) blocking. BSA is used in the conventional ELSIA protocol as a nonspecific binding blocking reagent. It is suggested that MPC unit prevented nonspecific adsorption effectively. Thus, the high signal/background (S/B) ratio assay was realized using the PMBN surface sprayed by ESD. Additionally, antibodies conjugated to PMBN kept its stability for a several days in a dry condition at 37 °C. The PMBN surface sprayed by ESD can produce the low detection limit, high sensitive, stable and reliable assay.

Furthermore, coating with PMBN by ESD can also apply to microchips on which a conductive substrate has been formed by patterning. We have fabricated polydimethylsiloxane (PDMS) based microchip to develop the microchip ELISA system (Figure 4). Chemiluminescence intensity was observed in this microchip system corresponding to the concentration of TSH on the surface coated BSA as a blocking reagent (Figure 5). Considering the case of BSA, adopting PMBN surface sprayed by ESD to this microchip will show high S/B ratio, and now it is under development.

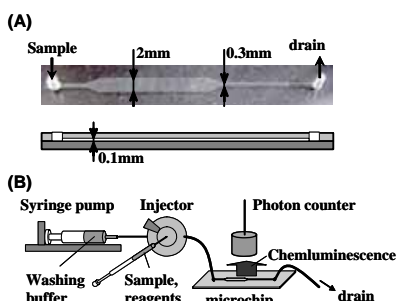


Figure 4. Microchip ELISA(A) Photograph of PDMS based microchip. (B) Schematic representation of microchip ELISA system.

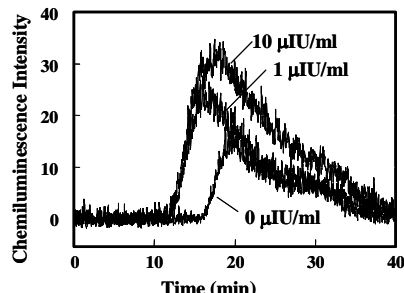


Figure 5. Detection of TSH from chemiluminescence signal in microchip. (Concentration of TSH = 0, 1, 10 μ IU/ml, Flow rate: 1 μ l/min).

4. Conclusions

We achieved high S/B ratio assay by the novel method of increasing the surface area for the immobilized antibody using ESD method and by decreasing the nonspecific binding applying the phospholipid polymer. The PMBN surface prepared by ESD can be used to yield a highly sensitive, stable, and reliable assay in the microchip.

References

1. J. Doshi, J. Reneker and D. H. J. Reneker, *Electrostat.*, 35, 151, (1996).
2. T. Konno, J. Watanabe and K. Ishihara, *Biomacromolecules*, 5, 342 (2004).
3. K. Ishihara and Y. Iwasaki, *J. Biomat. Appl.*, 13, 111, (1998).

BIO- DETECTION SYSTEM WITH BACTERIAL SPORE COLLECTION AND DETECTION CHIPS

Hisao Inami¹, Mitsuhiro Matsuzawa¹, Yasuhiko Sasaki¹, Shigenori Togashi¹, Ryo Miyake¹, Masahiro Kurihara¹, Kouichiro Tsuge² and Yasuo Seto²

¹Hitachi, Ltd, Ibaraki 312-0034, Japan

²National Research Institute of Police Science, Chiba 277-0882, Japan

Abstract

We have developed an autonomous bio- detection system (ABDS) for detecting biological threat agents (e.g., *Bacillus anthracis*) that performs continuous aerosol collection, spore germination, and detection. The ABDS, bacterial spore identification system uses micro-fluidic chips for aerosol impactor collection, spore germination, DNA extraction, and DNA amplification analysis. Using the ABDS, *Bacillus subtilis* spores can be detected within 2 hr.

Keywords: Bacteria, Spore, Collection, Detection, Micro-fluidic chip

Equipment and Method

(1) Concept of operation

One of the problems of conventional bio- detection is that it requires specialized skill for the very complex sample preparation and DNA extraction. As shown in Fig. 1, the ABDS consists of an air sampler, disposable chip A for spore collection and germination, disposable chip B for DNA extraction and amplification, and an analyzer. The chips are composed of two layers of silicon elastomer – polydimethylsiloxane – (PDMS). All processing is included in the disposable chips. Reagents necessary are packaged in these chips beforehand. A non-expert can operate the system because distributed pouring (a highly-specialized skill) is not necessary. Moreover, there is no risk of infection for operators or of contamination of the equipment.

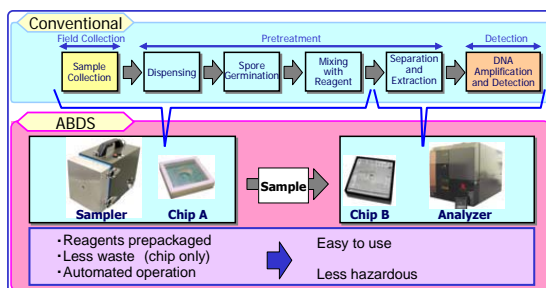


Fig. 1 Schematic illustration of analysis procedure with ABDS

(2) Aerosol collection

As shown in Fig. 2, chip A is set in the sampler. Impaction technology is applied to the suction part. Particles of the targeted size and weight are collected in the collection chamber of chip A. Smaller and lighter particles are carried away by air flow afterwards and are eliminated (Fig. 3(a)).

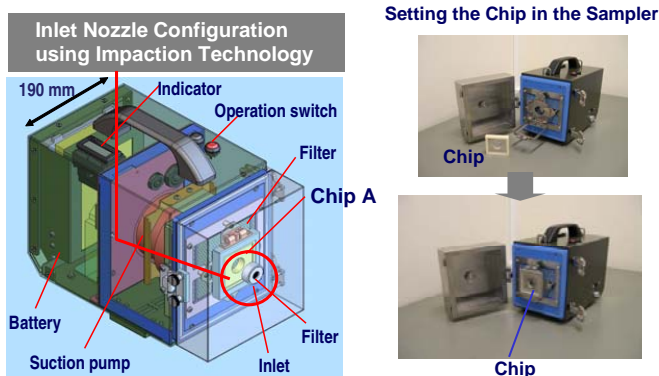


Fig. 2 Structure of Sampler with Chip A

(3) Germination of bacterial spores

Chip A is shown in Figs. 3 and 4. Reagents necessary for spore germination are stored in the surrounding passages. Chip A has the air connecting ports to supply air. The flow of all the reagents in the chip is controlled by on-off flow of compressed air from these ports. In the center of the chip is the chamber that performs bacterial spore collection and germination. After this takes place, chip A is placed in the analyzer (Fig. 5), and the reagents are serially introduced into the sample portion by compressed air, enabling spore germination [1] within 60 min (Fig. 6).

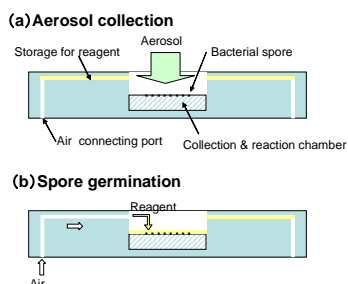


Fig. 3 Schematic illustration of sample collection and spore germination with Chip A

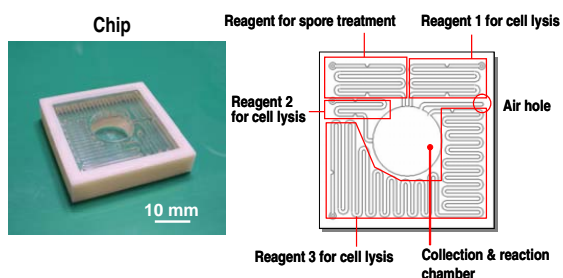


Fig. 4 Structure of Chip A

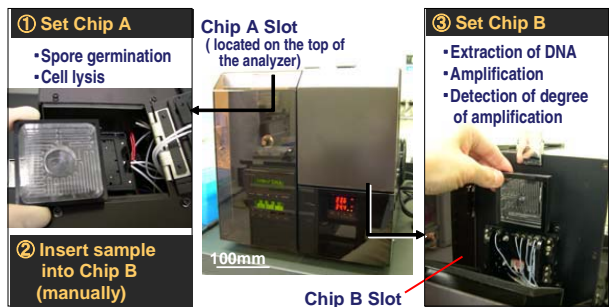


Fig. 5 Operational steps for analyzer

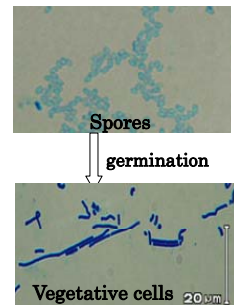


Fig. 6 SEM image of spore germination

(4) DNA extraction and amplification

The treated sample is transferred manually from chip A to chip B. Once chip B, with the DNA sample, is loaded into the analyzer, reagents necessary for DNA extraction and amplification are introduced one by one. The bacterial DNA is extracted through the extraction column , and the target DNA is amplified and detected using the ICAN method[2].

Results and discussion

The ABDS result for *Bacillus subtilis* spores (10^6 cfu/ml) is shown in Fig. 7. The amplification of the target DNA was observed within 30 min. The total period from sample collection to DNA amplification was less than 2 hr. Therefore, the ABDS can alert the airborne bacterial spore contamination considerably faster (within 2 hr) and easier than on-site air collection followed by tedious and specialized sample culturing and microbiological examination.

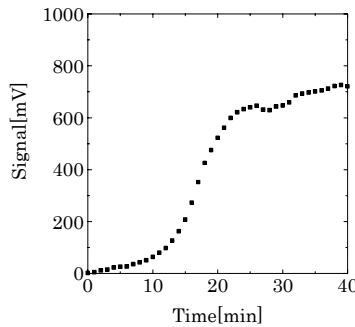


Fig. 7 *B. subtilis* spores DNA amplification using ABDS

References

- [1]. Y. Fujinami, M. Kataoka, K. Matsushita, H. Sekiguchi, T. Itoi, K. Tsuge and Y. Seto, Journal of Health Sciences, 50 (2), pp.126-132, (2004)
- [2]. H. Mukai, Rinsyou-byouri, 50 (5), pp.528-532, (2001)

PRECIPITATION BIOSENSOR BASED ON LAB-CHIP ACCOMPLISHING SELF-FLUID REPLACEMENTS VIA CAPILLARY FORCE

**Kwang Hyo Chung², Jung Woo Hong¹, Jun Hwang Lee¹, Hyeon-Bong Pyo²,
Byung Woo Kim³, Hyun C. Yoon¹**

¹Department of Molecular Science & Technology, Ajou University, Korea
²Biosensor Team, Electronics and Telecommunication Research Institute, Korea

³Department of Chemical Engineering, Sungkyunkwan University, Korea
(hcyoon@ajou.ac.kr)

Abstract

A novel polymer microfluidic chip for sample exchange via capillary force and a test of the device for an enzyme-catalyzed precipitation reaction are described. All the fluidic actuations in the device were run by a time-planned flow sequence and accomplished by only capillary force. The chip accomplishing self-replacement of samples was realized by designing the channels with theoretically derived equations for the capillary flow and stop. The chip was fabricated with polymer replication techniques which are suitable for the device fabrication with low price and single use. The test for a biochemical analysis using biocatalyzed precipitation reaction with the chip showed desired outcome. The presented microfluidic method would be applicable to various biochemical lab-chips with integrated washing steps or fluid replacement steps.

Keywords: Capillary force, Enzymatic analysis, Precipitation, Self-wash

1. Introduction

Microfluidic devices typically use external energy source such as a mechanical pump or a power supply to attain the precise control of multiple streams. A simple and compact microfluidic chip that does not use external energy for the fluid control would be very effective in the point of care testing. The surface tension is a well known surface force and natural force acting on the free surface of liquid, and it generates capillary pressure when the liquid contact with solid surface of a capillary. The device in this study was designed in such a way that the sample replacement in the reaction chamber would be accomplished by capillary force only [1].

For the application of the device in biochemical analysis, precipitation reaction was conducted on the chip. A precipitation method of horse radish peroxidase(HRP)-catalyzed precipitate formation reaction with 4-chrolo-1-naphtol(4-CN) was adopted [2]. 4-CN is a peroxidase substrate suitable for use in immunosensing procedures. This substrate produces an insoluble product that is blue in color and can be observed visually. This particular reaction was used because it is simple, persistent and the result can be seen with bare eye very easily. The reaction was induced to take place in the reaction chamber of the fabricated lab-chip (Figure 1).

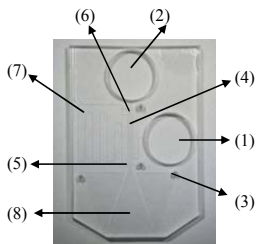


Figure 1. Configuration of the microfluidic chip: (1) Fluid inlet #1, (2) fluid inlet #2, (3) air vent, (4) reaction chamber, (5) stop valve #1, (6) stop valve #2, (7) side retarding channel, (8) waste chamber.

2. Experimental

The channels inside the chip were designed by theoretically derived equations for the capillary stop pressure and the capillary flow time. Numerical simulations were conducted to check the validity of equations and the performance of the designed chip.

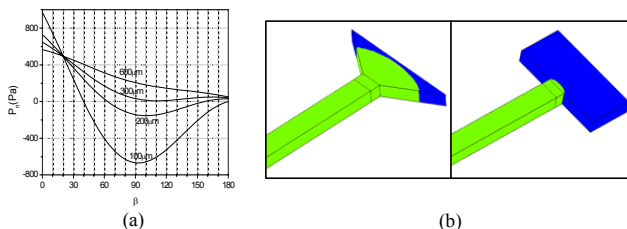


Figure 2. (a) Theoretical capillary pressure at an expanding channel with β (expansion angle) and width, (b) simulation

Figure 2 shows the exemplary results of the simulation. The polymer chip was intended to be disposable, and fabricated by sealing a hot-embossed PMMA substrate with an adhesive-coated PET film. The embossing master was of a single height for simple fabrication, and was obtained by nickel-electroplating on a SU8-patterned Ni-plate followed by CMP (Chemical Mechanical Polishing). The PET film was modified by plasma treatment to have a designed contact angle.

For biochemical analysis, a substrate solution consisting of 10 μ l of 4-CN (50 mM) and hydrogen peroxide were prepared and used. The prepared solution was dispensed in one liquid inlet and the enzyme HRP solution was deposited in another inlet. Then, the precipitation reaction was initiated and the change in blue color intensity in the reaction chamber was registered. The color intensity of the reaction chamber was numericalized to visualize the result in a graphical format.

3. Results and discussion

The actuation steps were demonstrated in Figure 3 and revealed a good performance. Liquid flows maneuvered through the predicted path of the fluidic chip successfully. Figure 4 shows the systematic procedure of the reaction and the change of color intensity in the reaction chamber. Since the precipitate had formed instantly when the two samples were mixed, sample exchange period in the reaction chamber was just enough to create the desired result.

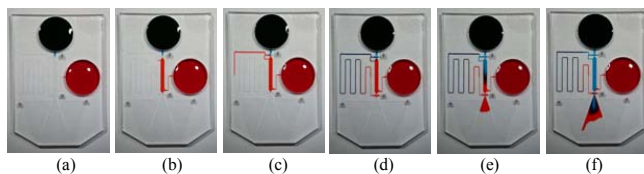


Figure 3. Flow sequence. (a) introduction of fluid 1 & 2 and operation of stop valve 2, (b) operation of stop valve 1 and filling the reaction chamber, (c) elimination of stop valve 2 and flow retardation at side channel, (d) elimination of stop valve 1, (e) filling the waste chamber, (f) replacement of fluids at the reaction chamber

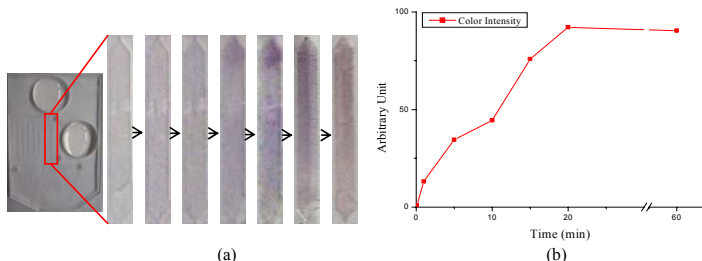


Figure 4. (a) A sequential view of the enzyme catalyzed precipitation reaction, (b) change in color intensity in the reaction chamber.

As can be seen in Figure 4b, the color intensity of the precipitate increased and leveled off after 20 minutes, exhibiting a typical pattern of enzymatic catalysis. An extension of this principle by using HRP-tagged antibody is currently underway. In conclusion, the presented microfluidic chip can be applicable to various lab-chips having integrated washing steps or fluid replacement steps. The performance of the bioanalysis could be enhanced by employing functionalized microbeads in the reaction chamber.

Acknowledgements

This research was supported by grants from the Basic Research Program of KOSEF (R01-2006-000-10240-0), the Regional Technology Innovation Program of MOCIE (RTI04-03-05), and the ERC(BSEP) of KOSEF.

References

1. D.R.Reyes, D.Iossifidis, P.A.Auroux, A.Manz, *Micro Total Analysis Systems.1. Introduction, theory, and technology*, Anal. Chem., 2002, 74, pp.2623-2636
2. H.C.Yoon, J.S.Ko, H.Yang, Y.T.Kim, *Stepwise surface regeneration of electrochemical immunosensors working on biocatalyzed precipitation*, The Analyst, 2002, 127, pp.1576-1579

SIMULTANEOUS BIOASSAYS ON SEVERAL PLUGS OF MAGNETIC PARTICLES

Ben J. K. Brown and Nicole Pamme

University of Hull, Dep. of Chemistry, Cottingham Road, Hull, HU6 7RX, UK
(n.pamme@hull.ac.uk)

Abstract

We introduce a very simple method for simultaneous bioassays based on plugs of magnetic particles within a microchannel.

Keywords: magnetic particles, immunoassay, parallel analysis

Introduction

Magnetic particles coated with specific biomolecules are commonly used as solid supports for DNA, protein and cell analysis (fig. 1). Typically millions of such particles are mixed with an analyte sample in a test tube. The particles are then retained in the tube by means of an external magnet and the supernatant is pipetted off. Multiple washing steps are required, making this batch procedure rather time-consuming.

Alternatively, plugs of magnetic particles can be immobilized inside a microfluidic channel (fig. 2). The particle plug can be flushed with reagents and released as desired. This has been demonstrated by several groups^[1] including for DNA hybridization,^[2] immunoassays^[3] and mRNA isolation.^[4] Such examples demonstrate the merits of miniaturizing analytical assays in terms of reduced sample volumes and faster reaction times. However, few attempts^[5] have been made to take advantage of another benefit of miniaturization: integrating several components onto a small footprint for simultaneous analysis of several sample components. Here, we demonstrate a simple method for the immobilization of several plugs of magnetic particles with different surface chemistries along a microchannel to undertake simultaneous analysis (fig. 3).

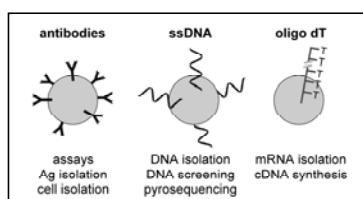


Figure 1: Magnetic particles can be used for a wide variety of bioassays.

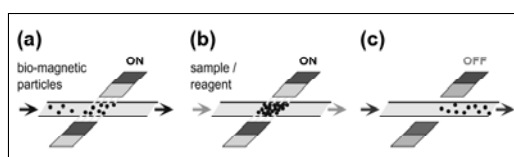


Figure 2: Magnetic particles can be handled elegantly in microfluidic channels by (a) stopping them in flow, (b) flushing with reagents and (c) releasing as desired.

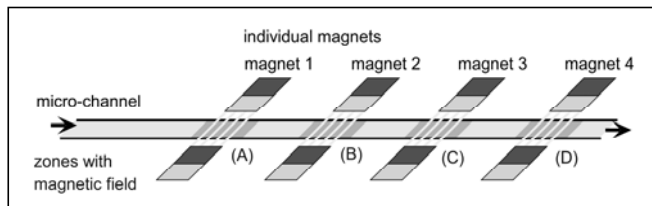


Figure 3: The principle of simultaneous analysis on plugs of magnetic particles. Over the length of a microchannel, particles are trapped in localized magnetic fields.

Experimental

For proof of concept, a simple fused silica capillary ($100\text{ }\mu\text{m}$ i.d.) was used as a microchannel and pairs of NdFeB magnets with a 3 mm gap were used to generate localized magnetic fields over the length of the microchannel (fig. 4). Fluid was pumped by means of a syringe pump. The maximum applicable flow rates to stop particles in flow were investigated for several types of magnetic particles ranging from $1\text{ }\mu\text{m}$ to $8\text{ }\mu\text{m}$ diameter (table 1). To load several plugs, initially one magnet pair was placed around the capillary and particles were stopped. After flushing with buffer solution, a second magnet was placed further upstream and another particle suspension was trapped. Thus, up to three plugs were immobilized over a channel length of 5 cm .

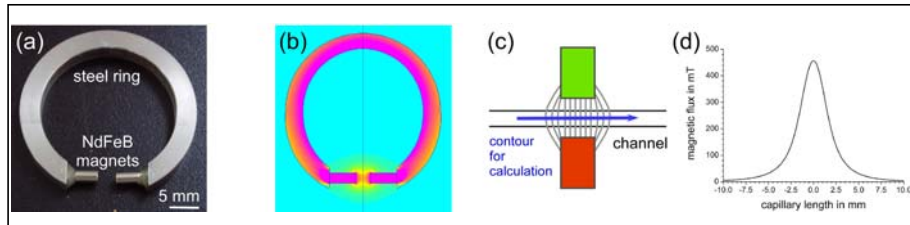


Fig. 4: (a) Localized magnetic fields were generated by a pair of NdFeB magnets glued to a steel ring. (b) Simulation of the magnetic field between the poles. (c/d) A calculation of the magnetic flux along a capillary positioned in the magnet gap shows that the field is localized over only a few mm of channel length.

Results and Discussion

As an example of a simultaneous bioassay, two small plugs with glycine and streptavidin coated particles ($2.8\text{ }\mu\text{m}$ Dynabeads) were formed and subsequently flushed with a solution of fluorescent biotin. The biotin bound to the streptavidin particles, hence fluorescence was observed from this plug (fig. 5). This reaction was merely chosen as an example assay due to the ready availability of the reagents. Many other assays and reactions could be performed using the same format.

Table 1: Maximum flow rates at which magnetic particles could be stopped in flow.

Particle Type and Supplier	Particle Diameter in μm	Maximum Flow Rate for Retention in mm s^{-1}
Dynabeads (Invitrogen)	1.0	0.5
	2.8	2.8
	4.5	4.1
Compel (Bangslabs)	3.2	0.8
	8.0	2.4
Micromer (Micromod)	4.0	1.5
	8.0	0.5

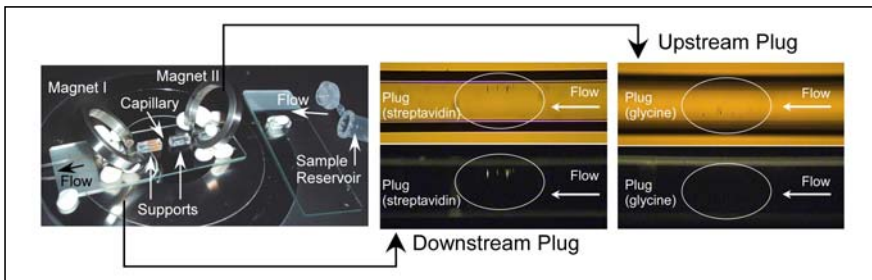


Figure 5. Example of a dual bioassay: (left) Photograph of the setup featuring two magnets. A plug of streptavidin coated Dynabeads was immobilized. Subsequently, further upstream a plug of glycine coated beads was formed. These plugs were then flushed with fluorescent biotin solution, rendering the streptavidin plug fluorescent and the glycine plug unchanged.

Conclusions

The method could be exploited further by utilizing a channel network to speed up loading of particles and to selectively release plugs into side streams. This assay platform is a technically quite simple yet universal device that can be applied to a wide range of bioanalytical reactions and, more desirably, could be combined with further sample treatment up- and downstream.

References

- (1) N. Pamme, *Lab on a Chip* **2006**, 6, 24-38.
- (2) Z. H. Fan; S. Mangru, et al., *Anal. Chem.* **1999**, 71, 4851-4859.
- (3) J. W. Choi; K. W. Oh, et al., *Lab on a Chip* **2002**, 2, 27-30.
- (4) G. F. Jiang; D. J. Harrison, *Analyst* **2000**, 125, 2176-2179.
- (5) K. Smistrup; B. G. Kjeldsen, et al., *Lab on a Chip* **2005**, 5, 1315-1319.

SINGLE CHAMBER BASED CELL CONCENTRATION, DNA EXTRACTION AND REAL-TIME PCR FOR RAPID PATHOGEN IDENTIFICATION

**Yoon-Kyoung Cho, Jeong-Gun Lee, Young-Sun Lee,
Jong-Myeon Park, Beom-Seok Lee and Christopher Ko**

Bio Lab, Samsung Advanced Institute of Technology, PO Box 111,
Suwon, 440-600, Republic of Korea
(dnachip@samsung.com)

Abstract

Recently we reported a novel cell lysis method utilizing a 808 nm laser and magnetic beads[1]. Addition of magnetic particles to the cultured bacteria solutions accelerated the heat transfer rates. As a result, only 40 seconds of laser irradiation effectively lysed pathogens including both Gram-negative and Gram positive bacteria and hepatitis B viruses. In this report, we used magnetic micro particles modified with target specific antibodies and thus we could separate and concentrate target pathogens from whole blood and could do rapid and efficient DNA extraction using the same laser irradiation method. Furthermore, the same chip can be used in the real-time microchip based PCR machine, GenSpector® TMC-1000[2] for the quantitative DNA analysis.

Keywords: **bacteria, virus, pathogen, cell concentration, cell lysis**

1. Introduction

Most of the biochip studies so far have pursued on single functionality and used purified DNA or homogeneous sample as an input sample. However, practical applications such as in clinical or environmental analysis require processing of complex fluids; e.g. whole blood, or contaminated food solution. Due to the complexity and the large volume requirement, most of the sample preparation steps still rely on the time-consuming traditional bench top methods. As a result, development of rapid and efficient sample preparation methods for “real” sample analysis remains as a major bottleneck for the realization of the micro total analysis system.

In our previous report [1], we demonstrated that single chamber based pathogen detection could be possible by simply transferring the same microchips from the hand-held cell lysis device, Laser-Irradiated Magnetic Bead System (LIMBS), to the real-time microchip based PCR machine, GenSpector® TMC-1000 [2]. However, the PCR detection was not possible for the real samples such as blood and cell or DNA concentration was not possible.

2. Theory

We report here an important extension of the LIMBS technique in which single chamber based, rapid PCR detection of pathogen from whole blood is achieved through the use of magnetic beads in dual purpose; (1) target cell separation and concentration

by using magnetic beads conjugated with target cell specific antibody and (2) rapid cell disruption aid in laser irradiated cell lysis step

3. Experimental

Fig. 1 shows the schematic diagram of the proposed experimental steps. First, target pathogen specific antibody conjugated magnetic beads are mixed with target samples such as blood or serum. Then, the sample and beads mixture is flowed in microchip equipped with Nd-magnet and the magnetic beads are captured in the chamber. Followed by washing, the chip is transferred to the LIMS device for the rapid cell lysis. Then, the same chip is loaded for the real-time PCR.

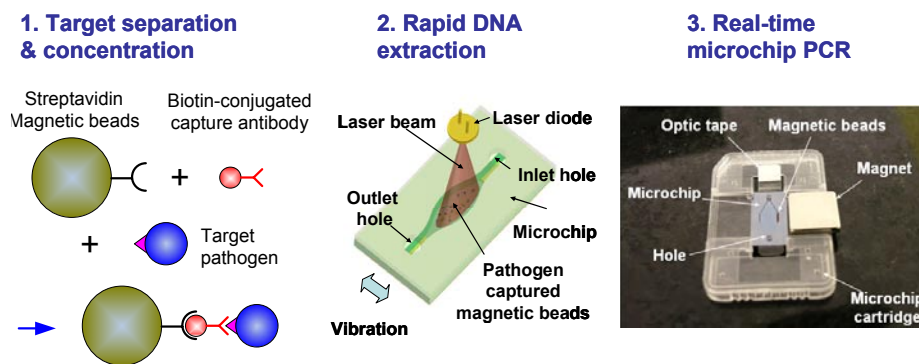


Fig. 1. Schematic diagram of the single chamber based cell concentration, lysis and real-time PCR for rapid pathogen detection. Antibody coated magnetic beads have dual functions; (1) target specific cell capture and (2) rapid cell disruption aid in laser irradiated cell lysis step. A microchip is compatible in all of the steps.

4. Results and discussion

Real-time PCR was conducted following the pathogen (bacteria or virus) separation and lysis using the methods described in Fig. 1. When the whole blood sample is used, PCR was not possible without the target separation and concentration step. However, the PCR results were comparable to the case when clean buffer was used if the proposed method is used. Target capture efficiency was over 95% both for the bacteria and virus separation and concentration.

5. Conclusions

We have demonstrated that rapid DNA isolation from raw samples such as whole blood or serum and the quantization of DNA concentration were possible using a single chamber based micro PCR chip. Total analysis time from front-end sample preparation to rapid real-time PCR detection could be within an hour. This method is rapid, efficient and does not require large volume or many kinds of buffers and therefore very adequate for the fully integrated DNA analysis system.

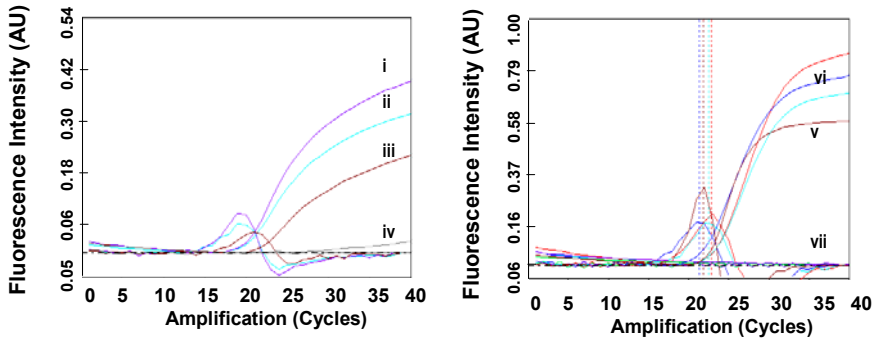


Fig. 2. Real-time PCR detection of bacteria (A) and virus (B) from whole blood using the single chamber based rapid assay. The experimental conditions are summarized in Table 1.

Table 1. Real-time PCR detection of bacteria (*E. coli*, 10^5 cell/ μ l) solution and virus (HBV, 10^3 cell/ μ l) from whole blood using the single chamber based rapid assay. The volume ratio of the bacteria solution and various buffer solution was 1: 3.

Pathogen	solution	Target separation & concentration step	Cp
Bacteria (<i>E. coli</i>) (10^5 cell/ μ l)	(i) PBS buffer	Used	19.40
	(ii) whole Blood	Used	19.43
	(iii) PBS buffer	Not used	21.05
	(iv) whole Blood	Not used	Not amplified
HBV DNA	(v) PBS buffer	Not used	21.79
Virus (HBV) (10^3 cell/ μ l)	(vi) Serum	Used	22.22
	(vii) Serum	Not used	Not amplified

References

- [1] J.-G. Lee, K. H. Cheong, N. Huh, S. Kim, J.-W. Choi, and C. Ko, *Microchip-based one step DNA extraction and the real-time PCR in one chamber for rapid pathogen identification*, Lab Chip, pp. accepted, (2006).
- [2] Y.-K. Cho, J. Kim, Y. Lee, Y.-A. Kim, K. Namkoong, H. Lim, K. W. Oh, S. Kim, J. Han, J. Park, Y. E. Pak, C.-S. Ki, J. R. Choi, H.-K. Myeong, and C. Ko, *Clinical evaluation of micro-scale chip-based PCR system for rapid detection of hepatitis B virus*, Biosensors and Bioelectronics, vol. 21, pp. 2161~2169, (2006).

MICROFLUIDIC DEVICE BASED ON SELF-ORGANIZED MAGNETIC BEADS : APPLICATION TO THE ON-CHIP ANALYSIS OF THE PRION PROTEIN

A. Le Nel^{1,2}, L. Korecka³, M. Slováková³, N. Minc^{1*}, C. Smadja², J.M. Peyrin², J.L. Viovy¹, M. Taverna²

¹Laboratoire PCC, Institut Curie (UMR/CNRS 168), Paris, France

²JE2495, Université Paris XI, Châtenay-Malabry, France

³Dept. of BBS, University of Pardubice, Czech Republic

Contact email : myriam.taverna@cep.u-psud.fr

Abstract

We present the development of a “lab-on-a-chip” entailing two microreactors based on the self-organization of magnetic beads, dedicated to the analysis of the Prion Protein (PrP). The enzymatic and the immunocapture reactors were based on the covalent immobilization of either proteinase K or antibodies. Then, these two analytical steps were integrated in a dual PDMS chip.

Keywords: magnetic beads, self-assembly, prion, digestion, immunocapture

1. Introduction

To-date, no method is available to diagnose Prion diseases in an early stage on living animals or humans, and the diagnosis can be secured only post-mortem. The main goal of this study was to design efficient microreactors to perform both protein digestion and immunocapture. A high density of magnetic beads (grafted with molecules like enzymes or antibodies) is immobilized in a microchannel between two magnets which create a non-uniform magnetic field collinear to the microchannel. The plug of beads gives rise to a relative low pressure drop thanks to the self-organization of the beads [1]. The resulting functionalized matrix has a small and relatively homogeneous pore size, well adapted to the protein sizes thus allowing for fast and reproducible protein reactions.

2. Enzymatic microreactor

After the optimization of the Proteinase K (PK) reactor for on chip digestion (previous work [2]), the reproducibility of the system has been tested. It included reproducibility of the digestion extent of the PK beads and reproducibility of the microreactor formation. A standard deviation of 3% has been found for each study. The reactor was then applied to the digestion of brain homogenates over-expressing the PrP of sheep. Solutions of PrP, pathological and normal, were digested in the same conditions (PK beads, temperature, buffers...). At a flow rate of 7 μ L/h, it was possible to differentiate between normal and pathological Prion Protein (figure 1). No bands appeared on

* Current address : Dept. Of Microbiology, Columbia University, NY, USA

Western Blot meaning that the normal PrP was fully digested. In contrast, pathological PrP present in infected brain was resistant to the digestion as evidenced by the intense spots on the subsequent western blot analysis. This is very encouraging because the difference between normal and pathological PrP is so pronounced that we can anticipate that this method could distinguish intermediate prion strains (normal PrP partly resistant to PK or pathological PrP highly PK sensitive).

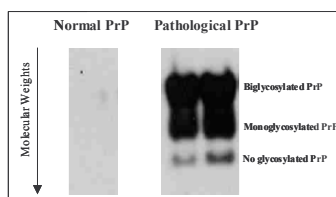


Figure 1: Western Blot of (normal and pathological) PrP solutions after on-chip PK digestion at a flow rate of $7\mu\text{L}/\text{h}$

3. Immunocapture microreactor

The anti-PrP antibodies (IgG) were covalently bound to the magnetic beads using two different methods ([3]): random and oriented immobilization. In the first one, the $-\text{NH}_2$ groups of IgG were bound to the $-\text{COOH}$ functional groups of magnetic particle using EDC (water soluble carbodiimide) and S-NHS (hydroxysulfosuccinimide). The second one involved two steps: first, the carbohydrate moieties located in the Fc fragment of IgG were oxidised using sodium periodate; in the same time, the $-\text{COOH}$ groups of beads were changed into $-\text{NH}_2$ groups using EDC, S-NHS and adipic acid. Finally, beads and antibodies were mixed together with sodium cyanoborohydrate to stabilize the linkage. Development and optimization of the reactor were performed using affinity chromatography methods (antigen-antibody reaction and recovery of the antigen by elution step) in batch-wise and on-chip experiments. The batch-wise experiments enable to quantify the antibodies bound to the magnetic beads. In our conditions, it was possible to immobilize $20\mu\text{g}$ of antibodies on beads with random immobilization and twice as much with the second method. On-chip, optimal flow rates for both the capture and the elution were determined.

4. Coupling of microreactors

The two analytical steps were then integrated in a dual PDMS chip (figure 2a)). Two systems of magnets were introduced to immobilize two different functions on the chip: digestion and capture. The primary device integrates PK digestion followed by the antibody capture to keep and analyze only the pathological PrP (figure 2b) et 2c)). For the moment, this process is made possible by successively closing the different access of the microchannel and changing the buffers.

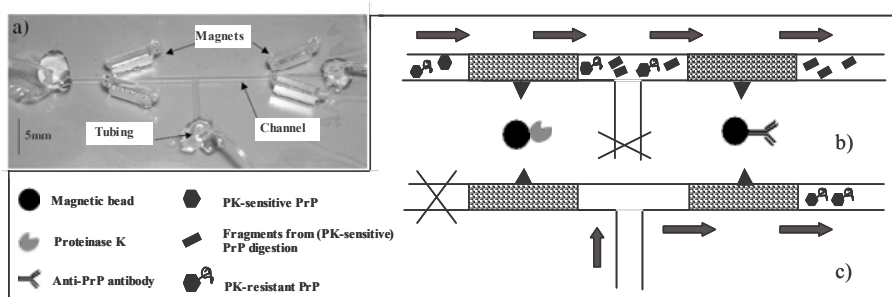


Figure 2: a) Photography of the PDMS dual chip. b) and c) Principle of the two-steps system: b) The protein mixture is first digested by the plug of PK beads and then passed through the immunoaffinity microreactor which will capture the non-digested PrP. c) Elution of the capture PrP by changing the pH of the buffer and recovery of the digested and concentrated fragments

5. Conclusion

For the first time, differential digestion of pathological and normal prion protein was demonstrated on a chip. This format leads to a spectacular “signature” for the presence of pathological protein. We proposed a new type of chip integrating two steps, enzymatic digestion and immunocapture, in order to combine the high specificity mentioned above with a very low limit of detection, thanks to a considerable concentration of the proteins of interest into a very small volume (a few hundred nL). These developments pave the route for the development of a Micro Total Analysis System able to perform diagnosis at an early stage in body fluids rather than post-mortem on brain samples

Acknowledgments

This work was supported in part by the French Ministry of Research/CNRS Programme “NMAC: Microproteolab” and by the European Project “NEUROTAS”.

References

- [1] M. Slováková, N. Minc, Z. Bilková, C. Smadja, W. Faigle, C. Fütterer, M. Taverna, J.L. Viovy, *Lab on a chip* 2005, pp. 935-942
- [2] A. Le Nel, N. Minc, M. Slováková, C. Smadja; J.M. Peyrin, M. Taverna, J.L. Viovy, *Proceeding of μTAS2005*, pp. 1552-1554
- [3] G.T. Hermanson, *Bioconjugate techniques*, Academic press, 1996

ELECTROKINETIC PRECONCENTRATION AND HIGHLY STACKING GEL ELECTROPHORESIS FOR ANALYSIS OF HIGH MOLECULAR WEIGHT PROTEIN COMPLEXES ON A PLASTIC MICROCHIP

Mohamad Reza Mohamadi***, Laili Mahmoudian*, Noritada Kaji*, Manabu Tokeshi*, Hiroshi Chuman** and Yoshinobu Baba****

* Department of Applied Chemistry, Graduate School of Engineering, Nagoya University, Japan

** Graduate School of Pharmaceutical Sciences, The University of Tokushima, Japan

***Health Technology Research Center, AIST, Japan

Abstract:

An efficient dynamic coating using methylcellulose and a non-ionic detergent (Tween-20) was developed which controlled protein adsorption onto the surface of microchannels on a microchip made of poly (methyl methacrylate), PMMA. Highly stacking microchip electrophoresis under non-denaturing condition was used for analyzing high molecular weight protein complexes on a plastic microchip. The method has the efficiency of 6×10^6 plate/m for a complex of mAb-HSA with MW of ~220kDa and with the detection limit of few pM.

Keywords: Microchip Electrophoresis, Protein, Preconcentration, Stacking

1. Introduction

Ever since the μ TAS was started, microchip electrophoresis (MCE) of proteins especially high MW proteins on polymeric microchips has been a challenge. The high sample adsorption on the surface of microchannel leads to peak broadening and low reproducibility in analysis. Covalent coating of the microchannel surfaces produces a stable coating which is favored for some applications like coupling the MCE system to a mass spectrometer. But as there is some difficulty to apply a covalent coating to the microchannels; thus, dynamic coating can be considered as an effective and easier way to reduce protein adsorption on the microchannels.

In the current research a new dynamic coating which includes methylcellulose and a non-ionic detergent (Tween-20) was developed which decreased the interactions between the protein samples and the surfaces of microchannels in a polymeric microchip made pf PMMA. Highly stacking MCE of high MW protein complexes under non-denaturing condition on a plastic microchip was achieved.

2- Experimental

An optimum concentration of Tween-20 (0.01%) and range of concentrations of methylcellulose (0.1% to 1.5%) in Tris-HCl 20mM, pH 8.3 was used as dynamic coating in all MCE experiments. The dynamic coating was included in the electrophoresis buffer which was loaded into the buffer waste (BW) reservoir and injected into the microchannels using a syringe pump just prior to the electrophoresis. An inverted fluorescence microscope, Axivert 135TV (Carl Zeiss, Tokyo, Japan), illuminated by a 100-W mercury arc lamp and a 10 /0.3 NA objective lens (Carl Zeiss) was used to view the protein separations. A HVS448 1500V, (LabSmith, Livermore, CA), power supply which was controlled by a PC has been used for MCE. A CCD camera, (EB-CCD, Hamamatsu Photonics, Hamamatsu, Japan), was used to capture the separation process. The captured photos were analyzed by image processing software (Cosmos32, Library Inc., Tokyo, Japan). The electropherogram was simulated for each separation from acquired data. After conditioning the electrophoresis, the MCE has been done on a home modified Hitachi microchip system attached to a HVS448 1500V, (LabSmith), power supply which was controlled by a PC.

A combination of field amplified stacking (FAS) and electrokinetic supercharging plus the sieving effect of methylcellulose solution in the microchannel was used to sharpen the peak for high MW protein complexes. To get the FAS effect the protein samples were first diluted by dd-H₂O In this method, then a terminating electrolytes (TE) includes a terminating anion (Gly⁻) was electrokinetically injected after the sample zone. The front head of the sample in the channel was the linear polymeric gel in a leading electrolyte (LE). During the separation the sample zone for high MW protein complex was stacked between terminating electrolyte and the sieving effect of the gel. The protein sample was also preconcentrated on the cross channel.

3- Results and discussion

Protein samples with range of MW up to 100kDa were separated on this system (Fig.1). The electrophoresis was non-denaturing which could be used for studying protein-protein interactions and protein complexes. Complexes of antigen-antibodies were chosen to study by this method. Like all the on chip immunoassays the peak related to the complex was broaden which diminished the detection limit. To address this problem different strategies like field amplified stacking (FAS) and electrokinetic supercharging which both previously had been applied on microchip electrophoresis [1,2] were tested. A combination of these two methods, as it was described in the experimental section, was found to be the best way to get a sharp peak for the immune complexes. Fig. 2 shows the stacking effect on the peak of a complex of a mAb-HSA with MW of ~220kDa. The system was applied for competitive immuneassay for quantitation of human serum albumin (Fig. 2). In Fig. 3 the standard curve shows the limit of detection which was 15pM of HSA. Quantitation of HSA in a real human serum sample was also conducted by this method. Other protein-protein complexes like enzyme-substrate were also separated by this method.

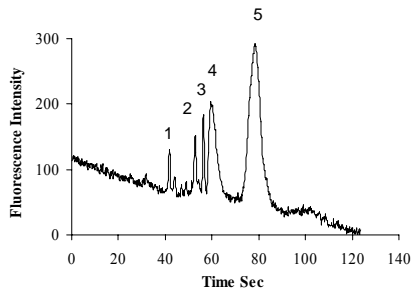


Figure 1. Electropherogram shows separation of three FITC labeled protein samples Trypsin inhibitor 20.1kDa (peaks 1& 2) BSA 66kDa (peak 4) and Amyloglucosidase 100kDa (peak 5) on a PMMA microchip under non-denaturing condition. Peak 1 is a degradant of BSA.

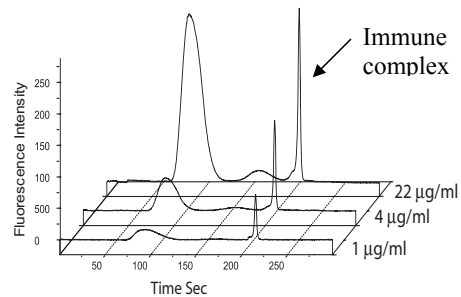


Figure 2. Electropherogram show separations of FITC labeled HSA and its complex with mAb-anti HSA. Different

concentration of HSA were incubated at RT for 20 min with 20 μ g/ml of antibody.

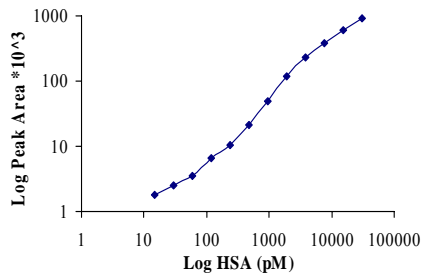


Figure 3. Serial dilutions of an FITC labeled HSA were incubated with a mAb-anti HSA (20 μ g/ml). Standard curve shows the correlation between peak areas of the immune-complexes against concentration of HSA.

Acknowledgments

This work has been partially supported by a grant from New Energy and Industrial Technology Development Organization (NEDO) of Ministry of Economy, Trade and Industry, Japan and a grant-in-aid from the Ministry of Education, Science and Technology, Japan.

References:

- [1] Xu Z., Ando T., Nishine T., Arai A., and Hirokawa T. *Electrophoresis* 2003, 24, 3821–3827.
- [2] Huang H., Dai Z., Xu F. and Lin B., *Electrophoresis* 2005, 26, 2254–2260.

FABRICATION OF THE CHEMICALLY-FUNCTIONALIZED CAPILLARY-ELECTROPHORESIS MICROCHIP BASED ON CAPILLARY-ASSEMBLED MICROCHIP (CAs-CHIP) TECHNIQUE

Seigi Takeda, Hideaki Hisamoto, and Shigeru Terabe

Graduate School of Material Science, University of Hyogo, Japan

(e-mail: hisamoto@sci.u-hyogo.ac.jp)

Abstract

A simple fabrication of the chemically-functionalized capillary electrophoresis microchip was demonstrated using the capillary-assembled microchip (CAs-CHIP) technique [1-4], which involved the simple embedding of the chemically-functionalized square capillary as separation capillary into a PDMS microchannel possessing same cross section to outer section of square capillary. Here, we used octadecylsilane (ODS)-modified square capillary as a separation capillary and found that the simple fabrication of CEC-chip was possible.

Keywords: capillary-assembled microchip, capillary electrochromatography, capillary electrophoresis, PDMS, square capillary

1. Introduction

Fabrication of capillary electrophoresis microchip is usually performed by micromachining procedure such as photolithography-chemical etching or molding. In order to integrate the functional separation mode, position-selective chemical modification of microchannel is indispensable. Photopolymerization and multiphase flow patterning are the common methods for this purpose, however, these methods have some experimental difficulties on integrating multiple functions on a single microchip [1]. On the other hand, we have been investigating the development of CAs-CHIP in a recent few years. CAs-CHIP is fabricated by simply embedding the functionalized square capillaries into a PDMS channel. Therefore, in contrast to the previously reported fabrication of electrophoresis microchip, our system has an advantageous feature of the simple integration of chemical functionality on a single microchip.

Here, we report an example of the fabrication, injection and capillary electrochromatographic (CEC) separation using ODS-modified capillary.

2. Experimental

After removing the polyimide coating, square capillaries were cut into appropriate length and embedded onto a lattice PDMS plate as shown in Figure 1. After bonding, reservoirs were attached at the other ends of capillaries. Concerning the fabrication of CEC chip, ODS-modified open-tubular square capillary was used instead of the bare separation capillary. Detection was carried out by the laser induced fluorescence detection using argon laser (488 nm).

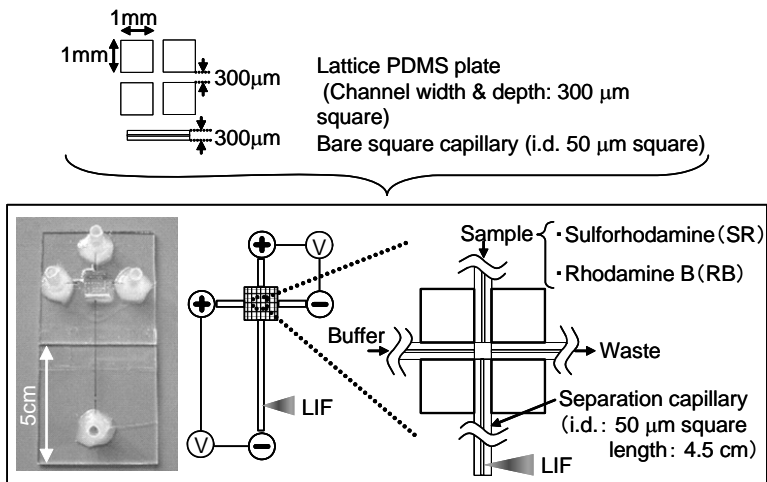


Figure 1. Fabrication of the capillary electrophoresis microchip based on CAs-CHIP technique.

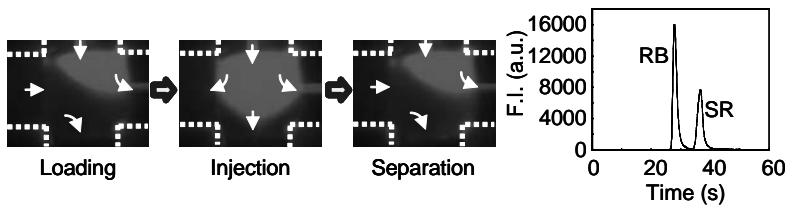


Figure 2. Fluorescence images showing “gated injection” procedure, and obtained electropherogram.

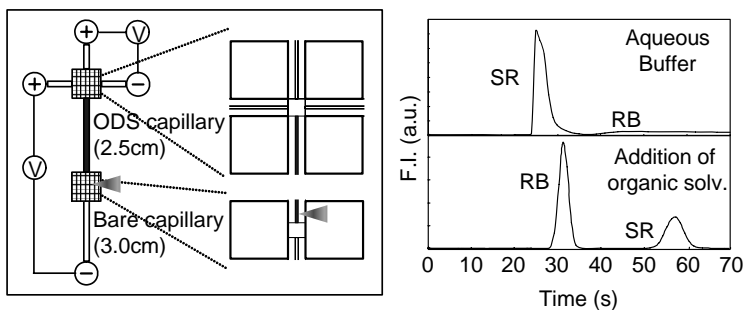


Figure 3. CEC chip using ODS-modified capillary, and typical electropherograms obtained by different eluent.

3. Results and discussion

In order to realize our concept, we first investigated the injection modes using the rhodamine B and sulforhodamine as test samples. Although “pinched injection mode” did not work due to the large dead volume at the crossing point of the channel, “gated injection mode” worked well and complete separation was achieved (see Figure 2).

In our case, chemically-functionalized capillaries can be easily implemented. As a typical example, we prepared ODS-modified capillary and used as a separation capillary. When the aqueous buffer was used as background solution, sulforhodamine was eluted first, and the rhodamine B was slowly eluted with long tailing due to the adsorption to the ODS surface. In contrast, when the buffer containing organic solvent was used, elution order was reversed (see Figure 3), indicating that the typical CEC separation mode worked well.

4. Conclusions

Simple fabrication of the chemically-functionalized capillary electrophoresis microchip was achieved. Sample injection using the gated injection mode enabled fairly good separation of test samples, although the fabricated chip had quite large dead volume at the crossing point. By employing the ODS-modified capillary, typical CEC separation behavior was observed. These results suggested that the wide applicability of CAs-CHIP in the field of separation science by simply replacing the chemically-modified capillaries in each purpose.

Acknowledgements

H.H. is grateful for the research funding sponsored by the Grant-in-Aid for Scientific Research from the Ministry of Education, Culture, Sports, Science and Technology, Japan, and Hyogo COE program from Hyogo prefecture, Japan.

References

- [1] H. Hisamoto, Y. Nakashima, C. Kitamura, S.-I. Funano, M. Yasuoka, K. Morishima, Y. Kikutani, T. Kitamori and S. Terabe, *Capillary-Assembled Microchip for Universal Integration of Various Chemical Functions onto a Single Microfluidic Device*, *Anal. Chem.*, 76, 3222-3228 (2004).
- [2] H. Hisamoto, S.-I. Funano and S. Terabe, *Integration of Valving and Sensing on a Capillary-Assembled Microchip*, *Anal. Chem.*, 77, 2266-2271 (2005).
- [3] H. Hisamoto, M. Yasuoka and S. Terabe, *Integration of Multiple-Ion Sensing on a Capillary-Assembled Microchip*, *Anal. Chim. Acta*, 556, 164-170 (2006).
- [4] H. Hisamoto, S. Takeda and S. Terabe, *Capillary-Assembled Microchip as a Deproteinization Device for Capillary Electrophoresis*, *Anal. Bioanal. Chem.* in press (2006).

IMPROVED PLASMA YIELD BY A NEW DESIGN OF MICROCHANNEL BEND STRUCTURES

C. Blatttert¹, R. Jurischka¹, I. Tahhan¹, A. Schoth¹ and H. Reinecke¹

¹Laboratory for Process Technology, Department of Microsystems Engineering (IMTEK), University of Freiburg, Germany

Abstract

Since most clinical chemistry tests are performed on cell-free serum or plasma, micro assay devices for blood tests require integrated on-chip microfluidics for separation of plasma or serum from blood. A new design of a microchannel bend separation device based on parallel microchannels results in improved blood plasma yield that is comparable to the filter performance of polyester membranes.

Keywords: blood, filter, lab-on-a-chip, microchannel bend, separation

1. Introduction

The microchannel bend was introduced at μ TAS 2004 as a novel blood separation technique [1]. The advantage of this technique is the robust and simple design for a cost effective mass production in plastics for disposable use and an easy integration into lab-on-a-chip systems. No integrated actuators like pumps or valves are necessary.

This paper reports an improved design of microchannel bend structures using parallel microchannels for the separation of blood plasma and blood cells. The result of the new design is a higher plasma yield compared to formerly presented devices.

2. Theory

The microchannel bend uses for the filtration of blood plasma and blood cells only physical (centrifugal force in the bend region) and hydrodynamic ("plasma skimming" due to significant flowrate differences in plasma and cell channel) separation mechanisms. In a previous paper, the effect of channel geometry variations in microchannel bends on blood cell separation efficiency was shown [2]. One result was increasing separation efficiency with decreasing plasma channel to cell channel flow rate ratio. This finding means that high separation efficiency involves low plasma yield. To overcome this drawback an improved design of the micro channel bend structures is presented that is based on a parallel arrangement of plasma channels.

3. Experimental

The basic separation device consists of a feed channel branching into a cell channel and a plasma channel (Figure 1). Different test chips have been fabricated in plastics. Typical channel dimension are shown in Table 1. Then, two different chips with the same geometry were compared by six consecutive test runs. These experiments were performed with diluted human blood (hematocrit: 9%).

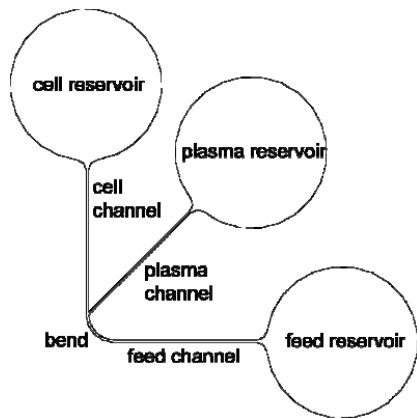


Figure 1: Schematic of a microchannel bend structure.

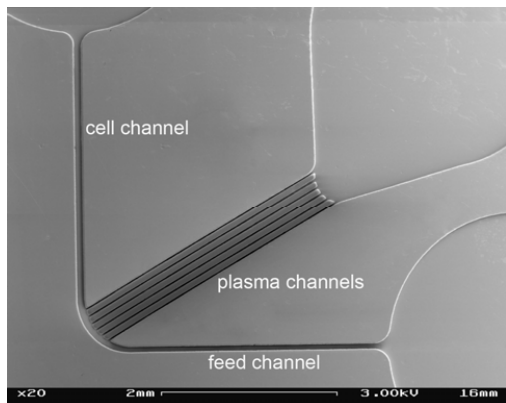


Figure 2: SEM picture of a device with 6 parallel channels.

The blood was infused into the chip by a syringe pump at an average feed velocity of 2.7 m/s. Figure 2 shows a device with the new design using 6 parallel plasma channels.

Table 1: Typical channel dimensions of a microchannel bend structure.

	width	depth	length	radius	diameter
feed channel	60 μm	70 μm	3 mm	-	-
cell channel	90 μm	70 μm	3 mm	-	-
plasma channel	20 μm	70 μm	3 mm	-	-
bend	-	-	0.8 mm	0.5 mm	-
reservoirs	-	-	-	-	3 mm

4. Results and discussion

Figure 3 and 4 show the run to run and chip to chip reproducibility of the micro channel bend separation technique for red blood cells (RBC) and white blood cells (WBC). The RBC separation efficiency varies between 98 % and 100 % for chip A and between 99 % and 100 % for chip B. The WBC separation efficiency varies between 97 % and 98 % for chip A and is 98 % for chip B in all runs. The plasma yield of these chips was about 15 %. Compared to a device with a single plasma channel the plasma yield could be increased by a factor of 6 with this design whereas the separation efficiency is unchanging for both devices.

One of the well established micro separation techniques for blood are polyester filter membranes [3]. Table 2 compares separation properties of Pall Hemasep V filter membranes with the parallel channel micro bend structure. The microchannel bend achieves a comparable plasma yield at a shorter separation time and lower consumption of surface area

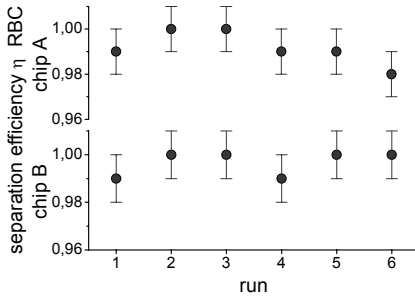


Fig. 3: Reproducibility of RBC separation efficiency.

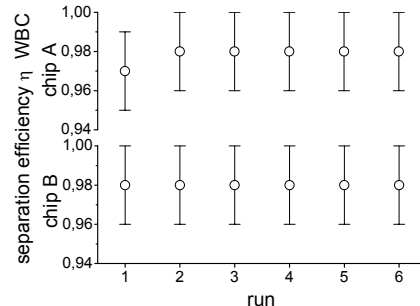


Fig. 4: Reproducibility of WBC separation efficiency.

Table 2: Properties of polyester filter membranes (Pall Hemasep [3]) in comparison to the micro channel bend structure with parallel plasma channels.

	plasma yield*	separation time	filter surface area
Pall Hemasep V	~ 15 %	10 sec	7.5 mm · 7.5 mm
microchannel bend	~ 15 %	4 sec	~ 5 mm · 5 mm

*Fraction of separated plasma volume compared to total blood sample volume of 40 µl.

5. Conclusion

The microchannel bend represents a competitive and reproducible separation technique. Contrary to filter membranes, the microchannel bend can be simply and monolithically integrated as filter device into lab-on-a-chip system.

Acknowledgement

This work was established within the project µTBC that was funded by the German Ministry For Education and Research (BMBF). Thanks apply to our project partners and Dr. W. Koester, University Hospital Freiburg, Department of Clinical Chemistry, for establishing and supporting the analyses of the blood specimens.

References

1. C. Blattert, R. Jurischka, I. Tahhan, A. Schoth, P. Kerth, W. Menz, Proc. of µTAS 2004, pp. 483-485
2. C. Blattert, R. Jurischka, I. Tahhan, A. Schoth, P. Kerth, H. Reinecke, Proc. of µTAS 2005, pp. 1352-1354
3. Pall Corporation - Life Sciences, Hemasep Filter Media. www.pall.com. 2005

HIGH PERFORMANCE ELECTROPHORETIC ANALYSIS ON CYCLOOLEFIN POLYMER MICROCHIPS

Fumihiko Kitagawa¹, Takafumi Suzuki², Jun Mizuno², Shuichi Shoji² and Koji Otsuka¹

¹*Department of Material Chemistry, Graduate School of Engineering, Kyoto University, Japan*

²*Department of Electrical Engineering and Bioscience, Waseda University, Japan*

(fkitagawa@mbox.kudpc.kyoto-u.ac.jp)

Abstract

This paper reports an application of cycloolefin polymer (ZEONEX) for affinity microchip electrophoresis (AMCE), and an improvement of the detectability for chiral analyses by using a thermal lens microscope (TLM) as a detection scheme and a sweeping technique based on a strong affinity between amino acids and proteins. In the chiral analysis of racemic tryptophan derivatized with a dye on the ZEONEX chip, the affinity sweeping by bovine serum albumin provided a 26-fold sensitivity enhancement compared to a conventional AMCE analysis.

Keywords: microchip electrophoresis, thermal lens microscope, sweeping, protein, chiral separation

1. Introduction

In the protein analysis by capillary electrophoresis (CE) and/or microchip electrophoresis (MCE), the adsorption of analytes onto the inner surface of the capillary or microchannel leads to analytical irreproducibility. To suppress the adsorption of proteins, several chemical modifications [1] for polymer microchips have been applied to MCE, but these techniques are inconvenient. Thus, the introductions of new polymer materials without any modifications are required in the MCE analysis for proteins. In our previous study, cycloolefin polymer (ZEONEX) which has been employed as a material for commercially available blood vials owing to its low adsorptivity was used as the base plate of the chip for the MCE analysis [2]. As a typical result, serum proteins were detected as a broader and weaker peak on conventional quartz chips due to serious adsorption, whereas on the ZEONEX chips a partial peak separation was obtained with ~200-fold increase in the peak height. Therefore, the result clearly demonstrated that the adsorption of proteins was suppressed on the ZEONEX surfaces.

In this study, by utilizing the low adsorptivity of proteins on the ZEONEX microchip, MCE chiral separation with a protein as a chiral selector (affinity MCE; AMCE) was investigated. It is well known that proteins have efficient chiral selectivities for a broader range of enantiomers because of highly controlled biological interactions, and various proteins have been used as chiral selectors in CE. However, proteins have been scarcely applied to AMCE since their surface adsorption interferes

the chiral analysis. Thus, the application of the ZEONEX chip is expected to achieve an effective chiral separation using protein as a chiral selector.

2. Experimental

A cycloolefin polymer (ZEONEX[®], ZEON Co.) microchip with a cross-type channel (width, 50 μm ; depth, 30 μm) was used for the chiral analysis of amino acid derivatives. A ZEONEX microchip was fabricated by O₂ plasma bonding of ZEONEX plate with the microchannel patterns. A sample solution was injected as a long plug into the separation channel by a gated injection technique. A thermal lens microscope (TLM, ITLM-11, Institute of Microchemical Technology) was employed for the detection of the nonfluorescent analytes.

3. Results and discussion

To achieve sensitive detection in AMCE on the ZEONEX chip, on-line sample preconcentration by affinity sweeping was developed. For affinity sweeping in AMCE, bovine serum albumin (BSA) was used as a chiral selector for tryptophan (Trp) derivatized with a dye for TLM detection. As shown in Figure 1, a Trp ($\text{pI} \sim 7$) solution dissolved in a neutral buffer was injected as a long plug into the separation channel filled with a basic buffer containing BSA ($\text{pI} \sim 4$). The zwitterionic Trp moves faster by the electroosmotic flow (EOF), while the negatively charged BSA slowly migrates toward the detection point. Owing to a higher affinity between Trp and BSA ($K_a = \sim 10^4$), the analytes in a long sample zone were swept by BSA to a narrow zone, so that the sharp peak is expected to be detected by the TLM.

Prior to the affinity sweeping experiments, it was confirmed that racemic Trp was successfully resolved by BSA under a conventional AMCE condition as shown in Figure 2a. This is the first demonstration for the chiral AMCE separation on the microchip. On the ZEONEX chip, the reproducible chiral analysis could be performed

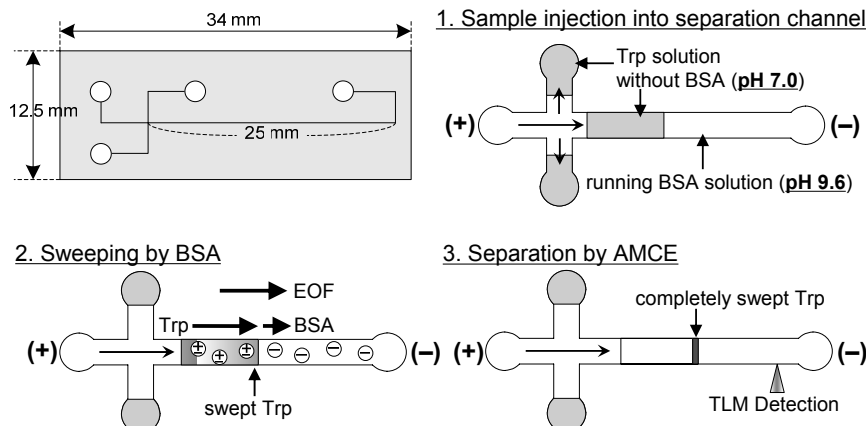


Figure 1. Schematic illustration of on-line sample preconcentration by affinity sweeping on the ZEONEX microchip.

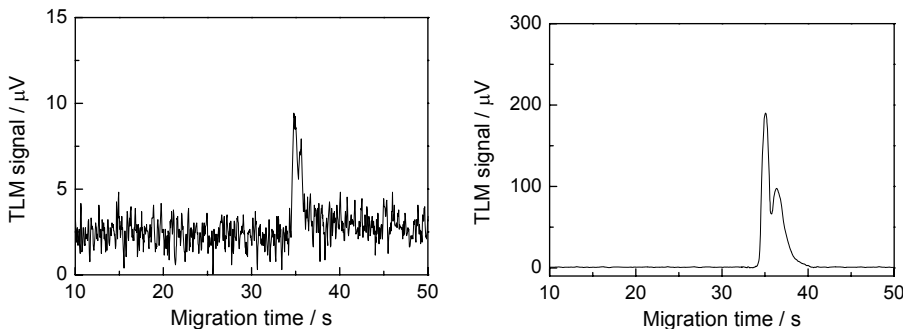


Figure 2. AMCE–TLM analysis of the derivatized Trp on the ZEONEX chip in (a) the presence and (b) the absence of BSA in the sample matrix. Background solution, 5.0 mg/mL BSA in 10 mM borate buffer (pH 9.6) containing 1.0 mM SDS; sample, (a) 1 μ M Trp in borate buffer (pH 9.6) containing BSA, (b) 1 μ M Trp in phosphate buffer (pH 7.0) without BSA; injection, (a) pinched injection, (b) gated injection for 3.0 s.

at least during ten consecutive runs despite containing BSA in the running buffer.

Figure 2b shows the AMCE–TLM analysis of the derivatized Trp on the ZEONEX microchip under the sweeping–AMCE condition. Due to the affinity sweeping effect, the 26-fold increase in detection sensitivity was achieved with resolution of 0.74. Thus, the combination of the affinity sweeping with MCE–TLM on the ZEONEX microchips provides the highly sensitive and high-speed chiral analyses.

4. Conclusion

Sensitive detection of amino acid enantiomers on the ZEONEX microchips was attained by the newly developed sweeping technique in the AMCE–TLM analysis. The affinity sweeping using BSA brought the 26-fold increase in the detection sensitivity and the acceptable chiral resolution for nonfluorescent Trp derivatives. Therefore, the affinity sweeping technique using protein chiral selectors on the ZEONEX microchips is expected to provide a high performance and highly sensitive MCE analyses for a broader range of enantiomers.

Acknowledgments

The authors thank Prof. T. Kitamori, Dr. A. Hibara (The University of Tokyo), Dr. M. Tokeshi (Nagoya University), and Mr. S. Hiki (Institute of Microchemical Technology) for their assistance in TLM measurements. This study is a part of joint researches, which are focusing on development of basis of technology for establishing COE of nano-medicine, carried out through Kyoto City Collaboration of Regional Entities for the Advancing Technology Excellence, JST.

References

- [1] J. Liu, T. Pan, A.T. Woolley, and M.L. Lee, *Analytical Chemistry*, **76**, 6948 (2004).
- [2] F. Kitagawa et al., *Proceedings of MicroTAS 2005*, pp. 331 (2005).

ONE-STEP IMMOBILIZATION OF CATIONIC POLYMER ONTO A POLY(METHYL METHACRYLATE) MICROCHIP FOR HIGH PERFORMANCE ELECTROPHORETIC ANALYSIS OF PROTEINS

Kei Kubota, Kenji Sueyoshi, Fumihiro Kitagawa and Koji Otsuka

Dept. of Material Chemistry, Graduate School of Engineering, Kyoto University,
Japan

Abstract

One-step covalent immobilization of poly(ethyleneimine) (PEI) onto poly(methyl methacrylate) (PMMA) substrates was investigated to achieve an efficient separation of basic proteins in microchip electrophoresis. The PEI treated PMMA chip showed a stable anodic electroosmotic flow and a reproducible migration of proteins compared with an untreated one. A baseline separation of two basic proteins was successfully achieved within 30 s only utilizing a separation length of 5 mm.

Keywords: microchip electrophoresis, protein analysis, surface modification, poly(methyl methacrylate)

1. Introduction

In microchip electrophoresis (MCE) analysis of proteins, sample adsorption onto the surface of a separation microchannel often reduces the separation efficiency and the analytical reproducibility. Dynamic coating of several polymers is known to be one of the useful approaches for suppressing the protein adsorption. However, desorption of coated polymers from the surface of the microchannel is sometimes problematic, so that the application of covalently immobilized polymer coating is required. As for glass microchips, covalent coating techniques based on silane chemistry have been applied, while for polymer chips such as poly(methyl methacrylate) (PMMA), only a few groups have reported the development of chemical modification procedures [1, 2]. Stable coatings were obtained by the covalent modifications, whereas these techniques require the use of organic solvents as reaction media and/or rinsing liquids, which would damage the PMMA surfaces. Therefore, a modification method with no organic solvents should be introduced to the PMMA microchip.

In this study, to obtain a stable coating with easy manipulations, the covalent immobilization of a cationic polymer with amino groups onto the surface of PMMA microchip by nucleophilic addition-elimination reaction [3] was investigated. High-molecular mass PEI which has a large number of amino groups and a positive net charge over a wide pH range was chosen as a surface modifier to suppress the adsorption of cationic proteins on the basis of a strong electrostatic repulsion force generated between PEI and analytes. The reaction between acylcarbon of PMMA and secondary amino groups in PEI dissolved in a basic aqueous solution is expected to proceed as shown in Fig. 1.

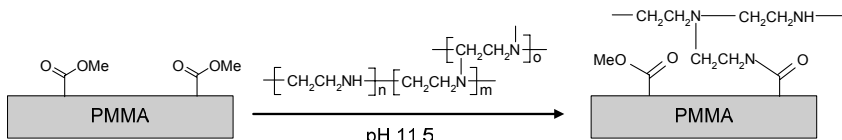


Fig. 1. Covalent immobilization of PEI onto the PMMA surface.

2. Experimental

A PMMA microchip has a simple cross-type channel ($100\text{ }\mu\text{m}$ width $\times 30\text{ }\mu\text{m}$ depth) with a total separation length of 38 mm. Immobilization of PEI onto the PMMA surface was performed as follows. The PMMA microchip was washed by soaking in methanol for 10 min, and rinsed thoroughly with deionized water. A solution of 10–20% (w/w) PEI in 100 mM borate buffer (pH 11.5) was pumped through the microchannel for 2 h using a syringe pump, followed by rinsing with deionized water for 20 min. The modified PMMA microchip was then dried at $30\text{ }^\circ\text{C}$ overnight. The background solution used throughout the experiments was 10 mM phosphate buffer (pH 4.0). Proteins were labeled with rhodamine B isothiocyanate (RBITC) for laser-induced fluorescence detection.

3. Result and discussion

To evaluate the immobilization of PEI, the electroosmotic flow (EOF) rate measurements on the prepared PMMA chips were performed. The EOF rate on the untreated PMMA chip was too small to detect an EOF marker since a net charge on the bare PMMA surface is nearly zero, leading to the weaker EOF. On the other hand, the PEI treated PMMA chip showed the anodic EOF and its mobility (μ_{eo}) was evaluated to be *ca.* $-1.3 \times 10^{-4}\text{ cm}^2/\text{V}\cdot\text{s}$. In addition, the endurance of the PEI modified PMMA chip was also investigated (Fig. 2). The day-to-day reproducibility of μ_{eo} was good with the relative standard deviation (RSD) of 5.2% ($n = 4$ within 32 days) in the dry storage condition at room temperature. This longer stability of the prepared microchip indicated that the loss of PEI was successfully suppressed by the immobilization through the covalent bond.

Prior to the MCE analysis, the adsorption of proteins on the PEI modified PMMA chip was evaluated. RBITC derivatized avidin (RBITC-AVI) was selected as a test analyte. In the adsorption test for RBITC-AVI, the following experimental procedure was performed. An RBITC-AVI solution was introduced to the microchannel. After 30 min, the microchannel was rinsed with deionized water for 2 h. By fluorescence

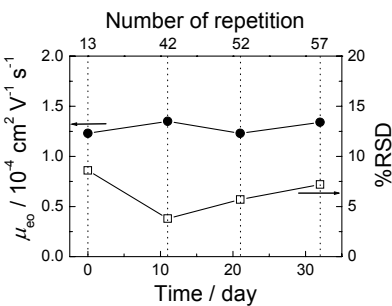


Fig. 2. Long-term stability of the PEI modified PMMA microchip. %RSD of μ_{eo} was calculated from five consecutive runs.

imaging measurements, it was confirmed that the PEI modification onto the PMMA chip could apparently reduce the surface adsorption of the cationic proteins.

In the MCE analysis on the PEI modified microchip, two proteins were successfully separated within 30 s only utilizing a separation length of 5 mm as shown in Fig. 3. While the migration time of the protein gradually increased during only four consecutive runs on an untreated PMMA chip, reproducible analyses were attained with the RSD of 0.9% by using the PEI immobilized microchip. These results demonstrated that the Coulombic repulsion force generated between cationic PEI and basic proteins could avoid the irreversible adsorption of the analytes onto the PMMA surface, which provided a high performance analysis medium for biogenic compounds.

4. Conclusion

One-step immobilization of cationic PEI was achieved onto the surface of PMMA substrates using nucleophilic addition-elimination reaction, which reduced irreversible adsorption of proteins. As a result, fast, efficient, and reproducible MCE analyses of cationic proteins were attained by using the PEI modified PMMA microchips.

Acknowledgments

The authors thank Mr. Kazuyoshi Kurihara (Hitachi Chemical) for supplying the PMMA microchip. This study is a part of joint researches, which are focusing on development of basis of technology for establishing COE of nano-medicine, carried out through Kyoto City Collaboration of Regional Entities for the Advancing Technology Excellence, JST.

References

- 1 A.C. Henry, T.J. Tutt, M. Galloway, Y.Y. Davidson, C.S. McWhorter, S.A. Soper, R.L. McCarley, *Surface modification of poly(methyl methacrylate) used in the fabrication of microanalytical devices*, Anal. Chem. 72 (2000) 5331–5337
- 2 J. Liu, T. Pan, A.T. Woolley, M.L. Lee, *Surface-modified poly(methyl methacrylate) capillary electrophoresis microchips for protein and peptide analysis*, Anal. Chem. 76 (2004) 6948–6955.
- 3 F. Fixe, M. Dufva, P. Telleman, C.B.V. Christensen, *Functionalization of poly(methyl methacrylate) (PMMA) as a substrate for DNA microarrays*, Nucleic Acids Res. e9 (2004) 32

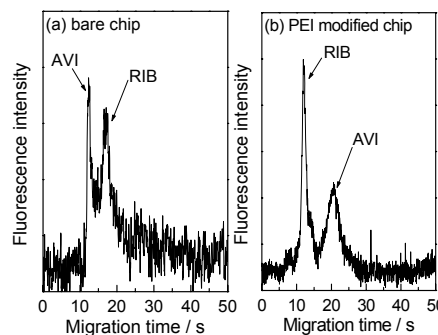


Fig. 3. MCE analysis of RBITC derivatized ribonuclease A (RIB) and AVI on the (a) bare and (b) PEI modified PMMA microchips.

A MICROLITER ELECTROKINETIC DEIONIZER FOR RAPID PROCESSING

Charlotte C. Kwong¹, Adam Huang², and Chih-Ming Ho¹

¹Department of Mechanical & Aerospace Engineering,
University of California, Los Angeles, CA 90095, USA

²Department of Mechanical Engineering,
University of Arkansas, Fayetteville, AR 72701, USA

Abstract

This paper reports a rapid deionizer with capability to reduce the conductivity of 20 μ l cell culture medium by 2 orders of magnitude in 15 minutes. To our best knowledge, this is the first deionizer in microliter scale addressing the low conductivity (<0.1mS/cm) prerequisite requirement for electrokinetic applications in rapid process.

Keywords: Deionizer, Ion Extraction, Electrokinetics, Dielectrophoresis, Cell Manipulation

1. Introduction

Electrokinetics techniques have been demonstrated to manipulate and separate particles in micron scale with great success. For instance, in lab-on-a-chip realization, Dielectrophoretic (DEP) technique is one of the potential candidates in the electrokinetics family to tackle separation tasks. The prerequisite for utilizing DEP approach is low medium conductivity [1] in the order of 0.1mS/cm. Biological medium unfortunately are highly conductive. Specifically, conductivity of bovine blood is ~8.0mS/cm, of human urine is ~10mS/cm, and of a popular cell culture medium, phosphate buffered saline (PBS), is ~14.5mS/cm.

Currently, high conductivity medium is inevitably replaced by mixture of culture medium and sugars to reach the DEP prerequisite low conductivity. This limits using DEP as a separation technique on integrated chip basis. By coupling our deionizer as a pre-stage in the module, this hinderer can be eradicated. To encounter for this challenge, we demonstrated a deionizer [2] by H filter [3] ion extraction principle earlier, the time taken was hours to reach the target conductivity. In contrast, our new deionizer only takes 15 minutes. We then can proceed to study the population distributions of various blood cells.

2. Experimental

A 3-chamber deionizer was developed by using dialysis membranes (Spectrum Laboratories, CA, USA) for sample isolation and carbon aerogel (Marketech Intl., WA, USA) as electrodes. 3 pieces of polycarbonate were machined into the left buffer chamber, center fluidic channel (Length: 20 x Height: 1 x Width: 2mm) piece and right buffer chamber. Carbon aerogel, dialysis membrane and silicone gaskets were sandwiched between each buffer chamber and the center fluidic piece. Electrical connection to the carbon electrodes was made through contact spring probes (Interconnect Devices, KS, USA) glued onto the buffer chamber pieces. Actual deionizer was shown in Figure 1a. Deionization was carried out through ion trapping

and electrolysis by applying voltage on two carbon aerogel electrodes as illustrated in Figure 1b. Carbon aerogel provided extremely high surface area as shown in SEM picture (Figure 2a & b). Each $2 \times 2 \text{ mm}^2$ electrode weighed 0.0415g used in the test, had an effective surface area of 16.61m^2 . On the other hand, dialysis membrane (MWCO 6k – 9k, Figure 2c & d) coupled in experimental setup could avoid cells of interest loss through diffusion into the side chambers.

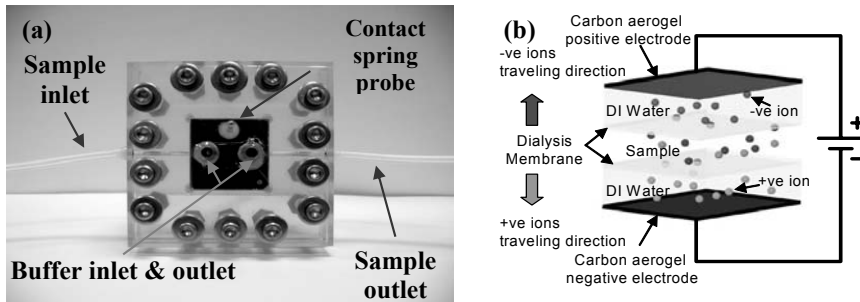


Figure 1. (a) Picture of the deionizer (b) Working principle of deionizer. Ions are attracted through the dialysis membrane towards the carbon aerogel electrode of opposite polarity where ion trapping and electrolysis occurs

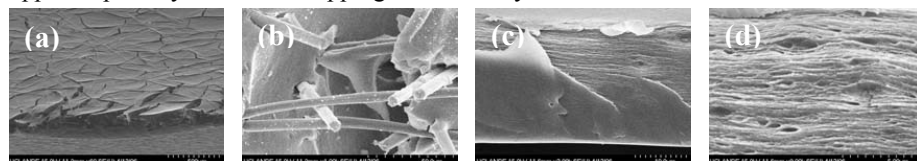


Figure 2. (a) SEM image of carbon aerogel electrode at 60X, showing their high area-to-volume ratio to trap ions effectively (b) SEM image of the same electrode at 1kX (c) SEM image of dialysis membrane (MWCO 6k – 9k) at 2.99kX (d) SEM images of the same membrane at 9kX, showing the overlapping layers

In this experiment, sample of 8.0mS/cm was formed by mixing PBS with deionized (DI) water. To make sure the dialysis membranes were wet before the experiment, the center fluidic channel was first flushed by $300\mu\text{l}$ DI water. Then $20\mu\text{l}$ sample was pumped into the center fluidic channel while the buffer chambers were filled up by DI water. To avoid generated gases accumulating on the carbon electrode, DI water was steadily pumped into each of the buffer chambers at $25\mu\text{l}/\text{min}$ by syringe pump during experiment. Contact spring probes were hooked up to DC power supply directly during experiment. Investigations were performed as a function of voltage (0 – 12V) at 20 minutes and function of time (0 – 20 minutes) respectively. Deionized samples were pumped out and collected at the end of experiments with the voltage on. All conductivity readings were measured by Horiba B-173 compact conductivity meter. The device was disassembled, thoroughly cleaned by DI water, two dialysis membranes were replaced and the device was reassembled after every measurement. Carbon aerogel electrodes also were replaced after high voltage runs.

3. Results and Discussion

Experimental results for final sample conductivity at 20 minutes as a function of voltage was plotted in Figure 3a. Conductivity dropped from initial conductivity, 8.0mS/cm to 1.05mS/cm after 20 minutes if 0V was applied. This reduction in conductivity was solely resulted from diffusion. On 12V, the conductivity was further reduced to 0.035mS/cm after 20 minutes. It is encouraging to note that at lower voltage, such as 8V, the 0.1mS/cm benchmark deionization task could also be accomplished from 8.0mS/cm to 0.098mS/cm in 20 minutes. Figure 3b shows the conductivity as a function of time for various voltages. The conductivity on 12V after 15 minutes was 0.042mS/cm. Once again, this could already fulfill the DEP prerequisite (<0.1mS/cm).

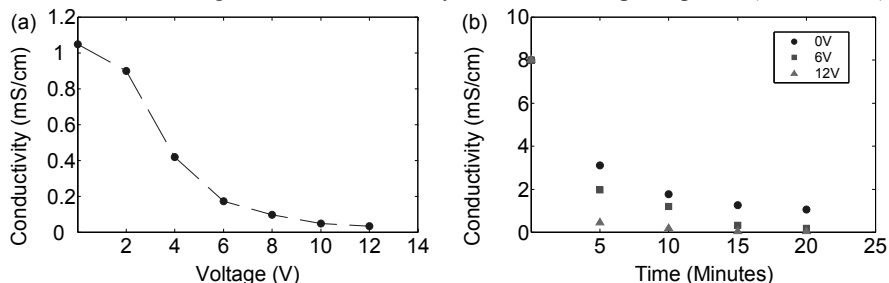


Figure 3 (a) Deionization results in 20 minutes as a function of voltage (b) Deionization results as a function of time for 0V, 6V and 12V

In this study, we observed a few critical operating conditions for this deionizer. First, the carbon aerogel electrode surfaces had to be wet at all times in order for the deionizer to work properly. Second, with no replacement of carbon aerogel electrodes after operating at high voltages, such as 12V, this deionizer would perform in a similar manner as if it was under 0V during the next run. We believed this was caused by the oxidation of the carbon aerogel electrode, not only preventing electrolysis to occur but also attenuating the established electric field. Another challenge we noted was the gold plated contact spring probes were corroded after prolonged usage. One possible solution is using platinum plated probes which can resist the attack of formed chlorine.

4. Conclusion

We successfully demonstrated a capable micro-deionizer to reduce medium conductivity by 2 orders of magnitudes in 15 minutes, which frees up one of the bottlenecks to utilize DEP techniques in chip integration.

Acknowledgements

This work is supported by NASA through NSBRI and partially supported by NIH, with co-operative agreement numbers NCC 9-58-317 and EB-00127 respectively.

References

1. X.-B. Wang *et. al.*, *Anal. Chem.*, 72 (4), pp. 832 – 839 (2000).
2. C. C. Kwong, N. Li, and C.-M. Ho, *Proc. SPIE*, Vol. 6003, 60030N (2005).
3. J. P. Brody, and P. Yager, *Sensor Actuator A – Phys*, 58, pp .13 – 16 (1997).

FLOW RATE INDEPENDENT PARTICLE FOCUSING AND SEPARATION BY CHAOTIC ADVECTION

Sungyoung Choi and Je-Kyun Park

Department of BioSystems, Korea Advanced Institute of Science and Technology (KAIST), KOREA

Abstract

We propose a new focusing and separation principle utilizing chaotic advection that there is no necessity for accurate control of flow rates and for the aid of sheath flow. In this principle, the slanted obstacle is used as a source to generate a secondary transverse flow, which enables to continuously focus and separate particles according to their sizes. This paper deals with chaotic focusing and separation results of microbeads.

Keywords: particle separation, chaotic advection, microfluidics

1. Introduction

Separation of heterogeneous particles holds an important part in biological analysis. To serve this need in microchips, various microfluidic separation principles have been introduced, using asymmetric bifurcation of fluid streams [1] and size-dependent particle alignment to a sidewall [2]. In the former two cases, sample fluids containing particles have to be injected into a microchip simultaneously with the sheath flow to confine the particles within a certain position of a fluid stream. This technology has a drawback that it requires accurate control of flow rates. Additionally, pressure perturbation can lead to the failure of separation. In spite of the successful development of microfluidic devices, microfluidics still has a challenge for the effective separation of microscopic particles.

2. Theory

The focusing and separation principle are shown in Figure 1 and 2. Slanted obstacles generate a lateral pressure gradient, which drive transverse flows shown in Figure 1b:

$$\eta \nabla^2 V - \nabla p = 0 \quad (1)$$

where η is the viscosity of the liquid, V is the velocity, and p is the pressure. At this moment, particles suspended in the fluid are deflected by the transverse flows along y-axis (Figure 1a). When they are focused to the one side of the wall, particle separation begins. Separation is achieved by the hydrodynamic interaction between particles and the obstacles. Particles which have comparable sizes with the obstacles are confined within the center of z-axis. In that region, transverse pressure gradient is not built (Figure 1b), which makes the particles keep their focused position (Figure 2a). We call this motion the “direct mode.” On the other hand, smaller particles which are relatively free from the confinement within the center of z-axis can oscillate following clockwise and counter-clockwise rotating flow (Figure 2, b and c). We call this motion the “oscillating mode.” This oscillation makes them deviate from their focused position.

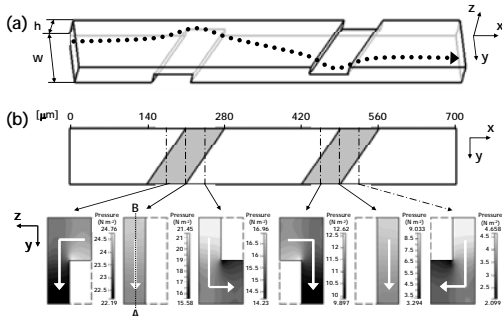


Figure 1. (a) Three-dimensional microchannel geometry with slanted obstacles. It is 50 micron high by 100 micron wide. (b) Top view of the channel geometry. The vertical cross sections show simulated pressure distributions along the channel.

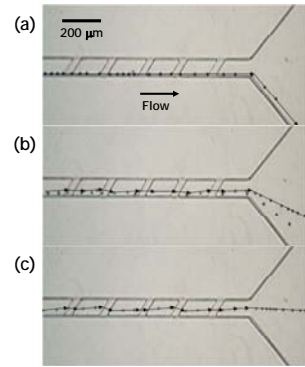


Figure 2. Particles passing the obstacles; (a) direct, (b) low-oscillating, and (c) high-oscillating mode.

3. Experimental

To demonstrate this principle, we microfabricated slanted obstacles with poly(dimethylsiloxane) (PDMS), which is the half of the channel in height. Patterns of upper and lower obstacles were formed on silicone wafer with SU-8 photoresist. Molded PDMS layers with upper and lower obstacles put with each other and bonded after oxygen plasma treatment. As a result, the slanted obstacles alternatively placed on the top and bottom wall of a channel (Figure 1a).

4. Results and discussion

As a model particle, polystyrene microbeads with diameters of 12, 15 and 20 μm were prepared in 0.2% Tween® 20 aqueous buffer. The positions of particles were individually measured in the expanded outlet region of 1 mm. Figure 3 shows the transition from direct to oscillating mode according to the decrease of particle diameter. The 20 μm particles which have the nearly same size as the obstacles took the direct mode. In contrast, the 12 and 15 μm particles oscillated with different magnitude. Smaller particles have higher oscillation magnitude (Figure 3). In addition to that, separation mode is not affected by the change of flow rate because of the increase of pressure gradient according to the increase of the flow rate (Figure 4). In this device, the 12 and 15 μm particles were separated within the range of 405.9 ± 112.8 and 186.7 ± 56 μm , respectively (Figure 5 and 6).

5. Conclusions

In this study, we have developed a new hydrodynamic separation principle utilizing chaotic advection. Since this device does not depend on the accurate control of flow

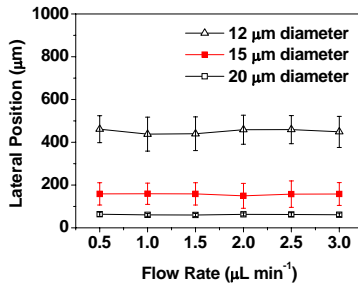


Figure 3. Measured particle positions as a function of flow rate and microparticle diameter.

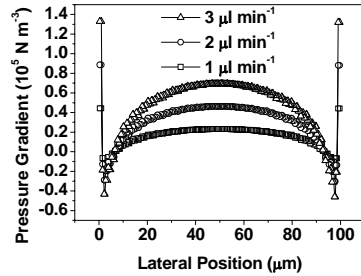


Figure 4. Plot of calculated pressure gradients along the line from A to B in Fig. 1b.

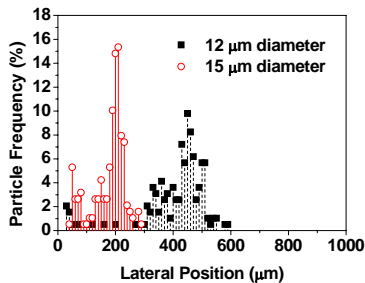


Figure 5. Continuous separation of microparticles with diameters of 12 and 15 μm at a flow rate of $1 \mu\text{L min}^{-1}$.

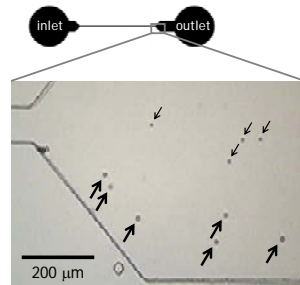


Figure 6. Separated microparticles. Small and large arrows indicate 12 and 15 μm particles, respectively.

rates and the aid of sheath flow, we believe that it can be easily applied to the purification of biological samples in portable microchips.

Acknowledgements

This work was supported by CHUNG Moon Soul Center for BioInformation and BioElectronics Center, KAIST. The microfabrication work was performed at the Digital Nanolocomotion Center.

References

1. L. R. Huang, E. C. Cox, R. H. Austin, J. C. Sturm, Science, Vol. 304, pp. 987-990 (2004).
2. M. Yamada, M. Nakashima, M. Seki, Anal. Chem., Vol. 76, pp. 5464-5471 (2004).

APPLICATION OF PARTIAL FILLING TECHNIQUE AND SWEEPING TO ELECTROPHORETIC ANALYSIS ON T-CROSS AND 5 WAY-CROSS MICROCHIPS

Kenji Sueyoshi¹, Hidenori Nagai², Shin-ichi Wakida², Junji Nishii²,
Fumihiko Kitagawa¹ and Koji Otsuka¹

¹The University of Kyoto, Nishikyo-ku, Kyoto 615-8510 Japan,

²National Institute of Advanced Industrial Science and Technology, AIST,
Midorigaoka, Ikeda, Osaka 563-8577, Japan

Abstract

This paper describes the study on the application of the partial filling technique to microchip micellar electrokinetic chromatography (PF-MCMEKC) by using a T- and 5 way-cross microchips which can successively introduce the pseudostationary phase and sample solutions. As a typical result, two fluorescent dyes which could not be separated by microchip zone electrophoresis were successfully resolved by PF-MCMEKC. Furthermore, the enhanced sensitivity was attained compared with that in conventional MCMEKC.

Keywords: partial filling technique, sweeping, microchip micellar electrokinetic chromatography

1. Introduction

In microchip electrophoresis (MCE), mass spectrometric (MS) detection is desired for a rapid identification of separated analytes. However, an insufficient separation ability is sometimes problematic in MCE-MS since a background solution (BGS) is limited to be volatile, and hence, various effective separation modes such as micellar electrokinetic chromatography (MEKC) can not be applied. To overcome this problem, the application of the partial filling (PF) technique [1] to the MCE analysis is required. Although Nelson *et al.* [2] reported the successful application of PF-MEKC to MS detection, such investigations have not been performed in MCE since a conventional cross-chip can inject only one solution despite the requirement of the successive injection of the pseudostationary phase (PSP) and sample (S). In this study, we applied

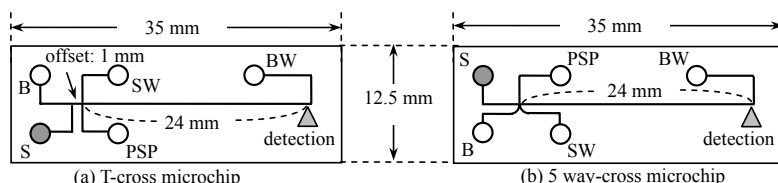


Figure 1. Schematic illustration of the (a) T-cross and (b) 5 way-cross microchips.
B, background solution; BW, running buffer waste; S, sample solution; PSP, pseudostationary phase solution; SW, sample solution waste reservoirs.

the PF technique to MCMEKC by using a T- or 5 way-cross channel microchips to improve resolution and the concentration sensitivity of the MCE analysis.

2. Theory

In the PF technique, the PSP solution is partially filled in front of the S plug, and S overtakes the PSP zone (Fig. 2a and 2b). The S can be separated during the migration in the PSP plug. After passing through the PSP plug, the separated S plugs are detected without any interference of the PSP (Figure 2c).

3. Experimental

Quartz microchips with a T-cross or 5 way-cross channel were fabricated by a photolithographic technique. The S and PSP solutions were injected by a gated injection method and the injection time of the S was controlled by the applied voltages. Electropherograms were obtained with a laser-induced fluorescence (LIF) detection scheme. Rhodamine derivatives (sulforhodamine B, SRB; sulforhodamine 101, SR101) were selected as the test analytes.

4. Results and discussion

On the T-cross chip, the PSP solution could be injected as a long plug by the gated injection technique and the S loaded in the offset channel could be introduced into the separation channel. To evaluate the analytical performance of the PF-MCMEKC, the mixture of rhodamine derivatives and sodium dodecyl sulfate (SDS) was selected as S and PSP, respectively. In PF-MCMEKC, two rhodamine derivatives, which were detected as one peak in microchip zone electrophoresis (MCZE) as shown in Fig. 3a, were well separated by the injection of the SDS plug (Fig. 3b). In addition, fluorescence imaging measurements revealed that the S zone became to the narrow band immediately after the injection of the S due to the sweeping effect which is caused by the incorporation of the sample molecules into the SDS micelles. During the migration in the SDS plug, the swept S zone was separated by the separation principle of MEKC. Finally, the S

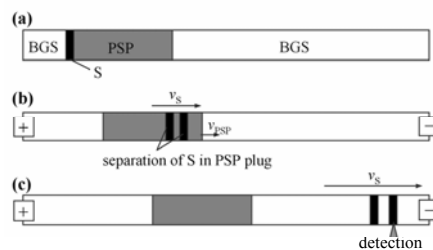


Figure 2. Schematic of the PF technique. (a) Injection of the S and PSP plugs, (b) separation of the S in PSP plug, and (c) detection of S without any interference from PSP.

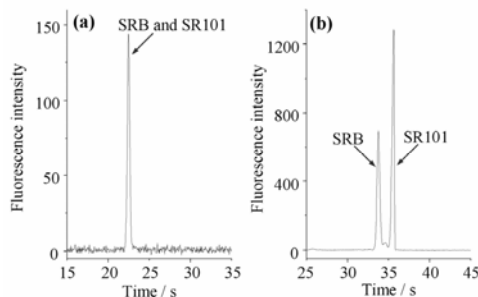


Figure 3. Electropherograms obtained by (a) MCZE with a conventional pinched injection and (b) PF-MCMEKC by using T-cross chip.

plug passing through the SDS plug was broadened, and it reached at the detection point. Thus, it was confirmed that PF-MCMEKC was successfully achieved by using the T-cross chip. As the injection time of the SDS solution increased from 0.5 to 3.0 s, resolution increased from 1.30 to 1.73 since the longer SDS plug would provide the larger phase ratio. Furthermore, *ca.* 10-fold improvement of the detectability was also attained by the sweeping.

To achieve further high sensitivity in PF-MCMEKC, the 5 way-cross chip was newly designed and fabricated, which enables to inject a larger volume of S. As a result, the peak height increased with increasing the injection time of S due to the sweeping effect (Fig. 4). At the injection time of 6.0 s, the 66-fold enhancement of the detectability of SR101 was achieved in comparison with conventional MCMEKC using the pinched injection technique (Figs. 4a and 4d). Additionally, the concentration efficiency was higher than that on the T-cross chip even under the same volume condition. This further enhancement of the efficiency observed on the 5 way-cross chip might be due to a specific field amplified effect during the S injection step.

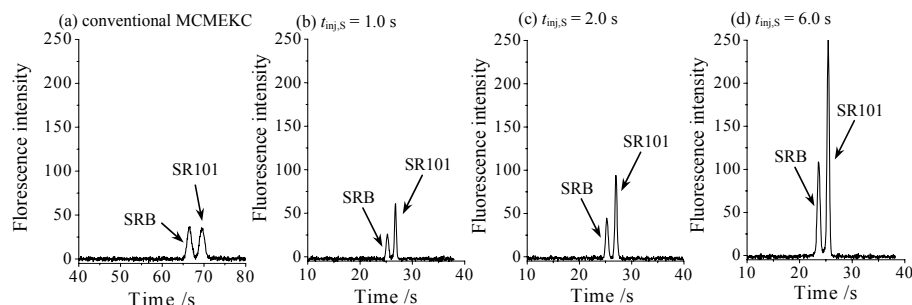


Figure 4. Electropherograms obtained by (a) conventional MCMEKC and (b)-(d) PF-MCMEKC by using 5 way-cross chip. S, (a) 1 μ M SRB and SR101; (b)-(d) 100 nM SRB and SR101; t_{inj} , injection time of S.

5. Conclusion

By using the T-cross and 5 way-cross form channel chip, the PF technique was successfully applied to MCMEKC. On the 5 way-cross microchip, the baseline separation of the rhodamine derivatives was attained with the 66-fold increase in the concentration sensitivity. The successful PF-MCMEKC is promising a high performance MCE-MS analysis.

References

- Y. Tanaka, S. Terabe, *Partial separation zone technique for the separation of enantiomers by affinity electrokinetic chromatography with proteins as chiral pseudo-stationary phases*, J. Chromatogr. A, Elsevier, 694, pp. 277-284, (1995)
- W. M. Nelson, Q. Tang, A. K. Harrata, C. S. Lee, *On-line partial filling micellar electrokinetic chromatography-electrospray ionization mass spectrometry*, J. Chromatogr. A, Elsevier, 749, pp. 219-226, (1996)

tmRNA PURIFICATION BY ELECTROPHORETIC FILTRATION FOR GENOMIC IDENTIFICATION OF BACTERIA ON-A-CHIP

Paul Vulto, Christoph Klaunick, Günter Igel, Gerald Urban

Laboratory for Sensors, Department of Microsystems Engineering (IMTEK),
Albert-Ludwigs-Universität Freiburg, Germany

Abstract

A microchip is presented that enables the purification of small RNA molecules by electrophoretic filtration. The chip consists of two embedded reservoirs with integrated electrodes connected by a gel separation channel. Purification efficiencies are analysed by real-time PCR.

Keywords: tmRNA, nucleic acid purification, electrophoretic filtration, phasguides, real-time PCR

1. Introduction

TmRNA is a bacterial RNA that has both messenger and transfer functions. It consists of relatively few nucleotides (< 400) and has been identified in all sequenced bacterial species [1]. Since tmRNA is a naturally amplified molecule (~1000 copies per cell for e.g. E.Coli), it is an interesting target for genetic identification. It is our goal to realize an automated, PCR-free (Polymerase Chain Reaction) microsystem for identification of bacteria based on their tmRNA sequence. The system will ultimately include full sample pre-treatment and an affinity-sensing platform. In this paper a device is presented that enables purification of tmRNA by electrophoretic filtration.

2. Principle

Electrophoretic filtration is similar to conventional chip electrophoresis. A sample is migrating electrically through a channel and a separation matrix (in this case an agarose gel) can be chosen such that small molecules travel faster than larger molecules. The small molecules are eluted from the gel in a purified form.

3. Microfabrication

Platinum electrodes are patterned on top of a Pyrex glass wafer. Microfluidic elements are patterned in a dry film resist (Ordyl SY330). A second Pyrex wafer containing drilled holes is then bonded to the bottom wafer. Connection pads are diced free by dicing the bonded chip half through. Gel is applied in the separation channel by pipette pressure, before starting an experiment.

Figure 2 shows the tmRNA purification chip. It contains input and output reservoir chambers that are connected through a channel, which is filled with gel. The reservoir

chambers contain integrated electrodes for electrophoretic actuation and phaseguides for a controlled liquid introduction and recovery [2].

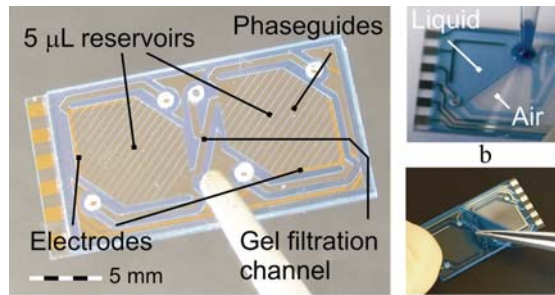


Figure 1. a) Electrophoretic filtration chip with two reservoirs of 5 μ L, a 6 mm gel separation channel and integrated platinum electrodes.

b) Phaseguides enable a controlled liquid introduction and recovery.

c) The chip has been fabricated and sealed under RNase-free conditions

4. Purification experiments

The chip is tested for a mixture of RNA and DNA and a phenolic extract of complete cells. The samples are purified through a 4% w/v NuSieve agarose gel under a constant current of 15 μ A. Since tmRNA is much smaller than its DNA, the ratio of RNA to DNA is considered a good indicator for purification efficiency. The relative quantity of RNA and DNA is determined using real-time PCR. A one-step reverse transcriptase PCR (RT PCR) is performed to determine the RNA and DNA quantity, while a non-RT PCR gives only information about the DNA quantity. A dilution series of a plasmid containing the tmRNA sequence is used for relative quantification. The RNA/DNA ratio is determined using the following formula:

$$\frac{|C_{RNA}|}{|C_{DNA}|} = \frac{E_{RT}^{(\Delta Ct(\text{plasmid}-RT_Sample))}}{E_{non-RT}^{(\Delta Ct(\text{plasmid}-non-RT_sample))}} - 1 \quad (1)$$

Where $|C_{RNA}|$ and $|C_{DNA}|$ stand for the plasmid-normalised concentrations of RNA and DNA. E_{RT} and E_{non-RT} stand for the efficiencies of the reverse transcribed and the non-reverse-transcribed reactions. The Ct value is the threshold cycle number, where the increase of fluorescence level is first detected.

5. Results

Figure 2 shows the electrophoretic migration of Xylene Cyanol through the gel path. Xylene Cyanol migrates through a 4% agarose gel with a velocity similar to a 150-basepair DNA element. Since Xylene Cyanol starts eluting from the gel after 2 minutes, it is expected that a 400 nucleotides RNA element needs at least 4 minutes to travel through the gel.

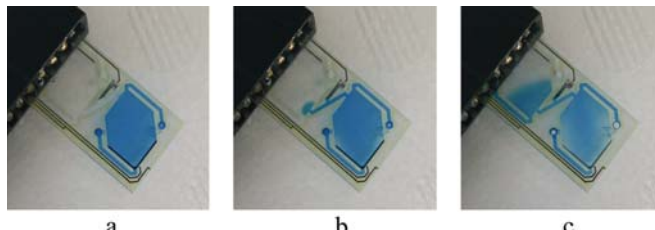


Figure 2. Electrophoretic migration of Xylene Cyanol through a 4% agarose gel.

a) Time = 0 min. b) Time = 2 min. c) Time = 11 min.

Table 1 shows the RNA/DNA ratio of the purified product. This ratio divided by the RNA/DNA ratio of the original sample gives us the purification factor. In reality the amount of purified RNA is higher then presented by the PCR results, since the reference plasmid does not account for inefficiencies in the reverse transcription process.

Table 1. Threshold cycle numbers and purification factors after relative quantification

Elution time (min.)	Ct-value RT PCR	Ct-value non-RT	RNA/DNA ratio	Purification factor
5	25	31	12	20
7	26	35	21	53
8	22	35	195	333
10	21	28	16	28
10 (Phenolic extract)	20	29	38	135

6. Conclusion

Purification from tmRNA by electrophoretic filtration on a microchip has been demonstrated. TmRNA has been effectively purified from a DNA/RNA mixture. In future work, more complex samples will be studied and the separation performance of various gels will be tested.

Acknowledgements

The authors would like to thank Dr. Barry Glynn for the provision of plasmids and assistance in biological analysis.

References

- [1] W. Schönhuber, G. Le Bourhis, J. Tremblay, R. Amann, S. Kulakauskas, Utilization of tmRNA sequences for bacterial identification, *BMC Microbiology*, pp. 1-20, (2001).
- [2] P. Vulto, G. Medoro, et al., Selective sample recovery of DEP-separated cells and particles by phaseguide-controlled laminar flow, *J. Micromech. Microeng.* 16, pp.1847-1853, (2006).

SU-8 MICROCHIPS FOR BIOMOLECULE ANALYSIS USING FREE ZONE ELECTROPHORESIS

T. Sikanen^{1,2}, L. Heikkilä², S. Tuomikoski³, R.A. Ketola², R. Kostiainen², S. Franssila³ and T. Kotiaho¹

¹Lab. Analytical Chemistry, Dept. Chemistry, University of Helsinki, Finland

²Div. Pharm. Chemistry, Faculty of Pharmacy, University of Helsinki, Finland

³Microelectronics Centre, Helsinki University of Technology, Finland

⁴DDTC, Faculty of Pharmacy, University of Helsinki, FINLAND

Abstract

This paper demonstrates the applicability of SU-8 microdevices for biomolecule analysis using free zone electrophoresis. Autofluorescence properties of SU-8 and its effect on the detection sensitivity through SU-8 microstructures are also evaluated.

Keywords: SU-8, electroosmotic flow, electrophoresis, autofluorescence

1. Introduction

Due to simple and low cost fabrication, polymer materials have replaced glass structures in many microfluidic applications. However, each polymer possesses its unique characteristics, e.g., surface chemistry and optical properties, which strongly affect the fluidic behaviour in polymer microchannels and define the applications and detection methods in which the specific polymer is best exploited. We have earlier demonstrated that SU-8 polymer maintains fairly dense surface charge, equal to glass surfaces, and is therefore advantageous for applications requiring high electroosmotic flow (EOF) [1]. In this study, we have evaluated the applicability of SU-8 for biomolecule analysis using free zone electrophoresis combined with fluorescence detection.

2. Experimental

We explored the compatibility of SU-8 with a number of buffer solutions commonly used in bioanalytical separations (Figure 1a). The electroosmotic (EO) mobilities for different buffer solutions were measured both in SU-8 and in glass microchannels by the current monitoring method. The separation conditions were optimized for fluorescent labelled amino acid, peptide and protein samples in terms of the separation voltage and buffer composition. Sensitivity of fluorescence detection through SU-8 microdevices was evaluated by filling the microchannels sequentially with dye solutions of increasing fluorochrome concentration. Signal-to-noise (S/N) ratios were measured for selected fluorochromes at three different fluorescence excitation/emission wavelengths through SU-8 and Borofloat™ glass microchannels of equal dimensions. The signal was collected with fixed illumination and amplifier settings for all concentrations and both materials, and S/N ratios calculated relative to the signal intensity at zero concentration.

3. Results and discussion

EO mobilities measured for SU-8 were equal to the mobilities in glass microchannels except for the buffers of pH≤4 (Figure 1a). These results are in line with our previ-

ous observation that SU-8 has strongly pH dependent EOF which reverses from cathodic to anodic at pH 3-4 [1]. Moreover, CAPS buffer (N-cyclohexyl-3-aminopropane-sulfonate) seemed to have interactions with SU-8 that did not occur with glass, resulting in significantly lower EOF in SU-8 than in glass microchannels (Figure 1a).

The high observed EOF was employed in biomolecule analysis using free zone electrophoresis. SU-8 microchannels showed good separation performance with migration time repeatability and plate numbers on the order of 2-3 % and 7,300-31,000 / 4.5 cm, respectively, under separation conditions optimized for amino acid and peptide samples. In Figure 1b a separation of six fluorescent labelled L-amino acids is illustrated. Currently, optimization of the separation conditions for protein analysis is underway. Protein separation by zone electrophoresis is often compromised due to multistep surface coating which is required to reduce non-specific adsorption. Our results suggest that SU-8 potentially provides good separation efficiency also for protein analysis due to its high EOF, yet clearly hydrophobic nature (contact angle >75° for aqueous solutions), which effectively eliminate protein adsorption.

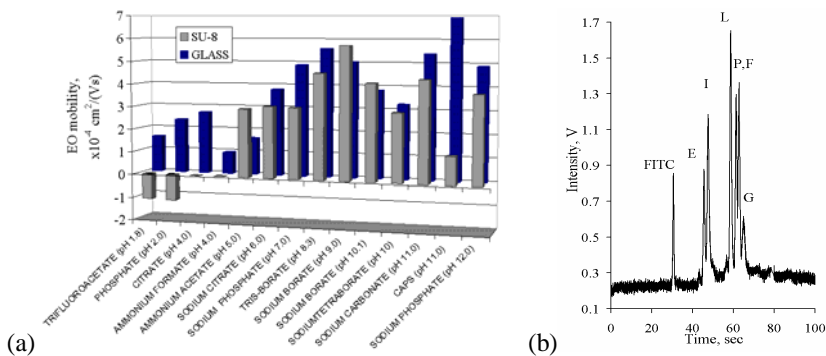


Figure 1. (a) Measured EOF mobilities for selected buffer solutions at 20 mM concentration and given pH in SU-8 (gray) and glass microchannels (black). (b) Separation of six L-amino acids (60 μM each, marked by their one letter abbreviations) in 20 mM sodium borate (pH 10.1); separation voltage +4.4 kV (800 V/cm); separation length 4.5 cm; microchannel dimensions 30 μm \times 22 μm \times 55 mm (w \times h \times L); L-amino acids labelled with a 3-fold excess of fluorescein isothiocyanate (FITC) in 40 mM NaHCO₃/acetone (1:1).

Since biomolecules are commonly detected as their fluorescent derivatives, we also evaluated the applicability of fluorescence detection in SU-8 microdevices. Many polymers absorb light at low UV/Vis wavelengths giving rise to autofluorescence [2], which results in reduced excitation efficiency and less sensitive detection of fluorescent analytes through polymer microchannels. According to UV/Vis spectra, SU-8 is known to be transparent at wavelengths above 390 nm. Nevertheless, we observed considerable background due to SU-8 autofluorescence even at wavelengths between 400-500 nm, and distinct differences in S/N ratios were measured through SU-8 and glass microchannels (Figures 2a-b). However, at wavelengths above 500 nm, that are typical for

rhodamine B based derivatives, equally sensitive detection (S/N ratios) was obtained through both materials (Figure 2c).

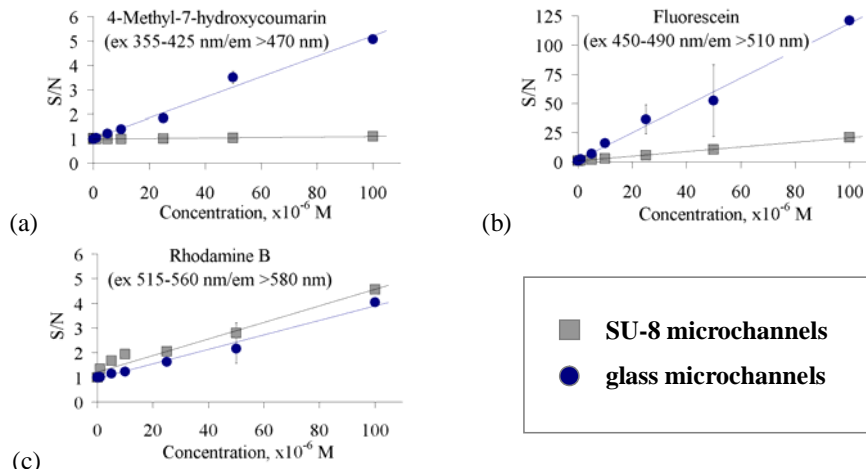


Figure 2. S/N ratios measured through SU-8 (gray squares) and Borofloat™ glass microchannels (black circles) at three different fluorescence excitation/emission wavelengths (filtered) with their specific fluorochromes: (a) 4-methyl-7-hydroxycoumarin, (b) fluorescein and (c) rhodamine B. (Note that the differences in S/N ratios between the three different fluorochromes are due to differences in their relative quantum yields.)

4. Conclusions

Microchannels fabricated of SU-8 polymer were shown to be compatible with and maintain high EOF in a wide range of buffer solutions. This enabled efficient biomolecule separations in SU-8 microchannels using free zone electrophoresis. Although limited sensitivity with fluorescence detection was observed due to SU-8 autofluorescence, such problems can be avoided by careful fluorochrome selection. In addition, SU-8 fabrication technology provides means to overcome sensitivity problems related to optical detection. For instance, an electrospray ionization interface can be integrated with the separation channel to enable mass spectrometric detection [3].

Acknowledgements

This work was financially supported by Academy of Finland (projects no. 51615 and 211019), University of Helsinki Research Funds and Finnish Cultural Foundation.

References

1. Sikanen, T., et al., Lab Chip 2005, 5(8), 888-896.
2. Piruska, A., et al., Lab Chip 2005, 5(12), 1348-1354.
3. Tuomikoski, S., et al., Electrophoresis 2005, 26, 4691-4670.

FAST SEPARATION OF λ - AND T2-DNA WITH ELECTRODELESS DIELECTROPHORESIS

J. Regtmeier, T.T. Duong, A. Ros*, D. Anselmetti

Bielefeld University, Experimental Biophysics, Germany

*Alexandra.Ros@physik.uni-bielefeld.de

ABSTRACT

The fast separation of long DNA via electrodeless dielectrophoresis in a simple and easy-to-fabricate microfluidic device is presented. An AC voltage is applied to an array of periodically arranged posts creating dielectrophoretic traps. Size-dependent migration velocities are obtained by applying an additional DC voltage, which drives the DNA through the structured microchannel. With this technique we are able to achieve fast and efficient separations of λ - and T2-DNA. The mechanism is analysed in terms of a Kramer's rate and a notable change in the diffusion coefficient of λ -DNA is observed.

Keywords: DNA, separation, dielectrophoresis, microfluidics

1. Introduction

The fast and reliable separation of large DNA molecules is still a demanding problem in separation science. The established method of slab gel electrophoresis with pulsed electric fields is very time consuming (10h up to 200h). Capillary electrophoresis with diluted gels represents a fast alternative, however with similar drawbacks in size limitation.

Harnessing the exerted forces of nonuniform AC electric fields onto polarizable objects is well established. By extending this method using a targeted combination of microstructures and electric fields, novel techniques for the separation of biomolecules can be developed. The ion cloud around DNA in aqueous solution renders it polarizable, thus a dipole can be induced enabling the interaction with inhomogeneous electric fields. Although the mechanism of DNA polarization is not yet understood in detail [1], it was experimentally demonstrated that DNA exhibits positive dielectrophoresis. The necessary nonuniform electric field can be designed with non-conducting posts and the DNA is trapped at the locations of the highest field gradient in between two posts known as electrodeless dielectrophoresis of DNA [2]. Ajdari and Prost made in 1991 a theoretical proposal to exploit dielectrophoresis for DNA separation [3]. In this paper, we extend these previous studies and present the first separation of λ - and T2-DNA in a microfluidic chip via electrodeless dielectrophoresis.

2. Methods

The monolithic separation chip is made of poly(dimethylsiloxane) (PDMS) based on soft lithography. Briefly, contact lithography of SU-8 on a Si-wafer is followed by casting PDMS from the SU-8 masterwafer. The cured and structured PDMS is peeled

off and, after an oxygen plasma treatment, it is covered with a glass slide which was previously spincoated with PDMS. Fig. 1 shows an electron micrograph of the injector (1) and the first two rows of the array of posts, which extends over 3.8mm in the separation channel (4). The channels are 95 μ m wide, the posts are 7.4 by 2.2 μ m with a spacing of 2.3 μ m and a row distance of 21.1 μ m. The DNA is dissolved in 10mM phosphate buffer containing 2mM NaCl, 1mM EDTA, 0.1% (v/v) POP-6, 2 μ l/ml β -mercaptoethanol and YOYO-1 for fluorescent staining and is injected via a cross injector. For the separation of λ -DNA (17.5pM) and T2-DNA (6pM), a sample plug is driven through the separation channel by a DC voltage (U_{DC}) of 12V applied between the electrodes in the reservoirs (3) and (4) with a distance of 7mm. An AC voltage (U_{AC}) of 60Hz, also applied at the electrodes (3) and (4), is increased incrementally from 150V to 189V, with steps of 0.6V every 3 seconds. When the final value is reached, the DC voltage is switched off, and a steady state electropherogram is recorded by scanning the fluorescence signal of the separated and trapped DNA zones in the structured channel.

Video sequences at 10 fps with single observable λ -DNA molecules are recorded for varying AC voltages at 60Hz with $U_{DC} = 12V$ and analysed in terms of trapping and migration times.

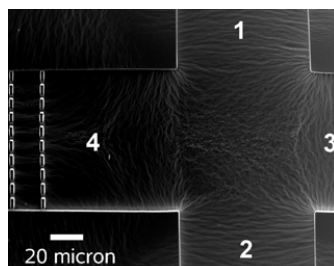


Figure 1. SEM image of a section of the microfluidic chip.

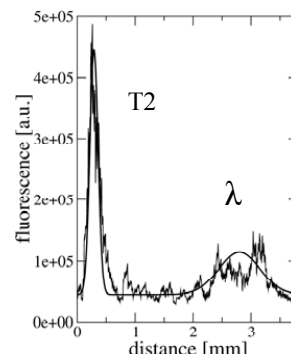


Figure 2. Electropherogram of λ - and T2-DNA with gaussian fits as a guide to the eye [4].

3. Results and Discussion

The successful separation of λ (48.5kbp)- and T2(164kbp)-DNA is shown in fig. 2 [4], with a separation time of only 200s. The T2-DNA is trapped at the beginning of the separation channel, whereas the λ -DNA molecules are only captured at a distance of 2.8mm from the injector. The sample is separated with baseline resolution.

The mechanism of the separation can be elucidated by comparing the Kramer's rate, i.e. the inverse time required to escape from a trap and to migrate to the next. Figure 3 shows the Kramer's rate of the two sorts of DNA versus U_{AC} . Above amplitudes of 125V the rates for the two DNA species differ significantly, clearly justifying the applied U_{AC} values in the separation experiment. One can conclude that the separation is

based on the faster escape of λ -DNA out of the trap. This can be due to different polarizabilities and to different diffusion coefficients of the two DNA species [3]. In order to investigate the unusual broadening of the λ -DNA peak in fig. 2, we determined the dispersion of the λ -DNA according to [5] (see fig. 4). With increasing trapping voltages, i.e. above 140V, the diffusion coefficient is significantly increased. This corresponds to longer trapping times (fig. 3) and explains the dispersion of the λ -DNA peak in fig. 2. The origin of this unusual increase is currently under experimental investigation.

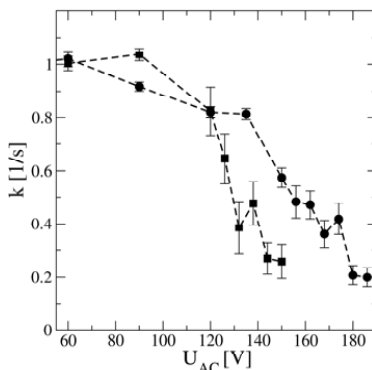


Figure 3. Kramer's rate k versus U_{AC} .

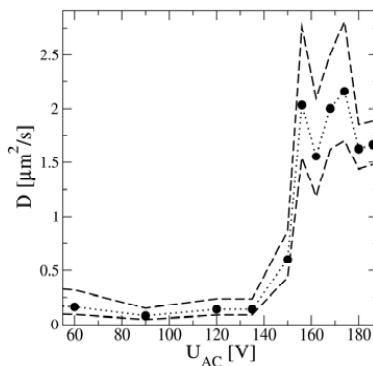


Figure 4. Diffusion coefficient of λ -DNA versus U_{AC} (dashed lines indicate the error).

4. Conclusion

Our new microfluidic method exploiting electrodeless dielectrophoresis enables the efficient separation of long DNA strands within only 200s. The mechanism of the separation can be understood in terms of a size dependent trapping of DNA manifested by the observed Kramer's rate for the escape out of the dielectrophoretic traps. We expect that this new separation method for long DNA molecules can selectively be adapted and optimized by tuning the electric driving parameters (AC and DC) to address an even broader size range in the future [4].

5. References

- [1] D. Porschke, Macrodipoles: Unusual electric properties of biological macromolecules, *Biophysical Chemistry*, 66, pp. 241 (1997)
- [2] C. Chou et al., Electrodeless Dielectrophoresis of Single- and Double-Stranded DNA; *Biophysical Journal*, 83, pp. 2170 (2002)
- [3] A. Ajdari, J. Prost, Free-flow electrophoresis with trapping by a transverse inhomogenous field, *PNAS*, 88, pp. 4468 (1991)
- [4] T.T. Duong, J. Regtmeier et al., Dielectrophoretic separation of DNA, submitted 2006
- [5] P. Reimann et al., Giant Acceleration of Free Diffusion by Use of Tilted Periodic Potentials, *PRL*, 87, 010602 (2001)

Ni PATTERN FOR GUIDING MAGNETIC BEADS SELF-ORGANIZATION : APPLICATION TO LONG DNA ELECTROPHORESIS IN DILUTE ARRAYS

Antoine-Emmanuel Saliba,¹ Charlie Gosse,² Nicolas Minc,³ Christophe Roblin,² Kevin Dorfman,⁴ and Jean-Louis Viovy¹

¹ Institut Curie, UMR168, Paris, France

² Laboratoire de Photonique et Nanostructures, LPN-CNRS, Marcoussis, France

³ Columbia Univ., NYC, USA

⁴ Univ. of Minnesota, Minneapolis, USA

e-mail address : jean-louis.viovy@curie.fr

Keywords : *DNA electrophoresis, magnetic beads, Ni pattern*

Abstract

Self-assembled matrices of magnetic beads have shown their potential to separate long DNA (>100 kbp). Because of their tunability, they represent an interesting alternative to arrays of posts obtained by microlithography. In this paper, a nickel template is used to nucleate the obstacles growth and thus organize the matrix around a predefined design. DNA molecules, 48 to 166 kbp long, were separated in minutes and the measured resolution was compared to theoretical predictions.

1. Introduction

When confined in a Hele-Shaw cell and submitted to a uniform magnetic field, a suspension of superparamagnetic particles self-organizes into a 2D array of columns with hexagonal order on short distances and glasslike order on long distances. Such arrays were used for fast electrophoretic separation of long DNA molecules [1]. Although self-assembled matrices have the advantage of simplicity, they cannot match microlithographic arrays for long range order and pore size monodispersity [2]. We address the latter challenge by patterning the lower face of the electrophoresis channel with a magnetic nickel template. Under a uniform external field, the nickel dots create local magnetic field gradients that attract beads and columns, imposing a predefined order. We demonstrate the ability to separate long DNA molecules with these matrices and our approach for studying the resolution of the DNA separation over a wide range of posts density.

2. Experimental

Hexagonal arrays of 1.2 μm diameter magnetic dots were obtained by standard lift-off technology (Fig. 1a). First, D263 float glass substrates, 210 μm thick, were cleaned with piranha. Patterns were then defined by optical lithography using a LOR5A – Ultra I-123

bilayer. After a two-step development in MF-26A and LDD26W, 150 nm of Ni was deposited by e-beam evaporation, using a 20 nm Ti under-layer to promote adhesion (Fig. 1b). Finally, lift-off was achieved by dissolving the Ultra I-123 in acetone and the LOR5A in EBR PG. We noticed that raw dots tend to come unstuck in water; consequently, we encapsulated them in a 350 nm silica coating by plasma enhanced chemical deposition (Fig. 1c). To complete the device, a PDMS replica of a microfluidic channel was sealed onto the patterned glass substrate. The magnetic beads suspension (\varnothing 500 nm – Ademtech) injection and the hydrodynamic flow regulation were performed with a pressure controller(Fluigent).

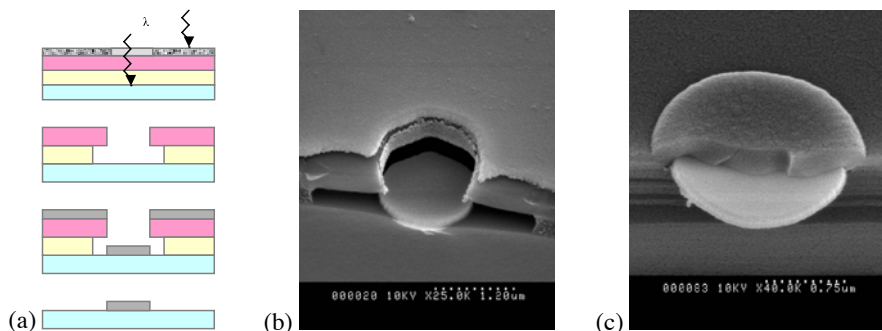


Figure 1. Nickel dots fabrication : Schematic representation of the lithographic and lift-off processes (a); SEM views of the dot before lift-off (b) and after encapsulation (c).

3. Results

To equal the ‘natural’ column spacing [3] with the dots one, as well as to avoid interstitial filaments, we empirically adjusted the channel height between 20 and 50 μm . In parallel, the column diameter was tuned by changing the bead concentration. Then, matrix hydrodynamic flow resistance and reproducible assembling/disassembling of the array were validated (Fig. 2).

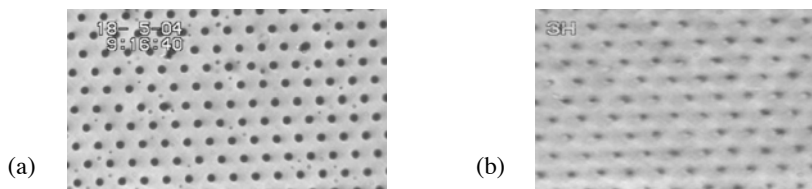


Figure 2. (a) Ni hexagonal array of 1.5 μm diameter dots spaced by 10 μm . (b) Magnetic columns self-assembled on the preceding Ni template, the optical microscopy view was taken few microns above the surface.

Recent experimental and analytical studies [4,5] of the DNA/columns collisions suggested that more dilute arrays should lead to higher a resolution per row of obstacles. This directed self-assembly method offers a flexible way to study the latter prediction. Highly regular columns arrays with spacing ranging from 4 to 30 μm can be used to perform DNA separation. Figure 3a represents an electropherogram of the separation between λ , 2λ , and T4 DNA obtained with a 7 μm post spacing. Resolutions between 1.1 and 1.4 indicate that in less than 2 minutes interesting performances can be obtained in such dilute arrays. Additionally, the resolution per row was calculated for different posts spacing (Fig. 3b). The agreement between experiment and theoretical predictions is satisfactory since the model has no adjustable parameters [5].

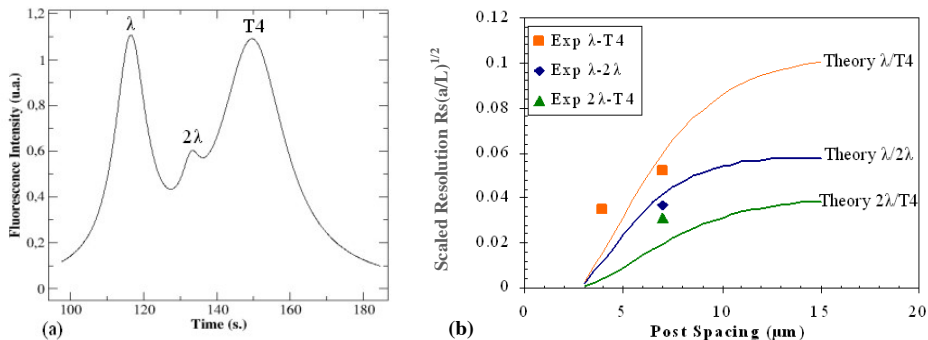


Figure 3. (a) Electropherograms for the separation of a λ , 2λ , and T4 DNA mixture under a 18.78 V/cm electric field and with a video detection at $L = 5$ mm from the injector. The post diameter was 2.6 μm and the spacing a was 7 μm . The resolution Rs between different species are : $\lambda / \text{T4} : 1.36$; $\lambda / 2\lambda : 1.33$; $2\lambda / \text{T4} : 1.11$. (b) Separation resolution per row as a function of the post spacing (2.6 μm column).

4. Conclusion

In this paper we emphasize the use of template directed self-assembly of magnetic columns for studying DNA separations. Tilted or sparse arrays can be obtained, allowing another step towards a detailed understanding of realistic separation systems.

References

- [1] Doyle et al., *Science*, **295**, 2237 (2002)
- [2] Kaji et al., *Anal. Chem.*, **76**, 15 (2004)
- [3] Liu et al., *Phys. Rev. Lett.*, **74**, 2828 (1995)
- [4] Minc et al., *Electrophoresis*, **26**, 362 (2005)
- [5] Minc et al., *Phys. Rev. Lett.*, **94**, 198105 (2005)

MULTIPLEX AFFINITY CAPILLARY ELECTROPHORESIS IN A SINGLE MICROFLUIDIC CHANNEL FOR GENE MUTATION ANALYSIS

Akira Inoue^{1, 2}, Kazuo Hosokawa¹, Toshiyuki Ito¹, Kae Sato¹, Kimiko Makino² and Mizuo Maeda¹

¹RIKEN, 2-1 Hirosawa, Wako, Saitama, 351-0198, JAPAN

²Tokyo University of Science, 2641 Yamazaki, Noda, Chiba, 278-8510, JAPAN

Abstract

This paper describes a novel method for multiplex gene mutation analysis using affinity capillary electrophoresis (ACE) in a single microfluidic channel. The multiplexing was realized by controlling the binding capacities of multiple probes immobilized to the sieving polymer matrix. Single-step detection of two point mutations is demonstrated with a simple step and procedure.

Key words: SNPs, Affinity electrophoresis, Multi-sample recognition, DNA-polymer conjugate, PDMS

1. Introduction

Multiplex DNA binding assay in a single microchannel is promising for high-throughput mutation analysis. For this purpose, several methods based on spatially defined recognition elements (i.e. microarray concept) have been reported [1, 2]. They required cumbersome and time-consuming fabrication steps such as photopolymerization of the hydrogel plugs. In this paper, we demonstrate that ACE enables multiplex DNA binding assay with a spatially homogeneous recognition element containing multiple probes [3].

2. Principle

The principle of this technology is shown in Figure 1. Here two mutations sites are assumed to be analyzed. The microchannel is filled with a polymer matrix having two DNA probes (1 and 2) complementary to parts of the wild type sequence (sample A). Electrophoretic migrations of single-stranded DNA samples are retarded by sequence-specific interactions with the probes. Sample A binds to the both probes and has the lowest mobility. Sample D has the both mutations and binds to neither probe. This DNA has the highest mobility. Sample B has one mutation and binds only to probe 1. Sample C has the other mutation and binds only to probe 2. Samples B and C have intermediate mobilities. The key issue is the separation between samples B and C. To do this, the binding capacities of the probes are designed to be unequal. In this example, probe 1 has a larger binding capacity than probe 2. Hence the samples D, C, B, and A reach the detector in this order (Figure 1b).

3. Experimental

For sample A, we chose an 18-mer model sequence identical to human c-Ki-ras gene codons 10–15 (Table 1). We examined the well-known point mutations at codons 12 and 13. Sample B had the codon 12 mutation, sample C the codon 13, and sample D the both. The probes, complementary to sample A, had different chain lengths: 7-mer for probe 1 and 6-mer for probe 2. The 5' ends of the samples were labeled with FITC. They were mixed in Tris-borate buffer at each final concentration of 1.0 μM . In some experiments, 0.5 μM samples were also used. For the probes, 5'-methacryloyl-modified oligonucleotides were synthesized by

Integrated DNA Technologies. Probe-poly(dimethylacrylamide) (PDMA) conjugate was synthesized through the same procedure as previously reported [4], except that the reaction mixture contained 100 μM probe 1 and 20 μM probe 2.

A microchip was fabricated by bonding a microscope slide glass and a poly(dimethylsiloxane) (PDMS) chip, which had been molded by standard soft lithography. For microchip electrophoresis, we utilized the autonomous solution handling technique, in which the high gas solubility in PDMS is exploited (Figure 2) [4]. Platinum electrodes were dipped into the reservoirs, and an electric field was applied.

4. Results and Discussion

Figure 3a shows the images of the multiplex gene mutation assay using four kinds of oligonucleotides (Table 1). Immediately after the electro-phoresis was started, the sample plug was compacted from 500 μm to 100 μm (Figure 3a, 2 s), which means 5-fold sample

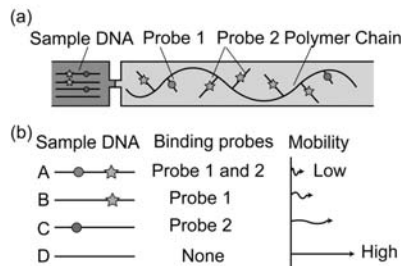


Figure 1. Principle of multiplex ACE.
 (a) The sample and the polymer solutions are merged at the passive stop valve (the pinched region, ref. 4).
 (b) Binding and migration behaviors of the samples.

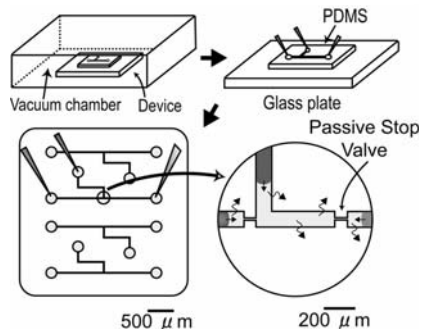


Figure 2. Procedures for the autonomous solution handling technique.

Table 1. Oligonucleotide sequences.

Name	Sequence ^{a,b}
Sample A	FITC-5'-GGA <u>GCT GGT</u> GGC GTA GGC-3'
Sample B	FITC-5'-GGA GCT AGT <u>GGC GTA</u> GGC-3'
Sample C	FITC-5'-GGA GCT GGT <i>TGC</i> GTA GGC-3'
Sample D	FITC-5'-GGA GCT AGT <i>TGC</i> GTA GGC-3'
Probe 1	5'-C TAC GCC-3'
Probe 2	5'-ACC AGC-3'

^aUnderlined sequences are complimentary to the probes.

^bItalic face letters denote mismatched bases.

preconcentration. This effect was caused by the discontinuous electrophoretic mobility at the entrance of the probe-PDMA conjugate. Then, the samples migrated at various speeds, and were completely separated (Figure 3a, 25 s). The successful separation is considered to be realized by the principle illustrated in Figure 1b. We confirmed the band assignment by taking electropherograms with various concentrations of the samples (data not shown). The effect of the probes on specificity was also confirmed by a series of control experiments with various probe compositions (Figure 3b). Namely, we tested PDMA without the probes, PDMA with only probe 1, PDMA with only probe 2, and PDMA with both of the probes at a uniform concentration. The results confirmed that the multiplex ACE required the two probes at different concentrations.

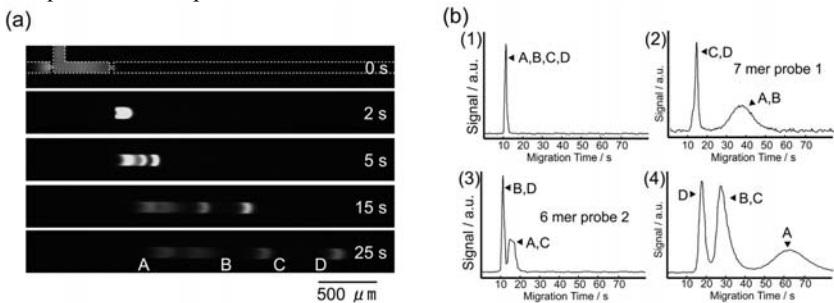


Figure 3. (a) Consecutive images of the multiplex ACE. Sample concentration, 1.0 μM for each; polymer matrix, 10% PDMA with 100 μM probe 1 and 20 μM probe 2; buffer, 50 mM Tris-borate (pH 7.4) with 10 mM MgCl_2 ; electric field, 50 V cm^{-1} . (b) Electropherograms with various polymer matrices: (1) 10% PDMA without the probes, (2) 10% PDMA with 100 μM probe 1, (3) 10% PDMA with 20 μM probe 2, and (4) 10% PDMA with the both probes at a uniform concentration of 50 μM .

5. Conclusions

We proposed a new methodology for multiplex gene mutation assay in a single microchannel. Cumbersome spatial addressing of the binding elements was evaded by the use of ACE with a newly devised multi-probe conjugate. The proposed method has a great potential for point-of-care testing of gene point mutations and single-nucleotide polymorphisms.

6. References

- [1] G. H. Seong, W. Zhan and R. M. Crooks, *Anal. Chem.*, 2002, **74**, 3372–3377
- [2] K. G. Olsen, D. J. Ross and M. J. Tarlov, *Anal. Chem.*, 2002, **74**, 1436–1441.
- [3] A. Inoue, T. Ito, K. Sato, K. Hosokawa, M. Makino and M. Maeda, *Chem. Lett.*, 2006, **35**, 658–659
- [4] T. Ito, A. Inoue, K. Sato, K. Hosokawa and M. Maeda, *Anal. Chem.*, 2005, **77**, 4759–4764.

MINIATURIZED TWO-DIMENSIONAL GEL ELECTROPHORESIS OF PROTEINS USING LOW-CONCENTRATION MULTIFILAMENT-SUPPORTING GEL FOR ISOELECTRIC FOCUSING

Tamao Odake¹, Kazutoshi Kamezawa¹, Kozue Miyata¹, Hiroki Hotta¹, Yasuaki Kojima², and Kin-ichi Tsunoda¹

¹Department of Chemistry, Gunma University, 1-5-1 Tenjiin-cho, Kiryu, 376-8615 Japan

²Mitachi Co. Ltd., 2-1284-33 Kohbayashi-cho, Isesaki, 379-2206 Japan

Abstract

A miniaturized two-dimensional gel electrophoresis (2-DE) system was constructed with a multifilament supporting-gel (MFS-gel) as a first-dimensional gel for isoelectric focusing (IEF). The MFS gel could provide low-concentration (2.5%T) polyacrylamide that reduced IEF time and improved transfer efficiency from the first-dimensional gel to the second one of especially high-molecular-weight proteins. The miniaturized system was applied to 2-DE separation of proteins and it was found that an hour and a half was enough to perform 2-DE. This system could be expected as a fast protein separation method for elucidation of cellular mechanism, disease diagnosis and screening.

Keywords: **two-dimensional electrophoresis, miniaturization, multifilament, protein, polyacrylamide**

1. Introduction

Two-dimensional gel electrophoresis (2-DE), where proteins can be separated according to their isoelectric point in the first dimensional isoelectric focusing (IEF) and their size in the second dimensional sodium dodecyl sulfate-polyacrylamide gel electrophoresis (SDS-PAGE), is a powerful separation tool in proteomic research. However, the conventional 2-DE needs handling skills, and long analysis time, at least two days. A commercially available immobilized pH gradient (IPG) dry strip gel is easier to handle. However, the concentration of the IPG strip gel is 4%T and is not suited for fast separation of high-molecular-weight proteins. Therefore, desired is a new 2-DE system that can provide fast separation of proteins including high-molecular-weight region without need of such technical skills.

We have proposed as a new IEF gel for 2-DE a low concentration polyacrylamide gel supported by a multifilament string: multifilament supporting-gel (MFS-gel) [1]. By using a multifilament string as an IEF gel support, the total acrylamide concentration of the gel could be reduced to 2.5%T with sufficient mechanical strength, and the gel was easily handled with tweezers. Due to the large pore of the low-concentration (2.5%T) polyacrylamide gel, proteins were focused faster than by using the conventional 4%T

gel. Also, proteins, especially in the high-molecular-weight region, were observed more clearly on the silver-stained 2D map than by using the 4.0%T gel, and as clearly as by using the agarose IEF gel.

To fasten electrophoretic separation, the miniaturization of the gel itself was considered effective as well. We constructed a miniaturized 2-DE system using the low-concentration MFS-gel as an IEF gel, and evaluated the miniaturized 2-DE system using proteins of a pI marker kit and high-molecular-weight region.

2. Experimental

The MFS-gel is shown in Figure 1. The MFS-gel was 1 mm in diameter and made according to the literature [1] with some modification. The MFS-gel was soaked in a solution containing carrier ampholytes before use, cut into appropriate length, and set in the groove on the IEF plate of the miniaturized 2-DE system shown in Figure 2. After a sample was applied and the plate was set on the IEF apparatus equipped with a water-cooling unit, separation voltage was applied. After IEF, the gel was removed from the groove with tweezers.

The miniaturized second-dimensional gel was 55 mm wide, 40 mm long and 0.75 mm thick. The MFS-gel was put on the top of the second-dimensional gel with agarose sealing. Three colored proteins such as C-phycocyanin (MW 264 kDa, pI 4.3), hemoglobin (MW 67 kDa, pI 7.2), and cytochrome c (MW 13 kDa, pI 9.6) were used to monitor IEF separation, and proteins of a pI marker kit and high-molecular-weight marker proteins were used to evaluate 2-DE separation performance. Silver staining was used to visualize proteins on the 2D gel.



Figure 1 MFS-gel.

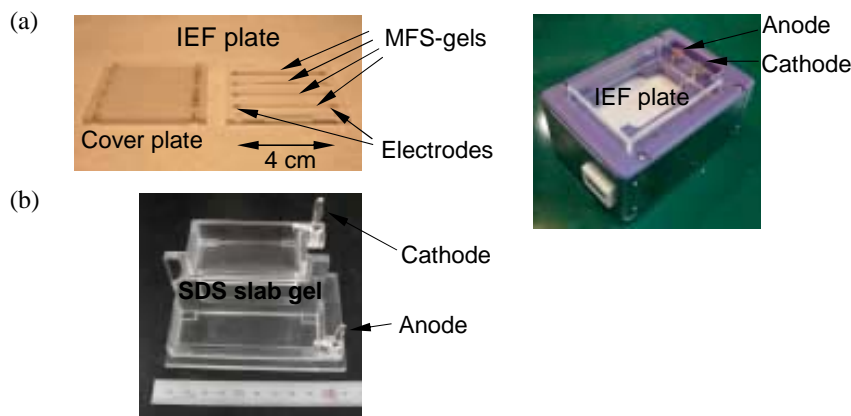


Figure 2 Apparatus for IEF (a) and SDS-PAGE (b) of the miniaturized 2-DE system using the MFS-gel.

3. Results and discussion

Using the low-concentration (2.5%T) MFS-gel of 4 cm, the mixture of three colored proteins, C-phycocyanin, hemoglobin, and cytochrome *c*, was separated in 8 min, which was about twice faster than using the same concentration of the MFS-gel of 7 cm. The miniaturized (short) MFS-gel was shown effective to fast IEF separation of proteins. Using the miniaturized 2-DE system, proteins of a pI marker kit were separated as shown in Figure 3. An hour was enough to perform the first dimensional IEF and it took 12 min in the second dimensional SDS-PAGE. Therefore, an hour and a half was enough to carry out 2-DE separation using the miniaturized system. High-molecular-weight marker proteins including thyroglobulin from bovine thyroid gland (MW 670 kDa) were applied to fast 2-DE separation using the miniaturized 2-DE system, and proteins of high-molecular-weight region above 200 kDa were successfully separated in an hour.

In conclusion, this miniaturized 2-DE system using the low-concentration MFS-gel was shown to be useful for fast separation of proteins including high-molecular-weight proteins. High-molecular-weight proteins such as membrane protein and thyroglobulin have an important role in the cellular transport and disease. Therefore, this system can be expected as a fast protein separation method for elucidation of cellular mechanism, disease diagnosis and screening.

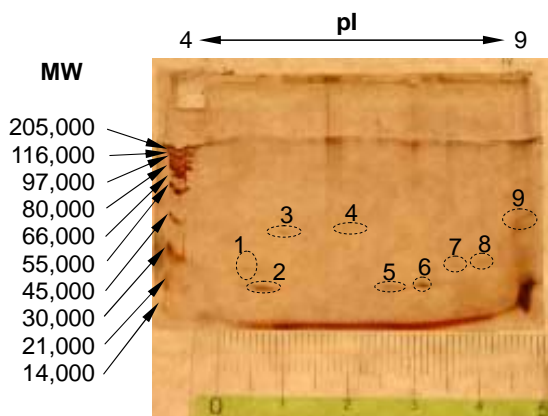


Figure 3 Fast 2-DE separation of proteins of a pI marker kit using the miniaturized 2-DE system. 1: Soybean trypsin inhibitor, 2: β -lactoglobulin A, 3: Bovine carbonic anhydrase B, 4: Human carbonic anhydrase B, 5: Horse myoglobin-acidic band, 6: Horse myoglobin-basic band, 7: Lentil lectin-acidic band, 8: Lentil lectin-middle band, 9: Trypsinogen

REFERENCES

1. J. Li, A. Ogasawara, T. Odake, T. Umemura, K. Tsunoda, *Anal. Sci.*, **20**, 1673-1679 (2004).

A NEW EXPLORATION IN ENHANCING THE RESOLUTION FOR HIGH-PERFORMANCE ANALYSIS OF MONO-SULFATE GLYCOSAMINOGLYCAN DISACCHARIDE ISOMERS ON A POLY(METHYL METHACRYLATE) CHIP

Yong Zhang^{1,2}, Guichen Ping³, Bingmei Zhu², Noritada Kaji², Manabu Tokeshi², Yoshinobu Baba^{2,4}

¹The University of Tokushima, 1–78, Shomachi, Tokushima 770–8505, Japan

²Nagoya University, Furo-cho, Chikusa-ku, Nagoya 464-8603, Japan

³Waseda University, 3-4-1 Ohkubo, Shinjuku, Tokyo 169-8555, Japan

⁴AIST, Hayashi-cho 2217-14, Takamatsu 761-0395, Japan

Abstract

The glycosaminoglycans (GAGs) labeled with 2-aminoacridone, hydrochloride (AMAC) were found to be prevented from adsorption to the surface of polymethylmethacrylate (PMMA) microchips by dynamic coating microchannel with methyl cellulose (MC). To obtain sufficient resolution of mono-sulfate GAG disaccharide isomers on microchip electrophoresis (MCE), buffer pH, β -cyclodextrin (β -CD), and 1,4-dioxane (DO) were systematically investigated. We found that the application of 1,4-dioxane (DO) dramatically improved the resolution of the analytes. Δ Di-triS, Δ Di-UA2S, Δ Di-4S, and Δ Di-6S were baseline separated within 75 sec. The theoretical plate was in the range of 5×10^5 – 1×10^6 m⁻¹.

Keywords: Microchip electrophoresis, Mono-sulfate glycosaminoglycan isomer, 1,4-dioxane, Resolution, Solvation effect

1. Introduction

GAGs are negatively charged disaccharide repeating units, usually containing a sulfated hexosamine and uronic acid. Those units compose a chain covalently linked to "core" proteins, forming proteoglycans (PGs). PGs are involved in regulating cell adhesion, migration and proliferation, thus become important effectors of cellular processes that constitute the basis of development and disease. These properties depend mainly on specific structures of the GAG moieties present in PGs. MCE attracts attention in separation and analysis by means of rapid separation speed, high performance and throughput, cost-effective, and the capability of system integration and multiplexing [1]. Thus, profiling of GAGs on MCE may be useful in allowing early clinical diagnosis of diseases and understanding life sciences.

2. Theory

Eq 1 gives the factors that can affect electrophoretic mobility.

$$\mu_{app} = \frac{q}{6\pi\eta r} \quad (1)$$

Where, μ_{app} is electrophoretic mobility, q is ion charge, η is solution viscosity, r is ion radius. Among these factors, we made our efforts to get a different r of Δ Di-UA2S, Δ Di-4S and Δ Di-6S so that they could show different mobility. And different r was realized by different solvation layer size around the analytes.

3. Experimental

Derivatization of Δ Di-4S, Δ Di-6S, Δ Di-UA2S and Δ Di-triS with AMAC was performed as described by Jackson and modified by Kitagawa *et al.* In this procedure, reductive amination was adopted. Firstly, sugar ring opened in acetic acid environment. Then the lone pair of amino groups of the label attacks the carbon of carbonyl groups of reducing sugars, forming the Schiff base. The Schiff base is acid-labile and is reduced with sodium cyanoborohydride to a stable secondary amine. Microchip electrophoresis was carried out on HITACHI SV1100 with a LED confocal fluorescence detector which provides a median excitation source of 470nm. The separation length is 3 cm [2].

4. Results and discussion

PMMA has a very hydrophobic surface, thereby causing strong adsorption of analytes, such as fluorescence dyes and proteins, on its surface. MC was found to be crucial for suppressing adsorption of the GAGs labeled with AMAC

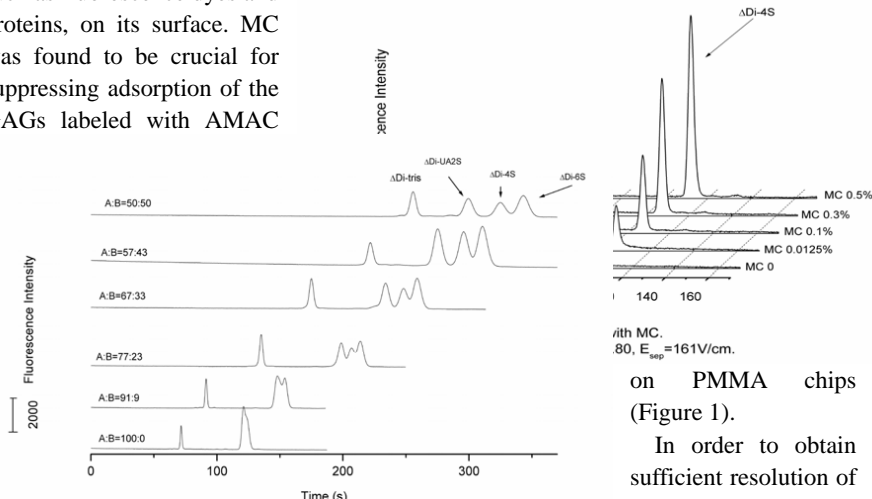


Figure 2. Effect of DO on enhancing resolution of GAG disaccharide isomers. A is running buffer, B is DO. 0.2 mol/L Tris-NaH₂PO₄ buffer, pH value 6.81, MC 0.5%, E_{sep} = 161V/cm.

with MC.
0.80, E_{sep} = 161V/cm.
on PMMA chips
(Figure 1).

In order to obtain sufficient resolution of

mono-sulfate GAG disaccharide isomers on MCE, buffer pH, β -CD, and DO were systematically investigated. As a result, there was no resolution by changing buffer pH. Partially resolution was obtained by using β -CD. DO in the running buffer was found to be critical for separation of mono-sulfate GAG disaccharide isomers on MCE (Figure 2). To decrease the analysis time, High electric field strength was studied on MCE.

5. Conclusion

Under the optimized conditions, baseline separation of Δ Di-4S, Δ Di-6S, Δ Di-UA2S and Δ Di-triS was obtained within 75 sec with the separation efficiency over 500,000 plates/m (Figure 3). The RSD values of mobility for four GAG disaccharides are less than 2.05% in ten different channels, and the detection limit for AMAC labeled mono-sulfate GAG disaccharides is 2.6×10^{-8} mol/L.

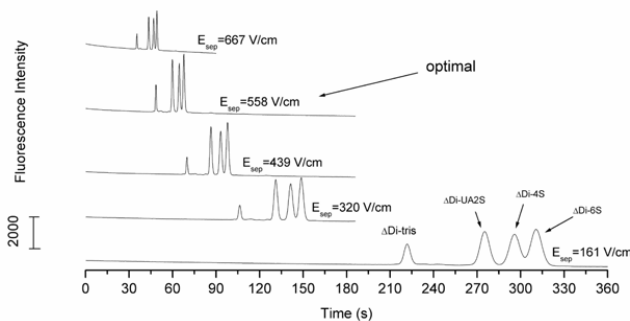


Figure 3. High speed separation of GAG disaccharides by increasing electric field strength. 0.2 mol/L Tris-NaH₂PO₄ buffer, pH 6.81, MC 0.5%, running buffer : DO = 57:43.

References

- [1] Khandurina, J., Guttman, A., *Microscale separation and analysis*, Curr. Opin. Chem. Biol. 2003, 7, 595–602.
- [2] Dang, F., Zhang, L., Jabasini, M., Kaji, N., Baba, Y., *Characterization of Electrophoretic Behavior of Sugar Isomers by Microchip Electrophoresis Coupled with Videomicroscopy*, Anal. Chem. 2003, 75, 2433–2439.

SELECTIVE PARTICLE SEPARATION AND DEPOSITION BY 3-D INSULATOR-BASED DIELECTROPHORESIS

Kai-Cheng Chuang, Li-Yu Chu, Maw-Shuan Jiang,
Tzu-Han Chuang, Chien-Chung Fu, and Shih-Kang Fan

¹Institute of Nanotechnology, National Chiao Tung University, Taiwan

²Institute of MEMS, National Tsing-Hua University (NTHU), Taiwan

³Department of Power Mechanical Engineering, NTHU, Taiwan

Abstract

A particle separator was demonstrated based on 3-D insulator-based dielectrophoresis (iDEP). Two droplets containing mixtures of 1- μm and 5- μm polystyrene beads were placed above and beneath a 200- μm -thick PMMA sheet. An array of X-ray lithography fabricated through microholes on the PMMA sheet generated the 3-D iDEP forces since it distorted the electric line passing through. When applying a proper AC signal, 1- μm beads were concentrated and deposited in the microholes, while 5- μm beads were expelled from the microholes by the 3-D iDEP forces.

Keywords: DEP, iDEP, Particle Separation, Particle Concentrator

1. Introduction

Dielectrophoresis (DEP) provides the motion of a particle by the interaction of a non-uniform electric field generated by microelectrodes with the induced effective dipole moment of the particle [1]. Besides using microelectrodes, in the cases of iDEP, non-uniform fields can be created by placing insulators in an originally uniform field [2]. As shown in Fig. 1, with the distorted electric lines, iDEP would attract suspended particles toward the microhole (high electric field strength) by positive DEP (pDEP) or repel them from the microhole by negative DEP (nDEP). The concept of iDEP was mostly applied and demonstrated on a 2-D microfluidic chip, i.e., thin liquid sheet with voltage applied in the longitudinal direction, where electric lines were merely regulated in 2-D. In this paper, 3-D iDEP was investigated on a PMMA sheet with through microholes sandwiched by two droplets

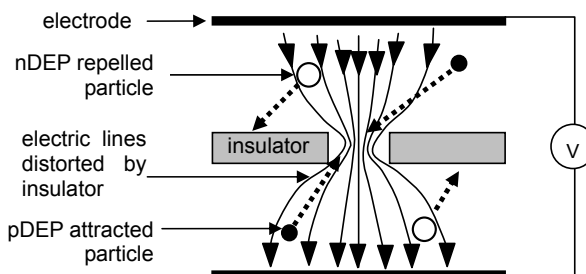


Figure 1.
Particles selectively trapped (pDEP, shown black) into or repelled (nDEP, shown white) from the microhole by iDEP.

2. Experimental

A droplet-based 3-D iDEP device was studied as shown in Fig. 2. Two droplets containing fluorescent polystyrene beads were placed above and beneath a 200- μm -thick PMMA sheet with an array of microholes (Fig. 3). The top droplet could be further manipulated by the above electrolyte (Na_2SO_4) droplet by mirror-EWOD across a PVDC sheet (12.5- μm -thick) [3]. The non-uniform electric field was established by applying voltage between two Teflon coated ITO glasses. Tested microholes, with opening of $10 \mu\text{m} \times 10 \mu\text{m}$ and $25 \mu\text{m} \times 25 \mu\text{m}$, were fabricated by deep X-ray lithography process on PMMA sheets with a thickness of 200 μm . Microholes were patterned by a 1.5 GeV synchrotron beam line with the exposure of 900 mA \times min/cm. PMMA sheets were then developed by GG developer at 40°C for 30 min. The X-ray micromachined 10- μm -wide microholes are shown in Fig. 3.

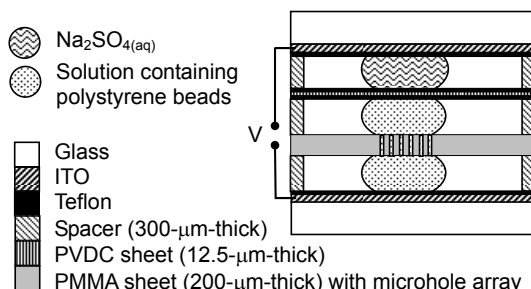


Figure 2. Configuration of a 3-D iDEP device.

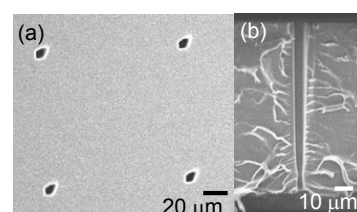


Figure 3. SEM image of microhole array (a) top-view (b) cross-sectional view.

3. Result and discussion

Basic 3-D iDEP phenomenon was first investigated by using 5- μm (in diameter) polystyrene beads. The beads were dispersed in water with the concentration of 1.4×10^7 number/mL and manipulated by applying a $140 \text{ V}_{\text{rms}}$ AC signal between two ITO glasses as shown in Fig. 2. 3-D iDEP was studied by monitoring the motion of dispersed 5- μm beads under various frequencies of the applied AC signal. It was observed that the 5- μm beads were repelled from the $25 \mu\text{m} \times 25 \mu\text{m}$ microholes by nDEP at the applied frequencies from 1 kHz to 100 kHz, as shown in Fig. 4.

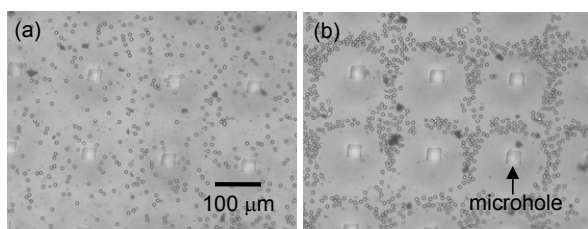


Figure 4. Demonstration of iDEP by 5- μm polystyrene beads. (a) Beads were evenly dispersed with no voltage was applied. (b) Beads repelled from microholes by nDEP when voltage was applied (100 kHz, $140 \text{ V}_{\text{rms}}$).

1- μm bead (1.8×10^9 number/mL) solution was then added and mixed with the 5- μm bead solution of equal volumes. As shown in Fig. 5(a)-(d), when 1 kHz 140 V_{rms} was applied, the 5- μm beads were repelled from the microholes by nDEP as expected. However, the 1- μm beads were attracted and trapped into the $10 \mu\text{m} \times 10 \mu\text{m}$ microholes. Therefore, by choosing proper particle, liquid medium, and frequency, beads can be selectively separated and stored in the microholes. After 2 min operation, the device was disassembled. The PMMA sheet was rinsed and cleaned by water gently and observed by fluorescent microscope after drying. The microscopic image (Fig. 5(e)) shows fluorescence at the microholes, proving the deposition of the polystyrene beads.

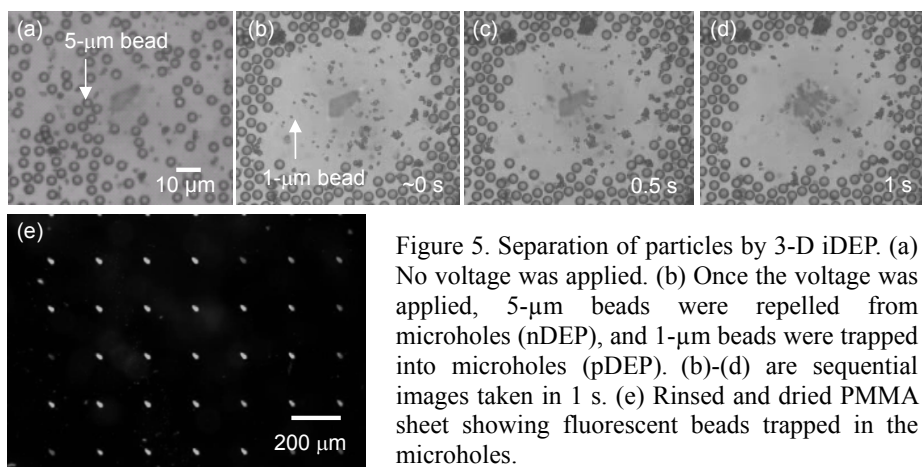


Figure 5. Separation of particles by 3-D iDEP. (a) No voltage was applied. (b) Once the voltage was applied, 5- μm beads were repelled from microholes (nDEP), and 1- μm beads were trapped into microholes (pDEP). (b)-(d) are sequential images taken in 1 s. (e) Rinsed and dried PMMA sheet showing fluorescent beads trapped in the microholes.

4. Conclusion

We demonstrated a particle separator by 3-D iDEP. By applying 1 kHz 140 V_{rms} across two droplets containing 1- μm and 5- μm polystyrene beads, 1- μm beads were concentrated into the through microholes on PMMA sheet between the droplets. Meanwhile, the 5- μm beads were expelled away from the through holes. The applied voltage can be decreased since most of the voltage was consumed across the PDLC sheet. Although the PDLC sheet is not beneficial to iDEP, it provides the ability of the manipulation of the droplet.

References

1. C. Yu, J. Vykoukal, D. M. Vykoukal, J. A. Schwartz, L. Shi, and P. R. C. Gascoyne, *A Three-dimensional Dielectrophoretic Particle Focusing Channel for Microcytometry Application*, Journal of MEMS, 14, pp. 480-487, (2005).
2. M. P. Hughes, *Strategies for dielectrophoretic separation in laboratory-on-a-chip systems*, Electrophoresis, Vol. 23, pp. 2569-2582, (2002).
3. K.-C. Chuang, and S.-K. Fan, *Direct Handwriting Manipulation of Droplets by Self-Aligned Mirror-EWOD across a Dielectric Sheet*, Proc. IEEE MEMS Conf. 2006, Istanbul, Turkey, pp. 538-541, (2006)

NOVEL PHYSICALLY ADSORBED POLYMER COATING ON PMMA MICROCHIP WITH MULTI CHANNEL ARRAY FOR HIGH-THROUGHPUT PROTEIN ANALYSIS

Hiroki Okada¹, Noritada Kaji¹, Manabu Tokeshi¹ and Yoshinobu Baba^{1,2}

¹Department of Applied Chemistry, Nagoya University, Furo-cho, Chikusaku,
Nagoya 464-8603, Japan,

²HTRC, AIST, Hayashi-cho 2217-14, Takamatsu 761-0395, Japan
(h051102d@mbox.nagoya-u.ac.jp)

Abstract

For protein analysis, polymeric microchip was extremely incompatible with protein samples. To overcome the incompatibility, we developed a novel physically adsorbed polymer coating, which was a new approach and different from conventional coating methods, on PMMA microchip using cellulose derivatives as the coating reagents. The coating method remarkably progressed analytical performance and we could successfully separate 5 proteins dependent of their own sizes with high reproducibility (RSD; within 3%, n=12) on coated PMMA microchip with 12 channels array.

Keywords: coating, cellulose derivatives, poly(methylmethacrylate) (PMMA), protein, high-throughput

1. Introduction

Polymeric materials are attractive materials for chip technology because of the potential of easy fabrication, low-cost and disposability. Unfortunately, they are highly incompatible with biological samples, in particular, proteins denatured with sodium dodecyl sulfate (SDS) which strongly adsorb to channel walls of PMMA via hydrophobic interaction and exhibit the electroosmotic flow (EOF)¹. The EOF disturbs the migration of proteins and therein, modification of channel walls of PMMA is necessary to suppress both the adsorption and EOF². However, the coating methods are under tailoring. Therefore, further investigation is needed.

2. Experimental

Proteins were labeled with Cy5 fluorescent dye and then denatured with SDS (2 %) and β -mercaptoethanol (0.1 M). Prior to electrophoresis, all of the channels were filled with a cellulose derivative (Figure 1) with desired concentration and then were dried for 1 day at room temperature in order to stabilize the coating. Next, the channels were filled with running buffers and electrophoresis was then performed.

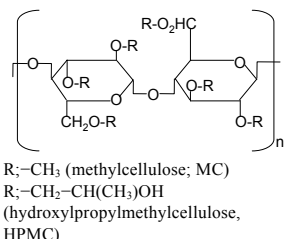


Figure 1

3. Results and Discussion

The water contact angle was decreased from 66.8° to 15.0° after using HPMC 2 as the coating reagent (Table 1), namely, the wall of channels became hydrophilic by the coating method. To examine the coating effect, we measured the mobility of EOF on non-coated and coated channel walls. The mobility of the EOF (μ_{eo}) on coated channel walls was approximately 2 order of magnitude lower than that on non-coated channel walls (Table 1). We thought that this phenomenon was responsible for the greater number of hydroxyl group of HPMC than that of MC, which was verified by using HPMC 2. The water contact angle and EOF decreased with increasing hydroxyl group of HPMC. Therefore, hydroxyl group affected the creation of the hydrophilic surface. We applied our coating method to 12 channel array microchip electrophoresis. On a 12 channels arrays PMMA microchip coated by HPMC 2, we could successfully separated 5 different proteins based on their own size with high reproducibility (within 3 %, $n=12$) using low viscosity polymer (4.5 cP), dextran, as a sieving polymer (Figure 2).

Table 1. Measurement of water contact angle and the mobility of EOF

coating reagent	angle (degree)	^b μ_{eo} ($\times 10^{-6} \text{ cm}^2 \cdot \text{V}^{-1} \cdot \text{s}^{-1}$)
none	$66.8 (\pm 0.15)$	$928.1 (\pm 0)$
MC	$23.0 (\pm 0.50)$	$11.9 (\pm 0.90)$
^a HPMC 1	$19.9 (\pm 0.20)$	$6.42 (\pm 0.18)$
^a HPMC 2	$15.0 (\pm 0.50)$	$5.64 (\pm 0.090)$

^a HPMC 2 has hydroxyl group more than HPMC 1, which was obtained by FT-IR spectroscopy and from data sheet provided by Shinetsu Chemical Co. Ltd.

^b Average of 4 measurements

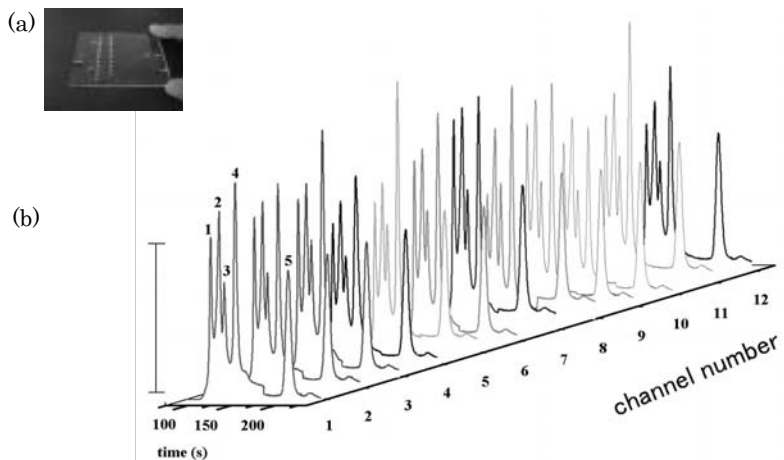


Figure 2. Twelve channels array electrophoresis. (a) Picture of microchip with 12 channels array. (b) Electropherograms of 12 channel array. Running buffer; 4 % dextran, 5 mM Tris-HCl and 3.5 mM SDS. The number of peak; 1 Tripsin Inhibitor (20.1 KDa), 2 Carbonic Anhydrase (29 KDa), 3 Ovalbumin (43 KDa), 3 Bovine Serum Albumin (68KDa) and β -galactosidase (114.6 KDa). Each protein concentration was 50 ng/ μ L. RSD of migration time of each protein was within 3 % ($n=12$). All the channel were coated with 0.15 % HPMC 2.

4. Conclusions

We developed the novel physically adsorbed polymer coating method, which was simple, novel and different from conventional coating methods, using cellulose derivatives as the coating reagent. It was revealed that hydroxyl group of a coating reagent mainly affected the creation of hydrophilic surface of channel walls of PMMA. In addition, this coating method was applied to 12 channel array electrophoresis and protein separation with high speed and reproducibility was achieved. This report recommended that our coating method was the key step to construct high-throughput protein analysis system on polymeric microchips.

Acknowledgements

The present work was supported in part by a Grant-in-Aid for Scientific Research from the Ministry of Education, Science and Technology (MEXT), Japan.

References

1. Nagata, H., Tabuchi, M., Hirano, K., and Baba, Y., Electrophoresis 2005, 26, 2247-2253.
2. Okada, H., Baba, Y., Proceeding of Micro Total Analysis Systems 2005, 334-336

DNA SEPARATION BASED ON THE GYRATION RADIUS EMPLOYING NANO-PILLAR WITH SQUARE ALLOCATION

Ryo Ogawa¹, Noritada Kaji², Sou Wakao², Shingi Hashioka¹,
Yoshinobu Baba^{2,3}, and Yasuhiro Horiike¹

¹National Institute for Materials Science, Japan

²Department of Applied Chemistry, Nagoya University, Japan

³Health Technology Research Center, AIST, Japan

Abstract

Our previous report explained the nano-pillars playing a role as a molecular sieve in DNA size separation. We investigate the sieving effect of nano-pillars with square allocation, and discuss the mechanism of DNA size separation. By applying the nano-pillars with square allocation, it is revealed that the sieving effect of nano-pillars has correlation with the gyration radius of DNA, and the nano-pillar chip can provide a method to separate DNA by size precisely.

Keywords: Nano-pillar, DNA size separation, Electrophoresis, Sieving effect, Gyration radius

1. Introduction

In the last μ TAS meeting, we reported DNA electrophoretic separation employing tilted (a) and square (b) allocations of nano-pillars shown in Fig. 1 [1], where four pillar

regions of 500 μ m length, namely the total pillar region of 2 mm length lined up in one section via 35 μ m pillar-free spacing

as shown in Fig. 2. However, the square type nano-pillars with 300 nm gap did not separate 10 and 38 kbp DNA fragments (see Fig. 3(a)), whereas the tilted allocation separated 10 and 38 kbp at the same 50V/cm electric field (see Fig. 3(b)). This failure in separation for the square allocation might result from higher velocity of DNA fragments due to excessive application of voltages. In this report, we take consideration the effect of applied voltage, and performed the further study of DNA separation employing

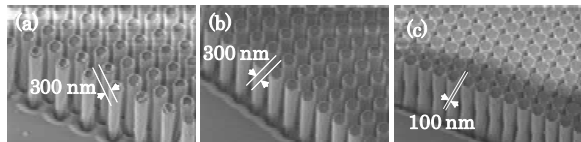


Figure 1. Nano-pillars with tilted allocation (a) and nano-pillars with square allocation (b). The gaps between pillars are 300 nm. Nano-pillars with square allocation and 100-nm gap (c).

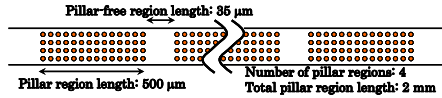


Figure 2. Dimension of nano-pillar regions.

nano-pillars with square allocation, and discuss the mechanism of DNA separation by nano-pillars with square allocations based on experiments of DNA size separation.

2. Experimental

The fabrication method of quartz nano-pillars was reported in ref. [2]. We employed the nano-pillars shown in Fig. 2 to separate the DNA fragments (1 kbp, 10 kbp and 38 kbp). The gaps of nano-pillars were 100nm and 300nm. Besides, in order to aim at separation of lower fragments, we fabricated twenty pillar regions of 215 μm length, namely the total pillar regions of 4.3 mm length lined up in one via 35 μm pillar-free spacing as shown in Fig. 4. Employing the nano-pillars with 300 nm gaps, we investigated the separation of λ DNA digested by HindIII.

3. Results and discussion

When electric field applied was decreased from 50V/cm to 30V/cm, the 1 kbp DNA (as a marker), 10 and 38 kbp were separated clearly after going through the whole pillar regions of 2 mm. As shown in electropherograms of Fig. 5, the nano-pillars with 100-nm gap (Fig. 1-c) separated 1 kbp and fragments length over 10 kbp, while the nano-pillars with 300-nm gap (Fig. 1-b) separated 38 kbps and fragments below 10 kbp. When we employed the nano-pillars with 300 nm gaps (shown in Fig. 6), 23 kbp and some fragments below 10 kbp were separated as shown in Fig. 6, where 50V/cm electric field was applied because 30V/cm application required longer separation time. The fragments below 10 kbp were not

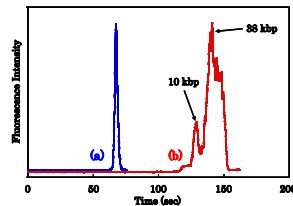


Figure 3. Electropherograms in square (a) and tilt (b) nano-pillars for 10 kbp and 38 kbp. Intensity of fluorescence stained DNA fragments was observed after DNA fragments traveled 2-mm pillar regions.

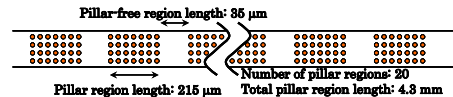


Figure 4. Dimension of nano-pillar regions.

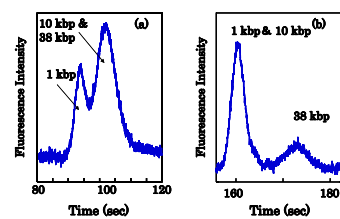


Figure 5. Electropherograms in square nano-pillars with 100 nm gap (a) and 300 nm gap (b) for 1 kbp, 10 kbp and 38 kbp. Intensity of fluorescence stained DNA fragments was observed after DNA fragments traveled 2-mm pillar regions.

separated in these nano-pillars, though the separation became clear as the DNA traveled farther.

Based on these results, we discussed the separation mechanism according to the gyration radius (Rg) of DNA estimated as $\sqrt{bL}/\sqrt{6}$, where b and L as Kuhn's length and contour length respectively. Rg of 1, 10, 23 and 38 kbp are 78, 245, 373 nm and 478 nm, respectively. We summarize DNA size separation results for the square allocation pillars as follows, where gap width is defined as “ g ”; (1) the 100 nm gap separates 1 and 10 kbp, and Rg 's corresponding to 1 and 10 kbp are 78 and 245 nm. (2) the 300 nm gap separates 10 and 23 kbp, and Rg 's corresponding to 10 and 23 kbp are 245 and 373 nm. Therefore, each gap exists between Rg 's corresponding to separated base pairs. As referring Fig. 7, when two kinds of DNA with $Rg > g$ and $Rg < g$ migrate within pillars, velocity of DNA with $Rg > g$ becomes lower than that of DNA with $Rg < g$, thus leading to separation due to the sieving effect.

4. Conclusions

Consequently, in the case of square allocation of nano-pillars, gap width less than the DNA fragments with given Rg and the more pillar regions allow to separate smaller base pairs at higher resolution. We conclude it can lead to the precise DNA size separation using nano-pillar chip.

Acknowledgements

This research was partially supported by the Ministry of Education, Science, Sports and Culture, Grant-in-Aid for Young Scientists (B), 17750078, 2006.

References

- [1] R. Ogawa, *et.al.*, μ TAS 2005, pp. 1012-1014
- [2] N. Kaji, *et.al.*, Anal.Chem., 76(1) (2004), pp.15-22.

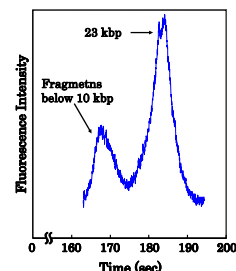


Figure 6. Electropherograms in square nano-pillars for 23 kbp and fragments below 10 kbp. Intensity of fluorescence stained DNA fragments was observed after DNA fragments traveled 2-mm pillar regions

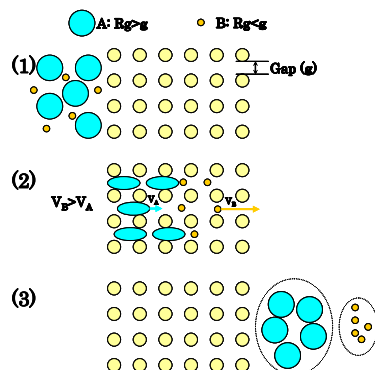


Figure 7. DNA separation of nano-pillars with square allocation.

μ-HOTPLATE ARRAY FOR MANIPULATION OF ADHESIVE CELLS BY MEANS OF IR DIODE LASER LIGHT

Helke Reinhardt, Petra S. Dittrich, Joachim Franzke and Andreas Manz
ISAS - Institute for Analytical Sciences Dortmund, Germany

Abstract

We demonstrate a simple approach for fast and localized heating in the dimension range of a single living cell. The heating is realized due to strong absorbance of infrared light by microsized particles or patterned surfaces (“μ-hotplates”).

Different materials are tested with respect to their applicability for laser induced optical heating and the effect on single living cells is explored.

The presented technique can be a versatile tool for initiation and modulation of biochemical or cellular reactions, reversible cell membrane opening, or for the control of cell growth.

Keywords: temperature control, cell handling, microarray, single cell observation

1. Introduction

Many processes in single cells strongly depend on temperature [1]. The ability to control the temperature within separate regions of a single living cell could be a tool for modulation or initiation of cellular responses. Since infrared light at 830 nm wavelength is hardly absorbed by the cells [2], it minimizes the interference of the multiple cumulative temperature-dependent effects and prevents cells from irreversible damage.

Heating of localized areas within microdevices is commonly achieved by Peltier devices or thin film resistive heaters. Such devices typically require a direct connection to a control device. Recently, some approaches have been presented for contactless heating of small volumes by means of light [3-4] or magnetic fields [5].

2. Experimental

To achieve microparticle enhanced optical heating, the light of a 830 nm continuous wave diode laser was focused by the microscope objective of a modified inverted microscope (Olympus IX 71) to a diameter of approximately 5 μm. A μ-hotplate was positioned at the beam spot of the laser light (Figure 1). Simultaneously, widefield illumination by a Hg-arc lamp was facilitated to directly observe the effects of optical heating via fluorescence microscopy.

We tested three different materials for μ-hotplates with respect to their absorbance and applicability. First, graphite powder suspended in PDMS was spincoated onto a 150 μm thick microscopy slide to a layer thickness of ~15 μm (Figure 2-A).

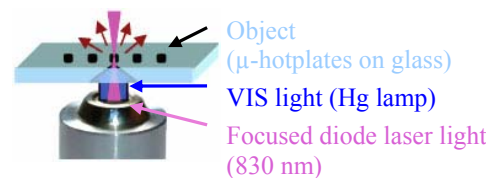


Figure 1. Principle of optical heating

In the second approach, carbon microarrays were produced by pyrolyzing microstructures made of SU-8 photoresist [6] (posts of 8 μm diameter and 5 μm height, Figure 2-B). Pyrolysis was done at 700 °C in a muffle furnace permanently flushed with nitrogen.

Alternatively, different structures of platinized gold (overall thickness ~220 nm) were produced (GeSiM, Großberkmannsdorf, Germany) on borosilicate glass (D263) of 145 μm thickness (Figure 2-C).

The effect of optical heating on living cells (colon cancer cells SW 480) was investigated. The cells were directly grown on poly-D-lysine covered glass slides, patterned with the absorbing material. A frame made of PDMS served as a cell chamber. Cell viability tests were performed using erythrosine B.

3. Results and Discussion

All tested materials are suitable for inducing slight temperature increases of a few K up to boiling of water, within less than a second, upon exposure to laser light of a few mW laser power.

Graphite particles lead to strong heating due to their high absorbance for IR light (Figure 3). However, the particles are inhomogeneously distributed and form aggregates, leading to a low reproducibility.

Laser light exposed to carbon μ -hotplates results in induced cell death for cells in direct contact (Figure 4-B: 22 mW, 1 s), depending on laser power and exposure time (summary see Table 1). By using higher laser power at 36 mW for 1 s, the cell is completely ruptured, (Figure 4-C) and the whole cell substrate becomes available, for example for single cells analysis. Lower laser power does not lead to induced cell death (Figure 4-A). Likewise, cells survive the direct exposure of IR light without the use of the μ -hotplates. Often bubble formation occurs due to the strong heating and the rough carbon surface.

Laser power of more than 60 mW for 1 s is necessary to induce cell death using

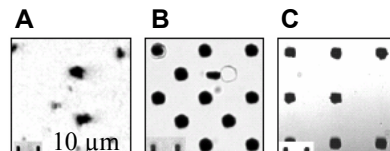


Figure 2. Microparticles and μ -hotplates: (A) graphite powder, (B) carbon and (C) Au-Pt-black μ -hotplates

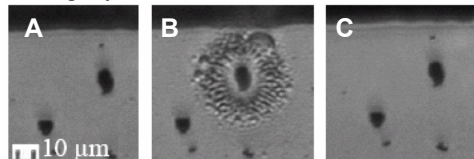


Figure 3. Boiling of water by heating graphite particles: (A) before and (B) after laser treatment (14 mW, 10 s); (C) after flushing with water

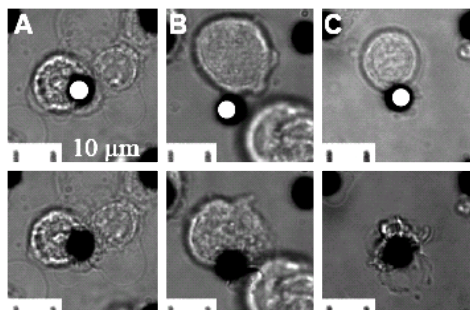


Figure 4. Images of cells grown on glass with carbon μ -assays before (top row) and after (bottom row) laser-induced heating for 1 s : (A) 14 mW: cell survives; (B) 22 mW and (C) 36 mW: cells die
○ - Position of laser spot

Au-Pt-black μ -hotplates (squares of $160 \mu\text{m}^2$), due to lower absorption of the laser light. Applying laser power of 25 mW for 1 s or less does not affect cell viability. Bubble formation can be prevented and produced on purpose at the edges of a hotplate.

Table 1. Survival rate of cells grown on glass with carbon μ -hotplates for various laser intensities, P, and exposure time, t

	P = 5 mW	P = 14 mW	P = 22 mW	P = 30 mW
t = 0.5 s	100%	100%	100%	50%
t = 0.75 s	100%	100%	100%	0%
t = 1 s	100%	100%	0%	0%
t = 2 s	100%	50%	0%	0%

4. Conclusions

The μ -hotplates made of carbon and Au-Pt-black give a good control over the survival of cells, since fast and defined heating is possible. In contrast to common heating systems, no direct connections are necessary. Therefore, it is a very flexible method, which can be easily implemented in any microchip. Also, this technique is suitable for moving small volumes and droplets.

Acknowledgment

Financial support by the European Community (CellPROM project, contract no. NMP4-CT-2004-500039 under the 6th Framework Programme for Research and Technological Development) is gratefully acknowledged. We thank U. Marggraf for the fabrication of the SU-8 structures and A. Neyer (University Dortmund, Germany) for kindly providing the cleanroom facility.

References

1. V. Zeeb, M. Suzuki and S. Ishiwata, *A novel method of thermal activation and temperature measurement in the microscopic region around single living cells*, J. Neurosc. Meth., 139, pp. 69-77 (2004)
2. K.C. Neuman, E.H. Chadd, G.F. Liou, K. Bergman and S.M. Block, *Characterization of Photodamage to Escherichia coli in Optical Traps*, Biophys. J., 77, pp. 2856-2863 (1999)
3. A.G. Skirtach, A.M. Javier, O. Kreft, K. Köhler, A.P. Alberola, H. Möhwald, W.J. Parak and G.B. Sukhorukov, *Laser-Induced Release of Encapsulated Materials inside Living Cells*, Angew. Chem. Int. Ed., 45, pp. 4612-4617 (2006)
4. G.L. Liu, J. Kim, Y. Lu and L.P. Lee, *Optofluidic control using photothermal nanoparticles*, Nature Materials, 5, pp. 27-32 (2006)
5. J.-H. Park, A.M. Derfus, E. Segal, K.S. Vecchio, S.N. Bhatia and M.J. Sailor, *Local Heating of Discrete Droplets Using Magnetic Porous Silicon-Based Photonic Crystals*, J. Am. Chem. Soc., 128, pp. 7938-7946 (2006)
6. A. Singh, J. Jayaram, M. Madou and S. Akbar, *Pyrolysis of Negative Photoresists to Fabricate Carbon Structures for Microelectromechanical Systems and Electrochemical Applications*, J. Electrochem. Soc., 149 (3), pp. E78-E83 (2002)

HIGH THROUGHPUT SINGLE CELL CLONE ANALYSIS

Sara Lindström¹, Rolf Larsson², Helene Andersson¹

¹ Royal Institute of Technology, Dept of Nano Biotechnology, 100 44 Stockholm,
Sweden

² Uppsala University, Dept of Medical Sciences, 751 85 Uppsala, Sweden
(sara@biotech.kth.se)

Abstract

A novel microplate has been developed for high throughput single cell/clone analysis. Rapid single cell seeding using a conventional FACS into micro wells allows several thousands of single cells to be cultivated, short-term (72 h) or long-term (10-14 days), and analyzed individually. The platform requires a remarkably low number of cells, a major advantage when screening limited amounts of patient cell samples. Analysis of single cell heterogeneity and colony formation related to drug sensitivity can be accomplished in a high throughput manner.

Keywords: single cell analysis, leukemia, high throughput, single clone analysis

1. Introduction

Most laboratory assays used for drug sensitivity/resistance testing today are based on measurements of average effects on the whole tumor cell population, making it difficult to study how individual cells differ from each other [1]. This platform [2] enables investigators to analyze characteristics of patient samples on a single cell level, leading to a more optimized treatment.

2. Materials

The plate consists of three levels: a bottom glass plate, an etched microgrid plate and a top membrane. It has the format of a microtiter plate to facilitate implementation in clinical labs (figure 1).

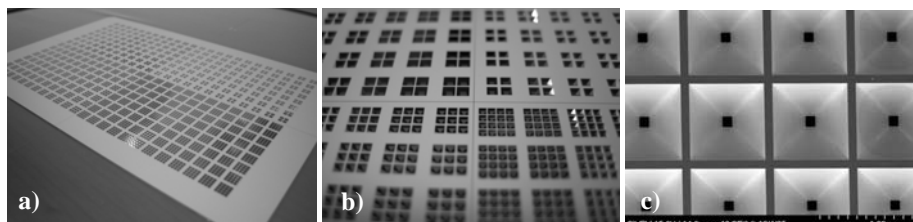


Figure 1. a) Whole plate (127 x 86mm). Version with 1536 to 6144 wells per whole plate. b) Different sizes of micro wells (volumes from 150nl to 500nl). c) Sloped walls for facilitated cell seeding.

The goal is to fit as many wells (currently 6144) as possible into the plate and maintain the possibility to seed individual cells using the FACS. There are two versions of the plate, one with an anodically bonded glass bottom and one that is clamped together with

a selected surface to enable surface modifications (ie. fibronectin, cell seed layers etc) of the whole bottom plate before assembly. Different membranes have been tested to optimize cell cultivation conditions and prevent evaporation.

3. Experimental

Cell seeding is performed by FACS, efficiently placing one cell in the centre of each well (figure 2).

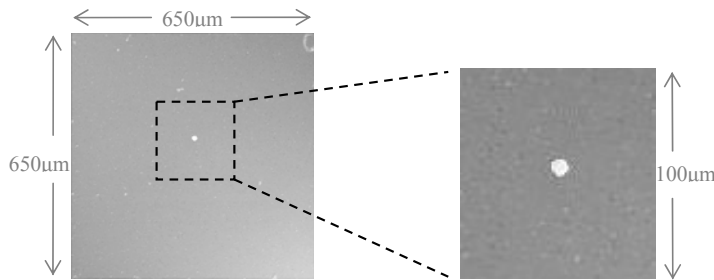


Figure 2. A fluorescently labeled single cell in one well directly after cell seeding.

4. Results and discussion

The time needed for seeding single cells in for example 300 wells is 5 minutes (i.e. one second per well) with a ~90% single cell occupancy per well. The FACS is also used for subsequent distribution of chemotherapeutic drugs, shown with lysis buffer in figure 3. This makes it possible to study different drugs and concentrations and their effects on single cells in high throughput.

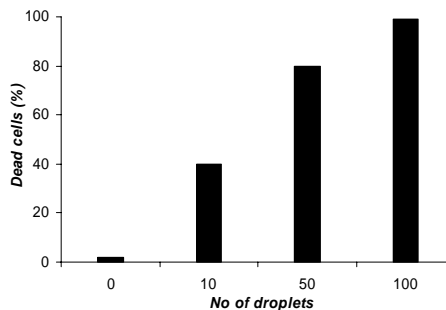


Figure 3. Percentage of dead cells (y-axis) after FACS distribution of lysis buffer (x-axis shows increased lysis buffer concentration) demonstrating the working concept of distributing drugs by FACS.

Leukemic K562 cells have successfully been seeded and cultivated in the plate up to 14 days (figure 4), followed by a staining procedure (MGG) and evaluation of viability and colony formation.

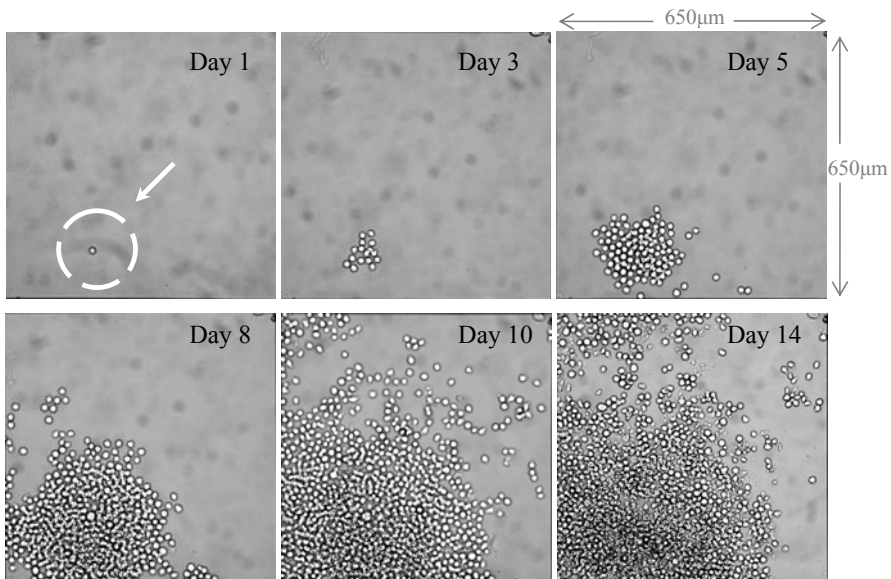


Figure 4. Colony formation in one well (day 1-14) starting with a single cell.

Patient samples (chronic lymphocytic leukemia) have been sorted in the same manner. Viability in the plate is comparable with other cell cultivation systems. Consumption of cells drastically decreases to 0.6% of the cells needed in conventional methods: a major advantage since the number of cells most commonly is the limiting factor when screening patient samples for drug sensitivity.

5. Conclusions

This novel device for high throughput single cell analysis has the potential to become an optimal diagnostic tool when studying tumor cells from for example leukemia patients with respect to heterogeneity, proliferation and apoptosis/sensitivity to chemotherapeutics at the single cell/clone level.

Acknowledgements

Financial support from PicoVitro AB is gratefully acknowledged. Kaj Kauko and Laurent Barbe kindly helped with the fluorescence imaging and FACS support was received from John Löfblom and Jan Grawé.

References

1. Freuhof JP and Bosanquet AG. *In vitro determination of drug response: a discussion of clinical applications*, PPO updates, 7, 1-16 (1993).
2. US patent # 6037171: *Cell culture microchambers in a grid matrix sandwiched between a planar base and semipermeable membrane*.

ON-CHIP HIGH-ACCURACY EVALUATION OF CELLULAR EPM VARIATION WITH CELL CYCLE PROGRESS THROUGH S-PHASE

Takanori Akagi^{1,2}, Masa Suzuki¹ and Takanori Ichiki^{1,2}

¹ School of Engineering, The University of Tokyo, 2-11-16 Yayoi, Bunkyo-ku
113-8656, Japan

² Center for Nano-Bio Integration, The University of Tokyo, 7-3-1 Hongo, Bunkyo-ku
113-8656, Japan
E-mail: akagi@sogo.t.u-tokyo.ac.jp

Abstract

We report the successful tracking of cellular electrophoretic mobility (EPM) evolution with the progress of a cell cycle using on-chip cell electrophoresis. After thymidine treatment, the EPM distribution of HL-60 cells apparently differed from that of nonsynchronized cells and seemed to follow a Poisson distribution. In order to clarify the reason for this observation, another improved procedure was adopted for more defined synchronization at the early stage of the S-phase. As a result, we were successful in tracking the evolution of the EPM distribution of cells, released from the arrested state at the early stage of the S-phase, with the progress of the S-phase. Moreover, an additional advantage of our methodology lies in its ability to allow simultaneous evaluation of EPM and GFP fluorescence. These results suggest that on-chip cell electrophoresis is a methodology powerful enough to track the cellular surface evolution through the cell cycle and is expected to be a promising analysis platform in various applications.

Keywords: Cell cycle, Electrophoretic mobility (EPM), Green fluorescence protein (GFP) assay, On-chip cell electrophoresis

1. Introduction

With the recent progress in biotechnology, the analysis of living cells has become increasingly essential. In particular, in cell therapy and tissue engineering, the evaluation of the cell cycle, that is, the cycle of cell duplication and division, is essential for achieving a full therapeutic effect because cellular function and response to drugs vary during the cell cycle [1, 2]. However, conventional tools for analyzing the cell cycle such as the fluorescence-activated cell sorter (FACS) are not suitable for cellular analysis in clinical applications because chemical invasion and damage to the cell membrane are not negligible. On the other hand, electrophoresis of cells is one of the techniques used to quantify the cell surface charge and to study events at the level of membranes of single cells. We have recently reported that the highly precise measurement of cellular electrophoretic mobility (EPM) using on-chip microcapillary electrophoresis (μ CE) is a promising methodology for identifying different species and states of living cells noninvasively [3]. We preliminarily reported its possible application to cell cycle evaluation using synchronized cells at various cell cycle stages [4]. In this paper, we report the successful tracking of cellular EPM evolution with the progress of the cell cycle using on-chip cell electrophoresis and discuss its biological relevance in clinical applications.

2. Experimental

In order to synchronize the cell cycle stage, human leukemic (HL-60) cells were cultivated with thymidine (1 mM) and leptomycin B (0.1 μ M) in accordance with the schedule illustrated in Figs. 1(a), 2(a) and 3(a). In order to confirm the synchronizing effect, collected

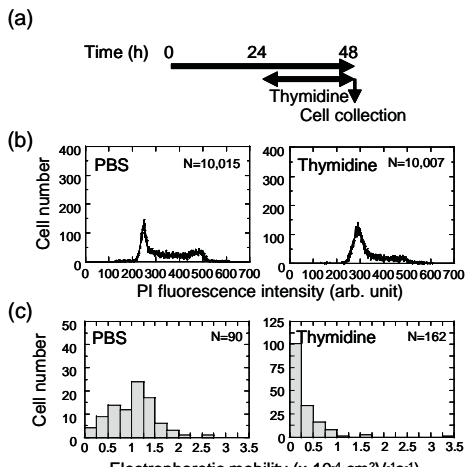


Fig. 1 Influence of the synchronizing effect of thymidine on DNA contents and EPM value of HL-60 cells. (a) Time scheme of thymidine treatment. (b) DNA content histograms of HL-60 cells treated with PBS for control (left) and thymidine (right). (c) EPM histograms of HL-60 cells treated with PBS for control (left) and thymidine (right). The EPM distribution after treatment with thymidine differed from that after treatment with PBS and followed a Poisson distribution.

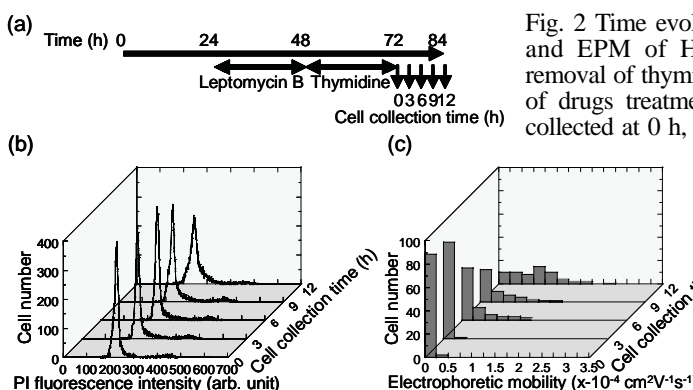


Fig. 2 Time evolution of DNA content and EPM of HL-60 cells after the removal of thymidine. (a) Time scheme of drugs treatment. HL-60 cells were collected at 0 h, 3 h, 6 h, 9 h and 12 h after the removal of thymidine. (b) Time dependent variation of DNA content distribution. (c) Time dependent variation of EPM distribution.

cells were stained with propidium iodide (PI) and the DNA content of the cells was analyzed by determining the fluorescence intensity of stained DNA using a flow cytometer (Beckman Coulter). In order to measure the EPM of HL-60 cells using μ CE chips, microchannels of 30 μm depth and 30 μm width were made by deep RIE on a 20 mm by 20 mm silica glass plate. The inner surfaces of microchannels were coated with the 2-methacryloyloxyethylphorylcholine (MPC) polymer. PBS(-) was used as a migration buffer. Movies of migrating cells, which were recorded using a high-speed charge-coupled device (CCD) camera, were analyzed using real-time particle tracking velocimetry (PTV) software. Electroosmotic flow (EOF) mobility was measured using charge-free beads. EPM was calculated by subtracting EOF mobility from apparent EPM. Electric field strength was constant at 100 V/cm in all the experiments.

3. Results and discussion

Firstly, we examined thymidine treatment as illustrated in Fig. 1(a) for preparing HL-60 cell samples synchronized at the S-phase. In order to confirm its synchronization effect, DNA content distributions of treated cells were measured using a flow cytometer with the PI treatment technique for dyeing DNA. We were able to confirm the drug-induced

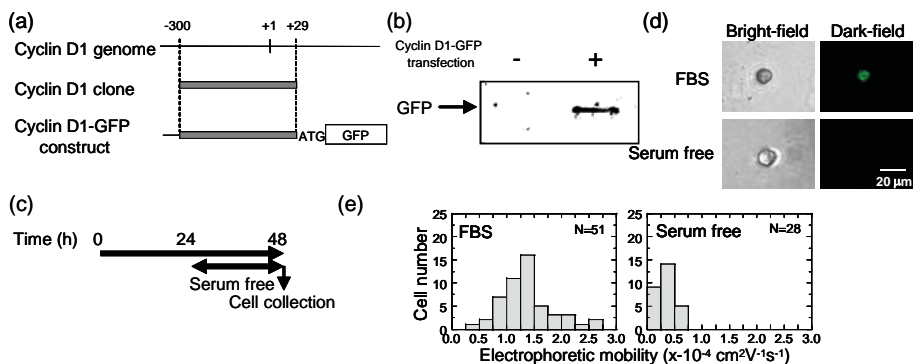


Fig. 3 (a) Gene map of a cyclin D1-GFP construct. (b) Western blot analysis of transfected HL-60 cell extracts with anti-GFP antibody. (c) Time scheme of serum treatment. (d) Microscope bright- (left) and dark-field (right) images of transfected HL-60 cell. (e) EPM distribution of transfected HL-60 cells.

synchronization at the S-phase (Fig. 1(b)). Then, EPM values of synchronized cells were measured, as shown in Fig. 1(c). The EPM distribution of thymidine-treated cells was apparently different from that of nonsynchronized cells and seemed to follow a Poisson distribution. Although the reason for this was not clear, we assumed that the observed unique distribution may be ascribed to ill-defined synchronization resulting from the adopted drug-treatment procedure. Namely, some cells are arrested at the early stage of the S-phase, whereas others are arrested at the late or some other stage. Therefore, another improved procedure (Fig. 2(a)) was adopted for more defined synchronization at the early stage of the S-phase. As a result, we were successful in tracking the evolution of the EPM distribution of cells, released from the arrested state at the early stage of the S-phase, with the progress of the S-phase. From the change in DNA content distribution (Fig. 2(b)), we confirmed the progress of DNA synthesis through the S-phase. At the same time, the EPM distribution gradually varied with the progress of the cell cycle through the S-phase (Fig. 2(c)). Thus, on-chip cell electrophoresis has been demonstrated to be a methodology powerful enough to track the cellular surface evolution through the cell cycle. Moreover, an additional advantage of our methodology lies in its ability to allow the simultaneous evaluation of EPM and fluorescence. Hence, cell cycle study using both EPM evaluation and green fluorescent protein (GFP) assay has been demonstrated. HL-60 cells were transfected with a fusion transgene of the GFP-coding region and 5'-flanking region of the human cyclin D1 gene, which is related to the progression of cells through the cell cycle (Fig. 3(a-b)). We confirmed GFP fluorescence and EPM variation depending on the presence of serum, namely, the G₁ arrest phenomenon (Fig. 3(c-e)). In summary, the on-chip cell electrophoresis system reported here is expected to be a promising analysis platform that is useful in various applications.

References

- [1] T. Akagi, et al., *Life Sci.* **72**, 1183-1197 (2003).
- [2] T. Akagi, et al., *J. Pharmacol. Exp. Ther.* **308**, 378-384 (2004).
- [3] J. N. Mehrishi, et al., *Electrophoresis* **23**, 1984-1994 (2002).
- [4] T. Akagi, et al., *Proc. Micro Total Analysis Systems 2005*, 373-375 (2005).

MAGNETO-MICROFLUIDIC DEVICE FOR APOPTOTIC CELL SEPARATION

Hyun-Seok Kim¹, Oh-Taek Son¹, Kunhong Kim²,
Sang Hyeob Kim³, Sung-Lyul Maeng³ and Hyo-Il Jung¹

¹Graduate School of Mechanical Engineering, Yonsei University, Korea

²Graduate School of Medicine, Yonsei University, Korea

³Cambridge-ETRI joint R&D center, IT convergence & components laboratory, ETRI
(E-mail : uridle7@yonsei.ac.kr)

Abstract

Separation of magnetically labeled cell has been a popular technique in cytometry. Normal Jurkat cells were treated with Chlorohexamide (CHX) and TRAIL to induce apoptosis. Apoptotic cells were treated with biotin functionalized fusion protein, C2A and streptavidin coated magnetic beads. The force balance between magnetic and drag force acting on the cells were calculated. The microfluidic device was designed accordingly. Results from our device were in a good agreement with those of the conventional flow cytometer, indicating our device can be used to sort apoptotic cells in a miniaturized system.

Keywords: microfluidic device, apoptosis, C2A protein

1. Introduction

Apoptosis as a term of programmed cell death is highly involved in the process of life that maintains homeostasis of tissues and organs in concert with proliferation, growth, and differentiation. Apoptosis is a good indication to check the efficiency of the drug compound as it is the first cellular process in the treatment of tumor with anti-tumor agent [1]. Fast detection of apoptotic cells *in vitro* can be used in high-throughput screening to monitor the efficiency of drug compounds [2].

In our study, we selectively labeled apoptotic cells with magnetic beads and applied external magnetic field to separate labeled cells. For the high efficiency of on chip separation, the design of microfluidic channel was optimized based on the analysis of force balance between magnetic and drag force. Finally, the result of microfluidic cell sorter was compared with FACS (Fluorescence Activated Cell Sorter).

2. Theory

The equation of motion resulted from integration of two forces, stokes drag and magnetic force is give by [3].

$$\Delta z = \frac{V_m \Delta \chi |\nabla B^2|}{12 \mu_0 \pi \eta R} t \quad (1)$$

Where V_m is the volume of paramagnetic material per bead, $\Delta \chi$ is the magnetic susceptibility of magnetic bead, B is the magnetic field intensity, μ_0 is the magnetic

permeability of free space, η is the viscosity of solution, R is the radius of a single cell coated with magnetic particles and t is the time.

The optimized microfluidic channel geometry is shown in Fig. 1. Because of asymmetric structure of outlets, required deflection of labeled cells in vertical direction is more than $25\mu\text{m}$. According to equation (1), we designed the length of main channel as 14mm long and flow rate of $5\mu\text{L}/\text{min}$ for inlet 2, $25\mu\text{L}/\text{min}$ for inlet 1 and 3.

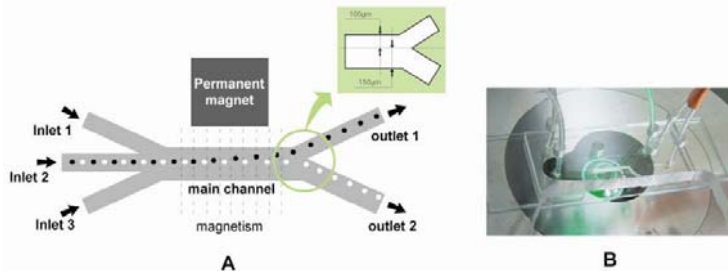


Figure 1. Schematic diagram (A) and photograph (B) of microfluidic channel.

3. Experimental

To obtain apoptotic cells, we treated normal Jurkat cells (1×10^6 cells/mL) with chlorohexamide ($10\mu\text{g}/\text{mL}$) and TRAIL ($500\text{ ng}/\text{mL}$). Biotin-C2A protein ($1\text{ mg}/\text{mL}$, $5\mu\text{L}$), drug treated Jurkat cells, (5×10^5 cells/mL, $200\mu\text{L}$) and CaCl_2 (200 mM , pH 7.4, $10\mu\text{L}$) were mixed and then incubated for 10 min. Then, streptavidin coated magnetic beads ($0.8\mu\text{m}$, 6×10^6 beads/mL, $10\mu\text{L}$) were added and mixed (Fig 2A).

The microfluidic channel was fabricated using conventional PDMS softlithography process [4]. We applied the SU-8 negative epoxy based photoresist (SU-8 2100, MicroChem Corp.) as a mold which is appropriate for making $130\mu\text{m}$ height of the channel. PDMS (DC-134, Dow Corning) was poured on the SU-8 mold and peeled off after baking.

Two syringe pumps (KDS scientific, CMA instruments) were connected to inlets as flow actuator. One is the buffer solution syringe, and the other two are the sample solution syringes. The microfluidic channel was placed on an optical microscope and monitored by a CCD camera (Fig. 2B).

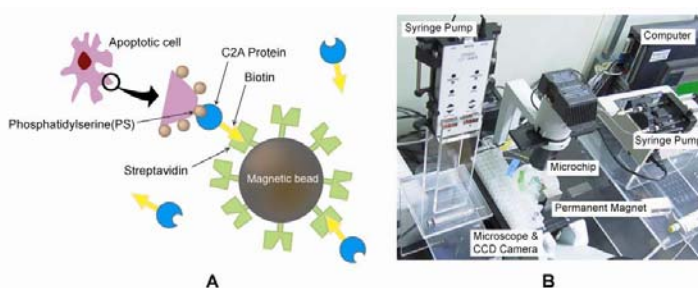


Figure 2. Principle of labeling apoptotic cells (A) and experimental setup (B)

4. Results and discussion

The rate of apoptosis in drug treated Jurkat cells are shown in Fig. 3A, 33% (early and late apoptotic cells). When we applied this sample in microfluidic cell sorter, 14.5×10^4 cells (36%) were separated from the total number of cells (40.8×10^4). Consequently, the efficiency of our device was 92% (Fig. 3B).

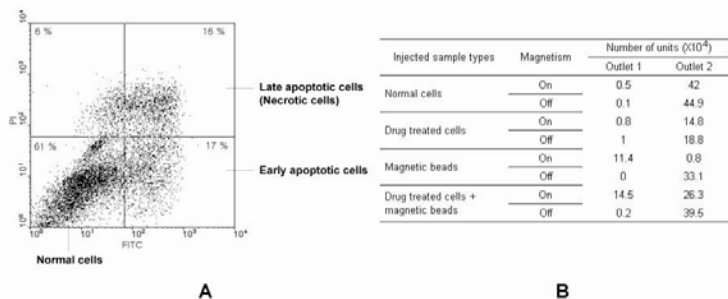


Fig. 3 FACS analysis of apoptotic Jurkat cells (A) and the result of our device (B)

5. Conclusion

In this research, we theoretically analyzed apoptotic cell mobility in microfluidic channel and fabricated the channel based on the analysis. The efficiency of the separation by our approach was comparable with that of the conventional cytometer analysis.

Acknowledgements

This work was supported by the Ministry of Information and Communication, Republic of Korea, under project No. A1100-0501-0073 and a grant from National Core Research Center (NCRC) for Nanomedical Technology of the Korea Science & Engineering Foundation. We are very much grateful to Dr. B. Davletov for his kind supply of C2A protein gene.

References

1. D. Myrick, D. Blackinton, J. Klostergaard, N. Kouattab, A. Maizel, H. Wanebo and S. Mehta, Paclitaxel-induced apoptosis in Jurkat, a leukemic T cell line, is enhanced by ceramide, Leukemia Research Vol. 23 pp.569–578 (1999)
2. S. D. H. Chan, G. Luedke, M. Valer, C. Buhlmann and T. Preckel, Cytometric Analysis of Protein Expression and Apoptosis in Human Primary Cells With a Novel Microfluidic Chip-Based System, Cytometry Part A, Vol. 55A pp. 119–125 (2003)
3. Q. Ramadana, V. Samperb, D. Poenara, C. Yub, On-chip micro-electromagnets for magnetic-based bio-molecules separation, J. Magnetism and Magnetic Materials Vol. 281 pp. 150–172 (2004)
4. D. C. Duffy, J. C. McDonald, O. J. A. Schueller, and G. M. Whitesides, Rapid Prototyping of Microfluidic Systems in Poly(dimethylsiloxane), Anal. Chem. Vol. 70, pp. 4974-4984 (1998)

Microbial Cells Trapping and Detection through Filter-based Microfluidic Devices

Zhu L., Peh X.L., Ji H.M., Feng H.H., Liu W.-T.

*Institute of Microelectronics, 11 Science Park Road, Science Park II, 117685,
SINGAPORE

Abstract

Trapping efficiency up to 90% with 12 microbial cells was achieved by optimizing sample delivery and filter design in a microfluidic device, and using a novel injection approach. Cell loss during sample delivery was significantly minimized by increasing the tubing diameter used for the connection between sample storage and micro-device. A hydrodynamic focusing approach was used to reduce cells contacting and adhesion on the walls of micro-channel and chip inlet. We also optimized the pillar design with a zigzag arrangement (13 μm in chamber depth and 0.8 μm in gap) to prolong the effective length of cell trapping, and to reduce the gap length between any two given pillar (i.e. pressure drop) at the filter region.

Keyword: trapping efficiency, microfluidic, lab-on-a-chip, microbial, pathogen, detection

1. Introduction

Two major sources of sample loss during sample introduction from macro to micro world are dead volume and surface adhesion. While dead volume could be minimized by proper design of the world-to-chip interface [1], surface adhesion, especially the adhesion of proteins and cells, has been the focus of many research papers [2,3]. Bare semiconductor and glass surfaces were found to be most attractive to cell adhesion, which could be effectively controlled by surface coating [4-5]. Besides the two major sources, we reported here two other sources of cell loss, which occurred at the interface between sample storage and delivery tubing and on the inlet walls of silicon chips. We were able to achieve trapping efficiency up to 90% with 12 microbial cells after the optimization of sample delivery, introduction and the filter design of a filter-based microfluidic device.

2. Experimental

A 1 mL plastic syringe is connected with polyvinyl acid coated fused silica capillary through a syringe needle and a capillary union. Capillaries used are of an inner diameter of 25, 76, 250, 530 μm , respectively, and were cut into various lengths, i.e. 4, 10, 18 and 30 cm. The capillary was then connected to a filter-based microfluidic filter chip (Fig. 1) through a chip holder [6].

3. Results & Discussion

To evaluate cell loss during sample delivery, solution containing 4- μm polystyrene

beads was pumped through a fused silica capillary from a 1 mL plastic syringe commonly used for sample delivery. Bead loss through a 30-cm capillary tube was observed, and the percentage of loss increased from 14.4% with 530- μm ID capillary to 46.5% with 25- μm ID capillary (Fig. 2a). Calculation of the intercepts at zero capillary length showed ~65 - 93% of total beads loss (after 30-cm capillary) happened at the interface between the syringe and capillary (Fig. 2b). By increasing the tubing diameter used for the connection between sample storage and micro-device, the cell loss was significantly minimized.

To further minimize severe cell adhesion on the inlet wall of a micro-device, a hydrodynamic focusing approach (Fig. 3) was used. This greatly reduced cells contacting and adhesion on the walls of micro-channel and chip inlet. Cell loss could also occur at the filter region mainly due to cell deformation. To prevent cells squeezing through gaps that are relatively smaller than the cell size, the gap size could be reduced. However, this could also lead to an increase in pressure drop over the filter region, causing further deformation and breakage of cells. Thus, we have optimized the pillar design with a zigzag arrangement (13 μm in chamber depth and 0.8 μm in gap) to prolong the effective length of cell trapping, and to reduce the gap length between any two given pillar (i.e. pressure drop) at the filter region (Fig. 1). The maximum working flow rate also increased from 20 $\mu\text{L}/\text{min}$ [4] to 100 $\mu\text{L}/\text{min}$.

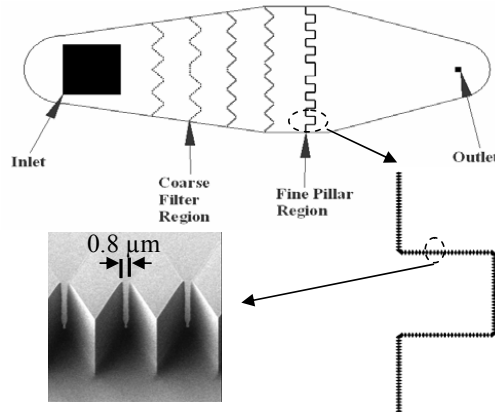
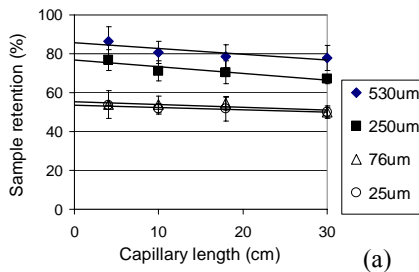
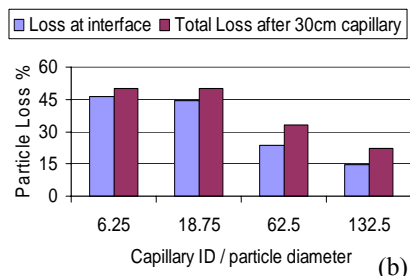


Figure 1. Schematic diagram of the diamond shaped pillar type filter design. Inset: SEM photo of the diamond shaped pillars.



(a)



(b)

Figure 2: (a) Retention of 4 μm particles after passing through fused silica capillary. (b) Loss of particles at zero capillary length and after 30 cm capillary.

4. Conclusion

After solving the potential cell loss during sample injection and trapping, the overall cell trapping efficiency with the integrated system was evaluated by injecting 150 μL of sample solution containing 12 *Cryptosporidium parvum* and 12 *Giardia lamblia* cells through a poly(vinyl alcohol) coated fused silica capillary (ID 250- μm). The trapping efficiencies for *C. parvum* and *G. lamblia* were improved from $79 \pm 11\%$ and $50.8 \pm 5.5\%$ without hydrodynamic focusing, respectively, to $90.8 \pm 5.8\%$ and $89.8 \pm 16.6\%$ with hydrodynamic focusing.

References

1. C.K. Fredrickson, Z.H. Fan, *Macro-to-micro interfaces for microfluidic devices*, Lab Chip, **4**, 526-533 (2004).
2. H. Lu, L.Y. Koo, W.C.M. Wang, D.A. Lauffenburger, L.G. Griffith, K.F. Jensen, *Microfluidic Shear Devices for Quantitative Analysis of Cell Adhesion*, Anal. Chem. **76**, 5257-5264 (2004).
3. P.D. Moreira, P.R. Marreco, A.M. Moraes, M.L.F. Wada, S.C. Genari, *Analysis of cellular morphology, adhesion, and proliferation on uncoated and differently coated PVC tubes used in extracorporeal circulation (ECC)*, J. Biomed. Mater. Res. B, **69B**, 38-45, (2004).
4. J.D. Cox, M.S. Curry, S.K. Skirboll, P.L. Gourley, D.Y. Sasaki, *Surface passivation of a microfluidic device to glial cell adhesion: a comparison of hydrophobic and hydrophilic SAM coatings*, Biomaterials, **23**, 929-935 (2002).
5. B.J. Kirby, A.R. Wheeler, R.N. Zare, J.A. Fruetel, T.J. Sheppard, *Programmable modification of cell adhesion and zeta potential in silica microchips*, Lab On A Chip, **3**, 5-10 (2003).
6. L. Zhu, Q. Zhang, H.H. Feng, S. Ang, F.S. Chau, W-T. Liu, *Filter-based microfluidic device as a platform for immunofluorescent assay of microbial cells*, Lab. Chip., **4**(4) 337-343 (2004).

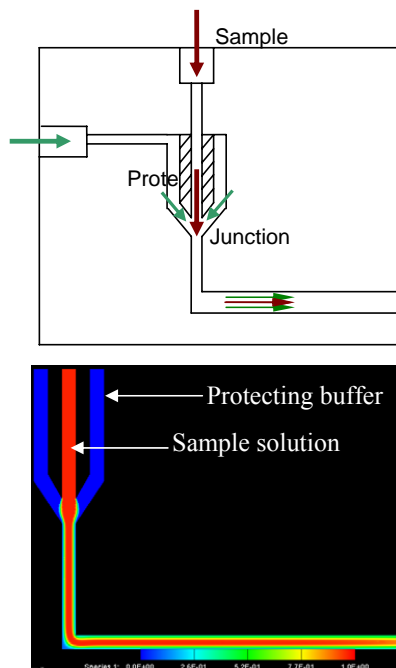


Figure 3: (a) Schematic drawing of hydrodynamic structure. (b) Simulation of the flow profile in micro-channel.

DISPOSABLE THERMOPLASTIC MICROCHIPS FOR CELLULAR AND BIOMOLECULAR ANALYSIS

Jonas Melin^{1,2}, Henrik Johansson¹, Malin Jarvius¹, Ola Söderberg¹, Jenny Göransson¹, Ulf Landegren¹, Mats Nilsson¹ and Jonas Jarvius^{1,§}

¹Dept. of Genetics and Pathology, Uppsala University, Sweden.

²Dept. of Engineering Sciences, Uppsala University, Sweden.

§To whom correspondence should be addressed.

E-mail: jonas.jarvius@genpat.uu.se

Abstract

We have developed a multipurpose microfluidic platform where actuators such as pumps and valves can be combined with excellent opportunities for mammalian cell growth and for sensitive fluorescence detection on inexpensive disposable chips, thus enabling a wide range of integrated microfluidic assay procedures. In this study we demonstrate a device for simultaneous detection of cells, stained for five different surface proteins, in three parallel flow channels.

Keywords: thermoplastics, injection molding, bonding, flow cytometry

1. Introduction

In order to fully exploit the benefits of microfluidics in biological applications, methods are needed to produce disposable microchips on a large-scale. However, unlike the successful production of solid-phase microarrays by integrated circuit fabrication techniques [1], large-scale implementation of similar principles for production of microfluidic systems has yet to be realized. We have developed a multipurpose platform where pumps and valves can be combined with excellent opportunities for mammalian cell growth and for fluorescence detection on inexpensive disposable chips, enabling a wide range of integrated microfluidic assay procedures [2]. Rapid compact disc injection molding techniques are used to produce structured microchips. In this study we have demonstrated the utility of the platform for fluorescence applications by fabricating a miniature flow cytometer, capable of simultaneously measuring three cell samples.

2. Experimental

Polymer microfluidic chips were produced by injection molding in combination with a scalable bonding process, described in detail elsewhere [2]. In brief, thermoplastic microfluidic chips were produced by compact disc injection molding by Åmic AB (Sweden). After dicing and silica deposition, a 200 µm thick PDMS-zeonor lid was bonded to the silica layer so as to create a closed channel, suitable for observation with a high-magnification objective.

Human blood was obtained from a healthy volunteer. Peripheral blood mononucleated cells were prepared by Ficoll (Pharmacia) separation. The cell-suspension was split into

three parts and each part was stained with two different antibodies (anti-CD19 PE + anti-CD3 FITC, anti-CD4 PE + anti-CD8 FITC, and anti-CD20 FITC + anti-CD4 PE, all from Dako) for 30 minutes at 4°C. The cells were washed by centrifugation 3 times and resuspended in PBS (137 mM NaCl, 2.7 mM KCl, 10 mM phosphate buffer, pH 7.4). The three differently stained lymphocyte samples were pumped through three parallel microchannels (50x40 µm cross section) with a syringe pump PHD-2000 (Harvard instruments) at a rate of 1 µL/min. A confocal microscope (Zeiss LSM 5 META) was used to detect the cells, operated in line-scanning mode across all three channels perpendicular to the direction of liquid flow. The microscope focus was set to the center of the microchannels and the pinhole was set to 400 µm, corresponding to a calculated optical slice of <5 µm in a Carl Zeiss Fluar 40x/1.3 NA objective. Typically, 10000 lines of 512 pixels were recorded, with a voxel time of 1.6 microseconds, resulting in a total data acquisition time of approximately 10 seconds. The line scan data were stored in a 24-bit rgb-TIF-file and analyzed by dedicated software written in MATLAB 6.5 (MathWorks, MA). The data obtained was verified by flow cytometry using a FacSORT instrument (Becton Dickinson).

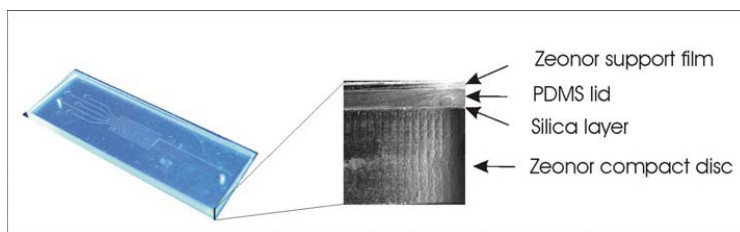


Figure 1. Left: A bonded microchip. **Right:** Cross-section of the bonded chip showing the PDMS-thermoplastic composite.

3. Results and Discussion

We have developed a platform for microfluidic analysis that combines the virtues of elastomer technology and high-throughput compact disc injection molding (figure 1). This has been possible by incorporating a recently developed technique for sealing and stacking thermoplastic microstructures, suitable for large-scale production of disposable chips [2]. The choice of polymer is open, allowing selection of the optimal material for a given application, based on e.g. chemical and optical properties or on price.

The favorable optical properties of the thermoplastic material Zeonor makes it an attractive choice for fluorescence applications, since auto-fluorescence levels are similar to those of glass [3]. We have demonstrated the utility of the platform by counting fluorescence-labeled cells that were pumped through three parallel microchannels (Fig 2A). Each channel contained cells labeled for two different surface proteins. From a single 10 second data acquisition three protein ratios could thus be obtained. For labeled lymphocytes we measured the ratios of CD19/CD3 to 0.07, CD8/CD4 to 0.33 and CD20/CD4 to 0.17, well in accordance with the corresponding ratios measured in a standard flow cytometer; 0.10, 0.32 and 0.14, respectively.

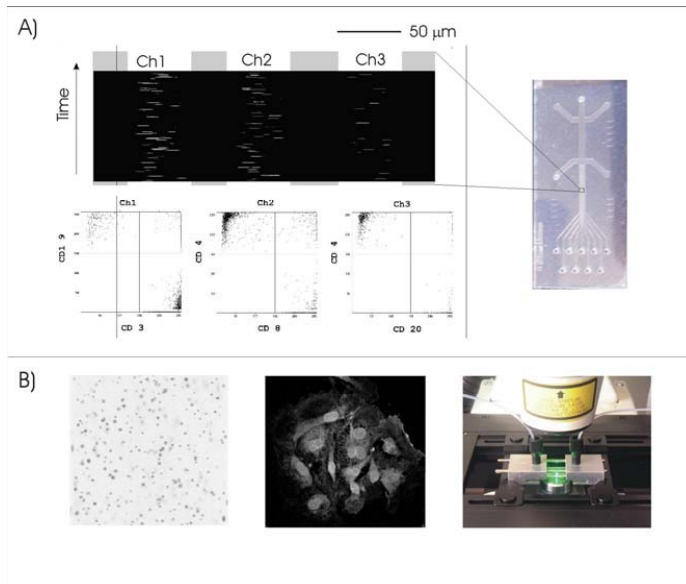


Figure 2. Illustration of analyses using the thermoplastic-PDMS platform. **A)** Fluorescence detection of five surface antigens in three independent microchannels. Three different surface proteins ratios were measured: CD19/CD3 was 0.07, CD8/CD4 was 0.33 and CD20/CD4 was 0.17, well in accordance with the standard flow cytometer data; 0.10, 0.32 and 0.14, respectively. **B)** From left to right, amplified single molecules detected in a homogenous flow system, single molecule detection of interacting Myc-Max proteins in a human endothelial cell line, and to the right instrumentation setup of the microchips and dedicated interface.

We have also used the platform in a number of biomolecular analysis formats (Fig. 2B) such as, cell culture, single molecule analysis both *in situ* and in a flow-system. Novel pump mechanisms, such as push-pull configurations, are also under investigation on the platform.

4. Conclusions

The platform presented here permits inexpensive production of integrated actuators possible, it supports mammalian cell growth, and has excellent optical properties for fluorescence detection.

References

1. Fodor, S.P. et al. *Nature* **364**, 555-556 (1993).
2. Melin, J. et al. *Anal. Chem.* **77**, 7122-7130 (2005).
3. Lamonte, R., McNally, D. *Plast. Eng.* **56**, 51-55 (2000).

THE MICRO PETRI DISH: A HIGHLY SUBDIVIDED MICROBIOLOGICAL GROWTH FORMAT FABRICATED BY MICRO-ENGINEERING A HIGHLY POROUS CERAMIC FOR DIAGNOSTICS, COUNTING AND SCREENING APPLICATIONS

Colin Ingham,^{1,2*}, Ad Sprenkels³, Johan Bomer³, Albert van den Berg³, Willem M. de Vos^{1,2} and Johan E.T. van Hylckama Vlieg^{1,4}

¹ Wageningen Centre for Food Sciences, Wageningen, NL

² Laboratory of Microbiology, Wageningen University, Wageningen, NL.

³ MESA+ Research Institute, University of Twente, Enschede, NL.

⁴ NIZO Food Research, Ede, NL.

Email: colin.ingham@wur.nl

Abstract

A microbial culture chip with an unprecedented number of culture areas (millions) has been manufactured by microengineering a porous aluminium oxide support. These chips have great potential in high throughput and diagnostic microbial culture.

Keywords: Microbial culture chip, porous aluminium oxide

1. Introduction

Microbial culture faces new challenges. Traditional growth formats such as the Petri Dish, whilst used for centuries, do not suit modern needs such as automation and high throughput. Furthermore, microbial culture from a few cells to the level of a visible colony or turbidity measurements is slow; taking from overnight for a rapidly growing organism such as *Escherichia coli* to >3 weeks for *Mycobacterium tuberculosis*. To meet the needs of microbial diagnostics, and industries such as manufacturing and food production, new growth formats are required. It is desirable that such formats are cheap and do not require complex technologies, such as robotics. MEMS techniques may help provide solutions here.

Microbial culture using porous materials as an inert support is well known. For example, dialysis membranes or nitrocellulose filters have been used for the growth of bacteria and fungi with the nutrients supplied through the pores from beneath (1, 2). However, such membranes have never been developed into high throughput or highly miniaturized formats. This may be due to the fact that the microengineering of these flexible and uneven filters and membranes is challenging. One alternative material that could be used is porous aluminium oxide, also known as Anopore. Microbial culture is possible on strips of this material with the nutrients supplied from beneath, allowing organisms on the upper surface to divide and create microcolonies (2-4). Growth of bacteria or fungi can be monitored at the single cell and microcolony level using a variety of microscopy techniques including fluorescence. The imaging properties are excellent due to a flat surface with low background fluorescence and the material is translucent when wet (2, 3). Furthermore, the high degree of porosity and inert nature of this material are useful. However, whilst aluminium oxides are used extensively within the MEMS and nanotechnology disciplines, highly subdivided microbial growth formats (100,000 to millions of culture areas) have never been made.

2. Theory

The challenge was to create a method of modifying a strip of porous aluminium oxide to create an array of highly precise culture areas that support microbial growth. The format needed to support culture of all culturable organisms and facilitate microbial cell analysis. Such a “culture chip” can be thought of as a large number of miniaturized Petri dishes. It is important that such chips should be relatively simple and behave in a reproducible and unbiased way; for example in viable counts or screening for mutants with altered properties.

3. Experimental

The solution to the problem was to bond an acrylic polymer over a sheet of porous aluminium oxide. Then reactive ion etching, directed by means of a shadow mask, was used to remove the acrylic polymer in selected locations leaving the material in place to provide cross-walls to segregate the different test areas. Finally, a sputtered layer of platinum was used to mask autofluorescence common to polymers. The solution was validated by culture of a series of very different microorganisms on the culture chip to utility, as described below.

Microengineering - Briefly: 36 x 8 mm strips of porous aluminium oxide (Anopore from Whatman, UK) were laminated over the entire surface using an acrylic film (from Ordyl). A silicon shadow mask was constructed and sputtered with a protective layer of 150 nm aluminium oxide. The mask was used to direct reactive ion etching (using a PlasmaTherm 790 parallel-plate reactive ion etcher) to remove the laminate in an array of square culture areas (7 x 7 to 150 x 150 μm). The culture areas of exposed aluminium oxide were separated by 20 μm wide and 10 μm high walls of intact laminate that acted as barriers against microbial cross-contamination then sputtered with platinum.

Culture and validation - Bacteria and fungi were cultured upon ethanol-sterilized chips placed upon the appropriate culture medium. Culture conditions were 6 h at 37 °C on L agar for *Escherichia coli*, 8 h at 37 °C (anaerobic conditions) for *Lactobacillus plantarum* WCFS1 and 7 h at 37 °C on Sabouraud agar for the yeast *Candida albicans*. Imaging was by transmission or fluorescence microscopy scoring compartments as supporting growth imaged by a Kappa CCD camera mounted on an Olympus BX41 microscope with the R, ImageJ and Excel software packages used for analysis.

4. Results and discussion

By etching techniques discrete growth compartments were constructed on the surface of the aluminium oxide. The result is a highly regular array (C.V. of dimensions < 5%) of miniaturized culture areas capable of supporting growth combined with *in situ* imaging (Fig 1) at densities ranging from 8200 to 360,000 growth areas cm^{-2} . This allows the creation of chips with 7 to 40 million of culture areas on a 96 well footprint: well within the range required for high throughput screening applications. Culture, containment of microbial growth within discrete areas has been demonstrated for *Lactobacillus plantarum* strain WCFS1 (Fig 1) and other micro-organisms suggesting a general applicability. For all organisms in the test panel > 99.5% of the culture areas could support growth and there were no obvious spatial biases across chips in terms of culturability.

5. Conclusions

Highly subdivided culture chips were created using MEMS techniques and shown to support microbial culture. The grid forms a highly regular framework for software to interpret

growth patterns and allows an unprecedented level of massively parallel culture. Additionally, unlike other miniaturized growth there are no problems with desiccation or aeration. We suggest that such culture chips are amenable to automation and may be valuable tools for high-throughput single cell biology, microbial diagnostics and counting, and screening.

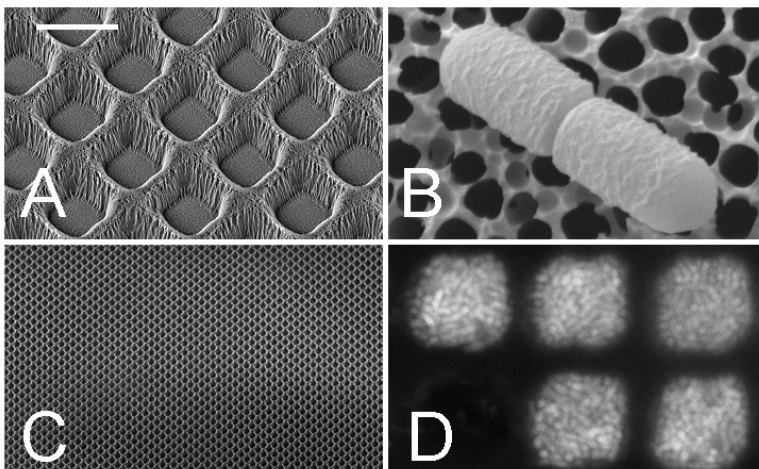


Figure 1. Example of culture format. (A) Scanning electron micrograph with porous base material marked. (B) Culture of *Lactobacillus plantarum* WCFS1 on chip surface imaged by SEM showing detail of aluminium oxide. (C) Overview of A. (D) Culture of *L. plantarum* WCFS1 within this format stained after growth with the fluorogenic dye Syto 9 and imaged by fluorescence microscopy. The inoculum was only a few bacteria per compartment, the organism has multiplied over a period of hours to fill the compartment but the walls are effective at protecting empty growth areas (such as the unstained area in the bottom left corner).

Acknowledgements

Thanks to LioniX B.V. for help with chip manufacture.

References

1. Nordbring-Hertz, B., Veenhuis, M. & Harder, W. (1984). Dialysis membrane technique for ultrastructural studies of microbial interactions. *Appl Environ Microbiol* 47, 195-197.
2. Jones, S.E., Ditner, S.A. Freeman, C. Whitaker, C.J. & Lock, M.A. (1989). Comparison of a new inorganic membrane filter (Anopore) with a track-etched polycarbonate membrane (Nuclepore) for direct counting of bacteria. *Appl Environ Microbiol* 55, 529-530.
3. McKenzie, C.H., Helleur, R. & Deibel, D. (1992). Use of inorganic membrane filters (Anopore) for epifluorescence and SEM of nanoplankton and picoplankton. *Appl Environ Microbiol* 58, 773-776.
4. Ingham, C.J., M. van den Ende, D. Pijnenburg, P.C. Wever and P.M. Schneeberger. 2005. *Appl. Env. Microbiol.* 71, 8978-8981.

MAGNETIC ON-CHIP DNA EXTRACTION IN A DROPLET BASED MICROSYSTEM

U. Lehmann¹, C. Vandevyver², V.K. Parashar¹, M.A.M. Gijs¹

1) Institute of Microelectronics and Microsystems

2) Research Commission EPFL-SNF

Ecole Polytechnique Fédérale de Lausanne (EPFL), Switzerland

Abstract

Magnetic droplet manipulation is a promising new approach towards the miniaturization of bioanalytical procedures. We present a system that combines droplet microfluidics and magnetic microparticles for the extraction and purification of DNA from μl -sized lysed cell samples. The DNA is detected on-chip via fluorescent microscopy or via an off-chip amplification step. We are able to extract and detect the DNA from as little as 10 cells in our system.

Keywords: droplet manipulation, magnetic particles, DNA extraction, cell lysis

1. Introduction

The miniaturization of processes for bio-analysis is an area of vast potential for droplet based microfluidic systems. In this respect the extraction of DNA from crude cell samples is gaining interest since most detection procedures rely on an amplification step that requires DNA of high purity. Here, we present a system (figure 1) that combines the magnetic manipulation of freely suspended droplets with bead-based DNA purification protocols. The use of small droplets as sample containers helps to reduce reagent consumption and processing time and in addition decreases the contact interfaces with the manipulation platform, thus minimizing problems of bio-molecule adsorption to sidewalls. The droplets are actuated via magnetic microparticles contained within, which act as force mediators and allow us to profit from the comparatively large force and long range of magnetic actuation [1]. These particles additionally serve as mobile substrates for the bio-molecules [2].

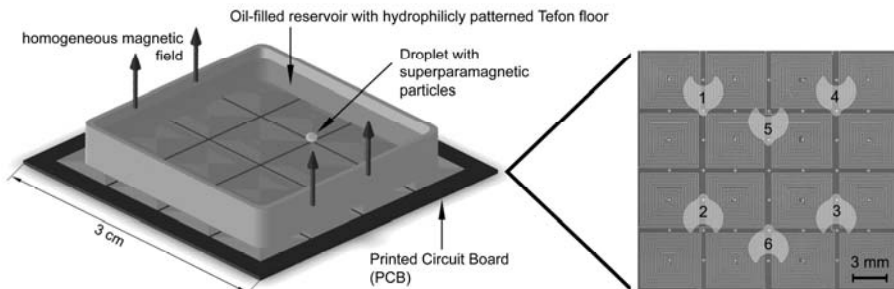


Figure 1. Schematics of the droplet manipulation system. The figure on the right-hand side demonstrates the placement of the 10 μl reservoirs that contain the different reagents for the DNA extraction (1: Lysis buffer, 2-4: washing reagents (ethanol), 5-6: elution buffer).

2. Purification Procedure and Setup

The stages of the on-chip DNA purification are schematically shown in figure 2. Starting from a set of six immobilized droplets of 10 µl, we are able to miniaturize a protocol for the extraction and purification of DNA from crude cell samples. The cells are lysed in a solution containing Guanidine thiocyanate, which also help to selectively attach the DNA to the magnetic silica particles. After extracting a small droplet containing the magnetic particles and the attached DNA from the immobilized lysis buffer droplet, the particle-and-DNA compound is passed through three stages of washing. Thus we are able to remove transferred cell debris or proteins, since these would inhibit subsequent steps of amplification. As a last step of the on-chip DNA extraction protocol, the purified DNA is eluted from the particles in a buffer of low ionic strength. Subsequently the eluted DNA can be either detected using fluorescent microscopy or it can be transferred to a step of amplification via Polymerase Chain Reaction (PCR).

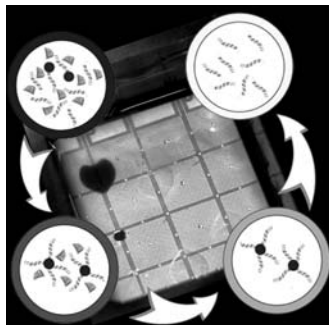


Figure 2: Schematic principle of the DNA extraction and purification process. First, the cells are lysed and the DNA is bound to the magnetic particles. The magnetic particles are separated from the initial droplet and washed in three stages. Finally the particles are mixed with an elution buffer where the DNA is removed

3. Experiments and Discussion

We tested the functionality of the proposed procedure using different concentrations of mammalian cells (Jurkat, ACC-TIB 152)[3]. The eluted DNA was detected via fluorescent microscopy using PicoGreen as quantification agent. Figure 3 shows the results of the on-chip detection, where we can clearly distinguish between different initial cell contents. Due to the low DNA concentration, which ranges from 60 pg for 10 cells to 6000 pg for 1000 cells in a 10 µl droplet, the fluorescent signal is close to the lower limit of detection. We additionally transferred the extracted and eluted DNA to a subsequent amplification step. This PCR-step also verifies if the extracted DNA is intact and sufficiently pure, because cells debris, proteins or lysis reagents generally inhibit the amplification. Figure 4 shows an agarose gel electropherogram of different samples, where the successful amplification of human β -actin proves the purity of the eluate. In the electropherogram, the difference in cell amounts is also visible, especially in the band of the unused primer. The intensity of the primer for 10 cells is significantly higher

than for 100 or 1000 cells which indicates differences in the concentration of the initial DNA material subjected to the amplification.

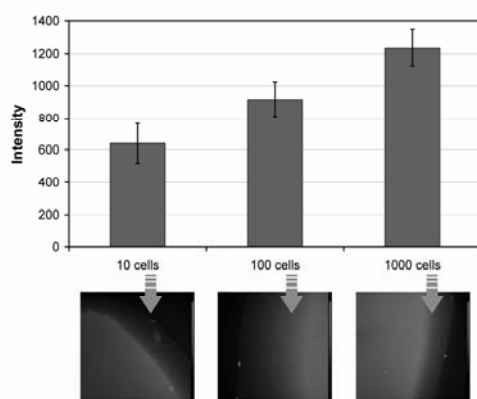


Figure 3. Fluorescent on-chip detection of the eluted DNA in a 10 μl droplet. The upper diagram shows the intensity of the fluorescence as determined from the fluorescent microscopy photographs below.

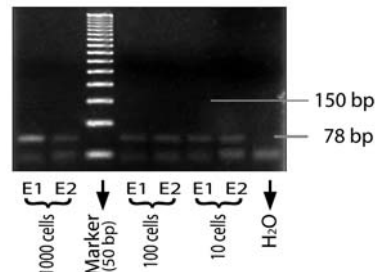


Figure 4. Agarose gel electropherogram of human β -actin after 35 cycles of PCR starting from 3 μl of eluate, which contains the DNA extracted from different concentration of Jurkat cells. The lowest band shows the primers whose consumption varies with initial cell number. (E1, E2: first and second elution; M: 50 bp ladder marker)

4. Conclusion

Our results demonstrate the potential of the presented 2D magnetic droplet manipulation system as a promising platform for bioanalytical applications. We were able to extract, detect and amplify the DNA of as little as 10 cells using sample volumes of 10 μl . The use of droplets allows an easy conversion of titerplate-based procedures onto a microchip, which will result in lowered reagent consumption, higher system sensitivity and less contamination.

References:

- [1] U. Lehmann, S. Hadjidj, V. K. Parashar, C. Vandevyver, A. Rida, and M. A. M. Gijs, "Two-dimensional magnetic manipulation of microdroplets on a chip as a platform for bioanalytical applications", *Sensors and Actuators B: Chemical*, vol. In Press, Corrected Proof.
- [2] M. A. M. Gijs, "Magnetic bead handling on-chip: new opportunities for analytical applications", *Microfluidics and Nanofluidics*, vol. 1, pp. 22-40, 2004
- [3] U. Lehmann, C. Vandevyver, V.K. Parashar, and M.A. Gijs "Droplet-Based DNA Purification in a Magnetic Lab-on-a-Chip", *Angewandte Chemie International Edition*, 45(19), pp. 3062-3067, 2006.

DEVELOPMENT OF A MICROCHIP-BASED FERTILIZATION AND CULTIVATION SYSTEM FOR IN VITRO PRODUCTION OF BLASTOCYSTS

**Kiichi Sato¹, Manabu Ozawa², Kazuhiro Kikuchi²,
Takashi Nagai³, and Takehiko Kitamori⁴**

¹Department of Applied Biological Chemistry, The University of Tokyo,
Yayoi, Bunkyo, Tokyo, 113-8657 Japan,

²National Institute of Agrobiological Sciences, Japan,

³National Institute of Livestock and Grassland Science, Japan,

⁴Department of Applied Chemistry, The University of Tokyo, Japan

Abstract

A microchip-based system for domestic animal breeding was designed and constructed. The microchip has a culture chamber and microchannels for medium supply. By using the system, porcine and mouse embryos were successfully fertilized and developed to the blastocyst stage.

Keywords: animal breeding, blastocyst, cell culture, embryos, in vitro fertilization

1. Introduction

In-vitro production of embryos of domestic animals is very important in livestock farming for lower cost. The current procedures are, however, rather troublesome and inefficient. Unlike other cells, controlling culture conditions suitable for the oocytes and embryos is severe; oxygen tension must be kept lower than the atmosphere (optimum: 5% O₂) and maintenance of these conditions, i.e. uterus or oviduct-like circumstances, is important for efficient culture of these cells. We thought that the circumstances could be easily realized in a microspace of a microchip. By applying our knowledge and technique to culture cells in a microchip [1,2], we developed a microchip-based in vitro embryo production system and porcine embryos successfully developed in vitro to the blastocyst stage.

2. Microchip fabrication

The concept of the system is illustrated in Fig. 1. The system has three steps, i.e. in vitro maturation and fertilization (IVF) of oocytes, and in vitro culture (IVC) of embryos to the blastocyst stage. Glass microchips were fabricated by photolithography and wet etching method. Each chip has culture chambers with 500 – 1,000 μm in diameter and connecting microchannels (50 μm in depth, 100 μm in width) (Fig. 2). Using this microchip, we examined the efficacy of IVF and IVC.

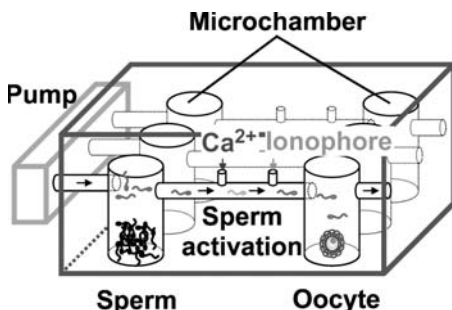


Fig. 1 Fundamental concept of the micro breeder system

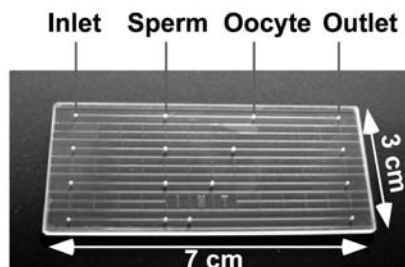


Fig. 2 In vitro fertilization and embryo culture microchip

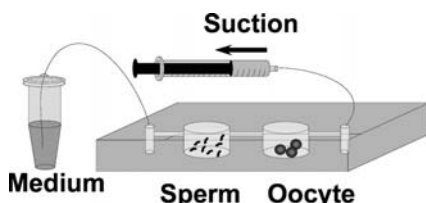


Fig. 3 Continuous flow fertilization and culture

3. In vitro fertilization

Porcine follicular oocytes were matured in vitro as previously described [3]. The matured oocytes were transferred to the microchamber, and frozen-thawed and preincubated boar epididymal spermatozoa [4] were put into the other chamber (10^5 spermatozoa/chamber). Then fertilization medium, which was equilibrated with a gas consisted with 5% CO₂ and 5% O₂ in advance, flowed continuously (10 μ L/h) for 3 h at 38.5°C to give the opportunity of the gametes to encounter and then followed by IVC medium for 7 h (Fig. 3). Fig. 4 shows the gametes during IVF in a microchip. Monospermic fertilization rate was calculated as 20%, which was comparable with that in the conventional method [3].

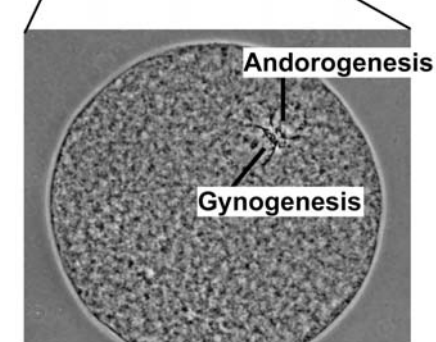
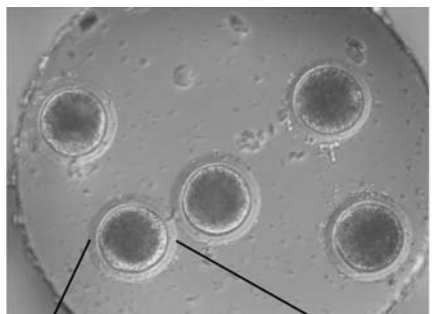


Fig. 4 Photographs of embryos fertilized in the microchip. Monospermic fertilization was confirmed.

4. Embryo culture

Porcine embryos and in vivo produced mouse embryos were cultured in the microchip. The IVC media were used after equilibrated in advance with the gas. The mouse embryos at the mono-cell stage and porcine embryos at the 2- to 4-cell stages were transferred into the microchambers and cultured at 37°C or 38.5°C, respectively, under continuous IVC medium flow (6 μ L/h) conditions. Fig. 5 shows photographs of the embryos after IVC for 4 days in microchip with a 700- μ m microchamber. All mouse embryos and 28% of porcine embryos developed to the blastocyst stage. The rate was almost the same as that of the conventional method. Optimization of the medium composition, flow conditions, and shape of the micro chamber may bring more efficient in vitro production of blastocysts.

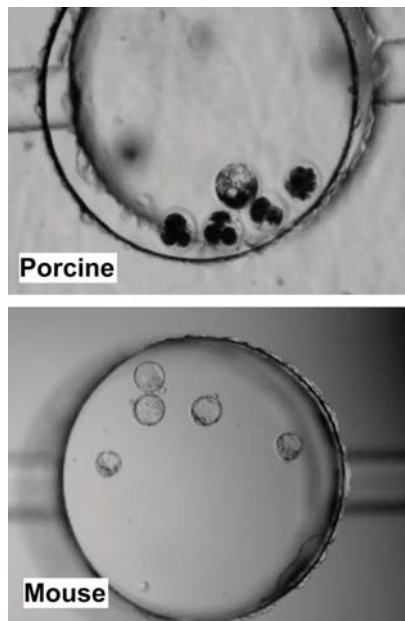


Fig. 5 Photographs of embryos cultured in the microchip

References

- [1] M. Goto, K. Sato *et al.*, *Anal. Chem.*, **77**, 2125-2131 (2005).
- [2] Y. Tanaka, K. Sato *et al.*, *Anal. Sci.*, **20**, 411-423 (2004).
- [3] K. Kikuchi *et al.*, *Biol. Reprod.*, **66**, 1033-1041 (2002).
- [4] K. Kikuchi, T. Nagai *et al.*, *Theriogenology*, **50**, 615-623 (1998).

FULLY-ROUND BURIED MICROCHANNELS IN GLASS FOR LATERAL PATCH CLAMPING

Wee-Liat Ong, Jack-Sheng Kee, Agarwal Ajay, Nagarajan Ranganathan,
Kum-Cheong Tang, and Levent Yobas*

Institute of Microelectronics, 11 Science Park Rd, S117685, Singapore

(*Contact: leventy@ime.a-star.edu.sg)

Abstract

We report on fully-round self-forming microchannels in phosphosilicate glass (PSG) for lateral patch clamping. These microchannels are fabricated by reforming doped glass layer in silicon trenches under heat and pressure; a process analogous to the heat-pulling/polishing glass patch pipettes. A gigaseal achieved with such microchannel on PC12 cells is also presented.

Keywords: lateral, patch clamp, self-forming, round microchannels, gigaseal

1. Introduction

Patch clamping is the “gold” standard for studying ion channels residing across cell membrane [1]. Known as a direct but skill-laden method, patch clamping can be transformed into a high-throughput assay by replacing glass patch pipettes with chips having an array of patch apertures [2]. Such approach could lead to a direct assay for high-throughput screening of drug candidates on ion channels.

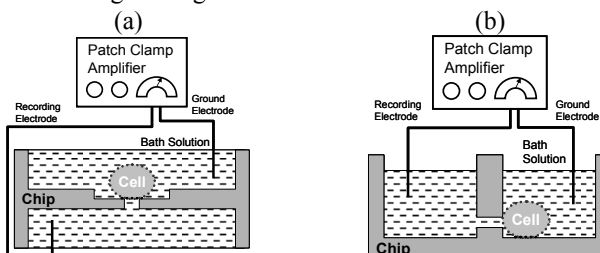


Figure 1. Diagrams of chip-based patch clamping on (a) planar, & (b) lateral apertures.

2. Patch Clamp Chip

Our approach employs a lateral aperture of a buried microchannel which differs from the reported planar patch apertures (figure 1). Advantages of the lateral patch clamping such as denser array, easier integration and packaging have been shown earlier using the patch apertures micromolded in poly(dimethylsiloxane) (PDMS) [3]. However, a round lateral aperture in glass which mimics the mouth of a conventional patch pipette is highly desired for an increased performance. By improving on our previously reported work [4], our present device demonstrates a buried microchannel in PSG with a circular aperture profile that is seamless and smooth similar to the mouth of a heat-polished patch pipette [1].

Major fabrication steps are illustrated in figure 2. Briefly, a $2\mu\text{m}$ -wide and $3.5\mu\text{m}$ -deep rectangular trench was formed on a silicon substrate using deep reactive ion etching. A $4\mu\text{m}$ -thick PSG was deposited on the substrate trapping a void inside the trench. Subsequent annealing step at 1150°C for 30 mins transformed the void into a cylindrical shape by reflowing PSG. A second lithography step created the bath and recording chambers exposing both ends of the buried microchannel. Additional annealing in oxygen ambient at 1050°C for 10 mins created 350-nm -thick thermal oxide on silicon and also smoothened the aperture edges. The aperture shape and size were controlled by trench's width/depth ratio, thickness of PSG, and annealing parameters. By varying these parameters, we fabricated circular microchannels at the length and diameter scale of $10\text{--}200\mu\text{m}$ and $0.2\text{--}1.5\mu\text{m}$, respectively. Figure 3 shows a fabricated buried microchannel. In figure 4, a 5-mm-by-5-mm patch clamp chip is shown before and after packaging with a PDMS layer having self-sealing interconnects.

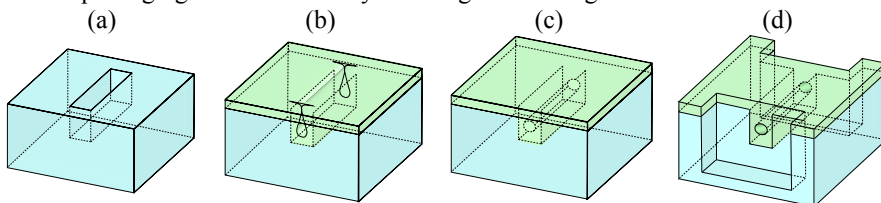


Figure 2. Major fabrication steps (a) trench etching (b) PSG deposition & void trapping (c) annealing & rounding void (d) chamber etching & exposing aperture.

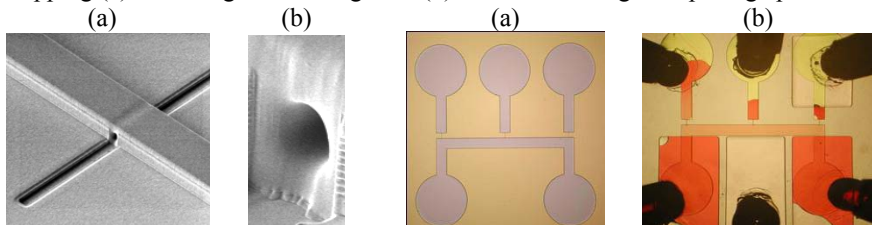


Figure 3. SEM images: (a) buried microchannel ($10\mu\text{m}$ long and $1.2\mu\text{m}$ diameter) and (b) a close-up view of the lateral aperture.

Figure 4. Photomicrographs of silicon chip with three patch-clamping sites: (c) before and (d) after the PDMS packaging undergoing fluidic characterization.

3. Experimental Results & Discussion

As presented in figure 5, electrical resistances (R) across electrolyte-filled microchannels of different length (L) confirm the classical relation $R = \rho L/A$ for a given cross-sectional microchannel area (A) and electrolyte resistivity (ρ). Seal formation capability of the apertures was tested on rat PC12 cells ($\varnothing \sim 10\mu\text{m}$ - $15\mu\text{m}$). The cells were introduced into the device after being prepared according to the protocol in [3]. By controlling the flow, individual cells were brought near to the patch aperture such that a gentle suction ($\sim 23\text{kPa}$) applied through the recording chamber could attract

and trap a nearby cell at the aperture (figure 6). Typical access resistance across a 1.3- μm -diameter and 20- μm -long microchannel was measured as $7.8\text{M}\Omega$. After capturing the cell, the resistance increased to $1.4\text{G}\Omega$ (figure 7). This level of seal could lead to a whole-cell or single channel recordings.

Such microchannels are easy to fabricate and package, and can be further integrated with microfluidics for a high-density patch-clamping array.

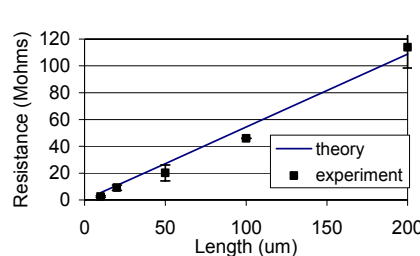


Figure 5. Access resistance across $1.3\mu\text{m}$ -diameter buried microchannels as a function of channel length ($\rho = 0.56 \Omega\text{m}$).

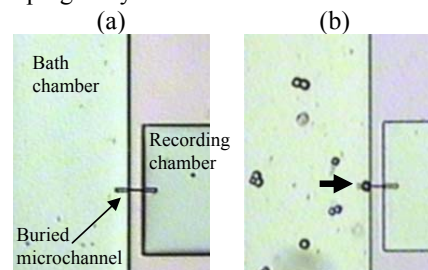


Figure 6. Photomicrographs (a) before & (b) after trapping a PC12 cell (arrow) by suction through buried microchannel ($1.3\mu\text{m}$ -diameter and $20\mu\text{m}$ -long).

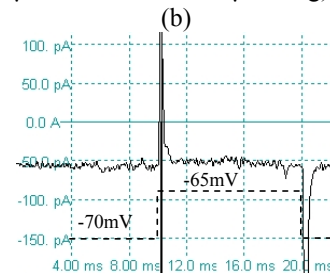
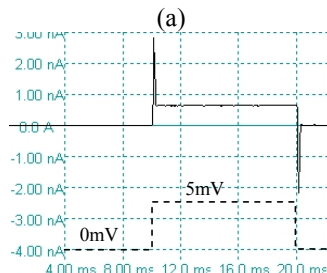


Figure 7. Typical current traces measured across a $1.3\mu\text{m}$ -diameter and $20\mu\text{m}$ -long buried microchannel in response to applied voltage pulse of $+5\text{mV}/5\text{ms}$ (dashed line) (a) before ($7.8\text{M}\Omega$) and (b) after ($1.4\text{G}\Omega$) capturing a PC12 cell (a negative 70mV bias was maintained to facilitate seal formation as in conventional patch clamping).

References:

1. B. Sakmann, E. Neher (Eds). Single Channel Recording. 2nd Ed., New York: Plenum, (1995)
2. C. Schmidt, M. Mayer, H. Vogel, *A chip-based biosensor for the functional analysis of single ion channels*, Angew Chem. Int. Ed Eng, 39, pp. 3137–3140, (2000).
3. J. Seo, C. Ionescu-Zanetti, R. Lai, L.P. Lee, *Integrated multiple patch-clamp array chip via lateral cell trapping junctions*, Appl. Phys. Lett., 84 (11), pp. 1973-1975, (2004).
4. L. Yobas, L. Zhao, J. Zhu, R.S. Kumar, R. Nagarajan, S. Liw, W.C. Hui, T.M. Lim and F.S. Sheu, *Self-forming lateral apertures in silicon microchannels for patch clamping*, Procc. Micro Total Analysis System, pp. 933-935, (2005).

THE ROLLING MOTION OF CARDIOMYOCYTES ON A DIELECTROPHORESIS CHIP

Yiling Qiu¹, Ronglih Liao² and Xin Zhang¹

¹Department of Manufacturing Engineering, Boston University, USA

²Brigham and Women's Hospital, Harvard Medical School, USA

Abstract

In this paper, we report a new mechanical motion of cardiomyocytes, rolling with respect to principal axis of the rod-shaped cardiomyocyte, caused by both AC electric forces and interactions between cells and substrate. The rolling motion can be an important motion in the alignment of the rod-shaped cardiomyocytes.

Keywords: Rolling, Cardiomyocytes, Dielectrophoresis

1. Introduction

The cell manipulating technologies of forming cell patterns are necessary in the research of the interaction between cardiomyocytes and other types of cells. Among the cell manipulating technologies, AC electric field manipulations, i.e. dielectrophoresis and electro-orientation, of the rod-shaped cardiomyocytes on a microfluidic dielectrophoresis (DEP) chip have been demonstrated in published reports [1,2]. However, within a period time since the cells are isolated from heart tissues, cardiomyocytes keep their rod-shaped geometry. It induces possibility of rolling with respect to principal axes of the cells which is driven by AC electric forces on a microfluidic DEP chip. The rolling motions of cardiomyocytes can enhance the efficiency of cell-alignment with AC electric forces.

2. Theory and Modeling

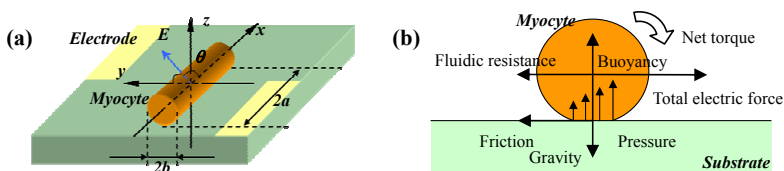


Figure 1: (a) The Cartesian coordinate and orientation of electric field. (b) The mechanical analysis of a cardiomyocyte on a microfluidic DEP chip.

The Cartesian coordinate system used for describing motions and geometry of the cardiomyocytes is shown in **Figure 1a**. AC electric forces can cause the translational motions of cardiomyocytes, such as dielectrophoresis, electro-orientation, etc., of which

the motions can be described in a 2D model in x-y plane. However, due to the friction between the cell and the substrate, these motions can be blocked. The specific rod shape of cardiomyocyte introduces possibility of rolling motions, as shown in **Figure 1b**. A cardiomyocyte in media is subjected to electric forces, which introduces a rolling torque with respect to the contact point between the cell and the substrate. When this rolling torque is high enough to overcome the fluidic resistance and the rolling friction generated by distributed pressure in contact area, the net torque can cause the rolling of cardiomyocytes. According to the model above, the angular accelerations of with respect x-axis (rolling acceleration, α_x) can be described as the following equation:

$$\alpha_x = \frac{4}{3} \pi a b \epsilon_m \operatorname{Re}(CMF) |\nabla \mathbf{E}^2| \sin \theta \quad (1)$$

where CMF stands for Clausius-Mosotti Factor, ϵ_m is the media dielectric constant. When the cell is approximately perpendicular to the electric field ($\theta=90^\circ$), the value of α_x reaches its apex, namely, rolling is relatively easy in this situation.

The finite element modeling results are shown in **Figure 2a**, describing the point-charge-like electric field generated by the sharp electrode tips in the vicinity. In the case of positive CMF, the positive gradient of electric field leads trapping forces toward the microelectrode tips when cardiomyocytes are injected into the chamber, as shown in **Figure 2b** and **2c**.

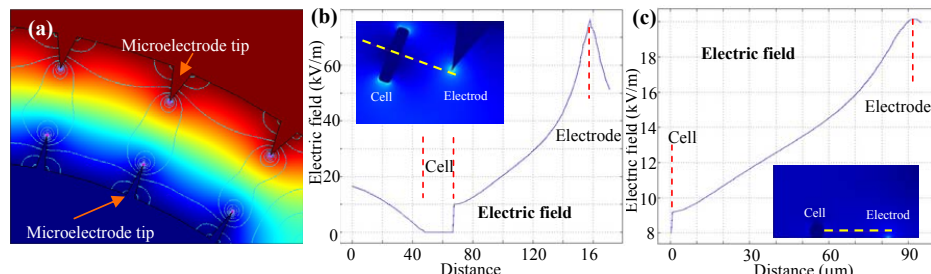


Figure 2. (a) The simulation result of electric field distributions in the vicinity of electrodes. The top (b) and side views (c) of electric field distribution on the dash line.

3. Experimental

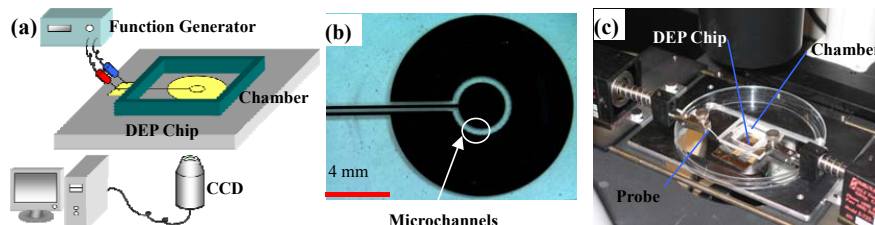


Figure 3. (a) Schematic of experiment setup. (b) The gold microelectrodes (c) The stage.

Figure 3 shows the schematic of experimental setup and the top view of microelectrodes. Such integrated microelectrodes were formed by patterning gold onto glass slides. In the experiment, the isolated cardiomyocyte media was injected into the customer-made chamber sealed with the microelectrodes slide, which was mounted on an inverted microscope ($200\times$).

4. Results and Discussion

The rolling of cardiomyocytes was observed with the peak to peak voltage of $10V_{p-p}$ and the crossover frequency of $2MHz$. **Figure 4** provides a series of pictures showing the rolling motion, as well as the trapping toward the microelectrode at the inner side. The cell was in translational motions when suspending in the media ($t<0$). After it sank to the bottom and the contact between the cell and the substrate established, the translation motions stopped ($t=0$) due to the friction. The initial rolling was relatively slow because the torque was slightly beyond the threshold. While the cell got closer to the outer microelectrode tip, the angular speed increased due to the larger electric force. The rolling was then slowed down because the trapping force toward the inner microelectrode moved the cell out of the area where the electric forces were approximately perpendicular to the cell long-axis. Finally, the cell stopped rolling ($t>40s$) while the trapping continued.

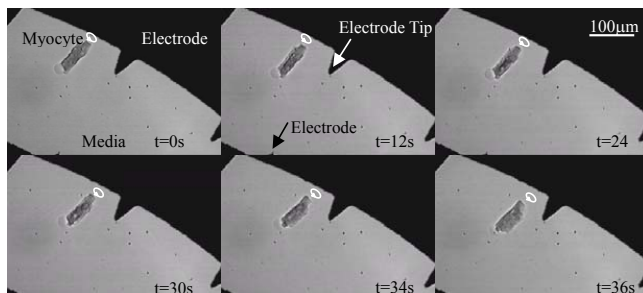


Figure 4. A series of picture showing rolling and dielectrophoresis of the cardiomyocyte. The rolling direction is indicated with circular arrows and straight arrows.

5. Conclusion

In this paper, we presented the rolling motions of rod-shaped cardiomyocytes on a DEP chip, which can be used for efficiently manipulating cardiomyocytes or other rod-shaped cells in the cell-patterning. It is also reinforcement to the understanding of the mechanical motions caused by AC electric field.

References

1. M. Yang and X. Zhang, MicroTAS'05, pp.367-369.
2. M. Yang, C. C. Lim, R. Liao and X. Zhang, MEMS'06, pp.8-11.

CELL GROWTH CONTROL USING CHEMICAL STIMULATION REGULATED BY MICROVALVE SWITCHING

Yuta Nakashima and Takashi Yasuda

Graduate School of Life Science and Systems Engineering, Kyushu Institute of Technology, 2-4 Hibikino, Wakamatsu-ku, Kitakyushu 808-0196, Japan

Abstract

This paper presents the testing of a cell differentiation control using a microfluidic device. The microfluidic device consists of a chamber, a microchannel, a microvalve, and a nano-hole array. Because these components are fabricated very close to one another, the microvalve switching allows precise control for releasing nerve growth factor (NGF) which enhances axonal outgrowth from a cell body. Experiments using PC12 cells showed that cell growth depended on the distance between the cell and the nano-hole array. Also, the cell differentiation was affected materially by the frequency and the duty factor of the valve switching.

Keywords: Cell differentiation, Chemical stimulation, Nano-hole, Microvalve

1. Introduction

Our purpose is to fabricate microfluidic devices which can control cell differentiation, and to apply them to restoring impaired or lost biological function. In order to control chemical stimulation to cells, we previously fabricated a microfluidic device consisting of a cell-culture chamber, a microvalve, and a nano-hole array for chemical release [1]. Because the hole diameter is much smaller than the cell size and the valve is located very close to the holes and the chamber, our device allows more precise control of chemical release than other groups' devices which release chemical solution through a micro-sized hole onto a cell trapped in a chamber [2, 3]. In this paper, we present the behavior of cells stimulated using the fabricated device, i.e., differentiation guidance of cells using release control of nerve growth factor (NGF) which is a protein that enhances axonal outgrowth from a cell body.

2. Design and fabrication

We designed a microfluidic device that consisted of a chamber for cell culture, a microvalve for controlling chemical release, and a nano-hole array for chemical release as shown in Fig. 1(a). The chamber and the microchannel were fabricated on the handle silicon layer and the device silicon layer of a SOI wafer, respectively. The microchannel measuring 100 μm in width and 10 μm in depth was fabricated directly below the chamber, and these were connected only by nano-holes. The nano-holes whose inside diameter was designed to be 0.5 μm or less were fabricated in a SiO_2 layer because the typical diameter of an axon terminal is 0.5 – 4 μm . The microvalve using different liquid surface tensions on a hydrophobic channel (covered with self assembled

monolayer (SAM), 1-octadecanethiol) and a hydrophilic channel (covered with SiO₂) was constructed at the T-shaped crossing of the microchannel. Figure 1(b) shows the schematic of liquid switching principle of the microvalve. When pressure is applied from the inlet, the inlet liquid will break into the hydrophobic channel and merge with the outlet liquid. If the inlet liquid includes NGF, it will diffuse into outlet liquid and eventually be released from the nano-hole array. As mentioned above, this device can precisely control releasing of NGF because the chamber, the microvalve, and the nano-hole array were fabricated very close to one another, and therefore chemical stimulation can be applied directly to cultured cells in the chamber. Figure 2 shows the SEM photograph of the chamber (a, b) and 100 nano-holes in the SiO₂ membrane (c, d). The chamber has an area of 200 μm x 200 μm, and 100 nano-holes were fabricated in one section of the chamber.

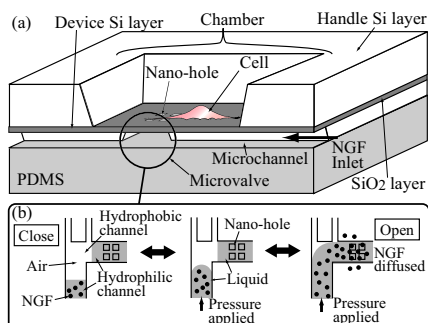


Fig. 1 Schematic of a microfluidic device.

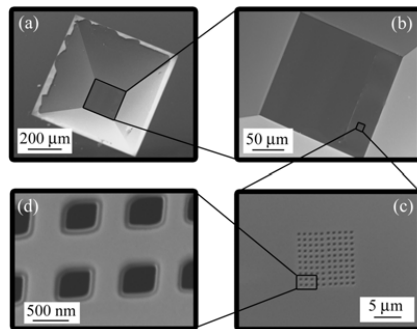


Fig. 2 SEM photographs of the device.

3. Experimental Results

We observed the growth of cultured cells while the microvalve was switched at 1 Hz. As shown in Fig. 3, the lower left cell that adhered to the surface elongated the axon toward the nano-hole array as time passed. On the other hand, the right side cell could not begin to differentiate because it did not adhere to surface at first. However, after it succeeded in adhering to the surface of the chamber two hours after the original stimulation was applied, the right side cell also demonstrated our intended movement manner, i.e. it elongated the axon toward the nano-hole array as time passed.

Figure 4 shows the transition of the cell size changed by chemical stimulation. We normalized the changing sizes of cells by their original size. Of the three conditions tested, only the cell that was located 70 μm away from the nano-hole array was differentiated 6 hours after stimulation. However, the size of a cell located 120 μm away from the nano-hole array remained almost constant, and that of a cell located 200 μm away decreased as time passed because the NGF concentration was not high enough to differentiate the cells in an area far away from the nano-hole array.

The cells cultured at 120 μm away from the nano-hole array were stimulated using NGF release regulated by switching the valve at two different duty factors that are the duration of the microvalve open in one switching cycle (Fig. 5). The cell began to differentiate after 2 hours when the duty factor was 0.6. When the duty factor was 0.5,

the size of a cell remained almost constant. Therefore, increase of the duty factor accelerates the cell differentiation.

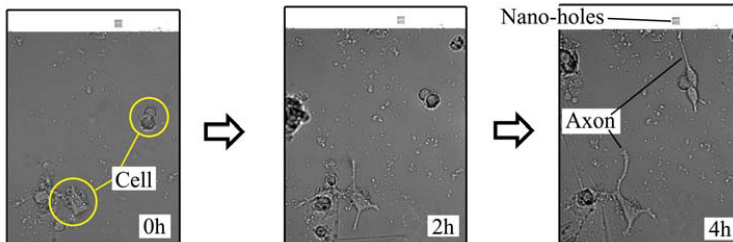


Fig. 3 Cell differentiation guidance on the fabricated microfluidic device.

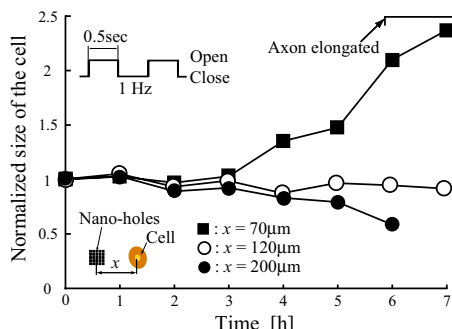


Fig. 4 Transition of the cell size depending on the distance from the nano-hole array.

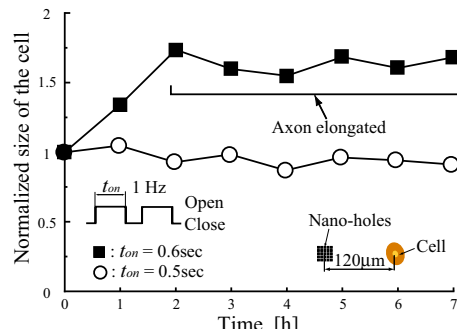


Fig. 5 Transition of the cell size depending on the duty factor of valve switching.

4. Conclusions

We showed that cell growth depends on the distance between the cell and the nano-hole array. We also demonstrated that cell differentiation can be guided by controlling the frequency and duty factor of the microvalve switching.

Acknowledgements

This work was supported by the “Development of Nanotechnology and Materials for Innovative Utilizations of Biological Functions” Project of the Ministry of Agriculture, Forestry and Fisheries of Japan, and also by a fund from the MEXT (Ministry of Education, Culture, Sports, Science and Technology) via the Grant-in-Aid for Scientific Research (B).

References

- Y. Nakashima *et al.*, “Microfluidic Device for Axon Elongation Control,” Tech. Dig. Transducers’05, pp. 1741-1744, 2005.
- S. Koster *et al.*, “Dispensing System for Localized Stimulation of Neural Cell Networks,” Proc. μ TAS, pp. 93-96, 2003.
- B. Le Piouf *et al.*, “Living Cells Captured on a Bio-microsystem Devoted to DNA Injection,” Materials Science and Engineering C, 12, pp. 77-81, 2000.

SINGLE MICROBE DISPENSING SYSTEM WITH MICRO MACHINED PARTICLE SENSOR

Tadashi Sano¹, Yasuhiko Sasaki¹, Hajime Ikuta² and Tatsuo Sumino²

¹Mechanical Engineering Research Laboratory, Hitachi, Ltd.

²Hitachi Plant Technologies, Ltd.

Abstract

We fabricated a dispensing system equipped with a particle sensor. This system acquires a single microbe from a mixture of various microbes in a solution. The microbe's passage through an orifice is detected electrically as resistance changes, and the single microbe is injected into a well by a dispenser. Experiments showed that 96% of particles were individually injected by the dispenser into wells successfully.

Key Words: microorganism, bacteria, bacterium, separation, dispensing, isolation

1. Introduction

In industries that use microbes, it is important to acquire new and pure strains of microbes efficiently. In sewage treatment, for example, by using a new bacterium that needs not any food to survive, we are able to have prospects of eliminating a major running cost. Figure 1 shows a well known method of microbe acquisition. In this method, a solution containing various kinds of microbes is fixed, and a single microbe is separated from the solution stochastically. Then, the microbe is cultivated, and a pure community of microbes is acquired. Finally, these microbes are analyzed to determine whether they are a new strain or a known strain. But this conventional method is inefficient because, during the process of separating and dispensing single microbes, many wells are found to contain no microbe or plural microbes. Therefore, we developed a dispensing system that dispenses single microbes efficiently after isolating and separating them using a microbe separation device. The period of operation required for separation using this system instead of the conventional method could be shortened by two orders of magnitude.

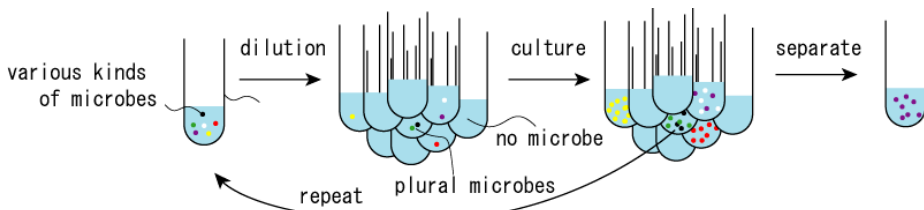


Fig.1 Conventional method for separation of pure microbes

2. Dispensing system

Photographs of the dispensing system and microbe separation device assembled in this research are shown in Figs. 2 and 3. This system's dispensing unit consists of a microbe separation device, pumps, and valves. It can dispense each microbe to one arbitrarily selected well created on a 96-well microplate set on the base of the dispensing system. The dispenser can move on three axes: X, Y, and Z. The dispenser, pumps, and valves are operated on the basis of a detection signal indicating the presence of a microbe. After dispensing a microbe to a well, the dispenser moves to the following well and dispenses another single microbe, and so on.

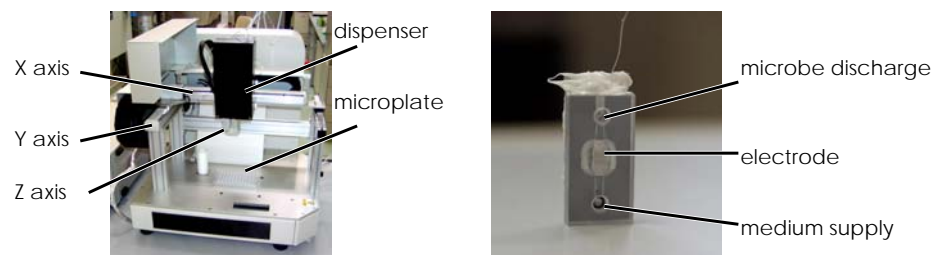


Fig.2 Picture of dispensing system
(600Wx500Dx700Hmm)

Fig.3 Picture of Microbe separation device

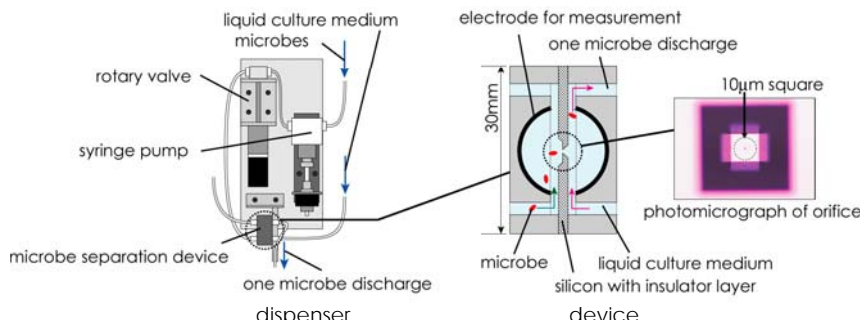


Fig.4 Structure of microbe separation device

The structure of the dispenser and microbe separation device is shown in Fig. 4. This device has an orifice made from a silicone plate using a wet etching process, and there are channels on both sides of the orifice formed by putting a resin piece with grooves in place. Electrodes are attached to every channel. Therefore, a microbe passing through the orifice is detected using an electrical sensing zone method. A pump supplying culture medium and another pump supplying microbes are connected to the device. These pumps

are operated by a microbe separation device that gives commands on the basis of the detection signals. When a microbe passes through the orifice, the system dispenses it to a well by suspending operation of the microbe pump and initiating operation of the culture medium pump.

3. Experimental result

We tested the dispensing system in automatic mode using 5-micrometer polystyrene particles as substitutes for microbes. The control screen we observed is shown in Fig. 5 (a). It took about 40 minutes to dispense these particles to all 96 wells. It is indispensable to dispense one microbe into one well for acquiring pure strains of microbes. Ninety-six percent of the particles were individually dispensed into the wells successfully. The four misses, representing an error rate of 4%, were caused by detection of a particle while another particle was being dispensed. This errors indicated that plural particles were dispensed. Two example waveforms of the particle-passage detection signal are shown in Fig. 5 (b). Fig. 5 (b) (i) shows a single particle's signal. This particle was successfully dispensed as a single particle in a well. Fig. 5 (b) (ii) shows two particles' detection signals, and these particles were dispensed together into a well.

References

- [1] Coulter W.H., Proc. Nat. Elec. Conf., pp.1034(1956)
- [2] R. W. LINES, The Electrical Sensing Zone Method, Spec. Publ. R Soc. Chem., No.102 pp.350-373 (1992)

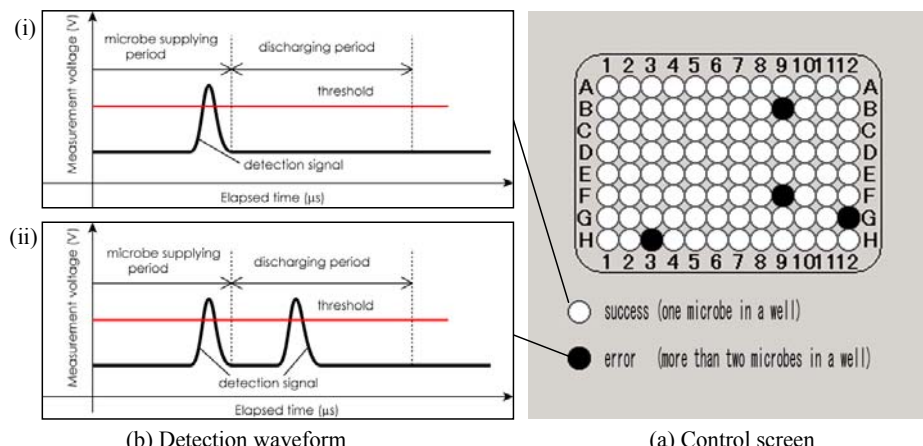


Fig.5 Experimental result of dispensing

ULTRASONIC MANIPULATION IN A MICROFLUIDIC CHIP FOR INDIVIDUAL HANDLING OF PARTICLES AND CELLS

Martin Wiklund, Jessica Hultström, Otto Manneberg and Hans M. Hertz

Biomedical & X-Ray Physics, Dept. of Applied Physics, KTH/Albanova,
SE-106 91 Stockholm, Sweden

Abstract

We have developed a microfluidic platform for individual particle handling by the use of ultrasonic standing waves. Elementary manipulation functions, useful in cell-based biotechnology applications, are demonstrated. Oblique coupling of ultrasound allows for any kind of high-NA optical microscopy, which is important for individual characterization of cells.

1. Introduction

Ultrasonic standing wave (USW) manipulation is a suitable technique for high-throughput, continuous separation, concentration or alignment of particles or cells in microfluidic systems. In flow-through systems, suspended particles or cells are focused into the pressure nodes of the standing wave, typically oriented parallel with the microchannel [1]. However, USW technology is primarily considered as a “coarse” and long-range tool for simultaneous manipulation of all particles inside the chip, in comparison to “sharp”, short-range tools such as laser tweezers or dielectrophoresis [2]. Here, we investigate USW-generated elementary manipulation functions (EMFs) for handling of individual or low numbers of particles or cells inside a microfluidic chip. The demonstrated EMFs may be used in different kinds of cell-based biotechnology applications, where step-by-step handling and individual characterization of the cells are important.

2. Experimental arrangements

The chip, illustrated in Fig. 1, consists of a glass-silicon-glass structure, compatible with label-free, high-resolution transmission microscopy. The ultrasound is coupled into the fluid channel by an external transducer combined with a refractive element in an oblique arrangement

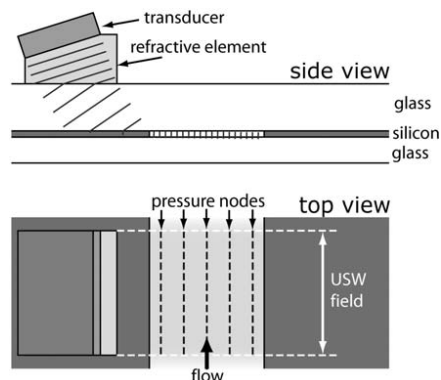


Figure 1. Schematic of chip and the USW transducer.



Figure 2. One-dimensional aggregation of 10 µm beads in four subsequent pressure nodes.

(cf. Fig 1), which allows both focusing and direction of the wave. The microchannel in the silicon layer has a cross section of $750 \mu\text{m}$ (width) $\times 40 \mu\text{m}$ (height). This elongated shape of the cross section is chosen for optimized microscopic view of all cells in the chip. Furthermore, since the channel height has the same scale as the cell size, the cells are rearranged into only one dimension in the pressure nodes (cf. Fig. 2).

3. Results and discussion

The most fundamental EMF is parallel alignment in multiple nodes (Fig. 3a). The number of nodes is chosen by the ultrasound frequency. The frequency may be tuned from the fundamental resonance at 2.12 MHz (equivalent to 2 nodes) to the fifth harmonic overtone at 13.4 MHz (equivalent to 13 nodes). Other EMFs are one-dimensional particle aggregation ('line-aggregation') (Fig. 2 and Fig. 3b) and fusion of line-aggregates by USW frequency shift (Fig. 3c). Line-aggregation can be used for distinction and numbering of individual particles (cf. Fig. 2) or cells (cf. Fig. 4), while fusion of line-aggregates may be used in cell-based assays. The method is also compatible with other manipulation tools, e.g., it is possible to combine the USW chip with dielectrophoretic manipulation for increased spatial precision [2].

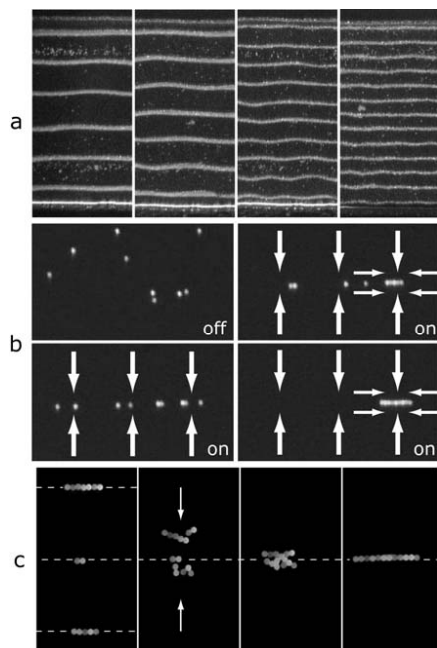


Figure 3. Parallel alignment in multiple nodes (a), one-dimensional aggregation (b), and fusion of one-dimensional aggregates (c).



Figure 4. One-dimensional aggregation of U-937 cells.

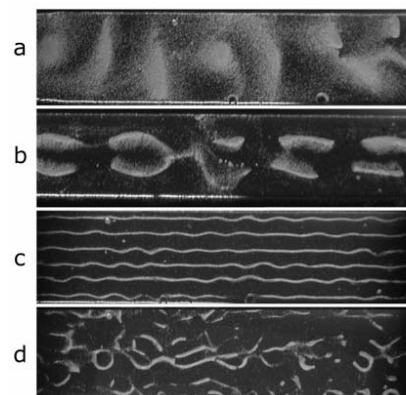


Figure 5. Complex patterns of the USW field by mode coupling and acoustic streaming at 1.48 MHz (a), 1.72 MHz (b), 6.20 MHz (c), and 6.61 MHz (d).

In miniaturized USW resonators, such as a microfluidic channel, the geometrical properties of the cavity are important for the shape of the nodes. This is illustrated in Fig. 5, where the transducer is driven at frequencies not matching the basic resonance condition (i.e., where the channel width corresponds to a multiple of half the acoustic wavelength). In such cases, complex mode coupling occurs, sometimes in combination with acoustic streaming.

4. Conclusions and outlook

The general goal of the work presented here is to design a flexible, multi-purpose and gentle cell handling system for surface-based and long-term biotechnology applications. An example of such an application is controlled cell differentiation ('cell programming') by surface-to-surface contact of a cell with a functionalized bead, or with another cell. Since the differentiation procedure is assumed to take long time (~days), USW manipulation is superior to alternative techniques from a viability point-of-view [3]. In this context, the experiment shown in Fig. 3c (fusion of one-dimensional aggregates) can be considered as a proof-of-principle experiment of a gentle cell handling device for 'cell programming'. Furthermore, our flat channel design is perfectly suitable for high-throughput and multiplexed USW cell handling, but still in the individual (one-by-one) format. This makes it possible to study not only the average properties, but to perform high-speed characterization of each single cell. In addition, our oblique USW coupling technique allows for either fluorescence-based or label-free (non-contaminating) optical characterization.

Acknowledgements

This work was supported by the European Community-funded *CelIPROM* project under the 6th Framework Program, contract No. NMP4-CT-2004-500039.

Keywords: Ultrasonic manipulation, cell handling, cell aggregation

References

1. A. Nilsson, F. Petersson, H. Jönsson and T. Laurell, Acoustic control of suspended particles in micro fluidic chips, *Lab Chip*, **4**, pp. 131-135 (2004).
2. M. Wiklund, C. Günther, R. Lemor, M. Jäger, G. Fuhr, H.M. Hertz, Ultrasonic standing wave manipulation technology integrated into a dielectrophoretic chip, *Lab Chip*, submitted.
3. J. Hultström, O. Manneberg, K. Dopf, H. M. Hertz, H. Brismar and M. Wiklund, Proliferation and viability of adherent cells manipulated by standing-wave ultrasound in a microfluidic chip, *Ultrasound Med. Biol.* (2006), accepted.

PROLIFERATION OF COS-7 CELLS TRAPPED BY STANDING-WAVE ULTRASOUND IN A MICROFLUIDIC CHIP

**Jessica Hultström, Otto Manneberg, Hans M. Hertz, Hjalmar Brismar
and Martin Wiklund**

Dept. of Applied Physics, KTH/Albanova, SE-106 91 Stockholm, Sweden
jessica.hultstrom@boxx.kth.se

Abstract

We study cell viability after ultrasonic-standing-wave trapping of low cell numbers in a microfluidic chip by recultivation of the trapped cells. The cell proliferation rate is estimated by counting of initial and final cell numbers and shows normal cell growth. The results demonstrate the potential of ultrasonic standing waves as a tool for gentle and long-term manipulation of low cell numbers in microfluidic systems.

Keywords: Ultrasonic manipulation, cell handling, cell viability, image analysis

1. Introduction and theory

Ultrasonic-standing-wave (USW) technology has potential to become a standard method for gentle and contactless cell handling in microfluidic chips. Cells are trapped in the ultrasonic pressure nodal planes by the long-range acoustic force, which may be designed to perform elementary manipulation functions [1]. However, in order to perform biologically accurate experiments on the trapped cells it is necessary that the ultrasonic cell manipulation is gentle.

2. Experimental arrangement

We investigate viability and proliferation of adherent COS-7 cells exposed to long-term USWs in a temperature-regulated microfluidic chip by a combination of several indicators of the cell state, i.e., fluorescence assays and automatic image analysis. Fig. 1a shows the USW resonant cavity where channel dimensions and ultrasound frequency have been carefully matched. The cells form two-dimensional aggregates of low cell numbers ($<10^3$) inside the chip as shown in Fig. 1b. These aggregates are trapped against a continuous flow of either cell culture medium or assay buffer and may be imaged by fluorescence microscopy. High-NA label-free cell imaging can be performed in an alternative arrangement using obliquely coupled USW enabling transmission light microscopy. Fig. 2 demonstrates USW-induced line-aggregation for distinction and numbering of cells in high-throughput applications.

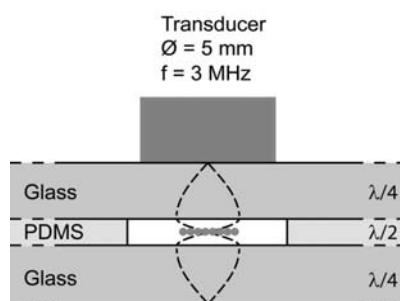


Figure 1a. Schematic of the chip.

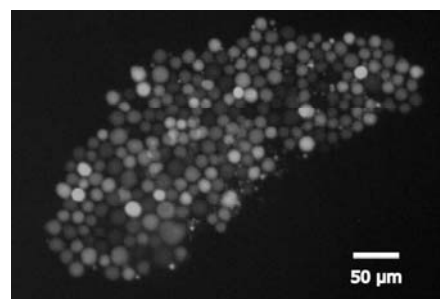


Figure 1b. Trapped two-dimensional fluorescently labeled cell aggregate.



Figure 2. COS-7 cells trapped in line aggregate in the new channel layout using obliquely coupled USW enabling the usage of transmitted light microscopy (20 \times objective).

To determine the cell state during USW exposure the cells were labeled with the direct viability indicator Calcein AM. For investigation of possible delayed cell damage we studied the proliferation rate of USW-exposed cell compared to non-treated control cells. Cell proliferation was measured by cell counting using image analysis tools after 2-3 days of cell cultivation (cf. Fig. 3) [2].

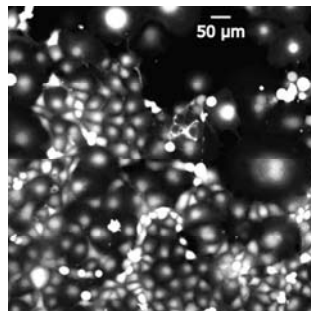


Figure 3. Recultivated COS-7 cells labeled with the viability indicator Calcein AM three days after USW exposure (partly overexposed).

3. Results and discussion

The cell growth after 2-3 days of recultivation, presented in Fig. 4, was estimated by comparing the initial and final number of cells. No deviations in the doubling time from expected values for adherent cells (24-48 h) were observed for COS-7 cells trapped at acoustic pressure amplitudes up to 0.85 MPa, and for trapping times up to 75 minutes. In contrast to the control cells, the USW-exposed cells also maintained the growth rate even at low cell numbers and cell concentrations. Thus, the results demonstrate the potential of ultrasonic standing waves as a tool for gentle and long-term manipulation of low cell numbers in microfluidic systems.

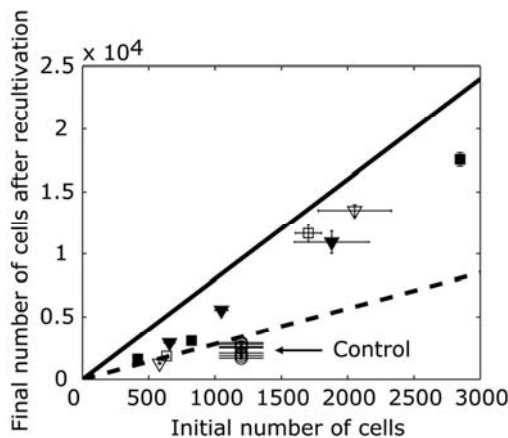


Figure 4. Cell growth was estimated by comparing initial and final cell numbers after 2-3 days of recultivation. Two experiments with USW exposure time of approx. 30 min [■, ▼] and two with exposure times approx. 60 minutes were performed [□, ▽]. Normal cell growth assuming doubling times of 24 [-] and 48 [--] hours are indicated. For comparison, untreated cells [○] were also cultivated.

Acknowledgements

This work was supported by the European Community-funded *CellPROM* project under the 6th Framework Program, contract No. NMP4-CT-2004-500039.

References

1. M. Wiklund, C. Günther, R. Lemor, M. Jäger, G. Fuhr, H.M. Hertz, Ultrasonic standing wave manipulation technology integrated into a dielectrophoretic chip, *Lab Chip*, submitted.
2. J. Hultström, O. Manneberg, K. Dopf, H. M. Hertz, H. Brismar and M. Wiklund, Proliferation and viability of adherent cells manipulated by standing-wave ultrasound in a microfluidic chip, *Ultrasound Med. Biol.* (2006), accepted.

MULTIPARAMETRIC OPTIMIZATION OF SILICON CHIP PROPERTIES FOR CONSISTENT SUCCESS IN ION CHANNEL RECORDINGS

T. Sordel^a, Y. Sinquin^a, F. Kermarrec^a, F. Sauter^b, C. Pudda^b, F. Chatelain^a, N. Picollet D'Hahan^a.

^aCEA, Life Science Division, Biopuces Lab, 17 rue des Martyrs, 38054 Grenoble France.

Tel +33 4 38 78 67 78 / fax +33 4 38 78 59 17 / picolletdhahan@dsvsud.cea.fr

^bCEA Grenoble, LETI, Laboratoire des Composants Intégrés pour le Vivant.

Keywords: planar patch-clamp, design of experiments, ion currents, silicon chips

1. Introduction

Successful planar patch-clamp recordings depend on surface and microhole characteristics that ideally should stabilize giga-seal formation. At this time, the most suitable material to conceive planar patch-clamp chips is glass: as for micropipettes, it allows obtaining high resistive seals with cell membrane. However, glass microfabrication processes are less common than those of silicon. Moreover, on silicon-based chips, seals often form with sub-gigaohm resistances [1]. Since silicon remains an attractive material for future electronic integration, our challenge is to find an ideal surface and optimal microhole characteristics improving the chips performance. We present here a systematic multiparametric study developed in order to determine and discriminate the influence of main silicon chip parameters on seal quality. In this study, we focus on results related to the microhole features (diameter and thickness) and to the surface quality (roughness and hydrophilic behavior).

2. A multiparametric study

Microhole diameters, silicon dioxide membrane thicknesses, roughness and hydrophilic behaviour were investigated as a function of the seal quality. Our flexible and modular system [2,3], in which the only disposable part is the silicon chip, makes it possible to test all chips configurations easily, such as membrane thickness (from 3 μm to 8.5 μm) and micropore size diameter (from 2.5 μm to 1.8 μm). In order to minimize the chips designs and to quantify the influence of all parameters, we implemented a Design Of Experiment (DOE), coupled to a systematic characterization study using SEM, AFM, contact angle drop and seal measurements.

3. Results

In order to obtain high hydrophilic surface, an oxygen plasma treatment was performed on the silicon dioxide surface. As a result, the contact drop angle of water decreased from 23° to less than 10° . Moreover, as observed in Figure 1, the success rate for seals higher than $100\text{ M}\Omega$ (i.e. the threshold value for seal resistance that allows recording ionic currents in the whole-cell configuration) was consecutively increased from 0% to 80% after plasma O₂ treatment. We also demonstrated that decreasing the pore diameter from 2.5 to 1.8 μm enhances the seal yield from 63% to 82%. Results obtained with the DOE strategy show that surface hydrophilic behavior is likely to be the most crucial parameter for the seal value, followed by the microhole diameter and the silicon oxide membrane thickness and surface roughness last.

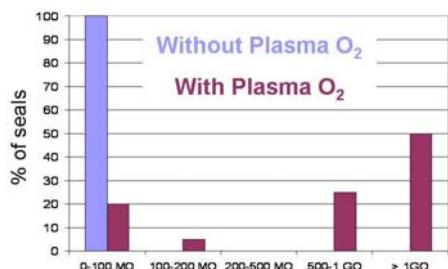


Figure 1: Distribution of seal resistances with and without oxygen plasma treatment. 25 seal resistance values were reported per chip.

The DOE strategy allowed manufacturing optimal chip design. As shown in Figure 1, more than 80% of seals are higher than $100\text{ M}\Omega$ and around 55% of seals are gigaseals. This chip design is therefore optimal for ion channel recordings and, as shown in Figure 2, usable for the most common voltage gated ion channels study and for IC50 values determination (Figure 3). In addition, a decrease of chip capacitance below 25 pF increased signal to noise ratio and therefore the sensitivity of ion currents recordings.

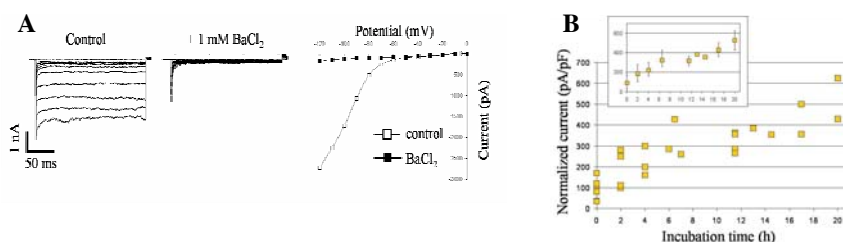


Figure 2 : Voltage gated ion currents recordings from CHO cells. **A.** Whole cell IRK1 currents. *Left:* potassium currents elicited with activating voltage steps from -100 mV to +100 mV. *Middle:* blocking effect of Ba²⁺ divalent (1 mM). *Right:* Current-voltage relationship curve. **B.** Time-dependent increase in BK(Ca) channel expression with Tetracycline incubation. Whole-cell current magnitude, evoked by depolarization to 120 mV and plotted as a function of the duration of Tet incubation. Current was normalized for cell size. The inset illustrates the mean current values (\pm S.E.M) at selected times.

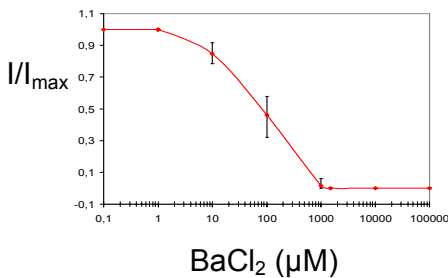


Figure 3 : Dose-response characterization demonstrated with BaCl₂, an IRK1 potassium channel inhibitor. 3 data per concentration. BaCl₂ IC50 (85 μ M \pm 20 μ M) matches published data.

4. Discussion and conclusion

This multiparametric approach is based on a DOE that allows performing a minimal number of experiments compared to a systematic incremental analysis to screen the major parameters influencing seal quality. The exploitation of such a set of experiments allowed to classify the most significant parameters influencing the seal formation and improved our seal success rate. By adding new microfabrication steps, further results will allow us to discriminate the effects of the microhole thickness and surface roughness.

5. Acknowledgements

We would like to thank F. de Crecy (CEA/Leti) for technical support and fruitful discussions on DOE methods and data analysis.

References:

- [1]. K.Schroeder et al. Ionworks HT: a new high-throughput electrophysiology measurement platform. *J. Biomol. Screen*, **5**, pp. 50-64, (2003)
- [2]. T.Sordel et al. Hourglass SiO₂ coating increases the performance of planar patch-clamp. *Journal of Biotechnology* **125**, pp.142-154, (2006)
- [3]. N. Picollet et al. A silicon-based “Multipatch” device. *Sensor Letters* **2**, 91-94, (2004)

RAPID CONCENTRATION OF BACTERIA USING 3-D ELECTRODELESS DIELECTROPHORESIS IN A PLASTIC CHIP

**Yoon-Kyoung Cho, Suhyeon Kim, Chinsung Park,
Kyusang Lee, Jeong-Gun Lee and Christopher Ko**

Bio Lab, Samsung Advanced Institute of Technology, PO Box 111,
Suwon, 440-600, Republic of Korea
(dnachip@samsung.com)

Abstract

A new electrodeless dielectrophoresis (DEP) chip utilizing microfabricated plastic membranes have been designed and tested for the first time, as far as we are aware. The DEP forces are significantly enhanced because there are two dimensional geometric constrictions in the proposed pore type traps compared to the one dimensional geometric constriction in the previously reported DEP traps using glass post arrays.

Keywords: Dielectrophoresis, Bacteria, Concentration, Cell Separation

1. Introduction

DEP has been employed to sort, manipulate, and concentrate a wide range of particle types including cells, bacteria, viruses, and DNA. The majority of DEP studies reported in the literature employ microfabricated metallic electrodes. However, the problems are that the electrodes are not chemically inert, gas bubbles can be formed due to the electrolysis, and the DEP force is effective only near the electrode surfaces. Recently, alternative ways to construct DEP trap, namely electrodeless (or, insulating) DEP, have been reported[1, 2]. In electrodeless DEP, the trap is formed by using geometrical constrictions in insulating substrates (e.g. quartz) instead of metallic microelectrodes. We report an alternative electrodeless DEP technique utilizing microfabricated plastic membranes.

2. Theory

To a first approximation the DEP force acting on an object is:

$$F_{DEP} = \alpha(\omega)E\nabla E \quad (1)$$

where $\alpha(\omega)$ is the polarizability of the object at the angular velocity ω , and E is the applied external field E . The DEP forces are significantly enhanced because there are 2-D geometric constrictions in pore type traps compared to the 1-D geometric constriction in the previously reported DEP traps using glass post arrays. Simulations using CFD-ACE (CFD Research, Huntsville, Alabama) suggested that the DEP forces in pore type traps (3D-EDEP) were always superior to that of the post type traps (2D-EDEP) regardless the shapes of the trap as shown in Fig. 1A.

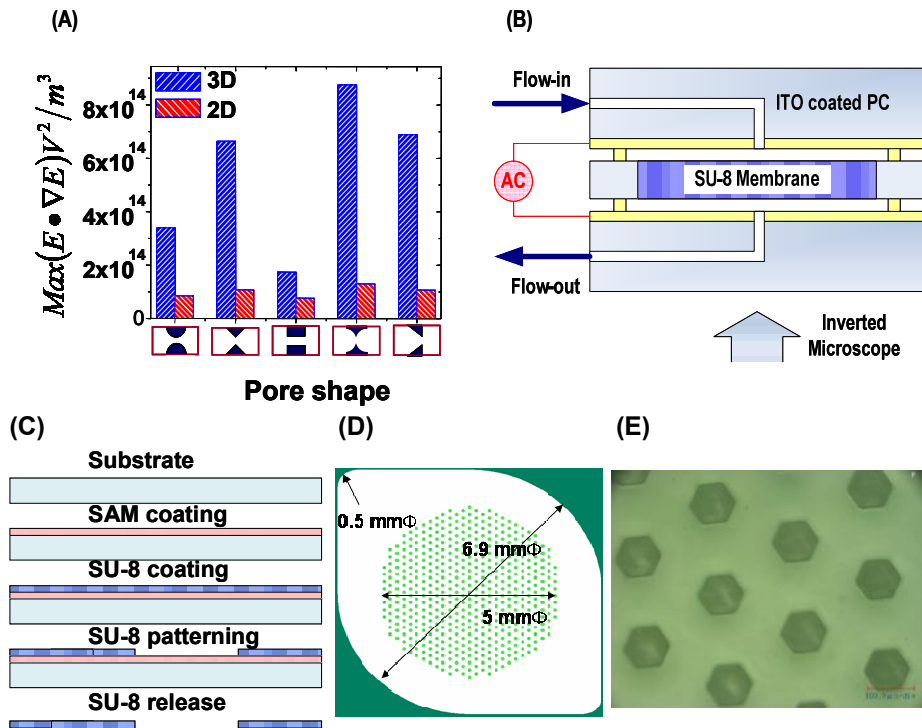


Fig. 1. (A) The simulation shows that the dielectric force normalized to the polarizability ($E \cdot \nabla E$) is significantly enhanced for 3D-EDEP case compared to the conventional 2D-EDEP chips regardless the shape of the trap. (B) Experimental set-up for visualization of bacteria concentration using dielectrophoresis. (C) Schematic diagram of the fabrication of SU-8 membrane chips (D) Mask layout of a chip (E) Optical micrograph of the chip showing the honey-comb type pores.

3. Experimental

As shown in Fig. 1B, ITO coated PC (poly carbonate) was used as top and bottom electrodes for the bacteria concentration using DEP. SU-8 membranes with specific geometric pore design have been fabricated and used as a 3D-electrodeless DEP trap.

4. Results and discussion

Previous DEP experiments from literature have been done at a very slow flow rate, if not at no-flow condition. However, for the rapid and efficient concentration, the device must be able to handle a large volume of sample in a short time. This is one of the major difficulties that have prevented DEP from being widely used in large volume applications.

In this report, the bacteria trapping experiments were conducted at a large flow rate, 100ul/min. Fig. 2A~2D show the fluorescence images of the trapped bacteria on the edge of the pores. Fig. 2E shows the effect of the frequency of the applied electric fields on the trapping efficiency. Quantitative analysis of the concentration efficiency (e.g. Fig. 2F) using very dilute samples, $< 10^5$ cell/ml, has been conducted using colony counting methods.

5. Conclusion

A new 3-D electrodeless dielectrophoresis (DEP) chip utilizing microfabricated plastic membranes have been tested for the application of the rapid concentration of bacteria. The membrane type plastic DEP chips have regular patterns of pores and the pore diameter varies along the pore depth. Because these kinds of pores have 2-D geometrical constriction, the DEP forces are significantly enhanced.

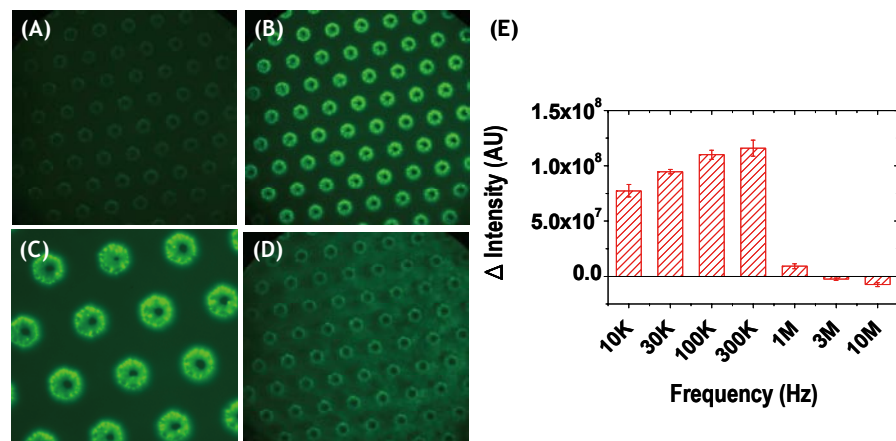


Fig. 2. (A) Bacteria solution (*E. Coli* : 1×10^7 cell/ml in DI) is flowing with flow rate of 100 ul/min. Electric field is turned off. (B) 1 min. after applying electric field, $E = 1280$ V/cm and $f = 300$ kHz. (C) Enlarged picture of the image (B) showing each bacterium trapped on the edge of the pores. (D) E-field is turned off and bacteria are released. (E) Effect of the frequency, 10 kHz ~ 10 MHz on the trapping efficiency. E-field (1280 V/cm) was on for 60 sec and off for 30 sec at each frequency. The maximum trapping efficiency was obtained at 300 kHz.

References

- [1] C. F. Chou and F. Zenhausern, *Electrodeless dielectrophoresis for micro total analysis systems.*, IEEE Eng. Med. Biol. Mag., vol. 22, pp. 62~67, (2003).
- [2] B. H. Lapizco-Encinas, B. A. Simmons, E. B. Cummings, and Y. Fintschenko, *Dielectrophoretic concentration and separation of live and dead bacteria in an array of insulators*, Anal Chem., vol. 76, pp. 1571~1579, (2004).

HIGH-YIELD ELECTROPORATION USING RF-MODULATED FIELD CONSTRICTION

Osamu Kurosawa¹, Hidehiro Oana², Hidetoshi Kotera³ and Masao Washizu^{2,4}

¹Advance Co., ²Dept. Mechanical Engineering, The University of Tokyo,

³Dept. Mechanical Engineering, Kyoto University,

⁴Center for Nano Bio Integration, The University of Tokyo

washizu@washizu.t.u-tokyo.ac.jp

Abstract

We have previously reported on an electroporation method based on field constriction, where a biological cell is immobilized on a micro-orifice opened on an electrically insulating plate, across which a pulse voltage is applied. Due to field constriction, most voltage drop occurs around the orifice, so that the voltage applied to the electrodes is impressed directly to the cell membrane on the orifice. The reversible membrane breakdown, i.e. poration, occurs exclusively at the orifice, at a voltage as low as 1-2 V. However, when the breakdown takes place, electrical current starts to flow through the opened pore, and induces breakdown at other location of cell membrane that could lead to cell destruction. In order to avoid such breakdown propagation, we present in this paper a method of using RF-modulated voltage. With the method, electroporation yield of 90% is achieved for the cells on a 10 x 10 orifice array.

Keywords: electroporation, cell, orifice, field constriction, RF-modulation

1. INTRODUCTION

When an electrical pulse is applied to the cell, and the induced transmembrane voltage V_m exceeds a critical voltage V_b , which is typically 1V for most cells, membrane breakdown occurs, and pores are formed on the membrane. If V_m is not too high, the breakdown is reversible, and the pores are spontaneously resealed. Electroporation is a method to bring foreign substances during this transient pore formation. Electroporation is conventionally done by exposing a cell suspension to a pulsed uniform electric field, however, because cells have size distribution, and the induced transmembrane voltage is size-dependent, appropriate V_m is induced only to the cells in a narrow size range, which result in low electroporation yield.

To solve the problem, we have recently developed an electroporation method based on field constriction at a micro-fabricated orifice [1]. The method uses an electrically insulating orifice plate on which a biological cell is immobilized (fig.1). When the voltage is applied, the field lines converge into the orifice and hence most voltage is concentrated around the orifice, so that poration occurs exclusively at the orifice. The method is inherently independent on the size and shape of the cells.

However, in experiments, we sometimes observe breakdown at locations other than on the orifice, and that often lead to cell disruption. We identified its cause to the

breakdown propagation. In this paper, we present the mechanism of the phenomenon, give a solution using Radio-Frequency (RF) modulated pulse, and demonstrate high-yield electroporation based on the RF pulse.

2. PRINCIPLE

Referring to fig.2, when the voltage V_{app} is applied, the breakdown first occurs at the membrane on the orifice, because most voltage drop is concentrated there due to field constriction, and a pore is formed. But then electrical current start to flow through the pore resistance R_{pore} , to charge the capacitance of the entire membrane C_m . The membrane voltage V_m (the voltage across C_m) builds up until $V_m = V_{app}$, so that next breakdown can occur anywhere.

Such breakdown can be avoided if the applied voltage is modulated. The time constant of charging is given by $\tau_c = C_m R_{pore}$, and is about $100\mu\text{s}$ for 100nm -sized pore. Therefore, if we use RF-modulated voltage (fig.3), whose period T_m satisfying the condition $T_m < \tau_c$, R_{pore} bears most voltage drop, and the voltage on C_m can be very small.

The RF-modulation improves the electroporation yield not only by avoiding breakdown propagation, but also through better pore formation. Persistent voltage on R_{pore} results in maintaining and expanding the pore by Maxwell stress, which is in contrast to the conventional method using simple stepwise pulse where the stress quickly decays with the time constant τ_c . Small voltage on the membrane might also minimize the damage to the membrane channels etc.

3. EXPERIMENTAL

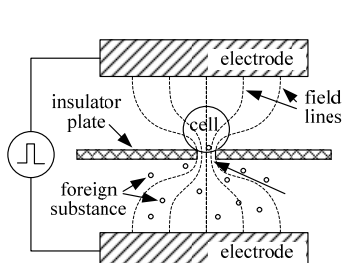


Fig.1 Electroporation using field constriction

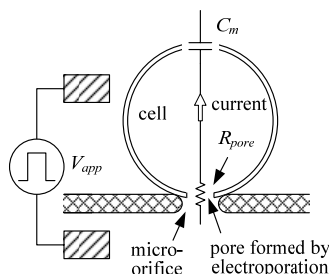


Fig.2 Equivalent circuit after pore formation

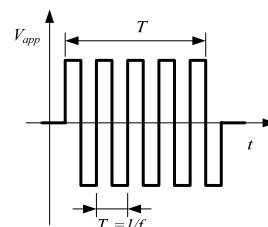


Fig.3 RF-modulated voltage pulse

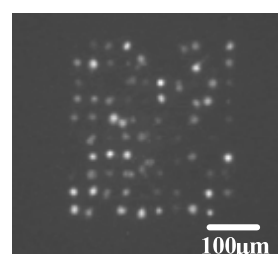


Fig. 4 Electroporation of 10×10 array of human monocytes,
 $1.5\text{V}, f_m = 50\text{kHz}, T=10\text{msec}, 5$ pulses

Experimental demonstrations are performed by using a DNA-binding fluorescence dye (YO-PRO1) as a tracer. The orifice plate is $7\mu\text{m}^t$ Kapton film, to which $2\mu\text{m}^\phi$ orifices are opened by laser machining. Fig.4 is the electroporation of a 10×10 array of human monocyte cells immobilized onto the orifice by aspiration. Successful introduction of the dye is observed in about 90% of the cells, which was not achievable with the pulse without modulation. No perceivable morphological change due to cell damage is observed after the electroporation. Fig.5 is the result with murine fibroblast L929, whose cell cycle is about 24 hrs. The adherent cell is first removed from culture dish with a standard protocol, at which moment the cells take nearly spherical shape. Then they are placed on the orifices by aspiration (fig.5 a), and a single RF pulse is applied. Fig.5 b-1) is the bright field image 18 hours later, where the cells have already started to proliferate on the orifice plate. Fig.5 b-2) is the fluorescence image of the same place, showing fluorescence from the cells. The fluorescence dye by itself is impermeable to the cell membrane, so this photo proves that the proliferating cells in the photo were in fact electroporated. Fig.5 c-1) and 2) are 47 hours after poration. Denser proliferation is observed, indicating cell division.

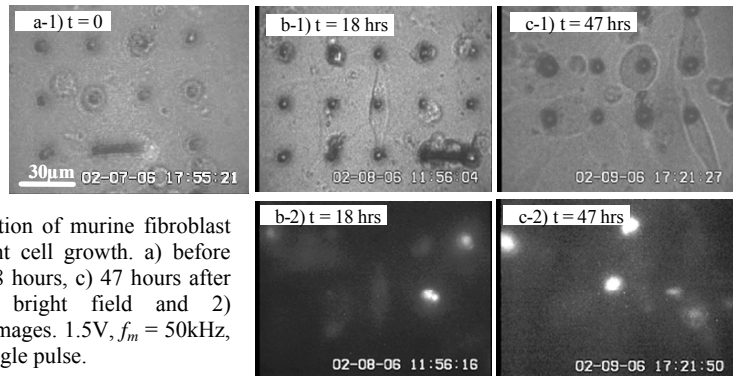


Fig.5 Electroporation of murine fibroblast and subsequent cell growth. a) before poration, b) 18 hours, c) 47 hours after poration, 1) bright field and 2) fluorescence images. 1.5V , $f_m = 50\text{kHz}$, $T=10\text{msec}$, single pulse.

4. CONCLUSIONS

The mechanism of breakdown propagation is clarified, and by using RF-modulated constriction field, high-yield, low cell-damage electroporation is achieved.

Acknowledgements

The authors would like to thank Prof. Akinori Noma, Dr. Satoshi Matsuoka of Kyoto University, Prof. Teruyuki Nagamune and Prof. Takashi Ushida of the University of Tokyo for valuable discussions. This work is supported in part by Grant-in-Aid for Scientific Research from NEDO, Kakenhi 18048008 and the Leading Project for Biosimulation of the Ministry of Education Japan.

References

1. M. Washizu et al.: "High-yield electroporation of cells using field constriction at micro orifices", Proc. micro-TAS2005, vol.2, p.1401-1403 (2005)

RED BLOOD CELL DEFORMATION UNDER EXTENSIONAL FLOW USING HYPERBOLIC CONVERGING SHAPE MICROCHANNEL

Sung Sik Lee, Yoonjae Yim, Kyung Hyun Ahn*, Seung Jong Lee

School of Chemical and Biological Engineering

Seoul National University, Seoul, 151-744, Korea

(* ahnnet@snu.ac.kr)

Abstract

The deformation of red blood cells (RBCs) was investigated under extensional flow. The extensional flow was developed by hyperbolic converging shape microchannel. RBCs were suspended in polyvinyl pyrrolidone (PVP) solution to facilitate deformation and pass through the microchannel. The images of deformed RBCs were captured by high-speed camera and the contrast was improved by band path filter. The degree of deformation was quantified in constant extensional flow region and compared to the result from simple shear flow. It was confirmed that the extensional flow is more efficient in the deformation of RBCs than simple shear flow.

Keywords: Hyperbolic converging, Extensional flow, Red blood cell, Deformability, Elongational Index

1. Introduction

The red blood cells (RBCs) can deform along the flow direction. This deformability is an important physiological factor and has been exploited as one of the clinical diagnosis methods for specific diseases [1-3]. While most studies deal with RBC deformation under simple shear flow, RBC deformation under extensional flow has not been heavily explored. To understand RBC deformation and its physiological meaning, however, it is desirable to investigate the phenomena under extensional flow.

The hyperbolic converging shape is one of the typical geometry to generate extension flow [4-5]. It offers the advantages of continuous monitoring of each RBC during deformation and of generating high extension flow rate. In this study, we investigated the deformation using hyperbolic shape microchannel.

2. Experimental

We designed a hyperbolic converging shape microchannel to obtain a constant extensional rate in specific as shown in Fig. 1. The sidewalls converge according to a hyperbolic equation of the form: $h(z)=1/(Az+B)$ where $A=3.0 \times 10^{-5} \mu\text{m}^{-2}$, and $B=1 \times 10^{-3} \mu\text{m}^{-1}$, unit of z is μm . The extensional strain rate to flow direction at center of channel was calculated by computational simulation (Fluent 6.1). We obtained the adequate constant extension rate corresponding to input flow rate.

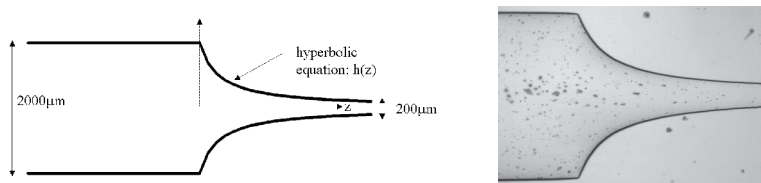


Figure 1. Design of hyperbolic converging microchannel for constant extension rate

Microchannels were fabricated by molding polydimethylsiloxane (PDMS, Sylgard 184, Dow) upon a silicon master. The microchannel was attached to PDMS-coated glass slide so that the microfluidic channels were surrounded by four PDMS surfaces. The plasma sterilizer (PDC-32G, Harrick) was used to bond the PDMS coated glass to PDMS channel. After plasma treatment, we placed the microfluidic device in an oven at 135°C for 72h to convert the microfluidic channels to uniformly hydrophobic surface. A small bandwidth interference filter (380-420nm) enabled the cells to appear as dark objects against a bright background (Fig.2). At each shear level, 1000 images were successively captured by high-speed camera. The degree of RBC deformation was quantified by Elongational Index (EI) defined as: $EI=(A-B)/(A+B)$, where A and B are the long and short axis of individual RBC image. RBCs in the specific area of interest were selected and their degrees of deformation were measured. They were suspended in polyvinyl pyrrolidone (PVP) solution to facilitate deformation.

3. Results and discussion

As we increased the input flow rate, RBCs were deformed by extensional flow at hyperbolic region. In order to compare the simple shear and extensional flow effect on the RBC deformation, EI's were plotted as a function of the applied stress (Fig 3). In both simple shear and extensional flow cases, the degree of deformation was saturated

at the specific level of ca. 0.5-0.6. At low stress region, it is confirmed that the extensional flow is much more efficient in the deformation of RBCs than the simple shear flow. From those results, we postulate that RBC motion and deformation mechanism are different in each flow field.

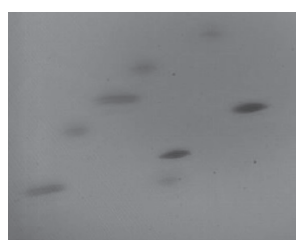


Figure 2. RBC deformation at extension stress=12.0Pa

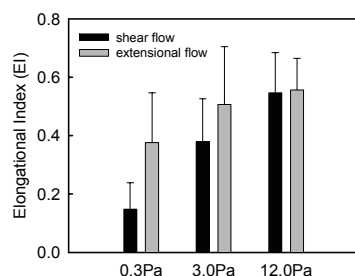


Figure 3. Comparison of EI value: shear flow and extensional flow

Acknowledgements

This work was supported by the National Research Laboratory Fund (M10300000159) of the Ministry of Science and Technology in Korea.

References

1. F. C. Mokken, M. Kedaria, C. P. Henny, M. R. Hardeman, and A. A. Gelb, The clinical importance of erythrocyte deformability, hemorheological parameter, Ann. Hematol. vol.64, pp.113-122, (1992).
2. S. S. Lee, N. J. Kim, K. Sun, J.G. Dobbe, M. R. Hardeman, J. F. Antaki, K. H. Ahn and S. J. Lee, Association between Arterial Stiffness and the Deformability of Red Blood Cells (RBCs), Clin. Hemorheol. Microcirc. vol.34, pp. 475-481, (2006).
3. R. M. Hochmuth, The micropipet and the mechanical deformation of cells, BMES Bulletin, vol.15, pp.35-39, (1991).
4. F. Feigl, F. X. Tanner, B. J. Edwards and J. R. Collier, A numerical study of the measurement of elongational viscosity of polymeric fluids in a semihyperbolically converging die. J. Non-Newtonian Fluid Mech. vol.115, pp.191-215, (2003).
5. G. C. Randall, K. M., Schultz and P. S. Doyle, Methods to electrophoretically stretch DNA: microcontractions, gels, and hybrid gel-microcontraction devices, Labchip, vol.6, pp.516-525, (2005).

MINATURIZED CELL CULTURE DEVICES FOR SPIRAL GANGLION NEURONS

Peter Norlin¹, Tommy Schönberg¹, Beata Kostyszyn², Christian Vieider¹
and Mats Ulfendahl²

¹Department of Industrial Micro- and Nanotechnology, Acreo AB, Sweden

²Center for Hearing and Communication Research, Karolinska Institutet,
Sweden

Abstract

We report the development of a miniaturized cell culture device intended for co-culture of embryonic spiral ganglion neurons and adult cochlea from mice. A cage-like cell culture chamber was designed which presents a barrier to the cell bodies of neurons, but allows the growth of neurites through narrow passages in the wall. The culture chambers are manufactured in PDMS and bonded to supports of glass, PDMS and a porous membrane. Initial culture tests using PC 12 cells showed that cells proliferated well and differentiated into neurons in all cell chambers.

Keywords: cell culture, spiral ganglion neurons, poly(dimethylsiloxane)

1. Introduction

Spiral ganglion neurons (SGN) are the primary sensory neurons whose dendrites connect to the hair cells in the cochlea of the inner ear, and whose axons join to form the cochlear nerve projecting to the cochlear nuclei in the brain stem [1]. To treat hearing loss, drugs need to be developed which stimulate regeneration of hair cells as well as SGNs. Several *in vivo* models are presently used to test for drugs effects. However, *in vivo* models have many obvious drawbacks, in the case of the mouse accentuated by the diminutive size of the inner ear and resulting complicated drug delivery. Hence, *in vitro* models aimed at screening of drugs for treatment of hearing loss are a highly desired complement. Here we report the development of miniaturized *in vitro* cell culture devices intended for co-culture of embryonic SGN and adult cochlea from mice.

2. Experimental

A cage-like cell culture chamber was designed (Figure 1) which presents a barrier to the cell bodies, but allows the growth of neurites through narrow ($\sim 5 \mu\text{m}$) passages in the wall (similar to the *canalliculi perforantes* in the cochlea). A cochlea preparation may be placed outside the cage in order to study the interaction between it and the neurons. The width of the cage is varied to enable studies of cell growth in different degrees of confinement.

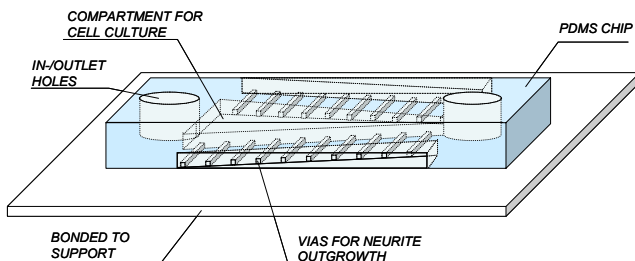


Figure 1. Schematic illustration of the cell culture device

The culture chambers were fabricated in poly(dimethylsiloxane) (PDMS), replicated against a lithographically defined SU8 resist mold with two levels (~350 µm and ~5 µm). In- and outlet holes were opened with a punching tool. The holes were sealed after cell injection by inserting plugs cut from pipette tips. Using the oxygen plasma method [2], the PDMS structures were bonded to three different supports: (1) A glass plate. Glass is well-established as a cell culture support and forms a good seal to PDMS. (2) A PDMS disc. PDMS shows good cell culture properties, possibly better than glass. (3) A permeable membrane of polyester (PET), available as a well-plate insert (Corning). By evaporating a thin film layer (~250 Å) of SiO₂ on the membrane we created a bondable surface on the polyester material.

Cell chamber prototypes were tested together with a PC 12 cell line, derived from a transplantable rat pheochromocytoma. The cells respond to Nerve growth factor (NGF) by induction of the neuronal phenotype. ~10 µl of cell suspension was injected into the cell culture chambers. Cells were cultured under standard growing conditions in DMEM medium supplemented with 15 % horse serum, 2.5 % fetal bovine serum, 2nM L-glutamine and 1 % penicillin/streptomycin. Differentiation of PC 12 cells was induced by adding NGF into culturing media. Cells were incubated for 16 days in 37 °C and 5 % CO₂. The medium was renewed every 2 days.

3. Results

Figures 2-3 show PDMS chips before bonding (two typical design versions). Chips bonded to different supports are shown in Figure 4. All devices are compatible with a multi-wellplate format (Figure 5). To verify that the permeable membrane was not clogged by SiO₂, the transport of water through the membrane was observed. It was found that water transported significantly faster through the oxide treated membrane than a non-treated control. Presumably this is explained by the hydrophilic properties of SiO₂.

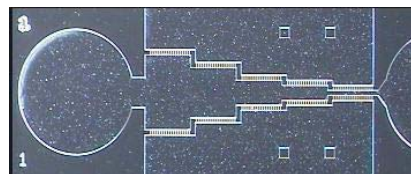


Figure 2. Photomicrograph of a PDMS chip (11 mm x 3.5 mm).

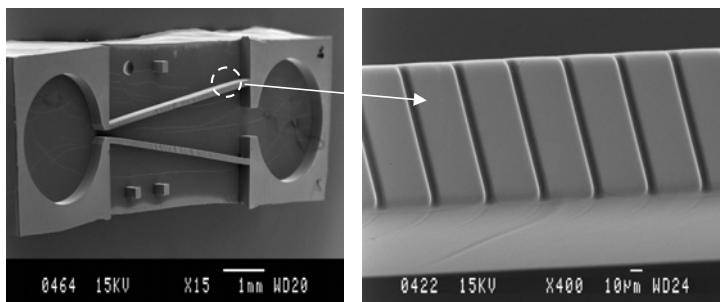


Figure 3. Scanning electron micrographs of a PDMS chip viewed from below (left) and close-up of neurite outgrowth channels formed in the wall of the chamber (right).



Figure 4. PDMS chips bonded to (from left to right) a porous membrane, a PDMS plate, and a glass plate (12 mm diameter).



Figure 5. The cell culture devices are compatible with a multi-wellplate format.

PC 12 cells proliferated well and differentiated into neurons within all cell chambers (Figure 6). Cells showed the tendency to be attracted to the openings in the chamber wall. However, since no outgrowth of neurites was observed, new prototypes with wider channels will be tested. Chambers bonded to glass and PDMS could be re-used several times after rinsing and autoclaving. No major difference in cell growth properties between glass and PDMS was observed. The interface between chambers and PET membranes appeared sufficiently strong in simple pull force tests in air, but adhesion problems appeared after one day in cell growth medium. Poly-ornithine coating was used in the chambers to stimulate cell adhesion. However parallel incubation of the cells in the chambers without any coating of the growth surface showed no significant difference in proliferation or differentiation of the cells compared to coated ones.

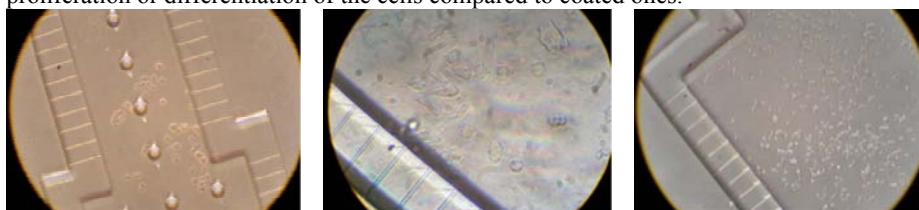


Figure 6. Photomicrographs of PC12 cells after (left to right) 3, 7 and 10 days in culture.

4. Conclusions

We have presented the first results of the design, manufacture and evaluation of a miniaturized cell culture device, intended for the study of e.g. drug effects on auditory cells and co-cultures of auditory cells with possible transplantation candidates. It was demonstrated that cells proliferated and differentiated into neurons in culture chambers with cell growth supports of three different types. On-going work addresses the optimization of the chamber design.

Acknowledgement

This research was supported by European Commission FP6 Integrated Project EUROHEAR, LSHG-CT-20054-512063.

References

1. M.C. Holley, *Drug Discovery Today*, **10**, 1269-82 (2005).
2. D.C. Duffy *et al.*, *Anal. Chem.*, **70**, 4974-84 (1998).

A POLYMER BIOCHIP FOR DETECTING INORGANIC AND ORGANIC PHOSPHATE USING PLANAR COBALT MICROELECTRODES

Zhiwei Zou, Jungyoup Han, Am Jang*, Paul L. Bishop*, and Chong H. Ahn

Microsystems and BioMEMS Laboratory,

Department of Electrical & Computer Engineering & Computer Science,

*Department of Civil & Environment Engineering, University of Cincinnati, USA

Abstract

In this work, a low-cost, miniaturized, multi-analyte polymer biochip, which can be used for measuring inorganic ($H_2PO_4^-$) and organic phosphate compounds (adenosine 5'-triphosphate, ATP and adenosine 5'-diphosphate, ADP), and pO_2 has been designed, fabricated, and characterized for environment monitoring.

Keywords: Phosphate sensor, cobalt electrode, biochip, oxygen sensor

1. Introduction

Phosphate measurement is essential in the monitoring of environmental pollution caused by the eutrophication of lakes and rivers; it is also required in the clinical diagnostics of hyperparathyroidism, vitamin D deficiency, and Fanconi syndrome.

Enzyme based phosphate sensors have been widely used, whereas the relatively high cost and instability of enzyme material limit their applications for inexpensive lab-on-a-chip. An alternative method uses cobalt-wire as the phosphate-selective electrode for potentiometric measurement. It displays high selectivity and sensitivity towards phosphate ions in aqueous solutions [1]. In our previous work, we have introduced BioMEMS fabrication technology to realize a planar cobalt microelectrode for on-chip inorganic phosphate detection; the cost, preparation and sensing time, and analyte consumption have been reduced by the miniaturized on-chip phosphate sensor [2].

2. Design and fabrication

The proposed system contains a novel on-chip cobalt microelectrode used for phosphate monitoring (Figure 2a), and an integrated Clark-type amperometric oxygen

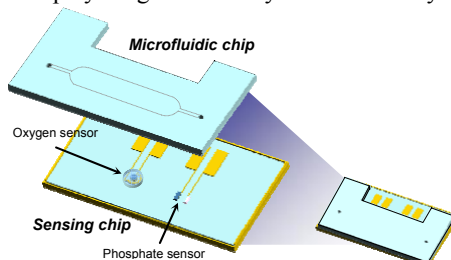


Figure 1. Schematic illustration of the polymer biochip for phosphate and pO_2 sensing.

sensor with gel-based solid electrolyte to monitor pO_2 (Figure 2b) [3], which has a noted effect on the cobalt electrode potential, since the potential mechanism involves the oxidation of cobalt. A polymer biochip has been achieved for rapid on-chip detecting of inorganic phosphate and pO_2 concurrently. In addition, the system also shows the capability for organic phosphate (ATP and ADP) measurement.

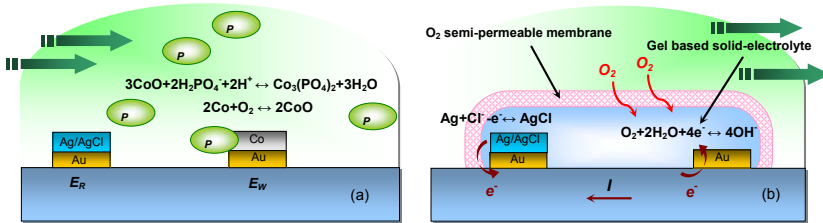


Figure 2. Working principle: (a) Potentiometric phosphate sensor with cobalt electrodes and (b) Clark-type amperimetric oxygen sensor with gel-based solid electrolyte and oxygen semi-permeable membrane.

The fabricated device consists of a polymer (Cyclic Olefin Copolymer, COC) microfluidic chip and a sensing chip which has a cobalt electrode based phosphate sensor and a solid electrolyte based oxygen sensor as shown in Figure 3. The detection circuit (Figure 4) developed in this research has been used as a portable system together with the polymer biochip at ease. The biochip is fabricated using the standard BioMEMS fabrication techniques and the detail has been reported previously [2, 3].

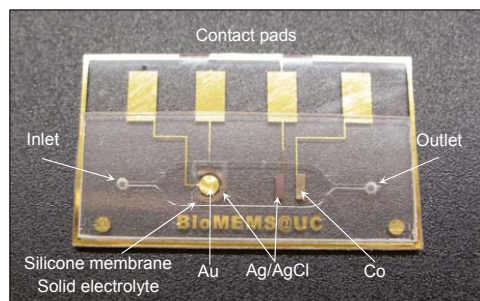


Figure 3. Photograph of the fabricated biochip.

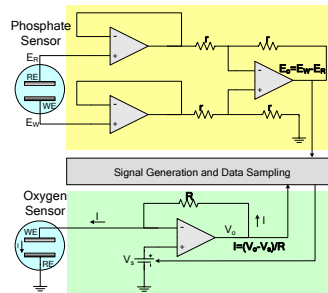


Figure 4. Detection circuits for the phosphate sensor and the oxygen sensor.

3. Results and discussion

Figure 5 presents the potentiometric response to different concentrations of inorganic phosphate (KH_2PO_4) at pH 5.0, and Figure 6a shows the calibration curve of sensor's response to different concentrations of organic phosphate (ATP and ADP). Moreover, the oxygen sensor has been characterized with different pO_2 in water as shown in Figure 6b.

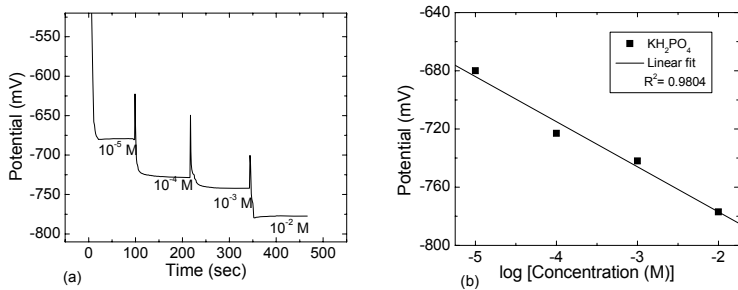


Figure 5. Potentiometric response of the phosphate sensors in different concentrations of KH_2PO_4 at pH 5.0: (a) Continuous measurement and (b) Calibration curve.

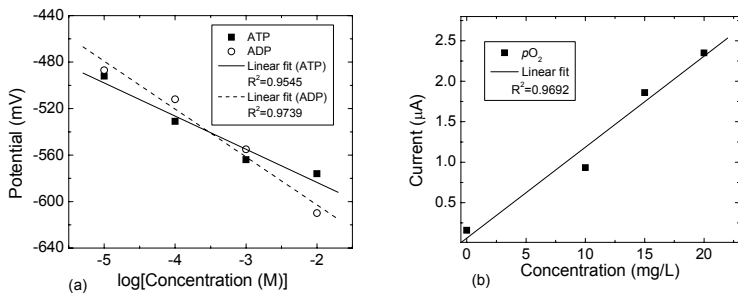


Figure 6. Calibration curves: (a) the phosphate sensors in response to different concentrations of organic phosphate compounds (ATP and ADP) in 15 mM KHP buffer at pH 5.0; and (b) the oxygen sensor in response to different $p\text{O}_2$ concentrations in aqueous solution.

4. Conclusions

A new polymer biochip for phosphate and oxygen sensing has been developed in this work. The sensing mechanism and fabrication technique ensure the very low cost and the high yield of the device, while also keeping the good performance. This inexpensive and rapid-response system can be large-scale field deployed for mass environmental data collections and also used for disposable point-of-care testing in clinical diagnostics.

Reference

1. D. Xiao, et al, Surface-modified cobalt-based sensor as a phosphate-sensitive electrode, *Anal. Chem.*, 67, pp. 288-291, (1995).
2. Z. Zou, et al, A disposable on-chip phosphate sensor with planar cobalt microelectrodes on polymer substrates, *Biosensor 2006*, Toronto, Canada, O77, (2006).
3. C. Gao, et al, Development of inexpensive biosensor array for point-of-care testing, *Proc. Micro Total Analysis Systems 2003*, Squaw Valley, USA, pp. 97-800, (2003).

AUTONOMOUS LABEL FREE OPTICAL DETECTION OF SPORES TRAPPING IN AN INSULATOR-BASED DIELECTROPHORETIC CONCENTRATOR

Poorya Sabourchi¹, Alfredo M. Morales¹, Blake A. Simmons¹, and Rafael V. Davalos^{*1,2}

¹Sandia National Laboratories, Livermore, CA, USA

²Biomedical Engineering, Virginia Tech-Wake Forest, Blacksburg, VA, USA

^{*}rvdaval@sandia.gov

Abstract

We present the effectiveness of coupling insulator-based dielectrophoresis (iDEP) with real-time optical feedback to rapidly concentrate and actively detect water-borne pathogens. Our approach has a threshold detection of 10^3 particles and can detect contaminations as low as 10^5 cells/mL at flow rates of $60 \mu\text{L}/\text{min}$ in less than a minute. The images and data presented were obtained using a compact and transportable standalone unit with an overall footprint of less than a half a cubic foot and weighs less than 10 pounds. As particles are collected, a measurable increase of the intensity in the trapping region was observed with a CCD camera, indicating particle concentration.

Keywords: Label free optical detection, dielectrophoresis, sample preparation

1. Introduction

Sample concentration is an essential step for the detection of biological pathogens in a microfluidic platform [1]. A variety of dielectrophoretic device architectures have been developed to support particle sorting and sample processing in microfluidic systems [2]. In insulator-based dielectrophoresis (iDEP), remote electrodes apply an electric field along a channel while insulating structures distort the field providing the spatial nonuniformities needed to drive dielectrophoresis [3].

Here we employ real-time optical feedback coupled with iDEP concentration to rapidly and actively detect water-borne pathogens. As particles are collected in the trap, a measurable increase in intensity at the trapping region was observed with a CCD camera, indicating particle concentration. In order to enhance the signal (average intensity of selected pixels between the insulating obstacles) we have employed a Gabor Filter for post-processing of acquired images. Gabor Filter, which is essentially a bandpass filter, optimally captures both local orientation and frequency information from an image [4]. This makes Gabor filtering attractive for images of spore concentration as they create texture during the trapping period. This approach has a threshold detection of 10^3 particles and can detect contaminations as low as 10^5 cells/mL at flow rates of $60 \mu\text{L}/\text{min}$ in less than a minute.

2. Experimental methodology

The images and data presented were all obtained with a compact transportable standalone unit with an overall footprint of less than a half a cubic foot and a weight of

less than 10 pounds. The system, as shown in Fig. 1, consists of a microfluidic chip and custom made manifold, which is integrated with an SVM340 (Labsmith, Livermore, CA), a commercially available optical platform.



Figure 1. Portable Setup: Images of (left) top view of the portable desktop iDEP unit with power supply and (right) underside showing the iDEP polymer device containing 8 separate channels.

The microfluidic chips are fabricated in a cyclic olefin copolymer, Zeonor® (Zeon Chemicals, Louisville, KY). The fabrication pipeline presented before [3] and depicted in Fig. 2, starts with the fabrication of the device features in a silicon wafer using standard photolithographic techniques (2a) and proceeds through the development of a metal stamp (2b) from which thousands of inexpensive disposable polymer chips can be replicated (2c).

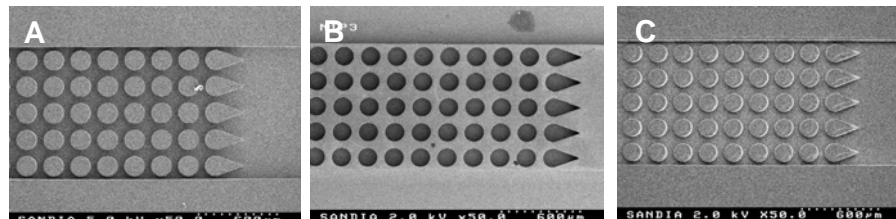


Figure 2. Chip Fabrication: Images depicting the fabrication route of a polymer-based iDEP device from the (A) Si stamp to (B) electroformed Ni stamp to (C) injection molded polymer replicate.

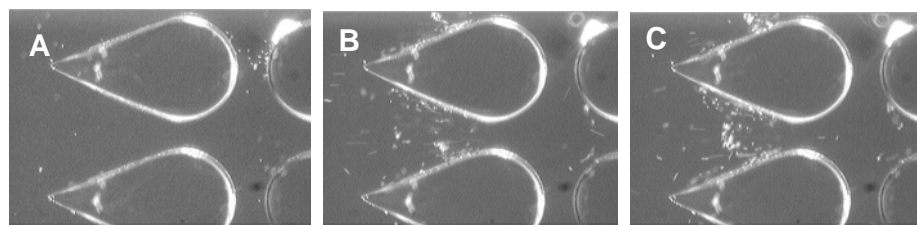


Figure 3. Optical Detection: Images depicting the fabrication route of a polymer-based iDEP device from the (A) image of the background without the particles at time zero (C) image of trapped spores after 30s (C) image of trapped bundle of spores after 55 sec.

3. Results and discussion

Fig. 3a shows the trapping region during the operation of the device before sufficient voltage is applied to concentrate the particles. Fig. 3b shows unlabeled spores bundles on the order of $5\mu\text{m}$ were introduced into the system at a concentration of 10^5 cells/mL and trapped using an applied field of 700 V/cm in a low conductivity buffer. As particles are collected in the trap, a real-time measurable increase of the intensity in the trap region is observed with a CCD camera, indicating that particles are being collected (Fig. 3c). The camera was controlled with the MATLAB Image Processing Toolbox (Mathworks, Natick, MA) and each frame was post-processed with a Gabor filtering algorithm to enhance particle texture intensity compared to background (Fig. 4a). Then, the average intensity of a specific area (defined in Fig. 4a) was plotted (Fig. 4b) for the period of one trapping cycle (60 sec).

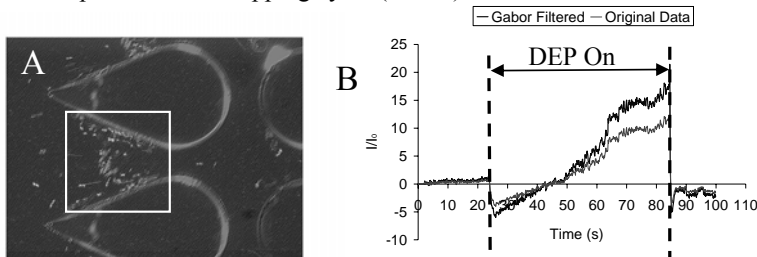


Figure 4. Image Processing and Analysis: (A) Gabor filtered image of trapped spores (B) Plot average intensity of a specific area (4a) for the period of one trapping cycle (60 sec).

The use of iDEP with optical feedback provides an autonomous mechanism to concentrate and detect when a sufficient number of particles of interest have been collected for downstream testing. Our approach has a threshold detection of 10^3 particles and can detect contaminations as low as 10^5 cells/mL at flow rates of $60 \mu\text{L/min}$ in less than a minute.

Acknowledgements

The authors acknowledge Allen Salmi, Karen Krafciak, and Pierre Ponce for their invaluable contributions to the project. Sandia is a multiprogram laboratory operated by Sandia Corporation, a Lockheed Martin Company, for the United States Department of Energy's National Nuclear Security Administration under contract DE-AC04-94AL85000.

References

1. Lapizco-Encinas, B.H., et al. *J. Microbiological Methods* **62**: 317-326, (2005).
2. Cummings, E.B., Singh, A. *Anal. Chem.* **75**: 4724-4731, (2003).
3. McGraw, G.J., Davalos, R.V., et al. *SPIE Proceedings* **5715**: 59-68, (2005).
4. Najarian, K., Splinter, R. *Biomedical Signal and Image Processing CRC*, (2006).

ALTERNATIVE METHOD FOR CURRENT COLLECTOR OF MICRO DIRECT METHANOL FUEL CELL USING CARBON PAPERS

Soo Ho Kim¹, Jermim Noh¹, Min Ku Jeon¹, Luke P. Lee² and Seong Ihl Woo^{1*}

¹ Department of Chemical and Biomolecular Engineering (BK21 Graduate Program) & Center for Ultramicrochemical Process Systems (CUPS), Korea Advanced Institute of Science and Technology (KAIST), 373-1, Guseong-dong, Yuseong-gu, Daejeon, 305-701, Republic of Korea.

² Department of BioEngineering, University of California, Berkeley, CA 94720, USA

Abstract

The alternative method for current collector was developed using carbon papers instead of thin film of metal. The flow field of the anode and cathode was made by the wet etching process of glass. The single cell test was performed with 1 M methanol solution and oxygen at room temperature. The open circuit voltage and maximum power density results show that the carbon paper is adequate for current collector owing to its high electrical conductivity.

Keywords: Micro direct methanol fuel cell, Microfabrication, Carbon paper, Current collector

1. Introduction

Microfabricated direct methanol fuel cells (DMFCs) have emerged as a candidate to compete with conventional power sources among various fuel cells because they does not need reformer or other pre-fuel processing parts [1]. The studies on micro-DMFC have been focused on the design of flow fields [2] and the materials for substrate [3]. However, the current collector has received much less attention although it affects cell performance. In this work, the alternative method for current collector was studied using carbon papers instead of thin film of metal.

2. Design and fabrication

Figure 1 shows the design of anode and cathode flow fields, including two serpentine channels. The width and length of the microchannel were 400 μm and 142.4 mm, respectively. The active area was 0.86 cm^2 and open area was 35.3 %. The flow field of anode and cathode was fabricated by the wet etching process of glass with a depth of 30 μm . Toray carbon paper was used as the current collector for anode. The carbon paper containing 20 wt % PTFE was used as the current collector for cathode. The schematic diagram and photograph image of the micro-DMFC were described in figure 2.



Figure 1. Design of flow field for anode and cathode

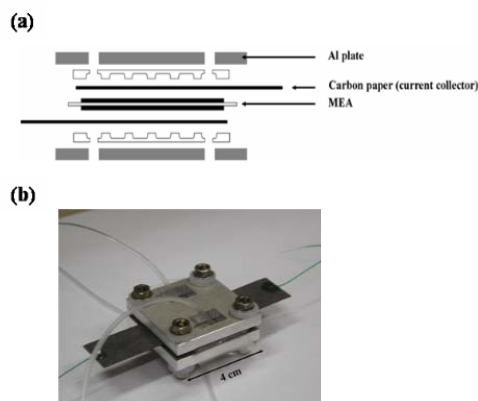


Figure 2. (a) Schematic diagram of the micro-DMFC. (b) Photograph image of the micro-DMFC

3. Results and discussion

Methanol aqueous solution of 1 M was prepared to test cell performance. A peristaltic pump (Masterflex L/S, Cole-Parmer Instrument Co., IL, USA) was used to feed the liquid fuel and control the flow rate. A gas flow meter was used to control the flow rate of oxygen. An electronic load system (EL-200P, DAE GIL ELECTRONICS Co. Ltd., Korea) was used to obtain polarization curve at a scan rate of 10 mA s^{-1} .

Figure 3 shows the polarization and power density curve of the micro-DMFC at room temperature. The feed rate of 1 M methanol solution was 0.30 ml min^{-1} and the oxygen flow rate was 100 ml min^{-1} . The open circuit voltage was 0.396 V and the maximum power density was 12.97 mW cm^{-2} as shown in Figure 3. This results show that the carbon paper is adequate for current collector owing to its high electrical conductivity.

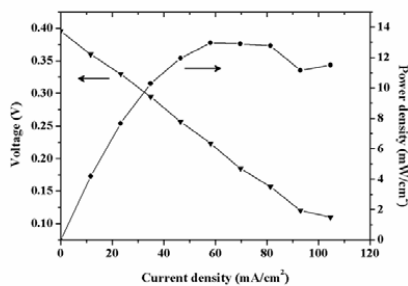


Figure 3. Performance of the micro-DMFC at room temperature

4. Conclusions

Micro direct methanol fuel cell was fabricated by MEMS technique. The flow field of the anode and cathode was made by the wet etching process of glass. The single cell test was performed with 1 M methanol solution and oxygen at room temperature. The open circuit voltage and maximum power density was 0.396 V and 12.97 mW cm^{-2} when the flow rate of the methanol solution and oxygen were 0.30 ml min^{-1} and 100 ml min^{-1} , respectively. This results show that the carbon paper is adequate for current collector owing to its high electrical conductivity.

5. Acknowledge

This research was funded by “Center for Ultramicrochemical Process Systems (CUPS)” sponsored by KOSEF (2006).

6. References

- [1] G. Q. Lu and C. Y. Wang, J. Power Sources, Vol.144, pp. 141-145, (2005).
- [2] C.W. Wong, T.S. Zhao, Q. Ye and J.G. Liu, J. Electrochem. Soc., Vol.152, pp. A1600-A1605, (2005).
- [3] H.-Y. Cha, H.-G. Choi, J.-D. Nam, Y. Lee, S.M. Cho, E.-S. Lee, J.-K. Lee and C.-H. Chung, Electrochim. Acta, Vol.50, pp. 795-799, (2004).

SEMI-AUTOMATIC MICROSYSTEM BASED SAMPLE PREPARATION FOR THE DETECTION OF BIOLOGICAL AGENTS

M. Ritzi, D. Dadic, F. Doffing, F. v. Germar, R. Gransee, K. S. Drese

Institut für Mikrotechnik Mainz GmbH

Abstract

A modular polymer-microchip system is presented on which bacteria are isolated from environmental samples either soil or dust samples or aqueous solutions followed by purification of the DNA. It is shown that commercial available DNA preparation kits can be transferred to micro-systems for automatic processing.

Keywords: Micro-system, sample preparation, biological agents

1. Introduction

Identification of biological micro-organisms in diverse samples is of increasing interest in different fields like for example environmental microbiology, clinical diagnosis or forensic analysis (see e.g. <http://www.ca.sandia.gov/>). While in earlier times bacteria were isolated and than cultured today micro-organisms were usually detected using PCR. In most cases identifying biological contaminants needs the concentration and isolation of DNA to get rid of specific substances like e.g. humic substances in soil which interfere with the following PCR. Sample preparation therefore represents a necessary pre-purification step for the downstream processes. Several kits are on the market for fast DNA purification and all of them need multiple handling operations. Using micro-fluidic devices in general provides a number of benefits like simplified use, increased reproducibility and analysis speed, reduced sample size and chemicals consumption, and lower contamination risk. Due to these advantages more and more effort is done to transfer standard analysis assays into lab-on-a-chip-systems [1, 2].

2. Experimental modular set-up

The developed sample preparation system [Fig. 1] comprises several modules which functions will be described in the following. Functionality of modules is proved using soil riddled with 10^{10} *E. coli* per gram mimicking natural background and $50 - 5 \cdot 10^5$ *Bacillus thuringensis* per gram representing a contamination to be detected. About 0.5 g soil are introduced into the syringe extractor where bacteria are extracted from the particles using a Molzym kit [www.molzym.com]. Unsolved particles are removed from bacteria suspension by a filter (pore size 10 µm). Bacteria suspension is then guided to the lysis module. Alternatively, aqueous solutions (25 ml) (e.g. from air samplers) can be pumped into the system where bigger particles like dust or soot are removed by a cascade of filters with decreasing pore sizes. On the last filter (pore size 0.22 µm) bacteria are collected. By a back flush with buffer solution bacteria are again driven to the lysis module. These two modes of operation are decided by the position of the two

turning valves. The subsequent process steps are sample-independent. Bacteria are lysed at 90°C. Evaporation of water is suppressed by a cooling channel. All necessary buffers are added to the sample at passive valves and mixed in meandering channels. Purification of DNA is performed by using the Molzym column with buffers of their PrestoSpinD Plant Kit. The remaining ethanol is removed from the column by the use of preheated air. A supplying chip module is used to preheat both dry air and elution buffer to 70°C. Additionally, this module contains reservoirs for washing and elution buffers. Eluted DNA sample is collected in a tube and 2-4 µl are needed for following PCR.

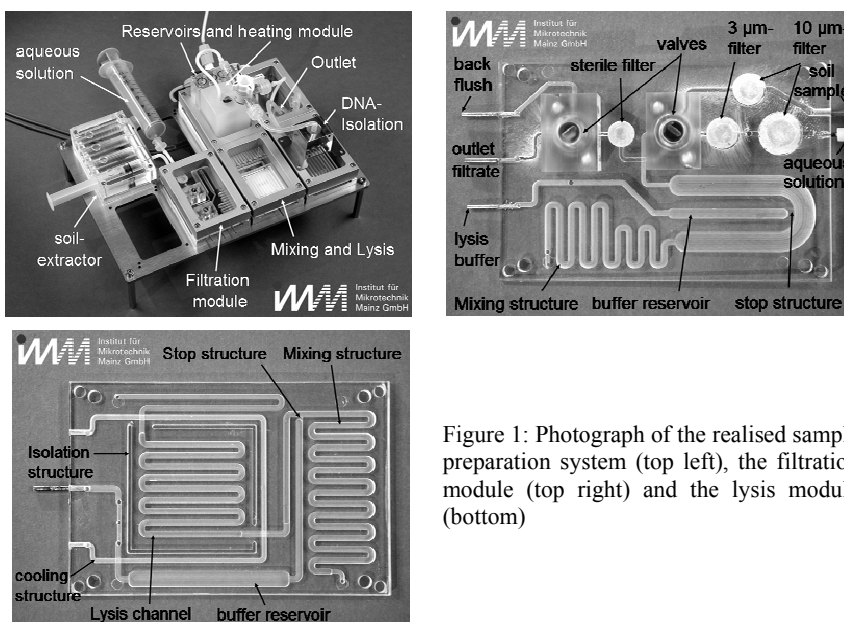


Figure 1: Photograph of the realised sample preparation system (top left), the filtration module (top right) and the lysis module (bottom)

3. Results and discussion

Automatically bacterial DNA preparation of soil or aqueous samples is realised within this modular set-up using a commercial available DNA purification kit. In a first approach we proofed functionality of the single modules [Fig. 2A-D] as there are the extraction, enrichment and lysis of bacteria, and the DNA-purification. Conditions (temp., times, vol.) of the original protocol were used. With conventional techniques about 10^3 specific bacteria within a background of 10^9 common bacteria purified can be detected [Fig. 2A]. In the following the functionality of the individual modules of the platform was verified. Filtration of bacteria from 15 ml aqueous solution on the filtration module followed by spintube preparation proofs efficient concentration of the bacteria [Fig. 2C] as well as lysis on chip seems to be efficient [Fig. 2D]. As shown in Figure 2E the combined modules (2) possess comparable results to the preparation using conventional spintubes (1) purifying $5 \cdot 10^9 E. coli + 10^6 Bac. Thur.$ from 0.5 g soil.

Experiments to show the detection limit of the full system are under process, but it is likely to be comparable to the macroscopic one.

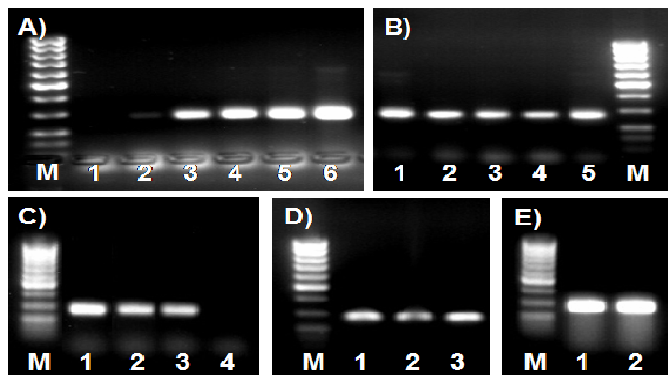


Figure 2: PCR-analysis in 2% agarose-gel of *Bacillus thuringiensis* DNA in 2 µl purified DNA sample (M = 100 bp marker); **A**) Spintube preparation of 0.5 g soil with $5 \cdot 10^9$ *E. coli* (1) + 10^2 (2), 10^3 (3), 10^4 (4), 10^5 (5), and 10^6 (6) *Bac. Thur.*; **B**) DNA-Isolation with purification module: $5 \cdot 10^9$ *E. coli* + 10^6 (1), 10^5 (2+3), and 10^4 (4+5) *Bac. Thur.*; **C**) Concentration of bacteria from 15 ml aqueous solution on filtration module: $5 \cdot 10^9$ *E. coli* + 10^5 (1), 10^4 (2), 10^3 (3) and 10^2 (4) *Bac. Thur.*; **D**) Lysis on chip: $5 \cdot 10^9$ *E. coli* + 10^5 (1), 10^4 (2), and 10^3 (3) *Bac. Thur.* in 200 µl buffer; **E**) Spintube preparation (1) and preparation with developed micro-system (2): $5 \cdot 10^9$ *E. coli* + 10^6 *Bac. Thur.* in 0.5 g soil.

4. Outlook

Next steps will be to optimise and automate the different modules followed by the integration of the single functions into one single chip system. The interesting question is if by automation, i.e. elimination of variability due to manual handling and contamination of sample, the macroscopic imitations can be overcome. Also, this preparation system can directly be combined with a microchip-based PCR [3] for analysis.

Acknowledgement

The presented work was supported by federal funding under the contract number E/E590/5Z013/4F169 and accomplished on behalf of the WIS (Wehrwissenschaftliches Institut, Dr. Stefan Köhne, Humboldtstraße 1, 29633 Munster).

References

1. Y.-F. Chen, J. M. Yang, J.-Jr. Gau, Ch.-M. Ho, Y.-Ch. Tai; Microfluidic System for Biological Agent Detection; <http://ho.seas.ucla.edu/publications/conference/2000>
2. I. Abdel-Hamid, A. Linnell, G. Bajszar and C. Call; Portable Microfluidic Biological Agent Detection System; <http://handle.dtic.mil/100.2/ADA433114>
3. G. Münchow, D. Dadić, F. Döffing, St. Hardt and K.S. Drese; Automated chip-based device for simple and fast nucleic acid amplification; Expert Rev. Mol. Diagn. 5(4), 613–620 (2005)

MICROFLUIDIC GLUCOSE BIOFUEL CELLS FOR POWER GENERATION FROM BIOFLUIDS

Makoto Togo, Akimasa Takamura, Tatsuya Asai, Takashi Abe
and Matsuhiko Nishizawa

Department of Bioengineering and Robotics, Graduate School of Engineering,
Tohoku University, Sendai 980-8579, Japan

Abstract

This paper reports on an implantable glucose biofuel cell generating electric power from body fluids, such as blood. By the use of enzyme as an anodic catalyst and vitamin K₃ as a harmless electron-mediator, we can realize the power generation from biofluids. We assembled a microfluidic biofuel cell to evaluate cell performance and stability in biofluids.

Keywords: biofuel cell, enzyme, vitamin K₃, micro-fabrication, implantable

1. Introduction

The biofuels cell use enzymes as electrode catalyst, and thus perform high reaction selectivity even in a very mild condition (room temperature, neutral pH etc.). Such properties allow us to design a simple and small cell structure (separator-less), and to generate electricity from mixed fuel solutions, e.g., glucose-containing body fluids[1]. These advantages enable biofuel cell to be an implantable power source. We have studied enzyme-based glucose biofuel cell[2], and in the present study we assemble the fuel cell system as a microfluidic-type device to evaluate the cell performance during a continuous operation.

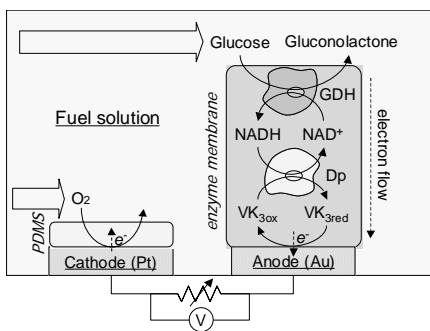


Figure 1. Schematic illustration of reaction schemes for the biofuel cell.

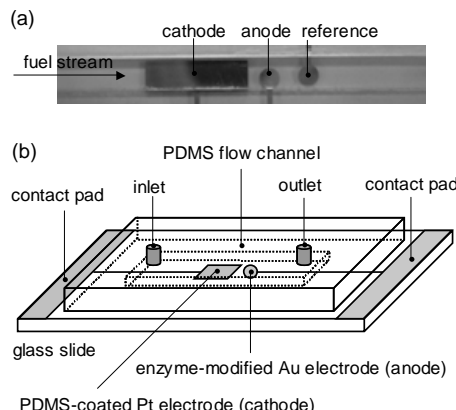


Figure 2. Structure of the microfluidic biofuel cell.

2. Experimental

Figure 1 shows the electrochemical reactions at anode and cathode [2]. The glucose oxidizing anode consists of two enzymes (diaphorase (Dp) and NAD dependent glucose dehydrogenase (GDH)), cofactor NAD and Vitamin K₃ (2-methyl-1,4-naphthoquinone) polymer as a harmless electron-mediator. The coating of PDMS particulate film on Pt cathode ensured selective O₂ reduction[3]. Figure 2 shows the microfluidic biofuel cell systems. Microfluidic chip-based biofuel cells were composed of a couple of electrodes and PDMS microchannel[4].

3. Results and discussion

The performance of the cell, with the enzyme-based anode and the PDMS-coated Pt cathode, was evaluated in a 37 °C phosphate buffer solution (pH 7.0) containing 5.0 mM glucose and 1.0 mM NADH under the flow rate of 1.0 ml/min (Figure 3). The open circuit voltage of 0.55 V and the maximum power density of 0.046 mW/cm² have been obtained. As shown in Figure 4, the output current was low at lower flow rates (0, 0.1 ml/min), and high at higher flow rate (1.0 ml/min), suggesting that the cell performance is partly controlled by fuel supply. It is worth noting that the diffusion of NADH into the enzyme-based membrane would be slow due to electrostatic repulsion. The studies on the previous incorporation of NADH within the membrane are now progressing.

Figure 5 shows the stability of the microfluidic biofuel cell. After 120 minutes of continuous operation in a buffer solution, the initial discharge current of 0.11 mA/cm² dropped to 0.085 mA/cm² (ca. 80 %). On the other hand, the discharge current in a bovine serum was half of that in a buffer solution, and dropped to 65 %. In a bovine serum, the reaction selectivity of electrodes is break down especially at the Pt cathode. In order to evaluate enzyme anode more precisely, we need to conduct experiment using tougher cathode like the enzyme cathode or the Ag|AgCl cathode.

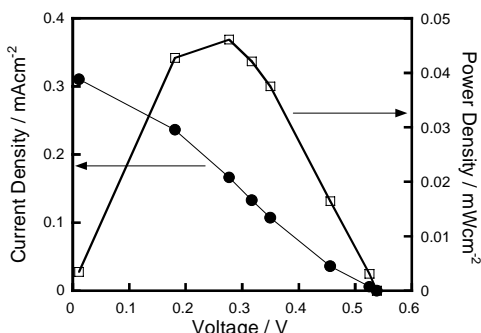


Figure 3. Cell performance in a phosphate buffer solution of pH 7.0 containing 1.0 mM NADH and 5.0 mM glucose, 1.0 ml/min, 37 °C.

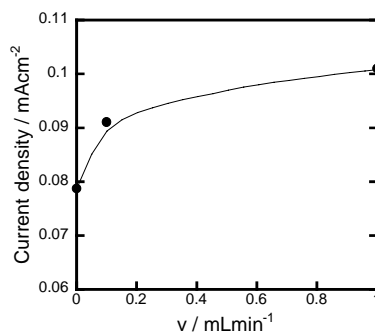


Figure 4. Discharge current ($R=30\text{ k}\Omega$) in various flow rate, 37 °C, phosphate buffer solution of pH 7.0 containing 1.0 mM NADH and 5.0 mM glucose.

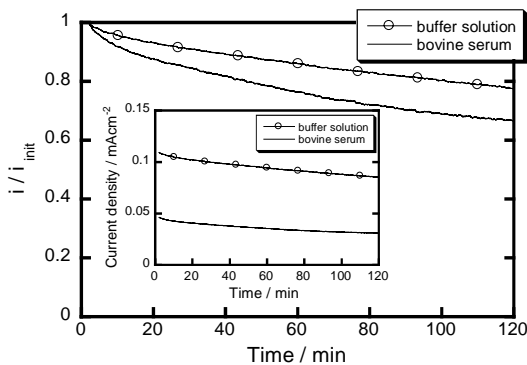


Figure 5. Stability of the discharge current ($R=100 \text{ k}\Omega$) under a (a) phosphate buffer of pH 7.0 containing 1.0 mM NADH and 5.0 mM glucose, (b) bovine serum containing 1.0 mM NADH, 1.0 ml/min, 37 °C.

4. Conclusion

We assembled a microfluidic biofuel cell to evaluate cell performance in biofluids. The power density of the biofuel cells was 0.045 mW/cm² in a 5.0 mM glucose and 1.0 mM NADH containing phosphate buffer solution of pH 7.0. By the reaction selectivity of electrode, the discharge current in a bovine serum was half of that in glucose buffer solution. To stabilize the biofuel cell performance in the biofluids, we are developing a highly selective cathode.

Acknowledgements

Author express appreciation to Dr. Kosuge and Dr. Fukasaku (Daiichi Pure Chemicals Co., Ltd.) for synthesis of mediator polymers. This work was partly supported by Health and Labor Sciences Research Grant from the Ministry of Health, Labor and Welfare of Japan. Glucose dehydrogenase was donated from TOYOBO.

References

- [1] A. Heller, *Aiche Journal*, **51**, 1054 (2005).
- [2] F. Sato, M. Togo, M. K. Islam, T. Matsue, J. Kosuge, N. Fukasaku, S. Kurosawa, and M. Nishizawa, *Electrochemistry Communications*, **7**, 643 (2005).
- [3] F. Mizutani, Y. Sato, Y. Hirata, and S. Iijima, *Analytica Chimica Acta*, **441**, 175 (2001).
- [4] M. Nishizawa, M. Togo, A. Takamura, T. Asai and T. Abe, *Technical Digest PowerMEMS 2005*, 177 (2005).

Genetic Conversion of Bacteria and its Application to Micro Direct Photosynthetic/Metabolic Bio-Fuel Cell (DPMFC)

**Keisuke Morishima¹, Akihiro Furuya¹, Takeyuki Moriuchi¹, Makoto Yoshida²
Masahiro Ota², and Yuji Furukawa³**

¹Department of Mechanical Systems Engineering,

Tokyo University of Agriculture and Technology, Koganei, Japan

²Faculty of Urban Liberal Arts, Tokyo Metropolitan University, Japan

³Management of Technology,
Tokyo University of Agriculture and Technology, Japan

Abstract

We have developed mediator-less direct photosynthetic/metabolic bio fuel cell (DPMFC) in which microparticles of polyaniline were adopted as electrodes to draw electrons from bacteria. In this paper, in order to inhibit hydrogen emission and increase power generation efficiency, we propose to utilize genetic manipulated bacteria, such as purple photosynthetic bacteria (PPBs) which are activated by organic compounds as well as emitting hydrogen in photosynthetic and metabolic processes for increasing power generation efficiency by applying gene manipulation to inhibit hydrogen emission. We assumed is that more electrons will be stored inside PPB if hydrogen emission is inhibited. As a result, the power density of gene manipulated bacteria became $10\mu\text{W}/\text{cm}^2$, that is higher than the normal one.

Keywords: Photosynthetic, Metabolic, Micro Bio Fuel Cell, Genetic manipulation, Bacteria

1. Introduction

A micro portable fuel cell has been on demand for a various field. A micro-photosynthetic/metabolic bio fuel cell [1] has been reported. This fuel cell makes electricity by using electrons which is extracted by mediators such as methylene blue from cyanobacteria. However, methylene blue does not have biocompatibility; furthermore, such mediators lose their function rapidly when exposed to light, hence, shortens the durability of cell and results in lower efficiency. To overcome these problems, we have developed a novel mediatorless direct photosynthetic/metabolic bio fuel cell (DPMFC) in which microparticles of polyaniline were adopted as electrodes to draw electrons directly from bacteria. [2] Nevertheless, the output is still low. Therefore, for increasing output, we selected PPBs as new fuel, and the electron generation efficiency of PPB is improved by applying gene manipulation technology. The objective of this research is to evaluate the usefulness of gene manipulation in increasing electrical output of bacteria based bio-fuel cells.

2. Biology of Purple Photosynthetic Bacteria

Fig.1 shows the photosynthetic and metabolic mechanisms of three types PPBs.

Normal-type PPB absorbed organic compounds for metabolizing. H₂ released inevitably by nitrogen-fixing enzyme (*nif*) of normal-type PPB. Some H₂ released is taken up into cell using the hydrogen-uptake enzyme (*hup*), which provides reducing power in the form of electrons. Therefore, the removal of these enzymes enables us to control electron generation capacity. Accumulation-type PPB was developed by removing *nif*, and emission-type PPB was developed by removing *hup* from normal-type PPB.

3. Working Principle of DPMFC

Fig.2 shows a schematic of the working principle of DPMFC. DPMFC has an anode chamber and a cathode chamber separated by a proton exchange membrane (PEM). Electrons are extracted from the electron transport chain of PPB, which is in contact with an electrode consisting of polyaniline, thus generating electricity. Fig.3 shows the structure of prototype DPMFC.

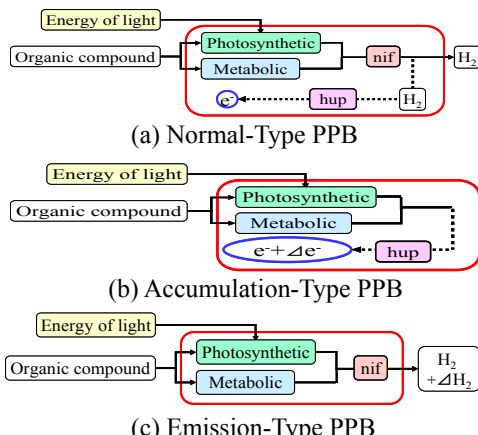


Fig.1 Photosynthetic and Metabolic Mechanisms of Three Types PPB

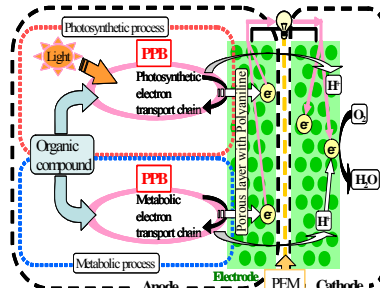


Fig.2 Working Principle of DPMFC

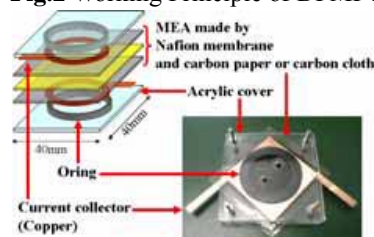


Fig.3 Structure of Prototype DPMFC

4. Experiments

DPMFC performance was evaluated on the basis of electric power, which was measured by connecting resistors (10 Ω to 1 kΩ) to DPMFC. PPB cultured for 3 days was used in all the experiments.

5. Results and Discussion

Table 1 shows the experimental result of the performance reproducibility evaluation. As a result, using genetic manipulated bacteria did not clearly increase electric power, and the electric power was unstable. Table 2 shows the experimental results of the assessment of the catalyst carrier. DPMFC performance was improved using a thin and

highly porous material, namely, carbon paper (0.11 mm thick), to increase the area of contact between the PPBs, polyaniline and Nafion117. Fig.4 shows the open-circuit voltage performance of DPMFC, and Fig.5 shows the electric power performance of DPMFC. From time course of electric power, the cell life was about 2 hours.

Table 1 Result of Performance Reproducibility Evaluation

Experi-mental number	Power density[μ W/cm ²]					Ave rage
	1	2	3	4	5	
Normal	7.8	5.3	3.5	5.4	2.2	4.9
Accumu-lation	7.6	8.1	4.0	4.5	2.8	5.4
Emission	6.6	4.5	4.6	3.1	4.6	4.7

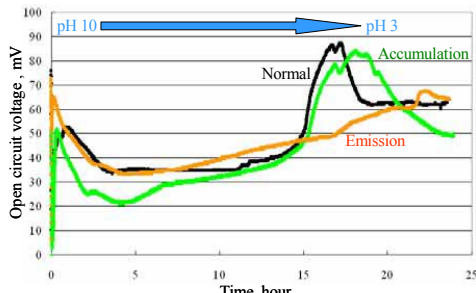


Fig.4 Open-Circuit Voltage Performance of DPMFC

Table 2 Results of Assessment of Catalyst Carrier

	Power density[μ W/cm ²]		
	Carbon paper 0.19mm thick	Carbon cloth	Carbon paper 0.11mm thick
Normal	1.6	4.1	8.4
Accumulation	3.6	9.0	10
Emission	1.3	5.5	5.3

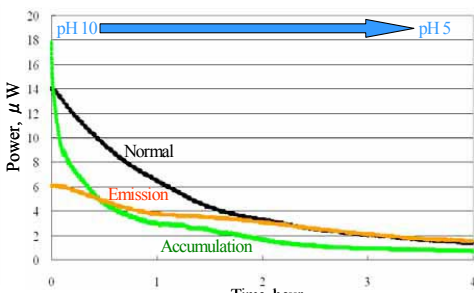


Fig.5 Electric Power Performance of DPMFC

6. Conclusions

There is not so much of a difference between three types of PPB in DPMFC performance. Nevertheless, it is highly possible that gene manipulation can improve the electric power output of accumulation-type PPB. We successfully show that the power density of genetic manipulated bacteria is higher than the normal one. This result tells us that there is huge possibility to use bio resources as energy sources in future.

References

1. K. B. Lam, M. Chiao, and L. Lin, "A Micro Photosynthetic Electrochemical Cell", *Proc. IEEE Conf. on Micro Electro Mechanical Syst. (MEMS 2003)*, Kyoto, Japan, Jan. 19-23, pp.391-394, (2003).
2. Y. Furukawa, T. Moriuchi and K. Morishima, "Design Principle and Prototyping of Direct Photosynthetic/Metabolic Bio Fuel Cell (DPMFC)", *J. Micromech. Microeng.* **16** (2006) S220-S225.

DEVELOPMENT OF HANDY ENVIRONMENTAL ATMOSPHERIC PARTICLE MEASUREMENT DEVICE BASED ON ON-CHIP TWO-CHANNEL MICRO COULTER COUNTER

Kazuhiro Miyamura^{1,2}, Yoshikuni Kikutani^{2,3}, Kazuma Mawatari^{2,3},
Mitsuo Kitaoka² and Takehiko Kitamori^{3,4}

¹ Horiba, Ltd., 2 Miyanoigashi, Kissyoin, Minami-ku, Kyoto 601-8510 Japan,

² The Research Association of Micro Chemical Process Technology, Japan,

³ Micro Chemistry Group, Special Research Laboratory for Optical Science, Kanagawa Academy of Science and Technology, Japan, ⁴ Department of Applied Chemistry, Graduate School of Engineering, The University of Tokyo, Japan
(E-Mail: kazuhiro.miyamura@horiba.com)

Abstract

A handy devise based on on-chip two-channel micro Coulter counters was developed for environmental atmospheric particle measurements. Size of the measurement device was 80 x 180 x 45 mm. It was designed to work with batteries and only 850 g in weight with batteries included.

Keywords: particle, Coulter counter, filter

1. Introduction

Suspended particulates, especially nanoscale ones, are possible cause of allergy and cancer, and on-site monitoring of such particles is one of the most important objectives in environmental analysis. We have developed a micro Coulter counter chip with two micro Coulter counters with 50 and 10 μm aperture sizes and could be applied to measurements of particle size distribution from 0.8 to 15 μm [1] (Figure 1).

In this paper, we report on a handy measurement device that we newly fabricated based on the two-channel micro Coulter counter chip.

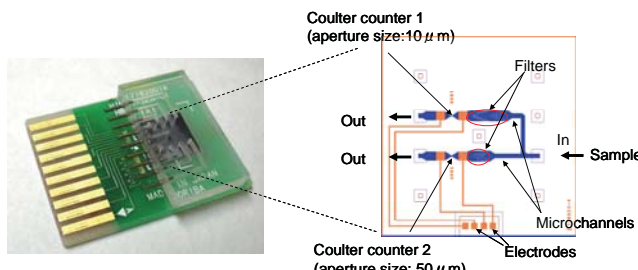


Figure 1. Photograph of the microchip with two-channel Coulter counters set in a chip holder (left) and structure of the microchip (right). Size of the microchip was 10 x 10 mm.

2. Experimental

Figure 2 shows a block diagram of the newly developed measurement device.

It was comprised of the Coulter counter chip, a diaphragm pump, valves, a waste reservoir, liquid level sensors and electric circuits.

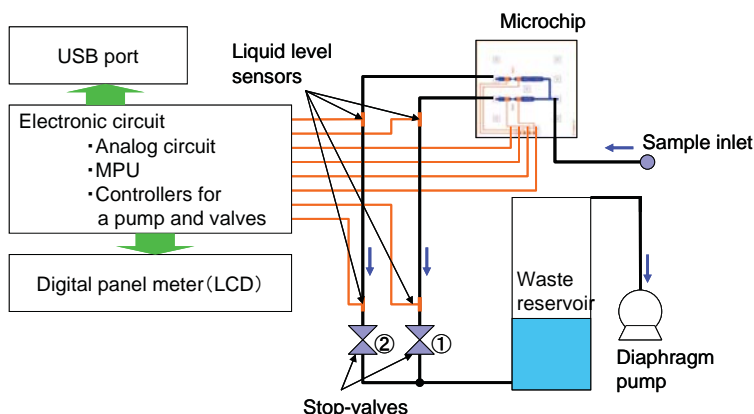


Figure 2. Block diagram of the particle size measurement device

Structure of the microchip was basically the same as in the previous report [1] (Figure 1). Namely, it was made of glass and silicon, and its size was 10 x 10 mm. It had two branches of microchannels having a Coulter counter with different aperture sizes (10 and 50 μm). Silicon pillars in the microchannels acted as filters to define particle-size-range introduced to the apertures. Particle size of 0.8 ~ 4 μm could be measured with the 10- μm aperture, and that of 4 ~ 15 μm could be measured with the 50- μm aperture.

Sequence of measurement was as follows:

- (1) A Coulter counter microchip was set in a chip holder unit and both electric and liquid connection was made. (The procedure is so simple that the microchip could be easily replaced and disposed.)
- (2) One of the two stop-valves was closed and a sample diluted by solvent was introduced to one of the Coulter counter using the diaphragm pump. Amount of sample solution passing through the counter was regulated to be 50 μL using liquid level sensors.
- (3) The stop-valve was opened and the other stop-valve was closed. The same amount of sample solution was introduced to the other Coulter counter.
- (4) Total number of particles was displayed in the digital panel meter. Size distribution data could be transferred to a PC using a USB cable.
- (5) Washing solution was introduced to the chip. The wastes were stored in the waste reservoir.

3. Results and Discussion

Figure 3 shows a photograph of the device.

Time required for the measurement was only one minute.

Improvement on the battery, the process control software, and noise shield to realize better S/N ratio is now on progress. New microchips with more than two Coulter counters for wider measurement range are also under development.

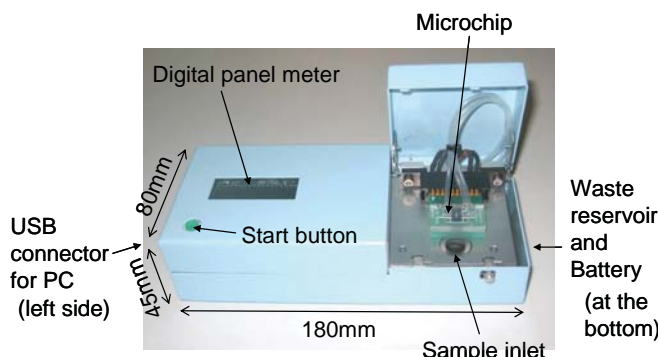


Figure 3. Overview of the particle size measurement device (80 x 180 x 45 mm, 850 g)

4. Conclusion

We developed a particle size measurement device based on an on-chip two-channel Coulter counters. Size of the device was as small as 80 x 180 x 45 mm, and its weight was only 850 g with batteries included. Measurable particle size range was from 0.8 to 15 μm . Total number of particles was displayed in the digital panel meter. Size distribution data could be transferred to a PC using a USB cable.

Acknowledgement

This research has been carried out as a part of “Micro-Chemical Technology for Production, Analysis and Measurement Systems” Project, with financial support from the New Energy and Industrial Technology Development Organization (NEDO), Japan.

REFERENCES:

- [1] K. Miyamura et al., Proc. μTAS 2005, 1495-1497.

EFFECTS OF FLUIDIC CONDITIONS ON THE DIFFUSION-BASED BIOLUMINESCENT DETECTION OF ATP IN MICROFLUIDIC DEVICE

Thuan-Hieu Tran¹, Young-Bum Kim¹, Yoon-Mo Koo^{1,2}, Jin-Hwan Kim³, Eun-Ki Kim¹ and Woo-Jin Chang²

¹Department of Biological Engineering, ²ERC for Advanced Bioseparation Technology, Inha University, Incheon 402-751, Korea

³ M&B GreenUs Co. Ltd., Seoul 152-021, Korea

Abstract

The effects of flow rates of ATP and reagent solutions and total flow rates on the bioluminescence were surveyed in microfluidic device. The optimum ratio of reagent, ATP and reagent solution through 3 inlet ports were 1.5:7:1.5. The optimum total flow rate and resulting retention time was 8 $\mu\text{l}/\text{min}$.and 15 sec, respectively.

Keywords: Microfluidic device, bioluminescence, luciferase, ATP

1. Introduction

Bioluminescence-based cell detection using ATP, luciferin and luciferase is one of the most popular techniques due to their high sensitivity and ease of operation. Several works have shown that the ATP dependent luminescent assay is a rapid and reliable detection method in quality control of beverages and foods, cosmetics, environmental control, clinical studies and public hygiene, etc [1,2]. The advantages of micro-total analysis system (μ -TAS) are high sensitivity, rapid operation and low cost for analysis [3]. Integration of ATP-based bioluminescent assay into the μ -TAS would contribute to the rapid detection of the contamination by cells with lower cost and higher sensitivity. However, the product of bioluminescent reaction (light) disappeared very quickly, different from conventional enzymatic reactions in which products are accumulated. Thus, survey on the optimum fluidic conditions is essential to obtain the better sensitivity of bioluminescent detection.

2. Experimental

HPLC grade water without chemiluminescence was used for all solutions after filtered by 0.2 μm filter. ATP (Sigma-Aldrich Co.) solution was made with HEPES buffer solution (pH 7.8). Luciferase-luciferin solution as reagent solution was made from Enliten ATP Assay System (Promega Co.).

The microfluidic device that has 3 inlets and 3 outlets was made of PDMS by soft-lithographic method. A serpentine-shape microchannel was designed in the middle of microfluidic device to increase the retention time of the solutions and enhance the sensitivity of detection. The width of microchannel was 200 μm all over the microfluidic device, except inlet and outlet channels which were 100 μm . The height of the microchannel was about 50 μm (Fig. 1).

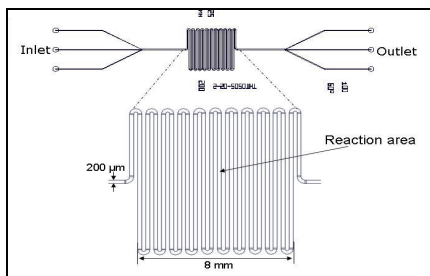


Figure 1. Schematic drawing of microfluidic device.

The home-made detector system was used to measure the amount of light produced by bioluminescent reaction. The detector system was composed of PMT (Hamamatsu Co.), DAQ system (NI Co.), and controlling program coded by LabVIEW 7.1. PMT was fixed on the bottom of the home-made dark box. The diameter of the circular active area of PMT was 8 mm and it was aligned on the serpentine-shape microchannel.

3. Results and discussion

ATP and reagent solutions were continuously infused into microfluidic device through 3 inlet ports by micro-syringes and syringe pumps. The percentage of ATP flow was changed from 10% to 90% while the total flow rate was kept constant at 1 $\mu\text{l}/\text{min}$ to determine the optimum content of ATP solution. In this case, the flow rates of reagent solutions were adjusted following the flow rate of ATP solution. The optimum ratio of reagent, ATP and reagent solution through 3 inlet ports was 15%:70%:15% (Fig. 2). The total flow rate was changed from 2 to 12 $\mu\text{l}/\text{min}$ while content of ATP solution was kept constant at 70%. The effect of infused position of each solution among 3 ports was tested. The optimum total flow rate was 8 $\mu\text{l}/\text{min}$ (Fig. 3).

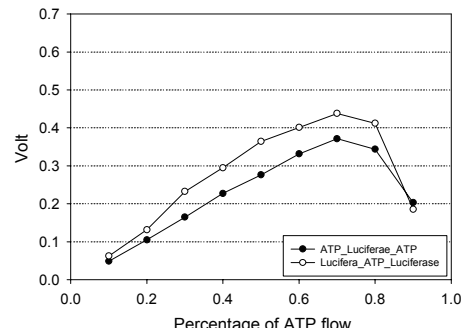


Figure 2. Effect of flow rate ratio between ATP and reagent solution with different infusion methods: reagent solution in the middle (closed circle) and ATP solution in the middle (open circle). The total flow rate was 1 $\mu\text{l}/\text{min}$.

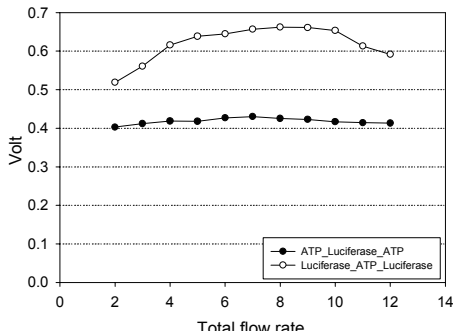


Figure 3. Effect of total flow rate with different infusion methods: reagent solution in the middle (closed circle) and ATP solution in the middle (open circle). The content of ATP solution was 70%.

The bioluminescent reaction completed before it is entered into the detection channel if total flow rate is lower than 8 $\mu\text{l}/\text{min}$ while it is uncompleted within reaction channel with larger than 8 $\mu\text{l}/\text{min}$, resulted in lower bioluminescence in both cases.

Bioluminescent reaction was affected from the position of ATP and reagent solutions. Higher bioluminescence was obtained when ATP solution was injected through the middle of 3 inlet ports. It is assumed that this is related with different diffusivities of ATP and luciferase molecules and the velocity profile of the flow within microchannel. Optical micrographs of the bioluminescence by the position of ATP solution is shown in Fig. 4. The area of bioluminescence is larger when ATP solution was infused in the middle of the ports.



Figure 4. Micrographs of bioluminescence in straight channel of microfluidic device with different infusion methods: ATP solution in the middle (A), reagent solution in the middle (B). ATP solution (10^{-3} M) occupied 70% of total 8 $\mu\text{l}/\text{min}$ of flow.

4. Conclusions

The position of ATP and reagent solution was the important factor for bioluminescent reaction in microchannel. The optimum fluidic conditions for bioluminescent reaction were determined as 8 $\mu\text{l}/\text{min}$ of total flow rate and 70% of ATP flow rate.

Acknowledgements

This work was supported by Core Environmental Technology Development Project for Next Generation (102-051-031), Ministry of The Environment, Korea.

References

1. A. Guadano, E. de Pena, A. Gonzalez-Coloma and J.F. Alvarez, *Development of a new bioluminescent mutagenicity assay based on the Ames test*, Mutagenesis, Vol.14 no.4 pp. 411-415, (1999).
2. S. Brolin and G. Wettermark, *Bioluminescence Analysis*, VCH Verlagsgesellschaft, NY, USA, pp.104-111, (1992).
3. B.H. Weigl, R.L. Bardell and C.R. Cabrera, *Lab-on-a-chip for drug development*, Adv. Drug Deliv. Rev., Vol. 55 no.3 pp. 349-377, (2003).

MICRO FIA USING SEGMENTED LAMINAR FLOW IN MICROCHANNEL AND ITS APPLICATIONS TO MULTI-COMPONENT ENVIRONMENTAL ANALYSES

Katsumasa Sakamoto^{1,2}, Tomohiko Kawakami^{2,3}, Yoshikuni Kikutani^{2,4}, Kazuma Mawatari^{2,4}, Hiroaki Nakanishi¹, Mitsuo Kitaoka² and Takehiko Kitamori^{4,5}

¹ Technology Research Laboratory, Shimadzu Corporation, 3-9-4 Hikaridai, Seikacho, Sorakugun, Kyoto 619-0237 Japan, ² The Research Association of Micro Chemical Process Technology, Japan, ³ Kaken Inc., Japan, ⁴ Micro Chemistry Group, Special Research Laboratory for Optical Science, Kanagawa Academy of Science and Technology, Japan, ⁵ Department of Applied Chemistry, Graduate School of Engineering, The University of Tokyo, Japan
(E-Mail: ksakamo@shimadzu.co.jp)

Abstract

A micro FIA system for environmental analyses was developed. In the newly developed system, lateral diffusion in a segmented laminar flow was utilized to obtain a flat concentration profile along the longitudinal direction of a microchannel. As a result, the system could be applicable to multi-component analyses without changing position of the detector.

Keywords: flow injection analysis, environmental analysis, laminar flow, segment flow, thermal lens

1. Introduction

In conventional flow injection analysis (FIA), a plug of sample solution is injected to a channel, and reaction proceeds with molecular diffusion at the front and rear boundaries of the sample plug. As a consequent, concentration profiles of chemical species along the channel become complicated and highly depend on diffusion coefficients, reaction rate constants and so on (Figure 1). Usually high flow rate conditions are necessary to enhance mixing efficiency.

In stead of longitudinal diffusion in a channel of conventional FIA, we utilized lateral diffusion in a segmented laminar flow in a microchannel to realize simple and efficient micro FIA.

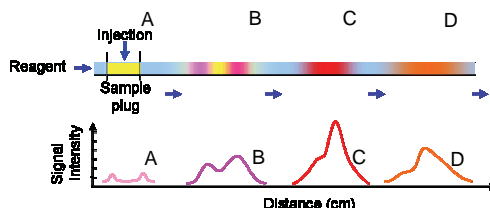


Figure 1. Concentration profile along a channel of conventional FIA. Mixing and reaction of sample and reagent proceed from the front and rear ends of the sample plug resulting in a complex profile along the channel.

2. Concept of micro FIA using Segmented Laminar Flow

Low Reynolds number flow inside a microchannel tends to be laminar, and when streams of two reagents are introduced to a Y-shaped microchannel, they flow side-by-side. Mixing is then proceeds with lateral diffusion through the interface between the two solutions. Because width of a microchannel is typically $\sim 100 \mu\text{m}$, lateral diffusive mixing rapidly completes. Segmented laminar flow can be made by introducing segment of sample solution to a Y-shaped microchannel. In the downstream section where lateral diffusive mixing being completed, segment with a flat concentration profile is formed (Figure 2). It makes data acquisition and interpretation very straightforward. Furthermore, the simple flat concentration profile makes it possible to carryout various analyses with a fixed detection point, whereas in conventional FIA, detection point must be changed along the channel depending on the analytical reactions used.

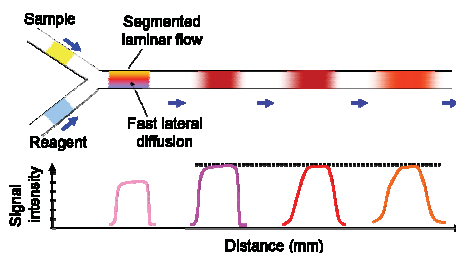


Figure 2. Concept of micro FIA using segmented laminar flow in a microchannel. Mixing and reaction proceed by rapid lateral diffusion through the interface along the microchannel, and almost flat concentration profile throughout the segment is formed.

3. Experimental

We developed a compact micro FIA system based on segmented laminar flow in a microchannel (Figure 3).

Two micro injectors, which could inject $2 \mu\text{L}$ of a sample, were used to introduce sample solutions and reagents for colorimetry to a Y-shaped microchannel. For detection of color change in the microchannel, thermal lens microscope (TLM) was used. TLM is a sort of photothermal spectrometer which could sensitively determine concentration of non-fluorescent molecules in very small sample volumes. SELFOC® microlens fixed on the

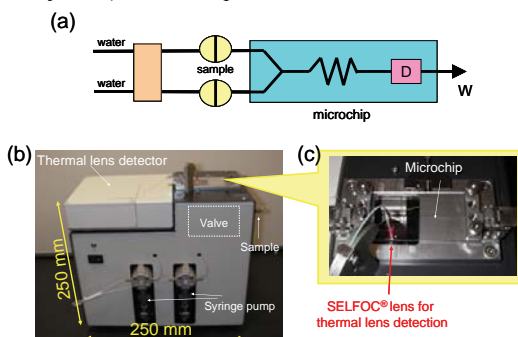


Figure 3. Micro FIA system for environmental pollutants. (a) Block diagram, (b) Photograph of the whole system, (c) Microchemical chip used in the system.

microchip was used to focus excitation and probe beams of the TLM.

4. Results

Figure 4 shows a typical signal obtained with the micro FIA system. As expected, flat and simple concentration profiles were observed. One sample analysis was finished within 1 minute.

We performed flow analysis of environmental pollutant, such as hexavalent chromium, copper and phosphoric acid of water. Figure 5 shows the results of environmental pollutant analyses.

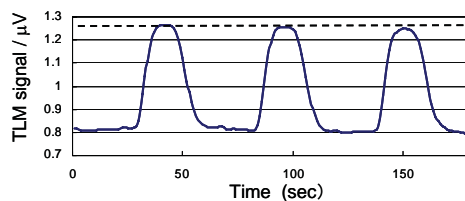


Figure 4. Typical signal of the micro FIA system (Analysis of Cr(VI) in water).

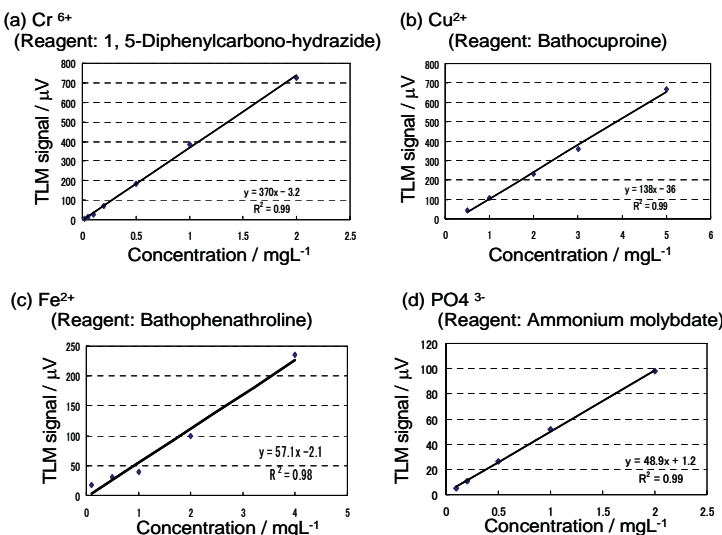


Figure 5. Results of environmental pollutant analyses using the Micro FIA system.

5. Conclusion

In this study, a micro FIA system for multi-component environmental analyses was developed. Unlike conventional FIA systems, in which a plug of sample solution is injected to a reagent flow, the newly developed system utilized segmented laminar flow in a Y-shaped microchannel. As a consequence, concentration profile along the channel was largely simplified and multi-component analyses could be carried out without changing position of the detector.

DISSOLVED OXYGEN MICROELECTRODE SENSOR FOR *IN SITU* BIOLOGICAL APPLICATIONS

Jin-Hwan Lee, Xingtao Wei, Tae-Sun Lim, and Ian Papautsky

Department of Electrical and Computer Engineering,
University of Cincinnati, Cincinnati, OH USA

Abstract

In this paper, a new penetrating dissolved oxygen (DO) sensor for *in situ* biological applications has been successfully demonstrated. HF-based etching technique was used to sharpen and recess sensor tips. The polymerized polypyrrole layer was used as an insulator. DO microelectrode sensors were fully characterized in saline, and exhibited a rapid and linear response in the 0-9 mg/L (0-21% O₂) range. The key advantages of this sensor include: 1) ability to penetrate samples to perform measurements; 2) small size for *in situ* measurements; 3) array structure for higher robustness; and 4) possibility of multi-analyte detection.

Keywords: Microelectrode, dissolved oxygen, recessed tip, polypyrrole

1. Introduction

Microelectrodes can be used to provide measurements of dissolved oxygen (DO) in ground water or wastewater, a key test in water quality and waste treatment process control, or measurements within undisturbed biofilms for assessing bioremediation. They can also be used to monitor compositional changes in liquids when only small quantities are available, such as soil pore water, and they can do this rapidly. The DO microelectrodes are commonly polarographic recessed cathode gold electrodes fabricated from pulled glass pipettes [1,2]. However, such microelectrodes are generally very fragile, are difficult to manufacture, have relatively short life time, and require trained personnel to use. They must be used in a laboratory under strictly controlled conditions. Further, due to the small signals involved these sensors are usually subject to electrical interferences and must be used inside a well-grounded Faraday cage.

To address these problems, we have recently developed an ORP microelectrode array [3]. Development of ion-selective sensor microelectrodes discussed here is the next logical step to implementation of an integrated multi-analyte sensor (Fig. 1). We believe these sensors will be sufficiently robust to be used in the field/point-of-care, capable of rapidly and accurately sensing analytes *in situ*.

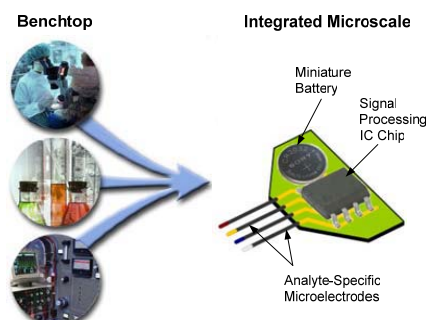


Figure 1. Concept of an integrated micro-electrode array sensor for *in situ* point-of-care/field-based measurements.

2. Design and Fabrication

Microelectrode sensor arrays were fabricated from borosilicate glass using an extension of the process we recently reported in [3] (Fig. 2). Initially, four 1-cm long glass probes were formed. In the first step of the etch process, the glass beams were transformed into microelectrodes by etching with a HF-based etchant followed by a gradual withdrawal to produce a taper. In the second etch step, microelectrode tips were further sharpened to approximately 200 nm using meniscus etching [3]. Sensors were packaged using PCB carriers and conductive silver epoxy was used to establish electrical connections to individual microelectrodes. Polymerized polypyrrole was used as an insulator electrodeposited on all surfaces of microelectrodes. A beveler was then used to remove the insulation and expose glass core material at the tip. In the final step, recess was formed in each tip by etching the core in HF. The underlying gold layer exposed inside the recess formed the sensing area. The recess is used to limit diffusion of oxygen.

3. Results and discussion

The recessed DO microelectrode arrays consisted of four 1 cm long microelectrodes at 450 μm center-to-center spacing. Representative results are shown in Fig. 3. The small size and angle (“syringe type”) of sensors tips will permit easier penetration of tissues and biofilms for biological applications. Using the recess process, we successfully created tips with $<1.7 \mu\text{m}$ recesses. Fig. 3 also illustrates the high quality of conformal

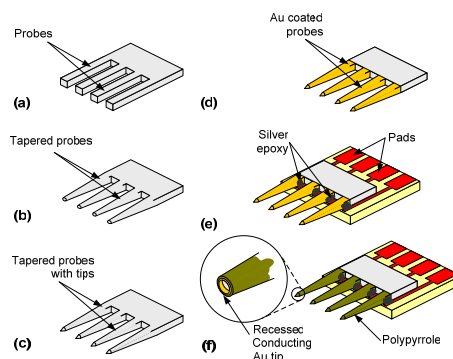


Figure 2. Recessed DO microelectrode array fabrication sequence. (a) Form glass probes by dicing; (b) taper probes in HF-based etchant; (c) use meniscus etching to sharpen probes; (d) deposit Au conductive layer; (e) use silver epoxy to establish electrical connections; (f) coat microelectrodes with polypyrrole insulating layer and recess tips by beveling and etching.

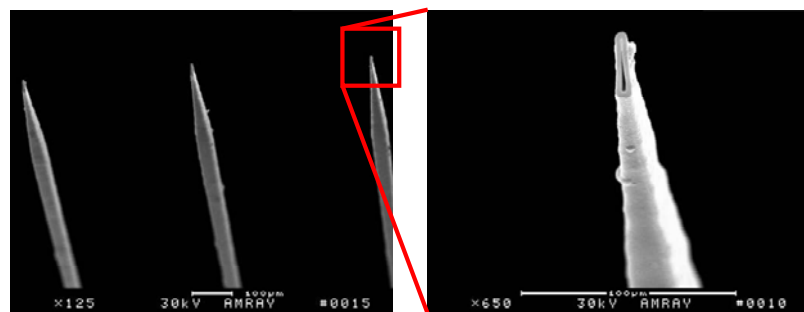


Figure 3. SEM of the recessed DO microelectrode array with about 1.7 μm recess.

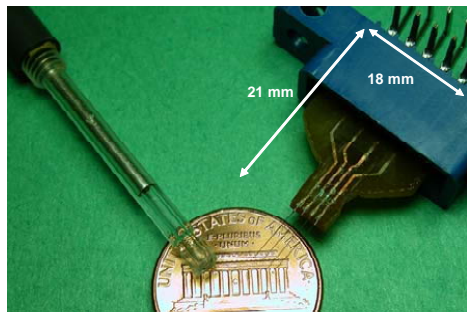


Figure 4. The recessed DO microelectrodes sensor array packaged on a PCB carrier with a commercial DO milli-electrode.

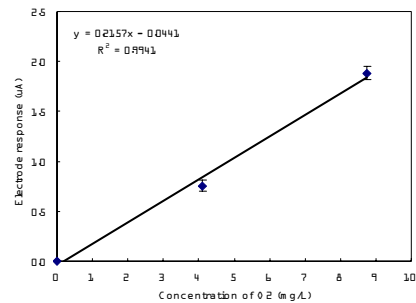


Figure 5. Calibration curve of the recessed DO microelectrodes array.

pinhole-free polypyrrole electrodeposition insulating polypyrrole layer was cured at 120 °C for 24 hrs. This increased its chemical resistance to HF and enhanced its dielectric properties. Film conductance was measured to be $<10^{-8}$ S. The tip sizes and overall dimensions of the fully packaged 4-probe DO array are compared with a commercial DO sensor in Fig. 4. The array structure which has four electrical isolated microelectrodes increases robustness.

The developed DO sensors were characterized using oxygenated saline in the 0 to 9 mg/L O₂ range. The microelectrode sensor was polarized at -750 mV (vs. Ag/AgCl reference electrode) for at least several hours prior to calibration in saline (0.85% NaCl solution) [1]. Testing solutions were made in saline by the oxygenation with pure nitrogen gas, a gas mixture of 10% O₂ and 90% N₂, and air (21% O₂). The commercial oxygen milli-electrode (MI-730, Microelectrodes Inc.) was used to verify oxygen concentrations. The sensor calibration curve (vs. Ag/AgCl reference electrode) is shown in Fig. 5. The sensor exhibited a fast (<10s) and linear response, making it ideally suited for *in situ* applications.

4. Conclusions

The new DO microelectrode sensors were successfully developed and characterized. Using the developed recess methodology, we demonstrated $<1.7\text{ }\mu\text{m}$ recessed microelectrode tips. The electropolymerized polypyrrole worked well as an insulating layer. In the long term, we expect this work will lead to *multi-analyte* microelectrode sensors, envisaging its numerous *in situ* biological applications.

Acknowledgement

This work was fully supported by the National Science Foundation (BES-0529217).

References

1. P. Bishop and T. Yu, *Water Sci. Tech.*, **39**, pp. 179-185 (1999).
2. R. A. Linsenmeier and C. M. Yancey, *J. Appl. Physiol.* **63**, pp. 2554-2557 (1987).
3. J.-H. Lee *et al*, *Sensors and Actuators B*, **115**, pp. 220-226 (2006).

NUMERICAL ANALYSIS AND MINERAL WATER MEASUREMENT IN CONFINED LIQUID ELECTRODE PLASMA-OPTICAL EMISSION SPECTROMETRY

Isao Kumagai¹, Hirokazu Matsumoto¹, Tamotsu Yamamoto²,
Eiichi Tamiya¹ and Yuzuru Takamura^{1,3}

¹School of Material Science, Japan Advanced Institute of Science and Technology

²Tenor, Inc.

PRESTO, Japan Science and Technology Agency

Abstract

The handy elemental analyzer using the plasma in a micro channel is developed in this paper. The micro channel with narrow part is filled with sample solution and high voltage is applied. Subsequently, bubble is generated in the narrow part of the channel, and plasma emits light in the bubble. This research optimized the micro channel shape by numerical simulation of the temperature and the nucleation frequency. Then, the nucleation position of the bubble and plasma is successfully fixed at the center in the flow channel for reproducible measurement. Moreover, elemental analysis of Na and K in commercially available mineral water was demonstrated.

Keywords: Liquid electrode plasma, Micro fluidic channel, Atomic emission spectrometer, Nucleation frequency

1. Introduction

We have developed a handy atomic emission spectrometer, namely liquid electrode plasma optical emission spectrometry (LEP-OES) [1-2]. The principle is simple. When voltage was applied in the micro fluidic channel that was filled with sample electrolytic solution, H₂O gas bubble was formed by Joule heating, and subsequently generated plasma emits light in the bubble. By analyzing the light, we can determine the atomic concentration in the sample solution. It is important to control the bubble position for stable and reproducible measurements. In this report, the temperature in the micro fluidic channel and the nucleation frequency of the bubble were calculated by numerical simulation and the results were compared to experimental ones. The shape of micro fluidic channel was optimized in order to fix the bubble nucleation position. Finally, the quantitative analysis was demonstrated using the commercially available mineral water.

2. Theory

The equations used for numerical simulation were follows. Heat conduction is (1).

$$\rho C_p \frac{\partial T}{\partial t} - \nabla \cdot (k \nabla T) = Q \quad (1)$$

Q is heat source from resistive heating in (2).

$$-\nabla \cdot (\sigma \nabla V) = Q \quad (2)$$

The nucleation frequency of the bubble is (3)

$$J_{ho}(T) = N_l \left(\frac{3 \sigma_l(T)^{\frac{1}{2}}}{\pi m_l} \right) \exp [G(T)] \quad (3)$$

Here, $J_{ho}(T)$ is value of the nucleation frequency of the bubble in unit of time and volume.

3. Experimental

Experimental setup is shown in Fig. 1. Microfluidic chip was made of PDMS and quartz glass plate by soft-lithography using SU-8 thick resist. Typical channel width and height were 400μm and 100μm, respectively. High voltage from 800V to 1500V was applied by pulse power supply using Pt electrodes. Optical emission spectra were analyzed by Ocean Optics USB2000 handy-type spectrometer. The plasma image was observed by microscope and recorded by high speed CCD camera in order to check the bubble position and its reproducibility.

4. Results and discussion

Fig. 2 is slice image of water temperature by 3D numerical simulation of electrostatic field and heat transfer in the channel at 80 μsec after the voltage of 1,200V is applied. Nucleation does not be taking in account in this figure. The highest temperature is at the four corners of the narrow channel because the electric current is most concentrated at those positions.

Fig. 3 shows the temperature and the estimated nucleation frequency (J_{ho}) at the corner as a function of the time. The nucleation frequency is increase drastically around 80μs, which corresponds to the experimentally observed nucleation time on the same condition.

Figure 4 shows the nucleation frequency distributions at 90 μs for two different shape channels that consist of (a) only straight wall, and (b) curved wall. In (b), the channel

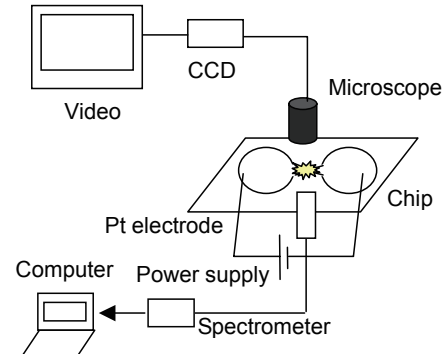


Fig. 1. Experimental setup

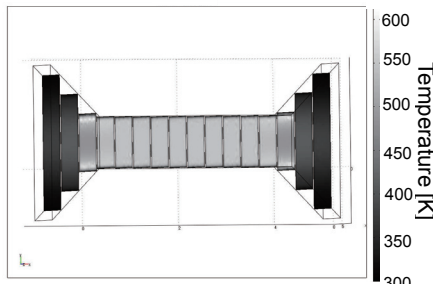


Fig.2. Temperature at 80μsec.

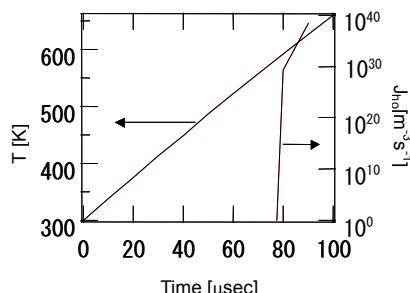


Fig.3. Temperature and nucleation frequency.

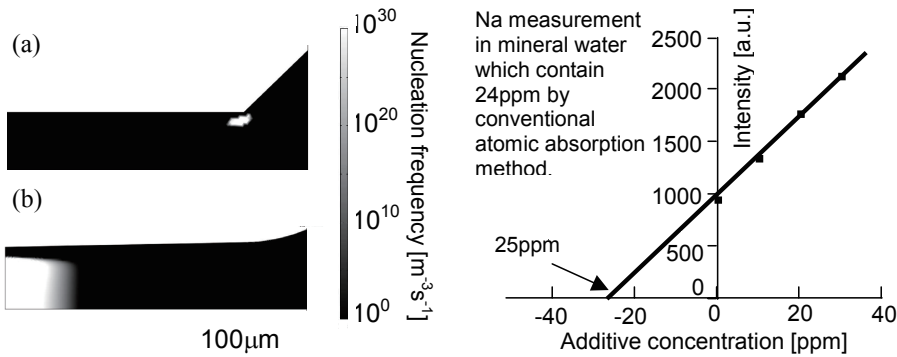


Fig.4. The bubble nucleation frequency at 90 μ s in (a) straight wall channel and (b) curved wall channel.

width was narrowed by 7% at center. With these small changes of shape, it is found that the position of the bubble and plasma can be fixed at the center as shown in figure 4 (b).

Finally, we tried to demonstrate quantitative analysis for practical sample. Figures 5 are Na and K concentration measurements in a commercially available mineral water by our apparatus. Standard addition method was used for quantification. The values of ours are close to those by conventional atomic absorption method.

5. Conclusions

In order to improve accuracy and reproducibility of LEP-OES, the numerical simulation was carried out for the temperature and the bubble nucleation frequency. The shape of micro fluidic channel was optimized and the bubble and plasma position was successfully fixed at the center of the channel. Finally, the Na and K concentrations in commercially available mineral water were successfully measured by this method.

Reference

- 1) H. Matsumoto, A. Iiduka, T. Yamamoto, E. Tamiya, Y. Takamura , *Proc. μ TAS2005*, vol. 1, pp. 427-429.
- 2) A. Iiduka, Y. Morita, E. Tamiya, Y. Takamura, *Proc. μ TAS2004*, vol. 1, pp. 423-427.
- 3) Van Stralen, S. and Cole, R., *Boiling Phenomena*, 1, Hemisphere Washington (1979)

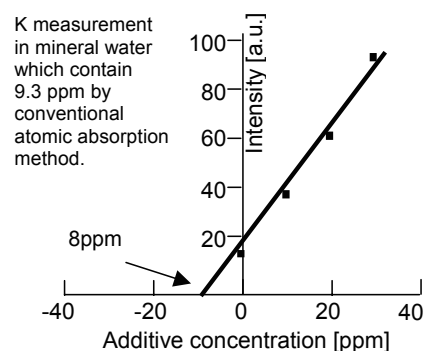
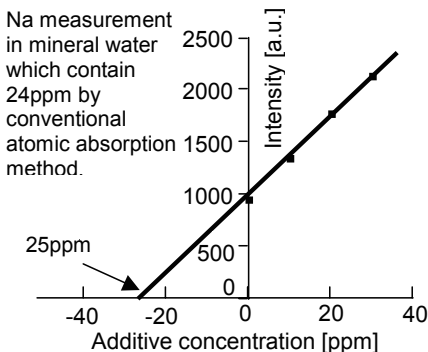


Fig. 5. Na and K measurement in commercially available mineral water by LEP-OES with standard addition method.

PASSIVE DISTRIBUTING METHOD FOR CELLULAR DIAGNOSTIC MICROWELL ARRAY USING SELF-REGULATING PINCHED FLOW

Kentaro Kawai¹, Masaki Kanai^{1,2}, Tatsuya Munaka^{2,3}

Hirohisa Abe², Akira Murakami³ and Shuichi Shoji¹

¹ Major in Nanoscience and Nanoengineering, Waseda University, Japan

² Technology Research Laboratory, Shimadzu Corporation, Japan

³ Graduate School of Science and Technology, Kyoto Institute of Technology, Japan

Abstract

We developed passive cell distributing method for cellular diagnostic microwell array. This method can distribute cells evenly and simultaneously to a number of microwells only by introducing cell suspensions from the inlet. In order to reduce the dispersion of the number of distributed cells to each microwell, we propose a novel concept of the self-regulating pinched flow. The self-regulating pinched flow is realized in a microchannel, which consists of the center micropillar colonnades and side channels. CFD simulations were carried out to optimize the design of the pinching area. Using a fabricated prototype device having 8 microwells, uniform distribution of the beads was obtained successfully. The coefficient of variation (CV) of the distributed bead in microwells was 29.3%.

keywords: passive distribution, microwell array, high throughput screening, self-regulating pinched flow

1. Introduction

In previous work, we reported a first prototype of cellular diagnostic microwell array using passive distributing method as shown Fig.1 [1]. This method achieved simultaneous cell distribution to a number of microwells with a simple channel configuration which consisted of multi-step T-shaped bifurcations. However, in this prototype, the number of distributed cells deviates greatly due to biased cell flow in the loading channel, as shown in Fig.2 [2]. At the downstream of the bifurcation, the cell flow is biased toward the vertical wall. This biased cell flow causes asymmetric

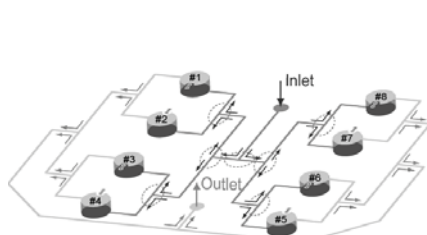


Fig.1 Schematic concept of the high-throughput cellular analysis device using passive distribution

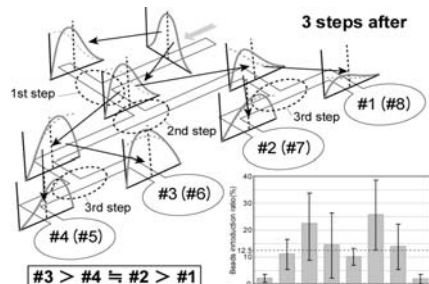


Fig.2 Beads flow profiles in each branches of the preliminary configuration.

distribution and this asymmetry is amplified at each step of the bifurcations. To solve this problem, we propose a novel concept of the self-regulating flow by applying the pinched flow concept [3].

2. Concept

Fig.3 shows the schematic of the self-regulating pinched flow concept. The self-regulating pinched flow is generated in the pinching area consists of a center micropillar colonnades and side channels. In this structure, cells flow along the micropillars while major of the carrier flows out between the pillars to the side channels. Since upper and lower carrier flows in the side channels are pinched at the outlet, the cells are expected to be focused at the center of the outlet. However, in case that the pinching area is symmetric, almost 100% cells flow out to the lower outlet (Fig.3(b)) due to the biased cell flow generated at the T-shaped bifurcation as shown in Fig.3(a). The use of the asymmetric pinching area realizes the correction of the biased cell flow and uniform distribution is obtained as shown in Fig.3(c). CFD simulations were carried out to optimize the structure of the pinching area.

3. Experimental and Results

A prototype device having 8 microwells was fabricated. Fig.4 shows the schematic design and SEM images of the device. Double line micropillars of isosceles right triangle ($10\mu\text{m}$ in two short sides) with $5\mu\text{m}$ interval are used. In preliminary evaluation, the flow stream in the pinching area was visualized using fluorescent beads ($1\mu\text{m}$ diameter) suspension as shown in Fig.5. The CFD simulation result of the

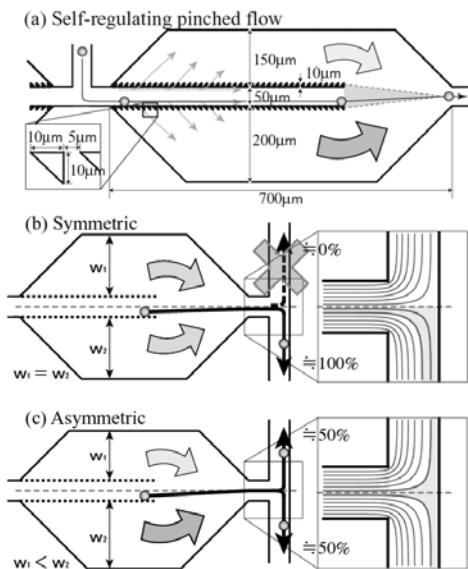


Fig.3 Schematic concept of the self-regulating pinched flow.

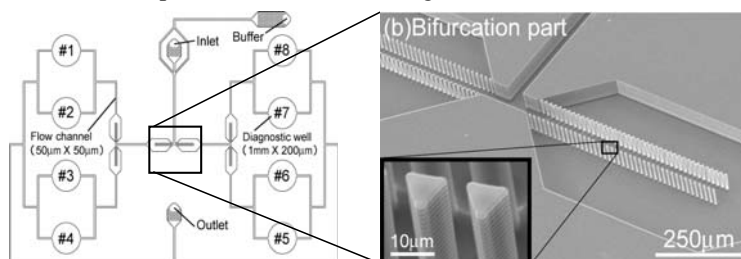


Fig.4 Schematic design of the prototype device (Center) and SEM images of a microwell and the self-regulating pinched structure (Both sides).

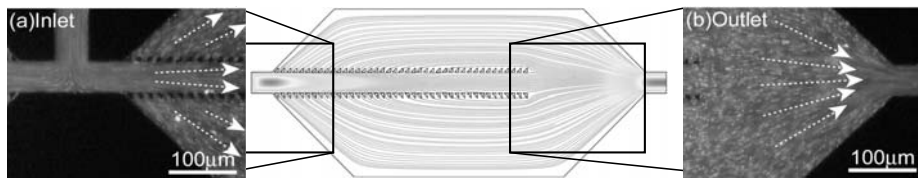


Fig.5 Streamlines of the CFD simulation result (Center) and those of the CCD image (a, b)

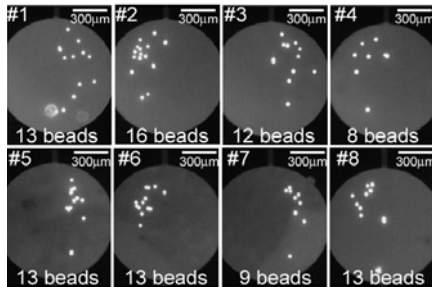


Fig.6 Fluorescent images of the distributed beads to 8 microwells of the prototype device.

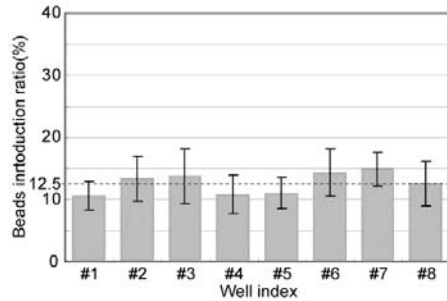


Fig.7 Bead distribution ratio in 8 microwells of the prototype device.
(Averaged over 10 measurements)

pinching area is also shown in the center of Fig.5. These results confirmed that the self-regulating pinched flow was obtained. Using 20 μm fluorescent beads as the samples, passive distribution was carried out. An example of the observed is shown in Fig.6. The bead distribution ratio with average of 10 measurements is shown in Fig.7. The results show the remarkable improvement compared to the previous results (Fig.2). CV of the average of eight microwells was 29.3%.

4. Conclusion

In order to improve the uniformity of the number of distributed beads by passive distribution, a new concept of self-regulating pinched flow was proposed. Using CFD simulation, we optimized the structure of the pinching area. Experimental results using fluorescent beads concluded that CV of the average of eight microwells improved from 94.9 % to 29.3%. We are currently going on further optimization of the design to extend the number of the arrayed microwell.

Acknowledgements

This work is partly supported by Japan Ministry of Education, Culture, Sports Science & Technology Grant-in-Aid for COE Research and 21st COE of Waseda University, Scientific Basic Research (A) No. 12450167, and Japan Society for the Promotion Science Grant-in-Aid for Creative Scientific Research No. 13GS0024.

References

- [1] M.Kanai, et al., MicroTAS'04, pp.126-128
- [2] K.Kawai, et al., Jpn. J. Appl. Phys. Vol. 45, No. 6B, 2006, pp. 5607–5613
- [3] Y.Sai, et al., MicroTAS'05, pp.346-348

POLYMER MICROVALVES WITH PRE-STRESSED MEMBRANES FOR TUNABLE FLOW-PRESSURE CHARACTERISTICS

Detlef Snakenborg, Henning Klank and Jörg P. Kutter

Technical University of Denmark

MIC - Department of Micro and Nanotechnology

DTU, Building 345 east

2800 Kgs. Lyngby, Denmark

phone: +45 4525 5785 - FAX: +45 4588 7762

Keywords: microvalve, polymer fabrication, integration

1 Abstract

A novel, inexpensive, polymer-based valve approach is presented that allows the combination of a check valve's rectifying properties with the possibility to actively control the flow rate in the forward (open) direction.

2 Introduction

The number of principles that have been developed for both passive and active microvalves during the past two decades is almost uncountable [1]. However, only very few principles take integrational aspects into consideration. The emerging change in the field of lab-on-a-chip devices from conventional MEMS materials to polymers opens new room for alternative fabrication technologies that allow rapid and economical production [2]. Yet, polymers are difficult to combine with conventionally fabricated MEMS devices. Further, polymer fabrication does not support the direct transfer of MEMS principles but demands new designs and approaches [3]. In this work, we present a microvalve that can easily be fabricated with polymer fabrication methods and integrated into existing systems [4]. A theoretical model describing the experimental results was developed and it was shown that the flow-pressure characteristics of the valve can be tuned by changing simple design parameters.

3 Fabrication and Experiments

The principle of the valve is depicted in Fig. 1. Between two rigid substrates (PMMA) an elastomer membrane (PDMS) is clamped. The membrane is provided with an incision (without removing material) using a custom-made tool. This slit is centered over a cavity, which is fabricated into the lower substrate. Applying a pressure from the top allows the membrane to expand into the cavity, which results in an opening of the slit (Fig. 1a). The geometry of the upper substrate prevents the membrane to expand if pressure is applied

from the bottom and therefore inhibits flow in the other direction (Fig. 1b). To support this effect, the fluidic through-hole in the upper structure is moved off-center with respect to the slit.

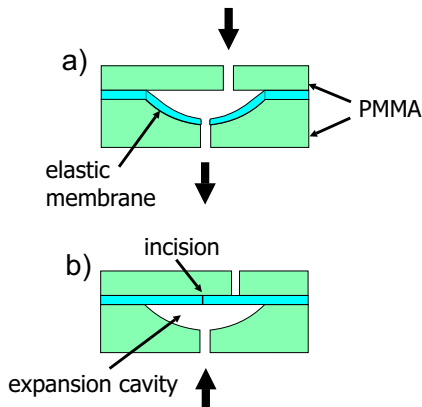


Figure 1: Working principle of the valve: an elastomer membrane is clamped between two rigid polymer substrates. A cavity in the bottom substrate allows the membrane to deflect, which results in an expansion of the slit (a). The off-center through-hole in the top substrate prevents the membrane to deflect if a pressure is applied from the bottom (b).

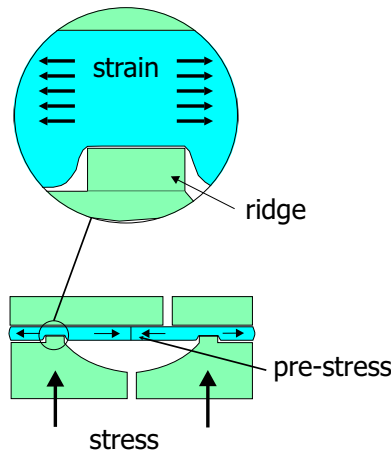


Figure 2: A concentric ridge around the expansion cavity exerts a local stress on the membrane that results in strain. This strain in turn pre-stresses the membrane. An external pressure has to exceed a certain threshold in order to deflect the membrane.

The novelty compared to commonly used check valves is the additional sealing that is provided by the closed slit of the elastic material. This is evidenced by the fact that no flow could be measured in the closed direction, even at applied pressures as high as 10 bar. The elasticity of the valve membrane not only supports the sealing in the closed state but additionally allows to actively control the flow-pressure characteristics in the forward direction. To utilize this effect while avoiding high forces, the geometry of the valve seat was modified by adding a concentric ridge (like a mesa) around the cavity, as shown in Fig. 2. Looking at the area enclosed by the ridge, this stress results in a strain and, because the stress is applied annularly, in a compression of the membrane and the slit. Hence, to deflect the membrane by an externally applied pressure a certain threshold has to be overcome first.

4 Measurements and Results

To estimate the influence of an externally applied stress on the flow rate in open direction a set of flow-pressure characteristics for a test-valve at varying stresses was determined,

as depicted in Fig. 3. It can be seen that the achievable flow rate at a certain pressure decreases as a result of increasing mechanical stress. Consequently, also the opening pressure of the valve is increased at elevated stress, as can be seen in Fig. 4. Additionally, Fig. 4 shows the flow rate in the opening direction for increasing stresses recorded at constant hydraulic pressure. Increasing the applied stress from, e.g., 0.8 N/mm^2 to 1.2 N/mm^2 can significantly reduce the flow rate, from $0.6 \mu\text{l/s}$ to $0.2 \mu\text{l/s}$. Entirely stopping the flow is also possible.

The conducted measurements show the potential to combine the present rectifying property of the membrane valve with the capability to actively adjust the flow in the forward direction.

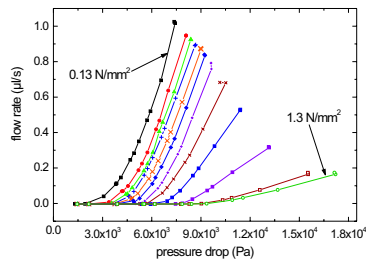


Figure 3: Measurement data of flow vs. applied pressure for a valve with an $800 \mu\text{m}$ cavity diameter using a $70 \mu\text{m}$ thick membrane with a $600 \mu\text{m}$ long slit. The set of curves shows the flow-pressure characteristics for different applied mechanical stresses.

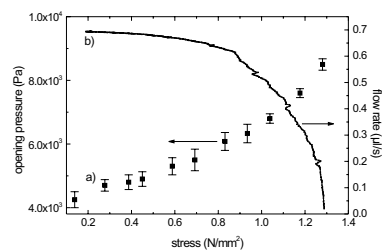


Figure 4: a) the opening pressure of the valve increases with increasing stress, b) as a result of increasing stress the flow rate at a constant applied pressure decreases.

References

- [1] W. O. Kwang and H. A. Chong. A review of microvalves. *Journal of Micromechanics and Microengineering*, 16(5):R13, 2006.
- [2] H. Becker and L. E. Locascio. Polymer microfluidic devices. *Talanta*, 56(2):267 – 287, 2002.
- [3] O. Rotting, W. Ropke, H. Becker, and C. Gartner. Polymer microfabrication technologies. *Microsystem Technologies*, 8(1):32–36, 2002.
- [4] A. Brask, D. Snakenborg, J. P. Kutter, and H. Bruus. Ac electroosmotic pump with bubble-free palladium electrodes and rectifying polymer membrane valves. *Lab on a Chip*, 6(2):280–288, 2006.

PROGRAMMABLE PNEUMATIC LOGICAL CIRCUITS FOR MICROFLUIDIC DEVICE CONTROL

William H. Grover, Erik C. Jensen,¹ Robin H. C. Ivester, and Richard A. Mathies

Department of Chemistry, University of California, Berkeley, CA 94720 USA

¹ Biophysics Graduate Group, University of California, Berkeley, CA 94720 USA

Abstract

Valve-based pneumatic logical circuits are demonstrated for the on-chip control of microfluidic lab-on-a-chip devices. In one powerful case, two “logical” valves impart latching behavior to a “working” valve. Vacuum or pressure pulses as short as 120 ms are used to latch the “working” valve open or closed. Arrays of these latching valve circuits can be controlled independently using an on-chip valve-based binary demultiplexer. Using these pneumatic logical circuits, n pneumatic inputs are used to control $2^{(n-1)}$ independent latching valves. By reducing or eliminating off-chip controllers, these pneumatic logical circuits can reduce the size, power consumption, and cost of lab-on-a-chip devices. A pneumatic XOR logic gate is also demonstrated, suggesting that extremely complex on-chip logical circuits are feasible.

Keywords: latching valves, multiplexing, pneumatic valves, digital pneumatic logic

The monolithic membrane valves and pumps developed previously by our group (Figure 1) [1] have enabled lab-on-a-chip systems for a variety of applications, including pathogen analysis [2], automated evolution of RNA catalysts [3], extraterrestrial amino acid analysis [4], and DNA computation using single nucleotide polymorphisms as binary bits [5]. In these applications, each on-chip pneumatic valve typically requires a dedicated off-chip solenoid valve controller. The size, power consumption, and cost of these off-chip controllers impose a practical limit on the number of independent pneumatic valve and pump operations that can be integrated into a lab-on-a-chip device.

To address this critical limitation, we present here the development of *programmable pneumatic logical circuits*—networks of on-chip valves that can be used to encode and control the operation of even the most complex microfluidic devices. In these circuits, on-chip monolithic membrane valves control the flow of pressurized and depressurized air and, in turn, other valves. Like transistors in microprocessors, the valves can be arranged into arbitrary logical circuits that encode the specific on-chip fluidic manipulations required for an assay. Pneumatic logical principles were used to design the latching valve circuits shown in Figures 1C and 2 [6]. In this circuit, two “logical” valves impart latching behavior to a third “working” valve. Vacuum pulses (~85 kPa) as short as 120 ms latch the working valve open for more than 2 minutes, and 120 ms pressure pulses (40 kPa) latch the working valve closed indefinitely. Since the latching valves retain their open or closed state even after all sources of vacuum and pressure are removed from the device, many latching valves can share a single controller through the binary demultiplexer circuit shown in Figure 3A. In this test

device, a four-bit valve-based demultiplexer routes 120 ms vacuum and pressure pulses from a single input to sixteen independent latching valves. All sixteen latching valves in the device in Figure 3A can be set open and closed according to any pattern every four seconds without errors. The multiplexed latching valves also retain their ability to control fluid flow: Figure 3B shows that vacuum and pressure pulses as short as 80 ms are adequate to reliably open and close one of the multiplexed latching valve against a 4 kPa fluid pressure head. Using the programmable pneumatic logic circuits presented here, $2^{(n-1)}$ independent valves can be controlled on-chip using only n off-chip controllers. Since these valves require only 120 ms vacuum or pressure pulses to latch open or closed for at least 2 minutes, *1000 independent on-chip latching valves could be controlled using only 11 off-chip controllers.*

Finally, the latching and demultiplexing circuits presented here are only two of many possible circuits that could be used to encode and control device operation on-chip. The six-valve XOR (exclusive-OR) pneumatic logic circuit shown in Figure 4 opens or closes a valve according to the XOR of the logical state (open or closed) of two other valves. Using pneumatic AND, OR, NOT, and XOR gates that we have developed, any Boolean logical function could be expressed on-chip as a circuit of valves. We expect that these pneumatic logical structures will play an important role in future microfluidic devices that integrate both the chemistry *and the logic* of assays on-chip.

- [1] W.H. Grover, A.M. Skelley, C.N. Liu, E.T. Lagally, and R.A. Mathies, *Sens. Act. B* **89**, 315–323 (2003).
- [2] E.T. Lagally *et al.*, *Anal. Chem.* **76**, 3162–3170 (2004).
- [3] B.M. Paegel and G.F. Joyce, Proceedings of the MicroTAS 2005 Conference, Boston, MA, USA, October 9–13, 2005, pp. 28–30.
- [4] A.M. Skelley *et al.*, *Proc. Natl. Acad. Sci. USA* **102**, 1041–1046 (2005).
- [5] W.H. Grover and R.A. Mathies, *Lab on a Chip* **5**, 1033–1040 (2005).
- [6] W.H. Grover, R.H.C. Ivester, E.C. Jensen, and R.A. Mathies, *Lab on a Chip* **6**, 623–631 (2006).

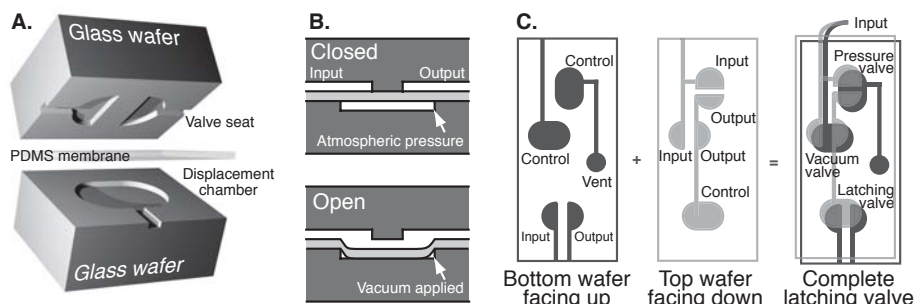


Figure 1. Exploded (A) and cross-sectional (B) views of a monolithic membrane valve. The valve is normally closed. When vacuum is applied to the displacement chamber, the PDMS membrane is pulled away from the valve seat and the valve opens, connecting the input and output channels. (C) Design and assembly of a latching circuit containing two “logical” valves that control a third “working” valve.

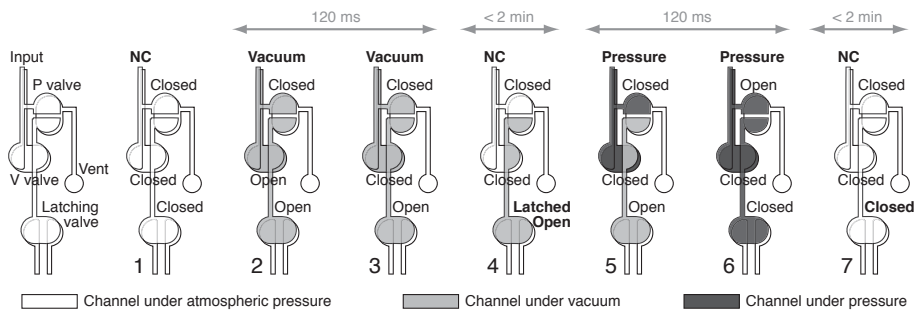


Figure 2. Operation of the latching valve circuit shown in Figure 1C. The vacuum, pressure, and latching valves are normally all closed (step 1). Vacuum applied to the Input is passed through the vacuum valve and opens the latching valve (step 2). In less than 120 ms, the vacuum valve passively closes (step 3) and the trapped vacuum holds the latching valve open for several minutes after vacuum is removed from the Input (step 4). Pressure applied to the Input (step 5) is passed through the pressure valve and closes the latching valve (step 6), which remains closed after pressure is removed from the Input (step 7). NC indicates “no connection” to the channel (only atmospheric pressure).

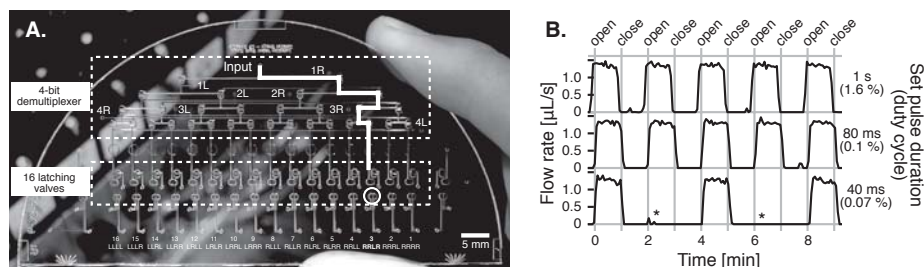


Figure 3. (A) Photograph of the latching valve demultiplexer. Each of the 16 latching valve circuits has a unique address determined by which demultiplexer valves must be open to actuate the latching valve. To open latching valve 3 (circled; address RRLR), vacuum is applied to the demultiplexer valves at 1R, 2R, 3L, and 4R, and a 120 ms vacuum pulse at the input is routed via the highlighted path to latching valve 3. (B) Fluid flow through multiplexed latching valve 3 as the valve is latched open and closed by vacuum and pressure pulses of different durations while running the program shown in Figure 3A. While 40 ms pulses occasionally fail to open the latching valve (*), pulses as short as 80 ms successfully latch the valve open and closed for at least one minute.

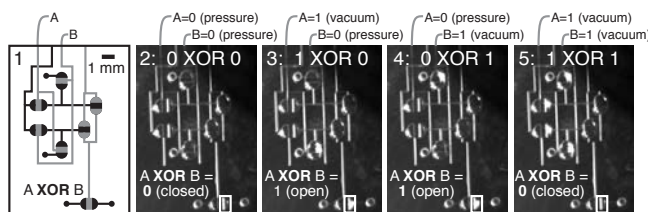


Figure 4. (1) Diagram of a six-valve pneumatic XOR (exclusive-OR) circuit. Vacuum (representing 1 or TRUE) or pressure (0 or FALSE) is applied to inputs A and B. The “A XOR B” readout valve opens if vacuum is applied to **either A or B**, and closes if vacuum is applied to **both A and B or neither A nor B** (a logical XOR). The open readout valves in photographs 3 and 4 reflect more light and appear brighter than the closed valves in photographs 2 and 4, indicating the correct results for an XOR gate.

AN OPTICAL RETRIEVAL MICROFLUIDIC SYSTEM FOR MICROARRAY APPLICATIONS

Wei-Heong TAN and Shoji TAKEUCHI

CIRMM, Institute of Industrial Science,
The University of Tokyo, Tokyo 153-8505, Japan
Phone: +81-3-5452-6650, Fax: +81-3-5452-6649,
Contact E-MAIL: tan@iis.u-tokyo.ac.jp

Abstract

We describe a simple device that hydro-dynamically traps beads in an array, and employs, for the first time, “optical-based” bubbles to release arrayed beads from traps. This device is simple to operate, robust and highly efficient. 100 micro-beads can be arrayed in less than 20 sec. Traps are also numbered for addressability and immobilized beads can be selectively released using bubbles. Typically, it takes less than 0.6 sec to retrieve a bead. Bubbles are formed by localized heating of aluminum patterns in the device using laser. This approach does not require complicated on-chip integrated circuits, greatly simplifying fabrication and allowing the device to be easily fabricated using a combination of traditional and soft lithography techniques. We also demonstrated the feasibility of this retrieval method by releasing beads selectively from the microarray.

Keywords : Microarray, Microbubbles, Hydro-dynamic traps, Release, PDMS

1. Introduction

Biological cell manipulation devices that use electrokinetic/magnetic forces [1,2] have complicated fabrication and control systems, while devices that use optical tweezers [3] might have problems with buffer change as they are weak against hydrodynamic forces. Here, we propose a device that uses hydrodynamic forces to trap particles. Particles are stably immobilized by the flow and chemicals/drugs can be easily introduced upstream. Selected particles can be retrieved using “optical-based” bubbles. The device is realized without complicated fabrication, and operation is straightforward.

2. Design and experimental

The concept of the trapping mechanism was presented in MEMS2006 [4] and is explained in Fig 1(a). A bead in the flow will be carried by the main stream into the trap (Trapping mode). Once the trap is filled, flow resistance is increased drastically along the straight channel, and the main flow is redirected along the loop channel. Subsequent beads will be carried along the loop channel, bypassing the filled trap (Bypassing mode). This design allows for one-bead-to-one-trap, and 100 micro-beads can be arrayed in less than 20 sec. Here, we incorporated a new release function and improved the trapping design to array beads as small as 15 μm . Moreover, traps arranged in parallel make screening of multiple chemicals feasible. Figure 2 shows a new strategy for releasing

trapped beads. Aluminum patterns function as heaters where bubbles form when illuminated with laser; Formed bubble displaces the trapped bead into the main flow and is carried towards the outlet. The device (Fig.3) is made by a combination of traditional and soft lithography techniques (Fig. 4).

3. Results and discussion

High speed camera images (Fig. 5) captured the instant at which a trapped bead was displaced by an “optical-based” bubble. The infra-red (IR) laser does not have any heating effect on water/cells, but causes localized heating when focused on aluminum patterns. When the IR laser was switched on, bubble formation was observed after 0.373s (Fig. 5c). The bubble displaced the bead out of the cavity (Fig. 5d), and the bead was carried along the loop channel towards the outlet (Fig. 5e-f). The bubble cooled down, shrank and disappeared in about 3 sec after the laser was switched off. Typically, it takes less than 0.6 sec to retrieve a bead. Studies on the effect of different laser settings on bead release probability at different flow rates revealed that higher power settings at short intervals are more efficient than low power settings at longer intervals (Fig. 6). This is because high power settings translate to higher heat generation and at short intervals, heat loss to forced convection is limited. To demonstrate the ease of operation of our trap-and-release device, beads were arrayed and selected beads were released to form patterned lines (Fig. 7). In the 1st row, after every 2 beads, 2 consecutive beads were released to form a “dash line”. In the 2nd row, after every 4 beads, 2 consecutive beads were released to form a “long-dash line”. No beads were released from the 3rd row, forming a “solid line” with the beads. All the beads were released from the 4th row to form an “empty line”. Beads have to be released from the upstream to the downstream of the flow. In this case, the beads were released sequentially from left to right. The entire procedure was accomplished within a few minutes using an X-Y stage.

4. Conclusions

The proposed device is highly amenable to automatic processing, and can be easily scaled up to cater for fast, high-throughput, and highly parallel screening. Our trap-and-release method can easily be extended to cells where it would be useful for drug screening/discovery and in the study of mutations as post-analyses can be performed on retrieved cells.

Acknowledgements

W.H. Tan thanks the Ministry of Education, Culture, Sports, Science and Technology, Government of Japan: MEXT for scholarship.

References

1. Manaresi, N. et al, 2003, J. Solid-State Circuits, 38, pp. 2297–2305.
2. Lee et. al., 2004, Appl. Phys. Lett. 85, pp. 1063–1065.
3. P.Y. Chiou et. al, 2005, Nature, 436, pp. 370-372.
4. Tan et. al., 2006, MEMS, pp. 534-537.

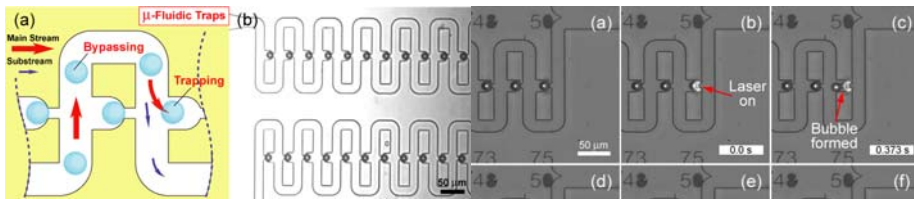


Figure 1. Photo of (a) μ -Fluidic Trap device (20×5 traps in series), and (b) close up of device with trapped beads.

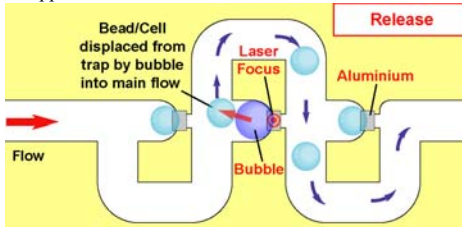


Figure 2. Schematic diagram showing the release mechanism using bubble. IR Laser is focused onto the aluminium pattern, causing localized heating and bubble formation. The formed bubble displaces the trapped bead/cell from the trap into the main flow.

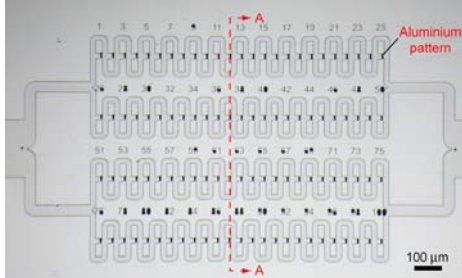


Figure 3. Photo of device consisting of 100 traps (4 parallel rows of 25 traps each) aligned with aluminium patterns. Traps are numbered for addressability.

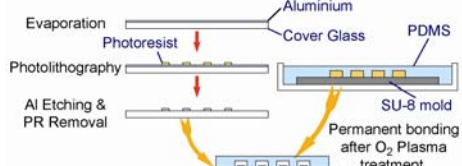


Figure 4. Process flow of device. The diagram corresponds to the cross-section AA in Fig. 3. Aluminium heaters are patterned using standard MEMS processes and channels are made from PDMS using soft lithography techniques.

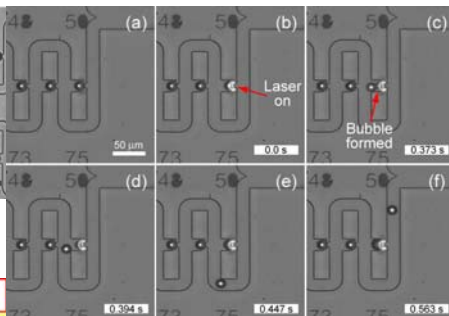


Figure 5. Sequence of high speed camera images showing the retrieval mechanism using bubble. Photo showing (a) trapped beads before application of laser, (b) application of IR laser, (c) bubble formation after 0.373s, (d) bubble displacing the bead out of the cavity, (e) bead being carried along the loop channel, and (f) bead moving towards the outlet. Bubble cools down, shrinks and disappears in about 3 sec after the laser was switched off, and another bead can enter the trap again.

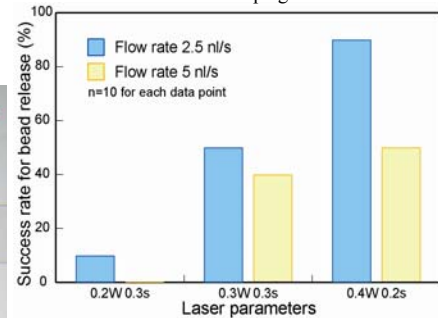


Figure 6. Success rate of bead release at different laser settings

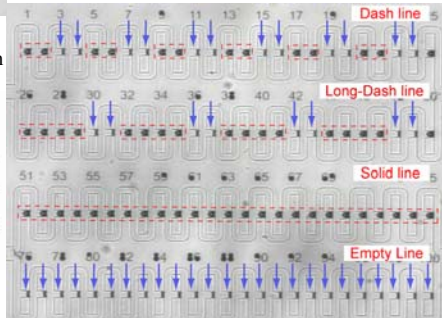


Figure 7. Photo of device with trapped beads. Arrow indicates position of released beads.

ACCURATE AND HIGH SPEED PARTICLES AND BIOMOLECULES SORTING MICROSYSTEM USING 3-DIMENSIONAL SHEATH FLOW

Takahiro Arakawa¹, Tokihiko Aoki¹,
Yoshitaka Shirasaki², Takashi Funatsu³ and Shuichi Shoji¹

¹Major in Nano-science and Nano-engineering, Waseda University

²Major in Bioscience and Biomedical Engineering, Waseda University

³Graduate School of Pharmaceutical Sciences, University of Tokyo

(arakawa@shoji.comm.waseda.ac.jp)

Abstract

High-speed particles and biomolecules sorter using thermoreversible gelation polymer and 3-dimensional sheath flow system was realized. The sol-gel transfer induced by the focused IR laser was used in this system. Double-deck structure made of PDMS and glass was adopted to realize the 3-dimensional sheath flow. High-speed sorting of about 3 ms and accurate sorting of 10^6 events were obtained.

Keywords: biomolecules sorter, high-speed sorter, accurate sorting, 3-D sheath flow, PDMS microchannel

1. Introduction

High throughput and high performance bimolecular sorting system is a basic tool for biological cell and proteome analysis. Various type of cell sorting system have been studied and developed. A high-speed particle sorter using combination of the sheath flow and repulsive dielectrophoretic force (DEP) has already reported [1]. However, electric stimulation sometimes influences the behavior of the biomolecules, for example, destroying the weak interaction of protein and organelle.

In our work, previous sorting system has been successfully operated to separate *E. coli* bacterial cells expressing green fluorescent protein (GFP) continuously for up to 6 hours [2]. And a high-speed 2-D sheath flow sorter using the thermoreversible gelation polymer (TGP) was reported [3]. Using the sorter described above, switching time of about 5 ms was realized. However, since the sorter has large flow resistance, the stability of sorting was influenced by the pressure fluctuation. For actual bio-applications, we present an improved high-speed particles and biomolecules sorter using 3-dimensional sheath flow system.

2. Principle and Design

The sorting mechanism of the sheath flow sorter is shown in Fig.1. The device has 3 inlets (two carriers and one sample flow) and 2 outlets (waste port and collection port). TGP solution containing samples is introduced from the center channel, which is sandwiched by carrier flows of TGP solution on both sides. When the target molecules are detected, focused IR laser is irradiated onto the waste port side flow of TGP solution, inducing gel transformation by thermal effect. It results in changing the sample flow direction to the collection port.

To improve the accuracy of the sorting, the flow resistances of the microchannels are decreased. The CFD simulation was used to optimize the channel structure. In order to reduce the flow resistance, cross sectional dimensions of all microchannels except the sample inlet are increased to 20 μm x 20 μm (Fig.2). The cross sectional dimensions of the sample inlet are 5 μm x 5 μm which is located topside of the carrier inlets. This

structure enables the 3-D sheath flow. By controlling the flow ratio of sample and carriers, the sample flow can be finely focused to realize accurate sorting.

3. Experimental section

To establish low cost disposable device, the channel structure was formed by PDMS. At first, positive photoresist of OFPR-800 LB 200CP was spin-coated and the sample channel pattern was transferred to the silicon substrate. 5 μm deep sample channel was etched by CCP-RIE. After the photoresist was removed using acetone, negative photoresist of PMER N-CA3000PM was spin-coated and patterned for 20 μm deep carrier channels. The double-deck structure was realized by the silicon and the photoresist mold. To transfer the master structures to PDMS, the liquid PDMS was casted. To fabricate PDMS microchannels having a small cross-sectional area, the casting PDMS of 5:1 ratio of resin to curing agent, was used instead of the normally used one (10 : 1). The PDMS microchannel and 170 μm -thick glass substrate were bonded after O₂ plasma treatment. Fig.3 shows the microchannel having a double-deck structure made of PDMS.

Fig.4 (a) and Fig.4 (c) show the confocal images of top view and cross-sectional view of the microchannel using rhodamine as the sample flow. Fig.4 (b) and Fig.4 (d) show the distributions of the fluorescent beads in the lateral and vertical direction. Sample flow was laterally focused to about 1.0 μm and vertically focused to about 5.0 μm at the sample to carrier flow ratios of 1/10. The switching behavior of this system was observed by CCD imaging system. The continuous video frames of the sorting operation are shown in Fig.5 (a) and Fig.5 (b). The obstacle bead and the target bead were at the total flow velocity of 3.5 mm/s. The switching time was about 3 ms, which was estimated from the setting duration of the IR irradiation and also estimated from the video image analysis. During 50 min operation, accurate sorting of 10⁶ events was realized.

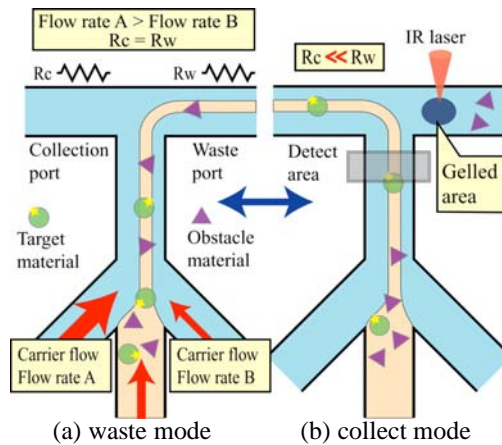


Fig. 1. Principle of the proposed particle and biomolecule sorter using TGP

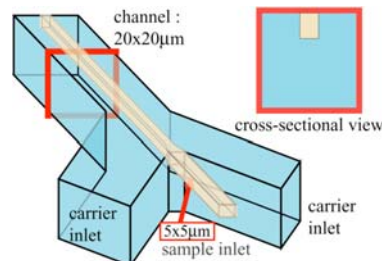


Fig. 2. Schematic view of the proposed 3-D sheath flow

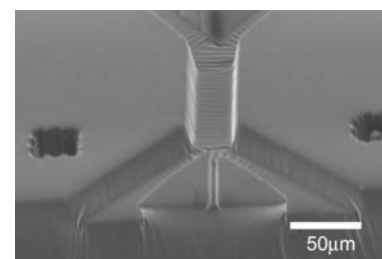


Fig. 3. Photograph of the fabricated microchannel

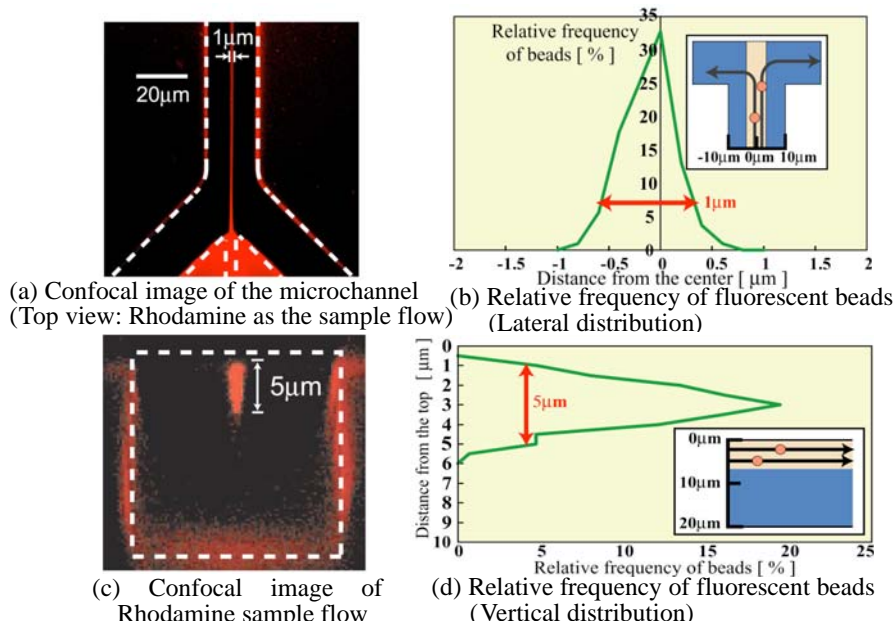


Fig. 4. Evaluations of the 3-D sheath flow using confocal

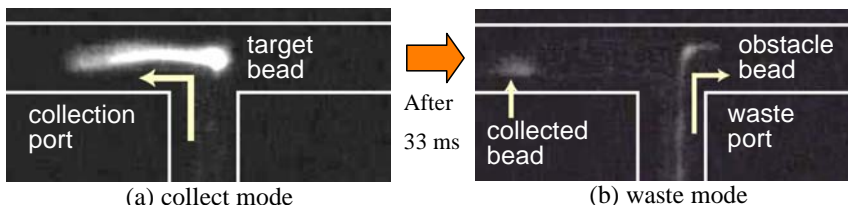


Fig. 5. Tracks of target and obstacle beads (frame rate 33ms, flow velocity 3.5mm/s)

4. Conclusion

High performance particles and biomolecules sorter using 3-D sheath flow was fabricated. Fast and reproducible sorting was obtained by optimizing the microchannel structure. Maximum sorting speed is about 3 ms and remarkable errors were not observed during 10^6 events. This system is applicable for the high-speed DNA separation and organelle sorting which are expected in biological and medical research field.

Acknowledgement

This development was supported by SENTAN JST, Japan Ministry of Education, Culture, Sports Science & Technology Grant-in-Aid for COE Research "Molecular Nano-engineering and Its Development into Microsystem" and SCOE "ASMew".

References

- [1] K. Takahashi et al., Nanobiotechnology, 2004
- [2] Y. Shirasaki et al., *Anal. Chem.* 2006, 78, 695-701
- [3] T. Arakawa et al., *Meas. Sci. Technol.* in press

MICROFLUIDIC PARTICLE ALIGNMENT FOR FLOW CYTOMETRIC APPLICATIONS UTILIZING HYDRODYNAMIC FILTRATION

Ryota Aoki¹, Masumi Yamada², Masahiro Yasuda¹, and Minoru Seki¹

¹Osaka Prefecture University, JAPAN and ²The University of Tokyo, JAPAN

Abstract

We propose here a new method for controlling particle positions in microchannels, which is one of the essential technologies in the field of flow-cytometric cell sorting and analysis. In this method, simple introduction of particle suspension into a specific microchannel enables focusing of particle positions into the center of the microchannel, utilizing the principle of hydrodynamic filtration. In this study, a microdevice with multiple branch channels was fabricated by regarding the microchannel structure as a resistive circuit, and the positions of micrometer-size polymer particles were controlled.

Keywords: microfluidic device, sheath flow, particle alignment, cell sorter

1. Introduction

Flow cytometry is a most-frequently used method to analyze and sort particles, especially cells and bio-particles, and has been realized in microfluidic format [1, 2]. In this method, particle positions in capillary or microchannel should be centered, since particle near the inner wall can not be properly detected. For this purpose, usually sheath flows are employed (Fig. 1), but complicated flow control is required, and particle concentration is decreased. In this study, we propose a new method to control particle positions in microchannel, without employing sheath flows.

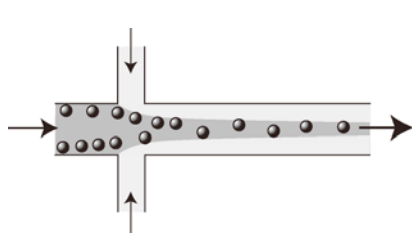


Figure 1. Control of particle positions using conventional sheath flows. Precise flow rate controls are indispensable. Liquid flow containing particles is dark-colored.

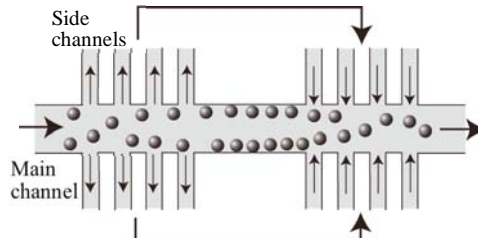


Figure 2. Principle of particle alignment. By simply introducing particle suspension, only the liquid flow is withdrawn into the side channels, and recombined into the mainstream, enabling the control of particle positions.

2. Principle

The basic principle for particle alignment is shown in Figure 2, in which a microchannel having multiple side channels is used. By continuously introducing a cell/particle suspension into the main channel, liquid flow without particles is

repeatedly removed from the main channel through side channels. Then in the downstream, by re-injecting the removed liquid flow from the side channels into the main channel, these liquid flows work as the sheath flows, and particle positions can be centered. Particle behavior at a branch point is shown in Figure 3. In the figure, the width of the region flowing into a side channel determined the aligned particle size. The flow rate distributed into each side channel is determined by the microchannel geometry, and they can be controlled when regarding the microchannel network as an analogue of a resistive electric circuit [3].

3. Experimental

PDMS-glass hybrid microdevices were fabricated using usual soft lithographic techniques. One of the fabricated microdevices is shown in Figures 4 and 5. This microdevice has one inlet, one outlet, main channel, and 146 (73×2) side channels. The width of the main channel is 25 μm , and that of the side channels is 10 μm . The depth of the microchannel is 13 μm . Fluorescing polymer microspheres, whose diameter is 5 μm , were used as model particles. The particles are suspended in an aqueous solution containing surfactant, and then introduced into the microchannel using a syringe pump.

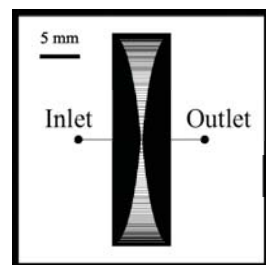


Figure 4. Microchannel design of the device. The size of the microdevice is 33 x 33 mm.

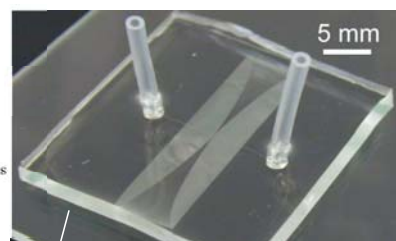
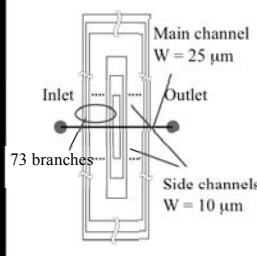


Figure 5. Photograph of the PDMS-glass microdevice.

4. Results and Discussion

Particle behavior in the microchannel near the outlet is shown in Figure 6. As can be seen, particles are precisely aligned near the center of the microchannel. Histograms showing the distributions of particle positions, near the inlet and outlet of the microchannel, are shown in Figure 7. Near the inlet, particles were randomly dispersed, while particles positions were centered after passing through multiple branch and

confluent points. These results show the ability of this method for the flow cytometric applications, due to the simplicity and applicability.

5. Conclusions

In this paper, we have presented a new method for particle alignment in a microchannel utilizing the principle of hydrodynamic filtration. This microfluidic device enables us to easily control the passage positions of particles in the microchannel. It is expected that this system will be able to apply various kinds of particle, such as cells and organelles, and be integrated into a cytometric platform.

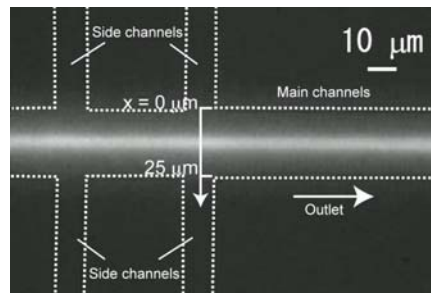


Figure 6. Behavior of the fluorescent particles in the main channel near the outlet. Particle positions are precisely focused in the center of the main channel.

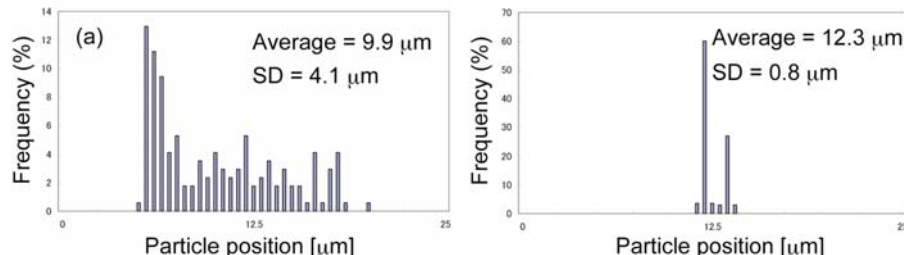


Figure 7. Distribution of particle positions: (a) near the inlet, and (b) near the outlet, when the flow rate was 5 $\mu\text{L}/\text{min}$. The horizontal axis (x-axis) corresponds to that in Fig. 6.

Acknowledgement

This study was supported in part by Grants-in-aid for JSPS fellows, Scientific Research B (16310101) from the Ministry of Education, Culture, Sports, Science, and Technology, Japan.

References

- [1] A. Y. Fu, C. Spence, A. Scherer, F. H. Arnold, S. R. Quake, *Nat. Biotechnol.*, 17, 1109 (1999).
- [2] M. A. McClain, C. T. Culbertson, S.C. Jacobson, J. M. Ramsey, *Anal. Chem.*, 73, 5334 (2001).
- [3] M. Yamada, M. Seki, *Lab Chip*, 5, 1233 (2005).

HARNESSING BIOLOGICAL MOTORS AND NANOSWITCHES FOR TECHNICAL APPLICATIONS

Viola Vogel

Department of Materials, ETH Zürich, Switzerland
(viola.vogel@mat.ethz.ch)

One key objective in bionanotechnology is to convert discoveries in the molecular sciences of how biological nanosystems work into new technologies even envisioning applications that can go far beyond their natural uses. Examples to be discussed will include the use of biological nanomotors to enable molecular manufacturing far away from equilibrium and the utilization of bacterial adhesion proteins as force-enhanced nanoadhesives.

Building assembly lines for nanocargo using motor proteins is motivated by the fact that a large number of specialized biological motors are used by cells to actively transport molecules and organelles along cytoskeletal filaments to defined locations. This ATP-driven process enables cells to dynamically reconfigure their intracellular building blocks to meet specific cellular tasks. Borrowing from nature, we are developing insights into how to engineer nanoscale transport systems based on biological motors that allow to shuttle cargo between user-specified locations. Methods have been furthermore developed to control the speed of the nanoshuttles with light, and we evaluated how various synthetic polymers affect the lifetime of these biomolecules embedded in integrated hybrid devices. We could also show that kinesin-driven transport can be utilized to drive the self-assembly of mesoscopic structures that would not form in the absence of active transport.

Asking how to utilize catch bonds that strengthen under loads was stimulated by our recent discovery that bacterial adhesion to surfaces can be enhanced under flow conditions. This is in contrast to common expectations since the adhesive strength of most receptor-ligand interactions is exponentially reduced if pulled apart by force. However, some receptor-ligand complexes exist that strengthen if strained which is the hallmark for catch bonds. Mechanisms of how these bonds work will be discussed as well as first technical applications.

References

1. H. Hess, G. D. Bachand, V. Vogel, **Powering nanodevices with biomolecular motors**, Chemistry, 10 (2004) 2110-2116
2. H. Hess, J. Clemmens, C. Brunner, R. Doot, S. Luna, K.-H. Ernst and V. Vogel, **Molecular self-assembly of “nanowires” and “nanospools” using active transport**, Nanoletters 5 (2005) 629-633
3. C. Brunner, K.-H. Ernst, H. Hess, V. Vogel, **Lifetime of biomolecules in polymer-based hybrid nanodevices**, Nanotechnology 15 (2004) S 540-548
4. W. E. Thomas, E. Trintchina, M. Forero, V. Vogel, E. Sokurenko, **Bacterial adhesion to target cells enhanced by shear-force**, Cell, 109 (2002) 913.
5. M. Forero, W. Thomas, C. Bland, L. Nilsson, E. Sokurenko, V. Vogel, **A catch-bond based smart nano-adhesive sensitive to shear stress**, Nanoletters, 4 (2004) 1593.
6. Thomas, W. E., Forero, M., Yakovenko, O., Nilsson, L., Vicini, P., Sokurenko, E., Vogel, V. (2005). **Catch Bond Model Derived from Allostery Explains Force-Activated Bacterial Adhesion**. Biophys J. 90 (2006) 753-64

CONTINUOUS-FLOW BIOMOLECULE SEPARATION THROUGH PATTERNED ANISOTROPIC NANOFUIDIC SIEVING STRUCTURE

Jianping Fu^{1,*} and Jongyoon Han^{2,3,*}

¹Department of Mechanical Engineering, ²Department of Electrical Engineering and Computer Science, ³Biological Engineering Division, Massachusetts Institute of Technology, Cambridge 02139, MA USA
(*e-mail address: jpfu@mit.edu, jyhan@mit.edu)

Abstract

We report a microfabricated anisotropic sieving structure (Anisotropic Nanofilter Array: ANA) for continuous-flow biomolecule separation. The designed structural anisotropy in the ANA causes different-sized biomolecules to follow different trajectories, leading to efficient separation. Continuous-flow Ogston sieving-based separation of short DNA and proteins as well as entropic trapping-based separation of long DNA were achieved, thus demonstrating the potential of the ANA as a generic sieving system for biomolecules of broad size scales.

Keywords: Nanofuidics, anisotropy, biomolecule separation, DNA, protein

1. Introduction

Efficient methods of separating and purifying biomolecules from a complex mixture are essential in biology and biomedical engineering. Recently, there has been great interest in switching from conventional porous gel media to patterned regular sieving structures, either by colloidal templating of self-assembled bead arrays or by various microfabrication techniques. However, the regular sieving structures reported in the literature so far have proven efficacious only for long DNA separation and their applicability to smaller, physiologically-relevant macromolecules remains questionable. Here we report a unique anisotropic sieving structure design and its implementation for continuous-flow separation of biomolecules of very broad biological size scales, based on two distinct sieving mechanisms: Ogston sieving [1] and entropic trapping [2].

2. Anisotropic Nanofilter Array (ANA)

The design of the ANA consists of a two-dimensional periodic nanofilter array (**Fig. 1**). The separation mechanism of the ANA relies on different sieving characteristics along two orthogonal directions within the ANA, which are perpendicular and parallel to the nanofilter rows. Upon application of two orthogonal electric fields E_x and E_y , negative-charged molecules assuming a drift motion in deep channels can be selectively driven to jump across the nanofilter to the adjacent deep channel. Molecular crossings of the nanofilter under the influence of E_x can be described as biased thermally activated jumps across free energy barriers at the nanofilter threshold [3]. For Ogston sieving, this energy barrier originates from the configurational entropy loss within the constriction

due to the steric constraints of the nanofilter wall, and this barrier favors molecules with a smaller size for passage (**Fig. 1A**) [1], resulting in a greater jump passage rate P_x and thus a larger stream deflection angle θ for shorter molecules. For molecules with diameters greater than the nanofilter constriction size, passage requires the molecules to deform and form hernias at the cost of their internal conformational entropy (*i.e.*, entropic trapping). Longer molecules can assume a greater jump passage rate P_x due to their larger surface area contacting the constriction and thus have a greater probability to form hernias that initiate the escape process, resulting in a larger deflection angle θ (**Fig. 1B**) [2].

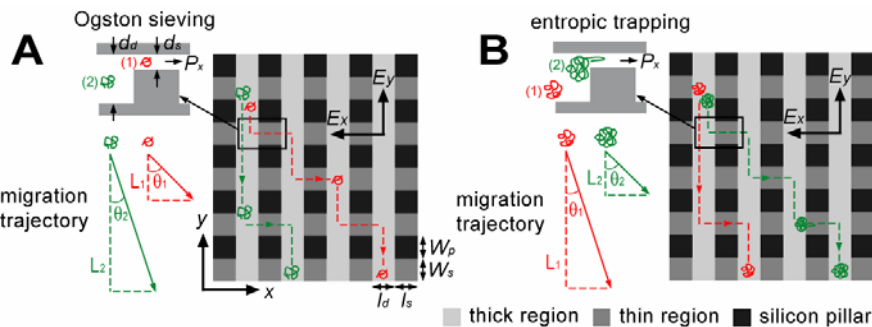


Figure 1. Schematic showing negatively charged molecules assuming bidirectional motion in the ANA under two orthogonal electric fields E_x and E_y . Dashed lines and arrows indicate migration trajectories projected onto the x - y plane for both the Ogston sieving (A) and the entropic trapping regimes (B).

3. Results and discussion

Figure 2 and Fig. 3 show separation results of a PCR marker sample (50–766 bp, rod-like rigid molecules with end-to-end distance of 16–150 nm, Ogston sieving) and λ DNA–Hind III digest (2.027–23.13 kbp, radii of gyration R_g : 140–520 nm, entropic trapping) through the ANA (with $d_s=55$ nm), respectively. A close look at the fluorescence images revealed that, as expected, for Ogston sieving of the PCR marker, shorter DNA fragments followed more deflected migration trajectories than longer ones, while for entropic trapping of λ DNA–Hind III digest, longer ones followed more deflected trajectories. From the fluorescence intensity profiles in Fig. 2, the size selectivity of the ANA in the Ogston sieving regime can be estimated to be about 5 nm [4]. The ANA is also capable of separating mixtures of proteins that have different molecular weights based on the Ogston sieving mechanism [1, 4].

Continuous-flow separation through the ANA should be applicable to other molecular properties (*e.g.*, charge density (pI) or hydrophobicity) that can lead to differential transport across the nanofilters. We believe the ANA can be used as a generic sieving structure to separate other particles of interest with nanoscale dimensions, including nanoparticles and nanowires, viruses and cell organelles.

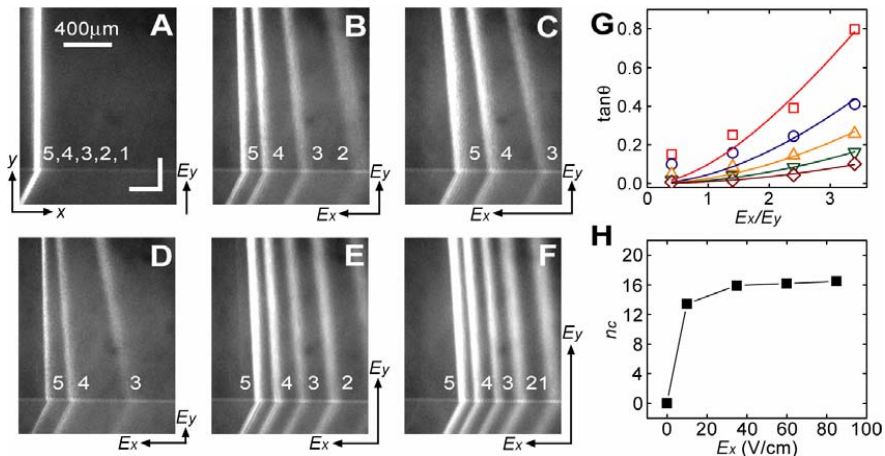


Figure 2. Ogston sieving of the PCR marker through the ANA. (A to F) Fluorescent photographs of the PCR marker stream pattern under different field conditions as indicated. White scale bar for electric field: 25 V/cm. Band assignment: 1, 50 bp; 2, 150 bp; 3, 300 bp; 4, 500 bp; 5, 766 bp. (G) $\tan\theta$ as a function of E_x/E_y at fixed $E_y=25$ V/cm (50 bp (\square), 150 bp (\circ), 300 bp (\triangle), 500 bp (∇), 766 bp (\diamond)). The solid lines are calculated theoretical curves [4]. (H) The effective peak capacity n_c on E_x when $E_y=25$ V/cm.

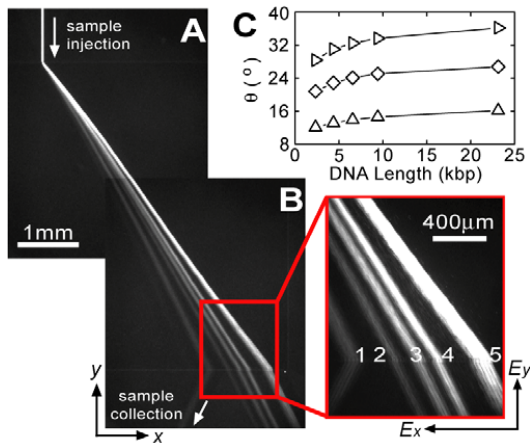


Figure 3. Entropic trapping of λ DNA-Hind III digest through the ANA. (A to B) Fluorescent photographs showing separation of λ DNA-Hind III digest with $E_x=185$ V/cm and $E_y=100$ V/cm. Band assignment: 1, 2.322 kbp; 2, 4.361 kbp; 3, 6.557 kbp; 4, 9.416 kbp; 5, 23.130 kbp. (C) θ as a function of DNA length with $E_y=100$ V/cm and E_x varied (E_x : 80 V/cm (Δ), E_x : 145 V/cm (\diamond), E_x : 185 V/cm (\triangleright)).

4. Reference

1. J. Fu, P. Mao and J. Han, *Appl. Phys. Lett.* **87**, 263902 (2005).
2. J. Han, S. W. Turner and H. G. Craighead, *Phys. Rev. Lett.* **83**, 1688 (1999).
3. J. Fu, J. Yoo and J. Han, *Phys. Rev. Lett.* **97**, 018103 (2006).
4. J. Fu, A. Stevens, S. Tannenbaum and J. Han, *submitted*.

NONLINEAR ELECTROKINETIC FLOW PATTERN NEAR NANOFUIDIC CHANNEL

Sung Jae Kim¹, Ying-Chih Wang², Hongchul Jang²,
Jeong Hoon Lee¹, and Jongyoon Han^{1, 3}

¹Department of Electrical Engineering and Computer Science,

²Department of Mechanical Engineering,

³Biological Engineering Division, Massachusetts Institute of Technology, USA

Abstract

We investigated the nonlinear electrokinetic flow near nanofuidic channels in the nanofuidic-preconcentrator. The ultra-fast vortices were generated near the nanochannel entrance due to the non-equilibrium electroosmotic flow (EOF). The size of the vortex was dependent on the microchannel depth and had critical effects on the preconcentration efficiency. We found out that the strong mixing due to the large vortex reduced the concentration gradient, which was necessary for strong concentration polarization. A shallow microchannel preconcentrator was made and an efficient preconcentration was achieved.

Keywords: Nonlinear electrokinetics, nanochannel, ion depletion, preconcentrator

1. Introduction

Nanofuidic channels thinner than ~50 nm demonstrate unique ion-permselectivity at moderate ionic buffer strengths, which can be utilized for various applications. We recently have demonstrated a nanofuidic protein preconcentrator which can efficiently concentrate proteins and peptides up to 10^6 fold [1]. Ions near nanochannel were depleted on the anodic side of nanochannels (concentration polarization) and both positively and negatively charged molecules were accumulated at the depletion boundary when coupled with tangential EOF. While the high accumulation speed of the device was attributed to the induced EOF [2] that could be generated by permselective ion current through the nanochannel, a detailed study of such a nonlinear electrokinetic flow is critically needed, for further development of nonlinear electrokinetic theory as well as for the optimization of nanofuidic preconcentrator. To explore this phenomenon in detail, we visualized the electrokinetic flow pattern inside and outside the ion depletion region by tracking the fluorescent nanoparticles in-situ.

2. Experiment

We investigated the electrokinetic flow in four different types of preconcentration device, as shown in Figure 1. For the experiment, 10 mM dibasic sodium phosphate buffer (dibasic, pH=8.7) was used. The tracer particle used in this work was 40nm and 500 nm carboxyl-terminated polystyrene beads. We also used positive and negative fluorescent dyes as molecular tracers.

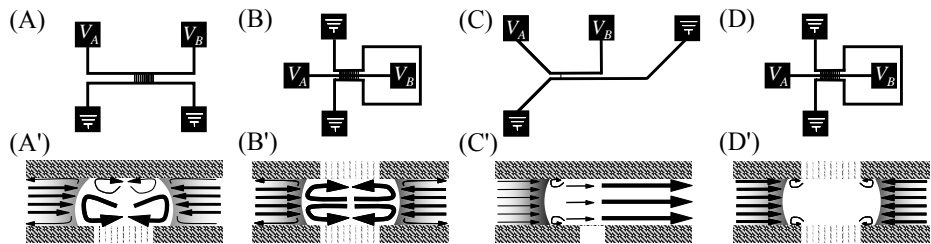


Figure 1. Schematics of four types of ion-preconcentrator: (A) single gate, (B) dual gates, (C) shallow single gate and (D) shallow dual gates channel. The dimensions of microchannel are $50 \mu\text{m} \times 12 \mu\text{m}$ ($W \times D$) in (A) and (B), $10 \mu\text{m} \times 1.5 \mu\text{m}$ in (C), and $50 \mu\text{m} \times 2 \mu\text{m}$ in (D). All nanochannels have the dimension of $5 \mu\text{m} \times 40 \text{ nm}$ ($W \times D$). The marked ('') figures indicate the schematics of flow patterns at $V_A = V_B$.

3. Results and Discussion

In the devices with deeper ($\sim 12 \mu\text{m}$) microchannels (Device A & B), we observed strong flow vortices (secondary EOF) generated around the nanofilter entrance, and they were immediately merged into bigger vortices as shown Figure 2. The formation of vortices was caused by the non-equilibrium electroosmotic slip velocity [3]. The flow velocity of the vortices, especially right beside the nano filter, was 10-times or more higher than that of the typical (primary) EOFs.

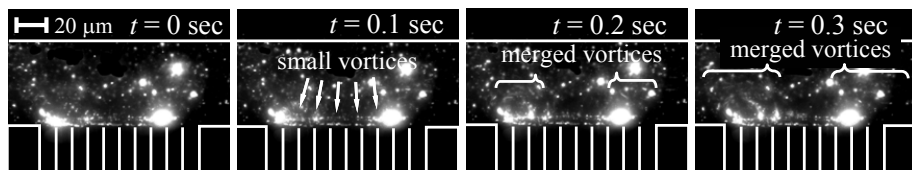


Figure 2. Time-dependent change of ion-depletion generation in the Device A.

The ion-depletion and ion-enrichment behaviors in Device A and B were presented in Figure 3. Strong vortices were generated to mix fluids inside the depletion region and caused a backflow outside of the depletion region.

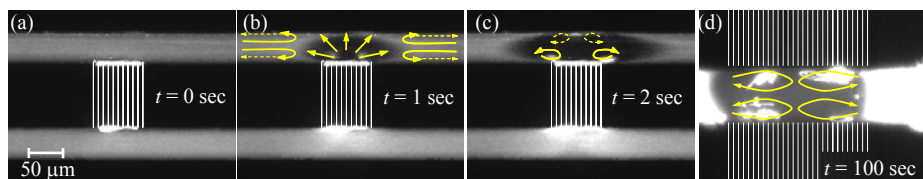


Figure 3. Electrokinetic behaviors in the Device A: (a)-(c) and Device B: (d). Dashed-arrow represents a lower velocity than that of the line arrow.

Using the two nanochannels on the both sides (Device B), the particles were more effectively collected because the vortices were evenly distributed, as shown in Figure

3(d). Such a strong vortex flow would induce fast mixing and dispersion of ion-depleted region near the nanochannel, which would prevent a further concentration polarization. Therefore, flow patterns were mostly vortex-like, and the overall preconcentration speed was low.

With a much thinner ($1.5\text{ }\mu\text{m}$) microchannel (Device C & D), however, qualitatively different flow behavior was observed. Fast, unidirectional flow was observed in the direction of the tangential electric field, which was at least $\sim 10\times$ faster than the normal EOF (Figure 4).

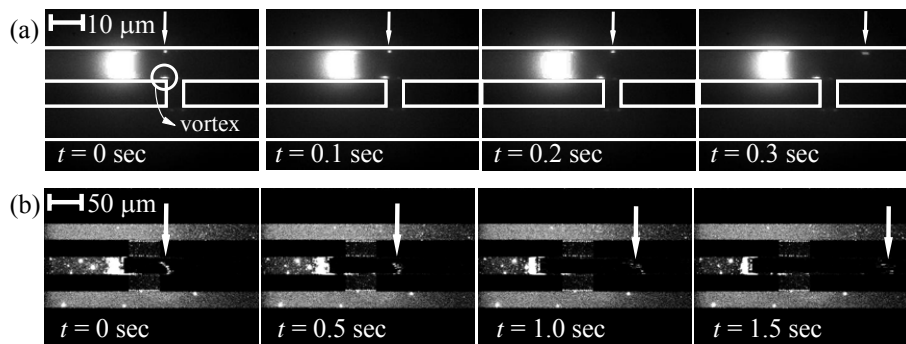


Figure 4. Electrophoretic migration using (a) Device C and (b) Device D. Estimated velocity of pointed particle is approximately (a) $140\text{ }\mu\text{m/sec}$ at $V_A = V_B = 10\text{V}$ and (b) $375\text{ }\mu\text{m/sec}$ at $V_A = 20\text{V}$ and $V_B = 15\text{V}$. (Background was subtracted from the image.)

Due to this flow, the preconcentration in this device was much faster. In addition, vortices were much smaller ($1\sim 2\mu\text{m}$) in the lateral dimension, which is correlated to the thickness of the microchannel. We hypothesize that smaller vortices in Device C and D would lead to less mixing and dispersion of the ion depletion region. As a result, much stronger concentration polarization occurs, possibly across the entire length of the microchannel, which leads to a unidirectional plug flow. The buffer solution after the preconcentration zone in the device loses its ion concentration at least down to $\sim 20\text{ }\mu\text{M}$, which was estimated by differential bead velocity in the two regions. This study could lead to novel electrokinetic flow pumping mechanism using nanochannels.

Acknowledgements

This work was partially supported by NIH Grants EB005743, GM68762, and CA119402. S. J. Kim was partially supported by Samsung Electro Mechanics. J. H. Lee was partially supported by KOSEF.

References

1. Ying-Chih Wang *et. al.*, *Anal. Chem.*, **77**, pp. 4293-4299, (2005).
2. S. S. Dukhin, *Adv. Colloid Interface Sci.*, **35**, pp. 173-196, (1991)
3. I. Rubinstein and B. Zaltzman, *Phys. Rev. E*, **72**, pp. 011505-1-011505-19, (2005).

OBSERVING AND TAMING BROWNIAN MOTION OF SILICON NANONEEDLE IN MICROMACHINED PDMS CHAMBER

Ersin Altintas¹, Karl F. Böhringer² and Hiroyuki Fujita¹

¹CIRMM/IIS, The University of Tokyo, Meguro-ku, Tokyo, 153-8505 JAPAN

²The University of Washington, Seattle, WA 98195, USA

ABSTRACT

This paper presents an effective way to obtain rotational motion of an encapsulated silicon nanoneedle in an appropriate cylindrical PDMS chamber containing liquid and to provide control over its Brownian motion by an external non-uniform AC electric field.

Keywords: Brownian motion, Brownian ratchet, nanosphere lithography, non-uniform AC field, PDMS

1. INTRODUCTION

Producing a net-unidirectional rotation from Brownian motion of a nanoneedle by 3-phase electrostatic rectification is under investigation (Fig. 1). Unlike in an electrostatic motor, Brownian motion provides the motive force; however, a periodically rotating electrostatic field rectifies this motion to produce a net rotation. This work aims at an engineering solution to novel, efficient nano-scale actuators exploiting Brownian motion inspired by biomolecular motors.

Brownian motion is the random motion of suspended micro/nano particles due to thermal fluctuations. Slender particles for the observation of rotation and the control of their motion—e.g. a nanoscopic needle—are preferable to widely used spherical beads whose rotation is indistinguishable. We have achieved taming, i.e. limiting the degree of freedom of Brownian motion of the nanoneedle by encapsulating it in a PDMS chamber and observed the alignment of the nanoneedle along the external electric field.

2. FABRICATION

We adopted nanobead masking; i.e. nanosphere lithography, in DRIE of silicon (Si) to prepare nanoneedles of

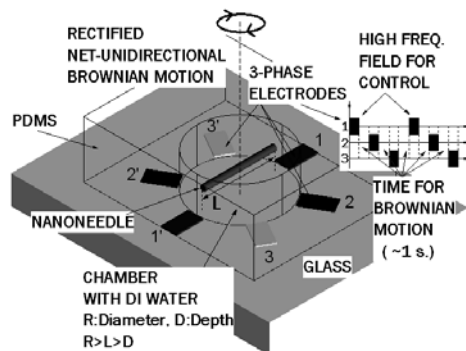


Figure 1. Conceptual design for micromachined Brownian motor.

$3.5\text{ }\mu\text{m}$ in length [1]. Si substrate is exposed to O_2 plasma, 3 minute-100 sccm at 50 watt in a RIE system, and diluted solution of beads (Bang Laboratories Inc., polystyrene beads, diameter=230 nm, 200(DIW):1(Original concentration)) is spin-coated to form an etch mask for anisotropic DRIE etching of Si. Subsequently, isotropic etching is applied to facilitate breaking of the nanoneedles at a specific length. Then, the sample is ultrasonicated and centrifuged (Fig. 2). It is refreshed by DI water to prepare the nanoneedle solution. Si nanoneedles with aspect ratios close to 20 are fabricated. For encapsulation, cylindrical PDMS chambers are prepared with an SOI mold [2]. Their diameters are 2, 4, 6 and 8 μm with a depth of $2.2\text{ }\mu\text{m}$. Triangular shaped Ni electrodes are fabricated onto coverglass by photolithography.

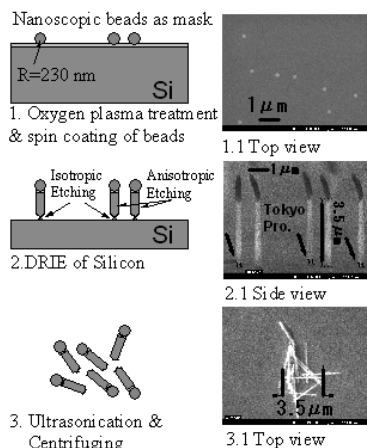


Figure 2. Fabrication of Si nanoneedles (1)Oxygen plasma treatment for enhancing hydrophilicity of the surface and spin-coating of beads. (2) DRIE of Si (3) Ultrasonication and centrifuging.

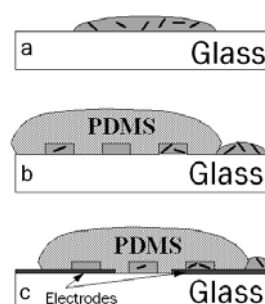


Figure 3. Experimental procedure (a) Introduction of nanoneedle solution onto the coverglass (b) Sealing PDMS chamber array and encapsulation of Si nanoneedles (c) Encapsulation and control of Brownian motion by electrodes microfabricated onto the coverglass.

3. RESULTS AND DISCUSSIONS

Rotational Brownian motion of an encapsulated $3.5\text{ }\mu\text{m}$ long- $\varnothing 200\text{ nm}$ Si nanoneedle was observed (Fig. 3ab, Fig. 4). The height of the chamber is less than the length of the nanoneedle and smaller than the chamber diameter; therefore the degrees of freedom are limited in vertical and translational direction. This can be understood from color change of the needle caused by defocusing during motions perpendicular

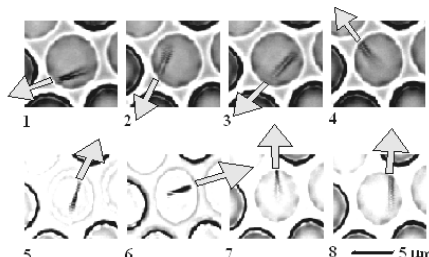


Figure 4. Rotational Brownian motion of a $3.5\text{ }\mu\text{m}$ long Si nanoneedle in a $6\text{ }\mu\text{m}$ - $2.2\text{ }\mu\text{m}$ PDMS chamber. Arrow is the reference for the direction. Captures are at different instants of time.

to the observation plane. After this verification, an electric field ($10V_{pp}$, 10 kHz) was applied to the encapsulated nanoneedle (Fig. 3c) between triangular shaped Ni electrodes. Although it could escape from the PDMS chamber during the observation, alignment of the nanoneedle with the field was observed with suppressed vertical motion (Fig. 5).

Following this, we made a flow cell between copper tapes (~80 μm in thickness) separated by $190\pm30\ \mu m$ on a coverglass. After a water droplet containing nanoneedles was introduced on the gap, coverglass was put over it and 1MHz square wave was applied between copper tapes. The Brownian motion of the needle was completely restricted with an electric field of 37 mV/ μm , while no control was possible around 2 mV/ μm . Partial alignments were observed around 5 mV/ μm (Fig. 6). Those data can lead to a proper region of operation for the Brownian motor to distinguish it from an electrostatic motor.

4. CONCLUSIONS

Rotational Brownian motion of an encapsulated Si nanoneedle in an appropriate disk-shaped PDMS chamber is observed. The alignment of the nanoneedle is achieved at 10 kHz-83 mV/ μm (avg.) external non-uniform AC electric field. 3-Phase rotational system is in progress.

ACKNOWLEDGEMENTS

The authors would like to thank to Prof. S. Takeuchi and his laboratory members in IIS, The University of Tokyo, for allowing the access to their utilities.

REFERENCES

- [1] Laine A. R. et al., *Nanobiotechnology*, 1(3), pp. 227-236, 2005
- [2] Arata H. et al., *Anal. Chem.*, 77(15), pp. 4810-4814, 2005

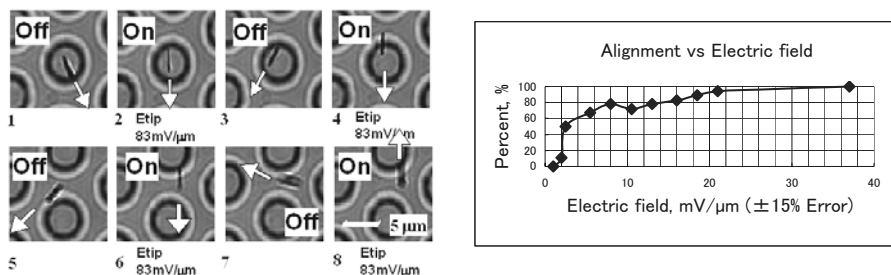


Figure 5. On/Off control of Brownian motion of a 3.5 μm long Si nanoneedle and alignment with a non-uniform electric field (10 kHz, 50% duty cycle, square wave AC). Vertical motion is limited. Regardless of sealing, attraction to the electrode can be seen. Arrow is the reference for the direction.

Figure 6. Alignment of nanoneedle in electric field.
(1MHz, 50% duty cycle, square wave)

OPTICAL DETECTION OF LIVING CELLS' REFRACTIVE INDEX VIA BUFFER MODULATION OF MICROFLUIDIC CHIP

W. Z. Song¹, X. M. Zhang¹, L. K. CHIN¹, C. S. LIM², A. Q. Liu¹, P. H. YAP³
and H. M. Hosseini¹

¹ School of Electrical & Electronic Engineering

² School of Chemical and Biomedical Engineering

Nanyang Technological University, Singapore 639798

³ DSO National Laboratories, Singapore 118230

(Email: eaqliu@ntu.edu.sg, Tel: (65) 6790-4336, Fax: (65) 6792-0415)

This paper reports the measurement of single living cells' refractive index (RI) using a Fabry-Perot (FP) cavity with buffer modulation of microfluidic chip. In the experiment, a single cell is captured in the cavity, and then the spectral shift in response to the buffer change with the presence/absence of cell can be used to determine the cell's RI and size. The microfluidic chip facilitates automatic detection and makes it promising for label-free drug screening.

Keywords: Fabry-Perot cavity, living cells, optofluidic microchip, refractive index

1. Introduction

Recent years has seen rapid increase of research interests in determining the cell physical parameters such as size, shape and RI as demanded by biological studies and cell-based drug screening [1]. RI has long been used to determine the concentration of solvents in a uniform solution [2]. For non-uniform medium such as living cell, the entire cell can be well represented by an effective RI. It is found that among all the ingredients, the protein is one of the main contributors in RI due to its abundance and high refractive index (about 1.50-1.58) [2]. Therefore, the effective RI is a key indicator to reflect the cell states (e.g., protein level) and to discriminate the cells (e.g., a normal cell from a cancerous cell of the same type). This paper proposes a simple but precise method for RI measurement implemented in a microfluidic chip.

2. Principle of detection

The principle of the detection method is shown schematically in Fig. 1, which consists of two aligned single mode fibers and a cell holder submerged in the buffer solution. The holder is to temporarily capture the cell during the measurement. The end facets of the fibers are high-

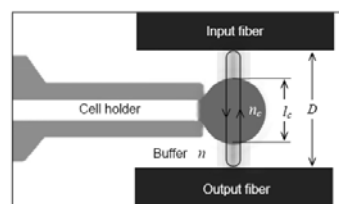


Figure 1 Schematic of Fabry-Perot cavity.

reflection coated so as to form the FP cavity. The fibers also serve as the optical input and output. The wavelength λ of the m^{th} FP mode in the output spectrum is given by $\frac{1}{2}m\lambda = nD + (n_c - n)l_c$, (n : RI of buffer, D : separation of fibers, n_c : RI of cell and l_c : cell size). In the measurement, two buffer solutions with slightly different RIs are used alternatively. Four spectra are obtained in response to the buffers change and the absence/presence of cell, i.e., λ_{n1} for buffer 1 without cell, λ_{n2} for buffer 2 without cell, λ_{c1} for cell in buffer 1, λ_{c2} for cell in buffer 2. By differentiating the wavelength values, it yields $l_c = D(1 - (\Delta\lambda_c / \Delta\lambda_n))$ and $n_c = n_1[1 + (\Delta\lambda_l \Delta\lambda_n) / (\lambda_{n1}(\Delta\lambda_n - \Delta\lambda_c))]$ where $\Delta\lambda_c = \lambda_{c2} - \lambda_{c1}$, $\Delta\lambda_n = \lambda_{n2} - \lambda_{n1}$, and $\Delta\lambda_l = \lambda_{c1} - \lambda_{n1}$. Both cell size and RI can be determined simultaneously.

The designed microfluidic chip is illustrated in Fig. 2(a) and the integrated chip is shown in Fig. 2(b). Buffer 1 and buffer 2 are injected alternatively from the inlets by syringe pumps into the main channel. This is one of the key steps to realize the differential detection method by varying the surrounding medium. In the cell inlet, the living cells in buffer 1 are injected one by one into the main channel for detection. The cell holder is a micropipette controlled by another syringe pump. A single cell can be captured when the pump works in the withdraw mode through a controllable valve, and it can be released and flushed away when the valve is shut off. In the microfluidic chip, microchannel and network scribed on PMMA substrate using 248nm excimer laser, which is then integrated with the fiber and holder. The gap of FP cavity between the input and output fibers is 35.5 μm . The end facets of the input and output fibers (Corning SMF-28) are coated with 40nm thick gold layer with reflectivity of 80%.

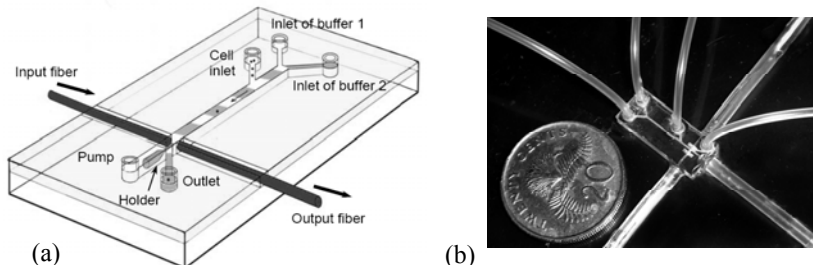


Figure 2 Microfluidic chip for single living cell detection using FP cavity:
(a) schematic of biochip design; and (b) photograph of an integrated chip.

3. Experiment results and discussions

The light source is a superluminescent LED with central wavelength of 1550 nm and bandwidth of 80 nm. The output fiber is connected to an optical spectrum analyzer. Buffer 1 (reference) is standard phosphate buffered saline (PBS) solution with nominal RI of 1.350. Buffer 2 is prepared by adding small amount of ethylene glycol (RI: 1.431) to the PBS so as to obtain a slightly higher RI. The measurement is conducted on the MDCK cell (Madin Darby canine kidney cell) with a size of 16 - 20 μm and an effective

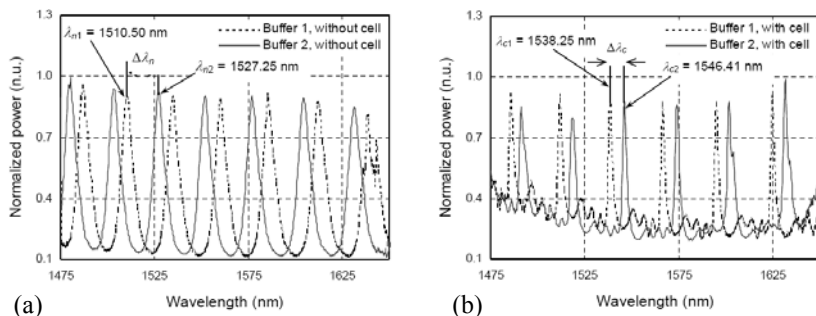


Figure 3 Optical transmission spectra with the change of buffer and cell: (a) buffers without cell; (b) buffers with cell

RI of 1.385 to 1.404. Fig. 3 shows the spectra obtained in the experiment. The measurement is repeated for four times by releasing and recapturing the same cell and the results are listed in Table 1. The cell RI has a standard deviation of $\pm 0.2\%$. However, the cell size has large fluctuation ($\pm 4.0\%$). This may be due to the fact that the captured cell is in different position and orientation, i.e. different l_c . In contrast, the effective RI is less dependent on the position and orientation as long as the central part of the cell is within the optical detection beam.

Table 1 Experiment results of RI of buffer and cell.

		Test 1	Test 2	Test 3	Test 4	Average	Standard deviation
Buffer 2 (PBS + ethylene glycol)	Refractive index	1.363	1.366	1.365	1.364	1.365	$\pm 0.1\%$ (accuracy)
MDCK cell	Refractive index	1.398	1.395	1.400	1.401	1.399	$\pm 0.2\%$
	Size (μm)	18.2	17.0	18.5	17.3	17.8	$\pm 4.0\%$

Conclusion

This paper presents a microfluidic chip to determine both the size and RI of single living cells with the advantages of high accuracy, easy control and continuous detection. It utilizes high-reflection coated fibers to form FP cavity in the microfluidic environment, and changes the buffer solution using microfluidic technology. The RI and size of the cell is measured simultaneously by differentiating the spectral shift. The experiment on MDCK cells measures an effective RI of 1.398 and an average cell size of 17.8 μm with accuracy of 0.1%. This microchip allows label free detection of single living cells in microfluidic environment with potential applications in cell biological research, disease diagnosis and cell-based drug screening.

References:

1. B. Kemper, D. Carl, J. Schnekenburger, I. Bredebusch, M. Schäfer, W. Domschke, G. von Bally, J. Biomed. Opt. **11**, 034005 (2006).
2. P. L. Gourley, J. Phys. D: Appl. Phys. **36**, 228 (2003).

INTEGRATED MICROFLUIDIC BILAYER LIPID MEMBRANE (BLM) ARRAYS

L. Hromada, Jr.¹, J. Kasianowicz², M. Gaitan², D. Millard¹, D. L. DeVoe¹

¹Department of Mechanical Eng., Univ. of Maryland, College Park, MD USA

²National Institutes of Standards and Technology, Gaithersburg, MD, USA

Abstract

An electrophysiological testing array has been developed in a polymer microfluidic format utilizing integrated Ag/AgCl electrodes. In-situ formation of bilayer lipid membranes can be formed at any one of the three fully enclosed, electrically addressable array sites. The array format allows for single or multiple simultaneous electrophysiological testing depending on desired testing conditions.

Keywords: BLM, Bilayer Lipid Membranes, Electrophysiology

1. Introduction

An integrated microfluidic system for the in-situ formation and sensing of bilayer lipid membrane (BLM) arrays is reported. The polymer chip combines multilayer microchannels for solvent and lipid delivery enabling automated BLM formation, and thin film Ag/AgCl electrodes for addressable electrophysiological sensing from each BLM site within the array. Artificial BLMs have been widely used to investigate fundamental electrophysiology kinetics including ion channel formation and transduction [1,2]. Standard macro-scale approaches suffer from several well-known issues, mainly poor BLM lifetimes, laborious formation techniques, and limited data collection throughput. Recently, microfluidic technology has been applied to BLM formation and sensing [3,4]. Suzuki, et al. [5] demonstrated a PMMA microfluidic device with multiple BLM sites; however the individual sites were not addressable. In a related device [6] the array sites were open-faced, thus limiting BLM lifetime and testing duration due to evaporation. The present work addresses these issues by automating the membrane formation process in a fully enclosed microfluidic chip.

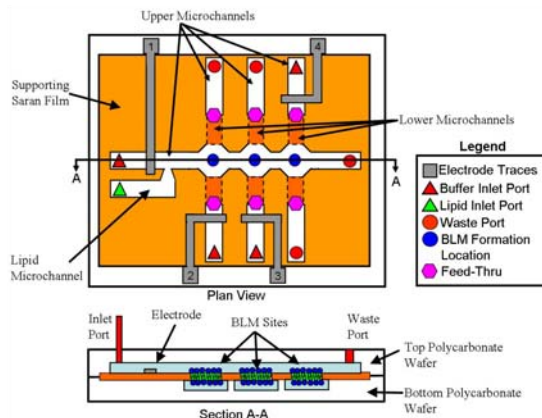


Fig. 1 Plan and section view of BLM microfluidic array device containing three sensing sites. A PVDC film containing thermally-formed BLM support holes is positioned between two imprinted PC chips. Integrated Ag/AgCl electrodes enable low-noise current monitoring.

2. Fabrication

The BLM device array consists of two polycarbonate (PC) substrates sandwiching a polyvinylidenechloride (PVDC) film, as shown in Fig. 1. Microchannels within each PC chip are aligned to BLM formation sites within the PVDC film. Microchannels 50 μm wide and 50 μm deep are fabricated in each PC layer by hot embossing. A 12 μm thick PVDC film is applied to the bottom PC substrate, and Ag/AgCl electrodes are deposited using an electrodeposition process reported by Polk et al.[7]. Briefly, Cr, Au, and Ag are evaporated using a shadowmask to 8 nm, 8 nm, 100 nm thickness, respectively. A 1-2 μm thick Ag film is then electroplated to improve electrode lifetime and stability. Finally, the top Ag film is chloridized to form stable and low-noise Ag/AgCl electrodes.

Next, 25 μm diameter BLM support holes are formed in the PVDC film by a traditional hot needle method. Feed-thru holes are also created using a hot needle to enable electrical connections to microchannels beneath the PVDC film. The PC and PVDC surfaces are hydrophilized by UV-ozone treatment to promote improved lipid solution control inside the microchannels using similar techniques report by [8].

Prior to alignment and thermal bonding, a minute amount of petrolatum was applied to the BLM formation site using a micromanipulator, ensuring a hydrophobic anchor region to promote stable BLM formation. Lastly, fluidic access is provided through a novel needle interface which simplifies fabrication, minimizes dead volume, and uses standard capillary connectors. A typical fabricated device is shown in Fig. 2.

3. Results and Discussion

The in-situ BLM formation process is described in Fig. 3 using a single site chip. The device is initially filled with 1M KCl (pH 6.7) buffer solution, and the lower reservoirs are sealed. Current monitoring for a ramp voltage input yields saturated output due to the low-resistivity salt bridge formed between the upper and lower electrodes (Fig. 3a). A plug of lipid solution (10 mg diphyanoyl PC in 1 mL hexadecane) is introduced into a side channel at a rate of 17 nL/min. As the lipid solution crosses over the BLM formation site, the output current drops in amplitude and transforms into a square wave (Fig. 3b). Finally, buffer solution is introduced from the left upper channel at a rate of 170 nL/min which begins to displace the lipid plug towards upper waste (Fig. 3c). As the lipid remaining within the 25 μm diameter hole thins, the square wave amplitude increases which is characteristic of capacitive lipid membrane formation.

Post BLM formation analysis of accompanying electrical signals yields a BLM capacitance of 2.5 pF. When dividing by the BLM formation area, a 0.5 $\mu\text{F}/\text{cm}^2$

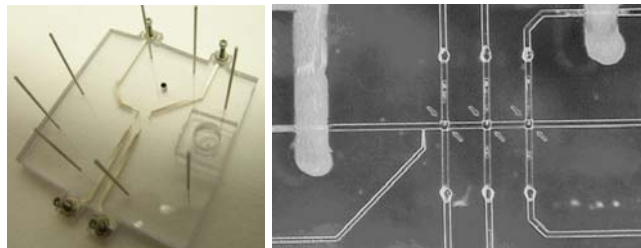


Fig. 2 Fabricated 50 mm square BLM array device with fluidic ports and electrode terminals (left), and view of sensing sites, lipid injection side channel, PVDC feed-thrus, and Ag/AgCl electrodes (right).

specific BLM capacitance is achieved which compares favorably to other reported ranges of specific BLM capacitances [1-6].

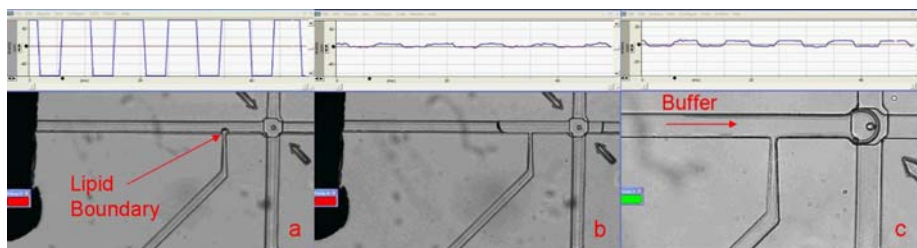


Fig. 3 Micrographs showing BLM formation process in which (a) lipid solution is injected from the side channel, forming a plug which (b) flows across the BLM formation site. Finally, (c) buffer solution displaces the lipid plug to the right resulting in BLM formation. Current monitoring through the AgCl electrodes is shown inset for each stage of the process.

Initial BLM device studies show the importance of microchannel surface hydrophilization via UV-ozone treatments prior to lipid injection. Untreated BLM array chips exhibited uncontrollable lipid responses usually in the form of wall wicking. On the other hand, treated BLM array chips demonstrate very plug-like lipid flow motion, which greatly improves controllability for precise movements.

4. Conclusions

In-situ formation of BLMs has been realized in an enclosed array format with integrated AgCl electrodes capable of stable and low-noise current measurements from individually-addressable membranes. The 3-element array explored here comprises a first step towards a fully integrated system for multiplexed ion channel measurements from BLM arrays. Future efforts will be directed towards electrophoretic transport of transmembrane proteins to populate individual membranes, and electrophoretic analyte separation prior to delivery to the sensing sites.

Acknowledgements

The authors acknowledge Jackie Viren for her help on this project. The authors are also grateful to Brian Polk (NIST, Gaithersburg, MD) for his insight on Ag/AgCl fabrication.

References

1. P. Mueller, D. Rudin, H. Tien, W. Wescott, *Nature*, 194, 1962, pp. 979-980.
2. W. Hanke, and W. Schlu, *Planar Lipid Bilayers*, Academic Press, 1993.
3. K. Funakoshi, H. Suzuki, and S. Takeuchi, *MicroTAS 2005*, pp. 951-953.
4. M. Sandison and H. Morgan, *MicroTAS 2005*, pp. 1249-1251.
5. H. Suzuki, K. Tabata, H. Noji, and S. Takeuchi, *Langmuir*, 2006, 22, pp. 1937-1942.
6. H. Suzuki, K. Tabata, Y. Kato-Yamada, H. Noji, and S. Takeuchi, *Lab on a Chip*, 2004, 4, pp. 502-505.
7. B. Polk, A. Stelzenmuller, G. Mijares, W. MacCrehan, and M. Gaitan, *Sensors and Actuators B*, 114, n1, 2006, pp 239-247.
8. C. W. Tsao, L. Hromada, J. Liu, D. L. DeVoe, Submitted to *Lab on a Chip*, 2006.

“BLOWING VESICLES”: A SIMPLE METHOD FOR DIRECT MICROENCAPSULATION IN LIPID VESICLES

Kei Funakoshi, Hiroaki Suzuki, and Shoji Takeuchi

Institute of Industrial Science (IIS), The University of Tokyo

Meguro-ku, Tokyo, 153-8505, Japan

Phone: +81-3-54526650 / Fax: +81-5452-6649

Contact E-mail: funako@iis.u-tokyo.ac.jp

Abstract

We developed a method for forming lipid vesicles from planar lipid membrane. On a chip device with a jet nozzle, lipid vesicles of about 480 μm were formed one-by-one by applying pulsed jet flows, similar to blowing soap bubbles from a soap film. In this method, desired reagents and micro particles were encapsulated inside large vesicles directly. Size of vesicles could also be controlled by adjusting the dispense time of pulsed jets.

Keywords: **lipid membrane, ultra giant vesicle, liquid jet dispenser**

1. Introduction

Lipid bilayer is the fundamental structure of cell membranes. And lipid bilayer can be formed as spherical vesicles with self-assembly of lipid molecules by suspending lipid powder in an aqueous phase. There are many applications of lipid vesicles as biocompatible capsules for gene transfections, drug delivery, and bio-reactors [1-3]. In conventional hydration methods, lipid vesicles with wide distributions (0.1-20 μm) are formed.

Recently, we have managed to form a planar lipid bilayer between two aqueous compartments on a chip [4]. Here, we utilize the planar bilayer to create lipid vesicles. Figure 1 shows the schematic diagram of our method inspired by soap bubble formation. Applying a pulsed jet flow from a small nozzle to the vertical lipid bilayer, a lipid vesicle is generated from the planar membrane. This method allows direct encapsulation of reagents into lipid vesicles, reducing the volume of reagents. In addition, the vesicle size can be controlled by adjusting the parameters of the jet dispenser (dispense time, pressure level, nozzle size, etc).

2. Experimental

The gourd-shaped well with a two intersectional chambers (diameter; 4mm, depth; 2 mm) was fabricated from a PMMA substrate (Fig. 2) with CAD/CAM system. To form the planar lipid membrane on a chip, the well was first filled with 15 μl of lipid solution (25mg /ml, in decane). Next, two water droplets (15 μl) were introduced with a micro

pipette into both chambers, forming two lipid monolayers at the interfaces of water/decane. The bilayer was formed when the two monolayers were contacted each other by increasing the volumes of the two water droplets. Then, a micro jet nozzle made from glass capillary (inner diameter; 25-60 μm) was brought near the lipid membrane (about 100 μm from the lateral side) with a micromanipulator system. The nozzle was connected to the air dispenser that can control time and pressure of the pulsed jets.

3. Results and discussion

As a pulsed jet (dispense time = 0 msec, air pressure = 60 kPa) of fluorescent solution (1 mM, calcein) was ejected at center of the planar lipid bilayer, a lipid vesicle containing fluorescent solution was generated from the planar lipid membrane into the aqueous phase. With this method, it was possible to form about 20 lipid vesicles one-by-one continuously from one planar lipid membrane by applying continuous pulsed jets (Fig. 3). Figure 4 shows the sequence of lipid vesicle formation captured by high speed camera. When a jet was applied, the center of the lipid membrane dramatically deformed, resulting in formation of vesicles (mean diameter; 480 μm). Depending on ejecting conditions, small satellites ($\sim 200 \mu\text{m}$) were sometimes created. Size distribution of primary vesicles showed near monodispersity with a C.V. of 6.1% (Fig. 5). Compared to varying the nozzle size, we found that varying the dispense time has a more significant effect on the size of vesicles (Table 1).

4. Conclusions

The formation of lipid vesicles on a chip with micro jet dispenser has been successfully demonstrated. The uniformly-sized vesicles of about 480 μm were formed one-by-one by applying pulsed jet flows, and exhibited a narrow size distribution. Size of vesicles could be controlled by adjusting the dispense time of pulsed jets. We believe that this method will provide a new strategy of lipid vesicles for constructing artificial cell systems, or bio reactor systems based on cell membrane-mimetic functions.

Acknowledgements

We thank Hiroyuki Noji at Osaka University for helpful discussions. This research was supported by Precursory Research for Embryonic Science and Technology (PRESTO), JST.

References

- [1] K. Sou, et al., Biotechno. Prog. 2003, 19, 1547-1552.
- [2] Y. Sato, et al., Chemical Physics Letters, 2003, 380, 279-285.
- [3] S. Fleischer, et al., Methods enzymol. 1989, 171, 191-394.
- [4] K. Funakoshi, et al., microTAS 2005, Vol. 2, pp. 951-953, 2005.

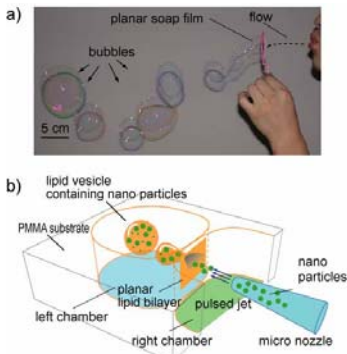


Figure 1. Our concept of "Blowing Vesicles."
 a) A photo of blowing soap bubbles. b) Schematic image of formation of lipid vesicles using pulsed jets. The solutions in the left and right chambers are separated by a planar lipid bilayer. Applying pulsed jets to the center of lipid bilayer, lipid vesicles containing desired reagents are formed.

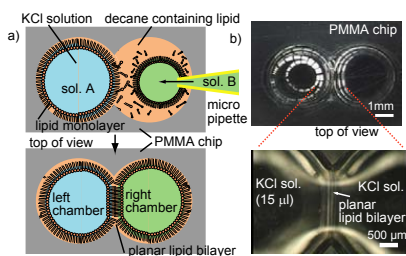


Figure 2. Preparation of a planar lipid bilayer.
 a) Schematic images of formation of a planar lipid bilayer between left and right chambers. b) Two droplets are formed in decane containing lipid (25 mg/ml) using micro-pipette.

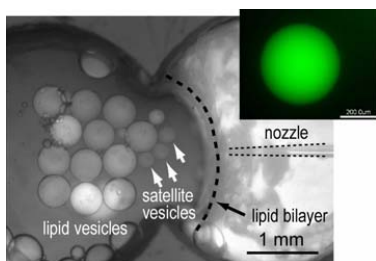


Figure 3. A microscopic image of many vesicles.
 Lipid vesicles containing fluorescent molecules were formed one-by-one by applying sequential pulsed jets.

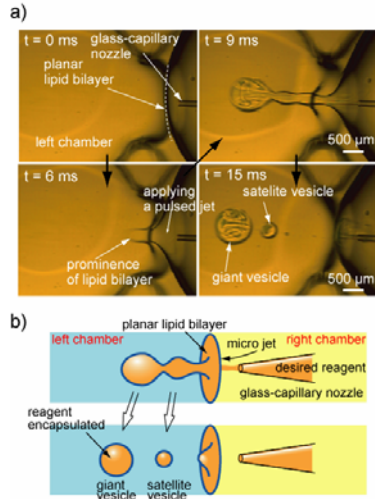


Figure 4. Sequential images of vesicle formations.
 a) High speed camera imaging of formation of a lipid vesicle. b) Schematic illustrates of the mechanism of the formation of giant vesicles and satellite vesicles from a planar lipid bilayer.

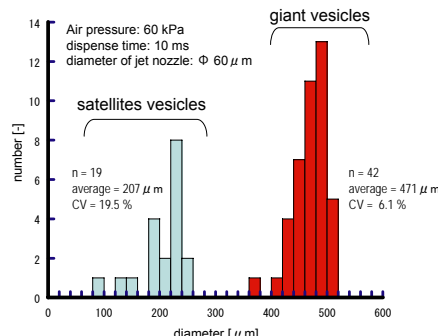


Figure 5. Histogram of vesicle size.

Table 1. Differences in the giant vesicle size with changes in the dispense time and nozzle diameter.

	case 1	case 2	case 3
nozzle size [µm]	60	60	25
dispense time [ms]	10	15	10
number of vesicles	42	7	20
average [µm]	471	646	484
CV [%]	6.1	13.7	5.8

MULTIPHASE MICROFLUIDICS NEAR THE SPEED OF SOUND

Axel Günther and Klavs F. Jensen

Department of Chemical Engineering, Massachusetts Institute of Technology
77 Massachusetts Ave., Cambridge, MA 02139, USA
(axelg@mit.edu)

Abstract

Microscale two-phase flows have often become synonyms for flow conditions at which interfacial forces dominate over viscous ones by several orders of magnitude. Instead, this contribution focuses on gas-liquid microflows where the opposite is true: inertia and viscous forces match or dominate interfacial ones. The presented configuration could provide a paradigm-shift for applications that require very large interfacial areas in microsystems, e.g., for conducting highly exothermic gas-liquid reactions. Devices based on such flow conditions are scalable, and provide an increase in throughput per channel by up to two orders of magnitude, compared with present systems.

Keywords: Microscale gas-liquid flow, multiphase microfluidics, microchemical systems, flow instability

1. Introduction

The characterization of microscale gas-liquid flow allows particular phase distributions to be selected (Fig. 1a). Our present contribution considers gas-liquid flows at very high velocities, hence large Capillary numbers, $Ca = U_b \mu / \sigma$, where σ is the interfacial tension, μ the viscosity of the liquid and U_b the velocity at which a bubble or fluid filament travels. Liquid films with very large surface areas are obtained that are attractive for conducting highly exothermic gas-liquid reactions (e.g. direct fluorination) since the reduced film thickness decreases liquid mass transfer limitations. Interfacial area and throughput are significantly increased compared to segmented or annular flows. Gas-liquid reactions have so far been performed under segmented or annular flow conditions and throughput was then increased by parallelization (scale-out) [1]. Segmented gas-liquid flows at small Capillary numbers, typically smaller than 0.01, have previously proven effective in enhancing mixing and reducing dispersion during nanoparticle synthesis [2] and can be described by classical low Reynolds number fluid mechanics methods [3].

2. Experimental

The considered microchannel network (a schematic is given in Fig. 1.b) has a rectangular cross-section (400 μ m wide, 380 μ m deep) was formed in silicon by DRIE and thermal oxidation. Anodic bonding against Pyrex provided optical access. Nitrogen and fluorescently labelled ethanol separately enter the chip, pass through 50 μ m wide pressure drop channels before they meet at a trapezoidal mixing section that leads into 40 μ m wide and 500 μ m long constriction, and is subsequently expanded to a 400 μ m wide outflow section with a gas-liquid separator [4] at its end.

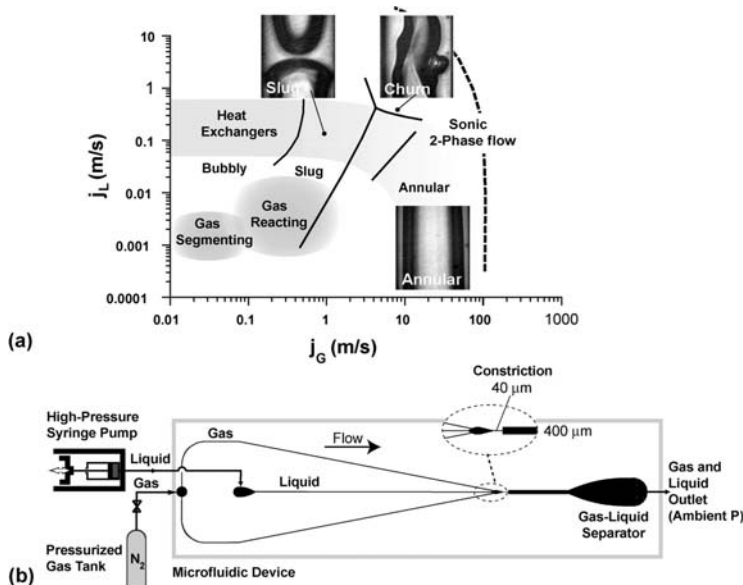


Figure 1. (a) Flow regime diagram for gas-liquid flow through a hydrophilic microchannel network of rectangular cross section ($d_h = 400\mu\text{m}$). Shaded regions show representative conditions for gas-liquid reactions and conditions where gas is used as a segmenting fluid to enhance mixing. (b) Schematic with the experimental setup of a microchannel network with $40\mu\text{m}$ wide and $380\mu\text{m}$ deep flow constriction that was used in the present study.

3. Results and Discussion

Figure 2a compares the magnitudes of gravitational and viscous forces with respect to interfacial ones in the form of the Capillary number and the Bond number, $g \rho d_h^2 / \sigma$. Liquid is delivered with a high-pressure syringe pump (Harvard Apparatus PHD 4400) and gas is directly fed from a pressurized cylinder, without *a priori* controlling the gas flow rate. Provided a sufficiently high pressure, the gas flow rate inevitably adjusts to the sonic two-phase flow limit in the narrow channel section. The resulting superficial gas velocity then only depends on the superficial liquid flow rate and exceeds several tens of meters per second. Note that a further increase of the inlet pressure does not increase throughput. Pulse-laser microscopy (pulse duration: 7ns) provides sharp fluorescence images of the gas-liquid phase distribution (Fig. 2b). Microchannel walls are covered with a thin liquid film that becomes unstable. Interfacial Kelvin-Helmholtz (KH) waves [5] and their disintegration into narrow fluid filaments can be observed. From double-exposure images, we have determined the velocity, U_b , at which fluid filaments travel to be greater than 10 m/s, Fig. 2d gives an example. Studying the dynamics of interfacial waves in channels that are narrower than $100\mu\text{m}$ is particularly attractive since the gas phase then remains laminar up to the sonic flow limit and the desired unstable films are not expected to disintegrate due to the influence of turbulence. According to classical KH theory, relative velocities between gas and liquid of approximately

5 m/s, which are exceeded in our experiments, are required for films to become unstable.

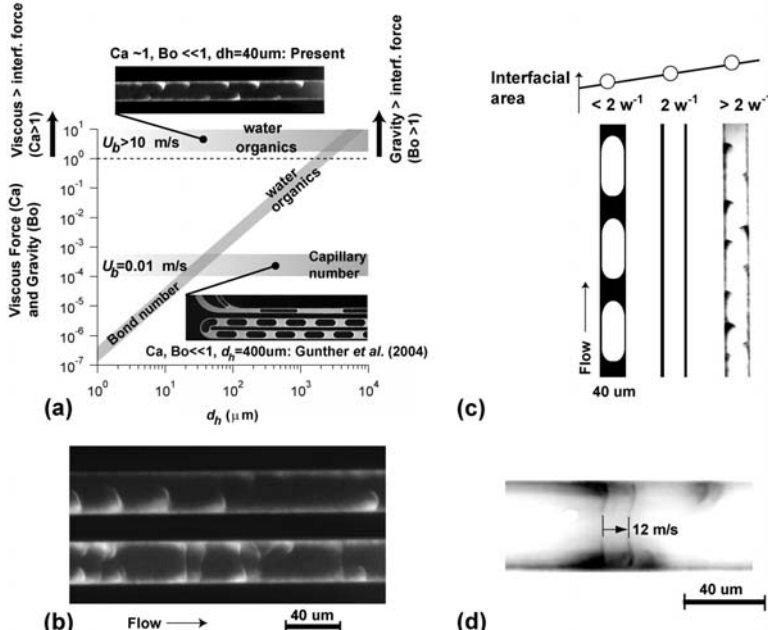


Figure 2. (a) Relative importance of viscous, gravity and interfacial forces as expressed by the Bond and Capillary numbers for a wide range of characteristic flow velocities and channel diameters. (b) Instantaneous images from pulsed-laser fluorescent micrographs. (c) Behavior of gas-liquid interfacial area for segmented flow (left), annular flow (center) and inverted fluorescent image of unstable waves (right) as observed by pulsed-laser fluorescent microscopy in a 40 μm wide and 380 μm deep microchannel near the sonic velocity limit. (d) Filament velocity determined in double-exposure fluorescence micrograph ($\Delta t = 1\mu\text{s}$).

References

1. N. de Mas, A. Günther, T. Kraus, M.A. Schmidt, K.F. Jensen, "Scaled-Out Multilayer Gas-Liquid Microreactor with Integrated Velocimetry Sensors" *Ind. Eng. Chem. Res.*, **44** (24): 8997 - 9013 (2005)
2. B.K.H. Yen, A. Günther, M.A. Schmidt, K.F. Jensen, M.G. Bawendi "A microfabricated gas-liquid segmented flow reactor for high temperature synthesis: the case of CdSe quantum dots," *Ang. Chemie, Int. Ed.*, **44** (34): 5447-5451 (2005)
3. G.I. Taylor "Deposition of a viscous fluid on the wall of a tube"; *J. Fluid Mech.* **10**: 11-5 (1961), F.P. Bretherton "The motion of long bubbles in tubes". *J. Fluid Mech.* **10**: 166-88 (1960)
4. A. Günther, S.A. Khan, M. Thalmann, F. Trachsel, K.F. Jensen "Transport and reaction in microscale segmented gas-liquid flow". *Lab Chip* **4**: 278-86 (2004)
5. S. Chandrasekhar "Hydrodynamic and Hydromagnetic Stability". International Series of Monographs on Physics, Oxford Univ. Press (1961)

ACOUSTIC SEPARATION OF PARTICLES WITH SIMILAR ACOUSTIC PROPERTIES BY MEANS OF MEDIUM DENSITY MANIPULATION

Filip Petersson¹, Lena Åberg² and Thomas Laurell¹

¹Dept. Electrical Measurements, Lund Institute of Technology, Sweden

²Div. Hematology and Transfusion Medicine, Lund University, Sweden

Abstract

Separation of micrometer sized and smaller particles is of fundamental importance in the biological and biomedical sciences. A number of methods are currently available. Acoustic separation, in particular, has got the potential to become a very powerful tool. Typically, one particle type is separated from parts of the suspending medium or two particle types are separated from each other. An approach to extend the applicability of the method through manipulation of the suspending medium is suggested. This offers the possibility to separate particles with similar acoustic properties. Furthermore, a more general acoustic separation method, termed Free Flow Acoustophoresis (FFA), is suggested for parallel and continuous separation, in combination with medium manipulation if desired.

Keywords: separation, ultrasound, radiation force, suspended particles, cells

1. Introduction

Acoustic forces have been used extensively for separation and manipulation of microparticles in various situations [1, 2]. In general, an acoustic standing wave is generated in a cavity filled with suspended particles and the resulting axial PRF (primary radiation force) is utilized to move the particles towards the nodes and/or anti-nodes. However, in separation applications, particles with similar acoustic properties have proven difficult to separate from each other. One possible way out is density and/or compressibility manipulation of the suspending medium, finding the balancing criterion that results in increased differences in the axial PRF.

2. Theory

The acoustic force equation, equation 1 [3], states that the magnitude of the axial PRF, among other things, depends on the density and compressibility of the suspending medium. The relative magnitude of the PRF affecting two particle types can therefore be changed by altering these properties (figure 1). The density can be manipulated by adding a substance, e.g. CsCl, which is used extensively as a density gradient and contrast medium.

$$F_r = -\left(\frac{\pi p_0^2 V_c \beta_w}{2\lambda}\right) \cdot \phi(\beta, \rho) \cdot \sin(2kx) \quad (1)$$

$$\phi = \frac{5\rho_c - 2\rho_w}{2\rho_c + \rho_w} - \frac{\beta_c}{\beta_w} \quad (2)$$

V_c is the volume of the particle, λ is the ultrasonic wavelength, p_0 is the pressure amplitude, x is the distance from a pressure node and ϕ is defined by equation 2. The density of the medium and particles are denoted ρ_w and ρ_c respectively and the corresponding compressibilities β_w and β_c respectively.

Mixtures of several particle types with similar acoustic properties can be separated by combining medium manipulation with FFA (figure 2) [4]. Thus, the fact that dissimilar particles types move at different rates in an acoustic standing wave field is utilized to create a particle gradient in a multi outlet chip, making parallel and continuous fractionation possible.

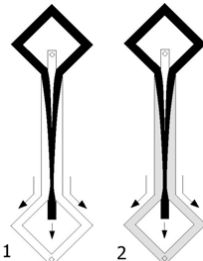


Figure 1: By manipulating the properties of the suspending medium two particle types (grey and black), that normally are affected similarly by the axial PRF (1), can be separated (2). To achieve this, a density increasing substance like CsCl can be added to the medium entering through the centre inlet.

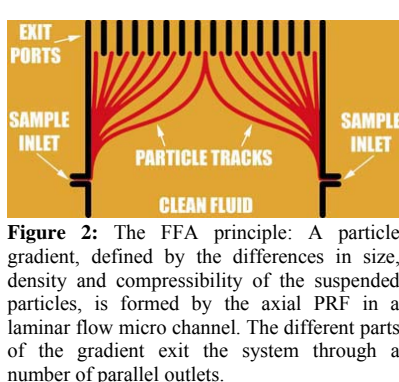


Figure 2: The FFA principle: A particle gradient, defined by the differences in size, density and compressibility of the suspended particles, is formed by the axial PRF in a laminar flow micro channel. The different parts of the gradient exit the system through a number of parallel outlets.

3. Experimental

Using an acoustic particle separation chip with three inlet channels and three outlet channels (figure 1) it was proven possible to separate polystyrene ($\rho = 1.05 \text{ g/cm}^3$) and polymethacrylate particles ($\rho = 1.22 \text{ g/cm}^3$) of equal size ($3 \mu\text{m}$) from each other. A mixture of the two particle types entered the chip through two side inlets (flow rate: $2 \times 0.025 \text{ ml/min}$) while a particle free medium entered through a centre inlet (flow rate: 0.15 ml/min). A half wavelength standing wave was generated between the side walls of the wet etched laminar flow silicon micro channel (width $\sim 370 \mu\text{m}$, depth $\sim 125 \mu\text{m}$) using a piezoelectric ceramic (actuated at 2 MHz). When the suspending medium was distilled water and the same medium entered through the centre inlet both particle types were moved, by the axial PRF, to the pressure node along the middle of the channel without any distinguishable separation. All particles subsequently exited through the centre outlet when the total side outlet flow rate and the centre outlet flow rate were equal (figure 3), i.e. 0.10 ml/min . When CsCl (0.22 g/ml) was added to the medium entering through the centre inlet the situation changed. The denser polymethacrylate particles moved to the centre of the channel, as earlier, while the polystyrene particles only moved slightly towards the channel centre (figure 4). The polystyrene particles were consequently collected in the side outlets while the polymethacrylate particles were collected in the centre outlet. Based on these

findings subsequent work targeted thrombocyte separation from erythrocytes, an important application in the blood banking sector. Thrombocyte separation from blood, using acoustic separation methods, has proven difficult to perform in saline solution (9 mg/ml), since both blood components behaved similarly in an acoustic standing wave field. The described medium manipulation principle was thus successfully utilized to separate erythrocytes and thrombocytes. The centre inlet was perfused by CsCl (0.22g/ml) in saline solution and the blood components, in blood plasma, were supplied via the side inlets.

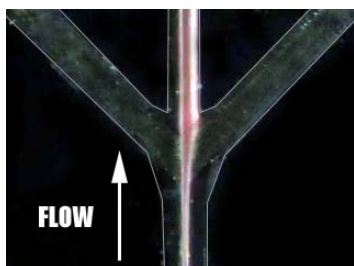


Figure 3: A mixture of 3 μm polystyrene (red) and polymethacrylate (white) particles in distilled water. Both particle types exited through the centre outlet when the standing wave was applied.

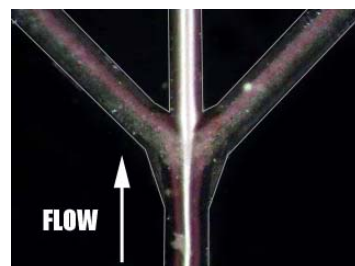


Figure 4: The same situation as in figure 3, with 0.22 g CsCl per ml distilled water in the centre inlet. The polymethacrylate particles exited through the centre outlet while the polystyrene particles exited through the side outlets.

4. Results and discussion

The resulting blood component fractions, collected from the centre and side outlets, showed a vast dominance of erythrocytes in the centre fraction (>96 % of the total number of erythrocytes) and thrombocytes in the side outlet fraction (>92 % of the total number of thrombocytes).

By combining medium manipulation principle with FFA, which is done simply by adding more outlets on the chip, complex separation tasks can be handled. Parallel and continuous separation of four particles types has been shown using an FFA chip with seven outlets. Experimental results have also shown that FFA has great potential in handling biological samples.

5. Conclusions

Medium density manipulation was shown to offer a way to separate particles with similar acoustic properties and is therefore likely to be a powerful tool in extending the applicability of acoustic particle manipulation and separation methods. In combination with FFA it opens a new route in parallel and continuous flow particle separation.

References

- [1] F. Petersson et al., *Anal Chem*, 77(5), pp.1216-1221, (2005).
- [2] M. Nilsson. et al., *Proc. Micro TAS 2005*, pp. 515-517, (2005).
- [3] K. Yoshioka. and Y. Kawashima, *Acustica*, 5, pp. 167-173, (1955).
- [4] F. Petersson and T. Laurell, *Proc. 12th Int. Symp. on FFF 2005*, P1, (2005).

MICROFLUIDIC CENTRIFUGATIONS IN A SPIRAL MICROCHANNEL

Wei Wang, Dongsheng Xu, and Zhihong Li

National Key Laboratory of Micro/ Nano Fabrication Technology, Institute of microelectronic, Peking University, Beijing, 100871, China

E-mail: zhli@ime.pku.edu.cn

Abstract

In this work, an Archimedean spiral microchannel was fabricated by the micromachining technology. When the operating pressure drop was about 0.7MPa, a high centrifugal acceleration up to 2,000g could be achieved in the sample fluid, and this high centrifugation was demonstrated to be able to separate white blood cells from a whole human blood effectively and efficiently.

Keywords: Microfluidic, centrifugation, spiral microchannel

1. Introduction

Integrating centrifugal operations into a single chip was indubitably important to build up a real sense micro-total-analysis-system. Recently, the microfluidic technique was treated as a prospective way to realize some kinds of centrifugal operations in a chip. A micrometer-sized lid-driven re-circulating flow was proposed to generate a radial acceleration up to $10^6 g$ ^[1], and this device was used to control rotations of biological particles of both micro- and nano-meter scale dimensions to investigate the effects of shear stresses on biological and chemical processes^[2]. In this work, an Archimedean spiral microchannel was fabricated by the micromachining technology to realize a microfluidic centrifugation in a single chip.

2. Principle and experimental protocol

As shown in Figure 1(a), when the sample flows through the channel with a high velocity, a centrifugation is developed due to the angular momentum induced by the small curvature of the microchannel. Particles embedded in the fluid thereby suffer the fluid's acts and depart from their original track towards the outer channel wall. In the experiments, indicated in Figure 1(b), a high pressure N₂ gas was used to provide the operational pressure at the inlet, which was recorded by a pressure gauge. Figure 1(c) exhibited the assembled chip, and the fabrication process of the chip was also schematically illustrated in Figure 1(d). Three outlet layouts were adopted as shown in the insert figures with outlet channel widths of 1/2, 1/3, and 1/4 of the main

microchannel one. Centrifuged bloods in the both outlets were numbered by an automated hematology analyzer (KX-21TM, Sysmex Corp., Japan).

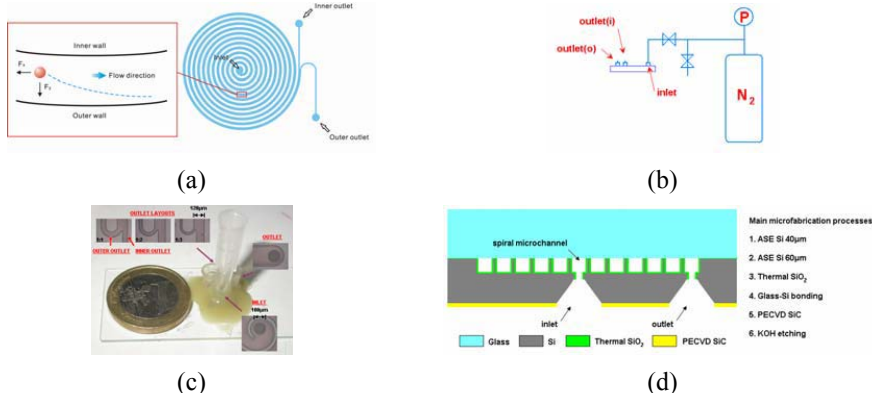


Figure 1 Principle and experimental setup of the proposed microfluidic centrifugation chip. (a) Schematic illustration of the chip and its working principle, (b) experimental setup, (c) photographs of the present chip with a coin for comparison, insert figures were the chip's inlet, outlet, and three outlet layouts, (d) the chip's cross-section structure and the main microfabrication processes.

3. Results and discussion

The numerical results, as shown in Figure 2(a), demonstrated that a high centrifugal acceleration ($a_{C,\max}$) up to 2,000g could be achieved in the present chip with a pressure drop of 0.7MPa. Figure 2(b) and (c) showed the centrifugation-driven displacements of the white blood cell and the red blood cell at the chip's bifurcation point from their original Y-positions when they entered the channel. The distinguishing trace performances of the white blood cell and the red blood cell could be attributed to their diameter difference. Effects of the secondary flow were also investigated and the results, which were exhibited in Figure 2(d), pointed out that there was a very small Dean number and it hardly had any impacts on cells separation in the experiments.

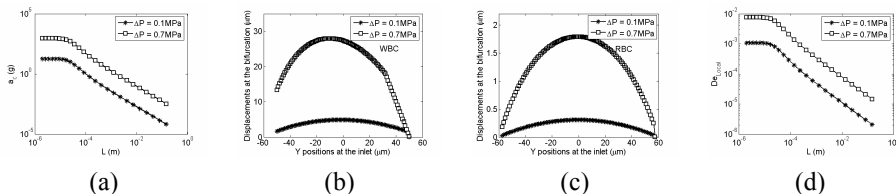


Figure 2 Numerical results of the present chip. a) Variation of centrifugal accelerations along the spiral microchannel with different pressure drops, b) cell traces of white blood cells, c) cell traces of red blood cells, d) variation of local Dean numbers along the channel.

Figure 3 showed the whole human blood cell separation results. It was clear that the

white blood cell which has a larger diameter can be enriched at the outer outlet no matter which the chip's layout was. In the layout I and layout II, the numbers of the white blood cell in the outer outlet were both nearly 6 times than those in the inner reservoirs and changed little with the working pressure drop increasing. When the outer outlet channel was 30 μ m wide, i.e. the layout III, the white blood cell number ratio was smaller than those in the other two layouts due to multifold effects, such as shear-induced particle migration. Separation performances of the red blood cells in the present centrifugal chip were also shown in Figure 3. The results indicated that due to the small diameter of the red blood cell, the present microfluidic centrifugation could not make the cells depart from their original traces notably, which was the same as the numerical prediction.

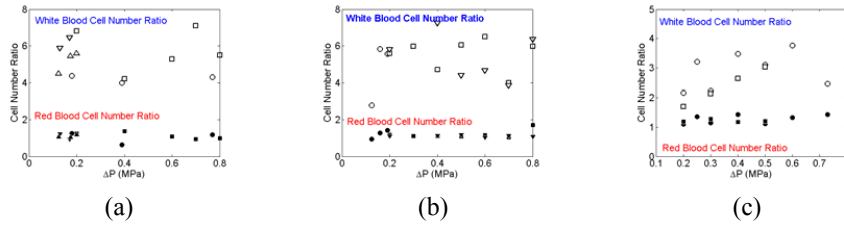


Figure 3 Whole blood cells separation in the present chip. a) Separation results of the 1:1 outlet layout, b) separation results of the 1:2 outlet layout, c) separation results of the 1:3 outlet layout.

4. Conclusions

In this work, an Archimedean spiral microchannel was presented to realize a continuous microfluidic centrifugation-in-chip and was used for the whole blood cell separation. The experimental results demonstrated that the present centrifugal acceleration was high enough to sedimentate the white blood cells to the outer channel wall and thereby to enrich these 20 μ m-diameter cells in the chip, while the red blood cells, which have a small hydraulic diameter, could not be separated by the present continuous microfluidic centrifugation in the chip.

Acknowledgement

The project was financially supported by National Natural Science Foundation of China (Grant No. 60576020 and 90607004). Wei Wang would like to thank the financial support by the China Postdoctoral Science Foundation.

References

- [1] Shelby, J.P.; Lim, D.S.W.; Kuo, J.S.; Chiu, D.T. *Nature*, **2003**, 425(4), 38.
- [2] Shelby, J.P.; Chiu, D.T. *Lab Chip*, **2004**, 4, 168-170.

WATER CONFINED IN EXTENDED-NANO SPACES STUDIED BY NMR SPECTROSCOPY: - A THREE-PHASE MODEL -

**Takehiko Tsukahara^{1,2}, Wataru Mizutani¹, Akihide Hibara¹, and
Takehiko Kitamori^{1,2}**

¹Department of Applied Chemistry, School of Engineering, The University of Tokyo 113-8656, Japan, ²CREST, Japan Science and Technology Agency, Japan. (e-mail: ptsuka@cl.t.u-tokyo.ac.jp)

Abstract

This report describes characterization of molecular motions of water confined in well-defined 10 nm – 100 nm scale channels on a microchip (called extended-nano spaces) based on NMR spectroscopy results. We found that the relaxation rates of water were increased by size-confinement in the range of not only 200 – 800 nm but also 4 - 40 nm, while the rates did not depend on the space sizes of 40 - 200 nm. These results could be expressed quantitatively by a three-phase exchange model suggesting that the water motions in extended-nano spaces are controlled by the fraction of three phases, including the bulk phase (S_B), the proton transfer phase (S_P), and the adsorbed phase (S_a).

keywords; Extended-Nano Space, Water, NMR, Relaxation, Proton transfer

1. Introduction

The study on water in confining geometries has attracted much attention in various fields of chemistry and biology. Many studies have reported that the water in 1 nm nanopore forms the S_a phase (~0.3 nm) with surfaces and the properties are similar to ice. On the other hand, we have expected that an extended-nano space can be an experimental tool for characterizing collective behaviors of liquid-phase water molecules, and investigated novel confinement-induced properties of water molecules by using spectroscopic methods. The time-resolved fluorescent measurements have shown that the water confined in a 330 nm space has higher viscosity and lower dielectric constant compared with bulk water [1]. Moreover, previous NMR studies have clarified that translation and proton mobility of water are modulated by size-confinement from the vicinity of 800 nm. These phenomena suggest that the S_P phase, consisting of loosely coupled water molecules located within about 100 nm from surfaces, exists in extended-nano spaces. [2].

However, limited information is available about how size-confinement affects the properties of water molecules in the size of 800 to 1 nm, and to what extent the water properties in these spaces are different from those in 1 nm nanopores. Therefore, in the present study, we characterize molecular motions of water in 10 nm scale extended-nano spaces by NMR spectroscopy, and develop a simple theoretical model.

2. Experimental

The 40 – 5,000 nm extended-nano spaces were fabricated on a quartz substrate by electron beam lithography and plasma (SF_6 , CHF_3) etching. The fabricated substrate was thermally laminated with a cover one, and then cut with a diamond cutter for using as NMR sample tube. Measurements of ^1H -NMR spectra were carried out with JEOL 500 MHz NMR spectrometer without spinning under nitrogen gas flow.

3. Results and Discussion

We examined the size-dependence of ^1H -NMR spin-lattice relaxation rates ($1/T_1$) of water. As shown in Fig. 1 (a), the $1/T_1$ values changed drastically from about 800 nm and increased with decreasing in sizes up to 200 nm. At below 200 nm, the $1/T_1$ values approached a constant value. When the size was further reduced until 4 nm-sized silica nanomaterial, an increase in $1/T_1$ values was observed again. Therefore, we compared our experimental $1/T_1$ values with theoretical ones based on a three-phase theory stating that the water in confined geometries is composed of three phases: a S_B phase, a S_P phase, and a S_a phase. The water molecules in the 800 – 5,000 nm size are dominated by the S_B phase and the $1/T_1$ values do not depend on the size. Since the S_P phase appears with decreasing sizes at around 800 nm, the $1/T_1$ values begin to change according to the interfacial area ratio of S_P phase to S_B phase. The S_P phase dominates water motions at less than 200 nm size, while the S_a phase with a thickness of 0.3 nm begin to affect water molecules with decreasing in sizes. Thus, the overall relaxation rate ($1/T_{1EXP}$) is expressed as follows as the weighted average of these phases:

$$\frac{1}{T_{1EXP}} = \frac{1}{T_{1B}} + \frac{\lambda A_1}{V_1} \frac{1}{T_{1P}} + \frac{\varepsilon A_2}{V_2} \frac{1}{T_{1a}} \quad (1 = S_P, 2 = S_a) \quad (1)$$

where $1/T_{1B}$, $1/T_{1P}$, $1/T_{1a}$, λ , ε , and A/V are the $1/T_1$ of S_B , $1/T_1$ of S_P , $1/T_1$ of S_a , thickness of S_a , thickness of S_P , and interfacial area ratio, respectively. When the thickness (ε) of S_P was presumed to be 50 nm, the $1/T_1$ values given by Eq. (1) were quite consistent with the measured $1/T_1$ data (See Fig. 1 (b)). On the other hand, the experimentally measured $1/T_1$ values in the size of 4 to 200 nm could be expressed by a two-phase model, which takes into account only the exchange of water between the S_P and the S_a phases as shown in Fig. 1 (c).

4. Conclusion

We examined the $1/T_1$ values of water confined in the space sizes of 4 – 5,000 nm, and clarified that novel confinement-induced nanospatial properties of water molecules appear in extended-nano spaces below 800 nm. In particular, it was found that the S_P phase dominates water molecules at less than 200 nm size. These results suggested that water motions in confining geometries are controlled by the weight averaged of the three S_B , S_P , and S_a phases.

References

1. A.Hibara, et al., *Anal Chem.* 74, 6170, (2002).
2. T. Tsukahara, et al., *submitted* (2006).

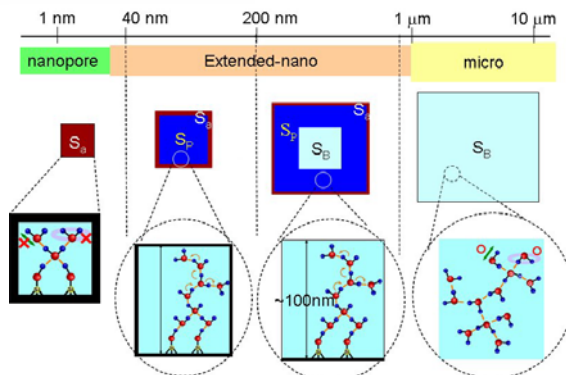
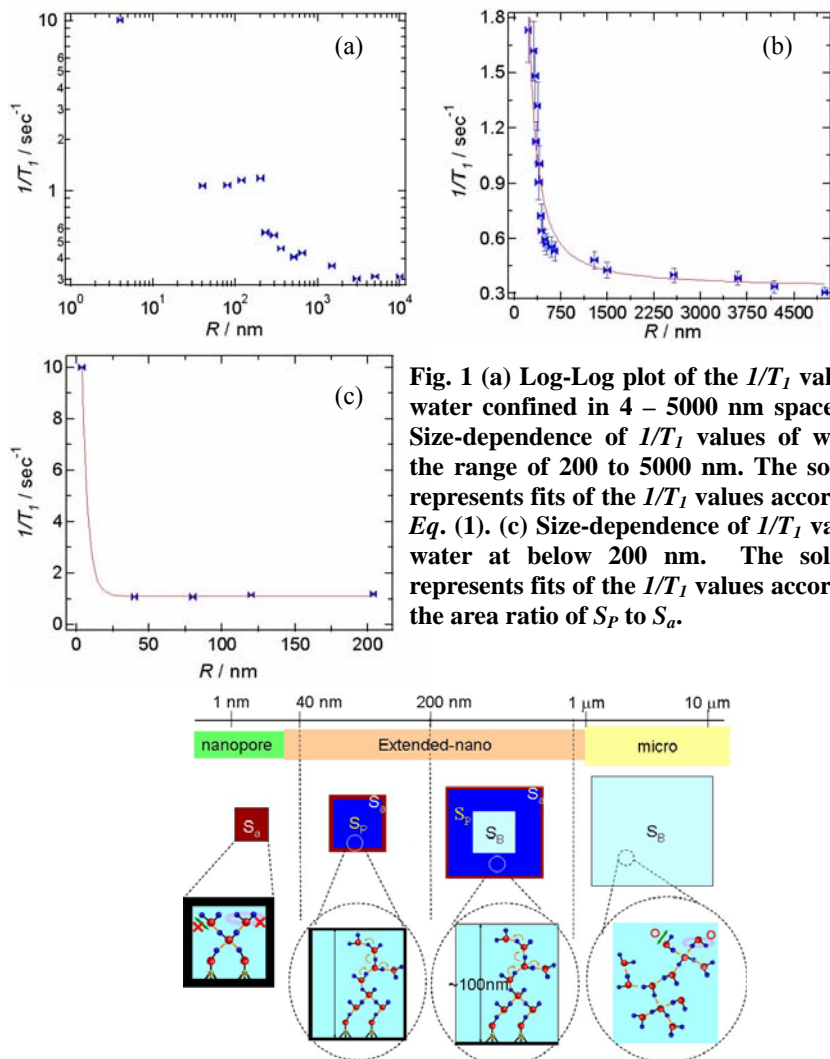


Fig. 2 Concept of three-phase model. In S_B , the water molecules have ordinary liquid structure and free translation and rotation. Slower translation and higher proton mobility is induced by the surfaces with keeping ordinary water structure. In S_a , the water is similar to ice and the translation and rotation are also inhibited.

VOLTAGE-GATED PROTEIN TRANSPORT THROUGH NANOPOROUS MEMBRANES

Anson V. Hatch and Anup K. Singh

Sandia National Laboratories, Livermore, CA, USA

(ahatch@sandia.gov, aksingh@sandia.gov)

Abstract

We report a novel means of fractionating proteins based on their voltage-dependent electromigration through nanopores of a polymer membrane. The nanoporous membranes were fabricated *in situ* in channels of a microchip using photopolymerization. The pores (1-10 nm) are small enough that proteins are excluded from passage with low applied electric fields, but increasing the field enables proteins to pass through. The magnitude of field required for a change in exclusion behavior is protein-specific with a correlation to protein size. Passage of proteins through the pores at higher field strengths could be attributed to partial unfolding or deformation of proteins due to the driving force of the applied field. The field-dependent exclusion mechanism could be useful as a multifaceted fractionation tool with single membranes or a network of membranes. Another exciting possibility is characterizing protein conformation, folding and stability based on field-dependent transport through nanopores.

Keywords: Nanopore, membrane, size exclusion, protein translocation

1. Introduction

Differentiating piecewise transport of biomolecules such as DNA and proteins through nanopores is promising for characterizing, counting, and sequencing biomolecules [1]. Nanoporous size exclusion membranes fabricated in microfluidic channels have also proven useful for concentrating proteins $\sim >10$ kDa in size over 1,000-fold to improve on-chip assay sensitivities [2]. We found that the applied field strength is a critical parameter determining protein exclusion. Protein exclusion was thus characterized for a range of electric field strengths and protein sizes.

2. Experimental

Narrow (~ 15 μm) cross-linked polyacrylamide (22% T, 6% C) membranes were fabricated *in situ* by laser photopolymerization within the etched channels of glass microchips (30 μm etch depth, 80 μm width, Caliper Life Sciences) (Figure 1) [2]. Polyacrylamide sieving gels (8% T 2.6% C) were also photopolymerized in separation channels immediately adjacent to the membranes so that fractions of excluded proteins could be analyzed by gel electrophoresis and LIF detection [2]. Fluorescent protein samples (10 nM) were concentrated at the membrane for different times depending on the applied field (longer times for lower applied fields) such that the time-voltage product was constant. Protein transport was also characterized by confocal imaging.

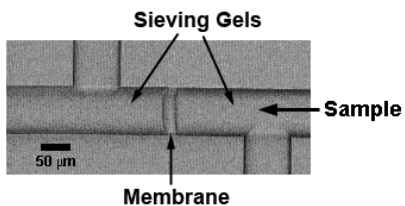


Figure 1. Micrograph of a photopolymerized nanoporous membrane in a glass microchannel.

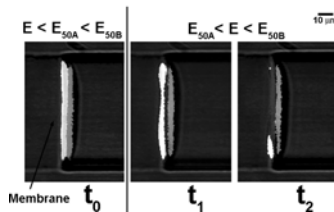


Figure 2. Labeled ovalbumin and IgG are excluded at low $E(t_0)$ but at higher $E(t_1, t_2)$, ovalbumin passed through the membrane while IgG remained excluded.

3. Results and discussion

At low field strength (E), proteins >10 kDa are excluded quite effectively and accumulated at the edge of the membrane as shown in Figure 2A. By increasing E , a threshold was reached where proteins were no longer excluded from the pores and began to migrate through. The exclusion threshold was unique for most proteins studied meaning that protein exclusion can be regulated over a wide size-range of proteins by simply adjusting the voltage. Figure 2 shows ovalbumin and IgG both excluded at low E (t_0 , 15 V/cm), but at higher E (50 V/cm) only IgG was excluded (t_1 , t_2) while ovalbumin passed through the membrane pores.

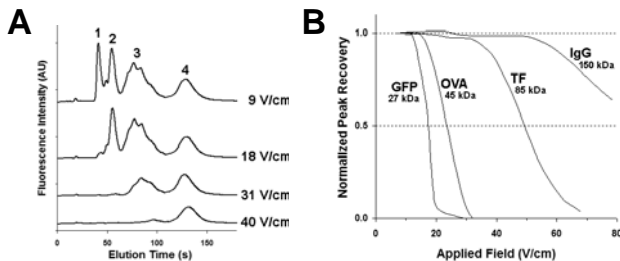


Figure 3. Protein exclusion quantified by PAGE separation analysis. A) Electropherograms of excluded proteins. At low E (9 V/cm), all 4 proteins were excluded. Proteins were stepwise removed from the mixture due to field-dependence of exclusion. B) Protein exclusion as a function of E for different size proteins (green fluorescent protein, ovalbumin, transferrin, and IgG antibody).

The relatively sharp and distinct field thresholds for proteins ranging from 27 - 240 kDa were exploited to piecewise remove proteins from a mixture by adjusting E (Figure 3). At low E across the membrane ($E=11$ V/cm), all 4 proteins in a mixture were excluded from the pores and then readily separated by integrated PAGE analysis. At different field strengths, it was possible to trap only 1, 2, or 3 of the 4 proteins while the other(s) passed through the membrane pores. The field-threshold of exclusion correlated with protein size.

Integrating a system of membranes gives additional flexibility for continuous fractionating and preconcentration of proteins in a dense network. This was

demonstrated with the simple case of 2 membranes (Figure 4). With E above the threshold for GFP at the first membrane, and E below threshold at the second membrane, GFP passed through the first membrane and was trapped at the second. The GFP was confirmed to be unaffected by passage through the membrane according to integrated PAGE analysis. This demonstrates the ease to which integrated analysis features could be coupled with each membrane in a network.

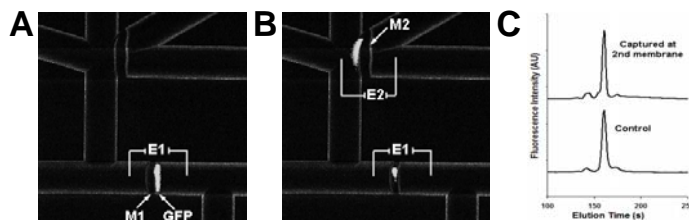


Figure 4. Field selective membrane network. A) GFP is excluded at the 1st membrane (M1) with $E_1 < E_{50}$. B) With $E_1 > E_{50}$, GFP passes through M1, but at M2 where $E_2 < E_{50}$, GFP is trapped. C) Integrated PAGE analysis shows no residual effects for GFP after passing through the pores.

4. Conclusions

A novel voltage-dependent exclusion of proteins by nanopores is demonstrated. This behavior was demonstrated for a number of proteins and a correlation was found between the voltage-threshold for exclusion and the protein MW. We postulate that voltage-dependent change in electromigration is a result of partial denaturation of proteins. The ability to selectively gate proteins at membranes is a promising means for manipulating and characterizing proteins. Applications include step-wise voltage-tunable fractionation of a complex protein mixture in a simple chip with just one membrane (no sieving gel or packed bed required).

Acknowledgements

This work was supported by the NIDCR (U01DE014961) and Sandia LDRD program.

References

1. D. Folgea, M. Gershaw, B. Ledden, D.S. McNabb, J.A. Golovchenko, and J.L. Li, "Detecting single stranded DNA with a solid state nanopore," *Nano Letters*, vol. 5, pp. 1905-1909, 2005.
2. A.V. Hatch, A.E. Herr, D.J. Throckmorton, J.S. Brennan, and A.K. Singh, "Integrated preconcentration SDS-PAGE of proteins in microchips using photopatterned cross-linked polyacrylamide gels," *Analytical Chemistry*, vol. 78, pp. 4976-4984, 2006.

Sandia is a multiprogram laboratory operated by Sandia Corporation, a Lockheed Martin Company, for the United States Department of Energy under contract DE-AC04-94AL85000.

NANOMECHANICAL PROTEIN PRESENCE AND CONCENTRATION DETECTORS BASED ON THE MECHANICAL STIFFNESS OF PROTEINS IN SQUEEZED NANO-GAPS

Won Chul Lee^{1,2}, Young-Ho Cho¹, and Albert P. Pisano²

¹Digital Nanolocomotion Center, KAIST, Republic of Korea

²Berkeley Sensor and Actuator Center, UC-Berkeley, USA

Abstract

We present a new class of the protein presence and concentration detector based on the mechanical stiffness measurement of protein-receptor layers in a squeezed nano-gap. It is experimentally verified that the present protein detector measures not only the protein presence and size at the reduced measurement uncertainty of $\pm 1.1\text{nm}$ but also the protein concentration at the sensitivity of 2.88N/mN .

Keywords: protein concentration detector, nano-gap actuator, protein stiffness, nanomechanical biodetector

1. Introduction

Previously, we presented the protein *presence and size* detector(Fig.1a) [1] based on the squeezed displacement measurement of $x_2(t)$ in Fig.2a. Both devices(Figs.1a and 1b) use the nanomechanical detection principle, where the actuator squeezes the protein-receptor layers in the nano-gap through a mechanical spring(k_s). This nanomechanical principle offers simple, inexpensive, and high-precision protein detection[1] compared to other principles[2,3]. The previous device[1], however, was unable to measure the protein *concentration* due to a couple of problems: 1) the distortion in the time-dependent squeezed displacement($x_2(t)$ in Fig.2a) that should be corrected by the time-dependent actuated displacement of $x_1(t)$; 2) the displacement measurement uncertainty of $\pm 7.4\text{nm}$ [1] caused by signal drift and noise.

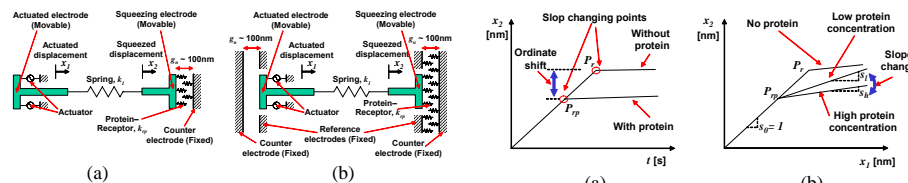


Fig.1 Comparison of the nanomechanical protein detectors: (a) the previous protein presence detector [1]; (b) the present protein presence and concentration detector, measuring the actuated and squeezed displacements using compensated displacement monitoring electrodes.

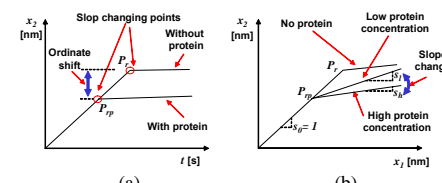


Fig.2 Working principle of the nanomechanical protein detectors: (a) the previous protein presence detection [1] using the relationship between the actuation time, t , and the squeezed displacement, x_2 ; (b) the present protein concentration detection using the relationship between the actuated and squeezed displacements, x_1 and x_2 .

In this work, we succeed to measure the protein concentration by solving the above-mentioned problems as follows: 1) We add an actuated nano-gap(Fig.1b) to measure $x_1(t)$ in addition to $x_2(t)$. We synchronize $x_1(t)$ and $x_2(t)$ to obtain the directed correlation(Fig.2b) between x_1 and x_2 , thus eliminating the distortion included in $x_1(t)$ and $x_2(t)$; 2) We use reference electrodes(Fig.2b) in both actuated and squeezed nano-gaps to compensate the signal drift and noise, thus reducing the displacement measurement uncertainty from $\pm 7.4\text{nm}$ to $\pm 1.1\text{nm}$. We also experimentally verify the selectivity, repeatability, and sensitivity of the nanomechanical protein detectors.

2. Working Principle

Figure 2b illustrates the protein detection principle, where the mechanical stiffness of protein-receptor layers is measured from x_1 - x_2 relationship. The squeezed receptor-protein layers provide added stiffness(k_{rp} in Fig.1) to the mechanical spring(k_s). The added stiffness changes the modulation line slope on x_1 - x_2 plane(Fig.2b). We measure the protein concentration from the modulation line slope(Fig.2b), while detecting the protein presence and size from the ordinate shift(Fig.2a).

3. Experiments and Results

We design(Fig.3) and fabricate the present detector(Fig.4). In experimental study, we characterize 1) the distortion in the time-dependent squeezed displacement, 2) the displacement measurement uncertainty, 3) the selectivity, 4) the repeatability, and 5) the sensitivity of the protein detectors. 1) The distortion, expressed by the t - x_2 nonlinearity(3.0%), is eliminated by the time-dependent actuated displacement of $x_1(t)$. 2) The displacement measurement uncertainty is reduced to $\pm 1.1\text{nm}$ (Fig.5) due to the compensated displacement monitoring electrodes. 3) The protein detection selectivity is verified by Fig.5a: The detector generates the size detection signal($12.1 \pm 2.3\text{nm}$) for receptor-active protein and the null detection signal for receptor-inactive protein. 4) The detection repeatability is demonstrated by Fig.5b: The detector measures the protein size($13.2 \pm 3.3\text{nm}$) for added protein. After the protein removal, the size detection signal returns to the initial state(null signal) indicating no protein. 5) We verify the sensitivity, where the slopes are obtained from the modulation lines(Fig.6a). For the protein concentration of $5\text{--}10\text{nM}$ (Fig.6b), the stiffness($n k_{rp}$) is measured in the range of $9.6\text{--}24.1\text{N/m}$ at the sensitivity of 2.88N/m/nM .

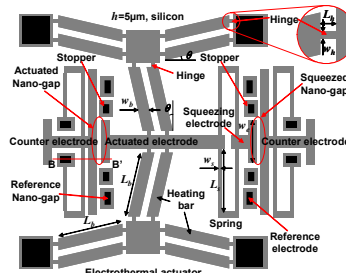


Fig.3 Top view of the protein presence and concentration detectors.

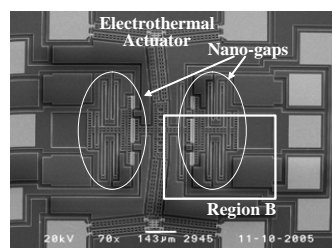


Fig.4 SEM photographs of the present protein detector.

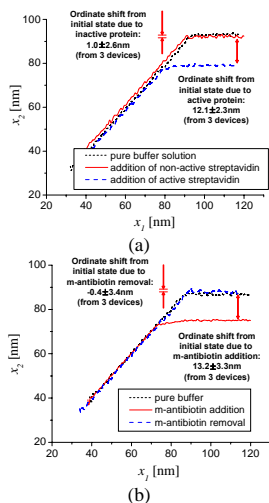


Fig.5 Experimental squeezed displacement, x_2 , for the actuated displacement, x_1 : (a) in the selectivity verification using receptor-active and receptor-inactive streptavidin; (b) in the repeatability verification using m-antibiotin.

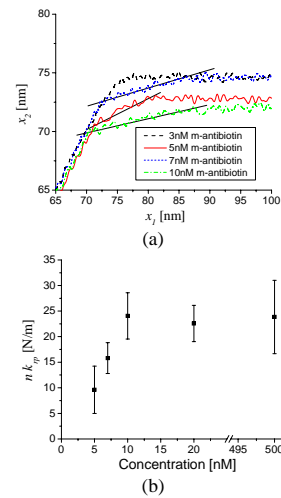


Fig.6 Protein concentration detection: (a) experimental squeezed displacement, x_2 , for the actuated displacement, x_1 ; (b) experimental stiffness of receptor-protein layers, $n k_{rp}$.

4. Conclusions

We presented, fabricated, and characterized a new class of the protein presence and concentration detector based on the mechanical stiffness measurement of protein-receptor layers in a squeezed nano-gap. It was experimentally verified that the present protein detector measures the size of the proteins, streptaavidin and m-antibiotin, as 12.1 ± 2.3 nm and 13.2 ± 3.3 nm at the measurement uncertainty of ± 1.1 nm, respectively, while showing the concentration detection sensitivity of 2.88N/m/nM in the m-antibiotin concentration range of $5\sim 10\text{nM}$.

Acknowledgements

This work has been supported by the National Creative Research Initiative Program of the Ministry of Science and Technology (MOST) and the Korea Science and Engineering Foundation (KOSEF) under the project title of “Realization of Bio-Inspired Digital Nanoactuators.”

References

1. W.C. Lee and Y.-H. Cho, *Nanomechanical protein detectors using electrothermal nano-gap actuators*, Proc. MEMS 2004, pp.629-632, (2004).
2. R Bashir, *BioMEMS: state-of-the-art in detection, opportunities and prospects*, Advanced Drug Delivery Reviews, www.sciencedirect.com, (2004).
3. J. Zhang, et al., *Vapor and liquid mass sensing by micromachined acoustic resonator*, Proc. MEMS 2003, pp.470-473, (2003).

INDUSTRIAL PRODUCTION BY MICRO CHEMICAL PLANTS

Shinji Hasebe

Dept. of Chem. Eng., Kyoto University, Nishikyo-ku, Kyoto 615-8510 Japan

Abstract

A project on micro-chemical process technology was executed during 2002 and 2006 under the supervision of the New Energy and Industrial Technology Development Organization, NEDO in Japan. The results of the project are introduced focusing on the industrial production by micro chemical plants.

Keywords: Micro reactor, Industrial production, Pilot plant

1. Introduction

To accelerate the development of micro chemical plant and microchip technologies, the Ministry of Economy, Trade and Industry, METI, in Japanese Government planned a national project named "High Efficiency Micro-Chemical Process Technology." In 2002, this project was started under the supervision of NEDO. In 2003, the project name was changed to "Production, Analysis and Measurement System for Micro-Chemical Process Technologies," and the project was successfully finished in March 2006. The project was managed by the Research Association of Micro Chemical Technology, MCPT, which was organized by 30 chemical and instrumental companies. The project consisted of three groups as shown in Fig. 1. In this manuscript, the results of the project are explained focusing on those of Group 1.

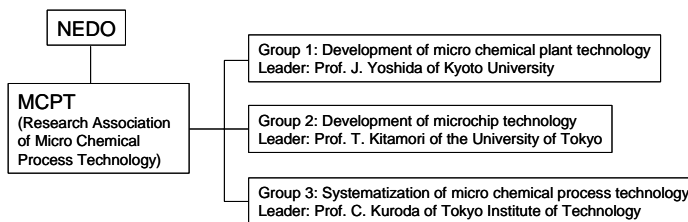


Figure 1 Structure of the Micro-Chemical Process Technology Project

2. Development of micro chemical plant technology

The major research themes of Group 1 in Fig. 1 are i) development of various types of micro reactors, micro mixers, micro energy transfer devices, and micro separators, ii) a study on the fundamental characteristics of micro systems, iii) a study on the design and operation methods of micro systems, and iv) synthesis of functional materials by micro systems and verification of the efficiency of the micro systems through the continuous operation of pilot plants. In this section, some results obtained in themes i) and iii) are explained.

a) Assembled type multi-stage micro reactor for catalytic reaction

The catalysts are deactivated during operation. Thus, how to regenerate the activity of the catalysts is the key problem to use catalytic reactor for real production. In the developed assembled type multi-stage micro reactors, a micro space of 100 – 1400 μm in depth is created by placing the membrane catalyst element and thermostable gasket alternately. In this structure, deactivated catalyst elements are easily replaced by reassembling the device. The developed micro reactor was used for hydrogen production [1].

b) Optimal shape design of the micro devices

The performance of the micro devices depends on the shape of the micro channel as well as the size of the devices. A shape design method based on simplified thermo-fluid models was proposed, and was applied to the design problem of a plate-fin micro reactor under constraints related to temperature and residence time distributions, pressure drop, and production specifications. Figure 3 shows an obtained reactor shape, and the numbering up structure satisfying the constraint on flow uniformity [2].

c) Control of the numbering-up plant

The residence time of each of the parallel micro devices should be constant to ensure the predetermined performance. By simulation and experimental works, it becomes clear that the pressure drop control structure shown in Fig. 4 is effective in making flow distribution uniform even if blockage occurs at one of the parallel devices [3].

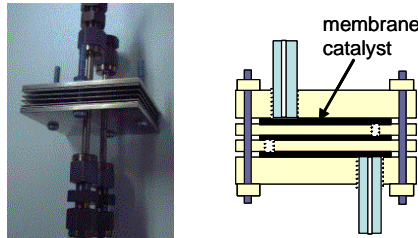


Figure 2 Membrane catalytic reactor

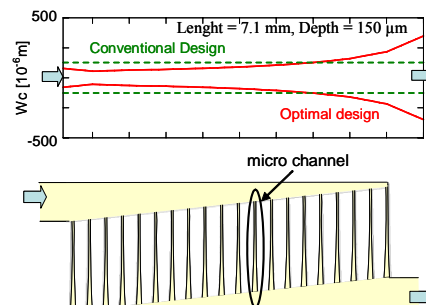


Figure 3 Optimization of plate-fin micromixer

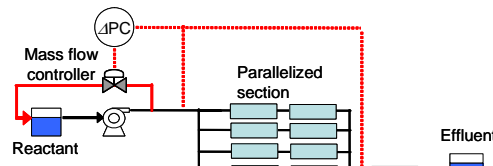


Figure 4 Pressure drop control structure

3. Pilot plants developed in the project

In the project, nine micro pilot plants were constructed and the efficiencies of the micro systems were verified.

1) Halogen-Lithium Exchange Process: Halogen-lithium exchange reactions of aryl bromides with n-butyllithium followed by trapping with an electrophile were achieved under non-cryogenic condition (0 °C). The pilot plant shown in Fig. 5 can produce 0.5 kg of desired product in 6 hours of continuous operation. .

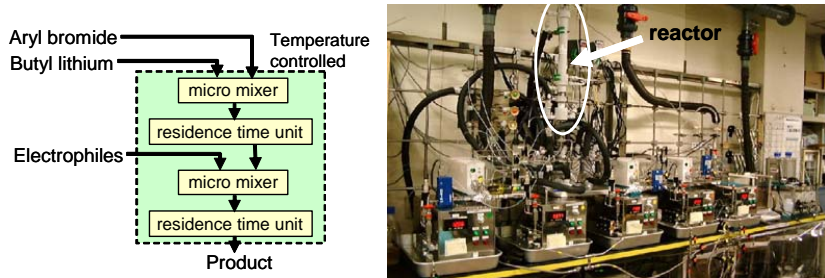


Figure 5 Process structure of Halogen-Lithium Exchange reaction (left) and pilot plant (right)

- 2) Grinard Exchange Process: A reaction of ethylmagnesium bromide with bromopentafluorobenzene was carried out at a plant consisting of a micro mixer and a shell & tube micro heat exchanger. The yield of Pentafluorobenzene was 97 % in short residence time (5 sec). 15kg of the product was obtained in 24 hours.
- 3) Swern Oxidation Process: Swern oxidation can be accomplished at temperatures of -20 °C to 20 °C, which is much higher than those for conventional macro batch reactors. Multilamination type micromixers are used for precise temperature control [4].
- 4) Radical Polymerization Process: A shell & tube micro reactor system consisting of five successive shells was developed for free radical polymerization. The polydispersity index of the product, butyl acrylate, was much smaller than that by a conventional batch reactor [5].

In addition to the above plants, the following micro plants were constructed: *Selective Oxidation with Hydrogen Peroxide*, *Polycondensation Process*, *Ultra-fine Particle Generation Process*, *Organic Particle Production Process*, *Selective Condensation Reaction Process*.

4. Conclusion

Through the Micro-Chemical Process Technology Project, it becomes clear that micro chemical plants have possibilities to be used for real production. The development of 9 pilot plants verifies that the period from the laboratory to the production plant can be shortened compared with conventional plants.

Reference

1. T. Maki, T. Ueyama and K. Mae, *Chem. Eng. Technol.*, **28**, pp. 494–500, (2005).
2. O. Tonomura, *et al.*, *Optimal Shape Design and Operation of Parallel Microreaction Channels*, CD-ROM of the 7th World Cong. of Chem. Eng., 10-14 July, Glasgow, Scotland, (2005).
3. T. Tominari *et al.*, *Operation Policy and Blockage Diagnosis for Micro Chemical Plants with Internal/External Numbering-up*, Preprint of IMRET 9, Setp. 6-8, Potsdam, Germany, (2006).
4. T. Kawaguchi *et al.*, *Angew. Chem. Int. Ed.*, **44**, pp. 2413-2416, (2005).
5. T. Iwasaki and J. Yoshida, *Macromolecules*, **38**, pp. 1159-1163 (2005).

CUSTOMIZED TRAPPING & ASSEMBLY OF MAGNETIC CARRIERS IN SINGLE & MULTIPLE POTENTIAL WELLS

Qasem Ramadan¹, **Daniel P. Poenar**², **Victor Samper**¹ and **Chen Yu**¹

¹Bioelectronics & BioMEMS Program, Institute of Microelectronics, 11 Science Park Road, Singapore 117685, ²Nanyang Technological University, Microelectronics Centre, EEE School, Singapore 639798

EMAIL: qasemr@ime.a-star.edu.sg

Abstract

This paper presents an efficient technique for trapping and assembly of micro-magnetic particles in confined spatial locations using customized designs of micro-coils (MCs). High magnetic field strengths and field gradients were achieved using MCs with several planar geometrical configurations of micro-wires of increased thickness and reduced width. Magnetic particles have been trapped and confined in single and an array of deep magnetic potential well corresponding to the MCs configuration.

Keywords: Magnetic Carriers, micro-coils, trapping

1. Introduction

Micro-scale magnetic separation has been demonstrated in several previous studies [1-2]. However, these devices do not allow confined or controlled trapping of the magnetic particles. In this paper we present the results of magnetic particles trapping and assembly at localized spatial locations with very steep magnetic potential wells generated by various designs of MCs having conductors with a 3:1 aspect ratio. These designs allow controlling the magnetic traps distribution and potential and the particles motion in their suspension. Fig. 1 shows a schematic drawing of the device with its major parts.

2. Simulation

The simulated magnetic flux density profiles of different MCs are presented in Fig.2. The looping profile was purposely varied in order to detect the effect of MC geometry on the generated magnetic flux and the particle assembly profile. When a ferromagnetic core is inserted within a MC (Fig. 2d), it offers a low reluctance path for the magnetic flux lines and therefore results in focusing the magnetic energy in a single deep potential well.

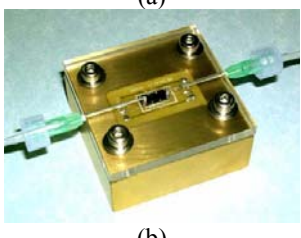
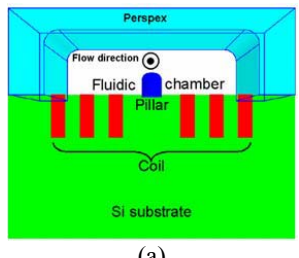
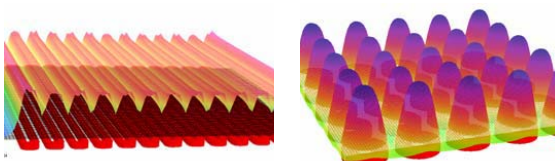
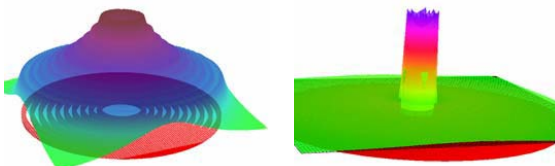


Figure 1: (a) Schematic cross-sectional drawing of the device with its major parts; (b) Final fluidic block with chip inserted in.



(a) Meander Shaped MC without magnetic pillars, $B_{\max} = 3.35$ mT
 (b) Current loop array without magnetic pillars, $B_{\max} = 4.3$ mT



(c) Spiral micro-coil without magnetic pillar ($B_{\max} = 25.5$ mT)
 (d) Spiral micro-coil with magnetic pillar, $B_{\max} = 0.105$ T

Figure 2: Magnetic flux density distributions at 1 μ m above the surface of different MCs. The conductor cross-sectional area is 10^{-10} m^2 with a current density of $J=10^9$ A/m^2 .

3. Experimental

The fabrication processes used to realize the devices presented in this study are described in detail in our previous publication [3]. Experiments to test the capability of the magnetic devices to trap magnetic beads were conducted using superparamagnetic particles (Estapor^R) with diameters ranging from 0.8 to 5 μ m. The sample was introduced into the chip by using a custom-built microfluidic connector block, syringe pump, and silicone tubing. Particle tracking was performed using an optical microscope with a CCD camera.

4. Results and Discussion

Each different device shows a different trapping profile and behaviour due to its particular structure. Fig.3 shows the particles distribution profile before and after injecting an electric current of 100 mA in different MCs. The particles align along a single wire (Fig.3a) or are periodically trapped along a meander shaped-MC (Fig.3b). The particles also concentrated within a single current loop (Fig.3c), an array of loops (Fig.3d), or at the centre of a spiral MC (Fig.3e & f). The spiral MC shows the highest field confinement in its central zone and, therefore, particles concentrate at a singular central point.

The number of trapped particles was counted by dividing the area of the MC into several divisions. For the meander MC similar numbers of particles were found in every

division (each division contains 2 conductors) over the whole surface of this device (Fig.4a). On the other hand, the concentration of trapped particles rapidly increases towards the centre of the spiral MC (Fig.4b). The magnetic particles confinement was more clearly observed for the spiral MC with a magnetic core where the beads rapidly accelerate towards the core and are trapped there.

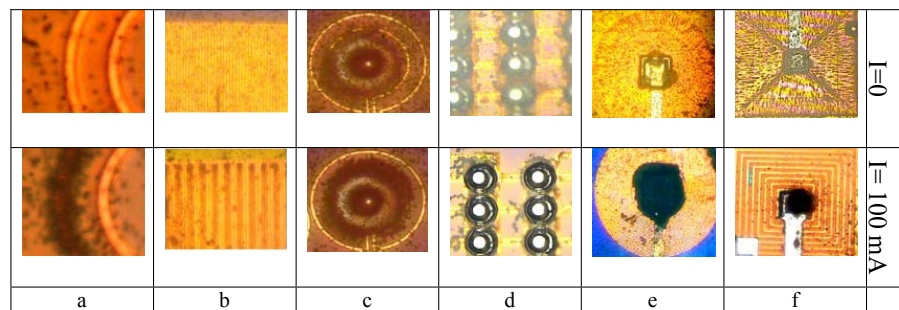


Figure 3: Trapping profiles of magnetic particles obtained by different MCs.

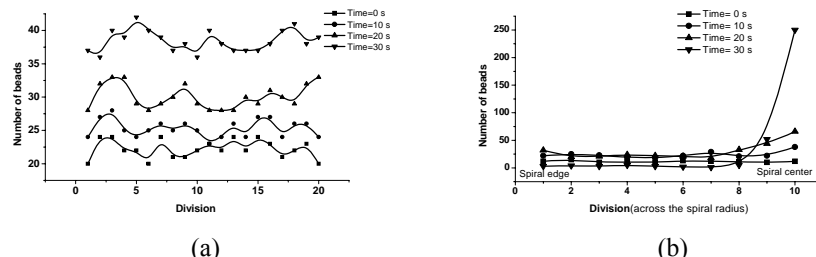


Figure 4: Trapping profile obtained from counting the magnetic particles within several divisions of a meander shaped MC (a) and spiral shaped MC (b) at different time intervals.

5. Conclusions

In Summary, our micro-fabricated coils efficiently maximize, concentrate, and selectively pattern micro-magnetic particles for an efficient magnetic immunoassay on a chip.

References:

1. H. Lee, A. M. Purdon, and R. M. Westervelt, Manipulation of biological cells using a microelectromagnet matrix, *Appl. Phys Lett.*, 85, 1063 (2004).
2. T. Deng, M. Prentiss, and G. M. Whitesides, Fabrication of magnetic microfiltration systems using soft lithography, *Appl. Phys. Lett.*, 80, 461 (2002).
3. Q. Ramadan, V. Samper, D. Poenaru and C. Yu, Fabrication of three-dimensional magnetic micro-devices with embedded micro-coils for magnetic potential concentration”, *J. Microelectromechanical Systems*, 15 (3) 624-638, (2006).

NATURE-INSPIRED MICRO-FLUIDIC MANIPULATION USING ARTIFICIAL CILIA

Jaap M.J. den Toonder, Dirk J. Broer, Murray Gillies, Judith de Goede,
Titie Mol, Wim Talen, Hans Wilderbeek

Philips Research Laboratories, 5656 AA Eindhoven, The Netherlands
(jaap.den.toonder@philips.com)

Abstract

We have developed polymer-based micro-actuators that can be set in motion electrostatically. When integrated in a micro-fluidic channel, the effect of the moving actuators resembles that of so-called "cilia" (beating microscopic hairs) that occur in nature and which are used for example in micro-organism propulsion. We have shown experimentally that, indeed, our artificial cilia can induce significant flow velocities of at least 75 $\mu\text{m/s}$ in a fluid with a viscosity of 10 mPas.

Keywords: **artificial cilia, polymer micro-actuators, electrostatics, micro-fluidics**

1. Introduction

Biochemical analyses of body fluids such as saliva, urine and blood give important information about health and disease. An important trend in this field is the transition of centralized lab analysis to cartridge-based near-patient testing using biosensors. An important aspect for a biosensor device are the micro-fluidics modalities that must take care of transportation, mixing and routing of the fluids within a micro-fluidic channel system. Typical sizes of the micro-fluid channel widths and heights range from several micrometers to several hundreds of micrometers. In this paper we show a novel method of active micro-fluidic manipulation, which is inspired by nature.

One particular micro-fluidics manipulation mechanism "designed" by nature is that due to a covering of beating cilia over the external surface of micro-organisms (e.g. Paramecium, Pleurobrachia, and Opaline), as shown in figure 1. A cilium can be viewed as a small hair or flexible rod (in protozoa: typical length 10 μm and diameter 0.1 μm) which is attached to the surface. The movement of individual cilia is asymmetric in nature, see figure 1, and allows effective transport of the organism. Apart from the propulsion of micro-organisms, other functions of cilia are in cleansing of gills, feeding, excretion, and filtering.

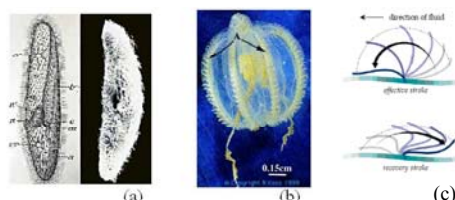


Figure 1: Two micro-organisms that make use of propulsion by cilia: (a) Paramecium, (b) Pleurobrachia; (c) motion of an individual cilium.

2. Artificial cilia

We have developed polymer composite micro-actuators which respond to an applied electrical by changing their shape. The typical structure of the actuators is that of a curled micro-beam, as shown in figure 2. On the glass substrate, an indium-tin-oxide (ITO) layer, covered by a dielectric layer, is present. The curled micro-beam itself consists of two layers, namely an acrylate film of 1 μm thickness, and a chromium film of about 10 nm thick. The processing conditions and the thermo-mechanical properties of these two layers determine the radius of curvature of the micro-beam. By applying a voltage difference between the ITO electrode and the chromium film, the micro-beam is attracted towards the surface and rolls out. After switching off the voltage, the micro-beam returns to its original shape by elastic recovery.

The actuators are fabricated using standard micro-technology, including a sacrificial layer etching step to partially release the actuators from the substrate and obtain the curled geometry. Working demonstrators have been made of surfaces containing arrays of the actuating elements with various sizes. Figure 2 shows fabricated micro-actuators with a length of 100 μm a width of 20 μm . The shape and movement of the micro-actuators resembles that of cilia, and therefore we call them artificial cilia.

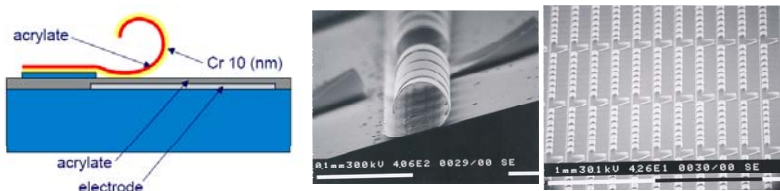


Figure 2: Electrostatically actuated polymer composite structures; left: schematic cross section of one actuator. Right: SEM pictures of actual micro-structures.

3. Experimental

To assess the ability of the artificial cilia to manipulate fluids, we have carried out basic flow visualization experiments. A thin layer of silicon oil, with a viscosity of 10 mPas, was deposited on the substrate containing the micro-actuators. The thickness of this film was about 1000 μm , so that the micro-actuators were completely immersed in the liquid. For visualization purposes, a low concentration of titanium particles (estimated size approximately 1 μm) had been dispersed in the silicone oil.

During the experiments, the electrical potential of the chromium film was kept at zero, whereas a block voltage between 80 and 0 V and with a frequency of 1 Hz was applied to the ITO electrode. The movement of the titanium oxide particles was observed using a light microscope and a high-speed camera, connected to image processing software used to produce movies of the recorded particle movement.

4. Results

Figure 3 depicts ten top-view snapshots from a movie of one actuation cycle of three by two microbeams, i.e. the total recording time is 1 second. The cross-sectional

shape of the microbeams at the times of the snapshots is also sketched. The beams are down in snapshot (d) and they are completely up in snapshot (i). The micro-actuators, in this case, have a length of 150 μm , a width of 20 μm , and are electrostatically actuated with a frequency of 1 Hz. The figure shows that fluid flow is indeed induced by the artificial cilia. Two titanium dioxide particles, indicated in the circles, are traced. From the visualized movement of these particles, it can be seen that the approximate velocity caused by the cilia movement, is 75 $\mu\text{m/s}$, which is significant even though the shape change and the actuation frequency of the artificial cilia is not optimized.

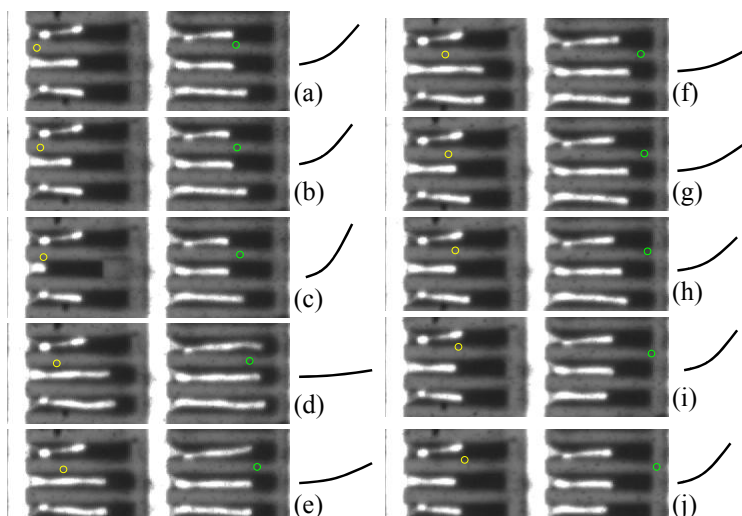


Figure 3: Visualization of flow induced by actuated microbeams (artificial cilia): snapshots from a movie showing a top view of 3 x 2 beams, length 150 μm , width 20 μm , actuated in silicone oil ($\eta = 10 \text{ mPa s}$) containing titanium oxide particles. One actuation cycle is shown (the beams are down in (d)), and the corresponding approximate cross-sectional shapes of the microbeams are sketched. Two titanium oxide particles are traced in time. Since the cycle time is 1 Hz, the approximate velocity of the tracer particles is 75 $\mu\text{m/s}$.

5. Conclusions

We have produced artificial cilia on the basis of polymer composite micro-actuators that can be set in motion by electrostatic means. When covering the wall of a microfluidic channel, the micro-actuator movement can induce significant flow velocities in the surrounding fluid. For the particular case we studied, velocities of 75 $\mu\text{m/s}$ in a silicone oil (10 mPas) were observed. Optimisation of the shape change of the actuators, as well as the electrical driving scheme, could improve the effectiveness. The concept of the artificial cilia could find interesting applications in micro-fluidic systems, especially when local fluid manipulation such as local mixing, or special flow pattern generation, are desired.

AN OPTICAL INJECTION SYSTEM USED FOR OPTIMIZATION STUDIES OF HIGH ASPECT RATIO LC COMOSS COLUMNS

**W. De Malsche^{1,2}, H. Eghbali¹, Jan De Smet¹, J.G.E. Gardeniers¹
² and G. Desmet¹**

¹Department of Chemical Engineering, Vrije Universiteit Brussel,
Belgium

²MESA⁺ Research Institute, University of Twente, The Netherlands

Abstract

A method was developed to evaluate the influence of the pillar configuration on the dispersion characteristics in pillar arrays intended for use in liquid chromatography. This method consists in uncaging a narrow plug of dye through a micromachined window. A proof-of-principle of the method is demonstrated and a first plate height determination was performed.

Keywords: uncaging dye, comoss, liquid chromatography, pillar array, injection

1. Introduction

Recent computational fluid dynamics (CFD) studies have shown that it would be highly desirable to replace the packed bed columns used in liquid chromatography by 2D structured pillar arrays [1]. Dimensional parameters such as pillar and wall spacing and pillar shape appear to be crucial for achieving higher efficiencies [2]. Even though optimal dimensional values are available by CFD studies, no experimental validation of these parameters has been performed so far. This is in part due to the fact that it is not straightforward to convert a proposed design into the desired pillar array without altering the original dimensions. Different process steps such as lithography, Bosch etching and even bonding give rise to minute alterations of an original design, which lead to large deviations of the predicted fluidic behaviour. Another issue is that in order to study band broadening in detail, a good injection system should be available. A challenging aspect is the high aspect ratio of the channels that are needed, making it extremely difficult to inject undisturbed and rectangular plugs [3].

2. Experimental

A virtual injection system is presented here which allows to create very wide and perfect rectangular plugs by means of an uncaging dye [4]. We fabricated a $30 \mu\text{m} \times 1 \text{ mm}$ window inside a pillar array channel, through which laser light could *in situ* create a fluorescent plug (Fig.1). Due to the positioning of the window in contact with the channel, no increase in peak width due to light diffraction effects occurs (Fig.2). Because of the configuration of our system (the laser is situated at the silicon side and the objective lens is at the glass side), the plugs could be observed from the exact moment that they are being generated. For the fabrication of the chip, we first etched the pillars by Bosch etching. Subsequently, 300 nm stress free silicon nitride was deposited to provide a transparent etch stop for subsequent KOH etching of the (100) silicon wafer. The thickness of the silicon nitride layer can be easily varied in order to increase the pillar dimensions and to decrease the microchannels between the pillars. This provides an easy method to vary submicron distances with a normal UV lithography equipment. Finally the pillar channel was sealed by anodic bonding to a Pyrex® substrate.

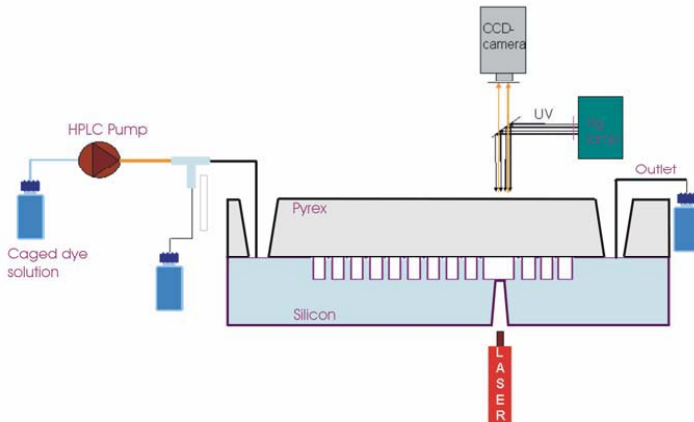


Figure 1. Setup showing operation principle. A solution containing 2 mg/ml of the caged dye bis-(5-carboxymethoxy-2-nitrobenzyl) ether dikaliump salt in DI water is pumped via a flow splitter through the pillar channel. Applying the laser light uncages a plug defined by the window by chemical modification. This generated plug is subsequently monitored by a CCD camera. On the bottom side of the wafer a 2 μm thick layer of PECVD SiO_2 and a 1 mm thick layer of PMMA was applied for improving the mechanical strength of the window (not shown).

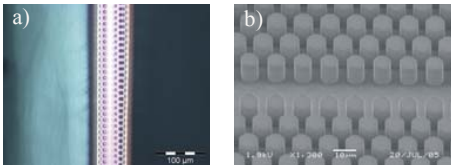


Figure 2. a) Bottom view of the injection window. The inclined walls are due to the KOH etching. The width of the window is about 30 μm , which is larger than the intended 10 μm due to errors on the wafer flat orientation and alligning.

3. Results and discussion

A plug was created in one of the channels with pillar diameters of 10 μm (Fig.3). A theoretical plate height value of $9,7 \pm 0,3 \mu\text{m}$ ($n=4$) was determined for the peak zone (Fig.4), based on a flow velocity of 0.94 mm/s. Experimental work is under way to evaluate and optimize the performance of different pillar configurations using the presented technique.

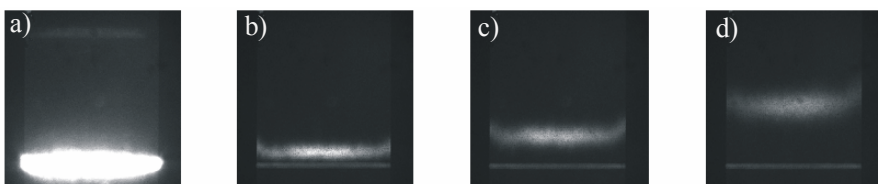


Figure 3. a) Optical injection at time 0 s by applying the laser source, b) a fluorescent plug becomes visible after turning of the laser at $t = 0.938$ s, the peak moves along the channel: c) $t=2.189$ s, d) $t=4.534$ s. It can clearly be seen that the flow velocity is faster at the side of the channel. This is due to a local low flow resistance and can be cancelled by optimizing the distance of the side wall to the closest pillar.

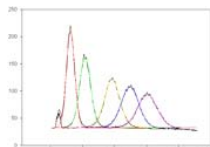


Figure 4: Plot of the intensity (a.u.) versus the distance travelled in the channel (mm). The intensity profiles were determined by discarding the region close to the side wall and averaging the intensities along the width of the channel.

4. Conclusions

We have fabricated a pillar array column with an integrated functionality that allows the creation of fluorescent plugs as narrow as 30 μm . This device can be used to evaluate the performance of different pillar configurations in terms of band broadening with the prospect of optimizing liquid chromatography on a chip.

REFERENCES

- [1] P. Gzil et al., *Anal.Chem.*, 2004, 76, 4501-4507
- [2] M. De Pra et al., *Proc. Micro Total Analysis Systems* 2005, 2, pp. 838-840
- [3] Chmela et al., *Lab Chip*, 2002, 2, 235-241
- [4] Sinton et al., *J. Micromech. Microeng.*, 2002, 12, 898-904.

LATERAL CELL SEPARATION IN MICROFLUIDIC CHANNEL BY 3D ELECTRODE DIELECTROPHORESIS

Lisen Wang¹, Steven Marchenko², Noo Li Jeon¹,
Edwin Monuki², Lisa A. Flanagan², Abraham P. Lee^{1,3,*}

¹Department of Biomedical Engineering, ²Department of Pathology,

³Department of Mechanical Engineering, E-mail: aplee@uci.edu

University of California, Irvine. 3120 Nature Sciences II, Irvine. CA. 92697

Abstract:

This paper presents a novel design and separation strategy for lateral sorting of cells in microfluidics by dielectrophoresis (DEP). Unlike most of the DEP separations in microfluidics which utilize planar electrodes inside microchannel to separate objects at different heights of the channel, we have developed a process to fabricate vertical electrodes in the side wall of the microchannels to generate non-uniform electric fields, thus DEP forces along the lateral direction of the channel. In our design, coupled DEP forces are used to laterally locate different cells at different equilibrium positions in the channel and the separated cells can automatically flow into different outlet reservoirs simultaneously. Experimental results with cells/beads separation and cell/cell have been demonstrated with this design. This novel separation strategy is more compatible with other sample preparation steps and can achieve automatic and parallel processing of target samples.

Keywords: Dielectrophoresis, lateral cell separation, flow cytometry, cell sorting

1. Introduction

Most of current DEP electrodes utilize planar electrodes on the surface of the substrate to generate DEP force along the vertical direction of the microchannel as those in field flow fractionation (FFF)-DEP [1]. The electric field decays exponentially with the height of the channel for the planar electrode configuration, and the DEP forces can only affect those particles close to the electrodes at the bottom of the channel. When configuring vertical electrodes in the side wall of the channel (Fig.1), electric field extend across all the volume of channel can be generated to avoid any dead electric field zone.

2. Principle of separation

We have developed a process to make vertical electrode embedded in the side wall of microchannel [2]. Interdigitated electrodes in the side wall of the channel are fabricated to generate the differential DEP force and a secondary DEP force is used to counter the first DEP force. When the mixed cell population is pumped into the channel, they are separated by the DEP forces in the separation zone and then flushed into different channel outlets by the through-flow, as in Fig.2a. Since the DEP force is determined by the frequency of the signal applied on the electrodes as well as the particle/medium's properties. With different frequencies and magnitudes of signals applied to these opposing sets of electrodes, the polarization factor of the cells can be tuned to make them balance at different points in the channel. As illustrated in Fig. 2b, the frequencies and amplitude can be tuned to have the "white cells" to be equilibrium at some position above the center line of the channel. When a cell is close to electrode #1, like the one at point A, the DEP force F_1 from electrode #1 is larger than the DEP force F_2 from electrode #2, the cell will be pushed towards the top electrodes (electrodes #2). With the movement away from the bottom electrodes, DEP force F_1 decreases and F_2 increases until it reaches an equilibrium position where F_1 equal to F_2 at point C. Meanwhile, the "grey cells" can be tuned to be equilibrium at some position below the center flow line and then these two types of cell can be sorted to different outlets automatically. The lateral separation strategy can be used to continuously separate cells

and is compatible with other sample preparation steps in microfluidics. Fig. 3 shows the simulated electric field distribution inside the channel with vertical electrodes in the side walls. The center of the channel has a minimum gradient of electrical field squared corresponding to a minimum DEP force. For particles with negative DEP properties, it is a stable equilibrium point and for positive DEP it is an unstable point. This equilibrium point can be tuned by varying the magnitude of the voltage applied. For two types of cells both with negative DEP forces, Fig.4 illustrates the principle of separation by applying two signals with different frequencies. The polarization factor K of these two cells can be tuned by the frequencies applied causing them to be positioned at different equilibrium points in the channel and separated by the flow lines.

3. Experimental Results

Most of cells experience negative DEP forces at low frequencies and positive forces at high frequencies in low conductivity medium [3]. To have a negative DEP effect, cells are resuspended in an isotonic medium at physiological pH and low conductivity (8.5 % sucrose (w/v), 0.3 % dextrose (w/v) dissolved in doubly deionized water, conductivity adjusted to 0.1 mS/cm with 1640 RPMI using ThermoOrion conductivity/pH meter). Experimental results successfully demonstrate the separation of polystyrene beads and cells (Fig. 5), and separation of two types of cells (Fig.6). For the cells/beads separation, both the cells and beads are experiencing negative DEP forces from the electrodes and they are continuously flow out of the channel to the outlets. For the cell-cell separation, only top electrodes are turned on the achieved the separation, the N115 cells are trapped to the top electrodes and HEK293 are repelled to the bottom of the channel. At the beginning of the experiment, only HEK293 cells flow into the bottom outlet, and when the DEP force is released, N115 cells will flow into the top outlet with the flow. With appropriate control of the flow rate, it is possible to balance the positive DEP force with the hydrodynamic force to prevent the stable trapping of the N115 cells and therefore to achieve continuously flow through separation.

4. Conclusion

We have developed a novel separation technology based on coupled DEP forces balancing effect. The principle has been introduced and experimental results have demonstrated the feasibility of this separation strategy. This continuous flow through separation system enables high throughput microfluidic sorting and could be a complementary platform to conventional flow cytometry.

Acknowledgments

This work was supported by funding from UCI and a grant from the Roman Reed foundation.

References

1. X. B. Wang, J. Vykoukal, F. F. Becker, and P. R. C. Gascoyne, "Separation of polystyrene microbeads using dielectrophoretic/gravitational field-flow-fractionation," *Biophys. J.*, vol. 74, no. 5, pp. 2689–2701, 1998.
2. Lisen Wang, Abraham P Lee, "Microfabrication Process for Polymer Microchannel with Embedded Vertical Electrodes for Microfluidic Applications". Proceedings of 2004 ASME: International Mechanical Engineering Congress & RD Expo Nov. 13-19, Anaheim California
3. Peter.R.C.Gascoyne, Jody. V. Vykoukal, "Dielectrophoresis-Based Sample Handling in General-Purpose Programmable Diagnostic Instruments". PROCEEDINGS OF THE IEEE, VOL. 92, NO. 1, JANUARY 2004

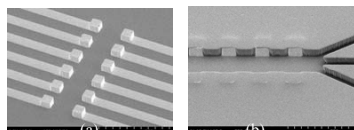


Figure 1. (a) SEM of vertical electrode before channel layer is constructed, (b) the final channel with electrodes embedded in the sidewall .

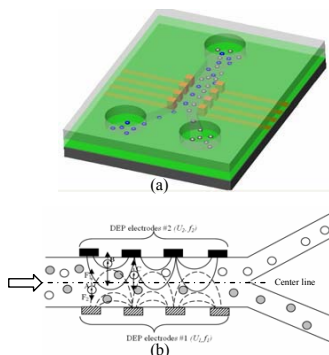


Figure 2. Schematic of the lateral separation principle by two coupled DEP forces. (a) Random distributed cell population come into the separation zone and separated to different equilibrium points and then flow in to different outlet channels. (b) The force balance plot of the cells in the separation zone.

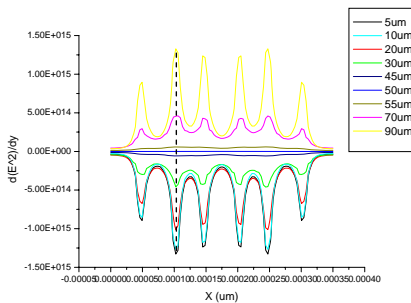


Figure3. Simulation results for the gradient of electric field squared along the width of the channel direction. The center of the channel has minimum electric field and close to the electrodes with maximum electrical field gradient therefore DEP forces.

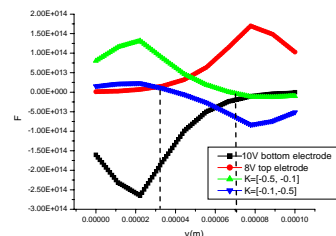


Figure4. Normalized DEP forces in the channel along the line as shown in Fig. 3. The equilibrium points (zero DEP forces) of two objects with different polarization factors can be tuned to away from the center as shown by the dashed line.

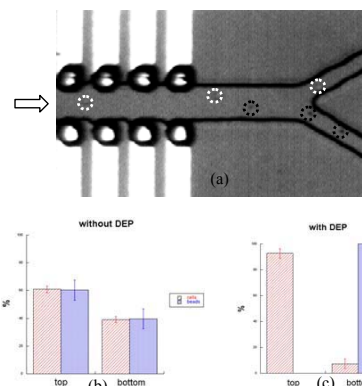


Figure5. (a) A snapshot of the separation of polystyrene microbeads and HEK293 cells. Cells (white circles) are sorted to top channel outlet and beads (black circles) are sorted to bottom outlet, (b) Free flow without DEP forces, (c) with DEP separation.

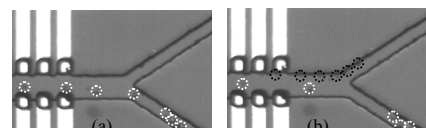


Figure6. Experimental results for the separation of HEK 293(black circle) and N115 (white circle) cells. (a) N115 cells repelled from the top electrodes and flow into the bottom channel, (b) HEK293 cells are released from the top electrodes and flow into the top channel.

A DIGITAL CENTRIFUGAL DROPLET-SWITCH FOR ROUTING OF LIQUIDS

Stefan Haeberle¹, Lars Naegele¹, Roland Zengerle^{1,2}, and Jens Ducréé^{1,2}

¹Laboratory for MEMS Applications, Department of Microsystems Engineering (IMTEK), University of Freiburg, Georges-Koehler-Allee 106, 79110 Freiburg, Germany (haeberle@imtek.de)

²HSG-IMIT – Institut für Mikro- und Informationstechnik, Wilhelm-Schickard-Straße 10, 78052 Villingen-Schwenningen, Germany

Abstract

A new centrifugal principle for the binary switching of droplets is presented. By means of the Coriolis force, the droplets are directed into a specific reservoir selected by the sense of rotation. To route a larger volume, the liquid is split into droplets by a centrifugally stimulated break-off at a hydrophobic nozzle. Employing this method, by far smaller flow rates can be routed compared to our recently introduced Coriolis flow switch for continuous flows [1,2]. This enables a robust and cost-efficient microfluidic process integration of preparative spin-column protocols requiring extended retention times.

Keywords: centrifugal microfluidics, hydrodynamic switch, droplets, liquid router

1. Introduction

Many sample preparation protocols, e.g. for DNA extraction require a centrifugal purification and concentration within so called spin columns. These protocols include the manual replacing of the collecting vessels. A current trend is the integration and automation of these handling steps using microfluidic technologies [3,4]. This requires a liquid switch enabling the binary routing of liquid flows. The flow rates in these protocols must be small ($\ll 1 \mu\text{L} / \text{s}$) as they have to meet the time frame of an optimal physicochemical binding within the solid phase, e.g. a membrane or aggregated beads. Our novel droplet-switch enables a fully binary switching of small flow rates and thus enables the complete implementation of extraction protocols on the centrifugal microfluidic platform [5].

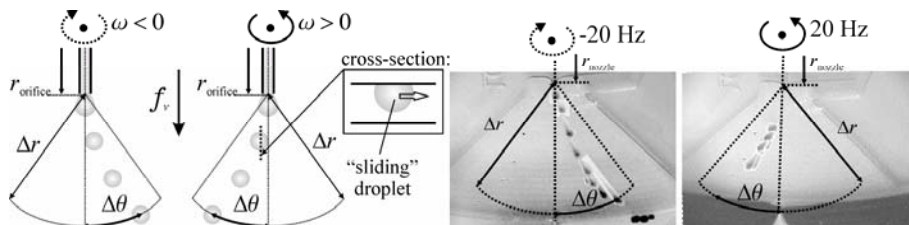


Figure 1. Left: Centrifugally induced dripping of water-droplets from a hydrophobic orifice. Depending on the sense of rotation, the droplets are either deflected to the right (clockwise) or to the left (counter-clockwise). Right: Typical trajectory of a sliding droplet obtained by superposing several stroboscopic images.

2. Functional Principle

The functional principle and proof of operation is depicted in Figure 1. A continuous water flow is split into single droplets at a hydrophobic orifice under the impact of the centrifugal force f_v . The droplets do not freely move through the chamber but they are sliding along the hydrophobically coated lid (see sketch of cross-section). The direction of the deflected droplet depends on the sense of rotation only. Several stroboscopic images, acquired under rotation, are overlaid in Figure 1 (right) to visualize typical droplet trajectories for a rotational frequency of 20 Hz. The radial bottom of the reservoir is pre-filled with oil in order to determine the impact-point of the water droplets and thus the displacement angle $\Delta\theta$.

Figure 2 surveys the displacement angle $\Delta\theta$ over the frequency of rotation v for a “sliding” droplet (Figure 1). Due to the low hydrodynamic resistance of the inlet channel, the critical frequency for a centrifugally stimulated break-off amounts to a few Hz, only. Towards elevated frequencies, the azimuthal displacement $\Delta\theta$ stabilizes at about 30° . The “free-flight” measurements at $v=10$ Hz, for which the lid has been removed from the chamber, suggest that the friction with the lid (“sliding”) reduces the azimuthal deflection of the droplet in that case.

In order to enforce a highly reliable binary routing, we introduce two discrete outlet channels. The upper and the lower picture sequences in Figure 3 (left) visualize the course of switching into the right (clockwise rotation) and left (counter clockwise rotation) outlet, respectively. Furthermore, to elevate the critical break-off frequency, the hydrodynamic resistance upstream of the nozzle has been significantly increased with respect to Figure 1.

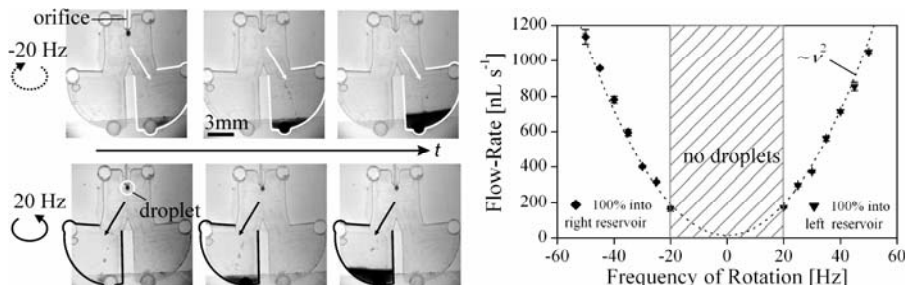


Figure 3. Left: The two picture sequences show the 100% digital switching of single droplets into one of two reservoirs (left or right). All water droplets are deflected into the right reservoir upon clockwise rotation (upper row of stroboscopic pictures) while all the liquid ends up in the left reservoir in the reverse sense of rotation (lower sequence). Right: Flow rates have been measured between 160 nL s^{-1} and $1.1 \mu\text{L s}^{-1}$, scaling with the square of the rotational frequency v .

Since no droplets break off at frequencies below 20 Hz and the displacement for a reliable switching is reached at frequencies of 20 Hz and higher, the switch possesses a “self-controlled” mechanism. This ensures that the droplet formation is suppressed within the interval $\nu < 20$ Hz where the azimuthal deflection would not be sufficient for a reliable binary routing. Figure 3 (right) indicates the elevated frequency threshold as well as the scaling of the flow rate with the square of ν .

Figure 4 shows how a complete microfluidic sample preparation structure could look like. A column of polymer beads (polystyrene, diameter: 47 μm) is retained at an aggregation step of $\sim 40 \mu\text{m}$ height upstream of the switch orifice. Different liquids can be flushed through the bead column and either be directed to the left or the right reservoir, depending on the sense of rotation. To visualize the liquid routing, first 10 μL of red ink have been placed into the reservoir connected to the switch and pumped at 70 Hz clockwise rotation into the right reservoir. Subsequently, green ink has been introduced and switched into the left reservoir (counter-clockwise rotation). The two liquids could be switched in a completely binary fashion into their designated reservoirs.

3. Conclusion and Outlook

We realized a self-controlled digital liquid router based on the centrifugally induced break-off and the Coriolis-induced deflection of droplets. Future work will be focused on implementation of common sample-prep protocols into our centrifugal “lab-on-a-disk” platform.

References

- [1] T. Brenner, T. Glatzel, R. Zengerle, and J. Ducr  e, *Lab on A Chip*, vol. 5, no. 2, pp. 146-150, (2005).
- [2] T. Brenner, T. Glatzel, R. Zengerle, and J. Ducr  e, in *Proceedings of μ TAS 2003*, Eds. M. A. Northrup, K. F. Jensen, and D. J. Harrison, pp. 903-906, (2003).
- [3] L. A. Christel, K. Petersen, W. McMillan, and M. A. Northrup, *J. of Biomech. Engineering-Transactions of the ASME*, vol. 121, no. 1, pp. 22-27, (1999).
- [4] J. W. Hong, V. Studer, G. Hang, W. F. Anderson, and S. R. Quake, *Nature Biotechnology*, vol. 22, no. 4, pp. 435-439, (2004).
- [5] J. V. Zoval and M. J. Madou, *Proceedings of the IEEE*, vol. 92, no. 1, pp. 140-153, (2004).

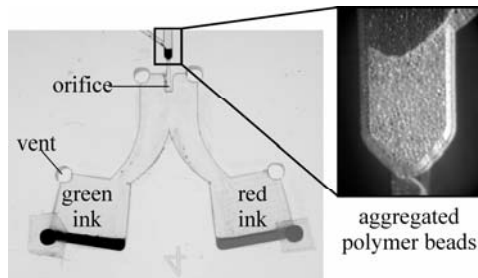


Figure 4. A centrifugal solid-phase extraction structure. Small polystyrene beads are aggregated upstream of the switch. First, red ink is injected and directed to the right, afterwards green ink is injected under counter-clockwise rotation, thus ending up entirely in the left reservoir.

A column of polymer beads (polystyrene, diameter: 47 μm) is retained at an aggregation step of $\sim 40 \mu\text{m}$ height upstream of the switch orifice.

PNEUMATIC MICROPUMPS UTILIZING TIME-DELAY PERISTALTIC ACTUATION

Chun-Wei Huang, Song-Bin Huang and Gwo-Bin Lee

Department of Engineering Science, National Cheng Kung University, Tainan 701,
Taiwan

E-MAIL: gwobin@mail.ncku.edu.tw

Abstract

This study reports a new pneumatic micropump featuring three membrane-enclosed air chambers with different volumes. When compressed air fills the chambers, the membranes are pushed downwards sequentially, resulting in the liquid in the underlying fluid channels to be pumped forward peristaltically. This new micropump can be operated by using a single electromagnetic valve (EMV). A maximum flow of 108 $\mu\text{l}/\text{min}$ is obtained at a driving frequency of 10 Hz and an air pressure of 25 psi (172.4 kPa) when a membrane with a thickness of 80 μm and a microchannel with a width of 500 μm is tested.

Keywords: Microfluidics, micropump, peristaltic actuation, MEMS

1. Introduction

Pneumatic micropumps driven by compressed air supplied by an external source have attracted considerable interest recently. Unger et al. fabricated an elastic polymer membrane arrangement and showed how it can be driven by compressed air to provide a micropumping or microvalving effect for microfluidic systems [1]. Peristaltic pneumatic micropumps provide an effective means of driving fluids in microchannels and can be readily integrated with bio-sensing chips [2]. Such a peristaltic pneumatic micropump requires three EMV switches to perform the pumping action. This paper therefore presents a new pneumatic micropump that can be driven by using a single EMV and a simple control circuit. This feature is very important for simplifying the control system of the microfluidic system and reducing the overall system size. The developed micropumps could be promising for micro total analysis systems.

2. Design and fabrication

The pneumatic micropump consists of three air chambers with different volumes and an underlying liquid microchannel. The schematic diagram of the micropump is shown in Figure 1(a). Figure 1(b) shows the cross-sectional view of the actuation mechanism of the micropump. When the compressed air is supplied to the air chambers, the flow

stopper is first activated to prevent liquid backflow. Then the chambers are filled up with compressed air sequentially from the smallest one to the largest one. The membranes between the air chambers and the liquid microchannel are then pushed downwards sequentially to pump the fluid toward $-X$ direction. The micropump is made of polydimethylsiloxane (PDMS) using soft lithography techniques and integrated with a micro flow sensor to monitor the flow rate of the samples and reagents [3]. A photograph of the assembled micropump integrated with the micro flow sensor and the microchannel is shown in Fig. 2.

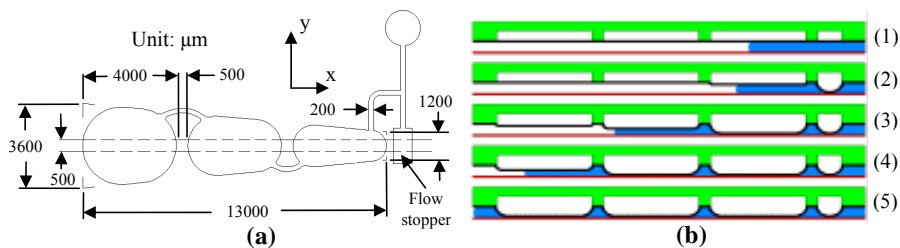


Figure 1. (a) Schematic illustration of the micropump. (b) Cross-sectional view of the actuation mechanism.

3. Results and discussion

The effect of the applied air pressure on the flow rate at different driving EMV frequency is explored and the results are shown in Figure 3. During the test process, the EMV driving frequency is varied sequentially to test the effect of the driving frequency.

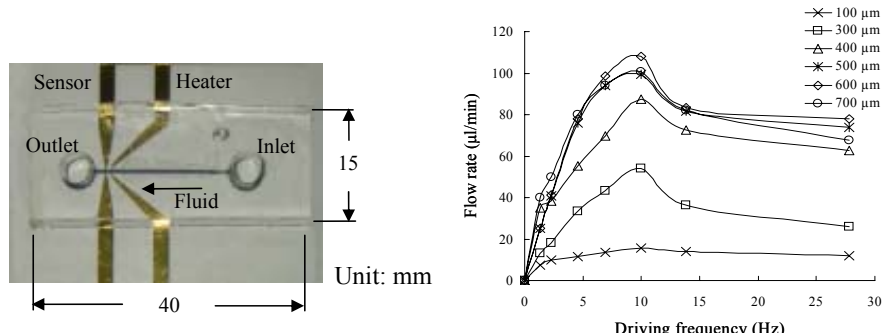


Figure 2. A micropump integrates with flow sensor to monitor the flow rate.

Figure 3. Effect of the applied air pressure on the flow rate at different driving frequencies.

In general, the flow rate increases with increasing driving frequency (at a constant

pneumatic pressure). However, the maximum flow rate at a constant applied pressure is limited by the fill and release times of the compressed air. If the operational frequency is too high, the air chamber cannot be completely filled and released, and the flow rate will start to fall. Finally, this micropump is integrated into a microfluidic system for cell culture application. Figure 4(a) shows the schematic illustration of the cell culture chip. The whole cell culture process including medium supply and cell harvest can be automated on a single chip. Figure 4(b) shows the CCD images of daily observation on cell culture. These images show that the human lung cancer cells can be successfully cultured using the developed automatic cell culture chip.

4. Conclusions

This study reports a new pneumatic pump whose operation is based on the time-delay peristaltic actuation effect caused by the sequential deflection of PDMS membranes. The pneumatic micropump is controlled by using a single EMV switch and a simple control circuit. More importantly, it was integrated into a microfluidic system for automatic cell culture and the human lung cancer cells can be successfully cultured.

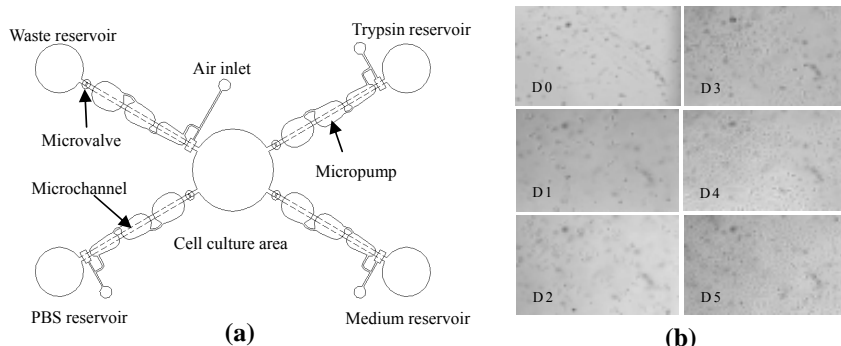


Figure 4. (a) Schematic illustration of the microfluidic cell culture system. (b) CCD images of daily observing.

References

1. M. A. Unger, H. P. Chou, T. Thorsen, A. Scherer and S. R. Quake *Monolithic microfabricated valves and pumps by multilayer soft lithography*, Science, 288, pp.113-116, (2000).
2. C. H. Wang and G. B. Lee *Automatic bio-sampling chips integrated with micro-pumps and micro-valve for disease detection*, Biosens. Bioelectronics, 21, pp.419-425, (2005).
3. N. Sabatè, J. Santander, L. Fonseca, I. Gràcia and C. Canè *Multi-range silicon micromachined flow sensor*, Sens. Actuators A, 110, pp.282-288, (2004).

MICROFLUIDIC INTEGRATION OF GEL-BASED REFERENCE ELECTRODES FOR ELECTROPHYSIOLOGICAL MEASUREMENTS ON CHIP

E. Dahan¹, M. Benabderrazik¹, T. Lehnert¹, V. Bize², J.-D. Horisberger² and
M.A.M. Gijs¹

¹ Ecole Polytechnique Fédérale de Lausanne (EPFL),
Institute of Microelectronics and Microsystems, Lausanne, Switzerland.
² Department of Pharmacology and Toxicology, UNIL, Lausanne, Switzerland.

Abstract

In this paper we present a novel integration method of Ag/AgCl gel-based reference electrodes in microfluidic systems. A simple fabrication process and the characterization of these stable and low-impedance electrodes is demonstrated.

Keywords : integrated reference electrode, Ag/AgCl micro-electrode, agar salt bridge, electrophysiology on-chip, liquid junction, capillary stop.

1. Introduction

Ag/AgCl wires connected via an agar salt bridge are the most common type of reference electrode used for measuring ionic currents through cell membranes. Ag/AgCl is a reversible but exhaustible electrode that has to be maintained in a constant Cl⁻-concentration environment. A gel-based salt-liquid junction provides a link between the Ag/AgCl wire electrode and the tested solution. Miniaturization is so far limited to needle-type reference electrodes [1] that can not be integrated into a microfluidic system. Microfabrication using Ag/AgCl thin- and thick-film deposition [2] have also been investigated for micro-electrochemical applications, but stability is limited due to consumption of AgCl. Here, we developed a system where the agar conductive gel junction is directly integrated into a fluidic microchip, solving stability problems related to the integration of Ag/AgCl thin films.

2. Principle of the microfluidic integration

This new microfluidic integration method of agar bridges is based on capillary force filling of suitable microchannels combined with capillary stop structures [3]. The principle is shown in fig. 1. Our system consists of a perfusion channel, e.g. for applying different test solutions to an immobilized cell, and a side channel for the electrode. The capillary stop structure consists of several finger-like constricted channels (50 µm wide, 100 µm high), designed to prevent the agar gel from entering the perfusion channel (500 µm high).

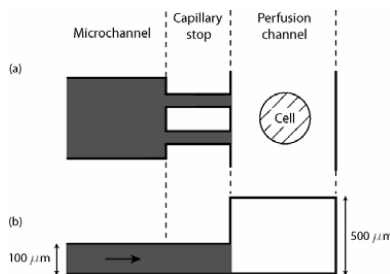


Fig. 1 : Design of the microchannel filled with agar gel (agar bridge) ending by a capillary stop structure connected to the perfusion channel. The position of the cell is represented by the hatched disc. **a)** Top view and **b)** side view.

3. Fabrication process

Dry agar powder dissolved in a 3M KCl solution is heated to 100°C and becomes a viscous fluid. The dimensions of the side channel have been properly chosen to allow self-filling with liquid agar by capillary force. Upon cooling, agar transforms into a gel and the test solution may flow in the perfusion microchannel without cross contamination. The Ag/AgCl wire electrode is connected via a small external on-chip electrolyte reservoir to the agar bridge. Multilayer SU-8 structures (Fig. 2a), made of two SU-8 layers (100 and 500 μm high), are used as a mold for the poly-dimethylsiloxane (PDMS) microchannels. An air plasma treatment makes the PDMS surface hydrophilic to enhance capillary filling.

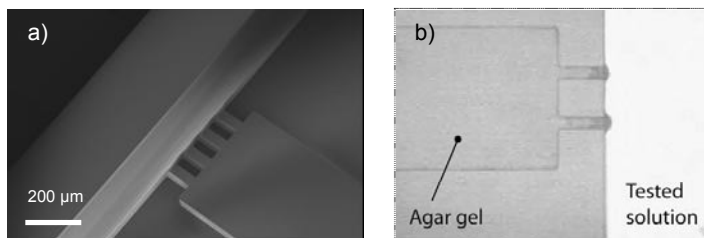


Fig. 2 : **a)** SEM picture of a SU-8 mold for PDMS microchannels with a two-layer structure (100 and 500 μm high). A capillary stop structure with a 4-finger end is shown here. **b)** Agar gel (colored with dye) blocked by a capillary stop structure (2 fingers) in a PDMS microchannel.

4. Experiments and results

Fluidic and electrical characterization of the whole electrodes (Ag/AgCl wire + salt bridge) have been performed. The agar gel stops are positioned at the side wall of the perfusion microchannel, as shown on fig. 2b. Since the impedance of one single integrated electrode can not be easily measured in our device, a symmetrical set-up was used. Two identical electrodes (resistance R) are face-to-face with a 3M KCl test solution flowing in the perfusion channel (resistance R_m) (fig. 3a). The impedance has been measured for increasing number of fingers in the capillary stop structure. Experimental results compare well with theoretical values as shown on the graph in fig. 3b. The electrodes are stable in time and can be stored for several days in the fridge (8°C). This type of integrated low-resistance electrode is a very suitable reference bath electrode for stable and accurate measurements, for instance on *Xenopus* oocytes with a voltage-clamp microsystem [4].

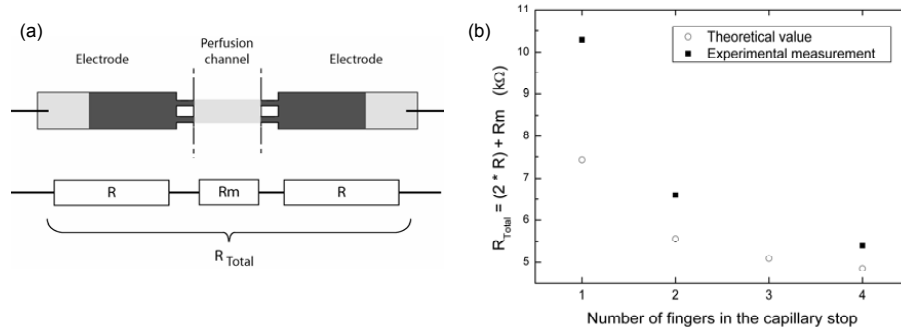


Fig. 3 : Measurement of electrode resistance: **a)** Equivalent electrical circuit of the tested structures. **b)** Theoretical and experimental results of R_{Total} for electrodes having different capillary stops.

References

- [1] T. Kitade, K. Kitamura, S. Takegami, Y. Miyata, M. Nagatomo, T. Sakaguchi, and M. Furukawa, "Needle-type ultra micro silver/silver chloride reference electrode for use in micro-electrochemistry," *Analytical Sciences*, vol. 21, pp. 907-912, (2005).
- [2] A. Simonis, M. Dawgul, H. Lüth, and M. J. Schonig, "Miniaturised reference electrodes for field-effect sensors compatible to silicon chip technology," *Electrochimica Acta*, vol. 51, pp. 930-937, (2005).
- [3] T.-S. Leu and P.-Y. Chang, "Pressure barrier of capillary stop valves in micro sample separators," *Sensors and Actuators A : Physical*, vol. 115, pp. 508, (2004).
- [4] E. Dahan, V. Bize, T. Lehnert, J.-D. Horisberger, and M. A. M. Gijs, "On-chip non-invasive voltage clamp on *Xenopus* oocytes," presented at MicroTAS, Boston, vol. 1, pp. 906-908, (2005).

INKJET MICROPUMP FOR PARALLEL MICROFLUIDIC TESTING

Fumio Takagi, Hiroshi Koeda, Rie Miyazaki and Shinichi Kamisuki
Seiko Epson Corporation, Japan

Abstract

In this paper we report on a new microfluidic system integrated with an inkjet micropump. The microfluidic system has 32 microchannels connected with individual nozzles of the inkjet. By ejecting droplets from the nozzles continuously, fluids in the microchannels can be transported at a constant flow rate. In order to demonstrate a pumping performance, streptavidin-biotin binding test and microfluidic ELISA test were carried out. This device can be used for the simultaneous analysis of multiple biomarkers toward point-of-care testing (POCT).

Keywords: micropump, inkjet, Point-of-Care

1. Introduction

Microfluidics has been considered as one of the most promising approach in POCT system, because microfluidics can reduce not only consumption of reagent and sample volume but also detection time and the system size. However, most of the present microfluidic systems use a syringe pump that is obstacle to downsizing the system, especially for multi-channel analysis. In order to address this issue, we adapted an inkjet dispenser to microfluidic system for use as a micropump. Since each microchannel is connected with an individual nozzle, the inkjet micropump can transport multiple fluids simultaneously at a sufficient flow rate for a microfluidic analysis. In this work we fabricated a compact microfluidic system integrated with an inkjet micropump and demonstrated biological reactions by means of a fluorescent and chemiluminescent detecting method.

2. Experimental

The fabricated device consists of a microfluidic substrate and an inkjet micropump as shown fig.1. The microfluidic substrate made of glass sheets has 32 microchannels that are individually connected with nozzles of inkjet.

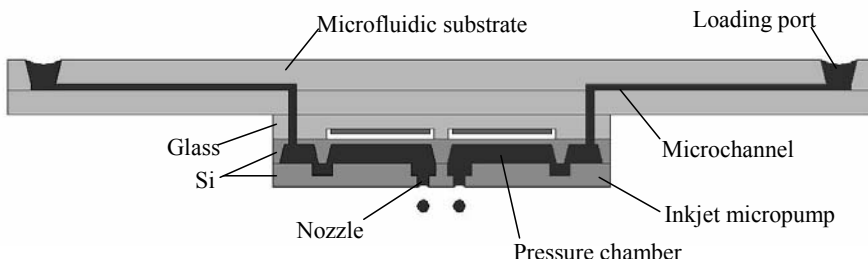


Figure 1. Schematic diagram of microfluidic system integrated with inkjet micropump

If all the nozzles are connected to the microchannels, the inkjet micropump is capable of transporting 128 fluids in parallel [1]. The design of the inkjet micropump is based on that of SEAJet® developed for POS (point-of-sales) printers [2][3]. Fig.2 illustrates a dispensing mechanism of the SEAJet® that is actuated by an electrostatic force generated between silicon membrane and ITO electrode on the Pyrex® glass. The size of the inkjet micropump is 13.8 x 12.4 x 0.76 mm³. The droplet volume is 14pl at a driving voltage of 26.5V.

For fabrication of the microfluidic substrate, grooves and through holes are engraved on two sheets of glass by sandblasting with a mask of photosensitive film patterned by photolithography. Thereafter, those glass sheets are glued together to form the microchannels. The size of the microchannel is 400μm wide and 100μm deep, and the diameter of the through hole is 200μm. The fabricating process of the inkjet is described elsewhere [1][2]. Finally, the inkjet micropump and the microfluidic substrate are aligned and bonded together. Fig.3 is a photograph of the fabricated microfluidic device with flexible print circuit (FPC) board.

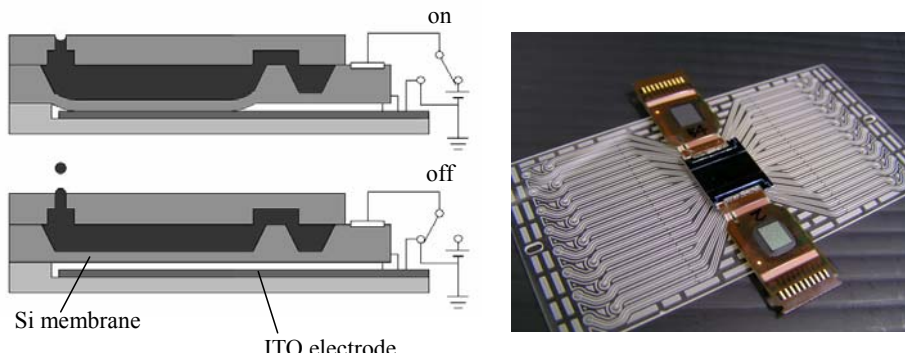


Figure 2. Working principle of SEAJet® based on Si membrane actuation

Figure 3. Photograph of the fabricated microfluidic device integrated with inkjet micropump

3. Result and Discussion

The flow rate was measured at a back pressure of nearly zero. The measurement result is shown in Fig.4 as a function of driving frequency. The flow rate is almost proportional to the frequency up to 5 kHz. At higher frequency than 5 kHz, the graph shows fluctuation that seems to be caused by the interaction with the fluidic resonant frequency. The coefficient of variation of the flow rate was less than 5 % in spite of the channel to channel variability of microfluidic length. Maximum flow rate was measured to be 8.2μl/min at 12 kHz frequency.

Using the fabricated device, streptavidin-biotin binding test was demonstrated. Prior to the test, biotin labeled BSA was filled and adsorbed on the surface of the microchannel. After removing non-adsorbed BSA by a wash buffer, FITC labeled streptavidin was supplied into a loading port and transported through the microchannel at a flow rate of 1μl/min. Finally, fluorescent intensity was detected by cooled CCD. Fig.5 shows a fluorescent image of the microchannel and the fluorescent intensity as a

function of streptavidin concentration. The loaded streptavidin was successfully detected for a wide range of concentration. Additionally, the microfluidic ELISA test was also carried out in the same manner. Mouse IL-2 (1ng/ml) was successfully detected with chemiluminescent substrate (SuperSignal® West Pico Chemiluminescent Substrate, PIERCE). Those results indicate that the inkjet micropump enables microfluidic analysis.

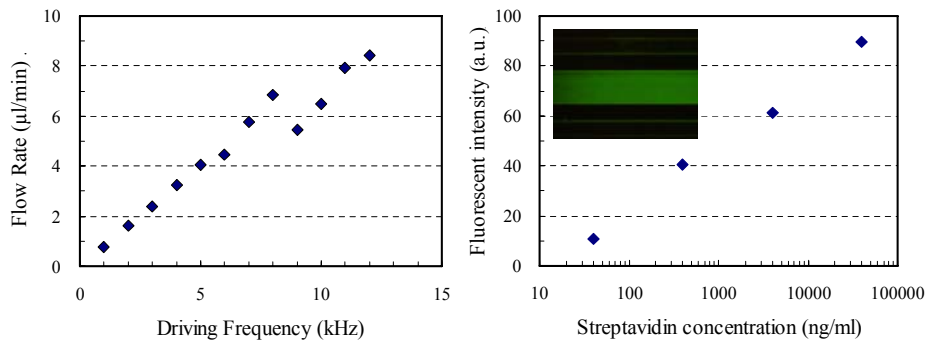


Figure 4. Flow rate as a function of driving frequency

Figure 5. Fluorescent intensity depending on streptavidin concentration and analyzed fluorescent image

4. Conclusion

An inkjet micropump for transporting parallel fluids has been proposed and successfully demonstrated for the microfluidic analysis. Due to the sufficient pumping performance and the integration of a lot of nozzles into a small size, the inkjet micropump gives the opportunity to be widely used for parallel analysis of various biomarkers towards point-of-care testing.

References

1. F.Takagi, R.Kurosawa, D.Sawaki, S.Kamisuki, M.Takai, K.Ishihara and M.Atobe, "Pico Liter Dispenser with 128 Independent Nozzles for High Throughput Biochip Fabrication", MEMS2004, pp.276-279
2. S.Kamisuki, M.Fujii, T.Takekoshi, C.Tezuka and M.Atobe, "A High Resolution, Electrostatically-Driven Commercial Inkjet Head", MEMS2000, pp.793-798
3. M.Fujii and T.Takekoshi, "The Development of a Static Electricity Actuated Inkjet Head for POS printers", IS&T's NIP18, 2002, pp.148-152

ULTRARAPID DROPLET MIXER FOR DIGITAL MICROFLUIDICS

K.P. Nichols and J.G.E. Gardeniers

MESA+ Institute for Nanotechnology

University of Twente, Enschede, The Netherlands

k.p.nichols@utwente.nl

Abstract

A novel AC electric field induced mixing device has been developed for integration into digital microfluidic systems. The device is capable of mixing 1 μl liquid droplets on a timescale of less than 100 ms when operated at 500 Hz, 250 V_{RMS}. A dielectric layer between the droplet and electrodes prevents Joule heating or current flow at these settings. Operating at higher or lower frequencies may degrade mixer performance.

Keywords: mixer, digital microfluidics, electrowetting, dielectrophoresis

1. Introduction

Digital microfluidics represents a new trend in microfluidic design utilizing discrete droplets manipulated on electrode arrays instead of continuously flowing fluid manipulated in microchannels [1].

Paik et al. have already described elegant mixers for digital microfluidics that mix droplets by “split-and-merge” mixing and “array” mixing [2]. The Paik et al. devices move droplets back and forth, essentially folding them to increase the droplet interfacial areas. However, the Paik et al. devices require approximately 3 seconds to mix droplets of a volume that can be equivalently mixed using our system in less than 100 ms.

The device presented here is compatible with existing electrowetting on dielectric (EWOD) digital microfluidic systems such as that described by Wheeler et al. [1] and could be easily integrated as a dedicated mixing component in a larger EWOD device.

2. Experimental

The device consists of four Au electrodes patterned on a planar surface (Figure 1), covered by a 5 μm SU-8 5 (MicroChem) dielectric layer and a 1 μm Teflon AF 601S1-x-6 (DuPont) film. The total device length is 4.4 mm with a width of 1.15 mm. The spiral appendages have a 40 μm width and a 60 μm inter-electrode gap.



Figure 1. Mixer Electrodes Pattern.

Mixing efficiency was analyzed using a Lambert Instruments HI-CAM high-speed camera to obtain videos of the mixing of 1 μl droplets of 10⁻⁵ M fluorescein with 1 μl DI water droplets (Figure 3). These videos were subsequently analyzed using MATLAB to determine the mean gradient of the variance as a function of time. For a given frequency, a value τ was calculated as the point at which 63% of the final value was reached. (Figure 2). Side views were not possible with the experimental setup utilized.

A standard signal generator and a Krohn-Hite 7602M amplifier operating at 250 V_{rms} generated AC voltages with frequencies ranging from 1 Hz to 260000 Hz. To load the device, electrodes 1 and 4 (Figure 1) were set high, and electrodes 2 and 3 were set low. To mix, electrodes 1 and 4 were grounded, 2 was set high, and 3 was set low.

3. Results and Discussion

Efficient mixing was achieved in two frequency regimes (Figure 2). The first efficient mixing regime extends from 150 Hz to 2250 Hz. The second efficient mixing regime extends from 46000 Hz to 260000 Hz.

In the 1 Hz to 150 Hz frequency regime, part of which was used by Paik et al. [2], mixing occurs only by folding and stretching of droplets and through “self-propelled” droplet motion [3]. As shown in figure 2, this regime is capable only of relatively inefficient mixing.

Highly efficient mixing (sub 100 ms for 1 μ L) was demonstrated in the 150 Hz to 2250 Hz regime. At the present time, we believe this is due primarily to a process analogous to AC electroconvection, though without the associated Joule heating. The 500 Hz column of Figure 3 clearly indicates the rapid homogenization possible when operating at this frequency.

Relatively inefficient mixing was found in the 2250 Hz to 46000 Hz frequency regime. A

representative example from this regime is shown in the 3000 Hz column of Figure 3. In the 467 ms image, there are clear diffusion barriers centered on the spiral mixer. Since these correspond to the regions of highest field strength, it is suspected that this effect is due to strong negative dielectrophoresis (DEP) forces. Negative DEP forces occur at different frequencies depending on the characteristics of a particle. However, these frequencies typically fall within this regime [4].

Efficient mixing was demonstrated in the 46000 to 260000 Hz regime. However, use of this regime is not recommended due to the difficulty of determining the cutoff for negative DEP forces for arbitrary particles. Additionally, electrolysis is possible as impedance decreases at high frequencies.

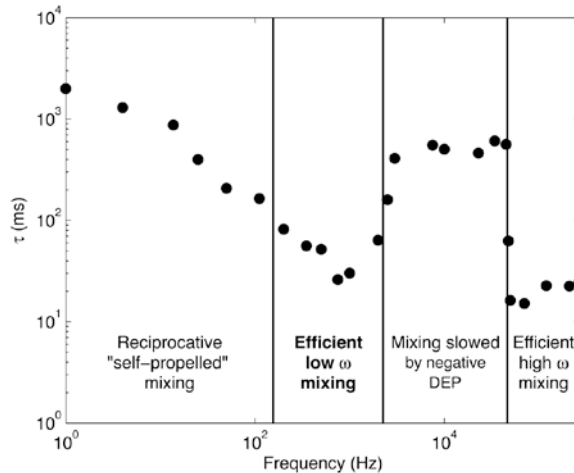


Figure 2. Mixing τ obtained by high-speed image analysis of the mixing of 1 μ L of 10⁻⁴ M fluorescein with 1 μ L of DI water. τ is defined as the point at which 63% of mixing is complete.

Higher frequencies were not investigated due to the limitations of the amplifier.

Additionally, it was demonstrated that at 500 Hz the mixing of fluorescein with KCl is unaffected by KCl molarities from 10^{-5} M to 5 M, and that no Joule heating occurs, which are critical for the device's suitability in chemical and biological applications.

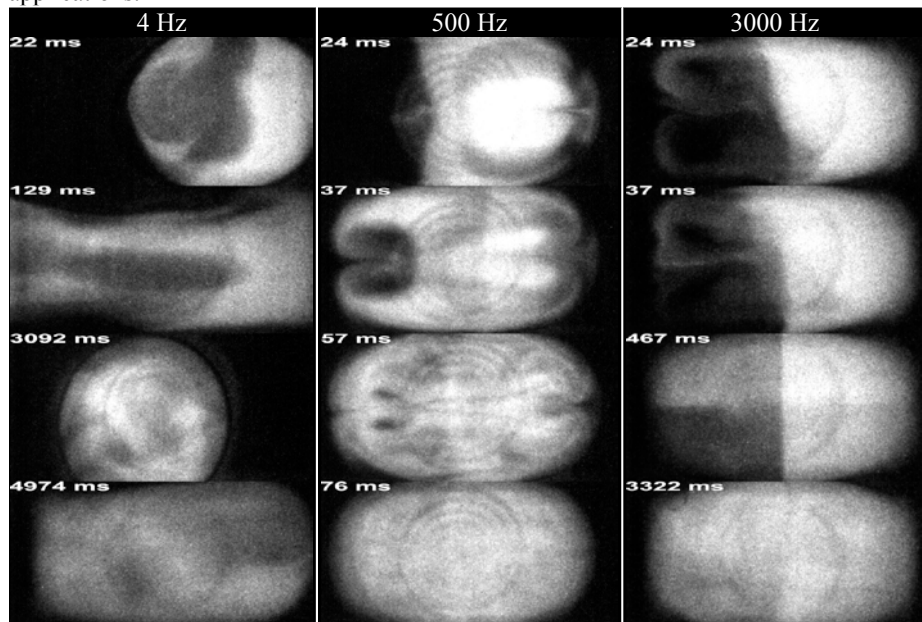


Figure 3. Representative images from videos of mixing behavior at 16 Hz (left), 500 Hz (center), and 3000s Hz (right). Mixing at 500 Hz is significantly faster than mixing at 4 Hz or 3000 Hz.

Acknowledgements

This research was financially supported by the Technology Foundation STW, applied science division of NWO and the technology program of the Ministry of Economic Affairs of The Netherlands (project no. 6626).

References

1. Wheeler, A.R., et al., Digital microfluidics with in-line sample purification for proteomics analyses with MALDI-MS. *Anal. Chem.*, 2005. 77(2), 534-540.
2. Paik, P., V.K. Pamula, and R.B. Fair, Rapid droplet mixers for digital microfluidic systems. *Lab on a Chip*, 2003. 3(4), 253-259.
3. Gunji, M. and M. Washizu, Self-propulsion of a water droplet in an electric field. *Journal of Physics D-Applied Physics*, 2005. 38(14), 2417-2423.
4. P.R.C. Gascoyne and J. Vykoukal, Particle separation by dielectrophoresis, *Electrophoresis* 2002, 23, 1973–1983.

CONTROL OF DROPLETS IN MICROCHANNELS THROUGH LASER-INDUCED THERMOCAPILLARITY

Charles Baroud[†], Jean-Pierre Delville[‡]

[†] LadHyX, Ecole Polytechnique, F-91128 Palaiseau cedex, France

(baroud@ladhyx.polytechnique.fr)

[‡] CPMOH, Université de Bordeaux I, F-33405 Talence cedex, France

Abstract

For droplets to be useful as microfluidic reactors, a robust and general technique needs to be developed to actively control their evolution. We present a contactless technique based on local heating of a water-oil interface which allows control over all the phases of the a droplet *life-cycle*.

keywords: Droplet microfluidics, Optical forcing, Marangoni flow

1. Introduction

The usefulness of droplets as microreactors depends on the ability to actively control their motion in microchannels. While some techniques exist to control drops on open substrates [1], there doesn't yet exist a general approach to control droplets inside microchannels during their formation, merging, and transport. Current work relies largely on the use of complex geometries in order to produce the required results on drops traveling inside microchannels [2, 3].

We demonstrate here a contactless technique that allows the control of all the steps of droplet microfluidics inside microchannels. It is based on the heating of an oil-water interface by a laser, which induces a thermocapillary flow along this interface. The flow in turn produces a force that "pushes" the droplet away from the laser. The combination of laser heating and a complex geometry allows active control of the drops.

2. Optically actuated valve

If implemented in a cross-shaped microchannel, this constitutes the first microfluidic valve for drop formation. The laser heating stops the advance of the water drop while allowing the surrounding oil to continue flowing, as shown in Fig. 1. The blocking time of the water drop increases with the laser power and so does the size of the drop thus produced.

3. Optically induced drop fusion

Other devices may be implemented based on this forcing technique. In particular, the merging of drops can be induced through thermocapillary pumping at two touching interfaces (Fig. 2). While the drops resist merging (especially in the presence of surfactants) due to the presence of a lubrication film between them, the laser may be used to induce the merging. This takes place since the thermocapillarity produces a flow from the hot point to the colder regions which evacuates the oil film. The typical time required to evacuate the film decreases with the thickness of the latter and drops therefore merge rapidly in microfluidic systems.

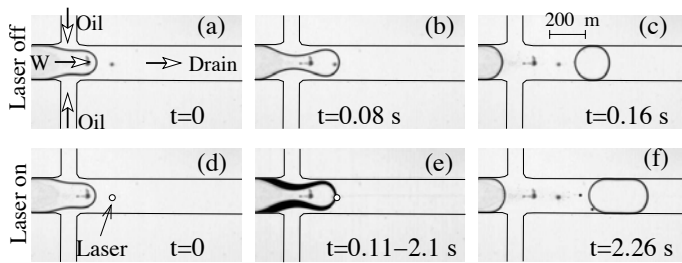


Figure 1: The valve mechanism: In the absence of a laser, water in oil drops are formed in a cross-shaped microchannel. Once the laser is illuminated, the water interface is completely blocked for several seconds while the oil continues to flow.

4. Combination of effects

Finally, these techniques may be combined together in order to force chemical reactions to start at the drop formation. This can be done with a single laser source if the channel geometry is chosen correctly, as shown in Fig. 3. In this case, two drops are formed in a single channel. Without the laser, the drops cannot be synchronized or forced to merge. However, the laser may initially be used as a valve to keep the downstream drop stationary until the upstream drop is detached. When the latter arrives, it pushes the downstream drop along and the two merge together as they cross the laser spot. In this way, a stationary may be used to perform two different tasks.

5. Conclusion

The results presented here represent the first demonstration of a complete set of tools for controlling drops in microchannels. Our technique also allows other operations such as sorting drops, controlling their division, or mixing their contents [4]. It does not require

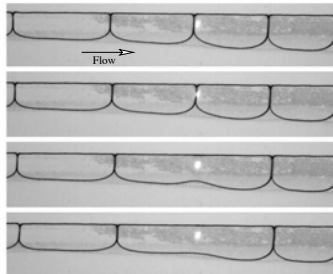


Figure 2: The merging mechanism: In the absence of a laser, drops do not merge due to the presence of a lubrication film between them. The local heating from the laser source however rapidly evacuates the oil film and forces the merging to occur.

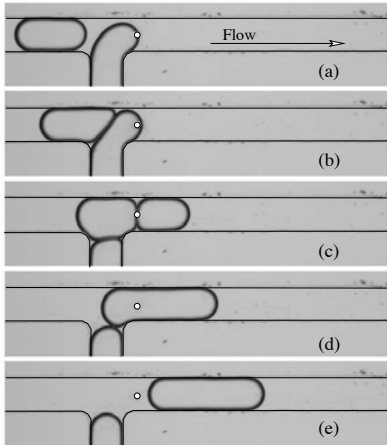


Figure 3: Combined blocking and merging: The presence of the laser allows the synchronization of drop formation and their merging.

special microfabrication or patterning, in addition to being completely contactless. The devices may therefore be reconfigured in real time by simply moving the laser beam position and several operations may be implemented in parallel while using a single laser beam, for example through holographic techniques. Finally, note that a fundamental understanding is now within reach through recent numerical modeling [4].

References

- [1] A.A. Darhuber and S.M. Troian. Principles of microfluidic actuation by modulation of surface stresses. *Annu. Rev. Fluid Mech.*, 37:425–455, 2005.
- [2] H.A. Stone, A.D. Strook, and A. Ajdari. Engineering flows in small devices: Microfluidics toward a lab-on-a-chip. *Annu. Rev. Fluid Mech.*, 36:381–411, 2004.
- [3] T.M. Squires and S.R. Quake. Microfluidics: Fluid physics at the nanoliter scale. *Rev. Mod. Phys.*, 77(3):977–1026, July 2005.
- [4] C.N. Baroud, J-P. Delville, F. Gallaire, and R. Wunenburger. Thermocapillary flow for controlling droplet motion in microchannels. *Phys Rev. Lett.*, Submitted 2006.

A DISPOSABLE ON-CHIP PRESSURE ACTUATOR USING IR-INDUCED THERMOLYSIS FOR SAMPLE TRANSPORT

Jungyoub Han, Soohyun Lee, and Chong H. Ahn

Microsystems and BioMEMS Laboratory

Department of Electrical and Computer Engineering and Computer Science
University of Cincinnati, Cincinnati, OH 45221-0030, USA

Abstract

In this work, a functional on-chip pressure actuator using infrared (IR) based heating scheme, which produces controllable pressure to transport a fixed-volume of fluid sample in lab-on-a-chip on demand has been designed, fabricated, and characterized. The pressure output of the developed device is controlled by the deposited amount of the solid energetic material, which can precisely transport the liquid sample to the required location. The device developed in this research provides a reliable solution to transport liquid samples in a microfluidic system, which responds to a pressing demand in biochemical and clinical analysis as part of the development of μ TAS.

Keywords: Microfluidic handling, Lab-on-a-chip, Solid energetic material, IR heating scheme.

1. Introduction

In this research, a disposable on-chip pressure actuator using the new non-contacted infrared (IR) –induced thermolysis scheme, which produces adjustable pressure to drive liquid samples on demand using one of the alternative safe solid energetic material (AMBN: 2,2' azobis(2-methylbutyronitrile), is designed, fabricated, and fully characterized with extension of the innovative sample transport method recently reported by Hong *et al.* at the University of Cincinnati [1].

2. Design and Fabrication

The on-chip pressure actuator is composed of only an IR heat source as an igniter and solid energetic material (AMBN) in a matrix format as shown in Fig. 2.

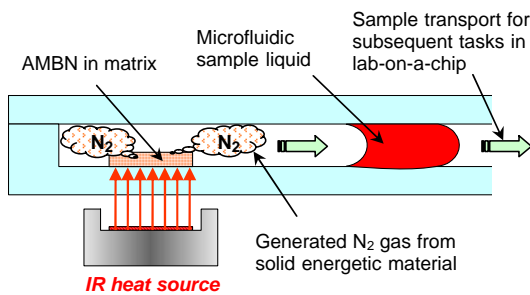


Figure 1. Schematic illustration of the on-chip pressure actuator using IR-induced thermolysis.

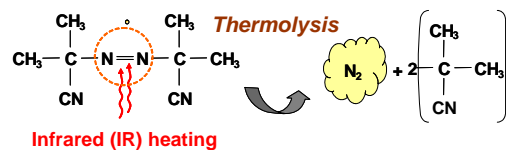


Figure 2. AMBN thermolysis mechanism.

Upon application of a specific temperature, AMBN dissociated and mainly produces nitrogen gas and free-radical [2]. Using the thermogravimetric analyser, thermolysis of AMBN has been obtained that the preliminary dissociation at 67 °C leads to the controlled release of only nitrogen gas, and the second dissociation occurs by 90 °C, which provides the operation range of IR heat source that causes AMBN to release nitrogen gas between 70 °C and 90 °C. The dynamic heat response of the IR heat source is characterized using LabView with a programmable power supply and a thermocouple.

A polymer material, cyclic olefin copolymer (COC) is chosen as the substrate, which has good optical transmittance and chemical resistance. Figure 3 depicts the temperature profile of AMBN matrix using CFD-ACE+™. The material properties including the thermal conductivity of the COC (0.13 W/mK) and AMBN matrix (0.12 W/mK) and the natural convection in the surfaces as boundary condition are applied to the simulation model. From the simulation, the AMBN matrix with design can meet the desired operation temperature range. To realize a disposable on-chip pressure actuator at a low-cost and simple fabrication, direct printing techniques without screen-mask is adopted for deposition of AMBN matrix on the substrate as illustrated in Figure 4 (a). Then, the device is integrated with a polymer microfluidic chip using room temperature UV bonding technique [3] as shown in Fig. 4 (b) and (c).

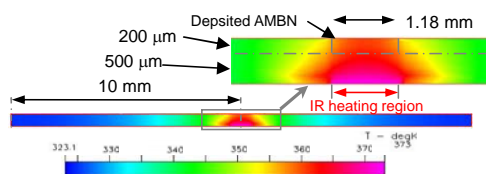


Figure 3. Thermal simulation result of temperature distribution of the cross-section.

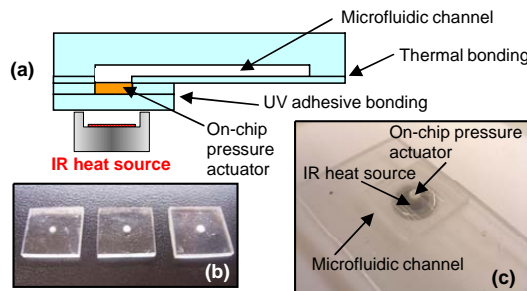


Figure 4. Integration of the on-chip pressure actuator with a microfluidic chip: (a) schematic cut view; (b) fabricated on-chip pressure actuator modules; and (c) photograph of the packaged device with IR heat source.

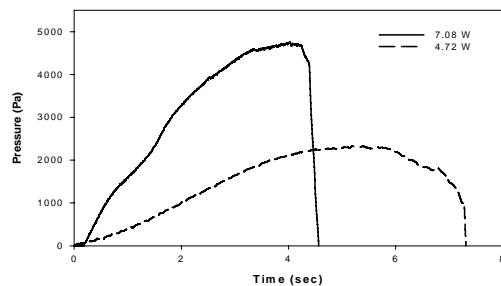


Figure 5. Generated gas pressure with different applied power to IR heat source in the open channel.

3. Experimental Results

The experiment shows that the output pressure from the AMBN can be controlled by the applied power as shown in Fig. 5. The captured video frames of the fluid which is transported using the on-chip pressure actuator are shown in Fig. 6. It takes around 3 seconds to drive the fluid out of the microchannel of 70 mm length. The input power of 5.16 W for 4 seconds is applied to the on-chip pressure actuator with various amount of AMBN until the maximum pressure was reached. The relationship between maximum pressure generation and different amounts of AMBN is shown in Fig. 7, and the relationship between movement of fluidic sample at the maximum pressure and different amounts of AMBN volume in Fig. 8.

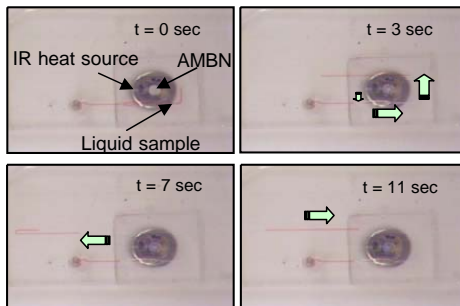


Figure 6. Captured video images at different time steps clearly demonstrating the on-chip pressure generation using IR-induced thermolysis for sample transport.

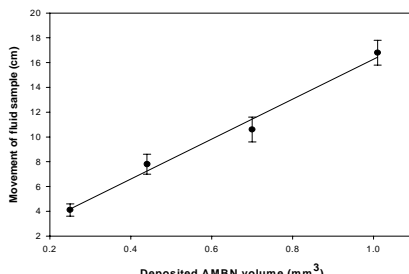


Figure 7. Movement of fluidic sample with different amounts of AMBN volume at the maximum pressure.

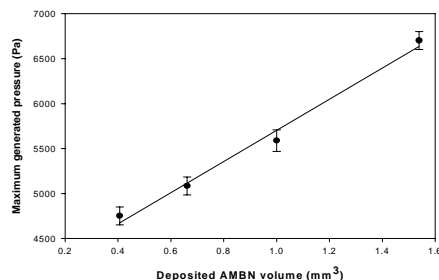


Figure 8. Maximum generated gas pressure with different amounts of deposited AMBN volume in the closed chamber of 7.69 ul.

4. Conclusions

A functional on-chip pressure generator using contactless infrared (IR) heating has been realized and fully characterized for driving liquid through the microchannels on polymer substrates. The solid energetic material generates non-toxic and biologically inert nitrogen gas, which is extremely suitable for applications in micro fluid actuating, and responds to a pressing demand in biochemical and clinical analysis as part of the lab-on-a-chip or μ TAS.

References

- [1] C.-C. Hong, et. al., Lab-on-a-Chip, vol. 3, pp.288-293, 2003.
- [2] E.T. Denizov, et. al., Handbook of Free Radical Initiators, Wiley-Interscience, 2003.
- [3] J. Han, et. al., MicroTAS'03, Squaw Valley, USA, pp. 1113-1116, 2003.

A MONOLITHIC 3D FLOW-FOCUSING DEVICE FOR THE FORMATION OF SINGLE/DOUBLE EMULSIONS IN A CLOSED/OPEN MICROFLUIDIC SYSTEM

Shih-Hao Huang^{1,2}, Wei-Heong Tan¹, Fan-Gang Tseng², and Shoji Takeuchi¹

¹ CIRMM, Institute of Industrial Science, The University of Tokyo, Japan

² Institute of MEMS, National Tsing Hua University, Taiwan

Abstract

We propose a planar 3D microfluidic flow-focusing device (MFFD) that can produce monodisperse single/double emulsions in a closed/open microfluidic system. By confining droplets to the central axis of the microchannel, we avoid the problem of wetting and successfully produced single emulsions for both water-in-oil (W/O) and oil-in-water (O/W) droplets utilizing the same device as well as double emulsions containing one to several internal droplets inside in the closed channel configuration. We also demonstrated the feasibility of forming W/O droplets and polymer microspheres in an open channel configuration by withdrawing fluid from the outlet channel. The unique fabrication provides flexibility for Lab-on-Chip microsystem.

Keywords: monodispersed droplets, double emulsions, SU-8, black photoresist

1. Introduction

This work is motivated by the increasing importance of droplets in many Lab-on-Chip applications [1] and the need for a simple device that can produce single/double emulsions without any surface modifications of channel walls [2]. Our device is compatible with standard MEMS fabrication procedures, and also allows the use of organic solvents which are incompatible with PDMS devices. We succeeded in operating the device in both closed/open channel configurations.

2. Design and Fabrication

Fig.1 (a)-(b) show schematic diagrams of the monolithic 3D MFFD to produce monodisperse single and double emulsion drops, respectively. Two or three immiscible fluids can be focused through the coaxial orifices. At the orifice, the inner liquid thread stays confined to the central axis of the microchannel, surrounded by the continuous phase. As the dispensed phase (inner fluid thread) does not wet channel walls, our proposed 3D MFFD can produce single emulsions for both water-in-oil (W/O) and oil-in-water (O/W) droplets utilizing the same device. Fig.1 (c) shows schematic diagrams of the cross section of 3D MFFD. The device consists of three layers of SU-8 resist structures to form the embedded coaxial orifices. CK-7800L black photoresist was

used to mask unexposed regions from exposure during the latter processes [3]. Here, open channel configuration refers to the 3D MFFD without PDMS cover.

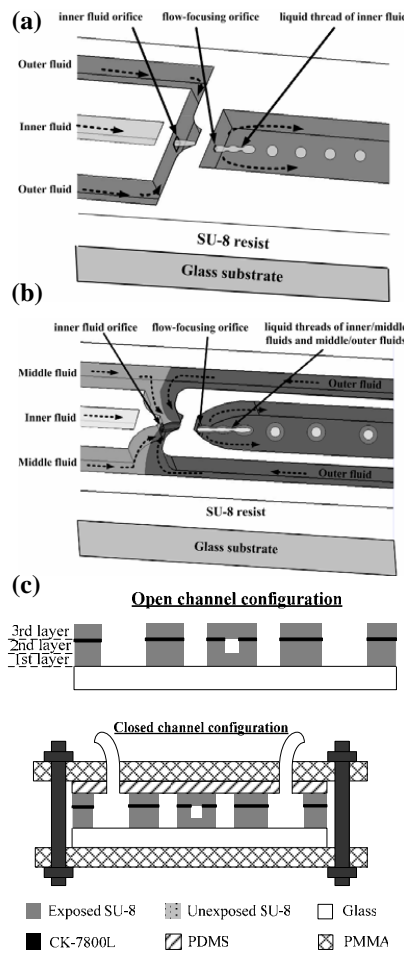


Figure 1 (a) and (b) show schematic diagrams of the 3D MFFD to produce monodisperse single emulsion drops and double emulsion drops, and (c) the cross section of 3D MFFD

3. Results and discussions

Fig.2 (a)-(b) show the variation of droplets' diameters with respect to flow rate ratio (Q_c/Q_d) of the continuous phase (Q_c) and dispensed phase (Q_d) in the closed channel configuration, where Q_d fixed at 0.6 $\mu\text{l}/\text{min}$ with $D_{\text{orifice}}=200\mu\text{m}$. Fluid treads for both O/W and W/O droplets can be clearly observed without any occurrence of phase inversion [2b]. Fig.3 (a) show the images of the coaxial tread breaking into “in-phase” and “phase-shifted” double emulsion drops in a closed channel configuration, each containing a single internal droplet. As break-up frequency of the inner fluid thread exceeded that of the middle fluid thread, double emulsions with multiple internal droplets were produced (Fig.3(b)). We also demonstrated the feasibility of forming W/O droplets and polymer microspheres in an open channel configuration by withdrawing fluid from the outlet channel. We filled up the microchannels with continuous phase. DI water or monomer was then added to the inner fluid reservoir. We withdrew the fluid from the outlet channel using a syringe with a tiny needle. Fig.4(a)-(e) shows W/O droplets produced in an open channel configuration by varying the withdrawal flow rate (Q_w). Polymer particles were obtained by the in-situ photopolymerization of monomer droplets passing through the UV irradiated area. Polymer particles were collected by heating the 3D MFFD to remove the DI water (Fig.4 (f)).

Reference

1. a) W. Jeong et. al., 2004, Lab chip, 4, pp. 576-80.; b) A. S. Utada et. al., 2005, Science, 308, pp.537-41.
2. a) M. Joanicot and A. Ajdari, 2005, Science, 309, pp.887-89.; b) M. Seo et. al., 2005, Langmuir, 21, 11614-11622.
3. S. H. Huang and F.G. Tseng, 2005, J. of Micromech. Microeng., 15, pp.2235-42

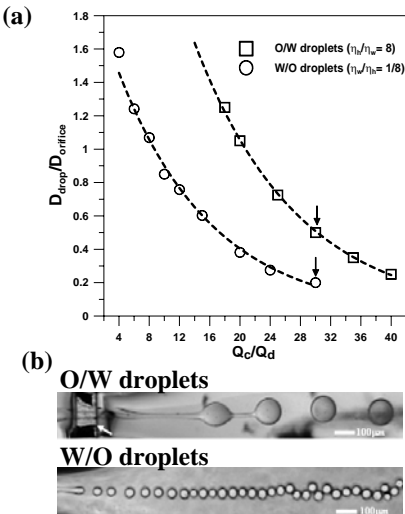


Figure 2 (a) shows the results of the droplets' diameters with respect to the flow rate ratio (Q_c/Q_d), and (b) the images of O/W and W/O droplets at $Q_c/Q_d=30$ indicated in (a).

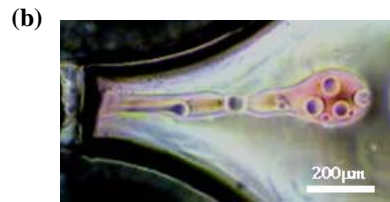
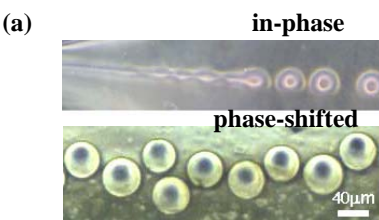


Figure 3 (a) images of in-phase and phase-shifted double emulsion, (b) Double emulsions with multiple internal droplets.

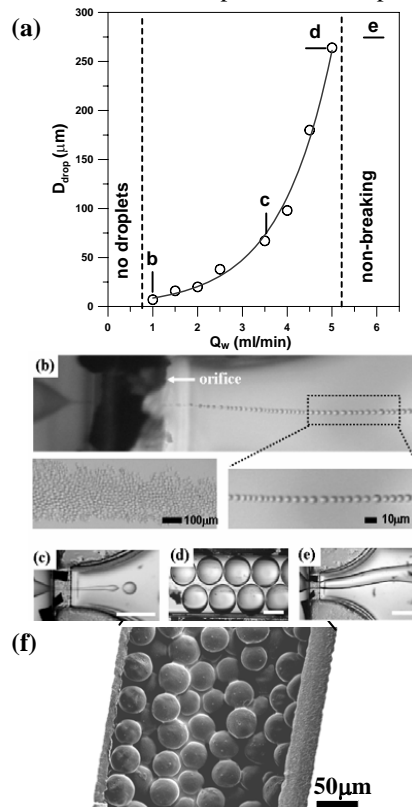


Figure 4 (a) W/O droplets produced by varying the withdrawal flow rate (Q_w) in an open channel configuration. (b)-(e) show the images indicated in (a). (f) polymer microspheres with 40 μm.

CHECKERED ELECTROSTATIC ACTUATOR FOR TWO-DIMENSIONAL MANIPULATION OF LIQUID DROPLETS

Kei Takenaka and Yasushi Goto

Hitachi, Ltd., Japan

Kei.takenaka.ma@hitachi.com

Abstract

A new electrostatic actuator for manipulating liquid droplets in μ -TAS was developed. This actuator has square electrodes ($300 \times 300 \mu\text{m}$) on a single plate. These electrodes are placed in a checkered arrangement and connected along either one of the two diagonal lines. This actuator can perform two-dimensional manipulation—moving, splitting, and merging—of an 80-nl liquid droplet on a single plate.

Keywords: electrostatic actuation, two-dimensional manipulation, liquid droplet, μ -TAS

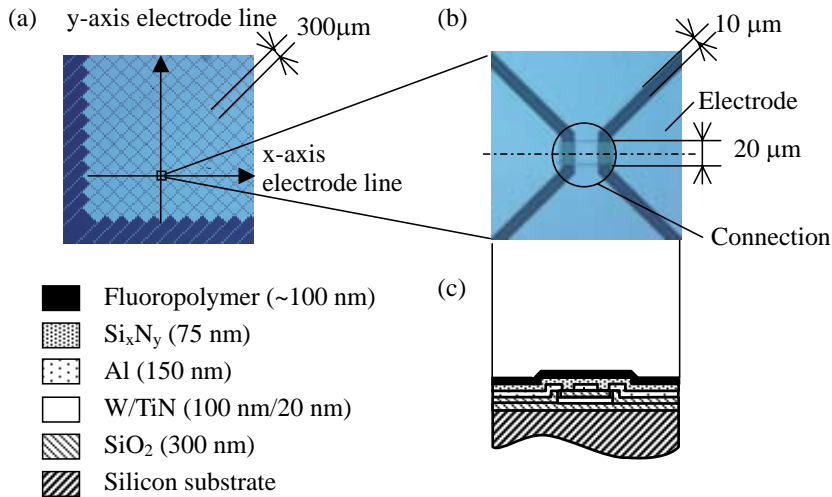
1. Introduction

Liquid-droplet manipulation actuators using electrostatic force—which require neither pumps nor valves and minimize dead-volume of reagents and samples in channels or reservoirs—have recently been attracting a lot of attention [1-4]. To apply these actuators to μ -TAS, liquid droplets should be manipulated in a two-dimensional plane. S.-K. Fan *et al.* reported a cross-reference EWOD device in 2003 [4]. This actuator has $M \times N$ intersect grids where N rectangular electrodes on bottom plate and M rectangular electrodes on top plate. Using this actuator, they demonstrated two-dimensional manipulation of liquid droplets at the intersection points of electrodes in two separate plates under an applied voltage. However, it is therefore structurally difficult to combine this actuator with analytical devices such as sensors, reactors, and heaters because rectangular electrodes are placed on both the top-plate and the bottom-plate. To combine this actuator and analytical devices, it is preferred that all electrodes of the actuator for manipulating liquid droplets are placed on the bottom plate and analytical devices are equipped with the top plate.

2. Theory and experimental measurement

We fabricated an electrostatic actuator on a single substrate for manipulating liquid droplets in a matrix. Plane views of the fabricated actuator are shown in Figs. 1(a) and (b). This actuator has square electrodes ($300 \times 300 \mu\text{m}$) placed in a checkered arrangement. All electrodes are connected along either one of the two diagonal lines of electrodes. The cross section of the fabricated actuator is illustrated in Fig. 1(c). Although the lines of electrodes connected in the horizontal direction (x-axis electrode line) and the lines of electrodes connected in the vertical direction (y-axis electrode line) intersect at their connections, both electrode lines are isolated electrically by a silicon-oxide film (300nm) and covered by a silicon nitride film (75nm) and a fluoropolymer

film (~100nm).



(a) Plane view (photo) (b) Enlarged view (photo) (c) Cross-sectional view
Fig. 1: Plane and cross-sectional views of the fabricated device

A schematic diagram of the fabricated device difference is created between the x-axis electrode which are selected by the selecting switches. The liquid droplet was moved to the cross point by electrostatic force between the x-axis and y-axis electrode lines. Furthermore, to select the adjoining electrode lines of each axis, the fabricated device can change the volume of the manipulated liquid droplets.

A cross-sectional view of the fabricated device with two spacers and a top plate is illustrated in Fig. 3. The spacers—a 30- μm -thick polyester two-sided tape (No5603; Nitto Denko)—are used to define the gap between the top plate and the device. A slide-glass-coated fluoropolymer (FS-1010TH; Fluoro Technology) is used as the top plate.

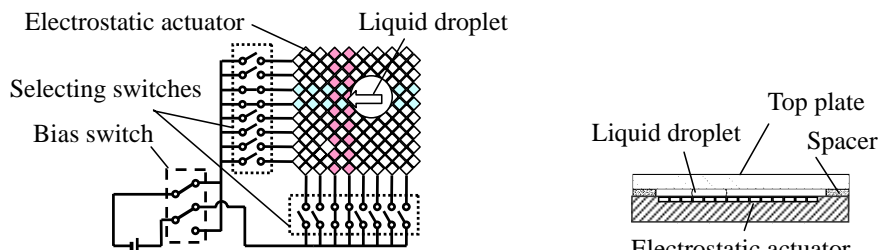


Fig. 2: Schematic diagram of the fabricated device

in Fig. 2. A potential difference is created between the x-axis electrode

, y-axis electrode lines,

which are selected by the selecting switches. The liquid droplet was moved to the cross point by electrostatic force between the x-axis and y-axis electrode lines. Furthermore,

to select the adjoining electrode lines of each axis, the fabricated device can change the

volume of the manipulated liquid droplets.

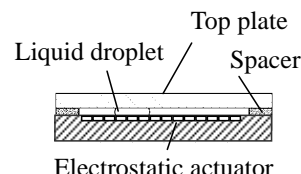


Fig. 3: Cross-sectional view of the test device

3. Results and discussion

The results of a droplet-manipulation experiment are shown in Fig. 4 as a series of pictures. The applied voltage is 30 V. An 80-nl liquid droplet was split in two by pulling it in opposite directions (1-6), the two liquid droplets were merged by pulling them toward each other (7-10), and the merged liquid droplet was moved (11-16). This figure shows that this electrostatic actuator can be successfully manipulated in a two-dimensional plane with only one plate. It is structurally easy to combine this electrostatic actuator with analytical devices because all electrodes of the actuator for manipulating liquid droplets are placed on a single plate.

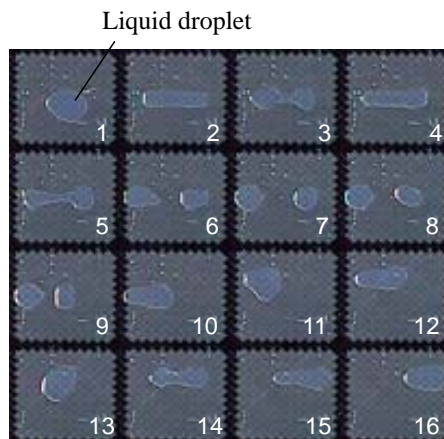


Fig. 4: Test results shown as a series of photos

4. Conclusions

A new electrostatic actuator for manipulating liquid droplets in μ -TAS was developed. This actuator has square electrodes placed in a lattice-shaped arrangement and connected along either one of two diagonal lines. It can move, split, and merge liquid droplets in a two-dimensional plane. Furthermore, as all electrodes of it for manipulating liquid droplets are placed on a single plate, it is structurally easy to combine this actuator with analytical devices on the other single plate. This means that the actuator is useful for manipulating liquid droplets for μ -TAS.

References

1. M. Washizu., IEEE Trans. Ind. Appl. 34, pp. 732-737, 1998
2. M.G.Pollack, R.B.Fair, A.D.Shenderov., Appl.Phys.lett., vol.77, pp.1725-1726, 2000
3. S.K.Cho, H.Moon, C.-J.Kim., J.MEMS., vol.12, pp.70-80,2003
4. S.-K. Fan, C. Hashi, and C.-J. Kim., Proc. IEEE 16th Int. Conf. MEMS (MEMS'03), pp. 694-697, 2003

SPONTANEOUS MICROFLOW OF MICROPILLAR ARRAY ELECTROSPRAY IONIZATION MICROCHIP

Nissilä Teemu^{1&2} Sainiemi Lauri³ Sikanen Tiina^{1&4} Kotiaho Tapio⁴

Franssila Sami³ Kostiainen Risto¹ Ketola Raimo Allan^{1&2}

¹ Div. of Pharm. Chem., Faculty of Pharmacy, Univ. of Helsinki

² Drug Discov. and Development Technology Center, Univ. of Helsinki

³ Microelectronics Center, Helsinki Univ. of Technology

⁴ Laboratory of Analytical Chemistry, Univ. of Helsinki

Abstract

A robust semiconductor micropillar array electrospray ionization (ESI) chip has been developed, fabricated and tested. The silicon chip has spontaneous transfer of liquids. Capillary forces and hydrostatic pressure affects the flow rate. ESI could be formed easily by applying high voltage to the chip. Via ESI interface the chip can be connected to a mass spectrometer.

Keywords: micropillar array, flow, capillary action, electrospray, ionization

1. INTRODUCTION

Micropillar arrays have shown to have strong capillary forces which enable transfer of liquids in the micro channels without external power, such as pumping [1]. Electrospray ionization-mass spectrometry (ESI-MS) is a well-known analytical technique, by which liquid samples can be directly analyzed with good sensitivity and selectivity. Various types of miniaturized ESI sources have already been manufactured using pumping or electroosmotic flow. The purpose of this work was to evaluate the spontaneous flow of liquids in micropillar array chips with varying diameters of the pillars and the distances between them. Furthermore, the tip of the micropillar array was used as a direct ESI tip, thus the whole microchip could be connected to a mass spectrometer.

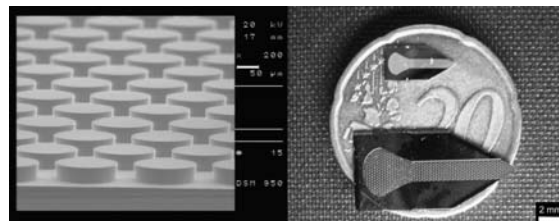


Figure 1: Micropillar array chip. SEM picture of shapes of micropillars and overview of the small and large size chips on a 20 cent euro coin.

2. EXPERIMENTAL

Micropillar array chips were fabricated to a silicon substrate. Pillar arrays were etched by deep reaction ion etching (DRIE) to a depth of $50\text{ }\mu\text{m}$. A scanning electron micrograph of a pillar array and the whole chip are presented in Figure 1. The shape of the pillars was round, and the diameters varied from 15 to $200\text{ }\mu\text{m}$ and the distances between pillars were from 1 to $80\text{ }\mu\text{m}$ from chip to chip. The cylindrical pillars were arranged in an equilateral triangular conformation [2]. The end of the channel containing the micropillar array was sharpened to enable ESI. The setup of combining a micropillar array with a PE Scieix API-300 triple quadrupole mass spectrometer for ESI-MS measurements is presented in Figure 4a. High voltage was applied to the sample section of the chip. Potential difference between the microchip and the first lens of mass spectrometer was 2.5 kV. The electric current between the chip and MS was about 100 nA. The sample, tetrabutylammoniumiodide in acetonitrile, was pipetted onto the sample section.

3. RESULTS AND DISCUSSION

The capillary flow at the micropillar array is a spontaneous feature based on the capillary action and is dependent on the diameters of pillars and the distances between them. Figure 3a shows that the flow rate clearly increases when the distance between the pillars one increased from $2\text{ }\mu\text{m}$ to $75\text{ }\mu\text{m}$. Figure 3b shows that the flow rate increases when the volume of solvent (ethanol) is increased from $2\text{ }\mu\text{l}$ to $8\text{ }\mu\text{l}$ indicating that hydrostatic pressure increases the spontaneous flow within the micropillar array. The flow rates presented in Figure 3 are suitable for direct ESI. The sharpened tip at the end of the chip allows stable Taylor cone and thus stable ESI (Figure 2). Mass spectrum of tetrabutylammonium by micropillar ESI chip shows abundant molecular ion at m/z 242, and thus proves both the spontaneous flow of the sample from the sample section to the tip of the microchip. It was also noticed that the flow rate of the liquid was increased when the ES voltage was turned on. That was because the ES sucks the fluid from the pillar array thus forming a significant force which moves the liquid in the micropillar array channel.

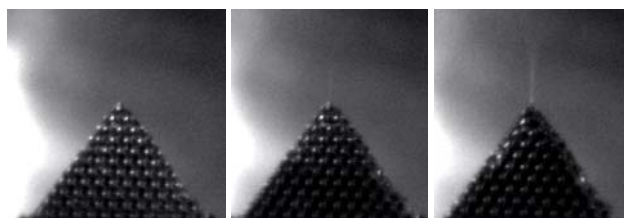


Figure 2: Formation of electrospray. Time between photos is 40 ms.

To summarize, we are able to analyze chemical compounds with silicon micropillar array ESI-MS chip, which provides spontaneous transfer of liquids. We can also control the flow rate of the chip by changing dimensions of micropillar array and hydrostatic pressure.

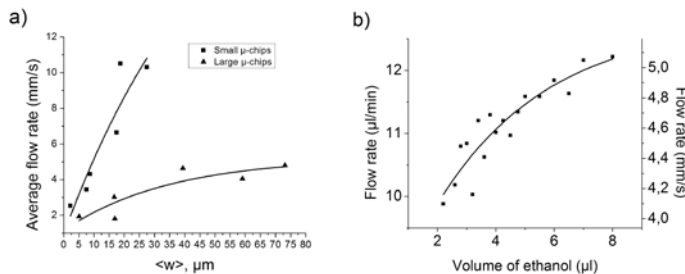


Figure 3: Spontaneous microflow at microarray pillars. a) The effect of the distance between micropillars $\langle w \rangle$ to the flow of ethanol in small (channels lengths = 5 mm) and large (channels lengths = 11 mm) chips. Introduced volumes of samples were 1 μl with small and 4 μl with large chips. b) The effect of the sample volume of dropped ethanol in the inlet to the flow rate of ethanol.

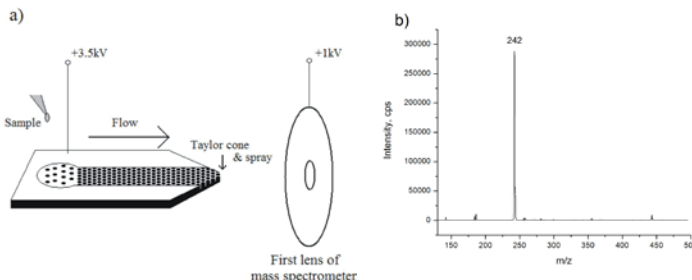


Figure 4: a) Principle of the measurement setup. b) Mass spectrum of tetrabutylammonium (molecular weight 242) measured with the micropillar-ESI-MS.

References

- Öhman Per Ove and Mendel-Hartvig Ib. Micro fluidic structures. Patent application, PCT/SE03/00919, WO 03/103835, 2003.
- Nico Vervoort et al. Importance and reduction of the sidewall-induced band-broadening effect in pressure-driven microfabricated columns. *Anal. Chem.*, 76:4501–4507, 2004.

MICROMIXING BIOLOGICALLY CROWDED AGENTS BY FOLDING PLUGS THROUGH PILLARS

Kum Cheong Tang¹, Rachmat Multi Wibowo², and Levent Yobas¹
¹Institute of Microelectronics, 11 Science Park Road, S117685, Singapore
²Nanyang Technological University, Singapore 639798
(Contact: leventy@ime.a-star.edu.sg)

Abstract

In this paper, we describe a microfluidic device for the rapid mixing of viscous sticky crowded agents. These agents were isolated in plugs and forced to pass through a series of pillars which caused mixing by inducing an oscillating interfacial shear.

Keywords: microfluidics, mixing, crowded agents, plug, shear

1. Introduction

The interior of a cell consists of densely-packed soluble molecules [1]. A single species concentration is relatively low but collectively, these molecules can occupy a significant 20 to 30% of the total volume (typically 50 to 400mg/mL). We call such a fluidic medium “crowded” [2 – 3]. Most biochemical reaction experiments are conducted in molecular concentrations between 1 to 10mg/mL (negligible crowding effects). We report a microfluidic device mixing viscous and sticky crowded media like bovine serum albumin (BSA). The *in vitro* study of reaction kinetics demands that the reactants be homogeneously mixed faster than the occurrence of the reaction itself [4].

2. Experimental

Mixing of crowded agents has been demonstrated in serpentine-shaped micromixers with bumpy edges [4]. Our device, made of polydimethyl siloxane (PDMS) using soft lithography [5], incorporates a series of pillars and provides a reasonable mixing efficiency by repeatedly folding and stretching plugs of crowded agents traversing through the pillars (figure 1). The channel of this micromixer contains repeated arrangement of small (50μm) and big pillars (80μm). The nominal length and depth of the channel are 30mm and 80μm, respectively. The first pair of the small pillars is located about 1mm from the cross-junction. The gap between the small pillars of a pair is fixed at 40μm, 60μm and 80μm as a design parameter.

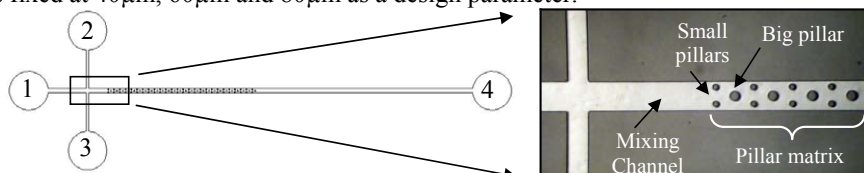


Figure 1. Layout and photomicrograph of the micromixer (1, 2, and 3 are inlets and 4 is outlet).

3. Results and discussion

Silicone oil (Dow Corning 200[®] viscosity 19.06 mPa-s) was injected into the device through inlets 2 and 3 while two separate streams of BSA solution were injected through inlet 1. Figure 2a shows the formation and mixing of BSA plugs (200mg/mL dissolved in phosphate buffered solution laced with two different colored dyes) in the 80μm-gap design. For all experiments, two BSA solutions were injected into inlet 1 at 0.05μL/min and silicone oil was injected into inlets 2 and 3 at 1μL/min, unless otherwise stated. Under steady flow, the oil pinches off the BSA solution at the cross-junction, creating plugs of BSA transported downstream through the pillars. Fluorescent dye was added to one BSA stream to visualize the mixing process (figure 2b). A surfactant Tween 20 (3% v/v) was added to oil to improve the plug stability. The length of the plug is roughly 250μm. We observed that without the pillars, the BSA plugs could not mix efficiently (figure 3). Fluid exchange between the two halves of the plug was minimal and fluorescent dye remained confined to only one BSA stream.



Figure 2. (a) Optical and (b) fluorescence photomicrograph of BSA plugs.

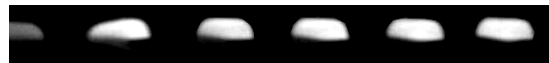


Figure 3. Inefficient mixing of BSA plugs without employing the pillars.

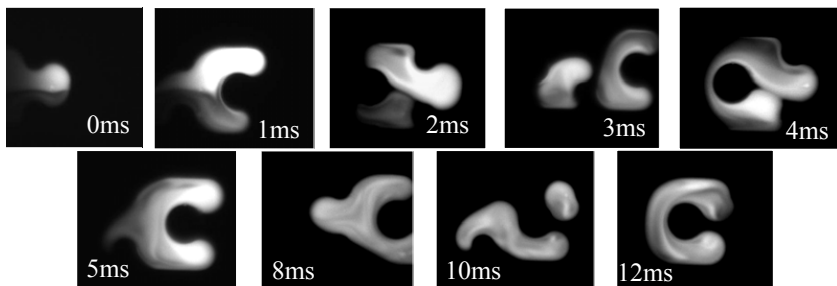


Figure 4. Mixing of BSA-BSA plugs.

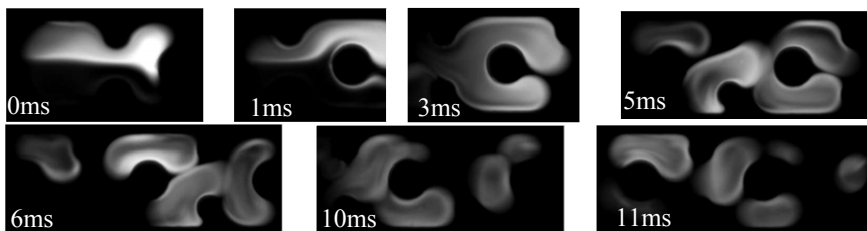


Figure 5. Mixing of BSA-Hb plugs.

Effect of the pillars (80 μ m-gap) on the mixing can be observed from the striations in the plugs captured at subsequent points in time (figure 4). The plugs stretched and split as they encountered a big pillar and re-combined as they squeezed between two small pillars (e.g. at 4ms). This cyclical action induced oscillating interfacial shear within the plug contents. After repeated cycles of stretching, splitting and re-combining, the dye within the plugs redistributed evenly. Complete mixing occurred at the 6th cycle 11ms after the first encounter with the pillars (a cycle is a set of two small and one big pillar). For the 40 μ m and 60 μ m-gap designs, complete mixing was observed earlier at the 4th (7ms) and 5th cycle (9ms), respectively. Figure 5 shows the mixing of BSA and hemoglobin (Hb) using the 80m-gap design. BSA and Hb flowed at 0.1 μ L/min (inlet 1) while oil at 1.3 μ L/min. Both BSA (containing fluorescent dye) and Hb were dissolved in PBS at 260mg/mL and 300mg/mL, respectively. Since Hb is almost twice as viscous as the BSA, mixing took a longer time (>20ms). Hence, the striations are not clearly visible within the first 11ms.

A plot of normalized fluorescence intensity of the plugs in different designs is given in figure 6. Mixing caused an overall decline in the intensity by redistributing the dye rapidly. This simple arrangement of pillars can be further optimized for the rapid mixing of the crowded media in the study of reaction kinetics.

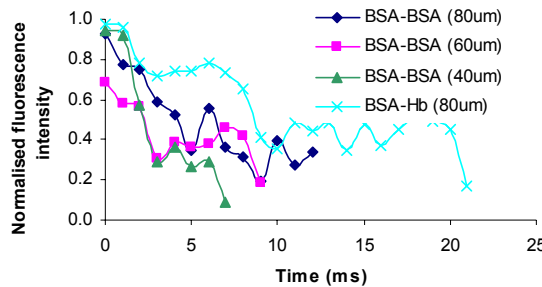


Figure 6. Normalized fluorescence intensity.

References

1. D. S. Goodsell, *The Machinery of Life*, Springer-Verlag, New York, 1993, p. 56.
2. R. J. Ellis, *Macromolecular crowding: obvious but unappreciated*, TRENDS in Biochem. Sci., 26 (2001) 597 – 604.
3. A.P. Minton, *The influence of macromolecular crowding and macromolecular confinement on biochemical reactions in physiological media*, The J. of Biol. Chem., 276 (2001) 10577 – 10580.
4. A. Liau, R. Karnik, A. Majumdar and J. H. D. Cate, *Mixing crowded biological solutions in milliseconds*, Anal. Chem., 77 (2005) 7618 – 7625.
5. J. C. McDonald and G. M. Whitesides, *Poly(dimethylsiloxane) as a material for fabricating microfluidic devices*, Accounts of Chem. Res., 35 (2002) 491 – 499.

MULTI-REAGENTS HIGH SPEED EXCHANGE FLOW SYSTEM FOR SINGLE BIOMOLECULAR DYNAMICS REAL TIME MONITORING

Yukiko Sato*, Takahiro Arakawa*, Tomoya Sameshima, Taro Ueno**,
Takashi Funatsu** and Shuichi Shoji***

* Major in Nano-science and Nano-engineering, Waseda University,

** Graduate School of Pharmaceutical Sciences, University of Tokyo

Abstract

We develop a multi-reagent high speed exchange flow system integrated with Total Internal Reflection Fluorescent Microscopy (TIRFM). The reagent switching time within 100 ms was obtained with high performance in-channel PDMS microvalves, the real time monitoring of a single protein behavior, the chaperonin GroEL - cochaperonin GroES rapid interaction, was performed. The fabricated TIRFM microflow system enables the observation of single biomolecular level very short time reactions of a few seconds.

Keywords: real time monitoring, single biomolecular detection, protein analysis, microflow system, PDMS microvalves

1. Introduction

The TIRFM technique has been applied for single biomolecular level observation under very low background light using evanescent field. It is produced just beyond the interface with penetration depth of 150 nm when a laser is incident on the substrate at above the critical angle [1]. Flat and pinhole-free glass surface reduces diffuse skylight, which is required in the investigation of single-molecule level proteins [2]. We developed no leakage and small dead volume monolithic PDMS microvalve systems [3]. However, the switching time was limited around 300 ms. High speed microvalve was requested for real time monitoring.

2. Experimental

Figure 1 shows the cross-sectional view of this system which consists of the glass microchannel with the observation area, and the PDMS pneumatically actuated membrane and air pressure channels of the active microvalves. The cross-sectional SEM photomicrograph of the monolithically

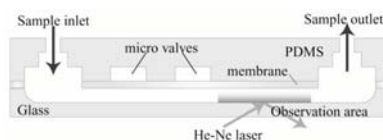


Figure 1 Cross sectional view of the in-channel microvalve system for TIRFM

fabricated in-channel valve is shown in Figure 2. We measured reagent exchange time of the microvalve system using a high speed CCD camera by applying stepped air pressure. The exchange time within 100 ms was obtained at the observation area. The flow system can control reagent injection volume of less than 5 nL. Combination of this high speed reagent exchange microflow system and TIRFM enables the real time monitoring of single biomolecular dynamic reactions. Imaging of the chaperonin GroEL - cochaperonin GroES interactions was chosen to show the capability of the single molecular level detection.

Figure 3 is a schematic of the immobilized GroEL and GroES interaction. Area (i) in Figure 3, GroEL is immobilized to the glass surface, while area (ii) is blank.

Figure 4 shows a sequential buffer and sample flows of the controlled by three microvalves for monitoring GroEL and GroES interactions. GroEL was introduced and immobilized to the glass surface (Figure 4(a)). Then residual GroEL was cleaned off with buffer, Term I (Figure 4(b)). High concentrated reagent of fluorescently-labeled GroES (Cy5-GroES) was injected for 1 sec, Term II (Figure 4(c)). Then buffer was introduced to clean off the unbound GroES, Term III (Figure 4(d)).

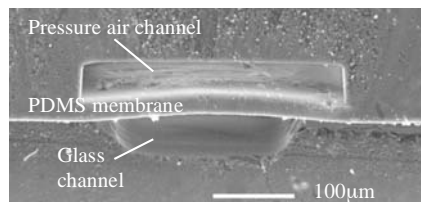


Figure 2 Cross-sectional SEM photomicrograph of the PDMS and Pyrex glass microvalve

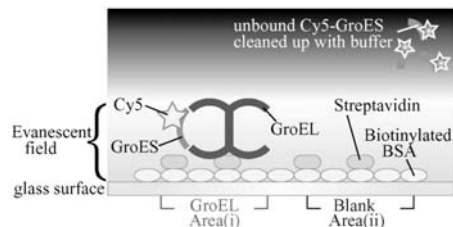


Figure 3 Schematic view of the interaction of GroEL and GroES on the glass surface

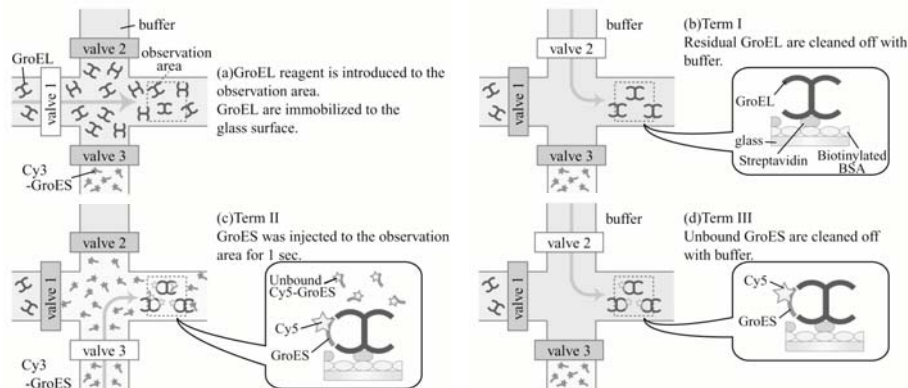


Figure 4 Sequence of the flow for monitoring GroEL and GroES interactions

3.Results

Figure 5 shows the TIRFM images at the observation area.

Figure 5(a) is the image of during Term I, 5(b) is that of during Term II, 5(c) is that of during Term III. Figure 6 shows time dependent fluorescence intensity at the observation area (i) (GroEL; red circle) and area (ii) (blank; blue circle) in Figure 5(c). Very low back ground noise was observed during Term I. When the GroES reagent was injected, fluorescence intensity was out of range during Term II. Right after the buffer was introduced for cleaning during Term III, the fluorescent intensity was remained at area (i) (GroEL), while that was decreased immediately to the background level at area (ii) (blank). The fluorescence intensity was decreased by the laser irradiation during Term IV.

Very short time protein reactions were observed by the microflow system.

4.Conclusions

Example of the monitoring the single molecular level interaction was performed. This result describes proposed microsystem is applicable for real time monitoring of the single biomolecular level interactions.

Acknowledgement

This development was supported by SENTAN JST, Japan Ministry of Education, Culture, Sports Science & Technology Grant-in-Aid for COE Research "Molecular Nano-engineering and Its Development into Microsystem" and SCOE "ASMew".

References

- [1]T. Funatsu et al., Nature, **374**, 555-559, (1995)
- [2]T. Ueno et al., Molecular Cell, **14**, 423-434, (2004)
- [3]T. Arakawa et al., μ -TAS 2004, pp381-383
- [4]T. Arakawa et al., Transducers2005, pp1489-1492

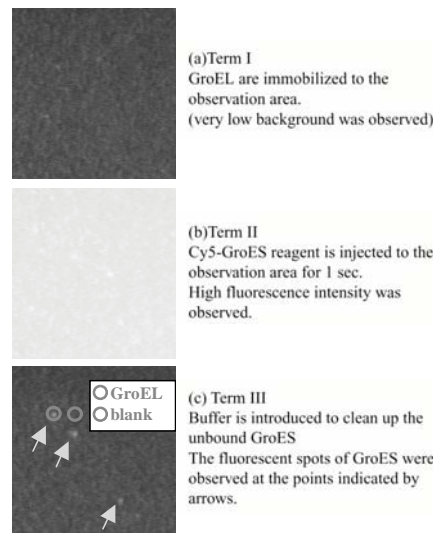


Figure 5 TIRFM images of the GroEL-GroES interactions

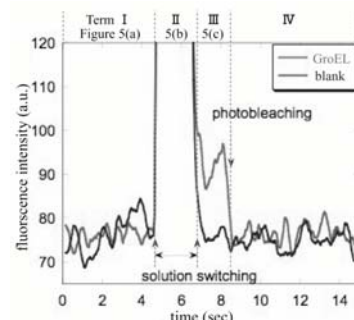


Figure 6 Time dependent fluorescence intensity at area (i) (GroEL) and area (ii) (blank)

BEAD IMMOBILISATION IN A PLANAR POLYMER MICROFLUIDIC ELECTROCAPTURE DEVICE

Mats Jönsson and Ulf Lindberg

Solid State Electronics Department, The Ångström Laboratory, Uppsala University.

P.O. Box 534, 751 21 Uppsala, Sweden.
e-mail: mats.jonsson@angstrom.uu.se

Abstract

The electrocapture technology has been utilized for capture of beads in a robust planar micro device with integrated ion selective electrodes. Capture and release of 2 μm beads is successfully demonstrated.

Keywords: electrocapture; concentration; beads; microdevice

1. Introduction

With the electrocapture technology charged biomolecules and particles can be immobilised in a flow channel by applying a local electric field [1]. Earlier electrocapture devices have been manufactured from polymer tubing and are therefore not easily incorporated in a lab-on-a-chip system nor has it been possible to study the effect of the electric field on the charged biomolecules in detail.

2. Experimental

A planar microfluidic electrocapture (ECD) device that captures and concentrates beads by a local electrical field has been assembled and tested. The presented device enables on-line observations of electrically manipulated beads in a micro channel. The design is based on a sandwich construction from a glass substrate and a PMMA-lid, using a patterned polyimide spacer to form the channel [2]. Capture and release of 2 μm polystyrene beads have been performed successfully at an applied potential of 300 V.

The planar capture device was designed to be simple, robust and easy to manufacture. The device is a sandwich construction of a lower support part and an upper lid part. The ion selective membrane used is Nafion. The lower support part and the upper lid part was first mounted separately and then assembled to form the channel, see figure 1

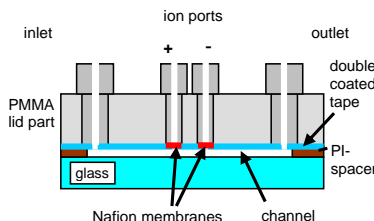


Figure 1. Cross section view of the planar capture device. The ion port distance is 10 mm and the total channel volume is 3.6 μL .

3. Results and discussion

The capture was observed and documented with an inverted fluorescence microscope, equipped with a digital camera. The assembled leak tight device is shown in figure 2. The capture behaviour is studied using a sample of 2 μm diameter polystyrene beads suspended in 0.2 M Tris-HCl Buffer, pH 7.4. The sample solution is introduced from a syringe pump into the capture device at a flow rate of 0.5 $\mu\text{L}/\text{min}$. The position of the capture zone is located 2 mm upstream from the centre of the ion selective membrane. A voltage of 300 V is applied for 15 min to capture an observable amount of sample, see figure 3. To describe the behaviour of the capture in the detail, a complex electrokinetic and hydrodynamic model is required since electrophoretic and electroosmotic forces [3] are likely to be involved. The presented results support the stacking principle suggested by Astorga-Wells and Swerdlow [4]. The most challenging task in building the device is to integrate the ion selective electrodes in a microdevice with a reliably bonded channel. By using a thick glass substrate, the device becomes mechanically stable and the PMMA-part is sufficiently thick for a robust design of the channel-to-tubing interface connections.

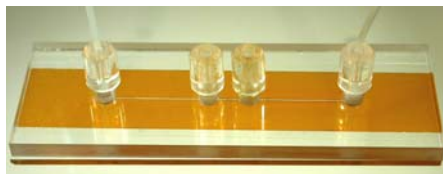
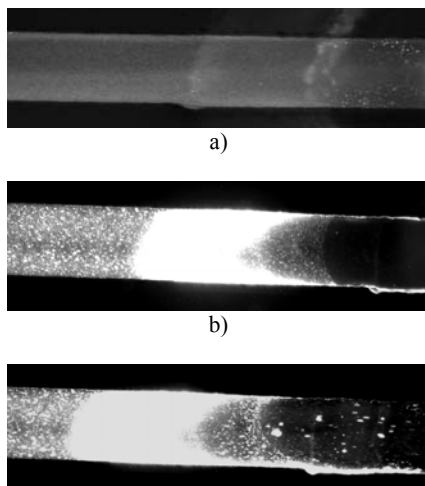


Figure 2. Photo of the planar capture device, view from above. The channel, length 60 mm, in the PI-spacer is seen through the PMMA lid part. The fittings for inlet, outlet and buffer reservoirs are connected.



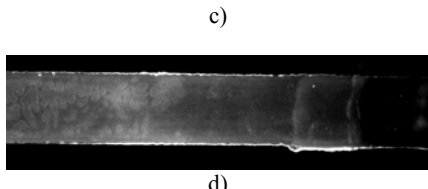


Figure 3. Picture sequence of the capture channel (width 0.8 mm, height 75 μm) with the flow direction from left to right. The photos of the captured beads are taken at a position 2 mm upstream from the downstream ion selective membrane, (a) continuous flow of sample, (b) capture of beads at applied electric field of 300 V for 15 min, (c) directly after the release the beads are released in clusters, (d) 10 minutes after the capture major part of the beads are released.

4. Conclusion

Capture and release of 2 μm beads is successfully demonstrated which shows potential for the planar electrocapture device to be used for biological samples.

References

1. J. Astorga-Wells, S. Vollmer, T. Bergman, and H. Jornvall, *Microfluidic systems and proteomics: Applications of the electrocapture technology to protein and peptide analysis*, Analytical Biochemistry, vol. 345, pp. 10-17, (2005).
2. M. Jönsson, U. Lindberg. *A planar polymer microfluidic electrocapture device for beads immobilisation*, J. of Micromechanics and Microengineering, in press.
3. A. J. Bard and L. R. Faulkner, *Electrochemical methods : fundamentals and applications*, 2. ed. New York: Wiley, (2001).
4. J. Astorga-Wells and H. Swerdlow, *Fluidic preconcentrator device for capillary electrophoresis of proteins*, Analytical Chemistry, vol. 75, pp. 5207-5212, (2003).

MOVING, MIXING, AND FILTRATION OF DROPLETS BY MAGNETIC FIELDS

Juergen Pipper*, Pavel Neuzil and Tseng-Ming Hsieh

Institute of Bioengineering and Nanotechnology,
31 Biopolis Way, The Nanos, #04-01, 138669 Singapore
jpipper@ibn.a-star.edu.sg

Abstract

We overlay surface-functionalized magnetic particles with mineral oil to turn free droplets into a virtual laboratory. The magnetic particles allow the droplet manipulation by magnetic fields and act temporarily as solid support for performing complex biochemical processes in sequence. A proof-of-concept experiment demonstrates how to isolate cells, lyse, and subject them to a real-time polymerase chain reaction (PCR) targeting a transfection vector-encoding gene in less than 20 min.

Keywords: Droplets, magnetic particles, μfilter, sample preparation, μPCR

1. Introduction

Several microfluidic systems have been reported for moving, merging, mixing, and splitting of droplets on surfaces, such as electrowetting [1], surface acoustic waves [2], or dielectrophoresis [3]. However, these methods lack the most important operation for performing sequential (bio)chemical processes: being able to purify starting material and/or reaction products from crude or complex mixtures. If a solid phase with affinity to any material of interest was part of a droplet-based system, such sequential processes were possible. To this end, the idea of incorporating magnetic particles to manipulate droplets by magnetic fields [4] presents an attractive option for realizing a micro total analysis system (μ TAS). Here, we present a modular chip-based microfluidic system for the (bio)chemical analysis of (body)fluids. Key feature of the system is a self-assembling droplet that is spontaneously formed on a hydro-/oleophobic surface by encapsulating an aqueous suspension of magnetic particles in an immiscible liquid (fig. 1a). By applying (electro)magnetic fields (fig. 1h), the droplet can be manipulated in the x, y-direction. Basic manipulations include moving, merging, mixing, filtering, and splitting of two or more droplets (fig. 1b-g).

2. Experimental results

Solid phase extraction of cells (Fig. 1b-g): a droplet containing a 100 nL suspension of $200 \mu\text{g } \mu\text{L}^{-1}$ Dynabeads® CD15 (Dynal Biotech) in 0.01 M phosphate buffered saline (PBS), pH 7.4 (Sigma-Aldrich)/ 1% bovine serum albumin (BSA) (Roth) was merged with a 10 μL droplet containing 0.1% transiently green fluorescent protein (pmaxGFP™)-transfected (amaxa) THP-1 cells (American Type Culture Collection) in a modified RPMI 1640 cell culture medium at a density of 5×10^6 cell/mL, mixed for 300 s, and washed successively for 20 s in two droplets containing 10 μL 0.01 M PBS/

1% BSA. At this stage, 30-40 purified THP-1 cells were immunocaptured onto the Dynabeads® CD15 (data not shown).

Cell lysis and polymerase chain reaction (PCR) (Fig. 2b): the 100 nL droplet containing the purified surface-bound THP-1 cells was moved onto the microfabricated heater, merged with a 3 µL droplet containing the PCR mixture, mixed for 20 s, and lysed at 100 °C for 60 s. A 99 base pair (bp) fragment of the pmaxGFP™ vector was the target gene and 5'-atg acc aac aag atg aag agc a-3', 5'-gtt ggt gcc gaa gtg gta gaa g-3', and 5'-FAM-aag gcg ccc tga cct tca gcc cct a-3'-Eclipse® Dark Quencher (Research Biolabs) were used as forward primer, reverse primer, and probe. The PCR was carried out using the *Taq* PCR Core Kit (QIAGEN) and consisted of 50 cycles of denaturation at 95 °C for 1 s and annealing/elongation at 60 °C for 4 s (Fig. 3a). For the no template control (NTC), non-pmaxGFP™-transfected THP-1 cells were used instead. The PCR product yield and specificity were verified by capillary electrophoresis using a Bioanalyzer 2100 (Agilent) (Fig. 3b).

3. Results and discussion

Being able to retain the immunocaptured THP-1 cells (Fig. 2a) after solid phase extraction (Fig. 1b-g) and to release their genetic material into the PCR solution is critical for performing the (bio)assay in sequence. Potential contaminants are either left behind in the cell culture suspension or removed during the washing process. Thus, only the purified surface-bound THP-1 cells are subjected to the subsequent process. Since the solid phase extraction of the THP-1 cells is accomplished within 300 s, working on ice is unnecessary.

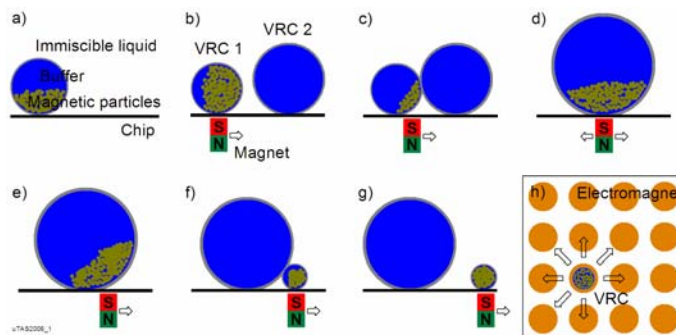


Figure 1: a) A self-assembling droplet is composed of an aqueous suspension of magnetic particles, covered by an immiscible liquid. b-h) A permanent magnet or h) an array of electromagnets is used to b) move, c) merge, d) mix, e, f) filter, and f, g) split the droplets. Only the material, which is immobilized on magnetic particles, is isolated during filtration (Fig. 2a).

4. Conclusion

For the first time, we demonstrate the integration of sample preparation into a drop-based microfluidic system.

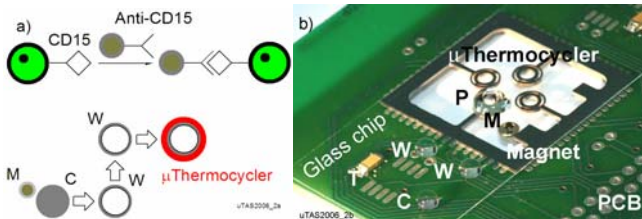


Figure 2: a) Schematic of the isolation of the pmaxGFPTM-transfected THP-1 monocytes from a cell culture suspension by immunoreaction with anti-CD15 coated magnetic particles according to figure 1b-g. b) Thereafter, the cells are thermally lysed, and subjected to a PCR. C (cell culture suspension), W (washing solution), P (PCR mix-ture), M (magnetic particles), T (temperature sensor for calibrating the PCR chip), PCB (printed circuit board).

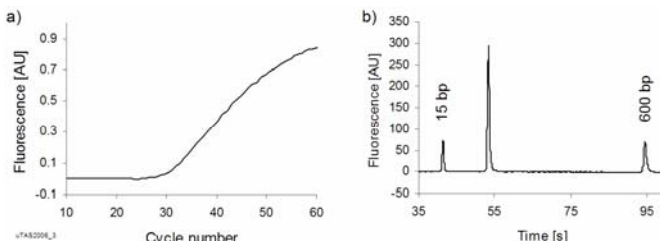


Figure 3: a) Real-time, TaqMan®-based PCR carried out in a droplet according to figure 2b with the pmaxGFPTM vector as target gene. b) Capillary electrophoresis data of the PCR product; the amplicon length is 99 base pairs.

References

1. M. G. Pollack, R. B. Fair and A. D. Shenderov, Electrowetting-based actuation of liquid droplets for microfluidic applications, *Appl. Phys. Lett.* 77, 1725-1726 (2000).
2. P. R. C. Cascoyne, J. V. Vykovakal, J. A. Schwartz, T. J. Anderson, D. M. Vykovakal, K. W. Current, C. McConaghay, F. F. Becker and C. Andrews, Dielectrophoresis-based programmable fluidic processors, *Lab on a Chip* 4, 299-309 (2004).
3. Z. Guttenberg, H. Mueller, H. Habermueller, A. Geisbauer, J. Pipper, J. Felbel, M. Kielpinski, J. Scriba and A. Wixforth, Planar chip device for PCR and hybridization with surface acoustic wave pump, *Lab on a Chip* 5, 308-317 (2005).
4. U. Lehmann, C. Vandevyver, V. K. Parashar, M. A. M. Gijs, Droplet-based DNA purification in a magnetic lab-on-a-chip, *Angew. Chem.* 45, 3062-3067 (2006).

Acknowledgements

This project was funded by the Institute of Bioengineering and Nanotechnology (IBN), the Agency for Science, Technology and Research (A*STAR), and the Biomedical Research Council (BMRC). We thank K. W. Leck for cell transfection/ culturing.

ADVANCED FLOW CONTROL OF LIQUIDS IN MICROFABRICATED CAPILLARY PUMPS

M. Zimmermann^{1,2}, P. Hunziker², E. Delamarche¹

¹ IBM Research GmbH, Zürich Research Laboratory, Säumerstrasse 4, CH-8803 Rüschlikon, Switzerland, Phone +41 44 724 86 00, Fax +41 44 724 89 66

² University Hospital Basel, Petersgraben 4, CH-4031 Basel, Switzerland
(ymz@zurich.ibm.com)

Abstract

This paper reports a method for accurately controlling the filling of capillary systems (CSs) by engineering capillary pumps (CPs). CPs can be used with liquids of different viscosities and serially connected CPs can force the liquids to flow in a sequence of predefined flow rates.

Keywords: autonomous, capillary pump, flow rate, immunoassay

Introduction

The CSs are microfabricated in Si, covered with Au, and have wettable flow paths; they can be used to miniaturize assays greatly and to perform fluorescence surface immunoassays with a sensitivity up to 1 pM using only 600 nL volumes of samples. [1] The flow conditions of liquids displaced in CSs have an important effect on the kinetics of binding between surface-immobilized receptors and analytes in solution. In addition, immunoassays comprise multiple binding, blocking, and rinsing steps, which typically necessitate different durations. [2] The laminar flow of solutions in microchannels can make rinsing efficiently done in a few seconds, whereas the immuno-capture of antigens necessitates incubation times of several minutes. [3] A regular flow in a microchannel is also desirable for replenishing depleted analytes and keeping diffusion profiles of analytes optimal compared to the advancement of the binding reaction. [4] In a CS, the volume of the flow path in front of a CP is negligible compared to the volume of a CP. Therefore, even though a CP is placed after the site where the assay takes place, the CP can be used to control the flow conditions of most of the liquid flowing through a CS.

Concept

Figure 1 shows a typical chip, having three independent CSs, each of which ends with one CP. We engineered CPs in such chips to control the flow conditions of liquids of various viscosities. We used water, PBS, 1% BSA in PBS (viscosity ~1 mPa s) and an intravenous perfusion solution containing 20% of human albumin (~4 mPa s) at room temperature. The contact angles of these liquids on the walls of the CS were similar (~30–50°). By varying the shape, characteristic dimensions, spacing and relative positions of the microstructures in the pumps, we were able to program very low flow rates of these liquids in the CSs, Figure 2, and to control the filling front of these liquids in the CPs, Figure 3. Control over the filling front of the liquid is important to prevent entrapping air in a CP, to permit different liquids to be sequentially displaced in

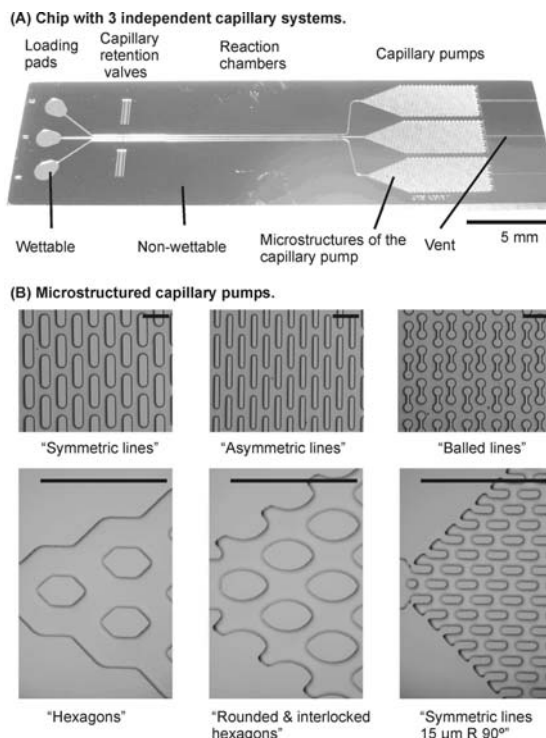


Figure 1. Photograph of a Si chip (covered with Au) having three CSs (A) and optical micrographs showing details of various types of CPs (B). Each CS may be used for one surface immunoassay, during which samples and reagents added to loading pads flow through the reaction chamber at a flow rate governed by the CP terminating the CS. The characteristic dimensions, spacing, and relative position of the microstructures in the CPs determine their filling behavior. The scale bars in (B) are 250 μm .

a CS with high temporal control, and to enable CPs to be used serially to program complex sequences of flow rates in a CS. In the later case, efficient connecting structures as shown in Figure 4 are important to ensure the complete filling of each successive CP.

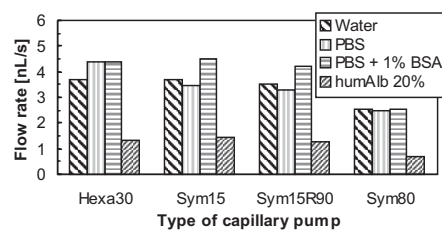


Figure 2. Flow rates of liquids having various composition and viscosity in a CS where the CP either contains 30- μm -wide rounded hexagons, 15- μm -wide lines, 15- μm -wide lines rotated by 90° with respect to the main axis of the pump, or 80- μm -wide lines. Although the viscosity of the filling liquid plays an important role on the filling rate, the filling rates can be accurately programmed for liquids of different viscosities.

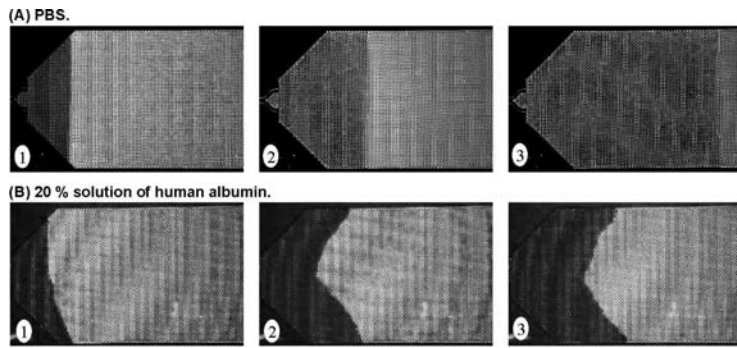


Figure 3. Optical micrographs showing the filling behavior of PBS (A) and a solution containing 20% of human albumin (B) in a capillary pump having 15- μm -wide lines, which are normal to the main axis

of the pump and symmetrically spaced (Sym15 CP). The higher viscosity of the solution in (B) induces more friction along the main axis of the lines, which favors more spreading of the liquid front in the pump than in (A). The scale bar is 1 mm.

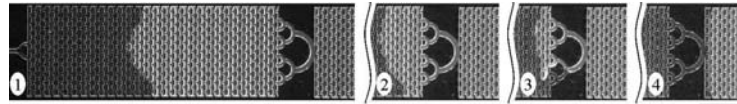


Figure 4. Optical micrographs showing the serial filling of two

CPs (“Sym” type having 60- μm -wide lines) with a 20% solution of human albumin. Owing to the pump design and to the connecting structures in between the pumps, the viscous liquid fills the first CP without entrapping air and then merges into one stream in the connecting structures before entering the second CP. The connecting structures are hierarchical bridges in which a filling liquid encounters zones with decreasing capillary pressure and increasingly strong pinning sites. The scale bar is 1 mm.

Outlook

The method presented here to structure CPs and to control the flow of liquids in CSs suggests that autonomous CSs can be programmed for exhibiting well defined flow characteristics. We expect advanced flow control in CSs to enable sensitive and fast portable immunoassays such as the ones needed for point-of-care applications.

References

1. S. Cesaro-Tadic et al. *High sensitivity miniaturized immunoassays for TNF- α using microfluidic systems*, Lab Chip 4, 563–569, (2004).
2. D. Wild, Ed. *The Immunoassay Handbook*, Nature Publishing Group, New York, (2001).
3. D. Juncker et al. *Autonomous microfluidic capillary system*, Anal. Chem. 74, 6139–6144, (2002).
4. M. Zimmermann et al. *Modeling and optimization of high-sensitivity, low-volume microfluidic-based surface immunoassays*, Biomed. Microdev. 7, 99–110, (2005).

NANOCHANNELS WITH INTEGRATED FABRY-PÉROT INTERFEROMETRY: A NEW TOOL FOR NANOFUIDICS

Jan Eijkel, Koen van Delft, Dragana Mijatovic, Niels Tas, Frieder Mugele
and Albert van den Berg

MESA+ Institute, Twente University, 7500 AE Enschede, the Netherlands

Abstract

1-D Pyrex nanochannels down to 6 nm height were fabricated with an on-chip integrated Fabry-Pérot interferometer enabling the real-time observation of channel filling without using fluorescent dyes. The interferometer consisted of two parallel silver mirrors on both sides of the nanochannel, spaced from it by 1 μm of SiO_2 . The filling speed of ethanol and water was observed, indicating respectively enhanced friction and decreased friction (slip flow).

Keywords: nanochannels, nanofuidics, Fabry-Pérot, capillary filling, slip flow

1. Introduction

Visualizing liquid inside 1-D nanochannels using light microscopy generally becomes highly problematic when the channel height is smaller than 20 nm. Dissolved fluorescent solutes can still be detected but do not give information on the liquid itself, since their behavior is also influenced by electrical (ion exclusion) and/or chemical (adsorption) influences. From the surface forces apparatus (SFA) a good visualization tool is known, namely the Fabry-Pérot interferometer (figure 1).^[1] The SFA however lacks the easy accessibility of the experimental space that is provided by nanochannels, and from which nanofuidic studies can benefit. We therefore married both technologies and manufactured a new tool for nanofuidics: nanochannels with an integrated Fabry-Pérot interferometer. In a first series of experiments we demonstrate the usefulness of this tool by observing the abnormal filling kinetics of 1-D nanochannels.

2. Experimental

A Fabry-Pérot interferometer was micromachined by depositing on two separate Pyrex wafers a 45 nm thick silver layer and covering it with 1 μm of PECVD silicon oxide. The structures were subsequently flattened by chemical mechanical polishing. On one of these wafers arrays of 100 1-D nanochannels with a length of 500 nm and heights of 6, 12 and 16 nm were manufactured by wet etching with a 0.5% HF solution, followed by DRIE of connecting 900 nm deep microchannels and powder blasting of access holes. Finally the two wafers were fusion-bonded at 400°C for 1 hour. A cross-section of the interferometer part and a top view of the entire chip are shown in figures 1 and 2. The optical setup consisted of a white light source with monochromator for the incident light and a microscope with CCD camera to receive the transmitted light (figure 4). A syringe pump was used for liquid introduction via access holes and microchannels to the nanochannels.



Figure 1. Left: Cross section of the interferometer part of the chip;
Right: Beam interference in a Fabry-Pérot interferometer

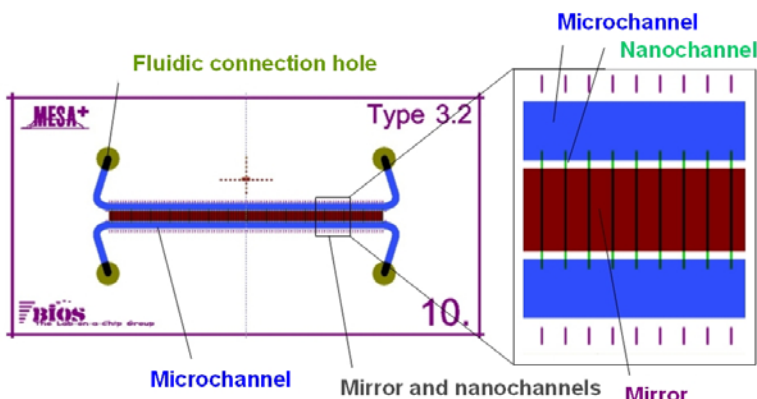


Figure 2. Top view of the nanofluidic device with integrated interferometer

3. Results and discussion

Figure 3 shows a sequence of images made during filling of 6 nm channels with ethanol and of 12 nm high channels with water. Figure 4 shows the meniscus position against \sqrt{t} , obeying the Lukas-Washburn equation [2]:

$$x(t) = \sqrt{\frac{\sigma \cos \theta d}{3\mu}} \cdot \sqrt{t} \equiv a_c \sqrt{t}, \quad (1)$$

where σ is the surface tension (Nm), θ the contact angle, d the channel height (m) and μ the viscosity (Pa s). Table 1 compares the experimentally determined slopes a_e with the theoretically determined ones a_c using equation 1, and gives $C = a_e/a_m$. Clearly ethanol fills the channels progressively slower than theoretically expected on downscaling, which can be attributed either to the electroviscous effect [2] or to the increasing influence of the surface roughness on downscaling (RMS = 0.7 nm). Interestingly, the water filling speed increases on downscaling. Close inspection of Figure 3 showed that for water the optical signal changed only gradually after passing of the meniscus while for ethanol the change was sudden. This seems to indicate a gradual change of the water content in the channels, possibly first inclusion and then dissolution of nanobubbles, with slip flow then explaining the unexpectedly rapid filling

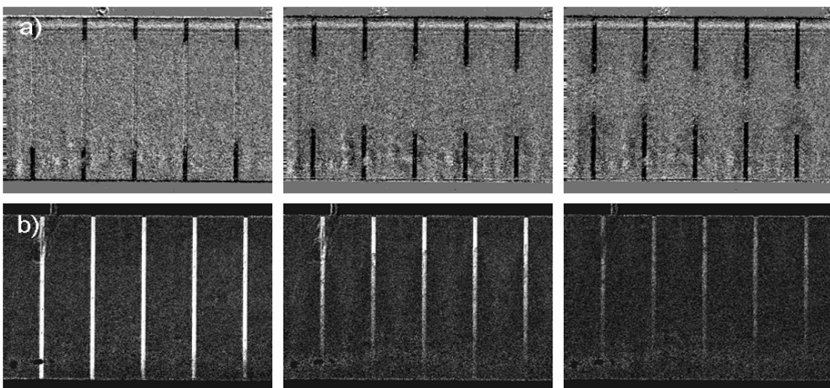


Figure 3 a) Filling of 6 nm channels with ethanol from both sides and b) filling of 12 nm channels with water from the bottom up. For image processing reasons filled channels appear dark in a), while empty channels appear bright in b).

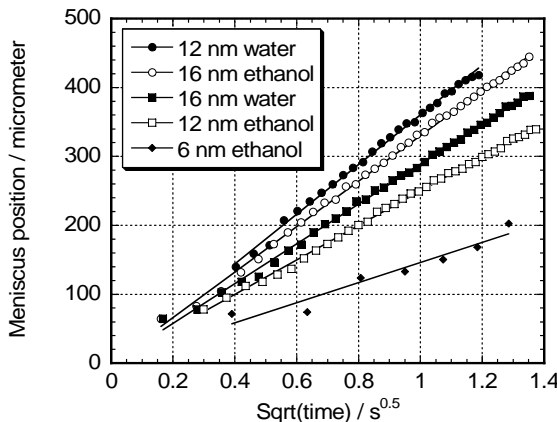


Figure 4 Filling curves : meniscus position versus $t^{0.5}$.

Channel height / nm	a_m [$\mu\text{m s}^{-0.5}$]	a_c [$\mu\text{m s}^{-0.5}$]	C
16.2nm (EtOH)	330	363	1.21
12.3nm (EtOH)	250	317	1.61
6.4nm (EtOH)	146	228	2.43
16.2nm (H ₂ O)	288	188	0.42
12.3nm (H ₂ O)	360	164	0.21

Table 1 Measured and calculated slopes of the filling curves. C is the ratio a_c/a_m .

1. J.N. Israelachvili, *Intermolecular and surface forces*, 2nd. Ed., Academic Press, London, 1992.
- 2 N. R. Tas, J. Haneveld, H. V. Jansen, M. Elwenspoek, and A. van den Berg, *Appl.Phys.Lett.* 85 (2004) 3274-3276.

A DELAYED MICRO MIXER MODULE FOR CONTINUOUS FLOW IMMUNOASSAY WITH PRELOADED REAGENT

Jaephil Do, Junhai Kai and Chong H. Ahn

Microsystems and BioMEMS Laboratory

Department of Electrical & Computer Engineering and Computer Science,
University of Cincinnati, Cincinnati, OH 45221 USA

Abstract

This paper presents a new micro mixer module utilizing delayed sample flow for a continuous flow immunoassay with preloaded reagents. A new micro mixer module that can combine and mix two small liquid plugs without air entrapment, has been designed, fabricated and characterized for the continuous flow immunoassay. This new mixing module will be an essential component for numerous on-chip immunoassays, including protein lab-on-a-chips toward point-of-care clinical diagnostics.

Keywords: Delayed Micro Mixer, Continuous Flow, Immunoassay, Lab-on-a-chip

1. Introduction

Immunoassay has been one of the most important assays in various clinical diagnostics on lab-on-a-chip platforms. Numerous reports for the assay have been published, but most previous works have suffered from sample preparation, which requires several reagent injections in sequence. A bulk syringe pump or micro pump is usually used to load the reagents or buffer solutions during the assay, but it becomes a major obstacle for developing the lab-on-a-chip toward point-of-care testing (POCT) [1].

In this sense, a continuous flow immunoassay utilizing preloaded whole immunoassay reagents on a chip can be a promising solution to address this challenge. A conventional multi-injection immunoassay and a new single injection continuous flow immunoassay are compared in Figure 1. To accomplish this, a new micro mixer

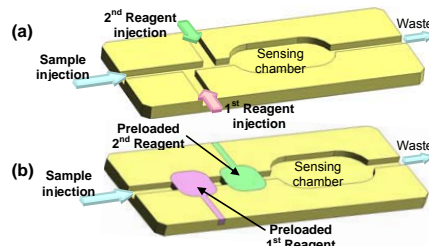


Figure 1. Schematic illustration of immunoassay on lab-on-a-chip: (a) a conventional multi injection immunoassay and (b) a new single injection continuous flow immunoassay with preloaded reagents.

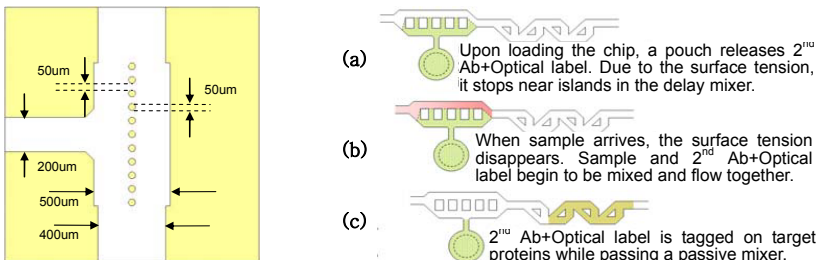


Figure 2. Design of delayed micro mixer and its operation sequence of delayed micro mixer module with preloaded immunoassay reagents.

module that can combine and mix two small liquid plugs without air entrapment, has been designed, fabricated and characterized for the continuous flow immunoassay.

2. Design and simulation

In the mixing module, two different micro mixers are required; namely a “delayed” micro mixer and an in-plane micro mixer as described in Figure 2. Specifically, the innovative delayed micro mixer as described in Figures 2 is an essential component for mixing the separated sample with immunoassay reagents such as buffer solution and primary or secondary antibodies.

The principle of operation is based on the pressure barrier that develops when the cross-section of capillaries changes abruptly into an expansion region between two cylindrical pillars. This serves to “hold” the first liquid that was pre-loaded [2]. When the second liquid flows past the pillar structure, it makes contact with the first liquid and the surface tension barrier is broken allowing concurrent flow of the two liquids. A downstream mixer can then mix the two liquids. The simulation results as a proof concept for the delayed micro mixer are shown in Figure 3. The maximum pressure barrier that a surface tension effect can hold is calculated at various surface contact angles and plotted in Figure 4.

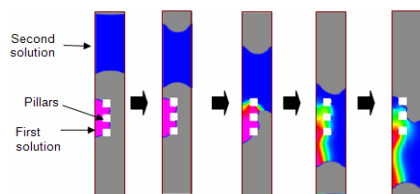


Figure 3. Simulation results as proof concept for a delayed micro mixer using CFDR-ACE+™ from CFD Corp.

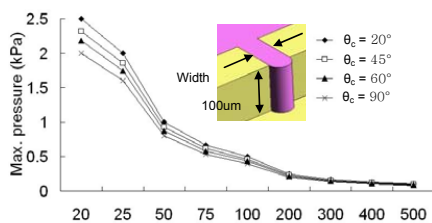


Figure 4. Plot of a maximum holding pressure of surface tension valve at various width and contact angle (θ_c) (channel height is fixed at 100μm).

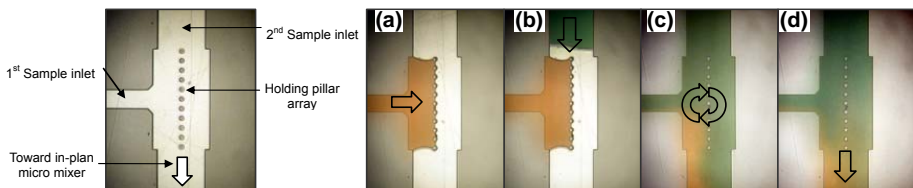


Figure 5. Photographs of the fabricated delayed micro mixer and operation sequences: (a) First sample preloaded and holding due to surface tension effect (b) second solution injection (c) break the meniscus of a held sample and (d) combined two samples flow into downstream in-plain micro mixer.

4. Experimental results

A delayed micro mixer is fabricated using PDMS casting on SU8 mold. The fabricated device is shown in Figure 5. As a delayed micro mixer, both the “hold” ability of the pillar array and the ability to mix the two liquid plugs need to be characterized. Holding and mixing capabilities of the delayed micro mixer were tested using DI water containing red and green dyes by flowing second liquid at flow rates of $10.0 \mu\text{L}/\text{hr}$. The achieved mixing sequences are shown in Figure 5. Also the maximum flow rates, at which the combined two samples can be flowed into downstream without any residue between pillars, were measured and plotted in Figure 6.

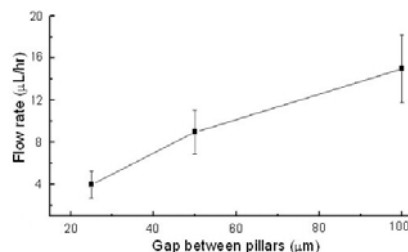


Figure 6. Plot of a maximum flow rate at which the combined two samples can be flowed into downstream without any residue between pillars. Flow rate was measured for different gap between pillars 25, 50 and 100 μm .

5. Conclusion

In conclusion, an innovative delayed micro mixing module for continuous flow immunoassay with preloaded reagent has been successfully developed in this work. This new mixing module will be an essential component for numerous on-chip immunoassays, including protein lab-on-a-chips toward point-of-care diagnostics.

Reference

1. Jin-Woo Choi, K. W. Oh, J. H. Thomas, W. R. Heineman, H. B. Halsall, J. H. Nevin, A. J. Helmicki, H. T. Henderson, and C. H. Ahn, “An integrated microfluidic biochemical detection system for protein analysis with magnetic bead-based sampling capabilities,” *Lab Chip*, Vol. 2, pp. 27–30, 2002.
2. P. F. Man, C. H. Mastrangelo, M. A. Burns and D. T. Burke, “Microfabricated capillary-driven stop valve and sample injector,” *Proceeding of The IEEE MEMS Conference ’98*, Heidelberg, Germany, pp. 45-50.

NATURE-INSPIRED ACTIVE MIXING IN A MICRO-CHANNEL

Vinayak Khatavkar, Patrick Anderson, Han Meijer and Jaap den Toonder
Materials Technology, Dutch Polymer Institute,
Eindhoven University of Technology, The Netherlands.

Abstract

We propose a novel design for an active micro-mixer that is inspired by the motion of ciliated micro-organisms occurring in nature. The conceptual design consists of an array of individually addressable, artificial cilia in the form of micro-actuators covering the micro-channel walls. Through numerical simulations we demonstrate the feasibility of the concept by showing that chaotic mixing can indeed be obtained under proper conditions even for a simple two micro-actuator configuration.

Keywords: mixing, chaotic advection, fluid-structure interaction, micro-actuators

1. Introduction

Many applications of micro-fluidics require efficient mixing of two or more liquids. Mixing at the micro scale usually occurs through a rather slow diffusion process due to inherent laminar flow conditions. To speed-up mixing, numerous novel passive and active micro mixers are being developed.^[1] We propose a new promising configuration for an active micro-mixer consisting of an array of individually addressable micro-actuators, covering the micro-channel walls, that can be actuated by an external stimulus such as an electric or a magnetic field. The motion of these micro-actuators can in turn induce either primary or secondary motion in the surrounding fluid leading to chaotic mixing. This idea is inspired by the motion of flagellated and ciliated micro-organisms.^[2]

2. Methods

We have developed a computational fluid-structure model to explore the feasibility of the concept and help design the optimal mixer configuration with respect to the mechanical and geometrical properties of the actuators as well as the actuation scheme. This model is based on a fictitious domain method and simulates both the micro-actuator motion as well as the concomitant fluid flow, fully capturing the fluid-structure (solid) interaction.^[3] The simulated fluid flow patterns resulting from the motion of single and multiple actuated elements under the action of a time-periodic forcing function are then analyzed using dynamical systems theory to quantify the mixing efficiency.

3. Results and discussion

The feasibility of our concept is demonstrated through a simple two micro-actuator design. As shown in Fig. 1, when a proper actuation scheme is used, two micro-actuators can indeed induce effective mixing by chaotic advection in a micro-channel.

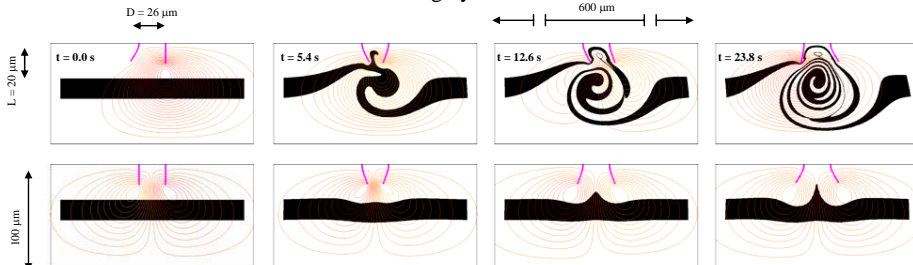


Figure 1. Visualization of mixing patterns by passive advection of a fluid strip (black) reveals actuation schemes that lead to ‘good’ (top row) and ‘poor’ (bottom row) mixing. The two micro-actuators (magenta) are actuated with a phase lag of 90° (top row) and 180° (bottom row) at a frequency of 4 Hz. The instantaneous flow streamlines are also shown (colored lines).

The dependency of mixing efficiency on the actuation scheme, shown in Fig 2, is less critical so long as its value is near the optimum value of 90°. For optimal mixing, it seems that the two micro-actuators should be placed as close to each other as possible, obviously taking care to avoid their collision, and they should preferably be actuated 90° out of phase (see Fig 3).

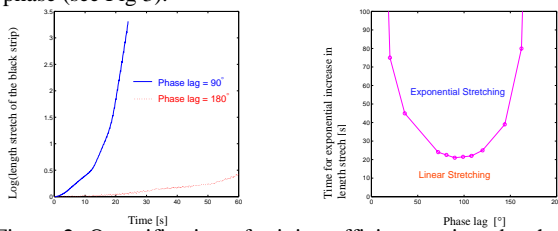


Figure 2. Quantification of mixing efficiency, given by the length stretch of fluid strip (left) is used to generate a phase diagram (right) where the optimal actuation scheme can be readily identified.

Furthermore, for micro-actuators smaller than 20 % of the channel width, the mixing effectiveness is higher when they are arranged on the same wall. However as shown in Fig 4, increasing the micro-actuator length improves the effectiveness of an opposite wall micro-actuator arrangement.

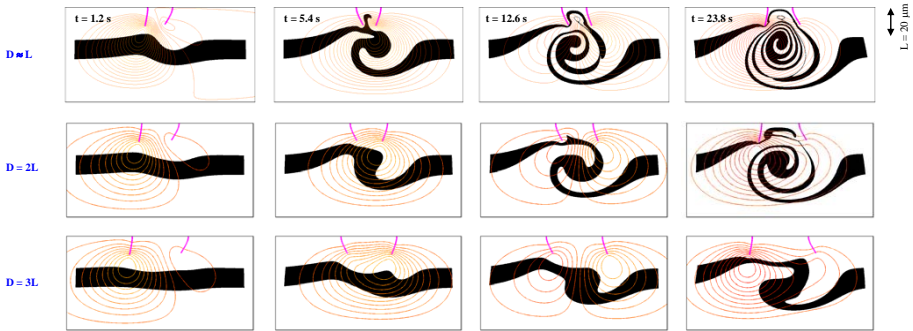


Figure 3. Mixing quality as a function of spacing (D) between the two micro-actuators of length (L). In all three cases, the two micro-actuators are actuated with a phase lag of 90° and at a frequency of 4 Hz.

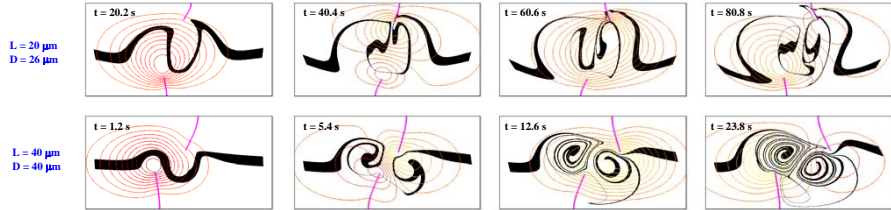


Figure 4. Improvement in mixing with an increase in the length (L) of micro-actuators for an opposite wall arrangement of the two micro-actuators. In both cases, the micro-actuators are actuated with a phase lag of 90° and at a frequency of 4 Hz.

5. Conclusions

Effective mixing by chaotic advection can be obtained with cilia-like micro-actuators integrated in a micro-fluidic channel. Our numerical simulations show that, with a well-chosen geometrical arrangement and actuation scheme, mixing can even be obtained with only two micro-actuators.

Acknowledgements

This work is sponsored by the Dutch Polymer Institute (Project no 532).

References

- [1] D.J. Beebe et. al., *Annu. Rev. Biomed. Eng.*, **4**, 261, 2002.
- [2] G.I. Taylor, *Proc. Roy. Soc. A*, **209**, 447, 1951.
- [3] R. van Loon et. al., *Int. J. Num. Meth. Fluids*, **46**, 533, 2004.

CENTIMETER-SCALE, DIAGNOSTICS INCUBATOR WITH INTEGRATED PERfusion

Jelena Vukasinovic¹ and Ari Glezer¹

Woodruff School of Mechanical Engineering, Georgia Institute of Technology

Abstract

Growing demands for long-term incubation of biologically faithful, high-density, 3-D, cultures during extended physiological studies require efficient perfusion platforms with functional microvasculatures that mimic the *in vivo* condition in a thermally regulated environment. While expensive incubation baths with thermostatically controlled water jackets and capillary action perfusion are available [1-2], their use is confined to specific experimental conditions. The interstitial nutrient and gas delivery remains diffusion limited over the long term and cultures decay metabolically. To overcome these problems, we describe simple fabrication, packaging and characterization of a compact, low-cost, diagnostics incubator with actively controlled perfusion that enables *in situ* monitoring of culture activity with a superior control of critical biological functions using convectively enhanced intercellular, mass, and, heat transport.

Keywords: incubator, microfluidics, perfusion chamber, PDMS, neuronal culture

1. Introduction

Emerging trends to culture neurons and other cell lines in 3-D systems demand efficient perfusion settings that overcome diffusion barriers in nutrient delivery and waste removal. Recent work [3-4] demonstrates the utility of convectively enhanced mass transport in growing high-density ($>10,000$ cells/mm³) engineered tissue constructs [3] and 700 μ m thick brain slices [4] in perfused culture chambers [5]. Miniature diagnostics incubator is an extension of this work to scale-down cell cultures and their microenvironments onboard an environmentally controllable, portable platform.

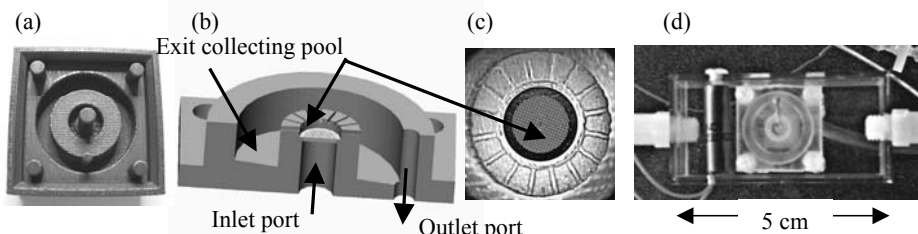


Figure 1. Perfusion platform (a) mold (b) vertical cross-section (c) culture chamber (d) incubator

2. Fabrication and Packaging

Perfusion chambers are rapidly prototyped by replica molding of PDMS over extruded 3-D thermoplastic molds, Fig. 1. Perfusing/cell attachment substrates are bonded to the

bottom of the cell culture life support chambers. Perfusion platform is encapsulated by an imaging accessible, membrane aerator [6] that maintains sterile, moist environment of appropriate acidity. Perfusion chamber, fluidics, flexible heater, and thermocouples are packaged within a 25 x 51 x 18 mm clear, heated enclosure (incubator).

3. Results and Discussion

Flow within the chamber, induced by simultaneous nutrient infusion and withdrawal of catabolites, is investigated experimentally using microPIV, Fig. 2. Culture is exposed to a direct flow of media issuing from an array of micronozzles normal to the tissue, and further improved by 3-D convection induced by microjet interactions and peripheral perfusate extraction [5]. Flow dynamics is elevation dependent and alters from the free flow of discrete jets; interactions among decelerating, broadening jets; to impingement flow along the membrane. Due to biased discharge through peripheral microchannels, a closely spaced array of impinging jets obtains a single, centrally located stagnation zone. Developing, central wall jet accelerates towards the exits due to merging of outflows from a number of adjoining wall jets. This strong wall jet deflects the axis of microjets located further away from the center of the chamber and their impingement is delayed or even prevented. Thus, jets emanating closer to the center of the chamber penetrate deeper into the cultured domain targeting the most vulnerable part of the tissue with the microjet axial trajectory reduction from the center towards the perimeter.

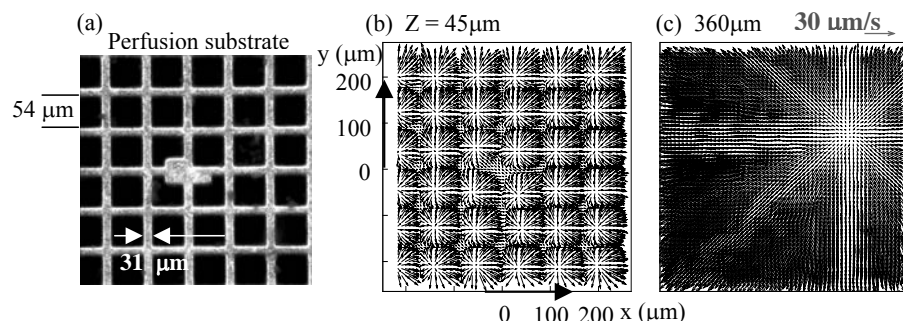


Figure 2. Particle image velocimetry measurements in planes parallel to the perfusion substrate and normal to the axe of microjets (a) field of view (b) spreading of discrete jets upon discharge (c) biased convection towards the exit microchannels at higher elevations

Forced flow of the appropriate gas mixture over the heater located on one side of the incubator heats the perfusion chamber located downstream. In operation, the chamber remains nearly isothermal so that the injected media reaches desired temperature of within its fluidic platform well before entering the culture chamber, with the heated length increasing linearly with the flow rate. Thermocouple measurements, Fig 3, reveal that the controlled media temperature just prior to injection at 10 $\mu\text{l}/\text{min}$, follows the air temperature inside the outer, collecting pool where perfusate leaves the chamber. Media temperature oscillates around $37 \pm 0.2^\circ\text{C}$ over an 8-hour period, upon turning the heater.

A PID controller coupled to a solid-state DC switching relay varies the heat flux dissipated by a heater. Owing to its $7\mu\text{l}$ of volume, culture chamber and the entire perfusion platform facilitate temperature control due to relaxed working conditions and low time constants with negligible delays before parameters reach desired values.

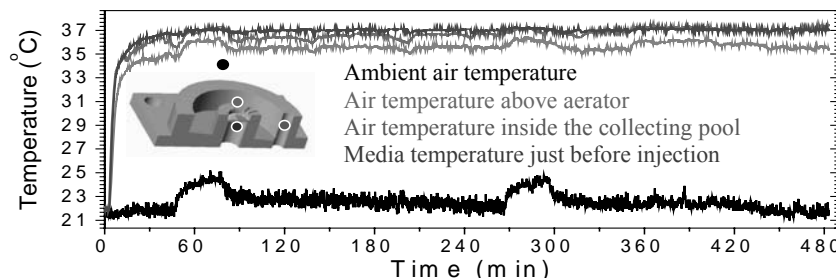


Figure 3. Temperature measurements over 8 hours

4. Conclusions

Centimeter-scale incubator alleviates many of the shortcomings of conventional, large-scale incubators such as unwanted cross-contamination and repeated analyses, imaging, interfacing and perfusion inaccessibility. The scale-down simplifies design, offers fast response times to physical changes, rapid exchange rates, and, reduces expenditures associated with specimen, reagents and power consumption. Modular design, simple packaging and interfacing facilitate the integration of sensors [7] or commercial multielectrode arrays. Relevant infrastructure remains outside the miniature incubator enclosure, thus keeping it inexpensive, simple to fabricate, and therefore disposable.

Active perfusion functionality enables the growth of 3-D organotypic cultures [3-4]. While in standard culturing the tissue decay begins at the center, a realized flow field in the present arrangement specifically targets this zone in delivering plethora of nutrients. At high enough exchange rates, a lateral reduction in nutrient concentration is deemed negligible as 3-D cultures exhibit fairly uniform viability throughout the volume [3].

Acknowledgements

This work is supported by the NIH 1 R01 EB00786.

References

1. Haas H.L., Schaefer B., and Vosmansky M., J. Neurosci. Meth. **1**:323-325, (1979).
2. Zbicz K.L. and Wright F.F., J. Neurophysiol. **53**:1038-1058, (1985).
3. Cullen D.K. et al., Proceedings of the IEEE EMBC 2006.
4. Rambani K. et al., Neuroscience 2006.
5. Vukasinovic J. and Glezer A., Proceedings of the ASME BIO 2006.
6. Potter S.M. and DeMarse T.B., J. Neurosci. Meth. **110**:17-24, (2001).
7. Zanzotto A. et al., Biotechnol. Bioeng. **87**: 243-254, (2004).

IMPROVED CARRIER MEDIUM EXCHANGE EFFICIENCY IN ACOUSTIC STANDING WAVE PARTICLE WASHING

Per Augustsson, Filip Petersson and Thomas Laurell

Department of Electrical Measurements, Lund University, Lund, Sweden
per.augustsson@elmat.lth.se

Abstract

A microfluidic device for particle washing was designed utilizing an acoustic standing wave field in a micro channel. Particles were focused in the center of the channel by the acoustic radiation force while the original carrier media was shifted sideways (orthogonal to the flow) at a number of consecutive wash fluid flow junctions along the main flow. Experiments were carried out in order to compare the washing efficiency to that of an earlier presented particle washing device. The new wash chip removed more than 95% of the original carrier fluid in a mix of 5 μ m polyamide beads and green food color as compared to the older device which removed only 60% at the corresponding conditions. The particle wash performance was shown to depend on the number of consecutive wash fluid flow junctions.

Keywords: Particle wash, acoustic radiation force, microfluidics, ultrasound

1. Introduction

Strategies for particle manipulation and spatial control in microfluidic systems are highly desired. In view of this, ultrasonic standing wave focusing has emerged as an attractive non contact mode of operation [1]. Earlier work by Petersson [2] has shown it possible to wash particles in a continuous flow utilizing acoustic standing wave forces. A carrier medium exchange with 95% recovery of particles while removing 95% of a contaminant was reported at a sample throughput of 100 μ l/min. This was accomplished by moving the particles acoustically from the contaminated medium near the channel walls into a stream of clear medium in the center of the channel.

When moving particles from one medium to another, large differences in acoustic and fluidic properties of the two media tend to diminish the medium exchange efficiency drastically. To further improve the washing performance, as reported in [2], a new device, less sensitive to media properties, was designed. Particles flowing through a micro channel were focused to the center of the channel by an ultrasonic standing wave while the medium was exchanged at a number of consecutive junctions. Fresh wash media was supplied along the junctions at one side while contaminated media was removed at the opposite side via the two corresponding bifurcation channel structures.

2. Theory

Briefly, a particle that is situated in an acoustic standing wave field will experience an acoustic radiation force towards either the nearest pressure node or the nearest pressure anti node. The size and direction of the force are determined by the differences in the acoustic properties of the particle and the liquid medium.

By actuating a micro channel with a piezoelectric ceramic, particles suspended in an aqueous medium can be moved from the side of the channel towards the center of the channel preventing them from escaping the channel via any side outlets. By creating a number of inlets and corresponding outlets along the main channel it is possible to switch away and replace any contaminated carrier fluid. The crossing lateral flow at each junction forces the band of particles to move close to the channel wall with the lateral wash fluid flow. After each junction the acoustic force will again move the particles back to the center of the main channel. At the next junction, the process of shifting out the contaminated fluid is repeated. As long as no particles are lost in the junctions the process can be repeated any number of times (Figure 1, left).

3. Experimental

The microfluidic channel was wet etched in <110> silicon using 30% KOH at 80°C. The depth of the channel was 190 µm and the width of the main channel was 375 µm. On one side of the main channel a bifurcation structure was placed that could supply the channel with clean aqueous medium at 2, 4 or 8 points along the channel. On the opposite side of the channel a similar bifurcation structure was used to wash away the contaminated medium. An older version of the washing channel, a so called 2Y-channel, was used to evaluate the performance of the design (Figure 1, right).

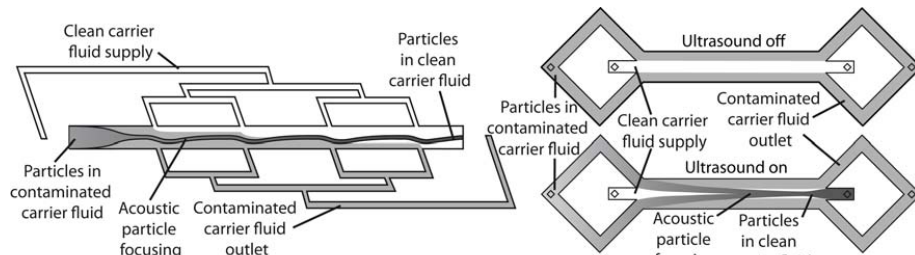


Figure 1. Schematic of the new particle wash chip (left), showing the initial acoustic focusing of the particles, followed by four sequential carrier fluid exchange steps, removing the original contaminated carrier fluid. The earlier presented 2Y-chip design, (right) where particles in a contaminated media enter the wash chip through the side inlets while clear media is supplied via the center inlet, was used as comparison.

A mixture of ultrasound doppler blood phantom containing 5µm Orgasol Polyamide spheres was contaminated with green food color (E104, E131). The particle concentration was $100 \cdot 10^6$ particles per ml. MilliQ water was used as clean carrier fluid into which the particles were to be moved. A small amount of detergent was added to the clean carrier fluid in order to prevent particles from aggregating.

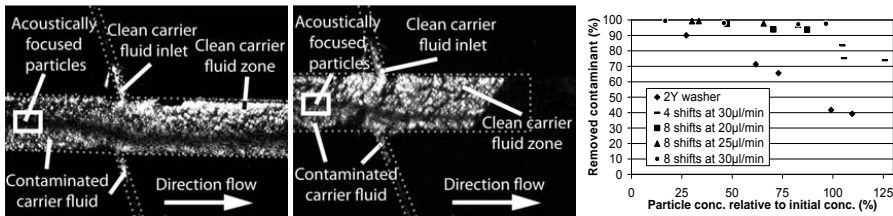


Figure 2. Acoustically focused beads passing the first and the last junction of a wash channel (left and middle). Diagram showing removed contamination vs. relative particle concentration, for the different washing devices (right). For the 8-junction channel the wash fluid flow per junction was varied from 20 µl/min to 30 µl/min.

Washing was carried out with the side shifter chip as well as on the older 2Y-chip using the same particle mixture. The throughput of particle sample was 100 µl/min in all experiments. Side shifter channels with 4 and 8 junctions were set to shift out 20-30 µl/min at each junction. The 2Y-chip was run using 170 µl/min of clean carrier fluid.

4. Results and discussion

The side shifter showed drastically improved washing ability as compared to the 2Y-chip. Approximately 80% of the contamination was removed for a channel with four wash junctions, whereas the 2Y-chip removed only 60% of the contamination. Using a channel with 8 side shifts, the removal of contamination was over 97%, still maintaining a particle recovery of 80%. The device could be tuned to wash away over 99% of the contamination but the recovery of particles dropped to 15-30% (Figure 2, right).

5. Conclusions

On chip particle washing utilizing acoustic forces may open routes to extraction and concentration of particles and cells from complex biological media. The continuous flow format and low dead volume makes it an attractive tool in the processing of valuable and minute biofluids in e.g. bioanalytical situations or in purification protocols. To become a competitive alternative to manual centrifugation methods the washing must be effective and rapid. This work shows that it is possible to design a device that can wash efficiently with low loss of particles by employing the presented side shifting strategy to remove the contamination. By increasing the number of shift junctions the washing efficiency can be expected to become even higher than the currently reported 97%.

References

1. A. Nilsson, F. Petersson, H. Jönsson and T. Laurell, *Acoustic control of suspended particles in micro fluidic chips*, Lab on a Chip 2004, 4, pp.131-135, (2004)
2. F. Petersson, A. Nilsson, H. Jönsson and T. Laurell, *Carrier Medium Exchange through Ultrasonic Particle Switching in Microfluidic Channels*, Analytical Chemistry 2005, Vol. 77, No 5, pp 1216-1221, (2005)

THE SPATIALLY FOCUSED REAGENT INJECTION SYSTEM USING 3-D SHEATH FLOW SCANNER INTEGRATED WITH SiO₂ MESH STRAINER

Yasuo Suzuki ¹, Masaki Kanai ^{1,2}, Takahiro Nishimoto ², and Shuichi Shoji ¹

¹ Major in nanoscience and nanoengineering, Waseda University, Japan

² Technology Research Laboratory, Shimadzu Corporation, Japan

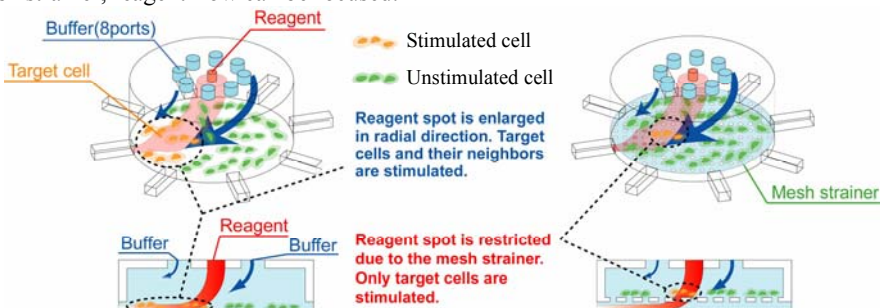
Abstract

We developed a spatially focused reagent injection system with improved 3-D sheath flow scanner. SiO₂ mesh strainer is formed in the microwell to improve spatial resolution of the reagent flow. This enables selective delivery of the reagent to target cell colonies cultivated in the microwell. To fabricate the SiO₂ mesh strainer, sacrificial layer etching of Si micro pillars is employed. Simulation and experimental results confirmed that a use of the mesh strainer improves spatial resolution of the induced reagent successfully.

Keywords : 3-D sheath flow, sample injection, cell analysis, micro mesh

1. Introduction

In the previous work, we reported a reagent injection system using 3-D sheath flow scanner [1], as shown in Fig.1(a). Reagent flow is surrounded by buffer flows introduced from eight buffer inlets. The direction and depth of the reagent flow are controlled by changing eight buffer flow rates. The reagent delivered to the target cell colonies and then cellular reaction such as protein productions is real time monitored by means of fluorescent microscopy observed from a bottom side (e.g. fluorescent anisotropy, FRET) [2]. In the previous configuration, reagent spot at the bottom is enlarged in radial direction, therefore the unexpected colonies besides the target colonies are also stimulated. To improve spatial resolution of the reagent injection, SiO₂ mesh strainer formed in the microwell is employed, as shown in Fig.1(b). Since the reagent flows through the openings of the mesh strainer, reagent flow can be focused.



(a) 3-D sheath flow scanner : previous work

(b) 3-D sheath flow scanner with SiO₂ mesh strainer

Fig.1 Schematic concept of 3-D sheath flow scanner

2. CFD Simulations

By CFD simulation (CoventorWare, Coventor Inc, USA), we investigated the reagent flow profiles and the reagent area profiles at the bottom in the previous microwell (Fig.2(a)) and the newly designed microwell (Fig.2(b-1)-(b-3)). Comparison between Fig.2(a) and the others indicates that the mesh strainer is helpful to control spread of the reagent flow efficiently. Fig.2(b-1)-(b-3) show that the positions of the reagent spot on the mesh strainer for various buffer flow rates. The results confirmed good controllability of the induced reagent positions.

3. Fabrication

From the CFD simulation results, prototype devices were designed and fabricated. The fabrication steps are shown in Fig.3. The microwell and inlets structure was formed by multi-step deep-RIE process of a silicon substrate [3]. The SiO_2 mesh layer is deposited by sputtering on Si micropillars, which are used as sacrifice layer (Fig.3(b)). After SiO_2 sputtering, Si micro pillars are etched (Fig.3(c)) and lid portions of SiO_2 layer are removed by BOE (Fig.3(e)). To realize free-standing structure of the mesh strainer, SiO_2 sputter condition was optimized to reduce residual stress. Fig.4 shows SEM images of the fabricated device which has SiO_2 mesh strainer of $5\mu\text{m}$ thick with $5\mu\text{m}$ diameter holes. The mesh strainer was stood up by the flow rate up to 60mL/min .

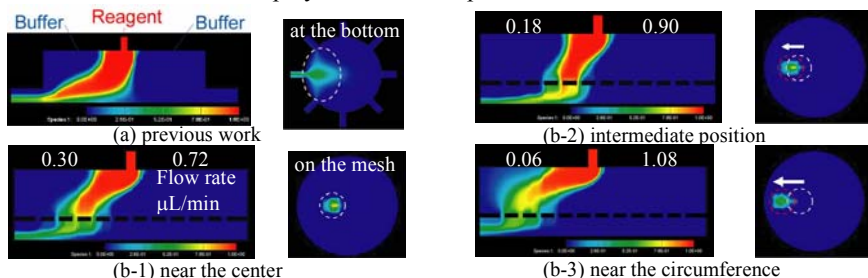


Fig.2 CFD simulation results of the reagent flow profile controlled by buffer flow rates

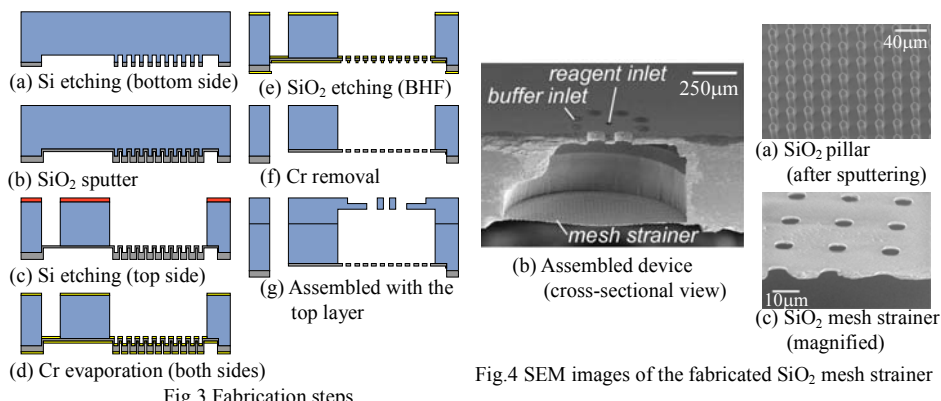


Fig.3 Fabrication steps

Fig.4 SEM images of the fabricated SiO_2 mesh strainer

4. Experimental

The reagent injection behaviors were evaluated with the fabricated device. The reagent flow of the fluorescent dye (Fluorescein, SIGMA) was introduced and observed by a fluorescent microscopy from the bottom side. The cross sectional image of the reagent flow and the reagent spot image on the mesh strainer were shown in Fig.5 and Fig.6 respectively. These results confirmed that the reagent flow was spatially focused on the mesh strainer. By controlling the buffer flow rates, reagent flow was scanned to any direction successfully, as shown in Fig.7 (a)-(d).

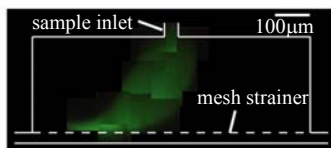


Fig.5 Cross-sectional image of the reagent flow observed by confocal microscopy

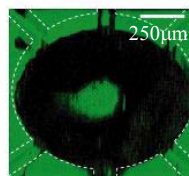
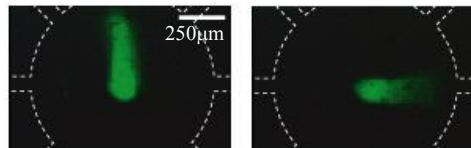
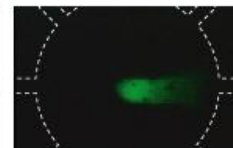


Fig.6 Fluorescent image of the reagent spot on the mesh strainer



(a) $\theta=0^\circ$



(b) $\theta=90^\circ$



(c) $\theta=180^\circ$

Fig.7 Fluorescence images of reagent flow controlled in the clockwise directions

5. Conclusions

A spatially focused reagent injection system for biological cell cultivating microwell using 3-D sheath flow scanner integrated with SiO₂ mesh strainer was proposed. After the feasibility studies using CFD simulation, the first prototype device with fine mesh strainer was successfully fabricated. To make the mesh strainer in the microwell, spatial resolution of the reagent flow was improved and fundamental feature of the spatially focused reagent injection system for cellular analysis was confirmed.

Acknowledgements

This work is partly supported by Japan Ministry of Education, Culture, Sports Science & Technology Grant-in-Aid for COE Research and 21st COE of Waseda University, scientific Basic Research (A) No. 12450167.

REFERENCES

- [1] H. Mikado, et.al. *μTAS2005*, pp557-559, 2005
- [2] T. Munaka, et.al *Proc. μTAS2003*, pp283-286, 2003
- [3] M. Kanai, et.al. *Sensors and Actuators A*, Vol.114, pp. 129-134, 2004

ELECTROLYSIS-DRIVEN DRUG DELIVERY FOR TREATMENT OF OCULAR DISEASE

Ellis Meng¹, Jason Shih², Po-Ying Li¹, Ronalee Lo¹, Mark S. Humayun¹, and Yu-Chong Tai²

¹University of Southern California, Los Angeles, CA 90089 USA

²California Institute of Technology, Pasadena, CA 91126 USA

Abstract

A new paradigm for treatment ocular diseases using micromachined drug delivery devices is explored as an optimal means of pharmacologic management. The device consists of a refillable reservoir, electrolysis pump, and cannula. Electrolysis-driven drug delivery provides flexible, long term treatment with only a single surgery.

Keywords: Drug delivery device, implant, electrolysis pump, parylene, ocular

1. Introduction

Many vision-threatening diseases, including retinitis pigmentosa, age-related macular degeneration, diabetic retinopathy, and glaucoma, are incurable and yet extremely difficult to treat with currently available therapies (oral, topical, injections, and sustained-release implants). In particular, the eye wall is an effective physical barrier that obstructs intraocular delivery of therapeutic levels of drug to specific treatment sites. Intraocular injections and sustained-release implants can be effective therapies, however, repeated injections or implantations are required (typically at 6 week intervals). Furthermore, device size and drug volume are severely limited by physiological space constraints [1, 2].

While several MEMS drug delivery platforms have been explored, none are suitable for long term management of ocular diseases. Specific requirements include broad drug compatibility, ability to be refilled for chronic use, minimally invasive implantation, variable dosing (continuous or bolus), and physiological sensing for feedback controlled delivery. We previously presented a passive, mechanically-operated MEMS drug delivery which did not have variable dosing capability or feedback control [3]. An electrolysis-driven implantable MEMS drug delivery system can meet these requirements. In addition, power consumption and heat dissipation are minimal facilitating chronic operation in the body.

2. Experimental

The drug delivery system is an assembly of two parts that form a refillable silicone reservoir (~50 μ L), electrolysis pump, and flexible parylene cannula (Fig. 1). During implantation, the integrated cannula crosses the sclera (eye wall) and is directed at the disease site. A pressure gradient generated by electrolysis acts on drug contained within the reservoir, forcing drug onto the disease site through the cannula. When drug is depleted from the reservoir, the chamber is repeatedly refilled by non-destructively puncturing the wall with a non-coring needle attached to a drug-filled syringe.

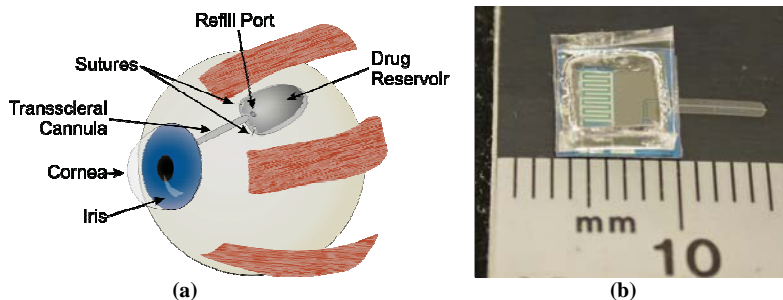


Figure 1. (a) Concept drawing of drug delivery device and (b) assembled drug delivery device

The base layer of the drug delivery device contains both the pump and cannula; a simplified fabrication process flow based on [4] (Fig. 3). The underside of the cannula is lined with an array of posts that facilitate its release from the silicon substrate. The free-standing cannula is 1 mm wide and formed from two parylene depositions (each 7.5 μm thick) (the fluid channel is only $100 \times 25 \mu\text{m}^2$ in cross section). A 70 μm thick SU-8 layer reinforces the parylene microchannel, preventing its collapse when a drug reservoir is bonded to the base chip. The top layer is a silicone rubber (Sylgard 184) reservoir fabricated by casting from conventionally machined molds. Silicone rubber can withstand multiple punctures by non-coring syringe needles (30 gauge) [3].

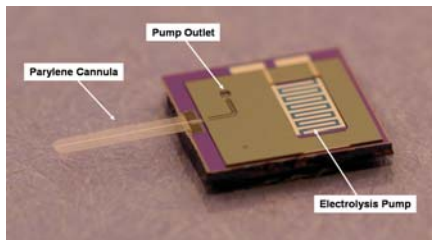


Figure 2. Electrolysis pump (Pt electrodes) and cannula integrated on base layer of drug delivery device

3. Results and Discussion

Pump performance was evaluated by using current to control DI water flow rate (Fig. 3). Data were obtained by observing movement of a meniscus in a volume-calibrated capillary over time and calculating the corresponding flow rate. Electrolysis pumping for delivering Betoptic (beta-blocker for glaucoma treatment) has been demonstrated (data not shown). In addition, the device performance is evaluated at body temperature (37°C) (Fig. 4). Finally, packaging is being developed to enable device evaluation in *ex vivo* porcine eyes and *in vivo* animal studies.

4. Conclusion

A new paradigm for intraocular drug delivery is presented in which electrolysis drives the delivery of drugs through a surface micromachined parylene cannula.

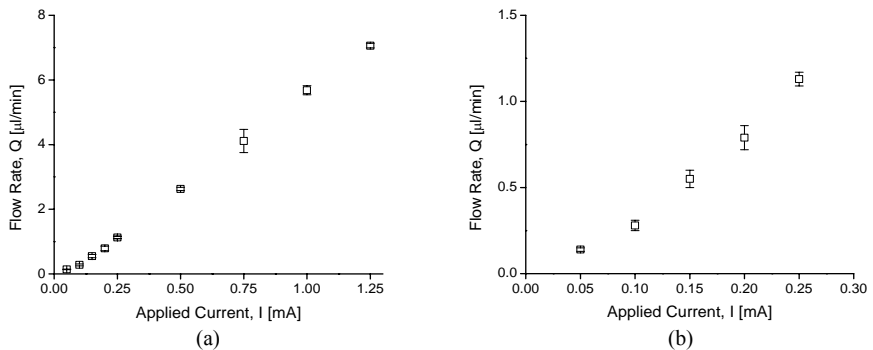


Figure 3. (a) Current-controlled pumping of DI water and (b) close-up of performance at lower flow rates (mean \pm SE, n=4)

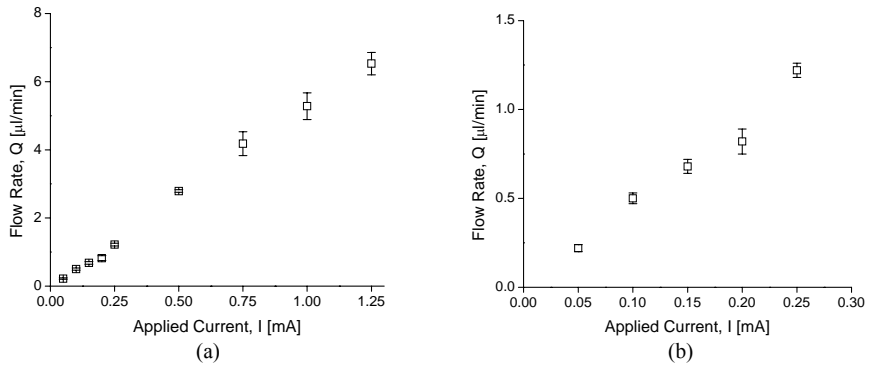


Figure 4. (a) Current-controlled pumping of DI water at 37°C and (b) close-up of performance at lower flow rates (mean \pm SE, n=4)

Acknowledgments

This work was funded in part by the Engineering Research Centers Program of the NSF under Award Number EEC-0310723 and Bausch & Lomb. We would like to thank Mr. Trevor Roper and members of the Biomedical Microsystem Lab.

References

- [1] D. H. Geroski and H. F. Edelhauser, "Drug delivery for posterior segment eye disease," *Invest Ophthalmol Vis Sci*, vol. 41, pp. 961-4, 2000.
- [2] D. C. Metrikin and R. Anand, "Intravitreal drug administration with depot devices," *Curr Opin Ophthalmol*, vol. 5, pp. 21-9, 1994.
- [3] R. Lo, K. Kuwahara, P.-Y. Li, R. Agrawal, M. Humayun, and E. Meng, "A Passive Refillable Intraocular MEMS Drug Delivery Device," in *International Conference on Microtechnologies in Medicine and Biology*. Okinawa, Japan, 2006, pp. 74-77.
- [4] J. Xie, Y. Miao, J. Shih, Y. C. Tai, and T. D. Lee, "Microfluidic platform for liquid chromatography-tandem mass spectrometry analyses of complex peptide mixtures," *Anal Chem*, vol. 77, pp. 6947-53, 2005.

A RAPID FIELD-FREE ELECTROOSMOTIC MICROPUMP INCORPORATING CHARGED MICROCHANNEL SURFACES

Segyeong Joo¹, Taek Dong Chung² and Hee Chan Kim¹

¹Department of Biomedical Engineering, Seoul National University, Korea

²Department of Chemistry, Sungshin Women's University, Korea

Abstract

A rapid field-free electroosmotic micropump (RFEP) was constructed incorporating separate anionic and cationic glass microchannel surface modifications and its performance was investigated. Two of the arms of the devised Y-shaped RFEP were coated with anionic and cationic polymers, respectively. Different charges localized on these interior surfaces produced electroosmotic flow in opposite directions when an electric field was applied along the two coated arms. The hydrodynamic pressure developed at the common junction of the three arms generated field-free flow, which responded rapidly and reversibly to the applied electric field. The flow rate of the devised RFEP was 98.4 nL min⁻¹ when 1.0 kV was applied in 10 mM phosphate buffer at pH 7.0.

Keywords: Micropump, Electroosmotic flow, Microfluidics

1. Introduction

Micropump is a key component in microfluidic system. Many micropumps with various operating principles were developed [1]. For those micropumps, micropump using electroosmotic flow (EOF) is suitable for miniaturizing system size and generating rapid-responding flow. However, EOF is sensitive to microchannel surface adsorption and high electric field of EOF causes problems, such as cell lysis [2]. Producing electroosmotically driven field-free flow on a microchip is a solution to the developing micropump for microfluidic system.

The key concept used in the present study was a 'T'-shaped channel network design with two arms with positively and negatively charged interior surfaces, respectively. The schematic in Figure 1 shows how the T-shaped channel works. Although an electric potential is applied across the charged horizontal arms, no field gradient exists in the

vertical channel, which is thus field free. Moreover, the fluid in the field free vertical channel can be made to move upwards (Figure 1(B)) or downwards (Figure 1(C)) by switching the polarity of the field applied potential across the two horizontal arms; it also respond reversibly to an applied voltage like a plain EOF.

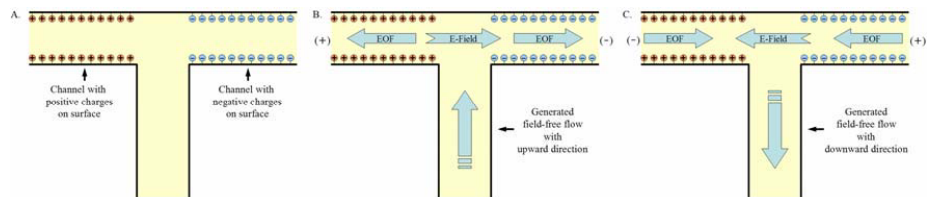


Figure 1. Schematic of field-free flow generation by modifying the surface of microfluidic chip.

2. Experimental Results

Figure 2 shows the schematic design of the proposed RFEP. The two upper arms with different interior surface charges and the vertical field-free channel were connected at the buffering region. Channel width and height is 30 μm and the diameter of buffering region is 300 μm . Glass chip was fabricated using general photolithography, etching and thermal bonding processes.

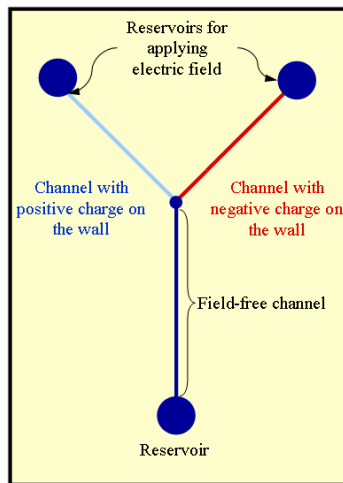


Figure 2. Schematic design of the proposed RFEP.

The output flow rates of the developed RFEP were measured by changing the applied voltages between the charged channel reservoirs. The channel was filled with 10 mM phosphate buffer (PB) at pH 7.0 and the resistance of the upper two arms was 148 M Ω . The slope of the flow rate versus applied voltage was 98.4 nL min $^{-1}$ kV $^{-1}$. Detailed results are shown in Figure 3, which shows that the flow rate increased linearly from 50 to 200 nL min $^{-1}$ as the applied potential was increased from 0.5 to 2.0 kV. These flow rates are rather slower compared with those previously reported for EOF micropumps. With the achieved pumping rate, we could transfer object with speed of 1.85 mm s $^{-1}$ when applied 1 kV assuming 30 μ m \times 30 μ m channel dimension.

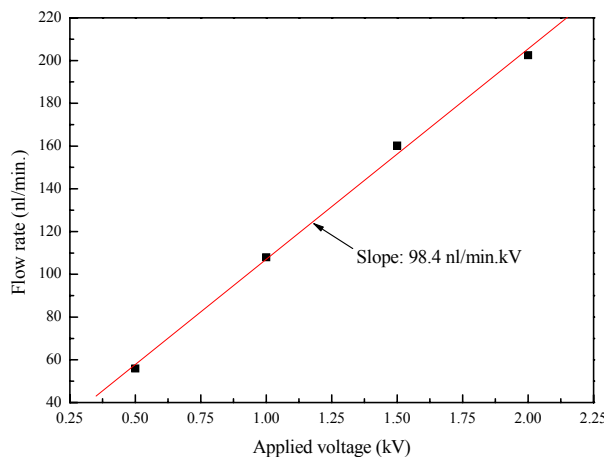


Figure 3. Flow rate versus applied electric field.

3. Conclusion

We have described a novel rapid field-free electroosmotic micropump (RFEP) which is driven by selectively coated microchannels. The devised RFEP was fabricated using general microfabrication techniques, thus ensuring its straightforward fabrication and combination with other microfluidic elements. The flow rate of the devised RFEP was found to be directly proportional to the applied electric field with a slope of 98.4 nL min $^{-1}$ kV cm $^{-1}$ in 10 mM PB at pH 7.0.

References

1. P. Woias, Proc. SPIE, 4560, 39-52 (2001).
2. P. C. H. Li, D. J. Harrison, Anal. Chem., 69, 1564-1568 (1997).

MICROFLUIDIC CONTROL FOR GRAVITY-DRIVEN ELISA APPARATUS

Jhy-Wen Wu and Nan-Kuang Yao

Medical Electronics and Device Technology Center,
Industrial Technology Research Institute, Hsinchu, Taiwan

Abstract

A microfluidic chip-based enzyme-linked immunosorbent assay (ELISA) for clinical diagnosis was developed. Through this chip, the Hepatitis C virus (HCV) dissolved in a serum sample was successfully determined with high sensitivity. This chip not only enabled to reduce the assay time from one hour to five minutes, but also it was achieved by simple manual operations. In addition, it did not use any activating power or peripheral supporting electromechanical facilities.

Keywords: ELISA, flow order control, gravity-driven, microfluidic chip

1. Introduction

Flow control is the basis of automatic reaction process for most biochemical analyses. The significant function requirements include (1) the capability to switch the flow, (2) correctly following the flow order, (3) the capability to define and control the flow amount, and (4) the capability to minimize the mixing of any two reactants. In 1992, Doring et al. [1] drove the deformation of the hanging arm via thermal expansion to switch the moving fluid direction. Lee et al. [2] presented a microchip capable of continuous sample switching and injection by integrating hydrodynamic focusing and valveless flow switching inside multi-ported microchannels.

2. Experimental

A microfluidic chip (Fig. 1) was made of PMMA plate (10cmx2cmx0.5cm), and mainly comprised a plurality of reactant wells arranged at different heights, a plurality of flow-control microchannels, and a reaction chamber having a collection channel with a winding shape. Each reactant well had an air-in vent. Each separate flow-control microchannel was connected to the bottom of its corresponding reactant well, and each pair of neighboring separate microchannel has a U-shape structure connecting the pair of neighboring separate microchannels. These separate microchannels were converged into the reaction chamber through the collection channel. Except for the first reactant,

the other reactants were initially stored in reactant wells, respectively, and sealed by tape. After the first reactant was loaded into the well, the chip was activated by placing in a inclining or standing position and the air-in vents were unsealed. The reactants flowed downward due to the gravity through a corresponding microchannel into the reaction chamber in the order specified by the height of the position of the reactant wells. The novel structures with different widths and lengths of the separate microchannels were utilized to increase the flow resistance of reactants (Fig. 2A), and were designed to guarantee each reactant correctly guided into the reaction chamber. When the first reactant flowed downward, it would pass by the branch of the U-shape structure (Fig. 2B) which connecting the second microchannel, and a small amount of reactant stopped at the branch due to the surface tension. When the second reactant in the neighboring microchannel flowed downward, the second reactant would merge the first reactant and be guided into the reaction chamber. The minimal mixing of reactants before entering the collection channel can be achieved due to the air block effect.

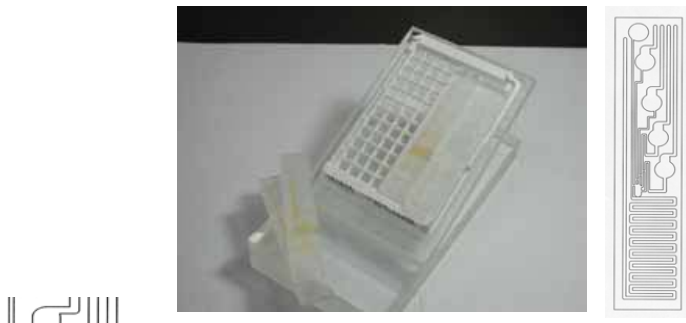


Figure 1. The microfluidic chip system.

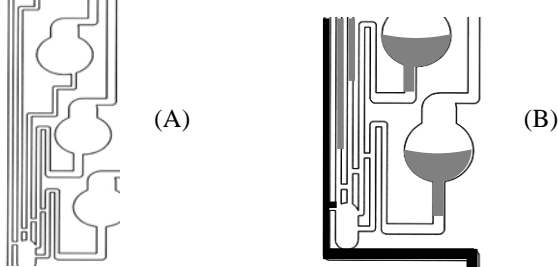


Figure 2. Layout of microfluidic chip. (A) The arrangement of geometric microchannel, (B) The horizontal connecting alley.

3. Results and discussion

In our experiments, the antigens were immobilized on the inner surface of the reaction chamber. While the five reactants, including first-degree antibody, buffer solution PBS, second-degree antibody with enzyme, buffer solution PBS, and chromogen TMB, were placed inside the five reactant wells, respectively. The total reaction time was about five minutes and the result was correct with highly sensitivity (Fig. 3). The OD value detected by ELISA reader was 1.297 for positive response and 1.002 for negative response, respectively.



Figure 3. The results of HCV test: (A) positive response, (B) negative response.

4. Conclusions

In this paper, we have shown the novel feature of this apparatus that the reactants flow into the reaction chamber in a desired order without using any external actuating power or device only by gravity. In comparison to conventional ELISA method, our method is greatly reduction of assay-time, simplifies the experimental procedure and achieves the real automated device. We believe that this kind of apparatus will serve as a very useful tool for biochemical analyses.

Acknowledgements

The authors would like to thank Dr. Luo-Hua Miao of Oncoprobe Biotech inc. in Taiwan for his support.

References

1. C. Doring, T. Grauer, J. Marek, M. Mettner, H. P. Trah, and M. Willman, Proc. IEEE Micro Electro Mechanical System Workshop, MEMS'92 (1992).
2. G. B. Lee, C. I. Hung, B. J. Ke, G. R. Huang, and B. H. Hwei, J. Micromechanics and Microengineering, 11, 567 (2001).

A NOVEL INTEGRATED MICROFLUIDIC SERS-CD WITH HIGH-THROUGHPUT CENTRIFUGAL CELL TRAPPING ARRAY FOR QUANTITATIVE BIOMEDICINE

Hansang Cho and Luke P. Lee

Biomolecular Nanotechnology Center, Berkeley Sensor and Actuator Center
Department of Bioengineering, University of California, Berkeley, CA 94720 USA

Abstract

Integrated microfluidic surface-enhanced Raman spectroscopy on a compact disk (SERS-CD) platform has been developed for high-throughput quantitative biomedicine. A smart design of a SERS-CD platform including efficient cell-trapping microfluidics, a locally integrated SERS probe, and a sample-accumulating concentrator is a solution for label-free high-throughput screening and detection. A SERS probe combined with a protein concentrator allows monitoring the dynamics of secreted proteins as a function of trapped cell density, accumulation time, and the induced centrifugal force. The design of centrifugal cell trapping microfluidics was characterized by using polystyrene beads and HeLa cells and the preliminary evaluation of a centrifugal sample concentrator on a SERS probe was accomplished by observing the increased Raman spectrum of Rhodamin 6G (R6G) as the molecule accumulated on the probe.

Keyword: quantitative cell analysis, centrifugal concentrator, centrifugal separation, cell trapping, SERS, SERS-CD

1. Introduction

Quantitative cell analysis requires both capabilities of effective cell trapping and sensitive detection of secreted proteins. Such trapping has been achieved by applying electro-kinetic force or hydraulic pressure, which requires complicated electrical connections or extensive tubing, making integration difficult. Therefore, a device in a CD format is attracting considerable attention because flow can be regulated by controlling the rotational speed of the device without any connection to external components [1] while providing a high throughput platform and easy integration with a detector [2]. In contrary to a conventional label-requiring fluorescence technique, a label-free optical technique based on SERS has been used in the detection of a large number of chemicals and biological molecules due to its high sensitivity and molecular specificity [3]. However, detecting molecules secreted from cells requires a strong enhancement because the molecules are secreted at low concentration. Therefore, the CD-based integration of a cell trapping microfluidics with a SERS probe and a sample concentrator will be useful for quantitative cell analysis.

2. System Design

A SERS-CD platform designed in a wafer format exerts a centrifugal force on randomly distributed cells and secreted molecules in the radial direction across the whole wafer.

The centrifugal force separates introduced cells from media and the cells are collected in trapping chambers. The trapped cells can secrete molecules activated by introduced chemical. The molecules are delivered only in the radial direction and accumulated on a SERS probe. The accumulated molecules are analyzed by measuring the Raman spectrum (Figure. 1).

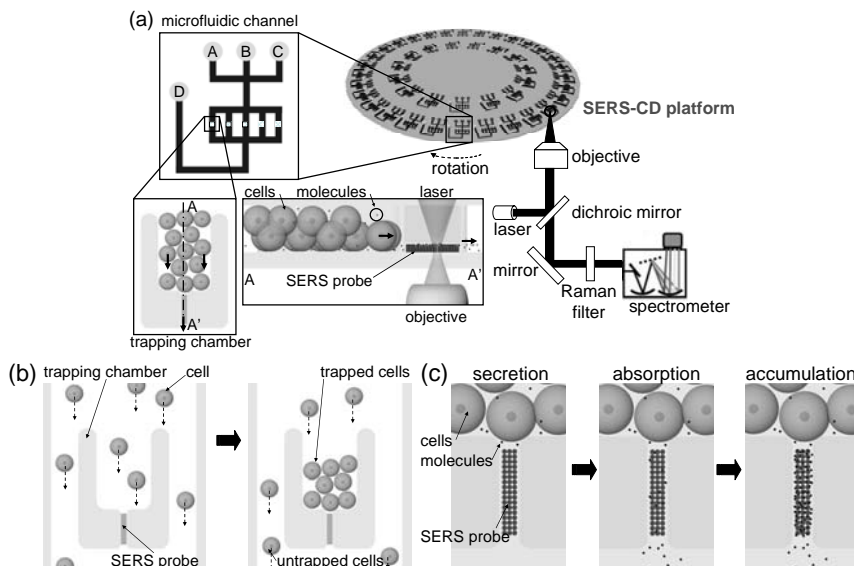


Figure 1. Schematic representation of an integrated SERS-CD platform for biomolecule detection.
 (a) A SERS spectroscopy and a SERS-CD platform. (reservoirs for activating chemicals (A), cells (B), media (C), and vent (D)) (b) Cell trapping schematics comparing cells before trapping (left) after trapping (right). (C) Sample concentrating cycle: secreted molecules are delivered (left), absorbed (center) and then accumulated on a SERS probe (right), which results in molecule concentrating.

3. Experimental

The microfluidic channels were fabricated by means of soft lithography. A negative photoresist (SU8-2050, MicroChem, MA) was spin-coated and patterned to make a mold for microfluidic channels with a thickness of 50 μm . A mixture of poly(dimethylsiloxane), (PDMS) prepolymer and a curing agent (SYLGARD 184 A/B, Dow Corning, MI) in a ratio of 10:1 was then cast against the molds to yield an elastomer replicas and then was cured for 2 hours in an oven at 70°C. A SERS-CD platform was fabricated by bonding the cured PDMS replica to a glass wafer of 4 inch in diameter by oxygen plasma treatment using a reactive ion etcher system for 20 s.

4. Results and discussions

The cell trapping and sample concentrating were characterized separately. The trapping efficiency was defined by the ratio of the number of filled trapping chambers to the total

number of chambers. Figure 2 shows that the trapping efficiency increased with increasing entrance width (W_{en}) and decreasing exit width (W_{ex}). Figure 3 shows that SERS enhancement was improved as the number of cycles increased and the intensity at 1509 cm^{-1} increased by 5 times after 7 cycles of concentrating.

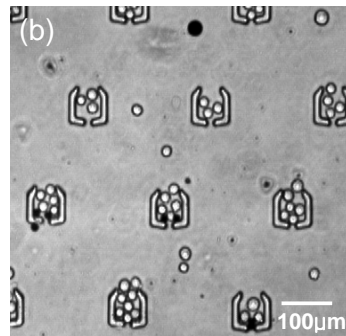
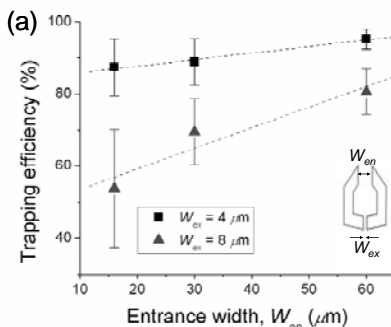


Figure 2. Characterization of centrifugal particle trapping. The characterization was achieved by measuring trapping efficiency with (a) polystyrene beads ($10 \mu\text{L}, 4.6 \times 10^7 \text{ particles mL}^{-1}$) and (b) HeLa cells ($10 \mu\text{L}, 4 \times 10^6 \text{ cells mL}^{-1}$) at 3,000 rpm for 3 minutes.

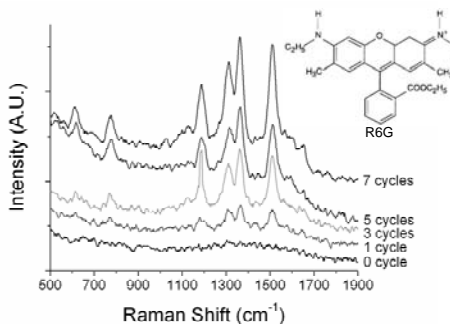


Figure 3. Characterization of centrifugal sample concentrating. The characterized was done by measuring SERS of R6G under 90 mW ($2.9 \text{ W}\cdot\text{cm}^{-2}$) of 785 nm photons and integration time of 10 s after every cycle of concentrating. A SERS probe was prepared by collecting Au particles of 80 nm on a glass substrate. R6G was introduced by dropping $1 \mu\text{L}$ in solution at the concentration of 1 mM , was delivered to the SERS probe by a centrifugal force. After each SERS measurement, the introducing of R6G was repeated.

5. Conclusions

High-throughput cell trapping and sample concentrating were demonstrated with a novel SERS-CD platform. Highest trapping efficiency was achieved at channels having largest entrance width and smallest exit width and SERS intensity became stronger as the number of concentrating of R6G increased.

Acknowledgements

This work was supported by Intel Corp.

References

1. A. Rothert, S. K. Deo, M. J. Madou et al., *Anal. Biochem.* **342**, 11 (2005)
2. S. A. Lange, G. Roth et al., *Angew. Chem. Int. Edn* **45**, 270 (2006)
3. K. Kneipp, H. Kneipp et al., *J Phys.-Condens. Mat.* **14**, R597 (2002)

ELECTROPHORETIC MANIPULATION AND ELECTROCHEMICAL ANALYSIS OF SINGLE CELL WITH THE MICROFLUIDIC DEVICE

Kuniaki Nagamine¹, Tomoyuki Yasukawa¹, Hitoshi Shiku¹,
Masahiro Koide², Tomosato Itayama², Tomokazu Matsue¹

¹ Graduated School of Environmental Studies, Tohoku University, Japan,

² National Institute for Environmental Studies, Japan

E-mail address: nagamine@bioinfo.che.tohoku.ac.jp

Abstract

We have fabricated a microfluidic device comprising a 100 pL scale analytical chamber for electrochemical measurement of cellular activities. The microfluidic main channel and the analytical chamber were fabricated using poly(dimethylsiloxane) (PDMS). The chamber contained two Pt microelectrodes served as an electrochemical working electrode and an electrophoretic electrode to manipulate cells into the chamber. Yeast cells were introduced to the chamber by the electrophoresis, and its β -galactosidase (β Gal) activities were characterized by amperometry. *p*-Aminophenol (PAP), generated by the enzyme-catalyzed hydrolysis of *p*-aminophenyl- β -D-galactopyranoside (PAPG), was detected electrochemically.

keywords: microfluidic device, single cell, electrochemistry, electrophoresis

1. Introduction

Microfluidic systems are attractive due to their potential as analytical tools with an enhancement of reaction efficiency. Microfluidic channels formed by patterned PDMS have been applied to the biosensors and cell manipulations. However, there are few reports of the systems combined with electrochemical biosensors and cellular manipulation in the fluidic channels. In this presentation, we developed a microfluidic device incorporating electrochemical detection and cellular manipulation systems. Moreover, the chamber electrode is utilized to measure single cellular activities of β Gal.

2. Experiments

Growth conditions of yeast cells

The yeast *Saccharomyces cerevisiae* Y190 strain with the medaka estrogen receptor α was kindly provided by Dr. Shiraishi. The expression of β Gal in Y190 strain was

induced by 17 β -Estradiol (E2) using two hybrid system (Figure 1, [1]). Before use, yeast cells were treated with 0.3 % TritonX-100 to facilitate the cell membrane permeability for the β Gal substrate, PAPG.

Fabrication of electrochemical microfluidic device

Pt electrodes were fabricated on the glass substrate by conventional photolithography, metal sputtering, and lift-off techniques. The lead wire was insulated with the SiO₂ layer which was also fabricated by micromachining techniques. Positive photoresist patterns of fluidic channels and chambers were fabricated on the electrodes and then PDMS was molded. After photoresist patterns were eluted by acetone, the resulting portions can be utilized for the channels and chambers. Figure 2(A) shows the photograph of electrochemical microfluidic device. The fluidic device was composed of the main channel (300 μ m in width, 10 μ m in height) and the chambers aside of the main channel (100 x 100 x 10 μ m, Fig. 2(B)). Two Pt working electrodes were positioned in the chambers used for electrochemical measurement (10 x 10 μ m) and electrophoretic manipulation (10 x 30 μ m).

Electrophoretic manipulation of single cell

The suspension of cells in 20.0 mM Hepes-NaOH buffer (pH 7.0) was injected into the main channel. A +2.0 V dc voltage against the large electrode, which was embedded in the main channel, was applied to the Pt microelectrode placed in the chamber in order to introduce cells into the chamber.

Electrochemical detection of β Gal activity in yeast cells

Z buffer solution (60.0 mM Na₂HPO₄, 39.7 mM NaH₂PO₄, 10.0 mM KCl, 1.0 mM MgSO₄) containing 7.4 mM PAPG was injected into the chamber with cells from the inlet of main channel and the device was allowed to stand for 10 min. Then the potential of +0.3 V vs. Ag/AgCl was applied to the working electrode in order to detect PAP release from yeast cells by β Gal reaction. Reference electrode was inserted to the outlet of the microchannel.

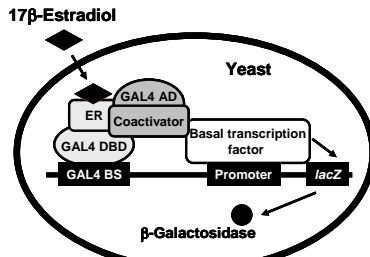


Figure 1. The principle of β Gal expression in *S. Cerevisiae* Y190 strain.

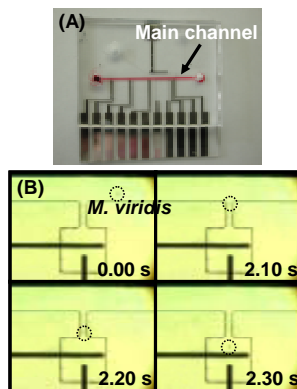


Figure 2. (A) The photograph of the electrochemical microfluidic device. (B) Electrophoretic manipulation of a single *M. viridis* cell in the channel.

3. Results and discussion

Figure 2(B) shows the electrophoretic manipulation of a single cyanobacterium *Microcystis viridis* cell in the microchannel. When +2.0 V dc voltage was applied to the Pt electrode in the chamber, flowing cell in the main channel was introduced into the chamber. In addition, the application of -2.0 V permitted to withdraw the trapped cell to the main channel. The electrophoresis method is found to be desirable and easy way to manipulate specific single cells in the population.

The β Gal activity of entrapped yeast cells was detected using this device. Figure 3 shows the oxidation current response for PAP generated from yeast cells cultured with and without 20.0 nM E2. 120 yeast cells were entrapped in the chamber. When +0.3V vs. Ag/AgCl was applied, the oxidation current responses were detected from the yeast cells exposed to E2. On the other hand, the current responses obtained from the yeast cells cultured without E2 are in the background signal level, suggesting that current response reflected the β Gal activity of the cells. We are currently carrying out the measurement of β Gal activity in single yeast cells using this microfluidic device.

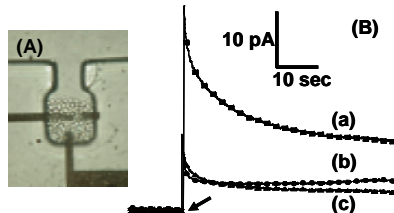


Figure 3. (A) The micrograph of the chamber entrapping 120 yeast cells. (B) The oxidation current for PAP generated from yeast cells cultured with (a) and without 20 nM E2 (b) when applying the voltage at 0.3 V vs. Ag/AgCl (indicated arrow). (c) indicates the current response of no cells.

4. Conclusion

In this study, we have performed the eletrophoretic manipulation of a single cell and the electrochemical detection of β Gal activity in yeast cells using the microfluidic device. This device would enable the high-throughput and long-term monitoring of gene expression against the drug candidates at a single cell level.

Acknowledgements

This work was partly supported by Grants-in Aid for Scientific Research from the Ministry of Education, Science and Culture, Japan. K.N. acknowledges the support obtained from a research fellowship of the Japan Society of the Promotion of Science. We thank Dr. F. Shiraishi for providing *S. cerevisiae* Y190 strain used for this study.

References

- [1] T. Nishihara et al, J. Health Sci., **46**, 282-298 (2000).

ACCELERATION OF ABSOLUTE NEGATIVE MOBILITY FOR PARTICLE SORTING IN A MICROFLUIDIC DEVICE

J. Regtmeier, R. Eichhorn, P. Reimann, A. Ros*, D. Anselmetti

Bielefeld University, Experimental Biophysics, Germany

*Alexandra.Ros@physik.uni-bielefeld.de

ABSTRACT

Recent designs in microfluidic devices extend common separation concepts by exploiting new non linear phenomena for molecular dynamics on a length scale of 10 microns and below, giving rise to novel manipulation tools and non-intuitive phenomena for microseparations. A rather paradoxical and new migration phenomenon termed absolute negative mobility (ANM) using thermal fluctuations in a non-equilibrium environment generates average motion of particles in the direction opposite to an applied static force [1]. Here, we propose how ANM can be accelerated in order to improve maximum velocities for future applications such as purification or sorting of colloidal particles, cells and cell compounds.

Keywords: absolute negative mobility, particle sorting, thermal noise, non linear dynamics

1. Introduction

ANM for colloidal particles in solution can be evoked in an array of periodically arranged rows of posts separated by alternating small and large gaps (see fig. 1). Polystyrene microbeads at low concentration in aqueous buffer solution are driven through this geometry by application of electric fields along the y -axis. Particle diameters and gap widths are chosen such that the beads can pass through the large gaps but not through the small ones. Thus, the small gaps together with the electric field act as traps. Conditions far from thermal equilibrium are realized by an unbiased AC-voltage U_{AC} switching periodically between $\pm U_0$. Upon application of a small static offset voltage U_{DC} and adequate driving parameters for U_{AC} ANM can be observed [1]. Numerical simulations of ANM adopted to experimental conditions are in very good agreement with our experimental observations [1]. Such calculations further reveal that this migration effect can be suitably tailored to drive colloidal particles of different size into opposite directions [2], thus providing a new tool for particle sorting in microfluidic device format. However, the maximum velocities achieved for ANM of μm -sized spheres are small, i.e. in the order of nm per second. Here, we focus on the adaptation of the post array geometry in order to reduce lateral diffusion times of colloidal particles in the microdevice and thus accelerate ANM of colloidal particles.

2. Methods

The motion of a single bead in the periodic microstructure is modelled by a stochastic Langevin dynamics as previously reported [1; 3]. The simulation is performed for colloidal particles with a diameter of 1.9 μm , a diffusion coefficient D of 0.13 $\mu\text{m}^2/\text{s}$ and a velocity v of 0.28 $\mu\text{m}/\text{s}$ at an applied voltage of 1V over the whole device. A

periodical driving, U_{AC} with an amplitude of $U_0 = 120$ V and a frequency of 0.03 Hz is used for the square geometry (fig.1a) and, correspondingly, U_{AC} with an amplitude of $U_0 = 90$ V and a frequency of 0.05 Hz for the layout in fig.1b. The monolithic poly(dimethylsiloxane) (PDMS) device is made by soft lithography, as previously reported [1]. Improved UV-lithography of SU-8 photoresist via a pre-designed photomask is achieved by a home built pneumatic mask contact device.

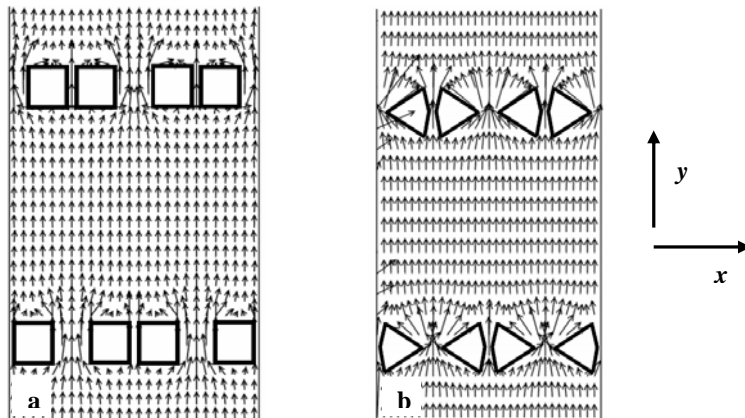


Fig. 1: Section of microstructured post array designs for ANM in a microchannel with simulated force field (arrows): a) Square posts and b) sharpened posts.

3. Results and Discussion

The probability for the particles to avoid a trap in the post array critically depends on the diffusion and the electrokinetic driving of the particles. Allowing a more efficient avoidance of the traps in lateral (x -) direction, one would expect faster ANM velocities. We have thus designed two new geometries in which the lateral dimension of the posts is decreased compared to our previous device [1]. In the first approach, square posts with a base of $4\mu\text{m}$ are envisaged (fig. 1a). In the second approach (fig. 1b) the posts are designed trapezoidally.

Numerical simulations within these two designs were performed for colloidal particles with a diameter of $1.9 \mu\text{m}$. Fig. 2a and 2b reveal that maximum velocities of ANM are enhanced up to a factor of 20 for case *a* and up to 30 for case *b*, respectively, compared to our previous study [1].

Based on these results we designed layouts adapted to fig. 1a and b on a master wafer photolithographically structured with SU-8 photoresist. Casting of PDMS resulted in corresponding PDMS microstructures as exemplarily demonstrated for the square design in figure 3. The electron microscopy image shows posts of $3.3 \times 3.3 \mu\text{m}^2$ base and a height of $9 \mu\text{m}$ in channels of equal height. The aspect ratio thus results in a value of three and the smallest post distance (serving as particle trap) resulted in $1.8 \mu\text{m}$. We could thus demonstrate the fabrication of improved geometries in order to accelerate ANM of colloidal particles with simple UV-lithography combined with PDMS casting.

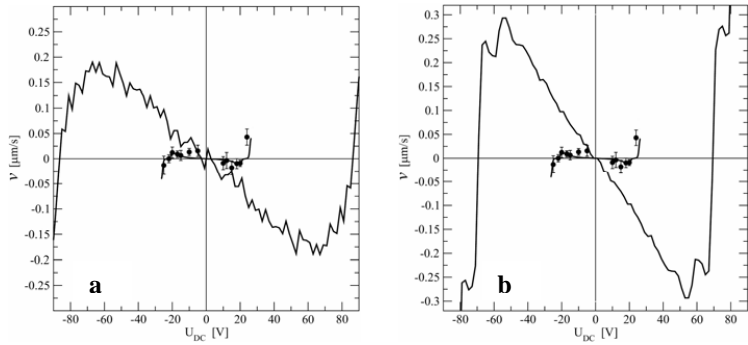


Fig. 2: Numerical simulation of particle velocity for 1.9 μm sized particles versus applied static offset force U_{DC} . a) Simulation for the design demonstrated in fig. 1a. For comparison, recently published [1] experimental data with numerical simulations are shown around the origin in both a) and b) (dots with line around the origin). b) Simulation for the design demonstrated in fig. 1b

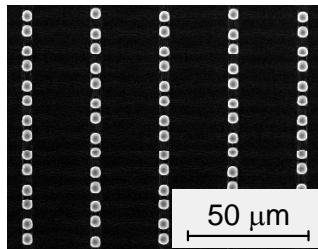


Fig. 3: Scanning electron micrograph of PDMS structures obtained for the square design according to fig. 1a.

4. Conclusion

Numerical simulations reveal that the non-intuitive migration phenomenon ANM can be accelerated by an optimized geometry. We demonstrate the fabrication of optimized post arrays in microfluidic channels by soft lithography with sufficiently high aspect ratio and sufficiently small post distance in order to trap colloidal particles $>1.8 \mu\text{m}$ diameter. The acceleration of ANM in both new designs for colloidal particles with pre-defined mobility and diffusion coefficients in aqueous solution is currently under experimental investigation.

5. References

- [1] Ros, A., Eichhorn, R., Regtmeier, J., Duong, T. T., Reimann, P., and Anselmetti, D., Brownian Motion: Absolute Negative Particle Mobility, *Nature* 2005. 436, 928
- [2] Regtmeier, J., Anselmetti, D., and Ros, A., Novel Migration Phenomena in Structured Microfluidic Devices, *Proceedings of μ TAS 2005*. 1, 340
- [3] Regtmeier, J., Eichhorn, R., Duong, T. T., Reimann, P., Anselmetti, D., and Ros, A., Particle Sorting by Absolute Negative Mobility in a Microfluidic Device, *submitted* 2005.

ENHANCED PROTEIN CAPTURE BY ULTRAFAST SAW DROPLET μ MIXING

Elisabeth Galopin, Alan Renaudin, Jean-Christophe Camart,

Vincent Thomy, Christian Druon, Pierre Tabourier

Institut d'Electronique, de Microélectronique et de Nanotechnologie
Villeneuve d'Ascq, FRANCE

Abstract

Lab-On-Chip applications require high quality surface chemistry and functionalization because it can affect stability, selectivity or recognition ability towards target molecules. As digitalized microfluidics is foreseen as a relevant technique to implement programmable biology, a simple active micromixing of droplets for microTAS applications using surface acoustic wave (SAW) is developed and characterised. Controlled acoustic streaming within microdroplets enables fast and homogeneous biointeractions, bringing high quality biological interfaces.

Keywords: Surface acoustic waves, microdroplet, micromixing, protein, biosurface interactions

1. Introduction

Within Lab On a Chip and MicroTotal Analysis Systems (μ TAS), fast and homogeneous interactions are needed. These interactions can occur between two biomolecules (micromixing) or between a biomolecule and surface, by the means of a bio-functionalized zone. Problems can be faced in functionalization, such as non specific adsorption, coffee stain effects [1] in DNA spotting... It is shown that SAW can favourably solve the exposed issues [2]. Besides, the will in clinical applications to work with smaller amounts of analytes and to enhance biosensing sensitivities leads to necessary think of reduced sample micro/nanofluidics. This tendency has given birth to discrete microfluidics. In this work, nanometric amplitude waves are generated by InterDigitized Transducers on a LiNbO₃ piezoelectric substrate, providing remote action on biological microdroplets [3].

2. Theory

In small volumes, hydrodynamic flows are characterised by low Reynolds numbers. Interaction can only occur by diffusion [4]. The use of SAW at the liquid-solid interface provides streaming effects in microdroplets [5-6], which enhance interaction and thus functionalization quality by bringing molecules in contact with the active surface. The proposed Lab-on-Chip allows an effective and rapid acoustic mixing of droplets in a controlled fashion for specific protein binding interactions.

3. Experimental

The resulting interaction was characterised using fluorescence and dilution-type measurements by contacting dyed molecule droplets with water droplet and observing

with a high definition video camera. Time series of SAW mixing within droplets, as exposed Fig.1, show the sequence leading to a fast homogeneous microdroplet.

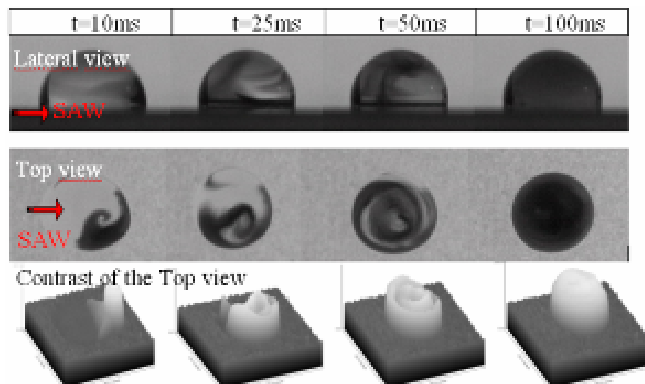


Figure 1. $10 \mu\text{l}$ droplet time series of SAW mixing at 28 dBm power transducer excitation: (up) lateral view, (middle) top view, (down) contrast.

4. Results and Discussion

Mixing efficiency is characterised by plotting the standard deviation to the mean signal versus time (Fig.2). Characteristic mixing times can be divided by at least 300.

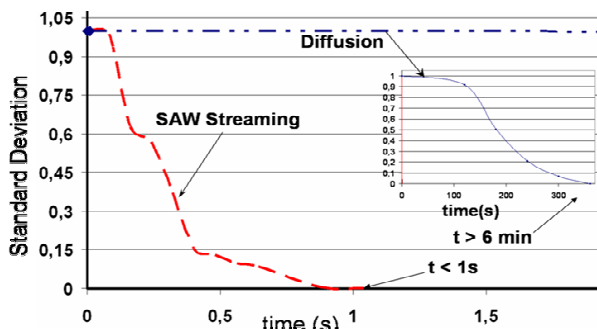


Figure 2. Normalised standard deviation to average luminosity signal for diffusion and for SAW-mixed droplets.

For biological applications the droplet carrying the biomaterial can be squeezed between the platform and a functionalized cover [7]. The same conditions were applied to a SAW-mixing of microdroplets with the cover. Recorded times scale are lightly superior by a few tens of milliseconds, however, thanks to increased surface exchanges, this configuration has huge potentialities in the field of biological micromixing systems.

Following these results, the mixing was applied to the biotin-streptavidin interaction. Temperature in the droplets was effectively controlled by maintaining SAW power at a value of 28 dbm in continuous mode, determined by preliminary calibrations.

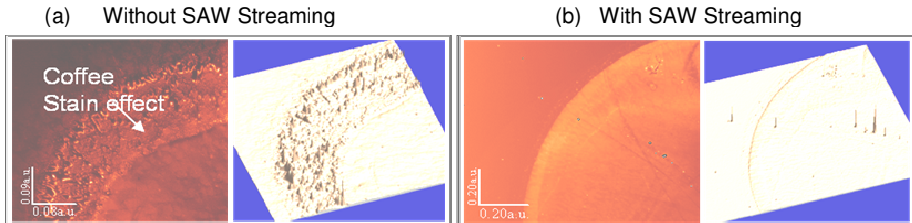


Figure 3: Fluorescence images of Cy3-streptavidin immobilised (1/4 view of 2 μL droplets manually spotted) and 3D view of the fluorescence intensity and homogeneity (a) without and (b) with SAW.

Surface homogeneity and intensity measurements comparing the interaction efficiency with and without acoustical streaming show a large improvement in the case of SAW streaming (Fig. 3).

5. Conclusion

SAW-based micromixing of biological liquids provides beneficial effects for on chip biological interactions. It enables the generation of highly homogeneous two-dimensional patterns of functional biomolecules and offers new prospects in the field of biological applications such as biorecognition or protein analysis.

Acknowledgements

The authors thank Rabah Boukherroub, Institut de Recherche Interdisciplinaire, Corentin Sriet, Institut de Biologie de Lille, and Farzam Zoueshtiagh, Laboratoire de Mécanique de Lille. Region Nord Pas de Calais and FEDER supported this work by their financial and equipment contribution.

References

- [1] R.D. Deegan, O. Bakajin, T. Dupont, F. Huber, S. Nagel and T. Wittel, *Capillary flow as the cause of ring stains from dried liquid drops*, Nature, 389, pp. 827-829, (1997).
- [2] Z. Guttenberg, H. Müllera, H. Habermüllera, A. Geisbauera, J. Pipperb, J. Felbelb, M. Kielpinska, J. Scribaa, A. Wixforth, *Planar chip device for PCR and hybridization with surface acoustic wave pump*, Lab on a Chip, 5, pp. 308-317, (2005).
- [3] A. Renaudin, P. Tabourier, V. Zhang, J-C. Camart, C. Druon, *SAW nanopump for handling droplets in view of biological applications*, Sens. & Act. B, 113, pp. 389-397, (2006).
- [4] V. Hessel, H. Löwe, F. Schönfeld, *Micromixers: a review on passive and active mixing principles*, Chemical Engineering Science, 60, pp. 2479-2501, (2005).
- [5] W. Nyborg, *Acoustic streaming*, Academic Press, San Diego, pp. 207-232, (1998).
- [6] W. Tseng, L. Lin, W. Sung, S. Chen, Gwo-Bin Lee, *Active micro-mixers using surface acoustic waves on Y-cut 128° LiNbO₃*, J. Microm. Microeng., 16, pp. 539–548, (2006).
- [7] A. Renaudin, K. Chuda , V. Zhang, X. Coqueret, J-C. Camart, P. Tabourier, C. Druon, *SAW Lab-on-Chip in view of protein affinity purification implemented from nanodroplet transport*, MicroTAS'05, pp. 559-601, (2005).

GIANT AMPLIFICATION OF REDOX CURRENT IN A NANOFUIDIC CHANNEL

Marcel A. G. Zevenbergen, Diego Krapf, Marc R. Zuidam and Serge G. Lemay

Kavli Institute of Nanoscience, Delft University of Technology, Lorentzweg 1,
2628 CJ Delft, the Netherlands

Abstract

We have developed a nanofuidic device consisting of a 300 nm high, water-filled cavity bounded by two parallel electrodes which amplifies the electrochemical signal from redox molecules inside the cavity by a factor of ~400 through redox cycling.

Keywords: Electrochemical sensing, redox cycling, nanofabrication

1. Introduction

The ability to electrically detect and manipulate single molecules in solution with high time resolution represents an ongoing experimental challenge in micro- and nanofuidics, analytical chemistry and lab-on-a-chip applications. Electrochemically active molecules are particularly suited for electrical detection through Faraday currents at appropriately biased electrodes. Few electrons per molecule are involved in these reactions, rendering direct detection virtually impossible. This difficulty can be overcome by fabricating two planar electrodes in close proximity to each other: a single molecule undergoing a random walk in the region between the electrodes reversibly serves as reactant and product, thereby shuttling multiple electrons between the electrodes. This so-called redox cycling process [1] is illustrated in Figure 1.

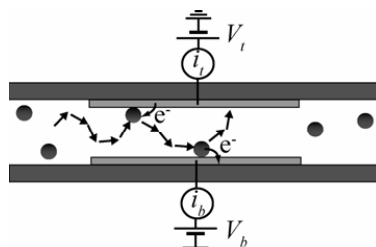


Figure 1. Illustration of the device concept. Electrochemically active molecules undergo a random walk between the two electrodes, thereby shuttling multiple electrons. V_t and V_b are the applied potential to the top and bottom electrode, while i_t and i_b are the corresponding measured currents.

2. Device Fabrication

We have developed a nanofluidic device consisting of a solution-filled cavity bounded by two parallel platinum electrodes separated by 300 nm. In brief, two planar electrodes separated by a silicon sacrificial layer were embedded in sputtered SiO₂. In the final step, the silicon layer was removed using a newly developed plasma etch process. This process uses a high-density, inductively-coupled SF₆ plasma with no added O₂, rendering the etching isotropic (Figure 2a).

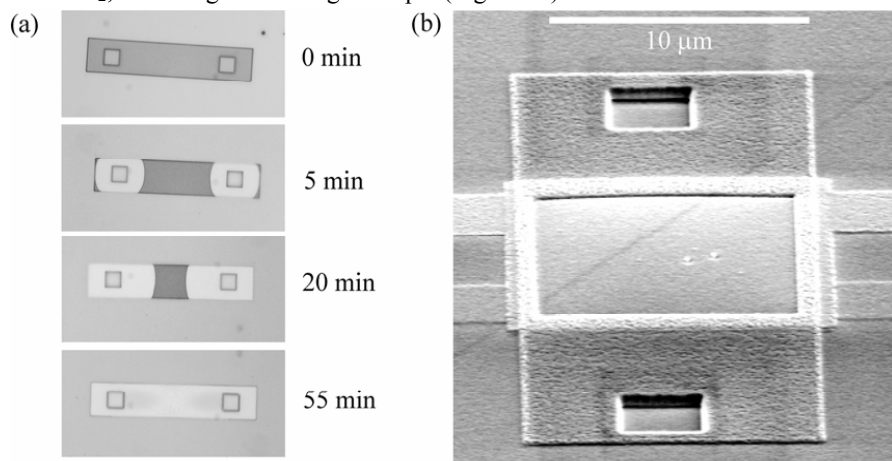


Figure 2. (a) Sacrificial etch of a 10 x 50 μm , 120 nm high Si test structure covered with 500 nm sputtered SiO₂. The plasma enters the cavity via two 5 x 5 μm access holes (squares). The etch proceeds gradually and after 55 min a channel is formed. (b) SEM image of a finished device. Fluid enters the 100 μm^2 area bounded by the parallel electrodes via two square entrance holes. Contacting wires can be seen on both sides.

3. Amplification of the electrochemical signal

The device achieves highly efficient redox cycling, resulting in the amplification of the electrochemical signal from redox molecules inside the cavity by a factor of ~400. This is demonstrated in Figure 3a. Because of the high concentration of inert salt (250 mM KCl), transport of the redox species (1mM ferrocenedimethanol) is entirely due to diffusion and the transport-limited steady-state current i_{ss} becomes

$$i_{ss} = eDAA_v c_0 z^{-1} \quad (1)$$

where $-e$ is the electron charge, D the diffusion constant ($4.7 \times 10^{-6} \text{ cm}^2/\text{s}$), A the area of overlap between the electrodes ($100 \mu\text{m}^2$), A_v Avogadro's number, c_0 the bulk concentration of redox-active molecules and z the distance between the electrodes. From the measured linear dependence of i_{ss} on the bulk concentration c_0 , the height of the cavity was determined to be 282 nm (Figure 3b), consistent with expectations.

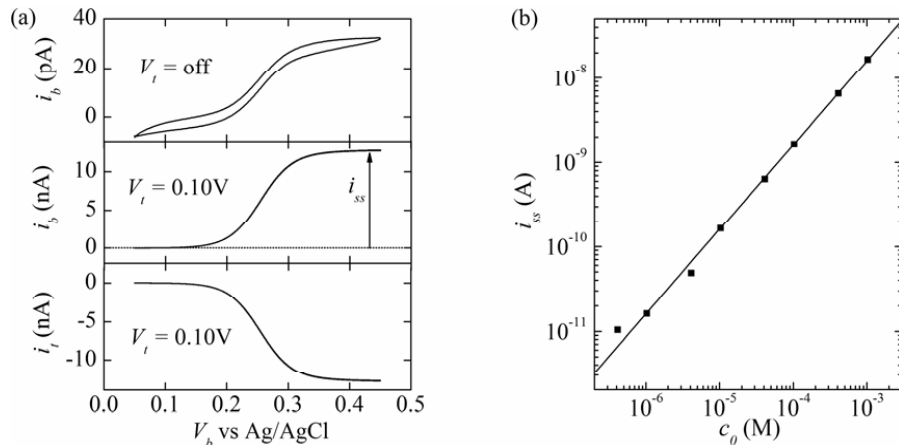


Figure 3. (a) Cyclic voltammetry (scan rate 1 mV/s) performed with the bottom electrode while the top electrode was electrically disconnected (top curve) and with $V_t = 0.10\text{V}$ (middle curve). The steady-state current i_{ss} is amplified approximately 400 times in the second case. The bottom curve represents the current through the top electrode obtained simultaneously with the middle curve. It is a mirror image of the current through the bottom electrode, indicating that nearly 100% of the generated product is cycled. (b) Transport-limited current i_{ss} versus concentration. The solid line is a fit to Eq. (1).

4. Mesoscopic fluctuations in the number of redox molecules in the cavity

Since the electrochemical current is proportional to the number of particles in the cavity, fluctuations in this current probe fluctuations of the number of particles in the cavity [2]. At the smallest concentrations investigated ($0.4\text{ }\mu\text{M}$), we observed excess current noise of 67 fA rms, corresponding to fluctuations of as few as 70 molecules inside the cavity.

5. Conclusion

We have developed a nanofluidic device consisting of two planar electrodes separated by 300 nm. Redox cycling amplifies the electrochemical current by a factor ~ 400 . Noise in the measured electrochemical current indicates sensitivity to fluctuations of as few as 70 molecules, and we expect that further downscaling will yield devices capable of detecting single redox molecules.

References

1. For a comprehensive review see C. Amatore in *Physical Electrochemistry* edited by I. Rubinstein (Marcel Dekker, New York, 1995).
2. M.A.G. Zevenbergen *et al.*, submitted.

MICROFLUIDIC BUBBLE ACTUATORS BASED ON HYDROGELS

Joerg Nestler¹, Karla Hiller¹, Thomas Otto² and Thomas Gessner^{1,2}

¹Center for Microtechnologies, Chemnitz University of Technology, Germany

²Fraunhofer Institute for Reliability and Microintegration (IZM), Chemnitz, Germany

Abstract

A low cost, super absorbing hydrogel is used for an electrolysis bubble actuator applicable for microfluidic valves and pumps. Advantages of such a rubber-like ionic polymer gel are a simple fabrication process compared to the use of liquids and improved performance of the actuator unit compared to water.

Keywords: micro fluidics, bubble actuator, electrolysis, hydrogel, lab on chip

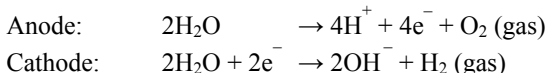
1. Introduction

Dosing and pumping small amounts of liquids is essential for the proper functionality of many Lab-on-Chip applications. Thus, fully integrated pumps and valves at an affordable price are desired to control the flow of a sample liquid, buffers or reference solutions.

The electrochemical generation of gas bubbles by electrolysis offers a great opportunity for cheap actuators with large deflection, high pressure and precise control of dosed volumes. Such bubble actuators have already been successfully demonstrated for microfluidics [1,2]. However, the integration of a liquid (e.g. water) can be critical for mass fabrication and may also cause problems concerning long-term stability. A Poly (acrylic acid)-based hydrogel was therefore investigated for its applicability as electrolyte, which combines the electrolytic and gas generating properties of water with a good processibility by screen printing or stencil printing.

2. Theory

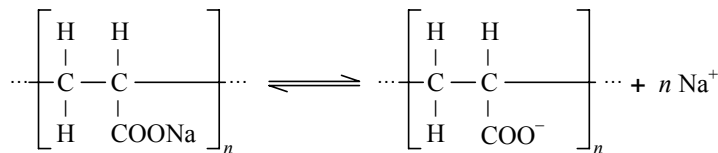
The electrolysis of water is the dissociation of water molecules into oxygen and hydrogen gas by means of a an electric current. The reaction is given by



Using pure water, this reaction is very slow. Increasing the ion content in the water for a given voltage increases the conductivity and thus the speed of the reaction.

Poly (acrylic acid) (PAA) is a so-called super absorbing polymer which is able to dramatically swell in water. The swollen state is referred to as a hydrogel, which mainly

consists of up to 99 wt% of water, but has a very high viscosity. When PAA is brought in contact with water, the weakly bonded sodium dissociate, leaving negatively charged polymer chains and movable sodium ions.



Using this effect, PAA not only “thickens” the water, but also increases its ion content, thus leading to a much faster electrolytic reaction.

3. Experimental

Silicon was used as substrate material for the actuators. After thermal oxidation, a thin (20nm) titanium layer was sputtered as adhesion layer, followed by a gold layer of 200nm thickness. The metals were then structured to form electrodes of different geometries. Chambers around the electrodes where subsequently formed by SU8 lithography, leading to cavity heights of around 360μm (Fig. 1).

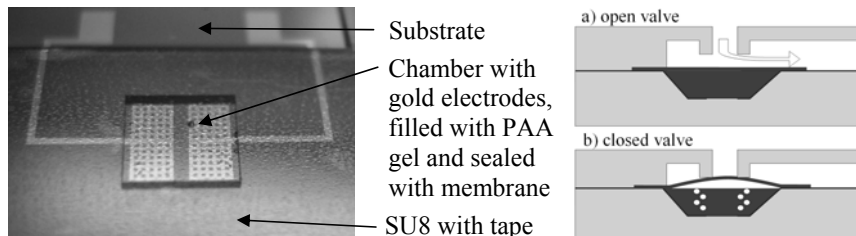


Figure 1. Picture of a fabricated test structure filled with PAA and covered with a tape as membrane layer (left) and schematic drawing of a bubble-gel valve (right).

Gels with three different PAA concentrations (0.7wt%, 0.42wt% and 0.35wt%) were prepared using PAA (Luquasorb1010, BASF) and deionised water. The first of these mixtures has rubber-gel like properties, whereas the last one is still more “liquid-like”. The SU8-chambers were filled with the PAA gel and sealed with tape of a thickness of 70μm (SWT10, Nitto Denko)

The membrane deformation and deflection was then measured by a stripe projection system. The dynamic properties such as the speed of deflection were measured by an auto-focus profilometer both for different electrode geometries and gel compositions.

4. Results and discussion

The actuators with chamber areas of 3x3mm², interdigital electrodes and a PAA concentration of 0.7wt% reached a deflection of more than 300μm (Fig. 2, left) within a time of about 12s at a voltage of 5V. Comparing the results for the different electrode

designs and PAA concentrations, it could be found that the performance of the actuator cell is mainly improved by a proper electrode design rather than a certain PAA concentration. As expected, interdigital (“int”) electrodes show the best performance due to the much lower resulting resistance of the electrolytic cell, which consequently leads to a higher current and faster bubble generation for a fixed voltage.

As shown in Fig. 2 (right), the PAA concentration also has impact to the conductivity of the gel. The conductivity and thus the speed of bubble generation increases with higher PAA content. However, this effect is much less important than the electrode configuration.

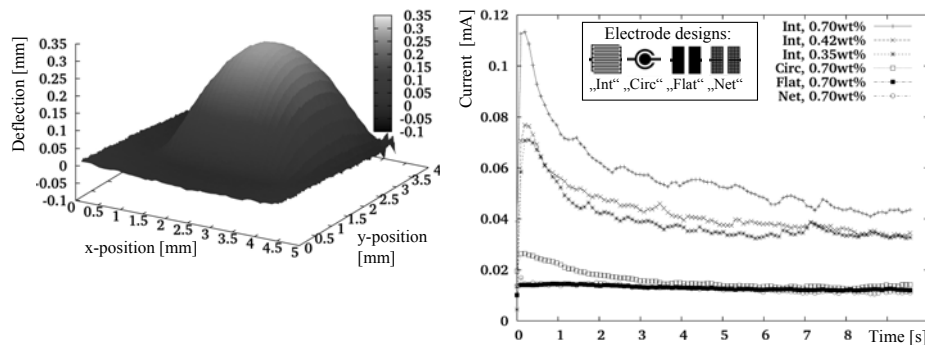


Figure 2. Actuator with an area of 3x3mm²: Maximum final membrane deflection before membrane delamination (left), and current for different PAA concentrations and electrode configurations over time at a voltage of 5V (right).

5. Conclusion

PAA has been successfully proved as a electrolytic material for a micro actuator. It offers the potential of simple integration while increasing the ion content of the electrolytic solution at the same time. Next steps will focus on tailoring the actuator for microfluidic actuation in fully integrated point-of-care devices.

Acknowledgements

This work has been founded by the European Commission under contract number 016768 and is part of the research project SEMOFS (Surface Enhanced Micro Optical Fluidic Systems).

References

- [1] C. Neagu et al., *The electrolysis of water: an actuation principle for MEMS with a big opportunity*, Mechatronics 10 (2000), pp.571-581
- [2] S. Böhm et al., *A closed-loop controlled electrochemically actuated micro-dosing system*, J. Micromech. Microeng. 10 (2000), pp 498-504

FABRICATION OF NOVEL HYDROPHILIC POLYMER NANOFUIDIC SYSTEM FOR BIOMOLECULES SEPARATION IN AQUEOUS FLOW

Tae-Ho Yoon, Lan-Young Hong, Chang-Soo Lee and Dong-Pyo Kim*

School of Applied Chemistry and Biological Engineering,
Chungnam National University, Daejeon, 305-764 Korea

Abstract

Channel structure with range 30 μm in width and 900 nm in height with weir structures was fabricated using novel hydrophilic polymer (HP) with contact angle to water in range 13~25° and soft lithography technique. The leak-free channel structures were built with strong bond to glass slide by plasma treatment, and the flow behavior was comparatively observed with that of the conventional PDMS channel structures. Aqueous solution could spontaneously flow only by capillary force through the fabricated HP nanochannels while no flow into PDMS channels due to the hydrophobic non-wetting nature. Moreover, PDMS did not exactly replicate the fine pattern of Si master, but HP revealed excellent replication fidelity in nanoscale patterns. And the HP exhibited additional advantages such as solvent resistance against organic solvents after crosslinking treatment, and high optical transparency in visible and ultraviolet region, easy bondability to glass slide. This novel HP must be promising as a matrix material of aqueous based nanofuidic devices such as biosensors, capillary electrophoresis units and microbioreactors.

Keywords: Nanofuidics, Hydrophilic Hybrid Polymer, DNA Separation

1. Introduction

Among the polymers used in soft-lithography, polydimethylsiloxane (PDMS) is one of the most promising materials for the microscale molding due to low-cost, easy fabrication and high optical transparency[1]. However, PDMS is a highly hydrophobic material, which makes difficult for transferring aqueous solutions within submicron size channels or networks[2]. A variety of methods dealing with these problems have been proposed, such as oxygen plasma treatment, silanization, adsorption of polymers and lipid coatings. But, these methods suffer problems of instability, heterogeneous surfaces properties, or difficulties in application.

Therefore, we developed novel hydrophilic hybrid polymer (HP) with excellent processibility and UV/thermal curability, which reveled low contact angle range at 13~23°, depending on the chemical composition. This patented organic-inorganic hybrid polymer was synthesized by homogeneously mixing the silica-titania complex with Tiron, $(\text{HO})_2\text{C}_6\text{H}_2(\text{SO}_3\text{Na})_2$, and organic coupling additive of diacrylate oligomer. Moreover, it is advantageous that the cured HP exhibited high resistance to several organic solvents (e.g. alcohols, acetone and hexane etc.) and UV/visible transparency and high replication fidelity.

2. Experimental

To fabricate HP nanochannel supported by PDMS as shown in Fig. 1, HP was spin-coated on the silanized Si wafer master with relief structure, then liquid PDMS was poured over the uncured HP layer, followed by curing at 60°C for 12 h. The HP structures with a series of 800 nm height of weir structure inside the 30 μm width and 900 nm of depth of the nanochannel was readily removed from the master without damage due to interfacial adhesion problem, indicating the excellent infiltration. And PDMS nanofluidic device was fabricated by without HP by general schemes to compare replication performance with HP hybrid nanofluidics. The leak-free nanofluidic system was fabricated by binding of plasma treated holed glass to the obtained HP nanochannel body. In order to confirm the replication of HP hybrid system, we utilized AFM (XE-100, PSIA Inc., USA), and optical microscope(DCS 104T, Sometech, Korea).

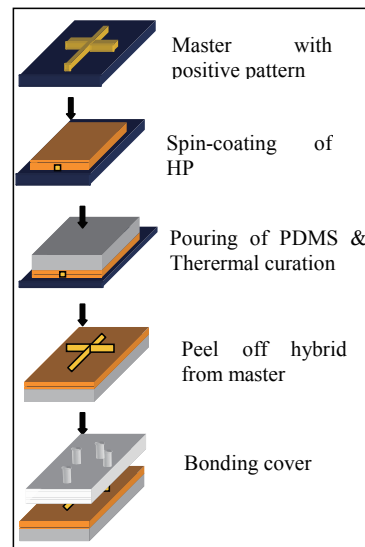


Fig. 1. Procedure for fabrication of HP hybrid channel.

3. Results and discussion

When nanofluidics was fabricated using HP hybrid, the comparison of pattern shapes on the master and the fabricated substrate were well matched respectively, which confirm the high fidelity of the replication process as shown in Fig. 2 (a) and (b). In contrast, PDMS hardly replicated the nano weirs with many defects due to low wettability as shown in Fig. 2 (a) and (c).

Moreover, AFM profile of the HP hybrid pattern displayed exact weir structure with 900 nm depths at both channel dam along the flow direction and ca. 800 nm heights at inside channel, as shown in Fig. 2(d) and (e). And the AFM profile across the channel showed that the dimension of deep part has 30 μm width and 800 nm heights, and the shallow part is only ca. 100 nm heights with the identical channel width. Alternative nanochannel with weir structure was fabricated using the same sealing technique with the holed glass

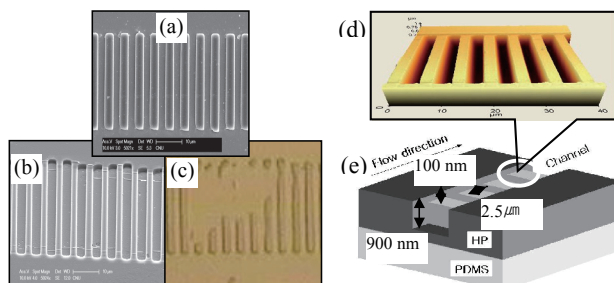


Fig.2. SEM and microscopic images of (a) master, (b) fabricated nanochannel with HP hybrid, (c) fabricated channel with PDMS, (d) AFM image and (e) schematic picture of nanochannel.

cover. When a drop of buffer solution was filled into hole, spontaneous flow was generated by capillary force along the channel over the deep part of 900 nm in depths and the shallow part of 100 nm in depth as shown in Fig. 3(a). Because the channel comprises narrow constrictions and wider regions that cause size-dependent trapping of biomolecules at the onset of a constriction. This process creates electrophoretic mobility differences, thus enabling efficient separation without the use of a gel matrix or pulsed electric fields [3]. Therefore, the fabricated hydrophilic nanofluidic system in Fig. 3 (b) could be easily applied to separate or analyze biomolecules such as proteins or DNA. To evaluate performance of nanofluidic capillary electrophoresis module, BSA-FITC protein was used as a model protein under 50mM Tris buffer and 10volts/mm of electric filed. In this case, protein migrated successfully by electric osmotic flow under electric filed.

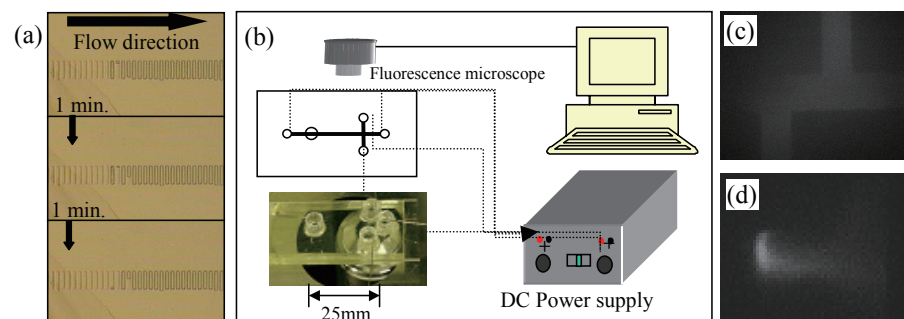


Fig. 4. (a) Aqueous flow pattern by wettability of HP polymer of fabricated nano channels in the weir pattern 30 μ m of widths and 100 nm-900 nm of heights with HP hybrid, (b) fabricated nanofluidic capillary electrophoresis(CE) module with power supply, controller, fabricated CE modules with pt electrode, (c) fluorescence image at sample loading step and (d) fluorescence image of BSA-FITC at separated region with $\Delta V = 10$ volts/mm.

4. Concluding remarks

In conclusion, we successfully fabricated a hydrophilic nanofluidic system with newly synthesized organic-inorganic HP material having excellent patterning compared to PDMS material. And the spontaneous aqueous flow enabled to separate or analyze biomolecules such as as proteins or DNA due to the different retention time in the nanochannel. Therefore, it is promising for the applications in the fields of aqueous biosensor and bioreactors to replace PDMS-based nanofluidic devices

References

1. X. Yu, D. Zhang, T. Li, L. Hao and X. Li, *Sens. Actuator A*, 108, pp.103-107 (2003).
2. G. Ocvirk, M. Munroe, T. Tang, R. Oleschuk, K. Westra and D. J. Harrison, *Electrophoresis*, 21, pp.107-115 (2000).
3. T. Wehr, R. Rodriguez-Diaz and M. Zhu, *Capillary electrophoresis of proteins*, Marcel Dekker, New York, pp. 18-20 (1998).

PHOTODEFINABLE PDMS FOR RAPID PROTOTYPING OF DISPOSABLE LAB-ON-A-CHIP SYSTEMS

Ali Asgar S. Bhagat, Preetha Jothimuthu and Ian Papautsky

Department of Electrical and Computer Engineering,
University of Cincinnati, Cincinnati, USA

Abstract

In this paper, we report a new and simple method of patterning polydimethylsiloxane (PDMS) directly using a photoinitiator. The new positive-acting photodefinable PDMS mixture is only sensitive to light <365 nm and thus can be processed under normal ambient light conditions outside a gold room. We successfully characterized the process and applied it to rapid prototyping of a disposable microfluidic device.

Keywords: Photodefinable PDMS, LOC, rapid prototyping, PDMS

1. Introduction

Considerable work in the area of lab-on-a-chip (LOC) has been done using PDMS. Properties such as low cost, chemical inertness, ease of fabrication, good reproducibility, low toxicity and high transparency have made this polymer very popular [1]. However, one critical drawback of PDMS fabrication methods is the need to use traditional photolithography processes to fabricate a master. There have been several attempts to make PDMS photosensitive, and thus directly patternable. Lotters *et al.* [2] succeeded in making PDMS act as negative resist, but, as it became photosensitive processing required a gold room. It also became O₂-sensitive and had to be processed rapidly. Another example is the photodefinable silicone Dow Corning [3] recently introduced to semiconductor packaging market. However, this product is similar to negative photoresist in terms of high cost and the need for clean room photolithography facilities.

2. Methods

In this work, PDMS was made photosensitive by using benzophenone photoinitiator. When benzophenone is irradiated at <365 nm, it creates a benzophenone radical which reacts with the vinyl group present in PDMS base (Sylgard 184) and prevents it from curing (via a linear chain of base monomer radicals). Figure 1 illustrates the proposed chemistry. During the post-exposure bake, the unexposed PDMS gets cured, while the exposed PDMS remains uncured

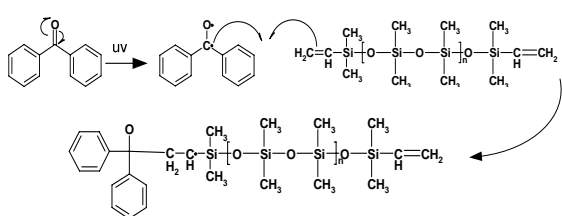


Figure 1. Benzophenone radical reacts with the vinyl group of the base monomer preventing it from curing.

and can be washed away in toluene (Figure 2). The photosensitive PDMS in this work is positive-acting, which simplifies LOC design and fabrication. Further, it is only sensitive to light <365 nm and thus can be processed under normal ambient light conditions.

To optimize the process, benzophenone was dissolved in 1 g of xylene and mixed with PDMS.

Table 1 summarizes the mass ratios of these parameters. The mixture was then spin coated on a glass wafer, and exposed (non-contact) with a UV light source for 8 - 12 min (aligner or a common black light) through a chromium or a transparency mask using non-contact exposure. The corresponding post-exposure bake time was approximately 50 s. The results were characterized with SEM and optical microscopy.

3. Results

The fabrication process was successfully demonstrated for height ranging from 10 μm to 60 μm . Figure 3 indicates the thickness of PDMS for varying spin speeds. Optimum feature definition was obtained using 2% (m) of benzophenone photoinitiator and PDMS monomer mixed at 10:1 (m/m) ratio with curing agent. Dimensions less than 100 μm were achieved with good definition using this mixture. Post-exposure bake carried out in a conventional oven yielded better edge definitions than hot-plate, likely due to more uniform heat transfer. Over-exposure of this mixture resulted in feature widening, just as commonly seen with conventional positive photoresists.

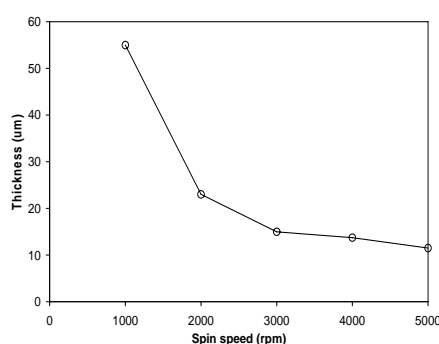


Figure 3. Spin speed vs. thickness plot for the photo PDMS mixture.

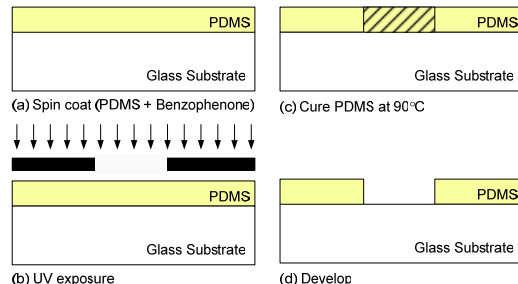


Figure 2. Fabrication sequence of *photoPDMS*.

Table 1. Summary of PDMS mixtures tested

Benzophenone : PDMS	Curing agent: PDMS base
1 : 1000	1 : 20
1 : 100	1 : 10
1 : 50	1 : 5
1 : 33	

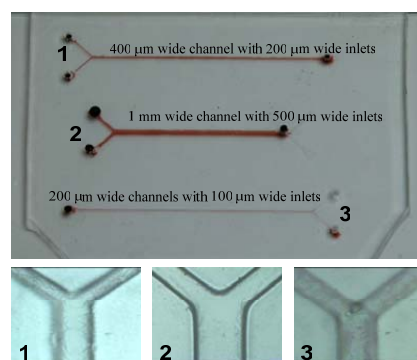


Figure 4. Microfluidic channels in *photoPDMS*. Red dye is added for better visualization.

Under-exposure or over-curing resulted in no patterns, similar to normal PDMS films.

To demonstrate feasibility of this new *photoPDMS*, a variety of microfluidic channels and components commonly used in LOC were successfully fabricated. Representative results are shown in Figure 4, which illustrates microchannels 20 μm deep with widths ranging from 100 μm to 1 mm. The channels were successfully bonded using oxygen plasma, as commonly done with normal PDMS, and characterized with 1 μM fluorescein solution. SEM image of a pattern fabricated using this process is shown in Figure 5. Due to non-contact exposure, sidewalls are rounded. Nevertheless,

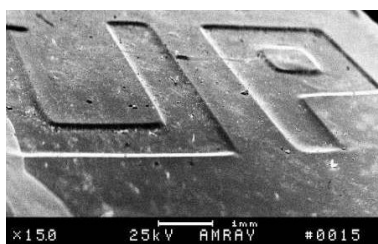


Figure 5. SEM of a pattern using the new *photoPDMS* mixture.

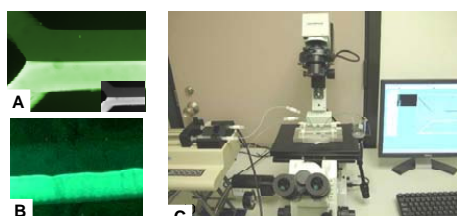


Figure 6. Epifluorescence images of the microchannel at the entrance (a) and 5 mm down the channel (b); 1 μM solution of fluorescein (pseudo-colored green) is on the bottom with water on top. (c) microfluidic test setup.

this is similar to isotropically etched glass and is acceptable for many microfluidic LOC devices and applications. The surface of the pattern shows many dust particles due to processing outside cleanroom. Microfluidic characterization showed good channel definition and no leakage (Figure 6), indicating strong adhesion and ability to be processed similar to normal PDMS.

4. Conclusions

A new simple method of patterning PDMS directly was successfully demonstrated for fabrication of microfluidic LOC devices. The *photoPDMS* is robust and could be processed even under normal ambient light. The critical advantages of the new material are: 1) directly photodefinition (no master); 2) processing in ambient light (no gold room) 3) positive acting (easier fabrication); 4) precise thickness control via spin coating; 5) simple preparation; and 6) all advantages of PDMS including low cost. The *photoPDMS* developed in this work will enable rapid prototyping of low-cost, disposable LOCs without clean room facilities, envisaging its numerous applications in the microfluidics and LOC fields.

Acknowledgement

This work was fully supported by the National Science Foundation (BES-0428600) and the University of Cincinnati Institute for Nanoscale Science and Technology

References

1. J. C. McDonald and G. M. Whitesides, *Acc. Chem. Res.*, **35**, 491-499 (2002).
2. J. C. Lotter *et al.*, *J. Micromech. Microeng.*, **7**, 145-147 (1997).
3. Patternable Silicones for Electronics, Product Data Sheet, Dow Corning (2005).

FABRICATION AND OPTICAL CHARACTERIZATION OF NANO-HOLE ARRAYS FOR MOLECULAR DETECTIONS

O. M. Piciu*, M. C. v. d. Krog†, M. W. Docter**, P. M. Sarro*, A. Bossche*

*Department of Microelectronics/DIMES, **Department of Applied Physics,
Delft University of Technology, Delft, Netherlands

Abstract: This paper reports the improved fabrication process and the optical characterization of different nano-hole arrays in thin metal films, to be integrated into a novel atto-liter titre plate device for high speed molecular analysis. Using electron-beam lithography and lift-off technique, different array structures with the hole-diameters between 150nm-200nm and pitch of 1050nm are fabricated in 200nm thick layer of gold-palladium (60/40) alloy on glass. The spectrum of the light transmitted through the fabricated arrays is measured. Applying Rhodamine on top of the hole-array reveals a 9 times increased fluorescent signal.

Keywords: nano-hole arrays, lift-off technique, enhanced light transmission

1. Introduction

A recently discovered optical phenomenon (i.e. light transmission through sub-wavelength apertures [1]) has been identified as a promising optical detection principle, allowing simple (massive) parallel read-out. Making use of the extraordinary properties of this transmitted light: enhancement of its intensity, small angular diffraction and spectral selection, we are developing an optical atto-liter titer plate device for high-speed molecular analyses.

The basis of this device is a nano-hole array in a thin metal film, where each hole serves as a reaction chamber. The optical detection can be made in two different ways:

1. Gathered molecules inside the holes change the optical properties of the transmitted light;
2. The transmission excites fluorochrome-bound molecules inside the holes and the emission is observed.

2. Technology

Hole-arrays in gold/palladium=Au/Pd (60/40) alloy on glass are fabricated. The general lines of the process are the same as for the previous fabrication of nano-hole arrays in gold (Au) [2]: we evaporate chromium and then spin a bi-layer (upper/under-layer) resist scheme on cleaned fused silica samples. The upper-layer of the resist is a negative tone; therefore patterning the holes with electron beam lithography, followed by development and reactive ion etching results in pillars on the location of the future holes. Afterwards, 200 nm of Au/Pd is electron-gun evaporated and the pillars are removed by lift-off procedure, resulting in an array of holes. The following changes leads to improvements of the arrays: 1. Replacing the Au by an Au/Pd alloy: due to the fact that the grains of Au/Pd are smaller than of Au, the shape of the holes is better

defined; 2. Increased thickness of Cr (30 nm): it allows us getting a more constant height measurement during the exposure, thus an improved focus; 3. A decreased under-layer thickness (\sim 670nm): this reduces the resist etching time and avoids problems as bending of the pillars, which may occur due to the high aspect ratio between their height and the cross-section area; 4. The exposure parameters in the electron beam pattern generator are changed into a beam step size of 5nm and a dose of $1500\mu\text{C}/\text{cm}^2$ for 175 nm holes; 5. The sample is orientated upside-down during lift-off in a higher temperature HNO_3 100% bath (45°C). Hanging the sample upside-down results in cleaner samples and the higher temperature results in faster etching and better removal of the chromium.

3. Results and discussion

Using the above presented technique, two types of hole-arrays are fabricated: 25 by 25 round-holes in Au/Pd with square and with hexagonal holes' distribution; the hole-diameter is between 150nm and 200nm and the pitch is 1050nm (e.g. see figure 1 a, b). To optically characterize the nano-hole arrays, we measure both spatial and spectral transmission through both types of holes' configuration, using Köhler illumination with an upright optical microscope (Leica DM-RXA) and a SpectraCube (Applied Spectral Imaging). The transmission spectra are calculated (corrected for background and illumination) and plotted in figure 1c for their reliable range (450 to 750 nm).

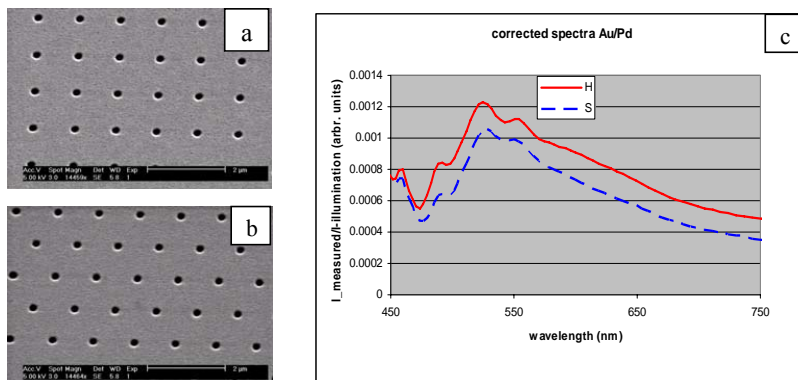


Figure 1. SEM picture of a hole-array with square hole' distribution a), and with hexagonal holes' distribution b), in 200nm of Au/Pd on glass, with the hole size of \sim 175nm and pitch of 1050nm. c) Spectra through square (S) and hexagonal (H) arrays.

Furthermore, we determine enhanced fluorescent transmission due to the periodicity of the arrays. We use an Olympus BX-FM upright microscope, an argon ion laser source (Reliant, Laser-physics, $\lambda = 514\text{nm}$) and 100x dry lens (numerical aperture = 0.75). Square holes' distributed arrays are coated with Rhodamine G6 (FLUKA), 0.05mM concentration. The light intensity is measured through the holes (named array = A), uncoated and coated with fluorescence solution, with and without a filter (Chroma

Technology Corp. excitation 540 nm, emission 560nm) for Rhodamine (555nm) and also through the bare glass in the same conditions (named marker = M). The results are divided to the unit area; 50 images are averaged and compensated for the used neutral density filter (ND) and exposure time. Afterwards they are corrected for the background light (see table 1).

Table 1 shows also the ratios (e.g. R_{AY}) between fluorescent signal and transmitted signal. To know the enhancement of the transmission through the arrays compared to the signal through bare glass the ratios R_{AY} and R_{MY} are compared after compensating for the auto-fluorescence, which is given by $(R_{AY}-R_{AN})/(R_{MY}-R_{MN})$ and has a value > 1. This means that the use of arrays gives us a higher signal compared to the bare glass.

option1	option2	option3	Intensity		
A	N	N	7.31E+03	$R_{MN}=MNY/(MNN-MNY)$	4.37E-07
A	N	Y	4.13E-02	$R_{MY}=MYY/(MYN-MYY)$	9.86E-05
A	Y	N	2.24E+04	$R_{AN}=ANY/(ANN-ANY)$	5.66E-06
A	Y	Y	2.05E+01	$R_{AY}=AYY/(AYN-AYY)$	9.15E-04
M	N	N	1.28E+07	$(R_{AY}-R_{AN})/(R_{MY}-R_{MN})$	9.26
M	N	Y	5.60E+00		
M	Y	N	1.52E+07		
M	Y	Y	1.50E+03		

Table1. Measurements' results and calculated ratios; option1: Array or Marker, option2: Rhodamine coating: Yes/No, option3: filter: Yes/No

4. Conclusions

Different nano-hole arrays with the hole size between 150nm and 200nm are fabricated in gold/palladium alloy (60/40) on glass, using negative tone electron beam resist, electron beam lithography and lift-off technique. In figure 2, the spectrum of the hexagonal holes' distribution in comparison with the spectrum of the square holes' distribution, shows a 20% increase in the transmitted light, as consistent with [3]. Furthermore, we use Rhodamine coated nano-hole arrays. From the ratios calculated in table 1, we see that the intensity of the fluorescent light through these periodical sub-wavelength apertures is enhanced with more then a factor of 9 compared to the fluorescence through the bare glass.

This supports the use of arrays in our novel atto-liter titre plate device for high speed molecular analysis.

Acknowledgements

This work was financially supported by the Dutch Government as part of the NanoNed program, under auspices of the Stichting voor de Technische Wetenschappen (STW) and was conducted in the Nanofacility Department of the Kavli Institute of NanoScience and DICES, TU Delft, The Netherlands.

References

1. T.W. Ebbesen, et al, Nature **391**, 667-669 (1998)
2. O. M. Piciu, et al, IEEE Sensors 2005, 452-455 (2005)
3. T. Thio, et al, Journal of the Optical Society of America. B **16**, 1743-1748 (1999)

THREE-DIMENSIONAL MICROSTRUCTURING OF PDMS INSIDE A MICROCHANNEL FOR FUNCTIONAL MICROFLUIDIC DEVICES

Shoji Maruo, Takuya Hasegawa and Kosuke Oishi

Dept. of Mechanical Engineering, Yokohama National University

79-5 Tokiwadai, Hodogaya-ku, Yokohama 240-8501, Japan

Abstract

We have developed a photocurable PDMS resin for making three-dimensional (3-D) PDMS-based microstructures via two-photon microstereolithography. By using a direct laser scanning method, freely movable microrotors were built into a microchannel and driven by light. The movable PMDS micromachines have potential for application to microfluidic devices and as micromanipulation tools for biological applications.

Keywords: Two-photon microstereolithography, PDMS, Microfluidic devices

1. Introduction

Poly (dimethylsiloxane) (PDMS) elastomer has recently attracted much attention for its ease of fabrication, optical transparency, low cost and biocompatibility. Notably, PDMS-based microfluidic devices are already in wide use in a range of applications such as in electrophoresis chips, cell sorters, and microvalves. In the normal microfabrication processes with PDMS elastomer, it is difficult to fabricate sophisticated 3-D microstructures owing to conventional molding processes. This drawback restricts the further functionalization of PDMS-based biochips.

In this paper, we report the fabrication process of 3-D PDMS-based microstructures via two-photon-absorbed photopolymerization. The two-photon process makes it possible to fabricate arbitrary 3-D microstructures at submicron resolution [1]. Although two-photon-absorbed photopolymerization of PDMS elastomer has been recently reported [2], the resultant 3-D microstructures were merely immovable solid models such as microcapillaries and micropillars on a glass plate. In contrast, we demonstrate that freely movable microstructures can be made from PDMS elastomer using direct laser writing. In addition, movable microstructures were built into a microchannel through *in situ* photopolymerization stimulated by focusing a femtosecond laser beam.

2. Two-photon microstereolithography with a photocurable PDMS resin

A photocurable PDMS resin was made by mixing PDMS prepolymer with a radical photoinitiator suitable for two-photon absorption at 0.4 wt %. Since the photoinitiator has a wide absorption range (310 to 420 nm), PDMS resin is suitable for two-photon-absorbed photopolymerization initiated by a near-infrared femtosecond pulsed laser beam.

The width and depth of drawing lines of the photocurable PDMS resin were measured for optimizing the exposure conditions for fabricating fine microstructures using two-photon microstereolithography. Figure 1 shows the dependence of the width and depth of the resultant line structures on laser power at a laser beam scanning speed of 10 $\mu\text{m}/\text{s}$. This indicates that submicron resolutions can be achieved by optimization of the laser power and beam scanning speed. The minimum width and depth were less than 350 nm and 750 nm, respectively.

As shown in Fig. 2, several types of 3-D microstructures were fabricated using the photocurable PDMS resin. Figure 2 (a) shows several alphabetical letters. Figure 2 (b) shows microrotors 10 μm in diameter with different thickness that were fabricated by stacking sectional shapes. These results demonstrate that complex microstructures can be fabricated with smoothly curved surfaces.

Freely movable microstructures were also fabricated using the direct laser writing method proposed in our previous work [3]. Microrotors 10 μm in diameter with a shaft 1 μm in diameter were fabricated without any assembly processes. The microrotor can be rotated in ethyl acetate by means of an optical trapping technique. In our method, a wing of the rotor is trapped by a focused laser beam. The rotor is then rotated by scanning the laser beam in circular mode. Figure 3 shows a rotating microrotor at a rotation velocity of 20 rpm.

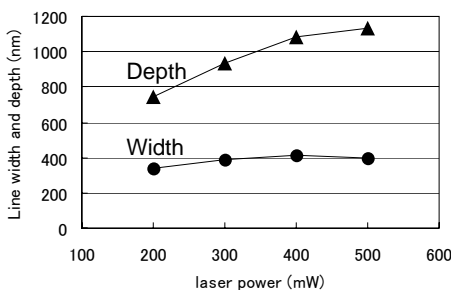


Figure 1 The dependence of line width and depth on laser power

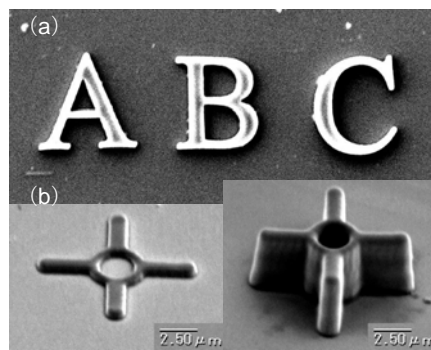


Figure 2 Microstructures fabricated by two-photon microstereolithography

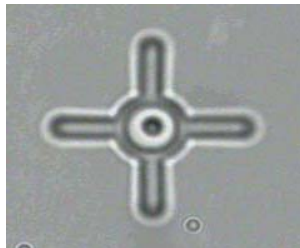


Figure 3 Optical driving of a microrotor

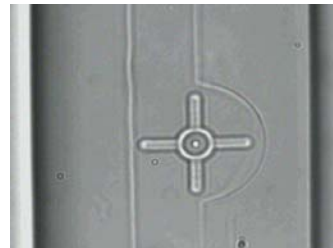


Figure 4 A microrotor with an outer casing fabricated inside a microchannel

Finally, we attempted to make a movable microrotor inside a microchannel filled with unsolidified resin. A squared glass capillary (inner diameter: 50 μm) was soaked in the photocurable PDMS resin and subjected to a vacuum in a desiccator to help filling with the photocurable PDMS resin. The glass capillary filled with the resin was set on the oil immersion objective lens for the *in situ* fabrication of a movable microrotor. As shown in Fig. 4, a movable microrotor 20 μm in diameter with an outer casing was fabricated inside the squared glass capillary. The microrotors are potentially useful for functional microfluidic devices such as micro flowmeters and micro stirrers. The *in situ* fabrication of functional microfluidic devices is likely to play an important role in the functionalization of simple microchannels made from glass, silicone and plastic.

3. Conclusions

A photocurable PDMS resin has been developed for two-photon microstereolithography. Several types of sophisticated 3-D microstructures with submicron resolutions were fabricated with the PDMS resin. Movable microstructures such as microrotors were also fabricated inside microchannels. The *in situ* fabrication of functional microdevices inside microchannels will be useful for functional biochips employed in single-cell analysis systems and cell sorters.

This research was supported in part by research grants from the Japan Society for the Promotion of Science (Grant-in-Aid for Young Scientists (A), Exploratory Research and Scientific Research in Priority Areas: Systems Cell Engineering by Multi-scale Manipulation).

References

1. S. Maruo, O. Nakamura, S. Kawata, *Opt. Lett.* **22**, 132 (1997).
2. C. A. Coenjarts and C. K. Ober, *Chem. Mater.* **16**, 5556 (2004).
3. S. Maruo, K. Ikuta and H. Korogi, *Appl. Phys. Lett.* **82**, 133 (2003).

SOFT LITHOGRAPHY WITHOUT USING PHOTOLITHOGRAPHY

Shih-hui Chao^{1,2}, Robert Carlson², and Deirdre Meldrum^{1,2}

¹Microscale Life Sciences Center

²Department of Electrical Engineering

University of Washington, Seattle, WA 98195-2500, USA

joechao@u.washington.edu

Abstract

Conventional poly(dimethylsiloxane) (PDMS) soft lithography relies on photolithography for fabrication of micropatterned molds.. Here, we present an alternative method to fabricate microfluidic devices using microscale PLasma Activated Templating (μ PLAT). The use of photoresist in soft lithography is replaced by patterned water droplets created using μ PLAT. As a result, device fabrication is less time consuming, more cost efficient and flexible, and ideal for rapid prototyping. Furthermore, this method has unique features that are difficult to achieve using photolithography.

Keywords: microscale plasma activated templating, μ PLAT, soft lithography, hydrophobicity, PDMS.

1. Introduction

Present day poly(dimethylsiloxane) (PDMS) soft lithography relies on photolithography to fabricate solid molds with features down to micrometer and nanometer scales [1]. However, for many applications in the literature that do not require fine feature resolutions, photolithography is complicated, expensive, and time-consuming. In contrast, using the presented μ PLAT method [2,3] to fabricate PDMS structures such as microchannels is an easier, faster, and less-expensive approach for microfluidic device prototyping.

2. Fabrication processes

μ PLAT is a method that creates hydrophilic patterns on polymer surfaces (i.e., PDMS surfaces) by masking them with microscale patterns and then exposing them to oxygen plasma. Only the exposed areas become hydrophilic. The fabrication steps for fabricating PDMS microchannels using a single plasma exposure are illustrated in the left row of Figure 1. The procedure involves 1) adhering a mask to the flat PDMS followed by plasma treatment for 1 minute in steps (a–b). 2) After plasma treatment, the mask is removed and the PDMS slab is dipped in 5% (v/v) glycerol-to-water solution in step (c). Patterned droplets only stay on the hydrophilic regions. 3) The last steps (d–e) demonstrate pouring uncured PDMS on the slab and curing it in a 65°C water-bath. The ports are then made by punching holes with an 18.5-gauge hypodermic needle to interface 1/32" PEEK tubing.

The masks for μ PLAT can be made of any materials that provide good adhesion with the treated surfaces, and compatible to the O₂-plasma treatment. For treating PDMS surfaces,

we have successfully tested masks made of PDMS, glass, silicon, SU-8 photoresist, overhead transparency (celluloid), aluminum, and bronze. The presented results were performed using overhead-transparency masks because they adhere to PDMS surfaces firmly and are easily removed without damaging either the mask or the substrate.

3. Feature resolution

To understand the resolution limits of μ PLAT, we micromachined 20-mm-long slits of widths from 100 μ m to 1 mm on an overhead transparency (Figure 2a) using a Nd:YAG laser. Eight PDMS chips were made using a same batch of 1:10 PDMS (Dow Sylgard 184) under the same conditions. Figure 2b shows one of the produced chips with all channels filled with color dyes. The yield rates of the channels show almost 100% success for dimensions larger than 400 μ m, with the yield decreasing at smaller scales (Figure 2c). The typical profile of the channels is rounded with an aspect ratio lower than 0.1 (Figure 3).

4. Modular prototyping

μ PLAT allows modularized fabrication: A microfluidic network can be made by multiple exposures of individual modules. The later plasma exposure steps duplicate the first exposure, as shown in Figure 1(g-j). Figure 4a shows the patterns cut by a razorblade on transparencies used in multiple exposures. Figure 4b shows various configurations of the two microfluidic modules, and Figure 4c shows photographs of products. For prototyping purposes, developers can use a collection of masks for individual modules (e.g., branches, ports, reactors, mixers...) to be combined to form a microfluidic network. The configuration of these modules can be adjusted depending on specific applications.

5. Conclusions

We demonstrate, for the first time, the use of water molds created by μ PLAT technique to fabricate PDMS microchannels. The use of μ PLAT water molds already promises more rapid, less expensive lab-on-a-chip device prototyping. Researchers without the access of photolithography facilities can produce PDMS devices from scratch in two hours.

Acknowledgements

We gratefully acknowledge the support of this research by the NIH NHGRI, Centers of Excellence in Genomic Science. We appreciate Professor R. Bruce Darling for providing the machining laser, John Koschwanez and Dr. Barry Lutz for helpful discussions.

References

1. D. C. Duffy, J. C. McDonald, O. J. A. Schueller, and G. M. Whitesides; "Rapid prototyping of microfluidic systems in poly(dimethylsiloxane)," *Analytical Chemistry*, Vol. 70(23) pp. 4974-4984 1998.
2. B. A. Langowski, and K. E. Uhrich; "Microscale plasma-initiated patterning (μ PIP)," *Langmuir*, Vol. 21(23) pp. 10509-10514 2005.
3. R. Carlson, J. Koschwanez, and D. Meldrum. Novel material patterning for electronic and magnetic components on PDMS. *microTAS*, Boston,(2005). 672-674.

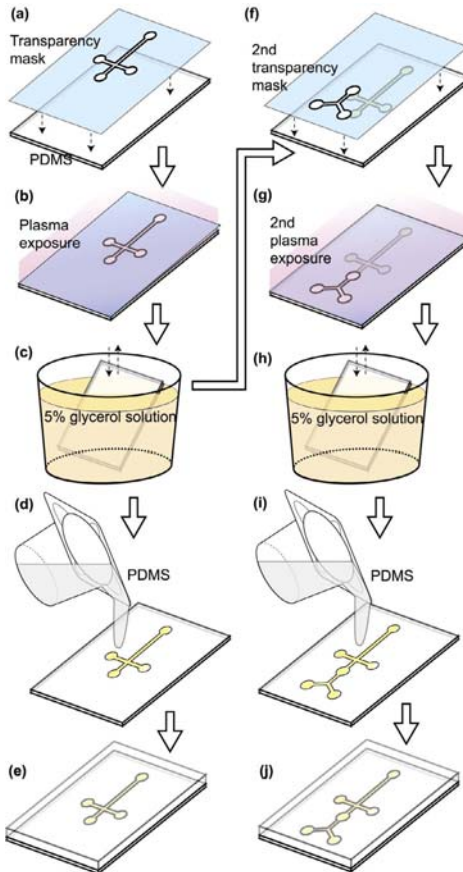


Figure 1. The fabrication process of PIP soft-lithography. (a) Adhering the transparency mask on a flat PDMS slab; (b) Exposing the PDMS to oxygen plasma; (c) Removing the transparency mask, dip-coating the PDMS slab with glycerol solution. The solution only beads up in the exposed region; (d) Pouring uncured PDMS on the flat PDMS slab; (e) Curing the channel layer PDMS. For secondary exposure, adhering the second mask to the desired region of the wet PDMS slab from (c); (g-j) Repeating steps (b-e).

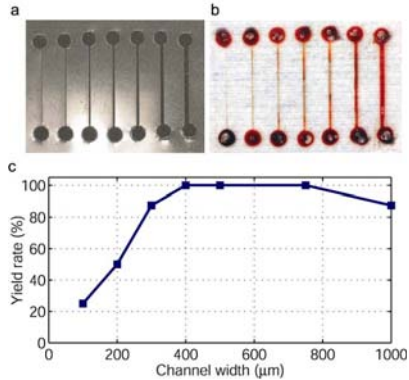


Figure 2. (a) Laser micromachined mask with slits from 100 μm to 1 mm widths. (b) Resulted channels filled with food dye. (c) Yield rates versus channel width.

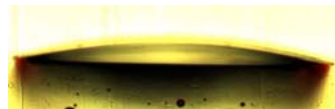


Figure 3. Cross-section view of a 750- μm -wide channel. The maximum height is $\sim 50 \mu\text{m}$.

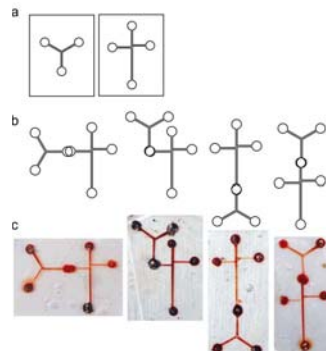


Figure 4. (a) Mask patterns of two microfluidic modules. (b) Geometric combinations of the two modules. (c) Resulted channels filled with food dye.

SINGLE CELL CAPTURE WITH FERROMAGNETIC ELEMENTS GROWN ON PDMS

John Koschwanez, Robert Carlson, Deirdre Meldrum

Department of Electrical Engineering, University of Washington, Seattle, WA

Abstract

Magnetic traps are fabricated by electrolessly depositing NiCoB alloy elements directly onto polydimethylsiloxane (PDMS) using a simple and inexpensive method. These traps are used to capture yeast cells attached to 50 nm paramagnetic beads.

Keywords: cell trapping, PDMS, magnetism, electroless plating, μ PLAT

1. Introduction

Here we report the magnetic capture and release of a single yeast cell using an inexpensive, quickly and easily fabricated, microfluidic device. The magnetic traps are made by electrolessly depositing ferromagnetic elements directly onto polydimethylsiloxane (PDMS). Using a process we call microscale PLasma Activated Templating (μ PLAT) [1], we have fabricated gold, carbon, zinc oxide, nickel-alloy, and copper patterns, which our group has employed in electrostatic and thermopneumatic actuators, thermocouples, optical structures, and magnetic elements. Previously reported methods of fabricating magnetic traps for particle capture involve electroplating, evaporation, sputtering, or vapor deposition on a silicon or glass substrate (review in [2]). Our group has previously reported trap fabrication on PDMS using lift-off masks and etch masks [3]. Other reported methods of metal placement on PDMS (not used for particle capture) have used electron beam evaporation [4], transfer from a silicon substrate [5], and electroless deposition using a polyelectrolyte brush [6].

Our fabrication method has many advantages: (i) Fabrication is quick and inexpensive and can be performed outside a cleanroom (after the reusable stamp molds are fabricated). (ii) The method is compatible with wafer scale mass production. (iii) The element fabrication can be easily integrated into a series of fabrication steps. (iv) The ferromagnetic elements can be placed on any layer in a multilayer PDMS device, and therefore (v) the distance between the element and the captured cell is limited only by alignment precision and a protective biocompatible layer. Reducing this distance increases the magnetic force at the capture site.

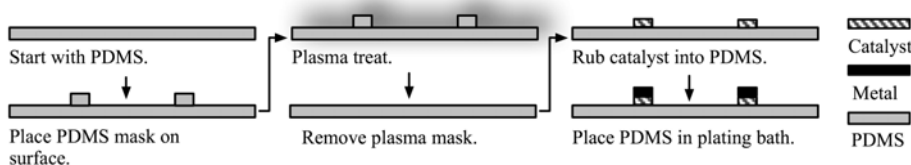


Figure 1. Schematic of ferromagnetic element fabrication

2. Microfabrication method

Figure 1 shows the microfabrication schematic. The substrate can be PDMS of any thickness and curvature provided that the surface conforms to a PDMS stamp. Both GE RTV 615 (General Electric, Waterford, NY) and Sylgard 184 (Dow Corning Corporation, Midland, MI) have been used as substrates and stamps. The stamp is made by casting PDMS on an SU-8 2025 (MicroChem, Newton, MA) mold. To fabricate the magnets, the stamp is placed on the substrate and treated in a plasma cleaner (Harrick, Ithaca, NY) at low power. Those areas that are shielded from the plasma by the stamp will be plated. Next, the palladium chloride catalyst (Sigma-Aldrich, St. Louis, MO) that has been ground using a mortar and pestle is rubbed into the PDMS using vinyl foam (Frost King, Mahwah, NJ); the catalyst will only adsorb to those areas shielded from plasma treatment (similar to graphite adsorption reported in [1]). The height of the catalyst was measured by atomic force microscopy (AFM) at 30-40 nm.

The structure is then placed in the nickel-cobalt plating bath up to 1 hour. The bath, partially based on [7], consists of 70 mM nickel sulfate hexahydrate, 30 mM cobalt sulfate heptahydrate, 0.10 M trisodium citrate, 24 mM Dimethylamineborane, and 1.0 mM thioglycolic acid (all chemicals from Sigma-Aldrich, St. Louis, MO). The bath is heated to 60 °C and adjusted to a pH of 7.00 using NaOH. After 1 hour, 6 samples of deposited metal elements were measured by AFM to be between 1080 and 1600 nm.

Figure 2 shows elements fabricated using a triangular stamp with an extended tip. To construct the capture device, a protective layer of PDMS is spun on the magnets and a PDMS microfluidic channel is bonded above the magnets.

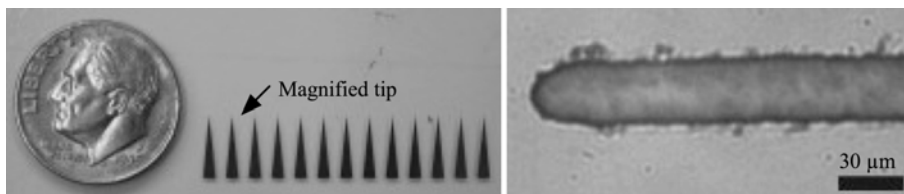


Figure 2. Ferromagnetic elements after plating for 1 hour. Top: an array of elements used to capture multiple cells (microfluidic channel not shown.) Bottom: 60X brightfield image of the straight extension at the end of one of the triangular tips.

3. Results

To test the device, we pumped biotinylated yeast cells attached to streptavidin-coated 50 nm paramagnetic beads (Miltenyi Biotec, Germany) into the channel. We find that 50 nm beads eliminate cell aggregation, unlike the larger beads used in other cell trapping demonstrations. When the ferromagnetic elements are externally magnetized using a small permanent magnet, a cell is captured (Figure 3). When the magnet is removed, the cell is released.

We have repeatedly tested the trapping ability of the microfabricated magnetic elements. We are now characterizing the trap force and integrating the device into a single-cell analysis system [3].

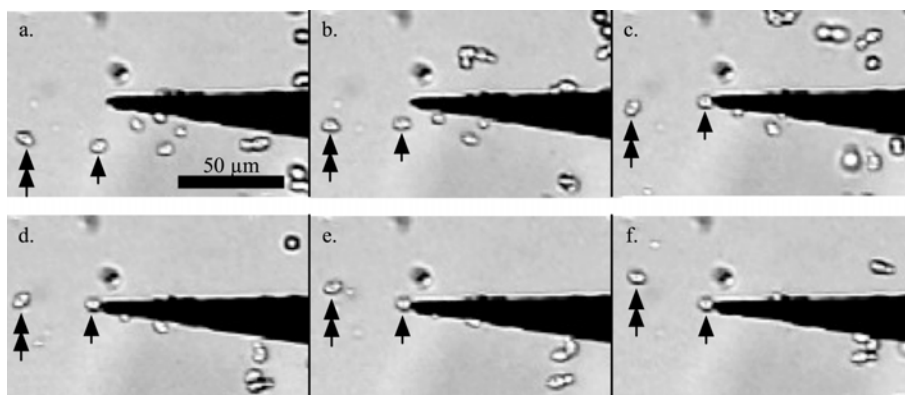


Figure 3. Single yeast cell capture. The images were taken 1 s apart. The cells are attached to 50 nm paramagnetic beads, which are not visible in the image. The cell marked with a single arrowhead is captured at the tip of the ferromagnetic element in frame c. The cell marked with a double arrowhead flows freely. The 2 stationary marks above the tip are optical debris.

References

- [1] R. Carlson, J. Koschwanez and D. Meldrum, Novel material patterning for electronic, magnetic, and optical components on PDMS, Proc. Micro Total Analysis Systems 2005, Boston, MA, pp. 672-674, (2005).
- [2] N. Pamme, Magnetism and Microfluidics, Lab on a Chip, 6, pp. 24-38, (2006).
- [3] J. Koschwanez, J. Wolfe, M. Holl, R. Carlson, D. Meldrum, Automated, Biomechatronic System to Study Single Cell Aging, Proc. Biomedical Robotics and Biomechatronics (BioRob 2006), IEEE, Pisa, Italy, pp. 959-964, (2006).
- [4] N. Bowden, S. Brittain, A. G. Evans, J. W. Hutchinson and G. M. Whitesides, Spontaneous formation of ordered structures in thin films of metals supported on an elastomeric polymer, Nature, 393, pp. 146-149, (1998).
- [5] K.S. Lim, W. J. Chang, Y. M. Koo and R. Bashir, Reliable fabrication method of transferable micron scale metal pattern for poly(dimethylsiloxane) metallization, Lab on a Chip, 6, pp. 578-580, (2006).
- [6] O. Azzaroni, Z. Zheng, Z. Yang, W. T. S. Huck, Polyelectrolyte Brushes as Efficient Ultrathin Platforms for Site-Selective Copper Electroless Deposition, Langmuir, 22, pp. 6730-6733, (2006).
- [7] T. S. N. S. Narayanan, A. Stephan and S. Guruskanthan, Electroless Ni-Co-B ternary alloy deposits: preparation and characteristics, Surface & Coatings Technology, 179, pp. 56-62, (2004).

FABRICATION AND CHARACTERIZATION OF NANOMETER SIZED GRAPHITIC CARBON ELECTRODES

Rongbing Du and Mark T. McDermott*

Department of Chemistry, University of Alberta, Edmonton AB, T6G 2G2,
Canada
(E-MAIL: mark.mcdermott@ualberta.ca)

Abstract

This paper reports the fabrication of nanosized carbon electrodes by using a combination of electron-beam lithography (EBL) and pyrolysis. The fabrication process and the characterization results are provided.

Keywords: Nanofabrication, Carbon Nano-Electrode, E-beam Lithography, Pyrolysis, Electrochemical Detector.

1. Introduction

Carbon nanostructures have been under intense scrutiny due to their promise in new devices with increased capabilities. By far, the most widely investigated carbon nanostructures are carbon nanotubes. The production of carbon nanotubes with controlled microstructure, size and shape is highly developed. However, despite a number of recent advances, the manipulation of carbon nanotubes to precise locations remains a challenge.¹ In this presentation, we report the fabrication of nanometer sized graphitic carbon structures using a combination of electron-beam lithography (EBL) and pyrolysis. EBL allows for the precise control of shape, size and location of these carbon nanostructures.

Graphitic carbon is a widely used electrochemical material due to a number of advantageous properties such as wide potential window, low cost, mechanical stability, and applicability to many common redox systems. In addition, the surface of carbon materials can be chemically tailored by covalent attachment of organic films. Recently, pyrolysis of photoresist has been used to prepare flat graphitic carbon films for electroanalytical² and molecular electronic³ applications. We are extending this concept to create nanometer sized graphitic carbon structures.

2. Experimental

The nanometer sized graphitic carbon structures were fabricated by using a combination of electron-beam lithography (EBL) and pyrolysis. EBL allows for the precise control of shape, size and location of these carbon nanostructures. Figure 1 depicts our procedure. First, a negative e-beam resist, Novolak SU-8 2000 is spin-coated onto a Si substrate. EBL is used to create structures in the SU-8 resist that are subsequently graphitized via pyrolysis in a vacuum sealed quartz tube at 1000°C.

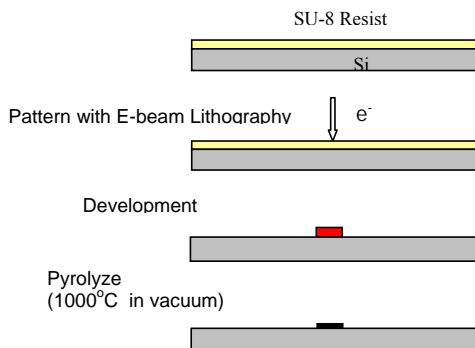


Figure 1: Fabrication process for graphitic carbon nano structures.

3. Results and discussion

Carbon nanostructures with a variety of shapes and sizes can be fabricated with this method. Figure 2 contains SEM images of a few examples of carbon nanostructures that we have created. Figure 2A and B show an example of a grid structure with 19 nm linewidths.

Part C is an array of carbon nanodots and part D is a representation of the University of Alberta seal featuring 50 nm linewidths.

We have carried out a number of characterizations of the pyrolyzed SU8 material. The graphitic microstructure of the pyrolyzed material was probed with Raman spectroscopy. These results indicate the material is highly graphitized. A 4-point probe measurement was used to determine the resistivity of carbonized SU8. A value of $1.1 \times 10^{-5} \Omega \text{ m}$ was obtained, which agrees well with that of other pyrolyzed materials [4]. The size and shape of the nanostructures have been characterized by scanning electron microscopy (SEM) and scanning force microscopy (SFM). The lateral sizes of the nano SU8 structure before and after pyrolysis are probed by SEM. The results show that the lateral size is maintained during the pyrolysis even for structures with widths of 18 nm. SFM results indicate a vertical shrinkage of about 80% after pyrolysis.

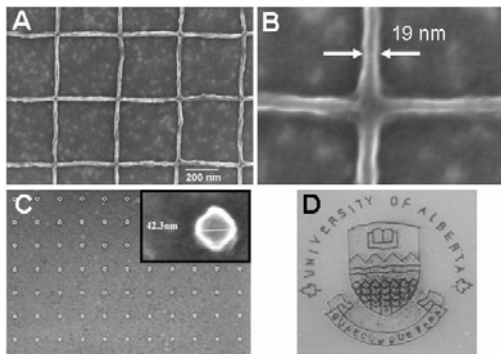


Figure 2: SEM images of graphitic carbon structures created by EBL and pyrolysis.

Finally, we are currently applying these structures as nano-electrodes. Figure 3 shows the cyclic voltammogram of 1 mM K₄[Fe(CN)₆] obtained at an 140- nm carbon nanoband electrode (shown in inset).

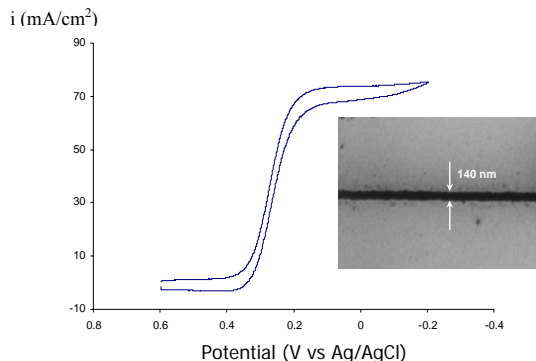


Figure 3: Cyclic voltammetry of 1 mM K₄[Fe(CN)₆] (1.0 M KCl) at a 140 nm wide graphitic carbon nanoband electrode (scan rate = 20 mV/s).

From the CV experimental result, we observed a limiting current plateau which is characteristic of radial diffusion to cylindrical ultramicroelectrodes. The observed behavior is also consistent with quasi-reversible electron transfer between K₄[Fe(CN)₆] and the graphitic carbon surface similar to that observed at more common carbon electrodes such as glassy carbon.

4. Conclusions

We demonstrate the fabrication of well-defined nano carbon electrodes by EBL and pyrolysis. The nano structure keeps constant in the lateral size, while vertical shrink about 80% after pyrolysis. The smallest size of nano carbon electrodes can approach to 20nm.

References

1. X.; M. H. Huang et al., *Controlled Placement of Individual Carbon Nanotubes*, NanoLett., 5, 1515-1518, (2005).
2. S. Ranganathan and R. L. McCreery, *Electroanalytical Performance of Carbon Films with Near-Atomic Flatness*, Anal. Chem., 73, 893-900 (2001)
3. S. Ranganathan et al., *Covaletly Bonded Organic Monolayers on a Carbon Substrate: A New Paradigm for Molecular Electronics*, NanoLett., 1, 491-494, (2001)
4. Madou MJ et al., *Electrical properties and shrinkage of carbonized photoresist films and the implications for carbon microelectromechanical systems devices in conductive media*, journal of the electrochemical society, 152, J136-J143, (2005)

A Low Temperature Bonding Technique for Microfluidic Chip Fabrication Using Soft-Cure SU-8 Sheet

Hirofumi Shintaku¹, Yasutoshi Hirabayashi¹, Teru Okitsu¹,
Satoyuki Kawano², Takaaki Suzuki¹, Isaku Kanno¹, and Hidetoshi Kotera¹
¹Kyoto University, Yoshida-honmachi, Sakyo-ku, Kyoto, 606-8501, Japan
²Osaka University, Machikaneyama-cho, Toyonaka, Osaka 560-8531, Japan

Abstract

In this paper, we propose a novel bonding technique using soft-cure SU-8 sheet under low pressure and low temperature. The pressure for the bonding process ($\sim 5\text{kPa}$) was significantly smaller than those of other bonding techniques ($\sim \text{MPa}$). This bonding process allows us to select a wide variety of materials such as fragile and low melting point materials.

Keywords: microchannel, SU-8, bonding, microfluidic chip

1. Introduction

SU-8 is widely used thick negative photoresist to fabricate micro-structures such as integrated microchannels. To fabricate a microchannel using SU-8, bonding process is necessary to seal the ceiling of microchannel. Conventionally, either adhesive layer [1] or high bonding pressure ($\sim \text{MPa}$) [2] is required to realize a reliable sealing of microchannel. In the present study, we have developed a bonding technique which can complete the bonding process under low pressure and low temperature using soft-cure SU-8 sheet.

2. Theory

The patterned soft-cure SU-8 sheet is fabricated on a silicone rubber substrate using standard SU-8 fabrication process. Because of the poor UV-light reflection at the interface between the substrate and the SU-8, incomplete cross-link layer of SU-8 is formed at the interface. This interfacial layer acts as an adhesive layer, thus the soft-cure SU-8 sheet can be bonded with another SU-8 structure.

Practically to fabricate the soft-cure SU-8 sheet, the SU-8 (SU-8 2100, MicroChem) was coated to be $130\mu\text{m}$ thick on the silicon rubber substrate and small holes for the fluidic port were patterned using UV-lithography. Then, the SU-8 sheet is peeled off from the substrate (see Fig.1).

2. Experimental

In order to demonstrate the applicability of the proposed bonding technique using soft-cure SU-8 sheet, a microfluidic chip for a Coulter type particle counter was fabricated. The fabrication process for the

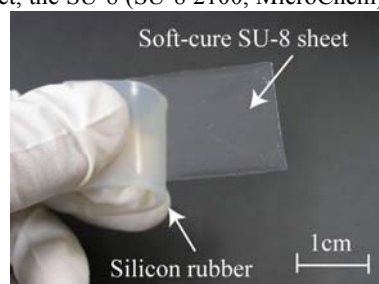


Figure 1. Soft-cure SU-8 sheet embedded inlet holes for fluidic port.

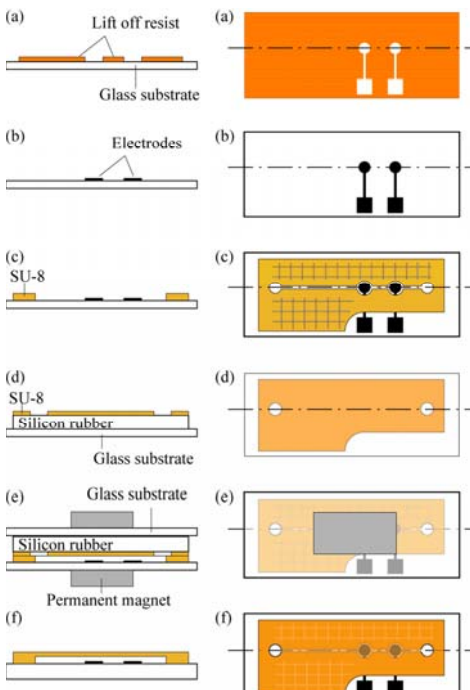


Figure 2. Fabrication process for a Coulter type particle counter using proposed bonding technique.

microscope (UH3, Olympus) and we confirmed that the interface area more than 90% was bonded completely. The details of the SU-8 interface were observed by a SEM image as shown in Fig.4. It is hard to see the boundary line between the SU-8 layer and soft-cure SU-8 sheet, implying that the boundary area of SU-8 was chemically combined.

Furthermore, we conducted an electric impedance measurement to apply the fabricated microfluidic chip to the particle counter. Clear signal (pulse-like signals) from the particles passing through the aperture was obtained as shown in Fig.5. This result indicates that the easy bonding technique developed here is reliable and applicable to fabricate a practical microfluidic chip.

We fabricated only a one-layer microfluidic chip using the proposed bonding technique in the present study. The proposed bonding technique, however, can be easily extended to fabricate two or multiple-layer microfluidic chip by accumulating the photo-patterned soft-cure SU-8 sheet. Therefore, this proposed bonding techniques allows us to develop a

microfluidic chip in Fig.2 is as follows; (a), (b) patterning Au electrodes on a glass substrate by lift-off process, (c) fabricating the SU-8 microchannel structure over the Au electrodes using UV-lithography, (d) fabricating soft-cure SU-8 sheet and (e), (f) aligning and bonding the wsoft-cure SU-8 sheet on the SU-8 microchannel. In order to complete the bonding process by cross-linking the soft-cure SU-8 sheet, the sheet and microchannel are pressed at ~5kPa using a pair of permanent magnets (Sm-Co Magnet, Magna) and heated on a hotplate at 60°C for 3hours. To eject the residual solvents in the soft-cure SU-8 sheet during the bonding process, a grid structure is fabricated in the microchannel layer of SU-8.

3. Results and discussion

Figure 3 shows (a) a photograph and (b) a micrograph of the fabricated microfluidic chip using the proposed bonding technique. The bonding quality was evaluated using acoustic

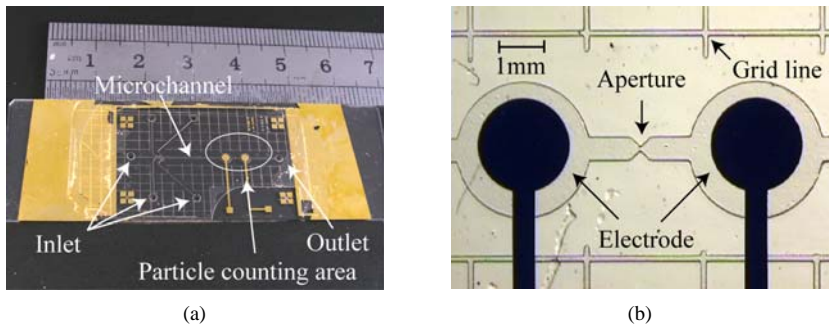


Figure 3. Photograph (a) and micrograph (b) of microfluidic chip fabricated by the proposed technique.
three dimensional microfluidic system.

4. Conclusions

Easy and reliable bonding technique for sealed-microchannel fabrication using soft-cure SU-8 sheet was proposed. The bonding quality was evaluated measuring bonding area and its applicability was confirmed measuring electrical impedance using the microfluidic chip. The results showed that the proposed bonding technique was appreciable and reliable to fabricate practical microfluidic chips.

Acknowledgements

This study is supported in part by grant-in-aids for JSPS Research Fellowships for Young Scientists (No.16001152) and Center of Excellence for Research and Education on Complex Functional Mechanical Systems (COE program) of MEXT, Japan.

References

- 1 S. Li et al., *J. Micromech. Microeng.*, 13, pp.732-738 (2003).
- 2 F.J. Blance et al., *J. Micromech. Microeng.*, 14, pp.1047-1056 (2004).

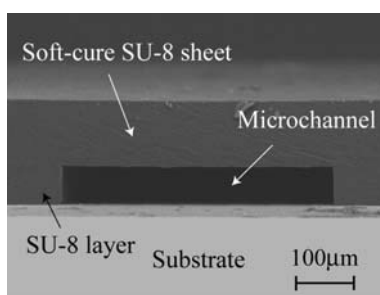


Figure 4. SEM image of microchannel sealed by the proposed technique.

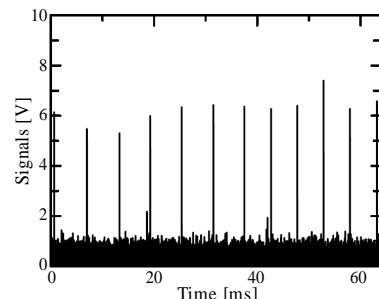


Figure 5. Signals obtained during the counting particles by the fabricated chip.

Three-dimensional Microfabrication for Biodegradable Polymers

Toward Implantable Micro Devices

Akira Yamada, Fuminori Niikura, and Koji Ikuta

Dept. of Micro/Nano System Engineering, Graduate School of Engineering, Nagoya University,
Euro-cho1, Chikusa-ku, Nagoya, Aichi 464-8603, Japan

Abstract

We have developed a novel three-dimensional microfabrication method for biodegradable polymers. Unlike conventional processes, our process satisfies high-resolution and high-speed requirements. The system design allows us the processing of micro-level forms by stacking up melted polymers from the nozzle. A single layer from the piled-up layers of extruded lines was observed to evaluate the resolution. The lateral and depth resolutions attained are 40 μm and 45 μm , respectively. Biodegradable polymers enable three-dimensional microstructures such as micro-pipes, micro-bends, and micro-coil springs to be manufactured in less than 15 min. The biocompatibility of the structure was evaluated using a cell line (PC12). A small vessel, with a transparent base, was fabricated using PLA and cells were cultivated in it. The cell morphology and the proliferation were then compared with the results obtained using the standard method. Our system renders it possible to produce toxic-free, and leakage-free devices. Our system is expected to have potential applications in optimum design and fabrication of implantable devices.

Keywords: Biodegradable polymer, Real Three-dimensional, High-resolution, High-speed, Biocompatible

1. Introduction

Biodegradable polymers, such as poly(lactide) (PLA), poly(glycolide) (PGA), and poly(lactide-co-glycolide) (PLGA), have been employed for use in medicine[1,2]. In recent years, advances in tissue engineering that can regenerate tissue and organ has generated a lot of interest[3,4] and a technology for fabrication of a scaffold is needed[5]. But, due to limitations in the fabrication technology, we can only acquire simple shape structures in the present circumstances. The fused deposition modeling (FDM) is a method that enables us to produce complicated three-dimensional structures and is usually used for prototyping industrial designs. The FDM is also applied for production of biodegradable implantable devices[5]. In this paper, we report a novel method for the fabrication of three-dimensional microstructures, with high-resolution and high-speed[6]. The biocompatibility of the microstructure is verified using a cell line.

2. Materials and methods

2.1 Biodegradable polymers and microfabrication system

PLA, PGA, and PLGA are thermoplastic resin, the resin melts down and drops in viscosity after being heated. Fig. 1 shows a basic principle of FDM. The melted polymer is extruded from a fine nozzle and the nozzle traces the XY surface based on a slice data. One layer is constructed and the process is repeated as the need arises. Fig. 2 is the schematic diagram of the fabrication system that we have developed. Resinous pellets are fed into the syringe and the temperature is elevated up to its melting point. The XYZ stage and the syringe are driven by a stepping motor, and these are in controlled by the PC. The fabrication process can be carried out automatically. The system is characterized by employing a small syringe to provide melted polymer, and pellet materials can be used directly into the syringe. Since our method does not need toxic solvents that results in bioincompatibility of the manufactured structure, it is suitable for various kinds of biodegradable polymers for medical use. As we have designed a fine nozzle ($\phi 50\mu\text{m}$) and optimized fabrication parameters, complicated three-dimensional microstructures can be fabricated with high-resolution at high-speed.

2.3 Biocompatibility test

Biocompatibility of the fabricated device is a crucial matter for use in medicine. We fabricated a small vessel using the fabrication system that we have developed and a cell line, PC12, is cultivated in it. A vessel

for cultivation is fabricated using PLA, which has a lower degradation rate. To observe the cell, a transparent base is necessary. To acquire a transparency, we chose optimized fabrication parameters and the appropriate molecular weight (M.W.) of material. The internal size of the vessel is $4.5\text{mm} \times 4.5\text{mm} \times 5\text{mm}$. Cells were cultivated at 37 degree centigrade and in a 5% CO_2 incubator by using a established protocol. The cultivated cells were evaluated in the aspect of its morphology and growth. The number of cells in the photo image of the optical microscope were counted and the cell morphology and growth curve were compared with the standard one.

3. Results

3.1 Evaluation of the resolution

A single layer from the piled-up layers of extruded line is observed to evaluate the resolution using the optical microscope. Fig. 3 shows that the lateral and depth resolutions attained are $40\ \mu\text{m}$ and $45\ \mu\text{m}$, respectively.

3.2 Microfabrication

We fabricated various shapes of biodegradable microstructures such as micro-pipes (Fig. 4), micro-bend pipes (Fig. 5), and micro-coil springs (Fig. 6) using PLA and PLGA. The time required to fabricate each structure is 3 to 12 min.

3.3 Biocompatibility

Fig. 7 shows a cultured PC12 cells after 42 hours of cultivation. The cells in the PLA vessel is shown in (a), and the cells in the standard vessel for control is shown in (b). The morphology of the cells cultured in the PLA vessel is normal and similar to those in the standard vessel.

The cell growth curve of both vessels are shown in Fig. 8. The number of cells are increasing up to 89 hours for both vessels. These results suggest that the biodegradable microstructure has sufficient biocompatibility.

4. Discussion

The resolution of the conventional FDM was at most several hundred micrometers[5], but we achieved $45\ \mu\text{m}$ by manufacturing a very fine nozzle and optimizing fabrication parameters. The time required to produce a microstructure is less than 15 minutes using our system. This merit is very profitable for use in

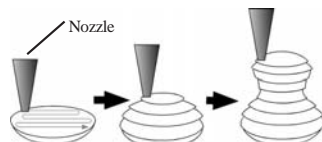


Fig. 1 Basic principle of fused deposition modeling.

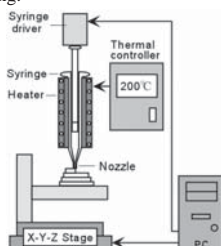


Fig. 2 Schematic diagram of the fabrication apparatus.

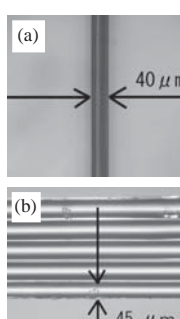


Fig. 3 Photographs of a layered line.
(a) Top-down view
(b) Side view

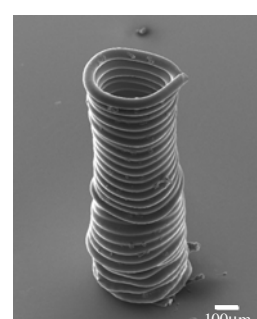


Fig. 4 SEM photograph of a micro-pipe. O.D.: 0.4mm, Height: 1.5mm, Fabrication time: 5.5min., Resolution: $48\ \mu\text{m}$, Material: PLA

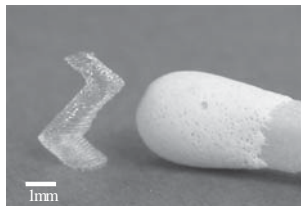


Fig. 5 A micro-bend pipe with matchstick.
O.D.: 1.5mm, Height: 4mm, Fabrication time: 12min., Material: PLA



Fig. 6 A micro-coil spring.
L.D.: 0.2mm, O.D.: 0.9mm, Pitch: 0.8mm, N=5, Fabrication time: 3min. Material: PLGA.

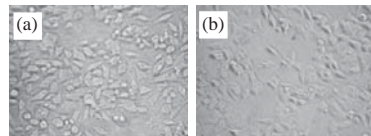


Fig. 7 Cultured PC12 cells after 42 hours of cultivation.
(a)In a PLA vessel, (b)Standard vessel for control.

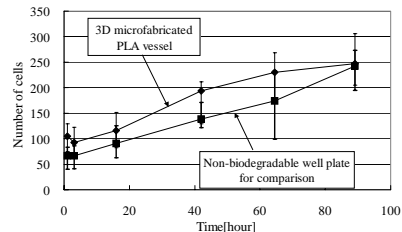


Fig. 8 Cell growth curve of PC12 cultured in PLA vessel and standard vessel.

medicine. The structure fabricated by conventional FDM had not attained biocompatibility due to the use of toxic solvents, that are indispensable in the pre-process. Our method is also able to handle almost all types of thermoplastic resin by employing a batch process. Conventional FDM is limited to only one or two resins. At the material dynamics, the size of the structure is assigned an order of square or cube, a size of the structure will be larger at most several percentages. Therefore, the strength of the microstructure has enough strength for fabrication of medical devices.

5. Conclusion

In this paper, we demonstrated a newly developed method for fabrication of three-dimensional microstructures from biodegradable polymers. We realized (1) Real three-dimensional microfabrication, (2) High-resolution ($45\mu\text{m}$), (3) High-speed (less than 15 min) fabrication, (4) Transparent structure that allows observation of its internal condition, (5) Sufficient Biocompatibility. The above results show the usefulness of fabrication system for future medicine.

Acknowledgment

This research was supported by a research grant from the Japan Society for the Promotion of Science (Research for the Future program: Grant No. JSPS-RFTF-96I00103) and a Grant-in-Aid for Scientific Research ((A)(2) 15206027).

References

- R. K. Kulkarni, K. C. Pani, C. Neuman, and F. Leonard, *Poly(lactic acid) for surgical implants*, Arch. Surg., 93, pp. 839–843, (1966).
- Y. Matsusue, T. Yamamoto, M. Oka, Y. Shikinami, S. H. Hyon, and Y. Ikada, *In vitro and in vivo studies on bioabsorbable ultra-high-strength poly(L-lactide) rods*, J. Biomed. Mat. Res., 26, pp. 1553–1567, (1992).
- R. Langer, and J. P. Vacanti, *Tissue engineering*, Science, 260, pp. 920–926, (1993).
- L. J. Bonassar, and C. A. Vacanti, *Tissue engineering: The first decade and beyond*, J. Cell. Biochem. Suppl., vol.30-31, pp. 297–303, (2002).
- D. W. Hutmacher, *Scaffolds in tissue engineering bone and cartilage*, Biomaterials, 21, pp. 2529–2543, (2000).
- K. Ikuta, A. Yamada, and F. Niikura, *Real Three-Dimensional Microfabrication for Biodegradable Polymers -Demonstration of High-Resolution and Biocompatibility for Implantable Microdevices*, The 26th Annual International Conference of the IEEE Engineering in Medicine and Biology Society (EMBS04), pp. 2679-2682, (2004).

FABRICATION OF ROBUST BIOCOMPATIBLE IN-PLANE MICRONEEDLES WITH SHARP 3-D TIP

Chun Yan Jin and Seung S. Lee

Department of Mechanical Engineering, Korea Advanced Institute of Science and Technology, 373-1, Guseong-dong, Yuseong-gu, Daejeon, Korea

Abstract

This paper presents two novel but simple fabrication technologies of robust biocompatible in-plane microneedles with sharp 3-D tip. One is to fabricate biodegradable PLLA microneedles using hot pressing process, and the other is to fabricate Ni microneedles coated with bio-inert parylene-C using electroplating, polishing, and CVD process. Both of the technologies use SU-8 deep microneedle mold which is fabricated with conventional inclined UV lithography.

Keywords: microneedle, inclined UV lithography, biocompatible

1. Introduction

Various fabrication technologies of microneedles have been developed over the past few years for painless, improved transdermal, and local drug delivery.

Microneedles are classified to out-of-plane and in-plane. For out-of-plane microneedles, the needle length is not defined lithographically but often by a removal process which is costly, time consuming, and difficult to control. On the other hand, the needle length of in-plane microneedles is defined lithographically and thus straight forward to control [1]. But most of the previous in-plane microneedles are not biocompatible and robust because they are made of brittle silicon or silicon compounds with 2-D thin feature [2-3]. To overcome those limitations, microneedles should be made by biocompatible material and have a shape thickened gradually from sharp 3-D tip to needle shank and base. Otherwise large insertion force will be caused by increased interfacial area [4].

This study addresses the fabrication process of biodegradable in-plane PLLA microneedles with sharp 3-D tip using inclined UV lithography, PDMS molding, and hot pressing processes and bio-inert parylene-C coated Ni microneedles with the same shape as PLLA microneedles using electroplating, polishing, and CVD processes.

2. Fabrication and results

Figure 1 shows the fabrication process of a deep SU-8 negative microneedle mold

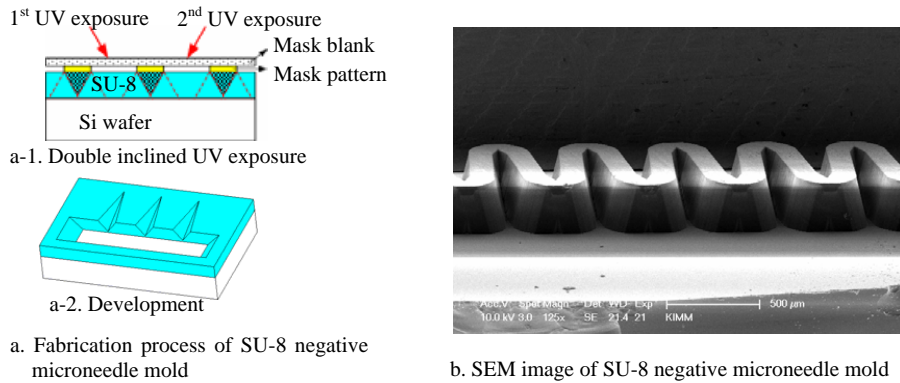


Figure 1. Fabrication process of SU-8 negative microneedle mold and the result.

and the result. The successive double inclined UV exposure and development lead to a deep negative microneedle mold (Figure 1. a-1 and 2). This method has advantages of using widely used and easily accessed UV light source and SU-8 photoresist. In addition, alignment is not required during double exposure process because the mask and SU-8 are vacuum contacted. The fabricated SU-8 negative microneedle mold has deep and inclined trenches and sharp edges as shown in Figure 1. b.

Figure 2 shows the fabrication process of PLLA microneedles with the SU-8 negative microneedle mold and the result. By double PDMS(Poly-Di-Methyl-Siloxane) molding processes (Figure 2. a-1 and 2), a PDMS negative microneedle mold is fabricated. Hot pressing process with PLLA beads makes the final microneedles using the PDMS

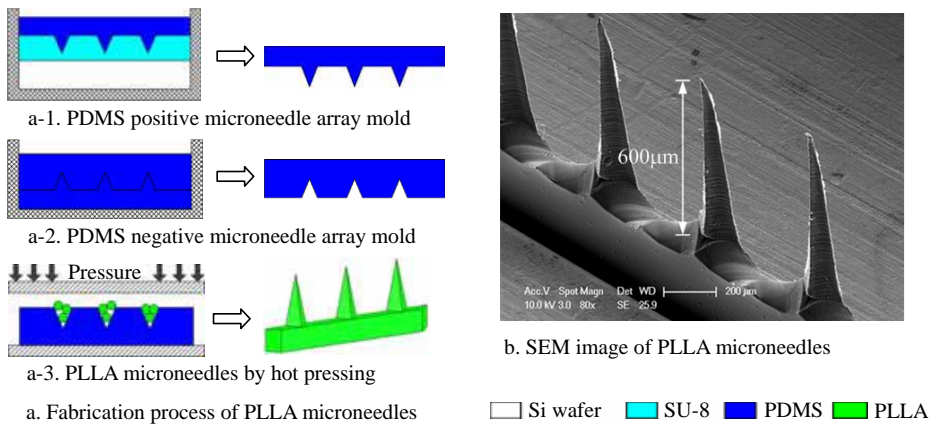


Figure 2. Fabrication process of PLLA microneedles and the result.

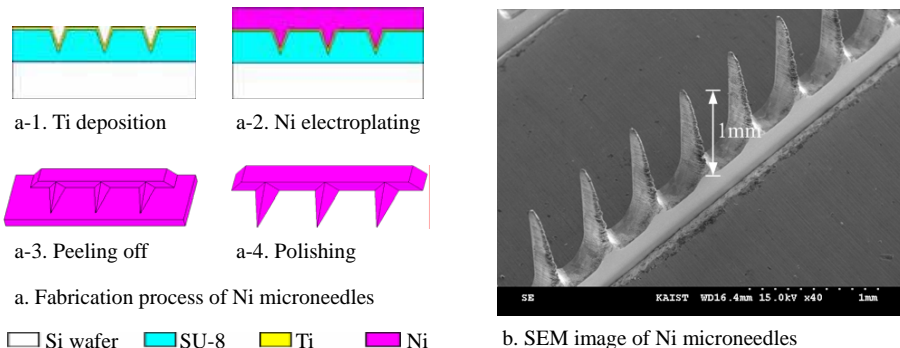


Figure 3. Fabrication process of Ni microneedles and the result.

negative microneedle mold (Figure 2. a-3). The fabricated microneedles are 600 μm long and have a shape thickened gradually from sharp 3-D tip to shank and base which is required for smaller insertion force and enough strength as shown in Figure 2. b. In addition, because PLLA is a bio-degradable material, PLLA microneedles can be used in bio-application field without remaining debris which are harmful to body.

The fabrication process of Ni microneedles and the result is shown in Figure 3. Ti deposition on SU-8 negative microneedle mold as a seed layer is followed by Ni over electroplating (Figure 3. a-1 and 2). After peeling off Ni from SU-8, undesired Ni part is polished and Ni microneedles are fabricated (Figure 3. a-3 and 4). As long as 1mm Ni microneedles are fabricated as shown in Figure 3. b. Since fabricated Ni microneedles have the same shape as the PLLA microneedles above, they have advantages which PLLA microneedles have except biodegradable. To use it in bio-application fields with safety, bio-inert parylene-C is coated on it using CVD.

References

1. Michael L. Reed, *et al.*, Microsystems for drug and gene delivery, Proc. IEEE, vol. 92, pp. 56-75, (2004).
2. Liwei Lin, *et al.*, Silicon-processed microneedles, J. Microelectromech. Syst., vol. 8, pp. 78-84, (1999).
3. Kazunari Oka, *et al.*, Fabrication of a micro needle for a trace blood test, Sensors and Actuators A 97-98, pp. 478-485, (2002).
4. Shawn P. Davis, *et al.*, Insertion of microneedles into skin: measurement and prediction of insertion force and needle fracture force, J. Biomech., vol. 37, pp. 1155-1163, (2004).

FAST PATTERN FORMATION OF POLYMER MICROSTRUCTURES INDUCED BY ULTRAHIGH ELECTRIC FIELD

Brian Pow and Mo Yang

Department of Health Technology and Informatics, Hong Kong Polytechnic University, Hong Kong

Abstract

The control of pattern-formation processes on surfaces and in polymer thin films is of increasing importance for technological application [1]. However, the long annealing time which range from tens of hours to around one hundred hour, blocks the wide application of this technique in fabrication of microstructured devices and templates. Here, we have developed a method for fast fabricating polymer microstructures based on ultra-high electric field induced self assembly and pattern formation.

Keywords: Polymer microstructures; Self assembly; Pattern transfer

1. Introduction

Fabrication of structures in the micron and nanoscale via self assembly has attracted much interest in recent years [1]. Self assembly methods range from fluidic self assembly of optoelectronic devices on silicon substrates (micron scale) to growing islands or quantum dots in heteroepitaxial film systems (nanoscale). These methods offer high throughput and low cost solutions compared to conventional patterning or lithography technologies, and they enable the fabrication of structures with dimensions beyond the wavelength of the light employed in most lithography processes [2]. The assembly of thin polymeric films into ordered structures induced by electrodynamic instability is a relatively new phenomenon that offers a simple way to form ordered microstructures on silicon substrates. Figure 1 shows the mechanism of electrohydrodynamic patterning.

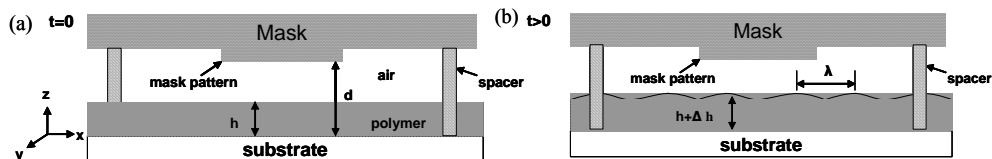


Figure 1: Schematic of electrohydrodynamic patterning. (a) Initial stage with a flat surface (b) The electrostatic pressure acting at the polymer-air interface causes instability in the film with a well defined wavelength. d is the mask-substrate spacing; h is the initial thin film thickness;

2. Experimental setup

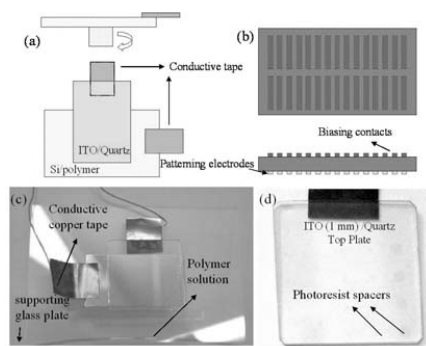


Figure 2 (a) A schematic of experimental setup (b) Replica of the master electrode for the pattern transfer. (c) Experimental setup for self assembly of polymer patterns. (d) ITO/quartz top plate (1mm×1mm) with photoresist spacers.

The setup in **Figure 2a** was enclosed in an aluminum oven equipped with a front observation window. The outside of the aluminum enclosure was covered with a layer of thermal insulating material. A temperature controller and a thermocouple controlled the temperature inside (**Figure 2b**). The assembly was placed between two pieces of copper tapes, which were connected to a voltage-stabilized power supply. For the bottom electrode/plate, a piece of conductive copper tape was applied right before spin coating the polymer (**Figure 2c**). For the top electrode, conductive copper tape was applied and the capacitor was formed with an offset configuration as shown in **Figure 2d**.

3. Results and discussion

Figure 3 shows results from a self assembly experiment for which the initial polystyrene thickness was 200 nm and the spacer thickness was 400 nm. The capacitor arrangement was heated to 170°C and a bias voltage of 120 V was applied across the capacitor. Figure 3(a) shows the initial stage of the flat thin film surface. After 5 minutes of annealing, the lateral distribution of the polymer is reminiscent of electrohydrodynamic instabilities seen in the polymer film (Figure 3(b)), resulting in islands of 2 μm in diameter. After 20 minutes of annealing, the average island diameter is 5 μm. Locally close packed arrangement of features were also noted, in the form of a hexagonal arrangement (Figure 3(c)). After 40 minutes of annealing in Figure 3(d), the average island diameter is 18 μm.

Figure 4 shows the results of two pattern replication experiments for line replica pattern. For Figure 4(a)-(d), pre-patterned ITO/Quartz top plates was used, where the

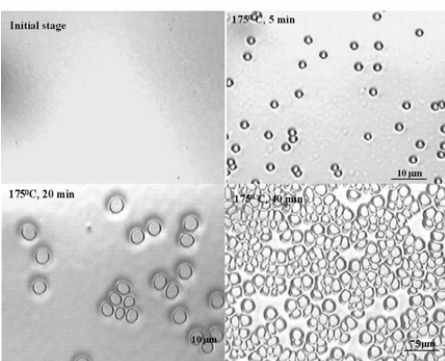


Figure 3 Self assembly of polystyrene structures at 170°C and applied bias of 120 V. (a) Initial stage (b) After 5 minutes of annealing, the average diameter of islands is 2 μm. (c) After 20 minutes, the average diameter of islands is 5 μm. (d) After 40 minutes of annealing, the average diameter of islands is 18 μm.

pattern was formed by conventional photolithography and wet etching. For the experiment shown in Fig. 8(a)-(b), the polystyrene film thickness was 200 nm and the spacer thickness was 600 nm. Complete formation was observed after 8 minutes of total processing time, as shown in Figure 4(d), and the average height measured was 410 nm and the average line width was 2 μ m.

Figure 5(a) shows the electrical field distribution in the polymer/air interface for the rod pattern. Figure 5(b) shows the line width as a function of annealing time for the above two cases. The islands of the polymer film continue to evolve to larger sizes with the increase of annealing time. From Figure 5(b), we can see that high electrical field permits appropriate annealing time to obtain stable and complete submicro or nano pattern.

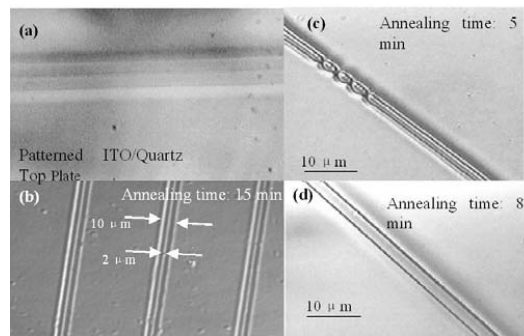


Figure 4 Replication process for line patterns. (a) Patterned Indium Tin Oxide (ITO)/quartz top plate. (b) The line width of the pattern is around 2 μ m after 15 minutes of annealing time when $V = 180V$. (c) The wider air gap needs shorter annealing time (8 min) and lower voltage (130V) to obtain the similar size. (d) Line formation after 8 minutes

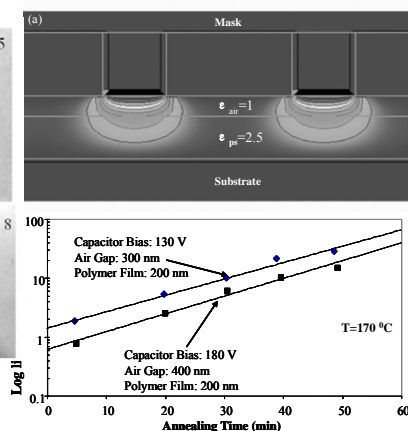


Figure 5 (a) Electrical field distribution in the polymer/air interface for the rod pattern. (b) Line width as a function of annealing time.

4. Conclusion

A method has been described for fast self assembly and template replication in polymers using ultrahigh electrical field. Beneficial is, in particular, the time required for pattern replication is significantly reduced from tens of hours to tens of minutes using the ultra-high electrical field. Potential applications of the method in the micron and nanometer scales include bio-fluidic MEMS, polymer optoelectronic devices and patterned templates for nanolithography.

References

- [1] YN Xia, JA Rogers, KE Paul and GM Whitesides Chem. Rev. 99, 1823, 1999.
- [2] G. Whitesides, JP Mathias and CT Seto, Science, 254, 1312-1319, 1991

THE MEMBRANE MICRO EMBOSSED (MeME) PROCESS FOR FABRICATING 3-D MICROFLUIDIC DEVICE FORMED FROM THIN POLYMER MEMBRANE

Masashi Ikeuchi and Koji Ikuta

Dept. of Micro/Nano Systems Eng., School of Eng., Nagoya University, Japan

Abstract

The newly developed “membrane micro emboss (MeME) process” realizes arbitrary 3-D microstructures made of thin polymer membrane, which is impossible with traditional microfabrication techniques. Using MeME process, unique microfluidic devices composed of only thin membrane were successfully fabricated. Due to its thin membrane structure, the microfluidic device offers much higher mass and heat transfer through microchannel walls compared to traditional microfluidic devices, and thus, opens up new application fields for microfluidic devices.

Keywords: Membrane, Polymer, Emboss, Mass transfer, Fabrication

1. Introduction

We report the development of MeME process for fabricating a microfluidic device formed from thin membrane - i.e. “membrane microfluidic device”. Distinctively, the microchannel is composed of thin membranes in the membrane microfluidic device (Fig.1a), whereas the microchannel is made inside thick substrates in the conventional microfluidic device (Fig.1b). The reduced thickness of the wall enables significantly enhanced heat and mass exchange between the inside and the outside of the microchannel. By utilizing these characteristics of the membrane microfluidic device, we can expand the overall application of microfluidic devices to temperature-dependent and environment-dependent reactions. Although there are various processes to fabricate μ TAS or MEMS devices, there are no processes applicable to fabricate membrane microfluidic devices we have proposed.

2. MeME Process

To realize the membrane microfluidic device, we have developed MeME process (Fig.2).

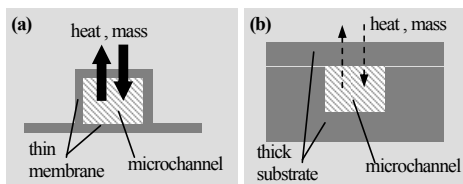


Fig.1 Schematic illustration of the cross-section of (a) membrane microfluidic device proposed here and (b) conventional microfluidic device made of thick substrates

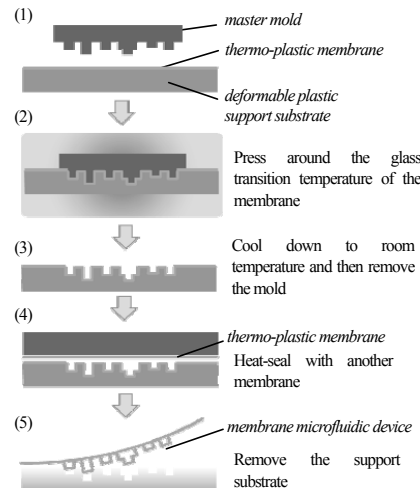


Fig.2 Fabrication process of the membrane microfluidic device by membrane micro emboss (MeME) process

This process needs a master mold, a thermoplastic polymer membrane and a deformable plastic support substrate. Firstly, the polymer membrane is set between the master mold and the support substrate. Secondly, they are heated to the glass transition temperature of the polymer membrane. Then, the master mold is pressurized against the membrane. During the pressurization, the membrane together with the support substrate is deformed to match the surface of the master mold. After cooling to room temperature, the master mold is separated from the deformed membrane. To fabricate sealed microchannels, another planar membrane is placed on the deformed membrane and heat-sealed. Lastly, the membrane microfluidic device is completed by dissolving the support substrate in a selective solvent. All of the process is done in an improvised tabletop microemboss device.

3. Process Conditions

We investigated the effect of the process conditions, including pressing time period, pressing speed and the property of support substrates. Poly-lacticacid (thickness=5 μm) was used as membrane material and paraffin was used as a support substrate. Longer time period resulted in smaller curvature at the bottom corner of the microchannel, but did not affect the height because it saturated before 250 seconds (Fig.3a). This result suggests that we can fabricate microchannels with different cross-sectional shape from only one master mold by just modifying the pressing time period. Higher pressing speed and the use of paraffin with higher melting point increased the height of the microchannel (Fig3 b,c). This was due to the increasing pressure against the membrane under these conditions (Fig.3d).

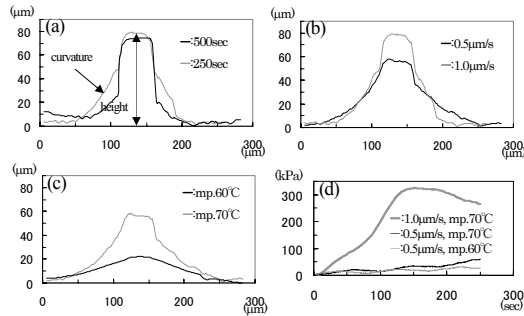


Fig.3 (a-c) Height profiles of the membrane microchannels with width of 50 μm under various process conditions: (a) pressing time period = 250sec, 500sec (b) pressing speed = 0.5 $\mu\text{m/s}$, 1.0 $\mu\text{m/s}$ (c) melting point (mp.) of paraffin = 60°C, 70°C (d) Pressure transitions during the MeME processes under several process conditions

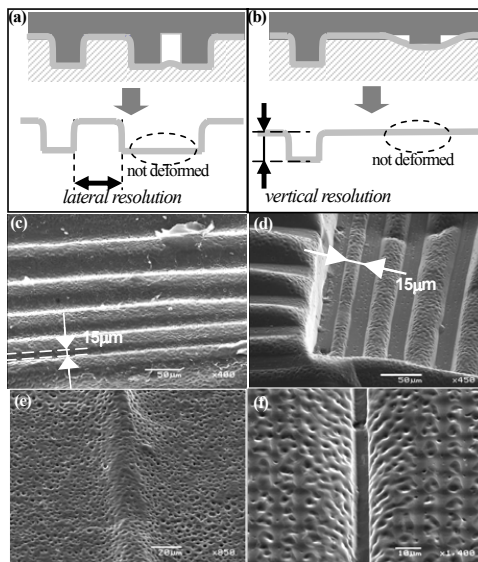


Fig. 4 (a) definition of the lateral resolution (b) definition of the vertical resolution (c, d) SEM of the upper and the under side of the deformed membrane for examining lateral resolution (e, f) SEM of the upper and the under side of the deformed membrane (height = 5 μm) for examining the vertical resolution, respectively

4. Process Resolutions

After setting optimal process conditions, the fabrication resolution both in lateral and vertical direction was investigated. The lateral resolution (Fig.4a) was found to be smaller than 15 μm (Fig.4c,d), and the vertical resolution (Fig.4b) was found to be around 1 μm (Fig.4e,f). These resolutions are sufficient for fabricating microfluidic devices. The resolutions can be much smaller with thinner membranes.

5. Prototype Fabrication

We have demonstrated the fabrication of highly branched microchannels formed from poly-lacticacid membrane with thickness of 5 μm . The honeycomb-like master mold (Fig.5a) was made by micro-stereolithography developed in our laboratory [1]. The surface of the mold was coated with fluorocarbon polymer for easy removal of the mold. After pressing the master mold against the membrane, the microstructures of the master mold were precisely transferred to the membrane (Fig.5b,c). The interface of the two membranes was tightly sealed after heat-sealing at 70C for 30 seconds (Fig.5d). Red solution was filled in the microchannels by capillary force. No leak or blockage of the microchannel was observed (Fig.5e). Thus, the membrane microfluidic device which has microchannels with width of 50 μm , depth of 50 μm and wall thickness of 5 μm was successfully fabricated using MeME process.

6. Conclusion

In summary, we have developed MeME process to fabricate membrane microfluidic devices with high precision, speed and simplicity. The process is applicable to various materials, since it requires only thermo-plasticity of the membrane material. The membrane microfluidic device proposed and developed here, will open the way to the new application of microfluidic devices for biological and chemical analysis, where temperature control and interfacial mass transfer have critical importance.

References

- [1] K. Ikuta and K. Hirowatari, Real three dimensional micro fabrication using stereo lithography and metal molding, Proc. of MEMS'93, pp.42-47, 1993

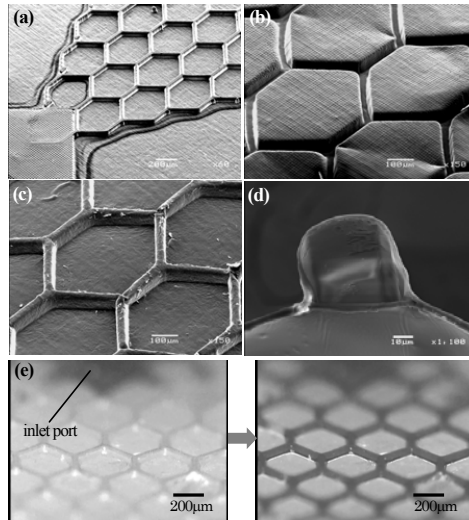


Fig.5 (a) SEM of the master mold (b) SEM of the underside of the membrane microchannel (c) SEM of the upperside of the membrane microchannel (d) SEM of the cross-section after heat-sealing (e) Optical microscopy of the membrane microfluidic device before and after filling red-colored water

SINGLE-STEP NIL OF MICRO AND NANOCHANNELS COMBINED WITH OPTICAL WAVEGUIDES FOR CHARACTERIZATION OF DNA MOLECULES

Søren Jacobsen¹, Jason P. Beech¹, Mikkel Schøler¹, Anders Kristensen²,
Jonas O. Tegenfeldt^{1*}

¹Division of Solid State Physics, Lund University, P. O. Box 118, SE-221 00
Lund, Sweden

*jonas.tegenfeldt@ftf.lth.se

²MIC-Department of Micro and Nanotechnology, Technical University of
Denmark (DTU), Building 345east, Oersteds Plads, DK-2800 Kongens Lyngby,
Denmark

Abstract:

A device is made for local excitation of stretched DNA. A nanochannel is combined with micron-scale access channels and a waveguide. The nanochannel ensures a stretched conformation of the DNA, thus opening up for linear analysis of the DNA with respect to *e.g.* length or attached specific probes. The waveguide provides local excitation either directly of the DNA or indirectly through a local point source of light. Here we report on a first step towards this goal with a simple single-step 3D nanoimprinting lithography (NIL) method to create a device with nanofluidic channels for stretching of DNA, integrated with waveguides for local optical excitation.

Keywords: NIL, nanofluidics, DNA analysis

1. Introduction

For linear direct optical analysis of DNA, such as fiber FISH[1] and optical mapping[2], the available resolution is limited by the poor elongation of DNA in conventional approaches [1,2] as well as by the diffraction limit. This can be solved by a *Scanning Nearfield Optical Microscope* (SNOM) on a chip implemented by local excitation of the DNA through integrated point sources of light in nanofluidic channels.

The nanofluidic channels have a two-fold purpose. They stretch the DNA [3] and they confine the DNA to a close proximity of the light source, ensuring nearfield optical imaging of the DNA.

2. Experimental

The device is designed with two micron-scale access channels (Fig 1). The channels are joined by a nanochannel in the center. Waveguides, positioned to illuminate the nanochannel and its content, are defined for end-butt coupling at the edge of the chip.

A silicon stamp for NIL was fabricated through a mix&match fabrication scheme: An initial photolithography step, using a positive process in 1.5 μm AZ 5214E resist, was performed to define alignment marks, waveguides and microchannels. This pattern was transferred \sim 2 μm into the silicon substrate through a reactive ion etch (RIE).

Subsequent electron beam lithography step, using a SU-8 resist, was performed to define the nanochannels. The pattern was transferred 200 nm into the substrate through a three-step RIE process. Finally the stamp was given an anti-sticking coating through vapor-phase adsorption of perfluorooctyl-trichlorosilane.

mrt-I T85 nanoimprint resist from micro resist technology GmbH ($T_g \sim 85^\circ\text{C}$) was spun on oxidized silicon wafers to a thickness of $\sim 2 \mu\text{m}$ and the full devices were imprinted in one single step: $T=200^\circ\text{C}$, $F=15\text{kN}$, $t=5 \text{ min}$. To seal the structures, borosilicate float glass wafers were covered with mrt-I T65 ($T_g \sim 65^\circ\text{C}$) to a thickness of $\sim 200 \text{ nm}$ and brought together with the device wafer: $T=69^\circ\text{C}$, $F=5\text{kN}$, $t=150\text{s}$. In this way a reliable sealing is ensured while still preserving the integrity of the device structure. Access holes for the microfluidic channels were made through sandblasting with $50 \mu\text{m} \text{ Al}_2\text{O}_3$ grains. Finally, the bonded devices were diced in an automatic dicing saw.

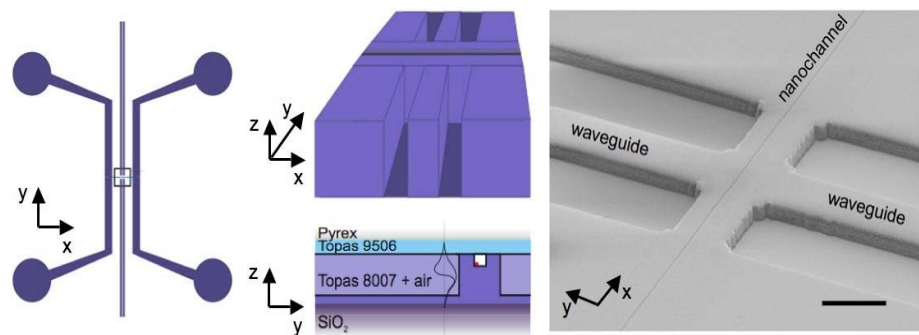


Figure 1. The design. (LEFT) Two microchannels with a total of four reservoirs are connected by a small nanochannel in the centre. The small central square indicates the location of the nanochannel and the cross sections as depicted above in the top and bottom center. (TOP CENTER) 3D view of the device along the waveguide. (BOTTOM CENTER) Sideview of the device. Topas 9506 corresponds to mrt-I T65, and Topas 8007 to mrt-I T85. (RIGHT) The actual device as imaged in a SEM. Scale bar is $10 \mu\text{m}$.

The device was mounted in a chuck and a multimode optical fiber was butt coupled to the device. An index matching gel was used to enhance the coupling efficiency.

3. Results and discussion

Fluorescently stained DNA was introduced into the large channel to a close proximity of the nanochannels and pulled into the nanochannels using electrophoresis. In this way the DNA was imaged both in the macroscopic channel and the nanochannel (Fig 2). At the intersection point of the nanochannel and the waveguide, the DNA is illuminated by light from an integrated waveguide.

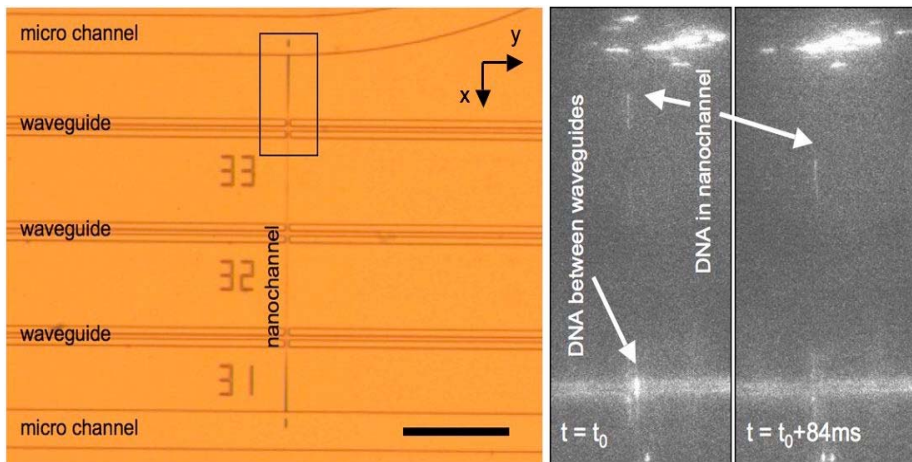


Figure 2. (LEFT) Optical microscopy image of the device. Scale bar is 100 μm . (RIGHT) Two subsequent frames in an area indicated by the rectangle in the left image. A fluorescence microscope was used with a 60x water immersion objective (NA1.0 and WD 2.0mm) and an EMCCD (Andor, Belfast, UK). TOTO-1 (Invitrogen, Carlsbad, California, US) stained lambda phage DNA is illuminated at the top of the field of view by a mercury lamp. The waveguide at the bottom is glowing slightly due to autofluorescence of the mrt-I T85 and the mrt-I T65. At time $t = t_0$ a single DNA molecule is illuminated locally by the waveguide.

4. Conclusions

The device has been demonstrated to work for stretching of DNA.

Next, point sources of light will be implemented in the nanochannel. These could be of three types: active components such as lasers and LEDs, passive components such as quantum dots and fluorescence enhancing particles such as metal or semiconducting particles and structures. It is important to keep in mind that for fluorescence enhancement, quenching is also present giving an optimal separation between the particle and the fluorophore on the DNA.

Acknowledgements

The work is partially supported through the EC-funded project NaPa (Contract no. NMP4-CT-2003-500120). The content of this work is the sole responsibility of the authors. Equipment was used that was purchased with the support from the Crafoord Foundation (Lund) and from the Knut and Alice Wallenberg Foundation (Stockholm).

References

- [1] R. J. Florijn *et al.*, Human Molecular Genetics **4** (5), 831-836 (1995).
- [2] Weiwen Cai *et al.*, PNAS **95** (7), 3390-3395 (1998).
- [3] J. O. Tegenfeldt *et al.*, PNAS **101** (30), 10979-10983 (2004).

SOLVENT-RESISTANT MICROFLUIDIC DEVICE FABRICATION USING RAPID MOLDING TECHNIQUE

Lung-Hsin Hung¹, Rita Kuo², Kenneth J. Shea³, and Abraham P. Lee^{1,4}

¹Department of Biomedical Engineering,

²Department of Electrical Engineering and Computer Science,

³Department of Chemistry,

⁴Department of Mechanical and Aerospace Engineering,

University of California at Irvine, USA

Abstract

This paper presents a simple and rapid microfluidic fabrication process for making devices with good chemical resistance at high resolutions. The molding replicate technique is used to fabricate thiolene-based microfluidic channels. The overall processes don't require specialized equipment or facilities and can fabricate channels with 3D geometry in single-step fashion. The fabricated thiolene-based microfluidic channels have widths from 10 μ m to 800 μ m but are not limited at this range, and the surface hydrophobicity is controllable by surface treatment. Toluene droplet generation in thiolene channels is demonstrated.

Keywords: Thiolene, droplets, organic solvent, channel fabrication

1. Introduction

Poly(dimethylsiloxane) (PDMS) molding technique is one of the most widely adapted microfluidic fabrication process. However, PDMS is incompatible with most organic solvents as it tends to absorb and swell upon contact. Devices made by glass or silicon require expensive and time-consuming processes. With the growing interest in using microfluidic systems for organic phase applications [1], the development of a reliable, low-cost, and fast turnaround fabrication process for solvent-compatible devices is desired.

Thiolene-based micro channels are resistant to swelling by most organic solvents and suitable for organic-phase applications. Thiolene-based devices were first developed using prototyping photolithography process [2,3]. Here we utilize the molding technique as an improved method to simplify the process and increase the channel design feasibility.

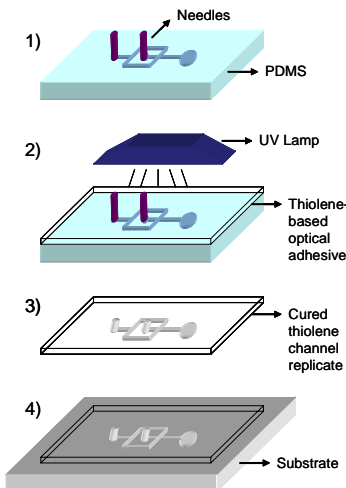


Figure 1. Thiolene channel fabrication processes. 1) PDMS mold and needles setup; 2) optical adhesive was cast and cured under UV exposure; 3) detached thiolene channel replicate; 4) The replicate sealed onto the substrate and the microfluidic device is formed.

2. Experimental

The fabrication process is shown in Fig. 1. Thiolene-based optical adhesive is poured onto PDMS molds, where needles are used to make room for tubing insertion after adhesive is cured. The adhesive cures rapidly under 265nm UV exposure. The exposure time is 10 minutes for 2mm film or less. After curing, thiolene channel replicate is detached and sealed to glass or thiolene substrate.

Toluene droplet generation is demonstrated using shear-focusing channel design [4] shown in Fig. 2(a). Toluene phase is sheared by continuous aqueous phase and monodispersed droplets are generated (Fig. 5). Toluene, which would swell PDMS but is a commonly used organic solvent, is chosen as the dispersed phase and water as the continuous phase. Two liquid phases are injected into the micro channels by syringe pumps separately and high speed camera is used to capture the real time images.

3. Results and discussion

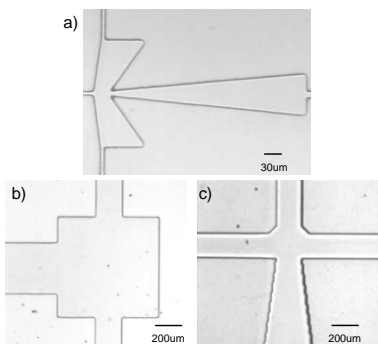


Figure 2. Replicate thiolene channel widths ranging from 10 μm to 800 μm .

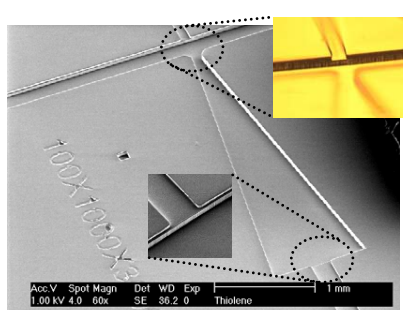


Figure 3. SEM image of 3D thiolene channels with 89 and 48 μm layers.

Fig. 2 shows various thiolene channel designs ranging from 800 μm to 10 μm , but are not limited to these dimensions and sizes. Thiolene adhesive has high replicate accuracy, therefore the channel size and resolution depend primarily on the quality of PDMS molds, which are disposable and easy to prepare. Another advantage using rapid molding method over photolithography is the ability to fabricate 3D channels in rapid and reusable fashion, without second layer photoresist developing, washing and alignments for every time use. SEM images show multi-depth thiolene channels of 48 μm and 89 μm heights (Fig. 3), which can be applied for microfluidic shear force control [5].

Cross-linked thiolene device is hydrophobic, while the surface hydrophobicity is adjustable by plasma treatment [6], and the relationship between thiolene surface hydrophobicity and plasma treatment time is shown in Fig. 4. Therefore the thiolene channels can be tuned to either hydrophobic or hydrophilic for water-in-oil and oil-in-water applications. To prove this concept, an organic-phase microfluidic experiment is demonstrated by toluene-in-water droplet generation. The fabricated thiolene device is subject to air plasma treatment to make the surface hydrophilic, and 20 μm monodispersed toluene droplets are generated as shown in Fig. 5.

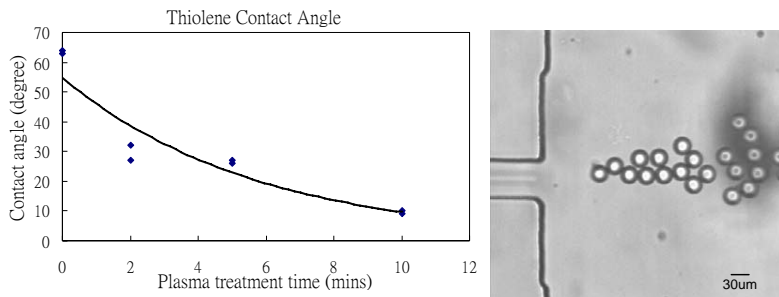


Figure 4. Thiolene surface hydrophobicity as a function of plasma treatment.

Figure 5. Toluene droplets generation in thiolene device without swelling or damaging the channels.

4. Conclusions

Thiolene microfluidic devices fabricated by rapid molding technique provide a simple and reliable platform for organic solvent-based processes. With the rapid developments in microTAS, this technique will be useful for various chemical and material syntheses applications.

Acknowledgements

The authors would like to acknowledge Larry Lai for his help on SEM imaging.

References

1. P. Gould, *Microfluidics realizes potential*, Materials Today, pp. 48-52, (2004).
2. C. Harrison, J. T. Cabral, C. M. Stafford, A. Karim, and E. J. Amis, *A rapid prototyping technique for the fabrication of solvent-resistant structures*, Micromech. Microeng., pp. 153-158, (2004).
3. Z. T. Cygan, J. T. Cabral, K. L. Beers, and E. J. Amis, *Microfluidic platform for the generation of organic-phase microreactors*, Langmuir, pp. 3629-3634, (2005).
4. L.-H. Hung, K. M. Choi, W.-Y. Tseng, Y.-C. Tan, K. J. Shea, and A. P. Lee, *Alternating droplet generation and controlled dynamic droplet fusion in microfluidic device for CdS nanoparticle synthesis*, Lab Chip, pp. 174-178, (2006).
5. E. M. Chan, A. P. Alivisatos, and R. A. Mathies, *High-temperature microfluidic synthesis of CdSe Nanocrystals in Nanoliter Droplets*, J. Am. Chem. Soc., pp. 13854-13861, (2005).
6. L.-H. Hung and A. P. Lee, *Optimization of droplet generation by controlling PDMS surface hydrophobicity*, Proc. IMECE 2004, 61737, (2004).

VIVO STUDY OF MECHANICAL PROPERTIES OF THE MONOLITHIC SILICON PROBES WITH FLEXIBLE PARYLENE CABLES FOR NEURAL PROSTHESES

Changlin Pang¹, Yu-Chong Tai¹, Sam Musallam², Cevat Ustun², Daniel S. Rizzuto², Richard A. Andersen², and Joel W. Burdick³

¹Caltech Micromachining Lab, California Institute of Technology

²Division of Biology, California Institute of Technology

³Department of Mechanical Engineering, California Institute of Technology
(Email: Changlin@its.caltech.edu)

Abstract

This work presents the new experimental results for a new monolithic silicon probes array with flexible parylene cables used for neural prostheses. A new technology developed in the Caltech micromachining lab provides great flexibility to fabricate silicon probes with large range of geometries. Instead of the brittle inorganic materials (e.g. SiO₂ or Si₃N₄), parylene is used as the insulating/protecting material on silicon substrate. Parylene is biocompatible and at the same time improves mechanical properties of the silicon probes. Animal tests have been done to validate the mechanical properties of the new silicon probes with different geometries. The results show that the probes have great improvements than other current silicon probes in mechanical properties. Successful chronic implantation shows that the probes are able to penetrate monkey's pia by hand insertion.

Keywords: Neural probes, silicon probes, parylene, neural prostheses

1. Introduction

An important common goal is to achieve cortex prostheses using implanted probes to interface with robotics by pure thoughts. The first beneficiaries are likely to be patients with spinal-cord injuries, peripheral nerve disease, or amyotrophic lateral sclerosis [1]. To achieve this, researchers are racing to make 3-D neural probes that can record cortex cognitive signals. Unfortunately, there are two major challenges toward the ideal devices. The first is the lack of long-term insulating/protecting biocompatible materials. The commonly used materials such as SiO₂ and Si₃N₄ are useful but they are brittle and have reliability issues for chronic use.

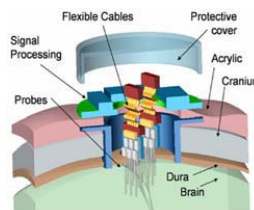


Figure 1. Schematic of cortical implantation using parylene cables.

The second problem is related to through-skull interconnect. Signals obtained by probes have to be cabled out of skull (Shown in Fig. 1). Flexible and biocompatible cables are simply crucial. Facing these two new aspects of research, a new 3-D silicon probes array with monolithic flexible parylene cables has been developed in the Caltech micromachining lab (Shown in Fig. 2) [2]. Firstly, the electrodes on the new probes are completely insulated by parylene, instead of the conventional SiO_2 and/or Si_3N_4 . Here, Parylene is highly desirable because only parylene has been proven to have the longest durability for over 3 years for implant insulation [3]. Secondly, this new probe technology allows the integration of monolithic flexible parylene cables, which further enable functional through-skull interconnect. At the same time, unlike other current silicon probes, for example, Michigan probes made by wet etching can only reach limited probe thickness, and need to open pia and even special guide tools for insertion because of mechanical weakness of the probes. This may cause bigger damage to the brain. Our new double side DRIE etching fabrication technology allows us to make the silicon probes strong enough to penetrate primates' pia. Animal tests have been done to validate the mechanical properties of our new silicon probes.

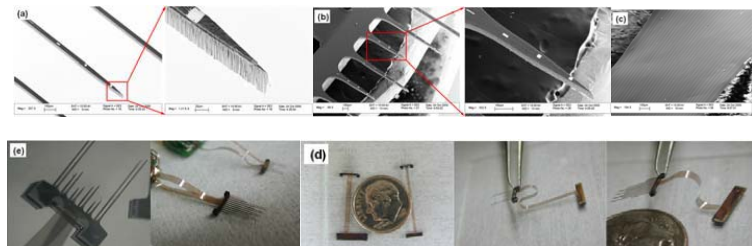


Figure 2. Pictures of the fabricated probes. (a) SEM pictures of the long shank probes; (b) SEM pictures of the short shank probes; (c) SEM picture of the parylene cable; (d) optical pictures of the 2-D probe arrays with parylene cables; (e) optical pictures of the 3-D probe arrays (4x2 with 32 electrodes and 8x2 with 64 electrodes) stacked by two 2-D probes plates.

2. Devices design and fabrication

In order to test the mechanical properties of the new silicon probes. Testing silicon probes are designed for vivo tests. The design parameters are shown in Fig. 3. The testing silicon probes are the same as the complete device except metal electrodes and parylene cables. A $10\mu\text{m}$ parylene layer is on top of the silicon probe's shank, so that the testing probes perform the same mechanical properties as the complete device. A fabricated testing silicon probe is shown in Fig. 4.

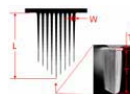


Figure 3. Parameters of the silicon probes for rigidity test.



Figure 4. A fabricated silicon probe for rigidity test.

3. Testing results and discussions

The testing silicon probes with different geometries are tested to penetrate rat's dura by hand insertion. The test results are shown in Table 1. The probes without top parylene layer are very brittle and all failed in the vivo tests. The results prove that parylene insulating/protecting layer makes greatly improvement of the probe mechanical properties. A chronic implantation of the testing silicon probe in rat's brain has been done to test the probe biocompatibility. The animal recovered very well after 7 days. As a common knowledge, rat's dura is a little bit thicker than primates' pia. A successful chronic implantation in monkey's cortex by penetrating monkey's pia is done using a complete device with metal electrodes and flexible parylene cables.

Table 1. Silicon probes rigidity vivo test results

Probe No.	Probe shank length L (mm)	Probe shank base width W (μm)	Probe shank thickness T (μm)	Top parylene layer thickness T1 (μm)	Testing results (penetrating rat's dura)
1	1.0, 1.5	75	150	10	successful
2	6.0, 6.5, 7.0, 7.5, 8.0	75	150	10	failed
3	8.0	100, 120, 140, 160, 180, 200	200	0	failed
4	6.0, 6.5, 7.0, 7.5, 8.0	200, 250	240	10	successful
5	6.0, 6.5, 7.0, 7.5, 8.0	175	100, 120, 140, 160, 180, 200	10	successful
6	6.0, 6.5, 7.0, 7.5, 8.0	150	100, 120, 140, 160, 180, 200	10	successful
7	6.0, 6.5, 7.0, 7.5, 8.0	125	100, 120, 140, 160, 180, 200	10	failed
8	6.0, 6.5, 7.0, 7.5, 8.0	100	100, 120, 140, 160, 180, 200	10	failed

4. Conclusions

The new parylene-embedded MEMS probes are developed, and the mechanical properties are validated by animal tests.

Acknowledgements

We would like to thank Mr. Trevor Roper for assistance with fabrication and the members of the Anderson lab at Caltech for help on vivo tests.

References:

1. S. Musallam, B. D. Corneil, B. Greger, H. Scherberger, R. A. Andersen, *Science* 305, 258 (July 9, 2004, 2004)
2. C. Pang et al., paper presented at the The 27th Annual International Conference of the IEEE Engineering in Medicine and Biology Society (EMBC 2005), Shanghai, China, September 1-4 Sept. 1-4, 2005.
3. E. M. Schmidt, J. S. McIntosh, M. J. Bak, *Med. Biol. Eng. Comput.* 26, 96 (1988 Jan).

FABRICATION OF SILICON NANOWIRE BRIDGE

**Kook-Nyung Lee, Suk-Won Jung, Won-Hyo Kim, Min-Ho Lee,
and Woo-Kyeong Seong**

Nano-mechatronics Research Center, Korea Electronics Technology Institute,
Seongnam-si, Gyeonggi-do, 463-816, Korea
(Email: plumpy@keti.re.kr)

Abstract

We have fabricated silicon nanowire bridges with conventional micromachining process including photolithography, anisotropic etching, and thermal oxidation of silicon substrate. Due to the anisotropic wet etching of (100) single crystalline silicon substrate in KOH solution, uniform and well-defined silicon nanowires were obtained, which had inverted triangular shape cross-section. Our fabrication process enabled us to obtain silicon nanowire bridges as small as 60 nm in diameter and 10 μm in length.

Keywords: silicon nanowire, nanowire bridge, nano bridge, thermal oxidation

1. Introduction

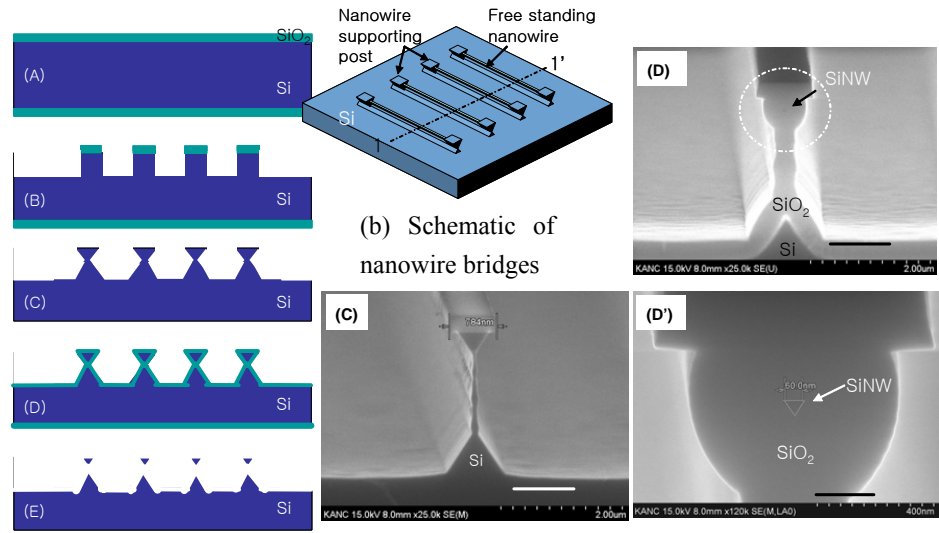
Nanowire has attracted much interest as essential parts for functional electronics devices because of its potential applications in nanoelectronics (1-3) and highly sensitive biosensor (4-5). Although research focused on the fabrication of nanowire using synthesis based bottom-up approach(3) has led to considerable achievements to date, lithography based top-down fabrication (6-7) still needs more works because of economic limitations. Here, we report simple and cost effective fabrication process of silicon nanowire bridges just using conventional micro-machining process.

2. Experimental

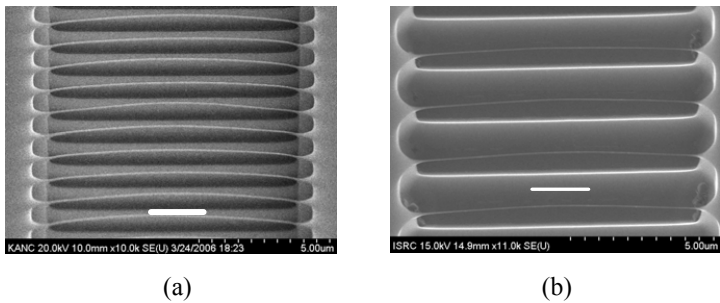
2. 1 Fabrication process

Silicon nanowire was simply fabricated by a conventional micro-machining technology based on photolithography, anisotropic etching, and thermal oxidation process. For overall approach to the fabrication, single crystalline silicon substrate was used with p-type (100)-oriented substrate characterized by 0.01-0.02 Ωcm and 10-30

Ω cm and n-type (100)-oriented substrate. All substrates were 100 mm in diameter (4 inch wafer). Electrical properties of silicon nanowire can be controlled by choosing a silicon substrate with an intended dopant type and concentration. Starting with thermal oxidation of silicon substrate, 0.8 to 1 μ m width lines of oxide layer are defined with a stepper photolithography. Silicon bulk anisotropic etching by deep silicon reactive-ion-etching(DRIE) and potassium hydroxide(KOH) solutions in sequence steps provides inverted triangular shape cross-section of silicon lines supported by narrower silicon pillars as shown in process step (C) in Fig. 1. Since anisotropic wet etching of single crystalline silicon in KOH solutions gives this triangular-like structure determined by (111) etch stop plane of silicon, (110)-oriented silicon lines reach uniform and constant diameter. Thermal oxidation of silicon substrate follows to produce a silicon nanowire with a sub-100 nm diameter near the center of an inverted triangle((D) in Fig. 1), while the supporting silicon pillar becomes completely oxidized. Nanowire becomes free-standing after the surrounding SiO_2 is removed (Fig. 2).



(a) Process flow(1-1') (c) SEM pictures of nanowire at the process step (C) and (D)
 Fig. 1 Fabrication process flow and schematic of silicon nanowire bridges. The scale bar corresponds to 1 μ m and 200 nm in (C and D), and in (D') respectivley, in the SEM pictures.



(a)

(b)

Fig. 2 Silicon nanowire bridges obtained by removing SiO₂. This freestanding nanowire shows uniform shape in diameter and slightly bends up by the beam stress. Nanowire is 10 μm in length and 100 nm and 60 nm in diameter in (a) and (b) respectively. The scale bar corresponds to 2 μm .

3. Results and discussion

Regardless of silicon substrate type, silicon nanowire was successfully obtained as a freestanding bridge, which has sub-100 nm diameter and 10 μm length. The uniform line shape of a released nanowire shows much improvement contrary to that of nanowire obtained by reactive-ion-etching(RIE) based process. Note that every process required to fabricate the nanowire is a very well-known conventional micro-machining process and consequently a well-controlled process can be obtained and a large-scale wafer level process is possible. We expect that the fabricated silicon nanowire bridges have many applications for nanowire based sensors and electronic devices.

References

1. X. Duan, C. Nlu, V. Sahi, J. Chen, J. Parce, S. Empedocles, J. Goldman, *Nature*, 425, 274 (2003)
2. Y. Cui, C. M. Lieber, *Science* 291, 851 (2001).
3. A. M. Morales, C. M. Lieber, *Science* 279, 208 (1998)
4. Y. Cui, Q. Wei, H. Park, C. M. Lieber, *Science* 293, 1289 (2003).
5. G. Zheng, F. Patolsky, Y. Cui, W. U. Wang, C. M. Lieber, *Nature Biotech.*, 23(10) (2005)
6. J. Kedzierski and J. Bokor, *J. Vac. Sci. Technol. B* 15(6), 2825 (1997)
7. O. H. Elibol, D. Morissette, D. Akin, J. P. Denton, and R. Bashira, *App. Phy. Let.*, 83(22), 4613 (2003)

ELECTRONIC DROP SENSING IN MICROFLUIDIC DEVICES USING AIR-LIQUID INTERFACE DETECTION: AUTOMATED OPERATION OF A NANOLITER VISCOMETER

Nimisha Srivastava and Mark A. Burns

Department of Chemical Engineering, University of Michigan Ann Arbor MI

Phone: 925-294-2507 Email: nsrivastava@sandia.gov

Abstract

We describe three droplet sensing techniques: a digital electrode, an analog electrode, and a thermal method. All three techniques use a single layer of metal lines that is easy to micro-fabricate and an electronic signal can be produced using low DC voltages. While the electrode methods utilize changes in electrical conductivity when the air-liquid interface of the droplet passes over a pair of electrodes, the thermal method is based on convective heat loss from a locally heated region. For the electrode method, the analog technique is able to detect 25nL droplets while the digital technique is capable of detecting droplets as small as 100pL. For thermal sensing, temperatures profiles in the range of 36°C and higher were used. Finally we have used the digital electrode method and an array of electrodes located at preset distances to automate the operation of a microfluidic viscometer. The viscometer is completely controlled by a laptop computer, and the total time for operation including setup, calibration, sample addition and viscosity calculation is approximately 4 minutes.

Keywords: electronic, automated, droplet, sensing, viscometer, microfluidics

1. Introduction

Microfluidic devices that utilize discrete droplets as tiny storage containers, mixers and miniaturized batch reactors are increasingly being used to perform complex multiplexed reactions, measurements and assays for chemical and biological applications [1]. A significant part in fully automating these devices is liquid droplet detection techniques that can determine in real time the location and velocity of multiple streams inside microfluidic channels. Since a droplet shares an interface with either air or another liquid at all times, the droplet may be sensed simply by detecting its advancing or receding interface. The ability to sense a liquid droplet by tracking an interface allows a variety of other non-optical detection techniques to be used that require minimal fabrication complexity and do not require derivatization of liquid sample.

2. Experimental

The detailed glass and silicon fabrication and experimental setup is outlined elsewhere [2]. Briefly microfluidic channels were prepared in annealed borosilicate glass using HF wet etching. Electrodes, resistive heaters and resistive temperature

sensors were fabricated on silicon using e-beam evaporation of Au, Ti and Pt followed by lift-off in acetone. A custom designed immersion gold printed circuit board (Advanced Circuits, Aurora, CO) serves as the platform for chip-to-world electrical connections. The diced silicon die is fixed to the PCB and the gold contact pads on the silicon are wire bonded. The glass die is then glued to the wire-bonded silicon die. The automated operation of the droplet sensors and the viscometer is via LabVIEW™ control program (National Instruments).

3. Droplet Sensing Techniques

We present three droplet sensing techniques: a digital electrode, an analog electrode, and a thermal method. A digital method reacts digitally, turning “on” when the air-liquid interface of the droplet passes over the sensor (Fig.1). An analog sensor, in addition to turning “on”, responds as a function of the droplet size (Fig. 2).

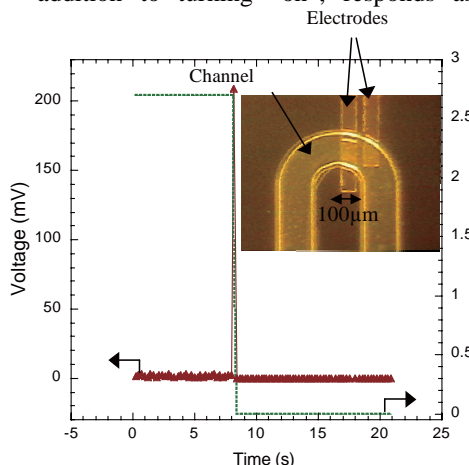


Fig. 1: Digital Electrode Based Droplet sensing. The peak in the voltage occurs when a drop passes over the electrode. The green dotted waveform is the voltage applied to the electrodes. The inset shows a pair of electrode inside a microchannel.

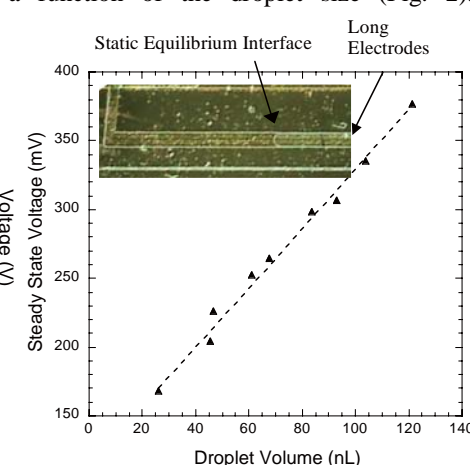


Fig. 2: Analog Electrode Based Droplet Sensing. The steady state voltage response is recorded which varies linearly with the size of the droplet. Inset shows the top view of a microfluidic channel and two long parallel electrodes that run all along the bottom surface of the channel. A drop of water is partly wetting the electrodes in the channel.

In our analog electrode based method, the voltage response from a pair of parallel electrodes indicates the location and volume of the droplet present over the electrodes. Figure 2 shows a device with parallel gold electrodes (400nm thick, 100μm wide and 100μm apart) fabricated along the bottom of a channel. A drop of water displaces air over the electrodes as it moves inside the channel, partially wetting the electrodes. The volume of water droplet over the parallel electrodes is proportional to the steady state response from the electrodes.

In our digital electrode sensing technique (Fig 1), pairs of electrodes are fabricated at pre-determined locations inside the microfluidic channel, and a constant DC signal

(~2.7V) is applied across each pair. The electrodes in each pair are placed close to each other (50 μ m apart) to achieve maximum conductance in the electrical circuit. As the liquid interface passes over the electrodes, a conduction path a non-zero voltage drop (>10mV) is observed (Fig. 1). When this happens, the power to the electrodes is turned off to prevent electrolysis and the time t is recorded. The entire spectrum of times along with the corresponding position of the electrodes provides the exact location of the liquid inside the channel as a function of time. The instant response of the electrodes to the presence of a liquid makes this an excellent method to dynamically track a moving liquid drop and was used to automate the operation of a nanoliter viscometer (Figure 3).



Fig.3: Automated and Portable Viscosity Measurement System. The setup consists of a microfluidic device with digital electrode sensors, external electronics, data acquisition accessories and a laptop computer.

A limitation of the electrode based sensing method is that it may only be used for electrically conductive liquids. The thermal method for liquid detection is based on convective loss of heat when a liquid drop passes over a localized region. The thermal sensor consists of an on-chip resistive heater and a resistive temperature detector (RTD) in close proximity beneath the channel (data not shown, [2]).

5. Conclusions

We have demonstrated several drop sensing methods of which the digital electrode method and an array of electrodes located at preset distances to automate the operation of a previously described microfluidic viscometer. The viscometer is completely controlled by a laptop computer, and the total time for operation including setup, calibration, sample addition and viscosity calculation is approximately 4 minutes. The present system of portable viscosity measurement may now be used as is in several applications including bedside patient monitoring for hyperviscosity syndrome.

Acknowledgements

The authors would like to acknowledge support from NIH through grants P01 HG01984 and R01 AI49541.

References

- [1] J. Atencia and D. J. Beebe. *Nature*, 2005, **437**, 648.
- [2] N Srivastava and M.A Burns, *Lab on a Chip*, 2006, **6**, 744

ELECTROCHEMICAL REAL-TIME PCR

Siu-Wai Yeung, Thomas Ming-Hung Lee and I-Ming Hsing*

Department of Chemical Engineering, The Hong Kong University of Science
and Technology, Hong Kong SAR, China

*Corresponding Author E-mail: kehsing@ust.hk

Abstract

In this work, we report the first electrochemistry-based real-time polymerase chain reaction technique for sequence-specific nucleic acid detection. This new technique builds upon all advantages of the well-established fluorescence-based counterpart such as short assay time (simultaneous target DNA amplification and detection). In addition, this electrochemical approach utilizes simple and miniaturizable instrumentation compared to the bulky and expensive optics required in the fluorescence-based schemes.

Keywords: real-time PCR, electrochemistry, solid-phase extension, ferrocene-dUTP

1. Introduction

The detection of specific deoxyribonucleic acid (DNA) sequences has a pivotal role in applications of medical diagnostics, forensic science, food and environmental monitoring, biodefense and many others. The real-time polymerase chain reaction (PCR) [1], which monitors the fluorescence signal associated with the amplified sequence at each PCR cycle, is now the most sensitive and specific quantitative DNA analysis method. Nevertheless, the bulky and expensive optics involved has confined its utilization in central laboratories. To enable on-the-spot rapid DNA identification, the optical signal transduction scheme would better be replaced by the electrochemical (EC) scheme, which has inherent advantages of simple instrumentation and low-cost. In fact, tremendous efforts have been devoted to EC DNA biosensors during the past decade [2]. Basically, the majority was based on the hybridization of the target sequence to an oligonucleotide capture probe immobilized on an electrode surface, followed by signal transduction with hybridization indicator. This post-amplification detection strategy significantly increases the overall assay time and makes quantitative analysis difficult. Towards the goal of real-time EC PCR, the key is to develop an EC sequence-specific detection methodology that is compatible with PCR and produces a signal proportional to the amount of amplicon. Among all the established indicators, ferrocene (Fc)-based redox marker is one of the most suitable candidates. To date, work has been done on the enzymatic labeling of PCR amplicon with Fc-deoxyuridine triphosphate (dUTP) [3], but real-time monitoring of the amplification process has not been reported yet. Herein, we demonstrate that the solid-phase extension of a capture probe immobilized on an electrode with Fc-dUTP during PCR results in an accumulation of electrochemical signal in the presence of the target template.

2. Experimental

All general chemicals were obtained from Sigma–Aldrich (St. Louis, MO) while PCR reagents were purchased from Invitrogen (Carlsbad, CA), unless otherwise stated. Indium tin oxide (ITO)-coated glass (Delta Technologies, Stillwater, MN) was first immersed in a solution of H₂O₂/NH₄OH/H₂O (1:1:5) at 80 °C for 5 min. Then, it was rinsed with water and dried with nitrogen gas. The hydrolyzed substrate was treated with a 10 % (3-glycidoxypropyl)trimethoxysilane in 95 % ethanol for 1 h. After silanization, the substrate was dried at 50 °C under vacuum. Next, it was incubated with 1 μM of an oligonucleotide probe (5'-NH₂-TTT TTT TTT TTT TTT TTT TTA AGG AAA CAG CTA TGA C-3') in phosphate buffer saline (PBS, 100 mM NaCl/10 mM sodium phosphate, pH 7.0) overnight. Excess probe was washed off with PBS.

The PCR master mix contained 1× ThermoPol reaction buffer (20 mM Tris–HCl, 10 mM (NH₄)₂SO₄, 10 mM KCl, 2 mM MgSO₄, 0.1 % Triton X-100, pH 8.8), 0.2 mM dNTPs (with 0.06 mM dTTP substituted by Fc-dUTP), 0.2 μM forward primer (5'-GTA AAA CGA CGG CCA G-3'), 0.2 μM reverse primer (5'- AAG GAA ACA GCT ATG AC-3'), 0.02 ng/μL M13mp18 template (Sigma), 0.5 μg/μL bovine serum albumin, and 0.02 units/μL Vent_r® (exo-) DNA polymerase (New England BioLabs, Ipswich, MA). The functionalized substrate was dipped into the mixture and subjected to the following thermal cycling profile: initial denaturation at 95 °C for 2 min; 25 cycles at 95 °C for 20 s, at 55 °C for 20 s, 72 °C for 10 s. Note that Fc-dUTP was synthesized according to King and co-workers' protocol [3], with minor modification on the purification procedure to improve the yield. After certain PCR cycles, the ITO-coated glass was removed from the PCR tube and rinsed with water. Finally, differential pulse voltammetric (DPV) measurements were performed using Autolab PGSTAT30 (Eco Chemie, The Netherlands) with a pulse amplitude of 100 mV and scan rate of 25 mV/s. Pt was used as the counter and pseudo-reference electrodes.

3. Results and Discussion

The EC real-time PCR technique is based on the solid-phase extension of the capture probe with Fc-dUTP, as schematically shown in Figure 1. During the PCR denaturation step (95 °C), the double-stranded amplicon is denatured into single-stranded form. At the annealing temperature (55 °C), the amplicon hybridizes with the immobilized extension probe in addition to the solution hybridization between the amplicon and primers. Thereafter, the probe is extended with the incorporation of Fc-dUTP by the polymerase. With this strategy, the redox signal, in proportion to the amount of amplicon, gradually builds up. The most prominent feature is the possibility to directly detect the electrochemical signal of the amplicon cycle-by-cycle. Figure 2 shows the DPV scans of the ITO electrodes after running different PCR cycles. The electrochemical signal from the incorporated Fc increases with the PCR cycle number. Control experiments, which either do not have the template or have nonspecific template, were studied to confirm that the detected electrochemical signal indeed originates from the specific extension of the immobilized probe. A close-to-flat line signal was obtained for the negative control after 25 cycles. It should be noted that, at a starting template amount similar to the optical based real time PCR, the onset spot (i.e.,

the point at which the signal is distinguishable from the baseline) for this EC scheme occurs earlier than that for the optical one (usually at 15 to 20 cycles). This is particularly attractive for ultra-fast DNA identification in point-of-care applications.

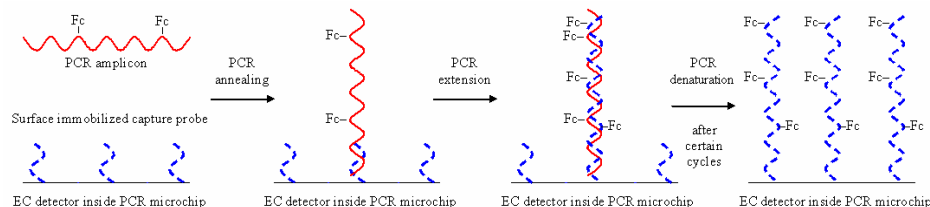


Figure 1. A schematic representation of the solid-phase extension of electrode surface-immobilized oligonucleotide probe for the EC real-time PCR technique.

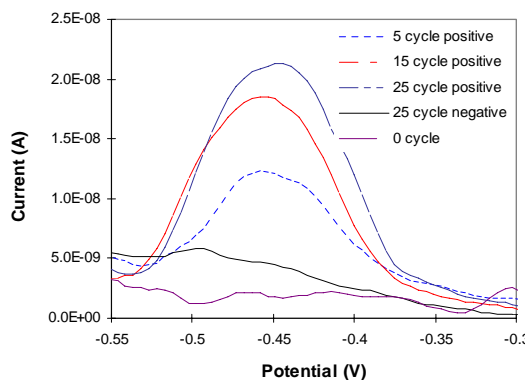


Figure 2. DPV scans showing the ferrocene signal at different PCR cycle numbers.

4. Conclusions

We have demonstrated a proof-of-concept experiment showing the utilization of solid-phase extension of the electrode surface-immobilization capture probe with Fc-dUTP for real-time PCR monitoring. Further work will be carried out to implement this new strategy in our previously developed integrated PCR-EC microdevice.

Acknowledgements

The authors thank the funding support from the Research Grants Council of the Government of Hong Kong Special Administrative Region (RGC Earmarked Grants# 601305).

References

1. T. Dorak, *Real-Time PCR*, Taylor & Francis, (2006).
2. T.G. Drummond, M.G. Hill and Barton J.K., *Nature Biotech.*, 2003, vol. 21, 1192.
3. W.A. Wllassoff and G.C. King, *Nucleic Acids Res.*, 2002, vol. 30, e58.
4. T.M.H. Lee, M.C. Carles and I.M. Hsing, *Lab Chip*, 2003, 3, 100.

ULTRASENSITIVE AND HIGH RESOLUTION UV ABSORBANCE DETECTION OF PROTEINS VIA INTEGRATED POLYMER MICROFLUIDICS

L. Zhu¹, C.S. Lee², and D.L. DeVoe¹

¹Department of Mechanical Engineering and ²Department of Chemistry and Biochemistry, University of Maryland, College Park, MD, USA

Abstract

An integrated UV absorbance detection system employing a novel silicon-in-plastic technology to seamlessly integrate bare UV photodiode chips into polymer microfluidic systems has been developed. Detection platforms fabricated using this approach exhibit exceptionally low mass detection limits down to 9.8 amol and sub-nanoliter detection volumes for bovine serum albumin (BSA) as a model protein.

Keywords: silicon-in-plastic, photodetector, protein, UV absorbance

1. Introduction

UV absorbance detection, widely used in capillary-based electrophoretic separations, enables direct label-free monitoring of peptides or proteins during high-resolution separations. However, UV absorbance detection suffers from low sensitivity in microfluidic systems due to inherently short optical pathlengths. Microfluidic detection cells with longer pathlengths have been reported, but with loss of spatial resolution due to the larger interrogated channel length [1] or limited optical resolution when using integrated detectors [2-4]. Here we report a new approach to seamlessly integrate bare photodetector chips into polymer microfluidics, enabling exceptionally high detection resolution and sensitivity beyond that achieved even in commercial capillary platforms.

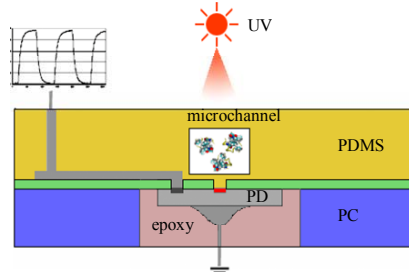


Figure 1. Schematic of the integrated UV absorbance detection system.

2. Fabrication

A schematic of the microfluidic system is shown in Figure 1, and the fabrication process is depicted in Figure 2. Fabrication is based on a previously reported silicon-in-plastic process [5]. Briefly, the photodetector chip is embedded into a polycarbonate substrate using an epoxy layer to level the exposed surface to within 1 μm . Parylene C is deposited as a passivation layer, and Au/Cr traces provide off-chip interconnects. Microchannels of varying dimensions are formed by micromolded PDMS and bonding to the substrate, with the active area of the photodetector aligned to the microchannel.

3. Experimental

A schematic of the experimental setup is shown in Figure 3. Bovine serum albumin (BSA) was used as a model protein. Diluted protein sample and 10 mM Tris buffer were

loaded into two syringe pumps connected to the input reservoir of the microchannel through a capillary T connector and nanoport fitting. A commercial UV detection system (Spectroflow-757) was modified for use as the UV source. Tris and BSA were alternately pumped through the channel for 10 min at a flow rate of 5 $\mu\text{L}/\text{min}$ at BSA concentrations down to 1 $\mu\text{g}/\text{mL}$. All testing was performed at 230 nm excitation in a dark room.

4. Results and discussion

Four devices with different photodetector chip sizes and microchannel dimensions were fabricated and tested. Table 1 summarizes the design parameters, detection volume and detection limit for the four devices. Figure 4 exhibits the time-domain data traces showing normalized changes in measured absorbance for three analyte concentrations (BSA at 100, 10, and 1 $\mu\text{g}/\text{mL}$) using chip design 2. As evident from this figure, BSA can be detected at 1 $\mu\text{g}/\text{mL}$ ($1.5 \times 10^{-8} \text{ M}$) with a signal-to-noise ratio of approximately 3. The results of the BSA dilution measurements for each design are shown in Figure 5. In this figure, the data points are averaged over 3 on/off cycles, with error bars reflecting $\pm 1 \sigma$ for each set of measurements. All designs exhibit good linearity between absorbance and analyte concentration at high concentrations, but with some deviation at lower concentrations.

5. Conclusion

Exceptionally low concentration and mass detection limits were achieved for BSA at 15 nM and 9.8 amol, respectively, with spatial resolution defined by the photodetector active area as low as 25 μm . These individual metrics show 1-2 orders of magnitude improvement over commercially available capillary UV absorbance systems. Further improvements are anticipated through the use of differential signal amplification for background cancellation.

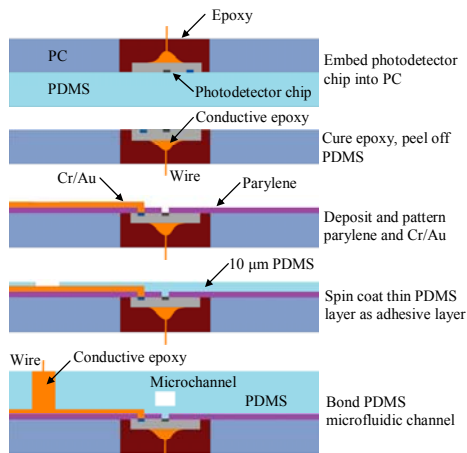


Figure 2. Fabrication process for the microfluidic detection platform.

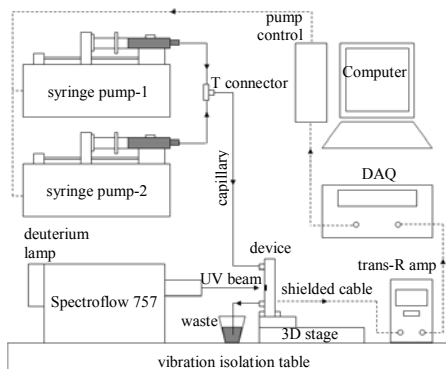


Figure 3. Schematic of the testing apparatus used for data collection.

Table 1. Summary of design parameters and characterization results for four different detection platform designs.

		Design 1	Design 2	Design 3	Design 4
Channel dimension	width	200 μm	500 μm	200 μm	90 μm
	depth	185 μm	400 μm	60 μm	215 μm
Active area of photodetector chip	(160 μm) ²	(70 μm) ²	(70 μm) ²	(25 μm) ²	
	minimum	4.74 nL	1.96 nL	0.29 nL	0.13 nL
Detection volume	maximum	5.92 nL	14.0 nL	0.84 nL	0.48 nL
	concentration	2 $\mu\text{g/mL}$ (30.1 nM)	1 $\mu\text{g/mL}$ (15.2 nM)	15 $\mu\text{g/mL}$ (227.3 nM)	5 $\mu\text{g/mL}$ (75.8 nM)
Limit of Detection BSA @ 230 nm	mass	9.5 – 11.8 pg (144 – 179 amol)	2.0 – 28.0 pg (30 – 212 amol)	4.3 – 12.6 pg (66 – 191 amol)	0.6 – 2.4 pg (9.8 – 36 amol)
	Dynamic range	25,000	50,000	3,300	10,000

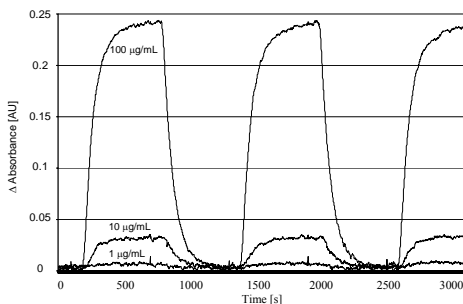


Figure 4. Time-domain data traces showing normalized changes in measured absorbance for three analyte concentrations (BSA at 100, 10, and 1 $\mu\text{g/mL}$) using chip design 2 (see Table 1).

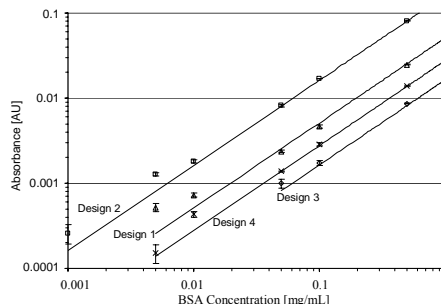


Figure 5. Calibration curves for all tested chip designs. Data points are average absorption measurements performed over at least 3 on/off cycles, with error bars reflecting $\pm 1 \sigma$ for each set of measurements.

References

1. K. Swinney, D. J. Bornhop, *Electrophoresis*, vol. 21, No. 7, pp. 1239-1250, 2000.
2. Z. H. Liang, N. Chiem, G. Ocvirk, T. Tang, K. Fluri and D. J. Harrison, *Analytical Chemistry*, vol. 68, No. 6, pp. 1040-1046, 1996.
3. N. J. Petersen, K. B. Mogensen and J. P. Kutter, *Electrophoresis*, vol. 23, No. 20, pp. 3528-3536, 2002.
4. T. Kamei, B. M. Paegel, J. R. Scherer, A. M. Skelley, R. A. Street and R. A. Mathies, *Analytical Chemistry*, vol. 75, No. 20, pp. 5300-5305, 2003.
5. L. Zhu, D. C. Meier, C. Montgomery, S. Semancik and D. L. DeVoe, in *Micro Total Analysis Systems 2005*, Boston, MA, pp. 482-484, 2005.

Integrating a Molecularly Imprinted TiO₂ Modified Microelectrode in a Microfluidic System for Detection of Nicotine

Chen-Hsun Weng¹, Cheng-Tar Wu², Kuo-Chuan Ho^{2,3} and Gwo-Bin Lee¹

¹Department of Engineering Science, National Cheng Kung University, Tainan, Taiwan

²Department of Chemical Engineering, National Taiwan University, Taipei, Taiwan

³Institute of Polymer Science and Engineering, National Taiwan University, Taipei, Taiwan

E-MAIL: gwobin@mail.ncku.edu.tw

Abstract

This study reports a micro-system capable of sensing nicotine (NIC) using a new combination of microfluidics, electrochemical sensing, and molecularly imprinting polymer (MIP) techniques. The sensing system can detect the concentration of NIC by fabricating NIC-imprinted TiO₂ sites on a microelectrode. The modular design of the sensing systems allows us to integrate a microfluidic control module and an electrochemical sensing module for a sensitive and selective detection of NIC in an automatic format.

Keywords: microfluidics, nicotine, MIP, micropump, LOC

1. Introduction

Nicotine is pyridine derivative alkaloid with fatal toxicity. Over the past two decades, there has been considerable interest in the development of methods for detection of nicotine. Several attempts have been made, including spectrophotometry, reversed high performance liquid chromatograph (HPLC), and potentiometry [1]. However, a compact and cost-effective NIC-sensing system is still in great need. In this study, we utilize the enabling microfluidics and electrochemical sensing techniques to form a NIC-sensing system. The selectivity of the sensing system can be improved by using a MIP film.

2. Design and fabrication

The microfluidic system comprises two zones, namely a microfluid-pumping zone and a NIC detection zone. A pneumatically actuated micropump drives the sample into the detection zone, which houses the NIC-sensing electrodes. In this study, the shape of the microchannel was streamlined in order to reduce the dead volume. This enhancement reduced the response time of the sensing operation and improved the uniformity of the sample flow. The microfluidic control module was fabricated using SU-8 molding and PDMS casting techniques. The working and counter electrodes (Pt) were deposited on a glass substrate by using an electron-beam evaporation process. The reference electrode (Ag) was then deposited on the same glass substrate. The Ag layer was treated using a solution of 1M FeCl₃ to form an AgCl layer. The preparation of modified working electrodes for nicotine detection was preformed by coating the MIP-TiO₂. Thus, the NIC imprinted TiO₂ modified electrode (Pt/TiO₂ [NIC]) can be used for NIC detection. The analyte, NIC, was

incorporated into the TiO_2 matrix and coated on a Pt electrode. The imprinting sites were created by sintering at 500 °C.

As shown in Fig. 1, three layers of PDMS and a glass substrate with the sensing electrodes can be modularly integrated for NIC sensing. A microfluidic chip comprising microchannels, a micropump, a microvalve was integrated with the electrochemical sensing electrodes which can specifically detect NIC by using the MIP technique. The pneumatic micropump was used to transport a precise amount of samples to the sensing electrodes [2]. Figure 2(a) shows the sensing electrodes located underneath the microfluidic control module. The dimensions of the chip are measured to be 5.5 cm x 2.5 cm. Figure 2(c) shows the three sensing electrodes patterned on a glass substrate with a dimension of 0.5 cm X 0.6 cm. The PDMS microfluidic control module and the electrochemical sensing module were then bonded together using an oxygen plasma treatment.

3. Results and discussion

In this study, a hand-held controller composed of a control circuit, three electromagnetic valve (EMV) switches and an air compressor was assembled to modulate the NIC sensing system. The compressed air can be injected into air channels to activate peristaltic micropumps. The pumping rate increases with the driving frequency and the applied air pressure as shown in Fig. 3. NIC was then electrochemically detected on a modified electrode made by the MIP technique. Amperometric detection of NIC was achieved by electropolymerizing a conducting polymer, poly(3,4-ethylenedioxythiophene) (PEDOT), on the electrodes. The sensing potential for a NIC-imprinted Pt electrode ($\text{Pt}/\text{TiO}_2[\text{NIC}]/\text{PEDOT}$) was 0.86 V (vs. Ag/AgCl/saturated KCl), as judged by the polarization curve as shown in Fig. 4.

Figure 5 shows a steady-state oxidation current response of NIC at 0.86 V at each concentration level varying from 0 to 5 mM. The linear detection ranged from 0 to 5 mM, with a sensitivity of $41.89 \mu\text{A}/\text{mM}\cdot\text{cm}^2$ and a detection limit of $1.8 \mu\text{M}$, respectively. Non-imprinted electrodes were also tested for comparison. To investigate the selectivity of the developed method, cotinine (COT) and glucose (Glu) were chosen as the interferences due to similar chemical structures (Fig. 6b). The corresponding current responses of NIC and its interferences were shown in Fig. 6(a). Experimental data show that the developed system can successfully detect NIC concentration with a high sensitivity and selectivity.

4. Conclusions

We reported a microfluidic device for nicotine sensing by using a new combination of microfluidics, electrochemical sensing, and MIP techniques. The detection system was integrated with a micropump which can continuously drive fluids into the NIC sensing zone. The developed device can successfully measure the concentration of nicotine with a sensitivity of $41.89 \mu\text{A}/\text{mM}\cdot\text{cm}^2$ and a detection limit of $1.8 \mu\text{M}$.

References:

1. K. Haupt, K. Mosbach, Vol.100, Chem. Rev., pp.2495-2504 (2000).
2. C. H. Wang, G. B. Lee, Vol.21, Biosens. Bioelectron., pp.419-425 (2005).

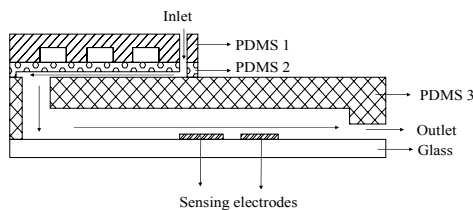


Fig.1 Schematic diagram of cross-sectional view of the modular detection system.

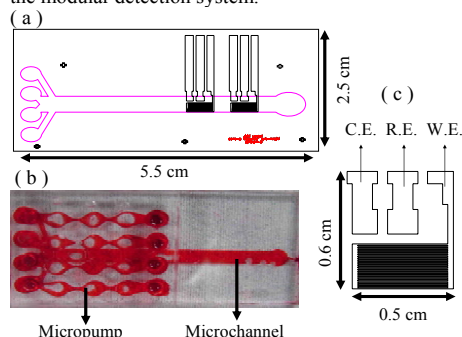


Fig.2 (a) Schematic diagram of microchannels with microelectrodes (top view). (b) A photograph of the microfluidic device. (c) The sensing microelectrodes comprising a counter electrode (Pt), a working electrode (Pt) and a reference electrode (AgCl/Ag).

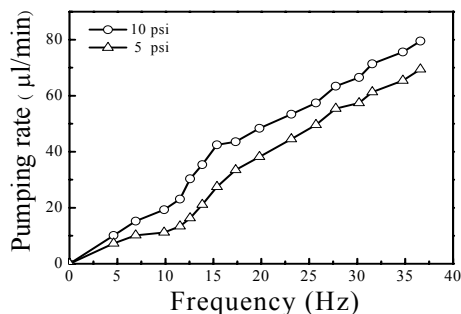


Fig.3 The maximum pumping rate is measured to be 79.5 $\mu\text{l}/\text{min}$ at a pressure of 10 psi and a driving frequency of 36 Hz.

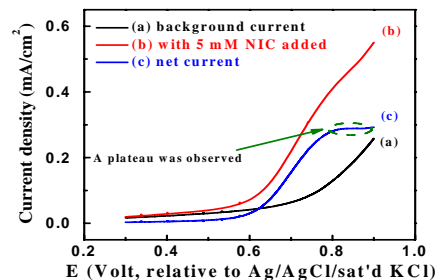


Fig.4 The polarization curve for the oxidation of NIC on the Pt/TiO₂[NIC]/PEDOT electrode. The scan rate is 1 mV/sec in 0.1 M KCl containing PBS solution (pH = 7.4).

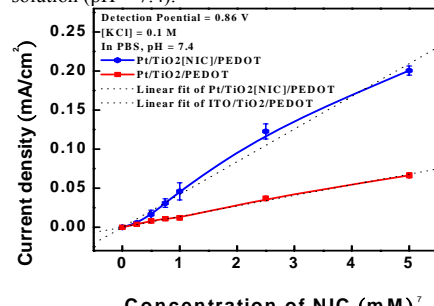


Fig.5 The calibration curves for the NIC-imprinted electrodes. Line (A): sensitivity is 0.042 $\text{mA}/(\text{mM} \cdot \text{cm}^2)$, Line (B): sensitivity is 0.014 $\text{mA}/(\text{mM} \cdot \text{cm}^2)$.

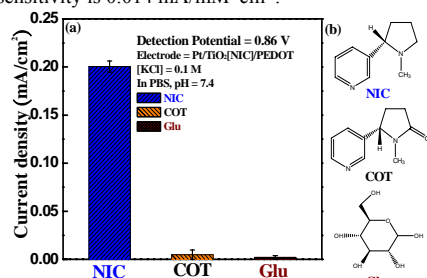


Fig.6 The interference effect. (a) The current densities of NIC, COT and Glu. (b) The chemical structures of NIC and its interferents.

MONOLITHICALLY INTEGRATED DYE-DOPED PDMS OPTICAL FILTERS FOR DISPOSABLE ON-CHIP FLUORESCENCE DETECTION

Oliver Hofmann¹, Xuhua Wang^{1,2}, Alastair Cornwell², Stephen Beecher², Amal Raja³, Donal D.C. Bradley², John C. deMello³ and Andrew J. deMello³

¹Molecular Vision Ltd., Bioincubator Unit, Bessemer Building,
Prince Consort Road, London SW7 2BP, United Kingdom

² Physics Department and ³Chemistry Department, Imperial College London,
Exhibition Road, London SW7 2AZ, United Kingdom

Abstract

We report on the fabrication of novel dye-doped PDMS microfluidic layers which concurrently serve as optical long-pass filters for on-chip fluorescence detection. In contrast to using discrete optical filters, doping of the microfluidic substrate presents a low-cost alternative affording high efficiency collection of the fluorescence signal.

Keywords: Fluorescence detection, integration, PDMS doping, optical filters

1. Introduction

On-chip fluorescence detection in a co-linear or “head-on” geometry often suffers from saturation of the detector with excitation light, masking any weak fluorescence signals. Typically long-pass filters are employed which selectively block out the lower wavelength excitation light while transmitting high wavelength fluorescence from the analyte (Figure 1).

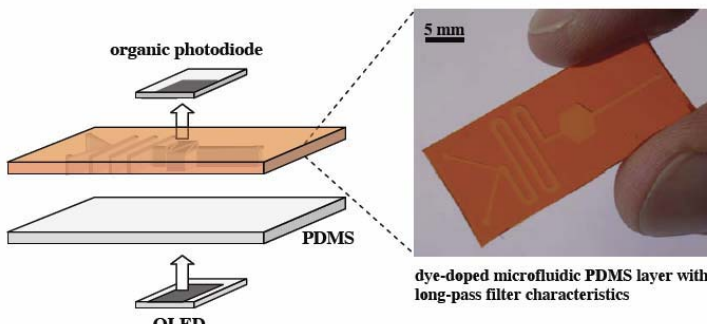


Figure 1 Schematic of monolithic optical long-pass filter use. In a co-linear detection geometry the excitation source and detector are positioned below and above the assembled microchip.

While the use of integrated interference and CdS filters has been reported [1], such filters are expensive and unsuitable for conformable elastomeric materials such as PDMS, a preferred substrate for low-cost disposable applications. We have overcome

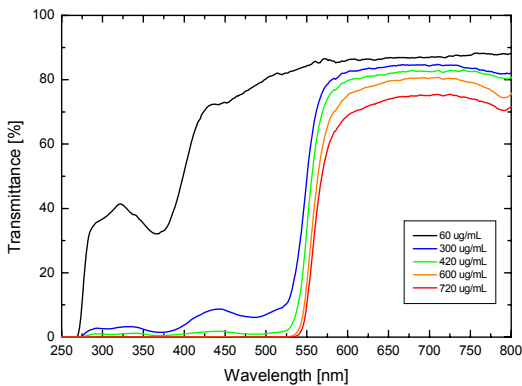


Figure 2 Transmission characteristics for Sudan II doped PDMS microfluidic layers.

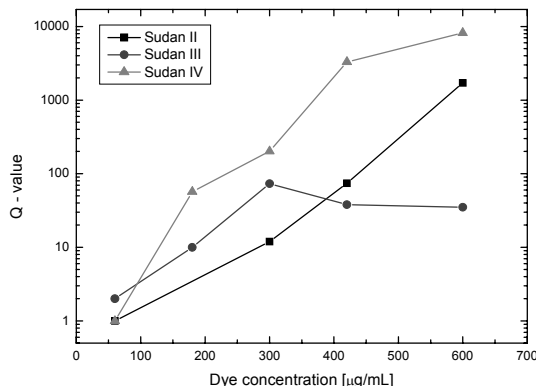


Figure 3 Attenuation factors Q for PDMS microfluidic layers doped with Sudan dyes.

layers doped with 1.2 mg/mL Sudan II, transmission values <0.01% at 500 nm and >80% at 570 nm were obtained, corresponding to an attenuation factor of ~10,000 or a potential sensitivity gain of 4 orders of magnitude (Figure 3). The performance of the long-pass filter in a co-linear detection geometry is illustrated in Figure 4. While 500 nm light is efficiently blocked, 600 nm light is transmitted at levels similar to undoped PDMS. The upper plot shows that for 500 nm excitation there is no detectable signal over the entire range, demonstrating both effective blocking and low auto-fluorescence. More rigorous tests with laser excitation and an integration sphere revealed auto-fluorescence levels below that of commercially available Schott-glass filters [2].

Furthermore the dye doped PDMS filters proved stable when exposed to polar solvents such as water and ethanol, indicating minimal dye leaching, while exposure to

this bottleneck by pre-polymerisation doping of PDMS with lysochrome dyes dissolved in small volumes of toluene [2].

2. Experimental

To fabricate the dye-doped PDMS microfluidic layers up to 30 mg of apolar Sudan II, III and IV dyes were dissolved in 1 mL toluene and then added to premixed PDMS monomer and hardener. After careful mixing the PDMS was poured over an SU-8 master comprising the micro-channel patterning and then cured at room temperature. The maximum dye load that could be incorporated without noticeable dye aggregation was 1.2 mg/mL with the toluene content kept below 10v/v-%.

3. Results and discussion

Out of the three tested dyes, Sudan II doping yielded best results with a sharp roll-on between low wavelength blocking and high wavelength transmission (Figure 2). The cut-on point was ~550 nm with a transitional region of ~50 nm. For 1-mm-thin PDMS

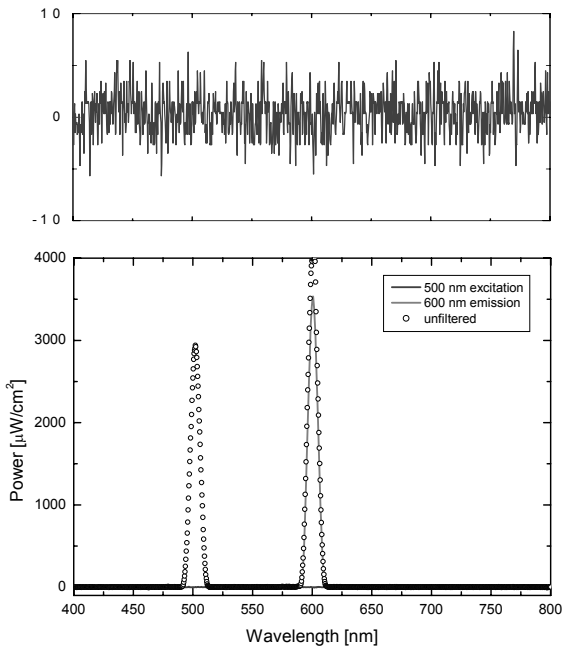


Figure 4 Co-linear detection with 1-mm-thin OD 4 Sudan II filter. The lower plot indicates that the 500 nm light is strongly attenuated while the 600 nm transmission is comparable to undoped PDMS. Top plot shows low light levels for 500 nm excitation.

UV and Ar Ion laser light resulted in only negligible changes, indicating good photostability. Favourable PDMS bulk properties such as elasticity, wettability and bonding characteristics were also retained.

4. Conclusions

In summary we have demonstrated excellent long-pass filter performance for the dye doped PDMS layers. Work is ongoing to extend the range of available long-pass filters into the blue and green spectrum to match commonly used light sources and fluorophores. In our efforts to develop disposable fluorescence detection systems for point-of-care diagnostics, we are also trying to fabricate short-pass filters to sharpen the output of integrated OLED light sources [3].

Acknowledgements

The Imperial College authors thank the UK Engineering and Physical Sciences Research Council (GR/R58949) and Molecular Vision Ltd. for funding this work. Molecular Vision Ltd. acknowledges support from the UK Biotechnology and Biological Sciences Research Council through its Small Business Research Initiative (grant 147/SBRI 19689).

5. References

1. J.R. Webster, M.A. Burns, D.T. Burke, C.H. Mastrangelo, *Anal. Chem.* 2001, 73, 1622.
2. O. Hofmann, X.H. Wang, A. Cornwell, S. Beecher, A. Raja, D.D.C. Bradley, A. J. deMello, J.C. deMello, *Lab Chip* 2006, 6, 981.
3. O. Hofmann, X.H. Wang, J.C. deMello, D.D.C. Bradley, A.J. deMello, *LabChip* 2005, 5, 863.

MICROFLUIDIC DATA ACUSITION FOR DIGITAL QUANTIFICATION USING AMPLIFIED SINGLE MOLECULE DETECTION

Jonas Melin^{1,2}, Jonas Jarvius¹, Jenny Göransson¹, Johan Stenberg¹,
Fredrik Nikolajeff² and Mats Nilsson^{1§}

¹Dept. of Genetics and Pathology, Uppsala University, Sweden.

²Dept. of Engineering Sciences, Uppsala University, Sweden.

[§]To whom correspondence should be addressed.

E-mail: mats.nilsson@genpat.uu.se

Abstract

Amplified single-molecule detection constitutes a scheme for biomolecule enumeration by transforming specific molecular recognition events at nanometer dimensions to optically detectable micrometer-sized DNA macromolecules. Unlike traditional ensemble average measurements, our detection approach preserves the discrete nature of the molecular population. At flow rates higher than 3 $\mu\text{l}/\text{min}$ confocal data acquisition results in a precision limited by Poisson counting statistics.

Keywords: single molecule detection, confocal detection

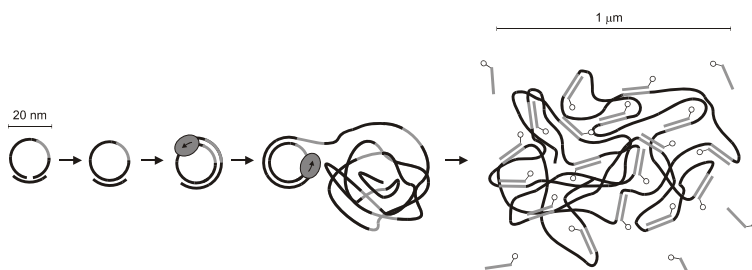


Figure 1. Principal mechanism for amplified single molecule detection.

1. Introduction

We have recently presented a method for amplified single-molecule detection [1]. The formation of one DNA circle as a result of recognition of one target is the first step in the digital signal transmission chain. This is achieved by a highly specific molecular probing reaction, employing so-called padlock probes. Padlock probes are linear synthetic DNA molecules that become circularized through enzymatic ligation upon identification of specific DNA targets [2]. Subsequently, each circular DNA molecule is copied using

rolling circle amplification (RCA), resulting in the creation of one rolling circle product (RCP) for each recognized target (figure 1). A fluorescently labeled DNA oligonucleotide is hybridized to the repeated sequence of the RCP generating a confined cluster of about 1000 fluorophores. These clusters are visible as bright objects with a diameter of approximately 1 μm when observed by fluorescence microscopy. The number of recognized targets can thus be quantified by counting these objects. RCP enumeration is achieved by pumping the liquid through a microchannel observed by line scanning confocal fluorescence microscopy across the channel. In this study we have investigated the influence of flow rate during confocal data acquisition.

2. Experimental

Polymer microfluidic chips were produced by high-throughput injection molding in combination with a scalable bonding process [3]. DNA circles were created by enzymatic ligation of padlock probes and RCA were performed by phi 29 DNA polymerase as described in [1]. The labeled RCP solution was pumped through the microchannel (200x40 μm cross section) at various flow rates. Data was acquired by operating a confocal microscope (LSM 5 META, Zeiss, Germany) in line-scanning mode with the scanning path perpendicular to the direction of liquid flow.

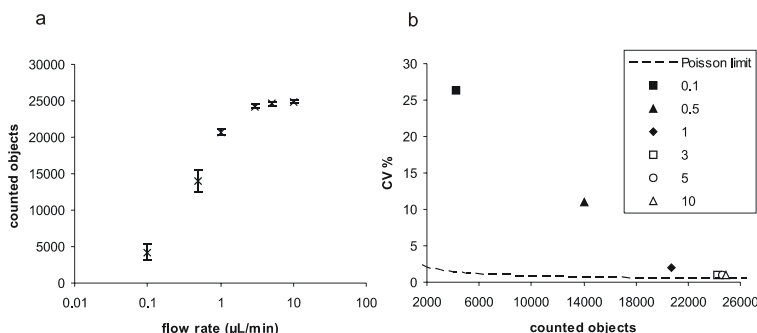


Figure 2. **a)** Counted objects as a function of flow rate using scanning confocal readout. **b)** The coefficient of variance (CV) calculated from the standard deviations in **a** are compared to the CV predicted by Poisson statistics.

3. Results and discussion

Within certain limits confocal readout is insensitive to flow rate variations (figure 2a). When acquiring data at a relatively high flow rate, around 10 $\mu\text{l}/\text{min}$ (figure 3a), consecutive scan lines are separated as a result of the liquid flow. Due to the parabolic flow profile the separation is larger in the central part of the flowchannel, compared to close the edges. The sampled volume are defined by the number of confocal volumes sampled, i.e.

the number of pixels in the rawdata file. If the flow rate is decreased to 3 $\mu\text{l}/\text{min}$ (figure 3b) this regime is still dominating, but the data contributing fraction of the volume passing the detector increases. Moderate variations in flow rate will thus not affect the sampled volume and consequently the number of detected objects, which explains the plateau in figure 2a. However, if the flow rate is substantially lowered below 3 $\mu\text{L}/\text{min}$ the laser will hit each object several times, since the distance between consecutive scan lines will be smaller than the object diameter (figure 3c) and the number of laser hits per object is dependent on the flow rate. The number of detected objects is therefore highly dependent on flow rate as shown for 0.1-3 $\mu\text{l}/\text{min}$ in figure 2a. When the sampled volume is defined by the confocal volume the precision is limited by Poisson statistics (3-10 $\mu\text{l}/\text{min}$ in figure 2b). Whereas when the sampled volume is flow limited (0.1-1 $\mu\text{l}/\text{min}$ in figure 2b) flow rate variations are likely to be the limiting factor of the overall precision, since the number of detected objects are highly dependent on the flow rate in this regime.

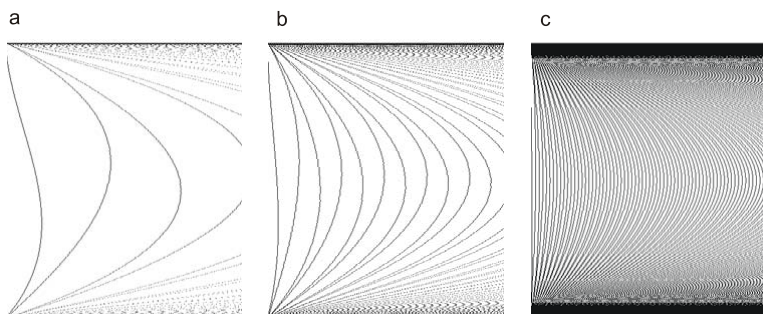


Figure 3. Line scan simulations of the liquid passing the laser at different flow rates. The part of the liquid hit by the laser is shown in black. **a)** 10 $\mu\text{l}/\text{min}$ **b)** 3 $\mu\text{l}/\text{min}$ **c)** 0.5 $\mu\text{l}/\text{min}$

4. Conclusions

The precision of the confocal readout format is limited by Poisson counting statistics if the flow rate is above 3 $\mu\text{l}/\text{min}$. In this regime the sampled volume is defined by the confocal optics ensuring that the same volume is sampled in each replicate. Below 3 $\mu\text{l}/\text{min}$ flow rate variations are likely to be the limiting factor for precision.

References

1. Jarvius, J. et al. *Nat. Methods* **3** (2006).
2. Nilsson, M. et al. *Science* **265**, 2085-2088 (1994).
3. Melin, J. et al. *Anal. Chem.* **77**, 7122-7130 (2005).

FABRICATION OF LIQUID CORE WAVEGUIDE ANALYTICAL CHIPS USING TEFLON AF AND THEIR ANALYTICAL FEATURES

Hiroki Hotta,¹ Hiromi Takiguchi,¹ Tamao Odake,¹
Tomonari Umemura,² and Kin-ichi Tsunoda¹

¹Department of Chemistry, Gunma University, Japan

²Department of Applied Chemistry, Nagoya University, Japan
(tsunoda@chem.gunma-u.ac.jp)

Abstract

We have successfully constructed a liquid core waveguide (LCW) analytical chip made from amorphous fluorinated polymer, Teflon AF-1600. The polymer has lower refractive index (1.31) than water, and therefore, LCW with an aqueous solution as a core could be formed using it as a clad material. We applied the chip to the flow colorimetric analysis of nitrite ion using the Griess-Saltzman reaction. Sensitivity improvement could be obtained by the extension of optical path-length of the LCW. The lower limit of detection for nitrite was ca. 20 ng dm⁻³. Sensitive and convenient colorimetric detection system could be achieved by using this LCW chip.

Keywords: Liquid Core Waveguide, Teflon AF, Nitrite Ion, Griess-Saltzman Reaction

1. Introduction

The sensitivity of absorbance spectroscopy can be improved by extending optical path-length using a liquid core waveguide (LCW), where a tubing cell as clad is filled with the solution which has a higher refractive index than that of the cell material. Recently, amorphous fluorinated polymer series, Teflon AF, which have lower refractive indices (1.29 ~ 1.31) than that of water (1.333), have been developed and an LCW with an aqueous solution as a core can be formed using the polymer. Long path-length analytical cells with Teflon AF tubing have been reported in spectrophotometric measurements [1,2]. The LCW technique has also been applied to μ -TAS chips to overcome the lower sensitivity of conventional optical detections due to their shorter path-length. Datta et al. preliminarily reported that the channels in a silicon microchip, whose walls were covered with Teflon AF, worked as LCWs and could be used to enhance the absorbance signals [3]. Recently, we also constructed a microchip fabricated by a quartz glass substrate whose inner surface was coated with Teflon AF-2400 (50 μ m thick). The sensitivity improvement in the absorbance, which was proportional to its path-lengths (30 mm), could be observed by the flow analysis of bromothymol blue (BTB) aqueous solution. However, a bonded surface between the quartz glass and Teflon AF film was separated when concentrated alkaline solution was

used as a sample. Therefore, in this study, we tried to fabricate a chip made from only Teflon AF, and apply the chip to the flow colorimetric analysis of nitrite ion.

2. Chip Design and Experimental Setup

Figure 1 shows the analytical chip made from only Teflon AF-1600, and its cross-sectional view is shown in Figure 2. A channel was mechanically carved in the Teflon AF sheet of 1 mm thickness, and then, the sheet was covered with another Teflon AF sheet (0.5 mm thick) by heat-sealing. The LCW was designed a half-circled shaped having 44 mm long, and optical fibers were attached to the channel to couple and out-couple with a source light. This chip was applied to the colorimetric detection of nitrite ion which could be detected colorimetrically as a colored azo dye product (λ_{max} : 545 nm) by using Griess-Saltzman reaction. Figure 3 shows the schematic diagram of the measurement system. A source light (He-Ne Laser: 543 nm) was introduced into the LCW, and the absorbance was monitored by using a photodiode detector. Saltzman reagent (1% sulfanilamide and 0.1% N-(1-naphthyl)ethylenediamine were dissolved in 10 % HCl aqueous solution) and a carrier solution (pure water) were flowed from pump A and B, respectively, and sample solutions were injected from the 6-way valve injector with a 50 μL sample loop. The reaction mixture was flowed into the LCW detector after flowing the reaction coil with 128 mm-long.

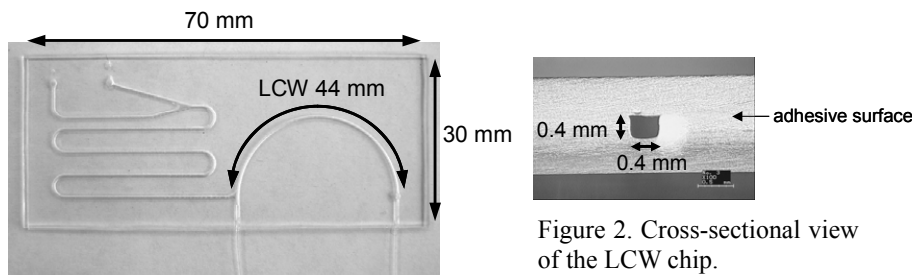


Figure 1. Teflon AF-1600 LCW analytical chip.

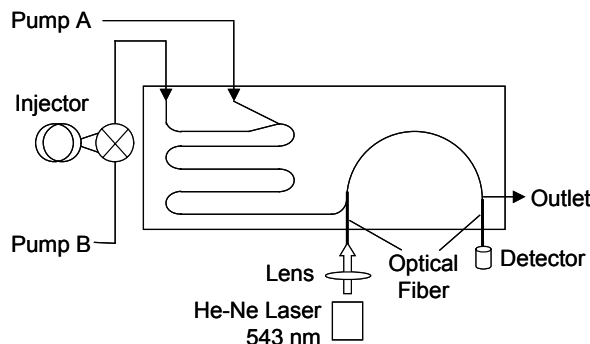


Figure 3. Schematic diagram of the measurement system.

3. Results and discussion

At first, a BTB aqueous solution was continuously flowed as a standard in order to verify the formation of the LCW. The increase of the absorbance proportional to the BTB concentration could be observed. This chip exhibited higher sensitivity than that expected from its path-length, i.e., 7.6 times higher than that with 10 mm cell. In the case of the colorimetric detection of nitrite ion, a sample solution was injected into the system through valve injector. Well-defined peaks proportional to the concentration of nitrite could be obtained as shown in Figure 4. These peak heights were increased with decreasing the flow rate, because the reaction coil (128 mm) was not long enough to complete the reaction. The calibration curve was linear up to 1000 mg dm^{-3} at 0.1 mL min^{-1} , and under the slower flow rate ($0.025 \text{ mL min}^{-1}$), the lower limit of detection could be obtained ca. 20 ng dm^{-3} for nitrite. This chip showed high durability for the acid, alkaline, and organic solvents. Sensitive and convenient colorimetric detection system could be achieved by using this Teflon AF chip.

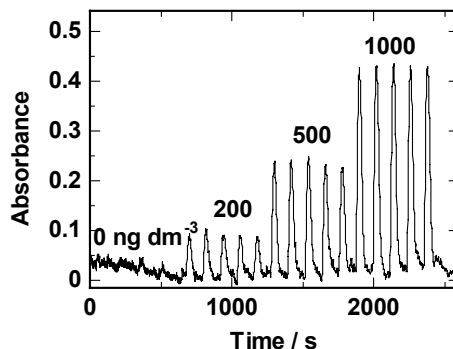


Figure 4. FIA chart of the colorimetric detection of nitrite ion. Flow rate: 0.1 mL min^{-1} .

References

1. H. Takiguchi, A. Tsubata, M. Miyata, T. Odake, H. Hotta, T. Umemura, and K. Tsunoda, *Anal. Sci.*, 2006, 22, 1017-1019.
2. R. D. Waterbury, W. Yao, and R. H. Byrne, *Anal. Chim. Acta*, 1997, 357, 99-102.
3. A. Datta, I.-Y. Eom, A. Dhar, P. Kuban, R. Manor, I. Ahmad, S. Gangopadhyay, T. Dallas, M. Holtz, H. Temkin, and P. K. Dasgupta, *IEEE Sens. J.*, 2003, 3, 788-795.

INTEGRATED ELECTROCHEMICAL SENSOR ARRAY FOR ON-LINE MONITORING OF YEAST FERMENTATIONS

E.E. Krommenhoek¹, J.G.E. Gardeniers¹, J.G. Bomer¹, A. Van den Berg¹, X. Li², M. Ottens², L.A.M. van der Wielen², G.W.K. van Dedem², M. Van Leeuwen², W.M. van Gulik², J.J. Heijnen²

¹MESA+ Institute for Nanotechnology, University of Twente, P.O. Box 217,
7500AE Enschede, The Netherlands

²Department of Biotechnology, Delft University of Technology, The Netherlands

Abstract

This paper describes the design, modelling and experimental characterization of an electrochemical sensor array for on-line monitoring of fermentor conditions in a miniaturized cell assay. The sensor array is capable of monitoring viable yeast concentration, dissolved oxygen concentration, pH and temperature.

keywords: **electrochemical sensors, impedance spectroscopy, ultramicro electrodes**

1. Introduction

In modern biotechnology, there is a strong demand for rapid screening of micro-organisms on the small scale [1, 2]. This work describes the development of an integrated sensor array suitable for application in parallelized micro bioreactors. The micro sensors are suitable for the detection of biomass, dissolved oxygen, pH and temperature. An electrochemical approach was chosen as electrochemical sensors are scalable, integratable, autoclavable and cheap when fabricated at high volumes. The sensor array has the same footprint as a 96-well micro titer plate.

2. Theory

Viable yeast concentration is determined from dielectric spectroscopy. For cells in an AC electrical field, interfacial polarization of the cell membrane occurs. If the signal frequency exceeds a so-called characteristic frequency, dielectric dispersion occurs. Therefore, the permittivity of the cell suspension decreases and its conductivity increases [3]. For a miniaturized electrode configuration with a high cell constant, the capacitance between the electrodes is very small and determination of the conductivity is preferable. The increase in conductivity is a measure for the biomass concentration.

The dissolved oxygen measurement is based on amperometric detection of oxygen reduction. The concentration gradient near the electrode at which oxygen is reduced is expressed by the Cottrell equation and states that the profile is in equilibrium within a few ms. and independent of convection for ultra micro electrodes (radius < 2.5 μm). Finite element simulations show the minimum electrode spacing required to prevent diffusion field overlap. The value is further reduced by recessing the electrodes (Fig. 1).

pH is measured with an ISFET, a FET-based device with a reference electrode in solution acting as gate contact. Site-binding processes at the oxide surface lead to a pH-

dependent threshold voltage. A platinum strip with a nominal resistance of 500 Ohm is included for temperature measurements.

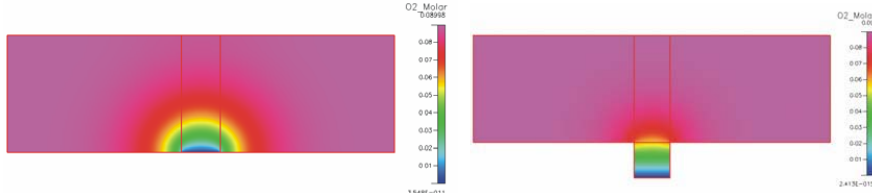


Figure 1: Finite element simulations of oxygen concentration near electrode. Left: electrode on flat surface; right: electrode recessed

3. Experimental

The sensors were fabricated on an oxidized silicon substrate using conventional microelectronic fabrication techniques. Doped ISFET drain-and source regions were defined using standard photolithographic processes and by deposition and oxidization of tantalum. Aluminum was used for metallization of the ISFETs. A lift-off process was used for deposition of the Ta/Pt structures for the other sensors. A photostructured layer of polyimide creates recessed arrays of ultra micro electrodes with a radius of 2 μm and isolates insensitive parts of the chip. Before post-exposure baking the polyimide, the devices were placed in oxygen plasma for 10 seconds to roughen the polyimide surface and thereby improve the adhesion of the Hysol® used to mount the devices on a PCB and to protect the bondwires. Microscope pictures of the sensor array and the ultra micro electrodes can be found in figures 2 a and b, respectively.

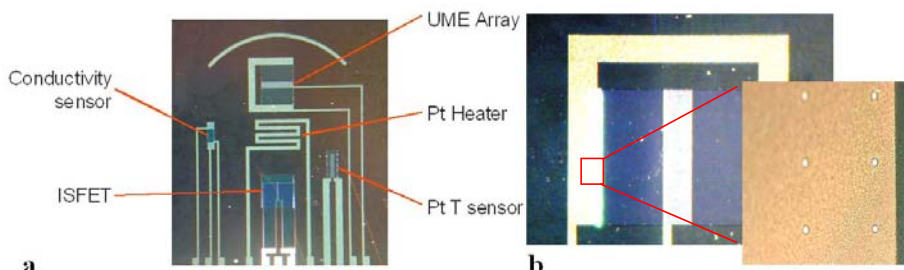


Figure 2: Microscope pictures of (a) sensor array and (b) dissolved oxygen sensor

4. Results and discussion

Measurements showed that the conductivity of a *S. cerevisiae* cell suspension increases for frequencies above 1 MHz (Fig. 3a). The increase scales linearly with the biomass concentration for yeast suspensions with different dilutions (Fig. 3b). Experimental results obtained in a supernatant solution showed that the current through the ultra micro electrode array scales linearly with the dissolved oxygen concentration with high selectivity when the electrode array is properly polarized. The flow dependence is negligible compared to that of a platinum macro electrode (Fig. 4).

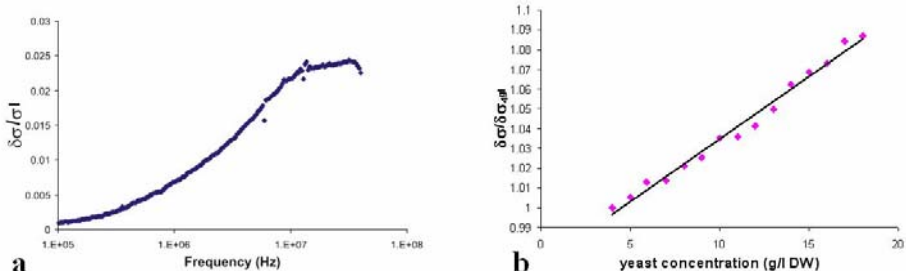


Figure 3: Conductivity variation versus (a) frequency and (b) biomass concentration

ISFET sensitivity equals -58 mV/pH unit. ISFET drift was reduced to 0.002 pH/hr by measuring differentially between an ISFET in a constant pH-environment and an ISFET exposed to pH-changes.

Characterization of the temperature sensor shows the resistance of the platinum strip increases linearly with temperature in the range of 20 – 45 °C with 0.22%/°C sensitivity.

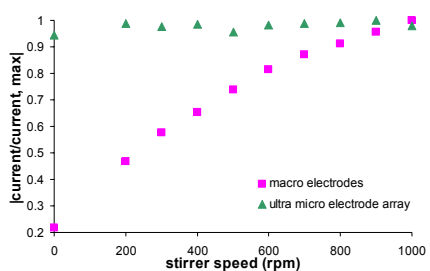


Figure 4: Flow dependence

5. Conclusion

This study shows the design, modelling and experimental characterization of an electrochemical sensor array suitable for on-line monitoring of the most relevant fermentor conditions, i.e. biomass concentration, dissolved oxygen concentration, pH and temperature. The sensors are fabricated using standard cleanroom processes. Experiments show that all sensors are sufficiently sensitive in the desired range.

Future work aims at integration of the sensor arrays in micro fermentors. The sensors will be operated sequentially in order to prevent crosstalk.

Acknowledgements

This work is funded by ACTS, which is part of the Dutch Research Council (NWO), DSM Anti-Infectives BV, Diosynth and Applikon BV.

References

1. Z. Zhang, N. Szita, P. Boccazz, A.J. Sinskey, K.F. Jensen, *A well-mixed, polymer based microbioreactor with integrated optical measurements*, Biotechnology and Bioengineering 93 (2), pp. 286-296, (2006).
2. M.M. Maharbiz, W.J. Holtz, R.T. Howe, J.D. Keasling, *Microbioreactor arrays with parametric control for high-throughput experimentation*, Biotechnology and Bioengineering 85 (4), pp. 376-381, (2004).
3. K. Asami and T. Yonezawa, *Dielectric behaviour of non-spherical cells in culture*, Biochimica et Biophysica Acta 1245, pp. 99-105, (1995).

INTEGRATED POLYDIMETHYLSILOXANE WAVEGUIDE FOR OPTICAL DETECTION

Jack Sheng Kee¹, Daniel Puiu Poenar², Levent Yobas¹

¹Institute of Microelectronics, Singapore

²Microelectronics Center, EEE School, Nanyang Technological University,
Singapore

(leventy@ime.a-star.edu.sg)

Abstract

A microsystem has been realized in poly(dimethylsiloxane) (PDMS) comprising a waveguide integrated with a microfluidic channel. The successful usage of the integrated PDMS chip was demonstrated for absorbance and fluorescence detection.

Keywords: Optical Detection, Polydimethylsiloxane, Waveguide

1. Introduction

Integration of various optical components in PDMS-based microfluidics provides a robust and disposable lab-on-a-chip while retaining the quality of optical detection [1]. Previously, both SU-8 based waveguide [2] and square-hollow PDMS waveguide [3] have been demonstrated for absorbance detection, while monolithic PDMS waveguide system has been shown to possess excellent optical properties [4]. Here, we demonstrate the integration of a square PDMS waveguide –with no additional cladding - with a microfluidic channel for absorbance and/or fluorescence detection.

2. Experimental

A PDMS waveguide with a cross sectional area of $150\mu\text{m} \times 125\mu\text{m}$ has been integrated orthogonally to a microfluidic channel of width $250\mu\text{m}$ using soft lithography. The channel was enclosed with a PDMS cover layer bonded using oxygen plasma treatment. The setup for absorbance and fluorescence measurements from the integrated microsystem is schematically described in Figure 1. The light source was a 5mm^2 blue (475nm) light emitting diode (LED). The intensity attenuation of transmitted light through the waveguide was investigated, including the case where an orthogonal misalignment was introduced in the LED position relative to the waveguide axis of symmetry. For absorbance measurements, a bandpass filter centered at 475 nm was used to ensure that the CCD receives no fluorescence emission. For fluorescence detection, a bandpass filter centered at 535nm was used to reduce background noise and the LED's light. The results from both detection methods were compared with those from a commercial plate reader (Perkin Elmer Victor 3) in absorbance mode (490nm) and in fluorometry mode (excitation at 485 nm and detection at 535 nm).

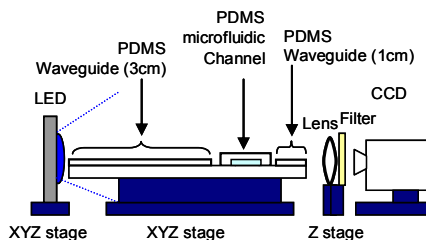


Figure 1. Experimental setup for the PDMS-based optofluidic microsystem

3. Results and discussion

The intensity attenuation of the PDMS waveguide was measured to be 0.047dB/cm (Figure 2) which compares well with earlier literature [4]. Figure 3 shows that a reduction of 10% in the intensity of light propagated through the waveguide occurs only after a 1mm lateral shift of the LED from the waveguide's axis of symmetry thus enabling the LED light source be coupled easily to the PDMS waveguide.

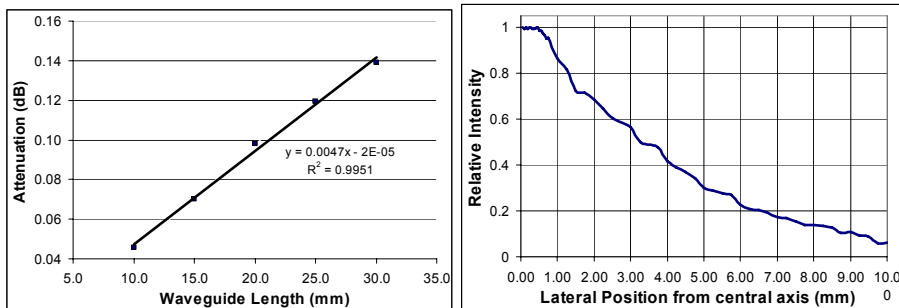


Figure 2. PDMS waveguide attenuation.

Figure 3. Intensity of light in PDMS waveguide with respect to the LED's axis.

In our integrated microsystem, the light is guided through a 3cm long PDMS waveguide to a 250 μ m-wide microfluidic channel and then through a 1cm long PDMS waveguide to the CCD camera. The light intensity was stabilized by feedback control of injecting different LED currents (Figure 4). Absorbance and fluorescence detection of the fluorescein (of concentration from 8.4×10^{-6} M to 0.305M) were studied (Figure 5).

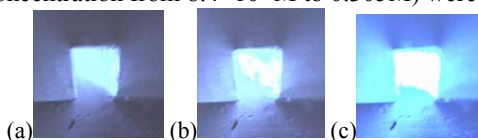


Figure 4. Microscope images at the face end of the PDMS waveguide when the input was illuminated with LED at the source current of (a) 40mA, (b) 80mA and, (c) 120mA.

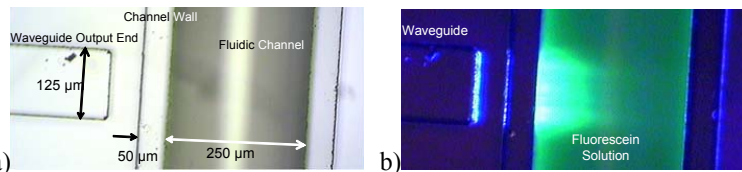


Figure 5. Top view of the waveguide-channel coupling as the light passing through the waveguide: (a) under external illumination; and (b) no external illumination.

Figure 6 shows that the absorbance detection by the PDMS waveguide is in excellent agreement with the Beer-Lambert Law. The differences in the slope and magnitude are due to geometrical discrepancy in optical path length and volume of the fluid analyzed (the 96 well plate and the 250 μm -wide microfluidic channel). In figure 7, the fluorescence detection is comparable with that of the commercial reader.

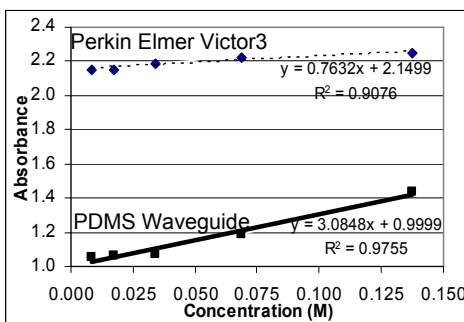


Figure 6. Comparison of absorbance measurement by a commercial reader and the PDMS waveguide microsystem.

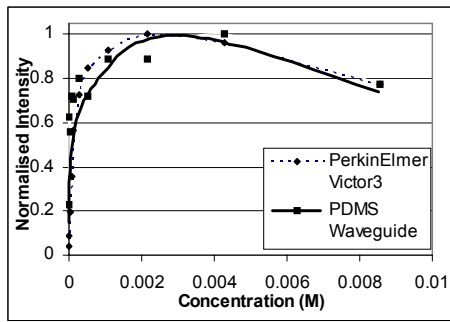


Figure 7. Comparison of fluorescence detection by a commercial reader and the PDMS waveguide microsystem.

4. Conclusions

Experimental results on absorbance and fluorescence detection corroborate the achievability of a PDMS waveguide monolithically integrated with a microfluidic chip. This realization provides a robust and cheap integration for lab-on-a-chip microsystems as neither laser sources nor fiber optics were utilized.

References

- Verpoorte E., *Chip Vision-optics for microchip*, Lab Chip, Vol. 3, pp. 42-52, (2003).
- Chang-Yen D., and Gale B., *An Integrated optical oxygen sensor fabricated using rapid-prototyping techniques*, Lab Chip, Vol. 3, pp. 297-301, (2003).
- Splawn B. G., and Lytle F. E., *On-chip absorption measurements using an integrated waveguide*, Anal. Bioanal. Chem., Vol. 373, pp. 519-525, (2002).
- Chang-Yen D. et al, *A Monolithic PDMS Waveguide System Fabricated Using Soft-Lithography Techniques*, J. of Lightwave Technology, IEEE, Vol. 23, No. 6, pp. 2088-2093, (2005).

PADLOCK PROBE-MEDIATED ROLLING-CIRCLE AMPLIFICATION IN MICROCHAMBERS, MONITORED AT THE SINGLE-MOLECULE LEVEL AND IN REAL-TIME

Jonas Jarvius[§], Olle Ericsson, Jonas Melin,
Mats Nilsson, and Ulf Landegren

Dept. of Genetics and Pathology, Uppsala University, Sweden.

[§]To whom correspondence should be addressed.

E-mail: jonas.jarvius@genpat.uu.se

Abstract

A new generation of rapid and efficient methods to detect genomic sequence variants and copy number changes could help bring about point-of-care analysis of the genomes of people and of microorganisms. In a novel approach to such molecular analyses we have demonstrated the feasibility of using general zip-code DNA microarrays for amplified single-molecule detection of padlock probes. We monitored the kinetics of solid-phase rolling-circle amplification (RCA) of padlock probes using phi 29 DNA polymerase.

1. Introduction

Methods for rapid detection of DNA sequences that represent markers for disease or drug metabolism, or for bacterial or viral infection, have the potential to permit cost-effective point-of-care diagnostics. Such assays must have sufficient sensitivity and specificity to resolve even single-nucleotide variants directly in the complexity of the human genome with no need for prior target sequence amplification.

Padlock probes are single-stranded oligonucleotides with target complementary sequences at both ends, connected by a backbone sequence [1]. Upon target recognition, the probes become circularized by enzymatic ligation, allowing single-nucleotide polymorphisms to be distinguished directly in total human genomic DNA. The reacted circular molecules serve as ideal substrates for RCA, generating long nucleic acid strands composed of repeats of complements of the padlock probe. By using padlock probes hybridized to oligonucleotides immobilized in a microarray, followed by on-chip RCA from the free 3' ends of the immobilized probes, long single-stranded products can be generated on the surface and subsequently detected using fluorescent hybridization probes. The reaction converts individual nanometer-sized probes to easily detectable micrometer-sized reaction products.

2. Experimental

To investigate the characteristics of array RCA we monitored the reactions in-real time using a confocal microarray scanner equipped with an in-house developed microchamber (fig 1a). A modified molecular beacon design was used for fluorescence detection of the RCA products to avoid quenching effects[2]. Probes were deposited on a planar surface and saturated with circularized DNA probes prior to initiating array RCA. We were also able to enumerate individual amplified RCA products within microarray features (fig 1b). Two padlock probes designed to discriminate single nucleotide variants were hybridized to the corresponding target sequences, followed by enzymatic ligation using T4 DNA ligase. Identical zip-code sequence and two specific sequences were encoded in the backbone of each probe. After ligation reacted probes were allowed to compete for hybridization to the same arrayed probe. This was followed by 45 minutes of RCA and subsequent hybridization of fluorophore labelled detection oligonucleotides specific for complements of each of the two probe variants. The objects were enumerated and classified using a Zeiss LSM 5 META confocal microscope and in-house developed software.

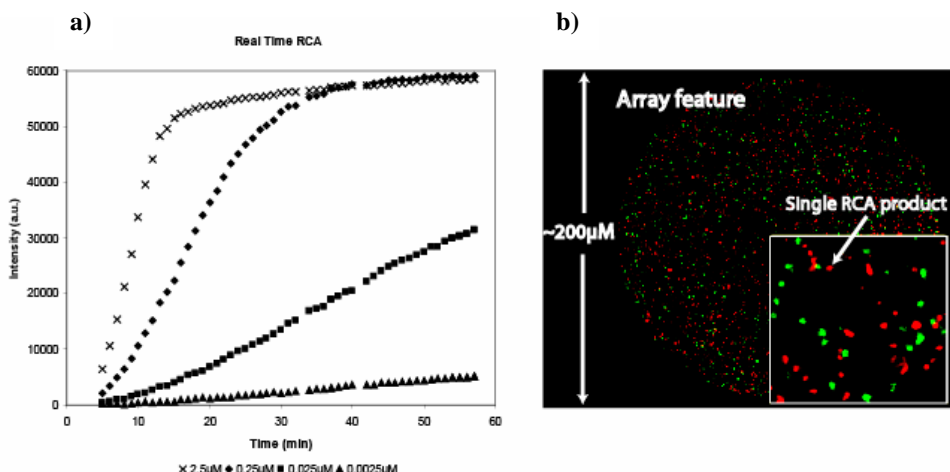


Figure 1 a) RCA was monitored in real-time in a micro chamber by confocal laser scanning. A microarray within the chamber comprised array features with four different probe concentrations which were saturated with RCA substrate. The RCA proceeded in a linear fashion for at least 60 minutes and the signal was proportionate to the amount of RCA substrate. **b)** Confocal laser microscope image displaying individual amplified molecules obtained from the RCA reaction in a microarray feature. Two separate classes of RCA products, red and green, are clearly observed using specific fluorescence-labeled oligonucleotides. The absence of yellow objects illustrates that individual objects indeed represent single amplification products.

3. Results and discussion

Padlock probes have been used for large-scale SNP analysis directly in unamplified genomic DNA[3]. We have also used amplified single-molecule detection of padlock probes for high precision analysis of *Vibrio cholerae* using a microfluidic setup[4]. The combination of amplified single-molecule detection of padlock probes and general purpose tag microarrays could enable highly parallel genetic analyses with very low limits of detection and high precision. On-chip RCA of specifically reacted probes is a powerful tool to amplify padlock probes hybridized to microarrays. The reaction proceeds linearly for at least 60 minutes and generates a confined product containing about 750 concatenated repeats complementary to the padlock probe after 45 minutes amplification. This approach illustrated herein may be exploited for rapid point-of-care diagnostics.

4. Conclusions

We have successfully detected individual amplified molecules representing padlock probes amplified by rolling-circle replication on microarrays, and we furthermore monitored the reaction in real-time using a modified molecular beacon design.

References

1. Nilsson, M., et al. *Science*, **265**, 2085-8 (1994).
2. Nilsson, M., et al. *Nucleic Acids Res*, **30**, e66 (2002).
3. Hardenbol, P., et al. *Nat. Biotechnol*, **21**, 673-8 (2003)
4. Jarvius, J., et al. *Nat. Methods*, **3**, (2006) in press

ULTRA WIDE BAND DIELECTRIC SPECTROSCOPY OF SINGLE CELL IN MICROFLUIDIC DEVICES

V. Senez^{1*}, A. Treizebré¹, E. Lennon^{2,3}, H. Ghandour¹, V. Mille¹, T. Heim¹,
T. Akalin¹, T. Yamamoto², N. Bourzgui¹, D. Legrand⁴, Y. Sakai^{5,2,3},
P. Supiot⁶, J. Mazurier⁴, T. Fujii^{2,3}, B. Bocquet¹

¹IEMN/CNRS-USTL-ISEN, ⁴UGSF/CNRS-USTL, ⁶GEPIFREM/CNRS-USTL,
University of Lille, France

²CIRMM/IIS, ³LIMMS/CNRS-IIS, ⁵CSE-OBE-IIS,
University of Tokyo, Japan

(*corresponding author: vincent.senez@isen.iemn.univ-lille1.fr)

Abstract

Various BioMEMS have been designed and fabricated in order to characterize the variation of the electrical properties of single cells during ligand-receptor interactions. We are interested in both dielectric (i.e. polarization) and vibrationnal (i.e. absorption) spectroscopy. Several devices are currently tested for low (<100MHz) and high (>40GHz) frequency measurements.

Keywords: Single Cell, Cell Signaling, Dielectric & Vibrationnal Spectroscopy, Planar Electrode, Transmission Line, THz.

1. Introduction

This work is focused in the area of ligand-receptor interaction analysis, working with a well-characterized biological model (ligand: lactoferrin, receptors: nucleolin and sulfated proteoglycans) [1]. The purpose is to be able to assign, in real time, a specific crossing pathway to a ligand/receptor pair, without the use of molecular labels. The classification is based on changes in the electrical properties of the cell. We propose to follow the various phases of assembly between the ligand (lactoferrin) and receptors (nucleolin and sulfated proteoglycans) present or not on a set of mutant CHO cell lines (Fig. 1a), and internalization of the ligands/receptors complexes into single cells. The assembly and intracellular fate (endocytosis, nuclear targeting) of the ligand/receptors complexes will be followed in real time by measuring their interaction with the electromagnetic waves. The spectra will be analyzed and compared with the results obtained from standard microscopy techniques.

2. Microdevices and Technologies

Permittivity and conductivity measurements of biological species across a range of frequencies provide information about their chemical status [2]. Access to a broad frequency range is absolutely necessary due to their size and chemical diversity. We have tested various methods for the immobilization of the cells: i) mechanical (Fig. 1b), ii) chemical (Fig. 1c) and 3) electrical (Fig. 1d). We have designed several structures for their characterization. In the low frequency range (LF) (<100MHz), we have fabricated

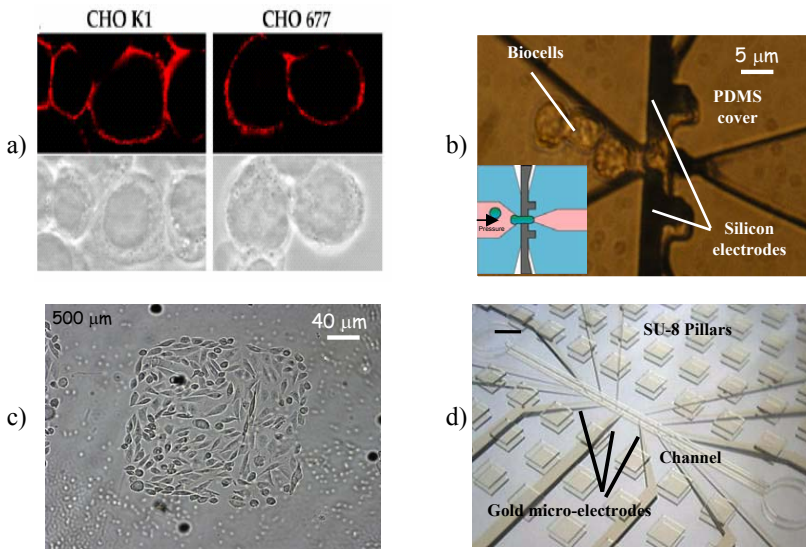


Figure 1: a) Binding of lactoferrine on two mutants of CHO cells. CHO 677 line do not allow endocytosis of lactoferrine; b) Single cell measurement set-up using deformability of cell between 3D silicon electrodes; c) Patterning and immobilization of CHO cells on glass substrate by surface treatment with OTS and amine; d) Microfluidic chip for dielectrophoretic immobilization of single cells.

coplanar and 3D electrodes sensors for impedance measurements (Fig. 2a). In the high frequency ranges (HF), we are using coplanar waveguide (CPW) for the microwave spectrum up to 220GHz and slotlines (CS) up to 1THz. We are also investigating a new propagation mode [3], known as a Goubau mode (GL), around a single conductor (Fig. 2b). We have demonstrated recently that the propagation is maintained if we reduce dramatically the diameter of this wire down to micrometer scale.

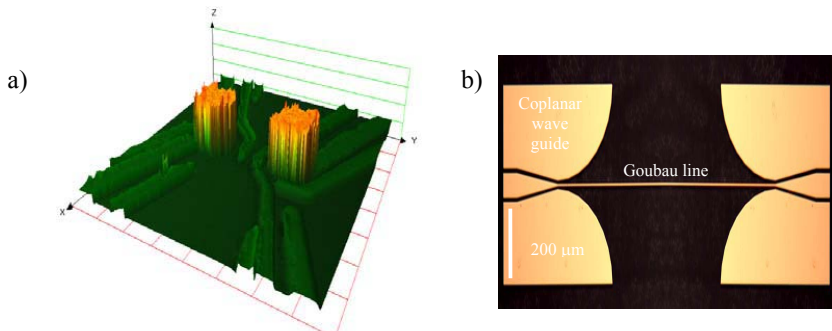


Figure 2: a) Details of 3D gold electrodes designed for the electrical impedance measurement of single cell; b) Top view of coplanar wave guide to Goubau line.

BioMEMS are fabricated on silicon or glass substrates with microfluidic parts in polymeric materials. We are using usually PDMS which has many well known advantages. However, it also shows disadvantages: fairly high losses ($\epsilon_r \approx 2.7$, $\tan\delta \approx 0.04$ in THz band), low Young modulus (<5 MPa) and difficulty to metallize. That is why we are also working with Plasma Polymerized TetraMethylDiSilOxane (PPTMDSO) deposited with cold nitrogen plasma [4]. Metallic patterns can be defined easily on PPTMDSO and its dielectric properties are fairly good.

3. Modelling and Measurements

The efficiency of our method depends on a correct design of the sensors (i.e.: coplanar electrodes or waveguide, 3D electrodes, GL, etc...) and a realistic model of the dielectric properties of the cell. We are using Comsol Multiphysics from COMSOL and Microwave Studio from CST (Fig. 3a) tools in the LFR and HFR, respectively. However, these FEM methods have to be coupled with a transport lattice (i.e.: SPICE like) approach to take into account the geometrical details of the cell [5] and to correlate features of the dielectric spectra with sub-components of the cell (Figs. 3b-c).

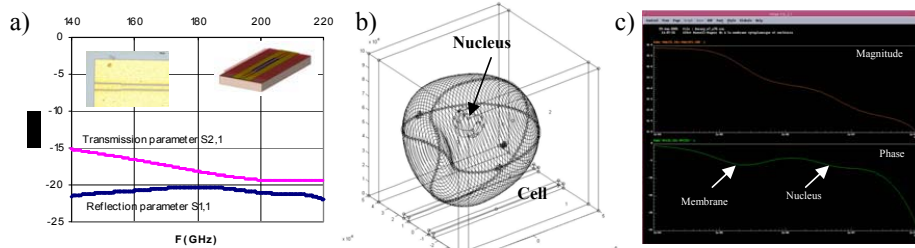


Figure 3: a) Transmission and reflexion coefficients simulated with Microwave studio (CST) for a CPW guide (see insert); b) Advanced model for cell-electric field interactions; c) SPICE simulation of the electrical impedance of a single cell showing membrane/nucleus effects.

Measurements are performed with impedance analyzers (SOLARTRON 1260+1296 or AGILENT 4294) in the LFR and with vectorial network analyzers (AGILENT XF & ANRITSU 37147C) in the HFR. The performances of the micro-devices in LF & HF are currently measured in dry and liquid conditions. Finally, we are also working on the integration of a discrete home-made LF measurement system foreshadowing a future CMOS solution.

4. References

- [1] D. Legrand *et al.*, Eur. J. Biochem., 271, pp.303-317, 2004.
- [2] J.R. Facer *et al.*, APL, 78, pp.996-998, 2001.
- [3] K. Wang *et al.*, Nature, 432, pp.376-379, 2004.
- [4] B. Bocquet *et al.*, Proc. SPIE, 5345, pp.118-129, 2004.
- [5] V. Senez *et al.*, Proc. Nanotech., Boston (USA), 1, pp. 99-102, 2004.

ACKNOWLEDGMENTS

Parts of this work have been carried out within the FENOTIP project funded by the French Research National Agency (ANR) as PNANO n°05-0244-A3 and the grant of Dr. E. Lennon was supported by the Japanese Society for the Promotion of Science (JSPS).

CORROSION RESISTANT INTEGRATED OPTICAL MICROSENSOR FOR NIR SPECTROSCOPY AND ITS APPLICATION IN MICROREACTORS

Sylwester Bargiel, Jan A. Dziuban, Rafał Walczak, Paweł Knapkiewicz,
Anna Górecka-Drzazga

Wrocław University of Technology, Faculty of Microsystem Electronics and
Photonics, Silicon Mechanics & Microengineering Laboratory, Poland,
e-mail: sylwester.bargiel@pwr.wroc.pl

Abstract

In this paper a silicon-glass optical microsensor for near-infrared spectroscopy of highly corrosive fluids is presented. The microsensor has been designed to control a course of a nitration reaction of toluene and other aromatic hydrocarbons, carried out in microreactor. The microsensor has low dead-volume (90 nl) and chemical resistance against concentrated sulphuric and nitric acids. The spectral NIR transmittance characteristics of various chemicals have been successfully measured.

Keywords: Optical sensor, NIR spectroscopy, nitration reaction, microreactor

1. Introduction

The nitration reactions of aromatic compounds are among the basic reactions used in chemical synthesis. These reactions often show extremely exothermic behaviour and as combined with chemically aggressive reactants (e.g. concentrated sulphuric and nitric acids) and explosion potential of many nitro compounds - can be placed amongst the most hazardous industrial processes.

Nevertheless, the recent achievements in microsystem technology have shown that nitration reactions can be safely carried out in microreactors [1,2]. High heat and mass transfer rates in microscale allow the reactions to be performed at higher temperature, providing high yields that are not achievable in conventional reactors. However, real time analytical monitoring of the final product of reaction is necessary to suppress the unwanted by-products [2]. Near-infrared spectroscopy (NIR) appears to be very useful for this purpose due to its capability of a real time, non-invasive monitoring of the chemical processes [3]. The application of NIR spectroscopy in microreactor requires a suitable microsensor characterized by the very low dead-volume and high chemical resistance against hot, concentrated nitric and sulphuric acids. Until now, integrated NIR microsensor able to work in so harsh environment has not been reported. This work concentrates on the development of such microsensor based on microsystem technology and optical fibers.

2. Experimental

The microsensor is composed of a silicon structure, a glass cover, and two multimode ($\phi=125/62.5\mu\text{m}$) glass optical fibres (Figure 1a). The fibres are positioned in alignment grooves at the opposite corners of the C-shaped fluidic channel (width 130 μm , depth 140 μm). The fluidic channel is completely separated from the optical fibres by the NIR transparent, 20 μm thick silicon “walls”, bonded anodically to the glass cover. The optical path-length is 5 mm and the dead-volume about 90 nl. As the side-walls and top wall of fluidic channel are made of silicon dioxide and borosilicate glass respectively, total chemical resistance of optical cell is ensured.

The fluidic channel and alignment grooves are etched into n-type, 380 μm thick, double-side polished, (100) oriented silicon substrate in DRIE process (A601E, Alcatel, France) (Figure 1b). This process has been optimised to obtain the vertical side-walls of the channel. The fluidic inlet/outlet holes are back-side etched into the silicon substrate using a photolithographically patterned 100 nm Al mask layer. The silicon substrate is wet oxidized again to obtain a 0.3 μm SiO_2 isolation layer. The silicon substrate is anodically bonded (450°C, 1.5 kV) to a Borofloat® 33 glass (Schott, Germany). High quality bonding process is required to ensure the leakproofness of the channel. Finally, the fibres equipped with ST connections are positioned in the alignment grooves and immobilized by a droplet of UV-curable optical glue UVO-114 (Epo-Tec, Germany). Figure 1c shows the complete device.

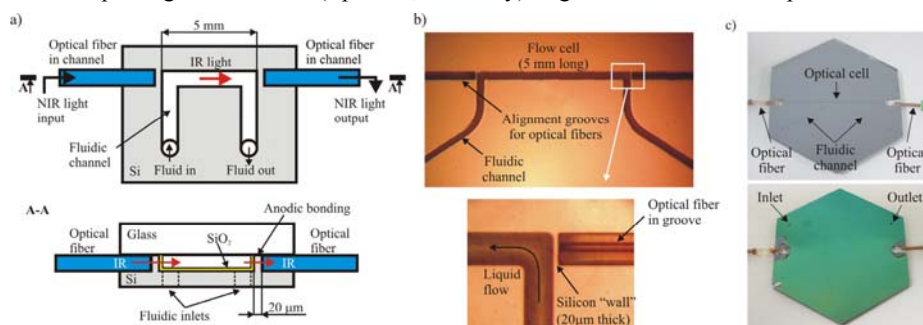


Figure 1. The NIR microsensor: a) construction scheme of the microsensor, b) details, c) top and bottom side of complete device.

3. Results and discussion

The fluidic channel has been filled with the concentrated nitric acid followed by the sulphuric acid, each for 24 hours. No damages have been observed, which confirms the desired chemical resistance of the microsensor.

The tests, carried out in the set-up presented in Figure 2a, have shown that the transmission of the NIR light through the empty optical cell occurs at wavelengths over 850 nm (Figure 2b). The spectral measurements of transmittance of water, benzene and

toluene have been performed. The transmittance has been calculated from the Beer-Lambert law as a ratio of the emerging light intensity, measured for the cell filled with each analyte, to the light intensity measured for the empty cell. According to the obtained spectra, water can be distinguished from benzene and toluene (Figure 2c). This is of great importance because the water content in reaction product is among the main indicators of the expected course of nitration reaction.

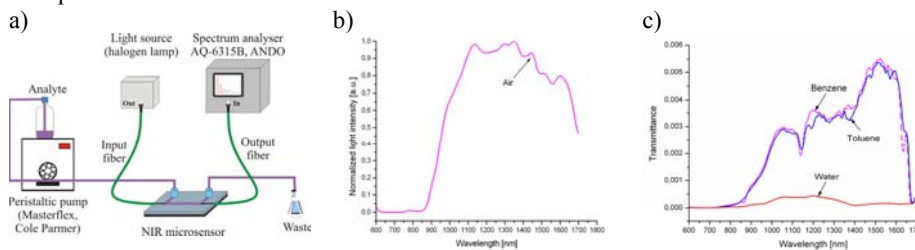


Figure 2. NIR spectral measurements: a) set-up, b,c) obtained transmittance spectra.

The obtained transmittance values are generally very low (<0.006). This is a result of low light intensity in optical cell caused by relatively small core diameter of optical fibers (62.5 μm) at long optical path (5 mm), as well as the surface roughness of DRIE etched side-walls of fluidic channel. However, the results indicate that the described microsensor can be used for the in-situ controlling of this chemical reaction in the microscale.

4. Conclusions

The silicon-glass optical microsensor for NIR spectroscopy of highly corrosive fluids has been developed. The microsensor has very low dead-volume (90 nl) and high chemical robustness against concentrated sulphuric and nitric acids. Tests have confirmed the usefulness of microsensor in NIR spectroscopy. The sensor is chemically and biologically inert and can be used for other, than pointed out here, purposes.

Acknowledgements

This work has been financed by the NEPUMUC project (contract no 014036) in the frame of 6 EC PR.

References

1. J.R. Burns, C. Ramshaw, *A microreactor for the nitration of benzene and toluene*, Proc. Fourth International Conference on Microreaction Technology, Atlanta, USA, (2000).
2. W. Ferstl et al., *Development of an automated microreaction system with integrated sensorics for process screening and production*, Chemical Eng. Journal, 101, pp 431-438, (2004).
3. L. Bokobza, *Near infrared spectroscopy*, J. Near Infrared Spectrosc. 6, 3 (1998).

A ROOM TEMPERATURE CMOS SINGLE PHOTON SENSOR FOR CHEMILUMINESCENCE DETECTION

Marek Gersbach^{1,*}, Yuki Maruyama^{2,*}, Cristiano Niclass¹, Kazuaki Sawada², Edoardo Charbon¹

¹Ecole Polytechnique Fédérale de Lausanne (EPFL), Lausanne, Switzerland

²Toyohashi University of Technology (TUT), Toyohashi, Japan

*both authors contributed equally to this work

keywords: chemiluminescence, bioluminescence, molecular assay, single photon detection, laminar flow.

Abstract

A room temperature single photon sensor array, fully integrated in CMOS, is presented for the detection of low-intensity luminescence. A Y-shaped microfluidic reactor is used as platform for the chemical reaction generating luminescence. Experimental results show that the system can reliably detect luminescence with a high signal-to-noise ratio even at low emission intensities.

Introduction

In this paper we present a novel, single photon sensor based, detection of luminescence. The sensor's core technology is a single photon avalanche diode (SPAD) array fabricated in 0.8 μ m CMOS technology [1]. Figure 1 shows a photomicrograph of the array.

A SPAD is a p-n junction biased above breakdown, where its optical gain is virtually infinite. When a photon is absorbed, with non-zero probability, an avalanche is triggered and subsequently quenched, thus generating a pulse synchronized with the impinging photon (Geiger mode of operation). Radiation intensity can be evaluated by counting pulses during the integration period and adjusting for fill factor and photon detection probability. Intensity signal-to-noise ratio (SNR) is limited in SPADs by dark count rate (DCR). This sensor exhibits one of the lowest DCR ever reported in a CMOS SPAD at room temperature (see Tab. 1.). Thanks to this noise performance, chemiluminescence can be detected with an SNR comparable to that of photomultiplier tubes (PMTs) and cooled CCDs but at a fraction of the cost, power dissipation, and size [2]. Thanks to its scalability, this sensor enables significantly higher lateral resolutions than large-area pixel solutions [3], [4]. In addition, thanks to the speed at which it is operated and its timing resolution, the sensor is indicated for fast low-emission experiments and simultaneous fluorescence-luminescence imaging.

Experimental

In our experimentation the reaction platform of Fig. 2 was demonstrated. The experiment involved Enhanced Chemiluminescence (ECL) plus Western Blotting Detection Reagents (Amersham Biosciences) and a secondary antibody, Anti-Mouse IgG (whole molecule) Peroxidase Conjugate (Sigma Aldrich) diluted in Tris Buffered Saline (20mM). The platform is a powerful tool for

monitoring luminol photon emissions, occurring when a ECL Plus solution reacts with a secondary antibody. Other kinds of enzymatic activities can also be evaluated with this platform. The reaction was monitored using the experimental setup described in Fig. 3. By means of a syringe pump, the reagents are forced through a Y-shaped microchannel under laminar flow conditions. The reaction takes place in the region where the two solutions are mixed through diffusion causing an anisotropic photon emission [5],[6]. A portion of this emission is collected by the optical system and concentrated over an area of 5x5 pixels. Photon counts are then evaluated independently using a 32bit counters.

Results and Discussion

The plots of Fig. 4 and Fig. 5 show the emission decay of chemiluminescence in a 10mm tube and in a 2mm channel. The plot of Fig. 6 shows the evolution of photon emission on a section of the channel perpendicular to the flow. Fig. 7 shows a measurement of the emission intensity along the laminar flow. All the measurements were performed at room temperature.

Performance	Min.	Typ.	Max.	Unit
Pitch		58		μm
Array size		32x32		-
Pixel Dark Count Rate (DCR)		5.5		Hz
Saturation			25	MHz
Wavelength range	350		1000	nm
Photon Detection Probability @ op. wavelength (530nm)		25		%
Power dissipation		6		mW

Table 1. Sensor performance at room temperature.

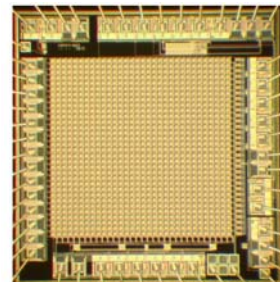


Figure 1. Photomicrograph of the SPAD array fabricated in CMOS technology.

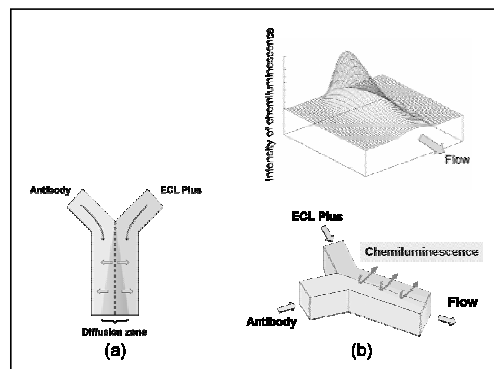


Figure 2. Schematic diagram of the reaction.. The inlet components mix at the intersection inducing photon emission. (a) Diffusion effect, (b) Image of photon emission distribution

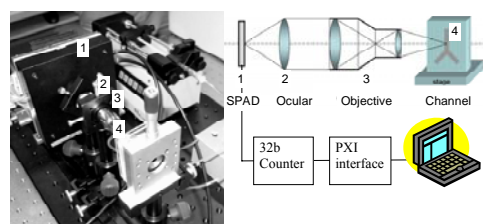


Figure 3. Experimental setup and schematic diagram.

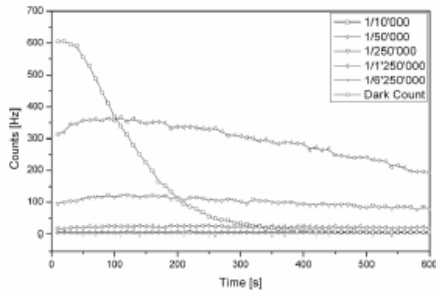


Figure 4. Chemiluminescence emission decay in a 10mm tube as a function of concentration. Dark count rate (DCR) is also plotted.

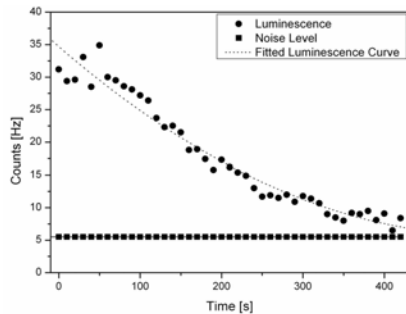


Figure 5. Chemiluminescence decay in a 2mm channel for a 1/10,000 concentration.

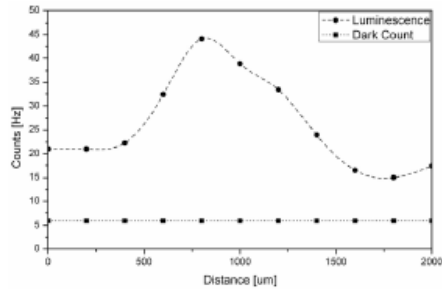


Figure 6. Photon emission distribution in a sweep perpendicular to the flow axis in a 2mm channel.

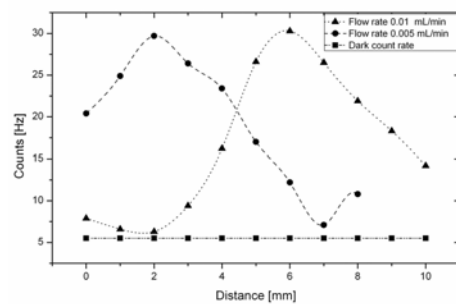


Figure 7. Photon emission distribution in a sweep parallel to the flow axis in a 2mm channel as a function of the chemical flux.

REFERENCES

- [1] C. Niclass A. Rochas, P.A. Besse, R. Popovic, and E. Charbon, "A 4μs Integration Time Imager Based on CMOS Single Photon Avalanche Diode Technology", to appear in *Sensors and Actuators: Physical*, 2006.
- [2] K. Feather-Henigan, S. Hersey, A. Johnson, G. M. Milosevich, and K. Hines, "Immunoblot Imaging with a Cooled CCD Camera and Chemiluminescent Substrates", *American Biology Laboratory*, pp. 44-46, June 1999.
- [3] H. Eltoukhy, K. Salama, and A. El Gamal, "A 0.18μm CMOS Bioluminescence Detection Lab-on-Chip", *Journal of Solid-State Circuits*, Vol. 41, N. 3, pp. 651-662, March 2006.
- [4] U. Lu *et al.*, "CMOS Chip as Luminescent Sensor for Biochemical Reactions", *IEEE Sensors Journal*, Vol. 3, N. 3, pp. 310-316, June 2003.
- [5] C. Oda, K. Sawada, T. Tsuchiya, H. Takao, M. Ishida, "Integrated Electrochemical DNA Sensors with Microfluidic Channel Reactor", *μ-TAS'03*, Vol. 1, pp. 371-374, October 2003.
- [6] K. Sawada, C. Oda, H. Takao, M. Ishida, "Smart Microfluidic Electrochemical DNA Sensors Integrated Signal Processing Circuits", *TRANSDUCERS'05*, pp. 279-282, June 2005.

NEUROTRANSMITTER SENSING DEVICE WITH MOLECULE-PERMEABLE PLATINUM FILLED IN NANO-HOLES

Takashi Yasuda, Kazuyuki Shinohara, and Tetsunori Hirata

Graduate School of Life Science and Systems Engineering, Kyushu Institute of Technology, 2-4 Hibikino, Wakamatsu-ku, Kitakyushu 808-0196, Japan

Abstract

This paper presents a novel microfluidic device for detecting glutamate electrochemically using enzyme reaction. The device consists of a cell-culture chamber, nano-holes filled with Pt black, a microchannel for storing enzyme solution, and three electrodes for electrochemical measurement. We measured response current when glutamate solutions were dropped onto the device, and succeeded in obtaining response current depending on the glutamate concentrations.

Keywords: Enzyme sensor, Neurotransmitter, Nano-hole, Platinum black

1. Introduction

Detection of neurotransmitters released from a single nerve cell is important to reveal intercellular communication mechanism and develop new medical cure for nervous disease. In order to detect glutamate from a single cell, we fabricated nano-holes for guiding glutamate to enzyme solution directly under a cell-culture chamber. This permits higher spatial resolution than the enzyme-immobilized electrodes [1, 2].

2. Design and fabrication

Figure 1 shows the schematic of a device which consists of a cell-culture chamber, nano-holes in a SiO₂ diaphragm, a microchannel for storing enzyme solution, and three electrodes for electrochemical measurement. The working electrode is made of Ti/Pt and covered with Pt black which fills the nano-holes. Because Pt black has a lot of nano-sized pores, glutamate having small molecular size of about 0.8nm permeates through the Pt black into a microchannel, while enzyme, glutamate oxidase, having large molecular size of about 8.2nm does not permeate into the cell-culture chamber. When glutamate is released from a cell, it will permeate through the Pt black in the nano-holes and encounter glutamate oxidase in the microchannel, and be oxidized by enzyme reaction, which will produce H₂O₂. When voltage of about 200mV was applied between the working electrode and reference electrode, H₂O₂ will be oxidized on the working electrode and electrons will flow into the electrode. Therefore, glutamate can be detected by measuring current on the electrode.

The device was fabricated as follows. First, a SiO₂ diaphragm was fabricated by the anisotropic etching of a silicon wafer. Next, nano-holes of 500nm in diameter were opened in a SiO₂ diaphragm by FIB etching. Then, after three Ti/Pt electrodes are patterned, Pt black is deposited only on the working electrode by electroplating until it fills the nano-holes completely. Finally, the device is mounted on a glass wafer with

PDMS spacers. Figure 2 shows the photograph of the whole device and the close-up views of the electrodes and the nano-holes filled with Pt black.

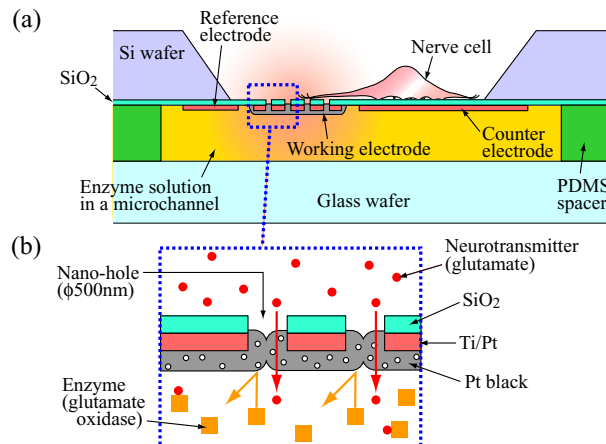


Fig. 1 Schematic of neurotransmitter detection.

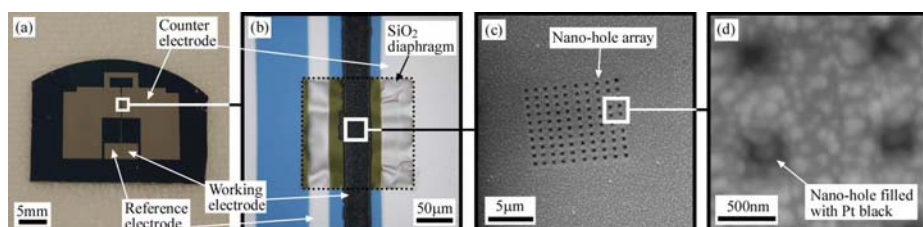


Fig. 2 Photographs of the fabricated device.

3. Experimental results

Molecule permeation through nano-holes filled with Pt black was tested using two fluorescent dyes, Rhodamine B and GFP, which have different molecular size of about 1.3nm and 6.8nm, respectively (Fig.3). This result indicates that glutamate molecules which are smaller than Rhodamine B molecules permeate through the Pt black while glutamate oxidase molecules which are larger than GFP molecules do not.

In order to verify the possibility of electrochemical measurement using the fabricated device, we measured response current when H_2O_2 solutions of 5mM and 10mM were dropped onto the chambers of the two devices which have nano-holes filled with or without Pt black. The large surface area of nano-porous Pt black generated larger current than the case without Pt black (Fig.4). Moreover, when glutamate solutions of various concentrations were dropped onto the device which included a glutamate oxidase solution of 50unit/ml in the microchannel, we succeeded in obtaining current responses that were dependent on glutamate concentration (Fig.5&6).

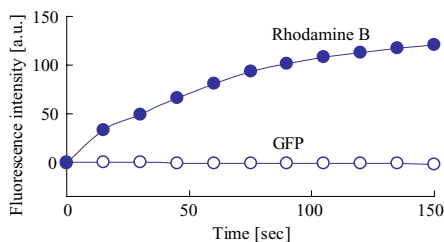


Fig. 3 Molecule permeation through the nano-porous Pt black.

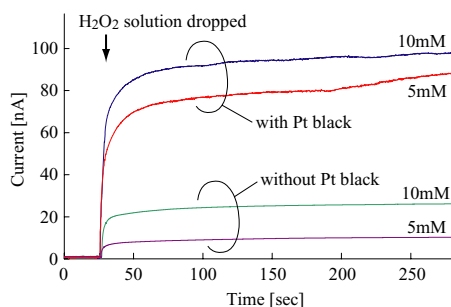


Fig. 4 Current response in case that H_2O_2 solutions were dropped onto the devices.

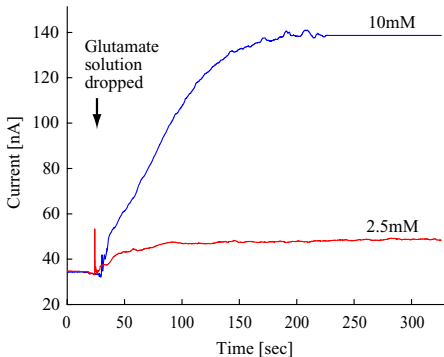


Fig. 5 Current response curves in case of two different glutamate concentrations.

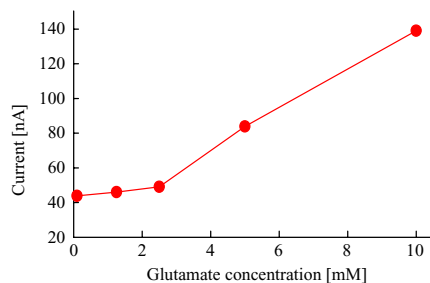


Fig. 6 Relationship between glutamate concentration and response current.

4. Conclusions

We fabricated the microfluidic enzyme sensor device which has Pt black filled in nano-holes. From several experiments, it was found that Pt black functions effectively as a glutamate-permeable filter which glutamate oxidase does not pass through, and that the device shows a fundamental performance required for glutamate sensing.

Acknowledgements

This work was supported by the “Development of Nanotechnology and Materials for Innovative Utilizations of Biological Functions” Project of the Ministry of Agriculture, Forestry and Fisheries of Japan, and also by a fund from the Ministry of Education, Culture, Sports, Science and Technology via Grant-in-Aid for Exploratory Research.

References

- [1] R. Kurita *et al.*, *Analytica Chimica Acta*, 441, pp. 165-174, 2001.
- [2] N. Kasai *et al.*, *Analytical Sciences*, Vol. 18, pp. 1325-1327, 2002.

NANOPARTICLE-BASED SERS IMAGING OF BIOLOGICAL ARRAYS

Francis Nsiah, D. Jed Harrison and Mark T. McDermott*

Department of Chemistry, University of Alberta, and National Institute of Nanotechnology/National Research Council, Canada

ABSTRACT

This paper reports a surface-enhanced Raman spectroscopic (SERS) method for high-sensitivity detection and reading of protein microarrays. The array fabrication is based on microfluidic patterning methods and detection relies on gold nanoparticle labeling procedures. The surface enhancement afforded by coupling metal nanoparticles to extrinsic labels is used to generate high-sensitivity detection.

Keywords: SERS, Microarrays, Gold Nanoparticles, Mapping

INTRODUCTION

The development of sensitive detection schemes for the detection of biomolecular interactions will lead to further advancements in areas such as proteomics, drug discovery and pathogen detection. The surface enhancement afforded by coupling metal nanoparticles to extrinsic labels has driven the exploration of Raman spectroscopy for biomolecule interaction detection.

Over the past year, we have been developing surface enhanced Raman spectroscopic (SERS) methods for the reading of protein microarrays. We have developed simple microfluidic patterning methods and nanoparticle labeling procedures to fabricate and read such microarrays. Results of our efforts in using Raman mapping in reading antibody-antigen arrays is also presented.

EXPERIMENTAL

The protein arrays were constructed in a three-step process as shown in Figure 1A. First, a polydimethylsiloxane (PDMS) microfluidic network is brought into conformal contact with planar gold substrate modified with mercaptoundecylamine. The protein antigen (bovine IgG) nonspecifically

Figure 1A. Array fabrication via microfluidic channels (μ FCs) in PDMS: (a) PDMS device is placed on NH_2 modified gold substrate, forming μ FCs; (b) Antigen (bIgG) patterned in lines via μ FCs; (c) Chip immersed in BSA to block non-specific adsorption; (d) Second set of μ FCs is placed perpendicularly

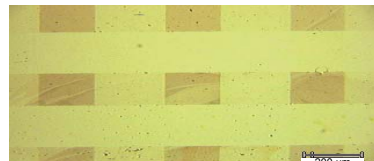
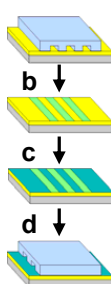


Figure 1B. Optical image of protein chip.

adsorbs to the $-NH_2$ surface. After delivering the antigens to the chip, the array surface was blocked with 0.1% BSA for 1 h. A second set of microfluidic channels are then used to deliver gold nanoparticle-labeled antibodies to the chip. A region of such an array is shown in the optical micrograph in Figure 1B.

RESULTS AND DISCUSSION

Figure 2 shows the nanoparticle labelled assembly. Antibodies are linked to the gold nanoparticles via a bifunctional, Raman reporter molecule, 5,5'-dithiobis(succinimidyl-2-nitrobenzoate) (DSNB) [1]. The nitrobenzene moiety of DSNB, located in close proximity to the Au nanoparticle, provides the SERS signal for detection as demonstrated by the SERS spectrum in Figure 2.

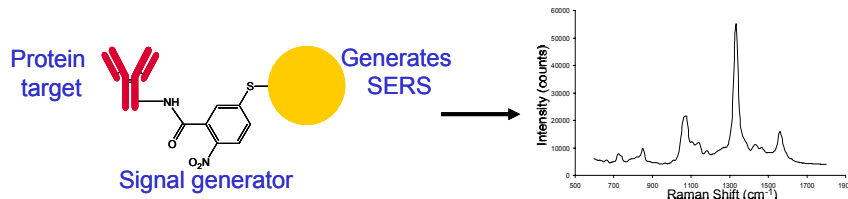


Figure 2. SERS of nanoparticle-labelled antibody

The reading of the protein microarrays was carried out by examining the individual spots on the chip. Figure 3 shows Raman spectra collected at different spots on the array surface. The intense spectrum measured in the regions where the antibody delivery microchannels intersected with the patterned antigen lines corresponds to the SERS spectrum of DSNB. Very small signals are measured elsewhere on the chip. Taken together, these observations demonstrate the ability of this method of read antigen-antibody interactions. Parallel reading of such arrays can be accomplished by Raman mapping. Figure 4 is a SERS map generated using the intensity of the symmetric NO₂ stretch (1332 cm^{-1}) to generate the contrast. For this array, the surface density of antigen was varied by delivering different solution concentrations of bovine IgG to the chip surface. The horizontal cross-sectional profile of antigen-antibody binding (not shown) illustrates that the measurement is quantitative with antigen surface density.

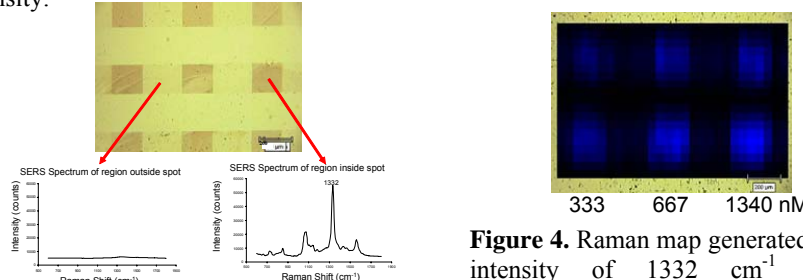


Figure 3. Spectroscopic reading of protein antigen microarray.

Figure 4. Raman map generated from intensity of 1332 cm^{-1} band. Concentrations indicated are those used to pattern the antigens on the chip surface.

Quantitative analysis of the binding of nanoparticle labeled antibodies with immobilized antigens has been carried out as well as investigation into multivalency of the binding event. Figure 5 is a binding curve constructed by plotting SERS intensities of the 1332 cm^{-1} band versus the solution density of antibody labeled nanoparticles. The adsorption constant, K_{ads} , for the binding of the nanoparticle labeled antibodies was determined using a single binding-site model (Langmuir isotherm). For the bovine IgG-anti-bovine IgG system studied here, $K_{\text{ads}} = 1.4 \times 10^{10}\text{ M}^{-1}$. This same antigen-antibody system was examined in a label-free assay with surface plasmon resonance where K_{ads} was determined to be $1.1 \times 10^7\text{ M}^{-1}$ [2]. The observed higher binding constants for our SERS measurements can be attributed to either a multivalent effect originating from multiple antibodies conjugated to each nanoparticle (inset of Figure 5) or signal enhancements inherent in Raman spectroscopy of nanoparticle systems (e.g., hot spots).

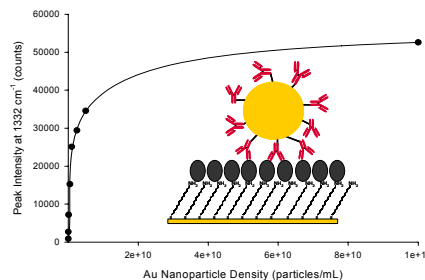


Figure 5. Quantitative binding curve generated from the intensity of 1332 cm^{-1} band as a function of nanoparticle density. This is a fit with a single-site binding model (Langmuir isotherm) with the use of band intensity as quantitative measure of binding.

CONCLUSIONS

Raman reporter molecules can be combined with nanoparticles for sensitive SERS detection of biological binding. In addition, the use of Raman mapping is a viable readout method for array chips has been demonstrated with interesting quantitative binding effects observed with the nanoparticle system.

ACKNOWLEDGEMENTS

This work has been supported by Genome Health Initiative (GHI) Canada, National Institute for Nanotechnology and the Department of Chemistry, University of Alberta.

REFERENCES

1. D. S. Grubisha, R. J. Lipert, H. Y. Park, J. Driskell, and M. D. Porter, *Analytical Chemistry* **75**:5936 (2003).
2. V. Kanda, J. K. Kariuki, D. J. Harrison, and M. T. McDermott, *Analytical Chemistry* **76**:7257 (2004).

HIGH-SENSITIVITY LOW-COST ON-CHIP CHEMILUMINESCENCE DETECTION BASED ON INTERGRATED ORGANIC PHOTODIODES

Rupa Das^a, Xuhua Wang ^{a,c}, Oliver Hofmann^c, John C. deMello^{b,c}, Andrew J. deMello^{b,c}, Donal D.C. Bradley ^{a,c}

^aEXSS Group, Dept. of Physics, Imperial College London, SW7 2AZ, UK

^bDepartment of Chemistry, Imperial College London, SW7 2AZ, UK

^cMolecular Vision Ltd., 21 Wilson Street, London EC2M 2TD

ABSTRACT

We report the use of novel low-cost disposable organic photodiodes for high-sensitivity detection of on-chip chemiluminescence assays. By planar integration of the photodiode, spatial matching of the pixel size to the microchannel dimensions and by chemically tuning the detector responsivity to the luminescence emission we have achieved sensitivities equivalent to PMT based detection. This bodes well for the applicability of our disposable detection systems to point-of-care diagnostic testing.

Keywords: integrated detection, organic photodiodes, chemiluminescence, disposable diagnostics

1. INTRODUCTION

Chemiluminescence (CL) offers a simple but sensitive means of monitoring low level analyte concentrations. CL is particularly attractive for portable microfluidic assays, because the CL reaction acts as an internal light source, thereby lowering instrumentation and power requirements while providing a low signal background. Traditionally CL assays have been monitored by expensive and non-portable externally mounted photomultiplier tubes (PMTs) and microscope based collection optics. More recently the use of silicon photodiodes has been reported on silicon microchips, which are still relatively high-cost and thus unsuitable for disposable devices [1]. Here we overcome this bottleneck by using solution processable organic photodiodes in combination with molded poly(dimethylsiloxane) (PDMS) based microfluidic chips, thereby providing a sensitive, low-cost, rapid prototyping and compact route towards disposable diagnostic devices.

2. RESULTS

We report polymer photodetectors made from a blend of regioregular poly(3-hexylthiophene) [P3HT] and 1-(3-methoxycarbonyl)-propyl-1-phenyl-(6,6)-C₆₁ [PCBM]. The blend was spin coated over an ITO-coated glass substrate on which a PEDOT:PSS injection layer had been previously deposited. Deposition of an aluminum cathode through a shadow mask completed the diode structure. The detector has a

photoresponse from 350 nm to 670 nm, with an external efficiency of ~60% at 510nm and a rise time of 1 μ s [2].

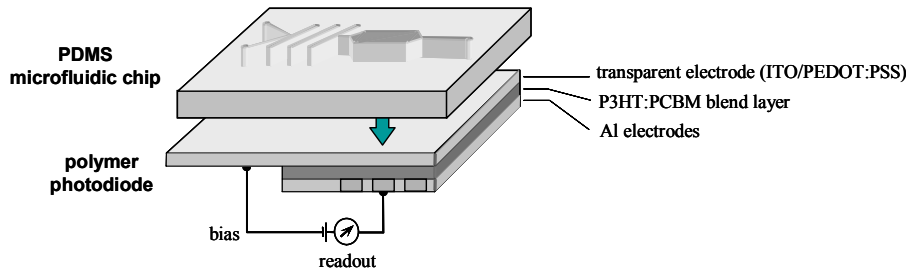


Figure 1: Schematic of the PDMS microfluidic chip with integrated low-cost polymer photodiode for on-chip CL based bioassay detection. The absence of a lightsource and the low power requirements of the polymer photodiode enable battery operation.

The microfluidic chip fabrication was based on standard soft lithography. standard photolithography used on negative SU-8 photoresist to make mold. PDMS (Dow Corning Sylgard 184), monomer and hardener mixed in a ratio of 10:1 (w/w), is poured onto the SU-8 master and cured at 65°C for 3 hours. Cured PDMS is then carefully peeled off the master. To form an enclosed channel, the structured PDMS layer is placed in conformal contact with the glass side of the polymer photodiode.

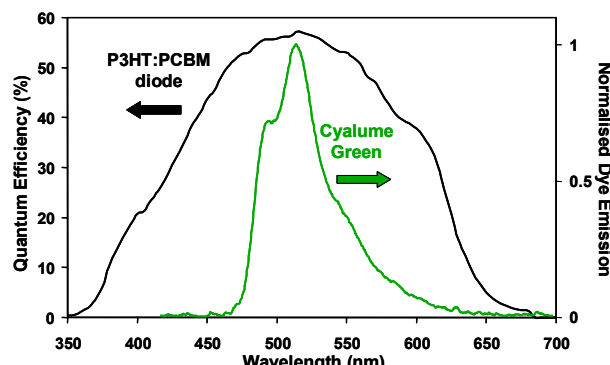


Figure 2: Quantum efficiency spectrum of P3HT:PCBM photodiode and normalised emission spectrum of the employed green CL dye. The emission spectrum of the green dye is well matched to the spectral response of the photodiode, enabling high-sensitivity detection.

To test the suitability of our integrated detectors for point-of-care testing we performed a peroxyoxalate CL based bioassay on-chip. Hydrogen peroxide was selected as the model compound for CL based quantitation because it is produced by a number of enzymes in the presence of specific analytes such as alcohol, glucose, and cholesterol. The CL reagents used were bis(2-carbopentyloxy-3,5,6-trichlorophenyl) oxalate

(CPPO), dimethylaminopyridine (DMAP) catalyst and 9,10-diphenylanthracene dye (cyalume green). The CL reaction was initiated by pumping the CL reagent/dye/catalyst and the hydrogen peroxide test solution into a Y-type micromixer. CL emission results from energy transfer from an excited state intermediate to the dye molecule (indirect CL). Figure 2 depicts the CL emission overlap with the spectral responsivity of the polymer detector.

The photodiode response was measured for varying hydrogen peroxide concentrations and then compared to results obtained with a microscope mounted high-sensitivity PMT. Figure 3 illustrates that the polymer detector and the high-sensitivity PMT have a comparable response with a hydrogen peroxide detection limit $<10 \mu\text{M}$.

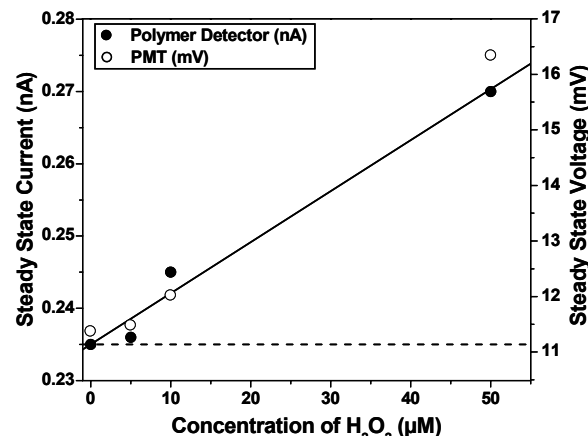


Figure 3: CL signal as a function of hydrogen peroxide concentration for polymer detector (●) and high-sensitivity PMT (○). The dashed line corresponds to the photodiode dark current. Note that for both detectors, a detection limit $<10 \mu\text{M}$ is obtained under non-optimised CL conditions.

3. CONCLUSION

While the presented results already demonstrate a 100-fold sensitivity gain compared to previous work with organic small molecule photodiodes [3], we anticipate a further 100 to 1000-fold improvement in the limit-of-detection by optimisation of the chemiluminescence assay, reduction of the background signal by light-proofing, and improvements to the photodiode fabrication protocol.

REFERENCES

- [1] A.M. Jorgensen, K.B. Mogensen, J.P. Kutter, O. Geschke; *Sens. Actuator B-Chem* 2003, 90, 15-21.
- [2] E.M. Barrett, X. Wang, P.N. Stavrinou, D.D.C. Bradley; unpublished
- [3] O. Hofmann, P. Miller, P. Sullivan, T. S. Jones, J.C. deMello, D.D.C. Bradley, A.J. deMello; *Sens. Actuator B-Chem* 2005, 106, 878-884.

DETECTION OF ANTIBODIES IN 10 μ m WELLS ON MICRO-ARRAYED CELL CHIPS BY 2D-SPR AFFINITY IMAGING

**Masayasu Suzuki¹, Shintaro Hane¹, Toyohiro Ohshima¹, Yasunori Iribe¹
and Tatsuya Tobita²**

¹Faculty of Engineering, University of Toyama, Toyama, 930-8555 Japan

²NTT Advanced Technologies Corporation, Atsugi, Kanagawa, 123-4567 Japan

Abstract

This paper reports the first success of mouse IgG detection in 10 μ m I.D. micro wells on micro-arrayed cell chips by using a two-dimensional surface plasmon resonance (2D-SPR) sensor, which features antibody production monitoring of a single B lymphocyte.

Keywords: Surface plasmon resonance, 2D-SPR, Microarray, Cell chip, IgG

1. Introduction

Detection and collection of antigen-specific B lymphocytes for the target antigen is quite important for the development of antibody medicines which are expected as “future medicines”. We are, in Toyama Medical-Bio Cluster Projects, developing the antigen-specific B lymphocytes screening system based on the micro-arrayed lymphocyte chip on which a quarter million of 10 μ m micro-wells, which are approximately the same size of human lymphocytes, are arranged. This screening system consists of a cell seeding units for micro-well array chips, a high resolution detection unit, and an automatic single cell collection unit. We engaged in the developments of novel sensor systems for micro-well array chips.

We focused on a 2D-SPR sensor [1] as a tool for immunochemical monitoring in the micro well. But conventional 2D-SPR sensors can be applied to only the spots over several hundreds μ m scale. In order to realize SPR imaging of 10 μ m wells, further improvements of resolution and sensitivity are required. Since SPR is based on surface waves, its sensitivity might be drastically decreased in small area such as 10 μ m well.

In this study, mouse IgG in micro wells was detected by using the high resolution 2D-SPR sensor (2D-SPR04A, NTT-AT) [2] which we have developed.

2. Experimental

Fig.1 shows the schematic drawing of the sensor system. The sensor system employed the high refractive optical system, 7X microscopic lens and cooled CCD camera. The micro-well array was prepared with a PDMS film on gold sensor film.

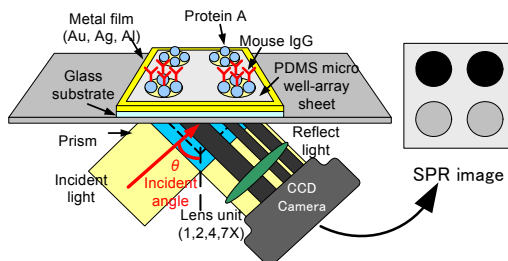


Fig.1 2D-SPR immunosensor for the micro-arrayed cell chip

Protein A was used as a receptor of mouse IgG, and was immobilized onto the gold by covalent binding via 4,4'-dithiodibutyric acid..

3. Results and discussion

With 10 and 30 μm I.D. micro wells, mouse IgG were detected. But little responses could be observed in 10 μm wells. This may caused by sensitivity decrease of SPR sensing in micro area. In order to improve the sensitivity of the SPR sensor, measurement conditions of SPR sensor was optimized. Sensitivity could be extremely improved by the optimization of measurement angle, exposure time, light source intensity and so on. For example, the maximum response was obtained when the measurement angle was set at (SPR angle – 0.5°) as shown in Fig.2.

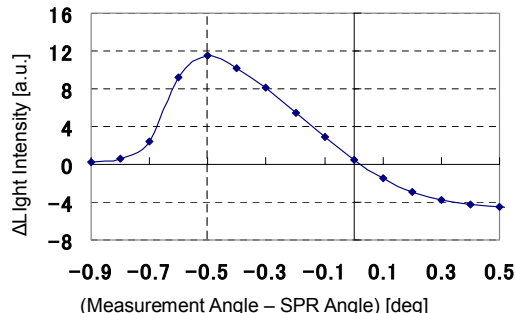


Fig.2 Measurement angles and sensor responses

By the optimization of measurement angle and exposure time of CCD camera, SPR sensitivity was improved by over 20 times, as shown in Fig.3 (at 20mg/ml glucose). Under this condition, IgG was measured in 10 and 30 μm micro wells. In 30 μm micro wells, sensor response to 0.1mg/ml mouse IgG was improved by 5 times. 0.01 mg/ml IgG also could be detected under the same condition. In 10 μm micro wells, 0.1 mg/ml IgG could be successfully detected with this micro-arrayed 2D-SPR sensor (SPR image was shown in Fig.4 and the sensor response was in Fig.5). These results show the possibility of the real-time monitoring for the antibody production by a single B lymphocyte in a micro well.

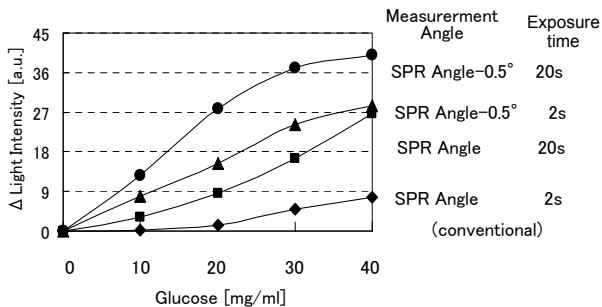


Fig.3 Improvement of SPR sensor sensitivity by optimization of measurement angles and exposure time

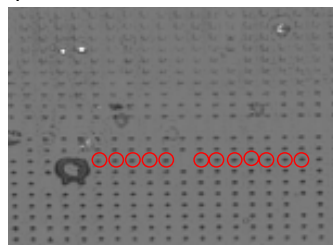


Fig.4 SPR image of 10 μm micro wells filled with mouse IgG

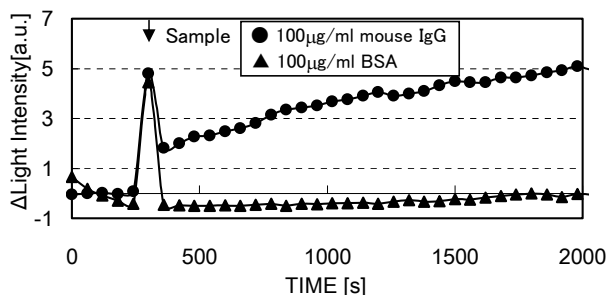


Fig.5 SPR sensor response to mouse IgG and BSA in 10 μm micro wells
(Averaged value obtained with 12 wells indicated with circles in Fig.4)

Acknowledgements

This study was partially supported by Toyama Medical-Bio Cluster Project and Gant-in-aid for Scientific Research on Priority Areas (No.445), both from MEXT.

References

1. J.M.Brockman *et al.*, *J.Am.Chem.Soc.*, **121**, 8044-51 (1999).
2. T.Tobita *et al.*, *Tech.Report of IEICE, OME2000-136*, pp.51-56 (in Japanese)

PYROLYZED CARBON FOR DETECTION OF BIOMOLECULAR INTERACTIONS USING ELECTROCHEMICAL IMPEDANCE SPECTROSCOPY

Jung A Lee*, Seong pil Hwang**, Kwang-Cheol Lee***, Ju hyoun Kwak**,
Se Il Park***, and Seung S. Lee*

*Dept. of Mechanical Engineering and **Dept. of Chemistry, KAIST

***Leading-Edge Technology Group, KRISS, Daejeon, Korea

ABSTRACT

We demonstrate the use of carbon electrode fabricated by pyrolysis process for biological applications. Pyrolyzed carbon electrodes from AZ 9260 are fabricated by photolithography and photoresist thermal decomposition in a N₂ atmosphere. The detection of avidin binding to the pyrolyzed carbon electrode modified with biotin as receptor is carried out successfully by measuring the electrochemical impedance change.

Keywords: Pyrolyzed carbon electrode, Electrochemical impedance spectroscopy, Biomolecular interaction detection

1. INTRODUCTION

Carbon has been one of the most popular materials due to properties such as wide electrochemical stability, low-background noise, and excellent biocompatibility. Pyrolyzed carbon microstructures, fabricated by photolithography and photoresist thermal decomposition in inert atmosphere, have been reported for various applications such as microbatteries, image sensors, and biochemical sensors [1~3]. Pyrolyzed carbon electrodes can have complex and fine shapes and are reducible compared to carbon ink by silk screen printing or carbon pastes. In this paper, we demonstrate the use of carbon electrode fabricated by pyrolysis process for biological applications. Biotin and avidin are selected as receptor-ligand model system and avidin detection is carried out on the pyrolyzed carbon electrode modified with biotin by measuring the electrochemical impedance change.

2. EXPERIMENTAL

Fig. 1(a) shows a schematic view of a device with a pyrolyzed carbon working electrode, an Au counter electrode, and a reference wire for electrochemical impedance measurement. The carbon electrode is modified with biotin for detection of avidin binding using the electrochemical impedance spectroscopy, as shown in Fig. 1(b). Fig. 2 shows the fabrication process of a pyrolyzed carbon electrode device for electrochemical impedance experiment. Positive photoresist, AZ 9260, is spin-coated at 5000 rpm onto the wafer with 0.8 μm-thick SiO₂ and developed after baking on a hotplate at 110°C. The pyrolysis of patterned AZ 9260 is carried out at temperature 1000°C for 30 min in a N₂ atmosphere. Fig. 3 shows the (a) thickness change, (b) surface roughness, (c) resistivity, and (d) specific contact resistivity (ρ_c) of pyrolyzed

carbon versus pyrolysis temperature between 600°C and 1000°C. The pyrolyzed AZ 9260 thickness decreases from 14% to 19% of the initial thickness as the temperature increases from 600°C to 1000°C. The resistivity decreases from 13.3 kΩ-cm to 9 mΩ-cm as the temperature increases from 700°C to 1000°C.

3. RESULTS

The electrochemical measurement system consists of an Au counter electrode, an Ag reference wire, and a carbon working electrode pyrolyzed at 1000°C with AZ 9260. The measurement is carried out in 100 µl of 10 mM PBS (pH 7.4) containing 10 mM KCl and 10 mM Fe(CN)₆ as electrolytic solution. The impedance spectra are measured from 2 kHz to 50 mHz at E=111 mV with 10 mV_{AC}. Fig. 4 shows FT-IR spectra of carbon electrode pyrolyzed at 700°C before and after O₂ plasma treatment. A carbonyl peak of plasma-treated carbon is apparent at 1585 cm⁻¹ and increases compared to plasma-untreated electrode. The carbon electrode is incubated in the ethanol with 50 mM EDC/NHS for 2 hr and then kept in the ethanol with 1 mg biotin (EZ-link amine-PEO₂-biotin, Pierce) for 2 hr. The biotin-modified carbon electrode is incubated for 1 hr in the 10 mM PBS (pH 7.4) with 10% triton X-100 to reduce non-specific binding of avidin. Fig. 6 shows cyclic voltammetry results of biotin-modified carbon electrodes before and after 500 µg/ml avidin binding. Fig. 6 shows the impedance measurement results on biotin/triton-modified carbon electrode before and after 500 µg/ml avidin binding compared to biotin/triton-unmodified electrode as a Nyquist plot. The noticeable increase of impedance modulus and phase is observed upon the avidin binding onto the carbon electrode modified with biotin compared to unmodified electrode. Fig. 7 shows the electron-transfer resistance (R_{et}) at the biotin-modified carbon electrodes versus avidin concentration between 50 ng/ml and 500 µg/ml. As the avidin concentration increases, R_{et} increases due to the enhanced avidin binding on the biotin-modified carbon electrodes. In this experiment, we employed the pyrolyzed carbon electrode for avidin detection using electrochemical impedance spectroscopy and avidin was detected successfully on the pyrolyzed carbon electrode modified with biotin by measuring the electrochemical impedance change.

4. CONCLUSIONS

We have fabricated carbon electrodes fabricated by pyrolysis process for biomolecular interactions. The pyrolysis of patterned AZ 9260 is carried out at temperature 1000°C for 30 min in a N₂ atmosphere, following 300°C for 3 hr at ramping rate of 10 °C/min. The pyrolyzed AZ 9260 thickness decreases from 14% to 19% of the initial thickness as the temperature increases from 600°C to 1000°C. The resistivity decreases from 13.3 kΩ-cm to 9 mΩ-cm as the temperature increases from 700°C to 1000°C. The detection of avidin binding to the pyrolyzed carbon electrode modified with biotin as receptor is carried out successfully by measuring the electrochemical impedance change.

REFERENCES

1. C. Wang, G. Jia, L. H. Taherabadi, and M. Madou, *J. Microelectromech. Syst.*, 14 (2), 348 (2005).
2. M. Liger and Y-C. Tai, 19th IEEE Int. Conf. on MEMS, 106 (2006).
3. K. Naka, T. Hashishin, J. Tamake, and S. Konishi, 19th IEEE Int. Conf. on MEMS, 518 (2006).

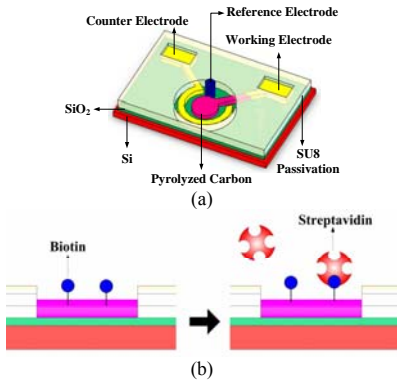


Figure 1. (a) Schematic view of a device with a pyrolyzed carbon working electrode, Au counter electrode, and reference wire for electrochemical impedance measurement and (b) a biotin-modified carbon electrode for detection of avidin binding.

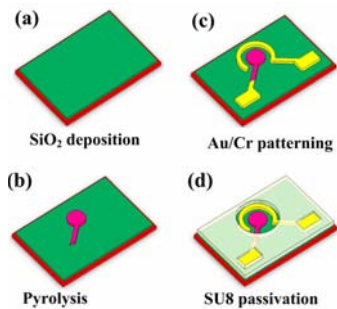


Figure 2. Fabrication process of a pyrolyzed carbon electrode device.

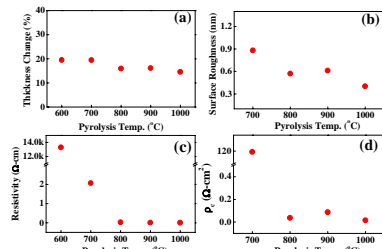


Figure 3. (a) Thickness change, (b) surface roughness, (c) resistivity, and (d) specific contact resistivity (ρ_c) of pyrolyzed carbon versus pyrolysis temperature.

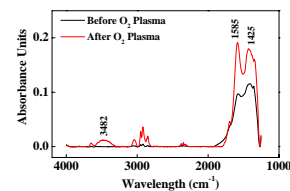


Figure 4. FT-IR spectra of carbon electrode pyrolyzed at 700°C before and after O₂ plasma treatment.

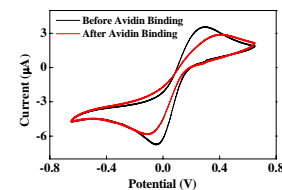


Figure 5. Cyclic voltammetry results of biotin-modified carbon electrodes before and after 500 µg/ml avidin binding.

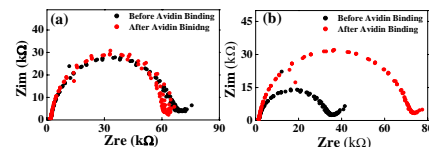


Figure 6. Faradaic impedance spectroscopy of (a) biotin/triton-unmodified and (b) biotin/triton-modified carbon electrodes before and after 500 µg/ml avidin binding as a Nyquist plot.

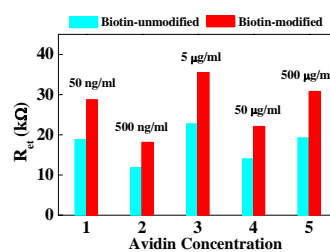


Figure 7. Change of the electron-transfer resistance (R_{ct}) at the biotin-modified carbon electrode as a function of avidin concentration. R_{ct} data are extracted from the corresponding Nyquist diagrams.

Kwang-Cheol Lee, Korea Research Institute of Standards and Science (KRISS), Daejeon, Korea, e-mail: kclee@kribs.re.kr

NON-SURFACE-BINDING LABEL-FREE QUANTIFICATION OF PCR PRODUCT WITH FAST AND SEQUENTIAL DETECTION CAPABILITY

Maesoon Im^{1*}, Seong-Jin Kim¹, Kyutae Yoo^{2*},
Jeoyoung Shim², Kyusang Lee², Younja Cho², Wonseok Chung²,
Christopher Ko², and Euisik Yoon³

¹Dept. of EECS, Korea Advanced Institute of Science and Technology (KAIST),
Republic of Korea

²Bio Lab, Samsung Advanced Institute of Technology, Republic of Korea

³Dept. of Electrical and Computer Engineering, University of Minnesota, USA

*Two authors contributed equally.

Abstract

This paper reports non-surface-binding, label-free PCR product quantification using a field effect transistor as a DNA sensor. Fast and sequential detection of DNA samples has been achieved without regeneration of sensing surface by using readout circuitry integrated with FET DNA sensors. In addition, various PCR amplicon concentrations are successfully quantified.

Keywords: DNA chip, PCR, field effect transistor, label-free detection, non-surface-binding, sequential detection

1. Introduction

It has been reported that field effect transistors (FET) can be used for the detection of PCR products [1, 2]. In the previous works, the detection was achieved by the surface-binding DNAs on the transistors. Therefore, prior to the detection of PCR products, the deposition of a positively charged layer, such as poly-L-lysine, on the sensing region was required for electrostatic association. The introduction of additional layers lengthens the total analysis time, and can be a noise source due to the variation of each deposition in case of sequential sensing. In this paper, we first present a fast, label-free FET sensor which detects PCR products with no surface binding mechanism.

2. Device Structure

Figure 1 shows a cross sectional view of the proposed FET DNA sensor. The device is fabricated by using standard 1.0 μm CMOS processes with an additional etching step in poly silicon gate region. The gate oxide (about 25nm) is exposed to sample solution as a sensing layer. Platinum layer is deposited and patterned to be used as a

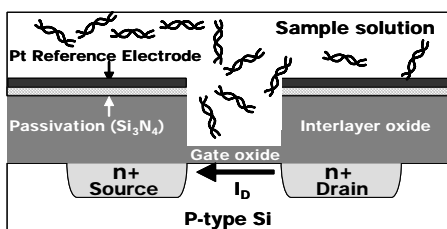


Figure 1. Cross section of the proposed field effect transistor for DNA detection.

reference electrode which applies bias voltage to the gate through electrolyte solution.

The surface potential on the gate oxide is determined by the negative surface charge formed at a given ionic strength from the reaction equilibrium of SiO₂ surface and pH 6 solution [3]. The influx of PCR amplicon solution of similar pH will change the surface potential mainly as a combined result of increased charge density and ionic strength. This event is detected by measuring the decrease in drain current resulting from the reduction of electron carrier concentration in the channel of field effect transistors.

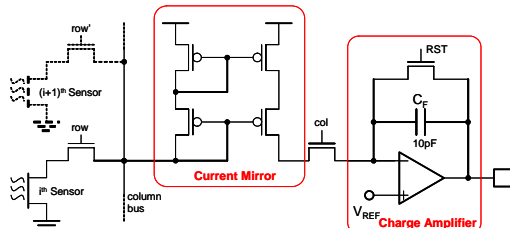


Figure 2. Schematic of integrated readout circuit.

The fabricated device consists of 16×12 arrays to collect statistically-sufficient data points at once. We designed n-type FET arrays with addressing and readout circuits. Each column has a current mirror and the whole array shares a charge amplifier as shown in Figure 2. The current mirror copies the current from a selected pixel and the charge amplifier converts current into voltage. Figure 3 shows the fabricated sensor chip, the magnified view of FET sensors and its custom jig. The chip is located inside the jig (shown in a dashed line) to be immersed in sample solution delivered through microfluidic channels.

3. Experimental Results

The PCR of 25 cycles has been performed for *Staphylococcus aureus* of 249-base-pair and 460-base-pair, respectively. Negative control samples employed the same protocol except for the plasmid template. Figure 4 shows the experimental results for PCR amplicon solutions and negative control samples. Since DNAs are not required to be bound to the sensor surface, fast and sequential detection of various DNA samples can be achieved. Sensing chamber is washed with 0.01mM phosphate buffer solution (pH 6) prior to every injection of samples. All fluids are introduced with a flow rate of 10mL/min. Figure 5 shows the response characteristics after introduction of PCR products. Response time is measured under 10 sec, which is by an order of magnitude faster than that of the previous work [1]. Various PCR amplicon concentrations are successfully quantified as shown in Figure 6. Surface potential increases monotonously as concentration increases.

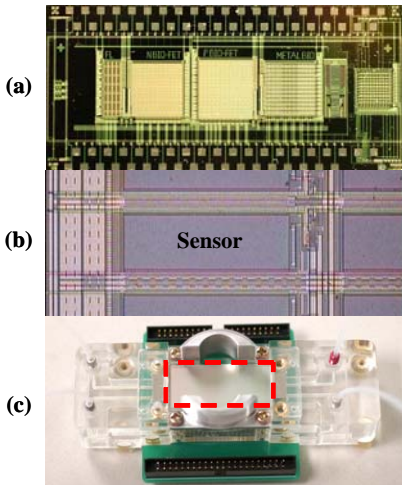


Figure 3. (a) Photograph of the fabricated DNA sensor chip; (b) Magnified view of a sensing element; (c) Microfluidic assembly jig in which the fabricated chip (dashed line) is loaded upside down.

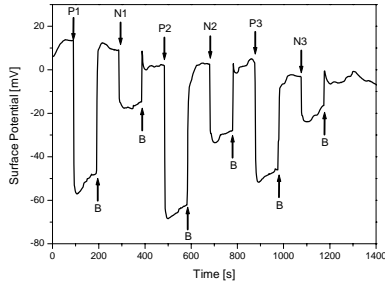


Figure 4. Sequential detection of various samples. “P” denotes PCR product injections while “N” denotes negative control sample injections. Number means different concentrations and template types: (1) 3ng/ μ L, 249bp, (2) 6ng/ μ L, 460bp and (3) 3ng/ μ L, 460bp. Arrows with “B” indicate the injection of 0.01mM phosphate buffer solution for washing.

4. Conclusions

We have demonstrated non-surface-binding quantification of PCR products using field effect transistors integrated with readout circuitry. DNA samples have been sequentially and instantly detected without renewal of sensing surface. Additionally, diverse concentrations of PCR amplicons have been successfully discriminated.

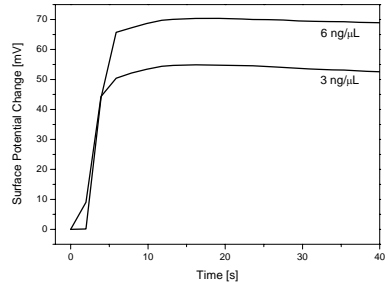


Figure 5. Sensor response after introduction of PCR product of 460bp *Staphylococcus aureus*.

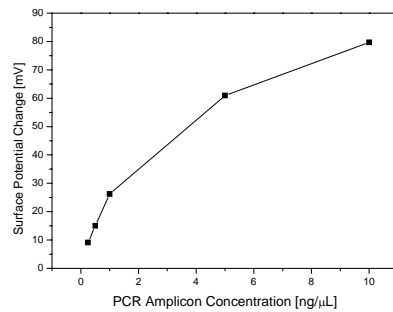


Figure 6. Quantification of five PCR amplicon samples. (0.25ng/ μ L, 0.5ng/ μ L, 1ng/ μ L, 5ng/ μ L and 10ng/ μ L)

References

1. C.-S.J. Hou, N. Milovic, M. Godin, P.R. Russo, R. Chakrabarti, and S.R. Manalis, *Label-Free Microelectronic PCR Quantification*, Anal. Chem., Vol.78, pp.2526-2531, 2006.
2. F. Pouthas, C. Gentil, D. Cote, G. Zeck, B. Straub, and U. Bockelmann, *Spatially resolved electronic detection of biopolymers*, Physical Review E, 70, 031906, 2004.
3. R.E.G. van Hal, J.C.T. Eijkel, and P. Bergveld, *A general model to describe the electrostatic potential at electrolyte oxide interfaces*, Advances in Colloid and Interface Science, Vol.69, pp.31-62, 1996.

A NEW APPROACH TO THE EVALUATION OF DIELECTROPHORESIS

Yukihsia Wada, Yoshio Tsunazawa and Naoji Moriya

Technology Research Laboratory, Shimadzu Corporation, Kyoto, Japan
wadayuki@shimadzu.co.jp

Abstract

We propose a new approach to measure the dielectrophoretic property of colloidal nanoparticles by diffraction intensity of a temporally induced grating. We obtained the dependence of dielectrophoresis on the frequency of the applied voltage for silica particles of 8nm in diameter by using the optical method.

Keywords: nanoparticle, dielectrophoresis, density grating

1. Introduction

Nanoparticles are widely used in many fields such as pharmaceuticals, biotechnology and semiconductor industry. The dielectrophoresis (DEP) is known as a efficient tool for handling nanoparticles [1][2], because DEP exerts forces to the particles with induced dipole moment toward the more intense electric field. Many reports described the function of DEP, however, the size of the particle concerned was mostly in the ranges of a micrometer or a sub-micrometer level, while we intended to deal with particles of 1nm -100nm in diameter. The difficulty of DEP for these small particles is the decreased sensitivity, because the DEP force is proportional to the third power of diameter of the particle.

2. Theory

To attain more sensitive detection, we propose a new technique, based on light diffraction from the periodic modulation of particle density induced by DEP. Increased sensitivity is due to the fact that many nanoparticles thus modulated serve to diffract light in phase to a particular diffraction order.

3. Experimental

We use the system shown in Fig.1, where the particles are contained in a sample cuvette having a pair (L and R) of comb electrodes, patterned by lithography on an inner side of the cuvette window. A picture of the electrodes is shown in Fig.2. A radio frequency (r-f) voltage applied between the two electrodes induces the DEP force to the particles, and the particles are forced to migrate toward the space between R and L, forming a density grating. Then, once again as in Fig.1, we illuminate the density grating by the collimated light. We can use the diffracted light intensity as a measure of the strength of DEP. Due to the special electrodes design as shown in Fig.1 and Fig.2, the pitch of the particle density grating (40 μ m) is twice as large as the teeth of the

electrode ($20\mu\text{m}$). Thus the first order diffraction from the density grating is separated from the undesirable diffraction from the electrodes.

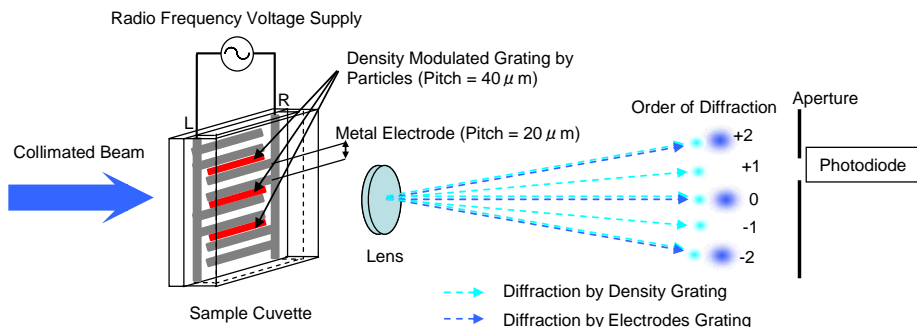


Figure 1. Schematics of the system.

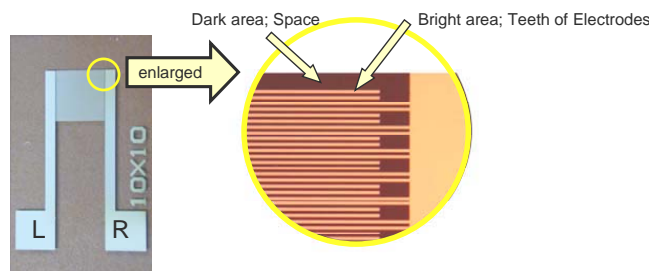


Figure 2. Picture of teeth of electrodes.
Bright Area; electrodes, Dark Area; space between teeth of electrodes.

3. Results and discussion

An example of measurement is shown in Fig. 3, which is a result with silica particles of 8nm in diameter. At the beginning, when the r-f voltage is turned on (DEP is ON) during 0.2 seconds, the signal increases, i.e., the particles migrate by DEP and form a density grating. When the DEP is off, the signal decreases exponentially towards the original level. The ten traces in the figure correspond to different frequency of applied voltage ranging from 200kHz to 500kHz . A plot of frequency dependence is shown in Fig. 4, where the ordinate is the diffraction intensity. Because the diffracted light power is proportional to the square of the density modulation of the particles [3], it can be related to the efficiency of the DEP.

The decay rate of the curves in Fig.3 is related with the diffusion coefficient of the particles. Then, the diffusion coefficient can be easily converted to the particle diameter based on the Einstein-Stokes relation, using the known viscosity and absolute temperature [4].

In addition to the silica particles mentioned above, we have carried out measurements

for polystyrene particles, protein suspensions (such as bovine serum albumin and cytochrome C) and nano particles of gold. So the proposed method is expected to have various fields of application in research and industry of nanoparticles.

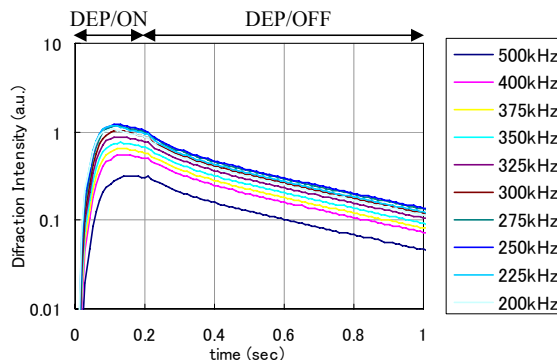


Figure 3. Raw trace of the diffraction intensity for silica particles of 8 nm in diameter.
DEP/ON; for measurement of DEP force, DEP/OFF; for measurement of the diffusion coefficient of nanoparticles.

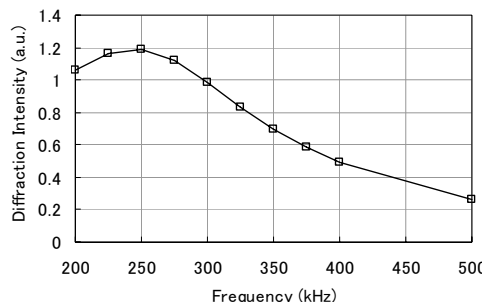


Figure 4. Frequency property for silica particles of 8nm in diameter.
The diffracted light power of 0.1 seconds after DEP start in Fig.3 was plotted

References

1. H.A. Pohl, *Dielectrophoresis*, (Cambridge University Press, 1978).
2. M.Washizu, S. Suzuki, O. Kurosawa, T. Nishizaka, T. Shinohara, "Molecular dielectrophoresis of biopolymers", IEEE Trans. on Industry Applications, 30, pp.835 – 843, (1994).
3. M.Terajima, "TRANSLATIONAL DIFFUSION OF INTERMEDIATE SPECIES IN SOLUTIONS", Res.Chem.Intermed, 23, pp. 853-901, (1997)
4. Y. Wada, S. Totoki, M. Watanabe, N. Moriya, Y. Tsunazawa, and H. Shimaoka, "Nanoparticle size analysis with relaxation of induced grating by dielectrophoresis", Opt. Express 14, pp. 5755-5764, (2006)

PEPTIDE BASED PROTEIN KINASE DETECTION USING A NANOMECHANICAL DYNAMIC MICROCANILEVER

**Kyo Seon Hwang^{1,2}, Jeong Hoon Lee¹, Dong Won Chun¹, Byung Hak Cha^{1,2},
Ga Young Han¹, Jung Ho Park², Eun Gyeong Yang¹, Dae Sung Yoon¹, and
Tae Song Kim¹**

¹Korea Institute of Science and Technology, Seoul 136-791, Republic of Korea

²Korea University, Seoul 136-701, Republic of Korea

E-mail: dsyoon@kist.re.kr, tskim@kist.re.kr

Abstract

A nanomechanical microcantilever promises to bring about revolution in the field of chemical and biological analysis system development. We report the peptide immobilized nanomechanical microcantilever operated in dynamic vibration mode for quantitative label-free detection of protein kinase A. The detection principle of dynamic cantilever is that specific interaction on the microcantilever surface lead to the dynamic response change of microcantilevers. We achieved the protein kinase A detection in the low concentration as much as 6.6 pM through measuring the dynamic response change of microcantilever.

Keywords: Nanomechanics, Microcantilever, Protein kinases, Peptide

1. Introduction

Protein kinases are key regulators of cell function that constitute one of the largest and most functionally diverse gene families. Protein kinases that serve as molecular switches are by definition highly dynamic proteins that can toggle between different conformational states [1]. Because of these important roles of protein kinases, they get to be major targets for drug delivery. In this point of view, to understand functions of protein kinases, a detection of small amount protein kinases is essential issue. Here, we report the quantitative detection of protein kinase A (PK A) on a nanomechanical dynamic microcantilever, described by resonant frequency shift.

2. Experimental

In order to achieve direct mechanical response, nanomechanical dynamic microcantilever was fabricated by using micromachining process. Fig. 1 shows the measurement schemes and a SEM photograph of the nanomechanical dynamic cantilever arrays designed for dynamic self-exciting and sensing. For active role of a sensor in the biomolecules interaction, we deposited a gold (50 nm) layer for the recognition layer on the nanomechanical dynamic microcantilever. After the gold deposition on microcantilever, the peptide inhibitor was immobilized by using calixcrown self-assembled monolayers and streptavidin. And then, we performed the biological passivation by using BSA as shown in Fig. 2. Before and after PK A was interacted with peptide inhibitor on the microcantilever, we measured the resonant frequency of the microcantilever. We calculated the resonant frequency shift values due to the PK A-peptide inhibitor interaction via measured resonant frequencies.

3. Results and discussion

We investigated the dynamic response change of the microcantilever caused by specific binding between PK A and inhibitor. Fig. 3 shows the experimental results of the mechanical response as a function of the PK A concentration ranging from 6.6pM to 66nM and we can achieve the detection limit up to pico molar level. This result (Fig. 3) manifest that the surface stress is proportional to the population of PK A - peptide inhibitor pairs, indicating that the intermolecular interactions between PK A - peptide inhibitor pairs generate the compressive stress [2]. Moreover, it clearly reveals that ATP affect PK A - peptide inhibitor interaction. The specific binding property of PK A and its inhibitor was validated by monitoring the resonant frequency of microcantilevers when they are dipped into the myoglobin antigen. When this happened, there was no resonant frequency shift of microcantilevers, indicating that the peptide inhibitor exhibit the specificity in binding of PK A. Fig. 4 shows the SPR analysis result of quantitative PK A - peptide inhibitor interaction. The results from Fig 3. and Fig. 4. indicate that nanomechanical dynamic microcantilever has high analytical sensitivity and wide dynamic range than SPR.

4. Conclusions

We demonstrated the label-free detection of protein kinases in the low concentration with the nanomechanical dynamic microcantilever. It indicates that microcantilever is

very useful tool to detect the biomolecules of small amount. Consequently, the nanomechanical cantilever can provide a simple, label-free electric detection for bioanalysis system.

Acknowledgement

The authors are grateful for the financial support by Intelligent Microsystem Center sponsored by Korea Ministry of Science and Technology as a part of the 21st century's Frontier R&D Projects (Grant MS-01-133-01) and National Core Research Center for Nanomedical Technology sponsored by KOSEF (Grant R15-2004-024-00000-0).

References

- [1] A. Johnson, et al., 101, Chem. Rev., 2243-2270 (2001).
- [2] J. H. Lee, et al., 84, Appl. Phys. Lett., 3187-3189 (2004).

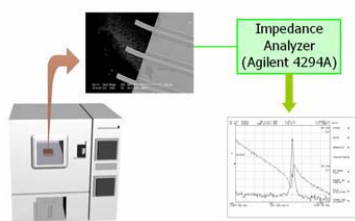


Figure 1. Measurement schemes and SEM photograph of the nanomechanical dynamic microcantilever arrays designed for dynamic self-sensing.

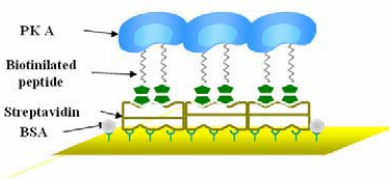


Figure 2. A schematic diagram showing the specific interaction between the peptide and protein kinase A.

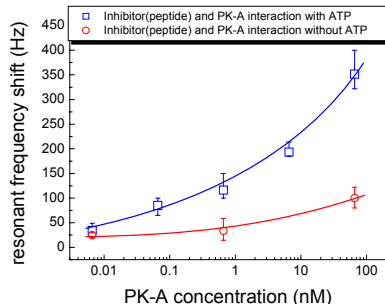


Figure 3. Resonant frequency changes as a function of PK A concentration.

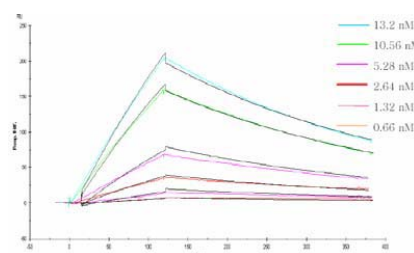


Figure 4. Surface plasmon responses as a function of protein kinase A concentration.

NANOSTRUCTURED SURFACE AS EWOD COUNTER ELECTRODE FOR MATRIX-FREE MASS SPECTROMETRY ANALYSIS

N. Verplanck¹, Y. Coffinier^{1,2}, M. Wisztorski³, G. Piret^{1,2}, C. Delhaye³, V. Thomy¹, I. Fournier³, JC. Camart¹, P. Tabourier¹ and R. Boukherroub^{1,2}

¹IEMN - UMR CNRS 8520, Cité scientifique, 59652 Villeneuve d'Ascq cedex, France

²IRI, Cité scientifique, 59652 Villeneuve d'Ascq cedex, France

³Laboratoire de Neuroimmunologie des Annélides, Cité scientifique, 59652 Villeneuve d'Ascq, France
(vincent.thomy@iemn.univ-lille1.fr)

Abstract

This paper reports on the preparation of a superhydrophobic nanostructured surface consisting of chemically modified silicon nanowires for the realisation of EWOD counter electrode and matrix-free mass spectrometry analysis. The main advantages associated with such a substrate are: (i) flow resistance of droplets considerably reduced, (ii) simple realisation of hydrophilic and functionalized pads in the superhydrophobic surface allowing analytes trapping and enhancement of the liquid/surface interaction, (iii) subsequent analysis by matrix-free desorption/ionization MS-DIOS on these pads.

Keywords: EWOD, Superhydrophobic surfaces, Silicon nanowires, DIOS-MS

1. Introduction

Current digital microfluidic systems are often based on the electrowetting on dielectric (EWOD) effect which allows droplet handling basic operation [1]. So far, the best EWOD results obtained for MALDI analysis concern a set up consisting of two parallel plates, a base and a cover preventing from evaporation, between which microdroplets of biological liquid are sandwiched [2]. Classically, the base is made of an electrode array coated with a bilayer composed of a dielectric and an amorphous fluoropolymer plane layer. The cover, working as a counter electrode, is made of a conductive substrate (i.e. silicon) coated with the same amorphous fluoropolymer layer.

This paper reports on the preparation of a superhydrophobic nanostructured surface consisting of chemically modified silicon nanowires (SiNWs) for the realisation of EWOD counter electrode and matrix-free mass spectrometry analysis. The main advantages associated with such a substrate are: (i) flow resistance of droplets considerably reduced, (ii) simple realisation of hydrophilic and functionalized pads in the superhydrophobic surface allowing analytes trapping and enhancement of the liquid/surface interaction, (iii) subsequent analysis by matrix-free desorption/ionization MS-DIOS on these pads.

2. Theory

The silicon nanowires used in the present study were prepared by the so-called vapor-liquid-solid (VLS) mechanism [3-6]. The fundamental process is based on metal catalyst directed chemical vapor deposition of silicon. In this technique, the diameter of the nanowires is determined by the diameter of the catalyst particles and therefore, the method provides an efficient means to obtain uniform-sized nanowires (Figure 1).

First, a thin film (4 nm thick) of gold was evaporated on a silicon (Si) substrate. Gold nanoparticles with a high size distribution were obtained due to metal dewetting on the surface. Exposure of the gold-coated Si surface to silane gas (SiH_4) at a pressure of 100 mT at 540°C for 60 min (Q: 40 sccm) led to silicon nanowires growth. The obtained nanowires are terminated by gold seeds according to the VLS growth mechanism. They display a mean diameter comparable to the diameter of the initial gold nanoparticles catalyst and are several microns long as evidenced by SEM image (Figure 2).

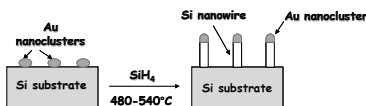


Figure 1. Silicon nanowires growth using VLS technique

Wettability of a solid surface is a characteristic property of materials and is controlled by both surface roughness and surface chemical composition. To reach superhydrophobicity, a combination of surface roughness and low surface energy is required [7]. In the present work, superhydrophobic SiNWs surfaces (contact angle ~ 150°) were prepared by the combination of surface roughness and chemical modification with octadecyltrichlorosilane [8]. The surface roughness can be controlled by the SiNWs density. The as-grown SiNWs display a roughness of several hundreds nanometers as estimated by AFM imaging.

3. Experimental

The bottom plates were fabricated by using standard microfabrication techniques. The bottom glass plate consists of an array of independently addressable control electrodes (1 mm²) patterned in a 10 nm thin nickel layer, which is further coated with a SU-8 layer (2 μm) as a dielectric (Figure 3). A hydrophobic layer of Teflon AF 1600 (20 nm) is then deposited (contact angle = 115°). Silicon nanowires are synthesized on silicon substrate (counter electrode) using the well-known Vapor-Liquid-Solid (VLS) technique (Presented in 2. Theory - Figure 1 and 2) [5]. The formation of a superhydrophobic layer on the silicon nanowires surface was achieved by chemical derivatization with octadecyltrichlorosilane (OTS) (contact angle = 149°) while the DIOS pads are prepared by a simple exposure of the octadecyl-terminated silicon nanowires surface to UV-ozone through a physical mask containing 20x50 μm² apertures. Thus, we can locally control the wetting properties of a macroscopic hydrophobic surface.

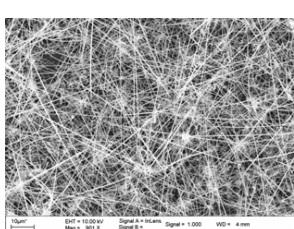


Figure 2: SEM view of SiNWs

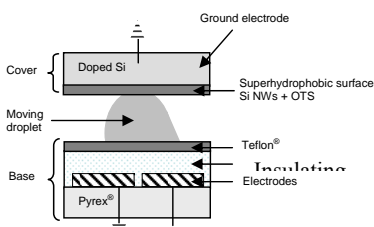


Figure 3: Set up of the EWOD platform

4. Results and discussion

The gap between two plates is 300 μm so that a 1 μL droplet of biological liquid (Substance P amide, 5.10 $^{-5}$ Mol.L $^{-1}$) can be moved under 68 V while 100 V were required to displace the same droplet with a classical cover (silicon wafer coated with Teflon). Finally, mass spectrometry analysis of the targets in the hydrophilic DIOS pads is carried out using MALDI TOF-TOF with no organic matrix. It has been shown that silicon nanowires can successfully be used as a substrate for MS analysis without any organic matrix [9] (Figure 2).

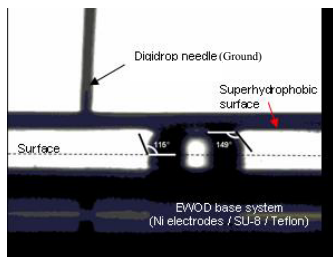


Figure 1: Droplet sandwiched between two plates system (base coated with Teflon, cover with NW / OTS)

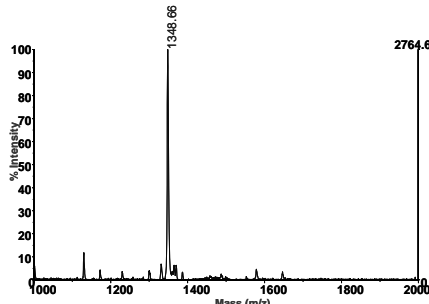


Figure 2: Mass spectrum of Substance P amide on VLS hydrophilic pad

5. Conclusions

EWOD and MALDI is often combined to allow sample displacement and analysis on the same chip. MALDI requires the use of a matrix which complicates the microsystem. We have shown that we can use superhydrophobic nanostructured counter electrode for EWOD displacement and as DIOS target. Moreover, the applied voltage dramatically decrease.

Acknowledgements

The Centre National de la Recherche Scientifique (CNRS) and the Nord-Pas-de Calais region are gratefully acknowledged for financial support.

References

- [1] S.K. Cho, H. Moon and C.J. Kim, *J. Microelectromech. Syst.* **12**, 70 (2003)
- [2] A.R. Wheeler, H. Moon, C.A. Bird, R.R. O. Loo, C.J. Kim, J.A. Loo, R. L. Garrell, *Anal. Chem.* **77**, 534 (2005)
- [3] R. S. Wagner, W. C. Ellis, *Appl. Phys. Lett.* **4**, 889 (1964).
- [4] Y. Cui, X. Duan, J. Hu, C. M. Lieber, *J. Phys. Chem. B* **104**, 5213 (2000).
- [5] B. Salhi, B. Grandidier and R. Boukherroub, *J. Electroceram.* **16** (2006) 15-21
- [6] B. Salhi, B. Gelloz, N. Koshida, G. Patriarche, R. Boukherroub, *Phys. Stat. Sol. (C)* (*accepted*)
- [7] N. A. Patankar, *Langmuir* **20**, 8209 (2004)
- [8] R. Boukherroub et al. (*to be published*)
- [9] E. P. Go, J. V. Apon, G. Luo, A. Saghatelian, R. H. Daniels, V. Sahi, R. Dubrow, B. F. Cravatt, A. Vertes and G. Siuzdak, *Anal. Chem.* **77**, 1641 (2005)

MEMS-BASED PICOLITER ELECTROCHEMICAL CELL ARRAY FOR THE FABRICATION OF OLIGONUCLEOTIDE CHIPS

Thierry Leïchlé¹, Emeline Descamps², Bruno Corso², Sébastien Laurent²,
Pascal Mailley², Thierry Livache², Jean-Bernard Pourcel¹,
Christian Bergaud¹ and Liviu Nicu¹

¹ Laboratory of Analysis and Architecture of Systems, CNRS, Toulouse, France

² SPrAM CNRS- CEA Grenoble, France

Abstract

An array of microcantilevers, allowing electrochemical reactions to take place inside picoliter droplets, was used to fabricate a simple DNA chip bearing two ODN probes as a proof-of-concept. The electrochemical cells consist of drops of electrolyte deposited onto a conductive substrate by microcantilevers that incorporate a fluidic channel patterned with a gold electrode. This tool allows structuring surfaces with micrometer size ODN spots through electro-co-polymerization of pyrrole and ODN bearing pyrrole monomer. The described procedure enables the rapid fabrication of biochips with a controlled probe density and ODN spots which conserve their specificity.

Keywords: Electrochemistry, Micropatterning, ODN chips, Polypyrrole

1. Introduction

In the last twenty years, DNA recognition based on its hybridization with oligonucleotide (ODN) probes has received increased attention, especially for the fabrication of ODN chips. This is mostly due to its potential for genetic material analysis as well as the possibility to diagnose genetic diseases. Lately, several tools have been developed in order to decrease the size of these chips by increasing their density [1]. This size reduction is pertinent only if the spots can be printed uniformly. This condition is necessary to properly compare fluorescence signals and validate results. Toward this aim, we propose a method relying on the use of a microcantilever-based deposition tool, presented in [2], that enables the electrodeposition of polypyrrole conjugated with biomolecules onto conductive substrates. Because the printed liquid droplet size and polymer film thickness are controlled by the contact time during deposition and the electropolymerization charge, reproducible spots can be created with this technique.

2. Experimental

Figure 1.a displays the process used for substrate structuration with polypyrrole spots using the cantilever array (shown in Figure 1.b). The ten cantilevers (fabricated as depicted in Figure 2) are loaded with an electrolytic solution containing pyrrole monomers by dipping them in a reservoir drop before being moved to a precise location

above a gold coated sample. The cantilevers are approached to the surface until mechanical contact occurs, leading to the creation of a liquid drop onto the surface. Typical drop diameters range from 5 to 25 μm . An electrochemical pulse of 2V is then applied between the anodically polarized gold substrate and the cantilever used as a counter-electrode. The pulse is applied during few tens of milliseconds, thus enabling polypyrrole electropolymerization onto the surface, before setting back the cantilevers from the surface. The resulting amperogram, e.g. the one shown in Figure 1.c., is used to verify the proper electropolymerization during the experiment.

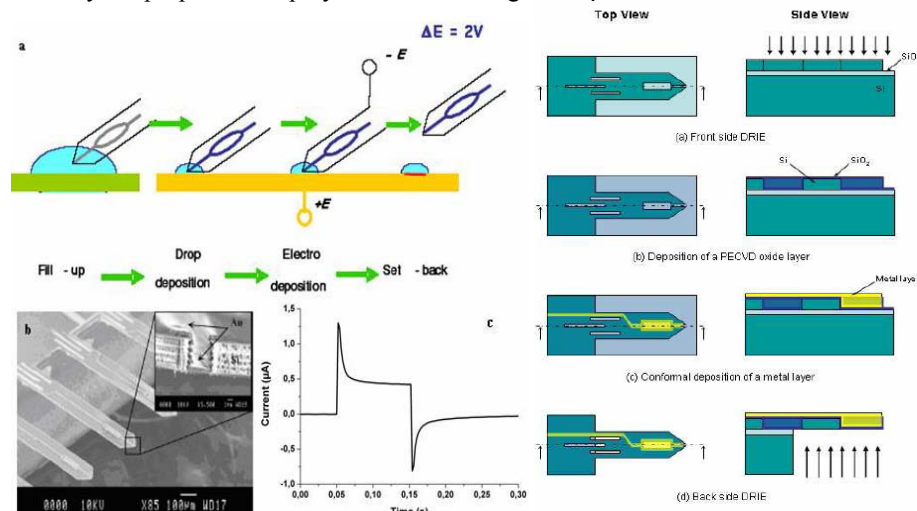


Figure 1. a. Principle of the electrodeposition process, b. SEM pictures of the cantilevers, c. typical resulting amperogram plot

Figure 2. Fabrication process of the cantilevers with metallic electrodes for local electrochemistry

3. Results and discussion

In such a context, ODN probes bearing pyrrole units were electrocopolymerized with unsubstituted pyrrole monomers at the gold surface leading to the localized deposition of biologically active and mechanically stable polymer films [3]. The electrodeposition process was done using an electrolytic aqueous solution containing sodium phosphate buffer saline as supporting electrolyte, pyrrole and pyrrole-ODN. Fluorescence was observed after hybridizing the spots with biotinylated complementary ODN, followed by a streptavidinphycoerythrin revelation, thus proving the biological functionality of the polymer spots. Furthermore, in order to demonstrate the specificity of the coatings toward their DNA targets, we have designed a simple biochip with two different ODN probes (M5 and CP). Figure 3 shows the fluorescence images, obtained after hybridization with M5 and CP complementary targets. As no fluorescence signal is observed on the non specific spots, specificity is demonstrated. Finally statistical operations were carried out on successively deposited droplets without any cantilever

refill (see Figure 4). The good reproducibility of the fluorescence signal provided by each spot highlights the reproducibility of the process and exemplifies the possibility to successively fabricate biochips without refilling the cantilevers.

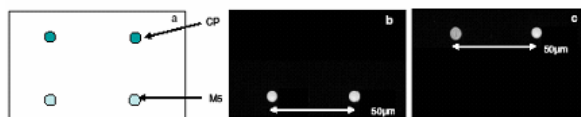


Figure 3. a. Schematic of a fabricated polypyrrole-ODN matrix with one row of CP and one row of M5 ODN, b. Fluorescence picture after hybridization with M5 complementary strand, c. Fluorescence picture after hybridization with CP complementary strand

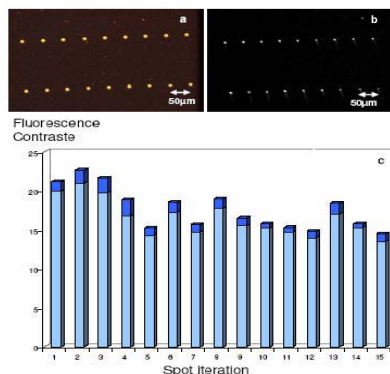


Figure 4. a. Drop optical microscope picture after electropolymerization and cantilever take-off, b. Fluorescence picture after hybridization and revelation. c. Evolution of the average contrast (clear blue) and of the contrast standard deviation (dark blue) calculated for the 10 concomitantly synthesized spots according to the number of deposited spot raw

4. Conclusions

In summary, we present a new electrospotting tool that enables the fabrication of biochips integrating micrometer size ODN spots. This new method of chip synthesis allows the rapid generation of reproducible and specific ODN spots in a parallel way.

Acknowledgements

The partial financial supports of the EC-funded project NaPa (Contract no. NMP4-CT-2003-500120) is gratefully acknowledged.

References

1. J. G. F. Tsai et al., Proc. of IEEE MEMS 2003 conf., pp. 295-298, (2003).
2. T. Leichlé et al., Appl. Phys. Lett. 88, 254108, (2006).
3. S. Szunerits et al., Electroanalysis 17(22), pp. 2001-2017, (2005).

NOVEL FLUORESCENCE DETECTION TECHNIQUE FOR NON-CONTACT TEMPERATURE SENSING IN MICROCHIP PCR

Sudip Mondal and V. Venkataraman

Department of Physics, Indian Institute of Science, Bangalore-560012, India

Abstract

DNA amplification using Polymerase chain reaction (PCR) in a small volume is used in Lab-on-chip systems involving DNA manipulation. For few microliters volume of liquid it becomes difficult to measure and monitor accurately and reproducibly the thermal profile. Conventional temperature sensors are either not biocompatible or too large and hence positioned away from the liquid leading to calibration errors. In this work we present a fluorescence based detection technique that is completely biocompatible and measures directly the liquid temperature.

Keywords: Fluorescence detection, microchip-PCR, SYBR Green, non-contact temperature sensor

1. Introduction

Fluorescence detection in chip-PCR is being used to monitor DNA amplification and calibrate the chip using melting curve analysis [1]. The most common dye used for PCR is double stranded-DNA (ds-DNA) binding SYBR green (SG). It is well known that fluorescence of most dye molecules decreases with temperature. Therefore one may expect that the SG fluorescence signal can be directly used to monitor and control the PCR mix temperature. There are however three problems in implementing this idea in conventional real time microchip PCR systems. First, fluorescence is typically recorded only once per cycle and therefore not suitable for continuous monitoring. Second, the fluorescence is proportional to ds-DNA amount and changes from cycle to cycle depending on the amplification. Lastly, the change in fluorescence with temperature is very small at the beginning of the PCR cycles due to the small initial concentration of template DNA.

In this work we show how these problems can be overcome in a 3 μL silicon-glass microchip that is heated by non-contact induction heating [2]. The technique uses a fast data acquisition system with a low noise Lock-in amplifier for collecting fluorescence data. The calibrated intensity is used to measure and control the in-situ temperature using computer controlled set point for PCR in the silicon-glass microchip.

2. Experimental

The PCR mix is prepared using 2X DyNAmo qPCR kit (Finzymes) containing SG and *Thermus brockianus* DNA polymerase. 50 μL of the mix contains 100 ng of Lambda DNA and 0.5 μM of forward and reverse primers. 6U of *Thermus aquaticus* polymerase is added in excess to overcome adverse surface adsorption effect in

microchip. For fluorescence feedback experiments we added separately 50 ng of a 100 base-pair DNA (called “sensor DNA”) apart from the template and primers in the mix.

SG fluorescence signal is collected using 470 nm blue excitation and 520 nm emission using a silicon photodiode. The photocurrent is measured using fast low noise data acquisition system using a Lock-in amplifier SRS-830 to monitor the fluorescence continuously [3]. For fluorescence feedback, photocurrent is used to compare with the set point provided from the computer.

Silicon-glass microchip is fabricated using MEMS techniques [2]. PCR is performed with 3 μ L volume in a silicon-glass microchip covered with 4 μ L of mineral oil. The microchip is cycled through the temperature cycles using induction heater. For comparison with temperature feedback control, a k-type thermocouple is attached to the secondary.

4. Results and discussion

Fluorescence profile of 30 PCR cycles amplifying Lambda DNA is shown in Figure 1A using thermal profile shown in the inset. The increase in fluorescence envelope indicates successful amplification. During the initial cycles, denaturation and extension fluorescence are very close and becomes well separated at the later cycles. A 100 base-pair sensor DNA is suitably chosen so that it is non-specific to the primers and does not get amplified. Its fluorescence therefore does not change from one cycle to the next (Figure 1B). This large “background” continuous fluorescence signal from the sensor DNA is calibrated against temperature and used to control the heater power during the PCR reaction of Lambda DNA.

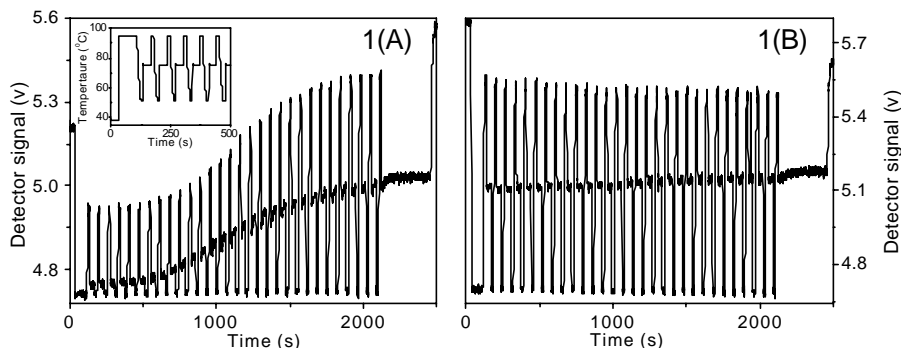


Figure 1: Fluorescence data during PCR of lambda DNA. (A)Normal amplification with inset showing thermal profile and (B) using sensor DNA.

In Figure 2, we compare the temperature and fluorescence data from the chip using conventional temperature control (2A and 2B) of a calibrated thermocouple sensor attached close to the chip with our novel fluorescence feedback control (2C and 2D). Adding sensor DNA to PCR saturates the amplification signal but allows the switching of temperature reproducibly between the set points required for PCR. We perform melting curve analysis before and after the PCR for product specificity.

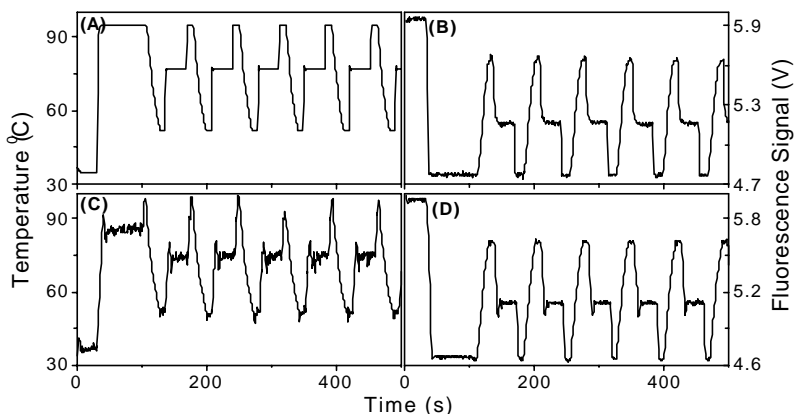


Figure 2: Comparison between temperature and fluorescence feedback control.

Figure 3A shows data corresponding to the sensor DNA before PCR and the amplified product after PCR for both temperature and fluorescence feedback control. This is also confirmed by gel electrophoresis figure 3B.

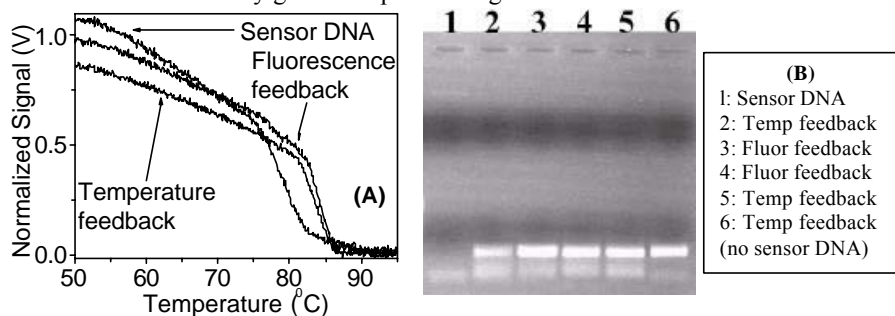


Figure 3. Confirmation of PCR with sensor DNA. Melting (3A) and Gel doc. (3B) of PCR product

5. Conclusions

In conclusion, we have demonstrated a novel method for non-contact temperature sensing and control of microchip PCR reactions using SYBR Green fluorescence detection.

References

1. L.A. Legendre et al, MicroTAS'05; A.R. Prakash et al., M35A, MicroTAS'05
2. D. Pal and V. Venkataraman, A portable battery-operated chip thermocycler based on induction heating, *Sens. Actuators A*, **102**, pp. 151-156 (2002).
3. S. Mondal and V. Venkataraman, In situ monitoring of polymerase extension rate and adaptive feedback control of PCR using fluorescence measurements, *J. Biochem. Biophys. Methods*, **65**, pp. 97-105 (2005).

DEVELOPMENT OF A GOLD-CAPPED NANOPARTICLE LAYER-BASED OPTICAL BIOSENSOR FOR LABEL-FREE DETECTION OF BIOMOLECULAR INTERACTION STUDIES

**Do-Kyun Kim, Minh Hiep Ha, Tatsuro Endo, Yuzuru Takamura and
Eiichi Tamiya**

School of Materials Science, Japan Advanced Institute of Science and
Technology, 1-1 Asahidai, Nomi city, Ishikawa 923-1292, Japan

Abstract

We developed a Localized Surface Plasmon Resonance (LSPR) based label-free optical biosensor. The gold-capped nanoparticle layer chip was applied to the LSPR-based optical biosensor for label-free monitoring the antibody-antigen reaction. For this purpose, the C-reactive protein (CRP) antibody was immobilized on the surface of gold-capped nanoparticle layer chip, which could recognize only CRP antigen. The detection limit was found to be 10 pg/ml by using the CRP antibody immobilized LSPR based label-free optical biosensor.

keywords: Gold-capped nanoparticle layer chip, label-free optical sensor, LSPR, CRP antibody-antigen reaction

1. Introduction

The excitation of LSPR by visible light at an incident wavelength, where resonance would occur, results in the appearance of intense absorption bands. The intensity and position of the SP absorption bands are characteristic of the type of the nanomaterial, the diameter of nanoparticles and their distribution. These methods can detect an immediate change in the interfacial refractive index (RI) of the surrounding medium [1], which is greatly affected by the attachment of biomolecules at the colloid-solution interface. Biomolecule binding induces a change in the color of the sensor substrate, thus providing an easily detectable optical signal. Mie theory predicts a red shift in the position of the absorbance peak (λ_{max}) and an increase in its intensity.

LSPR phenomena have been previously utilized to monitor biomolecular interactions by our group [2] and others [3,4]. In this research, we achieved the improvement of the sensitivity using the gold-capped nanoparticle layer chip that was applied to detect the antibody-antigen recognition reaction.

2. Experimental

For the fabrication of LSPR-based optical biosensor, the surface modified silica nanoparticles (diameter: 100 nm) were aligned onto the gold-deposited slide glass substrate by the Functional Self-Assembled Monolayer (SAM) between them, which is shown in Figure 1. Then, nanoparticle layer was also deposited with gold (300 Å) by using thermal evaporator. White light emerging from the optical fiber bundle was incident onto the gold-capped nanoparticle layer chip from the vertical direction. The reflected light was coupled into the detection optical probe of the optical fiber bundle and analyzed by the UV-visible spectrophotometer directly without the need of any external detectors, that making this detection easy and fast unlike the conventional SPR apparatus. All absorbance spectra were taken from 400 to 800 nm on the UV-visible spectrophotometer at room temperature. Figure 2 shows the LSPR optical properties of the gold-capped nanoparticle layer chip at each step of fabrication.

The experimental procedure for the immobilization of CRP antibody is shown in Figure 3. The antibody immobilization was carried out with an almost similar procedure to the formation of the gold-capped nanoparticle layer chip. The CRP antibody was immobilized on the gold-capped nanoparticle layer chip, which could recognize only CRP antigen. The CRP antibody-antigen reaction was performed by the introduction of different concentrations ($1 \mu\text{g} \sim 1 \text{ fg/ml}$) of CRP antigen solution for 1h onto CRP antibody immobilized gold-capped nanoparticle layer chip.

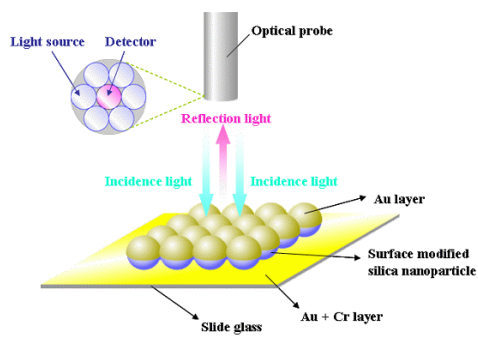


Figure 1. Experimental setup and construction of LSPR based label-free optical biosensor.

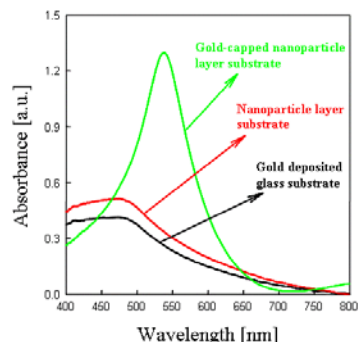


Figure 2. Optical properties for each step of fabrication of gold-capped nanoparticle chip.

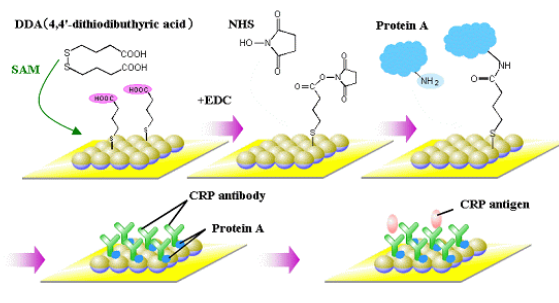


Figure 3. Experimental procedure for immobilization of CRP antibody on gold-capped nanoparticle layer chip and CRP antibody-antigen reaction.

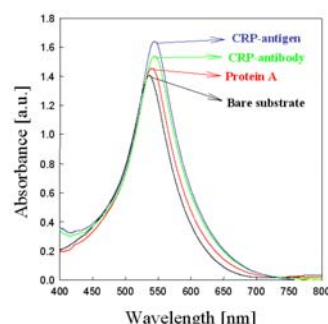


Figure 4. Optical properties for each step of CRP antibody-antigen reaction.

3. Results and discussion

Figure 4 shows the LSPR optical properties for each step of the immobilization of CRP antibody and the CRP antibody-antigen reaction. The peak absorbance and the wavelength of gold-capped nanoparticle layer chip were observed at 1.4 and 536nm, respectively. The optical properties evaluation of CRP antibody and antigen reaction

was carried out using the anti-CRP antibody immobilized LSPR-based optical biosensor. In the results, the optical properties of LSPR based label-free optical biosensor were shown to be able to distinguish reaction between CRP antibody and antigen on the surface of gold-capped nanoparticle layer chip.

In addition, The CRP antibody-antigen reaction was performed by the introduction of different concentrations of CRP antigen solution for 1h onto CRP antibody immobilized gold-capped nanoparticle layer chip. Subsequently, the optical properties evaluation of CRP antibody and antigen reaction was carried out. The detection limit was found to be 10 pg/ml by using the CRP antibody immobilized LSPR based label-free optical biosensor as shown in the Figure 5.

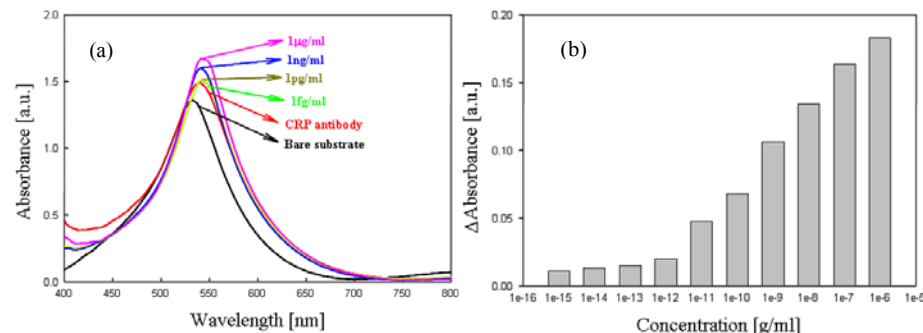


Figure 5. Optical properties and absorbance strength change according to concentration of CRP antigen by using LSPR based label-free optical sensor
(a) Optical properties (b) Absorbance strength change

4. Conclusions

In this report, the optical properties of LSPR based label-free optical biosensor were shown to be able to distinguish reaction between CRP antibody and antigen on the surface of gold-capped nanoparticle layer chip. We expect that this detection method using LSPR based label-free optical biosensor is possible to analyze conveniently with high sensitivity, because there is no necessity of labeling such as the enzymes and the fluorescent dye.

Acknowledgements

This work was supported by the Post-doctoral Fellowship Program of JAIST in Japan.

References

1. N. Nath and A. Chilkoti, A Colorimetric gold nanoparticle sensor to interrogate biomolecular interactions in real time on a surface, *Anal. Chem.*, **74**, 504-509, (2002).
2. T. Endo, K. Kerman, N. Nagatani, Y. Takamura and E. Tamiya, Label-free detection of peptide nucleic acid-DNA hybridization using localized surface plasmon resonance based optical biosensor, *Anal. Chem.*, **77**, 6976-6984, (2005).
3. T. Kalkbrenner, U. Håkanson and V. Sandoghdar, Tomographic plasmon spectroscopy of a single gold nanoparticle, *Nano. Lett.*, **4**, 2309-2314, (2004).
4. A. Dahlin, M. Zäch, T. Rindzevicius, M. Käll, D.S. Sutherland and F. Höök, Localized surface plasmon resonance sensing of lipid-membrane-mediated biorecognition events, *J. Am. Chem. Soc.*, **127**, 5043-5048, (2005).

PRESSURE AND SUPERCRITICAL CO₂ CONDITIONS IMPROVE THE ESTERIFICATION REACTION OF PHTHALIC ANHYDRIDE WITH METHANOL IN GLASS MICROREACTORS

F. Benito-López¹, R.M. Tiggelaar², R.J.M. Egberink¹,
J.G.E. Gardeniers², W. Verboom¹, A. van den Berg², and D.N. Reinhoudt¹

MESA⁺ Institute for Nanotechnology, University of Twente, Enschede,
The Netherlands

¹ Supramolecular Chemistry and Technology Group

² BIOS Lab-on-a-Chip Group

Abstract

We have developed a new microreactor platform for studying high pressure synthetic chemistry near/under supercritical conditions. A simple reaction, the esterification of phthalic anhydride with methanol, was studied at high pressures as well as under *sc*CO₂ conditions using a continuous flow glass microreactor. The unique design of this system is such that supercritical conditions can be generated in the microreactor, by controlling the pressure and temperature. The microreactor design allows to study the influence of different *p,T*-conditions on the rate constants in an easy way.

Keywords: microreactor, high-pressure, kinetics, supercritical CO₂

1. Introduction

High-pressure conditions can have a positive effect on the rate constant, yield, and selectivity of chemical reactions. However, work in this area has been limited due to the requirement of special equipment. The small characteristic dimensions of microreactors make them suitable for performing chemical reactions that need extreme conditions, like high pressures or temperatures, without extensive safety precautions. In this contribution the results of a study on the reaction kinetics of an esterification reaction are presented when performed in a glass microreactor under high pressures and supercritical CO₂ (*sc* CO₂) conditions.

2. Experimental

In Figure 1(a) a picture of the microreactor, made of Borofloat glass, is shown. It has two inlets for the introduction of pressurized fluids. In the following channel (70×30 μm², length 13.5 mm) mixing of the fluids takes place as well as the chemical reaction. This channel connects to a narrow channel (20×5 μm², length 177 mm), which acts as a hydraulic resistance that ensures a constant pressure in the reaction zone.

In this chip the esterification of phthalic anhydride in methanol was performed (Figure 1(b)). In Figure 2 the kinetic values are depicted as a function of pressure for different temperatures.

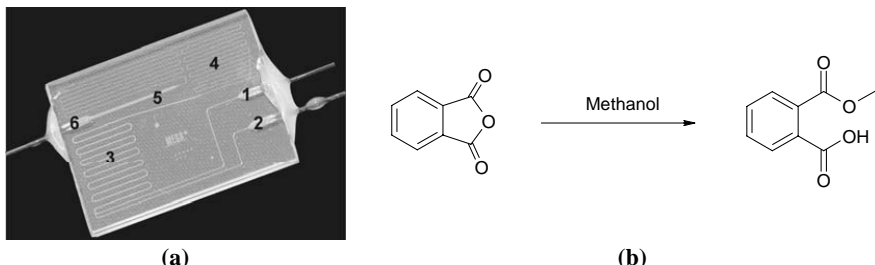


Figure 1. (a) Microreactor chip ($20 \times 15 \times 2.2$ mm). Legend: **1** inlet liquid- CO_2 , **2** inlet sample solutions, **3** reaction zone, **4** fluidic resistor, **5** expansion zone, **6** outlet.
(b) Scheme of the esterification of phthalic anhydride with methanol.

Substantial increases in kinetic values were found when the reaction was done at high pressures. For all investigated temperatures, there is a sharp increase in the rate constants. For instance, at 20°C 42-fold and 79-fold increases were found for a pressure increase of 90 or 110 bar, respectively. In Table 1 an overview is given of the rate constants obtained from experiments done at high pressures (90 and 110 bars) and for experiments where scCO_2 is used as cosolvent. scCO_2 is generated in the microreactor by changing the phase of $\text{CO}_2(l)$ by increasing the temperature of the reaction zone above the critical temperature (T_c) of CO_2 . When scCO_2 is used as cosolvent, at pressures of 90 and 110 bar very high enlargements of the rate constants were observed, for example, 161-fold and 296-fold increases at 40°C .

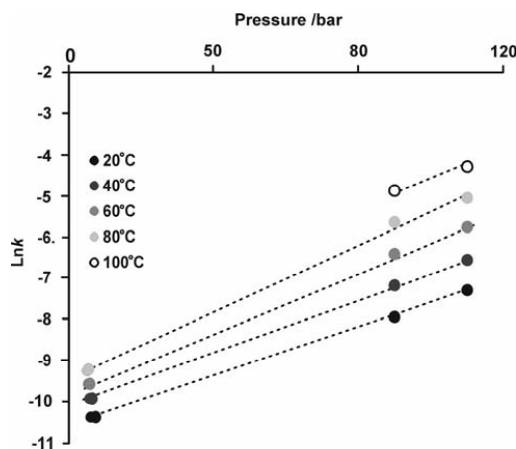


Figure 2. Kinetic values as a function of pressure for different temperatures.

3. Discussion

Theoretically, for labscale experiments a pressure of 110 bar should not affect the reaction kinetics. However, when performed in the microreactor, significant increases were found. These enlarged reaction rates might be attributed to the distinctive

conditions under which the continuous flow microreactor is operated, such as diffusive mixing under laminar-flow regime in small reaction volumes (~260 nL of the reaction zone) [1].

Table 1. Kinetic values for different temperatures at 90 and 110 bars with and without *scCO₂* as cosolvent.

T /°C	k /M ⁻¹ s ⁻¹ (90 bar) ^a		k /M ⁻¹ s ⁻¹ (110 bar) ^a	
	methanol	Methanol + <i>scCO₂</i>	methanol	Methanol + <i>scCO₂</i>
20	3.5×10^{-4}	--	6.7×10^{-4}	--
40	7.6×10^{-4}	1.2×10^{-1}	1.4×10^{-3}	2.0×10^{-1}
60	1.6×10^{-3}	1.8×10^{-1}	3.1×10^{-3}	3.1×10^{-1}
80	3.5×10^{-3}	2.7×10^{-1}	6.4×10^{-3}	4.6×10^{-1}
100	7.5×10^{-3}	3.6×10^{-1}	1.3×10^{-2}	6.9×10^{-1}

^a Mean values from duplicate experiments.

Other aspects, like material properties (hydroxy and silanol groups in the surface), could also play a role since the esterification reaction is acid catalyzed, and are currently examined. In case of *scCO₂* as cosolvent, extremely high rate constants were found. This is attributed to the unique properties of *scCO₂*, which dramatically change reaction rates with relatively small changes in temperature and pressure [2].

4. Conclusions

Clearly, the results of this study show that glass microreactors in continuous flow mode operated at high pressure conditions give rise to significant rate enhancements. Since temperature and pressure can be regulated and their influence on continuous flow reactions can be observed easily and fast, this microreactor has a great potential for high-throughput screening at high pressures. Implementation of high-pressure processes in microreactors offer important advantages in terms of safety and therefore makes high pressure research easier accessible.

Acknowledgements

This research is supported by the Dutch Technology Foundation STW, applied science division of NWO, and by NanoNed, a national nanotechnology program coordinated by the Dutch Ministry of Economic Affairs.

References

1. V. Hessel, C. Hofmann, P. Lob, J. Lohndorf, H. Lowe and A. Ziogas, *Aqueous Kolbe-Schmitt synthesis using resorcinol in a microreactor laboratory rig under high-p-T conditions*, Org. Proc. Res. Dev. **2005**, 9(4), pp. 479-489.
2. P.G. Jessop and W. Leitner, *Chemical synthesis using supercritical fluids*, Wiley, Germany (1999).

A DIGITAL MICROFLUIDIC SYSTEM TO FACILITATE PRESTEADY STATE KINETIC STUDIES USING MALDI-TOF MS

K.P. Nichols and J.G.E. Gardeniers

MESA+ Institute for Nanotechnology

University of Twente, Enschede, The Netherlands

k.p.nichols@utwente.nl

Abstract

A digital microfluidic system has been developed to facilitate studies of reaction kinetics using matrix-assisted laser desorption/ionization time-of-flight (MALDI-TOF) mass spectrometry. The device consists of an integrated mixer and individually addressable electrodes arranged to allow the combination of liquid droplets at well-defined time intervals. The device combines two droplets to initiate a reaction, then, with precise timing, combines a third droplet to quench the reaction, and finally combines a fourth droplet to form a matrix. The device was tested against a model protein tyrosine phosphatase system, and good agreement with results previously published using more time consuming analytical methods was found.

Keywords: MALDI, digital microfluidics, kinetic, protein tyrosine phosphatase

1. Introduction

MALDI-TOF mass spectrometry has been demonstrated as a useful tool in presteady state kinetic research by Houston et al., who combined it off-line with quench-flow methods to follow the appearance of a protein tyrosine phosphatase (PTPase) reaction intermediate [1]. Houston et al., were capable of measuring rate constants up to 30 s^{-1} . The device described within extends this technique to measure rate constants approximately 5 times greater.

MALDI-TOF allows for the determination of rate constants regardless of the incorporation of a chromophore, which is not possible with spectrophotometric studies of presteady state kinetics, and at a wide variety of buffer concentrations, which is difficult with electrospray ionization mass spectrometry. Both of these advantages are useful if one wishes to study enzymatic reactions at naturally occurring conditions. The primary shortcoming of MALDI-TOF is its limited ability to obtain quantitative measurements. However, quantitation is possible under specific conditions.

Wheeler et al. have already developed an electrowetting on dielectric (EWOD) digital microfluidic system for use with MALDI-TOF [4]. However, the Wheeler et al. device would have several drawbacks when used in kinetic studies. First, the Wheeler et al. device, being an EWOD system, requires a lid during droplet manipulation. While the lid can be manually removed, this step limits the device's throughput, and prevents immediate analysis of the crystallized product within the MALDI-TOF system.

Further, while Paik et al [3] have demonstrated droplet mixers for EWOD based systems, the Wheeler et al. device does not include these. The digital microfluidic device described within does not possess these disadvantages, and has the added advantage of lower fabrication cost, and ease of use.

As a model system, YOP51 PTPase [5] was analyzed. Deprotonated PTPases act as nucleophilic thiolates during their attacks on phosphates. Mass-spectrometric analyses of PTPases are possible due to the predictable formation of a covalent phosphoenzyme intermediate [1]. In this study, unphosphorylated enzyme is used as an internal standard to permit quantitation of the phosphorylated to unphosphorylated enzyme ratio, which is used to determine presteady state kinetic values.

2. Experimental

The digital microfluidic system used to obtain kinetic values consists of individually addressable Au electrodes (Figure 1), covered by a 5 μm SU-8 5 (MicroChem) dielectric layer and a 1 μm Teflon AF 601S1-x-6 (DuPont) film.

When voltage is applied across adjacent electrodes at 500 Hz, 250 V_{RMS}, liquid droplets quickly center themselves over the interelectrode gap. The incorporation of a spiral structure as an interelectrode gap acts as an efficient mixer [5].

Experiments were conducted by sequentially combining 0.7 μL buffered 50 μM YOP51 PTPase (Sigma) at pH 7.2 with its substrate, 20mM *p*-nitrophenyl phosphate (Acros), then quenching the reaction with 1 M dichloroacetic acid (Acros), and finally forming a matrix using 25 mg/ml ferulic acid in 2:1 H₂O/acetonitrile (Acros). Temperature was controlled at 30°C. Samples were directly analyzed on the digital microfluidic chip using MALDI-TOF.

Combination and mixing of droplets at well-defined time intervals was accomplished using a custom-built relay board interfaced with a laptop PC controlled using MATLAB. Each 0.7 μL droplet was initially loaded on one of the four outermost electrodes, and then brought into the center for rapid mixing. Hi-speed video analysis was used to measure average droplet speeds during transfer to the center of the device. The measured speeds were used to define zero points for the initiation of mixing.

Details of the model PTPase reaction are available elsewhere [1, 5]. However, in brief, the following equations were used to deduce the rate constants k_1 and k_2 :

$$C = \frac{k_2}{(k_2 + k_3)\left(1 + \frac{K_m}{[S]_0}\right)} \quad (1) \quad b = k_3 + \frac{k_2}{1 + \frac{(k_2 + k_3) \cdot K_m}{k_3 \cdot [S]_0}} \quad (2) \quad \frac{[EP]}{[E]_0} = C \cdot \left(1 - e^{-bt}\right) \quad (3)$$

Nonlinear regression using MATLAB was used to fit eq. 3 to K_m values obtained from literature [5], experimentally relevant concentrations, and scaled [EP]/[E]₀ data calculated as the peak height of EP divided by the sum of the EP and E peak heights.

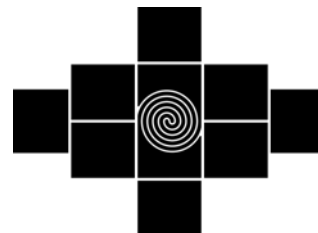


Figure 1. Electrode Pattern.

3. Results and Discussion

Presteady state rate constants determined using this system for YOP51 at pH 7.2, 30°C were found to be in good agreement with previously reported values [5] (Figure 3, f_{theory} vs. f_{meas}). While a high standard deviation was observed, the system throughput was high enough to generate sufficient Gaussian distributed data to overcome the noise associated with measurements so close to the theoretical limits of detection. The advantage of this system over that by Houston et. al is not greater accuracy of individual measurements, but higher throughput allowing for inaccuracy to be overcome.

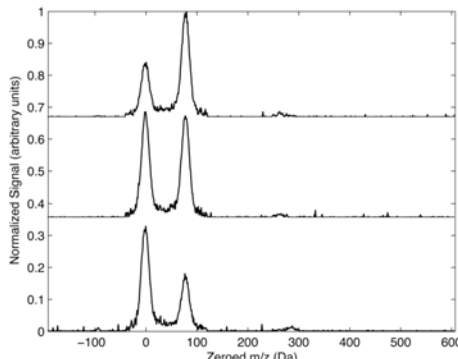


Figure 2. Typical scaled MALDI-TOF mass spectra acquired with fitted Gaussian distributions. The two peaks represent unphosphorylated and phosphorylated PTPase, respectively.

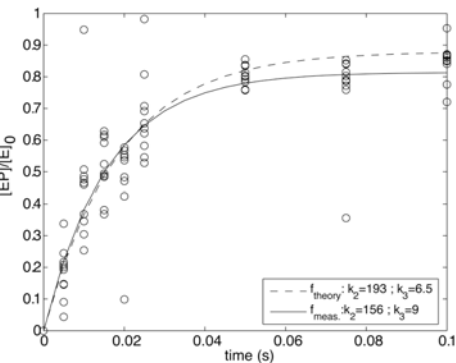


Figure 3. Transformed MALDI-TOF data fit to equation 3. The data represent rate constants significantly higher than what Houston et al. reported being able to determine.

Acknowledgements

This research was financially supported by the Technology Foundation STW, applied science division of NWO and the technology program of the Ministry of Economic Affairs of The Netherlands (project no. 6626).

References

1. Houston, C.T., et al., Investigation of enzyme kinetics using quench-flow techniques with MALDI. *Anal. Chem.*, 2000. 72(14): 3311-3319.
2. Nichols, K.P. and Gardeniers, J.G.E., Ultrarapid Droplet Mixer for Digital Microfluidics. *MicroTAS 2006*. Pages not yet determined.
3. Paik, P., V.K. Pamula, and R.B. Fair, Rapid droplet mixers for digital microfluidic systems. *Lab on a Chip*, 2003. 3(4), 253-259.
4. Wheeler, A.R., et al., Digital microfluidics with in-line sample purification for proteomics analyses with MALDI-MS. *Anal. Chem.*, 2005. 77(2), 534-540.
5. Zhang, Z.-Y., et al., Catalytic function of the conserved hydroxyl group in the PTPase signature motif, *Biochemistry* 1995, 34, 16389–16396.

ELECTROKINETIC TRANSPORT WITH STOKES FLOW IN MICROFLUIDIC-CHIP UNDER ASYMMETRIC CONDITIONS OF CHANNEL SURFACE

Myung-Suk Chun, Tae Seok Lee, and Il Tae Kim

Complex Fluids Research Lab., Korea Institute of Science and Technology
(KIST), PO Box 131, Cheongryang, Seoul 130-650, Republic of Korea
(contact: mschun@kist.re.kr)

Abstract

The behavior of the slip length and the long-range repulsion plays an essential role for design and operation in many of μ TAS devices. We have developed the explicit model incorporated together the finite difference scheme for electrokinetic flow in rectangular microchannels encompassing Navier's boundary slip. The externally applied body force originated from between the nonlinear Poisson-Boltzmann field around the channel wall and the flow-induced electric field is employed in the equation of motion. It is evident that the fluid slip counteracts the effect by the electric double layer (EDL) and induces a larger flow rate. Particle streak imaging by fluorescent microscope has been applied to microchannels designed to allow for flow visualization of dilute latex colloids underlying the condition of simple fluid. We recognized the behavior of fluid slip at the hydrophobic surface of polydimethylsiloxane (PDMS) wall, from which the slip length was evaluated for different conditions.

Keywords: microfluidic-chip, electrokinetic flow, fluid slip, colloid, particle streak

1. Introduction

Since hydrophobic materials have become attractive for use in MEMS fabrication of μ TAS devices, an understanding of the physics of either microfluids or nanofluids involving electrokinetic phenomena is significant. Many studies have contributed to the slip behavior in narrow channels, in which the Navier's fluid slip occurs in hydrophobic surfaces as depicted in Figure 1 [1,2]. A slip length β inferred from measurements is the local equivalent distance below the solid surface at which the no-slip boundary condition would be satisfied if the flow field were extended linearly outside.

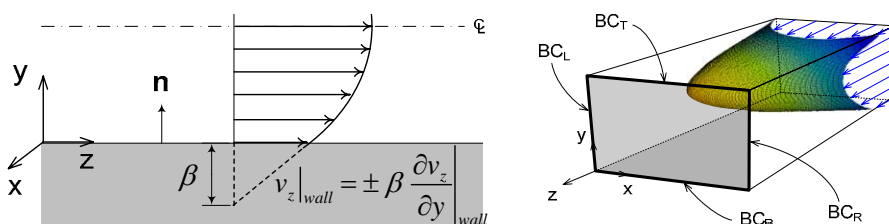


Figure 1. Fluid slip at hydrophobic surface (left), and channel with different BCs (right)

2. Theoretical consideration and computations

The surface of channel wall usually has inhomogeneous properties, due to a bonding with different materials in many of the μ TAS devices. As shown in Figure 2, computations were performed with asymmetric variations of both slip length and long-range repulsion, because the hydrodynamic and electric properties depend on the material of the wall [3]. Figure 3 exhibits that the fluid slip induces a higher flow velocity, while the presence of EDL retards the flow rate. If the slip is absent, a higher apparent viscosity and a higher friction factor would be predicted.

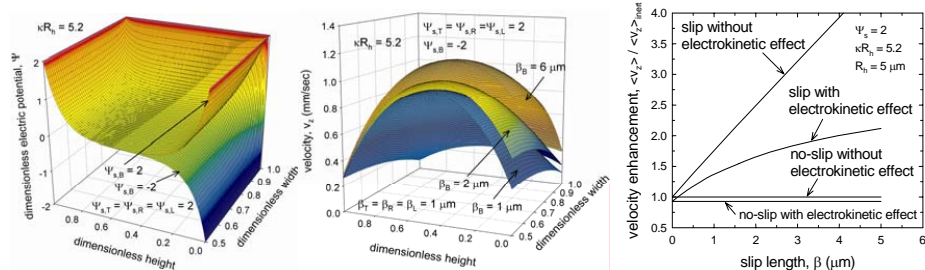


Figure 2. Simulation results of electric potential and velocity profiles in rectangular channel, $R_h = 5 \mu\text{m}$

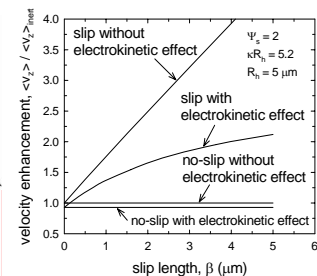


Figure 3. Effect of the slip and EDL on flow velocity

3. Microflow experiments

Experimental observations provide benchmark data for the verification of theoretical study and developing novel micro processes [4]. Microfabrication procedures based on the MEMS micromachining are employed to prepare the microfluidic-chip using molded PDMS and glass cover. The velocity profile of dilute latex colloids was obtained in the channel of PDMS-glass as well as PDMS-PDMS chip shown in Figure 4, by employing the fluorescent microscope with particle streak velocimetry (PSV) on a parallel uniaxial flow field [5]. A ratio of particle size to channel width is quite small, and the serpentine channel has also been considered besides the straight one.

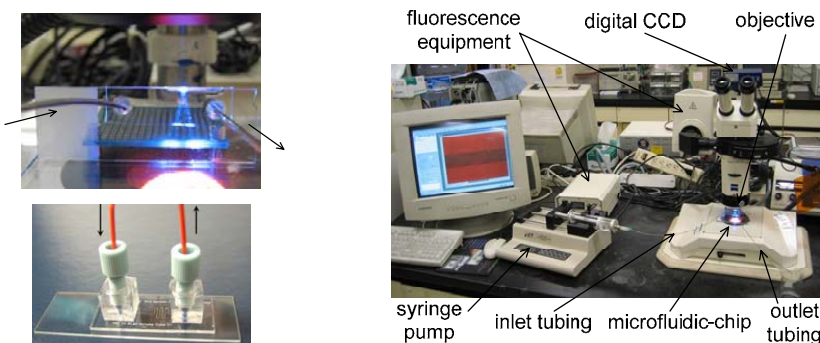


Figure 4. PDMS-glass and PDMS-PDMS chips (left), and experimental setup (right)

4. Results and discussion

In Figure 5, we observe the fluid slip at the hydrophobic surface of PDMS wall, which allows evaluation the value of slip length for different suspension conditions. The PDMS-PDMS channel resulted in a higher flow velocity than PDMS-glass one. Figure 6 shows that the slip length has a trend to decrease as the pH increases causing the stronger electrokinetic effect, but increases as the nominal shear rate increases.

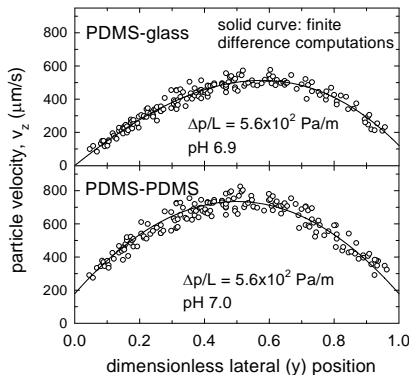


Figure 5. Uniaxial velocity profile in microfluidic-chip at 0.5 mM KCl solution

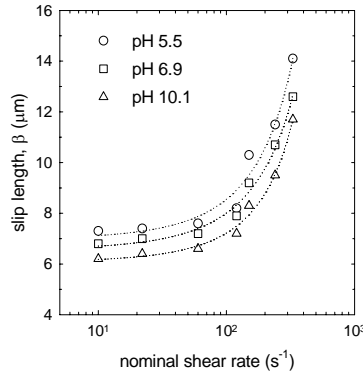


Figure 6. Variations of the slip length for different shear rate and pH

5. Conclusions

We developed the numerical scheme for electrokinetic flow with Navier's boundary slip in rectangular channels. The Stokes flow in confined spaces is influenced by the EDL, therefore, the fluid behavior in microchannels deviates from that described by the laminar flow equation in general. Newtonian fluid slip induces a larger flow velocity and then a lower friction factor would be predicted. The validity of the velocity profile determined by flow visualization was justified by comparing with the computational results, where a good agreement was found. Newtonian fluid slip at hydrophobic surfaces has been observed at the length scale of several micrometers, and it is available to obtain the dependency of slip length on the shear rate and suspension pH.

Acknowledgements

This work was supported by the KOSEF (R01-2004-000-10944-0) as well as the KIST (μ TAS Research: 2E19570).

References

- [1] D.C. Tretheway and C.D. Meinhart, *Phys. Fluids*, **14**, L9-L12 (2002).
- [2] Y. Zhu and S. Granick, *Phys. Rev. Lett.*, **88**, 106102/1-4 (2002).
- [3] M.-S. Chun, T.S. Lee and N.W. Choi, *J. Micromech. Microeng.*, **15**, 710-719 (2005).
- [4] M.-S. Chun, M.S. Shim and N.W. Choi, *Lab Chip*, **6**, 302-309 (2006).
- [5] M.H. Oddy, J.G. Santiago and J.C. Mikkelsen, *Anal. Chem.*, **73**, 5822-5832 (2001).

CONFOCAL MICROSCOPIC MEASUREMENT OF PROTON DIFFUSION IN CHEMICAL REACTING FLOW

Mitsuhisa ICHIYANAGI¹, Yohei SATO¹ and Koichi HISHIDA¹

¹Keio University, 3-14-1 Hiyoshi, Kohoku-ku, Yokohama, 223-8522 JAPAN
E-mail: ichiyanagi@mh.sd.keio.ac.jp

Abstract

A simultaneous measurement technique for velocity and pH distributions was developed to investigate proton diffusion in a chemical reacting flow. The present study employed micro-PIV and laser induced fluorescence (LIF) for the velocity and pH measurement, respectively. Two aqueous solutions were merged at the junction of the T-shaped microchannel. Proton concentration profiles for the non-chemical reaction (water and aqueous solution) agree well with theoretical profiles, and profiles for the chemical reaction (Two phosphate buffer solutions with different pH value) indicate the production and extinction of protons which were yielded by the buffering action.

Keywords: Velocity, pH, Micro-PIV, LIF, Confocal microscope, Buffering action

1. Introduction

A chemical reacting flow is controlled by the mixing and molecular diffusion whose condition is determined by the fluid velocity and the ion diffusion, especially protons. For further accurate control of chemical reactions, it is expected to establish a simultaneous measurement technique for the velocity and pH distribution, because it is realized to investigate the mixing and diffusion process in a chemical reacting flow. The objective of the present study is to investigate the mixing and diffusion phenomena of protons by utilizing micro-PIV [1] and LIF [2] with the confocal microscope.

2. Experimental Setup

Tables 1 and 2 represent particle properties for micro-PIV and dye properties for LIF, respectively. Figure 1 illustrates a schematic of the measurement system comprising of an inverted microscope, a confocal scanner, an Ar laser ($\lambda = 488$ nm) and a 3CCD camera. The depth of field for a conventional microscope is 7 μm [3], while

Table 1. Properties of fluorescent particles

Material	Polystyrene
Diameter of particles	1 [μm]
Density	1.055 [g/cm^3]
Absorption wavelength	488 [nm]
Emission wavelength	645 [nm]

Table 2. Properties of fluorescent dye

Material	Fluorescein sodium
Molecular weight	376.28
Absorption wavelength	494 [nm]
Emission wavelength	518 [nm]

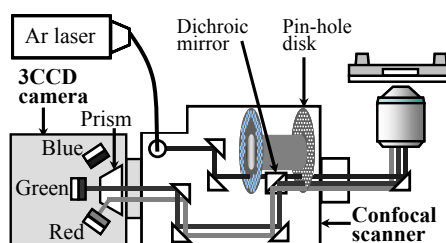


Figure 1. Schematic of measurement system.

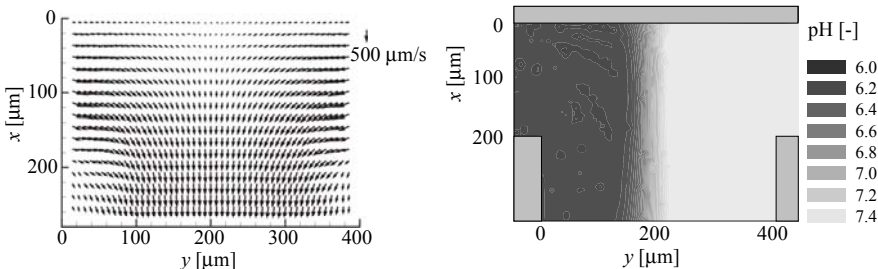


Figure 2. Velocity-vector map in the junction area at $z = 15 \mu\text{m}$ measured by micro-PIV in the case of the chemical reaction field.

Figure 3. Two-dimensional pH distribution in the junction area at $z = 15 \mu\text{m}$ obtained by LIF in the case of the chemical reaction field.

that for the present system is $1.4 \mu\text{m}$ [4], because out-of-focus fluorescence was excluded from the captured images by the pin-hole disk in the confocal scanner. The present system enables to separate the fluorescence of the particles from that of the dye, because the 3CCD camera separates RGB colors by the internal prism and the emission wavelength of the particles differs from that of the dye as shown in Tables 1 and 2 [5].

3. Results and Discussion

The present study employed a T-shaped microchannel whose width is $400 \mu\text{m}$ and its depth is $50 \mu\text{m}$ to form a mixing field in the junction area. The experiments were performed under the two conditions, that is, a non-chemical reaction field and a chemical reaction field with a buffering action. For the non-chemical reaction, ion-exchanged water (pH 6.2) and disodium hydrogenphosphate (pH 7.2) were injected into inlets A and B, respectively. For the chemical reaction, phosphate buffer solutions with pH 6.0 and pH 7.7 were injected into inlets A and B, respectively. Figures 2 and 3 exhibit the velocity-vector map by micro-PIV and the two-dimensional pH distribution by LIF, respectively, for the chemical reaction. Figure 4 shows the proton concentration distributions which were evaluated by the pH distributions of both cases. It is found that in the case of the chemical reaction, the two buffer solutions form the liquid-liquid interface, while in the case of the non-chemical reaction, the interface is not clearly observed due to the effect of the proton diffusion. The proton concentration distributions of the experiments were compared with those of the numerical simulation which were calculated by substituting the velocity maps by micro-PIV into the scalar transport equation. Figure 5 exhibits that in the case of the non-chemical reaction, the proton concentration profiles of the experiments agree well with those of the numerical simulation, while in the case of the chemical reaction, the numerical simulation shows smaller gradients of the proton concentration than those of the experiments, because this is caused by the equilibrium reaction of the phosphate buffer solutions ($\text{H}_3\text{PO}_4 \rightleftharpoons \text{H}_2\text{PO}_4^- + \text{H}^+$ which is well known as the buffering action). At $y < 200 \mu\text{m}$, the production of protons were yielded by the reaction that the equilibrium shifts to the right side, while at $y > 200 \mu\text{m}$, the extinction of protons were yielded by the reaction that the equilibrium shifts to the left side.

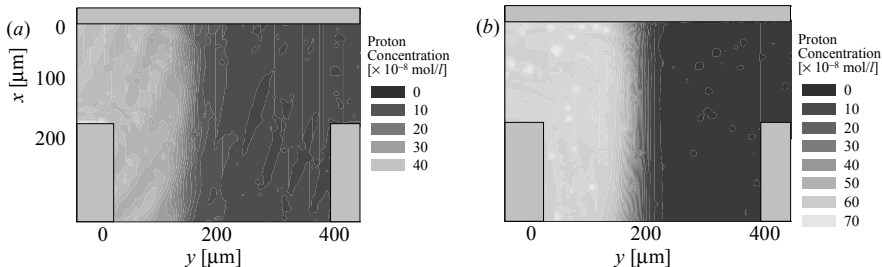


Figure 4. Proton concentration distributions obtained from pH distributions in the case of (a) the non-chemical reaction field and (b) the chemical reaction field.

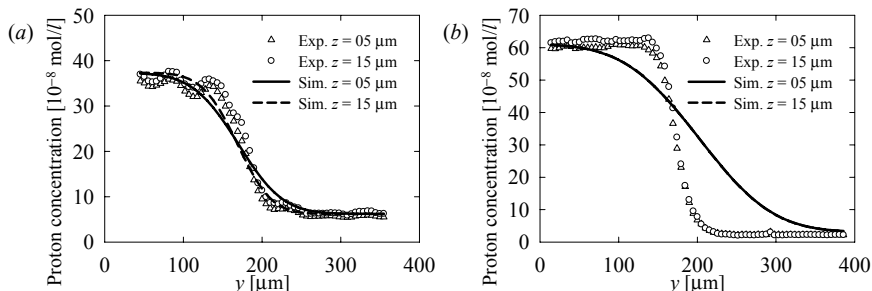


Figure 5. Proton concentration profiles obtained from experiment and numerical simulation at $x = 100 \mu\text{m}$ in the case of (a) the non-chemical reaction field and (b) the chemical reaction field.

4. Conclusion

A simultaneous measurement technique was developed by utilizing the confocal microscope in order to detect the velocity and pH distributions in a microchannel and investigate the mixing and diffusion phenomena of protons. The present technique was applied to the chemical reacting flow with the buffering action, and enables us to investigate the flow field with the production or extinction of protons. In the future, the present technique will contribute to evaluate a production term by the chemical reaction.

Acknowledgements

This work was subsidized by R&D for practical use of university-based technology from matching government and private funds, and the Grant-in-Aid for Scientific Research (No. 15206024) and the 21st century center of excellence for “System Design: Paradigm Shift from Intelligence to Life” from the Ministry of Education, Culture, Sports, Science and Technology in Japan.

Reference

1. Santiago, J. G. *et al*, *Exp. in Fluids*, **25**, pp. 316–319, (1998).
2. Sato, Y. *et al*, *Meas. Sci. Technol.*, **14**, pp. 114–121, (2003).
3. Meinhart, C. D. *et al*, *Meas. Sci. Technol.*, **11**, pp. 809–814, (2000).
4. Wilson, T., *Confocal Microscopy*, Academic Press, (1990).
5. Ichiyanagi, M. *et al*, *Proc. 13th Int. Symp. Appl. Laser Tech. Fluid Mech.*, (2006).

RAPID PHASE SPACE SURFACE GENERATION USING AN INTEGRATED MICROFABRICATED DEVICE REACTION DETECTION SYSTEM AND AUTOMATED CONTROL

Christopher Cullen,¹ Siva Krishnadasan,¹ John C. deMello,¹ Robert C.R. Wootton,² and Andrew J. deMello¹

¹Department of Chemistry, Imperial College London, South Kensington, London, SW7 2AZ, UK. ²Department of Pharmacy and Chemistry, Liverpool John Moores University, Byrom Street, Liverpool, L3 3AF, UK.

Phone: +44 207 5945866, Fax: +44 207 5945834

Abstract

The optimisation of reaction conditions is a vital process in the establishment of viable industrial synthetic routes. This paper shows a method for the rapid generation of high resolution chemical surfaces illustrating the effects on the reaction rates of the variation of ratios of reactants on imine formation.

Keywords: microreactor, reaction kinetics, reaction optimisation

1. Introduction

Conventionally the acquisition of information relating to reaction kinetics is a slow process with the reaction data typically measured by titrations. Even some of the more recent integrated methods of analysis have a limited scope for the rapid variation of reactant concentrations. Recently, it has been shown that continuous flow systems with integrated analysis can rapidly generate large amounts of reaction data.[1] [2]

The novel approach described herein allows the simultaneous alteration of the ratio of the reagents at fixed reaction times to generate phase space surfaces. These are generated using a continuous flow microfluidic reactor with online UV/vis spectroscopic detection. By automating control of hydrodynamic flow within the system phase space surfaces may be generated in a rapid and reproducible manner.

2. Experimental

The planar glass microfluidic reactor used in the current studies was fabricated using conventional wet etching techniques. The formation of benzylidene-phenyl-amine from aniline and benzaldehyde (Figure 1) is monitored with 0.5 mM reactant solutions in ethanol.

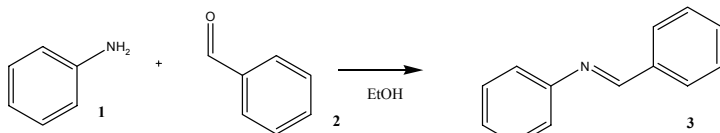


Figure 1. Reaction of aniline **1** and benzaldehyde **2** to form benzylidene-phenyl-amine **3**.

The reaction is well known to proceed readily at room temperature with the product demonstrating an absorption maximum at 310 nm. This is suitably resolved from the spectroscopic features of the reactants, allowing simple generation of phase space surface data. The variation in the extent of reaction is observed in real time by the transmittance of monochromatic light (at 310 nm) through a commercially available 1 mm path length flow cell in series with the microfluidic reactor. The hydrodynamic infusion of reagents is controlled by a LabView programme which allows incremental changes in pumping rates and the concentration ratios of reagents.

3. Results and discussion

Initial experiments with proportional incremental increases in the flow rates of both reagents were compared to stopped-flow and steady state experiments. The stopped-flow measurement show the reactions progress when the flow rate through the observation cell is suddenly stopped. The static point or steady state reaction profile was made with a series of transmittance readings at fixed flow rates, each corresponding to a fixed reaction time. The ramped method with incremental increases in flow rate of $0.1 \mu\text{l min}^{-1}$ each second gives a very dense set of data, with readings of transmittance every second unaffected by the short equilibrium times.

The kinetic traces for all three experimental modes are illustrated in Figure 2, and using calculations of the dead volume of the microreactor, showed good agreement with less than a 3 % variation.

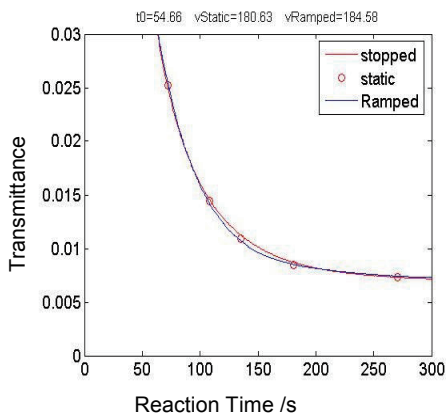


Figure 2. Reaction profiles of aniline with 1 equivalent of benzaldehyde to produce benzylidene-phenyl-amine measured by stopped-flow, static point and ramped methods

Subsequently a set of data obtained at fixed ratios of reactants with a gradual increase in volumetric flow rate (inversely proportional to reaction times) was used to generate a surface of reaction data (Figure 3). Data were also obtained at fixed flow rates with incremental variations in reactant concentration (Figure 4). The two space phase surface plots obtained independently by varying differing reaction parameters correspond closely showing the accuracy of this method.

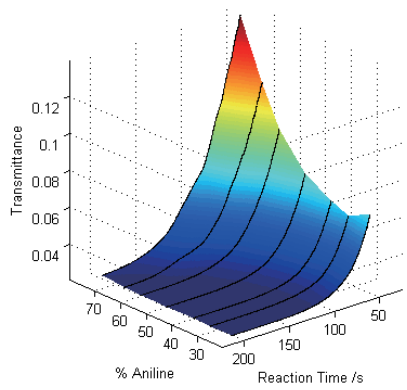


Figure 3. Phase surface plot generated from varying the reaction times at fixed ratios of reactants.

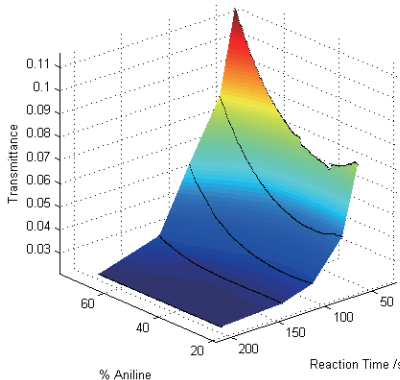


Figure 4. Phase surface plot generated from varying the ratios of reactants at fixed reaction times.

4. Conclusion

In conclusion, we have shown that reproducible and accurate high resolution chemical phase space surfaces can be generated from reactions within microfluidic devices using online UV/vis spectroscopy detection. The frequent and small incremental variations in flow rates allow a high density of data to be collected showing the effects of both reaction time and reactant concentrations on the efficiency of product formation, thus allowing the optimisation of reaction conditions. The automated reloading of syringes from reactant reservoirs means many runs can be sequentially programmed, providing a system capable of extruding a high density of reaction data very rapidly. A reaction surface can be generated within the period of a working day with a density of data that would take weeks-months using traditional titration methodologies.

Acknowledgements

The authors would like to thank GlaxoSmithKline and the EPSRC for their support of this work.

References

1. S.A. Leung, R.F. Winkle, R.C.R. Wootton and A.J. de Mello, *A method for rapid reaction optimisation in continuous-flow microfluidic reactors using online Raman spectroscopic detection*, *The Analyst*, **130**, 46 (2005).
2. H. Wensink, F. Benito-Lopez, D.C. Hermes, W. Verboom, H.J.G.E. Gardeniers, D. N. Reinhouldt and A. van der Berg, *Measuring reaction kinetics in a lab-on-a-chip by microcoil NMR*, *Lab on a Chip*, **5**, 280 (2005).

SIMULATION EXAMINATION FOR EXTRACTION ON OIL/WATER SURFACE

Ryo Anraku¹, Takahiro Asai¹, Kenji Uchiyama¹, Akihiko Hattori¹, Manabu Tokeshi², and Takehiko Kitamori³

¹NIPPON SHEET GLASS CO.,LTD., Japan

² The University of Nagoya, Japan

³The University of Tokyo, Japan

Abstract

In this study, we compared the extraction result on oil/water surface in a microchip between experiment and calculation. As a result, when the model considered flow was given the fitting constant as stopped flow experiment and computed, the extraction in the m-xylene at the channel exit became about half compared with the experiment value.

Keywords: Simulation, Multilayer flow, Microchannel, Microfluidics

1. Introduction

There is a solvent extraction as one of the unit chemistry operations in a microchip. After the model of oil/water surface formation in the micro channel is established, it is necessary to develop the solvent extraction model by the simulation.

We constructed a numerical computing model about the two-phase and multi-phase formation phenomenon in the micro channel, and have been proving the validity of the computing model by comparing it with the experiment.

This report is aims to construct models such as solvent extractions and interfacial reactions by using two-phase formation model that has been established. We report about comparison between result of computation and measurement by using the chip pattern for Co(II) wet analysis [1].

2. Experimental

Simulations

The amount extraction of cobalt complex on water/oil interface in the micro channel was calculated by the numerical analysis by using 2D reaction model as shown Figure 1. A commercial CDF code (FIDAP) solved the full Navier-Stokes equations using a finite element method approach.

To reproduce the solvent extraction, the extraction speed between the oil/water interfaces was set. The distribution coefficient was assumed to be one and it calculated. A reactive constant and the extraction speed were decided to fit the experiment result in the condition of stopped flow [2].

In the flow model, the oil/water interfaces position was decided by the free surface analysis at first. Next, the interface was fixed, and the extraction calculation was done using experimental conditions in the document [1].

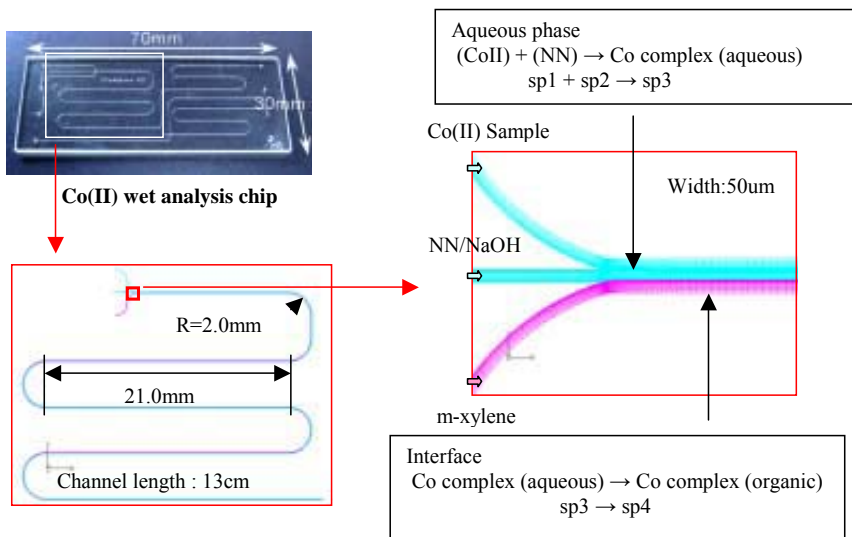


Figure 1. Co(II) wet analysis chip model

3. Results and discussion

Comparison between experiment and calculation

Figure 2 shows the result of the fitting the extraction constant in the condition of stopped flow. Moreover, the parameter used for the flow model is shown in Table 1. When the flow model was given the fitting constant and computed, the extraction in the m-xylene at the channel exit became about half compared with the experiment value. Because this model was steady calculation and interface was fixed, unsteady flow was not considered. But it is thought that the convection of the direction of the channel depth by the difference of the surface tension and disorder of flow actually exists, and it was suggested to promote the extraction in the micro channel.

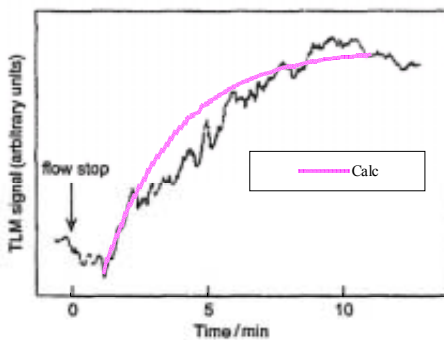


Figure 2. Fitting the experiment result in the condition of stopped flow

Table 1. Calculation parameter

Parameter	Unit	Value
Diffusion coefficient	M	1.0×10^{-5}
Initial concentration		
Co ²⁺ (sample)	M	1.0×10^{-7}
2-nitroso-1-naphthol(NN)/NaOH	M	3.4×10^{-5}
Reaction rate constant		
Complex generation reaction	1/s M	1.0×10^7 (fitting)
Co complex extraction	1/s	1.25×10^4 (fitting)

4. Conclusions

As a verification of the extraction model in the microchip, the extraction constant was identified from the stopped flow model, and the flow model was calculated by using this value. As a result, the amount of the extraction became half compared with the experiment. The factor of the extraction promotion by the flow is suggested. By examining the factor to promote the extraction of the disorder of the interface, the development of the unit chemistry operation model will become possible with the simulation in the future.

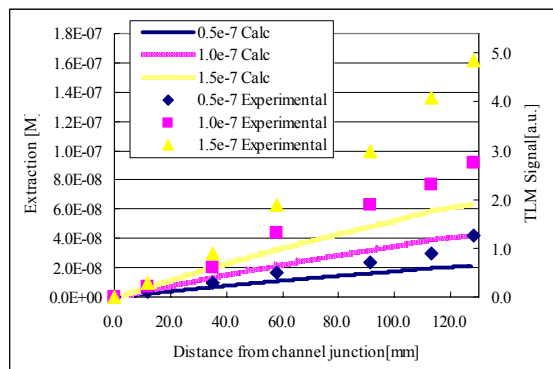


Figure 3. Relation between distance from the channel junction and extraction

References

- [1] Integration of a wet analysis system on a Microchip, Manabu Tokeshi, Tomoko Minagawa, Kenji Uchiyama, Akihide Hibara, Kiichi Sato, Hideaki Hisamoto, Takehiko Kitamori, MicroTAS(2001)
- [2] Integration of a wet analysis system on a glass chip determination of Co(II) as 2-nitroso-1-naphthol chelates by solvent extraction and thermal lens microscopy, Tomoko Minagawa, Manabu Tokeshi, Takehiko Kitamori, Lab on a Chip, 1, 72-75(2001)

MEASUREMENT OF ION DIFFUSIVITY AT THE ELECTROLYTE-GLASS INTERFACE BY EVANESCENT WAVE MOLECULAR TAGGING

Hiroki FUKUMURA¹, Mitsuhsia ICHIYANAGI¹ and Yohei SATO¹

¹Keio University, 3-14-1, Hiyoshi, Kouhoku-ku, Yokohama, 223-8522 JAPAN
E-mail: yohei@sd.keio.ac.jp

Abstract

A new measurement technique for ion velocity and diffusivity in the vicinity of interface is proposed for investigation of transport phenomena near the wall surface. This technique, which is called evanescent wave molecular tagging, utilizes caged fluorescent dye and evanescent wave illumination. Evanescent wave molecular tagging was performed in stationary flow and electroosmotic flow, and compared to molecular tagging with epi-fluorescent illumination. The ion diffusion near the wall surface can be also affected by the velocity gradient of the flow.

Keywords: Nanoscale, Electric double layer, Ion diffusion, Evanescent wave, Caged fluorescent dye

1. Introduction

Transport of analyte and reactant molecule in small liquid sample is the one of the most crucial phenomena involved in efficiency and functionality of micro-TAS [1]. The transport phenomena can be affected greatly by interface of liquid and wall as the surface to volume ratio increases. It is noteworthy to investigate experimentally transport phenomena, which is governed by velocity and diffusion of the molecule, in the vicinity of electrolyte-glass interface. The objective of the present study is to develop the measurement technique of ion velocity and diffusivity at the vicinity and to investigate the transport phenomena. The evanescent wave molecular tagging technique utilizes caged fluorescent dye and evanescent wave illumination.

2. Principle of evanescent wave molecular tagging

Evanescent wave generated by total internal reflection at the interface [2] as illustrated in Figure 1. Evanescent wave enables to excite fluorescent dye only of the order of 100 nm from the interface. Caged fluorescent dye [3] is initially non-fluorescent owing to attached caging groups. The dye restores the fluorescence when ultraviolet light irradiates the dye and cleaves the caging groups, which is well known as uncaging event. The schematic concept of evanescent wave molecular tagging is illustrated in Figure 2. Just after irradiation of a single pulsed ultraviolet laser, the evanescent wave illumination excites the uncaged fluorescent dye near the wall surface. The dye velocity and diffusivity were calculated by the displacement of the peak-value and the broadening of the fluorescent intensity profile fitted to Gaussian profile, respectively.

3. Experimental setup

The CMNB-caged fluorescein (Molecular Probes Inc.) was employed as the caged fluorescent dye which was dissolved with 0.5 mmol/l concentration in 10 mmol/l carbonate buffer at pH 9.5. Figure 3 shows an I-shaped microchannel comprised of a poly(dimethylsiloxane) (PDMS) chip and a borosilicate cover glass plate. The electroosmotic flow was generated by an application of 37 V/cm DC electric field. The present measurement system was shown in Figure 4. A continuous ultraviolet laser beam from an Nd:YVO₄ laser (1 W, $\lambda = 355$ nm) was used for the uncaging event. After attenuated and pulsed, the beam was focused into a laser sheet in a microchannel cross-section. For evanescent wave illumination, a 60 \times magnification oil-immersion objective lens ($NA = 1.45$) was employed. A laser beam from a diode pumped solid laser (30 mW, $\lambda = 473$ nm) was totally internally reflected on an interface between the borosilicate cover glass and the buffer solution. The characteristic penetration depth of the evanescent wave was 78 nm under the present experimental condition. For epi-fluorescent illumination, a mercury lamp was employed. Fluorescence from the uncaged dye was captured onto the CCD pixel sheet with 37 ms frame interval.

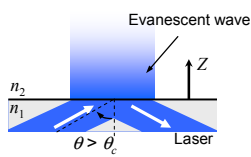


Figure 1. Schematic of evanescent wave illumination.

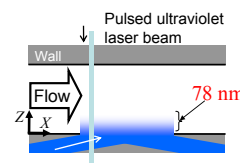


Figure 2. Schematic concept of evanescent wave molecular tagging.

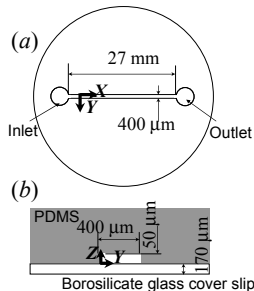


Figure 3. Schematic illustration of (a) top and (b) cross-sectional views of microchannel.

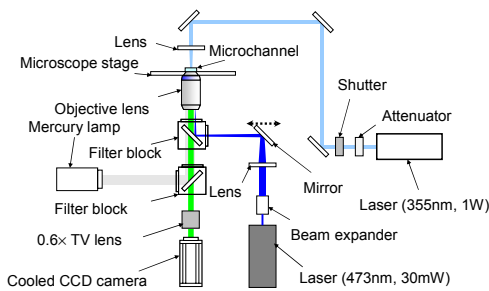


Figure 4. Schematic illustration of measurement system.

4. Result and discussion

Prior to the uncaged dye velocity and diffusivity measurement in the EOF, the diffusivity of the dye in a stationary flow was measured. Figure 5 shows the fluorescence intensity profiles at $y = 200$ μ m with epi-fluorescent and evanescent wave illumination. The diffusivity obtained by evanescent wave illumination was 5.33×10^{-10}

m^2/s , compared to $6.61 \times 10^{-10} \text{ m}^2/\text{s}$ obtained by epi-fluorescent illumination. These values are agreed with fluorescein diffusivities, $6.4\text{--}6.6 \times 10^{-10} \text{ m}^2/\text{s}$ and $4.37 \times 10^{-10} \text{ m}^2/\text{s}$ reported by [1] and [3], respectively.

Figure 6 indicates the velocity profiles of the EOF obtained by epi-fluorescent and evanescent wave illumination. The velocities obtained by epi-fluorescent illumination is larger than the velocities obtained by the evanescent wave illumination because of the Z-direction velocity gradient induced by the zeta potential difference between the bottom wall (borosilicate glass) and the top wall (PDMS) of the microchannel. Diffusivities in the EOF obtained by epi-fluorescent and evanescent wave illumination are $11.1 \times 10^{-10} \text{ m}^2/\text{s}$ and $8.79 \times 10^{-10} \text{ m}^2/\text{s}$, respectively. In the both illuminations, the diffusivities in the EOF are larger values compared to the diffusivities in the stationary flow. This fact indicates the ion diffusion even in the vicinity of the electrolyte-glass interface can be affected by the velocity gradient.

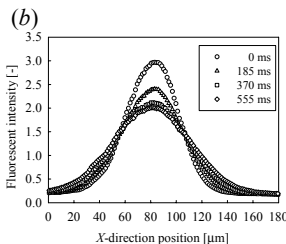
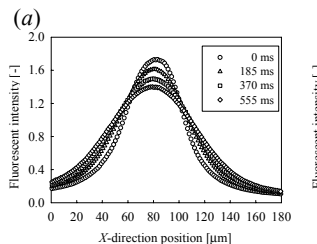


Figure 5. Fluorescent intensity profiles by (a) epi-fluorescent and (b) evanescent wave illumination in the stationary flow.

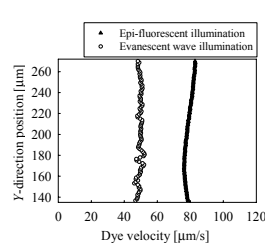


Figure 6. Velocity profiles of the electroosmotic flow.

5. Conclusions

A measurement technique of ion velocity and diffusivity in the vicinity of the electrolyte-glass interface was developed for investigation of transport phenomena near the interface. This technique was applied to the stationary flow and electroosmotic flow. The velocity profile and diffusivity of the uncaged fluorescein were obtained and compared to those obtained by using epi-fluorescent illumination. The diffusivity in the vicinity of the interface is also affected by the velocity gradient of the flow.

Acknowledgements

This work was subsidized by the Grant-in-Aid for Young Scientists (A) No.17686017 of Ministry of Education, Culture, Sports, Science and Technology and TEPCO Research Foundation.

References

1. Galambos, P. *et al.*, MicroTAS'98, pp.189–191, (1998).
2. Axelrod, D. *et al.*, *Ann. rev. biophys. bioengin.*, 13, pp. 247–268, (1984).
3. Paul, P.H. *et al.*, *Anal. Chem.*, 70, pp. 2459–2467, (1998).

PHOTOREACTIONS IN MICROREACTORS

Teijiro Ichimura,¹ Yoshihisa Matsushita,² Kosaku Sakeda,¹ Tadashi Suzuki,¹ Hideki Tanibata,³ and Toshiaki Murata⁴

¹Department of Chemistry and Materials Science, and ²Department of Chemistry, Tokyo Institute of Technology, Japan

³Mitsui Engineering & Shipbuilding Co., LTD, Japan

⁴Mitsui Zosen Plant Engineering, Inc., Japan

Abstract

A micro-flow system for photoreactions was developed and the processes of asymmetric photosensitized reactions, photocatalytic oxidation and reduction of aromatic compounds, and amine N-alkylation in microspace were examined. These model reactions proceeded very rapidly with considerably large photonic efficiencies. The results suggest the feasibility of a microreaction system on organic photoreactions.

Keywords: Photochemistry, Asymmetric Reaction, Photocatalyst, Endocrine Disrupters

1. Introduction

In the last decade, microreaction systems have been developed by using their distinct properties, such as short molecular diffusion distance, excellent heat transfer characteristics, laminar flow, and large surface-to-volume ratio. Although we can expect microreactors to exhibit higher spatial illumination homogeneity and better light penetration through the entire reactor depth in comparison to large-scale reactors, there are only several reports on photoreactions in microreactors. Thus we are investigating applications of microreactors on organic photoreactions. In this presentation we will report the study on asymmetric photoreactions and photocatalytic reactions in microreactors.

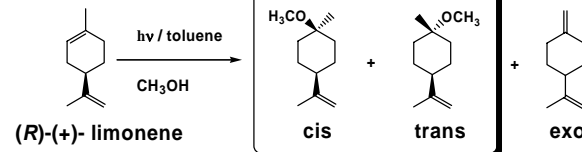
2. Experimental

Microreactors made of quartz which have a microchannel of 200-500 μm width, 10-500 μm depth were employed. The bottom and side walls of the microchannel were coated with a TiO₂ layer for photocatalytic reactions. Sample solution fed into the microreactor was irradiated by a KrF excimer laser (248 nm), the third and fourth harmonics of a Nd³⁺: YAG laser (355 and 266 nm), an OPO laser excited with the YAG laser, or UV light emitting diodes (UV-LEDs, 365nm, 10~500 mW).

3. Results and Discussion

The effects of residence time, reaction temperature, photon density, and excitation wavelength on photosensitized enantio- and diastereo-differentiating reactions were investigated. Photonic efficiencies of model reactions were considerably larger than those in conventional batch reactors. Further, the yield of photosensitized diastereodifferentiating addition of methanol to terpenes (Scheme 1) was greatly improved in the microreactor.

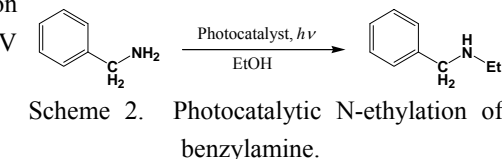
Photocatalytic oxidation of endocrine disruptors and reduction of aromatic compounds were investigated in a microreactor with



Scheme 1. Diastereodifferentiating addition of methanol to limonene.

immobilized photocatalytic TiO_2 layer. Apparent reaction rates in microreactors were much larger than those in conventional batch reactors [1, 2]. The photoreduction proceeded within 60 s to yield 10.7 % of benzylalcohol from benzaldehyde and 45.7 % of p-toluidine from p-nitrotoluene by the excitation of 365 nm UV-LED.

It has been known that N-alkylation of aromatic amines occurred by UV irradiation of Pt loaded TiO_2 (TiO_2/Pt) suspended in a variety of alcohols in conventional batch



Scheme 2. Photocatalytic N-ethylation of benzylamine.

reactors. Ohtani et al. [3] studied N-alkylation process of amines by the irradiation 400-W high-pressure mercury of TiO_2/Pt . They reported that N-alkylation of benzylamine occurred with the yield up to 84.4 % by 4 hours irradiation in ethanol solvent. They also reported that N-alkylation of amines could not be observed by the irradiation of Pt-free TiO_2 .

Observed photocatalytic processes of N-alkylation of aromatic amines in microreactors were considerably different from those in conventional batch reactors. The N-alkylation of benzylamine was studied in the photocatalytic microreactor of 300 μm depth excited with 365-nm UV-LEDs. The reaction proceeded very rapidly in the photocatalytic microreactor with immobilized TiO_2/Pt . The N-alkylation in ethanol proceeded within only 150 seconds to yield 85 % of N-ethylbenzylamine from benzylamine. In contrast to the result in batch reactors, we also successfully observed N-alkylation reaction of aromatic amines by using the microreactor with immobilized

Pt-free TiO_2 as well as TiO_2/Pt . The N-alkylation in ethanol proceeded within only 150 seconds to yield 43 % of N-ethylbenzylamine with Pt-free TiO_2 .

We further investigated an oxidation process of p-chlorophenol by using a gas-liquid-solid multiphase microreaction system. To produce high interfacial area between the phases, we introduced aqueous solution of p-chlorophenol and oxygen gas into a microchannel. The yield of photodegradation is shown in Fig. 1. The horizontal axis indicates the gas injection rate while the injection rate of sample solution was kept at a constant value of 10 $\mu\text{L}/\text{min}$. At a lower gas injection rate, micro-bubbles were formed and at a gas injection rate higher than 500 $\mu\text{L}/\text{min}$, a pipe-flow, the gas flowed through the center of the microchannel while the liquid flowed close to the photocatalyst surface, was formed. The reaction yield increased to 43 % at the irradiation time of 14 s in the pipe-flow while it was 10 % at the irradiation time of 75 s without injection of oxygen gas. Under the pipe-flow condition, the liquid phase is always saturated with oxygen even in the end part of the microchannel. In addition, as increasing the gas injection rate, the thickness of the liquid phase decrease. At the gas injection rate of 750 $\mu\text{L}/\text{min}$, the thickness of the liquid phase is estimated to be 25 μm . These facts may increase the reaction yield. The application of multiphase photocatalytic microreaction system on synthetic organic reactions will be further discussed.

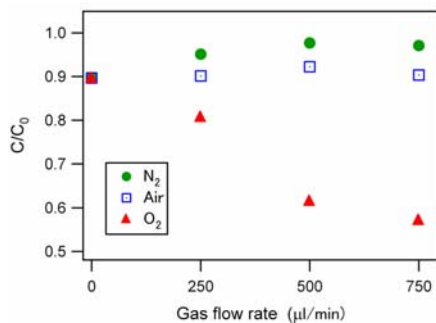


Fig. 1. Photocatalytic oxidation of p-chlorophenol ($1.1 \times 10^{-3} \text{ M}$) in a multiphase microreactor of 500 μm depth.

References

1. Y. Matsushita, S. Kumada, K. Wakabayashi, K. Sakeda, T. Ichimura, *Photocatalytic reduction in microreactors*, Chem. Lett., 35 pp. 410-411, (2006).
2. T. Ichimura, Y. Matsushita, K. Sakeda, T. Suzuki, *Photoreactions*, in *Microchemical Engineering in Practice*, ed. By T. R. Dietrich, Blackwell Publishing, (2006).
3. B. Ohtani, H. Osaki, S. Nishimoto, T. Kagiya, *A novel photocatalytic process of amine N-alkylation by platinized semiconductor particles suspended in alcohols*, J. Am. Chem. Soc., 108, pp. 308-310, (1986).

STREAMING CURRENTS AS A MEANS TO STUDY THE SURFACE CHARGE IN NANOFUIDIC CHANNELS

F.H.J. van der Heyden, D. Stein, D.J. Bonthuis, K. Besteman,
S.G. Lemay, C. Meyer and C. Dekker.

Kavli Institute of Nanoscience, Delft University of Technology,
Lorentzweg 1, 2628 CJ, Delft, The Netherlands.

Keywords: streaming current, surface charge, nanofuidics, charge inversion, power generation.

Streaming currents as a novel tool

Nanofuidics is an emerging field of interest because of its potential to study and manipulate fluids, nanoparticles, and molecules in lab-on-a-chip devices. Electrokinetic phenomena such as electro-osmotic flow and streaming currents, induced by the charged walls of a microchannel, will become increasingly important in the nano-regime because of the larger surface to volume ratio. Streaming currents are ionic currents that result from the pressure-driven transport of the net charge inside the electrical double layer at a charged surface (Fig. 1). As a result they are a probe of the electrostatics at the solid-liquid interface. We employed streaming currents in rectangular nanochannels as a sensitive tool to study the surface charge in a variety of conditions. Interpretation is straightforward because of the well-defined dimensions of our nanochannels.

The surface charge of silica

We studied the surface charge density, σ , of silica as function of salt concentration and channel height h using streaming currents. σ was found to increase with salt concentration because of the chemical equilibrium of the charge-determining silanol groups with protons in the water [1]. σ can be independently obtained by measuring the electrical conductance in the regime where the σ -induced countercharges dominate the conductance of the channel, i.e. at low salt in nanoscale geometries [2]. The σ thus obtained is much larger than the σ measured by streaming currents. This discrepancy is reconciled by invoking an additional surface conductance, the so-called Stern

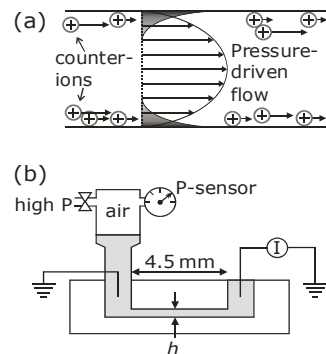


Fig. 1: (a) Schematic illustration of the origin of the streaming current. The fluid flow is modeled by the Navier-Stokes equation with the no-slip boundary, and the charge distribution by the exact solution of the Poisson-Boltzmann equation between parallel plates [1, 4]. (b) Sideview of the nanochannel with electrical and pressure connections. Channels of length 4.5 mm, width 50 μm , and height $h = 490$ nm were used, unless stated otherwise. The current scaled linearly with the pressure difference Δp , and we defined the streaming conductance, S_{str} , as the streaming current per Δp .

layer conductance, which dominates the channel conductance at low salt [5]. The Stern layer conductance was found to be the same for both K^+ and Li^+ -ions, whose bulk mobilities differ by a factor of 2, suggesting that mobile protons dominate the conduction in the Stern layer.

Charge inversion by multivalent ions

The effect of multivalent ions on the effective surface charge of silica was investigated in previously unexplored regimes of biological relevance [3]. Ions with $Z \geq 3$, with Z the valence, are known to accumulate strongly in the Stern layer, thereby causing the effective surface charge to flip sign. This effect is called charge inversion. Using streaming currents as a sensitive method up to high salt concentrations, we demonstrated charge inversion to occur for divalent ions at high concentrations (fig. 2). For $Z = 3$, extra monovalent salt was found to suppress, and even cancel, charge inversion (Fig. 3). This effect of the monovalent salt could be explained within the framework of strongly correlated liquid theory, by including the entropy of mixing and imposing the extra assumption that an ion cannot approach a surface closer than its radius. With these modifications, this model describes our data accurately for intermediate KCl concentrations (dashed curves). For higher concentrations, screening of the bare surface charge becomes dominated by monovalent ions in the Stern layer.

Power generation with nanochannels

Electrical power is harvested from the pressure-driven streaming current by connecting an external load resistor, R_L . Both the power (fig. 4) and the efficiency (not shown) were found to have maximum as function of R_L . Our results could be excellently modeled by characterizing the nanochannel through its linear electrokinetic response properties (inset and lines in fig. 4). These linear responses were obtained as fit

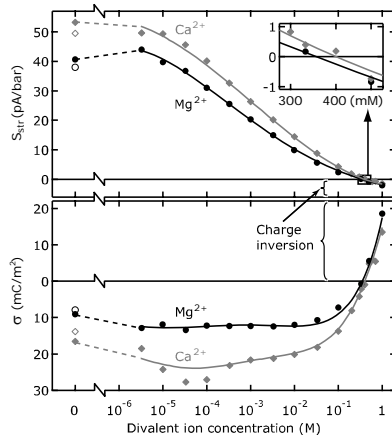


Fig. 2: S_{str} and σ as function of divalent ion concentration. The inset highlights the charge inversion concentration region. Lines are guides to the eye; open symbols are measurements after each sweep from low to high concentration.

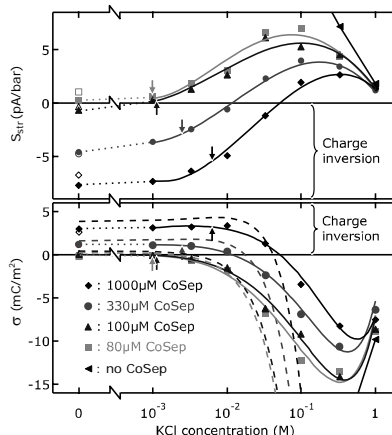


Fig. 3: S_{str} and σ as function of KCl concentration in the presence of trivalent CobaltSepulchrate (CoSep) ions. Solid lines are guides to the eye and dashed lines are model curves. Arrows indicate where KCl ions start to dominate the screening length.

parameters from measurements [5], and from calculations using nonlinear Poisson-Boltzmann theory [4]. These theoretical calculations for a constant σ as a boundary condition revealed that i) the highest efficiency occurs in the regime of double layer overlap, when co-ions are expelled from the nanochannels, ii) there exists an optimal σ for maximal efficiency, $h\sigma = 0.6 \text{ nm} \times \text{C/m}^2$, that balances tradeoffs between increased convective charge transport (when σ is raised), and resistive power dissipation, and iii) the fully-optimized efficiency that can be obtained from a fluidic system is ultimately determined by a single dimensionless parameter, that contains the mobility of the counterions (leading to a maximal efficiency of 7% for K^+ and 12% for Li^+) [4]. This theory is also applicable to the efficiency of electro-osmotic pumping. Our measurements in silica nanochannels confirmed the prediction that the efficiency was highest for low salt, where double layers overlap (fig. 5). However, the predicted dependence on counterion mobility and h were not observed, due to a dominating Stern layer conductance at low salt. A maximum efficiency of about 3 % was found for 75 nm-high channels. The efficiency is expected to be higher for materials with a lower Stern conductance.

- [1] F.H.J. van der Heyden, D. Stein and C. Dekker, "Streaming Currents in a Single Nanofluidic Channel", Phys. Rev. Lett. **95**, 116104 (2005)
- [2] D. Stein, M. Kruithof and C. Dekker, "Surface-Charge-Governed Ion Transport in Nanofluidic Channels", Phys. Rev. Lett. **93**, 035901 (2004)
- [3] F.H.J. van der Heyden *et. al.*, "Charge Inversion at High Ionic Strength Studied by Streaming Currents", Phys. Rev. Lett. **96**, 224502 (2006)
- [4] F.H.J. van der Heyden *et. al.*, "Electrokinetic Energy Conversion Efficiency in Nanofluidic Channels", Nano Lett., accepted for publication.
- [5] F.H.J. van der Heyden *et. al.*, "Power Generation by Pressure-Driven Transport of Ions in Nanofluidic Channels", Phys. Rev. Lett., submitted.

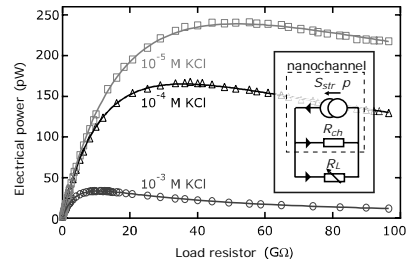


Fig. 4: The generated electrical power $P = \Delta V^2 / R_L$ as function of R_L for a few different KCl concentrations and $\Delta p = 4$ bar, where ΔV is the equilibrium potential difference across R_L . The data are excellently modeled (lines) by characterizing the fluidic channel through its linear electrokinetic response properties, S_{str} and R_{ch} , and using the electrical equivalent circuit (inset). R_{ch} is the electrical conductance of the nanochannel.

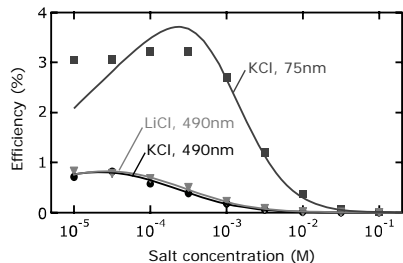


Fig. 5: The power generation efficiency as function of salt concentration for different channel heights and counter ions. Lines are calculations using a chemically varying σ to model the diffuse layer with an extra conductance to model the Stern layer.

IN-SITU MONITORING OF C-REACTIVE PROTEIN (CRP) ANTIGEN-ANTIBODY BINDING IN A LIQUID ENVIRONMENT USING A MICROMECHANICAL PZT THICK FILM CANTILEVER

Tae Yun Kwon^{1,2}, Jae Hong Park¹, Dae Sung Yoon¹, Hong Lim Lee² and Tae Song Kim¹

¹ Korea Institute of Science and Technology, Seoul, 130-650, Korea

²Department of Ceramic Engineering, Yonsei University, Seoul 120-749, Seoul, Korea

Abstract

The monolithic piezoelectric thick film cantilever device was fabricated for bio molecule recognition sensor. For biosensor applications, resonance frequency behavior of integrated microcantilever in various viscous liquids using electrical measurement method was investigated. In this study, we report on resonant frequency shift measurement based on a micromechanical cantilever for label-free detection of a CRP in a liquid environment..

Keywords : biosensor, PZT thick film, cantilever, Resonance frequency shift, CRP

1. Introduction

Microfabricated cantilevers have recently attracted considerable interest in relation to the development of a wide range of novel physical, chemical and biological sensors [1]. The real-time monitoring of a prostate-specific antigen specific binding in a liquid environment using a PZT thin film cantilever was reported [2]. In that study, severe deterioration of the resolution of the resonance peak was encountered due to a liquid damping, resulting in a drawback, in that the resonant frequency curves with respect to assay time showed large fluctuations. This was because the actuating force induced by the thin film cantilever is too small to overcome the high effective mass and viscous environment of the liquid. A primary advantage of the piezoelectric thick film device is that a large actuating force can be generated through a thick film in comparison with a piezoelectric thin film. Recently, we have succeeded in the fabrication of a monolithic piezoelectric thick film cantilever device on a Si substrate using a MEMS process [3]. In this study, for the application of microcantilever sensor to bio-molecule detection, we report the resonance frequency behavior of integrated microcantilever biosensor in various viscous liquids using electrical measurement method, and we report a result of on resonant frequency shift measurement based on a micromechanical cantilever with a PZT actuating

layer for label-free detection of a C-reactive protein in a liquid environment. For the bioassay in a liquid environment, a liquid test cell has been fabricated, using a bonding technique between PDMS bilayers.

2. Experimental

The PZT thick films were patterned onto the Pt/TiO₂/SiN_x/Si substrate by a screen printing method using a low pressure screen printing machine. The monolithic cantilevers were acquired from the patterned PZT thick film by the MEMS fabrication process suggested in Reference 3 (see Fig. 1). The PDMS liquid cells were made for the liquid test and the real-time bioassay (see inset in Fig. 1). For the mechanical test in a liquid environment, electrically insulating liquids (FluorinertTM, 3M) were employed as liquid media, and their absolute viscosities were 1.4, 3.4 and 4.7 cP at 25°C. For electrical and biological passivation, all cantilever samples were coated with parylene-C film. For the bioassay, a monoclonal anti-CRP of a 50 µg/ml concentration was immobilized on 3 mM Calixcrown SAMs, and the PBS solution containing 100 ng/ml CRP antigens was used for *in-situ* monitoring of the interaction between the antibody and the antigen.

3. Results and discussion

Fig. 2 shows the measurement results of the primary resonant frequency in various liquids. As seen in the plot, the cantilever operated well in various liquid environments. The primary resonant frequency shifted from a high to low frequency range with the increasing viscosity. It is worthwhile to note that the cantilever clearly showed its intrinsic primary resonant frequency (12.38 kHz) even at a high viscosity of 4.7 cP, corresponding to the viscosity range of whole blood. This means that a real-time assay using human blood or serum can be realized using the thick film cantilever. The cantilever has been used for the *in-situ* monitoring of a bioassay. Calixcrown SAMs were used as linker molecules. The assay protocol and process were described in Fig. 3. Fig. 4 shows the real-time behavior of the resonant frequency change of the cantilever with respect to the assay time, after the target solution injection (the CRP antigen and a negative control). As the CRP antigen of 100 ng/ml was injected into the liquid cell, the resonant frequency of the cantilever gradually decreased with time, showing a similar trend to the Langmuir adsorption isotherm. After approximately 20 min, the reaction between the CRP antigen and the antibody reached an equilibrium state.

4. Conclusion

In summary, the monolithic PZT thick film cantilever showed excellent long-term mechanical stability in various liquids, including one in the viscosity range of whole blood. Finally, we demonstrated that a real-time bioassay of a CRP was successfully performed using the monolithic piezoelectric thick film cantilever.

References

- [1] C. Hagleitner, A. Hierlemann, D. Lange, A. Kummer, N. Kerness, O. Brand, H. Baltes, *Nature*, **414**, 293 (2001).
- [2] K. S. Hwang, J. H. Lee, J. Park, D. S. Yoon, J. H. Park, T. S. Kim, *Lab Chip*, **4**, 547 (2004).
- [3] J. H. Park, T. Y. Kwon, D. S. Yoon, H. Kim and T. S. Kim, *Adv. Funct. Mater.*, **15**, 2021 (2005)

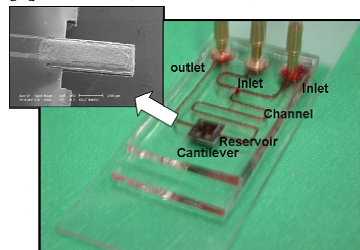


Figure 1. A SEM image of a piezoelectric thick film cantilever and a photograph of liquid cell fabricated using a bonding technique between the (PDMS) bilayers.

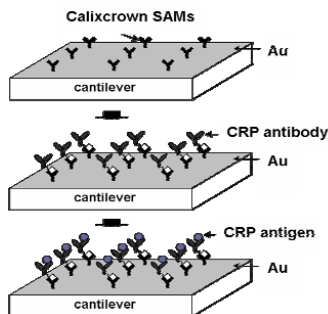


Fig. 3. A schematic diagram of the immobilization of CRP antibody on the cantilever surface and the subsequent interaction between the CRP antibody and the CRP antigen.

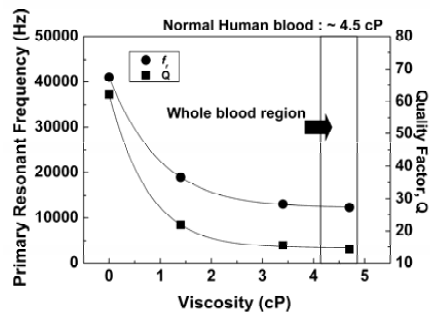


Figure 2. Resonance frequency behavior of the thick film cantilever in the liquid cell with respect to liquid viscosity

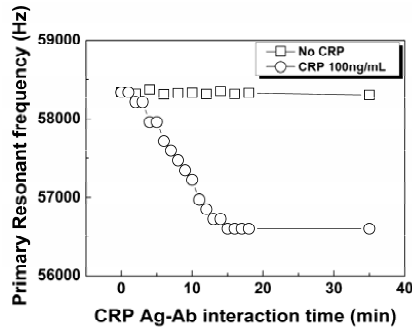


Figure 4. *In-situ* resonant frequency change after the injection of 100 ng/ml CRP antigen into the PDMS liquid cell

DETERMINATION OF BLOOD SUGAR USING MICROCHIP ELECTROPHORESIS

Eiki Maeda^{1, 2}, Masatoshi Kataoka³, Yasuo Shinohara^{1, 2}, Noritada Kaji⁴,
Manabu Tokeshi⁴ and Yoshinobu Baba^{3, 4}

¹The University of Tokushima, Shomachi, Tokushima 770-8505, Japan

²IGR, The University of Tokushima, Shomachi, Tokushima 770-8505, Japan

³HTRC, AIST, Hayashi-cho, Takamatsu 761-0395, Japan

⁴Nagoya University, Chikusa-ku, Nagoya 464-8603, Japan

Abstract

In this study, high-performance monitoring system for blood sugar was developed by using microchip electrophoresis with a plastic chip. A combination of a reductive amination as sugar labeling and sugar-borate complex formation realized highly selective detection of blood sugar even in a blood sample. This paper demonstrates that this system enables us to determine blood sugar with high sensitivity and high accuracy, and it will be applicable to clinical diagnosis.

Keywords: blood sugar monitoring, borate ion, electrophoresis, microchip, reductive amination

1. Introduction

Glucose is one of the most important substances for all mammals, and its concentration in the blood is strictly adjusted. Diabetes, which is a major health problem mechanism and shows hyperglycemia, causes a lot of critical complications. Therefore, it is very important to monitor and to control the blood sugar for diagnosis and effective treatment of diabetic. However, current clinical diagnosis needs milliliter-scale sample and reagent volumes. In this study, blood sugar monitoring system using microchip electrophoresis was developed to achieve reducing sample and reagent consumptions.

2. Experimental

All experiments were carried out using a Hitachi SV1100 microchip electrophoresis system, and performed on a microfabricated polymethylmethacrylate chip (Fig. 1). Borate buffer (200 mM, pH 8.5) contains 0.5% w/v methylcellulose was adopted from previous report as a migration buffer [1]. After collection of blood specimens from three healthy individuals, blood cell separation was performed followed by labeling of sugars. For the detection of reducing sugars, 2-aminoacridone (AMAC) was used (Fig. 2). Enzymatic reactions using hexokinase and glucokinase were performed for the peak identification. Moreover, the blood sugars in the three specimens were calculated

using standard curve obtained from AMAC-labeled glucose solution. Furthermore, as comparison of the quantitative accuracy, clinical assay (glucose-dehydrogenase method) using the same specimens was requested to SRL Inc.

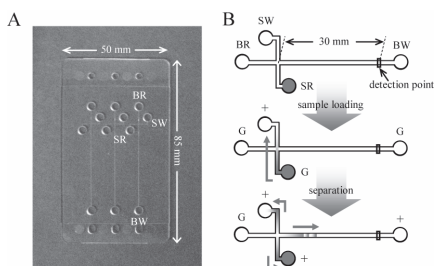


Figure 1. (A) Plastic chip with a simple cross-channel was used in blood sugar monitoring. (B) Electrokinetic sample injection process.

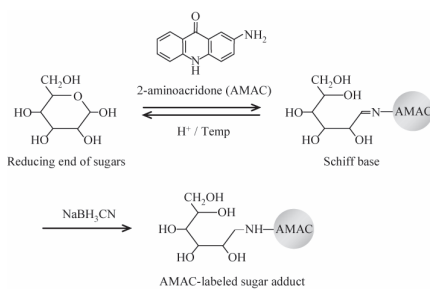


Figure 2. Reaction scheme for the labeling of reducing sugars with AMAC.

3. Results and Discussion

During electrophoresis, using the negative charge which derived from sugar-borate complex [2] as a driving force, AMAC-labeled sugars were migrated to anode side (Fig. 3). Reductive amination was occurred at reducing end of sugars, therefore it is

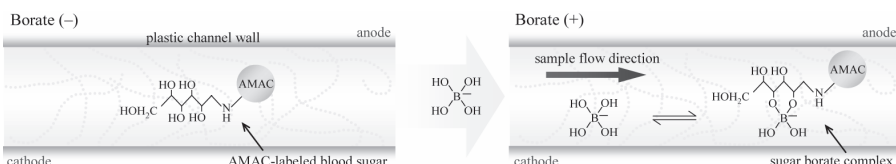


Figure 3. Schematic diagrams of sugar-borate complex formation in microchannel.

possible to detect sugars specifically in blood with which various biological molecules coexist. AMAC-labeled sugar in the blood specimen was detected in about 145 seconds with high selectivity (Fig. 4). By comparison with AMAC-labeled glucose in migration time, it was surmised that this peak was derived from glucose. The detected peak was identified as AMAC-labeled glucose by the enzymatic reactions (Fig. 5). The quantitative analysis was also performed and the linear correlation coefficient in the range of 1.0–300 μM of AMAC-labeled glucose solution was 0.999. The measurement values of AMAC-glucose were not affected by other sugars such as galactose, xylose and maltose. Then, the blood sugars in the three specimens were calculated from standard curve. The results obtained from microchip electrophoresis were very close to the reference values ($P = 0.034$) in SRL Inc (Table 1). Also, the sample volume and its concentration for one analysis compared with the current method

were reduced to 5% and 1.25%, respectively.

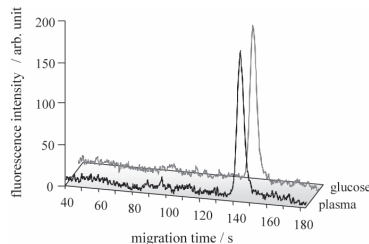


Figure 4. Electropherograms of AMAC-labeled blood sugar and glucose. Experimental conditions: Esep = 168 V/cm

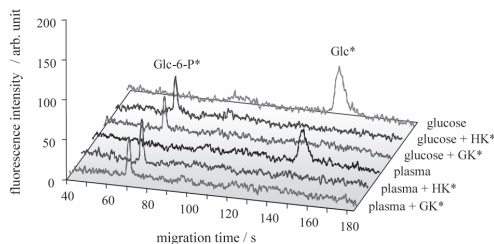


Figure 5. Electropherograms of AMAC-labeled blood sugar and glucose treated with or without phosphoenzyme.

Table 1. Calculated concentrations and reference values of each specimen.

blood specimen	peak height ^{a)}	blood sugar (mg/dl)	reference value ^{b)} (mg/dl)
A	1153	97.34	98
B	1324	111.43	107
C	2151	179.53	175

^{a)} Experimental conditions as in figure 4. All three blood specimens were diluted 20-fold with 0.2 mol/L borate buffer (pH 8.5) after derivatization.

^{b)} Clinical assay (glucose-dehydrogenase method) was requested to SRL Inc. using same blood specimens

4. Conclusions

We have presented high-performance monitoring system for blood sugar using microchip electrophoresis with a plastic chip. Blood sugar was detected with high sensitivity and high accuracy even in a blood sample. These results serve as a good basis for further research towards a real highly-integrated chip format that will be developed in near future, like the diagnostic chip which can perform clinical assay on one sheet.

References

1. E. Maeda, K. Hirano, Y. Baba, H. Nagata, M. Tabuchi, *Conformational separation of monosaccharide of glycoproteins labeled with 2-aminoacridone using microchip electrophoresis*, Electrophoresis, 27, 2002-2010, (2006).
2. W. J. Evans, E. J. McCourtney, W. B. Carney, *A comparative analysis of the interaction of borate ion with various polyols*, Anal. Biochem., 95, 383-386 (1979).

A MICROCHIP-BASED FLUORESCENCE POLARIZATION IMMUNOASSAY

Tomoya Tachi¹, Noritada Kaji¹, Manabu Tokeshi¹ and Yoshinobu Baba^{1,2}

¹Department of Applied Chemistry, Graduate School of Engineering, Nagoya University, Nagoya 464-8603, Japan,

²Health Technology Research Center, AIST, Takamatsu 761-0395, Japan,

Abstract

A simple and rapid immunoassay on a microchip has been developed by using fluorescence polarization measurement. We here report a microchip-based quantitative analysis of a kind of bronchodilator, theophylline, which is important for the treatment of asthma.

Keywords: microchip, immunoassay, fluorescence polarization, drug monitoring, theophylline

1. Introduction

Microfluidic devices have various advantages such as reduction in sample and reagent consumption, high reaction efficiency, short analysis time, simple operation, integration and automation. A microchip immunoassay is one of the good applications that make use of these advantages. However, a microchip immunoassay generally requires immobilization of antibodies or antigens and troublesome operations such as washing and reflowing, and therefore the overall assay process is not so fast. Although a diffusion immunoassay (DIA), which is simple operation and very rapid, has been proposed by Hatch et al. [1], there is much room for further improvement because diffusive transport during the early stages of binding between antigen and antibody is measured in the non-equilibrium state. In the present study, we have realized a fluorescence polarization immunoassay (FPIA) on a microchip. The FPIA method is also very simple and rapid. Moreover, since the FPIA developed here is assayed in the equilibrium state between antigens and antibodies, the reproducibility is very high. A FPIA method, a quantitative competitive immunoassay, is widely used for therapeutic drug monitoring at present [2]. We here report a FPIA method on a microchip for the determination of theophylline concentration.

2. Experimental

We here designed a microfluidic FPIA system in figure 1 and 2. Laser-induced fluorescence and microscope collection optics are used in this system, and polarizers are equipped at both the entrance and the exit of a dichroic mirror. Polarized fluorescence can be detected after mixing theophylline and fluorescence-labeled theophylline tracer, followed by anti-theophylline antibody on the microchip. In this experiment,

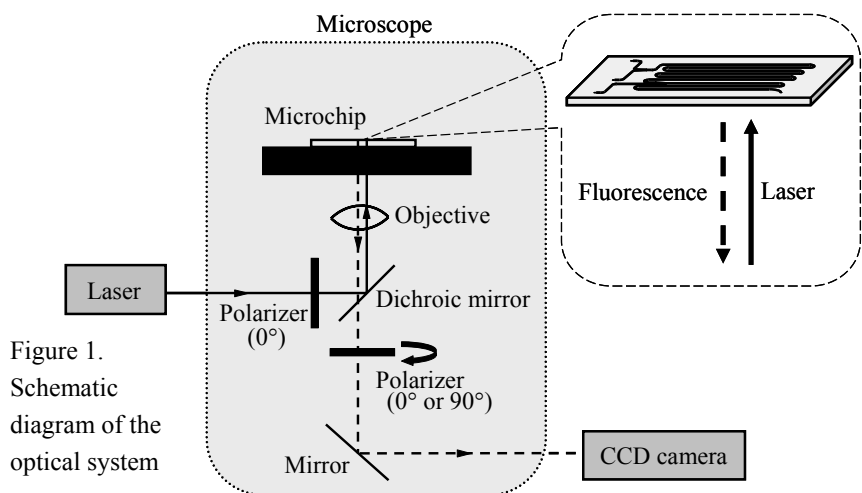


Figure 1.
Schematic
diagram of the
optical system

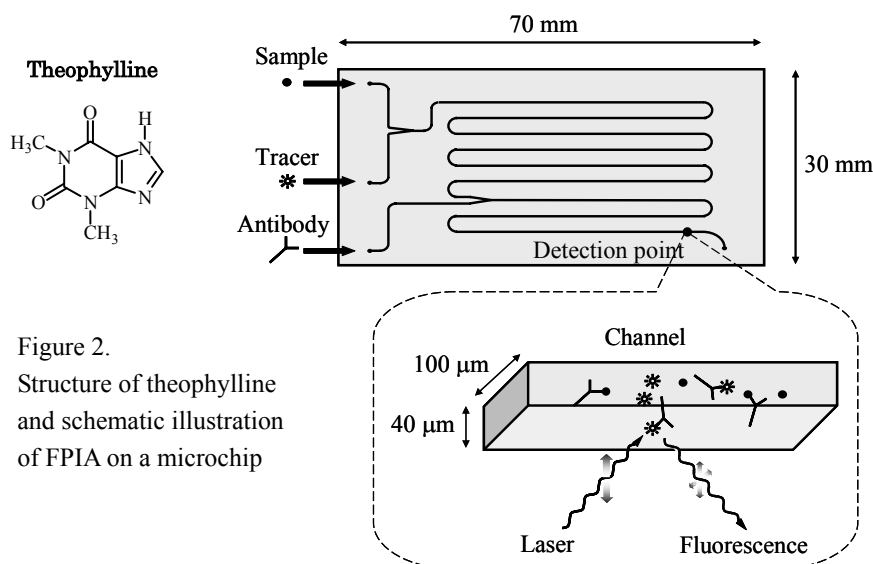


Figure 2.
Structure of theophylline
and schematic illustration
of FPIA on a microchip

tracer-antibody-complex, which is larger than tracer, emits more polarized fluorescence than tracer. Therefore, with increasing antigen concentration in a sample, the more polarization relaxation is observed since tracer-antibody-complex concentration is decreased and tracer concentration is increased. Various concentrations of theophylline standard are flowed into the microchannel with constant concentration of tracer and antibody.

3. Results and discussion

The plot of polarization value against theophylline concentration in this system is shown in Figure 3. The mixing of the solutions is complete at the detection point on this condition. As shown in this figure, the relaxation of polarization was observed with increasing theophylline concentration in the same manner as that of the bulk-scale assay.

The therapeutic range of theophylline concentration in serum is from 10 to 20 $\mu\text{g}/\text{mL}$. Figure 3 suggests that determination of theophylline concentration is feasible near the therapeutic range in this system. Furthermore, theophylline will be assayed within 1 minute by the optimization of the microchannel structures.

4. Conclusions

We have developed a simple and rapid immunoassay on a microchip by using fluorescence polarization measurement. A microchip FPIA is a tool that will be used for the analysis of various substances such as drugs, hormones and tumor markers, and it will be important in drug development, clinical medicine and the other fields in the future.

References

1. A. Hatch, *et. al.*, *Nature Biotech.*, **19**, 461-465 (2001)
2. M. E. Jolley, *et. al.*, *Clin. Chem.*, **27**, 1190-1197 (1981)

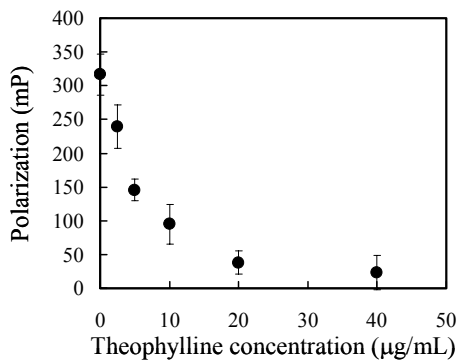


Figure 3.
Relationship between theophylline concentration and polarization
(mP; millipolarization units)

DISK-BASED PARALLEL CHEMILUMINESCENT DETECTION OF DIAGNOSTIC MARKERS FOR ACUTE MYOCARDIAL INFARCTION

L. Rieger¹, J. Steigert¹, M. Grumann¹, S. Lutz¹, G. Olofsson², M. Khayyami²,
W. Bessler³, K. Mittenbuehler³, R. Zengerle^{1,4}, and J. Ducr  e^{1,4}

¹Lutz Rieger, Laboratory for MEMS Applications,
Department of Microsystems Engineering (IMTEK), University of Freiburg,
Georges-Koehler-Allee 106, 79110 Freiburg, Germany

²Prolight Diagnostics AB, Sweden, ³IMMZ, Germany, ⁴HSG-IMIT, Germany

Abstract

We present a novel concept for the parallel detection of cardiac markers on a rotating lab-on-a-disk. Antigens indicating an acute myocardial infarction (AMI) are captured by a bead-based chemiluminescent ELISA procedure conducted under rotation on a polymer disk and detected by a photomultiplier (PMT). Parallel channel structures allow the quasi-simultaneous screening for different markers. To proof this concept, diluted, HRP-labeled myoglobin antibodies are captured with cardiac myoglobin coated beads. We obtain a CV of 12.4% and a $c_{min}=12.2 \text{ ng/ml}$ which is well below the myoglobin cut-off for the diagnosis of AMI [1]. Furthermore, two different antibody concentrations are read out simultaneously during spinning to demonstrate the capability of parallelization.

Keywords: cardiac marker, ELISA, parallel readout, centrifugal microfluidics

1. Introduction

So-called “lab-on-a-chip” systems for diagnostic point-of-care technologies attract a growing interest due to their immanent benefits of reduced turn-around times, their amenability for full process integration and automation, increased reliability, and minimized costs [2]. Among various lab-on-a-chip concepts, “lab-on-a-disk” [3,4] systems exploit centrifugal forces for metering, accelerated sedimentation of particles in biological suspensions, and mixing in order to run fully process integrated assays. In our approach, we implement a disk-based test to screen the relevant cardiac markers in parallel. This enables the early diagnosis of acute myocardial infarction in a single run.

2. Assay Principle

Polystyrene beads ($r_{bead} = 75 \mu\text{m}$) are coated off-disk with capture antibodies specific to the respective antigen ① and then aggregated in the disk-based detection chamber. On-disk, the plasma sample is incubated with the beads ② followed by horseradish peroxidase (HRP) labeled detection antibodies ③ in a flow-through procedure. Finally, a mixture of Luminol and hydrogen peroxide is transported over the beads ④. In this step, the HRP enzyme catalyzes the oxidation of Luminol to excite 3-aminophthalate which emits a photon upon relaxation [4] (Fig. 1-A). The photon count is hence a direct measure of the target antigen concentration in the sample.

3. Experimental Setup and Read-out Procedure

Our modular setup (Fig. 1-B) comprises a photomultiplier tube (PMT) and a centrifuge which spins a disposable polymer disk in the format of a standard CD.

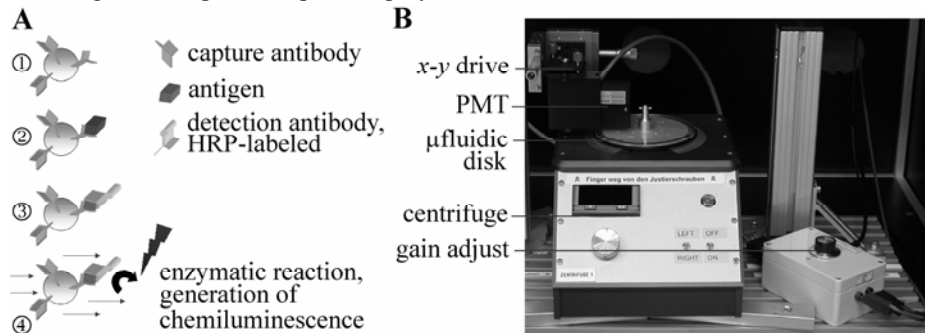


Figure 1. Assay principle and experimental setup. (A) Beads are first functionalized with capture antibodies off-disk ①. After bead aggregation, target antigens are transported into the detection chamber to form the specific antigen-antibody complexes ② which are coupled with HRP-labeled detection antibodies subsequently ③. The chemiluminescent reaction [5] is catalyzed by the HRP enzyme under constant flow of Luminol/H₂O₂ ④ and read out under rotation. (B) The measurement setup comprises a centrifuge with a disk holder, the PMT module, an electronics box for adjustment of the gain voltage, and an x-y drive for the positioning of the PMT relative to the disk.

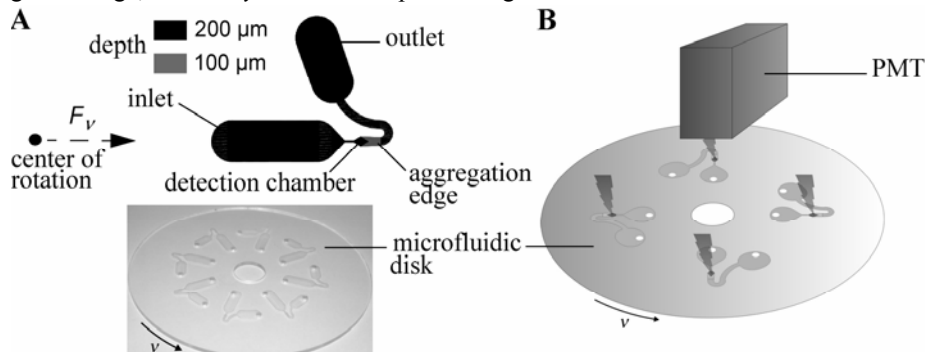


Figure 2. Microfluidic disk and read-out concept. (A) The chip with the format of a conventional CD features passive microfluidic elements, only: an inlet, a detection chamber, a geometrical barrier for bead aggregation, and an outlet. (B) For the parallel read-out, the disk is spun at a frequency ν and the chemiluminescent signal for each chamber is detected by a high-bandwidth PMT once per revolution.

Reagents are transported through the fluidic structures by the centrifugal force which is controlled by a designated frequency protocol $\nu(t)$. Each measurement channel on the disk (Fig. 2-A) features a set of passive microfluidic structures, i.e. an inlet, a detection chamber, an outlet ($h = 200 \mu\text{m}$), and a geometrical barrier for the bead aggregation

($h = 100 \mu\text{m}$). The chemiluminescent signal for each detection chamber is read out in parallel during rotation by the PMT (Fig. 2-B).

4. Results

For the validation of the concept, diluted HRP-labeled myoglobin antibodies are captured with human cardiac myoglobin coated beads. Our calibration curve (Fig. 3-A) features a CV of 12.4 % which represents 4 disks with 8 channels each processed on different days and a $c_{\min} = 12.2 \text{ ng/ml}$ as the lower limit of detection which is far below the myoglobin threshold at 100 ng/ml for the diagnosis of an AMI [1]. The capability for parallelization is demonstrated by the quasi-simultaneous read-out of two different antibody concentrations (500 ng/ml and 160 ng/ml, respectively) in Fig. 3-B.

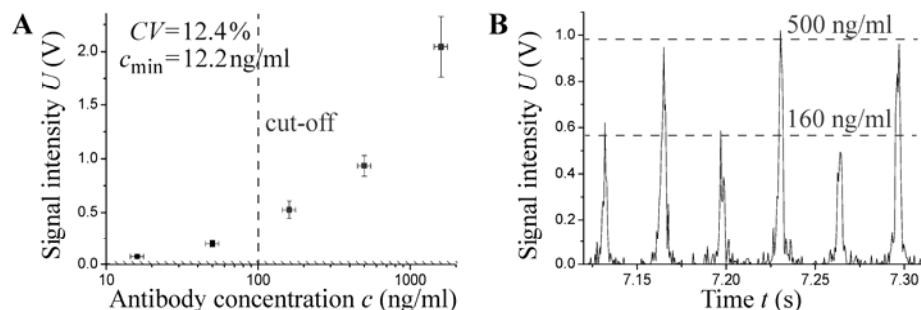


Figure 3. (A) Calibration curve for the myoglobin assay featuring a $CV = 12.4\%$ and a $c_{\min} = 12.2 \text{ ng/ml}$ which is far below the AMI cut-off at 100 ng/ml [1]. (B) Spectrum of the parallel read-out of two concentrations, 500 ng/ml and 160 ng/ml, respectively. The signals can easily be discriminated and are in agreement with the calibration curve.

5. Conclusion

We realized a versatile concept for the automated processing and high-speed (< 1 s) read-out of parallel chemiluminescent ELISAs. It is particularly suited for the early determination of AMI where three distinct cardiac markers, e.g. Myoglobin, Troponin-I, and CK-MB, have to be detected simultaneously. The simple and rugged concept is implemented in a modular setup comprising a PMT, a standard centrifuge, and an exchangeable polymer substrate containing passive fluidic structures which can thus readily be fabricated by standard polymer micromachining.

References

- [1] F. Apple *et al.*, Clinical Chemistry, 45:2, pp. 199-205, (1999).
- [2] A. van den Berg, E. Oosterbroek, Micro Total Analysis Systems, Elsevier Science, Amsterdam, NL, (2003).
- [3] M. Madou and G. Kellogg, Proceedings of SPIE, SPIE publisher, San Jose, 3259, pp 80-93, (1998).
- [4] J. Steigert *et al.*, J. Assoc. for Laboratory Autom., 10, pp. 331-341, (2005).
- [5] P. Whitehead, K. Kricka, J. Thorpe, Clinical Chemistry, 25, pp. 1531-1546, (1979).

CONTROLLED MICROFLUIDIC GENERATION OF LIPID SHELL-BASED PERFLUOROCARBON MICROBUBBLES FOR USE AS ULTRASOUND CONTRAST AGENTS

Kanaka Hettiarachchi¹, Esra Talu³, Marjorie L. Longo³, Paul A. Dayton⁴, Abraham P. Lee^{1,2}

¹*Dept. of Biomedical Eng., University of California, Irvine, USA*

²*Dept. of Mechanical & Aerospace Eng., University of California, Irvine, USA*

³*Dept. of Chem. Eng. & Materials Science, University of California, Davis, USA*

⁴*Dept. of Biomedical Eng., University of California, Davis, USA*

Abstract

A microfluidic flow-focusing method to produce micron-sized lipid shell-based perfluorocarbon (PFC) gas microbubbles for use as ultrasound contrast agents is demonstrated. The PDMS-based microfluidic devices feature expanding nozzle geometry with a 7 μm orifice width, and are robust enough for consistent production of microbubbles with runtimes lasting several hours. We are able to produce 5 μm microbubbles, which is an ideal size for current ultrasonic imaging techniques.

Keywords: Microbubbles, Contrast Agents, Ultrasound Imaging, Microfluidics

1. Introduction

FDA-approved ultrasound contrast agents are 1-5 micron bubbles encapsulated within a human serum albumin or phospholipid shell for stabilization. Due to the compressibility of their gas core, these stabilized microbubbles improve the sensitivity and specificity of diagnostic ultrasound imaging by increasing the reflection of sound waves, improving the accuracy of detecting organ functional abnormalities [1]. Ultrasound imaging systems can specifically detect the presence of microbubble contrast agents using detection techniques based on a bubble's resonant frequency or destruction threshold, which are properties dependent on bubble diameter.

Current production techniques create a highly polydisperse microbubble population with diameters as large as 20 μm . This limits imaging sensitivity since only a small percentage of the contrast agents have diameters which result in resonant frequencies optimized for the limited bandwidth of a clinical imaging system.

2. Theory

Microfluidic chambers provide an ideal platform for the controlled production of microbubble contrast agents with a much smaller size distribution. Several groups have recently developed microfluidic technologies for the generation of microbubbles [2,3], but to date no group has demonstrated microbubble production in the diameter range required for use as ultrasound contrast agents, or the feasibility of producing lipid shell-based perfluorocarbon gas microbubbles.

Our 2-dimensional flow-focusing device (Fig. 1a) features expanding nozzle geometry to generate monodisperse microbubbles. The bubble break-off location is focused to the narrowest point which incurs the highest shear force, the orifice (Fig. 1b), providing uniform control of bubble sizes [4]. Channel geometry in addition to the liquid and gas flow rates are used to control the bubble sizes.

3. Experimental

The devices were fabricated from a SU-8 master with the channels molded in poly(dimethylsiloxane) (PDMS) using standard soft lithography and rapid prototyping techniques. A high resolution 20,000 dpi photomask enabled designs having critical channel widths such as a 7 μm orifice and closely spaced filtering channels.

The recipe for microbubble preparation consisted of adding to a vial containing a 9:1 molar ratio of phospholipid to emulsifier a 10% aqueous glycerol/propylene glycol mixture. The probes DiI and NBD were added at 1 mol% for fluorescence microscopy studies. Table 1 defines the lipid shell and gas core components of the microbubbles.

Table 1. Microbubble composition

Component	Abbreviation	Name	Category
Shell	DSPC	1,2-distearoyl-sn-glycero-3-phosphocholine	Phospholipid
Shell	PEG-40 stearate	Polyoxyethylene 40 stearate (Myrij 52)	Surfactant emulsifier
Gas core	C ₄ F ₈ / N ₂	Octafluorocyclobutane / Nitrogen	Osmotic agents

Microbubbles were produced by flow-focusing, forcing a central stream of PFC and nitrogen gas and two side sheath flows of an aqueous mixture with the stabilizing lipid and emulsifier (Fig. 2). The gasses are supplied from pressurized tanks via flexible tubing and delivered into the chamber using a micro flow meter. The continuous lipid phase mixture is pumped at a constant flow rate using a digitally controlled syringe pump. A Nikon inverted microscope and high-speed camera is used to capture images and record movies of the microbubbles in the microfluidic device.

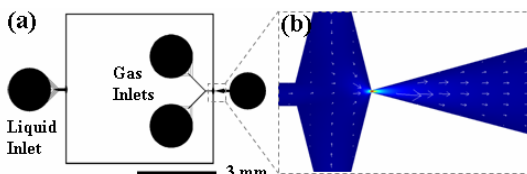


Figure 1. Schematic view of the microfluidic device layout and CFD flow simulation

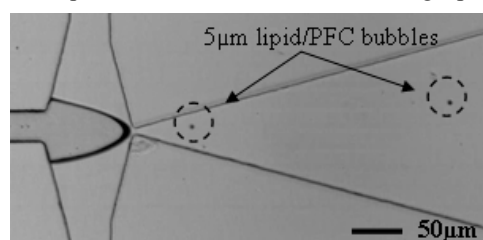


Figure 2. Microfluidic production of lipid shell-based PFC microbubbles

4. Results and discussion

As shown in Figure 3a, the DSPEC lipid monolayer shell stabilizes the microbubble by maintaining the inner gas core, while the PEG-40 sterate emulsifier helps to prevent coalescence [5]. Microfluidic generated microbubbles are visible in brightfield (Fig. 3b), and fluorescence microscopy confirms the existence of the coatings (Fig. 3c). The N₂/PFC gas mixture helps to maintain bubble size by setting an osmotic equilibrium with water-soluble gases, enabling the PFC gas to resist the Laplace and outer fluid pressures.

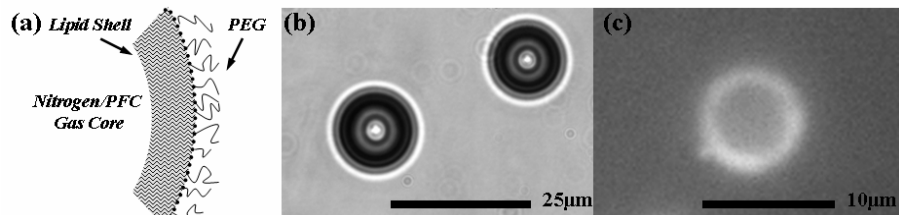


Figure 3. Microbubble structure with brightfield and fluorescence microscopy images

Production rates as high as one bubble per microsecond, or 6×10^7 bubbles per minute, have been measured. Studies on optimizing parameters for long-term stability after production are currently underway. The issue of creating long-lasting lipid shell-based PFC gas microbubbles in microfluidic systems poses interesting studies concerning the impact of device geometry and scale, flow parameters, and the synergy between shell, internal components, and surrounding medium on the stabilization of microbubbles.

5. Conclusions

With microfluidics technology, we can produce lipid shell-based PFC gas microbubbles in a size range compatible with ultrasound imaging. These systems allow custom-designing of ultrasound contrast agents with different gas cores and new shell materials for stabilization, and future targeted imaging and therapeutic applications.

Acknowledgements

The authors would like to thank Lisen Wang for microfabrication assistance, and funding from UC Discovery Grant BIO-ELE04-10462 and by the National Institutes of Health through the NIH Roadmap for Medical Research, Grant # 1 R21 EB005325-01.

References

1. P. A. Dayton and K. W. Ferrara, J Magn Reson Imaging, vol. 16, pp. 362-77, 2002.
2. P. Garstecki, I. Gitlin, W. DiLuzio, G. M. Whitesides, E. Kumacheva, and H. A. Stone, Appl. Phys. Lett., vol. 85, pp. 2649-2651, 2004.
3. J. M. Gordillo, Z. D. Cheng, A. M. Ganan-Calvo, M. Marquez, and D. A. Weitz, Phys. Fluids, vol. 16, pp. 2828-2834, 2004.
4. Y. C. Tan, V. Cristini, and A. P. Lee, Sensors and Actuators B: Chemical, vol. 114, pp. 350-356, 2006.
5. M. A. Borden, G. Pu, G. J. Runner, M. L. Longo, Colloids and Surfaces B-Biointerfaces, vol. 35, pp. 209-223, 2004.

RAPID, MULTIPLEXED COMPETITIVE IMMUNOASSAYS USING DISPOSABLE MICROFLUIDIC DEVICES AND SPR IMAGING

Kjell Nelson, Neil Geisler, Karman Tandon, and Paul Yager

Department of Bioengineering, Box 355061, University of Washington
Seattle, Washington, 98195 USA
(kjell@u.washington.edu)

Abstract

A technique has been developed for conducting multiple simultaneous competitive immunoassays on a single disposable microfluidic device. The assays require less than 50 μL of sample and are complete within 3 minutes. The analytical detection limit for a model small-molecule analyte (phenytoin, MW 252.3 Da) achieved using custom-built SPR imaging systems currently under development in our laboratory or by our local collaborators is approximately 1 nM (\sim 250 pg/mL).

Keywords: Competitive immunoassay, SPR imaging, point-of-care diagnostics

1. Introduction

The development of point-of-care (POC) diagnostic systems promises to significantly reduce health care costs and improve patient outcomes[1]. Among the primary requirements for such a system is the ability to rapidly and quantitatively measure a wide range of analytes simultaneously in a small sample. A platform concept for such a diagnostic system includes a reusable reader and a single-use, disposable microfluidic card that conducts the assay. Surface plasmon resonance imaging (SPRI) is a powerful detection technology with untapped potential for miniaturization and deployment in POC settings. Successfully using SPRI for clinical diagnosis requires the development of techniques for rapidly conducting multiple immunoassays using an inexpensive, disposable microfluidic device. Coupled to a miniature SPR imager, this microfluidic immunoassay platform will enable small, portable readers to measure an enormous range of analytical targets. We describe here a method for conducting simultaneous, quantitative competitive immunoassays on a disposable microfluidic device using the antiepileptic drug phenytoin as a model small molecule analyte.

2. Experimental

The device is comprised of three layers: 1) a 75mm x 25mm glass substrate coated with a 45nm-thick gold film, 2) a 3.7 mm wide channel laser-cut in a 12 μm thick MylarTM sheet (coated on both sides with 25 μm of pressure-sensitive adhesive), and 3) a 250 μm thick PMMA capping layer (Figure 1).

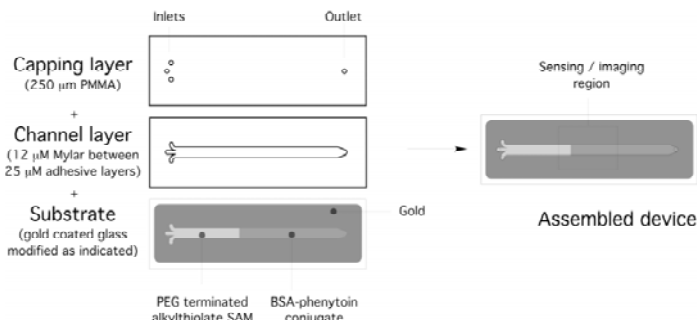


Figure 1. Diagram illustrating the surface preparation and device construction used for our SPR-imaging based microfluidic competitive immunoassays. The assembled device is a single-use disposable; the fluid interconnects between the device and the off-card pumps are not shown.

Prior to device assembly, the gold substrate is patterned with a PEG-functionalized alkylthiol SAM upstream of the SPR imaging region (to minimize non-specific protein adsorption to the channel walls) and a BSA-phenytoin conjugate within the imaging region. The assay is conducted by preparing buffered solutions of a monoclonal anti-phenytoin IgG premixed with varying amounts of phenytoin. These solutions are then pumped into the device inlets at equal flow rates (250 nL sec⁻¹ in the data presented here). Binding of the antibody to the immobilized BSA-phenytoin generates an SPR signal; presence of phenytoin in the sample solution will reduce the rate of antibody binding to the sensor proportional to the concentration of the competitor. Multiple fluid streams allow for simultaneous detection of a range of concentrations of a single analyte (using different concentrations in each stream) when the substrate has only one immobilized species, or for detection of multiple analytes if the substrate were patterned with different immobilized species. The channel dimensions and flow rates used ensure laminar flow and that lateral diffusion between fluid streams can be neglected[2].

3. Results

Antibody binding to the BSA-phenytoin functionalized substrate results in an increase in reflected intensity in the SPR image (Figure 2a). The addition of phenytoin reduced the rate of antibody binding in a dose-dependent fashion due to competition for antibody binding sites between solution phase phenytoin and the surface-immobilized BSA-phenytoin conjugate (Figure 2b). The assay responded linearly to a range of analyte concentrations (Figure 3). Intra- and inter-assay CV was less than 10% over this range (data not shown). The dynamic range of the assay can be controlled by varying the antibody concentration; reducing the antibody concentration to 25 nM permits detection of lower analyte concentrations with concomitant reduction in SPR signal.

4. Conclusions

We have demonstrated a method for conducting multiple simultaneous quantitative, competitive immunoassays for small molecule analytes using a disposable

microfluidic card and SPR imaging. Individual flow streams can be used for different patient samples, as run-time calibrators, or to detect multiple analytes. This method is well-suited for conducting rapid immunoassays for point-of-care diagnostics.

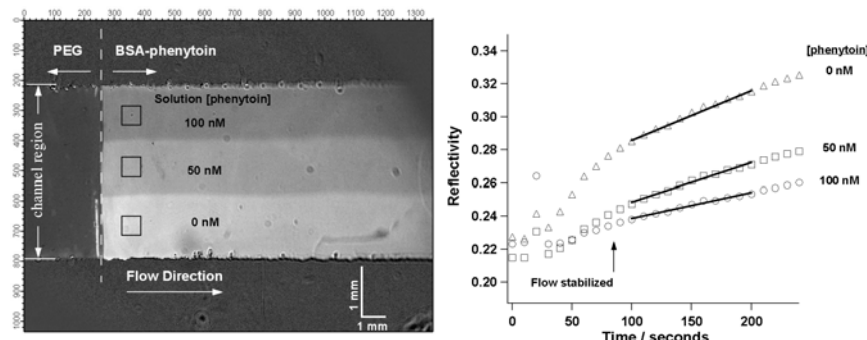


Figure 2a,b. Figure 2a (left): SPR difference image illustrating a typical experimental outcome following 3 minutes of fluid flow. Bright regions represent areas with accumulated antibody. Three solutions of phenytoin premixed with 250 nM anti-phenytoin were injected at 250 nL/sec/inlet. The black squares are the pixels used for the average percent reflectivity plotted in Fig. 2b (right). The assay response was quantitated using a linear fit (black lines, Fig. 2b) applied to the period of the assay following sample injection and concentration stabilization.

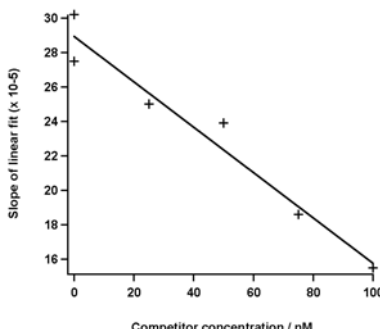


Figure 3. Dose dependence of rate of reflectivity change for 250 nM anti-phenytoin mixed with varying amounts of phenytoin.

References

- Yager, P. et al. Microfluidic diagnostic technologies for global public health. *Nature* 442, 412-418 (2006).
- Kamholz, A. E. & Yager, P. Theoretical analysis of molecular diffusion in pressure-driven laminar flow in microfluidic channels. *Biophysical Journal* 80, 155-160 (2001).

A CROSS-FLOW ELECTROPHORESIS MICROFLUIDIC DEVICE FOR DNA SAMPLE CONCENTRATION

Pedro Ortiz¹, Calum McNeil¹ and Alun Harris²

¹School of Clinical and Laboratory Sciences, The Medical School, University of Newcastle upon Tyne, Newcastle upon Tyne, NE2 4HH, UK

²School of Electrical, Electronic and Computer Engineering, Merz Court, University of Newcastle upon Tyne, NE1 7RU, UK

Abstract

A DNA sample concentration microfluidic device is presented. The concentration device uses cross-flow electrophoresis induced by integrated parallel coplanar electrodes along the bottom of a microfluidic channel. The performance of the device is demonstrated by fluorescence imaging of labelled DNA samples.

Keywords: DNA, sample concentration, cross-flow electrophoresis, microfluidics

1. Introduction

Concentration of DNA samples by electrokinetic methods has been widely used for analytical purposes in microdevices [1, 2]. The devices presented herein are stand alone functional units but have been designed to be easily integrated as part of a Lab-on-a-Chip system for genetic diagnostics, in which reagents, added during steps prior to detection, dilute the sample. This unit offers a simple solution to the DNA sample dilution problem, which is highly undesirable in this type of microsystem as this could result in a decrease in system sensitivity.

2. Device working principle

Figure 1a shows a cross section of a microchannel with integrated coplanar electrodes. Applying a DC voltage to the pair of parallel electrodes will establish an electric field in the channel perpendicular to the direction of flow. The presence of this electric field will induce electrophoretic migration of the circulating DNA molecules

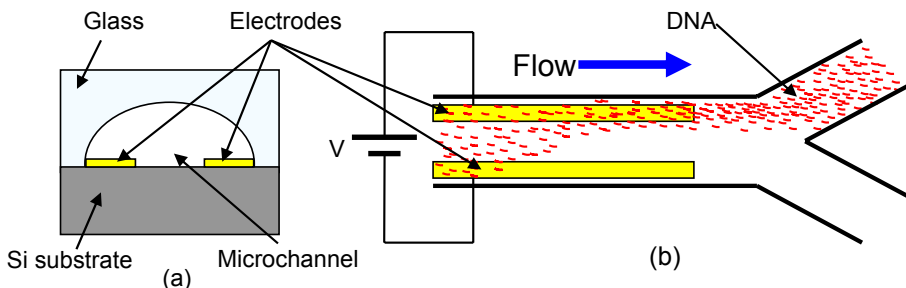


Figure 1. a) Cross-section of microchannel with integrated coplanar electrodes. b) Schematic of the working principle: The electric field established across the channel drives DNA molecules towards a region of high electrical potential.

towards the region of the channel with higher potential (Figure 1b). This creates a gradient in the concentration of DNA molecules across the microchannel as the sample flows through the active region of the channel. Splitting the flow further downstream in the middle of the channel results in two streams in which the one which originated on the side of the channel with the higher electrical field has a greater concentration of DNA molecules compared with its counterpart.

3. Experimental

Devices (Figure 2) were fabricated using standard cleanroom techniques. Microfluidic channels were etched on glass with an amorphous silicon hard mask using HF. Au electrodes were deposited on a Si substrate by evaporation onto an oxide insulating layer (5000Å) which had previously been deposited. Patterning of Au was performed by lift-off. The two substrates were then aligned and bonded using anodic bonding. The polarization of the electrodes was controlled with a PC using a Digital I/O card (PCI-6229, National Instruments) and an in-house program written in LabView (National Instruments).

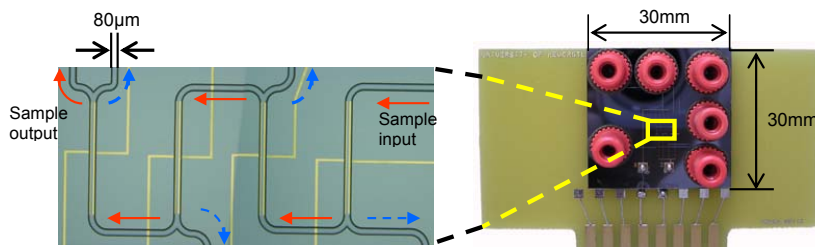


Figure 2. Photograph of a packaged four stage DNA concentration device and detail of microfluidic network with integrated gold electrodes. Solid arrows indicate the path followed by the DNA molecules in the channels and dashed arrows indicate waste channels.

In order to test the performance of the concentration devices, a set of experiments intended to image the deflection of the DNA molecules was carried out using a fluorescence imaging technique. Single stranded DNA (ssDNA) from salmon sperm (Sigma) was labelled with a fluorescent dye, TO-PRO3 (Invitrogen). Fluorescence imaging experiments were performed using an Olympus fluorescence microscope and a CCD camera.

4. Results and discussion

Figure 3 shows a typical image of a TO-PRO3 labelled DNA sample flowing through the channel with integrated parallel coplanar electrodes. A higher intensity of fluorescence can be observed on top of the electrodes due to reflection of the emitted light on the gold surface. Figure 3a shows that the fluorescence intensity is homogeneous in both streams after splitting the fluid at a Y junction when no voltage is applied. In contrast, Figure 3b shows how the fluorescence profile across the microchannel varies when a DC voltage of 3V is applied to the electrodes ($Q=1\mu\text{L}/\text{min}$). For voltages above 3V gas bubble formation was observed due to electrolysis of water.

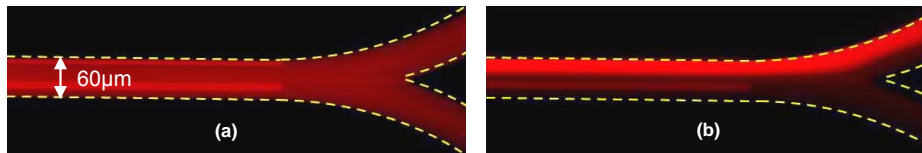


Figure 3. ssDNA ($100\mu\text{g/mL}$) labelled with fluorescent dye TO-PRO3 flowing through a $60\mu\text{m}$ wide channel ($Q=1\mu\text{L}/\text{min}$), (a) without applied voltage and (b) with an applied DC voltage (3V).

In order to increase the concentration capability of the system a device was designed and fabricated which repeated the operation described above four times. Figure 4a shows a fluorescence image of such a device. An increase in fluorescence intensity can easily be observed after each one of the stages. Figure 4b shows the concentration of the sample by an increase in fluorescence intensity measured after the flow split in each cross-flow electrophoresis stage.

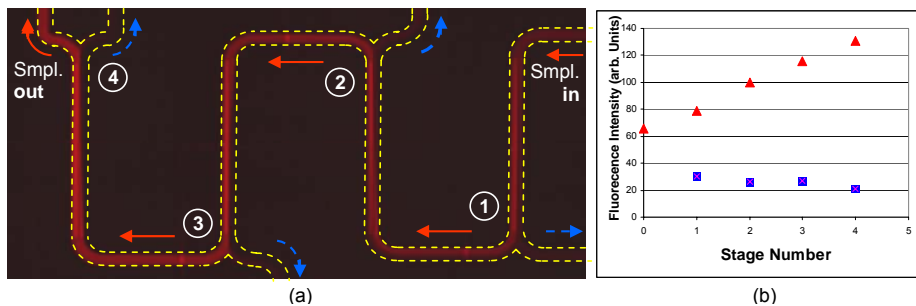


Figure 4. (a) ssDNA sample ($100\mu\text{g/mL}$) flowing through a four stage concentration device. ($Q=1\mu\text{L}/\text{min}$, applied potential = 3V). (b) Fluorescence intensity of the sample stream (\blacktriangle) and the waste stream (\blacksquare) after each concentration stage. The concentration of the input sample is indicated in stage 0. Solid arrows indicate the path followed by the sample and dashed arrows indicate the waste channels.

5. Conclusions

Concentration of DNA samples by cross-flow electrophoresis in microfluidic channels with integrated coplanar electrodes has been demonstrated. The device operates well at potentials up to 3V, however, at greater potentials bubble formation due to electrolysis of water is observed. Decreasing the dimensions of the microfluidic network (channel width and depth) as well as decreasing the inter-electrode separation should allow the generation of higher electric fields without the need to apply a voltage high enough to cause electrolysis of water.

References

1. C.H. Lin and T. Kaneta, *On-line sample concentration techniques in capillary electrophoresis: Velocity gradient techniques and sample concentration techniques for biomolecules*, Electrophoresis, 2004, 25, 4058-4073.
2. P.K. Wong, T.H. Wang, J.H. Deval, C.M. Ho, *Electrokinetics in Micro Devices for Biotechnology Applications*, IEEE-ASME Trans. on Mechatronics, 2004, 9 (2), 366-376.

A RAPID HIGH-SENSITIVITY IMMUNOASSAY UTILIZING A NOVEL ON-CHIP ELECTROKINETIC ANALYTE TRANSPORT METHOD

Tomohisa Kawabata, Chen Li, Xiaohui Bi, Celeste Kirby, Yihshing Shih, Luc Bousse, H. Garrett Wada, Mitsuo Watanabe, and Shinji Satomura

Wako Pure Chemical Industries, Mountain View, CA, and Osaka, Japan

Keywords: Diagnostics, Immunoassay, Isotachophoresis, Biomarkers

Abstract

We describe a novel high-sensitivity sandwich immunoassay that uses vacuum-driven assembly of three reagents on chip: an antibody-DNA conjugate, the sample, and a fluorescently labeled antibody. An isotachophoresis (ITP) sample stacking step then concentrates the DNA conjugate and the sample complexes, followed by a CE separation. In an assay for alpha-fetoprotein, a detection limit of around 1 pM is achieved. The CE separation enables the detection of the AFP-L3 component, which is a liver cancer biomarker.

1. Introduction

Diagnostic applications of microfluidic analysis technology require high sensitivity. Previous work on microfluidic immunoassay systems [1,2] has described integrated devices that achieved sensitivities around 1 nM, comparable to those in conventional immunoassays. However, the most valuable assays where microfluidic technology could be applied often require much higher sensitivity, in the picomolar range. The target application for our work is the detection of the different forms of alpha fetoprotein (AFP). AFP-L3, a Lens Culinaris agglutinin (LCA) binding form, has been shown to be a specific tumor marker for early stage liver cancer detection [3].

2. Description of the Assay

This paper describes a novel microfluidic device designed to achieve high sensitivities. The analytes, both AFP isoforms -L1 and -L3, are sandwiched by two antibodies, one of which is fluorescently labeled, and the other is conjugated to a DNA molecule. The DNA conjugated antibody provides mobility which concentrates and stacks the immunocomplexes by the ITP process. After the ITP stacking, the field is switched to an electrophoretic separation mode that separates the AFP isoforms in a gel containing LCA.

Controlled binding reactions between the sample and the two labeled antibodies are crucial in obtaining good quantitation and sensitivity. It is desirable for these reactions to occur on-chip, so the entire assay can be controlled and automated in the microfluidic device. Initial attempts to mix the sample and reagents by pressure driven flows in a long channel [6] proved to be unsatisfactory due to the variability in viscosity of real serum samples. As an alternative, we have developed an electrophoretically driven mixing method, where components are lined up by vacuum in a channel in an order of mo-

bility such that subsequent application of a field will drive them together and allow them to react. We have called this an Electrokinetic Analyte Transfer Assay (EATA). The geometry of the microfluidic device accurately defines the volumes of the reagents at the nanoliter scale, and thus eliminates pipetting errors (see Figure 1). Another advantage of the EATA method is that the DNA antibody is also concentrated by the ITP stacking before binding with the sample, thereby increasing the speed of the binding reaction. After the binding reactions and ITP stacking are completed, voltage application is switched to another well containing leading buffer [5], after which normal CE separation and detection occurs.

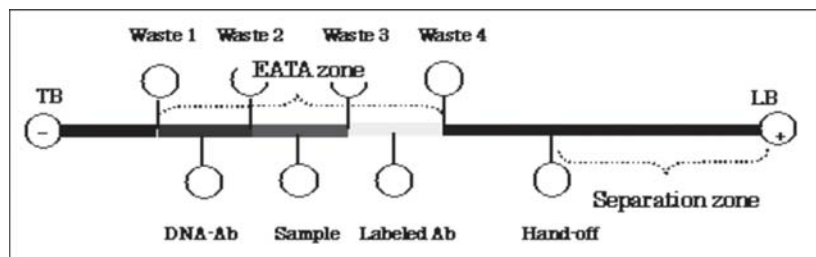


Figure 1: Conceptual Diagram of the EATA chip. Vacuum is applied to all four waste wells to create accurately defined plugs of sample, binding reagents, and buffers. The ITP step is initiated by applying a voltage between the LB and the TB wells. When the sample reaches the separation zone, the voltage is applied between the Hand-off and the LB wells

3. Results and Discussion

Figure 2 shows an example of an electropherogram of a 100 pM AFP sample, and Figure 3, a calibration curve showing a detection limit close to 1 pM. As seen in Figure 4, the degree of completion of the binding reactions depends on the magnitude of the electric field. The lower the field, the more time will be taken by the ITP step, and that will increase the degree of completion of the binding reactions. Another factor that helps the speed of the binding reactions is the large increase in concentration caused by the ITP stacking of the antibody-DNA complex.

References

- [1] N. Chiem, N. and D. J. Harrison, *Anal. Chem.*, 2005, 69(3) pp. 373-8.
- [2] V. Linder, S.K. Sia, and G.M. Whitesides, *Anal. Chem.*, 2005, 77(1) pp. 64-71.
- [3] H. Oka *et al.*, *J. Gastroenterol. Hepatol.*, 2001, 16(12) pp. 1378-83.
- [4] T. Kawabata *et al.*, *Anal. Chem.*, 2005, 77(17) pp. 5579-82.
- [5] Charles Park *et al.*, AICHE 2004 Annual meeting, Austin, TX.
- [6] H.G. Wada *et al.*, *NSTI-Nanotech 2005*, Vol. 1, p. 610.

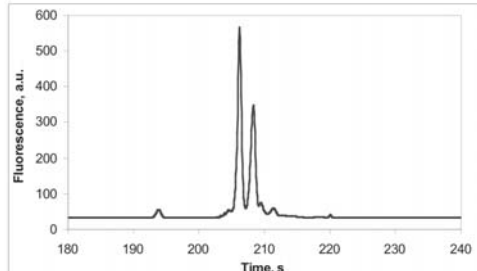


Figure 2: Electropherogram of the two sample peaks from the immunocomplex in the AFP assay. The left hand peak is for the AFP-L1 form, and the right hand peak comes from AFP-L3. The fraction of the total AFP present in the AFP-L3 form is a biomarker for liver cancer with improved sensitivity and specificity.

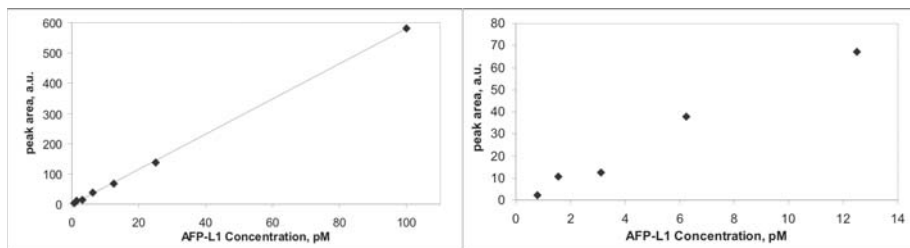


Figure 3: Titration curves for AFP-L1 in the 0 to 100 pM range, with on the right an enlargement of the 0 to 14 pM region. The left hand graph shows good assay linearity in this range ($R^2 = 0.9996$). The right-hand graph shows that at 1.6 pM the detected peak area was significantly higher than zero AFP-L1.

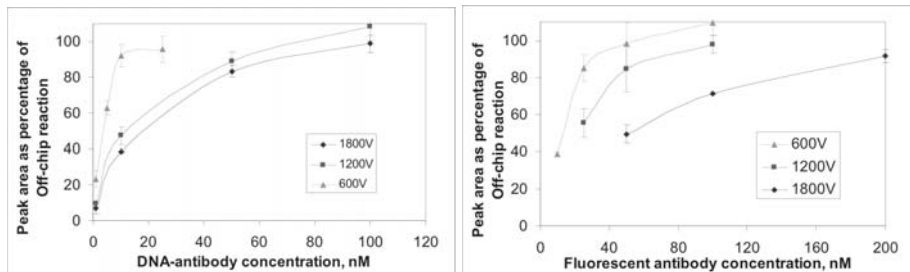


Figure 4: Completion percentages of the on-chip binding reactions as a function of the electric field. Lower fields allow more time for binding, and give higher binding levels. The left-hand graph shows data for the DNA-antibody, with the sample pre-incubated off-chip with the labeled antibody. The right-hand graph shows similar data for the fluorescently labeled antibody. All peak areas are normalized to those obtained by pre-incubation of sample and both antibody reagents for at least 30 minutes prior to on-chip ITP-CE.

IN VIVO CHARACTERIZATION OF IMPLANTABLE UNPOWERED PARYLENE MEMS INTRAOCULAR PRESSURE SENSORS

Po-Jui Chen¹, Damien C. Rodger^{1,2}, Rajat Agrawal², Ellis Meng²,
Mark S. Humayun², and Yu-Chong Tai¹

¹California Institute of Technology, USA ²University of Southern California, USA
E-mail: pjchen@mems.caltech.edu

Abstract

This work presents a complete suite of *in vitro* and *in vivo* characterizations of an unpowered, biocompatible, parylene-based micro-electro-mechanical-systems (MEMS) pressure sensor for intraocular pressure (IOP) sensing. *In situ* mechanical responses of the sensors facilitate real-time pressure readouts without power consumption/transduction. Two types of IOP sensors (high-sensitivity and needle-implantable) have been fabricated and characterized. *In vitro* and *in vivo* testing results have successfully demonstrated that the high-sensitivity IOP sensors can achieve mmHg-sensitivity pressure responses both on-bench and inside an enucleated porcine eye, while the needle-implantable IOP sensors can be implanted into a porcine eye through a needle and secured inside the eye. Using this new IOP sensor paradigm we can realize unpowered, real-time, faithful, and convenient IOP monitoring in glaucoma patients.

Keywords: In Vivo, Intraocular Pressure, Parylene, Pressure Sensor, Unpowered

1. Introduction

Unpowered parylene MEMS IOP sensors were described previously [1][2] and are essentially all-mechanical compliant structures inspired by a Bourdon tube (free-standing curved thin-walled tube). They are systematically deformed by a pressure difference applied between the pressure encapsulated in the tube/channel and the ambient pressure, realizing direct pressure measurement through observation of tube deformation. Therefore, after the IOP sensors are implanted on the iris of the eye, their visible IOP readouts can be observed with a microscope/stereoscope from outside the eye through the transparent cornea. Design, fabrication, and *in vitro* characterization of the novel IOP sensors were presented [2]. In this work, continuing the progress of this research, we have more extensively developed the IOP sensors and demonstrated practical *in vivo* pressure sensing in the mmHg range inside a real eye.

2. Experimental

By implementing state-of-the-art micromachining technology, two types of IOP sensors were microfabricated for characterization. Fig. 1 shows a spiral-tube sensor and a long-armed-tube sensor for high-sensitivity pressure responses, and Fig. 2 shows the needle-implantable IOP sensor. For the needle-implantable sensors, integrated packaging has been designed to facilitate secure anchoring and functionality of the

device after implantation on the iris of the eye [2]. All of these IOP sensors were monolithically micromachined so assembly processes were not required.

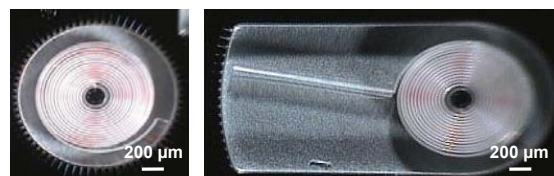


Figure 1. Microfabricated high-sensitivity parylene IOP sensors with 1.1-mm-diameter spirals.



Figure 2. Microfabricated needle-implantable IOP sensors: (left) Concept of integrated device packaging; (right) A fabricated device situated inside a 19-gauge needle.

3. Results and discussion

The micromachined IOP sensors were first tested on-bench to characterize their *in vitro* behaviors. Testing results of the needle-implantable sensors were previously reported [2]. For the high-sensitivity sensors their pressure sensitivity was 0.46 degree/mmHg in rotational trajectory with the spiral-tube design and 11.24 $\mu\text{m}/\text{mmHg}$ in lateral trajectory with the long-armed-tube design as shown in Fig. 3.

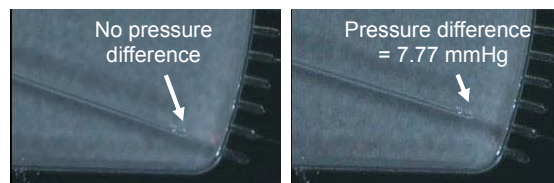


Figure 3. *In vitro* pressure response of the long-armed-tube sensor with a lateral sensing trajectory. Pressure difference is applied between inside and outside of the parylene tube.

Implantation has been conducted in several enucleated porcine eyes to characterize the *in vivo* performance of the IOP sensors. For the high-sensitivity sensors, a flat incision and suturing were performed to implant the devices. Testing results show that both the spiral-tube and long-armed-tube designs successfully registered IOP variations under observation with a surgical microscope. A real-time 8.72 $\mu\text{m}/\text{mmHg}$ IOP sensitivity was achieved with the long-armed-tube sensor as shown in Fig. 4. In addition, repeatable pressure responses of the sensors were confirmed by applying cyclic pressure variations. For the needle-implantable sensors, in spite of their minimally observable pressure

responses due to low optical magnification of the scope as shown in Fig. 5, preliminary testing of the tissue anchors has shown promise that the devices can be securely anchored on the iris even when vigorously pushing them using a blunt tube or shaking the eye. Further anchoring studies are underway to more precisely determine the reliability of the devices in the intraocular environment.

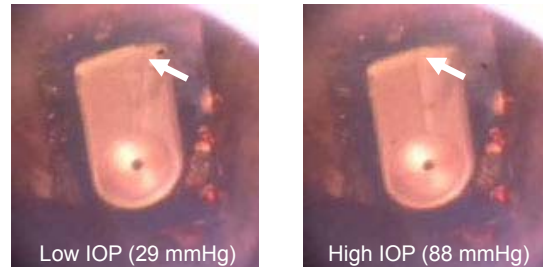


Figure 4. *In vivo* pressure response of the long-armed-tube IOP sensor.

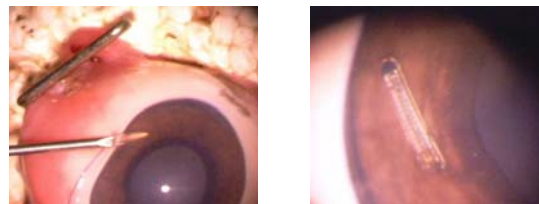


Figure 5. *In vivo* characterization of the needle-implantable IOP sensor: (left) Image of device implantation through a needle incision; (right) Device implanted inside the eye. The tissue anchors mechanically secure the device on the iris in the intraocular environment.

4. Conclusion

In this work both *in vitro* and *in vivo* characterizations of the developed pressure sensors have been successfully performed to prove the concept of unpowered IOP sensing. Testing data have yielded positive results toward realization of real-time IOP readout.

Acknowledgments

This work was supported in part by the Engineering Research Centers Program of the National Science Foundation (Award Number EEC-0310723) and by Bausch and Lomb.

References

- [1] P.-J. Chen, D.C. Rodger, M.S. Humayun, and Y.-C. Tai, "Unpowered Spiral-Tube Parylene Pressure Sensor for Intraocular Pressure Sensing," *Sensors and Actuators A: Physical*, 127(2), pp. 276-282, 2006.
- [2] P.-J. Chen, D.C. Rodger, E. Meng, M.S. Humayun, and Y.-C. Tai, "Implantable Unpowered Parylene MEMS Intraocular Pressure Sensor," *Proc. IEEE-EMBS MMB '06*, Okinawa, Japan, May 9-12, 2006, pp. 256-259.

AN EMPIRICAL MODEL FOR A PIEZOELECTRIC TISSUE CONTRAST SENSOR EMBEDDED IN A BIOPSY TOOL

Tao Li^{*} and Yogesh B. Gianchandani

*Engineering Research Center for Wireless Integrated Microsystems
University of Michigan, Ann Arbor, USA*

ABSTRACT

This paper describes an empirical model for a micromachined piezoelectric sensor located in a hollow cavity on the interior tip of a biopsy needle to aid in real time tissue differentiation during fine needle aspiration (FNA) biopsy. The disc-shaped sensor made from bulk lead zirconate titanate (PZT) has 50 μm thickness and 200 μm diameter. Samples such as oils and saline solution with controlled acoustic impedance ranging over $1.1\text{-}1.6 \times 10^6 \text{ Kg/m}^2$ were tested for calibration. A modified Butterworth-Van Dyke (BVD) equivalent circuit is used to model the PZT disc with tissue loading, and an empirical tissue contrast model shows an approximately proportional relationship between frequency shift and sample acoustic impedance.

Keywords: Piezoelectric Sensor, Resonance, BVD Circuits, Fine Needle Aspiration (FNA)

I. INTRODUCTION

While thyroid cancer results in <1% of cancer deaths, thyroid nodules, either benign or malignant, can be observed in ~20% of the general US population [1]. Since conventional ultrasound imaging cannot generally distinguish benign and malignant nodules, FNA biopsy is usually required to make a final diagnosis. This is typically performed with a thin needle of 20-27 gauge with outer diameter <1 mm, and is challenging in itself due to the precision required in acquiring the desired sample from the small target volumes for subsequent cytological examination. To aid the positioning of the biopsy needle, traditional ultrasound imaging is performed in real time. Despite the added complexity, this does not provide the necessary precision, and at least 2-5% of FNAs are read as non-diagnostic because of improper sampling [1-3].

We recently reported an in-situ device for detecting tissue contrast during FNA biopsy of thyroid nodules [4]. Intended to complement traditional ultrasound imaging, it uses a micromachined piezoelectric sensor embedded near the tip of a biopsy needle to distinguish tissue planes in real time. However, its practical use demands a predictive model for the interaction between the device and sample. In this paper an empirical model is developed based on new experimental results obtained from samples with known acoustic impedance.

II. DEVICE DESCRIPTION

The scheme for in-situ detection of tissue contrast during thyroid biopsy is shown in Fig. 1. A sensor made from bulk lead zirconate titanate (PZT) is integrated at the tip of the needle and is connected to a spectrum analyzer for real-time impedance measurement. Figure 2 illustrates the structure of the device. The creation of the cavity in the wall of the biopsy needle (Fig. 2b) leaves a thin, tailored, stainless steel diaphragm. A micromachined PZT disc (Fig. 2c) is located against the diaphragm (Fig. 2d). The varying acoustic impedance of the nearby tissue changes the vibrational characteristics of the diaphragm, and hence the mechanical boundary condition of the PZT disc. This is transduced into a change of its electrical impedance by the piezoelectric effect, and subsequently detected by the impedance spectrum analyzer, thus providing a measure of tissue contrast.

III. MEASUREMENT RESULTS

For the purpose of device calibration and modeling, the sensor was tested with samples that have known and controlled acoustic impedance (Z_a). These are oil samples and saline solution of varying concentration.

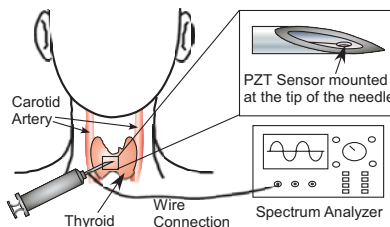


Fig. 1:
Schematic of the proposed tissue contrast sensor used for thyroid biopsy.

* Corresponding author: 1301 Beal Ave., Ann Arbor, MI, 48109, USA; Tel: 1-734-647-2040; Email: litz@umich.edu

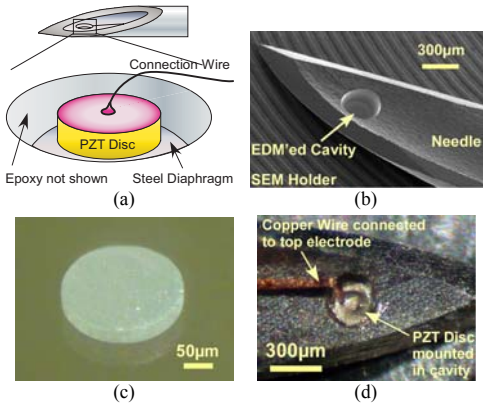


Fig. 2: (a) Schematics of the tissue contrast sensor in perspective view with sealing epoxy removed; (b) SEM image of a syringe needle tip processed by micro electro-discharge machining (μ EDM) to form the cavity for mounting PZT sensor. (c) Photo of a released PZT disc batch fabricated by SEDUS process [5] using batch micro ultrasonic machining to transfer a pattern defined by serial μ EDM. Diameter: 200 μ m. Thickness: 50 μ m. (d) Finished device before sealing epoxy is applied. Coated copper wire is used to make connection to the top electrode of the PZT disc. The stainless steel needle body is used as the ground electrode.

The sensor response was measured at a needle insertion depth of 5 mm for all cases. The Z_a of these samples ranged over $1.1\text{--}1.6 \times 10^6$ $\text{Kg/m}^2\text{s}$, with Z_a of common tissues toward the upper end of this range. In the experiment with saline samples, solution concentrations from 1% to 20% were tested; the measurement results are shown in Fig. 3. The measured frequency shift increased with greater saline concentration when the concentration was smaller than $\approx 3.5\%$, and remained approximately constant when the concentration became greater. This phenomenon is similar to that discussed in [6], and is possibly due to saturation of available cation binding sites on the sensor diaphragm. The sample acoustic properties obtained from literature and the experimental results of resonance frequency shift are used for the subsequent device modeling.

IV. DEVICE MODELING

The resonance frequency shift (Δf) of the piezoelectric sensor is dependent on both the mass loading effect and elastic properties of the samples [7]. The Z_a of a sample is the product of its density and acoustic velocity, the latter being further related to the elastic bulk modulus of the material. Thus, an empirical tissue contrast model can be built for the biopsy device by plotting the measured Δf versus Z_a , as shown in Fig. 4(a). The data used in this plot are from results described in Section III and previous results for porcine fat and muscle tissue discussed in [4]. The relationship is approximately proportional, as shown in the shaded area, considering the uncertainty in the acoustic properties of the samples.

The electrical characteristics of a free PZT disc in longitudinal vibration mode can be modeled by a lumped-element Butterworth-Van Dyke (BVD) equivalent circuit as shown in Fig. 5(a) [8]. In this circuit, C_0 is the clamped capacitance between the two electrodes of the PZT disc, and an infinite number of series LC_n ($n=1,3,5,\dots$) motional branches are connected in parallel, where n denotes harmonic modes of the mechanical

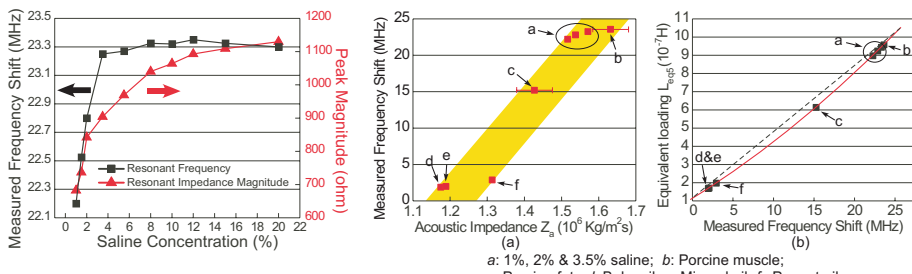


Fig. 3: Measurement results of saline sample with concentration between 1% and 20% shown as measured frequency shift and peak magnitude of impedance vs. saline concentration.

Fig. 4: (a) Measured resonant frequency shift vs. acoustic impedance of the samples. The error bars on the data for porcine samples indicate lack of certainty in the values of acoustic impedance Z_a . (b) Calculated equivalent loading L_{eqS} as a function of frequency shift for the samples. The dotted line indicates linear relation for comparison.

resonance of the disc. The first branch of L and C_1 corresponds to the fundamental resonance mode, and the n^{th} branch of L and C_n represents the n^{th} mode. The equations to determine the values of C_0 , L , and C_n can be found in [8].

A modification to this original BVD circuit is necessary to accommodate the loading effect. Inductors can be used to model mass loading such as a diaphragm

attached to a piezoelectric sensor [7]. These inductors are denoted as $L_{m(n)}$ in Fig. 5(b), and their values for such a diaphragm loading can be determined using equations provided in [7]. To include the tissue loading effect in the model, $L_{m(n)}$ can be extended by adding in series another equivalent loading inductance $L_{eq(n)}$. This additional inductance is an equivalent that includes the effect of both mass and elastic loading for modeling convenience. The frequency of each harmonic mode $f_{(n)}$, or equivalently the frequency of each electrical impedance peak can then be denoted as

$$f_{(n)} = \frac{1}{2\pi\sqrt{(L + L_{m(n)} + L_{eq(n)})C_n}}, n = 1, 3, 5 \dots \quad (1)$$

In the experiments, the 5th harmonic mode (at 176 MHz in air) was found to have a higher Q than the fundamental and 3rd harmonic mode, and was consequently selected for measurement. Therefore, the 3rd LC_n branch (for the 5th harmonic mode) of the modified BVD circuit is of the most interest. The calculated equivalent loading L_{eq5} for each of the samples used to build the empirical tissue contrast model is plotted as a function of the measured frequency shift Δf_5 in Fig. 4(b). The two plots in Fig. 4 provide the empirical tissue contrast model (i.e., the relationship of Z_a to Δf_5) and the relationship of L_{eq5} to Δf_5 . These relationships can be used with the modified BVD circuit model to relate the physical parameters of the device and samples to Δf for design and optimization of the sensor.

V. CONCLUSIONS

An empirical model has been built for the piezoelectric tissue contrast sensor based on experimental results and a modified BVD circuit model. This model established the relationship between the measured frequency shift and sample acoustic impedance, providing an effective approach to predict the interaction between the device and sample for its proposed practical use.

ACKNOWLEDGEMENT

This work was supported primarily by the Engineering Research Centers Program of the National Science Foundation under Award Number EEC-9986866.

REFERENCES

- [1] F. Pacini and L.J. De Groot, "Thyroid Neoplasia," *The Thyroid and its Diseases*, 6th ed., W.B. Saunders Company, 1996, updated online at <http://www.thyroidmanager.org>, May 2004
- [2] S. Takashima, H. Fukuda, and T. Kobayashi, "Thyroid nodules: clinical effect of ultrasound-guided fine-needle aspiration biopsy," *J. Clin. Ultrasound*, 22(9), pp. 535-42, Nov.-Dec. 1994
- [3] H. Gharib and J. R. Goellner, "Fine-needle aspiration biopsy of the thyroid: an appraisal," *Ann. Intern. Med.* 118(4), pp.282-9, Feb. 1993
- [4] T. Li, R.Y. Gianchandani, and Y.B. Gianchandani, "A bulk PZT microsensor for in-situ tissue contrast detection during fine needle aspiration biopsy of thyroid nodules," *Proc. IEEE MEMS 2006*, Istanbul, pp. 12-15, Jan. 2006
- [5] T. Li and Y.B. Gianchandani, "A micromachining process for die-scale pattern transfer in ceramics and its application to bulk piezoelectric actuators," *IEEE/ASME J. Microelectromechanical Systems*, 15(3), pp. 605-12, Jun. 2006
- [6] H. Zhang, M.S. Marma, E.S. Kim, C.E. McKenna, and M.E. Thompson, "Implantable resonant mass sensor for liquid biochemical sensing," *Proc. IEEE MEMS 2004*, pp. 347-50, Jan. 2004
- [7] H. Zhang, E.S. Kim, "Micromachined acoustic resonant mass sensor," *IEEE/ASME J. Microelectromechanical Systems*, 14(4), pp. 699-706, Aug. 2005
- [8] T. Ikeda, *Fundamentals of Piezoelectricity*, Oxford University Press, New York, 1990

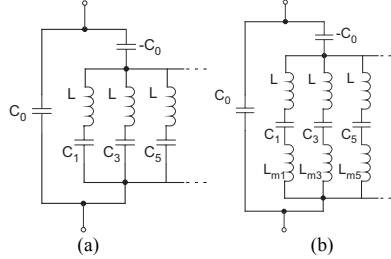


Fig. 5: BVD equivalent circuits of a piezoelectric resonator in longitudinal vibration mode. All loss mechanism ignored.
(a) free resonance; (b) with equivalent loading.

SINGLE CHAMBER DNA EXTRACTION AND AMPLIFICATION FOR PROSTHETIC JOINT INFECTION DETECTION

Lindsay A. Legendre¹, Weidong Cao¹, Kerryl Piper³, Jerome P. Ferrance¹, Robin Patel³ and James P. Landers^{1,2}

University of Virginia Department of Chemistry¹ and Pathology², Charlottesville, VA 22904 USA

Phone: 434-243-8658, Fax: 434-982-3048

Contact E-MAIL: landers@virginia.edu

³Mayo Clinic, Division of Infectious Diseases, Rochester, MN 55905 USA

Abstract

This work reports on the application of a microchip system integrating DNA extraction with infrared-mediated (IR) PCR amplification within a single chamber for the detection of bacterial infections within prosthetic joints. Results show not only the successful integration of DNA extraction and amplification in a single chamber, but an improvement over the PCR detection limit for bacterial infection when compared to conventional molecular biological methods.

Keywords: **microchip integration, DNA extraction, PCR, bacterial infection detection**

1. Introduction

Prosthetic joint implantation has improved the quality of life for many individuals, but up to 10% of these patients develop complications attributed to joint failure with one main cause being prosthetic joint infection (PJI) [1]. For detection of the infectious agents associated with PJI, a broad-range PCR assay has been developed to amplify a highly conserved region of 16S ribosomal DNA shared universally among bacterial species [1]; this method utilizes a commercial kit for extraction of bacterial DNA from a prosthesis sonicate followed by quantitative PCR (qPCR). For this assay, detection is limited to 168 16S rDNA starting copies, equivalent to the presence of 24 *Escherichia coli* cells, due to a small number of bacteria contaminating most reagents. A faster, more sensitive approach for detecting bacteria in sonicates, particularly those that could be used in the operating room, was sought to improve clinical management of PJI.

2. Theory

Two advantages of microfluidic devices are the inherent small volumes and the ability to integrate multiple sample processing steps into the same device, completely isolating the process and, among other advantages, decreasing the opportunity for contamination. We have previously reported integration of DNA solid phase extraction (SPE) with PCR in a glass microdevice for a variety of clinical samples [2], but a limitation of the method lies in the volume mismatch between the DNA elution volume and the PCR chamber volume. Extraction on a silica bead packed channel allows DNA elution in a volume of approximately 10 µL while the PCR chamber volume is typically

0.5 μ L or less, thus utilizing only a fraction of the purified DNA from the sample. Performing SPE and IR-PCR in a single chamber would provide an inherent advantage over previous microchip-based methods [2], in that all of the eluted DNA could be utilized in the amplification, improving detection limits by 1-2 orders of magnitude.

3. Experimental

A glass microdevice was designed that would allow for SPE of DNA and the subsequent IR-PCR to be performed in the very same chamber (**Figure 1**). Chitosan-coated magnetic beads, a recently reported DNA extraction solid phase [3], uses a pH-induced DNA release technique that provides efficient DNA recovery (92% \pm 4%) while eliminating the use of high salt solutions and organics (both potent PCR inhibitors) from the process. A simple external magnet controls the location of the beads in the chamber, eliminating the need for weirs or pillars and simplifying device design and fabrication. While previous SPE phases have been composed of materials incompatible with PCR [2], the chitosan coating does not affect the efficiency of PCR, allowing the beads to remain in the chamber during PCR.

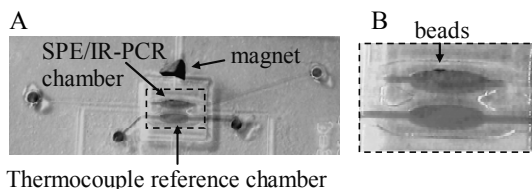


Figure 1. Picture of the microdevice containing magnetic beads. A) The microdevice was filled with dye for better visualization of the fluidic channels. B) A closer view shows the chitosan-coated magnetic beads held to the side of the chamber with the external magnet.

4. Results and Discussion

Microchips are ideal for a clinical application such as PJI, where background bacterial DNA interferes with the detection of low level infectious agents (i.e., low starting copy DNA detection). Performing PCR in larger volumes, such as 25 μ L, allows for more background bacterial DNA templates to be included in the reaction which can lead to a false positive diagnosis. By decreasing the volume required to perform PCR, less background DNA is available for the PCR. This is demonstrated in **Figure 2**, where negative controls are shown for PCR performed in both a 25 μ L qPCR and a 450 nL IR-PCR. The melt curve in **Figure 2A** identifies the product formed in the negative control as specific product based on its melting temperature while the electropherogram run post-microchip PCR shows no specific product has been amplified (**Figure 2B**). In addition, *trace a* in Figure 2B shows the successful amplification from only 68 16S rDNA starting copies, equivalent to just under 10 *E. coli* cells, improving the level of detection for the broad-range PCR over conventional methodology.

While small volumes inherent to microchips help overcome one obstacle with molecular methods for PJI detection, another benefit offered is integration of multiple processes. **Figure 3** shows successful integration of SPE and PCR in a single chamber.

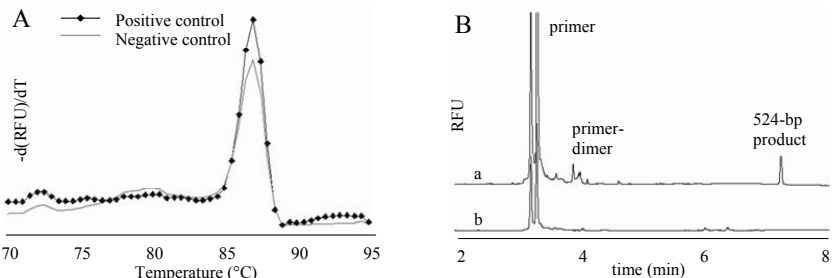


Figure 2. Comparison of PCR methods. A) A melting curve post-qPCR of both a positive control and negative control showing the products amplified during qPCR. The peak seen at 87 °C in both traces is indicative of the 524-bp product. B) Microchip IR-PCR of both a) a positive control with 68 16S rDNA starting copies and b) a negative control. The negative control fails to amplify in the microdevice.

Lysed cells are mixed with the beads in the chamber, the beads washed to remove cellular material and the DNA eluted from the bead surface into the chamber with the very PCR master mix that will be used for DNA amplification. PCR thermocycling required around 13 minutes while the extraction takes under five minutes. The benefits of the PJI microdevice over the conventional methods suggest that implementation of this device in an operating room could offer the speed and more sensitive detection of PJI desired by orthopedic clinicians.

5. Conclusions

A novel technique integrating SPE with PCR in a single chamber has been described using a chitosan phase with excellent DNA recoveries. Since the beads used for DNA extraction remain in the chamber during the PCR, all of the eluted DNA is utilized in the amplification process. As a result of the many advantages offered by a microfluidic device, improvements over molecular methods for PJI detection can potentially be improved when performed on the PJI microdevice.

References

- Trampuz, A., Steckelberg, J. M., Osmon, D. R., Cockerill III, F. R., Hanssen, A. D., Patel, R. *Reviews in Medical Microbiology*, 14, p1, (2003)
- Legendre, L. A., Bienvenue, J. M., Roper, M. R., Ferrance, J. P., Landers, J. P. *Analytical Chemistry*, 78, p1444, (2006).
- Cao, W., Easley, C. J., Ferrance, J. P., Landers, J. P. *Analytical Chemistry*, in press.

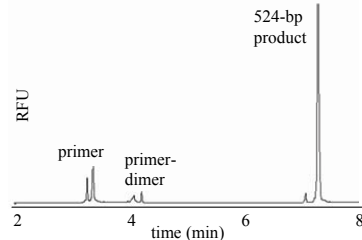


Figure 3. Resultant electropherogram from SPE/IR-PCR performed in the same chamber from 1.6×10^5 *E. coli* cells lysed in the SPE loading solution.

SYNPLIFIED MICROFLUIDIC PROCEDURE FOR BIOTINYL-OLIGONUCLEOTIDE BASED MICRO-IMMUNOASSAY SYSTEM

Yuichi Oku¹, Shuichi Akaba¹, Ryotaro Hara¹, Mamoru Umeda¹,
Manabu Tokeshi² and Takehiko Kitamori³

¹Nissui Pharmaceutical Co., Ltd., Ibaraki, Japan

²Graduate School of Engineering, Nagoya University, Nagoya, Japan

³ Graduate School of Engineering, The University of Tokyo, Tokyo, Japan
(e-mail: y-oku@yki.nissui-pharm.jp)

Abstract

We report here a new on-chip immunological assay system that can detect 100 pg/mL of Hepatitis B surface antigen (HBsAg) within 15 minutes by using a premixed reagent mixture and a semi-automated analyzer. This system is used only two reagents. One reagent is antigen-antibody reaction-related contents and the other reagent is an enzyme substrate. Instead of an antibody-immobilization in the microchannel, biotinyl oligonucleotide-immobilized microchannel was used for antigen trapping. As a result, our assay system required less time than the conventional step-by-step method.

Keywords: Diagnosis, Immunoassay, Thermal lens microscopy

1. Introduction



Figure 1. Semi-automated analyzer.

On-chip immunological detection using a beads-bed scheme has been reported [1]. Advantages of this method are high sensitivity and fast analysis. However, it was a little bit troublesome, and required complicated channel structures. For on-chip immunological detection, antibodies must be immobilized within the microchannels. To form a microchannel which fabricated on a polymer substrate, the bonding process using heating or chemical solvents is required, resulting that antibodies are

fatally damaged by these processes. To avoid these drawbacks, we developed simple structured microfluidic devices and new antibody immobilization method for the plastic substrate [2]. A unique surface modification technology recently developed, which fixed chemicals having primary amino group on the surface of channels after the channel formation (PrimeSurface®, Sumitomo Bakelite Co., Ltd.) was used for protein immobilization. We used this technology to immobilize biotinyl oligonucleotide. In this paper, we report a new on-chip immunological detection system using a newly designed polymer microchip, and a semi-automated analyzer (Figure 1).

2. Experimental

Microfluidic chip

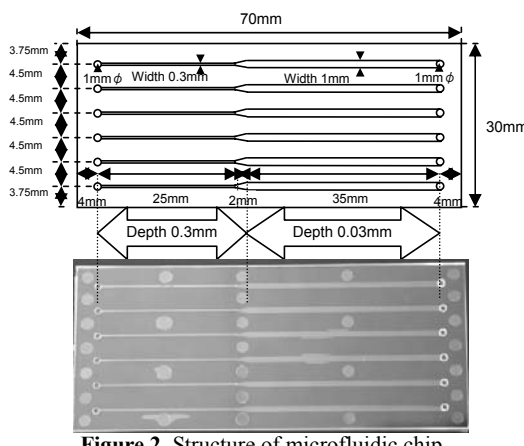


Figure 2. Structure of microfluidic chip.

Microfluidic chips were prepared by cyclopolyolefin polymer (Figure 2). A shallow part (30 μm depth) and other part (300 μm depth) were optimized for the binding reaction and detection, respectively. The substrate with channels and the flat substrate were sealed by heating. The surfaces of the channel were activated by the PrimeSurface® technology and then biotinyl oligonucleotide-NH₂ was flowed into the channels in order to immobilize biotinyl oligonucleotide.

Assay scheme and actuations of semi-automated analyzer

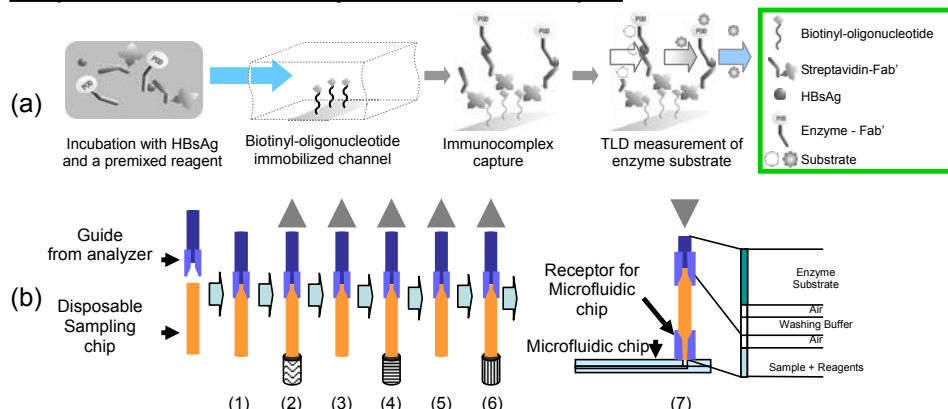


Figure 3. (a) Assay scheme and (b) actuations of the semi-automated analyzer.

Assay scheme and actuations of the semi-automated analyzer were shown in Figure 3. A sample was incubated together with streptavidin-labeled anti-HBsAg-Fab' and horseradish peroxidase-labeled anti-HBsAg-Fab' for 5 minutes. Then, its mixture was set in the analyzer. The assay procedures are as follows: (1) A guide attached to the head of nozzle picked up a disposable sampling chip (DSC). (2) Enzyme substrate was sucked into DSC. (3) Air was sucked into DSC. (4) Washing buffer was sucked into DSC. (5) Air was sucked into DSC again. (6) Mixture of sample and reagents was sucked into DSC. To protect carry-over, only DSC could keep this mixture. (7) Finally, five liquids and air layers were formed in the analyzer. And these liquid layers were injected into the microfluidic chip at an appropriate flow speed. And enzyme activities were measured with a thermal lens detector (TLD).

3. Results and Discussion

Sensitivity of HBsAg

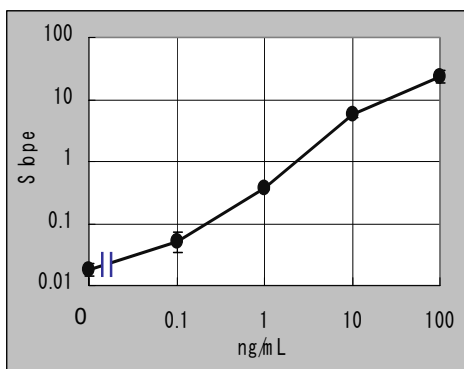


Figure 4. Sensitivity of HBsAg.

This system could measure 100 pg/mL of HBsAg using 15 μL of sample (Figure 4). Measurement time of this system was within 30 minutes including incubation of the sample and reagents. All key steps including the incubation (5 min.), injection into microfluidic chip (2 min.), washing and enzyme activity measurement (1.5 min.) were only 8.5 minutes in total. The semi-automated analyzer is just a prototype to confirm our idea. Although it took about 30 minutes for the assay, the overall analysis time can be within 15 minutes by improving the analyzer.

Evaluation of control sera

Table 1. Evaluation of control sera with this analyzer and the other methods. Gray colored cells were positive results.

	Unit	Infectrol® A	Infectrol® B	Infectrol® C	Infectrol® D	Infectrol® E
This analyzer	ng/mL	0.19	1.55	7.67	>100.00	0.00
Analyzer A	C.O.I.	0.98	6.09	30.13	>100.00	<1
Analyzer B	U/mL	0.25	1.40	6.30	140.97	0.00
Analyzer C	C.O.I.	2.60	14.11	58.90	882.60	<1
Analyzer D	IU/mL	0.29	1.70	8.03	>100	0.00
Teststrip E	—	—	+	+	+	—
Teststrip F	—	—	—	+	+	—
Teststrip G	—	—	+	+	+	—

Control sera for internal quality control were measured by this system. Infectrol® A-D are positive and Infectrol® E is negative samples, respectively. The results were summarized in Table 1. This analyzer could detect all positive sera although Analyzer A and 3 kinds of teststrip could not detect Infectrol® A as positive.

4. Conclusion

We established the high sensitive immunoassay system involving a semi-automated analyzer, equipped with a thermal lens detector, and cyclopolyolefin polymer-based chip. Fundamental assay procedures required only 8.5 minutes, and 100 pg/mL of HBsAg could be detected as a model of antigen. We believe this system can be applied to any kinds of binding assay.

Acknowledgements

This work was supported by the Grant from the New Energy and Industrial Technology Development Organization (NEDO), Japan.

References

- [1] K. Sato *et al.*, *Anal. Chem.*, **72**, 1144-1147 (2000).
- [2] Y. Oku *et al.*, *Proc. of μTAS 2005 conf.*, 1321–1323 (2005).

INTEGRATION OF ANTIBODY ARRAYS INTO A PREASSEMBLED MICROFLUIDIC DEVICE FOR ON-DEMAND IMMUNOASSAY

Masahiko Hashimoto, Hirokazu Kaji, Maria E. Kemppinen,
and Matsuhiko Nishizawa

Department of Bioengineering and Robotics, Graduate School of Engineering,
Tohoku University, Sendai 980-8579, Japan

Abstract

This paper describes a method to create a patterned surface within a microchannel by electrochemical means, which enables on-demand and site-specific immobilization of protein array after the device is fully assembled. High density protein immobilization is achieved by locating proteins to a three-dimensional microstructure. In addition, by first depositing a pattern of poly(ethylene glycol) (PEG)-based copolymer in the microchannel, a uniform protein pattern is obtained even in a stream flow.

Keywords: protein pattern, microchannel, electrochemical method, 3D microstructures.

1. Introduction

The controlled immobilization of unstable biomolecules such as proteins within a microfluidic channel is a critical step in many types of bioassays. We have previously reported a method to create a patterned surface within a microchannel by electrochemical means, “electrochemical bio-lithography”, which enables site-specific immobilization of antibody array after the device is fully assembled. Since the electrochemical surface reaction is fast enough to satisfy the diffusion-controlled case, the length of electrolysis period and channel height can control the size of protein-immobilized area. In addition, by using the stepwise electrochemical treatment, multiple types of protein arrays can be patterned within a single microchannel [1-3]. To make this approach more suitable for practical applications, three-dimensional microstructures were fabricated on the channel wall. Because the 3D microstructure increases the area of surface for protein attachment, the intensity of fluorescence signal increases in detection that uses a fluorescence-labeled probe. In addition, a pattern of anti-biofouling polymer that is not affected by the electrochemical treatment was introduced on the channel surface. By switching non-polymer regions from anti-biofouling to protein-adsorptive, it becomes possible to strictly define protein-adsorptive regions even when there is a stream flowing in the channel.

2. Experimental

The microfluidic device consists of three layers: a microelectrode-bearing glass substrate, a silicone rubber, and a substrate with the PDMS microposts or the PEG-patterned glass substrate (Fig. 1). PDMS microposts were fabricated by using molding technique with SU-8 photoresist. The PEG micropattern was prepared by using a PDMS microstamp.

After the microfluidic device was fully assembled, solutions of polyethylenimine (PEI) and heparin were passed through the microchannel, to form an electrostatically assembled multilayer on the channel wall. Subsequently, 0.1M PBS solution containing 25 mM KBr (pH 7.4) was

introduced into the channel and after the flow was completely stopped, a potential pulse of 1.7 V vs. Ag/AgCl was applied to each microelectrode in order to generate Br₂ (subsequently HBrO). Finally, a protein solution was run though the channel, followed by a wash with PBS.

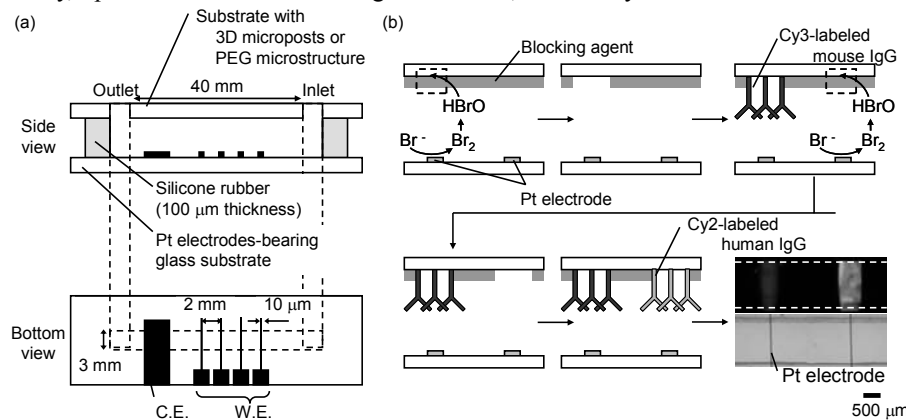


Figure 1. (a) Schematic representation of side and bottom views of the microfluidic device. (b) Schematic diagram outlining the electrochemical surface treatment within the microchannel, and fluorescence micrograph of the immobilized multiple antibodies.

3. Results and discussion

Fig. 2a shows a fluorescence micrograph of locally immobilized protein on the channel surface. The Cy3-labeled protein A was located on the opposite face of the electrodes, corresponding to the pattern of the electrode array. Fig. 2b shows the fluorescence intensity along the white line shown in Fig. 2a. The fluorescence signal obtained from the uneven surface is higher than that from flat surface, due to protein attached to the sidewall of microposts. Fig. 3 shows the plots of fluorescence intensity obtained from protein-immobilized region versus the specific surface area of the channel wall. It is obvious that the positive correlation between the fluorescence intensity with the increased specific surface area exists. This patterning technique is applicable to more complicated structures such as filter membranes, and their vast surface area would give highly enhanced signal.

There was a problem of lithographic treatment is affected by natural streams in

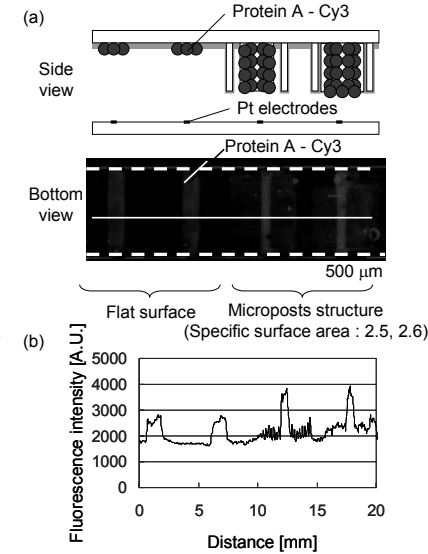


Figure 2. (a) Fluorescence micrograph of the protein pattern on the microposts structure and plane surface when surface was treated electrochemically. (b) Cross-sectional fluorescence intensity along the line in (a).

microchannels, since the diffusion layer of the electro-generated oxidant is shifted in the flow direction. In order to address this problem, we defined the regions of which the oxidant can and cannot switch the surface property by first depositing a patterned PEG-based copolymer on the channel wall (Fig. 4a). PEG is a typical anti-biofouling polymer, and is unaffected by our electrochemical treatment. We conducted the electrochemical treatment and subsequent immobilization according to the procedure shown in Fig. 1b. Fig. 4b shows a fluorescent micrograph of the Cy3-labeled protein A patterned on the channel wall. As can clearly be seen, the proteins adsorbed only on the regions without PEG-coating layer. Fig. 4c shows the fluorescence intensity, along the white line shown in Fig. 4b. Almost no fluorescence was observed on the surface of the PEG, providing high S/N ratio. Since the PEG micropatterns strictly restrict the areas on which proteins can potentially adsorb even in a stream, a constant amount of proteins can be immobilized and ensures reproducible experiments.

4. Conclusions

The microfluidic device with electrochemical bio-lithography enables the real-time and on-demand immobilization of protein arrays within the microchannel. It is expected that this methodology will make a large contribution to protein chip technology.

Acknowledgements

This study was supported by Industrial Technology Research Grant Program in 05 from NEDO of Japan, and by a Grant-in-Aid for Scientific Research B (No. 17310080) from the Ministry of Education, Science and Culture, Japan. M.H. acknowledges support from a research fellowship of the Japan Society for the Promotion of Science.

References

- [1] H.Kaji, M.Hashimoto, and M.Nishizawa, *Anal. Chem.*, 78,5469 (2006).
- [2] H.Kaji, K.Tsukidate, M.Hashimoto, T.Matsue, and M.Nishizawa, *Langmuir*, 21,6966 (2005).
- [3] H. Kaji, M. Hashimoto, K. Tsukidate, T. Matsue, M. Nishizawa, *MicroTAS'05*, pp. 1309 (2005).

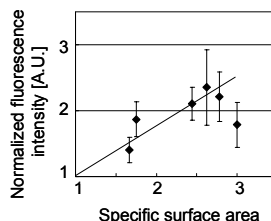


Figure 3. Plots of the specific fluorescence intensity versus specific surface area of micropost-structured substrate.

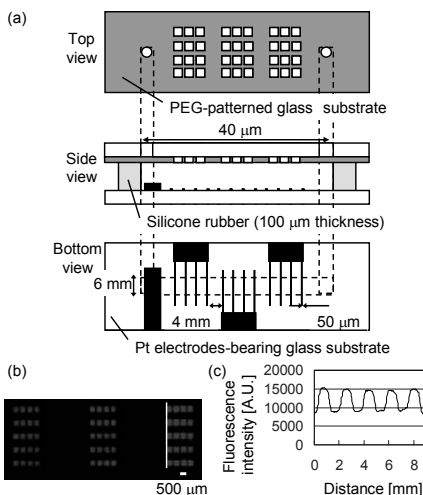


Figure 4. (a) Schematic representation of the microfluidic device which has PEG micropattern. (b) Strategy for the protein immobilization within pre-defined locations. (c) Fluorescence micrograph of the protein pattern restricted by PEG when surface was treated electrochemically three times. (d) Cross-sectional fluorescence intensity of the line in (c).

TEMPERATURE GRADIENT FOCUSING FOR ON-CHIP MONITORING OF ENZYME REACTION PRODUCTS IN COMPLEX SAMPLE MIXTURES

Matthew S. Munson, Jonathan G. Shackman, Laurie E. Locascio, and David Ross

National Institute of Standards and Technology, USA

Abstract

Temperature gradient focusing (TGF) is demonstrated as an analytical tool for conducting enzyme assays with short analysis times and little or no sample preparation. The technique's potential compatibility with clinical samples is also demonstrated. These results show that TGF enzyme analysis may be a suitable tool for conducting rapid, high sensitivity point-of-care assays.

Keywords: capillary electrophoresis, enzyme assay, temperature gradient focusing

1. Theory

TGF is a recently developed technique for the simultaneous concentration and electrophoretic separation of analytes in a microfluidic system [1]. TGF balances the electrophoretic velocity of ionic analytes with solution convection through a separation channel whose ends are held at different temperatures. The separation buffer is chosen so that the ionic strength, and therefore electrophoretic velocity, varies with temperature. The convective velocity can be adjusted so that the net velocity of the analyte (the sum of the electrophoretic and convective velocities) is zero at a unique point in the channel. TGF has been applied to small molecules, DNA, proteins, and particles [1].

2. Electrophoretic Exclusion Enables Complex Sample Analysis

The convective flow in TGF is dependent on electroosmotic flow (EOF), making it sensitive to surface fouling. However, because the convective and the electrophoretic velocity are opposed, it is possible to exclude unwanted classes of molecules from the separation channel. This mitigates the fouling problem without surface coatings through an exclusion effect. If the direction of convection is from waste to sample and electrophoresis is from sample to waste, any species located within the sample reservoir that is electrophoretically slower or of the opposite charge than the target analyte will remain in the sample reservoir. It therefore does not contact the surfaces of the separation channel and cannot affect EOF. This allows for the analysis of complex biological samples that would normally require time-consuming channel pretreatment or pre-analysis sample cleanup.

The exclusion effect is demonstrated with a protein known to adhere to many surfaces, bovine serum albumin (BSA). Repeated analyses of a sample containing 10 nmol L^{-1} fluorescein in a buffer consisting of 0.5 mol L^{-1} tris and 0.5 mol L^{-1} boric acid were conducted with BSA concentration varying from $80 \mu\text{g ml}^{-1}$ to 8 mg ml^{-1} . A voltage of 3 kV was applied to the 3 cm separation channel. The temperature gradient

($250\text{ }^{\circ}\text{C cm}^{-1}$) was applied over a 2 mm segment of the channel. The applied pressure was reduced at a rate of 1 Pa s^{-1} . The repeatability of the analyte peak position suggests the absence of variability in EOF over the course of the experiment. The variation in peak height is due to BSA binding fluorescein in the sample reservoir [2].

To confirm the impact of BSA fouling, a fresh device was used to focus carboxyfluorescein (CF) from a sample containing no BSA. The same device was then used to focus CF from a sample containing 10 mg ml^{-1} BSA. Finally, the channel was rinsed for 30 minutes with a 10 mg ml^{-1} BSA solution, rinsed for 10 minutes with buffer, and then used to focus CF from a BSA free sample. Five replicate scans were performed for each condition. No difference in the peak position for the scans conducted before rinsing the capillary with BSA was observed. After exposing the capillary to the BSA solution, the peak position was shifted by approximately 0.7 kPa . In addition, the scan to scan variability in peak position was significantly increased after flushing the capillary with BSA. These results clearly demonstrate that the BSA located in the sample is excluded from the channel during the analysis of CF. This electrophoretic exclusion can be applied to the analysis of any electrophoretically rapid analyte in the presence of slower molecules that interact unfavorably with the surface of the analysis channel. These types of interactions are one of the main difficulties in using electrophoretic analysis for complex sample mixtures.

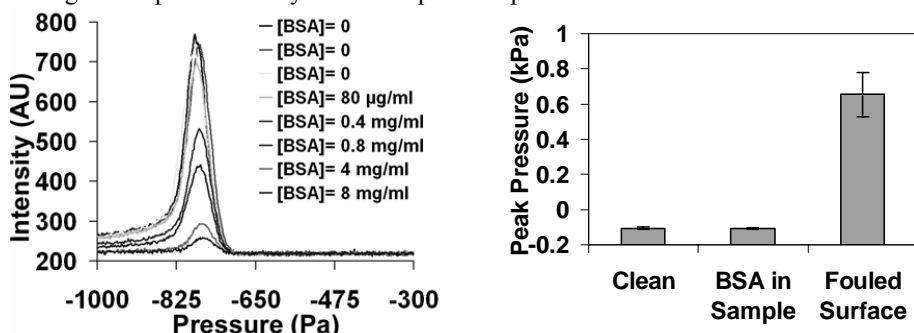


Figure 1: Exclusion of BSA from the separation channel is demonstrated by analyzing the samples that varied only in BSA concentration. Left: raw intensity profiles from TGF experiments show little variation in P_{\max} . Variation in peak height is due to association of BSA and fluorescein in the sample reservoir. Right: P_{\max} does not change when 10 mg ml^{-1} BSA is added to the sample. When the channel is intentionally exposed to BSA there is a large shift in P_{\max} and the variability of P_{\max} ($n=5$). This demonstrates that BSA in the sample is excluded from the channel. Error bars represent ± 1 standard deviation.

3. Monitoring biochemical reactions

The ability to monitor biochemical reactions is demonstrated using β -galactosidase (βgal) and fluorescein-di- β -d-galactopyranoside (FDG) as a model enzyme-substrate system. The enzyme βgal cleaves FDG twice to produce fluorescein [3]. The concentration of product (fluorescein) is representative of the average reaction rate over the course of the experiment. Therefore, we can use this technique to determine the impact of various reaction conditions on the enzyme reaction rate. As a demonstration,

we monitored the effect of incubation temperature and cofactor (Mg^{++}) concentration. Samples were incubated at room temperature and at 30 °C in the presence or absence of 1 mmol L⁻¹ Mg^{++} . Solutions containing a fixed starting concentration of FDG but varied enzyme concentrations were allowed to react followed by TGF analysis of the reaction products.

Interexperimental repeatability of approximately 6% ($n=3$) was observed, with limits of detection (LOD) of 800 ng ml⁻¹ with a 10 minute reaction time (Figure 2). Although the demonstrated LOD is significantly higher than previous reports (35 pg ml⁻¹) [4], these reports utilized a much longer analysis time (approximately 1 hour). In addition, previous reports also demonstrated problems with non-specific adsorption of the enzyme to the channel walls. Using TGF, the enzyme is excluded from the analysis channel eliminating this as a source of error. It is anticipated that this difference could simply be bridged by employing an LIF detection scheme, without the need for increased analysis time.

4. Conclusions

This report demonstrates the ability to use TGF to analyze enzyme concentration or as a research tool to determine the impact of reaction conditions on enzyme kinetics. This work also demonstrates that these measurements can be made in complex biological samples due to the electrophoretic exclusion that arises from the opposition

of convection and electromigration. These aspects of TGF-based enzyme assays could allow them to be a useful tool in point-of-care and clinical diagnostics.

References

- (1) Ross, D.; Locascio, L. E. *Analytical Chemistry* **2002**, 74, 2556-2564.
- (2) Penniston, J. T. *Experimental Eye Research* **1982**, 34, 435-443.
- (3) <http://www.probes.com>.
- (4) Craig, D., et al. *Analytical Biochemistry* **1995**, 226, 147-153.

Acknowledgements

The authors acknowledge the financial support of the NIST/NRC Postdoctoral Research Program

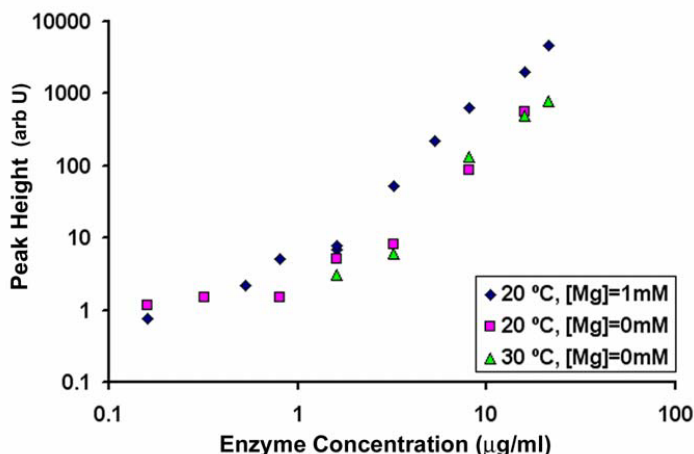


Figure 2: β Gal TGF enzyme assay. Enzyme concentration and assay conditions (incubation temperature, Mg^{++} concentration) were varied. The observed limit of detection was 800ng/ml. Enzyme and substrate were reacted for 10 minutes prior to TGF analysis.

SINGLE-BEAD ANALYSIS ON COMPACT DISK SHAPED MICROFLUIDIC DEVICE

**Hidenori Nagai¹, Yuka Narita^{1,2}, Masayuki Matsubara¹, Takashi Irie¹,
Keiitsu Saito^{1,2} and Shin-ichi Wakida¹**

¹National Institute of Advanced Industrial Science and Technology (AIST),
Ikeda, Osaka, 563-8577 Japan

²Kobe University, Kobe, Hyogo, 657-8501 Japan

keywords: Immunoassay, centrifugal flow, capillary burst valve, immunoglobulin A

Abstract

A compact disk shaped microfluidic device (Lab-on-a-CD) was developed to allow the evaluation of mental stress. Secretory immunoglobulin A (sIgA) was measured by a heterogeneous enzyme immunoassay (EIA) on the Lab-on-a-CD. For the microfluidic control by centrifugal force, we examined the relationship between the rotational speed and the microchannel profile. Using a sIgA-immobilized bead for a competitive antigen-antibody reaction, sIgA in standard samples could be quantified. It is expected that the Lab-on-a-CD would be suitable for miniaturization and automation of the processes in EIA.

1. Introduction

EIA has been widely used for various diagnoses. EIA utilizes an antibody with high molecular recognition and selectivity, and an enzymatic reaction that can amplify the detectable signal and enhance the sensitivity of the assay. However, the conventional EIA using a titer plate requires tremendous labor and long analysis time. To overcome these drawbacks, several papers on the integration of heterogeneous immunoassay systems into microfluidic devices have been published over the last decade [1,2]. In these devices, the miniaturized reaction fields had enhanced reaction efficiency, simplified procedures, reduced assay time, and lowered consumption of samples, reagents, waste and energy. In the case of a miniaturized EIA device, a large number of small beads were often applied instead of a solid phase immobilized antigen or antibody used in the wells of a titer plate. Though the number of beads in the microchannel needs to be exactly controlled in order to achieve accurate analysis, this is difficult. Moreover, such microfluidic devices generally require relatively large peripherals, such as pumps. Therefore, it would be unsuitable for EIA devices integrated on to a hand-held system.

Recently, compact disk-shaped microfluidic devices (Lab-on-a-CD) have been demonstrated for an integrated EIA using centrifugal force based fluid handling without mechanical pumps [3]. As centrifugal force can act on all the microfluids on the disk simultaneously, it is considered that a Lab-on-a-CD is suitable for parallel processing of a large number of assays.

This paper describes heterogeneous EIA on a Lab-on-a-CD using a single bead

immobilized with sIgA in each reaction reservoir. It was expected that the total area of the specific surface for antigen-antibody reaction would be uniform in a single bead analysis, and the backpressure to flow could be reduced. As centrifugal and capillary forces were examined for microfluidic control in the multi-step process (e.g., antigen-antibody reaction, bound/free separation, detection) in EIA, each step of EIA was automatically carried out according to the rotational speed of the Lab-on-a-CD.

2. Experimental

Lab-on-a-CDs were fabricated of PDMS for the examination of microfluidic control by centrifugal force. The relationship between rotational speed and microchannel cross section was examined; the channel width was varied from 20 μm to 1 mm, the location of the connected reservoir was varied from 1.5 to 3.5 cm from center of rotation, and the channel depth was examined at 40 and 100 μm . 1 μl of aqueous solution containing 400 $\mu\text{g/ml}$ BSA was injected into each injection reservoir. The Lab-on-a-CD was rotated at several speeds from 750 to 3000 rpm and the behavior of solution was observed using a stroboscope.

According to the experimental results for the centrifugal control, a Lab-on-a-CD for EIA was designed. Glass beads of size 1 mm in diameter were immobilized with sIgA and then treated with blocking solution. A sIgA-immobilized bead was loaded into each antigen-antibody reaction reservoir on the Lab-on-a-CD for EIA. Standard sIgA solution was reacted with horseradish peroxidase (HRP) labeled anti-sIgA antibody solution and then mixed with the blocking solution. 1 μl of the sample solution containing the immunocomplex was loaded into the injection reservoir. 1 μl of Amplex Red and H_2O_2 mixture was loaded into each detection reservoir. The Lab-on-a-CD was rotated to transport the sample solution to the reaction reservoir loaded with the sIgA-immobilized bead. After 10 min for competitive antigen-antibody reaction, the solution was flowed into the detection reservoir by second rotation. The fluorescence intensity was observed using a fluorescent imaging scanner.

3. Results and discussion

The centrifugal force can be defined by the angular speed of rotation, fluid density, surface tension, and geometry and location of the channels and reservoirs. The sample solutions were loaded into the Lab-on-a-CD for examination of microfluidic control and rotated with several speeds. To process each step of EIA using a Lab-on-a-CD, stop and flow of the solutions should be simultaneously controlled under the same rotational speed. As the results in the present research, 2000 rpm was the critical point to divide the flowing into the microchannels 40 μm deep as compared between 20 μm and 1 mm in channel width. The difference between the capillary forces to stop or flow the microfluids was calculated to be 2.78 times. Therefore, it was shown in the present research that microfluidic control based on centrifugal force could be set up by effective combination of the channel width and depth, which should differ by at least over three times.

The reservoir position and the channel profile on the Lab-on-a-CD for EIA were also investigated. In the present research, a single glass bead 1 mm in diameter was used as the sIgA-immobilized surface instead of the well bottom in a 96-wells titer plate. The surface areas

of the bead and well bottom were about 3.1 and 33 mm², respectively. Therefore, the amount of HRP-labeled antibody in an assay reduced in order to avoid saturation of the antibody in the antigen-antibody reaction. Figure 1 shows the calibration curve of the standard sIgA using the Lab-on-a-CD for EIA. The calibration curve showed good linearity until 66 µg/ml and the limit of detection (LOD) was 2.5 µg/ml (6.4 nM) of sIgA. In humans, the concentration of sIgA in saliva is typically in the range of 50-500 µg/ml; the value significantly decreases under mental stress [4]. Thus, the LOD is enough to detect the sIgA in saliva without any pretreatment, and thus, this assay may be expected to be suitable for daily management of mental stress.

4. Conclusion

We have successfully demonstrated that a CD-shaped microfluidic device could perform EIA for sIgA. Centrifugal force could be effectively controlled to manipulate the microfluids sequentially from each reservoir into the connected microchannel. A preliminary analysis of sIgA indicated that each process was automated by the rotary speed and the analysis time on the Lab-on-a-CD was only 30 min. The application of this Lab-on-a-CD would be also promising for a handheld system for rapid screening of pathogens and physical and mental disorders.

Acknowledgement

The present work was partially supported by Industrial Technology Research Grant Program in '05 from New Energy and Industrial Technology Development Organization (NEDO) of Japan.

References

1. K. Sato, M. Tokeshi, T. Odake, H. Kimura, T. Ooi, M. Nakao, T. Kitamori, *Anal. Chem.* 72, pp. 1144, (2000).
2. K. Schult, A. Katerkamp, D. Trau, F. Grawe, K. Cammann, M. Meusel, *Anal. Chem.* 71, pp. 5430, (1999).
3. S. Lai, S. Wang, J. Luo, L.J. Lee, S.-T. Yang, M.J. Madou, *Anal. Chem.* 76, pp. 1832, (2004).
4. E.A. Shirtcliff, D.A. Granger, E. Schwartz, M.J. Curran, *Psychoneuroendocrinology* 26 , pp. 165, (2001).

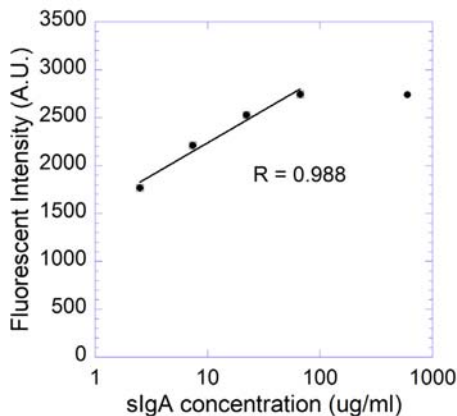


Figure 1. Calibration curve of standard sIgA using the Lab-on-a-CD for EIA.

A BEAD BASED DNA DIAGNOSTIC ASSAY USING NANOPARTICLE MEDIATED SERRS DETECTION WITHIN A LAB-ON-A-CHIP FORMAT

Paul B. Monaghan¹, Karen M. McCarnery², Alastair Ricketts², Rachel E Littleford² Frances Docherty², W. Ewen Smith², Duncan Graham², Jonathan M. Cooper¹

¹Dept.of Electronics and Electrical Engineering, University of Glasgow

²Dept. of Pure and Applied Chemistry, University of Strathclyde

Keywords: PCR, SERRS, microfluidics, beads

1. Introduction

There is a continued interest in the development of new on-chip protocols for the rapid determination of the causes of infectious disease. In this article we present a chip-based method for identifying *Chlamydia trachomatis*. This procedure combines elements of PCR, on-chip solid-phase sample clean-up and determination using Surface Enhanced Resonance Raman spectroscopy (SERRS). There have been several reports on the use of microspheres within chip-based systems due to the increase in surface area and the variety of surface chemistries to perform ligand-binding assays¹⁻³. In the assay reported here, we exploit the use of a packed bead-bed of functionalised microspheres retained within a microfluidic network in order to selectively capture the sample thus enabling the introduction of washing steps to remove background contributions. The use of this bead-based assay not only provides a solid-state clean-up format, but also provides short diffusion distances with the matrix to reduce the time and improve the efficiency of binding.

2. Experimental

An outline of the assay is described in figure 1. In this process, PCR for the target sequence for *Chlamydia trachomatis* was performed using a biotinylated primer off-chip resulting in a biotinylated amplicon. This enabled post-PCR selective capture of the amplified PCR target using streptavidin-coated beads, on-chip, in order to remove background contributions from the sample matrix. To implement this, a low-cost microfluidic chip with an integrated filter membrane retaining a bed of ~10 µm streptavidin functionalised microbeads was produced in PDMS using simple mold replication techniques

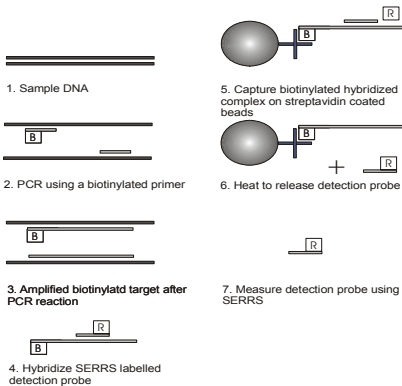


Figure 1. Outline of the assay principle

on an anisotropically dry-etched silicon master, see figure 2 (ii). This enabled quick and low-cost replication production of devices. After molding, the devices were permanently bonded using plasma oxidation. Fluids were controlled on-chip by a precision syringe pump.

The biotinylated product was flowed past and captured on the streptavidinated beads followed by a cycle of buffer washing stages. This served to remove contributions from the sample matrix. A complimentary SERRS active labelled (R6G) detection sequence was then hybridised to this product followed by further washing stages to remove excess detection probe, enabling determination of the analytical signal. In order to remove the Raman contribution of the polymer microspheres, the detection probe was thermally released from the beads. This was achieved by simply melting the biotinylated PCR target-detection probe duplex by locally heating the chip's bead-bed. After release, the detection probe was flushed downstream for determination. Colloidal silver nanoparticles were mixed with the released sample at the chip's intersection to provide a metallic surface in order to probe the system by SERRS. The sample was interrogated with a 532nm laser line and the SERRS signal was collected on an inexpensive fibre-coupled Ocean Optics miniature spectrometer. The SERRS spectrum acquired from this analysis is shown in figure 4.

4. Results and Discussion

Figure 3(i), top, shows the capture of biotinylated PCR product and hybridisation of the detection probe. In this instance, the detection probe was labelled with the Raman active and fluorescent active label, Rhodamine 6G. This enabled the hybridisation and release to be imaged by fluorescence. The lower image of figure 3(i) shows the same bead-bed after heating and thermal release of the labelled detection probe. The probe was flushed downstream to interact with colloidal silver nanoparticles in to derive the SERRS signal. A typical SERRS spectrum obtained from the bead bed is presented in figure 4. This spectrum contains each of the characteristic bands associated with the label attached the probe.

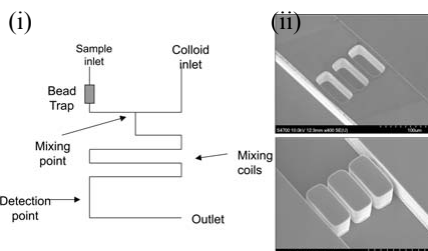


Figure 2 (i) Schematic layout of the device (ii) SEMs of Top-Si master. Bottom-molded PDMS device

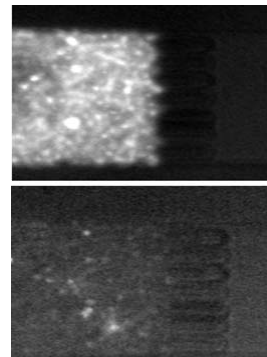


Figure 3 Top-capture and hybridisation. Bottom-The bead-bed after release.

All though not demonstrated here, a potential advantage of SERRS versus other methods is improved multiplex sequence detection capability without the need for additional instrumentation. This arises as a consequence of the sharp Raman fingerprints associated for each of the individual labels. This aspect will be investigated in the future. Using the reported procedure we have obtained a detection limit of 20nM for the labelled detection sequence using SERRS.

3. Conclusion

In this assay, we combine complimentary assay components in order to achieve an analytical solution to efficiently determine nucleic acid sequences of clinical relevance, in this case *Chlamydia trachomatis*. We have shown that a PCR mixture can be selectively captured on-chip followed by sample clean-up, release and interrogation on a low-cost platform using PDMS microfluidic devices. It is anticipated that future work will focus on multiplex determination of several sequences simultaneously. As such, this represents a positive contribution towards inexpensive low-volume genetic analysis for potential routine diagnostic applications.

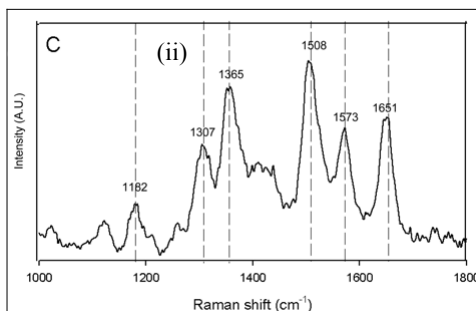


Figure 4. SERRS spectrum obtained from the R6G-labelled detection sequence on-chip

4. Acknowledgements

PBM and FD would like to acknowledge Scottish Enterprise for the financial support of this work. The Authors would also like to thank Prof. Paul Wallace of Quality Control for Molecular Diagnostics (QCMD), Glasgow, UK for his advice with regards to the PCR work.

5. References

- Verpoorte, E. *Lab on a Chip* 2003, 3, 60N-68N
- Andersson, H.; van der Wijngaart, W.; Enoksson, P.; Stemme, G. *Sensors and Actuators B-Chemical* 2000, 67, 203-208.
- Andersson, H.; van der Wijngaart, W.; Stemme, G. *Electrophoresis* 2001, 22, 249-257
- Docherty, F. T.; Monaghan, P. B.; Keir, R.; Graham, D.; Smith, W. E.; Cooper, J. M. *Chem. Comm.* 2004, 118-119

AUTOMATED MICRO-ELISA SYSTEM FOR ALLERGY CHECKER: A PROTOTYPE AND CLINICAL TEST

Toshinori Ohashi¹, Yoshinori Matsuoka¹, Kazuma Mawatari¹,

Mitsuo Kitaoka¹, Tadao Enomoto² and Takehiko Kitamori^{1,3},

¹The Research Association of Micro Chemical Process Technology, Japan.

²Dept. of Otolaryngology, Japan Red Cross Society, Wakayama Medical Center

³Graduate School of Engineering, The University of Tokyo, Japan

Abstract

We report a first prototype machine of an automatic and compact micro-ELISA system for clinical diagnosis of allergy. The excellent performances were verified in three times faster analysis time, one order smaller sample and reagents volume with enough sensitivity compared with conventional systems. The prototype was subjected to a clinical trial authorized by the Ethical Advisory Board and good correlations with conventional method have been verified with 82 allergy patients. We believe our system show most excellent performances as practical systems.

Keywords: micro-ELISA, allergy, thermal lens detection, clinical test

1. Introduction

Microchip-based ELISA system is expected one of useful applications, especially, in point-of-care (POC) clinical diagnosis. In previous papers, several micro-ELISA microchips have been reported. However, automatic and compact systems have not been realized due to the difficulty in achieving many sophisticated technologies in sample injection, pump, valve, connector, ELISA microchip, surface treatment, detection, automation, and the compact system design. In this presentation, we realized a prototype system for clinical diagnosis of allergy. We illustrate the details of the system and performances by testing the system in a clinical test.

2. Principle

The principle of our micro-ELISA on microchip is illustrated in Figure 1.

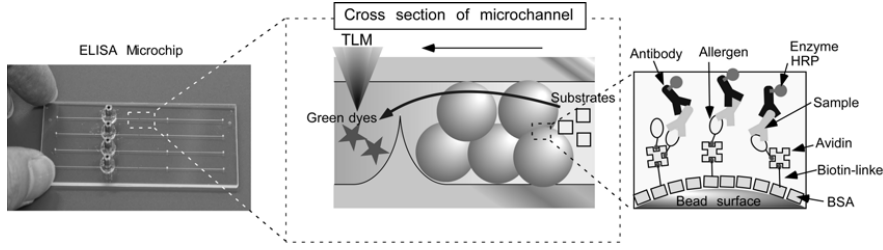


Figure 1 Principle of micro-ELISA on microchip

Polystyrene (PS) micro-beads were introduced into a microchannel, and allergens are linked on the PS surface. For decreasing background signals from non-specific bindings, BSA and biotin-avidin reactions were used for the surface chemistry. The dye solution was produced by an enzymatic colorimetric reaction in stop-flow condition, and the concentration was measured by thermal lens microscope.[1]

3. Experimental

Automatic micro-ELISA system

In Figure 2, our system and the components are illustrated. The samples and reagents are stocked in tubes on a tray. A PEEK tube sucks and injects the samples and reagents at a determined flow rate which was controlled by four syringe pumps. The change of the flow to a waste or a microchip can be controlled our original micro-valve. The PEEK tube is connected after sucking the samples and reagents, and immunoassay is conducted on the microchip and detected by our original on-chip thermal lens microscopes (TLM). All the moving components are driven with auto-stages controlled by software on PC.

Micro-beads preparation

PS micro-beads ($\Phi 45\mu\text{m}$) for total IgE determination were immobilized. PS micro-beads for specific IgE determination were coated with biotinated-BSA and then avidin (KPL) before introduction into a microchannel.

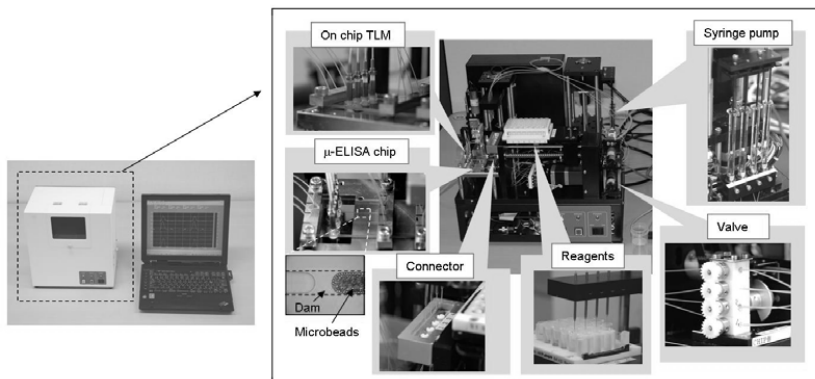


Figure 2 System (left) and the components (right) in our micro-ELISA

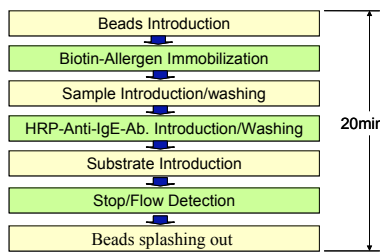


Fig.3 Typical procedure

the substrate solution of tetramethyl benzidine and H₂O₂ mixture (KPL) were injected.

Detection

Four on-chip micro thermal lens detection devices (micro-TLD) were utilized as an optical alignment free thermal lens detection system [2]. SELFOC micro lens was integrated on the top surface of the microchip at the 10mm downstream from the dam of the microchannel. The excitation wavelength used in this research was 635nm, and the detection wavelength was 750nm.

4. Results and Discussion

The typical signals are shown in Figure 4. The stop -flow reaction (1 min for stop) for the colorimetric reaction generated a peak signal, and the height was measured. The performance was compared with the conventional system. Our micro-ELISA system features small sample volume of 5μL (1/10 relative to the conventional methods), fast analysis time of 20 min (1/3), and low cost for reagents (1/10) in addition to the compact size. The sensitivity is 1 ng/ml (data not shown) and enough for allergy diagnosis. Finally, we conducted a clinical test to verify the applicability for practical uses in medicals or clinics. The good correlation was obtained ($r=0.891$, $n=82$) with a conventional method. Also, the results for specific IgE showed comparable correlation. We illustrate the details of the clinical test in my presentation.

5. Conclusions

In addition to allergen diagnosis, our system can be applied for various immunoassay systems just by changing the antigen or antibody on PS surfaces.

Acknowledgements

The present work was supported by the New Energy and Industrial Technology Development Organization (NEDO) of Ministry of Economy, Trade and Industry, Japan.

References

- [1] T. Ohashi *et al.*, Micro TAS 2004, A32100 (2004)
- [2] Y. Matsuoka *et al.*, Micro TAS 2004, A32640 (2004)

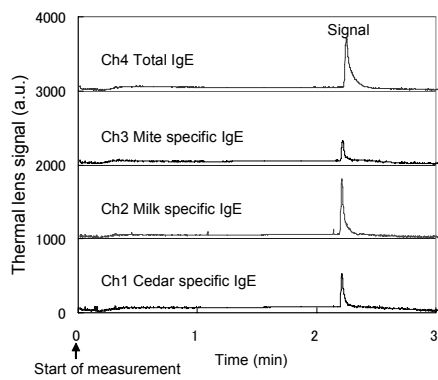


Figure 4 Typical signals for total IgE and specific IgE (mite, milk, and cedar)

Parallel Synthesis in an EOF-based Micro Reactor

Charlotte Wiles

Department of Chemistry, The University of Hull, Cottingham Road, Hull, HU6 7RX, UK.

Keywords: Electroosmotic flow (EOF), parallel synthesis, solid-supported catalysts, tetrahydropyranyl (THP) ethers and micro reactors

Abstract

Although an array of synthetic transformations have been successfully performed within micro fabricated reactors, no systems describe the scale-out of such reactions using electroosmotic pumping. With this in mind, we describe our initial evaluation of an EOF-based parallel reactor suitable for the high-throughput synthesis of tetrahydropyranyl ethers.

1. Introduction

In order to achieve the overall aim of synthesising analytically pure compounds within micro fabricated reactors, we recently described the incorporation of solid-supported reagents and catalysts into capillary based flow reactors (Figure 1), largely employing electroosmotic flow (EOF) as the pumping mechanism [1,2]. Although this approach enabled the synthesis of analytically pure compounds, without the need for additional off-line purification, the quantities of material produced (typically ca. 10 mg hr⁻¹) were not suitable for the target market *i.e.* the fine chemical or pharmaceutical industry, where greater throughputs are required. To address this shortfall, we began investigating a means of increasing the quantity of material synthesised, whilst retaining the advantages associated with reaction miniaturisation.

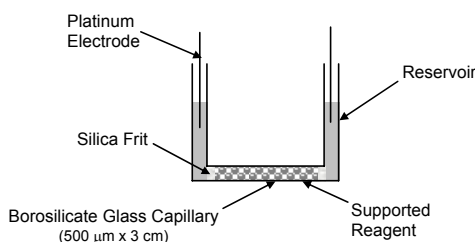


Figure 1. Single capillary reactor used for the evaluation of supported reagents and catalysts.

As Figure 2 illustrates, this was achieved by increasing the number of packed channels employed. In addition to the obvious increase in productivity, the parallel reactor can also be used for rapid reaction optimisation, catalyst evaluation or even for the parallel synthesis of multiple products.

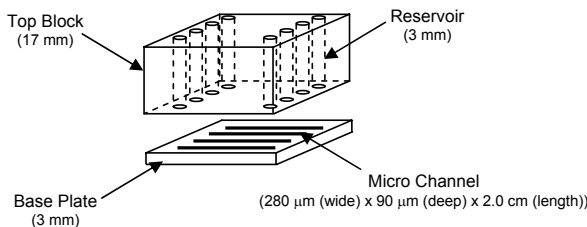


Figure 2. Schematic illustrating the EOF-based micro reactor used for the parallel synthesis of tetrahydropyranyl ethers.

2. Experimental

As Figure 2 illustrates, the fabrication of multiple micro channels, within a single base plate, enables reaction throughput to be increased four-fold, whilst retaining the reaction characteristics developed in single channel reactors. To construct the packed-beds, micro porous silica frits were placed at one end of the micro channels, once cured, silica-supported sulfonic acid (200-400 mesh size, 2.50 mmol g⁻¹) was dry-packed into the micro channels (Figure 3) (1 mg channel⁻¹) and a second micro porous silica frit used to retain the supported reagent. Prior to performing a reaction, the micro channels were primed with anhydrous MeCN to ensure a complete liquid circuit formed, enabling the mobilisation of reagents and products by EOF.

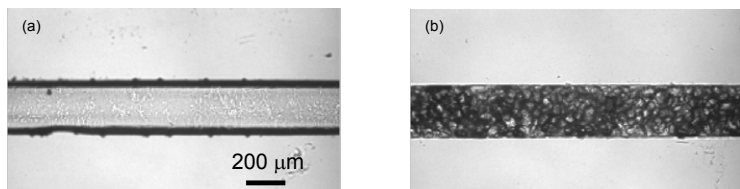


Figure 3. Optical micrograph of an (a) unpacked and (b) packed micro channel.

To synthesise an array of THP ethers, a premixed solution of 3,4-dihydro-2*H*-pyran and alcohol (1.0 M, 1:1) was placed in reservoir A, mobilised through the packed-bed and the reaction products collected in reservoir B in MeCN (40 μ l) (Figure 4). After 10 min, the reaction products were analysed by GC-MS, enabling the % conversion of alcohol to THP ether to be determined. Once optimised, the reactors were operated continuously, for 2.5 hr, in order to synthesise sufficient material for evaluation by NMR spectroscopy. To confirm the catalytic activity was attributed to the solid-supported acid, reactions were repeated using a series of silica gel packed channels, whereby no product formation was observed.

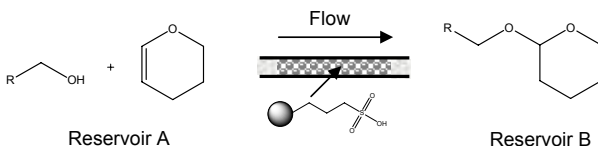


Figure 4. Schematic illustrating the general synthesis of THP ethers in a packed micro channel.

3. Results and Discussion

Using the synthesis of 2-benzyloxy-tetrahydropyran as a model reaction ($R = Ph$), system reproducibility was investigated by analysing the reaction products generated every 10 min, over the course of 2.5 hr. Using this approach, excellent reaction reproducibility was demonstrated ($n = 15$, conversion = 99.997 % and % RSD = 4.6×10^{-3}), confirming device stability and catalytic activity. With this in mind, the generality of the technique was subsequently investigated, as illustrated in Table 1.

Starting Material	Product	Flow Rate ($\mu\text{l min}^{-1}$)	Conversion (%)	Actual Yield (g)	Yield (%)
Benzyl alcohol	2-Benzylxy-tetrahydropyran	1.00	99.9	0.0287	99.9
Butan-1-ol	2-Butoxy-tetrahydropyran	1.50	99.9	N/A	N/A
Hexan-1-ol	2-Hexyloxy-tetrahydropyran	1.50	100.0	0.0418	99.8
Octan-1-ol	2-Octyloxy-tetrahydropyran	1.50	99.9	0.0480	99.7
Decyl alcohol	2-Decyloxy-tetrahydropyran	1.50	99.9	0.0541	99.8
Cyclohexanol	2-Cyclohexyloxy-tetrahydropyran	1.40	99.9	0.0386	99.9

Table 1. Summary of the results obtained for the synthesis of THP ethers in a single micro channel.

Having demonstrated the ability to synthesise an array of THP ethers in excellent yield and purity, the next step was to investigate the scale-out of the technique. Employing all four reaction channels, analogous results were obtained to those illustrated in Table 1; affording a throughput of ca. 50 mg hr^{-1} for 2-benzyloxy-tetrahydropyran.

4. Conclusions

Using the parallel reactor described herein, we are able to scale-out EOF-based reactions through the use of multiple packed channels, resulting in a robust reactor suitable for the continuous flow synthesis of fine chemicals.

5. References

1. C. Wiles, P. Watts and S. J. Haswell, *Tetrahedron*, pp. 8421-8429, 60 (2004).
2. C. Wiles, P. Watts and S. J. Haswell, *Tetrahedron*, pp. 5209-5217, 61 (2005).

Acknowledgements

Full financial support provided by the EPSRC (grant no. GR/S34106/01) is gratefully acknowledged.

ORGANIC SOLVENT MICRODROPLETS IN SURFACE-MODIFIED PDMS MICROCHANNELS

Daniel J. Holt,¹ Richard J. Payne,² Florian Hollfelder,³ Wilhelm T. S. Huck⁴ and Chris Abell.¹

¹University Chemical Laboratory, Lensfield Rd, Cambridge, CB2 1EW, UK.

²The Scripps Research Institute, 10550 N. Torrey Pines Rd, La Jolla, CA 92037, USA.

³Melville Laboratory for Polymer Synthesis, Department of Chemistry, University of Cambridge, Lensfield Rd, Cambridge, CB2 1EW, UK.

⁴Department of Biochemistry, 80 Tennis Court Rd, Old Addenbrookes Site, Cambridge, CB2 1GA, UK.

Abstract

The utility of PDMS microchannels as an environment for producing microdroplets of common organic solvents is presented in this paper. A combination of a fluorous channel coating and a novel, effective surfactant molecule is demonstrated to facilitate droplet formation in organic solvents, opening up possibilities for organic synthesis within this type of microenvironment.

Keywords: microdroplets, organic solvents, synthesis.

1. Introduction

The use of microdroplets within microfluidic devices is proving to be a fruitful approach to microscale chemical and biological reactions and high-throughput screening, especially using droplets as simple microreactors for kinetic studies [1] and simple chemical reactions [2]. Poly(dimethylsiloxane) (PDMS) is the most common material used to create this kind of microdevice, due to the ease of rapid prototyping possible with this substrate [3], but is known to be incompatible with more polar organic solvents [4]. As a result, creation of organic solvent droplets in microfluidic systems has not thus far been approached using PDMS microdevices.

2. Theory

Droplets can be generated at the confluence of two immiscible fluids in a microchannel, due to the shear forces between the two liquid phases. The use of a fluorous continuous phase permits droplets to be made from common organic solvents, where these do not swell PDMS. In order to ensure that the organic phase forms droplets smoothly, the surface tension between the channel walls and the continuous phase must be lower than that between the walls and the droplet phase. This can be achieved by coating the PDMS with a perfluorinated silane, which will react readily with the PDMS surface to create a highly fluorophilic layer on the channel wall. If an organic solvent is compatible with PDMS but does not form droplets an efficient surfactant can be added to the continuous phase to reduce the surface tension and promote droplet formation.

3. Experimental

Microdevices were created in PDMS using standard photolithography techniques. The channel geometry used in these experiments was a cruciform flow-focusing device with dimensions of 50 μm x 25 μm (W x H). Microchannels were coated with perfluoroctyltrichlorosilane by flowing the neat liquid through the channel for 15 minutes and flushing with air. The continuous phase comprised Fluorinert FC-77 with surfactants as detailed in Table 1. Solvents were examined for droplet formation within the device at a variety of flow regimes, and their dominant behaviors characterized.

4. Results and Discussion

The results of this preliminary study are outlined in Table 1. A representative sample of eleven common organic solvents were tested using this device design. A number of these did not produce droplets under any flow regime tested, and swelling of PDMS was seen for more polar solvents. A second class of solvents displayed droplet-forming properties which were dependant on the flow rate, and could be hampered by swelling of the PDMS. This

typically caused smaller droplets to be formed, rather than channel-width plugs. A third class of solvents, dipolar aprotics, were the most versatile and reliable at forming droplets. Within this class, acetonitrile was pre-eminent, producing droplets at a wide variety of relative and total flow rates (Fig. 1).

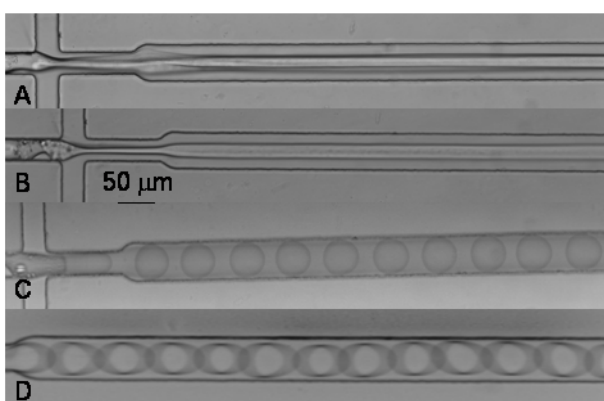


Figure 1. Behaviour of organic solvents in microchannels. Ethanol (A) and methanol (B) both coflow; DMF (C) and acetonitrile (D) both form droplets.

With the addition of a novel perfluoropolyalkyl-polyoxyethylene surfactant molecule X to the continuous phase, methanol droplet formation could be induced within microchannels (Fig. 2). Acetonitrile also formed more stable droplets using this surfactant. We rationalise this as the effect of a more efficient surfactant molecule lowering the surface tension between the two immiscible phases, and so increasing the capillary number, Ca . Studies on a number of other promising surfactant-like molecules are ongoing.

Table 1. Summary of the behaviour of a sample of organic solvents when introduced into a flow-focusing junction. Key: A = 30 % perfluoroctanol in FC-77; B = 10 % perfluoroctanol in FC-77; C = 5% trifluorotoluene in FC-77 (all w/w); D = 1 mM surfactant X in FC-77.

Solvent	Surfactant	PDMS Swelling	Dominant behaviour
Et ₂ O	A	Yes	Coflow
EtOAc	A, B, C	Little	Coflow
MeOH	A, D	None	Coflow (A) / Droplets (D)
EtOH	A	None	Coflow
THF	B, C	Yes	Droplets
Toluene	A, C	Yes	Droplets
CHCl ₃	A	Yes	Coflow / droplets
Hexane	A, C	Yes	Small droplets
DMSO	A, B	None	Jetting / droplets
DMF	B	None	Droplets
MeCN	B, D	None	Droplets

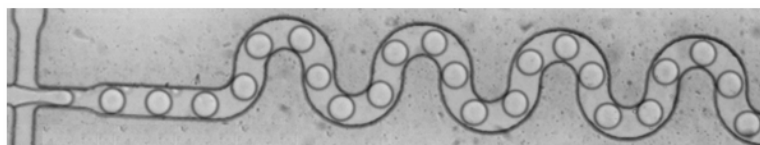


Figure 2. Droplets of methanol being formed at a flow-focusing junction in fluoruous oil with 1 mM fluorinated surfactant molecule X.

5. Conclusions

We have demonstrated the use of microfluidic devices for creating droplets of common organic solvents. This is achieved via a combination of a fluorophilic channel coating and an efficient surfactant to lower surface tension between the two phases and so promote droplet formation. The behaviour of these droplets does not differ in any significant respect from that of water droplets, and work is underway to use these solvent droplets as microreactors for organic synthesis.

Acknowledgements

The authors thank Christ's College, Cambridge and the RCUK for funding.

References

- [1] H. Song, R. F. Ismagilov, *J. Am. Chem. Soc.*, 2003, **125**, 14613.
- [2] J. Gerdts, D. E. Sharoyan, R. F. Ismagilov, *J. Am. Chem. Soc.*, 2004, **126**, 6327.
- [3] J. C. McDonald, D. C. Duffy *et. al.*, *Electrophoresis*, 2000, **21**, 27.
- [4] J. Ng Lee, C. Park, G. M. Whitesides, *Anal. Chem.*, 2003, **75**, 6544.

SCREENING MULTI-PHASE ENZYMATIC REACTIONS IN A MICROREACTOR SETUP

Kaspar Koch¹, Pieter J. Nieuwland¹, Hans E. Schoemaker²,

Marcel G. Wubbolts², Floris P.J.T. Rutjes¹ and Jan C.M. van Hest¹

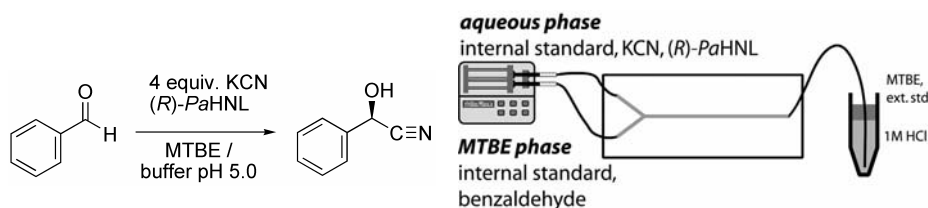
¹ Institute for Molecules and Materials, Radboud University Nijmegen
Toernooiveld 1, 6525 ED Nijmegen, The Netherlands

² DSM Research, PO BOX 18, 6160 MD Geleen, The Netherlands
Contact E-MAIL: k.koch@science.ru.nl

keywords: biocatalysis, synthesis, reaction optimization, multi-phase

1. Introduction

Hydroxynitrile lyases (HNLs) catalyze the reversible addition of hydrogen cyanide to prochiral aldehydes, resulting in optically pure cyanohydrins (Scheme 1). Traditionally, synthesis of enantiopure cyanohydrins catalysed by HNL was performed in aqueous media (single phase system)[1]. However, in several cases less satisfactory results were obtained with respect to enantiopurity and conversion. A significant advancement to overcome this problem was developed by Griengl *et al.*[2]. They showed that by employing a vigorously stirred biphasic system, chiral cyanohydrins could be prepared in excellent enantiomeric purity and high yields. We previously reported that we successfully carried out the synthesis of different cyanohydrins, using a crude lysate, in a microreactor setup without any clogging occurring[3]. In order to find the best conditions to synthesize cyanohydrins, different parameters have to be screened preferably in an automated fashion. This report describes the possibility to screen different parameters to find the optimal reaction conditions with our microreactor system.



Scheme 1. General scheme for the synthesis of cyanohydrins.

Figure 1. Schematic representation of the synthesis in the microreactor setup.

2. Experimental

Calibration

Three different solutions were made in order to calibrate the microreactor setup and to screen the different reaction parameters. Solution A (organic phase): containing 0.23 M benzaldehyde, 0.18 M anisole (internal standard) in MTBE. Solution B (aqueous phase): containing 0.92 M KCN, 10% (v/v) (*R*)-*PaHNL* crude lysate, 10 mg/mL *para*-nitrophenol (internal standard), 0.4 M citric acid buffer pH 5. Solution C (quench phase): 1 μ L/mL *meta*-bromoxylene (external standard) in MTBE. Over hundred quench vials were prepared containing 100 μ L 1 M HCl and 200 μ L solution C. Subsequently, five different amounts (10, 20, 30, 40 and 50 μ L) of solution A and B were added to five quench vials. These were analysed by chiral HPLC (Shimadzu VP equipped with a Chiralpak AD-H column) in order to construct the calibration curves.

Microreactor procedure

High pressure syringes (Harvard Apparatus) were charged with both solutions (A and B) and mounted on the syringe pumps and connected to the microchip via capillaries (microchannel dimensions: width 150 μ m, depth 30 μ m, total length 98 cm; HF etched; fabricated by Micronit Microfluidics BV). Total reaction volume, consisting of the microchannels and the outlet capillary, was 9 μ L. To initiate the reactions, the flow rate was set to the desired flow speed (i.e. 1 μ L/min for both pumps) and stabilised for 20 minutes. After this stabilisation period, the end of the outlet capillary of the microchip was placed into a microvessel (quench vessel) for 10 minutes (collection time). The collection of the samples was done automatically using a sampling robot (Gilson, ASPEC XL). 1 μ L of the MTBE quench phase was injected and analysed by chiral HPLC to determine the actual flow rates, conversion and enantioselectivity.

Lab-scale procedure

Solution A and solution B (total volume for ratio A:B 1:1 2 mL) were added to a reaction tube and stirred vigorously. Aliquots (100 μ L) were taken and directly quenched in the quench vials as described earlier at several time intervals.

3. Results and discussion

Before actually screening the selected enzymatic transformation, first the microreactor setup had to be validated for a multiphase system. We therefore examined if the “set flow” on the syringe pump corresponded to “actual flow” by using internal and external standards in the two syringes and quench vials. This is of utmost importance because the flow rate determines the actual residence time. We found that the most reliable results were obtained when syringes especially designed for high pressure applications were used. In all screening experiments the internal and external standards were added to calculate the actual residence time. After validation of the reliability of the microreactor setup an extensive screening experiment was performed. An aqueous flow containing enzyme ((*R*)-*PaHNL*) and KCN was mixed in the microreactor with an organic MTBE phase containing benzaldehyde (Fig. 1). In the synthesis of the corresponding cyanohydrin the residence time and the ratio of water/organic phase were

varied. All experiments (>100) were automatically handled, i.e. reaction mixtures collected by an autosampler, and analysed by chiral HPLC. This screening could be easily carried out within one day using only 250 μL of enzyme solution (crude lysate). If this screening was performed at lab-scale, at least 5 mL of lysate should be needed. The results from these experiments are depicted in Fig. 2a. It can be concluded that upon increasing the ratio water/organic phase, the conversion is rapidly increased, due to more enzyme and KCN. This effect is less significant compared to the parameter residence time. The enantiomeric excess in all experiments was $>99\%$. The experiments were also carried out at lab-scale (Fig. 2b). There is no significant difference in conversion between both methods, which implies that a vigorous stirred reactor is comparable with a microchannel in which the two phases are pumped through.

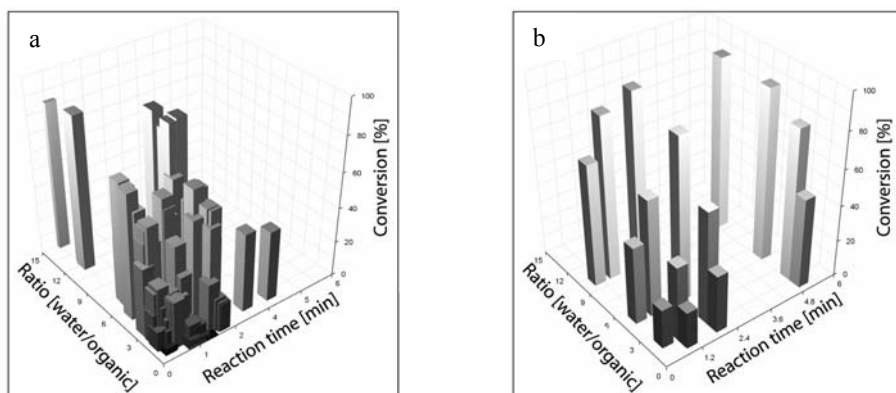


Figure 2. 3D-graph of the two screened parameters vs. conversion. a) microreactor b) lab-scale.

4. Conclusion

A method has been developed to determine the actual residence time, while conducting reactions in microreactors, by using internal and external standards. This is of utmost importance because of the significant error between the “set-flow” on the syringe pump and the “actual flow”. Furthermore, we have successfully developed a method and microreactor setup to screen an enzymatic reaction in a two phase system in an automatic fashion. There is no significant difference between the microscale setup, which means that we can screen reactions at microscale to find the best reaction conditions and use these conditions to synthesize the product at large scale.

References

- [1] K. Drauz and H. Waldmann (Eds.), Enzyme catalysis in organic synthesis : a comprehensive handbook, Wiley-VCH: Weinheim, Chapter 14.7, 974 (2002).
- [2] Griengl H. *et al*, Tetrahedron, 54, 14477-14486 (1998)
- [3] K. Koch, F.P.J.T. Rutjes, J.C.M. van Hest *et al*, MicroTAS '05, 924-925 (2005)

IONIC LIQUIDS IN A MICROREACTOR: PALLADIUM CATALYSIS

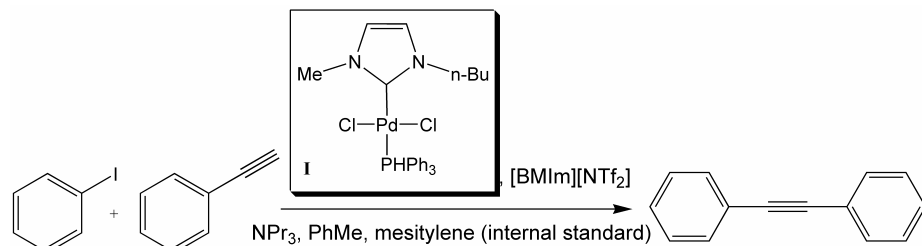
Pieter J. Nieuwland, Kaspar Koch, Jan C.M. van Hest and
Floris P.J.T. Rutjes

Institute for Molecules and Materials, Radboud University Nijmegen
Toernooiveld 1, 6525 ED Nijmegen, The Netherlands
Contact E-MAIL: p.nieuwland@science.ru.nl

keywords: reaction optimization, catalysis, ionic liquids, multi-phase

1. Introduction

Optimization of industrially relevant palladium catalyzed transformations remains a challenge, since for different substrates varying conditions are required. One of the benefits of single channel microreactors is the ability to rapidly screen reaction conditions with very small amounts of reagent and catalyst.



Scheme 1. The Sonogashira coupling of iodobenzene and phenylacetylene with a palladium catalyst in an RTIL

Two palladium catalyzed reactions have already been carried out in a microreactor by Ryu *et al.* [1][2]: a Heck coupling and a Sonogashira coupling. Normally these catalysts form solid/liquid heterogeneous systems, and are thus difficult to use in microchannels. However, when room temperature ionic liquids (RTILs) are used to dissolve the catalyst, a liquid/liquid two phase system can be applied. In this paper we present a systematic study of a Sonogashira reaction with Palladium catalyst I (Scheme 1) in the RTIL 1-butyl-3-methylimidazolium bistriflyl amide ([BMIm][NTf₂]), which was chosen for its relatively low viscosity.

2. Experimental

The Sonogashira coupling was performed in a microreactor and on lab-scale in a liquid/liquid two-phase system. The organic phase contained phenylacetylene (1 equiv, 0.42 M), iodobenzene (1.05 or 2 equiv), tripropylamine (1.66 equiv), toluene and mesitylene as an internal standard, while the ionic liquid phase contained catalyst I. GC-MS was used to determine the conversion. The effective catalyst concentration was 5 mol % in most series and 10 or 20 mol % in two different series.

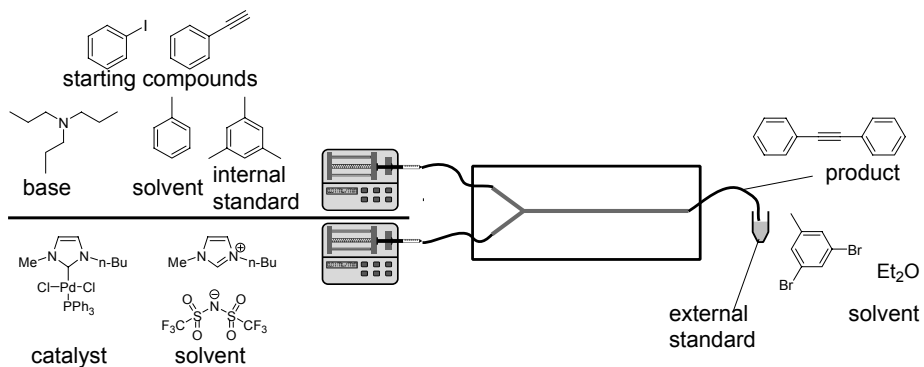


Figure 1. Microreactor setup

Microreactor (Fig. 1): High pressure syringes (Harvard Apparatus) were charged with both solutions and placed in syringe pumps. The syringes were connected to a pyrex microreactor (dimensions: width 150 μm , depth 30 μm , total length 98 cm; HF etched; fabricated by Micronit Microfluidics BV) via capillaries. The microreactor was suspended in a heated oil bath. The reaction time was varied by changing the pump rate. Aliquots were taken by collecting the outflow for 1 – 10 minutes.

Lab-scale: The organic phase (250 μL) and the RTIL phase (50 μL) were added together in a 2 mL vial, heated in an oil bath and stirred with a small stirring bar. Aliquots of 2 μL were taken at several time intervals.

3. Results and discussion

Fig. 2 compares the conversion as a function of time at 90 °C between microreactor and lab-scale, showing no significant difference in reaction rate. Furthermore, the reproducibility of the three micro-scale series is high.

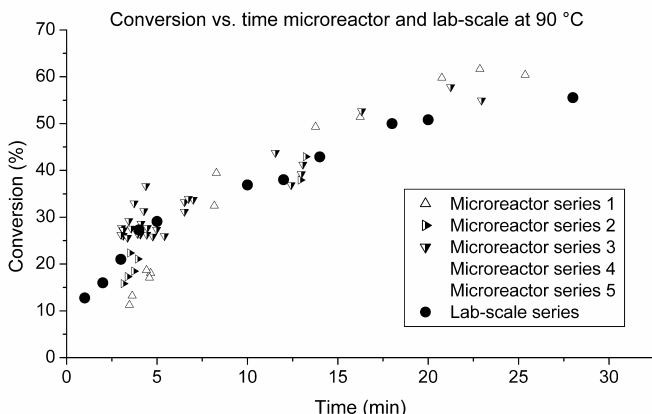


Figure 2. Reaction rate comparison micro-scale / lab-scale

Fig. 3 shows the conversion in microreactor experiments at 90 °C and higher temperatures. Series with elevated iodobenzene and catalyst concentrations are also shown. At 100 and 110 °C the conversion increases rapidly in the first minutes, but at longer reaction times the conversion is slightly lower than at 90 °C. This indicates a decreased activity of the catalyst, possibly due to decomposition.

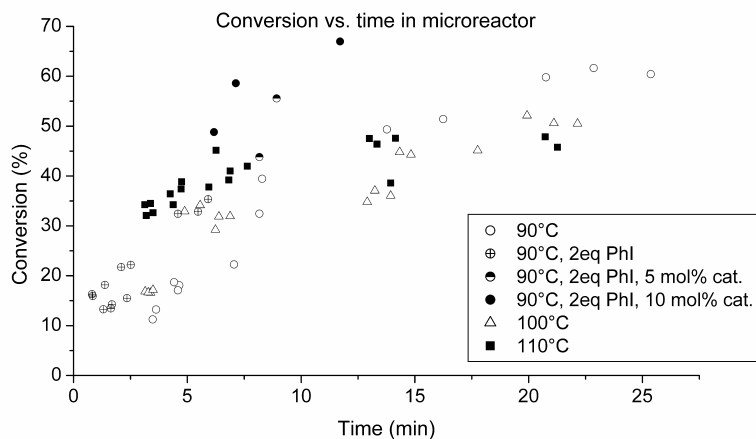


Figure 3. Reaction rate comparison microreactor at elevated temperatures

The concentration of iodobenzene has no influence on the reaction rate, but the conversion could be elevated by increasing the catalyst load. It is noteworthy to mention that the volume of catalyst / RTIL mixture required to measure a series of reactions at one temperature in triplo is approximately 15 μ L, for a single series of lab-scale experiments 50 μ L.

4. Conclusion

A Sonogashira coupling using RTILs was successfully performed in a microreactor. It was shown that reaction behavior in a microreactor is similar to lab-scale conditions, enabling fast catalyst screening. Furthermore it can be concluded that only a very small amount of catalyst and starting material is required to perform optimization yielding a large number of data points.

References

- [1] T. Fukuyama, M. Shinmen, S. Nishitani, M. Sato, I. Ryu, Org. Lett. 4, 1691 (2002)
- [2] S. F. Liu, T. Fukuyama, M. Sato, I. Ryu, Org. Proc. Res. Dev. 8, 477 (2004)

HIGH SURFACE AREA ANATASE MICROREACTORS FOR PHOTOCATALYSIS AND CHEMICAL SYNTHESIS

Alexander Iles*^{1,2}, Henrik Lindstrom² and Robert Wootton³

¹ Department of Chemistry, University of Hull, Hull, HU6 7RX, UK.

² National Institute for Materials Science (ICYS), Tsukuba, Japan.

³ Department of Chemistry, John Moores University, Liverpool, UK.

Email: a.iles@hull.ac.uk

Abstract

In this work we introduce a simple technique we have developed for depositing a robust, yet highly porous and active film of anatase titania onto the inside walls of a microreactor.

Keywords: Titanium Dioxide, Anatase, Photocatalysis, Microreactor.

1. Introduction

Photocatalytic microreactors containing immobilised titanium dioxide are of great interest to chemists and biochemists since they offer significant advantages over bulk scale systems and they can be used in a wide range of applications.^[1] However, a practical microfluidic photo-catalytic reactor must have a very large active surface area, be simple and cheap to produce, yet be robust enough to be used for long periods without maintenance. Previously reported systems have not met all of these rigorous requirements.^[2-5]

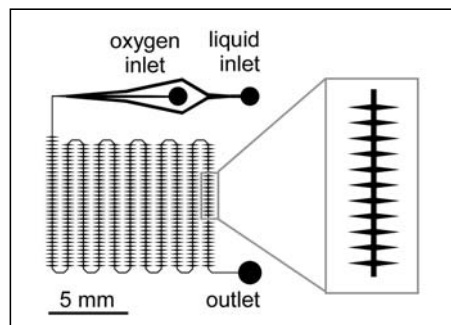


Figure 1: Schematic of the chip layout featuring a liquid inlet, a gas inlet for oxygen (if required), and a meandering channel with side lobes for increased surface area.

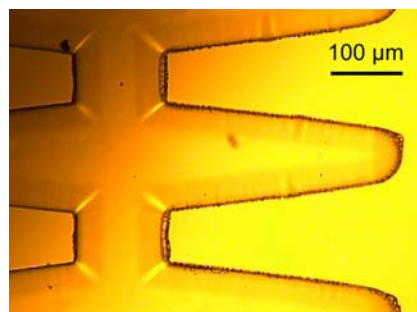


Figure 2: Photograph of a section of the microchannel after titanium dioxide deposition. The TiO₂ film appears uniform and without visible cracks.

2. Experimental

For this work, microfluidic reactor devices were fabricated from soda lime glass using laser lithography, wet-etching and conventional thermal bonding (fig. 1). A titania film coating was then deposited onto the internal walls of these devices by slip casting (fig 2). Cross sectional SEM measurements were made on a sectioned device (fig. 3), which revealed that the film was approximately one micrometer thick. The porosity of the film was found to be 67 % and BET measurements gave a surface area of more than $260 \text{ m}^2 \text{ g}^{-1}$, which is considerably higher than previously reported values for immobilised titania films within microreactors.^[4] XRD measurements showed that the film was 100 % anatase titania.

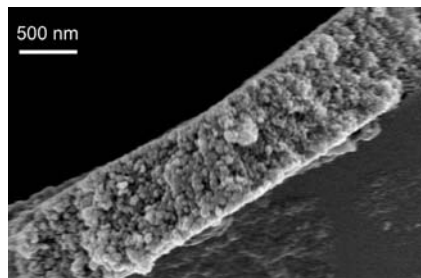


Figure 3: SEM picture of the cross-section of the deposited titanium dioxide showing the highly porous film composition and a film thickness of about 1 micrometer.

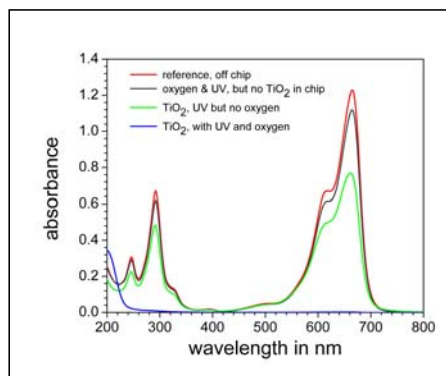


Figure 4: Absorbance spectra of three chip effluents and one reference solution: the methylene blue absorption peaks decreased according to the extent of degradation.

3. Results and discussion

To test their photocatalytic activity, a solution of 32 mg L^{-1} methylene blue was pumped through these devices at $2.5 \mu\text{L min}^{-1}$ while they were exposed to UV light. Experiments were performed with and without adding additional oxygen. UV-VIS absorption spectra of the effluent solutions were recorded. Typical spectra are shown in fig. 4. These results show the effectiveness of these titania coated microreactors in breaking down methylene blue, especially when oxygen was added. The methylene blue concentration was reduced by 98.5 % with a residence of only 15 s (table 1).

Table 1: Comparison of the methylene blue degradation for different experimental conditions: Using a titanium dioxide coated microchannel with oxygen plug flow and UV light, methylene blue was almost completely degraded within a few seconds.

Reaction Conditions	Residence time in s	Degradation of Methylene Blue in %	Degradation rate in % per s
Chip without TiO ₂ with UV and O ₂	15	8.9	0.59
Chip with TiO ₂ with UV	40	37.8	0.95
Chip with TiO ₂ with UV and O ₂	15	98.5	6.6

4. Conclusions

We have shown that it is possible to deposit a highly porous anatase film with a very high surface area onto the inside walls of microreactor devices and have demonstrated that they can be used for photocatalysis. These microreactors were found to be very robust and could operate for long periods of time without degradation. We have also shown how the addition of gaseous oxygen can be used to drastically improve the performance of photocatalytic degradation devices. Such devices can be used in an enormous range of different chemical and biochemical systems.

Acknowledgements

This work was supported by the Japanese Ministry for Education, Culture, Sports, Science and Technology (MEXT).

References

- (1) B. Jones, et al., *microTAS Proceed.*, **2005**, K. F. Jensen (edit.), Kluwer Academic Publishers, 286-288.
- (2) X. Li, et al., *Chem. Comm.*, **2003**, 964-965.
- (3) H. Nakamura, et al., *Chem. Eng. Journal*, **2004**, 261-268.
- (4) R. Gorges, et al., *J. Photochem. Photobio. A*, **2004**, *167*, 95-99.
- (5) G. Takei, et al., *Catalysis Comm.*, **2005**, *6*, 357-360.

RAPID GAS-LIQUID PALLADIUM CARBONYLATIVE CROSS-CO尤LING REACTIONS USING A GLASS FABRICATED MICROFLUIDIC CHIP FOR APPLICATIONS IN ^{11}C -RADIOLABELLING

Philip W. Miller,¹ Nicholas J. Long,¹ Andrew J. de Mello,¹ Ramon Vilar,¹ Jan Passchier² and Antony Gee²

¹Department of Chemistry, Imperial College London,

²PET Imaging Division, Translational Medicine and Genetics, GSK, Academic Centre for Clinical Investigation, Addenbrooke's Hospital, Hills Road, Cambridge (email: philip.miller@imperial.ac.uk)

Abstract

A series of gas-liquid palladium catalysed carbonylative cross-coupling reactions, forming secondary amides, were carried out using a glass fabricated microfluidic device. Improved yields from the microreactions were obtained in short reaction times (< 2 min) and were higher in all cases when compared to their corresponding batch reactions. We are currently in the process of applying our reaction set-up to [^{11}C]CO radiolabelling to be used in PET (Positron Emission Tomography) imaging.

Keywords: Carbonylation, cross-coupling, palladium, gas-liquid reaction, medical imaging, Positron Emission Tomography

1. Introduction

PET (Positron Emission Tomography) imaging is a rapidly emerging field in medical imaging. The synthesis of ^{11}C isotopically labelled compounds for use in PET scans is a particularly challenging area of chemistry.¹ These challenges arise from the short half-lives associated with positron emitters (^{11}C $t_{1/2} = 20.4$ min) and from the difficulties of working with radioactive compounds. Carbonylative cross-coupling reactions²⁻⁴ (Fig. 1) are becoming an increasingly important class of reaction in the synthesis of ^{11}C -labelled compounds⁵ owing to their convenient one step transitions to a number of biologically interesting functional groups.

Carbonylation reactions are conventionally carried out at elevated pressures of carbon monoxide in the presence of a palladium-phosphine catalyst and can take

many hours to go to completion. The rates of these reactions are dependent on a number of factors such as the aryl halide species, the nature of the catalyst, the nucleophilic species, the pressure and the temperature of the system. The insertion step of the carbonylative catalytic cycle can be rate limiting owing to the poor transport of carbon monoxide into the solution phase. This step of the catalytic cycle can be enhanced by

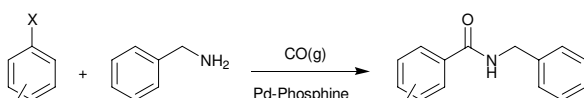


Figure 1. Synthesis of *N*-benzylbenzamides via the palladium catalysed carbonylative cross-coupling reaction.

increasing pressure in the system or by improving contact between gas and liquid phases; microreactor devices provide a potentially very useful way of doing this.^{6,7} Here we report a series of carbonylation reactions using a glass fabricated microfluidic chip with the aim of applying it to [¹¹C]CO radiolabelling reactions.

2. Experimental

The microfluidic device (figure 2a) was constructed from a glass substrate using chemical wet etching techniques. The liquid and gaseous reagents were introduced *via* separate entrance ports and mixed on chip using a mixing-tee configuration. Our reaction set-up (figure 2b) involved injecting a mixture of arylhalide, palladium-phosphine catalyst and benzylamine into the chip and mixing with a constant flow of CO gas heated; the device was heated to 150 °C. Liquid flow rates of 10 µl/min and gas flow rates of 2 sccm were used for these experiments which impose an annular type flow regime on the system generating high gas-liquid interfacial contact areas.

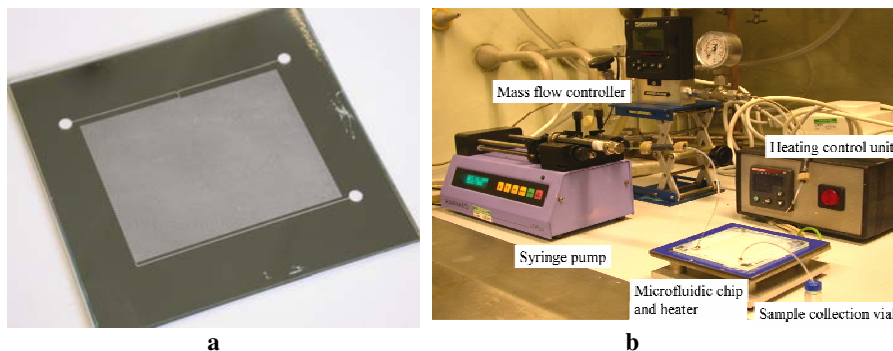


Figure 2. (a) A photograph of the microfluidic chip used in the carbonylation reactions. The channel is 5 metres long, 200 µm wide and 75 µm deep (volume = 75 µl). (b) Reaction set-up for the carbonylative cross coupling reaction using a microfluidic chip.

3. Results and Discussion

A series of different arylhalide substrates (table 1) with varying electronic properties were investigated for the carbonylative cross-coupling reaction with benzylamine and carbon monoxide using Pd(dppp)Cl₂ catalyst. The highest yield was obtained for entry 1 owing to the facile nature of the oxidative addition step of iodoaryl groups to palladium(0). In contrast entry 2, also an iodoaryl, gave lower yields (55%) due to the electron donating *para* methoxyl group slowing down the oxidative addition step. The bromoaryl substrates entries 3-5 gave high yields of amides owing to their electron withdrawing groups enhancing the oxidative addition step.

The insertion of CO into the catalytic cycle forming the acyl palladium(II) complex can be rate limiting owing to the poor transport of carbon monoxide into the solution phase. The increase in yields obtained by the microreactions can be attributed to the enhanced heat transfer and enhanced transport of CO gas into the liquid phase as a direct result of the increased interfacial gas-liquid contact area generated within our microfluidic device.

Table 1

Entry	Substrate	Yield (%) ^{††}
1		87
2		55
3		75
4		83
5		85

4. Conclusions

In conclusion a microstructured device has been used to perform gas-liquid carbonylation reactions to good effect. High yields of amide products were obtained in very short residence times (<2 min) for these conventionally slow reactions. Compared to traditional batch scale reactions, the gains in yields over this time period obtained demonstrate a distinct advantage in using microdevices for these gas-liquid phase reactions. We are currently in the process of adapting our reaction set-up to radiolabelling experiments using ^{11}CO for the synthesis of ^{11}C labelled amide and ester molecules.

Acknowledgements

We would like to express our thanks to GSK for the financial support of this project

References

1. G. Antoni, T. Kihlberg and B. Långström, *Handbook of Radiopharmaceuticals*, Wiley, 2003, Chpt. 5, 140.
2. H. M. Colquhoun, D. J. Thompson and M. V. Twigg, *Carbonylation Direct Synthesis of Carbonyl Compounds*, Plenum Press, New York, 1991, 37.
3. A. Schoenberg, I. Bartoletti and R. F. Heck, *J. Org. Chem.*, 1974, **39**, 3318.
4. A. Schoenberg and R. F. Heck, *J. Org. Chem.*, 1974, **39**, 3327.
5. F. Karimi and B. Långström, *J. Chem. Soc., Perkin Trans. 1.*, 2002, 2111.
6. P. W. Miller, N. J. Long, A. J. de Mello, R. Vilar, A. Gee and J. Passchier, *Chem. Commun.*, 2006, 546.
7. M. T. Rahman, T. Fukuyama, N. Kamata, M. Sato and I. Ryu, *Chemical Commun.*, 2006, 2236.

[†] Average of three runs based on the arylhalide and calculated by GC using diphenyl ether as internal standard.

DEVELOPMENT OF A NMR MEASUREMENT CHIP FOR IN-SITE MONITORING OF CHEMICAL SYNTHESIS

**Yutaka Takahashi¹, Ryo Sakai², Masamichi Nakakoshi³, Satoshi Sakurai¹,
Ryoji Tanaka¹, Hiroto Suematsu¹, Hiroaki Utsumi¹ and Takehiko Kitamori⁴**

1 Analytical Instrument Division, JEOL Ltd, JAPAN

2 Functional Chemicals R&D Laboratories, Nippon Kayaku Co., Ltd., JAPAN

3 Instrumental Analysis Center, Yokohama National University, JAPAN

4 Department of Applied Chemistry, The University of Tokyo, JAPAN

Abstract

Development of a micro device for NMR and its application for in-site monitoring of chemical synthesis were described. Since this device can be inserted into a 5 mm ϕ NMR sample tube, it is possible to carry out an in-site monitoring of chemical synthesis using a microchip combined with a standard NMR instrument. The performance was demonstrated the direct detection of the intermediates of Grignard reaction.

Key words: **NMR, Micro device, Interface, Intermediates, Chemical synthesis**

1. Introduction

Nuclear magnetic resonance (NMR) spectroscopy is expected as a powerful qualitative analytical detection method in microchip technologies. Several researchers have reported the developments of chip-based NMR probes [1]. These are not economic and not easy to use because a special NMR probe is necessary to carry out the microchip-NMR.

From such viewpoint, we developed a micro device to be used for a standard NMR probes and reported on it in previous meeting [2]. Since the micro device had a problem for tubing connections, we developed a newly designed micro device, which was named “MICCS” (Micro Channeled Cell for Synthesis monitoring), and it’s methodology with a NMR was named “MICCS-NMR”. MICCS-NMR was applied to the real-time monitoring of the intermediate of Grignard reaction.

2. Experimental

Fabrication: The photograph of newly designed the NMR micro device “MICCS” was shown in Fig.1. MICCS is composed of the plastic part for tubing connection and the glass part for reaction and detection. The glass part, fabricated on a Pyrex glass plate, was purchased from Institute of Microchemical

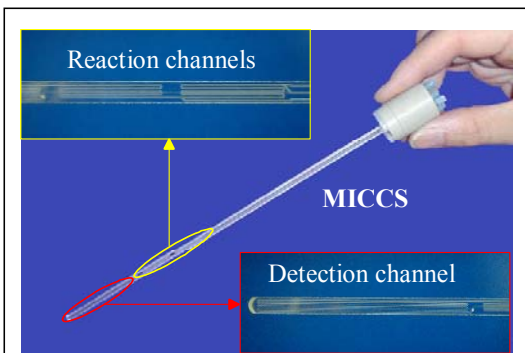
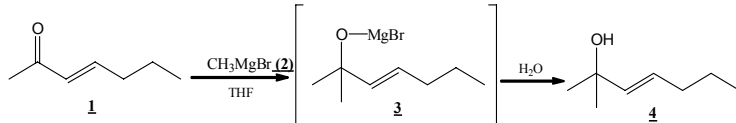


Figure 1. Photo of NMR micro device “MICCS”.

Technology, Co Ltd (Kawasaki, Japan). This part consists of reaction and detection channels; width was 300 μm and depth was 100 μm . The volume of the detection channel was ca. 8 μL . The plastic part, which was made from PEEK, was purchased from Takasago Electronic Co. Ltd (Nagoya, Japan). MICCS can be used with a standard 5 mm ϕ NMR probe because the glass part can be inserted into a 5 mm ϕ NMR sample tube

Instrumentation: NMR spectra were obtained on a JEOL JNM-ECA 600 (Akishima, Japan) with a standard 5 mm ϕ probe. Chemical solutions were delivered into channels using syringe pumps (MD1001 with BS-MD1200, Bioanalytical Systems Inc., West Lafayette, IN). Syringes and MICCS were coupled with fused-silica capillary tubing (150 μm ID x 375 μm OD). The tubing was directly connected into connection ports of MICCS using finger tight fittings. The glass part of MICCS was inserted into a sample tube and was mounted into a probe together with a sample tube holder and a rotor set.

Chemicals and synthesis: 3-hexene-2-one (**1**) was purchased from Tokyo Chemical Industry Co. Ltd. (Tokyo, Japan). Tetrahydrofuran (THF, dehydrated grade) and 1 M-MeMgBr (**2**, in THF) were purchased from Wako Pure Chemical Industries Ltd.



Scheme 1. Grignard reaction.

(Osaka, Japan). Dimethylsulfoxide-d₆ (DMSO-d₆) and acetone-d₆ were purchased from Sigma-Aldrich Inc. (St. Louis, MO) to use as a NMR lock. THF solutions of **1** (0.5 M) and **2** (0.5 M) were introduced into the channels of MICCS. Both solutions were mixed at Y-shaped channel and Grignard reaction was occurred as shown in Scheme 1. The reaction temperature was not controlled (room temperature). The total flow rate of two solutions was 4.0 μ L/min. The flow rate ratio of two solutions was changed while measurement (**2** / **1**; 4 / 0, 3 / 1, 2.5 / 1.5 and 1 / 3).

3. Results and discussion

The 2-D display of ¹H-NMR spectra obtained from the experiment of Grignard reaction was shown in Fig. 2. First, 4 μ L/min flow rate of the solution of **2** was introduced into MICCS, and then the solution of **1** was added. The flow rate ratio was consecutively

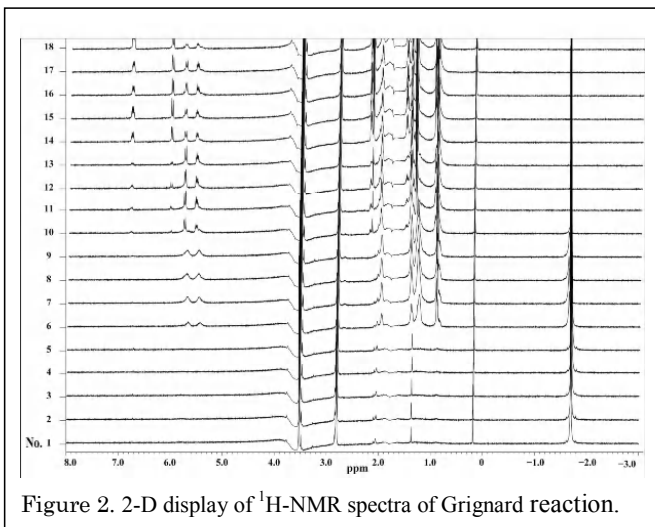


Figure 2. 2-D display of ¹H-NMR spectra of Grignard reaction.

changed as described above. These results indicate the expected intermediate (**3**) was probably observed at the spectra number 6 to 13, because these spectra were quite different from those of **1** and **4**. The details of this result will be discussed.

Acknowledgements

This work was supported by “Project of Micro-Chemical Technology for Production, Analysis and Measurement Systems” of New Energy and Industrial Technology Development Organization (NEDO), Japan.

References

- [1] C. Massin et al., J. Magn. Reson., Vol.164, pp. 242-255, (2003).
- [2] Y. Takahashi et al., MicroTAS04, Vol. 2, pp. 464-466, (2004).

EXPERIENCES WITH MESO- AND MICROFLUIDIC-BASED FLOW REACTORS FILLED WITH HETEROGENOUS CATALYSTS, USING HIGH TEMPERATURE AND HIGH PRESSURE

Ferenc Darvas, Csaba Csajagi, Zoltan Bajor and Richard Jones

Thales Nanotechnology Inc., Zahony utca 7, H-1031 Budapest, Hungary

Keywords: Thales Cube reactorsTM, CatCartTM, hydrogenation, organic iodide compound formation

1. Introduction

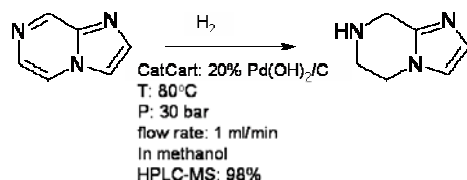
Exploring the high pressure, high temperature space segment of organic reactions by using efficient catalysts is a challenging opportunity offering radical shortening of reaction time combined with high yield and high purity of the product. Meso- and microfluidic-based flow reactors filled with heterogeneous- or immobilized homogeneous catalysts are suitable for this purpose, as the experience with Thales Cube ReactorsTM filled mostly with nanostructured catalysts demonstrates [1-6]. Cube ReactorsTM are belonging to the family of „mesofluidic” reactors, i.e. reactors which operating with somewhat thicker tubes (100 to 300 micron) than usual microfluidic reactors. Here we demonstrate the use of Cube ReactorsTM first of all for „unpleasant” reactions, like hydrogenation, and others, e.g. organic iodide compound formation.

2. Experimental

- The H-CubeTM reactor (Fig. 1/A) serves for hydrogenation. The hydrogen required is generated in-situ electrolytically by the device and combined with the substrate through a mixer. The hydrogen/substrate mixture can be heated and pressurized up to 100°C and 100 bar respectively. The mixture is then passed through the packed catalyst cartridge (belonging to the CatCartTM catalyst family shown in Fig. 1/C), where the actual reactions take place, and the products emerge into the collection vial within a short period of time (1-3 Minutes). The experience generated with the more than 100 H-Cube reactors worldwide shows that H-Cube is capable of hydrogenating a wide range of functional groups such as nitro-, alkene-, alkyne-, nitrile-, imine groups as well as performing N-/O-debenzylation, desulfurization and dehalogenation reactions. Here we present the use of the reactor for the selective hydrogenation of imidazo[1,2- α]pyrazine under the emphasized reaction conditions (Scheme 1).

- The other novel reactor, the X-CubeTM (shown in Fig. 1/B), works by flowing a reaction mixture or several separate reactants into the reactor using a dual pump-injector system. After mixing, the substrates enter a heater or cooler CatCartTM column where they can undergo reaction conditions of up to 200°C or down to -20°C respectively. The

reaction mixture may also be pressurized up to 150 bar. X-Cube can be used to perform reactions with without the use of an outside gas source. As a chosen reaction here we report an organic iodide compound formation from 3-chloro-7-nitroindole (Scheme 2). Furthermore, Table 1 summarizes all the reaction types those were performed at Thales or those are in potential interest.



Scheme 1. Selective hydrogenation of imidazo[1,2- α]pyrazine with the H-Cube™

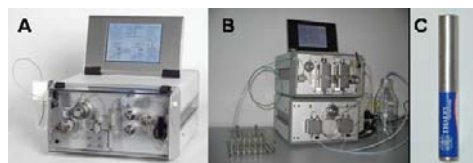
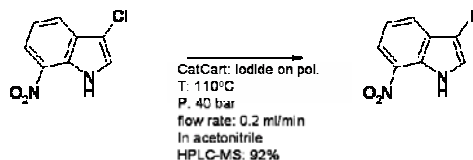


Figure 1. Thales Cube reactors with CatCart™: A: H-Cube™, B: X-Cube™, C: CatCart™



Scheme 2. Organic iodide compound formation with the X-Cube™

3. Results and conclusions

The results from the three chosen reactions mentioned above are summarized as follows: 1) The selective hydrogenation of imidazo[1,2-a]pyrazine in the H-Cube™ reactor resulted in 98% yield towards 5,6,7,8-tetrahydro-imidazo[1,2-a]pyrazine while the same reaction performed in batch mode results in 95% yield according to Pierre-Antoine et al. [7]. 2) The organic iodide compound formation performed in the X-Cube™ system showed 82% yield.

In summary, we have successfully performed high-temperature, high pressure meso and microfluidics-based catalytic flow reactions by using the Thales Cube reactor series which offer radical shortening of reaction time combined with high yield and high purity of the products. Furthermore these reactors can offer the advantages of developing high-throughput and scalable technologies with short optimization time and that of

running reactions in a safer, more controllable mode than normal batch reactors can provide.

Table 1. Summary of the reactions the X-Cube reactor was used for at Thales Nanotechnology. *These reactions are under study at Thales Nanotechnology.

Interesting reactions	Common reactions which are safer to perform with Thales Cube reactors	Industrially important reactions	In-situ reagent formations
C-C coupling:	Alkylation	Direct fluorination*	Synthesis of Grignard reagent
Sonogashira	Esterification	Nitration	Trimethylsilylation*
Negishi	Synthesis of halogenated compounds	Diazo compound formation*	Synthesis of butyl Li*
Stille	Synthesis of nitrile compounds	Hydrogenation	Synthesis of boronic acids*
Heck	Amide formation	Oxydation	Synthesis of Ar-ZnCl*
Suzuki	Hydrolysis	Carbonylation*	Azide formation
C-N coupling:	Epoxy-opening	Hantzsch reaction*	
Buchwald	Chlorination	Michael addition	
Aryl-ether formation:		Wittig synthesis*	
Ullmann		Peptides synthesis*	
		Knoevenagel synthesis*	
		Bromination	
		Friedel-Crafts acylation, alkylation	
		Ether decoupling	

Acknowledgements

Here we would like to Krisztian Niesz for his useful advice and comments.

References

- [1] R. Jones, L. Godorhazy, N. Varga, D. Szalay, L. Urge and F. Darvas, *Continuous-Flow High Pressure Hydrogenation Reactor for Optimization and High-Throughput Synthesis*, J. Combi. Chem., pp. 110-116, 8(1), (2006).
- [2] R. Jones, L. Godorhazy, D. Szalay, L. Urge and F. Darvas, *A novel method for high-throughput reduction of compounds through automated sequential injection into a continuous-flow microfluidic reactor*, QSAR Comb. Sci., pp. 722-727, 24(6), (2005).
- [3] C. Spadoni, R. Jones, L. Urge and Darvas F, *The recent advancements of hydrogenation technology and their implications for drug discovery research*, Chem. Today, pp. 36-39, January/February (2005).
- [5] B. Desai, O. Kappe, *Heterogeneous hydrogenation reactions using a continuous flow high pressure*, J. Combi. Chem., pp. 641-643, 7(5), (2005).
- [6] S. Saaby, K. R. Knudsen, M. Ladlow, S. V. Ley, *The use of a continuous flow-reactor employing a mixed hydrogen-liquid flow stream for the efficient reduction of imines to amines*, Chem. Commun., pp. 2909-11, 23, (2005).
- [7] B. Pierre-Antoine, C. Sablayrolles, J.-P. Chapat, J. Chem. Res., pp. 468-480, 2, (1984)

DNA SEPARATION ON NANOCHANNEL WITH PHOSPHOLIPID POLYMERS

Madoka Takai¹, Kyousuke Shimizu², Yu Nagase² and Kazuhiko Ishihara¹

¹Department of Materials Engineering, Center for NanoBio Integration, The University of Tokyo, 7-3-1 Hongo, Bunkyo-ku, Tokyo 113-8656, Japan

²Graduate School of Engineering, Tokai University, Japan
takai@mpc.t.u-tokyo.ac.jp

Abstract

DNA separation was carried out by use of microcapillary chip with nanochannel with different ζ -potential. The channel modified with PMSi (poly-[2-methacryloxyethyl phosphorylcholine(MPC)-co-3-methacryloxypropyltriethoxysilane (MPTS)]) showed small ζ -potential of around -10 mV comparing with the channel without modification having ζ -potential of -60 mV. T4 DNA (165.6 kbp), and λ DNA (48.5 kbp) were separated by an electric field and detected by a current change of nanochannel. The electromigration velocity was controlled on a surface ζ -potential, and an applied voltage, respectively. The rapid DNA separation has been achieved by modified PMSi nanochannel. The PMSi modified nanochannel could use several times after simple ultrasonic cleansing due to inhibit DNA adsorption on the surface of channel, which is additional significant function as well as the control of ζ -potential.

Key words: microchip electrophoresis, DNA separation, ζ -potential
2-methacryloxyethylphosphorylcholine (MPC) polymer, electrochemical detection,

1. Introduction

Microchip electrophoresis is one of the useful separation tools for genomics and proteomics. The materials for fabricating the microchip are mainly fused silica due to controllability of channel fabrication and optical transparency for fluorescence detection. The major problem on the material is adsorption of biomolecules such as DNA and proteins onto the surface of the inner capillary wall. When these biomolecules adsorb on the micro-, nano-scale channel, the microchip cannot be used, and it needs hard cleaning process for repeatable use, typically by alkali etching. 2-Methacryloxyethylphosphorylcholine (MPC) based polymers are well known as the excellent biocompatible materials, which can successfully suppress the adsorption of biomolecules[1]. In this study, we use the poly[(MPC)-co-3-methacryloxypropyltriethoxysilane (MPTS)](PMSi)[2] as the surface modification material for DNA separation by microchip based capillary zone electrophoresis.

2. EXPERIMENTAL

The microchip is designed for electrochemical detection, which is a good for damage-less detection method because fluoresce-labeled substance is not necessarily. Figure 1 shows the chemical structure of PMSi, and PMSi can react chemically with

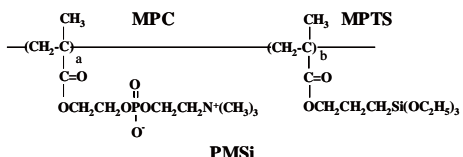


Figure 1. The chemical structure of PMSi.

quartz surface. The coating process is very simple. PMSi of 0.05 wt% ethanol solutions is flowed the channel for 3 min, and the chip is dried for 4 hr at 70 °C after elimination of polymer solution. The ζ -potential of the surface modified with PMSi was almost -10 mV in Tris-borate-EDTA (TBE) buffer. The Figure 2 shows the photograph and the channel design of DNA separation microchip. The channel was fabricated by photolithography and HF based wet etching using Au mask. 0.4 mg/mL of T4 DNA(165.6 kbp) and λ DNA(48.5 kbp) for each in TBE were prepared as stock solutions. The DNA separation solution is 0.5xTBE, catalase, glucose oxidase, glucose and DNA. Voltage is applied between the electrode 1 and 4, and the current on anode is measured by the potentiostatically.

3. Results and discussion

T4 DNA and λ DNA were separated obviously by used of nanochannel with and without PMSi modification. The data is shown in Figures 3(a), and (b), respectively. T4 DNA and λ DNA were detected by the increase of current at nanochannel. The considerable detection mechanism on the microchip is summarized in the Figure 4. After separation, DNA entered in the nanochannel with a change in configuration, the detection current, which is limited by the nanochannel, was increased by a passage of DNA through the nanochannel. The electromigration velocity was depended on the surface ζ -potential, and applied voltage, respectively. Therefore, it is thought that the detection time can be controlled by these parameters. Actually, the detection time of T4 DNA at 3 V of applied voltage became fast drastically at

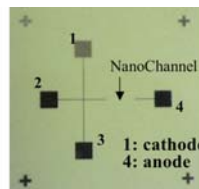


Figure 2. Photograph of DNA separation chip and the schematic illustration of nanochannel design.

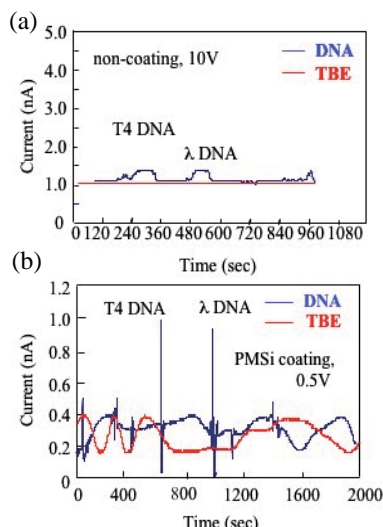


Figure 3. DNA separation of microchip electrophoresis by non-coated nanochannel at 10 V(a), PMSi modified nanochannel at 0.5 V(b)

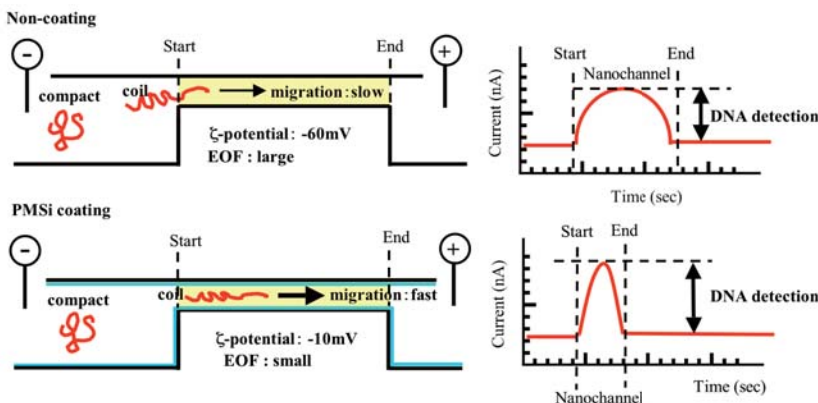


Figure 4. Considerable explanation of DNA separation by nanochannel elecrophoresis with current detection.

30.5 sec as seen in Figures 5. The difference of ζ -potential was observed as the current profile change and detection time. When the electroosmosis flow rate became large, the electromigration velocity of DNA decreased and it led to take a long detection time. Finally we checked repeatability of the non-coated, and PMSi modified microchips, respectively. The PMSi modified chip could use several times after simple ultrasonic cleansing due to no DNA adhesion on the nanochannel.

4. Conclusions

T4 DNA and λ DNA were separated by microcapillary chip with nanochannel showing negative ζ -potential. The detected peak current was indicated by passage of DNA through nanochannel and the detection time could be controlled by the applied voltage and ζ -potential. The PMSi modified surface showed excellent DNA adsorption resistance as well as controlling the ζ -potential.

References

1. K. Ishihara, H. Oshida, Y. Endo, T. Ueda, A. Watanabe, and N. Nakabayashi, *J. Biomed. Mater. Res.* **26**, 1543 (1992).
2. M. Takai, H. Onoda, K. Ishihara, Y. Takamura, and Y. Horike, *Proceedings of μ TAS 2004*, Vol.2, pp.115(2004).

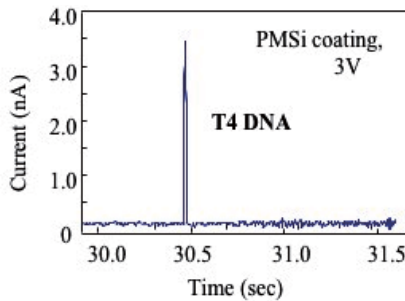


Figure 5. T4 DNA detection of microchip electrophoresis by PMSi modified nanochannel at 3 V.

DESALTING OF UREA FROM SALT-RICH PROTEIN SAMPLE FACILITATED BY COPPER (II) ION IN MICROFLUIDIC DECIVE

Kwang Suk Yang^{1,3}, Yun Suk Huh¹, Yeon Ki Hong², Won Hi Hong¹ and Do Hyun Kim^{1,3}

¹Korea Advanced Institute of Science and Technology, Daejeon 305-701 Korea

² ChungJu National University, Chungbuk 380-702 Korea

³Center for Ultramicrochemical Process Systems, Daejeon 305-701 Korea

Abstract

We present the simple and rapid microfluidic desalting systems, which are 3-phase desalting system using simple diffusion and (3+2)-phase desalting system based on the coupling of simple diffusion and affinity of urea. The facilitative desalting system is particularly useful for removal of urea and analysis of protein by mass spectroscopy because urea is removed by the mass transfer with the difference of concentration, molecular size and the affinity of urea to copper (II) ion resulting the complex. We also evaluated the activity and MALDI-TOF-MS spectrum of red fluorescent protein (RFP) for protein analysis.

Keywords: Protein pretreatment, desalting, micro-dialysis

1. Introduction

Sample preparation method of protein for the rapid analysis is an issue in development of genomics. The produced proteins must be in native and active conformation with removal of salts and by-produced products. But, currently used analytical procedures require extensive expertise, expensive equipments, and time. Conventional methods are inadequate for high throughput experiments and efficient recovery of target protein, and its activity control [1]. To overcome these limitations, we have investigated an effective microfluidic system for desalting and cleanup of sample protein from 8M urea mixture.

For the more effective desalting of urea, our microfluidic system is based on the coupling of simple diffusion and facilitative diffusion using copper (II) ion, which is ready to form $\text{Cu}^{2+}\text{-}(urea)_n$ complex as shown in Figure 1 [2].

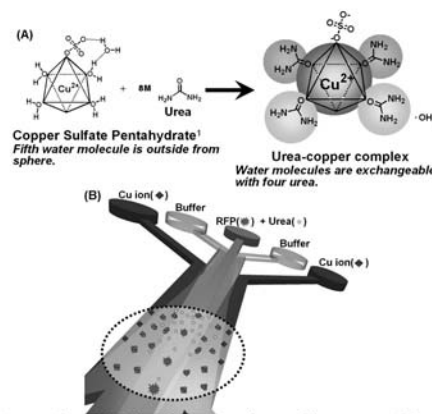


Figure 1. (A) The interaction of copper (II) sulfate pentahydrate with 8M urea; (B) Schematic illustration of Cu-urea reaction in the channel.

2. Design of Devices

Design of 3-phase and (3+2)-phase system for desalting of protein are shown in Figure 2, where the device of (3+2)-phase system is 4-cm-long, 500- μm -wide. For the stable laminar flow, 5 cm-long diffusion channel was formed at the inlet channel. Then, Cu^{2+} phase was added to the (3+2)-junction and was used for ‘active desalting’ process with the formation of Cu^{2+} -urea complex. The active desalting system of (3+2)-phase system is coupled process of diffusion and affinity of capturing of urea by Cu^{2+} .

3-phase system with 300- μm -wide and 4-cm-long channel was formed for the desalting of urea from sample solution using simple diffusion process, which is defined as a ‘passive desalting’.

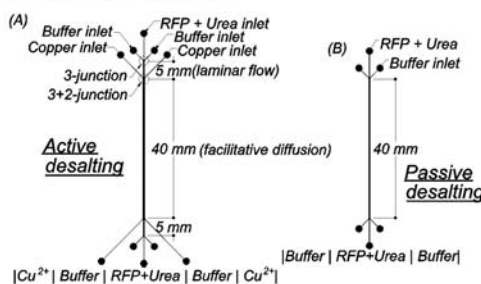


Figure 2. (A) (3+2)-phase system; (B) 3-phase system

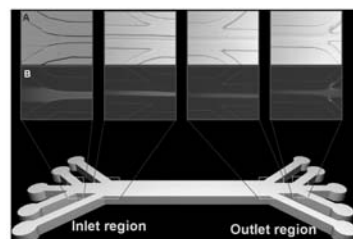


Figure 3. Sectional photographs of (3+2)-phase system. (A) optical microscope image; (B) fluorescence microscope image.

3. Experimental

PDMS molds were fabricated by using photolithography with the use of SU-8 on silicon wafer as a master, and bonded to microscope slides using oxygen plasma surface treatment [3]. The flow rate of center phase (RFP + 8M urea) was kept 0.5 mL/h, and that of both buffer (pH7, 10 mM Tris-HCl) side phases was varied 1.5~5.0 mL/h using syringe pumps. Formation and behavior of the laminar flow were observed with a fluorescence microscope shown in Figure 3.

The protein concentration was analyzed by Lowry method. The concentration of urea was determined by HPLC with a UV detector at 195 nm. The amount of copper (II) ion which crossed over from affinity phase to sample phase through buffer phase was determined by using atomic absorption spectrometry.

4. Results and discussion

Under the optimum flow rate (4 mL/h) of buffer phase, removal efficiency of urea was around 55% in the 3-phase system (Figure 4(A)). In the case of (3+2)-phase system, it gives removal efficiency of urea around 70% which is 15% higher than 3-phase system, where optimum flow rate of buffer phase was 3 mL/h (see Figure 4(B)).

In Figure 4(C), the increase of Cu^{2+} concentration increases removal of urea. But, recovery of RFP decreased sharply from 100 mM of Cu^{2+} . Figure 4(D) shows the effect of Cu^{2+} concentration in the center phase. From Figure 4(C) and 4(D), 50 mM of Cu^{2+} was optimum concentration for desalting in micro-device.

By the removal of urea, protein refolding was expected. So, fluorescence intensity recovery test was performed by using (3+2)-phase system. Fluorescence intensity of RFP was recovered around 17% from 64% of RFP + 8M urea solution as shown in Figure 4(E). Also, ~32% enhancement of signal intensity on MALDI-TOF mass spectra was observed by applying (3+2)-phase system in Figure 4(F).

5. Conclusions

Our investigation shows that the facilitative micro-desalting device was successfully achieved removal of urea for the analysis of proteins. In this study, we demonstrated two types of desalting system which are 3-phase desalting using simple diffusion and (3+2)-phase desalting based on the coupling of simple diffusion with affinity of urea for the effective removal of urea.

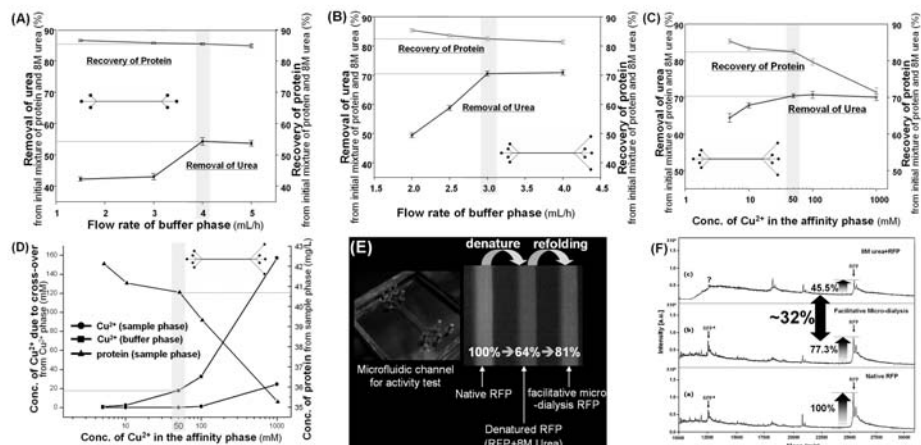


Figure 4. (A) Effect of flow rate of the buffer phase in 3-phase system; (B) Effect of flow rate of the buffer phase in (3+2)-phase system; (C) Effect of concentration of copper ion in (3+2)-phase system; (D) Effect of the copper ion concentration vs. RFP recovery and copper ion cross-over; (E) Activity of RFP from (3+2)-phase system; (F) MALDI-TOF spectra for protein analysis.

Acknowledgements

This work was supported by the Basic Research Program (grant No.R01-2004-000-10681-0) of the KOSEF, the Center for Ultramicrochemical Process Systems sponsored by KOSEF and the BK 21 project sponsored by KRF.

References

- M. T. Taylor, P. Belgrader, R. Joshi, G. A. Kintz, M. A. Northrup, 2001 Proc. μ TAS Kluwer Academic Publishers, Dordrecht, The Netherlands pp. 670-672, (2001).
- J. Liu, X. Chen, Z. Shao, P. J. Zhou, Appl. Polym. Sci. **90**, 1108-1112, (2003).
- Y. Xia, M. Mrksich, E. Kim, G.M. Whitesides, J. Am. Chem. Soc. **117**, 9576-9577 (1995).

MICROCHIP SOLID-PHASE-ENHANCED LIQUID-LIQUID EXTRACTIONS UTILISING HIGHLY SELECTIVE MOLECULARLY IMPRINTED POLYMERS AS CHEMORECOGNITION SOLVENT EXTRACTION AGENTS

Oliver Castell^{*,} Chris Allender^{*} David Barrow^{**}**

^{*} MRRU, Welsh School of Pharmacy, Cardiff University, Cardiff. UK.

^{**} metaFAB, Cardiff School of Engineering, Cardiff University, Cardiff. UK.

Abstract

Molecularly imprinted polymers (MIPs) are a class of artificial receptors that promise an environmentally robust alternative to naturally occurring bio-recognition elements of chemical sensing devices and systems [1]. This work reports for the first time the application of MIPs in microfluidic systems to enhance solvent extraction. This paper describes the use of MIPs as solvent extraction reagents in microfluidic biphasic solvent systems, their successful interface to aqueous sample media and the opportunities for utilisation of this unique system in novel microscale separation procedures. This study demonstrates the development of a novel multiphase flow microfluidic system utilising MIPs in the extracting phase to enhance both efficiency and selectivity of a simple two phase liquid extraction.

Keywords: **microscale, liquid extraction, solid-phase-extraction, solvent extraction, biosensing, molecularly imprinted polymers, multi-phase flow.**

1. Introduction

Liquid – liquid extraction, or solvent extraction, has been used for many years for chemical and biochemical purifications, separations, and enrichments. In conventional use the efficiency and selectivity of the technique is restricted. Following a recent study in which MIPs were used to enhance macro-scale extraction [2], and with the escalating interest in miniaturised, scalable and automated laboratory processes, this work presents the novel concept of highly efficient on-chip micro-extractions utilising MIPs as artificial receptors in multi-phase flow microfluidic systems.

2. Theory

Molecularly Imprinted Polymers (MIPs) offer simple, customisable, rugged and cost effective alternatives to biological recognition systems [1]. The methodology involves the introduction of analyte specific binding sites within rigid, cross-linked, three dimensional polymer matrices [3]. This is achieved

through the formation of pre-polymerisation complexes between the analyte (template) molecule and functionally complementary monomers and their subsequent polymerisation in a porogenic environment in the presence of cross-linking monomer(s). Template removal yields a functionally and spatially ordered imprinted site capable of rebinding the template molecule. Recognition is achieved through a combination of spatial and inter-molecular interactions between analyte and polymer functionality at the binding site.

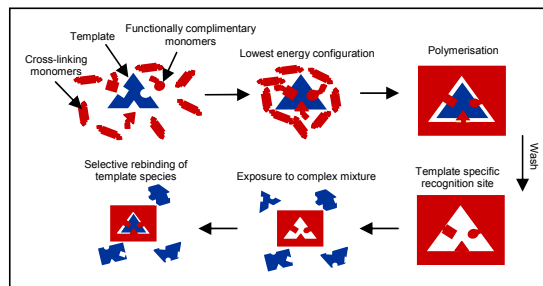


Fig 1. Schematic illustrating molecular imprinting methodology

Segmented flow regimes of alternating immiscible organic and aqueous fluid packets are characterised by each fluid packet having high internal mixing and a continually refreshing fluidic interface between contiguous fluid segments [4] (Fig 2). This unique mixing property is unusual as microfluidic systems overwhelmingly display laminar flow characteristics associated with low Reynolds number channel geometries. This important property allows the rapid attainment of chemical equilibrium between adjacent fluid phases [4].

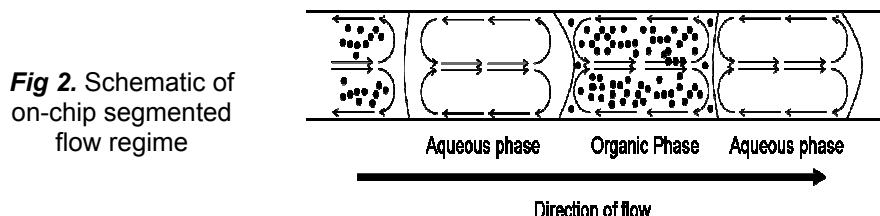


Fig 2. Schematic of on-chip segmented flow regime

The novel presence of solid-phase MIP particles in the organic liquid phase was predicted to enhance the specific transfer of analyte from the aqueous phase to the organic phase by maintaining a significant concentration gradient between the two immiscible fluid phases.

3. Experimental

Monodisperse propranolol imprinted polymer microspheres [p(divinylbenzene-co-methacrylic acid)] were prepared by precipitation polymerisation [2] (Fig 3). The affinity of the polymers for propranolol was

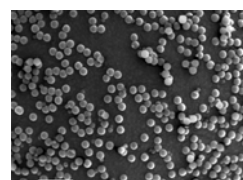


Fig 3. MIP microspheres

assessed by established techniques [2]. Segmented flow regimes were generated in a micromilled PTFE reactor incorporating T-junction geometry and a 35 cm channel length for extraction.

4. Results and Discussion

The MIP particles demonstrated greater affinity for the template species than did the non-imprinted polymer (control) particles (NIP) (Fig 4). On-line flow through UV absorbance spectrophotometry of the microfluidic segmented flow regimes demonstrated a significant increase in removal of propranolol from the aqueous phase in the presence of MIP compared to organic solvent (hexane) alone. UV absorbance data illustrates almost complete removal of propranolol from the aqueous stream. (Fig 6) The key property of this system is that this extraction would be *molecularly selective* [2].

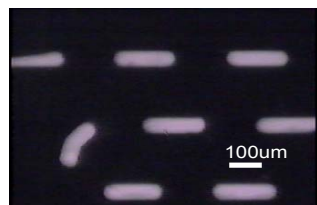


Fig 5. MIP enhanced segmented flow extraction fluorescent image

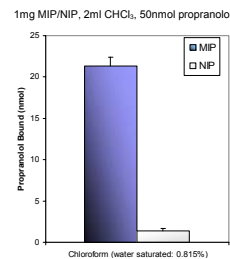


Fig 4. Propranolol bound to MIP and NIP (control)

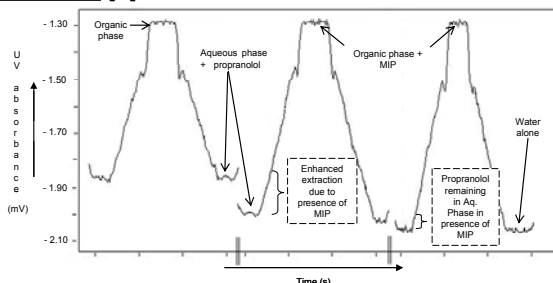


Fig 6. Composite on-line UV absorbance data for propranolol extractions into hexane ±MIP

5. Conclusion

This unique principle generates opportunities for on-chip MIP based extractions and chemical enrichments in industrial applications, offering commercial, ecological and practical advantages to traditional solvent extraction techniques. Ongoing work involves the incorporation of an integrated on-chip capillary force fluid phase separator to allow further analyte manipulations and recovery as well as quantitative analysis of MIP-enhanced extraction efficiencies.

References

- [1] C. Allender, C. Heard and K. Brain, *Molecularly imprinted polymers - Preparation, biomedical applications and technical challenges*. *Progress in Medicinal Chemistry*, 36, pp. 235-291, (1999).
- [2] O. Castell, C. Allender and D. Barrow, *Novel biphasic separations utilising highly selective molecularly imprinted polymers as biorecognition solvent extraction agents*, *Biosensors and Bioelectronics*, in press.
- [3] G. Wulff and A. Biffis, *Molecularly imprinted polymers - Man-made mimics of antibodies and their applications in analytical chemistry*. Elsevier, Oxford. (2001).
- [4] N. Harries, J. Burns, D. Barrow and C. Ramshaw, *A numerical model for segmented flow in a microreactor*, *Journal of Heat and Mass Transfer* 46, pp 3313 – 3322, (2003).

TOWARD DENATURING GRADIENT GEL ELECTROPHORESIS ON A CHIP

Tomoyuki Morita *, Takashi Matsumura *, Akiko Miya * and
Juan G. Santiago**

* Ebara Research Co., Ltd., Japan and

** Department of Mechanical Engineering, Stanford University, USA

Keywords: DGGE, denaturant, DNA separation, electroosmotic flow, electrophoresis

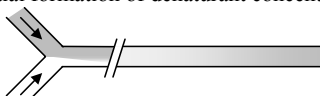
ABSTRACT

We present the concept of on-chip denaturing gradient gel electrophoresis (DGGE) and experimental studies to perform it. Our studies include a sensitive DNA labeling method available under highly denaturing conditions, a method to form a denaturant concentration gradient in a microchannel using electroosmotic flow (EOF), and evaluation of effectiveness of hydroxyethyl cellulose (HEC) as an on-chip DNA separation matrix and its temperature dependency. Our results demonstrated critical initial step toward the first achievement of on-chip DGGE.

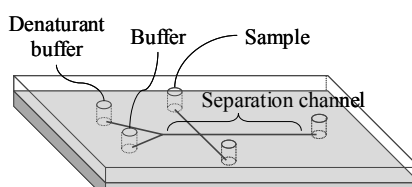
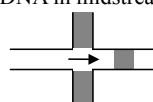
1. INTRODUCTION

DGGE is an electrophoretic method that can separate DNA fragments of equal length but different sequence [1]. DGGE is currently one of the most prevalent techniques in the analysis of microbial communities in environmental samples [2]. However, DGGE is time-consuming and difficult to reproduce across different gels. On-chip DGGE (Figure 1) has the potential to decrease analysis time and achieve good reproducibility. In order to achieve on-chip DGGE, we investigate a detection method available under highly denaturing conditions and a method to form a denaturant concentration gradient in a microchannel using EOF. We also evaluate the effectiveness of HEC as a DNA separation matrix and its temperature dependency.

1. Initial formation of denaturant concentration gradient at upstream Y-intersection



2. Injection of DNA in midstream intersection



3. Separation of DNA in denaturant gradient (can occur to the left or right of injection)



Figure 1. Concept of on-chip DGGE

2. EXPERIMENTAL

We used a microchip embossed in an acrylic substrate (Hitachi Chemical, Japan) for DNA electrophoresis and a glass microchip (IMT, Japan) for studying the formation of denaturant gradients. The background buffer was 40mM Tris-acetate, 10mM EDTA. The denaturant buffer also contained 7M urea and 40% formamide (typically referred to as a 100% denaturant buffer). We evaluated both the ULYSIS labeling system (platinum coordinative bond to the N₇ of guanine) and the YOYO-1 intercalated dyes (Molecular Probes, USA). We used HEC (MW: 9,0000-10,5000, Polysciences, USA) as a DNA separation matrix.

3. RESULTS AND DISCUSSION

We first compared the ULYSIS and YOYO-1 labeling methods. Figure 2 shows electropherograms of PCR products labeled with ULYSIS and YOYO-1. The ULYSIS sample has higher signal strength than the YOYO-1, suggesting that the ULYSIS approach preserves the degree to which DNA is denatured better than YOYO-1.

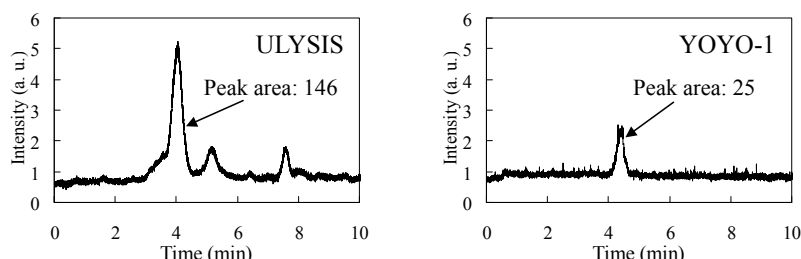


Figure 2. Electropherograms of PCR products (209bp) labeled with ULYSIS and YOYO-1 at 50°C. Buffer contained 80% denaturant and 1.75% HEC. Fluorophore used in ULYSIS system was Alexa Fluor 488.

We have achieved a denaturant gradient using EOF and simple diffusive mixing at a Y-shaped junction, as shown in Figure 3. We flowed both background and denaturant buffers (from the two wells on the left) and decreased the 100% denaturant buffer voltage at a steady rate to vary mixing ratio. We estimated the solutions were well mixed across the channel width within 5mm of the Y-junction.

Lastly, we have evaluated the selectivity (defined in Figure 4 caption) of 1.75% HEC (MW: 9,0000-10,5000) solution at temperatures. Figure 4 shows selectivity measurements (obtained on a microchip) and these are compared to data using an 8% polyacrylamide slab gel. The performance of HEC was superior to the traditional gel for all but the shortest DNA pair lengths.

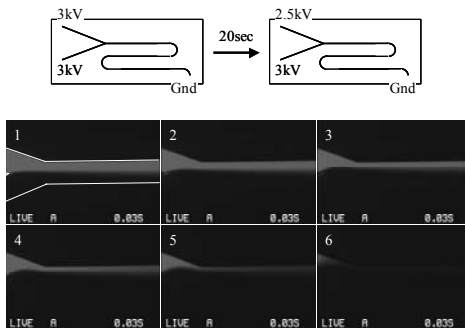


Figure 3. Schematic of test chip design (top) and results of mixing of a 100% denaturant buffer and a background buffer (bottom). The buffers contained 2% HEC. The 100 % denaturant buffer contained Rhodamine B as a surrogate of denaturant. The width and depth of the microchannels were respectively 100 μm and 40 μm . The interval between each image was 3 seconds.

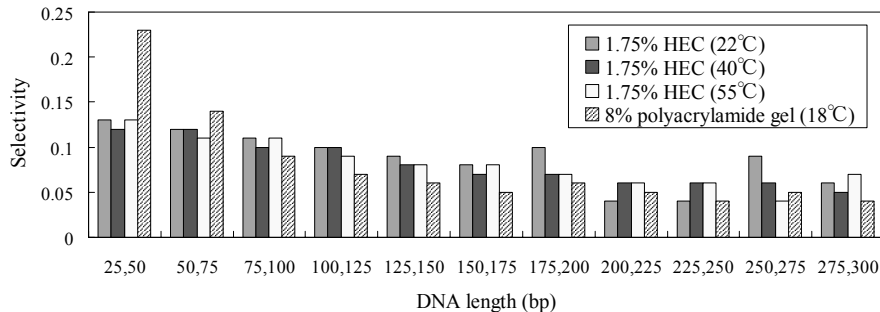


Figure 4. Selectivities of 1.75% HEC solution (from electrophoretic on-chip experiments) and 8% polyacrylamide gel. DNA sample was 25bp DNA ladder. The selectivity is defined as $\Delta\mu_{1,2}/\mu_{\text{avg}1,2}$, where $\Delta\mu_{1,2}$ is a difference in mobility and $\mu_{\text{avg}1,2}$ is the average mobility. The selectivity was calculated for each fragment pair indicated in the bottom.

4. CONCLUSIONS

The diffusive mixing and active EOF control strategy is effective, and ULYSIS is an effective method for labeling at these highly denaturing conditions. Our near-future work will involve combining these techniques and evaluating the performance of DGGE on a chip.

REFERENCES

- [1] S. G. Fischer and L. S. Lerman, Proc. Natl. Acad. Sci. USA, 1983, 80, 1579–1583.
- [2] G. Muyzer, E. C. de Waal and A. G. Uitterlinden, Appl. Environ. Microbiol., 1993, 59, 695-700.

ON-CHIP ISOTACHOPHORESIS USING ELECTROPHORETIC SPACERS

Tarun Khurana and Juan G. Santiago

Dept of Mechanical Engineering, Stanford University, Stanford CA 94305, USA

Abstract

We demonstrate an electrophoretic technique that simultaneously concentrates and separates trace fluorescent analytes on a chip. This technique is based on isotachophoresis and employs a leading electrolyte (LE), trailing electrolyte (TE) and electrophoretic spacers of intermediate mobility to separate analytes of interest. The analyte peaks obtained do not disperse and tunable resolution and concentrations can be achieved by choosing appropriate spacer concentration.

Keywords: Isotachophoresis, electrophoresis, spacers, single interface ITP

1. Introduction

Isotachophoresis (ITP) is a useful sample preconcentration technique and is often used prior to the capillary electrophoresis (CE) step to achieve the required sensitivity for trace analysis [1]. Sample ions to be stacked and separated are typically introduced between the leading and trailing electrolyte whose mobilities are respectively higher and lower than the mobilities of analyte ions. Under the influence of electric field, sample ions redistribute themselves in adjacent zones in the order of their mobility and these zones move at a same speed under steady state. Spacers are electrophoretic molecular species with mobilities intermediate to those of sample analytes. They segregate into positions between sample ions and serve to increase separation resolution. Spacers have been used in traditional CE systems to improve UV-based detection resolution [2,3]; but have not been used with fluorescence or on a chip. We present the use of electrophoretic spacers for on-chip ITP based separation and detection of fluorescent species.

2. Theory

In ITP, a trace analyte(s) concentrates in the region between background ions with mobilities that bound those of the analyte(s). For example, the leading and trailing ion pairs for the analyte species X_1^- , X_2^- and X_3^- in Fig. 1 are respectively (L^-, M_1^-) , (M_1^-, M_2^-) and (M_2^-, T^-) . The order of mobility, μ , to achieve the ITP/spacer condition is $\mu_L > \mu_{X_1} > \mu_{M_1} > \mu_{X_2} > \mu_{M_2} > \mu_{X_3} > \mu_T$. A mixture of analyte species and spacer electrolytes (M_1^- , M_2^-) is injected between the LE and TE. Upon application of an electric field from reservoir 3 to 1, the spacers separate into two distinct zones between the LE and TE. Analyte ions concentrate at the interfaces between these zones and, after a brief transient process, migrate at a steady velocity, with constant concentration and effectively uniform width.

3. Experimental

To demonstrate ITP separation with spacers, a sample mixture consists of three fluorescent species: Oregon Green carboxylic acid, fluorescein and Bodipy (Molecular Probes), with concentrations of ~100 nM. Two spacers, tris serine and tris phenylalanine at ~10mM (Sigma Aldrich), are injected between LE and TE. The leading electrolyte is 350 mM tris-HCl, pH adjusted to 10.2 and the trailing electrolyte is 50 mM sodium tetraphenyl borate. To achieve ITP concentration and separation, 1200 V potential is applied in the LE well and the TE well is grounded using a Labsmith (HVS448, 3000D) power supply. The separated and concentrated analyte peaks are observed using an Olympus epifluorescent microscope and CCD camera (Roper Scientific).

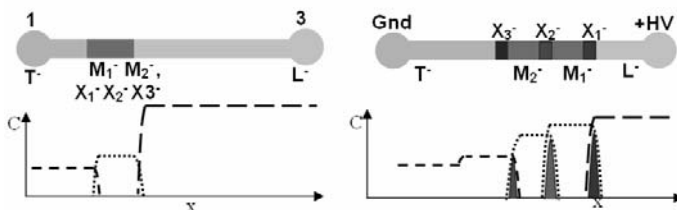


Fig 1. Schematic of the distribution the leading (L^-), spacer (M_1^- , M_2^-), trailing (T^-) and sample (X_1^- , X_2^- , X_3^-) ions at $t = 0$ and a later time ($t > t_{\text{separation}}$). The spacers M_1^- , M_2^- form ITP zones behind L^- on applying electric field and trace analyte ions accumulate at the interface of the spacers according to their mobility.

4. Results

Upon application of an electric field, the fluorescent species migrate towards the anode and separate and concentrate at the interfaces of anions that bound its mobility. In the steady state condition (~3 cm downstream), the analytes are separated by the spacers and the sample peaks are non-dispersive move with equal speed, as required by the ITP dynamics. Fig. 2 shows the spatio-temporal plot of the imaged intensity of the three analyte peaks. The diagonal traces in this plot of concentration versus position and time show that species migrate with no net dispersion and with identical speed (and the spacing between them stays constant). Figure 3 shows another set of experiments where spacers are eliminated one at a time from the initial analyte mixture. When a spacer separating two analyte peaks is eliminated, the two adjacent fluorescent analyte peaks merge into each other as shown in Fig. 3. This confirms that the analyte peaks are indeed separated by the non-fluorescent spacers.

5. Conclusion

We have successfully demonstrated the use of spacers for on-chip ITP-separation of fluorescent analytes. Improved resolution is achieved here because of self-sharpening nature of the analyte peaks. Resolution can be tuned by varying initial spacer

concentrations. This technique can be extended to a larger number of analytes by choosing appropriate spacer species.

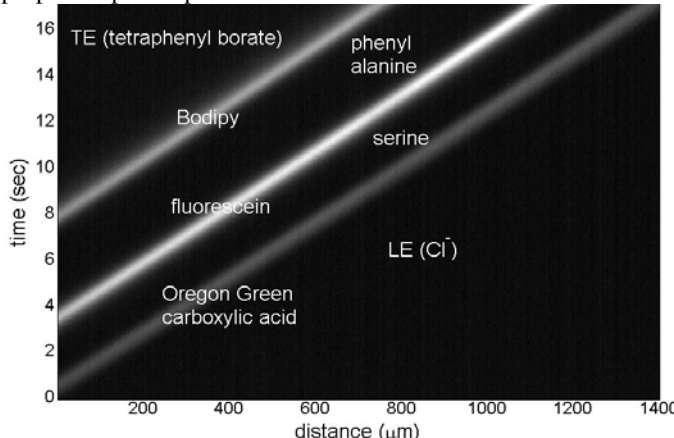


Fig 2. Plot of the fluorescence signal within the separation channel as a function of time and the streamwise coordinate, x . The three diagonal stripes show the motion of the three analyte peaks. These parallel bands demonstrate the peaks move at the same speed and with constant concentration as required by the ITP/spacer dynamics.

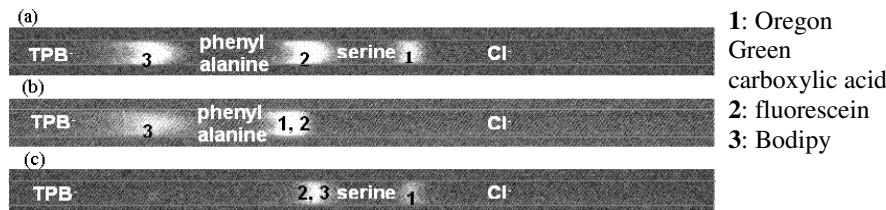


Fig 3. Raw images of the fluorescent analyte peaks inside a $50 \mu\text{m}$ wide (by $20 \mu\text{m}$ deep) microchannel. Shown are three experiments. In (a), both spacers phenyl alanine and serine are present in the sample mixture. In (b), only phenyl alanine spacer is used; and in (c) only the serine spacer is used. When one of the spacers is eliminated, the two adjacent fluorescent analyte peaks merge into a single peak as expected

References:

1. B. Jung B., R. Bharadwaj, J.G. Santiago, On-Chip million fold sample stacking using transient isotachophoresis, *Analytical Chemistry*, 2006, 2319-2327 (78).
2. F. Oerlemans, C. D. Bruyn, F. Mikkers, T. Verheggen, F. Everaerts, Isotachophoresis of urinary purines and pyrimidines: the use of spacers for identification, *Journal of Chromatography*, 1981, 369-379, (225).
3. I. Nagyova, D. Kaniasky, Discrete spacers for photometric characterization of humic acids separated by CE, *Journal of Chromatography*, 2001, 191-200, (916).

BIOMOLECULE AND ORGANELLE TRAP USING ELECTRIC AND HYDRODRAG FORCE FIELDS IN TAPER SHAPED MICROCHANNEL

Yuichi Tomizawa¹, Hiroaki Oose¹, Kunimitsu Ueno¹, Md Shameen Ahsans¹, Naoki Nagatani¹, Wako Nagasaka¹, Eiichi Tamiya¹, and Yuzuru Takamura^{1,2}

¹ School of Materials Science, Japan Advanced Institute of Science and Technology

² PRESTO, Japan Science and Technology Agency

Abstract

In this paper, trapping of cell organelles such as nucleus and mitochondria, and chromosome was reported using a taper shaped polydimethylsiloxane (PDMS) microchannel. The trap conditions for each biosubstance were investigated. In addition, trapping of biomolecules such as denatured RNA and protein (BSA) was also demonstrated using a silica glass chip, which has fine taper structure compared with PDMS ones.

Keywords: Biomolecule and organelle trapping, extraction, purification, molecular filter

1. Introduction

Extraction of a specific molecule or organelles from cells is one of the important issues for the understanding the biological phenomena from the point of embryology, tissue engineering, aging, and carcinogenesis. However, current microfluidic device technologies are not sufficient for extraction and purification of DNA, RNA and organelles from cells. We reported earlier a selective DNA trapping employing mutually reverse electric force and hydrodrag force field in a taper-shaped channel [1-2]. This time, we attempted to develop the trapping system for cell organelles (mitochondria and nuclei), chromosome and biomolecules of RNA and Protein (BSA) by the same principle. This technique can trap biomolecules selectively by tuning the ratio of the two forces with mild electric condition and relatively large structure compared to the case of dielectrophoresis [3]. The trapping technology using microfluidic devices has many advantages in bio-analysis. Our trap system needs no machine element. The size of microchannel is over 10 times larger than that of target biomaterials. For this reason, our channel is not easily blocked.

2. Preparation of biomaterials

The sample solution of nuclei was prepared by following steps. At first, cell density of HeLa was adjusted to $1 \times 10^6/\text{ml}$. The nuclei were extracted using Nuclear Extraction Kit (Chemicon International Inc). The nuclei were loaded with a fluorescent dye, YOYO-1 (Ex. Peak 491 nm, Em. Peak 509 nm). The mitochondria solution for a trap experiment was

prepared by following steps. A cell density of HeLal was adjusted to 2×10^7 /ml. The mitochondria were extracted using Mitochondria Isolation Kit for cultured cells (PIERCE). The nuclei were loaded with a fluorescent dye, Mito Red (Ex. Peak 560 nm, Em. Peak 580 nm). The sample solution of chromosome was prepared as follows. Chromosomes were extracted from BALL-1 cell. The chromosome were dyed with YOYO-1.

BSA staining solution was prepared as follows. Sodium dodecyl sulfate (SDS) of 1gm was taken into a 200ml beaker and 100ml of 0.1M Tris-HCl (pH= 6.8) was added in it. In an another 50ml beaker, 0.87 gm of bovine serum albumin (BSA) and 10 ml of distilled water was taken. From each of the above solutions, 0.5ml was taken into a test tube and boiled for one minute. 1 μ l SYPRO orange protein gel stain (Ex. Peak 470 nm, Em. Peak 570 nm) was taken into another test tube and 5ml of 7.5% acetic acid was added in it. Finally, from the content of each of these test tubes, 5 μ l was taken into a sample bottle and 80 μ l of 7.5% of acetic acid and 0.03mg of polyvinylpyrrolidone were added in it.

3. Experimental set up

A sample solution was introduced into a microchannel with triangle shape tapered structures. When sample biomolecule or organelle was driven by electric force and hydro drag force simultaneously in opposite directions, target biomaterials were then trapped near the triangle shape tapered structure. The trapping motion of each samples were observed under a fluorescence microscope. The observed fluorescence was intensified by the CCD camera. The fluorescence image was stored in PC as digital data (Fig 1.). The change of intensity of fluorescence was analyzed using SimplePCI software (Leeds Instruments).

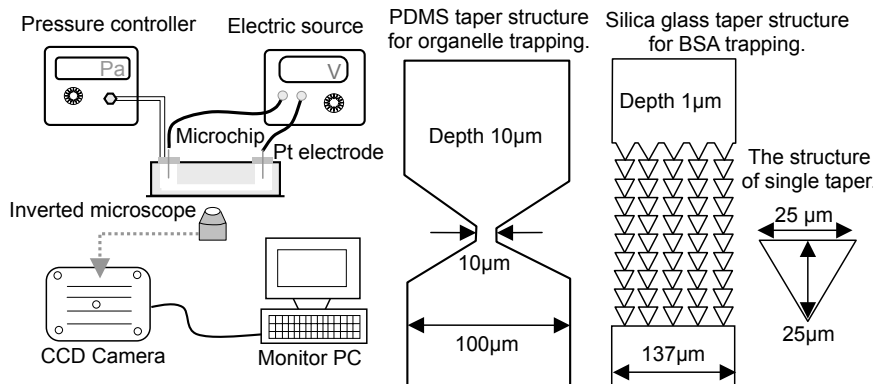


Fig 1. Experimental set up (left) and structure of the taper shape microchannel (right).

4. Results and discussion

The trap condition for nucleus, mitochondria and chromosome were investigated using a taper microchannel which was made from PDMS (polydimethylsiloxane) (Fig 2.). The trap condition of each organelle obtained as results of each experiment were shown in Fig 2 (right). We discovered that higher voltage and higher current were needed, in order to trap the smaller organelle. Addition to these, denatured RNA and Protein (BSA) samples were also successfully trapped (Fig 3) in the silica glass taper microchannel which has a more fine structure compared with PDMS microchannel.

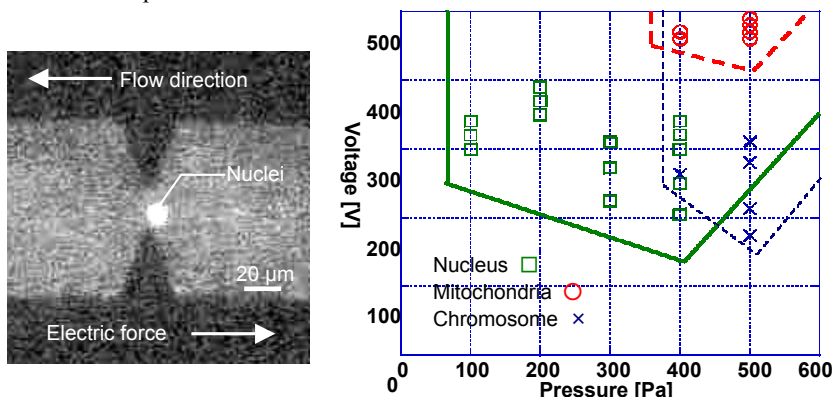


Fig 2. Fluorescence image of nuclei trapping (left) and trapping condition of organelles (right).

5. Conclusions

We successfully developed the trapping system for organelles (mitochondria and nuclei) in the cells, chromosome, RNA, and Protein (BSA). Our trap has a great potential for extraction and purification of target biomaterials from the cells in microfluidic chips. We consider that the trapping technology is a novel method for single cell analysis, single molecule detection, gene expression, and continuous PCR etc in the future.

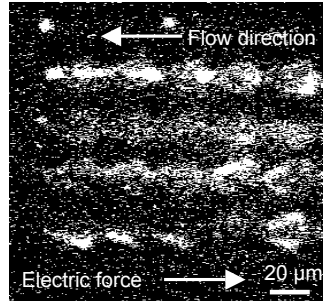


Fig 3. Fluorescence image of protein trapping.

References

1. Y. Takamura, et al., Proc of microTAS 2002, Nara, Japan, Vol 1, 317 (2002).
2. Y. Tomizawa et al., Proc of microTAS 2004, Malmö, Sweden, Vol 1 659 (2004).
3. Chia-Fu Chou, et al., Biophys. J., Vol. 83, 2170, (2002).

MICROCHIP ELECTROPHORETIC MOBILITY SHIFT ASSAY FOR DETECTING INTERACTIONS OF DNA-TRANSCRIPTION FACTOR NF κ B

Sonoko Inoue¹, Masatoshi Kataoka^{2,3}, Yasuo Shinohara², Noritada Kaji⁴,
Manabu Tokeshi⁴, Yoshinobu Baba^{3,4}

¹The University of Tokushima, Tokushima, 770-8505, Japan

²IGResearch, The University of Tokushima, Tokushima, 770-8505, Japan

³Health Technology Research Center, AIST, Takamatsu, 761-0395, Japan

⁴Department of Applied Chemistry, Nagoya University, Nagoya, 464-8603, Japan

Abstract

Microchip electrophoretic mobility shift assay (μ EMSA) has been developed for DNA-protein interaction study, and finally, we succeed in detecting the interaction of DNA and Nuclear Factor κ B (NF κ B) within only 200 s. Since the method provides quantitative data simultaneously, kinetics data analysis of DNA-protein interaction was also conducted.

Keywords: Microchip Electrophoretic Mobility Shift Assay (μ EMSA), Microchip Electrophoresis, DNA-binding Protein, NF κ B, Polymethylmethacrylate (PMMA)

1. Introduction

DNA-protein interaction plays a central role in many cellular functions including DNA replication, recombination, repair and transcription. One of techniques to study gene regulation is electrophoretic mobility shift assay (EMSA) which separates DNA and protein in equilibrium state in a solution based on a different binding stoichiometry. Although this technique gives a qualitative identification for sequence-specific DNA-binding proteins and enables the quantitative measurement of thermodynamic and kinetic parameters [1, 2], there are drawbacks such as time-consuming work and necessity of radioactive materials. In this study, by using polymethylmethacrylate (PMMA) microchip (Fig. 1), we have developed μ EMSA which permits rapid and quantitative assessment of DNA-NF κ B interaction.

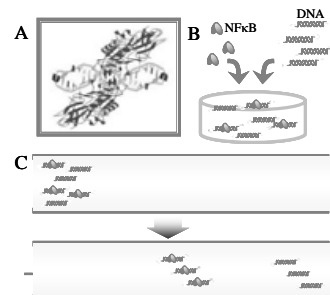


Figure 1. Overview of the experiments. (A) Structure of the human NF κ B homodimer-DNA complex. (B) Incubation and (C) electrophoretic separation of the mixture of NF κ B and oligonucleotide.

2. Experimental

Recombinant Human NF κ B (p50), which is a eukaryotic transcription factor and regulates a gene expression [3], was expressed in bacteria from a full-length cDNA and purified. NF κ B consensus oligonucleotides, which have the sequences 5'-AGTTGAGGGGACTTCCCAGGC-3' and 5'-GCCTGGGAAAGTCCCCCACT-3', were labeled with Cy5 at the 5' terminus. Nuclear extracts of HeLa cells were prepared by Nuclear Extracts Kit and were applied to μ EMSA as well as purified rhNF κ B. For microchip electrophoresis, Hitachi SV1210 microchip electrophoresis system was used with polymethylmethacrylate chips. Prior to electrophoresis, Cy5-labeled DNA probe and purified rhNF κ B, or nuclear extracts were incubated for 30 min in a binding buffer with nonspecific competitors poly d(I-C) and poly-L-lysine at room temperature. Conventional gel shift assay experiment was also conducted to evaluate μ EMSA.

3. Results and Discussion

The EMSA technique is based on a different migration behavior of free DNA molecules and DNA-protein complexes when subjected to non-denaturing gel electrophoresis. As shown in Figure 1, NF κ B and consensus 5'-Cy5-oligonucleotide

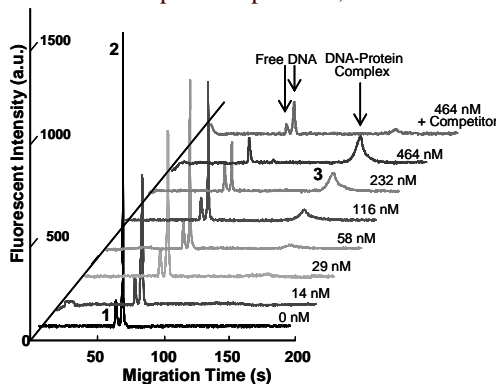


Figure 2. Separation of DNA-NF κ B complex and free-DNA under various concentrations of NF κ B indicated at the right edge.

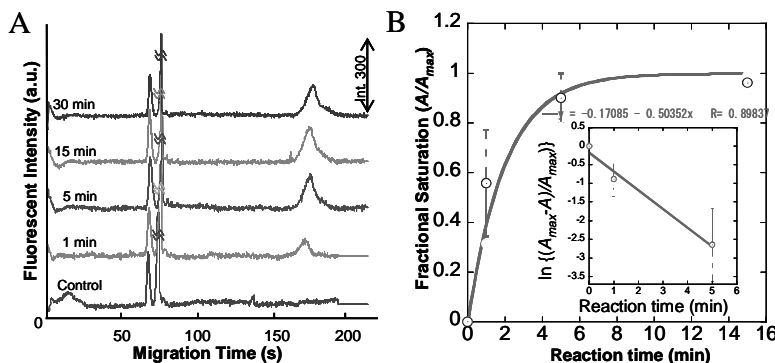


Figure 3. Monitoring of DNA-NF κ B complex formation. (A) Separation of DNA-NF κ B complex under various reaction time indicated at the left edge. (B) The time course of DNA-NF κ B binding reaction and determination of k_{obs} (inset).

were incubated in a binding buffer and applied to electrophoretic experiments. The mixture was separated into three peaks within 200 s and each peak was identified as the free-ssDNA, dsDNA, and the DNA-protein complex by competitive assay as indicated in Figure 2. The DNA-protein complex formation was monitored under various incubation times and the observed association constant k_{obs} was calculated at 0.50352 min^{-1} (Fig. 3). Nuclear extracts from HeLa cells were also applied to μ EMSA and NF κ B was specifically detected by competitive assay using consensus and non-consensus oligonucleotide (Fig. 4). However, the peak of DNA-protein complex in nuclear extracts showed retard compared with the purified protein experiment. It could be assumed that DNA-protein complex might be consisted of not only p50/p50 homodimer but also the other kinds of heterodimer. For further characterization, supershift assay should be performed by introducing antibody. These results suggested that this μ EMSA is a highly reliable for DNA-protein interaction study both in quantitative and qualitative aspects.

4. Conclusions

We have elucidated the impact of μ EMSA for qualitative and quantitative analysis of DNA-NF κ B interaction. The advances of μ TAS such as a multi-channel array system and an integrated system including cell digestion on a single chip will expedite our assay system to realize comprehensive analysis of functional genomics and proteomics.

References

1. A. S. Meyer, M. D. McCain, Q. Fang, A. E. Pegg, and T. E. Spratt, *Chem. Res. Toxicol.* **2003**, *16*, 1405-1409.
2. N. Y. Sidorova, S. Muradymov, and D. C. Rau, *Nucleic Acids Res.* **2005**, *33*, 5145-5155.
3. U. Zabel, R. Schreck, and P. A. Baeuerls, *J. Biol. Chem.* **1991**, *266*, 252-260.

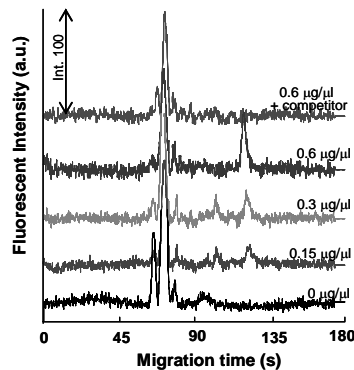


Figure 4. Separation of the mixtures of DNA and nuclear extracts from HeLa cells.

CONTINUOUS PARTICLE MANIPULATION IN MICROCHANNEL USING LASER RADIATION PRESSURE

Takatsugu MORIYA¹, Koichiro SAIKI¹ and Yohei SATO¹

¹Keio University, Hiyoshi 3-14-1 Kohoku-ku Yokohama 223-8522 JAPAN
Email: yohei@sd.keio.ac.jp

Abstract

Manipulation of substance groups is important process in a microfluidic device. In the present study, a technique which is able to manipulate substance groups using laser radiation pressure is developed. The laser radiation pressure for the present system is analyzed and the technique is applied in a flow field. Particle groups in the flow field are manipulated by the technique.

keywords: Laser radiation pressure, Optical manipulation, Submicron particles.

1. Introduction

Manipulation of substance groups is one of the important processes in a microfluidic device. Several substance manipulation techniques in microfluidic devices have been reported [1], [2]. In particular, optical tweezers enables a non-contact manipulation and have flexibility so that the technique limits an area of manipulation to several micro meters [3], [4]. In this technique, optically transparent substances such as cells and DNA are trapped at a focal point by laser radiation pressure in stationary fluids. However, continuous control is difficult in a flow field because substances are trapped at the focal point. The objective of the present study is to develop a continuous laser manipulation system that can manipulate groups of particles in the flow field.

2. Experimental setup

A laser focal area is shaped linearly by using a cylindrical lens (CL) to extend a manipulation area because a traditional focal point is not enough to manipulate particles in a flow field. Rotation of the cylindrical lens enables the focal area to rotate. To manipulate continuously, the laser beam profile is changed so that particles are moved

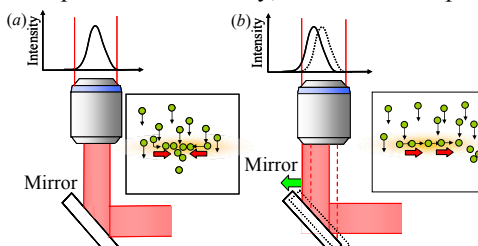


Figure 1. Schematic of the focal area (a) using cylindrical lens and (b) changing laser beam profile.

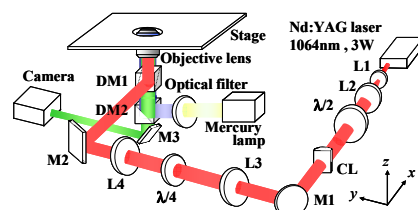


Figure 2. Schematic of experimental setup.

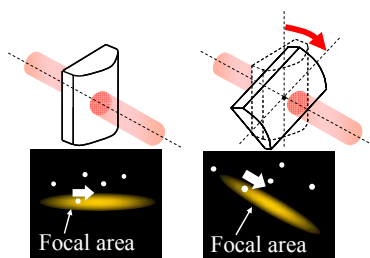


Figure 3. Schematic of cylindrical lens rotation.

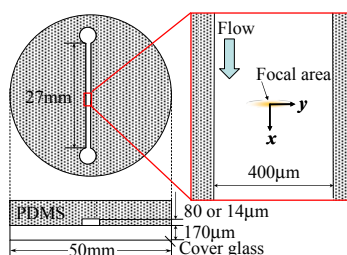


Figure 4. Schematic of I-shaped microchannel.

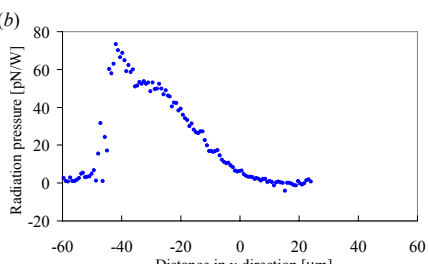
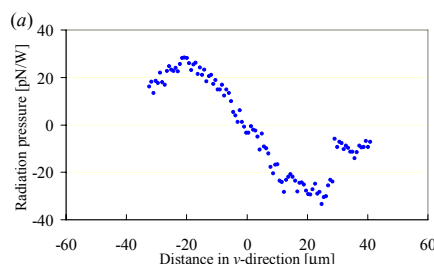


Figure 5. Result of distribution measurement of the radiation pressure in y -direction for the case of (a) using cylindrical lens and (b) changing laser beam profile by moving mirror.

in one direction in the focal area. To change its profile, the laser beam is moved by a moving mirror before entering an objective lens. Figure 1 illustrates a schematic of the changing of the focal area and the changing its profile. Figure 2 shows a schematic of experimental setup of the present study. Figure 3 exhibits a schematic of cylindrical lens rotation.

The optical radiation pressure in a system of the present study was investigated. Fluorescent particles whose diameter were $2 \mu\text{m}$, made of polystyrene (refractive index $n = 1.59$) in buffer solution ($n = 1.30$) were selected. Figure 4 shows the microchannel used in this study. The fluorescence of the particles was collected through a $40\times$ objective lens ($NA = 1.30$) and captured by either a CCD camera or a CMOS camera. Velocities of the particles were measured in a stationary fluid by Particle Tracking Velocimetry (PTV) which is a velocity measurement technique using a series of instantaneous images captured by the camera. The laser radiation pressure is given by Stokes's drag law which is derived by

$$F = -3\pi\mu D_p u_R \quad (1)$$

where F is the laser radiation pressure, μ is a dynamic viscosity, D_p is diameter of particles and u_R is a relative velocity between particles and buffer solution. In this study, the equation of laser radiation pressure assumes that the laser radiation pressure is equal to Stokes's drag force usually, because relaxation time of particles, 10^{-11} seconds, is enough shorter than frame rate of cameras, 10^{-2} seconds.

After measurement of the laser radiation pressure, the technique was applied in a flow field and particles were manipulated.

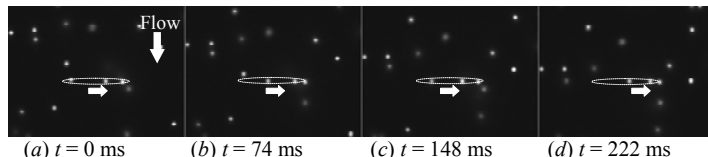


Figure 6. Time evolution of instantaneous image of optical manipulating particle by 0 degree of cylindrical lens rotation.

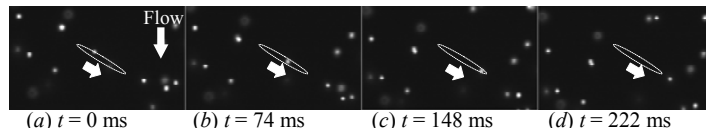


Figure 7. Time evolution of instantaneous image of optical manipulating particle by 30 degree of cylindrical lens rotation.

3. Results and Discussion

Figure 5 shows results of the optical radiation pressure measurements. The laser radiation pressure and plotted against distance of y -direction in Figure 5. The result shows that width of the area which is able to manipulate is about 50-60 μm and the fact which particle manipulation in one direction is confirmed by changing beam profile with moving mirror.

This technique is applied in a flow field. Figure 6 demonstrates the continuous manipulation in the cases in which the rotation angle of the cylindrical lens θ_{CL} is 0 and Figure 7 exhibits the case which θ_{CL} is $-\pi/3$ radians. The laser beam was able to manipulate the particles in any direction by rotation of cylindrical lens. At the laser focal area, particles were manipulated appropriately for each case.

4. Conclusion

The present study enables us to manipulate cells or DNA regionally and continuously in a flow field. This manipulation is expected to be used in microspace applications, such as separation, selection and mixing. These applications will help the development in the biochemical field to manufacturing new medicines or new food products.

Acknowledgements

This work was subsidized by the Grant-in-Aid for Young Scientists of Ministry of Education, Culture, Sports, Science and Technology (No. 17686017).

References

1. Devasenathipathy,S., et al, *Micro Total Analysis Systems 2003*, **1**, pp. 845-848,(2003).
2. Petersson, F., *Analyst*, **129**, pp. 938-943, (2004).
3. Ashkin, A., *Science*, **210**, pp. 1081-1088, (1980).
4. Ashkin, A. et al, *Optics Letters*, **11**, pp. 288-290, (1986).

HIGH THROUGHPUT CONTINUOUS SEPARATION BY ELECTRODELESS DIELECTROPHORESIS

Lujun Zhang, Florin Tatar and Andre Bossche

Dept. of Microelectronics, Delft University of Technology,
Mekelweg 4, 2628CD, Delft, the Netherlands

Abstract

We present a novel device for continuous separation in both time and spatial domain based on dielectrophoresis (DEP), where the non-uniform electric field is generated by means of a circular channel structure instead of conventional ac electrodes. Compared with the previously reported dielectrophoretic separation using electrode arrays [1], this device is more mechanically robust and chemically inert. And compared with the previously reported electrodeless dielectrophoretic separation methods [2], this device achieves higher throughput and continuous separation.

Keywords: separation, dielectrophoresis, electrodeless DEP

1. Introduction

The principle of the continuous electrodeless DEP separation in circular channel is illustrated in Figure 1. By applying a DC voltage over the circular chamber, a non-uniform electric field will be generated whose gradient directs towards the centre of the circle. The sample mixture is driven along the channel by the electro-osmotic flow. Due to the different DEP force magnitudes and directions, the particles with different DEP responses move continuously to the different location across the channel as they flow, thus continuously separated into the different outlets. Furthermore, the particles following the outer side path will be left behind, since the electro-osmotic flow at the inner side of the channel is faster than that at the outer side of the channel.

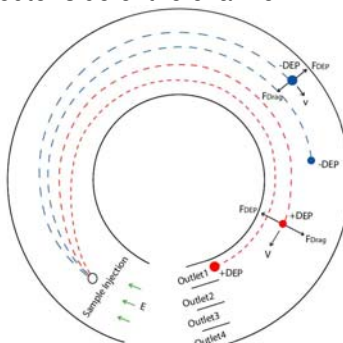


Figure 1. Schematic diagram of the dielectrophoretic separation in a circular micro-channel

2. Simulation

In Femlab 3.1i, a 3D channel model enclosed by a 50 μm inner circle and a 100 μm outer circle is built and the height of the channel is 40 μm . A 10V DC voltage is applied over the channel. To simulate the particle behavior in the micro-channel, the trajectory calculations are implemented in Matlab 7.0 after the field calculations are performed with Femlab 3.1i. Four particles of different size and dielectric properties are used, which are positive DEP particles with 5 μm and 10 μm radius, and negative DEP particles with 5 μm and 10 μm , respectively. The simulation result for the angle displacement of these four particles is shown in Figure 2, which verifies the particle separation in the time domain.

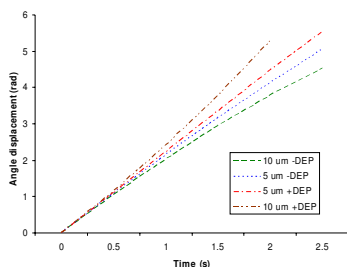


Figure 2. Simulation result for the angle displacement of 4 particles with different size and dielectric properties

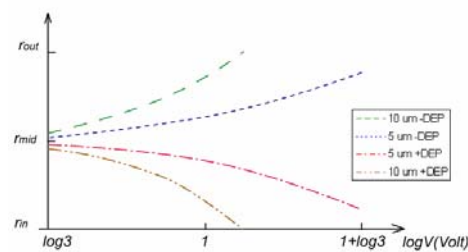


Figure 3. Particle positions across the outlets varying along the voltage applied over the circular channel

Varying the voltage over the channel, we simulated the particle's ending position across the outlet. The result is shown in Figure 3, r_{in} and r_{out} represent the inner side point and the outer side point of the outlet respectively, which verifies the separation in the spatial domain. With lower field intensity, the particles can be hardly separated due to the dramatically reduced DEP force which is proportional to the squared field gradient. While with higher field intensity, the greatly enlarged DEP force makes those particles over-separated with respect to the outlets as can be seen in Figure 3.

3. Fabrication

The main part of the fabricated device is shown in Figure 4. A silicon wafer is used as a substrate. A 2 μm layer of thermal oxide is firstly grown on both sides of the wafer. Then, 4 μm PECVD oxide is deposited on the back side of the wafer to serve as a mask for through holes etching. The Ti electrodes are fabricated with sputtering machine (TRIKON Sigma sputter coater) and plasma etching machine (TRIKON Omega plasma etcher). Through-holes are made by deep reactive ion etching at room temperature with the Bosch process, as

shown in Figure 5. Sequentially, a thick layer of SU-8 50 is coated on to the top the silicon substrate and pattern to form the side wall of the channel. To obtain a 40 μm thick SU-8 layer, 30 second spin coating with the speed of 4000 rpm/min is performed. And proximity mode with a 130 μm separation gap is chosen for exposure. Finally, the silicon substrate is aligned and bonded to a glass wafer using SU-8 adhesive bonding.

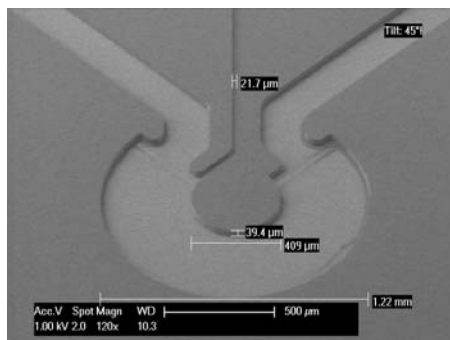


Figure 4. SEM picture of the separation channel with inlets, outlets and actuating electrodes

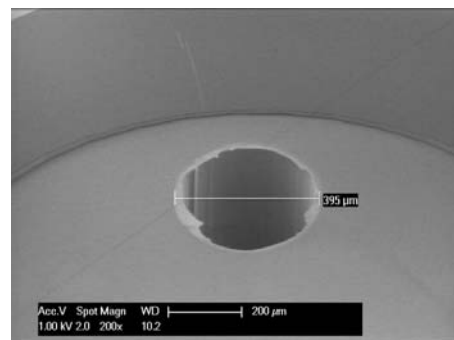


Figure 5. An inlet/outlet through-hole of 400 μm diameter etched with DRIE Bosch process

4. Conclusions

We have shown in this work design, simulation and fabrication of a novel device for continuous separation based on dielectrophoresis (DEP). Up to now, the simulation results have shown the separation in both time and spatial domain for the particles with different size and dielectric properties. And the device has been successfully fabricated as shown in Figure 4. The experiment is expected to be carried out soon to verify the design and the simulation method.

Acknowledgements

This research is under grants from The Dutch Technology Foundation (STW), Applied Science Foundation of NWO and the technology programme of Ministry of Economic Affairs, the Netherlands.

References

- 1 Pethig, R., Y. Huang, et al., *Positive and negative dielectrophoretic collection of colloidal particles using interdigitated castellated microelectrodes*, J. Phys. D Appl. Phys. 24, pp. 881-888 (1992).
- 2 C.F. Chou and F. Zenhausern, *Electrodeless dielectrophoresis for micro total analysis system*, IEEE Eng., pp. 62-67 (2003).

ELECTROPHORETIC SEPARATIONS IN SMALL SPACES: GRADIENT ELUTION MOVING-BOUNDARY ELECTROPHORESIS (GEMBE)

Jonathan G. Shackman and David Ross

National Institute of Standards and Technology, USA

Abstract

Microfluidic lab-on-a-chip devices employing capillary electrophoresis are currently constrained by limitations of on-chip separation lengths and injection schemes. These limits are exacerbated in multiplexed devices, with the number of access ports and off-chip equipment needed for injections increasing with the number of parallel analyses. We describe a novel injection-less separation method, Gradient Elution Moving-Boundary Electrophoresis (GEMBE), which can provide the highest number of electrophoretic separations possible for a given, limited chip area. The reduction in chip area is accomplished by combining moving boundary electrophoresis, which does not require the formation of an injected plug, with a temporally varying hydrodynamic counter-flow, which provides high resolution separations in very short microchannels.

Keywords: capillary electrophoresis, DNA, immunoassay, multiplex separations

1. Introduction

As the field of Micro Total Analysis Systems matures and moves in the direction of further integration, it is important to consider how many analysis elements can be accommodated into the small footprint of a microfluidic chip. Much of the work in the field has been to miniaturize conventional analysis techniques onto a planar chip format with minimal modifications to the basic operation mode of the technique [1]. However, conventional techniques are often optimized using macroscale, bench-top instruments. If device footprint is considered as a key parameter, the optimal process is likely to be different for microfluidic platforms. In this work, we take the example of electrophoretic separations and consider footprint as the primary limiting factor. Conventional electrophoretic separations begin with the injection of a discrete zone of sample and proceed with the electrokinetic migration and separation of that zone; microchip electrophoretic separations are performed similarly. However, if chip area is limited, two serious drawbacks to the conventional method exist: additional channels and fluid reservoirs are required to form the injection zone; and long channels are required for high-resolution or high peak capacity separations.

2. Theory

We have developed a new technique specifically avoiding these drawbacks to yield a much smaller footprint for electrophoretic separations: Gradient Elution Moving-Boundary Electrophoresis (GEMBE). Moving-Boundary Electrophoresis (MBE) [2] was chosen due to the elimination of injection structures; the sample solution is

continuously introduced into the separation channel and analytes are detected as steps when the sample boundary migrates past the detector. The stepwise output is differentiated yielding the familiar electropherogram. Gradient elution is accomplished by applying a controlled counter-flow that is varied over time. Only analytes with electrophoretic mobilities greater than the counter-flow can enter the separation channel. As the counter-flow is scanned from high to low flow rates, the different analyte boundaries begin their migration along the channel at different times allowing for high-resolution separations in very short channels.

3. Experimental

Both single capillary and multiplexed polymer microdevices were utilized (Fig. 1). For capillary experiments, a 3 cm long capillary (30 μm id; 360 μm od) was inserted between a polypropylene analyte reservoir and sealed block connected to a pressure controller with high voltage applied between the two ends. Microdevices were fabricated by computer numerical control milling into 380 μm thick polycarbonate (PC) sheets. Milled channels were 40 μm deep, 150 μm wide, and 1 cm long. The channels were thermally bonded to a PMMA piece milled to contain a common waste access port and 75 μL volume sample reservoirs. A pressure controller, used to regulate the hydrostatic pressure at the common waste port, was connected via PEEK tubing to an O-ring sealed lid at the access port. High voltage was applied to the pressure cell and sample reservoirs were grounded. Fluorescence microscope detection utilized arc lamp illumination, a CCD detector, and appropriate filter sets. Raw data was transformed by Savitzky-Golay smoothing [3] to obtain a derivative function.

4. Results and discussion

The viability of GEMBE was established with the quantitative separation of small dye molecules and various amino acids. GEMBE facilitates greater flexibility in selectivity when compared to conventional capillary zone electrophoresis, as the acceleration of the counter-flow (analogous to gradient slope in chromatography) becomes a separation parameter. It was found that high resolution separations could be achieved in short channels by varying the counter-flow velocity at a relatively slow rate (*i.e.*, low

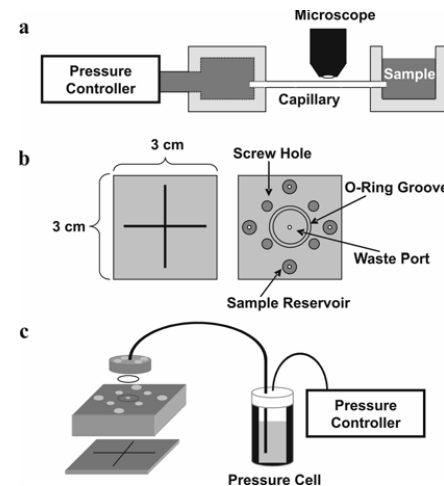


Figure 1. GEMBE instrumentation.
 (a) Schematic of capillary instrument.
 (b) Diagram of milled PC channels (black lines) and PMMA fluid handling block.
 (c) Schematic of microdevice in use. PC is bonded to PMMA; a lid is attached by screws with O-ring. Fluid delivery and pressure control is via a pressure cell.

counter-flow acceleration) while rapid, less-efficient separations could be obtained at high acceleration. Alternatively, non-linear accelerations could be used, such as step-and-hold to isolate single analytes (infinite resolution). The technique was further extended to the separation of single-stranded DNA using a sieving buffer, with baseline resolution of 15- and 17-mers of poly(cytosine) within 1 cm (Fig. 2). A competitive immunoassay for insulin was also demonstrated (Fig. 3) to show that large proteins can be investigated. A four-channel microdevice was used to separate fluorescein and carboxyfluorescein in parallel (Fig. 4). The result demonstrates that multiplexed analyses can be accomplished in short channels (1 cm) utilizing a single detector, one high voltage source, and a single pressure controller, with the throughput limiting factor being channel width and available detection field of view.

5. Conclusions

GEMBE is well suited to microfluidics when considering scalability as shown in parallel devices. The method provides high resolution separations in short microchannels without the additional access ports or equipment needed for injection formation.

References

1. P.S. Dittrich, *et al.*, Anal Chem, Vol 78, pp. 3887-3907 (2006).
2. A. Tiselius, Trans Faraday Soc, Vol 33, pp. 524-531, (1937).
3. A. Savitzky and M.J.E. Golay, Anal Chem, Vol 36, pp. 1627-1639 (1964).

Acknowledgements

The authors acknowledge the financial support of the NIST/NRC Postdoctoral Research Program.

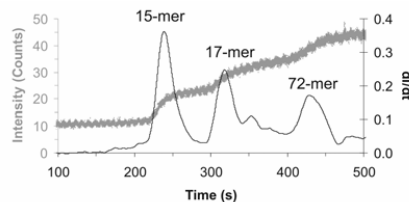


Figure 2. GEMBE separation of ssDNA poly(cytosine)-mers. Grey trace is raw intensity data. Black trace is transformed derivative.

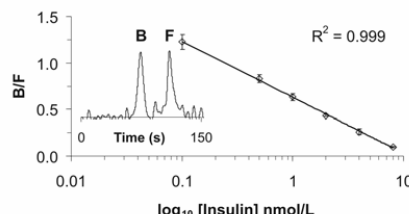


Figure 3. GEMBE insulin immunoassay calibration. Error bars are ± 1 SD ($n=3$). Inset shows separation of free FITC-insulin (F) and F bound to antibody (B).

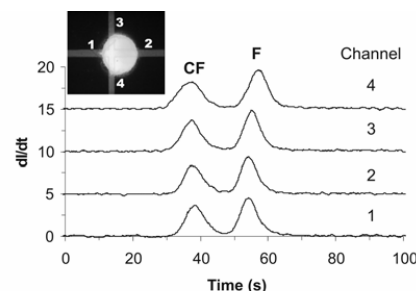


Figure 4. Simultaneous separation of fluorescein (F) and carboxy-fluorescein (CF) in a 4-channel device. Using CF as an internal standard, F inter-channel peak area RSD was 1%. Inset image shows the detection field and channel numbers.

ON-CHIP TEMPERATURE GRADIENT FOCUSING VIA JOULE HEATING: LOW-POWER SAMPLE CONCENTRATION AND SEPARATION

G.J. Sommer, S.M. Kim, E.F. Hasselbrink Jr.

Department of Mechanical Engineering

University of Michigan, Ann Arbor, MI, USA

Abstract

We present a rapid, low-power technique for concentration and separation of analytical proteins using a simple PDMS device. Joule heating along a variable-width channel supports the temperature gradient needed for focusing. A fundamental theoretical analysis and numerical simulation show agreement with experimental results and provide tools for device design.

Keywords: Temperature gradient focusing, Joule heating, separation, PDMS

1. Introduction

Temperature Gradient Focusing (TGF), introduced by Ross and Locascio in 2002 [1], has emerged as a viable separation technique in microsystems. In a previous work [2] we showed that a sufficient temperature gradient for TGF could be created simply using Joule heating in a variable-width microchannel. In this work we further analyze the temperature-dependent transport phenomena associated with TGF using a numerical simulation, and use our fundamental analysis in the design of a low-power concentration and separation PDMS device.

2. Theory

TGF is an electrophoretic technique that balances the average bulk flow of a buffer/analyte solution against the electrophoretic migration of the species. Because the electrophoretic mobility, μ_{ep} , of a species is temperature-dependent, the temperature gradient and E-field along the channel can be set up such that concentration will occur at a location x_{conc} if $u_{net} = u_{bulk} + u_{ep} > 0$ for $x < x_{conc}$ and $u_{net} < 0$ for $x > x_{conc}$.

The quasi-1D mass balance equation through a variable-width channel, considering only convective bulk flow and electrophoretic flux, can be written as:

$$A_i \frac{\partial c_i}{\partial t} = -\frac{\partial}{\partial x} [A_i (u_{bulk,i} c_i + u_{ep,i} c_i)] \quad (1)$$

where A is the area of the channel and c is the species concentration at location i . Assuming steady state and employing mass conservation, $\nabla \cdot (u_{bulk} A) = 0$, solving equation (1) yields:

$$\frac{c_{x=x1}}{c_{x=x0}} = \frac{(u_{bulk,x0} + u_{ep,x0}) A_{x0}}{(u_{bulk,x1} + u_{ep,x1}) A_{x1}} \quad (2)$$

In our device, Joule heating is used to induce a temperature gradient along the length of a variable-width channel. Assuming the channel dimensions of the channel

are much smaller than the glass and PDMS substrate in which it is formed, the 1-D heat equation considering only Joule heating and radial conduction through the substrate can be written as:

$$\frac{I^2}{\sigma_i(T_i)d_i w_i} = Kk \frac{T_i - T_\infty}{d_i} w_i \quad (3)$$

where I is the constant current through the channel, $\sigma(T)$ is the electrical conductivity, k is the thermal conductivity of the substrate around the channel, T_∞ is the ambient temperature, d is a length scale on the order of the channel depth, w is the channel width, and K accounts for the channel geometry ($O(1)$). Assuming $\sigma(T)$ is approximately proportional to the temperature difference, the temperature will vary roughly inversely with the width of the channel, thus providing a temperature gradient. Equations (2) and (3) will serve as rule-of-thumb approximations for this technique.

The mass transport, conservation, electroneutrality, and energy equations were discretized into a 1-D numerical model and solved using a Crank-Nicolson scheme at each channel location and time step using Matlab (Mathworks, Natick, MA). The simulation is used to predict the temperature, velocity, and concentration profiles under variable concentration conditions.

3. Experimental

The variable-width microchannel in Figure 1 was fabricated by casting PDMS over a SU-8 2010 (Microchem) silicon substrate mold. After punching vertical holes for reservoirs, the PDMS slab and a slide glass were plasma-treated and bonded together.

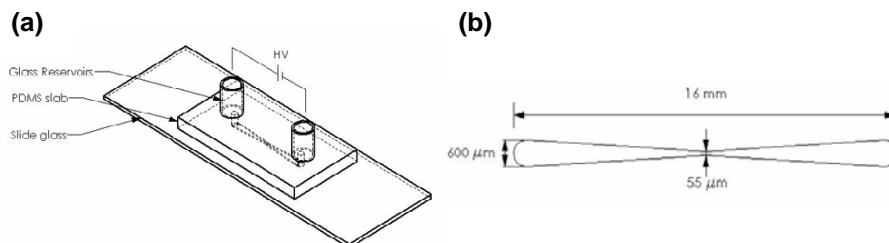


Figure 1 - (a) Schematic of PDMS system used. (b) Dimensions of microchannel. Depth = 18μm

FITC-labeled BSA and Fluorescein-Na were diluted into a solution of 900mM Tris, 900mM Borate buffer and loaded into the channel. 1200V was applied across the channel to concentrate and separate the sample.

4. Results and Discussion

Figure 2 shows the numerical simulation results for the expected (a) temperature profile, (b) bulk and sample net velocity profiles, and (c) concentration profile of Fluorescein-Na in 900mM Tris-Borate under 1200V for time=10sec. The higher temperature in the center of the channel causes a location of zero analyte net velocity, thus inducing convection.

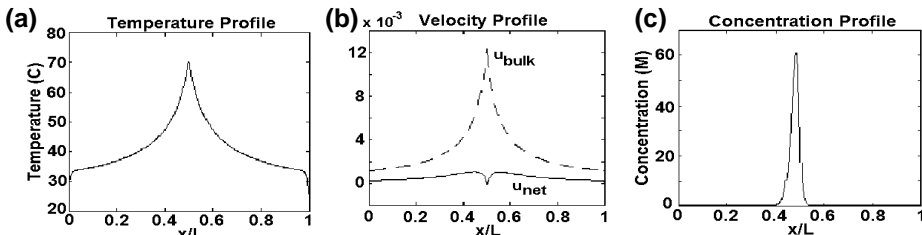


Figure 2 – Numerical simulation of concentration of Fluorescein-Na in 900mM Tris-Borate with 1200V applied at time=10sec. (a) Temperature profile. (b) Profiles of bulk fluid velocity (solid) and sample net velocity (dashed). (c) Concentration profile.

Figure 3 shows experimental concentration and separation of Fluorescein-Na and FITC-BSA under 1200V. At time=5min, both analytes are concentrated at the same location in the center of the channel. The continuous Joule heating causes the channel temperature to rise and the focusing locations ($u_{net} = 0$) for each species diverge causing the focused analyte plugs to separate.

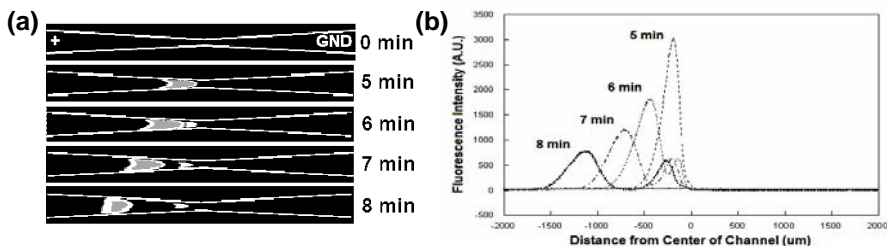


Figure 3 - Focusing of FITC-BSA and Fluorescein-Na in 900mM Tris-Borate buffer with 1200V applied. (a) Time-sequence images of center of channel. (b) Fluorescence intensity variations along centerline of channel, showing a clear separation of the two species after 8 minutes.

Because the same E-field is used for establishing a temperature gradient and sample transport, this system requires ~1/80th of the power needed for external temperature control. This energy savings enables potential implementation into portable devices.

5. Conclusion

We have demonstrated a simple, low-power technique for concentrating and separating analytical species in <10 minutes. The modest requirements allow for implementation into several lab-on-a-chip applications. A fundamental theoretical analysis and numerical model aid in the understanding of TGF via Joule heating and can be used in future device design.

References

- [1] D. Ross and L.E. Locascio, "Microfluidic Temperature Gradient Focusing", *Anal Chem*, **74**, 2556 (2002).
- [2] S.M. Kim, G.J. Sommer, E.F. Hasselbrink, Jr., "Electrophoresis with Temperature Gradients: Theory and Experiments", *Proc. MicroTAS 2005*, Boston, MA. (2005).

CONTINUOUS-FLOW PHASE-SEPARATION OF POLYMER SOLUTIONS IN MICROFLUIDIC AQUEOUS TWO-PHASE EXTRACTION SYSTEM

Woo-Jin Chang¹, Hye-Mee Park², Thuan-Hieu Tran² and Yoon-Mo Koo^{1,2}

¹ERC for Advanced Bioseparation Technology, Inha University,
Incheon 402-751 Korea

² Department of Biological Engineering, Inha University, Incheon 402-751 Korea
(wjchang@inha.ac.kr)

Abstract

Phase-separation properties of immiscible polymer solutions for continuous separation of biomolecules in microfluidic aqueous two-phase extraction system (MATPES) were surveyed. Concentrations and contact time of polymer solutions defined phase-separation time. Most of *E. coli* were continuously partitioned in dextran-rich phase.

Keywords: continuous-flow, aqueous two-phase extraction, phase-separation

1. Introduction

Effective preconcentration and separation of biomolecules in μ -TAS is very important to simplify the device, decrease the operation time and enhance the sensitivity of detection. Aqueous two-phase extraction system (ATPS) is used for the separation and fractionation of biomolecules because of its biocompatibility. ATPS is consisted of two immiscible solutions in bulk water, resulted in approximately 65~95% of high water content [1]. ATPS is generally constructed by the combination of one polymer (e.g. polyethylene glycol) and salt or second polymer (e.g. dextran). Partition coefficient (K) which is defined as ratio of the concentrations of molecules in both phases represents the separation efficiency. ATPS-based preconcentration and separation of biomolecules is a promising technique for microfluidic device. However, only a few applications of the ATPS in microfluidic device have been reported yet. Separation and fractionation of the aggregates of plant cells [2] and CHO-K1 cells [3] were reported. In this study, characteristics of phase-separation were surveyed with continuously infused polymer and buffer solutions and partition of *E. coli* was monitored in microfluidic device.

2. Experimental

Poly(dimethylsiloxane)(PDMS) microfluidic device was made by conventional soft-lithographic method. Dimension of the device is shown in figure 1. Poly(ethylene glycol)(PEG, M.W. 35,000, 15 % w/w, Fluka Co.), dextran (M.W. 40,000, 15 % w/w, Amersham Biosciences Co.) and PBS buffer were selected as model solutions for MATPES. All solutions were infused by syringe pumps (SP250, WPI Inc. Co.). PBS buffer or cell solution was injected through the middle port of three inlet ports. The optical micrographs were taken by fluorescence microscope (BX51, Olympus Co.) and CCD camera. *E. coli* cells were stained by LIVE/DEAD Baclight Bacterial Viability Kit

(L7012, Molecular Probes Co.) prior to use.

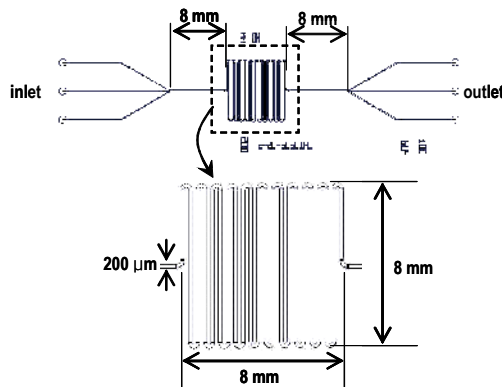


Figure 1. Dimension of microfluidic device which has 3 inlet and 3 outlet ports. The width and the depth of the microchannel is 200 μm and 50 μm , respectively.

3. Results and discussion

The concentration of polymers and contact time for phase-separation in microchannel are determined by ratio of infused solutions and total flow rate, respectively. Phase-separation was not occurred when the calculated concentrations of polymers were lower than around 2.5%. The interface between two polymer solutions was temporarily disappeared at the junction of two solutions, because each polymer is diffused into opposite polymer solution before stabilized. Each phase has less than 20% of another polymer which forms opposite phase, in general. Retention time of the solutions for phase separation was determined by monitoring the concentration profile of fluoresceine in microchannel. Phase-separation was completed within a few seconds in microchannel.

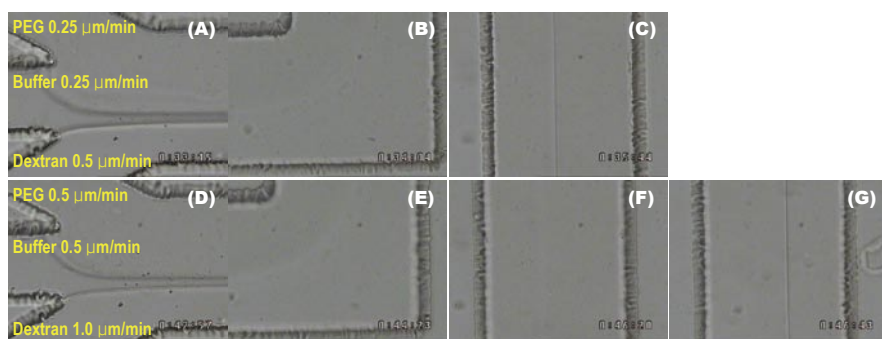


Figure 2. Micrographs at inlet junction (A, D), 0.8 cm (B, E), 1.6 cm (C, F) and 2.4 cm (G) from inlet junction with varying flow rates. It takes longer time for phase-separation with higher flow rates.

Asymmetric distribution of *E. coli* in developed microfluidic ATPS was observed. The effects of gravity on the distribution of cells can be ignored in microfluidic ATPS, different from macroscale ATPS. It is very difficult to obtain precise partition coefficient of cells in macroscale ATPS, because cells are precipitated on the interface by gravity.

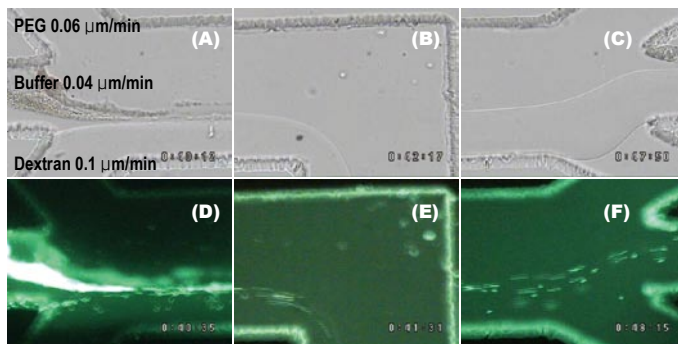


Figure 3. Bright field (A, B, C) and fluorescence (D, E, F) micrographs of *E. coli* in MATPES. Most of *E. coli* cells injected through middle port were partitioned into dextran rich phase.

4. Conclusions

Phase-separation properties of microfluidic aqueous two-phase extraction system were surveyed. Asymmetric distribution of *E. coli* cells in developed MATPES was observed. MATPES is believed to be a useful technique for the continuous fractionation and separation of biomolecules in microfluidic device.

Acknowledgements

This work was supported by grant No. (R0-2005-000-10927-0) from the Basic Research Program of the Korea Science & Engineering Foundation.

References

- [1] H. Hustedt, K.H. Kroner, U. Menge and M.R. Kula, *Protein recovery using two-phase systems*, Trends Biotechnol., 3, 139-144, (1985).
- [2] M. Yamada, V. Kasim, J. Edahiro and M. Seki, *Continuous cell partitioning using an aqueous two-phase flow system in microfluidic devices*, Biotech. & Bioeng., 87, 489-494, (2004).
- [3] K.-H. Nam, W.-J. Chang, H.-J. Hong, S.-M. Lim, D.-I. Kim and Y.-M. Koo, *Continuous-flow fractionation of animal cells in microfluidic device using aqueous two-phase extraction*, Biomed. Microdev., 7(3), 189-195, (2005).

MULTI-STAGE FREE-FLOW ISOELECTRIC FOCUSING FOR ENHANCED SEPARATION SPEED AND RESOLUTION

Jacob Albrecht and Klavs F. Jensen

Massachusetts Institute of Technology, 77 Massachusetts Ave., Cambridge,
Massachusetts 02139, USA

Phone: 617-253-6546, Fax: 617-258-8224

Contact e-mail: albrecht@mit.edu

Abstract

This work presents the first implementation of tandem stages for free-flow isoelectric focusing. Both simple analytical and rigorous computational models for IEF suggest device performance can be improved by utilizing multiple stages to reduce the time required for high resolution separations. A device to test this principle was designed and tested, with fraction analysis by SDS-PAGE. We report the initial results of device characterization, showing separation of four model proteins.

Keywords: Free flow electrophoresis, isoelectric focusing, prefractionation

1. Introduction

Isoelectric focusing (IEF) is often used to separate proteins in order to reduce sample complexity or as part of a 2-D separation, and has been performed in micro free flow electrophoresis format (FF-IEF) using isolated electrodes [1-3]. However in these systems, resolution is limited by high diffusive fluxes. To increase resolution, higher electric fields may be applied, but precipitation, Joule heating, and electrodynamic dispersion become limiting. A new technique to circumvent these limits to resolution involves designing a free-flow IEF chamber with outlet fractions that enter a second IEF stage.

2. Theory

Scaling arguments imply that the resolution of FF-IEF increases roughly with the square root of the channel width, but that the time to reach this resolution increases proportionally with the channel width. This suggests that by performing a separation in a narrow channel prior to a wider channel, the resolution can be reached in less time. Analogous to mechanical power, a free flow IEF stage can be “geared” for either speed or resolution; “shifting” enhances the overall performance of the device.

To examine this phenomena, a model developed previously [2] was expanded to include dynamic changes in focusing length and applied voltage. Figure 1 shows the simulated focusing (normalized to the channel width) of BSA under identical field strengths and residence times. As shown by the three cases presented in Figure 1, focusing within a 1mm wide channel (solid line) reaches steady state rapidly, but the high diffusive flux

prevents sharp focusing. Focusing within a 3mm channel (dotted line) has a higher final resolution, but requires approximately three-fold more time to reach steady state. By shifting from a 1mm channel at steady state to a 3mm channel (dashed line), the greater resolution of the wider channel is realized in 40% less time.

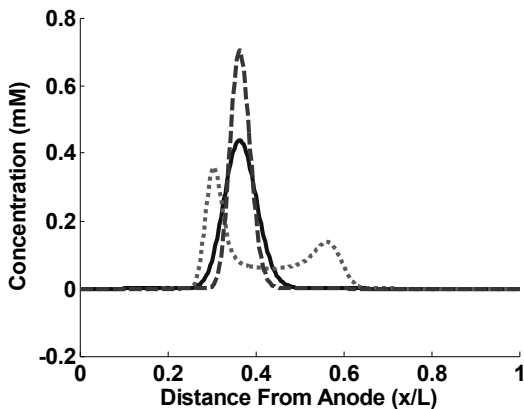


Figure 1: Simulation of BSA focusing with different channel geometries

3. Results and Discussion

A schematic of a device with two tandem stages is shown in Figure 2. The body of the device (a) is made of PDMS and is designed for a maximum of 3 inlets and 9 outlets. Post structures (b) define the polyacrylamide used to apply the electric field to the open sample channel. These UV-polymerized gels can be patterned without a photomask, and allow for arbitrary electric fields in each stage. The first stage is designed to perform a rapid prefractionation step with a steep pH gradient, while each of the three secondary stages are designed to perform a higher-resolution focusing step with a shallower pH gradient. The channel geometry at the splits has been optimized to ensure equal fluidic resistance for each outlet. A photo of the device is shown in Figure 3. Here, ten fluidic and six electrical connections are held in place by the PDMS without the need for epoxy.

An additional feature of the multistage devices is the ability to collect fractions for analysis, or orthogonal separations such as SDS-PAGE. A stained SDS-PAGE gel (Figure 4) of prefractionated amyloglucosidase, carbonic anhydrase II, trypsinogen, and trypsin inhibitor shows basic separation at a relatively low applied voltage (18V across each section). Amyloglucosidase focuses more tightly than the other three proteins due to its lower diffusive flux.

4. Conclusions

This work presents a two stage free-flow IEF device that is theoretically capable of fractionating proteins more efficiently than previous FF-IEF designs. We demonstrate in our initial tests the prefractionation of four model proteins prior to separation and

detection by SDS-PAGE, making these devices a potentially attractive alternative to more laborious isoelectric separation schemes.

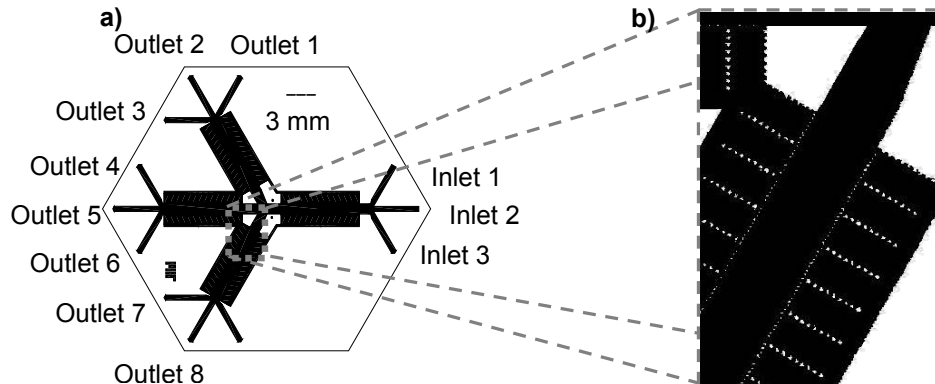


Figure 2: Schematic of multi-stage FF-IEF device.
Acidic ← pH → Basic

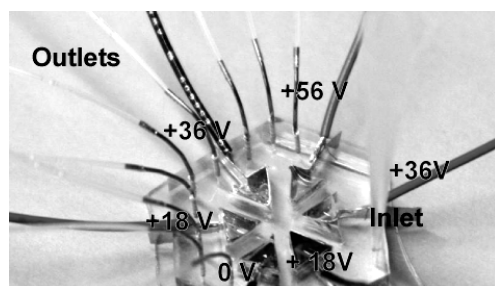


Figure 3: Photo of device in operation.

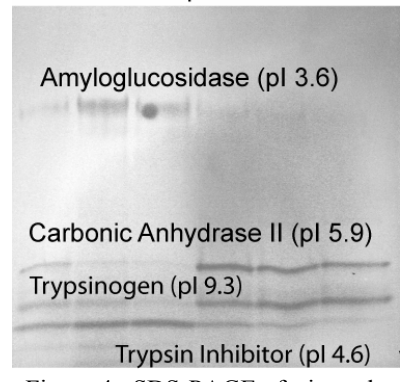


Figure 4: SDS-PAGE of six outlet fractions

Acknowledgements

The authors thank the National Institutes of Health (PSO-GM068762) for funding, as well as the staff of the MIT Microsystems Technology Laboratories for technical support.

References

1. Y. Xu, C.X. Zhang, D. Janasek, A. Manz, *Lab on a Chip* **3**, 224-227 (2003).
2. J. Albrecht, S. Gaudet, and K. F. Jensen., Proc. Micro Total Analysis Systems 2005, pp. 1537-1539.
3. Kohlheyer, D., Besselink, G. A. J., Schlautmann, S., Schasfoort, R. B. M., *Lab on a Chip* **6**, 374-380 (2006).

SENSITIVITY IMPROVEMENT FOR PEPTIDE/PROTEIN ANALYSIS IN MICROCHIP ELECTROPHORESIS-MASS SPECTROMETRY

Takahide Kameda¹, Fumihiko Kitagawa¹, Akihiro Arai², Koichi Suzuki²,
Shin Nakamura² and Koji Otsuka¹

¹ Graduate School of Engineering, Kyoto University, Japan

² Shimadzu Corporation, Japan

Abstract

This paper reports an analysis of biogenic compounds, *e.g.*, peptides and proteins, by microchip electrophoresis-mass spectrometry (MCE-MS) combined by using an electrospray ionization (ESI) interface with a spray tip and a liquid junction. To improve the reproducibility and the MS sensitivity of the MCE analysis, successive multiple ionic polymer layer (SMIL) coating was applied to a quartz microchip and/or a spray tip. In the MCE-MS analysis of biogenic compounds, a successful separation and selective detection was achieved. Toward a further improvement of the concentration sensitivity of peptides, the use of an on-line sample preconcentration method was investigated.

Keywords: microchip electrophoresis, mass spectrometry, ESI interface, biogenic compounds, on-line sample preconcentration

1. Introduction

Recently, the use of mass spectrometry (MS), which has the advantages of no needs for the derivatization of analytes and the structural information capability, as a detection scheme in microchip electrophoresis (MCE) has been developed. In MCE-MS, electrospray ionization (ESI) is regarded as the most suitable ionization method. A development of an ESI interface using sheath liquid for MCE-MS has been reported but the detection sensitivity decreased due to sample dilution by the sheath liquid. On the other hand, Terabe and co-workers have reported the fundamental study on MCE-MS coupled by a sheath less ESI interface, and successful analyses of basic drugs and peptides were achieved [1-2]. In this paper, we applied MCE-MS with the sheath less ESI interface to the analysis of peptides and proteins. To achieve a further improvement of the MS detectability for biogenic compounds, an application of on-line sample preconcentration technique was investigated.

2. Experimental

The detailed structure of the microchip and the ESI interface used in this study is shown in Figure 1. The quartz microchip with a simple cross-type channel coated

successively with polybrene and dextran sulfate (SMIL coating [3]) was employed to prevent the adsorption of analytes. The spray nozzle, which was a tapered fused silica capillary and was attached to the exit of the separation channel of the microchip, was employed to build the ESI interface. The bottom of the exit edge of the separation channel was fabricated as a flat plane to minimize the dead volume between the channel and the ESI spray tip. The ESI voltage was applied through the liquid junction reservoir.

3. Results and discussion

To evaluate the fundamental analytical performances in MCE–MS, two peptides, i.e., Pro–Leu–Gly amide and [Val^4] angiotensin, were used as test analytes. An electropherogram of these peptides is shown in Figure 2. These two peptides were successfully separated with resolution of 1.3 and detected within 70 s. Pro–Leu–Gly amide and [Val^4] angiotensin were detected as $[\text{M}+\text{H}]^+$ and $[\text{M}+2\text{H}]^{2+}$, respectively. Thus, faster and efficient separation, and selective detection of peptides were attained by the present MCE–MS system.

Toward an improvement of the MCE–MS analysis of proteins, effects of the SMIL coating were investigated. When a SMIL coated microchip and a bare spray tip were employed in the MCE–MS analysis of cytochrome *c*, a broader peak was observed, while in the SMIL coated spray tip a slightly sharper peak was obtained as shown in Figure 3(a). Using the SMIL coated spray tip brought the 2-fold decrease in the peak width. In the MS spectrum at 0.61 min, ten charge states ranging from +10 to +19 were observed as shown in Figure 3(b). The molecular weight of 12358 determined from the MS spectrum was accorded within a 0.5% difference of the

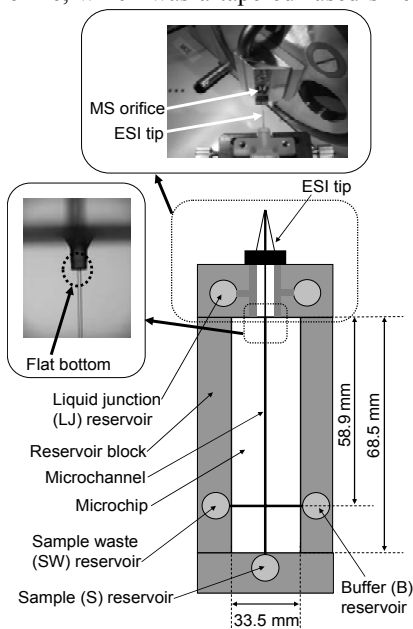


Figure 1. Schematic illustration of the microchip and ESI interface for MCE–MS.

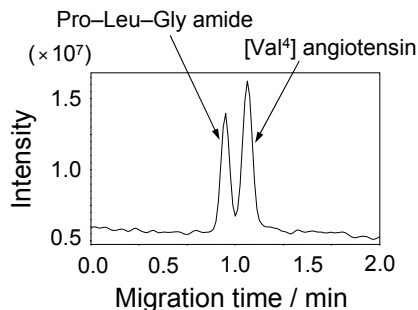


Figure 2. MCE–MS analysis of 100 ppm Pro–Leu–Gly amide and [Val^4] angiotensin. Background solution, 50 mM acetate acid (pH 2.8) containing 30% (v/v) acetonitrile; injection time, 0.5 s.

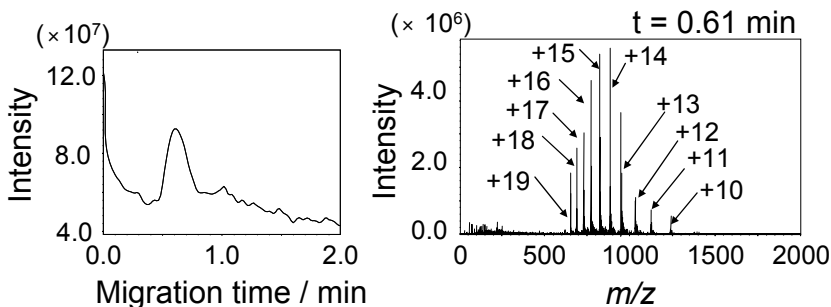


Figure 3. MCE-ESI-MS analysis of 100 ppm cytochrome *c* using the SMIL coated spray tip. Background solution, 50 mM acetate acid (pH 2.8) containing 30% (v/v) acetonitrile; injection time, 2.0 s.

literature value. However, the limit of detection of these proteins and/or peptides was *ca.* 10–50 ppm and the peak width was still broader, so that an on-line sample concentration technique should be introduced in the present MCE-ESI-MS system to attain an enhanced detectability.

Among several on-line sample preconcentration techniques, stacking, which is a facile concentration technique based on the conductivity difference between a sample matrix and background solution, is applicable to MCE-MS but the sufficient concentration might not be expected due to a limited conductivity range of the sample solution which should be electrophoretically injected into a separation channel. On the other hand, the dynamic pH junction technique which utilizes the electrophoretic mobility difference in the two zones with different pH is anticipated for an effective concentration of zwitterionic peptides and proteins since a larger change in their charge states is occurred at the pH boundary. Comparison of these techniques for the on-line preconcentration of peptides will be presented.

4. Conclusion

In the analysis of peptides and proteins, faster and efficient separation, and selective detection were successfully achieved by the present MCE-ESI-MS system. It should be noted that SMIL coating onto the inner surface of the spray tip brought a better efficiency and higher peak height for proteins. A combination of the MCE-ESI-MS analysis with on-line sample preconcentration is promising the rapid, sensitive, and selective analysis of peptides and proteins.

References

- [1] Y. Tachibana et al., *J. Chromatogr. A*, **1011**, 181 (2003).
- [2] Y. Tachibana et al., *J. Chromatogr. A*, **1025**, 287 (2004).
- [3] H. Katayama et al., *Anal. Chem.* **70**, 2254 (1998).

AUTOMATED ALL-FRACTIONS COLLECTION FOR MICROFLUIDIC SEPARATION

Dawid Zalewski¹, Stefan Schlautmann¹ and Richard B.M. Schasfoort¹

¹MESA+ Institute, University of Twente, the Netherlands

Abstract

An automated, electrokinetically controlled fractionator and collector for microfluidic separation is described. The fractionator is coupled to capillary electrophoresis. The separated sample fractions are detected and guided into collection channels. The device utilizes flow-lock technique, which enables selective spatial separation and collection of all fractions. The technique was demonstrated on model mixture.

Keywords: fraction collection, fractionation, capillary electrophoresis, electrokinetic separation

1. Introduction

Proteomics research requires combining multidimensional separation with detection, identification and other postprocessing methods. Those techniques are often incompatible and sample handling interfaces are needed to create efficient systems. The fraction collection of a sample separated by electrokinetic methods is a useful technique used as an intermediate step in a multidimensional analysis [1, 2]. An automated procedure provides a fast way of sample purification [3].

2. Theory

Accurate peak detection is crucial for a proper fractions' distribution. Using a conductivity or fluorescence signal threshold level as a criterion fails on noisy or biased data. Comparison of a local signal deviation, derived from l last samples, to a full length deviation (Equation 1) gives better results. The weighted average x_w is calculated with respect to current signal value and the threshold coefficient η is used for fine tuning. Data preconditioning (e.g. bias cancellation) can be applied if needed.

$$\sum_{i=n-l+1}^n \sqrt{\frac{(x_i - x_w)^2}{l}} > \eta \cdot \sum_{i=1}^n \sqrt{\frac{(x_i - x_w)^2}{n}} \quad (1)$$

3. Experimental

The device shown in Figure 1 was used to demonstrate the principle of operation. Channels were etched in a borosilicate glass wafer, followed by forming the liquid reservoirs by powderblasting. Subsequently the wafer was thermally bonded to another glass with deposited conductivity detection electrodes.

The operation sequence is shown in Figure 2. Sample fractions leaving the CE part are detected in the interfacial region by conductivity measurements. A real-time algorithm based on statistical signal analysis is employed for accurate recognition of an upcoming peak. The separation is then paused and the fraction is guided to an appropriate channel accordingly to the electrophoretic mobility calculated from the separation time measured in a preceding step. The same procedure repeats for the next fractions. As a result the fractions are sorted and stored in different channels. The process can be looped enabling sample concentration.

Three high-voltage power supplies are used to control the chip. The signal from a conductivity detector is acquired with Agilent 34401A multimeter. The instruments are controlled by in-house written native Windows software with a time resolution better than 25ms. The needed voltages, including electroosmotic backpressure compensation are found by deriving and solving an equivalent resistance matrix of the system for a given step. A microscope equipped with a mercury lamp for fluorescence detection and a CCD camera is used for visual inspection.

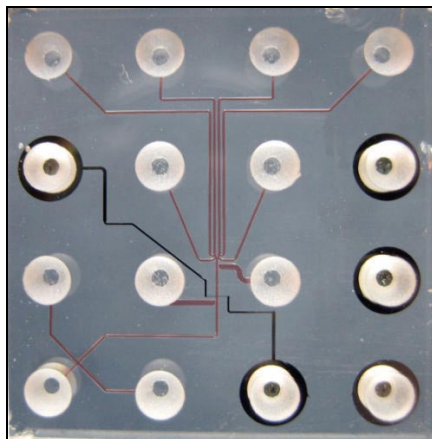


Figure 1. Top view of a chip. Dimensions are 20x20 mm. (Channels are filled with a die for visualization).

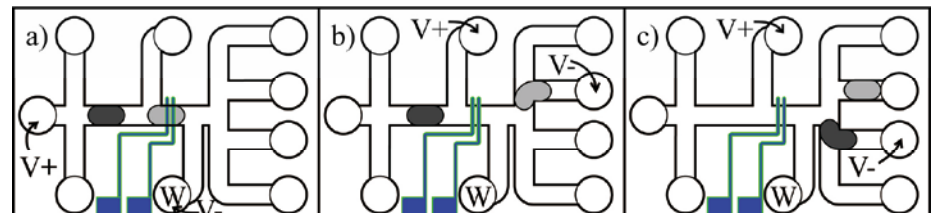


Figure 2. When the first sample fraction reaches the conductivity detector (a) the voltages are switched. The separation freezes and the detected fraction is guided into the appropriate collection channel (b). After it reaches the desired position the separation is resumed and procedure is repeated for other fractions (c). The unneeded portions can be dragged into the waste reservoir (W).

4. Results and discussion

The experimental results are shown in Figure 4. Separation and fractionating of two-component sample (Fluorescein and Rhodamine B) is demonstrated. The method of operating the separation and fractionation independently (flow-lock) and employing automated fraction detection provides an efficient way of sample collection when the amount of analyte is small and no part of it can be lost.

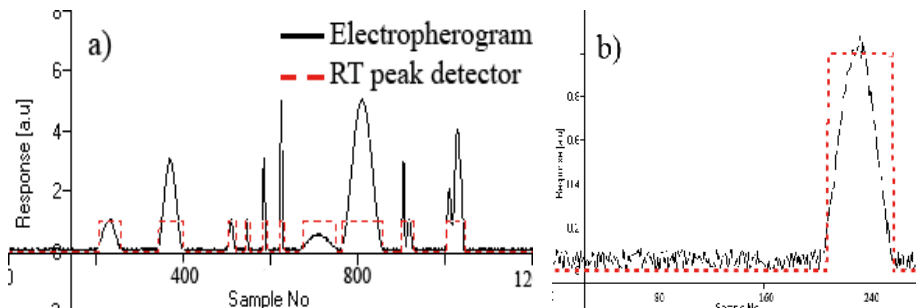


Figure 3. Output signal of a peak recognition algorithm (a). Electropherogram shown for comparison. The zoom box (b) contains the first peak. Even with a noisy input peaks are detected after reception of less than 5 first peak points.

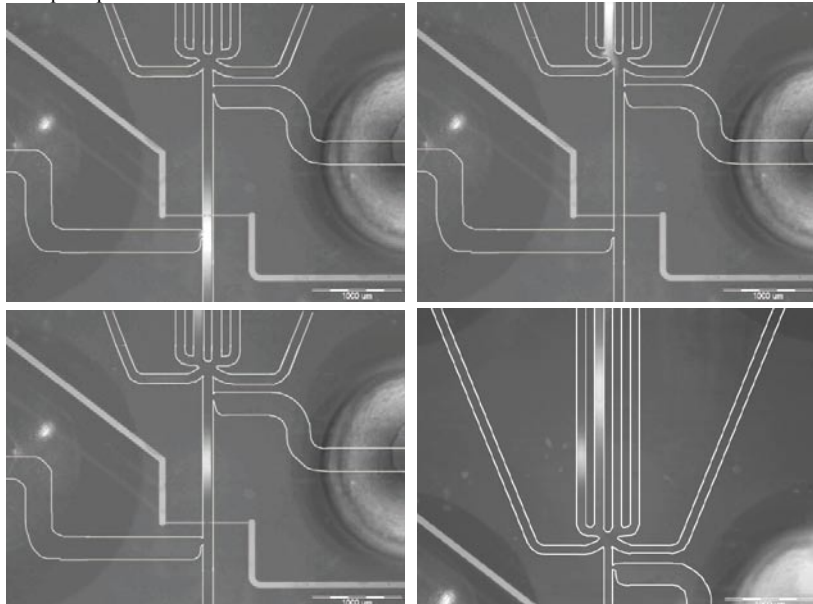


Figure 4. The sequence of images taken during CE separation/fractionation of a 1mg/ml Fluorescein, 1mg/ml Rhodamine B in 10mM Hepes. Complete separation of both fractions with automated fractionating into different collection channels is shown. (Channels outlines overlaid for readability)

References

1. M. Minarik et al., Fraction collection in micropreparative capillary zone electrophoresis and capillary isoelectric focusing, *Electrophoresis* 2000, 21, pp. 247-254
2. Zhen Wang et al., Valveless on-chip automated protein fractionator and collector utilizing electrokinetically manipulated sheath flow, *Proc. Micro Total Analysis Systems* 2005, pp. 1549-1551
3. J. Khandurina et al., Micropreparative fraction collection in microfluidic devices, *Anal. Chem.* 2002, 74, pp. 1737-1740

PUSHING THE LIMITS OF DETERMINISTIC LATERAL DISPLACEMENT DEVICES

Asger Vig Larsen¹, Jason P. Beech², Veysel Özkapıcı¹, Brian Bilenberg¹,
Anders Kristensen¹, Jonas O. Tegenfeldt^{2*}

¹MIC-Department of Micro and Nanotechnology, Technical University of Denmark (DTU), Building 345east, Oersteds Plads, DK-2800 Kongens Lyngby, Denmark

²Division of Solid State Physics, Lund University, P. O. Box 118, SE-221 00 Lund, Sweden

*jonas.tegenfeldt@ftf.lth.se

Abstract

We explore the scaling of devices based on deterministic lateral displacement with N, the longitudinal periodicity. By increasing N rather than decreasing the inter-obstacle distance devices can be made that have a small sub-micron critical size, yet are defined using standard UV-lithography with super-micron sized structures.

Keywords: microfluidics, separation device

1. Introduction

Deterministic lateral displacement (DLD) has been shown to be an extremely powerful technique for separation of particles on the micron scale with unprecedented high resolution[1] [2]. To expand the technique into separation of viruses and possibly single proteins, the critical size must be decreased to below 100nm.

2. Theory

DLD is based on pure geometrical effects and in its simplest form it acts as a cut-off filter sending particles larger than a critical size in one direction and smaller particles in another direction. The critical size is simply given by $R_{crit} = \alpha * d/N$, where the correction term α due to the parabolic flow of the liquid is typically $\alpha \sim 2.5$. d is the distance between posts and N is the number of rows in each spatial period.

To decrease the critical size, the three involved parameters above can be manipulated. The correction term, α , can be decreased by using flow techniques that are not associated with stick boundary conditions such as electrokinetic flow. Changing the inter-obstacle distance, d , is another alternative but it requires advanced nanofabrication. We have opted for increasing the periodicity, N . It has recently been investigated for larger structures[3]. Here we explore it for submicron separation.

3. Experimental

We have explored the scaling of the critical size, R_{crit} , with N . To this end we have made devices using single-step nanoimprinting lithography (NIL) with $N = 10, 20, 40$, and 100 with a constant post separation of $d = 1.0\mu m$ with an overall design as

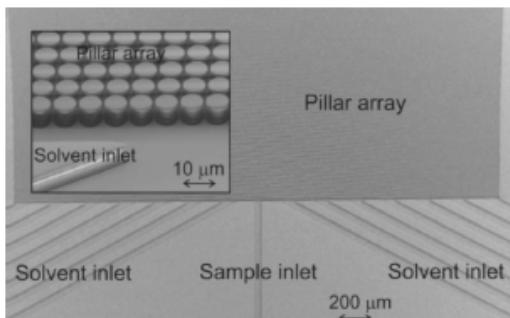


Figure 1. Details of a typical device (from [1]). SEM images of the separator device fabricated in a single layer of Topas grade 5013 before sealing with a Pyrex glass lid. The device height is 8.5 μm , the pillar diameter is 7 μm and the gap between neighboring pillars is 1 μm . The widths of the inlet channels are 50 μm . This shows a device with $N=10$ and critical radius 0.5 μm . Similar devices were made with $N=20, 40, 100$.

parabolic flow profile, the critical size is expected to be given by $R_{\text{crit}} = \frac{d}{\sqrt{3N}}$ (Fig 2).

4. Results and discussion

Since the resolution of DLD is often smaller than the size distribution of standard latex bead preparations we have developed a new protocol to characterize the device. To investigate the uncertainty in the DLD, we studied data from devices with $N=10$ and nominally a critical diameter of $2R_c \sim 500\text{nm}$.

From figure 3 it is clear that the bead population (diameter $510\text{nm} \pm 26\text{nm}$) is divided into two streams, one with beads smaller and one with beads larger than the critical size. The beads flowing in between the two main streams represent the uncertainty in the critical size of the separation in the device. Assuming a Gaussian size distribution of the

described in [1] (Fig 1). Changing N rather than d simplifies fabrication by allowing us to use the same process for all the devices. Only the design needs to be changed. This approach allows us to test a simple theoretical model that is based on the assumption of a parabolic flow profile in the device. In the DLD, the flow is divided into N streams with equal flow. Due to the stick boundary conditions (that lead to the parabolic flow profile) the stream adjacent to the post must therefore be wider than the central streams. This is the origin of the correction term. Assuming deep channels (depth is 8.5 μm) and taking into account the

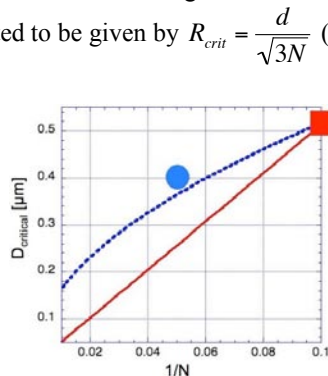


Figure 2. Plot of critical size versus $D_c = 2R_c \sim 1/N$. Dotted line corresponds to $D_c = 2\beta * 1\mu\text{m} / \sqrt{3N}$ and solid line corresponds to $D_c = 2\alpha * 1\mu\text{m} / N$ where the correction factors are chosen to fit measurements with device $N=10$: $\alpha = 2.57$ and $\beta = 1.41$. Measured critical sizes from devices with $N=10$ (square) and $N=20$ (circle) are indicated in the plot.

beads, and simply measuring the particle flow in the streams give a critical diameter of $2R_c \sim 514 \pm 3\text{nm}$. This represents an unprecedented 0.6% uncertainty in size characterization.

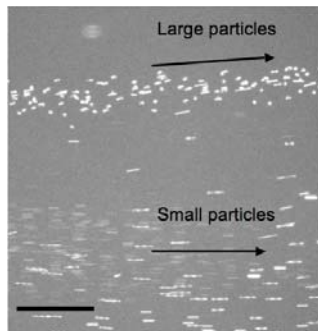


Figure 3. Results of separation of a collection of green fluorescent latex beads with a mean diameter 510 nm and a standard deviation of 26 nm. The distribution of bead sizes are divided into two separate streams, one containing beads of size smaller than the critical size and one of beads larger than the critical size. The beads in between represent the uncertainty of the method. Scale bar is 5 μm .

5. Conclusions

Future work will focus on decreasing the critical size of the device in several ways: decrease of distance between posts, d ; increase of N ; and manipulation of the flow so that the correction term approaches unity. Decrease of the correction factor can be achieved by increasing the velocity of the particles close to the walls of the posts by introducing close to slip boundary condition e.g. using electrokinetic movement of the latex microspheres.

Acknowledgments

The work is partially supported through the EC-funded project NaPa (Contract no. NMP4-CT-2003-500120). The content of this work is the sole responsibility of the authors.

References

- [1] B. Bilenberg, M. Hansen, D. Johansen, V. Özkapici, C. Jeppesen, P. Szabo, I. M. Obieta, O. Arroyo, J. O. Tegenfeldt, and A. Kristensen, *Topas-based lab-on-a-chip microsystems fabricated by thermal nanoimprint lithography*, Journal of Vacuum Science & Technology B **23** (6), 2944-2949 (2005).
- [2] L. R. Huang, E. C. Cox, R. H. Austin, and J. C. Sturm, *Continuous Particle Separation Through Deterministic Lateral Displacement*, Science **304**, 987-990 (2004).
- [3] D. W. Inglis, J. A. Davis, R. H. Austin, and J. C. Sturm, *Critical particle size for fractionation by deterministic lateral displacement*, Lab On A Chip **6** (5), 655-658 (2006).

FLOW CONTROL IN MICROFLUIDIC DEVICES WITH A PLANAR SEPARATION FORMAT

Margaret A. Lerch and Stephen C. Jacobson*

Department of Chemistry, Indiana University, Bloomington, IN 47405, USA

Abstract

We report strategies to control fluid flow in microfluidic devices with a planar separation format. Operation included using focusing channels to direct the sample into and through the sample transfer region prior to launching the sample in an orthogonal direction. This configuration minimized sample dispersion during the transfer process.

Keywords: flow control, electrokinetic transport, separations

1. Introduction

We have been investigating various strategies for performing two-dimensional separations on microfluidic devices. One such device has a planar format where the first dimension separation is performed in one axis, and the effluent from the first dimension is introduced orthogonally along a second axis for the second dimension separation. The planar format has an advantage over serially coupled separations in that the entire sample can be introduced from the first dimension into the second dimension. Various formats for coupling isoelectric focusing and capillary gel electrophoresis separations on microfluidic devices in a planar format have been reported [1-3].

Figure 1 shows a microfluidic device with a planar format where the first dimension separation is conducted in the vertical direction and the second dimension separation in the horizontal direction. The first step in designing this device was developing a method to transfer the sample with minimal dispersion because lateral dispersion of the sample plug in the planar region will diminish the quality of the separation. Our initial efforts began with conducting SIMION calculations to determine the shape of the equipotential lines in the planar region. The goal of these calculations was to determine the minimum number and spacing of channels needed to achieve parallel equipotential lines in the planar region. As the number of focusing channels increases, the equipotential lines become more parallel. With the SIMION calculations, the optimal spacing was empirically determined to be 80 μm center-

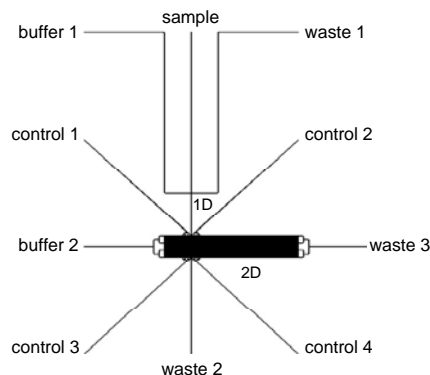


Figure 1. Schematic of a microfluidic device with a planar format. Each control channel in this design branches into 4 focusing channels near the planar region.

to-center between the 1D channel (or waste 2 channel) and the first focusing channel and 240 μm center-to-center between the first focusing channel and the remaining focusing channels.

2. Experimental

Microchannels were cast in poly(dimethylsiloxane) (PDMS) substrates using masters made from the negative tone photoresist SU-8 [4]. The PDMS substrate and glass coverplate were then permanently joined, after being exposed to air plasma for 40 s prior to contacting. Images were obtained using an inverted optical microscope (Olympus IX71) equipped with a high-pressure Hg arc lamp and CCD camera (Photometrics Cascade 512B). The CCD camera was controlled using IPLab imaging software. A 10 μM solution of disodium fluorescein in a 1 mM sodium tetraborate and 20 mM HEPES buffer was used as a fluorescent probe. For the electrokinetic transport, electrical potentials were applied to the reservoirs using custom-built high-voltage power supplies and controlled using LabView.

3. Results and Discussion

Microfluidic devices were designed and fabricated with the control channels branching into 1, 2, or 4 focusing channels near the planar region. Figure 1 is the CAD drawing for the 4 focusing channel design. Figure 2 shows a bright field image of the planar region between the 1D channel and the waste 2 channel for the four focusing channel design. The vertical dimension of the planar region is 1.6 mm in this image, and the second dimension contains 16 parallel channels. Figure 3 shows fluorescence images of sample being transported from the top of the planar region toward the bottom. In (b-c), the ratios of the electric field strengths in the focusing channels to the 1D channel (E_f/E_{1D}) are 1.0 and 4.1, respectively. As expected, the sample stream narrows with increasing E_f/E_{1D} . However, as this ratio increases

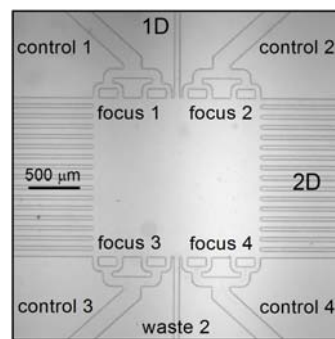


Figure 2. Bright field image of the sample transfer region on the microfluidic device with a planar format.

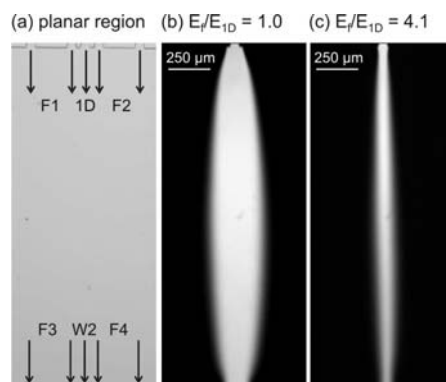


Figure 3. (a) Bright field image of the planar region between the 1D channel and waste 2 channel (W2). Fluorescence images of sample transport through the planar region with (b) $E_f/E_{1D} = 1.0$ and (c) $E_f/E_{1D} = 4.1$. This microchip is the 4 focusing channel design, but only 2 of the 4 focusing channels for each control channel are shown in (a). Arrows depict flow direction.

the sample stream becomes more diluted. Therefore, we examined the concentration to width ratio in order to determine optimum operating conditions. Figure 4 shows the stream width (4σ) in the center of the planar region and the concentration to width ratio for the 1 and 4 focusing channel designs. As seen in the figure, a substantial narrowing of the sample stream is observed moving from 1 to 4 focusing channels. Also, the concentration to width ratio improves tremendously. For the 4 focusing channel design, a maximum concentration to width ratio is achieved with $E_f/E_{ID} = 4.1$ corresponding to a minimum stream width (170 μm). In Figure 5, a sample plug is shown moving through the planar region. The plug undergoes minimal axial and lateral dispersion while traversing the planar region.

Acknowledgements

This work was supported in part by center grants from the Indiana 21st Century Research and Technology Fund and from the National Center for Research Resources at the National Institutes of Health (RR018942).

References

1. X.X. Chen, H.K. Wu, C.D. Mao, and G.M. Whitesides, *Anal. Chem.* 74, 1772-1778 (2002).
2. S.-W. Tsai, M. Loughran, and I. Karube, *J. Micromech. Microeng.* 14, 1693-1699 (2004).
3. Y. Li, J.S. Buch, F. Rosenberger, D.L. DeVoe, and C.S. Lee, *Anal. Chem.* 76, 742-748 (2004).
4. D.C. Duffy, J.C. McDonald, O.J.A. Schueller, and G.M. Whitesides, *Anal. Chem.* 70, 4974-4984 (1998).

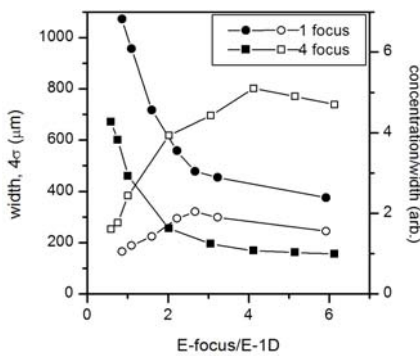


Figure 4. Variation of the stream width (solid symbols) and concentration to width ratio (open symbols) with ratio of the electric field strengths in the focusing and first dimension (1D) channels for 1 and 4 focusing channels.

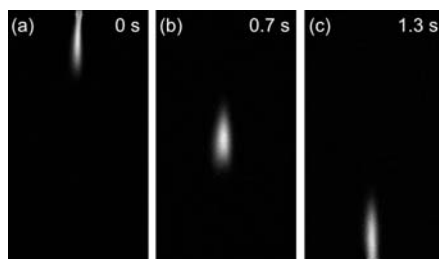


Figure 5. Fluorescence images of a sample plug traveling through the sample transfer region at (a) 0 s, (b) 0.7 s, and (c) 1.3 s. The E_f/E_{ID} ratio is 2.3, and the microchip is the 4 focusing channel design

MICROCHIP-BASED RAPID SAMPLE-PREPARATION FOR GAS-CHROMATOGRAPHY ASSAY OF AMPHETAMINE-TYPE STIMULANTS IN URINE SPECIMENS

Hajime Miyaguchi¹, Manabu Tokeshi², Yoshikuni Kikutani², Akihide Hibara^{2,3}, Hiroyuki Inoue¹ and Takehiko Kitamori^{2,3}

¹National Research Institute of Police Science, Kashiwa 277-0882, Japan

²Kanagawa Academy of Science and Technology, Kawasaki 213-0012, Japan

³The University of Tokyo, Bunkyo-ku, Tokyo 113-8656, Japan

Abstract

As the first application of pressure-driven microfluidics in forensic toxicology, a microchip-based liquid-liquid extraction for the gas-chromatography assay for amphetamine-type stimulants in urine has been developed. The interface consisting of 1-chlorobutane and alkalized urine was stabilized in the asymmetric microchannel modified partially with the capillarity restricted modification (CARM) method. As a practical demonstration, methoxyphenamine hydrochloride was administered to three healthy volunteers, and the concentration of methoxyphenamine in their urine was determined.

Keywords: Forensic toxicology, Solvent extraction, Amphetamines

1. Introduction

To analyze amphetamine-type stimulants (ATS) such as methamphetamine (MA) and amphetamine (AP), gas chromatography (GC) including gas chromatography/mass spectrometry (GC/MS) is extensively used in forensic laboratories because of its versatility and reliability. By way of sample preparation for GC analysis, conventional liquid–liquid extraction (LLE) has a widespread use, but it is not only laborious but also environmentally unfriendly due to the consumption of considerable amounts of organic solvents. One of the sophisticated approaches to achieve both laborsaving and small-scale sample preparation is to make use of microfluidics. Miniaturization of LLE using pressure-driven liquid manipulation has been extensively studied by Kitamori's group [1].

Properties of the surface inside a microchannel have a significant influence on flow configuration due to the relatively large interface area of microchannels. Recently, Hibara *et al.* developed a new concept of partial surface modification named the capillarity restricted modification (CARM) method that allows a partial surface-modification in a simple and reproducible fashion [2]. As an application of the CARM method, we investigated a microchip-based LLE for GC analysis of ATS in urine.

2. Experimental

The Pyrex glass microchip (Fig. 1) was purchased from the Institute for Microchemical Technology (Kawasaki, Japan). A modification reagent (2.5% (w/v) Trichloro(tridecafluoroctyl)silane (FAS-Cl) in α , α , α -trifluorotoluene (PhCF₃)) was employed for the CARM method [2].

The illustration of microchip-based LLE is shown in Fig. 1. Twenty microliters of an internal standard solution (0.5 μ g/ml mephentermine), 80 μ l of 0.25 M EDTA, 0.2 ml of 25% aqueous ammonia and 1.3 ml of water were admixed to 0.4 ml of a urine sample, and the aqueous mixture was delivered to the deep microchannel. 1-Chlorobutane was delivered to the shallow microchannel as the extraction solvent. Flow rates were controlled by a dual syringe-pump (Harvard). The flow rates were usually 10 μ l/min for 1-chlorobutane, and 50 μ l/min for the pretreated urine. Purging, stabilizing and sampling periods were 1, 1 and 3 min, respectively.

GC was carried out on a Hewlett-Packard HP5890 gas chromatograph equipped with a DB-5ms column (J&W), a flame ionization detector (FID) and an autosampler.

For the conventional LLE, 50 μ l of 5 M sodium hydroxide and 0.25 g of sodium sulfate were added to 1 ml of urine sample. After sodium sulfate was dissolved by vortex mixing, 0.5 ml of 1-chlorobutane was added, and vortexed for 1 min.

3. Results and discussion

Alkalization of urine is necessary to extract the basic stimulants, but the surface modification with a silanizing reagent would be damaged by alkali. Therefore, the durability of the modification on test chips (Pyrex glass, 1×1 cm) against 2.5% aqueous ammonia was evaluated by measuring the contact angle of the surface. The contact angle of the FAS-coated glass surface was obviously higher than that of the ODS-coated surface until 6 h (FAS, 109.5±1.1°; ODS, 100.9±2.9°). Because it is likely that higher hydrophobicity is necessary to stabilize the multiphase flow, the FAS modification was employed in this study. When processing pretreated urine with 1-chlorobutane on the CARM-processed microchip with FAS, the two-phase flow was well-controlled, and thus almost complete phase separation at the downstream junction was achieved, which is essential for microchip-based LLE especially for off-chip analysis.

The extraction efficiencies tend to increase with overuse of the microchip. A trend of the extraction efficiency of MA is shown in Fig. 2. In the beginning of a newly modified microchip, the extraction efficiency was about 20–30%, and a flat interface was observed at the boundary area (Fig. 2a). After about 7 h use, the undulated interface emerged (Fig. 2b–d) and the extraction efficiency started increasing. The extraction efficiency finally reached up to about 70%. This unexpected increase of the extraction efficiency may be attributed to intraphase turbulence-flows generated by undulation of

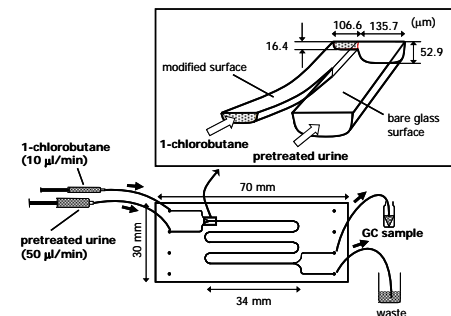


Fig. 1 Illustration of the microchip-based liquid-liquid extraction apparatus.

the interface. Although the overused microchip provided higher extraction efficiencies, the values were not very reproducible, and further additional uses finally resulted in a phase separation error.

In order to make an assessment on whether the microchip-based method was acceptable or not for a quantitative analysis, linearity was estimated with six concentrations, and some of the parameters about test method reliability were determined. The extraction efficiencies with the microchip-based LLE (26.1–31.1%) were much lower than those with the conventional LLE (97.3–106.2%), but the internal standard effectively compensates the deviation of the extraction efficiencies, which resulted in a good linearity ($r^2 > 0.9997$). Interday accuracy, intraday precision and interday precision of the microchip-based method were acceptable when employing the internal standard.

Quantitation of methoxyphenamine (MPN) in urine obtained from the three donors administered 50 mg of MPN hydrochloride orally was carried out with both the microchip-based LLE and the conventional LLE. The results of quantitation (3–27 µg/ml) were in agreement with each other. Owing to the pretreatment of urine, no difficulties arose throughout the microchip-based LLE process.

4. Conclusion

The present method requires 5 min extraction time, and approximately 100 µl of the solvent and urine to prepare a GC sample. We think that this study and future developments such as a subsequent flow-process and a small-volume GC injector are sure to contribute to the rapid automation analysis in forensic toxicology. We are investigating an on-line derivatization for GC/MS such as trifluoroacetylation that improves not only the peak shapes of GC but also the number of the mass fragments on electron ionization MS, and these improvements will contribute qualitative reliability. The study of the additional derivatization process is now under investigation.

References

1. M. Tokeshi, T. Minagawa, T. Kitamori, *Anal. Chem.* 72, 1711–1714 (2000).
2. A. Hibara, S. Iwayama, S. Matsuoka, M. Ueno, Y. Kikutani, M. Tokeshi, T. Kitamori, *Anal. Chem.* 77, 943–947 (2005).

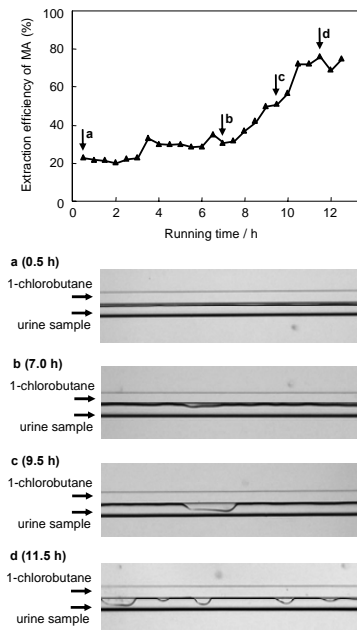


Fig. 2 Upper graph. Trend of the extraction efficiency of MA. Each point represents the data of the extract accumulated during the preceding 30 min. Lower graphs. Changes in the shapes of the interface at different running times.

A PROTEIN-ANALYSIS CHIP INTEGRATING AFFINITY CHROMATOGRAPHIC COLUMN AND ISOELECTRIC FOCUSING CHANNEL

Yutaka Koyama, Takehiko Kitamori and Kiyohito Shimura

Department of Applied Chemistry, The University of Tokyo,

7-3-1 Hongo, Bunkyo-ku, Tokyo 113-8656, Japan

shimura@cl.t.u-tokyo.ac.jp

Abstract

We report a protein-analysis microchip integrating specific capture by affinity chromatography (AC) and charge-based separation by isoelectric focusing (IEF). Ten fmol each of 4 kinds of peptide isoelectric point (pI) markers in 1 μ L of a sample was separated in an IEF channel of the protein-analysis chip.

Key words: **affinity chromatography, isoelectric focusing, electrophoresis, post-translational modifications, protein analysis**

1. Introduction

Multi-dimensional separation technologies are required for proteomics. The substantial loss of samples occurs at connective processes from one separation process to another. Loss-less connections are expected to be achieved in a micro TAS [1].

We made a Pyrex glass chip integrating AC and IEF. The device, in its final form, is expected to allow the analysis of a small amount of samples in a complex sample matrix and to provide valuable information about post-translational modifications, which are difficult to analyze in a simple way using previous procedures.

2. Theory

Zone electrophoresis (ZE) has long been a main stream of micro-channel separations in the development of micro TAS. Unfortunately the limited sampling volume of ZE obscured the merit of micro channels in the analyses of real samples. In contrast to ZE, the sampling volume of IEF can be as large as the total volume of the separation channel owing to its focusing nature. Direct application of IEF to biological samples, however, does not provide fruitful results because of their high complexity. Making use of the merit of a micro chemical chip in integrating multiple processes, we attempted to couple affinity chromatography and IEF in a microchip, in which a substantial part of the captured proteins by AC can be analyzed by IEF.

3. Experiment

A micro channel, 150 μm wide and 60 μm deep, was etched on a Pyrex glass plate (3 cm x 7 cm x 0.7 mm), and it was thermally bonded with the plate having platinum electrodes (Fig. 1). The gel beads for affinity capture were retained in the channel by means of a constriction at the end of the AC channel (25 mm long). The channel was coated with polydimethylacrylamide and connected to tubings via newly designed mechanical valves that were inserted between access holes and tubing connectors (Fig. 2). A confocal laser-induced fluorescence detection system was set at the upstream end of the IEF channel (25 mm long) (Fig. 3).

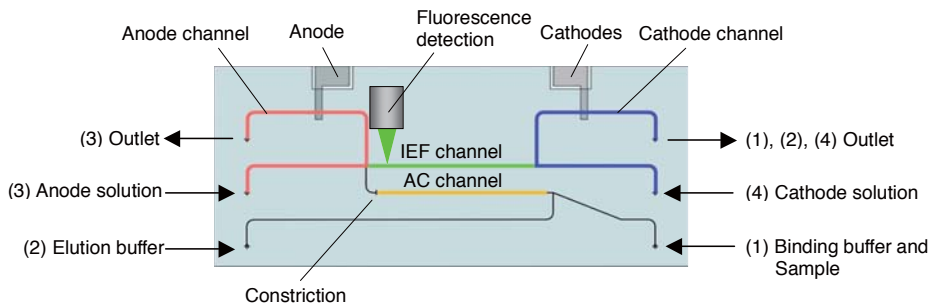


Fig. 1 AC-IEF chip and its operations

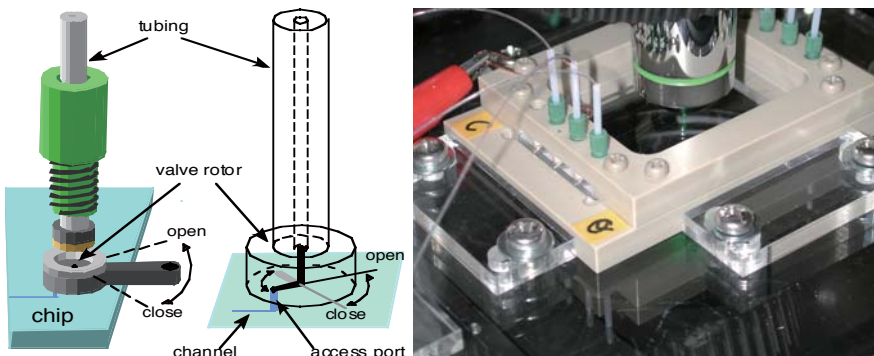


Fig. 2 Mechanical valve

Fig. 3 AC-IEF chip system

4. Result and discussion

A preliminary experiment was done without affinity beads. One μL of the sample solution containing four kinds of rhodamine-labeled peptide pI markers ranging from pI 3.64 to 9.56 each at 10 nM (10 fmol) was applied to the chip [2]. A part of the sample was trapped in the IEF channel by stopping the flow. An acidic anode solution and a basic cathode solution were introduced into respective electrode channels. Electric focusing was carried out for 4 min at 1 kV, and the whole IEF channel was scanned at a rate of 1 mm/s (Fig. 4). The separation pattern was retained for over 4 min under the electric field.

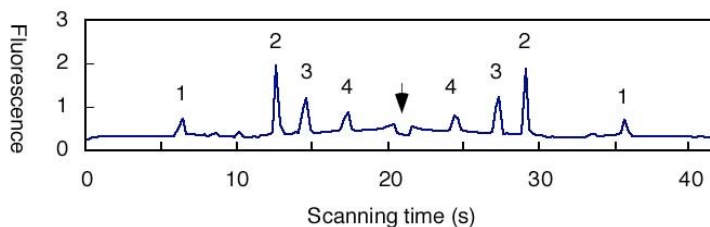


Fig. 4 IEF separation of four fluorescence-labeled peptide pI markers (10 fmol). The pI values of the peaks are (1) 3.64, (2) 5.53, (3) 7.58 and (4) 9.56. Scanning was returned at the arrow.

5. Conclusion

The concept of the system allows fast and precise analysis of a specific protein in a complex sample matrix at high sensitivity. The determination of isoelectric points should provide valuable information for identification of proteins and post-translational modifications that are of critical importance in proteomic analyses.

Acknowledgement

This study was supported by the Research Association of Micro Chemical Technology (NEDO), Japan.

Reference

- [1] Guzman, N.A., Phillips, T.M., *Anal. Chem.* 2005, **77**, 61A-67A
- [2] Shimura, K., et al., *Anal. Chem.* 2002, **74**, 1046-1053

DEVELOPMENT OF NEGATIVE DIELECTROPHORETIC CELLULAR PATTERNING SYSTEM FOR CO-CULTURING OF TWO DIFFERENT CELL TYPES

Masato Suzuki¹, Tomoyuki Yasukawa¹, Mariko Komabayashi², Akiko Inagaki², Yoshio Hori², Hitoshi Shiku¹, and Tomokazu Matsue¹

¹ Graduate School of Environmental Studies, Tohoku University, 6-6-11 Aramaki-Aza Aoba, Aoba, Sendai, 980-8579, Japan

² Tohoku University Biomedical Engineering Research Organization (TUBERO), 2-1 Seiryo, Aoba, Sendai, 980-8570, Japan
(msuzuki@bioinfo.che.tohoku.ac.jp)

Abstract

Biological cells have been manipulated in a microdevice by means of negative dielectrophoresis (n-DEP) to form a micropatterns with two different cell types. The device with interdigitated array (IDA) electrodes was used to manipulate cells and to create a periodical line patterns with cells on a cell culture slide that was placed on 30 μm above IDA electrodes. Mouse myoblast cells (C2C12) were used as model cells to regulate the cultivation in weaker electric field regions in the micropatterning device filled with a cell culture medium. Specifically, cells formed the line pattern within 30 sec on the cell culture slide when a 1 MHz ac voltage (12 Vpeak-to-peak) was applied to the IDA electrodes. Most of patterned cells adsorbed on the slide after several minutes incubation under the application of ac voltage. The micropatterning with alternate lines of two different cell types was achieved by subsequently injecting another cell suspension in the device, and applying ac voltage to a different set of IDA electrodes. The method based on n-DEP permits the quick and easy fabrication of micropatterns composed from two different cell types without chemical modification of substrates.

Keywords: dielectrophoresis, co-cultivation, cell-adhesion, micropatterning, cell manipulation

Introduction

The micropatterning with living mammalian cells has evoked a strong interest in many areas of biotechnology as well as in the fundamental studies of a cellular biology^[1]. To date, many techniques for the cell patterning have been reported. Most of these patterning methods, such as a soft-lithography^[2] and photo-lithography^[3], are to utilize the surface-recognition abilities of cells. These methods, however, require complex pretreatments of the substrate to be patterned by cells and are not suitable for co-cultivation of two different types of patterned cells. We present here a novel patterning method and co-cultivation of two-different types cells based on negative-dielectrophoresis (n-DEP)^[4] without the pretreatment of the cell culture slide.

Design of Negative Dielectrophoretic Micropatterning Device

Fig. 1 schematically depicts the principle of the patterning method with biological cells based on n-DEP. The n-DEP force directs the cells toward the weakest region of the non-uniform electric field and cells are patterned above the microband electrodes. The four phases interdigitated array (IDA) electrode with 50 μm widths and 100 μm gaps was used as a template for making the cellular patterns. A polyester film with 30- μm thickness was sandwiched by the IDA electrode and cell culture polystyrene slide. The patterning device was mounted under a microscope and filled with a suspension of mouse myoblast C2C12 cells (2.5×10^7 cells/mL) in Dulbecco's Modified Eagle medium supplemented with 5 % heat inactivated horse serum and 0.5 % streptomycin.

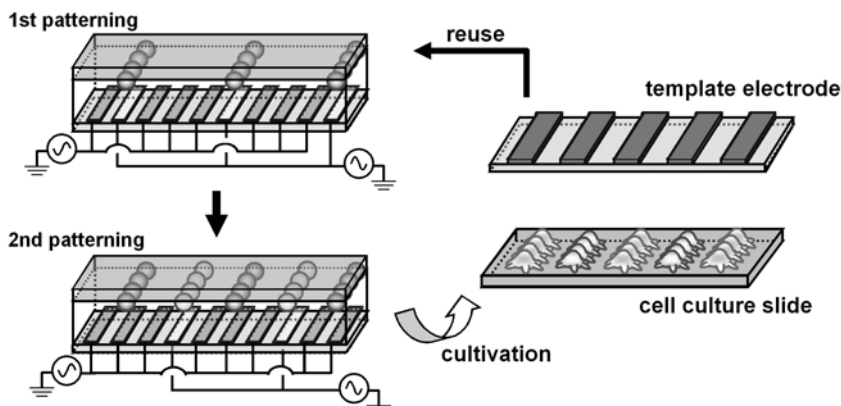


Figure 1. Principle of the patterning method in the present study

Results and Discussion

On applying the ac voltage (1 MHz, 12 Vpp) to the IDA electrode, almost all cells rapidly move with a repulsive force of n-DEP to the culture slide and form lines on it within a minute. Incubation for 5 min at room temperature under the voltage application allows the adsorption of the cells patterned on the culture slide (Fig. 2). The shape and number of cells depend on the cultivation time. The teardrop shape of cells is observed after 3 hr cultivation. The line patterns of cells are gradually disintegrated with the increase of the number of cells.

It should be noted that the present method allows the formation of other patterns between the lines previously formed with cells. AC voltage was applied to different set of IDA electrodes in order to fabricate second cell lines and, as a result, the second pattern was formed between the first lines of cells. Fig. 3 shows the resulting periodical patterns with 300 μm pitch of two different cell types. The first pattern of cells was stained with CellTracker Green CMFDA before fabricating the second pattern. In a fluorescent image in Fig 3(b), signals were obtained from the positions of the first pattern of cells. Multipatterning of different cell types can be achieved by utilizing the n-DEP-based method.

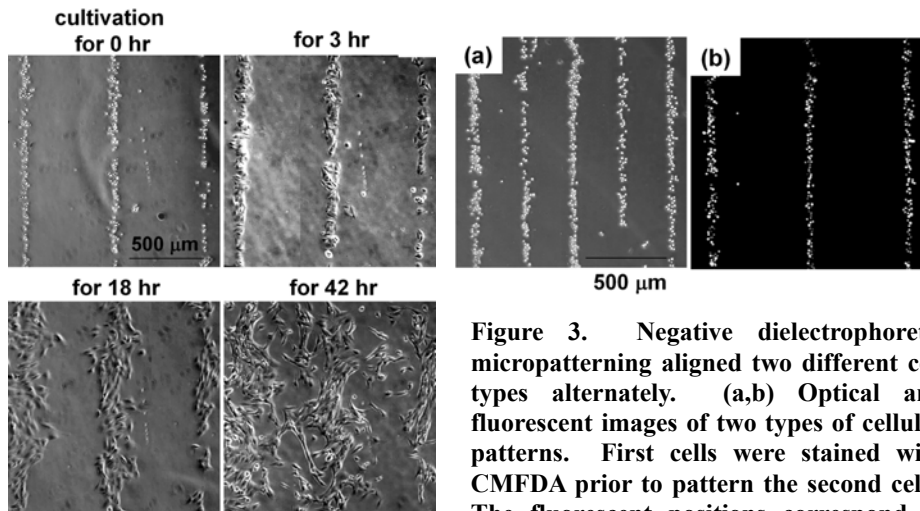


Figure 2. Optical micrographs of the patterned C2C12 cells on the cell culture polystyrene slide

Figure 3. Negative dielectrophoretic micropatterning aligned two different cell types alternately. (a,b) Optical and fluorescent images of two types of cellular patterns. First cells were stained with CMFDA prior to pattern the second cells. The fluorescent positions correspond to the first patterned cellular positions

Conclusion

We have developed a novel microdevice based on n-DEP for fabricating the micropatterns with two types of cells. Cell alignment can be done easily and quickly on the cell culture slide without the chemical pretreatment. This method will offer the great possibilities for the multipatterning of many cell types in order to develop the analysis system of cellular interactions.

Acknowledgements

This work was partly supported by Grants-in-Aid for Scientific Research (17750149) and for Scientific Research of priority areas (18048001) from the Ministry of Education, Science and Culture, Japan. M.S. acknowledges support from a research fellowship of the Japan Society for the Promotion of Science.

References

- [1] S. Raghavan, C. S. Chen, *Adv. Mater.*, **16**, 1303-1313, **2004**
- [2] R. Singhvi, A. Kumar, G. P. Lopez, G. N. Stephanopoulos, D. I. C. Wang, G. M. Whitesides, D. E. Ingber, *Science*, **264**, 696-698, **1994**
- [3] J. M., Corey, B. C. Wheeler, G. J. Brewer, *IEEE Trans. Biomed. Eng.*, **43**, 944-955, **1996**
- [4] (a) T. Matsue, N. Matsumoto, I. Uchida, *Electrochim. Acta*, **42**, 3251-3256, **1997**, (b) M. Suzuki, T. Yasukawa, Y. Mase, D. Oyamatsu, H. Shiku, T. Matsue, *Langmuir*, **20**, 11005-11011, **2004**

MICROSYSTEMS FOR ELECTROPHYSIOLOGICAL STUDY OF INVITRO NEURODERMATOLOGICAL CULTURES

Laurent Griscom¹, Ulysse Pereira², Jean-Pierre Pennec², Mathieu Ben¹, Laurent Misery²

¹BIMIS/SATIE CNRS UMR8029, ENS-Cachan-Bretagne, Campus de Ker Lann, 35170 BRUZ, FRANCE

²I3S – UBO, 5 avenue Foch, CHU MORVAN, 29609 BREST cedex

Abstract:

In this report, a biochip with multicompartiment campenot chambers was fabricated with PDMS for neuron and skin cell co-culture. The chambers are interconnected by microfluidic pathways, which allow the neurons to develop nerve endings in the skin compartment. Gold micro electrodes were integrated into the biochip.

Keywords: Cell Culture, PDMS, Microsystem, Microelectrode

Introduction

Study of interactions between the skin and the nervous system is an important domain for dermatologists concerned with maladies such as chronic pain or itch and for the cosmetics industry. In this study, PDMS microsystems were created for the effective in-vitro culture and separation of sensory neurons and skin cells. The different cell types are cultured in Campenot chambers [1] that are joined by multiple microchannels buried in the PDMS microsystem structure [2.,3]. These microchannels allow the neurons to grow axons that infiltrate the skin cells and form nerve endings. Separate electrophysiological measurements on the sensory neurons can then be made after stimulation of the skin cells by use of extra cellular microelectrodes integrated into the chip or patch-clamp recording.

Methods

The PDMS chip was fabricated using a two level SU-8 master to mold multiple copies that formed 10-20 micron wide (height 12 μ m) microchannels, and the 3mm cell chambers (height 1.2mm). A polymer-based surface treatment was applied to the glass substrate and PDMS microstructure to insure a long-term hydrophilic and biocompatible cell growth surface [4]. The substrate was made of plain glass slides or slides with gold microelectrodes.

Primary cell cultures were extracted from eight day old pigs, as the skin and neurons are thought to resemble human skin interactions more precisely than that of rats. The skin cells were mainly keratinocytes while the extracted neurons were dorsal root ganglions (DRG). After extraction and trypsinization the cells were placed into the chambers by pipette and cultured for 15 to 30 days.

Electrophysiological activity of the DRG was monitored in reaction to various stimulants and irritants applied to the skin cells, (capsaicin, histamine and heat). The stimulation of the skin cells was applied using 200 μ l of histamine or capsaicin at a concentration of 30 μ Mol/ml and the solutions were added to the medium during electrophysiological measurements and recorded for 10 Minutes.

Heat was applied using drops of hot water at 45°C Electrophysiological activity was measured using either an external patch-clamp apparatus that could be lowered into the chambers or by use of extracellular microelectrodes. The macro-patch clamp technique used to record the membrane currents operated under voltage clamped conditions in the cell-attached configuration [5,6]

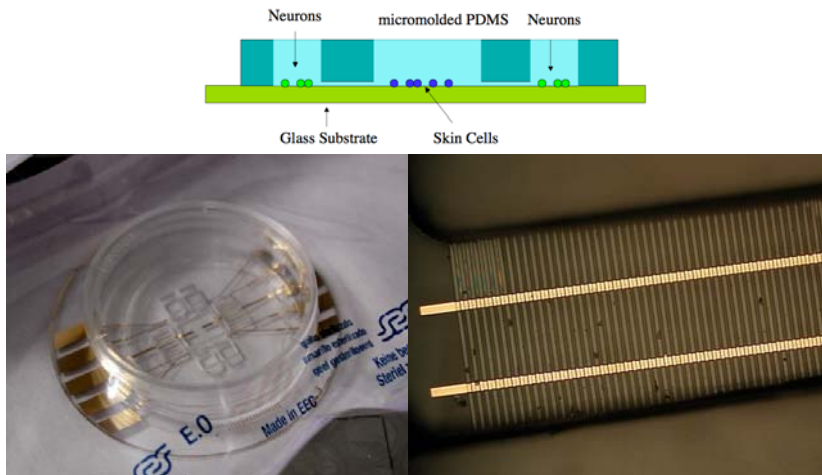


Figure 1: (Top) Schmatic diagram of PDMS microsystem with channels and wells placed on glass substrate. (Left) Photograph of PDMS microsystem with integrated gold microelectrodes on 50mm glass substrate, enclosed in a 35mm dish. (Right) 100micron wide gold electrodes included under the micro channels.

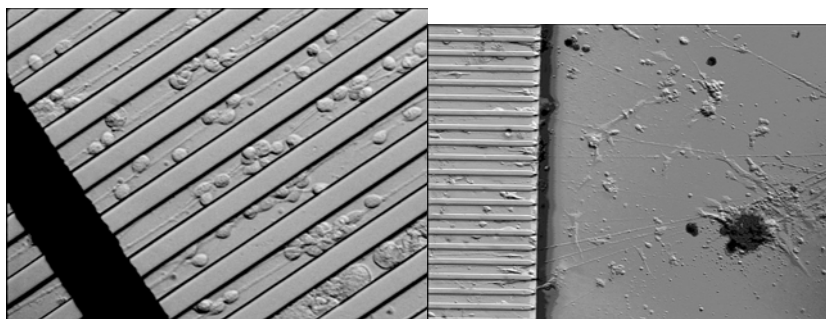


Figure 2: (Left) Microscope images of axons traversing the length of buried 20 microns wide multiple microchannels; the black band is the gold microelectrode. (Right) The axons in the neuron compartment are attracted to the microchannels which lead to the skin cell compartment.

Results

The surface treatment used in the microsystem assembly allowed the biological researcher to adequately fill the microchannels and wells with medium several weeks after fabrication due to the long-term hydrophilic effect. After seeding each compartment with the cells, axons from DRG neurons could be observed to extend into the skin compartment through the 1mm long microchannels after 1 week of culture.

Electrophysiological measurements were performed initially by patch-clamp on axons leading to the skin compartment. An increase in electrophysiological activity in the neuron cells was noted after the addition of heat (hot water drops) in the skin compartment.

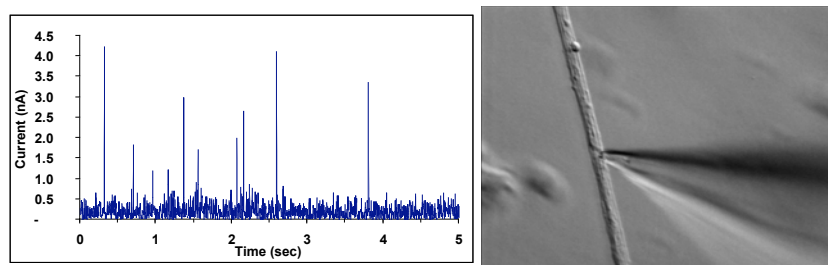


Figure 3: (Left) Spontaneous activity recorded from a neurite by extracellular patch clamp electrode, after application of heated medium (45°C) in the bath. (Right) image of patch clamp electrode in contact with a DRG axon.

References

- [1] R. Campenot, *Proc. Natl. Acad. Sci. USA* Vol. 74, No. 10, pp. 4516-4519, October 1977 Cell Biology
- [2] L. Griscom., P. Degenaar, B. LePioufle, E. Tamiya, & H. Fujita Techniques for patterning and guidance of primary culture neurons on micro-electrode arrays. Sensors and Actuators B: Chemical 83, 15-21 (2002).
- [3] Degenaar, P. et al. A method for micrometer resolution patterning of primary culture neurons for SPM analysis. Journal of Biochemistry 130, 367-376 (2001).
- [4] L. Griscom, G. Legeay, B. LePioufle, International Patent Demand N° PCT/FR2005/001162
- [5] J-P. Pennec et al. *Cell Mol Biol* (Noisy-le-grand). 2002 Jun;48(4):351-8.
- [6] J-P. Pennec et al. *Journal of Experimental Biology* 207, 3935-3944 (2004)

A MULTIELECTRODE MICROCOMPARTMENT PLATFORM (MUMP) FOR SPATIOTEMPORAL LOCALIZATION OF NEURONAL INJURY POTENTIALS

Surendra K. Ravula¹, Maxine A. McClain¹, Minsheng Wang², Jonathan D. Glass², A. Bruno Frazier¹

¹Georgia Institute of Technology, Atlanta, Georgia 30332 USA

²Emory University, Atlanta, Georgia 30322 USA

Abstract

This paper describes a multielectrode microcompartment platform (MUMP) for studying the electrophysiological effects of drugs on cultured neurons. We demonstrate the ability to culture neurons with extensions growing into adjoining compartments while maintaining fluid isolation between compartments. Furthermore, we describe the assembly of the microsystem and show the ability to record action potentials in the multicompartment system. The chemotherapeutic drug and neurotoxin vincristine is used as the test vehicle to demonstrate the effectiveness of the MUMP in studying the spatiotemporal localization of metabolic processes underlying chemotherapy-induced neuronal injury.

Keywords: DRGs, compartmented cultures, vincristine, injury potentials

1. Introduction

The convergence of microfluidics, microelectronics, and cell culture techniques has opened up new opportunities for the creation of hybrid neural microsystems [1]. Since these systems offer unparalleled spatiotemporal control over the biochemical microenvironment of a neuronal culture and the ability to incorporate many substrate-embedded electrodes under the neurons, they enable more sophisticated studies on the signaling mechanisms that govern neuronal physiology. In this work, we describe a specific example of this new system paradigm-a multielectrode microcompartment platform (MUMP) that incorporates a microfluidic compartment divider

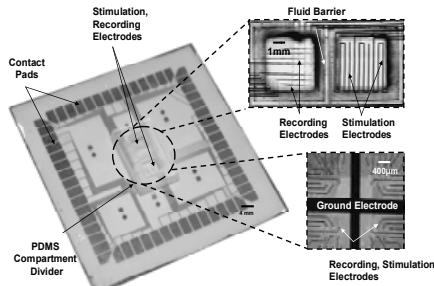


Figure 1. Assembled compartmented culture system. The microelectrode array (MEA) is fabricated using conventional semiconductor technology. The PDMS compartment divider is patterned with silicone grease and aligned to the electrode design on the MEA substrate. Insets show a close-up of two different fabricated MEAs with all of the stimulation and recording points exposed in the nitride insulating layer. The top inset also includes the compartment divider around the electrodes.

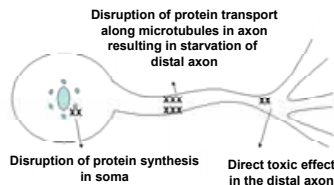


Figure 2. Potential metabolic pathways of vincristine-induced distal axonal degeneration.

with a multielectrode array (MEA) substrate (see Figure 1). The MUMP is used to study chemotherapy-induced distal axonal degeneration (DAD), a gradual degenerative condition that starts in the distal axon and proceeds proximally toward the cell body. By spatially dividing the neuron in the MUMP into two different drug compartments and monitoring the electrophysiological health of the neuron in both, we extend our work with vincristine, a chemotherapeutic drug, in compartmented cultures by examining its electrophysiological consequences. More specifically, we present evidence here that different spatiotemporally isolated mechanisms in the cell bodies and distal axons are responsible for vincristine neuropathy (see Figure 2).

2. Experimental Details

The system consists of a micromolded PDMS compartment divider that has microfluidic barriers and a 60-electrode fabricated MEA substrate [2].

Dorsal root ganglia (DRG) neurons were then plated in one of the compartments and allowed to grow axons into the adjacent compartment across a microfluidic barrier (see Figure 3). While allowing neurite extensions to grow across it, the barrier does not allow the fluid environments of both compartments to mix. The system was periodically checked for leakage by examining fluid levels and by changing the hydrostatic pressure in compartments that were known to be leaking.

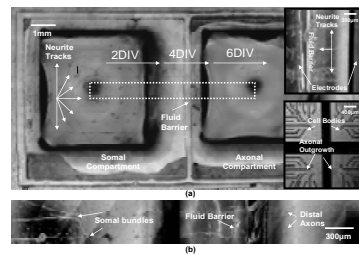
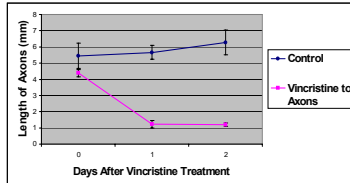


Figure 3. Culturing of dissociated DRG neurons in a two compartment system. (a) an 8-track neurite system. Neurons were plated in the left compartment and grew extensions along pre-patterned collagen tracks into the adjacent compartment after several days in vitro. The top inset shows three neurite tracks growing on the top electrode substrate in Figure 1. The bottom inset shows neurites growing on the bottom electrode substrate in Figure 1 before the compartment divider has been attached to it. (b) close-up of dashed box showing 2 of the 8 tracks.

Graph 1. Axonal degeneration due to vincristine-induced toxicity in a two compartment culture ($n=4$)



Values are mean \pm SEM. $P<0.001$ when vincristine sample compared to control at day 2.

3. Results and Discussion

After 10 days in culture, the neurotoxin and chemotherapeutic drug vincristine ($0.01\mu M$) was applied to the axonal compartment to induce axonal degeneration over a two day period (see Graph 1) [3]. The MUMP was then placed into a Multichannel Systems preamplifier setup (see Figure 4). To generate action potentials in the DRGs, a $2.5M$ solution of the depolarizing chemical KCl was applied to both compartments. Table 1 summarizes the electrophysiological results of applying vincristine to the axonal compartment over a two day period. Since these injury potentials change in both compartments, this data suggests that the degenerative phenotype is regulated by different spatiotemporally-isolated mechanisms in the cell bodies and distal axons.

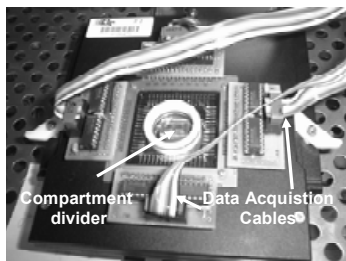


Figure 4. MUMP preamplifier recording setup with microfluidic compartment divider seated in the center of the MEA.

4. Conclusions

Taken together, these studies show that it is possible to culture neurons readily in the MUMP and that the system can be used to gather electrophysiological data from neurons cultured intercompartmentally. Moreover, through our experiments with vincristine, we have provided evidence that more than one spatially isolated mechanism could be involved in vincristine neuropathy. This knowledge may lead to the design of more effective pharmacological treatments for chemotherapy-induced neurodegeneration.

5. References

1. S. M. Potter and T. B. Demarse, "A new approach to neural cell culture for long term studies," *Journal of Neuroscience Methods*, vol. 110, pp. 17-24, (2001).
2. S. K. Ravula, J. D. Glass, and A. B. Frazier, "A microfabricated compartmented culture system for electrophysiological studies of neurons," presented at International Conference on Micro Total Analysis Systems, Boston, MA, (2005).
3. M. S. Wang, Y. Wu, D. Culver, and J. D. Glass, "Pathogenesis of axonal degeneration: parallels between Wallerian degeneration and vincristine neuropathy," *Journal of Neuropathology and Experimental Neurology*, vol. 59, pp. 599-606, (2000).

Table 1. Changes in localized injury potentials of DRGs during vincristine exposure (n=6)

	No Vincristine (Control)		Vincristine Added to Axonal Compartment	
	Somal Compartment	Axonal Compartment	Somal Compartment	Axonal Compartment
(Day 0) Number of Spikes	54±6	62±6	54±7	64±2
(Day 1) Number of Spikes	64±4	59±5	92±6	21±4
(Day 2) Number of Spikes	61±8	57±3	66±6	2±2

Values are mean \pm SEM. P<0.001 when axonal compartments are compared at day 2. P>0.05 when somal compartments are compared at day 2.

PERFUSED MULTIWELL TISSUE CULTURE PLATES WITH INTEGRATED MICROFLUIDIC SYSTEM

Karel Domansky¹, Walker Inman^{1,2}, Jim Serdy^{1,2}, Bryan Owens², Megan Whittemore¹, Laura Vineyard¹, Linda G. Griffith^{1,2}

¹Biological Engineering Division and Biotechnology Process Engineering Center, ²Mechanical Engineering Department,
Massachusetts Institute of Technology

77 Massachusetts Avenue, Cambridge, MA 02139, USA
domansky@mit.edu

Abstract

A new cell culture platform based on the multiwell tissue culture plate format has been developed. The novel approach provides perfused three-dimensional cell culture capability. The new capability is achieved by integrating microfluidic valves, pumps, and capacitors into the plate. The system provides a means to conduct high throughput assays for toxicology and metabolism. It can be also used for evaluation of long-term exposure to drugs or environmental agents or as a model to study viral hepatitis, cancer metastasis, and other diseases and pathological conditions.

Keywords: Cell-based assays, microbioreactor, multiwell tissue culture plates

1. Introduction

Recent reports indicate that it takes nearly \$800 million dollars and 10-15 years of development to bring a drug to market. Nearly 90% of the lead candidates identified by current in vitro screens fail to become drugs. One of the reasons for the high failure rate of drug candidates is the lack of adequate models. To address the problem, we have developed a new cell culture analog [1-3] amenable to routine use in drug development. It is based on the standard multiwell tissue culture plate format but it provides perfused 3D cell culture capability. The footprint of the new platform complies with international standards for multiwell plates and is in many respects compatible with the high throughput robotic systems in place at pharmaceutical and biotechnology companies.

2. Experimental

The perfused 12-microbioreactor array (Fig. 1) consists of a fluidic and a pneumatic manifold with a diaphragm sandwiched in between them. The fluidic manifold contains an array of 12 microbioreactor and reservoir pairs (Fig. 2a). Each microbioreactor/reservoir pair is fluidically isolated from all other microbioreactors on the plate. A key component of a microbioreactor is a scaffold for tissue morphogenesis. The scaffold can be, for example, a thin wafer (as shown in Fig. 2a) containing an array

of channels in which cells self-assemble into 3D pieces of tissue. Tissue in the scaffold is perfused by cell culture medium that is recirculated between a reactor and a reservoir by a built-in pneumatically driven bidirectional microdiaphragm pump with active valves (Fig. 2b). Diaphragms of all pumps and rectifying valves are actuated in parallel via three pneumatic lines connected to an electro-pneumatic controller.

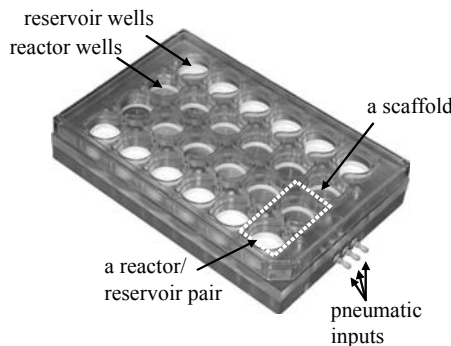


Figure 1. Microbioreactor array in the multiwell tissue culture plate format.

3. Results and discussion

Perfusion flowrate is determined by the volume pumped per cycle and cycle frequency. Actuation of the membrane in the pumps and valves generates flow pulsatility. To control it, we incorporated microfluidic capacitors between the pumps and the scaffolds. Fluidic capacitors absorb fluid during the pump emptying cycles and generate flow during the filling cycles. This results in damping the flow pulsatility. To determine fluidic capacitance $C = dV/dP$, we measured the displacement of capacitor membrane as a function of fluid pressure. From the membrane displacement, we calculated the volume of the fluid stored in the capacitor (Fig. 3a). Volume data from Fig. 3a as a function of absolute pressure are plotted in Fig. 3b and fitted with a polynomial function. First derivative of this function is the capacitance of the microfluidic capacitor. It is also plotted in Fig. 3b.

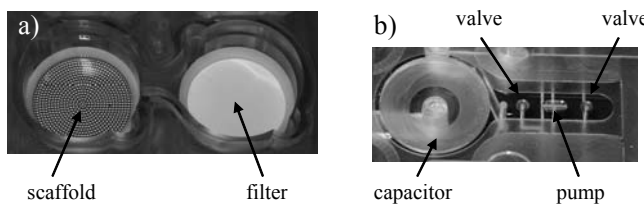


Figure 2. A microbioreactor/reservoir pair (a) and its pumping elements (b).

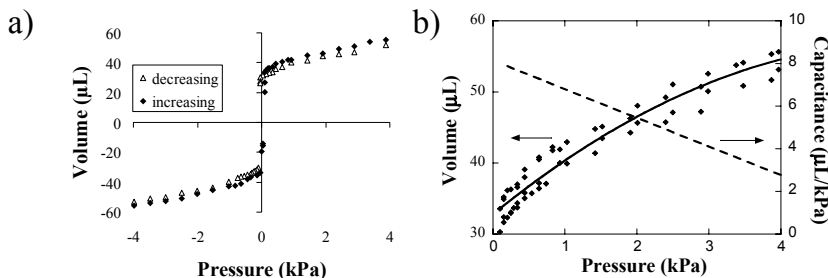


Figure 3. Capacitor volume as a function of the fluid pressure (a). Polynomial fit and capacitance as a function of the fluid pressure (b).

4. Conclusions

A novel platform for cell culture based on the multiwell tissue culture plate format has been developed. Key aspect of the new system is perfusion of 3D microtissue units by cell culture medium. Flow pulsatility is controlled by built-in microfluidic capacitors.

The system provides a means to conduct high throughput assays for toxicology and metabolism. It can be also used for evaluation of long-term exposure to drugs or environmental agents or as a model to study viral hepatitis, cancer metastasis, and other diseases and pathological conditions.

Acknowledgement

We want to thank DuPont – MIT Alliance, Pfizer, and NSF Biotechnology Process Engineering Center for financial support.

References

1. K. Domansky, W. Inman, J. Serdy, and L. G. Griffith, Perfused Microreactors for Liver Tissue Engineering, Proceedings of the 27th International Conference of the IEEE-EMBS, Shanghai, September 1 - 4, (2005).
2. K. Domansky, W. Inman, J. Serdy, and L. G. Griffith, 3D Perfused Liver Microreactor Array in the Multiwell Cell Culture Plate Format, Proceedings of the Ninth International Conference on Miniturized Systems for Chemistry and Life Sciences (μTAS), Boston, pp. 853-855, October 9 - 13, (2005).
3. K. Domansky, W. Inman, J. Serdy, and L. G. Griffith, Multiwell Cell Culture Plate Format with Integrated Microfluidic Perfusion System, Proceedings of SPIE, Microfluidics, BioMEMS, and Medical Microsystems IV, Vol. 6112, pp. 61120F-1 - 61120F-7, San Jose, January 23-25, (2006).

STACK AND MEASUREMENT OF ZEPTOMOLE NEUROTRANSMITTERS RELEASED FROM LIVING SINGLE CELLS ON A FASS-NANO-FLUIDIC CHIP WITH ELECTROCHEMICAL DETECTION

¹Ren-Guei, Wu, ^{1*}Fan-Gang Tseng, and ^{1,2}Chung-Shi Yang

¹Engineering and System Science Dept., National Tsing Hua University, Taiwan,
^{1, 2}National Health Research Institutes, Taiwan,

Abstract

This paper demonstrates the detection possibility of zeptomole level neurotransmitters released from two to three living PC-12 cells by employing FASS (the Field-amplified sample stacking) incorporated with a nano Pd-Pt-SWCNT (Pd-Pt nanostructure modified Single-wall carbon nanotube) electrode and integrated on a nano EC-CE (electrochemical capillary electrophoresis) chip. The detection limit can approach 0.5 nM (~ 38 zeptomole) dopamine with an S/N ratio > 2 for the releasing from two–three living cells.

Keywords: Zeptomole, Living single cells, Neurotransmitters, Carbon nanotubes (CNTs), Nano-fluidic chip

1. Introduction

The detection of single-cell-releasing is a challenging but important task for understanding single cell behavior. This paper proposes the integration of FASS, nano transitional channel, and nanostructured electrodes in CE-EC chip for exploring this possibility. FASS is a useful preconcentration technique and the highest reported FASS signal enhancement factor is roughly 500-1000 fold in microchip experiments [1]. Carbon nanotube-modified electrodes have been employed to sense dopamine and catechol in CE-microchip, demonstrated roughly 20-50 fold detection limit enhancement [2]. These two techniques will be integrated into a nano channel of EC-CE chip to further bring down sensing molecules close to the nano-structured electrode for 5-10 fold EC signal enhancement [3]. The expected total signal enhancement will be in the order of 4-5, which can bring down the detection limit of electrochemical detection from $\sim 10 \mu\text{M}$ into sub nM region, close to the level of single-cell-releasing.

2. Experiment and Results

The design and operation process are shown in Fig. 1(a). This chip was composed of two parts, the upper microchannel (L form) were used to trap the single cells by induced surface charge control electrodes in culture microchannel (width: 100 μm ; height: 50 μm) and then to pumping culture medium into the side main separation channel (width: 50 μm ; height: 50 μm), the lower nanochannel includes a ladder-shaped transitional reservoir and a line-shaped separation channel (width: 100 gradually to 50 μm ; height: 500 nm). SEM photograph shows the nano channel geometry and depth, in Fig 1(b)-(d). Before applied the separated electric-field, an inverted pre-concentration electric-field was used to stacking sample in front of the Nano-transitional channel.

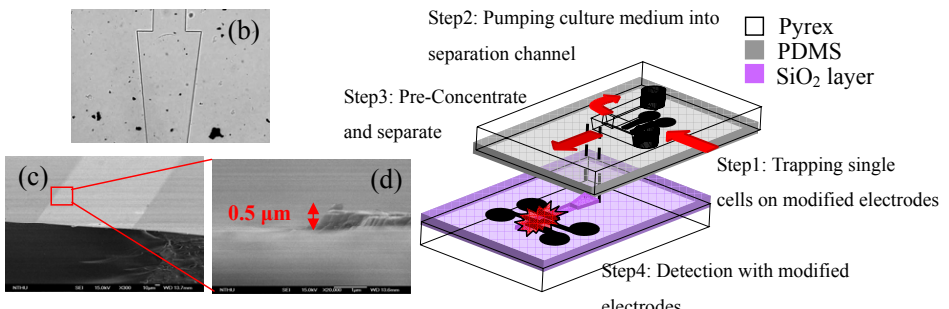


Fig.1 The On-Line Neurotransmitters measurement Process of a nano-FASS EC-CE Chip and (b)-(d) the SEM photograph of the nano-channel geometry and depth

The cells were trapped on electrodes by applied potentials from 0 to ± 10 V, the induced surface charge was adjusted to the isoelectric point of cell [4], as represented the simplified scheme in Fig. 2(a) and the process of a single cell trapping on collagen/SiO₂/Pt electrodes are shown in Fig. 2(b).

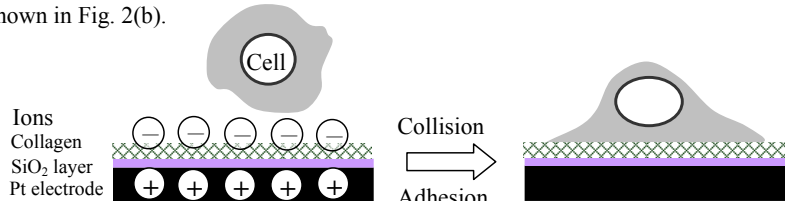


Fig. 2(a) The principle diagram of cell adhesion by induced surface charge electrode.

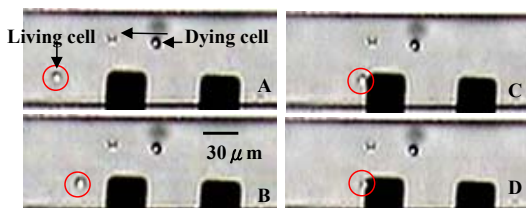


Fig. 2(b) The process of cell trapping on the collagen/SiO₂/Pt electrode

The process of FASS sample concentration is shown in Fig 3 (a) and (b) for a 100 nM Rhodamine B fluorescence dye. When the dye reaching the transitional reservoir and a separation voltage was then applied to the nano-separation channel, the fluorescence dye was rapidly concentrated into a narrow zone of 45 μ m had migrated about 100 μ m.

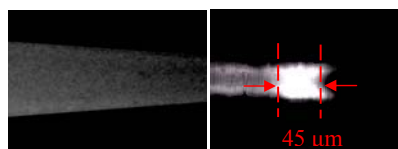


Fig. 3 Fig. 3 The FASS-CE concentration effect on Rhodamine B fluorescence dye.

In order to promote electrochemical detection, Pd nano-particles were electrodeposited on the Pt-based electrode. Finally, purified sCNTs were dissolved in nafion, dropped on the Pd-Pt electrode as a mediator for rapid electron transportation. Fig. 4 (a)-(c) shows the SEM photograph of the Pt-base、Pd-Pt、sCNT-Pd-Pt electrodes, respectively. Fig. 4 (d) shows the electrocatalysis efficiency of 10 mM $K_4Fe(CN)_6$ in 0.5 M H_2SO_4 on three modified electrodes, and only the one with sCNT-Pd-Pt coating carry out the maximum redox current.

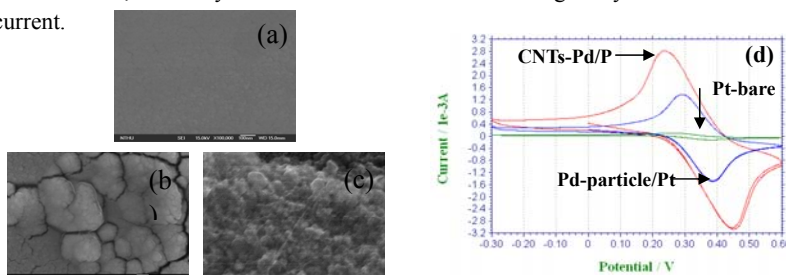


Fig. 4 (a)-(c) The SEM photograph of modified surface morphology of electrodes in three difference deposition step and (d) Cyclic voltammograms of 10 mM $K_4Fe(CN)_6$ in 0.5 mM H_2SO_4 of three modified electrodes.

Fig. 5(a) shows the living PC-12 cells growth state with NGF culture medium in microchannel on electrodes after two days. In here, it should be note that Trypan blue, a living membrane non-permeable dye was used to identify the cell living situation before 3 mM nicotine treatment to release dopamine. The detected signal from the releasing of two-three living cells is estimated as 0.5 nM when compared to that of a 1 nM standard dopamine solution, as shown in Fig. 5(b). Dopamine obtained from cell-lysing is also compared in the figure when 100 mM KCl was added in the same channel.

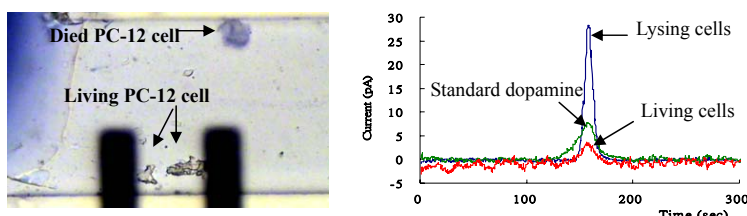


Fig. 5 (a) The living PC-12 cells with NGF culture and (b) Electropherogram of three conditions of culture medium: Green line, the standard (1 nM) dopamine. Red Line, the living cells with nicotine treated. Blue line, the cells lysing with KCl solution.

Reference

- [1] Byoungsok Jung, Rajiv Bharadwal, Juan G. Santiago, *AnzL. Chem.* 2006, 78, 2319-2327
- [2] Walter R. Vandaveer IV, David J. Fischer, *Electrophoresis* 2004, Vol. 25, issue 21-22, p.3528-3549
- [3] Ren-Guei, Wu, Fan-Gang Tseng, Chung-Shi Yang, *Nanotech* 2005, 625, p.728 - 731
- [4] Tai-Horng Young, Chih-Huang hung et al., *J. Colloid Interface Sci.* 2005, 258, p557-561

NOVEL PICOLITER COMPARTMENTAL MICROFLUIDIC CHIP DEVICES FOR HIGH-THROUGHPUT SINGLE-CELL SORTING AND ANALYSIS

Ramachandra Rao Sathuluri^{1, 2}, Masahito Kitamura², Shohei Yamamura², and Eiichi Tamiya²

¹Toyama New Industry Organization, 529, Takada, Toyama City, Toyama 930-0866, Japan

²School of Materials Science, Japan Advanced Institute of Science and Technology, 1-1, Asahidai, Nomi City, Ishikawa 923-1292, Japan

Abstract

In this study, we report development of novel compartmental microfluidic chip devices for high-throughput single-cell sorting and analysis of antigen-specific single B-cells before and after stimulation with an antigen from a bulk cell suspension in the aqueous compartments that are generated by the two-phase liquid systems in the Y-shaped microchannels (20 cm) made from poly(dimethylsiloxane) (PDMS) polymer. The effect of flow rates, viscosity of continuous phase (oil) and sample channel geometry on the size of aqueous compartments and cell sorting was studied. This chip system has the ability of sorting 1250 cells < 100 sec.

Keywords: Picoliter compartmental microfluidic device, multiplexing, two-phase liquids, single-cell analysis, high-throughput screening

1. Introduction

Sorting, screening and analysis of individual cells from a bulk suspension plays a pivotal role in the prognosis and early diagnosis of diseases thus facilitating timely and rightly treatment, while bulk analyses always gives averaged results. Though conventional flow cytometry known for its efficiency in cell sorting, they lack analysis of the same cell before and after stimulation with a particular stimulus. Therefore, we have constructed novel and inexpensive microfluidic chip devices coupled with two-phase liquid systems enabling high-throughput single-cell sorting and analysis of single B-cells from bulk lymphocyte suspensions in the picoliter aqueous compartments before and after stimulations with antigen of a choice (Fig. 1). The detection of a positive single B-cell was based on the increased intrinsic Ca^{2+} levels after stimulation with antigen, which we reported using microarray platform [1]. Further analysis of antibody DNA of positive cells would lead to development of a highly specialized monoclonal antibody as antibody medicine.

2. Experimental

The PDMS microchannel system (50 x 50 μm^2 wide and deep) as shown in Fig. 2a was constructed by casting PDMS (Sylgard 184 silicon elastomer, Dow Corning) over SU-8 50 photoresist (Microchem) mold on a silicon wafer by soft photolithography as previously described [2]. These devices were evaluated for establishment of compartmentalization of two-phase liquids (eosin liquid, mineral oil) under microsyringe pump pressure-driven force. The effect of flow rates of liquids, viscosity of oil phase (mineral oil, soybean oil, olive oil, perfluorodecaline) (Sigma) and sample channel geometry (20 x 50 μm^2 , 30 x 50 μm^2 , 50 x 50 μm^2) influence on the size of aqueous compartments as well as cell sorting was investigated.

The stability of high-throughput compartmental microfluidics was validated using high-density ($4.5 \times 10^{10}/\text{ml}$) of 1- μm size Fluoresbrite microspheres suspension (Polysciences). Further we have carried out the sorting of Fluorescent beads (6, 10- μm) ($2 \times 10^7/\text{ml}$) as model to the cell. Then, we have performed the sorting of mouse spleen

derived B-lymphocytes (1×10^6 cells/ml) that were labeled with $1\text{-}\mu\text{M}$ Fluo-4, fluorescent calcium indicator, (Ex. 494 nm, Em. 516 nm) (Molecular Probes) to monitor the single B-cell sorting and imaging, which was recorded using 12-bit CCD camera. The detection of a positive single B-cell is based on increased intrinsic Ca^{2+} levels after reaction with a stimulus.

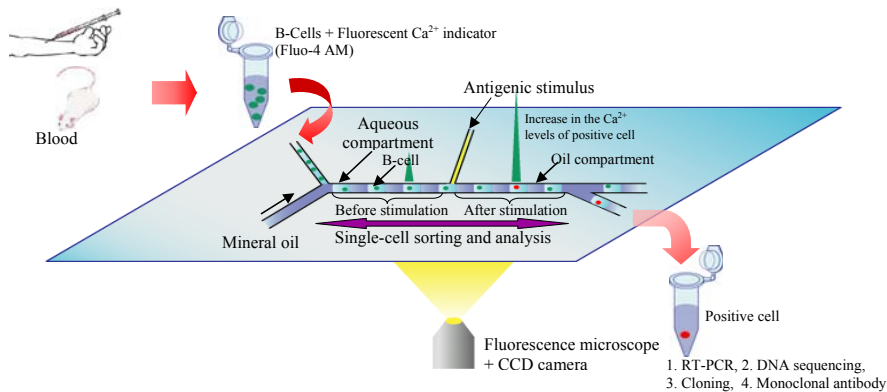


Fig. 1. Schematic illustration describing the novel picoliter compartmental microfluidic chip system for multiplexed single-cell sorting and detection of antigen-specific single B-cells from bulk suspension.

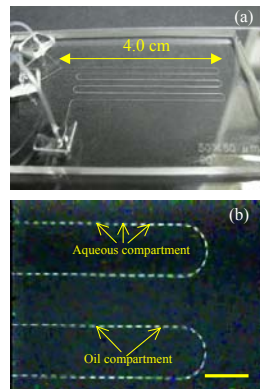


Fig. 2. Photograph of a microfluidic device (a), Fluorescent micrograph of picoliter compartments of eosin and mineral oil in the microchannels ($50 \times 50 \mu\text{m}^2$) (b), Scale bar indicates 1 mm.

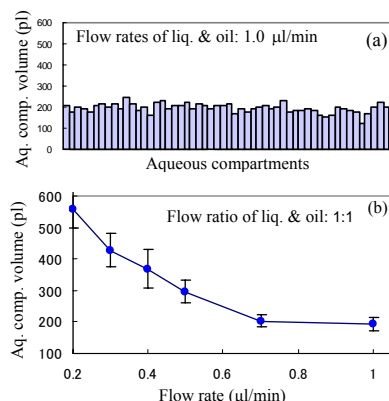


Fig. 3. Liquid distribution profile in the aqueous compartments of a chip (a), Effect of flow rates of two-phase liquids on the size of aqueous compartments generation in a microfluidic device with $30 \times 50 \mu\text{m}^2$ wide and deep sample channel and $50 \times 50 \mu\text{m}^2$ wide and height oil channel geometries (b).

3. Results and discussion

Fig. 2a shows PDMS-glass microfluidic chip devices with Y-shaped microchannel ($20 \text{ cm length, } 50 \times 50 \mu\text{m}^2$ wide and deep) established stable, continuous and alternate compartments of aqueous eosin and mineral oil under microsyringe pump pressure-driven force (Fig. 2b). Characterization of compartmental microfluidics revealed they generate picoliter-sized compartments of liquids ($\sim 190 \text{ pl}$) at a very high rate ($\sim 30 \text{ comp. /sec}$) distributing equal volumes of liquid in each aqueous compartment throughout microchannel at $1.0 \mu\text{l}/\text{min}$ flow rate of liquids suggesting stability of these

devices (Fig. 3a) and their size depends on the flow rates of both the liquids (Fig. 3b). By manipulating the sample channel geometries, the aq. compartment size could be made further smaller (~ 150 pl) which facilitate improved single-cell sorting (data not shown). The proof of stability of compartmental microfluidics demonstrated with high densities of Fluoresbrite microspheres (1- μm) suspensions (Fig. 4a). Studies on multiplexed sorting of beads (6- μm diameters), as a model to the cell, showed $\sim 65\%$ of the aq. compartments achieved single bead status at a flow rate of $0.1 \mu\text{l}/\text{min}$, whose imaging was recorded using high-speed, high-sensitive CCD camera (Fig. 5a). The intrinsic Ca^{2+} fluorescence from each B-cell was measured (Fig. 5b) using soft imaging system (analySIS, Germany) to identify a positive single B-cell before and after stimulations.

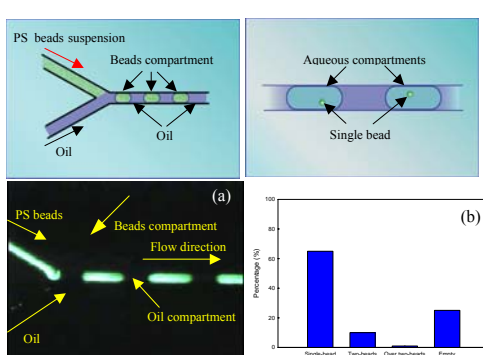


Fig. 4. Compartmentalization of high-density polystyrene beads (1- μm diameters) suspension and mineral oil in the microchannel ($50 \times 50 \mu\text{m}^2$) validating the proof of stability of compartmental microfluidics (a), Quantitative data on high-throughput single-bead (6- μm diameters) sorting using picoliter compartmental microfluidics (b), flow rates of both the liquids maintained at $0.1 \mu\text{l}/\text{min}$ each.

Fig. 5. Microscopic image showing sorting of single B-cell in aqueous compartment (a), Measurement of fluorescence from single B-cell in the aq.compartment (b), B-cells loaded with Fluo-4 and mineral oil served as aqueous and oil phases. Flow rates of the liquids maintained at $0.1 \mu\text{l}/\text{min}$ each.

4. Conclusions

The newly developed compartmental microfluidic system not only provide as a platform for high-throughput single-cell sorting and analysis system in diagnostic applications and also serve as a novel bio-analytical tool to perform rapid and sensitive assays to screen novel drugs at picoliter volumes on a single chip platform.

Acknowledgements

This work was funded by Toyama Medical Bio-cluster project of Toyama New Industry Organization sponsored by the Ministry of Education, Culture, Science and Technology.

References

1. S. Yamamura, H. Kishi, Y. Tokimistu, S. Kondo, R. Honda, R. Sathuluri, M. Omori, E. Tamiya and A. Muraguchi, Single-cell microarray for analyzing cellular response, *Anal. Chem.*, **77**, 8050-8056, 2005.
2. R. Sathuluri, S. Yamamura, Y. Takamura, and E. Tamiya, Multiplexed microfluidic devices for single-cell manipulation and analysis, *Proc. Micro Total Analysis Systems 2004*, Royal Society of Chemistry, UK, Vol. 1, pp. 61-63, (2004).

SINGLE-CELL ARRAY CHIP WITH CHAMBERS WHICH CAN ENCASE AND RELEASE B-CELLS USING THERMORESPONSIVE POLYMER

**Yoshiyuki Yokoyama^{1,2}, Shohei Yamamura², Satoshi Fujiki¹,
Katsumi Tanino¹ and Eiichi Tamiya²**

¹Toyama Industrial Technology Center, Takada 383, Toyama, 930-0866, Japan

²School of Materials Science, Japan Advanced Institute of Science and
Technology, Asahidai 1-1, Nomi, Ishikawa, 923-1292, Japan
(yokoyama@itc.pref.toyama.jp)

Abstract

We have developed the single-cell array chip with micro chambers which can encase and release B-cells using the volume change of a thermoresponsive polymer (PIPAAm). In order to fabricate the micro chambers made of PIPAAm on the substrate, a new PIPAAm photoresist using the chemically amplified system has been developed. And the chip with over 400,000 chambers could be obtained by photolithography. Using this chip, approximately 380,000 B-cells were able to be arrayed separately on one chip.

Keywords: micro array chip, single-cell analysis, B-cell, thermoresponsive polymer

1. Introduction

High throughput systems of screening and analyzing B-cells are under development [1], using a single-cell array chip (fig. 1). In this system, firstly, multiple B-cells are arrayed on the chip. Next, after antigens are added, B-cells which react specifically to the antigens will be detected. Finally, only a B-cell which shows a meaningful response will be collected; the gene sequence of the collected B-cell will be analyzed; and the results of the analysis will be used to develop monoclonal antibody medicine.

In this paper, a single-cell array chip has been developed. Depending on temperature, poly(*N*-isopropylacrylamide) (PIPAAm), a typical thermo-responsive polymers, swells or shrinks, changing its volume [2]. Using this volume change, we have developed a chip which can encase and release cells reversibly (fig. 2). When the chip temperature is 20 °C, the chambers swell; the chambers' diameters are decreased; and B-cells are encased within the chambers. Contrarily, when the chip temperature is at 35 °C, the chambers' diameters are increased since the PIPAAm shrinks; and the B-cells held within the chambers are released.

2. Experimental

We have developed a new PIPAAm photoresist using the chemically amplified system [3], in order to fabricate the micro chambers made of PIPAAm (fig. 3). First the PIPAAm copolymer was synthesized by radical-polymerizing *N*-isopropylacrylamide and 2-hydroxyethyl acrylate in the mole ratio of 80 to 20. Next, the resist solution was prepared by dissolving the PIPAAm copolymer, 2,4,6-tris [bis(methoxymethyl)amino]

-1,3,5-triazine which is a cross-linker, and bis(*t*-butylsulfonyl)diazomethane which is a photo-acid generator in 1-methoxy-2-propanol.

The resist film was fabricated by spin-coating onto silicon or glass substrates which were pretreated with a silane coupling agent. The negative patterns were transferred to the resist film by photolithography with a Xe-Hg lamp. A chip with over 400,000 chambers (10 µm width, 15 µm pitch, 3.5 µm depth) could be obtained (fig. 4).

3. Results and discussion

The chip was kept at various temperatures in water, and the changes in the chambers' diameters were observed. When the chip was at 35 °C, the PIPAAm shrank and the chambers' diameters became 10 µm. When the chip was at 20 °C, the PIPAAm swelled and the chambers' diameters became 6 µm. It was found that this behavior was reversible within 10 seconds and could be performed many times.

Next, the ability to catch and release polystyrene beads, which are dummy cells, was confirmed (fig. 5). First, bead suspension was placed on the chip while the chip was being kept at 35 °C. Next, the chip was cooled to 20 °C in order to swell the PIPAAm film swell and each chamber held a bead firmly owing to this swelling. Afterwards, the chip was washed with water of 20 °C to remove unheld beads. As a result, each chamber on the chip was able to hold a bead. Moreover, when the chip was heated to 35 °C, the PIPAAm film shrank and the beads were released from the chambers.

The chip was examined for its function to catch hold of real cells using mouse B-cells. It was found that when the chambers' diameters decreased, the B-cells, which have retractable membranes, were deformed and escaped from the chambers. Therefore, the volume of the swelling of the PIPAAm was increased with the adjustment of the concentration of the cross-linker, so that the chambers were able to encase the cells within completely (fig. 6). When the PIPAAm swelled, the cells were trapped securely within the chambers, and cells were not crushed but kept their spherical shape because the swelled chambers were made of soft hydro gel. Using this chip, approximately 380,000 B-cells were able to be arrayed separately on one chip.

4. Conclusions

We have developed a single-cell array chip with micro chambers which can encase and release B-cells using a thermoresponsive polymer. And cells can be arrayed on this chip individually and in high density.

Acknowledgements

This research and development was done by Toyama Medical Bio-cluster project and sponsored by the Ministry of Education, Culture, Sports and Science, Japan.

References

1. S. Yamamura, H. Kishi, Y. Tokimitsu, S. Kondo, R. Honda, R. Rao, M. Omori, E. Tamiya and A. Muraguchi, *Anal. Chem.*, **77**, 8050-8056 (2005)
2. G. Chen, Y. Imanishi and Y. Ito, *Macromolecules*, **31**, 4379-4381 (1998)
3. H. Ito and C.G. Willson, *ACS Sym. Ser.*, **212(2)**, 11-23 (1984)

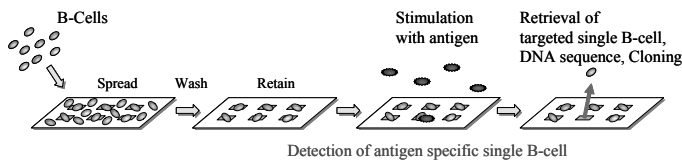


Figure 1. Schematic process for analysis of single B-cell using the single-cell array chip.

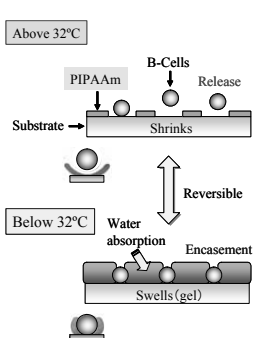


Figure 2. Chamber mechanism to encase and release cells using thermoresponsive polymer.

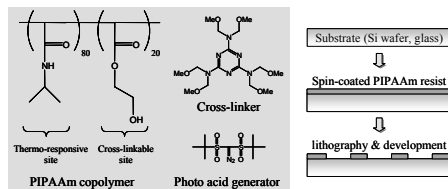


Figure 3. Chemical composition of the new PIPAAm photoresist, and patterning process by lithography.

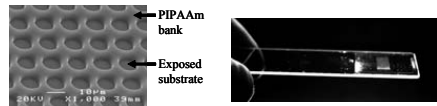


Figure 4. SEM image and real picture of the cell chip.

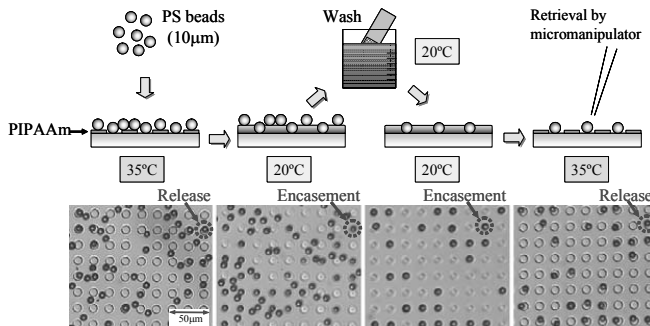


Figure 5. Encasement and Release of polystyrene beads separately by temperature control.

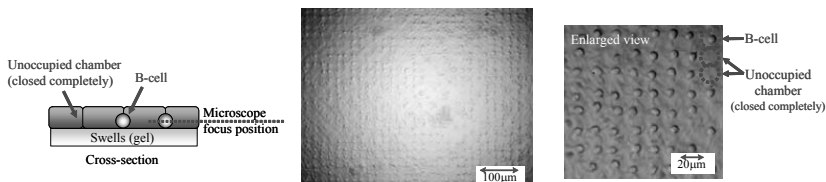


Figure 6. Microscopy image of mouse B-cells encased completely in swollen PIPAAm chambers at low temperature.

MECHANICAL STIMULATION OF ADULT VENTRICULAR MYOCYTES IN MICROFLUIDIC CHANNELS

Norbert Klauke¹, Godfrey Smith² and Jon Cooper¹

¹Dept. of Electronics, University of Glasgow, UK

²Institute of Biomedical and Life Sciences, University of Glasgow, UK

Abstract

This paper investigates the activation of isolated ventricular myocytes through a transient hydrodynamic force during regional perfusion in a microfluidic channel. Dams of variable height were integrated into the flow channel in order to partition the extracellular space around the cardiac myocyte. The central region of the cardiomyocyte was forced to replicate the shape of the dam structure. This permanent central compression did not effect the cellular response to electrical stimulation. Only the transient application of flow (1.3mm/s) directed towards the highest dam (6 μm) evoked the transient elevation of $[\text{Ca}^{2+}]_i$ and the transient cell contraction. The lower dams (<6 μm) enabled the microfluidic perfusion of separate regions of the cardiac myocyte without mechanical stimulation.

Keywords: Cardiomyocyte, action potential, stretch, mechanoelectrical feedback, flow rate

1. Introduction

The electrical activity of cardiomyocytes (action potential) controls their mechanical activity (contraction). Conversely, mechanical stimulation modulates the electrical activity of the cardiomyocyte, whereby a change in membrane stretch is sensed through mechanogated ion channels. The mechano-electric transduction in the whole heart has been termed electromechanical feedback to account for the heart rate modulation in response to ventricle filling [1]. The electrical activity of isolated ventricular myocytes has been studied in microfluidic channels during the superfusion of cellular regions, which were separated through dams integrated within the channel [2]. Here the recordings of mechanically stimulated Ca^{2+} transients evoked through the hydrodynamic stress at the dam during cell superfusion are presented. These findings were used to adjust the height and shape of the dam structure so that the separate cell regions could be superfused at the maximum flow rate (~1.3 mm/s) without mechanical stimulation.

2. Theory

The dam structure was introduced into the microfluidic channel to form a seal, which separated the extracellular space of the cardiac myocyte (Fig. 1). The seal narrowed the fluidic pathway until no flow was observed between the two compartments (Fig.2). The hydraulic pressure difference (ΔP) across the seal is the product of the flow resistance R and the average flow velocity v in the channel:

$$\Delta P = Rv \quad (1)$$

where the flow resistance is inversely proportional to the sectional area (A) of the channel:

$$R \propto 1/A \quad (2)$$

The electrical resistance between the two compartments was >20 M Ω [2] which corresponds to thickness of the fluidic path of <50 nm within the constriction. These simple

calculations suggest that substantial hydrodynamic stress can be generated in front of the dam even at the low flow rates used for superfusion.

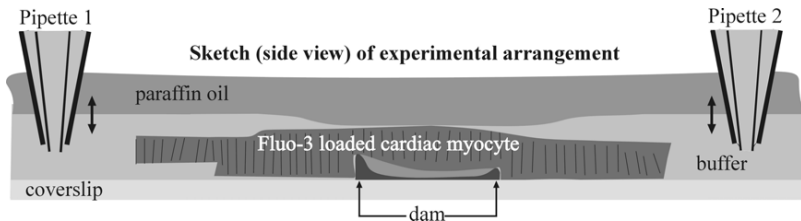


Figure 1: Illustration of the cardiac myocyte inside the microfluidic channel. Note the central region of the cell resting on the dam structure which defines the partition of the channel into two compartments. The channel lid is formed through an overlayer of paraffin oil through which the superfusion pipettes were inserted into the individual compartments using a piezo controlled z-translator.

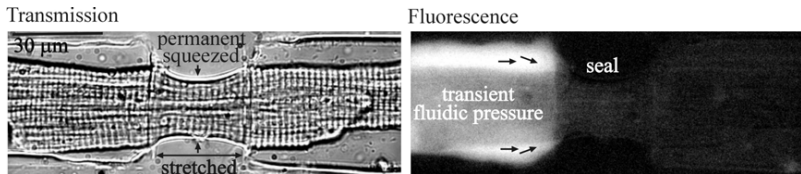


Figure 2: The central seal separates the cell ends hermetically as apparent on the fluorescence image. No dye (Fluoresceine) was detectable in the right compartment >5 min after dye injection into the left compartment.

3. Experimental

The central region of the cardiomyocyte was continuously squeezed and stretched in a fluidic constriction of paraffin oil, which formed a hermetic seal between the two ends of the cardiomyocyte thus preventing the flow along the cell surface in the constriction zone (Fig. 1; [2]). The sealant was confined between two hydrophobic dams 30 μm apart and 6 μm and 2 μm high, respectively, which were replica molded in a spin coated PDMS film (see [2] for methods). The regions of the cardiomyocyte in contact with the dams were forced to replicate the shape of this solid PDMS structure as revealed on confocal z-scans (Fig. 3). The constant mechanical load imposed through the combined stretch/compression did not affect the cardiac myocyte's response to the electrical stimulation using the integrated planar electrodes (Fig.4; [2, 3]). Both cell regions confined in the microfluidic channel were then superfused independently using two pressurized dual perfusion pipettes ([4]; flow rate <1.3mm/s) which were lowered from the oil overlayer into the cell chamber using a micropositioner (Fig. 1).

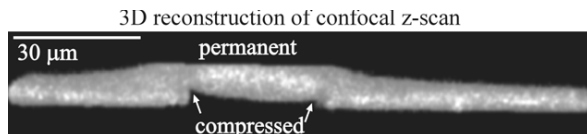


Figure 3: The dam structure generates a permanent deformation as indicated (arrows). Note the different height of the two dams.

Micrograph of experimental arrangement

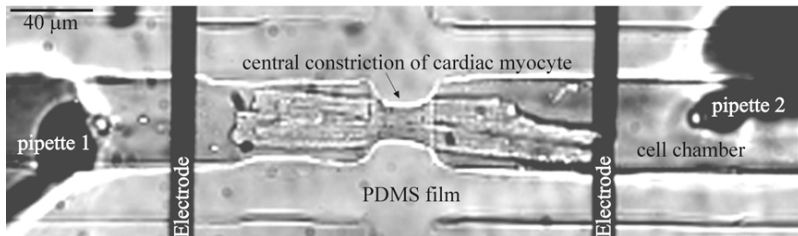


Figure 4: The cardiomyocytes were electrically stimulated using the integrated planar gold electrodes.

4. Results and Discussion

The superfusion of the cell end in contact with the higher dam (left in Figure 3) evoked a global synchronous rise in $[Ca^{2+}]_i$ and cell contraction, indicating an action potential. The cell response was transient during transient hydrodynamic stress (Fig. 5). Prolonged exposure to the microfluidic flow caused a sustained rise in the diastolic $[Ca^{2+}]_i$ and waves of $[Ca^{2+}]_i$ and contractions which lasted until the perfusion pipette was withdrawn from the cell chamber back into the oil (Fig. 5). The $[Ca^{2+}]_i$ and the cell contractions recovered immediately, thus allowing the repeated mechanical stimulation over a period of > 10 min. The application of fluidic pressure to the surface area in contact with the lower dam (2 μ m, right in Figure 3) or in the absence of the central constriction did not evoke a cellular response even at the maximal achievable flow velocity (1.3mm/s).

Representative recording of the $[Ca^{2+}]_i$ during mechanical stimulation

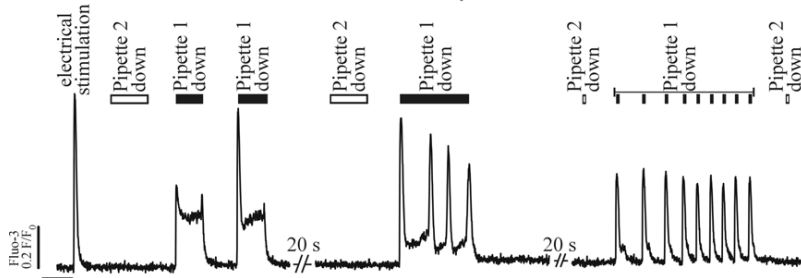


Figure 5: Ca^{2+} transients in response to hydrodynamic stress during the superfusion of the cellular region in contact with the higher dam (6 μ m).

5. Conclusion

The permanent mechanical load of a cardiac myocyte confined in a microfluidic constriction primes the cell towards the controlled electrical excitation in response to a transient hydrodynamic force.

- [1] M. J. Lab, Prog Biophys Mol Biol 71, 7-27.
- [2] N. Klauke, G. Smith, and J. Cooper, Biophys. J., in press.
- [3] E. White et al., Exp Physiol 78, 65-78.
- [4] O. Feinerman, and E. Moses, J Neurosci Meth 127, 75-84

FABRICATION OF A FLOW-TYPE MICRO CELL CHIP BASED ON PHOTO-INDUCED CELL CAPTURING

Yuichi Tada^{1,2}, Jun-ichi Edahiro¹, Kimio Sumaru^{1,*}, Toshiyuki Kanamori¹, Shinji Sugiura¹, Toshiyuki Takagi¹, Toshio Shinbo¹ and Yasuo Yoshimi²

¹ Research Center of Advanced Bionics, National Institute of Advanced Industrial Science and Technology (AIST), ² Shibaura Institute of Technology,

* 1-1-1 Higashi, Tsukuba, Ibaraki, 305-8565, JAPAN; k.sumaru@aist.go.jp

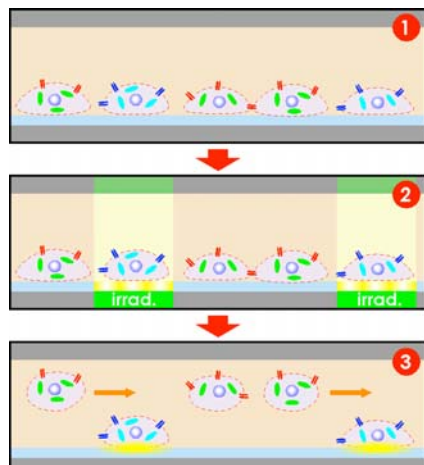
Abstract

By using a photo-responsive cell culture surface, which captures the cell strongly in response to light irradiation, we examined a novel layout of micro cell chip, in which living cells were immobilized in a prescribed arrangement in micro channels. We introduced a cell suspension into the micro channel, irradiated the near-UV light locally and washed with buffer solution. As a result of repeating these operation using two different kinds of cells, it was confirmed that the living cells of different kinds were placed in the prescribed positions in the micro channel without damaging their viability.

Keywords: flow-type micro cell chip, photo-induced cell capturing, microchannel

1. Introduction

Cell array chips have been studied actively aiming at effective analysis of pharmacologic effect of bioactive substances. In order to make such analysis more efficient, we examined a novel layout of micro cell chip, in which living cells were arranged in the prescribed locations in micro channels, by using a photo-responsive cell culture surface, which captures the cell strongly in response to light irradiation (**Fig.1**)¹.



2. Experiments

At first, we prepared a photo-responsive cell culture surface using a poly(N-isopropylacrylamide) functionalized with nitrospirobenzopyran (pNSpNIPAAm)¹. Then we put a piece of poly(dimethylsiloxane) having microchannel structure (width 600 μm , depth 200 μm) onto this photo-responsive

Figure 1. *In situ* cell manipulation implemented by photo-responsive cell capturing.

surface, and constructed a channel-type micro chip (**Fig.2**). In the microchannel of this chip, we arranged living cells of different kinds by repeating the following procedures. We seeded the cells on the micro channel uniformly by feeding a cell suspension, and kept it in an incubator for a prescribed period. Then we captured the cells in a certain area of the channel by irradiating locally the near-UV light (365 nm, 260 mW/cm²) for 2.5 min, and removed non-captured cells out of the irradiated area by washing the channel with phosphate buffer solution. We observed the microchannel in each step of the operation with a confocal scanning laser microscope.

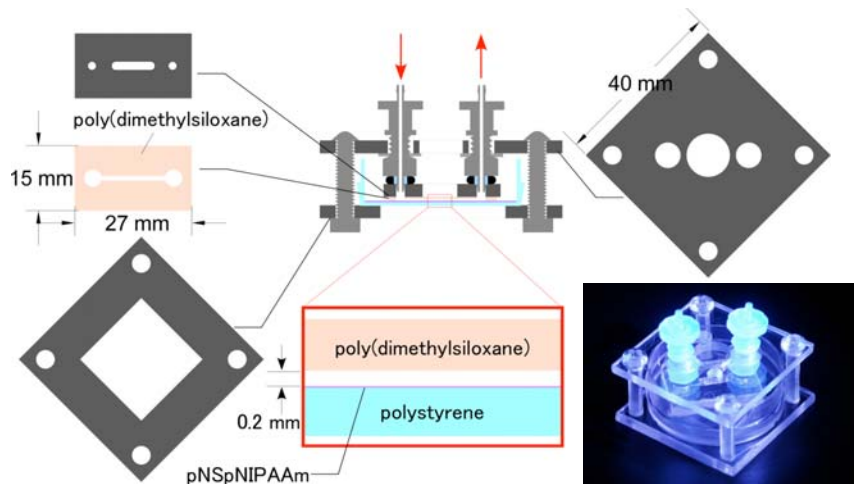


Figure 2. Construction and photographic image of a micro chip for fabrication of flow-type cell array based on photo-induced cell capturing.

3. Results and Discussions

The microscopic images of the microchannel in the respective steps of the operation are shown in **Fig.3**. By feeding a cell suspension, the CHO-K1 cells, which had been stained with a green fluorescent dye (CMFDA) in advance, were loaded onto the photo-responsive surface uniformly in the micro channel and incubated for 14 hours (**a**). After local light irradiation to trigger the cell capturing and subsequent washing with buffer solution, we obtained a cell domain in the prescribed area where CHO-K1 cells were captured firmly (**b**). After the incubation for 21 hours, however, the cells grew proliferously beyond the irradiated region indicating their highly maintained viability (**c**). Then the MDCK cells, which had been stained with a red fluorescent dye (CMTPX) in advance, were introduced into the micro channel (**d**), and the light was irradiated locally onto not only the area in which only MDCK cells existed, but also the area, in which the light had been irradiated in the previous step to capture CHO-K1 cells. After washing with buffer solution, the domains of MDCK cells were newly created after

local light irradiation and the washing (**e**). In this process, previously formed domain of CHO-K1 cells, which had grown proliferously beyond the irradiated region, was trimmed properly. This result suggested that the cell capturing effect induced by the light irradiation did not last for 1 day. Fluorescence observation of the resultant cell chip (**f**) indicated that the living cells of different kinds were immobilized in the prescribed arrangement in a closed microchannel.

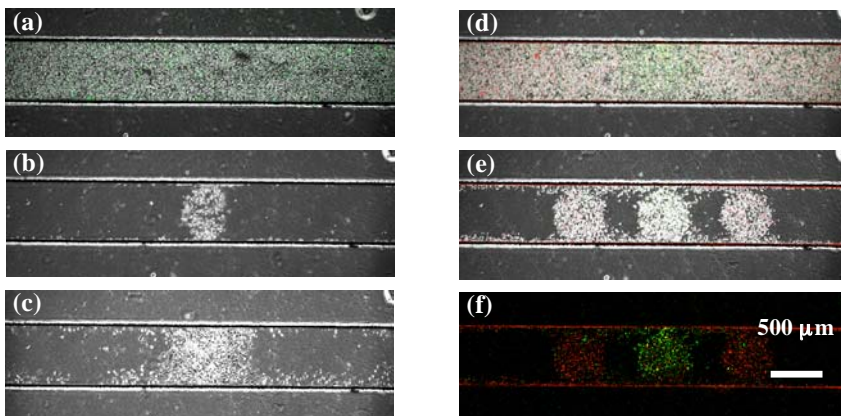


Figure 3. Microscopic images of microchannel in the respective steps of cell arranging operation based on photo-induced cell capturing.

4. Conclusions

Novel method to fabricate a flow-type micro cell chip was examined by using photo-induce cell capturing, which had been developed in our previous researches. As a result of the experiments using a channel type micro chip functionalized with a photoresponsive polymer, it was confirmed that the living cells of different kinds were placed in the prescribed positions in the closed micro channel without damaging their viability. The result of this study is expected to provide important guidance to fabricate a novel micro cell chip, which can realize the efficient matrix analysis of living cells responding to many bioactive substances.

Acknowledgement

This work was financially supported by Industrial Technology Research Grant Program in '05 from the New Energy Development Organization (NEDO) of Japan.

Reference

1. J. Edahiro, K. Sumaru, Y. Tada, K. Ohi, T. Takagi, M. Kameda, T. Shinbo, T. Kanamori and Y. Yoshimi, *In-situ Control of Cell Adhesion Using Photoresponsive Culture Surface*, *Biomacromolecules* , 6(2), 970-974 (2005).

SINGLE CELL TRANSFECTION DYNAMICS IN A MICROFLUIDIC SYSTEM

Na Li*, Pak Kin Wong*, James Lin**, and Chih-Ming Ho*

*Department of Mechanical & Aerospace Engineering,
University of California, Los Angeles, USA

**Department of Pediatrics, David Geffen School of Medicine,
University of California, Los Angeles, USA

Abstract

In this study, molecular beacons have been successfully transfected into living cells with high efficiency (80%~90%) inside a microfluidic system. This will enable a sensitive and specific method to monitor gene expression dynamics in single living cells. Fluorescence conjugated transfection reagent was adopted to investigate the transfection dynamics of molecular beacons. The development of microfluidic systems has facilitated real-time monitoring of individual cells, which revealed the transfection dynamics of molecular beacons at the single cell level.

Keywords: molecular beacon, transfection, microfluidics, gene expression dynamics, single cell

1. Introduction

Study of cell responses to various stimuli has important implications for biology and medicine. Compared to traditional cell culture systems, microfluidic cell culture systems have demonstrated advantages in generating the desired physical or chemical stimulations in space and time. However, their potentials to facilitate real-time screening of cellular responses have not been fully exploited. In this paper, we propose to use molecular beacons to monitor real-time gene expression dynamics of individual living cells inside a microfluidic cell culture system. Molecular beacons (Figure 1) have a stem-and-loop structure and undergo a spontaneous fluorogenic conformational change upon hybridization to the complementary nucleic acid target [1]. They have been shown to be extremely specific and sensitive in various applications. In this paper, transfection of molecular beacons was successfully demonstrated with high transfection efficiency inside a microfluidic system. Furthermore, single cell transfection dynamics were also investigated.



Figure 1. Schematic of specific RNA/DNA detection with molecular beacon

2. Experimental

We developed a microfluidic cell culture system (Figure 2). A PDMS microchannel (30um high, 1mm wide) was loaded into a heating chamber that is mounted on an inverted optical microscope. The entire setup was inside of a vertical clean bench, thus minimizing the possibility of contamination. Adoption of CO₂-independent cell culture

media (Invitrogen) has eliminated the need to control the CO₂ level inside the close chamber. Human embryonic kidney (HEK) 293T and Hela cells have been successfully cultured for up to one week in this system.

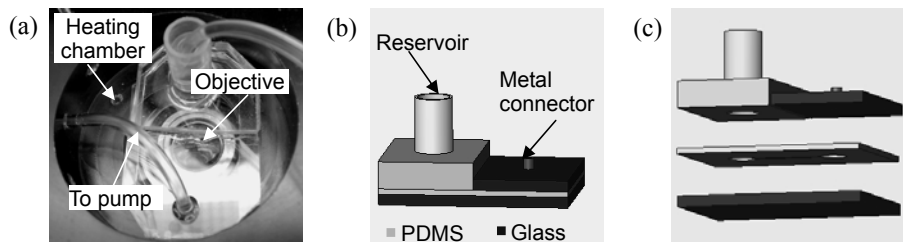


Figure 2. Microfluidic cell culture system. (a) Setup (b) Scheme of microfluidic device (c) Assembly of microfluidic device

3. Results and discussion

A molecular beacon that targets human beta-actin mRNA, was designed based on previous literature [2] and characterized. JetPEI™ (Polyplus transfection) was used to deliver the molecular beacon into 293T cells. As shown in Figure 3a, using concentrations that were optimal for 96-well plates resulted in lower transfection efficiency in the microchannel. This decrease may be attributable to the much greater surface-to-volume ratio at the scale of the microchannel, compared to a traditional cell culture system. After optimization for the microfluidic cell culture system, a high transfection efficiency of 80%~90% has been achieved (Figure 3b and c). For our molecular beacon, 2'-O-methyl modification was used to improve resistance to cellular ribonucleases. As shown in Figure 3d, transfection efficiency and mean signal-to-noise ratio (SNR) were similar between day I and day II, which suggests that the 2'-O-Me modified molecular beacons remains intact after 2 days.

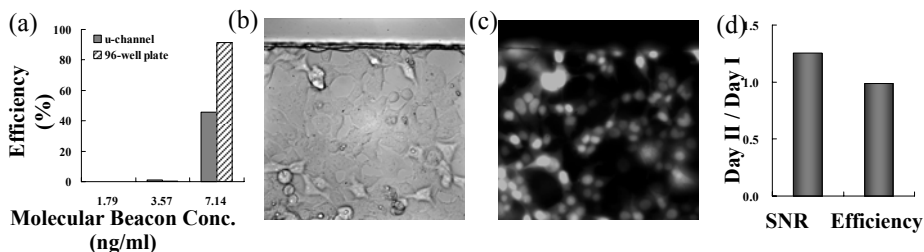


Figure 3. Transfection of beta-actin molecular beacons into 293T cells. (a) Comparison between microchannel and 96-well plate. Bright field (b) and fluorescence (c) images illustrating high transfection efficiency in microchannel at optimized condition. (d) Stability of molecular beacon inside of living cells

In the dynamics experiments, jetPEI-Fluor, a red fluorescent derivative of jetPEI, was used to transfet the green fluorescent labeled molecular beacons. This allows us to track jetPEI™/molecular beacon complexes. Data from a typical cell (Figure 4a) showed that the molecular beacon SNR began to increase significantly after 1 hour and

approached steady state in around 2hrs, whereas the SNR of jetPEI had minimal variation during the same time period. This implies that the jetPEITM/molecular beacon complex is taken up by cells within 2hr and that the additional time for the molecular beacon to reach the steady state may be attributed to other processes like the escape of jetPEITM/molecular beacon complex from the endosome, dissociation of the complex, and hybridization of molecular beacon to its specific mRNA target. This observation agrees with the proposed transfection mechanism in the literature [3]. Data from additional cells were plotted in Figure 4 b. Data of two individual cells and the average from the group of cells were highlighted. It was noted that the dynamics were similar between different cells. However, there was a relatively large difference in characteristic time to onset of transfection. This demonstrates that single cell studies provide information on cellular dynamics that may not be captured in aggregate data.

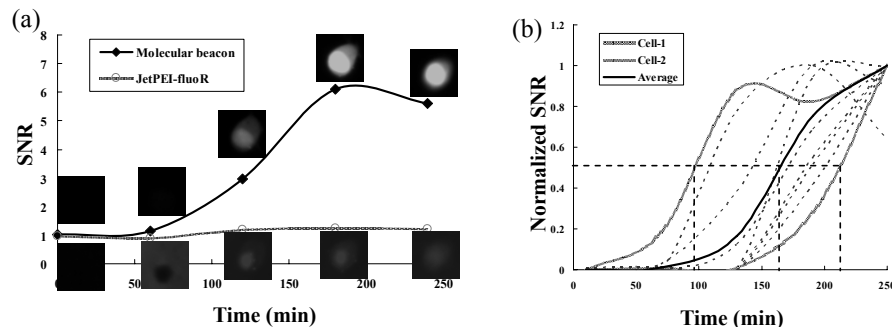


Figure 4. Transfection dynamics of molecular beacons with rhodamine-labeled jetPEI in a single cell (a) and group of individual cells (b).

4. Conclusions

The paper demonstrated that transfection of molecular beacons can be achieved inside a microfluidic system with a high efficiency. Results of single cell transfection dynamics showed that a microfluidic system can potentially be a powerful tool to explore the distinct mechanisms of various cellular internalization methods.

Acknowledgements

The work is supported by CMISE through NASA URETI program and NIH NIDCR.

References

1. S. Tyagi and F.R. Kramer FR, *Molecular beacons: probes that fluoresce upon hybridization*, Nat Biotechnol, 14, pp. 303-308, (1996).
2. D.L. Sokol, X. Zhang X, P. Lu, and A.M. Gewirtz, *Real time detection of DNA.RNA hybridization in living cells*, Proc Natl Acad Sci USA, 95(20), pp. 11538-11543, (1998).
3. O. Boussif, F. Lezoualc'h, M.A. Zanta, M.D. Mergny, D. Scherman, B. Demeneix, and J.P. Behr, *A versatile vector for gene and oligonucleotide transfer into cells in culture and in vivo: polyethylenimine*, Proc Natl Acad Sci USA, 92(16), pp. 7297-7301, (1995).

DEVELOPMENT OF A CELL CULTURE SYSTEM FOR DYNAMICALLY CONTROLLING CELL MOTILITY

Hirokazu Kaji, Takeaki Kawashima, and Matsuhiko Nishizawa

Department of Bioengineering and Robotics, Graduate School of Engineering,
Tohoku University, Sendai 980-8579, Japan

Abstract

We report a method for controlling the pattern of permissible cell migration and proliferation on a substrate in time and space. Using this method, a confluent monolayer of cells that is confined within a defined region is released into a neighboring region. Incorporated into the method is an electrochemical technique termed electrochemical bio-lithography that uses a scanning microelectrode to draw regions on the surface of the system that thereafter can support cell migration and growth.

Keywords: cell patterning, electrochemical method, cell migration, cell-based assay

1. Introduction

Cultured cells provide powerful systems for investigating mechanism for cellular motility. Micropatterning techniques including soft lithography are widely used to study and manipulate the behavior of adherent cells [1]. When cell patterning techniques are incorporated into cell motility assays, cells are first corralled within defined area(s) and then released in a controlled fashion [2-4].

Recently, we have been developing a surface patterning technique termed electrochemical bio-lithography, which can be conducted under typical physiological conditions [5-7]. Our technique uses a microelectrode to locally generate an oxidizing agent that then causes the rapid detachment of albumin or heparin from an underlying substrate. Subsequent adsorption on extracellular matrix (ECM) proteins on the newly exposed region induces local cell attachment.

Here, we report how this technique can be used with an *in vitro* cell motility assay. Figure 1 shows the essentials of the procedure. We defined the regions on which cells can and cannot grow and migrate by first depositing, in a defined pattern, the cell-resistant polymer (2-methacryloyloxyethyl phosphorylcholine (MPC) polymer in this study) on the surface of a glass substrate. This polymer is not contaminated by cells for longer cultivation periods than found for other nonbiofouling substances. Additionally, MPC is unaffected by our electrochemical treatment. Consequently, the edges of the polymer serve as nearly

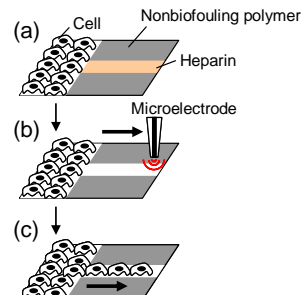


Fig. 1. General strategy for patterning cell motility using the microelectrode and a geometrically confined environment.

permanent boundaries for the regions on which the cells can grow and move. By then individually switching one or more nonpolymer regions from cell-repellent to cell-adhering, it becomes possible to strictly delineate the regions into which cells can migrate.

2. Experimental

The pattern of MPC polymer (Lipidure-CM5206E, NOF CORPORATION) was prepared by a micromolding technique. The PDMS micromold was reversibly bound to a glass substrate to form a microfluidic channel, followed by introduction of an MPC polymer/ethanol solution into the channel. After the ethanol was vaporized via the open end of the channel, the mold was gently removed from the substrate. Subsequently, heparin was deposited onto glass that was not covered with MPC polymer by first dipping the system into an aqueous solution of polyethyleneimine (PEI) for 20 min, then rinsing it with distilled water, and finally dipping it into an aqueous solution of heparin for 20 min.

For the generation of Br₂ (subsequently HBrO), we used a Pt-disk-type microelectrode (tip diameter, 10 μm) and a Ag/AgCl counter electrode both in phosphate-buffered saline (PBS) containing 25 mM KBr (pH 7.4). The microelectrode, with a constant potential of 1.7 V, was scanned at 100-200 μm s⁻¹ ca. 20 μm above the heparin complex to detach it from the substrate.

A subconfluent monolayer of HeLa cells was dissociated with a 0.25% trypsin solution, then suspended in serum-containing medium, and finally added to the assay system at a cell density of 1 x 10⁶ cells mL⁻¹. After 1 h of cultivation, the substrate was rinsed with medium to remove nonadherent cells and further incubated for 12 h in fresh medium. Subsequently, the cell-resistant regions of the now cell-patterned system that had not yet been treated with the microelectrode were so treated, and the entire system was incubated in serum-containing medium at which time cell motility assays were initiated.

3. Results and discussion

Figure 2 demonstrates that our system can be used as an *in vitro* cell motility assay. After HeLa cells were corralled within region *i* (Fig. 2a), the lanes of region *ii* were electrochemically treated. This treatment has no significant effect on the cells of region *i* because the concentration of the electrogenerated oxidant required to remove the PEI/heparin complex is an order of magnitude less than that needed to damage the cells [5]. After the electrochemical process, the entire system was incubated. Cells immediately began to migrate from region *i* to the lanes of region *ii* (Fig. 2b).

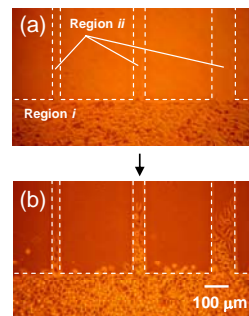


Fig. 2. Cell migration and growth in regions that were initially cell-repellent. (a) The micrograph shows that HeLa cells attached and spread only within region *i*. (b) Migration of cells from region *i* into region *ii* after electrochemical treatment and an additional 36 h cultivation.

The net distance that the cells migrated depended on the lane width, as summarized in Figure 3. The positive correlation between the cell migration rate with increasing lane width was obvious after 12 h of cultivation, whereas this tendency was obscured for 36 h owing to additional cell proliferation. We believe that the rate of cell migration correlates with spatial restriction(s) imposed on cell orientation(s). In narrower lanes, cells spread along the long axis of the lane because the cytoskeletons of the cells are compressed and oriented parallel to the lane edge. This restriction may obstruct the reorganization of the cytoskeletal filaments, which in turn would impede cell migration. For lanes wider than 50 μm , the cell migration rate is roughly constant. For these wide lane widths, the cellular environment is probably similar to that found for the usual culture environment, which is not spatially restricted.

Figure 4 shows the effects of antimigratory drugs on cell migration into areas that becomes accessible only after electrochemical treatment. Several other techniques that first confine and then release cells have been used to screen for potential drugs [2-4]. Compared with these techniques, our system directs mobile cells into defined regions, which in turn readily permits the relationship between cell motility and the biological effects of the compounds to be quantified.

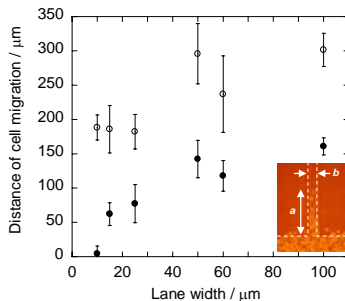


Fig. 3. Plots of cell migration distance versus lane width when cells were cultivated for 12 (●) and 36 h (○) following electrochemical treatment. The mean values of the cell migration distance ($\pm\text{SD}$) are those of at least four trials. The inset in the lower right corner is an example of a cell migration experiment, and the cell migration distance (a) and the lane width (b) are identified in the micrograph.

Acknowledgements

This study was supported by the Industrial Technology Research Grant Program in 2005 from NEDO of Japan, by a Grant-in-Aid for Scientific Research B (no.17310080), and by Scientific Research on Priority Areas (no.18048004) from the Ministry of Education, Science, and Culture, Japan.

References

- R. S. Kane, S. Takayama, E. Ostuni, D. E. Ingber, G. M. Whitesides, *Biomaterials* **20**, 2363 (1999).
- M. N. Yousaf, B. T. Houseman, M. Mrksich, *Angew. Chem. Int. Ed.* **40**, 1093 (2001).
- X. Jiang, R. Ferrigno, M. Mrksich, G. M. Whitesides, *J. Am. Chem. Soc.* **125**, 2366 (2003).
- G. Kumar, J. -J. Meng, W. Ip, C. C. Co, C. -C. Ho, *Langmuir* **21**, 9267 (2005).
- H. Kaji, K. Tsukidate, T. Matsue, M. Nishizawa, *J. Am. Chem. Soc.* **126**, 15026 (2004).
- H. Kaji, M. Hashimoto, M. Nishizawa, *Anal. Chem.* **78**, 5469 (2006).
- H. Kaji, T. Kawashima, M. Nishizawa, *Langmuir*, in press.

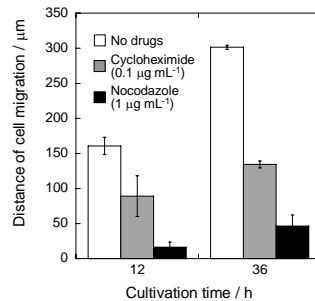


Fig. 4. Influence of drugs on the migration of HeLa cells into regions that support cell adhesion only after electrochemical treatment. A lane width of 100 μm was used for the assays. The mean values of the cell migration distance ($\pm\text{SD}$) of at least four trials are given.

SCREENING OF MOLECULAR LIBRARIES USING THE CONTINUOUS-FLOW, MICRO-MAGNETIC CELL SORTER

Sang-Hyun Oh¹, Amarendra K. Singh^{1,2}, Paul H. Bessette³,
Sophia A. Kenrick³, Jeffrey J. Rice³, Jiangrong Qian^{1,2},
Patrick S. Daugherty³, and H. T. Soh^{*1,2}

¹California Nanosystems Institute, ²Department of Mechanical Engineering,
³Department of Chemical Engineering, University of California-Santa Barbara

*E-mail: tsoh@engr.ucsb.edu

Keywords: *in vitro selection, magnetic cell sorting, high-throughput screening*

Abstract

A micromachined, two-stage, continuous-flow, micro-magnetic cell sorter is presented. Ferromagnetic microstrips were patterned in the micro-channel to generate a large magnetic field gradient, and the resulting magnetophoretic force deflected magnetically labeled cells toward a desired outlet in a laminar-flow buffer switching system. Using the sorter and superparamagnetic microbeads, we have demonstrated screening and enrichment of a peptide library based on its affinity towards the target antibody.

1. Introduction

Enrichment of rare cells based on their surface marker expression at a high throughput and purity is an important biomedical technique. Magnetic actuated cell sorters (MACS), wherein the target cells are labeled and sorted with magnetic microbeads, have been utilized for a wide range of biomedical applications¹⁻³. However, the precise control of magnetic and hydrodynamic forces that govern the purity and recovery of rare cells remains a challenge in conventional MACS. Microfluidics offers a compelling platform to precisely engineer these fields in self-contained and disposable microsystems. By combining Micro-magnetic Field gradient Generator (MFG) made of nickel microstrips³ with a laminar-flow buffer switching scheme⁴, we present a two-stage, continuous-flow micro-magnetic actuated cell sorter (cMACS) that is capable of exceptional enrichment (>770-fold) in a single pass at a high throughput (27,000 beads/second). Using the cMACS, we demonstrate, for the first time, the magnetophoretic screening of a molecular library in a microfluidic device, where a 10⁸-member microbial peptide library was screened and enriched for its affinity towards the target protein (α -FLAG M2 monoclonal antibody).

2. Experiments and Results

The cMACS is fabricated with PDMS molding of microfluidic channels (50 μ m height) on top of MFGs (200nm-thick nickel) on a glass substrate (Fig. 1). Magnetically labeled cells entering the first stage (Inset 1b) are guided into the second stage (Inset 1a) through the MFGs where they are deflected toward the collection outlet.

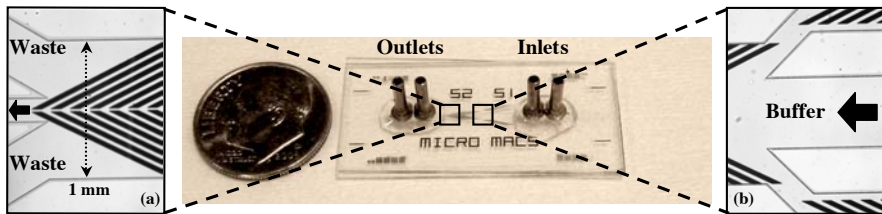


Figure 1. Two-stage cMACS using a buffer switching system: Micro-magnetic Field gradient generators (MFG; 20 μ m width, 200nm thickness) sequentially deflect magnetically labeled cells toward the center collection port.

Analytical calculation of magnetic field distribution in the vicinity of the MFG (Fig. 2a) clearly indicates strong gradient near the edges. When the MFGs are aligned at an angle to the flow direction, the velocity vectors of the labeled cells are significantly changed (Inset 2a), which results in an efficient continuous-flow sorting³. To quantify the purity, recovery, and throughput of the two-stage cMACS, a mixture of 0.1% magnetic beads and 99.9% polystyrene beads was processed at 27,000 beads/second. Most polystyrene beads are collected at the waste port without deflection (Fig. 2b), whereas magnetic beads are deflected by MFGs toward the collection port (Fig. 2c). In one round of continuous sorting, the fraction of magnetic beads increased from 0.1% to 77%, representing an enrichment factor of 770 (Fig. 3).

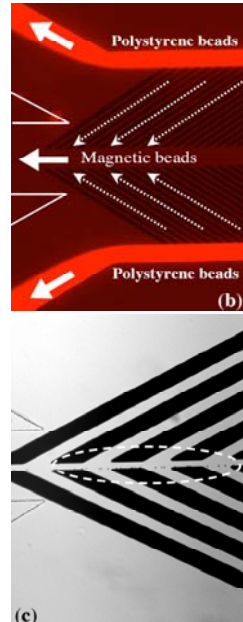
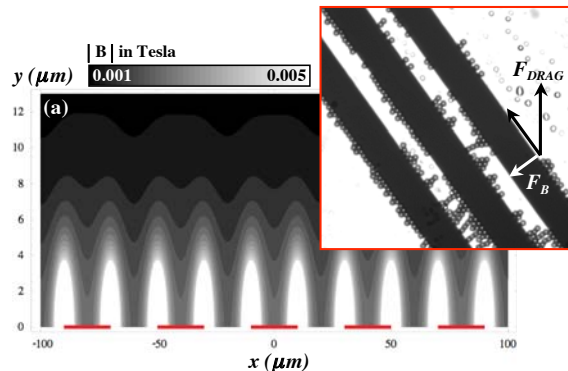


Figure 2: (a) The simulated magnetic field distribution $|B|$ near the MFG. Superparamagnetic particles are attracted toward high-gradient region ($F = m|\nabla B|$) near the line edge (inset). (b) Non-magnetic polystyrene beads move toward waste ports on both sides. (c) Magnetic beads are deflected by the MFG toward the collection port.

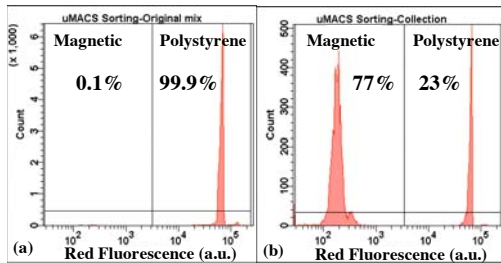


Figure 3. Single-pass enrichment of magnetic beads (1 μm) from non-magnetic (polystyrene, red-fluorescent) beads (2 μm) quantified by flow cytometry: (a) Initial mixture consists of 0.1% magnetic beads and 99.9% polystyrene beads (b) Final effluent consists of 77% magnetic and 23% non-magnetic beads (770X enrichment).

The cMACS was utilized to demonstrate *in vitro* selection of a peptide library against a target protein. A bacterial peptide library⁵ with $\sim 10^8$ members was incubated with biotinylated target protein and subsequently with streptavidin-coated 1 μm magnetic beads. Then the library was screened for target-binding peptides using the cMACS at 10^8 bacterial cells/hr. The fraction of target-binding members was quantified using flow cytometry after incubating the library with fluorescently conjugated target protein. After two rounds of cMACS, the purity of target-binding population increased from 0.03% (unselected) to 0.7%, 23.8%, respectively (Fig. 4).

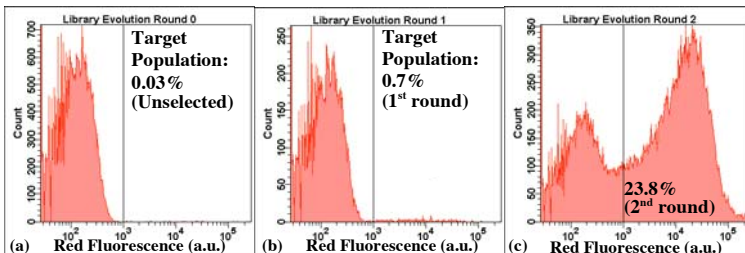


Figure 4. *In vitro* selection of a microbial peptide library for high affinity towards the target protein (α -FLAG M2 monoclonal antibody): The library ($\sim 10^8$ members) was first incubated with biotinylated target and subsequently with streptavidin-coated 1 μm magnetic beads. Then the cMACS screened the library for target-binding peptides and the screened clones were amplified overnight. The fraction of target-binding population in the library was analyzed by flow cytometry after incubating them with fluorescently labeled target. The intensity of red fluorescence (x-axis) indicates the expression level of target-binding peptides on each cell. (a) Unselected library (b) Following one round of cMACS, 0.7% of the population exhibit target-binding peptides (c) 23.8% of the population exhibit target-binding peptides after two rounds.

3. Conclusion

In conclusion, we demonstrated continuous-flow MACS that is capable of enriching magnetically labeled rare cells in two sequential stages with a high recovery and purity through precisely engineered local magnetic field gradient generators.

References

1. S. Miltenyi, W. Muller, W. Weichel, A. Radbruch, *Cytometry* **11** (1990), p. 231.
2. N. Pamme and A. Manz, *Analytical Chemistry* **76** (2004), p. 7250.
3. D.W. Inglis, R. Riehn, R.H. Austin, J.C. Sturm, *Applied Physics Letters* **85** (2004), p. 5093.
4. X. Hu *et al.*, *Proceedings of the National Academy of Sciences* (2005) Vol. 102, No. 44, p. 15757.
5. P.H. Bessette, J.J. Rice, P.S. Daugherty, *Protein Eng., Design & Selection* **17**, No. 10 (2004), p. 731.

MICRO CELL INCUBATOR WHICH CAN CONTROL THE pH OF CULTURE MEDIA THROUGH ON-CHIP INTEGRATED CO₂ GENERATOR

Yo Han Choi, Sang Uk Son, and Seung S. Lee

Korea Advanced Institute of Science and Technology

373-1, Guseong-dong, Yuseong-gu, Daejeon, Republic of Korea

Abstract

A novel micro cell incubator is described in this paper. In order to fabricate a small self-contained carbon dioxide supply unit, we adopted chemical production of carbon dioxide rather than compressed storage of the gas which requires huge tank. Carbon dioxide can be chemically produced by pyrolysis of sodium bicarbonate. The produced gas passes through a thin polymer membrane, and then liquid media separated from gas area by polymer membrane can uptake the gas.

Keywords: cell incubator, cell culture, carbon dioxide, sodium bicarbonate

1. Introduction and Theoretical Background

pH of animal cell culture media is controlled through the interaction of NaHCO₃ (sodium bicarbonate) in media with exogenously supplied CO₂ (carbon dioxide) in all most every incubator [1]. Consequently, it is inevitable that not only an incubator but also a large cylinder for compressed CO₂ must accompany the culture of animal cells. Therefore, any substitutive solution for supply of CO₂ without CO₂ cylinder may be one of the important points in the development of miniaturized portable cell incubators.

We previously reported a small chip which could generate CO₂ through chemical reactions [2]. Many kinds of gases including CO₂ are known to be able to pass through permeable polymer membranes such as PDMS (polydimethylsiloxane) [3], and it was reported that oxygen could be supplied into liquid medium through PDMS membrane [4]. The working principle is depicted in Fig. 1. NaHCO₃ begins to be decomposed at around 50 °C, and this pyrolysis is caused by an underlaid microheater. Several products including gaseous CO₂ are generated, which is described with a chemical equation as following;

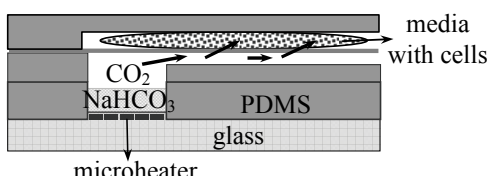


Fig. 1 Schematic view of working mechanism.

CO₂ flows through microchannel which is separated by thin PDMS membrane from upper structures; cell culture chambers. Then, CO₂ passes through permeable PDMS membrane from microchannel to diffuse into culture media.

2. Fabrication and Experiment

Fabrication process is depicted in Fig. 2. Microheaters were patterned through conventional photolithographic methods. The following PDMS layers with microstructures were made based on SU-8 (Microchem) molds which had been fabricated on silicon wafers (Fig. 3). The height and width of the mold for microchannel were measured to have 50 μm and 100 μm , respectively, and the height and diameter of mold for cell chambers are 100 μm and 5 mm, respectively. Thin PDMS membrane was made by spin-coating PDMS monomer solution on a Cr-coated silicon wafer. Fig. 4 shows a completed micro cell incubator, which is composed of a basal glass plate and four layers of PDMS.

SupT1 cell line which had been derived from human T cell lymphoma was used for culture test. Cells in RPMI 1640 (JBI) with 10 % of FBS (fetal bovine serum, JBI) were injected into the micro incubator (Fig. 5). The injected cells could be observed with semi-transparent structures as shown in Fig. 5. The magnified area in Fig. 5 are microchannels for gas. CO_2 was produced by connecting a 9-volt battery (6F22) to the electrodes of microheater. We are currently tuning the thickness of PDMS membrane and the amount of CO_2 for accurate control of pH.

3. Discussion

Several reports have described the culture of animal cells within microstructures including arrayed chambers [5]. However, the ambient conditions had to be maintained by continuously flowing pre-controlled media. The micro cell incubator reported in this

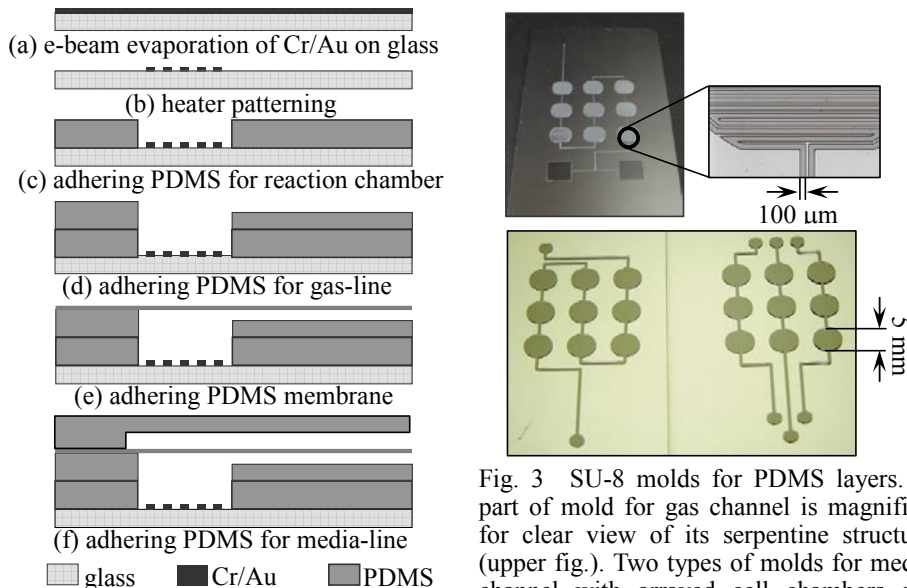


Fig. 2 Simplified fabrication process.

Fig. 3 SU-8 molds for PDMS layers. A part of mold for gas channel is magnified for clear view of its serpentine structure (upper fig.). Two types of molds for media channel with arrayed cell chambers are shown also at the lower figure.

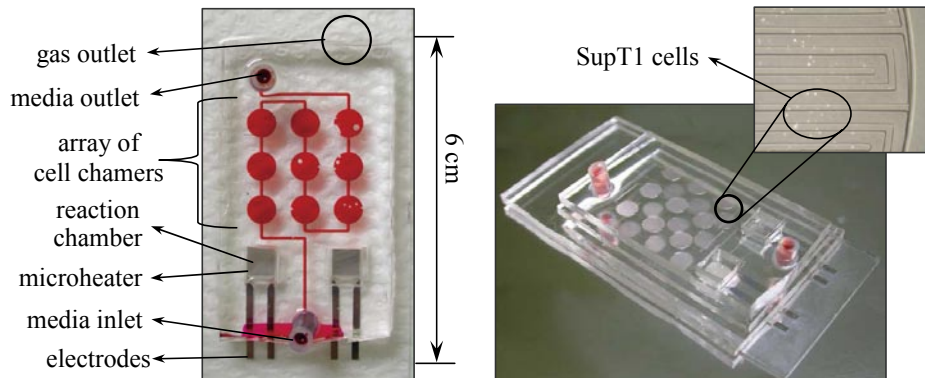


Fig. 4 A completed micro cell incubator. 0.5 % of Phenol Red solution is injected through media channel for clear demonstration. Note that gas-line layer is almost transparent.

Fig. 5 SupT1 cells in a cell chamber is shown as white dots. A circular cell chamber is superimposed on transparent PDMS structures including serpentine gas channels.

paper is a partially closed system which contains pH-controlling module. It is also easy to make varieties of arrays as shown in Fig. 3 for the culture with different conditions simultaneously. This micro cell incubator would be a model for to cell-based screening systems as well as portable cell incubator for outdoor use.

Acknowledgement

This research was supported by a grant (02-K14-01-005-1-2) from Center for Nanoscale Mechatronics & Manufacturing, one of 21st Century Frontier Research Programs, Ministry of Science and Technology, KOREA.

References

1. R. Ian Fresheny, "Culture of Animal Cells", 3rd ed., John Wiley & Sons, Inc., USA. (1994)
2. Yo Han Choi and Seung S. Lee, "Novel micro gas generator of carbon dioxide for actuation and gas source", in Proceedings of Micro Total Analysis Systems 2003, pp. 611-614. (2003)
3. S. G. Charati and S. A. Stern, "Diffusion of gases in silicone polymers: molecular dynamics simulations", *Macromolecules*, vol. 31, pp. 5529-5535. (1998)
4. Eric Leclerc, Yasuyuki Sakai, and Teruo Fujii, "Cell culture in 3-dimensional microfluidics structure of PDMS (polydimethylsiloxane)", *Biomedical Microdevices*, vol. 5, no. 2, pp. 109-114. (2003)
5. Paul J. Hung, Philip J. Lee, Poorya Sabourchi, Nima Aghdam, Robert Lin, and Luke P. Lee, "A novel high aspect ration microfluidic design to provide a stable and uniform microenvironment for cell growth in a high throughput mammalian cell culture array", *Lab Chip*, vol. 5, pp. 44-48. (2005)

A REVERSIBLY ASSEMBLED MICROFLUIDIC CHIP FOR CULTURE AND ANALYSIS OF SINGLE CELL ARRAY

Cécile Crozatier, Issa Tapsoba, Maël Le Berre, Stéphane Arbault,
Christian Amatore and Yong Chen

CNRS UMR 8640, Dpt. de Chimie, Ecole Normale Supérieure, France

Abstract

We present a new analytical device that integrates a parallel network of microelectrodes into a reversibly assembled microfluidic chip. With a novel cell handling technique, it is now possible to put live cells into confined analytical conditions during the least possible time, hence assuring their cellular integrity at all times. This permits the coupling of complex microfluidic experiments all the while keeping a strong biological meaning, comparable to those offered by macroscopic experiments.

Keywords: cell array, reversible assembly, electrochemical analysis, PDMS

1. Introduction

Microfluidics has been largely contributing to the miniaturizing of live cell analysis systems. However, while numerous types of biosensors and cell culture chambers have been developed and perfected, the integration of both onto the same device is still a challenge. Indeed, in the biological point of view, manipulating live cells in small channels and chambers as it is done in microfluidics is a form of stress that has yet to be quantified. Biological results obtained with the help of microfluidic devices are therefore not directly comparable to those already obtained at a macroscopic scale that are found in the literature.

Our idea is to use Micro-Aspiration [1], an innovative technique developed recently in our laboratory, to reversibly assemble microfluidic devices for precise handling and analyzing tasks, hereby confining and stressing the cells in the least possible way. In this paper, we present a new analytical device that integrates a parallel network of microelectrodes into a reversibly assembled microfluidic device intended for the investigation of oxidative stress mechanisms at the single-cell level.

2. Experimental

The device is divided into two parts (Figure 1.B1 & 1.B2). The lower part (Part I) is an array of linked culture chambers made in PDMS using the usual soft lithography techniques. The upper part (Part II) is an array of electrodes deposited on a glass substrate. The electrodes were fabricated by standard photolithography followed by lift-off of the deposited metal (Cr/Pt: 5/50nm). The formed metal tracks are then covered by an insulating layer (SiO_2 400nm) with openings (10 μm) for active areas, where black platinum was finally electro-deposited (Figure 1.B2).

After the assembly of part I onto a glass slide by aspiration (Figure 1.A), live murine macrophagous cells are distributed in the chamber array by flowing a cell suspension into the formed microchannels. After 15 minutes of cell stabilization in the chambers,

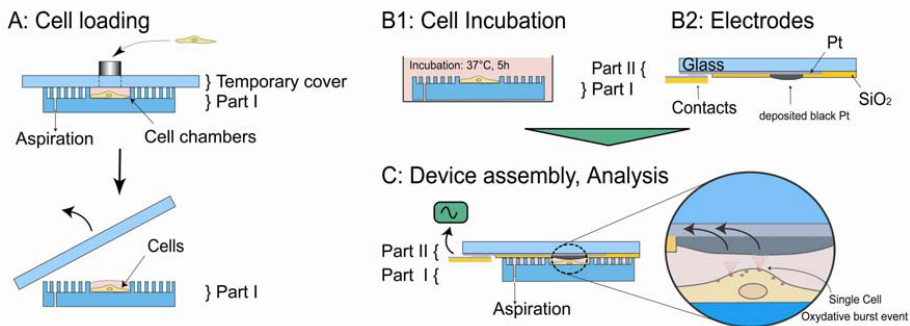


Figure 1. A: Cell loading in the culture chambers. By depressurizing the area of the PDMS chip surrounding the working channels, represented here by pillars, the former will be reversibly sealed onto the substrate. This type of seal can withstand up to 1 bar of pressure inside the working channels. B1: Part I is immersed in medium for Cell Incubation in cell culture conditions. B2: Description of the microelectrode array (Part II). C: Device Assembly and Analysis: the electrode array is aligned over the culture/detection chambers. The height (10 µm) of the chambers determines the average distance between cells and electrodes.

part I is disassembled and immersed in a DMEM culture medium and incubated (37°C, 5% CO₂) for at least 5 hours (Figure 1.B1). Finally, part I is withdrawn from the culture medium and directly reassembled onto the electrode array (Figure 1.C & 3). Micro-Aspiration ensures the evacuation of excess fluids and the perfect sealing of the device, making it ready for analysis tasks.

The reversible sealing of the device is simply assured by a depression established in a cavity surrounding to working fluidic channels that literally clamps the device onto the substrate with the help of only a tube and a vacuum pump.

3. Results and discussion

As a proof of concept, we chose to establish a setup in a reversibly assembled microfluidic device for the electrochemical monitoring of cellular oxidative burst events on an array of single cells.

Recently, a novel electrochemical approach has been introduced [2]. Based on the use of an ultramicroelectrode positioned in the close vicinity of a living cell, it enables the monitoring of single-cell release of electroactive species. Though the technique is well adapted for single cell analysis, it presents some important limits to the establishment of a solid model: it is time consuming and does not permit parallel investigation of a cell population. The microfluidic device presented here is an answer for such limits.

Figure 2 shows the successful detection of batch cell responses by one microelectrode of the array, hereby justifying their use in such a set-up. With the reversible assembling technique, it is possible to reuse for a number of time and in different configurations the same microelectrode array, making it easy to compare results obtained from different experiments.

Our cell handling technique provides numerous advantages to the chronoamperometry setup. After being precisely positioned in the chambers, the cells to be investigated

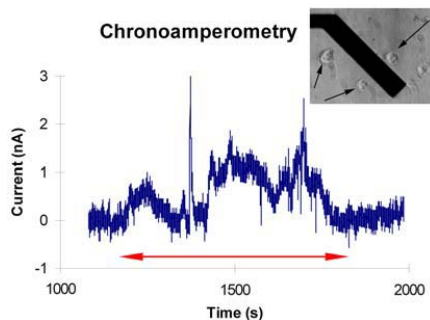


Figure 2. Response of a small population of ~20 murine macrophagous cells to an injection of Calcium Ionophore (A23187). The detection of excreted electroactive species is done on a single microelectrode (10 μm diameter ; Black Platinum microelectrode at 850 mV VS Ag/AgCl ref). The cells were deposited on the glass slide, around the microelectrode (see insert).

preserving their cellular integrity. Figure 3.A shows a microphotograph of a suitable cell for chronoamperometric experiments in the traditional setup, directly spread on a Petri dish, and figure 3.B shows a microphotograph of a cell loaded into a chamber: their physiologic similarities suggest a reliable and appropriate cell handling technique. Furthermore, since Micro-Aspiration permits a positive pressure in the microchannels, it makes this cell handling technique convenient and versatile, even giving the possibility to use multilayered device with valves and pumps.

4. Conclusion

The technique presented here allows a reliable setup for such delicate experiments as that of chronoamperometry on single cells. Furthermore, its simplicity and versatility offers new possibilities and outlooks for microfluidic applications in analytical science and cell biology.

Acknowledgments

This work was partially supported by European Commission through Project No. NMP4-CT-2003-505311 (Nabis) and Project No. NMP4-CT-2003-500120 (Napa). DGA is thanked for supporting Ph.D. grants.

References

- [1] M. Le Berre, C. Crozatier, G. Velve Casquillas and Y. Chen, Reversible assembling of microfluidic devices by aspiration, *Microelectron. Eng.*, vol. 83, pp. 1284–1287, (2006)
- [2] C. Amatore, S. Arbault, D. Bruce, P. de Oliveira, M. Erard and M. Vuillaume, Analysis of Individual Biochemical Events Based on Artificial Synapses using Ultramicroelectrodes : Cellular Oxidative Burst, *Faraday Discussions*, pp. 319-303, (2000)

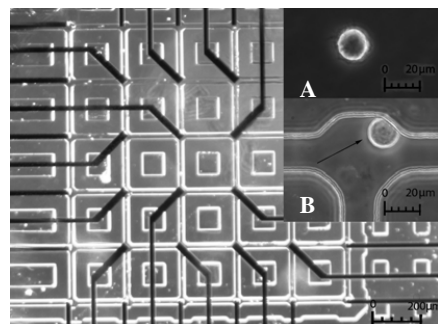


Figure 3. Microphotography of the assembled device. The linked culture/detection chambers (40 μm diameter) are aligned with the active parts (10 μm diameter) of the electrode array. Insert A shows a stabilized murine macrophagous cell in a Petri dish and insert B shows a stabilized cell in a chamber after incubation, before the analysis step.

have been recovering in the most usual cell culture configuration, hence cell culture configuration, hence

RAPID FLUORESCENCE-ACTIVATED CELL SORTING WITH OPTICAL-FORCE DEFLECTION IN A MICROFLUIDIC DEVICE

Thomas D. Perroud and Kamlesh D. Patel

Sandia National Laboratories, 7011 East Avenue, Livermore CA 94551, USA

ABSTRACT

We present our initial results on the integration of a fluorescence-activated cell sorter into a microfluidic platform for the study of macrophages. We show that hydrodynamically focused macrophages can be efficiently sorted into another laminar flow by optical-force deflection, similar to optical tweezers. Although high laser power is required for sorting macrophages, initial observations show no obvious laser damage to the cells.

Keywords: cell sorting, optical trapping, cytometry, FACS

1. INTRODUCTION

Microfluidic-based flow cytometry could potentially allow for the analysis of precious cell types (cells extracted from a biopsy sample or cancer cells) or avoid the biohazards of conventional droplet-based cell sorters. Furthermore, the integration of a fluorescence-activated cell sorter (FACS) with additional functional modules (such as intracellular immunoassays or cell lysis) represents an essential step towards the development of a complete analytical microdevice for studying cell populations. The use of optical trapping [1] as a sorting mechanism in a microfluidic-based FACS (μ FACS) has been recently demonstrated [2]. The non-invasive nature of optical forces and their resulting high sorting speed represent an attractive alternative over mechanical, dielectrophoretic, or electrokinetic sorting schemes for μ FACS. This paper reports on the development of a μ FACS integrated with intracellular immunoassays for a semi-quantitative proteomic characterization of macrophages, which are white blood cells - a component of our innate immune system. We present initial results on the high-throughput sorting of macrophages and their recovery as unstressed mammalian cells.

2. EXPERIMENTAL

Our setup consists of a 20 W continuous wave near-infrared (1064 nm) fiber laser for cell sorting and two 20 mW solid-state lasers (488 nm and 633 nm) for

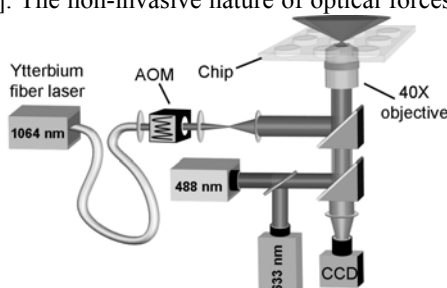


Figure 1. Scheme of a μ FACS. The fluorescence activation consists of two solid-state lasers (488 nm and 633 nm). The cell sorter consists of a fiber laser (1064 nm) and an acousto-optical modulator (AOM).

fluorescence detection. Following an epifluorescence configuration, all lasers are coaxially focused through the same 40X objective of an inverted microscope (Fig. 1). The sample flow can be either 7 μm polystyrene beads or RAW 267.4 mouse monocyte macrophages in an isopycnic PBS buffer (10% (v/v) Optiprep), whereas the sheath flow is PBS buffer only. In the microfluidic chip, cells are hydrodynamically focused into a single file by two feedback-controlled positive-pressure units to achieve high detection efficiency in the subsequent interrogation zone. In this region, the presence of a cell is detected through forward-scattering, and laser-induced fluorescence is used to probe cells for a particular protein-based assay. Both scattering and fluorescent signals of a cell passing through the interrogation region trigger an acousto-optical modulator to raster the near-infrared laser in the switching region. Cells in that region are trapped and deflected into another laminar flow stream for downstream binning.

3. RESULTS AND DISCUSSION

Two-dimensional hydrodynamic focusing was initially achieved in a commercially available chip [3], where one sheath flow focuses the cells along the wall of the channel (Fig. 2A). As the pressure in the sheath flow increases relative to the sample flow, the stream of the sample flow becomes narrower, thus focusing the particles along the wall. To achieve a more uniform linear velocity of the particles, we fabricated a second-generation chip that uses two sheath flows to focus the cells in the center of the channel (Fig. 2B).

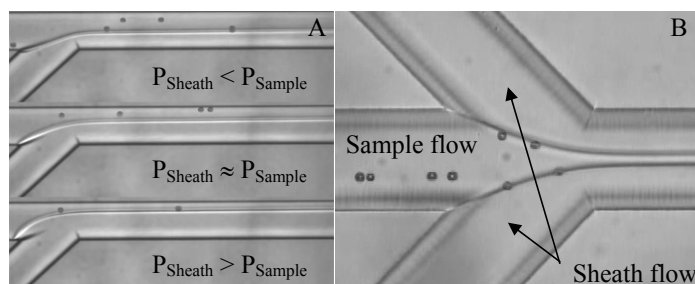


Figure 2. Hydrodynamic focusing using either design A, where only one sheath flow focuses cells along the wall, or design B, where two sheath flows focus cells in the center of the channel.

As a proof of concept for sorting cells using optical-force deflection, a 7 μm polystyrene bead is captured from a focused flow by the infrared laser beam (2 watts), translated to the other side of the channel, and subsequently released (Fig. 3). The estimated linear velocity of the flow from which the bead is captured is approximately 1 mm/s. Similarly, a macrophage focused along the wall of the channel is trapped, translated across the channel, and released in a different laminar flow (Fig. 4).

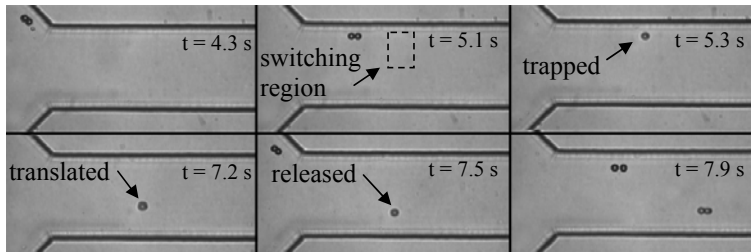


Figure 3. A time sequence of images showing a bead captured from a focused flow, translated to the other side of the channel, and released.

Our target goal for cell sorting is 10-20 cells/s with a 50% duty cycle. Since cells have a lower refractive index than polystyrene beads, higher laser power is required (on the order of several watts) for efficient trapping and deflection. Initial trapping and manipulating experiments with a 5 watts focused laser beam show no obvious physical damage or changes in the morphology of the macrophages.

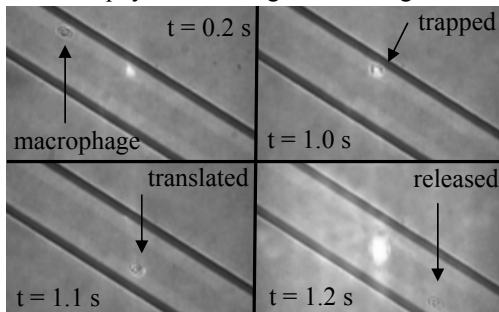


Figure 4. A time sequence of images showing a macrophage captured from a focused flow, optically deflected, and released.

Additionally, macrophages trapped at high power (5 watts) for at least 2 min do not become stained in a Trypan blue dead cell assay (data not shown). We are developing a more sensitive assay to determine whether the macrophages are accidentally activated by the near-infrared laser. In this immunoassay, we will measure the intracellular amount of cytokines, which are proteins produced after activation [4], thus directly monitoring the degree of activation of each macrophage.

4. CONCLUSIONS

Overall, our results are a promising step towards the sorting of macrophage subpopulations and their subsequent characterization on a single chip.

ACKNOWLEDGMENTS

Sandia is a multiprogram laboratory operated by Sandia Corporation, a Lockheed Martin Company, for the United States Department of Energy's National Nuclear Security Administration under contract DE-AC04-94Al85000.

REFERENCES

- [1] K. Svoboda and S. M. Block, Annu. Rev. Biophys. Biomol. Struct. 23, pp. 247-285, (1994).
- [2] M. M. Wang, et al., Nature Biotechnology 23, pp. 83-87, (2005).
- [3] Z. Palkova, et al., Cytometry Part A 59A, pp. 246-253, (2004).
- [4] A. J. Schuerwagh, et al., Cytometry 46, pp. 172-176, (2001).

A BIOPARTICLE DETECTOR AND ENRICHMENT PLATFORM USING INTEGRATED INSULATOR-BASED DIELECTROPHORESIS AND BIOIMPEDANCE MEASUREMENTS

Pierre Ponce¹, Blake A Simmons¹, Michelle Khine², and Rafael V Davalos^{*1,3}

¹Sandia National Laboratories, Livermore, CA, USA

²School of Engineering, University of California, Merced, CA, USA

³Biomedical Engineering, Virginia Tech-Wake Forest, Blacksburg, VA, USA

^{*}rvalaval@sandia.gov

Abstract

We have developed a bioparticle detection platform which combines insulator-based dielectrophoretic (iDEP) concentration with impedance feedback. The system continuously and selectively accumulates particles while electrical responses of the suspension at the trapping site are recorded. The operating conditions for trapping are determined by the physical and electrical properties of the target particle type. Recordings of phase offset, relative to the reference sensing signal, act as the principal monitoring indicators. These measurements enable us to detect the presence and the approximate concentration of biological contaminants in a sample. This study is the first to illustrate the potential of iDEP concentration in conjunction with impedance measurements. The results obtained from fluorescent beads and viable *B. subtilis* spores demonstrate the feasibility of using iDEP concentration with active impedance monitoring to detect biological pathogens collected from dilute samples.

Keywords: concentration, impedance, bacterial spores, bioMEMS, microfluidics

1. Introduction

Devices that detect health hazards in air and water supplies must be sensitive enough to detect low concentrations of pathogens. For example, less than a microgram of botulinum toxin is lethal to an average adult human [1]. Moreover, knowledge of the concentration of such particles can determine the toxicity level of a water supply and the appropriate measures needed to quickly resolve health crises.

The goal of this study is to establish the first steps towards realizing a self-contained platform that fully integrates the ability to concentrate bioparticles with a reliable method for detecting their presence. The trapping methodology is based on insulator-based dielectrophoresis (iDEP) [2]. This is a new iDEP device architecture that minimizes the trapping area to enhance the detection limit of the system. The small volumes of solution in the trap during detection makes the tracking of impedance changes a practical solution for detection [3, 4]. Detection is enabled by monitoring impedance changes through sensing electrodes located in the vicinity of the trapped particles. This publication demonstrates the feasibility of iDEP concentration coupled with impedance-based monitoring for rapid and sensitive detection of biologicals.

2. Experimental methodology

The microfluidic channel in our testing platform is fabricated on a polymer substrate Zeonor® (Zeon Chemicals, Louisville, KY). The insulating structures that facilitate particle trapping are formed by injection molding using a Ni stamp fabricated from a Si master, as detailed in [5]. All sample solutions use a low-conductivity ($1.52 \mu\text{S}/\text{cm}$) buffer. The device used is depicted in Fig. 1a. The detailed experimental conditions and setup used in the system for iDEP operations have been detailed in [2].

Impedance measurements and AC sensing signals were done using an SR830 DSP lock-in amplifier (Stanford Research Systems, Sunnyvale, CA). Baseline impedance measurements were taken in bulk solution and in a control microchannel to determine the electrical responses to different particle concentration levels. An AC probe signal of 50 mV amplitude (RMS) at a frequency of 2 kHz was used for all our trials.

Experiments conducted in rectangular control channels were used to compare our results to those obtained in the literature and our bulk measurements. The fluidic channel is 1 mm wide and 30 μm deep. The detection site within the channel consists of two 50- μm coplanar rectangular electrodes, separated by 150 μm . The electrodes are composed of thin Au film with a Ti adhesion layer. Their surfaces are then passivated with a ~0.4 μm -thick oxide layer (SiO_2) to prevent the occurrence of electrolysis in the solution and protect the sensing electronics.

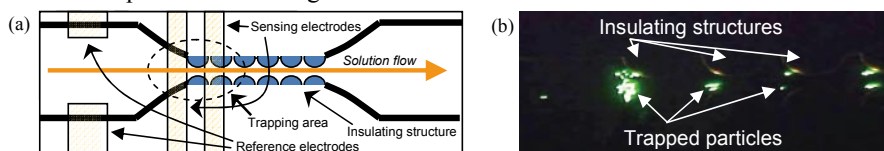


Figure 1. System layout. (a) labeled schematic of the channel. (b) image of trapping with iDEP.

3. Theory

The collection of individual particles within the medium can be modeled as a variable parallel resistance/capacitance pair, as shown in Fig. 2a. As the concentration of particles increases, the displacement of solution by those particles leads to changes in C_{Trap} and R_{Trap} . The cell constant, which affects measured resistances and capacitances, is affected by the dimensions and geometry of the electrodes and channel [6, 7]. Fig. 2b illustrates the test circuit used for measuring phases and currents. Based on our trap circuit model, we derive a formula that helps determine capacitive changes from the introduction of particles. The phase response is given by Eq. (1).

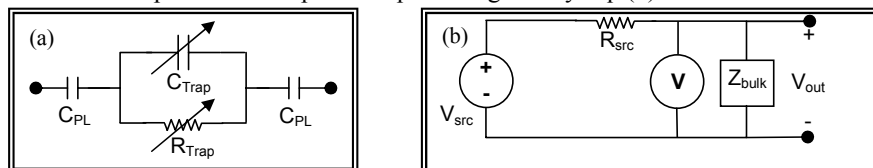


Figure 2. (a) Equivalent circuit depicting the changes in resistance and capacitance within the sensing region of the detection platform. (b) Test circuit used to monitor phase changes in the bulk solution. Z_{bulk} is the overall impedance modeled in (a).

$$\phi = \tan^{-1} \left(\frac{\omega C_{Trap} R_{Trap}}{(\omega^2 C_{Trap}^2 + 1)R_{src} + R_{Trap}} \right) \approx \tan^{-1} \left(\frac{\omega C_{Trap} R_{Trap}}{R_{src} + R_{Trap}} \right), \text{ for } \omega < 2\pi(2 \text{ MHz}). \quad (1)$$

4. Results and discussion

Fig. 1b shows the iDEP trapping of 2-μm beads in our device using an applied voltage of 400 V. The device performance was found to be similar to our previously published designs with the added benefit that the collected particles are acutely focused.

Table 1 summarizes the findings from experiments run on our control detection channel and compares them to experiments conducted in bulk solution using 20-mL glass vials. We calibrated Eq. (1) by applying AC signals to the 20-mL suspension volumes using stainless steel 1-mm electrodes (20 mm apart and without passivation). From these results, we estimate the resistance of the clean solution in the trap to be (R_{Trap}) approximately 2 MΩ. R_{src} , which accounts for parasitics and resistances to protect sensitive electronics, was chosen to be 10 MΩ.

Both sets of experiments display trends that correlate phase offset with particle concentrations in solution. This detection method can detect concentrations as low as 10^3 spores/mL. Past work on iDEP has demonstrated the capability of concentrating particles by a factor of 1000 within minutes [2]. The goal of our effort is to eventually develop a system that is capable of detecting low concentrations of bioparticles (~1 spore/mL) from a sample. The results of this study demonstrate that this detection limit should be attainable using iDEP with impedance monitoring.

Table 1. Baseline impedance measurements for *B. subtilis* in bulk tests ($n=5$)

Particle Concentration	Peak Phase Offset Relative to Clean (degrees) Bulk Tests	30μm x 50μm x 150μm channel
clean (no spores)	0.00 ± 0.04	0.00 ± 0.02
10^3 spores/mL	16.75 ± 0.15	0.05 ± 0.02
10^5 spores/mL	32.20 ± 0.14	0.19 ± 0.05
5×10^6 spores/mL	38.72 ± 0.25	0.24 ± 0.06
5×10^7 spores/mL	39.23 ± 0.08	0.33 ± 0.07

Acknowledgements

The authors thank B. Crocker, J. Brazzle, B. Haroldsen, G. McGraw, A. Salmi, K. Krafcik, J. van de Vreugde, S. Jamison, S. Ferko, Y. Syed, J. Rognlien, and P. Sabourchi for their contributions to this project. Sandia is a multiprogram laboratory operated by Sandia Corporation, a Lockheed Martin Company, for the United States Department of Energy's National Nuclear Safety Administration under contract DE-AC04-94AL85000.

References

1. S.S. Arnon *et al. JAMA*. **285**(8): 1059-1070, (2001).
2. B.H. Lapizco-Encinas *et al. J. Microbiol. Meth.* **62**: 317-326, (2005).
3. J. Suehiro *et al. J. Electrostat.* **57**: 157-168, (2003).
4. D.W.E. Allsopp *et al. J. Phys. D: Appl. Phys.* **32**: 1066-1074, (1999).
5. G.J. McGraw, R.V. Davalos *et al. SPIE Proc.* **5715**(6), San Jose, CA: 59-68, (2005).
6. P. Linderholm and P. Renaud. *Lab Chip* **5**: 1416-1417, (2005).
7. W. Olthuis *et al. Sens. Actuators B* **24-25**: 252-256, (1995).

SOFT-STATE BIOMICROFLUIDIC PULSE GENERATOR FOR FAST ENDOCYTIC RECYCLING ANALYSIS OF SINGLE CELLS

**Poorya Sabourchi, Cristian Ionescu-Zanetti, Navid Ghorashian,
and Luke P. Lee**

Berkeley Sensor & Actuator Center, University of California, Berkeley, USA

Abstract

We present the design, fabrication, and characterizations of an integrated soft-state biochemical pulse generator within single cell trapping device. Biochemical pulses are generated around trapped single cell array to study the kinetic response of membrane proteins. Hydrodynamic cell trapping via lateral channels allows the trapping of single cells from a bulk suspension. Microfluidic injection site adjacent to the cell-trapping channels enable the pulsed delivery of nanoliter volumes of biochemical reagent. Fast endocytic recycling of cells is studied under 0.5 Hz pulsed flow using a FM fluorescent dye and intensity results were compared to a simple compartment model.

Keywords: Soft-state Devices, Single Cell Analysis, Biochemical Pulses

1. Introduction

Analyzing individual cells will inherently be more accurate than any other cell-based sensor that relies on ensemble-averaged experiments. However, only few studies have carried out experiments on individual living cells using various microfluidic devices [1]. We recently introduced a microfluidic platform for high-throughput patch-clamp electrophysiology in which lateral cell trapping junctions enable hydrodynamic trapping of cells from a bulk cell suspension and electrophysiological recording [2]. We then developed a platform for rapid fluid exchange across the surface of a microfluidic channel at frequencies of up to 10 Hz [3]. We now present the design and characterizations of a soft-state biomicrofluidic pulse generator device where biochemicals are pulsed around single cells to study the fast endocytic recycling in cell membrane. Our method is simpler than existing methods of biochemical pulse generation based on scanning patch pipettes because no mechanical movement is required [4].

2. Design and Fabrication

The soft-state biomicrofluidic pulse generator device is fabricated using a two-layer SU-8 and soft-lithography of PDMS. The main channel and lateral fluidic channels are 50 and 3 μm in height respectively (Figure 1). Central to our setup is a fluidic injection system that uses a solenoid valve. Pulsed chemical reagents flow

through this injection system allowing characteristic response of single cell array to be performed in rapid succession.

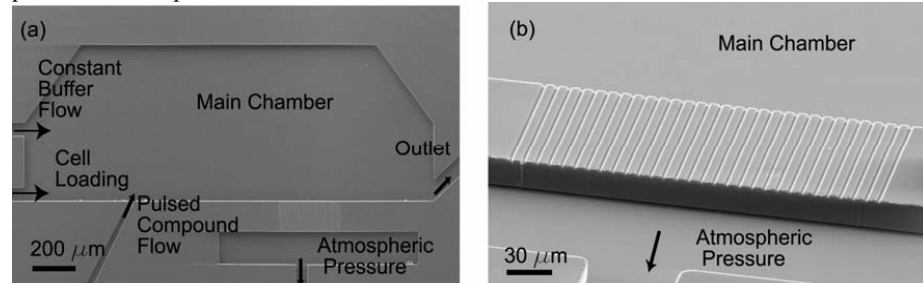


Figure 1. Device Design (a) An SEM image of the microfluidic device before bonding. A constant flow (left to right) is imposed in the main chamber, while a side capillary is used as an injection port. The main fluidic channel is 50 μm in height. (b) Close-up view of the trapping region. Each side channel had a width of 3 μm and height of 3 μm .

3. Experimental methodology

Suspended Hela cells were introduced from a syringe connected to cell loading port. As the cells entered the device, the pulse compound port and outlet were closed and the cell trapping port was opened to atmospheric pressure. This directed the flow of cells into the trapping sites (Figure 2 a-c). After opening outlet, closing cell loading port and flushing the cells with constant sterile buffer, Trypan blue was pulsed through the injection channel (Figure 2d). Chronological sequence of application and removal of Trypan blue around trapped single cells for 1 Hz pulsed flow is shown (Figure 2 e-d). After several pulses majority of the cells are still healthy and have not been stained.

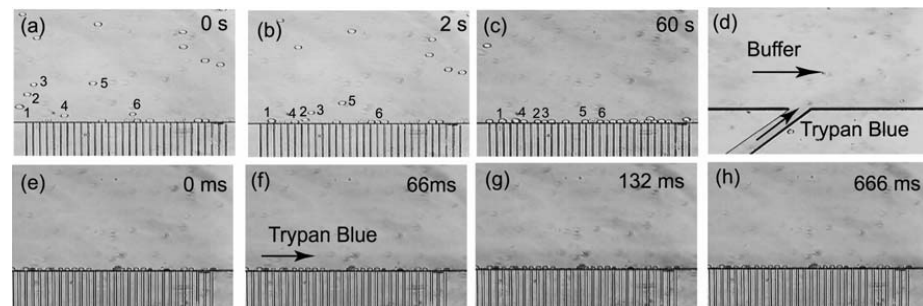


Figure 2. Viability Assay (a-c) Chronological sequence of sequential cell trapping. (d) Close-up view of the injection channel (e-h) Chronological sequence of application and removal of Trypan blue around trapped single cells for 1 Hz pulsed flow. After several pulses majority of the cells are still healthy and have not been stained.

3. Results and Discussion

Fast endocytic recycling of Hella cells cells is studied under 0.5 Hz pulsed flow using an amphiphilic fluorescent dye (FM 2-10) which reversibly partition into cell

membranes reversible (Figure 3 a-c) [5]. For compartment modeling transport from bulk to surface with mass transfer coefficient of $h = 6e-5$ m/s (Figure 3d) and then a three step kinetic model was used based membrane binding ($\alpha=1.71s^{-1}$), dissociation ($\beta=0.77s^{-1}$), internalization ($\gamma=0.0008s^{-1}$), and recycling ($\lambda=0.012s^{-1}$) of fluorescent molecules (Figure 3e). The intensity results and model is shown (Figure 3f) and they agree with accepted values for binding and endocytosis parameters [6].

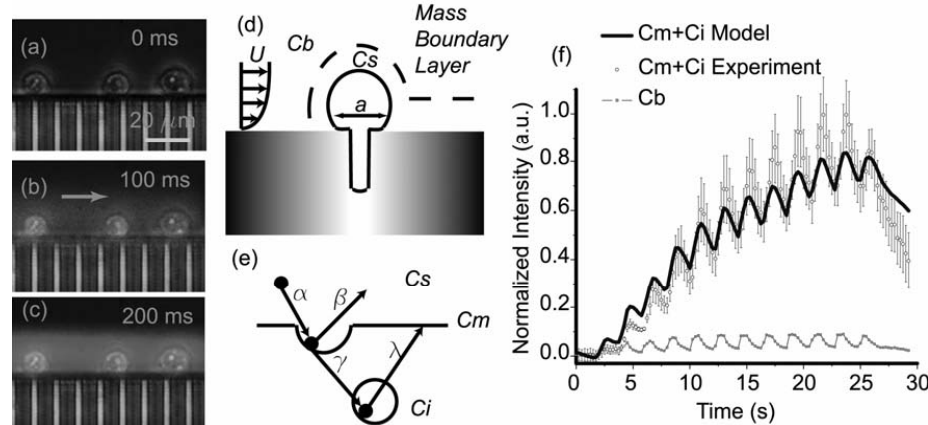


Figure 3. Compartment Modeling of Rapid Membrane Trafficking; (a-c) Chronological sequence of application and removal of amphiphilic fluorescent dye (FM 2-10) which reversibly labels cell membrane was used to characterize reversible binding kinetics of trapped single cells. (d) Transport from bulk to surface with mass transfer coefficient of $h = 6e-5$ m/s (e) Schematic of a three step kinetic model based membrane binding ($\alpha=1.71s^{-1}$), dissociation ($\beta=0.77s^{-1}$), internalization ($\gamma=0.0008s^{-1}$), and recycling ($\lambda=0.012s^{-1}$) (f) Fluorescent intensity measurement of FM-210 association to cells fitted to the kinetic model for 0.5 Hz pulse. The error bars represent standard deviation from three different trapped cells.

In summary, integrated biochemical pulse generator and single cell array trapping is designed, fabricated, and characterized. Membrane trafficking analysis at single cell level is performed under pulsed flow and the results of fluorescent bioassay were compared to simple compartment model of rapid membrane trafficking.

ACKNOWLEDGEMENTS

We thank Jeonggi Seo for help in SEM imaging. The device is fabricated in the microlab at UC Berkeley.

References

1. J. El-Ali, *et al.*, *Nature Insight* July (2006)
2. C. Ionescu-Zanetti, *et al.*, *PNAS*; vol. 102, no. 26, pp. 9112–9117, 2005.
3. P. Sabourchi, *et al.*, *Applied Physics Letters* 88, 183901 (2006)
4. J. Olofsson, *et al.*, *Proc. Natl. Acad. Sci.*; 102(23), 8097-8102.(2005).
5. F. R Maxfield, T. E. McGraw, *Nature Reviews MCB* 5, 121-132 (2004)
6. M. Hao, and F.R. Maxfield, *J. Biol. Chem.* 275, 15279–15286 (2000)

MICRO/NANO-PATTERNED SURFACES FOR CONTROL OF CELL ADHESION AND CELL FUNCTIONS: DIFFERENTIATION INTO ADIPOCYTES

Makiko Goto^{1, 2}, Kae Sato^{1, 3}, Takehiko Tsukahara^{1, 2}, Tomohiro Konno^{3, 4}, Kazuhiko Ishihara^{3, 4}, and Takehiko Kitamori^{1, 2, 3}

¹Department of Applied Chemistry, School of Engineering, The University of Tokyo, Tokyo, 113-8656, Japan,

²CREST, Japan Science and Technology Agency, Saitama, 332-0012, Japan

³Center for NanoBio Integration, The University of Tokyo, Japan

⁴Department of Materials Engineering, School of Engineering, The University of Tokyo, Japan

Abstract

Cell adhesion surfaces having micro/nano patterns and controlled chemical properties were fabricated. The patterning at a subcellular-scale should control the formation of focal adhesion formation that plays an important role in many cellular functions. We observed that preadipocytes adhered, proliferated on the surfaces, and were induced to differentiate. Individual cells adhered and grew on the patterns but confluent cell monolayers on nano patterns easily detached from the substrata. The micro/nano patterns provide cells with unique scaffolds controlling cell-matrix interactions at a subcellular scale.

Keywords: Nano patterning, cell adhesion, cell differentiation

1. Introduction

Cell adhesion plays a critical role in adherent cells because it triggers signal transduction inside the cells affecting cellular growth, proliferation or differentiation. Many studies on the interactions between cells and adhesion surfaces are reported. We focus adhesion surfaces patterned at a subcellular-scale (10-1,000 nm), the size reaching a focal adhesion (Figure 1). The focal adhesion plays a pivotal role in cell adhesion and signal transduction, and the patterning at a subcellular-scale should allow controlling morphology, proliferation, or differentiation of a cell. Our goal is the development of novel cell culture devices that can provide a variety of adhesion surfaces having defined physical and chemical properties allowing each kind of cells to function selectively. We already reported the fabrication of the patterned surfaces and the culture of mouse fibroblasts on them. The change of the cell shape was observed as the size of patterns was changed from 900 nm to 30 μ m [1]. In this study, we developed micro/nano patterns that control adhesion, growth, and the differentiation of preadipocytes cell line 3T3-L1 into adipocytes.

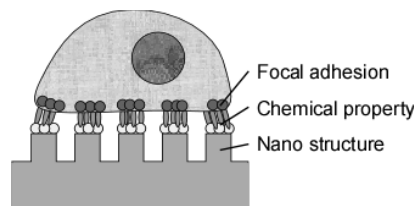


Figure 1. Cell adhesion surface with nano patterning

2. Experiments

Micro/nano structures were fabricated on quartz glass substrates by electron-beam lithography, metal sputtering, and lift-off methods. A gold and titanium layer in stripes was fabricated (Figure 2a). The gold surfaces were coated with 1-octadecanethiol (ODT), and then the quartz glass surface was coated with alkyl silane containing 2-methacryloyloxyethyl phosphorylcholine (MPC) polymer (Figure 2b). MPC polymer provides an inert surface for protein adsorption and adhesion [2], and we used MPC polymer as a barrier for protein adsorption and cell adhesion.

Fibronectin was adsorbed on the ODT-covered patterns, and then cells were seeded on the surfaces.

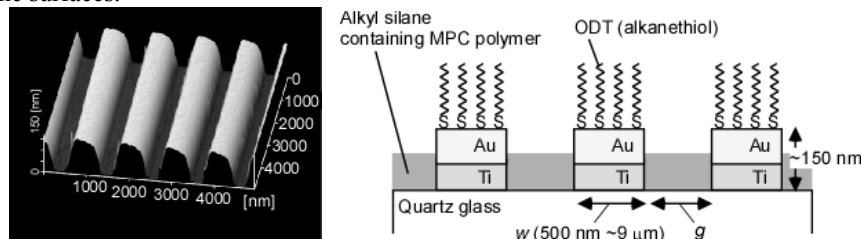


Figure 2. (a) A view of scanning electro microscope of nano patterns. (b) A cross view illustration of chemical modification with alkanethiol and alkylsilane.

3. Results and discussions

We defined the pattern scale with w , the width of a gold stripe, and with g , the gap between two stripes (Figure 2b). We fabricated two kinds of stripe patterns, pattern 1; $w = g$ and $w = 600 \text{ nm} \sim 9 \mu\text{m}$, and pattern 2; $w = 600 \text{ nm} \sim 9 \mu\text{m}$ and $g = 9 \mu\text{m}$ (fixed). In order to check the protein covering on nano patterns, the adsorbed fibronectin was immunostained (Figure 3). Fibronectin was adsorbed only on ODT layer on gold patterns. Mouse fibroblasts NIH/3T3 cells on the modified substrate did not attach on the quartz area modified with MPC polymer even at over confluent growth (Figure 4).

Mouse preadipocytes 3T3-L1 cells were cultured on the patterns. Cells attached on the patterns and elongated along the stripe (Figure 5a). On every pattern, cells proliferated and formed confluent monolayers, and then, some of the cell monolayers detached from the patterns (Figure 5b). On pattern 2, as w became smaller than $2 \mu\text{m}$, most monolayers started to detach from the surface. But when they were induced to differentiate into adipocyte by a treatment with dexamethasone, isobutylmethylxanthine, and insulin, cells differentiated into adipocytes (Figure 5c).

On nano scale patterns, cell-extracellular matrix (ECM) adhesion would be strong enough for individual cells to attach and proliferate, but when cells form a confluent monolayer, the balance of cell-cell adhesion and cell-ECM adhesion becomes unstable, and cell monolayers detach from the patterns, while the cells are still connected with each other. 3T3-L1 cells could differentiate into adipocytes on the patterns in the adipocyte-inducing media, although the cell-matrix adhesion was unstable. The effects of the nano patterning on the rate of cell proliferation and differentiation are under investigation.

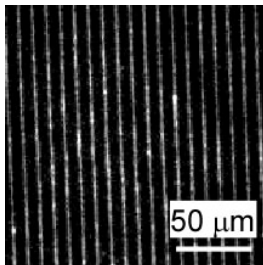


Figure 3. The fluorescent micrograph of the nano patterns, on which fibronectin was absorbed and immunostained (pattern2; $w = 530$ nm and $g = 9$ μ m).

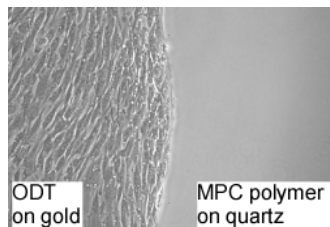


Figure 4. The micrograph of MIH/3T3 cells. cells were cultured over confluent, but didn't adhere on the quartz substrate modified with MPC polymer.

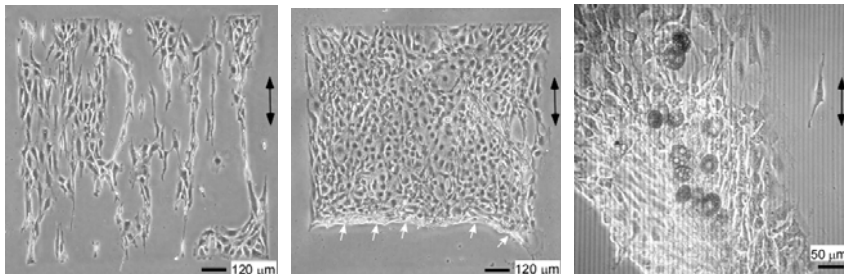


Figure 5. The micrographs of 3T3-L1 cells on pattern 2; $w = 600$ nm in (a) and (b), and $w = 550$ nm in (c). Black arrows in figures are the direction of stripes. (a) Elongated cells after 24 hours culture. (b) A confluent monolayer detaching from the pattern (the heads of white arrows) after 60 hours culture. (c) Cells differentiated into adipocyte in a cell monolayer and formed lipid droplets.

4. Conclusions

The micro/nano adhesion surfaces can provide cells with designed cell-matrix interactions and defined cell morphologies. Individual preadipocytes 3T3-L1 could adhere and proliferate on every pattern, but confluent cell monolayers on the nano patterns easily detached from the patterns.

The micro/nano patterning enables to form cell arrays and to control cell shape at a single cell level. Our study can contribute investigation of cell differentiation mechanisms by separating the action of major differentiation factors such as cell-cell communication, cell-ECM communication, and extracellular stimulation.

References

- [1] M. Goto, K. Sato, M. Yamato, A. Hibara, T. Kitamori, *Micro TAS '05*, pp. 1282-1284 (2005)
- [2] Y. Iwasaki, K. Ishihara, *Anal. Bioanal. Chem.* **381**, pp. 534-546 (2005)

EVAPORATION- AND PRESSURE- DRIVEN CLOSED-LOOP pH CONTROL IN A MICROLITER BIOREACTOR FOR HIGH-THROUGHPUT BIOPROCESSING

Zhiyu Zhang, Patrick Boyle, Ruben Kolfschoten, Paolo Boccazz,
Anthony J. Sinskey, Klavs F. Jensen
Massachusetts Institute of Technology, USA
(kfjensen@mit.edu)

Abstract

We present a polymer-based microbioreactor system for pH control and fed-batch culture of *Escherichia coli*. The microbioreactor is maintained at constant volume and water evaporation through the poly(dimethylsiloxane) PDMS oxygenation membrane “pumps” fluid through the system. Additions of acid, base, and glucose are driven by gas pressure and are closed-loop controlled by the pH and oxygen monitoring. Make-up water maintains the reactor at a constant volume.

Keywords: microbioreactor, microbial cell culture, pH control, evaporation-driven flow, microvalve

1. Instruction

We have previously demonstrated reproducible batch and continuous cell cultivation of *E. coli* in microliter microbioreactors with real-time and *in-situ* monitoring of optical density (OD), pH, and dissolved oxygen (DO) [1, 2]. Fed-batch operation, a very important method for bioprocess developments, allows control over environmental conditions in fermentations and is easily achieved by varying the volume. However, the volume is constrained in membrane based microfluidic systems. In order to satisfy this volume constraint, the fed batch micro reactor relies on water evaporation from the PDMS aeration membrane to create volume for acid, base, and glucose additions. The amounts are controlled by feedback of on-line pH and dissolved oxygen measurements. Excess evaporation is balanced by water addition.

2. Microbioreactor Setup

The fed-batch microbioreactor (Fig. 1) with integrated optical sensors consists of two thermally-bonded poly(methylmethacrylate) (PMMA) layers. The reactor chamber is covered by a spin-coated poly(dimethylsiloxane) (PDMS) membrane (100 μm) for evaporation and aeration. Mechanical assembly of this 220 μL device is enabled by a thick PDMS gasket and a PMMA cap. Details of the active mixing, optical sensors and measurements setup have been described previously [1].

Fig. 2 shows the microfluidic network and the control scheme for base addition in the microbioreactor. When dry air is flowing through the outer environmental chamber at 5 cm^3/min , water continuously evaporates through the PDMS membrane into the headspace above at a constant rate of 43 $\mu\text{L}/\text{hr}$, thus enabling fluid flow into the microbioreactor. A nitrogen gas cylinder pressurizes two liquid reservoirs to 0.7 atm and drives the liquid feeds. Liquid flowing out of reservoirs is controlled by

micro dispensing valves (INKX0514300A, The Lee Company). PEEK tubes with inner diameter of 50 μm and 58 cm in total length increase the flow resistance and limit the liquid injection volume to μL per valve opening. The microvalves are actuated by a Labview® program based on online pH measurements using a proportional and derivative (PD) controller. When valves are opened, working liquids from the reservoirs flow through the PEEK tubes and push strong acid and base solutions into the microbioreactor. A water reservoir at an elevated height of 25 cm replenishes water in the microbioreactor to maintain a constant volume.

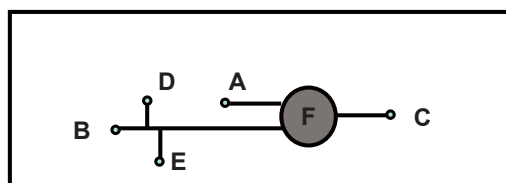


Figure 1. Schematic of microbioreactor used for pH control and fed-batch experiments. Port A – inoculation; B - water replenish; C – exit during inoculation; D – base feed; E – acid/glucose feed. F is the reactor chamber.

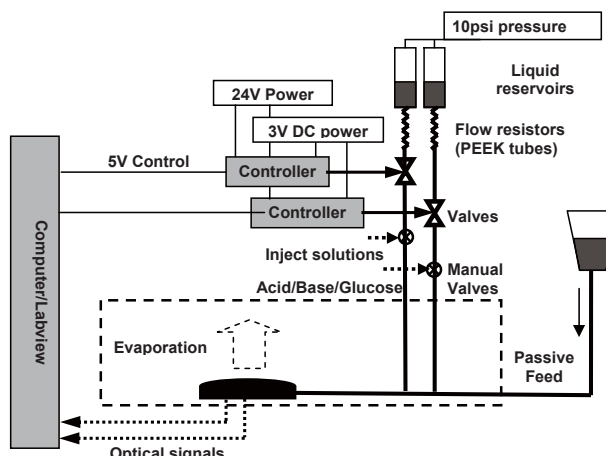


Figure 2. Schematic illustration of the microbioreactor system and control loops. The dashed line box indicates the environmental chamber containing the microbioreactor. Thick solid lines represent fluidic tubes and microchannels, while thin solid lines show electronic cables for power and signal transfer.

3. Results and Discussions

The pH value was successfully maintained within a certain range for *E. coli* fermentations (Fig. 3). Cells were physiologically healthier and remained active for longer period of time (as revealed by the dissolved oxygen curve), which in turn yielded significantly higher biomass concentration at the end of experiment.

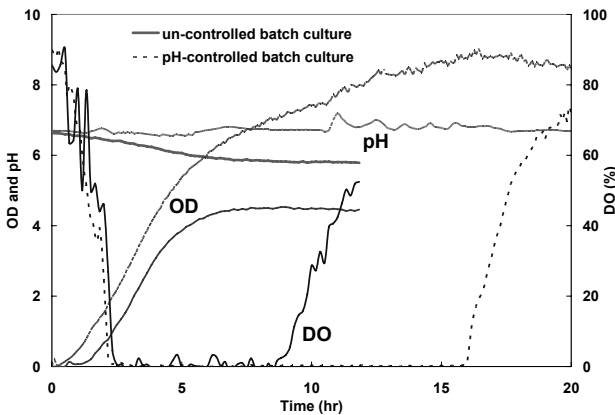


Figure 3. Comparison of *E. coli* cell cultures with (dashed lines) and without (solid lines) pH-control. The LB medium contained 8 g/L glucose, 0.1 mol/L MES, and KAN.

In another experiment (Fig. 4), the glucose feed was closed-loop controlled based on DO reading in the microbioreactor. 13 µg glucose was fed into the microbioreactor whenever the DO level rose above 62% saturation. As a result, the cell culture maintained aerobic metabolism for during major portions of the experiment.

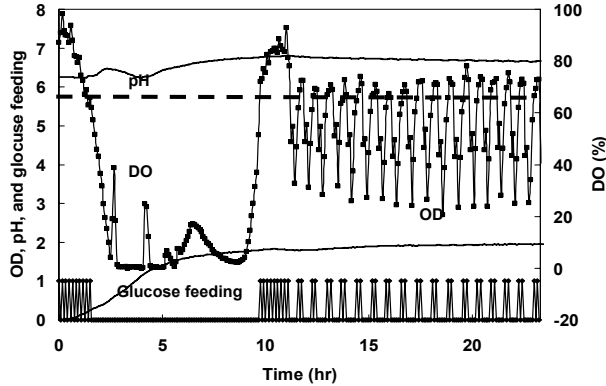


Figure 4. *E. coli* fed batch culture started with half LB medium contained 2 g/L glucose, 0.1 mol/L MES, and KAN. Feed medium contained 10 g/L glucose and the DO setpoint was at 65 % of air saturation level.

4. References

1. Z. Zhang, N. Szita, P. Boccazz, A. J. Sinskey, and K. F. Jensen, *Biotech.Bioeng.*, **2006**, 93, 286-296.
2. Z. Zhang, P. Boccazz, H.-G. Choi, G. Perozziello, A.J. Sinskey, and K.F. Jensen., *Lap Chip*, **2006**, 6, 906-913.

DROP IN DROP NANOLITER KINASE ASSAY MADE WITH HOT EMBOSSED DISPOSABLE MULTI CHANNEL DISPENSER

R. Steger¹, C. Mehne², N. Wangler¹, M. Hecke³, R. Zengerle¹ and P. Koltay¹

¹Laboratory for MEMS Applications, IMTEK, University of Freiburg,

² Institute of Microstructure Technology (IMT), University of Karlsruhe,

³ Institute of Microstructure Technology (IMT), Forschungszentrum Karlsruhe,
all Germany

Abstract

We present a new disposable “Dispensing Well Plate” (DWPTM) manufactured by hot embossing and its application for compound storage and processing of nanoliter assays by drop in drop technique. The DWP-dispensers have been manufactured by a new low cost process creating the 100 µm nozzles directly within the molding process. Fluorescence measurements indicate a good homogeneity of the dispensed volumes better than 5 %. The DWPTM was used to perform a kinase assay based on 100µM Rhodamine substrate with a total assay volume as low as 200 nL. The assay was arranged in a checker board structure on conventional microscope slides. Fluorescence read out showed an good quality of the reaction signals with a robust z-value of 0.57.

keywords: **microfluidic, nanoliter dispenser, miniaturized assays,
high-throughput-screening, HTS**

1. Introduction

There is a strong demand within the pharmaceutical und biochemical industry to create an increasing amount of data points within the high throughput screening in drug discovery [1]. On the other hand the costs of compound libraries and liquid handling have to be kept constant or should be reduced. One way to establish this is to reduce the assay volumes in the sub-µL range. Some research groups established solution phase based assays on slides or special nano-well plates [2, 3, 4]. One challenge within these developments is the precise and parallel handling of nanoliter volumes. The microfluidic DWPTM dispenser [5] is an appropriate tool for this task, which can be used as direct interface between the conventional storage in micro plates and the assay handling on slides and nanoplates.

2. Manufacturing process

The DWP-technology is characterized by arraying microfluidic dispensing units consisting of a reservoir, a capillary connection channel and a nozzle (fig.1). The pneumatically dispensed volume is defined precisely by the geometry of the nozzle and is greatly independent from actuation parameters. To manufacture the DWPTM we developed a hot embossing process using COC polymer. The mold insert was manufactured by high speed micromilling of steel (fig.2). By the hot embossing process

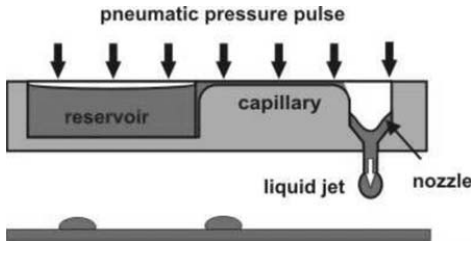


Fig. 1 Basis elements of the DWPTM dispensing process (schematic): reservoir, capillary and nozzle. Jet ejection occurs by pneumatic actuation and refilling by capillary forces when pneumatic pressure turned off.

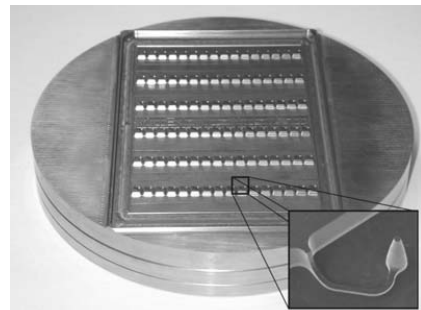


Fig. 2 Mould insert for a 96 channel DWP in the format of a micro well plate (127.7mm x 86.5 mm) with aspect ratios of 3 made by high speed micromilling of steel

the arrayed dispenser structures have been successfully replicated on the format of a microtiter well plate (fig.3) and in smaller 24-well format (35 mm x 26 mm). The nozzle orifices have been directly molded with a diameter of 100 µm with very good quality for contact less dispensing (fig.4).

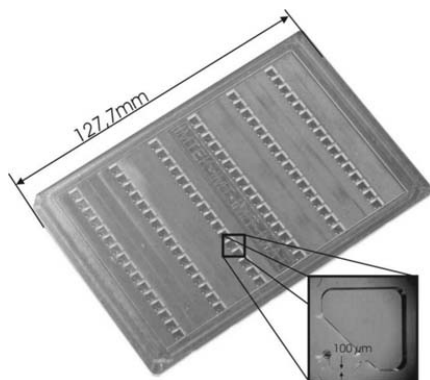


Fig. 3 Hot embossed 96 channel DWP in the format of a micro well plate (127.7mm x 86.5 mm) made from PMMA and COC with nozzles molded directly

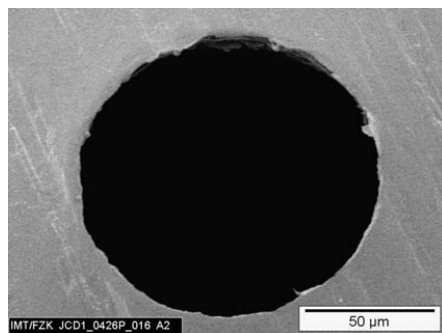


Fig. 4 DWP nozzle orifice made by direct embossing of through holes with a diameter of 100 µm. Sharp edged quality is important for good dispensing quality

3. Application test:

The hot embossed DWPTM plates have been used for storage tests. DMSO- and water-based buffers were filled in the reservoirs and dispensing quality was tested. Afterwards the filled DWP was stored at temperatures of -20°C several days. Tests showed no loss of the dispensing quality directly after defrosting (fig. 5). Hot embossed 24-channel DWPTM's have been used to perform a 200 nL kinase endpoint assay in a checker board

structure directly on a slide. Therefore 100 nL of HNPT-buffer and Trypsin in concentration of 200 U/ml were dispensed. Into these droplets either 100 nL of 100 μ M Rhodamine 110 substrate or pure buffer were dispensed in a checker board manner. The fluorescence read out showed an excellent signal response with no cross contamination (fig.6). In the pharmaceutical screening community a statistical parameter the Z-value [6] is used to evaluate and validate performance of assays. The Z-value for the checker board signals showed a robust value of 0.57 (1 from 6 measurements all with $Z' > 0,5$).

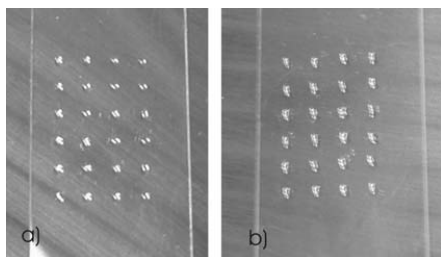


Fig. 5 4 x 6 droplet array with DMSO Buffer dispensed with hot embossed DWP a) before storage and b) after storage at -20°C directly after defrosting

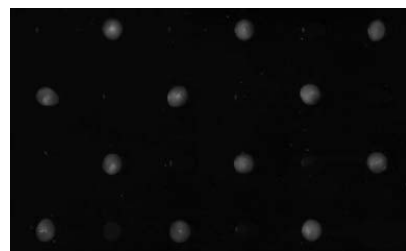


Fig. 6 Fluorescence read out of Kinase Assay with Rhodamine 110 substrate printed with the DWP in a checker board structure drop in drop with the enzymatic trypsin buffer (total volume 200 nL).

4. Conclusion

It was demonstrated that disposable plastic DWPTM made by hot embossing can be used for highly parallel dispensing of nanoliter volumes. With the disposable DWPTM plates miniaturized assays with a total volume of 200 nL consisting of 3 different components have been realized. The measured assay quality with a Z-value of 0.57 proofed a good dispensing quality. Therefore the DWPTM nanoliter dispenser is an interesting tool in creating higher throughput with low liquid volumes in pharmaceutical ultra-high-throughput-screening.

Acknowledgements

The support of the Landesstiftung Baden-Württemberg (Gromik-Project) is gratefully acknowledged. Thanks also to the HSG-IMAT in Stuttgart for support in mould manufacturing.

References:

- [1] Bergsdorf C., *Proceeding Screening Europe 2005.*, Geneva, Switzerland, February 2005.
- [2] Gosalia D., Diamond S., *Proceedings of the National Academy of Sciences of the USA*, July 2003 vol. 100 , pp. 8721-8726
- [3] Dietrich H. et al, *Analytical Chemistry*, Vol. 76, No. 14 July 2004. pp. 4112-4117.
- [4] Ma, Haiching et al, *Assay and Drug Development Technologies*, Vol. 3 No. 2, 2005, pp. 177-187.
- [5] Koltay P. et al, *Sensors and Actuators A-Physical*, Vol. 116 (3), 2004, pp. 483-491.
- [6] Zhang, J. et al, *Journal of Biomolecular Screening*, Vol 4 (2), 1999, pp. 67 – 73.

SYNTHESIS OF SPHERICAL MICROCAPSULES WITH NANO-PORES AND USE AS A POTENTIAL ENCAPSULANT

**Eun Ho Jeong¹, Sinoj Abraham², Takahiro Arakawa³, Il Kim²,
Shuichi Shoji³, Kyung Chun Kim¹ and Jeung Sang Go¹**

¹ School of Mechanical Eng., Pusan National Univ., 609-735, South Korea

² Dept. Polymer Science & Eng., Pusan National Univ., 609-735, South Korea

³ Major in Nano-science and Nano-engineering, Waseda Univ., 169-8555, Japan
micros@pusan.ac.kr

Abstract

The functional spherical microcapsules were produced through the innovative conjunction of the well-defined amphiphilic block copolymer and the stable droplet phase flow in the micro chemical plant. The microcapsules were formed to have hollow inner cavity and outer surface wall with nano-pores. To examine the potential of encapsulating foreign biochemical molecules, Congo-red dye was loaded into the microcapsule. The release performance in the specific surroundings such as temperature, pH and time was evaluated quantitatively.

Keywords: drug delivery, microcapsule, nano-pores, droplet, controlled release

1. Introduction

Recently, considerable interest has been shown in the fabrication of the nano-to-micrometer scale polymeric microcapsules with uniform and functional properties [1]. The potential utilization of polymeric microcapsules as encapsulants enabling the controlled release of drugs, dyes and enzymes has led to the speculation of a wide range of biomedical drug delivery designed to deliver a specific drug to a target place and to release it under the preferable environment such as pH, temperature and time [2,3].

This paper presents a novel method to fabricate polymer microcapsules with nanopores by using the droplet-based polymer self-assembly, together with the quantitative evaluation of its drug release performance as a potential encapsulant.

2. Self formation of microcapsules

The spherical microcapsules were successfully produced by utilizing the flow-through droplet-based supramolecular self-assembly in a crossed microchannel network (Fig. 1). The block copolymer of poly (styrene-b-methyl methacrylate) was synthesized to define amphiphilic polymer microstructure by the atom transfer radical polymerization (hereafter, ATRP) [4]. The molecular weight and the poly dispersity index (PDI) of the synthesized polymer was estimated by gel permeation chromatography (GPC) (Hewlett Packard Model 1100 series) equipped with a refractive index detector. The estimated values were 9837 g/mole and 1.08, respectively.

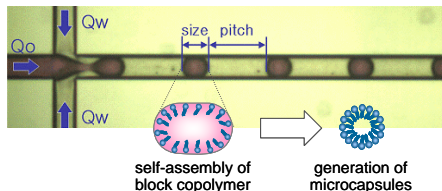


Figure 1. Microcapsule fabrication using the self-assembly of the block copolymer

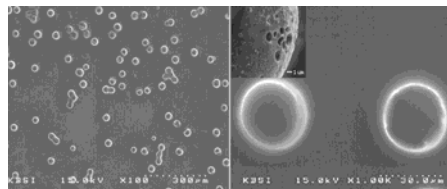


Figure 2. SEM images of the produced microcapsules with nano-pores on the surface.

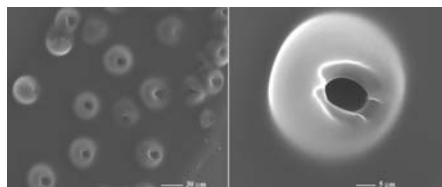


Figure 3. Visual characterization of the hollow microcapsule after O₂ plasma ashing of the surface.

Droplets can be obtained by introducing the immiscible fluids into the crossed inlet channel, which resulted in the flow-through droplet phase flow [5]. As an organic phase, PS-b-PMMA block copolymer was dissolved in the organic solvent of CH₂Cl₂ and was introduced into the middle channel with a flow rate of 10 μ l/min. The water containing 3 %wt PVA was flew from two side-channels with a flow rate of 5 μ l/min.

The stable droplet phase flow was obtained in the microchannel as visualized in Fig. 1. The 100 μ m-size droplets were drained from the outlet and dispersed in the de-ionized water. The size of droplets was decreased to about 50 μ m after 30 minutes. The size shrinkage occurred due to the release of solvent included in the droplet. After drying the microcapsules, the microcapsule with nano-pores was characterized by SEM image (Fig. 2) and its hollow cavity was also examined after O₂ plasma ashing of its wall surface (Fig. 3).

3. Evaluation of release performance

The Congo-red dye of a well-known azo-dye was loaded into microcapsule to examine encapsulation of foreign molecules and release performance under the specific surrounding (Fig. 4). The fabricated microcapsules were immersed into the distilled water (30 ml) containing dissolved Congo-red dye (6.5×10^6 g/cc) and sonicated over a day for the maximal degree of dye encapsulation. The about 20 % of dye from the solution was enclosed in the microcapsules.

The microcapsules were installed in the temperature-controlled UV cuvette containing KH₂PO₄/NaOH buffer solutions of pH 7 and pH 7.8. The UV profiles were obtained at three different temperatures of 30 °C, 50 °C and 70 °C. Fig. 5 shows the change in UV intensity with dye release at the temperature of 50 °C and the pH 7.8. The time dependence of dye release from microcapsules on the different conditions was represented in Figs. 6 and Fig. 7.

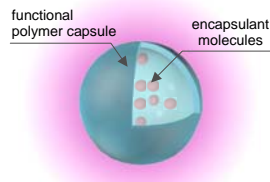


Figure 4. Environment-dependent release of the encapsulated molecules.

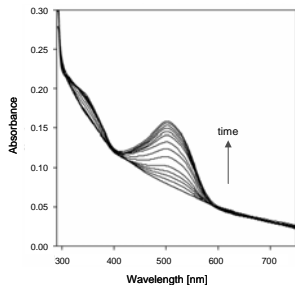


Figure 5. UV absorption spectra of the released Congo-red dye at pH 7.8 and 50 °C.

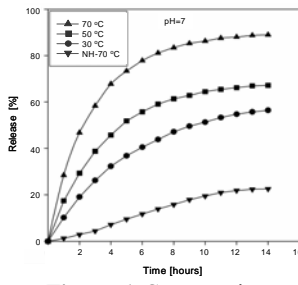


Figure 6. Comparative release performance at the pH 7.0 for four different temperatures.

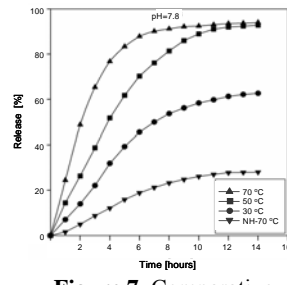


Figure 7. Comparative release performance at pH 7.8 for four different temperatures.

4. Conclusions

The well-defined microcapsules were successfully fabricated by utilizing the microfluidics techniques, morphological studies of the microcapsules were carried out using SEM and the hollow inner cavity of the microcapsules were demonstrated after performing plasma ashing. The versatility of these microcapsules as potential encapsulants were evaluated by incorporating Congo-red dye and the release performance were studied under various pH levels and temperatures.

Acknowledgements

This work was supported by Korea Research Foundation Grant funded by the Korean Government (MOEHRD) (KRF-042-D00016) and Japan Ministry of Education, Culture, Sports Science & Technology Grant-in-Aid for Scientific Basic Research No. 12450167

References

1. G. Ibarz, L. Dahne, E. Donath and H. Mohwald, *Smart micro- and nanocontainers for storage, transport and release*, Adv. Mater., 13, pp. 1324-1327, (2001).
2. I. Gill and A. Ballesteros, *Encapsulation of biologicals within silicate, siloxane, and hybrid sol-gel polymers: an efficient and generic approach*, J. Am. Chem. Soc., 120, pp. 8587-8598 (1998).
3. J. Guo, W. Yang, Y. Deng, C. Wang and S. Fu, *Organic-dye-coupled magnetic nanoparticles encaged inside thermoresponsive PNIPAM microcapsules*, Small 1(7), pp. 737-743 (2005).
4. K. Matyjaszewski, D. A. Shipp, G. P. McMurtry, S. C. Gaynor and T. Pakula, *Simple and effective one-pot synthesis of (meth)acrylic block copolymers through atom transfer radical polymerization*, J. Polym. Sci. Part A: Polym. Chem., 38, pp. 2023-2031 (2000).
5. S.J. Peng and R. A. Williams, *Controlled production of emulsions using a crossflow membrane*, Trans. IchemE, 76, pp. 894 (1998).

ON-CHIP CONSTRUCTION OF A MULTIFUNCTIONAL ENVELOPE-TYPE NANO DEVICE FOR A NON-VIRAL GENE DELIVERY SYSTEM

Hiroshi Kuramoto^{1,2}, Noritada Kaji⁵, Kentarou Kogure³, Manabu Tokeshi⁵, Yasuo Shinohara^{1,2}, Hideyoshi Harashima³ and Yoshinobu Baba^{4,5}

¹ The University of Tokushima, Shomachi, Tokushima 770-8505, Japan

² IGR, The University of Tokushima, Shomachi, Tokushima 770-8505, Japan

³ Hokkaido University, Sapporo 060-0812Japan,

⁴ HTRC, AIST, Hayashi-cho, Takamatsu 761-0395, Japan

⁵Nagoya University, Chikusa-ku, Nagoya 464-8603, Japan

Abstract

We developed a simple microdevice to construct a multifunctional envelope-type nano device (MEND) on a chip. MEND is an extremely efficient technology for a non-viral gene delivery system, however, the existing method to construct it is time-consuming, labor intensive, and tedious task. In the simple microdevice developed here, just by changing flow rate and concentrations of materials in microchip, we succeeded to construct MEND efficiently and easily.

Keywords: non-viral gene delivery system, microchip, DNA, multifunctional envelope-type nano device (MEND)

1. Introduction

Many gene carriers have been developed; however, most of them were insufficient in stability in blood stream, targeting ability to diseased cell/tissue, safety, and transfection efficiency as a gene delivery system. MEND is constructed by condensed DNA coated with lipid layers, to which the several functions is easily added, as shown in Figure 1. and has many advantages to overcome these drawbacks of other gene carriers, but we still need to develop a simple method for construction of MEND with high speed, high accuracy, and low-cost.

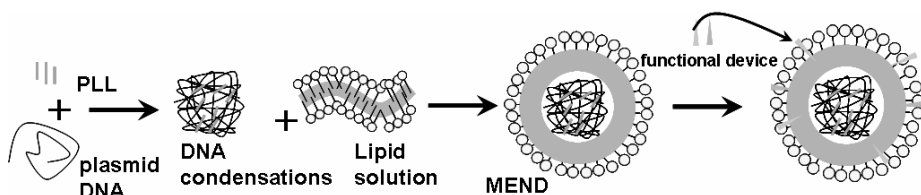


Figure 1. Schematic drawings of the preparation process of MEND.

2. Experimental

We fabricated the microchip that has three fluid channels (Figure 2). In this study, we examined the two processes of constructing MEND on microchip. The first process was DNA condensation process by poly-L-lysine (PLL) (Figure 3A). In this process, we applied plasmid DNA into channel A, d.d.water into channel B, PLL into channel C. The second process was coating process of DNA/poly-L-lysine condensates by lipid solution (Figure 3B). The lipid solution was composed of L- α -Phosphatidylethanolamine, Dicetyl phosphate, 1,2-disetearoyl-sn-glycero-3-phosphoethanolamine-N-[Methoxy(polyethylene glycol)-2000], n-Octyl- β -D-glucopyranoside. We applied lipid solution into channel A and B, DNA condensates into channel C. For constructing the targets on microchip, we examined various flow rate and concentrations of materials, and then, measured the diameter of targets by using dynamic light scattering (DLS).

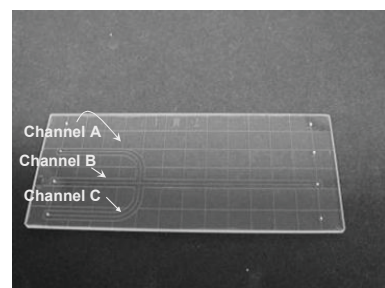


Figure 2. Photograph of a glass microchip

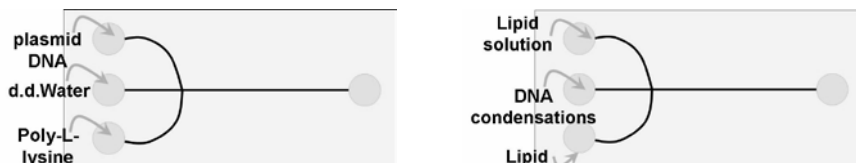


Figure 3. Schematics of the construction process of MEND on a microchip.
(A) DNA condensation process by PLL.
(B) Coating process of DNA/poly-L-lysine condensates by lipid layer.

3. Result and discussion

In the first step, we constructed DNA condensates on the microchip. In the second step, we constructed the prototype of MEND on the microchip. And then we determined if they were equal to existing DNA condensates and the prototype of MEND by using DLS (Figure 4B, 5B). We had already confirmed that the existing DNA condensates size was about 70~90nm (Figure 4A). And also we had already confirmed that the existing MEND size was about 100~120nm (Figure 5A). Figure 4 shows that the particle size of

DNA condensates were equal to existing DNA condensates. However, the target's ratio of total amount wasn't so high. Figure 5 shows that the particle size of the prototype of MEND was a slightly larger than the existing MEND.

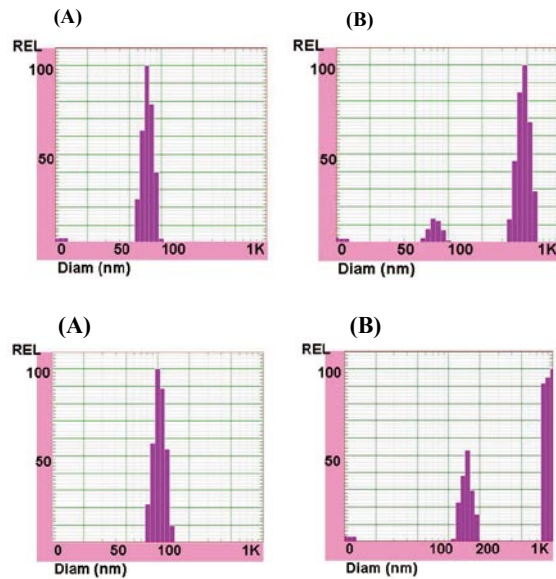


Figure 4. Comparison of the size distribution of DNA/poly-L-lysine condensates constructed (A) by the existing batch method and (B) on a microchip. The expected size of the condensate was in about 70 nm.

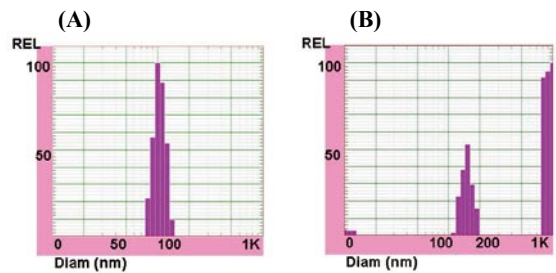


Figure 5. Comparison of the size distribution of MEND constructed (A) by the existing batch method and (B) on a microchip. Although the expected MEND ranged in size from 70 to 150 nm, the MEND constructed on a microchip was a slightly larger.

4. Conclusions

The simple device developed here has high ability in constructing DNA condensates and the prototype of MEND on the microchip. We could accomplish to increase speed and reduce costs in constructing it. We will be able to construct MEND less than 5 h, while we took about 34 h by the existing method. However, yield of MEND is not so high compared with the existing method. It may be attributable to the adsorption of MEND constructing materials onto the inner wall of a microchannel. The modification of the fluid channels in microchip will be one of the key issues to improve the efficiency of this device.

References

- [1] K. Kogure, R. Moriguchi, K. Sasaki, M. Ueno, S. Futaki, H. Harashima, *J. Control. Release*, 98, 317-323 (2004).
- [2] K. Sasaki, K. Kogure, S. Chaki, Y. Kihira, M. Ueno, H. Harashima, *Int. J. Pharm.*, 296, 142-150 (2005)

MICROCHIP-BASED OSTEOSIS SYSTEM FOR RAPID DRUG SCREENING FOR OSTEOGENESIS

**Kae Sato, Kazuyo Igawa Yuki Tanaka, Kiichi Sato,
Ung-il Chung, Takehiko Kitamori**

CNBI, The University of Tokyo, Bunkyo, Tokyo, 113-8656, Japan

Abstract

In the geriatric research field, osteoporosis is the major target of regenerative medicine and osteoblast is known as a key cell to osteoporosis. We developed continuous perfusion microfluidic cell culture system for osteoblast differentiation drug screening assays.

Keywords: cell culture, differentiation, drug screening, green fluorescence protein, thermal lens microscope

1. Introduction

Microchip techniques appear to provide some advantages for osteoblast differentiation drug screening, because the scale of the liquid microspace inside a microchip is fitted to the size of the cells. In microchambers fabricated on microchips, rapid and secure exchange of media or reagents was achieved by simple operations under continuous medium flows [1-2]. Because cells are cultured in a chamber for long time in the conventional differentiation experiments, reagent concentrations are gradually decreased and it is difficult to keep the constant concentration. Moreover, there is no high throughput and automated system for bioassay using a very small amount cells which is very important to drug screening researches. Therefore development of a microchip-based osteoblast differentiation bioassay system is very important and desirable. In this study, we developed continuous perfusion microfluidic cell culture system for osteoblast differentiation drug screening assays.

2. Experimental

The microchip was composed of two glass plates (30 mm × 70 mm). The

channels were 200 μm in width and 100 μm in depth. We used mouse MC3T3-E1 osteoblastic cells, which have a marker gene system expressing green fluorescence protein (GFP) under the control of osteoblast-specific promoters. MC-3T3 cells were cultured in the microchip with continuous perfusion of a medium at 37 °C (Fig. 1). Alkaline phosphatase (ALP), which is a basic marker of osteoblast maturation and osteogenesis, was measured using a histological stain and a thermal lens microscope (TLM). Cells were fixed for 15 minutes, incubated with a mixture of naphthol as-mx phosphate, N,N-dimethylformamide, and fast blue BB Salt, and analyzed by TLM.

3. Results and discussion

MC-3T3 cells were successfully cultured in the microchip. Bone morphogenetic proteins (BMPs), which are known as a group of the transforming growth factor-beta, were introduced to micro-cultured MC-3T3-E1 cells to stimulate the osteogenic differentiation. The cells treated with the stimuli showed fluorescent signals derived from induced GFP (Fig. 2). The expression of GFP was observed, ALP analysis was performed. ALP activity was analyzed using the thermal lens microscope (TLM). The measured signal intensity was dependent on BMPs stimuli. Therefore, a combination of the continuous perfusion flow culture system and GFP reporter assay has allowed sufficient performance for the screening of osteogenic compounds.

4. Conclusions

This system helps us monitor osteoblast differentiation easily, precisely and non-invasively. In near future, we will try to find the sufficient conditions for osteogenesis, and to discover osteogenic compounds using this system.

References

1. Y. Tanaka, K. Sato, M. Yamato, T. Okano, T. Kitamori, *J Chromatogr A*. 2006 1111: 233-7.
2. Y. Tanaka, K. Sato, M. Yamato, T. Okano, T. Kitamori, *Anal Sci*. 2004 20: 411-3.

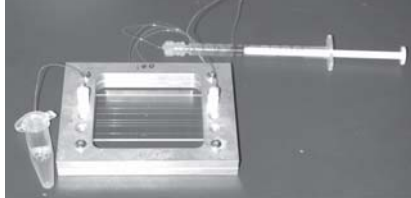


Figure 1. Continuous perfusion microfluidic cell culture system.

Microchip : Pyrex glass plates, 30 mm × 70 mm.
Microchannels : 200 μm in width and 100 μm in depth.

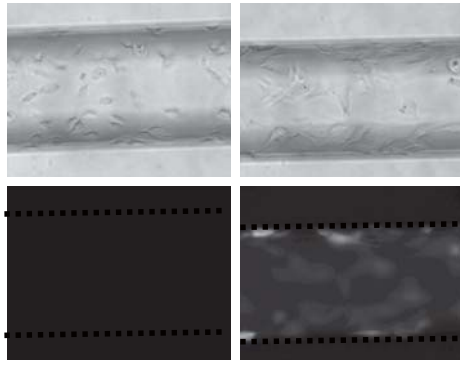


Figure 2. BMP-induced osteoblast differentiation.

GFP expression at day 4.
Cells:Col1a1-GFP MC3T3-E1
Culture Media:Osteogenic medium

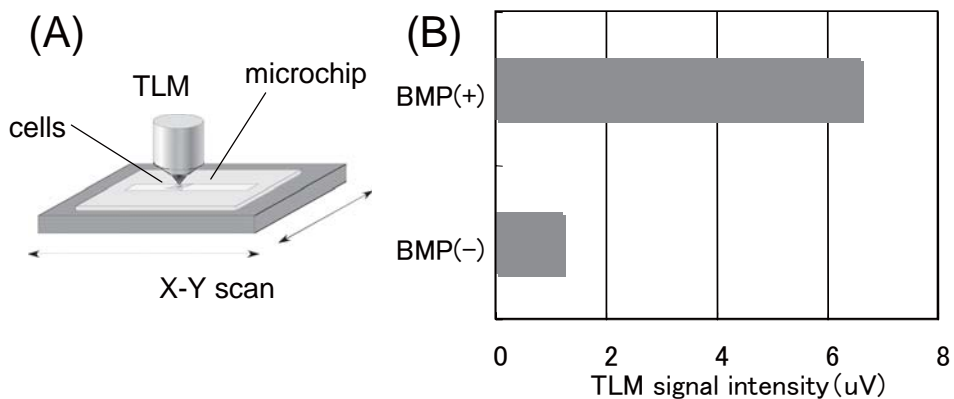


Figure 3. Alkaline Phosphatase (ALP) activity at day 4.

- (A) Detection system: thermal lens microscope (TLM); excitation beam, 633 nm;probe beam, 488 nm.
- (B) TLM detection of Alkaline phosphatase stain :Naphthol AS-MX
Phosphate, fast blue BB.

MICROFLUIDIC SELF-ASSEMBLY OF TUMOR SPHEROIDS FOR STUDIES OF ANTICANCER DRUG ACTIONS AND INTERACTIONS

Liz Y. Wu^{*}, Dino Di Carlo^{*}, and Luke P. Lee

Biomolecular Nanotechnology Center, Berkeley Sensor and Actuator Center

Department of Bioengineering, University of California, Berkeley, CA 94720 USA

Abstract

Multicellular tumor spheroids may provide a better model than monolayer culture of *in vivo* tumors for drug assays. We present a novel microfluidic method for self-assembly of tumor spheroids for these studies. Our device traps cancer cells hydrodynamically and spheroid formation is enhanced by maintaining compact groups of the trapped cells due to continuous perfusion. A large amount of tumor spheroids with a narrow size distribution can be formed in the device to provide a good platform for anticancer drug assays.

Key words: Self-assembly of spheroids, drug discovery, tumor spheroids, MCTS

1. Introduction

Multicellular tumor spheroids (MCTS) have recently received a great deal of attention in cancer research and have been applied to the evaluation of anticancer drugs since the 3D multi-cellular aggregates simulate more accurately the tumor micro-environment *in vivo* by reproducing nutrient and signal gradients and removing the effect of unnatural adhesion to artificial surfaces or gels [1]. For example, the IC₅₀ value of Taxol drug on MCF-7 cells spheroids was reported to be much higher than that of monolayer MCF-7 cells, and this information is valuable for clinical dosing. [2]

There are several techniques to generate MCTS, such as growth on non-adherent surfaces, in suspension [3], or by the hanging drop method [4], but most lack the ability to precisely control the number of cells in each spheroid or allow testing on the growth platform. Here we employed a purely hydrodynamic cell trapping method and precisely control the number of cells by the size of the traps (Fig. 1). We enhanced spheroid formation by maintaining compact groups of cells due to continuous perfusion (Fig. 2). After spheroid formation, drug assays may be performed immediately.

* These authors contributed equally to this work

2. Experimental

The microfluidic trapping array used for self-assembly of tumor spheroids was micromolded in PDMS (Fig. 2f). The bonded PDMS chambers maintain a sterile culture environment. We generated a non-adherent trapping array by flowing BSA or PEG into the device. MCF-7 suspension with 10^6 cells/ml was then loaded into the device until each trap in the device was filled with cells (Fig. 3a). Continuous media perfusion was controlled by syringe pump after cell trapping. Drug injection can then be conducted using the same channels. Spheroid formation was then observed using time-lapse phase contrast microscopy.

3. Results and Discussion

MCTS formation in the culture array is shown in Fig. 3. We observed tumor cells adhering to its neighboring cells in the same trap gradually under the time lapse microscope. The time for MCTS formation is approximately 24 hrs. To further investigate the structure of the spheroids, we dyed the cell membranes with C16-fluorescein and the cell nuclei with Hoechst (Fig. 3e, 3f). The fluorescent probes indicated separate cells were adhering to form a combined structure. This was further supported when after 24 hours of culture we applied high pressure and dislodged the entire spheroids – not individual cells. In Figure 3g a well-formed spheroid that was pushed out from one of the microfluidic traps is shown. Approximately 15% of spheroids partially adhered to the glass substrate, even after we coated the surface with BSA or PEG, indicating that improved non-adherent surface coatings are required. Different size MCTS were also generated by adjusting the size of culture chamber (images not shown).

4. Conclusions

A new method to self-assemble arrays of 3D tumor spheroids was demonstrated. The microfluidic chip was also capable of continuous media perfusion and a sterile culture environment. With this platform, anti-tumor assays can be done immediately after the spheroid formation right in the growth platform.

Acknowledgements

Liz Y. Wu was supported by Taiwan Merit Scholarship TMS-094-2-A-008 and Intel Research Fund. Dino Di Carlo was supported by a Whitaker Foundation Graduate

Fellowship and GSK.

References

- [1] Faute MAD et al. Clin Exp Metastasis 19: 161-168, 2002.
- [2] Nicholson KM et al. European Journal of Cancer Vol. 33, PP. 1291-1298, 1997
- [3] Kunz-Schughart et al., Kreutz M, Knuechel R. 1998. Int J Exp Pathol 79:1-23, 1998
- [4] Jens MK et al. Biotechnology and bioengineering 83:173-180, 2003

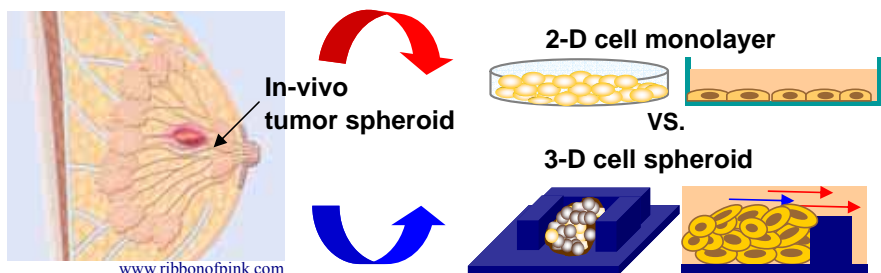


Figure 1. Formation of tumor spheroid. 3D tumor spheroids formed by trap geometry with additional perfusion control provides a better in-vivo like platform for anticancer drug analysis

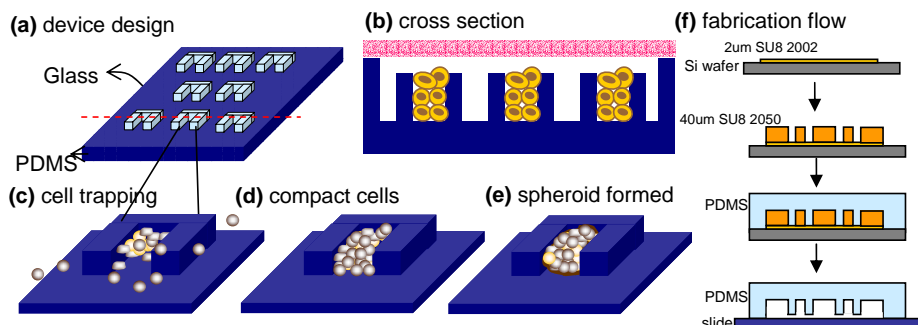


Figure 2. Self-assembly of tumor spheroid.

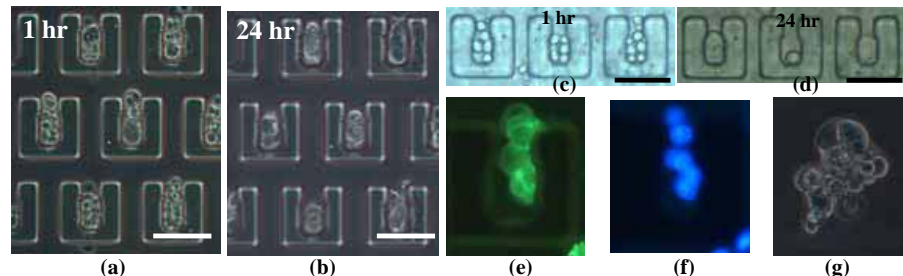


Figure 3. Spheroid culture results phase contrast image of the cells (a) 1hr after loading (b) spheroids formed in the trap array after 36 hrs of culture (c) dark field image of cells after loading (d) spheroids formation (e) image of C16-dyed cell membranes (d) image of Hoechst dyed cell nucleus (e) suspended spheroid taken out from the trap (Scale bar =100 μm)

NANOIMPRINTED FLUIDIC DEVICE FOR CONTINUOUS SEPARATION OF NANOPARTICLES

Keith J. Morton¹, James. C. Sturm¹, Robert H. Austin²
and Stephen Y. Chou¹

¹Department of Electrical Engineering,

² Department of Physics

Princeton University, Princeton, NJ 08544

Abstract

We demonstrate continuous flow bifurcation of nanoparticles using the principle of deterministic lateral displacement. Recently arrays of microfabricated posts, tilted relative to the fluid flow direction, were successfully used to separate DNA fragments [1], microbeads [1,2] and to fractionate whole blood [3,4]. We scale down this technique using nanoimprint lithography (NIL) to pattern a large-area array of nanofabricated posts and demonstrate for the first time bifurcation of 100nm and 200nm diameter fluorescent particles.

Keywords: Nanofluidics, Nanoimprint Lithography, Separation, Sorting, Etching

1. Introduction

Separation of biomolecules is a fundamental analytical tool in biology and the life sciences. Square grids of microfabricated posts, with their array axis tilted relative to the bulk fluid flow, have recently been used to successfully separate micron sized beads, DNA and whole blood [1-4]. These devices separate particles based on size. They exploit deterministic laminar flow around obstacles to achieve high-resolution, continuous-flow sorting. Particles that are smaller than a critical size follow the applied flow field through the obstacle array (Figure 1). Larger particles must follow the array axis which is tilted away from the flow field direction, creating a separation between the particle and the original streamline path. The gap between adjacent obstacles and the array tilt determine the critical radius [3] for particle displacement and therefore the size of the biomolecule being separated. We scale down this critical feature size using state of the art nanofabrication techniques to create large-area obstacle arrays with nanoscale gaps and demonstrate separation of nanoparticles.

2. Design and Fabrication

The large-area (1cm^2), two-dimensional nanopost arrays were fabricated by nanoimprint lithography (NIL) and reactive ion etching (RIE). With demonstrated sub-10nm patterning resolution [5], NIL is a low-cost, high-throughput alternative to serial-point-by-point nanopatterning techniques such as electron beam lithography. The NIL master mold (4" dia.) was made by interference lithography and RIE and was used to replicate multiple devices. The NIL was carried out using Nanonex NX-2000 imprint machine. The device area nanopillars were deep etched (Figure 1b) into the silicon

substrate using the BoschTM process (STS- Multiplex ICP etcher.) A photolithography patterned window defined the device sidewalls and was aligned to within 1° of the pillar array to produce multiple devices with varying tilt (Figure 1c). Inlet and outlet microchannels were patterned by a second photolithography layer and etched to match the pillar depth. The device was then cleaned and capped with a glass coverslip using oxygen plasma bonding.

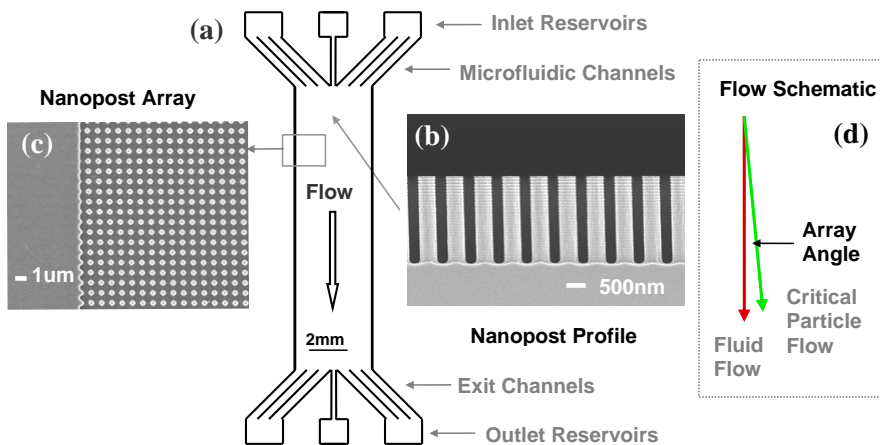


Figure 1: Nano Fluidic Sorting Device. (a) Device layout showing inlet reservoirs, microchannel feeds to the nanopillar array area and exit channels. (b) Cross-section scanning electron micrograph (SEM) of high-aspect ratio, 650nm diameter pillars on a 1um pitch grid. (c) SEM Top view of pillars showing the tilt angle of the two dimensional array relative to the device sidewall; (d) Particles larger than a critical radius cannot follow the applied flow field and must track along the tilt direction.

3. Results and Discussion

Visualization of fluorescent bead flow in the device is shown in Figure 2. A mixture of 100nm and 200nm diameter fluorescent polystyrene beads (Duke Scientific) enters the top of the device through the middle sample inlet port. Buffer solution, not containing beads, is introduced into the other two inlet reservoirs. This creates a hydrodynamic jet at the entrance to the nanopost array. As the mixture traverses the post array under hydrostatic pressure it is sorted into two streams. The smaller 100nm (red) beads follow the fluid flow streamlines while the 200nm (green) bead are displaced laterally as they travel through the post array resulting in clear separation between the two species.

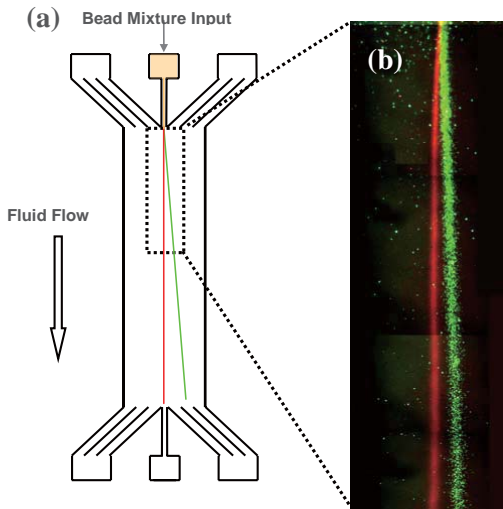


Figure 2: Bifurcation of 100nm (red) and 200nm (green) fluorescent beads in the nanofabricated sorting device. (a) Schematic showing bead mixture loading and flow through device. (b) Laser fluorescence microscope frame captures of beads moving through the device: initial bead mixture is separated according to particle size.

4. Conclusions

We have demonstrated continuous flow, high-resolution nanoparticle sorting by deterministic lateral displacement in an array of nanoposts. Using nanoimprint lithography we have fabricated obstacle arrays with nanoscale control of the critical gap size and have shown for the first time bifurcation of 100nm and 200nm diameter particles using this technique. The fabrication techniques presented here can be readily extended to even smaller gap devices for biomolecular sorting.

References

1. L.R. Huang, E.C. Cox, R.H. Austin and J.C. Sturm, Continuous Particle Separation Through Deterministic Lateral Displacement, *Science*, 304, pp. 987-990 (2004).
2. D.W. Inglis, J.A. Davis, R.H. Austin, J.C. Sturm, Critical particle size for fractionation by deterministic lateral displacement, *Lab on a Chip*, 6, pp.655-658 (2006)
3. S. Zheng, Y.-C. Tai, and H.L. Kasdan, MEMS Device For Continuous Blood Cell Separation, *Proceedings of MicroTAS 2005*, Boston, USA, pp. 385-387, (2005).
4. J.A. Davis, D.W. Inglis, K. J. Morton, D. A. Lawrence, L. R. Huang, S. Y. Chou, J. C. Sturm, R. H. Austin, Deterministic Hydrodynamics: Taking Blood Apart, *Proceedings of the National Academy of Sciences*, in press, (2006).
5. M.D. Austin, W. Zhang, D. Wasserman, S.A. Lyon and S.Y. Chou, 6nm Half-pitch lines and $0.04\mu\text{m}^2$ static random access memory patterns by nanoimprint lithography, *Nanotechnology*, 16, pp. 1058-1061, (2005).

EFFECTS OF APPLIED VOLTAGE AND CHANNEL CONFIGURATIONS ON DNA SIZE SEPARATION USING NANO FENCE MATRIX

Yoichi Tagaya¹, Masakazu Baba², Kenji Fukuzawa¹, and Yasunaga Mitsuya¹

¹Nagoya University, Furo-cho, Chikusa-ku, Nagoya, Aichi, 464-8603 Japan

²NEC Corporation, 34 Miyukigaoka, Tsukuba, Ibaraki, 305-8501 Japan

e-mail address: y_tagaya@nuem.nagoya-u.ac.jp

Abstract

We have demonstrated an effective biomolecule separation method using nanostructured channels based on a size exclusion chromatography (SEC). It has been revealed that a convex fence matrix is applicable to wide range separation in DNA sizes.

Keywords: microchip electrophoresis, separation size, voltage control, channel configuration

1. Introduction

Nanostructured microchannels for size separation of biomolecules are promising techniques in biotechnology because of the separation characteristics controlled by the artificially designed nanostructures and the total systems integrated with other functional components. Previously it was showed that nano fence matrix could be used for the SEC-type DNA separation [1]. In this study, we report the evaluation of separation voltage and the new design of nano fence matrix to achieve higher resolution.

2. Materials and Methods

The fence configurations in the microchannels are shown in Figure 1. The flat fence matrix has wide streets along the electrophoresis direction and narrow lanes perpendicular to the streets. In the SEC type separation using the flat fence matrix, the narrow lanes were designed for the passages of smaller molecules to detour as shown in Figure 1 (b). The feature of the convex fence matrix is that the lane width is changed at the halfway of the lane length. To evaluate separation performance, two kinds of DNA fragments were used: One is λ -Hin d III digest (0.1-23 kbp) as an example for longer DNA and the other is ϕ X 174-Hae III digest (72-1353 bp) as shorter one.

3. Results and discussion

Figure 2 (a) shows the electropherograms resulting from the flat fence matrix and

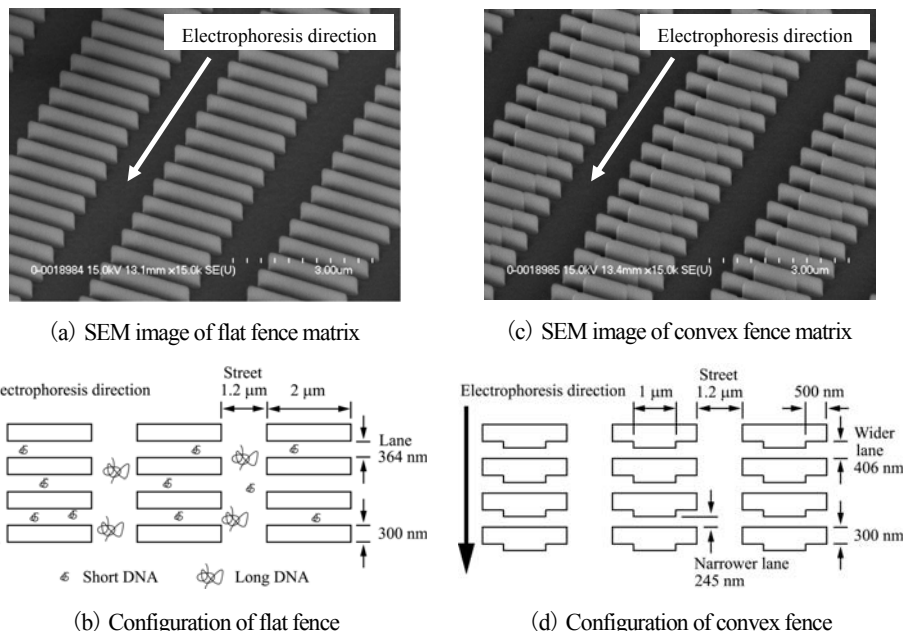


Figure 1. Scanning electron microscope (SEM) images and configurations of nanofabricated structures.

the longer DNA with the applied voltage as a parameter. From these results, we can see that the separation resolution is highest for the lowest voltage of 20 V. In addition, Figure 2 (b) shows the same results as Figure 2 (a) except for the shorter DNA indicating that the separation resolution is highest for the highest voltage of 100 V. These results reveal that lower voltage is preferable for the longer DNA, and higher voltage for the shorter one. Figure 2 (c) is the same results as Figure 2 (a) except for the flat fence matrix, that is, the results for the convex fence matrix using the longer DNA. It is found that the dependency of resolution on the applied voltage is substantially same as that for the flat fence matrix. Comparing between Figures (a) and (c), however, differences are noticeable in the case of higher applied voltage. The convex fence matrix enabled us to separate the peaks of 4, 6 and 9 kbp fragments from the peak of 23 kbp, while those peaks overlapped each other for the flat fence matrix. This enhancement in the separation performance brought by the convex fence matrix can be attributed to the fact that 4 to 9 kbp fragments were separated by the wider lane and the shorter DNA fragments by the narrower lane.

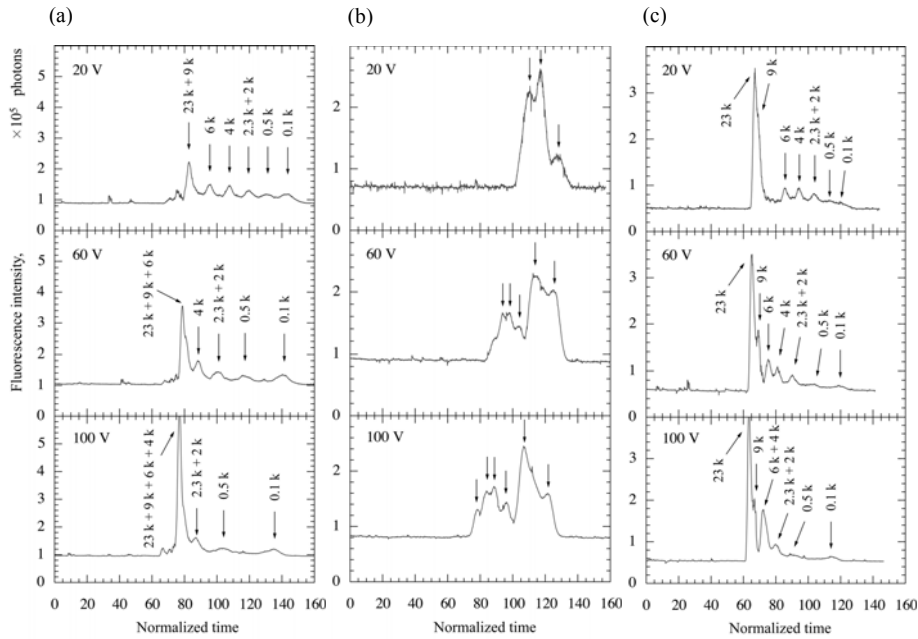


Figure 2. Electropherograms detected after passing through 8 mm nanostructured region. The time axes of 20 and 60 V results were normalized to be comparable with the 100 V results. (a) λ -Hin d III digest as longer DNA fragments (0.1-23 kbp) using the flat fence matrix. (b) ϕ X 174-Hae III digest as shorter DNA fragments (72-1353 bp) using the flat fence matrix. (c) λ -Hin d III digest using the convex matrix.

4. Conclusion

We performed the SEC-type DNA separations in the different applied voltages and design of nanostructures. It is found that a lower voltage is suitable for the separation of longer DNA fragments, and a higher voltage for shorter ones. In addition, the convex fence matrix has the advantage to separate 4 to 9 kbp fragments when even larger voltage is applied.

Acknowledgments

We thank to Shingo Yoneoka for the assistance of the experiments in this research.

References

1. M. Baba, et al., *DNA size separation using artificially nanostructured matrix*, Applied Physics Letters, Vol. 83, No. 7, pp. 1468-1470, (2003).

SELF-ASSEMBLED THREE-DIMENSIONAL NANOFLUIDIC SIEVES FOR BIOSEPARATION

Yong Zeng and D. Jed Harrison*

Department of Chemistry, University of Alberta, Edmonton, Canada

Abstract

This paper reports a biomolecular sieving system based on the use of ordered colloidal arrays to define the sieve structure. A fast and facile microfluidic colloidal self-assembly strategy has been developed to create nanofluidic sieves within microfluidic devices, with which fast separation of DNA and proteins of a wide size range can be achieved.

Keywords: Nanofluidics, molecular sieving, colloidal self-assembly, DNA, protein

1. Introduction

Micro-/nano-fabricated structures will provide means to improve the efficiency and speed of biomolecule separation [1,2]. Most micro-/nano-machined separation architectures were designed for large DNA molecules, generally due to technical challenges in accessing structures on the scale of small molecules, such as <10 nm for proteins. In addition, nanofabrication techniques demand sophisticated facilities and time-consuming procedures, and normally produce 2D architectures. Colloidal self-assembly offers a promising alternative to conventional nanofabrication for creating molecular sieving structures [3], but has suffered from the formation of cracks that prevent good separation performance. Herein we present a simple and facile strategy to construct ordered three-dimensional nano-sieves for fast size separation of biomolecules within microfluidic devices.

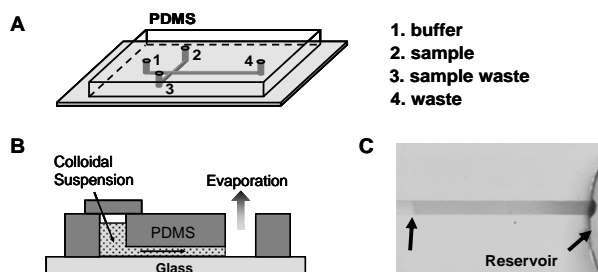


Figure 1. A) Layout of PDMS chip; B) Schematic of microfluidic colloidal self-assembly; C) A snapshot of packing 0.9 μm silica spheres in a 100 μm channel.

2. Experimental

PDMS microchips (Fig. 1A) were fabricated by standard soft lithography process. Reservoirs 1–3 were filled with aqueous suspension of silica colloids and were covered to prevent solvent evaporation. The suspension fills the channels spontaneously and evaporates from the open outlet at reservoir 4 (Fig. 1B). Evaporation triggers colloidal nucleation at the air-liquid interface, creating a one-directional flux for continuous growth of the bed. 4× TBE buffer was used to reduce EOF during electrophoretic separations; it also contains 4% 2-mercaptoethanol for DNA separation, or 0.1% SDS for proteins.

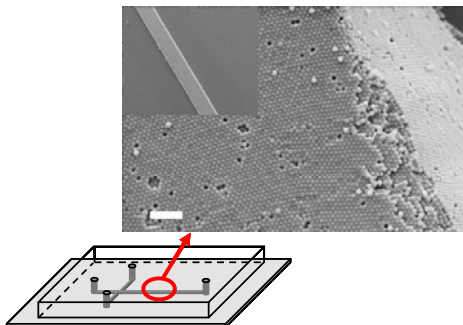


Figure 2. SEM images of an ordered 330 nm silica sphere array packed in a 100 μm channel. The scale bar is 2 μm for the high magnification.

3. Results and discussion

Microchannel confinement restricts drying to the opening of a channel, as demonstrated in Fig. 1C. The translucence of the packed section indicates the presence of interstitial water and shows there is no drying of the array within the microchannel. The arrays remain wet after the completion of self-packing, which avoids drying-induced cracks that jeopardize the separation performance. SEM images presented in Fig. 2 confirm that the spheres were closed packed, with long-range order over three dimensions. Nanometer-sized interstices in the close-packed sphere lattice create a periodic free-energy landscape for molecular sieving of nucleic acids and proteins based on their sizes.

Figure 3A shows that a DNA ladder of 100 to 2000 bp was well resolved within 0.7 mm and ~1.5 minutes in an array of 0.9 μm silica beads. Four consecutive runs of the same ladder were superimposed in Fig. 3B. The good run-to-run reproducibility indicates the stability of the colloidal array under the applied electric field. A 100-bp ladder was separated and log mobility was plotted

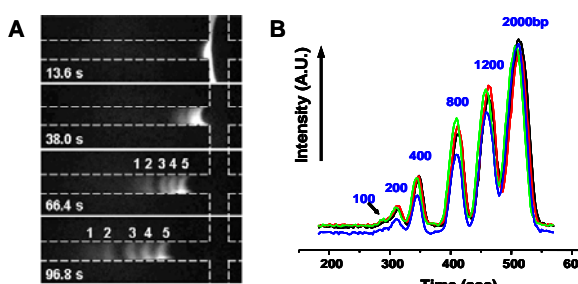


Figure 3. Separation of a dsDNA ladder of 100, 200, 400, 800, 1200, and 2000 bp in a 0.9 μm silica array. A) Time-elapsed fluorescence images ($E = 15 \text{ V/cm}$). The 100-bp band was missed due to its low concentration. B) Four runs obtained at 19.2 V/cm with a separation length $L = 5 \text{ mm}$.

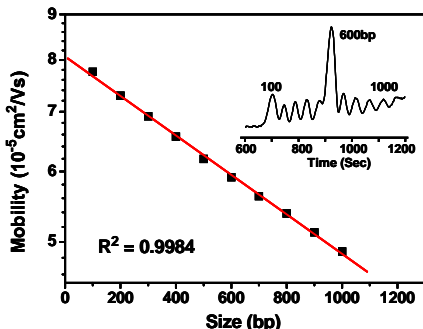


Figure 4. Semi-log plot of the mobility vs DNA size and its least-squares linear fit. The mobility of individual fragments was obtained by sorting a 100 bp ladder (900 nm silica beads, $E = 16.5 \text{ V/cm}$, $L = 9 \text{ mm}$) as shown in the inset.

against DNA size in Fig. 4. The good linearity of that plot confirms Ogston sieving as the governing mechanism of separation. The pore size can be readily tuned by varying the particle size to sort various molecules. Fig. 5 shows the separation of SDS denatured proteins using 160 nm beads. The plate numbers per meter were as high as $8 \times 10^5 \text{ m}^{-1}$, which is comparable with a microfabricated filter array [2] and with microsystems using a conventional polymer matrix [4].

4. Conclusions

We have established a microfluidic colloidal self-assembly approach for simple, fast, and economic fabrication of ordered, robust, three dimensional nano-sieves within a microfluidic system of channels. Using this type of sieve, fast size separation of DNA and proteins was demonstrated in a microchip system without the need of gels/polymers. The flexibility of pore size the arrays provide, and the extended long range order that is achievable suggest this methodology could ultimately outperform gel-based matrices.

Acknowledgements

We thank the Nanofab at University of Alberta for the facilities and the Natural Sciences and Engineering Research Council of Canada (NSERC) for funding.

References

1. J. Han, and H. C. Craighead, *Science*, 288, 1026-1029, (2000).
2. J. Fu, P. Mao, J. Han, *Appl. Phys. Lett.*, 87, 263902, (2005).
3. H. Zhang, and M. J. Wirth, *Anal. Chem.* 77, 1237-1242, (2005).
4. S. Yao, D. S. Anex, et al. *Proc. Natl. Acad. Sci. U.S.A.*, 96, 5372-5377, (1999).

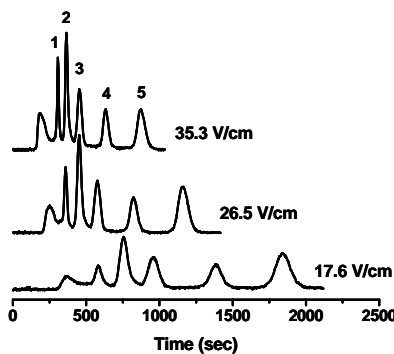


Figure 5. SDS separation of five proteins (160 nm silica particles, $L = 4 \text{ mm}$): (1) trypsin inhibitor, 20.1 kDa; (2) ovalbumin, 45 kDa; (3) BSA, 66 kDa; (4) phosphorylase B, 97 kDa; (5) β -galactosidase, 116 kDa.

INTEGRATED MICROREACTORS FOR SEQUENTIAL AND PARALLEL REACTIONS

Guodong Sui and Hsian-Rong Tseng*

Department of Molecular & Medical Pharmacology and Crump Institute for Molecular Imaging, David Geffen School of Medicine at UCLA, USA
(hrtseng@mednet.ucla.edu)

Abstract

In this presentation, I would like to introduce two new types of microfluidic circuits which have been recently developed in my research group at UCLA for performing sequential syntheses of radiolabeled imaging probes and parallel screening of an *in situ* click chemistry library.

Keywords: integrated microreactors, sequential reactions, parallel reactions, PET imaging probes, *in situ* click chemistry

1. Introduction

There are growing interests to explore microreactors for chemical reactions because they offer advantages over macroscopic reactors, such as reduced chemical consumption, rapid mixing, and improved control over mass and heat transfer. Many challenges remain, however, in the development of continuous-flow microreactors for (i) sequential syntheses whose individual steps require changing of solvents, reagents and conditions, and (ii) parallel reactions, where similar types of reactions are performed using different combinations of reagents, because the continuous-flow microchannels are plagued by cross-contamination from different reactions.

2. Results and Discussion

To overcome these challenges, two new types of integrated microreactors composed of microchannels and a number of functioning modules, e.g., pressure-driven valves/pumps and chaotic mixers have been demonstrated for performing sequential syntheses [1] of radiolabeled imaging probes and parallel screening [2] of an *in situ* click chemistry library. In the pilot study, several generations of integrated microreactors (**Figure 1**) were developed to execute five sequential chemical processes, including fluoride concentration, water evaporation, fluoride substitution, solvent exchange and hydrolytic deprotection, to produce short-lived (half-life is 110 minutes) positron emission tomography (PET) imaging probes, e.g., 2-deoxy-2-[¹⁸F]fluoro- D-glucose (FDG). This study suggested that integrated microreactors can generalize, accelerate, diversify and lower the cost of preparation for a wide range of molecular imaging probes.

Separately, another type of microreactors (**Figure 2**) were designed and fabricated to serve as an automated operation platform for parallel screening of 32 *in situ* click chemistry reactions with economy consumption of target biomolecules and reagents. We selected the known carbonic anhydrase II (bCAII) click chemistry system for this

proof-of-concept study. Here, acetylenic benzenesulfonamide ($K_d = 37 \pm 6$ nM) was used as the reactive scaffold (“anchor molecule”) for screening a library of 20 complementary azides in the presence of the template protein bCAII. The use of integrated microreactors in conjunction with in situ click chemistry promises the development of new inhibitor candidates more rapidly, less expensively, and with greater diversity. In principle, this integrated microfluidic platform can be extended not only to other in situ click chemistry libraries but also to other chemical libraries that require parallel screening platforms.

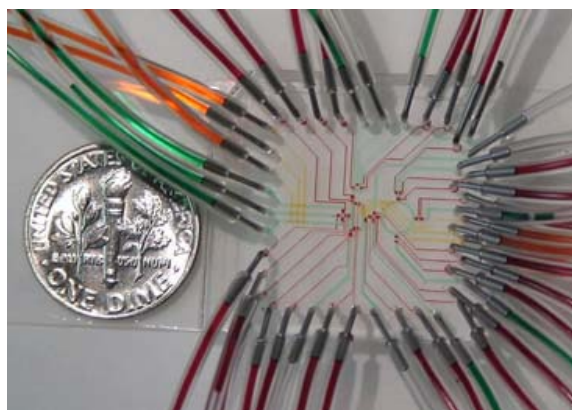


Figure 1. Optical image of the integrated microreactor utilized for sequential synthesis of PET imaging probes; a dime is present to calibrate the scale. The various channels were loaded with food dyes to help visualize the different components of the microreactor.

3. Conclusions

These two examples constitute a proof of principle for performing sequential and parallel reaction on the nanogram scale in an automated fashion. In addition to fundamental advantages such as low chemical consumption, precise control over reaction conditions, faster reaction kinetics, cost efficient and instant design/fabrication processes and fast redesign/improvement cycles. The integrated microreactors provide a whole new play field for chemists to test chemical reaction beyond the conventional setting.

In a broader playing field, our goal remains the creation of further integrated microfluidic technology platforms for the broader space in chemistry and biology beyond a single functioning platform on a chip. We will compile many different microfluidic platforms to produce a number of game systems: "Let's Play _____", where the blank is "chemical reaction circuits", "drug screening", "biomarker screening", "biochemical reaction kinetics", and "cancer diagnosis" etc. where execution is rapid and learning curves are steep.

Acknowledgment. The research was supported by the NIH NanoSystems Biology Cancer Center, the U.S. Department of Energy's Institute of Molecular Medicine, Siemens Medical Solutions USA Inc., and collaborations with Professors H.C. Kolb, N. Satyamurthy and M.E. Phelps at UCLA, J.R. Heath at Caltech and S.R. Quake at Stanford. GS thanks the UCLA SOMI program for a postdoctoral fellowship.

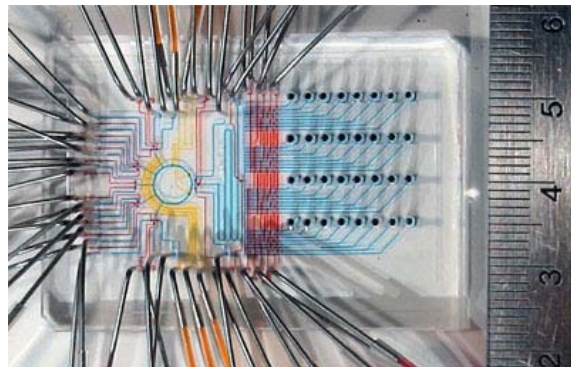


Figure 2. Optical image of the integrated microreactor utilized for parallel screening of an in situ click chemistry library; a ruler is present to calibrate the scale.

References

1. C.-C. Lee, G. Sui, A. Elizarov, C. J. Shu, Y.-S. Shin, A. N. Doole, J. Huang, A. Darion, P. Wyatt, D. Stout, H. C. Kolb, O. N. Witte, N. Satyamurthy, J. R. Heath, M. E. Phelps, S. R. Quake and H.-R. Tseng, *Multistep Synthesis of a Radiolabeled Imaging Probe Using Integrated Microfluidics*. *Science* **2005**, *310*, 1793-1796.
2. J. Wang, G. Sui, V. P. Mocharla, M. E. Phelps, H. C. Kolb and H.-R. Tseng, *Integrated Microfluidics for Parallel Screening of In Situ Click Chemistry Library*. *Angew. Chem. Int. Ed.* **2006**, *45*, 5276-5281.

PROTEIN SYNTHESIS IN A PLASTIC DEVICE FOR TOXIN DETECTION

Z. Hugh Fan^{1,2}, Qian Mei¹, Andrew Simon¹,
Carl K. Fredrickson¹, Wei Lian³, Shouguang Jin³

¹Department of Mechanical and Aerospace Engineering, ²Department of Biomedical Engineering, ³Department of Molecular Genetics and Microbiology, University of Florida, PO Box 116250, Gainesville, FL, 32611, USA
Email: hfan@ufl.edu; Fax: 352-392-7303

Abstract

Biological synthesis of proteins in a cell-free medium is implemented in a miniaturized plastic device. Protein synthesis can be inhibited by a toxin; this attribute is used as a sensing mechanism to detect toxins. Three proteins are simultaneously synthesized in an array device and their production yields are inhibited differentially by toxin simulants. Identification can be achieved based on the unique response pattern.

Keywords: toxin detection, protein expression, fluid manipulation, array

1. Introduction

Detection and identification of toxins are important for medical diagnostics, food/water safety testing, and biological warfare defense. Immunoassay is often the method used due to its simplicity and rapid analysis. Since immunoassay requires an antibody that is specific to the agent of interest, it cannot be used for detecting unknown or new agents because an antibody is simply not available. With the increasing ability to modify and engineer potential warfare agents, the ability to detect agents that have not been identified previously becomes more important.

To address this challenge, we are developing a detection method based on the mechanism of toxin actions. One of the mechanisms by which toxins cause toxic effects is to inhibit protein synthesis in cells [1]. For instance, ricin—a bioterrorism agent—kills people by inhibiting protein synthesis in a human being.

Biological synthesis (expression) of a protein includes the steps of gene transcription and protein translation. A gene is first transcribed into a messenger RNA, which is then translated into the corresponding protein. While protein expression is commonly implemented using *Escherichia coli* cells, it has also been realized in a cell-free medium employing a process called *in vitro* transcription and translation (IVT) [2]. In this work, three proteins are simultaneously synthesized in an array device. Their production yields are inhibited differentially by two toxin simulants. The resultant response pattern (or signature) of the array device can thus be used for detection and identification.

2. Experimental

Protein expression kits and reagents were obtained from Roche Diagnostics and Promega Corporation. Other reagents were mostly purchased from Fisher Scientific. Protein syntheses were implemented as described previously [3]. Either Western blotting or luminescence was used for measuring the yield of protein expression.

3. Results and Discussion

The device shown in **Fig. 1** consists of an array of units for expression of 3 different proteins. The top row of 3 units are for the positive controls, the second row for the negative controls, and other two rows for toxin samples with one repeat for enhanced precision. Each unit in the array device consists of a reaction chamber and a feeding chamber. Protein synthesis takes place in the miniaturized reaction chamber while the feeding chamber functions as the nutrient reservoir. The connection between them and a dialysis membrane provide a means to supply nutrients continuously, ensure proper mixing, and remove the reaction byproducts. These functions are critical to the protein production yield in a cell-free medium. The device was made from polymethylmethacrylate.

The concept is demonstrated by expressing three proteins, including green fluorescent protein (GFP), chloramphenicol acetyl-transferase (CAT), and luciferase. Their production yields are inhibited differentially by two toxin simulants, tetracycline (TC) and cycloheximide (CH). **Fig. 2a** shows the response pattern of the IVT array when TC is used whereas the response pattern of the same IVT array for CH is illustrated in **Fig. 2b**. The signals for the positive control are from the first row of 3 units in a device, in which GFP, CAT, and luciferase are synthesized in their respective expression mixture. These units are free of toxins. The

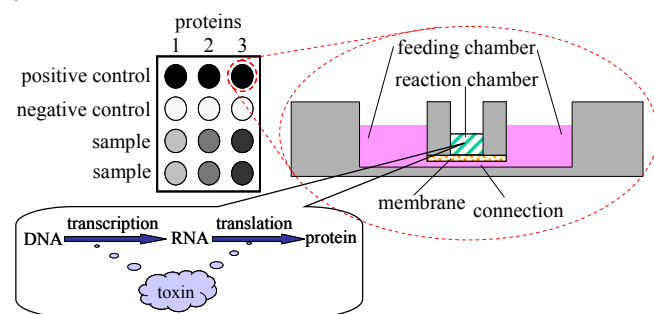


Figure 1. (top left) Device with an array of units. Darkness of the circles represents a hypothetical expression yield. (Top right, inside the dashed circle) Cross-sectional, expanded view of one unit. (Bottom left, in the call-out) Transcription and translation steps in each unit; and either step may be inhibited by toxins.

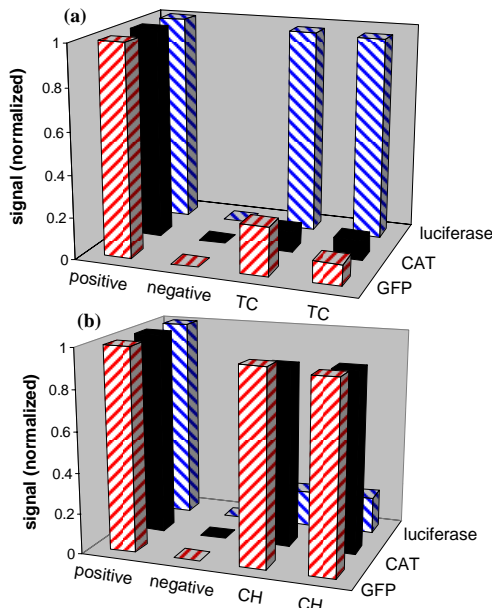


Figure 2. Response pattern of the IVT array for two toxin simulants, tetracycline (TC, a) and cycloheximide (CH, b).

signals for the negative control are from the second row of 3 units, in which the expression vector is not added. The signals for the samples are from the remaining two rows of 3 units, in which either 17 ng of CH or 25 ng of TC is added into the protein expression system. The significant difference in the response patterns between CH and TC clearly indicates that it is feasible to use the IVT array to detect and identify a toxin.

To detect a real toxin, ricin, we studied its inhibitory effects on luciferase expression by adding a series of concentrations of ricin into the IVT reactions in the miniaturized device. The calibration curve is shown in **Fig. 3**, in which the expression yield of luciferase (indicated by the luminescence) was plotted as a function of ricin concentration. The error bar of each data point indicates the standard deviation that is obtained from three repeat experiments. A linear relationship exists from 1 to 20 $\mu\text{g}/\mu\text{L}$, with the detection limit of less than 1 $\mu\text{g}/\mu\text{L}$.

The results in the inset of Fig. 3 confirm that the device design is proper. When IVT was implemented in a microcentrifuge tube, luciferase was synthesized in the first 0.5 hr and then the reactions ceased. In contrast, when it was in a miniaturized device with continuous feeding of nutrients and removal of byproducts, luciferase was continuously produced up to 4 hr. The yield of luciferase production in the miniaturized device is about 2.6 times higher than in a microcentrifuge tube.

5. Conclusion

A novel concept for toxin detection is presented based on toxin's inhibition of biological protein synthesis. We demonstrated the feasibility of the concept by expressing three proteins and obtaining the unique response pattern of the IVT array device for each toxin simulant.

Acknowledgement

This work is partially supported by the grant from the UCF-Space Research Initiative and the startup fund from the University of Florida. We would like to thank Dr. Brian Cain for the access to the luminometer.

References

1. Salyers, A. A.; Whitt, D. D. *Bacterial pathogenesis: a molecular approach*, 2nd ed.; ASM Press: Washington, D.C., 2002.
2. Spirin, A. S. *Trends Biotechnol* **2004**, 22, 538-545.
3. Mei, Q.; Fredrickson, C. K.; Jin, S.; Fan, Z. H. *Anal Chem* **2005**, 77, 5494-5500.

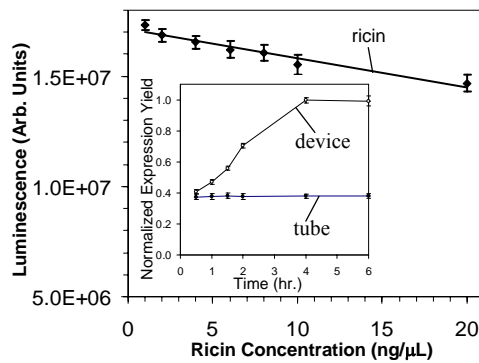


Figure 3. Calibration curve for ricin detection. (inset) Production yield of luciferase as a function of the expression time in a miniaturized device and in a microcentrifuge tube.

MULTI-STEP CONTINUOUS MICROCHEMICAL SYNTHESIS AND SEPARATION

Hemantkumar R. Sahoo, Jason G. Kralj and Klavs F. Jensen

Department of Chemical Engineering, Massachusetts Institute of Technology,
Cambridge, MA 02139, USA
(hemants@mit.edu)

Abstract

We demonstrate continuous flow multi-step chemical synthesis using three microreactors and two micro-phase-separators connected in series. Surface forces and preferential wettability characteristics of fluoropolymers are used for phase separation. The reactors are silicon-based microreactors. Carbamates are synthesized using the Curtius rearrangement reaction after extracting azides from aqueous phase into the organic phase. We also demonstrate parallel synthesis of a family of carbamates by splitting and branching out the reaction network.

Keywords: multi-step synthesis, liquid-liquid extraction, series, parallel, separation, carbamates

1. Introduction

There has been a continuing interest in multi-step continuous microchemical syntheses involving a separation step between two reaction steps [1]. In the present work, we have developed a continuous liquid-liquid phase separator and used it together with microreactors to perform continuous flow multi-step chemical synthesis.

2. Model Chemistry

The synthesis of carbamates using the Curtius rearrangement of isocyanates [2] serves as the model chemistry (Fig. 1) for demonstrating the multi-step microchemical synthesis. The reaction scheme involves the phase transfer reaction between aqueous azides and acyl chlorides requiring a liquid-liquid separation step, elimination of gas (N_2) in the formation of the isocyanate, and the liquid-liquid reaction of isocyanate with alcohol. Figure 2 shows a schematic of the setup used to synthesize the carbamates.

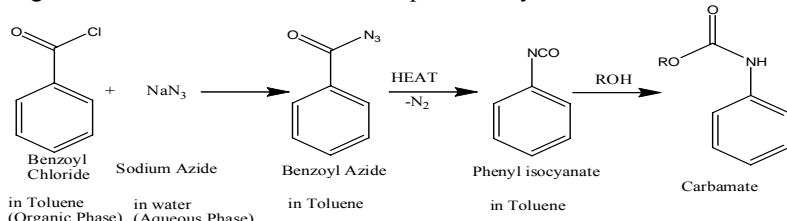


Figure 1. Carbamate synthesis scheme as case study

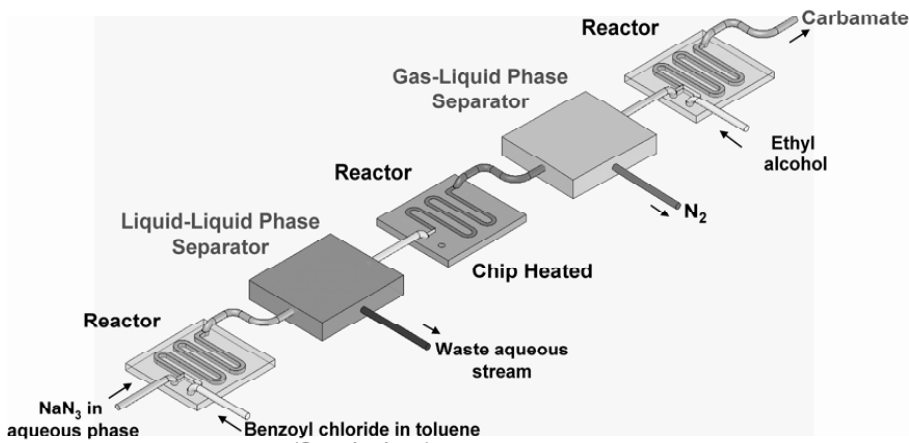


Figure 2. Schematic of the experimental setup for carbamate synthesis

3. Microchemical devices

Figure 3 shows the reactors used for the synthesis. All the three reactors were identical silicon based microreactors that have been used before for reaction optimization [3].

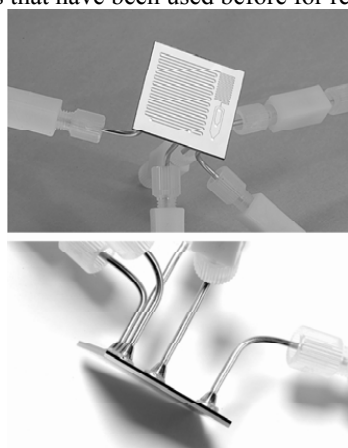


Figure 3 Microreactor used in the synthesis scheme

The development of the continuous liquid-liquid phase separator was based on the differences in surface energy of liquids resulting in preferential wetting and non-wetting characteristics as in our previous gas-liquid separators [4]. Figure 4 gives the details of the liquid-liquid phase separators. These devices also worked well as gas-liquid separators. We also used a different setup for the synthesis where the gas-liquid

separator worked on the basis of differences in gas and liquid density and this degassing holdup introduces a node for branching making parallel synthesis of analogous chemicals possible.

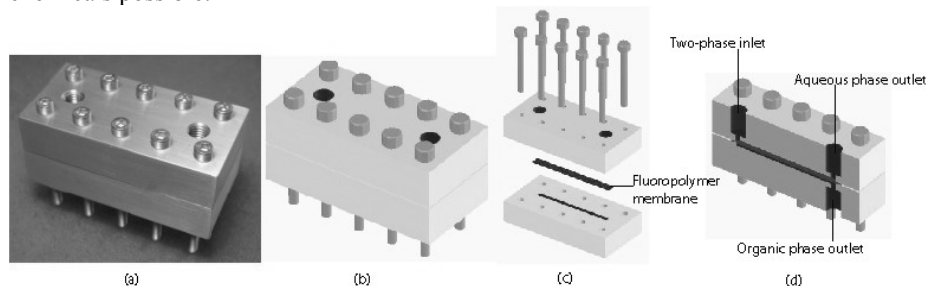


Figure 4. (a) Phase-separation device (b) Schematic of the device (c) Exploded view
(d) Sectional view

We performed parallel synthesis of methyl phenyl carbamate, ethyl phenyl carbamate and benzyl phenyl carbamate. The final carbamates were characterized using NMR measurements. Pressure-driven flow [5] was used to flow liquid out of the gas-liquid separator.

4. Conclusions

We have performed a continuous multi-step microchemical synthesis with separation, where we carried out three reactions with two separation steps in-between the reaction steps. We demonstrated series reactions and parallel synthesis. The salient features of this work include demonstration of solvent-switch operation, in-situ generation and consumption of hazardous intermediates such as isocyanates, safe operation of microreactor systems for high-energy chemistries, and small-scale production of chemicals in the neat form. The scheme involved three silicon microreactors, one liquid-liquid phase and one gas-liquid phase separator. Thus, we have realized a continuous, microscale version of a conventional batch synthesis scheme.

References

1. M. Tokeshi, T. Minagawa, K. Uchiyama, A. Hibara, K. Sato, H. Hisamoto and T. Kitamori, *Anal. Chem.* **74** (2002), p. 1565
2. C. Govindan, *Org. Proc. Res. & Dev.* **6** (1) (2002), p. 74
3. D. M. Ratner, E. R. Murphy, M. Jhunjhunwala, D. A. Snyder, K. F. Jensen, and P. H. Seeberger, *Chemical Communications*, **5** (2005), p. 578
4. A. Guenther, M. Jhunjhunwala, M. Thalmann, M. A. Schmidt, and K. F. Jensen, *Langmuir*, **21** (2005), p. 1547
5. C. Futterer, N. Minc, V. Bormuth, J.H. Codarbox, P. Laval, J. Rossier, and J.L. Viovy, *Lab Chip*, **4** (4) (2004) p.351

CAPILLARY ELECTROPHORESIS AND MICROCHIP

Shigeru Terabe

University of Hyogo, Emeritus Professor
280-52 Harimada-cho, Moriyama, Shiga 524-0012 Japan

Abstract

Advantages and disadvantages are compared between capillary and microchip formats from the viewpoints of electrophoresis and future prospect of microchip electrophoresis is discussed.

Keywords: capillary electrophoresis, microchip electrophoresis, electroosmotic flow, on-line sample preconcentration

1. Introduction

Capillary electrophoresis (CE) attracted great interests among separation scientists in 1980s because of potential high capability as an analytical separation technique. One of the major successes was separation of oligonucleotides for DNA sequencing in the early stage of CE developments. Application of CE to the analysis of proteins was not very successful, although CE was enthusiastically expected to replace conventional gel electrophoretic techniques. The major problem in protein analysis is adsorption on fused silica capillary wall. Separation of small molecules was successful in academic fields but CE is not widely accepted in industry as a general separation technique as high performance liquid chromatography (HPLC), which is ubiquitous in every industry.

Microchip format of CE appeared in early 1990s and gave us other functional capabilities in microscale separation. In particular, separations in micro channel combined with microvolume reactors for derivatization enabled the construction of the total microscale analysis system. Another attractive feature of microfabricated devices is a possible implementation of portable instruments and disposable microchips.

The author is a retired analytical chemist who spent most of his academic time in studying separation analysis, particularly CE. Therefore, he is unable to present new experimental results but can talk only about a history and some comments on the prospect of separation science.

2. Comparison between capillary and microchip formats in electrophoresis

Table 1 shows comparisons in performance between capillary and microchip formats. The advantage of microchip format is mainly in rapid analysis at the cost of resolution. Another remarkable advantage of microchip format is the flexibility of channel designs in two or three dimensions, while the capillary is simple cylindrical tubing with a constant diameter. Because of smaller sample sizes in microchip format the concentration detection sensitivity is low and absorbance detectors are rarely useful, which limits the range of analytes. The major advantage of the capillary format is high resolution compared with HPLC and microchip electrophoresis. One of the disadvantages of CE is low concentration sensitivity but this problem is almost solved

by using several on-line sample concentration techniques, which will be discussed in the lecture.

Table 1 Comparison between capillary and microchip formats in electrophoresis

Format	Capillary (50 μm i.d. x 25 cm)	Microchip (50 μm x 20 μm x 3 cm)
Material	Fused silica	Glass, plastic
Resolution	High ($N > 100,000$)	Low ($N < 10,000$)
Time	Medium (1- 30 min)	Fast (1-100 s)
Sample volume	1-10 nL	< 1 nL
Detection	UV, LIF, EC, MS, Conductivity	LIF, EC, MS, TLM, Conductivity
Sensitivity (Conc.)	μM (UV), nM (LIF)	nM (LIF)

3. Present status and future prospect of microchip electrophoresis

Problems in microchip electrophoresis are

- (1) Adsorption of proteins on the wall of microchannels.
- (2) Poor reproducibility in electroosmotic flow (EOF).
- (3) Limited detection capability.

Adsorption of proteins on the wall can be solved by several techniques developed in CE, probably the coating is a promising solution. Since EOF is not essential in electrophoretic separations except for capillary electrochromatography (CEC), complete suppression is one solution but no reliable technique is available yet. The control of EOF with external electric field may be a technique to be reconsidered because the advanced microfabrication techniques may be able to prepare microchannel with a constant radial external field. So far LIF is the only widely accepted detector in microchip electrophoresis and simple LIF detection systems with diode lasers specifically designed for the detection of particular analytes will be available.

The most probable application of microchip format in electrophoresis is high throughput analysis with multi channels designed for particular analytes in clinical analysis. If the analyte is defined, microchip electrophoresis systems can be constructed including sample pretreatments, optimized channel designs, detection schemes and surface treatments of channels. However, only few products based on microfabricated devices for routine analysis are commercially available. The most difficult issue will be the choice of target analytes.

Electrophoresis either in capillary or microchip format is one of the best techniques for the analysis of limited amounts of samples, such as single cell analysis. These techniques will be indispensable in bioanalysis. It is noted that electrophoretic separation is based on the principle different from that of chromatography and both separation techniques are complementary.

4. Conclusions

Most researches in microfabricated devices seem application oriented from the viewpoints of separation analysis probably because microchip format is not essential in fundamental researches. Therefore, the development of instruments for practical applications is strongly expected and an urgent issue.

STRETCHING THE LIMITS OF SEPARATION

Jason P. Beech, Jonas O. Tegenfeldt*

Division of Solid State Physics, Lund University, P. O. Box 118, SE-221 00
Lund, Sweden

*jonas.tegenfeldt@ftf.lth.se

Abstract:

We present a new type of stretchable elastomer microseparation device that is *adjustable* with nanoscale accuracy. Proof of principle has been demonstrated, and the device has potential use in a wide range of fields. In addition to general *adaptable* separation of bio-particles and biomolecules, it could be used for specific important applications such as virus purification for gene therapy and label-free suspension array for protein analysis. The wide range of uses and the potentially high impact of a successful use of the technique make it interesting and relevant to the broader scientific community.

Keywords: microfluidics, separation device

1. Introduction

Our device is based on deterministic lateral displacement (DLD), which has proven to be a very powerful technique for particle separation[1]. A DLD device is based on an array of obstacles in a microfluidic channel. As particles flow in the device, they will follow one of two trajectories: particles *larger* than the critical radius will move in a direction determined by the geometry of the device; particles *smaller* than the critical radius will move with the liquid flow. The critical radius is proportional to the distance between the obstacles. Although conventional DLD devices are capable of separation with a demonstrated *precision* of down to 10nm, it is very difficult to reach that level of *accuracy*, *i.e.* to design a device to have an accurately predetermined critical radius. This is especially relevant in situations when the size of a sample of interest varies or is not known accurately. To address these issues we have developed a device made in elastomeric PDMS where the separation is *tuned* on the nanometer-scale by stretching the entire device. The stretching changes the inter-obstacle distances, which in turn changes the critical radius of the separation.

2. Theory

The critical radius, R_{crit} , of a DLD device is simply given by the width of the first flow stream between the obstacles (see fig. 1B in ref [1]). With pressure driven flow, due to stick boundary conditions, the first flow stream is wider than the average width of the flow streams. This adds a correction term $\alpha \sim 2.5$ to the expression below. N is the number of rows in one spatial period and d is the distance between obstacles.

$$R_{crit} = \alpha \frac{d}{N} \quad (1)$$

When applying a strain to the entire device, the inter-obstacle spacing will change accordingly, thus changing the critical radius. An applied strain of 1% of the entire device will thus translate into a 1% change in the critical radius, thereby imposing modest demands on the required precision of the overall stretching for nanoscale adjustments of the critical radius.

3. Experimental

The tunable DLD device is made in PDMS using standard soft lithography procedures with a SU8 mold. The molded PDMS is attached to glass slides to seal the device. The glass acts as anchors for the device (Figure 1) and is attached to a microtranslation stage, which in turn is adapted for use in an inverted epi-fluorescence microscope. Fluorescent microspheres (Duke Scientific, Fremont California, US) of various diameters were suspended in aqueous solutions and used in the device, imaged with an EMCCD (Andor Technology, Belfast, UK)

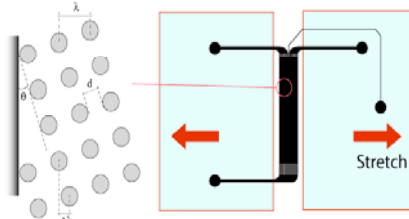


Figure 1. The device is held in a chuck designed to interface it with microfluidics *in situ* under a fluorescence microscope whilst simultaneously stretching it.

4. Results and discussion

The device is strained using a translation stage to change the distance, d , between obstacles and so change the critical size R_{crit} (Figure 2). The migration angle of $\theta = \theta_0 = 5.7^\circ$ corresponds to traces in fig. 2B and the migration angle of $\theta = 0^\circ$ to the traces in fig. 2C.

Assuming a Gaussian size distribution of the beads used in the experiment, the average migration angle, $\langle \theta \rangle$, as a function of critical size, R_{crit} , is fitted to an error function:

$$\langle \theta \rangle = \frac{\theta_0}{2} erfc\left(\frac{R_{crit} - x_0}{\sqrt{2}\sigma}\right) \quad (2)$$

Here x_0 is the average size in the bead population and σ is the standard deviation of the size distribution of the beads. θ_0 is given by $\tan \theta_0 = 1/N$. The fit to eq. 2 gives a relative standard deviation of 8% of the bead radius, which is consistent with the upper limit (12%) given for the standard deviation of the size distribution of the latex beads used. At the inflection point ($d=19.4\mu m$) the critical size equals the average size of the latex spheres so that $R_{crit}=5\mu m$ which gives a correction factor $\alpha = \frac{5\mu m}{19.4\mu m} 10 = 2.6$ for this particular device.

The root mean square error of the data to the fitted function corresponds to respectively 0.5° (vertical axis) and 130nm with respect to the cutoff radius (horizontal axis). This corresponds to a 2.5% error in determination of the cutoff radius.

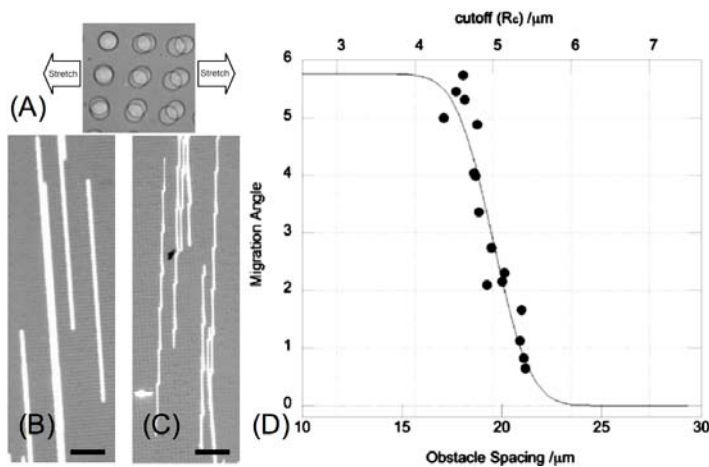


Figure 2. (A). Images of device before and after stretching. Scale bar is 300 μm . (B&C). 5 μm radius beads before (B) and after (C) stretching of the device. (D). Dependence of the average migration angle, θ , on the distance, d , between obstacles.

5. Conclusions

General applications of the device include e.g. real-time adaptation to changing conditions, real-time selection of fractions, creation of gradients in the obstacle array. Specific applications of the technique include label-free suspension arrays [2] where the binding of proteins to micrometer sized antibody-grafted particles are detected not by secondary antibodies but by the slight change in hydrodynamic radius of the particle upon binding of a protein. Accurate band-pass filtering can be implemented and targeted to a very specific size to within a few tens of nanometers. In this way a narrow range of sizes can be separated out which is particularly useful for virus purification with important implications for gene therapy[3].

Acknowledgments

The work is partially supported through funds from the Swedish Research Council (grant number 2002-5972) and the Knut and Alice Wallenberg Foundation (Stockholm).

References

- [1] L. R. Huang, E. C. Cox, R. H. Austin, and J. C. Sturm, *Continuous Particle Separation Through Deterministic Lateral Displacement*, Science **304**, 987-990 (2004).
- [2] F. F. Mandy, T. Nakamura, M. Bergeron, and K. Sekiguchi, *Overview and application of suspension array technology*, Clinics In Laboratory Medicine **21** (4), 713-+ (2001).
- [3] M. Nilsson, *et al.*, *Development of an adenoviral vector system with adenovirus serotype 35 tropism; efficient transient gene transfer into primary malignant hematopoietic cells*, Journal Of Gene Medicine **6** (6), 631-641 (2004).

INTEGRATED HIGH-PRESSURE 4-STAGE MICROPUMP FOR HIGH-SPEED MICRO GAS CHROMATOGRAPHY

Hanseup Kim, William H. Steinecker, Gordon R. Lambertus
Aaron A. Astle, Khalil Najafi, Edward T. Zellers, Luis P. Bernal
Peter D. Washabaugh, and Kensall D. Wise

Center for Wireless Integrated MicroSystems (WIMS)
University of Michigan, Ann Arbor, Michigan, USA

ABSTRACT

We report (1) the first demonstration of a microfabricated gas pump for multi-vapor analysis in a MEMS gas chromatograph (μ GC) system along with (2) detailed performance data on the micropump. The integrated 4-stage micropump consists of a monolithic ensemble of four pump chambers and five microvalves. Previously, we reported on the theory of operation, the individual technologies, and the fabrication of such designs [1-3]. In this paper, we report for the first time the high-performance data from the 4-stage micropump, including a maximum air flow rate of ~ 3.0 sccm and a pressure differential of ~ 7.0 kPa with a total power consumption of only ~ 15.1 mW. The micropump has an active area of 18.3×7.1 mm 2 , individual pumping membranes of 2×2 mm 2 , and has been operated for over 5 hours of intermittent tests over a six month period. Furthermore, it was combined with a microcolumn [4] and a micro-chemiresistor array detector [5] to form a functioning μ GC system where target vapors were transported by the micropump. The combined μ GC system successfully captured, separated, and detected the components of 4-vapor mixture under 7 seconds, which is the first MEMS-GC analysis operated by a MEMS-micropump.

Keywords: Integrated micropump and microvalve, peristaltic gas pump, micro gas chromatograph.

1. INTRODUCTION

A key factor that has hindered the development of totally integrated gas analysis microsystems is the lack of devices capable of providing efficient gas transport. The limited forces and volume displacements achievable in micro-scale make it difficult to produce sufficient pressure differentials and gas flow rates for practical use. The micropump described here uses a multi-stage (4-stage) configuration to obtain high net pressure differentials, and

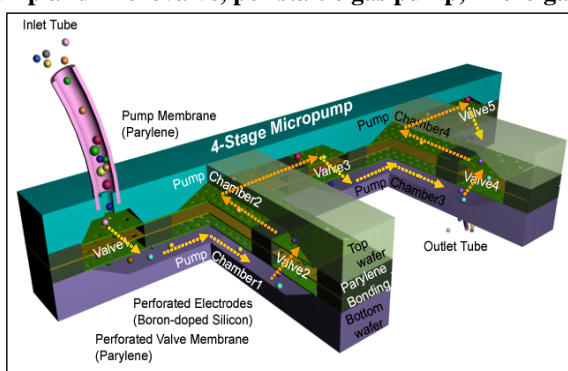


Figure 1: Illustration of an integrated 4-stage micropump for high-pressure generation. Arrows indicate the air flow path through the 4-stages.

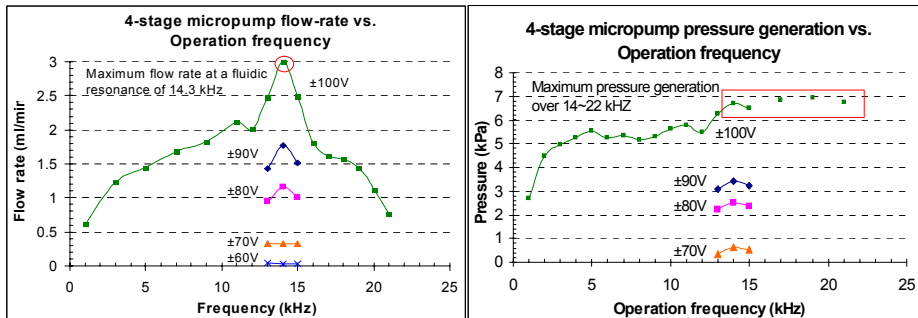


Figure 2: Measured flow rates (Left) and differential pressure (Right) over a wide range of operation frequencies under various voltages from the 4-stage micropump .

electrostatically actuated pumping membranes at a high-frequency fluidic resonance (>10 kHz) to obtain high flow rates [1]. The multi-stage configuration allows the pump to create small pressure differentials at individual stages but accumulate them into a high differential pressure. The high-frequency actuation of a membrane, enhanced by a fluidic resonance, leads to high volume displacements per unit period. Such a 4-stage micro gas pump has been fabricated by developing several microfabrication technologies [3], such as wafer bonding and membrane transfer with a flexible polymer, Parylene [2].

2. PUMPING PERFORMANCE OF A 4-STAGE MICRO GAS PUMP

The microfabricated micropump was operated at ± 100 V over a wide range of frequencies to determine the resonance frequency where the highest differential pressure and flow-rate are obtained (Fig. 2). After the resonance frequency was determined, the pump was operated at the resonance frequency under several different load conditions to obtain the differential pressure vs. flow rate performance curve(Fig. 3, Bottom Right). Test results show that the micropump has a fluidic resonance at 14.3 kHz where the highest flow of 3.0 sccm and maximum differential pressure of 7.0 kPa are obtained.

3. FIRST MEMS MICRO-GC ANALYSIS ENABLED BY A MICROPUMP

The micropump was serially connected to a chemiresistor array and a 25-cm micromachined separation channel, forming a complete μ GC system capable of capturing a sample mixture of airborne vapors, separating the components, and detecting them (Fig. 3). The chemiresistor array uses Au-thiolate monolayer-protected nanoparticle interfaces [5]. The DRIE-Si/glass micro-column is 25-cm long, has a cross-section of $140 \times 250 \mu\text{m}^2$, and uses a wall-coated dimethyl polysiloxane stationary phase [4,6]. The separation and detection of a mixture of acetone, benzene, toluene, and n-butylacetate in 7 seconds using atmospheric air as the carrier gas is shown in Figure 3. For this analysis, the micropump provided a flow of 0.2-0.3 sccm at 3.5 kPa differential pressure.

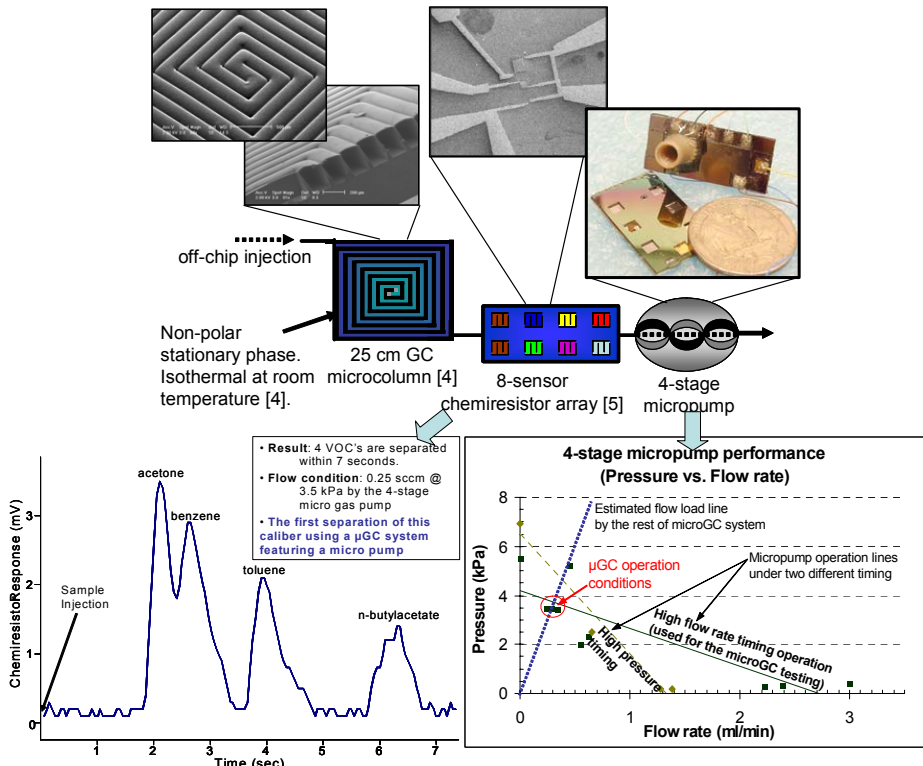


Figure 3: (Top) μGC testing set-up combining the micro pump, a microcolumn, and a chemiresistor array, (Bottom Left) the μGC chromatogram of 4 organic vapors, and (Bottom Right) measured differential pressure vs. flow rate performance curves for the 4-stage micro pump and the μGC system.

ACKNOWLEDGMENTS

The authors thank Shaelah M. Reidy and Dr. Masoud Agah for their contributions in coating microfabricated columns and microfabricating Si-Glass micro columns, respectively. This project is funded by the Engineering Research Centers Program of the National Science Foundation under Award Number EEC-9986866.

REFERENCES

- [1] A. A. Aslte, *et al.*, ASME 2005, IMECE 2005-81626.
- [2] H. Kim and K. Najafi, *JMEMS*, vol. 14, no. 6, pp. 1347-1355, 2005.
- [3] H. Kim, *et al.*, *μTAS 2005*, pp. 1173-1176.
- [4] G. L. Lambertus, *et al.*, *Anal. Chem.*, vol. 76, no. 9, pp. 2629-2637, 2004.
- [5] C.-J. Lu, *et al.*, *Lab On A Chip*, vol. 5, pp. 1123-1131, 2005.
- [6] M. Agah, *et al.*, *JMEMS*, vol. 14, no. 5, pp. 1039-1050, 2005.

Integration of surface microfluidics to closed-channel fluidics to realize a valveless multi-layer genetic analysis chip

Thirukumaran T Kanagasabathi, Ranjit Prakash, Karan VIS Kaler*
Biosystems Research and Applications Group
Schulich School of Engineering, University of Calgary, CANADA

1. Introduction

Microfluidic genetic analysis (μ GA) demonstrations, including our earlier work ^[1], and other integrated systems employing closed-channel devices are hampered in operation by a number of issues. Some of the issues include the requirement of valves and externally actuated pumps, problems pertaining to dead volumes, flow leakages, biochemical compatibility of valves and pumps, and an inability to precisely dispense and transport sub-microliter volumes of reagents sufficient for μ GA. To alleviate the above issues and furthermore benefit from the advantages of low-cost, low-reagent consumption of μ GA, we demonstrate a new approach on the unique integration of dielectrophoretic (DEP) liquid actuation, also referred as surface microfluidics^[2], to a multi-layer completely valveless PCR-CE (polymerase chain reaction – capillary electrophoresis) μ GA chip.

2. Materials and Methods

2.1 Fabricated Chip

The custom in-house fabricated glass μ GA chip (Fig1a) functionally integrates open and closed channel fluidics utilizing 3 independent fluidic and microelectrode layer structures for μ GA functionality. The device as shown in the schematic in Fig1b includes: (1) high-speed liquid actuation to both dispense and transport sub-microliter PCR reagents on the upper surface microfluidics layer, (2) an beneath second open-well PCR layer for genetic amplification and (3) a bottom third closed-channel CE fluidic layer for analysis. The functionality and first μ GA demonstration of this chip is presented below.

2.2 microGA Experiment -Droplet dispensing and mixing, PCR and CE analysis

In the top surface microfluidics layer, a 1 μ l droplet of (plasmid) DNA sample^[1] (under an oil cover) is positioned between and on top of a pair of coplanar microelectrode track (4000 μ m length, 30 μ m width, gap 30 μ m) and an excitation voltage is applied to the track electrodes. This non-uniform electric field exerts a DEP force on the droplet^[2], actuating a liquid finger along the length of the microelectrode track. This track is designed to terminate at an open well suitable for PCR and hence the actuated finger extends to the open PCR well containing the PCR master mix. When this projecting liquid finger merges with the PCR master mix, a small volume (about 10nl of DNA sample, corresponding to under 10% of the initial droplet) is dispensed from the droplet and mixed by diffusion with the PCR master-mix. Thermal cycling is then performed on the sub-microliter-mixed PCR master-mix in the open-well to amplify a genetic sequence in the DNA, specific to a primer sequence (5'-GCCAGGGTTTCCAGTCACGA-3' and 5'-

* kaler@ucalgary.ca, www.brag.ucalgary.ca

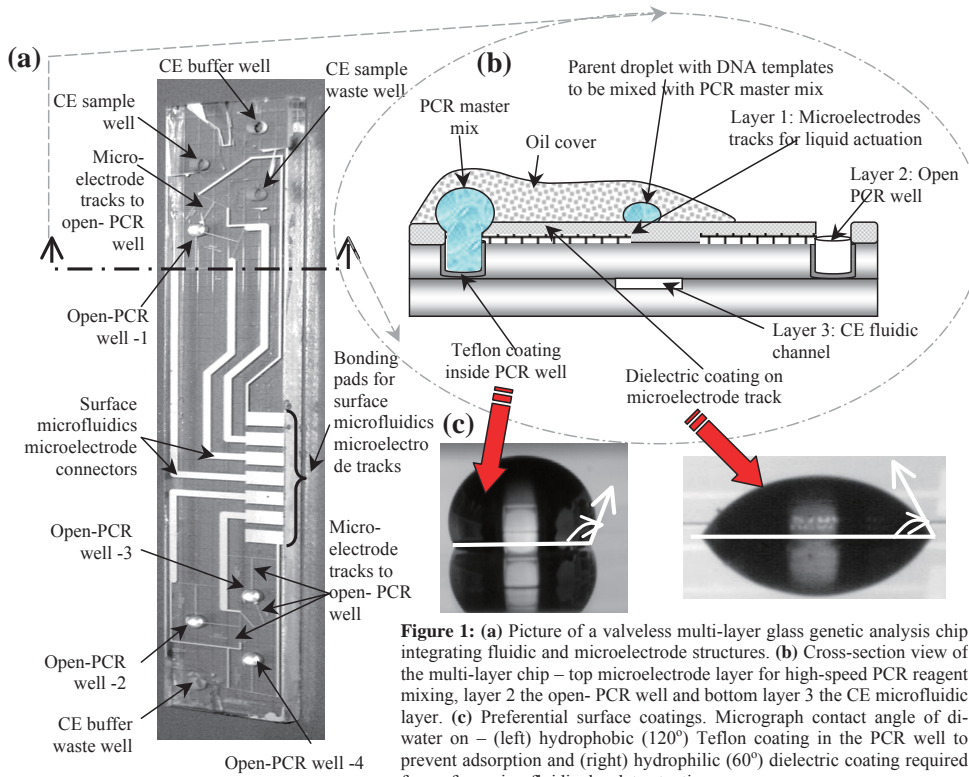


Figure 1: (a) Picture of a valveless multi-layer glass genetic analysis chip integrating fluidic and microelectrode structures. (b) Cross-section view of the multi-layer chip – top microelectrode layer for high-speed PCR reagent mixing, layer 2 the open- PCR well and bottom layer 3 the CE microfluidic layer. (c) Preferential surface coatings. Micrograph contact angle of di-water on – (left) hydrophobic (120°) Teflon coating in the PCR well to prevent adsorption and (right) hydrophilic (60°) dielectric coating required for surface microfluidic droplet actuation.

CAGGAAACAGCTATGAC-3)^[1] included in the PCR master mix. Finally, the PCR product is analyzed by CE integrated on-chip to accomplish μGA. The CE analysis of PCR in Fig 2 shows a DNA amplification peak of a 500bp PCR product at 242 sec, the size of which was verified from prior work^[1]. Furthermore, CE analysis of a negative control PCR (i.e. PCR in absence of template DNA) by conventional methods of the same PCR master mix (data not shown), resulted in only the primer peak, similar to that seen in Fig 2, and not a PCR product peak. The analogy of this control experiment and on-chip DNA droplet mixing to the PCR master mix in our chip validates successful sub-microliter DEP droplet mixing and rules-out false-positive data^[1].

2.3. Parameters for DEP droplet actuation

A combination of microelectrode geometries, excitation voltage and dielectric coating in the surface

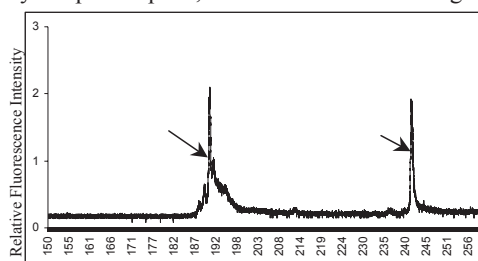


Figure 2: CE analysis of PCR on the integrated chip where DNA mixing with the PCR master mix was enabled by surface microfluidics.

microfluidic layer enable the successful realization of the sequential process of high-speed liquid actuation of the sample droplet containing the DNA. Hence based on prior work by Jones et al.^[2], we have experimentally determined these parameters for our chip. As shown in Fig 3, with a spin coated SU8 dielectric coating of $0.5\mu\text{m}$ and within a (sinusoidal) voltage range of 225V_{rms} and 237V_{rms} at 100 kHz , a linear velocity response of the droplet is observed. Microscope pictures of the DEP droplet mixing, where a liquid finger of the DNA droplet extends along the microelectrodes within milliseconds of applying 231V_{rms} at 100kHz is observed from images captured on a high-speed camera shown in Fig 4. Once the mixing occurs by merging of the DNA liquid finger with the larger PCR master-mix droplet at the end of the electrode ($t = 1.616\text{sec}$ in Fig 4), the voltage is switched off resulting in the break-up of the finger from the DNA sample droplet.

For successful liquid actuation a surface contact angle of about 60° is required while for PCR contact angle in excess of 100° is desired to retard adsorption^[1]. These requirements were achieved by preferentially coating (Fig 1c) the multi-layer chip with SU8 and Teflon, respectively.

3. Conclusion

In this work we have integrated liquid DEP actuation for sub-microliter droplet mixing to the PCR-CE method to realize a valveless multiplayer μGA chip. This integration approach can be further extended to a high throughput μGA system by incorporating multiple microelectrode tracks to a number of open PCR wells for array functionality.

References

- [1] A.R. Prakash, L M Pilarski, C Backhouse, K VIS Kaler, *MicroTAS 2005*, Vol. 1, pp. 145-147.
- [2] TB Jones, M Gunji, M Washizu, MJ Feldman, *Journal of Applied Physics* **2001**, 89, 1441.

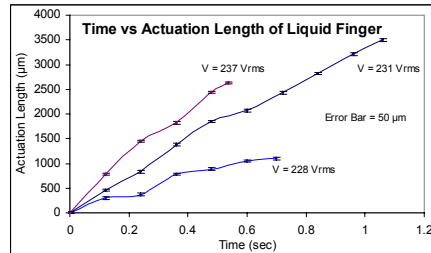


Figure 3: Experimental determination of optimal excitation voltage at 100 kHz for DEP liquid actuation. Electrode width (W) = 30 microns , gap (G) = 30 microns ; Thickness of dielectric coating = 0.5 microns .

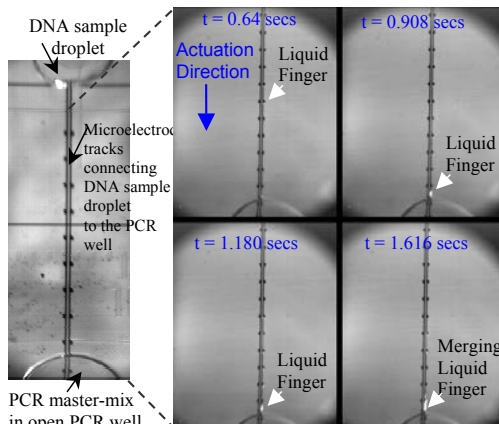


Figure 4: Time sequence response of DEP liquid actuation at an applied AC voltage of $231\text{ V}_{\text{rms}}$ and frequency 100 kHz .

Droplet-based High-Throughput Live/Dead Cell Assay

Eric Brouzes¹, Jeffrey Branciforte², Mariusz Twardowski², Dave Marran²,
Yue Suo², Yves Charles², Laurent Boitard², Michael P. Weiner²,
Jonathan M. Rothberg², Norbert Perrimon^{1,3} and Darren R. Link²

¹ Genetics Department, Harvard Medical School, Boston (MA), USA

² RainDance Technologies, Guilford (CT), USA

³ Howard Hughes Medical Institute, Harvard Medical School, Boston (MA), USA

Keywords: Droplets, Cells, Live/Dead assay

Abstract

We have developed an integrated live/dead assay for scoring the viability of cells encapsulated within droplets on a microfluidic device [1]. The device allows us to fuse [2] cell-containing droplets with dye-containing droplets. The combining, mixing [3], incubation and detection of cell viability are performed on-chip.

1. Introduction

The system uses discrete droplets as microreactors separated and transported by a continuous phase of fluorinated carrier fluid [3-7]. Each droplet moves as an independent nanoliter batch reactor. This compartmentalization ensures the coupling of genotype (or conditions) and phenotype [8]. By producing these microreactors and fusing them at a rate exceeding thousands of drops per second, we are enabling the screening of large libraries. We have focused our initial efforts on cells of the fruit fly *Drosophila melanogaster*. These cells have been used to complete a series of functional genomic RNAi screens that generated a wealth of information in signaling pathways, host/pathogen interaction and cell biology [9].

2. Experimental

Microfluidic devices were made using soft lithography techniques [10]. The dead cells were killed using ethanol. Cells are encapsulated in 50 μ m droplets either collected from a first chip and injected in the live/dead assay device, or directly encapsulated on the live/dead assay device. The live/dead assay device comprised a series of 5 modules that have been optimized for analysis of cell state.

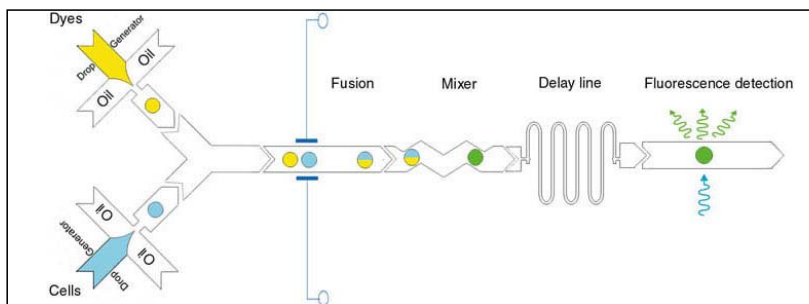


Figure 1: Schematic of the fluidics network of the live/dead assay

These modules are (Figure 1): 1) a set of two nozzles for encapsulation of both cells and fluorescent dye; 2) a fusion module; 3) a mixing module; 4) a delay line; and 5) a detection module to collect the fluorescent signal. Live cells and dead cells are respectively scored with Calcein-AM and Sytox Orange (Molecular Probes). The dyes were excited with a combination of two lasers (488nm and 555nm) and the signals collected by photomultipliers (PMT) associated with specific filters.

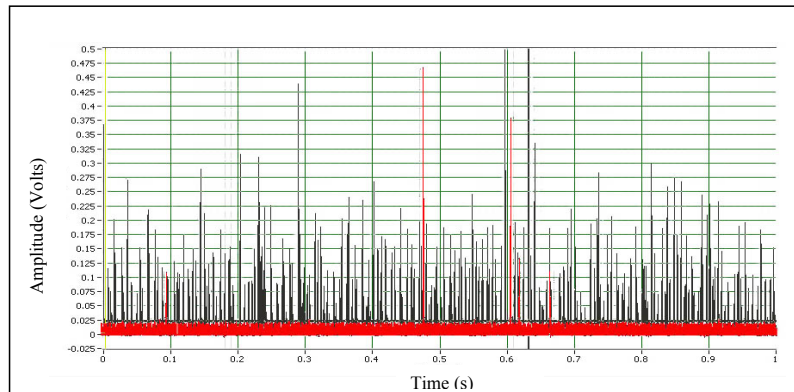
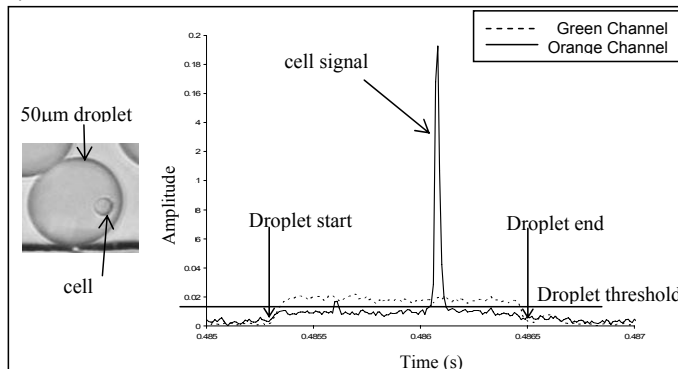


Figure 2: One-second raw signal trace (Black: Green channel; Grey: Orange channel). Live cells are scored with Calcein-AM (green signal) and dead cells with Sytox Orange (orange signal). The raw signal represents the signal recorded by the PMTs. Precisely, 287 cells are detected for 963 droplets in this example.

3. Results

A typical raw trace is shown in Figure 2, and Figure 3 shows the signal of a droplet containing a dead cell. The background signal of a droplet due to the Calcein-AM dye (dashed line) is sufficient to enable the detection of the droplets by the use of a threshold. In Figure 3, we can see that on top of the homogeneous signal there is a peak corresponding to a dead cell (Orange Channel). Typically the droplets and the peaks corresponding to the live and dead cells are detected using a set of specific thresholds. The droplet areas and the peak areas are integrated and further processed to correct the fluorescent cross-talk.

Figure 3:
Signal of a droplet containing a dead cell (peak in the orange channel), zoom from Figure 2.
Because the cells are discretely distributed in the droplet (see insert), the signal consists of a background component plus a localized peak due to the cell staining.



To validate our approach, we scored a 50-50 mixture of live and dead cells and checked that we were able to clearly distinguish both populations and find the right proportion. As seen in Figure 4, the two populations are clearly distinguishable, demonstrating that the combination of Calcein-AM/Sytox Orange is specific for identifying live/dead cells. In addition, the cell count of both populations shows that the ratio of live-dead cells is in the expected proportion.

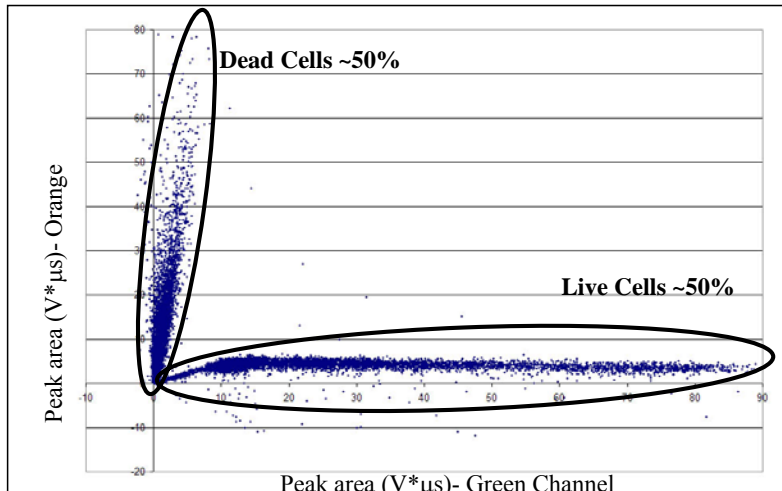


Figure 4: Analysis of a 50-50 mixture of live and dead cells. Scatter-plot of peak area in the green channel versus peak areas in the orange channel (the data are corrected for fluorescence cross-talk). 60,000 cells are detected in an equal proportion of live and dead cells. Comparatively only 6 peaks show a staining by both dyes. Note that negative values are due to the cross-talk correction.

4. Conclusions

We have developed an integrated live/dead assay for scoring the viability of cells encapsulated within droplets on a microfluidic device. Using this method we were able to determine the relative composition of a pre-mixed population of live and dead cells. We are now investigating how long cells can survive in these droplets and expanding the analysis to several mammalian cell lines.

- [1] S.L. Anna, N. Bontoux, and H.A. Stone, *Applied Physics Letters* **2003** 82 364-366.
- [2] W.-H. Tan and S. Takeuchi, *Micro TAS* **2005** 506-508.
- [3] J.D. Tice, H. Song, A.D. Lyon, and R.F. Ismagilov, *Langmuir* **2003** 19 (22) 9127-9133.
- [4] D.R. Link, S.L. Anna, D.A. Weitz and H.A. Stone, *PRL* **2004** 92 054503.
- [5] Y.-C. Tan, K. Hettiarachchi, M. Siu, Y.-R. Pan, and A. P. Lee, *JACS* **2006** 128(17) 5656–5658.
- [6] T. Thorsen, R.W. Roberts, F. H. Arnold, and S. R. Quake, *PRL* **2001** 86 4163.
- [7] S. Sugiura, M. Nakajima, S. Iwamoto, and M. Seki, *Langmuir* **2001** 17 5562.
- [8] D.S. Tawfik and A.D. Griffiths, *Nature Biotechnology* **1998** 16 652-656.
- [9] C.J. Echeverri and N. Perrimon, *Nature Review Genetics* **2006** 7(5) 373-84.
- [10] J. C. McDonald, D. C. Duffy, J. R. Anderson, D. T. Chiu, H. Wu, O. J. A. Schueller, G. M. Whitesides, *Electrophoresis* **2000** 21 27.

REAL-TIME FEEDBACK CONTROL OF DROPLET GENERATION FOR EWOD DIGITAL MICROFLUIDICS

Jian Gong and Chang-Jin "CJ" Kim

Mechanical and Aerospace Engineering Dept., UCLA, Los Angeles, U.S.A.

Abstract

We report the successful implementation of real-time feedback control of the droplet generation process on the electrowetting-on-dielectric (EWOD) digital microfluidics. Demonstrated in the air environment in this paper, the feedback allows precise ($< \pm 1\%$) droplet generation and also empowers users to prescribe the volume through software.

Keywords: EWOD, electrowetting, digital microfluidics, droplet generation

1. Introduction

Generating droplets of uniform volume is essential for the digital microfluidics systems, which use droplets as basic fluidic units. Recently we have shown that high uniformity ($\pm 2\%$) can be achieved by new firing sequence [1]. We have also confirmed accurate on-chip capacitive measurement of droplet volumes [1,2]. In the current paper, we develop feedback control system to defeat the random uncertainties and further improve the uniformity. Furthermore, the feedback allows generation of user-subscribed droplet volumes within a range determined by the hardware.

2. Method

Real-time feedback actuation has become possible through a new control board, capable of a fast capacitive sensing of the droplet volume and a precise construction of driving signals (Fig. 1(a)). A microcontroller from Microchip® can precisely control the high voltage driving signals for the EWOD actuation through a 14-bit digital-analog-converter (DAC) and a 32-channel on-board high voltage amplifier. A ring oscillator circuit is used to detect the capacitance between the driving EWOD electrode and the top grounding electrode, proportional droplet volume. The oscillation frequency of the circuit is inversely proportional to the capacitance and measured by a pulse counter in the microcontroller. Then the microcontroller decides the high-voltage driving signals according to the control algorithm in the program. By using a fast 20 MHz microcontroller and optimizing the program code, one cycle of sensing and driving can be completed within 1 ms. Considering the typical droplet moving speed under EWOD actuation is 1-10 mm/s, the control speed is fast enough for real-time control. An upstream PC defines the algorithm and downloads the program into the microcontroller.

One simple but efficient control algorithm is shown in Fig. 1(b). When the frequency (f) is detected by the pulse counter, the capacitance (C) is calculated. Driving signals at the creation site and reservoir will be controlled by the algorithm according to C to bring the droplet footprint area within the desirable range (between $c1$ and $c2$). When the droplet volume is within range, both the creation site and the reservoir will be energized until the liquid neck breaks and one droplet gets generated.

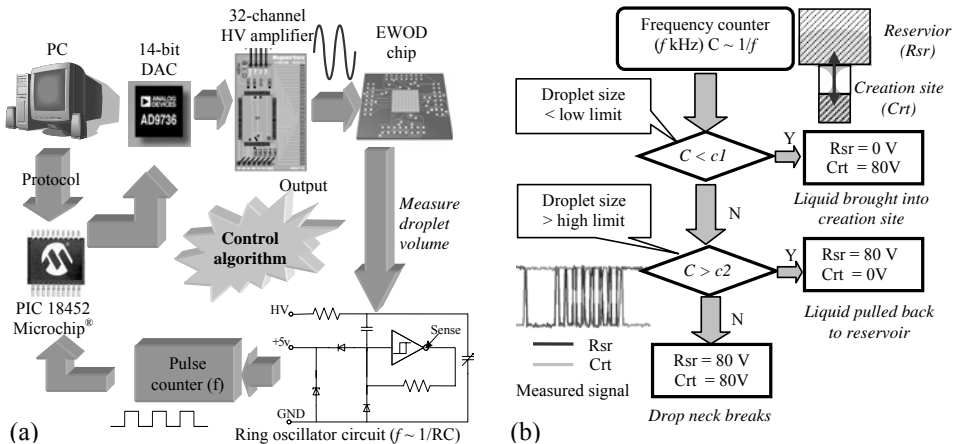


Figure 1. (a) Diagram of real-time feedback control hardware. (b) Feedback control algorithm for droplet volume control. c_1 and c_2 define the accuracy of droplet volume.

3. Results and discussion

Fig. 2 shows the results obtained on a printed circuit board (PCB) based EWOD chip [3] having the 1.5 mm x 1.5 mm electrodes and 100 μ m high channel. We compare droplet uniformities with and without the feedback. The standard deviation of the droplet volume distribution is 5x smaller with the feedback control. Fig. 3 also shows the excellent linear relationship between the droplet volume and the control parameter $1/f \sim C$. The smallest droplet we can generate is as small as 20% of the electrode size.

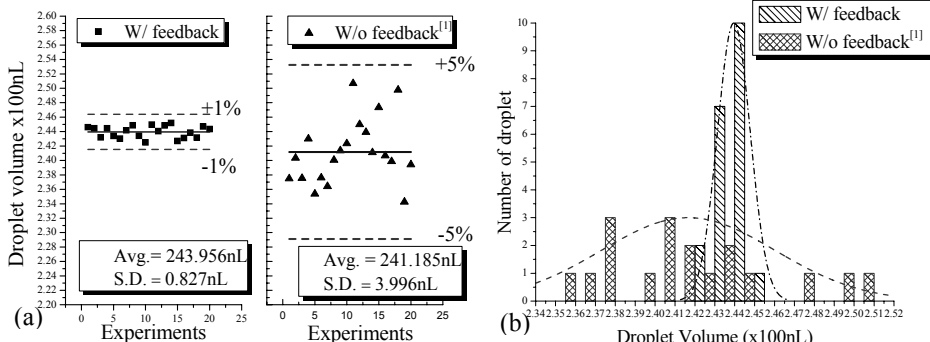


Figure 2. (a) Droplet volume generated with feedback control and without [1]. (b) Histogram of the data from (a) at every 1 nL volume increment.

With the new ability to accurately generate droplet volumes within a wide range, more sophisticated digital microfluidic operations can be designed, allowing new digital microfluidic operations not feasible before, such as high-order sample dilution. For example, for x10000 dilution, without feedback control the most efficient method is 1:1

mixing and cutting, requiring 14 operation cycles. On the other hand, with feedback control and variable droplet volume (down to 20%), only 6 cycles are needed. Fewer dilution cycles also improve the concentration accuracy with smaller accumulated error.

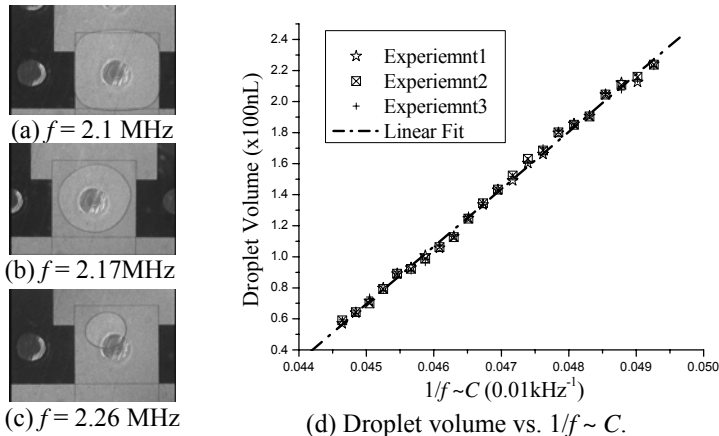


Figure 3. (a), (b), (c) are the snapshots right after droplet generation at certain feedback parameter f . (d) shows the linear relationship between volume and $1/f$ proportional to C .

5. Conclusion

We have successfully designed and implemented the real-time feedback control of the droplet generation process on the EWOD digital microfluidic chip, significantly improving the uniformity of the droplet volume (5x less standard deviation). Furthermore, the feedback allows the generation of varying volumes of droplets on a given electrode pattern. The former can improve device reliability by compensating for the uncertainties in the fabricated device and operation conditions, while the latter allows a new flexibility in designing sophisticated digital microfluidic applications.

Acknowledgements

This work has been supported by the NASA Institute for Cell Mimetic Space Exploration (CMISE) at UCLA and a gift from Wendy and Ken Ruby.

References

- [1] J. Gong and C.-J. Kim, Characterization and Design of Digitizing Processes for Uniform and Controllable Droplet Volume in EWOD Digital Microfluidics, Tech. Dig. Solid-State Sen. Act. Workshop, Hilton Head Island, SC, U.S.A., pp. 159-162 (2006).
- [2] N. Srivastavaa and M. A. Burns, Electronic Drop Sensing in Microfluidic Devices: Automated Operation of a Nanoliter Viscometer, Lab Chip, Vol. 6, pp. 744–751 (2006).
- [3] J. Gong and C.-J. Kim, Two-Dimensional Digital Microfluidic System by Multi-Layer Printed Circuit Board, Proc. Int. Conf. Micro Electro Mechanical Systems, Miami, FL, U.S.A., pp. 726-729 (2005).

PRODUCTION OF BIPHASIC ORGANIC DROPLETS AND PARTICLES OF GEOMETRICAL ANISOTROPY USING A TRI-PHASE LIQUID FLOW IN MICROCHANNELS

Takasi Nisisako¹ and Toru Torii²

¹Precision and Intelligence Laboratory, Tokyo Institute of Technology, R2-6, 4259 Nagatsuta-cho, Midori-ku, Yokohama-shi, Kanagawa, 226-8503, Japan

²Graduate School of Frontier Sciences, The University of Tokyo, 5-1-5 Kashiwanoha, Kashiwa-shi, Chiba, 277-8563, Japan
(nisisako@pi.titech.ac.jp)

Abstract

We report a tri-phase microfluidic technology that can produce picoliter-sized biphasic droplets and geometrically anisotropic polymer microparticles. Using a planar sheath-flowing regime, we generated biphasic droplets comprised of two immiscible organic fluids in co-flowing aqueous phase; these droplets formed Janus or core-shell structure by the balance of interfacial tensions among three liquid phases. Subsequent photo-polymerization produced nonspherical polymer particles such as hemispheric particles, and shells with a pore on their surfaces. The size and shape of droplets and particles were controllable by varying flow conditions. A scale-up approach by multiple-channel integration was also demonstrated.

Keywords: Microfluidics, Janus droplets, geometrical anisotropy

1. Introduction

Micro- and nano-particles with nonspherical shapes have wide variety of applications such as light-diffuser for optical films[1], building blocks for the supra-particular assemblies[2], etc. A conventional route to synthesize nonspherical particles is seed polymerization with controlled nucleation and growth steps; but flexible shape control is difficult and the range of particle size is limited. Although monodisperse ellipsoids, rods and disks have been prepared by polymerizing precursor droplets confined in microchannels[3, 4], this *in-situ* technique has several drawbacks, such as clogging and pressure loss in microfluidic devices. Here, we present a new microfluidic technique that can overcome the above-mentioned limitations.

2. Experimental

Microchannels (Fig. 1) were fabricated on a glass chip by the dry-etching technique;

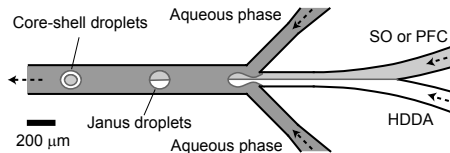


Figure 1. Schematic of a sheath-flowing geometry for producing biphasic organic droplets. Channel sizes are 100-200 μm in width and 100 μm in depth.

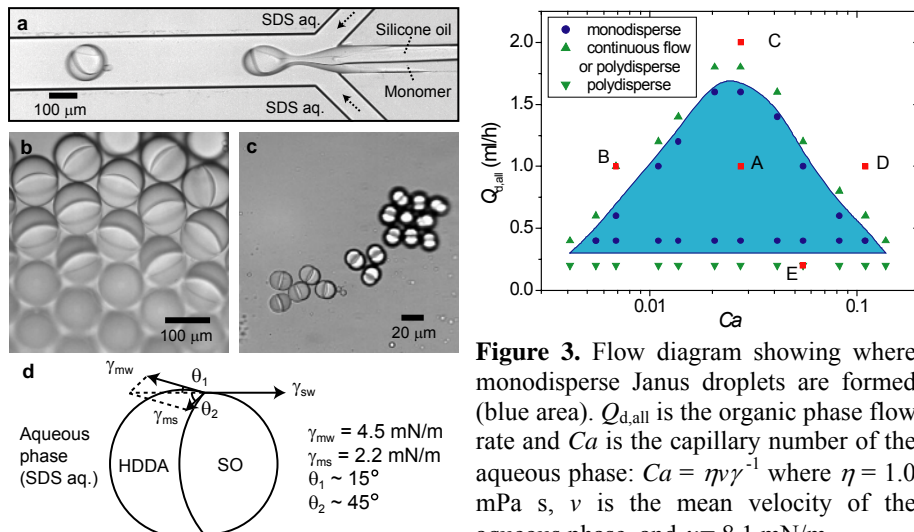


Figure 2. Biphasic Janus droplets: (a) Formation of Janus droplets consisting of silicone oil and monomer. Breakup rate is ~270 drops/s; (b) Primary Janus droplets; (c) Satellite Janus droplets; (d) A schematic showing the balance of three interfacial tensions. From the Young-Dupré equation, $\gamma_{sw} = \gamma_{mw}\cos\theta_1 + \gamma_{ms}\cos\theta_2 = 5.3$ mN/m.

solution of sodium dodecyl sulfate (SDS) or polyvinyl alcohol (PVA) was used as external aqueous phase. Photo-polymerization was performed outside the fluidic chip.

3. Results and Discussion

When SO was used with HDDA, biphasic Janus droplets were rapidly formed in coflowing aqueous phase by a shear-rupturing mechanism (Fig. 2a). Both “primary” and “satellite” droplets had similar Janus structure (Figs. 2b and c). They had asymmetric geometry because of the balance of three liquid-liquid interfacial tensions (Fig. 2d). Figure 3 shows flow conditions for producing monosized droplets; polydisperse droplets were formed when the total flow rate of the two organic phases was below 0.2 ml/h, because the organic stream became unstable due to the interfacial tension at the oil-oil interface. Subsequent polymerization produced monodisperse nonspherical particles (Fig. 4); the particle shape was controllable by changing the ratio of flow rates of the two organic phases. On the other hand, when PFC was the second organic phase, core-shell droplets enclosing PFC were formed reproducibly, because of the strong hydrophobicity of PFC. The number of cores was controllable by varying flow

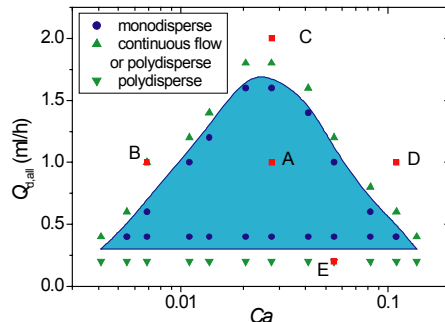


Figure 3. Flow diagram showing where monodisperse Janus droplets are formed (blue area). $Q_{d,all}$ is the organic phase flow rate and Ca is the capillary number of the aqueous phase: $Ca = \eta v \gamma^{-1}$ where $\eta = 1.0$ mPa s, v is the mean velocity of the aqueous phase, and $\gamma = 8.1$ mN/m.

we previously used a similar geometry for the synthesis of bicolored Janus particles for an electronic paper[5, 6]. An acrylic monomer (1, 6-hexanediol diacrylate, HDDA) was used as a polymerizable organic phase, and silicone oil (SO) or perfluorocarbon fluid (PFC) was used for the second organic phase. Aqueous phase: SDS aq. or PVA was used as external aqueous phase. Photo-polymerization was performed outside the fluidic chip.

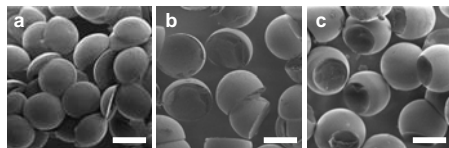


Figure 4. Particles of various shapes engineered by varying ratio of flow rates of HDDA (Q_m) and SO (Q_s): (a) Thin, truncated shape. $Q_m/Q_s = 0.25$; (b) Hemispheric shape. $Q_m/Q_s = 1$; (c) Particles with a dimple. $Q_m/Q_s = 4$. Scale bars are 100 μm .

conditions (Figs. 5a and b). We confirmed these core-shell geometries by confocal microscopy (Figs. 5c and d). Photo-polymerization of HDDA and evaporation of PFC produced macro-porous shells with a small pore on their surfaces (Fig. 5e). The production rate was easily scaled up by multiple-channel integration on a chip (Fig. 6).

4. Conclusion

We present a new route for the synthesis of polymeric microparticles with controlled shapes. The introduction of chemical anisotropies in addition to geometrical anisotropy would be a promising approach for the design of more functional colloids.

References

- [1] <http://www.tech-p.com/english/product/development/biconvex.html>
- [2] S. C. Glotzer, *Science* **306**, 419 (2004).
- [3] D. Dendukuri, et al. *Langmuir* **21**, 2113 (2005).
- [4] S. Xu, et al., *Angew. Chem. Int. Ed.* **44**, 724 (2005).
- [5] T. Nisisako, T. Torii, T. Higuchi, *Chem. Eng. J.* **101**, 23 (2004).
- [6] T. Nisisako, T. Torii, T. Takahashi, Y. Takizawa, *Adv. Mater.* **18**, 1152 (2006).

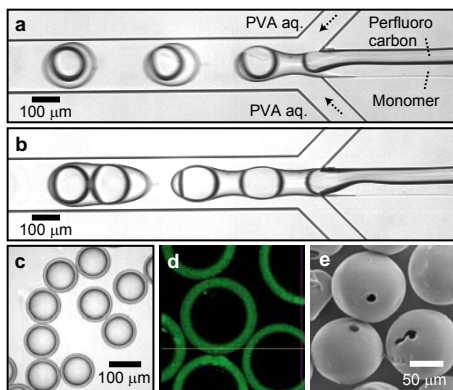


Figure 5. Core-shell droplets and particles: (a) Formation of core-shell droplets consisting of perfluorocarbon fluid (PFC) and monomer (HDDA); (b) Encapsulation of two PFC cores in a HDDA droplet; (c) Topview of core-shell droplets. CV was ~2 %; (d) A cross-sectional image obtained via confocal microscopy using fluorescent quantum dots; (e) Shells with a pore on their surfaces. Interfacial tension between PFC and aqueous phase (PVA aq.) was 17.1 mN/m.

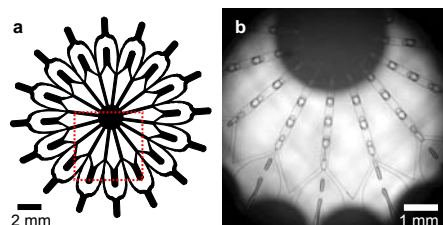


Figure 6. A numbering-up approach for mass-production of biphasic droplets: (a) A schematic of the 16-channel module. An output port is located in the center; (b) Formation of monodisperse core-shell droplets at 16 sheath-flow junctions. Production rate was ~ 40 ml/h.

MICROFLUIDIC DEVICE FOR CONTINUOUS AND HYDRODYNAMIC SEPARATION OF BLOOD CELLS

Masumi Yamada^{1,2}, Miyuki Matsuda³, and Minoru Seki^{3*}

¹The University of Tokyo, 7-3-1 Hongo, Bunkyo-ku, Tokyo 113-8656, Japan

²Tokyo Women's Medical University, 8-1 Kawada-cho, Shinjuku-ku, Tokyo 162-8666, Japan

³Osaka Prefecture University, 1-1 Gakuen-cho, Sakai, Osaka 599-8531, Japan

E-mail: seki@chemeng.osakafu-u.ac.jp

Abstract

We describe herein microfluidic devices for continuous and hydrodynamic separation of blood cells according to size. In our previous study, a new scheme for separating and concentrating particles utilizing microfluidic devices has been demonstrated, in which simple introduction of particle suspension enables both size-dependent concentration and separation. In this scheme, however, contamination of small particles into concentrated large particles could not be avoided, so separation efficiency was insufficient. We therefore improved the separation accuracy by employing flow splitting and recombining, and apply this method to the separation of blood cells.

Keywords: blood cell separation, hydrodynamic filtration, microfluidic device

1. Introduction

Separation of cells according to their physical or chemical properties is one of the essential techniques in the fields of biological research and medical care. A number of studies have been hitherto reported concerning separation of cells using microfluidic devices, including fluorescent-activated cell sorter [1, 2]. However, it cannot be said that versatile and useful microfluidic systems for cell sorting have been fully established.

In our previous study, we have proposed a scheme for continuous separation and concentration of particles and cells, utilizing laminar flow profiles in a microchannel network with multiple branch channels [3]. To overcome the disadvantages of the previous scheme, we proposed an improved scheme for particle separation, employing flow splitting and recombining. The principle is shown in Figs. 1 and 2. When the relative flow rate distributed to a side channel at a branch point is sufficiently low (Fig. 1 (a)), particles cannot go through the side channel, even when they are flowing near the sidewall. However, when the relative flow rate is increased, (Fig. 1 (b)), the size limit of particles that can go through the side channel is increased. By combining these flow states, particle positions in the main channel can be precisely controlled. That is, by repeating liquid flow removal from the main channel, and recombining into the downstream, particles are perfectly alignment onto one sidewall in the main channel.

Then, particles can be separated according to size, by increasing the relative flow rates into the outlet channels.

Blood cells are mainly composed of erythrocytes and leukocytes, whose shapes and sizes are entirely different. Also, since the population of leukocytes is $\sim 1/700$ that of erythrocytes, usual filtration can not be employed for preparation of leukocytes. Separation of blood cells is essential for various research and clinical scenes, so we tried to separate these cells as a model.

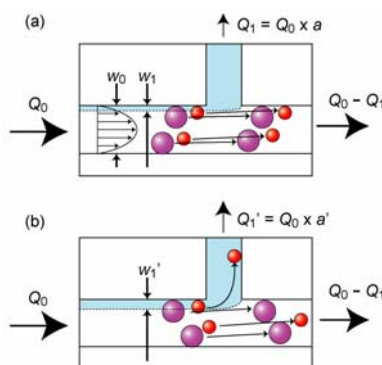


Figure 1. Schematic diagrams of particle behavior at a branch point. (a) When the relative flow rate into the side channel is sufficiently low, particles never go through the side channel (this flow state is called “flow split”). (b) When the relative flow rate is higher, the size limit of particles that can go through the side channels can be increased (“particle sorting”). The flow width w_1 determines the size of sorted particles.

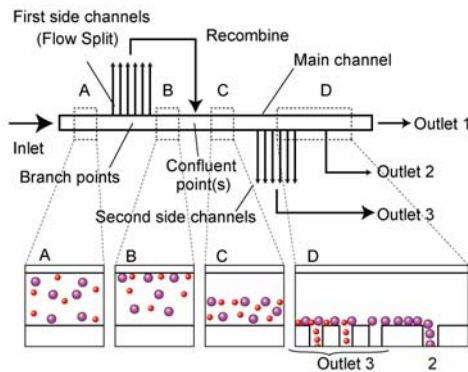


Figure 2. Principle of blood cell separation. By repeatedly splitting flow from the main channel and re-injecting, cell positions can shift toward one side wall (C). Then by repeatedly splitting flow through the second size channels on the other sidewall of the main channel, erythrocytes (small cells) are removed through outlet 3, while leukocytes (large cells) are perfectly aligned on one sidewall and collected from outlet 2.

2. Experimental

PDMS-glass hybrid microdevices were fabricated using usual soft lithographic techniques. One of the microchannel designs is shown in Fig. 3, which was designed regarding the microchannel network as a resistive circuit. There are one inlet, three outlets, 80 first and second side channels, respectively. Theoretically, $\sim 34\%$ of the liquid flow is split through the first side channels, while $\sim 80\%$ of the liquid flow is withdrawn through the second side channels. Also, it was expected that cells smaller than $\sim 6 \mu\text{m}$ would be recovered from Outlet 3, while cells with diameter of $6 \sim 20 \mu\text{m}$ would be collected from Outlet 2. Whole blood was diluted ($\times 10$) using PBS, and continuously introduced into the microchannel using a syringe pump with a flow rate of $20 \mu\text{L}/\text{min}$. The recovered cells were immobilized and stained on glass slides.

3. Results and Discussion

Cells recovered from each outlet and stained with Wright-Giemsa staining are shown in Fig. 4. As a result, 99.97% of the introduced erythrocytes were collected from outlet 3, while ~98% of leukocytes were collected from outlet 2. The concentration of leukocytes in Outlet 2 was increased 30-fold compared to the initial value. From these results, the potential of this microdevice for blood cell separation was successfully shown.

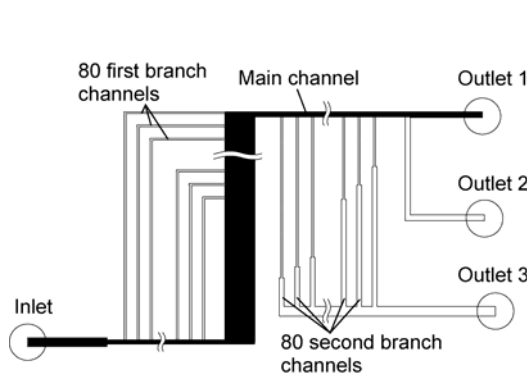


Figure 3. Schematic diagram of a microchannel designed for blood cell separation. The channel widths are 10~1000 μm , and the depth is $\sim 15 \mu\text{m}$. The main channel is shown in black. Drawing is not to scale.

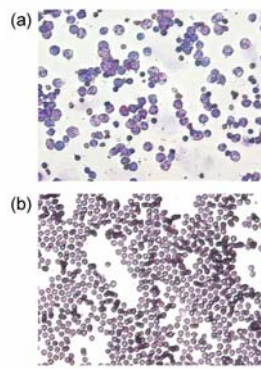


Figure 4. Photographs of blood cells collected from each outlet and stained on glass slides; cells collected from (a) outlet 2, and (b) outlet 3. The scale bar size is 100 μm .

4. Conclusions

Blood cells were successfully separated using the microfluidic devices. The presented scheme is advantageous since no chemical treatment is required to purify leukocytes, without damaging the cells. It is expected that this scheme will be applied to various biological materials.

Acknowledgement

This study was supported in part by Grants-in-aid for JSPS fellows, and Scientific Research B (16310101) from the Ministry of Education, Culture, Sports, Science, and Technology, Japan.

References

- [1] A.Y. Fu, et. al., *Nat. Biotechnol.*, 17, 1109-1111 (1999).
- [2] M. M. Wang, et. al., *Nat. Biotechnol.*, 23, 83-87 (2005).
- [3] M. Yamada and M. Seki, *Lab Chip*, 5, 1233-1239 (2005).

USING ACOUSTIC DIFFERENTIAL EXTRACTION TO ENHANCE ANALYSIS OF SEXUAL ASSAULT EVIDENCE ON A VALVELESS GLASS MICRODEVICE

Mikael Evander^{*1}, Katie M. Horsman^{*2}, Christopher J. Easley²,
James P. Landers^{2,3}, Johan Nilsson¹ and Thomas Laurell¹

^{*}equal contributors

¹Department of Electrical Measurements, Lund University, Lund, Sweden

Departments of ²Chemistry and ³Pathology, University of Virginia,
Charlottesville, USA

Abstract

The isolation of male and female DNA is an important step in the analysis of sexual assault evidence - a vaginal swab containing both epithelial cells from the female and sperm cells from the male. Forensic DNA analysis requires that the male and female fractions be separated in order to obtain a single-source DNA profile of the suspect. A novel microfluidic method using ultrasonic trapping and laminar flow valving has been developed to achieve this. The method utilizes an acoustic standing wave to retain the male fraction (sperm cells) while mobilizing the female fraction into a separate outlet. The retention of sperm cells was shown to be successful and the laminar flow valving was characterized using a mock sexual assault sample. The extent of the male fraction enrichment was determined using a biological sample containing sperm cells and lysed female epithelial cells, and showed a 16-fold enrichment which made an originally difficult-to-detect male DNA profile more readily detected. The microfluidic format also makes it possible to integrate this method with the downstream processing steps necessary for forensic DNA analysis.

Keywords: Acoustic trapping, differential extraction, forensic science

1. Introduction

The conventional isolation method used in the forensic DNA laboratories, *differential extraction*, is a time-consuming step, requiring up to 24 hours. It is neither highly amenable to automation, nor can it be easily integrated with other steps of the analysis. Therefore, a novel method of performing the isolation of male and female fractions from a biological material associated with sexual assault evidence has been developed; this has been termed Acoustic Differential Extraction (ADE).

2. Experimental

As with the conventional method, vaginal epithelial cells are selectively lysed upon desorption from a cotton swab. The sample, presumably containing sperm cells and female cell lysate, is infused in a 900 µm wide and 70 µm deep microfabricated glass channel. The glass channel is designed to work as a resonator cavity and reflector for the miniature piezoelectric transducers that are mounted at the bottom of the channel, as shown in Figure 1. Upon activation of the ultrasound, the sperm cells will be trapped in a standing wave [1] while free female DNA will not be retained due to its much smaller size. The sperm cells, trapped in the 3D fluidic space above the transducer, can be washed with buffer and the unretained biological material directed to an output

reservoir. Using laminar flow valving [2], the sperm cells can be released and directed into a separate output reservoir in anticipation of DNA analysis (see Figure 2).

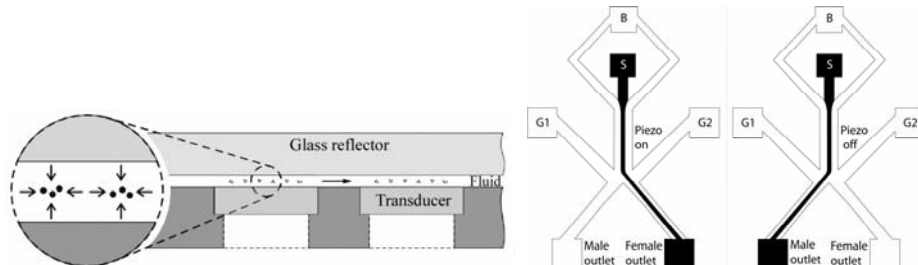


Figure 1: A cross-section schematic of the ultrasonic cell trapping zone. The sample is infused into a glass microchannel. When activating the transducers the sperm cells will be drawn to the pressure minima in the standing wave by the acoustic force field. The cells will be retained over the transducer until it is deactivated and then follow the buffer flow to the outlet reservoir for further analysis.

Figure 2: The sample is infused in inlet S and hydrodynamically focused through the buffer inlet B. Flow ratio control between the side inlets G1 and G2, enables the main flow to be directed either to a male or a female outlet. The laminar flow valving works in a continuous format making external valving obsolete.

With the purpose of evaluating the ADE microdevice for the collection of the two output fractions (male and female), preliminary work used a mock sexual assault sample using polystyrene microparticles to represent the sperm cells and Evan's Blue dye to represent the female cell lysate. The particles were trapped over the transducer and the dye was directed to the female outlet reservoir as shown in Figure 3. After washing the particles, the ultrasound was deactivated and the flow redirected in order to collect the particles in the male outlet reservoir.

A biological sample containing sperm cells and lysed female epithelial cells was subsequently tested by infusion into the device for five minutes while trapping the sperm cells over the transducer. The trapped sperm cells were washed with PBS for five minutes, then released and collected for analysis off-chip. DNA from the isolated cells was extracted using a commercial DNA extraction kit and analyzed with a duplex quantitative PCR assay [3] to show the sample purity. An example of the qPCR data obtained is provided in Table 1.

3. Results and Discussion

The qPCR-assay showed a 16-fold enrichment of the male fraction after the ADE. While the male DNA profile in the original mock sample (5% male) would be overwhelmed by the large mass of female DNA present (95%), ADE enrichment allowed for the sample obtained from the male outlet (85.4 % male) will be a predominately male profile and, therefore, more easily detected and interpreted.

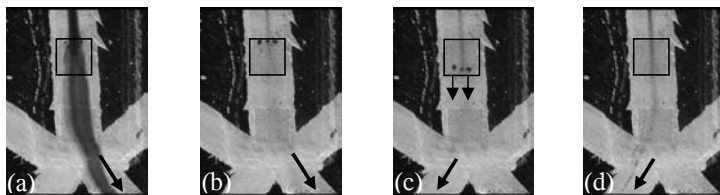


Figure 3: The laminar flow valving was characterized using a simulated sexual assault sample with Evan's Blue representing the female cell lysate and 10 μm polystyrene beads representing sperm cells. In (a), the mixed sample is infused into the device. The beads are trapped above the transducer (outlined) while the dye is washed into the right outlet. After 5 min of sample infusion, the channels are washed with buffer (b). After completed washing the outlet flow is redirected to the left outlet. The movement of the three dark spots between (b) and (c) indicates the release of the particles from the acoustic trap and in (d) the microbeads follow the buffer flow to the left outlet.

Table 1: A duplex quantitative PCR assay, measuring both male and total genomic DNA, was utilized to demonstrate the purity of the recovered fractions. Shown is the percentage of male and female DNA in the original mock sexual assault sample as well as the recovered fractions. A 16-fold enrichment of the male fraction was measured.

	<u>Percent Male</u>	<u>Percent Female</u>
Original Sample:	$5.1 \pm 0.5\%$	$94.9 \pm 9.3\%$
Male outlet reservoir:	$85.4 \pm 5.7\%$	$14.6 \pm 1.0\%$
Female outlet reservoir:	$0.5 \pm 0.04\%$	$99.5 \pm 8.0\%$

4. Conclusions

The results show that acoustic trapping should be exploitable for carrying out differential extraction of male and female fractions from sexual assault evidence. Moreover, highly-enriched male and female fractions can be obtained with the ADE technique, facilitated by laminar flow valving and circumventing the need for active valving. It is likely that this technique can be integrated with downstream chip-based sample processing, i.e., DNA extraction and amplification. Among other advantages, this method could significantly reduce the analysis time, potentially from 24 hours to roughly 60 minutes. The time savings, in combination with the possibility to create a fully automated system, gives the ADE technique the potential to enhance the means by which sexual assault evidence is processed in crime laboratories.

References

- Nilsson, M., Johansson, L. *et al*, *Acoustic trapping of cells in a microfluidic format*. $\mu\text{TAS} 2005$, Boston.
- Blankenstein, G., et al. *Flow switch for analyte injection and cell/particle sorting*. $\mu\text{TAS} 1996$, Basel.
- Horsman, KM., Hickey, JA. *et al*, *Development of a human-specific real time PCR assay for the simultaneous quantitation of total genomic and male DNA*. Journal of Forensic Sciences, 2006. **51**(4): p. 758-765

ISO-DIELECTRIC SEPARATION: A NEW METHOD FOR THE CONTINUOUS-FLOW SCREENING OF CELLS

M.D. Vahey¹ and J. Voldman¹

¹Massachusetts Institute of Technology, USA

Abstract

We introduce the first implementation of a method for the continuous-flow sorting of cells based specifically upon differences in their electrical properties. The method, which we call iso-dielectric separation (IDS), uses the dielectrophoretic (DEP) force in a liquid of spatially varying conductivity to map any electrically distinguishable phenotype to a unique position along the width of a microfluidic channel. The method is analogous to iso-electric focusing, with dielectric properties replacing surface charge as the basis for separation. IDS leverages the correspondence between the physiological state of a cell and its electrical properties to separate cells based upon such characteristics as viability or production of biomolecules [1]. Because IDS selects cells according to their generic electrical differences, it is possible to screen for such production without regard to the specific molecule being produced.

Keywords: Dielectrophoresis, continuous-flow screening, cell separations, conductivity gradient

1. Introduction

Conventional DEP separation methods typically sort cells based upon either the magnitude or the sign of the DEP force [2, 3], and are thus either strongly size-dependent, since the DEP force is proportional to cell volume, or intrinsically binary. Since screens generally involve heterogeneous populations with variations in cell size, these techniques lack the requisite sensitivity. An alternate method, DEP field-flow fractionation [4], balances the gravitational force with DEP levitation to sort cells approximately independent of their size. This approach, however, is not amenable to continuous-flow operation, since cells must be injected and collected in spatially confined plugs, and the separation occurs along the axis of flow. Furthermore, small cells such as bacteria do not settle to the defined heights needed for DEP-FFF. Because IDS offers continuous-flow sorting of particles into a continuum of electrical conductivities, it is possible to resolve highly diverse cell populations into arbitrarily many subpopulations with high throughput, independent of the sizes of the constituent cells.

2. Theory and Design

The IDS device consists of a 10 – 20 μm high PDMS microfluidic channel bonded to a Pyrex chip with gold electrodes patterned on it. Two fluids doped to different electrical conductivities enter the device and are sampled by a diffusive mixer to create a linear conductivity gradient in the separation channel. The cells enter this channel confined to the more highly conducting fluid; this way, the electrodes arranged across

the channel's diagonal serve as an n-DEP barrier, deflecting the cells across the channel in the direction of decreasing conductivity. This continues until the cells are sufficiently close to their iso-dielectric point that the drag force overwhelms DEP, and the cells are carried to one of the device's outlets for collection.

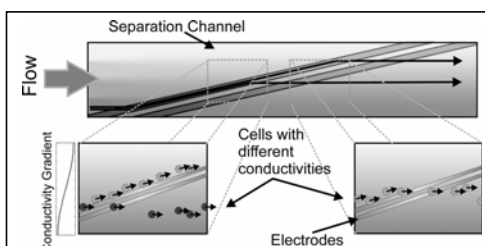


Figure 1: Device concept and operation. Electrodes along the channel's diagonal serve as DEP barriers, forcing cells to traverse the conductivity gradient until the DEP force is overwhelmed by drag and the cells flow downstream for collection.

Coupling between the physical domains relevant to the device's performance complicates the design of the device. We overcome these challenges by leveraging the advantages of microfabrication to create precisely defined geometries with disparate length scales. To maximize both the time over which the gradient attenuates by diffusion as well as the DEP force, we use a wide, shallow channel. Also of importance is the polarization of the electrically heterogeneous fluid by the electric field and the

electrohydrodynamic flows that are induced by this interaction. Confining the electric field to a small fraction of the channel's width results in a locally uniform conductivity and mitigates this coupling.

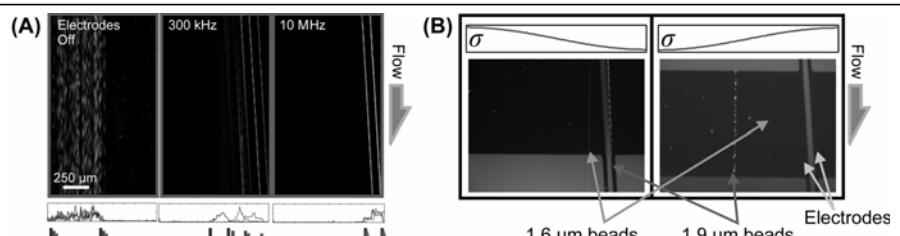


Figure 2: (A) Simultaneous separation of three types of polystyrene beads. (B) Selecting for conductivity in the presence of size variations; reversing the direction of the conductivity reverses the order in which the beads separate.

3. Results and Discussion

We have performed experiments using a broad array of particles and cells, including polystyrene beads, vesicles, and yeast. To demonstrate the analog nature of IDS, we flow three types of beads with different effective conductivities into the device simultaneously; at frequencies between 100 kHz – 1 MHz, we are able to resolve the three subpopulations, as shown in figure 2A. In the absence of a conductivity gradient, the same three beads are not resolved under the conditions of voltage, frequency and flow rate used in our device, suggesting that it is conductivity rather than size that governs the order of separation. This is supported further by the reversal of the IDPs of

two types of polystyrene beads upon reversing the direction of the conductivity gradient and using p-DEP as the basis for separation (figure 2B).

For a biological demonstration of IDS, we separate yeast based upon viability. Heat treatment of the cells compromises their membrane, causing the conductivity of the cytoplasm to decrease, as small ions are no longer confined within the cell [5]. As a result, viable cells exhibit successively higher electrical conductivities as the frequency is increased from ~100 kHz to ~1 MHz. Figure 3 shows the frequency- and conductivity-dependent separation of viable yeast cells from non-viable ones, with optimal separation occurring at ~600 kHz.

4. Conclusions

Technologies for continuous-flow screening of cells are currently in great demand. We have demonstrated through experiments involving both biological and synthetic particles a proof-of-concept for IDS as an emerging method for high throughput screens. The ability to sort cells based upon a phenotypic marker (viability) and perform non-binary separations in a method that is specific to electrical conductivity prepares us to apply IDS to screens of mutant libraries.

Acknowledgements: This work was supported by NIH grant (EB005753), MIT Buschbaum Fund, and the Merck/CSBi Graduate Fellowship.

References

1. Stephanopoulos, G., *Metabolic fluxes and metabolic engineering*. Metab Eng, 1999. **1**(1): p. 1-11.
2. Wang, X.B., et al., *Selective dielectrophoretic confinement of bioparticles in potential energy wells*. Journal of Physics D (Applied Physics), 1993. **26**, p. 1278-1285.
3. Markx, G.H., M.S. Talary, and R. Pethig, *Separation of viable and non-viable yeast using dielectrophoresis*. Journal of Biotechnology, 1994. **32**(1): p. 29-37.
4. Huang, Y., et al., *Introducing dielectrophoresis as a new force field for field-flow fractionation*. Biophysical Journal, 1997. **73**(2): p. 1118-29.
5. Huang, Y., et al., *Differences in the AC electrodynamics of viable and non-viable yeast cells determined through combined dielectrophoresis and electrorotation studies*. Phys. Med. Biol., 1992. **37**(7): p. 1499-1517.

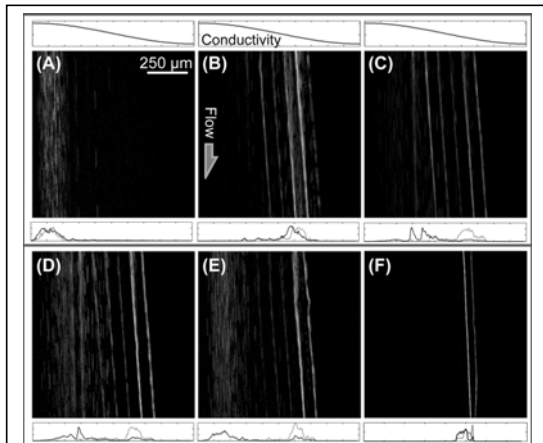


Figure 3: Live/dead separation of yeast using IDS with (A) electrodes off, (B) 200 kHz, (C) 400 kHz, (D) 500 kHz, (E) 600 kHz, and (F) 50 MHz.

LOW-VOLTAGE MICROFABRICATED PUMP BASED ON ELECTROOSMOSIS OF THE SECOND KIND

Trond Heldal¹, Tormod Volden¹, Janko Auerswald², Helmut Knapp²

¹IQ Micro Inc / Osmotex AS, Alpnach, Switzerland

²Swiss Center for Electronics and Microtechnology (CSEM SA), Alpnach, Switzerland

Abstract

A low-voltage micropump with no moving parts and based on standard MEMS fabrication has been developed. The pump has been characterized by pumping a variety of liquids, including de-ionized water, phosphate buffer saline, and aqueous solutions of sugars and alcohols, with pumping speeds up to 2 mm/s. The small power/voltage requirements and dimensions make the pump suitable for portable, embedded and implantable devices.

Keywords: micropump, nonlinear electrokinetics, EO2, low-power

1. Introduction

Based on recent findings in electrokinetics, in particular the discovery of “electroosmosis of the second kind” (EO2) [1], the pump design allows for liquid transport at much lower voltages (2–30 V) and field strengths (1.7 to 40 kV/m) than what is common in conventional electroosmosis and electrophoresis. The non-linearity of the EO2 also enables directed transport using an alternating field, thereby reducing negative effects associated with DC pumping (such as electrolysis, gas-evolution and concentration gradients).

2. Theory

EO2 can be observed at surfaces of unipolar conductors such as ion-exchange polymers, where electric field-induced concentration polarization results in a space-charge layer (see Fig. 1). Using circular geometries, the normal electric field component results in polarization, whilst the tangential component sets the charges in motion. The resulting EO flow is 1–2 orders of magnitude larger than for classical electroosmosis, for a given electric field strength. Other non-linear effects known as “AC electrokinetics” and “induced-charge electroosmosis” [2] are significantly weaker.

3. Experimental

The pump components are all fabricated inside the flow channel, resulting in a highly compact pumping device (see Fig. 2). The first prototype uses a PDMS channel of width 180 µm, height 50 µm and length 15 mm, covered by a glass plate. The driving electrodes, made out of deposited gold structures, are also placed inside the channel, with a spacing of 750 µm. The 3 ion-exchange actuator elements responsible for EO2 are 50-µm beads of sulfonated polystyrene. In another prototype 4 rows of 12 beads in a 780-µm-wide channel were used (see Fig. 3). The third prototype uses 6 molded 200-

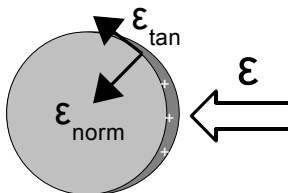


Figure 1. Transport mechanism: The normal electric field component ϵ_{norm} induces a space-charge layer on the ion-exchange element, while the tangential component ϵ_{tan} sets the charges in motion, resulting in EO flow.

μm cylinders (height 50 μm) of sulfonated polyether-ether-ketone (PEEK). Pumping performance was measured on aqueous solutions using fluorescent dyes or microbeads for flow visualization.

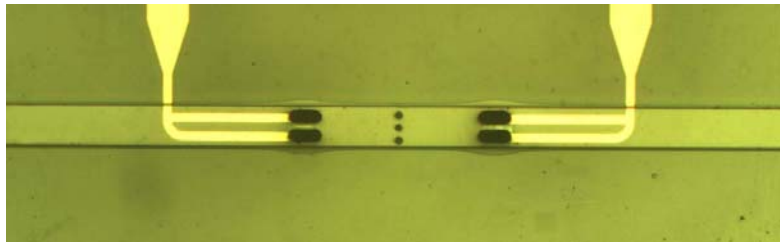


Figure 2. Micrograph of channel section containing the micropump. The active section consists of 50-μm-sized ion-exchange beads. The channel width is 180 μm, height 50 μm (rectangular) and length 15 mm.

4. Results and discussion

Table 1 summarizes the measured results for the first 3-bead prototype, together with the parameters of the electrical driving signal. Flow rates up to 2 mm/s were obtained, a strong pumping action taking the small pump size (area of induced charge approx 1/600 of total channel wall area) and the low driving voltage into account. The 48-bead system

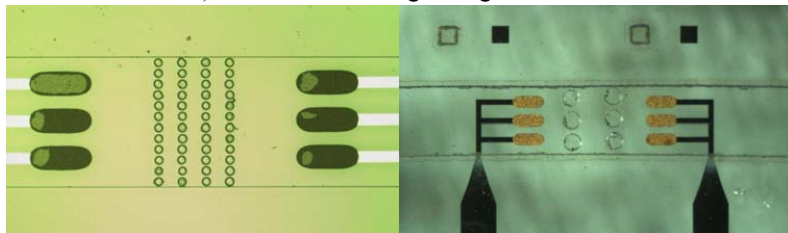


Figure 3. (left) 48-element pump using 50-μm-sized ion-exchange beads. (right) 6-element pump using molded ion-exchange cylinders. Electrode spacing: 1.2 mm.

showed flow rates of 0.01 mm/s for de-ionized water at a voltage of only 2 V

(1.7 kV/m). The somewhat weaker performance of the 6-cylinder system (0.1 mm/s at 10 V) can be explained by the larger distance between the active elements, allowing for backflow between the pumping regions. Generally, higher pumping velocities were obtained for lower frequencies and higher voltages. No degradation of flow was observed after pumping for 4 hours.

Currently, stronger pumps are being developed by adding more active elements and optimizing their structure. Smaller distance between the cylinders is expected to improve the performance of the 6-cylinder system. With the EO2 actuators distributed along the channel cross-section, the pumping effect and the corresponding volume flow scale with the width of the channel. Multiple actuators along the channel length increase the pumping pressure.

Liquids tested	Electric signal	Flow velocity
De-ionized water,	5–10 VDC,	0.01–2 mm/s
ethylene glycol (aq) 36/52%,	15–30 VAC (1–30 Hz)	(approx. 0.1–
methanol (aq) 3/10%,		20 nL/s)
PBS 0.02/0.2/2 mM [Na ⁺]		

Table 1. Pump performance of the first prototype, using liquids for life-sciences, fuel cell and liquid cooling applications. Counter pressure 1–4 mm water head. The AC signal is square-pulse with 20% duty-cycle and offset to obtain a zero DC component.

5. Conclusions

Micropumps based on electroosmosis of the second kind have been fabricated and demonstrated to pump liquids using low AC or DC voltages. Further work involves the use of higher numbers of active elements and optimizing their geometry and spacing to increase the pumping flow rate and pressure.

Acknowledgments

The authors would like to thank Professor Nataliya Mishchuk at the National Academy of Sciences of Ukraine for many helpful discussions. We are very grateful for the micromolding development by Vladislav Spassov. We would also like to thank Francis Cardot, Philippe Niedermann and the COMLAB crew in Neuchatel for their contributions to the microfabrication.

References

1. N.A. Mishchuk, P.V. Takhistov, Colloids and Surfaces A 95 pp. 119–131, (1995).
2. T.M. Squires, M.Z. Bazant, J. Fluid. Mech. 509 pp. 217–252, (2004).

DIRECTIONAL AND FREQUENCY-DEPENDENT FLOW CONTROL IN MICROFLUIDIC CIRCUITS USING PASSIVE ELASTOMERIC COMPONENTS

Christopher J. Easley¹, James M. Karlinsey¹, Daniel C. Leslie¹, Matthew R. Begley³, and James P. Landers^{1,2}

University of Virginia Departments of Chemistry¹, Pathology², and Civil Engineering³; McCormick Rd., Charlottesville, VA 22904, USA

Abstract

Discrete, passive components are shown to provide directional and frequency-dependent control over nanoliter-scale volumes on microfluidic devices. Complex fluidic circuits such as low-pass filters, converters, timers, and bandpass filters are proven functional. Time-responses of such networks can be modulated independently of fluid properties, by varying individual component dimensions and materials.

Keywords: fluidic capacitor, flow rectifier, fluidic timer, flow dampening, band-pass filter

1. Introduction

The design, characterization, and implementation of passive fluidic components for flow shaping represent an important new step towards designing more effective and portable microfluidic circuits. A discrete component for fluid storage and a rectifier for fluid flow are presented and modeled as a fluidic capacitor and fluidic diode, respectively. The passive flow rectifier (diode) is demonstrated to be functional with valve-based micropumps, eliminating the negative flow (pullback) problems typically encountered with these types of pumps. The fluidic capacitor can be used to control the time-response of fluidic circuits, including flow rate and response to cyclic inputs. The combination of these components and conventional microchannels (that function as fluidic resistors) enables fluidic circuits whose flow direction and magnitude can be modulated by changing a single pumping frequency. Thus, networks can be created that function as fluidic frequency filters (e.g. low-pass and high-pass), AC-DC converters, and timers. We propose that these directional and frequency-dependent passive flow control

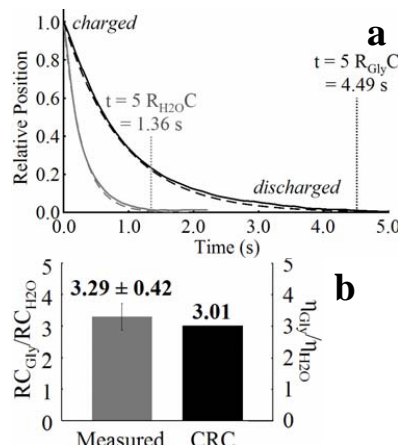


Figure 1. Experimental capacitor decay curves ($n=15$) matched well with predictions. (a) EFPI measurements allowed determination of discharging times ($t=5RC$) of the fluidic circuit and the (c) The ratio of time constants was within error of the viscosity ratios of the solutions, suggesting that the capacitance was independent of viscosity, η .

components provide a powerful complement to active microfluidic valves and may even present novel and robust alternatives to active valving.

2. Theory

With the advent of the microfluidics field, the analogy between electrical and fluidic circuits is gaining new momentum, particularly as electrical circuit simulations have proven effective for predicting microfluidic flow behavior and for designing chips [2-5]. The current work establishes initial design rules for fluidic circuits that enable directional and frequency-dependent control of flow. A commercially-available circuit simulation program was used for modeling and design of these fluidic networks.

Fig. 1A shows the discharging curves of a fluidic capacitor, which were obtained

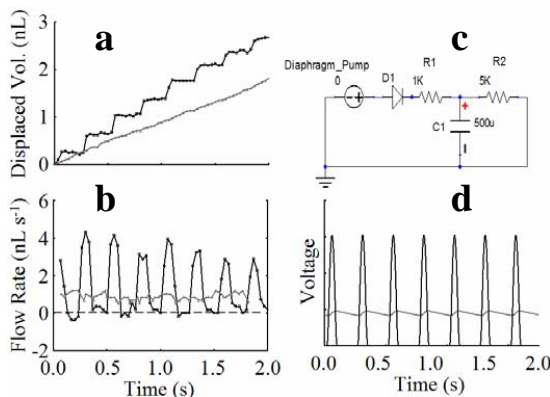


Figure 2. Fluidic low-pass filter or AC-DC converter. (a) Volumetric displacement and (b) flow rate curves before (black) and after (gray) the capacitor show that pulsatile flow was smoothed by the capacitor. A 4.0 Hz input frequency was filtered to an essentially constant flow rate of $\sim 1 \text{ nL}\cdot\text{s}^{-1}$. (c) The electrical circuit analog shows similar behavior when (d) the voltage is simulated with (gray) and without (black) the capacitor.

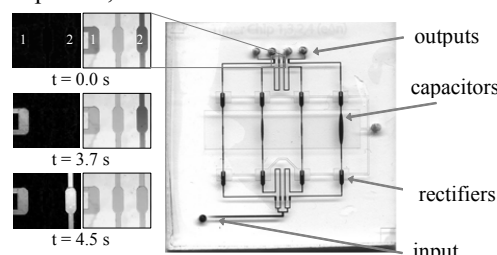


Figure 3. Passive fluidic timing was achieved with only a single syringe pump input using differential fluidic capacitances. The pump was initiated at $t = 0.0 \text{ s}$, at which time no flow was seen. At $t = 3.7 \text{ s}$, the smaller capacitor (channel 1) was charged, and flow was seen to break through the exit diode. The larger capacitor (channel 2) followed at $t = 4.5 \text{ s}$.

3. Experimental

The three-layer device configuration utilized in this work was adapted from the work of Grover et al. [7], including the normally-closed elastomeric valves utilized in portions of the work.

by measuring the poly(dimethylsiloxane) (PDMS) membrane deformation via extrinsic Fabry-Perot interferometry (EFPI) [6]. Such measurements match well with predicted behavior, with the ratio of time constants for water and 30% glycerol solutions ($n = 15$) independent of viscosity (Fig. 1B). This illustrates that the fluidic capacitance depends only on the membrane compliance, and hence can be modulated independently of the solution characteristics [5].

4. Results and Discussion

Combinations of these passive components provide the flexibility to create novel fluidic circuits. By combining a flow rectifier (diode) with the capacitor and resistor network, a microfluidic flow converter (from pulsatile to constant flow rate) was demonstrated (**Fig. 2a-b**) and shown to be in agreement with the AC-DC converter circuit model (**Fig. 2c-d**). This type of fluidic circuit provides the ability to use an on-chip cyclic pump to generate smooth (non-pulsatile) flow. The components were also arranged to achieve entirely passive fluidic timing in the absence of external actuation (e.g., vacuum- or pressure-based valving), eliminating the need for an active component (**Fig. 3**). Finally, the fluidic capacitor was used to tune the frequency-dependence of fluidic circuits (**Fig. 4a-b**), with the fluidic network shown to behave as a band-pass filter. As shown in **Fig. 4b**, the characteristic frequencies of fluidic networks can be shifted by altering the RC values using individual passive components. With further characterization of this frequency-dependent control, it should be possible to accurately meter flow rates and directionality with a single input source, eliminating the need for the overwhelming instrumentation that is typically necessary for microfluidic valving [1].

Acknowledgements

Funding for this work was provided through the American Chemical Society Division of Analytical Chemistry (ACS-DAC) in cooperation with Eli Lilly and Co.

References

- [1] T. Thorsen, S. J. Maerkl, S. R. Quake, *Science*, **298**, 580 (2002).
- [2] A. Ajdari, *C. R. Physique*, **5**, 539 (2004).
- [3] S. Attiya, A. B. Jemere, T. Tang, G. Fitzpatrick, K. Seiler, N. Chiem, D. J. Harrison, *Electrophoresis*, **22**, 318 (2001).
- [4] C. J. Easley, J. M. Karlinsey, J. P. Landers, *Lab on a Chip*, **6**, 601-610 (2006).
- [5] D. Kim, N. C. Chesler, D. J. Beebe, *Lab on a Chip*, **6**, (2006).
- [6] C. J. Easley, L. A. Legendre, M. G. Roper, T. A. Wavering, J. Ferrance, J. P. Landers, *Anal. Chem.*, **77**, 1038 (2005).
- [7] W. H. Grover, A. M. Skelley, C. N. Liu, E. T. Lagally, R. A. Mathies, *Sensors and Actuators B*, **89**, 315-323 (2003).

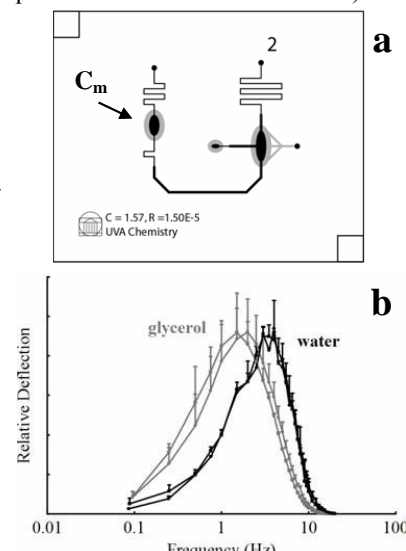


Figure 4. Fluidic band-pass filter. (a) The device design with the larger measurement capacitor (C_m) is shown here. (b) Frequency response curves (via EFPI) of devices with different C_m values. Note that the fundamental frequencies of the network was shifted due to the change in flow resistance.

GOLD MICROWIRE BRUSHES FROM NANOPARTICLE SUSPENSIONS FOR MAGNETOHYDRODYNAMIC PUMPING IN MICROFLUIDIC CHIPS

Jian-Bin Bao and D. Jed Harrison

Department of Chemistry, University of Alberta,
Edmonton, AB T6G 2G2, Canada

Abstract

We report an *in situ* technique for assembling conductive, gold microwires from nanoparticle (20 nm diameter) suspensions by applying a pulsed or ramped dc voltage. Nucleation at the anode results in dendritic growth of mobile microwires that can serve as electrical brushes between electrodes spaced up to 100 μm apart. When exposed to a magnetic field, the microwires experience a Lorentz force and are able to slip along the electrodes. The moving microwires drag the liquid in the microchannel and create a magnetohydrodynamic pump.

Keywords: Magnetohydrodynamic pumping, nanoparticle, microwire, self-assembly

1. Introduction

Magnetohydrodynamic (MHD) pumping has a potential for wide application in microfluidics, particularly in liquid chromatography and in microchips for NMR sample delivery. However, the large current density ($>100 \text{ mA/mm}^2$) required causes electrolysis of the solvent and evolution of gases, which usually disrupts flow in a microfluidic system. We describe the use of gold nanoparticle suspensions to create a highly conductive medium for MHD, in which high DC current densities can be generated at sufficiently low voltages to avoid inducing electrolysis of the solvent.

2. Experimental

A sandwich cell or open cell was fabricated to evaluate nucleation. Unipolar or bipolar voltage pulses or a continuously scanned voltage was applied to a gold nanoparticle suspension (0.5–2.5 wt. %) in the cell. The voltage was increased in intervals of 0.1 V (for the pulsed mode) or at a rate of 20 mV/sec (for the scanned mode), and the current was determined from the voltage drop across a resistance until a current jump was observed, from which we obtained a wiring voltage.

For MHD pumping, a mixture of nanoparticle and fluorescent bead suspension was injected in an electromagnetic channel (EMC) placed above a permanent magnet. When voltages were applied to the EMC, movement of the fluorescent beads, indicating flow

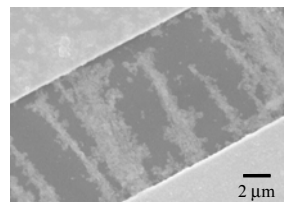


Fig. 1. SEM of microwires formed between electrodes on the walls of a fluidic channel.

in the channels, was recorded by CCD camera and the velocity was estimated from these movies, as done by Lemoff and Lee [1].

3. Results and Discussion

The mechanism of high conductivity of gold nanoparticle suspensions involves electrohydrodynamically induced nucleation and growth of microwires from the nanoparticles (Fig. 1). The microwires are sufficiently dynamic in nature to act as electrical brushes between the two sides of a flow channel, allowing high current densities, while being mobile enough to drag solvent with the wires as they are transported by the Lorentz force in the device, shown in Fig. 2. Motion due to the Lorentz force may break or bend the microwires, reducing surface contacts, or may

reduce the extent of their formation. Fig. 3 shows a drop in resistance of $\sim 1\%$ is observed when the magnetic field is abruptly removed from an electromagnetic channel.

The assembly of microwires from gold nanoparticle suspensions first requires a nucleation process. Sandwich cells were designed to evaluate nucleation. For a 2.5 wt. % gold nanoparticle suspension, the wiring voltage was 2.1 V (Fig. 4). For the same system, if unipolar voltage pulses or a continuously scanned voltage was applied, the wiring voltages increased to 2.7 V (Fig. 4). As the nanoparticle concentration increases (Fig. 5) or the spacing between electrodes decreases (Fig. 6), the

initial wiring voltage decreases. We also lowered the wiring voltage by enhancing the nucleation process. For instance, with silver as the electrodes, a voltage higher than 0.8 V injects silver ions in the vicinity of the anode, creating wires at

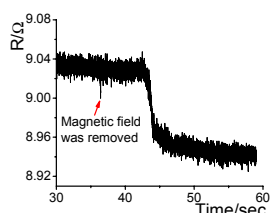


Fig. 3. The microwires were first assembled under a 0.5 T magnetic field in a 10 μm wide channel. When the field was removed, the resistance dropped about 1%.

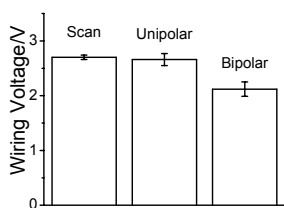


Fig. 4. Comparison of the experimental wiring voltages for 2.5 wt. % suspensions, obtained from sandwich cells.

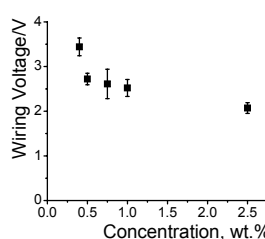


Fig. 5. Wiring voltages versus the concentration of the nanoparticle suspension.

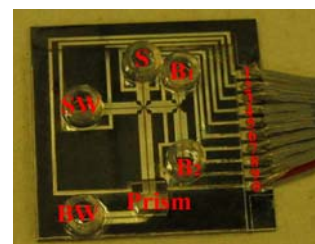


Fig. 2. Finished nano-MHD activated open-tubular LC chip (34 mm \times 34 mm). Flow velocities were measured in this device. Individually addressing each arm allowed control of the direction of flow at the intersection.

lower voltages (Fig. 6). Roughened electrode surfaces cause a non-uniform electric field that induces dielectrophoresis that enhances the assembly. Fig. 7 shows a drop of the wiring voltage with an asymmetric device when the dc dielectrophoretic effect is in the same direction as electrophoretic forces (tip + V). While the wires exhibit dendritic growth (see Fig. 1), wire formation is clearly not related to a Faradaic process, as it occurs at the anode rather than the cathode.

The MHD pumping velocity is inversely proportional to the microchannel cross-sectional area, therefore MHD pumping performance should be evaluated on the basis of linear flow rate per unit cross section. A pumping velocity of 0.1-0.2 mm/sec was realized by applying a DC voltage lower than 0.5 V to a gold nanoparticle suspension (1 wt. %) under a perpendicular DC magnetic field (~ 0.5 T). The velocity/cross section obtained from our nano-MHD is 10 times higher than those reported previously using electrolyte solutions as the working fluids [1-3].

4. Conclusions

The assembly of Au nanoparticles using a dc electric field into movable, conducting microwire brushes is previously unreported. The mechanism of wire formation and subsequent MHD pumping action is not fully understood, but the results are consistent with electrohydrodynamic flow and electrophoretic forces playing a significant role. The use of microwire brushes with MHD-pumped microfluidic devices is very promising, allowing the use of convenient permanent magnets and low voltages, so as to avoid electrolysis and heating due to eddy current effects. The operating voltage of the nano-MHD is in the range of a personal computer (PC) power supply. We could embed nano-MHD chips into a PC or integrate microfluidics and electronics into a single chip.

References

1. Lemoff, A. V., Lee, A. P. *Sens. Actuators B* **63**, 178-185 (2000).
2. Eijkel, J. C. T. et al. *Sens. Actuators B* **92**, 215-221 (2003).
3. Homsy A. et al. *Lab Chip* **5**, 466 - 471 (2005).

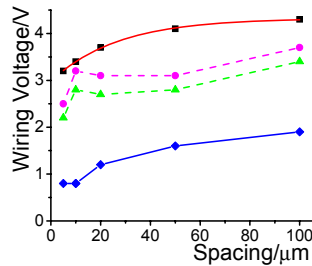


Fig. 6. Wiring voltages obtained from symmetric devices with different spacing. The top curve: fresh gold electrodes; bottom curve: fresh silver electrodes; dashed curves: gold electrode devices regenerated by ultrasound.

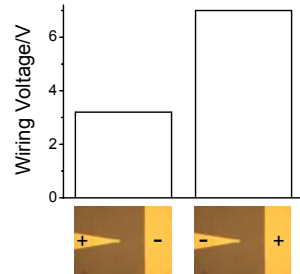


Fig. 7. Comparison of the wiring voltages obtained from asymmetric gold cells using a unipolar scanning method.

ON-CHIP CELLOMICS ASSAY: ARTIFICIAL RE-CONSTRUCTION OF TISSUE MODEL FOR CELL BASED DRUG DISCOVERY

Kenji Yasuda

Institute of Biomaterials and Bioengineering,
Tokyo Medical and Dental University
2-3-10 Kanda-Surugadai, Chiyoda-ku, Tokyo 101-0062 JAPAN
(e-mail: yasuda.bmi@tmd.ac.jp)

Abstract

We began a series of studies aimed at developing methods and systems of analyzing epigenetic information in cells, as well as that of genetic information, to expand our understanding of how living systems are determined. The role of epigenetic information on cells, which complements their genetic information, was inferred by comparing predictions from genetic information with cell behaviour observed under conditions chosen to reveal adaptation processes and community effects. A system of analyzing epigenetic information was developed starting from the twin complementary viewpoints of cell regulation as an 'algebraic' system (emphasis on temporal aspects) and as a 'geometric' system (emphasis on spatial aspects). The knowledge acquired from this study may lead to the use of cells that fully control practical applications like cell-based drug screening and the regeneration of organs.

Key words: **on-chip cellomics assay, epigenetic information, algebraic viewpoint, geometric viewpoint, photo-thermal etching, agarose microchamber array, multi-electrode array (MEA), synchronization, inheritance, adaptation, variability, individuality.**

1. Introduction

Knowledge about living organisms has increased dramatically during the 20th century and has produced the modern disciplines of genomics and proteomics. However, despite these advances, a great challenge remains in learning how the different living components of a cell are integrated and regulated. As we move into the post-genomic period, the complementarity of genomics and proteomics will become more apparent, allowing the connections between them to be exploited. However, neither genomics nor proteomics based only on genomic information can provide the knowledge needed to interconnect molecular events in living cells. The cells in a group are individual entities, and differences arise even among cells with identical genetic information that have grown under the same conditions. These cells respond differently to perturbations [1]. Why and how do these differences arise? Cells are minimum units determining their responses through genetic and epigenetic information like the history of interactions between them and fluctuations in environmental conditions affecting them. To

understand the rules underlying possible differences occurring in cells, we need to develop methods of simultaneously evaluating both the genetic and epigenetic information. In other words, if we are to understand adaptation processes, community effects, and the meaning of cell network patterns, we need to analyze their epigenetic information. We thus started a project focusing on developing a system that could be used to evaluate the epigenetic information in cells by continuously observing specific examples and their interactions under controlled conditions. The importance of understanding epigenetic information is expected to become apparent in cell-based biological and medical fields like cell-based drug screening and the regeneration of organs from stem cells, fields where phenomena cannot be interpreted without taking epigenetic factors into account.

We started a study on the “determination of genetic and epigenetic control processes in cells” using on-chip microfabrication techniques and cell-based analysis [2]. To understand the meaning of genetic information and epigenetic correlation in cells, we developed an on-chip single-cell-based microcultivation method. As we can see in Fig. 1, the strategy behind our method is constructive, involving three steps. First, we purify cells from tissue one by one in a nondestructive manner. We then cultivate and observe them under fully controlled conditions (e.g., cell population, network patterns, or nutrient conditions) using an on-chip single-cell cultivation chip or an on-chip agarose microchamber system. Finally, we do single-cell-based expression analysis through photothermal denaturation and single-molecule level analysis. In this way, we can control the spatial distribution and interactions of cells.

In this meeting, we explain the aims of our single-cell-based study and the single-cell-based cultivation/analysis system.

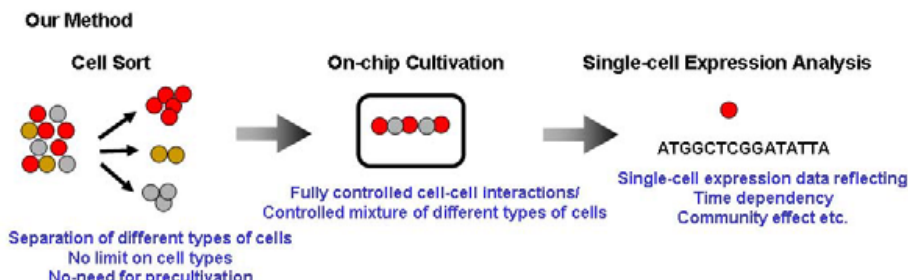


Figure 1. Our strategy: on-chip single-cell-based analysis.

2. Why on-chip cellomics assay? : Cultivation system for ‘algebraic’ and ‘geometric’ viewpoints

The first aim of our on-chip cellomics study is to develop methods and systems that enable the mechanism responsible for controlling (regulating) cells epigenetically to be analyzed. It is based on the idea that, although genetic information creates a network of biochemical reactions, its history as a parallel-processing recurrent network was

ultimately determined by the environmental conditions of cells, which we call epigenetic information. As previously discussed, if we are to understand the events in living systems at the cellular level, we need to bear in mind that epigenetic information complements the genetic information.

The advantage of this approach is that it removes the complexity in underlying physicochemical reactions that are not always completely understood and for which most of the necessary variables cannot be measured. Moreover, this approach shifts the view of cell regulatory processes from a basic chemical ground to a paradigm of the cell as an information-processing unit working as an intelligent machine capable of adapting to changing environmental and internal conditions. This is an alternative representation of the cell and can bring new insights into cellular processes. Thus, models derived from such a viewpoint can directly help in more traditional biochemical and molecular biological analyses that assist in our understanding of control in cells.

The main purpose of the study was to develop on-chip single-cell-based cultivation and analysis systems to monitor dynamic processes in the cell. We have used these systems to extend ideas from the genetic to the genetic-epigenetic network in investigating topics like variations in cells with the same genetic information, inheritance of non-genetic information between adjacent generations of cells, cellular adaptation processes caused by environmental change, the community effect of cells, and network pattern formation in cell groups (Figs. 2 and 3). After sufficient experimental observations, we can understand the role of epigenetic information in modeling more complex signaling cascades. This field has almost been entirely monopolized by physico-chemical models, which provide a good standard for comparison, evaluation, and development with our approach. The ultimate aim of our study is to provide a comprehensive understanding of living systems as products of both genetic and epigenetic information. It would permit us to describe the phenomena occurring in cell systems sufficiently well to be able to interpret and control them.

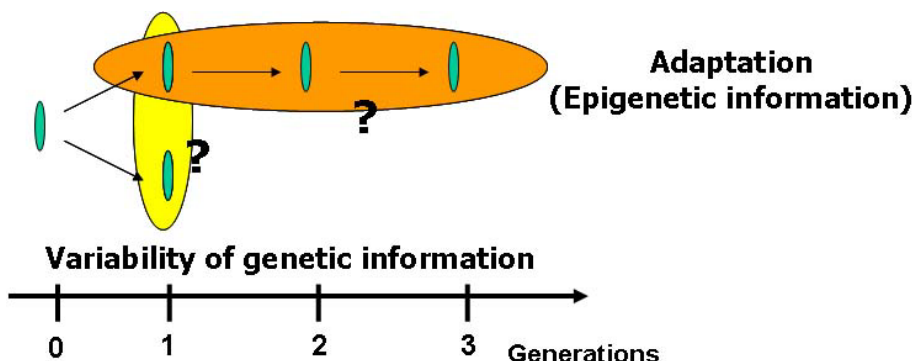


Figure 2. Aim of the single-cell based analysis (1): temporal aspect.

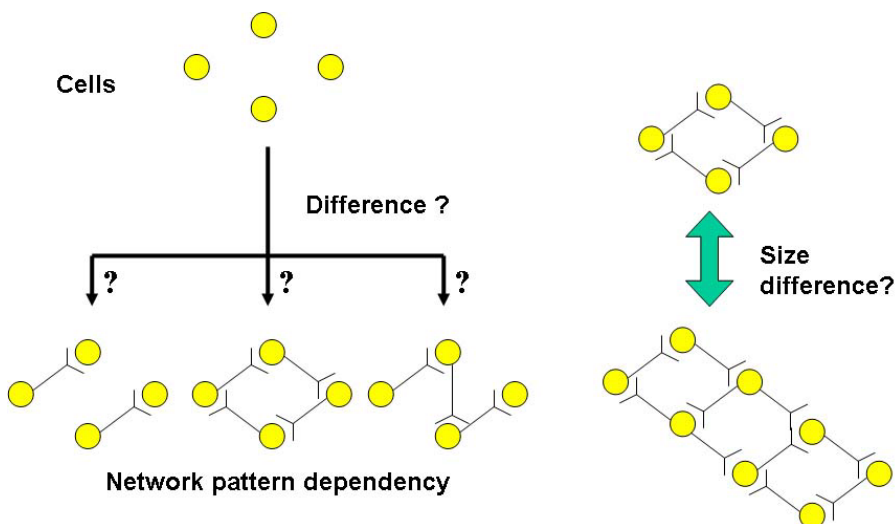


Figure 3. Aim of single-cell-based analysis (2): spatial aspect.

3. Example of ‘geometric’ viewpoint: On-chip agarose microchamber cultivation system

An approach to studying network patterns (or cell-cell interactions) and the community effect in cells was to create a fully controlled network by using cells on the chip (Fig. 3). For understanding the reaction of cells to the topography of the substratum, which occurs in the development and natural regeneration of tissue, a silicon wafer and a glass slide with holes and metal decorations have been created and tested. Though these conventional microfabrication techniques provide structures with fine spatial resolution, it is still hard to change the shape of these structures during cell cultivation, which is usually unpredictable and is only defined during cultivation. A variety of materials and several well-known methods, including bonding, sacrificial layer techniques, and lamination have been used to create tunnel-shaped microstructures between two microchambers. Creating small tunnels to connect two chambers without cells passing through is essential in cell cultivation. However, making these microstructures on a chip still requires a number of steps, and it is impossible to do during cell cultivation. We therefore developed a system consisting of an agar-microchamber (AMC) array chip, a cultivation dish with a nutrient-buffer-changing apparatus, a permeable cultivation container, and a phase-contrast/fluorescent optical microscope with a 1064-nm/1480-nm focused-laser-irradiation apparatus to create photothermal spot heating (Fig. 4). The most important advantage of this system was that we could change the microstructures in the agar layer even during cultivation, which is impossible when conventional Si/glass-based microfabrication techniques and microprinting methods are used.

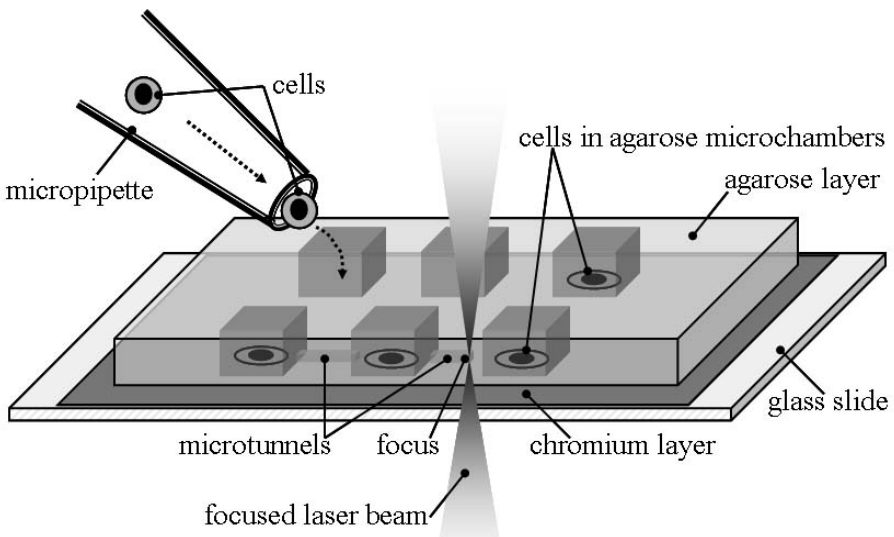


Figure 4. Agarose microchamber cell cultivation system with photo-thermal etching.

Figure 5 shows an example of this procedure. The micrographs are phase-contrast images of the growth of single hippocampal cells in three of the microchambers. When cultivation started, single cells were placed into the AMCs (Fig. 5(a)). Six hours later, single neurites elongated from the cells into the microchannels (Fig. 5(b)). At that time, because we found that the elongation of neurites was sufficiently stable, additional photo-thermal etching were done to connect two adjacent AMCs (Fig. 5(c)). Two hours after the additional photo-thermal etching (8-h cultivation), all three cells retained their shapes and continued the elongation (Fig. 5(d)). Finally, these three cells were connected counter-clockwise by the neurites. (Figs 5(e) and (f), 14 and 28-h cultivation). In contrast, if we had not used stepwise photo-thermal etching, cells in microchambers with two tunnels would have elongated both clockwise and counter-clockwise simultaneously and we would not have been able to distinguish in what direction the neurites had elongated.

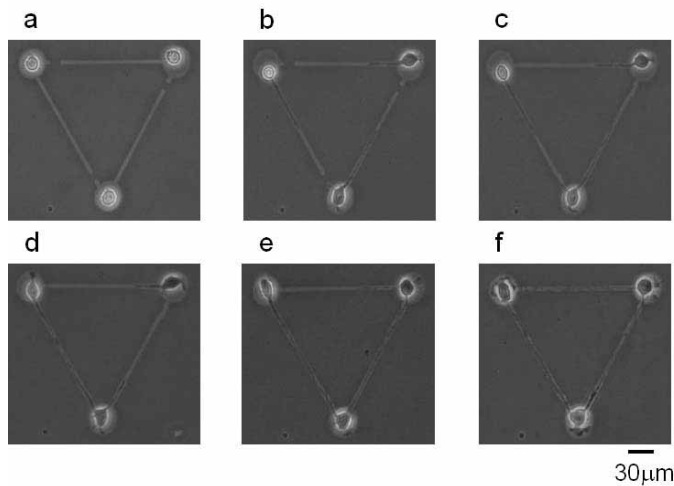


Figure 5. Stepwise formation of neuronal network pattern in rat hippocampal cells.

4. Conclusion

We developed and used a series of new methods of understanding the meaning of genetic and epigenetic information in a life system exploiting microstructures fabricated on a chip. The most important contribution of this study was to be able to reconstruct the concept of a cell regulatory network from the 'local' (molecules expressed at certain times and places) to the 'global' (the cell as a viable, functioning system). Knowledge of epigenetic information, which we can control and change during cell lives, complements the genetic variety, and these two kinds are indispensable for living organisms. This new kind of knowledge has the potential to be the basis of cell-based biological and medical fields like those involving cell-based drug screening and the regeneration of organs from stem cells.

Acknowledgements

The author acknowledges the assistance of all members of the Yasuda Lab. Financial support, in part by the Japan Science and Technology Agency (JST) and by Grants-in-Aids for Scientific Research from the Ministry of Education, Culture, Sports, Science and Technology of the Japanese government, is gratefully appreciated.

References

1. JL Spudich, DE Koshland Jr, *Non-genetic individuality: chance in the single cell*. Nature 1976, 262: 467-471.
2. K. Yasuda, Ch. 9 *On-chip single-cell cultivation systems: Enabling Algebraic and Geometric Understanding of Cells*. Lab-on-Chips for Cellomics (ed. Helene Andersson and Albert van den Berg), Kluwer Academic Publishers, Netherlands. (2004) .

GENERATION AND DELIVERY OF MONODISPERSE PICO-LITER DROPLETS OUT OF PDMS MICROCHIP INTO ACCELERATOR MASS SPECTROMETRY (AMS)

**Sung Jae Kim¹, Yong-Ak Song^{1,2}, Paul L. Skipper²,
Steven R. Tannenbaum², and Jongyoon Han^{1,2}**

¹Department of Electrical Engineering and Computer Science,
²Biological Engineering Division, Massachusetts Institute of Technology, USA

Abstract

We have developed a drop-on-demand microdroplet generator for the discrete dispensing of bio-samples into a bio-analytical unit, Accelerator Mass Spectrometry (AMS). The disposable PDMS microfluidic device can generate monodisperse droplets of pico-liter volume directly out of a plane sidewall of the microfluidic chip by an electrohydrodynamic mechanism. The droplet generation was accomplished without using either an inserted capillary or built-in tip. The minimum droplet volume was around 4 pico-liters, and the droplet generation was repeatable and stable for at least 30 minutes, with a typical variation of less than 2.0% of drop size. A computational simulation of the droplet generation verified the importance of controlling the surface wetting conditions for the droplet formation. Our microdroplet generator can be effective interfacing mechanism from a microfluidic chip to a non-chip bio-sensing unit, such as AMS or MALDI-MS.

Keywords: Microdroplet generator, drop-on-demand dispenser, EHD, PDMS microchip, AMS

1. Introduction

Dispensing a discrete amount of sample from microfluidic devices to macroscopic detectors such as Mass Spectrometry (MS) is an important world-to-chip coupling problem [1]. Among various MS techniques, AMS is ideally suited for direct coupling with microfluidic sample preparation devices, due to its high sensitivity in the order of attomole to zeptomole [2]. However, the current method for AMS sample injection requires manual dispensing of more than 1 μl sample volume. To address this issue, we have developed a pico-liter droplet dispenser as a discrete sample injection interface. It is a disposable PDMS device which generates regularly-sized droplets electrohydrodynamically, directly out of a microfluidic channel of the PDMS chip. No sophisticated ejection tip and external pumping is necessary for operation, and it is scalable to incorporate delivery of multiple samples from a single chip.

2. Experiment

In order to fabricate the droplet generator, the general PDMS chip fabrication process was used. Figure 1(a) shows the schematic of the PDMS chip. Two different types of the microchannels were built; A straight channel (Type I) with a dimension of 15 $\mu\text{m} \times$

$20 \mu\text{m} \times 5 \text{ mm}$ and a widened microchannel toward the opening (Type II) with a dimension of $20 \mu\text{m} \times 25 \mu\text{m} \times 5 \text{ mm}$. The opening of the second microchannel was expanded from $25 \mu\text{m}$ to $50 \mu\text{m}$ in width at an angle of 75 degrees. Both microchannels were covered by a separate PDMS plate containing a wedge shape with an inclined angle of 20 degrees. This wedge shape was to reduce the surface at the opening of the channel, thus minimizing the contact area between the sample liquid and the side wall. After bonding, the orifice of the device was coated with Teflon AF 1600 by brushing it over the PDMS surface. The coating provided a hydrophobic surface with a contact angle of ~ 110 degrees. Figure 1(b) provides a schematic illustration of the microdroplet generator system and the assembled system is shown in Figure 1(c).

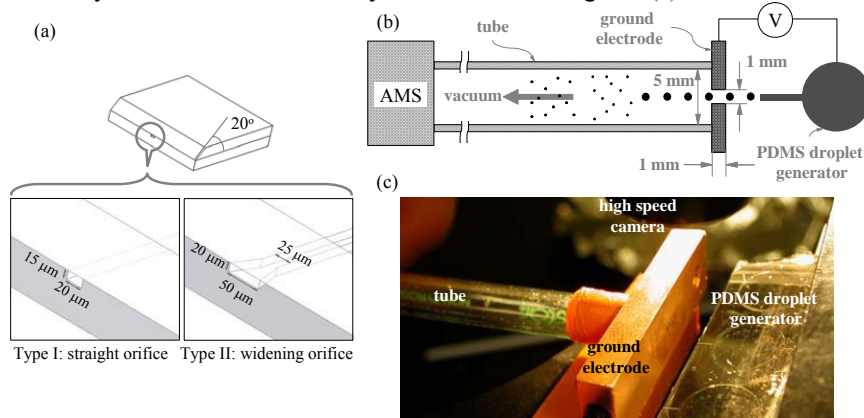


Figure 1. Schematic illustration of (a) two types of microdroplet generators; Type I with a straight channel and Type II with a widening exit at the end of the channel, and (b) experimental setup. The assembled system is shown in (c).

3. Results and Discussion

As shown in Figure 2(a), the Taylor cone-like structure was observed in the device without hydrophobic coating. In contrast, monodisperse droplets were generated from the Teflon-coated devices due to the low surface wettability as shown in Figure 2(b).

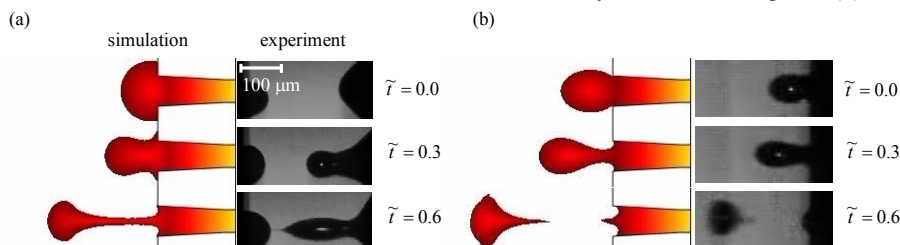


Figure 2. Numerical simulation and experimental results of the droplet generation from (a) a non-coated PDMS surface and (b) a Teflon-coated surface as a function of the dimensionless time unit.

Such a Taylor-cone like structure was found, both from experiments and numerical simulation, to generate instability and diversity in droplet size, due to a long tail behind the generated droplet. We have characterized the droplet generation process for various electric fields and solvent conditions. Figure 3 shows the generation of 0.1% acetic acid droplet which is a common solvent for AMS application.

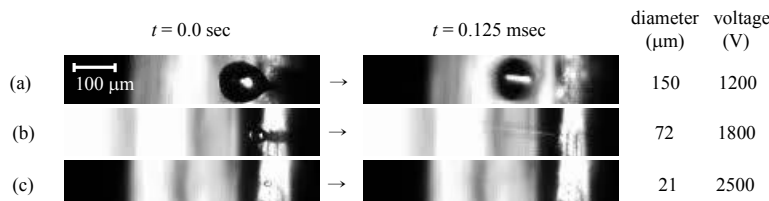


Figure 3. Generation of droplets with 0.1% acetic acid solution at a chip-to-electrode gap of 1 mm. Type I generator with Teflon coating was used.

Due to its lower surface tension compared to DI water ($\sigma_a \approx 50 \text{ dyne/cm}$ versus $\sigma_w = 71.97 \text{ dyne/cm}$), the droplets were formed without creating any sample residual tails at the outlet even in case of extremely small droplets. The minimum droplet size was ~ 4.2 pico-liters, and droplets were delivered horizontally, through the ground electrode opening into the tube, as far as 3cm. The droplet generation was repeatable and stable for hours, with a typical size variation of the drop size of less than 2.0%. The channel-geometry-enhanced droplet generation using Type II generator lasted for about 30 minutes without external pumping. The results obtained with various cosolvents are shown in Figure 4. This method is a low-cost droplet delivery method, which could find many uses in various microchip-to-world interfacing.

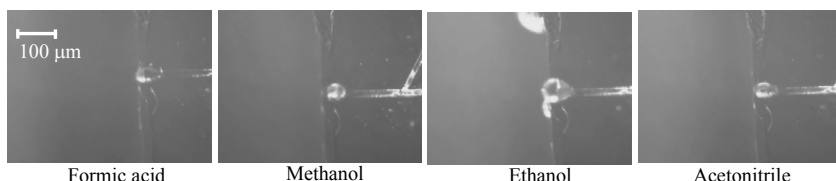


Figure 4. Microdroplet generation of various cosolvent solutions (0.1%) without external pumping. Type II generator with Teflon coating was used.

Acknowledgements

This work was supported by Grant R42CA084688 from the National Institutes of Health. S. J. Kim was partially supported by Samsung Electro Mechanics.

References

1. E. R. Lee, *Microdrop Generation*, CRC press, chapter 2-4, (2003).
2. R. G. Liberman, S. R. Tannenbaum, B. J. Hughey, R. E. Shefer, R. E. Klinkowstein, C. Prakash, S. P. Harriman, and P. L. Skipper, *Anal. Chem.*, **76**, pp. 328-334, (2004).
3. D. A. Saville, *Annu. Rev. Fluid Mech.*, **29**, pp. 27-64, (1997).

DIFFUSION-BASED FREE SOLUTION DNA HYBRIDIZATION AND TRANSPORT IN A NANOFUIDIC DEVICE

Sumita Pennathur¹, David Huber¹, Steve Rieu² and Kamlesh D. Patel¹

¹Sandia National Laboratories, Livermore, CA

²Brown University, Providence, RI

Contact e-mail: spennat@sandia.gov

Abstract

We report numerical, and experimental studies of diffusion-based, free-solution hybridization of nucleic acids in a nanofuidic device. We present continuum-based models for transport of oligonucleotides in a nanofuidic T-junction serpentine channel.

Keywords: DNA hybridization, nanofuidics, diffusion, NEMS

1. Introduction

Nucleic acid hybridization assays are essential tools for gene identification, genetic expression analysis, DNA sequencing, and clinical diagnostics. They are also expected to provide improvements in bioanalytical methods for pathogen detection and drug screening. Currently, the most common DNA hybridization assays use surface-bound probes and passive, diffusion-limited hybridization, which require large amount of DNA and long hybridization times[1]. Nanofuidic devices have a distinct advantage over conventional devices in that samples are confined to regions that are orders of magnitude smaller. Therefore, DNA hybridization studies within nanofuidic devices have the potential not only to decrease sample volumes, but also to reduce the time for target DNA to encounter its complement probe by a million-fold. Additionally, nano-confinement allows for the hybridization assay to occur in free-solution, so that there is no need to attach DNA probes to the surface, resulting in both a highly reusable architecture and improved hybridization efficiency [2].

2. Theory

Numerical simulations using our channel design are preformed using Comsol Multiphysics (Comsol, Inc.). Initial results suggest that, for submicron-scale fluidic channels, the diffusion and hybridization times for oligonucleotides to sample the width of a 50 nm x 50 nm cross-sectional channel is less than 500 s and 500 ms, respectively (Figure 1). In practice, oligonucleotides in nanofuidic devices have size-dependant diffusion coefficients and mobility values directly related to steric interactions with the

walls [3]. Therefore, experimental studies of transport, diffusion, and hybridization of free-solution DNA in a nanofluidic device are performed not only to validate the theoretical models, but also to provide data to estimate effective diffusion and mobility values for oligonucleotides of various lengths.

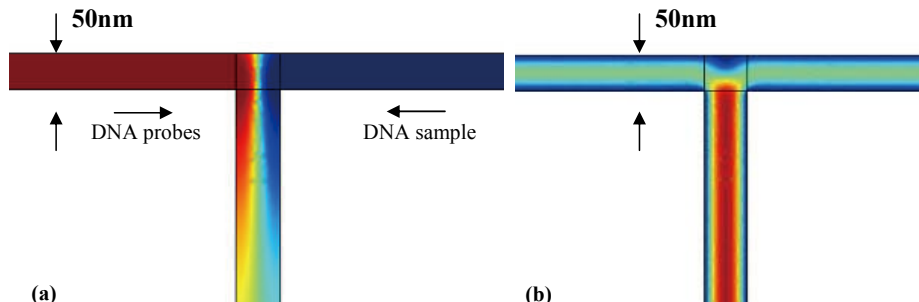


Figure 1. Numerical simulations of (a) concentration and (b) velocity profiles in a 50 nm x 50 nm nanometer sized fluidic channel with pressure-driven flow. Red regions indicate DNA probes (a) or regions of high velocity (b) while blue regions indicate DNA sample (a) or regions of lower velocity (b).

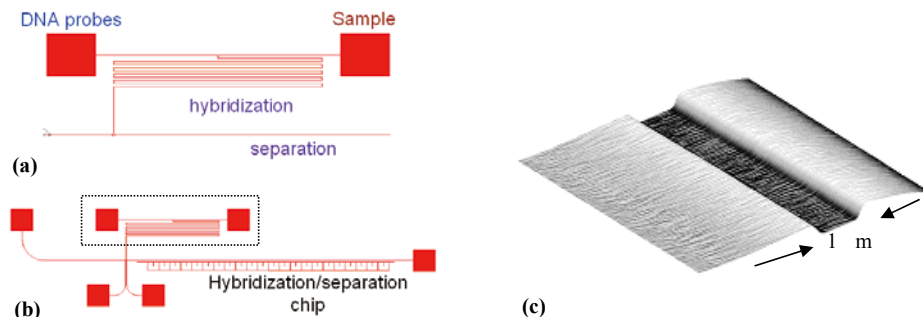


Figure 2: Schematic of DNA hybridization nanochannel device (a)-(b). The hybridization section of the device is shown in greater detail in (a). Tick marks are etched below the nanochannel separation region to aid in registration and quantization. (c) shows an Atomic force microscopy image of 50 nm deep x 1 m wide nanometer-scale channel. The image is representative of both the hybridization and separation parts of the channel.

3. Experimental

Nanofluidic devices were fabricated using conventional MEMS processing techniques in quartz substrates with nominal depths of 50, 250, and 1000 nm. (Figure 2) The interdiffusion and resulting hybridization of 10-100 bp DNA from the two liquid

streams is monitored optically using YOYO[®] intercalating fluorescent dye, a 488 ion-argon laser and/or mercury bulb with appropriate filter, and a CCD Camera (Cascade, Roper Scientific), allowing measurements of DNA concentrations on a continuous basis. From these measured concentrations, free solution size-dependent diffusion coefficients and mobility values of confined oligonucleotides are presented.

4. Results

The models and data demonstrate that the effective diffusion and mobility governing oligonucleotide hybridization and transport in nanochannels depends not only on bulk mobility and diffusion values but also on oligonucleotide length, bulk velocity, zeta potential, and background electrolyte concentration (Figure 3).

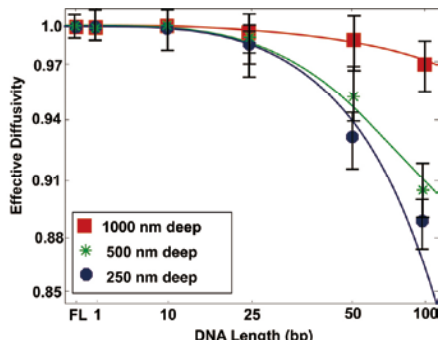


Figure 3: Nanochannel DNA diffusion model plotted against different values of DNA base pair length. Data values taken in 1000, 250, and 50 nm deep nanochannels with oligonucleotide lengths of 1 base (UTP), 10 bp, 25bp, 50bp, and 100bp with fluorescein as an end-tagged marker. Error bars reflect 95% confidence intervals for 3 realizations. Solid lines are linear least squares fit to the data points. Data shows that in nanochannels DNA diffusion depends not only on diffusion values but also on oligonucleotide length, bulk velocity, zeta potential, and background electrolyte concentration.

References

- [1] Kim, J. H-S. *et al.* "Characterization of DNA hybridization kinetics in a microfluidic flow channel." **Sensors and Actuators B**, 113 (2006) 281-189.
- [2] Benters, R. *et al.* "Dendrimer-Activated Solid Supports for Nucleic Acid and Protein Microarrays." **ChemBioChem**, vol2. 9(2001) 686-694.
- [3] Pennathur, S. *et al.* "Free-solution oligonucleotide separation in nanometer scale fluidic channels" *to be submitted to Lab on a Chip*, 2006.

ACKNOWLEDGMENTS

Sandia is a multiprogram laboratory operated by Sandia Corporation, a Lockheed Martin Company, for the United States Department of Energy's National Nuclear Security Administration under contract DE-AC04-94AI85000.

Miniturization of a High-Throughput Multi-Antigen Microfluidic Fluorescence Immunoassays

George Maltezos¹, Emil P. Kartalov², Vinh Nguyen¹, Clive R. Taylor² Axel Scherer¹

¹California Institute of Technology and ²University of Southern California

Keywords: Microfluidic, Immunoassay, Fluorescence, Antibody Detection

Abstract

The development of a miniaturized high-throughput multi-antigen microfluidic fluorescence immunoassay system is described. A 100-chamber PDMS (polydimethylsiloxane) chip performs up to 5 tests for each of 10 samples. In the particular study system, specificity of detection was demonstrated and calibration curves were produced for C-Reactive Protein (CRP), Prostate Specific Antigen (PSA), ferritin, and Vascular Endothelial Growth Factor (VEGF). The measurements show sensitivity at and below clinically normal levels (with S/N > 8 at as low as 10 pM antigen concentration). The chip uses 100 nL per sample for all tests. The developed system is an important step towards miniaturized derivative immunoassay applications in scientific research and “point-of-care” testing in medicine.

1. INTRODUCTION

Here we report on a high-throughput multi-antigen high-specificity high-sensitivity reproducible PDMS microfluidic system quantifying four representative blood analytes at the clinically relevant levels. An active microfluidic matrix (18) utilizes arrays of integrated micromechanical valves (19) to direct pressure-driven flow and multiplex analyte samples with immunoassay reagents. ELISA-like fluorescence immunostacks are formed in the microchambers at the intersections of sample and reagent channels. The fluorescence signals from these microchambers quantify the captured antigens. The 100-chamber prototype device can conduct 5 tests for each of 10 samples (with 2 replicates per sample-test combination). This test matrix could be expanded to significantly larger numbers (20). All test can be performed in parallel with digital read-out in less than 2 minutes of all tested quantities.

We chose blood analytes for initial validation of the system, because blood tests represent an example of routine use of immunoassays. The current “gold standard” clinical technology typically is based on ELISA and requires 0.5 to 2 mL of sample per test per patient. High kit and instrumentation costs dictate centralization of measurements to large clinical or reference laboratories, resulting in transportation and batch delays of up to 14 days between the phlebotomist appointment and the final results.

2. THEORY

In the modern healthcare environment of mounting costs and shrinking insurance coverage, decentralized “near-patient” or “point-of-care” testing has long been the holy grail of biomedical diagnostics. The main reason for this state of affairs is that the truly versatile systems are large and expensive, and therefore make centralization the only economically viable choice at present [1].

The current portable systems meet the first four requirements, but still fall short of satisfying the final one [1]. In particular, the glucometers measure only blood sugar, while iSTAT measures about a dozen analytes (gases, ions, hematocrit, and a single protein) in different combinations in hardwired cassettes. By comparison, a state-of-the-art large benchtop system (e.g. Roche’s Elecsys) can measure about 50 different analytes including many blood proteins. Thus versatility is an indispensable feature in any new device hoping to replace current benchtops and larger systems.

3. EXPERIMENTAL

An important development in this respect is the advent of multi-antigen microfluidic fluorescence immunoassay devices [2], which can measure up to 10 samples versus each of 5 tests. The device uses only 100 nL per sample for all tests and thus promises the eventual replacement of current phlebotomy with finger-prick blood tests.

Furthermore, the fundamental technology [3, 4] allows relatively straightforward expansion of the test matrix to 50x50, thereby providing a fast, highly-parallel simultaneous measurement of multiple analytes in multiple samples [1]. Hence, the system would satisfy the versatility requirement, while adequate specificity and sensitivity have already been demonstrated [2]. Low cost of the individual chips should not be a forbidding obstacle since they are made of inexpensive silicone using simple replication molding techniques.

4. RESULTS AND DISCUSSION

The final hurdle to overcome would be an inexpensive portable detection system. In the prototype system reported previously [2], the fluorescence signals from each of the 100 immunostack microchambers were recorded serially using a fluorescence microscope. The ironic result was that data collection took a disproportionately large fraction of the total experimental time, thereby undermining the advantages of the parallel chemical processing allowed by the microfluidic architecture. In addition, lab technicians and nurses at hospitals and physician’s offices cannot be expected to operate the desktop fluorescence microscopy system as a matter of course. A simpler, smaller, less expensive, parallel-acquisition system is the clear necessity. Herein, we report on a successful solution thereof.

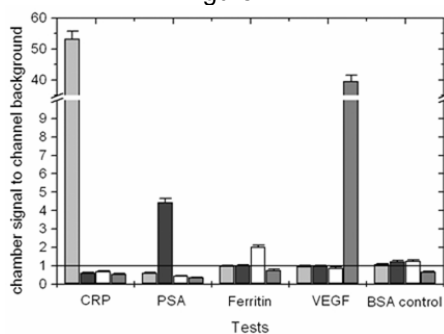
5. CONCLUSION

Our system uses an LED for excitation and a common consumer digital camera to image the fluorescence signal from the entire chip simultaneously, thereby providing an inexpensive way for a fast, parallel data acquisition. Other non-microscope systems [5-

[7] have been developed previously, but parallelization for large-scale immunoassay arrays could prove too difficult to fit architecturally [5, 6] or too expensive and time-consuming to assemble serially [7]. The chief novelty of our report is not the instrumentation itself but the demonstration that such a simple inexpensive system possesses sufficient sensitivity to detect analytes at biomedically relevant concentrations in microfluidic chips.

Figure 1 Specificity. Samples each containing 20 nM of a single antigen – CRP (light gray), PSA (black), ferritin (white), and VEGF (dark gray) – were fed in parallel into the test matrix. Each sample produced significant signal above background

Figure 1



References:

1. Gilbert, H.C. and Szokol, J.W. 2004. Point of Care Technologies. *Int. Anesthesiol. Clin.* 42 (2), 73-94.
2. Wang, J., Ibanez, A., Chatrathi, M.P., and Escarpa, A. 2001. Electrochemical Enzyme Immunoassays on Microchip Platforms. *Anal. Chem.* 73, 5323-5327.
3. Fruetel, J.A., Renzi, R.F., VanderNoot, V.A., Stamps, J., Horn, B.A., West, J.A.A., Ferko, S., Crocker, et al. 2005. Microchip separations of protein biotoxins using an integrated hand-held device. *Electrophoresis* 26, 1144-1154.
4. T. Thorsen, S.J. Maerkl, and S.R. Quake, *Science* 298, 580 (2002).
5. J. Seo and L.P. Lee, *Sensors and Actuators B*, 99, 615-622 (2004).
6. L. Pang, U. Levy, K. Campbell, A. Groisman, and Y. Fainman, *Optics Express*, 13 (22), 9003 (2005).
7. Y. Gambin, O. Legrand, and S.R. Quake, *Appl. Phys. Lett.*, 88, 174102 (2006).

OPTOFLUIDIC PARTICLE TRANSPORT IN LIQUID CORE PHOTONIC CRYSTAL FIBERS

Sudeep Mandal¹ and David Erickson²

¹Applied and Engineering Physics, Cornell University, USA

²Sibley School of Mechanical and Aerospace Engineering, Cornell University, USA
(de54@cornell.edu)

Abstract

Here we describe the optical guidance and transport of particles in a liquid-core photonic crystal fiber (PCF). We demonstrate the concentration of similar size particles into bands within the core of the fiber. Direct access to the optical mode along with low optical losses along the length of the core allow for precise particle concentration and separation.

Keywords: Optical chromatography, microfluidics, photonics, optofluidics

1. Introduction

The discovery that laser radiation could transfer its momentum to microscopic particles and thus be used to manipulate them has led to many innovative applications for micro total analysis systems. The recent interest in “Optofluidics” has led to a series of advanced implementation of such techniques to achieve all-optical control and sorting of particles into advanced and highly integrated microfluidic systems [1]. One exciting possibility is the development of on-chip optical chromatography systems (e.g. [2]) which have the potential to enable ultra-precise particle concentration and separation. At present the major limitation of such systems has been that the light-particle interaction length is limited by the focal depth of the free space optics to at most a few hundred microns. This limits the efficiency with which precise separations can be conducted. In this work we demonstrate a solution to this problem through the coupling of microfluidics with liquid core photonic crystal fibers (LCPCFs).

2. Theory

PCFs consist of a periodic lattice of air capillaries surrounding the core (see Figure 1(a)) which creates a photonic bandgap in the cladding causing light of the corresponding wavelengths to be guided within the hollow core [3]. In this work we selectively fill this hollow core with aqueous based solutions of micro and nanoparticles. The LCPCF now guides light via a total internal

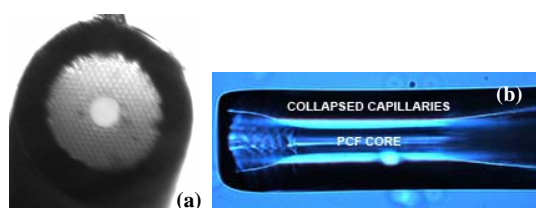


Figure 1. (a) Micrograph of end face of a PCF.
(b) Micrograph of PCF with collapsed capillaries at fiber end.

reflection mechanism as its core refractive index is higher than the average cladding index. The dielectric particles in liquid are guided by the optical scattering force exerted by the light coupled into the liquid-core. This axial force F_z experienced by the particles is dependent on both its size and refractive index. It is given by:

$$F_z(z) = 1.33 \frac{P_0}{c} \frac{128\pi^5 a^6}{3\lambda^4} \left(\frac{m^2 - 1}{m^2 + 2} \right)^2 e^{-\gamma z} \int I(r, z) dA \quad (1)$$

where a is the particle radius, P_0 is the input power of the laser, λ is the wavelength of the incident laser radiation, m is the effective refractive index of the particle in the liquid medium, γ is the attenuation coefficient of the fiber, $I(r, z)$ is the normalized transverse mode profile of the light propagating in the fiber and dA is the differential area element of the projection of the particle surface area on a plane perpendicular to the direction of propagation of light. The equation of motion of the particle in the liquid core is given by

$$m\ddot{z} = F_z(z) - mg - 6\pi\eta_{water}a\dot{z} \quad (2)$$

3. Experimental

In our experiments we used a hollow-core PCF having 20 μ m core diameter. We selectively fill the core with water by fusing the capillaries at the fiber ends using a fiber splicer [4] (See Figure 1(b)). The experimental setup is shown in Figure 2. The 40x objective at the end of the fiber is used to image the near field pattern of the emerging laser beam. Once proper light guidance through the liquid filled core was confirmed, we introduced a small quantity of 3 μ m fluorescing polystyrene particles into the water. Particles in the path of the 488 nm laser beam are pushed axially upwards through the fiber end. As shown in Figure 3, they rise up through the core and form a stationary band at a particular height where the optical force is balanced by the weight of the particle.

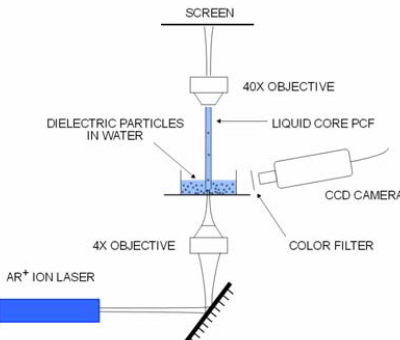


Figure 2. Experimental Setup

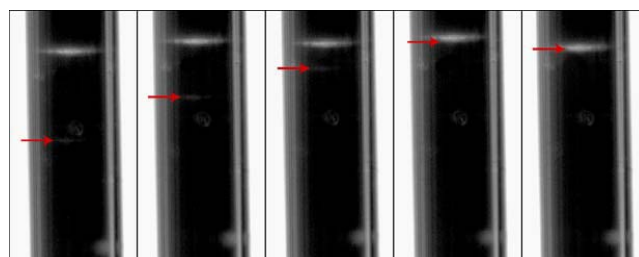


Figure 3. Sequence of a 3 μ m polystyrene particle rising up through the PCF and getting trapped at the band. At this position the optical force equals the weight of the particle.

4. Results and discussion

We have demonstrated the concentration of similar particles into distinct bands. Ongoing experiments will try and characterize the effect of multi-mode guidance of light in the fiber and the separation of different size particle bands in this setup. We also propose a technique (Figure 4) for achieving optical chromatography in an integrated lab-on-chip setup. This consists of a PCF embedded in a PDMS channel. The liquid containing a mixture of particles is electrokinetically driven through the core while the laser is coupled into the core in the opposite direction. Particles of different sizes will accumulate into bands at different positions along the core where the viscous drag forces would balance the axial scattering force exerted by the light coupled into the core. The interaction length for optical chromatography using our proposed technique is orders of magnitude larger than current optical chromatography systems [2].

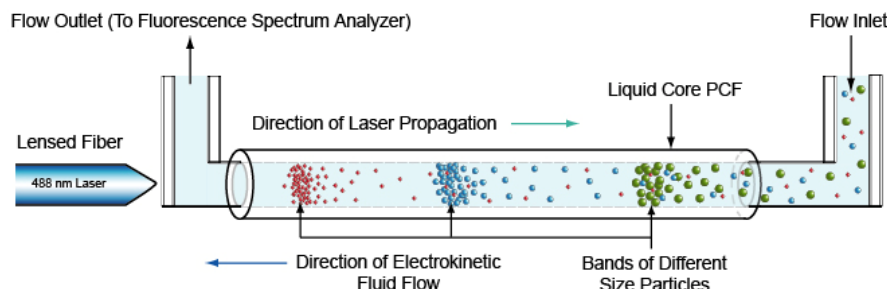


Figure 4. Schematics of an integrated microfluidics device incorporating liquid-core PCFs for optical chromatography.

5. Conclusions

Here we have illustrated a novel technique for particle concentration, trapping and separation which could have significant application in microfluidic cell sorters and rapid pathogen detection.

References

1. M. P. MacDonald, G. C. Spalding and K. Dholakia, "Microfluidic sorting in an optical lattice" *Nature* vol. **426**, pp. 421-424, (2003).
2. A. Terray, J. Arnold, and S. J. Hart, "Enhanced optical chromatography in a PDMS microfluidic system," *Opt. Express* **13**, 10406-10415 (2005).
3. J. C. Knight, "Photonic crystal fibres," *Nature* **424**, 847-851 (2003).
4. L. Xiao, W. Jin, M. S. Demokan, H. L. Ho, Y. L. Hoo, and C. Zhao, "Fabrication of selective injection microstructured optical fibers with a conventional fusion splicer," *Opt. Express* **13**, 9014-9022 (2005).

PCR BY MOVING A FREE DROPLET OVER DIFFERENT TEMPERATURE ZONES

Tseng Ming Hsieh, Yi Zhang, Juergen Pipper,* and Pavel Neuzil

Institute of Bioengineering and Nanotechnology,
31 Biopolis Way, The Nanos, #04-01, 138669 Singapore
jpipper@ibn.a-star.edu.sg

Abstract

This paper presents a novel miniaturized polymerase chain reaction (PCR) system that performs PCR by moving a free droplet over different temperature zones on a micromachined chip. The free droplet comprises magnetic particles, the PCR sample(s) and mineral oil, which together form a so-called virtual reaction chamber (VCR). The movement of the droplet is driven by magnetic forces and guided by a permanent magnet fixed onto a programmable two-axis linear stage. The micro-machined chip possesses four individual heating units, which are maintained at 95, 50–60, and 72 °C to create two or three different temperature zones. A successful PCR is demonstrated by moving the droplet over three different temperature zones operated at 95, 50, and two times 72°C for 45 cycles. The amplified PCR product is verified by capillary electrophoresis (CE).

Keywords: droplet, magnetic particles, virtual reaction chamber (VRC), PCR, lab-on-a-chip

1. Introduction

Since its invention in the 90s, the PCR has become an inalienable tool in molecular biology [1]. Two basic strategies are used: in the classic approach, a stationary PCR sample is thermocycled between two or three different temperatures [2], whereas under time-space-conversion, a PCR sample is moved through/ over three or four different temperature zones [3]. Here we present a PCR system, in which thermocycling is achieved by moving a VRC – a free droplet composed of magnetic particles, a PCR sample, and mineral oil – over three different temperature zones by magnetic forces (Fig. 1). Carrying out the PCR in this format enables fast heating/ cooling rates and running multiple samples simultaneously.

2. Results and discussion

The four different temperature zones of the PCR chip were made of micro-machined platinum thin film heaters/ temperature sensors and controlled by pulse-width modulation (PWM) using the proportional-integral-derivative (PID) method. We used a thin disposable glass or plastic substrate for separating the VRC from the PCR chip. By doing so, cleaning the ‘precious’ PCR chip to prevent carryover/ contamination between subsequent PCR runs was unnecessary. The miniaturized thermocycler was mounted onto a programmable two-axis linear stage, and a permanent magnet was fixed underneath. Moving the PCR chip, while keeping the VRC at a fixed position, would ease real-time monitoring during the PCR with a fluorescence microscope. To minimize the friction between the VRC and the glass substrate, its

surface was rendered both hydrophobic/ oleophobic by teflonizing.

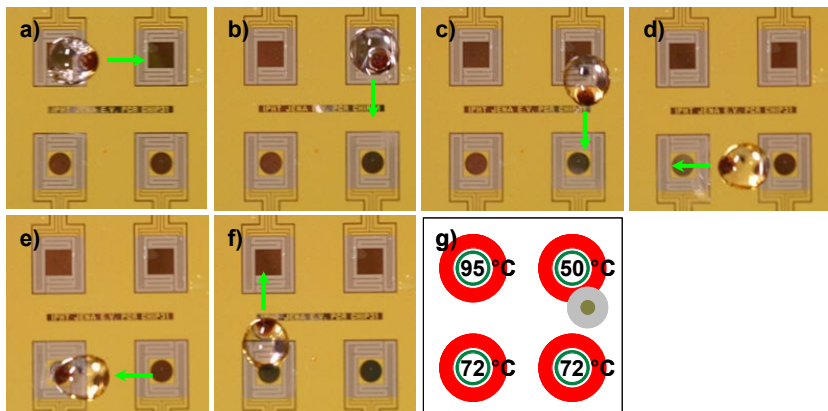


Figure 1. A series of images taken during PCR. The VRC was moved from a) the denaturizing to b) the annealing and c, d, e) elongation zone, which were kept at g) 95, 50, and two times 72 °C, respectively. The volume of the VRC was 5 µl. Overlaying the PCR mixture with mineral oil prevented evaporation.

To perform the PCR, the four heating units were maintained at 95, 50, 72, and 72 °C. The temperature profile along the paths was simulated by finite element analysis (FEA) (data not shown) and verified by infrared imaging (Fig. 2a, b). Since the droplet was moved within 1 s from one heater to another, heating (cooling) rates of 23 (−45) °C were realized.

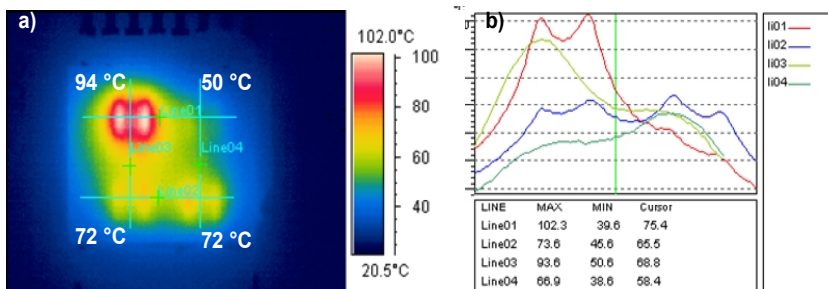


Figure 2. a) Infrared image of the thermal distribution of the glass substrate placed on the PCR chip. b) The thermal profiles for the single paths showed that the different temperature zones were effectively thermally decoupled from each other.

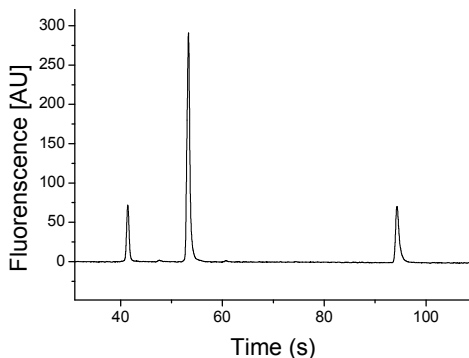


Figure 3: CE data. The first and third peak were two DNA size markers of 15 and 600 base pairs (bp), respectively. The amplicon had a length of 99 bp.

3. Experimental

We used the PCR Core Kit from QIAGEN. The PCR mixture was composed of 23 μL water, 10 μL 5 \times Q-Solution, 5 μL 10 \times PCR Buffer, 5 μL 10% bovine serum albumin (BSA) (Roth), 1 μL 10 mM dNTPs, 2.5 μL 10 μM each forward and reverse primer, 0.5 μL *Taq* polymerase, and 0.5 μL of a vector encoding the green fluorescent protein (pmaxGFP) (amaxa) as template. The PCR was performed according to the following thermocycling protocol: 45 cycles of denaturation for 5 s at 95 °C, annealing for 5 s at 50 °C, and two times elongation for 5 s at 72 °C (Fig. 1 a-f). The PCR product was verified by CE using a Bioanalyzer 2100 (Agilent).

4. Conclusion

The miniaturized PCR system demonstrated in this work is able to perform ‘fast’ PCR, because the heating/ cooling rate is independent from the thermal mass of the thermocycler. Utilizing disposable glass or plastic substrates help eliminating carry-over/ cross contamination and keeping operational costs low. Furthermore, this droplet-based approach can easily be integrated with sample preparation using surface-functionalized magnetic particles.

References

1. R. K. Saiki, S. Scharf, F. Falooma, K. B. Mullis, G. T. Horn, H. A. Ehrlich and N. Arnheim, Enzymatic amplification of beta-globin genomic sequences and restriction site analysis for diagnosis of sickle cell anemia, *Science* 230, 1350–1354 (1985).
2. M. A. Northrup, B. Bennet, D. Hadley, P. Landre, S. Lehew, J. Richards and P. Stratton, A miniature analytical instrument for nucleic acids based on micro-machined silicon reaction chambers, *Anal. Chem.* 70, 918–922 (1998).
3. M. U. Kopp, A. J. de Mello and A. Manz, Chemical amplification: continuous-flow PCR on a chip, *Science* 280, 1046–1048 (1998).

Numerical and Experimental investigations into a Novel Cell Sorter Utilizing Continuous Cascade Squeeze-Jumping Effect

Che-Hsin Lin^{1,2}, Cheng-Yan Lee¹ and Lung-Ming Fu³

¹Department of Mechanical and Electro-mechanical Engineering, ²Center for Nanoscience & Nanotechnology,

National Sun Yet-Sen University, Kaohsiung, 804, Taiwan

³Graduate Institute of Materials Engineering, National Pingtung University of Science and Technology, Pingtung, 912, Taiwan

chehsin@mail.nsysu.edu.tw

Abstract

This paper presents a novel technique for the continuous sorting and collection of microparticles in a microfluidic chip using a cascaded squeeze-jumping effect. In the proposed approach, microparticles of different sizes are separated from the sample stream using sheath flows and are then directed to specific side channels for collection. The sheath flows required to separate the particles are generated using a single high voltage supply integrated with a series of variable resistors designed to create electric fields of different intensities at different points of the microchip. Numerical simulations are performed to analyze the electrical potential contours and flow streamlines within the microchannel. Experimental trials show that the microchip is capable of continuously separating microparticles with diameters of 5, 10 and 20 μm , respectively. Importantly, the high performance of the microchip is achieved without the need for a complex control system or for sophisticated actuation mechanisms such as embedded microelectrodes, ultrasonic generators, or micropumps, and so forth.

Keywords: squeeze-Jumping effect, microfluidic, sheath flow, cytometer

1. Introduction

Miniaturized cell sorter devices have been already attracted lots of interest for researchers who work on Bio-MEMS. Many cell sorting devices have been successfully demonstrated using dielectrophoresis forces [1], or optical tweezing forces [2] and magnetic forces [3]. However, the fabrication process of these devices relies on a thin-film deposition process to construct the metal electrode such that the procedure is complicated, time-consuming, and cost ineffective. Therefore, the benefits come with the miniaturization are hindered.

The current study presents a novel technique for the continuous sorting and collection of particles in a microfluidic chip using a cascaded squeeze-jumping effect. In the proposed approach, a simple electrokinetic flow system is used to generate a cascaded set of sheath flows to sort microparticles of different sizes and to direct them to specific channels for collection and counting. A microchip is designed and fabricated using low-cost glass slides, and its sorting performance is evaluated experimentally

using the conventional metrics of the cell recovery ratio and the cell sorting yield ratio.

2. Experimental

The working principle of the proposed microfluidic device is shown in fig. 1. The main concept of the proposed method is based on that microparticles are unable to flow within a stream with the width of smaller than their diameter. Big particles will jump from its flow stream into the neighboring sheath flow by squeezing the sample stream while small particle will still flow stable in the sample flow. A cascade channel for generating sheath flows with different widths is utilized to sort microparticle with different sizes. Figure 2 shows Schematic illustration of the sheath flow squeezed effect, and is used to describe the theoretical model and derived formulas for predicting the flow width of the focused sample stream and the squeezing force on for the particles in the microchannel.

3. Results and discussion

Figure 3 presents a simplified schematic for experimental setup. Figure 4 presents the experimental and numerical flow fields of the squeezing phenomena at the first stage of the cascade channel. Figure 5 shows the corresponding flow velocity and acceleration profiles of the flows and the jumping forces provided by positive acceleration values at the squeezed region for big particles to move into the neighboring sheath flow stream. Figure 6 shows the continuous images of 20 and 10 μm microparticles jumping into the neighboring sheath flow and a mixed microparticles of 5, 10 and 20 μm can be separated successfully by the proposed novel method. This result confirms that the squeeze-jumping effect is feasible to force big particles to move into the neighboring sheath flow for continuous particle sorting.

4. Conclusions

This paper reports an innovative method for continuous particle sorting using a special microfluidic phenomenon of squeeze-jumping effect. Results confirmed the proposed micro device can successfully separate microparticles with different sizes. Similar concept can be adopted to sort biological cells such as stem cells, embryos, oocytes out of a mixed cell sample. It is the authors' believe that this simple approach will give substantial impacts on cell separation technology.

Acknowledgements

The financial support from National Science Council of Taiwan is acknowledged.

Reference

- [1] D. Holmes and H. Morgan, *Inst Phys Conf Ser*, 107 (2004).
- [2] F. C. Cheong, C. H. Sow, A. T. S. Wee, P. Shao, A. A. Bettoli, J. A. van Kan, and F. Watt, *Appl Phys B-Lasers Opt.*, **83**, 121 (2006).
- [3] J. Manent, K. Oguievetkaia, J. Bayer, N. Ratner, and M. Giovannini, *J Neurosci Meth.*, **123**, 167 (2003).

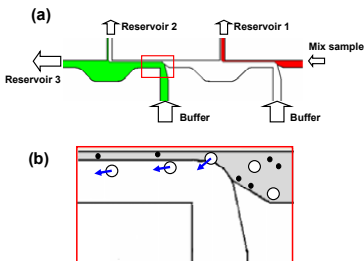


Fig. 1 (a) Schematic diagram of the working principle for the proposed cell sorter. (b) An enlarged picture for explaining the squeezing effect. Big particles will jump from their original flow stream into the neighboring sheath flow with small stream width.

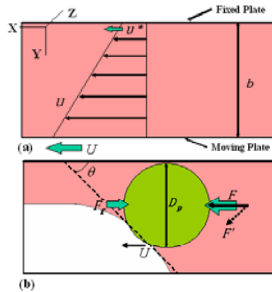


Fig. 2 Schematic illustration of the flow distribution in the squeezed sample flow (a) and the force act on the particle at the barrier (b). Consider a flow between two horizontal and parallel plates as figure. Assume that there is a flow barrier between the sample and sheath flows.

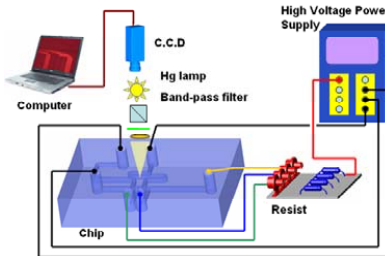


Fig. 3 Schematic illustration of the experimental setup for the proposed cell sorter. Note that only one power supply is required for the system. Multi-stage sheath flows with different widths were then induced for squeezing the sample particles.

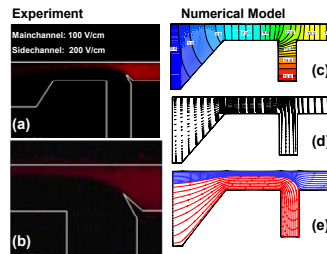


Fig. 4 Experimental flow contours (a, b) and numerical results of (c) electrical potential contours, (d) velocity vectors and (e) the streamline plots.

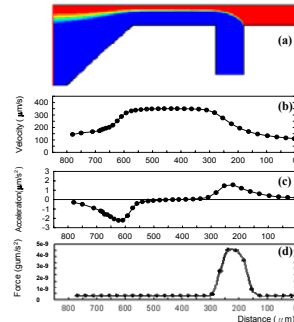


Fig. 5 calculated (a) flow field (b) velocity profile and (c) acceleration profile (d) squeezed force on particle at the first-stage squeeze region. Note that the values for the velocity and acceleration were estimated at the interface of the sample and sheath flows.

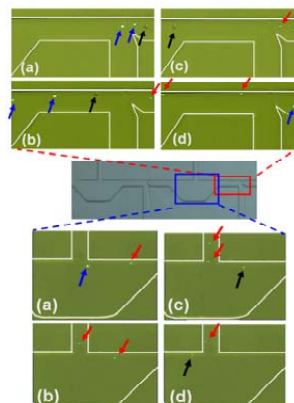


Fig. 6 Continuous images of microparticle sorting in the microchip.

A Novel Artificial Renal Microchip Employing Polymeric Nanofibers Membrane

*Kwang Ho Lee, **Jae Gwan Kim, ***Duck Joong Kim
Sang Hoon Lee, Byoung Goo Min

^Interdisciplinary Program in Biomedical Engineering Major, Seoul National University

**School of Mechanical and Aerospace Engineering, Seoul National University

***Dept. Biomedical Engineering, College of Medicine, Korea University

****Dept. Biomedical Engineering, College of Medicine, Seoul National University

E-mail: mountrain@myriad.snu.ac.kr

Abstract

In this study, a novel artificial renal replacement system is presented using a biocompatible polymeric nanofibers and MEMS technology. Usually, a classical artificial renal replacement system employs a semi-permeable membrane based hemodialyzer that replaces an ability of the kidney by removing metabolic toxins through diffusion and hydraulic pressure gradients. But, it has some limits in efficient filtration of metabolic byproducts (e.g.: urea, creatinine, and so on). We have developed PDMS based artificial renal microchips (AR chip) integrating biocompatible polymeric nanofibers which are utilized for the filtration of blood. Here, we demonstrate a novel artificial renal chip by integrating a high efficient biocompatible polymeric nanofibers membrane with the PDMS based micro-fluidic platform. Via the optimization of PDMS micro fluidic channel network and the multiple packaging of nanofibers membrane, we will realize the portable and wearable artificial kidney system.

Keywords: Artificial kidney, Artificial Renal Microchip (AR chip), Nanofiber, Electrospinning

1. Introduction

State-of-the-Art in Artificial Renal Replacement Therapy (Artificial Kidney)

Hemodialysis is a procedure that replaces the normal functions of the kidney by removing toxins, electrolytes, and fluid by purifying the patient's blood through an artificial semipermeable membrane (it is called a hemodialyzer or artificial kidney). Recently, researchers have improved this type of extracorporeal hemodialysis in relation mostly to biomaterials and to the design of critical disposable devices [1]. End-Stage Renal Disease (ESRD) patients are chronic hemodialysis which requires three days of four-hour hemodialysis sessions per one week. However, the treatment remains inconvenient because many patients have to make frequent visits to hospitals. The main clues to overcome such inconvenience in relation to the extracorporeal hemodialysis system are (1) a reduction of dimensions and (2) improvement of filtration efficiency. In conclusion, we have demonstrated the feasibility of chip-based hemodialysis, and we expect that our method suggested in this paper will be applied in the development of small and light-weighted dialyzer for the realization of portable hemodialysis system.

2. Materials and Experiments

Fabrication of of Artificial Renal microchip

Polyurethane (PU) and polyethersulfone (PES) are useful as materials for biomedical

devices. These materials were chosen because it is good blood compatibility, chemical stability, mechanical properties, mass transport properties and specially, excellent characteristic of fiber forming [2]. Generally, nanofiber filter increases the filtration efficiency for broad particle sizes [3], and for this reason, we used nanofiber web as a semi-permeable membrane through electrospinning process. And we fabricated the platform of the AR chips by using PDMS and nanofiber web and by following a soft lithographic method. Figure 1(a) is a schematic diagram of AR chips. We fabricated the PDMS platform by bonding two PDMS layers on which the patterns of upper and lower fluidic channels (width: 300 μm , and height: 150 μm) were engraved. We had produced each layer by using the SU-8 replication mold, as reported previously [4].

Evaluation of filtration capability

For our experiments concerning filtration properties, we used human whole blood and dialysate (Hemosol B0; a commercially produced bicarbonate-buffered hemofiltration replacement solution, Hospal). Into the inlet of the upper channel (which we will call the “blood channel”) and the lower channel (which we will call the “dialysate channel”), we introduced the blood and the dialysate respectively by using a syringe pump (KDS 100, KD Scientific Co.). The flow rate of the blood flow was Q_b : 1 ml/min and the dialysate flow was Q_d : 1 ml/min. We measured the reduction of urea, creatinine, and vitamin B12 concentration from the filtered blood.

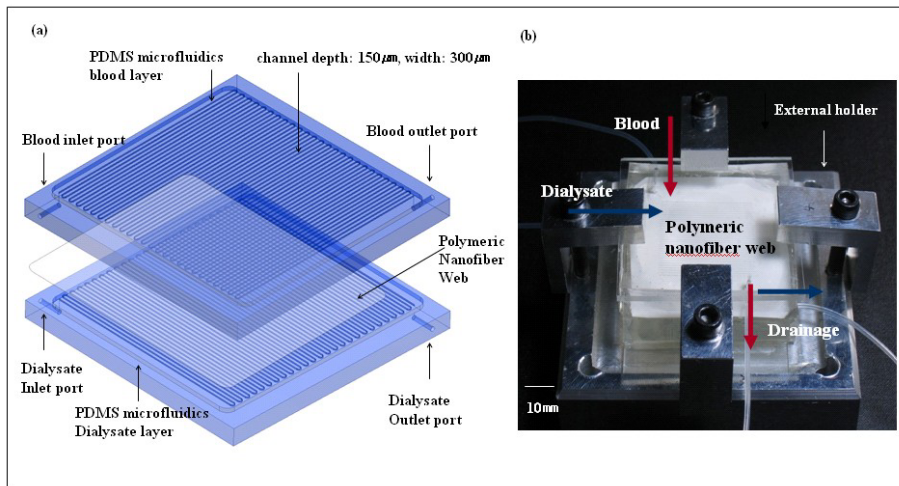


Figure 1. Fabrication of the artificial renal chip: (a) Schematic of PDMS-based hemodialysis chip containing polymeric nanofiber, (b) The fabricated AR chip and the fluidic network.

3. Results and Discussion

We have carried out many experiments to discover the optimal conditions for the fabrication of a good nanofiber membrane. The molecular weights of the urea, creatinine, and Vitamin B12 are 60, 180, and 1,180 Dalton (Da) respectively. The urea and the creatinine are low-molecular-weight species, while the vitamin B12 is a middle-molecular-weight species. As expected, all the AR chips effectively filtered the urea and the creatinine, and the clearances of these 4 chips were almost the same. However, the

clearance of vitamin B12 was quite different. The filtration of vitamin B12 in the nanofiber membrane was much higher than that in commercial membranes.

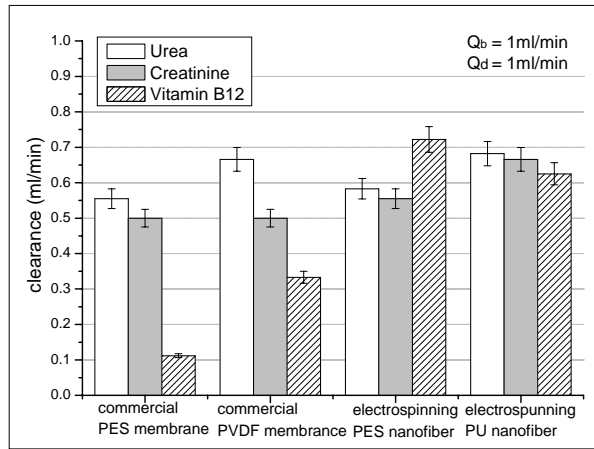


Figure 2. The clearance of urea, creatinine and vitamin B12 according to the inserted membrane

4. Conclusion

Until now, this microfabricated device could ultimately provide a smaller, less invasive and less expensive therapy for ESRD, and enables it to be portable and potentially wearable. For further improvements, we should (1) increase the surface area by multi-stacking the PDMS channels and the nanofiber membrane and (2) immobilize some specific proteins on the surface of the nanofiber web to capture the specific proteins that diffusion cannot, itself, remove

5. Reference

- [1] S. H. Yea, J. Watanabea, M. Takaia, Y. Iwasakib, and K. Ishihara, "Design of functional hollow fiber membranes modified with phospholipid polymers for application in total hemopurification system", *Biomaterials*, 2005, **26**, 5032–5041.
- [2] T. H. Grafe, and K. M. Graham, "Nanofiber Webs from Electrospinning", *The 5th International Conference of the Nonwovens in Filtration*, Stuttgart, 2003.
- [3] K. H. Lee, H. Y. Kim, Y. J. Ryu, K. W. Kim and S. W. Choi, "Mechanical Behavior of Electrospun Fiber Mats of Poly(vinyl chloride)/Polyurethane Polyblends", *Journal of Polymer Science, Part B: Polymer Physics*, 2003, **41**, 1256-1262.
- [4] S. H. Lee, W. J. Jeong, and D. J. Beebe, "Microfluidic valve with cored glass microneedle for microinjection", *Lab on a Chip*, 2003, **3**, 164-167.

CONTINUOUS MICROFLUIDIC CELL/PARTICLE SEPARATION VIA COMBINATION OF ELECTROOSMOTIC AND HYDRODYNAMIC SPREADING

Z. G. Wu¹, Y. F. Yu¹, A. Q. Liu¹, P. H. Yap³, C. S. Lim² and H. M. Hosseini¹

¹ School of Electrical & Electronic Engineering

² School of Chemical & Medical Engineering

Nanyang Technological University, Singapore 639798

³ DSO National Laboratories, Singapore 118230

(Corresponding author: Tel (65) 6790-4336, Email eaqliu@ntu.edu.sg)

Hydrodynamic spreading separation is an important technique for cells or particles sorting. In this paper, an electroosmotic flow (EOF) and a hydrodynamic flow are combined to control the spreading behavior for continuous cells or particles separation. The hydrodynamic spreading of fluids can be adjusted arbitrary with a tunable applied voltage. This spreading behavior is investigated through numerical simulation and experiment study. Based on the experimental results, particles of two different sizes, 10 and 2 μm , are separated. The experimental results are compared with the numerical results. The suggested technique provides a simple, flexible and versatile way for microfluidic cell sorting.

Keywords: Separation, electro-osmotic flow, hydrodynamic spreading, cell sorting

1. Introduction

Research on microfluidic devices for cell or particle separation has attracted strong interest from both of academia and industry. Various separation techniques including fluorescent-activated cell sorting, dielectrophoresis-activated cell sorting, magnetic-activated cell sorting and flow fraction cell sorting have been investigated. Thus far, the flow fraction or hydrodynamic spreading is one of the simplest techniques with high throughput. Cells or particles are sorted based on their respective sizes using a simple geometry design [1-2], where the spreading behavior of the flow for cells or particles separation can be affected by flow rate and viscosity ratio of the co-axis fluids among a pressure driven flow system [3]. In this paper, the spreading behavior for continuous cells or particles separation using a hydrodynamic flow system combined with an electroosmotic flow system is investigated. The hydrodynamic spreading behavior is studied through numerical simulation that is compared with experiment results. The two different sizes of particles are separated based on the hydrodynamic spreading behavior of fluids, which is controlled and adjusted arbitrary by the electroosmotic flow through a tunable applied voltage.

2. Principle of separation

Electroosmosis refers to the fluid flow that occurs when there is an electric double layer at a solid-liquid interface that arises from an electrostatic attraction between a charged surface and ions. When an external electric field is applied, the mobile positive ions in a diffuse layer move towards the cathode, resulting in a bulk fluid movement by dragging along the essentially electrically neutral bulk fluid that is far away from the microchannel wall. In general, the driven force of the electroosmotic flow is weaker than the pressure flow. However, when the pressure amplitude of the two flows is closely equal, the effect of the electroosmotic flow becomes very significant influence for the pressure driven flow. The hydrodynamic spreading of fluids is adjusted arbitrary by the electroosmotic flow control through the tunable applied voltage.

Figure 1 shows the principle of particle separation via hydrodynamic flow for cell or particle separation controlled by EOF. One fluid stream with different particles (sample flow) is converged to another fluid stream without particles (carrier flow) through a small channel. When the voltage is applied to the carrier fluid, the hydrodynamic behavior of the fluids changes according to the driven voltage of EOF. Since the fluid stream without particles occupies a broader channel width, when the amplitude of the applied voltage is proper, the larger particles are aligned against the channel wall and immersed in the carrier fluid, but the smaller particles remain changed in the original sample fluid. Through an abrupt channel amplified mechanism, the larger particles are forced into the carrier flow and the small particles are kept in the sample flow. The particles are then separated and can be collected into the different outlets.

The hydrodynamic spreading behavior controlled by electroosmotic flow is simulated using CFD-ACE⁺, the numerical simulation results of the fluid spreading behavior along the channels are shown in Fig. 2. The top branch occupies broader width than the bottom one when the voltage is applied.

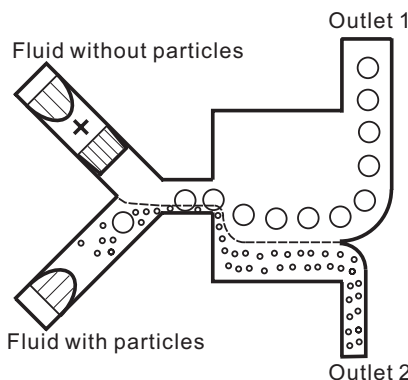


Fig. 1 Schematics of particle separation using hydrodynamic spreading behavior through EOF control.

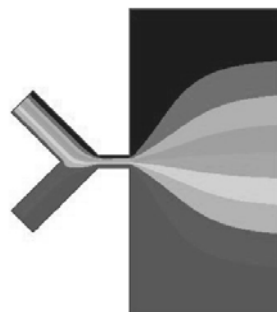


Fig. 2 Numerical simulation result of hydrodynamic spreading behaviors.

3. Experimental results and discussions

The biochip was fabricated using standard soft-lithography with polydimethylsiloxane (PDMS). Fig. 3 (a) shows the pure hydrodynamic spreading using fluorescent dye. Fig. 3 (b) shows that the hydrodynamic spreading behavior is controlled by the electroosmotic flow. The two experiment results show that the spreading behavior changes significantly with and without electroosmotic flow control.

The mixed particles with different diameters of 2 μm and 10 μm are put in one inlet. Deionized water is used as the carrier flow that is put in the other inlet and kept at a height which is the same with the one in the mixed particles. When the applied voltage on the carrier flow is raised, the carrier flow occupies the broader channel width and the sample flow occupies the narrower channel width. The larger particles are aligned against the channel wall and forced into the carrier flow, the small size particles remain at the bottom as shown in Fig. 4. As a result, the particles with different sizes are separated. Higher voltage is applied to enhance the separation effect.

Conclusions

A technique of continuous particles separation using hydrodynamic fluid spreading through electroosmotic control is investigated. The hydrodynamic spreading behavior is studied through numerical simulation and verified by experimental results. The separation of particles with two different diameters is demonstrated. This technique provides a simple, flexible and versatile way for cell sorting using biochip.

References

1. M. Yamada, M. Nakashima and M. Seki, 2004, *Analytical Chemistry*, pp. 5465-5471.
2. M. Yamada and M. Seki, 2005 *Lab Chip*, pp. 1233-1239.
3. Z G Wu, D. N Ghista and A. Q. Liu, *Proc. APCOT 06*, 25-28 June, Singapore, pp. 143.

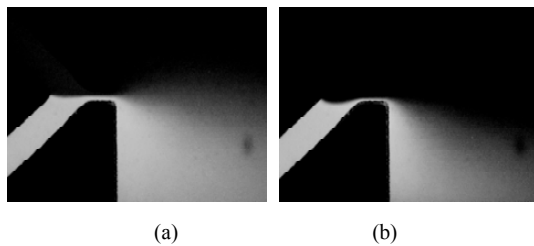


Fig. 3 Photograph of hydrodynamic spreading (a) without electroosmotic flow and (b) with electroosmotic flow control.

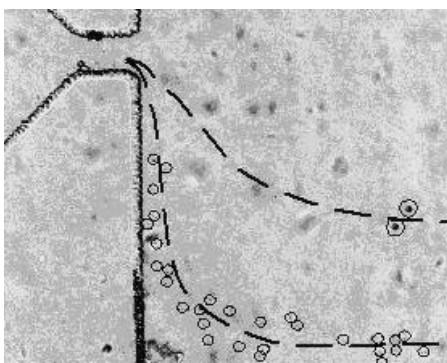


Fig. 4 Photograph of particles separation. The top dash line indicates the track of large particles (10 μm) and the bottom dash line indicates the track of smaller particles (2 μm).

TOWARDS MICROCHIP BIOSENSORS: PASSIVE MICROCHAMBER WASHING USING INLET-PRESSURE DIFFERENCE

Byung-Kwon Kim,¹ Sang-Youn Yang,¹ Sung-Jin Kim,² and Haesik Yang¹

¹Department of Chemistry, Pusan National University, Korea (hyang@pusan.ac.kr)

²Biosensor Group, Electronics and Telecommunications Research Institute (ETRI), Korea

Abstract

Microfluidic washing techniques that are essential to many microchip-based bioassays are still premature for practical applications. Here, we propose a passive washing protocol for microchip-based bioassay applications; this approach uses the inlet-pressure difference between two solution inlets, and it employs a washing valve that regulates the merging of two solutions. The inlet-pressure difference is induced by capillarity. Sample and washing solutions merge at the washing valve, and the passive washing process occurs just after the merging. The washing volume and direction are regulated by controlling the volume of solutions injected to the inlets. In addition, the washing speed can be programmed by controlling the microchannel width. As a model bioassay, the binding of biotin-4-fluorescein inside a reaction chamber is quantified by using the passive washing. The passive washing protocol provides a simple but effective microfluidic washing method.

Keywords: washing, capillary-driven flow, inlet pressure, biosensor, biotin

1. Introduction

The biospecific binding in many lab-on-a-chips occurs on solid surface in a microchamber. To measure the binding with high sensitivity, it is necessary to remove unbound species in the microchamber. Thus, it is important to wash the microchamber effectively. Generally, mechanical pumps or electrochemical pumps have been employed for microfluidic washing. However, these pumps make the whole system bigger and complex. Here, we propose a simple passive washing scheme. We regulate the shape of solution drops at the inlets to control the inlet pressure.

2. Principle

The operation principle is shown in Figures 1 and 2. The inlet pressure (ΔP) is determined by the Laplace equation:

$$\Delta P = P_{\text{sol}} - P_{\text{air}} = \frac{2\sigma}{R} \text{ or } -\frac{2\sigma}{R}$$

where P_{sol} and P_{air} are the pressures in the solution and air phases, respectively, σ is the surface tension of the solution, and R is the mean radius of curvature of the solution drop. When the sample solution merges with the washing solution at the washing valve, ΔP at the sample-solution inlet (SI) is smaller than at the washing-solution inlet (WI) ($\Delta P_{\text{SI},i} < \Delta P_{\text{WI},i}$) (Figure 2d). This pressure difference induces fluid flow from the WI to the SI until two inlet pressure values become equal ($\Delta P_{\text{SI},f} = \Delta P_{\text{WI},f}$) (Figure 2d) [1]. As a result, the solution

in a reaction microchamber is washed with a washing solution. The volume used for washing depends on the initial volume of two inlets.

3. Experimental

The microchip is made of a cyclo-olefin copolymer (COC) plate that was coated with bovine serum albumin (BSA) and an adhesive tape. The COC plate was hot-embossed with a nickel master that was fabricated using SU-8.

4. Results and discussion

The shape change of a liquid drop was monitored during washing process (Figure 3a-b). The volume of SI increases because of the passive washing induced by the inlet-pressure difference, while that of WI decreases. To check the efficiency of passive washing, fluorescence images were also obtained during washing process (Figure 4a-d). The fluorescence signal of fluorescein decays with change of sample solution to washing solution in the reaction microchamber. Fluorescein in the microchamber was completely removed after 5 s for 350 μm -wide fluidic resistor, indicating that a fast and effective washing has been achieved. The time needed for a complete washing is longer for a thinner channel that has a larger fluidic resistance (Figure 4e). As a model bioassay application, the specific binding of biotin-4-fluorescein on streptavidin surface was tested (Figure 5a). The biotinylated BSA was spotted on the reaction chamber of the COC plate, and then streptavidin was immobilized. On this microchip, a solution of phosphate buffered saline containing 1% (w/v) BSA (PBSB, pH = 7.4) and biotin-4-fluorescein was injected to the SI. After 10 min, a PBSB solution was injected to the WI. The amount of specifically bound biotin-4-fluorescein was determined by a fluorescence microscope. Passive washing eliminates most of unbound biotin-4-fluorescein molecules in the microchamber (Figure 5b). The calibration curve for biotin-4-fluorescein in Figure 5c indicates that the passive washing process are effective in removing unbound biotin-4-fluorescein and that this unique approach is practical to simple microfluidic devices required in heterogeneous phase bioassays.

5. Conclusions

We have demonstrated a simple but effective microfluidic washing protocol for bioassay applications. Our approach has the following advantages: (1) it does not require any internal or external pumps for microfluidic washing; (2) it enables facile macro-to-micro interface via solution dropping; (3) the washing speed can be programmed by controlling the fluidic resistance (changing channel width); (4) the washing direction and volume can be controlled by the volume of solution drops injected to the two inlets; and (5) a waste chamber is not necessary because the SI also acts as a waste chamber.

References

1. S.-J Kim, Y. T. Lim, H. Yang, Y. B. Shin, K. Kim, D.-S. Lee, S. H. Park, and Y. T. Kim, *Anal. Chem.* **77**, pp. 6494-6499 (2005).

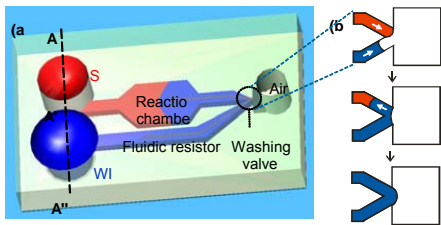


Figure 1. (a) Schematic view of the microfluidic device. (b) Schematic of solution flows at the washing valve before and after the merging of two solutions.

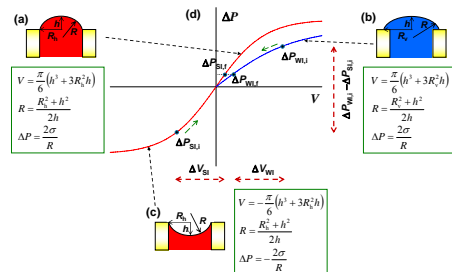


Figure 2. Schematic of the relationship between ΔP and V at solution inlets. (a) $V > 0$, $R_v = R_h$; (b) $V > 0$, $R_v > R_h$; and (c) $V < 0$, $R_v = R_h$. (d) Schematic graph of ΔP vs. V during the passive washing process

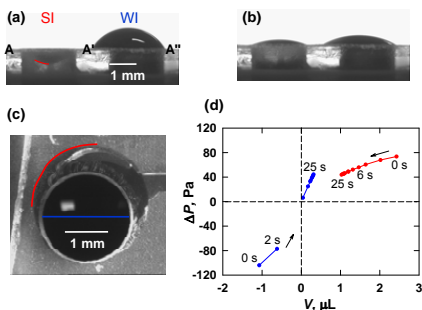


Figure 3. Side view of two solution drops at the inlets during the washing (a) before the merging of two solutions and

(b) 40 s after the merging. (c) Top view of a drop at the WI after the washing. (d) ΔP and V calculated from side views of solution drops.

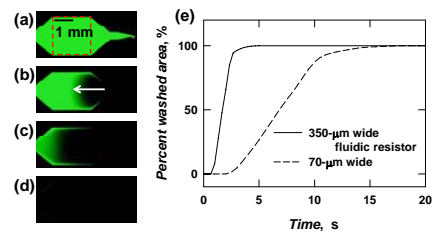


Figure 4. (a)-(d) Fluorescence images during passive washing. The channel width is 350 μm . The images were obtained (a) before the merging of two solutions, (b) 1 s, (c) 2.5 s and (d) 5 s after the merging. (e) Time dependence of the percent washed area.

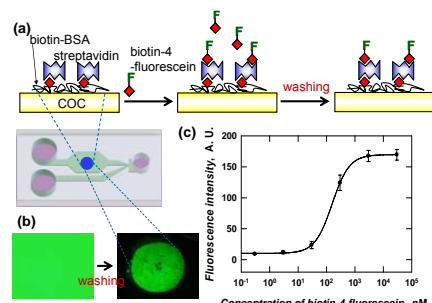


Figure 5. (a) Schematic representation for bioassay surface and the preparation procedure. (b) Fluorescence image obtained at a 300 nM biotin-4-fluorescein solution before and after passive washing (c) Dependence of fluorescence intensity on biotin-4-fluorescein concentration.

AC ELECTROOSMOTIC MICROMIXER: VISCOSITY AND IONIC STRENGTH DEPENDENCE OF MIXING TIME

Naoki Sasaki¹, Takehiko Kitamori^{1,2,3}, and Haeng-Boo Kim^{1,2,3}

¹ School of Engineering, The University of Tokyo, Bunkyo, Tokyo, 113-8656, Japan

² Kanagawa Academy of Science and Technology, Kawasaki, Kanagawa, 213-0012, Japan

³ CREST, Japan Science and Technology Agency, Kawaguchi, Saitama, 332-0012, Japan

Abstract

We present viscosity and ionic strength dependence of mixing time in AC electroosmotic micromixer. Rapid mixing was achieved for the viscosity up to 3 mPa s and for the ionic strength up to 10^{-3} . Rapid fluorescence staining of DNA with the mixer was also demonstrated.

Keywords: AC electroosmosis, micromixer, active mixer, microelectrode, staining

1. Introduction

Efficient mixing of fluids in microchannel is required for many chemical and biochemical applications. In the previous paper, we reported that our AC electroosmotic micromixer worked in a shorter mixing time compared with the reported micromixers [1]. In this paper, viscosity and ionic strength dependence of mixing time was studied, since the magnitude of AC electroosmotic flow (AC-EOF) depends on these parameters.

2. Principle

Figure 1 shows cross section of a microchannel with a pair of coplanar electrodes. Applying an AC voltage to the coplanar electrodes induces AC-EOF [2]. In the microchannel, the circulating flow is induced due to the confined space. Mixing of fluids is achieved by arranging the electrodes in parallel to the channel and inducing the circulating flow perpendicular to the flow of the fluid in microchannel, as shown in Figure 2. Efficient mixing of fluids is achieved by the use of meandering electrodes which can make periodical changes in both direction and velocity of the AC-EOF along the fluid streams and can accelerate mixing of the fluids.

3. Experimental

Aqueous fluorescein solution and water was used as test solutions. The two solutions were introduced to the mixer with a syringe pump, and AC voltage (20 V_{p-p}, 1 kHz) was applied to the electrodes. Viscosity and ionic strength of test solutions were adjusted by ethylene glycol and KNO₃, respectively. Mixing processes were visualized by a fluorescence

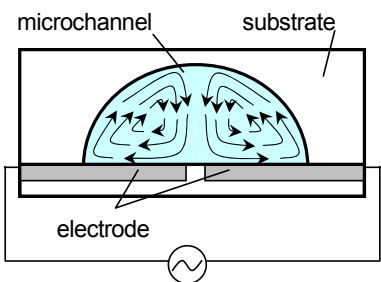


Figure 1. Cross section of a microchannel with a pair of coplanar electrodes. The direction of AC-EOF is indicated by arrows.

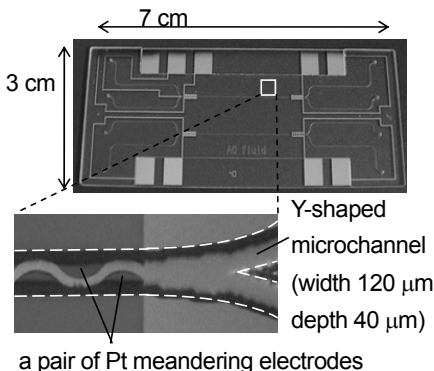


Figure 2. Photos of AC-EOF micromixer.

microscope equipped with a CCD camera. Mixing index and length was defined as described previously [1]. Since linear dependence was observed between mixing length and flow velocity, mixing time, T_{mix} , was defined as the slope of the regression line.

4. Results and discussion

T_{mix} increased in a linear fashion with viscosity as shown in Figure 3. This can be attributed to the decrease of AC-EOF, because it is predicted that AC-EOF is inversely proportional to the viscosity [2]. For the viscosity of 3 mPa s, T_{mix} was 0.6 s, which was 20-fold shorter than that of diffusional mixing. On the other hand, T_{mix} increased in a linear fashion with logarithm of ionic strength as shown in Figure 4, although it is difficult to predict ionic strength dependence of AC-EOF theoretically. For the ionic strength of 10^{-3} , T_{mix} was 0.5 s.

Rapid mixing and reaction with the mixer was demonstrated by fluorescence staining of DNA as shown in Figure 5. Before applying the AC voltage, DNA reacted with the

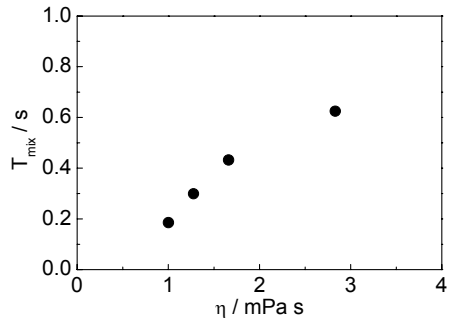


Figure 3. Viscosity dependence of T_{mix} .

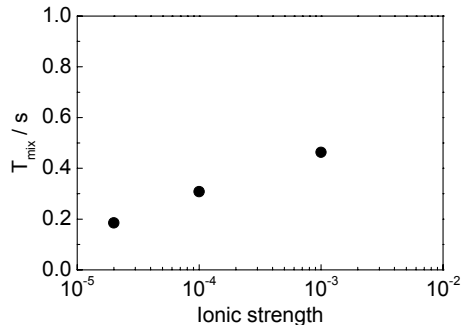


Figure 4. Ionic strength dependence of T_{mix} .

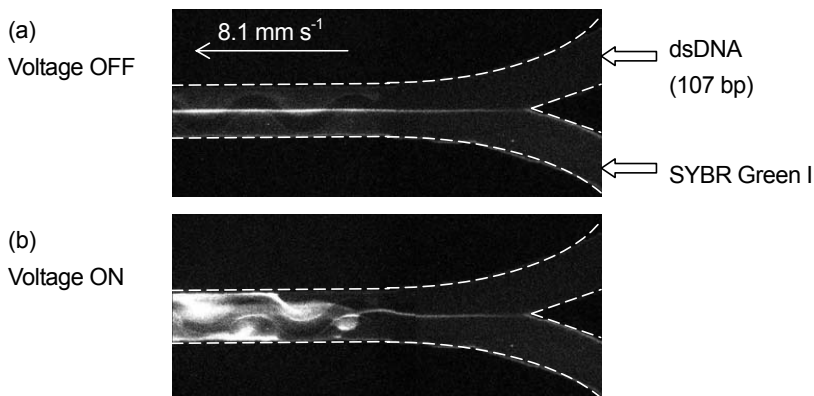


Figure 5. Fluorescence images of dsDNA (107 bp) stained with intercalator, SYBR Green I (a) without AC-EOF and (b) with AC-EOF.

intercalater at the boundary of the streams because of small diffusion coefficients of DNA ($\sim 10^{-7} \text{ cm}^2 \text{ s}^{-1}$) as shown in Figure 5(a). In contrast, by applying the AC voltage, two streams were rapidly mixed and fluorescence by intercalation was observed from whole of the channel (Fig. 5(b)).

5. Conclusion

We studied viscosity and ionic strength dependence of mixing time in AC electroosmotic micromixer. Rapid mixing was achieved for the viscosity up to 3 mPa s and for the ionic strength up to 10^{-3} . Rapid fluorescence staining of DNA with the mixer was also demonstrated. The present mixer can be a powerful tool for rapid mixing and reaction, which enables us to realize highly efficient chemical and biomedical analysis and organic synthesis in microfluidic devices.

Acknowledgements

The authors acknowledge Grants-in-Aid from the Ministry of Education, Culture, Sports, Science and Technology (MEXT), Japan (No. 14050024 on Priority Areas (417)) for support of part of the research.

References

- [1] N. Sasaki, T. Kitamori, H.-B. Kim, *Lab Chip*, **6**, 550-554 (2006).
- [2] N. G. Green, A. Ramos, A. Gonzalez, H. Morgan, A. Castellanos, *Phys. Rev. E*, **61**, 4011-4018 (2000).

RECIPROCATING DIAPHRAGM MICROPUMP FOR HIGH PRESSURE MICRO-CHEMICAL PROCESSES

Takanori Aono*, Akira Koide*, Ryo Miyake*, Mitsuo Kitaoka
and Takehiko Kitamori*****

*Mechanical Engineering Research Laboratory, Hitachi, Ltd., Japan

**The Research Association of Micro Chemical Process Technology, Japan

***Department of Applied Chemistry, School of Engineering, University of Tokyo, Japan

Abstract

We developed a high-pressure diaphragm micropump comprised of a pumping chamber and two active valves. It was made from stainless-steel substrates with high durability and chemical resistance against alkali and organic solutions. Three piezoelectric stack actuators were utilized for controlling the pumping stroke and closing the active valves. The micropump could pump liquids into micro channels smoothly with low flow rates (0.6~30 $\mu\text{L}/\text{min}$) under high-pressure conditions (up to 1.2 MPa) and was suitable for micro-chemical processes.

keywords: stainless steel, diaphragm, piezoelectric stack actuator, active valve

1. Introduction

Small pumps that can accurately drive very small amounts of liquids are required in most of the micro-chemical systems with functional micro channels. At MicroTAS'05, we had reported on our original diaphragm micropump comprised of a pumping chamber and two valves driven by three piezoelectric-stack actuators [1]. Weak point of this micropump was its low operational pressure (0.15 MPa). However, high-pressure conditions of about 1.0 MPa are often encountered in miniaturized chemical systems.

In this work, we improved the structure of the active valves to overcome this problem of pressure tolerance.

2. Initial design

Figure 1 shows the developed micropump. It had three SUS316 stainless-steel substrates (top, diaphragm, and chamber). The stainless-steel substrates have a higher durability and a higher chemical resistance. The top substrate had three through-holes, in which the piezoelectric-stack actuators were assembled. The diaphragm substrate had a pumping diaphragm and two valve diaphragms: an inlet and an outlet one. The chamber substrate had inlet/outlet holes, two connecting sections, and a pumping chamber. Tubes connect the micropump and the reservoir or the micro channels through inlet and outlet holes, relatively.

3. Improved design and evaluation

In the initial design, the active valves had been closed by press the diaphragm to the surrounding inlet/outlet holes. Loose contact between them had caused the relatively

low-pressure tolerance of the micropump. In the improved design, we used a resin tube for connection between the micropump and a micro channel or a reservoir. And we let the resin tube to stick out slightly into the chamber. When the diaphragm was pressed the tube end, the resin tube was elastically deformed and the active valve was sealed tightly enough to work under a high-pressure condition.

Figure 2 shows a photograph of the developed micropump. The three stainless-steel substrates were bonded using thermal diffusion bonding technology. The pump is 20 mm wide, 20 mm long, and 20 mm high.

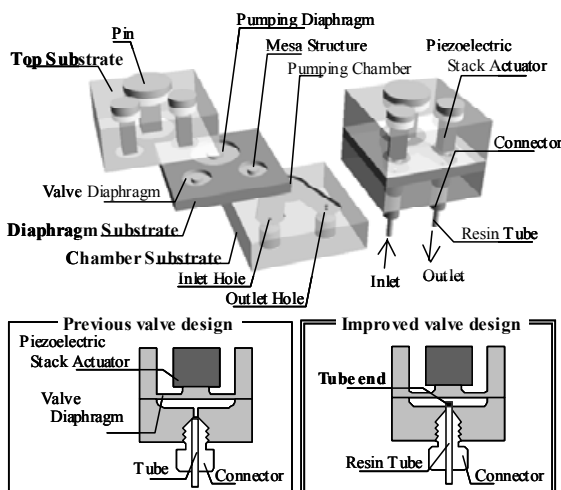


Figure 1 Three dimensional image of micropump

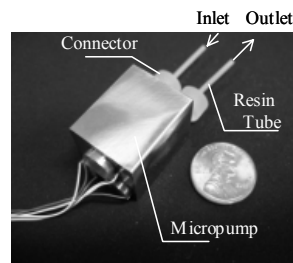


Figure 2 Photograph of micropump

Figure 3 shows the operation sequence of the micropump. First, the inlet valve was opened, and the pumping chamber and the outlet valve were closed. The pumping chamber was gradually opened to suck liquid into the pumping chamber. After the inlet valve was closed and the outlet valve was opened, the liquid in the pumping chamber was pushed out by the pumping diaphragm gradually going down. Finally, the valves were returned to the initial state and a cycle was completed. Rectangular wave voltages ranged from 0 to 100 V and triangular wave voltages ranged from 0 to 50 V were used for actuating piezoelectric-stack actuators of the inlet/outlet diaphragms and of the pumping diaphragms, respectively. The rectangular wave for controlling the inlet/outlet valves enabled to keep closed/opened condition, and the triangular wave for pumping chamber made it possible to gradually pump and suck.

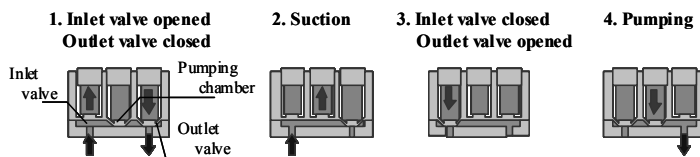


Figure 3 Operation mode of micropump

Figure 4 shows the dependence of the flow rate of the micropump on the frequency of the voltage waves. Flow rate was nearly proportional to the frequency. When the frequency was increased from 0.2 to 30 Hz, the flow rate increased from 0.6 to 30 $\mu\text{L}/\text{min}$. Improving the design enable to the active valves to work under high-pressure conditions thus increased the flow rate by about 500 %.

Figure 5 shows the dependence of the closed pressure of the micropump on the frequency of the voltage waves. The closed pressure was proportional to the frequency from 1 to 15 Hz, it gradually saturated about 1.2 MPa at 40 Hz.

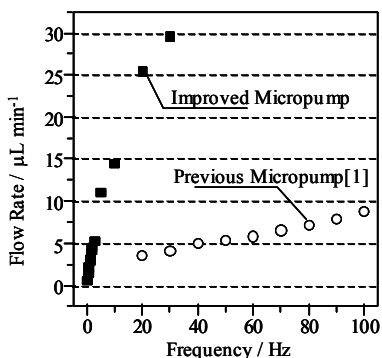


Figure 4 Dependence of flow rate on frequency

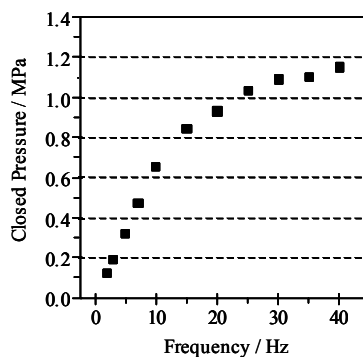


Figure 5 Dependence of closed pressure on frequency

4. Conclusion

Improving the valve design of our reciprocating diaphragm micropump for micro-chemical processes to enable the valves to work under high-pressure conditions could pump liquid into micro channels at flow rates ranging from 0.6 to 30 $\mu\text{L}/\text{min}$ under high-pressure conditions (~1.2 MPa). This micropump is now well suited for use in miniaturized chemical systems with functional micro channels.

Acknowledgements

This research was supported by a grant from the New Energy and Industrial Technology Development Organization, Japan.

References

- [1] T. Aono, A. Koide, R. Miyake, T. Kitamori, MicroTAS'05, p.p. 1186-1189

THE DIGITAL GENERATION OF ANALOG CHEMICAL SIGNALS

L. Chen, F. Azizi and C. H. Mastrangelo

Dept. of Electrical Engineering and Computer Science
Case Western Reserve University, Cleveland, OH, 44106, USA

Abstract

A 4-bit continuous flow, concentration digital-to-analog converter utilizing switched PDMS microfluidic networks was fabricated and tested. This converter produces discretized analyte concentrations controlled by a time-varying digital word; hence it is suitable for the generation of arbitrary dynamic analyte signals. Several analyte waveforms (sawtooth, cosine, and ramp) were generated at flows of 2 $\mu\text{L}/\text{min}$ and frequencies of 0.6-4 mHz.

Keywords: dynamic fluidic signals, dynamic mixers

1. Introduction

The generation of controlled dynamic chemical signals has many applications in the life sciences ranging from analyte-ligand analysis to the understanding and modulation of cellular response. Inspite of its importance, most of the work to date has focused on the generation of static signals with microfluidic mixing networks. These networks provide a multitude of mix-ratio outputs from two or more input flows [1-3] hence are commonly used for generation of static chemical gradients and parallel titration analysis. In [4] mixing networks were driven by external dynamic input flows to generate time-dependent output signals, and [5] reports the dynamic switching of gradients utilizing on-chip valves.

This paper reports for the first time, the utilization of digitally switched mixing networks for the generation of arbitrary dynamic chemical signals. In particular, we have fabricated and tested a 4-bit microfluidic continuous flow *concentration digital-to-analog converter* (or C-DAC) as described below.

2. A Continuous Flow C-DAC Structure

The C-DAC generates an arbitrary concentration of analyte within a specific analyte range and bit resolution; hence with this device one can generate analyte *waveforms*. The C-DAC consists of two mixing networks, M1 and M2, a digitally controlled flow multiplexer and a mixing resistor as shown in Fig. 1. Flows of analyte and solvent are input to mixing network M1, producing equal flow outputs of binary weighted analyte concentration. For a specified digital control bit input, the multiplexer valves select the corresponding bit outputs and route the bit flows to either the terminating mixing resistor or the waste line. Flow in the mixing resistor is maintained constant by selecting

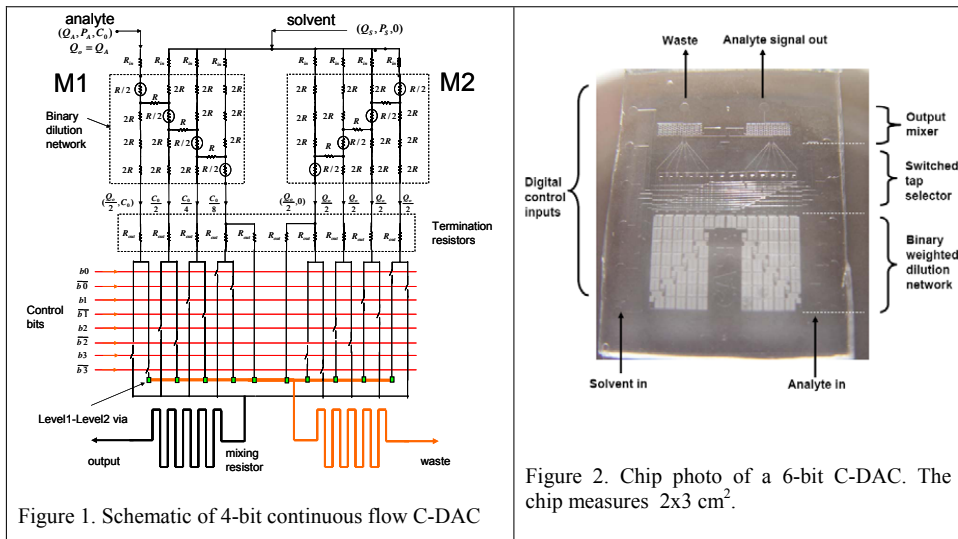


Figure 1. Schematic of 4-bit continuous flow C-DAC

either the bit flow from M1 or an equal flow of solvent from M2. Mixing in the network takes place at the circled flow resistors. Under these flow conditions and under the assumption of perfect mixing, the analyte concentration at the mixing resistor output is $C_{out} = \frac{C_o}{N} \cdot \sum_{i=0}^{N-1} b_i \cdot 2^{-i}$ where C_o is the input analyte concentration and N is the number of control bits.

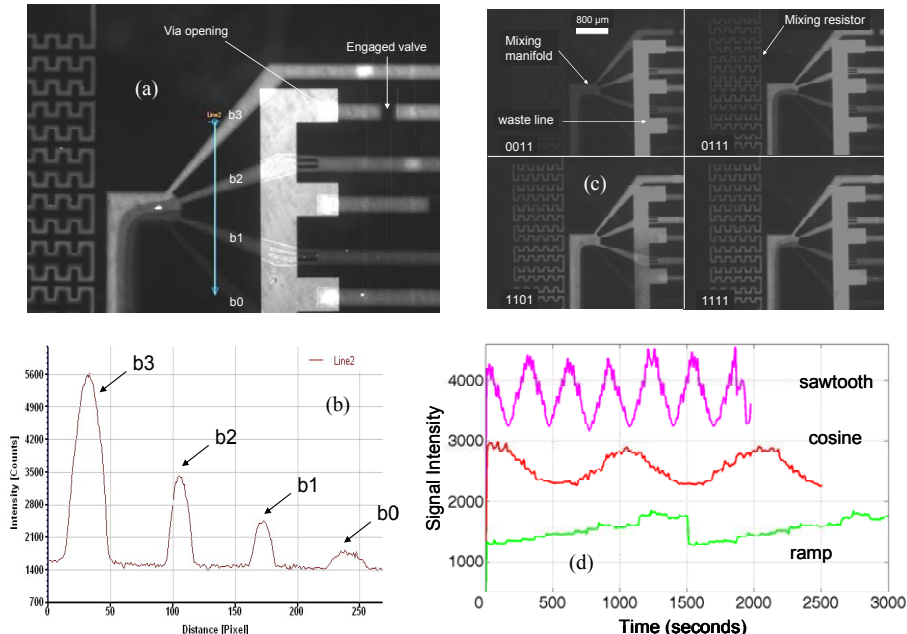
Figure 2 shows a photograph of a larger 6-bit C-DAC. Chips were constructed using a double-layer PDMS process [6] with integrated pneumatic valves and through-level vias. These vias permit the crossing of separate fluidic lines.

3. Experimental results

A 4-bit C-DAC chip was tested with a water-soluble fluorescent tracer dye (Risk Reactor, IFWB-C0 Clear Blue) as well as fluorescein as indicators of analyte concentration. Lines of dye and water were connected to the input chip and were pressurized at about 40 PSI to generate the internal flows. The fluorescent intensity of the output signals was recorded with an Olympus MVX10 epifluorescence microscope equipped with a Hamamatsu intensified camera. Figs. 3(a)-(b) show fluorescence photographs of the flow multiplexer outlet showing the binary-weighted intensities of the bit flows. Figs. 3(c)-(d) shows photographs of fluorescent images corresponding to different mixing codes. Fig. 3(d) shows the generation of several dynamic signals with the C-DAC at flow rates of 2 $\mu\text{L}/\text{min}$ with frequencies between 0.6-4 mHz. An important consideration in this device is the settling time of the switched mixed signal. If the exit mixing resistor is sufficiently long, the output mixer behaves as a dispersive low-pass filter that smears the signal thus eliminating much of the exit transients, but at

Figure 2. Chip photo of a 6-bit C-DAC. The chip measures $2 \times 3 \text{ cm}^2$.

the same time limiting the slope of the output signal. In this device the practical cutoff was about \sim 30 mHz. This cutoff can be increased at higher driving pressures and flow velocities.



Figs. 3(a)-(d): (a) image of different bit flows being mixed on the exit manifold. The bit flow is either mixed or re-routed to a waste line and replaced with an equal volume of solvent. (b) fluorescence intensities of binary weighted analyte concentrations. (c) Images of the mixing at different bit codes. (d) intensity at C-DAC outlet showing the generation of arbitrary dynamic analyte signals.

References.

1. X. Jiang, J. M. K. Ng, A. D. Stroock, S. K. W. Dertinger and G. M. Whitesides, A miniaturized, parallel, serially diluted immunoassay for analyzing multiple antigens, *J. Am. Chem. Soc.*, Vol. 125, pp. 5294-5295, (2003).
2. S. C. Jacobson, T. E. McKnight, and J. M. Ramsey, Microfluidic devices for electrokinetically driven parallel and serial mixing, *Anal. Chem.*, Vol. 71, pp. 4455-4459, (1999).
3. S. K. W. Dertinger, D. T. Chiu, N. L. Jeon and G. M. Whitesides, Generation of gradients having complex shapes using microfluidic networks, *Anal. Chem.*, Vol. 73, pp. 1240-1246, (2001).
4. F. Lin, W. Saadi, S. W. Rhee, S.-J. Wang, S. Mittal, and N. J. Leon, Generation of dynamic temporal and spatial concentration gradients using microfluidic devices, *Lab-on-a-chip*, Vol. 4, pp. 164-167, (2004).
5. D. Irimia, S-Y. Liu, W. G. Tharp, A. Samadini, M. Toner and M. C. Ponzanansky, Microfluidic system for measuring neutrophil migratory responses to fast switches of chemical gradients, *Lab-on-a-chip*, Vol. 6, pp. 191-198, (2006).
6. M. A. Unger, H. P. Chou, T. Thorsen, A. Acherer, S. R. Quake, Monolithic Microfabricated Valves and Pumps by Multilayer Soft Lithography, *Science*, Vol. 288, pp. 113-116, (2000).

PNEUMATIC MICRO DISPENSER SYSTEM WITH NO DEAD VOLUME FOR PORTABLE MICRO CHEMICAL DEVICE

Tadahiro Hasegawa*, Fumiuki Omatsu*, Toshiyuki Tsuji*, and Koji Ikuta**

*Dept. of Mechanical Eng., Osaka Institute of Technology, JAPAN,

**Dept. of Micro System Engineering, Nagoya Univ. , JAPAN

Abstract:

Two kinds of switching micro fluidic chips called “Dead volume-free” micro fluidic chip for portable micro chemical devices have been developed successfully. The 10-directional switching valve chip and the sampling chip as components of the air pressure drive micro dispenser system were developed successfully. The first one is the sampling chip that divides liquid every 1 μ L or 0.5 μ L without any dead volume of sample by decompressing and compressing the air. This simple operation is caused by our original novel detection method of micro fluid and check valves of hat shape. The second is the switching valve chip that can select the outlet. This chip has a special rotary mechanism consisting of silicone rubber ring for leak-preventions and the precise auto-positioning mechanism. This chip can switch ten outlets by built-in micro solenoid (1N, 6V DC) under high leakage pressure (higher than 500kPa). Since the both of chips were fabricated using our original “hybrid microstereolithography” (hybrid-IH process), micro assembling and bonding are not needed.

Keywords : Micro dispenser, 10-directional switching valve, Check valves, Photosensor, Hybrid microstereolithography

1. Introduction

Biochemical IC proposed by Ikuta [1] is useful for not only micro-TAS but also “portable” micro chemical devices such as portable health care devices. Dispensing devices that can efficiently divide sample in the chip are needed. A novel sliding micro dispensing device was reported by Kuwata et al. [2]. This device is capable of dispensing liquids in nanoliter range precisely. However, unmeasurable dead volume of liquid exists because of dividing a part of liquid injected into the channel. We speculated that the actuator with large power was needed to slide the glass. In this paper, we realized micro dispenser system without any dead volume for portable micro chemical devices.

2. Operation principle of pneumatic micro dispenser system

This dispenser system consists of the micro sampling chip and the micro multi-directional switching valve chip (Fig.1). These micro chips are stacked up by “Silicon rubber coupling method [3]”. First of all, liquid is sucked through check valve by the decompressing air in the chip. At the same time as detecting liquid with photosensor, it is cut out by switching to the pressurizing operation. Liquid that divided into a constant amount is injected through the other

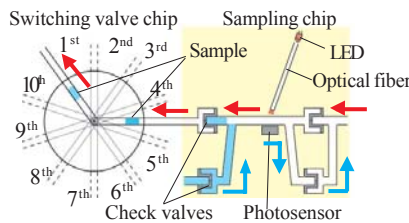


Fig.1 Concept of micro dispenser system without any dead volume

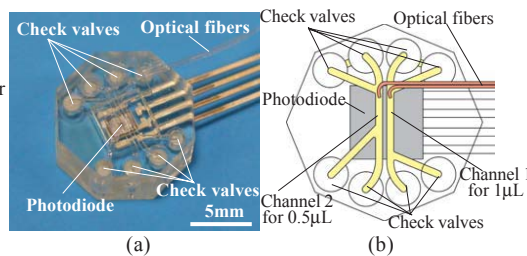


Fig.2 Micro sampling chip that can be cut out in 1 μL or 0.5 μL
(a) prototype (b) schematic design

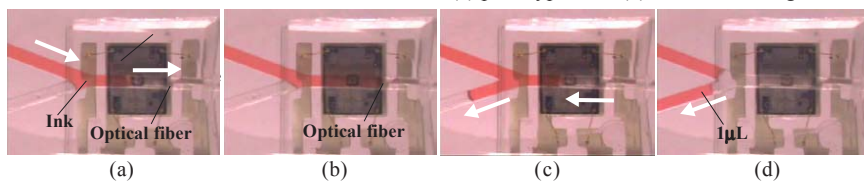


Fig.3 Sequential photographs of dispensing procedure
(a)decompression operation (b)detection of liquid
(c)pressurization operation (d)cutout for desired liquid amount

check valve without dead volume. In addition, by switching outlets with the multi-directional switching valve, dispensed liquids can be injected to several channel.

3. Air pressure drive micro sampling chip

Fig.2 shows the micro sampling chip that can divide liquids every 1 μL or 0.5 μL without any dead volume. The micro sampling chip consists of our original novel detection method of micro fluid and check valves of hat shape. First, the detection method of the micro fluid utilized total refraction of infrared rays. The infrared rays is irradiated through the optical fiber set up on the channel diagonally. If liquid is injected into the channel, the refractive index on the surface of the channel changes and the infrared rays is refracted to the photosensor. Therefore, not only passage of the fluid into the channel but also its existence can be detected as TTL level. Secondly, the silicone rubber of the hat shape that functions itself as a one-way valve was developed. The check valve is a simple structure to insert it at the channel during polymer solidification process. This check valve has opening pressure of $3.0 \pm 0.4\text{kPa}$ and can withstand over 300kPa. The route of liquid is automatically controlled by check valves (Fig.3).

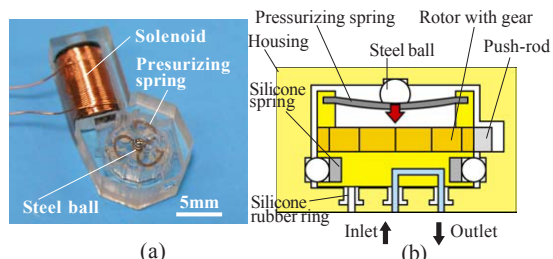


Fig.4 10-directional switching valve chip with built-in solenoid
(a) prototype (b) Cross sectional view

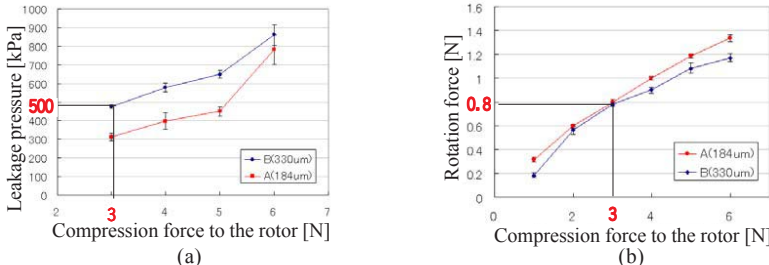


Fig.5 Optimal design of multi-directional switching valve chip
(a) Leakage pressure (b) Rotation force

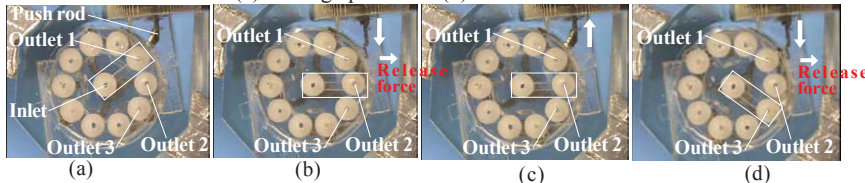


Fig.6 Sequential photographs of switching procedure
(a) position at outlet 1 (b) after switching to outlet 2
(c) push-rod returning to initial position (d) after switching to outlet 3

4. Multi-directional switching valve chip with rotary mechanism

The world's first 10-directional micro switching valve was developed by us [5]. Initially, the valve was operated manually to confirm the switching principle with the rotary mechanism. Next, the micro solenoid drive switching valve chip was developed for simple and quick operation (Fig.4). Positioning and detection of present location at the outlet were achieved with the latch mechanism without necessity of positioning. The insertion of all parts including the rotor during the fabrication of the housing succeeded by using our original hybrid microstereolithography [4]. To build the solenoid into the chip, the valve design parameters (the height of the silicon rubber ring and the compression force to the rotor) affecting the valve performance (the leakage pressure and the rotation force of the rotor) were optimized (Fig.5). Ten outlets were switched by the built-in micro solenoid (1N, 6V DC) smoothly and accurately (Fig.6).

5. Conclusions

Pneumatic micro dispenser system without any dead volume was proposed. The micro sampling chip that can divide liquids every 1 μ L or 0.5 μ L without any dead volume and the 10-directional switching valve chip with built-in micro solenoid as the component of this system were developed successfully. These module type micro fluidic chips should be the key device for portable and wearable micro chemical device in near future.

References

- [1] K.Ikuta, K.Hirowatari, T.Ogata: MEMS94, pp.1-6, (1994)
- [2] M.Kuwata, K.Sakamoto, Y.Murakami, et al.: μ -TAS04,pp.602-604, (2004)
- [3] T.Hasegawa and K.Ikuta: μ -TAS2001, pp.377-378, (2001)
- [4] K.Ikuta, S.Maruo, T.Fujisawa, A.Yamada: MEMS99, pp.376-387, (1999)
- [5] T.Hasegawa, K.Ikuta, and K.Nakashima: μ -TAS03, pp.215-218, (2003)

MANUFACTURING SIZE-CONTROLLED GELATIN MICROPARTICLES USING A MICROFLUIDIC CHIP

**Yu-Cheng Lin¹, Keng-Shiang Huang¹, Shian-Chin Lai², Yu-Jen Lai²,
Po-Wen Lin^{1,2}, Chih-Hui Yang^{2*}**

¹Department of Engineering Science, National Cheng Kung University,
Tainan, Taiwan

²Department of Biological Science & Technology, I-Shou University,
Kaohsiung, Taiwan

*Tel: +886-7-657-7711, Fax: +886-7-657-7057

Email: chyang@isu.edu.tw

Abstract

This study is to prepare monodisperse gelatin microparticles using a microfluidic chip. We have demonstrated that one can control the size of gelatin microparticles from 100 μm to 400 μm in diameter (with a variation less than 10%) by altering the relative sheath/sample flow rate ratio. The proposed microfluidic chip is capable of generating relatively uniform micro-droplets and has the advantages of actively controlling the droplet diameter, and having a simple and low cost process, with a high throughput. Experimental data show that when given a steady continuous phase (oil flow), the emulsion size increases with the increase in average velocity of the dispersed phase flow (sample flow). In addition, the size distribution of the resulting chitosan microspheres is narrow (about Polyindex = 1) which is suitable to provide the optimal release rate in the administration of controlled release drugs.

Keywords: gelatin, size-controlled, microfluidic

1. Introduction

Gelatin microparticles have characteristics of biodegradability and weak antigenicity suitable for medical and pharmaceutical applications [1]. Several methodologies for gelatin microparticles preparation have been described in the literature, including precipitation, spraying, emulsion techniques, and others [2-3]. However, the resulting size and size distribution of the microspheres cannot be easily controlled by these methods. Control of the particle size and its distribution is important for controlled-release drug delivery, because they influence the clearance rate from the body and ultimately determines the drug dosage. Basically, an ideal particle size and a uniform size can provide an optimal release rate.

Our strategy is based on a focusing on the forming a uniform self-assembling sphere structure, so-called water-in-oil (w/o) emulsions, in the cross-junction microchannel. These fine emulsions containing 1 % (w/v) gelatin and 1 % (w/v) genipine were then undergo crosslinking for 20 min, resulting in water-insoluble gelatin particles.

2. Experimental

The developed chip is fabricated by a CO₂ laser machine on a conventional poly methyl methacrylate (PMMA) substrate. The microfluidic chip has three inlet ports, one cross-channel, and three outlet ports (Fig. 1). Experiment data showed that the sample fluid was compressed by a shear force (oil flow) to form an arrow shape and then be separated into emulsions of about 100-400 μm in diameter (Fig. 2). In addition, the size and gap of the droplets are tunable by adjusting the relative sheath/sample flow rate ratio (Fig. 3).

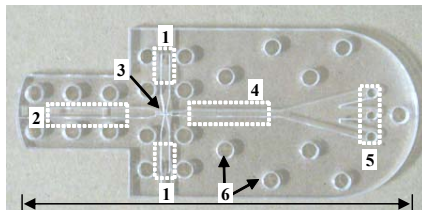


Fig. 1 Schematic drawings of the microfluidic chip: 1. oil inlet, 2. sample inlet, 3. cross-junction channel, 4. observation chamber, 5. outlets, 6. screw holes for binding. (scale bar 10 cm)

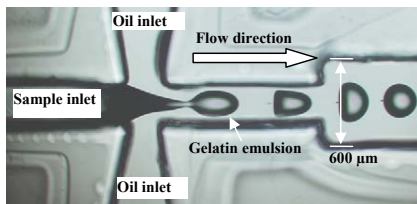


Fig. 2 Gelatin microemulsions are generated at the cross-junction with oil: 1.0 mL/min and water: 0.1 mL/min. The broadened channel (600 μm in width) near the outlet of the cross channel is designed for slowing down the flow and enhance the analysis observation. (The arrow indicates the flow direction)

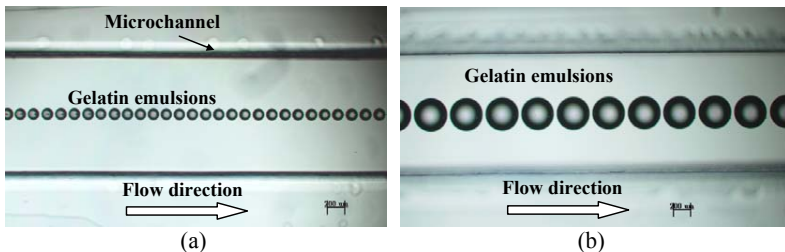


Fig. 3 The developed microfluidic chip is capable of generating relatively uniform micro-droplets. Enlarged microscope view of the size-controlled emulsions formation at observation chamber (1000 μm in width) under (a) oil: 1.0 mL/min, water: 0.01 mL/min, (b) oil: 1.0 mL/min, water: 0.1 mL/min. (scale bar 200 μm)

3. Results and Discussions

Experimental data showed that the size distribution of the resulting gelatin microspheres is very narrow (Polyindex = 1), as shown in (Fig. 4). When given a steady oil flow (sheath flow), the size of emulsion increases with the increase of the sample flow (Fig. 5).

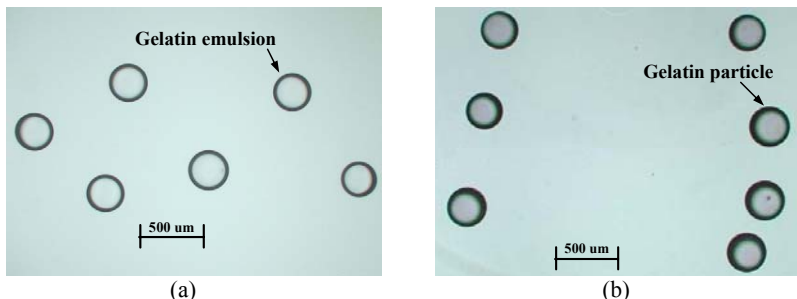


Fig. 4 The uniform size distributions of gelatin microparticles formed are observed in collection reservoir under the condition of oil: 1.0 mL/min and water: 0.07 mL/min. Enlarged microscope view of (a) Before cross-linked gelatin emulsions and (b) after cross-linked with 1 % genipine gelatin particles. (scale bar 500 μm)

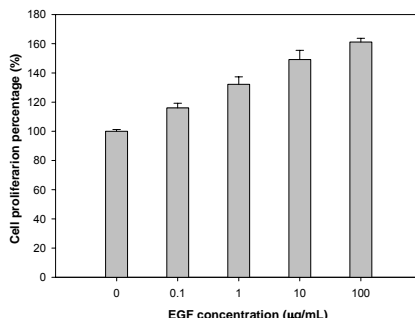


Fig. 5 Relationships between particle size and flow rate of aqueous solution under fixed oil flow rate.

4. Conclusions

The developed method turns out to be one of the most efficient methods for the production of monodisperse genipin-gelatin micro-hydrogels. The microfluidic chip is easy to fabricate and set-up, and is easily programmed to generate a large set of size-controlled gelatin microparticles. The approach in manipulation of uniform gelatin microparticles will provide many potential usages for pharmaceutical applications.

REFERENCES

- [1] M.A. Vandelli, F. Rivasi, P. Guerra, F. Forni, R. Arletti, *Int. J. Pharm.*, 2001, **215**, 175.
- [2] M. Luck, K.F. Pistel, Y.X. Li, T. Blunk, R.H. Muller, T. Kissel, *J. Control Release*, 1998, **55**, 107.
- [3] S. Iwamoto, K. Nakagawa, S. Sugiura, M. Nakajima, *Pharm. Sci. Tech.*, 2002, **3**(3), 25.

HYDROPHOBIC PLATING TECHNIQUE FOR FABRICATION OF MEMS SLIDE VALVE

Michio Takayama^{1,2}, Yoshikuni Kikutani^{2,3}, Kazuma Mawatari^{2,3},
Mitsuo Kitaoka² and Takehiko Kitamori^{3,4}

¹ Olympus Corporation, 2-3 Kuboyamachyo, Hachiouji, Tokyo 192-8512 Japan,

² The Research Association of Micro Chemical Process Technology, Japan,

³ Micro Chemistry Group, Special Research Laboratory for Optical Science,
Kanagawa Academy of Science and Technology, Japan, ⁴ Department of Applied
Chemistry, Graduate School of Engineering, The University of Tokyo, Japan
(E-Mail: m_takayama@ot.olympus.co.jp)

Abstract

Micro slide valves with glass/silicon/glass three-layered structures were fabricated using MEMS technologies. A part of the silicon layer, in which microchannels connecting the top and bottom sides were fabricated, could be slid to switch flow path between microchannels in the two glass layers.

In order to suppress leakage, hydrophobic plating technique was applied to the surface of the sliding valves. The valves were tested under pressure of between 0 and 200 kPa. With the hydrophobic Ni plating, water leakage was reduced to 1/50 of that with the non-coated valve.

Keywords: micro valve, hydrophobic plating, slide valve

1. Introduction

Inexpensive and disposable micro valves that enable few to few tens nano-liter dispensing are desired for micro biochemical applications.

There exist various micro valves based on MEMS technologies, such as passive valves utilizing surface tension of the liquid and diaphragm valves. However quantitative injection irrespective of physical parameters of the liquid, such as viscosity, is not possible with those micro valves.

Sample injection valves for HPLC can be used for quantitative injection, because in those valves channels with defined volumes slide between the flow paths for loading and dispensing. Problems are that the volumes are too large for micro-TAS and they are too expensive for biochemical applications where disposable devices are desired to prevent carry over problems.

We have successfully developed a sliding quantitative nano-liter dispensing device, wherein sections of a glass microchip were cut and were slid for switching connections between the microchannels [1]. In this paper we tried to fabricate less expensive micro slide valves using MEMS technologies.

2. Structure and Fabrication of Slide Valve

Figure 1 shows structure and fabrication scheme of the slide valve. It consisted of three layers (glass/silicon/glass), and middle part of the silicon layer could be slid. Three channels were vertically penetrating the sliding part, and the glass layers had two channels. By sliding

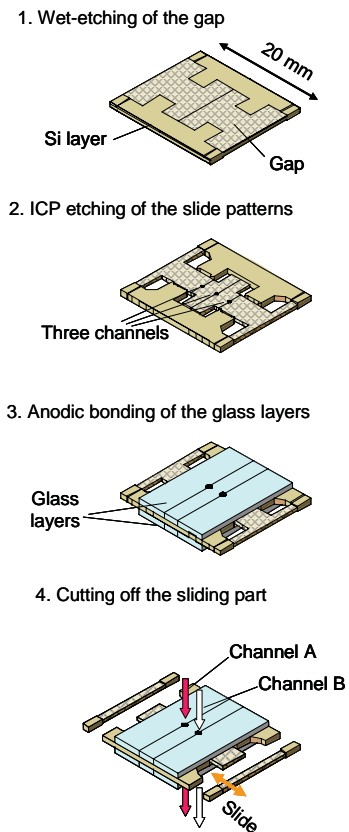


Figure 1. Structure and fabrication scheme of the slide valve

μm , and some hydrophobic coating should be made on the surface. More strongly hydrophobic the surface was, the larger the gap could be. Fluorocarbon coating of the gap surface using Cytop (Asahi Glass Co., Ltd., Japan) did not work well because the silicon and glass layers stuck together under the conditions of anodic bonding. So we applied hydrophobic plating method. Teflon particulates dispersed Ni plating was deposited on a Ni layer. Because of conductivity of the Ni layer, sticking

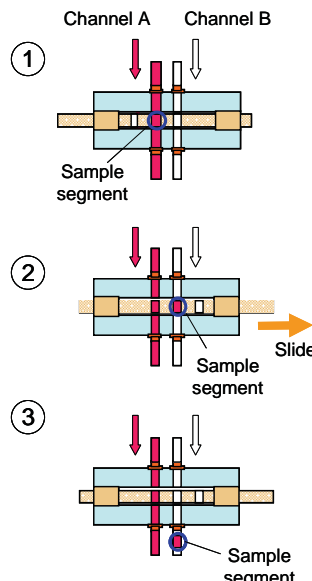


Figure 2. Working principle of the slide injection valve

the silicon part, a segment of solution A with defined volume could be injected to the solution B (Figure 2). Figure 3 shows a photograph of the slide valves.

We examined several fabrication methods for the slide valve. In order to prevent the sliding part to stick to the glass layer, a gap had to be etched. In order to prevent leakage at the gap, the gap must be smaller than $10 \mu\text{m}$.

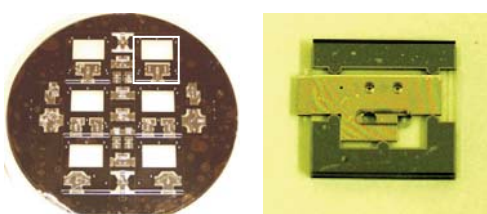


Figure 3. Photographs of the slide valve
Left: Before cutting off. Right: After cutting off

between the silicon sliding part and the glass could be prevented. We used Cr coating of the Ni layer during the patterning process to avoid unwanted oxidation of the Ni surface. And we used Al film instead of Ti for electrostatically fix the substrate during ICP etching process to avoid silicon dioxide residues that caused error in the anodic bonding.

3. Results and Discussion

The valves were tested under pressure of between 0 and 200 kPa. With the hydrophobic Ni plating, water leakage was reduced to 1/50 of that with the non-coated valve.

Three-way and rotary valves tend to be structurally complicated, and it is difficult to make them thin enough to be incorporated in microchips. We fabricated two- and three-way slide valves with the same fabrication technique (Figure 4). A small microchip as thin as 3.3 mm could be made by bonding the slide valve and a PDMS sheet with microchannels (Figure 5).

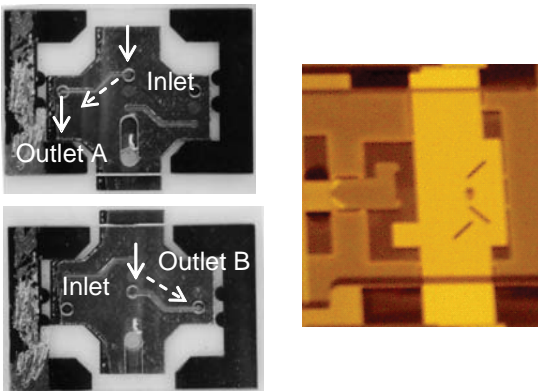


Figure 4. Two-way (left) and three-way (right) slide valves

4. Conclusion

We fabricated relatively inexpensive micro slide valves using MEMS technologies. Hydrophobic plating technique was used to suppress leakage at the sliding parts. Two-way and three-way slide valves fabricated using this method was so thin that they could be integrated in a microchemical chip as thin as 3.3 mm.

References

- [1] M. Kuwata et al., Proc. MicroTAS 2006, 602-604.

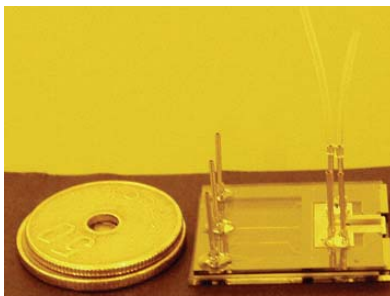


Figure 5. Microchemical chip with a slide valve

LASER CONTROLLED PICO-FRACTION UNIT FOR NANO-BIODEVICES

Toshihiko Ooie¹, Masato Tanaka¹, Tomonori Nakahara¹, Shinji Hyodo²
Yasuo Shinohara³ and Yoshinobu Baba^{1,4}

¹AIST, Health Technology Research Center, Japan

²Toyo Manufacturing Co., Ltd., Japan

³Institute for Genome Research, The University of Tokushima, Japan

⁴Graduate School of Engineering, Nagoya University, Japan

Abstract

In this research, a laser controlled liquid ejection unit for electrophoresis chips and integrated nano-biodevices was developed. Explosive vapor bubbles formed on a thin metal foil in a channel during laser irradiation effectively ejected biopolymer samples of the water solution from the channel to outside. The samples before and after ejection were analyzed by SELDI-TOF MS.

Keywords: nano-biodevice, pico-fraction, laser, bubble, electrophoresis

1. Introduction

Micro fluidic devices are powerful tools for the analysis of DNA, protein and other biopolymer samples. However, they have no fraction function that enables further analysis and/or the use of separated samples. For plastic-based disposable chips, complex systems such as piezoelectric actuators, micro valves [1] and micro heaters are not suitable because of their costs. We developed a laser controlled fraction unit, which has a laser unit outside and minimum additional parts in chip, a piece of metal foil as a beam absorber and an ejection port.

2. Design and Experimental

To realize a simple fraction unit, we set a piece of thin metal foil ($135\mu\text{m} \times 135\mu\text{m} \times 2\mu\text{m}$), which absorb laser beam from a pulsed laser unit outside the chip (Figure 1). The PMMA chip with micro channel, of which width and depth are approximately $100\mu\text{m}$ and $30\mu\text{m}$, respectively, was formed by injection molding. A polyester (PE) film, of which thickness was $50\mu\text{m}$ (including adhesive), was used for the cover film.

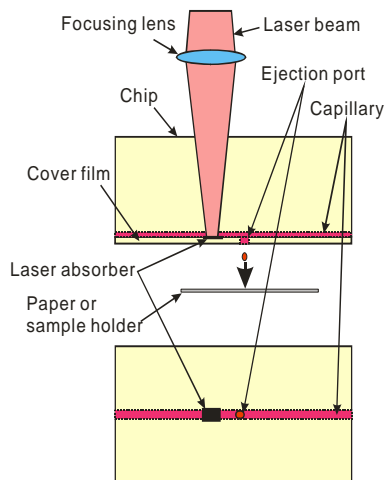
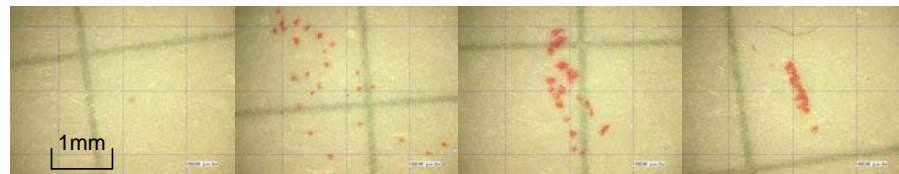


Figure 1 Schematic representation of a capillary chip used for the experiment. A titanium foil (thickness: $2\mu\text{m}$) was used for laser absorber.

An ejection port through the film was formed by the irradiation of focused fs-laser. In addition, two wells for reserved sample are at the each end of the capillary. A single-mode fiber laser, of which output power and wavelength were 40W in CW and 1060nm, respectively, was used to heat laser absorber in the capillary.

A diluted red ink was ejected to a white graph paper at a distance of 5mm from the ejection port to observe the ejection patterns. Protein samples (cytochrome c:0.1mg/ml of water and 1mg/ml of water, BSA:0.1mg/ml of water and 1mg/ml of water) were ejected to a protein chip array for SELDI-TOF MS (surface-enhanced laser desorption ionization-time of flight mass spectrometry) to compare their molecule size between before and after ejection.

3. Results and Discussion



(a)109 μ J, 60pulses (b)115 μ J, 60pulses (c)120 μ J, 30pulses (d)150 μ J, 30pulses

Figure 2 Ejection patterns at various laser pulse energy.

Figure 2 shows ejected patterns of red ink at a distance of 5mm from the ejection port. The frequency and the pulse width of the laser were constant at 1Hz and 2 μ s, respectively. From these patterns, ejection rates (ejection time/pulse number) at various laser pulse energy were estimated (Figure 3).

Ejection rate increases up to 0.85 with increasing laser pulse energy. For further increase of ejection rate, the optimization of the port shape is necessary.

Figure 4(a) and (b) show the SELDI-TOMS signals of BSA before and after ejection. The intensity is not proportional to the sample concentration and the pulse number, however, the signal of ejected sample indicates no significant difference from the signal of original sample. Similar results were obtained in cytochrome c (Figure 4(b) and (c)).

4. Conclusion

A novel function unit for electrophoresis chip and other integrated nano-biodevices was developed. The laser controlled pico-fraction unit successfully ejected protein samples without the change of their mass spectra.

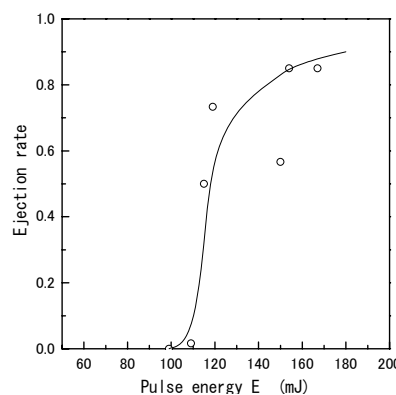


Figure 3 Relationship between laser pulse energy and ejection rate.

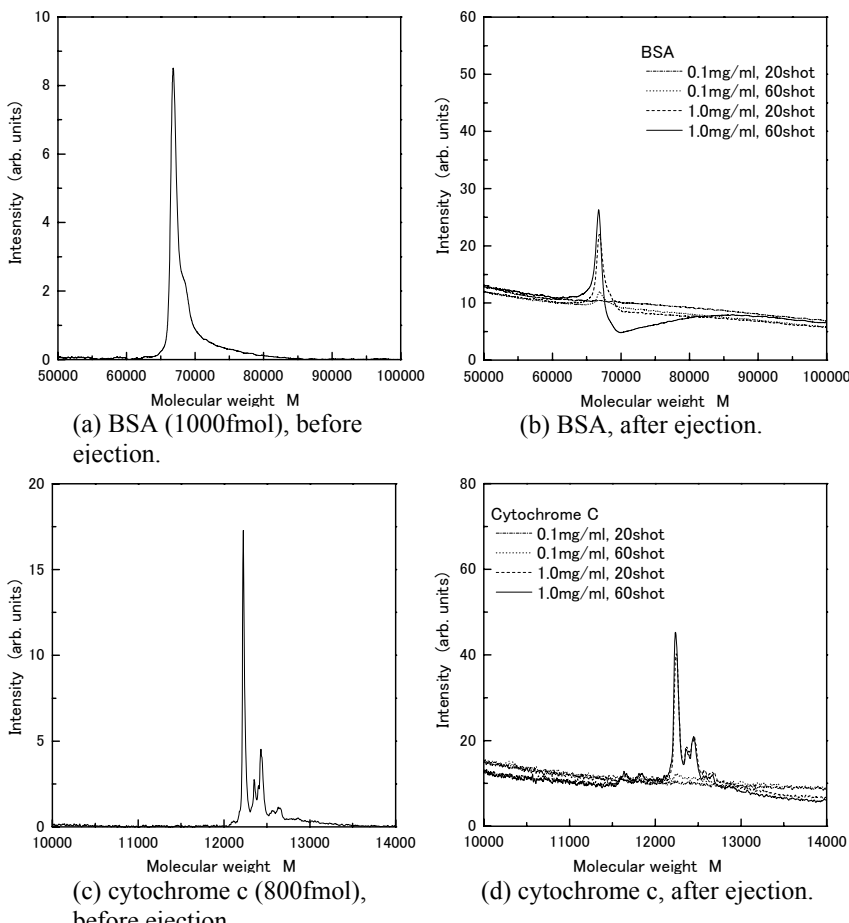


Figure 4 SELDI-TOF MS signals of BSA and cytochrome c, before and after ejection.

Acknowledgements

This work was supported by Ministry of Economy, Trade and Industry (METI), METI-Shikoku and Shikoku Technology Promotion Center (STEP) as the Regional Consortium Project.

References

1. K.Hosokawa and R. Maeda, A pneumatically-actuated three-way microvalve fabricated with polydimethylsiloxane using the membrane transfer technique, *J. Micromech. Microeng.* pp.415-420,10(2000).

MICRO FLUIDIC DEVICES IN 1 mm CUBE SHAPE FOR FLOW CONTROL IN A MICRO CHEMICAL CHIP

Yukimitsu Sekimori¹ and Takehiko Kitamori²

¹Nagano Keiki Ltd., co., Nagano, Japan

²The University of Tokyo, Tokyo, Japan

Abstract

This paper reports a series of micro fluidic devices, including pressure sensors, valves, and pumps, which have been developed for flow control in a micro chemical chip. All these micro fluidic devices have structure of 1mm cube, and they were embedded in a micro chemical chip. We succeeded in construction of a micro fluidic system using these devices.

Keywords: Pressure sensor, Valve, Pump, flow control

1. Introduction

Recently, integration of chemical operations onto micro chemical chips is drawing attentions. Microchannels of a typical width of 100 μm are fabricated in microchips, and various chemical operations such as mixing, reaction, extraction and separation can be carried out in the micro space. Efficient and environmentally amiable analytical systems with small samples and chemical synthesis systems can be constructed by using these micro chemical chips. Fluid control in a microchannel is a critical issue in such micro chemical systems. For fluid control in a microchannel, pressure sensors and micro valves that satisfy following specifications are necessary: miniaturized structure and high chemical resistance. And the devices should be installed anywhere in a micro chemical chip. In addition, they should be small so that disturbance to the flow and dead volume problems can be minimized. It is also important to develop installation method of the flow control devices to a micro chemical chip. We have examined some conventional devices for pressure control and have found that no existing devices satisfied all these requirements.

2. Characteristic of the devices

a) Pressure sensor element

Fig. 1 shows a pressure sensor element that we have developed. The sensor element was a 1 mm cube comprised of a diaphragm made of silicone a diaphragm support made of glass. Its diaphragm was coated with SiC.

The pressure sensor element has following features: small size, high chemical resistance, and high pressure resistance.

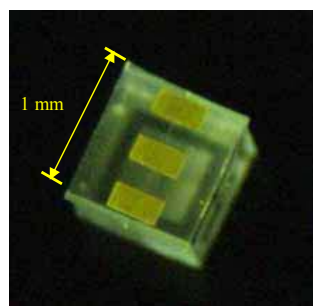


Fig. 1: Picture of the pressure sensor element

A square hole was fabricated in a cover plate of a micro channel, and the sensor element surrounded by chemically inert glue on its sidewalls was embedded in the square hole so that its diaphragm was in the same plane of the ceiling of the micro channel. Pressure at an arbitrary point could be measured by changing the position of the square hole.

The installation method of the sensor element in a micro chemical chip has following features: wide choice of material of the micro chemical chip, free choice of embedment position in the micro chemical chip, small dead volume, and negligible disturbance to the micro flow.

b) Micro valve

Fig.2 shows a sectional view of the developed valve. A 1 mm glass cube wound by chemically inert rubber was embedded in a square hole just the same as that for the pressure sensor.

When the glass cube is pushed into the microchip, the rubber deforms to fill in the microchannel, and the valve closes. When the pushing is stopped, the rubber will return to the original form, and the valve opens. By controlling the amount of pushing, aperture of the valve can be controlled.

Pressure-resistant ability of the valve was 1 MPa or more with either liquid or gas.

c) Micro pump

Fig.3 shows a sectional view of the newly developed micro pump. In a rectangular hole aligned along a micro channel, four rubber coated glass cubes were placed in line. Each cube had the same function as the above-mentioned micro valve. An external gear pushed these glass cubes periodically and in sequence so that they worked as a peristaltic pump.

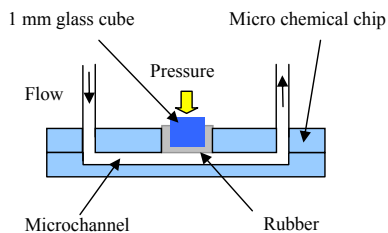


Fig.2 Sectional view of the micro valve

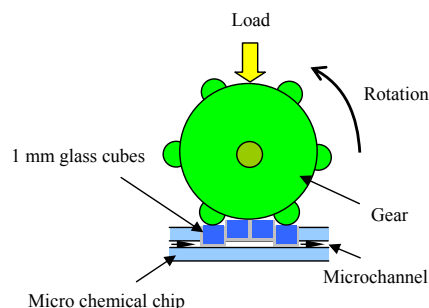


Fig.3 Sectional view of the micro pump

3. Micro chemical chip with the fluidic devices

Fig. 4 shows pictures of a micro chemical chip with the micro fluidic devices. The Pyrex glass chip (30 x 70 x 1.4 mm) had microchannels with 100 μm in width and 40 μm in depth, two rectangle holes for pumps, and five square holes for two pressure sensors and three valves.

In the microchip for fluidic control, only minimum components of the valve, the pump and the

pressure sensors were attached to the microchip. Namely, the valve and the pump were divided into a part to be actuated and a controller, and only the former was attached to the microchip. The pressure sensor elements were embedded into the microchip, while electric circuits of the pressure sensors were not.

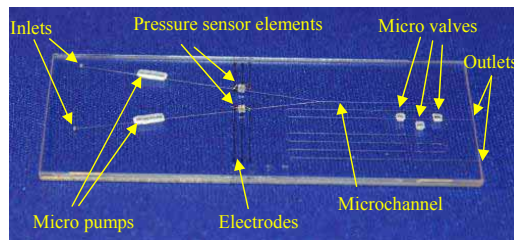


Fig.4 Picture of a micro chemical chip equipped with the 1mm cubic micro fluidic devices

4. Results

We tested the micro chemical chip with flow control devices in typical liquid control experiments: switching and mixing of two solutions. Two sets of micro pumps drove the two solutions, and two micro pressure sensors measured the pumping pressures. Micro valves were used for switching and regulation of the micro fluids. These devices were controlled by a controller comprised of the actuators for pumps and valves and sensor circuits for sensors. It was confirmed that the micro fluidic devices worked as intended.

The controller was quite simple and flexible, and can be easily applied to a micro chemical chip with a different configuration. A micro chemical chip with minimum components of the micro flow control devices can be manufactured with relative ease and with low costs, so that it could be disposable.

5. Conclusions

We have succeeded in development of a total micro fluidic system, which included 1mm cubic devices for driving, regulating and monitoring micro fluids.

Acknowledgements

This work was supported by the New Energy and Industrial Technology Development Organization (NEDO) of the Ministry of Economy, Trade and Industry, Japan.

Reference

- [1] Y. Sekimori, Y. Yoshida, T. Kitamori, *Proceedings of IEEE Sensors 2004*, pp. 516-519.
- [2] Y. Sekimori, M. Kitaoka, T. Kitamori, *Proceedings of Eurosensors XIX*, MP67

POLYMER BASED MEMBRANE DEVICES FOR SOLID-LIQUID EXTRACTION

**Yuji Murakami^{1,2}, Katsumasa Sakamoto^{1,3}, Kazuma Mawatari^{1,4},
Yoshikuni Kikutani^{1,4}, Masashi Higasa², Hiroaki Nakanishi³,
Mitsuo Kitaoka^{1,3}, Takehiko Kitamori^{4,5}**

¹The Research Association of Micro Chemical Process Technology, Japan,

²New Frontiers Research Laboratories., Toray Industries, Inc., Japan,

³Technology Research Laboratory, Shimadzu Corporation, Japan,

⁴Kanagawa Academy of Science and Technology, Japan,

⁵Graduate School of Engineering, The University of Tokyo, Japan

Yuji_Murakami@nts.toray.co.jp

Abstract

A novel method for solid-liquid extraction with a reciprocating current is proposed and demonstrated. Polymer based membrane devices for the extraction were fabricated with a proposed film-assisted method. The methods could reduce the extraction time.

keywords: extraction, filtration, polymer chip, soil analysis, heavy metal

1. Introduction

The official method for heavy metal analysis in soil requires 6 hours for extraction of 50g sample per test. In order to develop a portable on-site total analysis system, we tried to reduce the extraction time, the sample amount, and laborious procedure. Solid-liquid extraction requires, at least, a filtration unit, which should be disposable. However, microfluidic membrane devices are usually complicated, unable to integrate on a chip, and easy to leak. In this research, we have proposed and demonstrated a novel method for solid-liquid extraction with a reciprocating current. The method to incorporate a membrane into polymer based microfluidics was proposed and used to fabricate disposable devices for the extraction.

2. Experimental

Grooves on top (4mm in thick) and bottom (1mm) plates were formed by hot-embossing method on acryl plates. The top plate was drilled to make through holes

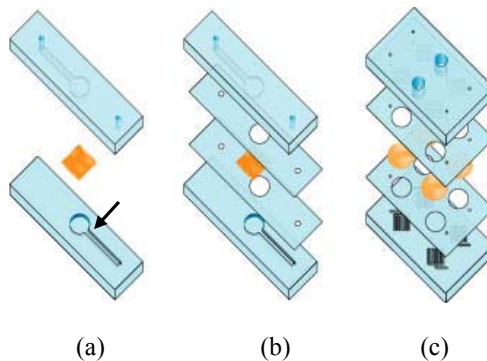
as two access ports (2mm in diameter) and a sample chamber (10mm in diameter). Membrane filters were sandwiched between thin acryl films with holes, and sealed by hot press. The top plate, the membrane film, and the bottom plate were bonded also by hot press. Model soil was put into the sample chamber and the chamber was tightly covered with an o-ring and a screw lid. Each access port was then connected to a reciprocating syringe pump synchronous to the other (Figs 1). Concentration of the extracted metal was measured by colorimetric method.



Figures 1 Fabricated two-lanes membrane device (left) and flow system (right).

3. Results and discussion

Because the typical thickness of the filter membrane is the same as the typical depth of the channel, a simple press bonding (Fig.2a) resulted in choking of the channel at the edge of the reservoir. To integrate with other functional element on a chip, however, channels should be drawn across the edge of membrane filtration element. To overcome the choking problem, we proposed a film-assisted method (Fig.2b). Thin polymer films incorporated into a membrane filter at the first step of

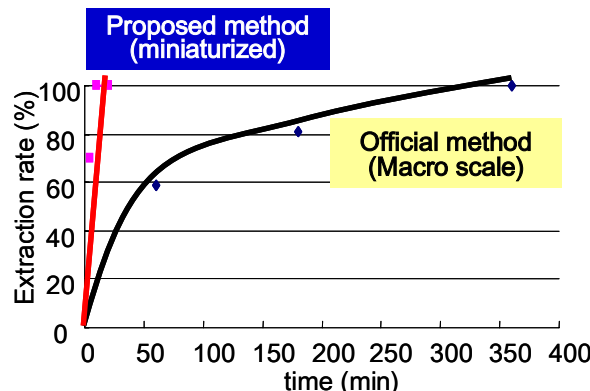


Figures 2 Schematic representation of a simple (a) and film-assisted (b) bonding in a normal membrane device, and film-assisted bonding for reciprocating current extraction of 2 lanes (c). Arrows show the choking points.

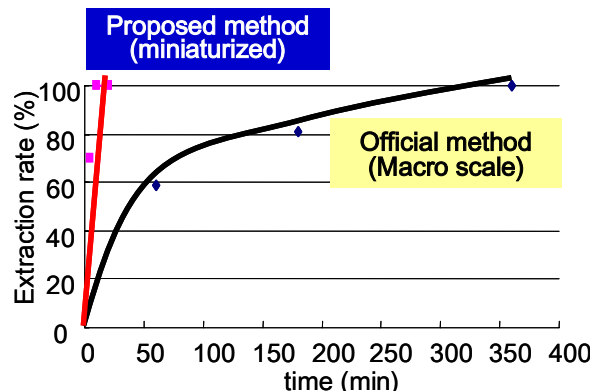
the fabrication, which was then bonded with microfabricated plates. The method enabled us to integrate other microfluidics on the same chip. The fabricated microchip (Fig.2c) was durable ($> 1\text{ MPa}$) enough to perform following method.

At the beginning of the research, we tried to employ ultrasonication in a microfluidics for the rapid extraction, resulting in a poor reproducibility due to variance of particle size of test soil. Next, the employment of a reciprocating current gave positive results in a preliminary study with a macro device, and then the devices in a microfluidics format were fabricated. Figure 3 shows a schematic representation of the extractor. Hexavalent chromium was extracted from 100 mg model soil (1/500 of the official method) and compared to the official method by a auto shaker. Results of extraction rate (Figure 4) suggest that the proposed method can reduce the time for extraction down to 15 min (official: 6h).

Microextraction using reciprocating current on a membrane chip with a film-assisted bonding method was fast, highly efficient, and easy to integrate other analytical unit such as reactor and detector.



Figures 3 Schematic cross-sectional view of the membrane device for reciprocating current.



Figures 4 Comparison of the extraction rate of hexavalent chromium from a model soil. In the case of the official shaking extraction, 50 g of sample was shook at 200rpm with the amplitude of 4cm. In the case of proposed reciprocating current method, 100mg of sample was repeatedly flowed.

SLIDING MICRO VALVE DEVICE FOR NANO LITER HANDLING IN MICROCHIP

Masahiro Kuwata^{1,2}, Takehiko Kitamori³

¹ Corporate Research & Development Center, Toshiba Corporation, Japan
(masahiro.kuwata@toshiba.co.jp)

² The Research Association of Micro Chemical Process Technology, Japan

³ The University of Tokyo, Japan

Abstract

This paper reports a novel sliding micro valve system, which is capable of switching and injecting liquids with quantitative accuracy in nano liter range without any dead volume in microchip. Surface treatment of slide structure prevents leaks under a pressure of 5 MPa. Since the device is made of Pyrex glass and fluorocarbon coating, it has high chemical tolerance. Sequential process of switching and quantitative injection (10nL) was performed to justify the applicability of this device.

Keywords: **microvalve, micromachining, flow injection analysis**

1. Introduction

It is important for quantitative multiple analysis to switch samples rapidly in microchip. The fundamental concept and the test results of sliding micro valve as injector device and multi-dispensing device were reported at past MicroTAS conferences [1,2]. The sliding micro valve structure can be extended to other functions serially and parallel (injection, switching, dispensing, and so on) in accordance with the intended use by modifying the channel structure.

2. Device structure

A valve integrated microchip and microscope pictures are shown in Fig. 1. The size of the microchip is about 70 x 30 mm. The depth and width of all channels are 40 μ m and 100 μ m, respectively. A part of microchip was cut in parallel with each other. And the valve part slides in parallel with right-and-left parts. The channels in microchip are disconnected and reconnected with this slide movement. Thus, it works as switching and injection valve each other. The width of the valve part is 3mm.

Before these were cut, these channels in left-center-right parts were originally single channel. Thus, when these are reconnected, the shape, depth and width are same. Therefore there is no dead volume left between these channel connections.

Surface treatment of slide structure is very important for pressure tightness. The contact surfaces of each part are coated with fluorocarbon resin to prevent leakage of liquid from the gaps of slide structure. This surface treatment works well for pressure tightness. All the valves can withstand a pressure difference of at least 5MPa.

Since this device is comprised of glass partly coated with fluorocarbon resin, it can be used for almost all kind of fluids including organic solvent, acid, alkaline.

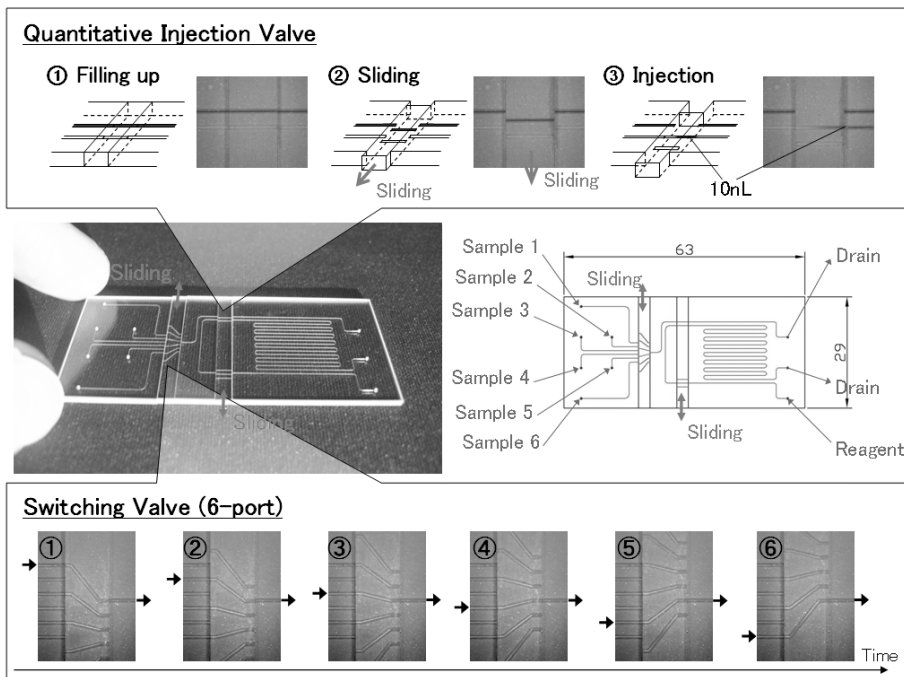


Figure 1. Structure of sliding micro valve device and microscope pictures.

3. Experiments

As a check of fundamental performance of switching valve device, changeover time was measured. Sunset Yellow solution (1.0×10^{-2} M) and water were switched. The signal was detected by thermal lens microscope at the point 28mm (volume 90nL) from switching valve. Typical result is shown in figure 2. In this system, switching valve embedded in microchip, and there is little dead volume left in valve structure. Thus it is possible to change the sample quickly. In the case of $1.0\mu\text{L}/\text{min}$, these samples changed within a few second.

As the fundamental application

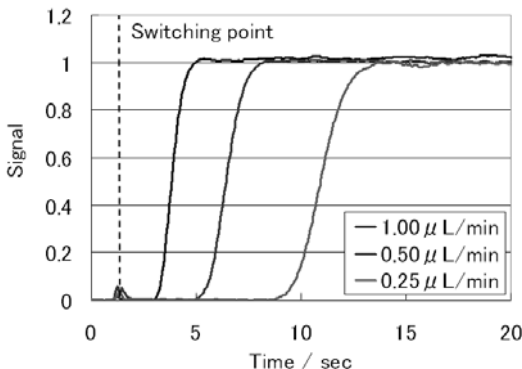


Figure 2. Typical result of changeover time measurement.

of this system, sequential process of switching and quantitative injection was performed. Three sunset yellow solution having concentration 1.0, 2.0, 3.0×10^{-2} M were switched and injected. The injection volume is 10nL. The signal of the injected samples were detected with thermal lenses microscope. Typical result is shown in figure 3. Switching and injection valve are integrated on a microchip and the volume between switching valve and injection valve is so little (distance 17mm, volume 57nL) that injection samples were quickly changed. Thus, the whole sequential process of three measurements for three samples was completed within 135sec. The residual liquid between contact surfaces of slide structure is so little that there is no problem in cross contamination of samples.

4. Conclusions

This paper describes the integration of injection and switching function on a microchip. This proposed system is expected to serve a number of analyses in micro-scale.

Acknowledgements

A part of the study presented in this paper was supported by New Energy and Industrial Technology Development Organization (NEDO), Japan.

References

1. M. Kuwata, T. Kawakami, K. Morishima, Y. Murakami, H. Sudo, Y. Yoshida, T. Kitamori, Sliding Micro Valve Injection Device for Quantitative Nano Liter Volume, Proc. Micro Total Analysis System 2004, pp.342-344, (2004).
2. M. Kuwata, K. Sakamoto, Y. Murakami, K. Morishima, H. Sudo, M. Kitaoka, T. Kitamori, Sliding Quantitative Nanoliter Dispensing Device for Multiple Anaysis, Proc. Micro Total Analysis System 2005, pp.602-604, (2005).

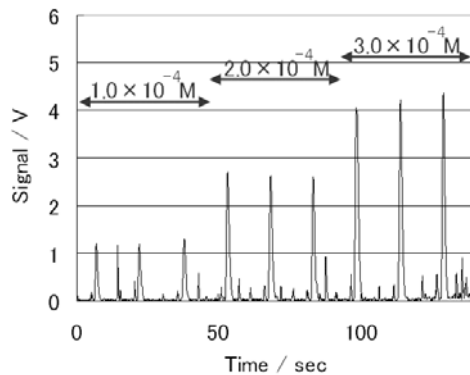


Figure 3. Typical result of sequential process of switching and quantitative injection. (Three measurements for three samples.)

FABRICATION OF PREMITIVE SPHERICAL MICROPUMP POWERED BY CARDIOMYOCYTES: MICRO SHERICAL HEART

Yo Tanaka¹, Kae Sato¹, Tatsuya Shimizu², Masayuki Yamato²,
Teruo Okano², Takehiko Kitamori¹

¹The University of Tokyo, Bunkyo, Tokyo, 113-8656, Japan

²Tokyo Women's Medical University, Shinjuku, Tokyo, 162-8666, Japan

Abstract

We have created a micro spherical heart-like fluidic device powered by spontaneously contracting cardiomyocyte sheets. This device was fabricated by wrapping a beating cardiomyocyte sheet exhibiting large contractile forces, around a fabricated hollow elastomeric sphere (5 mm diameter, 250 μm polymer thickness). Fluid oscillations in a capillary connected to the hollow sphere induced by the synchronously pulsating cardiomyocyte sheet were confirmed, and the device continually worked for at least 5 days in this system. We anticipate that this device might be applied for various purposes including a bio-actuator for medical implant devices that relies on biochemical energy, not electrical interfacing.

Key words: Cardiomyocyte, Heart, Bio-microactuator, Cell sheet, Hollow sphere

1. Introduction

Recently, efficient biochemical devices incorporating cells into a miniaturized chemical system have been frequently reported as the scale of a microspace is accommodated to cell sizes and processing capabilities. While biochemical reactors or analysis systems exploiting cellular biochemical functions are the mainstream, we proposed to exploit cardiomyocytes to integrate a mechanical function into a microspace and created a cardiomyocyte pump as a prototype bio-microactuator previously [1]. However, that fundamental design is a typical reciprocating displacement type with associated inefficiencies (i.e., unused volumes due to complicated compartment interfacing from centimeter-dimensional chip sub-structures and push-bars too massive to realize truly integrated fluidic devices exploiting complete cell-driven potential). Here, we demonstrate new fabrication methods to create a more realistic, heart-like spherical micropump powered by beating cardiomyocytes without waste compartments: a micro-spherical heart pump.

2. Experimental

Fig. 1 shows the design of a micro spherical heart powered by cardiomyocytes. This design represents only fundamental function, similar to the earliest primitive heart (one chamber, no valves) as in tubular hearts of annelids (e.g. earthworms). To improve mechanical transduction and fluid dynamic performance, we utilize a previously reported cultured cardiomyocyte sheet shown to exhibit cooperative

contractile forces produced by collectively synchronous, pulsatile properties across larger-scale dimensions [2].

A fabricated hollow sphere made of flexible polymer: PDMS is contracted by the rolled, attached cardiomyocyte sheet. Fabrication process of a hollow sphere with capillaries we have newly developed is shown in Fig. 2. Briefly, it was fabricated by dissolving a sugar ball after dispensing and solidifying PDMS prepolymer on the ball. Then, a prepared neonatal rat cardiomyocyte sheet detached from a temperature responsive dish was wrapped around the hollow sphere by aspirating the medium and incubated at 37°C for 1 hour to attach to the hollow sphere. A fabricated hollow sphere (about 5 mm in diameter, 250 μm in thickness) with connected capillaries (200 μm in inside diameter) is shown in Fig. 3A. The hollow sphere after transplantation of a cardiomyocyte sheet is shown in Fig. 3B.

3. Results and Discussion

Reliable maintenance of cell phenotypic contractile activity in the sheet produced periodic contractile-expansion motion of the PDMS micro spherical heart. In order to visualize the resulting fluid behavior in the attached capillaries, spherical polystyrene tracking particles (1 μm diameter) were dispersed in cell culture medium within the capillaries (Fig. 4A). Just after attachment of a cardiomyocyte sheet, particle movements were observed directly using a phase contrast microscope with an objective lens (40 \times , 0.60-NA) focused on the center of the capillary at 37°C. Time-course of the displacement (x) for a select particle near the center of the capillary is plotted in Fig. 4B, black line. Displacement at $t = 0$ s was defined as $x = 0 \mu\text{m}$. The fluid oscillating frequency was 0.4 Hz and the maximum linear displacement was 70 μm . This fluid motion was obviously produced by the cardiomyocyte sheet, because a tracking particle did not move practically before cardiomyocyte sheet transplantation (gray line in Fig. 4B). The device continually worked for at least 5 days.

4. Conclusions

In this report, we have demonstrated new fabrication methods to create a novel micro spherical heart-like pump prototype, and demonstrated its pumping mechanism and capabilities. Regular fluid motion in a capillary connected to the hollow pumping sphere was confirmed, with the device working continuously over 5 days. This bio/artificial hybrid fluidic device is a fully integrated, wireless mechanochemical converter, exploiting a spherical heart-like pumping structure. Pumping action is driven with only chemical energy input from culture milieu without any requirement for coupled external energy sources, unlike conventional actuators. Our demonstrated device would be applied in various purposes such as drug-delivery systems.

5. References

1. Y. Tanaka, K. Morishima, T. Shimizu, A. Kikuchi, M. Yamato, T. Okano, T. Kitamori, *Lab Chip*, **6**, 362-368, (2006).
2. T. Shimizu, M. Yamato, Y. Isoi, T. Akutsu, T. Setomaru, K. Abe, A. Kikuchi, M. Umezu, T. Okano, *Circ. Res.*, **90**, e40-e48, (2002).

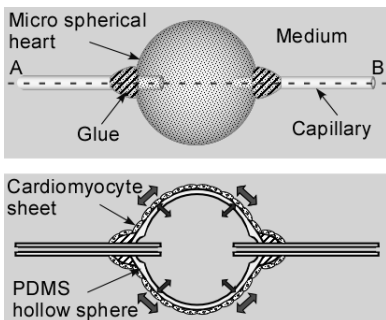


Figure 1. Design of a micro spherical heart. A cardiomyocyte sheet covers the hollow sphere entirely. (Upper) Schematic view. (Lower) Cross-sectional view along line A-B.

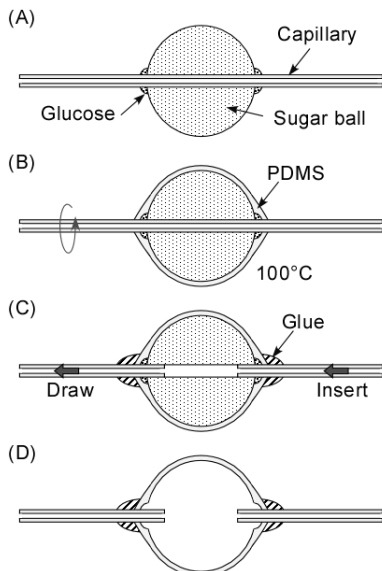


Figure 2. Fabrication process of a PDMS hollow sphere. (A) Threading a capillary through a hole on a sugar ball, and applying melted glucose around the hole to prevent penetration of PDMS prepolymer. (B) PDMS dispense and solidification while rotating above a hotplate at 100°C. (C) Drawing and insertion of capillaries to make them be into the sphere partly and attachment of them to the sphere by glue. (D) Dissolving the sugar ball by water.

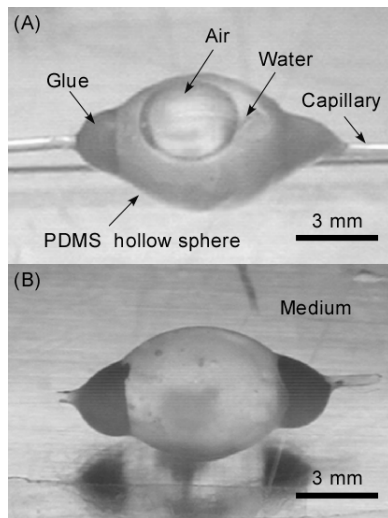


Figure 3. Photos of a hollow sphere. (A) A fabricated PDMS hollow sphere. (B) A hollow sphere immersed in medium after transplantation of a cardiomyocyte sheet.

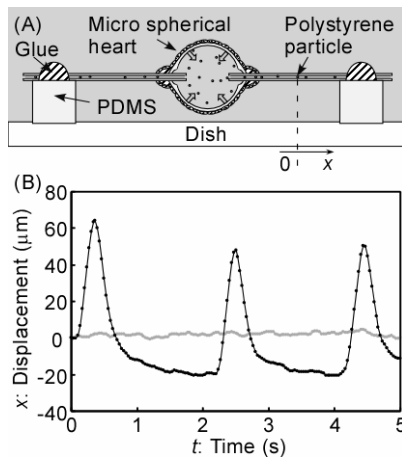


Figure 4. Fluid observation in a capillary. (A) Schematic view describing the observation method and a measured parameter (x). (B) Displacement time-course of one particle near the center of the capillary for 5 s at 37°C. Gray and black plots indicate particle displacement before and after cardiomyocyte sheet transplantation, respectively.

HIGHTHROUGHPUT ENZYME INHIBITION ASSAYS ON A CAPILLARY BASED SEQUENTIAL INJECTION SYSTEM

Wen-Bin Du, Qun Fang*, Zhao-Lun Fang

Institute of Microanalytical Systems, Department of Chemistry,

Zhejiang University, Hangzhou, China, 310028

fangqun@zju.edu.cn

ABSTRACT

We demonstrate an automated microfluidic sequential injection analysis system using a short fused-silica capillary, slotted-vial array sample injection system and laser induced fluorescence detection, which efficiently manipulates sample and reagent solutions in the nanoliter range. The present system was applied in a enzyme inhibition assay using β -galactosidase with a high throughput of 300 h^{-1} and low sample consumption of 4.2 nL .

KEYWORDS: sequential injection analysis, enzyme inhibition assays, microfluidics, capillary

1. INTRODUCTION

Sequential injection analysis (SIA),¹ as a new generation of flow injection analysis (FIA), has now developed into a well-established technique enjoying broad acceptance, owing to improvements in the degree of automation, sample/reagent economy as well as reliability compared to conventional FI systems. However, so far effects on miniaturization of SIA are rarely reported. Davidsson et al.² coupled a microfluidic chip with macroscale injection valves and pumps for construction of an enzyme based μ -biosensor. Pu et al.³ recently reported a microchip-based electroosmotic flow pump, and applied it with a macroscale six-way selection valve in a capillary-based SIA system for enzyme inhibition analysis.

2. EXPERIMENTAL

The system setup is as described in Fig 1. A 6-cm long fused-silica capillary with a secondary layer of polyacrylamide inside the bore (eCAP Neutral Capillary, Beckman Coulter) functioned as a sampling probe, reactor, as well as a flow-through detection cell. The outlet of the capillary was fixed and connected to a horizontally oriented waste reservoir, which provided liquid level differences for inducing gravity driven flows in the capillary. An auto-sampling system consisting of a pair of gears driven by a programmed stepping motor and a set of horizontally fixed slotted-vials,⁴ was employed to sequentially introduce samples and reagents into the capillary. The slotted-vials for containing samples and reagents were produced from 0.2-mL microtubes (Porex, Petaluma, CA) by fabricating 0.9-mm wide, 1.0-mm deep slots on the conical bottom of the tubes. On-column detection was achieved using a home-made laser-induced fluorescence detector with an excitation wavelength of 473 nm.⁵ Sample and reagents

zones were sequentially introduced via gravity driven flow by scanning the capillary tip through the vial slots, while vials containing sample, reagent and carrier were sequentially rotated to the probe in an order of carrier, enzyme, inhibitor sample 1, substrate, carrier, enzyme, inhibitor sample 2, substrate, etc.⁶ The sequentially injected train of solutions was transported through the capillary to the detection point and then to waste by the gravity drive. The enzyme inhibition assay was based on the inhibition of the β -galactosidase enzyme by an inhibitor sample (diethylenetriamine pentaacetic acid, DTPA), impeding the conversion of the substrate (fluorescein digalactoside, FDG) to fluorescent hydrolysates, fluorescein mono- β -D-galactopyranoside (FMG) and fluorescein via the enzyme.

3. RESULTS AND DISCUSSION

In this work, the slotted-vial array sample injection system was combined with a short fused silica capillary to produce a highly efficient and simple μ SIA system that is capable of sequentially introducing hundreds of nanoliter sample/reagents at high throughputs without resorting to conventional valves and pumps and microfabricated chips. Sequentially injected zones were rapidly mixed by diffusion and convection within the carrier flow, demonstrating a behavior that conformed well to the Taylor dispersion model.⁷

The potential for using the present system in high-throughput drug discovery was demonstrated by employing the β -galactosidase enzyme inhibition system as a model. Optimization of experimental parameters was carried out with preliminary experiments on effects of reaction rate, sample volume and flow rate. The difference between the liquid levels of the capillary and waste reservoir was set to 15 cm, corresponding to a flow rate of 4.2 nL/s to achieve sufficient mixing and enzyme reaction. The introduction times for inhibitor sample, substrate and enzyme solution were set to 1 s, respectively, resulting in a net sample/reagent consumption of 4.2 nL for each determination. Figure 2 displays the results of enzyme inhibition studies. With enzyme and substrate zones separated by a DTPA solution with different concentrations from 0 to 2.0 mM, the reaction rate decreased due to the inhibition of DTPA on the activity of the enzyme, initially forming a tallest peak that was basically Gaussian, and at higher concentrations

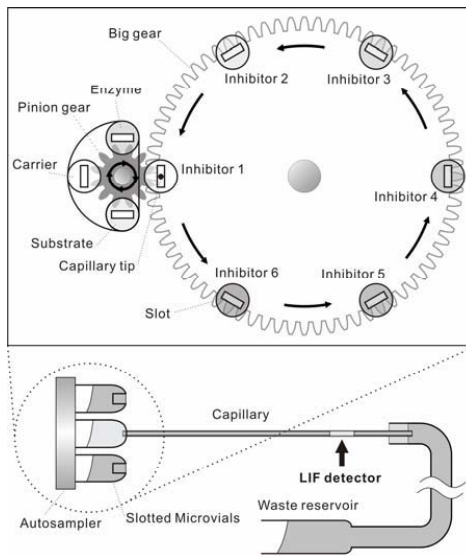


Figure 1. Schematic diagram of the μ SIA system. (not to scale).

producing a complete depression in the middle of the peak. A linear relationship was obtained between $\log C_{DTPA}$ (mM) and percentage inhibition in the range of 0.1-2 mM DTPA with a regression equation of $PI = 0.476 \log C_{DTPA} + 0.738$, $r^2 = 0.9932$. A precision of 2.7% RSD ($n = 5$) was obtained for 0.5 mM DTPA with a maximum possible throughput of 300 h⁻¹ deduced based on the peak width.

4. CONCLUSIONS

In the present work, without resorting to pumps, valves and microfabrication techniques, a simple capillary based microfluidic analysis system (CBMAS) was developed to perform SIA manipulation of multiple nanoliter volume liquids. We believe that the ultra low-cost μ SIA methodology developed in this work has great potentials in bioanalysis involving precious samples and reagents, particularly those that involve the sequential mixing of several solutions. The approach also provides a powerful means for online process monitoring and high-throughput screening.

ACKNOWLEDGMENTS

This work has been supports by the National Natural Science Foundation of China (Grant 20575059) and National Education Ministry (Grant NCET-05-0511).

REFERENCES

- [1] J. Ruzicka and G. D. Marshall, *Anal. Chim. Acta* 1990, 237, 329.
- [2] R. Davidsson, F. Genin, M. Bengtsson, T. Laurell and J. Emneus, *Lab Chip* 2004, 4, 481.
- [3] Q. S. Pu and S. R. Liu, *Anal. Chim. Acta* 2004, 511, 105.
- [4] W. B. Du, Q. Fang, Q. H. He and Z. L. Fang, *Anal. Chem.* 2005, 77, 1330.
- [5] J. L. Fu, Q. Fang and Z. L. Fang, *Anal. Chem.* 2006, 78, 3827.
- [6] Q. Fang and W. B. Du, Chinese Patent, Appl. No.: 200610049830.9, 2006.
- [7] W. E. van der Linden, *Trends Anal. Chem.* 1987, 6, 37.

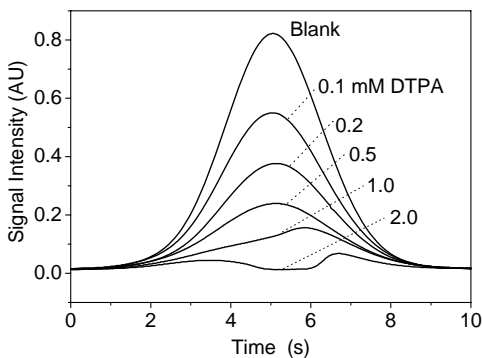


Figure 2. Enzyme inhibition assays obtained by varying the inhibitor concentration.

NOVEL 3-D IMPELLOR-SHAPED FERROMAGNETIC MICRO-STIRRER BAR AND ITS USE FOR ACTIVE MICROMIXING

Arun K. Nallani¹, Jeong-Bong Lee², David B. Wallace³, and Donald J. Hayes³

¹ Intel Corporation, 5000 W. Chandler Blvd., Chandler, AZ, 85226

² University of Texas at Dallas, 2061 N. Floyd Rd., Richardson, TX, 75080

³ MicroFab Technologies, Inc., 1104 W. Summit Ave., Plano, TX, 75074

Abstract

We report the development of a high efficiency magnetic microfluidic mixer based on a novel 3D impellor-shaped ferromagnetic micro-stirrer bar. The 3D impellor-shaped micro-stirrer bar with 31.6° inclined angle is fabricated using tilted (55°) SU-8 exposure technique. The 3-D inclined micro-stirrer bar causes 3-D perturbation of fluids resulting in rapid mixing in microscale. When compared with a vertical straight sidewall micro-stirrer bar, approximately 20% of mixing efficiency enhancement is achieved.

Key Words: SU-8, 3D impellor, ferromagnetic, stirrer, mixing

1. Introduction

Rapid, high efficiency mixing of fluidic species in microscale is essential for various microfluidic applications. Microscale mixing is challenging due to the inherent laminar flow of fluids in micro-scales. Laminar flow is demonstrated in Fig. 1a using dyed water-based liquid species flowing through a sealed PDMS microchannel (Fig. 1b). Molecular diffusion across fluidic interface is known to cause mixing in microscale, but it is limited due to slow mixing rates [1]. Lagrangian chaos is another mechanism known to be effective in micro-scale mixing [2] which occurs only in 2-D time-dependant or 3-D flows, which requires perturbations created by 3-D microstructures. The fabrication of true 3-D microstructures has not been fully realized yet [3].

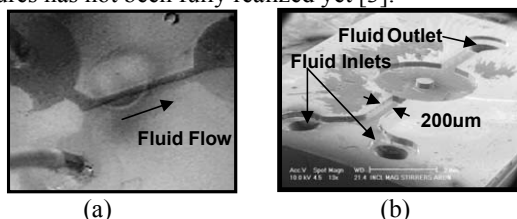


Fig. 1(a) Laminar flow of fluid illustrated by flow of green and pink dyed water based fluid species, (b) PDMS micro-channel.

2. Design and Fabrication

We designed a novel true 3-D impellor-shaped micro-stirrer which can be realized by tilted SU-8 exposure technique (Fig. 2a). Due to the refractive index difference between

air and SU-8, with an incident angle of 55° , the tilt angle of the SU-8 mold obtained is 31.6° . $\text{Ni}_{0.81}\text{Fe}_{0.19}$ permalloy is electroplated through the mold (Fig. 2b) to create 3-D impellor-shaped micro-stirrers. Various shapes and dimensions of straight and inclined sidewall micro-stirrers are fabricated (Fig. 2c, d). The micro-stirrers are heterogeneously integrated onto a center post built in PDMS microchannel (Fig. 1b) and the channels are plasma bonded onto glass substrates to form sealed micromixers. Holes, defined into the microchannel, form the fluidic inlets and outlets.

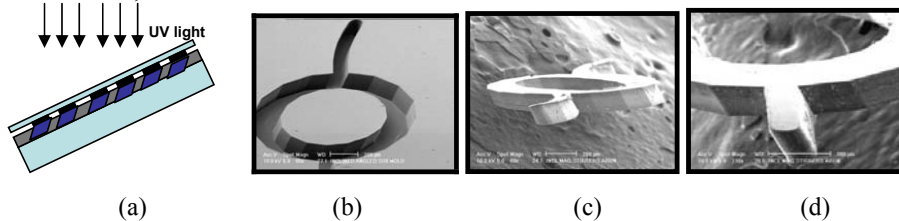


Fig. 2(a) Tilted SU-8 exposure; SEM images of; (b) inclined SU-8 mold; (c) 3-D curved inclined micro-stirrer; (d) 3-D straight inclined micro-stirrer.

3. Characterization

The micro-stirrer is actuated by placing the micromixer on a Cimerec Thermolyne stirring plate and microstirrers' rotational speeds are measured using a stroboscope (Movistrob model 500). The fluid flow through the micro-channel is set-up using controlled suction force applied from the outlet end using Microfab Inc., Pneumatics control unit model CT-PT-04. For quantitative evaluation of mixing efficiency, still images of mixing are captured using a camera and are analyzed using color analysis software (Able image analyzer v2.1).

4. Results and Discussion

Fig. 3(a-d) shows the mixing efficiency as a function of micro-stirrer's rotational speeds for the 3-D inclined impellor-shaped micro-stirrer. The mixing is quantitatively correlated by analyzing the pixel color intensity difference seen across a straight line on the output side of the micro mixer. Better mixing makes more uniform color at the output end which corresponds to a flatter contrast curve (Fig. 4). It is shown that 3D inclined microstirrer works better than the vertical sidewall stirrer (Fig. 5). The inclined micro-stirrer shows approximately 20% of mixing efficiency enhancement over the vertical sidewall microstirrer (Fig. 6). The improvement in mixing efficiency for the inclined micro-stirrers is because they are designed to operate such that during rotation, one blade forces the fluid in the upward direction while the other forces the fluid in the downward direction, thus causing the Lagrangian chaos required for rapid mixing in microscale.

5. Conclusions

A novel 3-D impellor shaped magnetic micro-mixer is developed and improved performance, based on Langrangian Chaos, is demonstrated. This novel true 3-D

impellor-shaped micro-stirrer bar-based microfluidic mixer will be useful for various microfluidic applications.

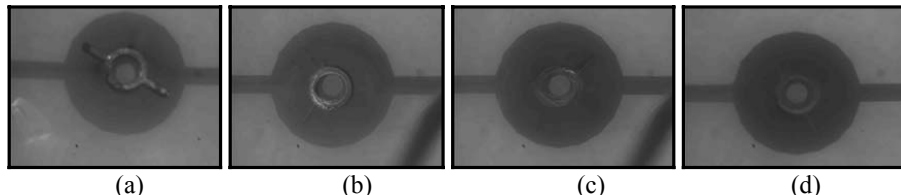


Fig. 3 Images of microfluidic mixing w/ 3-D straight inclined bar w/ (a) 0 RPM (b) 200 RPM (c) 800RPM and (d) 1000 RPM speeds.

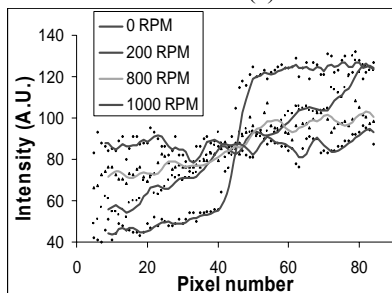


Fig. 4 Contrast profiles for different rotational speeds.

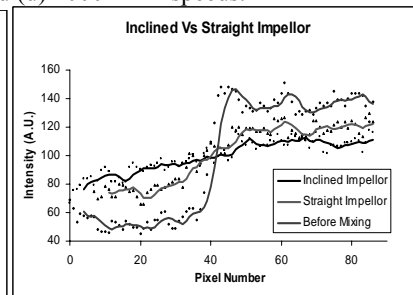


Fig. 5 Contrast profiles for the 3-D inclined vs. vertical sidewall straight impellor.

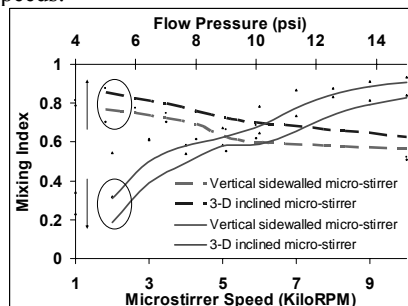


Fig. 6 Mixing Index as functions of pressure and micro-stirrer speed for the novel true 3-D impellor shaped micro-stirrer and vertical side-wall micro-stirrer.

References

1. C. Campbell, B. Grzybowski, *Microfluidic mixers: from microfabricated to self-assembling device*, Trans. R. Soc. London, A, 362, pp. 1069-1086, (2004).
2. J. Ottino, *The kinematics of mixing*, Cambridge, ISBN 0521368782, (1989).
3. L. Lu, K. Ryu and C. Liu, *Microstirrer and array for microfluidic mixing*, IEEE J. MEMS, vol. 11, issue 5, pp. 462-469, (2002).

HIGH-EFFICIENCY IN-VITRO SELECTION OF DNA APTAMERS USING A DIELECTROPHORESIS- ACTIVATED CELL SORTER (DACS)

Eric T. Lagally*, Xiaoyuan Hu*, Yanting Zhang*, Lisan Viel*, Jeffrey B.-H. Tok[§], Theodore M. Tarasow[§], and H.T. Soh*

*California Nanosystems Institute and Department of Mechanical Engineering,

University of California – Santa Barbara, Santa Barbara, CA

[§]Chemistry and Materials Science Directorate, Lawrence Livermore National Laboratory, Livermore, CA

Abstract

Current techniques for the *in-vitro* selection of high-affinity molecular recognition reagents usually require large volumes and intensive manual labor, leading to poor selection efficiency and reproducibility. In this work, we demonstrate the first SELEX process in a microfluidic device, utilizing the dielectrophoresis-activated cell sorter microchip (DACS) to screen an aptamer library. High-affinity aptamers can be generated in only two rounds of SELEX, representing a five-fold improvement in selection efficiency.

Keywords: *in-vitro* selection, aptamer, dielectrophoresis, SELEX

I. Introduction

Systematic Evolution of Ligands through Exponential Enrichment (SELEX) is a promising technique for the isolation of high-affinity nucleic acid molecular recognition reagents [1]. The resulting DNA or RNA aptamers demonstrate high affinity and specificity to a wide variety of target molecules, including proteins, carbohydrates, and small molecule targets [2]. In addition, aptamer libraries can be large ($> 10^{15}$ members), chemically synthesized and modified, are stable during long-term storage, undergo reversible denaturation and are amenable to amplification through the Polymerase Chain Reaction (PCR).

SELEX involves three steps: binding of a DNA or RNA pool to the target molecule, selection of bound aptamers, and amplification of these aptamers for the next round of selection. SELEX is typically manually intensive and requires many necessary rounds of selection, resulting in months of time to achieve convergence. Microfluidics offers an attractive platform to improve the efficiency of the SELEX process through more stringent control of selection conditions, which results in fewer necessary selection rounds. Furthermore, microfabrication also provides the opportunity to significantly decrease the need for manual labor by integrating multiple process steps in a single device. The advent of dielectrophoresis-based microfluidic deflection systems in particular provides a possible method for the separation of bound aptamer-target complexes from unbound aptamers, resulting in enhanced selection efficiency. By

immobilizing the target on a solid phase (e.g. polymer microsphere), microfluidic separations may be performed with very high efficiency. Here we demonstrate a novel use of our DACS device [3] to screen a DNA pool for high-affinity aptamers against human alpha-thrombin.

II. Materials and Methods

An aptamer library was synthesized consisting of 6×10^{14} unique sequences, each 85 bp long and containing a 40 bp internal randomized region flanked by primer hybridization sequences on both sides (Figure 1A). Next, SELEX was performed (Figure 1B); the library was reacted with biotinylated target molecule (human alpha-thrombin) and this mixture was then bound to microspheres using biotin-streptavidin chemistry.

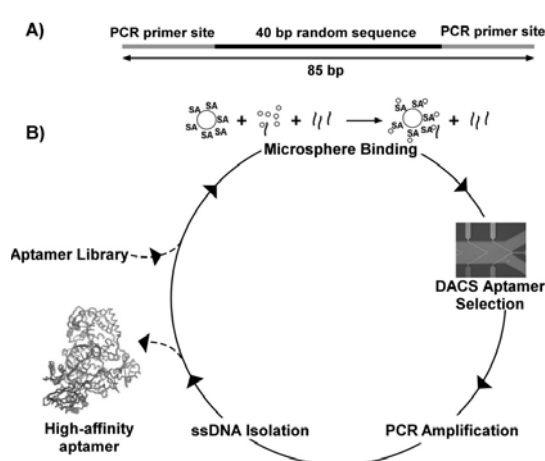


Figure 1. A) 85 bp aptamer library with 40 bp random sequence. B) SELEX protocol using DACS chip. High affinity aptamers bind to biotinylated target, and these complexes are bound to streptavidin-conjugated microspheres. Aptamers with no affinity for the target remain unbound. Isolation of bound aptamers is performed using the DACS chip, followed by PCR amplification and single strand generation. Repeated rounds yield high-affinity aptamers against the desired target.

The DACS chip (Figure 2A) was used to separate the aptamer sequences with affinity for the target molecule by sorting out the bead-bound aptamers from the mixture. In this configuration, the laminar flow within the DACS device directs unbound aptamers to the waste channels while bead-bound aptamers are dielectrophoretically deflected by the electrodes and funneled into the center collection channel (Figure 2B). The quadrupole electrodes of DACS were powered at 20 volts peak-to-peak at 1 MHz and the flow rate was 500 $\mu\text{L}/\text{hr}$. Following selection, the bound aptamers were PCR amplified using biotinylated primers and a streptavidin column was utilized to generate single strands for the next round of selection.

Flow cytometry was used to monitor the purity and the convergence of the isolated aptamer pools. Following each round of selection on the DACS device, 1% of the purified DNA pool was re-amplified using Cy5-labeled primer. The resulting fluorescently labeled aptamers were directed against thrombin-conjugated microspheres and the aggregate affinity of the pool was observed as the mean fluorescence intensity per microsphere.

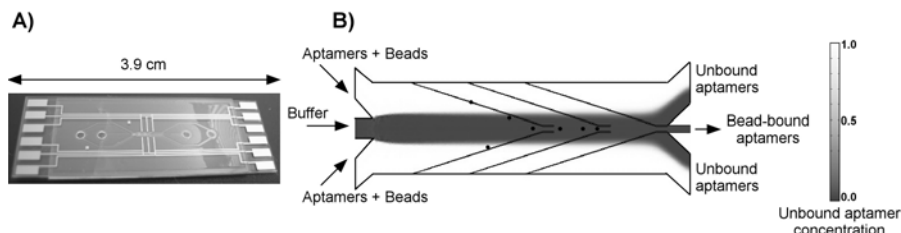


Figure 2. A). A micrograph of the Dielectrophoresis-Activated Cell Sorter (DACS) chip. B) Simulated concentration profile of the unbound aptamers during the DACS operation; bead-bound aptamers are deflected into the center collection channel, while unbound aptamers flow to waste.

III. Results and Conclusions

Figure 3 presents histograms of the Cy5 fluorescence collected from fluorescently labeled aptamers following two rounds of selection against human alpha-thrombin. The increase in fluorescence from the initial library towards the fluorescence seen from the positive control (a published thrombin aptamer [4]) in only two rounds represents an approximately five-fold improvement in the affinity enhancement per round compared to conventional SELEX performed manually (data not shown). This first screening of an aptamer library in a microfluidic system demonstrates rapid convergence and significantly higher efficiency for the isolation of aptamers with affinity towards the target molecule.

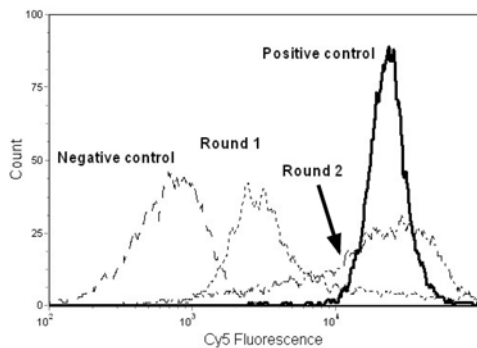


Figure 3. Fluorescence enhancement of aptamer binding to microsphere-immobilized human alpha-thrombin over two rounds of microfluidic SELEX. Enhanced affinity of the aptamer pools to thrombin is demonstrated by higher mean fluorescence values as a function of selection round.

References

1. Tuerk, C. and Gold, L., *Science*, 1990, 249, 505-510.
2. Proske, D., Blank, M., Buhmann, R. and Resch, A., *Appl. Microbiol. Biotechnol.*, 2005, 69, 367-374.
3. Hu, X. Y., Bessette, P. H., Qian, J. R., Meinhart, C. D., Daugherty, P. S. and Soh, H. T., *PNAS*, 2005, 102, 15757-15761.
4. Bock, L. C., Griffin, L. C., Latham, J. A., Vermaas, E. H. and Toole, J. J., *Nature*, 1992, 355, 564-566.

FABRICATION OF AN ON-CHIP NMR MICROFLUIDICS DEVICE

L. L. Sohn,¹ J. L. Herberg,² B. D. Harteneck,³ D. R. Myers,¹ and J. A. Liddle³

¹Dept. of Mechanical Engineering, University of California, Berkeley, CA 94720 USA

²Lawrence Livermore National Laboratory, Livermore, CA 94550 USA

³Lawrence Berkeley National Laboratory, Berkeley, CA 94720 USA

Abstract

We discuss our first steps toward the development of an on-chip NMR device that has the potential to probe and image single cells. We describe a novel technique we have developed for fabricating three-dimensional microcoils on a chip. Our fabrication protocol is general and therefore can be applied to different coil dimensions and different coil materials.

Keywords: *NMR, microfluidics, microcoils*

1. Introduction

Cell metabolism can change drastically due to naturally occurring fluctuations in the internal cell state and in environmental conditions. At a basic molecular biology level, it is important to gain an understanding of such fluctuations and their relationship to the dynamics of genetic and protein networks. Unfortunately, existing approaches to probing cell state, e.g. fluorophore tagging, suffer from a variety of limitations such that monitoring the dynamic state of a cell *in vivo* is not possible. Clearly, though, there is a great need for such a technology. Here, we present the development of an on-chip NMR device that has the potential to probe and image single cells.

2. Theory

The signal-to-noise ratio (SNR) of a three-dimensional (3D) micro-coil is directly proportional to \sqrt{Q} where $Q = 2\pi f L / R$, f is the operating frequency, L is the coil

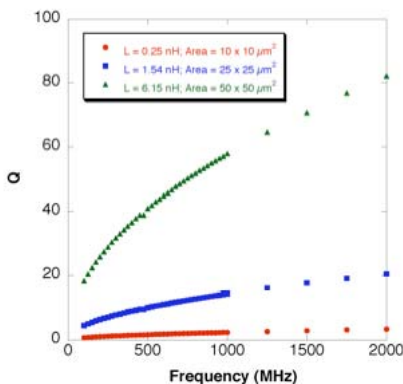


Figure 1: Calculated Q for a copper 3D micro-coil that is $\ell = 200 \mu\text{m}$ -long and consists of $N = 20$ turns. The Q vs frequency is shown for three cross-sectional areas (and therefore, inductances) of the coil: $10 \times 10 \mu\text{m}^2$ (circle); $25 \times 25 \mu\text{m}^2$ (square); and $50 \times 50 \mu\text{m}^2$ (triangle).

inductance, and R is the coil resistance. The coil inductance is defined as $L = (\mu_0 N^2 A) / \ell$ where μ_0 is the magnetic permeability of free space, N is the number of coil turns, A is the cross-sectional area of the coil, and ℓ is the coil length. Because R is determined by the resistivity of the metal used, the Q of a 3D micro-coil is largely dependent on the inductance L , and in turn, A the cross-sectional area of the coil. We have calculated the Q vs frequency of an $N = 20$ turns, $\ell = 200 \mu\text{m}$ -long copper solenoid having three different inductances: $L = 0.26 \text{ nH}$ (circle); $L = 1.54 \text{ nH}$ (square); and $L = 6.15 \text{ nH}$ (triangle) (Figure 1). Our calculation is for an ideal 3D micro-coil and does take into account the skin effect of copper at high frequencies. It does not, however, take into account stray capacitances and inductances associated with leads and the fluid that will eventually run through the coil. Regardless, our calculation does show a dramatic range of Q 's obtainable with our micro-coil when we simply change the cross-sectional areas (and therefore, the inductances) of the coil, itself.

3. Experiment

The fabrication steps we have developed to create our 3D micro-coils are summarized in Figure 2. As shown, the different steps include using a combination of conventional photolithography, electroplating, and photoresist leaching. Our protocol is general so that we can fabricate either gold or copper coils. Figure 3 shows a completed gold 3D micro-coil fabricated on a silicon substrate. As shown, it is an $N = 20$ turn coil which has a cross-sectional area A of $10 \times 10 \mu\text{m}^2$ and a length $\ell = 205 \mu\text{m}$.

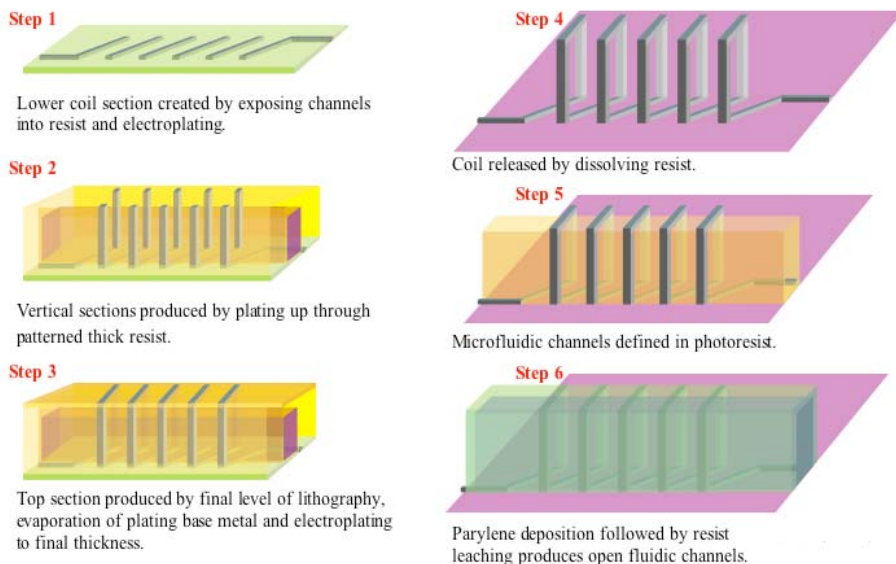


Figure 2: Fabrication steps to create 3D micro-coil.

Once our micro-coils are fabricated, they are coated with $\sim 2.5 \mu\text{m}$ of parylene (Fig. 3B). This, in conjunction with a PDMS microfluidic channel (Fig. 3C), electronically isolates the micro-coil from the fluid flowing through the coil.

4. Results and Discussion

Preliminary electronic measurements of our micro-coils are promising. The resistance of a gold micro-coil prior to annealing is 3.5Ω . After annealing, the resistance reduces to 3.0Ω . Much of the resistance measured is due to the micro-coil pads and leads that are on average $500 \mu\text{m}^2$ in area. We intend to reduce the size of the pads and leads to thus decrease the resistance. The inductance of a gold micro-coil is 5.0 nH , which corresponds to an estimated Q value of approximately 1 at a frequency of 100 MHz.

5. Conclusions

In this paper, we discuss our first steps toward the development of an on-chip NMR device that has the potential to probe and image single cells. We describe a novel technique we have developed for fabricating three-dimensional microcoils on a chip. Our fabrication protocol is general and therefore can be applied to different coil dimensions and different coil materials.

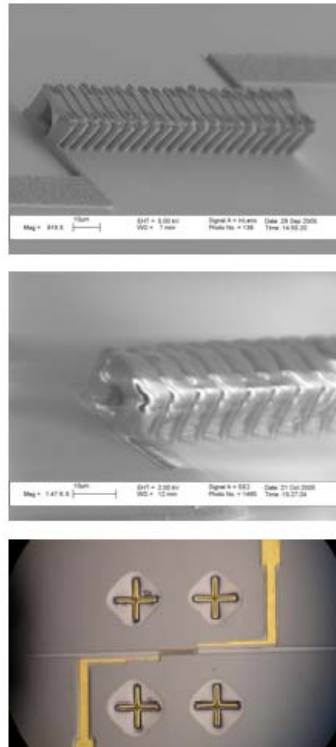


Figure 3: A) Scanning electron micrograph (SEM) of a gold 3D micro-coil. B) SEM photo of a gold 3D micro-coil coated with $2.5 \mu\text{m}$ of parylene. C) Optical view of a sealed device that includes a PDMS-based microfluidic channels and the 3D micro-coil.

A LOW POWER, MICROMACHINED, PROPORTIONAL VALVE FOR DRUG DELIVERY

Allan T. Evans¹, Jong M. Park*, Ryan P. Taylor², Tyler R. Brosten², Gregory F. Nellis², Sanford A. Klein², Jeffrey R. Feller³, Louis Salerno³, and Yogesh B. Gianchandani¹

¹*Department of Electrical Engineering and Computer Science, University of Michigan, Ann Arbor*

²*Department of Mechanical Engineering, University of Wisconsin, Madison*

³*NASA Ames Research Center, Moffett Field, CA 94035*

ABSTRACT

This paper describes a proportional valve that regulates viscous liquid media, intended for use with elastic reservoir/pumps in a portable drug delivery system. The valve is fabricated in a partially open state to permit flow even in the absence of applied power. At room temperature, piezoelectric actuation from -30 V to 60 V causes modulation of oil (viscosity 4.5 cP) flow rates in the range of 250-460 $\mu\text{l}/\text{min}$, while consuming as little as 0.136 μW of power. The valve is micromachined from bulk silicon and Pyrex glass. The entire packaged structure, including the actuator and housing, is 0.8 cm^3 .

Keyword: microvalve, piezoelectric actuation, drug delivery, flow modulation

1. INTRODUCTION

Elastic reservoir pumps are attractive for delivering liquids in portable applications since they do not consume any electrical power. However, the output varies with the fill level and delivery pressure [1]. These output variations can be corrected by using a proportional microvalve to regulate the pump. For applications that demand prolonged deployment and extended battery life, valves that consume little power are necessary. Using a normally open valve reduces energy consumption because it allows a nominal liquid flow rate without having to apply any power. This type of valve also provides greater control by allowing the flow rate to be either increased or decreased from its default liquid delivery rate. A number of micromachined valves have been reported in the past [5-14], but they have not addressed the needs of this particular application. Electrostatic valves typically require voltages >100 V, and are limited in operating pressure and range of flow modulation. Thermal and magnetic valves consume significant power. A piezoelectric valve used for this system greatly reduces energy consumption while overcoming the drawbacks of other actuation schemes. With proper control electronics and a coin cell battery, the entire portable system could interface with an individual through a catheter (Fig. 1).

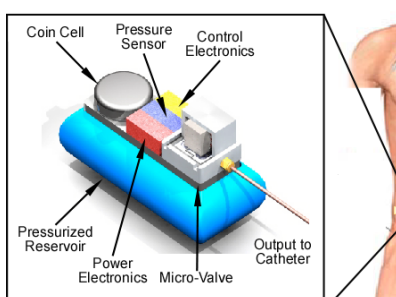


Fig. 1: Proposed system schematic. Expanded view of a side patch connected micro-valve controlled portable drug delivery system.

Typical chemicals that might be delivered with a micropump include insulin, hormonal and pain management drugs, and any other liquid phase drugs that are preferably delivered in a gradual manner. (Table 1). These chemicals have a range of viscosities that must be taken into account in any portable delivery system design.

Table 1: Typical drug delivery flow rates.

Drug Name	Delivery Rate
Morphine	20-167 $\mu\text{l}/\text{min}$ [2]
Pethidine	10-250 $\mu\text{l}/\text{min}$ [2]
Epidural	0-200 $\mu\text{l}/\text{min}$ [3]
Insulin	2-350 $\mu\text{l}/\text{min}$ [4]

Corresponding author; tel: 734 615 7136; fax 734 763-9324; email: evansall@umich.edu

This paper presents preliminary investigations into using a normally open piezoelectric microvalve and an external passive reservoir [15] to demonstrate low power liquid flow modulation within the same ranges currently used to continuously deliver pain relief drugs such as morphine.

2. VALVE DESIGN AND FABRICATION

The valve is constructed from bulk silicon and glass, with a piezoelectric (PZT) stack actuator and a glass-mica (Macor™) ceramic cap. The PZT provides power-efficiency, high force, and proportional actuation. A buried oxide layer in an SOI wafer acts as an etch stop for deep reactive ion etching of silicon, so the valve flexures have uniform thickness. A recess is wet etched into a glass wafer to accommodate the PZT displacement. The inlet and outlet holes are formed using electrochemical discharge machining. The SOI and glass wafers are anodically bonded, diced, and prepared for assembly with the ceramic cap and PZT stack. To create a normally-open valve, the PZT stack is energized during the assembly process, so that it shortens after assembly. Finally, the finished valve is attached to a Macor header to interface with the passive reservoir/pump and standard tubing.

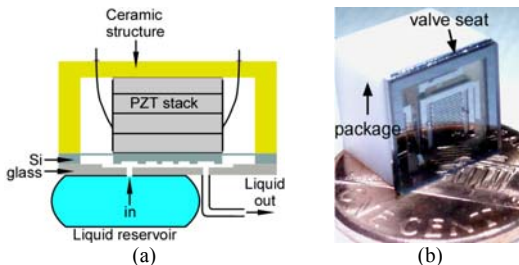


Fig. 2: (a) The valve cross-section showing the assembled ceramic-PZT-Si-glass structure and associated liquid reservoir. (b) A photograph of the completed assembled valve structure placed on a United States penny.

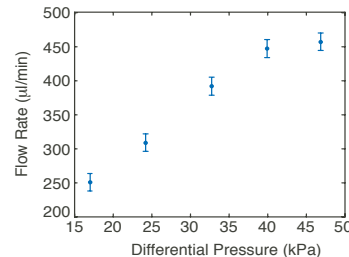


Fig. 3: Flow rate through un-actuated valve (0 V) across various pressures. At lower pressures the flow rate changes linearly with pressure.

3. VOLTAGE AND FREQUENCY FLOW RATE REGULATION

Preliminary tests were performed at room temperature using oil (viscosity 4.5 cP) to provide solution viscosity greater than saline water. For every test, a liquid reservoir was pressurized with regulated nitrogen gas to control and simulate varying pressures that might be generated from a passive source. The valve outlet was exposed to atmospheric pressure to create a pressure difference across the valve. Flow rates were determined by calculating the mass change in an outlet reservoir over a two minute time period.

In the first test (Fig. 3), the liquid flow rate was monitored as input pressure was varied. The flow rate varied linearly with the differential pressure over a range of 250-460 $\mu\text{l}/\text{min}$; the corresponding differential pressure drop was 16-47 kPa. In the next experiment (Fig. 4), the valve was actuated by increasing and decreasing the voltage with different inlet pressures. Flow rates were tested over a range of input pressures (108-142 kPa), and could be altered from the un-powered, partially open flow rate by as much as 50 $\mu\text{l}/\text{min}$.

A frequency test was conducted in which the microvalve was actuated with a 50 Hz, 0-60 V square wave with varying duty cycle (Fig. 5). This provided more uniform linear control across inlet pressure than DC control. These results suggest that either voltage or frequency can be used to regulate the flow rate. DC operation consumed 0.136 μW and AC operation used 45 mW. As expected, DC regulation consumes less power. AC modulation is less efficient because of capacitive losses in the piezoelectric actuator.

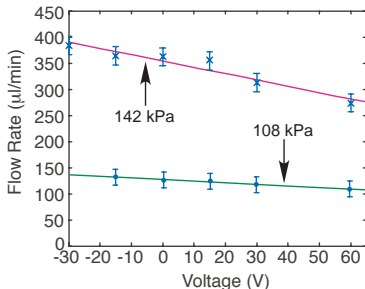


Fig. 4: Flow rate versus voltage actuation from -30 V to 60 V. Results are recorded for two inlet pressures, while the outlet is held constant at 101 kPa. Actuation is more pronounced with greater inlet pressure.

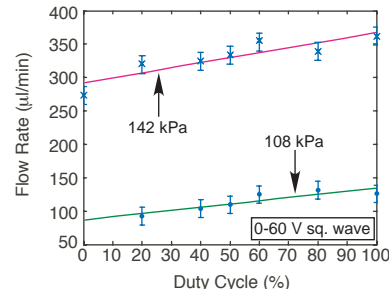


Fig. 5: Flow rate changes versus duty cycle for two inlet pressures. The actuation voltage was a 50 Hz square wave from 0-60 V. This method does not rely on the linearity of piezoelectric actuation.

4. CONCLUSIONS

The experiments described in this effort demonstrate that a piezoelectric microvalve actuated with varying DC voltages can adequately regulate liquid flow from a passive pump/reservoir. Furthermore, a power efficient, portable, high flow rate drug delivery system is realizable with these components.

ACKNOWLEDGEMENTS

These devices were fabricated at the Michigan Nanofabrication Facility. This work was supported primarily by NASA under award NNA05CP85G.

REFERENCES

- [1] B. Ziaie, et al., "Hard and Soft Micromachining for BioMEMS: Review of techniques and examples of applications in microfluidics and drug delivery," *Advanced Drug Delivery Reviews*, 56(2), 2004, pp. 145-72
- [2] E. Charlton, "The Management of Postoperative Pain," *Update in Anesthesia*, Issue 7, Article 2, 1997, pp. 1-7
- [3] L. Visser, "Epidural Anaesthesia," *Update in Anesthesia*, Issue 13, Article 11, 2001, pp. 1-4
- [4] "The Medtronic MiniMed 2007 Implantable Insulin Pump System," http://www.minimed.com/professionals/products/implantable_pump/eu.html
- [5] J.K. Robertson, K.D. Wise, "A Low Pressure Micromachined Flow Modulator," *Sensors and Actuators A*, 71(1-2), 1998, pp. 98-106
- [6] N. Vandelli, D. Wroblewski, M. Velonis, T. Bifano, "Development of a MEMS Microvalve Array for Fluid Flow Control," *J. Microelectromechanical Systems*, 7(4), 12/1998, pp. 395-403.
- [7] C.A. Rich, K. D. Wise, "A High-Flow Thermopneumatic Microvalve with Improved Efficiency and Integrated State Sensing," *J. Microelectromechanical Systems*, 12(2), 4/2003, pp. 201-8
- [8] M.J. Zdeblick, "A Microminiature Electric-to-Fluidic Valve," *1987 International Conference on Solid-State Sensors and Actuators*, pp. 827-9
- [9] T. Ikehara, H. Yamagishi, K. Ikeda, "Electromagnetically Driven Silicon Microvalve for Large-Flow Pneumatic Controls," *Proceedings of the SPIE - The International Society for Optical Engineering*, v. 3242, 1997, pp. 136-44
- [10] M.A. Huff, J.R. Gillbert, M.A. Schmidt, "Flow Characteristics of a Pressure-Balanced Microvalve," *1993 International Conference on Solid-State Sensors and Actuators*, pp. 98-101
- [11] S. Shoji, B. VanderSchoot, N. deRooij, M. Esashi, "Smallest Dead Volume Microvalves for Integrated Chemical Analyzing Systems," *1991 International Conference on Solid-State Sensors and Actuators*, pp. 1052-5
- [12] R. Duggirala, A. Lal, "A Hybrid PZT-Silicon Microvalve," *J. Microelectromechanical Systems*, 14(3), 2005, pp. 488-97
- [13] P.W. Barth, et al., "A Robust Normally-closed Silicon Microvalve," *1994 Solid-State Sensor and Actuator Workshop*, Hilton Head Island, pp. 248-250
- [14] L. Choonsup, Y. Eui-Hyeok, S. M. Saeidi, J.M. Khodadadi, "Fabrication, characterization, and computational modeling of a piezoelectrically actuated microvalve for liquid flow control," *J. Microelectromechanical Systems*, 15(3), 2006, pp. 689-96
- [15] J.M. Park, et al, "A Piezoelectrically Actuated Ceramic-Si-Glass Microvalve for Distributed Cooling Systems," *2006 Solid-State Sensor and Actuator Workshop*, Hilton Head Island, pp. 248-251

A Microfluidic Device for Droplet-based DNA-PNA Hybridization and Separation

Shohei Kaneda¹, Kotaro Somei², Koichi Ono³, Takatoki Yamamoto¹, and Teruo Fujii¹

¹IIS, The University of Tokyo, Meguro-ku, Tokyo, 153-8505 Japan

²Tokyo Institute of Technology, Yokohama, Kanagawa, 226-8503 Japan

³Enplas Laboratories, Inc, Kawaguchi, Saitama, 332-0034 Japan

(shk@iis.u-tokyo.ac.jp)

Abstract

A microfluidic device for droplet-based liquid handling by using two types of vent structure is presented. Two different samples were segmented into 330 pL droplets and merged together for hybridization by pneumatically manipulation. Then, electrophoresis was conducted on the same device for analysis of the reaction products.

Keywords: Droplet(s), Electrophoresis

1. Introduction

The development of microfluidic devices for droplet handling has attracted significant attention in the research field of μ TAS in recent years. Several methods have been thus proposed to manipulate droplets by electrostatic force [1], dielectrophoretic force [2], hydrodynamic force [3], and pneumatic force [4]. Although there're still some issues to be discussed, the pneumatic handling of droplets is one of the promising ways because of its intrinsic minimal side effects on bio/chemical reactions and compatibility with conventional separation (e.g., chromatography, electrophoresis, etc.) schemes. Therefore, we have continuously been pursuing the techniques for the droplet handling using pneumatic force, which is controlled through vent structures [4, 5] with an external automated pneumatic control system. Here, we present a droplet handling microfluidic device combined both droplet-based reactions and electrophoretic separation processes in order to realize the seamless analysis coupled with reaction by fully automated operations. As a demonstration, ssDNA and PNA (peptide nucleic acid) hybridization and electrophoretic separation were successfully carried out.

2. Experimental

The device consists of a fluidic chip made of PDMS and a glass substrate on which Au/Cr electrodes are patterned (left side in Fig. 1). The fluidic chip has four liquid ports (L1~4) and four pneumatic ports (P1~4) which connect to a PC controlled air pressure tank unit (HIP-240, Arbiotec, Japan). The two electrodes are patterned with 16.5 mm spacing on the glass substrate. The fluidic chip has three working regions (right side in Fig. 1A'~C'). All pneumatic channels are connected to each liquid channel through ‘microcapillary vent array’ (MVA1~3: w 4 μ m, h 2.5 μ m, pitch 4 μ m) [4]. By applying positive or negative air pressure to the liquid channels through the MVAs, introduction and formation of droplets and merging operation of liquid can be carried out. All liquid channels are connect to ‘main channel’ (in Fig. 1B’, C’) through ‘stop vent’ (SV1,

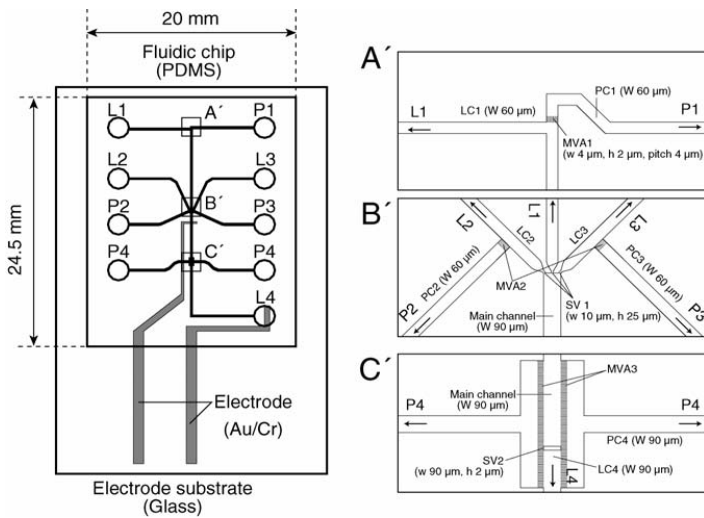


Figure 1. Schematic drawing of the microfluidic device. The three working regions are magnified in the right side. The four pneumatic ports are connected to a PC controlled air pressure tank unit via silicone tubes.

2). The stop vents work for positioning operation of liquid. These two types of vent structure are based on the hydrophobicity of PDMS and its small cross section. All channels height is 25 μ m.

3. Results and discussion

The performance of the device was evaluated by conducting the reaction of DNA-PNA (peptide nucleic acid) hybridization followed by electrophoretic separation. First, a HEC polymer solution (1.2 % Hydroxyethyl cellulose in 1X TBE buffer) works as a sieving matrix in L1, the ssDNA (72 mer, 4 μ M) solution in L2, and the PNA (15 mer, 4 μ M) solution in L3 were introduced into each channel and positioned at each SV1 by applying negative pressure of 5 kPa at P4 (Fig. 2A). Simultaneously, the polymer solution in L4 for salt bridge was introduced and positioned at SV2 (Fig. 2B). Second, The ssDNA solution was segmented into 330 pL droplet and injected into the main channel to be stopped at SV2 by applying positive pressure of 40 kPa for 1 sec at P2 (Fig. 2C). Similarly, the droplet of the PNA solution was formed and merged with the ssDNA droplet (Fig. 2D). Third, by applying positive pressure of 40 kPa at P1 and negative pressure of 5 kPa at P4, the polymer solution in L1 was metered, injected into the main channel and merged with the droplet of PNA-ssDNA conjugate solution (Fig. 2E, F). Then the second polymer solution works as salt bridge and the PNA-ssDNA conjugate droplet were merged by applying negative pressure of 20 kPa at P4. Finally, electrophoresis was conducted by applying 35 V (21.9 V/cm) between the two electrodes (Fig. 2H, I). Since PNA is electrically neutral [6] while DNA is negatively charged, the PNA was kept at the initial location while ssDNA was traveled through the PNA region during electrophoresis. The ssDNA would be mixed through the PNA region, so that both PNA and ssDNA droplets were not needed to be premixed completely by diffusion before electrophoresis. The weak peak shown in Fig. 2J corresponds to the ssDNA/PNA hybrid. The

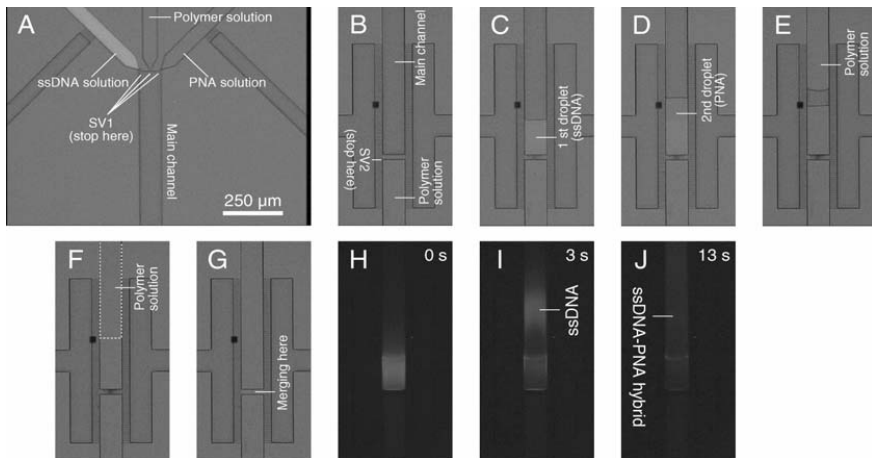


Figure 2. Captured video images of droplet-based liquid handling for ssDNA-PNA reaction and separation. (A) The solutions were introduced and stopped at each SV1. (B) The polymer solution for salt bridge was introduced and stopped at SV2. (C, D) The ssDNA and PNA droplet were segmented, injected into main channel and merged together. (E, F) After 1 min, segmented polymer solution for sieving matrix was injected and merged with the droplet. In this premixing, the ssDNA and the PNA solutions are not mixed completely by diffusion. (G) The droplet was merged with the salt bridge polymer solution. (H) Electrophoresis was conducted by applying 35 V (21.9 V/cm). (I, J) The ssDNA/PNA hybrid has smaller mobility than ssDNA. The ssDNA was stained by SYBR Gold.

mobility of ssDNA/PNA hybrid is lower than the ssDNA due to the uncharged nature of the PNA molecules [6]. Although, the efficiency of reaction is not so high in the current condition, the whole operations were executed within 3 min in an automated manner.

4. Conclusion

A droplet-based microfluidic device for hybridization/separation analysis was developed and it was confirmed that the whole process for the analysis could be conducted within 3 min in a fully automated manner. The present fundamental methodologies for droplet based multi-step operations could lead to further complication and automation in high-throughput analytical systems for nucleic acids, proteins, etc.

References

- [1] G. Michael, et al., *Appl. Phys. Lett.*, 77, pp. 1725-1726, (2000).
- [2] T. B. Jones, et al., *J. Appl. Phys.*, 89, pp. 1441-1448, (2001).
- [3] T. Nisisako, et al., *Lab on a Chip*, 2, pp. 24-26, (2002).
- [4] K. Hosokawa, et al., *Anal. Chem.*, 71, pp. 4781-4785, (1999).
- [5] S. Kaneda, et al., *Proc. µTAS 2003*, pp. 1279-1282, (2003)
- [6] P. E. Nielsen, et al., *Science*, 254, pp. 1497-1500, (1991).
- [7] A. Basile, et al., *Electrophoresis*, 23, pp. 926-929, (2002).

CONTINUOUS SEPARATION OF BLOOD PLASMA USING SEDIMENTATION IN A MICROCHANNEL

Sang Youl Yoon¹, Sung Yang², Joon-Ho Moon¹ and Kyung Chun Kim¹

¹School of Mechanical Engineering, Pusan National University, Busan, Korea

²Department of Bioengineering, The Pennsylvania State University, PA, USA

(e-mail: kckim@pusan.ac.kr)

Abstract

This paper reports a continuous, real time blood plasma separation method using sedimentation of blood cells in a microchannel. The design of a separation device and the efficiencies of separation are described in this paper. The device was made of PDMS (Polydimethylsiloxane). The functionality of the device is tested using a heparinized human whole blood.

Keywords : Blood Plasma, Separation, Microchannel, BioMEMS, Sedimentation

1. Introduction

Most clinical blood tests require cell-free serum or plasma. In order to obtain full blood test capabilities on a chip, it is essential to have a device, which can separate blood components within a chip. Current microfluidic technologies provide the separation of blood plasma from whole blood by using either mesh-type filters or diffusion based filtration systems in the device [1-3]. One of the biggest concerns of these devices is a clogging of cells for the filter type devices and a relatively long diffusion times of blood cells for the diffusion based filtration devices. In order to overcome these bottlenecks, a novel microfluidic device for continuous blood plasma separation is introduced. The operating principle is simply based on the sedimentation effect of RBCs within the microchannel. Hence, this study aimed to develop a continuous, real time blood plasma separation method using sedimentation of blood cells in a microchannel.

2. Design and Fabrication of Blood Plasma Separation Device

Figure 1 shows a schematic drawing of the operating principle of the device. Red blood cell has higher density ($\rho_{RBC} \approx 1100 \text{ kg/m}^3$) than blood plasma ($\rho_{BP} \approx 1030 \text{ kg/m}^3$).

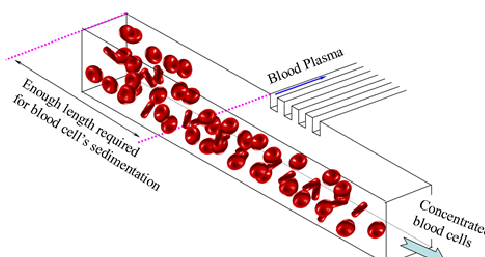


Fig. 1. Schematic drawing of the operating principle

Therefore, due to the sedimentation of blood cells on bottom of the channel, only plasma can be collected to blood-plasma separation channel using branch channels with low depth. The device was precisely designed to obtain maximum sedimentation of blood cells and to optimize the flow rate of separated blood plasma at the bifurcation region by control of pressure drops through the channels and CFD simulation (CFD-ACE+, CFD Research Corp.). The device was expected to derive the blood plasma of 0.5% of main blood flow rate through each separation channel and 9% of the inlet flow rate through 20 branch channels when the inlet flow rate is $0.1\mu\text{l}/\text{min}$.

The device was made of PDMS (Polydimethylsiloxane) and bonded with a glass plate by means of plasma bonding. The semi-3D shaped mold was fabricated with double layered and exposed SU-8 PR. The branched plasma channel had $10\mu\text{m}$ depth and $20\mu\text{m}$ width, while the whole blood channel had $90\mu\text{m}$ depth and $150\mu\text{m}$ width. A SEM image of the PDMS device is shown in Fig. 2.

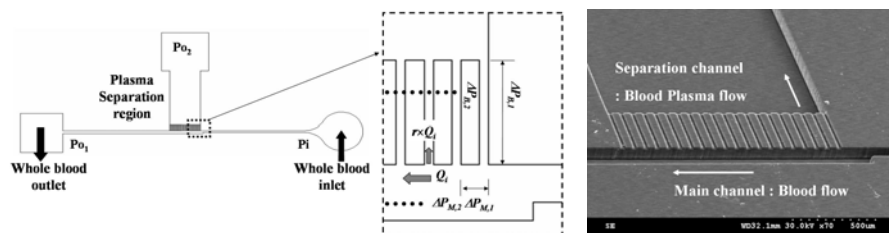


Fig. 2 Device design and SEM Image of the plasma separation region (X70)

3. Blood Plasma Separation Results and Discussion

The performance of the device was tested using a heparinized human whole blood. Figure 3 shows sedimentation depths of blood cells versus flow rates for both measurements and calculations at a $5000\mu\text{m}$ away from the inlet port. The depth of the cell-free layers varied from $10\mu\text{m}$ to $27\mu\text{m}$ according to inlet flow rates, and the depths were sufficient for the separation of the blood plasma.

Photographs of blood flow around the separation region during the blood plasma

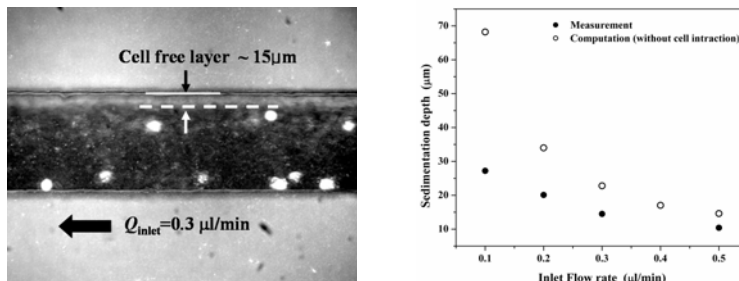


Fig. 3 RBC's sedimentation depths according to inlet flow rates at 5mm away from the inlet ; side view of the separation region during blood plasma separation (left) and relationship between sedimentation depth and inlet flow rate (right)

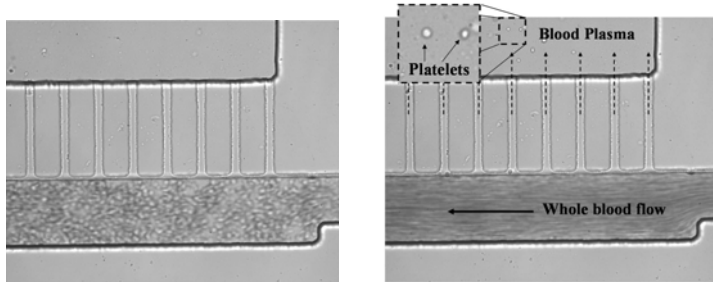


Fig. 4 Photographs of the plasma separation region ; Inlet hematocrit = 45 %,
 $Q_{\text{inlet}} = 0.1 \mu\text{l}/\text{min}$ (left), and $Q_{\text{inlet}} = 0.3 \mu\text{l}/\text{min}$ (right)

Table 1 Blood plasma separation results

$Q_{\text{inlet}} (\mu\text{l}/\text{min})$	$Q_{\text{Branch}} (\mu\text{l}/\text{min})$	$Q_{\text{Branch}}/Q_{\text{inlet}} (\%)$	$Q_{\text{Plasma total}}/Q_{\text{inlet}} (\%)$
0.1	0.00043	0.43	8.6
0.3	0.001	0.33	6.7

separation are shown in fig. 4. No RBCs was traveling into the plasma channels, although a few of platelets were observed in the separated blood plasma. Table 1 shows the separation efficiencies estimated from the measured flow rates at both main and plasma channels. The separated plasma volume was about 8.6% of the total amount of the whole blood and about 20% of the total amount of the blood plasma at the case of $Q_{\text{inlet}} = 0.1 \mu\text{l}/\text{min}$. The separation efficiency was in well agreement with the expected. The total separation efficiency could be increased by simply adding separation channels.

4. Conclusion

The continuous, real-time blood plasma separation was successfully demonstrated using a heparinized human blood. By utilizing the sedimentation effect of blood cells within a microfluidic channel, only the purified blood plasma could be collected in continuous, real time fashion. It is expected that the proposed device can be applied to continuous, real time fluid sampling for biomedical various applications.

Acknowledgement

This study was supported by a grant of the Korea Health 21 R&D Project, Ministry of Health & Welfare, Republic of Korea. (02-PJ3-PG6-EV05-0001)

References

1. B. He, L. Tan, and F. Regnier, *Micofabricated Filters for Microfluidic*, Analytical SystemsAnalytical Chemstry, Vol. 71, no. 7, pp. 1464-1468 (1999)
2. P.K. Yuen, et al, *Microchip Module for Blood Sample Preparation and Nucleic Acid Amplification Reactions*, Genome Research, pp. 405-412 (2001)
3. B.H. Weigl and P. Yager, *Microfluidic Diffusion-Based Separation and Detection*, Science, 283(5400), pp. 346-347 (1999)

FLOW CHARACTERISTICS OF NANOCHANNEL ELECTROOSMOTIC PUMPS

Duckjong Kim, Sang-Jin Park and Eui Soo Yoon

Micro/Bio Fluidics Team, Korea Institute of Machinery and Materials, Korea

Abstract

Nanochannel electroosmotic pumps with various pumping channel width are fabricated and tested to check if the pumping performance is enhanced with decreasing pumping channel size in sub-micron scale.

Keywords: electroosmotic pump, nanochannel

1. Introduction

Several researchers demonstrated electroosmotic (EO) pumping through microchannels fabricated in CMOS-compatible processes[1, 2]. In spite of continued performance improvements for microchannel EO pumps, a major drawback to these pumps is their low efficiency. Therefore, it is a very significant issue to enhance the performance of the EO pump. Recently, Min et al.[3] theoretically showed that the pumping power can be significantly increased by reducing the pumping channel size.

Therefore, in this work, if the pumping performance is enhanced with decreasing pumping channel size in sub-micron scale is experimentally investigated.

2. Experimental work

The nanochannel EO pump fabricated using standard MEMS technology is shown in Fig.1. The height and the length of 100 pumping channels are 20 μm and 100 μm , respectively. The pumping channel width is varied from 0.5 μm to 1 μm . The nanochannel EO pumps are tested in the experimental setup shown in Fig.2. Initially, the pump is filled with DI water. To evaluate the back flow characteristics of the pump, compressed nitrogen gas whose pressure is controlled is infused into the pump and the movement of DI water in the pump is observed through a microscope. For EO pumping

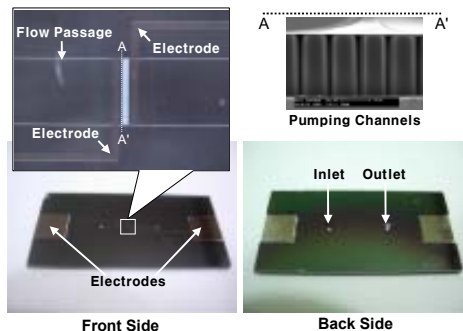


Figure 1. Nanochannel electroosmotic pump

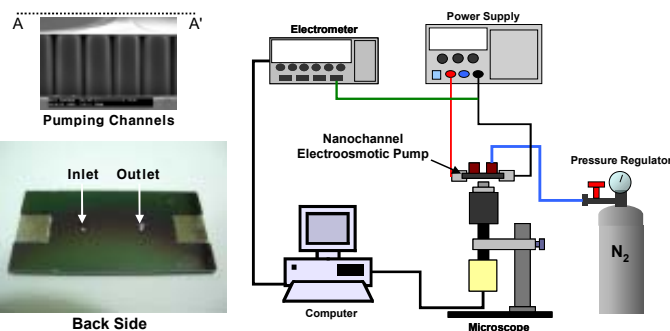


Figure 2. Experimental setup

without bubble generation, a small voltage difference of 4V is applied to electrodes in the pump.

3. Discussion

Test results are summarized in Figs.3-5. Fig.3 shows that the maximum pressure increases with decreasing pumping channel width. This can be accurately predicted by numerical simulation. On the other hand, Fig.4 shows that the maximum flow rate decreases with decreasing pumping channel size. The discrepancy between the experimental data and the theoretical prediction seems to be caused by the partial filling of pumping channels. Only 13-22% of pumping channels are estimated to be filled with DI water. Consequently, since the maximum pressure increase with decreasing pumping channel size balances the maximum flow rate decrease, the size effect on the pumping power and the efficiency is not significant in the tested range as shown in Fig.5. In addition, Fig.5 shows that the pumping performance deteriorates with decreasing pumping channel size beyond the tested range due to the electric double layer overlap. Although the experimental results show that the pumping performance is not effectively enhanced with decreasing pumping channel size when the ratio of the

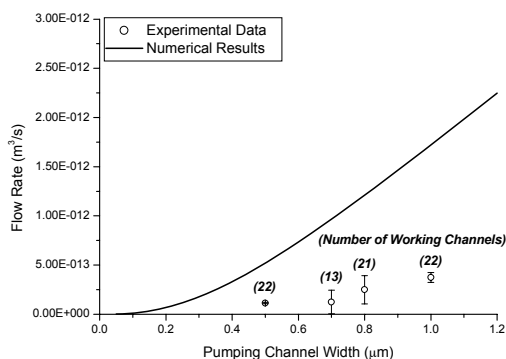
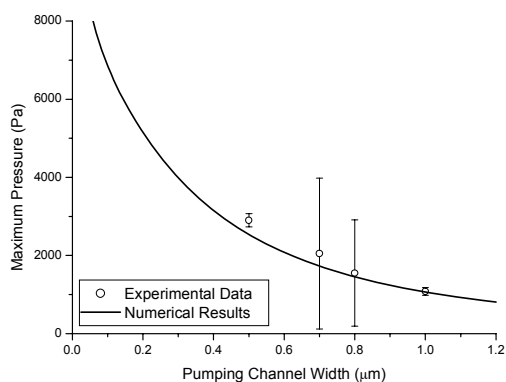


Figure 4. Maximum Flow Rate

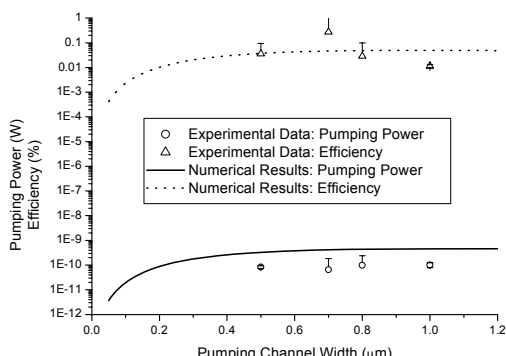


Figure 5. Pumping Power and Efficiency

channel size to the electric double layer thickness is small, it is expected that the size effect on the pumping power and the efficiency becomes significant as the ratio of the channel size to the electric double layer thickness increases.

4. Conclusions

Nanochannel EO pumps, whose pumping channel size is varied from $0.5\mu\text{m}$ to $1\mu\text{m}$, are fabricated and tested. Test results show that the pumping performance is not effectively enhanced with decreasing pumping channel size in sub-micron scale when the ratio of the channel size to the electric double layer thickness is small.

References

1. C. H. Chen, S. Zeng, J. C. Mikkelsen, Jr. and J. G. Santiago, IMECE'00, pp. 523-528.
2. D. J. Laser, A. M. Myers, S. Yao, K. F. Bell, K. E. Goodson, J. G. Santiago and T. W. Kenny, Transducers'03, pp. 151-154.
3. J. Y. Min, D. Kim and S. J. Kim, Sensors and Actuators: B, in press.

THE SERIAL DILUTION CHIP FOR CYTOTOXICITY AND CELL DIFFERENTIATION TEST

Choong Kim^{1, 2}, Kang Sun Lee¹, Sung Shin Ryu¹, Kyung Sik Shin¹, Kyu Jung Lee², Ji Yoon Kang¹ and Tae Song Kim¹

¹Microsystem research center, Korea Institute of Science and Technology, Korea

² School of Mechanical Engineering, Korea University, Korea
(jykang@kist.re.kr)

Abstract

This paper proposes two types of serial dilution devices generating linear and logarithmic concentration gradient. The designs of serial dilution chips were based on the adjustment of flow rate to obtain desired dilution ratio, so that they are not affected by molecular size, flow rate, and diffusion length. The performance of linear dilution chip was verified with image analysis of tryphane blue solution and cytotoxicity test. The percentage of cell viability was linearly proportional to the concentration of PFA with the standard deviation of 0.05 %. The experiment of logarithmic dilution chip also demonstrated that the concentrations of outlet was logarithmically linear and was in accordance with that of dilution by manual pipetting.

Keywords: serial dilution, logarithmic dilution, concentration gradient, cytotoxicity

1. Introduction

Serial dilution is essential for almost all chemical/biochemical applications, such as cytotoxicity testing [1] and experiments for the differentiation of stem cells [2]. To obtain concentration gradient with a single operation in a microfluidic device, molecular diffusion in a combined stable laminar flow were reported [3] [4]. However, the concentration profiles were affected by molecular size, flow rate, and diffusion length. Hence, we developed two types of serial dilution devices to solve those problems. The performances of the chips were verified through the image analysis of diluted solutions and cell toxicity test.

2. Principles

First, we developed a dilution chip generating a linear concentration profile for cytotoxicity testing. The dilution ratio is controlled by changing a number of channels, which determines the total amount of flow into chambers [5] (Figure 1 and 2). Second, we designed a dilution device for a logarithmic concentration profile, because the experiment of stem cell differentiation is usually done in a logarithmic scale [2]. Figure 3 depicted the schematic and concept of the chip; whereas the inlet flow of chemical is diluted at the 1st intersection of buffer flow, and then, the diluted fluid meet buffer flow again at the 2nd intersection. Hence, the concentrations of consecutive chambers are exponentially diluted. The concentrations of chemicals in the outlet chambers are defined by the relationship, $C_n/C_{n-1}=\eta$, where η is the dilution ratio and C_n and C_{n-1} are the concentrations of nth and (n-1)th outlet chambers respectively. The logarithmic

concentration profile was obtained by designing an appropriate microfluidic circuit using an electric circuit simulation. However, only the adjustment of flow rate in the fluidic circuit was not sufficient to realize the logarithmic dilution chip because the laminar flows did not fully merged at junctions without a proper mixer. Hence, the Tesla mixer was inserted between intersections for perfect operation of the logarithmic dilution chip

3. Experiments and results

To measure the dilution ratio of linear dilution chip, the water-soluble tryphane blue and de-ionized water were injected at the flow rate of 50 $\mu\text{l}/\text{min}$ into the chemical and buffer inlet port respectively. Cell toxicity was tested by the injection of diluted toxic chemical, PFA (paraformaldehyde), followed by tetrazolium-based colorimetric MTT assay to observe cell viability. The Tesla micromixer and logarithmic dilution chip was characterized by mixing of red dye and DI water. Images captured by a CCD camera were analyzed by the color intensity of dyed water. The analysis of the color intensity of the linear dilution chip indicated that the tryphane blue diluted in linear scale was in agreement with the theoretical value (Figure 4). The plot in Figure 5 shows that the percentage of cell viability is linearly proportional with the concentration of PFA with the standard deviation of 0.05 %. The linearity of concentration of the dilution chip was superior to that of manual pipetting. Figure 6 showed that the red-dye was diluted in logarithmic scale in agreement with a manual method and the simulation result of logarithmic dilution chip (CFD-ACE⁺) guaranteed the dilution ratio was not affected by flow rate (data not shown).

4. Conclusions

We developed a dilution chip generating a linear concentration profile and a logarithmic concentration profile for cytotoxicity testing and cell differentiation. The percentage of cell viability was linearly proportional to the concentration of PFA and the concentration profile from logarithmic dilution chip was in agreement with that from manual pipetting. We believe that this microfluidic system can be applied to not only biochemical experiment, but also for various screening system, such as optimization of chemical reactions.

Acknowledgement

This research was supported by the Intelligent Microsystem Center (IMC; <http://www.microsystem.re.kr>), which is carrying out one of the 21st Century's Frontier R&D Projects sponsored by the Korea Ministry of Commerce, Industry and Energy

References

- [1] Dinender Kumar et al., *Biochem. & Biophys. Res. Comm.*, 2005, 332, 135-141.
- [2] Frederic Bost et al., *Biochem. J.*, 2002, 361, 621-627.
- [3] H. B. Mao et al., *Anal. Chem.*, 2002, 74, 379.
- [4] Xingyu Jiang et al, *J. Am. Chem. Soc.*, 2003, 125, 5294-5295
- [5] Hyunwoo Bang et al., *J. Micromech. Microeng.*, 2004, 1165-1170

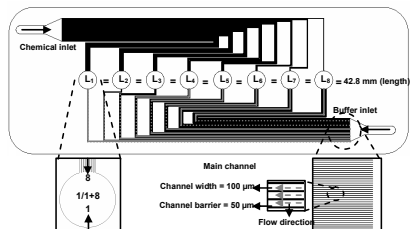


Figure.1 Schematic of serial dilution chip for cytotoxicity testing.

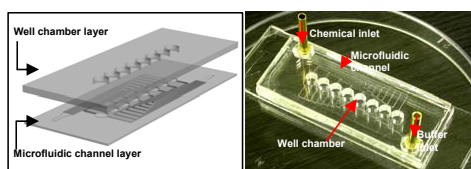


Figure.2 Fabricated PDMS serial dilution chip (consist of microfluidic channel layer and well chamber layer).

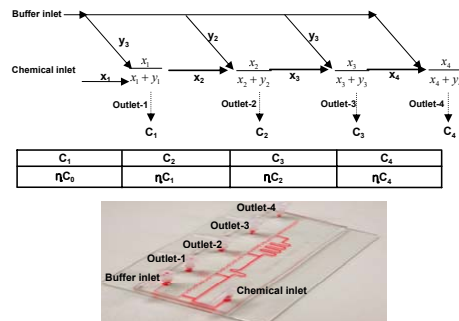


Figure.3 Concept and schematic of a dilution device for logarithmic scale concentrations profile and mixer simulation.

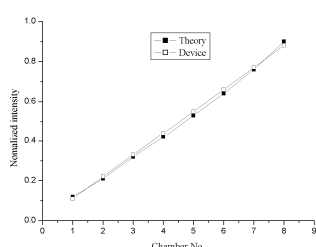


Figure.4 Intensities of Tryphane blue solution.

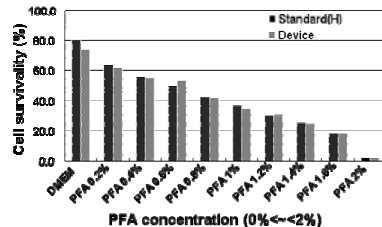
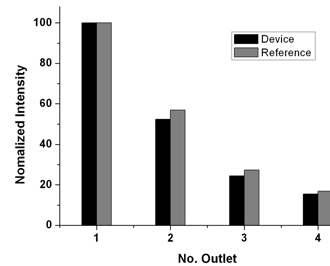
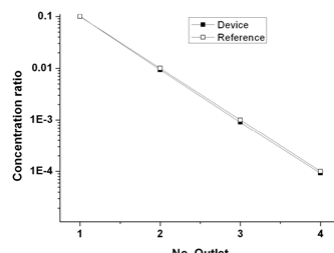


Figure.5 Measurement of cell viability with MTT assay (PFA 0.2 %~1.8 %).



(a)



(b)

Figure.6 (a) The analysis of color intensity of chip and reference method, (b) The concentration of a solution of chip and reference method.

FLUID FLOW STUDY IN A ROTARY GATE MICROVALVE

Rajesh Luharuka¹ and Peter J. Hesketh^{1,2}

¹G. W. W. School of Mechanical Engineering, Georgia Institute of Technology,
Atlanta, GA 30332 USA
²peter.hesketh@me.gatech.edu

Abstract

Flow characterization of a rotary gate microvalve is performed with both gas (N_2) and liquid (H_2O). The microvalve is tested in three different flow configurations and the results are summarized. Maximum gas flow of up to 0.5slpm was obtained at a moderate pressure drop of 40kPa in microvalves of size $4 \times 4\text{mm}^2$. Flow modulation of over 100 was achieved.

Keywords: gate microvalve, rotary, micromechanism, microfluidic

1. Introduction

A rotary gate microvalve is designed for flow modulation in a microfluidic system that operates at high flow rate or uses colloidal solution. A few different designs of gate microvalves have been reported in the literature [1]; all of which use a thermally-based actuation process for switching. This work is targeted towards developing an electromagnetically actuated gate microvalve to overcome the limitations posed by the previous designs such as slow switching, large size, and/or high energy consumption. The gate in this design rotates in-plane between its two stable positions (bistable) when actuated by an inductor, thus opening and closing the inlet/outlet orifice on the substrate. This paper is focused on the fluid flow study in this microvalve.

2. Design

The scanning electron micrographs in Figure 1(a,b) shows different components of the rotary gate microvalve. A suspended mass that acts like a gate rotates in the plane of the chip to regulate flow between its ports. The gate is suspended by a novel fully compliant in-plane rotary bistable micromechanism (IPRBM) [2] that advantageously constraints the gate in all degrees of freedom except for in-plane rotational motion. Multiple inlet/outlet ports provide flexibility of three different flow configurations as shown in Figure

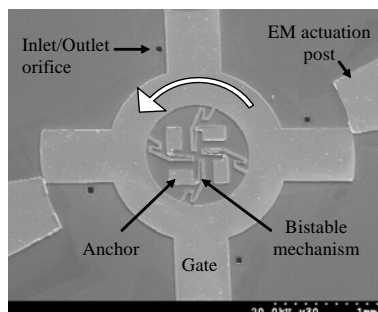


Figure 1. SEM image of normally open rotary gate microvalve

2(a-c). The microvalve is made of Permalloy ($\text{Ni}_{80}\text{Fe}_{20}$), a soft magnetic material. Two pairs of diametrically opposing posts are positioned relative to corresponding gates extending from the central mass, wherein an electromagnetic (EM) actuation at the posts causes the mass to rotate from first angular position to second angular position. Flow characteristics in this microvalve depend on various design parameters such as port size, gate width, gap size, micromechanism stiffness, and flow configuration.

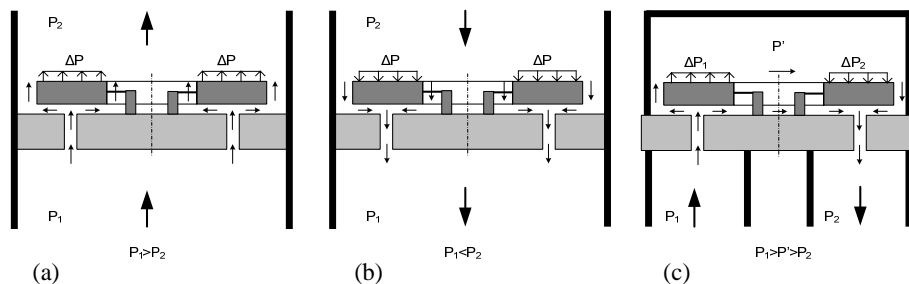


Figure 2. Different flow configurations in the microvalve and the pressure acting on the gate; (a) forward-flow; (b) reverse-flow; and (c) cross-flow

3. Experimentation and Results

The microvalve is characterized for both gas (N_2) as well as liquid (deionized H_2O) flow. The microfluidic tests are performed by pumping the fluid at a constant mass flow rate and recording the resulting pressure drop across the valve at equilibrium condition.

In the open state flow tests, gas (N_2) and liquid (deionized H_2O) flow rate of up to 500sccm and 20sccm, respectively was measured at a pressure drop of 40kPa. Gas flow is compressible at high flow rates and the maximum flow rate is limited by the number and size of inlet orifice. Liquid flow is incompressible and dominated by viscous forces due to low Reynolds number.

In the closed state, the flow configuration is important to flow resistance (see Figure 3). In forward flow condition, the pressure drop acts adversely on the gate causing the gap to widen with increasing differential pressure. Therefore, as a result of the widening of the gap, the flow modulation approaches unity at a higher flow rate. In the reverse flow configuration, the differential pressure across the gate assists in closing the gap thus providing a better fluidic seal. And finally, in the cross-flow configuration, a tilting moment acts on the gate due to the change in the direction of flow (as seen Figure 2(c)). This results in good seal at the outlet orifice of the microvalve. The flow results have been summarized in Table 1, which are based on results from 10 different microvalve designs.

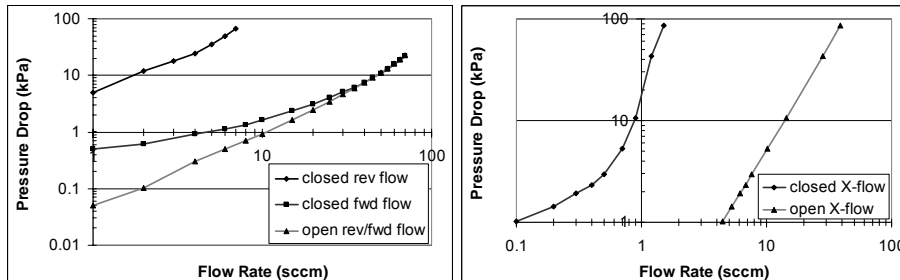


Figure 3. Nitrogen flow characteristics in a rotary gate microvalve (gate width=500 μ m; orifice size=60 μ m; gap size=11 μ m; gate thickness=15 μ m)

Table 1. Fluidic performance of the rotary gate microvalve

Performance Parameter	Units/Config.	Gas (N ₂)	Liquid (H ₂ O)
Differential pressure ¹	kPa	40	40
Max. flow rate ²	sccm	500	25
Open to closed flow ratio ³			
Rev. Flow		50 - 100	100-150
Cross Flow		40 – 80	150 – 200
Fwd. Flow		< 10	< 10

¹ characterization pressure drop; ² fwd and rev flow configuration; ³ open:close flow resistance

5. Conclusions

This fluid flow study in rotary gate microvalve presents the fluidic performance under different flow configurations. The flow modulation achieved in this design is higher than those reported in the previously developed thermal actuation based gate microvalves. The fluidic performance can significantly improve by including a valve seat, increasing the orifice size, and providing additional orifice/gate at the periphery of the annulus rotor mass.

Acknowledgements

We are grateful to Prof. David W. Rosen (director of RPMI at Georgia Tech) for providing laboratory facilities for rapid prototyping.

References

1. S. Braun, S. Haasl, S. Sadoon, A. S. Ridgeway, W. Van Der Wijngaart, and G. Stemme, *Small footprint knife gate microvalves for large flow control*, IEEE Transducers, Seoul, South Korea, pp. 329-332 (2005).
2. R. Luharuka, P. J. Hesketh, *In A fully compliant, in-plane rotary, bistable micromechanism*, ASME IMECE, Orlando, FL, pp. 481-485 (2005).

ELECTROACTIVE NANOWELL ARRAYS FOR PARTICLE TRAPPING AND DETECTION

Bernardo Cordovez and David Erickson

Sibley School of Mechanical and Aerospace Engineering, Cornell University, USA

Keywords: Nanowell Sensor, Electrophoresis, Electroosmosis, Dielectrophoresis

Abstract

We describe the development of electroactive nanowells that exploit extremely localized electrokinetic effects in order to guide and confine nanoparticles into targeted nanohole arrays. Immediate applications include high throughput single cell active trapping and accurate rapid unlabeled cell screening.

Introduction

Recently, a series of techniques have been demonstrated for single cell trapping in microwell arrays (e.g. [1]). While these techniques enable discrete optical observation of the biological targets, their passive nature limits the degree of inherent functionality. Here we present an electro-active nanowell platform for precise, parallel manipulation of individual nanoparticles and biotargets to discrete nanowell sites. In our devices, coupled electrophoretic, electroosmotic and dielectrophoretic effects are used to guide individual nanoparticles to the desired well site. The highly localized electric field in the microwell sites enables very strong particle trapping. This field concentration also enables us to exert thermal and chemical control over the nano-environment through manipulation of Joule heating [3] and electrolytic reactions.

Device Fabrication and Results

Nanowell arrays are made by spinning a 5 micron thick photoactive polyimide layer on top of an Indium Tin Oxide (ITO) coated glass slide. Microwells with sizes ranging from 6 to 25 microns in diameter were then photolithographically defined in the polyimide, leaving the well structure shown in Figure 1. In order to close the circuit, we then place a top ITO conductor separated from the bottom layer by two 70 micron spacers. After fabricating, plasma cleaning and assembling the nanowell architecture, a 0.1 mM phosphate buffer solution containing 1.9 micron polystyrene beads is then flowed from an open ended microfluidic channel (not shown) to the microwell device. The

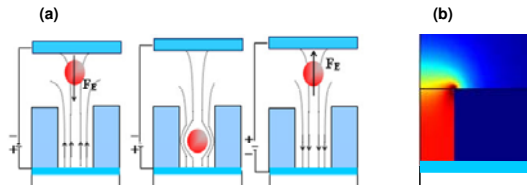


Figure 1: Electroactive Nanowell

(a) Particles are driven, sensed and repelled from the well depending on the polarity. (b) Axisymmetric finite element simulation displaying strong electric field concentration inside microwell.

polystyrene particles used in this experiment are carboxyl modified, giving them a small negative charge.

In this experiment (Figure 1), we apply a 5V DC field to drive 1.9 μ m polystyrene beads into the wells, and after reversing the polarity we observe particle rejection from the wells to the bulk of the channel. As Figure 2 illustrates, by applying a positive voltage on the bottom electrode, the polystyrene beads are driven from the bulk of the channel into the well, and by reversing the polarity they are ejected.

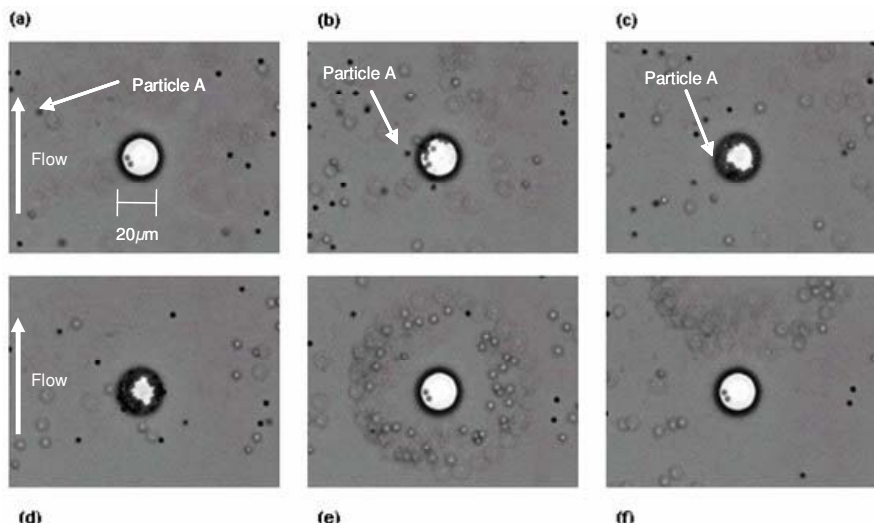


Figure 2: Time lapse illustrating particle attraction and repulsion of 1.9 μ m polystyrene beads in a 20 μ m well. Conditions are a velocity field of 30 μ m/s under a 5 Volt potential. (a) Unoccupied Microwell. Note: Two particles adhered onto ITO surface before experiment was performed (b) Particle attraction begins and beads are drawn into well. (c) Well after 15 seconds of attraction. (d) Microwell after 30 seconds of attraction. (e) Particles are rejected abruptly as polarity is switched (f) Ring-like pattern remains and drifts due to superimposed velocity field.

We have determined that even though electrophoresis is able to transport the particles to the targeted wells, there is a strong electroosmotic (EO) effect, generating a small recirculating velocity field in the proximity of the microwells. The electroosmotic effect manifests itself as follows: During attraction, particles immediately adjacent to the well are repelled radially away from it, while particles immediately above it are drawn into the well and trapped. When we reverse the polarity, particles are drawn in towards the well but are then repelled out of plane as they approach the well's edge. We believe this effect is enhanced by dielectric charging, since increasing ion accumulation in the double layer should increase the zeta potential at the polyimide/solution interface.

A Finite Element Analysis model (Figure 3) was constructed to further characterize the various electrokinetic contributions. The resulting transport streamlines comprising the superposition of the pressure driven flow and the electroosmotic,

electrophoretic and dielectrophoretic trapping elements are displayed. We can appreciate that the streamlines near the edges of the well point radially outwards, displaying the electroosmotic velocity generated at the walls of the polyimide. Dielectrophoresis was found to be small, except near the well edges. As well sizes approach submicrometer dimensions, however, this effect is expected to become more significant

In order to provide single well addressability, we are currently modifying our top and bottom ITO conductors by patterning interdigitated electrodes on the ITO glass slide. After patterning aligned microwells on the bottom electrodes, a top ITO electrode is aligned orthogonally, providing the ability to electrically probe a single microwell as shown in Figure 4. Furthermore, since particles have a characteristic length on the same order as that of our wells, well occupancy should greatly affect the field lines and impedance spectra [2].

Conclusions and Future Work

In this work we demonstrate effective particle trapping and repulsion from nanowells by manipulating extremely localized electrokinetic effects.

This work was has been made possible by the National Science Foundation through the NanoOptofluidic Sensors the grant NSF/CTS 0529045. (M. Plesniak, Grant Monitor)

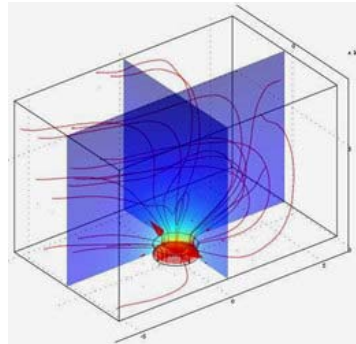


Figure 3: Finite Element Simulation: 3-D Finite Element Simulation displaying velocity stream lines in potential field.

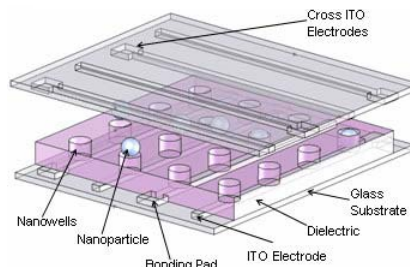


Figure 4: Current Device Setup: Cross Electrodes Layout enabling single well trapping and rejection in Nanowell Array.

References

- [1] Kang, M.; Trofin, L.; Mota, M.; Martin,C.R. "Silica Nanotube 3-D Microwell Arrays for Protein Assays," *Anal. Chem.* **77**, 6243-6249. (2005)
- [2] Rettig, J.R.; A. Folch. "Large-Scale Single-Cell Trapping And Imaging Using Microwell Arrays" *Anal. Chem.*, **77** (17), 5628 -5634. (2005)
- [3] Wu, J.; Ben Y.; Chang, H.C. "Particle detection by electrical impedance spectroscopy with asymmetric-polarization AC electroosmotic trapping" *Microfluidics and Nanofluidics* **1**, 161–167 (2005).
- [4] Erickson, D., Sinton, D., Li, D. "Joule Heating and Heat Transfer in Poly(dimethylsiloxane) Microfluidic Systems" *Lab on a Chip* **3**(3) 141-149 (2003).

ON-SITE SIZE-SELECTIVE PARTICLE SAMPLING USING MESOPOROUS POLYMER MEMBRANE MICROFLUIDIC DEVICE

Masashi Ikeuchi and Koji Ikuta

Dept. of Micro/Nano Systems Eng., School of Eng., Nagoya University, Japan

Abstract

A microfluidic device composed of three-dimensionally formed mesoporous polymer membrane was proposed and developed using “membrane micro embossing (MeME)” process. Unlike existing microfluidic devices adding filtration components to microchannels, the whole surface of the microchannel itself works as a large filter in this device. This unique structure realizes high-throughput “onsite size-selective sampling”, which is applicable to miniaturization of preparation steps in biological analyses. We have successfully fabricated microchannels composed of mesoporous membrane with tunable pore diameter and porosity. On-site size-selective sampling using microbeads ranging from $\phi 0.1\mu\text{m}$ to $\phi 15\mu\text{m}$ was demonstrated.

Keywords: Porous, Membrane, Filtration, Separation, Fabrication

1. Introduction

Size-selective sampling, such as blood cell separation from whole blood and protein extraction from cell lysate etc., is the first step for general biological analysis processes. Conventional microfluidic devices, however, focus mostly on downstream steps, such as separation or detection. Thus, sampling process is still usually carried out at bulkier scale using pipettes and tubes. To miniaturize the whole process on a microfluidic device and realize the real portable analysis device, we must embed filtration function in the device.

In existing reports on microfluidic devices for filtration, the structure of the filtration component is classified into two types.

1) An array of microstructures (beads, pillars, wires etc.) placed in the microchannel works as a filter (Fig. 1a) [1].

2) A large membrane filter is placed on the inlet of the microchannel (Fig. 1b) [2].

The problem of the first type structure is the clogging of the microchannel due to its small filtration area. In contrast, the problem of the second type structure is the occupation of large

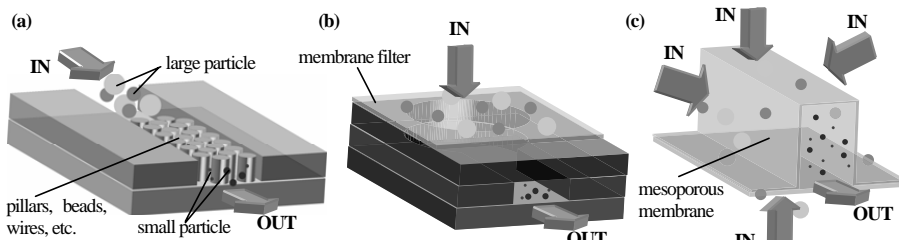


Fig.1 Schematic illustration of the three types of microfluidic device for on-site size-selective sampling. (a) An array of microfabricated structures (pillars, beads or wires etc.) placed in the microchannel works as a filter. (b) A large membrane filter is placed on the inlet of the microchannel. (c) Newly proposed “3-D membrane microchannel structure”: Whole surface of the microchannel wall, which is composed of thin mesoporous membrane, itself works as a large filter.

area for packaging, which works against the miniaturization of the device. Ideally, filtration components should have larger area for filtration, yet occupy smaller area for packaging.

To solve this paradox, we have proposed third type structure - “3-D membrane microchannel structure” (Fig.1c). In this structure, the whole surface of the microchannel wall, which is composed of three-dimensionally formed mesoporous membranes, itself works as a large filter. This unique structure offers both the larger filtration area and the smaller area for packaging. By using this novel structure, miniaturized high-throughput size-selective sampling device can be realized. Here, we have developed the prototype device and demonstrated the on-site size-selective sampling.

2. Fabrication of the mesoporous polymer membrane microfluidic device

At first, we fabricated mesoporous polymer membrane using spin-coating following phase-separation technique. Poly-lacticacid solution dissolved in dioxane-water mixed solvent was spin-coated on a glass substrate and dried in vacuo. The pore diameter and the porosity were tunable by adjusting the polymer content in the solution and the water content in the dioxane (Fig.2a,b).

Then the mesoporous membrane was formed to microchannel structure using MeME process developed in our laboratory (Fig.3). To the best of our knowledge, MeME is the only process applicable for three-dimensional micro-forming of mesoporous polymer membrane.

Fig.4 shows the SEM of the upper and the down side of the microchannel before sealing. The microchannel structure of the master mold was precisely transferred to the membrane, while preserving the mesoporous structure of the membrane (Fig.4a,b). No leakage or breakage was observed by filling the microchannel with red solution (Fig.5a,b). Though there were many pores penetrating through the microchannel wall, the solution was kept inside the microchannel due to surface tension.

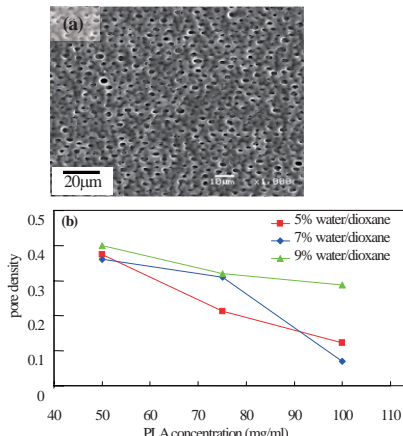


Fig.2 Mesoporous polymer membrane fabricated by spincoating following phase separation. (a) SEM of the mesoporous poly-lacticacid (PLA) membrane fabricated from 100mg/mL PLA/Dioxane solution containing 7% water. (b) Relation between pore density and PLA concentration in solution.

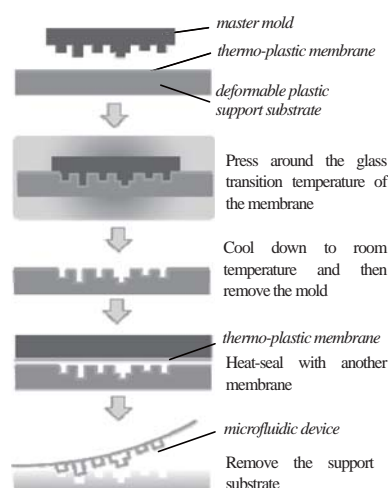


Fig.3 Fabrication process of the microfluidic device composed of thin membrane by membrane microemboss (MeME) process

3. Size-selective separation

We demonstrated the on-site size-selective sampling using suspension of microbeads ranging from $0.1\mu\text{m}$ to $15\mu\text{m}$ in diameter. Once the outside of the microchannel was filled with suspension, the suspension liquid started to flow through the wall due to surface tension. Microbeads larger than $1\mu\text{m}$ in diameter were trapped on the outer surface of the microchannel, while microbeads smaller than $1\mu\text{m}$ in diameter flowed through the microchannel wall (Fig.5c,d). This result shows that the microchannel itself worked successfully as a size-selective filter with $1\mu\text{m}$ cut-off diameter.

4. Conclusion

In summary, we have proposed and demonstrated on-site size-selective sampling with the unique microfluidic device composed of three-dimensionally formed mesoporous polymer membrane. By combining this sampling device with conventional microfluidic devices for separation and detection, the miniaturization of the whole analysis process can be achieved. The mesoporous membrane microchannel structure can also be extended to various fields, such as liquid-liquid and liquid-gas reaction, by utilizing the large interfacial areas and the short diffusion distance.

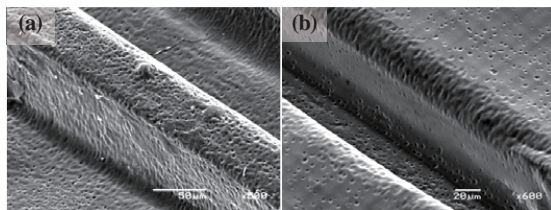


Fig.4 SEM images of the upperside (a) and the downside (b) of the microchannel made of mesoporous polymer membrane before sealing. Both the width and the height of the microchannel was $50\mu\text{m}$, and the thickness of the membrane was $5\mu\text{m}$. The images show the precise transfer of the microchannel structure to the membrane using MeME process. The mesoporous structure of the membrane was preserved throughout the process.

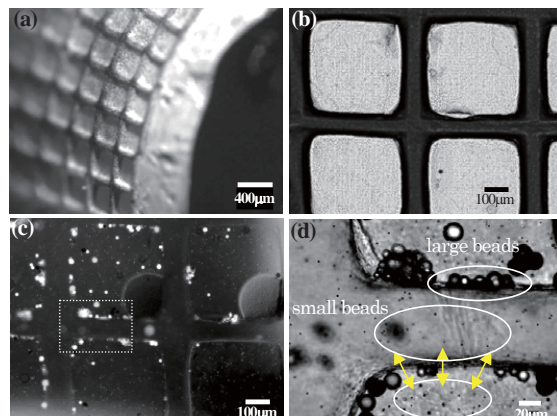


Fig.5 Microfluidic device composed of mesoporous polymer membrane. (a) Optical microscopy of the device filled with red colored water, (b) Magnified view of the (a). Although there were pores penetrating through the membrane, water is kept inside the microchannel due to surface tension, (c) Fluorescent microscopy of the device during size-selective sampling of the microbeads ($\phi 0.1\mu\text{m} \sim \phi 15\mu\text{m}$), (d) Magnified view of the white-dotted area in (c). Large beads ($>\phi 1\mu\text{m}$) were trapped on the microchannel wall, whereas small beads ($<\phi 1\mu\text{m}$) flowed through the wall. The wall of the microchannel worked successfully as a size-selective filter with $1\mu\text{m}$ cut-off diameter.

References

1. Y. Tezuka et. al., DNA size separation employing micro-fabricated monolithic nano-structure, Proc. Micro Total Analysis Systems 2002, pp.212-214, (2002).
2. S. Thorslund et. al., A hybrid poly(dimethylsiloxane) microsystem for on-chip whole blood filtration optimized for steroid screening, Biomed Microdevices, vol.8, pp.73-79, (2006).

PICOLITER-SIZED GEL COMPARTMENT ARRAY FOR HIGH-THROUGHPUT CELLULAR ANALYSIS

Tetsuya Shibanuma¹, Masumi Yamada², Masahiro Yasuda¹,
and Minoru Seki¹

¹Osaka Prefecture University, 1-1 Gakuen-cho, Sakai, Osaka 599-8531, JAPAN

²The University of Tokyo, 7-3-1 Hongo, Bunkyo-ku, Tokyo 113-8656, JAPAN

E-mail: seki@chemeng.osakafu-u.ac.jp

Abstract

In this study, we describe a simple and versatile system for immobilizing small amount of cells in microchannel, using picoliter-sized gel compartments. Utilizing gas permeability and hydrophobicity of PDMS microchannel, picoliter-sized aliquots of sodium-alginate solution were dispensed in parallel, and then gelled by contacting with CaCl₂ solution. We have successfully shown that single cells could be accurately immobilized in each compartment, and this system can be applied to the single cell cultivation and analysis. The presented system is useful for various biological studies, such as population dynamics of cells and assessment of drug efficacy on cells.

Keywords: cell trapping, cell cultivation, single cell analysis, gel formation, calcium alginate gel

1. Introduction

Cell immobilization and cultivation in microscale have great potentials for high-throughput cellular analysis. Among various methods for immobilizing biomaterials, hydrogels-based methods are useful due to its simplicity and biocompatibility. Several studies on cell immobilization using hydrogels in microchannels have been reported [1, 2], however, it was difficult to precisely form ultra-low-volume gels in microchannel, which will be advantageous for manipulation of single cells. In this study, therefore, we propose a reliable and simple system for immobilizing and cultivating small amount of cells by forming picoliter-sized calcium alginate gels in microfluidic devices.

2. Experimental

The principle to form an ultra-small gel in one compartment is shown in Figure 1. First, sodium alginate solution containing cells is introduced into the microchannel (Fig. 1(b)). Next, air is introduced into the microchannel, dispensing an aliquot with precise volume in the compartment (Fig. 1(c)) due to the hydrophobicity and gas permeability of PDMS. Then, CaCl₂ solution is introduced, and calcium alginate gel is immediately formed by the diffusive mixing of Ca²⁺ ion into the compartments (Fig. 1(d)). The number of cells can be controlled by changing the cell concentration and/or compartment size.

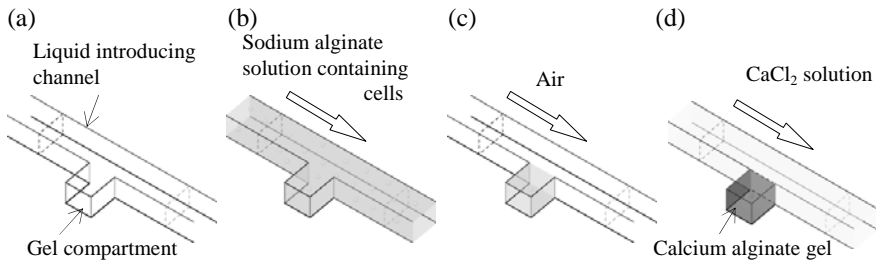


Figure 1. Procedure for gel formation. (a) Microchannel structure having a compartment. (b) By introducing sodium alginate solution containing cells into the microchannel, the compartment is filled with the suspension. (c) Then small aliquot is dispensed by introducing air. (d) Finally CaCl_2 solution is introduced to form a Ca-alginate gel containing cells.

PDMS microdevices were fabricated with usual soft lithographic techniques. Each microdevice has 10 channels, and there are 100 or 200 gel compartments per one microchannel. In order to improve reproducibility of the formed gel volumes, the depth of the compartments was varied from 10 to 40 μm , while that of the introducing channel was unchanged (40 μm).

3. Results and discussion

As a result, 25~100 pL gels were accurately formed (Figure 2), and it was revealed that a large difference in the depths contributed to the improved reproducibility of the gel volume.

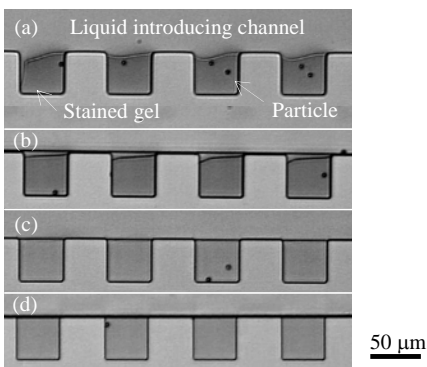


Figure 2. Photographs of the formed picoliter gels. The depth of the liquid introducing channel was 40 μm , while those of the gel compartments were (a) 40 μm , (b) 30 μm , (c) 20 μm , and (d) 10 μm , respectively. The gel volumes were 100~25 pL.

Next, single cells/particles were immobilized in gel compartment using standard polymer particles in a compartment as model. The distribution of the number of

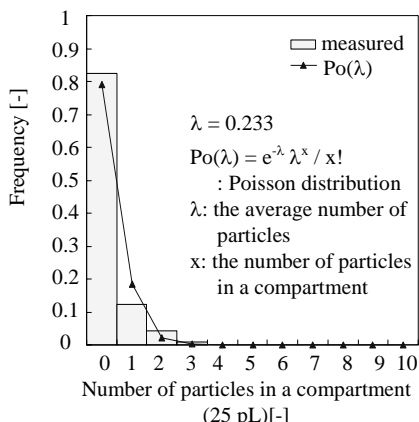


Figure 3. Distribution of the number of particles, in comparison with Poisson distribution.

particles is shown in Figure 3, in comparison with Poisson distribution. The experimental results well corresponded to the theoretical estimation. Then, yeast and *E. coli* cells were immobilized and cultivated in the device. As shown in Figures 4 and 5, most of the cells were singly immobilized and cultivated in the gel compartments, demonstrating the possibility for single cell cultivation and analysis. The relation between the initial *E. coli* cell concentration and the ratio of cell-containing compartments is shown in Figure 6. As a result, easy estimation of cell populations could be also performed using this method. By combining with other microfluidic operations such as concentration gradient generation, this system will be more useful.

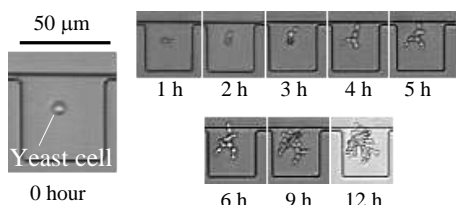


Figure 4. Single yeast cell cultivated in the gel compartment.

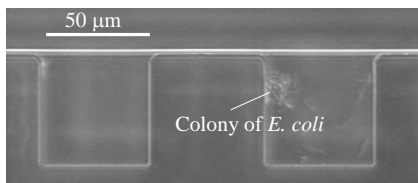


Figure 5. Single *E. coli* cell cultivation (24 hours after inoculation).

4. Conclusions

Picolarter-sized gel compartment array has been proposed, in which cell-containing multiple gels with accurate volume can be generated, and high-throughput cellular analysis can be performed. As an application, cultivation of single bacterial cells were successfully immobilized and cultivated in the gel compartments.

Acknowledgements

This study was supported in part by Grants-in-aid for JSPS fellows, and Scientific Research B (16310101) from the Ministry of Education, Culture, Sports, Science, and Technology, Japan.

References

- [1] T. Braschler, R. Johann, M. Heule, L. Metref and P. Renaud, *Lab Chip*, 5, 553-559 (2005).
- [2] M. Yamada, T. Hirano, M. Yasuda and M. Seki, *Lab Chip*, 6, 179-184 (2006).

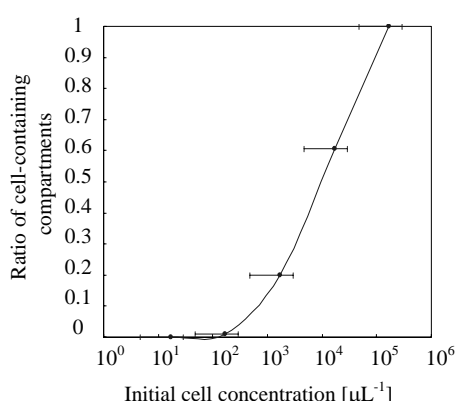


Figure 6. Ratios of the compartment with *E. coli* cells varying the initial cell concentration.

VENOUS VALVE LIKE MONO-LEAFLET MICRO VALVE AND ITS INTEGRATION WITH PUMPING SYSTEM

JeongYun Kim^{1,2}, JuYeoul Baek^{1,2}, YongDoo Park^{1,2}, Kyung Sun^{1,2}, and SangHoon Lee^{1,2*}

¹Department of Biomedical Engineering, Korea University, Anam-dong
Seongbuk-Gu, Seoul, 136-701 Korea

²Korea Artificial Organ Center, Korea University, Anam-dong Seongbuk-Gu, Seoul,
136-701 Korea (dbiomed@korea.ac.kr)

Abstract

Delivery of small volumetric-sensitive materials using a micro pumping system has become a pressing issue in the fields of chemistry, biology, and medicine. In this paper, we present a simple check valve whose operation mimics that of venous valves which is constructed via the *in-situ* fabrication method[1]. We constructed the micro pumping system by combining two venous-like check valves with an oscillating polymeric diaphragm driven by pneumatic force. We evaluated the performance of the pumping system, and also we investigated the feasibility of a novel PDMS-based micro total cell culturing system(μ TCCS) having addressable cell-delivering and cell culturing functions on a single platform.

Keywords: Micropump, check valve, *in-situ* photopolymerization, micro total cell culturing system (μ TCCS)

1. Introduction

In microfluidic devices, the safe transportation of sensitive samples (e.g.: DNA, protein, cells, chemicals, or drugs) with minimal dead volumes has become a central issue[2]. For this purpose, the delivery elements (e.g.: valve and pump) should be elastic material like tissue, biocompatible and easily integrative into other microsystems such as microreactors, micro assay systems, and cell culture chambers. In this paper, We constructed the simple micro pumping system using the photopolymerizable soft hydrogel, and evaluated the performance of the pumping system and integrated this pumping system into the PDMS-based μ TCCS.

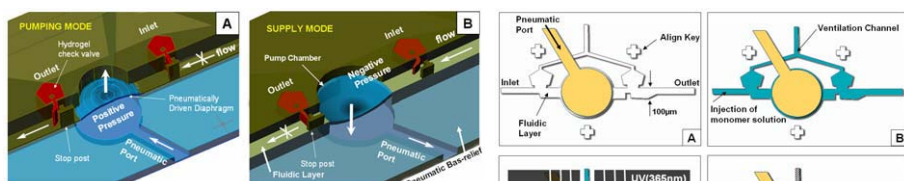


Figure 1. The 3-D schematic view of the pumping system

Figure 2. Micro fabrication of valve via *in-situ* photopolymerization

2. Fabrication

The 3-D schematic view and the operating principle of the pumping system are illustrated in Figure 1. The system consists of a PDMS platform including an oscillating membrane and two polymerized check valves. Figure 2 illustrates the fabrication scheme of the check valve. Into the inlet of the PDMS-based platform (a), the monomer solution (4-hydroxybutyl acrylate(89.67 wt.%) + DMPA(3.07 wt.%, used as a photoinitiator) + EGDMA(1.02 wt.%, used as a crosslinker) + Triton X-100(6.25 wt.%, used as a lubricant)) was introduced using the a syringe pump (b). Using photomask, all the regions were masked except the leaflet before radiation of the UV light (4200 mW/cm^2) (c). The alignment of photomask was carried out by using our homemade aligning system [3]. Then, the dashed area was polymerized(d). Finally, we rinsed the remaining unpolymerized monomer solution by using a PBS buffer solution.

To applied the pumping system to μ TCCS, we used 4 switch valves here, and 3 of them regulated the flow to the cell culture chambers to present the capability to deliver different volumes. To make more cells adhere and proliferate, we modified the surface of culture chamber by coating with fibronectin as extracellular proteins.

3. Experimental

The fabricated pumping system was evaluated under diverse conditions. By changing the pumping frequency, the controller regulated the mean flow rate. Last, we prepared mouse fibroblast cells, and the cell that passed through the pumping system were cultured in the μ TCCS with a 3 Hz pumping rate and incubated for 24 hours.

4. Results and discussion

In check valve, We determined the proper composition of the crosslinker to be 0.55 wt. %, and the fabricated leaflet exhibited very soft operations, like a venous valve. The lubricant (triton X-100) plays a very important role in the smooth, non-sticking operation of the leaflet. The lubrication is a very important factor in the successful operation of check valves. And, we establish and evaluated the micropump using this check valve. The flow rates of the micropump according to the pumping frequency were measured, and the results are plotted in Figure 3. As the pumping ratio increased, the flow rates increased almost linearly, and this indicates that we can regulate the delivered volume by changing the pumping frequency. We found that our pumping system can deliver a sample with a volume resolution of 100 nl, a value that is much smaller than the values of other device [1]. Furthermore, we integrated the micropump with micro total cell culture system(μ TCCS). Figure 4 is the a photograph from the top view of μ TCCS.

Finally, we pumped mouse fibroblast cells at the 1 Hz pumping frequency and at the 0.4 psi pumping pressure and transported them to the 3 different-sized cell culture chambers which coated the fibronectin to more cells adhere and porliferate. We have cultured the pumped cells 24 hours and carried out the cellular viability test and the Live/Dead assay. The Live/Dead assay shows that 95% of the fibroblast cells were alive after 24 hours. This finding means that the cells that had passed through the complex integrated pumping system were undamaged by the pumping system and alive well in the PDMS-based cell culture chamber.

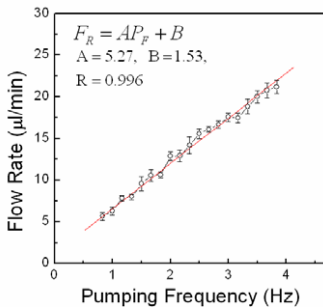


Figure 3. Changes of flow rate to the change pumping frequency

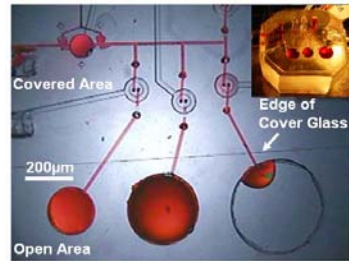


Figure 4. (a) Micrograph of the μ TCCS in operation

5. Conclusions

Through the proper use of materials and the simple in-situ fabrication method, we have established the technology to fabricate a freely movable microstructure inside the microfluidic channel. Based on this technology, we have created the micro check valve whose operation mimics a venous valve and have realized micro pumping system by integrating 2 micro check valves with the oscillating membrane. This micropump system can deliver solutions with a resolution of 100 nl per one stroke, and the delivered volume can be regulated precisely in relation to a pumping frequency. Furthermore, As we applied this micropump on the micro total cell culture system, a small volume of cell suspension media can be delivered to a specific chamber without damaging the cells because all the components consist of soft materials. And the delivered cells were cultured well in the culture chambers. One practical advantage of our device is that cells in any kinds of container (e.g.: flask, dish, bottle and well) can be transported through the use of a simple small tube. We expect that the important potential applications of our pumping system concerns multiple screening chips, including delivery function in a small volume range or drug delivery system

Acknowledgements

This study was supported by a grant from the Korea Health 21 R&D Project, Ministry of Health & Welfare, Republic of Korea (0405-ER01-0304-0001) and the Brain Korea 21 Project in 2006.

References

1. D. J. Beebe, J. S. Moore, J. M. Bauer, Q. Yu, R. H. Liu, C. Devadoss, B. H. Jo, *Functional hydrogel structures for autonomous flow control inside microfluidic channels*, Nature, 2000, 404, pp. 588–590
2. C. Yamahata, C. Vandevyver, F. Lacharme, P. Izewska, H. Vogel, R. Freitag, M.A.M. Gijs, *Pumping of mammalian cells with a nozzle-diffuser micropump*, Lab Chip, 5, pp. 1083–1088, (2005).
3. J.Y. Kim, J.Y. Baek, K.A. Lee, S.H. Lee, *Automatic aligning and bonding system of PDMS layer for the fabrication of 3D microfluidic channels*, Sensors & Actuators A, 119, pp. 593–598, (2005).

MICROFLUIDIC FLOW DISTRIBUTORS GENERATING CONCENTRATION GRADIENTS FOR BIOCHEMICAL ASSAY

Takaya Hirano¹, Masumi Yamada², Masahiro Yasuda¹
and Minoru Seki^{1*}

¹Osaka Prefecture University, 1-1 Gakuen-cho, Naka-ku, Sakai, Osaka 599-8531,
Japan

²The University of Tokyo, 8-3-1 Hongo, Bunkyo-ku, Tokyo 113-8656, Japan
*seki@chemeng.osakafu-u.ac.jp

Abstract

We propose here microfluidic systems for generating multiple concentration conditions, linear- and exponential-gradient generators. In these systems, by continuously introducing two kinds of solutions into the microdevices, multiple concentrations can be accurately formed. Especially in the case of linear-gradient generator, the formed stepwise concentrations are not affected by the flow rate, which is a major advantage compared to previously reported schemes for gradient generation. Also, in the exponential-gradient generator, the experimental concentrations and flow rates well corresponded to theoretical values. As an application of the presented systems, we successfully performed biochemical assay using bacterial cells.

Keywords: gradient, microfluidic device, high-throughput screening, cell analysis

1. Introduction

Preparing multiple concentration conditions is essential for high-throughput chemical/biochemical processing, such as the estimation of influence of drugs or chemicals on cells. In general, microfluidic devices are suitable for parallel and multiple operations, therefore, several schemes for generating multiple concentration conditions have been proposed [1, 2]. These schemes are versatile for conducting high-throughput analysis, although they have both advantages and disadvantages. In this study, we propose two systems for generating multiple concentrations conditions, utilizing the laminar flow systems in 3-D microfluidic network.

2. Linear gradient generator

The principle of linear gradient generator is shown in Fig. 1. When two kinds of solutions are continuously introduced into the microchannel structure, the mixing ratio at a confluence point is determined by the lengths of the distribution channels. So by changing the lengths of the distribution channels stepwise, multiple concentration conditions can be

accurately generated.

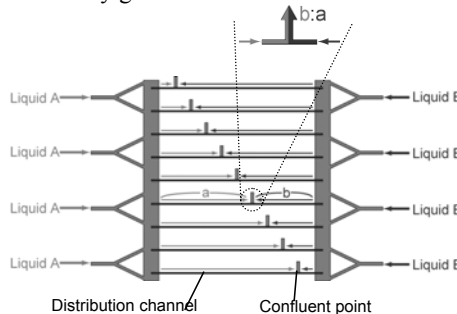
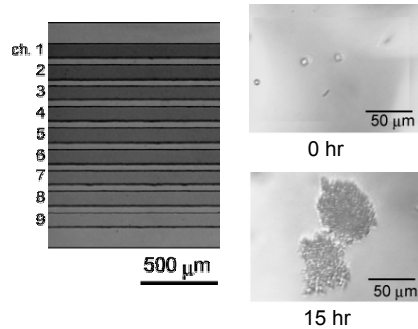


Figure 1. Principle for generating linear concentration conditions. When the lengths of the distribution channels for Liquid A and B are a and b , respectively, the mixing ratio will be $b:a$.

We fabricated PDMS microdevices (Fig. 2), and estimated the ability of the microdevice via colorimetric assay using water-soluble blue dye. As can be seen from Fig. 3 (Left), it was confirmed that the stepwise concentrations could be accurately formed, without the influence of the flow rate. Also, biochemical application was successfully performed using yeast cells, as shown in Fig. 3 (Right).



3. Exponential gradient generator

Preparing exponential concentrations is more frequently employed for various biological applications. Therefore, we performed the generation of exponential gradient by employing stepwise dilution. The microchannel design is shown in Fig. 4 (a). By precisely designing the microchannel network, regarding the microchannel as a resistive circuit (Fig. 4 (b)),

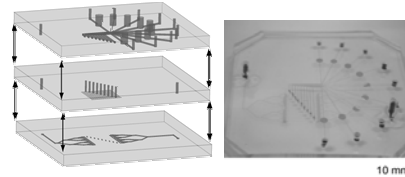


Figure 2. A schematic diagram and a photograph of the PDMS microdevice for linear-gradient generation. This microdevice is composed of three PDMS plates having different microchannel configurations. There are two inlets, nine cultivation chambers, and nine outlets. The mixing ratios of the two liquid flows are 1:9 ~ 9:1.

Figure 3. (Left) Photograph showing the generated stepwise concentrations at the detection point. (Right) Photographs of yeast cells immobilized and cultivated in the cultivation chamber in the microdevice. Ethanol concentrations were varied, and its influence was successfully evaluated (data not shown).

flow rate distributions at a branch point can be freely controlled. In this microdevice, when the diluting and concentrated solutions are continuously introduced with a flow-rate ratio of 2:1, the concentrated solution is diluted approximately one-tenth at each confluent point (CP_1 and CP_2). Accordingly, exponential and multiple concentration conditions (0%, 1%, 10%, and 100%) can be acquired.

To estimate the distribution ratio at each branch point, micro-particles were introduced, and the distribution ratio was calculated. As can be seen from Table 1 (Upper), the experimental distribution ratios well corresponded to the theoretical values. Also, the exponential concentrations could be successfully formed (Table 1 Lower).

3. Conclusions

It was successfully demonstrated that the presented systems are advantageous to prepare multiple concentration conditions. By increasing the number of the generated concentrations, more accurate biochemical processing would be conducted. Also, these systems would be applied for various biochemical experiments by immobilizing cells or biomacromolecules in the downstream.

References

- (1) NL Jeon, SKW Dertinger, DT Chiu, IS Choi, AD Stroock, GM Whitesides, *Langmuir*, 16, 8311 (2000).
- (2) X Jiang, JMK Ng, AD Stroock, SKW Dertinger, GM Whitesides, *J. Am. Chem. Soc.*, 125, 5294 (2003).

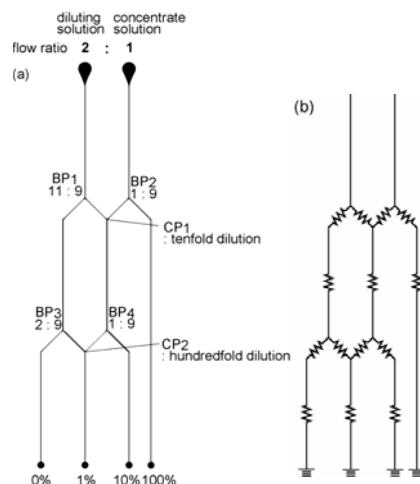


Figure 4. (a) Schematic diagram of the microchannel structure for exponential gradient generation. The microchannel is composed of wide and narrow channel segments. (b) Schematic diagrams of a resistive circuit corresponding to the microchannel network.

Table 1. (Upper) Theoretical and experimental values of the ratio of flow rates at each branching point. (Lower) Theoretical and experimental values of the concentrations at each outlet.

	BP1	BP2	BP3	BP4
theoretical	10.99 : 9.01	1.47 : 8.53	2.61 : 8.39	2.01 : 7.99
measured (particle)	11.76 : 8.24	1.35 : 8.65	2.25 : 8.75	2.19 : 7.81
	Outlet 1	Outlet 2	Outlet 3	Outlet 4
theoretical	0 %	2.82 %	14.03 %	100 %
measured (particle)	0 %	2.58 %	14.08 %	100 %

'WET' AC ACTUATED MICROFLUIDIC MICROPOROUS ARRAY FOR PATTERNING DIFFUSIBLE GRADIENTS DURING CELL CULTURE

Tushar Bansal¹, Meng-Ping Chang² and Michel M. Maharbiz^{1,3}

¹Department of Electrical Engineering and Computer Science, ²Department of Mechanical Engineering, ³Department of Chemical Engineering, University of Michigan, Ann Arbor, USA

ABSTRACT

This work presents a class of 'wet' MEMS elastomer-metal electrostatic actuators that can actuate in air, oil or water environments with no external fluidic connections, have actuation voltages as low as 1 V, and are made with biocompatible materials. Moreover, the hybrid devices are compatible with common PDMS microfluidic fabrication processes [7]. We present initial results on 5 x 5 arrays of actuated drug-dosing pores using this technology. These arrays are capable of patterning the spatio-temporal dosing profile of aqueous molecules into cell or tissue culture [1, 9].

Keywords: Microfluidics, electrostatic actuation, chemical microgradients, two-dimensional diffusion

1. INTRODUCTION

Microgradients of diffusible chemicals are essential for understanding many of nature's developmental processes; several groups have begun developing devices to study these gradients [2, 3, 4]. Specifically, we are interested in controlling the chemical microgradients that lead to differentiation and morphogenesis in tissue and primary cells. The large number of independent valves needed for this task motivated the development of all gold and polymer-gold (**PoGo**) wet MEMS valves presented here. Each valve actuator was required to operate in aqueous environments, have low actuation voltages and be compatible with cell culture surface functionalizations and coatings. Additionally, we wanted the technology to be compatible with simple PDMS microfluidic fabrication processes.

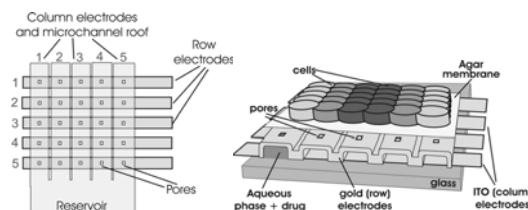


Figure 1 a) Top view and b) orthogonal view of the actuated pore array; hybrid PDMS-Au devices have an additional PDMS coat and the gold layer is patterned into flexures (see Figure 2).

This 'pull-in' voltage is given as:

$$V_{PI} = \sqrt{\frac{8k(g + (t_{ox} \cdot \epsilon_{rL}) / \epsilon_{ox})^3}{27\epsilon_0\epsilon_{rL}A_{cap}}} \quad (1)$$

where:
k = spring constant; t_{ox} = passivating oxide thickness
g = gap; ϵ_{ox} = oxide permittivity;
 A_{cap} = capacitor area; ϵ_{rL} = dielectric permittivity

Even though dielectrics such as water ($\epsilon_{rL}=80$) provide very low pull-in voltages, their use has historically been limited due to the problems related with electrolysis [5],

2. THEORY

Electrostatic actuation is a well known process in 'dry' MEMS. On applying a potential between two parallel plates, electrostatic forces pull both the plates together. If the plates are held apart by a linear spring, the maximum range of travel is limited to 1/3 of the original gap after which electrostatic force exceeds the spring force and the gap collapses.

anodization [5] and electrode polarization [6]. The devices presented here use an AC voltage signal to induce electrostatic forces between electrodes at the top and bottom of a microfluidic channel to collapse it; in this sense, they could be described as self-actuating ‘Quake’ valves [7]. In order to operate in water, a 5 MHz square wave with no DC bias is necessary to prevent double layer screening of the electrostatic forces [8]. Note that as water has such a high dielectric constant, the thickness of any passivating oxides cannot be ignored in the pull-in voltage calculations (Eq. 1) [10]. The **PoGo** devices using PDMS flexures were built due to the polymer’s very high elasticity (140%). In contrast, gold has a yield strength of 100MPa.

3. EXPERIMENTAL

A. Fabrication

Two types of actuators are possible (Fig. 2). In the all-gold version (Fig. 2h1), a final photoresist coat, lithography and gold etch defined the pore size ($5\text{ }\mu\text{m}$) and the exposed contact pad areas. In the hybrid PDMS-gold designs (Fig. 2h2), the gold ‘roof’ was patterned into very compliant flexures and PDMS was then spun on. By design, the elastomer served as the principal mechanical flexure. Photoresist was then removed by immersing the chip overnight in acetone. Pads were wire-bonded to a carrier PCB board.

B. Experimental Setup

Upright and inverted microscopy were done with a ZEISS Axioskop and a Nikon TE2000, respectively. Surface profilometry was carried out using a Zygo New View 5000. For fluorescent imaging and dosing, a mixture of de-ionized water and a Tris(2,2'-bipyridyl)dichlororuthenium(II) hexahydrate (Sigma) fluorophore was loaded in a reservoir and entered the microchannels through capillary action. Devices were also filled and tested with mineral oil (results are not presented here). Voltages were applied using a Keithley 2400 Sourcemeter.

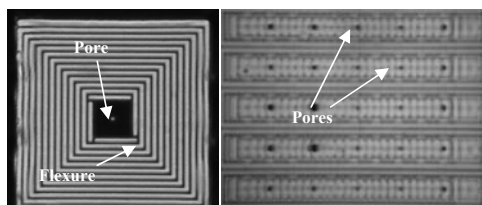


Figure 3. a) Single design of a gold-PDMS membrane b) A 5×5 array of all gold membrane

deflection profile of an un-actuated and an actuated all-gold pore. The measured peak current per actuation is less than $1\text{ }\mu\text{A}$. Figure 5 shows deflection vs. voltage amplitude (at 5 MHz) for an all-gold pore. It is important to note that neither cells nor cell medium

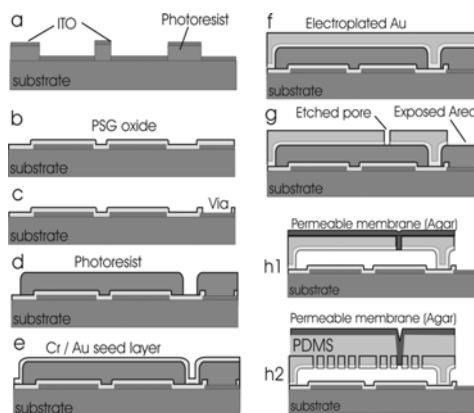


Figure 2. Fabrication process flow. The devices were fabricated on $4''$ glass substrates. Indium tin oxide (ITO) electrodes were sputtered (2000 \AA) and patterned through lift-off process and annealed at $750\text{ }^{\circ}\text{C}$ in Rapid Thermal Anneal (RTA) oven. A thin layer of oxide ($0.4\text{ }\mu\text{m}$) was deposited via PECVD and annealed in RTA at $700\text{ }^{\circ}\text{C}$. Contacts were timed etched through the oxide in 49% BHF (0.1 $\mu\text{m}/\text{min}$). A $5\text{ }\mu\text{m}$ thick resist was spun and patterned into desired microchannel geometries. Cr/Au ($150\text{ \AA}/1500\text{ \AA}$) was then evaporated onto the chip to form the ground electrode. $1.5\text{ }\mu\text{m}$ of gold was electroplated at a current density of 2 mA/mm^2 .

4. RESULTS AND DISCUSSION

Functional arrays of both types of devices and various flexure styles were fabricated. Figure 3a shows a fabricated representative PDMS-gold valve; Figure 3b shows a 5×5 all-gold valve array. **PoGo** devices have been designed to work between 1-5V. The all-gold devices are designed to work at 20-25V. Figure 4 shows the

will experience large electric fields (or electrolysis) as the field is confined below the cell culture area and the device is insulated by a membrane. Figure 6d shows the microgradient profile of a single actuated pore. In this image, the pore was left open for 180 seconds (Fig. 6a), then actuated and closed (Fig. 6b). Once actuated, the intensity decreases and the fluorophore diffuses out. Figure 6c shows a multi-pore section of the array, with the upper channel filled with fluorophore and showing diffusion. Multiple actuated pores with different release sequences can be used to pattern spatio-temporal gradients into cell and tissue culture.

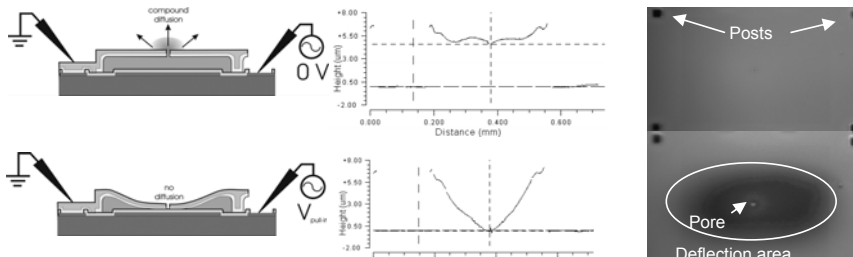


Figure 4. (top row) Undeflected (bottom row) Deflection with a 26 V amplitude, 5 MHz signal. From left to right: Schematic cross-section, profilometry cross section and visual confirmation of deflection (using inverted microscopy).

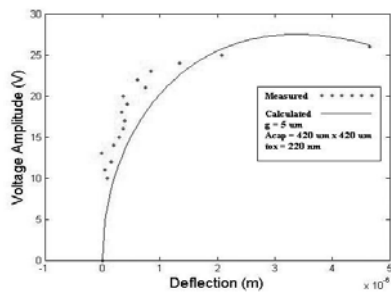


Figure 5: Pull-in voltage vs. deflection

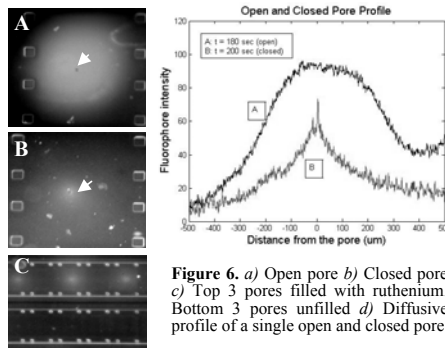


Figure 6. a) Open pore b) Closed pore
c) Top 3 pores filled with ruthenium.
Bottom 3 pores unfilled d) Diffusive profile of a single open and closed pore

5. CONCLUSION

We have designed, fabricated and tested a class of 'wet' MEMS polymer-gold (**PoGo**) electrostatic actuators. These independent valves work at low pull-in voltages and are capable of integrating with microfluidic devices.

6. ACKNOWLEDGEMENTS

The authors would like to thank the staff of MNF and Professor Mark Burn's lab. This work was funded by NSF grant ECS 0601528.

7. REFERENCES

- [1] B.G. Chung, F. Lin and N.L. Jeon, *Lab Chip*, 2006.
- [2] N.L. Jeon, H. Baskaran, S.K.W. Dertinger, G.M. Whitesides, L.V. de Water, M. Toner, *Nature Biotech*, 20, July 2002.
- [3] J.W. Allen, S.N. Bhatia, *Biotechnol Bioeng* 82: 253–262, 2003.
- [4] J. Park, T. Bansal, M. Pinelis and M. M. Mahabirz, *Lab Chip*, 2006.
- [5] K. R. Zavadil, M. A. Rising, and P. C. Galambos, Proc. Electrochemical Society Microfabricated Systems and MEMS VI, Series PV2002-6, Pennington, NJ, 2002, pp. 44–152.
- [6] J.W. Judy, *Smart Mater. Struct.*, vol. 10, pp. 1115–1134, Nov. 2001.
- [7] M.A.Unger, H.P. Chou, T. Thorsen, A. Scherer, S.R. Quake *Science* 288: 113-116 (2000).
- [8] T. L. Sounart, T. A. Michalske, K.R. Zavadil, *JMEMS*, vol.14, No.1, pp 125-133, Feb 2005.
- [9] M. C. Peterman, J. Noolandi, M. S. Blumenkrantz, H. A. Fishman, "Localized chemical release from an artificial synapse chip," *PNAS*, Vol. 101, no. 27, July 2004, pp. 9951-9954.
- [10] B. Legrand, A.-S.Rollier, D. Collard, L. Buchaillot, *Applied Physics Letter*, 88, 034105 (2006)

A MICROELECTROLYTIC DEVICE FOR ELECTRONICALLY CONTROLLED NITRIC OXIDE MICROGRADIENT GENERATION

P. Padmanabhan^{1†}, Z. Zhou^{2†}, B. Wu², J. Park³,
M. E. Meyerhoff², and M. M. Maharbiz³

¹Department of Applied Physics, Department of Biomedical Engineering,
University of Michigan, USA

²Department of Chemistry, University of Michigan, USA

³Department of Electrical Engineering, University of Michigan, USA

Abstract

We present the first micro-electrolysis device for the electronic control of nitric oxide (NO) release using a high molecular weight polyethylene imide (HMW PEI) pH sensitive NO donor. The device consists of Ti/Pt electrodes patterned on a glass wafer under a poly-dimethylsiloxane (PDMS) membrane used to contain the aqueous donor solution. The device operates on the premise that the electrolysis of water generates protons at the anode of the electrochemical cell, lowering the local pH of the electrolyte, triggering the release of NO from the donor. Using sets of electrodes, various spatio-temporal gradients of NO dosage can be achieved for *in vivo* or *in vitro* studies.

Keywords: nitric oxide, microfluidics, microgradient, electrolysis

1. Introduction

In the past two decades, nitric oxide has been shown to have vital physiological effects [1]. While materials and devices that passively release NO have been well documented, they do not allow for the modulation of release levels *in situ*. Additionally, previous attempts at active electronic control of NO generation have made use of toxic compounds or complicated constituents which are not amenable to biological research [2,3]. In order to generate biomedically useful, controllable NO gradients, we utilize a novel class of water soluble pH sensitive NO donors in conjunction with a microdevice capable of generating precise pH gradients, allowing for NO generation.

2. Theory

The device utilizes a HMW PEI compound which releases NO in acidic environments according to the mechanism shown in Figure 1 [4]. At pHs above 10, the donor is chemically inert and releases only trace amounts of nitric oxide. The device operates by using the electrolysis of water to generate protons at the anode of an electrochemical cell, generating a local pH decrease and releasing NO.

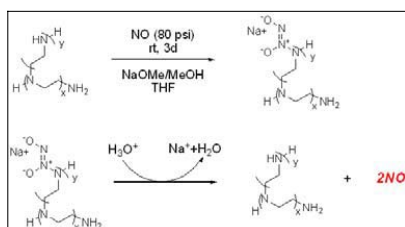


Figure 1. Mechanics of HMW PEI nitric oxide release

3. Experimental

Two versions of an NO generator chip were used. In the first, an array of Ti/Pt anodes 5 μm in width and 1.2 cm in length and a single cathode with a 2 mm width were patterned on a Pyrex wafer using lift off. A PDMS gasket was placed over the

[†]Authors contributed equally

electrode region to retain the NO donor solution over the active electrode area. The current through the electrodes was modulated using a current source (Kiethly). All NO release measurements were made in a 100 mL argon-sparged glass jar connected to an NO Analysis System (Sievers NOA 280i).

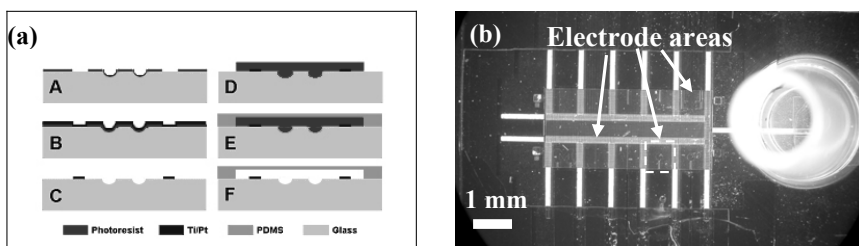


Figure 2. (a) Fabrication process for version 2 of the NO generation chip: (A) HF glass etch to form microchannels for electrolyte loading; spin coat and pattern photoresist for electrode definition, then (B) Ti/Pt (500Å/1500Å) evaporation as electrode material, then (C) pattern electrodes using lift off, then (D) spin coat and pattern photoresist for PDMS cavity formation, then (E) spin coat PDMS, and finally (F) strip photoresist in acetone to form cavity. (b) chip level picture of version 2 of the chip.

The second version, a modification of a design presented by Park *et. al.*, added a PDMS membrane 5 μm above the glass surface [5]. Note that the NO donor (and the supporting electrolyte) are thus sequestered beneath the gas-permeable PDMS membrane (Figure 2a) and do not come into contact with the external environment (i.e. cell culture medium or *in vivo* surroundings). The second version of the chip also used ten independent anodes with different geometries that allowed for the formation of various pH and NO gradients. Each anode reservoir region was fed via the etched glass channels. All NO release measurements were made using the same procedure as for version 1, above.

LysosensorTM Green DND-153 (Invitrogen) was used to fluorescently image the pH gradients. For this indicator, fluorescence intensity increases as solvent acidity decreases. Unfortunately, the fabricated electrolyte channel was too thin (5 μm) to provide enough signal for a quantitative readout. In order to image the generated pH gradients, the PDMS membrane was removed and replaced with a glass coverslip which increased the thickness of the trapped aqueous indicator layer and reduced filling unevenness.

4. Results

Figure 3 shows the concentration of NO in the analysis chamber versus time for the first version of the chip at potentials of 1.5 V and 2.5 V applied between the anode and cathode. Similarly, Figure 4 shows the concentration of NO at current steps of 20 μA , 40 μA , and 50 μA . Each increase in applied bias potential or current resulted in a corresponding increase in NO concentration. By varying the potential or current, we can achieve relatively stable NO release for several minutes. For high fixed voltages, the current swung widely; this was linked to changes in electrolyte conductivity which caused a great deal of instability. For high NO generation rates, current control was preferable. At lower voltages, such as those used to generate Figure 4, these swings were negligible.

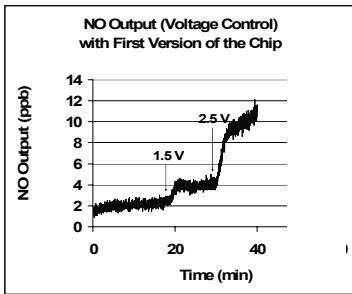


Figure 3. Concentration of NO in the chamber with voltage control for the 1st version on the chip.

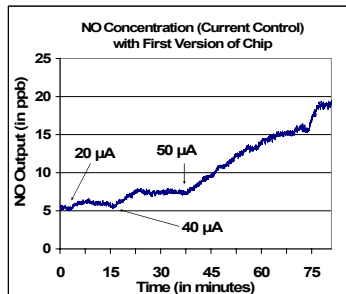


Figure 4. Concentration of NO in the chamber with current control for the 1st version of the chip.

Figure 5 shows the concentration of NO in the analysis chamber versus time for the second chip design (with PDMS membrane) at current steps of 6 μ A, 7 μ A, 9 μ A, and 13 μ A. The concentration at 9 μ A and 13 μ A showed an oscillatory behavior that appears to be caused by a periodic gas bubble formation and purging beneath the PDMS reservoir.

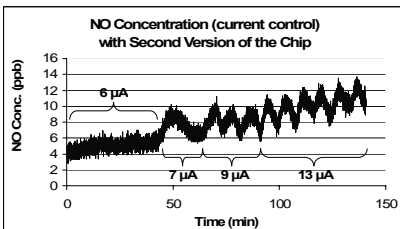


Figure 5. Concentration of NO in the analysis chamber with current control for the second version of the chip (electrode area was approximately $3.22 \times 10^{-9} \text{ m}^2$)

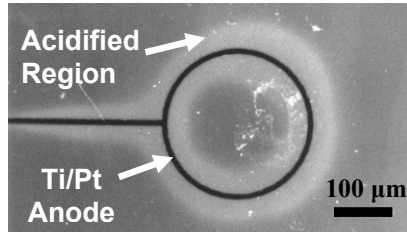


Figure 6. Image of pH gradient taken with Lysosensor™ Green DND-153. Background emission intensity corresponds to pH 7. Brighter regions indicate acidification

Figure 6 shows a pH gradient generated with the chip loaded with a pH 7 solution. A well defined cloud of acidified electrolyte forms around the electrode area when current is applied. Currently, we are working towards increasing the PDMS reservoir height to obtain a stronger fluorescent signal. Fluorescent imaging of the pH gradient will allow us to optically interrogate the pH during NO generation and use this to calculate NO levels at various points over a given gradient field.

References

- [1] D. L. Mooradian, T. C. Hutsell, L. K. Keefer, *J Cardiovasc Pharmacol.*, vol. 25, No. 4, pp. 674-678, April 1995.
- [2] A. D. McGill, Y. Yang, J. Wang, L. Echegoyen, P. G. Wang, *Methods in Enzymology*, vol. 301, pp. 235-242, 1999.
- [3] Y. Chi, J. Chen, and K. Aoki, *Inorg. Chem.*, vol. 43, pp. 8437-8446, 2004.
- [4] Z. Zhou, G. M. Annich, Y. Wu, and M. E. Meyerhoff, "Development of Polymeric Water-Soluble Nitric Oxide Donors for Potential Applications in Hemodialysis" *Biomacromolecules*, manuscript in preparation.
- [5] J. H. Park, T. Bansal, M. Pinelis and M. M. Maharbiz, *Lab on a Chip*, 6, pg. 611-622, 2006

CONTINUOUS-FLOW PARTICLE SORTING AT LOW APPLIED ELECTRIC FIELDS USING ELECTRODELESS DIELECTROPHORESIS IN RIDGED POLYMERIC MICROSTRUCTURES

A. Ezekiel Smith, Benjamin G. Hawkins, Yusef A. Syed, Brian J. Kirby
Sibley School of Mechanical & Aerospace Engineering, Cornell University,
Ithaca, NY

Abstract

We present a microfluidic device capable of sorting particles in a solution of physiological salinity. It effectively manipulates particles at electric fields as low as 30 V/cm and does so at high speeds and over small length scales. This device is designed around cheap, mass producible fabrication techniques allowing for facile incorporation into existing analytical systems.

1. Introduction

This work presents continuous-flow particle sorting at low applied electric fields (30 V/cm) using electrodeless DEP[1-4] in ridged polymeric microfluidic channels. Particle manipulation and sorting is critical in analysis of cellular systems and subpopulations, water monitoring, soil analysis, and colloidal synthesis. In contrast to previous work in electrodeless or insulative DEP, which typically require fields above 500 V/cm [3, 4], this device operates at the low electric fields required when using solutions of physiological salinity. It also offers advantages over other particle processing techniques in its ability to sort particles over small ($\sim 100 \mu\text{m}$) spatial scales and rapid ($< 1\text{s}$) time scales. These advantages combine to enable cell sorting in growth media, facilitating analysis of cells immediately following culture.

2. Design Methodology

Our design efficiently relates dielectrophoretic particle properties to particle motion via a geometrically defined ridge that creates spatial electric field perturbations. Particle motion by DEP is a second-order effect due to the polarization of a particle and its surroundings in the presence of a non-uniform electric field. Equation 1 gives particle velocity, u_{DEP} , as a function of its dielectrophoretic mobility, μ_{DEP} , and the electric field gradient.

$$\vec{u}_{\text{DEP}} = \mu_{\text{DEP}} \vec{\nabla}(\vec{E} \cdot \vec{E}) \quad (1)$$

This system sorts particles using a micro-channel geometry that transduces particle dielectric properties to transverse spatial position in continuous flow. We use electrodeless DEP due to its inherent simplicity, eliminating the need for integrated electrodes and the fouling attendant with their use. Whereas previous work demonstrated DEP by an array of insulating posts (a 2-D design) [1], our approach extends this technique to 3-D using channel constrictions in depth to create spatially non-uniform electric fields. The channel ridge perturbs the spatial distribution of the electric field, creating particle-dependent dielectrophoretic forces and deflection. Curvilinear sorting ridges as shown in Fig. 1 are designed such that the dielectrophoretic forces vary spatially across the channel

width. Particles are deflected transversely until they reach the position at which dielectrophoretic forces no longer prohibit particle transport across the ridge.

$$\vec{u}_{EK} = \mu_{EK} \vec{E} \quad (2)$$

The electromigration of a particle, u_{EK} , is linear with electric field and electrokinetic mobility, μ_{EK} , as shown in Eq. 2. As a result of controlled particle deflection, the downstream flow consists of a distribution of particles in which the particle dielectrophoretic mobility varies continuously across the channel width. This distribution can then be routed to multiple outlets, and specific subpopulations can be analyzed.

3. Experimental

The demonstrated device has a multilevel microchannel geometry formed by two lithographic steps that overlay ridges (constrictions in depth) onto an otherwise uniform channel. A Zeonor 1020R substrate (Zeon Chemicals) is hot embossed on a Silicon master fabricated using two lithographically defined layers and etched using a Bosch process. The embossed piece is drilled for fluidic access and bonded to a Zeonor blank to enclose the channel. To demonstrate system behavior, 1 and 2 μm carboxylate-modified Flu-oSpheres® were visualized via inverted fluorescent microscopy.

Pressure-driven and electroosmotic flows are used in conjunction to independently control drag, electrophoretic, and DEP forces. This allows DEP effects at low electric fields to be amplified by tailoring the applied pressure and electric field to reduce particle velocities. DC electric fields were used to simultaneously reduce particle velocities throughout the flow field (due to electrophoresis in the opposite direction to fluid flow) and induce particle-dependent deflection at the ridge structure (due to DEP).

4. Results and Discussion

Deflection of a single particle type demonstrates the fundamental mechanism for particle deflection and allows quantification of the relation between applied electric field and particle deflection. Particle distributions are approximately uniform in the absence of an electric field (Figure 2a). Applying a potential between the system reservoirs, how-

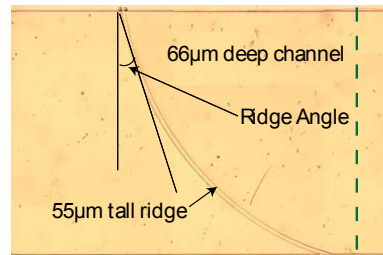


Figure 1. Device overview with curvilinear ridge marked showing dimensions of 6:1 ridge constriction. The green dashed line marks the position of the slice for Fig 3 & 5.

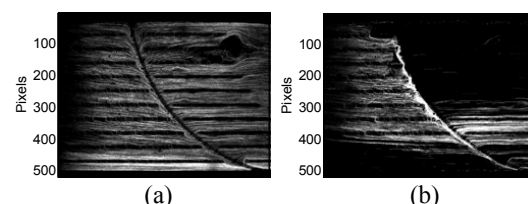


Figure 2. Time-averaged particle fluorescence micrographs of left-to-right flow over curvilinear ridge.(a): Pressure driven flow left to right(b): $E=60\text{V}/\text{cm}$.

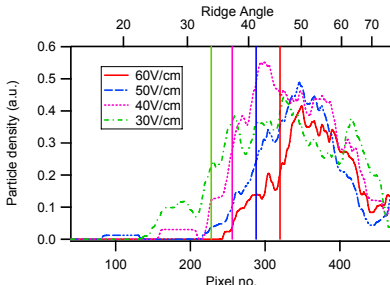


Figure 3. Output particle density along the vertical dashed line in Figure 1. Vertical bands denote location of peak half height, which is displayed in Figure 4. Pixel number refers to y pixel of Figure 2.

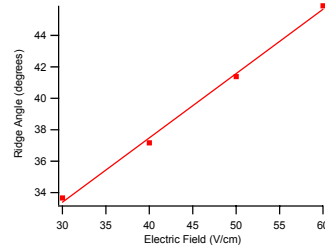


Figure 4. Ridge angle (defined in Fig 1) determined from half peak amplitude of particle densities.

ever, results in particle deflection to the lower region of the field of view (Figure 2b). Because particle deflection all occurs at the sorting ridge (rather than slowly throughout a device), the process is effectively instantaneous (<1 s). For a given particle type, deflection increases with the applied electric field (Fig 3). Defining the “critical ridge angle” as the geometric ridge angle at the half-height of the particle distributions, it can be shown that the distribution can be varied linearly and precisely with electric field (Fig 4). Through this precise control, the device can be tuned to operate for a wide range of μ_{DEP} and μ_{EK} .

Deflection of a mixed particle sample demonstrates how varying DEP mobilities can be used to sort particles in continuous flow. Time-averaged exit particle density distributions of a two component system (Fig 5) show how a mixed input stream can be separated into its constituents. This demonstrates the validity of the design and forecasts its ability to form concentration and pretreatment stages in lab-on-a-chip systems.

References

- Cummings, E.B. and A.K. Singh, *Anal. Chem.*, 2003. **75**(18): p. 4724-4731.
- Chou, C.F., et al., *Biophysical Journal*, 2002. **83**(4): p. 2170-2179.
- Barrett, L.M., Skulan, Andrew J., Cummings, Eric B., Singh Anup K., Fiechtnar, Gregory J., *μ TAS*. 2005. Boston, MA: Transducer Research Foundation, Inc.
- Cummings, E.B., *s. IEEE Eng. Med. Bio.*, 2003. **22**(6): p. 75-84.

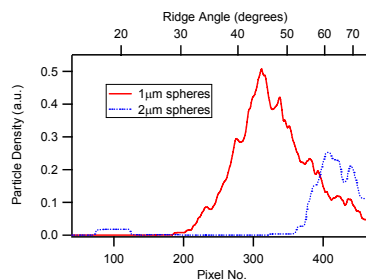


Figure 5. Particle sorting of microspheres of differing μ_{DEP} . Profiles are particle distributions at the dotted line in Figure 1. $E = 50\text{V}/\text{cm}$. Pixel number refers to y pixel of Figure 2.

A PASSIVE MICROFLUIDIC DROPLET FUSION DEVICE WITH 100% FUSION EFFICIENCY

Wei-Yu Tseng^a, Yung-Chieh Chen^b, Lung-Hsin Hung^a, Abraham P. Lee^{c,d}

^a Department of Chemical Engineering and Material Science

^b Electrical Engineering & Computer Science

^c Department of Biomedical Engineering

^d Department of Mechanical and Aerospace Engineering

204 Rockwell Engineering Center, University of California at Irvine, Irvine, CA 92697

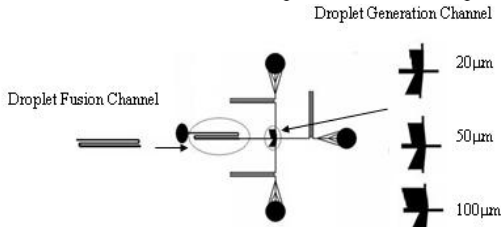
Abstract

We demonstrate here a droplet fusion device with 100% droplet fusion. This device includes an asymmetry wings double T-junction droplet generator and expanding droplet fusion channel. The asymmetry double T-junction generate stable and separate droplet pairs and the long expansion channel make droplets within a pair contact and have enough time to complete fusion process. This passive microfluidic device can reach 100% fusion efficiency.

key words : microfluidics, droplets, fusion, double T-junction

Introduction

Controlled droplet fusion in microfluidic device provides precise reagent mixing control for small scaling chemical reaction and biological detection. Previous works to achieve controlled droplet fusion are by exploiting the velocity difference between droplets to fuse large and smaller droplets or by stable droplet generation by double T-junctions and a velocity gradient tapering junction which can provide duration of collision and fusion[1,2,3,4]. However, unstable droplet generation lead to only 95% droplet fusion efficiency in the first design. In the second design, even double-T junction offer stable droplet generation, the time of the droplet pairs exiting in the fusion chamber is not always longer than the duration time of the collision and fusion of droplets and the maximum fusion efficiency can only reach 80%. Beside the problems mentioned above, the unfused droplets also cause uncontrollable further droplets fusion which cause non-uniform size fused droplets and the separation problems of fused and unfused droplets and. Here, we present a separate and stable droplet pair generation from an asymmetry double T-junction design and 100% droplet fusion inside long expanding droplet fusion channel (Figure 1).



Design of the droplet generator

An ideal 100% droplet fusion include a stable and separation droplet pair generator and a droplet fusion channel which can make droplet collision and provide enough time for droplet pairs fusion. Double T-junction design can

Figure 1. The droplet fusion device contains asymmetry wings droplet generation design and expanding long fusion channel.

offer stable but not separate droplet pairs in microfluidic device. In order to achieve stable and separate droplets pair generation, the alternating double T-Junction generator design was improved so that the double T-Junction includes asymmetric wings to facilitate the shortening of **D** and increasing of **d** as shown in Figure 2. Since the droplet generation frequency from each side of the double T-junction is constant, the distance **2D** between two droplets from the same T junction is constant (Figure 2). In symmetric designs [3, 4], since the droplets generate at same cross section alternatively, gaps between droplets from different sides will be **D**. In asymmetry design (Figure 2b), with the offset of the shearing junctions, D is shortened and the distance d between two pairs of droplets is increased at the same time.

Result and Discussion

As mentioned above, the separate droplets can be generated by the offset of the shearing junction. Figure 3 shows the droplet pairs separation results of different offset designs from $20\mu\text{m}$, $50\mu\text{m}$ to $75\mu\text{m}$. The distances D and d are compared in table 1. As the offset distance **g** increases, **D** decreases and **d** increases. This offset distance also results in unequal-size droplet generation from the double T-junction because the shearing point which is not in same cross section results in different shearing force. The smaller droplets are generated from the offset junction and the larger droplets are generated from the original junction. The ratio of the droplet sizes are constant in different offset device shown in table 1. The ratio between the flow rates to obtain 1:1 droplet generation ratios is strongly dependent of the size of the droplet ratio as shown in table 2.

The long expansion channels with two U-turn shape designs are used for droplet fusion. Its purpose is to remove the oil between droplet pairs to induce contact by expanding the channel width and to offer enough contact time for the droplet collision and fusion. The width of the expansion channel can range from $80\mu\text{m}$ - $120\mu\text{m}$ and the length of the channel is 4cm. In figure 4, all droplet pairs are generated from $100\mu\text{m}$ offset asymmetry generator, travel to the fusion channel and fused at the first U-turn shape design. The 100% droplet fusion efficiency has been achieved under different water flowrate at constant water flowrate ratio as shown in figure 5. When the water flow rate is lower than $0.3\mu\text{l}/\text{min}$, the droplet generation becomes unstable and the fusion efficiency drops to 40% dramatically. The fused droplets are monodisperse with less than 2% variation in size.

Conclusion

This novel system provides a highly controlled droplet generation with synchronization of unequal-size droplet generation combined with a droplet fusion microfluidic device with 100% droplet fusion efficiency and equal-size fused droplets. This design can be integrated with other microfluidic designs and is a promising tool for chemical syntheses and bioanalytical tests.

Reference

- [1] H. Yang, C. C. Park, Y.T. Hu, Physics of Fluids 13(5), pp.1087-1106 (2001)
- [2] Yung-Chieh Tan, Jeffrey S. Fisher, Alan I. Lee, Vittorio Cristini, Abraham P. Lee, Lab on a Chip, 2004, 292-298.
- [3] Helen Song, Joshua D. Tice, Rustem F. Ismagilov, Angewandte Chemie International Edition, 2003, 768-772

[4] L.-H. Hung, K.M. Choi, W.-Y. Tseng, Y.-C. Tan, K.J. Shea, and A.P. Lee, *Lab on a Chip*, vol. 6, 1-6, 2006.

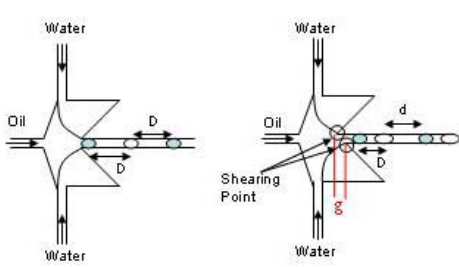


Figure2.(a)In symmetry wings design, distance of droplets from the same stream is 2D and droplets distance from different stream is D. (b) In asymmetry wings design, the offset of the shearing point shortens the droplet distance D and increases the distance d between droplet pairs.

g	Distance D within the droplet pair	Distance d between the droplet pair
20 μm	95.7 μm	103.6 μm
50 μm	79.1 μm	186.6 μm
75 μm	30.5 μm	297.5 μm

Table 1. The relationship between distances **D** and **d** at different offsets

g	Size ratioo	Flow rate ratio
20 μm	1:11:1	1.07:1
50 μm	1.24:1	1.36:1
75 μm	1.55:1	1.67:1

Table 2. The size ratio increased with the offset and the flow ratio to maintain 1:1 droplet

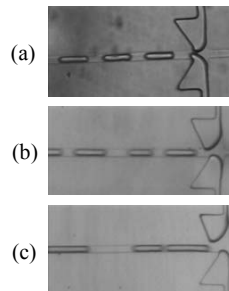


Figure3. (a)20 μm offset (b) 50 μm offset (c)75 μm offset asymmetry double T-junction

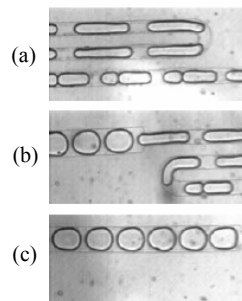


Figure4. (a) Each pair of droplets enter the fusion chamber and contact each other (b) At the u-turn channel, droplet fused (c) fused droplets are monodispersed

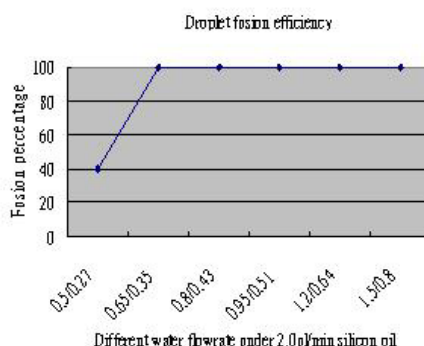


Figure 5. 100% droplet fusion efficiency can be achieved at varied water rate. The fusion efficiency drops when the flowrate is too low to have stable alternative droplet generation.

A SIMPLE COMPOSITE CAP SEALING OF INTEGRATED NANO/MICROFLUIDIC CHANNEL DEVICES BELOW 20 nm AT ROOM TEMPERATURE

Jian Gu^{*}, Ravi Gupta^{*}, Chia-Fu Chou^{**}, Qihuo Wei^{*,#}, Frederic Zenhausern^{*}

^{*}Biodesign Institute, Arizona State University, Tempe, AZ 85287, USA

^{**}Institute of Physics, Academia Sinica, Taipei 11529, Taiwan, ROC

[#]Liquid Crystal Institute, Kent State University, Kent, OH, USA
(email: cfchou@phys.sinica.edu.tw; Jian.Gu@asu.edu)

Abstract

A composite cap sealing process with precise dimension control, low pressure operation and permanent bonding at room temperatures has been demonstrated for the fabrication of 1D, 2D nanochannels (confinement in one and two dimensions, respectively), and integrated nano/microfluidic devices with a micro- to nano-scale interface. Channel size below 20 nm has been successfully sealed. Aspect ratio of $< 4 \times 10^{-5}$ has been achieved for 1D nanochannels.

Keywords: microchannels, nanochannels, sealing, nano-microfluidic interface

Nanofluidic structures have attracted many attentions recently due to the unique fluidic behaviors on the nanoscale [1] and the capability of biomolecule manipulation at confined environments [2, 3]. Integrated nano/microfluidic devices with micro-nano interface are also important for potential total-analysis-system at the nanoscale[4]. A straightforward way of fabricating integrated nano/microfluidic channels with proper interface is by cap sealing of nano- to micro-trenches. However, most of previous methods of cap sealing (such as anodic bonding [5], fusion bonding [5], modified nanoimprinting [2] etc.) require high pressure and/or high temperature. Here we report an extremely simple sealing process for the fabrication of 1D and 2D nanofluidic channels and the integration of nano/ microfluidic devices using a composite cap. The composite cap sealing process requires no or very low pressure, works at room temperature with high throughput and low cost.

Figure 1 shows a schematic of composite cap sealing process: a thin layer of PSQ (polysilsesquioxane) is spun on a cover glass and then thermally cured; nano- and micro-trenches with sloped micro-nano interface and loading holes are etched into Si or glass substrate; sealing is realized by oxygen plasma treatment of PSQ film and contact of two substrate surfaces (a thin silica layer is created by O₂ plasma treatment of PSQ film). Due to large plasma-treated surface energy and flexibility of the cap, the pressure for conformal sealing is small (usually less than 30 psi). We find that bonding between the composite cap and substrate is

spontaneous. Bonding wave has been observed after two surfaces making the initial contact. The bonding strength increases with time, and permanent bonding can form within one minute of initial contact with a proper plasma treatment. A small pressure (< 2 atm) at the beginning of the bonding will help the permanent bonding formation.

1. Composite cap by spinning PSQ on cover glass and O₂ plasma treatment



2. Sealing of nano-, micro- trenches with micro-nano interface and loading holes



Figure 1. Simple simultaneous sealing of nano-, microfluidic channels with micro-nano interface by a composite cap at room temperature.

For sealing of 1D nanofluidic channels, trenches with a width from 3 μm to 500 μm and a depth from submicron to sub-20 nm were first fabricated on a thermally oxidized Si wafer surface by photolithography and dry etching, and subsequently sealed by composite cap sealing. Because of the spontaneous bonding, the channels are either self-sealed or sealed by applying a tiny force (< 1 N) in making an initial surface contact for the bonding to propagate. 1D nanochannels with a depth down to 18 nm and aspect ratio below 4×10^{-5} have been demonstrated (Fig. 2). To our knowledge, this is the lowest aspect ratio of nanochannel reported to date.

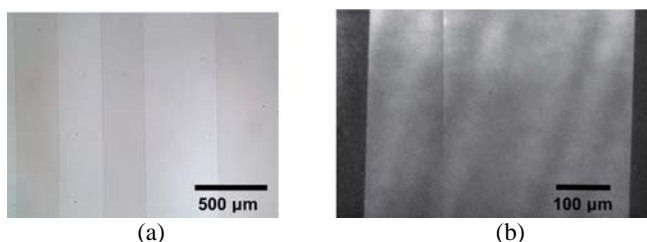


Figure 2. Bright field (a) and fluorescent images (b) of sealed 1D nanochannel with a depth of 18 nm and aspect ratio < 4×10^{-5} .

For sealing of 2D nanofluidic channels, nano trench array of 120-nm-width and 320-nm-period was etched into thermally oxidized Si wafer surface by nanoimprinting and pattern transfer techniques with a nanograting mold, and then sealed by the composite cap process. 2D nanochannel array has been sealed successfully, sometimes with the help of a small pressure (< 2 atm) to bring the two surfaces in contact at the beginning of the bonding. Dense 2D nanochannel array and integrated nano/microfluidic devices with sloped micro-nano interface were also fabricated and utilized for stretching double-stranded DNA (Fig. 3).

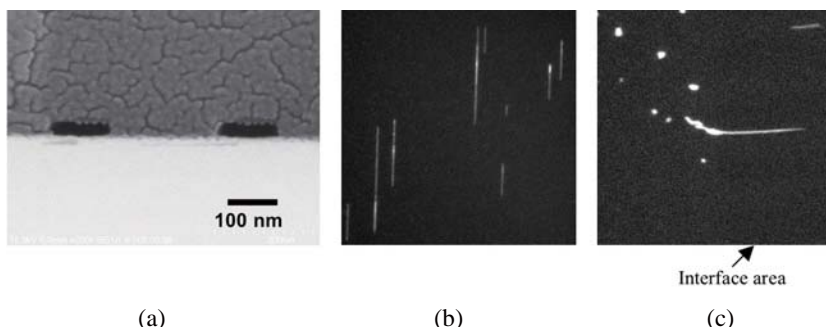


Figure 3. Cross-sectional SEM image of sealed 2D nanochannel (a) and fluorescent images of DNA stretched in 2D nanochannels (b) and at the micro-nano interface area (c).

In summary, a composite cap sealing process has been demonstrated for the sealing of 1D, 2D nanofluidic channels and integrated nano/microchannel devices with a micro-to-nano interface at room temperature. The demonstrated critical feature size can be sub-20 nm with the potential of shrinking down further due to the low-pressure operation of the sealing process. 1D nanochannel with an ultralow aspect ratio of $< 4 \times 10^{-5}$ and 2D nanochannel array have both been successfully sealed by the composite cape sealing. DNA pre-stretching at micro-to-nano interface in an integrated nano/microfluidic device was also observed.

The authors thank NanoOpto Corp. for providing nanograting mold for the fabrication of 2D nanochannel arrays.

- [1] N. R. Tas *et al.*, Applied Physics Letters **85**, 3274 (2004).
- [2] L. J. Guo, X. Cheng, and C. F. Chou, Nano Letters **4**, 69 (2004).
- [3] J. O. Tegenfeldt *et al.*, Proc. Natl. Acad. Sci. U.S.A **101**, 10979 (2004).
- [4] D. J. Beebe, G. A. Mensing, and G. M. Walker, Annu. Rev. Biomed. Eng. **4**, 261 (2002).
- [5] P. Mao, and J. Y. Han, Lab on a Chip **5**, 837 (2005).

PALM TOP SIZED DETECTION SYSTEM WITH MICRO CHEMICAL CHIP

Akihiko HATTORI¹, Yoshinori MATSUOKA², Mitsuo KITAOKA²,
Takehiko KITAMORI³

¹ Nippon Sheet Glass Co., Ltd., Japan

5-8-1, Nishi-Hashimoto Sagamihara-City Kanagawa, 229-1189, Japan

E-mail: AkihikoHattori@mail.nsg.co.jp

TEL +81-42-775-1520, FAX +81-42-775-1531

² The Research Association of Micro Chemical Process Technology, Japan

³ The University of Tokyo, Japan

Abstract

We have been achieved to development a palm top sized photo-thermal lens spectroscopy detection system with micro chemical chip, in which all devices required for thermal lens measurement such as light sources, optical multiplexer and so on were integrated in the small box. The detection system was free from optical alignment problems. The system developed here had good performance. The limit of determination for Ni complex standard solution was evaluated to be 1.0×10^{-5} (Abs).

Keywords: *Photo-Thermal Lens Spectroscopy, SELFOC® Micro Lens, Micro Chemical Chip*

1. Introduction

Smart integration of glass micro chemical chip system, ultra high sensitive quantitative analysis, and compact detection devices are essential issues in μ -TAS. Recently, Thermal Lens Microscope detection system (TLM) to analyze trace amount of chemical substances with micro chemical chips was developed by Kitamori et al. [1]. However the conventional TLM was not small enough to set up the practical μ -TAS. In this work, availing very small SELFOC® Micro Lens (SML) as an objective lens and an optical multiplexer, the palm top sized Photo-thermal Lens Spectroscopy Detection System (TLDS) has been achieved.

2. Principle and Design of Thermal Lens Spectroscopy Detection (TLD)

A schematic illustration of TLM in a micro channel is shown in figure 1. The principle of measurement for TLM has been described elsewhere [1-3]. Availing the SML as an objective lens and an optical multiplexer as shown in figure 2, the optical system of TLDS was designed. The SML is the most popular radial graded-index (GRIN) lens and it has features of parabolic refractive index distribution in a glass rod, cylindrical shape with flat ends, and adequate chromatic aberration. The chromatic aberration of SML can be controlled arbitrarily by changing materials and the lens size.

The excitation and probe beams propagated through the single-mode optical fibers were made to be coaxial using the optical multiplexer in figure 2. The optical multiplexer was consisted of a dielectric filter sandwiched in between two SML (see

Fig.2). As the dielectric filter has characteristics both of reflecting the beam emitted by laser diode 1 (excitation beam) and transmitting the beam emitted by laser diode 2 (probe beam), these beams were made coaxial and were introduced into the single-mode optical fiber.

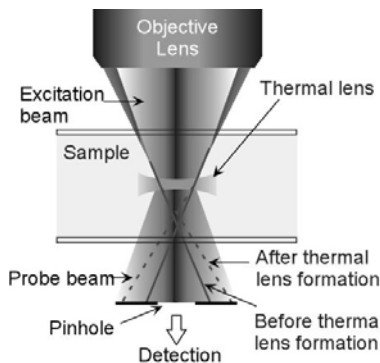


Fig.1 Principle of TLM

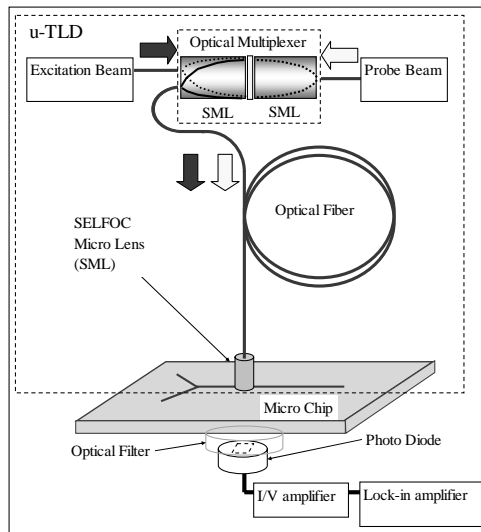


Fig.2 Optical system with SML

3. Palm Top Sized Detection System with Micro Chemical Chip

Fig.3 shows a schematic and photograph of on-chip detection device. Fig.4 shows a photograph of the Palm Top Sized Detection System with Micro Chemical Chip. Firstly, the performance of this detection system with standard solution of Ni phthalocyanine tetrasulfuric acid, 4Na salt was measured. The calibration curve assumed smooth linearity in the range from 1×10^{-8} to 1×10^{-5} mol/L. The value of determination limit was 1×10^{-8} mol/L (1.0×10^{-5} Abs). Excellent repeatability and reproducibility of photo-thermal signal intensities were also confirmed. The values of coefficient of variation in these measurements remained less than 3%.

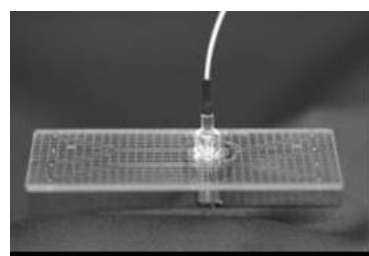
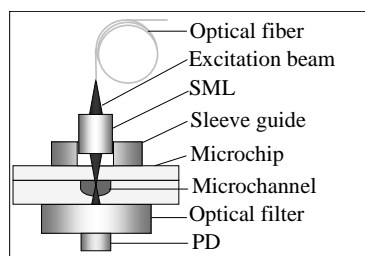


Fig.3 Schematic and photograph of on-chip detection device

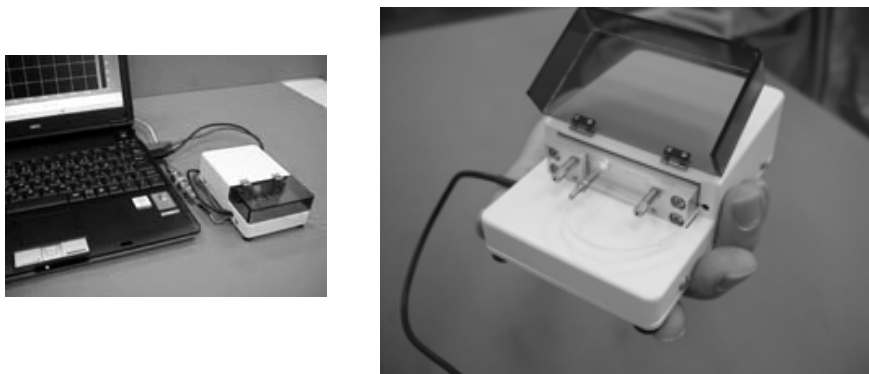


Fig. 4 Palm Top Sized Detection System with Micro Chemical Chip

This system can be operated with a notebook PC and the operation electric power can also supplied from a notebook PC by using a USB connector.

4. Conclusion

We have described the miniaturization of thermal lens detection system based on an optical fiber and SELFOC® micro lens. This palm top sized system developed here showed excellent performance for detection of nonfluorescent molecules despite the miniaturization of optical components. This system developed here will be used more widely in the future, for example POCT (point of care testing), on site monitor and so on. Practically, we are in the progress of developing a chip-based enzyme-linked immunosorbent assay system now.

Acknowledgements

This work was supported by “Project of Micro-Chemical Technology for Production, Analysis and Measurement Systems” of New Energy and Industrial Technology Development Organization (NEDO), Japan.

References

- [1] M. Harada, K. Iwamoto, and T. Sawada, “Photothermal microscopy with excitation and probe beams coaxial under the microscope and its application to micro particle analysis,” *Anal. Chem.*, 65, pp238-2940(1993).
- [2] S.E Bialkowski, Photothermal Spectroscopy Methods for chemical Analysis, Wiley, New York, (1996).
- [3] M. Tokeshi, M. Uchida, K. Uchiyama T. Sawada, and K. Kitamori, Single- and countable-molecule detection of nonfluorescent molecules in liquid phase, *J. Luminescence*, 83-84, pp. 261-264(1999).

INTEGRATION OF MULTIPLE ANALYTICAL PRINCIPLES ON A CAPILLARY-ASSEMBLED MICROCHIP (CAs-CHIP): MULTIPLE PROTEASE ACTIVITY AND ELECTROLYTE SENSING

**Terence G. Henares, Masayuki Takaishi, Naoya Yoshida,
Hideaki Hisamoto, and Shigeru Terabe**

Graduate School of Material Science, University of Hyogo, Japan

(e-mail: hisamoto@sci.u-hyogo.ac.jp)

Abstract

A general and simple implementation of simultaneous multiparametric sensing in a single microchip is presented by using a capillary-assembled microchip (CAs-CHIP) [1-4] integrated with reagent-release capillaries (RRCs), acting as various biochemical sensors. A novel “drop-and-sip” technique of fluid handling is performed with a microliter droplet of a model sample solution containing proteases and divalent cations that passes through the microchannel with the aid of a micropipette as a vacuum pump, concurrently filling each RRCs via capillary force. This RRC-based CAs-CHIP can be exploited for clinical diagnostics, drug discovery and systems biology applications.

Keywords: capillary-assembled microchip, capillary force, “drop-and-sip”, multiparametric sensing, protease activity

1. Introduction

The simultaneous multiparametric sensing in a single microfluidic device is inevitably an important aspect of miniaturized system since it provides minimal reagent/sample consumption while detecting a range of analytes. However, specific panel of analytes require a particular surface chemistry to activate a given microchannel surface for certain biochemical analysis, hence, making the integration of different analytical principles in a single microfluidic device more complicated.

Here, we demonstrated the simple and simultaneous detection of various proteases (trypsin, chymotrypsin, thrombin and elastase) and electrolytes (Mg^{2+} , Ca^{2+} and Zn^{2+}) in a single microfluidic device by integrating the enzymatic cleavage and complexation reactions as different analytical principles implemented into the RRC-based CAs-CHIP.

2. Experimental

The RRC-based CAs-CHIP was prepared by embedding various 2.3-mm RRCs and plugged capillaries onto the PDMS microchannel network (Fig. 1). To realize the multianalyte sensing without reagent diffusion and leakage, a facile technique called “drop-and-sip” was implemented. A microliter volume of sample was “dropped” on the inlet hole and “sipped” using a micropipette on the outlet hole, generating a long sample plug while allocating part of the solution into the RRCs by capillary force. The detection of protease activities and electrolytes were carried out using a fluorescence microscope.

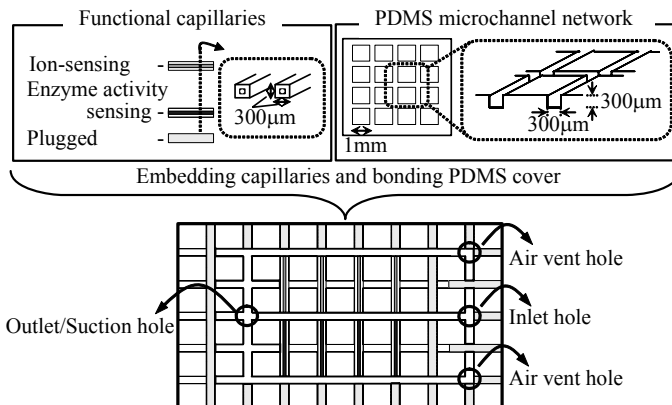


Figure 1. RRC-based CAs-CHIP for multiparametric sensing

3. Results and discussion

The molecular probe inside the RRC is immobilized with the aid of polyethylene glycol as polymer scaffold and release/react upon contact with sample solution. Examples of the enzyme activity- and ion-sensing results are shown in Figure 2. Both RRCs displayed a typical response, *i.e.*, it can sense changes in analyte concentration with a nanoliter volume of sample.

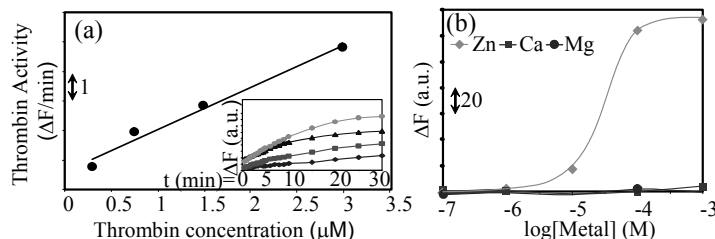


Figure 2. (a.) Boc-Asp(OBzl)-Pro-Arg-MCA immobilized capillary for thrombin activity sensing at various thrombin concentration (\blacktriangle 0.3, \blacksquare 0.74, \blacktriangledown 1.5 and \blacklozenge 3.0 μM) (b) Zinc-sensing capillary response with different Zn^{2+} ion concentrations and its selectivity over Ca^{2+} and Mg^{2+} ions.

The “drop-and-sip” technique proves to be the most compatible fluid handling methodology for the RRC-based CAs-CHIP because it prevents reagent diffusion and leakage from the capillary. Using a micropipette as vacuum pump, the contact time of the sample plug was ca. 0.55 second that was enough time to fill the RRCs by capillary force, since the theoretical capillary filling time is ca. 0.008 second.

Combining both simple methodologies of the RRC and “drop-and-sip”, the over-all simple-to-use property of RRC-based CAs-CHIP was realized. Figure 3 demonstrated

the simultaneous sensing of various proteases, cations and pH. The microchip effectively showed fluorescence detection of 8 different analytes.

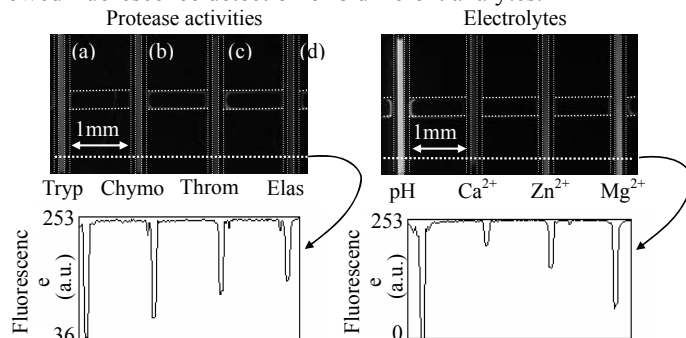


Figure 3. Simultaneous detection of the proteases activities and the metal ion concentrations using a single CAs-CHIP. The specific substrates used for each proteases are as follows, (a) Boc-Gln-Ala-Arg-MCA; (b) Suc-Ala-Ala-Pro-Phe-MCA; (c) Boc-Val-Pro-Arg-MCA; (d) Suc(OMe)-Ala-Ala-Pro-Val-MCA. Sample solution contains proteases ($0.04 \mu\text{M}$ trypsin (Tryp), $0.04 \mu\text{M}$ Chymotrypsin (Chymo), $0.74 \mu\text{M}$ thrombin (Throm) and $1.0 \mu\text{M}$ elastase (Elas)) and electrolytes ($100 \mu\text{M}$ Ca^{2+} , Mg^{2+} and Zn^{2+}).

4. Conclusions

The ease of integrating multiplex panel of analytical principles was successfully achieved. The easy-to-use nature of the RRC-based CAs-CHIP can be exploited for the analysis of biological samples.

Acknowledgements

T. H. acknowledges for the Monbukagakusho Scholarship from the Japanese government and H.H. is grateful for the research funding sponsored by the NEDO Grant for Industrial Technology Research (05A37702a), the Grant-in-Aid for Scientific Research from the Ministry of Education, Culture, Sports, Science and Technology, Japan, and Hyogo Science and Technology Association, Japan.

References

- [1] H. Hisamoto, Y. Nakashima, C. Kitamura, S.-I. Funano, M. Yasuoka, K. Morishima, Y. Kikutani, T. Kitamori and S. Terabe, *Capillary-Assembled Microchip for Universal Integration of Various Chemical Functions onto a Single Microfluidic Device*, *Anal. Chem.*, 76, 3222-3228 (2004).
- [2] H. Hisamoto, S.-I. Funano and S. Terabe, *Integration of Valving and Sensing on a Capillary-Assembled Microchip*, *Anal. Chem.*, 77, 2266-2271 (2005).
- [3] H. Hisamoto, M. Yasuoka and S. Terabe, *Integration of Multiple-Ion Sensing on a Capillary-Assembled Microchip*, *Anal. Chim. Acta*, 556, 164-170 (2006).
- [4] H. Hisamoto, S. Takeda and S. Terabe, *Capillary-Assembled Microchip as a Deproteinization Device for Capillary Electrophoresis*, *Anal. Bioanal. Chem.* in press (2006).

CHEMILUMINESCENT DETECTION IN A CUSTOMISED MICROFLUIDIC CHIP WITH INTEGRATED PROTEIN MICRO-ARRAY

C. A. Marquette¹, A. Homsy², K. Heyries¹, D. Hoffmann²,
L. J. Blum¹ and M. G. Loughran²

¹Laboratoire de Génie Enzymatique et Biomoléculaire, Université Lyon 1, France

²Tyndall National Institute, Cork, Ireland

Abstract

Protein microarrays for allergen diagnosis were integrated in microfluidic chips. The integrated microfluidic chip enabled chemiluminescence (CL) detection of human IgG antibodies with detection limit of 60 pM (or 9 ng/ml) within 30 min.

Keywords: Chemiluminescence, HPTS, micro-fluidics, protein micro-array,

1. Introduction

Chemiluminescence is an established and sensitive analytical technique for microarray detection, due to its very high signal to noise ratio [1]. A convenient reversible procedure was used to bond a polydimethylsiloxane (PDMS) microarray substrate to complimentary microfluidic multi-reaction chambers. This customized protein microfluidic system incorporated six interconnected reaction chambers to facilitate rapid, parallel, high throughput screening (HPTS) of different proteins. The complete protein microchip was assembled by careful alignment of protein-modified PDMS substrate with a complimentary SU-8 microfluidic chip (Fig. 1). In each reaction chamber, protein micro-assay occurred between the specific immobilized proteins and the complimentary peroxidase labelled antibodies.

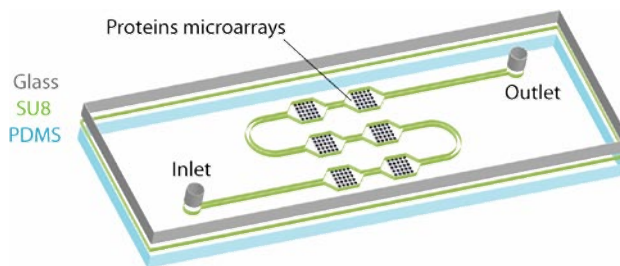


Fig. 1: Schematic of the integrated protein micro-assay system. The upper lid/surface of the reaction chamber was made of SU-8 microchannels on a glass substrate. The bottom substrate was composed of PDMS and contained spotted protein microarrays.

Modelling of the microchip geometry with Coventor Software provided an assessment of the necessary alignment for efficient fluid transfer [2]. Optimal fluid transport occurred at the center of each reaction chamber (Fig. 2).

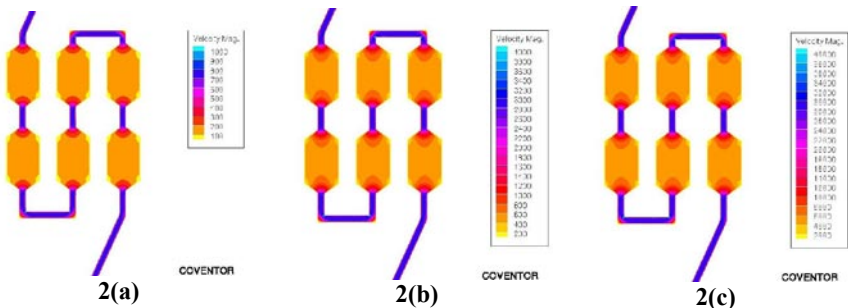


Fig. 2: Fluid velocity in the microchip determined by computer simulation with Coventor™ software: (a) Flow rate = $1.25 \mu\text{l}/\text{min}$, (b) Flow rate = $5 \mu\text{l}/\text{min}$, (c) Flow rate = $50 \mu\text{l}/\text{min}$ (velocity magnitude is $\mu\text{m}/\text{s}$).

2. Materials and methods

The microarrays were prepared by spotting protein solutions (1,3 nL in 0.1M carbonate buffer pH 9) on a PVC master, drying and covering the spots with liquid Sylgard 184 Polydimethylsiloxane (PDMS). This PDMS-protein matrix was cured at 100°C for 20 min then peeled from the master. The SU-8 microchannels (depth 80 μm , width 400 μm , length 76 mm) were fabricated via standard lithography procedures on glass wafers. PDMS inlet and outlet ports were permanently bonded to the upper glass surface of the microchip to ensure leak proof connection.

The fluidic characteristics of this protein microanalysis system were determined experimentally under a continuous reagent flow of 0.5 - 50 $\mu\text{l}/\text{min}$. The on-chip chemiluminescent immunoassay was initiated by saturation with VBSTA (veronal buffer containing 0.5% Tween20 and 1% BSA) for 30 min at a flow rate of $1.125 \mu\text{L}/\text{min}$. The antibodies solution, containing rabbit anti-protein and peroxidase anti-rabbit IgG at concentrations of 1 $\mu\text{g}/\text{ml}$, was then injected at a flow rate of $0.5 \mu\text{l}/\text{min}$ for 30 minutes. The chip was then washed with VBS at a flow rate of $5 \mu\text{l}/\text{min}$ for 20 min and filled with the chemiluminescent measurement solution ($220 \mu\text{M}$ luminol, $500 \mu\text{M}$ hydrogen peroxidase and $200 \mu\text{M}$ para iodo phenol in VBS buffer).

A sensitive CCD imaging system (Intelligent Dark Box II, Fuji Film) enabled direct quantification of the proteins immobilized in the microarray via peroxidase catalyzed CL. All experiments were performed at room temperature.

4. Results and discussion

The homogeneity of the sample distribution within the microfluidic chambers was confirmed by the flow of peroxidase labeled anti-human IgG in a biochip composed of 96 identical spots of human IgG. The chemiluminescent image obtained is presented in Fig. 3(a) and confirms reproducible distribution of the fluid throughout the system. The presence of occasional bubbles leads to spot missing.

Fig. 3(b) shows the results obtained using a biochip prepared with internal non-specific testing spots composed of spotted bovine serum albumin (BSA). Only the specific spots (lactoglobulin and peanuts lectin) of the microarrays produced chemiluminescent signals, whereas the signals onto the negative control spots remained at the background value.

Fig. 3(c) shows complementary chemiluminescent intensity signals obtained with a microarray composed of spotted lactoglobulin, peanuts lectin and human IgG and incubated concomitantly with anti-lactoglobulin, anti-peanuts lectin and anti-human IgG. As shown, the three proteins were detected after a unique sample injection with good signal to noise value. The detected amount of the 3 different proteins was 17 ng after 30 minutes incubation at room temperature.

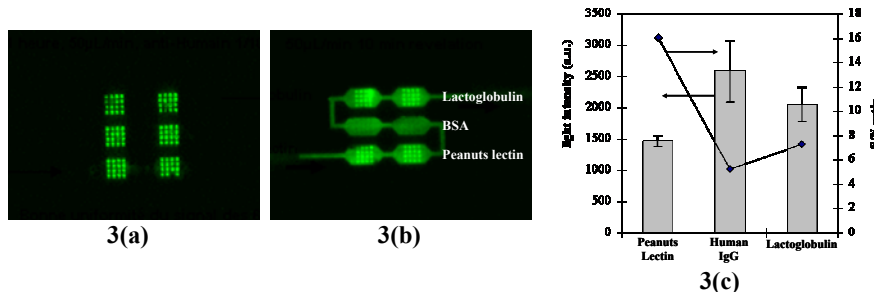


Fig. 3: CCD measurement of the associated chemiluminescent signal. (a) Homogeneity of sample distribution determined at a flow rate of 0.5 μ l/min, peroxidase labeled anti-human IgG concentration of 1 μ g/ml. (b) Simultaneous chemiluminescent immunoassay of anti-lactoglobulin, anti-peanuts lectin and anti-human IgG antibodies within the within the microfluidic system. (BSA proteins provide internal standard to confirm non-specific binding). (c) Measured chemiluminescent signal and signal to noise ratio for the three proteins tested concomitantly in (b). Peroxidase labeled anti-rabbit IgG concentration of 1 μ g/ml.

5. Conclusions

The detection of anti-lactoglobulin, anti-peanuts lectin and anti-human IgG was successfully achieved in a microfluidic environment, and our results are comparable with conventional protein microassay systems [3-4].

Acknowledgements

The authors acknowledge the EU FP6 project “Nanospad” and the Nano2Life mobility program for the financial support.

References

1. C.A. Marquette, L.J. Blum, *Direct immobilization in poly(dimethylsiloxane) for DNA, protein and enzyme fluidic biochips*, Analytica Chimica Acta, 506 (2), 127-132 (2004).
2. D. Hoffmann, M. Curtin, E. Moore, M. Loughran, *Development of an integrated microsystem for injection, transport and manipulation of encoded microbeads*, Lab on a Chip, submitted (2006).
3. D.S. Wilson, S. Nock, *Recent developments in protein microarray technology*, Angewandte Chemie International Edition, 42 (5), 494-500 (2003).
4. K.Y. Tomizaki, K. Usui, H. Mihara, *Protein-detecting microarrays: Current accomplishments and requirements*, ChemBioChem, 6 (5), 783-799 (2005).

THREE-DIMENSIONAL BIOLOGICALLY-ACTIVE NANOSTRUCTURED ARCHITECTURES IN POLYMER-BASED MICROFLUIDIC DEVICES FOR BIOMARKER DETECTION

Guofang Chen¹, Catherine Situma¹, Steven A. Soper¹ and Robin L. McCarley¹

¹Department of Chemistry and Center for BioModular Multi-Scale Systems, Louisiana State University, Baton Rouge, LA 70803, USA

Abstract

We report a novel three-dimensional (3D) DNA analysis device consisting of ultra-high-aspect-ratio polymer nanopillars prepared by a templating polymerization pattern-transfer method followed by a direct-write photochemical patterning approach to produce functional scaffolds for the immobilization of molecular recognition probes to nanopillars. These nanopillars can be integrated into microfluidic channels for producing high-surface-area supports for these probes to increase assay sensitivity and dynamic range, as well as rapid response times due to microfluidic addressing of the array. Anodic aluminum oxide (AAO) was used as the template for the nanostructures as well as the molding tool for the microfluidic network. The AAO template consisted of nanopores with a close-packed hexagonal geometry. The device demonstrated high-speed hybridization kinetics with detection limits on the order of femtmoles.

Keywords: Nanopillars, microfluidics, nano-templating, biomarker detection

1. Introduction

Microarray strategies have been widely utilized in life science research and diagnostics due to their ability to monitor many analytes in parallel when configured in a 2D format on a solid support. For detecting extremely low concentrations of solution targets from mixed populations, the microarray must possess high sensitivity and specificity. Unfortunately, one of the limitations associated with current microarray technologies is their limited immobilization capacity, which significantly affects the assay's dynamic range and offers poor sensitivity due to the low surface concentration of the probes. In addition, slow mass transfer to the surface results in long assay times. We have developed a novel, 3D microarray format situated within a microfluidic network consisting of ultra-high-aspect-ratio functionalized polymer nanopillars by adopting a nano-templating polymerization pattern-transfer method coupled to direct-write photochemical functionalization of the nanopillars [1-3].

2. Experimental

Anodic aluminum oxide (AAO) [1] was used as the template for nanopatterning as well as the molding tool for microstructure fabrication. The microstructures were fabricated

via lithographic and wet-etch processing of the closed-packed hexagonal nanoporous AAO [4]. Complex micro-patterns with different shapes and aspect ratios could be

prepared with vertical sidewalls using this etching technique. The microfluidic channel integrated with poly(methyl methacrylate), PMMA, nanopillars was prepared via cast-molding and nano-template polymerization pattern-transfer following embossing of the microstructures using the AAO template supported on

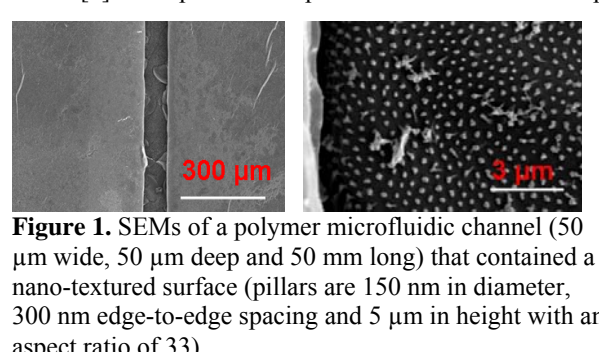


Figure 1. SEMs of a polymer microfluidic channel (50 μm wide, 50 μm deep and 50 mm long) that contained a nano-textured surface (pillars are 150 nm in diameter, 300 nm edge-to-edge spacing and 5 μm in height with an aspect ratio of 33).

aluminum (see Figure 1). Integration of these nano-textured surfaces directly within the microfluidic network provided a 50-fold increase in probe load compared to a planar 2D surface of the same size. The templated nanopillars could be functionalized through UV exposure at 254 nm resulting in surface-confined carboxylates that allowed covalent attachment of 5'-amino- terminated DNA probes directly to their surface using EDC coupling agents.

3. Results and discussion

Our 3D polymer nanopillars increased the array measurement sensitivity and dynamic range through the production of higher surface loads of probes per unit area by adding a third dimension to each element of the array. When coupled to microfluidic addressing, the system showed high-speed hybridization kinetics due to enhanced mass transfer to the surface with detection limits for solution oligonucleotide targets in the femtomolar regime. Figure 2 shows near-infrared (near-IR) fluorescence images resulting from planar and nano-textured PMMA serving as the support for monitoring hybridization-based assays. In the case of the planar PMMA surface, the array generated weak fluorescence against a uniform background (see Figure 2a). The image also showed a high degree of non-uniformity in the signal as well as poor spot definition. On the other hand, the fluorescence image of the PMMA nanostructured microarray showed stronger fluorescence with well-defined and more uniform spots (see Figure 2b). The fluorescence intensity from the nanostructured PMMA substrate increased by ~100-fold when compared to that of a planar PMMA substrate. In addition, two control experiments were carried out to confirm that the observed fluorescence signals were due to specific hybridization of the ‘target’ to its complementary probe. The experiments involved spotting of dye-labeled complementary targets onto the UV-modified surface of a PMMA nanopillar array and planar PMMA. We did not observe any fluorescence against the background in both cases. These experiments showed that there was little non-specific binding of the ‘target’ to the surface of either UV-modified PMMA nanopillars or planar substrates.

4. Conclusions

Our 3D biologically-active nanostructured architectures situated in polymer-based microfluidic devices provided a higher load of the biomarker probe by increasing the available surface area, thus improving the detection sensitivity of the microarray assay. In addition, these nanopillars could be integrated into a microfluidic element using a simple nanotemplating technique that does not require the use of expensive lithography methods, such as e-beam lithography. These nanopillar DNA microarrays can be coupled to an allele-specific ligation assay carried out in a thermal cycling polymer microchip to provide the ability to detect point mutations in certain genes with both high sensitivity, large dynamic range and rapid assay times when the microarray is poised within a microfluidic element.

Acknowledgements

We acknowledge funding from NIH, NSF EPSCoR (EPS-0346411) and the State of Louisiana.

References

1. H. Masuda and K. Fukuda, *Ordered metal nanohole arrays made by a two-step replication of honeycomb structures of anodic alumina*, Science, 268, 1466-1468 (1995).
2. R. L. McCarley, B. Vaidya, S. Wei, A. F. Smith, A. B. Patel, J. Feng, M. C. Murphy and S. A. Soper, *Resist-free patterning of surface architectures in polymer-based microanalytical devices*, J. Am. Chem. Soc., 127, 842-843 (2005).
3. G. Chen, J. G. Bolivar, S. A. Soper and R. L. McCarley, *Highly efficient protein capture and enzyme reactor beds based on ultra-high-aspect-ratio nanostructures (UHARHS)*, Proc. Micro Total Analysis Systems 2005, Boston, MA, USA, pp.1261-1263 (2005).
4. A. -P. Li, F. Müller, A. Birner, K. Nielsch and U. Gösele, *Fabrication and microstructuring of hexagonally ordered two-dimensional nanopore arrays in anodic alumina*, Adv. Mater., 11, 483-486 (1999).

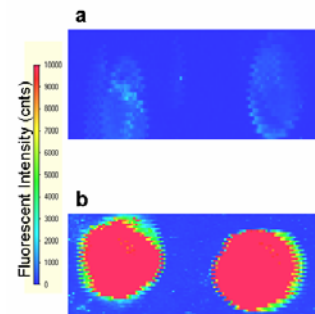


Figure 2 Near-IR scanning confocal fluorescence images of DNA microarrays patterned on a planar 2D PMMA surface (a) and a PMMA nano-textured surface containing high aspect ratio PMMA nanopillars (b). The DNA probes consisted of a random 17-mer sequence that was attached to the PMMA via EDC coupling. The DNA microarrays were incubated with a near-IR fluorescently-labeled solution complement.

INTEGRATED CMOS-COMPATIBLE SILICON NANOWIRE SENSOR WITH EFFICIENT SAMPLE DELIVERY

I. K. Lao*, A. Agarwal, H. H. Feng, N. Balasubramanian, D. L. Kwong
Bio-Electronics & Bio-MEMS, Institute of Microelectronics, Singapore

Abstract

A CMOS-compatible silicon nanowire (SiNW) sensor developed by self-limiting oxidation process is integrated with a micro channel for high sample delivery efficiency through either direct lining or hydrodynamic focusing. pH sensing result of the integrated sensor is reported.

Keywords: integrated micro system, silicon nanowire sensor, self-limiting oxidation, hydrodynamic focusing, sample delivery

1. Introduction

In recent years, chemical and biological detection utilizing nano-structures, such as nano-crystal, nanotube and nanowire has been gaining interest due to their superior performances [1]. Nano-structure with a large surface area to volume ratio provides high sensitivity, permitting prominent detection. Among them, SiNW is the most desirable nano-structure for an integrated system by taking the advantages of mature IC technology. To realize a SiNW sensor, SiNW has to be aligned and assembled on a metal electrode in a robust and well-controlled manner. Secondly, sample molecules have to pass the SiNW for detection. Overly relying on the high sensitivity of nanowire without consideration to mass transport can bring a detection limit [2].

In this study, we use self-limiting oxidation process [3] to fabricate SiNWs with lengths of 10, 20, 50 and 100 μm . Compared with other methods such as vapor-liquid-solid (VLS) method [4], self-limiting oxidation is completely CMOS-compatible, and the most important, it avoids post-synthesis alignment and assembly of SiNW. To reduce the mass transfer effect of sample molecules, micro fluidic channel with either direct lining or hydrodynamic focusing [5] is integrated with the SiNW sensors for efficient sample delivery.

2. Experimental

Fabrication of the integrated SiNW sensor is shown in Figure 1. Trenches are formed in Si wafer by UV photolithography and dry etching to obtain silicon fin structures. The fins are then oxidized in dry oxygen. The oxidation process is self-limiting because of the dynamic build-up stress, forming nanowires along the centre of the fins. The nanowires are released by trimming down the oxide and connected with metal electrodes. SU-8 is used to fabricate micro channels on top of the SiNW.

3. Results and discussion

Figure 2 shows a SEM image of our 100- μm SiNW. Synthesis of such long

nanowires is challenging using VLS method while their assembly is troublesome using reported sophisticated manipulating methods [1]. On the contrary, our SiNW eliminates such complex assembly and alignment problems. Figure 3 shows a cross-sectional TEM image of a SiNW. The SiNW is anchored on a silicon wafer to improve its mechanical strength. The diameter of SiNW is 20 nm in this work, but SiNWs with smaller diameters can also be fabricated.

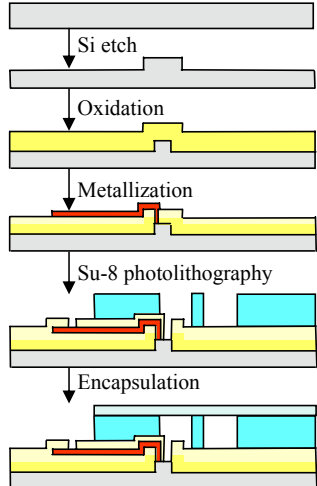


Figure 1. Process flow of an integrated SiNW sensor.

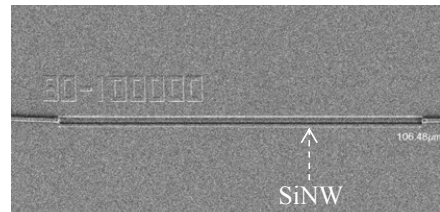


Figure 2. A SEM image of a 100- μm SiNW.



Figure 3. A cross-sectional TEM image of a SiNW with a diameter of 20 nm. An oxide layer is deposited to protect SiNW during sample preparation.

In our integrated system, Su-8 micro channels are fabricated for sample delivery. Su-8 is chosen due to its simple photolithography process which is compatible with our SiNW. It also provides a wafer-level integration and precise alignment between the channel and the nanowire as compared with reported PDMS channel [4]. Considering sample delivery efficiency and pressure inside the micro system, direct lining of the nanowires to micro channels is adopted for 50- and 100- μm nanowires while hydrodynamic focusing [5] is applied for 10- and 20- μm nanowires (Figure 4).

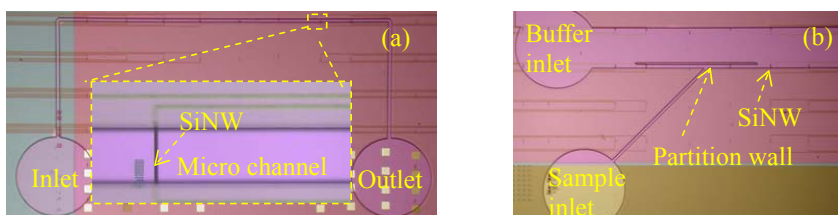


Figure 4. Optical images of integrated SiNW sensors. Micro channels for (a) direct lining for 50- μm SiNW and (b) hydrodynamic focusing for 20- μm SiNW.

Figure 5 shows I-V characteristic of the integrated SiNW sensor. The linear I-V

dependence indicates an ohmic contact between the SiNW and metal electrodes, which is critical for electronic and sensing applications as poor contact has an ambiguous effect on sensing performance [6].

To demonstrate a SiNW sensor for detection, the conductance of a SiNW at different pH solutions is measured (Figure 6). Drop in conductance is observed with pH increment. This is consistent with principle due to the depletion of positive surface charge which acts a lower positive gate voltage on our n-type SiNW. Through surface functionalization of the nanowire [1], the nanowire can act as a bio-sensor.

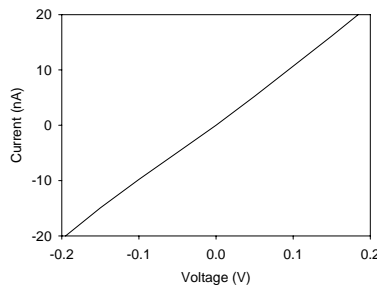


Figure 5. Current-voltage measurement of a SiNW sensor.

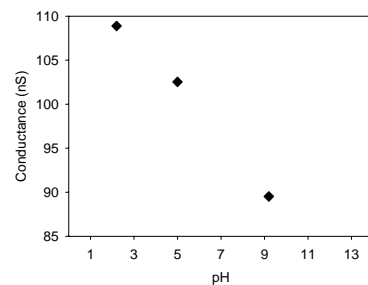


Figure 6. Electrical conductance change on pH sensing of a SiNW at 0.2 V.

4. Conclusions

In conclusion, we demonstrate a CMOS-compatible SiNW sensor with efficient sample delivery.

References

1. K. Wanekaya, W. Chen, N. V. Myung, A. Mulchandani, *Naowire-based electrochemical biosensors*, *Electroanalysis* 2006, 18(6), 533.
2. P. E. Sheehan and L. J. Whitman, *Detection limits for nanoscale biosensors*, *Nano Letters*. 2005, 5, 803.
3. A. Agarwal, N. Balasubramanian, N. Ranganathan, R. Kumar, *Silicon nanowires formation in CMOS compatible manner*, Proc. International Conference on Materials for Advanced Technologies 2005 (2005).
4. G. Zheng, F. Patolsky, Y. Cui, W. U. Wang and C. M. Lieber, *Multiplexed electrical detection of cancer markers with nanowire sensor arrays*, *Nature Biotechnology* 2005, 23, 1294.
5. I. K. Lao, A. Agarwal, H. H. Feng, N. Balasubramanian, D. L. Kwong, *Micro hydrodynamic focused channel for sample delivery control in an integrated CMOS-compatible silicon nanowire sensor*, in Proc. of Eurosensors XX, Goteborg, Sweden, Sept 17-20, 2006, in press.
6. R. J. Chen, H. C. Choi, S. Bangsaruntip, E. Yenilmez, X. Tang, Q. Wang, Y.-L. Chang and H. Dai, *An investigation of the mechanisms of electronic sensing of protein adsorption on carbon nanotube devices*, *Journal of American Chemical Society* 2004, 126, 1563.

DEVELOPMENT OF AUTOMATED LIQUID HANDLER FOR MICROFLUIDIC REACTOR ARRAY FOR HIGH-THROUGHPUT SCREENINGS OF PROTEIN CRYSTALLIZATION CONDITIONS

Tetsu Isomura¹, Toshiharu Shiraishi², Seiichiro Kishishita³, Mikako Shirouzu³, Michiteru Nishino¹, Atsushi Someya², Shigeyuki Yokoyama³, Minoru Seki⁴ and Shigetoshi Sugio¹

¹ZOEGENE Corporation, Japan, ²ARBIOTEC, Ltd., Japan, ³RIKEN Genomic Sciences Center, Japan, ⁴Graduate School of Engineering, Osaka Prefecture University, Japan

Abstract

Previously we have reported a novel screening system in search for protein crystallization conditions using microfluidic reactor array [1], with which the required volume of the protein solution decreases drastically. Here we report the advance of the system including a development of an automated liquid handler. The improved microchip consists of four blocks of 48 reaction chambers whose metering volume are 6 nL, and 192 conditions can be screened with only 2 μ L (0.5 μ L for each) of the protein solution. The liquid handler can control microfluidic reactor array system automatically by real-time monitoring of backpressure. It is equipped with four pumping heads that have sensors to monitor backpressure of microchannels on a microchip, and four non-contact dispensers. The system correctly handled various kinds of aqueous solutions, including salts, organics and polymers, while operation time depended on the properties of liquids. While 0.5 μ L of protein solution was dispensed in the microchannel for protein, 288 nL was effectively utilized for crystallization (the ratio of dead volume: 42.5%). A typical operation time to set up 96 different conditions on the microchip was 40-60 min. from dispensing, transporting and mixing solutions to sealing all wells with oil in a fully automatic manner.

Keywords: crystallization, microfluidic reactor array, automation, protein, screening

1. Introduction

High-throughput crystal structure determination of proteins has been a key technology for structural genomics and structure-based drug design. Crystallization of protein is one of the problematic steps as tens of mg of protein sample is consumed to screen conditions from which a protein can be crystallized. Nano-liter liquid handling is required to reduce the protein consumption, however, viscosity and surface tension of solutions used for crystallization are so different that precise control of dispensing volume is not easily achieved. We have reported microfluidic reactor array [1, 2] can reduce the amount of required volume dramatically, here we report a recent development of an automated liquid handler for microchips to which the microfluidic

reactor array system is applied for protein crystallization screening.

2. Experimental

The liquid handler and the microchip are depicted in Fig 1. The liquid handler is equipped with four pumping heads that have sensors to monitor backpressure, and four non-contact dispensers. The dispensing system can discharge 0.5 μL of various liquids without dead volume, and is free from touch-off procedure that reduces reproducibility. It also has a compressor, a temperature-controllable incubator for four protein solutions and two 96-well plate stockers for precipitants, one dispenser and one pumping head for sealing oil, and several uniaxial drive units. PDMS microdevices were fabricated as described before [1, 2] with small modification; PMMA is adopted for the top plate to increase rigidity. The microchip consists of four blocks of 48 reaction chambers with one microchannel for a protein solution and 48 microchannels for precipitant solutions. Its metering volume is 6 nL, and 192 conditions can be screened with only 2 μL (0.5 μL for each) of the protein solution within the SBS standard dimension.

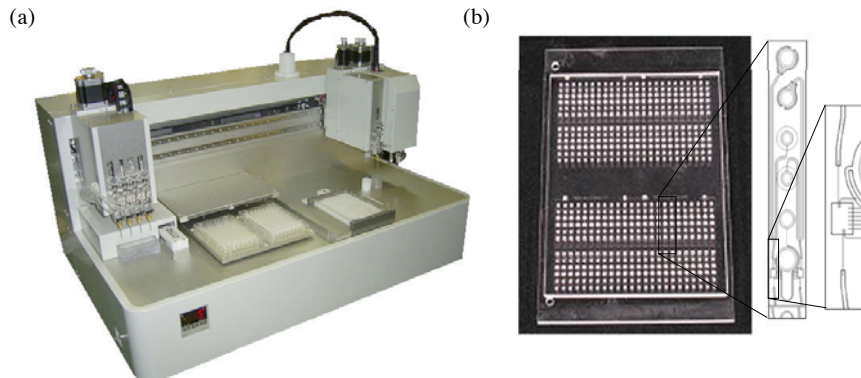


Figure 1. Developed automated liquid handler and structure of microchip.
(a) Appearance of the liquid handler (b) Picture and details of the microchip

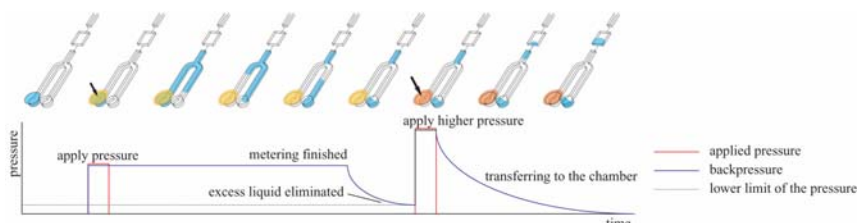


Figure 2. Schematic diagram and behavior of the backpressure. Backpressure decreases after excess liquid is eliminated. Higher pressure let the nano-sized liquid into the reaction chamber.

3. Results and Discussion

We found automatic control of microfluidic reactor array technology can be achieved by real-time monitoring of backpressure. The concept is shown in Fig. 2. After

introduction of liquid and metering, backpressure is reduced as surplus liquid is eliminated and the vent is opened up to the air. This monitoring system is available for various kinds of aqueous solutions, including salts, organics and polymers, and it makes robust against dispensing volume error.

The system correctly handled liquids with rather extreme behaviors (Table 1), and operation time depended on the properties of liquids and the structure of the microchannel (Table 2). While 0.5 μL of protein solution was dispensed in the microchannel for protein, 288 nL was effectively utilized for crystallization (the ratio of dead volume: 42.5%). Fig. 3 shows pictures of liquids transported in the chambers before introducing a protein solution. A typical operation time to set up 96 different conditions on the microchip was 40-60 min. from dispensing, transporting and mixing solutions to sealing all wells by oil in a fully automatic manner.

Table 1. Correctly handled liquids

a. Metering channel for precipitant	b. Metering channel for protein
Water	Water
30% isopropylalcohol	10 mg/mL Lysozyme
30% polyethyleneglycol 8000	50 mg/mL Lysozyme
3 M ammonium sulfate	10 mg/mL Catalase
1.5 M ammonium sulfate, 20% glycerol	
100 mM Bicine pH 9.0, 10% PEG20000, 2% Dioxane	

Table 2. Required time for operation

Channel	Liquid	Metering	Total of Pumping	Total*
Precipitant**	Water	20 s	41 s	51 s
	30% isopropylalcohol	20 s	44 s	55 s
	100 mM HEPES, 20 % PEG10000	73 s	102 s	114 s
Protein	Water	45 s	71 s	88 s

* Total time includes dispensing ** Four channels at a time

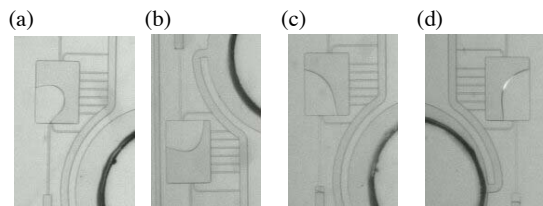


Figure 3. Pictures of the introduced liquids. Water(a), solutions of Crystal Screen HTTM (Hampton Research); tube #D01 (b), #C12(c), #H2(d)

Acknowledgements

We thank Precision Shibasaki Co., Ltd for manufacturing precision mechanical equipment and Mitsubishi Chemical Engineering Corporation for gracious consultation.

References

1. M. Yamada, C. Sasaki, T. Isomura and M. Seki, MicroTAS2003, 449-452 (2003)
2. M. Yamada and M. Seki, Anal. Chem., 76, 895-899 (2004)

MICROFABRICATION OF BARCODED MICROPARTICLE ARRAYS FOR MINIATURIZED AND MULTIPLEXED SINGLE NUCLEOTIDE POLYMORPHISM DETECTION

Zheng-liang Zhi,^a Shouhei Yamamura, Yusuru Takamura and Eiichi Tamiya

School of Materials Science, Japan Advanced Institute of Science & Technology, Japan

^aPresent address: School of Biological Sciences, University of Liverpool, UK

Email: zzhi@liv.ac.uk

Abstract

This paper describes a new and generic microarray platform using microfabricated barcoded microparticles for interrogating multiple DNA hybridization events and for single nucleotide polymorphism (SNP) detection. By coupling a DNA ligation extension reaction, this multiplexed approach was applied to detect SNP where the barcoded particles were used to track multiple reactions and events from DNA arrays in a high-throughput manner. A nano-deposited multilayer of poly-L-lysine (PLL) and poly-L-glutamic acid (PLGA) was introduced onto the monolayer covered particle surfaces to improve fluorescence detection. This approach was used to determine SNP at position -308 within a human gene for tumor necrosis factor (TNF-alpha).

Keywords: microarray, microfabrication, multiplexing, barcoding, single-nucleotide polymorphism

1. Introduction

SNP detections may facilitate not only the process of disease diagnosis but also the practice of preventative and curative medicine. Here we report a miniaturized and multiplexed method for high-throughput SNP detection using barcoded microparticle arrays coupled to an oligonucleotide ligation extension reaction. In our previous works, a new type of microparticle-based barcoding platform technology has been developed using microfabrication techniques. The barcoded Ni microparticles were used as the building blocks for multiplexed bioassays involving multiple biomaterial attachment, detection and identification.¹⁻³ The proposed multiplexing approach for SNP detection is based on an existing SNP assay protocol using allele-specific oligonucleotide ligation (Fig. 1). The SNP assay relies on distinguishing between two DNA molecules differing by one base by hybridization and ligation. The genotype of the target sequence was determined by determining whether the oligonucleotide probe complementary to the DNA sequencing was ligated to a fluorescence labeled reporter oligonucleotide or not. By monitoring the change of fluorescence intensity on the individual particle which was tagged with a sequence of DNA probe, SNP in a target DNA sample (SNP from G to A, C and T at position -308) within the TNF-alpha gene was selectively detected.

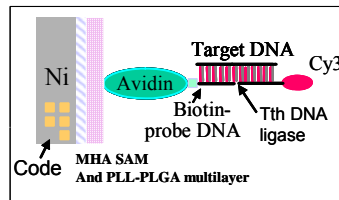
2. Experimental

Barcoded Ni microparticles ($100 \times 200 \times 5 \mu\text{m}$) were fabricated using photolithographically created photoresist patterns as the template for microparticles that were replicated by electrodeposition

technique. The particles were first coated with a self-assembled monolayer (SAM) of 16-mercaptohexadecanoic acid (MHDA), then a multilayer of PLL (20,700 MW) and PLGA (97,800 MW) was deposited using electrostatic layer-by-layer nanodeposition.⁴ Finally, streptavidin was immobilized by adsorption. Biotinylated DNA probes were each attached to a given type of particle *via* biotin-streptavidin chemistry. The synthetic oligonucleotides (with 6 thymines as a spacer in the probes) related to the genotypes of TNF-alpha were acquired from Fasmac (Kawaga, Japan) and had following sequences: Probe A: biotin-5'-tttttacccgtcc. Probe B: biotin-5'-tttttacccgtct. Probe C: biotin-5'-tttttacccgtcca. Probe D: biotin-5'-tttttacccgtcgg. Target 1 (position 297-317): tgagggcatgggacgggt. Reporter DNA: 5'-catgcccta-Cy3.

For attachment of DNA probes onto the particles, each set containing 10–20 particles was added a specific biotinylated DNA probe (0.1 μ M). After washing off the unbound probes, the particle sets were combined together. A 20 μ L of mixture of 0.1 μ M target DNA and reporter DNA-Cy3—diluted with 2% casein solution in 10 mM Tris buffer (pH 7.4), 0.5 M NaCl and 0.01 M EDTA—was added and incubated for 10 min. Tth DNA ligase (ABgene, UK) (1 unit) in 20 μ L of 5 fold diluted ligase buffer was added to the particles and incubated at room temperature for 2 hours. The particles were then washed at 50 °C and then spread onto a \sim 5 \times 5 mm area of a slide, the resulting fluorescence pattern from the microscopic particle zones was imaged with a MZFLIII fluorescence microscope (Leica, Germany) equipped with a cooled charge-coupled device camera (AxioVision 3.0, Carl Zeiss Inc., Swiss). The signal amplification was achieved by acquiring the imaging with an integration time of 20 s.

Fig. 1. Scheme showing the principle of ligase-mediated SNP detection on a barcoded microparticle. A three-component-DNA hybridization format was used to capture target DNA. Streptavidin is shown as avidin. The DNA ligase was used to increase the selectivity of hybridization. The signature (barcode) on the microfabricated particle was used for target/probe identification.



3. Results and discussion

To increase the fluorescence detection efficiency and overcome the fluorescence quenching problem on metallic surface, we used a SAM of MHDA to insulate the surface. The fluorescence intensity was further improved by layer-by-layer nano-deposition of a multilayer of poly-L-lysine (PLL) and poly-L-glutamic acid (PLGA) on the SAM,⁴ followed by streptavidin immobilization (Fig. 2). Nine layers of PLL/PLGA were necessary to achieve maximal fluorescence intensity.

The developed protocol was validated by applying it to the multiplexed determination of SNP from G to A, C and T at position -308 within a TNF-alpha gene. Fig. 3 shows that a selective discrimination against a single-base mismatch is achieved. In the experiment, four oligonucleotide probes (probe A, B, C, and D) individually attached on the different type of microparticles were used to sense one DNA target (tumor necrosis factor gene). After hybridization and reaction with DNA ligase, the particles were washed under a stringent condition (50 °C). Only one DNA probe with a sequence exactly pairing the target showed fluorescence signal on the particles, indicating selective detection.

Fig. 2. Fluorescence detection of DNA hybridization on metallic particles: increase of number of PLL-PLGA layers between MHDA and streptavidin increased fluorescence intensity. 0.1 μ M target DNA and reporter DNA-Cy3 were applied for all hybridization events.

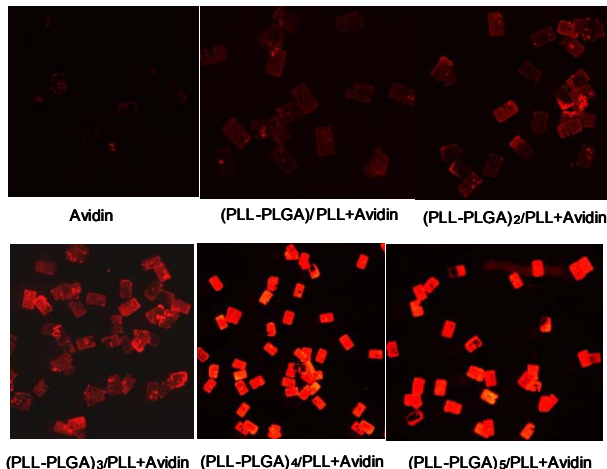
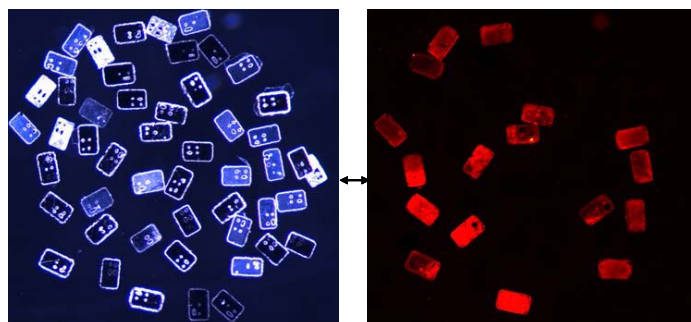


Fig. 3. Barcoded microparticle array for multiplexed DNA hybridization and SNP detection. Bright field (left) and fluorescence (right) images are shown. Only the same type of particles attached with DNA probe A showed fluorescence signals.



4. Conclusions

Multiplexed detection of DNA hybridization and SNP was successfully achieved by using barcoded microparticle arrays coupled to a DNA ligation extension reaction using Tth DNA ligase.

Acknowledgements

Z.-L. Zhi acknowledges Japan Society for Promotion of Science for a short-term invitation fellowship.

References

- [1] Z.-L. Zhi, Y. Morita, S. Yamamura and E. Tamiya. *Chem. Commun.*, 2005, 2448.
- [2] Z.-L. Zhi, Y. Morita, Q. Hasan and E. Tamiya. *Anal. Chem.*, 2003, 75, 4125.
- [3] Z.-L. Zhi, Y. Murakami, Y. Morita, Q. Hasan and E. Tamiya. *Anal. Biochem.*, 2003, 318, 236.
- [4] Z.-L. Zhi and D. T. Haynie. *Macromolecules*, 2004, 37, 8668.

“SPOT-IN-SPOT” HYBRIDIZATION OF OLIGONUCLEOTIDES DEPOSITED ON A GLASS SLIDE BY A MICROCANTELEVER-BASED DEVICE

N. Berthet^{**}, T. Leïchlé^{**}, E. Trévisiol^{*}, J.-B. Pourcier^{**}, D. Saya^{**}, C. Bergaud^{*}, L. Nicu^{**}, and J. M. François^{*}

^{*}Biochips Platform, Génopôle de Toulouse Midi-Pyrénées, INSA, France
^{**}Laboratory of Analysis and Architecture of Systems, CNRS, Toulouse, France

Abstract

The contact deposition device “Bioplume” was used for successive superposed depositions of two synthetic oligonucleotides on a glass slide. This so called “spot-in-spot” hybridization proved that microcantilevers can deposit drops of active biomolecules of 20µm diameter. This methodology is the first step towards surface functionalization of Micro-Electro-Mechanical Systems (MEMS).

Keywords: Spot-in-spot hybridization, Silicon microcantilevers, Contact deposition

1. Introduction

Parallel to the rapid progress in microfabrication, the field of biotechnology instruments is evolving towards miniaturization with reduced use of analyte quantities, multiplexing and higher sensitivity. As biosensors are getting smaller, coating their surface with bioactive layers is becoming an important challenge that requires alternative methods other than the immersion technique since it can be damaging for fragile microcircuits and is not selective for coating active areas.

Therefore, methods have recently been developed to carefully address droplets at the micrometer scale. While Bietsch et al [1] have used ink-jet printing to functionalize microcantilevers with various solutions, we recently developed an alternative technique relying on direct contact deposition [2]. The depositing tool, called “Bioplume”, consists of an array of micromachined silicon cantilevers with an integrated fluidic channel fixed to a xyzθ motion control system developed in the laboratory (figure 1).

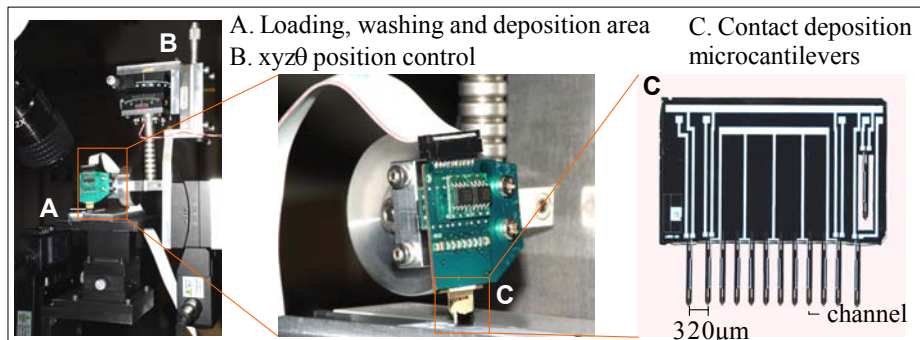


Figure 1 : Cantilever-based contact deposition device "Bioplume"

One of our requirements is to develop a device which can deposit precisely biomolecules several times at the same location without altering their biochemical properties. As a proof of this concept, we chose to examine the hybridization of two complementary oligonucleotides both deposited with “Bioplume”. Preliminary experiments demonstrated the feasibility of using microcantilevers for spotting the complementary oligonucleotide on top of the previously immobilized one, without cross-contamination. This is a “spot-in-spot” hybridization process.

2. Experimental

Deposition was performed using “Bioplume” (figure 1). Loading was done by immersing the cantilevers in the liquid to be arrayed, the slit being filled by capillary action. Droplet formed when the tip of the cantilever came in contact with the surface. Washing was carried out by dipping the microcantilevers into water. The solid supports used were proprietary aldehyde-dendrimer-coated glass slides [3].

Three oligonucleotides were used : the amino-modified oligo “35-mer NH₂” for the covalent linkage with the aldehyde-surface, its complementary sequence “15-mer Cy5” labelled with the red fluorophore Cy5 and an other oligonucleotide, “15-mer Cy3”, functionalized with the green fluorophore Cy3 for the study of cross-contamination and for the superposition experiments. Fluorescence measurements were obtained with the laser scanner Axon 4100A.

Buffers were chosen according to classical microarray protocols. All washing and treatment steps were performed with caution to avoid movement of the slides.

3. Results and discussion

3.1. Washing of microcantilevers

The washing test showed that a 15 minutes rinse resulted in a > 96% removal of the previously deposited solution (data not shown). At this stage, this result is adequate for this application, although it merits further optimisation for better reproducibility and confidence.

3.2. Spots superposition

To test the ability of the “Bioplume” device to deposit twice at the same position, Cy5 and Cy3 labelled oligonucleotides were addressed “spot-in-spot” on a glass slide.

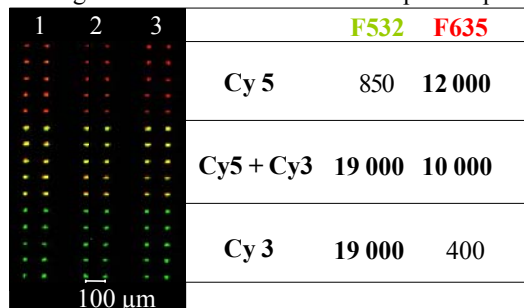


Figure 2 : “Spot-in-spot” deposition with micrometer scale precision.
Superposition of Cy5 and Cy3 (20 μm diameter spots).

As shown in figure 2, correct overlay of the spots was obtained as yellow spots were detected by the laser scanner where the red and green fluorescent drops overlap, thus demonstrating the mixture of both compounds. Due to the fact that the resolution of our scanner is 5 μ m/pixel and that the spots have a diameter of 20 μ m, the quality of the image is not ideal, but it is sufficient to detect “spot-in-spot” hybridization.

3.3. “Spot-in-spot” hybridization

Since the precision of the device was sufficient to overlay 20 μ m spots, “spot-in-spot” hybridization of several molecules of DNA could be considered. Arrays of 20 μ m diameter spots of “15-mer Cy5” were superposed with 20 μ m diameter spot arrays of immobilized “35-mer NH₂” or with buffer alone (negative control). After 30 minutes hybridization and a washing step to remove non-hybridized oligonucleotides, specific fluorescent signals were obtained at the locations where both “35-mer NH₂” and “15-mer Cy5” oligonucleotides were spotted (figure 3).

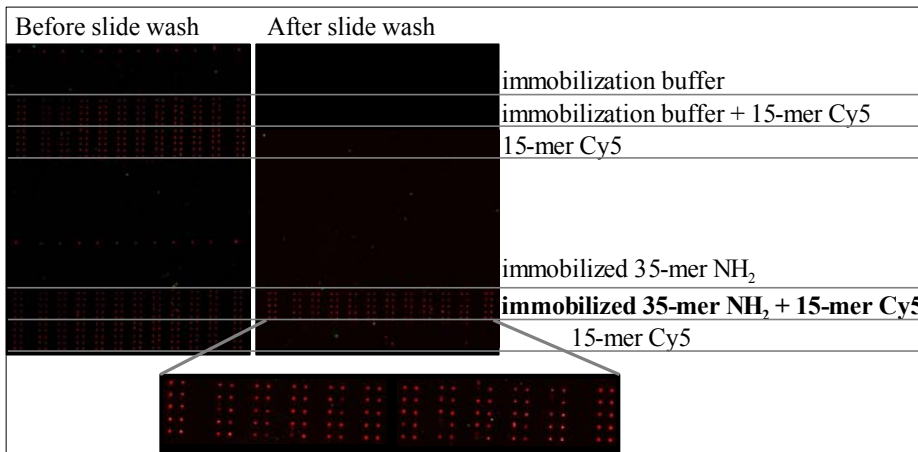


Figure 3 : “Spot-in-spot” hybridization of oligonucleotides on a glass slide using “Bioplume”.

4. Conclusion

Our “Bioplume” prototype was shown to allow successive superposed spotting of active biomolecules within micrometers. This method should enable local functionalization of MEMS sensing devices without mechanical damage of active surfaces, and contrary to ink-jet printing, without temperature or pressure stress on biomolecules. Further experiments are ongoing to validate “spot-in-spot” interactions of proteins.

Acknowledgements

- [1] A. Bietsch et al., *Nanotechnology* **15** (2004), pp. 873–880
- [2] P. Belaubre et al., *Proc. Transducers* (2005), pp. 648-651.
- [3] E. Trévisiol et al., *New J.Chemistry* **27** (2003), pp. 1713-1719

AUTOMATED CONTINUOUS FLOW POLYMERASE CHAIN REACTION IN INDEPENDENT MICRODROPLETS.

Max Chabert, Kevin D.Dorfman* and **Jean-Louis Viovy**.

Institut Curie UMR168. 26, rue d'Ulm. 75005 Paris. France.

jean-louis.viovy@curie.fr

Abstract.

We present a fully automated system for performing continuous sampling, reagent mixing and Polymerase Chain Reaction (PCR) in microdroplets transported in immiscible oil. Reproducible amplification, negligible cross contamination and low detection limits were demonstrated in continuous operation on numerous consecutive sample drops. The system, which opens the route to strong reagents and labor savings in high throughput applications, was validated on the clinically relevant quantification of progesterone receptor gene expression in human breast cancer cell lines.

Keywords: PCR, droplets, continuous flow, automation, interface.

1. Introduction.

Miniaturization of PCR systems has inspired many research groups and led to the invention of various original microfluidic devices. However, most of these remained at the proof of concept stage, and were lacking automation and reproducibility to compete with classical thermal cyclers. Previous attempts to mimic benchtop systems required complicated and expensive microfabrication steps [1]. We present here a totally automated, simple PCR device based on droplets microfluidics, comprising an original "world to chip" interface and on-line detection of the reaction products [2].

2. Experimental setup.

The different components of our system are presented in figure 1. Reactions are carried out in 1 μ L aqueous droplets transported in a 760 μ m i.d. Teflon capillary by fluorinated oil containing 0.5 % wt. fluoroalcohol surfactant. Temperature cycles are provided by winding the capillary around a cylinder divided in three distinct heating zones. Absence of cross-contamination between neighboring droplets was confirmed by quantitative PCR [3]. New samples and reagents are automatically aspired from a custom microtiter plate and combined, while a continuous flow of previously formed droplets is maintained in the reaction region. Endpoint product detection is achieved in the reaction capillary using Sybrgreen I staining and classical laser induced fluorescence.

* Current address: CEMS, U. Minnesota, 421 Washington Ave. S.E., Minneapolis, MN 55455 USA

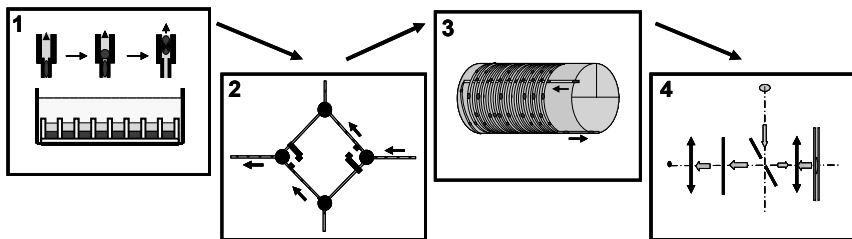


Figure 1. Experimental setup. 1. Sequential injection and mixing of two primary droplets from a MTP with three superimposed liquid levels (sample at the bottom of the wells, carrier fluid above, and plate entirely covered with cleaning solution); 2. Combination of sequential injection and storing of new samples with continuous flow of previous droplets; 3. Heating cylinder; 4. LIF detection.

3. Results.

Figure 2 presents the result of a contamination and reproducibility test on 19 consecutive droplets: non-amplified drops produce a weak and reproducible fluorescence signal (Sybrgreen background signal), confirming the absence of cross-contamination on numerous droplets, while amplified samples show a very reproducible positive signal. A curve accounting for the detection limit (LOD) of our system is shown in figure 3. Each amplified drop is separated from its neighbor by a negative drop to set a baseline and ensure an unbiased LOD measurement, and the initial DNA concentration is doubled between each consecutive positive drop. We successfully detected as low as 50000 initial template molecules with an amplicon length of 572 base pairs. The temperature cycling in figure 2 and 3 was 94°C for 30 s, 55°C for 30 s and 72°C for 60 s.

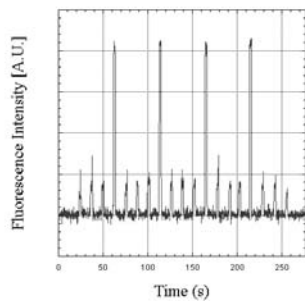


Figure 2. 19 consecutive drops. All drops contain enzyme mix and primers, but only one drop over four initially contains DNA.

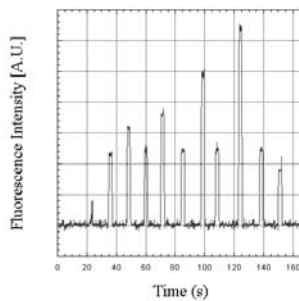


Figure 3. Limit of detection of the system. First detectable drop: third peak.

We finally applied our system to the detection of the progesterone receptor gene in a cancer cell line (T47d), and successfully detected it (figure 4), opening the way of direct application of high throughput PCR for diagnosis. Various temperature cycling programs, enzymes and fluorescent probes were used in our system, confirming the flexibility of our method. For instance, figure 5 presents the detection of the reference gene RPLPO using fluorescent probes and the qPCR core reagent kit (Eurogentech), with a temperature cycling of 30 s at 95°C and 60 s at 65°C. This mix however requires a long activation time and is therefore not well suited for use in our system, accounting for the low positive signal.

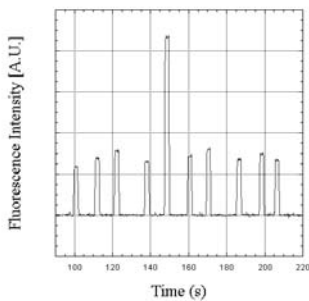


Figure 4. Detection of the PR gene (fifth drop) using Sybrgreen premix for quantitative PCR (temperature cycling: 30 s at 95°C and 60 s at 60°C).

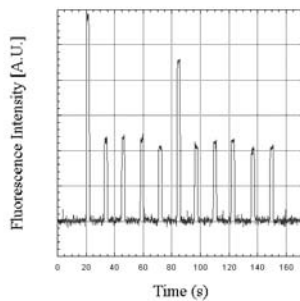


Figure 5. Detection of RPLPO. The first cleaning drop exhibits a fluorescence signal, corresponding to human genomic DNA contamination, efficiently removed.

4. Conclusion.

Our present system can run and analyze 3000 PCR reactions a day in continuous mode, and there is no hindrance for downscaling it to droplet volumes of the order of 100 nL, thus multiplying throughput by a factor of at least ten. Quantitative PCR can be easily integrated in the future by using fluorescence imaging of the droplets at each turn around the cylinder. Moreover, besides high throughput PCR, our fully integrated microdroplets platform can be used in a wide range of chemical or biological reactions, and can therefore be a useful tool for various applications in disciplines ranging from chemistry to biotechnologies.

References.

- [1] J. Liu, C. Hansen, S. R. Quake, *Solving the "World-to-Chip" Interface Problem with a Microfluidic Matrix*, Anal. Chem. 75, 3700-3704 (2003).
- [2] M. Chabert, K.D. Dorfman, P. de Cremoux, J. Roeraade and J-L Viovy, *in preparation*.
- [3] K.D. Dorfman, M. Chabert, J-H. Codarbox, G. Rousseau, P. de Cremoux, J-L. Viovy, *Contamination-Free Continuous Flow Microfluidic Polymerase Chain Reaction for Quantitative and Clinical Applications*, Anal. Chem. 77, 3700-3704 (2005).

A DISCONTINUOUS, EMBEDDED WAVEGUIDE AND MICROLENS SYSTEM FOR MULTIPLEX SINGLE MOLECULE DETECTION IN POLYMER MICROFLUIDIC SYSTEMS

Jason Emory,^{1,3} Ren Yang,^{2,3} Wanjun Wang,^{2,3} and Steven A. Soper^{1,2,3}

Department of Chemistry,¹ Department of Mechanical Engineering,²

Center for BioModular Multi-Scale Systems³

Louisiana State University, Baton Rouge, LA 70803, USA

Abstract

We present a technique for spatial multiplexing single-molecule detection for the analysis of point mutations and other biomarkers via an LDR-spFRET assay. Single fluorescent molecular beacons were interrogated by a laser beam launched into an embedded discontinuous waveguide fabricated from a negative tone resist. Microlenses fabricated from SU-8 were used to focus the excitation beam to the center of a series of microfluidic channels and also to couple excitation light from waveguide-to-waveguide. Fluorescent photons from detection zones of multiple channels were collected on a CCD camera operated in a time-delayed interrogation (TDI) mode. As a test of the system, double-stranded DNA molecules (λ -DNA and pBR322) were labeled with an intercalating dye, TOTO-3, which was used to identify each based on the intensity of the photon bursts generated by the stoichiometric nature of the labeling.

Keywords: Waveguide, Multiplexing, Microfluidics, Single Molecule Detection

1. Introduction

Several cancer-related diseases have been determined to be highly associated with a number of mutations in genomic DNA that can be used as biomarkers for diagnosis, prognosis or monitoring disease recurrence. One such cancer is colorectal cancer (CRC); it has been shown that point mutations within the *K-ras* gene occur early in tumorigenesis and therefore, show promise as biomarkers for diagnostic screening. There are 19 different point mutations in the *K-ras* gene that occur in CRC, all of which must be tested for securing reliable clinical assessment of the disease.

2. Theory

Previous work in our lab focused on the development of ligase detection reactions coupled to single-pair fluorescence resonance energy transfer (LDR-spFRET) using molecular beacons to detect point mutations in genomic DNA rapidly and efficiently using microfluidic systems.¹ However, the assay as configured could only screen for a single mutation at a time. The multiplexing capacity of the assay could be increased by imaging the detection zone of multiple channels onto a CCD. The single molecular beacons are then interrogated using a laser beam launched into an embedded

discontinuous waveguide fabricated from the negative tone resist, SU-8, with the discontinuities generated by the fluidic channels (see Figure 1). The difference in refractive index between PMMA ($n = 1.45$) and SU-8 ($n = 1.58$) produces total internal reflection within the intra-channel space. The waveguide irradiates a series of fluidic channels with the light coupling from waveguide-to-waveguide accomplished by spherical microlenses formed at the terminus of each waveguide (see Figure 2). The microlenses were formed using a unique off-axis, dual lithography approach, in which a double exposure (45° with respect to the substrate surface) of the SU-8 resist was invoked to create the spherical lenses.²

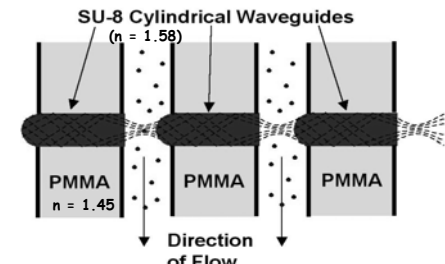


Figure 1. Discontinuous waveguides integrated into PMMA microfluidic channels. The waveguides contain a three-dimensional spherical microlens to focus the excitation light and couple its output into the next waveguide

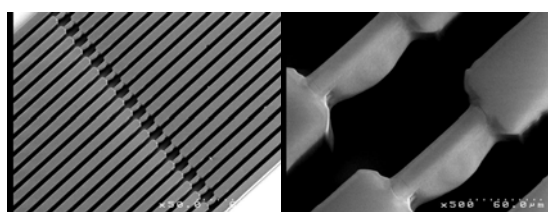


Figure 2. SU-8 microlens array fabricated by off-axis, dual lithography. The micrographs show the fluidic channels (20) and the waveguides with the microlens poised at one end of the waveguide

3. Experimental

A polymer-based microfluidic chip made from PMMA was hot embossed using a high-precision micromilled brass master. The negative tone resist, SU-8, was spin coated onto the chip followed by two exposures that were preformed at 90° with respect to each other to form two perpendicular cylinders. The intersection of the cylindrical light beams formed a spherical-shaped microlens. The SU-8 was then baked for 20 min and developed with 1-methoxy-2-propyl acetate. λ -DNA and pBR322 were diluted in 25 mM borate buffer, pH 9.1. The bis-intercalating staining dye, TOTO-3 (642 ex / 661 em) was added at a 5:1 bp:dye molar ratio. The samples were shuttled through the microfluidic channels by electrokinetic pumping at $E = 125$ V/cm. The channels were interrogated by a 635 nm laser diode launched into the microfluidic chip and subsequently imaged by a CCD operated in a TDI mode; the net velocity of the molecules through the field of view was matched to the parallel shift of the CCD.

4. Results and Discussion

Initial testing of the integrated fluidic/optical system was carried out using double-stranded DNA molecules (λ -DNA and pBR322) labeled with the intercalating

dye, TOTO-3. The DNAs could be identified based on the intensity of the photon bursts generated in each fluidic channel due to the stoichiometric nature of the non-covalent labeling. The data was plotted in a histogram of molecular events versus intensity (see Figure 3). The pBR322 was loaded into the device at a 10-fold higher copy number, which is consistent with the number of events seen for the lower amplitude bursts. The ratio of the mean burst intensity was 5.7, which is in close agreement to the length ratio of the DNA (λ -DNA / pBR322 = 11.3.)

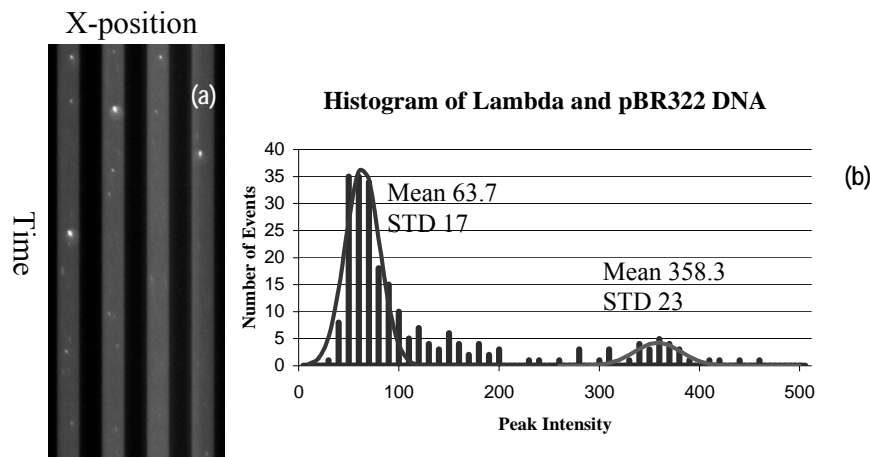


Figure 3. (a) Time-delayed integration image of λ -DNA and pBR322 traveling electrokinetically through a Gaussian laser beam ($\lambda_{\text{ex}} = 635 \text{ nm}$). (b) Histograms of the peak intensities versus number of events from TDI images shown in (a). The histograms were fit to Gaussian functions from which the mean burst amplitude and standard deviations were derived from.

5. Conclusions

The detection technique allowed spatial multiplexing of a series of microfluidic channels to collect histograms of single-molecule photon bursts that were fit to Gaussian functions to arrive the means and standard deviations. The full interrogation of the embedded waveguides and microlens into the microfluidic chip will create improved SNR need for the single-pair FRET beacons.

REFERENCES

- [1] Wabuyele, M. B.; Farquar, H.; Stryjewski, W.; Hammer, R. P.; Soper, S. A.; Cheng, Y.; and F. Barany, Approaching Real-Time Molecular Diagnostics: Single-Pair Fluorescence Resonance Energy Transfer (spFRET) Detection for the Analysis of Low Abundant Point Mutations in K-ras Oncongenes, *J. AM. CHEM. SOC.*, 125, USA 6937-6945, (2003).
- [2] R. Yang and W. Wang, Out-of-plane polymer refractive microlens fabricated based on direct lithography of SU-8, *Sens. Actuators A*, 113, USA, 71-77, (2004).

DISPOSABLE SINGLE-USE PUMPS BASED ON A WAFER-LEVEL PROCESS

Björn Samel, Julien Chretien, Rui Feng Yue, Patrick Griss, Göran Stemme

Microsystem Technology Lab, School of Electrical Engineering

Royal Institute of Technology (KTH), SE-10044 Stockholm, Sweden

Abstract

In this work we present the development of disposable single-use microfluidic pumps fabricated entirely on wafer-level scale which operate in the range of microliters. The proposed micropumps are based on a temperature sensitive silicone elastomer composite, consisting of PDMS and expandable microspheres and successfully demonstrated precise liquid volume control both at low and high flow-rates.

Keywords: micropump, disposable, wafer-level

1. Introduction

Developments in the field of micro total analysis systems (μ TAS) [1,2] aim at miniaturization and integration toward systems for applications, such as drug screening, drug delivery, cellular assays, protein analysis, genomic analysis and handheld point-of-care diagnostics. Such systems offer to reduce liquid reagent consumption, increase sensitivity and speed of analysis, but require the integration of various components such as pumps, valves, mixers, etc. Conventional MEMS processing techniques and materials (i.e. silicon and glass) make fabrication of these components sometimes complicated and costly. Therefore, new actuation principles and materials with the advantages of low cost, easy integration, high reliability, and compact size are required to promote the development of sophisticated microfluidic systems. Several new actuation principles and materials suitable for that purpose have recently been reported [3-5]. Some designs are limited by the need for localization of the active medium at specific positions, which hinders integration and development towards technically mature systems. Our group previously suggested the use of a single-use thermally responsive PDMS composite (i.e. expandable microspheres mixed with a PDMS matrix) as an innovative actuation principle solving the issue of localization [6]. Local actuation of the composite is achieved using a lithographically defined heater. In this paper we present fully integrated single-use micropumps based on the expanding composite which are entirely fabricated using wafer-level processes. The pumps are made of low-cost materials only and address precise integrated active dosing in the microliter range. The principle of operation for single-use pumps is described in Figure 1. Precise control of the composite expansion is achieved by means of integrated heaters. Sufficient voltage applied to the integrated heaters results in filling of reservoirs with the composite and release of initially stored liquid as a consequence.

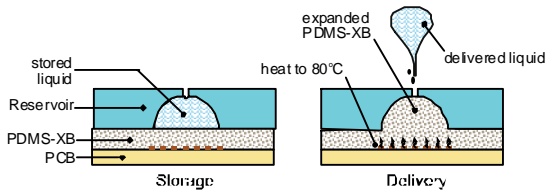


Figure 1: Schematic of the working principle showing the device before and after actuation. Upon heat the PDMS-XB composite expands and consequently fills out a reservoir resulting in dispensing of initially stored liquid.

pre-polymer, degassing in vacuum, spinning on the PCB at 200rpm and subsequently curing at 65°C (Figure 2a). Reservoirs are cast in PDMS by replica molding. Reservoir regions are first defined lithographically on a silicon wafer using standard photoresist (Shipley 1813). On top of these regions defined volumes of UV-curing epoxy (Epotek-OG142-13) are placed using a commercially available Eppendorf research® manual pipette. PDMS is poured over the master and cross-linked at 120°C. Additionally, access holes are punched out of the reservoir layer (Figure 2b).

The imprinted PDMS reservoirs are bonded to the previously fabricated stack of PCB/PDMS-XB by oxidizing both layers in oxygen plasma, aligning and bringing them into conformal contact (Figure 2c).

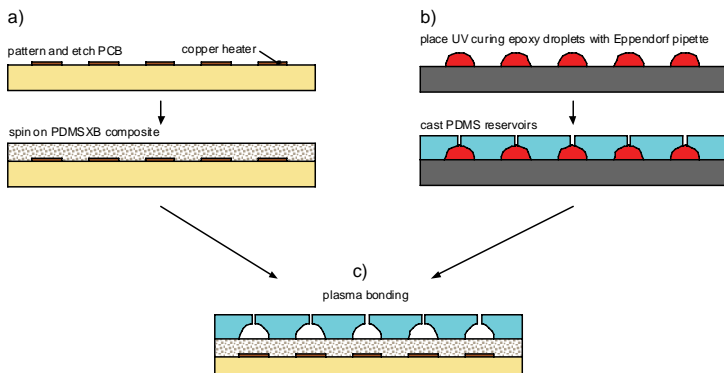


Figure 2: Process flow of the principal fabrication steps: a) First a PCB is lithographically patterned and PDMS-XB composite subsequently spun on and cured. b) A master for replica molding is fabricated by placing UV-curing epoxy with an Eppendorf pipette on predefined resist patterns on a silicon substrate. PDMS is cast over the master and subsequently cured. c) The PDMS reservoir layer from b) is plasma bonded to the fabricated stack of PCB/PDMS-XB from a).

Figure 3a shows the fabricated master depicting the spherically shaped reservoirs on the wafer substrate. Expanding the bare composite only, i.e. no reservoir attached; results in expansion profiles facilitating conformal filling by the expanded composite into the spherically shaped reservoirs which is shown in Figure 3b.

2. Fabrication

The devices are fabricated in a multilayer fashion (Figure 2). First microheater patterns are lithographically defined on printed circuit boards (PCB) to enable localized heating. The expandable composite is obtained by mixing PDMS and XB at a ratio of 300mg/ml liquid PDMS

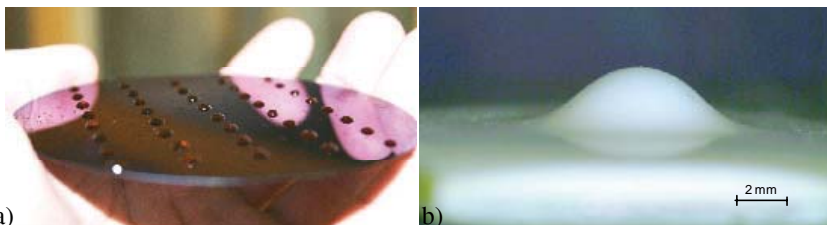


Figure 3: Photograph showing the fabricated master mold for replica molding. UV-curing epoxy was placed over the entire wafer using an Eppendorf pipette. The resulting structures have a predefined volume and conform well to the resulting spherical shape of the expanding composite profile (right).

3. Experimental

For measurement purposes capillary tubing was located on top of the access holes in the reservoir layer. Needles were inserted to seal the access holes and provide support for casting additional PDMS over the structures. Removal of the needles enabled filling the reservoirs under vacuum with glycol and ethanol based colored dye diluted in DI water. Volume measurements were conducted by using the advancing liquid meniscus in a precision glass-capillary as the measure of dispensed liquid. 37 consecutive measurements at a mean power of 800mW were made showing a mean dispensed volume of 3.5 μ l with a relative standard deviation of 5.7% (Figure 5). The dynamic response of the devices for this configuration showed displacement of liquid at flow-rates ranging from 7 μ l/h up to 500 μ l/h.

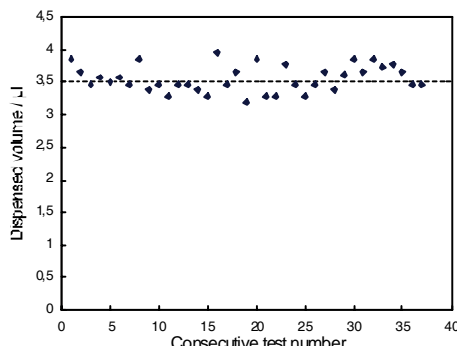


Figure 5: Result of 37 consecutively dispensed liquid volumes showing a standard deviation of 5.7%. The initial liquid volume of the Eppendorf was set to 5 μ l during fabrication.

4. Conclusion

We have shown single-use disposable microfluidic pumps fabricated on wafer-level scale allowing fully automated high-volume production. The electrically controllable pumps do not require external liquid control and are capable of delivering liquid both at high and low flow-rates. The latter is an indispensable prerequisite for e.g. transdermal drug delivery applications [7].

References:

- 1 Harrison, D.J., van den Berg, A. (Eds.) MicroTotalAnalysisSystems '98, Kluwer Academic Publishers: Dordrecht, 1998
- 2 Manz, A., Becker, H., (Eds.), Top. Curr. Chem., 194, Springer-Verlag: Berlin, Germany, 1998
- 3 Liu, R.H., Yu, Q. and Beebe, D.J., Journal of Microelectromechanical Systems, 11 (1), 45-53 (2002)
- 4 Carlen, E.T., Mastrangelo, C.H., Journal of Microelectromechanical Systems, 2002, 11 (3), pp. 165-173
- 5 C.-C. Hong, S. Murugesan, S. Kim, G. Beaucage, J.-W. Choi and C.H. Ahn, Lab-on-a-Chip 2003, 3, pp. 281 – 286.
- 6 B. Samel, J. Melin, P. Griss, and G. Stemme, Proc. of MEMS, Jan30-Feb3 2005 , Miami, USA.
- 7 N. Roxhed, B. Samel, L. Nordquist, P. Griss, G. Stemme, Proc. of MEMS, Jan22-Jan26 2006, Istanbul, Turkey.

A HANDHELD IMMUNOSENSING DEVICE BASED ON LOW-COST SELF-CONTAINED MICROCHIPS AND FERROMAGNETIC ACTUATION

Cedric Robillot*, Jane Fitzpatrick*, Stephen Grimmer*, Brett Kettle*,
Dalibor Dadic** and Klaus Drese**

* Cleveland Biosensors Pty Ltd, Brisbane, Australia,

** Institut für Mikrotechnik Mainz GmbH, Mainz, Germany

Abstract

A handheld biosensor capable of sensitive quantification of small organics, large proteins and pathogens has been developed. The Biofiniti® system is based on a low-cost, fully autonomous, hand-held electronic device designed to control and read disposable, mass-produced microchips (Fig 1). All fluidic and detection elements are integrated into self-contained cartridges, including; reagent storage, sample metering, pumping, magnetic capturing and electrochemical detection.

Keywords: handheld, point-of-care, immunoassay, ferromagnetic actuation, self-contained



Figure 1. Biofiniti® handheld sensor

1. Introduction

A large number of Point-Of-Care (POC) analyses are currently performed using lateral-flow devices. While they can be mass-manufactured at low cost, these devices display limited quantification and multiplexing abilities. There is a need for accurate disposable devices that require minimal user intervention and can be used at the point of decision. 'Lab-on-a-chip' technologies can provide an

alternative to lateral-flow devices but their competitiveness and commercial applicability are still to be demonstrated.

2. Theory

A large number of high performance detection and microfluidic technologies have been described in recent years but their integration into simple and rugged low-cost devices has remained a technical challenge.

To increase the ruggedness of the system, the Biofiniti® injection-molded cartridge does not connect fluidically to the low-cost reader and does not contain any moving part. The need for actuated valves has been circumvented by relying on the properties of two ferrofluidic pumps [1] integrated into a series of closed fluidic loops [2]. The fully programmable system can perform complex fluidic sequences at variable and reversible flow rates ranging from 1 μ L/min to 100 μ L/min.

Organic and protein targets are detected by an immuno-magnetic capture assay coupled with liposome amplification. Briefly, the sample is mixed off-chip with magnetic beads and marker-loaded liposomes, both conjugated to biological receptors. A drop of the reaction mixture is placed onto the chip and the sample is automatically metered, before being flowed along the channels onto a magnet where the beads are captured and the biological complexes washed with buffer. A lysis reagent is then flowed over the liposomes to release the marker they contain over the electrode, resulting in a direct amplification and generating the signal which is analyzed by the device [3].

3. Experimental

D-dimer is a fibrin degradation product that is used in the diagnosis of thrombotic (blood clot producing) diseases and conditions. Briefly, an anti D-dimer antibody was conjugated to tosylactivated 2.8 μ m magnetic beads (Invitrogen). A second antibody recognizing another epitope on the D-dimer molecule was conjugated to liposomes. The sample was mixed with the beads and the labeled liposomes for 3 min before being injected into the disposable cartridge. Including the incubation step, the whole assay lasted approximately 12min and included a calibration phase.

4. Results and discussion

Figure 2 shows the results obtained at high and low quantification range. The Biofiniti® device displays an excellent linearity and good reproducibility in both ranges.

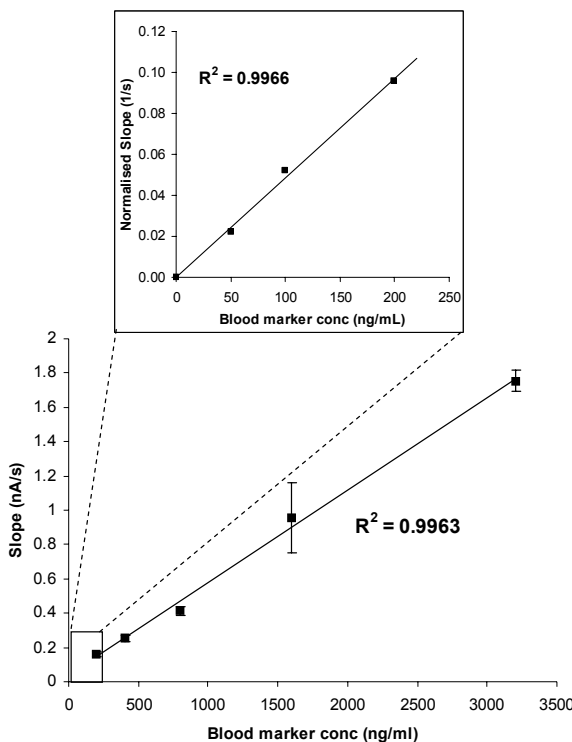


Figure 2. D-dimer detection in plasma using the Biofiniti® handheld sensor

5. Conclusions

The sub-15 min sandwich assay has also been demonstrated for the low-range quantification of other blood markers and a competitive version of the assay is currently applied to the quantification of small freshwater toxins between 0.1 μ g/L and 10 μ g/L.

By integrating complex fluidic features and electronic sensing elements into a low-cost injection-molded microchip, the Biofiniti® device provides a commercial alternative for the POC quantification of complex targets in difficult matrices.

References

- [1] Hatch, A., Kamholtz, A. E., Holman, G., Yager, P., Bohringer, K. "A ferrofluidic magnetic micropump", Journal of Microelectromechanical Systems, 10(2), 215-221, 2001.
- [2] PCT/AU2005/001341.
- [3] Kwakye, Sylvia D. "A micro-total analysis system based on nucleic acid sequence recognition", Thesis (M.S.)--Cornell University, May, 2002.

MICROFLUIDIC FLOW INJECTION ANALYSIS SYSTEM WITH AN ON-CHIP INTEGRATED PUMP DRIVE BASED ON CAPILLARY AND EVAPORATION EFFECTS

**Zhang-Run Xu, Chong-Hui Zhong, Yan-Xia Guan, Jian-Hua Wang and
Zhao-Lun Fang**

Northeastern University, Research Center for Analytical Sciences,
Shenyang, China
(E-mail: fangzl@mail.edu.cn)

Abstract

A microfluidic flow injection analysis (FIA) system was developed integrating a micropump based on capillary and evaporation effects onto a glass chip, with an array of slotted vials serving as a continuous sample injection device. The performance of the μ FIA system was demonstrated by photometric determination of Fe(III) using o-phenanthroline/hydroxylamine. A precision of 1.6% RSD ($n=11$) was obtained with a sampling volume of 420 nL Fe(III) at a sampling frequency of 50/h.

Keywords: Microfluidics, integration, micropump, FIA, spectrophotometry

1. Introduction

Since the introduction of the concept of miniaturized total analysis systems [1], rapid progress has been made in the development of lab-on-a-chip systems with multiple integration of various functional components. Several research groups have reported on miniaturizing flow injection analysis on lab chips, with different degrees of integration [2-4], including the integration of valves and peristaltic pumps on the chip [3]. However, generally such systems are not designed for the continuous introduction of a series of samples, but only for a few discrete samples preloaded in on-chip sample reservoirs, while the off-chip peripheral equipment (e.g. solenoid valves, pressurized gas, and the required computer programming) of liquid drives are all much larger than the chip itself, and therefore obstacles for achieving portability still remain.

Recently, our group reported a micropump based on capillary and evaporation effects that required no peripheral equipment [5], and which offers full potentials for on-chip integration. In this work, the pump was integrated on a microfluidic chip-based FIA system equipped with a continuous sample injection device based on an array of slotted vials.

2. Experimental

A sampling probe, micromixer and micropump were integrated on a glass chip (Figure 1), on which was fabricated a Y-configuration channel (about 50 μ m deep, 400

μm wide), with positive structures of a herringbone design in the main channel for inducing chaotic mixing [6]. Photometric measurements downstream of the mixer were achieved using a light emitting diode (LED) as light source (with optical mask), and an optical fiber/PMT combination for collecting and detecting the absorbed light on the opposite side of the channel. The high-throughput sample introduction system composing of an on-chip capillary sampling probe and an array of horizontally positioned slotted sample vials [4] were adopted in this system. Valveless nanoliter sample injection was achieved by linearly scanning the slots of the vial array across the silica capillary probe, while the flow was driven out from the waste by the integrated evaporation pump. The micropump consisted of an on-chip 3 mm i. d. cavity, surrounding which was fixed a 10-mm section of an 8-mm-i.d. plastic tube in which was push-fitted a tight roll of 5-cm long filter paper plug.

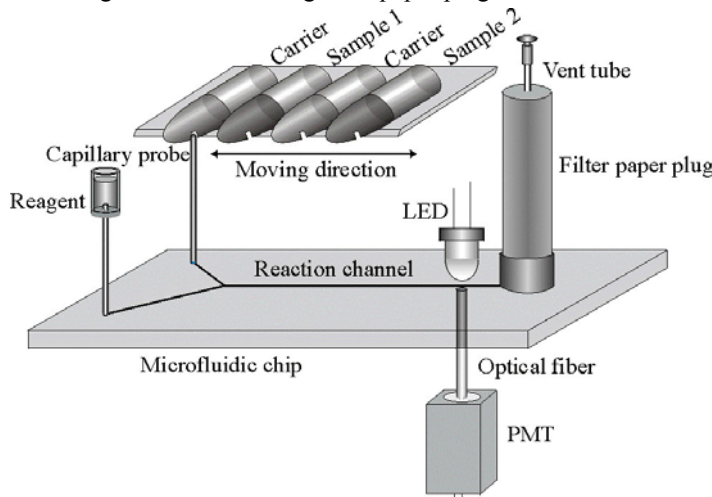


Figure 1. Schematic diagram of the microfluidic FIA system with an on-chip integrated pump drive based on capillary and evaporation effects, with slotted-vial array sample presentation.

3. Results and discussion

This easily fabricated pump was capable of continuously providing stable flow-rates over hours of operation without any peripheral equipment. With the ambient temperature and relative humidity fluctuating within 90 min in the ranges 20-21°C, and 30-31%, respectively, an average flow rate of 2.14 $\mu\text{L}/\text{min}$ was obtained, with a precision better than 1.6% RSD ($n=46$).

The performance of the integrated microfluidic FIA system was demonstrated using the photometric determination of Fe(III) with o-phenanthroline/hydroxylamine as

a model system, and a green LED. With a sampling volume of 420 nL Fe(III) (0.75 mM) standard solution at a sampling frequency of 50/h, a precision of 1.6% RSD (n=11) was obtained. A linear response range of 0.6-3.0 mM Fe(III) was obtained with a regression equation of $A=4.6\times10^{-3}C-6\times10^{-4}$ ($r^2=0.9949$) (Figure 2). The limit of detection for Fe(III) was 0.06 mM (3σ). The integrated FIA system featured simplicity in processing multiple samples, small size, low cost, and relatively good stability.

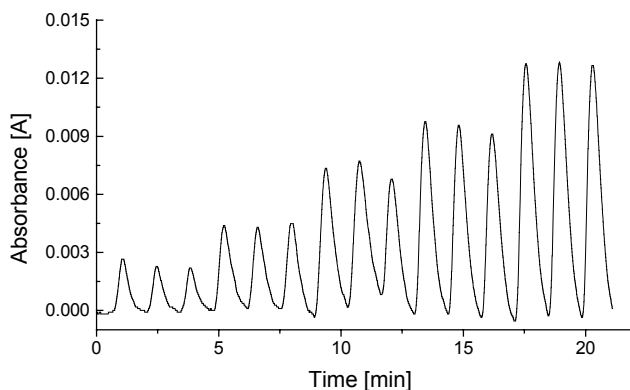


Figure 2. Typical recordings of sequentially injected 0.6, 1.2, 1.8, 2.4, and 3.0 mM Fe(III) standards.

Acknowledgements

The authors gratefully acknowledge support from Natural Science Foundations of China for this work. The authors are also grateful to Mrs. Xiao-Feng Fan, Mrs. Hong-Xin Jia and Prof. Zhi-Yong Wu for inspiring discussions.

References

1. A. Manz, N. Gruber, H.M. Widmer, *Sens. Actuators B*, B1: 244-248, (1990).
2. R.N.C. Daykin, S.J. Haswell, *Anal. Chim. Acta*, 313: 155-159, (1995).
3. A.M. Leach, A.R. Wheeler, R.N. Zare, *Anal. Chem.*, 75: 967-972, (2003).
4. W.B. Du, Q. Fang, Q.H. He, Z.L. Fang, *Anal. Chem.*, 77: 1330-1337, (2005).
5. Y.X. Guan, Z.R. Xu, J. Dai, Z.L. Fang, *Talanta*, 68: 1384-1389, (2006).
6. F. Fang, Z.Y. Wu, Z.R. Xu, J. Dai, Z.L. Fang. *Proceedings of the 3th Chinese National Conference on μTAS*, pp. 37-38, (2005).

DEVELOPMENT OF A MICRO ELISA SYSTEM FOR RAPID COLON CANCER DIAGNOSIS FROM TISSUE CELLS

Hisao Nakanishi^{1,2}, Mitsuo Kitaoka² and Takehiko Kitamori^{3,4}

¹ Sumitomo Bakelite Co., Ltd., Kobe, Hyogo 651-2241 Japan,

² The Research Association of Micro Chemical Process Technology, Japan,

³ Micro Chemistry Group, Special Research Laboratory for Optical Science, Kanagawa Academy of Science and Technology, Japan,

⁴ Department of Applied Chemistry, Graduate School of Engineering,
The University of Tokyo, Japan

ABSTRACT

In order to realize micro enzyme-linked immunosorbent assay (ELISA) of a tumor marker carcinoembryonic antigen (CEA) from tissue cells, we developed a rapid cell disruption method using a Shirasu porous glass (SPG) filter integrated in a plastic microchip. CEA concentration in serum diluted sample solutions after the cell disruption was analyzed by a newly developed micro ELISA system.

Keywords: **cell disruption, Shirasu porous glass (SPG), filter, ELISA, cancer diagnosis**

1. INTRODUCTION

A micro ELISA method using antigen-antibody reaction on microbeads packed in a microchannel has many advantages such as small sample and reagent consumption, and short assay time [1]. Till now, sample for micro ELISA systems were limited to serum samples. If micro ELISA systems can be applied to tissue samples, new application such as an on-site analysis in an operating room would become possible.

We successfully detected a tumor marker carcinoembryonic antigen (CEA) from colon cancer cells by combining a cell disruption microchip with a Shirasu porous glass (SPG) filter and a micro ELISA system.

2. EXPERIMENTAL

Figure 1 shows a block diagram of the total system comprised of a cell disruption chip and a semi-automatic micro ELISA system for detection of CEA.

In the cell disruption microchip, SPG filter was utilized. SPG filter has many characteristics beneficial for integration in a microchannel. Its pore size can be controlled from 0.1 to 20 μm . It is easily shaped into various forms. And it tolerate high pressure (200 ~ 280 MPa). Figure 2 shows a porous structure of SPG.

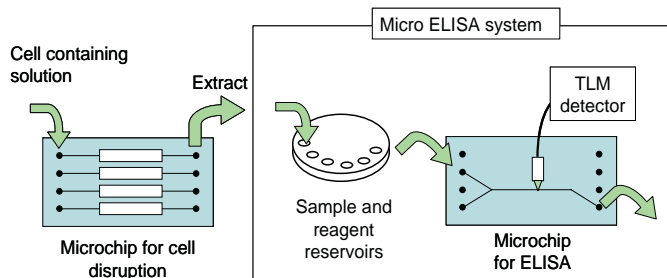


Figure 1. Schematic of the micro ELISA system for colon cancer diagnosis from tissue cells

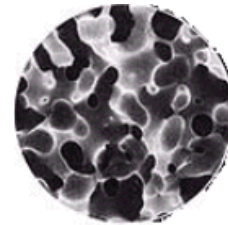


Figure 2. Porous structure of a SPG filter

A semi-automatic micro ELISA system for CEA (Figure 3) was developed by applying techniques reported by Sato et al. [1]. Mouse anti-human CEA-coated polystyrene micro beads were stacked at a dam in a microchannel. After sample solution containing CEA reacted with the antibody, mouse anti-human CEA conjugated with HRP was introduced. Then activity of the fixed HRP was assayed with TMB and H_2O_2 by a detection using a thermal lens micro detection device. Reagents and sample solutions were stored in reservoirs and automatically delivered in sequence to a microchip using a syringe pump. Because sample in cancer diagnosis contains hazardous things, the chip holder and TLM detector were specially made to allow easy replacement of the microchip.

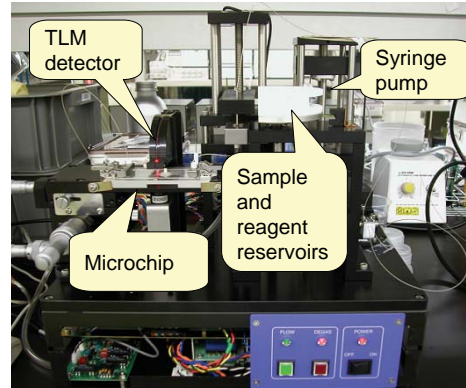


Figure 3. Micro ELISA system for CEA

3. RESULTS AND DISCUSSION

We found that by passing cells through a SPG filter, cell disruption could be completed in few seconds, while it takes more than one hour in conventional cell disruption. Furthermore, whereas in the conventional method, cell residue has to be removed with a centrifuge

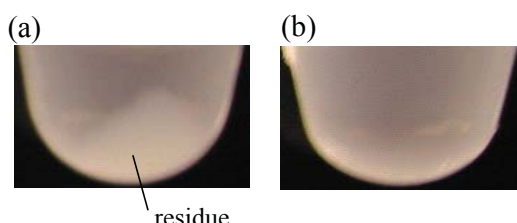


Figure 4. Centrifugally separated extract solutions
 (a) Extract of conventional cell disruption methods
 (b) Extract of cell disruption using SPG filter

after disruption, cell residue does not pass through SPG filter and protein extract could be obtained immediately (Figure 4). We fabricated rods of SPG and integrated them into a plastic microchip (Figure 5).

Buffer-diluted medium containing LS180 colon cancer cells was passed through the microchip with SPG filters and obtained solution was analyzed. CEA was successfully determined and the effectiveness of the method was confirmed.

Using the micro ELISA system, down to 0.1 ng/mL of CEA could be detected even with serum diluted sample solutions (Figure 6), and it was confirmed that this micro ELISA system could be applied to a real protein extract.

5. CONCLUSIONS

A microchip with SPG filters was developed for rapid cell disruption. A micro ELISA system capable of determining down to 0.1 ng/mL of CEA in serum diluted sample solutions was also developed. By combining these two technologies together, rapid colon cancer diagnosis from tissue cells became possible.

ACKNOWLEDGEMENTS

This study was supported by the New Energy and Industrial Technology Development Organization (NEDO), Japan.

REFERENCES

- [1] Kiichi Sato et al., *Lab Chip*, **4**, 570-575 (2004).

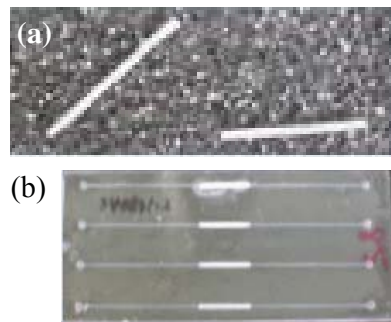


Figure 5. (a) SPG filters and (b) plastic microchip containing SPG filters.
Size of the SPG filter was
0.5 x 0.5 x 10 mm

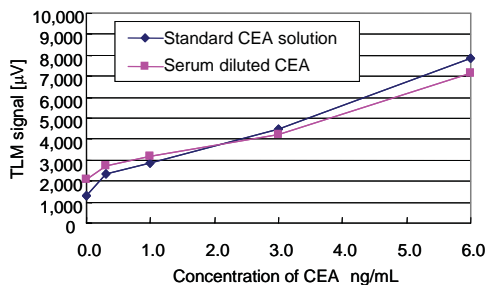


Figure 6. Calibration curves of CEA obtained with the Micro ELISA system

EFFICIENT MINIATURIZED SYSTEMS FOR MICROWAVE HEATING ON MICRODEVICES

Angelique Sklavounos¹, Daniel J. Marchiarullo², Susan L.R. Barker²,
James P. Landers^{2,3} and N. Scott Barker¹

Departments of ¹Electrical and Computer Engineering, ²Chemistry and

³Pathology, University of Virginia, Charlottesville, VA 22901;

Abstract

Efficient heating of microliter-sized chambers of water and PCR buffer solution is achieved through the use of microwave dielectric heating. Microwave power (1 W, 2-6 GHz) is delivered to the heating chamber via a microstrip transmission line integrated with the microdevice. Thermocycling of PCR buffer solution is demonstrated between 30 °C and 90 °C, with an average heating rate of 40 °C/sec and cooling rate of 65 °C/sec. Use of microwave components designed for wireless communication systems will allow development of a pager-sized thermocycler capable of battery powered operation.

Key Words: microwave dielectric heating, transmission lines, PCR

1. Introduction

The use of microwave dielectric heating has been demonstrated for a variety of chemical and biological reactions including drug synthesis[1] and the polymerase chain reaction[2,3]. Cavity resonators, similar to a microwave oven, have been utilized for such applications, but are clearly not suitable for miniaturized, portable devices. Alternatively, a microwave integrated-circuit source coupled to a microstrip transmission line can be used to deliver microwave power to specific locations on a microdevice. In previous work, microwave transmission lines for microchip heating were demonstrated to operate efficiently near the resonance frequency of water (~19 GHz)[4,5]. The cost for a microwave source at this frequency (~\$1000 US) may be prohibitive to development of a commercially-viable, microwave-mediated heating system. However, a lower frequency (2-6 GHz) system incorporating careful circuit design to match the equivalent electrical input impedance of the heating well to the impedance of the microwave source (typically 50 Ω) circumvents this problem. Recent wireless communications technologies (e.g., 802.11a/b/g) have driven the development of low-cost (~\$5 US) power amplifiers capable of delivering >1 W of microwave power (2-6 GHz range). Use of these components within a microchip system will allow production of a pager-sized thermocycler capable of operating with a 9 V battery.

2. Design and Experimental

Initial designs for the microwave microchips used glass/polyimide substrates with 1 μL heating wells as shown in Figure 1. The Debye equation for water is used to find

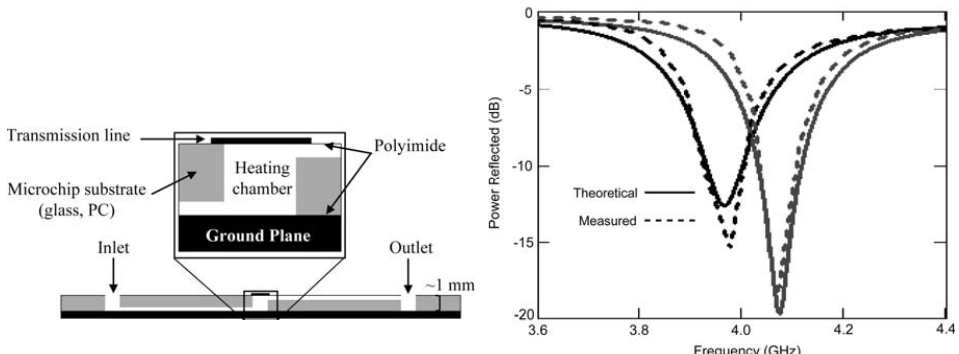


Figure 1: Side view of the microwave heating chip. Microwave energy is guided along the transmission line and delivered to the heating well.

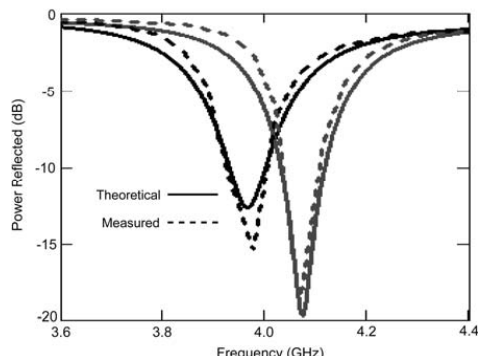


Figure 2: Comparison of the theoretical model with experimental data for two different matching networks.

the equivalent electrical input impedance of the heating well and the matching circuit is designed using microstrip transmission lines. The measured and modeled reflected-power versus frequency for two different matching circuits for these chips is shown in Figure 2. As can be seen, the reflected power is better than -15 dB (3% of incident power) at 3.97 GHz for the first design and nearly -20 dB (1% of incident power) at 4.08 GHz for the second design, demonstrating efficient transfer of the microwave power to the water in the heating well.

Experimental results were achieved using glass or polycarbonate microchips sealed with polyimide. Transmission lines were fabricated from copper and applied to the polyimide layer. Microwave power was generated using a microwave synthesizer amplified up to 1 W and then coupled to the transmission lines through SMA connectors. Temperature detection was performed using an inserted thermocouple, after experiments were performed to verify minimal effects from microwave interaction with the thermocouple.

3. Results

A microwave power amplifier capable of delivering up to 1 W in the 2-6 GHz range was used to demonstrate microwave dielectric heating in the glass/polyimide chip. The microwave power was square-wave modulated between 1 W and 0.5 mW with a period of 5 sec. Figure 3 shows thermocycling of PCR buffer between 30°C and 90°C , with an average heating rate of 40°C/sec and cooling rate of 65°C/sec . These temperature transition rates show this approach to heating will be competitive with other reported means of chip-based heating [6-8].

In order to increase the maximum temperature achieved with the applied microwave power, the same heating well geometry was implemented with a polycarbonate/polyimide substrate used for its lower thermal conductivity. Figure 4 shows heating of PCR buffer in this polymeric chip. The temperature reaches approximately 100°C at the center frequency of the matching circuit (5.863 GHz), seen

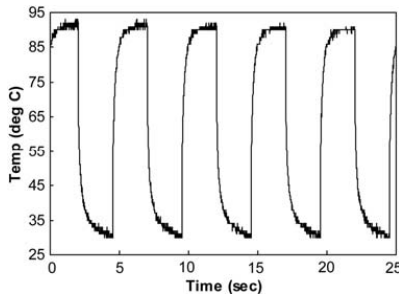


Figure 3: Demonstration of rapid thermocycling of PCR buffer in a glass chip using on chip microwave heating.

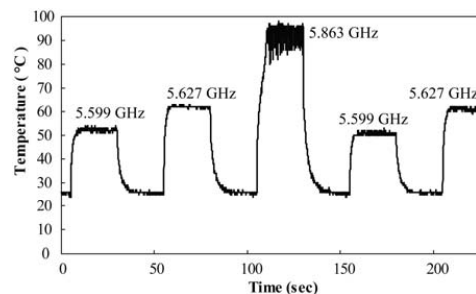


Figure 4: Temperature cycling of PCR buffer in a polycarbonate chip at specified frequencies. The contents of the chamber boiled during the third cycle (5.863 GHz).

as the ‘noise’ in the sensed temperature where the solution boils, while the temperature reaches 62 °C and 53 °C at 5.627 GHz and 5.599 GHz, respectively. This presents the clear possibility of controlling temperature in a frequency-dependent manner.

4. Conclusions

This paper has demonstrated the ability of microwave dielectric heating to quickly and efficiently heat microliter volumes in microdevices using relatively low power (~1 W) at frequencies well below the resonance frequency of water. This is achieved by integrating microstrip transmission lines and the required matching networks directly onto the microdevice. The thermocycling rates presented in this paper demonstrate that dielectric microwave heating can be used for efficient, fast thermocycling and that near reaction-rate limited PCR is possible using this method. The efficiency and speed combined with the low cost and small size of the microwave power components will facilitate the development of an affordable, pager-sized, battery-operated thermocycler.

5. References

1. C.O. Kappe and D. Dallinger, *The impact of microwave synthesis on drug discovery*, Nature Rev Drug Discovery 5 (1): 51-63 Jan 2006.
2. K. Orrling, P. Nilsson, M. Gullberg, and M. Larherd, *An efficient method to perform milliliter-scale PCR utilizing highly controlled microwave thermocycling*, Chem. Comm., 2004, 790-791.
3. C. Fermer, P. Nilsson, and M. Larhed, *Microwave-assisted high-speed PCR*, Euro J. of Pharmaceutical Sciences. 18 2003 129-132.
4. B. F. Barenburg, J. Burdon, Y. Chan, X. Dai, S. Gallagher, P. Grodzinski, R. Marrero, V. Nair, D. Rhine, and T. Smekal, *Microfluidic devices with monolithic microwave integrated circuits*, U.S. Patent 6,605,454 August 12, 2003.
5. S. G. Sundaresan, B. J. Polk, D. R. Reyes, M. V. Rao, and M. Gaitan *Temperature Control of Microfluidic Systems by Microwave Heating*, Proc. Micro Total Analysis Systems 2005, 657-658.
6. C. J. Easley, J. M. Karlinsley, and J. P. Landers *On-chip pressure injection for integration of infrared-mediated DNA amplification with electrophoretic separation*, Lab on a Chip, 6(5) 2006, 601-610.
7. M. Hashimoto, P. Chen, M. W. Mitchell, D. E. Nikitopoulos, S. A. Soper, and M. C. Murphy *Rapid PCR in a continuous flow device*, Lab on a Chip, 4(6) 2004, 638-645.
8. E. T. Lagally, C. A. Emrich, and R.A. Mathies *Fully integrated PCR-capillary electrophoresis microsystem for DNA analysis*, Lab on a Chip, 1(2) 2001, 102-107.

Microbead Based Total Analysis System for Hepatitis C Detection

Tae Seok Sim¹, Bo-Rahm Lee², Sang-Myung Lee², Hyo-Jin Yoon², Min-Soo Kim¹, Yoon-Sik Lee², Byung Gee Kim² and Yong-Kweon Kim¹

¹School of Electrical Engineering and Computer Science

²School of Chemical and Biological Engineering, Seoul National University
(Contact e-mail: sim93@snu.ac.kr)

Abstract

This paper describes a micro total analysis system for hepatitis C detection. We proposed a novel immunoassay method using two kinds of beads and heat which is simpler, easier and faster than the conventional enzyme-linked immunosorbent assay (ELISA) method. The proposed immunoassay method was realized on a single microchip and computer based control system for temperature and valve actuation was also implemented using integrated circuit board and LabVIEW program.

Keywords: Immunoassay, Bead, PDMS pneumatic microvalve, Microheater.

1. Introduction

The enzyme-linked immunosorbent assay (ELISA) is the most common immunoassay method in the clinical diagnoses and biochemical researches. However, this method has some drawbacks such as long assay time, complex procedures and expensive reagents. Up to now, several kinds of microchip has been developed to solve these problems, but most of them were focused on the miniaturization and integration of the conventional immunoassay. Although there were some variations in the detection method, the immunoassay on a microchip still needed complex chemical reactions and the labeling procedure in the end of assay to decide whether the target protein exists or not [1, 2]. However, the needs for several chemical reactions and labeling are not preferable to realization and automation of the assay system on a microchip. Furthermore, the complex procedures increase the contamination chances, manual handlings and off-chip reactions. We proposed a novel immunoassay method using two kinds of beads to solve these problems. One is used for capturing and releasing the target protein from the mixture of proteins and the other is used for the digestion of the captured target protein. Heat was applied when the captured target protein was released and digested. RNA aptamer was used instead of antibody for its functional alteration characteristic along with temperature. The target protein was selectively captured from the mixture of proteins in the first reaction chamber and transferred to the second reaction chamber filled with the trypsin immobilized beads. Then the digested target protein can be easily identified using the MALDI TOF MS. Since the proposed assay method does not need any chemicals but buffer solution and labeling procedure, it is simpler, easier and faster than any other immunoassay methods originated from ELISA.

2. A bead based temperature controllable microchip

Figure 1-(a) shows the structural schematic drawing of the bead-based temperature

controllable microchip. The microchip consists of PDMS micro fluidic device, glass cover, silicon structure and Pt electrodes. The PDMS micro fluidic device includes four micro pneumatic valves and microchannel. The pneumatic valves are normally open and have a push-down structure. The control channel is located on the flow channel so that pressure is applied in the upper channel to deflect the membrane downwards. The glass cover has four holes for inlet and outlet of each reaction chamber. In the silicon structure, there are two reaction chambers ($3.13 \mu\text{l}$). Each reaction chamber has a column of posts ($60 \times 60 \times 200 \mu\text{m}^3$) for bead packing. Since the trypsin immobilized on the beads is highly sensitive to the high temperature, two reaction chambers are thermally isolated by removing unnecessary silicon parts to reduce the thermal interferences derived from the high thermal conductance of the silicon. When the valve 1 and valve 4 are activated, two reaction chambers can be operated independently. The other mode is connection mode. When the valve 2 and the valve 3 are activated, two reaction chambers are connected through the microchannel so that the solution can be transported from reaction chamber 1 to reaction chamber 2.

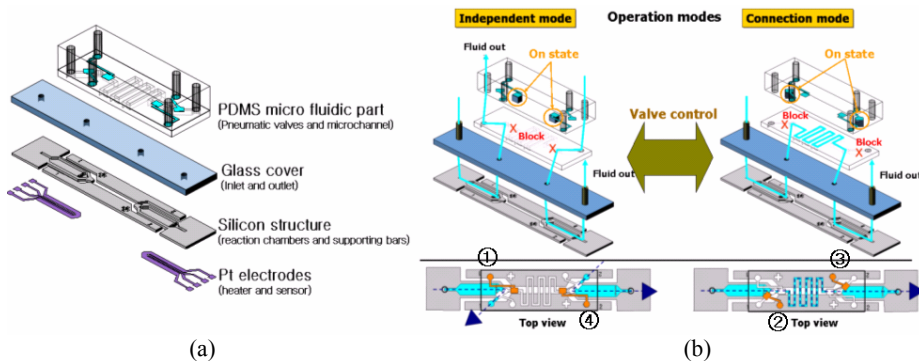


Figure 1. A schematic view of the microchip. (a) structure, (b) operation modes.

3. Experiment using μ TAS and results

Figure 2-(a) shows the complete analysis system. The microchip can be controlled and monitored using computer by plugging in to the chip loader located on the interface board. The overall reaction sequences on a microchip are depicted in figure 2-(b). The first reaction chamber was packed with the PEG-grafted bead on which RNA aptamer of HCV replicase is immobilized. This bead can be prepared by coating of organosilane, grafting of PEG on PS bead and immobilizing of RNA aptamer [2]. The second reaction chamber is packed with the PEG-grafted bead on which trypsin is immobilized covalently. First of all, $20 \mu\text{l}$ mixture of proteins (HCV replicase, HCV helicase, BSA, ovalbumin) was injected into the first reaction chamber and then incubated for 5 min at 25°C . After incubation, the first reaction chamber was washed with buffer intensively to remove non-specifically adsorbed protein. The captured HCV replicase was released from beads through protein denaturation by heating the first reaction chamber at 85°C for 1 min. $20 \mu\text{l}$ HCV replicase was transferred to the second reaction chamber packed

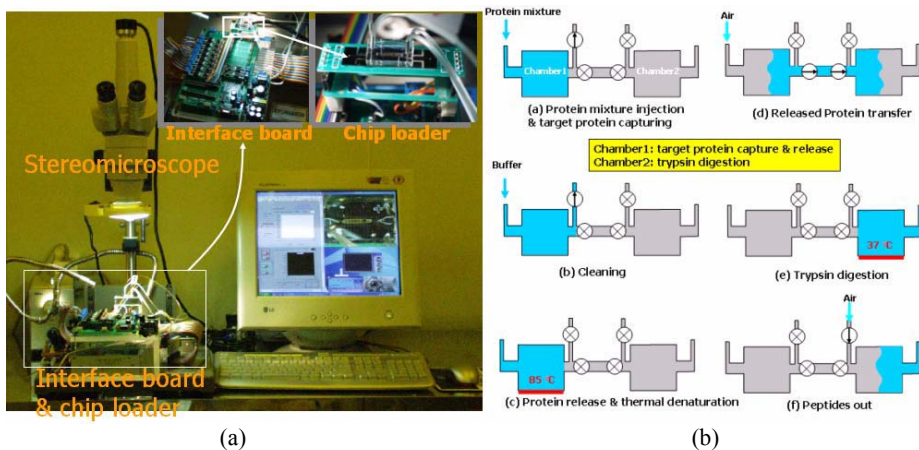


Figure 2. Total immunoassay system (a) and total immunoassay procedures (b).

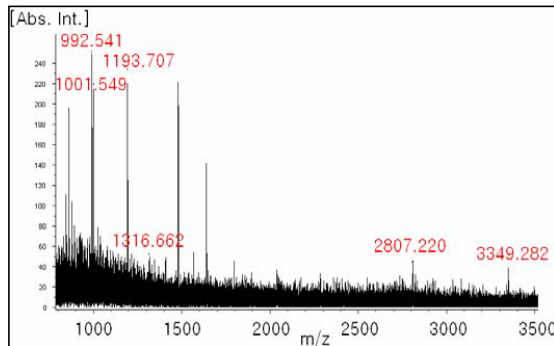


Figure 3. MALDI MS spectrum of the HCV replicase

4. Conclusions

In this work, a bead based μ TAS for detection of the HCV replicase and sample preparation of the detected protein prior to the MALDI TOF MS has been successfully implemented and verified its probabilities in clinical diagnosis and biochemical research.

References

1. Kiichi Sato, Manabu Tokeshi, Tamano Odake, Hiroko kimura, Takeshi Ooi, Masayuki Nakao, and Takehiko Kitamori, *Integration of an Immunosorbent Assay System: Analysis of Secretory Human Immunoglobulin A on Polystyrene Beads in a Microchip*, Anal. Chem., 72, pp. 1144-1146, (2000).
2. Min-Soo Kim, Woo-Jae Chung, Su-Hyung Cho, Byung-Gee Kim, Yoon-Sik Lee and Yong-Kweon Kim, *Study on Bead-based Micro Biochip and Analytical System for Protein Detection*, TRANSDUCER'S 03, Boston, USA, pp. 1267-1270, (2003).

with trypsin-immobilized PS beads and incubated for 10 min at 37 °C to digest HCV replicase into peptides. 20 μ l solution was eluted from microchip finally and analyzed with MALDI-TOF. As a result, we could acquire six matched peaks (12 % sequence coverage) of HCV replicase within about 20 min using a fabricated microchip and a control system (figure 3).

FABRICATION OF PMMA MICROCHIP INTEGRATED WITH GOLD NANOPARTICLE WORKING AND DECOUPLE ELECTRODES FOR HIGH PERFORMANCE CEEC APPLICATIONS

Ching-Mou Chen¹, Guan-Liang Chang¹, Kuo-Tang Liao², Hsuan-Jung Huang^{2,4} and Che-Hsin Lin^{3,4*}

¹Institute of Biomedical Engineering, National Cheng Kung University, Tainan, 701, Taiwan, ROC

²Department of Chemistry, ³Department of Mechanical and Electro-mechanical Engineering, ⁴Center for Nanoscience & Nanotechnology, National Sun Yat-sen University, Kaohsiung, 804, Taiwan, ROC
chehsin@mail.nsysu.edu.tw

Abstract

This study presents a PMMA-based capillary electrophoresis (CE) chip integrated with on-chip gold nanoelectrode ensemble (GNEE) as the working and decouple electrodes for high performance CEEC detection of dopamine and catechol biosamples. Microchips with two electrode configurations are designed fabricated and evaluated in this paper. Results show the charge current amplitude and baseline drift are significantly reduced while using NEE as the decoupler under high separation voltage conditions. The calculated S/N ratio of the sample peaks increases from 8.329 to 43.259 for the GNEE decoupler design. The use of GNEE for both working and decouple electrodes provides excellent performance over the conventional bulk electrode design. The proposed method is highly potential for developing a high performance CEEC chip for bioanalytical applications.

Keywords: PMMA, GNEE, Decoupler, CE-EC, Charge current

1. Introduction

Recently, studies on the nanoelectrode ensemble (NEE) for high performance electrochemical detection have become one of the interested research topics because of the excellent electrochemical characteristics of the nanoelectrode ensemble[1]. The most attractive advantages of NEE include ultrafast electron transfer reactions, high signal-to-noise ratios and lower detection limits. Since the Faradaic current on a NEE is proportional to the total geometric surface area of the ensemble, and while the background current is proportional only to the area of the electrode elements [2]. Therefore, NEE is also a good candidate for using as a decouple electrode in CE-EC systems.

In the present study, PMMA microfluidic chip integrated with GNEE was fabricated using a simple and novel process. Charge current and background noise level from GNEE and planar platinum electrodes were measured under different applied separation

electric fields. Biosamples of dopamine and catechol were adopted to evaluate the detection performance of the proposed CE-CE microchip device.

2. Experimental

Figure 1a shows the schematic for the design of the CE channel. In order to compare the electrode material effect in chip-based electrochemical detection system, three kinds of electrode configuration were tested in this study. (Figure 1b) Note that the counter/reference electrodes were Pt for all case and the exposed area for the GNEE electrodes were 3 mm x 150 μm . Figure 2 present a simplified schematic for the fabrication process of the GNEE CE-EC microchip. The GNEE film was directly hot-press onto the pre-patterned Pt electrode first then the microfluidic channel was sealed using a solvent containing alcohol and 1,2-dichloroethane under room temperature[3]. Figure 3 shows the photo image of the GNEE CE microchip. The experimental setup for testing the proposed microchip is given in Figure 4.

3. Results and discussion

Figure 5 shows the measured charge current from Pt decoupler and GNEE decoupler, results shows that charge current has reduced obviously in high separation voltage (above 120 V/cm) for GNEE decoupler design. Figure 6 shows that the microchip with GNEE decoupler provides a smooth, stable and much lower baseline noise in compare with conventional Pt decoupler. Results confirmed the good performance of GNEE electrode on removing the induced charge current. Figure 7 shows the electropherograms of detecting 1 mM dopamine and 1 mM catechol mixture obtained using the microchip equipped with bulk Pt decoupler and GNEE decoupler. A significant lower background current was found while using GNEE decoupler such that the signal response is much higher than the one obtained using bulk Pt decoupler. The calculated S/N ratios of the signal peaks are 8.329 and 43.259, respectively.

4. Conclusions

A simple yet high performance fabrication process was developed for fabricating the proposed microchip device in low-cost PMMA substrates. The detection results of the proposed microchip device using GNEE as the working and decouple electrodes show higher S/N ratio for the sample peaks than the conventional Pt electrodes. The proposed microchip device is feasible for achieving high performance, low detection limit and low cost CE-EC detection.

Acknowledgements

The financial support from National Science Council of Taiwan is greatly acknowledged. (NSC95-2320-B-110-001)

Reference

1. P. Ugo, L. M. Moretto, S. Bellomi, V. P. Menon, C. R. Martin, *Anal. Chem.* **68**, 4160 (1996).
2. N. P. Beard, C. X. Zhang, A. J. DeMello, *Electrophoresis* **24**, 732 (2003).
3. C. H. Lin, L. M. Fu, C. H. Tsai, C. H. Chao, C. W. Lan, 13th International Conference on Solid-State Sensors, Actuators and Micorsystems (Transducers' 05), 944 (2005).

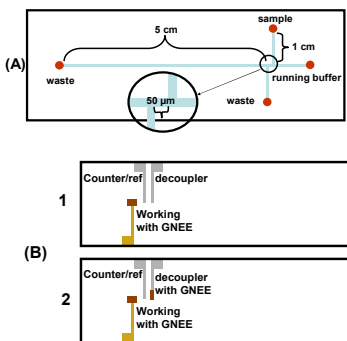


Fig. 1 (A) Design of the microchannel use in the study (B) Two kinds of electrodes layout (1) GNEE working electrode with bulk Pt decoupler (2) GNEE working and decouple electrodes.

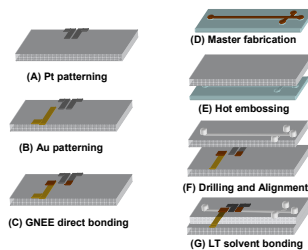


Fig. 2 A simplified schematic for the fabrication process of the GNEE CE microchip.

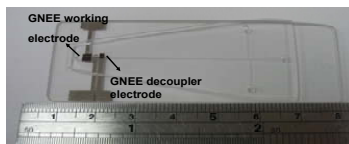


Fig. 3 Photo image of fabricated GNEE CE microchip.

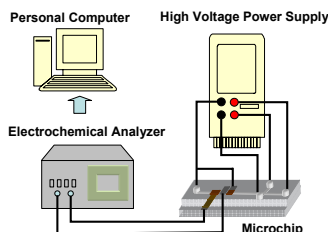


Fig. 4 Schematic diagram of experimental setup for CE-EC microchip with integrated GNEE.

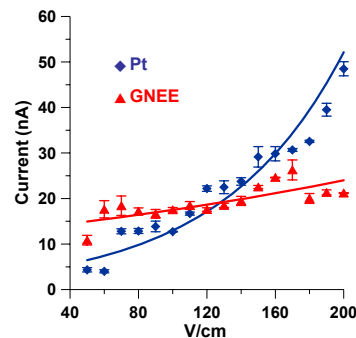


Fig. 5 Charge current response of GNEE and BGE (bulk gold electrode) electrodes under different separation voltages. Buffer: 10 mM MES buffer (pH=6.1).

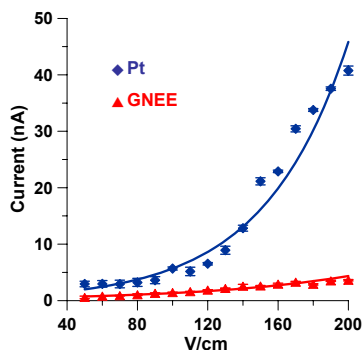


Fig. 6 Baseline drift level from GNEE and BGE (bulk gold electrode) electrode under different separation voltages. Buffer: 10 mM MES buffer (pH=6.1).

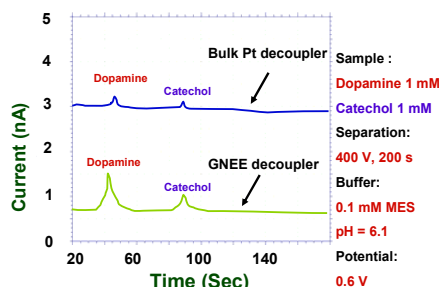


Fig. 7 Electropherograms of detecting the mixture of 1 mM dopamine and 1 mM catechol using type 1 and type 2 electrode configuration.

ON-CHIP pH SENSING WITH GEL MICROBEAD POSITIONED BY OPTICAL TWEEZERS

Hisataka Maruyama¹, Fumihiro Arai² and Toshio Fukuda¹

¹Department of Micro-Nano Systems Engineering, Nagoya University, Japan

²Department of Bioengineering and Robotics, Tohoku University, Japan

Abstract

A local pH sensing method in a microchip using a functional gel-tool was developed. We used salting-out gel-tools impregnated with Bromothymol Blue (BTB), which is a pH indicator. The gel-tool is made of ENT-3400, which is hydrophilic photocrosslinkable resin [1]. The primary constituent of ENT-3400 is polyethyleneglycol (PEG). A solution mixed with ENT-3400, BTB, high concentrations of electrolytic solution are stirred, and gel beads impregnated with BTB are obtained. Gel-tools are cured by UV-ray and adhere to the glass, but we can manipulate them by the optical tweezers. We can measure pH value locally from the color of gel-tool using calibrated color information in YCrCb color space. We succeeded in measuring local pH value with the pH sensing gel-tool by manipulating and locating it at the desired point in the microchip.

Key Words: Gel, Measurement, pH, optical tweezers, Lab-on-a-chip

1. Introduction

Environment measurement in a microchip is important to the on-chip experiment. Conventionally, the environmental dependence of fluorescent reagents was used for measurement of the environmental condition such as pH and temperature. However, this method requires filling the reagent in the microchip at measurement [2]. Although measurement is possible by a microsphere, whose surface is modified by fluorescent reagents and indicators, it takes time to modify the surface [3]. In case of fabricating sensors in a microchip by microfabrication, the sensing area is fixed and it is difficult to measure the desired location. In this research, we propose a functional gel-tool, which contains an indicator to measure the local environmental condition in a microchip. We used gel beads, which are generated by salting-out of ENT-3400. BTB was contained in the gel-tools as a pH indicator. Gel-tool is manipulated by optical tweezers and pH value is calculated from color information acquired by CCD camera.

2. Gel-tool contained a pH indicator

Figure 1 shows a schematic of pH sensing using gel-tool in a microchip. Gel-tool is made by salting-out of ENT-3400 (Kansai Paint) which is hydrophilic photocrosslinkable resin. Main component of ENT-3400 is PEG. We can manipulate salting-out gel-tool by optical tweezers in a water because the relative refractive index of PEG (1.42) is higher than that of water (1.33). A salting-out gel-tool and the fabrication method of pH sensing gel-tool are shown in Figs. 2 and 3. The gel-tools were fabricated by agitating mixture of 0.9 g ENT-3400, 0.3g BTB, and 2.4g 20wtpercentage KCl

solution. Since gel-tools are cured by UV-ray irradiation and adhere to glass surface, the gel-tools can be arranged in an arbitrary pattern. Fabrication of gel-tools takes a few minutes and is shorter than that of the surface modification [3]. Size adjustment of gel-tool is possible because uncured gel-tools fuse by attaching. Gel-tools can be used as a carrier of cells because the tool adheres to cells by attaching. Color information on gel-tools acquired by CCD camera(XC-555, Sony) is converted from RGB to YCrCb by eq. 1.

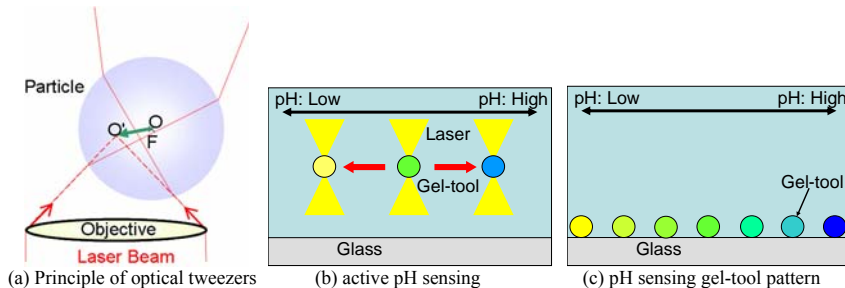


Fig. 1 A schematic of pH sensing gel-tool

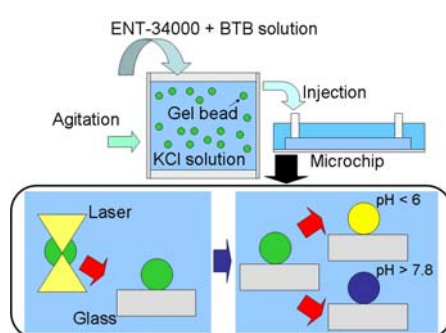


Fig. 2 A schematic of generation of pH sensing gel-tool

3. Experimental

The calibration results are shown in Figs. 4 and 5. We used gel beads of which size is from $5 \mu\text{m}$ to $15 \mu\text{m}$. There is proportional relation between pH and Cr, Cb. The measurement precision of pH is about 0.1 and that of Cb is about 0.27. In experiment, we applied Cr value for calculating pH value and pH value is calculated by equation 2. Figure 6 shows a schematic of active pH sensing. We shuttled gel-tool between pH4 and pH8 by optical tweezers at $50 \mu\text{m}/\text{s}$. Gel-tool can be manipulated at over $150 \mu\text{m}/\text{s}$. We confirmed the repeatability of pH detection from Fig. 7 and achieved the active sensing of local pH value in a microchip. Fig. 8 shows the arrangement of pH sensing gel-tool in the microchip. After the size adjustment, gel-tools were arranged on the glass and changed their color depending on pH of a solution. Adhered gel-tools did not removed from glass even by 894 mm/s flow speed. Local environment measurement was achieved by using pH sensing gel-tool in a microchip.

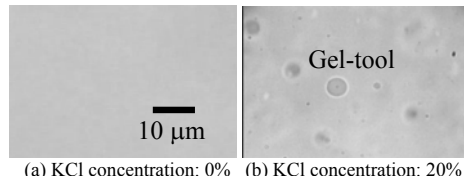


Fig. 3 Photograph of salting-out gel-tool

$$Y = 0.299R + 0.587G + 0.114B$$

$$Cr = 0.5000R - 0.419G - 0.081B \quad (1)$$

$$Cb = -0.169R - 0.419G + 0.500B$$

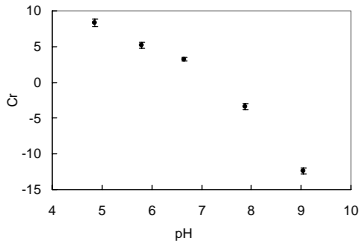


Fig. 4 Relation between pH and Cr

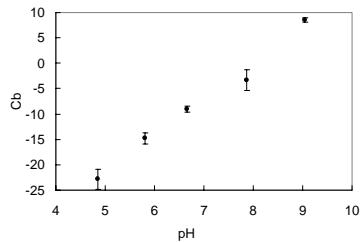


Fig. 5 Relation between pH and Cb

$$pH = -0.2153 * Cr + 7.2101 \quad (2)$$

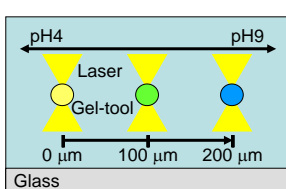


Fig. 6 A schematic of active pH sensing

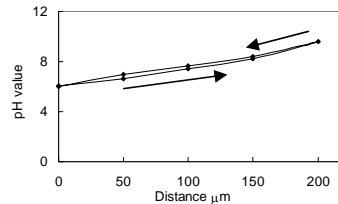
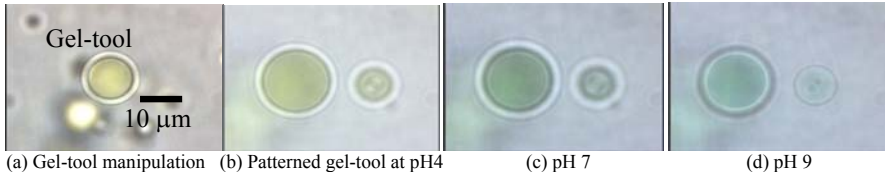


Fig. 7 Change of pH value



(a) Gel-tool manipulation (b) Patterned gel-tool at pH4 (c) pH 7 (d) pH 9
Fig. 8 On-chip pH sensing using pH sensing gel-tool

4. Conclusions

We proposed the pH sensing gel-tool for local environment sensing in a microchip, and active pH sensing and arrangement of pH sensing gel-tool pattern were demonstrated. The method enables us to make the on-chip measurement easy. This measurement method for environmental condition will make great contributions for cell biology.

5. Acknowledgement

This research is supported by The Ministry of Education, Culture, Sports, Science and Technology Grant-in-Aid for Scientific Research (17040017).

References

- [1] F. Arai, H. Maruyama, T. Fukuda and T. Katsuragi, Proc. of μ TAS2003, pp. 21-24, 2003 (Oral)
- [2] H. Akimoto, S. Saeki, et. al., Proc. of μ TAS2005, pp. 1476-1478, 2005
- [3] Jin Ku Cho, Lu Shin Wong, et. al., Chemical Communications, pp. 1470-1471, 2004

A BIOMIMETIC MEMS NEUROTRANSMITTER DETECTOR

Stephan T. Koev^{1,2}, Li-Qun Wu³, Gregory F. Payne^{3,4}, and Reza Ghodssi^{1,2,4}

¹Department of Electrical and Computer Engineering,

²Institute for Systems Research,

³University of Maryland Biotechnology Institute,

⁴Bioengineering Graduate Program,

University of Maryland, College Park, MD 20742, USA

(Corresponding author: ghodssi@umd.edu)

Abstract

We demonstrate, for the first time, micromechanical detection of the neurotransmitter dopamine and its discrimination from ascorbic acid. Microcantilever sensors were fabricated and coated with the polysaccharide chitosan by electrodeposition. The cantilevers were used for electrochemical oxidation of dopamine solution. The products of this reaction crosslink the chitosan film and create a tensile stress, bending the cantilever out of plane considerably. By contrast, electrochemical oxidation of ascorbic acid solution does not cause chitosan crosslinking and appreciable cantilever bending. This method is an improvement over conventional electrochemical dopamine detection techniques (e.g. cyclic voltammetry) that are highly non-specific.

Keywords: chitosan, dopamine, microcantilever, neurotransmitter

1. Introduction

Dopamine is one of the main neurotransmitters in the brain and is being extensively studied by neurobiologists [1]. Its release and regulation have been linked to human behavior, drug addiction, and a number of diseases. However, methods of detecting dopamine in nerve tissues and cultures with high spatial resolution and specificity are still needed. One common method for dopamine detection *in situ* is cyclic voltammetry [2] based on electrochemical oxidation of the analyte and measurement of the resulting current. However, this method is prone to false positives since other molecules in the solution such as ascorbic acid also oxidize and conduct current. Here, we use a micromechanical sensor to enhance the specificity of dopamine detection based on the polysaccharide chitosan. Previously, we have demonstrated chitosan as a biointerface that can be electrodeposited as a thin film and biofunctionalized [3,4]. In this work, we enlist a biomimetic approach to transduce electrochemical dopamine oxidation into mechanical changes of the chitosan film [5,6]. This approach mimics the quinone tanning reactions used by insects to harden their outer shell. Specifically, insects enzymatically oxidize dopamine-like compounds to crosslink and harden their shells.

2. Sensor Design

The sensor is a cantilever beam composed of layers of Si₃N₄, Au/Cr, and chitosan

with thickness 500nm, 100nm, and 1.5 μm respectively on a Si substrate (**Fig. 1, 2**). This device is fabricated by standard lithographic and etching techniques. Chitosan is electrodeposited by applying negative potential to the metal layer while immersed in a chitosan solution. The length of the cantilever is 100 μm , the width is 40 μm , and its calculated spring constant is 400nN/ μm . Changes in the residual stress of the chitosan film due to crosslinking cause differential bending of the cantilever. This out-of-plane displacement is measured in liquid by a custom modified optical interferometer (Veeco NT1100).

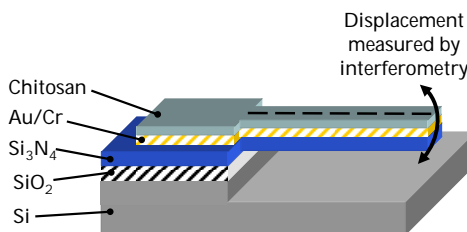


Figure 1. Schematic cross section of MEMS neurotransmitter sensor. The scans of cantilever bending in later figures are taken along the dashed line.

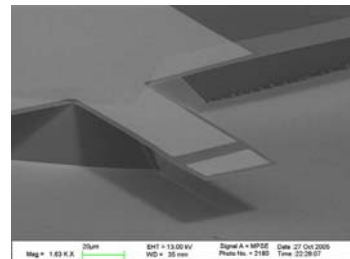


Figure 2. SEM of fabricated cantilever. The notch at the tip was used in some designs to facilitate optical measurements of cantilever displacement.

3. Experimental Results

The specificity of the sensor was tested in response to electrochemical ascorbic acid oxidation and dopamine oxidation. The device was immersed in the respective solution, and a positive potential was applied to the cantilever electrode (0.9V) for 30s. Both the ascorbic acid and dopamine solutions were adjusted to have a pH of 7.5 and a

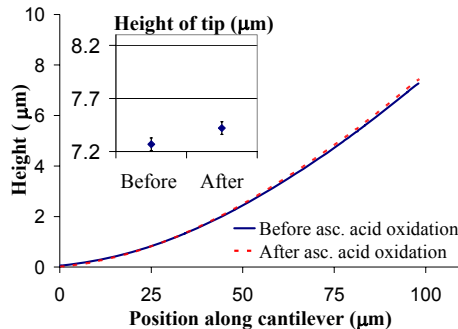


Figure 3. Scans along cantilever with chitosan before and after ascorbic acid oxidation (measured in DI water). The small differences in beam bending are caused mainly by measurement error, which is estimated to be 30nm at the tip.

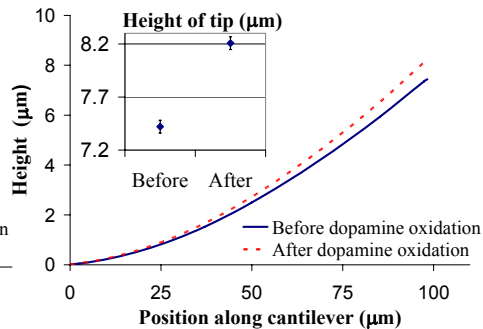


Figure 4. Scans along cantilever with chitosan before and after dopamine oxidation (measured in DI water). The chitosan generates tensile stress, bending the beam up by 800nm at the tip.

concentration of 0.1M. The sample was rinsed and immersed in deionized water (DI) for measurement before and after each oxidation reaction. The vertical cantilever displacement was measured through the DI.

Fig. 3 shows cantilever bending due to ascorbic acid oxidation. The initial displacement is caused by the initial residual stress of the chitosan, and the oxidation of ascorbic acid does not cause appreciable changes in cantilever bending. **Fig. 4** shows the response of the same cantilever to dopamine oxidation. Considerable differential bending occurs in this case since the chitosan is crosslinked by the oxidation reaction products and its residual stress is increased. The calculated stress change based on approximately 800nm displacement of the tip is 1.8MPa. The response could be further enhanced by optimizing cantilever geometry and increasing the chitosan thickness.

4. Conclusion

We have harnessed the mechanical responsivity of chitosan to electrochemical oxidation products to detect the neurotransmitter dopamine and discriminate against other oxidizable molecules. This MEMS-based method is expected to significantly improve dopamine detection capabilities for a better understanding of the role of this important neurotransmitter in the brain.

Acknowledgments

The authors would like to thank the Laboratory for Physical Sciences (LPS) and the National Science Foundation (NSF) for funding this work; the staff at LPS and the University of Maryland Nanocenter for assistance with cleanroom facilities; and colleagues at the MEMS Sensors and Actuators Lab for useful discussions.

References

- 1 B. J. Venton and R. M. Wightman, "Psychoanalytical electrochemistry: dopamine and behavior," *Analytical Chemistry*, vol. 75, pp. 414A-421A, 2003.
- 2 Q. Wu, M. E. A. Reith, R. M. Wightman, K. T. Kawagoe, and P. A. Garris, "Determination of release and uptake parameters from electrically evoked dopamine dynamics measured by real-time voltammetry," *Journal of Neuroscience Methods*, vol. 112, 2001.
- 3 L.-Q. Wu, A. P. Gadre, H. Yi, M. J. Kastantin, G. W. Rubloff, W. E. Bentley, G. F. Payne, and R. Ghodssi, "Voltage-Dependent Assembly of the Polysaccharide Chitosan onto an Electrode Surface," *Langmuir*, vol. 18, pp. 8620-25, 2002.
- 4 H. Yi, L.-Q. Wu, W. E. Bentley, R. Ghodssi, G. W. Rubloff, J. N. Culver, and G. F. Payne, "Biofabrication with Chitosan," *Biomacromolecules*, vol. 6, pp. 2881-2894, 2005.
- 5 L.-Q. Wu, M. K. McDermott, R. Ghodssi, and G. F. Payne, "Mimicking Biological Phenol Reaction Cascades to Confer Mechanical Function," *Advanced Functional Materials, In Press*, 2006.
- 6 L.-Q. Wu, R. Ghodssi, Y. A. Elabd, and G. Payne, "Biomimetic Pattern Transfer," *Advanced Functional Materials*, vol. 15, pp. 189-195, 2005.

FABRICATION OF POLYDIMETHYLSILOXANE(PDMS) MICROLENS FOR CELL DETECTION BY LIGHT SCATTERING

Sewan Park¹, Yongwon Jeong¹, Jinseok Kim¹, Kihwan Choi²,
Hyeon Cheol Kim¹, Doo Soo Chung² and Kukjin Chun¹

¹School of Electrical Engineering, Seoul National University, Korea

²School of Chemistry, Seoul National University, Korea

Abstract

In this paper, we present a polydimethylsiloxane (PDMS) microfluidic chip consisting of an integrated PDMS microlens for cell detection based on laser light scattering.

Keywords: microlens, PDMS, scattering

1. Introduction

The goal of the micro total analytical system (μ TAS) is to create a miniaturized lab-on-a-chip eventually for point-of-care. One of the key issues is to integrate a high-sensitivity detection system. Optical flow cytometry is the method of choice for many applications in clinical diagnostics. The method is mostly based on the simultaneous detection of laser light scattering and laser-induced fluorescence.¹⁾ The integrated PDMS microlens on the PDMS microfluidic chip, as shown in figure 1, enabled an easy alignment of the laser source and detector, and moreover enhanced the sensitivity and selectivity of the laser light scattering detection.

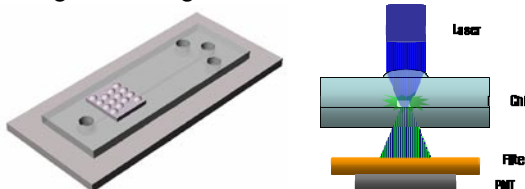


Figure 1. Fabrication process of PDMS microlens

2. Fabrication

We designed a plano-convex refractive PDMS microlens with focal length of 4 mm, a diameter of 750 μ m and a height of 58 μ m on the PDMS chip to focus an excitation laser with a spot size of 500 μ m onto a channel with a width of 100 μ m. The microlens and microfluidic chip were fabricated using PDMS. PDMS was selected as the material of the microlens because of its good optical properties, low cost, low interfacial free energy, easy modification of surface properties and biocompatibility, moreover, the PDMS microlens was compatible with the PDMS chip well in terms of bonding process and homogeneous refractive index. The fabrication process of the PDMS microlens is shown in figure 2.

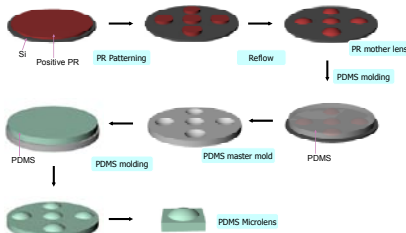


Figure 2. Fabrication process of PDMS microlens

The PDMS microlens was fabricated by replica molding. A master mold, concave-shaped, was fabricated by PDMS molding using a lens made by photoresist(PR) reflow. The heated PR was reflowed into a lens shape under the influence of surface tension.²⁾ The focal length of the PR microlens is controlled by the initial PR thickness before reflow and the diameter of the cylindrical pattern. The PDMS microlens was molded using a PDMS master mold. By this procedure, the peeling-off process was feasible, because the cured PDMS and liquid PDMS layer were not crosslinked together. SEM images of PR mold, PDMS master mold and PDMS microlens is shown in figure 3.

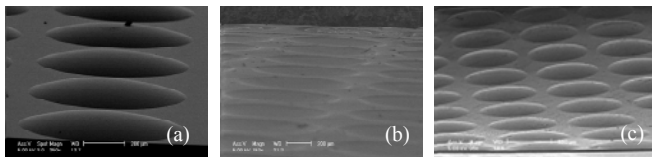


Figure 3. SEM images of (a) PR mold, (b) PDMS master mold and (c) PDMS microlens

A simple PDMS microfluidic chip with a T-channel was fabricated to integrate the PDMS microlens and test the efficiency of the microlens. Figure 4 shows the image of the fabricated PDMS microfluidic chip with the PDMS microlens

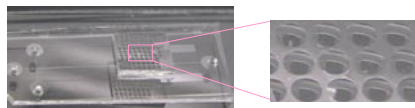


Figure 4. Image of fabricated PDMS microfluidic chip with PDMS microlens

3. Experimental

Light scattering detection method is a generic approach to cell or particle detection, because no time-consuming labelling step is required without the need for washing. In the laser scattering detection method, the spot size of the beam through the microfluidic chip is important to obtain the largest light scattering intensity, and consequently to obtain a good selectivity and sensitivity. To verify efficiency through the microlens, relative scattering intensities at a channel point with and without the microlens were measured. The cell detection setup using light scattering is shown in figure 5.

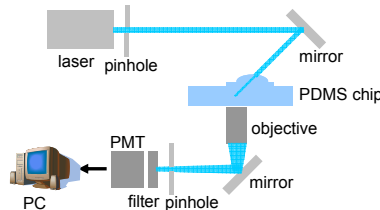


Figure 5. Cell detection setup using laser light scattering

The setup was interfaced with a PC using a data acquisition (DAQ) card and LabView as software. We used red blood cells (RBCs) as a cell sample.

4. Results and discussion

It can be seen in figure 6 that scattering intensities with the microlens were found to be much higher than those without the microlens. The scattering signals give information about cell size and shape. Larger cells generally have a higher scattering intensity. The more excitation laser light was focused into a channel, the more scattering signal was detected. The intensity of scattering signal at the detector as background noise became much smaller by using the microlens. Therefore, sensitivity and selectivity was increased by the microlens.

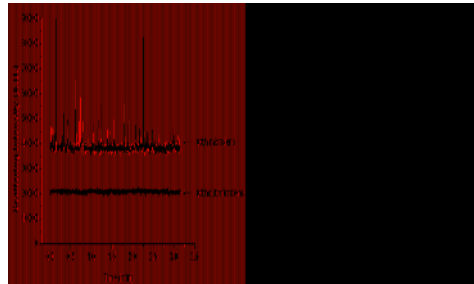


Figure 6. The scattering intensity of red blood cells

5. Conclusions

The PDMS microlens integrated on the PDMS microfluidic channel was verified to improve the laser intensity, and consequently selectivity and sensitivity of laser light scattering detection using red blood cells (RBCs).

References

1. Nicole Pamme, et al., *Counting and sizing of particles and particle agglomerates in a microfluidic device using laser light scattering*, Lab Chip, Vol. 3, pp.187-192, (2003).
2. Popovic, Zoran D., et al., *Technique for monolithic fabrication of microlens arrays*, Applied Optics, Vol. 27, pp.1281-1284, (1988).

A NOVEL, LOW-COST, COMPACT, LASER POINTER DRIVEN SURFACE PLASMON RESONANCE SYSTEM

Rahber Thariani and Paul Yager

Department of Bioengineering, University of Washington, Seattle, USA

Contact email: thariani@u.washington.edu

ABSTRACT

We demonstrate a novel and extremely low-cost method of building a surface plasmon resonance (SPR) microscope using a laser-pointer and an inexpensive and novel scattering, acoustic despeckler. Most SPR microscopy systems use incandescent sources which do not exhibit speckling, at the expense of increased energy consumption, weight, expensive filters and optics. An inexpensive laser pointer has been used as the source, coupled with an extremely cost-effective acoustic despeckler removing interference patterns in the images. No filter sets are required. This paper describes the elements composing the system and exhibited experimental characteristics.

Keywords: surface plasmon resonance, microscopy, laser, speckle

1. INTRODUCTION AND THEORY

Surface plasmon resonance is a phenomenon based on charge-density oscillations existing at the interface of two media with dielectric constants of different signs such as noble metals and glass. The charge-density waves are induced when the wavevectors of incoming photons are in resonance with the wavevectors of the surface plasmons for a given frequency. The surface plasmon wave is TM-polarized and the matching of wavevectors is characterized by a drop in the intensity of photons reflected from the interface. Fields associated with surface plasmons extend into the media surrounding the interface and are exponentially decaying. The surface plasmons are thus sensitive to changes in the media around them; this is manifested as a change in reflectivity as a function of near surface-refractive index.

Immunosensors based upon SPR consist of measurements of the reflected intensity from a surface sensitive to an analyte by deposition of the specific antibody. As analyte deposits upon the surface, the refractive index changes resulting in a change in reflectivity. Within certain limits, the change in reflectivity is linearly proportional to the change in refractive index. SPR immunosensors offer considerable advantages over other assay types including label-less detection and real-time tracking. With SPR microscopy [1,2] multiple types of antibodies can be arrayed upon the same surface allowing for rapid multi-analyte detection.

2. EXPERIMENTAL

The general scheme is illustrated in Figure 1. A commercially available (Laserglow.com, Toronto, Canada) laser pointer centered at 593.5 nm is used. This laser pointer can be operated with batteries; however we use here a 3V DC adaptor to reduce power variations. Lasers with a shorter wavelength can also generate surface plasmons, however, the use of Au coated substrates precludes the use of wavelengths shorter than 550 nm due to strong Au absorption. This particular laser was chosen since the output is highly polarized and thus the need for a separate polarizer is eliminated, which makes the system highly compact. The laser is mounted on a 5-axis + rotation stage (Newport,

CA) which is used align the laser and rotate it to the appropriate polarization (TM) for the generation of surface plasmons.

The despeckler is a modified audio transducer (Creative, Singapore) rapidly oscillating a scattering surface. The efficacy of the despeckler is evidenced in Figure 2, which shows images observed with the despeckler inactive (Figure 2a) and active (Figure 2b). An inexpensive Pixelink (Ontario, Canada) CCD camera was used for image collection. As we can see from the images the despeckler is highly effective in flattening the image. A frequency of 100Hz with an integration time of >50ms provided the optimal amount of speckle reduction.

To test the system efficacy a clean glass slide was coated with a 1nm layer of chromium (for adhesion) followed by a 45 nm layer of Au using an electron-beam evaporator. The Au surface was cleaned for 30 minutes using an UV-ozone cleaner. Four 5 μ L spots of Texas-Red labeled bovine serum albumin (BSA, Molecular Probes, OR) at a concentration of 1mg/mL in phosphate-buffered saline were deposited upon the Au coated slide using a micro pipette. Incubation for 45 minutes took place in a humidity controlled chamber, after which excess BSA was pipetted away. A Mylar flowcell [3] was then constructed on the Au coated slide and multiple rinses of PBS performed. The slide was then imaged through the SPR microscope and with the resulting image shown in Figure 3a. To verify that it was indeed the patterned BSA viewed with the SPR microscope, the slide was then viewed under a conventional epifluorescence microscope (Zeiss, 2x objective, TRITC filter set). Results are seen in Figure 3b where the correlation between the SPR microscope and the image fluorescence microscope image can be clearly seen. The SPR image is highly compressed in the horizontal axis due to the incident angle of the laser beam being around 71 degrees.

3. CONCLUSIONS

A simple, compact and low-cost SPR microscope driven by a laser pointer is demonstrated. A simple acoustic scatterer is used to despeckler the resulting microscope image. The system developed is highly scalable and may enable micro-analytical systems where inexpensive label-less detection of spatially distributed analytes is required.

4. ACKNOWLEDGEMENTS

We acknowledge Dr. Tim Chinowsky, Dr. Elain Fu and Dr. Kjell Nelson for helpful discussions. Funding was provided by the Cardiovascular Training Grant administered by Dr. Mike Regnier and the Bill and Melinda Gates Foundation Grant 399.

5. REFERENCES

1. E. Fu, J. Foley and P. Yager, Wavelength-tunable surface plasmon resonance microscope. *Review of Scientific Instruments* **74**, 3182-3184 (2003)
2. E. Fu, T. Chinowsky, J. Foley, J Weinstein and P. Yager, Characterization of a wavelength-tunable surface plasmon resonance microscope. *Review of Scientific Instruments* **75**, 2300-2304 (2004)

3. A. Hatch, A. Kamholz, K Hawkins, M Munson, E Schilling and P. Yager, A rapid diffusion immunoassay in a T-sensor. *Nat Biotechnol.* **19**(5):461-5(2001)

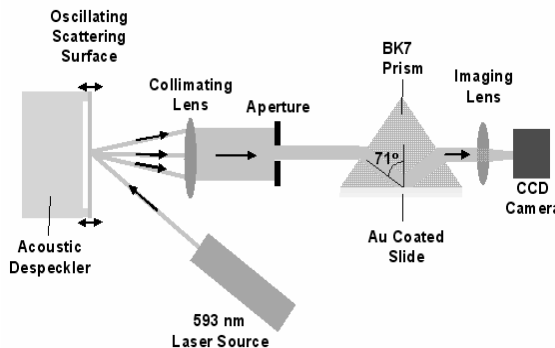


Figure 1) Schematic of the SPR microscopy system. The high resonance angle of 71 degrees can be clearly seen resulting in images with highly compressed in the x-axis. The acoustic despeckler consists of scattering aluminum foil over a vibrating speaker.

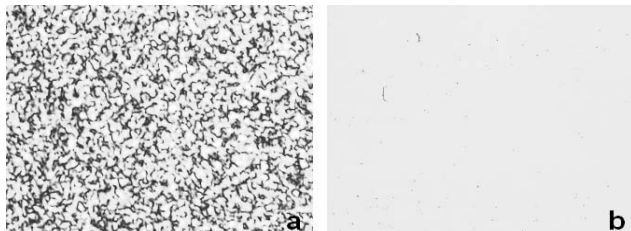


Figure 2a) Image obtained without despeckler. The interference patterns making the obtaining of an image are clearly seen. **2b)** With acoustic despeckler engaged the image field is flattened and highly uniform allowing for image acquisition.

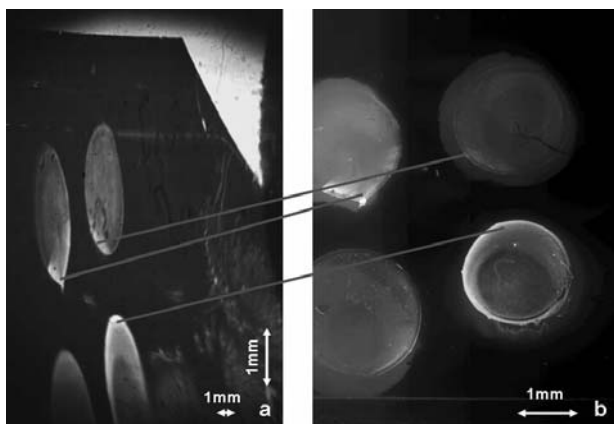


Figure 3a) SPRM image of patterned 1mg/mL fluorescently labeled BSA (Texas Red, Molecular Probes) incubated for 45 minutes. Compression in x-axis due to the high resonance angle is clearly seen. The edge of the channel is also visible, exhibiting high reflectivity.
3b) Fluorescent image of the same pattern (Zeiss ICM-405). Correlation between images obtained by different modalities is clearly demonstrated.

CAPACITIVE SURFACE STRESS-BASED CHEMO-MECHANICAL SENSOR

Si-Hyung "Shawn" Lim¹, Srinath Satyanarayana², Arunava Majumdar³

¹Center of Integrated Nanomechanical Systems (COINS), University of California, Berkeley, CA94720, USA (shlim@me.berkeley.edu)

² Dept. of Mechanical Engineering, University of California, Berkeley, CA94720, USA (ssrinath@me.berkeley.edu) (currently at Intel Corp.)

³ Dept. of Mechanical Engineering, University of California, Berkeley, CA94720, USA (majumdar@me.berkeley.edu)

Abstract

Chemical sensing experiments have been demonstrated using a capacitive surface stress-based chemo-mechanical sensor array and alkanethiol sensor coating layers. A dedicated capacitance measurement board with sub-femto farad accuracy and an in-built temperature controlled stage for the sensor chip were designed and fabricated for multiplexed sensing experiments with the sensor array. Sensor responses to example sensing targets like water and IPA vapors at different concentrations were measured. To minimize undesired thermal and chemical absorption responses, an updated sensor design has been proposed also.

Keywords: membrane, capacitive sensing, surface stress, chemical and biological sensing

1. Introduction

Surface stress sensors using micro machined silicon cantilevers have been demonstrated in chemical and biological sensing [1, 2]. However, the design, geometry and performance of these sensors are limited by the high stiffness of the silicon-based materials used in their fabrication. Recently, a novel parylene micro-membrane surface stress sensor array (Figure 1) using capacitive signal readout for chemical sensing applications was presented [3]. The micro-membrane sensor exploits the low elasticity modulus, better chemical resistance and biocompatibility of parylene when compared to the silicon-based materials used in traditional microfabrication.

In this paper, a dedicated capacitance measurement board with sub-femto farad accuracy and an in-built temperature controlled stage for the sensor chip are designed and fabricated. Chemical sensing experiments using miniaturized sensing platform are demonstrated using the fabricated sensor array and alkanethiol sensor coating layers. Furthermore, an updated sensor design is proposed to minimize undesired thermal and chemical absorption responses.

2. Device and Sensing Platform

When selective chemical/biological reactions occur between the target and probe molecules on the sensor surface, the changes in the intermolecular forces induce a

surface stress change which causes the membrane to change curvature and deflect as shown in Figure 1. The sensor deflection changes the effective gap between the two electrodes and changes the capacitance. Figure 2 shows sensing platform including a single-ended capacitance measurement circuit (A), on-board temperature control system (B), target vapor generation/control system (C), and integrated chemical sensing chamber (D).

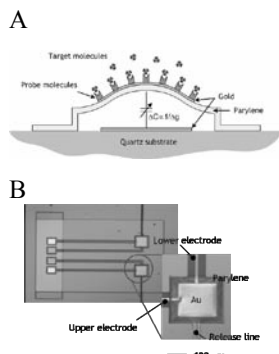


Figure 1. Capacitive membrane sensor.

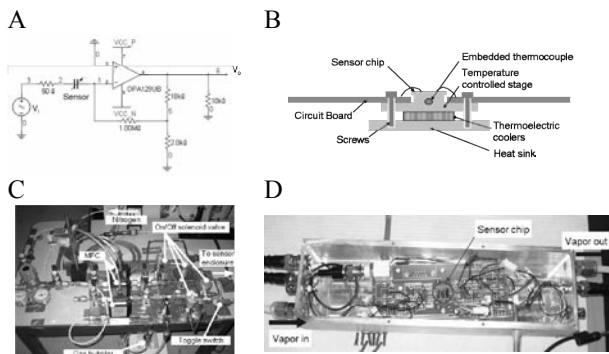


Figure 2. Sensing platform.

3. Preliminary experiment

Temperature response for each of the sensors used in the chemical sensing experiment was measured to test the proper release of the sensor membrane (Figure 3A). Two different alkanethiol coatings [11 Mercapto 1 undecanoic acid (MUA) $\text{SH}-(\text{CH}_2)_{10}-\text{COOH}$ and 11 Amino 1 undecanethiol (AOT) $\text{SH}-(\text{CH}_2)_{11}-\text{NH}_2$] were used as sensing layers in the multiplexed measurement. Sensor response to example sensing targets like water and IPA vapors at different concentrations were measured (Figure 3B and 3C). The preliminary experiments for IPA and water vapor sensing showed promising results and based on the measurement noise the sensor resolution were estimated to be ~ 30 ppm and ~ 200 ppm for IPA and water vapor respectively.

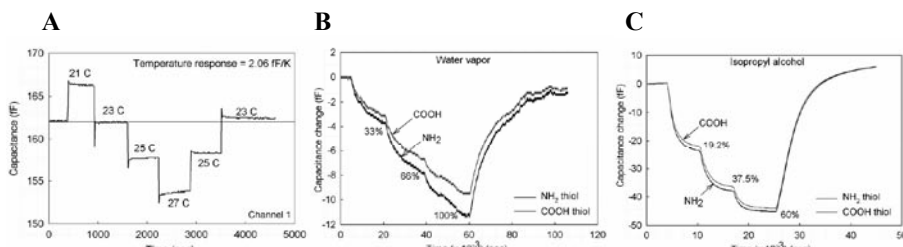


Figure 3. Experiment results. A. Temperature response. B. Water vapor response. C. Isopropyl alcohol response.

4. System Update

The preliminary experiment results for simple test vapors were promising. However, the strain mismatch between membrane and the thin film coating materials can generate undesired structural deformation for 1) thermal environment change and 2) chemical absorption into the membrane. To compensate those undesired sensor responses in a membrane-type bio-chemical sensor, a new sensor design has been proposed as shown in Figure 4. By putting another coating layer on the bottom of the membrane structure, those undesired sensor responses can be self compensated. The great reduction of the undesired thermal response provides the possibility to remove the substrate temperature controller in a usual bio-chemical sensor platform. Especially, in a portable or stand alone product, this unique design will greatly reduce power consumption. Sensors using the compensated design are currently under fabrication. In the near future, its performance will be demonstrated on a newly designed chemical sensing board as shown in Figure 5.

5. Conclusion

Chemical sensing experiments have been demonstrated using a capacitive surface stress-based chemo-mechanical sensor, alkanethiol sensor coating layers, and a dedicated capacitance measurement board. To minimize undesired thermal and chemical absorption responses, a thermal and chemical absorption compensation design was proposed.

Acknowledgements

The authors would like to thank Microfabrication Laboratory, UC Berkeley for providing microfabrication facilities. This work was supported by National Science Foundation.

References

1. T. Thundat and A. Majumdar, *Microcantilevers for Physical, Chemical, and Biological Sensing: Sensors and Sensing in Biology and Engineering*, New York: Springer-Verlag, 2003.
2. L. Pinnaduwage, H.-F. Ji, T. Thundat, Moore's law in homeland defense: an integrated sensor platform based on silicon microcantilevers, *IEEE Sensors Journal* 5, 2005.
3. Srinath Satyanarayana, Daniel T. McCormick, Arun Majumdar, Parylene micro membrane capacitive sensor array for chemical and biological sensing, *Sensors and Actuators B: Chemical*, 2006.

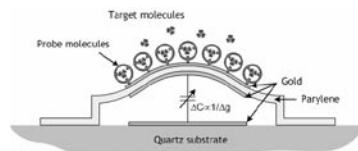


Figure 4. Modified capacitive membrane sensor design

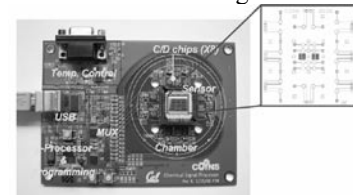


Figure 5. Updated chemical sensing board

Potentiometric drug transport analysis using oocyte-based field effect transistor

Toshiya Sakata^{1,2} and Yuji Miyahara^{1,2}

¹Biomaterials Center, National Institute for Materials Science, 1-1 Namiki,
Tsukuba, Ibaraki 305-0044, Japan

²Center for NanoBio Integration, The University of Tokyo, 7-3-1 Hongo,
Bunkyo-ku, Tokyo 113-8656, Japan

Abstract

We report the potentiometric drug transport analysis using an oocyte-based field effect transistor (FET), which is based on potentiometric detection of extracellular potential change at cell membrane/gate insulator. The time course of interfacial voltage can be monitored during the uptake of common substrate mediated by the transporter at the cell membrane using the oocyte-based FET. The platform based on the oocyte-based FET is suitable for a convenient and inexpensive system for drug screening in pharmaceutical lead discovery.

Keywords: potentiometric detection, drug screening, transporter, oocyte-based field effect transistor

1. Introduction

We have been investigating a new device for detection of bio-molecular recognition events using field effect devices, which is based on potentiometric measurement of molecular charges at a gate insulator/solution interface. So far we have succeeded in a direct detection of various DNA recognition events such as hybridisation, intercalation, primer extension and so on, and have found further the possibility of single nucleotide polymorphism (SNP) typing and DNA sequencing using field effect devices [1-7]. In this paper, we propose an oocyte field effect transistor (oocyte FET) for drug transport analysis, which is a FET combined with *Xenopus* oocytes, and investigate the electrical characteristics of oocyte FET with a transporter expressed at the oocyte membrane. In addition, we report on the possibility of non-invasive cell analysis and drug screening using oocyte FET.

2. Methods

Both the fabricated FETs and the commercial ISFETs (BAS Inc.) were used for the experiments in the present study. The FETs were immersed in a phosphate buffer solution (0.025 M Na₂HPO₄ and 0.025 M KH₂PO₄, pH 6.86, Wako) with an Ag/AgCl reference electrode with saturated KCl solution and oocyte was fixed on the gate area of FETs (**Figure 1**). The electrical characteristics of the FETs such as the gate voltage (V_G)-drain current (I_D) characteristics were measured in a pH 6.86 phosphate buffer solution at room temperature using a semiconductor parameter analyzer (4155C, Agilent). The threshold voltage shift ΔV_T was determined after introduction of common

substrates to oocyte-based FETs. The ΔV_T was defined as a difference of the V_G - I_D characteristics at a constant drain current of 700 μ A. The time course of ΔV_T during uptake of common substrates was monitored using a circuit with which the potential change at the interface between an aqueous solution and the gate insulator can be read out directly at a constant drain current. In the present study, the gate voltage and the drain current were set to be 1 V and 700 μ A, respectively.

3. Results and Discussion

We have prepared two types of oocyte-based FETs; one is the oocyte-based FET with transporter, the transportocyte FET; another is the oocyte-based FET without it, the control oocyte FET. Using these oocyte-based FETs, differential measurements were performed in order to eliminate the common background noises such as temperature change, change in ion concentration and so on. Also, the reference FET without oocyte was prepared in order to take account of the effect of oocyte fixed at the gate surface of the oocyte-based FET. When an estrone-3-sulfate (E3S) as a common substrate was introduced into two kinds of oocyte FETs and the reference FET, the interfacial potential of the transportocyte FET increased with uptake of E3S mediated by hOATP2 (human organic anion transporting peptide 2) transporter while the control oocyte FET and the reference FET showed little interfacial potential change, corresponding to the V_T shift (**Figure 2**). This result was in agreement with the experimental results performed by BD Gentest, Inc., which were based on uptake of [3 H]-labelled E3S by mediated hOATP2 transporter. Moreover, we could realize the quantitative analysis of E3S uptake using oocyte field effect devices (**Figure 3**), which was estimated as the flat band voltage (V_F) shifts in C-V characteristics using the field effect device different from transistor. Therefore, we have found out the possibility of a label-free and non-invasive drug

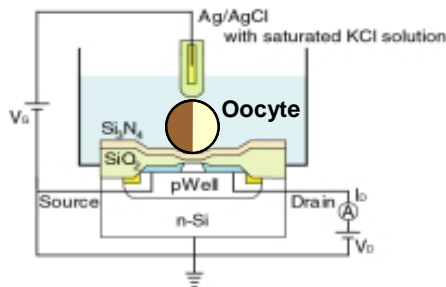


Figure 1. Diagram for measurement of electrical characteristics using oocyte field effect transistor.

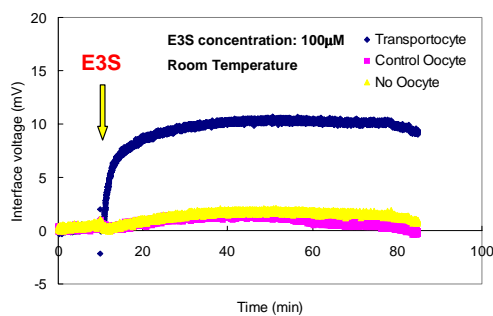


Figure 2. Direct detection of uptake of E3S substrate using oocyte field effect transistors.

transport screening using the oocyte field effect devices such as the oocyte FET.

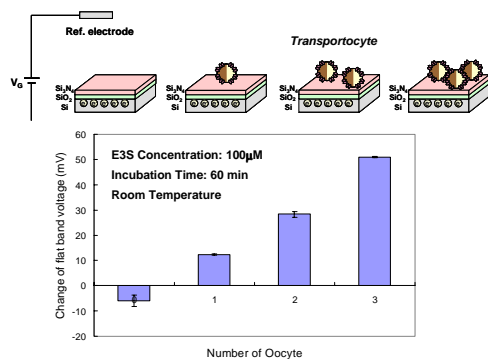


Figure 3. Quantitative analysis of uptake of E3S substrate using oocyte field effect devices.

oocyte-based FET is suitable for a safe, fast and convenient detection system for drug screening in pharmaceutical lead discovery.

Acknowledgments

The authors wish to thank Drs. Y. Horiike, J. Tanaka, H. Otsuka and S. Kita of National Institute for Materials Science in Japan, Mr. Y. Nakajima of Ryokusei M.E.S. Co., Ltd. in Japan and Mr. M. Kamahori of Hitachi Ltd. in Japan for their help and useful discussions.

References

1. T. Sakata, M. Kamahori and Y. Miyahara, *Materials Science and Engineering C* **24**, 827 (2004).
2. T. Sakata, M. Kamahori and Y. Miyahara, *Japanese Journal of Applied Physics* **44 No.4B**, 2854 (2005).
3. T. Sakata, S. Matsumoto, Y. Nakajima and Y. Miyahara, *Japanese Journal of Applied Physics* **44 No.4B**, 2860 (2005).
4. T. Sakata and Y. Miyahara, *ChemBioChem* **6**, 703 (2005).
5. T. Sakata and Y. Miyahara, *Biosensors and Bioelectronics* **21**, 827 (2005).
6. T. Sakata and Y. Miyahara, *Angewandte Chemie International Edition* **45**, 2225 (2006).
7. T. Sakata and Y. Miyahara, *Biosensors and Bioelectronics* in press (2006).

4. Conclusion

We have shown the potentiometric drug transport analysis using the oocyte-based FET, which is based on potentiometric detection of extracellular potential change derived from exchange of molecular charges mediated by transporting peptides at cell membrane. The time course of interfacial voltage change could be monitored during the uptake of common substrate mediated by the transporter without labeling materials and fracturing oocytes.

The platform based on the

BIOMOLECULAR MOTOR-DRIVEN SELECTIVE BINDING AND CONCENTRATING OF PROTEIN ANALYTES

T. Kim¹, L. J. Cheng², M.-T. Kao³, E. F. Hasselbrink¹, L. J. Guo², E. Meyhöfer^{1,3}

¹University of Michigan Department of Mechanical Engineering, 2350 Hayward Street, Ann Arbor, MI 48109 USA, ²Department of Electrical Engineering and Computer Science, ³Department of Biomedical Engineering

Abstract

We successfully demonstrated a biomolecular motor-driven microfluidic device that can detect target molecules from an analyte stream and then preconcentrate them at a horseshoe-shaped collector. This device removed approximately a few thousand molecules per second from the analyte stream, and the fluorescent signal from collected, labeled molecules at the collector increases up to five orders of magnitude within an hour.

Keywords: Biomolecular motors, microtubules, pre-concentrator

1. Introduction

We recently introduced the concept of biomolecular motors (BMMs) as nanoscopic, stand-alone, highly efficient, and low power prime-movers for μ TAS systems [1]. In this work we demonstrated that derivatized microtubules, propelled by kinesin, are able to bind and transport proteins away from an analyte stream. Recent work has demonstrated guiding microtubules along straight line using chemical patterning or mechanical nanotacks of kinesin [2-4] and rectifying their motility in the same direction using an arrow head pattern in microchannels [1,2]. In this paper, we develop a method to not only capture, but subsequently concentrate specific proteins at a fixed spot on a microchip for sensitive detection with a high NA objective.

2. Experiment

Fig. 1a shows the schematic of a biomolecular motor-driven device for selective binding and concentrating molecules. Biotinylated microtubules are loaded at the left side of an analyte stream with fluorescently labeled streptavidins, and observations are made at the collector located on the opposite side of the analyte stream. Fig. 1b shows SEM pictures of a microfabricated device. Microfluidic channels and a horseshoe-shaped collector were made via HF-glass wet etching and lithography, and nanotacks

on a coverslip were fabricated with CYTOPTM via nanoimprinting technology [2]. Low temperature SU-8 bonding made possible integration of these two parts. First, SU-8 was spun on RIE-treated PDMS. Second, the SU-8 was selectively transferred only onto the junctions of the glass substrate. Third, the glass substrate and the coverslip were bonded by exposing to UV and then cured under 50 kPa of pressure and at the temperature of 75 °C.

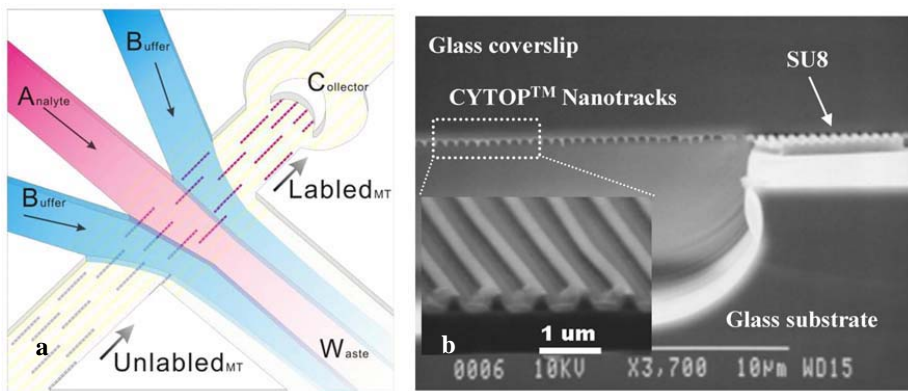


Fig. 1 (a) Schematic view of a biomolecular motor-driven selective binding and concentrating device. Unlabeled microtubules at left are translocated by kinesin towards the collector at right. They are guided to move straight across the analyte channel by nanotacks and bind fluorescently-labeled streptavidins from the analyte stream. The labeled microtubules are aggregated at the horseshoe-shaped collector. (b) The SEM images of the wet-etched glass substrate for microfluidic channels and nanoimprinted CYTOPTM nanotacks on a coverslip. SU-8 was selectively transferred to the junctions between the glass substrate and the coverslip as a sealant.

3. Results and discussion

We accomplished straight motion of the microtubules along CYTOPTM nanotacks across a pressure-driven flow by using previously reported method [2-4]. We can see the translocation of the microtubules (white spots in Fig. 2) because they are labeled by an analyte stream. We can also see most of the labeled microtubules accumulate at the deadlock of the collector. We believe that the collection of microtubules proceeds by the following mechanism: first, the leading ends of the microtubules are trapped into the gap which is likely to be generated at the fringe of the collector (between the top glass substrate and the bottom nanotacks during bonding process). Second, microtubules trapped in the collector decrease the number of locally available, active kinesins,

thereby reducing the transport efficiency. In addition, microtubules are linked together since each streptavidin molecule can bind four biotins. Using this collection mechanism we found that, for example, in case of a 2 nM analyte sample concentration the fluorescent intensity at the collector increases up to five orders of magnitude.

In summary, a novel biomolecular motor-driven molecular concentrator was designed, fabricated, nanotracks were integrated into the microfluidic device, and the feasibility of BMM-based molecular sorting assay was demonstrated. This approach promises integration of other microanalysis steps for complete stand-alone μ TAS systems.

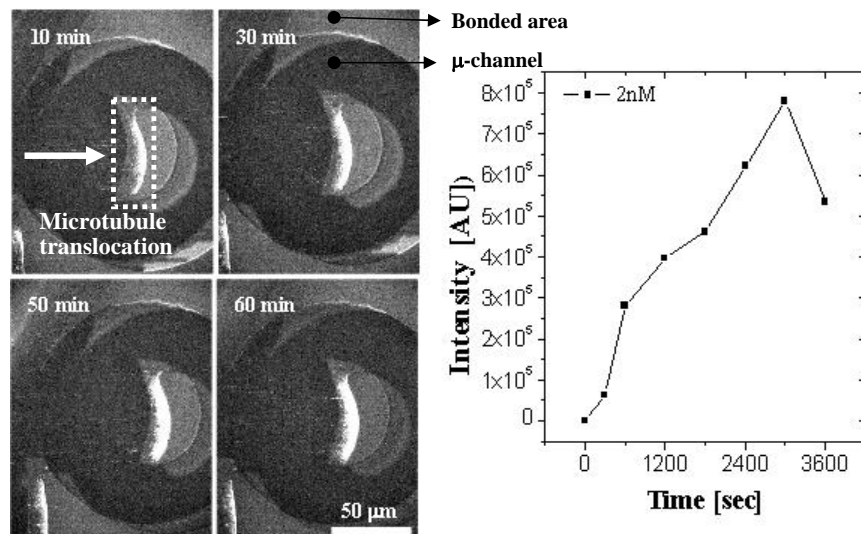


Fig. 2 Left: image sequences of microtubules heading toward the horseshoe-shaped collector. The white spots indicate the movement of microtubules bound with target molecules from a stream of analyte with time. Most of microtubules translocated by kinesin are concentrated around the collector indicated by a dot-line rectangle. Right: accumulation of the microtubules increases the fluorescent intensity, which was measured by summing up the intensity of every pixel in the dotted rectangle (80 by 240 pixels corresponding to 26 by 77 μ m).

4. References

1. T. S. Kim, H. K. Nanjundaswamy, C.-T. Lin, S. Lakämper, L. J. Cheng, D. Hoff, E. F. Hasselbrink, L. J. Guo, K. Kurabayashi, A. J. Hunt, E. Meyhöfer, μ TAS, pp 33-36, 2003.
2. J. R. Dennis, J. Howard, V. Vogel, Nanotechnology 10, 232-236, 1999.
3. Cheng, L. J., Kao, M. T., Meyhöfer, E., Guo, L. J., Small 2005, 1, 409-414.
4. Lin, C. T., Kao, M. T., Kurabayashi, K., Meyhöfer, E., Small 2006, 2, 281-287

DEVELOPMENT OF LOW-COST SURFACE ENHANCED RAMAN SCATTERING SUBSTRATES WITH SILVER NANO-PARTICLES USING THE MODIFIED SILVER MIRROR REACTION FOR ULTRA-SENSITIVE AND ON-SITE DETECTIONS

Katsuhito Kurooka and Norihisa Miki

Keio University, Yokohama, Kanagawa, 223-8522 Japan

Abstract

Ultra-sensitive as well as on-site detections are strongly demanded in the field of detection technology, which can be achieved by μ TAS utilizing surface enhanced Raman scattering (SERS). In this paper, we propose manufacturing of the SERS substrates with silver nano-particles utilizing the modified silver mirror reaction, where dispersants are added to the conventional silver mirror solution. The processes are very simple and completed in only 15 minutes at extremely low cost. The SERS substrate exerted extremely high Raman enhancement factor of 10^6 . We fabricated a μ TAS device containing the SERS site. It successfully showed remarkably high Raman enhancement with good repeatability. The fabricated SERS substrate and μ TAS device herein are low cost and exhibit good repeatability and thus, are readily applicable to ultra-sensitive and on-site detections in various applications.

Keywords: SERS, silver nano-particle, silver mirror reaction, ultra-sensitive and on-site detection, biosensor

1. Introduction

The surface enhanced Raman scattering (SERS), exploiting high field enhancement on the surface of metal nano-particles, exerts the spectrum with an intensity approaching 10^{14} to 10^{15} higher than that of conventional Raman spectrum [1]. Hence, it is expected to be applied to ultra-sensitive detection and analysis of proteins, virus, biosensors etc. Manufacturing of high-performance SERS substrates enabling electromagnetic field enhancement is crucial and has been widely investigated. Nano-scale silver structures have been most frequently used to achieve high Raman enhancement, which can be formed by deposition of silver on nano-structured PDMS [2] and aggregation of silver colloids in solution onto the surface of a glass substrate [3]. However, the SERS substrates developed so far have issues of time and cost for manufacturing and repeatability of the Raman enhancement. The objective of our work is to develop a μ TAS device that achieves ultra-sensitive and on-site detection by employing SERS. We propose manufacturing of SERS substrates with silver nano-particles utilizing modified silver mirror reaction and the μ TAS device containing the SERS site. The proposed SERS substrates can be manufactured in 15 minutes at extremely low cost with good repeatability and thus, are advantageous over those developed previously.

2. Experimental

The SERS substrate with silver nano-particles is fabricated utilizing modified silver

mirror reaction, where dispersants are added to the conventional silver mirror solution (silver nitrate solution + ammonia water), as illustrated in Figure 1. (a) After adding ammonia water, DI water and the dispersant to the silver nitrate solution, agitate them and produce the silver nano-particle solution. (b) Add a reducing agent and dip a glass substrate in the silver nano-particle solution simultaneously. Silver nano-particles deposit on the glass substrate surface and the glass substrate is taken out after 120 seconds and rinsed by DI water. The processes are completed in only 15 minutes.

Figure 2 (a) and (b) shows the SEM and FESEM images of the fabricated SERS substrate with the optimal conditions of the modified silver mirror reaction denoted in Table 1, respectively. The silver nano-particles 10-50 nm in diameter are formed on the substrate uniformly. Figure 2 (c) shows an image of the fabricated μ TAS device containing the SERS site. The fabrication processes are; Silver nano-particles are locally formed onto the glass substrate. Subsequently, bond the molded PDMS whose surface is activated by oxygen plasma to the substrate to form micro-channels. In experiments, samples, such as Rhodamine6G (R6G), are introduced into the micro-channels.

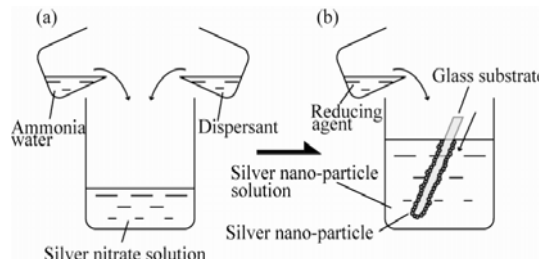


Figure 1. Silver mirror reaction processes

Table 1. Optimal conditions of silver mirror reaction

Condition	
Silver nitrate concentrate	5wt%
Reaction time	120 seconds
Solution temperature	25 degrees C
Reducing agent	Hydrazine
Dispersant	Copolymer with acid group

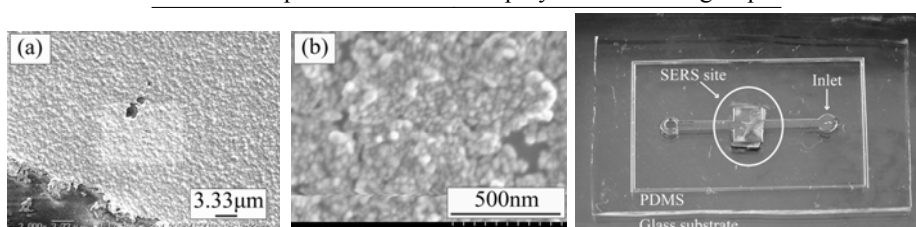


Figure 2. (a) A SEM image and (b) a FESEM image of the SERS substrate. (c) Fabricated μ TAS device

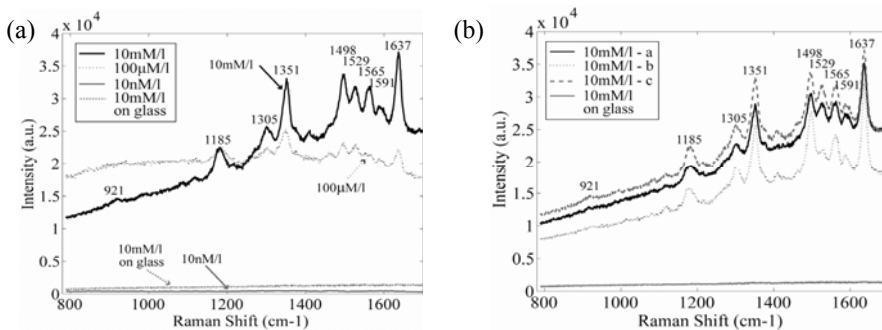


Figure 3. (a) SERS spectra of 10mM/l to 10nM/l R6G on the SERS substrate and 10mM/l R6G on the pristine glass substrate. (b) SERS spectra of 10mM/l R6G from randomly selected three points on the SERS site and that of 10mM/l R6G on the pristine glass substrate.

3. Results and discussion

Figure 3 (a) shows the SERS spectra of 10mM/l to 10nM/l R6G on the SERS substrates and the Raman spectrum of 10mM/l R6G on the pristine glass substrate. The laser was Ar laser (532nm), and the integration time of spectra acquisition was 3sec. For the signal of 10mM/l R6G from the SERS substrate, high Raman enhancement was observed compared to that from the glass substrate. By comparing the SERS spectrum of 10nM/l R6G from the SERS substrate and that of 10mM/l R6G from the pristine glass substrate, the Raman enhancement factor of the SERS substrate was found to be more than 10⁶.

Figure 3 (b) depicts the SERS spectra of 10mM/l R6G at randomly selected three points on the SERS site in the μTAS device. The laser was Ar laser (532nm), and the integration time of spectra acquisition was 3sec. Good repeatability with respect to the measurement position was successfully demonstrated with extremely high Raman enhancement, though the laser is irradiated R6G on the SERS site over PDMS.

4. Conclusions

We proposed the μTAS device with the SERS site, which was fabricated utilizing the modified silver mirror reaction. The fabrication processes of the SERS substrate are very simple, quick and extremely low cost. The SERS substrate exerted an extremely high Raman enhancement factor of 10⁶. The μTAS device successfully demonstrated high Raman enhancement with good repeatability, verifying the feasibility that the device can be applied to ultra-sensitive and on-site detection in various applications.

Acknowledgements

This research was supported by Asahi Glass Foundation.

References

1. Amy M. Michaels et al, J. Phys. Chem. B, Vol.104, pp. 11965-11971, (2000).
2. Gang L. Liu and Luke P. Lee, MicroTAS'05, Vol.2, pp. 1003-1005, (2005).
3. Katherine C. Grabar et al, J. Am. Chem. Soc., Vol.118, pp. 1148-1153 (1996).

Flowing Thermal Lens Micro Flow Velocimeter with On-Chip Microlens and Detachable Optical Fibers

**Yoshikuni Kikutani^{1,2}, Kazuma Mawatari^{1,2}, Kenji Katayama^{1,2},
Yoshinori Matsuoka^{2,3}, Takashi Fukuzawa³, Akihiko Hattori³,
Mitsuo Kitaoka², Manabu Tokeshi^{1,4} and Takehiko Kitamori^{1,4,5}**

¹ Micro Chemistry Group, Special Research Laboratory for Optical Science,
Kanagawa Academy of Science and Technology, Kanagawa 213-0012, Japan,

² The Research Association of Micro Chemical Process Technology, Japan,

³ Nippon Sheet Glass Co., Ltd., Japan, ⁴ Institute of Microchemical Technology, Japan,

⁵ Department of Applied Chemistry, Graduate School of Engineering,
The University of Tokyo, Japan (Contact E-Mail: ykikutani@pop12.odn.ne.jp)

Abstract

Flowing thermal lens micro flow velocimeter (FTL-MFV) is an optical detector for measurement of flow rate in microchannel without disturbing the microfluid. By using optical fibers and micro rod lenses, we have fabricated a series of small FTL-MFVs. In this paper, we report on a FTL-MFV with an on-chip microlens, that we newly developed to simplify optical alignment process needed for FTL-MFV measurements. Performance of FTL-MFV was also improved by using an on-chip microlens.

Keywords: thermal lens, flow velocimeter, microlens, on-chip lens

1. Introduction

We had developed flowing thermal lens micro flow velocimeter (FTL-MFV) for measurement of flow rate inside a microchannel [1]. In FTL-MFV, thermal lens produced in a microchannel with an excitation beam pulse is used as a tracer, and the flow rate is determined from the time required for the thermal lens to reach the downstream detection point. By selecting the wavelength of the excitation beam to coincide with the absorption band of the solvent, thermal lens can be produced without adding anything to the fluid. Sensitive lock-in synchronous measurement enables detection of a thermal lens with very small temperature rise, so that FTL-MFV causes extremely slight disturbance to the fluid.

The excitation and probe beams of FTL-MFV are irradiated to the microchannel through a microlens, and accurate alignment of the lens to the microchannel is needed for the measurement.

This paper reports on significant improvement in usability and performance of the FTL-MFV by using on-chip microlens and detachable optical fibers.

2. Experimental

Figure 1 illustrates structure of the on-chip FTL-MFV. A SELFOC® microlens in a lens holder was bonded to a pedestal bonded on a glass microchemical chip. Single-mode optical fibers for the excitation and probe beams were bundled together in a special glass ferrule, and the ferrule was bonded to a metal sleeve with a slit. The ferrule and the lens holder were of the same diameter, so that they could be easily connected and detached with the aid of the

metal sleeve. The metal sleeve had a metal head with a notch indicating the position of the two optical fibers. Only by setting the notch towards the upstream direction, alignment of the FTL-MFV completed. Distance between the excitation and probe beams was 70 μm . A multi-mode optical fiber for receiving the probe beam was fixed on the other side of the microchemical chip in a similar way using a pedestal, a metal sleeve and a glass ferrule. In fixing the on-chip lens and the receiver fiber at optimized positions, we have applied technique for fabrication of on-chip thermal lens detection device [2] with some modification considering difference between the two devices.

Figure 2 shows a photograph of a microchemical chip with on-chip lenses for FTL-MFV. Width and depth of the microchannel was 200 and 90 μm .

Flow rate of water was measured using 1480 nm IR laser as the excitation beam.

3. Results and Discussion

Figure 3 shows correlation between flow rate and phase shift of FTL-MFV signal, which is a linear function of traveling time of

the thermal lens. Measurements were carried out at two different but equivalent positions of the channel with repeated attachments and detachments of the optical fibers. The data showed good reproducibility, and it was verified that measurement of FTL-MFV could be very easily done only by connecting optical fibers to an on-chip lens at a point of measurement.

In addition to the enhanced usability, dynamic range of FTL-MFV was also expanded by fixing the microlens on a microchemical chip, because of reduction in vibrational noise with the fixed microlens (Figure 4).

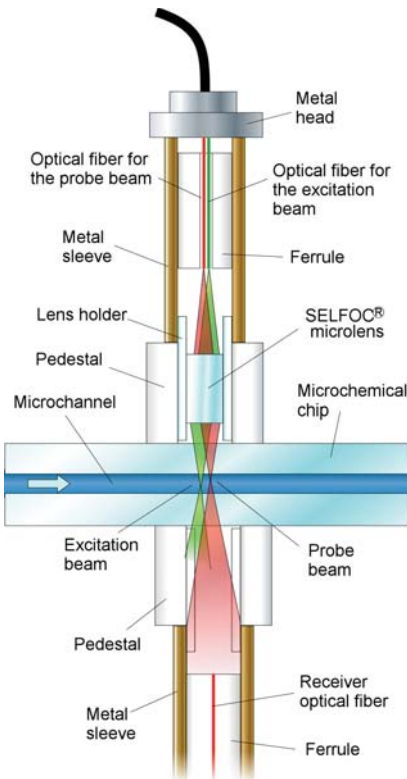


Figure 1. Structure of on-chip FTL-MFV.

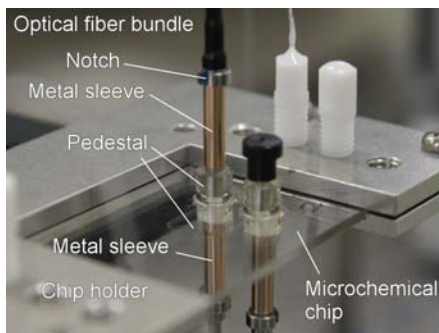


Figure 2. Microchemical chip with on-chip FTL-MFV.

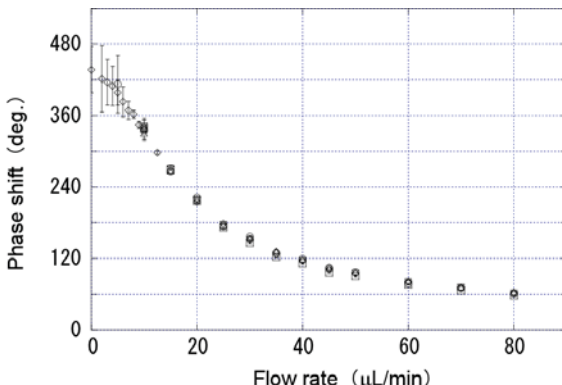


Figure 3. Flow rate dependence of phase shift of on-chip FTL-MFV signal. Modulation frequency of the excitation beam: 327 Hz. Data were taken with two different but equivalent on-chip microlenses. (Lens 1: $\circ \diamond \square$, Lens 2: $\triangle \nabla$)

4. Conclusion

A flowing thermal lens micro flow velocimeter with an on-chip microlens and detachable optical fibers was developed. The on-chip microlens greatly improved usability of the flow sensor by simplifying optical alignment process, and it was also effective in improving performance of the sensor by reducing vibrational noise.

Acknowledgements

This work has been done with a financial aid of the New Energy and Industrial Technology Development Organization (NEDO), Japan.

REFERENCES:

- [1] Y. Kikutani et al., Proc. μ TAS 2005, 970-972.
- [2] Y. Matsuoka et al., Proc. μ TAS 2004, Vol.2 452-454.

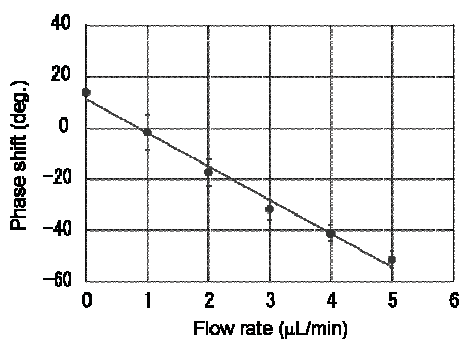


Figure 4. Flow rate dependence of phase shift of on-chip FTL-MFV signal at low flow rates. Modulation frequency of the excitation beam: 17 Hz.

PHOTOTHERMAL SPECTROSCOPY USING DIFFRACTION GRATING NANOCHANNELS FOR DETECTION IN NANO SPACE

Kotaro Oda¹, Kazuma Mawatari², Sho Asada¹, Akihide Hibara¹ and Takehiko Kitamori^{1,2}

¹The University of Tokyo, Bunkyo, Tokyo, 113-8656, Japan

²Kanagawa Academy of Science and Technology,
Kawasaki, Kanagawa, 213-0012, Japan

Abstract

We report a new photothermal spectroscopy using diffraction grating nano channels for detection in nano space. Photothermal effect was detected as intensity change of a diffracted probe beam due to refractive index change of heated sample solution inside nanochannels. The concept was verified by nanochannels of ~nm width × ~nm depth. The LOD (Limit of Detection) for Sunset Yellow solutions was 1.0×10^{-5} Abs. Further development to get higher sensitivity utilizing “Alternate diffraction grating method” is now investigated.

Keywords: nano channel, photothermal detection, diffraction grating

1. Introduction

Micro chemical process has many advantages for example small sample volume, rapid and effective reaction and small instruments. But detection in micro channel without fluorescent modification is very difficult. Thus we have developed original photothermal spectroscopy “Thermal Lens Microscope (TLM)” for sensitive detection of samples without fluorescent modification in micro-sized channels, and TLM has been proved to have comparable sensitivity to LIF method and wide applicability to spectrophotometric detection method for micro space. [1] However, in nano space ($<1\mu\text{m}$), generation of thermal-lens is difficult in principle, because the diameter of thermal-lens is beyond the size of nano space and glass has much higher thermal conductivity than water. In this study, we developed a new photothermal spectroscopic method for nano space by using diffraction grating nano channels. In this presentation, we verified and studied the details of the principle of this method. Furthermore, novel nanochannel structure to realize sensitive detection was suggested.

2. Principle and Experiment

The principle of diffraction grating nano channels spectroscopy is illustrated in Figure 1. Many nano channels (width, depth and period $\sim 10^2\text{nm}$) were placed inside the quartz glass

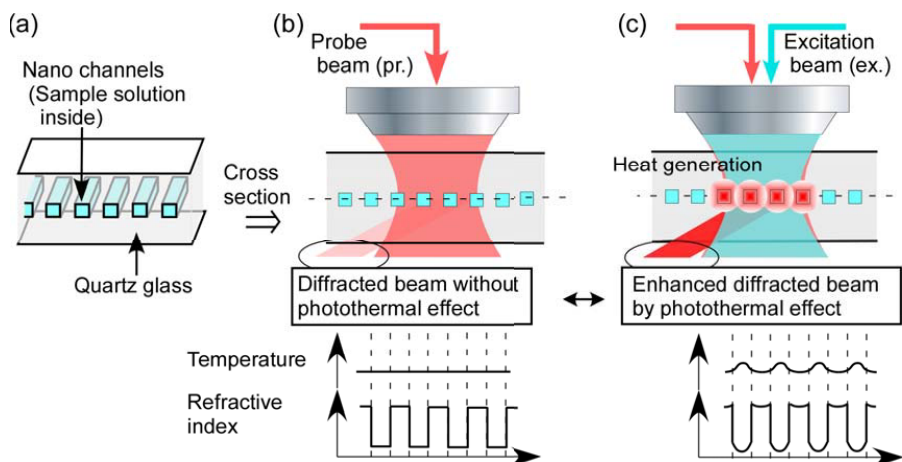


Figure 1. Principle of diffraction grating nano channels
 (a) Structure of diffraction grating nano channels (b) Cross-section drawing and distribution chart of temperature and refractive index when ex. OFF and (c) ON

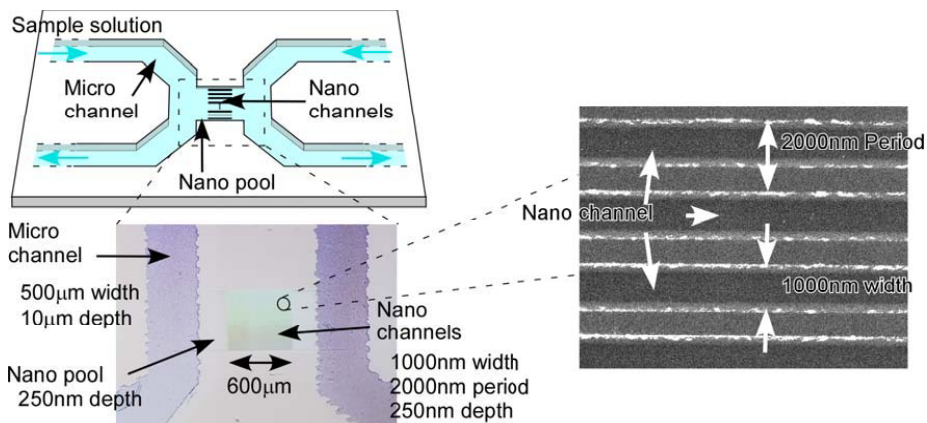


Figure 2. Design of chip, close-up of diffraction grating and SEM image of nano channels
 plate like a diffraction grating (Figure 1(a)). a continuous probe beam (pr. 633nm) introduced to diffraction grating nano channels (Figure 1(b)) made numerous diffracted beam by the refractive index differential between glass and solution. Next, an intensity-modulated excitation beam (ex. 488nm) was coaxially introduced to nano channels with the probe beam and yield heat generation at the nano channels (Figure 1(c)).

Heat generation yielded a change of refractive index differential between glass and solution, and changed the intensity of diffracted probe beam.

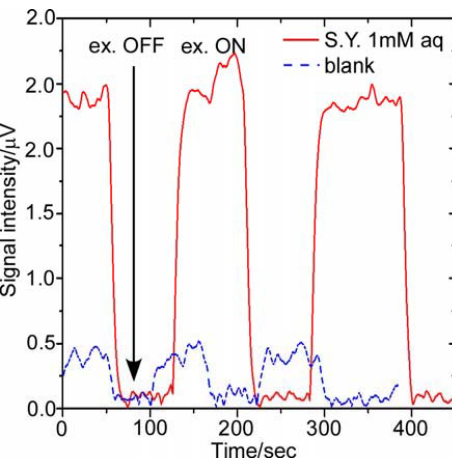
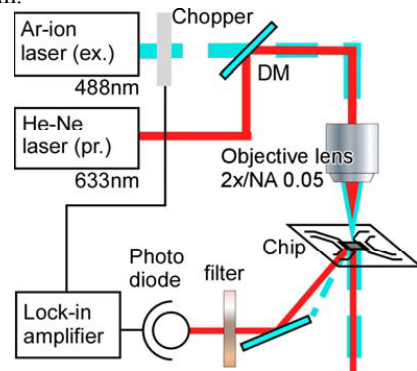
To verify this principle, a chip designed as Figure 2 was fabricated and used, and optical system was prepared as Figure 3. Photodiode and Lock-in amplifier were used to detect signal from diffracted probe beam and to decrease noise level. Intensity change of diffracted probe beam as an amplitude of the lock-in amplifier was recorded as signal intensity. Aqueous solutions of Sunset-yellow (S.Y.: dye) and pure water were used as samples and blank.

3. Results and Discussions

The raw signal data (sample: S.Y. 1mM aq and blank) is shown in Figure 4. The signal intensity differential of both sample and blank (pure water) was determined as “signal”. The signal was in proportion to the sample concentration. Thus the principle of this method could be validated, and ability to detect in nano space was suggested. In current research, the LOD of this method was 1.0×10^{-5} Abs. This value was worse than that of TLM (for $\sim 10^2 \mu\text{m}$ size channel, LOD: 5.0×10^{-7} Abs). It is preferable to get as high sensitivity as TLM for nano chemical process detection use. To get higher sensitivity, we are now investigating new method using “Alternative diffraction grating”. This method has an advantage in being able to kill background which has been a problem of thermal lens spectroscopy. Background free can be yielded because initial intensity of the detected beam is zero and the signal from solvent of the sample is canceled in principle. Thus we can get very high S/B ratio, and amplification of signal will become able, and higher sensitivity will be established. Detail will be described in the presentation.

References

1. T. Kitamori et al, “Thermal lens microscopy and microchip chemistry,” Analytical chemistry 76, 52A-60A (2004)



PHOTOTHERMALLY ENHANCED PHASE-CONTRAST MICROSCOPE FOR SENSITIVE VISUALIZATION OF NON-FLUORESCENT SAMPLES

Ken Oikawa¹, Akihide Hibara^{1,2}, and Takehiko Kitamori^{1,2}

¹The University of Tokyo, Bunkyo, Tokyo, 113-8656, Japan

²Kanagawa Academy of Science and Technology, Kawasaki, Kanagawa, 213-0012, Japan

Abstract

This paper describes the development of a non-scanning photothermal imaging method by CCD-based optics. By utilizing visible excitation laser and lamp-based illumination with phase-contrast optics, image-acquiring time was 4 min for 100 $\mu\text{m} \times 100 \mu\text{m}$ areas. In the present stage, the system could detect 7.5×10^{-6} absorbance while normal microscope can visualize 10^{-3} absorbance.

keywords: photothermal, visualization , absorbance

1. Introduction

Imaging technique is important in micro-nano science. Fluorescence microscopy is a powerful tool for visualizing fluorescent substances. In order to widen applicability of imaging methods, highly sensitive measurement of absorbance distribution is also desired.

Photothermal spectroscopy (PTS) measures thermal energy released during non-radiative relaxation after photo-absorption. A thermal lens microscope (TLM) is one of PTS. We have demonstrated usefulness and effectiveness of TLM in various applications including ultrasensitive determination in microfluidic devices [1]. By scanning a sample on a microscope stage, TLM can visualize non-fluorescent substances sensitively. However we have achieved a direct observation of cytochrome c in a neuroblastoma-glioma hybrid cell [2], the system took 1 hour to 900-point scan. Therefore, a novel and rapid imaging technique is desirable, where high sensitivity of TLM should be inherited. In this study, we developed a phase-contrast microscope enhanced by photothermal effect and achieved high-speed photothermal imaging.

2. Theory

Figure 1(a) illustrates a block diagram of conventional TLM. Since an excitation and probe lasers are focused tightly, photothermal effect occurs in restricted volume. In order to visualize sample distribution, the microscope stage should be scanned. Figure 1(b) illustrates master conception of our novel photothermal imaging system. The excitation laser is loosely focused, where the spot size is 100 μm in diameter. A phase-contrast optics and CCD camera are installed for detection of photothermal effect, where phase shift by photothermal effect can be detected as light

intensity change.

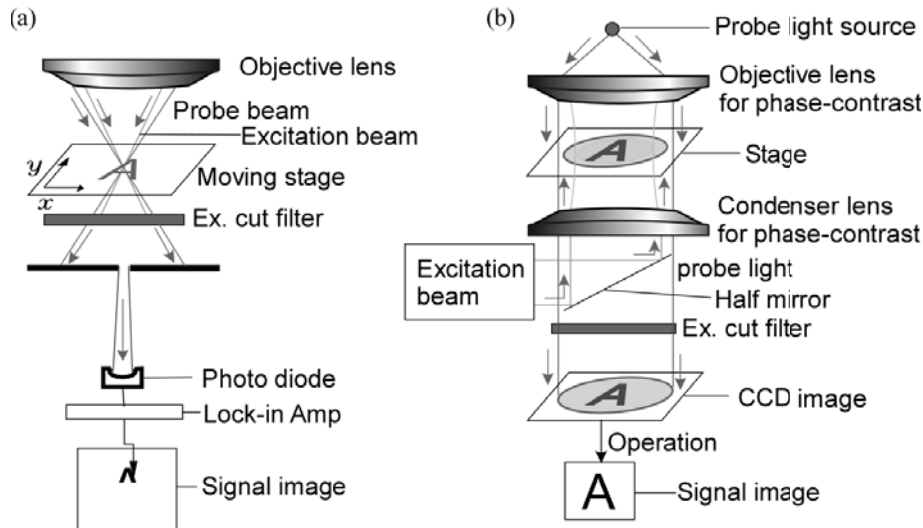


Figure 1. Master concept of (a) scanning-TLM and (b) photothermally enhanced phase-contrast microscope. This system used large laser spot, large detector, and fixed stage.

3. Result and Discussion

For fundamental investigation, a fused-silica microchip was prepared, where two parallel microchannels having a width of $4\text{ }\mu\text{m}$ and a depth of 250 nm were fabricated as shown in Figure 2(a). In order to eliminate shadow due to refractive index boundary, trans-decahydronaphthalene (decalin) was used as solvent. When dye solution was introduced to the microchannels, no channel structure was visible because absorbance of the solution was very low and refractive index was matched with the substrate.

Figures 2(b) and 2(c) show phase contrast images of the microchannels filled with dye solution without and with the excitation, respectively. Acquiring time for each image was 2 min. While no image was detected in Figure 2(b), clear channel structure was detected in Figure 2(c). Figure 2(d) shows an difference image between Figures 2(b) and 2(c), which corresponds to net photothermal signal due to light absorption by the solution in the microchannels. Figure 2(e) shows the signal intensity profile in the direction across the two microchannels. Judging from signal-to-noise ratio in the graph (20.7) and absorbance, a limit of detection ($S/N=2$) was determined as 7.5×10^{-6} absorbance. The width of signal distinguished from baseline was estimated to be 9.8

μm while the width of microchannel was $4 \mu\text{m}$. The broadening signal peak width was due to the effect of thermal diffusion, which is expected to eliminate by mathematical treatment. Total image-acquiring time was 4 min and achieving shorter image-acquiring time than conventional scanning-TLM method. The LOD for absorbance of dye solution by this method was roughly 1000 times superior to a normal microscope. Sensitivity should be increased for imaging of lower absorbance such as dye in organella.

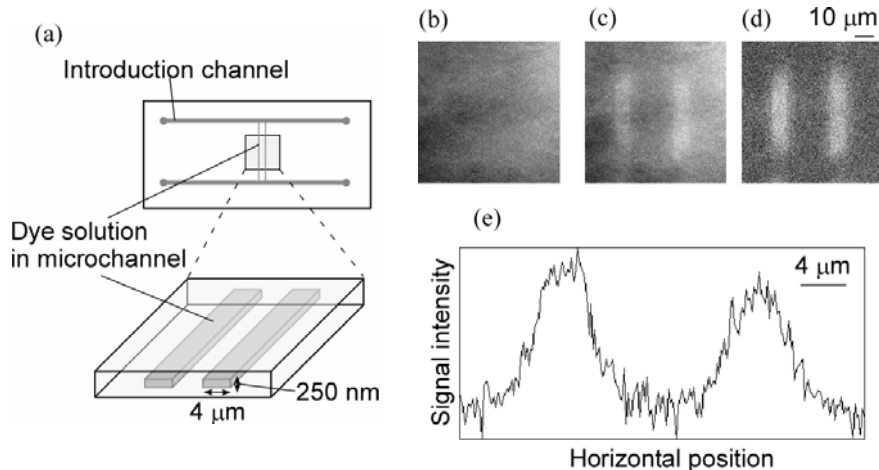


Figure 2. (a) Imaging area. Substrate was made from fused silica. (b) An image before excitation. Dye solution was too weak to see without excitation laser. (c) An image after excitation. Dye solution became visible as excited. (d) Brightness difference between (b) and (c). The refractive index change was clearly distinguished. (e) Horizontal cross section plot of (d). S/N ratio is 20.7 and detection limit was determined as 7.5×10^{-6} absorbance. The peak is broadening from 4 mm to 9.8 mm.

4. Conclusion

We have developed the photothermally-enhanced phase-contrast microscope. Acquisition time of this method was shorter than that of conventional photothermal one. When we achieve higher speed and more sensitive imaging, some applications are expect such as cytometry in nano-channel.

References

1. Tokeshi M, Uchida M, Hibara A, Sawada T, Kitamori T Vol. 74 (2001), *Analytical Chemistry*, pp. 2112-2116
2. Tamaki E, Sato K, Tokeshi M, Sato K, Aihara M, Kitamori T Vol. 74 (2002), *Analytical Chemistry*, pp 1560-1564

MICROFLUIDIC SPOTTING CHIP FOR LABEL-FREE PROTEIN MICROARRAYS

Eric Flaim, Mark T. McDermott and D. Jed Harrison

Department of Chemistry, University of Alberta, Edmonton, Alberta, Canada
National Institute of Nanotechnology, Edmonton, Canada

Abstract

A polydimethylsiloxane (PDMS) microfluidic spotting device has been developed for microarray fabrication on gold patterned surface plasmon resonance (SPR) biosensor slides. Photoresist pillar arrays for polydimethylsiloxane (PDMS) shadow masks were formed to create micro-sized Au spots by thermal evaporation. Au patterned SPR slides provide increased contrast for SPR imaging and reduced non specific adsorption. Devices, composed with 24 or 96 gold spots were fabricated and tested. Such devices allowed for organic and aqueous solution delivery and immobilization, and single spot addressability. Coupling to a 96 spot microtiter plate makes the 96 spot chip compatible with existing technologies and techniques, allowing for complete user customizability of microarray fabrication.

Keywords: SPR imaging, protein microarray, PDMS, microfluidics

1. Introduction

Protein microarrays have the potential to become even more useful in clinical diagnostics than DNA arrays, however, a number of barriers remain along the road to successful development. Detection by fluorescence is much less convenient than for DNA, due to the challenges of protein labeling. This has made Surface Plasmon Resonance (SPR) a very attractive alternative for the detection of the binding of biological molecules onto functionalized Au coated glass slides.¹ Improving the contrast and precision of SPR-read protein microarrays, and developing convenient fabrication methods for protein microarrays are two of the challenges of this methodology addressed in this work.² In particular, protein arrays require measurements of tens to hundreds of different binding sites (spots), rather than the thousands needed for DNA studies. This is, in part, simply because of the lack of availability of large protein sets. Further, the proteins studied by research teams will vary so greatly that a commercial chip-set is much less likely to be available than it is for DNA. We are developing a microfluidic system that will allow the individual laboratory to transfer up to 96 spots from microtitre plates to protein microarray chips for SPR readout. This “personal use” concept will create a highly flexible laboratory tool.

2. Design

Fabrication of 24 and 96 microfluidic spotting device for SPR sensors. SPR occurs only at the surfaces of coinage metals when certain conditions of wavelength and angle

are met. To localize the SPR response and minimize the background signal generated across the whole surface of an SPR sensor chip, patterning of $500 \times 300 \mu\text{m}^2$ Au spots was utilized. PDMS was cured against an array of photoresist posts of appropriate dimensions on a Si substrate, while pressure was applied from above, to create patterned through holes in a PDMS membrane. This membrane was used as a shadow mask during metal deposition. Flow channels ($100 \mu\text{m}$ wide, $40 \mu\text{m}$ deep) were formed using standard photolithographic and PDMS curing procedures. Figure 1a shows an aligned 24 Au spot SPR slide to a PDMS microchannel device. For increased spot density a 96 spot/48 sample device was fabricated (Figure 1b). A dense fluidic network delivers solution to a 1 cm^2 area on the SPR sensor, using a flow resistance balanced network to couple to the wells of a microtitre plate. This device consists of 2 PDMS layers, one containing the channel features, and a second thin layer allowing for sample flow to the Au spots on the glass SPR slide.

3. Results and Discussion

Organic Solution Immobilization. The 24 spot device was used to simultaneously immobilize 4 different alkyl thiols dissolved in 100% ethanol. Undodecal alkyl thiols with $-\text{NH}_2$, $-\text{COOH}$, $-\text{OH}$ and $-\text{CH}_3$ functional groups were passed through the PDMS microfluidic channels and allowed to immobilize for 2 hours at a

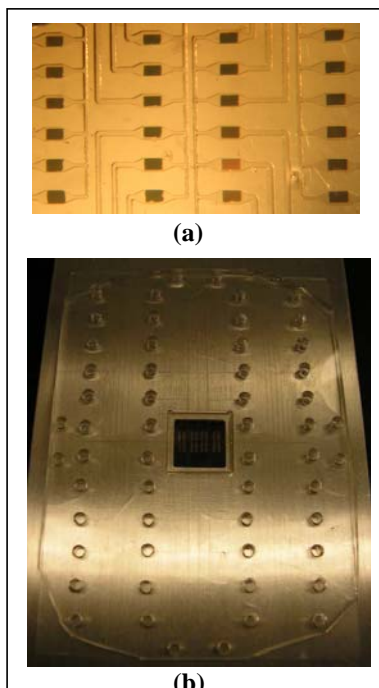


Figure 1. (a) Aligned PDMS device to Au patterned SPR slide (b) 96 Au spot device.

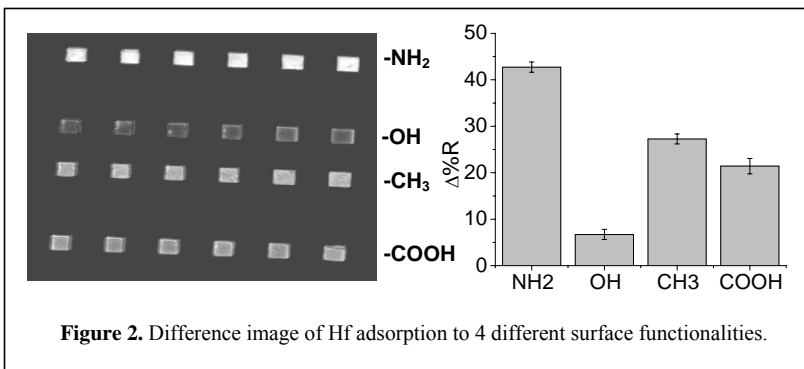


Figure 2. Difference image of Hf adsorption to 4 different surface functionalities.

concentration of 2 mM. Due to the small exposed surface area to volume ratio of the ethanol solutions within the microchannels there was limited solution evaporation on the time scale of immobilization. A solution of 430 nM human fibrinogen (Hf) was then flushed through the SPR and the subsequent signal was observed for each type of functionalized surface. Figure 2 shows the difference image collected upon non-specific physical adsorption of Hf to the various surface chemistries along with their respective % reflectivity.

Specific Addressing. The 24 and 96 spotting devices were used for direct immobilization of different proteins to various spots. Antibodies to the proteins were then passed over the sensor surface within the SPR, to monitor specific binding of the antibody/antigen pair through an increase in reflectivity (Figure 3).

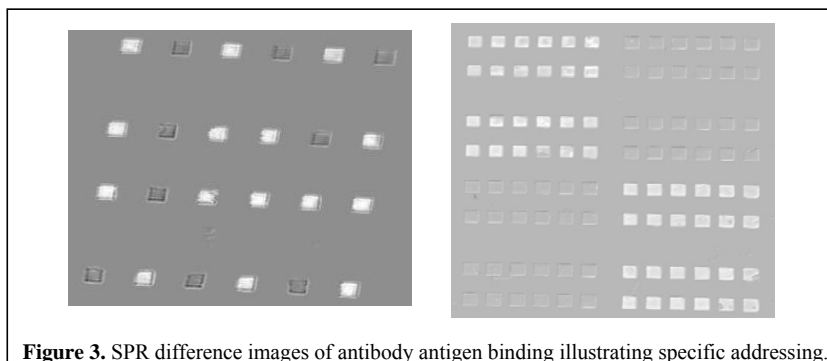


Figure 3. SPR difference images of antibody antigen binding illustrating specific addressing.

4. Conclusions

Two low density microfluidic spotting devices for label free protein microarrays have been developed for use with SPR. These devices resulted in high contrast images with zero background, and well defined, reproducible sensing regions. The design allow immobilization from aqueous or organic solutions from a PDMS device, without evaporation or leakage. Since the PDMS microchannels are either in conformal contact with a glass slide, as in the case of the 24 spot device, or irreversibly bonded to a thin PDMS sheet, such as in the 96 spot device, strong seals are formed and maintained. We have demonstrated delivery of multiple organic samples, investigated simultaneously within one experiment. Specific addressing of spots is achievable with these devices, allowing for complete customizability of surface immobilization. The system described should be able to meet the goals of providing a flexible, personal use, 100-spot density, protein chip system, that can be mated with current laboratory practice.

5. References

- (1) Vetter, D. *Journal of Cellular Biochemistry* 2002, 79-84.
- (2) Kanda, V.; Kariuki, J. K.; Harrison, D. J.; McDermott, M. T. *Analytical Chemistry* 2004, 76, 7257-7262.

NANOCAVITY NETWORK-BASED IMPEDANCE SENSOR FOR MOLECULAR DIAGNOSTICS

J. Tanner Nevill, Dino Di Carlo, and Luke P. Lee

Biomolecular Nanotechnology Center, Berkeley Sensor and Actuator Center
Department of Bioengineering, University of California, Berkeley, CA 94720 USA

Abstract

We demonstrate label-free detection of a molecular binding event using a nanocavity network-based impedance technique. A micro-affinity column of biotinylated beads is packed inside of a glass microchip, and the binding of avidin occludes the nanocavities between beads and is measured as a change of impedance through the packed column. We developed a model that indicates a ~8% increase in resistance upon saturated binding of avidin to the 1 μm diameter beads in the column. Preliminary data in 0.84 μm beads indicates a 20% increase in resistance upon saturation with avidin.

Keywords: Impedance sensor, microparticles, bead-based analysis, label-free

1. Introduction

Bead-based analysis methods are emerging as efficient techniques for molecular diagnostics due to the high surface to volume ratio, versatility in surface-chemistry, and ability to manipulate the beads with microfluidics [1, 2]. We present a unique label-free method to detect biomolecular binding based on impedance changes through a nanocavity network formed by packing microparticles or nanoparticles in microfluidic channels. This method requires no fluorescent labeling of analyte and allows a simple readout of binding through impedance at a given frequency.

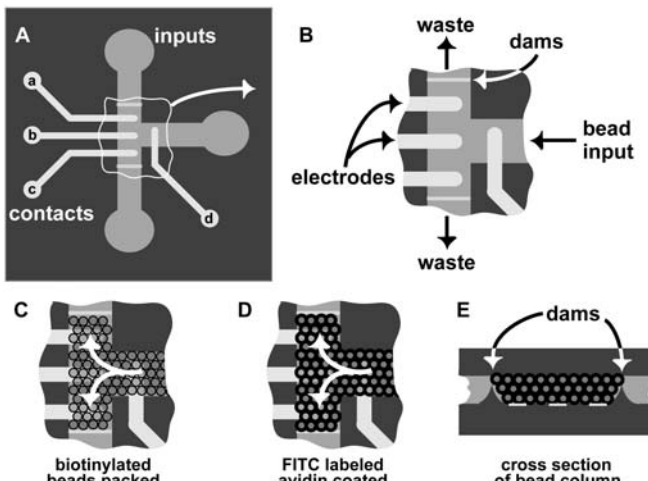


Figure 1. (A) Layout of the device, (B) active region consists of dams to trap beads with integrated electrodes, (C) beads are packed and resistance is measured, (D) sample is introduced and change in resistance is measured, (E) cross section of column, which shows dam structure.

The demonstrated microfluidic integration of the nanocavity system is also advantageous, allowing easy introduction of analyte solution and measurement buffer.

Previously, it has been shown that beads coated with a protein will lead to an increased resistance of a nanopore they are passing through, when compared to the uncoated bead [2]. In that situation a time dependent dynamic measurement of resistance is required, and beads must be pre-treated before analysis. However, in our system, the measurement is made in a stationary nanocavity system which is directly treated with analyte (Fig. 1). Binding of analyte then decreases the cross-sectional area of the void space and increases the measured resistance across the nanocavity system.

2. Theory

Resistance changes through nanocavity systems were modeled using a geometric model a closely-packed array of microparticles (Fig. 2). This model will give the upper limit on expected changes since a less than crystalline pack is expected. Using the unit cell described in Figure 2A we calculated the z-dependent cross sectional areas and perimeters (Fig. 2B) and total unit cell resistance. Knowing the perimeter, and assuming saturated binding, we calculated the obstructed area of the nanocavity with binding of various size molecules. For various size microparticles and biomolecules, the resistance increase upon binding is

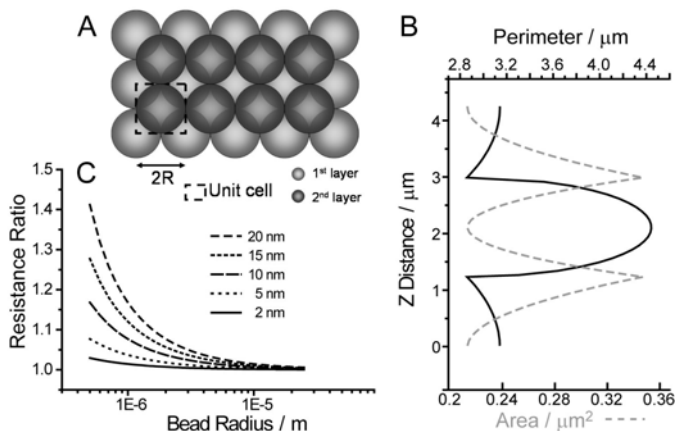


Figure 2. (A) Packed microparticles lead to z dependent areas and perimeters that repeat with the unit cell, defined here. Perimeters allow calculation of obstructed area with binding of biomolecules. (B) The z dependence of area and perimeter through a nanocavity system created by 3 μm radius microparticles. (C) Resistance ratio upon binding as a function of the bead pack radius is plotted for various sized biomolecules.

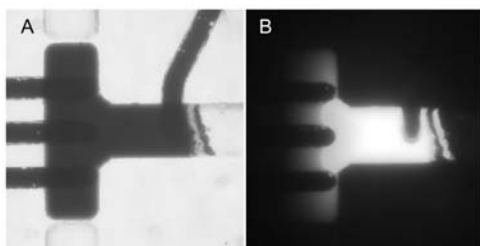


Figure 3. (A) Optical micrograph of the active region after biotinylated beads have been packed. (B) Fluorescent micrograph of beads after binding with FITC conjugated avidin.

plotted in Fig. 2C. This analysis suggests 1 μm diameter or smaller bead sizes for $\sim 10\%$ change in resistance for an average protein molecule of 50 \AA in diameter.

3. Experimental

Dams were created in a glass substrate using a single-step wet etching process. Electrodes were patterned onto another glass substrate via electron beam evaporation, and the two pieces were aligned and thermally bonded after input and contact regions were drilled. Polystyrene beads (0.84 μm in diameter) functionalized with biotin were packed into a micro-affinity column, creating a nanocavity network. The beads were then coated with an avidin solution. The avidin was fluorescently labeled in order to confirm binding (Fig 3). Impedimetric measurements were made with a Novocontrol impedance analyzer.

4. Results and Discussion

Figure 4 shows the impedance magnitude and phase angle between electrodes ‘a’ and ‘d’ before beads are loaded, after beads are loaded, and after the beads are coated with avidin. Buffer was flushed through the device before each measurement was made. The resistance values are plotted in Figure 5 for electrodes ‘a-c’ with ‘d’ as a common reference electrode (Fig 2A).

Acknowledgments

NDSEG Fellowship for JTN, Whitaker Fellowship for DD, and GlaxoSmithKline.

References

1. E. Verpoorte, “Beads and chips: new recipes for analysis”, *Lab Chip.* **3**, 60N-68N (2003).
2. O. A. Saleh and L. L. Sohn, “Direct detection of antibody-antigen binding using an on chip artificial pore”, *Proc. Natl. Acad. Sci.* **100**, 820-824 (2003).

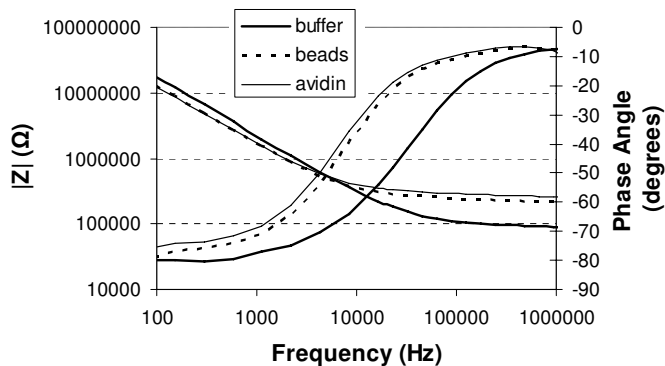


Figure 4. Raw impedimetric data from electrode ‘a’.

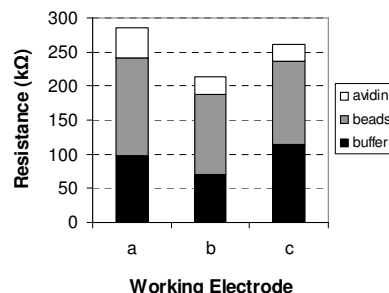


Figure 5. Resistance values for each electrode extracted from best fit to RC equivalent circuit.

SPREADING SMALL SIGNALS OVER LARGE AREAS: ELECTROCHEMICAL AMPLIFICATION IN AN SPR IMAGING SENSOR ARRAY

Melissa S. Hasenbank, Elain Fu, and Paul Yager
University of Washington, Seattle, WA, USA

Abstract

This paper demonstrates a recently reported lateral signal amplification phenomenon [1] in an array format. The amplification reaction involves the enzyme horseradish peroxidase (HRP) and the colorimetric substrate 3,3',5,5'-tetramethylbenzidine (TMB). Briefly, the enzyme signal is amplified by the formation of a precipitating enzyme product, which is detected by surface plasmon resonance (SPR) imaging. With HRP immobilized directly to the SPR sensor surface, the precipitate is also shown to form at remote locations. This lateral spread of an amplification signal is demonstrated in a microfluidic array format, where multiple electrically isolated gold regions patterned with small amounts of enzyme are shown to undergo rapid and significant amplification on each gold-coated region. This approach may be extended to enable the rapid and sensitive detection of multiple analytes in parallel.

Keywords: Electrochemistry, signal amplification, SPR imaging

1. Introduction

In an effort to improve the detection sensitivity of biosensors, a number of biocatalytic signal enhancement schemes have been developed. For example, enzymes and precipitating substrates have been used extensively to increase the detection signal of low analyte concentrations [2, 3]. The HRP/TMB enzymatic precipitation reaction is well documented in the literature [4]. In brief, the reaction cycle begins as hydrogen peroxide oxidizes HRP. The oxidized enzyme then converts TMB from its normal reduced state to a colored oxidized form, which may be induced to form a blue precipitate [5]. In the same reaction, HRP is reduced to its resting state, renewing the reaction cycle. The accumulation of the precipitate near the sensor surface increases the local refractive index, which may be quantified with SPR.

As shown in Figure 1a, traditional enzyme amplification schemes involve the localized conversion of substrate to product directly at the enzyme site. In contrast, in the lateral signal amplification scheme utilized in this work, which is depicted in Figure 1b, significant amounts of the signal-amplifying product form at sites remote from the immobilized enzyme [1]. This report demonstrates this lateral amplification of an enzyme signal in a microfluidic array format.

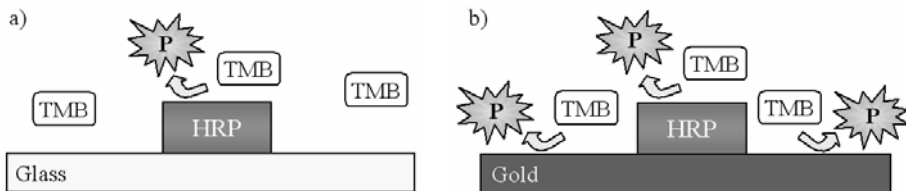


Figure 1. (a) Schematic of the traditional HRP/TMB amplification reaction on an insulator. HRP immobilized on a non-conductive substrate converts TMB to product (P) at the enzyme. (b) Schematic of the lateral HRP/TMB amplification reaction on a conductor, where the product also forms at sites remote from the original sites of enzyme activity, increasing the lateral extent of the signal.

2. Experimental

Electrochemical amplification arrays were demonstrated using a custom-built SPR microscope [6]; glass slides selectively patterned with gold and HRP; and a TMB substrate solution, containing hydrogen peroxide and precipitating agents. Arrays consisting of fifteen isolated $1\text{ mm} \times 1\text{ mm}$ gold-coated regions were fabricated by applying a custom shadow mask during the electron beam evaporation of 1 nm chromium followed by 45 nm gold. HRP was patterned onto a small area in the center of each gold region using a piezoelectric microdispensing system. The TMB solution was then introduced, initiating TMB oxidation and precipitate formation, which were monitored by SPR microscopy. At the imaging conditions used in this work, increases in refractive index, e.g., due to precipitate formation, correspond to increases in intensity. To quantify the extent of signal amplification, the change in percent reflectivity (%R) for representative regions was calculated using custom LabVIEW programs.

3. Results and Discussion

The SPR images in Figure 2 depict a patterned array before and after precipitate formation. In Figure 2b, the dark rectangular regions and the surrounding brighter regions within the fifteen rectangular regions represent the patterned HRP and the precipitate, respectively. The remaining regions are the glass substrate. Within each enzyme-containing gold region, extensive

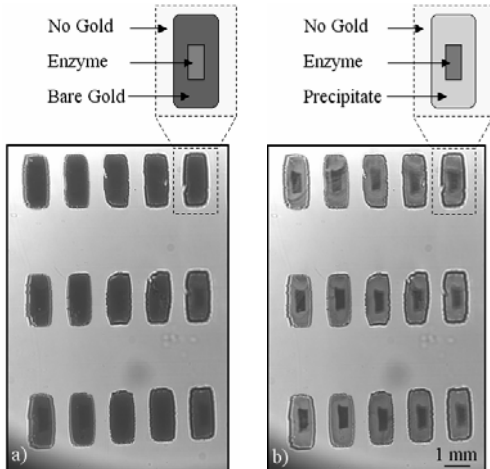


Figure 2. SPR images before (a) and after (b) precipitate formation in individual array regions. Each sample consisted of 15 isolated gold regions surrounded by glass. Enzyme was patterned in the center of each gold region, and precipitate formation was observed after the addition of the TMB solution. The SPR instrument foreshortens the image in one dimension.

precipitate formation was observed in electrically connected regions remote from the HRP molecules. Small regions of HRP may be amplified as much larger regions of precipitate, where the extent of lateral spread is determined in part by the lateral extent of the gold. Measurement of the SPR signal within each gold-patterned region showed that the precipitate formation was rapid and significant, with a greater than 30% increase in %R occurring within one minute.

4. Conclusions

We have demonstrated the potential of a novel electrochemical amplification system in an array format, which holds promise for improving the sensitivity of SPR imaging assays. This format may be used for the rapid, amplified detection of multiple analytes in parallel. Preliminary results indicate that this lateral signal amplification is at least semi-quantitative. Additional experiments to further investigate the quantitative potential and to demonstrate this lateral amplification phenomenon in an assay are planned.

Acknowledgements

Financial support was provided by the NIDCR (Grant Nos. T32 DE07023 and U01 DE014971).

References

1. Hasenbank, M.S., E. Fu, and P. Yager, *Lateral spread of an amplification signal using an enzymatic system on a conductive surface*, Langmuir, in press.
2. Alfonta, L., I. Willner, D.J. Throckmorton, and A.K. Singh, *Electrochemical and quartz crystal microbalance detection of the cholera toxin employing horseradish peroxidase and GM1-functionalized liposomes*, Analytical Chemistry. **73**(21): p. 5287-5295, (2001).
3. Kim, M.-G., Y.-B. Shin, J.-M. Jung, H.-S. Ro, and B.H. Chung, *Enhanced sensitivity of surface plasmon resonance (SPR) immunoassays using a peroxidase-catalyzed precipitation reaction and its application to a protein microarray*, Journal of Immunological Methods. **297**: p. 125-132, (2005).
4. Josephy, P.D., T. Eling, and R.P. Mason, *The horseradish peroxidase-catalyzed oxidation of 3,5,3',5'-tetramethylbenzidine - Free-radical and charge-transfer complex intermediates*, Journal of Biological Chemistry. **257**(7): p. 3669-3675, (1982).
5. McKimm-Breschkin, J.L., *The use of tetramethylbenzidine for solid phase immunoassays*, Journal of Immunological Methods. **135**: p. 277-280, (1990).
6. Fu, E., T. Chinowsky, J. Foley, J. Weinstein, and P. Yager, *Characterization of a wavelength-tunable surface plasmon resonance microscope*, Review of Scientific Instruments. **75**(7): p. 2300-2304, (2004).

NANOPARTICLE ENHANCED SPR IMAGING FOR PROTEIN MICROARRAYS

Chris Grant, Francis Nsiah, Jed D. Harrison, and Mark T. McDermott

Department of Chemistry and National Institute for Nanotechnology,
University of Alberta

Abstract

This work presents a study focused on improving the sensitivity of surface plasmon resonance (SPR) imaging for protein microarrays. The research examines the effects of nanoparticle size and binding valency on observed SPR signal.

KEYWORDS: SPR imaging, protein microarrays, gold nanoparticles, multivalent interactions

1. Introduction

Surface plasmon resonance is a well known label-free optical technique used to monitor binding interactions. Employing SPR in an imaging format permits the monitoring of multiple interactions in parallel; therefore it can be used as a read-out tool for microarray experiments. Since the late-1990's researchers have employed nanoparticles in SPR systems. The focus has been in two areas: improving the sensing platform [1] and biomolecule modification through nanoparticle mass tags [2]. Mass tags, such as latex and gold nanoparticles, have been used to increase a biomolecules mass and therefore the SPR signal observed upon binding. The work presented utilizes modified nanoparticles as mass tags and as a pathway to exploit multivalent interactions on protein chips.

2. Theory

SPR is a surface sensitive technique that detects binding based on local changes in refractive index at and/or near the microarray surface. Incorporation of gold nanoparticles into the binding moiety increases the refractive index change upon binding to the microarray surface and therefore the signal observed. Furthermore, each nanoparticle is coated with numerous antibody molecules opening pathways for multivalent interactions between the modified nanoparticle and proteins immobilized on the surface of the microarray. The collective effect is an enhancement of the observed binding constant.

3. Experimental

In this research microarray substrates were fabricated to permit facile biomolecule patterning through the use of a handheld pipette. First, a thin film of chromium then gold is thermally evaporated through a deposition mask onto a freshly cleaned glass surface. Second, the remaining exposed glass surface is modified with a fluorinated

silane polymer to render the glass hydrophobic, allowing aqueous solutions to be confined to the gold spots.

Once modified, the microarray chips were prepared for protein immobilization by formation of an amine terminated self-assembled monolayer (SAM). SAMs were formed overnight in an ethanolic solution of $\text{HS}(\text{CH}_2)_{11}\text{NH}_2$. Following monolayer formation, solutions of rabbit IgG, bovine IgG, and bovine serum albumin (BSA) were spotted on the surface and allowed to adsorb for 1 hour. The surface of the array was rinsed and the binding of anti-rabbit IgG (a-rIgG) and nanoparticles modified with anti-rabbit IgG was monitored using SPR imaging. Two different sizes of nanoparticles were used, 5 nm and 30 nm particles.

4. Results and discussion

Shown in figure 2 are the SPR difference images showing antibody (a) and modified nanoparticle (b) binding to rabbit antigen on the microarray surface. In both cases, antibody and nanoparticle modified with antibody, it can be noted that binding occurs specifically to the rabbit IgG. There is minimal non-specific adsorption to BSA and no cross-reactivity with bovine IgG. Therefore, binding of the modified nanoparticle is specific and governed by antibody-antigen interactions.

The next step involved evaluating the enhancement obtained by the presence of gold nanoparticles. For this, binding curves were created by incubating the microarray surface with increasing concentrations of antibody modified 5 nm or modified 30 nm particles. The results of these binding studies are shown in figure 3. Curve fitting software was used to fit the data and obtain a quantitative measure of the nanoparticle enhancement observed (table 1). The presence of a modified 5 nm particle decreased the dissociation constant over 10% while the modified 30 nm particle had a much greater effect, decreasing the dissociation constant by over 80%. The observed enhancement can be explained in terms of the greater refractive index change that occurs when an antibody modified

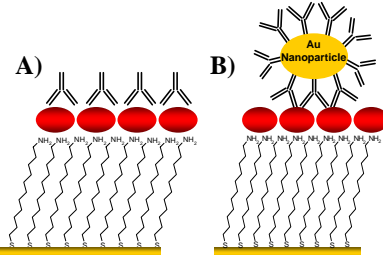


Figure 1. Cartoon representation demonstrating capture of antibody (a) and antibody modified nanoparticle by immobilized antigen. Drawings not to scale.

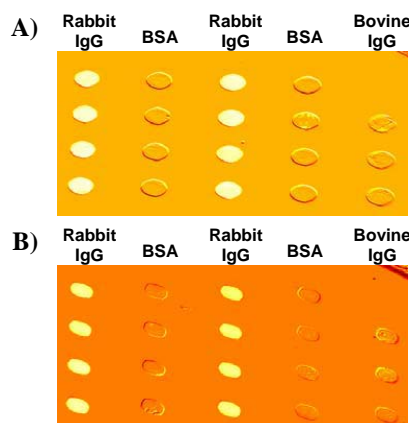


Figure 2. SPR difference image following incubation in 1300 nM a-rIgG (a) and 55 nM a-rIgG modified 30 nm particle (b).

nanoparticle binds to the microarray surface relative to an unmodified antibody molecule (see fig. 1). Also, the presence of numerous antibody molecules per gold nanoparticle permits multivalent binding to the microarray surface, increasing the observed binding strength.

5. Conclusions

Nanoparticle mass tags provide an effective means to increase observed binding constants with SPR imaging. In this work, incorporation of a 30 nm particle modified with anti-rabbit IgG decreased the dissociation constant 7 fold over the control experiment. Further research in this area will provide greater insight into the mechanism of this enhancement and permit the monitoring of low affinity interactions using this technique.

Acknowledgements

The authors would like to thank Dr. John-Bruce Green (University of Alberta), the National Research Council (NRC), and the Department of Chemistry and National Institute for Nanotechnology at the University of Alberta.

References

- [1] L. Andrew Lyon, M.D.M., Patrick C. Smith, Brian D. Reiss, David J. Pena, and Michael J. Natan, Vol. 54, Sensors and Actuators, pp. 118-124, (1999).
- [2] Ursula Pieper-Furst, W.F.M.S., Axel Warsinke, Vol. 550, Analytica Chimica Acta, pp. 69-76, (2005).

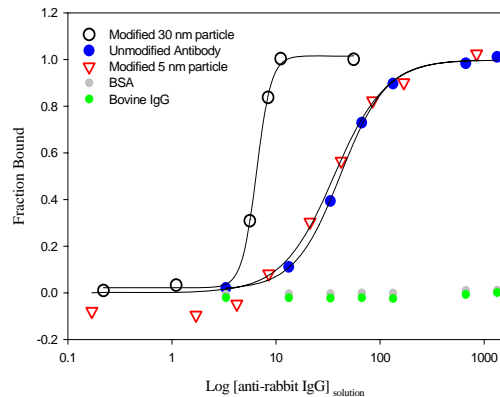


Figure 3. Binding curve for capture of anti-rabbit IgG and nanoparticles modified with anti-rabbit IgG.

Table 1. Curve Fitting Parameters

	K _{D,Het} (nM)	R ²	Slope Factor
Antibody (Ab)	41.7 ± 1.0	0.999	2.0 ± 0.1
5 nm + Ab	36.1 ± 1.2	0.996	1.7 ± 0.4
30 nm + Ab	6.5 ± 1.0	0.999	6.2 ± 0.6

SINGLE CELL DIFFERENTIAL IMPEDANCE SPECTROSCOPY ANALYSIS USING HIGH DENSITY HYDRODYNAMIC CELL TRAPPING ARRAYS

Daniele Malleo*, Dino Di Carlo†, J. Tanner Nevill†, David Holmes*,
Luke P. Lee†, Hywel Morgan*

*School of Electronics and Computer Science, University of Southampton, UK

†Department of Bioengineering, University of California at Berkeley

Abstract

We present a novel device for performing differential impedance spectroscopic analysis of single cells hydrodynamically captured in an array of trapping sites. The method combines the advantages offered by impedimetric analysis used for flow cytometry with the ability to capture multiple single cells and perform long-term transient and steady state analysis. We have tested the device by capturing single polystyrene beads and HeLa cells and measuring differential impedance responses.

Keywords: Single Cell Analysis, Differential Impedance Spectroscopy

1. Introduction

Impedance spectroscopy is by no means a novel method of analysis for tissues, cells and biomolecules[1]. Perhaps surprisingly, while other electrical methods of

manipulation and sorting based on the dielectric properties of biological samples (dielectrophoresis, electrorotation) have found widespread utilization since the introduction of microfabrication and photolithography techniques, and in fact have greatly benefited from the inclusion in the μTAS and lab-on-chip paradigms, impedance spectroscopic methods have rarely been employed for the analysis of single cells, except for the case of flow cytometers.

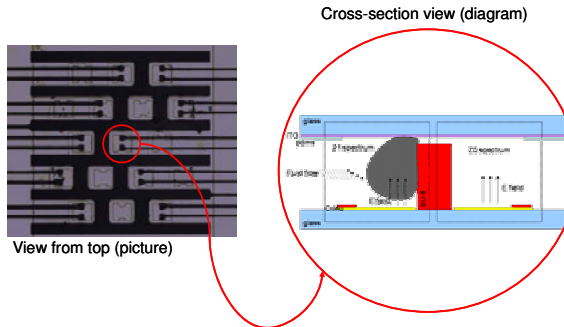


Figure 1 The differential nature of the measurements decreases sensitivity to local fluctuations in temperature and medium ionic strength and also normalizes the readings for differences in electrode shape, areas and coverage, as well as counterelectrode wetting conditions.

Impedance spectroscopy is a label-free, all electrical method of analysis which allows quantitative measurements of cell characteristics and changes in their membrane, cytoskeleton and nucleus elicited by the introduction of chemical compounds.

The impedance signal from a biological sample is resultant from the combination of electrical resistance and molecular and ionic polarization following excitation by an electric field. Different processes are responsible for the polarization of biological tissues and cells. In the frequency range between 10 kHz and 10 MHz, the effective permittivity (a measure of polarizability) of biological cells undergoes a dispersion, commonly attributed to the accumulation of charges at the interfaces between the membrane and the aqueous phases (i.e. the cytoskeleton and the bathing medium). Traditionally, impedance measurements have been performed on bulk quantities of cells [2]; these are not sensitive to the occurrence of rare events and do not allow the identification of outliers in the data; temporal averaging effects also affect measurements performed to an ensemble of cells making it impossible to record and identify fast kinetic events. To address these issues we have fabricated a device, which utilising metal electrodes aligned to SU-8 cell traps allows the analysis of single cells following their hydrodynamic capture. The trap design follows closely the one demonstrated by D.D. in [3]. Whereas impedance flow cytometers [4] only probe cells for a fraction of a second and at high frequencies, this device allows a full spectrum scan, and the analysis of a cell can take place continuously for as long as needed or desired.

2. Fabrication

The chip is fabricated employing standard microfabrication techniques: evaporation and patterning of metal electrodes via wet-etch process, spinning and photolithographic patterning of SU-8 negative photoresist. ITO coated slides (Sigma-Aldrich) were clamped to the SU-8 structures to form channels and function as a common ground electrode. Trapping sites were designed for differential measurements and optimally sized for capture of single cells.

3. Results and discussion

As a proof of concept we loaded the device with a solution of 1% polystyrene

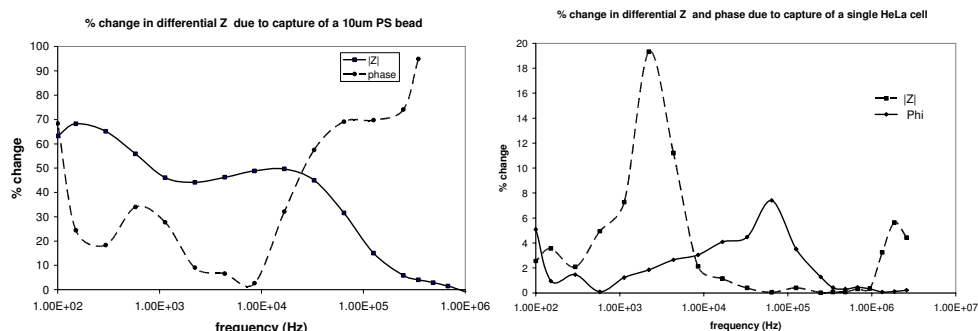


Figure 2 Differential Impedance Spectra for single bead (left) and single HeLa cell (right). HeLa cell provokes a stronger differential phase response.

beads, 10 μ m in diameter, and following their capture in the traps, measured the impedance response. The impedance following capture of a single bead shows a significant increase (>50%) over frequencies up to 10 kHz. We also loaded and detected presence of a single HeLa cell in a trap. As expected the response due to a single cell is weaker (changes averaging ~5% across the spectrum were detected, with a 20% peak at 5kHz) than the response elicited by a polystyrene bead of similar size, due to the dielectric differences between cells (which respond like shells containing a medium as conductive as the external electrolyte) and beads (which are solid spheres of dielectric material). In fact, the system is more sensitive to changes in the phase response at higher frequencies (10kHz < f < 1 Mhz) when looking at HeLa cells. Already Cheung et al. had shown in [3] that where changes in |Z| do not allow successful discrimination, it might be necessary to rely on phase response changes.

In the current design, the device employs a large ground electrode, which while simplifying the fabrication process and relaxing the alignment tolerances - negatively affects the sensitivity of the impedance readings. This occurs because the metal lines that connect the measuring electrodes to the peripheral pads for external connection also run parallel to the ground electrode, thus contributing to a parasitic capacitance which reduces the sensitivity of the device to changes in impedance. To address this issue and improve the sensitivity of the measurements, we plan to pattern the ground electrode, thus reducing its active area to the location of the trapped cells only.

4. Conclusions

We have presented a device for performing differential impedance measurements of single cells captured in an array of trapping sites. We have shown that we can successfully detect presence of single HeLa cells. We are currently improving the device to electrically monitor the transient behavior of cancer cells exposed to anti-tumoral agents by exploiting the changes induced in the dielectric properties of the membrane and cytoskeleton.

Acknowledgements

Daniele Malleo was supported by the UK Interdisciplinary Research Centre in Bio-Nanotechnology. The Whitaker Foundation provided support for Dino Di Carlo.
J Tanner Nevill would like to acknowledge NDSEG fellowship and GlaxoSmithKline

References

- [1] Foster KR, Schwan HP, Dielectric properties of tissues and biological materials - A critical review, *Critical Reviews in Biomedical Engineering* 17 (1): 25-104 1989
- [2] K. Asami and T. Yamaguchi , Dielectric spectroscopy of plant protoplasts, *Biophysical Journal*, Vol 63, Issue 6 1493-1499, 1992
- [3] Di Carlo D, Aghdam N, Lee LP, Single-cell enzyme concentrations, kinetics, and inhibition analysis using high-density hydrodynamic cell isolation arrays, *ANALYTICAL CHEMISTRY*, 78 (14): 4925-4930 JUL 15 2006
- [4] Cheung K, Gawad S, Renaud P, Impedance spectroscopy flow cytometry: On-chip label-free cell differentiation,*CYTOMETRY PART A* 65A (2): 124-132 JUN 2005

Surface Modification of Silicon Nanowires for the Development of Biosensor Chip

**Mira Kim^{1,2}, Kook-Nyung Lee¹, Suk-Won Jung¹, Woo-Kyeong Seong¹,
Dong-Sik Shin², and Yoon-Sik Lee²**

¹Nano Mechatronics Research Center, Korea Electronics Technology Institute,
Gyeonggi-do, 463-816 Korea

²School of Chemical and Biological Engineering, Seoul National University, Seoul
151-744 Korea

Abstract

We have studied on an electrical detection of biomolecule using silicon nanowire (SiNW) chips that were obtained by nanowire transfer method. The ability of SiNW for sensing surface charge change was checked in various buffer solutions after glutamic acid was coupled to the silicon surface. Protein bindings on the SiNW were verified through biotin-streptavidin experiment. For finding optimal sensing condition for protein binding and sensitive analysis, various spacers with different chain length were introduced to the surface of SiNW.

Keywords: silicon nanowire, biosensor, protein binding, surface modification

1. Introduction

Silicon nanowire (SiNW) has attracted much interest in view of their unique properties, which provide high sensitivity, permitting real time label-free electrical detection and easy fabrication into high density nanoscale devices. So SiNW has been studied extensively as a prospective diagnosis sensor because of their ability for rapid and direct analysis of chemical and biological samples. Here, we report preliminary results of surface modification of SiNW chips for pH sensing and the detection of biomolecule..

2. Experimental

2. 1. Fabrication of SiNW device

Well-aligned nanowires were obtained by micro-machining technology and were transferred onto an oxidized silicon substrate and the electrodes were fabricated for SiNW device (**Fig. 1.**).

- a. Thermal oxidation
- b. Photolithography
- c. Si anisotropic dry etching
 - ✓ Reactive ion etching
- d. Si anisotropic wet etching
- e. Si nanowire thinning
 - ✓ Thermal oxidation
- f. SiO₂ etching
- g. Nanowire transferring
- h. Removing nanowire fabricated substrate
- i. Photoresist (PR) removing
- j. Contact electrodes fabrication

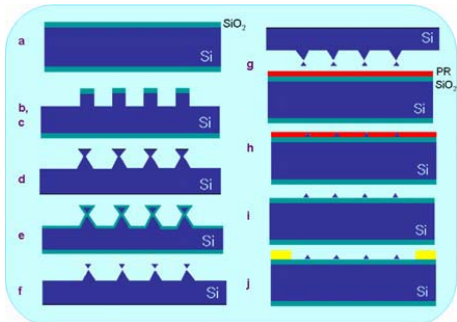


Fig. 1. Fabrication process of silicon nanowire (SiNW)

2. 2. Conductivity test of SiNW according to pH change

Aminopropylsilane group was introduced to SiNW and glutamic acid was coupled to the amine groups of the surface. The ability of SiNW for sensing surface charge change was checked under various buffer solutions. (Fig. 2.).

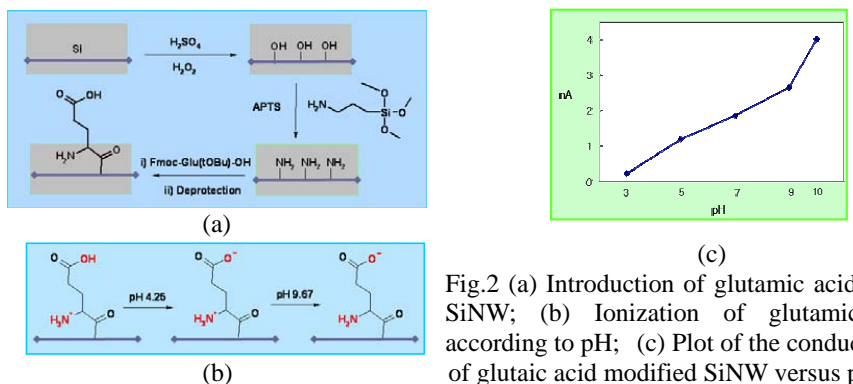


Fig.2 (a) Introduction of glutamic acid to the SiNW; (b) Ionization of glutamic acid according to pH; (c) Plot of the conductance of glutamic acid modified SiNW versus pH

2.3 Real time detection of streptavidin-biotin binding

Protein bindings on the SiNW were observed through the binding of streptavidin (17nM) on the biotin coupled SiNW. The binding event was easily checked by the increase of conductivity. To find the optimal binding condition, the distance between the biotin and the SiNW surface was controlled by introducing ϵ -aminocaproic acids(E) and β -alanines(B). We measured the initial conductivity signal (for 3 second) ratio of 170nM streptavidin to the saline buffer(S/B) according to the spacer length.

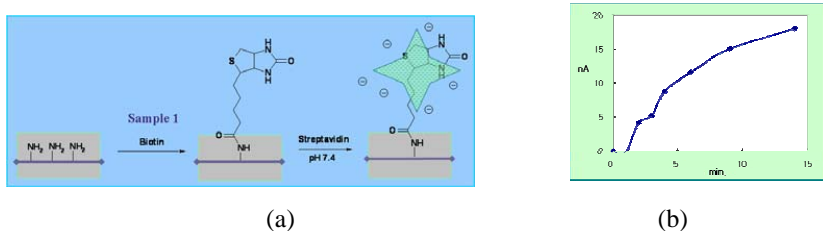


Fig. 3. (a) Introduction of biotin to the SiNW and detection of streptavidin; (b) Real-time detection of streptavidin on SiNW

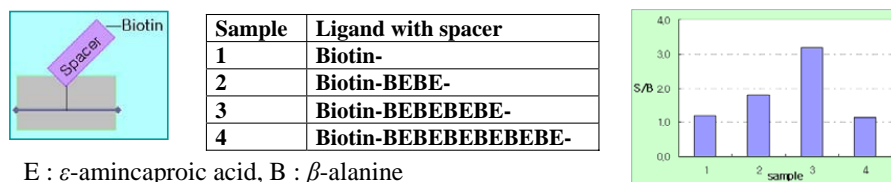


Fig. 4. Spacer effect on the initial conductivity measurement

3. Results and discussion

Conductivity of SiNW was changed according to the surface charge condition caused by protonation/deprotonation of the surface anchored functional groups of glutamic acid. At lower pH condition, the conductivity change of SiNW was less sensitive to the pH change. But the conductivity was sharply increased when the pH was passed the pKa of alpha-amino group. When streptavidin was bound to the biotin on the SiNW surface, the conductivity was increased and reached maxima after <30 min of incubation. Because streptavidin ($\text{pI}=5\sim6$) was negatively charged at the experimental buffer condition (pH7.4), the conductivity was increased as the amount of streptavidin was increased through binding. The longer spacer brings the better bindings of streptavidin, but caused the loss of sensitivity of SiNW, showing optimal spacer length for the detection of biomolecules. In conclusion, we have demonstrated a nano system which can detect a pH change of an aqueous solution and the *in-situ* binding event of biomolecules on SiNW.

References

W. Wang, C. Chen, K. Lin, Y. Fang, and C. M. Lieber, PNAS, Vol. 102, pp. 3208

IN-SITU FLOW VELOCIMETER IN MICROCHIP USING NEAR-FIELD HETERODYNE GRATING METHOD

Kenji Katayama¹, Yoshikuni Kikutani², and Takehiko Kitamori³

¹Chuo University, 1-13-27 Kasuga Bunkyo Tokyo 112-8551, Japan

²Kanagawa Academy of Science and Technology,
3-2-1 Sakado, Takatsu-ku, Kawasaki City, Kanagawa, 213-0012, Japan

³The University of Tokyo, 7-3-1 Hongo Bunkyo Tokyo 113-8551 Japan

E-mail: kkatayama@chem.chuo-u.ac.jp

Abstract

A simple optical technique was developed for flow rate measurements in a microchip using a simple optical setup. In principle, the motion and intensity of the photothemally excited grating-pattern was optically monitored. The dynamic range of flow rate measurement was 0.17 to 670 mm/s, which covers most chemical applications in a microchip.

keywords: *flow velocimeter, optical detection, heterodyne detection, in-situ*

1. Background

As the microchip sciences have progressed rapidly in recent years, much attention has been paid for methods for controlling a very small amount of liquid inside microchannels. Velocimeter for microchip has to satisfy the condition that it should not disturb fluid stream, and to realize in-situ measurement at specific points. However, fluid velocity is usually obtained indirectly by measuring the fluid quantity of liquid coming out of a microchip. There are a few possible methods for measurement of flow rate in a microchip. One of them is CMOS thermal sensor where change in thermal profile due to flow is detected using a CMOS sensor, but it is difficult to fabricate inside a microchip. Another one is particle image velocimer (PIV), but it is not in-situ measurement because particles are introduced inside a microchannel. Photothermal methods are suitable for in-situ measurements, and recently a new photothermal technique, near-field heterodyne grating (NF-HDG) method, has been developed and it features compact optical setup and high sensitivity. In this report, in-situ velocimeter for microchip has been developed by applying NF-HDG method to a microchip.

2. Principle

Detailed principle of NF-HDG method was published elsewhere[1], and a brief explanation is given here. When pump light is irradiated on a grating fabricated on a top surface of a microchip, liquid inside a microchannel is irradiated like a striped pattern. If light-absorbing molecules are inside a microchannel, light is absorbed and heat is generated like the same striped pattern shown in fig.1(a). Since the refractive index of liquid depends on temperature, the striped pattern works as a temporal grating (thermal grating). When probe light is incident on the same grating shown in fig.1(b), a part of the probe light is diffracted by the grating at the top surface (reference light), while the rest of light is also diffracted by the thermal grating (signal) after passing through the grating on the surface. The mixed light of

signal and reference was detected by putting a detector at the 1st order diffraction spot, and this type of measurement is called heterodyne detection, which improves sensitivity of the signal. This heterodyne signal intensity depends on the phase difference between the signal and reference. Since the phase of the signal changes depending on the liquid velocity, the velocity can be measured by the intensity of the heterodyne signal. (Compare fig.2(b) and (c).)

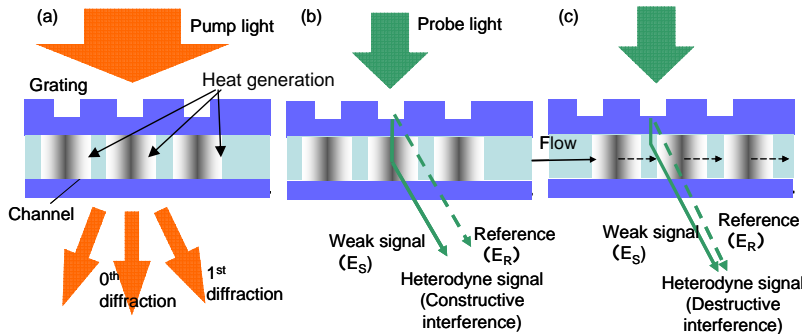


Fig.1 Principle of the velocimeter based on photothermally induced thermal grating; (a) heat deposition like a stripe pattern on liquid inside a microchannel, (b) and (c) heterodyne signal generation when the diffractions at a top grating and thermal grating are constructively and destructively interfered, respectively.

3. Experiments and discussions

A microchip was prepared to have a transmission grating on a top surface of a microchip. (grating spacing: 20-80 μm , grating depth: <1 μm). (fig.2) In the optical setup, pump and probe light has wavelength of 532 and 633 nm in wavelength, respectively, and they were set collinearly and incident on the grating at the top surface. One of the 1st order diffraction light was detected by a photodiode. The pump light is mechanically chopped at 330 Hz, and a heterodyne signal was extracted by a lock-in amplifier. Rhodamine 6G aqueous solution (0.1 mM) was used as a sample solution. The channel size of a microchip has 100 and 30 μm in width and depth, respectively.

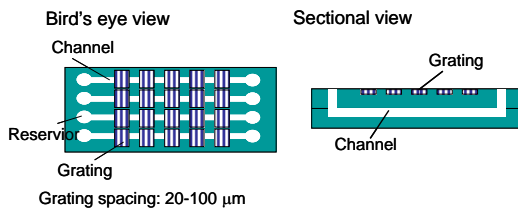


Fig.2 Bird's eye view and sectional view of a manufactured microchip with gratings above microchannels.

The dependence of liquid velocity is shown in Fig.3. In the vertical axis, values were obtained by subtracting the heterodyne signal intensity at the liquid velocity of v from that at 0 mm/s. (v : liquid velocity) The value decreased as the liquid velocity, and reversed and started to increase around 20 mm/s and was saturated for higher velocities. It is possible to measure fluid velocity in the range of 0.11-670 mm/s, though the calibration method should be established because of this curve calibration curve.

One thing that should be considered carefully is the relation between the signal intensity change, flow rate and chopper frequency. During one period of chopper frequency ($1/f$), the thermal grating moves the distance v/f (v : flow rate). When this distance is a multiple of the grating period, the same condition for a signal is satisfied as long as the proposed principle is valid. However, the signal intensity change gradually increased after 20 mm/s. This flow rate is roughly close to the rate where flow travels for the distance of the grating spacing for the period of the chopper frequency. This means the proposed principle of detection is only valid for low flow rates <20 mm/s, and it is assumed that a different principle holds for high flow rates.

It is assumed that the thermal grating was smeared from a grating-like thermal profile due to high rates and that the smeared pattern of the thermal profile diffracted the probe light beam. In this case, diffracted light would be emitted in a wide range of directions, and some component was projected in the 1st order diffraction and it was mixed with the reference field.

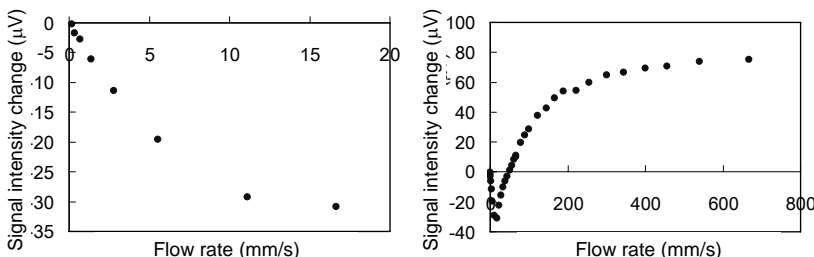


Fig.3 Dependence of heterodyne signal intensities on the liquid velocity for low and high flow rate regions. The heterodyne signal at 0 mm/s is subtracted from that at v mm/s.

4. Summary

Using a new photothermal method, NF-HDG method, wide range of flow velocity inside a microchannel was successfully measured. It is possible to measure 0.11-670 mm/s, which corresponds to 0.33-2000 $\mu\text{l}/\text{min}$. Since this velocity range covers most of microchemical applications, it is expected that this method is useful as an in-situ monitoring of flow rate inside a microchannel.

References

- [1] K. Katayama, et al. *Chem. Phys. Lett.* **377**(5-6), 589-594 (2003), *Appl. Phys. Lett.* **82**(17), 2775-2777 (2003).

MICROFLUIDIC IMPEDANCE ASSAY FOR MONITORING ENDOTHELIN INDUCED CARDIOMYOCYTE HYPERSTROPHY

Mo Yang¹ and Xin Zhang²

¹Department of Health Technology & Informatics, Hong Kong Polytechnic University, Hong Kong

²Department of Manufacturing Engineering, Boston University, USA

Abstract

In this paper, we report a new cardiomyocyte-based impedance sensing system with the assistance of dielectrophoresis cell concentration to monitor the dynamics process of Endothelin-1 induced cardiomyocyte hypertrophy.

Keywords: Cardiomyocyte hypertrophy, Impedance sensing, Endothelin-1

1. Introduction

Cardiac hypertrophy is an established and independent risk factor for the development of heart failure and sudden cardiac death that may be regulated by growth factor such as Endothelin-1 (ET-1). The majority of existing techniques to monitor hypertrophy in vitro is based on fluorescence probes designed to show morphological and biochemical alterations indicative of cardiomyocyte hypertrophy [1]. In this paper, a new cardiomyocyte-based impedance sensing system with the assistance of dielectrophoresis cell concentration is reported to monitor the dynamics process of Endothelin-1 induced cardiomyocyte hypertrophy.

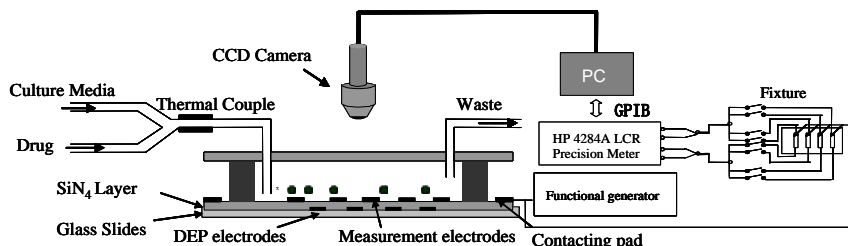


Figure 1: Simplified cross section of impedance based biosensor system with dielectrophoresis concentration.

2. Experimental setup

The cross section of the packaged device is shown in Figure 1. All fluids were injected into the chips using motor driven micropump. The flow rate in the main

channel of the bioprocessor was controlled by adjusting the pressure applied at the injector. The flow rate through the incubation chamber was controlled by applying a back-pressure at the chamber output using pressurized nitrogen. In this biochip, external valves at the input and output tubes were used to isolate the chip from the injection system during incubation. Figure 2(a) shows the biochip mounted onto a custom-made heated flow chamber with a built-in RTD temperature sensor. Electrical connections to the chips were established by using probes mounted on micromanipulators attached to the heated platform. Figure 2(b) shows the schematic chip layers. Figure 2(c) shows the top view of the biochip. DEP electrodes (Al) were used to concentrate cells from a dilute sample to form the cell monolayer with tight junctions and impedance electrodes (Cr-Au) were used to monitor the cardiomyocyte hypertrophy after the cell monolayer formation. Figure 2(d) shows the equivalent circuit model for impedance analysis.

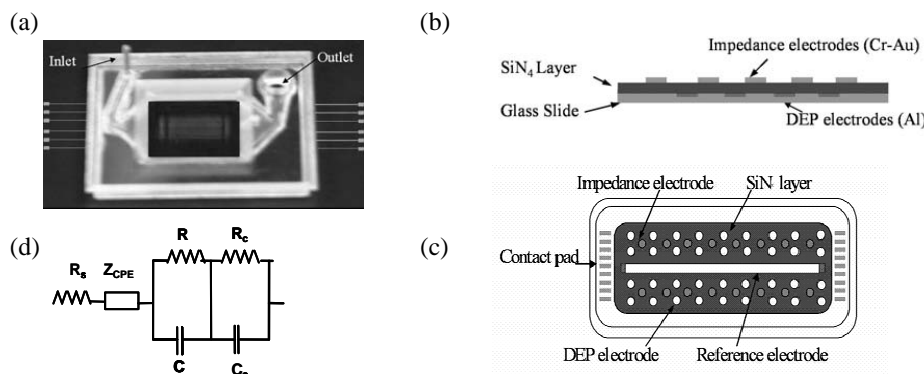


Figure 2: (a) Photograph of device with flow chamber; (b) Scheme of chip layer; (c) Scheme of chip top view; and (d) Equivalent circuit for analysis.

3. Results and discussion

To assess the effects of ET-1 on the extent of cell-substrate adhesion, the changes in cell-substrate impedance were monitored after the addition of ET-1. Typical results are shown in **Figure 3a**. The addition of 100 nM induced a rapid increase in impedance after an initial lag phase of around 0.3h. ET-1 induced a significant increase in normalized resistance (**Figure 3b**). The effect of DEP concentration on the impedance spectrum with addition of ET-1 was also explored for two cases: 4.6×10^3 /mL and 5.3×10^4 /mL (**Figure. 4(a)**). DEP cell concentration method clearly increased the cell number on the impedance detection microelectrodes, the sensitivity of hypertrophy detection and made the low concentration sensing possible for very dilute cell suspensions. The correlation between fitting circuit components (R_c and C_c) and Endothelin-1 concentration shows a higher sensitivity if using R_c as the sensing parameter (**Figure 4(b)**). Studies herein were carried out to examine the feasibility of this impedance sensing system for Endothelin-1 induced cardiac myocyte hypertrophy.

An equivalent circuit model was also introduced to fit the impedance spectrum to fully understand the impedance sensing system.

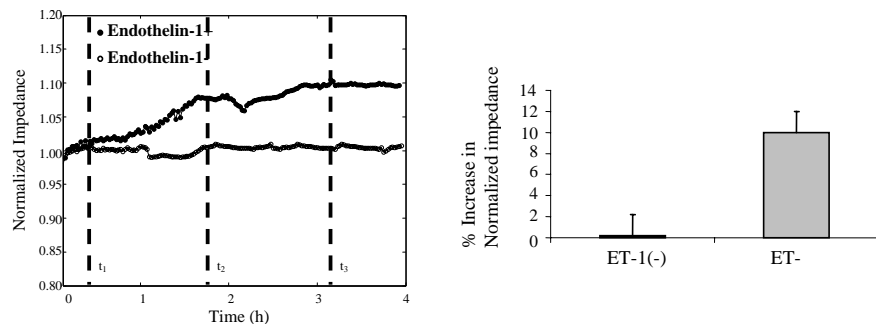


Figure 3: (a) Effects of ET on adhesion of cardiac myocytes to the Extracellular Matrix (ECM); (b) Comparison of percentage increase in normalized resistance after addition of ET-1.

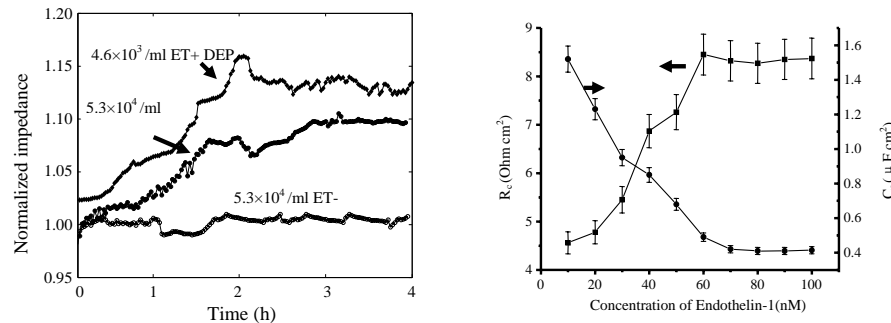


Figure 4: (a) Normalized impedance of cardiac myocytes injected into the bioprocessor at various concentrations; (b) Equivalent circuit parameter showing the correlation of variation of impedance to cardiomyocyte behavior.

5. Conclusion

In this work, a new cardiomyocyte-based impedance sensing system with the assistance of DEP cell concentration was developed to monitor the dynamic process of Endothelin-1 induced cardiomyocyte hypertrophy. By integrating the DEP cell concentration system with the impedance sensing device, we were able to significantly increase the sensitivity of the impedance system, which would reduce the time for detection by a significant factor.

References

- [1] Y. Fukuda, Y. Hirata, S. Taketani et al., Biochem Biophys Res Commun 164: 1431–1436, 1989

QUANTITATIVE TEMPERATURE MEASUREMENT OF MICRO-ELECTROPHORETIC FLOW USING TWO-COLOR LASER-INDUCED FLUORESCENCE

Souichi Saeki*, Junichi Funakoshi*, Takashi Saito*,
Kazuyuki Nakamura** and Teruo Nishida**

*Graduate School of Medicine, Yamaguchi University, JAPAN

**School of Medicine, Yamaguchi University, JAPAN

keywords : Optical measurement, Visualization, 2CLIF, Quantitative measurement, Electrophoretic flow

Recently, it is quite significant to construct a quantitative temperature measurement technique due to the integration of micro-electrophoresis systems. In general, Laser-induced Fluorescence (LIF) is used to measure the temperature field in a microchannel. However, this method strongly depends on the excitation intensity distribution which is generated by spatio-temporal intensity fluctuation of light itself and configuration of microchannel. Therefore, it is necessary to calibrate within each local region in image even when the observation area is fixed completely.

In our previous study, "Two-Color Laser-induced Fluorescence" (2CLIF) was proposed as quantitative temperature measurement in microchannel flow. Two fluorescent dyes were used as temperature dependent and independent dyes, which are excited by one excitation light. Fluorescences emitted from respective dyes could be separately acquired as two fluorescence images. The undesirable influence of excitation light could be eliminated in a ratio image calculated from the obtained images, because fluorescence intensity was an approximately linear function of excitation one. Therefore, it was possible to measure the temperature field quantitatively and simplify temperature calibration. Thus, 2CLIF was applied to the measurement of temperature distribution in microchannel and micro heat-transfer phenomenon was evaluated experimentally. In this paper, we represents the application of this method for micro-electrophoretic flow.

Figure 1 shows a schematic view of the experimental setup structured by epi-fluorescence microscope and 2-camera adopter. 2-camera adopter can split the fluorescences from two dyes into particular wavelength bands, then the images can be obtained by the two cooled-CCD cameras. In this experiment, Rhodamine B (0.02mmol/l) and Rhodamine 110 (0.002mmol/l) were used as temperature dependent and independent fluorescence dyes, respectively. To apply to micro-electrophoretic flow, acetate buffer (100mmol/l) was dissolved to test solution. It was injected to microchannel by a syringe pump, and then sealed up. Two fluorescence images were obtained, and then the ratio image was calculated by dividing the Rhodamine B fluorescence image with Rhodamine 110 fluorescence image.

Figures 2 and 3 show the normalized fluorescence intensity distribution of Rhodamine B and normalized ratio value distribution at 20.0 [degree C] in temperature calibration experiment, respectively. The spatial error of ratio value was reduced about 90 % as compared with the one of Rhodamine B. Therefore, the proposed method is not in need of calibration within each local region. Figure 4 and 5 shows the temperature calibration curve of normalized fluorescence intensities and ratio value, respectively. As shown by Fig.6, the ratio value has not only temperature dependency, but also 86% smaller spatial error than single fluorescence intensity. Consequently, the present method can quantitatively measure a temperature field with the average accuracy 1.23 [degree C], and temperature sensitivity 1.32 [%/degree C].

Figure 6 shows a schematic view of micro-electrophoresis. Three platinum wires are put into each outlet of a glass-made microchannel. Electrophoretic flow was generated by changing applied voltage of wires from 0V to 2kV. Figures 7 and 8 shows temperature distribution in observation area before electrophoretic flow was generated and after 30 seconds, respectively. We consider this method can clarify joule-heating generated by hi-voltage applied in micro-electrophoretic devices.

Word Count: 500

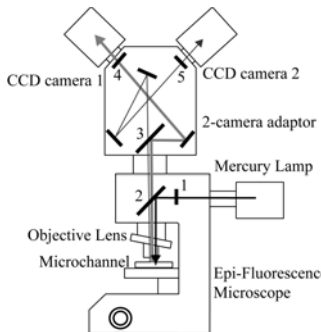


Fig.1: Schematic view of experimental setup. 1. excitation filter 470-490nm, 2. dichroic mirror 505nm, 3. dichroic mirror 565nm, 4. absorption filter 510-550nm, 5. absorption filter 580nm

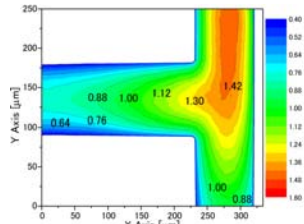


Fig.2: Normalized intensity distribution of RhodamineB ($T=20[\text{degree C}]$)

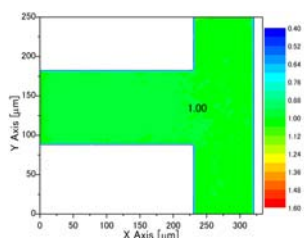


Fig.3: Ratio value distribution ($T=20[\text{degree C}]$)

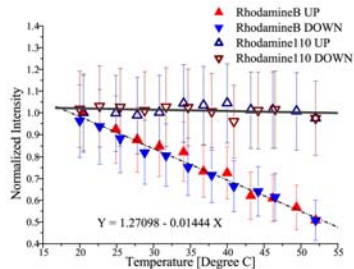


Fig.5: Calibration curve between temperature and normalized intensity of Rhodamine110 and RhodamineB

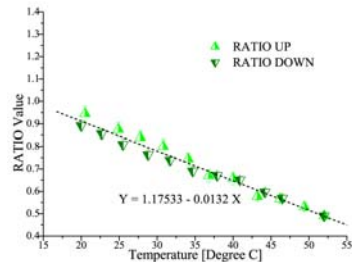


Fig.5: Calibration curve between temperature and ratio value

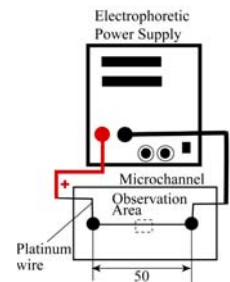


Fig.6: Schematic view of micro-electrophoretic flow measurement experiment

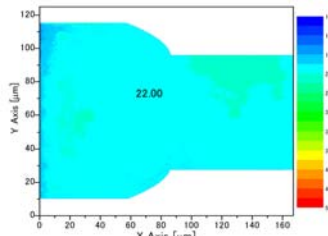


Fig.7: Temperature distribution in micro-electrophoretic flow (before)

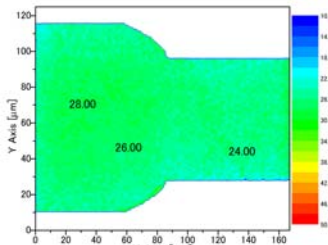


Fig.8: Temperature distribution in micro-electrophoretic flow (after 30 seconds)

OPTICAL AND IMPEDANCE DETECTION FOR ANALYSIS OF DNA HYBRIDISATION ON ENCODED MICRO-PARTICLES

David Holmes^{1,2}, Andrew Whitton^{1,2}, Gabriel Cavalli-Petraglia¹, Shahanara Banu¹, Sam Birtwell³, Gerasim Galitonov³, Hugo Martins¹, Cameron Neylon¹, Nikolay Zheludev³ and Hywel Morgan²

¹School of Chemistry, ²School of Electronics and Computer Science,
³School of Physics, University of Southampton,
Highfield, Southampton, UK

Abstract

We present a microfluidic device for the analysis of microfabricated “barcoded” particles. The optical (fluorescence and diffraction) and impedance properties of the SU8 particles are measured as they flow through the device. Electrical measurements are used to size the particles and trigger the data acquisition. The diffraction pattern produced by the individual particles uniquely identifies the particle and its chemical history (e.g. the DNA sequence on the particle surface). Fluorescence measurements are used to identify whether hybridisation of fluorescently labelled DNA has occurred.

key words: DNA, impedance, encoded particles, hybridisation, diffraction

1. Introduction

The limiting factor in high throughput combinatorial chemistry is the inability to analyse the massive number of molecules produced. This bottleneck is a major problem for the big pharma and others working in such fields as drug screening, DNA analysis, etc. [1]. To this end we have developed a microfluidic device capable of rapidly analysing the optical and impedance properties of individual encoded (optically barcoded) polymer particles [2] as they flow through the device. The particles are used as solid supports for the analyte under investigation (DNA in the present case). Each particle is identifiable by its optical diffraction pattern; allowing correlation between this unique code (associated with the particle’s chemical history) and the fluorescence and impedance measurements performed on the particle. We present data showing the system’s ability to detect DNA hybridisation on the surface of such encoded particles and distinguish between complementary and non-complementary sequences.

2. Materials and methods [3, 4]

Microfluidic chips were constructed as follows: 200 nm of platinum was evaporated onto 700 µm thick 4” pyrex wafers. The metal layer was patterned to form electrodes and polyimide used to form the flow channels. Two identically processed wafers were thermally bonded (EVG520/620, aligner bonder). Chips were diced from the wafers and inlet and outlet holes were drilled in the individual chips for fluidic access.

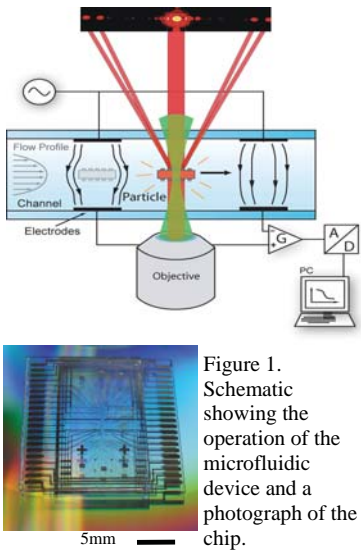


Figure 1. Schematic showing the operation of the microfluidic device and a photograph of the chip.

Two pairs of detection electrodes in the channel allow impedance measurements at various frequencies. The signal is read using a high-speed instrumentation amplifier and lock-in amplifiers (SR844, Stanford Research). A low frequency (500 kHz) signal was used to trigger data collection and size the particle. Data was digitised using a 16-bit A/D card (National Instruments) and stored for post-processing.

DNA was attached to the SU8 particles as follows: particles were functionalised with an Fmoc-6-aminohexanoic acid spacer using standard amide coupling conditions (HOBr, TBTU, DMF). After deprotection, the amino groups were reacted with succinic anhydride in basic media to provide carboxylic acid groups on the particle surface. 5'-amino ssDNA (single stranded DNA) probes were attached to the carboxylic surface through amide coupling using EDC (Imidazole buffer). Particles were washed with Tween20 (0.02 %). ssDNA sequences (labeled with Cy5 at the 5' end) were incubated with the DNA coated SU8 particles in SSCE buffer. Samples were heated for 1 min at 90 °C, shaken for 2 hrs at 45 °C and overnight at 35 °C. After hybridization particle samples were washed in PBS (0.05 % Tween20) and analysed on the microfluidic device and a commercial flowcytometer.

The barcoded particles were fabricated in SU8-5 with 1000 ppm Ni colloid (to increase the optical contrast). 50 nm thick sacrificial layer of Al was used to allow release of the SU8 particles from the silicon substrate.

The flow channel was imaged through an objective lens (x20 0.75 NA, Nikon). Light from a HeNe laser (632.8 nm, 10 mW) was focussed into the channel. Fluorescence emission was collected via the objective. The light was filtered (660 ± 20 nm), passed through a pinhole (50 μm) and detected using a photomultiplier. A second laser (532 nm, 20 mW) was used to read the barcodes (this time forming a narrow beam of collimated light emitted from the same objective). The far-field optical diffraction pattern was read using a CCD placed on-axis above the chip. The 0-order and 1st-order diffraction spots produced by the particle were read to identify the code.

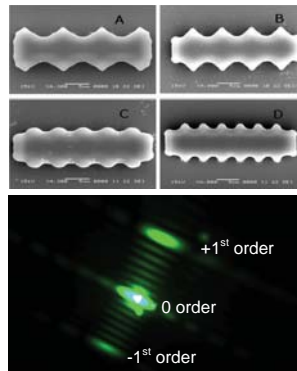


Figure 2. SU8 barcodes (length = 20 μm). The diffraction pattern from particle B is shown. The pattern is analysed as the particle flows in the microfluidic channel. Real time analysis is performed to identify the particle by measuring the distance between the 0 order and the ± 1 st order.

3. Results and discussion

Figure 1 shows a schematic diagram of the system. The particles enter from the left and flow through the device. Dielectrophoresis is used to orientate the particles before they pass through the detection region. A photograph of the microfluidic chip is also shown.

Figure 2 shows the barcoded particles fabricated in SU8 and a diffraction pattern from one of the particles. Figure 3 shows data obtained from a mixture of two particle types (i.e. different codes with different DNA sequences on their surface) incubated with fluorescently labelled DNA; particles with complementary DNA fluoresce while those with the mismatch sequences (non-hybridising) have a lower fluorescence. Data from the microfluidic device is shown in figure 3 (b) and compares favourably with that from a commercial flowcytometer (BD-FACSAria) figure 3 (a).

4. Conclusions

Diffractive barcodes were fabricated from SU8 using photolithography. DNA chemistry was performed on these particles. A microfluidic device was developed and shown to be capable of analysing the barcoded particles. The optical (diffraction pattern and fluorescence) and electrical properties of the particles were analysed as the particles flow through the system. We show the utility of the system to recognize DNA hybridization events on the surface of the particles. We are currently investigating the use of the system for DNA sequencing and other bio-chemical assays. Theoretical predictions suggest that several million distinct patterns can be encoded using particles of 50 μm in length [2], we are investigating this using nano-embossing techniques.

Acknowledgements

This work was supported by Research Councils UK through the Basic Technology Programme (GR/S23513/01). We thank the cleanroom staff of CMI at EPFL, Switzerland.

References

- [1] Brenner, S., et al. *Gene expression analysis by massively parallel signature sequencing (MPSS) on microbead arrays*, Nat Biotech, **18**, pp 630-634, 2000
- [2] Banu, S., et al, *Microfabricated barcodes for particle identification*, MME2005, Sweden, pp 252-255, 2005.
- [3] Morgan, H., et al, *High speed simultaneous single particle impedance and fluorescence analysis on a chip*, Current Applied Physics, **6**, pp 367-370, 2006.
- [4] Gawad, S., et al. *Micromachined impedance spectroscopy flow cytometer for cell analysis and particle sizing*, Lab Chip, **1**, pp 76, 2001.

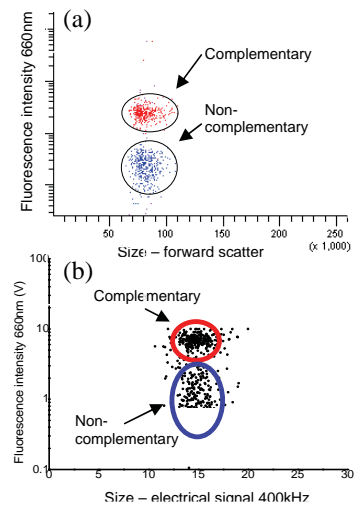


Figure 3. Comparison of (a) FACS and (b) microfluidic chip data for hybridised and un-hybridised DNA.

TRANSIT TIME OF COLLOIDS IN CHEMICALLY FUNCTIONALIZED ARTIFICIAL PORES

Andrea Carbonaro¹, Lucy Godley² and Lydia L. Sohn¹

Mechanical Engineering Department, University of California, Berkeley, CA USA¹
Section of Hematology/Oncology, Department of Medicine, The University of Chicago, Chicago, IL USA²

Abstract

We have developed a microfluidic device that measures the transit time of colloids flowing through an artificial pore functionalized with proteins. The sensing apparatus is purely electronic and consists of measuring the width of the electronic pulses generated when the colloids flow one by one through the pore. Having a resolution of $\sim 50 \mu\text{s}$, we are able to detect the increase in transit time due to the interactions between the colloids and the protein-coated pore walls.

Keywords: *artificial pore, electronic sensing, protein-protein interaction*

Introduction

Although the resistive-pulse sensing technique has been employed widely to sense, quantify, and determine the size of biological and artificial species such as colloids, cells, and DNA, very little attention has been given to the width of the electronic pulses generated when the analyte blocks the flow of current between the electrodes. In this paper, we measure the pulse widths of polystyrene colloids when they flow through a chemically-functionalized artificial pore, and we investigate the change in transit time due to the interactions between the colloids and the pore walls.

Theory

The transit time of colloids through the pore is based on resistive-pulse sensing technique: a non-conductive particle passing through a pore blocks the flow of current, thereby leading to a transient increase, or pulse, in the pore's electrical resistance. Electronic pulses can be characterized in terms of their magnitude and width: the first is strictly related to the size of the particle, whereas the latter gives the time spent by the particle inside the pore (Figure 1).

In a Poiseuille flow combined with an electrokinetic flow, the transit time, τ , of a sphere flowing through a pore of radius R is given by L/V_p (1), where L is the pore length, and V_p is the particle velocity, which can be expressed as [1]: $V_m(1-x^2)(c_1 - c_2x^5) + V_e$ (2), where V_m is the Poiseuille velocity at the center of the pore, V_e is the electrokinetic velocity, x is the fractional distance from the axis, and c_1 and c_2 are two correction coefficients which take

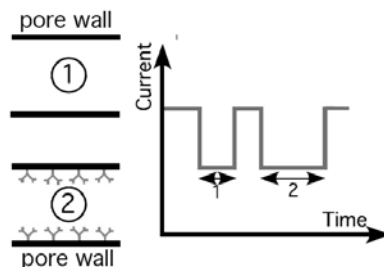


Fig. 1: Principle of proteins-colloids interaction detection.

into account the wall effects and the sedimentation velocity of the particle.

When the particle flows near a wall functionalized with proteins, the interaction between the particle surface and the protein results in a force, which is function of the nature of the interaction, the protein concentration inside the pore, and the shear rate of the flow. Based upon these assumptions, we can rewrite the velocity of the sphere inside a chemically functionalized pore as: $(V_m(1 - x^2)(c_1 - c_2x^5) + V_e)c_3$ (3), where c_3 is a correction coefficient that is introduced to model the particle-wall interaction. The values of c_3 are comprised between 0 (permanent bond) and 1 (no interactions).

Experimental

Our microfluidic device consists of a 15 μm -wide, 15 μm -high, and 800 μm -long pore connecting two 30 μm -deep reservoirs. The device was fabricated using standard soft-lithography and molding techniques: photolithography was first used to pattern a master of the pore and reservoirs. Next, the master was cast in a polydimethylsiloxane (PDMS) slab that was subsequently sealed to a glass slide with previously patterned Ti/Pt electrodes.

The chemistry used to functionalize the pore consists of three steps: the oxygen plasma-cleaned glass surface is first treated with 3-aminopropyltriethoxysilane (APTES) to make amino groups appear. Second, a hetero-bifunctional cross-linker (ANB-NOS) is coupled with the amino-silane groups. Third, proteins are attached covalently to ANB-NOS cross-linker through activation with UV light.

The link between the proteins and the cross-linker is achieved by incubation of the proteins inside the pore after the device fabrication. Incubation allows also the adsorption of proteins on the PDMS walls of the pore [2].

For our experiments, we used 9.95 μm SuperAvidin coated polystyrene colloids (Bangs Labs). The pore was functionalized using human Annexin V (R&D Systems), and the colloids were conjugated with anti-human Annexin V (R&D Systems). We performed all of our measurements using a four terminal probe technique to thus measure the pore current. A constant pressure of 10.5 kPa (1.5 psi) was used to drive the colloids ($\sim 3.5 \times 10^5$ colloids/ml) through the pore.

Results and discussion

Figures 3A and B show the current across the pore as colloids flow through it. In particular, Figure 3A shows a typical measurement of SuperAvidin coated colloids flowing through a non-functionalized pore. In Figure 3B, SuperAvidin coated colloids were first conjugated with biotinylated anti-human Annexin V antibody (5 $\mu\text{g}/\text{ml}$) and then run through a pore functionalized with human Annexin V (50 $\mu\text{g}/\text{ml}$). There is a clear difference in pulse width as the colloids flow through a pore functionalized with Annexin V, whereas we did not measure any significant change in pulse magnitude.

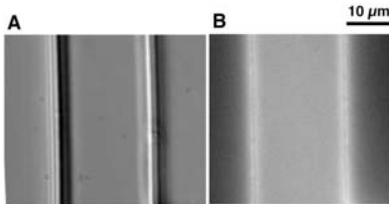


Fig. 2: A - optical image of a PDMS channel filled with PBS; B - fluorescent image of a functionalized PDMS channel.

To test the specificity of this interaction between the antibodies on the colloids and Annexin V on the pore walls, we also run a control experiment (Figure 4). Column *a* shows the mean transit time measured without any antibodies on the colloids or pore functionalization (6.70 ± 0.24 ms). When SuperAvidin coated colloids flow through a pore functionalized with Annexin V, we measured a mean transit time of 7.20 ± 0.50 ms (column *b*). We explain this shift in transit time as the result of non-specific interactions between the colloids and the Annexin V functionalized pore walls.

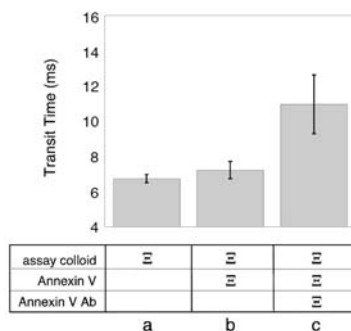


Fig. 4: Summary of the mean transit time of colloids when flown in different conditions.

Conclusions

In this paper we demonstrate our ability to use the resistive pulse sensing technique to sense the interactions between colloids flowing through an artificial pore and the chemically functionalized pore walls. We are currently working toward developing a more accurate model of the colloid–pore wall interactions and also using this technique to detect biomarkers on the cell surface [3].

Acknowledgements

The authors would like to thank Prof. H. Huang for the helpful discussions and Dr. A. Radenovic for the assistance in the use of the fluorescent microscope.

References

1. L. I. Berge, *J. Colloid Interface Sci.*, **135**, 283, 1990.
2. S. Karrasch, M. Dolder, F. Schabert, J. Ramsden, and A. Engel, *Biophys. J.*, **65**, 2437, 1993.
3. A. Carbonaro, L. Godley, L. L. Sohn, in preparation, 2006.

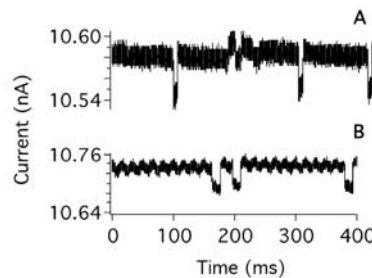


Fig. 3: Current versus time as colloids flow through the pore.

10.95 ± 1.69 ms is the mean transit time that was found when the colloids conjugated with anti-human Annexin V were flown through a pore functionalized with Annexin V (column *c*). We attribute this increase in transit time in the presence of specific interactions between the colloids and the coated pore walls. These results clearly show that the presence of protein on the pore walls affects the flow of colloids flowing through it. We also demonstrate that the sensitivity of our electronic measurements allows to distinguish between specific and non-specific interactions.

A MICRO SPR (SURFACE PLASMON RESONANCE) SENSOR WITH AN INTEGRATED PHOTODETECTOR

Hyungseok Pang¹, Hyoung J. Cho², and Patrick L. LiKamWa¹

¹College of Optics & Photonics: CREOL & FPCE, University of Central Florida, USA

²Department of Mechanical, Materials & Aerospace Engineering,
University of Central Florida, USA

ABSTRACT

SPR (surface plasmon resonance) sensors have been widely used in chemistry and biology to study binding affinity and kinetics. In this work, we report a novel integrated approach to a SPR sensor. Our sensor consists of a polymer waveguide and a MSM (metal-semiconductor-metal) photodetector on a GaAs substrate. This planar integration enables the direct opto-electric signal conversion without resorting to a separate bulk optical component and facilitates further integration of a light source. We have designed, fabricated and tested a micro SPR sensor with an integrated MSM photodetector. We have verified the functionality of a waveguide-based SPR sensor and a MSM photodetector in this first phase investigation.

Keywords: SPR sensor, Photodetector, Integrated optics, Polymer waveguide

1. INTRODUCTION

Most of commercially available Kretschmann type SPR sensors consist of a light source, a polarizer, a prism, and a photodetector. From this configuration, bulk optical components are unavoidable; therefore it is difficult to make a small planar device. An alternative approach to miniaturization of the SPR sensor utilizes a waveguide with spectral interrogation [1]. However, the planar miniaturization of the light source and detection parts has not yet addressed. A novel design concept of a photodetector-integrated SPR sensor is introduced in this work.

2. DESIGN

The device consists of a waveguide-based SPR sensor head and a MSM photodetector coupled to the end of the waveguide. Figure 1 illustrates the sensor structure, in which a 3-D view and a

cross-sectional view are shown in (a) and (b), respectively.

3. FABRICATION

The fabrication process starts with a MSM photodetector on a GaAs substrate. A silicon dioxide layer was deposited and patterned as a buffer layer for the suppression of dark current between electrodes and also for the improvement of the breakdown characteristics. Interdigitated electrodes with 2.5 μm -width and gap sitting on GaAs substrate convert the light coupled to metal-semiconductor-metal region into an electrical signal. A silicon oxynitride layer was deposited and patterned to have high thickness in a SPR sensor head region to minimize the coupling of the guided light into the GaAs substrate while its thickness was reduced in a MSM photodetector region to maximize the light coupling.

A 1.3 μm -width and 0.6- μm depth groove was patterned on the siliconoxynitride layer between the sensor head and the photodetector, forming a reversed-ridge type waveguide with SU-8 polymer layer. A 50 nm-thick and 750- μm length of gold sensing layer was deposited on the waveguide to construct a SPR sensor head. As a final step, CytopTM layer was patterned over the MSM photodetector region with a 200-nm thick metal cover layer. The cover layer is for preventing any background light from entering the MSM photodetector and for preserving the internally reflected light. The fabricated device is shown in Figure 2.

4. TEST

A waveguide-based SPR sensor head and a waveguide-coupled MSM photodetector were tested separately. In the experiment, a light from a Ti-Sapphire tunable laser was focused with a microscope objective lens and launched into the waveguides. For the SPR sensor head test, a range of refractive index liquids were applied on the sensor head and wavelengths were scanned from 730 nm to 800 nm. The end facet of the device was imaged with another microscope objective lens. The signal was collected with an external photodetector. The electrical signal strength depending on the coupled light intensity was measured for the characterization of the waveguide-coupled MSM photodetector. Figure 3 shows a schematic representation of the experiments.

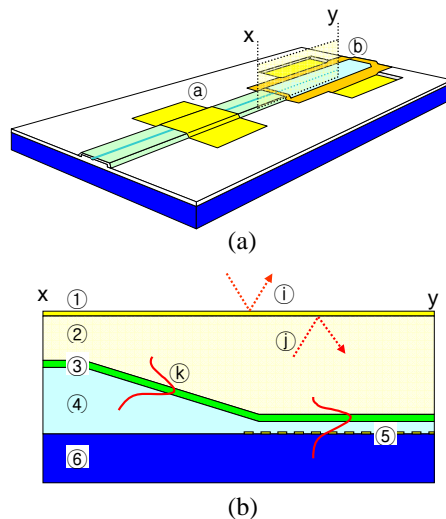


Figure 1.
(a) 3-D view of the device;
① SPR sensor head and
② MSM photodetector
(b) Cross sectional view of a guided light coupling region
① Metal Layer for Light Screening
② Cytop Layer
③ Su-8 Waveguide
④ Siliconoxynitride Buffer Layer
⑤ MSM Photodetector Electrodes
⑥ GaAs Substrate
(i) External light blocked by layer ①
(j) Internal light reflected by layer ①
(k) Light guided along the waveguide



Figure 2. Fabricated Device

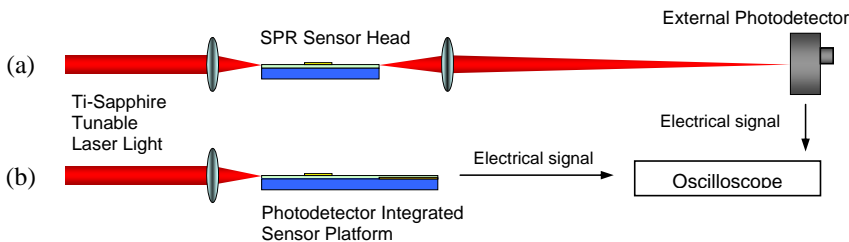


Figure 3. Experimental set up for (a) a SPR sensor head (b) MSM photodetector-integrated sensor

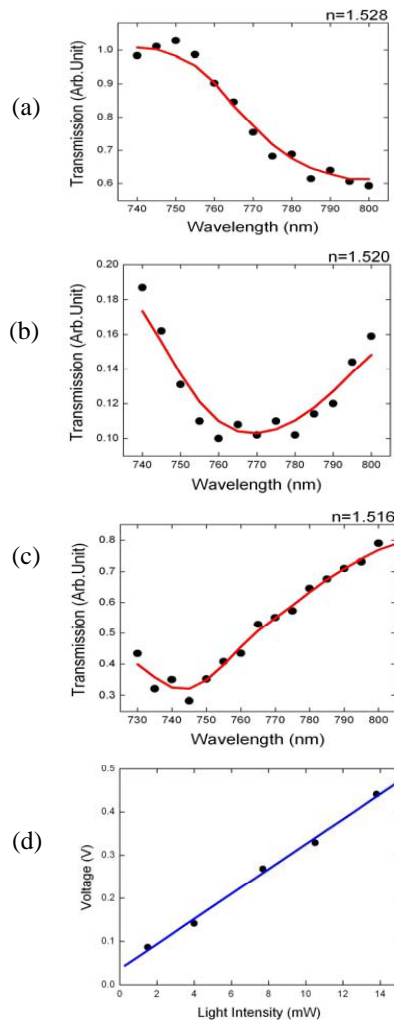
5. RESULTS AND DISCUSSION

Figure 4 (a), (b) and (c) show SPR absorption spectrum variation depending on the refractive index of the sample liquid that was applied on the sensor head within the scanned wavelength range, which verifies the functionality of the SPR sensor head. Figure 4 (d) shows electrical signals from the integrated photodetector. The electrical signal is linearly dependent upon the plug-in light intensity. The test results showed working conditions of the individual component. The verification of the sensor function as a whole is under way. This development promises a fully integrated SPR sensor system based on integrated optics.

REFERENCES

- [1] J. Dostalek, J. Ctyroky, J. Homola, E. Brynda, M. Skalsky, P. Nekvindova, J. Spirkova, J. Skvor, and J. Schrofel, "Surface plasmon resonance biosensor based on integrated optical waveguide," *Sensors and Actuators B-Chemical*, vol. 76, pp. 8-12, 2001.

Figure 4. (a)-(c) SPR absorption spectrum variation depending on refractive index of sample liquid and (d) electrical signal strength depending on the waveguide coupled light intensity.



EXTRACTION BEHAVIOR OF LANTHANOID(III) SPECIES USING DIHEXYL-N,N-DIETHYLCARBAMOYLMETHYLPHOSPHONATE IN THE MICROCHEMICAL CHIP

Yuya Takahashi, Hiroyasu Hotokezaka and Yasuhisa Ikeda

Research Laboratory for Nuclear Reactors, Tokyo Institute of Technology, Japan

Abstract

In order to separate actinoid(III) (An(III)) from lanthanoid(III) (Ln(III)) efficiently using microchemical chip, we have studied the extraction behavior of Sm(III) from aqueous phase to organic containing dihexyl- N,N -diethylcarbamoylmethylphosphonate (CMP). From the results, distribution rates (D) increase with increasing CMP, NO_3^- concentrations. These extractions are achieved within 2-3 s.

Keywords: radioactive liquid wastes, extraction, thermal lens microscope lanthanoid(III), dihexyl- N,N -diethylcarbamoylmethylphosphonate,

1. Introduction

In the reprocessing of spent nuclear fuel, radioactive liquid wastes containing transuranium elements and fission products (FPs) are produced. For environmental safety, it is necessary to separate long-lived radionuclide, especially the separation of An(III) from Ln(III) . Usually, it is difficult to separate An(III) from Ln(III) , because of their similarity of chemical properties. One of the methods for separating them is a liquid-liquid extraction using selective extractants. CMP (Figure 1) has been known to be one of selective extractants for An(III) and Ln(III) [1-2]. However, the conventional liquid-liquid extraction methods using CMP do not have high performance on the viewpoints of decontamination factor (DF). Using microchemical chip extraction, following advantages can be expected to be produced, (1) short time extraction (2) forming multi-phase laminar flow [3]. Hence, it may be expected that nuclides would be separated efficiently in the microchemical chip. In this work, extraction behavior of Sm(III) in the microchemical chip was studied using thermal lens microscope (TLM), which is suitable for detecting the species in microchemical chip [4-5].

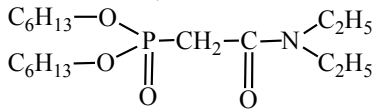


Figure 1. Structural formula of CMP.

2. Experimental

The LiNO_3 solution was prepared by dissolving LiNO_3 into 0.01 M ($M = \text{mol} \cdot \text{dm}^{-3}$) HNO_3 . $\text{Sm}(\text{NO}_3)_3$ was dissolved in LiNO_3 and HNO_3 solutions. These were used as the aqueous solutions. CMP was diluted with tetrachloroethylene was used as an organic phase.

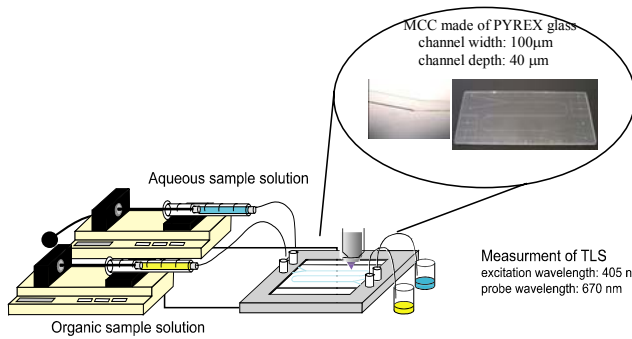


Figure 2. Apparatus for experiment.

An experimental setup for microchemical chip extractions is shown in Figure 2. In the extraction experiments, aqueous solutions were introduced in microchemical chip by microsyringe pump at 300 $\mu\text{l/h}$, and organic solutions of 0.8 M CMP, 1.0 M CMP, and 1.5 M CMP were introduced at 200, 140, 50 $\mu\text{l/h}$, respectively. These two solutions form two-phase laminar flows in microchannel shown in Figure 2. To determine Sm(III) concentrations, thermal lens signal (TLS) intensities of Sm(III) solutions in microchannel were measured by thermal lens microscope (TLM). TLS intensities of Sm(III) in aqueous phases were increased linearly with increasing concentrations of Sm(III) (Figure 3)[6]. By using these plots, Sm(III) concentrations in aqueous phases at various positions in microchannel were analyzed and plotted against the length from the interflow point (contact length) (Figure 4). Conventional liquid-liquid extraction were carried out with volume ratios, which were consistent with flow rate ratios of aqueous and organic solutions.

3. Results and discussion

Figure 4 shows the plot of Sm(III) concentration against the contact length for the extraction using 1 M LiNO₃ as aqueous phase and 0.8 M CMP as organic

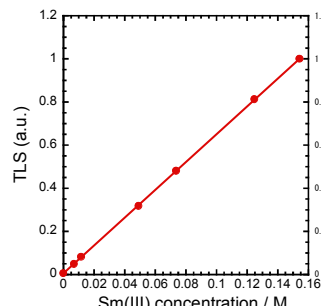


Figure 3. A plot of TLS intensities against [Sm(III)] in aqueous phase (3.0 M HNO₃) in MCC.

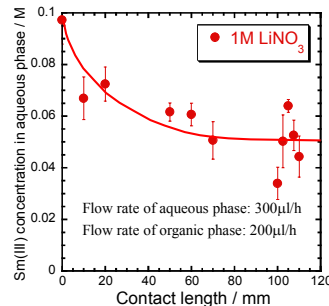


Figure 4. A plot of [Sm(III)] in 1 M LiNO₃ phase vs. contact length in MCC.

phase. It was found that Sm(III) concentrations decrease with contact length and that the extraction equilibrium is achieved at 100mm from the interflow point. These indicate that the extraction equilibrium is reached by 2-3 s. D values of Sm(III) extractions were shown in Tables 1 and 2. The D values are increase with increasing concentrations of CMP and NO_3^- . The D values in MCC system were consistent with those in the conventional liquid-liquid extraction. Furthermore, as mentioned above, the extraction of Ln(III) using MCC can be performed very rapidly.

This leads to the decrease in the radiation damage of extractants and diluents, and to the reduction of second radioactive wastes. Therefore it would be possible to achieve several extractions in short time to make high separation factors.

References

1. E. P. Horwitz, A. C. Muscatello, D.G. Kalina, and L. Kaplan, *Sep. Sci. Technol.*, **16**, pp. 417, (1981).
2. W. W. Schulz, L. D. McIsaac, *ISEC 77*, **21**, pp. 619, (1979)
3. H. Hotokezaka, M. Tokeshi, M. Harada, Takehiko Kitamori, and Y. Ikeda, *Prog. Nucl. Energ.*, **47**, pp. 439, (2005)
4. T. Kitamori, M. Tokeshi, A. Hibara, and K. Sato, *Anal. Chem.*, **76**, pp. 52A, (2004).
5. K. Uchiyama, A. Hibara, H. Kimura, T. Sawada, and T. Kitamori, *Jpn. J. Appl. Phys.*, **39**, pp. 5316, (2000).
6. K. Binnemans, C. Gorller-Waland, *Chem. Phys. Lett.*, **235**, pp. 163, (1995)

Table 1 Distribution ratios of Sm(III) in the extraction using the microchemical chip and the conventional liquid-liquid extraction at different nitrate condition.

	1 M LiNO_3	3 M HNO_3
Conventional liquid-liquid extraction	1.4 ± 0.0	1.9 ± 0.1
Microchemical chip extraction	1.5 ± 0.5	2.0 ± 0.1

Organic phase: tetrachloroethylene containing 0.8 M CMP.

Table 2 Distribution ratios of Sm(III) in the extraction using the microchemical chip and the conventional liquid-liquid extraction at different CMP concentrations.

	0.8 M CMP	1.5 M CMP
Conventional liquid-liquid extraction	1.9 ± 0.1	3.2 ± 0.1
Microchemical chip extraction	2.0 ± 0.1	3.5 ± 0.2

Aqueous phase: 3 M HNO_3 solution containing Sm(III).

DEVELOPMENT OF LIQUID/LIQUID OPTICAL WAVEGUIDE WITH MISCELLY SOLVENTS AND ITS APPLICATION TO THE OBSERVATION OF 1-ANILINO-8-NAPHTHALENE SULFONATE AT THE TETRAHYDROFURAN/WATER INTERFACE

**Hiromi Takiguchi, Sohto Asanuma, Hiroki Hotta, Tamao Odake,
and Kin-ichi Tsunoda**

Department of Chemistry, Gunma University, Japan
(tsunoda@chem.gunma-u.ac.jp)

Abstract

Constructed were liquid/liquid optical waveguides (LLWs), which have a liquid-core/liquid-cladding structure. In particular, the characteristics of the tetrahydrofuran (THF)/water LLW were investigated and this LLW was applied to the observation of the ion-pair extraction of a solvatochromic fluorophore, 1-anilino-8-naphthalene sulfonate (ANS), and hexadecyltrimethyl- ammonium ion (CTA) from the water phase to the THF phase.

Keywords: Liquid/liquid Optical Waveguide, Tetrahydrofuran, 1-Anilino-8-naphthalene Sulfonate

1. Introduction

Liquid/liquid optical waveguides (LLWs), which have a liquid-core/liquid-cladding structure, have firstly been proposed by us [1, 2]. The LLWs have been fabricated by using the flow of liquids from concentric glass capillaries into an outer glass capillary. Both immiscible solvents (e.g., toluene/water, diethyl ether/water and etc.) and miscible solvents (e.g., tetrahydrofuran (THF)/water, 5%NaCl aqueous solution/water, and etc.) can be used to form the LLWs. Our purpose is to use the LLWs as tools for studying the liquid/liquid interfaces, although the concept of the LLW has recently been extended to the microchip, and its potentialities as an optical switch and an evanescent coupler in micro-fluidic chips have also been investigated by Wolfe, et al and Tang, et al [3-5].

In this work, firstly, the characteristics of the THF/water LLW were investigated. Then, we set up a simple question in order to evaluate the LLW as a tool for studying the interfaces. That is, can we directly observe the solvent extraction process between miscible solvents with the LLW? To answer the question, we selected the ion-pair extraction of 1-anilino-8-naphthalene sulfonate (ANS) and hexadecyltrimethyl- ammonium (CTA) from the water phase to the THF phase as an example and the behaviors of the ion-pair in the LLW were studied.

2. Experimental

The experimental set up of the THF/water LLW and its photo are shown in Figures 1 and 2, respectively. The outer capillary was a quartz tube (1.1 mm i.d., 150 mm long) and the inner capillary was a stainless tube (0.31 mm i.d., 0.51 mm o.d., 100 mm long). The outer and inner capillaries were assembled with T-joints, and the inner capillary was partially inserted into the outer capillary. THF ($n_D = 1.41$) flowed into the inner capillary as the organic phase, while water ($n_D = 1.33$) or an aqueous solution flowed into the outer capillary as the aqueous phase. An optical fiber (SF-112, Sumita Optical Glass, Inc., Japan, 0.175 mm o.d., UV transmitted, NA = 0.20) was inserted into the inner capillary. The source light, which was provided by a Nd-YAG laser (15 Hz, 355 nm, 4 mJ), was introduced into the inner flow through the optical fiber. Fluorescence signals and scattering lights from the LLW were collected through the light guide, which was placed close to the surface of the outer capillary and was moved from the tip of the inner capillary to the end of the LLW along with the outer capillary. Then, the light signals were sent to a multichannel CCD detector (PMA-11, Hamamatsu Photonics Co., Japan) and spectra of 350-700 nm were obtained. The gravity-driven method was applied to send the solutions where their flow rates were adjusted with changing the levels of their surfaces in the reservoirs.

3. Results and discussion

The LLW was stable up to at least 150 mm in the range of 1 to 2 cm s^{-1} of linear velocities of both flows. The most stable LLW was obtained at ca. 11.3 for the ratio of the aqueous phase flow rate to organic phase where the linear velocities of water and THF were almost the same.

The ion-pair formation of ANS and CTA and its extraction could be observed at pH 11 with the bulk solution system of toluene and water, while they did not occur at pH 3 and 7. Thus, the aqueous solution containing 10 μM of ANS and CTA at pH 11 was

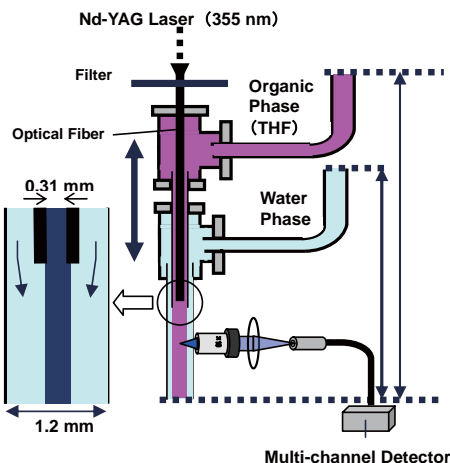


Figure 1 Schematic Diagram of THF/Water LLW.



Figure 2 THF/Water LLW. ANS (10 μM) was added to the THF phase.

used for the outer flow of the LLW, and the fluorescence spectra of ANS were monitored along with the outer capillary of the LLW. The changes in the intensity at 484 nm and the λ_{max} of ANS spectra at pH 3 and 11 were shown in Figure 3. The data at pH 3, where the ion-pair formation did not occur, were also taken for the comparison. At pH 3, almost the same results as those without the addition of CTA were obtained, i.e., the gradual increase in the intensity and no change in the λ_{max} of 484 nm, which corresponds to that of ANS in ca. 70% THF, were observed. On the other hand, the further blue shift of the λ_{max} was clearly observed at pH 11. The fluorescence of ANS increased then turned to decrease at the middle course of the LLW (Figure 3), while that at 472 nm (λ_{max} , ca. 95% THF) gradually increased (data is not shown) and the wavelength of 472 nm became the λ_{max} of the spectra after ca. 90 mm from the tip (Figure 3). Such blue-shift was not observed without CTA at pH 11 (data is not shown). Moreover, the existence of CTA in the bulk solution of the mixture of THF and water did not bring any spectral change of ANS fluorescence. It means that the ion-pair formation itself does not cause the spectral change of ANS in the THF/water mixture. These facts strongly suggest that the accelerated diffusion of the ion-pair into the THF phase, which caused the further blue shift of the λ_{max} , was clearly observed; the λ_{max} of 472 nm corresponds to that in ca. 95% THF. In other words, the extraction process between miscible solvents could be observed using this LLW technique.

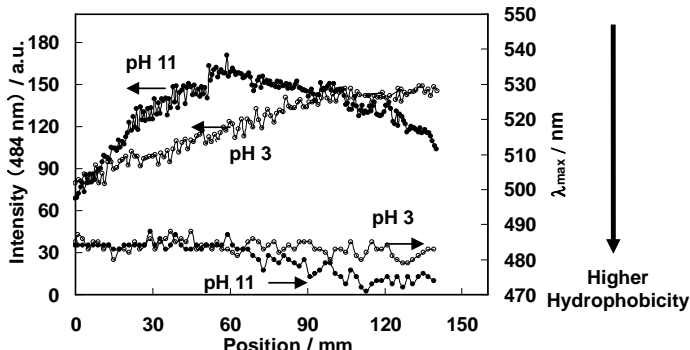


Figure 3 Intensity and λ_{max} of ANS fluorescence spectra with THF/water LLW. The aqueous solution containing 10 μM ANS and 10 μM CTA was used as the outer flow. The length of the LLW was ca. 150 mm. The linear velocity of both phases was 1.1 cm s^{-1} .

References

1. H. Takiguchi, et al., *Appl. Spectrosc.*, **57**, 1039-1041 (2003).
2. H. Takiguchi, et al., *Anal. Sci.*, **21**, 1269-1274 (2005).
3. D.B. Wolfe, et al., *Proc. Natl. Acad. Sci. U.S.A.*, **101**, 12434-12438(2004).
4. B.T. Mayers, et al., *Anal. Chem.*, **77**, 1310-1316(2005).
5. K.Y. Tang, et al., *Appl. Phys. Lett.*, **88**, 061112/1-061112/3 (2006).

EVALUATION OF HYBRIDIZATION KINETICS OF MOLECULAR BEACONS WITH NUCLEIC ACIDS USING PICOLITER MICROFLUIDIC DROPLET WITH MILLISECOND RESOLUTION

Albert Tsung-Hsi Hsieh¹, Jen-Hao Pan¹, Yuh Adam Lin¹, Abraham P. Lee^{1,2}

¹Biomedical Engineering, ²Mechanical and Aerospace Engineering,

University of California, Irvine, U.S.A.

Abstract

A microfluidic droplet analysis platform is developed for evaluating the hybridization kinetics of nucleic acid assays. In this platform molecular beacons (MB) and different sequence of nucleic acids are rapidly mixed in picoliter droplets and flown one-by-one through microchannels. Specific nucleic acid hybridization is evaluated by the accumulated fluorescence emitted from the droplets. This process does not require immobilization and stringent washing processes and is highly sensitive compared to conventional nucleic acid detection methods. The hybridization rates of MB with nucleic acids are determined by the mixing efficiency in picoliter-sized microdroplets. The hybridization kinetics is observed at millisecond resolutions. This nucleic acid assay platform can be the basis for an integrated rapid nucleic acid detection system that is programmable and requires only a few micro liters of sample

Keywords: FRET, molecular beacon, hybridization, micro-droplet, micro-mixer

1. Introduction

Molecular beacon (MB) is a unique class of fluorescence resonance energy transfer (FRET) molecules. The biochemical and optical properties of a MB makes it useful as a molecular probe for assays that do not require hybridization solid substrates or washing steps in conventional nucleic acids detection methods [1]. Molecular beacons are synthesized as single stranded nucleic acid molecules that are constructed by stem and loop structures. A MB becomes fluorescent only when the probe encounters the complementary target ssDNA as show in figure 1. MB also has outstanding capability for the selective detection of single nucleotide polymorphism (SNP) and multiplex target nucleic acid detection [2]. Kinetic measurement of fast chemical reactions in bulk solution is difficult due to two major problems typical of diffusion-based reactions: Slow mixing rate for reagents and large reagent dispersions. Since the mixing efficiency is not fast enough in flows with low Reynolds number, these problems still exist in microfluidic biochemical system [3].

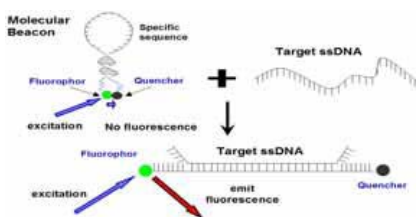


Figure 1. The stem portion of the MB remains closed, if no complimentary ssDNA exists in the solution and has very low background fluorescence intensity. The MB will be fluorescent once it hybridizes with its complementary target ssDNA. After MB hybridized with its target ssDNA, the signal to noise (background) ratio of fluorescence intensities can reach as high one hundred with optimal design.

2. Experimental

The design schematic of a PMRI platform device is shown in figure 1. When the aqueous phase flows into the center channel from two different inlets, the merged single stream is pinched-off by the shear force from the side oil streams and forms the picoliter droplets. The PMRI devices were fabricated in polydimethylsiloxane (PDMS) by using soft lithography techniques. The PDMS replica and a clean microscope glass slide were treated with air plasma for 1 min and brought together to form an irreversible seal. Polyethylene tubing was inserted into the inlets of the microfluidic channel. Syringe pumps were used to drive the liquid into the microchannels. The height of the channel is 50 μm , and the length of channel is 25 mm.

The microfluidic-based droplet system developed by our lab and others [4] was designed to extract the kinetic parameters of hybridization between MB and target ssDNA as shown in figure 2. The reagents are rapidly mixed in microdroplets as it is moving in a winding channel [5]. The hybridization reaction was recorded with 100 milliseconds resolution. We can observe that fluorescence of MB fills entire droplet after the fourth turn of the winding microchannel, i.e. around 500 μm position as shown in figure 3. Since the velocity of droplet is 8625 $\mu\text{m/sec}$, the mixing time is around 58 ms. The fluorescence image of the MB hybridization was acquired by a 10 seconds accumulated exposure. The total required solution is less than 400 nanoliter. Based on this result, we know the MBs hybridize to the targets instantly once mixing starts. With the rapid mixing in picoliter droplets, we are able to evaluate the hybridization kinetics of MB both in varying the length of MB stem portion and the concentrations of target ssDNA as shown in figures 4 and 5. The hybridization reaction between MBs and target nucleic acids involves both the binding of loop portion with target nucleic acid binding, and the opening of the hairpin structure. The sequence of molecular beacon (MB-BRCA1) for complementary DNA detection is Cy3-5'-CCTAGCCCTATGTATGCTTTGTTG T-GGCTAGG-3-BHQ2. The sequence of complementary DNA (cDNA) for MB-BRCA1 is 5'-TAAC-ACAACAAAGAGATACATAGG-GTTT-3'. We designed another three different DNA sequences to characterize the kinetics of MB hybridization. "SNP-M" sequence has single nucleotide polymorphism at the center of the cDNA sequence: 5'-TAAC-ACAACAAAGAaCATACATA GG-GTTT-3'. "2NP-ME" sequence has two nucleotide polymorphisms. They are located at the middle and end portions of cDNA: 5'-TAAC-ACAACAAAGAaCATACATgGG-GTTT-3'. "3NP-M" sequence has three nucleotide

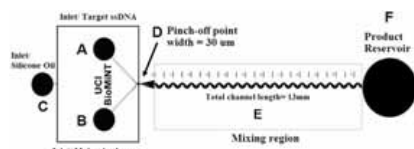


Figure 2. The layout of the designed picoliter droplet generation system and the winding channel for mixing. Pinch-off area channel width is 30 μm . The width, height and length of microchannel in the mixing region are 75 μm , 50 μm and 25 mm respectively. The angle at turning corner of the winding channel is 90 degree. The droplet diameter is 54.5 μm and volume is 238.5 picoliter.

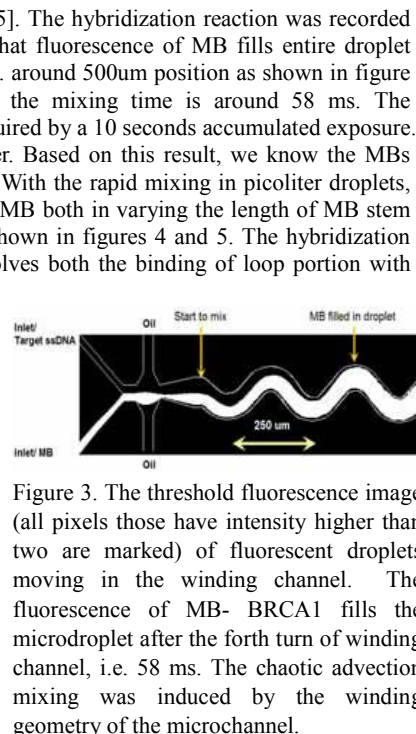


Figure 3. The threshold fluorescence image (all pixels those have intensity higher than two are marked) of fluorescent droplets moving in the winding channel. The fluorescence of MB-BRCA1 fills the microdroplet after the forth turn of winding channel, i.e. 58 ms. The chaotic advection mixing was induced by the winding geometry of the microchannel.

polymorphisms. They are all located at the middle of cDNA: 5'-TAAC-ACAACAAAGatATACATAGG-GTTT-3'.

3. Results and conclusions

All the MB and nucleic acids hybridization measurements were implemented under same conditions. The concentration of MB is 0.5 μ M and all DNA concentrations are 2.5 μ M. Figure 4 shows the comparison of the fluorescence intensities changes of MB-BRCA1 when it hybridized with above mentioned four DNA sequences. The 3NP-M sequence has the lowest fluorescence intensity and it is close to the background of molecular beacon. The 2NP-ME has the fluorescence intensity slightly higher than the 3NP-M, since it has only two nucleotides polymorphism. The fluorescence intensity of SNP-M sequence is about two and half times higher than the 2NP-ME one, but it is still much lower than the complimentary DNA. This result shows that this designed molecular beacon is very selective and sensitive to single nucleotide polymorphism.

The hybridization process consists of the following three steps: (1) the target ssDNA adheres to part of the loop domain of the MB, which remains closed, (2) as the number of stem portion base pair “unzipped”, the stem portion gradually opens. (3) hybridizing with the rest of loop portion, and the stem portion totally opens. Of these three steps, the reaction-determining steps are (1) and (2), since it takes time for the target nucleic acids to overcome the energy barrier of separating stem portion. This microfluidic droplet platform can have hybridization event resolutions as high as a few milliseconds. Future work will remove barriers to evaluate the hybridization kinetics at millisecond resolution by optimizing the mixing rate of reagents, flow velocity of the droplets, and the sensitivity of CCD camera.

Acknowledgement

The authors would like to gratefully acknowledge, Professor James Brody, Joseph Harris, Dr. Alan Lee, Dr. Wajeeh Saadi of Biomedical Engineering, University of California, Irvine and Dr. T. J. Fu for their precious suggestions and generosity to let us use their lab equipments.

References

- [1] S. Tyagi, F. R. Kramer, *Nature Biotechnology*, 14 (3): 303-308, 1996
- [2] S. A. E. Marras, F. R. Kramer, S. Tyagi, *Gen. Ana. Bio. Eng.*, 14 (5-6): 151-156 FEB 1999.
- [3] C. W. Xi, L. Raskin, S. A. Boppart, *Biomedical Microdevices* 7 (1): 7-12 Mar. 2005
- [4] Y. C. Tan, Jeffrey Fisher, Abraham P. Lee, *Lab-on-a-chip*, 4, 292-298 (2004)
- [5] H. Song, J. D. Tice, and R. F. Ismagilov, *Angew. Chem., Int. Ed.* 42, 768, (2003)

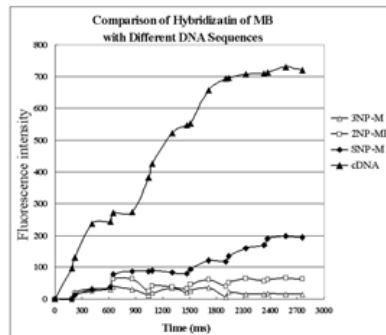


Figure 4. Comparison of hybridization of MB-BRCA1 with difference DNA sequences.

NMR STUDY ON THE TAUTOMERIC EQUILIBRIUM OF ACETYLACETONE CONFINED IN EXTENDED-NANO SPACE

Kyousuke Nagaoka¹, Takehiko Tsukahara^{1,2}, Akihide Hibara^{1,3}, Haeng-Boo Kim^{1,2,3} and Takehiko Kitamori^{1,2,3}

¹The University of Tokyo, Bunkyo, Tokyo, 113-8656, Japan

²Japan Science and Technology Agency, Kawaguchi, Saitama, 332-0012, Japan

³Kanagawa Academy of Science and Technology, Kawasaki, Kanagawa,
213-0012, Japan

Abstract

We examine size-dependence of the tautomeric equilibrium between keto and enol tautomers of acetylacetone (Hacac) in water confined in hundred-nanometer-sized channels on a microchip (called extended-nano space) by using ¹H-NMR spectroscopy. The results showed that keto tautomers of Hacac increase with decreasing in the sizes, and that water polarity changes by size-confinement.

keywords; tautomeric equilibrium, NMR, extended-nano space, dielectric constant, acetylacetone

1. Introduction

Micro-nano chemical systems on a chip have been received much attention for a variety of applications in chemical analysis. We have focused on that an extended-nano space has become an experimental tool for characterizing behaviors of liquid-phase molecules. Previously, we have studied size-confinement effects on physicochemical properties of water molecules. By capillarity and time-resolved fluorescent measurements of water confined in extended-nano spaces, we have clarified that viscosity and dielectric constant of the confined water were different from those in bulk water [1]. NMR relaxation measurements of confined water showed slower intermolecular motions and higher proton mobility rather than bulk water [2]. Such unique properties may enable to influence on the chemical equilibrium and reactions in solutions.

Hence, we examine size-dependence of keto-enol tautomeric equilibrium of Hacac, which is strongly dependent on polarity of solvents such as dielectric constant (ϵ) in water (See Figure 1), and discuss the size-confinement effects on the polarity of water molecules.

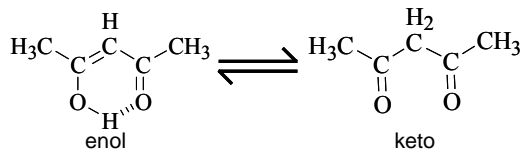


Figure 1. keto-enol equilibrium of Hacac

2.Experimental

Extended-nano spaces (equivalent diameter: 202 nm - 3000 nm) were fabricated on the synthetic quartz glass by electron beam lithography and plasma etching. The fabricated plate was thermally bonded with cover plate in a vacuum furnace at 1080°C, and was cut in 4 mm width by diamond cutter (See Figure 2). Measurements of ¹H-NMR spectra were carried out with JEOL 500 MHz NMR under nitrogen gas flow.

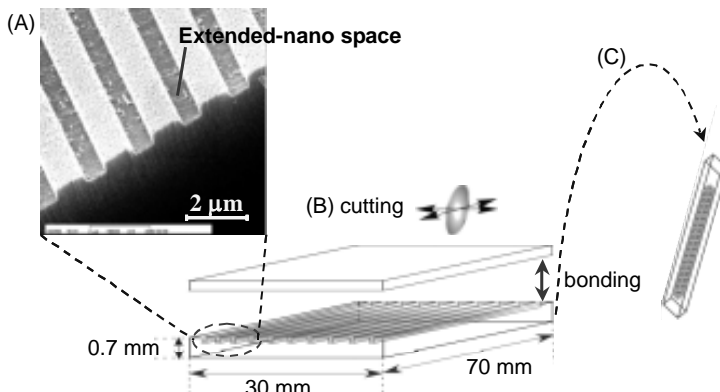


Figure 2. Fabrication scheme of extended-nano space for NMR measurements

(A) SEM image after EB lithography and etching (B) bonding and cutting
(C) introduction to NMR tube

3.Results and discussion

We made ¹H-NMR spectrum measurement of Hacac in water, and evaluated keto-enol equilibrium of Hacac based on peak area ratio of methyl group of keto form to that of enol one ($K_{EQ} = [\text{keto}]/[\text{enol}]$). As shown in Figure 3, keto form of Hacac increased drastically with decreasing the sizes at around 500 nm. The K_{EQ} values of bulk and 202 nm are 3.7 and 4.8, respectively. The tendency of K_{EQ} corresponds to enhancement of polarity by size-confinement, because keto form of Hacac increases with increasing in polarity of solvent.

To explain such phenomena, we measured temperature-dependence of keto-enol equilibrium of Hacac confined in extended-nano spaces at 0 to 30°C, and examined size-confinement effects on thermodynamic parameters such as

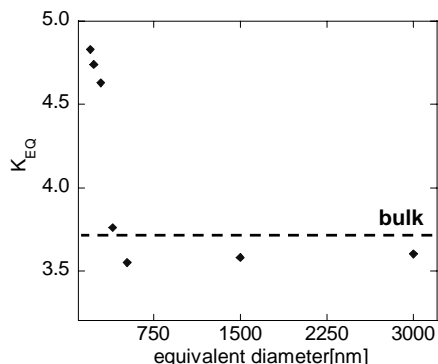


Figure 3. Size-dependence of peak area rate ($K_{EQ} = [\text{keto}]/[\text{enol}]$) of Hacac confined in extended-nano space, in the range of 202 to 3000 nm at 20°C. The dotted line is the K_{EQ} value in bulk water ($K_{EQ}=3.7$).

enthalpy (ΔH) and entropy (ΔS) due to van't Hoff's plot ($\ln K_{EQ} = -\Delta H/RT + \Delta S/R$). Figure 4 shows size-dependence of ΔH and ΔS of Hacac in water. Both ΔH and ΔS values decreased with decreasing in sizes at around 500 nm. The reduction means that keto form of Hacac is energetically and structurally stable. From these results, we concluded that in bulk space the Hacac and water have hydration structures as shown in Figure 5(a), while in extended-nano spaces the water molecules form well-ordered hydrogen bonding networks from surface and the C=O of Hacac molecules and water molecules are structured as shown in figure 5(b). This would result in changes of polarity of water by size-confinement.

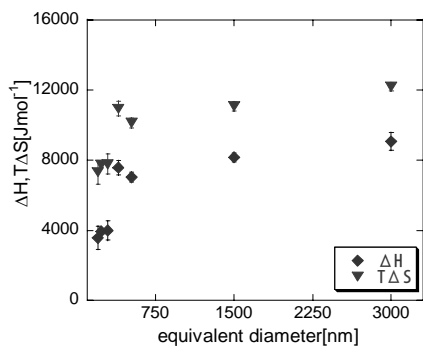


Figure 4. Size-dependence of enthalpy (ΔH) and entropy (ΔS) of Hacac confined in extended-nano space, in the range of 202 to 3000 nm

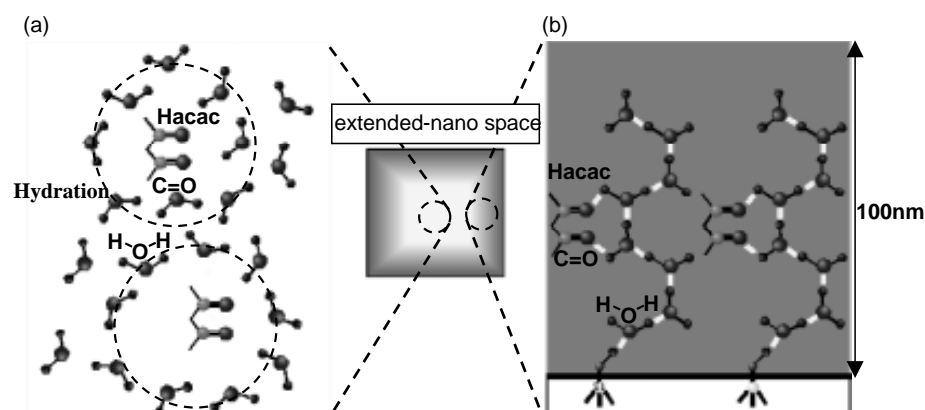


Figure 5. Concept model of water and Hacac (a) bulk space: hydration structure (b) extended-nano space: the C=O of Hacac molecules and water molecules are structured

REFERENCES

- [1] A. Hibara, T. Saito, H.B. Kim, M. Tokeshi, T. Ooi, M. Nakao, and T. Kitamori, “Nanochannels on a fused-silica microchip and liquid properties investigation by time-resolved fluorescence measurement,” *Anal. Chem.*, 2002, **74**, 6170.
- [2] T. Tsukahara, A. Hibara, T. Kitamori, “NMR studies on molecular structures and dynamics of water confined in nanochannels,” *Proceedings of μTAS 2004*, 2004, 189.

FUNDAMENTAL PROPTIES OF MICRO SUPERCOOLING FLOW

Akihide Hibara,^{1,2,3} Shinya Matsuoka,¹
Masaharu Ueno,¹ and Takehiko Kitamori^{1,2}

¹Department of Applied Chemistry, School of Engineering, The University of Tokyo, 7-3-1 Hongo, Bunkyo, Tokyo, 113-8656, Japan

²Microchemistry Group, Kanagawa Academy of Science and Technology, 3-2-1 Sakado, Takatsu, Kawasaki, Kanagawa 213-0012, Japan

³PRESTO, Japan Science and Technology Agency, 4-1-8 Honcho, Kawaguchi, Saitama 332-0012, Japan

Abstract

Fundamental properties of micro supercooling flow were demonstrated. We found that the freezing temperature of water depends on surface properties and size. The lowest freezing temperature was observed as -28 °C in the 70-μm-wide microchannel modified with hydrophobic group. Then, we confirmed the freezing temperature was independent of flow. Furthermore, we found micro supercooling flow can be realized for organic solvents.

1. Introduction

Micromodel fluid in microchannels has attracted attention as a special fluid having characteristics which are not observed on a macro scale. Water can remain in a supercooled liquid state at a temperature below the melting point where ice nucleation may be prevented. According to classical nucleation theory, the rate of nucleation depends on the number of water molecules. We have reported micro supercooling flow formation and its application to asymmetric synthesis [1]. However, fundamental properties of the micro supercooling flow have not been elucidated. In this paper, in order to clarify fundamental properties of the supercooling flow, freezing temperature was measured.

2. Experimental

Figure 1 shows experimental setup for measurement of freezing temperature inside microchannels. The microchips were put on a temperature controlling stage. Distilled water was introduced by a syringe pump into the microchannel. In the freezing point measurements, the flow in the microchannel was stopped except when measuring flow-dependence. The phase transition in the microchannels were judged from CCD images. At the beginning of the measurements, microchip temperature was controlled at 5 °C and kept there 5 min. Then, temperature was decreased at the rate of 1.0 °C/min until the pre-selected temperature was reached, and water in the microchannel was observed for 10 min. If freezing was observed during this time, this temperature was recorded as the freezing point. If it was not seen, the stage temperature was increased to 5 °C (initial state), and then, the temperature was

decreased ($1.0\text{ }^{\circ}\text{C}/\text{min}$) until the next selected temperature was reached, and water was observed for 10 min again. This operation was repeated until the water froze and the freezing point was recorded.

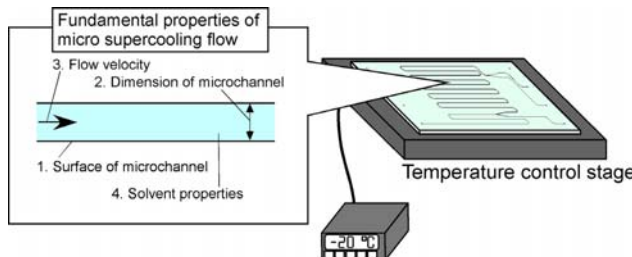


Figure 1 Illustration of experimental setup. The microchip is fixed on a temperature control stage, and liquid in the microchannel is observed by a microscope.

3. Results and discussion

Figure 2 shows the freezing point in the microchannels having a various dimensions. The diamond and circle show the freezing point in the microchannels having a bare glass surface and a hydrophobic surface, respectively. The hydrophobic surface was prepared by modifying octadecylsilane (ODS) group. In case of the hydrophobic surface, the freezing point of water decreased with decreasing the dimension. This tendency indicates that possibility of nucleation decreased with reducing surface area or liquid volume, which coincided with the classical nucleation theory. Contrastively, in case of the bare surface, the freezing point was $-15\text{ }^{\circ}\text{C}$ and was independent of the dimension. Generally saying, interactions between bare glass surface and water include various complicated phenomena. Although we cannot decide the reason why the freezing point was independent of the dimension, some chemical interaction governed the freezing process.

Table 1 Dimensions of the microchips and freezing points of water in the microchannel having hydrophobic or hydrophilic surfaces.

Microchip #	Width (μm)	Depth (μm)	Freezing temperature of water ($^{\circ}\text{C}$)	
			Hydrophilic surface	Hydrophobic surface
1	70	30	-15	-28
2	100	40	-15	-28
3	120	190	-15	-28
4	190	90	-15	-22
5	240	120	-15	-20
6	300	150	-15	-20

Next, we verified dependence of the freezing temperature on flow rate in the microchannel having a $100\text{-}\mu\text{m}$ width with a hydrophilic glass surface. The flow rate

was set from 0.1 $\mu\text{l}/\text{min}$ to 2.0 $\mu\text{l}/\text{min}$, which corresponds to averaged flow velocity of 0.42 mm/s to 8.33 mm/s. The freezing point was independent of the flow rate.

Figure 2 shows degree of freezing of several normal alcohols. Degree of supercooling is defined as $(T_m - T_f)/T_m$, where T_f is experimental freezing temperature, and T_m is melting point (literature value). Here, we found micro supercooling flow can be applied not only for aqueous solution, but also for various kinds of organic solvent.

By utilizing these features, the micro supercooling flow can be utilized in organic synthesis, analytical chemistry, physical chemistry and biochemistry.

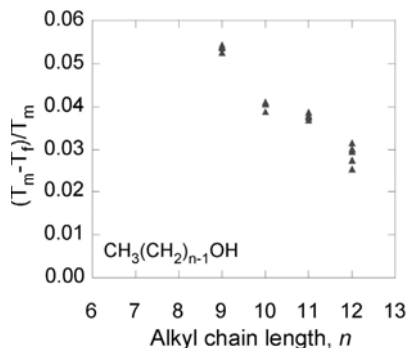


Figure 2 Degree of supercooling of several normal alcohols.

4. References

- [1] S. Matsuoka, A. Hibara, M. Ueno, and T. Kitamori, *Supercooled micro flows and application for asymmetric synthesis, Lab on a Chip* **6** 1236-1238 (2006)

IN-SITU MEASUREMENT OF THE PHOTOOXIDIZATION PROCESS OF ALKANETHIOL SELF-ASSEMBLED MONOLAYERS USING DUAL-CHANNEL QUARTZ CRYSTAL MICROBALANCE

Takashi Abe, Hiroshi Kato, Xinghua Li, Matsuhiko Nishizawa
Tohoku University, 6-6-01, Aoba-ku, Sendai 980-8579, Japan

Abstract

We demonstrate in-situ measurement of the photooxidation process of alkanethiol self-assembled monolayers using a Dual-channel Quartz Crystal Microbalance (D-QCM) sensor that uses spherically contoured resonators to acoustically separate sensing channels for simultaneous compensation of environmental disturbances. Using a photolithographic method to make the D-QCM, the reference channel used in parallel with the sensing channel has almost the same resonant frequency and temperature coefficient of frequency. As a result, mass changes of 10-pg order accuracy were observed under strong ultraviolet radiation over 4 days. Using the D-QCM, we can success to measure photoconversion from thiolate to sulfonate during UV irradiation

Keywords: Microfabrication, QCM, SAM, Dual-channel, Photooxidization

1. Introduction

Generally, the sensor response is not associated with the quantity being measured because of environmental drift such as temperature. It is well known that photooxidation by UV exposure leads to temperature drift. Frequency errors due to this temperature drift limit the accuracy of the mass measurement. For example, an AT-cut resonator (9 MHz fundamental mode) shows at least a 1 ppm frequency shift for each 1 K of temperature change. This frequency error of 1 ppm equates to several molecular layers of water. Therefore, mass change can not be accurately determined during strong UV irradiation.

To compensate for the environmental disturbance and provide sub-atomic-layer resolution, we have developed a Dual-channel Quartz Crystal Microbalance (D-QCM) using the photolithographic method. The use of photolithography is very important because two sensors need to be fabricated spatially close in order to cancel environmental disturbances. For miniaturization, it is known that the reduction of unwanted spurious responses is of paramount importance to avoid vibration coupling[1]. In order to reduce the generation of spurious modes and obtain a high quality resonator, we decided to fabricate a convex shaped QCM. Conventionally, the convex crystal resonator has been produced by polishing and has some problems, for example, difficulty in miniaturization and bulk fabrication and surface damage on the polished side. Recently, we have developed reactive-ion etching technology for quartz and glass [2] and this technology has been applied to the manufacture of convex type quartz-crystal resonators [3,4]. Combining the photolithographic and dry etch processes offers new promising approaches to the manufacture of QCMs with high Q, small diameters and monolithic integration on a substrate.

2. Experimental

The schematics of the experimental set-up and the optical photograph of the D-QCM are shown in Figure 1. The dimensions of fabricated QCMs are 1 mm diameter electrodes and 2 mm convex shallow formation. The thickness of the AT-cut quartz crystal is 100 μm . The resonator array having resonant frequencies within the frequency difference of 50 ppm was selected for the use as the D-QCM. The optimum convex

height was chosen to acoustically separate the resonator. In this study, all resonators used for the D-QCM were etched at least 3% of total thickness. The mass resolution of the fabricated sensor was evaluated by electroplating nickel on the electrode. The mass resolution was estimated at about 10 pg/Hz.

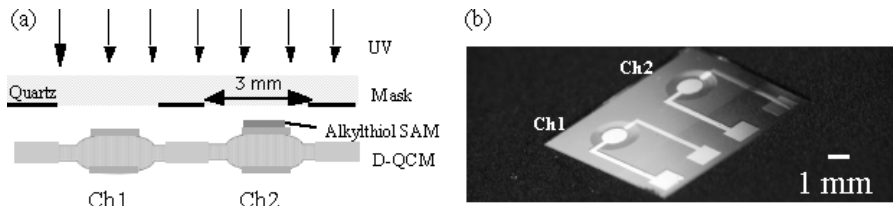


Figure 1 Schematic and photograph of D-QCM. (a) Experimental set-up for in-situ measurement of photooxidation using D-QCM. (b) Photograph of the D-QCM chip.

3. Results and discussion

The frequency response to variations in intensity of UV light are shown in Figure 2. Here, the reference channel is channel 1 (Ch1) and the sensing channel is channel 2 (Ch2). UV light from a high-pressure mercury lamp (HAMAMATSU, LC5) was radiated uniformly. For example, the difference in resonant frequency between Ch1 and Ch2 was about 0.2 Hz for 0.18 mW/cm² and about 0.6 Hz for 0.89 mW/cm² at 254 nm. The positive shift in resonant frequency due to the radiation is explained by the absorption of UV light. It should be noted that there was no acoustical interference with the sensor response when one of the resonators was masked. Of course, the sensor response of the masked resonator shows gradual frequency drift because of thermal transmission from the UV exposed region.

The photooxidation of a self-assembled monolayer was measured to show the usefulness of the D-QCM. The sensing electrode was dipped into an 0.01 mM ethanolic solution of decanethiol (Mw. 174.3) for 10 min. The frequency shift because of the binding is about 140 Hz. The UV intensity was held constant at 0.6 mW/cm² (254 nm). High-pressure mercury lamp is employed for monitoring the slow photooxidation of alkanethiol. Figure 3 shows the frequency responses with exposure of UV light on the monolayer. To show the utility of the D-QCM, the frequency response measured by a single QCM (S-QCM) is shown in Figure 3(a). This shows that the frequency drift depends on the environment. Under the exposure of strong UV light, in-situ measurement is impossible by using the S-QCM. On the other hand, the frequency shift measured by the D-QCM detects an interesting phenomenon as shown in Figure 3(b). The frequency decreased gradually over time. This change is explained by oxidation of

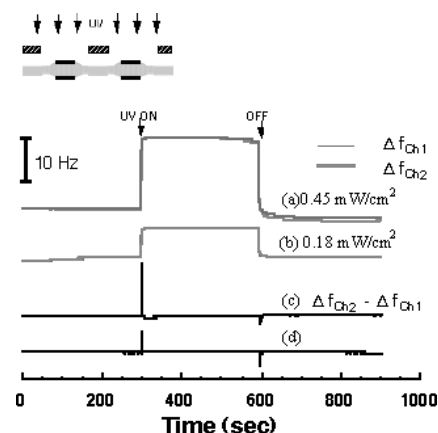


Figure 2 Frequency responses for Ch1 and Ch2 and the differences during exposure to UV light. (a) Frequency responses (0.45 mW/cm^2). (b) Frequency responses (0.18 mW/cm^2). (c) Frequency difference (0.45 mW/cm^2). (d) Frequency difference (0.18 mW/cm^2)

thiol groups. It is well known that UV (254nm) radiation breaks the Au-S bond and oxidizes the sulfur atom forming SO_3 [5]. The high-pressure lamp used in this work emits very weak intensity of light with a wavelength of 254 nm. Thus, the photooxidation was completed after 4-days-irradiation of UV light. Without any films on Au, no change was measured when the lamp was turned off. To check the reproducibility, we tried the measurement repeatedly. Figure 3(c) shows the frequency shift with UV exposure measured again after the photooxidation was completed. The frequency gradually increased when the lamp was turned on. After the lamp was turned off, the frequency decreased with the total frequency change within 2 Hz (equal to 20 pg). Here, the temperature at the resonator is raised up to about 60 degrees centigrade. It is reasonable to explain the frequency shift by water desorption and adsorption on the photooxidized monolayer.

4. Conclusions

In-situ measurement of the photooxidation process of alkanethiol self-assembled monolayers was demonstrated by using a D-QCM sensor. It should be noted that in-situ measurement of photooxidation is not reported in any earlier study of SAMs on Au before this study. The D-QCM will be one of the key analytical tools for in-situ measurements of interfacial phenomena under environmental disturbances.

Acknowledgements

This work was supported by the Ministry of Education, Culture, Sports, Science and Technology, Grant-in-Aid for Young Scientists (A).

References

- [1] W. Shockley, D.R. Curran, D.J. Koneval, *J. Acoust. Soc. Am.* **41**, 981 (1967).
- [2] a) T. Abe, M. Esashi, In Proceedings of Transducer'99, pp.1246-1249 (1999). b) T. Abe, M. Esashi, *Sens. Actuators A* **82**, 139(2000).
- [3] L.Li, M. Esashi, T. Abe, *Appl. Phys. Lett.* **85**, 2652 (2004).
- [4] T.Abe, H. Shimamoto, X. Li, *Jpn. J. Appl. Phys.* **45**, 5283(2006).
- [5] N.J. Brewer, S. Janusz, K. Critchley, S.D. Evans, and G.J. Leggett, *J. Phys. Chem. B* **109**, 11247 (2005).

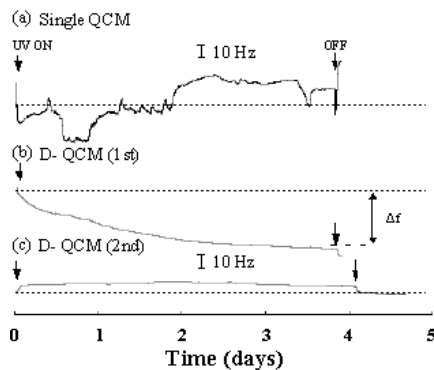


Figure 3 Frequency responses of alkanethiol monolayer coated sensor during exposure to UV light. (a) The frequency response measured by S-QCM. (b) The frequency response measured by D-QCM. (c) The frequency response measured by D-QCM for the UV exposed monolayer until photooxidation was completed.

A NEW MICROSTRUCTURED REACTION-CALORIMETER AS SCREENNING TOOL FOR THERMOKINETIC AND SAFETY PARAMETERS

J. Antes, D. Schifferdecker, S. Loebbecke, H. Krause

Fraunhofer Institute for Chemical Technology ICT, 76327 Pfinztal, Germany

Contact E-mail: aj@ict.fhg.de

Abstract

A microreactor based reaction calorimeter is described, which can be used as a screening tool for the evaluation of thermokinetic parameters in real time.

Keywords: reaction calorimetry, reaction enthalpy, thermokinetic

1. Introduction

For the chemical industry a “minimal time to market” is a crucial factor. For deciding the best way of a chemical synthesis, lots of detailed information about thermokinetics and safety parameters is needed in early phases of process development. These parameters are usually measured with reaction calorimeters, such as the RC1 from Mettler-Toledo [1], [2]. However, commercially available reaction calorimeters require an unfavourable large test volume of about 0.3 – 2.0 l and thus a relatively huge amount of test substance. Hence, the safety analysis of fast exothermic reactions with such reaction calorimeters raises several problems. The control of the reactor temperature and a sufficiently rapid mixing are difficult to achieve. This may cause significant selectivity and safety problems.

2. Experimental

To overcome the drawbacks of commercially available calorimeters, a new small reaction calorimeter with a hold-up of only 100 µl has been developed (Fig. 1a, 1b). The µl-calorimetric device consists of a flat microreactor made of glass. The microreactor is embedded between thermoelectric modules as heat-flow sensors, whereby the upper seebeck element is segmented in eight miniaturized seebeck elements to achieve a spatial resolution of the reaction enthalpy (Fig 2, 3). The entire calorimeter is placed into a thermostated unit to prevent the influences from the environment.

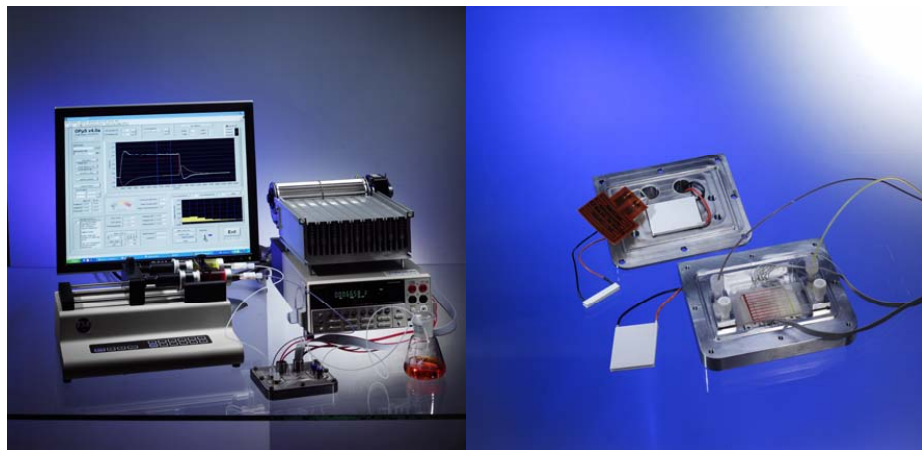


Fig. 1a: Experimental set-up of the new screening tool

Fig. 1b: Measuring cell of the reaction calorimeter with a reactor made of glass

Pulsation-free syringe pumps are used for the control of the reactants flow rates. Reaction processing and data acquisition are computer-controlled by using LabVIEW-programmed automation software.

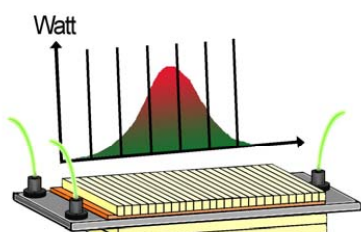


Fig. 2: Segmented seebeck elements for the spatial resolution of measured heat flows

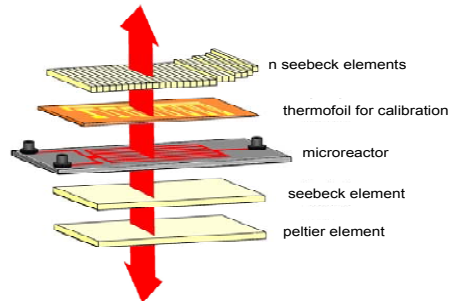


Fig. 3: Sandwich setup of a microreactor embedded between thermoelectric modules

The calorimetric measurement is performed by measuring continuously the heat flow that is released by the chemical reaction in the microreactor through the Seebeck elements. The generated voltage signals of the Seebeck elements are directly proportional to the reaction enthalpy of the chemical reaction. The measurement can be performed isoperibolic or isothermal. For isothermal measurements an additional PID controlled Peltier element is needed to achieve isothermal conditions in the microstructured reactor even in highly exothermic reactions.

3. Results and discussion

The new μl calorimeter has a very small time constant of about 3 s which is a factor 20 smaller than that of conventional calorimeters. The performance and the accuracy of the new device have been demonstrated based on several exemplary reactions, e.g.:

- the nitration of toluene with 100 % nitric acid: in Fig. 4 the measured heat release is plotted versus the volume flow of the toluene. The linearity of the calorimetric measurement confirmed that the conversion was complete at the end of the microreactor and the reaction enthalpy could therefore be estimated. The heat of reaction can be determined from the slope of the measured heat flow, i.e. 110 kJ/mol (literature: -115 to -135 kJ/mol).

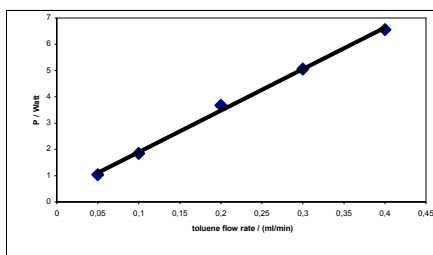


Fig. 5: Nitration of toluene: measured heat release as a function of toluene flow rate



Fig. 6: Hydrolysis of acetic anhydride, spatial resolution of the measured heat flow

- the hydrolysis of acetic anhydride with 10 M hydrochloric acid (measured reaction enthalpy at 25°C: 58 kJ/mol (literature: -57 to -62 kJ/mol). The progress of the reaction is shown in Fig. 6. The spatially resolved measurement of the heat flow along the flow direction permits an easy and fast characterisation of thermokinetic parameters.

4. Conclusion

The advantages of the new microreactor based reaction calorimeter can be summarized as the following:

- Reaction calorimetry in real time, no time-consuming calibrations
- Small reaction volume ($100 \mu\text{l}$), minimum substance consumption
- Safe analysis of potentially dangerous reactions, even critical process conditions can be investigated
- Fast screening of reaction and process conditions
- Isothermal measurement even of fast and strongly exothermic processes
- Working at steady state conditions avoids problems related to the time constant

References

- [1] Mettler Toledo, <http://www.mt.com>
- [2] R. Riesen, B. Grob, Swiss Chem. 7 (1985) 39-43

MECHANISM OF REACTION EFFICIENCY ENHANCEMENT IN MICROCHANNELS STUDIED BY SPECTROSCOPIC VISUALIZATION AND NUMERICAL SIMULATION

**Hirofumi Kawazumi¹, Kenichi Kanno¹, Masayuki Fujii¹,
Yoshiko Yamaguchi², Hideaki Maeda^{2,3}**

¹Department of Chemistry, Kinki University Kyushu, Iizuka, 820-8555, Japan

²National Institute of Advanced Industrial Science and Technology (AIST),
Micro-space Chemistry Laboratory, Tosa 841-0052, Japan

³Graduate School of Engineering Sciences, Kyushu University,
Kasuga 816-8580, Japan

Abstract

The mechanism of high reaction efficiency of an organic condensation reaction and an enzyme hydrolysis in microreactors was studied by using the on-line visualization and numerical simulation for spatial distribution of the products. The characteristic fluidic behavior appeared to play an important role in the reaction efficiency enhancement.

Keywords: Yield, condensation, enzyme hydrolysis, fluidics

1. Introduction

Miniaturized chemical analytical systems have been attracted interest owing to the advantages of fast analysis time, reduction of reagent consumption, portability and disposability. Furthermore, in terms of reaction time and yield better performances of some reactions have been demonstrated in microreactors with a few hundred micrometer dimensions [1]. To control the reactions and design the reactors, we should take into account the characteristic fluidic behavior such as laminar flow in the microchannel. In this report, the mechanism of the reaction efficiency enhancement is studied by using spectroscopic visualizations and numerical simulations for spatial product distributions in microchannels.

2. Experimental

Two reactions of condensation and enzymatic hydrolysis showed the increase of

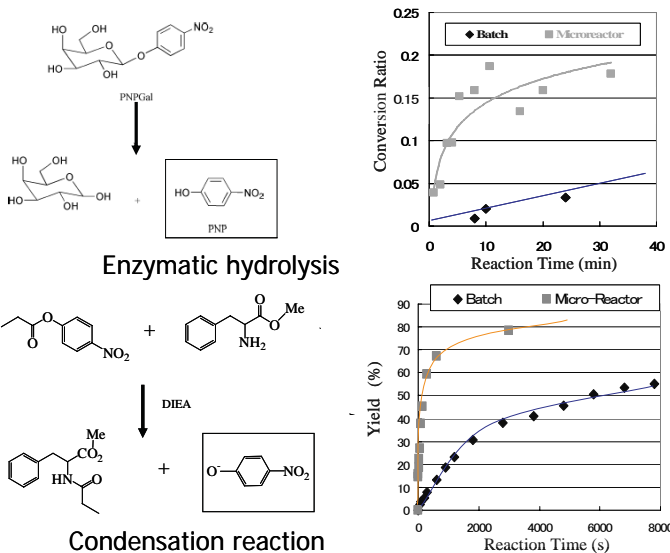


Figure 1. Reaction efficiency enhancement in a microreactor.

the reaction yield and the acceleration of the reaction rate in a Y-shape mixing microreactor, as shown in Figure 1. The product from the outlet of the microreactor was collected and analyzed with HPLC. In the on-line visualization, the colored product, p-nitrophenol (PNP), was measured in the absorption by using a microscope with 16-bits resolution CCD camera. The fluidic behavior was also visualized by using color pigments [2] and an acid-base indicator of phenolphthalein. The numerical simulations carried out with FLUENT (Fluent Inc., Lebanon, NH, U.S.A).

3. Results and discussion

Figure 2 presents a typical fluidic behavior of the laminar flow. The results from the on-line visualization indicate non-linear reaction progress along the flow and non-uniform product distribution across the microchannel. This feature is understood

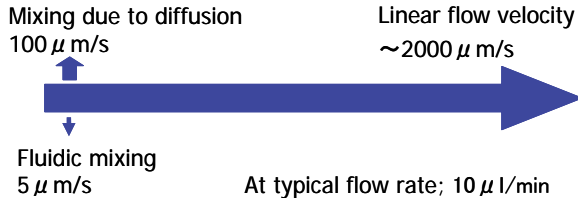


Figure 2.
Fluidic behavior in a laminar flow resulting from
spectroscopic visualization.

with the characteristic flow behavior in Figure 2. In the microreactor overall, however, the reaction rate constant in the microchannel is the same as that in the bulk reactor.

The numerical simulations carry out in order to relate quantitatively these spectroscopic measurements to the mechanism of the reaction efficiency enhancement. Figure 3 presents the product accumulation in each small part of a cross section of the microchannel. The reaction time is calculated from the channel length at the observation points and the flow rate. A larger acceleration is observed at the center part resulting from the starting material mixing in high initial concentrations at the laminar flow interface. Furthermore, the laminar flow efficiently brings the reaction product at the center region of the microchannel because the linear velocity distribution of the flow is parabolic and the lateral diffusion is suppressed in the laminar flow. Therefore, the product around the center is transported efficiently to the outlet and the product yield might result in the high efficiency in Figure 1.

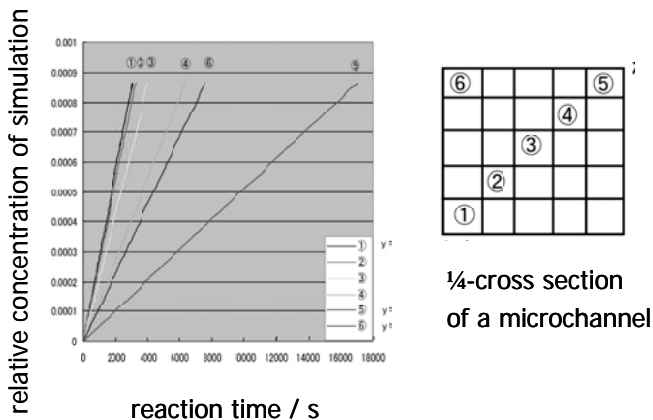


Figure 3. Numerical simulation of product yield in each partial cross section.

References

1. P. D. I. Fletcher, S. J. Haswell, E. Pombo-Villar, B. H. Warrington, P. Watts, S. Y. F. Wong and X. Zhang, *Tetrahedron*, **58**, 4735-4757 (2002); K. Kanno, H. Kawazumi, M. Miyazaki, H. Maeda and M. Fujii, *Aust. J. Chem.*, **55**, 687-690 (2002).
2. H. Kawazumi, A. Tashiro, K. Ogino and H. Maeda, *Lab on a Chip*, **2**, 8 – 10 (2002).

THE EFFECT OF SUPERHYDROPHOBIC SU-8 PATTERNEDE SURFACES ON THE RESPONSE OF THE QUARTZ CRYSTAL MICROBALANCE

P. Roach; C.R. Evans; G. McHale; N.J. Shirtcliffe and M.I. Newton

School of Biomedical and Natural Sciences, The Nottingham Trent University,
Clifton Lane, Nottingham UK NG11 8NS

Abstract

SU-8 photoresist was used to construct 5 micrometer diameter pillar arrays on quartz crystal microbalance (QCM) surfaces spaced 10 micrometers centre to centre, with varying heights from 5 to 25 micrometers. Liquid responses of the patterned QCMs are reported for a series of glycerol-water mixtures to cover a broad density-viscosity product range. Hydrophobic chemical treatment of the patterned surfaces was also conducted, with contact angle measurements being studied to assess the wetting state. The frequency spectra were recorded and fitted to a Butterworth van Dyke model, allowing changes in frequency, resistance, dissipation and a Newtonian liquid check to be carried out.

Keywords: QCM, SU-8, superhydrophobicity

1. Introduction

Amongst the most widely used acoustic wave devices is the quartz crystal microbalance (QCM). The first quantitative model for solid films attached to a quartz surface was given by Sauerbrey [1], relating frequency change to added mass per unit area. If the QCM is placed in a liquid the oscillatory motion of the crystal is damped by the entrained liquid and decays within a characteristic penetration depth [2,3]. The Kanazawa and Gordon equation describes both a frequency shift and a damping of the crystal resonance proportional to the square root of the density-viscosity product of the liquid.[3]

It is recognized in the literature that surface roughness can enhance the response of an acoustic wave sensor [4,5]. A number of models have been proposed for this effect, including Martin *et al*'s suggestion of a trapped mass of liquid acting as a rigid mass load [6,7] in addition to the Kanazawa and Gordon liquid response. Further, Theisen *et al* [8] have suggested that for a thickness shear mode device a high contact angle on a rough surface can trap gas and hence cause a trapped mass response dependent on the hydrophobicity of the surface. Thompson *et al* [9-11] have suggested that interfacial slip may occur so that a contact angle dependent response might exist even on a smooth surface. Ellis *et al* [12] have provided a predictive model showing how the equilibrium contact angle on a QCM surface might lead to interfacial slip. Recently, McHale and Newton have shown how a hydrodynamic slip boundary condition can provide a theoretical basis for either a trapped mass response or an interfacial slip response [13].

2. Experimental

The work presented is an extension of earlier research [14] in which we investigated the effect on the resonant frequency of a QCM of systematically patterning layers of SU-8 photoresist. 5 micrometer diameter features were patterned onto a QCM crystal, Figure 1, and subsequently chemically modified to produce superhydrophobic surfaces (i.e. water contact angles >150°). A range of glycerol/water mixtures were investigated to cover a broad density-viscosity range. The full resonant curves were fitted to a Butterworth van Dyke model allowing trends in frequency change and dissipation to be examined as well as a Newtonian liquid check. Varying feature heights were examined and measurements compared to flat surfaces, before and after chemical modification.

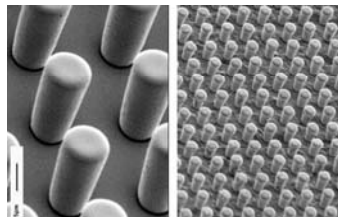


Figure 1. Electron micrograph of a typical SU8 pattern on a quartz crystal microbalance

3. Results and Discussion

Results showed a clear trend in frequency shift corresponding to the Kanazawa and Gordon model for all SU-8 structures except those being 10 micrometers tall, which gave rise to reproducible positive frequency shifts (referenced to water) for high % glycerol solutions (>90%), Figure 2.

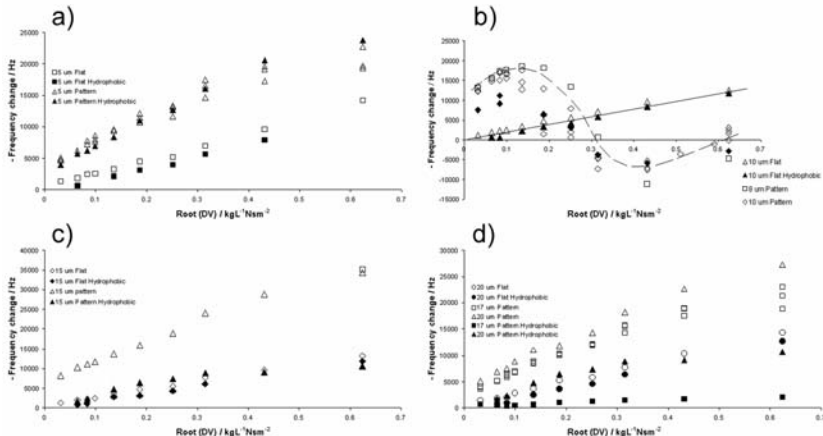


Figure 2. Frequency shifts referenced to water, shown with respect to square root viscosity-density product for varying % glycerol solutions; a) 5, b) 10, c) 15 and d) 20 micrometers thick flat and patterned layers. Trend lines in b) are added as guides only

Interestingly for these surfaces a non-Newtonian liquid response was also observed. After hydrophobisation lower frequency changes were observed for all patterned structures above 5 micrometers tall. Dissipation trends followed this pattern, with all surface patterns having a linear relationship between the change in dissipation relative to water and the square root of the viscosity-density product of the liquid, except those 10 micrometers tall, Figure 3. Hydrophobisation of the patterns also reduced the change in dissipation. The results presented clearly indicate that the combination of surface topography and surface chemistry can have a strong influence on the solid-liquid interfacial coupling as assessed using the response of the quartz crystal microbalance.

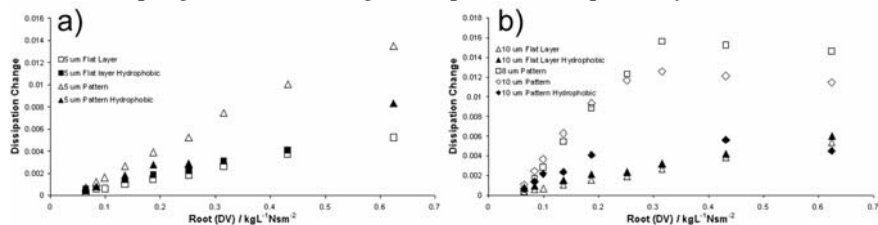


Figure 3. Dissipation changes referenced to water, shown with respect to square root viscosity-density product for varying % glycerol solutions for a) 5 and b) 10 micrometer flat and patterned layers.

4. Acknowledgements

The authors' acknowledge the financial support of the UK EPSRC.

5. References

1. G.Z.Sauerbrey, *Z. Phys.* 155, (1959) 206-222
2. S.Bruckensteiner and M.Shay, *Electrochim. Acta* 30 (1985) 1295-1300
3. K.K.Kanazawa and G.J.Gordon, *Anal. Chem.* 57, (1985) 1770-1771
4. R.Schumacher, G.Borges and K.K. Kanazawa, *Surf. Sci.* 163, (1985) L621-L626
5. R.Schumacher, J.G.Gordon and O.Melroy, *J.Electroanal. Chem.* 216, (1987)127-135
6. S.J.Martin, G.C.Frye, A.J.Ricco and S.D.Senturia, *Anal. Chem.* 65, (1993) 2910-2922
7. S.J.Martin, *Faraday Discuss.* 107, (1997) 463-476
8. L.A. Theisen, S.J. Martin and A.R. Hillmann, *Anal. Chem.* 76, (2004) 796-804
9. M.Thompson, A.L.Kipling, W.C.Duncan-Hewitt, L.V.Rajakovic and B.A.Cavic-Vlasak, *Analyst* 116, (1991) 881-890
10. M.S.Yang and M.Thompson, *Langmuir* 9, (1993) 1990-1994.
11. M.S.Yang, M.Thompson and W.C.Duncan-Hewitt, *Langmuir* 9, (1993) 802-811
12. J.G. Ellis, G. McHale, G.L. Hayward and M. Thompson, *J. Appl. Phys.* 94, (2003) 6201-6207
13. G. McHale and M.I. Newton, *J. Appl. Phys.* 95, (2004) 373-380
14. C.R.Evans, G.McHale, N.J.Shirtcliffe, S.M.Stanley and M.I.Newton, *Sensors and Actuators A*, 123-124 (2005) 73-76

CONTROLLED DELIVERY OF CALCIUM GATED MthK CHANNELS INTO AN ON-CHIP BILAYER LIPID MEMBRANE FOR ELECTROPHYSIOLOGY MEASUREMENTS

Michele Zagnoni*, Mairi E. Sandison*, Robert J. Wood**, Peter L. Roach** and Hywel Morgan*

* School of Electronics and Computer Science, University of Southampton, U.K.

** School of Chemistry, University of Southampton, U.K.

Abstract.

On-chip biological systems, such as bilayer lipid membranes (BLMs) into which proteins can be artificially reconstituted, have the potential for highly sensitive biochemical detection, particularly when coupled to an electronic and/or optical read-out system. In this work, the on-chip delivery, activation and recording of calcium gated potassium channels were investigated.

Keywords: bilayer lipid membrane, vesicle fusion, electrophysiology.

1. Introduction

Automation and reliability are fundamental biosensor requirements, with the final aim of producing a portable, fully automated sensor array platform remaining an open challenge [1,2]. However, the methods reported to date have either shown poor reproducibility or have not been amenable to automation or to the straightforward injection of protein containing solutions. In order to simplify and improve the reproducibility of this process, we now present a simple polymer microdevice, in which BLMs were formed using an air-exposure technique that rapidly induces the thinning of an initially thick lipid film. The acquisition of electrophysiological measurements of ligand gated ion channels represents a suitable test for on-chip BLM platforms, in order to develop and assess the sequence of individual processes required for a complete lab-on-a-chip system. This sequence comprises: the formation of a stable biological support (BLM) as described above, a controlled protein delivery procedure, the activation of the protein gating mechanism and finally, the electronic data acquisition.

2. Experimental

MthK channels (Fig. 1) [3] were expressed in *E. coli* BL21 (DE3) and were isolated by extraction into decylmaltoside, followed by Ni^{2+} affinity and gel filtration (S200) chromatographies, yielding 1 mg purified protein per litre of cell culture. For biophysical studies, MthK was reconstituted into POPE/POPC/Ergosterol liposomes to give a final concentration of 0.01 mg/mL (molar ratio lipid:protein 10000:1) in order to obtain the desired numbers of channels per vesicle: dried lipid mixture was rehydrated using 720 mM KCl, 8 mM HEPES, pH 7.4 and solubilised with decylmaltoside (22 mM). The solution was sonicated (6 minutes) and MthK added. This mixture was gently agitated for 10 mins at room temperature before the removal of detergent using pre-washed biobeads (four additions of 100 mg beads over four hours). This procedure resulted in the reconstitution of the channels into liposomes (approx. 90 nm in diameter). Subsequently, two different procedures were tested to achieve the required fusogenic proteoliposomes: freeze-thaw-sonication and extrusion. The first procedure relies on the formation of joined vesicles (JV), obtained as described in [5], while the latter gives proteoliposomes of equal size (400 nm in diameter) by extrusion of

lipids, ergosterol and proteins through a polycarbonate membrane. MthK proved stable to both procedures and neither sonication nor extrusion appeared to damage the protein.

The device was fabricated from PMMA (Fig. 2) using a combination of hot embossing and solvent bonding techniques (as described previously in [4]). After filling the entire device with buffer solution, the upper well was drained through the connecting channel. A small volume (<1 μ L) of lipid solution (10 mg/mL 7:3 POPE:POPC in decane) was then pipetted into the well, the majority of the solution flowing into the trench surrounding the aperture, leaving only a thin film over the aperture itself. Following a further injection of buffer, the well was again drained and the remaining lipid film left exposed to air for a short period of time (10-30 s). Once the lipid film had thinned sufficiently, the well was once more filled with buffer. As the device was produced from thin, transparent PMMA films, the thinning of the lipid film could be observed optically, and therefore the optimal point for the final buffer injection could be readily determined. The capacitance was also simultaneously monitored, so as to measure the thinning of the lipid film after the short air-exposure period.

3. Results

The air-exposure technique described above proved to be highly reproducible, with the initially thick lipid film thinning to produce a stable BLM in ~90% of tests (although occasionally more than one air-exposure period was required). The MthK proteoliposomes were successfully fused with an on-chip BLM (Fig. 2) using a previously published technique [6], where each fusion event is marked by a current spike, thus enabling the number of reconstituted channels to be estimated. Following this controlled protein delivery, the ion channel current was recorded after the activation of the MthK gating mechanism by addition of the Ca^{2+} ligand. After vesicle fusion events (Fig. 3), a 10 mM Ca^{2+} concentration was created in the reservoir where vesicles were injected (*cis*). *Cis* and *trans* sides contained 150 mM KCl, 8 mM HEPES, pH 7.4 and 720 mM KCl, 8 mM HEPES, pH 7.4 respectively. This represents a favourable condition for inducing fusions and was maintained also after protein insertion. The results obtained show the channel's activity and voltage dependency (Fig. 4), which correspond to the literature [3] by presenting a non-symmetrical response to positive (8-9 pA jumps) and negative (4-5 pA jumps) applied potentials.

4. Conclusions

The on-chip BLM system described provided stable and reproducible results and this work demonstrates the potential applicability of the system for future drug screening analysis and is encouraging for the development of fully automated biosensor systems.

Acknowledgements

This work is supported by the 6th Framework Programme of the European Commission under the contract NMP4-CT-2005-017114 "RECEPTRONICS". The MthK pQE70 expression plasmid was a kind gift from Youxing Jiang.

References

1. T. Ide, Yanagida, *Biochem. and Biophys. Research Communications*, **265**, 1999, pp. 595-599.
2. H. Suzuki, K.V. Tabata, H. Noji, S. Takeuchi, *Langmuir*, **22**, 2006, pp. 1937-1942.
3. Y. Jiang, A. Lee, J. Chen, M. Cadene, B.T. Chait, R. MacKinnon, *Nature*, **417**, 2002, pp. 515-522.
4. M.E. Sandison and H. Morgan, *J. Micromech. Microeng.*, **15**, 2005, pp.139-144.
5. D.J. Woodbury, *Meth. In Enzymol.*, **294**, 1999, pp. 319-339.
6. M.R.R. de Planque, G.P. Mendes, M. Zagnoni, M.E. Sandison, K.H. Fisher, R.M. Berry, A. Watts, H. Morgan, *IEE Proc. Nanobiotechnology*, **153**, 2006, pp. 21-30.

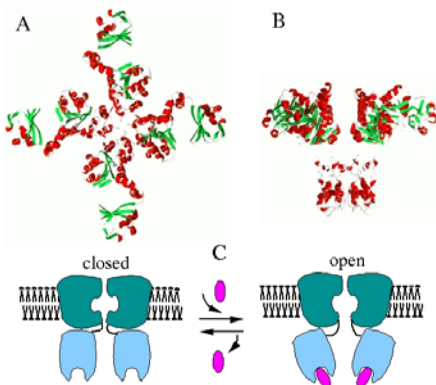


Figure 1. MthK channel [3]. (A) Top view of structure of the calcium gated potassium channel MthK, all four subunits shown. (B) Side view of MthK channel with two subunits shown for clarity. MthK is a homotetramer, each subunit consisting of two domains. One is the gating ring (large domain at the top of structure B) which controls the opening of the pore upon binding of Ca^{2+} ions, as demonstrated in (C). The second domain forms the smaller membrane-spanning pore which is the path through which K^+ ions migrate.

Figure 3. Current trace showing vesicle fusion events and channel activity. Vesicle fusions are characterised by transient current spikes, due to the degradation of nystatin/ergosterol channel incorporated into the vesicles, which were used as markers for controlling the number of fusions [5]. As shown in the highlighted region, after Ca^{2+} delivery, channel activity was observed. A 500 mM KCl gradient is present across the BLM (150mM-700 mM, 8 mM HEPES), as necessary for vesicle fusion, and a 100 mV potential was maintained throughout the process.

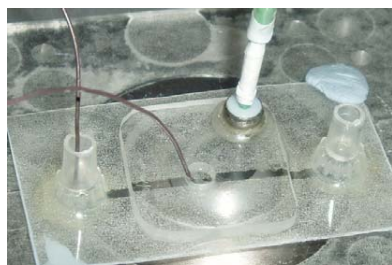


Figure 2. (a) Chip structure. In the centre (circled red) is an aperture where the bilayer is formed, which connects a lower fluidic channel and an upper well. A second channel runs outwards from a trench in the base of the well.
 (b) PMMA chip on which BLM formation and vesicle delivery are performed. Ion channel current is recorded through Ag/Ag-Cl electrodes.

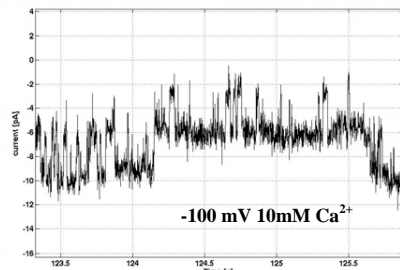
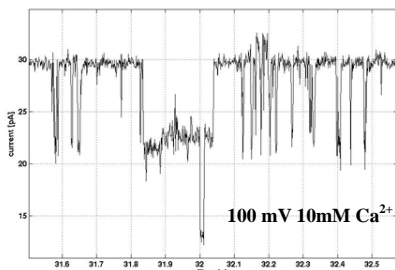
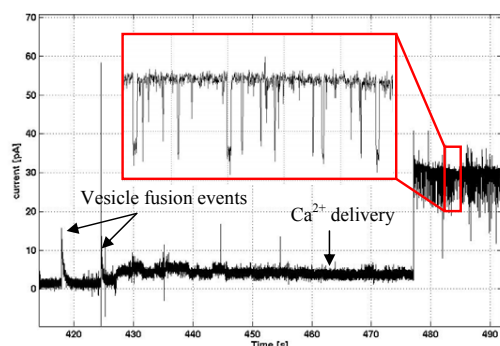


Figure 4. Electrophysiological analysis of MthK channels in a BLM. MthK exhibits a voltage dependency (100 mV left trace, -100 mV right trace). Both recordings were acquired at 1 kHz and a digital low-pass filter at 500 Hz was then applied.

VIABILITY AFTER ON-CHIP SINGLE-CELL MICRO-ELECTROPORATION FOR THE STUDY OF MACROPHAGE SIGNALING PATHWAYS

Eunice S. Lee^{1,2,3}, Sheri-Michele S. Bachelor¹, Zohora Q. Iqbal¹,
Luke P. Lee^{2,3}, and Rafael V. Davalos^{1,4}

¹Sandia National Laboratories, Livermore, CA, USA

²Biomolecular Nanotechnology Center, Berkeley Sensor and Actuator Center

³Department of Bioengineering, University of California, Berkeley, CA, USA

⁴Biomedical Engineering, Virginia Tech-Wake Forest University, Blacksburg, VA, USA
Email: rvdaval@sandia.gov

Keywords: single-cell electroporation, transfection, microfluidics

1. Introduction

In many biological systems the single cell is considered the relevant functional unit. For example, the immune response is carried out by a loosely-coordinated population of cells which is largely driven by the relatively few cells present at the site of infection. Thus, in order to fully understand the behavior of the population one must first understand that of the individual cells which drive it. While genetic engineering can be a valuable tool in such endeavors, certain cell types are recalcitrant to genetic engineering. Macrophages, for instance, are immune cells primed for defense against invading microbes; confronted with foreign nucleic acids, they typically transition into attack mode, confounding their study by genetic means. The shortcomings of genetic engineering may be circumvented through delivery of proteins (e.g., extra copies of endogenous proteins, inactivating antibodies, pathogen-derived toxins) directly into the cell. This can be accomplished using liposomes, bulk electroporation, or microinjection. The first two techniques are typically applied to large populations of cells, and consequently suffer from high degrees of cell-to-cell variability; the last typically damages the cells.

Micro-electroporation (EP) techniques have been developed to enable the delivery of exogenous proteins into single cells [1, 2]. In contrast to bulk EP, which employs high voltage ($\geq 1000V$) to permeabilize large populations ($\geq 10^5$) of cells, micro-EP methods use low-voltage ($< 10V$) electric pulses to permeabilize single cells. Our approach differs from other single-cell approaches in that minimal cell deformation is used to trap the cell. We show that significant cell deformation eventually causes cell death regardless of EP. Since cell response to foreign proteins occurs several hours after introduction, viability after EP is crucial for study of signaling pathways. We demonstrate that our method does not (in and of itself) interfere with the physiology of the cell to any significant degree. To our knowledge, this is the first study of viability after EP has been initiated.

2. Experimental

Device fabrication – We have developed a microfabricated, polydimethylsiloxane (PDMS) single-cell EP device in which single cells can be trapped at individual trapping locations (Fig.1a). Electrical and fluidic connections were made using Cytoflux

manifold (Fluxion Biosciences, CA). During EP, an electric field is applied across the cell, from the trapping channel to the main channel (Fig. 1b). There are two unique features of our design: (1) a cupped trapping area, which reduces cross-flow from the main channel and thereby, enables immobilization of the cell with minimal pressure, and (2) a high seal between cell and the trapping channel is not required to induce EP, minimizing cell deformation.

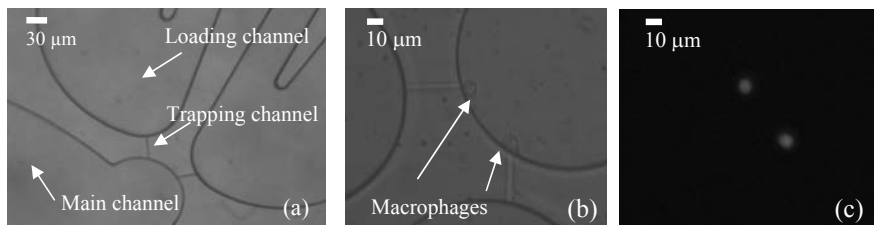


Fig. 1 - (a) Device layout, (b) bright-field image of macrophages trapped on trapping channels, and (c) fluorescent image of macrophages trapped on trapping channels.

Cell preparation – RAW264.7 is an adherent murine macrophage cell line. RAW264.7 cells were cultivated under standard conditions and resuspended to a final concentration of 1×10^6 cells/mL. The cells ($1 \mu\text{L}/\text{mL}$) were incubated with Calcein AM (Invitrogen) at 37°C for 20 min and not removed. Calcein AM is membrane permeant, but becomes fluorescent and impermeant in living cells upon cleavage by intracellular esterases.

Electroporation verification protocol – Single cells were trapped using negative pressure and Labview™ was used to generate and deliver electrical pulses. The electrical test and measurement circuitry used is described elsewhere [3]. 100 ms pulses of various amplitudes (0.7 V, 1.2 V, and 2.5 V) were applied across the trapped cell. In addition to electrical measurements, fluorescent assays were used to document the escape of Calcein from the cell during EP.

Viability assay – After an electric field is applied, the cells were released from the trapping channel and their viability monitored to verify that they were not adversely affected by the electrical pulses. Fluorescent snapshots were captured every 30 min for 3 hrs. Viable cells will continue to fluoresce.

3. Results and discussion

Electroporation verification- Fig. 2 demonstrates verification of EP. We found using single 100 ms pulses that 0.7 V pulses had no effect on the membrane, 1.2 V pulses reversibly open the membrane, and 2.5 V pulses irreversibly opened the membrane.

Viability assay after electroporation - Fig. 3 demonstrates long-term viability after reversible EP (1.2 V for 100 ms). We found that deformation due to trapping eventually caused cell death regardless of EP. Mechanically-stressed cells show a sharp decrease in fluorescence at 1.5 hours, presumably due to cell death. In contrast, undamaged cells showed no such decrease in fluorescence.

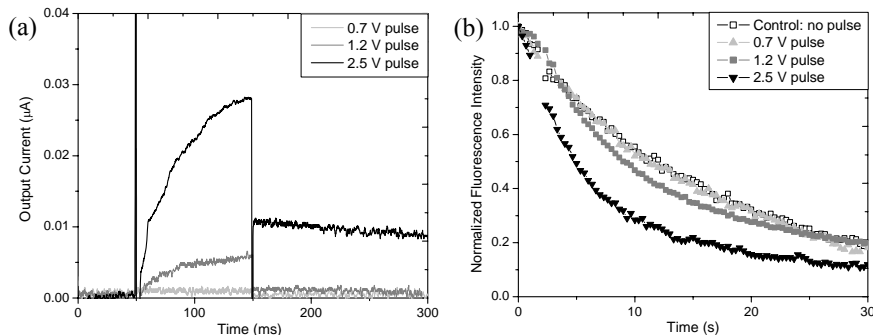


Fig. 2 – Verification of single-cell EP (a) Output current versus time. During EP, an increase in current is seen. (b) Fluorescent intensity versus time. When EP occurs, Calcein dye within the macrophage is released and a decrease in fluorescence is seen. Photobleaching is accounted for the control.

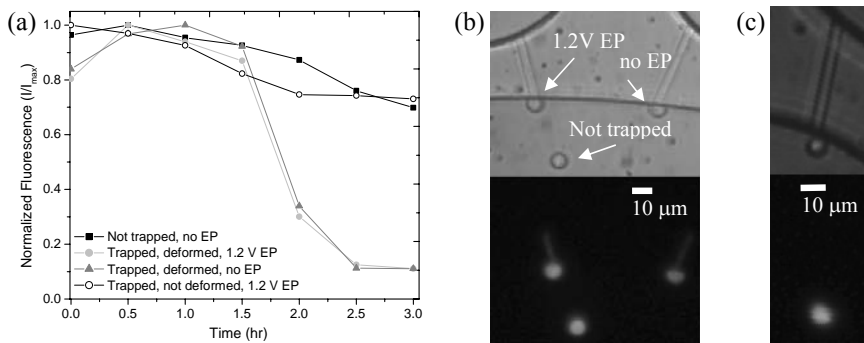


Fig. 3 – Long-term viability after EP. (a) Fluorescence intensity versus time. (b) Bright-field and fluorescent images of trapped and deformed macrophages and a control macrophage (not trapped). (c) Bright-field and fluorescent images of an undamaged cell when trapped.

Conclusion

We have developed a micro-EP technique to deliver precise quantities of proteins into cells. Trapping is achieved with minimal cell deformation, in contrast to other single-cell electroporation approaches. We demonstrated that cell deformation has negative long-term consequences. Our technique does not interfere with the physiology of the cell to any significant degree and is suitable for signaling pathway studies.

Acknowledgements

This work was performed by Sandia National Laboratories for the US Dept. of Energy, contract DE-AC04-94AL85000. We acknowledge funding from the Laboratory Directed Research and Development Program.

References

- [1] M. Khine, et al., *Lab on a chip*, 5 (2005) 38-43.
- [2] R.E. Diaz-Rivera, et al., *Biomedical Microdevices*, 8 (2006) 25-34.
- [3] E. S. Lee, et al., *Bioelectrochemistry*, 69 (2006) 117-125.

Microfluidic Systems Integrated with Pumping/Mixing and Separation Devices for Virus Detection

Kang-Yi Lien¹, Cheng-Yu Liu², Jr-Lung Lin², Hao-Yu Tseng², Wan-Chi Lee², Huan-Yao Lei³ and Gwo-Bin Lee^{1,2}

¹Institute of MEMS Engineering, National Cheng Kung University, Tainan, Taiwan

²Department of Engineering Science, National Cheng Kung University, Tainan, Taiwan

³Department of Microbiology and Immunology, National Cheng Kung University, Tainan, Taiwan

E-MAIL: gwobin@mail.ncku.edu.tw

Abstract

The study presents a new microfluidic system integrated with three functional devices of pumping, mixing and separating for virus sample pretreatment, analysis and detection. By using antibody-conjugated magnetic beads, the virus sample can be purified, enriched and detected with a higher sensitivity and selectivity. Moreover, the integrated micro-system can perform automatic incubation, transportation, mixing, and purification, possibly making it a crucial platform for future biological and medical applications.

Keywords: magnetic bead; mixer; separator; microfluidics; RT-PCR; virus detection

1. Introduction

Recently, micro-electro-mechanical-systems (MEMS) technology and micromachining techniques have enabled the miniaturization of biomedical devices and systems. Transportation, mixing and separation of fluids in microfluidic systems has been critical for miniaturized biomedical systems. Many approaches have been reported to drive fluids inside microchannels. Among them, pneumatic micropump is one of the most commonly used and reliable methods [1]. A rapid and efficient mixing device is also necessary in a chemical reaction or bio-detection system. Microfabricated rotary pump was developed to transport the flow and enhance the mixing performance in the microchannels as well [2]. A micro-total-analysis-system (μ -TAS) which integrates sample pretreatment, separation, transportation, reaction and detection can be realized if several crucial issues have been addressed properly. One of the major challenges for μ -TAS is for sample pretreatment, which has been widely explored recently [3]. For example, magnetic bead-based immunoassay performed on an integrated microfluidic biochemical analysis system was demonstrated [4]. In this study, a hand-held micro-system has been developed to purify and enrich bio-samples, and detect target virus with a higher sensitivity and specificity by using antibody-conjugated superparamagnetic beads.

2. Design

The target viruses were first captured by mixing with magnetic beads conjugated with specific antibody (Figs. 1(a)&(b)), and then purified and enriched by using a magnetic field generated by utilizing an on-chip bio-separator module which consisted of the microcoils (Fig. 1(c)). After washing out the unstable substances in the biological medium, the virus

samples were transported into a reverse transcription polymerase chain reaction (RT-PCR) chamber for nucleus acid amplification (Fig. 1(d)). A photograph of the integrated microfluidic chip is shown in Fig. 2(a). Note that three devices, including a bio-separator, a microfluidic control and a temperature control module, are integrated onto a single chip. Figures 2(b), (c) and (d) show SEM imagines of 2D, 3D microcoils and a rotary pump, respectively. The rotary pump was designed for sample transportation and mixing simultaneously such that viruses can be conjugated with the superparamagnetic beads.

3. Results and discussion

The characterization of the integrated microfluidic chip was first performed. Figure 3 shows the relation between the pumping rate and the driving frequency at different driving air pressures. The optimum operation of the fluid pumping rate was then chosen at a pressure of 20 psi and a frequency of 17Hz. The rotary pump can also work as a mixer for a rapid mixing. Significant mixing was observed (Fig. 4). Additionally, the magnetic field and the temperature generated by the 2D/3D microcoils were measured at different currents and shown in Fig. 5. They were facilitated to design 2D microcoils with the optimum thickness of 12 μ m. The applied current was chosen to be 0.5 A to avoid denaturing the bio-sample due to the temperature over 37°C. Meanwhile, a magnetic field of 30 Gauss can be produced to capture the magnetic beads conjugated with the target virus. Finally, Dengue virus serotype 2 with a detection gene of 171 bps was successfully amplified using the developed microfluidic RT-PCR chip. The detection limit was found to be 10²pfu/ml (Fig. 6a). The specificity of the microfluidic RT-PCR chip was also demonstrated as shown in Fig. 6b.

4. Conclusions

The current study has successfully demonstrated a hand-held, integrated microfluidic system. Samples have been effectively mixed, collected and purified in the automatic one-step process. Moreover, the new integrated microfluidic system can become a crucial platform in biological and medical applications for rapid clinical diagnosis of viruses.

Acknowledgements

The authors would like to thank partial financial supports from the National Science Council in Taiwan (NSC 94-3112-B-006-002, NSC 95-2218-E-006-026) and the MOE Program for Promoting Academic Excellence of Universities (EX-91-E-FA09-5-4).

References:

1. C. H. Wang and G. B. Lee, Journal of Micromechanics and Microengineering, Vol. 16, pp. 1-8 (2006).
2. H. P. Chou, M. A. Unger, and S. R. Quake, Biomedical Microdevices, Vol. 3, pp. 323-320 (2001).
3. A.J. de Mello, and N. Beard, Lab Chip, Vol. 3, pp. 11N-19N (2003).
4. J. W Choi, K. W. Oh, J. H. Thomas, W. R. Heineman, H. B. Halsall, J. H. Nevin, A. J. Helmicki, H. T. Henderson and C. H. Ahn, Lab Chip, Vol. 2, pp. 27-30 (2002).

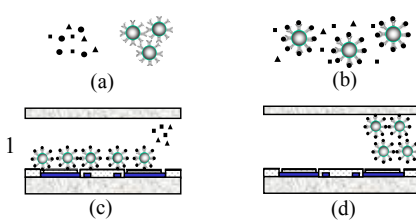


Fig.1 Experimental process of the integrated microfluidic RT-PCR system.

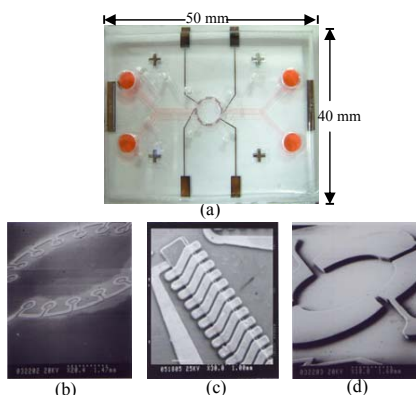


Fig.2 A photograph of the integrated microfluidic RT-PCR chip (a), SEM images of 2D (b), 3D (c) microcoils and a rotary pump (d).

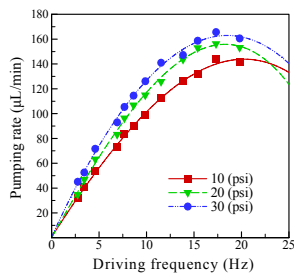


Fig.3 Relation between the pumping rate and the driving frequency at different air pressures.

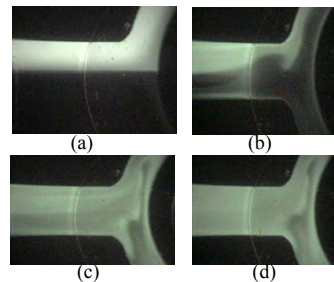


Fig.4 A series of images showing that two different samples can be well mixed by using the rotary pump.

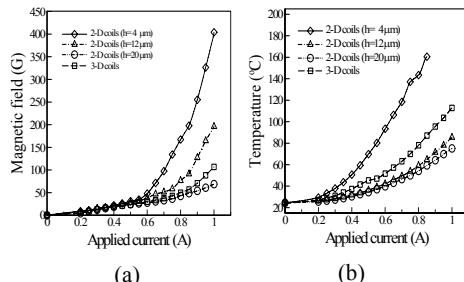


Fig.5 The magnetic field and temperature at different applied currents.

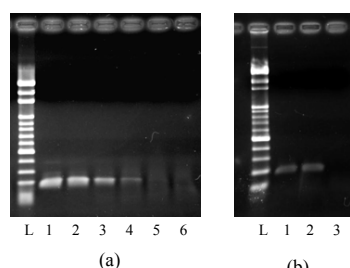


Fig.6 Slab-gel electropherograms of dengue virus. (a) The detection limit of Dengue viruses was 10^2 pfu/ml (lane 5). (b) Dengue virus in clinical serum (lane 1: positive control; lane 2: using magnetic beads; lane 3: without magnetic beads). Note that Lane "L" represents the 100-bp ladder DNA markers.

ELECTROTRANSFECTION IN MICROCHANNEL: A SHORTCUT TO ITS UPTAKE MECHANISM

**W. G. Lee¹, H. Bang¹, J. A. Kim², J. Lee¹, H. Yun¹, J. Park², K. Cho², A. Riaz³,
Y. S. Shin⁴, N. C. Jung², C. Chung², D.-C. Han¹ and J. K. Chang²**

¹School of Mechanical and Aerospace Eng., Seoul National Univ., South Korea

²Digital Bio Technology, Inc., South Korea

³Dept. of Bioengineering, University of California, Berkeley, USA

⁴Div. of Chemistry and Chemical Eng., California Institute of Technology, USA

Abstract

Here we investigated real-time uptake phenomena of foreign DNA molecules into living mammalian cells in electroporation using microchannels.

Keywords: Electrotransfection, microchannel, microcapillary, uptake mechanism

1. Introduction

Electroporation is a well-known gene transfection method to deliver a specific functional DNA into living mammalian cells with electric pulsations [1]. However, still unknown is the basic mechanisms of DNA transfer and intracellular response to the external electric pulses [2-3]. To disentangle these problems, we recently developed a novel method for electrotransfection using microchannel [4] or microcapillary [5].

2. Methodology

One of the advantages of microchannel-type electroporation is *in-situ* visualization of uptake phenomena of molecules into cells, which makes it possible to profoundly investigate the basic mechanisms of DNA transfer and intracellular response to the external electric pulses. Moreover, a uniform electric field in these narrow regions enabled us to enhance both cell survivability and transfection efficiency with few side effects which many conventional devices often had. More recently, we achieved a direct visualization of uptake mechanism of small and macro molecules into living mammalian cells especially in silica nanoparticles suspended medium. Silica is widely used as a biocompatible material, and its nanoparticles are strongly believed to play a double role in an intracellular transporter as well as a DNA condenser around the surface of cells [6]. Many experimental observations at single-cell level were made to explore the unknown uptake mechanism using single- and multi-microchannel equipped on an electroporation tool kit (refer to the Method section of ref. [4]). Several image analyses on directionality and polarity of uptake materials were performed: propidium iodide (PI), green fluorescent protein (GFP), FITC-siRNA, YOYO1-pEGFP (statistical data were not shown), and two classes of fluorescent dye-doped silica nanoparticles (SiNPs) such as 30nm PI-doped core SiNPs and 70 nm tetramethylrhodamine (TMR)-doped core-shell SiNPs. A wide variety of cell lines were statistically investigated [5] and quantitatively recorded using an interactive processing of JAVA program (data were not shown here). In this study, samples were prepared with HeLa cells (300 μ L of 1.5×10^6 cells/mL), YOYO1-pEGFP (6 μ L of 1 μ g/100 μ L), and SiNPs (100 μ L of 0.3mg/mL). The sample (40 μ L) was injected into the inlet of a single rectangular microchannel (50 μ m \times 400 μ m \times 2 cm, in height, width, and length) fabricated with a cover glass as a

bottom plate. Cell viability was measured to be around 97% prior to the experiments. Note that all electrical parameters were optimized to the electroporation protocol of HeLa cells (335V/cm electric field, 35 ms pulse width, 1s period between two square wave pulses). All images were taken using a 12 bit cooled CCD (Cooke SensiCam QE) on inverted microscope (IX71, Olympus) with a 100 \times objective lens (NA 1.4). The camera exposure time was 2 ms and no delay time was applied. Note that the degree of electroporation was strictly dependent on dimensional properties of instrumental environments: electrode type, and size and material of chamber [4]

3. Results and discussion

For 30nm PI-doped core SiNPs, PI dyes were likely to be permeated from their shallow outer shell, and thus produced cloudy PI complexes that were rapidly synthesized with intracellular molecules during electroporation. Figure 1 shows sequential images of YOYO1-labeled pEGFP uptake into a single HeLa cell ([a] to [t]) at two-pulse protocol ([b] and [l] indicate the time of electric pulsation).

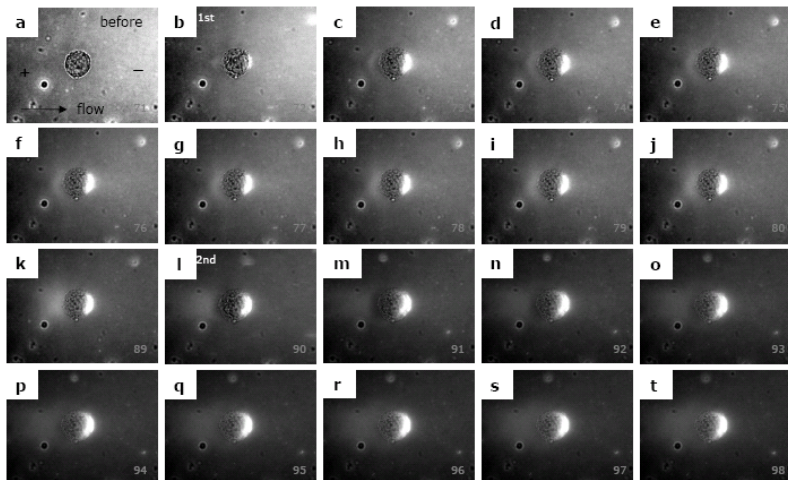


Fig. 1. Real-time observation of DNA uptake in 30 nm PI-doped core SiNPs-suspended media.

More DNA was gathered around the cell surface in 70nm TMR-doped SiNPs-suspended media while such phenomena were little found in only DPBS media as shown in Fig.2. These findings imply that SiNPs can condense more DNA near cell surface. A relative increase of fluorescence intensity of DNA uptake in SiNPs-suspended media was observed possibly due to a simultaneous movement of SiNPs into cells. Figure 2 shows sequential images of YOYO1-labeled pEGFP uptake into a single HeLa cell ([a] to [e]) at two-pulse protocol ([b] and [d] indicate the time of electric pulsation). Here note that the second and the fourth rows show normalized images of the first and the third rows respectively. In our experiments, the sizes of silica nanoparticles were measured using TEM, which showed 30 nm and 70 nm in a dry form (TEM images were not shown here). Note that hydrodynamic diameters of them may get larger than those in a dried state with 15% increase.

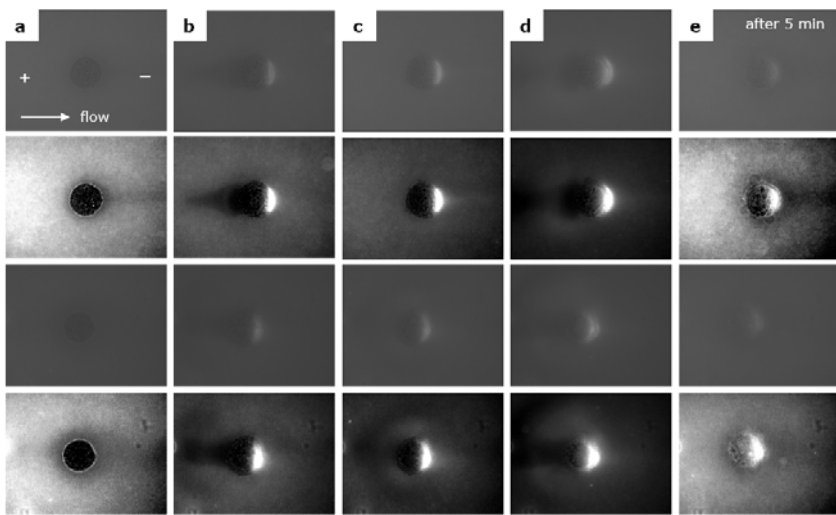


Fig. 2. Comparison between DNA uptake in DPBS with Mg^{2+} and Ca^{2+} (upper two rows) and DNA uptake in 70 nm TMR-doped core-shell SiNPs-suspended media (lower two rows).

4. Conclusions

In this study, uptake phenomena of electrotransfection were observed and visualized in real-time by using a microchannel-type electroporation. We strongly believed that a simple conversion of macro to micro dimension in an effectively induced area of electric field would be able to unveil unknown uptake phenomena of electrotransfection. Furthermore, a full understanding of these uptake mechanisms would open up a new vista to feasible applications of electrically mediated gene or cell therapy.

Acknowledgements

This work was supported by a grant of the Korea Health 21 R&D Project, Ministry of Health & Welfare, Republic of Korea (02-PJ10-PG4-PT02-0042).

References

1. D. Luo and W. M. Saltzman, *Synthetic DNA delivery systems*, Nat. Biotech. **18**, pp. 33-37, (2000).
2. M. Golzio, J. Teissié, and M.-P. Rols, *Direct visualization at the single-cell level of electrically mediated gene delivery*, Proc. Natl. Acad. Sci. **99**, pp. 1292-1297, (2002).
3. D. Luo and W. M. Saltzman, *Thinking of silica*, Gene Ther. **13**, pp. 585-586, (2006).
4. Y. S. Shin, K. Cho, J. K. Kim, S. H. Lim, C. H. Park, K. B. Lee, Y. Park, C. Chung, D.-C. Han, and J. K. Chang, *Electrotransfection of mammalian cells using microchannel-type electroporation chip*, Anal. Chem. **76**, pp. 7045-7052, (2004).
5. Refer to the website of <http://www.microporator.com>
6. H. Ow, D. R. Larson, M. Srivastava, B. A. Baird, W. W. Webb and U. Wiesner, *Bright and stable core-shell fluorescent silica nanoparticles*, Nano Lett. **5**, pp. 113-117, (2005).

GIANT PROTEOLIPOSOME ARRAY IN MICROCHAMBERS

**Nozomu Yamanaka, Kaori Kurabayashi, Kei Funakoshi,
Hiroaki Suzuki and Shoji Takeuchi**

The University of Tokyo, Institute of Industrial Science, 4-6-1 Komaba,
Meguro-ku, Tokyo 153-8505, Japan

Phone: 81-3-5452-6650, Fax: 81-3-5452-6649

E-MAIL: nozomu@iis.u-tokyo.ac.jp

Abstract

This paper describes two novelties which will contribute to the precise examination of the functions of membrane proteins. First, we describe a method to reconstitute purified membrane proteins in giant liposomes (giant proteoliposomes). Second, we established a system to observe the chemical/physical responses of liposomes by confining them in microchamber arrays during the perfusion of surrounding solution through a semi-permeable membrane. Since the position of proteoliposomes does not change during perfusion, we can continuously observe the response of single liposomes. Using this technique, we successfully detected the function of water channel, human aquaporin1 (hAQP1), by observing rapid shrinkage of its proteoliposomes due to the change in osmotic gradient.

Keywords: Giant liposome, Aquaporin, microchambers

1. Introduction

Giant proteoliposomes have been used to evaluate functions of membrane proteins [1]. However, methods for making giant proteoliposomes were complex [2], and membrane proteins may be inactivated during the process. Therefore, there is a need for a simpler preparation process. We employed human aquaporin 1 (hAQP1) as a membrane protein in this paper because the activity of reconstituted hAQP1 into liposomes is easily estimated by changing the osmotic pressure [3]. For the reasons mentioned above, we attempted to make giant proteoliposomes in a single step, and measured the activity of reconstituted hAQP1 in microchambers.

2. Experimental

Preparation of Giant proteoliposomes: The obtained hAQP1 cDNA from ATCC was subcloned into the plasmid, and the hAQP1 plasmids were transfected into HEK293 cells. The membrane fractions containing hAQP1 proteins were obtained by centrifuging cell lysates, and glycerol was added to obtain a final concentration of 10 %. Phosphatidylcholines (PC), phosphatidylethanolamine (PE), cholesterol in chloroform were mixed with DI. The mixed solution was dripped onto a glass substrate and dried. The membrane fraction solution containing hAQP1 was then dripped over lipids and dried for 15 mins. By adding 0.1M sucrose solution, giant liposomes containing hAQP1

spontaneously formed as shown in Fig. 1. Giant proteoliposomes were incubated with anti-hAQP1 and FITC-labeled second antibody. Reconstituted hAQP1s were observed by fluorescence microscopy.

Preparation of Microchambers: Parylene (thickness =10 μm) was deposited onto the glass. A layer of aluminum was then deposited. Immediately after this process, photoresist was spun, and patterned by standard optical lithography. The exposed photoresist was developed to form the mask for aluminum etching. The exposed Parylene was etched with O₂ plasma to form the microchambers. Finally, the aluminum mask was removed with aluminium etchant.

Measurement of hAQP1 activity: Solution containing fluorescence labeled giant proteoliposomes and 0.1M glucose solution were poured over the microchambers. After 30 mins, the microchambers containing giant proteoliposomes were covered with a cellulose membrane to prevent outflow of liposomes from microchambers when hypertonic solution was added. Hypertonic solution (0.5 M glucose) was then introduced over the cellulose membrane, and the changes in diameter of giant proteoliposomes induced by osmotic pressure were observed by fluorescence microscopy at 5 seconds interval for 30 seconds (Fig. 3). The change of relative volume in a giant proteoliposome was estimated from the following equation, provided that a giant proteoliposome was spherical.

$$\text{The volume of a giant proteoliposome at any time: } V_{(t)} = 4(3.14 \times r_{(t)})^3 / 3 \quad (1)$$

$$\text{The change of relative volume in a giant proteoliposome: } V_{(t)} / V_{(0)} \quad (2)$$

We also did similar measurements to giant proteoliposomes without hAQP1.

3. Results and Discussion

We observed binding of anti-hAQP1 antibody in giant proteoliposomes with hAQP1s (Fig. 2), confirming that hAQP1s were successfully reconstituted in giant proteoliposomes using our new method. In contrast, this reaction was not observed in giant proteoliposomes without hAQP1s (data not shown). When hypertonic solution was added, both giant proteoliposomes with and without hAQP1 shrank as liposome is permeated by water (Fig. 4). However, the change in diameter of giant proteoliposomes with hAQP1 was more intense than that of giant proteoliposomes without hAQP1. This is because water passes easily through the hAQP1 into the liposome. Our proposed method is simple, fast, and can make giant proteoliposomes with the membrane proteins retaining their activities. In addition, the technique of covering microchambers with a cellulose membrane can immobilize giant proteoliposomes while simultaneously allowing us to change the suspending solution.

Reference

- 1 M. Schwarz et al., *J Biol Chem.* 1994, 269 (47): 29481-29489
- 2 K. Bacia et al., *J Biol Chem.* 2004, 279 (36): 37951-37955
- 3 A.N. Van Hoek et al., *Biochemistry.* 1993, 32 (44): 11847-11856

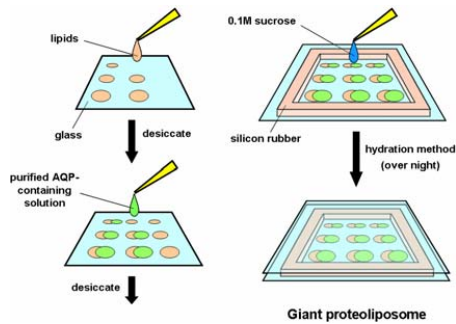


Figure 1. Procedures for making giant proteoliposomes.

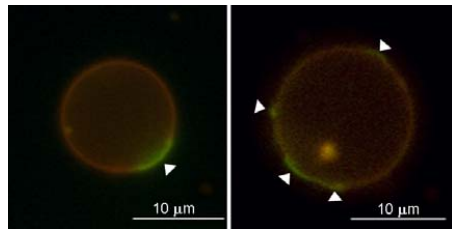


Figure 2. Fluorescent images of giant proteoliposomes. Lipids were stained with Dil (red). hAQP was labeled with anti hAQP1 as primary antibody, and FITC-labeled anti mouse IgG antibody was attached as secondary antibody (Green, arrow).

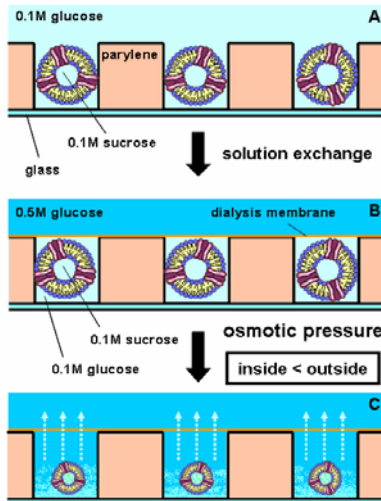


Figure 3. Schematic of the observation system for proteoliposomes using microchamber array. (A) Giant proteoliposomes sink and get trapped in microchambers due to the difference in specific gravity. (B) They were immobilized by covering the microchambers with dialysis membrane. Solution above the membrane was exchanged to hypertonic solution. (C) Osmotic pressure-induced change of liposome volume.

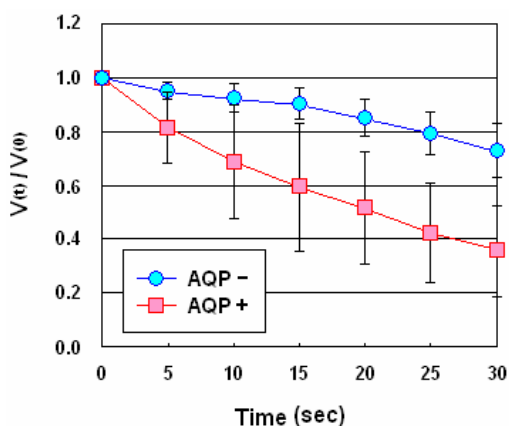


Figure 4. Change in volume of giant liposomes. Circle represents giant proteoliposome without hAQP1 group (AQP-, n = 15), and Square represents giant proteoliposome with hAQP1 group (AQP+, n = 15). The volume of AQP+ group decreased drastically. In contrast, the volume of AQP- group decreased slowly.

NANONEEDLE FIELDS FOR BIOLOGICAL INTERACTION WITH CELLS

M. Denoual¹, M. Chiral¹, O. De Sagazan², B Le Pioufle¹

¹Biomis-Satie ENS-Cachan antenne de Bretagne Bruz, France

²STMicroelectronics, France

This paper presents results and potentialities of a newly proposed nanostructured device covered with sharp polysilicon nanoneedles for biological applications. Such device could find applications in electrophysiological recording and genetic material transfection.

Keywords : nanoneedles, nanopuncturing, intracellular recording.

1. Introduction

Thank to a specific process, we are able to fabricate surfaces covered with sharp nanoneedle fields. Those surface were developped for biological purpose. The first step of our experimentation was to study the viability of cell cultures over such surfaces. The second step was to study more accurately the interaction between the nanoneedles and the biological cells. The fabrication process of the nanoneedles and the results of those paramount experimental steps are revealed in the result part, then the biological application under consideration is presented.

2. Results

A chlore based etching process allows us to produce fields of polysilicon nanoneedles with various densities (4 nanoneedles/ $100\mu\text{m}^2$ up to 40 nanoneedles/ $100\mu\text{m}^2$) and height (7 to $12\mu\text{m}$) (Figure 1). Compared to existing techniques, this process allows combining both high aspect-ratio nanoneedles and high densities of nanoneedles; those characteristics are usually obtained separately ([1-3]).

In [4], we have demonstrated the long-term viability and even the proliferation of cells cultured over those nanoneedle fields as illustrated in Figure 2. We have also shown that thanks to their extremelly sharp profil (tip diameter between 100 and 200nm typically), those nanoneedles allow the nanopuncturation of the cells membrane. This has been demonstrated through confocal imaging of cells culture over the fields (Figure 3.c.).

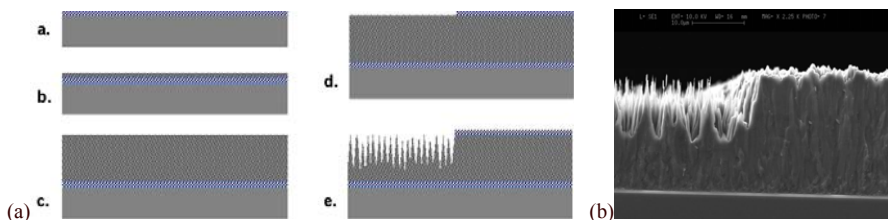


Figure 1. (a) Fabrication process of the nanoneedle fields. An oxide layer is grown over a silicon substrate for insulating purpose **a**. A polysilicon seed layer is deposited through LPCVD **b**. An epitaxial growth is performed at high temperature to reach 10 to 20 μ m thick polysilicon layer **c**. An oxide mask is performed to protect non-etched areas **d**. The polysilicon is etched with chlore based chemistry with an RIE equipment, that step forms the nanoneedles **e**.
 (b) SEM sideview showing the sharpness and aspect ratio for a high density field during the etching process. The scale bar is 10 μ m.

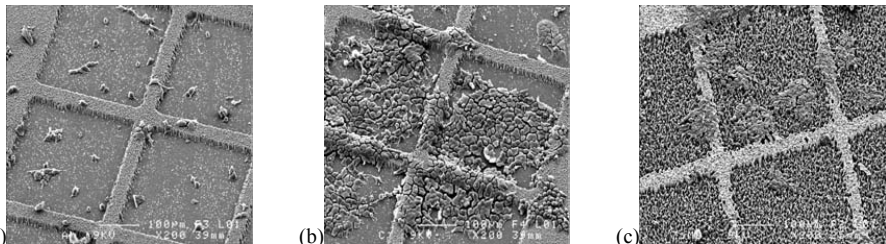


Figure 2. SEM pictures of cell cultures over nanoneedle fields at different development time. (a) cells over a low-density nanoneedle field after 24 hours. (b) on a low-density field after 7 days, the cell population has grown. (c) on a high-density field after 7 days, here also the population has grown.

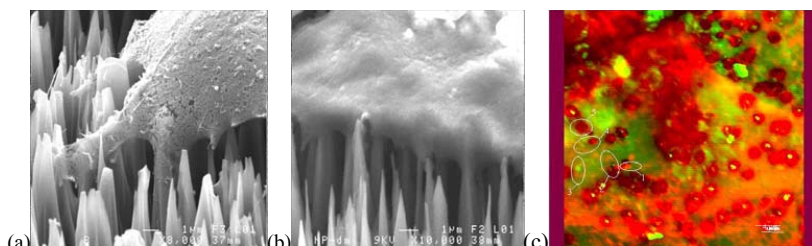


Figure 3. (a and b) SEM close views of cells over high-density nanoneedle fields. Tight interaction between the cell's membrane and the nanoneedles is observed; (c): confocal view of a cell over a low-density nanoneedle field after 72h culture. Texas- Red fluorescent marker was used to mark the actin protein. Scale bar is 4 μ m. White circles show some of the correspondences between the nanoneedles and the pores in the membrane of the cell.

3. Conclusion and forecast

We now propose the use of these nanostructured devices for intracellular potential recording of neuronal cells. For intracellular potential recording purpose the nanoneedle will be metallized with chromium and gold (Figure 4). Positioning of the neuronal cells will be realized through 3D structuration of the device as already performed with planar microelectrodes arrays in [5,6].

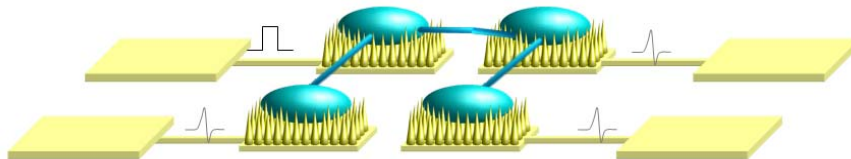


Figure 4. Schematic of the device for intracellular recording of neuronal cells. The nanoneedles are metallized to form nanostructured electrodes able to puncture the cells membrane for intracellular recording.

The metallized nanoneedles will then present an increased area compared to flat microelectrodes. But over all, they will allow intracellular recording which implies 2 or 3 orders of magnitude gain on the recorded signal compared to flat microelectrodes. Compared to intracellular micrelectrodes [7], the device will allow the simultaneous study of sets of several neuronal cells over a long period of time.

References

1. J. Zahn, N. Talbot, D. Liepmann and A. Pisano, *Microfabricated polysilicon microneedles for minimally invasive biomedical devices*, Biomed. Devices, 2(4), pp. 295-303, (2000).
2. I. Obataya, N. Nakamura and J. Miyake *Nanoscale Operation of a Living Cell Using an Atomic Force Microscope with a Nanoneedle*, Nano Lett., 5(1), pp. 27–30, (2005)
3. D. V. McAllister, M. G. Allen, M. R. Prausnitz, *Microfabricated Microneedles for Gene and Drug Delivery*, Biomed. Eng, 2, pp. 289-313, (2000).
4. M. Denoual, M. Chirat, B. LePioufle, *Cells cultures over nanoneedle fields*, Nanobiotechnology Journal, 1(4), pp. 389-394, (2005).
5. M. Denoual, L. Griscom, H. Toshiyoshi, H. Fujita, *Double-Height Accurate Micro-Molding Method for Three-Dimensional PDMS Structures*, Jpn. J. of Appl. Physics, 42(7A), pp. 4598-4601, (2003).
6. F. Morin, M. Denoual, L. Griscom, B. LePioufle, H. Fujita, E. Tamiya, *Controlling Cell Development by Microfluidic Techniques: a Step towards Whole-Cell Biosensors with Defined Biological Features*, Proc. of Micro Total Analysis System 2002, Japan, (2002).
7. Y. Hanein, K. F. Böhringer, R. C. Wyeth and A. O. D. Willows, *Towards MEMS Probes for Intracellular Neuronal Recording*, Sensors Update - Sensor Technology - Applications - Markets, 10(1), H. Baltes, G. K. Fedder, J. G. Korvink, pp. 47-75, (2002).

SIMULATING KINESIN/MICROTUBULE-BASED MOLECULAR SHUTTLE MOVEMENTS

Takahiro Nitta¹, Akihito Tanahashi¹, Motohisa Hirano¹, and Henry Hess²

¹Dept. of Mathematical and Design Engineering, Gifu Univ.,
Gifu, 501-1193, Japan

²Dept. of Materials Science and Engineering, Univ. of Florida,
Gainesville, FL 32611-6400, USA
(e-mail: nittat@cc.gifu-u.ac.jp)

Abstract

A computer simulation for kinesin/microtubule-based molecular shuttles has been developed. This simulation tool reproduced transport and detachment properties of the molecular shuttles. Use of this simulator enables the rational designs of the elements for Lab-on-a-Chip devices integrated with the molecular shuttles *in silico*.

Keywords: Molecular motor, off-lattice Monte-Carlo simulation, Computer-aided design

1. Introduction

Kinesin/microtubule-based molecular shuttles (MS) are a bio-inspired transport system for Lab-on-a-Chip devices. Functionalized microtubules loaded with nano-scale cargo are transported by kinesin motors along pre-determined tracks connecting modules on the chips, where assembly, sorting, and detection are carried out. The modules are constructed with microfabrication techniques, and carry out specific tasks, such as rectifying or sorting MS by confining and redirecting MS movements. The geometric layout of the modules determines their efficiency, quantified by the number of MS moving in the intended direction and of the number of MS being lost due to detachment from the surface. Here, we present a computer simulation which reproduces both the transport properties and the detachment of MS. This simulation tool provides for the first time a method for rationally designing MS modules.

2. Method

The trajectories of MS were modeled as two dimensional random walks confined within regions describing the module structures. Until MS crossed one of the boundary segments, the random walks were generated according to the method described in detail elsewhere [1]. When a shuttle crossed one of the segments, the guiding rule was applied; it was decided if the shuttle is redirected along the segment or

detached from the surface, according to calibrated guiding probabilities. The calibrated guiding probabilities were obtained from experimentally determined guiding probabilities [2, 3] and a semi-analytical model for MS movements along the boundaries. The calibrations were required because of the difference in spatiotemporal resolutions of between experiments and our simulation. If the shuttle detached from the surface, the iteration was stopped. Otherwise, the shuttle was redirected along the segment and the iteration was continued. Movements of 1,000 MS were analyzed for each geometry.

3. Results and discussion

Single wall or edge (experimental data by Clemmens *et al.* [2]): Figure1 shows the results on MS guiding by single edge or wall of chemical (A), topographical (B), and combined guiding (C). Corresponding to experimental spatial resolution, we counted as guided MSs which traveled more than 0.5 μm away from the wall after the collisions. The reproduced guiding probabilities were in good agreement with the experimental ones [2].

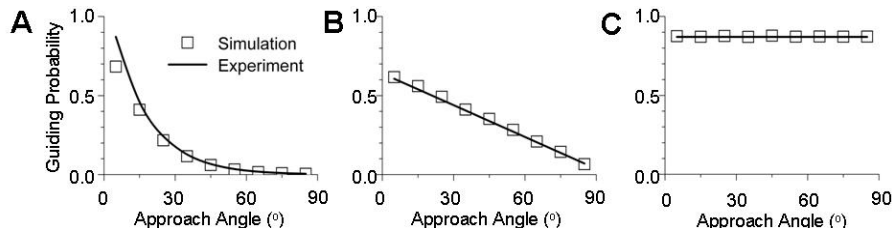


Figure1. Reproduced guiding probabilities are shown as open squares (A, chemical track; B, guiding channel; C, guiding channel with chemical selectivity). Solid lines are experimental data fits [2].

Straight Channel (experimental data by Clemmens *et al.* [4]): We implemented the guiding rule for topographical walls into our previous simulator for straight channels. The average distance between two wall collisions of the simulated MSs trajectories were $13.4 \pm 7.0 \mu\text{m}$ ($N=2927$, experiment: $16.6 \pm 7 \mu\text{m}$, avg. \pm SD), $17.7 \pm 8.7 \mu\text{m}$ ($N=2833$, experiment: $17 \pm 8 \mu\text{m}$), and $26.5 \pm 14.3 \mu\text{m}$ ($N=2634$, experiment: $24 \pm 14 \mu\text{m}$) for channel width of 1.5, 2.5, and 5.5 μm , respectively. Collision angles against the channel walls were $18.2 \pm 7.5^\circ$ (experiment: $11 \pm 7^\circ$), $20.7 \pm 9.0^\circ$ (experiment: $17 \pm 9^\circ$), and $25.2 \pm 11.9^\circ$ (experiment: $28 \pm 21^\circ$) for channel width of 1.5, 2.5, and

$5.5 \mu\text{m}$, respectively. These results were in good agreement with the experimental data by Clemmens *et al.* [4]

Rectifier (experimental data by van den Heuvel *et al.* [3]): We implemented the guiding rule into our previous simulator for the rectifier which van den Heuvel investigated. The result is in good agreement with their observation (Figure 2B). Tuning geometrical parameters, the rectifier length (L), the radius of the circular segments (R), and the offset between the inlet and outlet (d), improved the guiding efficiency and reduced the detachments of MS (Figure 2C). This is around 40 % reduction of MS detachment and 20 % increase of rectification efficiency from the original structure investigated by van den Heuvel *et al.*

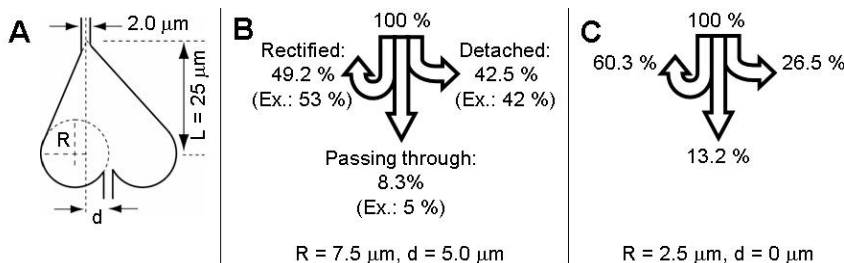


Figure 2. Rectifier geometry (A) and fractions of MSs rectified, passing through and detached from the rectifier of the geometry of $R = 7.5 \mu\text{m}$ and $d = 5.0 \mu\text{m}$ (B) and $R = 2.5 \mu\text{m}$ and $d = 0 \mu\text{m}$ (C) are shown. In B, experimental data [3] are shown in parentheses for comparison.

4. Conclusion

A simulation tool for MSs has been developed which facilitates the rational design of individual guiding structures. For the first time, the possibility of detachment from the surface after a wall collision of the shuttle has been included in the simulation. This improvement enables predictions of not only transport [1] but also detachment properties of MSs.

References

- [1] Nitta, T. et al., *Lab Chip*, **6**, 881-885 (2006)
- [2] Clemmens, J., et al., *Langmuir*, **19**, 10967-10974 (2003)
- [3] van den Heuvel, M.G. L, et al., *Nano. Lett.*, **5**, 1117-1122 (2005)
- [4] Clemmens, J., et al., *Langmuir*, **19**, 1738-1744 (2003)

Development of an Assay System for ABC Transporters Reconstituted in an Artificial Lipid Bilayer

H. Suzuki*, K. V. Tabata**, H. Noji**, and S. Takeuchi*

*The University of Tokyo, Institute of Industrial Science, Komaba 4-6-1,
Meguro-ku, Tokyo 153-8656, JAPAN

e-mail: hsuzuki@iis.u-tokyo.ac.jp, takeuchi@iis.u-tokyo.ac.jp

**Osaka University, The Institute of Scientific and Industrial Research, Mihogaoka
8-1, Ibaraki, Osaka 567-0047, JAPAN

Abstract

We have been developing a measurement system for membrane transport across a reconstituted planar lipid bilayer to examine the functions of transporter proteins [1]. In this system, an artificial planar lipid bilayer is pressed on the Parylene microchamber array (typically 0.1~1 pL in volume), and transporter proteins are reconstituted by vesicle fusion. Fluorescently labeled molecules (substrates) transported across the bilayer will be accumulated in microchambers, and the concentration is measured as fluorescent intensity. In this report, S/N ratio of fluorescent measurement was improved by reducing the fluorescence outside microchambers, and incorporation of human ATP binding cassette (ABC) transporters into the planar lipid bilayer was confirmed by single molecule fluorescent imaging.

Keywords: ABC transporter, Artificial lipid bilayer, Microchamber array

1. Introduction

In living cells, membrane proteins in plasma membranes regulate transport of various materials. Artificial planar lipid bilayers have been a powerful tool for the study of such membrane proteins [1-4]. Functions of ion channel proteins can be detected as electric current using electrophysiological techniques. However, there has not been any standard quantitative measurement method for the transport of non-ionic molecules (*e.g.*, proteins, lipids, and drugs) [5]. In particular, there is a huge demand for assay technology of ABC transporters known to excrete anti-cancer drugs out of cancer cells. The final goal of this project is to explore the absolute transport flux of transporters at single molecular level. Here, we report latest developments toward this single molecular transport assay.

2. Experimental Setup and Procedure

Conceptual diagram of our transport assay system is shown in Fig. 1. We utilize a microchamber array to confine transported molecules (substrates) in tiny volumes. To do this, an artificial planar lipid bilayer, where transporters are to be incorporated, is pressed on microchambers. Fluorescently labeled substrates accumulate in microchambers as they are transported across the bilayer, and are detected using a fluorescent microscopy. Previously, we reported that the transport of fluorophores through peptide nanopores (α -hemolysin) was observed [6] using total internal reflection fluorescence microscopy (TIRFM).

Microchambers, 10 μm in diameter and 3 μm in depth (0.23 pL in volume), were fabricated as follows. A few tens of nanometers of aluminum and 3 μm Parylene were deposited and patterned on a glass coverslip [6]. Aluminum layer reduces the generation of unwanted evanescent field outside the chambers to improve the S/N ratio in TIRF observation, while it is not thick enough to completely block the bright field observation during bilayer formation. Finally, the surface was coated with hydrophilic polymer (MPC polymer [7], PC modifier P, AI Bio-Chips Co., Ltd.) with a technique provided from the manufacturer. A planar lipid bilayer was formed separately at the 150 μm aperture opened at the bottom of the plastic upper chamber (7 mm in inner diameter) using a method described in Ref. 8 (Fig. 2a). Bilayer formation was confirmed by observing a faint circular edge inside the aperture in bright field observation. Then, it was pressed on a microchamber array by lowering the upper chamber with a manipulator. Bilayer membrane does not rupture since MPC polymer works as a molecular cushion Lipid

bilayer formation was still visible through the thin layer of aluminum. After the bilayer forming and pressing were completed under the bright field observation (Fig. 2b), it was switched to the fluorescent observation.

3. System Characterization

The detectable concentration range of fluorescent molecules inside microchambers was examined with a custom-made TIRFM. Sulforhodamine solution with different concentration was prepared and spread over the microchambers, and the image was captured with a cooled CCD camera (ORCA-ER, Hamamatsu Photonics). The thin layer of aluminum reduced the background emission outside chambers up to 50%, improving the S/N ratio (Figs. 3b). The calibration curve, in which brightness is plotted against the concentration, shows better linearity and less deviation with the aluminum coated chamber chip than transparent ones (Fig. 4). Thus, the smallest detectable concentration became as small as 1 nM, which corresponds to only 140 fluorescent molecules in a 0.23 μL microchamber.

4. Reconstitution of human ABC transporter into the planar bilayer

As a step toward the transport flux measurement, incorporation of human ABC transporter, multidrug resistance associated protein 2 (MRP2) was confirmed by single molecule fluorescent imaging. In this observation the bilayer was pressed on the planar glass instead of the microchamber chip, which is the same observation system as in ref. 8. Inside-out vesicles (membrane fraction) of S9 insect cells overexpressed with MRP2 proteins was kindly provided by GenoMembrane, Inc. MRP2 proteins were labeled with lectin fluorescent probe (concanavalin A, tetramethylrhodamine conjugate, C860, molecular probes) that binds to the sugar chain of MRP2. To facilitate the fusion into the planar bilayer, vesicles were incubated in buffer containing 500 mM KCl and 10% glycerol for 20 minutes, and buffer containing 100 mM KCl was added in 1:1 volume ratio. This process produces osmotic difference between inside and outside of vesicles to induce instability in the membrane. Vesicle solution (0.06 mg/mL in final concentration) was injected in the upper chamber. After a few minutes, bright spots moving around started to appear in TIRFM imaging (Fig. 5). In this experiment image was captured by an electron multiplication CCD camera (C9100, Hamamatsu photonics). They move according to the Brownian motion in 2-D plane, indicating labeled proteins are incorporated in the planar bilayer. Diffusion coefficient was calculated to be $2.5 \times 10^{-8} \text{ cm}^2/\text{s}$ from the trajectories (Fig. 5b). Since it is on the same order with the coefficient of other membrane proteins reported [8], we can conclude that the incorporation of MRP2 was successful.

5. Discussion and remarks

Here we reported our progress in developing the system to measure the transport flux of transporter proteins at single molecular level, yet there are still many challenges to be addressed. The transport flux in protoliposome uptake experiments were reported as 10-100 pmol/mg/min with human ABC transporters (MRP2) [9], and ATPase activity of bacteria ABC transporters were reported as 0.1-1 $\mu\text{mol}/\text{mg}/\text{min}$ [10]. Presuming the size of each transporter is approximately 170 kDa and 130 kDa, turnover simply calculated from these numbers becomes $1.3 \times 10^{-7} - 1.3 \times 10^{-6}$ and $1.7 \times 10^{-3} - 1.7 \times 10^{-2}$ translocation per minute, respectively. We aim to examine these numbers by measuring the substrate transport of single proteins [11].

References

- [1] C. Miller Ed., *Ion Channel Reconstitution*, 1986, Plenum Press.
- [2] H. Suzuki et al., *Lab-on-a-Chip*, 2004, 4(5), 502-505.
- [3] H. Suzuki et al., *Langmuir*, 2006, 22(4), 1937-1942.
- [4] H. Suzuki et al., *Biosensors and Bioelectronics (Short Comm.)*, 2006, articles in press.
- [5] R. Peters, *Annu. Rev. Biophys. Biomol. Struct.*, 2003, 32, 47-67.
- [6] H. Suzuki, K. V. Tabata, H. Noji, S. Takeuchi, *Proc. MEMS* 2006, 482-485.
- [7] K. Ishihara, *Sci. Technol. Adv. Materials*, 2000, 1, 131-138.
- [8] T. Ide and T. Yanagida, *Biochem. Biophys. Res. Commun.*, 1999, 265, 595-599.
- [9] R. Masereeuw et al., *J. Am. Soc. Nephrol.*, 14, 2741-2749, 2003.
- [10] E. Steinfels et al., *Biochemistry*, 43, 7491-7502, 2004.
- [11] a) Y. Rondelez et al., *Nature* 2005, 433, 773-777.; b) Y. Rondelez et al., *Nature Biotech.*, 2005, 23(3), 361-365.

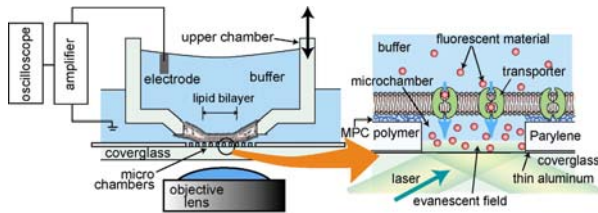


Fig. 1 Conceptual diagram of the optical detection system for membrane transport using lipid bilayer microchambers. An artificial lipid bilayer formed at an aperture in the upper chamber is pressed on microchambers made on a coverglass. After incorporation of target membrane proteins (transporters), fluorescent labeled molecules transported by membrane proteins are detected by fluorescent imaging with TIRFM.

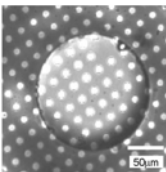
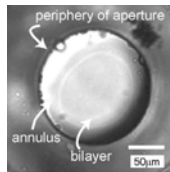


Fig. 2 (a) Lipid bilayer (10 mg DOPC / mL n-decane) formed at the aperture of the upper chamber immersed in electrolyte (10 mM MOPS+100mM KCl). (b) Lipid bilayer pressed on the microchamber array.

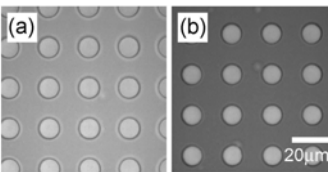


Fig. 3 Fluorescent image of microchambers with 1mM sulforhodamine. (a) Without and (b) with thin aluminum layer between the substrate and parylene layer.

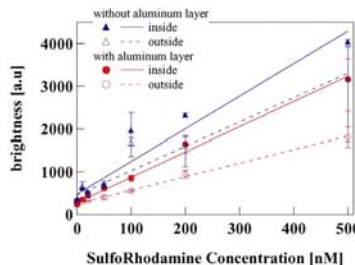


Fig. 4 Fluorescent intensity of sulforhodamine in microchambers with different concentration, with and without an aluminum layer.

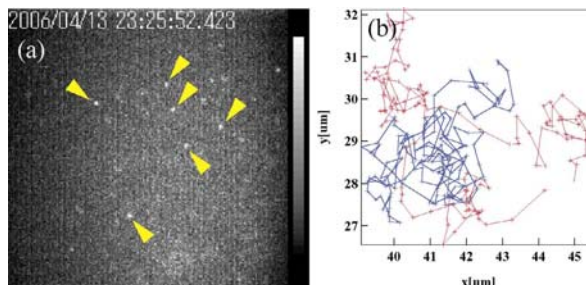


Fig. 5 (a) TIRFM image of single MRP2 proteins (marked with yellow arrows) incorporated in the artificial lipid bilayer pressed on a glass substrate. Fluorescently labeled proteins move according to the Brownian motion in 2-D plane of the bilayer. (b) Trajectories of single MRP2 proteins in Brownian motion. Diffusion coefficient was $2.5 \times 10^{-8} \text{ cm}^2 \cdot \text{s}^{-1}$.

LIPID BILAYER MEMBRANE FORMATION BY SOLVENT EXTRACTION IN A MICROFLUIDIC CHANNEL

Noah Malmstadt, Michael A. Nash, Robert F. Purnell, and Jacob J. Schmidt

Department of Bioengineering, University of California, Los Angeles, California, 90095, USA; noahmalm@ucla.edu, schmidt@seas.ucla.edu

Abstract

Membrane channel proteins have many potential applications, but realizing these applications requires new, automatable methods for fabricating lipid bilayer membranes. We have developed a technique for lipid membrane formation in a microfluidic device that relies on material-mediated extraction of solvent from a droplet of lipid solution. This technique, which is fully automatable, forms high-quality membranes with the capacity to host and measure channel proteins at the single molecule level.

Keywords: Lipid, membrane, bilayer, PDMS, extraction

1. Introduction

Membrane channel proteins play essential physiological roles, including: controlling interactions between cells and their environment, facilitating signaling, and helping to regulate the composition of the cytosol. These properties have made ion channels prime targets for drug discovery.[1] Similarly, the central role ion channels play in cardiac action potential generation has made them necessary targets for screening against unintended interactions with all novel drugs.[2] Membrane channels have also been the subject of intense recent research as engineered sensors capable of chemical detection at the single-molecule level[3] and there is significant effort toward exploiting these channels for rapid DNA sequencing[4]. Each of these applications requires the measurement of ion transport through channel proteins.

Accomplishing these measurements requires embedding channel proteins in lipid bilayer membranes. Unfortunately, current techniques for fabricating bilayers require skilled operators and are not amenable to automation.[5] An automatable membrane fabrication technology is necessary in order to realize the potential applications of membrane channel proteins for high-throughput screening and autonomous sensing.

A microfluidic platform would be ideal for these applications, and several microfluidic-based methods for membrane fabrication have been proposed.[6, 7] These systems are modifications of traditional membrane fabrication techniques; they require the presence of air in microfluidic channels during membrane formation and are not immediately amenable to automation. We have developed a novel automatable approach to membrane formation based solvent extraction from a droplet flow. A droplet of lipid-containing organic solution is formed in an aqueous flow stream in a channel fabricated from poly(dimethylsiloxane) (PDMS). The organic solvent partitions into the PDMS, leaving behind the lipid to self-assemble into a bilayer.

2. Experimental

Devices were constructed entirely from PDMS using standard polymer molding

techniques. Devices consisted of two layers of channels, one through which the working fluids were flowed and in which membranes were formed, the other which acted as valves on the fluidic layer, according to the technique of Unger et al.[8] Fluidic channels were fabricated with cross-sectional dimensions of 100 μm wide \times 35 μm high; valve channels were 200 μm wide \times 50 μm high. The device also contained integrated Ag/AgCl electrodes for electrical interrogation of membranes. Syringe pumps generated the desired flows. A biphasic flow configuration was obtained by controlling (with valves and pumps) two immiscible input streams. These input streams met at a 90° junction to combine into a single output stream. Droplet flows were formed from an aqueous phase (consisting of 1 M KCl buffered by 5 mM Hepes at pH 7) surrounding an organic lipid solution droplet (0.025 wt% of the lipid diphylonylphosphotidylcholine (DPhPC) in 1:1 squalene:n-decane and 50 ppm perfluorooctane).

Once a droplet (with a volume of about 2 nL) was formed, it was moved (using a syringe pump operating at 15 $\mu\text{L}/\text{h}$) into a region of the device between the electrodes which was then isolated from the rest of the device by two valves. The solvent was allowed to partition from the droplet into the PDMS from which the device was constructed, and the subsequently formed membrane was monitored electronically.

3. Results and Discussion

Figure 1 shows the time course of solvent extraction from a lipid-containing droplet. The solvent can be clearly seen partitioning into the PDMS device over the course of 4 minutes, bringing the two aqueous-organic interfaces together. During this extraction process, the capacitance of the droplet was measured (Figure 2). This capacitance is related to the droplet or membrane thickness by modeling the membrane as a parallel plate capacitor. For such a system the capacitance is given by $C = \epsilon A/d$, where ϵ is the permittivity of the lipid ($2.4 \times 10^{-11} \text{C}^2/\text{J}\cdot\text{m}$), A is the membrane area (given by the channel cross-section, measured by profilometry from the device mold to be $3500 \mu\text{m}^2$), and d is the thickness of the droplet/membrane. Figure 2 shows the capacitance steadily increasing until the point at 9 s, where it jumps to a plateau level. Over a series of experiments, this plateau capacitance was found to correspond to a thickness of $4.8 \pm 0.6 \text{ nm}$, as expected for a molecular bilayer of

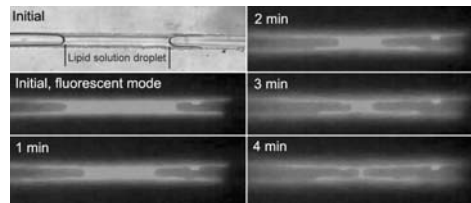


Figure 1: A time series of micrographs showing extraction of solvent from a droplet of lipid solution. The organic phase is dyed with the nonpolar fluorophore Nile Red. The channel width is 100 μm .

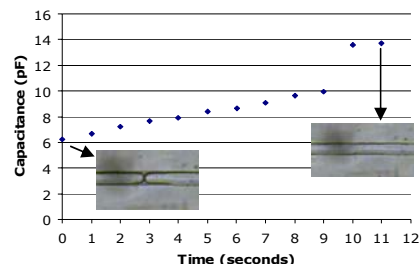


Figure 2: Capacitance measurements of the thinning droplet. Micrographs of the channel taken at the beginning and end points of the graph are shown. Although nothing is visible in the channel at $t=11\text{sec}$, the resistance of the channel remains high ($>1\text{G}\Omega$), and the value of the capacitance, 14 pF, corresponds to a bilayer membrane thickness (see text).

DPhPC. Membrane resistance was consistently measured at > 50 GΩ.

To confirm that these membranes were biologically functional, we incorporated the membrane channel protein α-hemolysin (αHL) into them. αHL was included in the aqueous phase at a concentration of 1 ng/ml and the voltage across the membrane was clamped at 80 mV while the current through the membrane was monitored. The insertion of αHL molecules into the membrane could be observed as discrete jumps in membrane conductance, as shown in Figure 3. Each of these conductance jumps is consistent with the known conductance value for a single molecule of αHL: 0.8-1 nS.

4. Conclusions

Solvent extraction from a lipid solution droplet in a microfluidic channel is a simple approach to fabricating lipid bilayer membranes. This technique does not require operator intervention: extraction and membrane formation occur spontaneously as a function of material properties. Membranes formed in this manner form a high-resistance seal and are capable of hosting membrane channel proteins and obtaining conductance data from these proteins with single-molecule resolution.

Acknowledgement: We thank Stephen Cheley for the kind donation of α-hemolysin.

References

- 1.Bennett, P.B. and H.R.E. Guthrie, *Trends in ion channel drug discovery: Advances in screening technologies*, Trends in Biotechnology, **21**(12) pp. 563-569, (2003).
- 2.Viskin, S., et al., *Long QT syndrome caused by noncardiac drugs*, Progress in Cardiovascular Diseases, **45**(5) pp. 415-427, (2003).
- 3.Bayley, H. and P.S. Cremer, *Stochastic sensors inspired by biology*, Nature, **413**(6852) pp. 226-230, (2001).
- 4.Kasianowicz, J., et al., *Characterization of individual polynucleotide molecules using a membrane channel*, Proc. Natl. Acad. Sci. U.S.A., **93** pp. 13770-13773, (1996).
- 5.Mueller, P., et al., *Reconstitution of cell membrane structure in vitro and its transformation into an excitable system*, Nature, **194** pp. 979-980, (1962).
- 6.Sandison, M.E. and H. Morgan, *Rapid fabrication of polymer microfluidic systems for the production of artificial lipid bilayers*, Journal of Micromechanics and Microengineering, **15**(7) pp. S139-S144, (2005).
- 7.Suzuki, H., et al., *Highly Reproducible Method of Planar Lipid Bilayer Reconstitution in Polymethyl Methacrylate Microfluidic Chip*, Langmuir, **22**(4) pp. 1937-1942, (2006).
- 8.Unger, M.A., et al., *Monolithic microfabricated valves and pumps by multilayer soft lithography*, Science, **288**(5463) pp. 113-116, (2000).

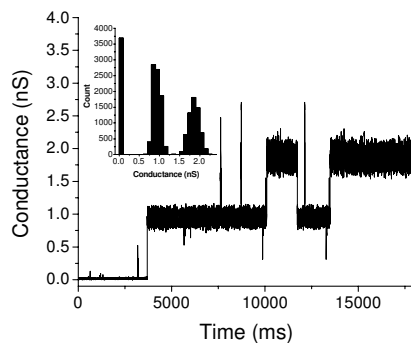


Figure 3: A conductance trace of a membrane with a constant applied voltage of 80 mV in the presence of αHL. Individual αHL insertion events can be seen as discrete jumps in membrane conductance. Inset: a histogram of conductance data, showing 0, 1, and 2 αHL molecules inserted in the membrane.

MONODISPERSE LIPOSOMAL GENE CARRIER FORMULATION IN PICOLITER MICRO-REACTOR FOR CONSISTENT AND EFFICIENT GENE DELIVERY

Albert Tsung-Hsi Hsieh¹, Yuh Adam Lin¹, Jen-Hao Pan¹, Abraham P. Lee^{1,2}

¹Biomedical Engineering, ²Mechanical and Aerospace Engineering,
University of California, Irvine, U.S.A.

Abstract

We developed a picoliter micro reactor and incubator system to formulate monodisperse cationic lipids and DNA complexes. The monodisperse micro reactor and incubator was designed and fabricated based on the microfluidic droplet formation devices which developed by our lab and others. Compared with the conventional irreproducible lipoplex preparation using hand-shaking or vortexing processes for mixing, the microfluidic platform developed for lipoplex formulation demonstrates the ability to rapidly and uniformly mix cationic lipid and DNA, resulting in the generation of lipoplex with narrower size distribution and smaller average size. This system enables an integrated process with constant mixing and incubation, and reproducibility of the lipoplex formulation.

Keywords: Gene transfection, lipoplex, micro-droplet, micro-reactor, micro-mixer

1. Introduction

The cationic lipid based liposomal carriers are reported as the most attractive non-viral and efficient carrier for delivering drugs, plasmid DNA, and shRNA for pharmaceutical and therapeutic applications [1]. Advantages of liposomal vectors include safety, lack of immunogenicity, ability to package large DNA molecules, and ease of preparation. The size of lipoplex (complexes of cationic lipid and DNA) dictates the efficiency of gene transfection [2]. The order of mixing of cationic lipid and DNA, their mixing rate, and their mixture incubation time are factors that determine the lipoplex sizes during sample preparation [3]. The conventional lipoplex preparation process involving hand shaking or vortexing for mixing is normally irreproducible. It results in large size distribution of lipoplexes, and it further affects the efficiency of gene transfection. A method able to consistently formulate monodisperse lipoplex assemblies is important for reproducibility of gene transfection or gene therapy experiments.

2. Experimental

The Picoliter volume Micro Reactor and Incubator (PMRI) system we developed is a promising solution for applications mentioned above. Advantages of using microfluidic droplet based devices have recently been reported, including the rapid mixing of liquids that are normally hindered in low Reynolds number single phase laminar flow systems [4,5]. The design schematic of a PMRI platform device is shown in figure 1. When the diluted 1:1 (DOTMA/DOPE) liposome formulation of cationic lipids (DOTMA=N-[1-

(2,3-dioleyloxy)propyl]-*N,N,N*-trimethyl-ammonium-chloride, DOPE=1,2-Dioleoyl-sn-glycero-phosphatidylethanolamin)[1] and DNA vector in cell medium flow into the center channel from two different inlets, the merged single stream is pinched-off by the shear force from the sheath oil streams and form picoliter droplets. Traditionally, the order of the addition of cationic lipid and DNA and mixing rate affect the resulting lipoplex size and homogeneity. In the PMRI platform, the lipids and DNA are simultaneously injected into the micro-reactor, thus minimizing lipoplex size differences. Once inside the droplet, the cationic lipids and DNA vector start to mix instantly due to the chaotic advection resulting from the droplet moving in the rendering channel as shown in figure 2.

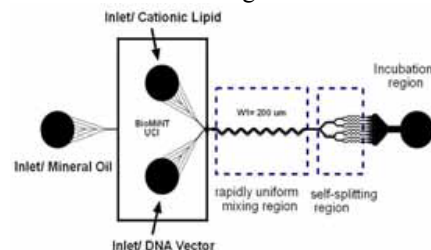


Figure 1. Schematic layout of multi-channel picoliter volume incubator generation channel.

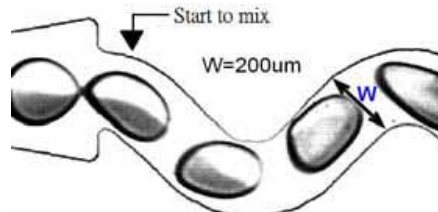


Figure 2. Rapidly uniform mixing region. Two reagents are mixed in micro-droplets by chaotic advection flow as the droplet moves in the rendering channel. No moving parts are needed for mixing.

After all lipids and DNA vector molecules are uniformly distributed in the micro droplet reactor, the primary droplet is split into eight smaller droplets in the serial-splitting channel design as shown in figure 3. This enables the rapid production of large numbers of picoliter droplets. Moreover, the mixing ratios of reagents are more

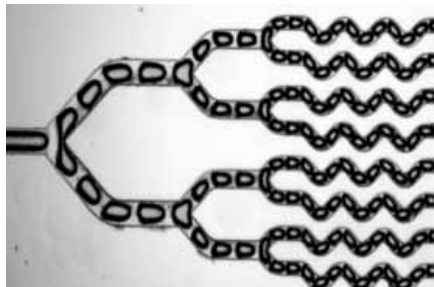


Figure 3. Series of droplet self-splitting region. One droplet splits into eight 14.1 picoliter volume droplets (dia.=30 um) by using serial-splitting channels. There are followed with advanced mixing channels before the incubation.

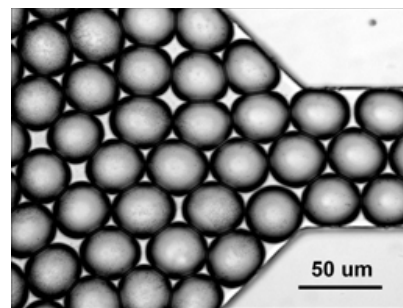


Figure 4. Mixtures of lipid/ DNA molecules are incubating in monodisperse 14.1 picoliter volume droplets, serving as micro-incubator for lipoplex formulation.

precisely controlled than in the single channel configuration. By utilizing designed serial self-splitting channels, the monodispersed picoliter volume (14.1 pl) incubators are generated as shown in figure 4. Normally, the incubation time for cationic lipid–DNA mixture is proportional to the size of the lipoplex due to aggregation.

3. Results and discussion

As seen in figure 5 the size distribution of lipoplex prepared by the PMRI platform has narrower size distribution peak than those generated by conventional method, and the average lipoplex size is smaller. The PMRI system we developed for lipoplex formulation demonstrates the ability to rapidly and uniformly mix cationic lipid and DNA simultaneously, and generates a narrower lipoplex size distribution. The most important advantage of PMRI is that it enables an integrated process for mixing and incubation, and the results are reproducible.

Acknowledgement

The authors would like to thank Prof. Stephen White and Dr. Hirotaka Sasaki in Dept. of Physiology and Biophysics, and Prof. Philip L. Felgner in Virus Research Center of UC Irvine for and lipoplex characterization and facilities access.

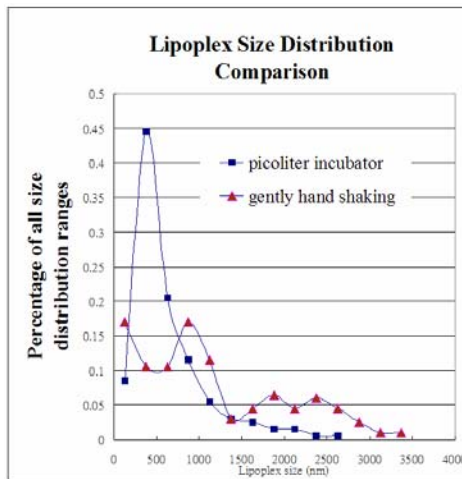


Figure 5. The comparison of the lipoplex size distributions. The solid line with rectangular represents the lipoplex prepared by PMRI and the solid line with triangle represents the lipoplex preparation by conventional hand-shaking method. The lipoplex prepared by PMRI platform method shows the result has a narrower size distribution peak and smaller average size. Lipoplex size was measured by dynamic light scattering (DAWN HELEOS, WYATT)

References

- [1] P. L. Felgner and G. M. Ringold, *Nature*, 337: 387-388 (1989)
- [2] P. C. Ross, and S.W. Hui, *Gene Ther.* 6:651–659, (1996)
- [3] Pedroso de Lima, M. C. et al. *Adu. Drug. Deliu. Reu.* 47:277–294 (2001).
- [4] Y. C. Tan, Jeff Fisher, Abraham P. Lee, *Lab-on-a-chip*, 4, 292-298 (2004)
- [5] Albert T.-H. Hsieh, L. H. Hung, Abraham P. Lee, *Proceeding, MicroTAS 2005*, Boston, 1327-1329.

HAND-OPERATABLE MICRO FLUIDIC ARRAYS FOR SINGLE CELL TRAPPING, PRECISE DRUG DOSAGE BY 3D'S PASSIVE MICRO VALVES AND SNARES

T. J. Chen, F. G. Tseng and C. S. Yang

Engineering and System Science Department, National Tsing Hua University,
Hsinchu, Taiwan

Abstract

This paper introduces a hand controllable single cell trapping and incubation network passively employing surface tension force to gently manipulate individual cell for single-cell-based research. The operations of bath registration of single cell array, precise parallel dosage for individual channel in nl resolution, and the replacement of incubation solution repeatedly have been successfully demonstrated in this work. This simple system can be operated by hands with pipette and polymer absorbent without the need of precise active control means.

Keywords: single cell manipulation, cell array, cell trapping, surface tension, check valves

1. Introduction

Single cell trapping, incubation and observation have been becoming important in cell biology to understand single cell behaviors and cell to cell interactions. There have been many methods developed for single cell manipulation and incubation in micro environment, including manually depositing cells into micro well arrays [1], pneumatically driving cells into micro fluidic channel [2], optical tweezers [3], or dielectrophoresis [4]. Most of the methods employed active ways for single cell manipulation, raising the questions about the interaction of manipulation energy with the target cells. This paper introduces another approach, by the employment of surface tension force passively [5][6], single cell can be gently manipulated with minimum impact. The whole fluidic system can be operated by hand with the precision of fluid volume in nl resolution, and the operatable processes including bath registration of single cell array, precise parallel dosage for individual channel, and the replacement of incubation solution repeatedly.

2. Experimental

The overall system is schematically shown in Fig.1A, revealing that the chip is clamped by two PMMA plates with fluidic inlet and outlet reservoirs. The detail of the cell incubation chip is revealed in Fig. 1B, consisting of wide channel for fluidic dispensing, narrow channel for fluid withdrawing, and center chambers for single cell trapping and incubation. Fabrication process is shown in Fig.2, involving 3-layer SU-8 structures for channels, 3D passive fluidic valves, and cell snares.

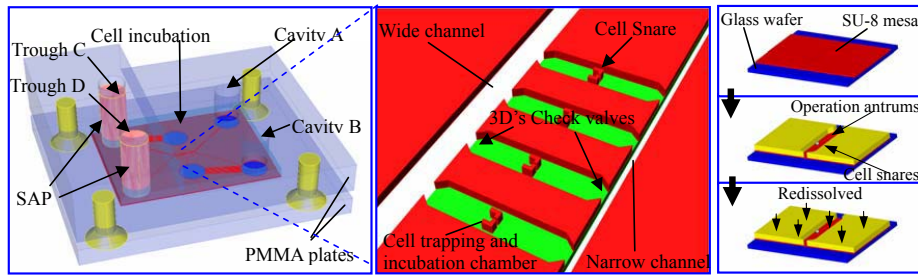


Fig.1A Schematic view of the cell incubation system

Fig.1B Arrays of operation antrums

Fig.2 Fabrication process of the

Fig.3 illustrates the operation processes of single-cell trapping and incubation. The medium with cells is dripped into the wide channel and flows into each of the center chamber by capillary force but stop at the chamber end with passive valves. Each snare is designed for allowing only one cell by the characteristic of flow filed. The residual medium in the wide channel can be withdrawn away but remaining the solution inside the center chambers by employing capillary pressure difference [6]. The solutions in the center chambers can be withdrawn later-on after usage by connecting the medium in the center chamber from the narrow channel with larger capillary pressure and then pull out, as shown in Fig. 4. This process can be repeated many times as desired and precise volume of solution can be delivered into the center chambers in a batch manner with only the rough process operated by hand.

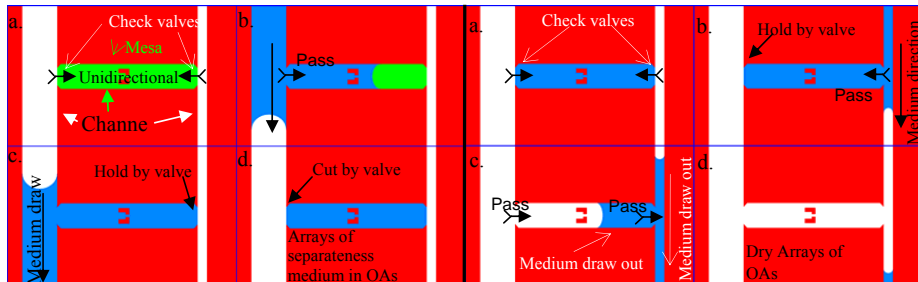


Fig.3 Single cell registration and precise dosage control in the center chambers.

Fig.4 solution withdraw from the center chambers

3. Results

The process of single cell trapping is demonstrated in Fig. 5A. When single cell trapped inside the snare and fill the center gap, flow will not be allowed to flow into the center of snare thus brings the rest of the cells passing by without accumulation inside the snare. This process can be operated in an array format and as shown. Fig. 5B demonstrated two different type cells can be trapped inside snares with different gap designs.

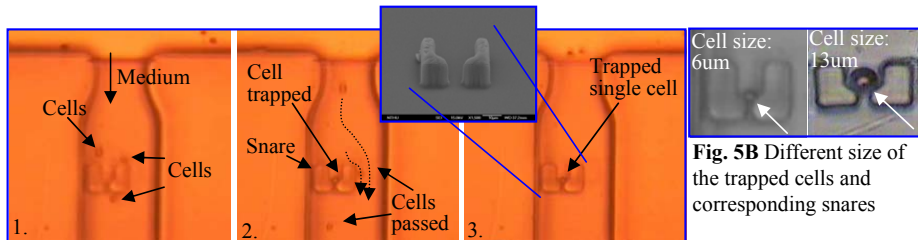


Fig. 5A single cell trapping process driven by capillary flow

The process of successful precise fluid dosage control and fluid replacement process inside center chambers is shown in Fig. 6. All are operated by hands with pipette and polymer absorbent by passively employing capillary related effects, thus carry out minimum impact on the target cells.

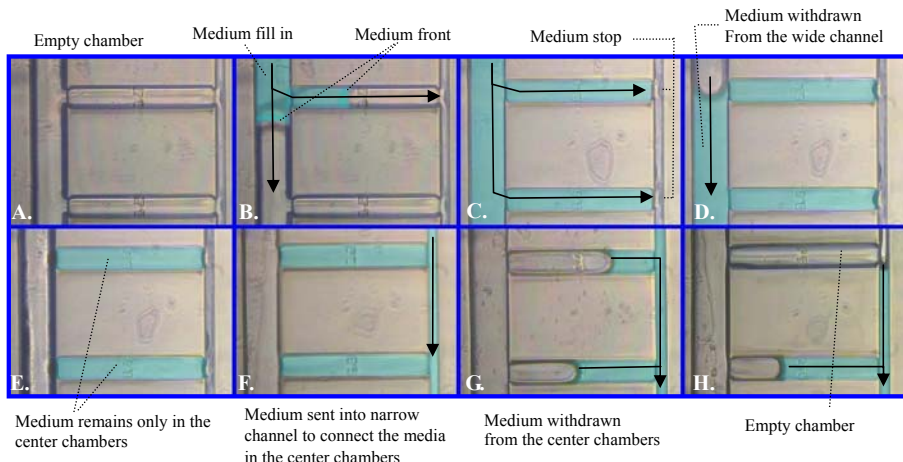


Fig.6 Operation process for fluid fill in and withdraw from micro chambers with precise volume control.

4. References

- [1] G.T.A. Kovacs, C.W. Storment, M. Halks-Miller,C.R. Belczynski, C.C.D. Santina, E.R. Lewis, N.I. Maluf, *IEEE Transactions on Biomedical Engineering*, Vol. 41, no. 6, June 1994, pp. 567-577.
- [2] Dongeun Huh, WeiGu, Yoko Kamotani, James B Grotberg and Shuichi Takayama, *Physiol. Meas.* 26 (2005) R73–R98.
- [3] Svoboda K., Block S. M. , *Annu Rev Biophys Biomol Struct* 23:247-85. 1994.
- [4] Joel Voldman, *Micro Total Analysis Syst.* '00. 431-434 (2000)
- [5] Shih-Chang Lin, Fan-Gang Tseng, Yi-Chin. Tsai , *Proceedings IEEE MEMS-03*, pp. 299-302, Jan. 19-23, 2003
- [6] F.-G. Tseng , K.-H. Lin, H.-T. Hsu, and C.-C. Chieng, *Sensors and Actuators A* , Vol. 111, pp. 107-117, 2004.

FORMATION OF THREE-DIMENSIONAL LIPID MEMBRANE STRUCTURES ON A MICROCHIP

Petra S. Dittrich¹, Martin Heule², Philippe Renaud², Andreas Manz¹

¹ISAS – Institute for Analytical Sciences, Dortmund, Germany

²Swiss Federal Institute of Technology of Lausanne (EPFL), Lausanne, Switzerland

e-mail: dittrich@isas.de

Abstract

In this work we present a method to generate three-dimensional lipid structures by extrusion of a lipid membrane through microholes, fabricated in a silicon chip that is sandwiched in between a two-layer microfluidic device. The mechanism of the formation process is investigated for different experimental conditions such as varying flow rates and membrane compositions.

Keywords: cell membrane, self-assembly, microhole, soft-matter devices, artificial cell

1. Introduction

Three-dimensional (3D) lipid structures, such as lipid vesicles and tubes, are a versatile tool in micro- and nanotechnology [1-3]. They could serve as containers for conducting biochemical processes, and for encapsulation of reagents or cells [4,5]. They are simple models for cells and cell organelles due to similarities in size and membrane composition. Moreover, a lipid tube can function as a transport channel to deliver samples, or as a separation channel for electrophoresis to analyze reagent mixtures [6].

In this study, a novel formation pathway for three-dimensional lipid structures is developed and investigated. It combines top-down photolithography techniques and the self-assembling ability of polar lipids. Photolithography techniques are utilized to fabricate microholes that provide the requirements to form lipid structures with predictable size and to align and guide vesicles and tubes in microstructured channels.

2. Experimental

The microfluidic device (Figure 1) is fabricated as described before [7]. It comprises of a silicon slide with microholes (diameter 3 µm) sandwiched between microfluidic channels made in polydimethoxysiloxane (PDMS, Sylgard 184, Dow Corning).

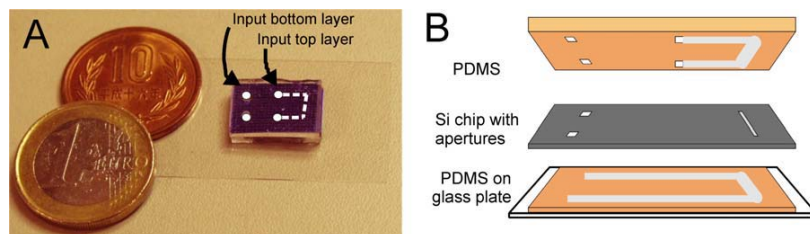


Figure 1: (A) Photograph of the device. A silicon chip comprising of the area with microsized holes is inserted between two PDMS layers composing microfluidic channels. Liquid reservoirs and the microchannel in the top layer are drawn in white color. (B) Scheme of the device (not to scale).

To facilitate the formation of the lipid structures, the microholes are coated with a lipid membrane that is stained with the fluorescent dye Dil-C18 (Invitrogen). Afterwards, the microdevice is assembled, connected to the tubing system, and top and bottom fluidic channels are filled with aqueous solution.

Various types of lipids with different chain length and with saturated and unsaturated chains were investigated (see Table 1, all lipids purchased from Avanti Polar Lipids).

Table 1: List of lipids used for micro-extrusion. The numbers in the abbreviation specify the length of the carbon hydrogen chains and the number of double bonds.

Lipid	Abbreviation
1,2-Dilauroyl-sn-Glycero-3-Phosphocholine (DLPC)	12:0 PC
1,2-Dimyristoyl-sn-Glycero-3-Phosphocholine (DMPC)	14:0 PC
1,2-Dipalmitoyl-sn-Glycero-3-Phosphocholine (DPPC)	16:0 PC
1,2-Distearoyl-sn-Glycero-3-Phosphocholine (DSPC)	18:0 PC
1,2-Dioleoyl-sn-Glycero-3-Phosphocholine (DOPC)	18:1cis PC
1,2-Dielaidoyl-sn-Glycero-3-Phosphocholine	18:1trans PC
1-Palmitoyl-2-Oleoyl-sn-Glycero-3-Phosphocholine	16:0-18:1 PC
1,2-Dioleoyl-sn-Glycero-3-Phosphate (DOPA)	18:0 PA

3. Results and discussion

The lipid membrane is extruded through the microholes upon applying a flow either in the top or in the bottom channel. Both the geometrical restriction by the small aperture and the difference of the flow rates between top and bottom side of the microholes determine form and length of the vesicles and tubes. A low pressure difference results in the formation of vesicle bunches with spherical and cylindrical shapes. The cylindrical structures partly resile, when the flow is stopped (Figure 2).

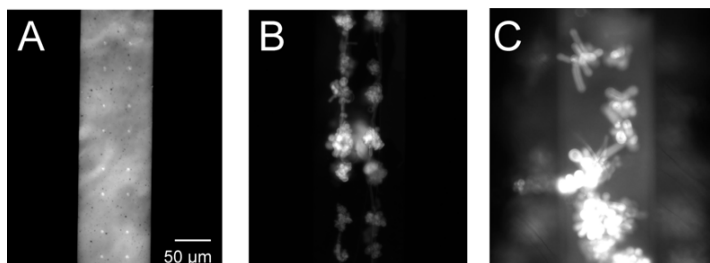


Figure 2: (A) Micrometer sized holes are fabricated in the silicon chip, and covered with a lipid layer that is stained with a fluorescent dye. If a flow is applied inside the top channel, spherical (B) or cylindrical (C) lipid structures are formed at each hole (here from the lipid 12:0 PC).

A strong pressure difference, produced by a high flow rate in the bottom layer, favors the formation of lipid tubes. The formed lipid tubes have a homogeneous diameter of $\sim 3 \mu\text{m}$ and a length of several hundred μm up to 1.5 cm (the length of the used microchannel). They remain stable when the flow is reduced or stopped, but bending and twisting could be observed (Figure 3).

The fabrication pathway is a common method to produce tubes from various kinds of lipids. However, the experiments were conducted at room temperature. Vesicle and tube formation was not observed for DPPC (16:0 PC) and DSPC (18:0 PC). These lipids have a high phase

transition temperature of 41 °C (DPPC) and 55 °C (DSPC), and exhibit a highly ordered gel phase at room temperature rather than a less ordered liquid crystal phase, which is necessary for the formation of three-dimensional lipid structures.

Occasionally, some of the created lipid tubes form helices when the flow is stopped. It occurs most regularly for the lipid DLPC, but helical-like structures can also be observed for other lipids (14:0 PC, 18:1 cis PC, DOPA). The mechanism is unknown so far, and will be subject of the future work.

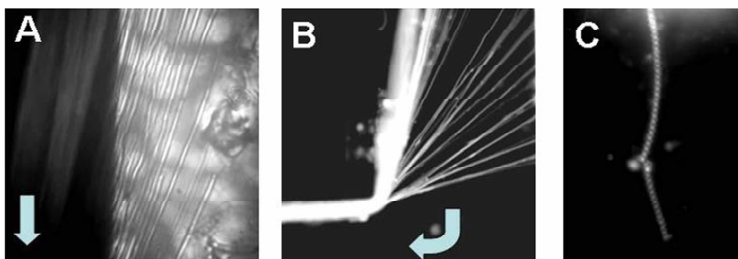


Figure 3: Formation of tubes by micro-extrusion using different lipids. Arrows indicate flow direction. (A) Tube formation directly at the microholes of the silicon chip (lipid: 14:0 PC). The area with the microholes appears bright, the microchannel is dark. (B) The tubes formed at the microholes are collected into one channel (lipid: 16:0-18:1 PC). (C) Helical structures formed by a tube made of the lipid 18:1cis PC.

4. Conclusion and outlook

The presented microdevice facilitates the formation of vesicles and tubes in an automated manner. The lipid vesicles could be generated with high speed by this technique, which allows the utilization as microreactors in applications, where large numbers of individual microreactors need to be screened. The formed lipid tubes can potentially be used for transport channels as well as for the construction of flexible microfluidic networks.

Acknowledgments

Financial support by the European Community (*CellPROM* project, contract No. NMP4-CT-2004-500039 under the 6th Framework Programme for Research and Technological Development) is gratefully acknowledged. We thank U. Marggraf for fabrication of PDMS masters, and A. Neyer for kindly providing the cleanroom facility.

References

- [1] J. M. Schnur, *Science* 262, pp. 1669-1676, (1993).
- [2] E. Evans, H. Bowman, A. Leung, D. Needham, D. Tirrel, *Science* 273, pp. 933-935, (1996).
- [3] M. Karlsson, M. Davidon, R. Karlsson, A. Karlsson, J. Bergenholtz, Z. Konkoli, A. Jesorka, T. Lobovkina, J. Hurtig, M. Voinova, O. Owar, *Annu. Rev. Phys. Chem.* 55, pp. 613-649, (2004).
- [4] P. Walde, S. Ichikawa, *Biomolecular Eng.* 18, pp. 143-177, (2001).
- [5] Y.-C. Tan, K. Hettiarachchi, M. Siu, Y.-R. Pan, A. P. Lee, *J. Am. Chem. Soc.* 128, pp. 5656-5658, (2006).
- [6] M. Tokarz, B. Akerman, J. Olofsson, J.F. Joanny, P. Dommergues, O. Owar, *Proc. Natl. Acad. Sci. USA* 102, pp. 9127-9132, (2005).
- [7] P.S. Dittrich, M. Heule, P. Renaud, A. Manz, *Lab Chip* 6, pp. 488-493, (2006).

DYNAMIC SINGLE CELL CULTURE ARRAY

Dino Di Carlo, Liz Y. Wu, Luke P. Lee

Biomolecular Nanotechnology Center, Berkeley Sensor and Actuator Center
Department of Bioengineering, University of California, Berkeley, CA 94720 USA

Abstract

We demonstrate perfusion culture of arrays of individually trapped cells with dynamic microfluidic control of cellular environment, high maintenance of cell isolation, and low cell death. Hydrodynamically trapped cells were shown to adhere and divide at a comparable rate to cells grown randomly on the same glass substrate. This technique will be useful in quantitative single cell studies that require perfusion of drugs or switching of solutions. Isolated cells in arrays allow facile image processing and eliminate effects of cell-cell communication on results.

Keywords: cell array, cell culture, hydrodynamic trapping

1. Introduction

Other techniques that allow single cell arrays of adherent cells in most cases require protein patterning of the surface or chemical treatments [1]. In other cases, cell number and cell-cell interactions are more difficult to control [2]. Here we present a technique in which no chemical treatments are required and single cell loading is easily performed in less than 30 seconds by flow of a solution of cells into the device. There is no pretreatment of glass or PDMS surfaces to enhance or reduce cell binding or adherence.

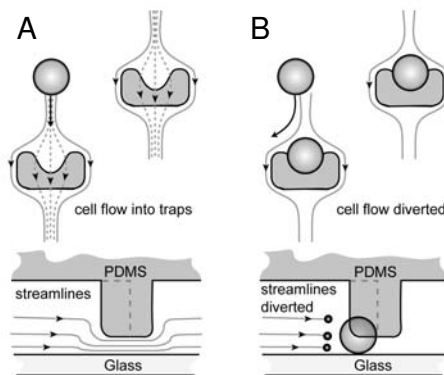


Figure 1. High density single cell isolation. (A-B) Two-layer (40 μm and 2 μm) cup-shaped PDMS trapping sites allow a fraction of fluid streamlines to enter the traps, which is reduced after trapping as the fluidic resistance increases. Trapping probability decreases with each cell trapped. Drawing is not to scale.

2. Experimental

The microfluidic device was designed, fabricated and characterized for cell trapping previously (Fig. 1) [3]. We now present data on single cell viability and growth after trapping. HeLa cells growing in the array at $t = 0$ hr, 12 hr, and 24 hr are shown in Fig. 2. Trapped cells are seen to divide normally and become adherent in a similar fashion to cells grown on the glass slide used as the substrate for the device.

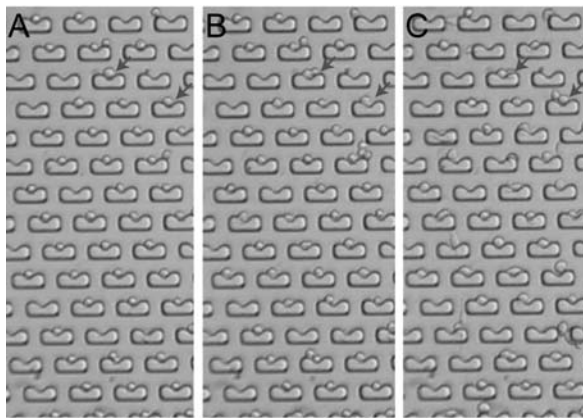


Figure 2. Arrayed single cell culture over 24 hours. Cells were cultured under continuous perfusion of media + 10% FBS with an average velocity ($2.5 \mu\text{m s}^{-1}$). Pictures are shown at times (A) 0 hrs, (B) 12 hrs, and (C) 24 hrs. The arrows indicate cells that undergo cell division within this time period.

3. Results and Discussion

The dynamics of adherence, cell death, and division are plotted for the device as well as a control substrate in Fig. 3. The time for which 50% of cells are adherent ~ 14 hours is matched in both the device and the control substrate. Individual cell behavior in the trapping structure is plotted over time in Figure 4. Here it is observed that after cell division both cells are retained in the trapping structure. Adherent morphology identical to the control situation is also observed with possible attachment to the PDMS structure during adherence the difference in some cases.

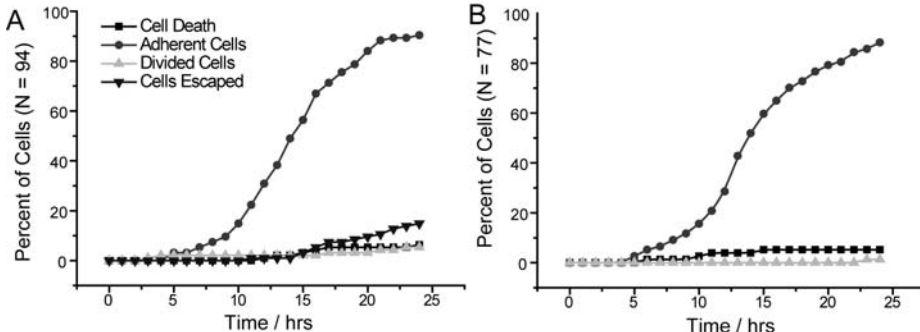


Figure 3. Characterization of cell adhesion and division in the single cell array. (A) Cell adhesion, division, and death are reported over time for individual cells in the single cell array. (B) The same characteristics plotted for culture on a control glass slide.

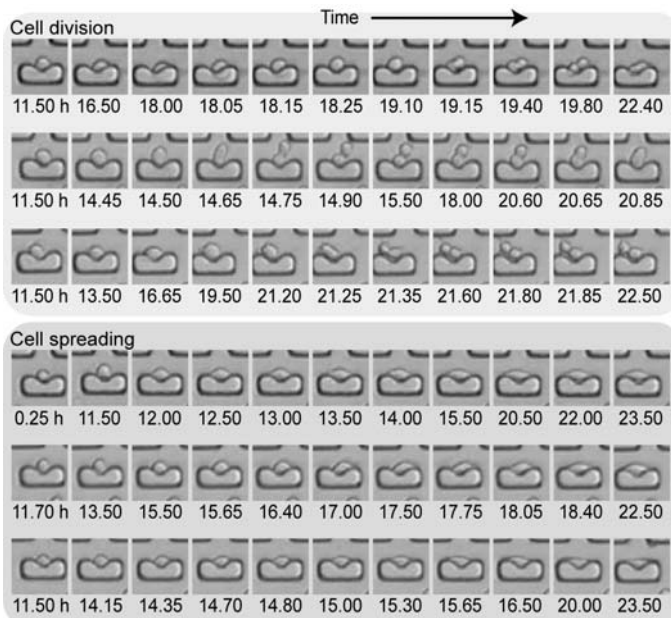


Figure 4. Characteristics of growth for single trapped cells. Frames from a movie of cell growth in the array are shown demonstrating both cell division (first three rows) and morphologies indicative of cell adhesion (rows 4 through 6). Time is shown below the frames in hours. After division daughter cells remained within the trapping region.

4. Conclusions

We argue that this novel and robust technique for arraying adherent cells in a microfluidic environment will enable many studies of quantitative single cell biology on both short and long timescales.

Acknowledgements

D. D. was supported by a Whitaker Foundation graduate fellowship and GSK. L.Y. W. was supported by Intel and Taiwan Merit Scholarship (TMS-094-2-A-008).

References

- [1] Ostuni E, Chen CS, Ingber DE, et al. *Selective deposition of proteins and cells in arrays of microwells*. Langmuir. 17 (9), 2828-2834 (2001).
- [2] Chin V Sanga S, Taupin P, et al. *A microfabricated platform for studying stem cell fates*. Biotechnology and Bioengineering. 88 (3), 399-415 (2004).
- [3] Di Carlo D, Aghdam N, Lee LP. *Single-cell enzyme concentrations, kinetics, and inhibition analysis using high density hydrodynamic cell isolation arrays*. Analytical Chemistry. 78(14), 4925-4930 (2006).

INFLUENCE OF APOPTOTIC CELLS ON MACROPHAGES AND INDUCTION OF PHAGOCYTOSIS STUDIED IN PDMS MICROCHIPS USING PHOTOSTABLE STAINING

Séverine Le Gac¹, Istvan Vermes² and Albert van den Berg¹

¹ BIOS, The Lab-on-a-Chip group, University of Twente, ² Department of Clinical Chemistry, Medisch Spectrum Twente, Enschede, The Netherlands
s.legac@ewi.utwente.nl

Abstract

We report here on the study of the interactions between apoptotic cells and macrophages by using time-lapse imaging and PDMS microchips. Cells are stained with fluorescent probes, and introduced in a shallow ($<20\text{ }\mu\text{m}$) and small (i.d. $100\text{ }\mu\text{m}$) microchamber. Time-lapse imaging enabled us to observe three types of interactions or processes. We also developed novel photostable staining agents specific to apoptotic cells and based on Qdots-probes.

Keywords: apoptosis, cellular interactions, PDMS chips, time-lapse studies, Qdots.

1. Introduction

Apoptosis is a genetically controlled event occurring during normal development, and its dysregulation is linked to diseases [1]. Apoptotic cells end up as apoptotic bodies whose clearance is done by macrophages through phagocytosis. A key-step in this process is the activation of macrophages via “eat-me” signals sent by apoptotic cells. Thereafter macrophages identify apoptotic bodies by specific molecular recognition. This work aims at studying macrophage role and the interactions between apoptotic cells and macrophages using microscopy and time-lapse imaging. For that purpose, both cell types are placed in a microchamber containing a few cells, and enabling thereby cell-to-cell interaction studies.

2. Experimental

2.1 Chip fabrication and preparation. PDMS microchips are fabricated using a casting procedure against a silicon mold that was first produced using DRIE techniques, and bonded after plasma-based surface activation. For chip bonding we mainly use thin glass mounted on appropriate chamber plates for confocal microscopy. PDMS chips are finally coated so as to ensure macrophage adherence and culture for ~ 1 day and cell survival.

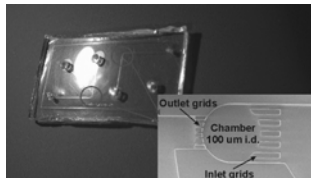
2.2 Cell handling and imaging. HL60 cells and macrophages RAW 264.7 are grown in supplemented RPMI+ and DMEM mediums, respectively. Apoptosis is induced using either drugs (camptothecin at $6\text{ }\mu\text{M}$) or 5-min UV irradiation at 254 nm .

Macrophages are stained using a permanent fluorescent agent. Apoptotic cells are stained using 3 dyes reflecting cell stage in the apoptotic cascade; TMRE stains the mitochondria

of viable cells, Annexin V-Alexa Fluor B647 the cellular membrane by recognition of PS moieties externalized during apoptosis (early stage), and YOPRO-1 the nuclei of dead cells (later stage) [2]. CLSM studies are performed on a Zeiss LSM 510-meta system using a 63X oil immersion objective. Care is taken to keep samples at 37°C during the experiments.

3. Results and discussion

Ideally, a few macrophages are stained, introduced in a chip and grown for ~ 1 day. Following this, stained apoptotic bodies are added, and cells are imaged. Nonetheless, a series of issues must be addressed for cell culture on chips and efficient time-lapse imaging.



Photograph of a PDMS microchip with an enlarged view (SEM picture) of the culture chamber. Macrophage 4 days after Qdots-based staining, and grown in a chip for 3 days.

3.1 Macrophage culture and staining. Macrophage adhesion and culture demand proper PDMS coating and a reliable staining procedure is also mandatory. BSA coating enables macrophage culture for up to 4 days. Macrophages were first stained with an organic dye (BODIPY), but various problems arose linked to the difficulties of on-chip staining, cell cross-staining and the low photostability. Therefore, macrophages are stained with Qdots before their introduction in the microchip.

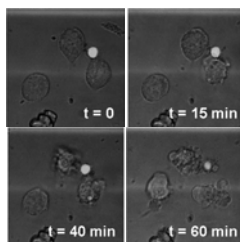


Figure 3. Macrophage (red) activation upon close contact with an apoptotic body (blue and green).

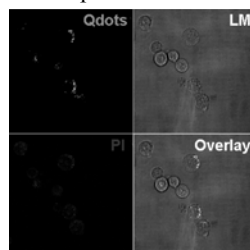


Fig. 4: Macrophages (Qdots, green) after one night incubation with apoptotic bodies (PI, red).

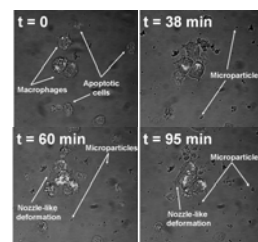


Fig. 5: Eating of microparticles released by apoptotic bodies (PI, red); attraction and deformation of macrophages (Qdots, green).

3.2 Macrophage activation. Co-culture of macrophages and apoptotic cells led us to various observations. Macrophages placed in close contact with apoptotic bodies are activated, indicating that signals were caught by the macrophages (Fig. 3). After overnight incubation of macrophages with PI-stained apoptotic bodies, red dots appear in macrophage

cytoplasm, demonstrating phagocytosis (Fig. 4). Apoptotic cells release microparticles [3], leading thereby to macrophage deformation to catch those microparticles (Fig. 5).

3.3 Qdots-probes for apoptosis imaging. Reliable and stable staining agents are mandatory for both time-lapse and frequent imaging: the whole process is long (>1h) but interesting events are very fast (<1min). As organic dyes are prone to bleaching upon prolonged exposure to light, we came to develop Qdots-based staining agents for specific recognition and imaging of apoptotic cells [4]. They are functionalized with a protein, Annexin V which specifically interacts with phosphatidylserine. With such Qdots cells can be imaged both more frequently and for longer periods without fading, enabling thereby prolonged studies and observation of fast events.

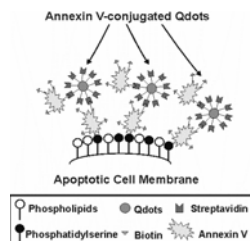


Fig. 11: Staining of apoptotic cell membrane using Qdots-based Annexin V probes, the latter being prepared through a streptavidin-biotin interaction

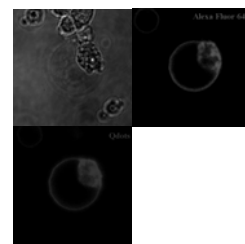


Fig. 12: Apoptotic cell stained with Annexin V-coupled agents, Alexa Fluor 647 (red) and with Qdots-based probes (pink).

4. Conclusion

Several types of interactions between apoptotic cells and macrophages were visualized. Although apoptotic body engulfment was demonstrated, it was not visualized. This may be accounted by two facts. Firstly, phagocytosis is a very temperature-dependant process and, secondly, staining of cells using an Annexin V-based agent hides PS moieties on their surface. This may hinder cell recognition by macrophages as PS moieties are involved in the process of recognition.

Acknowledgements

We would like to thank Paul ter Braak for his help in cell culture and Jiaje Li for his help in the clean-rooms for the fabrication of the silicon masters.

References

1. D. R. Green and G. Kroemer, *Science*, 305, pp 626 (2004).
2. C. Munoz-Pinedo; D.R. Green; A. van den Berg, *Lab On A Chip*, 5, pp 628-633, (2005).
3. J.H.W. Distler; L.C. Huber et al., *Apoptosis*, 10, pp 731-741, (2005).
4. S. Le Gac; I. Vermes; A. van den Berg, *Nanoletters*, in press, (2006).

MODELING THE BEHAVIOR OF MICROTUBULES IN THE PRESENCE OF ELECTRIC FIELDS FOR BIOMOLECULAR MOTOR-DRIVEN μ TAS

T. Kim¹, M.-T. Kao², E. F. Hasselbrink¹, E. Meyhöfer^{1,2}

¹University of Michigan Department of Mechanical Engineering, 2350 Hayward Street, Ann Arbor, MI 48109 USA, ²Department of Biomedical Engineering

Abstract

We have demonstrated that E-fields can be used as novel, active directional controls for biomolecular motor-driven μ TAS systems. In this work, we suggest a cantilever model for describing the deflections of microtubules in the presence of E-fields. Such model provides guiding scientific principles for engineering biomolecular motors and microtubules into μ TAS systems.

Keywords: Biomolecular motors, microtubules, directional control, electric fields

1. Introduction

We previously presented advantages of biomolecular motor (BMM)-powered μ TAS systems over traditional biochemical analysis instrumentation: motor-driven μ TAS systems can be nanoscopic, stand-alone, and highly efficient [1]. One of the main engineering hurdles to designing BMM-powered devices is controlling the direction of transport. Recent work has demonstrated guiding of translocating microtubules along straight lines using chemical patterning of kinesin, mechanical nanotrails and rectifying their motility (so that they all translocate in the same direction) using mechanical patterns [2, 3]. We have also developed an active control method to control the direction of translocation of microtubules on kinesin-coated surfaces using E-fields, which generate electrophoretic forces on (negatively charged) microtubules [4]. In this paper, we present a model that describes our observations of microtubule translocation in the presence of E-fields.

2. Results and Discussion

As seen in Fig. 1, experimental observations suggest that under a sudden application of an E-field parallel to the surface, but normal to the translocation direction, the leading end of the microtubule bends like a cantilever while the remainder of the microtubule is fixed via surface-attached kinesins. The bending is towards the anode, because the negatively-charged microtubule is attracted by dominating Coulombic (electrophoretic)

force. However, at the same time, viscous drag forces due to electroosmotic flow are imposed on the microtubule against the Coulombic force.

Modeling this as a cantilever-beam with uniform loading not only requires detailed understanding of electrokinetic and hydrodynamic mechanisms, but also requires that several mechanical and electrical properties of microtubules are measured: 1) the charge density ($q'_{MT} = 256e^-/\mu\text{m}$), 2) the viscous drag per unit length ($C\eta\mu_{EOF}\mathbf{E}$, where C is the perpendicular drag coefficient of a long cylinder [$C=4\pi/[\ln(\lambda_{MT}/2r_0)+0.84]$], λ_{MT} in length and r_0 in radius), η is the viscosity of buffer solutions (0.91×10^{-3} Pa·s), μ_{EOF} is electroosmotic mobility ($(1.49\pm 0.21)\times 10^{-4}$ cm 2 /Vs) and \mathbf{E} is the strength of E-fields), and 3) the flexural rigidity of the microtubules ($EI=(1.0778\lambda_{MT}^2-3.3589\lambda_{MT}+5.7332)\times 10^{-25}\text{Nm}^2$).

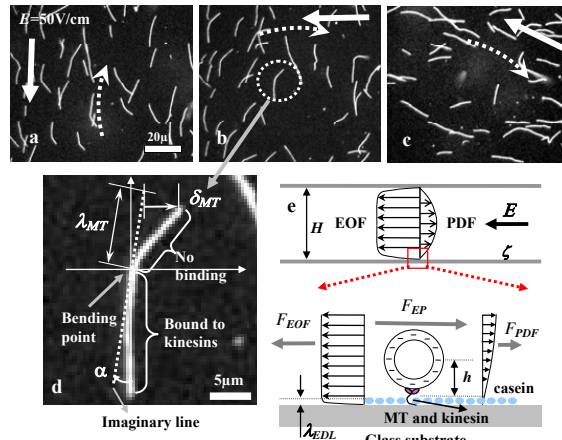


Fig. 1 Transient bending behavior of microtubules controlled to translocate along an arbitrary dotted-line circle after a 90° directional change of a 50 V/cm E-field. In (a), the applied E-field points downwards, which imposes forces on microtubules to redirect them upwards. (b) When the direction of the E-field vector (large arrow) is suddenly changed to the left, the leading ends of microtubules bend rightwards immediately. (c) After a short time, the remainder of each microtubule becomes aligned as well (the direction of the E-field is slightly biased by 26° for next direction control). (d) An example of a momentarily cantilevered microtubule. The length (λ_{MT}), the biased angle (α), and the maximum deflection (δ_{MT}) were obtained via manual image processing. (e) The electrophoretic force (F_{EP}), the viscous drag caused by EOF (F_{EOF}), and the viscous drag caused by PDF (F_{PDF}) are uniformly imposed on the microtubule and parallel to the E-field. The microtubule (MT) and kinesin are not to scale. The distance from the surface to the axis of the microtubule, h is about 21.5 nm [5] and the λ_{EDL} is less than 1 nm. The height of the microchannel, H , is about 75 μm and ζ denotes zeta-potential of glass surfaces ($\zeta = -18.7$ mV). The thickness of casein layer has been reported to be about 8 nm [5].

When the model includes all these properties, the uniform loading, ω , by an E-field of \mathbf{E} becomes $\omega = (q'_{MT} + C\eta\mu_{EOF})\mathbf{E}$, and the nonlinear deflection ($\delta_{nonlinear}$) of a cantilever beam is given by the following series solution [6]:

$$\delta_{nonlinear} = \sin(\psi_0)\lambda_{MT} - \frac{\omega \cos^2(\psi_0)}{EI} \lambda_{MT}^4 - \left(\frac{\omega}{EI} \right)^2 \frac{\sin(\psi_0) \cos^2(\psi_0)}{360} \lambda_{MT}^7 - \left(\frac{\omega}{EI} \right)^3 \left[\frac{\cos^4(\psi_0)}{10368} - \frac{13\sin^2(\psi_0)\cos^2(\psi_0)}{129600} \right] \lambda_{MT}^{10} + \dots \quad (1)$$

Note that the first two terms of Eq. 1 represent the linear solution from the cantilever beam deflection. Here, ψ is the slope at an arc length from the free end of the cantilever beam and the maximum deflection angle of the free end ψ_0 is obtained from the following equation.

$$0 = \psi_0 - \frac{\omega}{EI} \frac{\cos(\psi_0)}{6} \lambda_{MT}^3 - \left(\frac{\omega}{EI} \right)^2 \frac{\sin(2\psi_0)}{360} \lambda_{MT}^6 + \left(\frac{\omega}{EI} \right)^3 \left[\frac{\cos^3(\psi_0)}{5184} - \frac{\sin(\psi_0) \sin(2\psi_0)}{25920} \right] \lambda_{MT}^9 \quad (2)$$

We compare our linear and nonlinear models with experimental observations (Fig. 2) and observe that a significant deviation of the linear model in the presence of strong E-fields. However, our nonlinear model predicts the behaviors of microtubule translocation and deflection under E-fields rather well; it also predicts an optimum E-field strength for active and continuous control of the direction of microtubule translocation. In summary, our model reveals useful design principles and makes possible the systematic design of actively-controllable μ TAS systems that integrate BMM and microtubule-based transport systems.

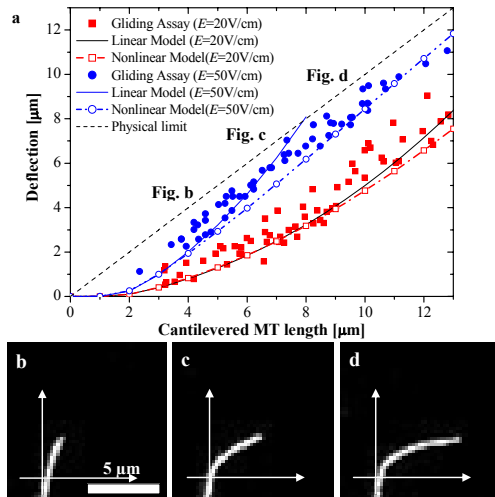


Fig. 2 In (a), the maximum deflections of microtubules are shown under 20 V/cm and 50 V/cm E-fields. The squares denote the experimentally observed deflections under 20 V/cm. The dash-dot line with squares represents the nonlinear model and the dash-dot line represents the linear model. The circles denote the experimental deflections under 50 V/cm. The dash line and the dash line with circles represent the simple linear model and the nonlinear model, respectively. From (b) through (d), the microtubule represents gradual deflections as it translocates and its cantilevered length increases with time under 50 V/cm.

3. References

1. Kim, T. S., Nanjundaswamy, H. K., Lin, C.-T., Lakämper, S., Cheng, L. J., Hoff, D., Hasselbrink, E. F., Guo, L. J., Kurabayashi, K., Hunt, A. J., Meyhöfer, E., μ TAS 2003, 33-36.
2. Lin, C. T., Kao, M. T., Kurabayashi, K., Meyhöfer, E., Small 2006, 2, 281-287
3. Hiratsuka, Y., Tada, T., Oiwa, K., Kanayama, T., Uyeda, T. Q. P., Biophys. J. 2001, 81, 1555-1561.
4. Kim, T. S., Kao, M.-T., Hasselbrink, E. F., Meyhöfer, E., μ TAS 2005, 1, 1234-1236.
5. A. J. Hunt and J. Howard, PNAS 1993, vol. 90, pp. 11653-11657
6. Frisch-Fay, R., Butterworths 1962, 162-174.

MICROFLUIDIC CELL CULTURE CHIP EMPLOYING POLYMERIC NANOFIBER MEMBRANE

SungRak Kim^{1,3}, KiHwa Lee¹, KwangHo Lee², JuYeoul Baek¹,
YongDoo Park¹, Kyung Sun¹ and SangHoon Lee¹

¹ Dept. of Biomedical Engineering, Korea Univ., South Korea

² Interdisciplinary Program in Medical and Biological Engineering Major, Seoul
National University, South Korea

³Korea Materials and Anslysis Corp.(K-MAC), South Korea

Abstract

In this paper, we have developed cell chip employing polymeric nanofiber membrane which was used for the better diffusion of nutrition or other materials such as growth factor and for the scaffold of cell culture, and we evaluated the function of this chip by culturing the human mesenchymal stem cells (hMSCs) which have large potential applications in the tissue engineering.

keywords: cell culture chip, nanofiber, Human mesenchymal stem cell(hMSC), tissue engineering

1. Introduction

Cell culture in a microfluidic chip has many advantages over conventional culture dishes and these cell chips were broadly applied in the cell-based assays, high throughput screening and the basic cell study [1]. Recently, the porous membrane has been employed in the cell chip as a scaffold for the better attachment of cells or a perfusion and most of these membranes are commercial products [2-3]. In this paper, we have developed cell chip employing polymeric nanofiber membrane and cultured the Human mesenchymal stem cells (hMSCs) which have large potential applications in the tissue engineering.

2. Fabrication of cell chip

The schematic diagram of our cell chip is illustrated in Figure 1(a). The upper of the chip is cell culturing chamber and the lower of the chip is fluid delivery channel. The top of cell culture chamber was opened to allow the cell and media delivery by using micropipette. The fabrication process of the cell chip is shown in Figure 1(b). The PDMS platform was fabricated via the standard softlithography process and the polymeric nanofiber membrane was incorporated between the upper and lower layer. The nanofiber membrane was produced by the electrospinning method and the material of nanofiber was polyurethane. The nanofiber membrane was cut with the 9 mm x 9 mm size, and it was placed at the 'X' position in the Figure 1(b) and the fabricated cell chip was sterilized by using the E.O gas sterilizer.

3. Experiments

Human MSCs were cultured in DMEM with 10% (v/v) fetal bovine serum and 1% (v/v) antibiotics containing penicillin and streptomycin in a humidified incubator (5%

CO_2 , 37°C). Cells from passage six were seeded on the nanofiber sheets with final concentration of 2×10^5 cells/ml and incubated overnight. Cells were fixed with 4% para-formaldehyde for 30 minutes. Actin filaments were visualized by staining with actin-palloidin for cytoskeletal structure.

4. Results and discussion

The cell chip was successfully constructed and Figure 2 demonstrates photograph of fabricated cell chip including nanofiber membranes and bonding of nanofiber membrane and PDMS platform was carried out via oxygen plasma surface-treatment. Both the upper and lower layers bonded stably and we found no leakage at the bonded region, and the semitransparent nanofiber membrane is visible in this Figure. Figure 3 demonstrates the SEM image of produced polyurethane nanofiber membrane. We have developed the process to fabricate the nanofiber membrane efficiently, and the conditions are listed in Table 1. The diameters of nanofiber were ranges from 100 nm to 500 nm and the solutions were well diffused through this membrane. Onto the cell culture chamber, we dropped the human MSC-suspension media, while we introduced the cell culture media slowly into the lower fluid channel and filled the whole lower channel. Afterward, we have incubated cells at the CO_2 incubator for 3 days and the nutrition and media were supplied through the membrane during incubation time. Figure 4(a) demonstrates the MSCs cultured on the conventional culture dish. After 3 days' incubation, we have dyed the actin filaments of hMSCs and Figure 4 (b) illustrates the fluorescent image of dyed cells which were cultured on the nanofiber membranes. Cells on the nanofiber survived well, adhered stably on the surface of nanofiber and spread uniformly on the membrane. Even though cellular morphology does not align on the nanofiber, some actin filament showed the specific orientation within the cells.

5. Conclusion

Recently, nanofiber membranes have been broadly applied in the diverse fields, especially in the filtration. In this paper, we have showed two feasibilities: (1) the nanofiber membrane can be integrated with the PDMS based microfluidic and (2) the nanofiber membrane can be utilized as scaffold for the cell culture. The nanofibers has high surface to volume ratio and much materials can be immobilized on the surface of nanofiber. So, we expect that this nano-membrane based chip will be applied in many fields if we functionalize the surface of nanofibers with appropriate materials such as cell growth factors or drugs.

Acknowledgement

This study was supported by a grant of the Ecotechnopia 21 Project, Ministry of Environment, Republic of Korea (052-041-037)

REFERENCES

- [1] Paul J. Hung, Philip J. Lee, Poorya Sabourchi, Robert Lin, Luke P. Lee, Vol. 89, Biotechnology and Bioengineering(2005), pp. 1-8
- [2] Yoshihiro Ito, Ji Zheng and Yukio Imanishi, Vol. 18, Biomaterials(1997), pp. 197-202
- [3] Vinay V. Abhyankar, David J. Beebe, microTAS2005(2005), pp. 148-150

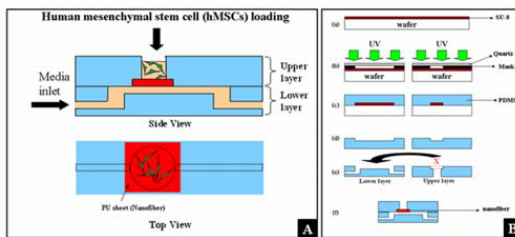


Figure 1. (a) Schematic diagram of cell chip (b) The standard softlithography process

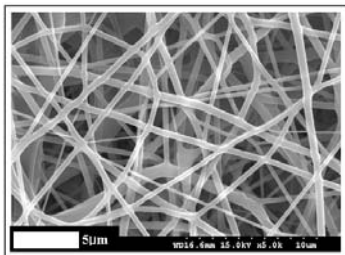


Figure 2. The SEM images of produced PU nanofibers

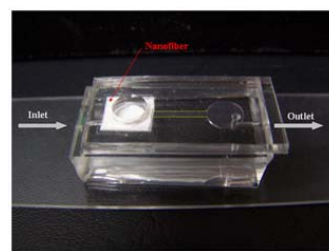


Figure 3. The photograph of fabricated cell chip including nanofiber membranes

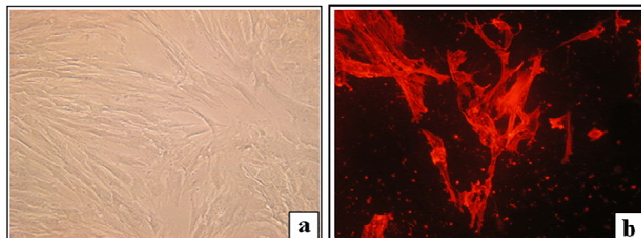


Figure 4. (a) The optical image of the hMSCs cultured on the conventional culture dish (b) The fluorescent image of cells which were cultured on the nanofiber membranes incorporated inside cell chip

Parameter	Polyurethane
Solution Concentration (%wt)	12
Solution flow rate (ml/min)	2.5
Tip-to-collector distance (cm)	7
Deposition time (hr)	8
Electric field strength (kV)	11
Characteristics	GFF

Abbreviations are: GFF: good fiber forming

Table 1. Summary of fiber forming conditions (the evaluation of fiber web was carried out by SEM image inspection)

The 10th International Conference on Miniaturized Systems for Chemistry and Life Sciences (μ TAS2006)
November 5-9, 2006, Tokyo, Japan

SAXS IN A μ TAS – A NEW APPROACH TO STRUCTURE:FUNCTION STUDIES OF BIOLOGICAL MACROMOLECULES

Bente Vestergaard¹, Lise Arleth², Detlef Snakenborg³, Katrine Toft^{1,3}, Jes Jacobsen⁴, James M. Flink⁴ and Jörg P. Kutter³

¹Biostructural Research, Dept. Medicinal Chemistry, Danish University of Pharmaceutical Sciences, DK-2100 Copenhagen, Denmark

²Biophysics Group, Dept. Natural Sciences, The Royal Veterinary and Agricultural University, DK-1871 Frederiksberg, Denmark

³ μ TAS group, MIC - Dept. of Micro and Nanotechnology, Technical University of Denmark, DK-2800 Kgs. Lyngby, Denmark

⁴Novo Nordisk A/S, Novo Alle, DK-2880 Bagsværd, Denmark

Abstract

A μ TAS for structural investigation of biological macromolecules and their complexes is being developed. The μ TAS features a 200 nl sample chamber for Small-angle X-ray Scattering (SAXS) analysis.

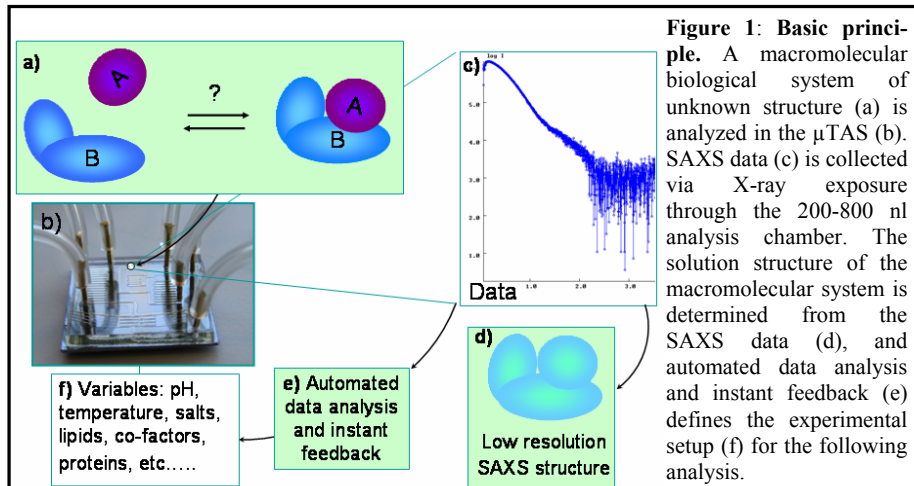
Keywords: structural biology, high-throughput, automated data analysis, microfluidic front-end, small-angle X-ray scattering

1. Introduction

Proteins are dynamic macromolecules that can undergo conformational changes or form complexes with other biological molecules. Elucidation of these suprastuctural features lies at the heart of an understanding of the structure:function relationship [1, 2]. Still, such features are difficult to investigate using established methods for structural characterization. One reason is that in order to get a comprehensive picture it is necessary to examine the macromolecules under many different solution conditions, which today is very demanding both in terms of time and sample consumption.

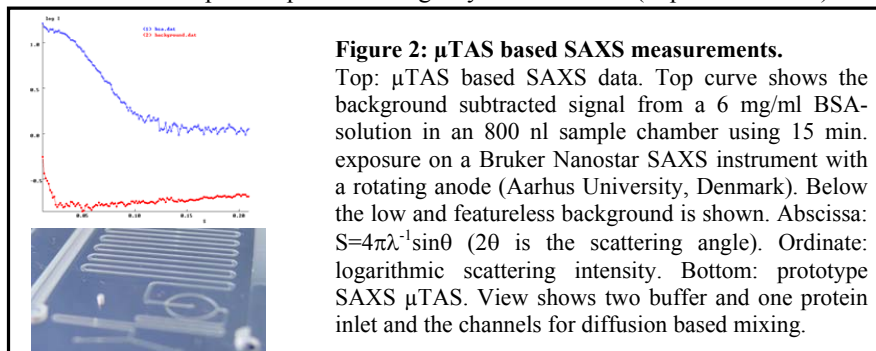
Here, we describe the development of a system combining state of the art from two areas: microfluidics and small angle X-ray scattering. Microfluidics for high-throughput screening of a large solution parameter space while using minute amounts of rare biomacromolecules. And SAXS as the tool for elucidating suprastuctural features and detecting experimental conditions defining borderlines between suprastuctural states (see Fig. 1 for a conceptual overview). Such a system also has the potential to enable screening of, e.g., formulation of bio-drugs and solubilization of membrane proteins. Furthermore, powerful software for automated data-analysis is developed, allowing direct feedback to the microfluidic front-end. Thus, rational navigation in the multidimensional experimental space becomes possible allowing pinpointing of structurally and functionally relevant areas of investigation, borders between various functional states, or structurally stable experimental windows of potentially labile biological systems. Ultimately, the SAXS/ μ TAS system enables time-resolved studies

of biological processes, using already established microfluidic techniques [3, 4] in combination with our high-throughput screening.



2. Experimental

Various polymers were tested for their X-ray absorption and diffraction characteristics on a rotating anode X-ray source (Aarhus University, Denmark) using 15 minute exposure times. A prototype polystyrene (Goodfellow) μ TAS has been developed using direct micro-milling. Proteins and buffer components mix by simple diffusion in channels with dimensions adapted to the final sample chamber of down to 200 nl. The μ TAS is sealed by a 125 μ m coverlid using thermal bonding. SAXS measurements on a solution of bovine serum albumin at 6 mg/ml in 50 mM Hepes, pH 7 in a prototype polycarbonate (PC) μ TAS with an 800 nl sample chamber were performed on rotating anode based instruments (Risø National Laboratory and Aarhus University, Denmark). Automated background subtraction and Indirect Fourier Transformation is at present pursued using Bayesian statistics (unpublished data).



3. Results and discussion

	Mylar	Kapton	PMMA	PC	PVC	PS	PETG	glass
Machinability	-	-	+	-	+	+	+	-
Bonding	N.A.	-	+	-	-	+	+	-
Cleaning	-	+	-	-	-	+	-	+
x-ray transmission	-	-	+	+	-	+	+	+
x-ray diffraction	-	□	+	+	□	+	+	+
x-ray endurance	N.A.	+	-	-	N.A.	+	-	+

Table 1. Polymer characteristics.

Machinability: no burr, smooth surfaces (prevention of bio-buildup). Bonding: High quality, vacuum compatibility, high strength. Cleaning: resistance to acid, base and ethanol. X-ray transmittance: high (optimizing signal:background). X-ray diffraction: not acceptable. X-ray endurance: high (high number of experiments performed before structural damage). Score: + (positive), - (negative), □ (neutral).

First successful protein measurements have been performed in a 800 nl sample chamber on a rotating anode based SAXS instrument (see Fig. 2). To our knowledge, this has never been demonstrated before. A proof of concept illustrating the diversity of possible structural investigations is under establishment.

4. Conclusions

A polymer-based prototype μTAS has been developed featuring simple mixing capabilities for protein and buffer solutions and an integrated X-ray transparent analysis chamber with 200-800 nl probe volume with an X-ray interaction path-length of 1 mm.

Acknowledgements

The authors acknowledge funding from Novo Nordisk A/S, Dept. of Micro and Nanotechnology/DTU, The Danish Research Councils (NABIIT, FSS) and DANSYNC, and beamtime at MAXLAB, Aarhus University and Risø National Laboratories.

REFERENCES

1. M.G. Clarey, J.P. Erzberger, P. Grob, A.E. Leschziner, J.M. Berger, E. Nogales, M. Botchan, *Nature Struct Mol Biol*, E-pub ahead of print (2006)
2. K. Lindorff-Larsen, R.B. Best, M.A. Depristo, C.M. Dobson, M. Vendruscolo, *Nature* 433, 128-32 (2005)
3. L. Pollack, M.W. Tate, N.C. Darnton, J.B. Knight, S.M. Gruner, W.A. Eaton, R.H. Austin, *Proc. Natl. Acad. Sci. USA* 96, 10115-10117 (1999)
4. R. Barrett, M. Faucon, J. Lopez, G. Cristobal, F. Destremaut, A. Dodge, P. Guillot, P. Laval, C. Masselon, J. Salmon. *Lab on a chip* 6, 494-499 (2006)

LOW COST MICROFABRICATED SILICON CHIP FOR MEMBRANE PROTEIN MONITORING

Bruno Le Pioufle^{1,3}, Christophe Yamahata², Kei Funakoshi², Hiroaki Suzuki², Agnès Tixier-Mita¹, Hiroyuki Fujita¹, Shoji Takeuchi¹

¹ LIMMS-CNRS/IIS, The University of Tokyo, Japan

² Institute of Industrial Science, The University of Tokyo, Japan

³ CNRS-SATIE/BIMIS, ENS Cachan, France

Abstract

In this paper we show the feasibility on using silicon batch-fabricated non planar microsized aperture for the monitoring of membrane proteins inserted in a lipid bilayer reconstituted on this aperture. A low cost chemical etching protocol was used for micromachining the aperture. This work is a first step towards integrated silicon biochips designed for membrane protein recording.

Keywords: Membrane proteins, hemolysin, Silicon, wet etching, Patch-clamp

1. Introduction

The membrane protein structure and functions are still barely explored, as these proteins only keep their functionalities if they are inserted in a lipidic double-layer. First prototypes of glass [1] or polymer [2] biochips recreating a biomimetic environment with the purpose of membrane protein characterization have been recently published. Potential application of such kind of biochips are huge in the pharmaco-toxicology domain, as membrane protein are key components in cancer and in drug rejection.

In this paper we show that a micro-aperture obtained by means of silicon microtechnology, could be used as a support for lipid bilayer reconstitution, and permitted the monitoring of membrane proteins. The feasibility of producing such batch fabricated silicon membrane protein chips, is crucial for future high throughput screening (HTS) arrays were electronics integration will be needed.

2. Experiments

Both oxidized faces of a (100) silicon wafer are patterned prior to wet etching with KOH and TMAH. The resulting perpendicular V-grooves, following {111} planes in silicon, produce a non planar aperture at their intersection, as shown on Fig. 1, which dimensions can be precisely controlled [3]. On Figure 2, we show a SEM view of the obtained non planar micro-aperture.

The processed silicon chip was then sandwiched between two 2mm thick Silicone sheets, in which open chambers were defined, shut by two glass layers (see Fig. 4). Both chambers (60µl) were filled with the buffer including the membrane protein at one side. The chip surface was then covered by the lipid layer using around 3 microliter of 1,2-Diphytanoyl-sn-Glycero-3-Phosphocholine (DphPC, Avanti Polar lipids) diluted in

Decane at 5 mg/ml concentration. The obtained lipid layer closing the aperture made through silicon is shown on Figure 3.

The membrane protein we used for the experiment was α hemolysin, which concentration was 0,18 μ g/ml, in 0,9 mM MOPS + 0,1M KCl buffer. This protein is used by bacteria to kill cells, as inserted in their cytoplasmic membrane, nanopores are created, increasing drastically the conductivity of the membrane, and leading to the cell lysis. For the monitoring of the conductivity between the CIS and TRANS sides of the artificial membrane, we used a patch-clamp amplifier (Nihon Kohden, CEZ-2400, Japan). A photo of the complete setup is presented Figure 4.

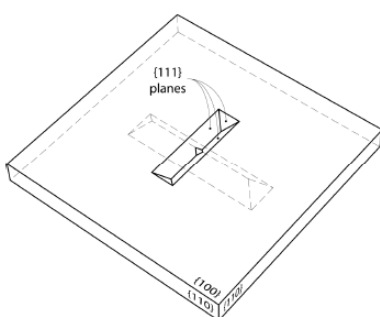


Figure 1. Schematic view of the aperture microfabrication by means of perpendicular V-grooves etching.

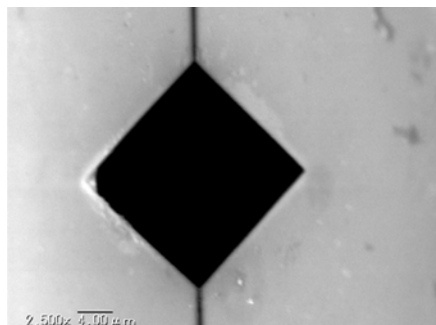


Figure 2. SEM view of the micromachined pore. The non-planar aperture is here 18 micron large (side dimension)

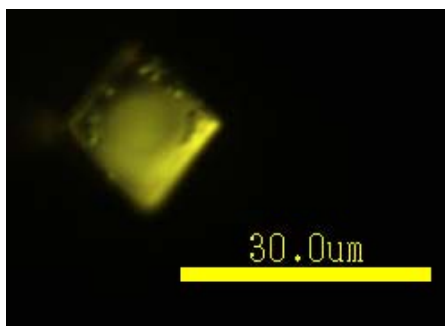


Figure 3. microscope view of the lipid layer formed on the aperture made through silicon.

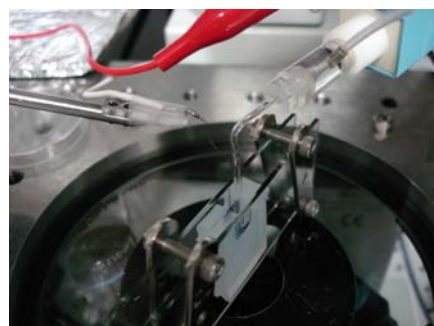


Figure 4. The experimental set-up: the CIS and TRANS side chambers are made in silicone rubber, sealed by two glass slides. Electrical recording is made by a patch-clamp amplifier.

3. Results and discussion

As shown on Figure 5, we could record the steps of current, each step corresponding to the insertion of a single membrane protein in the artificially reconstituted membrane. The recording of the electrical activity of the α -hemolysin proves that the lipid layer closing the aperture made through silicon, was a bilayer, and therefore proves the feasibility of reconstituting lipid bilayer on non-planar micro apertures in silicon. As the method used to obtain these nanopores is robust, highly reproducible, and low-cost, it opens perspectives for the HTS of membrane proteins activities.

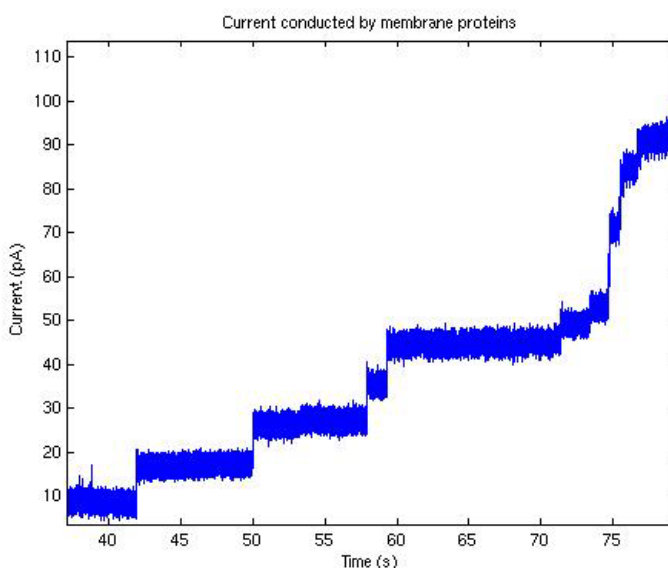


Figure 5. Recorded current through the α -hemolysin membrane proteins. A current step occurs when membrane protein units, inserted in the artificial membrane, assemble and become to be functional.

Acknowledgements

We are thankful to the VLSI Design and Education Center where the masks were fabricated (VDEC, Univ. Tokyo). We thank the Japan Society for Science Promotion and the Ministry of education for their support.

References

- [1] Fertig N et al., Phys Rev E, Vol 64, 040901, 2001
- [2] H. Suzuki et al., Langmuir 22, pp. 1937-1942, 2006.
- [3] A. Tixier-Mita et al., Transducers '03, pp. 250-253, 2003.

DIRECT MONITORING OF B- TO A-DNA CONFORMATIONAL TRANSITION AT A SINGLE MOLECULE LEVEL INDUCED BY ETHANOL IN MICROFLUIDIC DEVICES

Kentaro Fujiyoshi¹, Noritada Kaji¹, Manabu Tokeshi¹, Yoshinobu Baba^{1,2}

¹Department of Applied Chemistry, Nagoya University, Nagoya 464-8603, Japan

²Health Technology Research Center, AIST, Takamatsu 761-0395, Japan

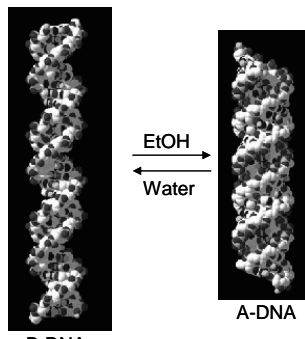
Abstract

This paper presents the development of a direct monitoring system of conformational transition from B- to A-DNA in microfluidics devices. Well-controlled laminar flows produced elongated large single DNA molecules onto chemically modified surfaces, and furthermore, ease of liquid-exchange operation of microfluidics devices enabled dynamic observation of B- to A-DNA conversion.

Keywords: Polydimethylsiloxane(PDMS), DNA, B- to A-DNA conversion, DNA stretching

1. Introduction

The conformation of DNA is sensitive to hydration and the conformational transition from B- to A-DNA could be induced by an increase of ethanol or salt in the solution, and as a result, the DNA became short and thick (A-form: 0.26 nm/base pitch, B-form: 0.34 nm/base pitch) as shown in Fig. 1. Extensive studies have been done to explore the B- to A-DNA transition by x-ray crystallography, FTIR, NMR, and CD [1]. In this study, by taking advantages of microfluidics devices, the unique optical approach to monitor B- to A-DNA conversion has been developed.



2. Experimental

Our approach mainly consists of two processes: deposit stretched DNA molecules onto a coverslip and consecutive operation of liquid exchange. As shown in Fig. 2, we fabricated a PDMS microchannel which has four branch channels and mounted it onto a 2-aminopropyltriethoxysilane modified coverslip. Bacteriophage λ -DNA (48.5 kbp) was deposited and stretched onto the coverslip by well-controlled laminar flows in a microchannel (Fig. 3). After the stretched DNA molecule arrays were prepared, the solution

Figure 1. Ethanol induces conformational transition from slender B- to short and thick A-DNA.

composition was changed by shifting a flow in the branched channel from DNA, YOYO-1, to water or different concentration of ethanol solution (10%, 20%, 30%, 40%, or 50% (v/v)). Fig. 4 shows the fluorescence images of stretched DNA in deionized water (a) and in 30% (v/v) ethanol solution (b). Since single DNA molecules were arrayed with high degree of uniformity with less overlapping and artifacts, reliable evaluation of the length of stretched DNA molecules could be possible. Theoretical lengths of B- and A-DNA are 16.49 μm (0.34 nm/bp \times 48.5 kbp) and 12.61 μm (0.26 nm/bp \times 48.5 kbp), respectively.

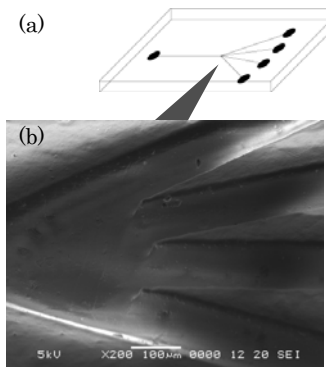


Figure 2. PDMS microchannel for direct monitoring of B- to A- DNA conformational transition. (a) A schematic drawing of PDMS microchip. (b) A SEM image of branch point of the microchannel.

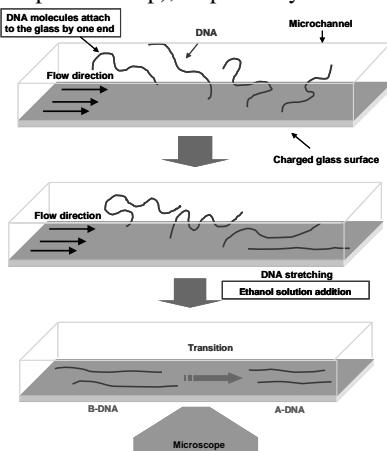


Figure 3. The scheme of deposition of stretched DNA in the microchannel and observation of conformational transition from B- to A-DNA by adding ethanol solution.

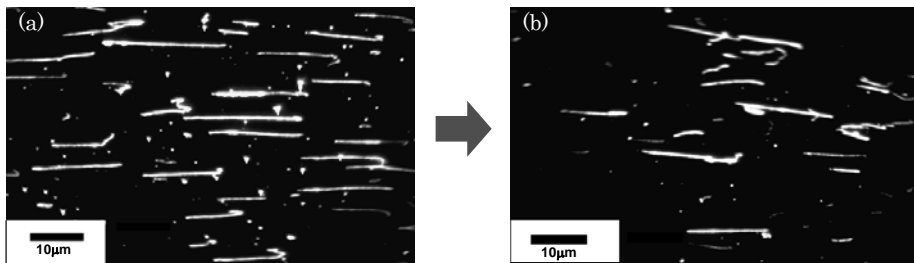


Figure 4. Fluorescence images of stretched λ -DNA (a) in deionized water, and (b) in 30% (v/v) ethanol solution.

3. Results and discussion

The statistical measurements of DNA length in different conditions shows that average length of DNA molecules in water is 18.26 μm , which is corresponding to B-DNA (Fig. 5a)

and DNA molecules which were exposed by ethanol solution after the fixation onto a coverslip were shrank in proportion as increase of ethanol concentration (Fig. 5), which may be attributable to A-DNA. Measured DNA lengths are slightly longer than the theoretical values, since lengths of DNA molecules were increased by the intercalation of the fluorescent reagent. These results demonstrated that our approach could not only analyze the conformational changes of DNA from B- to A-form but also directly monitor their changes.

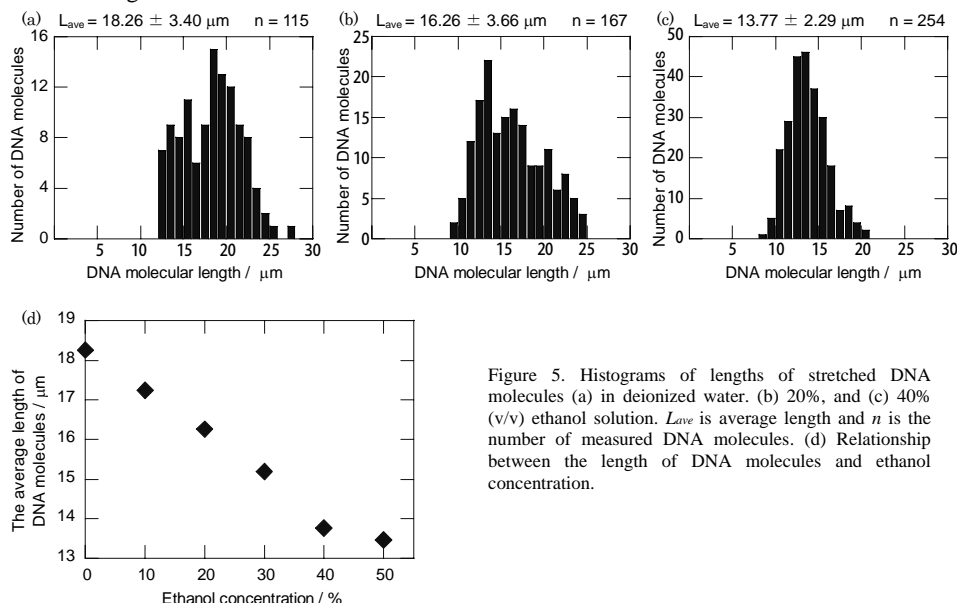


Figure 5. Histograms of lengths of stretched DNA molecules (a) in deionized water, (b) 20%, and (c) 40% (v/v) ethanol solution. L_{ave} is average length and n is the number of measured DNA molecules. (d) Relationship between the length of DNA molecules and ethanol concentration.

4. Conclusions

We have developed direct monitoring of the conformational transition at a single molecule level in microfluidic devices. Since some DNA binding proteins recognize an intermediate structure between A- and B-DNA [2], to understand the functions of DNA-interacted proteins concerning DNA structure become increasingly important. Our approach could give a new insight into functional genomics and transcriptomics.

References

- [1] R. E. Dickerson, and H.-L. Ng, *Proc. Natl. Acad. Sci., USA*, 2001, 98, 6986-6988.
- [2] X. J. Lu, Z. Shakked, and W. K. Olson, *J. Mol. Biol.*, 2000, 300, 819-840.

PREPARATION OF CELL-SIZED LIPOSOMES OF CONTROLLED SIZE CONTAINING LONG GENOMIC DNA

**Maël Le Berre¹, Marie-Alice Guedea-Boudeville², Yong Chen¹
and Damien Baigl¹**

¹CNRS UMR 8640, Dpt. de Chimie, Ecole Normale Supérieure, France

²CNRS UMR 7057, LMSC, Université Paris 7, France

Abstract

This article describes a method to prepare cell-sized liposomes of controlled size and containing long genomic DNA. Liposomes were obtained by the electroswelling of micro-printed lipid films of various motif sizes while duplex giant DNA (T4 DNA) was inserted during the swelling procedure. We found that the motif size of the micro-patterned lipid film controlled the final size of liposomes and that reversibly compacted DNA molecules could be inserted in the liposomes with a yield of about 10%.

Keywords: Artificial cell, micro-contact printing, liposome, DNA

1. Introduction

In nature, up to 2 m of genomic DNA materials is packaged to fit within narrow micrometric spaces, such as the nucleus of eukaryotic cells or the capsid of viruses. The preparation of artificial cell-sized liposomes with a controlled size and containing genetic materials is thus of great interest to investigate and understand the hierarchical self-organization and gene regulation in living complex systems. However, the double challenge of i) preparation of monodisperse liposomes and ii) insertion of long genomic DNA molecules inside liposomes has never been achieved up to now. Here, we describe a novel method that combines micro-contact printing technology, electroswelling formation of liposomes and DNA compaction methodology.

2. Experimental

Figure 1 shows a schematic representation of our method to prepare cell-sized liposomes of controlled size and containing long genomic DNA. First, a L- α -phosphatidylcholine (EPC) lipid solution (10 mg/mL in a 10:1 chloroform/methanol mixture) was spread on a temporary substrate (e.g., ITO) and dried under vacuum for one hour to obtain a well-organized dry and thin lipid film. Then, a PDMS stamp was used to transfer the lipid film with a desired pattern onto ITO-coated glass slides. Next, liposomes were obtained by the electroswelling (2 V, 10 Hz, 10 hours) of the micro-patterned lipid film in a 0.1 M sucrose solution. We used PDMS stamps with two motif sizes (dots of 15 and 30 μ m in diameter, respectively).

For DNA insertion experiments, molecules of genomic duplex T4 DNA (166,000 base pairs) were first compacted by spermine, a tetravalent cationic polyamine, (figure 3) and added to the solution for liposome swelling. This was obtained by the successive addition of 10 mM Tris-HCl buffer ($pH = 7.4$), 10 μ M spermine, 0.1 μ M fluorescent

dye DAPI, 0.1 μ M DNA in the 0.1 M sucrose swelling solution. For the observation and after the swelling, the solution containing the liposomes was extracted from the cell for electroswelling and mixed (1:2 v/v) with a 0.1 M glucose solution adjusted in osmolarity (110 mOsmol/L). After 2 hours, almost all liposomes had fallen down to the bottom of the observation cell by gravity and were observed using an Axiovert 200 inverted microscope (Zeiss) equipped with a 100 \times oil-immersion objective lens.

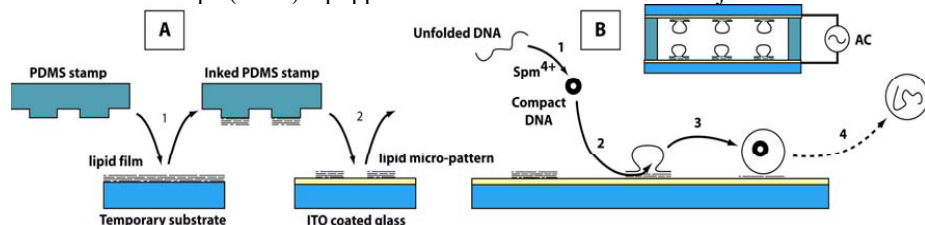


Figure 1. Schematic procedure of the preparation of liposomes of controlled size and containing long genomic DNA. A. Transfer of a lipid micro-pattern on an ITO-coated glass: 1) the PDMS stamp is inked by transferring a dry lipid film from a temporary substrate to the motifs of the stamp; 2) the lipid is stamped onto an ITO-coated glass slide. B. Electroswelling of liposomes from the lipid micro-pattern and simultaneous DNA insertion: 1) individual molecules of genomic T4 DNA (166,000 base pairs) are compacted in the presence of spermine (Spm^{4+}), a tetravalent cationic polyamine; 2) Toroidal condensates of such compacted DNA (approx. 90 nm in outer diameter) enter the liposomes while they are swelling under AC electric field. 3) When the electroswelling has been completed, liposomes detach from the surface. 4) Under appropriate conditions, compacted DNA may be unfolded due to the reversible nature of DNA compaction phase transition.

3. Results and discussion

Our micro-printing technique combines i) the simplicity of microcontact printing [1] and ii) a control deposition of the lipid film (thickness, organization) [2]. We found that the size of final liposomes is directly controlled by the motif size of the PDMS stamp, in agreement with [1-2]. Figure 2 shows two arrays of liposomes obtained after the swelling for 2 hours of micro-patterned lipid films with a motif size of 30 (left) and 15 μm (right), respectively. There is a clear increase in the mean diameter of obtained liposomes with an increase in the lipid motif size.

Up to now, usual techniques to include DNA inside a liposome (electroporation, swelling) have been limited to short DNA fragments (up to a few thousands base pairs). To insert very long molecules of genomic DNA, we used the fact that single molecules of long duplex DNA fold reversibly in the presence of multivalent counter-

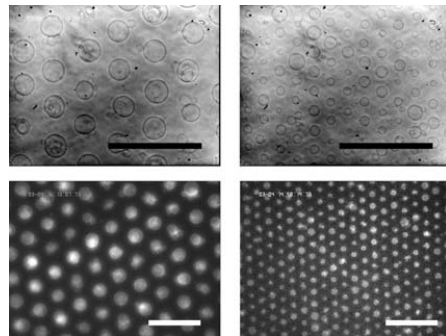


Figure 2. Phase-contrast (top) and Fluorescence (bottom) microscopy images of liposomes formed on the lipid pattern after 2 hours of electroswelling (2V, 10 Hz). The lipid patterns consisted of hexagonal arrays of lipid dots having a diameter of 30 μm (left) and 15 μm (right), respectively. Liposomes are made fluorescent by the use Rhodamine-Phosphatidylethanolamine, a fluorescent lipid. For each picture, scale bar is 200 μm .

ions into a very dense compact state [3]. Figure 3 shows the single-chain compaction of T4 DNA by spermine (Spm^{4+}) prior to the swelling of liposomes. Thus obtained DNA condensates have a toroidal shape with an outer diameter of ca. 90 nm (Fig. 3c).

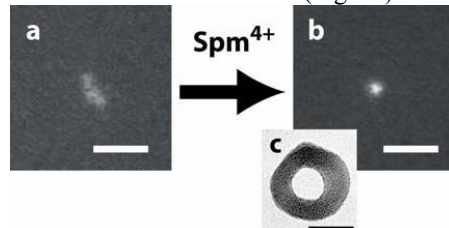


Figure 3. Single-molecule compaction of genomic T4 DNA (166,00 base pairs, 0.1 μM in 10 mM Tris-HCl buffer, $pH = 7.4$) by spermine (Spm^{4+}). Without spermine, all DNA molecules are in the unfolded elongated coil state. After sufficient addition of spermine, all DNA molecules fold individually into a dense compact state. a) Fluorescent microscopy (FM) image of an unfolded DNA molecule in the absence of spermine. Scale bar is 5 μm . b) FM image of compacted DNA molecule after addition of 10 μM spermine. Scale bar is 5 μm . c) Transmission Electron Microscopy (TEM) image of the compacted DNA molecule. Scale bar is 50 nm.

Figure 4 shows typical fluorescence microscopic images of a liposome obtained after swelling in a sucrose solution containing the compacted DNA molecules. In this figure, a compact DNA molecule can be seen as a fluorescent blue spot (fluorescence from DAPI-labeled DNA) freely moving within the fluorescent yellow liposome (fluorescence from fluorescein-labeled phospholipids composing the membrane of the liposome). The yield of such DNA insertion in cell-sized liposomes was estimated to be about 10%.

4. Conclusion

The method presented here, based on the electroswelling of micro-patterned lipid films and DNA compaction methodology, allows for the formation of cell-sized liposomes of controlled size (in the range 10–50 μm) and containing long genomic DNA. With a better yield in DNA insertion, it should pave the way for the controlled bottom-up preparation of artificial cells.

References

1. P. Taylor, C. Xu, P. D. I. Fletcher, and V. N. Paunov, A novel technique for preparation of monodisperse giant liposomes, *Chem. Commun.*, vol. 14, pp. 1732–1733, (2003)
2. K. Kurabayashi and S. Takeuchi, Formation of monodisperse giant liposomes using micro-patterned lipid films, *Proc. Micro Total Analysis Systems 2005*, pp. 1455–1457, (2005)
3. D. Baigl and K. Yoshikawa, Dielectric control of counterion-induced single-chain folding transition of DNA, *Biophys. J.*, vol. 88, pp. 3486–3493, (2005)

INTRACELLULAR RECORDING AND CALCIUM MEASUREMENT IN A SINGLE NEURON OF *APLYSIA* USING A NANO-PROBE

Masaki Shuzo¹, Tomoki Kazawa², Koutaroh Okada³,
Ryohei Kanzaki², and Isao Shimoyama¹

¹Graduate School of Information Science and Technology,
The University of Tokyo, Japan

²Research Center for Advanced Science and Technology,
The University of Tokyo, Japan

³Graduate School of Agriculture, Kyoto University, Japan

Abstract

“Nano-probe” is a tool for simultaneous measurement of Ca^{2+} concentration and a membrane potential in a single neuron. In addition, this system also has other functions such as drug injection and electrical stimulation. In this paper, we measured the Ca^{2+} concentration from a single neuron of *Aplysia* using the probe. This data was compared with the data which was acquired by conventional CCD method.

Keywords: nano-probe, Ca^{2+} concentration, fluorescence, *Aplysia*

1. Introduction

Recently, not only recording the neural activity, but also simultaneous measurement of ion concentration from a single cell is necessary for biological function analysis. Because Calcium ion especially plays a great role in a living thing, it is important to investigate it. Ca^{2+} concentration of the *in vivo* brain is measured as the intensity of fluorescence which is caused from fluorescent indicators injected in the target region. The CCD attached in the microscope is often used for the imaging method. Although this CCD method is suitable for two dimensional measurement, it is not enough in the following points. First, the excitation light does not reach the deep region because of

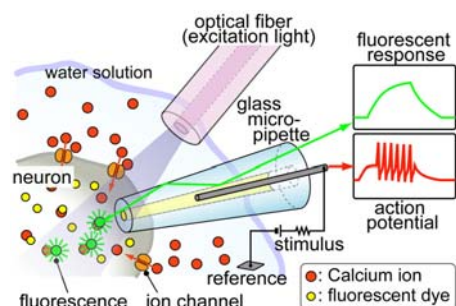


Figure 1. Concept of nano-probing system.



Figure 2. Photo of fabricated nano-probe.

the absorption by organizations. Second, the excited fluorescence attenuates during the propagation to the photo detector. As a result S/N ratio lowers, and it is necessary to lower the time resolution by taking long sampling time or to lower the spatial resolution by binning. So the actual phenomenon might not be able to be measured if the target region is deep or fast response is occurred.

On the contrary, using a “nano-probe” reported here, the excitation light is illuminated from the neighborhood of the target cell, and it is possible to measure the weak fluorescence from the tip of the probe which is inserted into the cell. In addition, the nano-probe provides the functions such as intracellular recording, electrical stimulation, and drug injection. The conceptual sketch and a photograph of the nano-probe are shown in Fig. 1 and Fig. 2, respectively. Characteristics of the nano-probe such as injection and photo-detection ability were reported in [2]. The first biological data from a single neuron of *Aplysia* using the nano-probe was reported in Transducers ’05 [3]. In this paper, we compared the data measured by the nano-probe and the data of the minimum pixel acquired by the CCD method at the same time.

2. Experimental

The target cell was a neuron of a buccal ganglion from an *Aplysia kurodai*, which was about 100 μm in diameter. The nano-probe was inserted into the cell body by about 40 μm from the horizontal direction (Fig. 3). Consequently, the fluorescent dye, OGB-1, was introduced by current injection using the probe. The electrical stimuli of 1, 3, and 10 seconds were applied to the neuron every minute by the probe. The current intensity was set to 5 nA. During the stimuli, the neuron was firing and the Ca^{2+} concentration became high. The change of fluorescence intensity was acquired by the nano-probe and CCD (HiSCA C6790-81, HAMAMATSU). The data of CCD was processed by the imaging software (AQUACOSMOS, HAMAMATSU). Sampling rate was set to 100 Hz for the probe, and 1 Hz for CCD in consideration of S/N ratio.

3. Results and discussion

To compare the data of CCD with the nano-probe data, the relative fluorescent change $\Delta F/F$ was calculated from one pixel at the probe tip of acquired images. The calculated $\Delta F/F$ image around the probe tip was shown in Fig. 4 which was enlargement view of the box in Fig. 3. Fig. 5 shows the results of the nano-probe and CCD marked by the asterisk in Fig. 4. Both results were almost consistent because the photo detection area of the probe was almost equal to the area of one pixel of the CCD image. The former was $0.785 \mu\text{m}^2$ in the FDTD simulation [3], and the latter was equivalent to $1 \mu\text{m}^2$. It should be noted that the sampling rate of the probe (100 Hz in this experiment) was much faster than the rate of CCD (1 Hz). The CCD managed to acquire the response of the stimulation of 1 second. But it was difficult to measure when the stimulation duration was less than 1 second. On the other hands, it could measure the response to the stimulation of 0.1 seconds with the sampling rate of 100 Hz because the probe has high light detecting ability (data is not shown). The nano-probe has the advantage in the condition where the response is faster or the signal is weak.

4. Conclusion

Ca^{2+} concentration was simultaneously measured in order to compare the methods of nano-probe and CCD. Although both results were almost consistent in this paper's condition, the nano-probing system has an advantage because it has an ability to measure the fluorescence from a tiny area of a three dimensional target with high sampling rate.

References

1. R. Yoshida, *et al.*, Calcium Imaging for Detection and Estimation of Spike Activities in *Aplysia* Neurons, *Zoological Science*, vol. 18, pp. 631-643, (2001).
2. S. Nagasawa, *et al.*, Calcium Concentration Measurement by Local Fluorescent-Dye Injection, *Sensors and Actuators B: Chemical*, vol. 102, pp. 7-13, (2004).
3. S. Nagasawa, *et al.*, Integrated Multi-Functional Probe for Active Measurements, *Proc. Transducers 2005*, vol. 2, pp. 1230-1233, (2005).

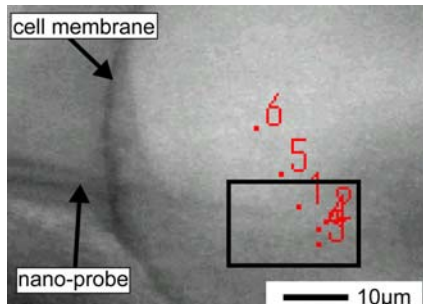


Figure 3. Measurement from an *Aplysia*'s single neuron.

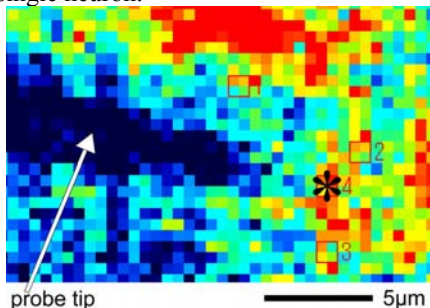


Figure 4. Ca^{2+} imaging around the probe tip. The color shows the fluorescence intensity. The nano-probe data was compared with the one pixel of CCD (marked by asterisk).

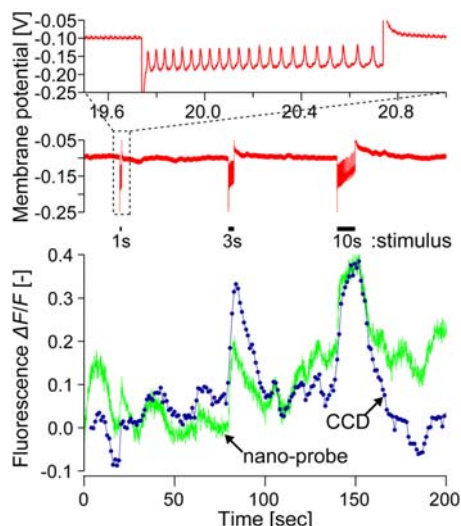


Figure 5. Comparison data between CCD and nano-probe. While electrical stimuli of 1, 3 and 10 seconds were applied, the fluorescence was measured. Sampling rate of fluorescence measurement was adjusted to 100 Hz for the nano-probe and 1 Hz for the CCD. The data of CCD was from one pixel marked by the asterisk in Fig. 4.

BIO-ACTUATED POWER GENERATOR USING CULTURED CARDIOMYOCYTES ON A POLYMER WIRE

Tomoji Ishisaka¹, Hiroshi Sato², Yoshitake Akiyama¹,
Yuji Furukawa¹, and Keisuke Morishima¹

¹Department of Mechanical Systems Engineering, Tokyo University of Agriculture and Technology, Koganei, Japan

²National Institute of Advanced Industrial Science and Technology, Japan
(E-mail: morisima@cc.tuat.ac.jp)

Abstract

A novel bio hybrid micro power generator using cardiomyocytes on a polymer wire was fabricated. Cultured cardiomyocytes convert chemical energy into kinetic energy efficiently and beat themselves autonomously. PZT fiber was utilized for cell immobilized substrate and electro-mechanical coupling material. In this paper, two preliminary experimental results were shown to prove this principle.

Keywords: Bio MEMS, Cardiomyocyte, PZT Fiber, Chemical Energy, Power Generator

1. Introduction

Natural cellular activities are increasingly exploited for micro analytical systems, biochemical reactors. We have proposed novel use of pulsating heart cells as mechanical micro actuators [1-2]. In this study, we propose a novel bio hybrid micro power generator using cardiomyocytes on a polymer wire. Cultured cardiomyocytes convert chemical energy into kinetic energy efficiently and beat themselves autonomously.

2. Principle of bio-actuated power generator

The principle of the bio-actuated power generator is that heart muscle cells are immobilized on a nylon wire, let it expand and contract, and this heartbeating force converts to a PZT fiber mechanically, and then the electrical energy is generated by piezoelectric effect. PZT fiber was utilized for cell immobilized substrate and electro-mechanical coupling material. Figure 1 (b) shows SEM image of a cross sectional view of PZT fiber. Figure 2 shows principle of bio-actuated power generator.

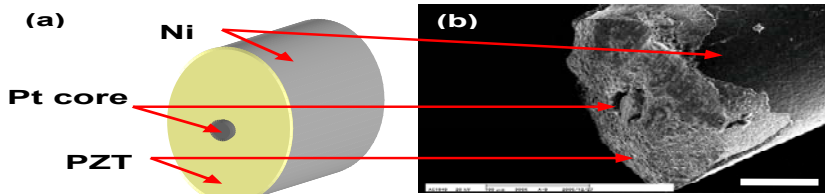


Figure 1. (a) Schematic view of PZT fiber, (b) SEM image of a cross sectional view of PZT fiber, scale= 100μm

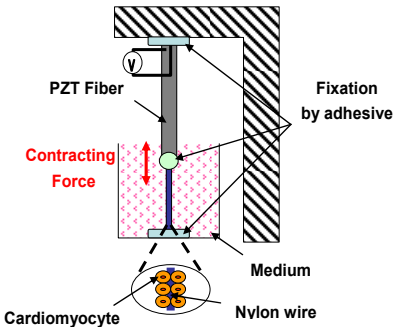


Figure 2. Principle of bio-actuated power generator with heart muscle cells and PZT fiber

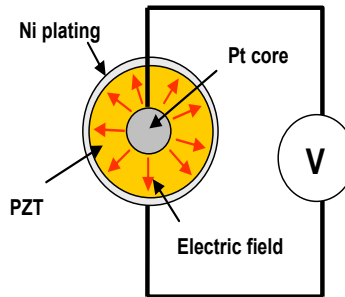


Figure 3. Principle of electric generation using PZT fiber

3. PZT fiber with Pt core

The PZT fiber consists of a liner PZT with a platinum core and plated with nickel, as shown in Figure 1. This unique structure of PZT fiber provides very easy set up to apply electric field and very sensitive application. In the above system, the electrical energy is generated by piezoelectric effect when the PZT fiber expanded, as shown in Figure 3.

4. Experimental

In this paper, two preliminary experiments were done to prove principle of the bio-actuated power generator.

First, the pulling experiment of the PZT fiber using a bimorph actuator as a model of cardiomyocytes was done (Figure 4). To convey the expansion force and contraction force of the nylon wire to the PZT fiber, they were glued together and each edge was fixed. To measure its frequency response, the nylon wire pulled it at heartbeat frequency (1 ~ 2Hz) using a bimorph actuator. The force that the nylon wire pulled the PZT fiber was tested with 4mN, 8mN and 11mN.

Second, the cardiomyocytes were cultured on the nylon wire. The diameter of the nylon wire is 150 μ m. A structure with a groove was made of PDMS was used to fix a nylon wire. These were sterilized UV light and the nylon wire was coated with fibronectin. Then, primary neonatal rat cardiomyocytes were seeded at the nylon wire in the dish. The dish which the nylon wire was in was filled with nutrient medium (Figure 5) and incubated at 37 degrees, CO₂ 5%.

5. Result and discussion

The result of the first experiment shows that the PZT fiber had a good response at heartbeat frequency and generates a voltage. Figure 6 shows the experiment results measured with an oscilloscope (Frequency = 2Hz). The PZT fiber generates 20mV using the bimorph actuator.

Figure 5 shows the cardiomyocytes (2nd day after culture) on the nylon wire. The cardiomyocytes beat themselves on it. From this result, we assume that more tension force is achieved if the density of cardiomyocyte on the nylon wire is much larger.

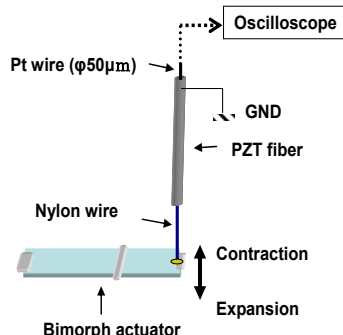


Figure 4. Pulling experiment of the PZT fiber using bimorph actuator

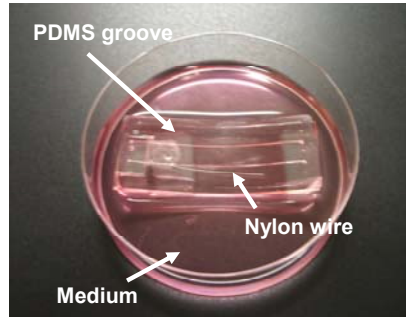


Figure 5. State of culture

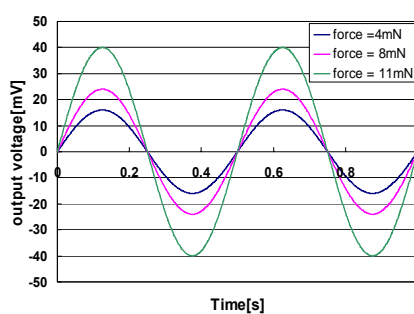


Figure 6. Output voltage of the PZT fiber, frequency = 2Hz

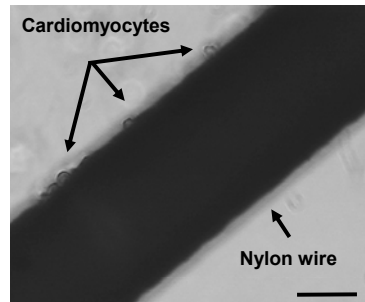


Figure 7. Microscopic image of Cardiomyocytes on the nylon wire, scale = 100μm

6. Conclusions

We confirmed a frequency response of the PZT fiber when the nylon wire glued with PZT fiber was pulled at heartbeat frequency (1 ~ 2Hz) using a bimorph actuator and the cardiomyocytes on the nylon wire were successfully cultured. These results show that power generation by the cardiomyocytes is possible. This novel bio-actuated power generator will open a new energy harvesting system for medical application

Reference

1. K. Morishima, Y. Tanaka, M. Ebara, T. Shimizu, A. Kikuchi, M. Yamato, T. Okano, and T. Kitamori, *Sensors and Actuators B, Chemical*, 119, 345–350, (2006).
2. Y. Tanaka, K. Morishima, T. Shimizu, A. Kikuchi, M. Yamato, T. Okano, and T. Kitamori, *Lab on a Chip*, 6(2), 230-235, (2006).

ARTIFICIAL LIFE FORMS IN MICROFLUIDIC COMPUTERS

Goran Goranović^{1,3}, Steen Rasmussen² and Peter E. Nielsen³

¹MEMPHYS-Center for Biomembrane Physics, University of Southern Denmark, 5230 Odense M, Denmark, goran@memphys.sdu.dk

²Self-organizing systems, EES 6, MS-D462, Los Alamos National Laboratory, Los Alamos NM 87545, USA, steen@lanl.gov

³Department of Medical Biochemistry and Genetics, University of Copenhagen, Blegdamsvej 3, DK-2200, Copenhagen N

Keywords: microfluidic computers, protocells, artificial life, life-support

1. Introduction

The electronically programmable microfluidic technology [1], termed microfluidic computers [2] or chemical Turing machines [3], represents a significant improvement over the traditional lab-on-a-chip technology enabling detailed online control of fluids and chemistry on microfluidic chips. In particular, evolution of bio-molecular interactions involving various XNA molecules, lipids, etc. can be monitored and/or programmed in sequential and parallel ways not previously possible. This in turn opens avenues for realizing both natural and artificial metabolic-information pathways within microfluidic-based structures. Moreover, it enables the life-support of entirely new living systems - protocells - that present a transition from nonliving to living matter [4].

2. Microfluidic computers

A microfluidic computer consists of a fluidic layer with a network of microchannels, superposed on layer with programmable electrodes (and actuators) controlling the flow, Fig. 1(a). In addition, a detection equipment, e.g., a camera mounted on a fluorescent microscope, collects read-outs from the chip and sends the data to a PC where it is real-time processed and fed-back to the system to adjust the actuating voltages. With such a feed-back programmable platform, one can precisely regulate the intake (timing and placement) of chemical reactants within the system during the course of a reaction - a major advantage over traditional methods relying on manual control. A specially important part of a microfluidic computer is the realization of iterative, or loop operations, essential for evolution on a chip. To enable this, both microfluidic hardware and voltage-adjusting software need to possess “circularity”, as shown in Fig. 1(a).

3. Evolution on a chip

In-vitro enzyme independent molecular evolution has two main problems not fully resolved: (1) a robust and evolvable self-replication with a high yield, and (2) an increase in the complexity of molecular interactions, both of which seem to be crucial traits of living entities.

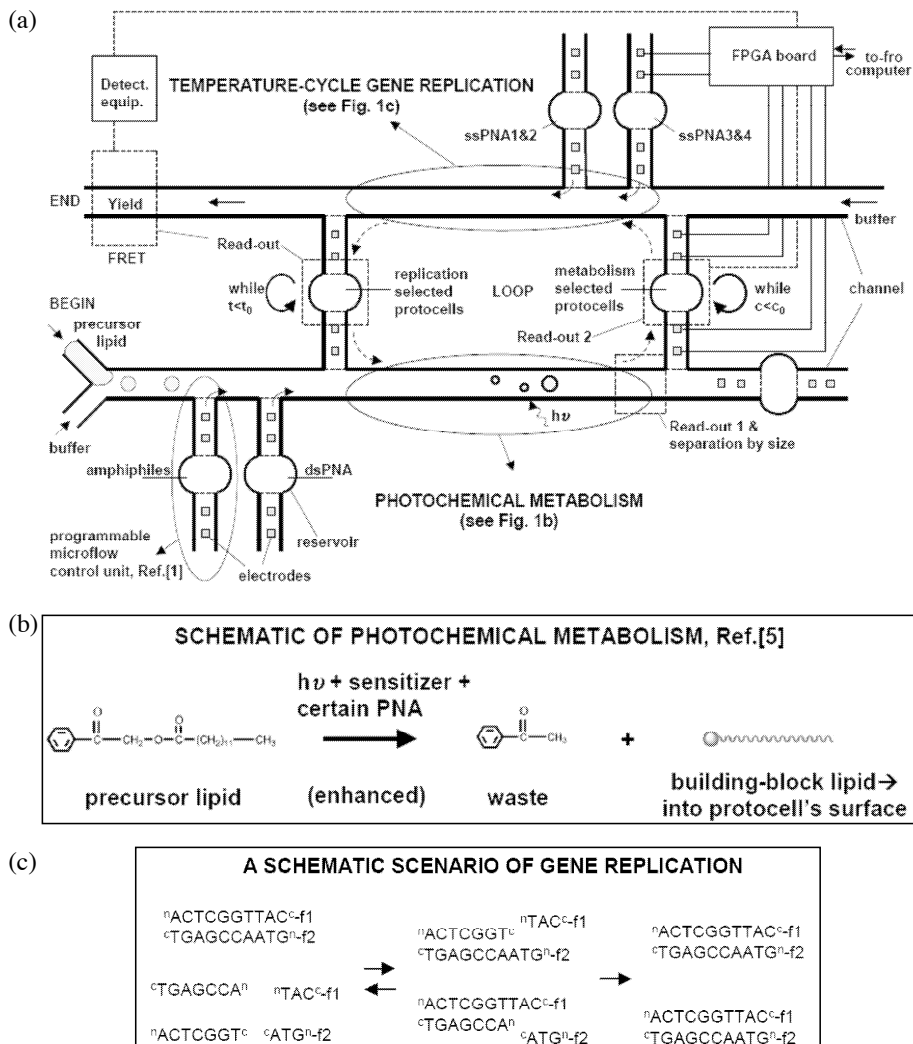


Fig.1 (a) Schematic of a microfluidic computer and the program for life-support and evolution of the protocells from [5]. The microflow control units are linked to a PC via Field-Programmable-Gate-Array (FPGA) and can be online programmed through feed-back loops based on the fluorescent read-outs (dashed rectangles). Time-controlled injection of amphiphiles and double-stranded peptide nucleic acid (dsPNA) to the fatty-acid droplets initiates the self-assembly; after the photo-induced/gene-mediated lipid metabolism, (b), the protocells can be selected based on the metabolic activity; further evolution involves temperature-driven kinetics of dsPNA with single-stranded PNA (ssPNAs), devised to give the FRET signal upon replication. (c) (f1, f2 - fluorophores).

The 10th International Conference on Miniaturized Systems for Chemistry and Life Sciences (μ TAS2006)
November 5-9, 2006, Tokyo, Japan

The strength of microfluidic computers is their ability to optimize individual processes (e.g. only self-replication) via loop operations, but also the possibility of optimizing evolution of more complex couplings between different chemical systems (e.g. genetic and metabolic). Our aim here is to show that two initially decoupled processes, self-replication and metabolism, can be integrated within a microfluidic computer into a synergistic gene-metabolism cycle characteristic for minimal protocells [5]. The idea is to evolve and select the protocells both for their replication as well as their metabolic abilities, or in other words, to increase the complexity of replicators by assisting them to do more than just replicate - in this case catalyze a metabolism.

The life-cycle of the protocell is based on the self-assembly and division of lipid (fatty acid) micelles whose growth is driven by a simple photochemical process and controlled via genetic variability of informational peptide nucleic acid (PNA) replicators. As shown in Fig.1(a) the photo-induced metabolism and gene replication are at first spatially decoupled, allowing them to be separately fine tuned, and then linked together by time-resolved flow control. After the first batch of protocells is self-assembled (the amphiphiles and the genes attached onto the precursor-lipid droplets), the simple metabolism, driven by light, is initiated where a photosensitizer in conjunction with genes enables the production of protocellular building blocks from resources, Fig. 1(b). This affects the size of the initial resource "swollen" protocells. Since the metabolic yield depends on the genetic sequence, selection (e.g., by size, velocity) is possible in the microfluidic channel in the first leg of the cycle, see bottom part of Fig. 1(a). The preselected protocells, containing double stranded PNA, then undergo temperature/concentration-controlled reactions with single stranded PNA oligomers in order to initiate replication, Fig.1(c). A fraction of the protocells is returned to the cycle and further evolved whereas most are collected and FRET analyzed. We are currently experimentally investigating various stages of this concept, first of its kind.

4. Acknowledgment

This work was supported by the European Union integrated project PACE (EU-IST-FP6-FET-002035).

References

1. U. Tangen, P. F. Wagler, S. Chemnitz, G. Goranović, T. Maeke, J. S. McCaskill, *An electronically controlled microfluidic approach towards artificial cells*, Proc. ECCS 05, Paris, (2005).
2. G. Goranović, *Microfluidic approach to the onset of life*, Seminars in Astrobiology, NORDITA Copenhagen, Nov 2005.
3. S. H. Muggleton, *2020 computing: Exceeding human limits*, Nature 440, 409-410, (2006).
4. S. Rasmussen, L. Chen, D. Deamer, D. Krakauer, N. Packard, P. Stadler, and M. Bedau, *Transition from nonliving to living matter*, Science 303, 963-965, (2004).
5. S. Rasmussen, L. Chen, M. Nilsson, S. Abe, *Bridging nonliving and living matter*, Artificial Life 9, 269-316, (2003).

MICROFLUIDIC IN-VIVO THERMAL PERTURBATION OF SELF-ASSEMBLED DROSOPHILA EMBRYOS TO STUDY THE ROBUSTNESS OF CELLULAR GENETICS

Gabriel T. Dagani^{1,2}, Jean R. Fakhouri^{1,2}, Weon Gyu Shin^{1,2},
John C. Sisson³ and Xiaojing Zhang^{1,2}

¹Department of Biomedical Engineering, ²Microelectronics Research Center,

³Department of Molecular Cell and Development Biology,

The University of Texas at Austin, USA

Abstract

We report the immobilization of Drosophila embryos on oil-covered self-assembled monolayers (SAMs) inside a microfluidic channel for thermal perturbation of embryos using laminar flows. We analyzed the fluid and heat transport in the microchannels using both numerical simulation and fluorescence thermometry. Thermally perturbed cellular events of gastrulation along the embryo membrane were captured in real-time using differential interference contrast (DIC) imaging. Unnatural asynchrony was observed when the embryo was exposed to a binary flow of 35°C at the posterior end and 20°C at the anterior.

Keywords: drosophila, embryo, thermal perturbation, self-assembly, microfluidics

1. Introduction

The ability to maintain genetic functions under varying conditions has long been considered an essential characteristic of biological networks. Injection of membrane-impermeable macromolecules, such as peptides and oligonucleotides, can alter or assay genetic functions. A complementary method is to modulate the external cellular environment at well-controlled spatial-temporal resolution. Recently, microfluidic devices were used for the thermal perturbation of a Drosophila embryo to study the symmetry of patterning during development [1]. However, the accuracy and throughput of perturbation are limited by the manual positioning process of the embryos using adhesive tapes and staining the embryos outside of the microfluidic channel. In this paper, we report the self-assembly of Drosophila embryos on oil-covered monolayers (SAMs) inside a microchannel for immediate feedback on highly characterized thermal perturbation.

2. Experimental Setup and Device Fabrication

A Y-junction microfluidic device is designed to inject two distinct thermal flows towards assembled embryos with sharp temperature step. The self-assembly pads are fabricated on a substrate and then covered with microfluidic channels, formed with rapid prototyping of polydimethylsiloxane (PDMS). As shown in Figure 1, the Cr/Au pads were prepared on glass cover slips using a lift-off process. The glass was submersed in 1mM octadecanethiol (ODT) [2] to form the hydrophobic SAMs sites. Halocarbon 700 oil (HCO) was then applied before the channel was plasma bonded to the glass substrate.

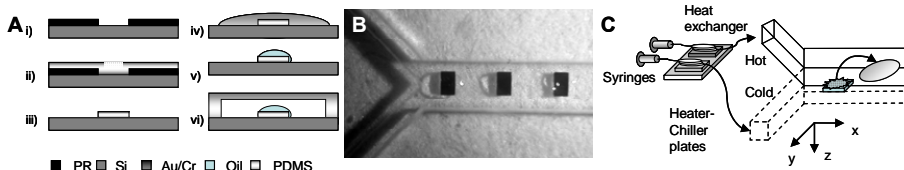


Figure 1. Microfluidic Y-junction device with self-assembly pads for binary thermal perturbation of embryos. (A) Microfabrication process of microfluidic device with self-assembly pads. (i) Pads definition, on a glass coverslip (ii)-(iii) lift-off process through evaporation of Cr/Au, (iv)-(v) treated with ODT, and covered with HCO, (vi) Plasma-bonding of substrate to PDMS channel. (B) Optical micrograph of a finished device with an array of gold pads covered in oil. (C) Set-up: the thermal flows are controlled using a syringe pump connected to a heat exchanger on heater/chiller plates.

3. Results and Discussion

The thermal profile around the embryo was modeled using FLUENT®. Embryo assembly and detachment is achieved through flow rate regulation (Fig. 2A). For self-assembly at 1-4 ml/min, the simulated flow force exerted on the embryo is an order of magnitude less than the measured detachment forces of $8.9\mu\text{N}$ [3] of the pads (Fig. 2B). Simulations show the temperature distribution narrows by 50% as flow rate doubles (Fig. 3A), widens by 85% for embryos displacement downstream from $200\mu\text{m}$ to $800\mu\text{m}$ (Fig. 3B), and widens at the top and bottom of the channel by a factor of 3 because of heat convection (Fig. 3C). Parallel thermal perturbation of aligned embryos is feasible due to the uniform temperature profiles across the embryos (less than 2% variation) (Fig. 3D). Intensity measurements of Rhodamine B dye were used for temperature characterization of two distinct thermal flows (Fig. 3E). The duration of cellular events of pre-gastrulation for an assembled embryo were recorded in real-time using a DIC enabled microscope (Fig. 4A-E). Control measurements showed a 25% increase in growth rate as temperature was increased from 24°C to 35°C . In addition, embryo development was observed to exhibit unnatural asynchrony when exposed to a binary flow of 35°C at the posterior end and 20°C at the anterior inside the microfluidic device (Fig 4F-G). The microfluidic self-assembly devices show great promise for fine spatial and temporal control over a developing embryos and cells for examining thermal robustness in various developmental stages.

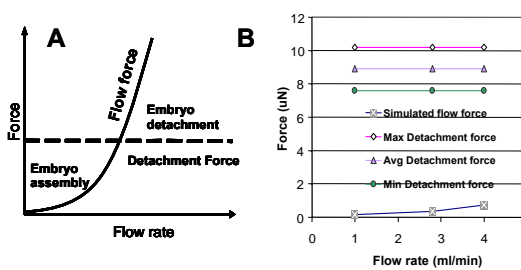


Figure 2. Flow rate control for embryo transport within microfluidic channels. (A) Two operating modes, assembly and detachment, of the microfluidic thermal perturbation device. (B) Comparison of flow forces (simulated) versus detachment forces (measured) for $250\mu\text{m} \times 100\mu\text{m}$ self-assembly pads.

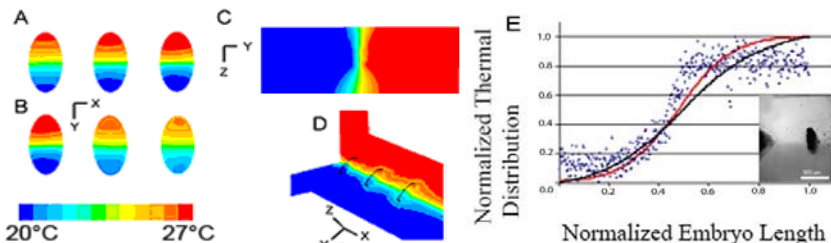


Figure 3 Numerical and experimental characterization of temperature distribution for embryos under binary thermal perturbation. (A) Effect of flow rate. Left to right (mL/min): 1, 2.8, and 4 at $x=200\mu\text{m}$ from the junction. (B) Effect of embryo displacement. Left to right (μm): $x=200$, 800, 1500 at $4\text{mL}/\text{min}$ (C) YZ cross section overlapping an embryo located at the bottom of channel at $x=200\mu\text{m}$. (D) Simulated result of temperature distribution around three embryos in microchannel at $x=200\mu\text{m}$, $800\mu\text{m}$, $1500\mu\text{m}$ at $4\text{mL}/\text{min}$. (E) Measured temperature distribution around a *drosophila* embryo is in good agreement with the simulations. Legend: experimental (♦) and simulation results at $4\text{mL}/\text{min}$ (—) and $1\text{mL}/\text{min}$ (—) for $(27^\circ\text{C} \rightarrow 20^\circ\text{C})$ for a normalized temperature distribution over the length of an embryo. Embedded: optical micrograph demonstrating temperature characterization using Rhodamine B dye. Temps recorded: $\sim 27^\circ\text{C}$ (dark) and $\sim 20^\circ\text{C}$ (light) with $\pm 1^\circ\text{C}$ deviation.

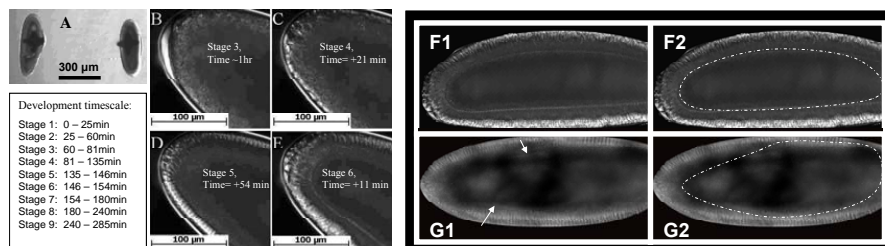


Figure 4. Time elapsed DIC images of embryo growth at posterior at 24°C until gastrulation (A) Optical micrograph of a dechorionated embryo assembled onto $150\mu\text{m} \times 150\mu\text{m}$ 'cross' pads. (B) Stage 3: syncytial division 9, polar bud formation; (C) Stage 4: Syncytial divisions 10-13, pole cell formation; (D) Stage 5: Cellularization; and (E) Stage 6: Onset of gastrulation.(F1,F2) Image of furrow front (dotted line) movement in Stage 6 at 24°C control embryo(G1,G2) Unnatural advancement of the furrow front on posterior(left-side) (35°C), versus the anterior (right-side) (20°C).

References

- [1] E. M. Lucchetta, et. al, *Nature* 434: pp. 1134–1138, (2005).
- [2] R. W. Bernstein, et. al, *Sens. Actuators, A*, 114: pp. 191-196, (2004).
- [3] X. J. Zhang, et. al, *JMEMS* 14: pp. 1187-1197, (2005).

BIO-ACTUATED BULB-SHAPED FLUIDIC DISPENSER POWERED BY HEART MUSCLE CELLS

Keisuke Morishima, Yoko Hori, Yoshitake Akiyama, and Yuji Furukawa

Department of Mechanical Systems Engineering,
Tokyo University of Agriculture and Technology, Koganei, Japan
(E-mail: morisima@cc.tuat.ac.jp)

Abstract

This paper reports a novel autonomous bio-microactuator powered by primary cultured cardiomyocytes. To exploit contractions of cardiomyocytes, we fabricated a PDMS bulb-shaped dispenser and allowed cardiomyocytes directly adhere to it. The displacement of the bulb-shaped dispenser by cardiomyocytes was larger than previous report.

Keywords: Bio MEMS, Cardiomyocyte, Chemical Energy, Microactuator, Mechanobiology

1. Introduction

Much attention has been directed to micro-total analysis systems (μ -TAS) and lab-on-a-chip, devices fabricated by microfabrication technology. A various kinds of efficient bioreactors, biosensors and bioassay systems have been produced by fusion of cell biology and various technologies. Those devices utilize only chemical or bio-chemical properties of cells.

Our group has focused on kinetic energy generated by cells and already reported that the micro bio-actuator, utilizing spontaneous contractions of primary cultured cardiomyocytes, can be driven by only chemical energy of biological reaction in living cells without electrical or mechanical energy[1-3]. However, this micro bio-actuator has low conversion efficiency of myocardial contractions to drive flow for practical use. To improve this issue, we propose that isolated cardiomyocytes from the heart of a neonatal rat are plated on a polydimethylsiloxane (PDMS) thin film and adhere tightly to it. In the previous studies, the cell-sheet engineering using temperature-responsive polymer was utilized. It enables us to collect a cultured cell-sheet by only temperature reduction without any damage of the cell-cell junction. It is, however, difficult to mount and fix the cell-sheet on the PDMS

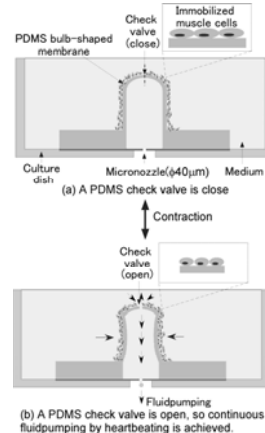


Fig.1 A principle of fluidpumping of bio-actuated bulb-shaped fluidic dispenser. A PDMS check valve is actuated by heart cell pulsating synchronously.

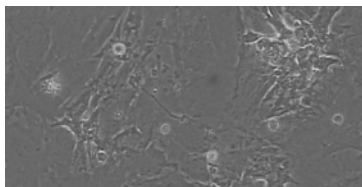


Fig. 2 Phase-contrast micrographs of cardiomyocytes one week in culture.

structure of a micro actuator. For this reason, the contractile force of cardiomyocytes was not able to bring out maximally for fluid drive.

This paper describes to design and fabrication of a novel bio hybrid micro fluidic dispenser using cardiomyocytes and micromachined mechanical components.

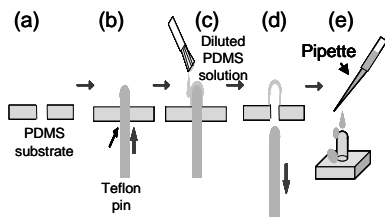


Fig.3 A schematic diagram of fabrication method of PDMS based bulb-shaped membrane structure and assembly process of a muscle-powered fluidic dispenser. (a), (b) Teflon pin was inserted through a hole on PDMS substrate. (c) Diluted PDMS solution was thin-layer coated. (d) PDMS thin membrane was baked at oven, and then teflon pin was pulled out. (e) Primary neonatal rat cardiomyocytes were directly seeded on PDMS bulb-shaped membrane structure.

allows the dispenser pump out a small amount of volume of fluid synchronously.

Primary neonatal rat cardiomyocytes were prepared according to following procedures. Cardiac ventricles of 1-day-old Wistar rats were digested at 37°C with collagenase in Dulbecco's phosphate buffered saline (DPBS, Ca^{2+} and Mg^{2+} free). Isolated cells were suspended in the culture medium, DMEM/F-12 supplemented with 10% FBS and 0.2% penicillin-streptomycin solution (Figure 2). The primary cell suspensions were prepared at above 1×10^6 cells / ml.

A bulb-shaped dispenser was made of PDMS without photolithography. The procedure was shown in Figure 3. Finally the primary cell suspensions were seeded on a

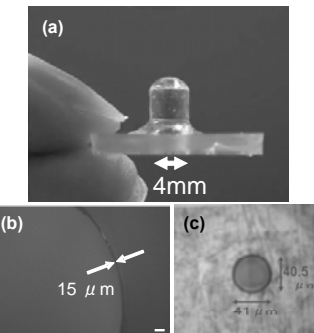


Fig.4 Photo of a prototype of PDMS bulb-shaped fluidic dispenser. (a) a whole view. (b) a cross sectional image of bulbed-shaped membrane(15μm thickness). (c) a micronozzle fabricated by micro discharge machining.

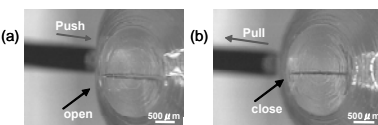


Fig.5 Photo of test of a PDMS check valve by pushing & pulling. A very small slit window was opened (a) and closed (b).

2. Material and Method

The principle of the proposed bio hybrid micro fluidic dispenser is shown in Figure 1. Cardiomyocytes are immobilized on a PDMS bulb-shaped thin membrane (15μm thickness). The check valve is closed while cardiomyocytes are relaxing; it is open autonomously while they are contracting spontaneously. A micromachined nozzle

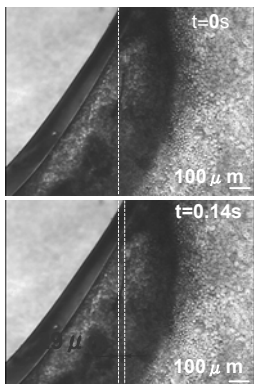


Fig.7 Microscopic image of pulsating cell-immobilized PDMS based bulb-shaped membrane and displacement of membrane per one pulse was 29 μ m.

fabricated by micro discharge machining for fluid dispensing.

3. Results and discussion

Figure 5 shows a photo of test of a PDMS check valve by pushing & pulling. We succeeded in fabricating and testing a very small slit window, which was opened and closed. A microscopic image of cell-immobilized PDMS based bulb-shaped membrane structure from top view, is shown in Figure 6. A whole structure was filled with medium and was incubated at 37 degrees centigrade, CO₂ 5%. A group of cardiomyocytes were pulsating synchronously. Next, displacement of a thin membrane structure by cardiomyocytes was measured. A microscopic image of pulsating cell-immobilized PDMS based bulb-shaped membrane is shown in Figure 7. Result of displacement of membrane per single twitch was 29 μ m. Compared previous results [1-3], a displacement of a thin membrane structure was relatively large.

4. Conclusions

We confirmed that it is possible to achieve much more efficient force just when plating on the PDMS thin membrane directly without using cell-sheet engineering. These results show that fluid dispensing power and efficiency by heart muscle cells are large enough to deliver a small amount of volume of fluid in a microspace.

References

1. K.Morishima, Y. Tanaka, M. Ebara, T. Shimizu, A. Kikuchi, M. Yamato, T. Okano and T. Kitamori, *Sensors and Actuators B*, 119, 345–350, (2006).
2. Y. Tanaka, K. Morishima, T. Shimizu, A. Kikuchi, M. Yamato, T. Okano, and T. Kitamori, *Lab on a Chip*, 6(2), 230-235, (2006).
3. Y. Tanaka, K. Morishima, T. Shimizu, A. Kikuchi, M. Yamato, T. Okano, T. Kitamori, *Lab on a Chip*, 6(3), 362 - 368, (2006).

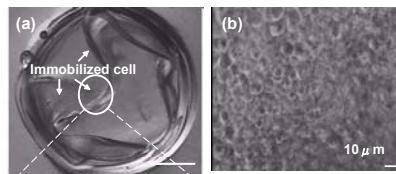


Fig.6 Microscopic image of cell-immobilized PDMS based bulb-shaped membrane structure from top view.

bulb-shaped thin membrane coated with fibronectin.

Figure 4 shows a photo of a prototype of PDMS bulb-shaped fluidic dispenser. Thickness of bulb-shaped membrane was 15 μ m around a whole structure to realize high efficient mechanical energy conversion. A micronozzle, 40 μ m in a diameter, was

fabricated by micro discharge machining for fluid dispensing.

DYNAMIC STUDIES OF PORE FORMING TOXINS USING A MICROFLUIDIC CELL ARRAY

Dino Di Carlo*, Josephine Shaw*, and Luke P. Lee

Biomolecular Nanotechnology Center, Berkeley Sensor and Actuator Center
Department of Bioengineering, University of California, Berkeley, CA 94720 USA

Abstract

Systematic studies of pore formation mechanisms of toxins in mammalian cell membranes are critical for understanding infectious disease as well as the biomimetic design of artificial toxins to target cancer cells for lysis. In this paper, dynamic studies of the pore formation mechanism of the bacterial toxin Streptolysin O (SLO) are accomplished by using a microfluidic single cell trapping array. HeLa cells are maintained isolated in hydrodynamic traps while a step concentration of SLO monomers is introduced into the device. Using fluorescent imaging analysis and computational modeling, we attempt to characterize the poration mechanism of the toxin by comparing the results to existing models. We observe that the existing models cannot be completely supported by the experimental data and a hybrid model has been created, involving discrete stochastic reaction kinetics to better explain the variability in the single cell behavior.

Keywords: single cell analysis, pore-forming toxins, membrane poration

1. Introduction

We utilized microfluidic single cell trap arrays to analyze and better understand the pore formation mechanism of SLO. The use of a microfluidic single cell trap array is advantageous to other techniques because the dynamics of membrane permeability in a large quantity of individual cells can be determined for identical experimental conditions. A comparable off-chip experiment could be done by isolating single cells with a micropipette and switching solutions around the cell but throughput would be much decreased and cells would not experience identical conditions necessary for quantitative analysis of pore formation.

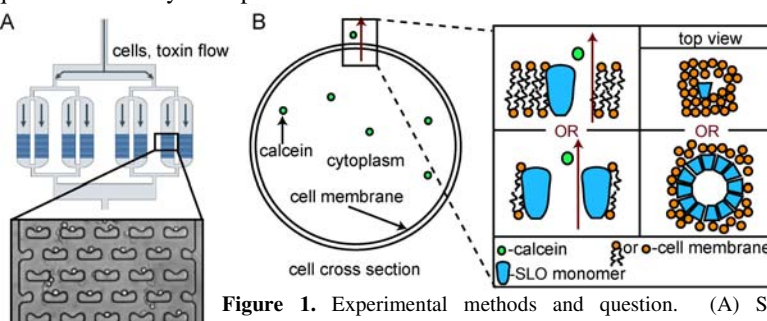


Figure 1. Experimental methods and question. (A) Schematic and micrographs of the microfluidic device for single cell trapping. (B) Mechanism of intensity measurements and varied pore-formation models.

We chose to study SLO, part of a large family of cholesterol dependent pore-forming toxins that bacteria produce to assist pathogenesis, because of the unknown mechanism of pore formation. There are conflicting models in the literature between pore formation occurring before the complete assembly of the oligomerized toxin ring or only after assembly has occurred [1]. We attempt to address this question using single cell analysis of permeability dynamics, and the modeling of diffusion of Calcein dye through porous membranes with varied pore sizes depending on the model.

2. Experimental Methods

The device was fabricated from PDMS and glass as described previously [2]. Introduced reagents were supplied through a branching introduction channel to individual trapping arrays. HeLa cells were dyed with Calcein AM and were flowed into the device. The cells were maintained isolated in hydrodynamic traps while SLO monomers were quickly introduced (Fig. 1). Then, the fluorescent intensity of the cells was monitored over time (Fig. 2). Only one trapping array was observed during an experiment, and the speed of reagent introduction was characterized to be ~ 250 ms using a 40kD fluorescein conjugated dextran solution. The experiment was carried out at concentrations of 100U/mL (.091 µg/mL) and 10kU/mL (9.1 µg/mL). Later, computer simulations were used to compare the experimental data to the existing hypotheses and to further characterize the pore formation mechanism of SLO.

3. Models and Simulations

The two existing hypotheses concerning the pore formation mechanism of SLO were modeled and simulated using Matlab. Due to the inadequacies of these models, we developed a hybrid discrete model involving probabilities and random variables to determine whether or not monomers oligomerized and whether or not they formed a transmembrane pore. Taking into consideration the geometrical conflicts of calcein exiting through pores in the cell membrane, the effective pore area (A_p) was calculated as follows:

$$\frac{A_p}{A_0} = (1 - a/r_p)^2 (1 - 2.104a/r_p + 2.09(a/r_p)^3 - 0.95(a/r_p)^5),$$

where A_0 is the actual pore area, r_p is the radius of the pore, and a is the radius of a solvated calcein molecule, taken to be 8.0 Å. Then, we employed Fick's first law of diffusion and the dependence of calcein intensity on the number of calcein molecules to model the decrease in intensity over time.

4. Results

The experimental data from two different monomer concentrations give similar behaviors, in which there is first a delay between introduction and initial membrane permeation, and then only smooth transitions in slope while the intensity decreases (Fig. 2). However, both initial models fail to account for the initial delay from the time of toxin introduction to the time of the initial decrease in intensity.

Hence, the hybrid model introduces four probability-dependent variables at each time step, which include the average number of monomers binding to the membrane, the probability that monomers and oligomers will oligomerize in a time step, the probability that monomers and oligomers form a transmembrane pore for a given oligomer size, and a measure of particle mobility in the membrane. We used the same

parameters to find best fit curves for the experimental data at both concentrations, increasing only the average number of monomers bound for the higher concentration. However, noting that there exists a widespread variation in the intensity curves from cell to cell, it is evident that only a stochastic model could produce a variation to match the experimental results (Fig. 3).

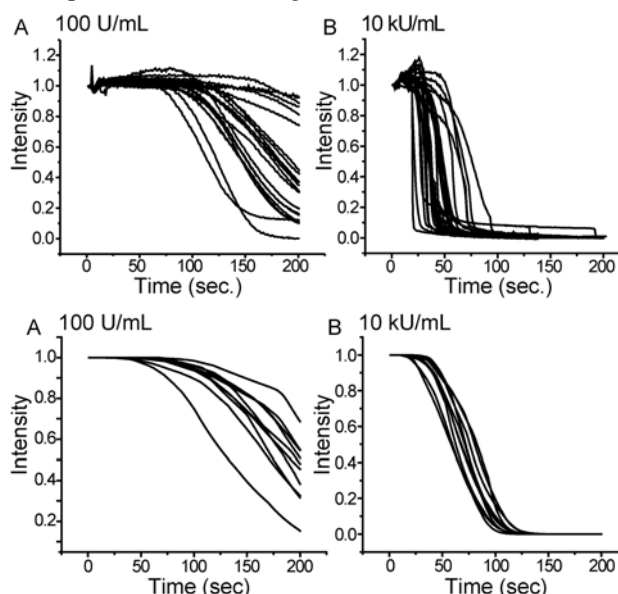


Figure 2. Experimental results of single cell pore-formation. (A) The intensity loss curves for calcein leakage from SLO-porated single cells with 100 U/mL SLO introduced in a stepwise fashion. (B) Intensity curves for 10 kU/mL SLO with a step introduction. For both cases notice a delay time before intensity loss. Each curve represents one cell.

Figure 3. Simulation results of single cell pore-formation. (A) Stochastic simulation of intensity loss due to pore-formation with a hybrid model that allows pore insertion before complete assembly. For 100 U/mL SLO. (B) Stochastic simulation results are shown for 10 kU/mL SLO. 10 simulations shown per concentration.

5. Conclusions

From the experimental and simulation results of single cell pore formation, it is evident that neither the whole pore model nor the monomer insertion model adequately describes the pore formation mechanism of SLO. As suggested by the initial delay, the pore formation mechanism of SLO must sometimes include a certain amount of oligomerization before creating a transmembrane pore; however it does not seem to be necessary for the entire pre-pore complex to be formed before poration, as shown by the smoothness of the intensity curves. Furthermore, only discrete stochastic processes can account for the variation seen among all the cells in any given experiment. The hybrid model thus is able to better match the initial delay time as well as the variation.

References

- [1] Palmer M, et al. Assembly mechanism of the oligomeric streptolysin O pore: the early membrane lesion is lined by a free edge of the lipid membrane and is extended gradually during oligomerization. *The EMBO Journal* (1998) 17, 1598–1605
- [2] Di Carlo D, Aghdam N, Lee LP. Single-cell enzyme concentrations, kinetics, and inhibition analysis using high-density hydrodynamic cell isolation arrays. *Analytical Chemistry* (2006) 78:14, 4925-4930

Note: definition of U (unit): one unit causes 50% lysis of 2% red blood cell suspensions in phosphate buffered saline, pH 7.4, after incubation at 37 °C for 30 min.

*Authors had equal contribution.

ELECTRIC FIELD INDUCED PROTEIN CRYSTALLIZATION

Muhammad Imran Al-Haq^{1,2}, Hidenori Tsuchiya¹, Toru Torii¹,
Hiroki Yamazaki², and Etsuo Shinohara²

¹Graduate School of Frontier Sciences, University of Tokyo, Kashiwanoha 5-1-5,
Kashiwa 277-8562, Japan

²TechnoMedica Co. Ltd., 5-5-1 Nakamachidai, Yokohama 224-0041, Japan
(e-mail: mialhaq@yahoo.com)

Abstract

A device has been fabricated to set up electric-field-induced protein crystallization experiments. The effect of external electric field (EF) on the crystallization of thaumatin and hen egg-white lysozyme (HEWL) was investigated. All experiments were set as a microbatch method in paraffin oil. The main advantages of having electric field-induced protein crystallization are shorter time required to obtain crystals, less nucleation (i.e. number of crystals) with bigger size of crystals.

Keywords: Electric field, large-size protein crystals, reduced nucleation.

1. Introduction

Our group has been working on fabrication of various devices for protein crystallization, e.g., electrostatic actuation and merging of droplets^[1]. Its later version was able to make an array of the merged droplets^[2]. Further improvements brought a robot that does all steps from droplet generation to imaging & storage^[3]. Here we are presenting another device that performs protein crystallization under electric field (EF) and can be used independently or with our robot^[3]. We use our own developed plastic film tray (PFT) for setting up the experiments. The PFT is fabricated by using a plastic film (Polyvinylidene chloride, PVDC) and it acts as an insulator between the electrode and the protein. The characteristics of the device are summarized in the Table 1 and shown in Fig. 1. The PFT (Fig. 2) has two parts: a

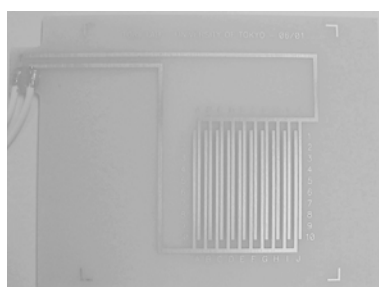


Fig. 1. An electrode panel

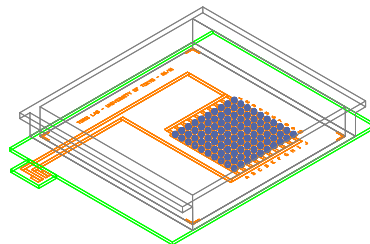


Fig. 2. Schematic of a plastic-film tray (PFT) placed over an electrode panel.

holder (made of polycarbonate) and the plastic film. The PFT, containing oil, protein solution, and precipitants, is placed on an electrode panel (Fig. 1) and connected to a power supply.

Table 1. Characteristics of the electrode panel

	Value
Substrate material	Polyimide
Electrodes material	Copper
Insulator thickness (t)	10µm
Electrode width (w)	800µm
Electrode gap (g)	200µm
Color	White

2. Experimental

Various crystallization experiments were carried out with (EF) and without (NEF) applying an external EF. The potential was varied from 0 to 280 V for HEWL (Fig. 3) and 0 to 270 V for thaumatin (Figs. 4-5). Droplets of protein and precipitant (each having volume of 500 nL) were dispensed in the centre of the electrode and the two droplets were merged. An array of droplets was hence formed and the electrode panel was plugged into the power supply and placed inside an incubator at 18°C. The images were taken at periodic intervals and data for number of crystals formed in each drop were taken. The crystal size was measured by using software.

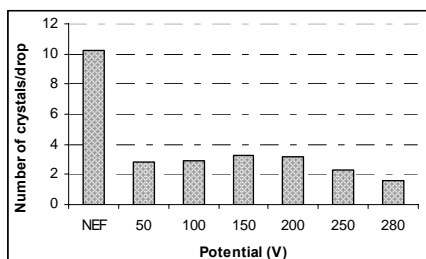


Fig. 3. Number of HEWL crystals/drop

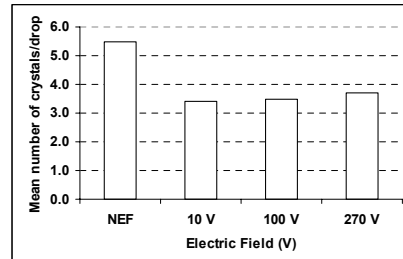


Fig. 4. Mean number of Thaumatin crystals

3. Results and Discussion

Comparative analyses on thaumatin and HEWL crystals have demonstrated that an application of external EF had positive effects. For example in the case of HEWL, the mean number of crystals in the NEF drops was 10, whereas for the samples in EF (0~280V) the mean crystals ranged from 2~4 (Fig. 3). In the case of HEWL, when the potential was 265 V or more the drop expanded due to the electrowetting effect (Fig. 6). In fact, only one HEWL crystal was obtained in about 65% of the drops under EF^[4]. Similar trend was found by Taleb et al.^[5] by using 750 kV/m.

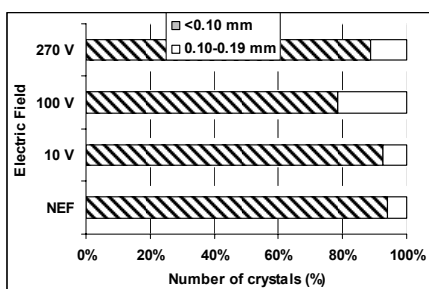


Fig. 5. Number of crystals (%) of a particular size at a specific electric field condition (voltage) after 24 h

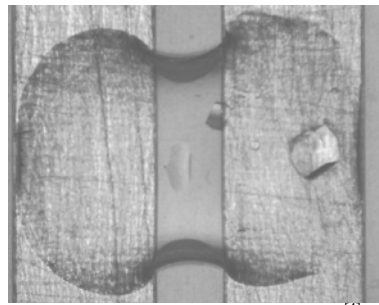


Fig. 6. Electrowetting effect (HEWL)^[4]

Application of EF reduced the nucleation rate of HEWL^[4]. Similar trend was also found for thaumatin. The mean number of thaumatin crystals for NEF was 5.4 crystals per drop and for the EF sample, it ranged from 3.2 – 3.8 (Fig. 5) and percentage of larger-sized thaumatin crystals in 100 V was more than the other conditions tested (Fig. 6).

4. Conclusions

The main advantages of having electric field-induced protein crystallization are (a) shorter time required to obtain crystals, (b) less nucleation/number of crystals, and (c) bigger size of crystals.

References

1. M. Hirano, T. Torii, T. Higuchi, & H. Yamazaki. A droplet-based protein crystallization device using electrostatic micromanipulation. Proc. Micro Total Analysis Systems 2004, Royal Soc Chemistry, Cambridge, UK, Vol. 2, pp. 148-150 (2004)
2. M. I. Al-Haq, E. Lebrasseur, W.K. Choi, T. Torii, H. Yamazaki, E. Shinohara, & T. Higuchi. High Throughput compact protein crystallization device. Proc. Micro Total Analysis Systems 2005, Transducers Research Foundation, California, USA, pp. 277-279 (2005).
3. M. I. Al-Haq, E. Lebrasseur, W.K. Choi, T. Torii, H. Yamazaki, E. Shinohara, & T. Higuchi. High-Throughput protein crystallization system employing electrostatic droplet actuation technique. Advances in Protein Crystallization, South San Francisco, Select BioSciences LLC, CT, USA [Proc. on CD] (2006).
4. M. I. Al-Haq, E. Lebrasseur, W.K. Choi, H. Tsuchiya, T. Torii, H. Yamazaki, E. Shinohara, & T. A device for electric-field-induced protein crystallization. J. App. Crystallography (submitted).
5. Taleb, M., Didierjean, C., Jelsch, C., Mangeot, J. P., Capelle, B. & Aubry, A. *J. Cryst. Growth*, **200**, 575-582 (1999)

MICRO SU-8 CHAMBER FOR PCR AND FLUORESCENT REAL-TIME DETECTION OF *Salmonella* spp. DNA

JLM Schulze, D Verdoz¹, J Berganza¹, G Olabarria¹,
J Berganza, J Elizalde and JM Ruano-López

MEMS/MST Department, IKERLAN-IK4 S.Coop., 20500 Mondragón, Spain.

¹Gaiker-IK4, Centro Technológico, 48170 Zamudio, Spain

Keywords: SU-8, PCR, Cy5, fluorescence, bonding

Abstract

We present the first SU-8 only Polymerase Chain Reaction (PCR) micro-device. Using a wafer level process, we tightly bond the SU-8 chamber with a layer of SU-8 itself, yielding a permanently sealed, transparent, durable chamber cover. We successfully amplified *Salmonella typhimurium* DNA and observed amplification product formation through the SU-8 cover during thermocycling with Cy5 labelled probes and TOPRO-3 DNA intercalator.

1. Introduction

The miniaturisation of PCR in SU-8 (a transparent, rigid and biocompatible polymer) by photolithography and bonding is of particular interest due to low cost and simplicity promising standardised, batch-produced, highly integrated, disposable Lab-on-a-Chip devices.

2. Chip Optimization

We have adapted our existing full-wafer SU-8 bonding and release protocol [1] for the bonding of layers of variable thickness, making possible the sealing of chambers several millimetres wide with SU-8 covers that can contain the pressures developed



Fig.1: Vertical cut across a 4 mm wide SU-8 PCR chamber on a 700μm Pyrex substrate.

during thermocycling. Figure 1 shows a vertical cut across a 4mm wide SU-8 PCR chamber. The SU-8 sealing cover is created on a separate Kapton substrate, bonded to the chamber and released from the Kapton to form a tight permanently sealing, free, transparent, low cost and durable chamber cover. Inlet holes are simply patterned into the resin without the need for any drilling or etching. Our 5.0μL, 190μm high, 3mm wide, 12mm long SU-8 PCR chamber (fig. 2-3), fabricated on a Pyrex substrate,

integrates six Ti/Pt (12nm/130nm) heaters with parallel heater elements and a resistive 1.2mm long sensor which measures only the hottest area of the chamber. The rhombus-shape facilitates pipetted liquid injection and extraction at the inlets/outlets. Conventional parallel heating elements are sensitive to asymmetries in the electrical contacts. We have developed a special shape of the heater's electrical contact pads which force the current to feed evenly into each heating element (20 μ m wide, 5mm long and 50 μ m spaced) yielding any contact pin displacements irrelevant. With this we reduced the maximum current variation between heater elements to only 0.04 μ A and achieved temperature uniformity.

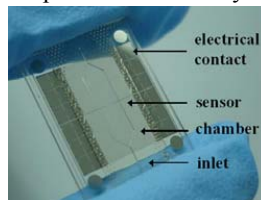


Fig. 2: Top view of the SU-8 PCR chip.

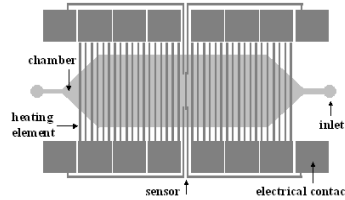


Fig. 3: Schematic top view of the PCR chip.

3. Experimental

For thermocycling, part of a 15 μ L PCR mixture (containing respectively 0.2 μ M Cy5/BHQII probe or 0.1 μ M TOPRO-3 intercalator for fluorescent detection, 0.5 μ M each primer, 1U Taq Polymerase) is pipetted into the chamber. The chip inlets are sealed by a plastic plug in a PMMA capsule (fig. 5-6). In this capsule, the chip is automatically aligned and can easily be mounted and replaced. The capsule's integrated PCB, electrical pins and electrical connectors eliminate the need for glue or wire bonding to make electrical contact. The packaging capsule is then placed under an epifluorescent microscope with a photomultiplier tube or CCD camera.

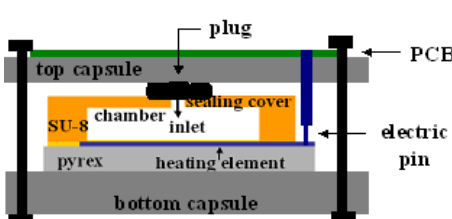


Fig. 4: Vertical cut view of the packaging capsule.

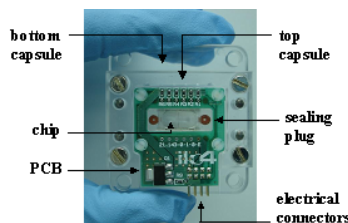


Fig. 5: Top view of the packaging capsule.

4. Results

Figure 6 shows the result of agarose (2%) gel electrophoresis of the amplification product with line 1 indicating the 100bp molecular weight markers, line 2 showing the successful on-chip amplification of the 158bp *Salmonella typhimurium* CECT 443 and line 3 giving the negative control (on-chip amplification with water instead of DNA).

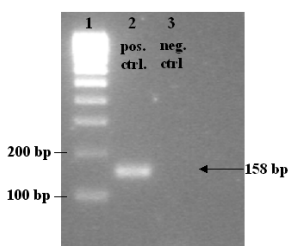


Fig. 6: Result of gel electrophoresis.

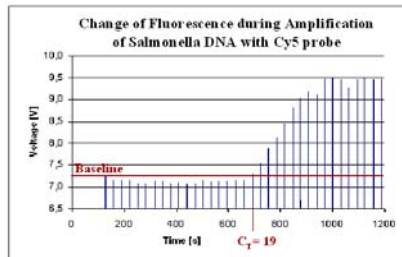


Fig. 7: Change of Fluorescence during amplification.

We also observed in real-time on-chip amplification product formation through the SU-8 cover during thermocycling with fluorescent CY5 molecular probes and TOPRO-3 intercalator (fig. 8-9). Only few articles [2] show (SYBR Green) fluorescent on-chip amplification product images. The change in fluorescence shows typical exponential signal increase after (threshold) cycle 19. After cycle 30 the signal plateau is reached (fig 7).

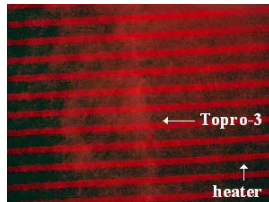


Fig. 8: Fluorescent image after amplification with TOPRO-3.

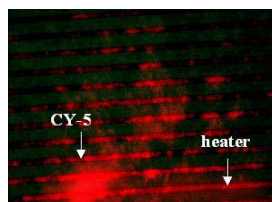


Fig. 9: Fluorescent image after amplification with a specific Cy5 probe.

5. Conclusion

We successfully amplified and fluorescently detected a 158 bp molecular marker from *Salmonella typhimurium* genomic DNA in our PCR chamber, fabricated completely in SU-8, sealed for the first time with a single layer of SU-8 itself. We are currently optimising conditions for quantitative real-time PCR product specification in our SU-8 chamber. We also work on integrating our PCR application with microfluidic control features and substituting pyrex with plastic substrates for truly low-cost, disposable devices.

References

1. M Agirregabiria, FJ Blanco, J Berganzo, MT Arroyo, A Fullaondo, K Mayora, JM Ruano-López, Fabrication of SU-8 multilayer microstructures based on successive CMOS compatible adhesive bonding and releasing steps, *Lab on Chip*, 5, pp. 545-552, (2005)
2. Z Zhao, Z Cui, D Cui, S Xia, Monolithically integrated PCR biochip for DNA amplification, *Sensors and Actuators A*, 108, pp. 162-167, (2003)

CONTINUOUS-FLOW POLYMERASE CHAIN REACTION (PCR) DEVICE USING A DISPOSABLE POLYMER DISK

Kwang Hyo Chung, Se Ho Park, Dae-Sik Lee and Hyeon-Bong Pyo

Biosensor Team, Electronics and Telecommunication Research Institute, Korea
(hyo@etri.re.kr)

Abstract

This paper presents a new type of continuous-flow polymerase chain reaction (CF-PCR) device, which can successfully amplify a human genome DNA in less than 10 minutes. A disposable polymer disk equipped with a long spiral microchannel is installed into a miniaturized heating device for the PCR. Uniform temperature distribution of heating blocks and fast thermal transition of moving sample realize a stable and fast PCR. The disk of single use and the heating device of simplified flow and thermal controls are unique in the literatures. The present CF-PCR device gives enhanced PCR performance in speed, size and control.

Keywords: PCR, continuous-flow, DNA, polymer disk

1. Introduction

Polymerase chain reaction (PCR) is a general and important process in genetic science. Recently, the miniaturized PCR devices have attracted a lot of interests due to its various advantages over conventional PCR thermocyclers. Many research groups have addressed the need for a PCR device with high amplification efficiency, enhanced speed, high-throughput, low sample consumption, automation, free of contamination and low cost. Continuous-flow PCR is highly suitable for the rapid amplification [1-2]. Here, we present a new type of CF PCR device, which realizes fast human DNA amplification under very simple fluidic and thermal control using a unique disposable polymer disk. The design and fabrication of the heating unit and the polymer disk will be explained and the PCR experiment using the present CF PCR device will be shown.

2. Experimental

The design of the microchannel in the disk is shown in Figure 1. The DNA amplification is accomplished by continuously pumping the DNA samples through the single spiral microchannel (length~0.54m) at a constant flow rate, while the DNA samples experience temperature change of three steps for PCR, i.e., denaturation, annealing and extension steps, per each cycle. In order to keep the cycling time per each cycle constant, the width of the channel continuously decreases as the channel goes from center (inlet) to border (outlet). The width of the

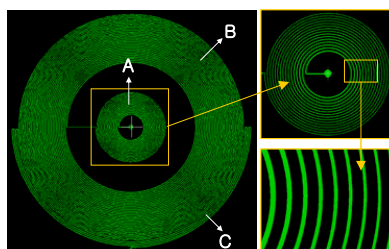


Figure 1. Spiral microchannel in the disk. A: Pre-denaturation zone, B: Cycling zone, C: Post-extension zone.

microchannel varies from 54 μm to 150 μm and the depth is fixed at 80 μm . The pre-denaturation and the post-extension zones are included before and after the 30 cycles' PCR zone, respectively. Both the additional zones pose the flow time of 10 % of the central cycling time.

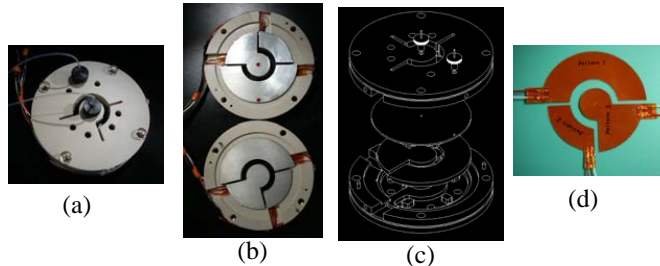


Figure 2. The CF-PCR device. (a) heating unit, (b) open view of heating unit with the heating blocks, (c) structure of the heating unit, (d) film heater.

Figure 2 shows the structure of the present CF-PCR device and the disk heating unit. The PCR cycle time is modulated by the pumping rate of the syringe pump connected to the inlet fluidic connector. The fan-shaped heating blocks are equipped with film heaters on their backside and are separated for thermal isolation (see Figure 2(b) & (d)). A temperature controller maintains the temperatures of the heating blocks at constant values. The top and bottom heating blocks facing each other are aligned, and their temperature is set to the same. The disk is tightly sandwiched with the heating unit for efficient heat transfer. The fluidic tubing and sealing are automatically established between the disk and the heating unit by aligning the top and bottom parts of the heating unit (Figure 2(c)). For thermal isolation and mechanical strength of pressing, the PEEK was used as the material of the clamp and air-trench was installed between the clamp and the film heaters.

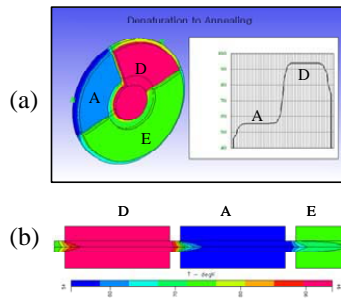


Figure 3. Simulation using CFD-ACE+. (a) Temperature distribution of heating unit, (b) Temperature transition along the channel with sample flow.

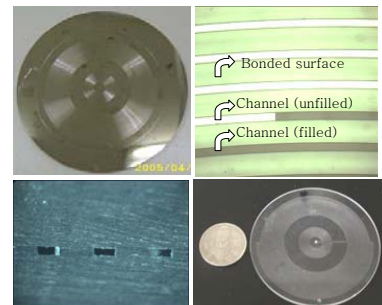


Figure 4. Disk fabrication. (a) Ni master, (b) Plan view of thermally bonded channel, (c) Cross section of thermally bonded channel , (d) The fabricated polymer disk.

Figure 3 demonstrates simulation results. The temperature uniformity of each blocks and thermal isolation between blocks are good.(Figure 3(a)) The temperature of pumped sample is changed quickly even at high flow rate.(Figure 3(b)) The polymer disk is hot embossed with a nickel master and thermally bonded with polymer sheet as shown in Figure 4. COC(Cyclo-olefin-copolymer) is used as the polymer due to its good thermal stability and bio-compatibility. The master is fabricated by the electroplating on the microchannel made from silicone DRIE process. The bonded disk is highly reliable for high pressure flow and the deflection of the channel after thermal bonding is very small(less than 5 μ m). Figure 4(d) shows the fabricated polymer disk, of which the diameter is 66mm and the thickness is 1.4mm.

3. Result and discussion

Figure 5 demonstrates a PCR amplification result using of 480-bp human N-acetyltransferase DNA, which is known as a marker of bladder cancer. The dynamic coating method using BSA(Bovine Serum Albumin) is utilized for preventing the surface adsorption of PCR components. The results indicate the present device can conduct reproducible and fast PCR.

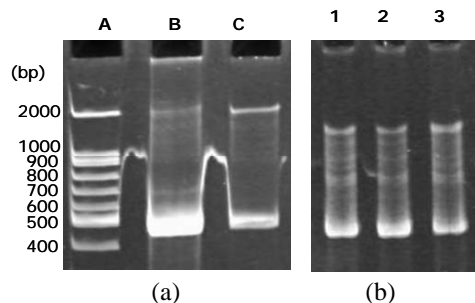


Figure 5. Gel electrophoresis of PCR results. (a) Lane A: Marker, Lane B; using a commercial PCR thermocycler (60min.); Lane C: using the present CF-PCR device(9min.). (b) Using the present CF-PCR device. Lane 1: 36min., Lane 2: 18min., Lane 3: 9min..

References

1. M.U. Kopp, A.J. de Mello and A. Manz, "Chemical amplification: continuous-flow PCR on a chip", *Science*, vol. 280, pp. 1046-1048 (1998).
2. C. Zhang, J. Xu, W. Ma, and W. Zheng, "PCR microfluidic devices for DNA amplification", *Biotechnology Advances*, vol. 24, iss. 3, pp. 243-284 , (2006).

RESTRICTION ENZYME ASSAY IN FEMTOLITER MICROCHAMBER

Liza Lam, Koji Ishizuka, Shouichi Sakakihara and Hiroyuki Noji

Institute of Scientific and Industrial Research, The Osaka University, Japan

Email: lizalam@sanken.osaka-u.ac.jp; hnoji@sanken.osaka-u.ac.jp

ABSTRACT

We report here our work on single-molecule restriction enzyme assay using a femtoliter microchamber. Our previous studies [1] have shown that femtoliter microchambers made of poly-dimethylsiloxane (PDMS) allowed us to measure biomolecule reactions at a single-molecule level without immobilization. In this study, we explore the potentials of encapsulating and manipulating single DNA molecules in new microchambers fabricated using acrylamide gel. The conventional use of acrylamide proves that this material has no unfavorable interactions with these biomolecules. Moreover, this novel approach delivers several advantages over typical PDMS microchambers due to the porous structure of acrylamide gel. Such structure permits ion/enzyme migrations and it has been demonstrated that electric field can be easily applied through the gel matrix. By exploiting this feature, cleavage reaction of DNA molecules in a microchamber has been initiated and directly observed under optical microscopy at the single-molecule level. The results obtained show that this is an extremely sensitive and fast detection technique for restriction enzyme assay. With the aim to extend this method, further DNA analyses such as DNA stretching under alternating electrical field can also be realized in order to measure the length of DNA fragments with high yield.

Keywords: Femtoliter microchamber, restriction enzyme, magnesium ions.

1. INTRODUCTION

The discovery of various enzymes having the ability to modify and synthesize DNA molecules led to numerous breakthroughs in DNA enzymology. A group known as restriction enzymes, which cleave DNA molecules, serves as a powerful tool for gene manipulation and pharmacological applications. Restriction enzyme basically binds onto a specific recognition sequence of a DNA molecule, and then cleaves it. The way in which a particular enzyme cuts a specific base sequence is always the same and reproducible despite the type of DNA molecules it is reacting with. Therefore, this enzyme offers a simple, reliable way to determine the position of a specific recognition sequence on a DNA molecule of interest. For several decades, it has been the interest of many scientists to exploit this technique for effective DNA analysis [2].

2. MATERIALS AND PROCEDURES

For our experiments, 48.5 kbp λ DNA molecules (16.5 μ m in full length) have been stained with SYBR Gold dye to visualize the activities of individual molecules. The

restriction enzyme chosen for our study, BamHI (source: *Bacillus amyloliquefaciens*) [3] cuts the λ DNA molecule into six different fragments, ranging from 5.5 kbp to 16.8 kbp in the presence of magnesium ions, a required cofactor. λ DNA molecules and BamHI enzymes in the sample solution are trapped within the femtoliter microchambers by pressing a microneedle on the surface of the gel against the glass slide. Direct observation of the activities within the femtoliter chambers, which are fabricated using 14% polyacrylamide (AA) gel, has been carried out as shown in Figure 1. The image was obtained through a fluorescence microscope equipped with a mercury light source, a 12% ND filter and an image intensifier unit (Hamamatsu Photonics C8600-05).

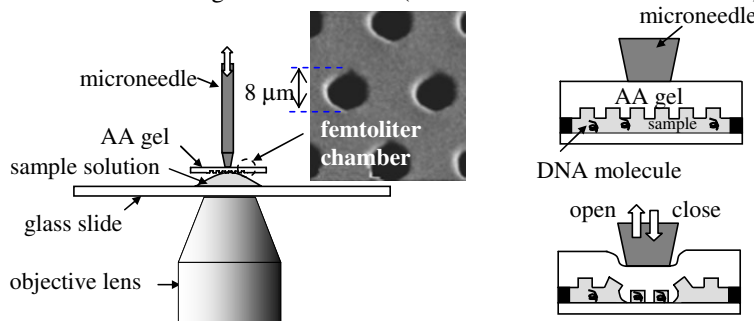


Figure 1: Experimental setup for encapsulating DNA molecules in microchamber

The initiation of restriction enzyme reactions such as controlling the incubation temperature and incubation time for each assay have been found to be unsuitable in our investigation. By applying a d.c. current across the AA gel using external electrodes, magnesium ions (Mg^{2+}) can move through the gel matrix and enter the microchambers. This method of introducing Mg^{2+} to trigger the reaction proves to be a more viable approach for our application. Furthermore, in general, the presence of Mg^{2+} are usually required for most restriction enzymes assays.

3. RESULTS AND DISCUSSIONS

Within the microchamber, the confined λ DNA molecule undergoing restriction enzyme reaction under the influence of restricted Brownian motion has been observed as shown in Figure 2.

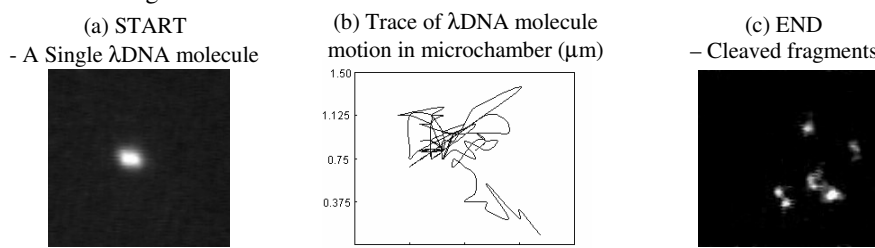


Figure 2: Results of restriction enzyme assay in microchamber

The complete cleaving process of the encapsulated single λ DNA molecule using BamHI is continuously observed. Mg^{2+} triggering has also allowed full control of initiating the reaction. Figure 3 describes the relationship between the rate of initiating reaction and current magnitude with respect to the electrodes' positions and the electrodes separation distances (reference to the inset on the right).

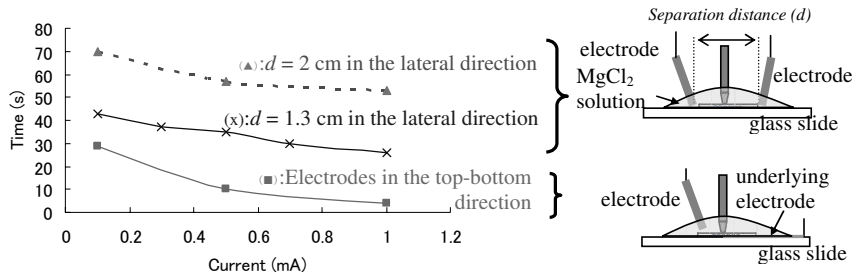


Figure 3: Influence of electrodes' positions on the relationship between the time required for initiating reaction and current.

Based the diffusion model of ion flux under the influence of a potential difference, the time required to initiate reaction can be theoretically estimated.

$$\frac{\partial c}{\partial t} = -D \left[\left(\frac{\partial^2 c}{\partial x^2} \right) + \left(\frac{zFV}{RTI} \right) \left(\frac{\partial c}{\partial x} \right) \right]$$

where c is Mg^{2+} concentration, t is time, x is distance, D is the diffusion constant in AA gel [4], V/I is the unit potential, z is number of positive charges, F is Faraday constant and RT is the thermal energy.

4. CONCLUSION

Restriction enzyme assay has been carried out within the novel femtoliter chamber, hence enabling direct observation. Subsequent analyses such as stretching of encapsulated DNA fragments (an example of an initial experiment shown in Figure 5) are currently investigated.

REFERENCES

- [1] Y. Rondelez G. Tresset, T. Nakashima, Y. Kato-Yamada, H. Fujita, S. Takeuchi, H. Noji, *Nature*, 433, pp. 773-777, (2005).
- [2] B.Garcia-Barreno, T.Delgado, J.A.Melero, *Journal of Virology*, pp. 801-808, (1996).
- [3] M. Newman, T. Strzelecka, F. D. Dorner, I. Schildkraut, A. K. Aggarwal, *Science*, 269, pp. 656-663, (1995).
- [4] L. Pavesi, A. Rigamonti, *Physical Review E*, 51, 4, pp. 3318-3323, (1995).

*The 10th International Conference on Miniaturized Systems for Chemistry and Life Sciences (μ TAS2006)
November 5-9, 2006, Tokyo, Japan*

Figure 4: Comparing experimental results and theoretical analysis

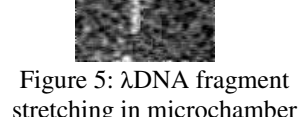
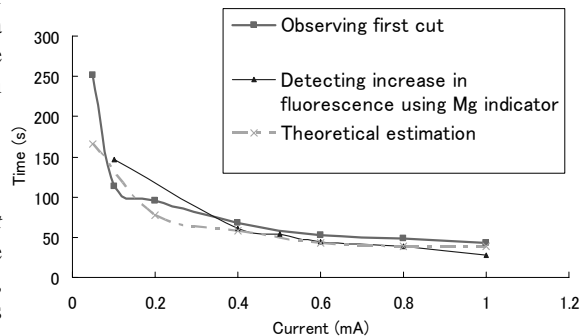


Figure 5: λ DNA fragment stretching in microchamber

A PLASTIC LAB-ON-A-CHIP FOR HIV DIAGNOSTICS USING RT-PCR AND DYNAMIC DETECTION

Soohyun Lee, *Sung-Woo Kim and Chong H. Ahn

Microsystems and BioMEMS Laboratory

Dept. of Electrical & Computer Engineering & Computer Science

University of Cincinnati, Cincinnati, Ohio 45221, USA

*Molecular Neurobiology Laboratory, McLean Hospital, Harvard Medical School
Belmont, MA 02478, USA

Abstract

In this paper, a plastic lab-on-a-chip, which can perform RT (Reverse Transcription), PCR amplification, and consecutive on-chip fluorescence detection, has been developed and applied for the rapid detection of HIV as a point-of-care testing.

Keywords: RT-PCR, On-chip Detection, Micro Pinch-Valves, Infrared Thermocycles

1. INTRODUCTION

Recently, there has been a large demand for the development of a point-of-care (POC) diagnostic kit for the early and rapid detection of HIV by analyzing DNA. With on-chip PCR amplification [1, 2], one of the most commonly used detection methods on the diagnostic chips is agarose gel-based electrophoresis, but the method usually requires a long analysis time. If capillary electrophoresis (CE) is used, it also needs a high voltage to operate the chip [2]. So, both methods are not suitable for the point of care testing (POCT). So, in this research, a new functional plastic lab-on-a-chip as described in Figure 1, which can perform RT-PCR using non-contact infrared (IR) thermocycles and provide dynamic on-chip fluorescence detection, has been developed and characterized for the HIV diagnostics.

In order to functionally control all processes required on the chip, a micro pinch valve using flexible silicone tube, which was developed by our group [3], was embedded into the chip to control assay sequence, enduring high inner pressure during PCR thermocycles. So, actuator pins to pinch the silicone tubes are mounted on the cap of the analyzer.

2. DESIGN AND FABRICATION

The plastic lab-on-a-chip consists of three different chambers for RT incubation, PCR amplification and on-chip detection, respectively (Figure 1 (b)). The mechanism of pinch valve is illustrated in Figure 1(c). This lab-on-a-chip was fabricated with Cyclic Olefin Copolymer (COC) using injection molding technique. Flexible silicone tubes were assembled over the areas of pinch valve and then thermal bonding process was performed as shown in Figure 2.

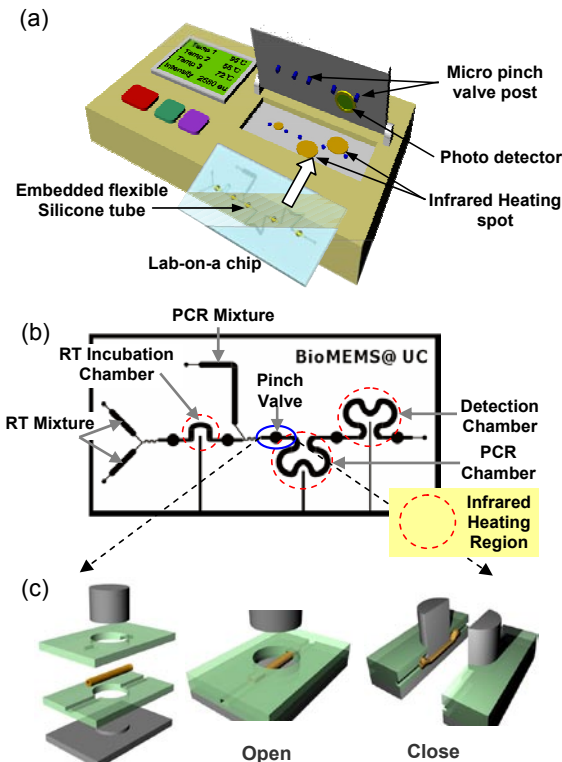


Figure 1. Point-of-care diagnostic system: (a) Chip and analyzer; (b) Functional lab-on-a-chip for seamless RT-PCR and dynamic detection; and (c) Mechanism of embedded micro pinch valves.

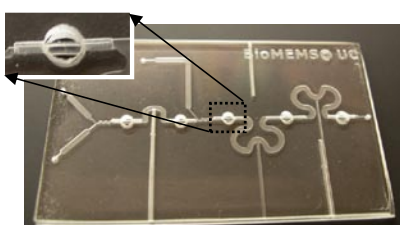


Figure 2. Microphotograph of fully disposable Lab-on-a-chip consists of RT incubation chamber, PCR reactor, detection chamber and embedded flexible silicon tubes

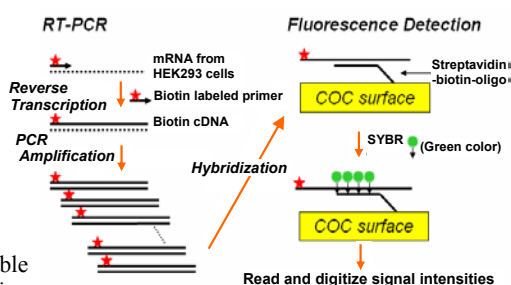


Figure 3. Sequence of bio-reaction on the fabricated chip.

Figure 3 shows the entire sequence of bio-reaction process on the chip. RT mixture and RTase were inserted into the RT incubation chamber through two different inlets. After incubation, RT and PCR mixture were injected into the PCR chamber. Upon the completion of PCR thermocycles using IR, PCR sample was moved into the detection chamber on which streptavidin-biotin-oligo already adsorbed. When the PCR sample is loaded to detection chamber, it is heated up at 65 °C and incubated for hybridization. And then SYBR green dye which has high binding affinity to the minor groove of double strand DNA is inserted into detection chamber for the fluorescent detection.

3. RESULTS AND DISCUSSION

The binding reaction of different concentration of FITC labeled streptavidin on COC surface is characterized first to verify how much streptavidin-biotin-oligo adsorbs on COC surface directly. Then, agarose gel electrophoresis has been performed as a reference as plotted in Figure 5. The results obtained from the on-chip RT-PCR shows acceptable amplifications. Finally, dynamic detections of HIV assay from the on-chip after RT-PCR have been successfully performed as shown in Figure 6, which clearly demonstrates dynamic on-chip fluorescence signals proportional to the number of PCR thermocycles.

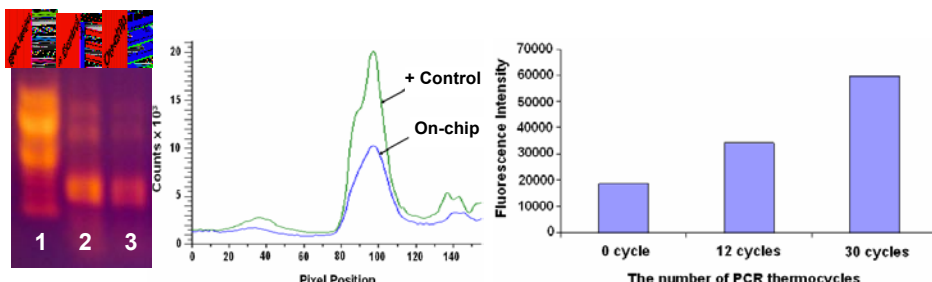


Figure 5. Agarose gel electrophoresis of PCR products as a reference: (a) Lane 1 shows 100 bp DNA ladder for reference; lane 2 is + control result from commercial equipment; lane 3 is on-chip amplification result. (b) Quantification measurement between lane 2 and 3 using scanner

Figure 6. Dynamic quantification measurement of HIV as fluorescence intensity after 0, 12 and 30 PCR thermocycles on lab-on-a-chip

4. CONCLUSION

Fully functional plastic lab-on-a-chip, which can perform RT incubation, PCR amplification and on-chip dynamic detection, has been developed and fully characterized for HIV diagnostics. Full optimization of the chip for HIV diagnostics is currently under evaluation. The new platform of plastic lab-on-a-chip with RT-PCR and dynamic detection will envisage a promising disposable point-of-care diagnostics for numerous infectious diseases in low cost.

REFERENCES

1. Jing Wang *et al.*, A disposable microfluidic cassette for DNA amplification and detection, *Lab on a chip*, 2006, **6**, pp. 46-53.
2. J. Khandurina *et al.*, Integrated System for Rapid PCR-Based DNA Analysis in Microfluidic Devices, *Anal Chem.*, 2000, **72**, pp. 2995-3000.
3. J. Han *et al.*, A Functional Disposable Lab-on-a-chip with Embedded Micro Pinch Valves for Whole Blood Analysis, *Proc. MicroTAS'05*, pp. 43-45.

CHARACTERIZATION OF mRNA DETECTION DEVICE IN LIQUID PHASE

Ryuji Yokokawa¹, Soichiro Tamaoki¹, Takashi Sakamoto²,
Akira Murakami², Susumu Sugiyama¹

¹Ritsumeikan University, 1-1-1 Noji-higashi, Kusatsu, Shiga 525-8577, Japan

²Kyoto Institute of Technology, Matsugasaki, Sakyō-ku, Kyoto 606-8585, Japan

Abstract

Focusing the earnest demand for mRNA detection in liquid phase for transcriptome analysis, we have developed a detection system using a fluorescent microscope. Our OMUpy2 probe hybridizes with an oncogene, c-fos mRNA, and emits fluorescence corresponding to mRNA concentration (Fig. 1). In order to detect the hybridization with high sensitivity, we optimized a detection area with keeping the sample volume in nanoliter range. Detectable number of molecules in the area is drastically decreased to 228 amol from pmol range in conventional liquid phase detection [1]. Autofluorescences of PDMS components were also investigated to minimize background noise, and S/N ratio increased 3.3-fold by the optimum filter setup.

1. Introduction

Transcriptome analysis based on the on-chip technology for personalized medicine has been proposed as an attractive medical treatment. Our target, c-fos mRNA, plays an important role in the transcription control as a factor during cell proliferation. However, c-fos RNA overexpresses and turns cells cancerous due to unknown factors. Therefore, cellular canceration can be detected by quantifying c-fos mRNA in a cell.

Conventional mRNA analysis has been performed in solid phase to detect a small amount of mRNA, and it involves several time consuming processes: purification of mRNA from samples, preparation of probes on the microarray, RT-PCR for amplifying cDNA, and the

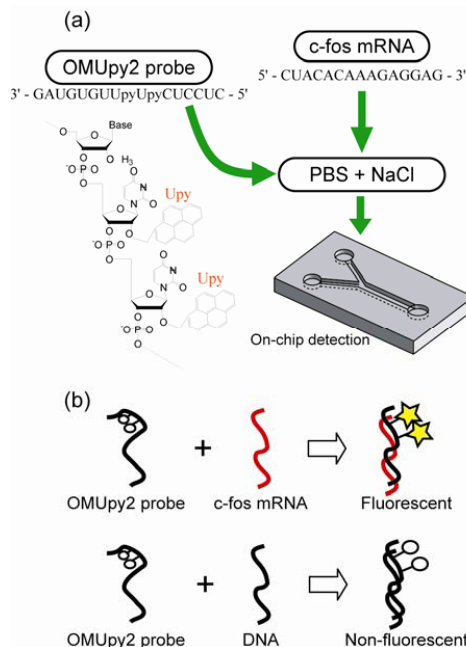


Figure 1. A schematic illustration of mRNA detection. (a) Fluorescence is detected only when the OMUpy2 probe hybridizes with c-fos mRNA in PBS including NaCl. (b) OMUpy2 probe can hybridize with a complementary DNA but not fluorescent.

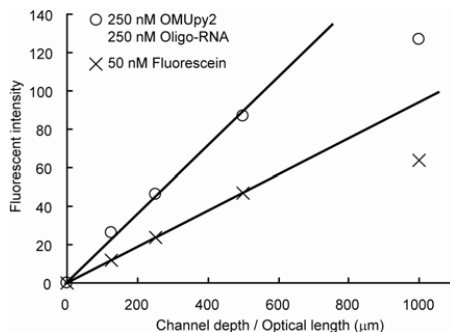


Figure 2. Relationship between fluorescent intensity and channel depth. Two samples, 250 nM OMUpy2 hybridized with 250 nM oligo-RNA and 50 nM fluorescein, were measured for depth optimization.

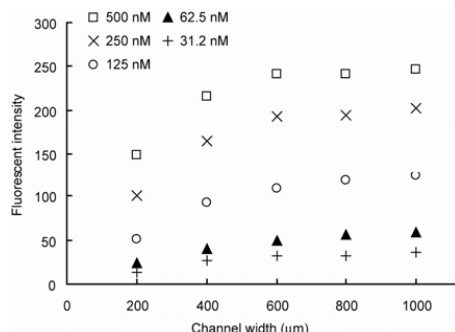


Figure 3. Relationship between fluorescent intensity and channel width. Five different concentrations of OMUpy2 hybridized with oligo-RNA were investigated for width optimization.

hybridization between probes and samples. Therefore, alternative rapid detection in liquid phase has been proposed for the on-site diagnosis, because a fluorescent signal can be sequentially detected on a chip right after hybridization. Liquid phase detection is an essential technology for personalized medicine.

2. Experimental

We previously developed a probe, OMUpy2, for c-fos mRNA detection [2]. The probe hybridizes with c-fos mRNA specifically, and generates fluorescence in liquid phase (Fig. 1). A synthesized RNA identical to c-fos mRNA was prepared for our experiments due to limited sample access. Fluorescent samples were prepared by hybridized 1 μM OMUpy2 probe with 1 μM oligo-RNA, and diluted by 10 mM PBS containing 0.1 M NaCl (pH 7.0) for experiments.

Microfluidic devices were fabricated by PDMS molding, and channel structures were sealed by a quartz substrate. Channels prepared for depth and width optimization were 125-1000 μm in depth and 200-1000 μm in width. The detectable concentration of hybridized sample was explored using the optimized channel size. Fluorescent intensities from several concentrations were measured.

OMUpy2 probe is excited by the wavelength of 340 nm, which is also known to be an excitation wavelength for PDMS. Autofluorescence from PDMS can be background noise, and decrease S/N ratio. We have evaluated autofluorescences from five PDMS components provided by Shin-Etsu Chemical. Based on the result, S/N ratios depending on emission filters were measured, and filter setup was optimized.

3. Results and Discussion

Linearities between fluorescent intensity and channel depth/width are retained up to 500 μm deep and 400 μm wide as shown in Fig. 2 and Fig. 3. Depth and width are not

effectively work over these values, though fluorescent intensity slightly increases. Concerning the detectable concentration and reduction of sample consumption, we utilized a channel 500 μm deep and 200 μm wide. Fluorescent intensity linearly increases with the increase of concentrations without fluorescent loss (Fig. 4). The lowest detectable concentration was successfully decreased to 1.9 nM, which corresponds to 228 amol in the detection area.

Autofluorescence spectra of five PDMS components are plotted in Fig. 5. The cross-linker has higher intensity than other four components in all the scanned range. These background noises degrade the probe signal at 480 nm. Signal-to-noise ratios are calculated assuming four common filter setups. The ratio obtained by a band-pass filter of 480 ± 15 nm is larger than others. Utilizing the optimized filter setup, the S/N ratio increased 3.3 times at an OMUpy2 concentration of 7.8 nM (data not shown).

Combining optimizations for device and detection setup, it will become possible to detect the small number of molecules in a diagnosis device for personalized medicine.

Acknowledgements

PDMS components were supplied by Shin-Etsu Chemical Co., Ltd. This work was partially supported by the 21st century COE program, the Ministry of Education, and Kyoto nanotechnology cluster funded by ASTEM.

References

- [1] M. Ohnishi, "Development of a microcapillary column for detecting targeted messenger RNA", 19th MSB Kobe 2005, p. 135
- [2] A. Mahara, et al., "Bispyrene-Conjugated 2'-O-Methyloligonucleotide as a Highly Specific RNA-Recognition Probe", *Angew. Chem. IntEd.*, Vol. 41, No. 19, pp. 3648-3650, (2002)

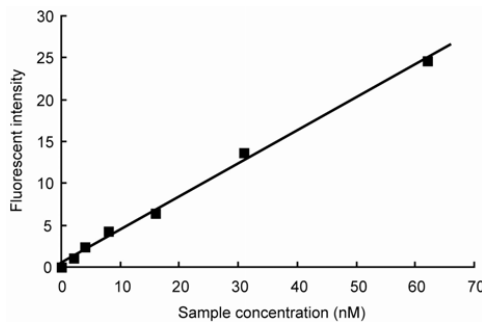


Figure 4. Relationship between fluorescent intensity and OMUpy2 concentration. The same concentration of OMUpy2 and oligo-RNA were hybridized, and the intensity was measured in a channel (width: 200 μm , depth: 500 μm).

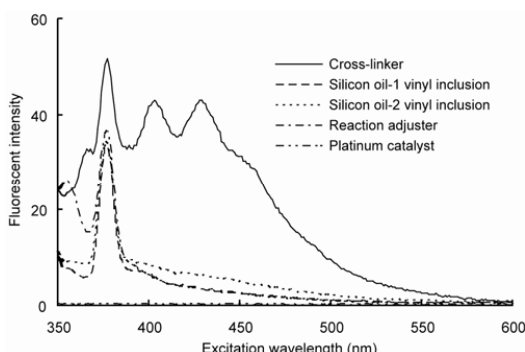


Figure 5. Fluorescent spectra of five components of PDMS. The scanned wavelength was from 350 nm to 600 nm.

DIFFERENT DISTRIBUTION OF LYSOZYME, GDNCL, AND CTAB DURING PROTEIN REFOLDING IN MICROFLUIDIC CHANNEL

TOSHIRO KOBORI, TOSHIO OHTANI, AND YUKIO MAGARIYAMA

National Food Research Institute,
National Agricultural and Food Research Organization
2-1-12 Kannondai, Tsukuba 305-8642, Japan

Abstract

Most of artificial refolding processes involve dilution of denaturant by excess amount of detergent, causing a low yield of refolded proteins. We investigated application of microfluidic channel to the dilution step. Lysozyme refolding was used as an experimental standard. Lysozyme, GdnCl, and CTAB were differently distributed in the channel, which was successfully predicted by a mathematical model considering substitution reaction between GdnCl and CTAB. Additional simulations suggest conditions necessary for further efficient refolding, such as CTAB concentration, channel width, and flow rate.

keywords: microfluidic channel, protein refolding, diffusion

1. Introduction

Recombinant proteins frequently form insoluble, inactive inclusion bodies in transformed microorganisms. To obtain active proteins from the inclusion bodies, we want an easy protein-refolding process. A fundamental idea involves unfolding of the inclusion bodies using denaturants, followed by a gradual dilution of the denaturants to accurately fold into native conformations with proper functions. However, the dilution reduces a yield of the final products.

In the present study, we applied a microfluidic channel to a refolding method to improve the dilution step. In the original method [1], lysozyme unfolded by GdnCl is added to 100 volumes of a detergent, CTAB, and eventually, CTAB gradually substitutes for GdnCl. Cycloamylose then supports a proper refolding after the CTAB-GdnCl substitution reaction.

2. Experimental results

We constructed a glass channel with four inlets and four outlets (Fig. 1, Institute of Microchemical Technology Co., Ltd) to analyze a substitution reaction of CTAB for GdnCl bound in lysozyme. 0.1~0.5% CTAB ran from the inlets #1, #3, and #4, whereas, 1, 5, or 10 mg/ml lysozyme denatured by 1, 2, or 4 M GdnCl also ran from the inlet #2. Flow rates were adjusted to 0.005, 0.01 or 0.025 ml/min. Concentration changes of lysozyme, GdnCl and CTAB were estimated by HPLC analyses with GF-310HQ column (50% CH₃CN/50 mM NaNO₃, 0.4 ml/min, 40 °C).

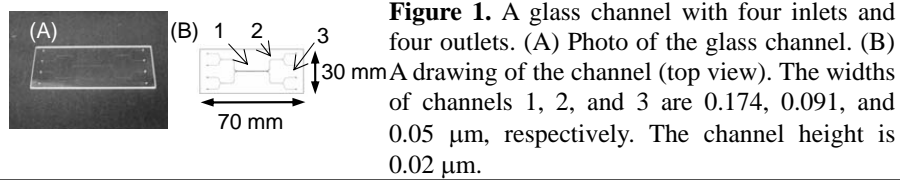


Figure 1. A glass channel with four inlets and four outlets. (A) Photo of the glass channel. (B) A drawing of the channel (top view). The widths of channels 1, 2, and 3 are 0.174, 0.091, and 0.05 μm , respectively. The channel height is 0.02 μm .

Typical concentration changes of lysozyme, GdnCl, and CTAB are shown in Figure 2. Lysozyme exhibited a slow change compared to GdnCl and CTAB (Fig. 2). A concentration change of CTAB largely depended on lysozyme concentration, and lysozyme with higher concentration suppressed CTAB diffusion. These results suggest that different distribution of lysozyme, GdnCl and CTAB in a channel could be simply explained based on their diffusions and exchange reactions among them.

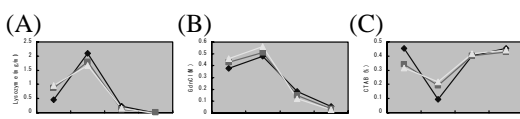


Figure 2. Typical examples of concentrations of lysozyme, GdnCl, and CTAB after passing through the channel.

(A) Lysozyme concentration. (B) GdnCl concentration. (C) CTAB concentration. The condition is 0.5% CTAB from inlets #1, #3, and #4, and 5 mg/ml lysozyme and 1 M GdnCl from inlet #2. Flow rate: 0.005 (black); 0.01 (grey); and 0.025 (white) ml/min.

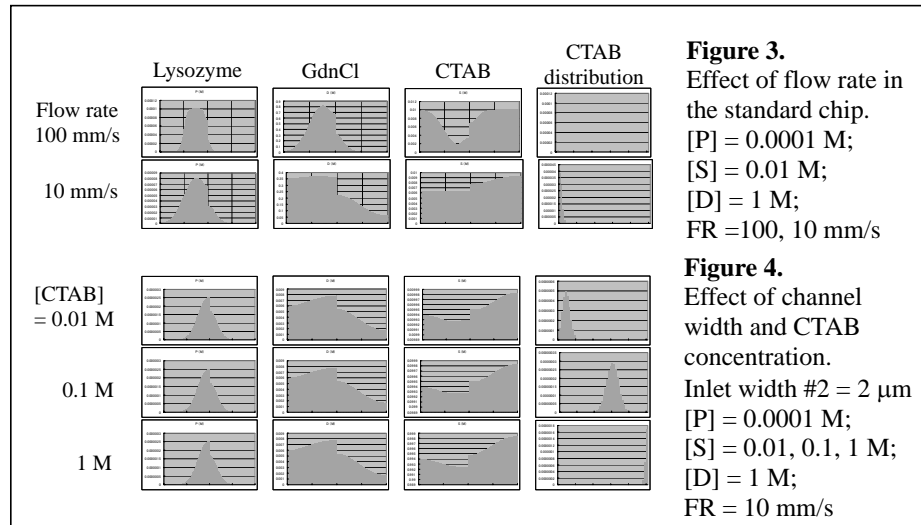
3. Numerical simulations

Distribution of each component in the microfluidic channel was numerically simulated based on the following assumptions: (i) A single lysozyme molecule contains fifty binding sites for GdnCl/CTAB, (ii) GdnCl (CTAB) bound at a binding site of lysozyme is substituted for CTAB (GdnCl), and (iii) The substitution rate constants are identical.

Distributions of each component were calculated based on the above model. Typical distribution patterns agreed with the experimental results. The patterns were dramatically changed upon reduced flow rate (Fig. 3), indicating that the flow rate would contribute to the efficient exchange reaction in the channel. Slight substitution of CTAB for GdnCl was predicted.

We then investigated effects of the channel widths and the CTAB concentration on the reaction. A narrow width of the inlet #2 (2 μm) resulted in a sharp distribution of lysozyme (Fig. 4), compared to the reaction in the standard chip (Fig. 3). Slow flow rate (10 mm/s) accomplished ~60% substitution of CTAB for GdnCl even in 0.01 M CTAB. A combination of high concentration of CTAB (1 M) and the reduced flow rate (10 mm/s) realized full substitution without wide diffusion of lysozyme (Fig. 4). Therefore, these simulations suggest that the narrow inlet #2 for lysozyme, the high concentration of CTAB, and the reduced flow rate would allow the exchange of GdnCl for CTAB that

was sufficient for further reactions for the lysozyme refolding. The conditions have been optimized for a practical use.



4. Conclusion

We applied a microfluidic channel to the dilution step of lysozyme unfolded by GdnCl with CTAB, which was a key step for the cycloamylose-mediated protein refolding. From the experimental results and the numerical simulations in this study, we obtained the basis for designing an optimal microfluidic channel for the dilution step.

Acknowledgements

This work is supported by Ministry of Agriculture, Forestry and Fisheries of Japanese Government.

References

1. Machida S, Ogawa S, Xiaohua S, Takaha T, Fujii K, Hayashi K. (2000) FEBS letters, 486(2), pp. 131-135.

HOMOGENEOUS DNA MELTING ANALYSIS FOR MUTATION SCANNING USING NANOLITER VOLUMES

Scott O. Sundberg¹, Jenny Greer², Carl T. Wittwer³, Robert J. Pryor³,
Oluwole Elenitoba-Johnson³, and Bruce K. Gale²

¹Department of Bioengineering, University of Utah

²Department of Mechanical Engineering, University of Utah

³Department of Pathology, University of Utah

Abstract

Solution-phase, homogeneous DNA melting analysis for heterozygote scanning was performed in 10 nL and 1 nL reaction volumes on a custom microchip and melt curves were in agreement with the gold-standard 10 μ L HR-1™ melting instrument (Idaho Technology, Salt Lake City, UT). The microchips were characterized for no surface coating and a bovine serum albumin (BSA) coating applied to the microchannels. It was found that BSA improved the reproducibility and S/N for melting analysis.

Keywords: DNA melting, mutation scanning, SNP genotyping, xurography

1. Introduction

In 1997 DNA melting analysis was introduced [1], using a double-stranded DNA fluorescent dye to detect single nucleotide polymorphisms (SNPs) and to perform mutation scanning following the polymerase chain reaction (PCR) for DNA amplification. This analysis method is advantageous over other DNA analysis systems because it is less complicated, fast, and prevents contamination of the sample and environment due to its closed-tube technique. Solution-phase or “homogeneous” melting analysis on a microchip is advantageous over microscale systems using hybridized oligonucleotides [2] due to the minimization of chip fabrication complexity and reduction in analysis time.

2. Materials and methods

Xurography [3] was used to create the microchips, using a knife plotter to cut out channel structures from double coated tape (9019, 3M, St. Paul, MN) and sandwiching patterned tape between glass slides, Figure 1(A&B). A Peltier heater and J-type thermocouple, with thermal grease at interfaces, were used for temperature control, Figure 1(C). Detection used a modified inverted microscope with optics designed for the double-stranded dye LCGreen® Plus (Idaho Technology), a photomultiplier tube and module (Hamamatsu, Bridgewater, NJ), and all hardware was operated using LabView 7.1 (NI, Austin, TX). PCR was performed on the DNA sample and then transferred to an HR-1™ instrument for a high-resolution reference melting curve. The sample was then injected into a microchip for melting within 10 nL and 1 nL volumes.

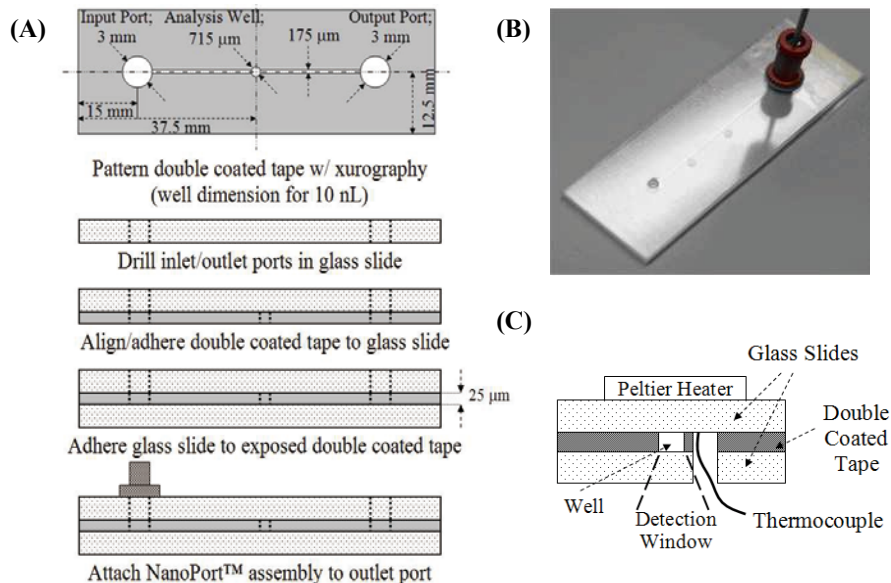


Figure 1. Fabrication process for microchip (A); photograph of final microchip assembly (B); and schematic of microchip well detection and temperature control (C).

3. Results and discussion

Table 1 compares S/N of melts with no microchannel coating and BSA (2.5 mg/mL). BSA coated channels provided a higher S/N and a more reproducible system. Figure 2 shows negative derivative melting plots of homozygous wild-type and heterozygous DNA for a SNP within an 84-bp fragment of *ATM* exon 17, where the heterozygotes were easily distinguished from the homozygotes by comparing the melting curve shape. Both 1 nL and 10 nL melts are in good agreement with the 10 µL HR-1™ melt curves. Temperature shifts between plots is due to a Peltier heater temperature gradient and varying thermocouple placement between microchips. It was found that the homozygous wild-type S/N values were 51, 69, and 2450 and the heterozygous mutant S/N values were 59, 63, and 2800, reported from smallest to largest volumes.

Table 1. S/N calculations of microchannels with no coating and with BSA coating.

Run #	S/N	
	No Coating	BSA
1	29.8	40.2
2	37.5	67.8
3	27.7	53
4	no melt	54.9
5	22.3	70.7

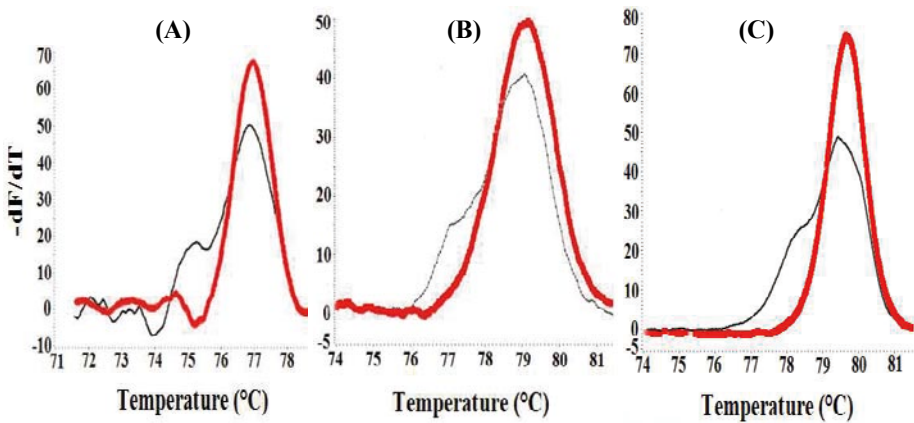


Figure 2. Negative derivative plots for the microchip (A:1 nL, B:10 nL) and the HR-1™ (C:10 μ L) using the *ATM* exon 17 target. Homozygous wild-type template (thick line); heterozygous mutant template (thin line).

4. Conclusions

Mutation scanning can be performed using homogeneous DNA melting analysis within nanoliter volumes. The 1,000 and 10,000-fold reduction in sample volume from the 10 μ L HR-1™ to 10 nL and 1 nL microchips does result in a lower S/N, but is still adequate for mutation scanning and would also work for SNP genotyping. It was further seen that the Xurography fabrication method provided adequate microchips for testing this chemistry. The next step for this research is to add PCR amplification with melting analysis within the microchip and move to an array format. Such a system could provide an inexpensive, high-throughput mutation scanning platform.

References

1. K. Ririe, R. Rasmussen, and C. Wittwer, *Product differentiation by analysis DNA melting curves during the polymerase chain reaction*, Anal. Biochem., 245, pp. 154-160, (1997).
2. A. Dodge, G. Turchatti, I. Lawrence, N. Rooij, and E. Verpoorte, *A microfluidic platform using molecular beacon-based temperature calibration for thermal dehybridization of surface-bound DNA*, Anal. Chem., 76, pp. 1778-87, (2004).
3. D. Bartholomeusz, R. Boutte, and J. Andrade, *Xurography: rapid prototyping of micro-structures using a cutting plotter*, IEEE J. MEMS, 14, pp. 1364-74, (2005).

INTEGRATED PCR AND THERMAL MELT ANALYSIS ON A MICROFLUIDIC CHIP

Deborah Boles*, Michele Stone*, Esther Huang**, Ming Wu**,
Roger Dettloff**, Aaron Rulison**, Javier Farinas**, and Ivor Knight*

*Canon U.S. Life Sciences, Inc., Rockville, MD, USA

**Caliper Life Sciences, Inc., Mountain View, CA, USA

ABSTRACT

We have modified and tested the microfluidic LabChip® system [1] to integrate thermal melt analysis and PCR in a continuous flow format utilizing reaction volumes of several nanoliters. Results demonstrate high resolution thermal melt analysis at ramp rates up to 1°C/s. To our knowledge, this is the first demonstration of a continuous flow system integrating PCR and thermal melt analysis.

Keywords: PCR, DNA Melting Analysis, LabChip Device, Genotyping

1. INTRODUCTION

Differentiation of PCR products by fluorescent melting analysis was first introduced in 1997 [2], and has since been demonstrated as a reliable genotyping technique for diagnostic applications [3]. Conventional instrumentation for thermal melt analysis utilizes slow thermal ramp rates (0.1 – 0.2 °C/s) to allow for heat transfer to reaction volumes in the microliter range [4]. Reducing volumes to the nanoliter scale permits rapid PCR cycling and thermal ramp rates for identification of targets in significantly reduced analysis time. Furthermore, the ability to perform continuous flow PCR greatly simplifies the integration of different biochemical reactions from sample preparation to analysis.

2. EXPERIMENTAL

The microfluidic chip, Figure 1, consisted of two bonded quartz plates; one piece with etched channels, the other piece with nine metal traces and through holes to serve as reagent reservoirs. A capillary inserted perpendicular to the plates allowed samples to be introduced into the channels directly from a microtiter plate by pressure driven flow.

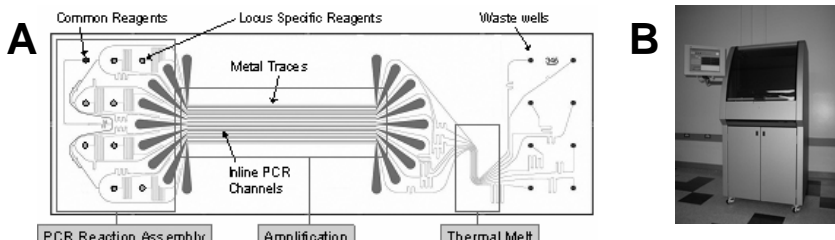


Figure 1: A schematic of the microfluidic chip design for integrated PCR and thermal melting (A) and the instrument (B).

DNA samples introduced via the capillary were mixed with Taq polymerase, SYBR Green I and dNTPs stored on the chip. The mixture was then split into 8 parallel channels each of which was supplied with a different set of locus specific reagents (probes, primers and MgCl₂). Samples were introduced serially onto the chip with buffer spacers between adjacent samples. Varying power levels were applied to the metal traces to rapidly cycle the temperature of the samples flowing through the amplification region. The thermal cycling required for PCR is accomplished by passing electrical current through the metal traces to heat portions of the channel while fluid contacting the backside of the microfluidic device is alternatively employed to rapidly cool that portion of the channels.

After amplification, samples in the detection region were thermally melted by ramping the temperature of a Peltier heater block beneath the detection region. Separate Peltier heaters are utilized to allow for independent temperature control of the waste and reagent wells to 25 °C. Fluorescence was measured and converted to plots of the negative derivative of fluorescence as a function of temperature.

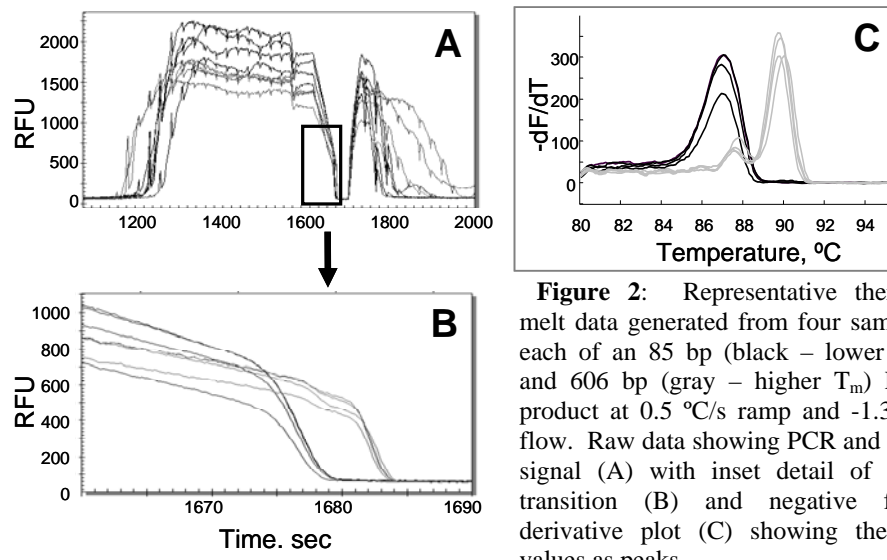


Figure 2: Representative thermal melt data generated from four samples each of an 85 bp (black – lower T_m) and 606 bp (gray – higher T_m) PCR product at 0.5 °C/s ramp and -1.3 psi flow. Raw data showing PCR and melt signal (A) with inset detail of melt transition (B) and negative first-derivative plot (C) showing the T_m values as peaks.

3. RESULTS AND DISCUSSION

A study of melting temperature of two PCR products, 85bp and 606bp, was performed in the apparatus using the double-stranded DNA binding dye SYBR Green I. Figure 2 shows the typical melting profile for the two products, when PCR and thermal melt are integrated. Figures 2A and B show the raw melt curves where fluorescence drops off most steeply as the DNA melts. In Figure 2C the melting transitions can easily be seen as peaks and are reported as T_m values. Note that the higher T_m, 606bp, product has a

complex melting curve with two transitions that are easily resolved in this device. A comprehensive study of the effect of flow rate on T_m values at two thermal ramp rates was performed using the same two PCR products. In these experiments PCR was performed off-chip and melt analysis was performed in the chip. Figure 3 shows that at each ramp rate, T_m values were consistent across all flow rates. Table 1 shows that ΔT_m , the parameter that differentiates the PCR products, was consistent across all tests, ($\Delta T_m = 3.7 \pm 0.05 ^\circ\text{C}$).

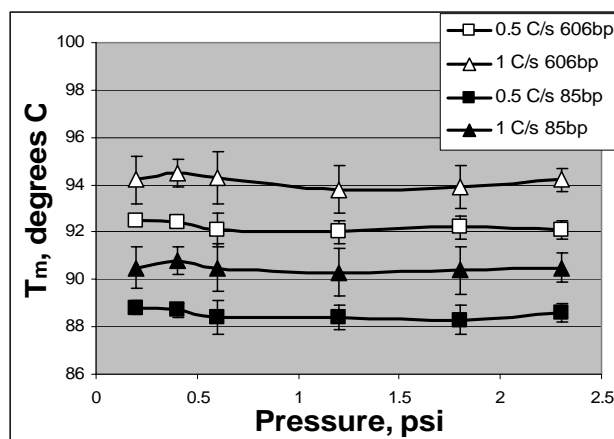


Figure 3: Effect of pressure on T_m of PCR products at different ramp rates. Each data point is a mean of 4-7 experiments. Error bars are standard deviation values.

Table 1: Comparison of T_m values for two PCR products across all flow rates and ΔT_m between the two PCR products across all flow rates for the experimental results shown in Figure 3.

Thermal Ramp Rate (°C/s)	Mean T_m Values \pm SEM (°C)		Mean ΔT_m \pm SEM (°C)
	85bp	606bp	
0.5	88.5 ± 0.08	92.2 ± 0.08	3.7 ± 0.05
1	90.5 ± 0.07	94.2 ± 0.11	3.7 ± 0.05

REFERENCES

- [1] J. Baker, et al. Proceedings of 7th International Conference on Micro Total Analysis Systems, 1335-1338, (2003).
- [2] K.M. Ririe et al, Product differentiation by analysis of DNA melting curves during the polymerase chain reaction, Analytical Biochemistry 245:154-160, (1997).
- [3] T.R. Gingeras et al, Fifty years of molecular (DNA/RNA) diagnostics, Clinical Chemistry 51:661-671, (2005).
- [4] M.G. Herrmann et al, Amplicon DNA melting analysis for mutation scanning and genotyping: cross-platform comparison of instruments and dyes, Clinical Chemistry 52:494-503, (2006).

A MINI AUTOMATIC PROTEIN FRACTIONATOR AND COLLECTOR

Zhen Wang, D Jed Harrison*

Department of Chemistry, University of Alberta, Edmonton, Alberta, Canada

Abstract

In this paper, we demonstrate an electrokinetically pumped protein fractionator and collector with 36 fractionation channels. The sample stream is shielded by sheath buffers so it can be delivered to any of 36 fractionation channels without contaminating the inlets of other channels. Sequential fractionation and collection at a fixed time interval was controlled by a high voltage relay box. This fractionator can be coupled with isoelectric focusing (IEF) separation of protein samples upstream. A two channel fractionator was used to investigate the IEF conditions.

Keywords: electrokinetics, isoelectric focusing, fractionation, protein, sheath flow

1. Introduction

A protein analysis platform on microchip is a challenging yet promising goal. The complex protein sample must undergo separation and fractionation before further analysis. Several fractionators have been reported. [1,2] In our previous work, [3] we developed an 8-channel fractionator that utilized sheath flow “protection” to prevent cross-contamination, and a peak selection method to selectively collect the fractions of interest. One of the drawbacks of this design is that the sample must be detected to be selected. Here we present a 36-channel fractionator, demonstrating that a high density fractionator is compatible with the sheath flow protection method, and that these devices can be used in the fraction/unit time method employed by conventional instruments, which requires that a large number of fractions be collected. The sample stream was fractionated into individual channels using electrokinetic driving force. A high voltage relay box was used to control the flow switching at a fixed time interval. No physical valve is involved in this system and no peripheral mechanical parts are required, making the device simple to use and easy to couple to other techniques.

2. Experimental

The microchips were made of O211 glass. The fluorescence images were collected by CCD camera. A PMT was used to capture the electropherograms. Voltage control was realized with a power supply and high voltage relay, controlled by a Labview program. Data collection was done using a National Instruments data acquisition card.

3. Results and discussion

The fractionator chip layout consists of 18 fractionation channels on each side, as shown in Figure 1. Channels were etched to different depths with a two-mask

process, in order to focus the electric field to give high sheath flow rates. Pspice software was used to simulate the current in each channel to estimate the flow rate of sheath buffer and sample (expressed in percent flow), Figure 2. The fluorescence images in Figure 3 illustrate the tight focus that was achieved across a distance of 2750 μm , with fractionation into 36 channels. Figure 4 shows the sequential flow switching at a fixed time interval. The sample stream and the inlets of fractionation channels were isolated by the sheath buffers, preventing cross contamination, a common problem in electrokinetically-valved devices.

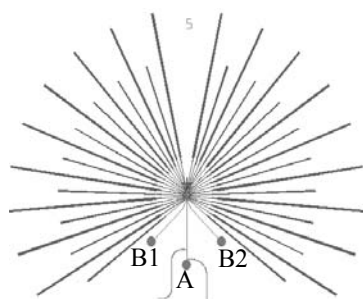


Figure 1 Chip layout of the fractionator Reservoir A was loaded with fluorescein, reservoir B₁ and B₂ with buffer for the sheath flow. The fractionation channels were grounded.

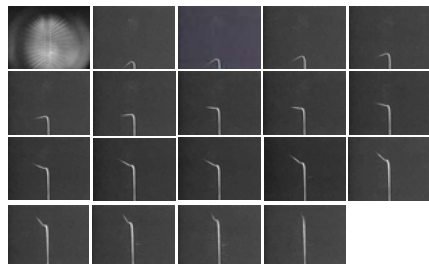


Figure 3 Images show the fractionation of flow into each channel. The sheath flow keeps the fluorescein stream tightly focused.

The fractionator will be coupled with isoelectric focusing (IEF). The high loading capacity and preconcentration characteristic of IEF make downstream analysis easier. IEF has been demonstrated on chip. [4,5] In our work, to combine the separation with the fractionation, one-step IEF is required, so the sample can only be loaded into a

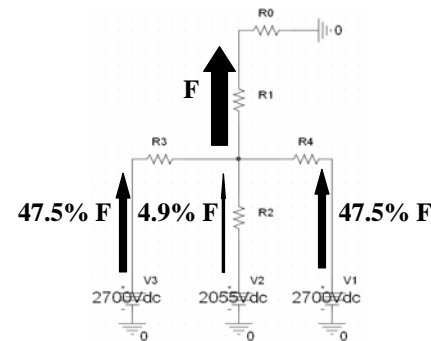
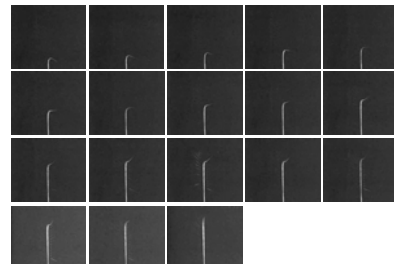


Figure 2 P-spice simulation of the channel impedances and predicted percent flow is also shown



portion of the separation channel. Both these requirements make IEF more difficult on-chip. To study the IEF conditions, a simpler fractionator design was used, as shown in Figure 5. We found that the length of the IEF channel, the buffer composition of sample and the concentration of the anolyte and catholyte all have effects on IEF. However, the most important factor is the distance between the anode reservoir and the injection plug. For the design in Figure 5(a), no good IEF could be achieved under any buffer conditions tested. However, as we shortened the distance between the anode reservoir and the injection plug (Figure 5b), three proteins with close pI values were separated nicely.

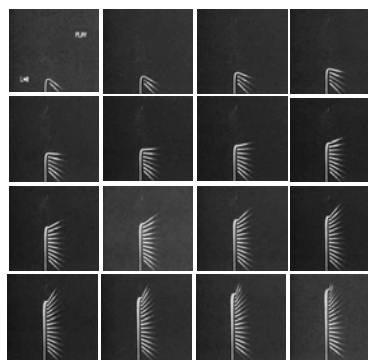


Figure 4 Images show the sequential fractionation of flow into each channel. The sheath buffer isolates the sample stream from the inlets of fractionation channels.

4. Conclusion

A high density fractionator is demonstrated for use with an integrated separation method. The conditions required for isoelectric focusing of proteins and delivery into the fractionator were determined. The design should be useful as a component of a larger more complex, integrated protein processing system.

References

- (1) Müller, O., Foret, F., Karger, B.L. *Anal. Chem.* 1995, 67, 2974
- (2) Tulock, J.J., Shannon, M.A., Bohn, P.W., Sweedler, J.V. *Anal. Chem.* 2004, 76, 6419
- (3) Proceeding of μ TAS 2005 conference, 1549-1551, Boston, USA.
- (4) Huanchun Cui *et al*, *Anal. Chem.*, 2005, 77, 1303-1309.
- (5) Ying-Chih Wang *et al*, *Anal. Chem.*, 2004, 76, 4426-4431.

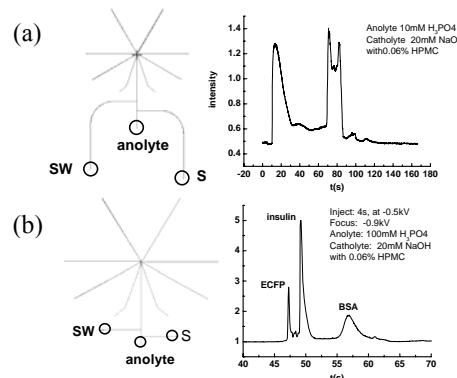


Figure 5 The distance between the anode reservoir and the injection plug is around 200 μ m in Figure 5b which gives a good separation compared to 2 mm in Figure 5a.

MICROCHIP-BASED ELECTROPHORETIC ANALYSIS OF LOW ABUNDANT UNKNOWN MUTATIONS USING SITE-SPECIFIC NICKING AND LIGATION ENZYMES

Rondedrick Sinville, Shawn Llopis, Hanna Pincas, Francis Barany, Steven A. Soper

Louisiana State University, Dept. of Chemistry, Baton Rouge, LA 70803
Weill Medical College of Cornell University, Dept. of Molecular Biology, New York, NY 10021

Abstract

A polymer-based microfluidic device was used to electrophoretically sort enzymatically cleaved and/or resealed fluorescently-labeled oligonucleotide products generated from an allele-specific ligase detection reaction (LDR) and/or endonuclease V (EndoV)/LDR mutation scanning assay. Analyses were conducted using microchannels formed via hot embossing of *LiGA*-generated high aspect ratio microstructures, which were subsequently filled with linear polyacrylamide (LPA). These separations were aided by the use of a novel surface modification procedure developed for poly (methyl methacrylate) (PMMA), which minimized the electroosmotic flow (EOF) and non-specific analyte-wall interactions; it was shown to provide increases in peak efficiencies ($>1.3 \times 10^6 \text{ m}^{-1}$) compared to pristine surfaces ($\sim 5 \times 10^5 \text{ m}^{-1}$). LDR products indicative of colorectal cancer point mutations were successfully separated in ~4 min, while unknown p53 mutations were elucidated using EndoV with a subsequent reduction in noise upon resealing of incorrectly nicked DNA using ligation.

Keywords: microchip electrophoresis, endonuclease V, ligase detection reaction

1. Introduction

The onset of colorectal cancer has been linked to a host of well characterized point mutations that occur primarily within codons 12 and 13 of the *K-ras* oncogene as well as unknown sporadic p53 tumor suppressor gene mutations. The presence of these mutations can be used as biomarkers for early detection or monitoring disease progression. These methods must take into account the relatively high abundance of stromal cells in the sample (as low as 1 mutated cell/500 normal cells). Two strategies conducive to microchip electrophoretic separations have been implemented to detect these mutations, which make use of enzymes that recognize PCR amplified mutational sites for the detection of both known and unknown mutations: ligase detection reaction (LDR) assays and the endonuclease V (EndoV) / LDR mutation scanning assays.

2. Theory

LDR is based on an allele-specific ligation of two complementary primers (common and discriminating), which flank a point mutation and hybridize to the target DNA. EndoV effectively nicks DNA at mutation sites within generated heteroduplexes

of two fluorescently labeled sequences in addition to some miscleavages, which can be subsequently resealed using ligation in real-time to reduce non-target signals [1,2]. These assays can be performed on a polymeric microchip for the electrophoretic sorting of the products provided the device minimizes zone dispersion, electroosmotic flow (EOF) and potential analyte-wall interactions.

3. Experimental

High aspect ratio microstructures (HARM) fabricated using mold inserts generated via *LiGA* were hot-embossed into poly(methyl methacrylate), PMMA. To provide sufficient plate numbers and to keep the device footprint small, channel turns were geometrically designed to reduce zone dispersion induced by race track effects (25 $\mu\text{m} \times 120 \mu\text{m} \times 11 \text{ cm}$) (see Figure 1). In addition, the device was built with a deep channel to improve detection limits when incorporating confocal fluorescence readout.

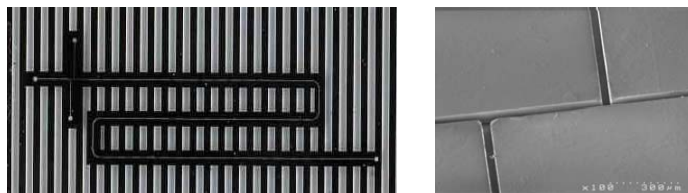


Figure 1. Micrograph of a nickel mold insert fabricated using *LiGA* containing high aspect ratio microstructures measuring 25 $\mu\text{m} \times 120 \mu\text{m} \times 11 \text{ cm}$ (left) and a micrograph (100X magnification) of a 500 μm offset injection T in the PMMA microchip, which provided a 150 μL injection volume (right).

To minimize the EOF and non-specific analyte-wall interactions, we developed and applied a coating scheme to covalently attach linear polyacrylamides (LPAs) to amine-terminated PMMA channel walls using a polymer grafting procedure (see Figure 2).

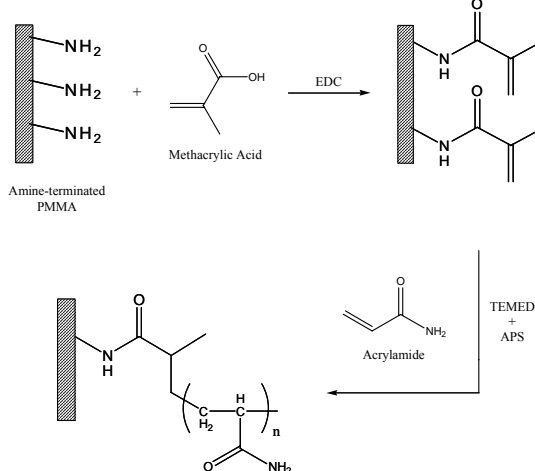


Figure 2. Chemical modification procedure used to coat PMMA with LPA. The grafting-from procedure involved UV activation of the PMMA surface to create surface-confined carboxylates, which could be reacted with a diamine to produce an amine-terminated surface. This was subsequently reacted with methacrylic acid, which served as the foundation for forming the linear polyacrylamide.

The microchip was filled with replaceable LPA matrices and detection was accomplished with an in-house built laser-induced fluorescence (LIF) system. For all samples, an injection plug (150 pL) was defined by the 500 μ m offset T and the separation was affected using a 125 V/cm field strength.

4. Results and Discussion

Initial studies of the LPA-coated PMMA microchips using dye-labeled oligonucleotides demonstrated an EOF that was reduced nearly one-order of magnitude compared to the pristine material, yielding plate numbers $>1.3 \times 10^6 \text{ m}^{-1}$ in comparison to $\sim 5 \times 10^5 \text{ m}^{-1}$ for pristine PMMA. Separations of multiple 780 nm dye-labeled LDR products and discriminating primers (20-65 bp) with mutant-to-normal ratios of 1:100 were achieved (see Figure 3B). Using two-color excitation (532, 780 nm), dye-labeled EndoV cleaved top and bottom strand p53 mutations of 168 and 195 bp, respectively, were separated and analyzed. A four-fold decrease in background signals were produced upon LDR treatment (see Figure 3A).

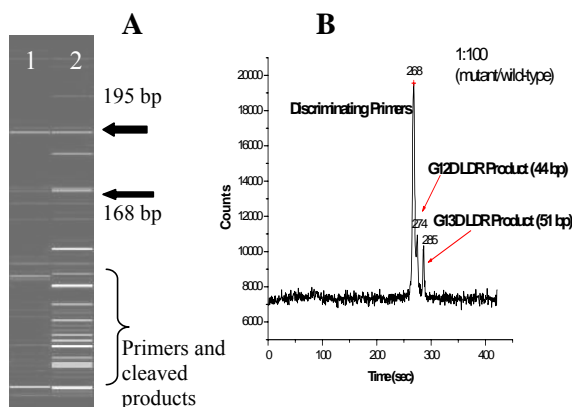


Figure 3. (A) Fluorescence image of EndoV nicked PCR products from a p53 gene region containing sporadic mutations. The EndoV treated PCR products (lane 2) were subsequently treated with ligase enzyme to repair nicked DNA at fully matched sites (lane 1). (B) Low abundance (1:100; mutant-to-normal) LDR products separated using 4% LPA in the PMMA microchip.

5. Conclusions

Using high aspect ratio, surface-modified PMMA microchips allows for the rapid separations for two novel mutation detection and mutation scanning strategies. The ability to both probe and detect mutations in a multiplexed fashion with rapid turn-around times makes this combination a viable alternative for cancer detection.

References

- [1] Pincas, H.; Pingle, M.R.; Huang, J; Lao, K; Paty, P.B.; Friedman, A.M.; and F. Barany, High Sensitivity Endo V Mutation Scanning Through Real-time Ligase Proof-reading, *Nucleic Acids Research*, 32(19), e148 (2004)
- [2] Khanna, M.; Park, P.; Zirvi, M.; Cao, W.G.; Picon, A.; Day, J.; Paty, P.; and F. Barany, Multiplex PCR/LDR for Detection of K-ras Mutations in Primary Colon Tumors, *Oncogene*, 18, 27-38 (1999)

MULTICHANNEL REVERSE TRANSCRIPTION-PCR MICRODEVICE FOR RAPID MULTIPLEX GENE EXPRESSION ANALYSIS

Nicholas M. Toriello¹, Chung N. Liu² & Richard A. Mathies^{1,3}

¹UCSF/UC Berkeley Joint Graduate Group in Bioengineering; ²Department of Chemical Engineering; ³Department of Chemistry; University of California, Berkeley, CA 94720, USA; toriello@berkeley.edu

Abstract

A microdevice is developed for rapid RNA analysis that integrates 1-step reverse transcription and 30 cycles of PCR (RT-PCR) amplification with capillary electrophoresis (CE) separation and fluorescence detection of the amplicons. The 4-layer glass-PDMS-glass-glass hybrid microdevice integrates microvalves, on-chip heaters and temperature sensors, nanoliter reaction chambers (380 nL) and 5-cm long CE separation channels. The direct integration of these processes results in attomolar detection sensitivity (<11 template RNA molecules or ~0.1 cellular equivalents) and rapid 45 min analysis, while minimizing sample waste and eliminating contamination.

Keywords: RT-PCR, RNA profiling, capillary electrophoresis, integrated RT-PCR microdevice, biomarker analysis

1. Introduction

The rapid profiling of gene expression levels and measurement of low abundance RNA transcripts is essential in fundamental studies of pathogenesis, single-cell assays, developmental biology and stem cell research. The techniques currently employed for gene expression profiling suffer from poor sensitivity and precision, expensive raw material usage, along with laborious and time-intensive protocols. To address these limitations, we have designed a highly-sensitive, fast, reliable and automated multichannel microdevice capable of detecting low RNA transcript levels (~11 copies) from multiple genes of interest. The microdevice performs RNA amplification by RT-PCR with only 30 cycles of PCR amplification followed by capillary electrophoretic analysis of the amplified product using laser induced fluorescence in <45 min [1].

2. Microdevice

The 4-layer glass-PDMS RT-PCR microdevice integrates all the elements necessary to amplify RNA and analyze the products from four different samples simultaneously [2]. This includes a glass manifold wafer and PDMS elastomer membrane for fluidic control, integrated heaters, temperature sensors, reaction chambers (380 nL) for thermal cycling and 5-cm long separation channels for amplicon sizing (Figure 1).

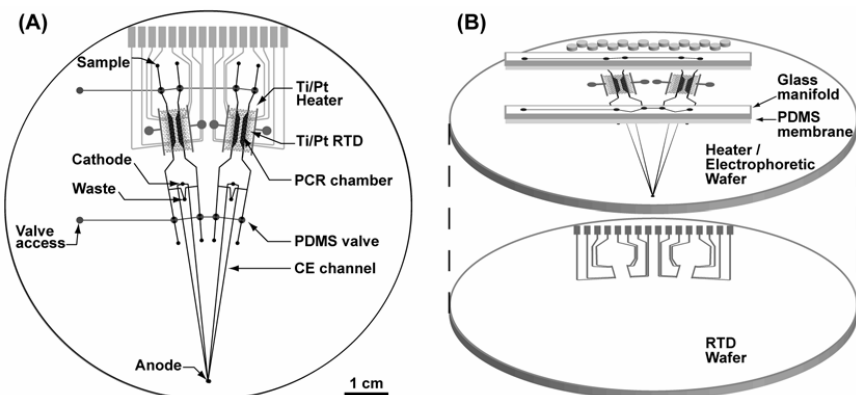


Figure 1. (A) Schematic of integrated multichannel RT-PCR microdevice. (B) The integrated microdevice is a 4-layer glass-PDMS hybrid structure. The top most wafer is a glass manifold for fluidic actuation. The second layer is a flexible PDMS membrane forming the microvalves. The glass heater/electrophoretic wafer contains resistive heaters on the top side along with glass reaction chambers and CE channels etched on the back side. The bottom glass RTD wafer contains Ti/Pt temperature sensing units.

3. Results and Discussion

A 1-step multiplex RT-PCR amplification from 10 pg of DNase treated *E. coli* RNA with primers specific to the malate dehydrogenase (*mdh*) and gyrase B (*gyrB*) genes, produce 204 bp and 235 bp amplicons, whose intensities correctly reflect the enhanced (4x) abundance of *mdh* transcripts relative to *gyrB* (Figure 2B). The microdevice also demonstrates the expected correlation between initial template concentration and amplicon peak height with a LOD of 10 fg of total *E. coli* RNA (~0.1 cellular equivalents and ~11 copies/reactor). The requisite control without reverse transcriptase is performed to ensure proper RNA amplification (Figure 2F).

The RT-PCR microdevice enables rapid tumor biomarker detection based on splice variant analysis from human tissue RNA. The *RBBP8* gene is used as a tumor biomarker in this study because it undergoes a shift in its splicing pattern (Figure 3 Top). RT-PCR amplification and subsequent electrophoretic separation from normal breast tissue RNA generates the expected amplicon. The tumor breast tissue RNA samples generate both splice variant amplicons because it is excised from tissue that contains both normal and tumorigenic cells (Figure 3).

4. Conclusions

In summary, a 4-lane fully integrated RT-PCR microdevice was developed to amplify femtograms low copy number) of RNA in submicroliter (380 nL) volumes followed by the direct electrophoretic separation and detection of the RT-PCR

amplicons. Since the average *E. coli* cell contains ~100 fg of RNA, the successful amplification and detection from 10 fg of RNA demonstrates that the RT-PCR microdevice is capable of analyzing single cells and low copy number transcripts (~11 copies/reactor) [3]. The ability to perform high sensitivity RT-PCR followed by genetic analysis also enables the use of this device for genetic analysis of viral pathogens.

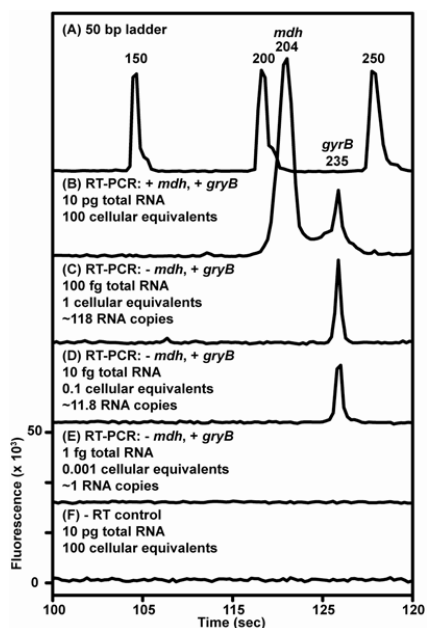


Figure 2. (A) 50 bp sinzing ladder. (B) Multiplex RT-PCR amplification and CE analysis from 10 pg of DNase treated *E. coli* RNA (C) RT-PCR amplification from of a 235 bp section of the *gyrB* gene on 100 fg of RNA. Companion analysis is performed on 10 fg (D) and 1 fg (E) of RNA in the reactor. (F) Control experiment on 10 pg of RNA in the absence of RT.

References

- Toriello, N.M.; Liu, C.N.; Mathies, R.A. *Anal. Chem.*, submitted.
- Liu, C.N.; Toriello, N.M.; Mathies, R.A. *Anal. Chem.* **2006**, *78*, 5474-5479.
- Toriello, N.M.; Douglas, E.S.; Mathies, R.A. *Anal. Chem.* **2005**, *77*, 6935-6941.

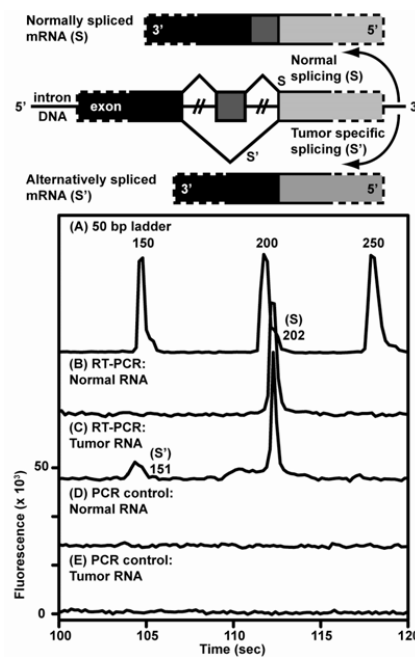


Figure 3. (Top) Schematic of normal *RBBP8* splicing (S) and tumor specific splicing (S'). (B) RT-PCR analysis of the *RBBP8* gene from 9.5 ng of normal breast tissue RNA generating a single amplicon (202 bp). (C) Tumor breast tissue RNA produces the expected 202 bp product and the 149 bp tumor specific splice variant.

Integrated Microfluidic System for the Processing of Membrane Proteins Isolated From Stem Cells

Małgorzata A. Witek*, Guofang Chen*, Hamed Shadpour*, Indu Khaterpal*,

Darwin Prockop***, Carl A. Gregory***, Robin L. McCarley*, and Steven A. Soper*

* Department of Chemistry and Center for BioModular Multi-Scale Systems (CBM²)
Louisiana State University, Baton Rouge, LA 70803, U.S.

** Pennington Biomedical Research Center, 6400 Perkins Rd., Baton Rouge, LA 70808, U.S.

*** Center for Gene Therapy, Tulane University, New Orleans, LA 70112, U.S.

Abstract

The work presented here will describe an integrated microfluidic system for membrane protein isolation and analysis. The integrated system consists of two modules: (i) a solid-phase protein capture module, and (ii) a two dimensional electrophoretic separations platform.

Keywords: protein, Lab-on-a-Chip/Microfluidics, electrophoresis

1. Introduction

Adult stem cells are undifferentiated cells that reproduce daily to provide certain specialized cells and are created from hemopoietic stem cells.^[1, 2] Pluripotent stem cells offer the possibility of a renewable source of replacement cells and tissues to treat a myriad of diseases. To develop more treatments, however, two basic questions concerning stem cells must be answered. First, how do stem cells remain unspecialized and regenerate for many years, and second, what factors inside and outside of the cells trigger stem cell differentiation. [1, 2] *Identifying the surface membrane proteins in stem cells at various stages of differentiation and in different developing tissue types is essential for controlling stem cell differentiation for various biomedical applications.*

2. Experimental

Fabrication of free-standing polymeric nanopillars. Methyl methacrylate monomer containing initiator and 1% wt. PMMA particles was introduced into the anodic alumina oxide (AAO) matrix. Polymerization was initiated by the exposure to UV light (254 nm) and lasted 30 min. After polymerization, PMMA cover plate (0.5 mm) was bonded using “Plastic Welder” to the AAO matrix containing formed PMMA. The replication template was removed from the assembly with saturated HgCl₂ and phosphoric acid. After dissolving the template the PMMA nanopillars were thoroughly washed with distilled water and allowed to freeze dry at -80°C. [3]

Fabrication of Microdevices. Microchips for performing the analyses were prepared by hot-embossing into poly(methyl methacrylate), PMMA, from a brass master fabricated via high precision micro-milling. [4]

Biotinylation of Cells. Cells were suspended in 0.15 M sodium phosphate buffer (PBS), pH 7.0-8.5 with Biotin/DMF solution and were allowed to incubate for 40 min. The unreacted biotin was removed by centrifugation of the product at 200 x g for 3 minutes. This was repeated twice. Cells were stored at 4°C in 0.05% sodium azide.

Immobilization of Streptavidin on UV-modified surfaces. UV exposed polymer pieces are incubated with agitation for 10 h in a 40 mM EDC (1-ethyl-1-(3-dimethylaminopropyl)carbodiimide) with 100 mM phosphate buffer (pH=7.0) containing Avidin or Streptavidin. Reaction was incubated at room temperature for 2~4 hr followed by the rinse with buffer.

Protein Separation. Sodium dodecyl sulfate microcapillary gel electrophoresis (SDS μ -CGE) and micellar electrokinetic chromatography (MEKC) were used as the separation modes for the first and second dimension of the electrophoresis, respectively. [5] The microchip incorporated a 30-mm SDS μ -CGE and a 10-mm MEKC dimension length. All channels were 20 μ m wide and 50 μ m deep. The SDS μ -CGE was performed using SDS 14-200 sieving matrix with 12 mM TRIS/HCl, 0.1% w/v (3.5 mM) SDS, pH 8.5 containing 0.05% w/v MHEC, and the MEKC was conducted using 12 mM TRIS / HCl, 0.4% w/v SDS, pH 8.5 containing 0.05% w/v MHEC as the dynamic EOF suppressor. Electrokinetic injection and separation were used with field strengths up to 0.4 kV/cm. Alexa Fluor 633 conjugated proteins were detected using laser-induced fluorescence with excitation/emission at 633/652 nm. [5]

3. Results and Discussion

The solid phase protein capture module consisted of free-standing PMMA nanopillar arrays with high aspect ratios (6-10) (Figure 1). These PMMA nanopillars, were 175-250 nm in diameter and 1 μ m in height.[3] Nanostructures were UV-irradiated to form carboxylate moieties on the surface, which were later utilized in process of protein immobilization on the PMMA surface. An NHS/EDC coupling reactions was adapted for streptavidin immobilization onto nanopillars.

Biotinylated molecules (e.g., proteins, DNA, RNA, etc.) can be easily detected with streptavidin derivatives or efficiently captured on streptavidin-coated solid supports (e.g., resins, magnetic beads, microtiter plates, chips). Integration of the nanostructures into microfluidic devices is performed for high-efficiency capture of target

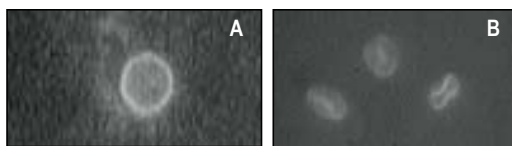


Figure 1. SEM of PMMA nanopillar array

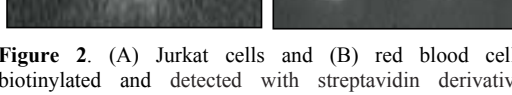


Figure 2. (A) Jurkat cells and (B) red blood cells biotinylated and detected with streptavidin derivative (AlexaFluor 488).

membrane biotinylated proteins. Figure 2 shows micrographs of (A) Jurkat cells and (B) red blood cells biotinylated and detected with streptavidin derivative (AlexaFluor 488). The elution of the biotinylated molecules from (strept)avidin-coated PMMA nanopillars can be achieved by the use of photocleavable biotin derivatives that can be

released using 300-360 nm light, or by incubation with SDS, urea/ thiourea solution and exposure to 94°C.

The second microfluidic module consists of a 2D protein separation unit. An SDS μ -CGE and MEKC were used as the separation modes for the first and second dimension of the electrophoresis, respectively. Effluents from the first dimension are repetitively transferred into the second dimension every 0.5 s of run time in the first dimension with the electrophoresis run time in the MEKC dimension being 10 s. Average plate numbers for a mixture of 10 proteins was 4.8×10^4 and 1.2×10^4 were obtained in the first and second separation dimensions, respectively. The plate heights was 0.62 and 0.87 μ m. The 2D separation of 10 investigated proteins was performed in ~12 min and provided a peak capacity of ~1,000 (Figure 3).

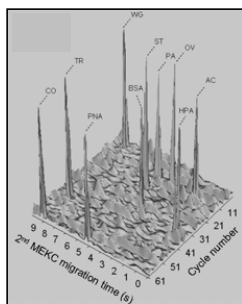


Figure 3. A three-dimensional image of the electropherogram with the cycle number plotted versus the MEKC migration time. A 2D separation was performed with a 30 nM protein mixture: wheat germ agglutinin (WG, 38 kDa), actin (AC, 43 kDa), ovalbumin (OV, 45 kDa), protein A (PA, 45 kDa), streptavidin (ST, 53 kDa), bovine serum albumin (BSA, 66 kDa), lectin HPA (HPA, 70 kDa), transferrin (TR, 80 kDa) concanavalin A (CO, 104 kDa), and lectin PNA (PNA, 110 kDa).

4. Conclusions

Recognition of the molecular pathways that promote stem cell differentiation would allow the control of cell and tissue growth for specific purposes. Membrane proteins can be analyzed by the use of presented modules. The benefit of a coupled 2D separation of protein is demonstrated by its high peak capacity as compared to its constituent 1D peak capacities. Fabrication of both separation channels in PMMA eliminates dead volumes between separation dimensions, improving the separation efficiency.

5. References

- [1] Gregory, C. A.; Gunn, W. G.; Reyes, E.; Smolarz, A. J.; Munoz, J.; Spees, J. L.; Prockop, D. J. *Ann. N. Y. Acad. Sci.* **2005**, *1049*, 97-106.
- [2] Munoz, J. R.; Stoutenger, B. R.; Robinson, A. P.; Spees, J. L.; Prockop, D. J. *Proc. Natl. Acad. Sci. U. S. A.* **2005**, *102*, 18171-18176.
- [3] Chen, G., Bolivar, J. B., McCarley, R. L., Soper, S. A. , Boston 2005; 1261-1263.
- [4] Hupert, M. L.; Guy, W. J.; Llopis, S. D.; Situma, C.; Rani, S.; Nikitopoulos, D. E.; Soper, S. A. *Proc. SPIE-Int. Soc. Opt. Eng.* **2006**, *6112*, 61120B/61121-61120B/61112.
- [5] Shadpour, H.; Soper, S. A. *Anal. Chem.* **2006**, *78*, 3519-3527.

RAPID PROTEIN CRYSTALLIZATION BY MICRO OSMOTIC SCREENING SYSTEM

Po-Hsiung Chan and Yu-Chuan Su

Department of Engineering and System Science
National Tsing Hua University, Hsinchu, Taiwan

Abstract

We have successfully demonstrated a micro osmotic screening system that grows protein crystals in hours with microgram samples. Employing the control capabilities realized by osmosis, each protein sample can be screened for crystallization conditions over extended ranges. In the prototype demonstration, 6 x 8 arrays with an overall size of 20 x 24 x 2.5 mm³ are fabricated and tested in the crystallization experiments. Crystallization conditions for lysozyme, catalase, thaumatin, and xylanase are identified within 2 to 3 hours while consuming less than 20 µl of protein solution each. As such, this osmotic system pioneers a new class of rapid screening schemes for high-throughput protein crystallization.

Keywords: Protein crystallization, osmosis, microfluidics

1. Introduction

In the post genomic era, one of the most challenging works is to investigate the structure-function relationship of encoded proteins on a genome-wide scale. X-ray crystallography has proven to be a versatile method in structural genomics. Despite high demand, the determination of protein structure remains a laborious and often unreliable task, mainly because of the difficulty in growing diffraction-quality crystals. Previously, researchers have proposed various macro-scale [1] and microfluidic [2-4] schemes for high-throughput protein crystallization. Although these approaches are capable of setting up hundreds of nanoliter-sized trials in minutes, the overall sample consumptions remain high if each trial can only screen for a limited range of crystallization conditions.

2. Principle

In the most popular hanging drop scheme, separate protein and reference solutions are enclosed in the same chamber. Over the crystallization process, water (in vapor form) is driven out of the protein solution because of the concentration difference between two solutions. The whole process is pre-determined and irreversible once it proceeds. For our new scheme shown in Fig. 1, protein and reference solutions are separated by a semi-permeable membrane, which allows only water to pass. Since the direction and flow rate of water across the membrane (and therefore concentrations of the protein solution) can be actively manipulated by tuning the osmotic pressure of reference solution, the new scheme is capable of controlling the crystallization process in a real-time manner. The phase-space trajectories of two osmotic crystallization processes with different initial states are shown in Fig. 2. During the processes, the trajectories can move forward and backward in various speeds when searching the optimal nucleation

conditions. In this way, each sample can be screened over extended ranges to achieve a higher hit rate. Once nucleated, the trajectories turn right and switch into meta-stable zone for high-quality crystal growth.

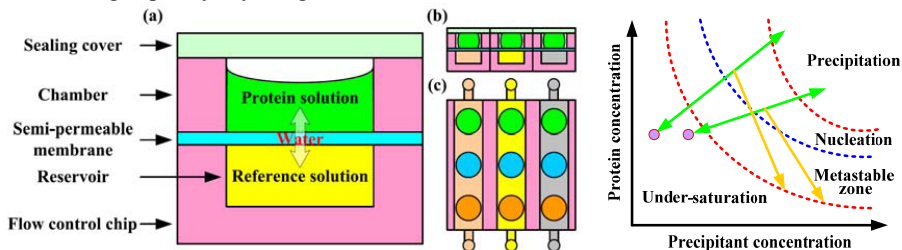


Figure 1: Structure of the osmotic screening system: (a) and (b) cross-sectional views of unit and array and (c) top view

3. Experimental

The prototype systems, 6×8 arrays with 6 independent reservoirs underneath, are made of polymeric plates and assembled by hot-melt and heat-curable adhesives as shown in Fig. 3. The overall size of the arrays is 20 mm x 24 mm x 2.5 mm as shown in Fig. 4. 48 crystallization trails, with 2 initial concentrations of a specific protein, 4 pH values of solutions, and 6 precipitating agents including NaCl, $(\text{NH}_4)_2\text{SO}_4$, CaCl_2 , Na/K tartrate, Na citrate, and PEG 3350, are performed on each array. While screening, the concentrations of protein solutions are controlled by tuning the osmotic pressure of underneath reference solutions. These trails are performed at 4 °C and inspected under an optical microscope for crystal nucleation and growth. In this work, totally 4 proteins including lysozyme, catalase, thaumatin, and xylanase are used for testing.

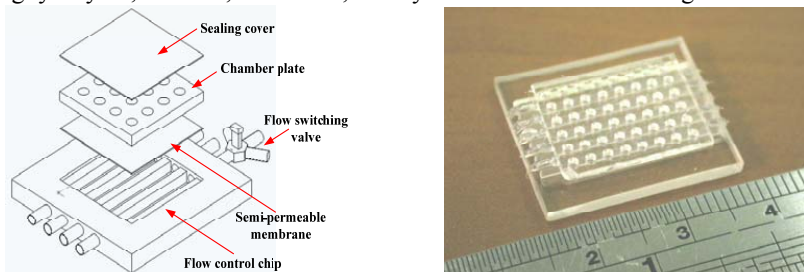


Figure 3: Assembly of the osmotic system

Figure 4: Photography of the prototype system

4. Result

Fig. 5 shows images of the crystals obtained in the 15 (out of 48) successful trials while lysozyme is screened. The conditions of these successful trials concur with the data revealed by other existing screening techniques. In our experiment, crystals are formed in less than 3 hours and some of them have dimensions larger than 100 μm , which are large enough for x-ray diffraction studies. Large crystals are then extracted, mounted, flash-froze in cryoloops, and subsequently exposed to a laboratory x-ray

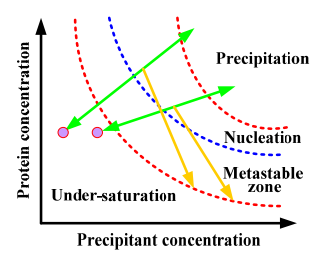


Figure 2: Trajectories of 2 osmotic crystallization processes through a simplified 2-D phase space

source. Fig. 6 shows a high-resolution diffraction pattern for a single lysozyme crystal grown in our crystallization experiments. Furthermore, screening trails with catalase, thaumatin, and xylanase also result in successful crystal growth as shown in Fig. 7.

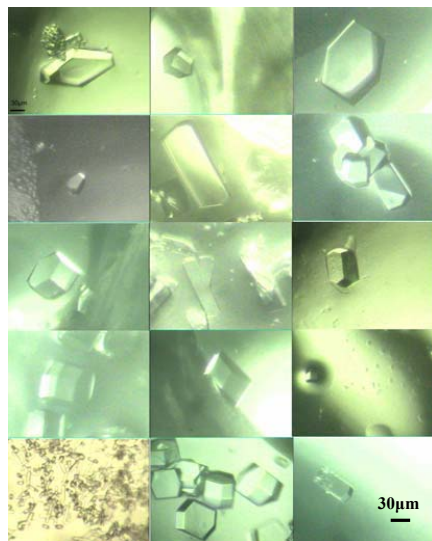


Figure 5: Images of lysozyme crystals after 3 hours

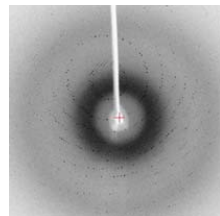


Fig. 6: X-ray diffraction pattern from a grown lysozyme crystal

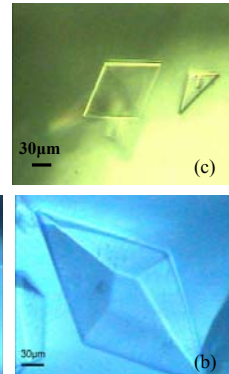


Figure 7: Images of catalase (a), thaumatin (b), and xylanase (c) crystals

5. Conclusion

A micro osmotic screening system that grows protein crystals in hours with microgram samples has been successfully demonstrated. In the prototype demonstration, crystals of lysozyme, catalase, thaumatin, and xylanase are grown in 3 hours with less than 20 μl of protein solution each. X-ray diffraction experiments are also performed and the results indicate that diffraction-quality crystals may be formed in the proposed osmotic micro-system.

Acknowledgement

This work is supported in part by the National Science Council of Taiwan (Grant number: NSC 94-2218-E-007-050.)

References

1. A. McPherson, Crystallization of Biological Macromolecules. Cold Spring Harbor Laboratory Press, 1999
2. C.L. Hansen, E. Skordalakes, J.M. Berger, and S.R. Quake, "A Robust and Scalable Microfluidic Metering Method that Allows Protein Crystal Growth by Free Interface Diffusion," PNAS, vol. 99, pp. 16531-36, 2002
3. B. Zheng, L.S. Roach, and R.F. Ismagilov, "Screening of Protein Crystallization Conditions on a Microfluidic Chip Using Nanoliter-Size Droplets," JACS, vol. 125, pp. 11170-71, 2003
4. M. van der Woerd, D. Ferree, and M. Pusey, "The Promise of Macromolecular Crystallization in Microfluidic Chips," JSB, vol. 142, pp. 180-187, 2003

A SINGLE HUMAN CHROMOSOME MANIPULATION AND GENE DETECTION VIA TRACE VOLUME PCR AMPLIFICATION USING MICROTWEEZER PROBE AND MICROCHAMBER ARRAY

Masato Saito ^(1,2), Kazuhisa Nakagawa ⁽³⁾, Tetsuya Takekawa ⁽⁴⁾, Keiichiro Yamanaka ⁽²⁾, Yuzuru Takamura ⁽²⁾, Gen Hashiguchi ⁽⁴⁾ and Eiichi Tamiya ⁽²⁾

⁽¹⁾ Toyama New Industry Organization, 529 Takada, Toyama 930-0866 Japan, ⁽²⁾ School of Materials Science, Japan Advanced Institute of Science and

Technology, 1-1 Asahidai, Nomi, Ishikawa 923-1292 Japan, ⁽³⁾ Institute of Industrial Science, University of Tokyo, 4-6-1 Komaba Meguro-ku, Tokyo 153-8505 Japan ⁽⁴⁾ Faculty of Engineering, Kagawa University, 2217-20

Hayashi-cho, Takamatsu, Kagawa 761-0396 Japan

Abstract

We have studied a new approach to analyze the genetic information and expression by the physical manipulation of the human chromosomes or biomaterials. We developed two procedures; the first one was the development of a silicon microchamber for polymerase chain reaction (PCR) in trace volume and the gene detection from a single chromosome directly. The second one was the development of a novel microtweezer probe, and the direct manipulation of human chromosome. In this report, we have achieved to collect a specific single human chromosome using microtweezer, and amplified Rhesus D (RhD) gene, which is found as only one copy on the chromosome-1 of the human genome by performing trace volume PCR on the microchamber chip.

Keywords: microtweezer probe, trace volume PCR, chromosome, microchamber array, manipulation

1. Introduction

The chromosome is a complex that consists of DNA and proteins, and DNA base sequences reach about three billion base-pairs for the human genome. Genome sequencing is a time consuming and high-cost procedure. However, all the information from the whole genome is not always needed. Therefore, a new analytical technique that can include these spatial elements is required for chromosome or genomic research. On the other hand, we have developed a microchamber array for PCR amplification [1] and a tweezer probe [2], individually. Those devices are effective to analyze biomaterials. In this research, we combined these devices and targeted human chromosome as a model case. This chromosome chip system may also be applicable to other organisms, which the genome sequences have not been identified yet.

2. Experiment

We fabricated the silicon microchamber array, which had 50 nL volume of each chamber (Fig. 1). Fabrication process was described elsewhere [1]. Moreover, we developed the novel tweezer-type probe devices (Fig. 2) for the manipulation of the biomaterials i.e. a single human chromosome. The tweezer probe tips were opened and closed with applying the voltage. Fabrication procedure was described elsewhere [2]. Two kinds of human metaphase chromosome samples were prepared. One was kindly provided by Professor K. Fukui from Osaka University, which contained no cell

membrane and cytoplasm etc. [3] and the other was prepared from the human lymphocyte cells according to the standard protocol [4].

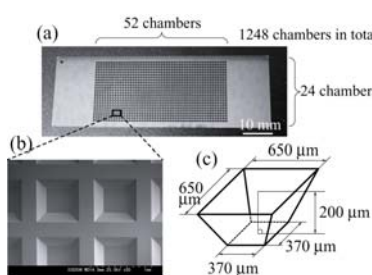


Fig. 1. The fabricated microchamber array. Each chamber volume was approximately 50 nL.

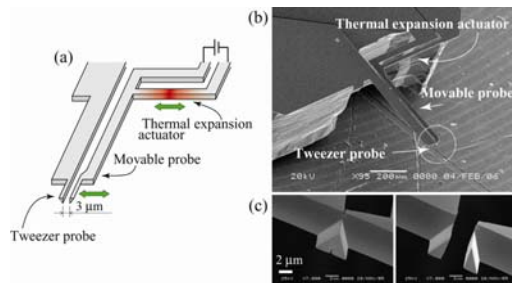


Fig. 2. Development of the tweezer probe. To capture the samples, the movable probe was operated with (c, left) and without (c, right) applied voltage.

3. Results and discussion

The whole human metaphase chromosomes, which contained no cell membrane and cytoplasm etc. [3], were distributed into 48 microchambers using nano-liter dispenser. The average number of the dispensed chromosomes per chamber was 80.7 ± 9.4 chromosomes. PCR amplification was performed on each microchamber after dispensing RhD gene specific primers and fluorescence (TaqManTM) probe. The fluorescence was detected using the DNA microarray scanner (Fig. 3b). The positive chambers with chromosomes released a high fluorescence signal compared with the negative ones without chromosomes. Thus, the specific DNA amplification from chromosomes was possible on the microchamber chip.

The chromosome-1, of which the whole chromosome was fixed on the slide glass, was peeled away from the substrate surface using the glass capillary, and was collected using tweezer probe with closing by the applied voltage (Fig. 4a). Thus, the position of the glass capillary and the tweezer probe tips were controlled using the micromanipulator. Then, the collected chromosome-1 was released into the microchamber (Fig. 4b) and used as the template DNA. Only one chromosome-1 was put into seven microchambers. After PCR amplification, positive signals could be obtained from five microchambers (Fig. 5b).

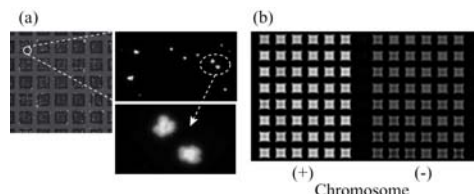


Fig. 3. Microchamber array PCR amplification from the whole human chromosome.

4. Conclusion

Here we report the successful amplification of a specific gene from a single-chromosome in the microchamber chip. Additionally, we developed a knife-type

AFM probe to dissect the chromosome and biomaterials, and performed the precise manipulation of the chromosome under AFM operation [5]. In the future, it is expected that the analysis of a specific portion of not only a chromosome but also other biological samples i.e. cells, DNA, etc. could become possible by the established method.

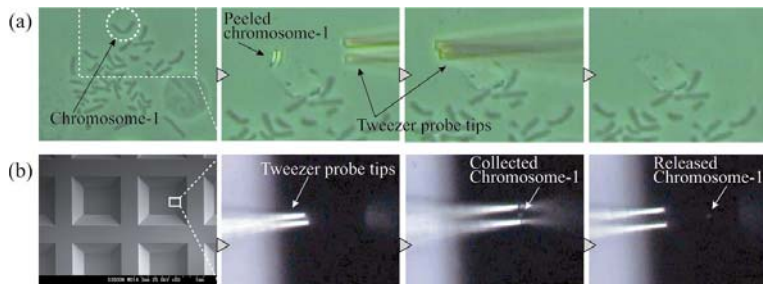


Fig. 4. The collection and the rearrangement of the chromosome-1 using the tweezer probe. (a) The chromosome-1 was peeled away from the substrate surface using the glass capillary, and was collected with the tweezer closed by the applied voltage. Thus, the position of the glass capillary and the tweezer probe tips were controlled using the micromanipulator. (b) The tweezer probe tip with the collected chromosome-1 was put into the microchamber, and was opened. The probe tips were pressed onto the sidewall of the microchamber. Then, the collected chromosome-1 was released into the microchamber.

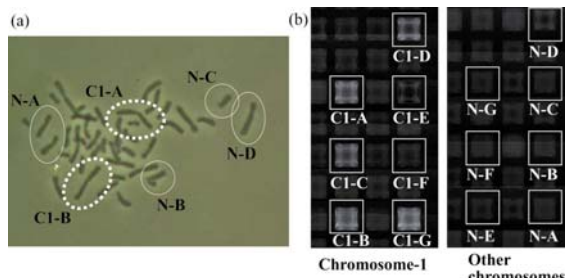


Fig. 5. On-chip specific DNA amplification from a single chromosome-1. Samples of the whole chromosome were prepared as shown in (a). Only one chromosome-1 sample as indicated with the C1-A or C1-B in the dashed circles, were picked, and put into one microchamber using tweezer

probe as shown in Figure 4. Other chromosomes from N-A to -G, which were not chromosome-1, were used as the negative controls. After the PCR amplification of the RhD gene from a single chromosome-1, five positive signals in seven microchambers could be obtained.

References

- [1] Y. Matsubara et al, Anal. Chem., 76, 6434-6439, (2004).
- [2] T. Takekawa et al, Transducers'05, Digest Tech. Papers, Korea, 2005, p. 621-624.
- [3] J. R. Gosden, Methods in Molecular Biology, 29, Humana Press, New Jersey, 1994, pp. 1-10.
- [4] S. Uchiyama et al, J. Biol. Chem., 280, 16994-7004, (2005).
- [5] M. Saito et al, Sens. Actuators A, 130-131, 616-624, (2006).

MICROFLUIDIC METHOD FOR THERMAL CYCLING BY MICROWAVE DIELECTRIC HEATING

Pierre-Alain Auroux^{1,2}, Jayna J. Shah^{1,3}, James Booth⁴, Mulpuri V. Rao³, Laurie E. Locascio⁵, Michael Gaitan¹.

1: NIST, Semiconductor Electronics Division, Gaithersburg, MD 20899, USA

2: KT Consulting, Inc., Antioch, CA 94509, USA

3: George Mason University, Department of Electrical and Computer Engineering, USA.

4: NIST, Electromagnetics Division, Boulder, CO 80305-3328, USA.

5: NIST, Analytical Chemistry Division, Gaithersburg, MD 20899, USA.
E-mail: pierre-alain.auroux@nist.gov

Abstract

We report on temperature time domain and spectral measurements for on-chip microwave thermocycling. In particular we observe enhanced specificity of the heating of a targeted sample compared to conventional heating block-based thermocyclers. Spatial control of the temperature in the device is implemented by delivering microwave energy to specific locations in the microfluidic chip. Our device characterization shows a linear response between the rise in temperature and the applied power as predicted by theory. On-chip thermocycling by microwave dielectric heating is characterized and compared to a commercial heating block-based thermocycler. This method is applicable to any reaction where fast and accurate heat transfer is required. We are currently developing PCR-based applications based on this technique.

Keywords: thermocycling, microwave, dielectric heating, PCR, DNA

1. Introduction

This paper assesses the impact of on-chip microwave heating for thermocycling and will demonstrate its advantages over conventional heating block approaches. Not only are precise temperature control and rapid temperature cycling vital capabilities for forensic PCR-based protocols, but sharp temperature transitions also greatly enhance the purity of PCR products [1]. However conventional thermocyclers, as they operate at the macro-scale, still present increased reaction times due to the thermal inertia of the heating/cooling blocks. With microwave heating the energy is locally and specifically delivered to the sample, therefore enhancing heating and cooling rates and reducing reaction times [2]. We present in this abstract a new approach for on-chip thermocycling aimed at DNA amplification based on this heating technique. To our knowledge no data have been reported regarding on-chip microwave thermocycling.

2. Experimental

Our experimental set-up comprises a micromachined microfluidic chip and an x-band waveguide (see Figure 1). Since the plastic chip has low microwave absorption, power/heat can be delivered directly to the fluid. In contrast, conventional methods require the conduction of heat through the device to the fluid.

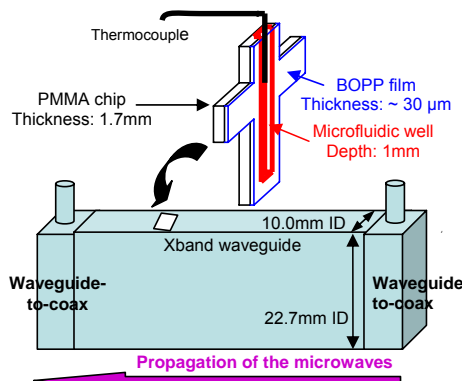


Figure 1. A rectangular x-band waveguide was used to heat the microfluidic device. A slot machined into one of the walls of the waveguide allowed the introduction of the microchip inside the microwave instrument. An amplifier was coupled to the waveguide, enabling the delivery of up to 50W of power over the 8-12GHz frequency bandwidth of the waveguide.

microchip (~15%), which demonstrates that the empty cell absorbs virtually no power. However a power dissipation of ~30% is registered with a cell filled with water: 15% of the incident energy is specifically transmitted to the sample. Figure 3 shows a linear relationship

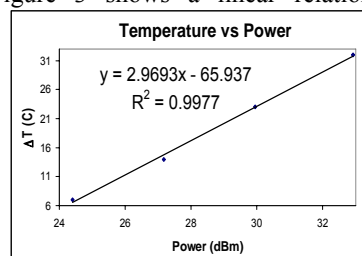


Figure 3. Characterization of the temperature response during on-chip microwave heating. Several input powers were tested whilst the temperature of the system was monitored. In accordance with theory a linear correlation was obtained.

waveguide (see Figure 1). Since the plastic chip has low microwave absorption, power/heat can be delivered directly to the fluid. In contrast, conventional methods require the conduction of heat through the device to the fluid.

Figure 2 shows a spectral measurement of the power dissipation for an empty waveguide, as well as a waveguide with a device with and without fluid over the frequency range 8 to 12 GHz. The power dissipated in an empty waveguide is similar to the energy dissipation in a waveguide with a

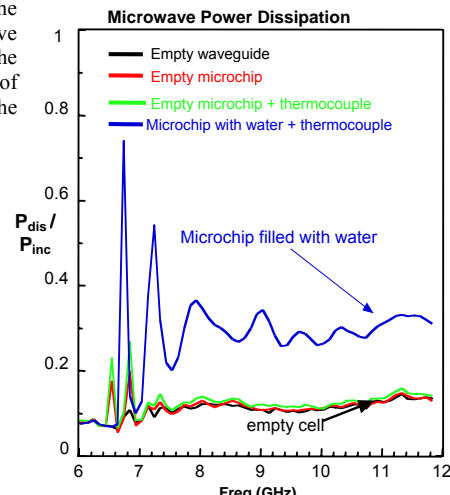


Figure 2. Broadband spectrum of microwave power dissipation through the setup. The plot is constructed from Scattering (S) – parameters measured at room temperature and calculated according to the equation $A + R + T = 1$, where $A = P_{\text{dis}}/P_{\text{inc}}$, $R = |S_{11}|$, and $T = |S_{21}|$. The microwave power dissipated into the empty microchip and the empty microchip containing thermocouple was approximately the same as the power dissipated into the empty waveguide. At 11 GHz, 15 % of the incident power was found to be dissipated into the water sample, 130 μL .

between the absorbed power and the temperature as would be expected. In Figure 4 we characterize on-chip thermocycling by microwave heating and observe a heating rate of 6°C/s.

3. Discussion and Conclusion

We demonstrated that microwave energy was specifically delivered on-chip to the sample with no interferences from the polymeric material. This result, in accordance with theory, underlines an advantage of microwave heating over Peltier-based systems, with which the microchip dissipates energy prior heating the sample. A linear dependence of the increase of temperature with the input power was observed. This calibration curve therefore further validates our microwave set-up, as theory and experimental data are in agreement. Finally we performed on-chip thermocycling with heating and cooling rates greater than those achieved on a conventional thermocycler. The data presented in this paper are in agreement with theory and therefore form a solid foundation for our future work.

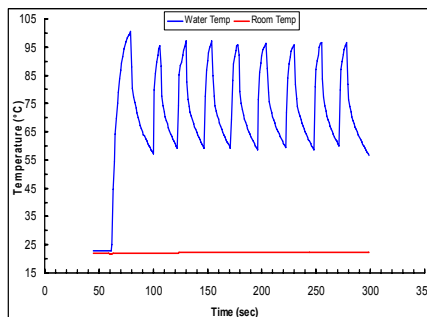
4. Acknowledgements

This work is sponsored by the National Institute of Justice Office of Science and Technology. Financial support for J.J.S. was provided by NIST under Grant #60NANB4D1132.

5. References.

- [1] C.T.Wittwer and D.J.Garling, Rapid cycle DNA amplification: time and temperature optimization, *BioTechniques* 10 (1991) 76-83.
- [2] C.Fermer, P.Nilsson, and M.Larhed, Microwave-assisted high-speed PCR, *Eur.J Pharm.Sci* 18 (2003) 129-132.

A- On-chip Thermocycling



B- Macro-scale Thermocycling

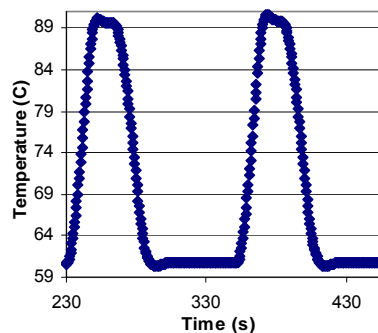


Figure 4. Comparison between on-chip and macroscale thermocycling. A: On-chip temperature cycling of 68µL of Di-H₂O with applied power of 20W. The average heating rate for this system was 5.96°C/s and a cooling rate of 2.23°C/s. These rates were higher than those obtained on a conventional thermocycler (respectively 1.69°C/s and 1.36°C/s) with a 25µL sample (B)

MICROFLUIDIC POLYMERIC INTEGRATED SELECTIVE ENRICHMENT TARGET FOR MALDI MS PEPTIDE PROFILING

Simon Ekström*, Lars Wallman*, Göran Helldin**, György Marko-Varga***
and Thomas Laurell*

* Lund Institute of Technology, Lund University, Sweden.

** MicroPlast AB, Skara , Sweden

*** Department of Analytical Chemistry, Lund University, Sweden

Abstract

A disposable polymeric Integrated Selective Enrichment Target (ISET) concept suitable for solid-phase microextraction of samples prior to MALDI MS peptide profiling of serum and plasma samples is presented.

Keywords: Mass Spectrometry, Proteomics, Peptide Profiling, Biomarkers

1. Introduction

Biological fluids such as blood, saliva, semen and urine present a convenient screening and diagnostic specimen for clinical analysis. Mass spectrometry (MS) analysis of low molecular weight biomarker patterns (<20 kDa) in serum or plasma can be used both to discover new biomarkers and as diagnostic classifiers [1, 2]. In order to fully utilize this methodology a highly qualitative sample preparation step is a prerequisite for a satisfactory MS-readout. We have previously presented an Integrated Selective Enrichment Target (ISET), realized in silicon, that can be used for solid-phase microextraction of samples prior to MALDI MS [3, 4]. While a silicon microfabricated ISET can provide the high throughput and reproducibility required for peptide profiling and clinical proteomics, the fact that a device used for such applications has to be disposable makes the use of silicon prohibitive. Further, patient serum or plasma samples are available in fairly large volumes (1-200 mL) and in order to increase the number of detected low abundant biomarkers in the sample a higher sample loading capacity is desirable.

2. Experimental

Disposable polymeric ISET devices were realized by injection moulding, in polyetheretherketone (PEEK), Figure 1. The ISET targets were manufactured to be 2 mm thick and comprise an array of perforated nanovials. Each array position (nanovial) has an inlet (1mm) and an outlet hole ($50 \pm 5 \mu\text{m}$), defining a volume of ca. 0.7 μL (compared to 40 nL for the silicon microfabricated ISET). This volume can be filled with a media, e.g. beads, selective for enrichment and purification of biomolecules prior to MALDI MS.

The conductivity necessary for the MALDI process was obtained either by deposition of a 50-100 nm thick gold layer or by using a conductive PEEK material.

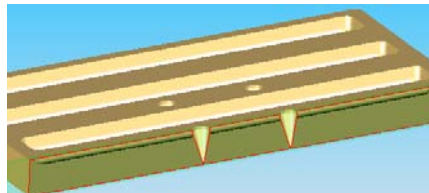


Figure 1. ISET device manufactured in PEEK, with a flat analysis zone.

3. Results and discussion

The core of the ISET sample preparation is that the fluid handling is performed straight through the device, Figure 2. The fundamental mass spectrometry performance of the surface of the polymeric ISET device was investigated and found to provide similar mass accuracy and resolution as compared to stainless steel MALDI targets.

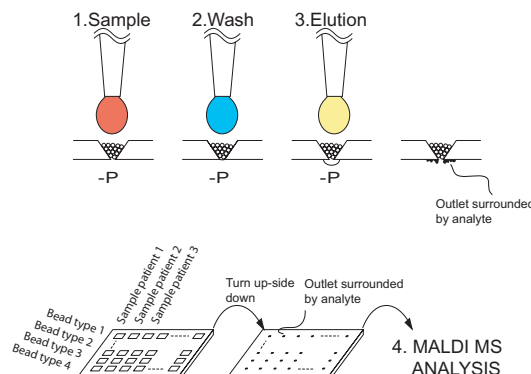


Figure 2. The principle of the ISET sample preparation can be described in four steps; (1) sample is drawn through the packed beads, or transferred to the nanovial while bound to the beads, and after washing (2) the sample is eluted (3) with matrix solution onto the ISET backside via the applied under pressure across the plate. The ISET is subsequently loaded into the MALDI MS instrument facing the back side up and each MALDI spot is analyzed (4).

The ISET sample preparation was applied to perform peptide profiling of human seminal plasma, which has implications in both prostate cancer and reproductive diseases. Figure 3 shows the mass spectrometric biomarker read-out after hydrophobic capture using the polymeric ISET (138 peaks observed in the mass range 900-6000 Da) and the commercial ZipTip technology (18 peaks in the mass range 900-6000 Da). By using additional types of beads different specificity and/or elution conditions for the ISET analysis the number of unique peptide ion peaks increases dramatically.

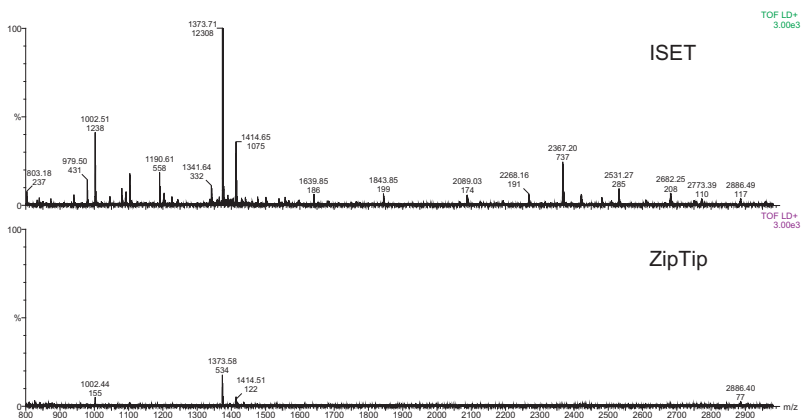


Figure 3. Mass spectrum (800-3000 Da) obtained after ISET respective ZipTip sample preparation of 200 μ L crude seminal plasma diluted 5 fold with 2 M UREA/0.1 % SDS. Note that y-axis normalized to 3000 counts.

4. Conclusions

The ISET sample preparation and presentation allows for easy multiplexing and high sensitivity analysis of biomarkers. The reduced fluid handling obtained with ISET sample preparation minimizes sample losses and can be performed by standard pipetting robotics. The disposable polymeric ISET concept increases the number of different sample preparation protocols that can be accommodated and significantly reduces the cost per analysis.

References

- (1) L.A. Liotta and E.F. Petricoin, *J. Clin. Invest.*, 2006, **116**, 26-30
 - (2) J. Villanueva, *et al.*, *J. Clin. Invest.*, 2006, **116**, 26-30,
 - (3) S. Ekström, *et al.*, *Electrophoresis* 2004, **25**, 3769-3777
 - (4) S. Ekström, *et al.*, *J. Proteome Research* 2006, **5**, 1071-1081

ENCAPSULATION OF MOUSE STEM CELLS IN ALGINATE BEAD BY MICROFLUIDIC CHIP

Su Kyoung Chae^{1,2}, In Hye Lee¹, Choong Kim¹, Chang Ha Lee², Ji Yoon Kang¹, and Tae Song Kim¹

¹ Microsystem Research Center, Korea Institute of Science Technology, Korea,

² Dept. of Chemical Engineering, Yonsei University, Korea

Abstract

A highly efficient droplet-generating microfluidic chip for encapsulating cells with hydrogel is presented. The chip has channels of several tens of micrometers for extruding alginate aqueous solution containing the P19 embryonic carcinoma stem cells and immiscible mineral oil. The cross junction of two heterogeneous flows was able to generate alginate droplets based on Rayleigh-Plateau instability. The electrostatic stabilized alginate solution was prepared by mixing 0.05 % poly-L-lysine and 1 % alginate solution. The diameter and the frequency of alginate droplets were controlled by the concentration of alginate solution and the velocity of running fluids. The alginate droplets in oil flowed into reservoir of calcium ion solution and reacted with ions instantaneously to form hydrogel bead. As a result, cells were quickly encapsulated in synthesized alginate hydrogel beads of 100~200 μm in diameter in microfluidic chip. These encapsulation beads were applicable to the encapsulation of single or several stem cells leading to the embryonic body formation for stem cell differentiation.

Keywords: encapsulation, micro droplet, microfluidic chip, hydrogel bead

1. Introduction

This study presents a highly efficient microfluidic chip for cell encapsulation using micro droplet generation with two immiscible solutions. Microfluidic droplet techniques have been developed recently in bioengineering and tissue engineering [1], and it was applied to generate polymer beads. Especially, technology to trap single or several living cells in hydrogel is rapidly developed, because the spheric gel has advantages of producing micro-sized compartment for living cell cultivation. Alginate gel is a popular matrix material in tissue engineering to block antibody and is well known to be suitable for the culture of mammalian cells like hepatocytes or islet cells. Recently, a method for cell entrapment and release on a microchip was reported [2] using geification of alginate hydrogel at the boundary of two laminar flows. However, the formation of continuous and uniform hydrogel was difficult and the trapped cells in hydrogel could not be transferred to other reservoir for the successive process like cell culture or analysis. Hence, we developed a method for encapsulating living cells in an alginate bead required for the various post-processes such as cell-based assay and culture of embryonic stem cell culture.

2. Experiment Methods

Microfluidic channels were fabricated by pouring polydimethoxysilane (PDMS, Sylgard 184, Dow Corning) on a silicon wafer containing SU-8 mold. The channel dimensions are shown in Figure 1. After encapsulation of P19 EC cells in alginate beads, they were treated with poly-L-lysine and alginate. P19 EC stem cells were cultured in Dulbecco's Modification of Eagle Medium (DMEM) supplemented with 10% FBS, where the cell density was $1.0 \times 10^7 \text{ cells}/\mu\text{l}$.

3. Results and discussion

We designed and fabricated a microfluidic chip for the continuous generation of alginate hydrogel beads encapsulating live cells. The droplet-generation chip consists of a cross junction for focusing alginate solution with oil and a downstream channel to calcium ion reservoir. The alginate aqueous solution contains P19 EC stem cells to be encapsulated during gelling. The chip was able to form alginate droplets in oil owing to Rayleigh-Plateau hydrodynamic instability of immiscible fluids (Figure 2). The interfacial tension at the alginate aqueous stream becomes unstable due to the perturbation of shear stress and the aqueous flow reduced its surface area by breaking up into spherical segments [3]. The flow ratio of aqueous solution and oil was optimized 10:1 and the diameter of alginate droplet was decreased as the flow rate of oil increased (Figure 3). The alginate emulsion flowed through channel and finally reacted with calcium ion solution in reservoir to form hydrogel beads of 100~200 μm in diameter instantaneously (Figure 4). However, alginate beads were polymerized too fast to form perfect spherical beads. Spherical beads with tails were synthesized like quotation mark. To make perfect spherical hydrogel, we added PLL (poly-L-lysine) to increase the viscosity of droplet to retain the shape of droplet and retard the reaction of calcium ion. Finally we obtained almost perfect spherical beads encapsulating cells as shown in Figure 5. The upper panels in Figure 5 showed the beads without cells and the lower ones present the capsules containing stem cells. The concentration of added PLL was adjusted since the composition of aqueous solution is different from that of culture media. The cells in the beads were successfully cultivated in hydrogel beads after liquefying inner alginate gel. The encapsulated P19 EC cells could aggregate without attaching to the wall of hydrogel and formed embryonic body for differentiation. Therefore, the alginate beads containing live cells can be applied to the study on the differentiation of stem cells in microfluidic platform and we also believe compartment-based cell based assay will be feasible with encapsulated cells. Since the capsules are manipulated far more easily than the single cells, they can be transferred to the next processes such as suspended or perfusion culture in bioreactor.

4. Conclusion

We developed a microfluidic chip providing continuous encapsulation of living cells in 3D spherical alginate hydrogel with uniform size and shape. It could be used for the differentiation of encapsulated stem cells through embryoid body (EB) formation. Furthermore suspension culture of single cell might be feasible to study stochastic intracellular processes and behavior of individual cells.

Acknowledgements

This research has been supported by the Intelligent Microsystem Center, which carries out one of the 21st century's Frontier R&D Projects sponsored by the Korea Ministry of Commerce, Industry and Energy and a KIST GRANT Program sponsored by KIST.

References

- [1] Klavs Jensen and Abraham Lee, Lab on a Chip, 4, 2004, pp31N-32N
- [2] Thomas Braschler et al, Lab Chip, 5, 2005, pp553-559
- [3] Zhihong Nieet al, J. Am. Chem. Soc. 127, 2005, pp8058-8063

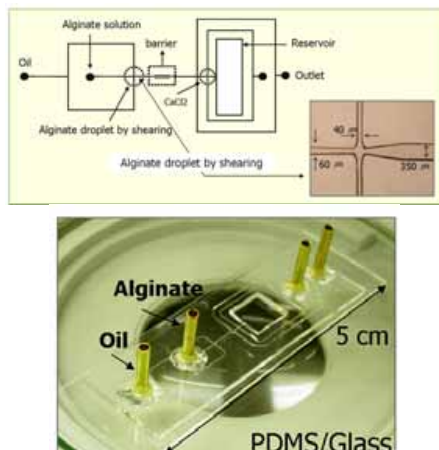


Fig. 1: Schematic of alginate microfluidic chip

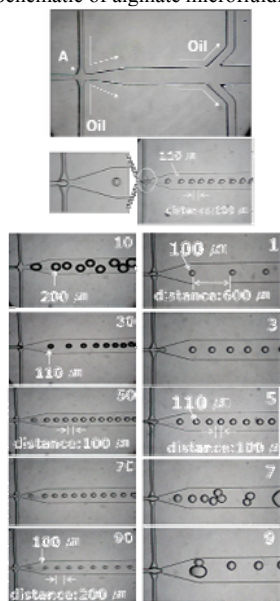


Fig. 2: Microscope image of the PDMS channel: Alginate solution-in-oil alternating microdroplet generation

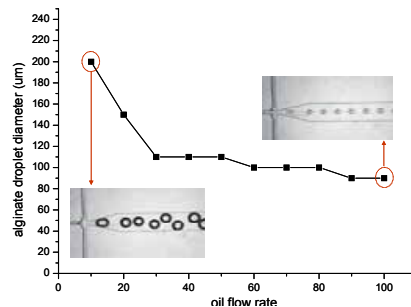


Fig. 3: droplet size on various oil flow rate (alginate = 5, constant): droplet diameter decreases relative oil flow rate increases.

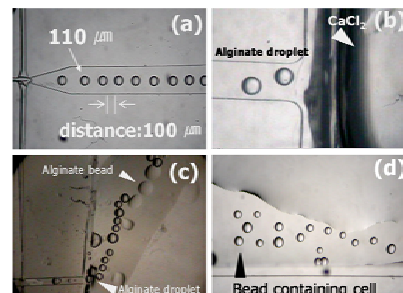


Fig. 4: Formation of calcium alginate bead by microfluidic chip

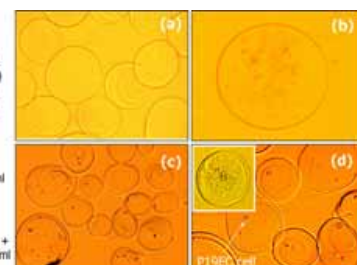


Fig. 5: P19EC cell trapping microcapsules beads

A CELL SWITCHING MICROSYSTEM FOR SINGLE CELL SORTING APPLICATION VIA ENHANCED DIELECTROPHORESIS DESIGN

Wen-Yu Chang and Cheng-Hsien Liu

Micro-System and Control Laboratory, Department of Power Mechanical Engineering,
National Tsing Hua University, Taiwan, ROC.

Abstract

This paper presents the design and experimental results of our cell switching microsystem. Via the enhanced dielectrophoresis design, the constructed spatial electric field can manipulate the target cells to the desired path and locations. In the upstream of microfluidic channel, the bow-tie-shape DEP electrode array focuses the randomly distributed inlet cells into a line. In the downstream of microfluidic channel, the multi-DEP switching electrodes sort out individual single cell to individual immobilization region, which has the quadruple DEP electrodes to trap individual cell for further cell analysis such as gene delivery.

Keywords: dielectrophoresis, biochip, cell manipulation

Introduction

Manipulation of biological cells via MEMS devices has become an important branch of biotechnology during the past decades. Owning to the dimension match with the molecules of micrometer in size, numerous techniques in hydrodynamics¹, optodynamics², electrodynamics³ and other fields have been developed for biological applications. Hydrodynamic manipulation usually needs multiple external pumps and high pressure driving flow for sorting applications. Optodynamics, such as optical tweezers, use high-energy laser power to hold/trap objects. The high energy might degrade the cell viability. In this paper we present a cell switching microsystem via the enhanced dielectrophoresis design for single cell manipulation with the characteristics of good cell viability, multifunction and microsystem integration.

Theory and microsystem design

Dielectrophoresis (DEP) manipulation is applied via the interaction between the applied electric fields and polarized particles. The positive/negative DEP force the polarized particles to move toward the regions with high/low electric density, respectively. In this research, we demonstrate the functions of cell alignment, multi-cell switch/sorting, and cell trapping in an array by either positive or negative DEP at different regions in our microsystem chip, as shown in figure 1. A commercial software CFDRC is used to simulate the electric fields, microfluidics and cell manipulation in our design. Figure 2(a) and 2(b) show the E-square distributions in the alignment region and the switching/sorting region, respectively, under the DEP operation. While the randomly distributed inlet cells flow in the main upstream microchannel, they will be

repelled to the area of the local electric field minimum via the negative DEP operation on the bow-tie-shape DEP electrode array. Hence, the cells can be lined up and focused while flowing through the alignment region. Then the individual cell is guided and switched to different microchannels by the invisible electrical barricade, which is constructed by the adjacent DEP sorting electrodes, based on the programmed DEP voltages. Next, via the positive DEP, the quadruple DEP electrodes in the downstream microchannel form the high electric density regions near the electrode edges to trap the individual cell at the immobilization region. The E-square distribution at the immobilization region is simulated as shown in figure 2(c).

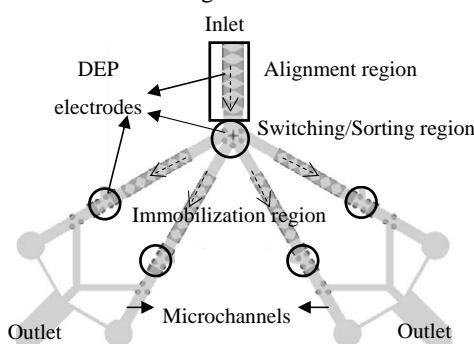


Figure 1. The schematic diagram of the cell-switching microsystem, including the functions of cell alignment in the main upstream microchannel, cell switching/sorting in the junction and cell immobilization in the downstream microchannel.

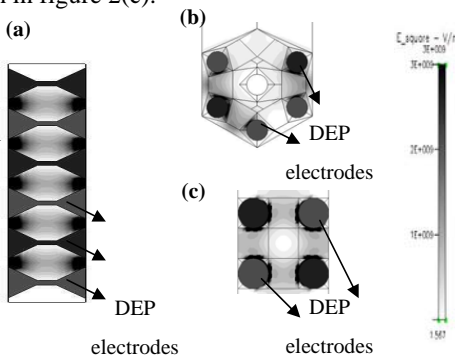


Figure 2. The CFDRC simulation for E-square distribution under the applied ac potential of 1 V_{pp} at 10 KHz. (a) The local electric field maxima appears to focus inlet cells to the center line of alignment region. (b) The invisible electrical barricades at the switching/sorting region are formed to guide the cell into the desired branch. (c) The local electric field maxima are formed near the edges of the quadruple electrodes at the immobilization region.

Experimental results

The cell switching microsystem chip is micromachined by using glass as the substrate, Al layer as the DEP electrodes. The microchannel is formed by using SU8. PDMS is used as the top cover. HEK 293 cells of $10\text{--}15 \mu\text{m}$ in diameter are used for demonstration in this paper. The DEP electric fields are applied by using 5 V_{pp} at 1 MHz for the positive DEP manipulation and 5 V_{pp} at 10KHz for the negative DEP manipulation, respectively. Figure 3 shows the experimental result of the alignment function. The cells in the upstream microchannel are randomly distributed before the negative DEP is turned on, as shown in figure 3(a). When the negative DEP is on, the cells entering from the inlet can be focused pass through the microchannel in a line without a chaotic manner, as shown in figure 3(b). Afterwards, the individual cell can be switched/sorted to the desired branch by the invisible electrical barricade. The cell

trace for the demonstration of switching/sorting function is shown in Figure 4. Finally, for the biological applications like cell electroporation, the individual cell is trapped to the immobilization electrode via the positive DEP operation as shown in Figure 5.

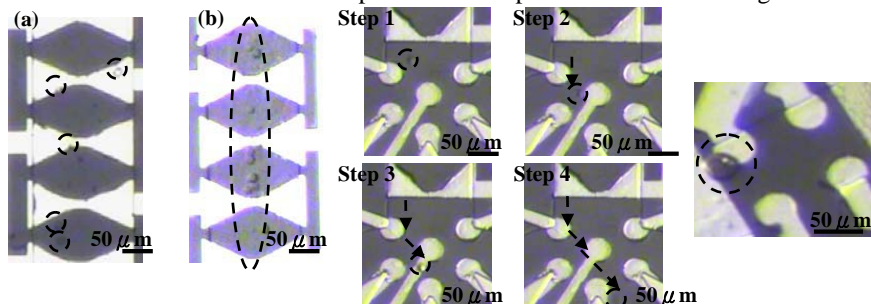


Figure 3. The demonstration for the function of cell alignment at the alignment region. (a) The randomly distributed cells flow through the microchannel when the DEP is off. (b) The cells are aligned to the centerline of the microchannel under the operation of negative DEP.

Conclusions

In this research, we demonstrate a cell switching microsystem with the integration of cell alignment function, sorting function and trapping function via the enhanced dielectrophoresis design. Experimental results show that the HEK 293 cells are successfully manipulated with good cell viability.

Acknowledgements

The authors thank to Nano Facility Center, National Nano Device Laboratory and Nano-Science and Technology Center for the fabrication facility support. The authors also thank Professor Hwan-You Chang and Miss Yun-Ru Pan for the supply of cells as well as valuable discussion. This work was supported by the National Science Council under grant NSC-94-2215-E-007-001.

Reference

1. C. C. Chen, S. Zappe, O. Sahin, X. J. Zhang, E. E. M. Furlong, M. Fish, M. Scott and O. Solgaard, *Transducer* 03, 2003, 659-662.
2. J. Enger, M. Goksor, K. Ramser, P. Hagberg and D. Hanstorp, *Lab Chip*, 2004, (4), 196-200.
3. P. H. Li and D.J. Harrison, *Anal. Chem.*, 1997, 69, (8), 1564-1568.

HIGH-DENSITY SPHEROID ARRAYS FOR 3-D LIVER CELL CULTURE AND SECRETION ANALYSIS

Mimi Y. Zhang, Dino Di Carlo, Liz Y. Wu, and Luke P. Lee

Berkeley Sensor & Actuator Center
UCSF/UCB Joint Program in Bioengineering
University of California, Berkeley, CA, USA

Abstract

To effectively coalesce otherwise monolayer liver cells (hepatocytes) seeded into microfluidic channels, we present a high-density cell-trapping array chip for rapid three-dimensional hepatocyte spheroid self-assembly. Moreover, by modifying trap geometries, spheroids of varying sizes can be formed in order to optimize the spatial microenvironment for improving cell viability and function. Preliminary sensitivity analysis of albumin secretion detection demonstrates the feasibility of using an optimized chemiluminescent immunoassay to determine the albumin concentrations in the range of 1 ng/mL to 500 ng/mL.

Keywords: spheroid, cell culture array, hepatocyte, cell-trapping

1. Introduction

Traditional monolayer cell culture methods cause hepatocytes to quickly lose their differentiated liver-specific functions. Microfabricated 3-D bioreactors address many of the issues associated with traditional liver cell culture such as providing more *in vivo*-like spatial cell-cell interactions with physiological flow conditions (Figure 1).

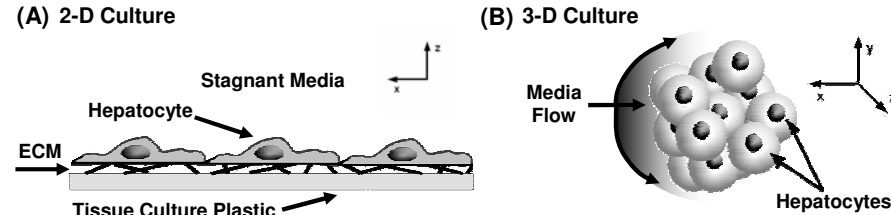


Figure 1. (A) Traditional 2-D monolayer cell culture on a dish without media flow. (B) Hepatocyte spheroid with 3-D cell-cell contact and continuous media flow.

Past efforts toward preparing multicellular hepatocyte aggregates (spheroids) have been made in traditional rocker-plate, porous foam block, and microarray chip cultures in order to maintain liver-specific functions *in vitro* [1]. However, these approaches employ static culture methods which are unable to simulate physiological flow conditions. Furthermore, the ability to analyze cell viability and function in a high-throughput manner is hindered due to the opaque substrates used in all three systems.

Previously, we demonstrated the feasibility of large-scale single cell trapping using purely hydrodynamic methods in a PDMS device [2]. Here we report an improved device design with 1) individually addressable trapping channels for functional assay analyses of spheroid secretions, and 2) physiologically relevant trap sizes for spheroid formation: 25-100 μm square with 50 μm depth (Figure 2).

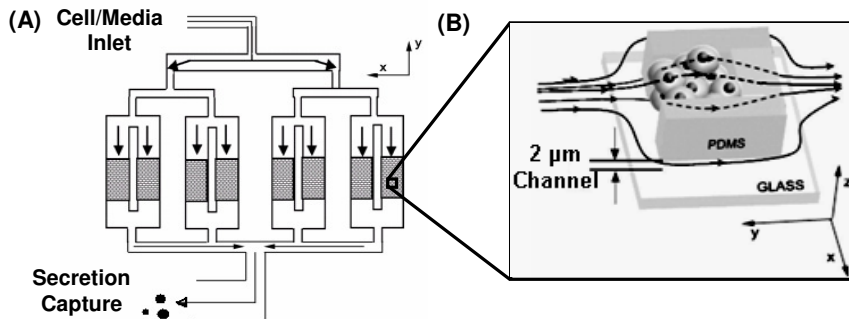


Figure 2. (A) Schematic of the device. Trapping arrays present physical barriers to multiple cells and spheroid formation occurs. Cell secretions are collected from individually addressed channel outlets. (B) Hepatocyte spheroids self-assemble due to hydrodynamic flow while a 2 μm channel facilitates effective trapping.

2. Experimental

The chips are fabricated using a two-layer SU-8/PDMS molding process. Three different trap sizes: 25 μm x 25 μm , 50 μm x 50 μm , and 100 μm x 100 μm , all with depths of 50 μm were designed and tested to sustain viable and functional HepG2/C3A (human hepatoma) cells (Figure 3). Cell viability, proliferation, and liver-specific function in terms of albumin secretion were characterized in the spheroid array device for each trap size (25-, 50-, and 100- μm -square) and compared with static control cultures on 12-well plates over two days. LIVE/DEAD and Hoescht nuclei stains (Molecular Probes, Auckland, NZ) and Trypan Blue (0.4%) stain (Sigma Chemical Co., St. Louis, MO) were used to test for viability and proliferation in devices and control 12-well plates, respectively. A high-sensitivity chemiluminescent immunoassay was developed to measure albumin secretion concentrations as low as 1 ng/mL (Figure 4).

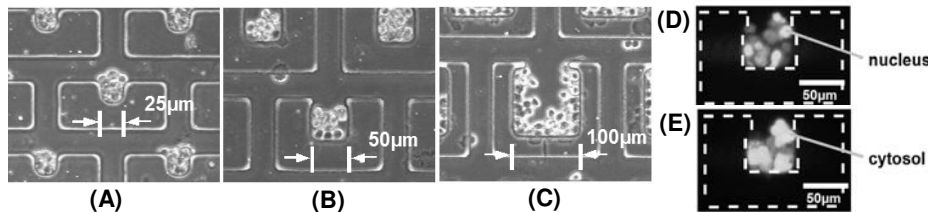


Figure 3. HepG2/C3A cells loaded into 50- μm -deep traps (into the page) measuring (A) 25 μm sq., (B) 50 μm sq., and (C) 100 μm sq. Spheroid self-assembly after 24-hours media perfusion: (D) fluorescently labeled with Hoescht 33258 DNA stain, and (E) LIVE stain, in 50 μm sq. traps (dashed outline).

3. Results and Discussion

Preliminary on-chip cell culture experiments were successfully performed on the three trap-size designs to evaluate albumin secretion as compared with monolayer controls. Specific albumin secretion improved in 3-D spheroids over traditional plate culture in a 2-day trial, supporting our hypothesis that the spheroid configuration induces more differentiated, liver-specific functions than in monolayer cultures (Figure 5). Further testing will be performed in order to verify that 3-D culture is superior in the long-term.

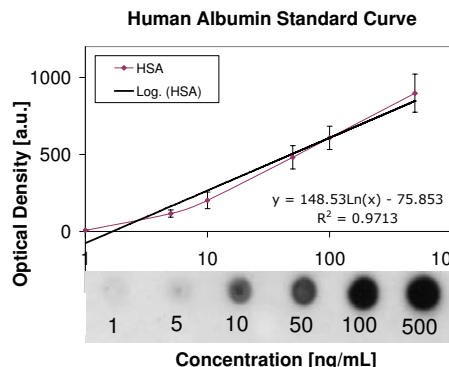


Figure 5. Dot blot sensitivity testing demonstrating the feasibility of detecting albumin secretions in the range of 1 ng/mL to 500 ng/mL.

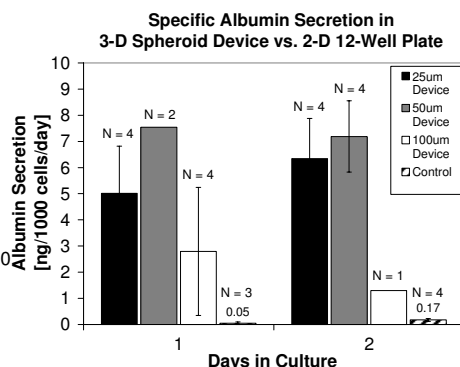


Figure 4. Specific albumin secretion in HepG2/C3A cells in device and control culture environments over 2 days. Error bars represent standard deviation.

4. Conclusions

This cell trapping array is addressable, continuously perfused, and capable of supporting HepG2/C3A cells. Furthermore, size-dependent spheroid physiology, cell-cell interactions, and cell-ECM interactions can be studied in this platform. In the future, we hope to improve the device's usability in order to accommodate the demands of high-throughput pharmacological, toxicological and metabolic screening.

Acknowledgements

We would like to thank Philip Lee and Terry Johnson for useful contributions on technical aspects, Jonathan Pegan for on-chip testing and data analysis, and J. Tanner Nevill for his help with device microfabrication.

References

1. S. L. Nyberg *et. al*, *Liver Transplantation*, **11**(8): 901-910 (2005), Y. Fujii *et. al*, *J. Biomater. Sci. Polymer Edn.*, **11**(7): 731-745 (2000), J. Fukuda, and K. Nakazawa, *Tissue Engineering*, **11**(7/8): 1254-1262 (2005).
2. D. Di Carlo *et. al*, *Analytical Chemistry*, **78**(14), 4925-4930 (2006).

A SINGLE-CELL ELECTROPORATION LAB CHIP VIA THE INTEGRATION OF DIELECTROPHORESIS MANIPULATION AND AC ELECTROKINETIC PUMP

Pang-Chih Liu and Cheng-Hsien Liu

Department of Power Mechanical Engineering, National Tsing Hua University,
Taiwan, R.O.C.
Micro-Systems and Control Laboratory

ABSTRACT

In this paper, we report the development and experimental results of a single cell electroporation Lab-chip via the integration of the enhanced dielectrophoresis manipulation and the embedded AC electrokinetic pump. By applying individual input AC voltage with different frequency, cells are manipulated in our device based on their electric property. Yoyo1 fluorescent probes are pumped to the electroporation region and get inserted into the target cell via our Lab-chip design. This research has demonstrated the pioneer of single-cell DEP manipulation with the integration of AC electrokinetic pump in a monolithic chip for bio-tech research like electroporation, which could be applied to the applications of drug screening and cancer study.

Keywords: dielectrophoresis, AC electrokinetic pump, single-cell, electroporation

1. INTRODUCTION

In recent years, a growing interest for the control of fluid pumping via electrokinetic effects such as electrothermal flow and electroosmosis has been developed in the field of micro-fluidics [1]. These studies provide many fundamental and important tools like pumping and mixing mechanism when they come to the development of Lab-on-a-chip and micro-total-analyses system (μ -TAS). The manipulation of bio-particles like cells, DNA and protein is also important for biological and medical applications. With recently fast growing MEMS technology, a number of novel ideas and studies related to the manipulation of micro-objects have been proposed [2].

2. LAB-CHIP DESIGN AND FUNCTIONS

The goals in our Lab-chip design are to manage a population of cells via enhanced dielectrophoresis manipulation in a micro channel and repeatedly sort out single cell to accomplish the process of bio-electroporation as shown in Figure 1. In our Lab-chip design, glass wafer is used as the chip substrate and the Al layer is adopted as the electrodes to achieve the functions of dielectrophoresis and AC electrokinetic fluid pumping. The micro channels are formed via the SU-8 photo-lithography process. Finally, the PDMS with injection and extraction holes is bonded together with the glass substrate. Figure 2 (A)-(D) illustrate the operation principles and manipulation processes of our Lab-chip. After the buffer with cells is injected into the micro chip via a syringe pump, the positive-DEP force from the P-electrode pair restricts the cells to stop in the middle of the $20\mu\text{m}$ wide micro channel and stay in a line as shown in Figure 2 (B). By applying the AC voltage with different frequency on the N-electrode pair, negative-DEP force could be generated to push adjacent cells in the middle of the micro channel to the opposite direction. This separation/sorting function is illustrated in Figure 2 (C). The single cell could then be separated and sorted out. Then another positive-DEP force from the Trapping-electrode pair is used to attract this single cell

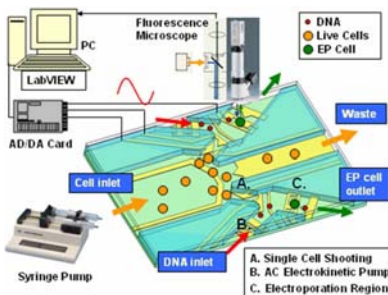


Figure 1. Illustration of our Lab-chip for single cell electroporation.

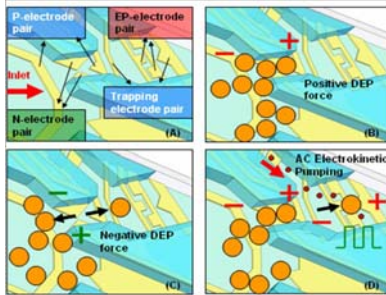


Figure 2. The operation principles of single cell sorting and electroporation in our Lab-chip.

forward to the electroporation region as shown in Figure 2 (D). Yoyo1 fluorescent probes are pumped into the electroporation region via the embedded AC electrokinetic pump and get inserted into the target cell via this Lab-chip design.

3. BIO-EXPERIMENTAL DEMONSTRATION AND RESULTS

Figure 3 shows the experimental results of the AC electrokinetic pumping simultaneously during the live cell manipulation. The small electrode has a width of $4\mu\text{m}$. The large electrode has a width of $25\mu\text{m}$. The small gap and the large gap are $8\mu\text{m}$ and $23\mu\text{m}$, respectively. The design of this AC electrokinetic pump is modified from Mphololo's report [3]. The AC electrokinetic pumping velocity in the DEP buffer is characterized up to $30\ \mu\text{m/s}$ under the applied AC voltage of $2\ \text{Vp-p}$ at $200\ \text{kHz}$. This AC electrokinetic pump is embedded in our Lab-chip to drive yoyo1 fluorescent probes to the electroporation region.

The function for single cell shooting/sorting mechanism is demonstrated as shown in Figure 4. MDCK (Madin-Darby canine kidney) cells and DEP buffer are pumped into the Lab-chip with a flow rate of $10\ \mu\text{m/s}$. At the time $T=5\ \text{sec.}$, the positive DEP force on the P-electrode is turned on. The target cells are attracted into the micro-channel. The amplitude and frequency of the applied voltage on the P-electrode are $3\ \text{Vp-p}$ and $10\ \text{MHz}$, respectively. Then the AC voltage on the N-electrode is turned on to generate negative DEP force in the middle of the micro-channel right after the positive DEP force is turned off. The amplitude and frequency of the applied voltage on the

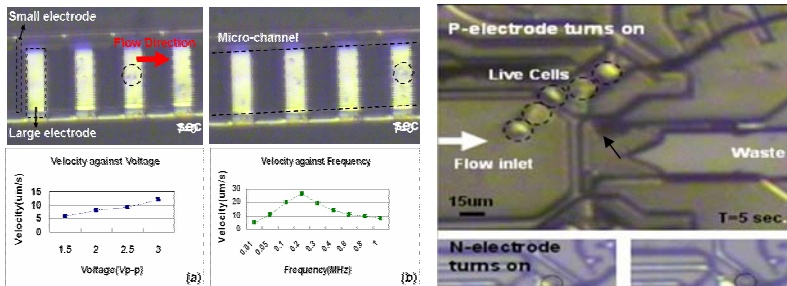
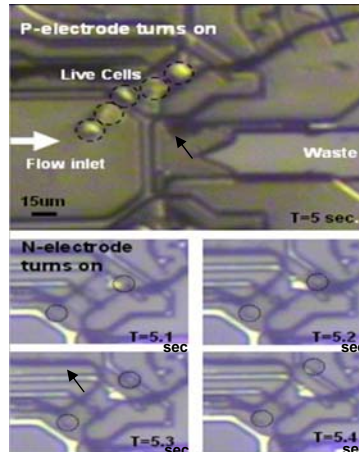


Figure 3. The experimental results of the AC electrokinetic pump simultaneously during the live cell manipulation in our Lab-chip design.

Figure 4. Experimental results demonstrate the single cell shooting function in our device.



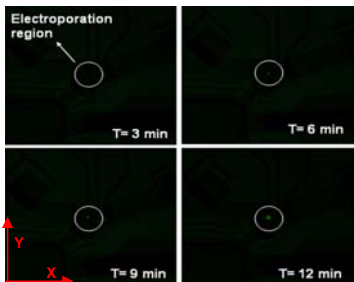


Figure 5. The time-sequence pictures of single-cell fluorescent intensity between 3 and 12 minutes.

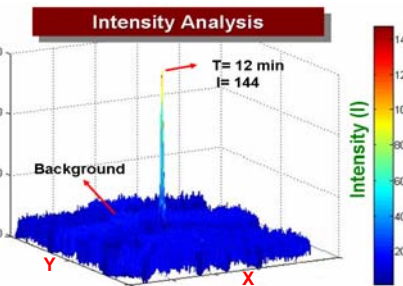


Figure 6. Fluorescent intensity diagram of Figure 5 is analyzed via the image processing toolbox offered by MATLAB.

N-electrode are 3 Vp-p and 10 kHz, respectively. During the time period between 5.1 and 5.4 seconds, the single cell is successfully sorted out of the micro-channel. Then another positive DEP electrode is turned on to attract the sorted-out single cell to the castellated electrodes, which perform the cell electroporation function. AC electrical voltage of 2Vp-p at 200 kHz is applied to the embedded AC electrokinetic pump to transport the yoyol fluorescent dye to the electroporation region in three minutes. Three times of 5V/ 100ms electrical pulses are applied on the castellated electrodes to achieve the function of cell electroporation. Figure 5 shows the time-sequence pictures of single-cell fluorescent intensity between 3 and 12 minutes. We use the Image Processing Toolbox in MATLAB to analyze the fluorescent intensity. The result is shown in Figure 6. After 12 minutes, the intensity of the fluorescence gets saturated and the maximum intensity is about 144 (0~255). If we continue exciting the fluorescence of the cell by 488 nm light source after 15 minutes, the fluorescent intensity decays progressively.

4. CONCLUSIONS

The design, analysis and experimental results of a Lab-chip for single cell electroporation via the integration of the enhanced dielectrophoresis manipulation and the embedded AC electrokinetic pump are reported in this paper. Single cell is sorted out successfully via the positive and the negative DEP forces generated from the DEP electrodes in our Lab-chip. Yoyol fluorescent probes are pumped into the electroporation region and inserted into single MDCK cell. Up to date, based on our knowledge, this research has demonstrated the pioneer of single-cell DEP manipulation with the integration of AC electrokinetic pump in a monolithic chip for bio-tech research like electroporation.

ACKNOWLEDGEMENT

The authors thank the Nano-Science Center and Technology and the Semiconductor Research Center for the micro-fabrication facility support. The authors also thank Professor Hwan-You Chang and Miss Yun-Ru Pan for the valuable discussion as well as the supply of cells and yoyol probes. This work was supported by the National Science Council under grant NSC-94-2215-E-007-001.

REFERENCES

- [1] H. A. Pohl, *Dielectrophoresis*, Cambridge University Press, Cambridge, UK, 1978.
- [2] Chen-Ta Ho, Ruei-Zeng Lin, Wen-Yu Chang, Hwan-You Chang and Cheng-Hsien Liu, "Rapid heterogeneous liver-cell on-chip patterning via the enhanced field-induced dielectrophoresis trap", accepted and to be published by Lab on a chip.
- [3] M. Mpholoa, C.G. Smith, A.B.D. Brown, "Low voltage plug flow pumping using anisotropic electrode arrays," Sensors and Actuators B **92** 262–268, 2003.

FACILE IMAGE-BASED CELL SORTING USING OPTO-FLUCS (OPTO-FLUIDIC CELL SORTING)

Joseph Kovac¹ and Joel Voldman¹

¹Electrical Engineering and Computer Science,
Massachusetts Institute of Technology, USA

Abstract

We present a new approach for sorting cells based upon visual information, termed opto-fluidic cell sorting (OPTO-FluCS). This technique uses a combination of hydrodynamic and optical scattering forces to array, image, and then sort many individual cells. Our device combines the strengths of microscopy-imaging in space and time—with the ability to array cell populations and isolate cells of interest in an intuitive, user-friendly fashion. We successfully demonstrate image-based sorting based on fluorescence localization, a sort unavailable with flow-assisted cell sorting.

Keywords: Cell sorting, microwell array, optical manipulation, optofluidics

1. Introduction

We have developed technology to sort cells based upon visual information. Our opto-fluidic architecture obtains sorting information through microscopy, predicated on temporal and spatial behavior of cells. While flow-assisted cell sorting (FACS) allows higher throughput, it bases sorts on whole-cell fluorescence at a single timepoint. Our approach scales effortlessly, requiring no electrical interconnects or support electronics to address cells [1]. Sorting of a single cell takes seconds, allowing for collection of larger numbers of cells than is practical with micropipette/micromanipulator systems [2]. While laser capture microdissection (LCM) has been used to sort non-viable cells from microwell arrays [3], its live-cell sorts require the use of proprietary films. Our opto-fluidic array architecture scales effortlessly to array sizes in excess of 20,000 sites, contains no interconnects, allows for diverse surface functionalization, requires seconds to remove a cell of interest, and provides for simple retrieval of released viable cells.

2. Architecture Design

There are two important elements to our system. First is a microfluidic chamber (Figure 1) with a PDMS well array that we use for simple passive cell loading via sedimentation and subsequent flushing (Figure 2A-B). After visualizing cells using any desired microscopy technique (phase, fluorescence, etc.), we note the positions of cells of interest. Second, we use a straightforward optical system to couple a laser onto the imaging axis. We remove a target cell by focusing the laser through an inexpensive objective onto the cell; the optical scattering force pushes the cell into the flow (Figure 2C). The optical intensity and energy-density levels that we apply to cells are orders of magnitude below those found harmful in conventional, high-numerical aperture optical tweezers, and thus our approach is unlikely to damage cells [4].

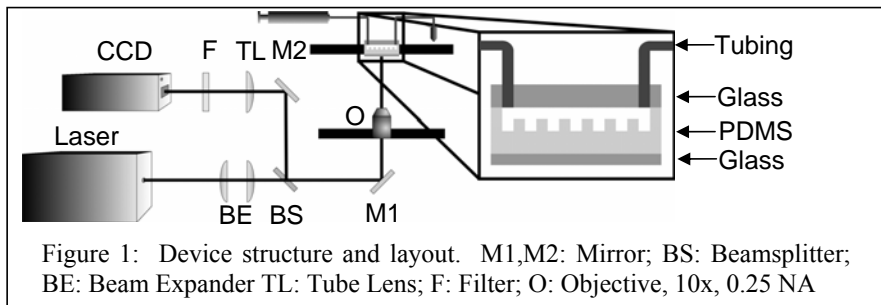


Figure 1: Device structure and layout. M1,M2: Mirror; BS: Beamsplitter; BE: Beam Expander TL: Tube Lens; F: Filter; O: Objective, 10x, 0.25 NA

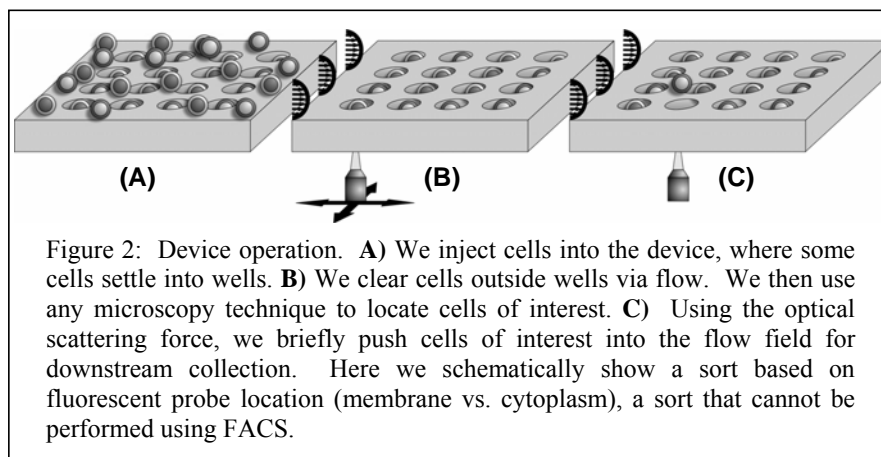


Figure 2: Device operation. **A)** We inject cells into the device, where some cells settle into wells. **B)** We clear cells outside wells via flow. We then use any microscopy technique to locate cells of interest. **C)** Using the optical scattering force, we briefly push cells of interest into the flow field for downstream collection. Here we schematically show a sort based on fluorescent probe location (membrane vs. cytoplasm), a sort that cannot be performed using FACS.

3. Results and Discussion

As a first demonstration, we loaded orange- and green-labeled HL60 cells randomly into the device, imaged them, and then sorted out the orange-labeled cells (Figure 3).

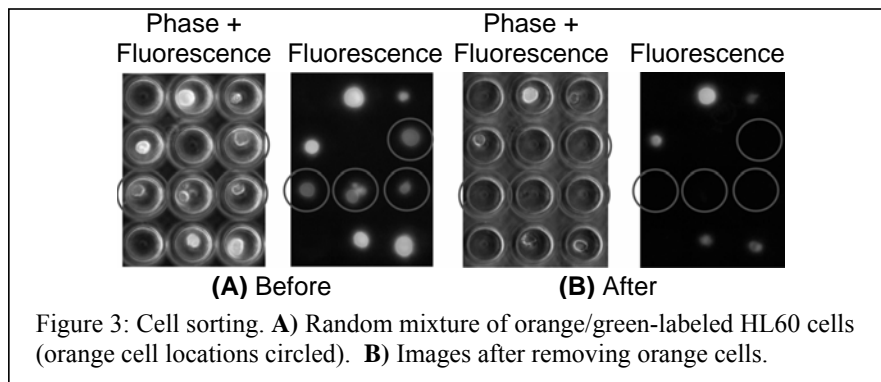
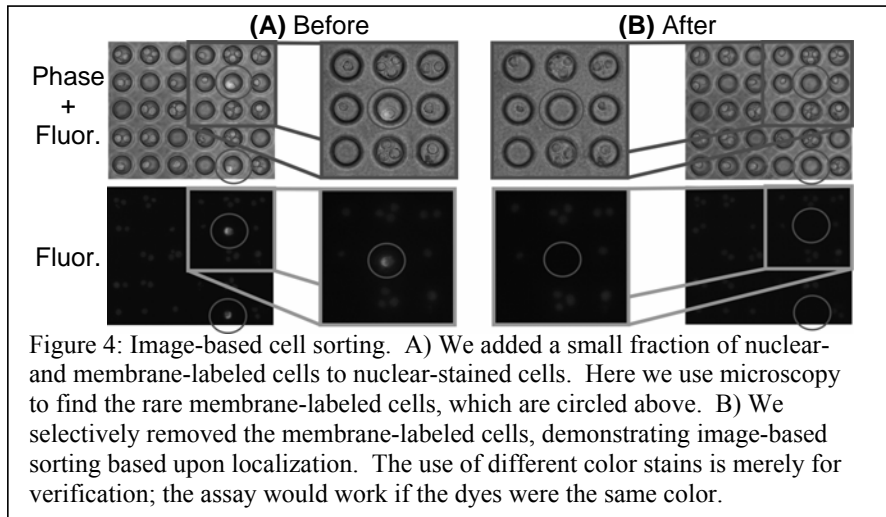


Figure 3: Cell sorting. **A)** Random mixture of orange/green-labeled HL60 cells (orange cell locations circled). **B)** Images after removing orange cells.



We demonstrated true image-based sorting by loading the device with nuclear-stained cells and a small fraction of nuclear- and membrane-stained cells (Figure 4). Using microscopy, we identified the cells with membrane stain and sorted them from the cells only labeled with nuclear stain. This demonstrates image-based sorting based upon localization, an assay that cannot be performed using flow cytometry.

4. Conclusions

Our results demonstrate the feasibility of sorting cells via microscopy in a user-friendly fashion. The simplicity of the optical system allows for straightforward incorporation of the system into widely used microscopes. Using this novel architecture, we aim to sort cells predicated on complex phenotypes in realms where traditional flow-assisted cell sorting (FACS) falls short.

Acknowledgements: We thank David Appleyard, Dr. Stanley Hong, Prof. Matthew Lang, and Prof. Dennis Freeman for their advice. This work was supported in part by the NIH, the Singapore-MIT Alliance, and a National Defense Science and Engineering Graduate Fellowship.

References

1. Taff, B.M. and J. Voldman, A scalable addressable positive-dielectrophoretic cell-sorting array. *Anal. Chem.*, 2005. 77(24): p. 7976-7983.
2. Yamamura, S., et al., Single-cell microarray for analyzing cellular response. *Anal. Chem.*, 2005. 77(24): p. 8050-8056.
3. Revzin, A., et al., Development of a microfabricated cytometry platform for characterization and sorting of individual leukocytes. *Lab Chip*, 2005. 5(1): p. 30-37.
4. Wang, M.M., et al., Microfluidic sorting of mammalian cells by optical force switching. *Nat. Biotechnol.*, 2005. 23(1): p. 83-87.

MICROCARRIER ENABLED MICROFLUIDIC ASSAYS OF ANCHORAGE DEPENDANT CELLS

Jamil El-Ali and Klavs F. Jensen

Massachusetts Institute of Technology, Cambridge, MA 02139, USA
(kfjensen@mit.edu)

Abstract:

We present the use of microcarriers as a method to greatly expand the cell types available for microchip based cell assays that rely on fluidic transport of cell suspensions through functional zones. Cells attached to the microcarriers remains viable and responsive to cell stimulation even after flow at high linear velocities through microfluidic systems.

Keywords: Microcarrier, Cell signaling, Protein pathways

Introduction:

Many microchip based cell assays rely on fluidic transport of cell suspensions through functional zones, such as cell sorting areas [1] or cell stimulation and lysis zones [2]. Most mammalian cells are adherent and anchorage dependant cells that can only be put in suspension by treatment with a proteolytic agent such as trypsin. However, this treatment and the loss of adhesion severely perturb the biological machinery of the cells causing interference in many assays. Instead we show that by attaching the cells to microcarriers cells can be suspended while retaining their normal anchorage dependent functionality. We further demonstrate this technique in a microfluidic device for cell signaling applications (i.e., studies of protein expression). Large microcarrier particles (100 μ m-1000 μ m), not suitable for transport in microfluidic systems, have preciously been utilized in cell culture systems, both conventional and microscale [3], because of the increased surface to volume ratio that can be achieved with microcarrier culture. The use of smaller carriers in microfluidic systems is, however, not trivial because below a certain (cell dependant) size geometric effects can induce apoptosis in the cells [4].

Experimental

To minimize geometrical effects while keeping the beads sufficiently small for compatibility with microfluidic devices, we have used medium sized beads (30 μ m-50 μ m) for cell attachment. The beads were coated with collagen in order to enhance cell adhesion. HeLa cells were incubated with the beads in a 25mL spinner flask under gentle stirring for 24 hours before experiments. To test the applicability of the microcarriers for cell based assays a microfluidic device was fabricated using soft lithography in a PDMS layer that was bonded to 50mm x 75mm glass slide. The main channel is 3 m long, 300 μ m wide and 200 μ m deep with 3 inlets for the microcarrier suspension, cell stimulus, and gas (Figure 1). The latter can be used to create segmented

gas liquid flow for enhanced mixing [2]. The channel length ensures long residence times in the system even at relatively high linear velocities, which represents a worst case scenario with respect to the influence of shear in the fluidic system on cell viability and function.

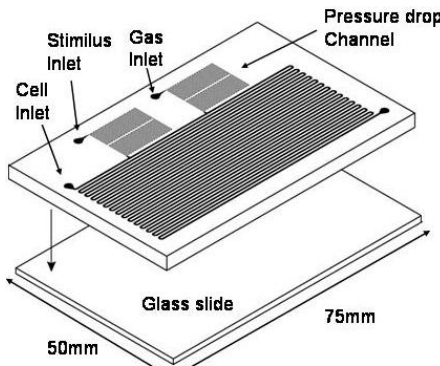


Figure 1. Schematic of the microfluidic system, with inlets for microcarrier introduction, cell stimulus and a gas inlet that can be used to form segmented gas-liquid flow. The main channel is 300 μ m wide, 200 μ m deep and approximately 300cm long.

Results

After 24 hours of incubation of HeLa cells with the beads in a 10:1 ratio, almost all cells adhered to the microcarriers and normal cell behavior such as cell division could be observed (Figure 2).

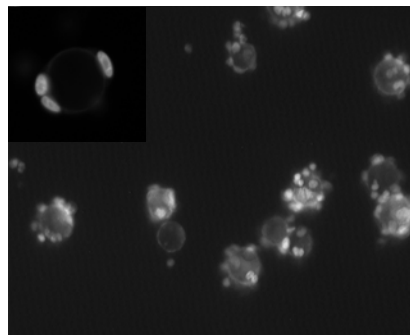


Figure 2. HeLa cells attached to collagen coated microcarrier beads. The histones in the nuclei have been transfected with green fluorescence protein (GFP) while the mitochondria in the cells have been dyed with a red fluoresce dye. Inserted in the upper left corner of the figure is a close up of what appears to be HeLa cells that have undergone cell division as indicated by the two closely separated nuclei.

Even after the microcarriers with the cells were flowed through the microfluidic system at an average linear velocity of ~14mm/s (50 μ L/min) the cells remained viable and no difference could be observed in cell attachment compared to the populations in the spinner flask (Figure 3A). As an application in cell pathway activation, we have found that cells on the microcarriers continue to respond strongly to EGF and TNF stimulation, with a clear increase in the activated ERK signal of the cell stress sensitive MAP kinase pathway (Figure 3B). This shows that microcarrier techniques are applicable for cell signaling assays.

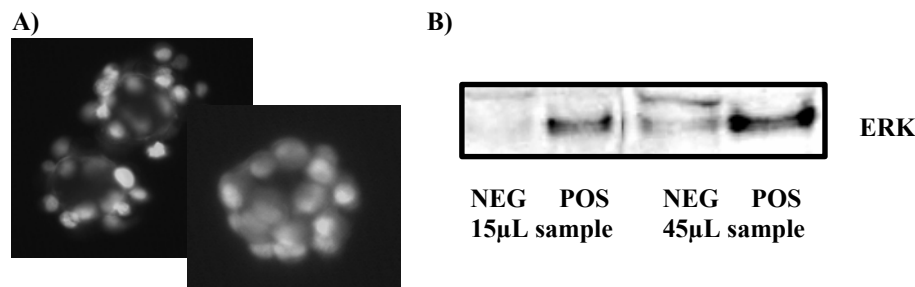


Figure 3. A) To the left is a micrograph close up of microcarriers after flow through the microfluidic system at 50 μ L/min. The cells appear to be attached to the same extend as those on the microcarriers directly from the spinner flask (Figure 2). To the right is a micrograph of regular (non-GFP) HeLa cells stained with a green viability dye after flow through the microfluidic system. All cells are viable after flow through the device. B) Western blot of P-ERK from cell lysates of HeLa cells on microcarriers. Lanes marked "POS" are from cells treated with EGF/TNF while lanes marked with "NEG" are from untreated cells. There are clear signals (scaling with sample size) in the positive samples. The negative control samples only show a weak signal.

Acknowledgments: This research was funded by National Institutes of Health (GM-68762)

References:

- [1] Fu, A. Y. et al., "An integrated microfabricated cell sorter", *Analytical Chemistry* **74**, 2451-2457 (2002).
- [2] El-Ali, J. et al., "Cell stimulus and lysis in a microfluidic device with segmented gas-liquid flow" *Analytical Chemistry* **77**, 3629-3636 (2005).
- [3] Nishino, T et al., "Cell culture and response assay total system for protein secretion on a microchip, μ TAS 2005, p930-932
- [4] Chen, C. S. et al., "Geometric control of cell life and death", *Science* **276**, 1425-1428 (1997).

CELL SYNCHRONIZATION USING DIELECTROPHORESIS

Unyoung Kim¹, Chih-Wen Shu², Karen Y. Dane¹,
Jean Y. J. Wang², and H. T. Soh^{*1}

¹University of California, Santa Barbara, USA

²University of California, San Diego, USA

(*E-mail: tsoh@engr.ucsb.edu)

Abstract

Currently available synchronization methods are not capable of achieving all three parameters of performance: non-invasiveness, high yield, and high synchrony. We present a dielectrophoresis activated cell synchronizer (DACS_{Sync}) – a microfluidic device that is capable of non-invasively achieving cell synchrony in mammalian cells. Using human breast ductal carcinoma cell line as a model system, we demonstrate a purely dielectrophoretic fractionation of cells in G1/S phase from an asynchronous mixture. DACS_{Sync} offers the potential for non-invasive synchronization which is capable of achieving high yield and synchrony by the use of arrayed devices that operate in parallel.

Keywords: Cell cycle, cell synchronization, dielectrophoresis, continuous-flow cell sorting

1. Introduction

The cell cycle is an essential mechanism through which all living beings reproduce. For biological and biomedical research, synchronization of cells at a specific phase is an important capability, especially for drug screening applications where cell cycle-regulated events are targeted for therapeutic or diagnostic use¹. Synchronization is currently accomplished by cell arrest using metabolic drugs^{2,3}, centrifugal elutriation⁴, or through the use of “baby machines”⁵ in the case of bacterial cells. However, such methods typically suffer from disruption of natural physiology by chemical treatment and low yield; to date, there is no reported methodology to achieve cell synchrony for all cell types. In this work, we report on a dielectrophoresis activated cell synchronizer which is non-invasive and capable of achieving efficient cell synchrony for a wide range of cell types.

2. Theory

The use of dielectrophoresis activated cell synchronizer (DACS_{Sync}) was investigated with the human breast ductal carcinoma cell line (MDA-MB-231) as a model system, wherein the device was used to separate the cells in G1/S and G2/M phases from an asynchronous population in a continuous-flow manner. The device exploits the fact that dielectrophoretic force is proportional to the cell’s volume (i.e.: $\sim r^3$). Multiple sets of electrodes are used to create a dielectrophoretic force-field that fractionizes the

heterogeneous cell population into subpopulations based on their sizes (Fig. 1a). The viscous drag and repulsive dielectrophoretic forces were calculated to simulate concentration profiles for two different cell sizes representing cells in G2/M phase (Fig. 1b) and G1/S phase (Fig. 1c). The simulation shows effective fractionation of cells based on size at the outlet (Fig. 1d).

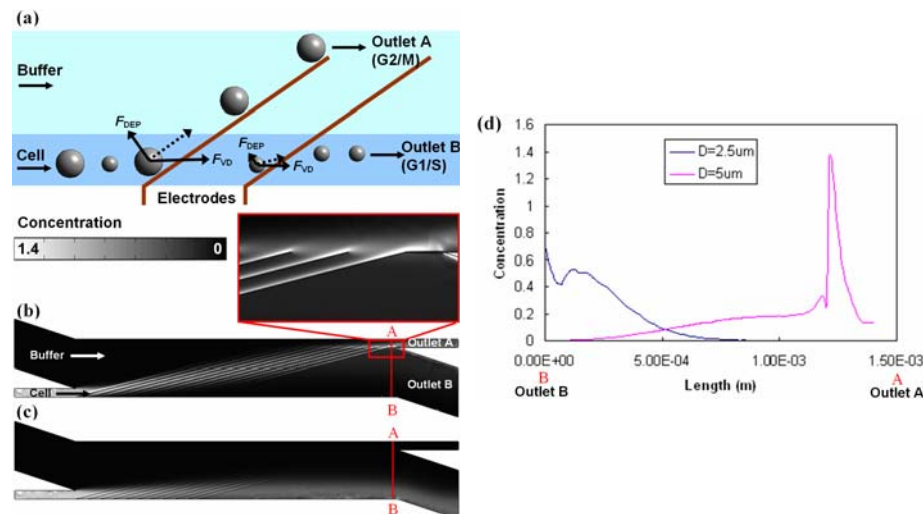


Figure 1. (a) Operational principle of DACSync: A volume-dependent dielectrophoretic force fractionizes an asynchronous population into subpopulations based on the size of the cells. Larger cells in G2/M are deflected to outlet A, while smaller ones in G1/S are going to outlet B. (b) Simulated concentration profile for $D=5\mu\text{m}$. (c) for $D=2.5\mu\text{m}$. (d) Cross-section (A-B in Fig 1a and 1b) plot of concentrations shows effective separation at the outlet.

3. Experimental

The device is fabricated with polyimide channel ($30\mu\text{m}$ height) between top and bottom glass substrates with Ti-Au (500nm thickness) electrodes (Fig. 2a). Cells entering the sample inlet are focused and aligned into a single line (Fig. 2b) using a series of DEP deflectors which ensures that all cells reach a uniform velocity and vertical position. Subsequently, the cells encounter a set of fractionization electrodes wherein the separation occurs (Fig. 2c). The larger cells (G2/M) are deflected into outlet A, whereas smaller cells (G1/S) pass through toward outlet B.

4. Results and discussion

The efficiency of synchronization was analyzed by flow cytometry. The cells were fixed and stained with propidium iodide (PI), fluorochromes which intercalate into DNA. Thus, by measuring a cell's DNA content, the phase of the cell can be evaluated. Initially, the ratio of the cells in G1/S phase to G2/M phase was 3.3:1 (Fig. 3a). After

synchronization, the ratio was increased to 6:1 enriching the G1/S-phase cells by two fold in the outlet B (Fig. 3b).

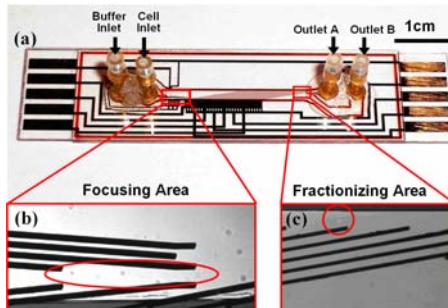


Figure 2. (a) The dielectrophoresis activated cell synchronizer is fabricated with polyimide spacer between two glass substrates containing Ti/Au quadrupole electrodes. (b) Cells enter the focusing area and line up. (c) Larger cells get deflected into the outlet A while smaller cells pass through the electrodes and enter the outlet B.

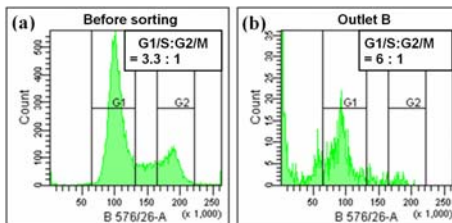


Figure 3. Cells in G1/S phase get enriched by two fold after synchronization. (a) Initial population consists of a ratio of 3.3:1 in G1/S to G2/M-phase cells. (b) Outlet B population consists of a ratio of 6:1 in G1/S to G2/M-phase cells.

References

1. J. Jackman and P. M. O'Connor, *Methods for synchronizing cells at specific phases of the cell cycle*, Current Prot. In Cell Bio. 8.3 (1998)
2. J. Gong, F. Traganos, and Z. Darzynkiewicz, *Growth imbalance and altered expression of cyclins B1, A, E, D3 in MOLT-4 cells synchronized in the cell cycle by inhibitors of DNA replication*, Cell Growth Differ. 6, 1485-1493 (1995)
3. R. T. Schimke, A. L. Kung, D. F. Rush, and S. W. Sherwood, *Differences in mitotic control among mammalian cells*, Cold Spring Harbor Symp. Quat. Biol. 56, 417-425 (1991)
4. P. K. Davis, A. Ho, and S. F. Dowdy, *Biological methods for cell-cycle synchronization of mammalian cells*, Biotechniques 30, 1322-1324 (2001)
5. C. E. Helmstetter, M. Thornton, N. B. Grover, *Cell-cycle research with synchronous cultures: An evaluation*, Biochimie 83, 83-89 (2001)

MICROFLUIDICS FOR CONTROLLED SINGLE CELL MICROINJECTION

Andrea Adamo and Klavs F. Jensen

Massachusetts Institute of Technology, Cambridge, MA 02139, USA
(aadamo@mit.edu)

Abstract

We report a microfluidics method for microinjection of cells. Cells are lined up in a microfluidic channel by geometry control and brought to the needle by fluid flow. The flow rate of the cell to the needle, the acceleration to pierce the cell by the needle, and the subsequent release of the injected cell are accomplished by manipulating pressure drops in the fluid channels with poly(dimethylsiloxane) (PDMS) pneumatic valves. Fluorescently labeled Dextran demonstrates microinjection and cell viability is explored with vital dyes.

Keywords: microfluidics, cell microinjection, polymer microfabrication

1. Introduction

The delivery of nucleic acids, proteins and small molecules across cell membranes into living cells is a key step in many biological experiments. Methods to introduce material into cells include chemical methods (synthetic vectors), biological vectors (viral vectors) and physical methods. Synthetic vectors are relatively cheap and efficient on selected cell types but they are associated with toxicity and produce non-quantitative delivery (*i.e.*, it is not possible to determine how much DNA is delivered into each cell). Biological vectors are more effective than synthetic vectors, but they are expensive and time consuming. Moreover, biological vectors can deliver only relatively short DNA sequences and, as in the case of synthetic vectors, they are rarely quantitative and can have toxic side effects. At present, manual microinjection is considered the most reproducible method, but it is expensive, slow and requires highly specialized operators [1]. Fujitsu has recently developed an automated microinjection robot that automates the capture of cells on a microchip pattern and the corresponding movement of the needle [2]. To our knowledge, the present microfluidic device is the first example of single cell manipulation and injection.

2. Device principle

In traditional microinjection a moving needle is manually positioned on the cell membrane to be pierced. In the present microfluidic device (Figures 1 and 2), cells are lined up in a micro channel by geometric control and brought to the needle by fluid flow control. The flow rate of the cell to the needle, the acceleration to force the cell onto the needle and piercing the membrane, and the subsequent release of the injected cell are accomplished by manipulating pressure drops in the fluid channels with poly(dimethylsiloxane) (PDMS) pneumatic valves. Each cell is injected with a micro

needle placed in the device with known volume of a desired solution. After injection, each cell flows to a collection reservoir, and the system is ready to inject the next cell.

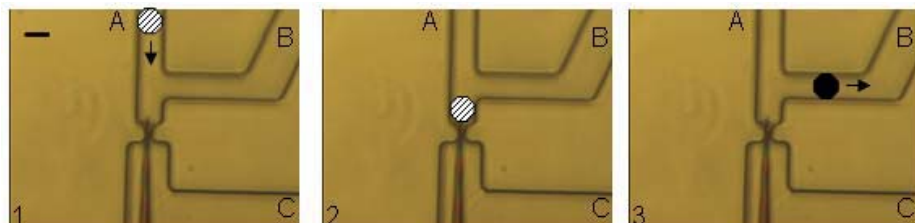


Figure 1: Schematic of microinjection device operation. Frame 1: a solution with suspended cells flows into channel A and the suspension fluid is drained thru channel C (the valve in channel C is opened and the valve in channel B is closed). Frame 2: a cell reaches the needle, it is pierced and injected. Frame 3: The valve in channel C is closed and channel B is opened so that the injected cell is carried away by the fluid.

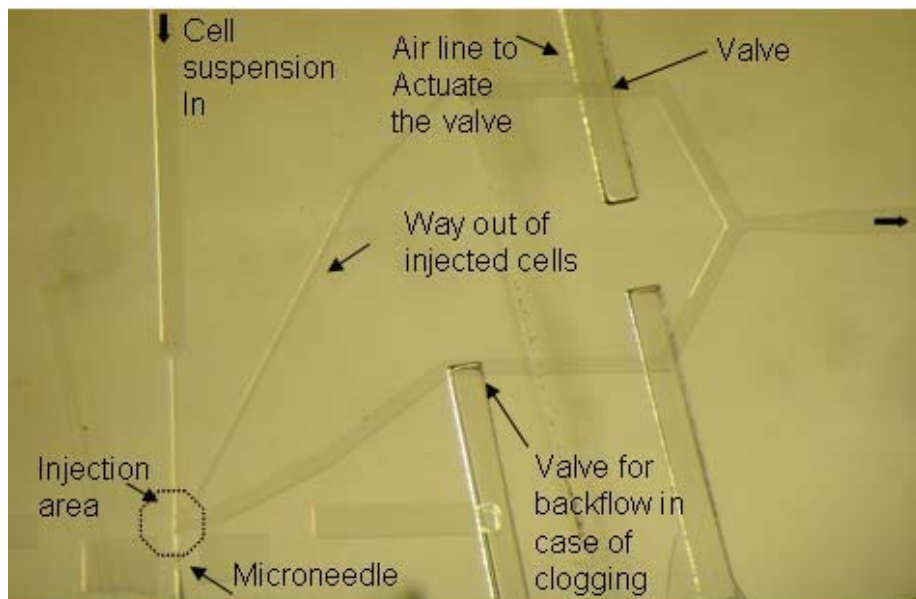


Figure 2: PDMS microfluidic device for single cell microinjection.

2. Experimental

The microinjection system (Figure 2) was constructed in PDMS by standard softlithography techniques. A micro needle made from a pulled glass capillary (tip

internal diameter 0.5 micron) was inserted and positioned in the device with the help of a micrometer stage and a stereo microscope.

In the experiments, a solution of cells was introduced in the microchannels system. Channel geometry and flow positioned the cells on the microinjection needle, one at a time. Cells were pierced, microinjected, released from the needle, and moved into a reservoir. Injection of fluorescent Dextran (tetramethylrhodamine MW 10000, Molecular probes, USA) demonstrated microinjection as the compound was sufficiently large to be unable to cross the cell membrane. The viability of cells flowing through the system without injection as well as cells injected with Dextran was explored by vital dyes. Figure 3 shows a cell (dyed for visualization purposes with orange acridyne, a vital dye) being pierced by the needle. Figure 4 shows the same cell being inject with Dextran, the fluorescence reveals both needle and cell. The viability of injected cells after injection was probed by the absence cell coloration in the presence of Trypan Blue

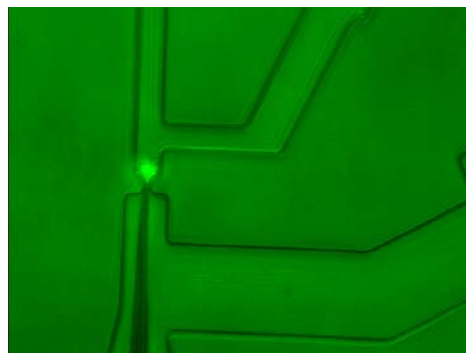


Figure 3: Injection area with a cell dyed with Acridine Orange (vital dye) for visualization purposes

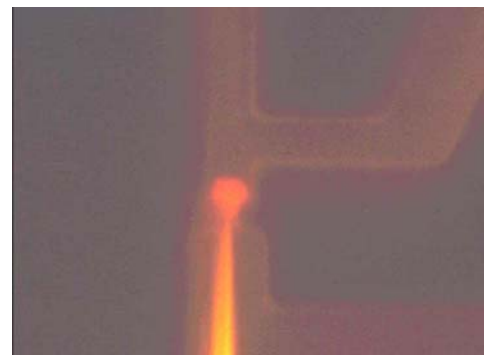


Figure 4: Injection area with a cell injected with red fluorescent dye (dextran, tetramethylrhodamine) Also the filled needle can be recognized

4. Conclusions

We have demonstrated the fabrication and operation of a microfluidic device for microinjection into cells. Further testing with gene transvection is being performed to evaluate the system for specific biological applications.

References

1. Chou TH, Biswas S, Lu S, *Gene delivery using physical methods: an overview*. Methods Mol Biol. 2004;245:147-66
2. http://www.fujitsu.com/us/news/pr/bsg_pr-2005-08-10-ci-release.html

96-WELL SINGLE-CELL ELECTROPORATION ARRAYS: REAL-TIME MONITORING AND FEEDBACK CONTROL OF MEMBRANE RESEALING KINETICS

Michelle Khine*, Cristian Ionescu-Zanetti**, Andrew Blatz**,
Lee-Ping Wang**, and Luke P. Lee***

*College of Engineering, UC Merced

Fluxion Biosciences Inc. and *Department of Bioengineering, UC Berkeley

Abstract

Rapid well-controlled intracellular delivery of drug compounds, RNA, or DNA into a cell -- without permanent damage to the cell -- is a pervasive challenge in basic cell biology research, drug discovery, therapeutic gene delivery, and molecular medicine. To address this challenge, we have developed a bench-top system comprised of a control interface, with mating disposable 96-well-based microfluidic systems, that enables the manipulation, monitoring, and characterization of an array of single-cells. Using this set-up, we individually electroporate an array ($n=15$) of Hela cells in suspension with low applied voltages (0.4V-0.8V) and insert otherwise impermeable Calcein (Invitrogen, MW=622) and Orange Green Dextran 514 (Invitrogen, MW = 70,000) by electrophoresis (-200mV) within seconds.

Keywords: single-cell, electroporation, intracellular, therapeutic gene delivery, molecular medicine

Introduction

Leveraging the principles of single-cell electroporation [1-4], in which transient pores can be induced in a cell's membrane when the transmembrane potential exceeds the dielectric breakdown voltage of the membrane (0.2 -1.5 V) [5], we have developed a multi-electroporation system that allows parallel operation (i.e. $n=15$) and monitoring of each cell's response electrically and optically (fluorescence) (Figure 1).

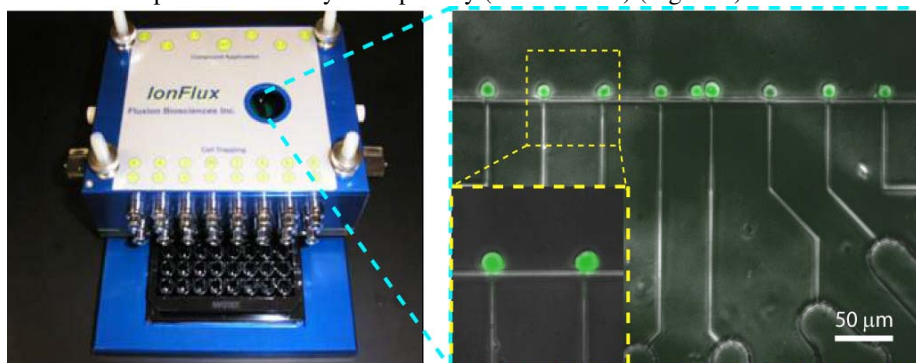


Figure 1. Arrayed electroporation. An array of fluorescently (Calcein) labeled Hela cells trapped in the 96 well device (inset). The device, on the bottom of the 96 well-plate, is housed in the IonFlux interface for electrical and pneumatic control.

Experimental Data

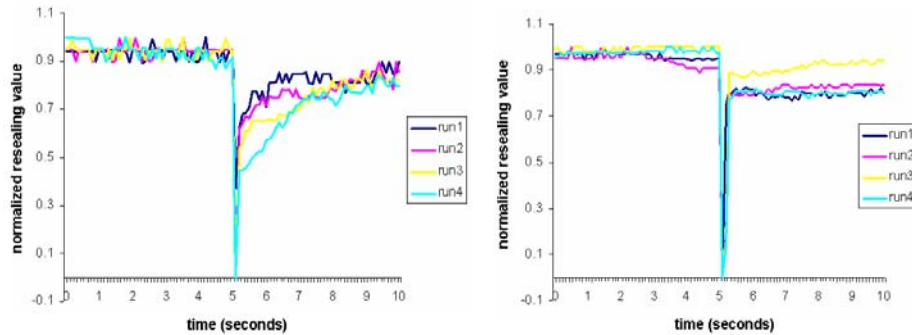


Figure 2. Resealing: effect of the Control Loop. (a) resealing after electroporation of a cell without control loop 4 times. (b) resealing after electroporation of the same cell with the control loop 4 times.

By holding the cell at a low voltage (10 mV) to measure the resistance immediately after the applied electroporation protocol, resealing kinetics can be also resolved (Figure 2a). Such time resolution was not previously attainable with other electroporation setups. From this, we can determine resealing time constants for various pulse conditions (Figure 3). We also developed a graphical user-interface program that automatically releases the electric field after an electroporation event has occurred (Figure 4). As is evident from Figure 2, in which the same cell was electroporated without the control loop 4 times, and then 4 times with the control loop (intensity renormalized after each subsequent run), resealing kinetics improve dramatically with the feedback loop.

With this algorithm, electroporation conditions no longer need to be set a priori using test cells as with other commercially available systems. With our program, after the cell is electroporated, the electric field is released. In this way, we can ensure the cell is electroporated (voltage incrementally until electroporation) and then immediately

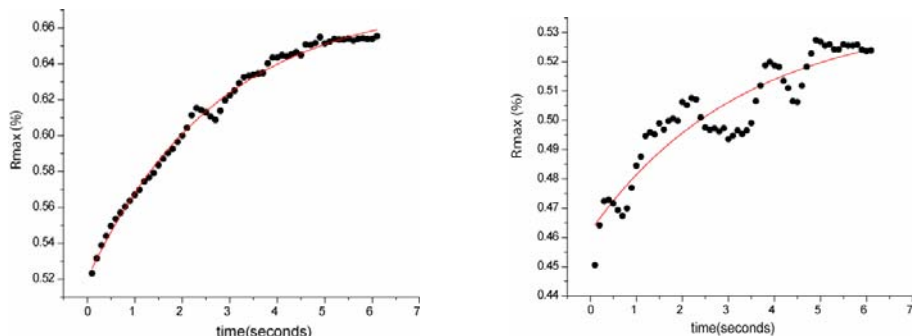


Figure 3. Resealing kinetics for two cells. By fitting to an exponential, the time constant for 50% resealing (t_{50}) was determined. The average time constant is 1.75s.

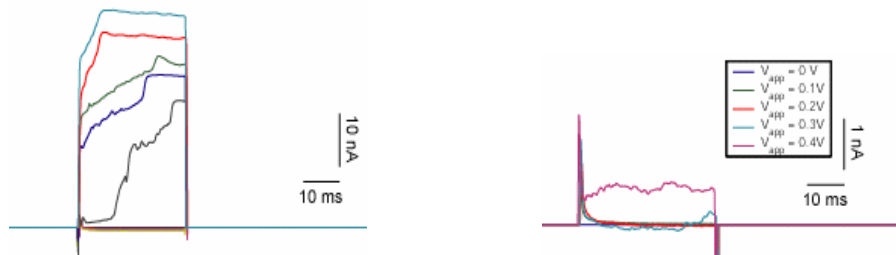
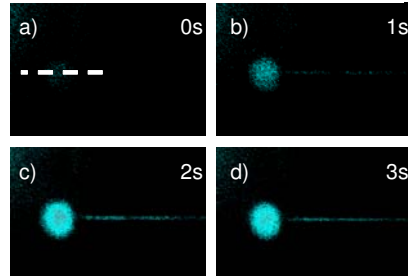


Figure 4. Membrane poration with and without control loop. (a) Without control loop – cell keeps getting electroporated (b) With control loop, the voltage is released after the electroporation event (jump in current, here at 0.4V) is detected.

released after this event. The control loop allows for multiple electroporation events without irreversible damage to the cell. We also rapidly introduced dyes of various molecular weights via electrophoresis. Holding the cell at -200mV immediately after electroporation drove Calcein into the cell within 3 seconds (Figure 5), which by diffusion alone took upwards of 30 seconds (data not shown).



Conclusions

In summary, we have demonstrated that we can (1) electroporate an array of single-cells ($n=15$) using very low applied voltages (0.4–0.8V) (2) ensure electroporation (3) monitor the cell's resistance before, during, and after electroporation (4) ensure that the cell reseals in a timely manner (5) reversibly electroporate the same cell up to 10 times and (6) introduce compounds via electrophoresis within seconds.

Acknowledgements

Funding Source: National Institute of Health NIGMS 1 R43 GM075509-01

References

- 1.Lundqvist, J. A., Sahlin, F., Aberg, M. A. I., Stromberg, A., Eriksson, P. S., Orwar, O. (1998). *Proc. Natl. Acad. Sci. U. S. A.* 95: 10356-10360.
- 2.Nolkranz, K., Farre, C., Brederlau, A., Karlsson, R.I.D., Brennan, C., Eriksson, P.S., S.G.Weber, Sandberg, M., Orwar O. (2001) *Analytical Chemistry*, 73, 4469-4477.
- 3.Huang, Y, Rubinsky B.(2003) *Sensors and Actuators A* 104, 3, 205-212.
- 4.Khine,M., Lau, A.D., Ionescu-Zanetti, C., Seo,J.,Lee,L.P. (2005). *Royal Society of Chemistry Lab on a Chip* ,5, 38–43.
- 5.Weaver, J.C. (1993) *J.Cell. Biochem* 51:426-435.

Figure 5. Fast calcein loading. (a-d) Within a 3 sec time span, membrane impermeable Calcein is loaded into the cell using an electrophoretic driving force. (e) The cell intensity measured across a cell section (dotted line in a).

HIGH THROUGHPUT ELECTROPORATION MICROCHIP FABRICATED BY SINGLE-MASK INCLINED UV LITHOGRAPHY

Takaaki Suzuki¹, Hideo Yamamoto¹, Masataka Ohoka², Atsuhiro Okonogi³, Hiroyuki Kabata³, Isaku Kanno¹, Masao Washizu⁴ and Hidetoshi Kotera¹

¹ Kyoto University, Yoshida-honmachi, Sakyo-ku, Kyoto 606-8501, Japan,

² ASTEM, Yoshida-honmachi, Sakyo-ku, Kyoto 606-8501, Japan

³ HMRO, Kyoto University, Yoshida-konoecho, Sakyo-ku, Kyoto 606-8501, Japan

⁴ The University of Tokyo, 7-3-1 Hongo Bunkyo-ku, Tokyo, 113-8656, Japan

(takaaki@me.kyoto-u.ac.jp)

Abstract

We propose a high throughput electroporation microchip simply and rapidly fabricated by inclined UV lithography using a single photoresist layer on a mask. To confirm the validity of the proposed single-cell analysis chip, we demonstrated high-yield electroporation for mouse erythroleukemia (MEL) cells with the membrane impermeant substances, Trypan blue and nuclear transport factor CFP-importin β .

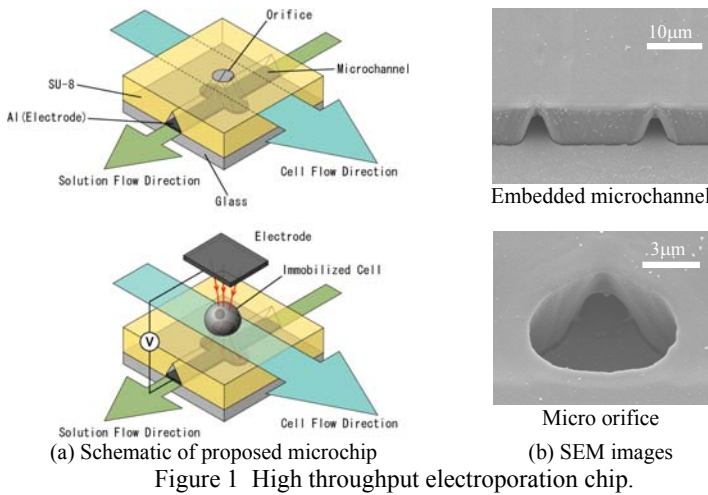
Keywords: Single cell analysis, electroporation, inclined UV lithography

1. Introduction

Electroporation induces structural rearrangements of the cell membrane by high electric field. Cellular responses to externally fed chemicals can be observed by temporarily increasing the cell membrane's permeability. Recently, some electroporation microchips have been proposed for high-throughput introducing impermeant substances such as DNA, proteins, dyes or drugs [1, 2]. In previous research literature, the authors have proposed a novel single-mask fabrication method for single cell analysis chips using inclined UV lithography to expose a single layered SU-8 coated on a patterned mask [3]. In this paper, we fabricated a high-throughput microchip by the proposed lithography, and demonstrated the electroporation for MEL cells with two assays with Trypan blue and CFP-importin β .

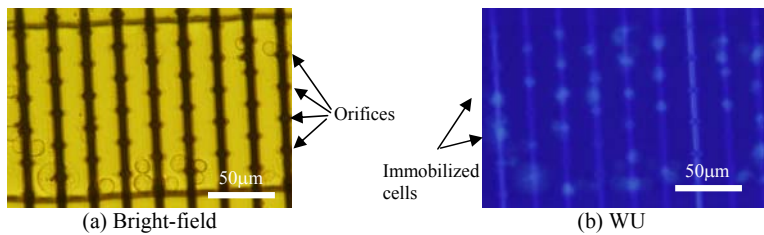
2. Experimental

A schematic and photographs of the high throughput electroporation chip are shown in Fig.1. The cells in the upper microchannels are immobilized at the high density arrayed orifices on the insulative SU-8 layer by negative pressure of the syringe pump. By applying a voltage between a metal mask at the bottom and a top electrode with field constriction [4], the immobilized cells are electroporated with the impermeant substances in the lower microchannel. We demonstrated the proposed system by introducing impermeant substance, e.g. Trypan blue and CFP-importin β .



3. Results and discussion

The cells in the upper microchannels are immobilized at the high density arrayed orifices by negative pressure of the syringe pump as shown in Fig.2. Firstly, a demonstration with MEL cells was carried out by electroporating the membrane impermeant dye Trypan blue, which can accumulate within the cell and appear a dark blue color. It is confirmed that Trypan blue introduced into the chip was fed to the cell's interior by the electroporation with the proposed chip as shown in Fig.3. As different assay experiment, time lapse images of the nuclear transport factor CFP-imporin β entering the MEL cell are shown in Fig.4. It can be seen that the CFP-imporin β accumulated within the cell nucleus and the fluorescent intensity was increasing with time. After the electroporation, we observed that mitochondria emitted fluorescence with Mit-E- Ψ Mitochondrial Permeability Detection Kit AK-116 (Biomol). It is seems that the cells are still alive after electroporating with the proposed chip using field constriction.



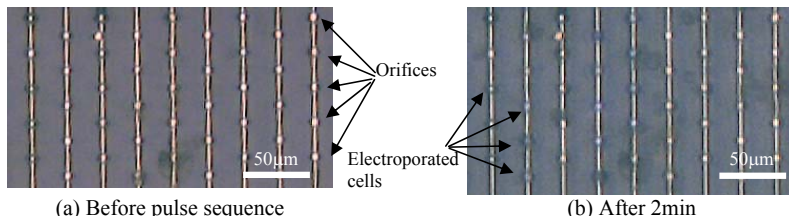


Figure 3 Electroporation of MEL cells immobilized at arrayed orifices with Trypan blue.

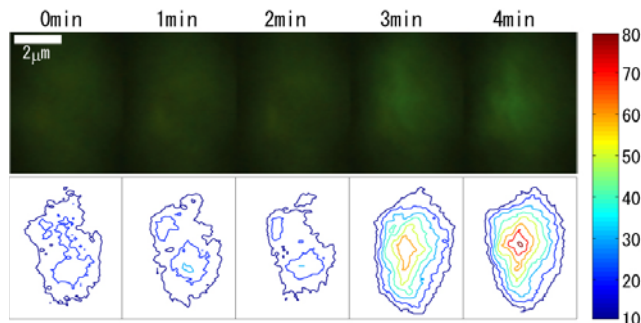


Figure 4 Time lapse images of CFP-importin β entering MEL cell.

Acknowledgements

This study is a part of Kyoto City Collaboration of Regional Entities for the Advancement of Technological Excellence of JST on the basis of research results supported in part by Mizuho Foundation for the Promotion of Sciences, and Center of Excellence for Research and Education on Complex Functional Mechanical Systems (COE program) of MEXT, Japan. The CFP-importin β was obtained by Prof. Makio Tokunaga (National Institute of Genetics) and Prof. Naoko Imamoto (RIKEN).

References

- [1] M. Khine, A. Kau, C. Ionescu-Zanetti, J. Seo and L. P. Lee, *Lab on a Chip*, vol.5, pp.38-43, 2005.
- [2] Y. Huang and B. Rubinsky, *Sens. Actuators A*, Vol.104, pp.205-212, 2003.
- [3] T. Suzuki, T. Tokuda, N. Fujiwara, H. Yamamoto, Isaku Kanno, M. Washizu and H. Kotera, *MicroTAS'05*, pp.1183-1185.
- [4] M. Washizu, Y. Wake, O. Kurosawa, H. Oana, S. Matsuoka, A. Noma and H. Kotera, *MicroTAS'05*, pp.1401-1403.

FLOW-LESS CENTRIFUGATION-FREE WASHING AND INCUBATION WITH SINGLE-CELL RESOLUTION

G. Medoro¹, A. Fittipaldi¹, A. Simoncelli¹, L. Altomare², R. Guerrieri²,
N. Maresi¹

¹ Silicon Biosystems, Italy

²ARCES, The University of Bologna, Italy

Abstract

In this paper we present a method to implement the equivalent of a complex incubation and washing protocol with single-cell resolution in a miniaturized lab-on-a-chip device (DEPArray™) without the need of centrifugation nor fluid flow.

Keywords: single-cell, dielectrophoresis, centrifugation, fluorescence, lab-on-a-chip

1. Introduction

Ubiquitous sample preparation steps involving cells, such as washing and incubation with fluorescent labels are traditionally implemented with centrifuges, resulting in significant cell losses when using small cell loads, as well as relatively high volumes of reagents. Attempts to miniaturize these process steps have been reported [1], but still rely on flow through devices, implying the use of pumps with sustained flows of reagents. This paper demonstrates how it is possible to implement the equivalent of a complex incubation and washing protocol with single-cell resolution in a miniaturized lab-on-a-chip device (DEPArray™) without the need of centrifugation nor fluid flow.

2. Protocol description

DEPArray™ platform is based on moving dielectrophoretic cages [2,3]; an array of electrodes implements tens of thousands of micro-cages on a bidimensional space; each micro-cage (which size is comparable with those of cells) is capable to entrap an individual cell, the position of which can be reconfigured by software making thus possible a selective movement of each cell along any path in the whole device. The DEPArray™ is equipped with two micro chambers each of which can be loaded with a different buffer (figure 1) making thus possible the implementation of the following protocol:

1. Sample and reagent loading: (figure 1,a) 1 μ l of celcein buffer solution (1 μ M.) is loaded in the reagent chamber; (figure 1,b) 2 μ l of PBS is loaded in the main chamber; (figure 1,c) 1 μ l of sample containing human chronic myelogenous leukemia K562 cells (5×10^5 cells/ml.) suspended in PBS are loaded in the same chamber;

2. Cell routing: (figure 1,d) cells are entrapped in a regular pattern; one cell is selected and routed from the original position into the reagent chamber while all the other cells are kept suspended in the original position;
3. Incubation: (figure 1,e) once arrived in the reagent chamber the selected cell is kept suspended for 5 minutes, enough to complete the staining process;
4. Washing: (figure 1,f) the stained cell is moved back into the original position (PBS buffer); passing from the reagent chamber to PBS the cell is consequently washed; a fluorescent signal is expressed selectively by the stained cell as shown in figure 2.

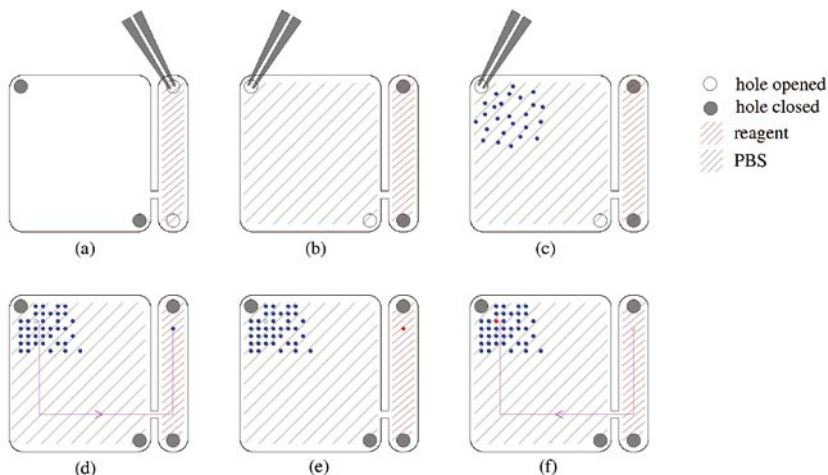


Figure 1: (a) Reagent Loading: the reagent is loaded on the right side of the chip (reagent chamber); the holes of the main chamber should be closed; (b) Buffer Loading: the buffer is loaded on the left (main chamber); the holes of the reagent chamber should be closed; (c) Cell Loading: cells are injected in the main chamber; (d) Cell Routing: cells are organized into micro-cages; one cell is moved into reagent chamber; (e) Incubation: the cell is kept suspended in the reagent chamber; (f) Washing: the cell is moved back to the original position.

3. Discussion

Notable advantages of this approach in comparison with standard techniques include:

High resolution: the protocol is effective at level of single cell, while standard protocols can only be executed on the whole sample without any selectivity;

Functional integration: this procedure can be used as a building-block and can be easily integrated in a complete analytical process-flow substituting external sample preparation steps; this is of paramount importance in the perspective of system integration of cell-based analytical devices;

Operates on living cells: DEPArray™ is gentle with cells and guarantees viability and proliferation [4];

Reduce timings and costs: since the protocol does not require active fluid flow or manual procedures, it is applicable also when very small amounts of sample and reagents are available (few microliters are enough to fill the whole microchamber device) while hundreds of microliters are normally required in standard procedures.

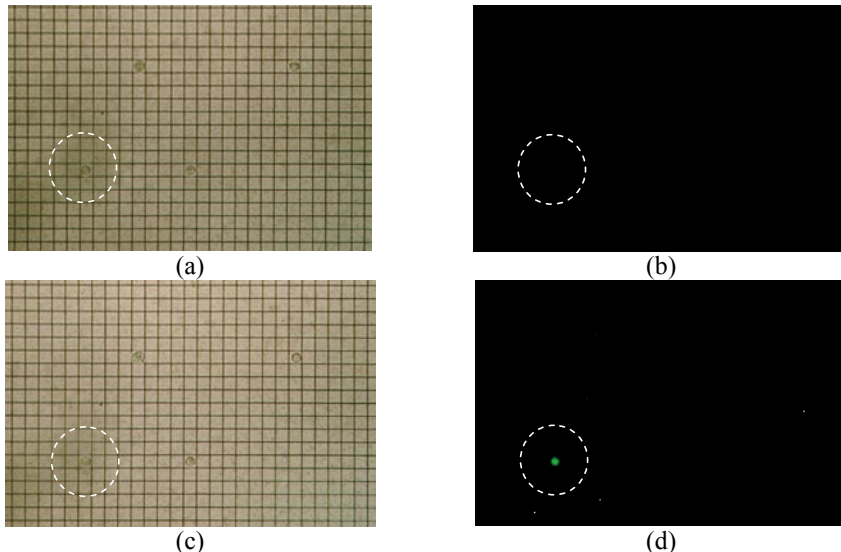


Figure 2: comparison between the cell position and fluorescence before (a-b) and after (c-d) cell dipping in calcein; at beginning the cells are organized into a regular pattern (a); no cell appears fluorescent (b); the cell identified by a dotted circle is moved in the reagent chamber, incubated and moved back to the same initial position (c); only this cell is now fluorescent (d).

3. Conclusions

In conclusion a complex incubation and washing protocol with single-cell resolution has been presented. The protocol has been implemented in a miniaturized lab-on-a-chip device without fluid flow or mechanical centrifugation.

References

1. U. Sager et al., "Cell Immersion and Cell Dipping in Microfluidic Devices", *Lab Chip*, 4, 148-151 (2004).
2. G. Medoro et al., "CMOS-only Sensors and Manipulator for Microorganisms", *Proc. IEDM*, 415-418 (2000).
3. N. Manaresi et al., "A CMOS Chip for Individual Cell Manipulation and Detection", *IEEE JSSC*, 38, 12 (2003).
4. A. Fuchs et al., "Electronic sorting and recovery of single live cells from microliter sized samples", *Lab Chip*, 6, 121-126 (2006).

METHOD FOR SELECTIVE CELL LYSIS BASED ON DIELECTROPHORESIS

Gianni Medoro¹, Melanie Abonnenc¹, Antonio Fittipaldi¹, Alessandro Simoncelli¹, Aldo Romani², Roberto Guerrieri² and Nicolò Maresi¹

¹ Silicon Biosystems, Italy,

² ARCES, The University of Bologna, Italy

Abstract

A method for selective cell lysis based on dielectrophoresis is presented. As far as we know this is the first time that this procedure is demonstrated with the resolution of a single cell in a pool of thousands, opening a wide range of applications in the field of single-cell biology based on lab-on-a-chip.

Keywords: lab-on-a-chip, cell, lysis, dielectrophoresis, cage

Introduction

The method for selective cell lysis presented in this paper is based on the use of a programmable lab-on-a-chip (DEPArray™) which uses dielectrophoresis to manipulate cells; the same force is exploited to get controlled lyses with the resolution of a single cell. This technique can be adopted to implement the following experiments:

1. sorting of living cells: sorting one or more cells of interest is possible simply by destroying all the other cells and recovering the whole sample;
2. survival cell analysis and sorting: in case more than one cell line is present in the sample, the parameters can be chosen to act selectively on a specific cell line making in this way possible an identification or a selection of the cell type;
3. selective DNA cell extraction: extracting the DNA is possible from one or more cells combining the dielectrophoretic trap force with a fluid flow; the cell of interest is lysated and the DNA is moved toward the exit transported by fluid flow while all the other cells in the sample are retained inside the chip;

Compared to other techniques [1] based on dielectrophoresis, the proposed approach offers the unique advantages of single-cell resolution (from one to hundreds or thousands of cells can be processed in parallel) and functional integration (the method can be combined with single cell manipulation and detection presented in [2]).

Device description

A prototype microelectronic lab-on-a-chip (DEPArray™) for massively parallel manipulation of cells based on moving dielectrophoretic cages [2] has been used; the core of DEPArray™ is an array of 100.000 programmable electrodes by which up to 25.000 micro-cages can be realized; each micro-cage (which size is comparable with those of cells) is capable to entrap an individual cell if negative dielectrophoresis is established; depending on the nature of buffer (and cells) the dielectrophoretic

behaviour can change from negative (nDEP) to positive (pDEP) simply changing the operating frequency of the applied voltages [3]; in case of nDEP cells are attracted toward the minima of the electric field (corresponding to the cage centers) while in case of pDEP cells are attracted to the maxima of the electric field (corresponding to electrode edges).

Protocol description

Selective cell lysis can be obtained as described in figure 1. In the first step of the protocol an array of cages is established by applying $3.3\text{Vpp}@50\text{kHz}$ to a first pattern (figure 1,a). The cells are consequently organized and trapped in nDEP into the cages. In the second step, the voltages change to $3.3\text{Vpp}@1200\text{kHz}$, switching to pDEP, and simultaneously a different pattern is applied (figure 1,b). This new pattern creates localized field maxima around in-phase electrodes, which are set in correspondence of each target cell (only one in the case of figure). The high field ($3.3\text{V}/1.2\text{ m}=2.75\text{MV/m}$) at selected electrode gaps causes a trans-membrane potential which is lethal for the target cell, but the field gradient vanishes at the location of neighbouring non-target cells, which slowly fall-down and remain approximately in the position where their cage was originally located. After five seconds the first pattern and frequency are restored, so that remaining cells are levitated again in nDEP cages.

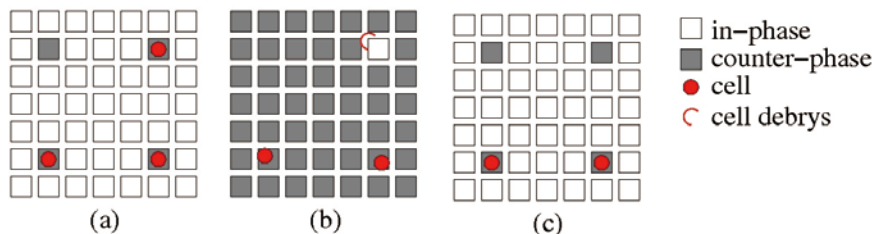


Figure 1 (a) an array of cages is obtained using first pattern ($3.3\text{Vpp}@50\text{kHz}$); a cage is localized where a counter-phase voltage is applied (the same phase is applied to the lid); an in-phase signal is applied to all the other electrodes; (b) selected cell lyses require a change of the voltage pattern and frequency; 1.2MHz is used as frequency and a pattern composed of a counter-phase signal in the target position and an in-phase signal to all the other electrodes; (c) finally the original pattern is applied.

Experimental results

As proof-of-concept, a simple experiment is reported in figure 2. Selective sequential lysis of two out of three cells (namalwa cells suspended in a solution of Mannitol 280mM and 6.25mM KCl) in a small portion of the chip. Persisting fluorescence of non-target cells demonstrates that neighbouring cells are unharmed.

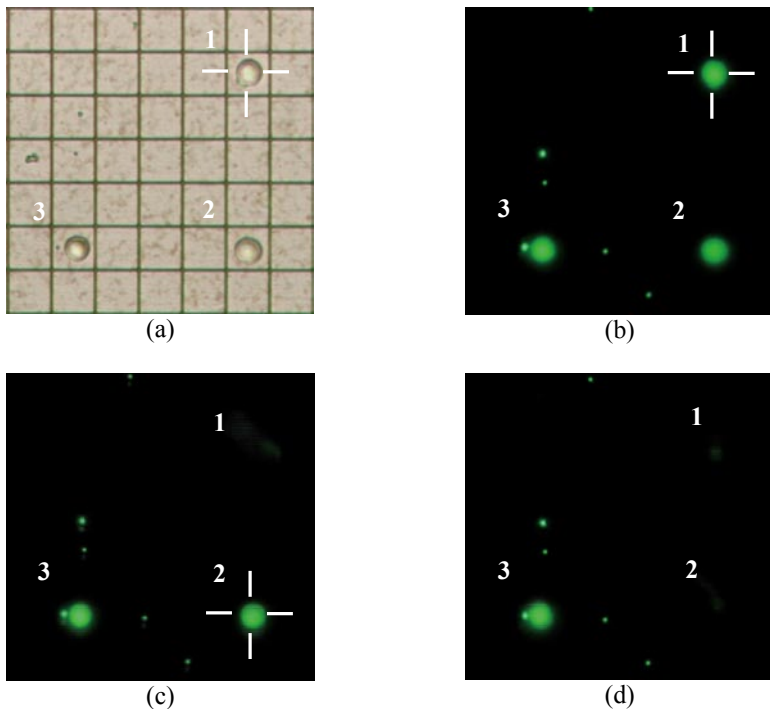


Figure 2: Snapshots from a sequence of selective cell lyses: (a) three cells are organized into a regular pattern; all cells -loaded with calcein- are fluorescent (b); cell N.1 is selected and destroyed first (c) followed by cell N.2 (d); at the end only cell N.3 is alive and still perfectly fluorescent.

Conclusions

In conclusion a method for selective cell lysis based on dielectrophoresis has been presented. This method offers the unique advantages of single-cell resolution and functional integration.

References

1. A. Menachery and R. Pethig, "Controlling cell destruction using dielectrophoretic forces", IEE Proc.-Nanobiotechnol., Vol. 152, No. 4, (2005).
2. N. Minaresi et al., "A CMOS Chip for Individual Cell Manipulation and Detection", IEEE Journal of Solid State Circuit, 38, 12 (2003).
3. X-B. Wang et al. "A unified theory of dielectrophoresis and travelling wave dielectrophoresis", J. Phys. D: Appl. Phys., 27, 1571-1574 (1994).

A CELL-RELEVANT MICROGRADIENT ENVIRONMENT

Thomas Frisk¹, Susanna Rydholm², Helene Andersson³,
Hjalmar Brismar², Göran Stemme¹

¹Microsystems Technology, Royal Institute of Technology,
SE-100 44 Stockholm, Sweden

²Cell Physics, Royal Institute of Technology

³Nanobiotechnology, Royal Institute of Technology
tfrisk@kth.se

Abstract

A device for microgradient cell environment has been designed, built and successfully evaluated with gel embedded MDCK cells.

Keywords: gradient, cells, culture, 3D

1. Introduction

With confocal microscopy new knowledge in cell physiology is acquired daily. However, most cell assays today are carried out either as multiwell plate assays, or in standard petridish assays. These two methods have different features and foci, but they have in common the large amount of cells submitted for treatment and imaging. In order to study only a few cells on a more detailed level[1, 2] in a relevant context, we have designed, built, and evaluated a microfluidic system. It features 1) immobilization of cells in three dimensions, 2) transportation of cell nutrients and treatments as well as removal of residual products, 3) an extremely stable and physiologically relevant gradient of chemical concentration distribution around the cell. Previous efforts in this field by our group revealed a few very important issues, indicating that microfabrication would be the enabling technology for experiments on cells in asymmetric environments.

2. Experimental

The ‘micromolar per micrometer’ gradient chip was manufactured with standard microfabrication methods including two soft masks and photolithography, DRIE and anodic bonding of 300 µm thin silicon to 170 µm thin glass. The smallest cell assay chamber measures length 100 µm by width 100 µm and height 50 µm.

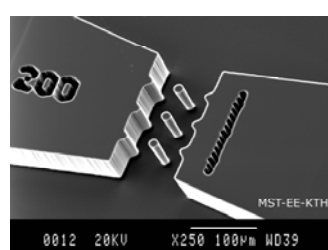


Figure 1. Gel cavity before glass lid bonding and backside hole etching.

Also larger chambers were manufactured with lengths ranging up to 500 μm . For long-time assays, position stability of the gel (and thus embedded cells) is of great importance.

Anchoring of the gel is accommodated through small pillars (20 μm diameter) in the cell-gel chamber/cavity as well

as bumps in the walls of the cavity (figures 1 & 2).

Filling of the cavity with cell-gel mixture is done with a nl syringe pump (figure 3).

The chamber volume ranges from 5 nl to approx. 15 nl. After filling, incubation in 37°C for 30 min results in a gel with cells secured in three dimensions. Through the two perfusion channels (0.1-0.5 $\mu\text{l}/\text{min}$), treatment and nutrients can be delivered in well controlled manner. The very small

distance (100 μm) between the channels enables a gradient of concentration

distribution which is

physiologically relevant and close to in-vivo-like dimensions. A larger distance between the channels would have meant larger concentration differences needed, thus treating cells close to the channels with non-relevant, poisonous concentrations.

3. Results and discussion

The time stability of the gel was studied with fluorescein in one channel and PBS in the other channel. The development of the gradient can be seen in figure 4.

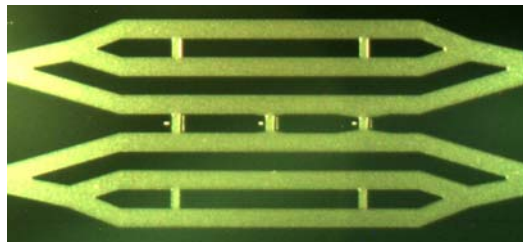


Figure 2. Fluidic system with 2+2 reference cavities and 3 cavities in middle with different lengths, here 300 μm , 400 μm and 500 μm . The varying lengths enables three different gradient slopes within the same chip. Perfusion channel widths 500 μm .

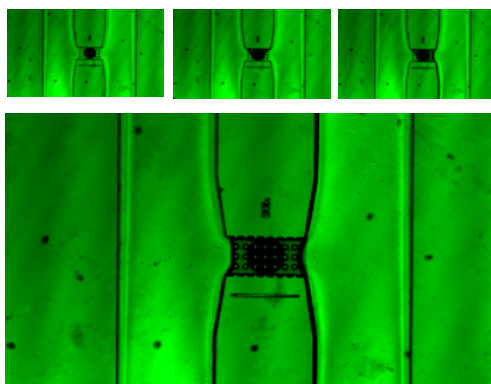


Figure 3. Filling sequence. 15 nl with cell-gel-mixture deposited with syringe pump with 10 μl syringe set to dispense 10 nl.

After three hours the gel was still intact, non-moving, thus stable both in its physical properties as well as its transportation (diffusion) accommodating function. Viable cells in ECM gel in the 100 x 100 μm cavity and in 100 x 300 μm cavity are shown in figures 5 and 6.

4. Conclusion

The new device has been tested with perfusion treatment of cells embedded in extracellular matrix gel, with the gel itself being a diffusion limiting barrier causing a chemical gradient acting on the cells, as well as acting as a fluid barrier causing ‘short circuits’ of the two flows, and immobilizing cells in true 3D, thus

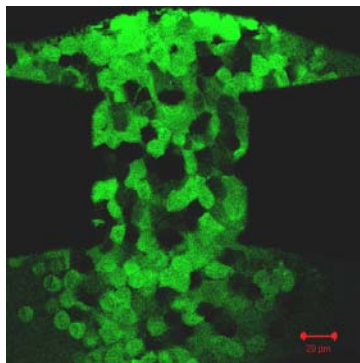


Figure 5. Cells embedded in ECM gel in a 100 μm long and 100 μm wide cavity. A slight overfill is visible. Cell density $12 * 10^6$ per 100 μl . Staining done with fluo-4 20 min.

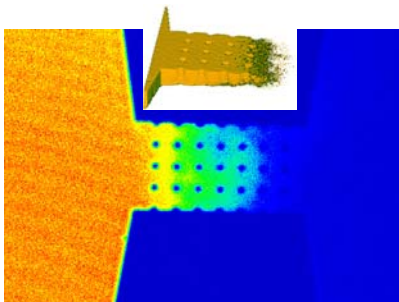


Figure 4. Fluorescein diffusing through Matrigel ECM gel. Insert shows 3D concentration view.

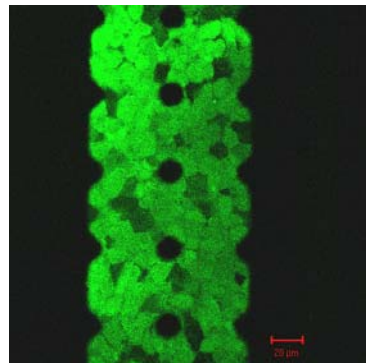


Figure 6. Cells embedded in ECM gel in the 300 μm long and 100 μm wide cavity. Cell density $12 * 10^6$ per 100 μl . Staining done with fluo-4 20 min.

mimicking the in-vivo situation well. The small dimensions enable physiologically relevant osmolarities and studies of individual cellular reactions to dual treatments.

References

- 1 S. Takayama, E. Ostuni, P. Leduc, K. Naruse, D.E. Inger, and G.M. Whitesides, Subcellular Positioning. *Nature*, 2001. 411: p. 1016.
- 2 D.M. Thompson, K.R. King, K.J. Wieder, M. Toner, M.L. Yarmush, and A. Jayaraman, Dynamic Gene Expression Profiling Using a Microfabricated Living Cell Array. *Anal. Chem.*, 2004. 76: p. 4098-4103.

MICROFABRICATED DEVICE FOR CONTROLLED STIMULI OF PRIMARY CILIA

Susanna Rydholm¹, Thomas Frisk², Helene Andersson³, Göran Stemme²,
Hjalmar Brismar¹

¹Cell Physics, Royal Institute of Technology, SE-106 91 Stockholm, Sweden

²Microsystems Technology, Royal Institute of Technology

³Nanobiotechnology, Royal Institute of Technology

Abstract

We present an improved device and method for studying cellular response on microfluidic controlled stimuli of primary cilia. The primary cilium functions as a mechano-sensor in renal tubular epithelium. Malfunction of cilia has been implicated in polycystic kidney disease as well as other kidney abnormalities. Bending of cilia will give rise to an intracellular calcium signal [1,2,3], but little is known about the importance of flow direction, magnitude and duration to the calcium response. Our preliminary results indicate flow speed sensitivity.

Keywords: cilia, cell, flow, sensitivity

1. Introduction

Cilia are hair like structures with a diameter of approximately 250 nm extending from 2 to more than 10 μm from the surface of the cell. Two types of cilia exist, motile and non-motile. The non-motile type is also called the primary cilium since there is only one present on each cell. The primary cilium is present in virtually all epithelial cells, functioning as a flow sensor via intracellular calcium when bent by a mechanical force. Malfunction of the cilia results in pathological processes such as polycystic kidney disease. Figure 1 shows a mechanical model of the primary cilium.

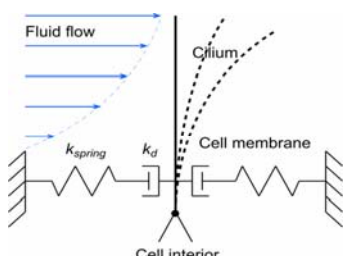


Figure 1. Mechanical model of cilium.

Although it is established that the primary cilium is an important flow sensor, little is known about the dynamic properties of cilia in sensing fluid flow. It is likely that for the physiological function, not only the presence of a flow but also the direction, magnitude and duration is of importance. Those parameters have not been possible to study on a cellular level previously.

Our approach to address these questions is based on the development of micro fluidic structures that allows control of mechanical and biochemical parameters on a submicrometer scale. The structures also allow the use of high resolution microscopy for studies of the dynamics in cilia function as well as the system generating intracellular calcium signals.

2. Experimental

The microfluidic structure consists of two orthogonal channels with inlets and outlets (figure 2) to enable orthogonal flows. The channels dimensions are 500 $\mu\text{m} \times 50 \mu\text{m}$. A 1 mm diameter opening through the silicon in the channel cross (not shown in figure 2) enables cell seeding. The structure was manufactured through standard microfabrication methods, including two soft masks, photolithography, DRIE and anodic bonding of 300 μm thin silicon to 175 μm thin glass. This thin glass is necessary to enable high resolution confocal microscopy imaging.

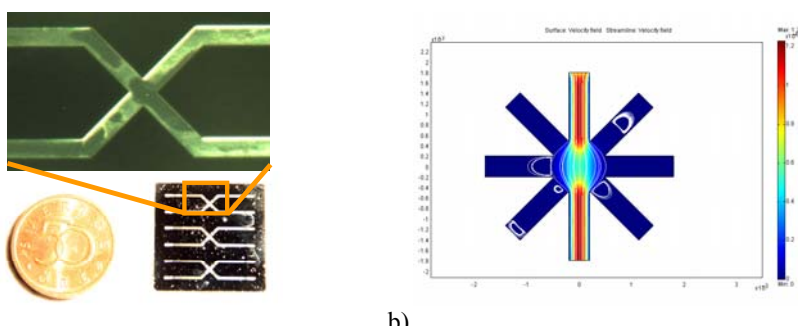


Figure 2 a) Silicon-glass chip. Channel dimensions: width = 500 μm , depth = 50 μm . Flow rates: 10-100 $\mu\text{l}/\text{s}$. b) FEM simulation of flow in microfluidic model system. Flow speed is less than half in the center cross compared to in the channels.

Flow control is achieved with a syringe pump and a 10 μl syringe. This setup enables a non-pulsating flow down to 0.5 μl per minute, corresponding to an approximate flow rate of 1 μm per second in the channel. Flow characteristics were investigated through the use of fluorescent beads in the flow and recording of their trajectories. Also a FEM analysis of the flow pattern was performed (figure 2b).

MDCK-cells (kidney epithelial cells, passages 10-20) were seeded into the chip at the concentration of 1 million cells per ml and cultured for three to four days to develop cilia (figure 3). During culture the chip was inserted in culture medium in the incubator at 37 °C. Cell staining was performed with the calcium sensitive fluorescent dye fluo-4 (5 μM) during 20 minutes. Intracellular calcium levels are then registered as variations of fluorescence intensity. A 20 to 30 minutes stabilization period was used before each flow test, as the cells need some time to recover after stimuli.

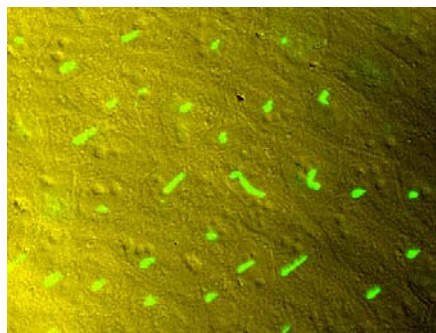


Figure 3. Ciliaforming MDCK cells. Majority of cells forms cilia, with lengths ranging from 2 μm to 4 μm . Culture time 3 days. Cell contours vaguely visible.

3. Results and discussion

Response times at a flow rate of 2 $\mu\text{l}/\text{min}$ (about 5 $\mu\text{m}/\text{s}$) were in the order of 5-10 s. Response times at 4 $\mu\text{l}/\text{min}$ (about 10 $\mu\text{m}/\text{s}$) were of similar magnitude 5-8 s. Response times at 7.5 $\mu\text{l}/\text{min}$ (about 10 $\mu\text{m}/\text{s}$) were in the 3-5 s range. Figure 4 shows graphs on intensity increase at flow stimuli. Differences in response times could be due to position in channel (parabolic flow profile), different cellular ability to respond or due to exhaustion after multiple consecutive flow starts and stops.

Reaction times at flow of 2 $\mu\text{l}/\text{min}$ (approx. 5 $\mu\text{m}/\text{s}$) were in the order of 5-10 s. Reaction times at 4 $\mu\text{l}/\text{min}$ (approx. 10 $\mu\text{m}/\text{s}$) were of similar magnitude 5-8 s. Reaction times at 7.5 $\mu\text{l}/\text{min}$ (approx 20 $\mu\text{m}/\text{s}$) were in the 3-5 s range. See figure 4 for graphs on intensity increase on flow stimuli. Reaction time spread could be due to position in channel (parabolic flow profile), different cellular ability to respond or due to cell exhaustion after multiple consecutive flow starts and stops.

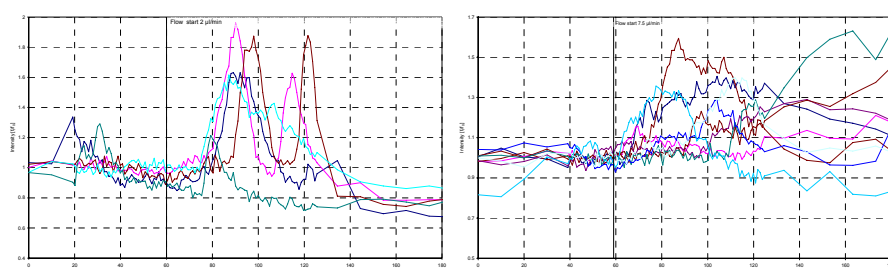


Figure 4. Intensity data recordings from cells stimulated with (top) 2 $\mu\text{l}/\text{min}$ (approx. 10 $\mu\text{m}/\text{s}$ at cilium level) and 7.5 $\mu\text{l}/\text{min}$ (approx. 40 $\mu\text{m}/\text{s}$).

4. Conclusions

Miniaturization through micromachining enables structures for precise flow directionality, laminar flow profiles and minimization of flow disturbances. On a cellular level we have now showed the response to controlled flow induced ciliar movement and the flow sensitivity of cilia. Our preliminary results indicate flow speed sensitivity.

References

1. Bending the MDCK Cell Primary Cilium Increases Intracellular Calcium, H. A. Praetorius, and K. R. Spring, Journal of Membrane Biol., **184**, 71 (2001).
2. Effect of flow and stretch on the $[\text{Ca}^{2+}]_i$ response of principal and intercalated cells in cortical collecting duct, W. Liu, et al., Am. J. Physiol. Renal Physiol., **285**, 998, (2003)
3. Polycystins 1 and 2 mediate mechanosensation in the primary cilium of kidney cells, S. M. Nauli, et al., Nature Genetics, **33**, 129, (2003)

INSIGHTS INTO NEUTROPHIL POLARIZATION MECHANISMS THROUGH THE USE OF MICROFLUIDIC DEVICES

Daniel Irimia and Mehmet Toner

BioMEMS Resource Center, Center for Engineering in Medicine and Surgical Services, Massachusetts General Hospital, Shriners Hospital for Children, and Harvard Medical School, Boston, MA 02114

Keywords: microstructured membrane, chemotaxis, gradient, neutrophil, mechanistic model

Better understanding of neutrophil polarization and migratory responses has direct implications in developing new therapeutic approaches to wound healing, inflammation, or cancer. Although many of the signaling molecules involved have been already characterized using sophisticated molecular biology tools, the mechanisms through which these components interact to produce cellular responses are less well understood. Here we present some new insights into neutrophil sensing mechanisms that we gained by using a basic engineering approach enabled by microfluidic devices.

We developed a general concept of pneumatically actuated, microstructured membranes to expose neutrophils to precise spatial and temporal changes of chemical gradients. Current experimental techniques that rely on the use of micropipettes positioned close to cells, and which can be turned on and off, or quickly displaced from one side of a cell to the other, produce gradients that are notoriously difficult to control and are easily perturbed by external factors. Using the new microfluidic devices that incorporate microstructured membrane structures into microfluidic gradient generators, we were able to expose neutrophils to precise spatial and temporal changes of chemical gradients [1]. Less than 4 seconds were needed for the formation of a gradient in a channel initially containing no chemical, or to switch between any two preformed chemokine gradients (Fig.1).

An axi-symmetric microstructured valve was designed to allow the creation of circumferentially uniform, fast changing chemical conditions around cells for the study of fast temporal stimuli in the absence of spatial gradients [2]. Cells and the reagents were trapped under a microstructured membrane with two concentric structures in a configuration that allowed the rapid change of solutions around the cell while preserving the spatial uniformity on the cell circumference. We measured the uniformity of concentration on a 200 μm diameter circle and estimated that less than 1% deviations from uniform conditions occurred on the circumference of a 20 μm diameter cell during exposure to the solutions loaded in the intermediate compartment (Fig.2).

The response of resting, primary human neutrophils to the newly established gradient was gradual. Spherically shaped, resting neutrophils began forming ruffles on their entire surface immediately after the exposure to a gradient. With time, the protrusions on cell surface decreased in number while increasing in size, until morphology characteristic of full polarization, represented by a leading edge and uropod, was achieved (Fig.1). Upon stimulation with a circumferentially uniform, temporal gradients, neutrophils transiently polarize in random directions and then quickly reverse to un-polarized state (Fig.2).

Starting from the observations of the initiation of neutrophil polarization and the adaptation to changes in the direction or average concentration of chemotactic gradients, we proposed a new hypothesis for neutrophil chemotactic response based on a temporal mechanism for gradient sensing. Our observations suggest that two temporal sensing mechanisms, one global (over the entire cell body) and one localized (leading edge), collaborate to direct neutrophil responses to microenvironment changes. While increasing averaged chemokine stimulation over the entire cell surface reinforces neutrophil polarization and directional migration, decreasing stimulation leads to polarization collapse and neutrophil stop. We implemented these mechanisms into a mechanistic model for neutrophil polarization and initial results suggest that known biochemical reactions form an adaptive control mechanism of extreme sensitivity. One important feature of the model is that it captures the oscillatory behavior of neutrophils during the initial polarization (Fig.3). In addition, this model could provide and explanation for the neutrophil responses to spatial and temporal chemotactic gradient changes observed in other experiments[3].

Through these examples, we demonstrate how microfluidic devices for controlling time and space of chemical gradients are poised to become enabling technologies for biomedical research into the biology of neutrophil chemotaxis.

REFERENCES:

1. Irimia, D., S.Y. Liu, W.G. Tharp, A. Samadani, M. Toner, and M.C. Poznansky, *Microfluidic system for measuring neutrophil migratory responses to fast switches of chemical gradients*. Lab Chip, 2006. **6**(2): p. 191-8.
2. Irimia, D. and M. Toner, *Cell handling using microstructured membranes*. Lab Chip, 2006. **6**(3): p. 345-52.
3. Jeon, N.L., H. Baskaran, S.K.W. Dertinger, G.M. Whitesides, L. Van de Water, and M. Toner, *Neutrophil chemotaxis in linear and complex gradients of interleukin-8 formed in a microfabricated device*. Nature Biotechnology, 2002. **20**(8): p. 826-830.

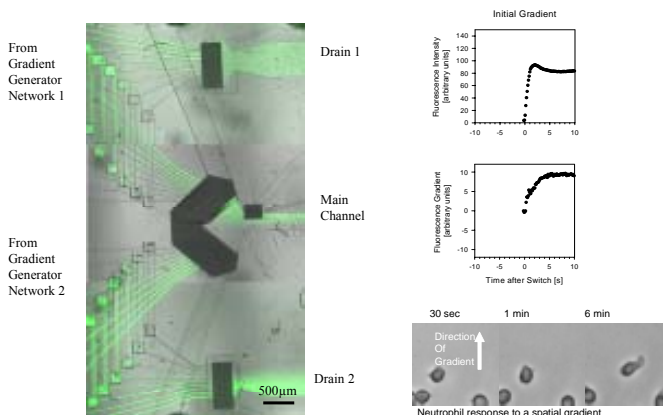


Fig.1. Neutrophil responses to the formation of spatial gradients. A microfluidic device consisting of two gradient generator networks have been combined through the use of an ensemble of microstructured valves. A new chemotactic gradient could be formed around neutrophils in less than 5 seconds. Neutrophils polarize in the direction of the gradient after a series of "trial and error" events.

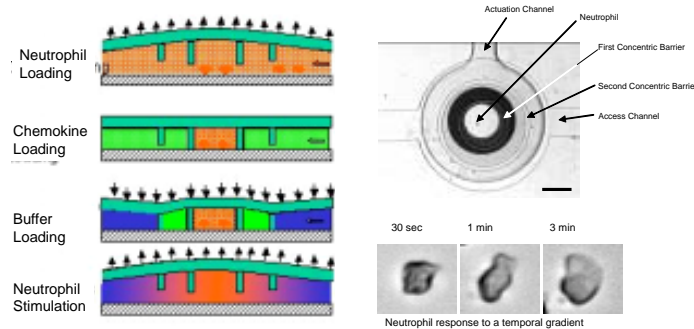


Fig.2. Neutrophil responses to the formation of temporal gradients. A microstructured membrane has been employed to create two concentric compartments around one neutrophil. Upon actuation, neutrophils were exposed to a circumferentially uniform concentration of chemokine that varied with time. Neutrophils polarize in a random direction.

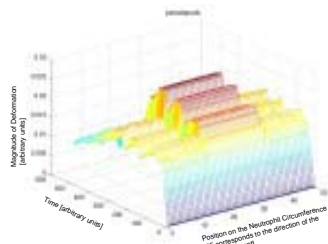


Fig.3. A mechanistic model has been developed to simulate the formation of pseudopods on the circumference of neutrophils following stimulations with spatial and/or temporal stimuli.

TRAPPING & CHEMICAL DOSING OF SUSPENDED CELLS IN HYDRODYNAMIC TWEEZER ARRAYS

Barry R. Lutz,^{*} Jian Chen,[†] Daniel T. Schwartz,[‡] and Deirdre R. Meldrum^{*}

^{*}Microscale Life Sciences Center, University of Washington, USA

[†]Department of Chemical Engineering, University of Washington, USA

Abstract

Hydrodynamic tweezers use audible-frequency oscillations around fixed obstacles in a microchannel to create non-contact traps for single cells. We describe trapping, fluorescence measurement, and chemical treatment in arrays of suspended cells.

Keywords: cell trapping, steady streaming, suspension cells

1. Introduction

Dynamic measurements of single cell behavior require a method of holding single cells in place for measurements while delivering chemical nutrients, reagents, and indicators. Hydrodynamic tweezers suspend single cells in steady streaming eddies created by a gentle oscillating flow without the need for physical contact or external fields [1, 2]. Steady streaming is a well-studied phenomenon, but it has recently been applied in microfluidics for cell transport [3] and cell lysis [4], as well as the trapping described here. We have shown that picoNewton trapping forces are created under conditions comparable to arterial blood flow [1], and traps can be numbered-up to create trapping arrays that tolerate net fluid flow [2]. Here, we show that net flow can be used to perform dosing and washing steps needed for assays on single suspension cells.

2. Experimental

The device (Fig. 1) creates cell traps in a microchannel containing fixed cylinders (radius, a) by oscillating the fluid at audible frequency (ω) and small displacement amplitudes ($s \sim 0.1a$). Fluid ports allow injection of cell sample, fluorescent indicators, and dye-free medium directly into the trapping array (Fig. 1, *Lower*). An ITO-coated conductive slide serves as a resistive heater to maintain cell culture temperature (37 °C).

3. Results and Discussion

For the case of a single cylinder in a sinusoidal oscillation, four symmetric eddies are created around the cylinder [5], and each eddy suspends a cell at the channel midplane [1]. Figure 2A shows the two pairs of symmetric eddies around a single cylinder when net flow is superimposed on the oscillation. Cells carried in the flow are captured by upstream eddies (Fig. 2B), while downstream traps typically remain vacant.

Trapped objects appear only to rotate (~1-10 Hz for conditions here) for low amplitude (Figs. 3A and 3B) or under pulsed illumination, while the oscillation of trapped objects is apparent at higher amplitudes (Figs. 3C and 3D). Experiments and calculations show that even large oscillation amplitudes have little effect on the fluorescence intensity integrated over the trap area (e.g., 5% for $s/a=0.1$, not shown).

For single isolated cylinders, we have shown that the trap strength is controlled via the oscillation conditions [1], and cells remain trapped under flowrates up to 1 cm/sec [2]. Fig. 4 shows flow images in arrays for pure oscillation (Fig. 4A) and two superimposed net flow velocities (Figs. 4B and 4C). Because the steady streaming originates from a thin boundary layer near the cylinder [5], close spacing of cylinders has little effect on the flow and trapping behavior compared to single isolated cylinders.

The ability to exchange the fluid medium is an essential feature of fluorescence-based assays requiring wash steps as well as dynamic chemical stimulus experiments. Fig. 5 illustrates chemical dosing and washing in an array by switching between flow of a fluorescent dye and dye-free buffer. For flow velocities compatible with moderate strength traps, dye can be delivered uniformly throughout the array (Fig. 5B) and washed away (Fig. 5C) with an exchange time of about 30 seconds. Faster exchanges are possible in stronger traps, and a portion of the array can be dosed by simultaneous flow of dye and buffer.

Fig. 6 illustrates steps used to perform a fluorescence vitality assay on an array of trapped T-cells. Cells incubated off-chip with a fluorescent vitality indicator (C_{12} -resazurin) are injected into the channel, where they are trapped in suspension by upstream eddies (Fig. 6A and 6B). Fluorescence background from excess dyes prevents measurement of cell fluorescence (Fig. 6C) unless a wash step is performed. In Fig. 6D, the fluorescence signal from metabolizing cells is measured without background interference after switching flow to dye-free medium. Here, exchange of the medium for washing or chemical dosing can be accomplished while cells are held in suspension.

4. Conclusions

The ability to perform chemical dosing and washing steps is necessary for many fluorescence-based optical assays as well as dynamic stimulus experiments. Hydrodynamic tweezers use gentle fluid forces created by audible frequency oscillations to suspend cells in a flowing stream without requirement for cell modification or external fields that may perturb cell behavior.

Acknowledgements

We thank the NIH/NHGRI Genome Training Grant administered by the UW Genome Sciences Department; the Microscale Life Sciences Center, an NIH Center of Excellence in Genomic Science (Co-directors Prof. Deirdre Meldrum (PI) and Prof. Mary Lidstrom); and the Boeing-Sutter Endowment for Excellence in Engineering (Prof. Daniel Schwartz) for funding this work.

References

1. Lutz, B.R., J. Chen, and D.T. Schwartz, *Anal. Chem.* **78**, 5429-5435 (2006).
2. Lutz, B.R. and D.R. Meldrum. *MicroTAS 2005*. Boston, MA.
3. Marmottant, P. and S. Hilgenfeldt, *Proc Natl Acad Sci USA* **101**, 9523-9527 (2004).
4. Marmottant, P. and S. Hilgenfeldt, *Nature* **423**, 153-156 (2003).
5. Lutz, B.R., J. Chen, and D.T. Schwartz, *Phys. Fluids* **17**, 023601 (2005).

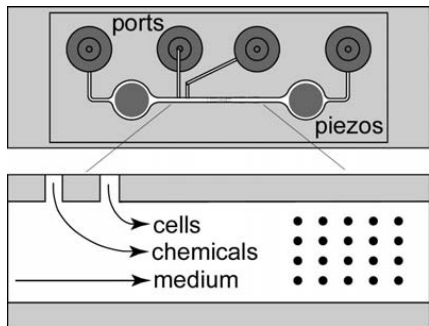


Figure 1. Schematic of the trapping flow cell. Fluid ports introduce cell sample, medium, and dye; piezoelectric discs oscillate fluid in the central channel; Traps are created around each cylinder.

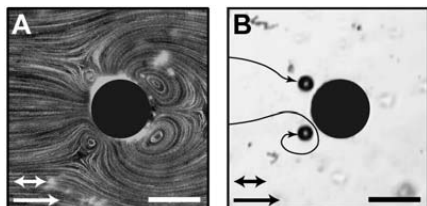


Figure 2. Particle capture from a flow stream. (A) Combined steady streaming and net flow. (B) Upstream traps capture particles from the flow, while downstream traps typically remain empty. Scale bars 100 μm , $\omega=1875$ Hz.

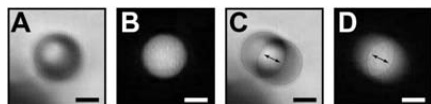


Figure 3. Bright-field (A,C) and fluorescence (B,D) images of trapped beads at two amplitudes. Scale bars 5 μm .

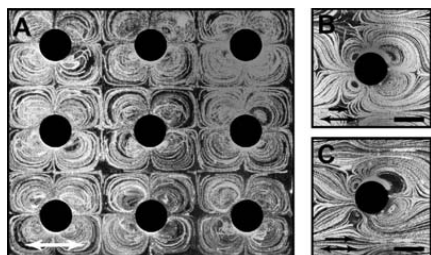


Figure 4. Flow in a trapping array for oscillation only (A) and oscillations with net flow (B, ~ 100 $\mu\text{m}/\text{s}$; C ~ 200 $\mu\text{m}/\text{s}$). Scale bars 100 μm , $\omega=1875$ Hz.

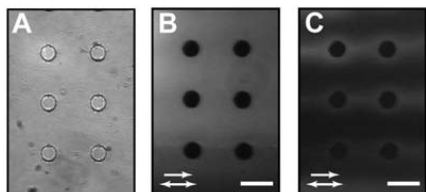


Figure 5. Bright-field (A) and fluorescence images showing injected fluorescein dye (B) and washing of dye by buffer flow (C). Scale bars, 200 μm .

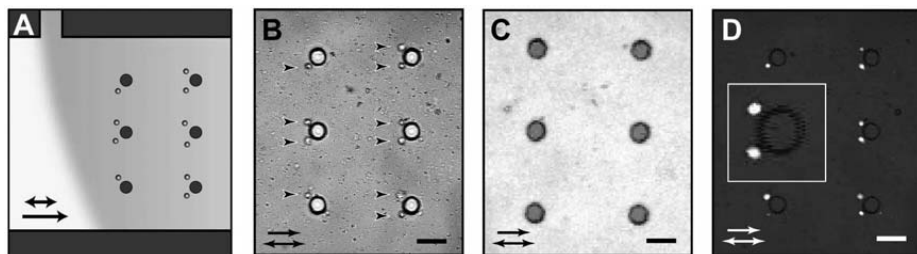


Figure 6. Cell vitality assay in a trapping array. (A) Schematic of cell loading in dye medium. (B) T-cells captured by upstream traps. (C) Fluorescence image of dye background. (D) fluorescence image of live cells after wash. Scale bars 200 μm , $\omega=4000$ Hz.

MICROFLUIDIC DEVICES FOR THE ASSEMBLY AND CULTURE OF THREE-DIMENSIONAL MULTI-CELLULAR CONSTRUCTS WITH DIFFUSION-LIMITED MICROENVIRONMENTS

M. Pinelis¹, R. W. Kasinskas², R. T. Borno¹, J. H. Park¹, E. Chu³,
N. S. Forbes² and M. M. Maharbiz¹

¹Department of Electrical Engineering and Computer Science, University of Michigan,

²Department of Chemical Engineering, University of Massachusetts, Amherst,

³Department of Biomedical Engineering, Johns Hopkins University

Email: pinelis@umich.edu

Abstract

We present a simple microfluidic method for the assembly and continuous culture of three-dimensional multi-cellular constructs. The technique is particularly useful for generating micro-environmental niches (such as hypoxia and acidosis) in non-vascularized tissue. The technique: 1) allows the rapid, parallel assembly of dozens of three-dimensional constructs with controlled shapes, sizes and interfacial gas transfer rates, 2) can be extended to adherent cells (which are normally grown in single monolayers) using functionalized glass beads, 3) permits long-term continuous culture and perfusion of the constructs.

keywords: bioMEMS, cell culture, microenvironment, three-dimensional, hypoxia

1. Introduction

Three-dimensional multi-cellular constructs play an increasingly important role in studies of tissue engineering, cancer and drug delivery [1,2,3,7,8]. Both mechanical and chemical cell-to-cell interactions play a role in the development of both normal and diseased states of tissue [4]. Unlike two-dimensional monolayer culture, 3D constructs capture some of the complexity of solid tissue [1]. In cancer biology, multi-cellular tumor spheroids are currently being used as *in vitro* models for studying the development of tumor malignancy and drug response assays [1,5,8]. As such, we have developed a class of device to study the micro-environmental niches created within tissue constructs as a result of diffusion limitations. These include, for

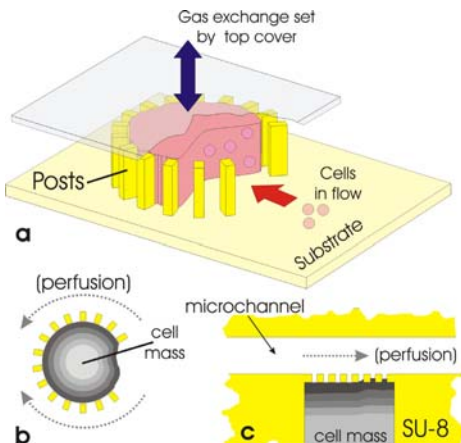


Figure 1 a) Schematic view of device operation, b – c) different ‘basket’ geometries generate different diffusion gradients (shown schematically in varying shades of gray).

example, the lack of oxygen (hypoxia) and the pH change at the center of multi-cellular masses. Traditional macroscopic culture techniques for assembling three-dimensional isotropic constructs have a number of drawbacks: large size and shape variability during culture, imaging and microscopy difficulties inherent in spheroidal cell masses, and the practical difficulties of maintenance and passaging of cultured constructs [5].

2. Design and Fabrication

Fig. 1 illustrates the device concept and geometry. To assemble the multi-cellular constructs, individual cells in suspension were flown into microchannels containing arrays of embedded posts ranging in size and spacing from 10-30 μm ; these posts are arranged so as to form ‘baskets’ of desired shapes and sizes. As cells flow by, some fraction become trapped in these ‘baskets’ and assemble into cylindroids and cubes (Figs. 4, 6-8). Fabrication is shown in Fig. 2.

3. Results



Figure 3 (left) Scanning electron micrograph of devices before assembly. Due to the high aspect ratios (1:10 to 1:20), the posts are fragile and can break off or stick to each other during handling.

cultured them for 24 hours, **2)** demonstrated the feasibility of quantifying diffusional limitations of a dense tissue mass with a fluorescent oxygen-sensitive Tris(2,2'-bipyridyl)dichlororuthenium(II) hexahydrate fluorophore (Figure 5), **3)** assembled three-dimensional constructs with 50 micron diameter glass beads (G.Kisker, Germany) intercalated with adherent C2C12 myoblast cells, **4)** assembled three-dimensional constructs with 50 micron diameter glass beads (G.Kisker, Germany) intercalated with adherent HeLa cancer cells, cultured them for 72 hours and imaged them with LIVE/DEADTM cell viability assays (Figure 7), and **5)** cultured clusters of colon carcinoma cancer cells for 1 week (Figure 8).

4. Discussion

We are currently assembling, culturing and monitoring constructs of C2C12 myoblasts (which have a known sensitivity to oxygen during differentiation), colon carcinoma cells (which are a common non-vascularized tumor model [8]; these cells aggregate without the need for beads) as shown in Figure 8 and HeLa cancer cells (Figure 7). Constructs have been cultured in the devices for 7 days; month-long cultures are in progress. These results and pH, oxygen and LIVE/DEADTM assays of the hypoxic microenvironments are the topic of a forthcoming manuscript and will be presented at the conference [6].

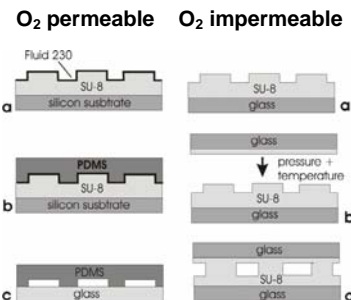


Figure 2 Fabrication flow. Two similar processes are used to yield either oxygen permeable or oxygen impermeable ‘baskets’. (left) Lithographically-patterned SU-8 is used to mold spun PDMS. The PDMS is then bonded to a glass wafer. (right) Lithographically-patterned SU-8 is bonded to a glass substrate using Microform film (Microchem, Newton, MA).

Using this device, we have: **1)** assembled 200-micron thick *Zinnia* plant cell cylindroids with patterned diameters ranging from 200 to 800 microns (Figure 4, 5) and

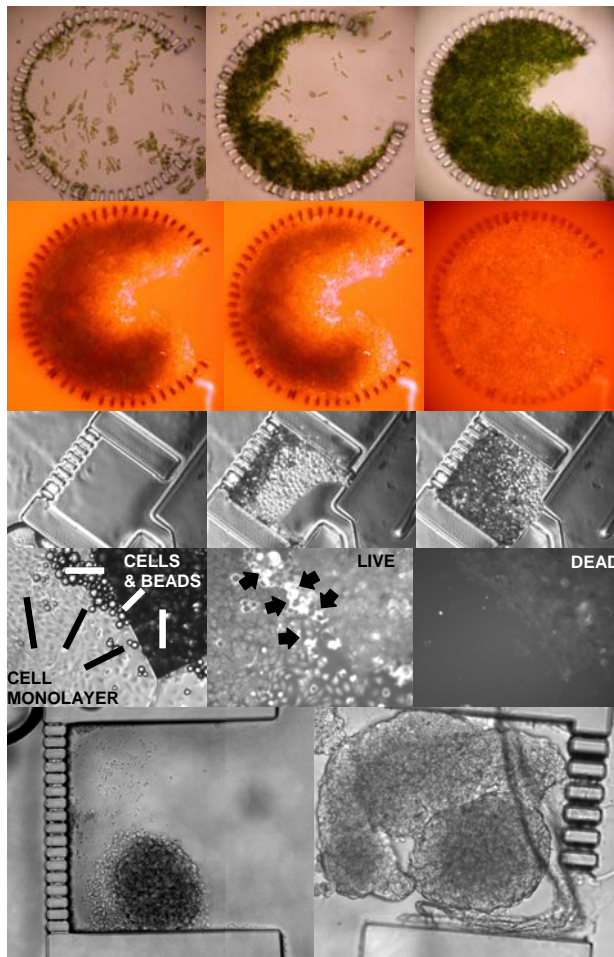


Figure 4 (row 1) Optical micrographs of *Zinnia* plant cell assembly into an 800 micron diameter cylindroid. Frames are approximately 15 minutes apart; device design accommodated transient fluidic resistances of filling cylindroids.

Figure 5 (row 2) Time course of oxygen-sensitive ruthenium fluorophore diffusion into a partially assembled 800 micron cylindroid. Frames are 2 seconds apart.

Figure 6 (row 3) Optical micrographs of 400x400x150 μm^3 well being filled with glass beads. Frames are approximately 5 minutes apart.

Figure 7 (row 4) Optical and corresponding LIVE/DEADTM fluorescence micrographs at the SU-8 edge of a 120 micron-tall well filled with glass beads and HeLa cells after 72 hours in culture. Middle image corresponds to live cells and right image corresponds to dead cells. In bead constructs, cells prefer to proliferate on the fibronectin-coated bead surface (arrowheads).

Figure 8 (row 5) Optical micrographs of 400x400x150 μm^3 wells loaded with colon carcinoma cell spheroids after 52 hours in culture.

References

1. J. M. Kelm, N. E. Timmins, C. J. Brown, M. Fussenegger and L. K. Nielsen, *Biotechnol Bioeng* 83, pp. 173-180, (2003).
2. R. M. Sutherland, *Science* 240, pp. 177-184, (1988).
3. P. J. Hung, P. J. Lee, P. Sabourchi, N. Aghdam, R. Lin and L. P. Lee, *Lab Chip* 5, pp. 44-48, (2005).
4. G. Hamilton, *Cancer Lett* 131, pp. 29-38, (1998).
5. N. S. Forbes, L. L. Munn, D. Fukumura, R. K. Jain, *Cancer Research* 63, pp. 5188-5193, (2003).
6. M. Pinelis, R. W. Kasinskas, R. T. Borno, J. H. Park, E. Chu, N. S. Forbes and M. M. Mahabirz, *manuscript in preparation*.
7. C.J. Flaim, S. Chen, S. N. Bhatia, *Nature Methods* 2, pp. 119-125, (2005).
8. R. W. Kasinskas and N. S. Forbes, *Biotechnol Bioeng* 94, pp. 710-721, (2006)

Sample Preparation for the Analysis of Gluten from Foodstuff in a Modular Chip-Platform

v. Germar, F; Doffing, F; Frese, I; Gransee, R; Drese, K S; Bermudo, M C*;
O'Sullivan, C**

Institut für Mikrotechnik Mainz GmbH, Carl-Zeiss-Straße 18-20, D-55129 Mainz

*Universitat Rovira i Virgili, Avinguda Països Catalans, 26, 43007 Tarragona, Spain

** Institut Ciatalà de Recerca i Estudis Avançats, Passeig Lluís Companys 23, 08010
Barcelona, Spain

1 Introduction

A modular system is presented for the sample preparation to detect coeliac disease toxic gluten from unprocessed and processed foodstuff to enable food producers a reliable labeling of their products. This system comprises all functionalities from the extraction of solid food samples to a detection module with a fluorescence based quantitative ELISA-detection.

Coeliac disease is an inflammatory disease of the upper small intestine and results from gluten ingestion in genetically susceptible individuals and is the only life long nutrient-induced enteropathy. The only treatment for celiac disease is a strict gluten free diet, with the longer the individual fails to adhere to this diet, the greater the chance of developing malnutrition and other complications. Today, there is no standardized system that extracts all the gluten components, ethanol soluble gliadins and insoluble glutenins, and determines the concentration of "toxic" sequences. This paper presents a module for the extraction of gluten from flour and from processed food samples in a single step. After extraction a small sample volume, where all unsolved sample particles are removed by centrifugation, is delivered to a micro system in which the sample is further processed for an immunochemical assay. Here, a disposable polymer chip for an optical detection with included optical components is presented.

2 Extraction

A drawing of the μ -extractor is shown in fig. 1a. The weighted sample is filled into a silicon tube. A peristaltic pump is kneading the sample intensively to mimic the vigorous mixing step of the lab scale protocol. Underneath the tube there is a heating element enabling extraction temperatures up to 90° C, which is needed for processed samples while flour extraction can be performed at RT. The extraction was done in 5 min. After the extraction the sample is centrifuged by a lab centrifuge and the supernatant is analysed by a Bradford assay. The performance of the flour extraction was comparable with the lab scale results (tab. 1) tested with different kinds of flour, cookies, zwieback and spiked flour samples. It could be shown that the presented μ -extraction module can transfer extraction steps like vigorous mixing and heating in a macro format into a micro system. Additionally, the transfer from large quantities of sample and buffer that can be handled with standard lab equipment like a normal balance to subsequent modules dealing with microscale volumes was successful.

Sample	Lab-Extraction	μ -Extractor
flour, RT (Spain)	14.49 ± 1.16 mg/ml	14.61 ± 2.51 mg/ml
flour, 85°C (Spain)	16.50 ± 1.17 mg/ml	16.50 ± 0.21 mg/ml
flour, RT (Germany)	12.54 ± 0.43 mg/ml	17.86 ± 1.84 mg/ml
baked dough, 85°C	15.97 ± 1.01 mg/ml	15.47 ± 1.72 mg/ml
cookie, 85°C	4.80 ± 0.40 mg/ml	2.83 ± 0.35 mg/ml
zwieback, 85°C	14.47 ± 2.61 mg/ml	10.79 ± 1.35 mg/ml
spiked samples, 0 mg	1.48 ± 0.03 mg/ml	1.38 ± 0.13 mg/ml
spiked samples, 10 mg	25.11 ± 0.92 mg/ml	10.00 ± 1.00 mg/ml

Tab. 1: Comparison of extraction results of different samples between the chip based system and the lab scale protocol.

3 Centrifugation

The major amount of the sample remains unsolved during extraction. Thus, a filtration step is necessary before the sample processing for the ELISA assay. Lab scale protocols require a centrifugation step in a lab centrifuge for approx. 5 min. A micro centrifuge (fig. 1b) was build up that enables the incorporation into the modular chip system with an automatic mode for filling in the sample and emptying the supernatant. This micro centrifuge comprises an electric motor, that allows 4500 g at 15000 rpm, fixed in a metal frame. Two chips made of PMMA are inserted on the axis of the motor. The lower chip is static and contains the fluidic connection to other chip modules. For rotation the electric motor and the rotor chip is lifted up and lowered to obtain the supernatant that can be directly used for the subsequent steps. No other filtration step is necessary to achieve the same efficiency as standard laboratory centrifuges.

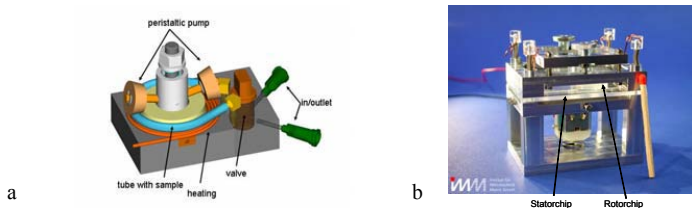


Fig. 1a: Construction drawing of the μ -extractor. b: Picture of the μ -centrifuge as a single module.

4 Complete Sample Preparation

Flour was extracted and directly centrifuged by the μ -extractor and centrifuge and analysed by a Bradford assay to show the overall performance of all extraction modules. This was compared with extractions using the macro protocol. With the μ -device 12.01 ± 0.91 mg/ml protein were extracted compared to 9.76 ± 1.45 mg/ml with the lab protocol. Thus, the successful transfer of the sample preparation from the lab to the μ -scale could be shown.

5 Multi-Functional Valves

A core part of the whole system is a set of valves (fig 2a). They all consist of a rubber disk which is pressed to the chips by a spring and a piston. Due to different layouts of slits cut into the disks, the valve can be used for metering fluids, for merging two plugs, for the distribution of reagents with a minimum of cross contamination or for switching

between the loading and extraction mode of the extractor module. The valves operate under pressures up to 7 bar and can be designed to have a minimal dead volume.

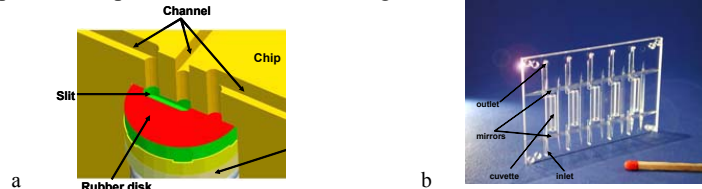


Fig. 2a: Cross section of the flat disk valve. Fig. 2b: Picture of the optical detection chip for 5 parallel immunoassays.

6 Optical Detection Chip

An optical detection chip was developed with a cuvette volume of $15 \times 2 \times 1 \text{ mm}^3$ (fig. 2b). A polymer inlet is incorporated on which antibodies against gluten are immobilized to perform an ELISA assay inside of this channel. The sensitivity of the system was tested with fluorescence dyes in transmission and fluorescence. The in- and outcoupling of light is done by integrated, total reflecting mirrors fabricated by ultra precise milling (fig 3a). No additional optical parts like beam forming optics are needed. The performance of the chip was tested with different dilutions of methyl umbelliferone between 0.1 and 10 $\mu\text{g}/\text{ml}$ for the transmission experiments at 370 nm. The same samples were used for a reference measurement in a conventional 1 cm cuvette with an UV-VIS spectrometer Lambda 900 from Perkin Elmer (fig. 3b).

Beside the detection channel there are two extra mirrors which collect the emitted light of fluorescence measurements. Fluorescence experiments were performed with 5, 6 carboxy fluorescein and methyl umbelliferone between 0.04 and 10 $\mu\text{g}/\text{ml}$ (fig. 3c). The excitation wavelength was 492 nm and the emitted light 515 nm. At concentrations below 1 $\mu\text{g}/\text{ml}$ the correlation coefficient of a linear fit was 0.999. This sensitivity fits the needs for the determination of gluten by an ELISA assay.

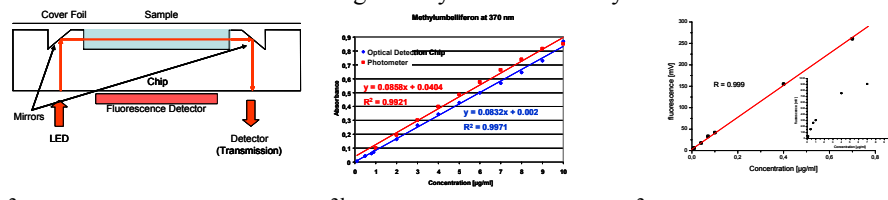


Fig. 3a: Scheme of the light path in the optical detection chip 3b: Transmission measurements with methyl umbelliferon at 370 nm, blue: chip measurements, red: standard lab spectrometer. 3c: Fluorescence of 5,6 carboxy fluorescein. The linear fit refer only to concentrations below 0.7 $\mu\text{g}/\text{ml}$, the insert shows the results over the whole concentration range up to 10 $\mu\text{g}/\text{ml}$.

Acknowledgement

This study has been carried out with financial support from the Commission of the European Communities, specific RTD programme 'Quality of Life and Management of Living Resources', QLK1-2002-02077, 'Quantification of Coeliac Disease toxic gluten in foodstuffs using a Chip system with integrated Extraction, Fluidics and biosensoric detection'. It does not necessarily reflect its views and in no way anticipates the Commission's future policy in this area.

DNA STRETCHING METHOD USING A FLOW INDUCED BY LASER IRRADIATION UNDER AC ELECTRIC FIELD

Michihiko Nakano¹, Kazunori Takashima¹, Shinji Katsura²
and Akira Mizuno¹

¹Toyohashi University of Technology, Toyohashi, Aichi, 441-8580 Japan

²Gunma University, Kiryu, Gunma, 376-8515 Japan

mizuno@eco.tut.ac.jp

Abstract

A micro-vortex is generated around an infrared laser focus where an intense AC electric field is applied. We used this opto-electrostatic micro-vortex to stretch individual long DNA molecules. When T4-phage DNA molecules were introduced into the opto-electrostatic micro-vortex, they were stretched around the laser focus. In addition, it was possible to keep it in stretching form for more than 30 sec. Using this method, length of DNA molecules can be measured without fixing to a substrate.

Keywords: DNA manipulation, conformational change, opto-electrostatic micro-vortex, DNA stretching

1. Introduction

Direct observation of fluorescent-labeled single DNA molecules, especially for at stretched shape, can be used for mapping, or for investigations on interactions with proteins and dynamics of bio-macromolecules. In this study, we used a micro-vortex induced by laser irradiation and an AC electric field to stretch long DNA molecules, T4 DNA (166 kbp, 53 μm). When an infrared (IR) laser beam was focused in the middle of two parallel electrodes, between them an AC electric field was formed, an opto-electrostatic micro-vortex, OEMV, was generated as illustrated in Fig. 1 [1]. The flow velocity can easily be controlled by varying the laser power, strength and frequency of the AC electric field. Position of the OEMV can be changed by moving the laser focus. The OEMV can stretch the long DNA molecule without tethering it to a substrate.

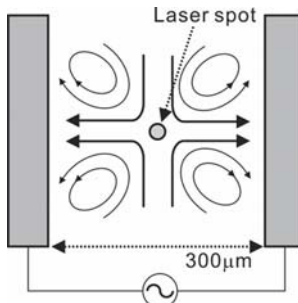


Figure 1. Flow, the OEMV, induced by laser irradiation and AC electric field. Black

solid arrows indicate the direction of the flow.

2. Experiment

The chromium microelectrodes were fabricated on a glass slide using standard photo-lithographic technique. An inverted fluorescent microscope equipped with a laser manipulation system was used for observation and laser focusing. In the system, the IR laser (Nd:YAG, 1064 nm, cw) was focused through an objective lens (x100, N.A.: 1.30). The T4 DNA molecules were stained with fluorescent dye YOYO-1. The DNAs were suspended in 10 mM Tris-HCl (pH 8.0) containing anti-fade reagents. The AC voltage source was connected to the microelectrodes. The DNA solution was applied on the glass slide with the microelectrodes, and covered with a cover glass. The solution was sealed using a manicure to avoid evaporation.

3. Results and discussion

When the OEMV was generated in the DNA suspension, the DNA molecules moved with the flow and were stretched around the laser focus due to the opposed flow. Figure 2 shows the stretching of T4 DNA with 70 kV/m, 1 MHz and 135 mW. The stretching could be maintained at the center of the OEMV by positioning the laser spot at the center of the T4 DNA molecule. The stretched shape could be maintained for at least 30 sec. Figure 3 shows the length distributions of the T4 DNA molecule under two different conditions of the OEMV. Lengths of T4 DNA molecule were measured as $27.3 \pm 8.7 \mu\text{m}$ and $49.9 \pm 8.9 \mu\text{m}$ for the flow velocities of $20.9 \pm 5.8 \mu\text{m/sec}$ (160 kV/m, 1 MHz and 80 mW), and $118.7 \pm 35.3 \mu\text{m/sec}$ (160 kV/m, 1 MHz and 135 mW), respectively. It can be observed clearly that the difference in the tension caused by different flow velocities resulted in the difference in the lengths of the stretched DNA molecules.

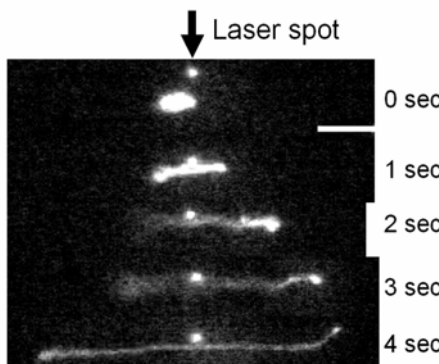


Figure 2. Fluorescent images of T4 DNA molecule undergoing stretching. Each image is a series in time proceeding from top to bottom. The time interval between each image was one sec. The conditions were 70 kV/m, 1 MHz and 135 mW. The white bar at the top right indicates 10 μm .

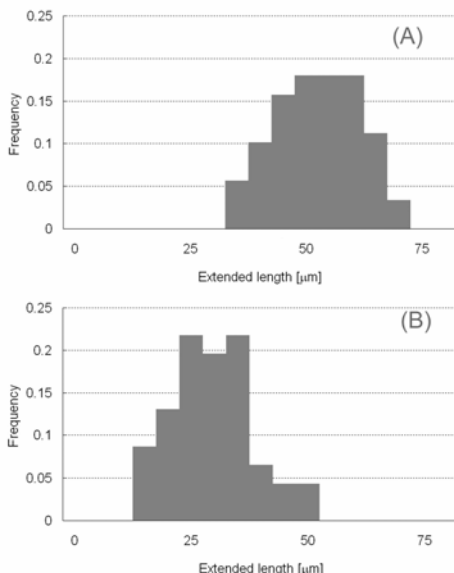


Figure 3. Length distribution for T4 DNA molecules extended by the flow of OEMV. The conditions were 160 kV/m, 1 MHz and 80 mW (A), and 160 kV/m, 1 MHz and 135 mW (B). In both cases, the ratio of the fluorescent dye was 4 bp/dye. These histograms show the results from measuring 46 (A) and 89 (B) T4 DNA molecules. The bin width is 5 μm .

4. Conclusions

The opposed flow of the OEMV stretched the long DNA molecule, T4 DNA. This method permits stretching of DNA molecules without tethering them to a substrate.

References

1. A. Mizuno, M. Nishioka, Y. Ohno, and L. D. Dascalescu, IEEE Trans. Ind. Appl. **31**, 464 (1995).

METAPHASE CHROMOSOME MANIPULATION USING NEWLY DEVELOPED AFM PROBES

Keiichiro Yamanaka⁽¹⁾, Tetsuya Takekawa⁽²⁾, Kazuhisa Nakagawa⁽³⁾, Masato Saito⁽¹⁾, Yuzuru Takamura⁽¹⁾, Gen Hashiguchi⁽²⁾ and Eiichi Tamiya⁽¹⁾

⁽¹⁾School of Materials Science, Japan Advanced Institute of Science and Technology, 1-1 Asahidai, Nomi, Ishikawa 923-1292 Japan, ⁽²⁾Faculty of Engineering, Kagawa University, 2217-20 Hayashi-cho, Takamatsu, Kagawa 761-0396 Japan, ⁽³⁾Institute of Industrial Science, University of Tokyo, 4-6-1 Komaba Meguro-ku, Tokyo 153-8505 Japan

Abstract

We have studied the development of a new procedure based on atomic force microscopy (AFM) for the analysis of metaphase chromosome. The aim of this study was to obtain the detailed information about the specific location of genes on the metaphase chromosome. In this research, we performed the manipulation of the metaphase chromosome by using novel AFM probes (knife-edged probe and tweezer-type probe) to obtain the fragments of chromosome with a smaller size than the ones obtained using the conventional methods; such as glass microneedles. We could pick up the fragment of the metaphase chromosome that was dissected with the knife-edged probe by using our tweezer-type probe.

Keywords: AFM; manipulation; chromosome; microtweezers; nanoprobe

1. Introduction

The chromosome is aggregated to high density during the metaphase of cell cycle. It may be said that the metaphase chromosome is essence of DNA-protein complex because the DNA forms various three-dimensional structures that are concerned with the regulation of gene expression. To obtain the specific gene on the metaphase chromosome, several reports using microdissection methods by micromanipulators have been published [1]. For example, microdissection of specific chromosomal regions was obtained under an inverted microscope using glass microneedles controlled by a micromanipulator. This method has the merit of obtaining several types of probes, either previously known chromosomal probes, or chromosomal DNA from an unknown origin. However, the conventional methods are not suitable for the analysis of more than 10 million base pairs, or hundreds to thousands of individual genes, because of the limited size of the microneedles for miniaturization. In this research, we introduce the metaphase chromosome manipulation by novel AFM probes to obtain the smaller size fragment of chromosome. AFM has the ability to perform the measurement of force spectroscopy and the manipulation of submicron order.

2. Experimental

Human metaphase chromosome was prepared from human lymphocytes, which were obtained from the whole human peripheral blood according to the standard protocols. Metaphase chromosomes solution was dropped onto glass slides or silicon substrate,

and air-dried until use. To confirm the picked up chromosome fragment, the absorbed chromosome on the substrate was stained with a fluorescent dye, YOYO-1(EX: 491 nm, EM: 509 nm) (Fig. 1).

To obtain the chromosome fragment in AFM operation, we fabricated the tweezer-type AFM probe using micromachining technology [2] as shown in Figure 2. In order to facing sharp wedged probes, we have developed a new fabrication method combined with anisotropic etching of silicon by KOH solution and local oxidation of silicon (LOCOS) techniques. At first, SiN deposition on a SOI wafer and a narrow slit opening in the SiN and the SOI was performed. LOCOS and SiN removal by RIE and KOH etching made {111} faces along with the slit. Afterwards, photoresist patterning and vertical silicon etching was done by ICP-RIE.

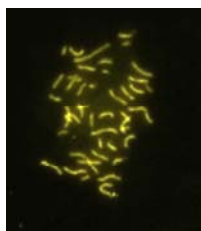


Fig. 1. Stained metaphase chromosome with fluorescent dye (YOYO-1).

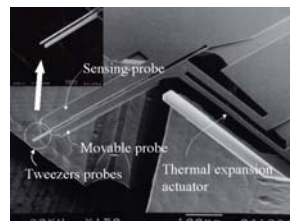


Fig. 2. SEM image of the tweezer-type AFM probe.

3. Results and discussion

The tweezer-type probe had two thin wedged-type arms. One arm (called as the sensing probe) was utilized for imaging as an AFM probe, and the other arm (called as the movable probe) was utilized for manipulation. The movable probe had a function that was closely related to the amount of the applied voltage (Fig. 3). Furthermore, the movable probe did not cause damage to the biological sample, while imaging in the tapping mode, because we designed the resonant frequency of the movable probe at a lower value than the sensing probe.

In our previous work, we fabricated the knife-edged AFM probe (Fig. 4) that was appropriate for the dissection of metaphase chromosome and DNA [3]. The metaphase chromosome, which was dissected and translocated with this knife-edged AFM probe, was imaged using the sensing probe in tapping mode. The tweezer-type AFM probe was operated to position the fragment of the chromosome between the sensing probe and the movable probe. Afterwards, in order to make the contact between the two probes on the substrate, the loading force was increased while controlling the amplitude reference, the amplitude reference was set at -1.10. The amplitude reference was a relative indicator of the loading force in SIITM AFM operation. As the electric power (30 V) was applied to the tweezer-type probe, the movable probe closed and sandwiched the fragment of chromosome. After the operation of picking up the fragment, no fragment was observed on the substrate by means of AFM imaging (Fig. 5), and fluorescence could be observed at the tip of the tweezer-type probe (Fig. 6).

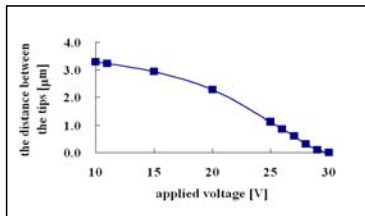


Fig. 3. The distance between the sensing probe and the movable probe. The distance is closely related to the amount of the applied voltage.

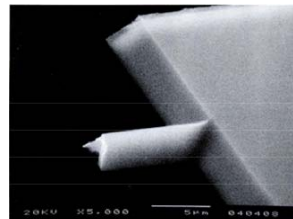


Fig. 4. SEM image of knife-edge probe.

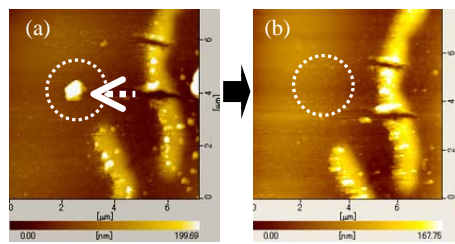


Fig. 5. AFM images of the translocation and the pick-up of metaphase chromosome. (a) after dissection and translocation by using knife-edged probe and (b) after picking up by using tweezer-type probe. After the operation of picking up the fragment, there is no fragment in area surrounded by the dashed line.

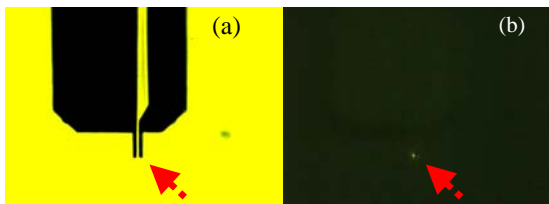


Fig. 6. The observation of tip of tweezer-type AFM probe. (a) bright field and (b) fluorescence field. Fluorescence of chromosome fragment could be observed at the tip of the tweezer-type probe.

4. Conclusions

We picked up the fragment of the metaphase chromosome that was dissected with the knife-edged probe by using our tweezer-type probe. It is expected that the nano-scale manipulation of biological samples, especially chromosomes, has become possible, and further analysis of the specific portion of a chromosome can be performed by the established analytical methods.

References

- [1] G. P. Bates, B. J. Wainwright, R. willson and S. D. M. Brown, Mol. Cell Biol., 6, 3826- 3830 (1986)
- [2] T. Takekawa, K. Nakagawa and G. Hashiguchi, Transducers'05, Digest Tech. Papers, 621- 624 (2005)
- [3] M. Saito, K. Nakagawa, K. Yamanaka, Y. Takamura, G. Hashiguchi, and E. Tamiya, Sensors and Actuators A. 130-131, 616-624 (2006)

A NOVEL FRAMEWORK OF MAKING PLA/PLGA POLYMER MICRO NEEDLES PATCH FOR BETTER SKIN PIERCING AND DRUG RELEASE

S. Chiu⁽¹⁾, H. Huang⁽¹⁾, C. Y. Chuang⁽²⁾, C. Fu^{(1)*}

⁽¹⁾Institute of MEMS,

⁽²⁾Department of Biomedical Engineering and Environmental Sciences,
National Tsing-Hua University,
No.101, Kuang-fu Rd., Sec. II, Hsinchu 300, Taiwan R.O.C.
E-mail: ccfu@mx.nthu.edu.tw*

Abstract

We presented in this paper a novel framework of making biodegradable polymer micro needles patch. Through this framework, the fabricated micro needles patch has better skin piercing ability and superior drug release control without the “initial burst” as before. In this paper, we introduced our fabrication approach, preparation methods and the produced patches. We have also executed piercing experiments on artificial skin and real human skin.

Keywords: Microneedles, transdermal drug delivery

1. Introduction

Many reports have been published to fabricate micro needles over the past ten years. One of the most important potential applications is the patch with micro needles array on it for efficient drug delivery purpose [1]. Meanwhile, our lab has successfully developed several unique methods to fabricate micro needles, such as solid micro needles array (figure 1), hollow needle array integrated with fluidic chips (figure 2) and even compliant polymer needles patch on flexible membrane (figure 3) and so forth [2][3][4]. Most of them can surely be replicated to different functional material, such as biodegradable PLGA (poly lactic-co-glycolic acid) when targeting on drug releases as shown in the figure 4.

In order to adapt the fabricated PLGA needles for drug release purpose, however, there are two essential issues have to be considered: The first one is the piercing ability. The PLGA needles are usually too soft to penetrate the outmost of the skin, the stratum corneum, which is from different body parts depends on where the patch to be applied. The basic idea of successful piercing is to ensure the fracture force of the needle can be larger than the insertion force when the needle into the skin [5].

The second issue is that PLGA is usually not easy to control the drugs release to prevent the “initial burst” problem, which is the phenomenon that a large part

of encapsulated drug is released in a short a time just after administration. The phenomenon happens very often when encapsulating injecting formulations in microspheres made from PLGA to provide long-term drug release.

We purpose a new framework composing of two layers as show in the figure 5. We employed PLA firstly as the needle material, which provides not only a tougher mechanical property to contribute a stronger fracture force, but also an outer shell to prevent the “initial burst” problem of the second layer, which has been proven valid by Matsumoto et al. in the microspheres’ case [6]. The second layer was made from appropriate blends of PLGA and drugs to furnish sufficient medical dose.

Besides the successful manufacturing of different micro needles, various piercing experiments have been conducted using different sorts of PLA/PLGA with the two-layer framework not only on real human skin surfaces (figure 6(a)(b)), which properties may vary in different conditions and different people, but also on different artificial skins made from standard silicone rubbers (with stand hardness index (shore 0-20A)) (figure 6(c)(d)) getting a more comprehensive insight of the piercing ability of the fabricated PLA micro needles. The *in vivo* test with albumin as marker in mice is executing.

Reference

1. D. McAllister, P. Wang, S. Davis, J-H Park, P Canatella, M.Allen, and M. Prausnitz, “Microfabricated needles for transdermal delivery of macromolecules and nanoparticles: Fabrication methods and transport studies” PNAS, vol. 100, no. 24, Page 13755–13760, November 25, 2003.
2. C. Fu, H. Huang, “Different Methods for the Fabrication of UV-LIGA Molds using SU-8 with Tapered De-molding Angles”, *Microsystems Technology* in Press.
3. H. Huang, C. Fu, “Out-of-plane Polymer Hollow Micro-needle Array Integrated On a Microfluidic Chip”, Proceeding of IEEE Sensors in Irvine, Nov. 2005.
4. H. Huang, C. Fu, “Out-of-plane Polymer Hollow Micro-needle Array Integrated on a Flexible Membrane”, Proceeding of ISNMT-2 in Taiwan, March 2006.
5. Sh. Davis, B. Landis, Z. Adams, M. Allen, M. Prausnitz, “Insertion of microneedles into skin: measurement and prediction of insertion force and needle fracture force”, *Journal of Biomechanics* 37 Page 1155–1163, 2004.
6. A. Matsumoto, Y. Matsukawa, T. Suzuki, H. Yoshino, “Drug release characteristics of multi-reservoir type microspheres with poly(dl-lactide-co-glycolide) and poly(dl-lactide)”, *Journal of Controlled Release* 106(1-2), Page 172-180, Aug 2005.

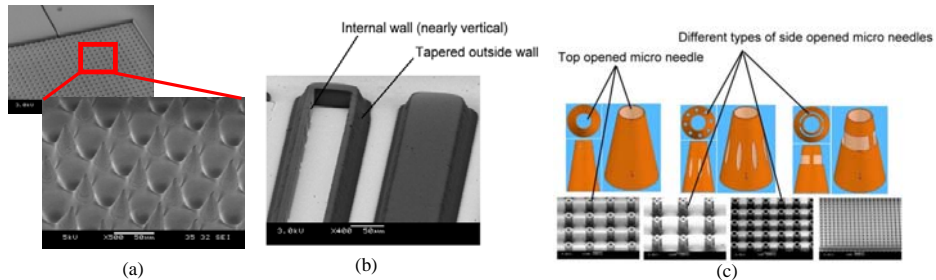


Fig. 1: (a) Fabricated polymer micro needles array by the purposed back-side exposure method in this study. Out-of-plane polymer micro needles with a height of 65 ~ 210 μm and an outer diameter between 20 ~ 100 μm have been successfully realized. (b) An example result made by the combinational method. The outside wall had a larger tilting angle, while the internal wall had a smaller tilting angle (nearly vertical) can be made by one lithography step. (c) Different kinds of hollow polymer micro needles can be fabricated through the purposed method.



Fig. 2 The micro needles array has been successful realized with fluidic channel systems by the purposed method in this study.

Fig. 3 The needles array fabricated on a flexible membrane substrate for compliant applications has been successfully realized in this study. The substrate employed here was PDMS.

Fig. 4 PLA micro needles array (900 needles in $0.5 \times 0.5 \text{ mm}^2$ area) fabricated by replication through a PDMS intermediate mold in this study.

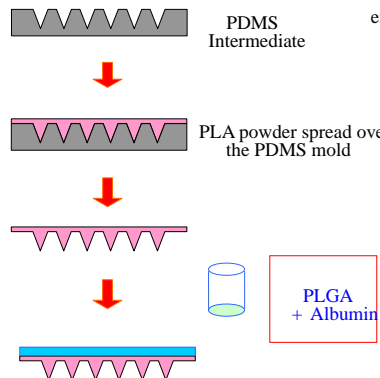


Fig. 5 The two-layer framework of the PLA/PLGA soft micro needle patch purposed in this study. We employed PLA firstly as the needle material, which provides a tougher mechanical property to contribute a stronger fracture force, and an outer shell to prevent the “initial burst” problem of the second layer. The second layer was made from appropriate blends of PLGA and drugs to furnish sufficient medical dose.

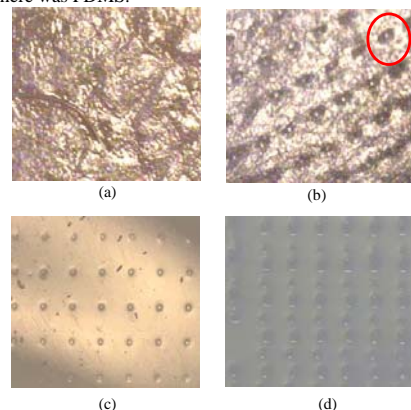


Fig. 6 Optical micrographs showing piercing experiments. (a) the human skin of hand back of an Asian people before piercing. (b) after piercing by a fabricated PLA needles array. (c) test result using artificial skin: Cica-Care[™] from Smith+Nephew Corp. (d) test result using simulated agarose gel with the standard hardness range of human skin.

HYDRODYNAMIC MANIPULATION AND SELECTIVE IMMOBILIZATION OF GIANT LIPOSOMES

Kaori Kurabayashi¹ Bruno Le Pioufle² and Shoji Takeuchi^{1,2}

CIRMM-IIS¹, LIMMS/CNRS-IIS²

The University of Tokyo, 4-6-1 Komaba, Meguro-ku, Tokyo, 153-8505, Japan

Phone: 81-3-5452-6650, Fax: 81-3-5452-6649, Contact E-MAIL:

kaorik@iis.u-tokyo.ac.jp

Abstract

This paper describes an approach based on the use of microfluidic device for producing, handling and arraying giant liposomes. Two prototypes are proposed in order to investigate the feasibility of these different steps that would be finally integrated in a single chip. Using a first micro-fluidic device we succeed to produce different types of giant liposomes by electroformation method, and to transport and collect by combining DC electric fields and fluidic flow. Using a second device made of micro-holes array on a Parylene thin film formed over microfluidic channels, the selectively immobilization of the liposomes was achieved.

Keywords: Giant liposome, Electroformation, Microfluidic Channels, Parylene, PDMS

1. Introduction

The usage of giant liposomes (over 10 μm in diameter) has increased in various fields [1] where the direct observation of lipid membrane is required (e.g. the studies on membrane proteins [2]). However, presently, there exist no simple all-in-one device for preparation, manipulation and immobilization of the giant liposomes, and such a device could greatly advance research in these fields.

We propose a new approach of all-in-one microfluidic device for producing, handling and arraying giant liposomes. Benefits of using microfluidic device for liposome applications include (i) only minute amount of reactants is needed for liposome preparation, and (ii) parallel micro channels and chambers allow several liposome operations to be performed simultaneously.

In this research, we prove this concept using two prototypes. The first device (Fig. 1) shows the feasibility of production, transportation and collection of giant liposomes on the same chip, while we demonstrate immobilization of giant liposomes using the second device (Fig. 3).

2. Experimental

2.1 Production, collection and transportation of liposomes (first device)

Figure 1 shows illustration of the device for producing giant liposomes by the electroformation method [3] and manipulating them. It made up of micro channels and chambers in PDMS (Sylgard 184 Silicones Elastomer, Dow Corning) and sandwiched

by two ITO glasses ($10 \Omega/\text{sq}$, custom-coated by Shintoku-Glass, Japan). Firstly, as shown in Fig. 2(a-i), giant liposomes were prepared by the electroformation method (AC, 10 Hz, 1.5 V) at the bottom of each chamber. Secondly, these liposomes were collected to top of the chamber by applying DC voltage (2 V) (Fig. 2b-i). Finally, the giant liposomes were transformed through the microfluidic channels using a microfluidic flow (Fig. 2c-i).

2.2 Immobilization of liposomes (second device)

The immobilization device is illustrated in Fig. 3. Figures 4 show cross-section view of the fabrication process of the device. Micro-holes array etched onto Parylene film formed over microfluidic channels made out of silicon using deep reactive ion etching DRIE process. Liposomes were introduced into the top chamber, and negative pressure was applied through the channel under the holes in order to immobilize the liposomes selectively.

3. Results and Discussion

Using the first device, we succeeded in producing simultaneously two types of fluorescently-stained giant liposomes at the bottom of each chambers on a single chip (Fig.2a-ii, iii). These liposomes were transported from bottom to top of the chamber by applying DC voltage (not shown) because they contain negatively charged lipids (phosphatidic-acid, PA). Finally, they were transported to the microfluidic channels using a microfluidic flow (Fig.2c). As shown in the simulation of the flow field in the chamber (Fig.2c-ii), the flow velocity was negligible near the top and bottom of the chamber. Thus, giant liposomes produced at the bottom of the chamber (Fig.2a-i) were not removed by the flow. It was confirmed that only liposomes in the area of the flow path shown in Fig.2(c)-ii could be carried away.

As shown in Fig. 5, we managed to trap and array various kinds of liposomes (red and green liposomes) at specific places using the second device of the micro-holes array. Advantages of this second device include: (i) ease of fabrication process, (ii) ease of observation, as Parylene is transparent, and (iii) ability of trapping various types of liposomes in a single device using the several fluidic channels under the holes.

4. Conclusions

This work demonstrates the feasibility of electroformation and handling (i.e. producing, collecting, transporting and arraying) giant liposomes in micro devices. Based on these technologies, we are currently developed fully integrated giant liposomes biochips as platforms for membrane protein analysis.

Reference

- 1 P.L. Luisi and P. Walde, *Giant Vesicles*, (John Wiley & Sons, LTD, 2000) pp. 3-9
- 2 G. Tresset and S. Takeuchi, *Analytical Chemistry*, 77, pp. 2795-2801, (2005)
- 3 M.I. Angelova and Dimitrov, D S, *Faraday Discuss. Chem. Soc.* 81, pp.303-311 and 345, (1986)

Production, transportation and collection

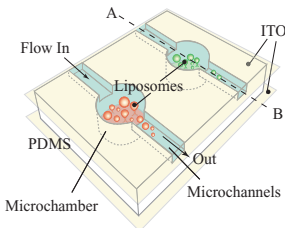


Fig.1 Schematic view of the microfluidic device with microfluidic channels and micro-litter chambers. Two types of liposomes were prepared by electroformation in each PDMS micro chamber (2000 μm in diameter, 665 μm in depth). They can be collected and transported through the channels (300 μm in wide, 235 μm in depth).

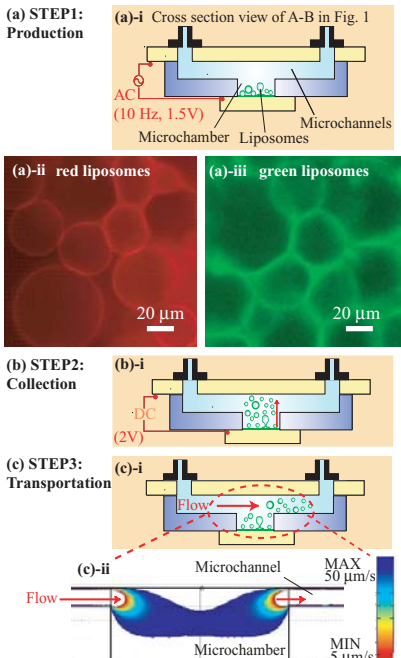


Fig.2 (a)-i Illustration of liposome production at the bottom of the microchamber. (a)-ii,iii Photographs of electroformed giant liposomes dyed red (DiI) and green (DiO) at each chamber. (b)-i Collection of the liposomes by DC. (c)-i Transportation of the giant liposomes with fluid control. (c)-ii Simulation result of the flow path of the chamber. Only velocities between 5-50 $\mu\text{m}/\text{s}$ are represented in this figure.

Immobilization

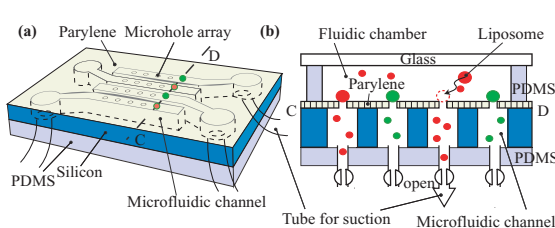


Fig.3 (a) Schematic view of a device for selective immobilization of liposomes. Microholes are formed on a Parylene thin film over microfluidic channels. (b) Cross section view (C-D) of the device. A chamber for introducing liposomes. Microfluidic channels for liposomes suction.

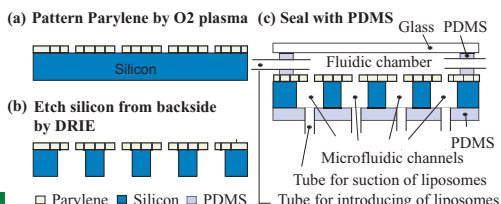


Fig.4 Fabrication of the Parylene microholes over microfluidic channels.

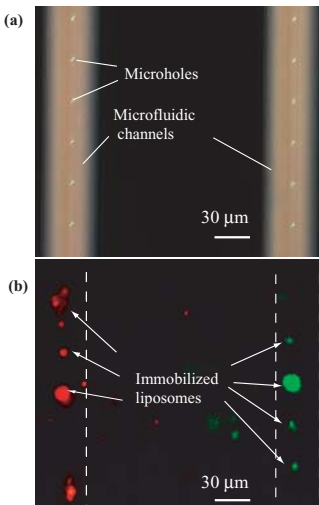


Fig.5 (a) Bright field view of Parylene microhole arrays on microfluidic channels. Thickness of Parylene was 5 μm . Mean diameter of the hole was 3.41 μm (CV: 6.4 %). (b) Fluorescence view of selective immobilization of red (dyed by DiI) and green (DiO) liposomes.

RAPID ON-CHIP HETEROGENEOUS BONE-CELL PATTERNING VIA THE ENHANCED DIELECTROPHORESIS TRAP FOR TISSUE ENGINEERING APPLICATION

Chen-Ta Ho¹, Ruei-Zeng Lin², Hwan-You Chang² and Cheng-Hsien Liu¹

¹ Department of Power Mechanical Engineering, ² Institute of molecular medicine, National Tsing-Hua University, Taiwan, R.O.C.

Abstract

A bone-mimetic cell-patterning technique for on-chip reconstructing heterogeneous osteocytes and hydroxyapatite particles via the design of enhanced field-induced dielectrophoresis (DEP) trap is demonstrated and reported in this paper. We mimic the morphology of the Haversian canal system of bone tissue to design the concentric-radial-tip-array electrodes for DEP operation. Well-defined and enhanced spatial electric field gradients are created for the in-parallel manipulation of massive individual cells and particles to form the biomimic pattern via vertical/horizontal DEP operation alternatively. Experiment results show that the osteocytes are positioned to form the shape of multiple concentric rings interlaced with pearl chain array of hydroxyapatites, which form bone-mimetic pattern. Good cell viability after cell-patterning is observed.

Keywords: dielectrophoresis, cell patterning, bone, tissue engineering

1. Introduction

Recent progresses in tissue engineering are devoted to develop the cell-based artificial tissues to restore and improve functional tissue for human organ's regeneration and transplantation. Cell patterning techniques which provide the basic cell blocks for rebuilding functional tissue play a crucial role in tissue engineering and drug screening [1]. Traditional porous and biodegradable scaffolds are used to bleed cells under physical and chemical cues for inducing cellular differentiation with proper functions. Nevertheless, most tissue engineering capabilities deal with relative simple tissues and fail to arrange heterogeneous cell types to reconstruct the complicated tissues. Recent advances in cell patterning focus on chemically modifying cell-adhesive substrate by photolithography, microcontact printing, and microfluidic patterning for enhancing cell-substrate adhesion [2]. These indirect methods are effective. However, they require complicated pretreatments and are limited by natural cellular adhesion which is slow and irregular. Active cell-patterning techniques such as ink-jet patterning and laser-guided writing are capable of handling different cell types [3], but the patterning resolution of jet-based printing and the laser energy loading on cells via optical tweezers are still the concerns. Thus, the development of high-resolution cell patterning to reserve cell-cell interactions with good cell viability is important and challenging. Here, we present a rapid cell-patterning technique for the on-chip reconstruction of the heterogeneous bone pattern with high patterning resolution and good cell viability.

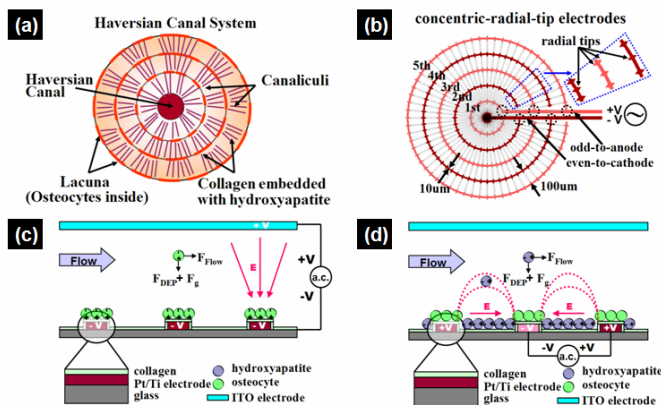


Figure 1. (a) The illustrated configuration of one classic unit of bone tissue, the Haversian canal system. (b) The geometric design of the concentric-radial-tip-array electrodes. (c) The operation principle of bone cell patterning in our bio-chip. The osteocytes are captured and patterned onto the concentric ring electrodes via the vertical DEP manipulation. (d) The hydroxyapatites are then patterned to from the pearl chain array in-between the first patterned osteocytes via the horizontal DEP manipulation.

2. Biochip Design and Operation Principle for Bone Cell Patterning

Field-induced DEP has been widely applied to the manipulation of micro-particles in microfluidics for years. DEP could offer the features of rapid cell manipulation and is easy for operation without the need of pretreatments to open its value on cell patterning. Our previous work reported the first successful demonstration of lobule-mimetic liver cell pattern [4]. We highlighted the concept- the control of the electric-field gradient is equivalent to the control of the cell-pattern. Following up with this platform, we dedicate to reconstruct the bone-mimetic pattern. We mimic the morphology of the Haversian canal system to design the concentric-radial-tip-array electrode for DEP operation, as illustrated in Figure 1(a)-(b). Through this specific electrode design, well-defined spatial electric field gradients are created. Osteocytes are firstly guided and positioned via the vertical DEP operation to generate the shape of multiple concentric rings. The horizontal DEP, then, micropatterns hydroxyapatite particles with pearl chain array interlaced in vacant spaces between rings adjacent to form the desired bone-mimetic pattern, as shown in Figure 1(c)-(d).

3. Experimental Setup

Sucrose medium with osteocytes and hydroxyapatites is used between the top ITO glass and the bottom glass substrate, which has Pt/Ti concentric-radial-tip-array electrodes on the top. Function generator is used to produce the ac signals for vertical and horizontal DEP manipulations. Cell patterning demonstration is recorded via a fluorescent microscope and a CCD-camera connected to a computer.

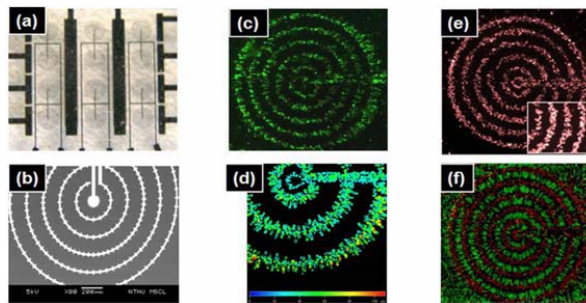


Figure 2. (a)-(b) The design of micromachined DEP electrodes. (c) *In-situ* fluorescence-based viability assay of patterned osteocytes. (92% cell viability) (d) Confocal image of the patterned and stacked osteocytes. (e)-(f) Demonstration of the heterogeneous bone-mimetic pattern. *In-situ* fluorescent images show that the red osteocytes and the green hydroxyapatites are micropatterned to reconstruct the bone-mimetic pattern.

4. Experimental Results and Discussions

Figure 2(a)-(b) show the design of micromachined DEP electrodes. Experimental results show that osteocytes can be well manipulated with positive DEP under the applied voltage of $5\text{ V}_{\text{p-p}}$ at 1 MHz. The hydroxyapatite-coated latex particles are manipulated under the applied voltage of $5\text{ V}_{\text{p-p}}$ at 100 KHz. Figure 2(c) shows the *in-situ* fluorescence-based viability assay of patterned osteocytes. The good cell viability (92%) is demonstrated. Confocal image shows the osteocytes are piled up with a height of $60\mu\text{m}$ in average (Figure 2(d)). After patterning the osteocytes above the concentric- radial-tip-array electrodes via the vertical DEP operation, medium is replaced to the culture medium to keep stable cell-substrate adhesion. Then, hydroxyapatites are micropatterned to form the pearl chain array interlaced at the vacant space between the patterned osteocytes to achieve the heterogeneous integration of bone pattern, as shown in Figure 2(e)-(f).

5. Conclusions

The fine cell patterning technique capable of manipulating heterogeneous cell types, providing high resolution pattern and reserving cell-to-cell interaction is crucial and important toward functional artificial tissues. In this paper, we demonstrate the on-chip heterogeneous bone-tissue-mimetic pattern via the enhanced DEP trap. Osteocytes are positioned to form the pattern of concentric rings interlaced with the hydroxyapatite particles aligned into the pearl chain array. The good cell viability after cell patterning is also demonstrated in this paper.

References

- [1]. D.R. Albrecht, V.L. Tsang, R.L. Sah and S.N. Bhatia, *Lab Chip*, **5**, 111-118, (2005).
- [2]. H. Andersson and A.V.D. Berg, *Lab Chip*, **4**, 98-103, (2004).
- [3]. D. Falconnet, G. Csucs, H. Garndin and M. Textor, *Biomaterials*, **27**, 3044-3063, (2006).
- [4]. C.T. Ho, R.Z. Lin, W.Y. Chang, H.Y. Cheng and C.H. Liu, *Lab Chip*, **6**, 724-734, (2006).

MICROFLUIDIC CELL-BASED ASSAYS BY 3D CELL CULTURE IN A PEPTIDE SCAFFOLD

Minseok S. Kim, Sunki Chae, Wonhye Lee, and Je-Kyun Park

Department of BioSystems, Korea Advanced Institute of Science and Technology (KAIST), Korea

Abstract

This paper describes a novel cell culture platform for 3D cell immobilization as well as a dose-dependant cell-based assay by forming linear concentration gradient inside a peptide scaffold of a microchannel. A sol-gel transition peptide hydrogel, Puramatrix™, was first adopted in microfluidics. As the mixture of the peptide hydrogel and human hepatocellular carcinoma cells (HepG2) was flowed and gelled in the middle of a main channel by diffusion of media, we could simply fabricate a stripe-shaped peptide scaffold. Encapsulated HepG2 were cultivated in the 3D microenvironment and applied to cytotoxicity assays using Triton X-100.

Keywords: 3D cell culture, peptide hydrogel, hydrodynamic focusing, concentration gradient, cell-based assay

1. Introduction

Microfluidic systems have been taken notice of breakthrough to improve credibility of cell-based assays and high-throughput screening (HTS) in drug discovery. Recently, several trials of 3D cultivation in microfluidics have been demonstrated by the report that 3D cultivation can be reverted to *in vivo*-like original state of cells rather than 2D cell culture [1, 2]. However, studies for various cell-based assays based on the cyto-compatible 3D cell culture have been rarely reported. In this study, we demonstrate a cell culture platform enabling both 3D cell culture and *in situ* dose-dependant cell-based assays.

2. Experimental

The device was designed as shown in Figure 1a and was fabricated by photolithography and poly(dimethylsiloxane) (PDMS) replica molding (Figure 1b). Sol-gel transition of a peptide hydrogel is the basis for 3D cell immobilization. To work the scheme, it needs sol-gel transition material (Puramatrix), a material

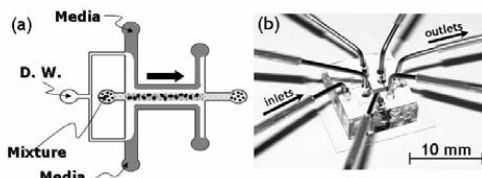


Figure 1. (a) Design of a microfluidic device for 3D cell culture. (b) Picture of the fabricated device.

making it gelation (media), and a material controlling sol-gel transition (distilled water). Distilled water was used to control the transition at the interval of two fluids.

3. Results and discussion

A mixture of Puramatrix and HepG2 was flowed in the middle of the main channel (Figure 2a). Then, distilled water was immediately turned off and both sides of media were contacted to the mixture within a few seconds (Figure 2b). When the media were close to the mixture, the mixture was also turned off. At this time, media were diffused into the mixture and the cells existed in the peptide hydrogel were 3-dimensionally encapsulated (Figure 2c). Finally, as distilled water was flowed again, the immobilized peptide scaffold can be seen without being washed away (Figure 2d). Consequently, we could simply fabricate a stripe-shaped micro-scaffold and control the scaffold width (CV: 5.8%, n=7) by hydrodynamics. They showed well-immobilized peptide scaffold in the middle of a main channel and the immobilized cells were cultured by perfusion for 3 days. Compared to conventional flask culture, the 3D cultured cells were severely clustered and aggregated each other as tumor's nature (Figure 3, a and b), whose morphologies were significantly different from those of cells in 2D culture (Figure 3, c and d).

After fabricating a strip-shaped peptide scaffold, fluorescein was flowed by one side of media inlet and medium was flowed by the other side of media inlet. Figure 4a represents concentration gradient profiles at distance from the center of a main channel (mixture inlet). Three cases of experiments were performed where no scaffold, a stripe-shaped Puramatrix scaffold, and a scaffold having HepG2 were included. In no scaffold, linear profile was only shown at an interface area of two streams. On the other hand, linear concentration gradient profile was formed at all cross-sectional area in both scaffolds. Figure 4b shows a fluorescence picture forming linear concentration profile in a main channel. The dotted line area indicates the position of a peptide scaffold. To evaluate the linear profile shown in a nonporous peptide scaffold, CFD simulation

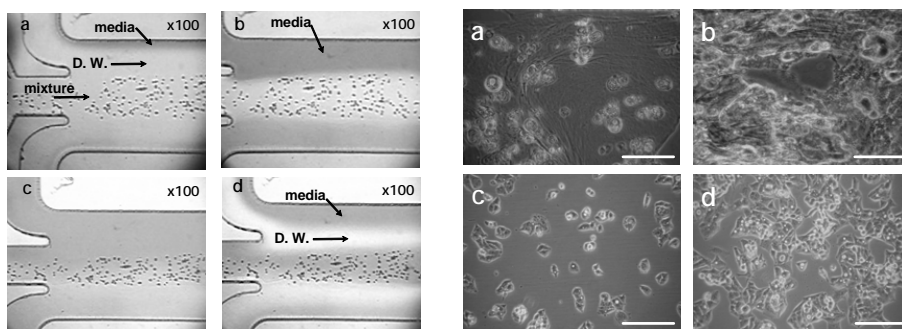


Figure 2. Pictures of 3D cell immobilization in the middle of a main channel

Figure 3. (a) and (c) are initial condition, (b) and (d) are after 60 h. All scale bars are 100 μm .

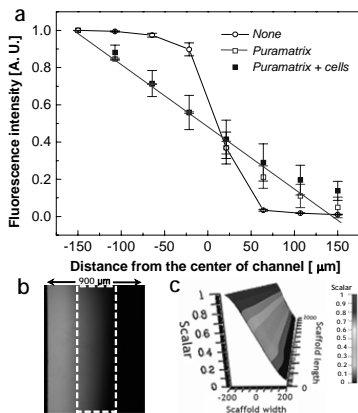


Figure 4. Concentration profiles at distance from the center of main channel.

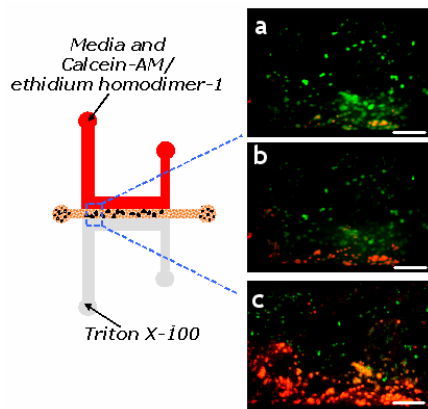


Figure 5. Toxicity test as concentrations of Triton X-100 (all scale bars are 100 μm).

(CFD-ACE) was carried out. Figure 4c displays the front side view of a scaffold. By this characteristic, toxicity test after 3D cell immobilization was conducted in the same device (Figure 5). Toxicant (Triton X-100) and media were injected at the same time where toxicant concentration gradient was generated. Live/dead cytotoxicity test solution (Molecular probes, OR) was flowed and pictures for cell viability were captured after sequential treatments with (a) 0.005%, (b) 0.01%, and (c) 0.02% Triton X-100. The result showed that as the higher toxicant (Triton X-100) concentration gradient forms, the wider dead zone of cells in the peptide scaffold represents.

4. Conclusions

A novel microfluidic device for 3D cell culture as well as *in situ* cell-based assays was developed. The stripe-shaped scaffold had highly linear concentration gradient at all cross-sectional area of a scaffold and the phenomenon was evaluated by CFD simulation. By the cellular study, it was evaluated that the microfluidic device is available for rapid acquisition of massive amounts of dose-response curves such as IC_{50} and EC_{50} values.

Acknowledgements

This research was supported by the Ministry of Commerce, Industry and Energy (MOCIE, Korea) and by the KRIIBB Initiative Research Program (KRIIBB, Korea).

References

- Y. -C Toh, S. Ng, Y. M. Khong, V. Samper, H. Yu, Assay Drug Dev. Techn., Vol. 3, pp. 169-176 (2005).
- A. Abbott, Nature, Vol. 424, pp. 870–872 (2003).

A PNEUMATIC MICRO CELL STIMULATOR FOR THE DIFFERENTIATION OF HUMAN MESENCHYMAL STEM CELLS (hMSCs)

Woo-Young Sim¹, Sin-Wook Park¹, Sang-Sik Yang¹,
Sang-Hyug Park², and Byoung-Hyun Min³

¹Dept. of Electronics Eng., ²Dept. of Biomedical Eng.,

³Dept. of Orthopaedic Surgery, Ajou University, Suwon, 443-749 Korea

Abstract

This paper presents the fabrication and test of a pneumatic micro cell chip which can induce stem cells to differentiate into specific body cell types. The micro cell chip actuated by a pneumatic force is designed to apply hydraulic pressure to human mesenchymal stem cells (hMSCs) cyclically. It provides a new generation of cell culture, stimulation and analysis devices for stem cell research and tissue engineering.

Keywords: Micro cell stimulator, Cell-MEMS, Stem cell, Tissue engineering, Regenerative medicine

1. Introduction

Stem cells have the remarkable potential to develop into many different cell types in the body. Especially, mesenchymal stem cells (MSCs) are well-characterized population of the adult stem cells that have no immune rejection and ethical objections in clinical uses. The common method to get specific cells/tissues derived from MSCs is used by biochemical factors (e.g. cytokines and growth factors). Recently, new method using the mechanical stimulation is reported [1, 2]. The conventional methods to experiment with stem cells have several drawbacks such as large number of cell culture surfaces and samples, bulky incubators, large fluid volumes, and expensive human labor and equipment [3].

2. Structure and fabrication

MEMS cell stimulators are designed to culture stem cells and apply the mechanical stimulation for research on the differentiation of stem cell. We focus our device on the chondrogenesis (i.e. differentiated to cartilage or bone) of hMSCs. Compared with the previous researches, the cell chip in this paper has some inherent potentials such as the reduction of the necessary quantity in stem cells, the cost reduction in process, and the increase of throughput.

The schematic diagram of a MEMS cell stimulator is shown in Figure 1. MEMS cell stimulator is based on the pneumatic actuator with a flexible diaphragm. It consists of five layers of poly(dimethylsiloxane)(PDMS; Sylgard 184, Dow-Corning) and glass (Borofloat-33) substrates. The device is largely comprised of an air chamber and several cell-media chambers. The cell-media chamber layer has five columns with three chambers connected by microchannels. The gasket and cell-media chamber with

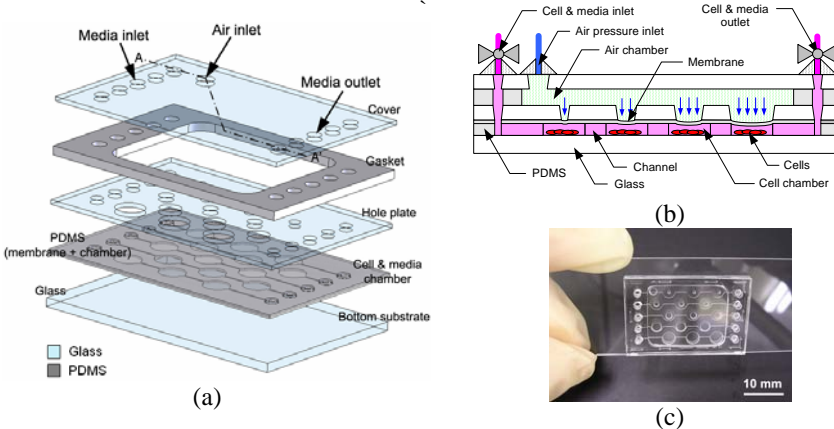


Figure 1. A micro cell stimulator actuated by a pneumatic force: (a) exploded view, (b) cross-sectional view (A-A'), (c) photograph of the fabricated cell chip.

a membrane are formed in PDMS by the standard molding-process. An air chamber part, including hole-plate, gasket and cover, is fabricated by the powder blasting process. To apply the various pressures simultaneously, hole diameters are designed differently. The fabricated device is shown in Figure 1(c).

3. Experimental

The device is initially filled with mixed solution, hMSCs (human mesenchymal stem cells) and culture medium by the syringe pump. After confirming the cells were attached to the bottom of the chamber for 12 h in incubator, hMSCs are exposed to cyclic compressive stimulus (frequency 1 Hz, pressure 5 KPa) for 10 minutes every 12 hours during 5 consecutive days. The changes of stimulated MSCs are examined by means cell surface marker staining in a monolayer using fluorescein isothiocyanate PE and PE-Cy5 conju-gated anti-human mono clonal antibodies, CD90 (Thy-1) and CD29 (Integrin). The osteogenic differentiation of hMSCs under the mechanical stimulus has been evaluated by ALP (alkaline phosphatase) staining.

4. Results and discussion

Figure 2 shows the images of cell status in cell chip. In the ALP staining, the calcium accumulation in osteogenesis is significantly higher than in control after 5 days of stimulating. Actin staining shows that skeletal fibers are enhanced by stimulation. CD 90 and 29 expressions are positive in MSC and decrease with the times under the stimulation.

As the result, CD markers and ALP expression show strongly positive result in the stimulation group. In this system, human bone marrow stem cells may be induced into having differentiation cells by a MEMS cell stimulator. Few studies are available with regard to the proper level of mechanical stress, including the magnitude, duration, and

frequency that could mimic the natural condition of differentiation of MSC.

5. Conclusions

A pneumatic micro cell stimulator, which can apply various pressures simultaneously, is developed and tested. We show the possibility that hMSCs can be changed into differentiated cells by mechanical stimulation. The feasibility of MEMS cell stimulator as a convenient and effective tool for stem cell research and tissue engineering is demonstrated.

Acknowledgements

This research project was funded by grant No. (R01-2003-000-11614-0) from the Basic Research Program of the Korea Science & Engineering Foundation (KOSEF).

References

- [1] C. Perka, et al., *J. Biomed. Mat. Res. A*, 52, pp. 543-552, 2000.
- [2] J. D. Kisiday, et al., *J. Biomechanics*, 37, pp. 595-604, 2004.
- [3] D. Beebe, A. Folch, *Lab chip*, 5, pp. 10-11, 2005.

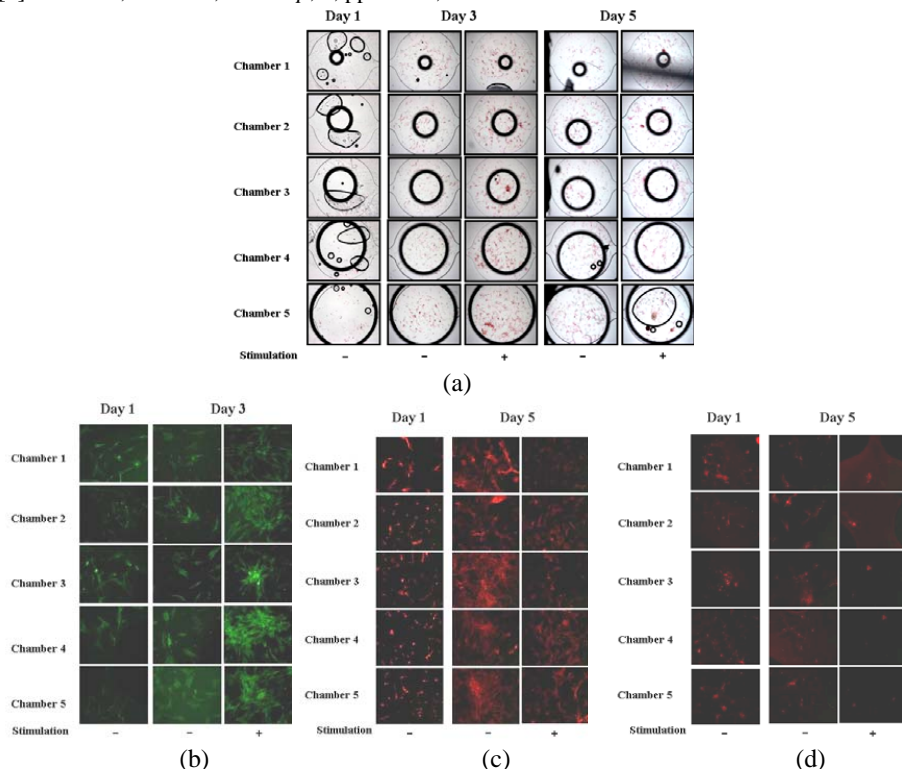


Figure 3. Micrographs of hMSCs (human mesenchymal stem cells) under the cyclic compressive stimulation during 5 days (frequency: 1 Hz, Pressure: 5 KPa). (a) ALP staining, (b) Actin staining, (c) CD 90 staining, (d) CD 29 staining.

TEMPERATURE, FLOW AND GLUCOSE SENSORS INTEGRATED WITH A SPIRALLY-ROLLED POLYMER TUBE FOR CARDIOVASCULAR MONITORING

Chunyan Li, Jungyup Han, Pei-Ming Wu and Chong H. Ahn

Microsystems and BioMEMS Laboratory

Department of Electrical & Computer Engineering & Computer Science

University of Cincinnati, Cincinnati, Ohio, 45221 USA

Abstract

An integrated physical and biochemical sensor module mounted on a flexible spiral microstructure for smart micro catheter for measuring physiological data (temperature/flow rate) and metabolic data (glucose concentration) in cardiovascular monitoring was developed and characterized in this work. The developed smart flexible micro tube system will provide a generic platform for micro catheter application assembling patient-specific and various microsensors, which can result in “smart” catheters with additional microsensors, microactuators, and wireless signal communication modules.

Keywords: spirally-rolled polymer microtube, smart microcatheter, microsensors, cardiovascular monitor

1. Introduction

Critically ill patients require continuous temperature monitoring and many parameters that determine biosensor performance are highly temperature dependent. Blood flow helps to understand many pathological conditions since many diseases alter the blood flow and can detect blood clots in the arterial system. So, the integration of temperature, flow and glucose sensors on a catheter can contribute to better diagnostic and therapy assessment. In the development of a functional microcatheter, wiring, assembling, and packaging processes has been investigated as one of the most challenging tasks due to its high manufacturing cost and most packaging approaches use the commercially-available catheter to attach miniature sensors as our previous work [1]. Our new “polymer microtube” with microsensors can be fabricated in plane and then construct a 3D tube structure by spirally rolling. When this flexible microtube is inserted through the blood stream, it has

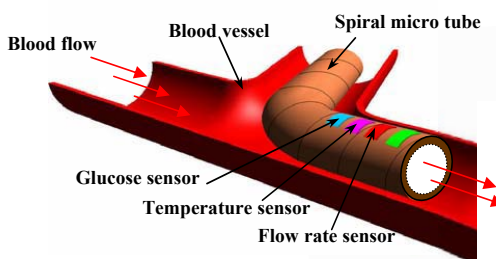


Figure 1. Conceptual drawing of a complex sensor module for smart micro catheter.

advantages without hurting the vessel and interfering the normal blood flow (Figure 1).

2. Design and Fabrication

Ti/Au RTD (resistance temperature detector) was fabricated as a temperature sensor. A current was passed through the RTD and the change of voltage with temperature was measured. Flow sensor adopted the principle of constant temperature anemometry. So, in addition to the temperature sensor, another Ti/Au RTD was connected to one arm of a Wheatstone bridge and heated by an electrical current. When the fluid is flowing, it convects heat away from the RTD and the bridge balances the amplifier that drives current through the RTD, heating it to keep constant temperature. The bridge voltage, V , represents the heat transfer and is thus a direct measure of the velocity of flow. The main principle for glucose detection is based on glucose oxidation by glucose oxidase and the by-product, hydrogen peroxide is measured on the working electrode [2]. Ti/Au RTD and glucose sensor were fabricated on the 25 μm thick Kapton film and spirally rolled as described in Figure 2. The other Kapton strip was rolled from opposite direction to make a braided structure for improved axial, flexural and torsional rigidity. Sensor principles and fabricated devices are shown in Figure 3.

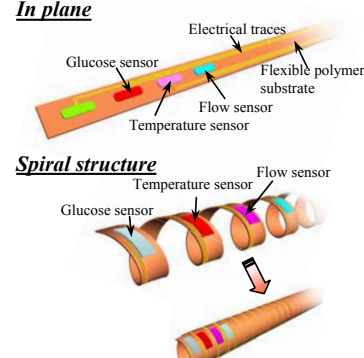


Figure 2. Illustration of the proof-of-concept the spiral microstructure with temperature, flow and glucose sensors fabricated from planar process.

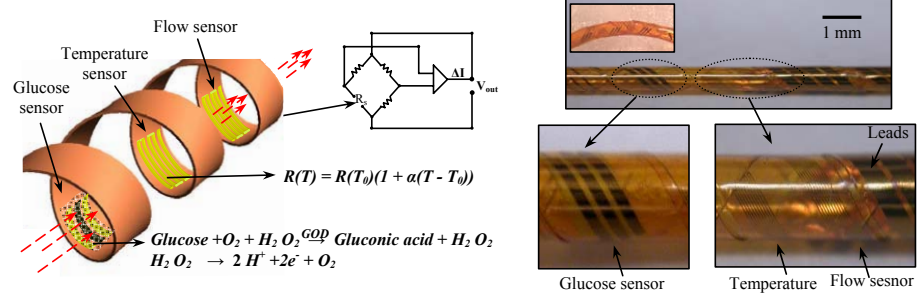


Figure 3. Fabricated devices: (a) Working principle and (b) photograph of the fabricated spirally-rolled Kapton tube (OD = 880 μm) with fabricated temperature, flow rate and glucose sensors inside.

3. Experimental results

A constant direct current ($I = 1 \text{ mA}$) was used to drive the circuit and the temperature was monitored by inserted thermocouple at the same time. Figure 4 shows the measure resistance variation versus temperature. The TCR value of Ti/Au film derived is 0.003 K^{-1} . Figure 5 shows the voltage output as a function of different

viscosity sugar water flow rate. A 3 mA bias current was applied and got the sensitivity of 3.06 mV/(ml/min). The glucose sensor performance under different temperatures with combined temperature sensor was recorded as shown in Figure 6, in which a significant temperature dependency was observed.

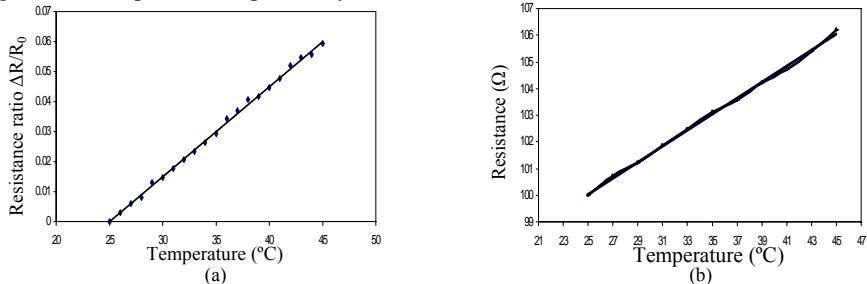


Figure 4. Temperature sensor characterization: (a) calculated TCR = 0.003 K^{-1} at applied current $I = 1 \text{ mA}$ and (b) RTD resistance versus the environment temperature monitored by the inserted thermocouple measured at the same time.

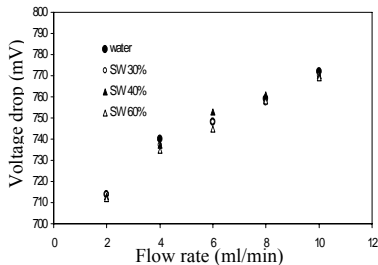


Figure 5. Flow sensor characteristic for different viscosity sugar water (1, 3.165, 7.145 and 93.85 cP) at constant temperature mode. Sensitivity is 3.06 mV/(ml/min).

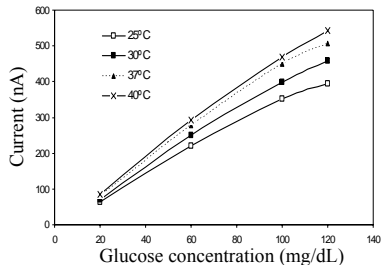


Figure 6. Measured peak current versus different glucose concentrations at different temperature for the tube with OD = $880 \mu\text{m}$.

4. Conclusions

In this work, temperature, flow and glucose sensors were successfully integrated on a $25 \mu\text{m}$ thick Kapton film and rolled spirally for different micro diameter tubes, then the sensors were fully characterized. The braided structure provides enough axial and flexural rigidity for the cardiovascular catheterization. This new method showed great possibilities for new low cost “smart” tube with multi-sensors for the cardiovascular in-vivo monitor.

References

1. C. Li, et al, Polymer flip-chip bonding of pressure sensors on flexible Kapton film for neonatal catheters, Proc. of the 17th IEEE MEMS pp. 749-753, (2004).
2. C. Li, et al, A new spirally-rolled polymer microtube with biosensors for smart microcatheter, MicroTAS'05, Boston, USA, pp. 1203-1205, (2005).

A FLUIDIC MOTHERBOARD INCLUDING FLUIDIC AND OPTICAL INTERCONNECTIONS, HAVING MODULAR FUNCTIONALITY FOR OPTICAL ANALYSIS IN MICROFLUIDIC SYSTEMS

G. Perozziello¹, D. Snakenborg¹, Z. Zhang², J. P. Kutter¹, O. Geschke¹

¹Dept. of Micro and Nanotechnology, Tech. University of Denmark, Lyngby, DK

²Dept. of Chem. Engineering, Massachusetts Institute of Technology, MA, USA

Keywords: motherboard, optic connections, fluidic interface, plug'n'play function

1. Abstract

In this work, we propose a new polymer-based microfluidic motherboard that integrates polymer-based waveguides and fluidic networks providing both fluidic and optical interfaces between microfluidic systems and the outer world (Figs.1 and 2).

The motherboard facilitates interconnections of several microfluidic systems for multiplexed and simultaneous analysis. Moreover, it offers a modular network for microfluidic chips, allowing more complex microfluidic process flows, where each microchip has a particular function [1].

2. Introduction

Microfluidic and optical interconnections between devices, interfaces between the environment and the devices, as well as housing the devices are critical issues to be considered where a platform for modular and multiplexed bio-chemical analysis is to be provided. Integrating and interfacing optical elements is a difficult task. The fluidic motherboard we developed offers a reliable method to interconnect, at the same time, fluidically and optically several microfluidic systems with ease of use.

3. Fabrication

The motherboard includes microfluidic channels machined into the bottom side of the substrate using micromilling technology. Through-holes allow connection to the top-layer. To seal the channels, a 1.5 mm thick PMMA plate is bonded thermally. Waveguides are directly machined into a spin-coated “doped” PMMA layer (with a higher refractive index than the substrate) on the top side by milling parallel grooves with a width down to 80 μm [2]. Additionally, pins are fabricated, which are part of the fluidic interconnections and allow the alignment of a chip with the waveguides of the motherboard [3]. To establish high density microfluidic interconnections between the motherboard and external tubes, detachable and re-usable PDMS sockets have been utilized [4]. For interconnecting the polymer waveguides to the light source and to the detection system, PDMS optical plugs integrating spherical lenses aligned to several optical fibers on the other side have been fabricated [5]. The optical connector plugs

allow focusing of light from the optical fiber to the waveguide and vice versa, thus alleviating alignment issues. The motherboard integrates polymer microfluidic systems having fluidic channels, waveguides and, additionally, custom made o-rings allowing alignment to the connection pins of the motherboard (Fig. 3). The individual chips are attached to the motherboard by just pressing them onto the alignment pins (Fig. 4). A sealed fluidic connection between chip and motherboard is ensured by the deliberate mismatch in diameter between the o-rings of the chip and the pins of the motherboard.

4. Experiments

Static fluidic tests have been performed to investigate the limits of the motherboard fluidic interconnections. Regarding the optical connector plugs, insertion loss measurements have been performed as a function of induced misalignment and the results have been compared with those obtained using a cleaved fiber. Finally, measurements of the optical losses using different connections have been performed and compared with those performed in the motherboard. For this purpose, light from an appropriate source ($\lambda=637$ nm) has been coupled to a detector via different connections, such as fiber-fiber, fiber-chip-fiber, fiber-motherboard-chip-motherboard-fiber, after which the results were compared.

5. Results

The results in Fig. 5 indicate that the optical plug displays a much greater tolerance to misalignment than standard fibers, showing a slow increase of insertion losses even in presence of misalignment. Optical measurements showed a recorded power of 300 μW when directly connecting one fiber to another fiber. For the connection fiber-chip-fiber the power went down to 150 μW . For the connection motherboard-chip-motherboard the power decreased to 4 μW . Taking the connection fiber to fiber as reference, an overall loss of 18 dB was measured in the motherboard (Fig. 6). Finally, leakage of liquids was detected at 3.2-3.5 bar and located in connection with the PDMS fluidic socket.

6. Conclusion

In conclusion, a new type of fluidic motherboard has been presented based on an inexpensive fabrication approach. It shows a very robust design allowing an easy interconnection of several microsystems providing auto alignment of fluidic and optical interconnections at the same time.

References

1. T. S. J. Lammerink, et al., Proc. of MEMS'96. IEEE, 389-394, 1996
2. D. Snakenborg et al., J. of Micromech. and Microeng. 16:375-381, 2006
3. P. Galambos et al., Micro-Electromech. Systems Division (MEMS), 3:723-730, 2001
4. R. B. Darling, TRANSDUCERS'01. EUROSENSORS XV, vol.2: 974-977, 2001
5. G. Perozziello et al., Proceedings of μ TAS 2005 Conference 1155-1157, 2005

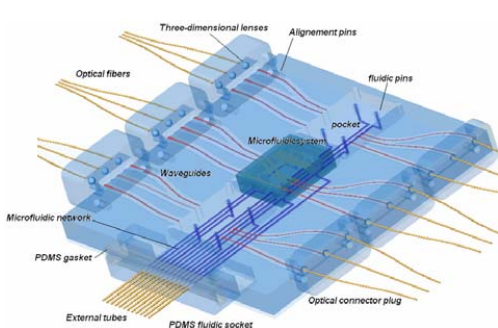


Figure 1: Three-dimensional view of the motherboard designed using a CAD software.

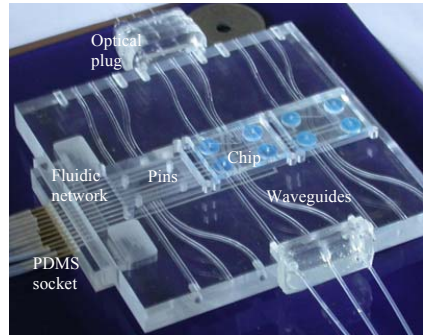


Figure 2: Isometric view of the motherboard, the chips, the optical plug and the PDMS socket.

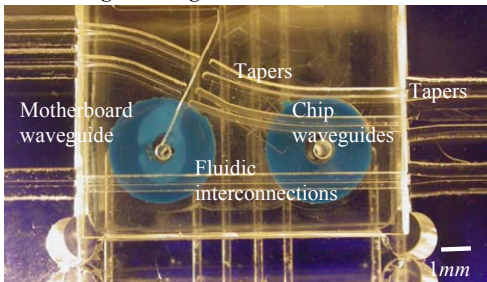


Figure 3: Close-up of the top view of the chip connected to the motherboard

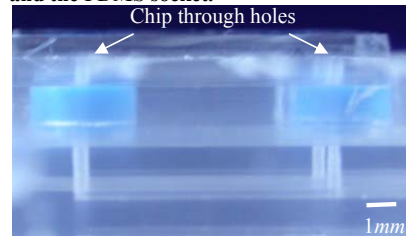


Figure 4: Close up of the integrated interconnections while the chip is plugged into the motherboard where perfect alignment between through holes of the chip and motherboard is seen.

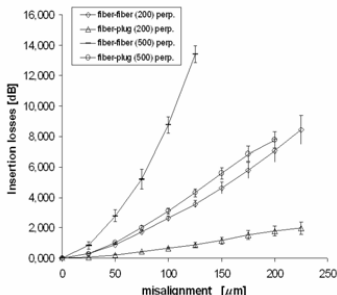


Figure 5: Insertion losses versus induced misalignment through an optical plug-fiber connection compared with the same losses measured through a fiber-fiber connection.

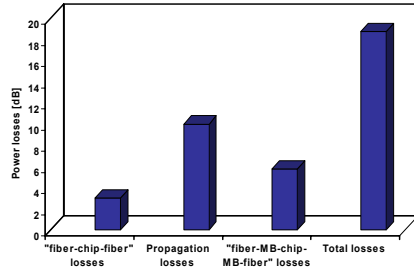


Figure 6: Optical power loss measurements through fiber-chip-fiber connections, propagation losses in the waveguides, insertion losses at fiber-MB-chip-MB-fiber connections, and total losses.

DIRECTED FLUIDIC SELF-ASSEMBLY OF MICROSCALE TILES

Mike Tolley¹, Victor Zykova¹, Hod Lipson^{1,2}, David Erickson¹

¹Sibley School of Mechanical and Aerospace Engineering, Cornell University, USA

²Computing and Information Science, Cornell University, USA

ABSTRACT

In this paper we present a novel microfabrication method in which regular, micro-scaled units are made to self-assemble into arbitrary, reconfigurable structures. We describe a series of experiments that involve the assembly of silicon microtiles in a multilayer PDMS microchamber. By controlling the local flow conditions in a microchannel array, the attraction, bonding, migration, and rejection of individual and paired microtiles are demonstrated.

Keywords: self-assembly, microfluidic, microtile, nanofabrication, digital matter

1. INTRODUCTION

Self-assembly has the potential to provide a scalable alternative to current direct-write/direct-manipulation microfabrication techniques [1]. One of the challenges of self-assembly is the fabrication of arbitrary (non-regular) structures such as those routinely achieved using top-down techniques. Our goal is to create a form of programmable “digital matter” in which desired structures are assembled from simple, microscale units which control their assembly by manipulating local fluidic forces (Figure 1). This self-assembly is directed by power, communication, and actuation provided to the units at the substrate. Here, we present an initial set of experiments designed to demonstrate the first layer of assembly and disassembly. Simple fluidic control is used to assemble individual and paired silicon microtiles in a PDMS microchamber. We also compare the effectiveness of various tile designs, substrate outlet designs, and assembly media.

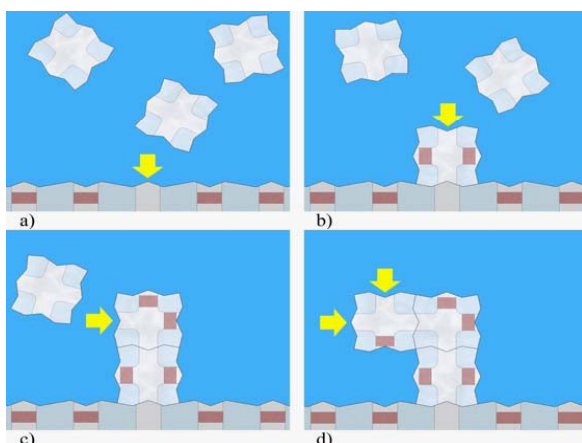


Figure 1. Directed Fluidic Self-Assembly Concept

a) Fluid flow (indicated by arrows) into a substrate attracts a nearby unit. **b)** Once attached, the unit draws power from the substrate to activate on-board valves (dark bands) and direct fluid flow through internal channels. **c)** The directed fluid attracts new units at desired locations. **d)** New units continue this process of directing fluid flow to assemble the next layer until the structure is complete.

2. FABRICATION

We fabricated solid, 30 μm thick, square silicon tiles with lengths ranging from 100 μm to 500 μm by etching and releasing the top layer of a silicon-on-insulator (SOI) wafer (Figure 2, left). Two self-alignment side patterns were fabricated. The first (Figure 3e-f) is four-fold rotationally symmetric but does not align when inverted. The second pattern (Figure 3a-d) is flip-invariant but has half the potential bonding sites since each tile has two different side patterns. The multilayer self-assembly chambers were fabricated by molding a 100 μm thick layer of poly(dimethylsiloxane) (PDMS) over 70 μm thick positive photoresist (SU-8) and bonding it to a glass surface. Various outlet designs were tested (see Figures 3, 4) and the design with single, narrow nozzles (Figure 2, middle) was found to minimize bonding errors. A second, thick layer of PDMS with pneumatic channels was overlaid on the fluidic layer (Figure 2, right) in order to valve the outlets. This allowed precise control over the shear conditions in the chamber.

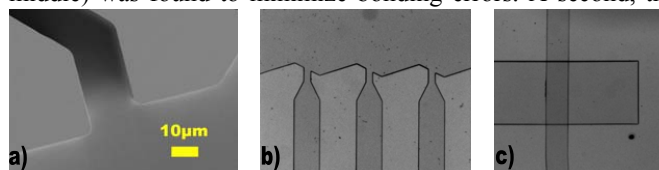


Figure 2. Fabrication of Microtiles and Assembly Chamber

a) SEM image of etched 100 μm Si tiles. b) Fluid outlets and patterned substrate of PDMS microchamber. c) Pneumatic channel (horizontal) overlaid on fluidic channel (vertical).

3. EXPERIMENTAL RESULTS

Single-tile experiments demonstrated our ability to attract, bond and reject a microtile from a patterned PDMS substrate (Figure 3a-d), as well as to migrate a tile along the substrate from one bonding site to the next (Figure 3e-f). In multi-tile experiments, we were able to attract tiles to the substrate, bring them together to self-assemble (Figure 4a-c), migrate the assembly along the substrate, and reject them (Figure 4d-f). Tile-tile and tile-substrate alignment was successful with both side patterns, but migration was more successful with the rotationally symmetric tiles. Tile assembly was conducted in three fluids: deionized water (Figure 4d-f), a 5% surfactant solution (Figures 3e-h,4a-c),

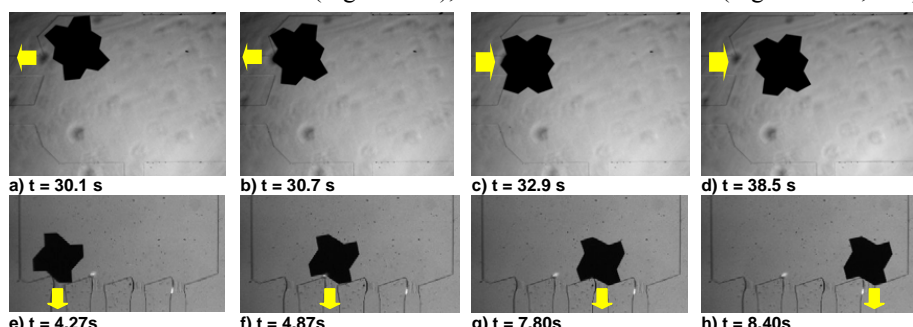


Figure 3. Single Tile Experiments a-d) Fluid flow (indicated by yellow arrows) into and out of a substrate channel attracts and then repels a 500 μm silicon tile in silicone oil. e-h) A 500 μm silicon tile in a 5% surfactant solution is made to migrate along a substrate by selectively opening and closing chamber outlets to direct fluid flow as indicated.

and silicone oil (Figure 3a-d). Tile movement and self-alignment was more successful in the surfactant solution and silicone oil experiment. Pressures in the range of 1-4 psi drove the flow enough to successfully move the tiles in the deionized water and the surfactant solution experiments. Much higher pressures (10-15psi) were required to manipulate the tiles in the silicone oil experiments. The pneumatic valves completely shut off fluid flow into the outlets under applied pressures in the range of 17-20psi.

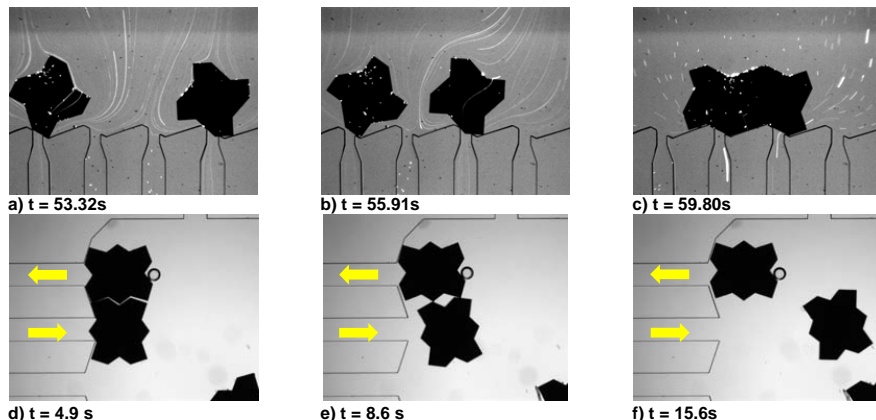


Figure 4. Multi-tile Experiments **a-c)** Two tiles are assembled on a substrate by selectively opening and closing outlet valves. 3 μ m fluorescent particles help visualize the assembly fluid's flow profile. **d-f)** Fluid flow in the directions indicated disassembles two 500 μ m silicon tiles in deionized water.

4. CONCLUSIONS

We have presented a new microfabrication paradigm in which structures are assembled from regular units with limited actuation and control. An initial series of experiments were described in which patterned micron-scale silicon tiles were made to self-assemble on a patterned substrate in a multilayer PDMS microchamber. Successful attraction, bonding, movement and rejection were demonstrated for individual and paired tiles. The effectiveness of various tile shapes and sizes, assembly chamber designs, and assembly fluids were compared. These experiments represent the first steps in the development of a novel microfabrication system based of directed microfluidic self-assembly.

ACKNOWLEDGEMENTS

This work has been funded in part by the US National Science Foundation program for Materials Processing and Manufacturing, Engineering Design, grant number 0634652. Mike Tolley would also like to thank the Natural Sciences and Engineering Research Council of Canada for their support through the Postgraduate Scholarship program.

REFERENCES

- [1] G. M. Whitesides and B. A. Grzybowski, Self-assembly at all scales, *Science* v. 295, Washington, USA, pp. 2418–2421, (2002).

MICROFLUIDICS ON A CONVENTIONAL, 10-\$ CDROM DRIVE: ALL-IN-ONE DETERMINATION OF THE HEMATOCRIT

L. Riegger¹, M. Grumann¹, J. Steigert¹, R. Zengerle^{1,2}, and J. Ducr  e^{1,2}

¹Lutz Riegger, Lab for MEMS Applications, Department of Microsystems Engineering (IMTEK), Univ. of Freiburg, Georges-Koehler-Allee 106, 79110 Freiburg, Germany

²HSG-IMIT, Institute for Micromachining and Information Technology, Germany

Abstract

We present a novel method to measure the hematocrit (*Hct*) of untreated whole blood on a conventional CDROM drive by simple visual inspection. After the manual introduction of an unmetered volume, all further processing steps including the bubble-free priming of the measurement capillary, the metering to a defined volume, and the sedimentation of the red blood cells are run automatically in the drive during a 4-minute period of centrifugation. The hematocrit can be read out at the phase boundary between the plasma and the sedimented cellular pellet on the disk-imprinted calibrated scale.

Keywords: CDROM, hematocrit, bubble-free priming, centrifugal microfluidics

1. Introduction

Among the various lab-on-a-chip concepts, “lab-on-a-disk” [1] systems exploit centrifugal forces for metering, accelerated sedimentation of particles in biological suspensions, and mixing in order to run fully process integrated assays. In general, these systems require expensive lab-based centrifuges for the precise control of the rotational frequency as well as the acceleration and deceleration which is not well compatible with point-of-care applications. In our approach, we “abuse” a conventional, 10\$ - PC-CDROM drive to implement a fully automated test for one of the most relevant parameters in medical diagnostics and routine blood screening - the hematocrit.

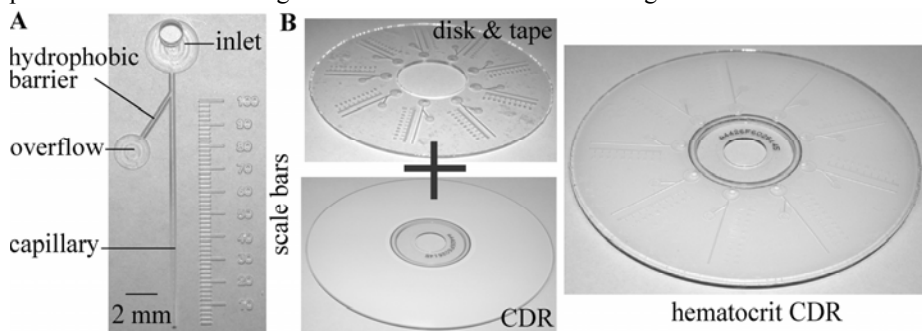


Figure 1. (A) The hematocrit structure features an inlet, an overflow confined by a hydrophobic barrier for metering, and a sedimentation capillary. Imprinted scale bars facilitate the hematocrit read-out by visual inspection. (B) The microfluidic disk is micromachined in PMMA and features a nine-fold degree of parallelization. After being surface modified, the disk is bonded to a conventional CDR by a double-sided tape.

2. Microfluidic Structure and Disk Fabrication

The hematocrit structure (Fig. 1-A) is CNC-micromachined into a PMMA disk with a tapered tool, yielding walls sloped at 45°. It comprises an inlet reservoir, an overflow channel featuring a hydrophobic barrier for metering, and a hydrophilized, 2-level capillary for sedimentation including a rounded dead end (Fig. 2-A). The capillary measures a radial length of 25 mm, a depth of 300 μm and widths of 300 μm and 900 μm for the bottom and the top, respectively. Next, a double-sided adhesive tape is sandwiched between the disk and a conventional, pre-written CDR (Fig. 1-B).

3. Priming

The priming initiates by centrifugally assisted capillary motion of tiny “swords” along the critical edge between the tilted walls and the sealing (“wicking”). After reaching the blind end of the channel, the blood progresses inbound along the opposite critical edge until it arrives at the hydrophobic barrier, thus triggering the reverse filling of the blind capillary across its entire cross section (Fig. 2-B) [2].

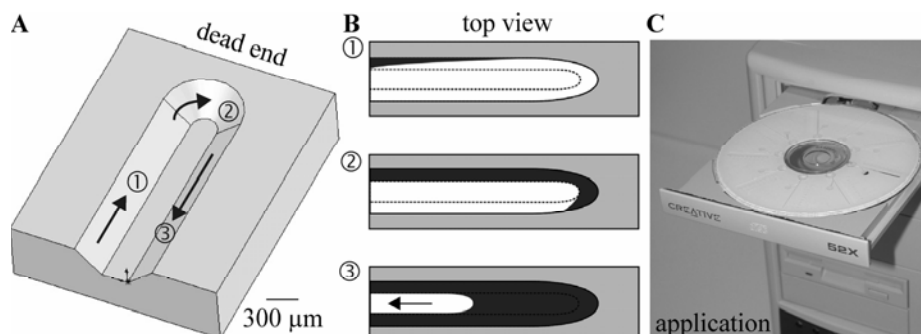


Figure 2. (A) Channel profile of the blind end of the capillary featuring walls which are sloped at 45° to increase the effect of capillary wicking. (B) The blood propagates towards the dead end along the critical edge presented by the boundary between the channel wall and the lid ①, ② until it reaches the hydrophobic barrier on the opposite side to initiate the reverse filling of the capillary leading to a complete evacuation of the channel ③ [2]. (C) The test disk can be readily “played” in any conventional CAV (constant angular velocity) CDROM drive. For safe operation, the rotational speed is limited via the ASPI hardware protocol to 6000 rpm (i.e., 30X).

4. Experimental Processing and Results

Unmetered samples of whole blood are introduced into the inlet reservoirs and the disk is inserted into the CAV-type CDROM drive. In order to define the spinning frequency and the spinning duration, the rotational speed is limited via the ASPI hardware protocol to 6000 rpm (i.e., 30X) and the disk-based data track of a defined size is completely read by the computer. During the acceleration phase, the capillary is primed and the blood sample is precisely metered (Fig. 3-A). After sedimentation, the

hematocrit can directly be read out by visual inspection on the disk-imprinted, calibrated scale bar (Fig. 3-B). With a 5- μ l sample of blood, only, we obtain a CV of 4.3%, a time-to-result of 4 min, and a high linearity ($R^2 = 0.999$) between the disk-based hematocrit determination and the reference measurement [3] (Fig. 3-C).

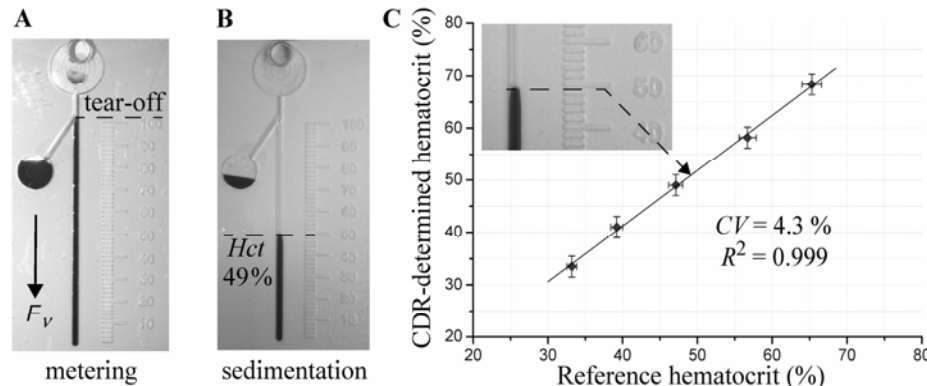


Figure 3. (A) After an unmetered volume of whole blood is applied to the inlet reservoir, the capillary is primed and a precise volume of whole blood is metered during acceleration in the CDROM drive. (B) After sedimentation, the absolute hematocrit can be determined with the calibrated scale imprinted along the channel. (C) The CV of 4.3 % and the high linearity of $R^2 = 0.999$ allow accurate measurements. It should be noted that the CV is governed by the visual readout (i.e., one scale bar = 2% Hct).

5. Conclusion

We introduced a novel hematocrit test on an unmetered sample of untreated whole blood drawn from the finger tip. The test is carried out automatically by a conventional, PC-controlled CDROM drive. The technology can be easily applied to all tests based on readout by visual inspection (e.g., agglutination tests). The aspect of using a ubiquitously installed, 10-\$ device technology in combination with disposable substrates that are very close to standard polymer mass fabrication opens promising perspectives for a cost-efficient implementation of microfluidic technologies at the end-user level, e.g. patient home care and sports medicine.

Acknowledgement

The authors thank the federal state of Baden-Württemberg (contract 24-720.431-1-7/2) for partial financial support of this project.

References

- [1] M. Madou and G. Kellogg, LabCD: A centrifuge-based platform for diagnostics, Proceedings of SPIE, SPIE publisher, San Jose, 3259, pp 80–93, (1998).
- [2] L. Rieger et al., Bubble-free priming of blind capillaries for high-accuracy centrifugal hematocrit measurements, Proc. μ TAS 2005, TRF, pp. 796-798, (2005).
- [3] HCT 142 Hematocrit turbidimetric test, Diaglobal GmbH, www.diaglobal.de.

CALORIMETRIC MEASUREMENT CLINICAL CHIP FOR HOME MEDICAL DIAGNOSIS

Yasuhiro Horiike¹, Hiroko Koda¹, S.-H.Chang¹, Ryo Ogawa¹,
Shingi Hashioka¹, Masao Nagai² and Hiroki Ogawa²

¹National Institute for Materials Science, Japan

²Adbic Incorp., Japan

Abstract

A calorimetric measurement chip system was developed using the centrifugal force, which enabled us to separate of blood collected by a painless needle, meter and mix both plasma and reagents. The chip function was confirmed for observation of curing course of hyperlipemia.

Key words; clinical chip, calorimetric measurement, centrifugal force, blood collection, toreharose

1. Introduction

A calorimetric measurement chip system has been developed to prevent life style related diseases at home [1]. The system aims at the following functions; (1) electronic collection of whole blood of 6 μL using a painless needle, (2) a chip operation using only centrifugal force, (3) simultaneous separation and metering of the blood, (4) mixing of 50~100 of reagents : 1 of plasma and (5) development of freeze-dried reagents for long-term preservation.

2. Chip Operation

The chip structure consisting of three layers and the actual chip are shown in Fig. 1(a) and (b). As shown in Fig. 2, rapid acceleration until reaching to a stationary rotation at a 1st layer separates plasma upward and blood cells downward in a zigzag

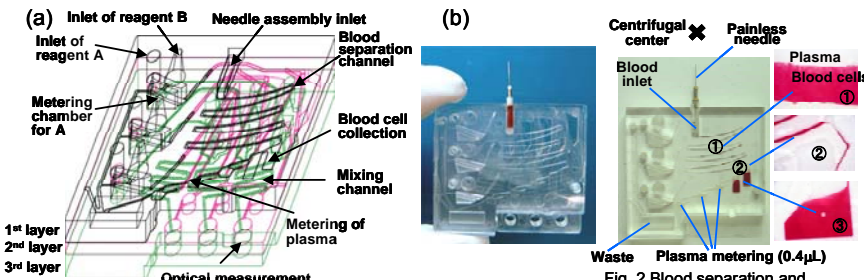


Fig. 1 Three levels structure of the chip (a) and Photograph of the chip (b)

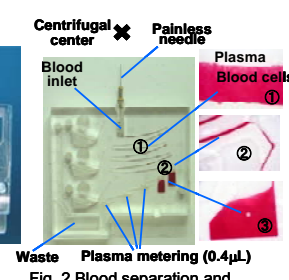


Fig. 2 Blood separation and simultaneous metering of plasma

channel. Then, blood cells are first captured at a final channel, and plasma passes over blood cells, thus falling into three metering chambers with a volume of $0.4 \mu\text{L}$. Figure 3 (a-d) shows a series of photographs which demonstrate these metering, transport and mixing processes of plasma and reagents A ($18\mu\text{L}$) and B ($6\mu\text{L}$), where colored inks were used for the observation. The reagent A introduced to the 1st inlet in (a) is metered by the centrifugal force together with plasma in (b). After rotating the chip at 90 degrees, centrifugal force transports both reagent A and plasma to the 2nd layer and shaking serves mixing/ reaction of them at five min. At the same time, the reagent B introduced to the 2nd inlet is transported to the 3rd layer by passing through the 2nd layer and is metered by centrifugal force. Finally, the reagent A and plasma mixture in the 2nd layer and the reagent B in the 3rd layer are mixed employing a zigzag channel (see Fig. 4), whose inner wall has protuberances, causing turbulence. Figure 5 (a-d) shows a series of the mixing progress of two solutions with and without fluorescent dye. A special feature of the zigzag channel is that an outside flow in an upper channel undergoes turbulence in presence of protuberances and in turn an inside flow in a lower channel undergoes turbulence. Repeating of the process accomplished the well mixing.

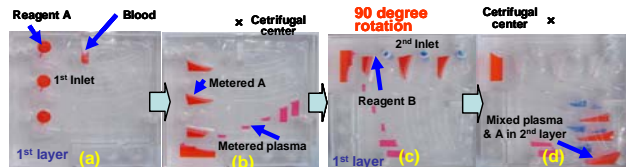


Fig. 3 Metering and mixing processes of reagent A/plasma and reagent B.



Fig. 4 Mixing zigzag channel.

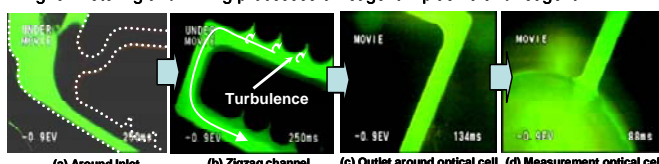


Fig. 5 Mixing process at zigzag channel. At (b), outside flow in an upper channel undergoes turbulence and inside flow in a lower channel undergoes turbulence.

3. Measurement

For practical use of the chip, long-term preservation of reagents was also studied. After A and B reagents A and B for triglyceride (Wako Junyaku) were added to toreharose at 10 weight % and were freeze-dried. As shown in Fig. 6, any decay was not observed even after one month.

Since a researcher in our laboratory suffered from abnormal high triglyceride level, course of the values were measured by taking a tablet of Mevalotin of a lipid-lowering agent (Sankyo Pharmacy) for about 4 months as shown in Fig. 7 employing the present chip, which was

introduced by blood collected using both visualization of blood vessel with NIR and detection of vessel position due to potential measurement between an arm surface and vessel

(see Fig. 8)[2] and freeze-dried triglyceride reagents+10% treharose (see Fig. 9) recovered by purified water. We confirmed gradual decrease of the value.

4. Conclusions

This chip allows us to test representative items of triglyceride, total-cholesterol and HDL. The capability is expected to prevent life style related diseases.

References

- [1] A. Oki, et. Al., Jpn. Appl. Phys., 42 (2003), pp.3722-3727.
- [2] H. Ogawa, et. al., M. A. Northrup, et. al. (Eds.) *Micro TAS 2003*, (2003) pp. 741-744.

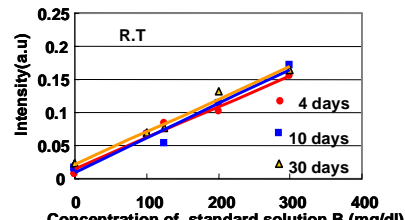


Fig. 6 Day-dependent decay characteristics of Triglyceride reagent B + 10% Treharose

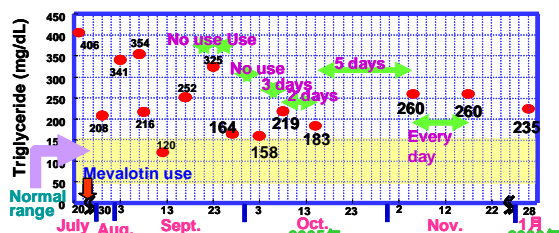


Fig. 7 Day-dependent triglyceride level by use of "Mevalotin", which is a lipid-lowering agent made by Sankyo Pharmacy



Fig. 8 (a) Monitoring of position of blood vessel by NIR irradiation, (b) Blood collection using needle

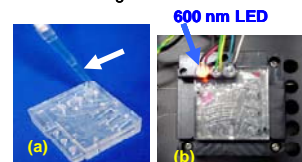


Fig. 9 (a) Introduction of freeze-dried reagent recovered to solution, (b) Actual measurement

A MICROFLUIDIC DEVICE FOR PRACTICAL LABEL-FREE CD4+ T CELL COUNTING OF HIV-INFECTED SUBJECTS

Xuanhong Cheng¹, Daniel Irimia¹, Meredith Dixon², Kazuhiko Sekine¹,
Utkan Demirci¹, Lee Zamir², Ronald G. Tompkins¹, William Rodriguez²,
Mehmet Toner¹

¹Surgical Services and Center for Engineering in Medicine, Massachusetts General Hospital, Harvard Medical School, and Shriners Hospital for Children,

²Partners AIDS Research Center, Massachusetts General Hospital and Division of AIDS, Harvard Medical School, and Brigham and Women's Hospital Boston, Massachusetts, 02114

Abstract

Practical HIV diagnostics are urgently needed in resource-limited settings. To address the limitations of current expensive, technically demanding and/or time-consuming approaches for CD4+ T cell counting, we have developed a simple microfluidic device, which specifically isolate CD4+ T lymphocytes with high efficiency directly from 10 microliters of unprocessed, unlabeled whole blood. CD4 counts determined under a microscope in our device matched measurements by conventional flow cytometry. This device can be used for simple, rapid and affordable CD4 enumeration in point-of-care and resource-poor settings.

Key words: AIDS diagnosis, CD4 counts, resource-poor setting, point-of-care

1. Introduction

Of the 40.4 million people infected with HIV globally, more than 35 million live in significant resource limited settings[1]. In the process of managing HIV+ subjects, counts of CD4+ T cells have proven to be essential biological indicators[2].

Currently, CD4+ T cell enumeration is obtained with either flow cytometers or bead-based non-cytofluorographic methods. The technical and operational needs limit their reach in resource-limited areas worldwide[3]. In this paper, we present the development of a functional microfluidic device for CD4 counting that requires no sample handling or specific labeling. The device is operated by injecting 10 μL of whole blood at a controlled flow rate, followed with rinsing and counting all the captured cells. This device can be combined with simple optics to form a low-cost, rapid CD4 cell counting system appropriate for resource-limited and point-of-care settings.

2. Experimental

Microfluidic devices were fabricated in PDMS using standard clean room techniques[4]. Freshly fabricated devices were modified using silane chemistry. Experiments were performed by flowing whole blood through the devices at desired flow rates and rinsing off unbound cells with buffer. The cells were stained with fluorescent antibodies for identification and counted manually under a microscope.

Sample flow-through and rinse buffer were collected from the outlet of the devices into eppendorf tubes and centrifuged to concentrate the cells for flow cytometry.

3. Results and Discussion

We first studied the effect of shear stress on capture specificity within the microfluidic device using whole blood from healthy, HIV-negative subjects. Within a shear stress window of 1 – 3 dyn/cm², we captured almost exclusively CD4+ T lymphocytes and minimal number of monocytes, the other type of CD4 receptor-presenting cells in circulating blood (Figure 1). We next studied the capture efficiency and discovered the same shear stress window, within which >90% of CD4+ T cells were isolated from 10 µL of unprocessed whole blood in less than 5 minutes (Figure 2).

After validating the device performance with blood from healthy subjects, we used the device to capture CD4+ T cells from HIV-infected subjects by first injecting HIV+ whole blood at a flow rate of 5 µL/min (1.7 dyn/cm²) for 2 minutes and rinsing non-specific cells afterwards. The number of isolated cells is manually counted to obtain CD4 counts. CD4 counts from the microfluidic chip were found to match those by conventional flow cytometry over the absolute CD4 count range of 200 – 800 cells/µL (Figure 3). The microfluidic chip also demonstrated the ability to discriminate clinically relevant CD4 count thresholds with sensitivity and specificity greater than 0.85.

4. Conclusions

We demonstrate a simple, quick and inexpensive CD4+ T cell counting device based on microfluidic cell affinity chromatography operated under controlled shear stress. Minimum handling procedures, rapid operation, simple device design and potential high-throughput detection makes this strategy a promising candidate for managing HIV patients in resource-limited settings.

Acknowledgements

We thank Dr. Shashi Murthy and Mr. Octavio for technical assistance. This work was supported by the National Institute of Biomedical Imaging and Bioengineering, National Institutes of Health, the Bill and Melinda Gates Foundation, and the Doris Duke Charitable Foundation.

References

1. Joint United Nations Programme on HIV/AIDS, World Health Organization (December 2005) AIDS Epidemic Update: December 2005.
2. Department of Health and Human Services (October 6, 2005) Guidelines for the Use of Antiretroviral Agents in HIV-1-Infected Adults and Adolescents.
3. Crowe, S., Turnbull, S., Oelrichs, R. & Dunne, A. Monitoring of human immunodeficiency virus infection in resource-constrained countries. *Clinical Infectious Diseases* **37**, S25-S35 (2003).
4. Murthy, S. K., Sin, A., Tompkins, R. G. & Toner, M. Effect of flow and surface conditions on human lymphocyte isolation using microfluidic chambers. *Langmuir* **20**, 11649-11655 (2004).

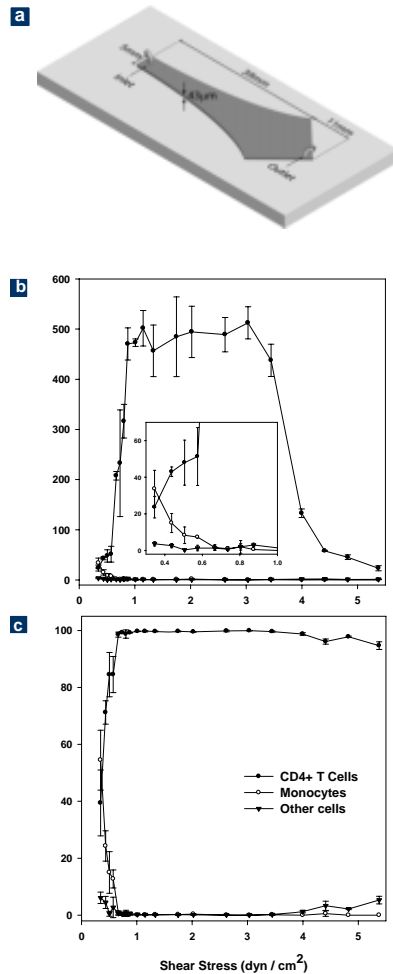


Figure 1. Effect of shear stress on cell adhesion in the Hele-Shaw devices using whole blood from healthy subjects. (a) Geometry of the Hele-Shaw device. The Hele-Shaw device offers a linear variation of shear along its central line. It was used in this study to screen the optimal shear stress for cell capture. (b) Adhesion of CD4+ T cells (solid circles), monocytes (empty circles) and other cells (solid triangles) in response to shear stress. (c) Composition of the surface captured cells as a function of shear stress.

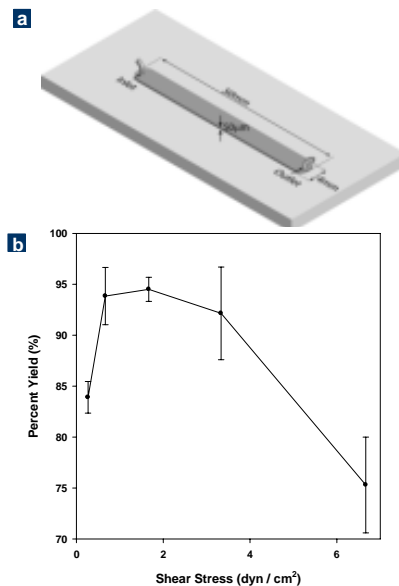


Figure 2. Effect of shear stress on capture yield in the linear devices using whole blood from healthy subjects. (a) Geometry of the linear cell count device used for CD4 T cell counting. (b) Capture yield at different shear stress.

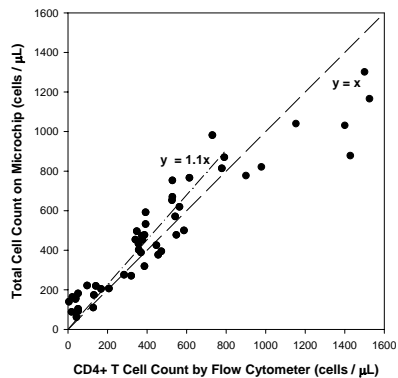


Figure 3. Correlation of total cell counts in the linear microchip versus absolute CD4 counts by flow cytometer, using whole blood from 46 HIV+ adult subjects.

HIGH THROUGHPUT MICROFLUIDICS

Ivar Meyvantsson¹, Jay Warrick¹ and David J. Beebe^{1,2}

¹Dept. of Biomedical Engineering, Univ. of Wisconsin - Madison, WI, USA

²University of Wisconsin Comprehensive Cancer Center, Madison, WI, USA

Abstract

Microfluidic systems hold promise to have a major impact across multiple fields of scientific inquiry. In order to make microfluidic systems accessible to the scientific community at large an important challenge is to simplify operation with existing infrastructure. We present a platform based on a passive pumping mechanism that requires neither external connection tubes nor integrated interconnects and can be operated using off the shelf lab automation.

Keywords: High throughput screening, automation, passive devices

1. Introduction

At least two hurdles can be identified that stand in the way of widespread adoption of microfluidic systems. First, microfluidic technology is not directly accessible to the average scientist. Existing microfluidic systems typically require new equipment (e.g. syringe pumps) and new methods causing a threshold for adoption. Second, many microfluidic methods are not amenable to high throughput operation. Although gradients and laminar flow interfaces have been employed for parallelism, the range of experimental parameters is limiting. Pneumatic valves have been used to address very large arrays, with great success in specific application areas [1]. Still there is a need for alternative approaches to high throughput microfluidics to expand areas of application.

We present a platform based on favorable scaling of surface tension effects, where the difference in pressure inside droplets of unequal volume drives flow in a passive device [2]. This allows the use of off-the-shelf liquid handling robotics (figure 1) to perform all assay functions while retaining and expanding the microfluidic functional space. The platform employs a large number of individually addressable microfluidic networks enabling the study of a large parameter space in each array.

2. Methods

Microfluidic channels were prepared by soft lithography. Two layer molds were created using SU-8 100 (Microchem Corp.) on 6 inch silicon wafers. The first layer defined microfluidic channel networks and the second layer was comprised of posts that formed holes in the PDMS replicas and

served as access ports to the networks. PDMS structures were placed on a polystyrene surface (Omnitray, Nunc) with a microtiter plate footprint.

Two different tools were used to deliver liquid to the devices, a handheld 8-channel electronic pipette (Brand GmbH, Germany), and a low-cost single probe automated liquid handler (223 Sample changer, Gilson Inc., USA) shown in figure 1 a). Fluorescein isothiocyanate (FITC, Sigma), fluorophore-labeled BSA (Molecular Probes), and fluorescent microspheres (Molecular Probes) were used to visualize fluid patterns.

3. Results

We employed off the shelf software to control robotic pipettor delivery and removal of small (1-10 l) drops to and from the access ports of microfluidic arrays (figure 1a, and 2a-b). We demonstrated that laminar flow can be produced with passive pumping and showed application for patterning cells (1b).

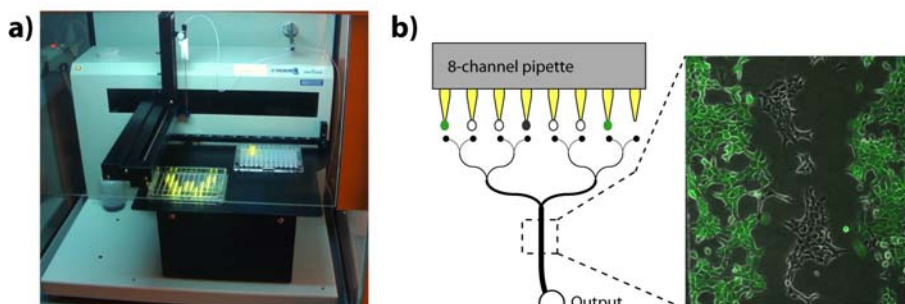


Figure 1. a) Existing robotic liquid handling equipment (shown here is the Gilson 223 Sample changer) can be used to perform fluid transfers to realize wide variety of biochemical and cell-based assays as well as syntheses. The device shown contains an array of 192 micro-chambers, 68 of which were loaded with FITC. Evaporation was reduced by placing a perforated plastic film on top of the device. b) Using an eight-channel electronic pipettor, seven stream laminar flow was produced (one tip unused). Adherent cells were patterned via laminar flow of seven streams, four containing media (white drops), and three containing cell suspensions (NMuMG, ATCC). Counting from left to right the first and last cell colonies expresses GFP (green), while the second does not (grey).

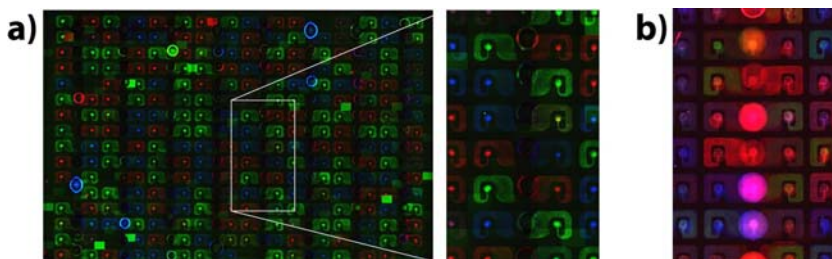


Figure 2. Highly parallel operation of simple microfluidic units. Shown is a device containing an array of 128 co-culture units, consisting of two chambers with separate inputs and a shared output in the center. a)

Fluorescent beads of three different colors were delivered to the structures according to a pre-programmed, random pattern. b) Chambers were coated with fluorescently labeled bovine serum albumin (BSA) prior to delivery of fluorescent beads. For protein addition, washing and bead seeding a total of 3200 fluid manipulation steps were performed using the liquid handling instrument shown in fig. 1

4. Discussion

The tube-less platform is scalable, on the device and system level, and absence of physical connections enables discrete access. Thus, each device is not limited to a single cell type or a dose response to a single soluble molecule. Rather, any given molecule or combination of molecules can be tested against any given cells, allowing more efficient coverage of larger parameter space without loss of microfluidic functionality. Importantly, devices are directly compatible with high throughput automated liquid handling and readout instruments.

5. Conclusions

We have demonstrated a tube-less platform that supports existing microfluidic functionality. We have shown that the platform is compatible with traditional fluid handling tools, facilitating use by biology researchers and pharmaceutical developers using existing infrastructure.

Acknowledgments

This work is supported by ARMY-BCRP Grant, NIH K25 Award.

References

1. T. Thorsen, S. J. Maerkl, and S. R. Quake, "Microfluidic large scale integration," *Science*, vol. 298, pp. 580 – 584, 2002.
2. G. M. Walker and D. J. Beebe, "A passive pumping method for microfluidic devices," *Lab on a Chip*, vol. 2, pp. 131 – 134, 2002.

MICROFABRICATED BIOPROCESSOR FOR NANOLITER-SCALE SANGER DNA SEQUENCING

Robert G. Blazej¹, Palani Kumaresan² and Richard A. Mathies^{1,3}

¹UCSF/UC Berkeley Joint Bioengineering Graduate Group,

²Department of Mechanical Engineering, and ³Department of Chemistry,
University of California, Berkeley, CA 94720, USA

Abstract

Utilizing hybrid glass-PDMS construction, we have developed an efficient, nanoliter-scale microfabricated bioprocessor that integrates all three key Sanger sequencing steps—thermal cycling, sample purification and capillary electrophoresis (CE)—into a microdevice capable of read-lengths equivalent to those used in the sequencing of the human genome. The bioprocessor incorporates a range of advanced technologies including miniaturized temperature sensing, nanoliter-scale Sanger extension reactions, microvalves/pumps, DNA affinity-capture and high-performance capillary electrophoresis. Lab-on-a-chip level integration enables sequencing of 556 continuous bases with 99% accuracy from only 1 femtomole of DNA template in a 250-nL reactor. The performance of this miniaturized DNA sequencer provides a benchmark for evaluating the ultimate cost and efficiency limits of Sanger sequencing.

Keywords: DNA sequencing, genetic analysis, capillary electrophoresis

1. Introduction

Sanger sequencing is remarkable in its ability to generate long and accurate DNA sequence reads. Alternative sequencing technologies [1,2] produce shorter, less accurate reads, a drawback that could significantly limit their usefulness in complex *de novo* genome sequencing and in the detection of biologically significant structural variations. The growing need for complete, whole-genome sequences and the importance of genome structure in speciation, evolution, disease and cancer [3], require that we use microfluidics to drive the cost, efficiency and scalability of long-read Sanger sequencing to its ultimate limit.

2. Experimental

The bilaterally-symmetric bioprocessor presented in **Figure 1** contains two independent DNA sequencing systems [4]. Functional elements are photolithographically patterned on three 100-mm-diameter glass wafers and assembled with a featureless PDMS membrane. The top two glass wafers are thermally bonded to form enclosed all-glass capillary electrophoresis channels and reaction chambers with integrated resistive temperature detectors (RTDs). Contact bonding between the fused top wafers, a PDMS membrane, and the bottom manifold wafer creates three-dimensional interconnects and microvalves/pumps [5].

Energy-transfer dye-terminator Sanger sequencing reagent containing 1 femtomole of DNA template is rapidly thermal-cycled in the 250-nL reaction chamber (35× 95 °C,

12 s; 60 °C, 55 s). The completed reaction is pumped by the microvalves to the capture/purification unit containing an affinity-capture matrix. An applied electric field drives the sequencing reaction products into the capture matrix where the desired DNA extension fragments selectively hybridize and concentrate at 30° C while residual reagents that would interfere with injection pass through to a waste reservoir. At 70° C the purified sequencing sample is released from the capture matrix, cross-injected onto the capillary electrophoresis channel, and resolved at 167 V/cm.

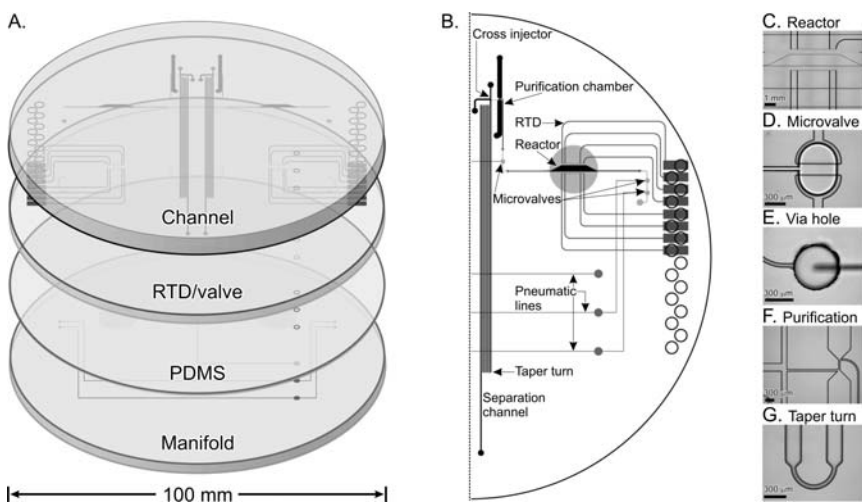


Figure 1. Integrated Sanger sequencing bioprocessor. Panels show the hybrid glass-PDMS microdevice layers (**A**), one complete DNA sequencing system (**B**), and component microphotographs (**C-G**).

3. Results and Discussion

Fluorescence quantitation of the sequencing reaction products after thermal cycling and purification indicates that 25 femtomoles of product are concentrated 200-fold into a 1.2-nL band of capture gel at 20 μ M. Given 1 femt mole of starting template in a 35-cycle linear amplification reaction, extension fragment production and purification is 71% efficient. Only 3.6 femtomoles of product is cross-injected into the separation channel yielding a total sample delivery efficiency of 10%.

Four-color sequence data were collected in under 35 min and processed with the Cimarron 3.12 base caller and Phred to generate base calls with accuracy estimates. **Figure 2** displays sequence data generated on the integrated bioprocessor in which 556 bases were read with 99% accuracy as compared to the known pUC18 sequence. Comigrating unincorporated fluorescently labeled terminators are absent in the sequencing trace, indicating their complete removal by the capture/purification process.

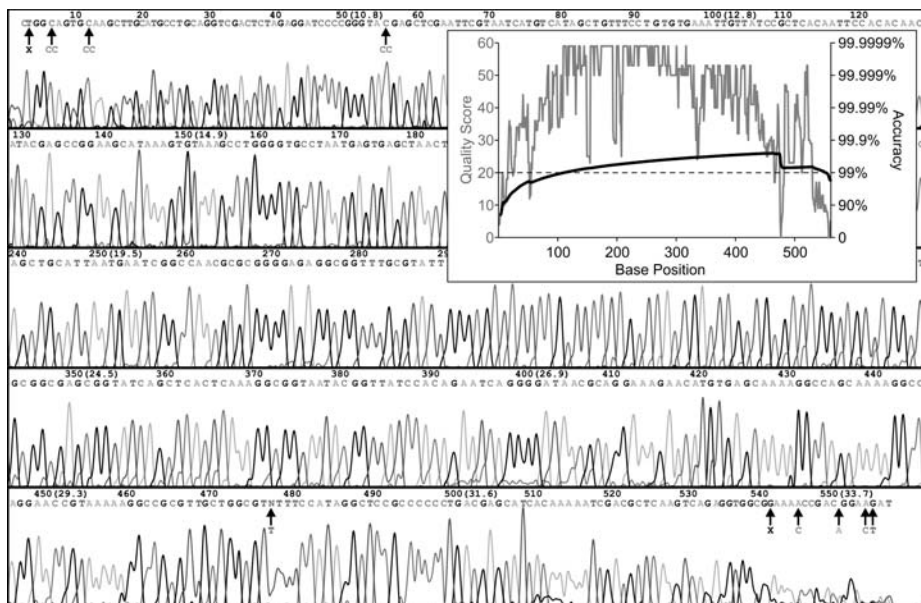


Figure 2. Sequence data generated on the integrated bioprocessor from a 750-bp pUC18 PCR amplicon. Automatic base calls, position, and elapsed time are given above the electropherogram. Mismatches with the consensus sequence are indicated by black arrows. Inset shows base call error probabilities and predicted read length.

4. Conclusions

The microdevice presented here is perhaps the most complex and functional nucleic acid processor ever constructed and represents a key step in the development of a bench-top platform capable of *de novo* sequencing plant and animal genomes. Current research is focused on eliminating inherent cross-injection inefficiencies through novel injection techniques that will enable Sanger sequencing from 100 attomoles or less of DNA template. Such ultra-low-template reactions approach the ultimate limits of Sanger sequencing, thus bringing into reach the goal of extremely-low-cost, long-read DNA sequencing.

References

- [1] Shendure J. *et al.*, *Science* **309**, 1728-1732, (2005)
- [2] Margulies M. *et al.*, *Nature* **437**, 376-380, (2005)
- [3] Check, E., *Nature* **437**, 1084-1086, (2005)
- [4] Blazej R.G. *et al.*, *Proc. Natl. Acad. Sci. USA*, **103**, 7240-7245, (2006)
- [5] Grover W.H. *et al.*, *Sens. Actuator B-Chem.* **89**, 315-323, (2003)

INTEGRATED MICROFLUIDIC SYSTEM FOR PROTEOMICS USING MIXED-SCALE STRUCTURES AND MALDI-TOF-MS

Harrison K. Musyimi, Hamed Shadpour, Guofang Chen, Robin L. McCarley,
Kermit K. Murray and Steven A. Soper

Department of Chemistry and Center for BioModular Multi-Scale Systems,
Louisiana State University,
Baton Rouge, Louisiana 70803, U.S.A

Abstract

A typical sample processing pipeline for proteomics entails a series of laborious and low throughput steps that often results in long analysis times and sample loss, thereby affecting the overall efficiency and outcome of the measurement. We have assembled a polymer-based microfluidic system that includes most of the protein processing steps into a single wafer and can be interfaced to several different mass spectrometer platforms for protein identification. The system was fabricated via micro-replication technologies from polymers and possessed the ability to analyze ~900 proteins in a single sample in an automated fashion with a total processing time <1 h.

Keywords: Proteomics, polymer microchips, two-dimensional separations, nanostructures, mass spectrometry

1. Introduction

We describe herein an integrated microfluidic-based protein analysis system, which can be interfaced to a variety of different biological mass spectrometers (MS), such as MALDI or ESI. Figure 1 shows a schematic of the device, which consisted of several processing units, including a cell lysis and protein extraction unit, a two-dimensional (2D) electrophoresis unit, a solid-phase nano-reactor and a micro-capillary electrochromatography (μ -CEC) unit. The system input is whole cells that were lysed and the protein components isolated using nanopillars decorated with thermally-responsive polymers. The isolated proteins were then separated using on-chip 2D electrophoresis and subsequently digested in a solid phase nano-reactor consisting of nanometer-pillars functionalized to allow covalent attachment of proteolytic enzymes for digesting the individual proteins for MS fingerprinting.

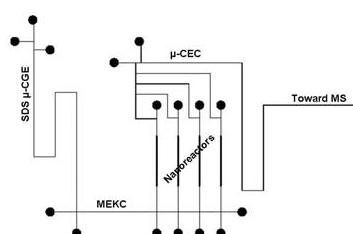


Figure 1. Schematic layout of the integrated polymeric microfluidic chip, which was prepared via hot-embossing from a mold insert. The nanostructures were prepared using a nanotemplating method from AAO.

2. Theory

The microfluidic network for the 2D separation employed two electrophoretic techniques, which were selected to be sodium dodecyl sulfate micro-capillary gel electrophoresis (SDS μ -CGE) in the 1st dimension followed by micellar electrokinetic chromatography (MEKC) as the 2nd dimension. The 2D separation unit possessed a calculated orthogonality of 77% and a peak capacity of 897.¹ The 2D separation unit was made from poly(methyl methacrylate), PMMA, which was selected due to its favorable physiochemical properties for this application.² A typical 2D separation could be carried out in <12 min.

3. Experimental

To produce the prerequisite structures, PMMA was hot-embossed from a brass mold master fabricated using high-precision micromilling.³ The nano-reactors and solid-phase extraction bed contained nanopillar arrays situated within a micro-channel and were fabricated using a nano-templating technique.⁴ A patterned anodic alumina oxide (AAO) template supported by aluminum, which was shadow printed via Ar ion sputtering of an Al target into the appropriate locations within the fluidic network, was ultra-sonicated followed by filling the nanopores with methyl methacrylate (MMA) monomer containing benzoin methyl ether and 1% PMMA powder. The polymerization occurred under UV-254 nm light with the sacrificial AAO template removed using phosphoric acid and a freezing drying technique. Trypsin was surface-immobilized onto the nanopillar structures following UV-254 nm exposure and incubation with 1-ethyl-3-[3-dimethylaminopropyl] carbodiimide hydrochloride (EDC). For protein capture, the nanopillars were dynamically coated with poly(N-isopropylacrylamide), pNIPPAm. Meso-scale pNIPPAm films have contact angles of 71° above its liquid critical solution temperature (LCST) and 50° below.

4. Results and discussion

To affect isolation of a series of proteins from whole cell lysates, nanopillar arrays (see Figure 2B) were dynamically coated with pNIPPAm, which showed super-hydrophobicity at a temperature above its LCST (contact angle ~90°) and super-hydrophilicity below its LCST (contact angle ~0°), which served as a highly efficient solid-phase capture-bed for hydrophobic proteins (see Figure 2A). Following protein isolation, a 2D SDS μ -CGE x MEKC separation was performed, which produced an efficiency, resolution and peak capacity of >10⁵ plates, >4 and ~897, respectively (see Figure 2C).¹ The sorted protein components could then be digested using a nanopillar solid-phase proteolytic reactor (see Figure 2B). The proteolytic nano-reactor was tested with several proteins to evaluate its performance, which indicated improved protein identification efficiencies due to fast (<4 s digestion times) and efficient (>80% sequence coverage) proteolytic digestions (see Figure 2D). The generated peptides from the proteolytic digestion could be separated using μ -CEC of the peptide fragments by coating the PMMA surface with a C18 hydrophobic phase following UV-activation of the PMMA surface to create a functional scaffold of carboxylate groups. The automated analysis could be completed by interfacing the microfluidic system to MALDI MS via a rotating ball interface.⁵ Peptide mass maps obtained from MALDI MS could be used to identify the proteins present in the sample.

5. Conclusions

We have designed and evaluated the performance of an integrated polymer-based microfluidic system consisting of mixed-scale structures for analyzing proteins in an automated fashion. The system can be multiplexed for high-throughput analyses and has the potential for accelerating biomarker discovery and performing diagnostics.

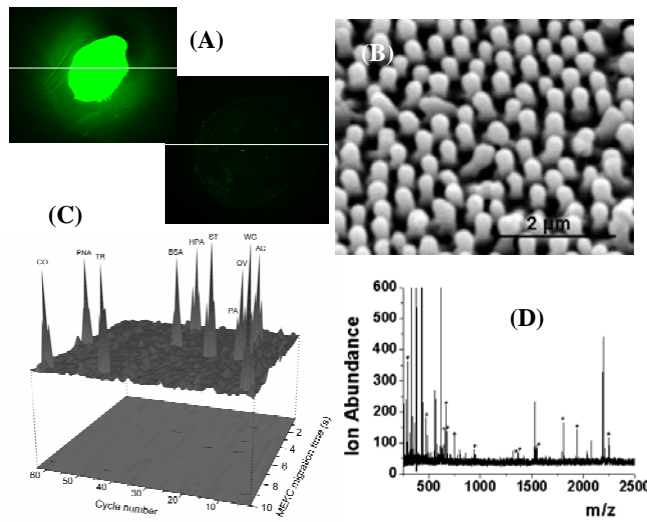


Figure 2. (A) Nanopillars that were dynamically coated with pNIPPAm and used to capture avidin that was labeled with a fluorescent dye. The first image shows the material above its LCST, in which the protein is captured and the second micrograph shows the release of avidin by dropping the temperature below the LCST. (B) Micrograph showing high aspect ratio (>340) nanopillars fabricated by nano-templating using AAO. The pillars were 60 μm in height and 175 nm in diameter with a 285 nm edge-to-edge spacing. (C) 2D SDS μ -CGE x MEKC electrophoretic separation of proteins. The detection was accomplished using laser-induced fluorescence of proteins labeled with Alexa-Fluor 633. (C) Mass spectrum showing the MALDI-TOF-MS analyses of peptides fragments generated from cytochrome C that were subjected to solid-phase proteolytic digestion using trypsin immobilized onto nanopillars

The authors would like to acknowledge financial support of this project from the National Institutes of Health and the National Science Foundation.

Acknowledgements

The authors would like to acknowledge financial support of this project from the National Institutes of Health and the National Science Foundation.

References

1. H. Shadpour, S. A. Soper, *Analytical Chemistry*, **78**, **2006**, 3519-3527.
2. H. Shadpour, H. Musyimi, J. Chen and S. Soper., *Journal of Chromatography A* **1111**, **2006**, 238-251.
3. M. L. Hupert, W. J. Guy, S. D. Llopis, H. Shadpour, S. Rani, D. E. Nikitopoulos and S. A. Soper, *Microfluidics and Nanofluidics*, **2006**, ASAP.
4. G. Chen, J. G. Bolivar, S. A. Soper and R. L. McCarley, *MicroTAS*, **2005**, 1261-1263.
5. H. Musyimi, J. Guy, D. Narcisse, K. Murray and S. Soper, *Electrophoresis* **26**, **2005**, 4703-4710.

MICROFLUIDIC PLATFORM FOR LIQUID CHROMATOGRAPHY – TANDEM MASS SPECTROMETRY (LC-MS/MS)

Jason Shih¹, Yunan Miao², Terry D. Lee², and Yu-Chong Tai¹

¹California Institute of Technology, Pasadena, CA, USA

²Beckman Research Institute, Duarte, CA, USA

Email: jshih@mems.caltech.edu

Abstract

We have developed a microfluidic chip capable of performing liquid chromatography – tandem mass spectrometry (LC-MS/MS). These chips were fabricated using our parylene surface micromachining technology. Key components included a mixer, sensors for measuring the flow rate and fluid composition, separation column, and electrospray nozzle. Feedback from the sensors was used to control pneumatically-driven pumps to produce the desired flow profile.

Keywords: Liquid Chromatography, Flow Control, Flow Sensors

1. Introduction

The recent trend in LC is towards miniaturization. The demand for higher sensitivity and better resolution separations has led to a reduction in scale. Nanoflow LC is now in widespread use and uses columns with an ID of <50 um; particles <5 um in diameter; and flow rates on the order of 100 nL/min. Microfluidic technologies are an ideal way to achieve these requirements and can also be used to make further reductions in scale.

Previously, we demonstrated that we could successfully carry out reverse phase (RP) separations using a fully-integrated standalone chip [1], but the short 1 cm column, as well as the lack of sensors, limited performance and caused the separations to be inconsistent, a characteristic essential in any LC system. The chips described here address both these problems and included the following: a passive mixer to form the solvent gradient; a 4.2 cm separation column; and an electrospray nozzle for on-line MS analysis. Most importantly, we also integrated sensors onto the chip to monitor the flow rate and eluent composition.

2. Theory

Several different types of separations are routinely used today. By choosing an appropriate stationary phase and mobile phase, the analyte can be separated based on charge, hydrophobicity, size, as well as many other molecular properties. In particular, we are focusing on RP separations. In these separations, the sample is first loaded onto a hydrophobic stationary phase. A solvent gradient, in which the polar component of

the eluent (generally acetonitrile or methanol) is increased over time, is then run through the column and the analytes are eluted in order of hydrophobicity. Precise control over the gradient is necessary to obtain repeatable and high performance separations. This technique is the backbone of most proteomic analyses.

The output of our separation is coupled to a MS using electrospray ionization (ESI). ESI involves the generation of a very fine aerosol via a nozzle. This process is facilitated by a high electric field concentration at the nozzle tip. ESI results in the ionization of the analytes prior to MS quantification.

To measure the flow rate, we will be measuring the time-of-flight (TOF) of an electrochemical pulse. The pulse was produced by applying a short, high voltage pulse to a pair of electrodes which produced an excess and depletion of ions at the corresponding electrodes. These ion pulses were then detected downstream by measuring the impedance of the passing fluid. At the same time, the impedance of the fluid also yielded a measurement of the composition of the fluid.

3. Experimental

The chips were fabricated using our developed parylene surface-micromachining technology. We started off by growing and patterning a 4000 Å oxide layer on a silicon wafer. Then, a 5 um parylene layer was deposited and patterned using oxygen plasma. This created the foundation for our freestanding electrospray nozzle. A 2000/200 Å Pt/Ti layer was then deposited and patterned using lift-off. This single metal layer was used to define the sensors as well as the electrode for establishing the electrospray potential. Next a sacrificial photoresist layer was spun on and patterned. This layer would eventually be removed and was used to define all the fluidic structures. Before a second 10 um parylene layer was deposited to completely define our channels, a DRIE process was used to etch trenches on either side of every channel. These trenches were subsequently filled with parylene and helped to anchor the second parylene layer to the substrate. The second parylene layer was then patterned and a final 50 um SU-8 layer deposited to encapsulate the channels. Finally, to make the electrospray nozzle freestanding, the silicon underneath the nozzle was etched away using XeF₂, a gas phase isotropic silicon etchant. Prior to use, the photoresist inside the channels needed to be dissolved away using acetone. A photo of the final chip is shown in Figure 1.

To test the chip, the column was first packed with the desired stationary phase. The chip was then connected to two pressurized solvent reservoirs, one containing a 40/60/0.1 (water/acetonitrile/formic acid) solution (referred to as Pump B) and the other containing a 100/0/0.1 solution (Pump A). The pressure in these reservoirs was directly controlled using electrically controlled pressure regulators. An autosampler was placed inline between Pump A and the chip. For separation experiments, the autosampler was commanded to load a pre-determined amount of sample. This sample plug was then injected onto the column using pump A. Once the sample had been completely loaded, pump B started up and the desired gradient was delivered. During the gradient formation, the flow rate and exact solvent composition was controlled using feedback from the sensors and appropriately varying the pressure on both pumps.

4. Results and Discussion

A typical separation result is shown in Figure 2. This particular separation used a 3 cm long column packed with 5 μm C₁₈ support. 250 fmol of a BSA digest was used as a sample and the solvent gradient was programmed to go from 0 \rightarrow 30% acetonitrile at a constant rate of 1%/min. The separations obtained were very similar to those obtained when connecting our column to a commercial LC nanoflow pump.

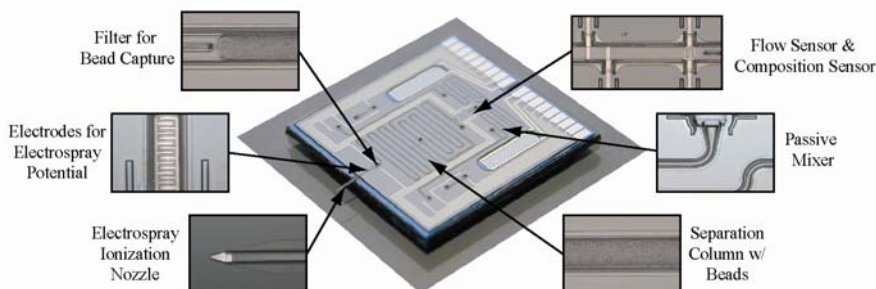


Figure 1: Photograph of the fabricated chip.

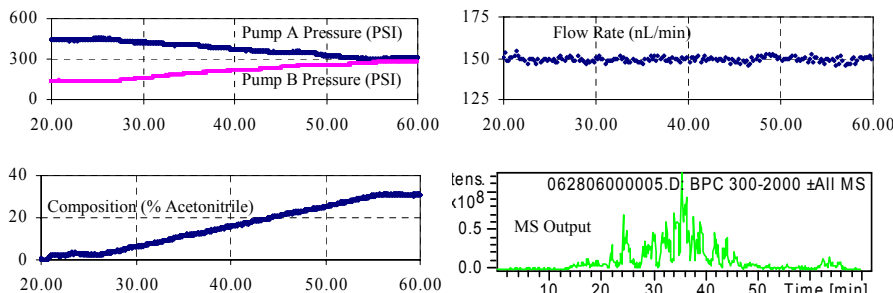


Figure 2: Typical separation result shown with sensor data and pump pressures.

5. Conclusions

We have successfully demonstrated a chip capable of LC-MS/MS. By using integrated sensors for flow control we are able to achieve much better control over the gradient compared to previous chip designs. This has lead to an improvement in repeatability and separation performance.

References

1. J. Xie, Y. Miao, J. Shih, Y.C. Tai, and T.D. Lee, *Microfluidic Platform for Liquid Chromatography-Tandem Mass Spectrometry Analyses of Complex Peptide Mixtures*, Analytical Chemistry, American Chemical Society, USA, pp. 6947-6953, (2005).

MICROFLUIDIC DEVICE FOR HIGH-THROUGHPUT IMMUNOFLUORESCENT STAINING OF SIGNALING PROTEINS IN ATTACHMENT-DEPENDENT CELLS

C. Joanne Wang*, Raymond Cheong*, and Andre Levchenko

Whitaker Biomedical Engineering Institute, Johns Hopkins School of Medicine
Baltimore, Maryland, 21218 United States
alev@jhu.edu. *Equal contribution.

Abstract

Immunocytochemistry is an established, high-content, genetically-noninvasive way of assaying signal transduction events, but is limited by the speed of manual analysis and cost of materials. We developed a microfluidic device to automate this assay in a high-throughput way with far less materials, and the device offers the additional advantages of providing temporally precise chemical delivery and uniform staining conditions. We demonstrate the power of the device with a detailed time-course of NF- κ B activity in response to the inflammatory cytokine TNF α .

Keywords: System biology, signal transduction, cell culture, immunoassay, cell analysis

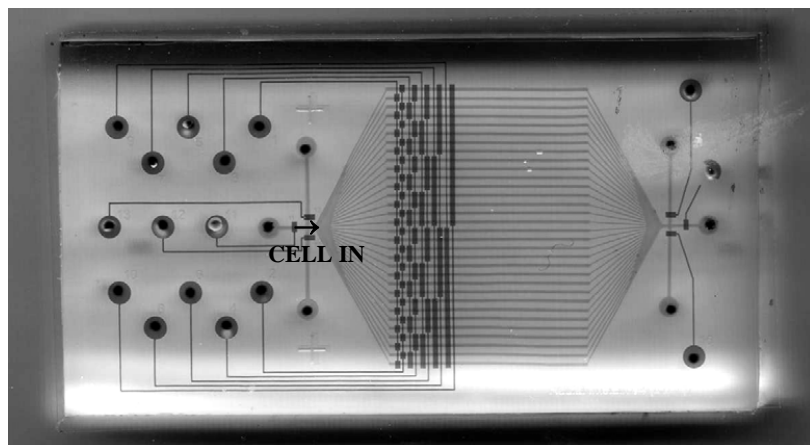
1. Introduction

Intracellular signal transduction involves a variety of molecular-level events occurring dynamically in space and time. One well-established strategy to track a specific molecule's spatio-temporal dynamics is to chemically fix the cells, then utilize immunostaining to visualize the location and the quantity of the molecule *in situ* [1]. This technique is most useful for measuring the effect of some stimulus at various time points, but it is difficult to apply stimuli for a precise duration, so the temporal resolution of the acquired data is coarse. In addition, throughput is severely limited by the speed of the manual analysis, and the cost of the materials (antibodies and cells). By exploiting the small scale and precise chemical delivery capability conferred by microfluidics, we have developed a multilayered PDMS device that automates immunofluorescent (or immunohistochemical) staining of cells, thereby enabling high-throughput characterization of the complex dynamics of interacting signaling pathways.

2. Results and Discussion

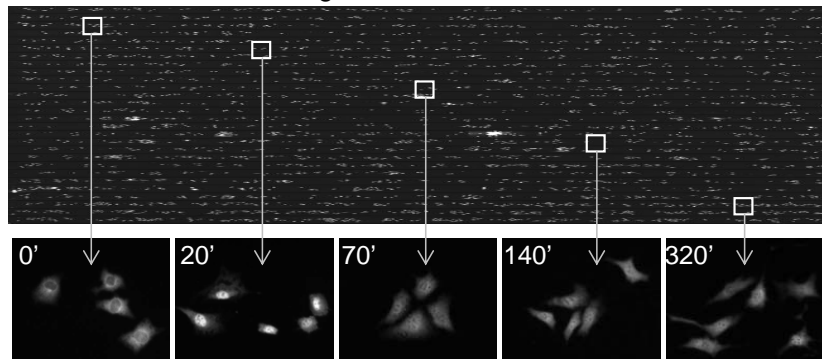
The immunostaining automation device shown in Fig. 1 consists of a monolithic 2-layer PDMS chip sealed with a glass coverslip, which is fabricated using techniques described previously [2]. The channels at the bottom layer are used for cell culture and stimulation, while the top layer channels actuated fluid delivery via multiplexing valves. When setting up for a typical experiment, the chip's control ports are connected to an array of Lee-solenoid-valves, and the bottom channel ports to the individual 1cc syringe reservoirs containing stimulation, fixation, or antibody solution.

Figure 1. Microfabricated high-throughput immunostaining PDMS device. The parallel light gray channels are where the cells reside. They are stimulated and immunostained *in situ*. The dark gray channels are the multiplexing micromechanical membrane valves that actuate fluid delivery.



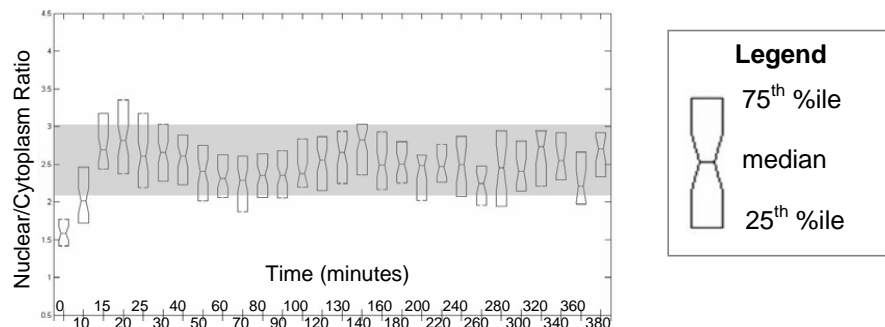
The glass substrate of the cell culture chamber was coated by introducing 0.1% gelatin (Sigma) into the device for at least 30 minutes, then overnight serum-starved cells were introduced into the 32 parallel culture chambers via a common inlet and allowed to attach for 3 hours. To introduce stimulants (e.g. TNF-alpha (Roche)) dissolved in cell media to each chamber, a computer automation program triggers the on-chip micromechanical multiplex valves and delivers the pressure-driven stimulant flow into the chosen culture chamber at the different time points specified by the experimenter so that the end of all stimulation periods coincided. To simultaneously stop and preserve the signal transduction events that are taking place inside the cells at that particular time instant, ice-cold PBS (Invitrogen) was introduced into all chambers followed immediately by 4% paraformaldehyde (Electron Microscopy Systems) for 20 minutes. Cells were permeabilized with 0.1% Triton X-100 (Sigma) for 5 min and blocked with 10% goat serum (Sigma), with PBS washes in between. Stimulated cells in all chamber were incubated with appropriate primary antibody (that tags the signaling molecule of interest) followed by fluorescent dye-conjugated secondary antibody. The location and intensity of the signal present in the cells were imaged using a motorized Zeiss inverted epifluorescence microscope equipped with a Cascade 512B II CCD camera and controlled by a custom autofocus script (Fig. 2). Using MATLAB (Mathworks), the images were flatfield-corrected, stitched together, and quantified. Briefly, the Hoechst image was used to determine the nuclear region for each cell and the average staining intensity in this region was compared to background. For each cell type and time point, 100-300 cells were analyzed in this manner to ensure statistical significance.

Figure 2. Chip image of stimulated NIH 3T3 (mouse fibroblast) cells immunostained *in situ* with anti-P65. Zoomed-in views showed endogenous NF- κ B temporal activity in NIH 3T3 cells stimulated with 10ng/mL TNF α .



We have employed the device to make time course measurements for characterizing the response of the NF- κ B pathway to TNF- α stimulation (Fig. 3). A variety of different experiments can be performed in high-throughput with the appropriate choice of cultured or biopsied cells, chemicals, and treatment pattern. Compared to traditional techniques, our device provides considerable time and materials savings, and allows quantification of cell's spatio-temporal response to stimulus.

Figure 3. NF- κ B activity profile in response to 10ng/mL TNF- α stimulation.



4. References

1. D. Barken, C.J. Wang, J. Kearns, R. Cheong, A. Hoffmann, A. Levchenko, Comment on "Oscillations in Nf-KappaB Signaling Control the Dynamics of Gene Expression", *Science*, 308, pp. 52a- 52a, (2005).
2. M.A. Unger, H.P. Chou, T. Thorsen, A. Scherer, S.R. Quake, Monolithic Microfabricated Valves and Pumps by Multilayer Soft Lithography, *Science*, 288, pp. 113-116, (2000).

Automated Two Dimensional Microfluidic Protein Profiling Combining IEF and SDS Gel Electrophoresis

J.S. Buch¹, J. Liu², S. Yang², C.-W. Tsao², T. Song¹, P. Sivanesan¹,
K. Phalnikar¹, C.S. Lee³, and D.L. DeVoe²

¹Calibrant Biosystems Inc.
Gaithersburg, MD, USA

²Dept. of Mechanical Engineering, ³Dept. of Chemistry and Biochemistry
University of Maryland, College Park, MD, USA

Abstract

A fully automated multidimensional protein separation system is presented as a high-throughput alternative to traditional 2-D PAGE for comprehensive protein profiling and biomarker discovery. Here we present recent developments enabling separation of complex protein mixtures using a new chip design, a substantially modified fabrication process including the use of UV-ozone surface treatments, and *in situ* photopolymerization of poly(ethylene glycol)-based gel plugs to control pressure-induced flow in selected regions of the chip.

Keywords: Isoelectric Focusing, Gel Electrophoresis, 2-D PAGE

1. Introduction

Despite its low throughput and laborious operation, 2-D PAGE remains a key proteomics technology in large part due to its high peak capacity, enabling the separation of many thousands of proteins in a single run. We have previously reported a multidimensional microfluidic technology designed to replicate the functionality of 2-D PAGE, but with more than an order of magnitude improvement in throughput [1,2]. The work described here is based on the prior system, which was validated using simple mixtures of model proteins, but with significant modifications including a new polymer microfluidic chip design and fabrication process to enable high resolving power for complex protein mixtures, and a fully-automated interface for on-chip preparation, separation, and detection.

The microfluidic system provides an initial separation of intact proteins in a first-dimension microchannel by non-native isoelectric focusing (IEF), providing a charge-based separation and concentration of constituent proteins within the mixture. The focused proteins are then simultaneously transferred to an array of orthogonal second-dimension microchannels for parallel, size-based SDS gel electrophoresis. Simultaneous monitoring of each microchannel in the second-dimension array is performed by a linear scanning laser-induced fluorescence detection system. While previous work has shown that the 2-D separation technology can theoretically provide peak capacities over 10,000, earlier attempts to achieve high resolution separations from complex samples have not been successful due to complications inherent in previous chip designs.

2. Results and Discussion

The multidimensional separation process using the new chip design (Fig. 1) consists of the following steps: (a) flush chip with DI water and buffer; (b) fill entire network with PEO gel; (c) fill acid, base, SDS, and dye channels; (d) flush IEF channel with ampholytes and sample; (e) apply voltages to acid/base reservoirs; (f) focus sample in IEF channel; (g) apply voltages to introduce SDS and dye to IEF channel; (h) incubate SDS and protein, electrokinetically transfer proteins to second dimension channel array, and perform SDS gel electrophoresis in 2nd dimension.

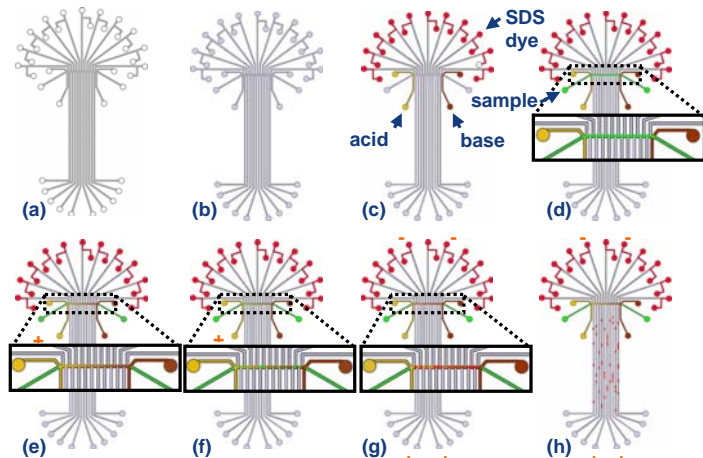


Fig. 1 Separation process flow schematic for a 10-channel chip.

A critical challenge in realizing separations in complex microfluidic networks is the prevention of bulk flow resulting from residual pressure within the network, for example due to small amounts of trapped air within the reservoirs. This problem is particularly acute as the number of reservoirs increases, and for interconnected networks where hydrodynamic crosstalk between channels can readily occur. To eliminate this problem, which has previously prevented effective separations in our 2-D chips, poly(ethylene glycol) (PEG) gel plugs are photopolymerized within selected regions of the chip prior to introduction of the poly(ethylene oxide) (PEO) sieving matrix. In one approach outlined in Fig. 2, PEO gel is introduced into an air-filled chip up to the IEF channel. The IEF and upper channels are then filled with PEG-functionalized monomer/cross-linker [3], and *in situ* UV-photopolymerization of short PEG plugs is performed using a quartz mask to define the exposure area. The PEO gel is then pumped toward the IEF

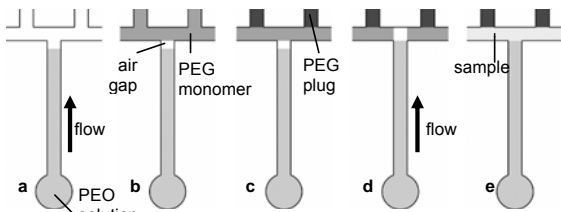


Fig. 2 Preparation of PEO/PEG gels.

channel to remove any residual air gap; and finally the IEF channel is flushed with ampholyte and sample. Similarly, PEG gel plugs are photopolymerized within the short channels leading to the acid and base reservoirs. This step ensures that acid and base may be pipetted into these reservoirs after sample is introduced without disturbing the sample/PEO interface due to hydrodynamic flow.

A comprehensive instrumentation platform has been developed to provide computer-controlled chip preparation, separation, and detection in a fully automated system. The system uses a reusable electrofluidic manifold which enables reliable interfacing to the disposable polymer chips. Images of the automated instrumentation platform are presented in Fig. 3. This platform also includes a multichannel LIFD detector which scans over the ends of each second dimension microchannel at a frequency of several Hz to ensure complete detection of all separated protein bands. The system also includes a thermoelectric cooler which maintains chip temperature below 10 °C during separation, enabling higher voltages for improved separation speed and resolution. The multidimensional separation of *E. coli* cell lysate by this platform is shown in Fig. 4 when using a 32-channel chip. Improved separation performance is

directly enabled by the use of the PEG gel plugs, ensuring reliable compartmentalization of reagents on chip and eliminating unwanted hydrodynamic flow, resulting in improved reproducibility for the multidimensional protein separation system. In addition, the presence of the PEG-based gel plugs allow for precise introduction of different first and second dimension separation media, improving the ability to automate the chip preparation process.

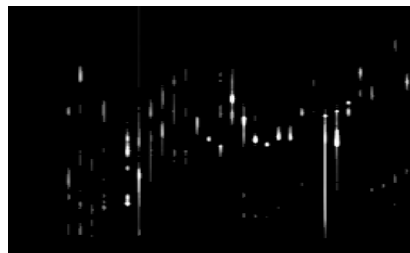


Fig. 4 Pseudo-gel image of *E. coli* cell lysate separation using a 32-channel chip.

References

1. Y. Li, J.S. Buch, F. Rosenberger, D.L. DeVoe, and C.S. Lee, *Anal. Chem.*, 76, 742-748, 2004.
2. J.S. Buch, Y. Li, Y.-X. Wang, J.W. Cooper, D.L. DeVoe, C.S. Lee, *Proc. Micro Total Analysis Systems 2004, Transducers Research Foundation*, 384-386, 2004.
3. J. Liu, X. Sun, P.B. Farnsworth, M.L. Lee, *Analytical Chemistry*, 78, 4654-4662, 2006.

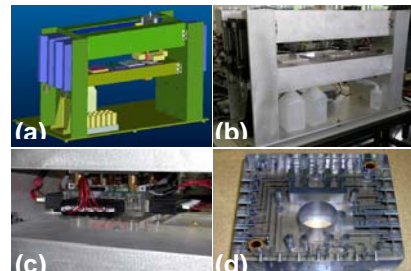


Fig. 3 Automated 2-D chip processing station: (a) solid model, (b) fabricated station, and detailed views of the manifold (c) with and (d) without electrofluidic interconnects.

SENSITIVE CHIRAL ANALYSIS METHOD FOR MICROCHIP BY CIRCULAR DICHROISM UV THERMAL LENS MICROSCOPE (UV-CD-TLM)

Kazuma Mawatari¹, Shun Kubota² and Takehiko Kitamori^{1,2}

¹Kanagawa Academy of Science and Technology (KAST), Kanagawa, Japan

²The University of Tokyo, Tokyo, Japan

(kmawatari@world.odn.ne.jp)

Abstract

We report a novel sensitive chiral analysis method for microchip-based synthesis or screening system of chiral compounds based on the circular dichroism (CD) thermal lens microscope (TLM) in UV wavelength region for wide range of chiral analysis: UV-CD-TLM. The UV (266 nm) excitation laser beam was phase-modulated and used to detect TL effects for the light absorption of left circularly polarized (LCPL) or right circularly polarized (RCPL) beam. We illustrated the principle of UV-CD-TLM, and more than 5 orders higher sensitivity was verified than that in conventional CD spectrometer.

Keywords: Thermal lens microscope, chiral analysis, circular dichroism, UV, pulsed laser

1. Introduction

Recently, microchip chiral synthesis and analysis systems are becoming of particular interest to the pharmaceutical field, where the goals are integration of multiple functions such as synthesis, screening, detection, and biological evaluation on a single integrated microchip to realize high-throughput systems. For this purpose, fast and sensitive detection method is one of the challenges. Conventionally, CD spectrometry was utilized for macro-scale high-throughput chiral analysis without chiral separations. However, the sensitivity is linearly dependent on the optical pathlength or volume of the sample and becomes quite low in micro-scale analysis.

In previous papers, we reported a first CD-TLM for sensitive chiral analysis on microchip in visible wavelength region. Excellent performances have been demonstrated in about 6 orders higher sensitivity in mass unit compared with that in sophisticated CD spectrometers. The capability of chiral recognition without chiral separation was also demonstrated. However, visible wavelength limits the range of application, because wide range of chiral compounds including proteins show light absorption in UV wavelength region.

In this report, we extend the applicability of our sensitive CD-TLM to UV wavelength region with a pulsed UV laser due to its wide wavelength tunability, high

power and the compact size.

2. Principle of UV-CD-TLM

Figure 1 shows basic principle of UV-CD-TLM for sensitive and selective chiral analysis on microchip. The basic principle is same as visible continuous wave (CW) CD-TLM in which the phase of the excitation beam was modulated to make LCPL and RCPL beam, and the strength of light absorption for each beam is measured as TL signal intensity and phase with a lock-in amplifier. However, the pulsed laser is used for excitation in UV wavelength, which makes difficult for detection with the lock-in amplifier. Therefore, we applied quasi-continuous wave (QCW) excitation, and realized phase-modulation for measurement of CD effect by thermal lens signal.

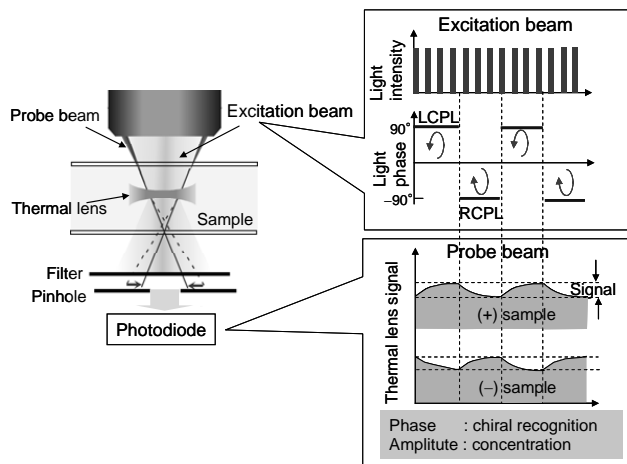


Figure 1 Principle of CD-TLM by LCPL and RCPL

3. Experimental

Figure 2 shows the instrument of UV-CD-TLM. The excitation beam was a YAG laser (wavelength 266 nm, power 25 mW, repetition 80 kHz). The linearly-polarized excitation beam was phase-modulated by a pockels cell (KD*P), and the polarization direction was turned by 90 degree with half-wave voltage applied to the pockels cell. The frequency is set at 1.2 kHz. Then, a quarter-wave plate changed the linearly-polarized beam to RCPL or LCPL. The probe beam is He-Ne laser (wavelength 633 nm, power 15 mW). These two beams were made coaxial with a dichroic mirror and introduced to UV objective lens (NA 0.4) and focused into microchannel to generate TL effects. The transmitted beams were again made coaxial, and the excitation beam was cut by an interference filter and only the probe beam was introduced to a photodiode through a pinhole. The output was fed into a lock-in amplifier, and the phase and amplitude were analyzed for chiral recognition and concentration determination, respectively.

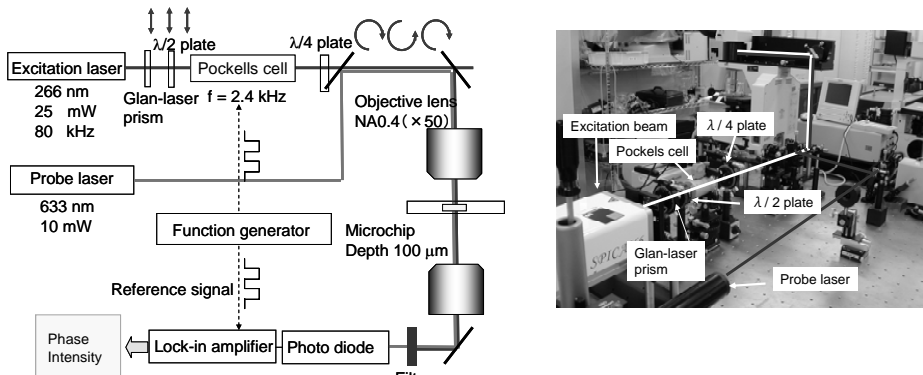


Figure 2 Instrument of UV-CD-TLM (left) and the picture (right)

4. Results and discussion

The signal intensity and phases were measured for (+)-camphor sulphonic acid (CSA), (-)-CSA, and racemic-CSA. We successfully recognized the chirality by measuring the phases, and no signal intensity was observed for racemic-CSA. The basic principle was verified. The performance was evaluated by investigating the detection limit in concentration as shown in Figure 3. The calibration curves showed good relationship, and the phases were successfully used for chiral recognition. The detection limit was $\sim 8 \times 10^{-4}$ M, and the value was at least 1 order superior to UV-CD spectrometers. The most important facto is the sensitivity in absolute amount, and the value is 5 orders superior considering the detection volume.

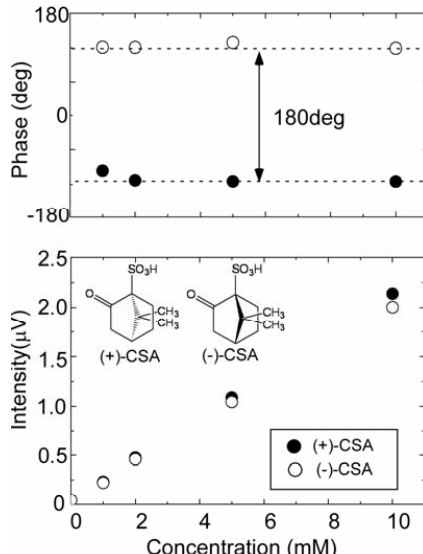


Figure 3 Calibration curve for (\pm) CSA

5. Reference

- [1] M.Yamauchi, K.Mawatari, A.Hibara, M.Tokeshi, and T.Kitamori, "Circular-dichroism thermal lens microscope for sensitive chiral analysis on microchip," *Anal. Chem.* 78, 2646-2650 (2006).

SINGLE-NUCLEOTIDE POLYMORPHISM DETECTION WITH THIN MEMBRANE TRANSDUCER

Misun Cha, Ilchaek Kim, Junbo Choi, Junghoon Lee

School of Mechanical and Aerospace Engineering

Seoul National University, San 56-1, Shinlim, Kwanak, Seoul Korea 151-742

Abstract

We present a thin membrane transducer that can detect a single base pair mismatch or a single nucleotide polymorphism (SNP). A highly specific molecular interaction on an extremely thin and flexible membrane surface causes the deflection of the membrane due to surface stress change which can be measured by a compact capacitive circuit.

Keywords: Thin membrane transducer, PDMS, DNA hybridization, SNP

1. Introduction

Mechanical transduction of bio/chemical events has recently attracted significant interests due to advantages in high specificity and label-free assays. Microcantilever techniques, mainly employing optical detection of the deflection, have been especially popular for those purposes. Reactions such as DNA hybridization [1], antigen-antibody binding [2], and also nonbiological reactions in vapor [3] were observed to cause the deflection of cantilevers. The optical detection, however, requires a bulky and expensive setup. It is also cumbersome to handle extremely flexible microcantilevers in a liquid. Recently, thin polymer membranes as sensing elements have been introduced, offering a device structure superior to that of the cantilever approaches [4,5]. This work presents the first demonstration of a single nucleotide polymorphism (SNP) detection capability of the polymer membrane device. Sensitivity and selectivity required for the SNP detection were enabled by the use of a very thin ($\sim 1 \mu\text{m}$) PDMS membrane (Young's modulus = $\sim 1 \text{ MPa}$) formed in a dome shape.

2. Device Concept

Fig. 1 illustrates the concept of the membrane transducer used. The specific molecular interaction on the extremely thin and flexible surface causes the deflection by a surface stress. This deflection is measured through the use of the membrane as shown in the figure. The membrane

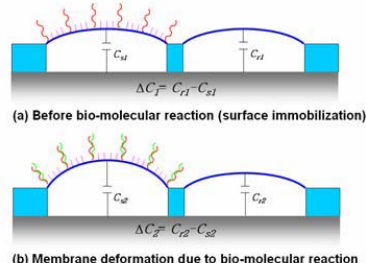


Fig.1 Concept of Thin Membrane Transducer

separates the upper liquid space and the lower cavity, enabling a capacitive detection that remarkably simplifies the overall configuration compared with the optical detection used in micro-cantilever approaches. The dome-like structure provides the good mechanical rigidity against the external disturbances, especially the flow pressure variation. More importantly, both tensile and compressive stresses can be detected when the dome shape becomes flatter or more bulged up respectively. Also, as depicted in Fig. 1, the effect of other disturbances such as pressure or temperature variation and nonspecific adsorption of liquid or other chemicals can be rejected by the differential sensing.

3. Experimental

Fig. 2 shows the fabrication process for the device. The detailed description of the fabrication process is shown elsewhere [4]. The view of PDMS device fabricated is shown in Fig 3. A single stranded thiolated DNA of 16-mer oligonucleotide at 1 μM concentration was immobilized on the gold-coated membrane.

Table 1. Oligonucleotide sequence	
Thiolated probe DNA	5'- $(\text{CH}_2)_6$ -TAG CCG ATA TGC GCA T-3'
Complementary DNA	3'-ATC GGC TAT ACG CGT A-5'
Noncomplementary DNA	3'-CGA TTA GCC GTA TAC G-5'
Distal single base SNP	3'-ATC GGC TAT ACG CGT C-5'
Proximal single base SNP	3'-GTC GGC TAT ACG CGT A-5'
Internal two base SNP	3'-ATC GGC TCG ACG CGT A-5'

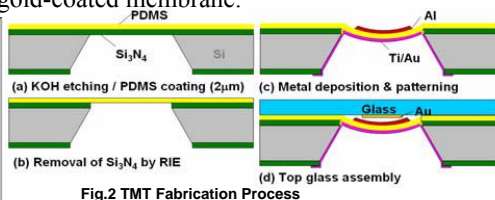


Fig.2 TMT Fabrication Process

In order to improve the accessibility of DNA probe to targets and avoid physisorption during hybridization, 1 mM MCH (6-mercaptop-1-hexanol) was treated as a spacer. Then, solutions (100 μl at 1 μM concentration of DNA) in 1M PBS (phosphate buffered saline, pH 7.0) buffer containing various sequences shown in Table 1 were applied.

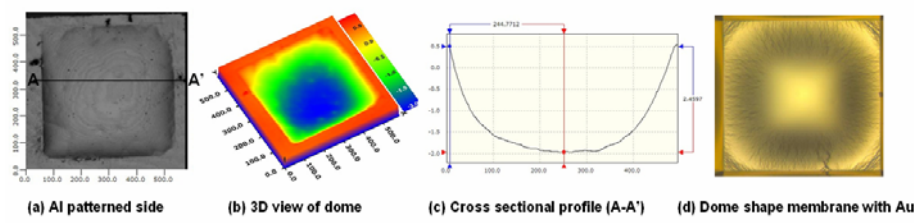


Fig.3 Dome Shape Membrane (Au-PDMS-Al)

4. Results and Discussion

Fig. 5 shows the capacitance variation for the hybridization experiments with all five cases. First, it is clearly shown that the perfect match and mismatch hybridization can

be sharply discriminated. While the mismatched sample caused little capacitance change, the perfectly matched sample caused the well-defined capacitance decrease vs. time. This means that the membrane deflected upward by the compressive stress when there was matching hybridization. The nanomechanics of this behavior has been explained elsewhere with micro-cantilever experiments and analysis [5,6], and our experiments confirm the behavior expected. The TMT demonstrated the SNP capabilities in discriminating the position of the SNP as well as the difference between the single mismatch and double mismatch hybridization. While the mismatch hybridization at the very end of the sequence shows a similar behavior to that of the perfect match hybridization, the mismatch at the bottom showed the behavior similar to the mismatching case. It is intriguing that the increase of capacitance, therefore the downward deflection due to tensile stress, was observed with the internal double mismatch hybridization case. We believe these behaviors can also be explained if a molecular-nanomechanical model is considered, and can be applied to other ligand-receptor reactions including specific protein interactions, which will eventually provide various protocols for disease diagnostics and drug research.

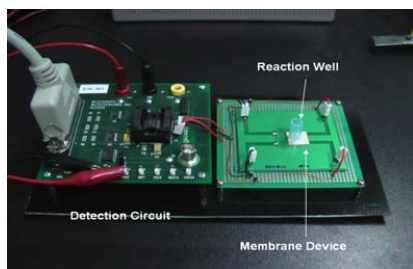


Fig.4 Experimental Setup with Capacitive Electronics

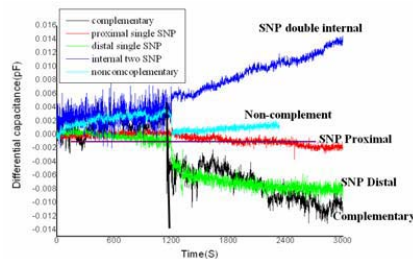


Fig.5 Experimental Results for DNA Hybridization

5. References

1. Fang Tian, et al, Anal. Chem.; **2005**; 77(6) pp 1601 – 1606.
2. G. Wu, et al, Proc. Natl. Acad. Sci. USA **98** (2001), pp. 1560–1564.
3. R. Berger, et al, Science 1997, 276, 2021-2024.
4. R. Rodriguez, J. Chung, K. Chung, J. Lee, Proc. ASME IMECE 2004.
5. S. Satyanarayana, D. T. McCormick, A. Majumdar, Sensors and Actuators B 115 (2006) 494–502
6. J. Fritz, et al, Science. 2000;**288**:316–318.
7. K.M. Hansen, et al, Anal Chem. 2001 Apr 1;73(7):1567-71.

MEASUREMENT AND MODELING OF DNA MOTION IN MICROCHANNEL INCLUDING FREQUENCY DEPENDENT ELECTROPHORESIS AND ELECTRO-OSMOTIC FLOW

Momoko Kumemura¹, Christophe Yamahata¹, Naoyoshi Sakaki¹, Gen Hashiguchi², Dominique Collard³ and Hiroyuki Fujita¹

¹Institute of Industrial Science, The University of Tokyo, Japan

²Faculty of Engineering, Kagawa University, Japan

³LIMMS-CNRS/IIS, The University of Tokyo, Japan

Abstract

This paper proposes a convenient way to model DNA motion in micro-channel induced by electrophoresis (EP) drift in which frequency dependent electro-osmotic (EO) flow is taken into account. Subject to ac EP, DNA oscillation amplitudes are measured from video traces and both EP and EO mobilities are successfully extracted by first order time delay model.

Keywords: Microfluidic, Electrophoresis, Electro-osmotic, DNA, modeling

1. Introduction

To capture single DNA by MEMS gripper [1], a microfluidic device with open access is under investigation, Fig.1. The device includes micro channels that are appropriate to isolate DNA molecules [2]. To bring the molecules one by one in the collecting well, DNA are moved by pulsed EP. This technique requires a precise control of DNA motion which is subjected to direct EP but also by a reverse EO drag flow [3,4]. A dynamic motion model is required, that is proposed in the following parts.

2. Experimental set up

For the model development, the EP experiments are performed in a symmetric microfluidic device having 2 holes (inlet and outlet) with access channels and 10 parallel microchannels in its central part. The device is filled with DI water containing λ -DNA. The part of interest of the device is plotted in Fig.2.

When low frequency ac voltage is applied between the electrode in the inlet hole and the counter electrode localized just ahead of the parallel microchannels, the DNA exhibit oscillating motions induced by EP drift. The oscillation amplitudes in the access channel are recorded thanks to the DNA fluorescent traces with a slow video acquisition as shown in Fig.3. The oscillation amplitudes are recorded for ac voltage amplitudes ranging from 0.5V to 10V with frequencies varying from 10Hz to 1KHz.

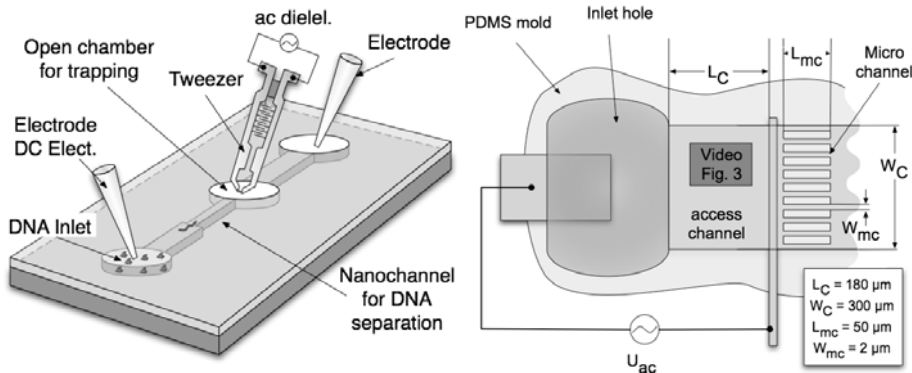


Figure 1: Principle for DNA isolation by micro-channel and capture by MEMS tweezer

Figure 2: Schematic top view of the microfluidic device. The channel high is 4 μm

2. DNA oscillation modeling

The negative charged DNA are subjected to 2 opposite forces : a direct EP force than move DNA by conduction to positive voltage and a opposite drift that is induced by the osmotic flow, liquid displacement induced by the interface positive charges motion drag. The direct EP velocity ($\mu_{ep} * E$) is built up instantaneously while the inversed EO flow ($-\mu_{eo} * E$), requires a delay time, τ , to be fully established. μ and E refer to mobilities and electrical field, respectively. The DNA velocity amplitude, V_{DNA} , is calculated thanks to the electromechanical equivalent circuit model of Fig. 4.

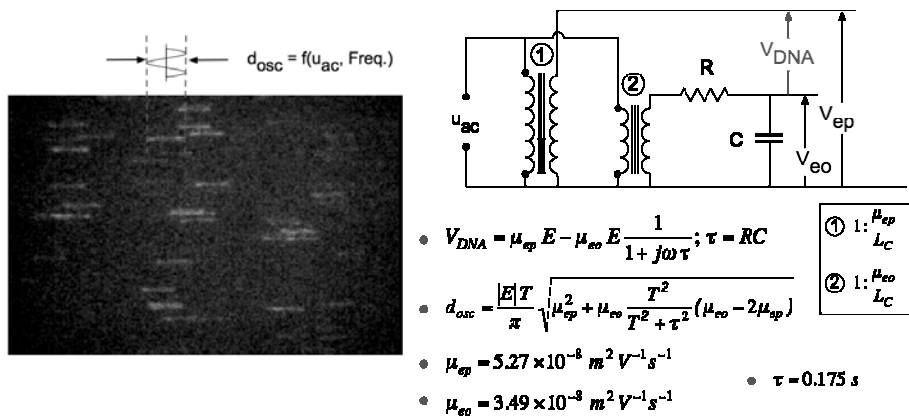


Figure 3: Trace of the DNA oscillating motion due to ac voltage

Figure 4: Equivalent circuit model for the DNA oscillation amplitude and extracted parameters

The 3 parameters of the model (μ_{ep} , μ_{eo} , τ), are extracted by fitting the experimental recorded DNA motion amplitude. An unique set of parameter (see value in Fig.4) provides an very good agreement between the model and the all the experimental data ranging from 10Hz-1KHz with ac voltage amplitudes (0.5-10V), as it is shown for 2 voltage amplitude in Fig. 5.

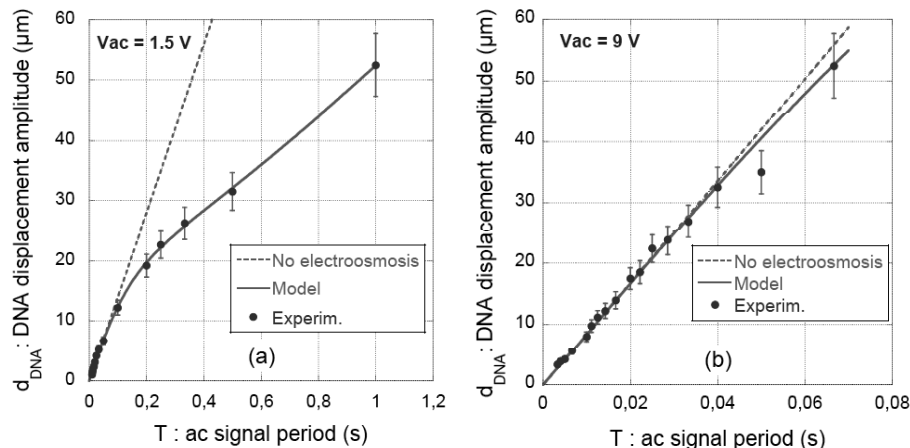


Figure 5: DNA displacement amplitude, d_{DNA} , plotted versus signal periods ($T=1/frequency$) for (a) 1.5 V and (b) 9V signal amplitudes. The model, formula and data from Fig.4 are given by the red line and the experimental data by the black dots with error bars. The curve without electroosmotic effect (dotted line) is also plotted. The effect of inversed EO drag is obvious for frequency lower than 10Hz ($T>0.1s$).

4. Conclusion

This proposed model proves to be efficient to analyze and simulate EP and OS flow in microfluidic channel. Thanks to this model, optimized conditions for pulsed EP have been found that systematically isolate and bring DNA molecules one by one in the collecting well (Fig.1).

Acknowledgements

We are thankful to the VLSI Design and Education Center (VDEC, University of Tokyo).

References

- [1] G. Hashiguchi et al., Anal.Chem. 75, p. 4347, 2003.
- [2] M. Kumemura, et al., Microtas 2005. 9, p. 521-523, 2005.
- [3] A. Manz et al., Journal of Micro-mech. and Micro-engineering 4, pp 257 -265, 1994.
- [4] A. Brask et al., Sensors and Actuators B: Chemical 92, pp. 127-132, 2003.

A HUMAN PROTEIN ATLAS FOR NORMAL AND CANCER TISSUES

Mathias Uhlen

Department of Biotechnology, AlbaNova University Center,
Royal Institute of Technology, Stockholm, Sweden

Antibody-based proteomics provides a powerful approach for the functional study of the human proteome involving the systematic generation of protein-specific affinity reagents. We have used this strategy to construct a comprehensive, antibody-based protein atlas for expression and localization profiles in 48 normal human tissues and 20 different cancers (1). The Human Protein Atlas is publicly available (www.proteinatlas.org) and contains, in the first version, approximately 400,000 high-resolution images corresponding to more than 700 antibodies towards human proteins. Each image has been annotated by certified pathologists to provide a knowledge base for functional studies and to allow queries about protein profiles in normal and disease tissues (2). We have recently (3) used the antibody reagents for validation of potential biomarkers to Mantle Cell Lymphoma (MCL) as well as high-throughput biomarker analysis of thousands of serum samples using a reverse array format (4). Our results suggest it should be possible to extend this analysis to the majority of all human proteins thus providing a valuable tool for medical and biological research, in particular for biomarker analysis in various patient cohorts.

Reference: (1) Uhlen M, Ponten F. (2005) Antibody-based Proteomics for Human Tissue Profiling. *Mol Cell Proteomics* 4(4): 384-393, (2) Uhlen et al (2005) A human protein atlas for normal and cancer tissues, *Mol Cell Proteomics*, 4(12):1920-1932, (3) Ek et al (2006) From gene expression analysis to tissue microarrays - a rational approach to identify therapeutic and diagnostic targets in lymphoid malignancies. *Mol Cell Proteomics*. 2006 Mar 8; (e publ. ahead of print), (4) Janzi et al (2005) Serum microarrays for large scale screening of protein levels. *Mol Cell Proteomics*. 4(12):1942-7.

AUTHORS INDEX

A

- Abbas, Shaghayegh 122
Abe, Hirohisa 500
Abe, Takashi 269, 479, 1330
Abell, Chris 864
Åberg, Lena 540
Abgrall, Patrick 188
Abonnenc, Melanie 1504
Abraham, Sinoj 1002
Adamo, Andrea 1492
Agarwal, Ajay 434, 1208
Agrawal, Rajat 834
Ahn, Chong H. 467, 588, 618, 1432, 1546, 1432, 1546
Ahn, Kyung H. 461
Ahsans, Md Shameen 900
Akaba, Shuichi 843
Akagi, Takanori 173, 413
Akalin, Tahsin 738
Akin, Demir 37
Akiyama, Yoshitake 1405, 1414
Albrecht, Jacob W. 921
Al-Haq, Muhammad Imran 1420
Allender, Chris 891
Altinas, Ersin 525
Altomare, Luigi 1501
Amatore, Christian 981
Andersen, Richard A. 702
Anderson, Patrick D. 621
Andersson, Helene 22, 410, 1507, 1510
Anraku, Ryo 59, 798
Anselmetti, Dario 383, 648
Antes, Juergen 1333
Aoki, Ryota 515
Aoki, Tokihiko 512
Aono, Takanori 1106
Aota, Arata 107
Arai, Akihiro 924
Arai, Fumihiro 233, 1247
Arakawa, Takahiro 86, 512, 603, 1002

- Arbault, Stephane 981
Arefi-Khonsari, Farzaneh 80
Arleth, Lise 1390
Asada, Sho 1274
Asai, Takahiro 59, 798
Asai, Tatsuya 479
Asanuma, Sohto 1318
Asthana, Amit 179
Astle, Aaron A. 1037
Auerswald, Janko 1061
Augustsson, Per 627
Auroux, Pierre-Alain 1465
Austin, Robert H. 1014
Azizi, Farouk 1109

B

- Baba, Masakazu 1017
Baba, Yoshinobu 236, 353, 395, 401, 404, 813, 816, 903, 1005
Bachelor, Sheri-Michele S. 1345
Baek, Ju Yeoul 1175, 1387
Baigl, Damien 1399
Bajar, Zoltan 882
Balasubramanian, Narayanan 1208
Bang, Hyunwoo 281, 1351
Bansal, Tushar 1181
Banu, Shahanara 1306
Bao, Jian-Bin 1067
Barany, Francis 1450
Barbier, Valessa 80
Bargiel, Sylvester 741
Baribier, Valessa 77
Barker, N. Scott 1238
Barker, Susan L. R. 1238
Baroud, Charles N. 585
Barrow, David 891
Bashir, Rashid 37
Bashkin, John 278
Bastiaansen, Cees W.M. 221
Bedair, Mohamed 203
Beebe, David J. 1564
Beech, Jason 696, 930, 1034

- Beecher, Stephen 720
Begley, Matthew R. 1064
Ben, Mathieu 945
Benabderrazik, Mariam 576
Benito-Lopez, Fernando 783
Berganza, J 1423
Berganza, Javier 1423
Bergaud, Christian 774, 1217
Bergquist, Jonas 326
Bermudo, M. C. 1522
Bernal, Luis P. 1037
Berthet, Nathalie 1217
Bessette, Paul H. 975
Bessler, Wolfgang 819
Besson, Eric 194
Besteman, Koen 807
Bhagat, Ali Asgar S. 663
Bi, Xiaohui 831
Bilenberg, Brian 930
Birtwell, Sam 1306
Bishop, Paul L. 467
Biyani, Manish 209
Bize, Vincent 576
Blatttert, Christoph 146, 359
Blatz, Andrew 1495
Blazej, Robert G. 1567
Blum, Loic J. 1202
Boccazzi, Paolo 996
Bocquet, Bertrand 738
Böhringer, Karl F. 122, 263, 525
Boitard, Laurent 1043
Boles, Deborah J. 1444
Bomer, Johan G. 425, 729
Bonthuis, Douwe J. 807
Bontoux, Nathalie 7
Booth, James 1465
Borno, Ruba T. 1519
Bossche, Andre 666, 909
Boukherroub, Rabah 771
Bousse, Luc 831
Boyle, Patrick 996
Bradley, Donal D.C. 720, 753
Branciforte, Jeffrey 1043
Brian, Ballios 203
Brismar, Hjalmar 449, 1507, 1510
Broer, Dirk J. 218, 221, 561
Brosten, Tyler 1148
Brouzes, Eric 1043
Brown, Ben J.K. 344
Bruus, Henrik 47
Buch, Jesse 1579
Burdick, Joel W. 702
Burg, Thomas 40
Burns, Mark A. 708
- C**
- Camart, Jean-Christophe 771, 651
Cao, Weidong 840
Carbonaro, Andrea 1309
Carlson, Robert 672
Carlson, Robert H. 675
Case, Marianne J. 122
Castell, Oliver 891
Cavalli-Petraglia, Gabriel 1306
Cha, Byung Hak 768
Cha, Misun 1585
Chabert, Max 1220
Chae, Su Kyung 1471
Chae, Sunki 1540
Chan, Po-Hsiung 1459
Chang, Chia-Hsien 1558
Chang, Donald C. 28
Chang, Guan-Liang 1244
Chang, Hwan-You 1537
Chang, Jun Keun 281, 1351
Chang, Meng-Ping 1181
Chang, Tsung Chain 305
Chang, Wen-Yu 1474
Chang, Woo-Jin 488, 918
Chang, Yu-Chi 134
Chang, Yu-Fen 137
Chao, Shih-hui 672
Charbon, Edoardo 744
Charles, Yves 1043
Charlot, Samuel 188
Chatelain, Francois 110, 452
Chatterjee, Debalina 125, 128
Chen , Yu 558
Chen, Ching-Mou 1244

- Chen, Guofang 1205, 1456, 1570
Chen, Jian 1516
Chen, Li 1109
Chen, Ming-Hung 161
Chen, Peilin 197
Chen, Po-Jui 176, 834
Chen, Tsung-Ju 1372
Chen, Yong 7, 981, 1399
Chen, Yu 317, 323
Chen, Yung-Chieh 1190
Cheng, L. J. 1265
Cheng, Xuanhong 1561
Cheon, Jinwoo 320
Cheong, Raymond 1576
Chetouani, Hichem 110
Chiba, Seiki A 278
Chin, L. K. 528
Chiral, Magali 1357
Chiu, Shao-Yin 1531
Cho, Hansang 642
Cho, Hyoung J. 1312
Cho, Keunchang 281, 1351
Cho, Sung K. 31
Cho, Yoon-Kyoung 347, 455
Cho, Young-Ho 552
Cho, Younja 762
Choi, Junbo 1585
Choi, Kihwan 1253
Choi, Sungyoung 371
Choi, Wonjae 34
Choi, Yo H. 978
Choi, Young Hoon 95
Chong, Ser Choong 317
Chou, Chia-Fu 1193
Chou, Qiong-Ru 137
Chou, Stephen Y. 1014
Chretien, Julien 1226
Chu, Eric 1519
Chu, Li-Yu 398
Chuang, Cheryl CY 1531
Chuang, Kai-Cheng 134, 398
Chuang, Tzu-Han 398
Chuang, Yun-Ju 161
Chuman, Hiroshi 353
Chun, Dong Won 768
Chun, Kukjin 1253
Chun, Myung-Suk 789
Chung, Chanil 281, 1351
Chung, Doo Soo 1253
Chung, Kwang Hyo 311, 341, 1426
Chung, Neon C. 1351
Chung, Peter M.-Y. 71
Chung, Sang K. 31
Chung, Seok 281
Chung, Taek Dong 636
Chung, Ung-il 1008
Chung, Wonseok 762
Chung, Yung-Chiang 305
Coffinier, Yannick 771
Collard, Dominique 182, 1588
Collins, John 116
Cooper, Jon 68, 963
Cooper, Jonathan M 855
Cordovez, Bernardo 1166
Cornwell, Alastair 720
Corso, Bruno 774
Crozatier, Cecile 981
Csajagi, Csaba 882
Cullen, Christopher J. 795
Cupelli, Claudio 53
- D**
- D Jed Harrison 1447
Dadic, Dalibor 1229
Dadic, Dalibor 476
Dagani, Gabriel T 1411
Dahan, Elodie 576
Dandy, David S 224
Dane, Karen Y 1489
Dang, Fuquan 236
Darvas, Ferenc 882
Das, Rupa 753
Daub, Martina 329
Daugherty, Patrick S. 975
Dauphinot, Luce 7
Davalos, Rafael V. 470, 987, 1345
Dayton, Paul A. 822
de Goede, Judith 218, 561
De Malsche, Wim 564

- de Mello, Andrew J. 200, 720, 753,
795, 876
- de Mello, John C. 720, 753, 795
- De Sagazan, Olivier 1357
- De Smet, Jan 564
- de Vos, Willem M. 425
- Dekker, Cees 807
- Delamarche, Emmanuel 612
- Delhaye, Caroline 771
- Delville, Jean-Pierre 585
- Demirci, Utkan 1561
- den Toonder, Jaap M.J. 218, 561, 621
- Denoual, Matthieu J. 1357
- Descamps, Emeline 774
- Desmet, Gert 564
- Dettloff, Roger 1444
- DeVoe, Donald L. 119, 531, 714,
1579
- D'hahan, Nathalie 452
- Dharmatilleke, Saman 143
- Di Carlo, Dino 1011, 1283, 1292,
1378, 1417, 1477
- Di Leonardo, Roberto 68
- Dittrich, Petra S. 407, 1375
- Dixon, Meredith 1561
- Djafari-Rouhani, Mehdi 74
- Do, Jaephil 618
- Docherty, Frances 855
- Docter, M. W. 666
- Doffing, Frank 476, 1522
- Domansky, Karel 951
- Domeier, Linda A. 155
- Dorfman, Kevin 386, 1220
- Drese, Klaus S. 476, 1229, 1522
- Druon, Christian 651
- Du, Rongbing 254, 678
- Du, Wen-Bin 1136
- Dube, Markus 329
- Ducrée, Jens 329, 570, 819, 1555
- Dumond, Jarrett J. 149
- Duong, Thanh Tu 383
- Dziuban, Jan 741
- E**
- Easley, Christopher J. 1055, 1064
- Edahiro, Jun-ichi 966
- Eddings, Mark A. 44
- Eggerink, Richard J.M. 783
- Eghbali, Hamed 564
- Eichhorn, Ralf 648
- Eiichi, Tamiya 1214
- Eijkel, Jan C.T. 615
- Ekström, Simon 1468
- El-Ali, Jamil 1486
- Elenitoba-Johnson, Oluwole 1441
- Elizalde, Jorge 1423
- Emory, Jason M. 1223
- Endo, Tatsuro 780
- Endo, Toshiaki 233
- Enomoto, Tadao 858
- Epilepsia, Aziel 122
- Erickson, David 1085, 1166, 1552
- Ericsson, Olle 735
- Esteve, Alain 74
- Esteve, Daniel 188
- Evander, Mikael 1055
- Evans, Allan 1148
- Evans, Carl R 1339
- F**
- Fakhoury, Jean R. 1411
- Fan, Hugh 1026
- Fan, Jeff 116
- Fan, Shih-Kang 134, 398
- Fang, Qun 1136
- Fang, Zhao-Lun 1136, 1232
- Farinas, Javier 1444
- Feller, Jeffrey 1148
- Feng, Han Hua 419, 1208
- Ferrance, Jerome P. 272, 840
- Fittipaldi, Antonio 1501, 1504
- Fitzpatrick, Jane 1229
- Flair, Eric 1280
- Flanagan, Lisa A. 567
- Fletcher, Daniel A. 308
- Flink, James M. 1390
- Forbes, Neil S. 1519
- Fournier, Isabelle 771
- Francois, Jean Marie 1217
- Franssila, Sami 152, 380, 597

- Franzke, Joachim 407
Frazier, A. Bruno 948
Fréchet, Jean M. J. 227
Fredrickson, Carl 1026
Frese, Ines 1522
Frisk, Thomas W 1507, 1510
Fu, Chien-Chung 398, 1531
Fu, Elain 1286
Fu, Jianping 519
Fu, Lung Ming 1091
Fujii, Masayuki 1336
Fujii, Teruo 65, 738, 1151
Fujiki, Satoshi 960
Fujita, Hiroyuki 182, 525, 1393, 1588
Fujiyoshi, Kentaro 1396
Fuke, Masafumi 16
Fukuda, Toshio 233, 1247
Fukumura, Hiroki 801
Fukuzawa, Kenji 1017
Fukuzawa, Takashi 1271
Funakoshi, J. 1304
Funakoshi, Kei 534, 1354, 1393
Funano, Shun-ichi 299
Funatsu, Takashi 512, 603
Furukawa, Yuji 482, 1405, 1414
Furuya, Akihiro 482
- G**
- Gaitan, Michael 119, 251, 260, 531, 1465
Gale, Bruce K. 44, 293, 1441
Galitonov, Gerasim 1306
Galopin, Elisabeth 651
Gan, H. 89
Gardeniers, Han J.G.E. 83, 564, 582, 729, 783, 786
Garrell, Robin L. 125, 128
Gee, Antony 876
Geisler, Neil 825
Gellberg, Mats 4
Gersbach, Marek 744
Geschke, Oliver 1549
Gessner, Thomas 657
Ghandour, Hala 738
Ghodssi, Reza 1250
- Ghorashian, Navid 990
Gianchandani, Yogesh B. 837, 1148
Gijs, Martin A.M. 428, 576
Gillies, Murray 218, 561
Glasdam Jensen, Thomas 47
Glass, Jonathan D. 948
Glatzel, Thomas 53
Glezer, Ari 624
Go, Jeung S. 1002
Godin, Michel 40
Godley, Lucy 1309
Golden, Joel P. 113
Gondoin, V. 257
Gong, Jian 1046
Goranovic, Goran 1408
Göransson, Jenny 4, 422, 723
Gorecka-Drzazga, Anna 741
Gosse, Charlie 386
Goto, Makiko 993
Goto, Yasushi 594
Goyal, Sidhartha 263
Graham, Duncan 855
Grainger, David W 224
Gransee, Rainer 476, 1522
Grant, Chris F 1289
Greer, Jenny 1441
Gregory, Carl A. 1456
Griffith, Linda G. 951
Grimmer, Stephen 1229
Griscom, Laurent 945
Griss, Patrick 1226
Grover, William H. 506
Grumann, Markus 329, 819, 1555
Gu, Jian 1193
Guan, Yan-Xia 1232
Gue, Anne-Marie 74, 188, 194
Guedea-Boudeville, Marie-Alice 1399
Guenther, Axel 537
Guerrieri, Roberto 1501, 1504
Guillo, Christelle 272
Gumpenberger, Thomas 185
Guo, L. J. 1265
Gupta, Ravi 1193
Gutmann, Oliver 329

H

Ha , Mihn Heip 780
Haapala, Markus 152
Haeberle, Stefan 570
Haguet, Vincent 110
Hahn, Young Ki 320
Han, Dong Kyun 248
Han, Dong-Chul 281, 1351
Han, Ga Young 768
Han, Jongyoon 519, 522, 1076
Han, Jungyoup 467, 588, 1546
Hane, Shintaro 756
Hara, Ryotaro 843
Harada, Takahiro 86
Harasima, Hideyosi 1005
Harris, Alun 828
Harris, Kenneth D. 221
Harrison, D. Jed 170, 254, 750, 1020,
1067, 1280, 1289
Harteneck, Bruce D. 1145
Hasebe, Shinji 555, 1121
Hasegawa, Tadahiro 1112
Hasegawa, Takuya 669
Hasenbank, Melissa S. 1286
Hashiguchi, Gen 1462, 1528, 1588
Hashimoto, Masahiko 846
Hashioka, Shingi 404, 1558
Hasselbrink, Ernest F. 13, 915, 1265,
1384
Hata, Hidetoshi 131
Hatch, Anson V. 549
Hattori, Akihiko 59, 798, 1196, 1271
Hawkins, Benjamin G. 1187
Hayes, Donald J. 1139
He, Huiqi 28
He, Mei 170
He, Xinya 224
He, Yan 1
Heckele, Mathias 999
Heijnen, Sef J. 729
Heikkilä, Liisa 380
Heldal, Trond 1061
Helldin, Göran 1468
Henares, Terence G. 299, 1199

Heng, Chew Kiat 317, 323
Henry, Charles S 224
Herberg, Julie L. 1145
Hertz, Hans M. 446, 449
Hesketh, Peter J. 1163
Hess, Henry 1360
Hettiarachchi, Kanaka 822
Heule, Martin 1375
Heydt, Richard 278
Heyries, Kevin 1202
Hibara, Akihide 107, 245, 546, 936,
1274, 1277, 1324, 1327
Higasa, Masashi 1127
Hiller, Karla 657
Hirabayashi, Yasutoshi 681
Hirano, Motohisa 1360
Hirano, Takaya 1178
Hirata, Tetsunori 747
Hisamoto, Hideaki 299, 356, 1199
Hishida, Koichi 792
Ho, Chen-Ta 1537
Ho, Chih-Ming 242, 368, 969
Ho, Kuo-Chuan 717
Hoffmann, Daniel 1202
Hofmann, Oliver 720, 753
Hollfelder, Florian 864
Holmes, David 1292, 1306
Holt, Daniel J 864
Holtz, William J. 230
Homsy, Alexandra 1202
Hong, Jennifer S. 251
Hong, Jung Woo 311, 341
Hong, Lan-Young 660
Hong, Won Hi 888
Hong, Wu 242
Hong, Yeon Ki 888
Hori, Yoko 1414
Hori, Yoshio 942
Horiike, Yasuhiro 404, 1558
Horisberger, Jean-Daniel 576
Horsman, Katie M. 1055
Hosoi, Yosuke 209
Hosokawa, Kazuo 19, 206, 389
Hosseini, H. M. 528, 1097

Hotokezaka, Hiroyasu	1315	Inagaki, Akiko	942
Hotta, Hiroki	392, 726, 1318	Inami, Hisao	338
Howe, Roger T.	230	Ingham, Colin J.	425
Howell, Peter B.	113	Inman, Walker	951
Hromada, Lou	531	Inoue, Akira	389
Hsieh, Tseng-Ming	609, 1088, 1321, 1369	Inoue, Hiroyuki	936
Hsing, I-Ming	711	Inoue, Sonoko	903
Hu, Xiaoyuan	1142	Ionescu-Zanetti, Cristian	990, 1495
Huang, Adam A.	368	Iqbal, Zohara Q.	1345
Huang, Chun-Wei	573	Iribé, Yasunori	756
Huang, Esther	1444	Irie, Takashi	852
Huang, Hao-Hsuan	305	Irimia, Daniel	1513, 1561
Huang, Heng-Chi	1531	Isailovic, Dragan	1
Huang, Hsuan-Jung	1244	Ishihara, Kazuhiko	212, 215, 236, 335, 885
Huang, Keng-Shiang	305, 1115	Ishisaka, Tomoji	1405
Huang, Shih-Hao	591	Ishizuka, Koji	1429
Huang, Song-Bin	573	Isomura, Tetsu	1211
Huang, X.Y.	89	Itayama, Tomosato	645
Huber, David	1079	Ito, Toshiyuki	389
Huck, Wilhelm T S	864	Ivester, Robin H. C.	506
Huh, Yun Suk	888	J	
Hui, Wing-Cheong	317	Jacobsen, Jes K.	1390
Hultström, Jessica	446, 449	Jacobsen, Soeren	696
Humayun, Mark S.	633, 834	Jacobson, Stephen C.	933
Hung, Lung-Hsin	699, 1190	Jaffrezic, Nicole	194
Hunt, Alan J.	13	Jahn, Andreas	119, 251
Hunziker, Patrick	612	Jang, Am	467
Hutchison, J. Brian	260	Jang, Hongchul	522
Hwang, Kyo Seon	768	Jang, Jin	34
Hwang, Seong P.	759	Jang, Jung-Tak	320
I		Jarvius, Jonas	4, 10, 422, 723, 735
Ichikawa, Naoki	71	Jarvius, Malin	4, 422
Ichiki, Takanori	173, 209, 413	Jeandey, Christian	110
Ichimura, Teijiro	804	Jensen, Erik C.	506
Ichiyanagi, Mitsuhsisa	792, 801	Jensen, Klavs F.	257, 537, 921, 996, 1029, 1486, 1492
Igawa, Kazuyo	1008	Jeon, Min Ku	473
Igel, Günter	377	Jeon, Noo Li	567
Ikeda, Yasuhisa	1315	Jeon, Sung Il	311
Ikeuchi, Masashi	693, 1169	Jeong, Eun H.	1002
Ikuta, Hajime	443	Jeong, Ok Chan	62
Ikuta, Koji	684, 693, 1112, 1169	Jeong, Yongwon	1253
Iles, Alexander	873	Ji, Hong Miao	317, 323, 419
Im, Maesoon	762		

- Jiang, Maw-Shiuan 398
Jin, Chun Yan 687
Jin, Qing-Hui 50
Jin, Shouguang 1026
Jin, Zongwen 320
Jing, Lim-Jing 317
Johansson, Henrik 4, 10, 422
Jones, Richard 882
Joo, Segyeong 636
Jösson, Mats 606
Jothimuthu, Preetha 663
Jousse, Fabien 77
Jung, Hyo-II 416
Jung, Hyun Jung 248
Jung, Suk-Won 705, 1295
Jurischka, Reinhold 146, 359
- K**
- Kabata, Hiroyuki 1498
Kai, Junhai 618
Kaji, Hirokazu 846, 972
Kaji, Noritada 353, 395, 401, 404, 813, 816, 903, 1005, 1396
Kaler, Karan VIS 1040
Kameda, Takahide 924
Kamezawa, Kazutoshi 392
Kamisuki, Shinichi 579
Kamiya, Shoko 233
Kanagasabapathi, Thirukumaran T. 1040
Kanai, Masaki 500, 630
Kanamori, Toshiyuki 966
Kaneda, Shohei 65, 1151
Kang, Ji Yoon 1160
Kang, Joo H. 320
Kang, Seong Ho 1
Kanno, Isaku 131, 681, 1498
Kanno, Kenichi 1336
Kanzaki, Ryoei 1402
Kao, M.-T. 1265, 1384
Karlinsky, James M. 1064
Kartalov, Emil P. 1082
Kasianowicz, John 531
Kasinskas, Rachel W. 1519
Kataoka, Masatoshi 813, 903
Katayama, Kenji 191, 1271, 1298
- Kato, Hiroshi 1330
Katsura, Shinji 104, 1525
Kawabata, Tomohisa 831
Kawaguchi, Yoshizo 185
Kawai, Kentaro 500
Kawakami, Tomohiko 296, 491
Kawano, Satoyuki 131, 681
Kawashima, Takeaki 972
Kawazumi, Hirofumi 1336
Kayyami, Masoud 819
Kazawa, Tomoki 1402
Kazoe, Yutaka 101
Keasling, Jay D. 230
Kee, Jack S. 732
Kee, Jack-Sheng 434
Kemppinen, Emilia M. 846
Kenji, Yasuda 1070
Kenrick, Sophia A. 975
Kermarec, Frederique 452
Ketola, Raimo A. 380, 597
Kettle, Brett 1229
Khan, Saif A. 257
Khatavkar, Vinayak V. 621
Kheterpal, Indu 1456
Khine, Michelle 987, 1495
Khurana, Tarun 897
Kikuchi, Kazuhiro 431
Kikutani, Yoshikuni 191, 296, 431, 485, 491, 936, 1118, 1127, 1271
Kim, Byung Gee 1241
Kim, Byung-Kwon 1100
Kim, Byung-Woo 341
Kim, Chang Jin (C.-J.) 1046
Kim, Chong 1160
Kim, Do Hyun 95, 780, 888
Kim, Dong-Pyo 179, 660
Kim, Duck Joong 248, 1157, 1094
Kim, Eun-Ki 488
Kim, Franklin J. 284
KIm, Haeng-Boo 245, 1103, 1324
Kim, Hak-Sung 320
Kim, Hanseup 1037
Kim, Hee Chan 636
Kim, Hyeon Cheol 1253

Kim, Hyun-Seok	416
Kim, Il	1002
Kim, Il Tae	789
Kim, Ilchaek	1585
Kim, Jae Gwan	1094
Kim, Jae Hoon	248
Kim, Jeong Ah	1351
Kim, Jeongyun	1175
Kim, Jin-Hwan	488
Kim, Jinseok	1253
Kim, Jungkyu	293
Kim, Kunhong	416
Kim, Kyung C.	1002
Kim, Kyung Chun	1154
Kim, Minseok S.	1540
Kim, Min-Soo	1241
Kim, Mira	1295
Kim, Sang Hyeob	416
Kim, Sehwan	34
Kim, Seong-Jin	762
Kim, Soo Ho	473
Kim, Suhyeon	455
Kim, Sun Min	915
Kim, Sung Jae	522, 1076
Kim, Sung Rak	248
Kim, Sung-Jin	1100
Kim, SungRak	1387
Kim, Sung-Woo	1432
Kim, T. S.	1265, 1384
Kim, Tae Song	768, 810, 1160
Kim, Unyoung	1489
Kim, Won-Hyo	705
Kim, Yong-Kweon	1241
Kim, Young-Bum	488
Kinoshita, Haruyuki	65
Kirby, Brian J.	1187
Kirby, Celeste	831
Kishishita, Seiichiro	1211
Kitagawa, Fumihiro	158, 362, 365, 374, 924
Kitagawa, Hiroaki	290
Kitamori, Takehiko	10, 59, 107, 191, 245, 296, 431, 485, 491, 546, 798, 843, 858, 879, 936, 939, 993, 1008, 1103,
	1106, 1118, 1124, 1127, 1130, 1133, 1196, 1235, 1271, 1274, 1277, 1298, 1324, 1327, 1582
Kitaoka, Mitsuo	191, 296, 485, 491, 858, 1106, 1118, 1127, 1196
Klank, Henning	503
Klauke, Norbert	963
Klaunick, Christoph	377
Klein, Sanford	1148
Knapkiewicz, Paweł	741
Knapp, Helmut	1061
Knight, Ivor T.	1444
Knudsen, Scott	40
Ko, Christopher	347, 455, 762
Kobori, Toshiro	1438
Koc , Yasemin	200
Koch, Kaspar	870, 867
Koda, Hiroko	1558
Koeda, Hiroshi	579
Koev, Stephan T.	1250
Kogure, Kentarou	1005
Koide, Akira	1106
Koide, Masahiro	645
Kojima, Yasuaki	392
Kolfschoten, Ruben	996
Koltay, Peter	999
Komabayashi, Mariko	942
Konishi, Satoshi	62
Konno, Tomohiro	212, 215, 993
Koo, Yoon-Mo	488, 918
Korecka, Lucie	350
Kornbluh, Roy	278
Korri-Youssoufi, Hafsa	194
Koschwanez, John H.	675
Koshizuka, Seiichi	86
Kostiainen, Risto	152, 380, 597
Kostyszyn, Beata	464
Kotera, Hidetoshi	131, 458, 681, 1498
Kotiaho, Tapio	152, 380, 597
Kovac, Joseph R.	1483
Koyama, Yutaka	939
Krafcić, Karen L.	155
Kralj, Jason G.	1029
Krapf, Diego	654

- Krause, Horst 1333
Krishnadasan, Siva 795
Kristensen, Anders 696, 930
Krommenhoek, Erik E. 729
Kruijer, Wiebe 22
Kubota, Kei 365
Kubota, Shun 1582
Kuester, Uwe 53
Kumagai, Isao 497
Kumar, Angelee 284
Kumaresan, Palani 1567
Kumemura, Momoko 182, 1588
Kuo, Rita 699
Kuramoto, Hiroshi 1005
Kurabayashi, Kaori 1354, 1534
Kurihara, Masahiro 338
Kurita, Ryoji 302
Kurooka, Katsuhito 1268
Kurosaki, Ryozo 185
Kurosawa, Kiyoko 296
Kurosawa, Osamu 16, 458
Kutter, Jörg P. 47, 503, 1390, 1549
Kuwata, Masahiro 1130
Kwak, Ju H. 759
Kwon, Tae Yun 810
Kwong, Charlotte C. 368
Kwong, Dim Lee 1208
- L**
- Lagally, Eric T. 1142
Lai, Shian-Chin 1115
Lal, Rakesh 25
Lam, Liza 1429
Lam, Wilbur 308
Lam, Y. C. 89
Lambertus, Gordon R. 1037
Landegren, Ulf 4, 10, 422, 735
Landers, James P. 272, 840, 1055,
 1064, 1238
Lao, Ieng Kin 1208
Larsen, Asger V. 930
Larsson, Chatarina 10
Larsson, Rolf 326, 410
Laurell, Thomas 314, 540, 627, 1055,
 1468
Laurent, Sébastien 774
Le Berre, Mael 981, 1399
Le Gac, Severine 1381
Le Nel, Anne 350
Le Pioufle, Bruno 182, 1357, 1393,
 1534
Leach, Jonathan 68
Lee, Abraham 116, 567, 699, 822,
 1190, 1321, 1369
Lee, Beom-Seok 347
Lee, Bo-Rahn 1241
Lee, Chang-Soo 660
Lee, Chau-Hwang 137
Lee, Cheng S 714, 1579
Lee, Cheng Yan 1091
Lee, Dae-Sik 311, 1426
Lee, Eunice S. 284, 1345
Lee, Gwo-Bin 573, 1348
Lee, Hong Lim 810
Lee, Hong-Joo 179
Lee, J. 1351
Lee, Jeong Hoon 522, 768
Lee, Jeong-Bong 1139
Lee, Jeong-Gun 347, 455
Lee, Jin-Hwan 494
Lee, Joonmo 281
Lee, Jung A 759
Lee, Junghoon 1585
Lee, Jun-Hwang 341
Lee, Kang Sun 1160
Lee, Ki B. 287
Lee, Ki Hwa 1387
Lee, Kook-Nyung 705, 1295
Lee, Kwang -C. 759
Lee, Kwang Ho 1094, 1387
Lee, Kyu Jung 1160
Lee, Kyusang 455, 762
Lee, Luke P. 284, 473, 642, 705, 990,
 1011, 1283, 1292, 1345
Lee, Sang Hoon 248, 1094, 1175,
 1387
Lee, Sanghyun 13
Lee, Sang-Myoung 1241
Lee, Seok Woo 275

Lee, Seong J.	461	Lim, Si-Hyung	1259
Lee, Seung S.	275, 687, 759, 978	Lim, Tae-Sun	494
Lee, Soo Hyun	588, 1432	Lim, Ti-Meng	317
Lee, Sung S.	461	LIM, Tit Meng	323
Lee, Tae Seok	789	Lin, Che Hsin	1091
Lee, Terry D.	1573	Lin, Che-Hsin	1244
Lee, Thomas MH	711	Lin, Hong-Ping	305
Lee, Won Chul	1348, 1351	Lin, James	969
Lee, Won Gu	281, 552	Lin, Jiunn-Yuan	137
Lee, Wonhye	1540	Lin, Jr-Lung	1348
Lee, Yi-Kuen	28	Lin, Po-Wen	1115
Lee, Yoon-Sik	1241, 1295	Lin, Qiao	92
Lee, Young-Sun	347	Lin, Ruei-Zeng	1537
Legendre, Lindsay A.	840	Lin, Yen-Chen	134, 305, 1115
Legrand, Dominique	738	Lin, Yuh A.	1321
Lehmann, Ulrike	428	Lindberg, Ulf	606
Lehnert, Thomas	576	Lundstrom, Henrik	873
Lei, Huan-Yao	1348	Lindstrom, Sara	410
Leichle, Thierry	774, 1217	Link, Darren	1043
Lemay, Serge G.	654, 807	Lipson, Hod	1552
Lennon, Erwan	738	Littleford, Rachel E	855
Lerch, Margaret A.	933	Liu, Ai Qun	528, 1097, 1474, 1480
Leslie, Daniel C.	1064	Liu, Cheng-Hsien	1537
Levchenko, Andre	1576	Liu, Cheng-Yu	1348
Lewis, Roxanne	203	Liu, Chung N.	1453
Li, Chen	831	Liu, Gang L.	284
Li, Chunyan	1546	Liu, Jing	50
Li, Hong	80	Liu, Pang-Chih	1480
Li, Hungwang	1	Liu, Wen-tso	419
Li, Na	969	Livache, Thierry	774
Li, Po-Ying	633	Liw, Saxon	317
Li, Tao	837	Llopis, Shawn	1450
Li, Thomas H.	308	Lo, Ronalee	633
Li, X	729	Locascio, Laurie	119, 251, 260, 849, 1465
Li, Xiaonan	729	Loebbecke, Stefan	1333
Li, Xinghua	1330	Lomas, Tanom	140
Li, Zhihong	543	Long, Nicholas J.	876
Lian, Wei	1026	Longo, Marjorie L.	822
Liao, Kuo-Tang	1244	Loughran, Michael G.	1202
Liao, Ronglih	437	Low, Hong Yee	149
Liddle, J. Alexander	1145	Luharuka, Rajesh	1163
Lien, Kang-Yi	1348	Lutz, Barry R.	1516
LiKamWa, Patrick L.	1312	Lutz, Sascha	329, 819
Lim, C. S.	528, 1097		

M

Mabius, David L. 164, 167
Maeda, Eiki 813
Maeda, Hideaki 1336
Maeda, Mizuo 19, 206, 389
Maeda, Ryutaro 71
Maeng, Sung-Lyul 416
Magariyama, Yukio 1438
Maharbiz, Michel M. 1181, 1184,
 1519
Mahmoudian, Laili 353
Mailley, Pascal 774
Majumdar, Arun 1259
Makino, Kimiko 389
Malleo, Daniele 1292
Malmstadt, Noah 1366
Maltezos, George 1082
Manabu, Tokeshi 1005
Manalis, Scott 40
Manaresi, Nicolò 1501, 1504
Mandal, Sudeep 1085
Manneberg, Otto 446, 449
Manz, Andreas 407, 1375
Marchenko, Steven 567
Marchiarullo, Daniel J. 1238
Marko-Varga, Gyögy 1468
Marquette, Christophe A. 1202
Marran, Dave 1043
Martens, Stefan 56
Marty, Antoine 188
Maruo, Shoji 669
Maruyama, Hisataka 1247
Maruyama, Yuki 744
Mastrangelo, Carlos 1109
Mathies, Richard A. 506, 1453, 1567
Matins, Hugo 1306
Matsubara, Masayuki 852
Matsuda, Miyuki 1052
Matsue, Tomokazu 645, 942
Matsumoto, Hirokazu 497
Matsumoto, Masahiro 269
Matsumura, Takashi 894
Matsuoka, Shinya 1327
Matsuoka, Yoshinori 296, 858, 1196,

1271

Matsushita, Yoshihisa 804
Matsuzawa, Mitsuhiro 338
Mawatari, Kazuma ... 296, 485, 491, 858,
 1118, 1127, 1271, 1274, 1582
Mazurier, Joel 738
McCarley, Robin L. 855, 1205, 1456,
 1570
McClain, Maxine A. 948
McDermott, Mark T. 254, 678, 750
 1280, 1289
McHale, Glen 200, 1339
McNeil, Calum 828
Medoro, Gianni 1501, 1504
Mehne, Christian 999
Mei, Qian 1026
Meijer, Han E.H. 621
Meldrum, Deirdre 672, 675, 1516
Melin, Jonas 4, 10, 422, 723
Ménétrier, Laure 98
Meng, Ellis 633, 834
Meyer, Christine 807
Meyerhoff, M. E. 1184
Meyhöfer, E. 1265, 1384
Meyvantsson, Ivar 1564
Miao, Yunan 1573
Mijatovic, Dragana 615
Miki, Norihisa 1268
Millard, D. 531
Miller, Philip W. 876
Min, Byoung Goo 1094
Min, Byoung-Hyun 1543
Minc, Nicolas 350, 386
Misery, Laurent 945
Mitra, Bhaskar 25
Mitsuya, Yasunaga 1017
Mittenbuehler, Klaus 819
Miya, Akiko 894
Miyaguchi, Hajime 936
Miyahara, Yuji 1262
Miyake, Ryo 338, 1106
Miyamura, Kazuhiro 485
Miyata, Kozue 392
Miyazaki, Rie 579

- Mizuno, Akira 104, 1525
Mizuno, Jun 158, 362
Mizutani, Fumio 302
Mizutani, Wataru 546
Moghbel, Reza 116
Mohamadi, Mohamad Reza 353
Mol, Titie 218, 561
Monaghan, Paul B 855
Mondal, Sudip 777
Monuki, Edwin 567
Moon, Joon-Ho 1154
Morales, Alfredo M. 155, 470
Morgan, Hywel 1292, 1306, 1342
Morishima, Keisuke 191, 482, 1405,
1414
Morita, Tomoyuki 894
Moriuchi, Takeyuki 482
Moriya, Naoji 765
Moriya, Takatsugu 906
Morton, Keith J. 1014
Mott, David R. 113
Mueller, Claas 146
Mugele, Frieder 615
Mulherkar, Rita 25
Multi Wibowo, Rachmat 600
Munaka, Tatsuya 500
Munson, Matthew S. 849
Murakami, Akira 1435
Murakami, Yuji 1127
Murata, Toshiaki 804
Murphy, Brian M 224
Murray, Kermit K. 1570
Musallam, Sam 702
Mushfique, Hasan M. 68
Musyimi, Harrison K. 1570
Myers, David R. 1145
- N**
- Naegele, Lars 570
Nagai, Hidenori 374, 852
Nagai, Masao 1558
Nagai, Takashi 431
Nagamine, Kuniaki 645
Nagaoka, Kyousuke 1324
Nagasaki, Wako 900
Nagase, Yu 885
Nagatani, Naoki 900
Najafi, Khalil 1037
Nakagawa, Kazuhisa 1462, 1528
Nakahara, Tomonori 1121
Nakakoshi, Masamichi 879
Nakamura, Kazuyuki 1304
Nakamura, Shin 924
Nakanishi, Hiroaki 491, 1127
Nakanishi, Hisao 1235
Nakano, Michihiko 104, 1525
Nakashima, Yuta 440
Nallani, Arun K. 1139
Narazaki, Aiko 185
Narita, Yuka 852
Nash, Michael 1366
Nellis, Gregory 1148
Nelson, Kjell E. 825
Nemoto, Naoto 209
Nestler, Joerg 657
Neuzil, Pavel 332, 609, 1088
Nevill, J. Tanner 1283, 1292
Newton, Michael I. 200, 1339
Neylon, Cameron 1306
Nguyen, N.T. 89
Nguyen, Vinh 1082
Nichols, Kevin P. 582, 786
Niclass, Cristiano 744
Nicu, Liviu 774, 1217
Nielsen, Peter E. 1408
Nieuwland, Pieter J. 867, 870
Niikura, Fuminori 684
Niino, Hiroyuki 185
Nikolajeff, Fredrik 326, 723
Nilsson, Andreas 314
Nilsson, Johan 1055
Nilsson, Mats 4, 10, 422, 723, 735
Nishida, Teruo 1304
Nishii, Junji 374
Nishimoto, Takahiro 630
Nishino, Michiteru 1211
Nishizawa, Kazuki 335
Nishizawa, Matsuhiko 269, 479, 846,
972, 1330

Nisisako, Takasi	1049	Otsuka, Koji	158, 362, 365, 374, 924
Nissila, Teemu J.	597	Ottens, Marcel	729
Nitta, Takahiro	1360	Otto, Thomas	657
Niwa, Osamu	302	Owens, Bryan	951
Noh, Jermim	473	Ozawa, Manabu	431
Noji, Hiroyuki	1363, 1429	Özkapici, Veysel	930
Nonogi, Mari	245	P	
Norlin, Peter	464	Padgett, Miles	68
Novak, Lukas	332	Padmanabhan, Prashant	1184
Nsiah, Francis	750, 1289	Pamme, Nicole	344
O		Pan, Jen-Hao	1321, 1369
Oana, Hidehiro	16, 458	Pang, Changlin	702
Obenschain, Keith S.	113	Pang, Hyung-Seok	1312
Oda, Kotaro	1274	Papautsky, Ian	494, 663
Odake, Tamao	726, 1318	Parashar, Virendra K.	428
Odake, Tamao	392	Park, Chinsung	455
Ogawa, Hiroki	1558	Park, Dae J.	266
Ogawa, Ryo	404, 1558	Park, Hae-Sim	320
Oh, Eunkeu	320	Park, Hye-Mee	918
Oh, Sang-Hyun	975	Park, Jae Hong	810
Ohashi, Toshinori	858	Park, Jae Y.	266
Ohoka, Masataka	1498	Park, Jaehyun	1184, 1519
Ohshima, Toyohiro	756	Park, Je-Kyun	34, 320, 371, 1540
Ohtani, Toshio	1438	Park, Jong	1148
Oikawa, Ken	1277	Park, Jong-Myeon	347
Oishi, Kosuke	669	Park, Jung Ho	768
Okada, Hiroki	401	Park, Junha	281
Okada, Koutaroh	1402	Park, Jun-Hong	179
Okano, Teruo	1133	Park, Kidong	37
Okitsu, Teru	681	Park, Sang-Hyug	1543
Okonogi, Atsuhito	1498	Park, Sang-Jin	1157
Oku, Yuichi	843	Park, Se Ho	1426
Olabarria, Garbióe	1423	Park, Se I.	759
Oleschuk, Richard	203	Park, Sewan	1253
Olofsson, Goeran	819	Park, Sin-Wook	1543
Omatsu, Fumiyuki	1112	Park, Yong Doo	1175, 1387
Ong, Wee-Liat	56, 434	Passchier, Jan	876
Ono, Koichi	1151	Patel, Kamlesh	1079
Ooie, Toshihiko	1121	Patel, Kamlesh D.	984
Oose, Hiroaki	900	Patel, Robin	840
Ortiz, Pedro	828	Paumier, Guillaume	74
Oshima, Marie	65	Payne, Gregory F.	1250
O'Sullivan, C	1522	Payne, Richard. P. J.	864
Ota, Masahiro	482	Peh, Xue Li	419

Pelrine, Ron	278	Rao, Mulpuri V.	1465
Pennathur, Sumita	1079	Rasmussen, Steen	1408
Pennec, Jean-Pierre	945	Rasooly, Julia	308
Pereira, Ulysse	945	Ratner, Buddy	263
Perozziello, Gerardo	1549	Ravula, Surendra K.	948
Perrimon, Norbert	1043	Regis, Jonnathan	164, 167
Perroud, Thomas D.	984	Regtmeier, Jan	383, 648
Perry , Carol C.	200	Reimann, Peter	648
Perumal, Jayakumar	179	Reinecke, Holger	146, 359
Pettersson, Filip	314, 540, 627	Reinhardt, Helke	407
Peyrin, Jean-Michel	350	Reinhoudt, David N.	783
Phalnikar, Koustubh	1579	Renaud, Philippe	1375
Piciu, Oana M.	666	Renaudin, Alan	651
Pincas, Hanna	1450	Reyes, Darwin R.	260
Pinelis, Mike	1519	Reyne, Gilbert	110
Ping, Guichen	395	Rhieu, Steve	1079
Piper, Kerryl	840	Riaz, Asif	1351
Pipper, Juergen	332, 609, 1088	Rice, Jeffrey J.	975
Piret, Gaelle	771	Ricketts, Alistair	855
Pisano, Albert P.	552	Riegger, Lutz	329, 819, 1555
Poenar, Daniel P.	558, 732	Ritzi, Marion	476
Ponce, Pierre	987	Rizzuto, Daniel	702
Porntheerapat, Nisaporn	140	Roach, Paul	200, 1339
Post, Janine N.	22	Roach, Peter L.	1342
Potier, Marie-Claude	7	Robillot, Cedric	1229
Pourciel, Jean-Bernard	774, 1217	Roblin, Christophe	386
Pow, Brian	690	Rodger, Damien C.	834
Prahlad, Harsha	278	Rodriguez, Isabel	143, 149
Prakash, A. Ranjit	1040	Rodriguez, William	1561
Prockop, Darwin	1456	Romani, Aldo	1504
Pryor, Robert J.	1441	Ros, Alexandra	383, 648
Pudda, Catherine	452	Ross, David	849, 912
Purnell, Robert	1366	Rossier, Jean	7
Pyo, Hyeon-Bong	311, 341, 1426	Rothberg, Jonatahn M.	1043
Q		Ruano-López, J.M.	1423
Qian, Jiangrong	975	Rulison, Aaron	1444
Qiu, Yiling	437	Rutjes, Floris P.J.T.	870
R		Rutjes, Floris P.J.T.	867
Rafeah, Siti	317	Rydholm, Susanna	1507, 1510
Raghavan, Srinivasa R.	251	Ryu, Sung Shin	1160
Rahong, Sakon	140		
Raja, Amal	720		
Ramadan, Qasem	558		
Ranganathan, Nagarajan	56, 434		
		S	
		Saarela, Ville	152
		Sabounchi, Poorya	470, 990
		Saeki, Souichi	1304

Sahoo, Hemantkumar R.	1029
Saiki, Koichiro	906
Sainiemi, Lauri	597
Saito, Keiitsu	852
Saito, Masato	1462, 1528
Saito, Takashi	1304
Sakai, Ryo	879
Sakai, Yasuyuki	738
Sakaki, Naoyoshi	1588
Sakakihara, Shouichi	1429
Sakamoto, Katsumasa	296, 491, 1127
Sakamoto, Takashi	1435
Sakata, Toshiya	1262
Sakeda, Kosaku	804
Sakurai, Satoshi	879
Salerno, Louis	1148
Saliba, Antoine-Emmanuel	386
Samel, Björn	1226
Sameshima, Tomoya	603
Samper, Victor	323, 558
Sanchez, Javier	326
Sandison, Mairi E.	1342
Sano, Tadashi	443
Santer, Mark	53
Santiago, Juan G.	894, 897
Sarajlic, Edin	182
Sarkar, Aniruddh	25
Sarro, P. M.	666
Sasaki, Naoki	1103
Sasaki, Seiichi	239
Sasaki, Yasuhiko	338, 443
Sathuluri, Ramachandra Rao	957
Sato, Hiroshi	1405
Sato, Kae	389, 993, 1008, 1133
Sato, Kiichi	431, 1008
Sato, Tadatake	185
Sato, Yasunobu	206
Sato, Yohei	101, 239, 792, 801, 906
Sato, Yukari	302
Sato, Yukiko	603
Satomura, Shinji	831
Satyanarayana, Srinath	1259
Sauter, Fabien	452
Sawada, Kazuaki	744
Saya Daisuke	1217
Schasfoort, Richard B.M.	927
Scherer, Axel	1082
Schifferdecker, Daniel	1333
Schlautmann, Stefan	927
Schmidt, Jacob J.	1366
Schoemaker, Hans E.	867
Schøler, Mikkel	696
Schönberg, Tommy	464
Schoth, Andreas	146, 359
Schulze, Janette L. M.	1423
Schwartz, Daniel T.	1516
Seki, Minoru	515, 1052, 1172, 1178, 1211
Sekimori, Yukimitsu	1124
Sekine, Kazuhiko	1561
Senez, Vincent	738
Seo, Hye K.	266
Seong, Woo-Kyeong	705, 1295
Serdy, Jim	951
Seto, Yasuo	338
Shackman, Jonathan G.	849, 912
Shadpour, Hamed	1456, 1570
Shah, Jayna J.	1465
Shastry, Ashutosh	25, 122, 263
Shaw, Josephine	1417
Shea, Kenneth J.	699
Shepherd, Heather	125
Shibamura, Tetsuya	1172
Shih, Jason	633, 1573
Shih, Yihshing	831
Shiku, Hitoshi	645, 942
Shim, Jeoyoung	762
Shimizu, Kyousuke	885
Shimizu, Tatsuya	1133
Shimizu, Toshimi	233
Shimoyama, Isao	1402
Shimura, Kiyohito	939
Shin, Dong-sik	1295
Shin, Kyung Sik	1160
Shin, Weon Gyu	1411
Shin, Young Shik	1351
Shinbo, Toshio	966
Shinohara, Etsuo	1420

- Shinohara, Hidetoshi 158
Shinohara, Kazuyuki 747
Shinohara, Yasuo 813, 903, 1005,
 1121
Shintaku, Hirofumi 131, 681
Shiraishi, Toshiharu 1211
Shirasaki, Yoshitaka 512
Shirouzu, Mikako 1211
Shirtcliffe, Neil J. 200, 1339
Shiu, Jau-Yeh 197
Shoji, Shuichi 86, 158, 362, 500, 512,
 603, 630, 1002
Shu, Chih-Wen 1489
Shuzo, Masaki 1402
Sibarani, James 212
Sikanen, Tiina 380, 597
Sim, Tae Seok 1241
Sim, Woo-Young 1543
Simmons, Blake A. 155, 470, 987
Simon, Andrew 1026
Simoncelli, Alessandro 1501, 1504
Singh, Amerendra K. 975
Singh, Anup K. 549
Sinquin, Yann 452
Sinskey, Anthony 996
Sinville, Rondedrick 1450
Sisson, John C. 1411
Situma, Catherine 1205
Sivanesan, Ponniah 1579
Skipper, Paul L. 1076
Sklavounos, Angelique 1238
Slovakova, Marcela 350
Smadja, Claire 350
Smith, A. Ezekial 1187
Smith, godfrey 963
Smith, W Ewen 855
Snakenborg, Detlef 503, 1390, 1549
Söderberg, Ola 4, 422
Soh, H. T. 975, 1142, 1489
Sohn, Lydia L. 1145, 1309
Somei, Kotaro 1151
Someya, Atsushi 1211
Sommer, Greg J. 915
Son, Oh-Taek 416
Son, Sang Uk 128, 978
Song, Seung Yeon 311
Song, T. 1579
Song, Tao 1579
Song, Wuzhou 528
Song, Yong-Ak 1076
Song, Young Soo 95
Soper, Steven A. 1205, 1223, 1450,
 1456, 1570
Sordel, Thomas 452
Sprinkels, Ad 425
Srinivasan, Uthara 230
Srivastava, Nimisha 708
Ssenyange, Solomon 254
Stachowiak, Jeanne C. 308
Stachowiak, Timothy B. 227
Steiger, Reinhard 999
Steigert, Juergen 329, 819, 1555
Stein, Derek 807
Steinecker, William H. 1037
Stemme, Göran 1226, 1507, 1510
Stenberg, Johan 723
Stone, Michele R. 1444
Studer, Vincent 7
Sturm, James C. 1014
Su, Yu-Chuan 1459
Sudor, Jan 74, 194
Suematsu, Hiroto 879
Sueyoshi, Kenji 365, 374
Sugii, Yasuhiko 107
Sugio, Shigetoshi 1211
Sugiura, Shinji 966
Sugiyama, Susumu 1435
Sui, Guodong 1023
Sumaru, Kimio 966
Sumino, Tatsuo 443
Sun, Kyung 248, 1175, 1387
Sundberg, Scott O. 1441
Sundin, Melker 47
Suo, Yue 1043
Suzuki, Hiroaki 182, 534, 1354, 1363,
 1393
Suzuki, Kenji 19
Suzuki, Koichi 924

Suzuki, Masaé	413	Tanahashi, Akihito	1360
Suzuki, Masato	942	Tanaka, Masato	1121
Suzuki, Masayasu	756	Tanaka, Ryoji	879
Suzuki, Takaaki	131, 681, 804, 1498	Tanaka, Yo	1133
Suzuki, Takafumi	362	Tanaka, Yuki	4, 10, 1008
Suzuki, Yasuo	630	Tandon, Karman L.	825
Suzuki Yukihito	86	Tang, Kum Cheong	600
Svec, Frantisek	227	Tang, Kum-Cheong	434
Syed, Yusef A.	1187	Tanibata, Kazuki	804
T		Tanino, Katsumi	960
Tabata, Kazuhito V.	1363	Tannenbaum, Steven R.	1076
Tabeling, Patrick	77, 80, 98	Tapsoba, Issa	981
Tabourier, Pierre	651, 771	Tarasow, Theodore M.	1142
Tachi, Tomoya	816	Tas, Niels R.	615
Tada, Yuichi	966	Tasselli, Josiane	188
Tagaya, Yoichi	1017	Tatar, Florin	909
Tahhan, Isam	146, 359	Tatoulian, Michaël	80
Tai, Yu-Chong	176, 633, 702, 834, 1573	Taverna, Myriam	350
Takagi, Fumio	579	Taylor, Clive R.	1082
Takagi, Toshiyuki	966	Taylor, Justine	254
Takahashi, Yutaka	879	Taylor, Ryan	1148
Takahashi, Yuya	1315	Tegenfeldt, Jonas O.	696, 930, 1034
Takai, Madoka	212, 215, 335, 885	Terabe, Shigeru	299, 356, 1032, 1199
Takaishi, Masayuki	1199	Thariani, Rahber	1256
Takamura, Akimasa	479	Thomy, Vincent	651, 771
Takamura, Yuzuru	497, 780, 900, 1462, 1528	Thorslund, Sara	326
Takashima, Kazunori	104, 1525	Tiggelaar, Roald M.	783
Takayama, Michio	1118	Tixier-Mita, Agnés	182, 1393
Takeda, Seigi	356	Tobita, Tatsuya	756
Takei, Go	245	Toft, Katrine N.	1390
Takekawa, Tetsuya	1462, 1528	Togashi, Shigenori	338
Takenaka, Kei	594	Togo, Makoto	479
Takeuchi, Shoji	182, 290, 509, 534, 591, 1354, 1363, 1393, 1534	Tok, Jeffrey B.-H.	1142
Takiguchi, Hiromi	726, 1318	Tokeshi, Manabu	59, 353, 395, 401, 798, 813, 816, 843, 903
Talen, Wim	218, 561	Tolley, Michael T.	1552
Talu, Esra	822	Tomer, Mehmet	1561
Tamaoki, Soichiro	1435	Tomizawa, Yuichi	900
Tamiya, Eiichi	497, 780, 900, 957, 960, 1462, 1528	Tompkins, Ronald	1561
Tan, Helen M. L.	173	Toner, Mehmet	1513
Tan, Wei-Heong	290, 509, 591	Toriello, Nicholas M.	1453

- Trevisol, Emmanuelle 1217
Tsao, Chia-Wen 1579
Tseng, Fan-Gang 161, 591, 1372, 954
Tseng, Hao-Yu 1348
Tseng, Hsian-Rong 1023
Tseng, Wei-Yu 1190
Tsuchiya, Hidenori 1420
Tsuge, Kouichiro 338
Tsuiji, Toshiyuki 1112
Tsukahara, Takehiko 546, 993, 1324
Tsunazawa, Yoshio 765
Tsunoda, Kin-ichi 392, 726, 1318
Tsutsui, Hideaki 242
Tuantranont, Adisorn 140
Tuomikoski, Santeri 380
Twardowski, Mariusz 1043
- U**
- Uchiyama, Kenji 59, 798
Ueno, Kunimitu 900
Ueno, Masaharu 1327
Ueno, Taro 603
Ulfendahl, Mats 464
Umeda, Mamoru 843
Umemura, Tomonari 726
Urban, Gerald A. 377
Ustun, Cevat 702
Utsumi, Hiroaki 879
- V**
- Vahey, Michael D. 1058
Valero, Ana 22
van Dedem, Gijs W.K. 729
van Delft, Koen M. 615
van den Berg, Albert 22, 83, 425, 615, 729, 783, 1381
Van der Heyden, Frank H.J. 807
van der Krogt, M. C. 666
Van der Linden, Anthony J. 218
van der Wielen, Luuk A.M. 729
van der Wouden, Egbert J. 83
van Gulik, Walter M. 729
van Hest, Jan C.M. 870
van Hest, Jan C.M. 867
van Hylckama Vlieg, Johan E.T. 425
van Leeuwen, Michiel 729
- van Nieuwkastele, Jan W. 22
van Oosten, Casper L. 221
Vandevyver, Caroline 428
Venkataraman, V. 777
Verboom, Willem 783
Verdoy, Dolores 1423
Verlpanck, Nicolas 771
Vermes, Istvan 1381
Vestergaard, Bente 1390
Vickers, Jonathon J 224
Vieider, Christian 464
Viel, Lisan 1142
Vilar, Ramon 876
Vinet, Francoise 74
Vineyard, Laura 951
Viovy, Jean-Louis 350, 386, 1220
Vitalis, Tania 7
Vogel, Viola 518
Voldman, Joel 1058, 1061, 1483
von Germar, Frithjof 476, 1522
Vreeland, Wyatt N. 119, 251
Vukasinovic, Jelena 624
Vulto, Paul 377
- W**
- Wada, H. Garrett 831
Wada, Yukihisa 765
Wakao, Sou 404
Wakida, Shin-ichi 374, 852
Walczak, Rafal 741
Wallace, Danid B. 1139
Wallman, Lars 1468
Wallow, Thomas I. 155
Wang, Chiaochun Joanne 1576
Wang, Jean Y. J. 1489
Wang, Jian-Hua 1232
Wang, Lee-Ping 1495
Wang, Lisen 567
Wang, Min S. 948
Wang, Wanjun 1223
Wang, Wei 543
Wang, Xuhua 522, 720, 753
Wangler, Nicolai 999
Warrick, Jay 1564
Washabaugh, Peter D. 1037

- Washizu, Masao 16, 458, 1498
Watanabe, Mitsuo 831
Wei, Qihuo 1193
Wei, Xingtao 494
Weiner, Michael P. 1043
Wen, Jian 272
Weng, Chen-Hsun 717
Whittemore, Megan 951
Whitton, andrew 1306
Wiklund, Martin 446, 449
Wilderbeek, Hans T.A. 218, 561
Wiles, Charlotte 861
Willaime, Hervé 77, 80
Wise, Kensall D. 1037
Wisitsoraat, Anurat 140
Wisztorski, Maxence 771
Witek, Małgorzata A. 1456
Wittwer, Carl T. 1441
Wong, Pak Kin 969
Wong, Sek-Man 317
Woo, Seong Ihl 473
Wood, Robert J. 1342
Woottton, Robert C.R. 795, 873
Wu, Biyun 1184
Wu, Cheng-Tar 717
Wu, Jhy-wen 639
Wu, Li-Qun 1250
Wu, Liz Y. 1011, 1378, 1477
Wu, Ming 1444
Wu, Pei-Ming 1546
Wu, Ren-Guei 954
Wu, Zhigang 1097
Wubbolts, Marcel G. 867
- X**
- Xie, Ling 317
Xu, Dongsheng 543
Xu, Yan 215
Xu, Zhang-Run 1232
- Y**
- Yager, Paul 825, 1256, 1286
Yamada, Akira 684
Yamada, Masumi 515, 1052, 1172, 1178
Yamaguchi, Yoshiko 1336
- Yamahata, Christophe 182, 1393, 1588
Yamamoto, Hideo 1498
Yamamoto, Takatoki 1151
Yamamoto, Tamotsu 497
Yamamura, Shohei 957, 960, 1214
Yamanaka, Keiichiro 1462, 1528
Yamanaka, Nozomu 1354
Yamato, Masayuki 1133
Yamauchi, Ryuji 233
Yamazaki, Hiroki 1420
Yan, D.G. 89
Yang, Bozhi 92
Yang, C. 89
Yang, Chih-Hui 1115
Yang, Chung-Shi 954, 1372
Yang, Eun Gyeong 768
Yang, Haesik 1100
Yang, Kwangsuk 888
Yang, Mo 690, 1301
Yang, Ren 1223
Yang, Sang-Sik 1543
Yang, Sang-Youn 1100
Yang, Shuang 1579
Yang, Sung 1154
Yao, Nan-kuang 639
Yap, Eric Peng Huat 528, 1097
Yasuda, Masahiro 515, 1172, 1178
Yasuda, Takashi 440, 747
Yasukawa, Tomoyuki 645, 942
Yeung, Edward S. 1
Yeung, Siu-Wai 711
Yi, Zhang 1088
Yim, Yoon J. 461
Yobas, Levent 56, 317, 323, 434, 600, 732
Yokokawa, Ryuji 1435
Yokota, Yoshimi 302
Yokoyama, Shigeyuki 1211
Yokoyama, Yoshiyuki 960
Yoo, Kyutae 762
Yoon, Dae Sung 768, 810
Yoon, Eui Soo 1157
Yoon, Euisik 762

- Yoon, Hyun C. 311, 341
Yoon, Sang Youl 1154
Yoon, Tae-Ho 660
Yoshida, Makoto 482
Yoshida, Naoya 1199
Yoshimi, Yasuo 966
Yue, Rui Feng 1226
Yun, Hoyoung 281, 1351
Yusuru, Takamura 1214
- Z**
- Zagnoni, Michele 1342
Zalewski, Dawid R. 927
Zamir, Lee 1561
Zellers, Edward T. 1037
Zendejas, Frank J. 230
Zeng, Yong 1020
Zengerle, Roland 53, 329, 570, 819, 999, 1555
Zenhausern, Frederic 1193
Zevenbergen, Marcel A.G. 654
Zhang , X. M. 528
Zhang, Chunyan 332
Zhang, Lujun 909
Zhang, Mimi Y. 1477
Zhang, Xiaojing 1411
Zhang, Xin 164, 167, 437, 1301
Zhang, Yanting 1142
Zhang, Yong 395
Zhang, Zhiyu 996, 1549
Zhao, Jian-Long 50
Zhao, Yi 164, 167
Zhao, Yuezun 31
Zheludev, Nickolay 1307
Zhen Wang 1447
Zheng, Jinjian 1
Zheng, Xiaoyu 167
Zhi, Zheng-liang 1214
Zhong, Chong-Hui 1232
Zhou, Zhengrong 1184
Zhu, Bingmei 395
Zhu, Liang 419
Zhu, Likun 714
Zhuang, Gui-Sheng 41, 50
Zimmermann, Martin 612

SUBJECT INDEX

- μPLAT 672, 675
μTAS 594
1,4-dioxane 395
10-directional switching valve 1112
1-anilino-8-naphthalene sulfonate 1318
2-C LIF 1304
2-D PAGE 1579
2D-SPR 756
2-methacryloxyethylphosphorylcholine (MPC) polymer 885
2MPC brush 212
3D 1519, 1507
3D cell culture 1540
3D impellor 1139
3D microfluidic integration 188
3D microstructure 846
3D sheath flow 512, 630
3D3C 65
3-dimensional flow 71
- A**
- ABC transporter 1363
absolute negative mobility 648
absorbance 1277
AC electrokinetic pump 1480
AC electroosmosis 1103
accelerator mass spectrometry (AMS)
 1076
accuracy 296
accurate sorting 512
acetylacetone 1324
acoustic node formation 13
acoustic radiation force 47, 627
acoustic separation 314
acoustic streaming 47, 116
acoustic trapping 1055
action potential 963
active mixer 1103
active mixing 116
active valve 1106
actuators 278
adsorption 227, 236
- affinity chromatography 389, 939
AFM 1528
Ag/AgCl microelectrode 576
agar salt bridge 576
AIDS diagnosis 1561
alignment 275
allergy 320, 858
amphetamines 936
anatase 873
angular momentum 68
animal breeding 431
anisotropy 519
Antibody detection 1082
apheresis 314
Aplysia 1402
apoptosis 416, 1381
aptamer 1142
Aquaporin 1354
aqueous two-phase 95, 918
array 1026
artificial cell 1399
artificial kidney 1094
artificial life 1408
artificial lipid bilayer 1363
artificial muscles 278
artificial pore 1309
artificial renal microchip 1094
artificial vessel 248
artificial-cilia 561
artificial cell 1375
asymmetric reaction 804
atomic emission spectrometer 497
ATP 488
ATR-readout 329
autofluorescence 380
automated data analysis 1390
automatic design 113
automation 1220, 1211, 1564
autonomous 612
- B**
- B- to A-DNA conversion 1396

bacteria	338, 347, 443, 455, 482
bacterial infection detection	840
bacterial spore	987
bacterium	443
band-pass filter	1064
barcoding	1214
batch process	275
B-cell	960
bead	1241, 606, 855
bead-based analysis	1283
bilayer lipid membrane	531, 1342
bilayers	1366
bioarray	185
biocatalysis	867
biochemical pulses	990
biochip	467, 1474
biocompatible	684, 687
biodegradable polymer	684
biofluid-activated battery	287
bio-fouling	263
biofuel cell	479
biogenic compounds	924
biointerface	335
biological agents	476
biological sensing	1259
bioluminescence	488, 744
biomarker	831, 1205, 1453, 1468
bioMEMS	987, 1154, 1405, 1414, 1519
bio-microactuator	1133
biomolecular interaction detection	759
biomolecular motors	1265, 1384
biomolecule separation	519
biomolecule trapping	900
biomolecules sorter	512
biosensor	810, 1100, 1268, 1295
biosilification	230
biosurface interactions	651
biotin	1100
black photoresist	591
blastocyst	431
blood	272, 314, 359
blood cell separation	1052
blood collection	1558
blood compatibility	248
blood plasma	1154
blood sugar monitoring	813
bonding	155, 422, 464, 681, 1423
bone tissue engineering	1537
borate ion	813
Brownian motion	525
Brownina ratchet	525
B-type natriuretic peptide	302
bubble	1121
bubble actuator	657
bubble-free priming	1555
buffer capacitance	83
BVD Circuits	837
C	
Ca ²⁺ concentration	1402
cage	1504
caged fluorescent dye	801
calcium alginate gel	1172
calorimetric measurement	1558
cancer diagnosis	1235
cantilever	810
capacitive sensing	1259
capillary action	597
capillary burst valve	852
capillary electrochromatography	356
capillary electrophoresis	356, 849, 912, 927, 1567
capillary electrophoresis (CE)	1453
capillary filling	615
capillary force	341
capillary force	1199
capillary pump	612
capillary stop	576
capillary-assembled microchip	299, 356, 1199
capillary-driven flow	1100
carbamates	1029
carbon dioxide	978
carbon nano-electrode	678
Carbon nanotubes (CNTs)	954
carbon paper	473
carbonylation	876
cardiac markers	819

cardiomyocyte	437, 963, 1133, 1405,
1414	
cardiomyocyte hypertrophy	1301
cardiovascular monitor	1546
cascade	1091
case II diffusion	155
catalysis	870
cavitation streaming	116
CD4 cells	326
CD4 count	1561
CDROM	1555
CE-EC	1244
cell	1504, 1510
cell adhesion	197, 269, 993
cell aggregation	446
cell analysis	630, 1178, 1576
cell array	197, 981, 1372, 1378
cell chip	756
cell concentration	347
cell cultivation	1172
cell culture	260, 431, 464, 945, 978,
1008, 1378, 1519, 1576	
cell culture array	1477
cell culture chip	1387
cell cycle	413, 1489
cell differentiation	440, 993
cell disruption	1235
cell handling	407, 446, 449
cell incubator	978
cell lysis	347, 428
cell manipulation	368, 942, 1474
cell membrane	1375
cell microinjection	1492
cell migration	972
cell patterning	173, 242, 972, 1537
cell separation	455, 1058
cell sheet	1133
cell signaling	1486
cell sorting	515, 567, 984, 1097, 1187,
1483	
cell synchronization	1489
cell to cell communication	642
cell trapping	642, 675, 1172, 1372,
1477, 1516	
cell viability	449
cell-adhesion	942
cell-based assay	972, 951, 1540
cell-MEMS	1543
cells	458, 540, 1043, 1507
cellular interactions	1381
cellulose	236
cellulose derivative	401
centrifugal	642
centrifugal flow	852
centrifugal microfluidics	570, 819,
1555	
centrifugal processing	329
centrifugal separation	642
centrifugation	1501, 1522
channel configuration	1017
channel fabrication	699
chaotic advection	371, 621
charge current	1244
charge inversion	807
check valve	1112, 1175, 1372
chemical energy	1405, 1414
chemical microgradients	1181
chemical sensing	1259
chemical stimulation	440
chemical synthesis	879
chemiluminescence	744, 753, 1202
chemotaxis	1513
chiral analysis	1582
chiral separation	362
chitosan	1250
chromosome	1462, 1528
cilia	1510
circular dichroism	1582
clinical chip	1558
clinical test	858
coating	401
cobalt electrode	467
co-cultivation	942
collection	338
colloid	257, 789
colloidal self-assembly	1020
comoss injection	564
compartmented cultures	948

competitive immunoassay	825
compliance	92
compound formation	882
computational modeling	62
computer-aided design	1360
concentration	455, 606, 987
concentration gradient	1160, 1540
condensation	1336
conductivity	708
conductivity gradient	1058
confocal detection	723
confocal microscope	792
confocal microscopy	65
conformational change	1525
consistency	296
contact angle	107
contact angle hysteresis	122
contact deposition	1217
continuous flow	618, 918, 1220, 1426
continuous-flow cell sorting	1489
continuous-flow screening	1058
contrast agents	822
controlled release	1002
copolymer	242
cototoxicity	1160
Coulter counter	182, 485
cross-flow	323
cross-flow electrophoresis	828
crowded agent	600
CRP	810
CRP antibody-antigen reaction	780
crystallization	1211
culture	1507
current collector	473
Cy5	1423
cyclic olefin copolymer	203
cytometry	984, 1091
D	
DDM	236
DDMS	663
dead-end filling	44
decoupler	1244
deformability	461
deionizer	368
denaturant	894
dendrimer	311
density grating	765
desalting	888
detachable connector	191
detection	338, 419
dextran	28
DGGE	894
diagnostics	831, 843
diamagnetism	110
diaphragm	1106
dielectric constant	1324
dielectric elastomer	278
dielectric heating	1465
dielectric spectroscopy	738
dielectrophoresis	34, 37, 125, 368, 383, 398, 437, 455, 470, 567, 582, 645, 765, 909, 942, 1040, 1058, 1142, 1166, 1187, 1474, 1480, 1489, 1501, 1504, 1537
differential extraction	1055
differential impedance spectroscopy	1292
differentiation	1008
diffraction	1306
diffraction grating	1274
diffusion	1079, 1438
digestion	350
digital matter	1552
digital microfluidics	98, 125, 582, 786, 1046
digital pneumatic logic	506
dihexyl-N,N-diethylcarbamoylmethyl- phosphonate	1315
DIOS-MS	771
directional control	1384
Disposable	1226
disposable diagnostics	753
dissolved oxygen	494
DNA	16, 383, 828, 1306, 519, 1396, 912, 1426, 19, 1005, 1020, 1588, 1399, 1465
DNA analysis	696
DNA chip	762

DNA detection	206
DNA electrophoresis	386
DNA extraction	428, 840
DNA hybridization	1079, 1585
DNA manipulation	1525
DNA melting	1441
DNA melting analysis	1444
DNA purification	272
DNA separation	660, 885, 894
DNA sequencing	1567
DNA size separation	404
DNA stretching	16, 1396, 1525
DNA-binding protein	903
DNA-polymer conjugate	389
dopamine	1250
double emulsions	80, 230, 591
double T-junction	1190
DRGs	948
drop	708
drop-and-sip	1199
droplet	56, 65, 77, 95, 98, 125, 128, 332, 570, 609, 699, 1002, 1043, 1088, 1190, 1220
droplet generation	86, 134, 1046
droplet manipulation	428
droplet microfluidics	122, 263, 585
droplet mixing	1040
drop-on-demand	1076
drosophila	1411
drug delivery	308, 633, 1002, 1148, 1531
drug discovery	1011
drug monitoring	816
drug screening	1008, 1262
dynamic coating	236
dynamic fluidic signals,	1109
dynamic mixers	1109
E	
E-beam lithography	678
EHID	1076
electroactive polymers	278
electric double layer	101, 801
electric field	104, 1384, 1420
electrocapture	606
electrochemical analysis	981
electrochemical detection	224, 678, 885
electrochemical impedance spectroscopy	759
electrochemical method	846, 972
electrochemical sensing	654, 729
electrochemistry	254, 645, 711, 774, 1286
electrodeless dielectrophoresis	909
electroformation	1534
electrohydrodynamic	125
electrokinetic	368, 1447
electrokinetic control	95
electrokinetic flow	789
electrokinetic injection	41
electrokinetic separation	927
electrokinetic transport	933
electrokinetic trapping	50
electroless plating	675
electrolysis	657, 1184
electrolysis pump	633
electronic sensing	1309
electroosmosis	1166, 1588
electro-osmotic controlled	1097
electroosmotic flow	74, 215, 239, 380, 636, 894
electroosmotic pump	1157
electrophoresis	380, 404, 813, 894, 897, 1121, 1151, 1166, 1456, 1588
electrophoretic filtration	377
electrophoretic flow	1304
electrophoretic mobility	413
electrophysiology	531, 1342
electrophysiology on-chip	576
electroporation	22, 25, 458, 1480, 1495, 1498
electrospinning	1094
electrospray	597
electrospray deposition	335
electrospray mass spectrometry	254
electrostatic actuation	594, 1181
electrostatics	561
electrotransfection	1351

- electrowetting 125, 128, 582, 1046
ELISA 299, 639, 819, 1235, 1522
elongational index 461
emboss 693
embryo 431
emulsion 98, 77
emulsion-templating 230
encapsulation 1471
encoded particle 1306
endocrine disrupter 804
endonuclease V 1450
endothelin-1 1301
energy conversion 287
enhanced light transmission 666
environmental analysis 491
enzymatic analysis 341
enzyme 479
enzyme assay 849
enzyme hydrolysis 1336
enzyme inhibition assays 1136
enzyme sensor 747
EO2 1061
EOF 83, 861
equation of continuity 65
ESI interface 924
etching 152, 254, 1014
etching anisotropy 137
evanescent wave 101, 801
evaporation-driven flow 996
EWOD 31, 128, 134, 771, 1046
extended-nano space 546, 1324
extensional flow 461
extraction ... 900, 1127, 1315, 1366, 1522
- F**
- fabrication 693, 1169
Fabry-Perot cavity 528
Fabry-Perot interferometer 615
FACS 984
FEFC 83
FEM 92
femtoliter microchamber 1429
femtosecond laser machining 13
ferrocene-dUTP 711
ferromagnetic 1139
ferromagnetic actuation 1229
field constriction 458
field effect transistor 762
filter 359, 485, 1235
filtration 1127, 1169
Fine Needle aspiration (FNa) 837
flow 597, 1510
flow control 933, 1124, 1573
flow cytometry 422, 567
flow dampening 1064
flow field fractionation 119
flow injection analysis 491, 1130, 1232
flow instability 537
flow modulation 1148
flow oder control 639
flow rate 612, 963
flow rectifier 1064
flow sensor 1573
flow velocimeter 1271, 1298
flow velocity measurement 170
flow-focusing 56
flow-type micro cell chip 966
fluid manipulation 1026
fluid slip 789
fluidic 113, 1336
fluidic capacitor 1064
fluidic interconnections 152
fluidic interface 1549
fluidic resistor 92
fluidic timer 1064
fluid-structure interaction 92, 621
fluorescence 101, 1082, 1402, 1423, 1501
fluorescence detection 720, 777, 1435, 1522
fluorescence polarization 816
fluorine-enhanced oxidation 167
forensic science 1055
forensic toxicology 936
fraction collection 927
fractionation 927, 1447
free flow electrophoresis 921
freezing point 1327

fret	1321
fusion	1190
G	
gas chromatography	936
gas-liquid reaction	876
gate microvalve	1163
gel	233, 1247
gel electrophoresis	1579
gel formation	1172
gelatin	1115
gene delivery	284
gene expression	7
gene expression dynamics	969
gene transfection	22, 1369
genetic algorithm	281
genetic analysis	1040, 1567
Genetic manipulation	482
genotyping	1444
geometrical anisotropy	1049
GFP assay	413
giant liposome	1354
gigaseal	434, 1534
glass chip	140
glass microfabrication	152
glucose sensor	266
glycosaminoglycan isomer	395
GNEE	1244
gold nanoparticle	206, 305, 750, 1289
gold-capped nanoparticle layer chip .	780
gradient	1178, 1507, 1513
grafting	212
graphitic carbon	254
gravity-driven	639
green fluorescence protein	1008
Griess-Saltzman Reaction	726
gyration radius	404
H	
handheld	1229
heart	1133
heat-controlled microelectrode	311
heat-sensitive polymer	311
heavy metal	1127
HeLa cell	28
hematocrit	1555
hemolycin	1393
heparin	248, 326
hepatocyte	1477
heterodyne detection	1298
high AR nanochannel	13
high efficiency	25
high performance	53
high speed sorter	512
high throughput	410
high throughput screening	500, 1564
High viability	25
high-pressure	783
high-resolution	684
high-speed	684
high-throughput	401, 1390
high-throughput screening	975, 999, 1178
HIV	326
hollow sphere	1133
hot embossing	143, 158
HPTS	1202
HTS	999
human IgE	320
human mesenchymal stem cell(hMSC) ...	1387
Hybrid microstereolithography	1112
Hybrid Si/polymer integration	188
hybrid tooling	146
hybridization	1306, 1321
hydrodynamic filtration	1052
hydrodynamic focusing	1208, 1540
hydrodynamic spreading	1097
hydrodynamic switch	570
hydrodynamic trapping	1378
Hydro-dynamic traps	509
hydrogel	657
hydrogel bead	1471
hydrogenation	882
hydrophilic	194
hydrophilic hybrid polymer	660
hydrophobic contrast	194
hydrophobic plating	1118
hydrophobicity	672
hyperbolic converging	461

hypoxia	1519
I	
iDEP	398
IgG	756
image analysis	449
immunoassay	224, 299, 305, 335, 344, 612, 618, 816, 831, 843, 852, 912, 1082, 1229, 1241, 1576
immunocapture	350
immunoglobulin A	852
immunosensor	302
impedance	987, 1306
impedance sensing	1301, 1283
impedance spectroscopy	729
implant	633
implantable	479
in situ click chemistry	1023
in vitro fertilization	431
in vivo	834
inclined UV lithography	687, 1498
incubator	624
industrial standard	296
infrared	1432
injection molding	146, 422, 1468
injury potential	948
inkjet	579
inlet pressure	1100
in-situ	1298
in-situ photopolymerization	1175
integrated	56
integrated detection	753
integrated micro system	1208
integrated micropump	1037
integrated microreactors	1023
integrated optics	1312
integrated processes	1453
integrated reference electrode	576
integration	503, 720, 1040, 1232
interface	879, 1220
interfacial tension	107
intermediates	879
intracellular	1495
intracellular recording	1357
Intraocular pressure	834
in-vitro selection	975, 1142
ion channel	531
ion current	452
ion depletion	522
ion depletion bridge	50
ion diffusion	801
ion extraction	368
ionic liquids	870
ionization	597
IR heating	588
IR laser	104
isoelectric focusing	921, 939, 1447, 1579
isolation	443
isotachophoresis	831, 897
J	
Janus droplet	1049
jet injector	308
joule heating	915
K	
kinetic	786, 1411
L	
LabChip device	1444
label free optical detection	470
label-free	1283
label-free detection	762
label-free optical sensor	780
lab-on-a-chip	7, 31, 68, 359, 588, 618, 657, 717, 1088, 1247, 1456, 1501, 1504
lab-on-a-display	34
laminar flow	491, 744
lanthanoid(III)	1315
Laplace pressure	245
large-size protein crystal	1420
laser	1121, 1256
laser induced fluorescence	792
laser micromachining	185
laser radiation pressure	906
latching valves	506
lateral	434
lateral cell separation	567
LDEP	134
leukemia	410
levitation	110

life-support	1408
lift-off technique	666
ligase detection reaction	1450
lipid	1366
lipid membrane	534
lipid nanotube	233
lipoplex	1369
liposome	119, 251, 1399
liquid chromatography	564, 1573
liquid core waveguide	726
liquid crystal display (LCD)	34
liquid droplet	594
liquid electrode plasma	497
liquid extraction	891
liquid jet dispenser	534
liquid phase detection	1435
liquid router	570
liquid/liquid optical waveguide	1318
liquid-liquid extraction	1029
live/dead assay	1043
living cell	528, 954
LOC	663
logarithmic dilution	1160
lotus leaf	161
low Reynolds number	116
low-power	1061
LSPR	780
luciferase	488
lysis	37, 1504
M	
magnesium ions	1429
magnetic bead	350, 386, 1348
magnetic carrier	558
magnetic cell sorting	975
magnetic particle	344, 428, 609, 1088
magnetism	675
magnetohydrodynamic pumping	1067
magnetophoretic immunoassay	320
MALDI	786
manipulation	1462, 1528
Mapping	750
Marangoni flow	585
masking	140
mass spectrometry	152, 924, 1468,
	1570
mass transfer	693
MCTS	1011
measurement	1247
mechanistic model	1513
mechanobiology	1414
mechanoelectrical feedback	963
medical imaging	876
membrane	44, 549, 693, 1169, 1259
membrane poration	1417
membrane protein	1393
MEMS	323, 573
mesoporous platinum	266
metabolic	482
micro array chip	960
micro bead assays	53
micro bio Fuel cell	482
micro cell stimulator	1543
micro chemical chip	1196
micro connector	191
micro device	879
micro direct methanol fuel cell	473
micro dispenser	1112
micro droplet generator	1076
micro electroporation	28
micro flow	534
micro gas chromatograph	1037
micro mesh	630
micro mixer	618
micro optics	332
micro particle sampler	31
micro PCR	332
micro pinch valve	1432
micro PIV	239
micro reactor	861
micro total cell culturing system	1175
micro valve	1118
microactuator	621, 1414
microarray	19, 329, 407, 509, 735, 750, 756, 1214
microbeads	185
microbial	419
microbial cell culture	996
microbial culture chip	425

- microbioreactor 951, 996
microbubble 509, 822
microcantilever 768, 1250
microcapillary 1351
microcapsule 1002
microcarrier 1486
microchamber 290, 1354
microchamber array 1363, 1462
microchannel 59, 281, 681, 798, 846,
 966, 1154, 1351
microchannel bend 359
microchemical system 537
microchip 813, 816, 1005
microchip electrophoresis 224, 353,
 362, 365, 395, 885, 903, 924, 1017,
 1450
microchip electrophoretic Mobility Shift
 Assay (microEMSA) 903
microchip integration 840
microchip micellar electrokinetic chromato
 graphy 374
microchip-PCR 777
microcoils 558, 1145
microcontact printing 19, 1399
microdevice 606
microdialysis 888
microdroplet 110, 651, 864, 1369,
 1471
microelectrode 494, 945, 1103
microELISA 858
microenvironment 1519
microfabrication 473, 479, 1214,
 1330
microfilter 323, 419, 609
microflow system 603
microfluidic cell sorter 416
microfluidic centrifugation 543
microfluidic channel 497, 1438, 1534
microfluidic chip 338, 639, 681, 1471
microfluidic computers 1408
microfluidic device 185, 212, 311,
 488, 515, 645, 669, 957, 1052, 1178
microfluidic devices 669
microfluidic mixing 116
microfluidic reactor array 1211
microfluidic structures 47
microfluidic-chip 789
microfluidics 37, 41, 44, 59, 68, 71,
 74, 98, 107, 128, 140, 155, 170, 179,
 224, 272, 278, 329, 371, 383, 419, 561,
 573, 588, 600, 624, 627, 636, 657, 717,
 798, 822, 828, 855, 930, 969, 987, 990,
 999, 1034, 1049, 1082, 1085, 1091,
 1115, 1136, 1145, 1163, 1181, 1184,
 1190, 1202, 1205, 1223, 1232, 1280,
 1345, 1411, 1456, 1459, 1492, 1516,
 1552, 1588
microgradient 1184
microheater 1241
microhole 1375
microlens 1253, 1271
micromachining 173, 1130
micromanipulation 233
micromixing 104, 651, 1103, 1369
microneedle 687, 1531
microorganism 443
microparticles 1283
micropatterning 164, 194, 269, 942
microPCR 609
micropillar array 597
micro-PIV 47, 65, 89, 131, 792
microplasma 173
micropore 182, 266
micropump 104, 573, 579, 636, 717,
 1061, 1175, 1226, 1232
microreactor 257, 741, 783, 795, 873,
 1369
microreactor array 290
microscale 891
microscale gas-liquid flow 537
microscopy 1256
microsensor 1546
microsputtering 774
microstructured membrane 1513
microsystem 476, 945
microtile 1552
microtool 233
microtube 248

- microtubules 1265, 1384
microtweezer 1462, 1528
microvalve 440, 503, 996, 1037, 1130,
 1148
microwave 1465
microwave dielectric heating 1238
microwell array 242, 500, 1483
microwire 1067
milling 146
miniaturization 392
miniaturized assays 999
MIP 717
mitochondrial 10
mixer 113, 582, 600, 621, 1139, 1348
modeling 1588
molding 161
molecular assay 744
molecular beacon 969, 1321
molecular filter 900
molecular imprinted polymer 891
molecular medicine 1495
molecular motor 1360
molecular nanomedicine 284
molecular surgery 16
molecular sieving 1020
monodispersed droplets 591
monolithic 272
motherboard 1549
MPC polymer 335
mRNA-protein fusion 209
multi droplet 1151
multi sample recognition 389
multifilament 392
multifunctional envelope-type nano device
 1005
multilayer flow 59, 798
multiparametric sensing 1199
multi-phase 867, 870
multi-phase flow 107
multiphase microfluidic 537
multiplex separations 912
multiplexing 506, 957, 1214, 1223
multi-step synthesis 1029
multivalent interaction 1289
multiwell tissue culture plate 951
mutation scanning 1441
N
nano channel 1274
nano imprint lithography 143
nano patterning 993
nano wet etching 50
nano-biodevice 1121
nanobridge array 705
nanochannel 149, 522, 615, 1157,
 1193
nanofabrication 143, 654, 678, 1552
nanofiber 1094, 1387
nanofluidic 74, 519, 660, 1079, 696,
 615, 807
nanofluidic chip 50, 954
nano-gap actuator 552
nano-hole 440, 747
nano-hole array 666
nanoimprint lithography 149, 1014
nanoliter dispenser 999
nanoliter droplet 134
nanomechanical biodetector 552
nanomechanics 768
nano-microfluidic interface 1193
nanoneedle 1357
nanoparticle 119, 251, 765, 1067
nanopillar 404, 1205
nanopore 182, 266, 549, 1002
nanoprobe 1402, 1528
nanopuncturing 1357
nanoscale 801
nanoscale probe array 37
nanosphere lithography 525
nanostructure 167, 197, 266, 1570
nano-templating 1205
nanowell sensor 1166
nanowire bridge 705
nanowires 771
nebulizer 152
needle-free 308
NEMS 1079
neural probes 702
neural prostheses 702

- neuronal culture 624
 neurotransmitter 747, 954, 1250
 neutrophil 1513
 NFkB 903
 Ni patterning 386
 nicotine 717
 NIL 696
 NIR spectroscopy 741
 nitration reaction 741
 Nitric Oxide 1184
 Nitrite Ion 726
 NMR 546, 879, 1145, 1324
 non linear dynamics 648
 non-biofouling surface 212
 non-contact temperature sensor 777
 Non-cross-linking interaction 206
 non-fouling surfaces 263
 nonlinear electrokinetics 522, 1061
 non-surface-binding 762
 Non-uniform AC field 525
 non-viral gene delivery system 1005
 nozzle 176
 nucleation frequency 497
 nucleic acid 317
 nucleic acid purification 377
 numerical simulation 41
- O**
 ocular 633
 off-lattice Monte-Carlo simulation 1360
 oligonucleotides chips 774
 'on the fly' photopolymerization 248
 on-chip cell electrophoresis 413
 on-chip detection 1432
 on-chip lens 1271
 on-line sample preconcentration 924
 oocyte field effect transistor 1262
 optic connection 1549
 optical chromatography 1085
 optical detection 732, 1298
 optical filters 720
 optical forcing 585
 optical manipulation 906, 1483
 optical measurement 1304
 optical sensor 741
- optical trapping 984
 optical tweezer 68, 233, 1247
 optimal design 281
 optimization 113, 293
 optoelectronic tweezers 34
 opto-electrostatic micro-vortex 104, 1525
 optofluidic 1085, 1483
 optofluidic microchip 528
 organelle trapping 900
 organic iodide 882
 organic solvent 699, 864, 1327
 organix photodiode 753
 orifice 56, 458
 osmosis 1459
 oxygen sensor 467
- P**
 padlock probe 4, 10, 735
 palladium cross-coupling 876
 paper battery 287
 parafilm 161
 parallel 861, 1029
 parallel analysis 344
 parallel reactions 1023
 parallel readout 819
 parallelization 77
 partial filling technique 374
 particle 485
 particle alignment 515
 particle concentrator 398
 particle electrophoresis 89
 particle method 86
 particle motion 62
 particle separation 371, 398, 1097
 particle sorting 648
 particle streak 789
 particle wash 627
 parylene 176, 633, 702, 834, 1534
 passive device 1564
 passive distribution 500
 patch clamp 182, 434, 1393
 pathogen 347, 419
 patterning 245
 PCR 200, 332, 762, 840, 855, 1088,

1220, 1238, 1423, 1426, 1444, 1465	
PDMS autofluorescence	1435
PDMS doping	720
PDMS microchannel	512
PDMS microchip	1381
PDMS microvalves	603
PDMS pneumatic valve	1241
PDMS surface modification	173
PEG hydrogel	242
peptide	768
peptide hydrogel	1540
peptide profiling	1468
perforated membrane filter	31
perfusion chamber	624
peristaltic actuation	573
peristaltic gas pump	1037
permanent magnets	110
personalized medicine	1435
PET imaging probes	1023
pH	792, 1247
pH control	996
phaseguides	377
phase-separation	918
phosphate sensor	467
Phospholipid polymer	215
photocatalysis	873
photocatalyst	245, 804
photochemistry	804
photodefinable PDMS	663
photodetector	714, 1312
photografting	227
photo-induced cell capturing	966
photoiniferter	212
phononics	1085
photooxidization	1330
photopatterning	203
photopolymerization	260
photosensor	1112
photosynthetic	482
photothermal	1277
photothermal detection	1274
photo-thermal lens spectroscopy	1196
photothermal nanoparticle	284
pico-fraction	1121
picoliter compartments	957
piezoelectric	308
piezoelectric actuation	1148
piezoelectric sensor	837
piezoelectric stack actuator	1106
pillar	323
pillar array	564
planar electrode	738
planar patch-clamp	452
plasma	314
plasma initiated patterning	672
plasma surface modification	269
plastic lamination	287
platinum black	747
plug	600
plug'n'play functionality	1549
plymer emboss	693
PMMA	236, 1244
pneumatic valves	506
pneumatic vibrator	62
point-of-care	326, 579, 1229, 1561
point-of-care diagnostics	825
poly(methyl methacrylate)	365, 401
polyacrylamide	392
polydimethylsiloxane (PDMS)	7, 19, 44, 71, 80, 161, 275, 299, 326, 356, 389, 464, 509, 525, 624, 669, 672, 675, 732, 915, 945, 981, 1076, 1253, 1280, 1366, 1396, 1534, 1585
polyelectrolyte	260
polymer	155, 164
polymer actuator	221
polymer chemistry	218
polymer chip	1127
polymer disk	1426
polymer fabrication	503
polymer material	224
polymer micro-actuators	218
polymer microchip	158, 1570
polymer microfabrication	1492
polymer microstructure	690
polymer monolith	170, 227
polymer physics	218
polymer waveguide	1312

polymer-micro-actuators	561
polymethylmethacrylate (PMMA)	903
polypyrrole	494
polypyrrroles electrodeposition	774
polysilazane glass	179
pore-forming toxins	1417
porous	1169
porous aluminum oxide	425
porous silica	230
positron emission tomography	876
post-translational modifications	939
potentiometric detection	1262
powder blasting	140
power generation	807, 1405
power source	287
precipitation	341
preconcentration	50, 353, 522, 1265
prefractionation	921
pressure Sensor	834, 1124
pressure-assisted	164
prion	350
protease activity	1199
protein	353, 362, 392, 401, 519, 651, 714, 1020, 1211, 1447, 1456
protein analysis	362, 392, 401
protein antiadsorption	519
protein array	651
protein binding	714
protein C2A	1020
protein capture	1211
protein chip	1447
protein concentration detector	1456
protein crystallization	1459
protein expression	1026
protein immobilization	209
protein kinases	768
protein microarray	1202, 1280, 1289
protein pathways	1486
protein pattern	846
protein pretreatment	888
protein refolding	1438
protein separation	311
protein stiffness	552
protein translocation	22, 549
protein tyrosinephosphatase	786
protein-protein interaction	1309
proteomics	203, 1468, 1570
protocells	1408
proton transfer	546
proximity ligation	4
pulsatile flow	131
pump	68, 1124
purification	900
pyrolysis	678
pyrolyzed carbon	759
PZT Fiber	1405
PZT thick film	810
Q	
QCM	1330, 1339
quantitative cell analysis	642
quantitative temperature measurement	1304
quantum dots	1381
R	
radiation force	314, 540
radioactive liquid wastes	1315
rapid photocopying	663
RCA	735
reaction calorimetry	1333
reaction enthalpy	1333
reaction kinetics	795
reaction optimization	795, 867, 870
reactive ion etching	137, 167
real three-dimensional	684
real time monitoring	603
real-time detection	735
real-time PCR	377, 711
recessed tip	494
red blood cell	461
redox cycling	654
reduced nucleation	1420
reduction ratio	293
reductive amination	813
refractive index	528
regenerative medicine	1543
relaxation	546
release	509
reliability	296

resonance	837	sequential reactions	1023
resonance frequency shift	810	serial dilution	1160
resource-limited settings	1561	SERRS	855
restriction enzyme	16, 1429	SERS	750, 1268
reversible assembly	981	shear	600
RF modulation	458	shear stress	56
RNA	317, 1435	sheath flow	515, 1091, 1447
RNA profiling	1453	Shirasu porous glass (SPG)	1235
rolling	437	shrinkage	275
rolling-circle amplification	4	sieving effect	404
rotary micromechanism	1163	signal amplification	1286
round microchannels	434	signal transduction	1576
RT-PCR	7, 1348, 1432, 1453	silica	257
S		silicon	1393
SAM	1330	silicon chip	452
sample concentration	828	silicon microcantilevers	1217
sample delivery	1208	silicon nanopillar	137
sample injection	630	silicon nanowire	705, 1295
sample plug	41	silicon nanowire sensor	1208
sample preparation	317, 470, 476, 609	silicon probe	702
scanning radical microjet	173	silicon-in-plastic	714
scattering	1253	silver enhancement	305
screening	1211	silver mirror reaction	1268
sealing	1193	silver nano-particle	1268
sedimentation	1154	simulation	59, 86, 798
segmented-flow	257, 491	simulation of complex fluids	53
SELEX	1142	single biomolecular detection	603
self assembly	119, 251, 350, 690, 1067, 1375, 1411, 1552	single cell	7, 10, 645, 738, 969, 981, 1480, 1495, 1501
self-assembly of spheroids	1011	single cell analysis	410, 957, 960, 990, 1172, 1292, 1417, 1498
self-contained	1229	single cell manipulation	22, 1372
self-forming	434	single cell observation	407
self-limiting oxidation	1208	single clone analysis	410
SELFOC micro lens	1196	single interface ITP	897
self-regulating pinched flow	500	single molecule detection	4, 723, 735, 744
Self-wash	341	single molecule detection	1223
sensitivity	1510	single-cell electroporation	1345
sensor	708	single-nucleotide polymorphism	1214
separation	323, 359, 383, 443, 540, 909, 915, 933, 1014, 1029, 1154, 1169	size effect	28
separation device	930, 1034	size exclusion	549
separation size	1017	size reduction	19
separator	1348	size-controlled	1115
sequential injection analysis	1136		

- slide valve 1118
slip flow 615
smart microcatheter 1546
SNP 10, 389, 1585
SNP genotyping 1441
sodium bicarbonate 978
soft lithography 179, 242, 672
soft-matter devices 1375
soft-state devices 990
soil analysis 1127
solid energetic materials 588
solid-phase 209
solid-phase extension 711
solid-phase-extraction 891
solid-supported reagents 861
solvation 395
solvent extraction 891, 936
sorting 1014
spacers 897
speckle 1256
spectrophotometry 1232
spheroid 1477
spiral ganglion neurons 464
spiral microchannel 543
spirally-rolled polymer microtube .. 1546
splitting 128
spore 338
spot-in-spot hybridization 1217
SPR Imaging 825, 1280, 1286, 1289
SPR sensor 1312
square capillary 299, 356
squeeze-jumping effect 1091
stacking 353
staining 1103
stainless steel 1106
stamping 16
steady streaming 1516
stem cell 22, 1543
stereoscopic observation 71
stimuli-responsive polymers 74
stirrer 1139
streaming current 807
stretch 963
structural biology 1390
SU-8 146, 380, 591, 681, 1139, 1339, 1423
submicron particle 906
sub-micron-aperture 176
supercooling 1327
supercritical CO₂ 783
superhydrophobic 161, 1339
superhydrophobic surface 197, 200, 771
superparamagnetic nanoparticles 320
surface acoustic waves 651
surface activation bonding 158
surface adsorption 200
surface characterization 122
surface charge 807
surface modification 107, 203, 215, 227, 239, 260, 365, 1295
surface modification 215
surface plasmon resonance 302, 756, 1256
surface plasmon resonance imaging . 206
surface stress 1259
surface tension 1372
surface treatment 80
surfactant wettability 269
suspended particles 540
suspension cells 1516
sweeping 362, 374
SYBR Green 777
synthesis 861, 864, 867
system biology 1576
- T**
- targeted delivery 25
tautomeric equilibrium 1324
Teflon AF 726
temperature control 407
temperature gradient focusing ... 849, 915
templating 251
tetrahydrofuran 1318
theophylline 816
therapeutic gene delivery 1495
thermal 708
thermal lens 491, 1271
thermal lens detection 858

thermal lens microscope	362, 843, 1008, 1315, 1582	
thermal noise	648	
thermal oxidation	705	
thermal perturbation	1411	
thermocycling	1465	
thermokinetic	1333	
thermolastic	422	
thermoreponsive polymer	960	
thin film ITO	293	
thin membrane transducer	1585	
thiolene	699	
three-dimensional electrode	28	
THz	738	
time-lapse studies	1381	
tissue engineering	1387, 1543	
titania	257	
titanium dioxide	873	
titration	245	
tmRNA	377	
toreharose	1558	
toxin detection	1026	
trace volume PCR	1462	
transfection	969, 1345	
transient charging	83	
transient electroosmotic flow	89	
transmission line	738, 1238	
transporter	1262	
trapping	558	
traveling wave micropump	131	
tumor spheroids	1011	
two phase flow	77, 98	
two-dimensional diffusion	1181	
two-dimensional electrophoresis	392	
two-dimensional manipulation	594	
two-dimensional separations	1570	
two-phase liquid	957	
two-photon microfabrication	669	
U		
ultra giant vesicle	534	
ultramicro electrode	729	
ultra-sensitive and on-site detection	1268	
ultrasonic manipulation	446, 449	
ultrasound	540, 627	
ultrasound imaging	822	
uncaging dye	564	
uniform temperature	293	
unpowered	834	
uptake mechanism	1351	
UV absorbance	714	
UV light actuation	221	
UV-LIGA	146	
V		
validation	296	
valve	1124	
valveless PCR-CE	1040	
velocity	792	
vesicle fusion	1342	
V-groove	182	
vincristine	948	
viral	317	
virtual electrode	34	
virtual reaction chamber	332	
virus	37, 347	
virus detection	1348	
viscosity	708	
visualization	1277, 1304	
vitamin K3	479	
voltage control	1017	
W		
wafer level	275, 1226	
wall-free microfluidics	194	
washing	1100	
water	546, 1327	
water in oil	290	
water monitoring	1187	
waveguide	732, 1223	
wet etching	1393	
wettability	245	
X		
xurography	1441	
Y		
yield	1336	
Z		
zeonor	155	
zeptomole	954	
zeta potential	89, 101, 239, 885	
ZnO	200	